Current Topics and Trends on Durability of Building Materials and Components

Carles Serrat, Joan Ramon Casas and Vicente Gibert (Eds.)

Current Topics and Trends on Durability of Building Materials and Components

Proceedings of the XV edition of the International Conference on Durability of Building Materials and Components (DBMC 2020)
Barcelona, Spain
20 – 23 October 2020

Edited by

Carles Serrat
Dept. of Mathematics

Joan Ramon Casas
Dept. of Civil and Environmental Engineering

Vicente Gibert
Dept. of Architectural Technology

Universitat Politècnica de Catalunya-BarcelonaTECH, Catalonia, Spain

A publication of:
International Center for Numerical Methods in Engineering (CIMNE)
Barcelona, Spain

Current Topics and Trends on Durability of Building Materials and Components

Carles Serrat, Joan Ramon Casas and Vicente Gibert (Eds.)

First edition, October 2020

ISBN: 978-84-121101-8-0

Cover: Basilica of the Sagrada Família. Spiral staircase inside the Nativity towers. Photo (c) Pere Vivas. Triangle Books. Sagrada Família.

Printed by: Artes Gráficas Torres S.L., Huelva 9, 08940 Cornellà de Llobregat, Spain

TABLE OF CONTENTS

PREFACE

Built environment (buildings, bridges, dams, highways...) is facing a dramatic increase of deterioration cases worldwide, mainly due to the lack of proper inspection and maintenance. Maintaining the safety and serviceability of the infrastructure assets is of crutial importance for the owners/stakeholders, and the society in general, but at the same time still limited resources remain available to this end. Academics, professionals and owners involved in the management of the built infrastructure have taken positive steps to develop more comprehensive measures and conduct better maintenance activities to better invest the limited funds. However, correct funding policies require a proper knowledge of the deterioration and damaging processes involved in the aging buildings. To this end, the series of conferences devoted to the Durability of Building Materials and Components (DBMC) have provided an excellent state of the knowledge and advancement since many years on the subject of durability and performance of the built environment. In fact, along more than 40 years, the main focus and topics of the different conferences have evolved according to the evolution of the existing and the appearance of new problems to be faced by the architectural/engineering community regarding durability of the construction assets.

Following the success of previous conferences, the 15th International Conference on Durability of Building Materials and Components (DBMC 2020) held in Barcelona from 20th to 23th of October 2020, covered all major aspects related to durability, from the more traditional ones such as building physics and durability, service life prediction, durability of historical buildings, to the most recent requiring the attention of the construction community as life-cycle assessment and sustainability, BIM technology and durability, and the influence of natural hazards and climate change on the durability of new and existing structures. Also new in this conference is the creation of awards to the student´s contribution (best paper, best poster and best oral presentation) and the launching of a grant for non-profit organizations of students in a projects contest for funding collaborative projects related to built infrastructures in developing countries.

However, the novelties in this edition of the conference have not been only restricted to the content of the scientific/technical/social subjects. In fact, the format has been also completely changed from the previous editions due to the impact of the COVID-19 pandemic situation. The declaration of the pandemic just few months before the celebration of the conference in June of 2020, provoked not only the shift to the new dates in October, but also the need to derive on a fully online conference. In this sense, DBMC 2020 has become the first fully online conference of the series.

The Organizing Committee has devoted its main efforts to prepare an attractive conference in the new online format in a limited period of time. We thank the confidence and collaboration of the prospective participants, which, in turn, had to accomodate themselves to the new scenario in a short time. The effort from all of us, organizers and participants, and the interest of the international community has been confirmed by the high response to the call for papers despite all negative constraints for travelling and networking. At the end, 368 preliminary abstracts were received at the Conference Secretariat. About 85 percent of them (313 in total) were invited by the Scientific Committee to submit extended abstracts and full papers, for oral or poster presentations in DBMC 2020. Finally, the scientific programme consisted of five keynote plenary sessions, 242 contributed papers (allocated in 13 special sessions and 23 conference topic sessions -in four parallel tracks- and one poster session) and a final round table on the

implications of a changing climate on a sustainable built environment. In total, 351 participants (30 percent of whom were students), from 41 different countries, have made DBMC 2020 an unforgettable experience.

Abstracts and full papers, including keynote lectures and technical papers have been assembled in a printed Book of Abstracts and an e-Book of Proceedings, respectively. They become a permanent record of the DBMC 2020 scientific contribution. This record is an effort to serve as a valuable reference on the recent developments in durability of the built environment. All the contents is also available at the webpage of the conference http://congress.cimne.com/DBMC2020, and in open access at https://www.scipedia.com.

As a DBMC 2020 Organizing Committee, we would like to take this opportunity to express our sincere thanks to all participants (keynotes, discussants, special sessions organizers, chairs, authors and attendees) for their contributions, to the membres of the Scientific Committee for their dedicated work and to the members of the Local Organizing, UPC Institutional, and Steeering Committees for the time and effort they have devoted to making DBMC 2020 a successful event despite the pandemic constraints and for their unconditional support to all important decisions we had to make along all the preparation process, and mainly in the last eight months. Last, but not least, our kind acknowledgement on one hand to the CIMNE Conference Secretariat, led by Bea, for their constant and helpful collaboration, and on the other hand to Cristina for her invaluable assistance. Thank you all!

Barcelona, October 2020

Carles Serrat (Chair)

Joan Ramon Casas

Vicente Gibert

ORGANIZING ASSOCIATIONS

American Society for Testing and Materials (ASTM)

International Council for Research and Innovation in Building Construction (CIB)

International Union of Testing and Research Laboratories for Materials and Structures (RILEM)

National Institute of Standards and Technology (NIST)

National Research Council Canada (NRC-CNRC)

ORGANIZERS AND COMMITTEES

ORGANIZING COMMITTEE

Carles Serrat i Piè
Chair
Department of Mathematics
EPSEB, Barcelona, Spain

Joan Ramon Casas i Rius
Department of Civil and Environmental Engineering
ETSECCPB, Barcelona, Spain

Vicente Gibert i Armengol
Department of Architectural Technology
ETSAB, Barcelona, Spain

STEERING COMMITTEE

Organizing Members

- Geert De Schutter, RILEM (Chair)
- Jennifer Keegan, ASTM
- Jorge De Brito, CIB
- Christopher C. White, NIST
- Michael Lacasse, NRC-CRC

Members at Large

- Robert Amor, The University of Auckland, New Zealand
- Carmen Andrade, CIMNE, Spain
- Christian Brischke, University of Göttingen, Germany
- Bruno Daniotti, Politecnico de Milano, Italy
- Vasco Peixoto De Freitas, FEUP, Portugal
- Peter Flüeler, m ETH/EMPA, Switzerland
- Dariusz Gawin, University of Lodz, Poland
- Julien Hans, CSTB, France
- Vanderley John, USP, Brazil
- Chun-Qing Li, RMIT University, Australia
- Isabel María Martínez, IETcc-CSIC, Spain
- Hiroyuki Miyauchi, BRI, Japan
- Shiro Nakajima, Utsunomiya University, Japan
- Carles Serrat, Universitat Politècnica de Catalunya-BarcelonaTECH, Spain
- Kiang Hwee Tan, NUS, Singapore
- Nil Turkeri, ITU, Turkey

UPC INSTITUTIONAL COMMITTEE

- Francesc Torres (Chair), President of UPC-BarcelonaTECH
- Jordi Berenguer, Vice-rector for Knowledge Transfer and Innovation of UPC-BarcelonaTECH
- Inmaculada Rodríguez, Dean of Barcelona School of Building Construction (EPSEB)
- Pedro Díez, Dean of Barcelona School of Civil Engineering (ETSECCPB)
- Félix Solaguren-Beascoa, Dean of Barcelona School of Architecture (ETSAB)
- Albert Cuchi, Dean of Vallès School of Architecture (ETSAV)
- Eugenio Oñate, Chair of Executive Council of the International Center for Numerical Methods in Engineering (CIMNE)
- Carles Serrat, Chair of the DBMC 2020 Conference

SCIENTIFIC COMMITTEE

Chairs
- Joan Ramon Casas (Co-Chair), UPC-Barcelona TECH, Spain
- Carmen Andrade (Co-Chair), CIMNE, Spain

Vice-Chairs
- Antonio Aguado, UPC-Barcelona TECH, Spain
- Túlio Bittencourt, University of São Paulo, Brazil
- Nele De Belie, University of Ghent, Belgium
- Ravindra Gettu, IIT Madras, India
- Rade Hajdin, IMC GmbH, Zürich & Belgrade Univ.
- Michael Lacasse, NRC Construction Research Centre, Canada
- Fernanda Rodrigues, Universidade de Aveiro, Portugal
- Elisabetta Rosina, Politecnico di Milano, Italy
- Ana Silva, IST, Lisbon, Portugal
- Alfred Strauss, BOKU, Vienna, Austria

Members
- Bijan Adl-Zarrabi, Chalmers University of Technology, Sweden
- Mark Ahrens, University Bochum, Germany
- Ahu Aydogan, City College of New York, USA
- Diana Bajare, Riga Technical University, Latvia
- Véronique Baroghel-Bouny, IFSTTAR, France
- Pablo Daniel Benítez-Mongelós, National University of Itapúa, Paraguay
- Umberto Berardi, Ryerson University, Canada
- Susan A. Bernal, University of Leeds, Leeds, UK
- Hans Beushausen, UCT, South-Africa
- Tomasz Blaszczynski, Poznan University of Technology, Poland
- Violeta Bokan-Bosiljkov, U. Ljubljana, Slovenia
- Mark Bomberg, Syracuse University, NY, USA
- Alessandra Bonazza, CNR, Italy
- Anatolijs Borodinecs, Riga Technical University, Latvia
- Lars Boström, SP, Sweden
- Kathryn Bourke, Whole Life Ltd, Watford, UK
- Thomas Braml, Bundeswehr University Munich, Germany
- Christian Brischke, University of Goettingen, Germany
- Zeynep Basaran Bundur, Özyegin University, Istanbul, Turkey
- Stefan Burtscher, TU Wien, burtscher consulting GmbH, Austria
- Guido Camata, University G. D´Annunzio, Chieti Pescara, Italy
- Jan Carmeliet, ETH Zürich, Switzerland
- Diana Car-Pušic, University of Rijeka, Croatia
- Robby Caspeele, University of Ghent, Belgium
- Anna Cellmer, Koszalin University of Technology, Poland
- Michael Chew, National University of Singapore, Singapore
- Sheila M.A. Conejos, School of Science and Technology, Singapore University of Social Sciences, Singapore
- Anca Constantin, Ovidius University of Constanta, Romania
- Bart Craeye, University of Antwerp, Belgium
- Paulo Cruz, University of Minho, Portugal
- Meri Cvetkovska, Ss. Cyril and Methodius University in Skopje, Republic of Macedonia
- Martin Cyr, INSA Toulouse, France
- Bruno Daniotti, Politecnico di Milano, Italy
- Jorge De Brito, Instituto Superior Tecnico, Technical University of Lisbon, Portugal
- Gianmarco De Felice, Università degli Studi Roma Tre, Italy
- Vasco Peixoto De Freitas, U. Porto, Portugal
- Dominique Derome, EMPA, Switzerland

- Josée Duchesne, Université Laval, Quebec, Canada
- Vilma Ducman, Slovenian National Building and Civil Engineering Institute, Slovenia
- Miren Etxeberria, UPC-BarcelonaTECH, Spain
- Flora Faleschini, Università degli Studi di Padova, Italy
- Ines Flores-Colen, Instituto Superior Técnico, University of Lisbon, Portugal
- David Garcia, UPC-BarcelonaTECH, Spain
- Dariusz Gawin, Lodz University of Technology, Poland
- Hua Ge, Concordia University, Montreal, Canada
- Jennifer Gerbi, U.S. Department of Energy, USA
- Michel Ghosn, City College New York, USA
- José Manuel Gómez Soberón, UPC-BarcelonaTECH, Spain
- Klodian Gradeci, SINTEF Building and Infrastructure, Trondheim, Norway
- Elke Gruyaert, KU Leuven, Belgium
- Lars Gullbrekken, SINTEF Building and Infrastructure, Trondheim, Norway
- Guillaume Habert, ETH Zürich, Switzerland
- Carl-Eric Hagentoft, Chalmers University of Technology, Sweden
- Tomáš Hanák, Brno University of Technology, Czech Republic
- Michael Hansen, TU Hannover, Germany
- Laia Haurie, UPC-BarcelonaTECH, Spain
- Shuichi Hokoi, Kyoto University, Japan
- Vít Hromádka, Brno University of Technology, Czech Republic
- Aletheia Ida, University of Arizona, USA
- Simo Ilomets, Tallinn University of Technology, Estonia
- Kei-Ichi Imamoto, Tokyo University of Science, Japan
- Joanna Janicka, University of Warmia and Mazury in Olsztyn, Poland
- Hans Janssen, KU Leuven, Belgium
- Pär Johansson, Chalmers University of Technology, Göteborg, Sweden
- Harald Justnes, SINTEF, Norway
- Targo Kalamees, Tallinn University of Technology, Estonia
- Mohammad Arif Kamal, Aligarh Muslim University, India
- Janis Kaminskis, Riga Technical University, Latvia
- Amnon Katz, Technion, Haifa, Israel
- Jacek Katzer, Koszalin University of Technology, Poland
- Miroslav Komljenovic, University of Belgrade, Serbia
- Kinga Korniejenko, Cracow University of Technology, Poland
- Jana Korytárová, Brno University of Technology, Czech Republic
- Jarek Kurnitski, Tallinn University of Technology, Estonia
- Joao Labrincha, University of Aveiro, Portugal
- Roman Lackner, UIBK, Innsbruck, Austria
- Akos Lakatos, Universiy of Debrecen, Hungary
- Paulo Laurenço, University of Minho, Portugal
- Elizabeth Laycock, Sheffield Hallam University, UK
- Agnieszka Lesniak, Cracow University of Technology, Poland
- Mae-Ling Lokko, Rensselaer Polytechnic Institute, USA
- Barbara Lothenbach, EMPA, Duebendorf, Switzerland
- Zoubir Lounis, National Research Council Canada, Canada
- Lyuben Lyubenov, University of Structural Engineering & Architecture, Bulgaria
- Ana Mandic Ivankovic, University of Zagreb, Croatia
- Mihajlo Markovic, University of Banja Luka, Bosnia and Herzegovina
- Ivan Marovic, University of Rijeka, Croatia
- Isabel Milagre Martins, LNEC, Portugal
- Berardo Matalucci, SHoP Architects, USA
- Jose Matos, University of Minho, Portugal
- José António Raimundo Mendes da Silva, Universidade de Coimbra, Portugal
- Esperanza Menéndez Méndez, Institute of Construction Science Eduardo Torroja (CSIC), Spain
- José Filipe Miranda-Melo, University of Porto, Portugal
- Eva Møller, Technical University of Denmark

- Sergio Montelpare, University G. D´Annunzio, Chieti Pescara, Italy
- Travis Moore, National Research Council Canada, Ottawa, Canada
- Martin Morelli, Aalborg University, Copenhagen, Denmark
- Vahid Nik, Lund University, Sweden
- María Nogal, Delft University of Technology, the Netherlands
- Takafumi Noguchi, University of Tokyo, Japan
- Ehsan Noroozinejad, Graduate University of Advanced Technology, Iran
- Daniel Oliveira, University of Minho, Portugal
- Fernando Pacheco Torgal, University of Minho, Portugal
- Ainars Paeglitis, Riga Technical University, Latvia
- Cedric Patapy, Laboratoire Matériaux et Durabilité des Constructions – INSA Toulouse/UPS, France
- Marco Perino, Politecnico di Torino, Italy
- Ruut Peuhkuri, Aalborg University, Copenhagen, Denmark
- Edyta Plebankiewicz, Cracow University of Technology, Poland
- Gul Polat, Istanbul Technical University, Turkey
- Ioana Popescu, IHE Delft Institute for Water Education, the Netherlands
- Andres J. Prieto, Universidad Austral de Chile, Valdivia, Chile
- John Provis, University of Sheffield, UK
- Elzbieta Radziszewska-Zielina, Cracow University of Technology, Poland
- Laura Rampazzi, University of Insubria, Italy
- Nuno Ramos, FEUP, University of Porto, Portugal
- Jacek Rapinski, University of Warmia and Mazury in Olsztyn, Poland
- Marzieh Riahinezhad, National Research Council Canada, Ottawa, Canada
- Pere Roca, UPC-BarcelonaTECH, Spain
- Hugo Rodrigues, Polytechnic of Leiria, Portugal
- Staf Roels, KU Leuven, Belgium
- Petra Rüther, SINTEF Building and Infrastructure, Trondheim, Norway
- Hiroaki Saito, Ashikaga University, Japan
- Antonio Sansonetti, CNR, Italy
- Amaia Santamaría, Universidad del País Vasco, Bilbao, Spain
- Mats Santamouris, University of Athens, Greece
- Karma Sawyer, U.S. Department of Energy, USA
- Erik Schlangen, TU Delft, the Netherlands
- Lina Seduikyte, Kaunas University of Technologies, Lithuania
- Dmitrijs Serdjuks, Riga Technical University, Latvia
- Igal M. Shohet, Ben-Gurion University of Negev, Israel
- Carey Simonson, University of Saskatchewan, Canada
- Gintautas Skripkiunas, Vilnius Gediminas Technical University, Lithuania
- Mohamed Sonebi, Queens University, Belfast, UK
- Wil Srubar, University of Colorado Boulder, USA
- Sudip Talukdar, British Columbia Institute of Technology, Burnaby, Canada
- Kiang Hwee Tan, National University of Singapore, Singapore
- Luping Tang, Chalmers University of Technology, Sweden
- Fitsum Tariku, British Columbia Institute of Technology, Burnaby, Canada
- Nicola Tarque, Pontificia Universidad Católica del Perú, Perú
- Akos Torok, Budapest University of Technology and Economics, Hungary
- Milan Trivunic, University of Novi Sad, Serbia
- Nil Türkeri, Istanbul Techn Univ, Turkey
- Maria Rosa Valluzzi, University of Padova, Italy
- Joris Van Acker, UGent, Belgium
- Keith Van de Riet, University of Kansas, USA
- Nathan Van Den Bossche, Ghent University, Belgium
- Philip Van Den Heede, Ghent University, Belgium
- Humberto Varum, University of Porto, Porto, Portugal
- Marius Vendrell, University of Barcelona, Spain
- Anne Ventura, IFSTTAR, France
- Yury Villagran, LEMIT, La Plata, Argentina

- Martins Vilnitis, Riga Technical University, Latvia
- Eva Vitkova, Brno Univeristy of Technology, Czech Republic
- Jeroen Vrijders, Belgian Building Research Institute, Belgium
- Johan Vyncke, Belgian Building Research Institute, Belgium
- Lin Wang, Concordia University, Montreal, Canada
- John A. Wells, Crosier Kilgour and Partners Ltd., Winnipeg, Canada
- Guang Ye, TU Delft, the Netherlands
- Joan Lluís Zamora, UPC-BarcelonaTECH, Spain
- Mariano Angelo Zanini, Università degli Studi di Padova, Italy
- Cristina Zanotti, University of British Columbia, Canada
- John Zhai, University of Colorado Boulder, USA
- Xiaohai Zhou, EMPA, Switzerland
- Valentina Žileska-Pancovska, Ss. Cyril and Methodius University in Skopje, Republic of Macedonia

LOCAL ORGANIZING COMMITTEE

Chair
- Vicente Gibert, UPC-BarcelonaTECH, Spain

Members
- Cindy Abbott-Brito
- Ronny S. Guarderas-Luna
- Laia Haurie, EPSEB
- Beatriz D. Médola
- Climent Molins, ETSECCPB
- Joan Moreno, ETSAV
- Ana-Belén Onecha, ETSAB
- Javier E. Peñuelas
- Verónica Royano
- Alejandra Valencia-Arboleda

SUMMARY

KEYNOTES

SPECIAL SESSIONS

CONFERENCE TOPICS SESSIONS

CONTENTS

KEYNOTES

SPECIAL SESSIONS

Approaches to Hygrothermal Simulation for Assessing Durability Related to Climate Change

Organized by Travis Moore (NRC, Canada) and Michael Lacasse (NRC, Canada)

Biomimetic and Bioinspired Approaches for Enhanced Durability of Cementitious Materials

Organized by Wil Srubar (University of Colorado Boulder, USA)
and Zeynep Basaran Bundur (Özyegin University, Istanbul, Turkey)

Degradation of Coating Materials and its Relation to Durability of Structures

Organized by Takafumi Noguchi (University of Tokyo, Japan) and Kei-ichi Imamoto (Tokyo University of Science, Japan)

Durability and Field Tests of Thermal Insulating and Innovative Constructive Solutions

Organized by Ines Flores-Colen (IST, University of Lisbon, Portugal) and Nuno Ramos (FEUP, University of Porto, Portugal)

Durability and Performance of Building Envelopes

Organized by Klodian Gradeci (SINTEF Building and Infrastructure, Trondheim, Norway) and Petra Rüther (SINTEF Building and Infrastructure, Trondheim, Norway)

Durability Considering Climate Change and Natural Hazards

Organized by Michael Lacasse (NRC, Canada) and Travis Moore (NRC, Canada)

Environmental Factors and Durability

Organized by Tomasz Blaszczynski (Poznan University of Technology, Poland)

Life Cycle Costs in Construction Projects

Organized by Vít Hromádka (Brno University of Technology, Czech Republic) and Edyta Plebankiewicz (Cracow University of Technology, Poland)

Modern Sustainable Building Materials and Technologies

Organized by Elzbieta Radziszewska-Zielina (Cracow University of Technology, Poland)

Performance Over Time of High-Performance Insulation and Reflective Building Envelope Materials

Organized by Umberto Berardi (Ryerson University, Canada) and Marco Perino (Politecnico of Turin, Italy)

Remote Sensing of Building Condition

Organized by Joanna Janicka (University of Warmia and Mazuri in Olsztyn, Poland) and Jacek Rapinski (University of Warmia and Mazuri in Olsztyn, Poland)

Slags in Cement-based Materials

Organized by Flora Faleschini (Università degli Studi di Padova, Italy) and Amaia Santamaria (Universidad del País Vasco, Bilbao, Spain)

Soft Computing Tools and Sustainable Building Construction and Maintenance

Organized by Diana Car-Pušic (University of Rijeka, Croatia) and Ivan Marovic (University of Rijeka, Croatia)

CONFERENCE TOPICS SESSIONS

Asset and Maintenance Management

Organized by Ana Silva (IST, Lisbon, Portugal)

Building Pathology and Durability

Organized by Túlio Bittencourt (University of São Paulo, Brazil)

Building Physics and Durability

Organized by Antonio Aguado (UPC-BarcelonaTECH, Spain)

Durability Approach for Historical and Old Buildings

Organized by Elisabetta Rosina (Politecnico di Milano, Italy)

Durability of Materials, Systems and Components

Organized by Ravindra Gettu (IIT Madras, India)

IT / BIM and Durability

Organized by Rade Hajdin (IMC GmbH, Zürich & Belgrade Univ)

Large Sample Size Studies in Durability

Organized by Fernanda Rodrigues (Universidade de Aveiro, Portugal)

LCA, Sustainability and Durable Construction

Organized by Nele De Belie (University of Ghent, Belgium)

Service Life Prediction Methodologies

Organized by Alfred Strauss (BOKU, Vienna, Austria)

LECTURES

XV International Conference on Durability of Building Materials and Components
DBMC 2020, Barcelona
C. Serrat, J.R. Casas and V. Gibert (Eds)

Prescription of Maintenance Interventions by the New Generation of Eurocodes for Climate-Change Resilient Structures

Maria Nogal[1]

[1] Faculty of Civil Engineering & Geosciences, Delft University of Technology, Netherlands
m.nogal@tudelft.nl

Abstract. *The new generation of structural Eurocodes will include climate change adaption measures in order to enhance the climate resilience of infrastructures across Europe. This paper discusses the impact that climate change might have on reinforced concrete structures subjected to corrosion, and the associated challenges of the standardisation of adaptation measures. A resilience-based framework is proposed for the adaptation of structural codes to climate change-induced actions. Such an approach aims to provide the required adaptive capacity to the new structures in order to be able to respond to the uncertain future minimising the investment under unlikely scenarios. In that way, the strategy can be summarised as a climate change-adapted design plus an in-design maintenance plan. Future actions, such as mapping the future climate-related drivers of corrosion, the determination of the design values of these drivers, and the prescription of maintenance activities, should be further investigated. Although this paper focuses on the new structures that will be designed with the new codes, some of the insights can be extrapolated to the existing structures.*

Keywords: *Corrosion, Climate change, Resilience, Maintenance, Eurocodes.*

1 Introduction

The pressure imposed by climate change has reached all sectors within the European Commission, which is now forced to take adaptation measures. In Union Innovation (2013), they acknowledged action gaps in a context where late responses could result in non-affordable economic, social, and environmental costs. Consequently, they proposed a road-map to include climate change adaptation considerations where technical standards were identified as an effective strategy to enhance the climate resilience of infrastructures across Europe.

In the construction sector, the first generation of EN Eurocodes was launched in 2007 with the aim to homogenise structural design within the Member States. The second generation of Eurocodes is planned by 2023, which will reflect the new market needs (e.g., new materials and construction techniques) and also the European commitment with the sustainable development goals. Therefore, the second generation of Eurocodes is planned to incorporate the adaptation of structural design to climate change.

Within the long list of impacts upon structures caused by climate change, corrosion has been identified as a priority theme, as it has been estimated that the increased maintenance and repair costs worldwide resulting from the acceleration of the corrosion process due to climate change might be of hundreds of billions of dollars annually (Bastidas-Arteaga & Stewart (2015)).

doi:10.23967/dbmc.2020.241

In this context, this paper discusses the adaptation strategy to be applied to the new generation of Eurocodes in relation to the corrosion of reinforced concrete (RC) structures. At present, the structural corrosion is addressed in EC2 (2005).

It is noted that the impact of climate change on man-made systems has a large component of uncertainty, given that the future climatic scenarios mainly depend on the evolution of the global sociopolitical context. Therefore, including climate change adaptation measures in the design phase of buildings and infrastructure is challenging because underestimating its impact would result in significant societal consequences, whereas overestimating it would imply an unnecessarily waste of resources. A resilience-based approach is proposed to address the issue, where the adaptation measures included in the design phase should tackle part of the impact of climate change, and during the service phase, upgrading mechanisms should be implemented to guarantee the system is prepared for the non-accounted impact of climate change if the evolution of climate change requires it.

Therefore, this work aims to provide an overview of the problem of corrosion induced by climate change to better understand the need for a resilience-based approach to address the standardisation process. The general framework proposed for the adaptation to climate change by the new generation of structural Eurocodes is outlined and the associated challenges are further discussed.

The remaining document is organized as follows; Section 2 provides an overview of the impact of climate change in Europe on the main drivers of the structural corrosion, Section 3 presents the corrosion problem in the context of climate change. In Section 4, the need for a resilient-based approach is discussed in the context of the standardising process. Finally, in Section 5 some conclusions and future research lines are drawn.

2 Climate Change in Europe

The durability of RC structures is threatened by the increment of carbon dioxide (CO2) concentration levels and climate change entailing variations in temperature and atmospheric humidity. These three parameters are the principal environmental drivers of corrosion.

To study the expected variations of air temperature and relative humidity (RH), the Representative Concentration Pathways (RCPs) proposed by IPCC (2014) are used. They are the so-called RCP2.6, RCP4.5, RCP6.0, and RCP8.5 scenarios, with RCP2.6 being closer to the scenario aimed by the Paris Agreement and RCP8.5 relating to the business-as-usual scenario. There exists a consensus amongst climatologists that RCP2.6 is naively optimistic, thus in practicality, the RCP4.5 is very often proposed as the potential optimistic scenario.

The definition of each scenario allows climatologists to determine the general atmosphere patterns and oceanic circulation dynamics at the global scale. Then, through complex processes of downscaling, climate changes at a regional level can be estimated with a significant level of confidence for each scenario providing a horizontal resolution of up to 0.11^o (about 12 km).

In Europe, it is clear that climate change will increase air temperature. The extent of the variation will depend on the geographical location, period of the year, and scenario considered; for instance, North Europe, which is the most affected area when analysing air temperature,

Table 1: Variation of air temperature due to climate change in Europe. The level of agreement among climatic models is given in brackets: L-low, M-medium, H-high, V-very high.

Area	Winter	Summer	Autumn	Spring
	(DJF)	(JJA)	(SON)	(MAM)
	RPC4.5			
North Europe	2^o-8^o (M)	0^o-6^o (H)	2^o-6^o (H)	2^o-6^o (M)
Central Europe	0^o-4^o (H)	0^o-4^o (H)	0^o-4^o (M)	0^o-2^o (V)
Mediterranean area	0^o-4^o (H)	2^o-4^o (H)	0^o-4^o (H)	0^o-4^o (H)
East Europe	2^o-6^o (H)	0^o-4^o (M)	0^o-4^o (H)	0^o-4^o (H)
	RPC8.5			
North Europe	4^o-10^o (M)	2^o-6^o (H)	2^o-6^o (H)	2^o-8^o (H)
Central Europe	2^o-4^o (V)	2^o-4^o (V)	2^o-6^o (H)	2^o-4^o (H)
Mediterranean area	2^o-4^o (V)	2^o-6^o (M)	2^o-6^o (H)	2^o-4^o (V)
East Europe	2^o-6^o (M)	2^o-6^o (H)	2^o-6^o (H)	2^o-6^o (H)

presents increments ranging between 4^o-10^o during the winter months (December to February) under the RCP8.5, whereas the RCP4.5 provides increments of 2^o-8^o during winter. The range of values is given by the use of different climatic models. Table 1 summarises the variation of air temperature due to climate change in Europe.

The impact of climate change on the RH is smaller. Regardless of the climatic scenario considered, only during the summer months (JJA), Europe might experiment reductions of up to 10% of the RH.

It is noted that an important source of the uncertainty of the climate estimations is linked to the uncertainty regarding the trajectory of greenhouse gas emissions (i.e., the RPC considered), which depends on factors such as the economic and societal trends. In the present context, this type of uncertainty cannot be reduced. Nevertheless, considering one or another scenario might differ in billion of euros in the long term. This should be kept in mind when updating the structural codes.

3 Impact of Climate Change-Induced Corrosion

3.1 Corrosion Mechanisms

RC corrosion refers to the phenomenon of the corrosion of the steel reinforcement of concrete caused by the infiltration into the concrete members of carbon dioxide, which reduces concrete pH till values below the steel passivisation threshold, and chloride, which reduces concrete alkalinity. Both processes are affected by temperature and RH.

When studying the RC corrosion, the stage characterised by the ingress process of the CO2 and chloride ion into concrete is known as the initiation stage. In this stage, it is of interest to determine the chloride concentration at the rebar level and also when the carbonation reaches this level, that is, the carbonation depth.

Several studies have analysed the impact of climate change in the carbonation ingress process when assuming different CO2 levels, RH, and temperature conditions. As shown in Table 2, the estimated increments of the carbonation depths are up to 45% by 2100 under the RCP8.5

Table 2: Effect of climate change on the carbonation and chlorine ion ingress processes in RC structures.

Ref.	Location	Assumptions	Estimation		Scenarios	
			Target	Value	Baseline	Target
CARBONATION INGRESS PROCESS						
Talukdar et al. (2012)	Canada	(a) increasing mean yearly temperature, (b) increasing duration of the hot season, (c) constant RH over time, and (d) increasing concentration of CO2	carbonation depths of non-pozzolanic, unloaded concrete structures	increment of 45%	year 2000	A1FI, year 2100
Talukdar & Banthia (2013)	Mumbai, London, New York City, Sydney, Toronto, Vancouver	(a) time dependent temperature	carbonation depths	increments between 27% and 45% (15 and 35 mm)	year 2000	A1FI, year 2100
Saha & Eckelman (2014)	Boston metropolitan area	(a) increasing temperatures, (b) increasing concentrations of CO2	carbonation depths	increment of 40%	year 2000	A1FI, year 2100
Peng & Stewart (2014)	China	(a) CO2 concentration, (b) local temperature, and (c) RH variable over time	carbonation depths	increment of 45%	year 2010	RCP8.5, year 2100
Mizzi et al. (2018)	Malta	(a) increasing CO2 concentration, and (b) increasing temperatures	carbonation depths for different concrete grades	increment up to 40%	RCP 2.6	RCP 8.5, year 2070
CHLORINE ION INGRESS PROCESS						
Saha & Eckelman (2014)	Boston metropolitan area	(a) increasing temperatures, (b) increasing concentrations of CO2	chloride penetration depths	increment of 12%	year 2000	A1FI, year 2100
Xie et al. (2018)	China	(a) increasing temperatures	chloride concentration at the rebar level of offshore RC bridges	increments of 6%-15%	year 2000	RCP8.5, year 2100
Khatami & Shafei (2017)	U.S. Midwest region	(a) increasing temperatures, (b) decreasing, constant and increasing RH, and (c) increasing surface chloride concentration	chloride concentration at the rebar level	increment of 37%	RCP2.6, year 2100	RCP8.5, year 2100

scenario (or the equivalent A1F1 scenario given by the SRES, Nakicenovic et al. (2000)) when comparing with the year 2000. It is noted that the results are very sensitive to local exposure conditions (Talukdar & Banthia (2013)).

In the case of the impact of climate change to the chlorine ion ingress process, the studies report more modest values, though still relevant, for the increment of chloride concentration at the rebar level when comparing the 2000-year values to the RCP8.5 by the end of century, reaching values around 15% (see Table 2). Khatami & Shafei (2017) report larger values, as they introduce in their model an increment of use of de-icing salts as a consequence of the observed consumption in the USA, which increased 200% in the last 25 years.

The second stage of the corrosion is known as propagation stage, which occurs once that the corrosion of the reinforcing steel is initiated, and finishes with the loss of steel area, cover cracking and spalling, and loss of the bond between steel and concrete. Whereas the initiation stage dominates the service life of the structure, the propagation stage lasts only a few years. For instance, Xie et al. (2018) report that the corrosion propagation stage of the offshore RC structures in China designed according to MOHURD (2008) would last less than one year considering future climatic conditions.

3.2 Impact on Reliability and Service Life

As a consequence of climate change, both the reliability and service life of RC structures are highly impacted. The extent of this impact depends on the geographical location, the structural codes used for design, and the climatic scenario considered. Table 3 summarises some of the findings regarding the impact of climate change on the reliability and service life of RC structures by the end of this century if the most pessimistic scenario, i.e., the business-as-usual scenario, is considered. Even when the compound effect of the carbonation- and chlorination-induced corrosion has not been studied yet, the enormous impact that climate change has on structural durability cannot be ignored.

Table 3: Impact of climate change on reliability and service life of RC structures.

Ref.	Location	Assumptions	Estimation		Scenarios	
			Carbonation-induced	Chloride-induced	Baseline	Target
M. G. Stewart et al. (2011)	Australia	(a) Increased CO2 levels, temperature and humidity, (b) different exposure classifications of the Australian code AS3600 (2009)	Increment of damage risk over 400% for inland arid or temperate climates	Increment of damage risk up to 15%	year 2000	A1B & A1FI, year 2100
Saha & Eckelman (2014)	Boston metropolitan area	(a) Structural design according to ACI (2011)	Reduction of service life of 26 years. Penetration depths in 60% of existing buildings exceeding the recommended cover thickness by 2050.	Reduction of service life of 10 years	year 2000	A1FI, year 2100
Pakkala et al. (2019)	Finland	(a) Changes in ambient T, RH and wind-driven rain, (b) different locations with respect to the solar radiation	Increment of corrosion rates of up to 200% during winter in coastal areas facing to the South		year 2000	A2, year 2100
Bastidas-Arteaga & Stewart (2015)	Continental, oceanic and tropical environments	(a) Increasing temperatures and length of hot periods, and (b) increasing RH	Lifetime reductions ranging up to 18%		year 2000	year 2100

4 Structural Codes

4.1 Adaptation Measures

The limit state of RC corrosion should include two phenomena, the cracking of concrete due to the sub-products generated by the corrosion and the reduction of effective steel cross-section, both occurring during the propagation stage. While the first is more related to aesthetic issues and the latter is linked to the structural integrity, the functionality of the structural member will determine which of the two phenomena is more critical. Given that the integrity of a structural member affected by corrosion will depend on the applied loads and structural configuration, its study becomes very case-specific and difficult to be generalised. Thus, when defining standardised strategies to adapt to climate change, it is better to focus on the initiation stage, which implies a larger portion of the structural service life and is less dependent on the applied loads and structural configuration.

Structural codes worldwide share a similar rationale when addressing the problem of corrosion; they focus on structural durability. Figure 1 generalises this approach. There exist two decision variables in regard to the structural design affecting the RC corrosion, that is, materials

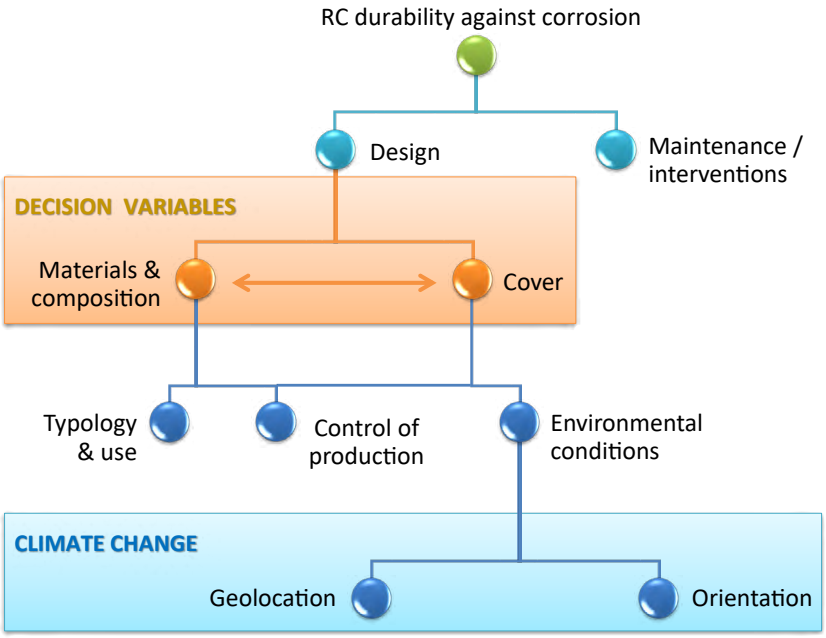

Figure 1: Rationale of structural codes to guarantee the structural durability against RC corrosion.

and composition and cover depth. Both of them are related, as the selection of a more dense concrete allows for a reduction of the cover depth. To determine these values, aspects such as typology and use, the control of production and the environmental conditions must be considered. Initially, the new environmental conditions given by climate change should be reflected here.

Regarding the materials and composition, two possible solutions can be taken, either improving steel corrosion resistance, e.g., through low carbon, stainless or galvanised steel reinforcement and glass-fiber reinforced polymer rebars, or improving concrete durability by increasing the concrete grade, the water-cement ratio or applying concrete coatings. In addition, other concrete mixes, such as blended and alkali-activated (AA) cement, can be used that present higher density matrices than the standard and commonly used Portland cement (PC). The structure of their matrices reduces the permeability of the harmful substances. In addition, the AA slag cement, where the slag substitutes part of the PC, presents higher resistance to corrosion and its production generates lower greenhouse gas emissions than PC. Despite the slag cement has been used in the USA for more than 100 years, the feasibility of replacing PC blinders should be further investigated.

Nevertheless, it is estimated that the measures required to adapt to climate change, such as increasing design cover by up to 8 mm or increasing concrete compressive strength by one grade would imply an increment of 1-3% of the construction costs (M. Stewart et al. (2012)). Other authors (Bastidas-Arteaga & Stewart (2016); M. Stewart & Bastidas-Arteaga (2019)) have addressed the cost-benefit analysis of increasing the cover thickness to 5 or 10 mm in

different structural components under different climate scenarios. They conclude that in many cases, this measure is not cost-effective. The factors affecting the efficiency of this type of adaptation measures do not depend only on the structural typology and member size, but also on the climatic conditions and the future discount rate.

Keeping in mind the impact that Eurocodes has in the economy of the State Members, standardising adaptation measures in a context of high uncertainty, where if the impact of climate change is underestimated by considering very optimistic scenarios, it would result in a significant reduction of the service life of new infrastructure and buildings, or if it is overestimated, in unnecessarily expensive investment. Apparently, there is not a fair solution.

4.2 Resilience-Based Approach

In the last years, there has been a clear shift from the traditional risk-oriented approaches to a perspective based on resilience. The need for a resilience-based approach has been made evident in those cases where either, the lack of knowledge about the potential hazards or their level of uncertainty was so large that the existing risk was underestimated. For that reason, the problem of climate change along with its associated uncertainty is pushing decision-makers to implement measures that boost resilience (Nogal & O'Connor (2018a); Val et al. (2019)). In this point it is important to note that risk- and resilience-based approaches are not incompatible; on the contrary, the latter complements the first one by adding a temporal dimension to the problem (Nogal & O'Connor (2018b)) and proposing a number of strategies to increase the preparedness level of the system and so allow for an adaptive response over time.

Therefore, to approach the issue of climate-change induced corrosion from a resilience-based view, the adaptation measures should be twofold. On the one hand, the measures addressing the impact of climate change that is certain should be implemented in the design stage, through cost-effective measures. More sustainable concrete mixtures might play an important role in this stage. On the other hand, the uncertain impact of climate change should be covered in a post-design stage, that is, through maintenance. In that regard, Eurocodes should prescribe specific maintenance in relation to climate change. It is clear that there is room for improvement in terms of maintenance in the present standards, as they merely define maintenance, mentioning that the structure will be adequately maintained.

Such an approach implies a number of challenges. The values of CO2 concentration levels, temperature and atmospheric humidity associated with low values of uncertainty should be determined based on the climate models for the end of the structural design life. Let's call them certain thresholds (CTs) of the corrosion drivers.

The maintenance strategies, which should be studied during the design phase, should state the frequency of the maintenance activities in which the updated information regarding climate change will be used to determine the short- and medium-term actions. Also at the design phase, a number of potential actions should be included considering the future climatic scenarios along with their economic cost. Finally, an economic program to face the potential structural upgrades should be included to guarantee the economic viability of the project. It is noted that some of the required maintenance interventions are usually less cost-effective than the measures adopted

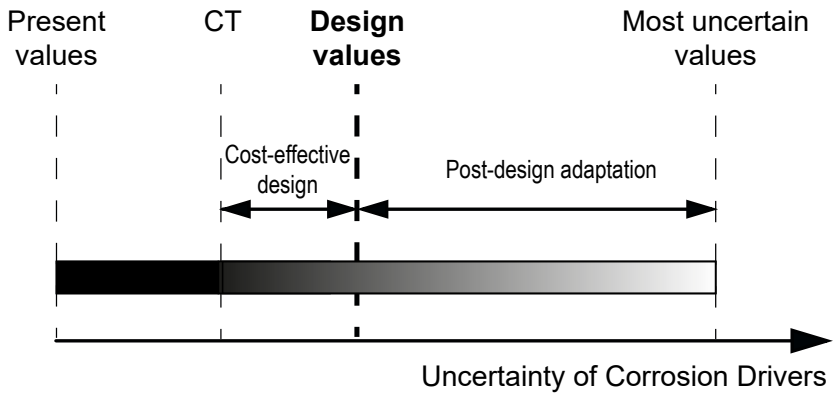

Figure 2: Representation of the design value of the corrosion drivers based on the cost-effectiveness of the adaptation measures and the uncertainty regarding the future value of the corrosion driver.

in the initial design. Therefore, the most cost-effective design should not cover only the CTs of the corrosion drivers, but more uncertain values in order to minimise the life cycle cost (see Figure 2). In other words, the new generation of Eurocodes should provide a design value of the corrosion drivers that will be established based on both, the uncertainty regarding the future value of the corrosion driver and the cost-effectiveness of the adaptation measures.

5 Conclusions

Beyond the geographical differences across countries, the main challenge of standardising "low-cost and no-regret adaptation measures" (Union Innovation (2013)) in the context of structural codes is posed by the uncertainty related to climate change, which mainly depends on the trajectory of greenhouse-gas emissions. For this reason, a resilience-based strategy for coping with climate change-induced corrosion has been suggested in this paper. Such an approach aims to provide the required adaptive capacity to the new structures in order to be able to respond to the uncertain future minimising the investment under unlikely scenarios. In that way, the strategy can be summarised as a climate change-adapted design plus an in-design maintenance plan. It is highlighted the need for an improvement of the structural Eurocodes in the area of maintenance.

Although the impact of climate change on temperature and atmospheric humidity is of interest in the context of RC corrosion, the CO2 levels should be also considered. The maintenance activities, which will be defined according to the on-going weather-related variables and CO2 emissions will further motivate countries to reduce their CO2 emissions in order to minimise their medium and long-term investments. Note that whereas climate change is a global issue, CO2 concentrations have an important local component, and thus, the proposed strategy will penalize more heavily those areas producing a larger amount of CO2.

This paper has shown a general framework for the adaptation of structural codes to climate change-induced actions under a resilience-based approach. Specific actions, such as mapping the future climate-related drivers of corrosion, the determination of the design values of these drivers, and the prescription of maintenance activities, should be further investigated.

ORCID

Maria Nogal: http://orcid.org/ 0000-0001-5405-0626

References

ACI. (2011). Building code requirements for structural concrete and commentary..

AS3600. (2009). AS3600 (2009), concrete structures. *Standards Australia, Sydney*.

Bastidas-Arteaga, E., & Stewart, M. (2015). Damage risks and economic assessment of climate adaptation strategies for design of new concrete structures subject to chloride-induced corrosion. *Structural Safety*, *52*, 40–53.

Bastidas-Arteaga, E., & Stewart, M. (2016). Economic assessment of climate adaptation strategies for existing reinforced concrete structures subjected to chloride-induced corrosion. *Structure and Infrastructure Engineering*, *12*(4), 432–449.

EC2. (2005). *En 1992 eurocode 2: Design of concrete structures.* Brussels: CEN.

IPCC. (2014). *Climate change 2014: synthesis report.* IPCC Geneva, Switzerland.

Khatami, D., & Shafei, B. (2017). *Climate change impact on management of deteriorating bridges: A case study of US Midwest Region* (Tech. Rep.).

Mizzi, B., Wang, Y., & Borg, R. P. (2018). Effects of climate change on structures; analysis of carbonation-induced corrosion in reinforced concrete structures in Malta. In *Iop conference series: Materials science and engineering* (Vol. 442, p. 012023).

MOHURD. (2008). Code for durability design of concrete structures..

Nakicenovic, N., Alcamo, J., Grubler, A., Riahi, K., Roehrl, R., Rogner, H.-H., & Victor, N. (2000). *Special report on emissions scenarios (SRES), a special report of Working Group iii of the intergovernmental panel on climate change*. Cambridge University Press.

Nogal, M., & O'Connor, A. (2018a). Considerations of resilience management in transportation. *Domains of resilience for complex interconnected systems.*, 107.

Nogal, M., & O'Connor, A. (2018b). Resilience assessment of transportation networks. *Routledge Handbook of Sustainable and Resilient Infrastructure*, 199.

Pakkala, T. A., Köliö, A., Lahdensivu, J., & Pentti, M. (2019). Predicted corrosion rate on outdoor exposed concrete structures. *International Journal of Building Pathology and Adaptation*.

Peng, L., & Stewart, M. (2014). Spatial time-dependent reliability analysis of corrosion damage to RC structures with climate change. *Magazine of Concrete Research*, *66*(22), 1154–1169.

Saha, M., & Eckelman, M. J. (2014). Urban scale mapping of concrete degradation from projected climate change. *Urban Climate*, *9*, 101–114.

Stewart, M., & Bastidas-Arteaga, E. (2019). Corrosion of concrete and steel structures in a changing climate. In *Climate adaptation engineering* (pp. 99–125). Elsevier.

Stewart, M., Wang, X., & Nguyen, M. (2012). Climate change adaptation for corrosion control of concrete infrastructure. *Structural Safety*, *35*, 29–39.

Stewart, M. G., Wang, X., & Nguyen, M. N. (2011). Climate change impact and risks of concrete infrastructure deterioration. *Engineering Structures*, *33*(4), 1326–1337.

Talukdar, S., & Banthia, N. (2013). Carbonation in concrete infrastructure in the context of global climate change: development of a service lifespan model. *Construction and Building Materials*, *40*, 775–782.

Talukdar, S., Banthia, N., Grace, J., & Cohen, S. (2012). Carbonation in concrete infrastructure in the context of global climate change: Part 2– Canadian urban simulations. *Cement and Concrete Composites*, *34*(8), 931–935.

Union Innovation. (2013). Communication from the Commission to the European Parliament, the Council, the European Economic and Social Committee and the Committee of the Regions. *A new skills agenda for Europe. Brussels*.

Val, D. V., Yurchenko, D., Nogal, M., & O'Connor, A. (2019). Climate change-related risks and adaptation of interdependent infrastructure systems. In *Climate adaptation engineering* (pp. 207–242). Elsevier.

Xie, H., Wang, Y., Gong, J., Liu, M., & Yang, X. (2018). Effect of global warming on chloride ion erosion risks for offshore RC bridges in China. *KSCE Journal of Civil Engineering*, 1–7.

XV International Conference on Durability of Building Materials and Components
DBMC 2020, Barcelona
C. Serrat, J.R. Casas and V. Gibert (Eds)

A Methodology for Assessment of Building Assembly Air Leakage Moisture Response, Condensation Risk, and Expected Durability When Subjected to Projected Future Climate Loads

David G. Kayll[1], Maurice Defo[2], Travis V. Moore[3] and Michael A. Lacasse[4]

[1] Morrison Hershfield Limited, Building Specialty Services,
2932 Baseline Rd., Ottawa, ON, Canada, dkayll@morrisonhershfield.com

[2] National Research Council, Construction Research Centre,
1200 Montreal Rd., Ottawa, ON, Canada, Maurice.Defoe@nrc-cnrc.gc.ca

[3] National Research Council, Construction Research Centre,
1200 Montreal Rd., Ottawa, ON, Canada, Travis.Moore@nrc-cnrc.gc.ca

[4] National Research Council, Construction Research Centre,
1200 Montreal Rd., Ottawa, ON, Canada, Michael.Lacasse@nrc-cnrc.gc.ca

Keywords: *Climate Change, Durability, Air Barrier, Moisture Response, Condensation.*

1 Introduction

In the 1980's and early 1990's, extensive analysis on air barrier system performance was conducted (Lux and Brown, 1989, Ojanen and Kumaran, 1995, Di Lenardo *et al.,* 1996) such that rational reference points for wall assembly design could be developed under historical Canadian climate patterns. The underlying intent was aligned with the fundamental needs to a) reduce energy use, and b) control condensation within moisture sensitive materials of a wall assembly.

This research work led to the development of the CAN/ULC S741 *Standard for Air Barrier Materials – Specification* and CAN/S742 *Standard for Air Barrier Assemblies – Specification*. Within these standards, performance criteria was established for the performance rating of air barrier materials and performance classification of air barrier assemblies based upon maximum allowable air leakage rates. The final component of this work was intended to be the development of a design approach that would integrate air barrier assembly performance with a building's design needs. Unfortunately, funding for the completion of this research and integration into building codes was halted before this work could be completed and published.

In the preparation of the 1995 National Building Code of Canada, under Part 5 *Environmental Separation*, there was a desire to define performance criteria for air barrier materials and air barrier assemblies. Since the research was not yet completed on air barrier assembly requirements, the ability to educate the design community on meeting minimum criteria was not yet possible. Hygrothermal computer modelling was still in its infancy and required significant assumptions on material performance to predict water vapour and moisture movement through assemblies, let alone the physics of air movement and condensation deposition. It was therefore accepted that codification of air barrier assembly performance was not reasonably practical.

By 2011 the Canadian Commission on Building and Fire Codes determined that it was

doi:10.23967/dbmc.2020.183

appropriate to consider air barrier assembly performance criteria in the National Building Code of Canada. The Standing Committee on Environmental Separation was tasked to:

> "*Develop quantifiable/explicit air leakage requirements for assemblies …and investigate the feasibility of creating a design approach to air leakage that would mimic the risk-based approach used for structural design where assemblies are designed to resist specified loads.*" (CCBFC 2011)

Parallel with this activity was the initiative to update CSA S478 *Guideline for Durability of Buildings*, with an emphasis on how appropriate building envelope design could be accomplished using the breakthroughs and improvements in computational hygrothermal modelling and analysis that had occurred in the intervening 20 years.

2 The Problem

In the development of the necessary changes to the National Building Code of Canada to adopt and implement a rational air barrier assembly design approach, it was identified that an exterior wall assembly durability risk assessment must assess whether various agents of deterioration will result in the;

- Shortening of the expected predicted service life of associated structural components, with resulting structural damage or risks of collapse, and/or
- Promotion of mold growth within the assembly, with resulting occupant health risks.

Air leakage through an exterior wall can be a significant contributor to these increased risks if resulting condensation moisture within the assembly leads to corrosion of metals, promotion of organic component deterioration, eg., wood decomposition, and/or promotion of mold growth. In order to assess the sensitivity of various wall assemblies to rates of air leakage, the following analysis methodology was developed.

3 Analysis Methodology

An analysis methodology was developed as described below. This paper focuses this analysis on one set of the variables to allow for assessment of the validity of the methodology.

Air leakage and its impact on wall assembly durability related to condensation and mold growth is a relative function of the following criteria:

1. Building occupancy characteristics – the internal hygrothermal loads imposed on the wall assembly. Different occupancy types affect interior hygrothermal loads. For the preliminary analysis in this paper, a residential occupancy was selected.
2. Building height – Building height directly influences wind loads and, therefore, air leakage rates (Shaw and Tamura, 1977). For this preliminary analysis, a single building height group was selected; a "low rise", 3½ storey residential property (<10 m tall).
3. Wall assembly composition – In this methodology, wall assemblies are assessed by the level of moisture tolerance of specific materials, the ability of the assembly to redistribute moisture within the assembly, and the ability of the assembly to dissipate moisture before it can cause deterioration or mold growth. For this preliminary analysis, a single wall assembly type was selected; a wood-framed wall with brick cladding reference wall, W1, as described in Section 3.1. Being of wood-frame construction, with the exterior masonry

cladding structurally attached to the wood studs, this assembly configuration is considered at relatively higher risk of potential negative impacts from moisture.

4. Building location climate characteristics – the historic and predicted future climate characteristics taken from a selected location in Canada. For the purposes of this initial analysis, the historic and future climate loads for the city of Winnipeg, Manitoba were selected as a baseline; Climate Zone 7A, 5670 HDD (NBC 2015). See Section 3.3.
5. Wall assembly air leakage rate – Variations in air barrier assembly air leakage rate were used to assess durability response. For the purposes of this initial analysis, air exfiltration due to imperfections in the air barrier system was calculated assuming air leakage rates of 0.05, 0.15 and 1.0 L/(s•m^2)@75 Pa. The first two represent air barrier assembly classifications A1 and A3 (CAN/ULC S472, 2011), while the final value was used to provide a quality check on the modelled results. An air leakage rate of 0.0 was also modelled to give a baseline for comparison of results and the ability to assess the impact of wind-driven rain without air leakage. The air leakage path is described in Section 3.2.

3.1 Reference Wall (W1)

Figure 1 shows the configuration of reference wall (W1). This wall assembly was chosen as an initial reference since a similar wall assembly was analyzed during the development work of the early 1990's (Ojanen and Kumaran, 1995, Di Lenardo *et al.,* 1996). This provided an initial comparison of this new methodology to the approach taken previously. The reference wall W1 has an effective RSI of 3.0 W/(m^2•K), which just meets current minimum thermal performance requirements for a low-rise residential Canadian building in Zone 7A that uses heat recovery ventilation (NBC, 2015). The results of this initial analysis should not be used to make design decisions. This approach was selected to facilitate comparisons of the results to earlier work.

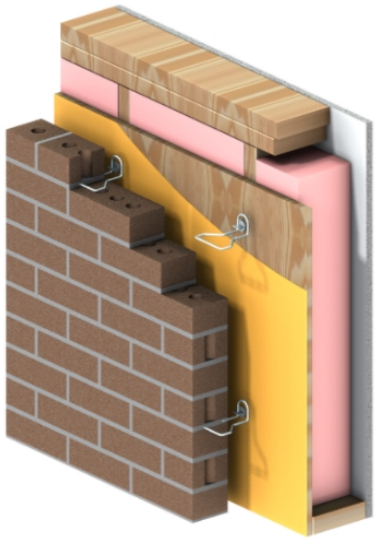

Figure 1. Reference wall (W1) schematic.

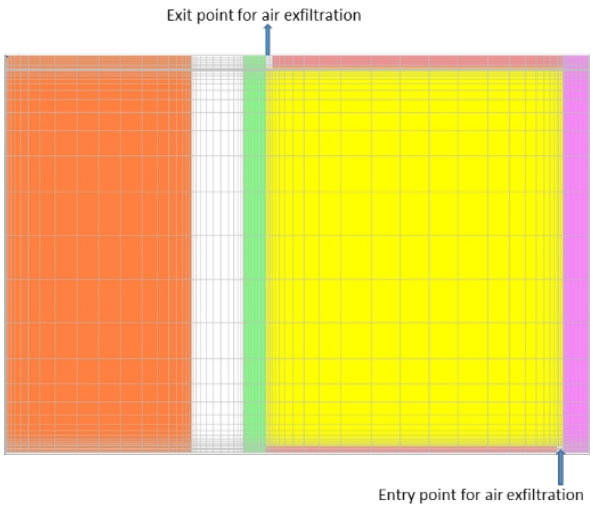

Figure 2. Modelled path of air movement.

The reference wall W1 comprises, from exterior to interior:

- Brick masonry (90 mm)

- Drainage cavity (25 mm)
- Exterior sheathing membrane (30-min building paper, 0.22 mm)
- Exterior oriented strand board sheathing (11 mm)
- Wood stud (spruce, 140 mm)
- Cavity insulation (glass fibre batt, 140 mm)
- Vapour barrier (6-mil polyethylene, 0.15 mm)
- Gypsum wallboard, primed and painted (12.7 mm)

3.2 Air Flow Path

To implement the air flow calculations, it was assumed that the air exfiltration occurs through an orifice in the air barrier system. The area of the orifice was estimated using the equation for sharp-edged orifice (ASHRAE, 2017). The orifice area was computed for each air leakage rate, assuming a rectangular orifice shape with a width of 0.05 m, the thickness of the opening was computed for each air leakage rate.

The risk of moisture condensation increases when the exfiltration path is longer, i.e., when air enters the insulation cavity at the bottom right corner and exits at the top right corner or vis-versa (Ojanen and Kumaran 1995). For this paper, it was assumed that air penetrates the cavity through a crack between the interior drywall and the flooring via imperfect contact between the bottom plate and the vapour barrier and exits through an opening between the top plate and the OSB sheathing, as shown in Figure 2.

3.3 Climate Data

Climate change weather data has been developed by the National Research Council that allows for balanced hygrothermal assessment of future building design needs (Gaur *et al.*, 2019). The data is comprised of hourly time-series of climate variables necessary to undertake hygrothermal simulations for a baseline time-period spanning 1986–2016 and 31-year long future time-periods when global warming of both +2°C and +3.5°C are projected (referenced to the baseline time-period). The climatic datasets were generated to capture the effects of the internal variability of the climate on future climate projections in fifteen hourly realizations that are part of the datasets derived from the large ensemble of climates simulated by the Canadian Regional Climate Model, version 4 (CanRCM4), each initialized under a different set of initial conditions in the CanESM2 global climate model. The generated datasets do not capture the uncertainty in climatic projections that may arise from the use of other global and regional climate models in simulating the regional climate and future climate projections.

For this study, only the 31-year time-periods corresponding to global warming of +3.5°C were considered; 1986-2016 Historical (“H”), and 2062-2092 Future (“F”). Each timeline comprises 15 realizations or runs. Since it can be onerous to consider all runs, it was decided that, for this preliminary study, only the median run (based on moisture index, MI) was selected from each timeline. The moisture index (Cornick and Dalgliesh, 2003) of a run was calculated as the average of the 31 yearly MI of that run.

For hygrothermal simulations in this study, two representative years were selected from the median run of the Historical and Future climate data. Since the purpose of the simulation is to address condensation risk, the first and second years were; 1) the year with the average annual temperature, and 2) that with the lowest annual temperature, of the 31-year data of the run. They

correspond respectively to the years 2008 and 2003 for Historical data, and 2092 and 2063 for Future data. Figure 3 compares the temperature, rain, relative humidity and wind speed profiles for the city of Winnipeg in the two years selected. The trend observed for the whole run is also present in the two-year data. It can be observed that; average temperature increases between the two timelines, while the wind speed decreases marginally. Rain and RH do not vary in average between the two timelines but more extreme annual RH values will be present in the future.

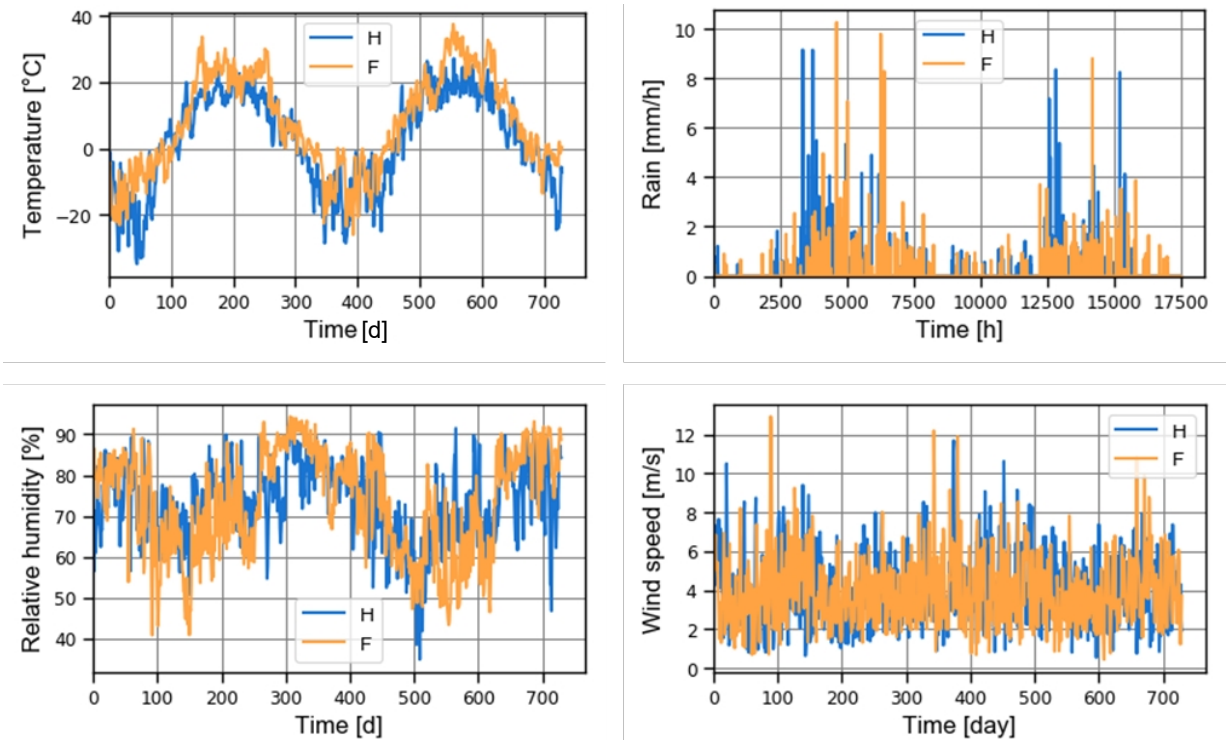

Figure 3: Comparison of the temperature, relative humidity, wind speed, and hourly rain distributions for the two years of historical and future climate data selected for hygrothermal simulations. Day 0 or hour 0 corresponds to January 1st of the first year.

3.4 Hygrothermal Model Used

DELPHIN 5, v5.9.4, was used for hygrothermal simulations. Important features of DELPHIN are its ability to handle wind-driven rain deposition and shortwave/longwave radiation as part of boundary conditions, as well as air leakage, moisture, and heat sources. A 2D configuration of the wall consisting of the vertical section passing through the insulation cavity was considered. This excludes the wood studs.

3.5 Boundary Conditions

Hourly data of climate loads (temperature, RH, wind velocity, wind-driven rain, shortwave and longwave radiations) on the cladding exterior surface were prepared according to DELPHIN specifications. Wind-driven rain was calculated using the ASHRAE (2016) standard method. Outdoor and indoor pressures were derived from differential pressure. The indoor T and RH were computed assuming that the building is equipped with heating and air conditioning with a

dehumidifier. Using ASHRAE (2016) formula, the indoor T varied from 21°C to 24°C and the indoor RH varied from 46% to 50%. For initial conditions, the T and RH of all layers were set to 21°C and 50% RH. As well the initial pressure was set to 101.3 kPa. Other parameters used for boundary conditions are summarized in Table 1. All material properties were obtained from the NRC material property database (Kumaran *et al.,* 2002).

Table 1. Boundary Conditions.

Boundary Conditions	Outdoor	Indoor
Heat transfer		
Convective heat transfer coefficient, α (W/m^{2}K)	$5.82 + 3.96\,V$*	8**
Shortwave absorption coefficient	0.6	-
Cladding longwave emission coefficient	0.9	-
Ground longwave emission coefficient	0.9	-
Ground albedo	0.1	-
Moisture transfer		
Water vapour transfer coefficient β (s/m)	$\alpha \times 7 \times 10^{-9}$	5.9 x 10^{-8}
Air leakage		
Air convection coefficient (s/m)	2	2

*: V is the wind velocity (m/s)
**: Indoor heat transfer coefficient encompasses both the convective and the radiative components

4 Results

The results of the preliminary analysis work relate to a combination of the following variables in the overall evaluation matrix:

- Residential occupancy
- Higher risk wall assembly
- Historical and Future weather data
- Low-rise building height
- Colder climate zone
- Air leakage rates of 0.0, 0.05, 0.15, and 1.0 L/(s•m^2)@75 Pa

The initial year was considered a conditioning year to allow stabilization after the initial boundary set points. Results are presented for relative humidity only, as the conditions for mold development were not reached over the two year simulation. Only results for the second year are discussed.

Preliminary results show that, based on the air path used, either; a) the bottom portion of the OSB in contact with the insulation, or b) the top left surface of the bottom plate, are more susceptible to condensation. For this paper, the results for the top left surface of the bottom plate was used to compare the impact of air leakage rates and climate change.

4.1 Effects of Air Leakage Rate and Climate Change

Figure 4 and 5 show the relative humidity profiles for each air leakage rate for the top left surface of the bottom plate for the reference wall (W1), for Historical (Figure 4) and Future (Figure 5) climate scenarios. Some key observations can be made:

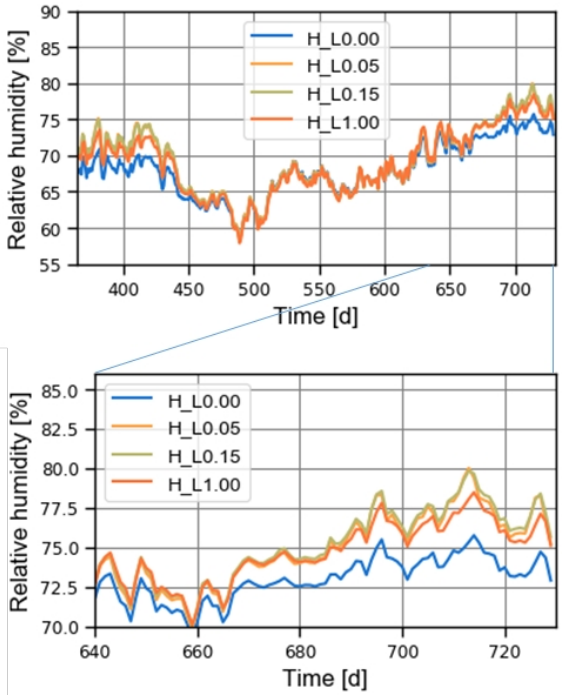

Figure 4. RH profiles, top left surface of bottom plate, reference wall (W1). Historic weather data.

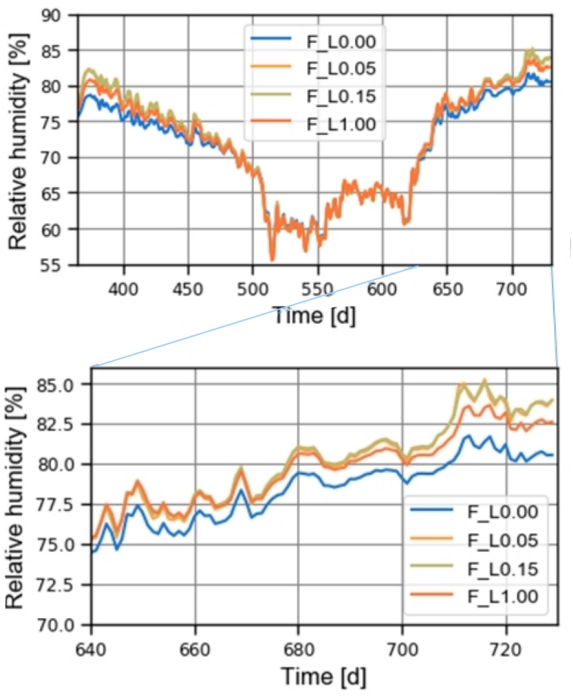

Figure 5. RH profiles, top left surface of the bottom plate, reference wall (W1). Future weather data.

Air Leakage Rate:

- All curves follow the same general profile as the 0.0 air leakage rate.
- All curves indicate that they have not normalized after the conditioning year, suggesting the length of simulation is insufficient to identify the final trends in moisture loading.
- Air leakage rates of 0.05 and 0.15 give almost identical results, regardless of climate scenario. Both of these air leakage rates show increased RH over the 0.0 rate.
- Air leakage rate of 1.0 has lower RH compared to 0.05 and 0.15. This is due to the cavity warming from the higher rate of warm air leakage (Ojanen and Kumaran 1995)

Climate Change:

- Differences of up to 4% for Historical climate and 5% for Future climate are found between the case with no air leakage and the cases with leakage rates of 0.05 and 0.15.
- The Future climate model shows that up to 85% RH is reached in wood materials, while in the Historical climate model, up to 80% is reached.
- Future climate data shows an increase of up to 8% in RH over Historical climate.
- Future climate shows sustained increase in RH versus Historical climate after the 710 day mark in the simulation. Historical climate shows a decrease in RH while Future climate shows sustained increase.
- The RH has not normalized for both climate scenarios, suggesting that the length of simulation is insufficient to provide suitable information on moisture loading.

5 Conclusions

This preliminary work is intended to document a methodology for assessment of air leakage rate and climate change on wall assembly durability. The initial assessment demonstrates that results that indicate the relative wall assembly performance under different air leakage rates can be used to establish inputs into a durability analysis. The results also demonstrate that differences between historical and future climate data suggests the methodology has merit.

However, it was also determined that conducting hygrothermal simulation using two years of climate data does not provide sufficient output data to assess stabilized moisture trends and mold development risks. Since mold development risk is a key criteria for long term durability assessment, future analysis work must use longer simulation durations.

Also critical is the length of the simulation "conditioning" time frame to allow the assembly component normalization of temperature and moisture conditions. Longer simulation timeframes will provide a better understanding of required conditioning durations.

Future work must analyze different; climate zones, building heights, building occupancies, wall assembly composition, and formal durability risk assessments for each result to understand the importance of air barrier performance on durability in a changing climate.

ORCID

David Kayll: https://orcid.org/0000-0002-3854-9408
Maurice Defo: https://orcid.org/0000-0001-9212-6599
Travis Moore: https://orcid.org/0000-0002-4920-9193
Michael Lacasse: https://orcid.org/0000-0001-7640-3701

References

ANSI/ASHRAE. (2016). ASHRAE Standard 160-2016. *Criteria for Moisture-Control Design Analysis in Buildings*. Atlanta: ASHRAE.

ASHRAE Handbook – Fundamentals (2017). ASHRAE, Atlanta.

CAN/ULC S472 (2011), Standard for Air Barrier Assemblies – Specification, Underwriters Laboratories Canada

CCBFC Canadian Commission on Building and Fire Codes (2011). Mandate letter to Standing Committee on Environmental Separation.

Cornick, S.M. and Dalgliesh, W.A. (2003). *A Moisture index to characterize climates for building envelope design*. National Research Council Canada 45658

Di Lenardo, B., Brown, W.C., Dalgleish, W.A., Kumaran, M.K. and Poirier, G.F. (1996) *CCMC Technical Guide for Air Barrier Systems for Exterior Walls of Low-Rise Buildings* Masterformat Section: 07272,

Gaur, A., Lacasse, M. and Armstrong, M. (2019). *Climate data to undertake hygrothermal and whole building simulations under projected climate change influences for 11 Canadian cities*. Data, 4(2), 72. National Research Council Canada

Kumaran M.K., Lackey, J.C., Normandin, N. and Van Reenen, D. (2002) *Summary Report From Task 3 of MEWS Project at the Institute for Research in Construction - Hygrothermal Properties of Several Building Materials*. National Research Council Canada

Lux, M.E. and Brown, W.C. (1989). *An air barrier for the building envelope*. Proceedings of Building Science Insight '86. National Research Council of Canada, Ottawa. NRCC 29943.

National Building Code Canada 2015 (NBC), Codes Canada

Ojanen, T. and Kumaran, M.K. (1995). *Effect of exfiltration on the hygrothermal behaviou of a residential wall assembly: Results from calculations and computer simulations*. Symp. on Moisture Problems in Building Walls, (pp. 157-167). Porto, Portugal.

Shaw, C.Y. and Tamura, G.T. (1977). *The Calculation of Air Infiltration Rates Caused by Wind and Stack Action for Tall Buildings*. National Research Council Canada 761, ASHRAE Transactions, 83,2, pp 145-158.

XV International Conference on Durability of Building Materials and Components
DBMC 2020, Barcelona
C. Serrat, J.R. Casas and V. Gibert (Eds)

Effect of Selected Moisture Reference Year on the Durability Assessment of Wall Assemblies under Future Climates

Sahar Sahyoun[1], Hua Ge[2], Chetan Aggarwal[3], Maurice Defo[4] and Travis Moore[5]

[1] Ph.D. Student, Concordia University, Montreal, Canada; s_sahyo@concordia.live.ca

[2] Associate Professor, Concordia University, Montreal, Canada; hua.ge@concordia.ca

[3] Ph.D. Student, Concordia University, Montreal, Canada; c_agga@encs.concordia.ca

[4] Associate Research Officer, Construction Research Centre, National Research Council Canada, Ottawa, Canada; Maurice.Defo@nrc-cnrc.gc.ca

[5] Research Council Officer, Construction Research Centre, National Research Council Canada, Ottawa, Canada; Travis.Moore@nrc-cnrc.gc.ca

Abstract. *Hygrothermal simulations are commonly used to evaluate the moisture damage risk of building envelopes over the long-term. For such assessment to be accurate, a proper selection of representative climate data is required. A common method is the selection of a moisture reference year from a set of available long-term climate data. For instance, the IRC-led research consortium MEWS (Moisture Management of Exterior Wall Systems) developped the Moisture Index (MI) approach, which consists of a wetting and a drying function. Therefore, the reference year selection would be based on the MI ranking. ASHRAE 160 is adopting a procedure named "the severity index" for the selection of moisture reference year. Combining climate loads and durability criteria, this method allows to select more "severe" weather years, thus providing a more representative ranking of the weather data. The objective of this paper is two-fold. First, to compare the selection of the moisture reference year based on two different approaches for both historical and future climate loads. Second, the effect of chosen representative years is evaluated and compared to long-term simulation periods (of 31-years) based on the durability of building assemblies. The methodology includes hygrothermal simulations of two different types of wall assemblies located in three different Canadian cities under a changing climate. In general, higher mold index values were obtained by the long-term simulation and MRYs using Isev. Comparing the results of different models under future climates, the three methods were in good agreement, except for a brick wall facing WDR in Ottawa and Vancouver. This might be due to the Isev correlations were developed based on a north-facing stucco wall. In addition, for a north-facing wall, an extremely low mold index was predicted for Vancouver, compared to WDR direction. Thus, considering a north-facing wall as a criterion for performance evaluation might misrepresent the reality in some locations. Hence, both WDR and North orientations should be considered. A further study will be carried out to investigate the performance evaluation of Isev method for different types of wall systems and orientations.*

Keywords: *Moisture Reference Year, Durability,Wind-Driven Rain, Mold Index, Climate Change.*

1 Introduction

With the increased concern of climate change, severe rainfall events are more likely to happen. Therefore, water penetration in wall assemblies, resulting from the coupled action of rain and wind, may cause moisture to accumulate in building envelopes which can lead to degradation

of building materials; thereby, reducing their performance and service life. Heat, air and moisture (HAM) simulation tools are typically used to determine the risk to deterioration of buildings' elements. However, these tools neccessite the selection of representative climate data, as well as a good understanding of the moisture conditions, in order to provide an accurate assessessement (Delgado *et al.,* 2012). Therefore, a moisture reference year is usually selected from existing long-term climate data to represent a climate that allows a correct evaluation of the moisture stress on the building envelope (Zhou *et al.,* 2016).

Different methods were introduced in the past and have been used to define moisture reference years (Hagentoft and Harderup, 1993; Harderup, 1994; Geving, 1997; Kalamees and Vinha, 2004; and Zhou *et al.,* 2016). The IRC-led research consortium MEWS (Moisture Management of Exterior Wall Systems) developped the Moisture Index (MI) approach, which includes wetting and drying indices (Cornick *et al.,* 2003). The wetting index (WI) can be represented by the mean annual total horizontal rainfall or the annual wind-driven rain load. The drying index (DI) is based on the yearly evaporation potential – meaning the total hourly difference between the saturation vapor ratio and actual vapor ratio of the ambient air. Besides, ASHRAE (2010) has further developed MRY selection measures, combining climate loads and durability criteria to select more "severe" weather years, thus providing a more representative ranking of the weather data. This new approach – the Severity Index (Isev), consists of a simple equation that would be used to calculate the predicted damage function value for each year. Salonvaara *et al.* (2010) have demonstrated that Isev is the most reliable and the most accurate among all available methods in selecting the most severe years in terms of hygrothermal performance for climates in North America.

The objectives of this paper is to compare the selection of the moisture reference year based on the moisture index (MI) and the severity index (Isev) methods for both historical and future climate loads. The effect of representative years on the durability assessment of building assemblies is evaluated under different moisture loads including rain leakage. A comparison is thus made between the effect of selected representative years and the long-term simulations on the durability of building assemblies.

2 Methods

2.1 Weather Data

Weather data were provided by the National Research Council of Canada (NRC). A continuous time-series[1] of hourly climate data was prepared for a baseline time-period spanning from 1986-2016 and a 31-year long future time-period selected for when projected global warming of 3.5°C is expected to be reached in the future (Gaur *et al.,* 2019). According to projections from Environment and Climate Change Canada (2018), future projected data of a 3.5°C increase, will be reached between 2062-2092. Each data set includes 15 realizations; however, only the median realization based on MI was used.

[1] The full dataset can be accessed from: 10.17605/OSF.IO/UPFXJ.

2.1.1 Selection of Reference Years

The selection of reference years was made with the intention to test wall assemblies under more representative design weather years in the selected timelines. Moisture Index (MI) and severity index (Isev) have been chosen as the indices for selecting the reference years. Both methods were used to select one (1) year as the reference year.

Following the previous work performed at NRC (Cornick et al., 2003), MI for every hour (MI_h) was calculated as a function of hourly wetness (WI_h) and dryness (DI_h) indices. WI_h is calculated as normalized accumulated hourly rainfall. Dryness index (DI_h) was calculated as a function of the difference between saturation vapor pressure and vapour pressure of the ambient air (Δ_{vp}). The saturation vapor pressure, p_{vs}, was calculated using Equation (1), retrieved from the ASHRAE Handbook of Fundamentals (ASHRAE, 2009).

$$\ln(p_{ws}) = \begin{cases} \frac{C_1}{T} + C_2 + C_3T + C_4T^2 + C_5T^3 + C_6T^4 + C_7\ln(T) & for\ T < 0 \\ \frac{C_8}{T} + C_9 + C_{10}T + C_{11}T^2 + C_{12}T^3 + C_{13}\ln(T) & for\ T \geq 0 \end{cases} \quad (1)$$

Where, C_1 = -5.6745359 E+03; C_2 = 6.392524 E+00; C_3 = -9.6778430 E-03; C_4 = 6.2215701 E-07; C_5 = -5.6745359 E+03; C_6 = -9.4840240 E-13; C_7 = 4.163501 E+00; C_8 = -5.8002206 E+03; C_9 = 1.3914993 E+00; C_{10} = -4.8640239 E-02; C_{11} = 4.1764768 E-05; C_{12} = -1.4452093 E-08; C_{13} = 6.5459673 E+00; and T denotes the ambient temperature (K).

The magnitude of Δp_v is calculated using Equation (2):

$$\Delta p_v = p_{vs} - p_v \quad (2)$$

Wetting and drying indices are normalized following Equation (3):

$$I_{normalized} = (I - I_{min})/(I_{max} - I_{min}) \quad (3)$$

Normalized values of Δp_v were used as DI_h magnitudes. Wetting and drying were assumed to be of equal importance and thus they were given equal weight in the determination of the moisture index (MI_h).

$$MI_h = \sqrt{(1 - DI_{h,norm})^2 + {WI_{h,norm}}^2} \quad (4)$$

Based on ASHRAE (2010), the severity index (Isev) for each year is calculated according to Equation (5):

$$I_{sev} = 108307 - 241.E_v - 1391.I_{cl} - 312326.\phi + 183308.r_{wd} + 15.2.p_v + 27.3.T^2 + 261079.\phi^2 - 0.00972.p_v^2 \quad (5)$$

Where, E_v is the solar radiation (W/m^2) incident on the wall; I_{cl} is the cloud index (0-8); ϕ is the relative humidity; r_{wd} is the wind-driven rain (kg/m^2.h) on the wall; p_v is vapor pressure (Pa), and T is the ambient temperature (°C). As specified by the method, Isev was calculated for the orientation receiving the least solar radiation (North). All the weather parameters were calculated in terms of annual average values for each year; using the number of hours during that year.

Once both annual average MI and Isev values were available, the years comprising the chosen time-period were ranked in ascending order, and the year corresponding to the 97th percentile, (ranked second out of the 31 years) in each time-period was chosen as the MRY. Figure 1 shows the annual average values of MI and Isev at each location, for a wall facing North.

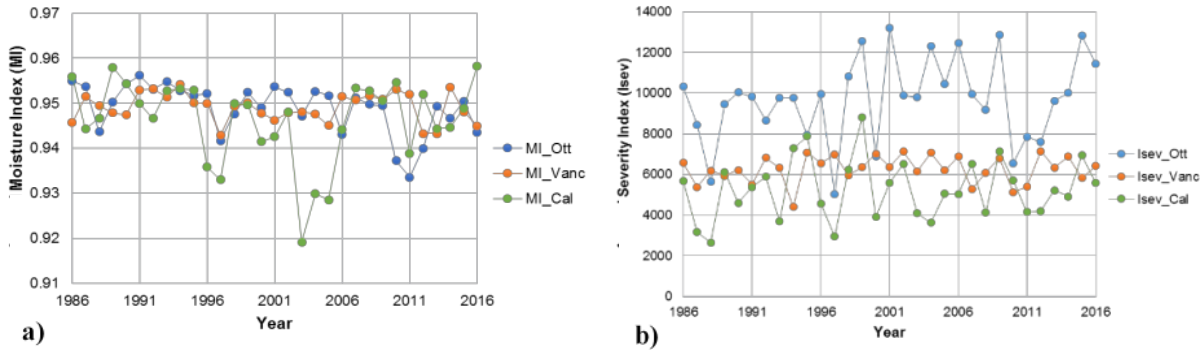

Figure 1. Comparison of annual moisture index MI (a) and Isev (b) in Ottawa (Ott), Vancouver (Vanc) and Calgary (Cal) for a North-facing wall based on historical data.

Table 1 summarizes the selected MRYs based on different locations under historical and future time-periods.

Table 1. Summary of selected moisture reference year and their MI and Isev values.

City	Data	MRY (MI)	MRY (Isev)
Ottawa	Historical	2010 ***(0.937)***	2009 ***(12856.4)***
Ottawa	Future	2085 ***(0.918)***	2069 ***(18720.0)***
Vancouver	Historical	2012 ***(0.943)***	2002 ***(7132.8)***
Vancouver	Future	2075 ***(0.921)***	2092 ***(9766.5)***
Calgary	Historical	2005 ***(0.928)***	1995 ***(7874.8)***
Calgary	Future	2089 ***(0.903)***	2092 ***(11198.8)***

2.2 Wall Assemblies

Two (2) wood frame wall assemblies, typical of Canadian residential building practice, were selected for this study. They differ only in their cladding type: stucco (19 mm) and brick (90 mm). A drainage cavity of 25mm and 10mm was designed for the brick and the stucco wall, respectively. Figure 2 shows the configuration of the wall assemblies.

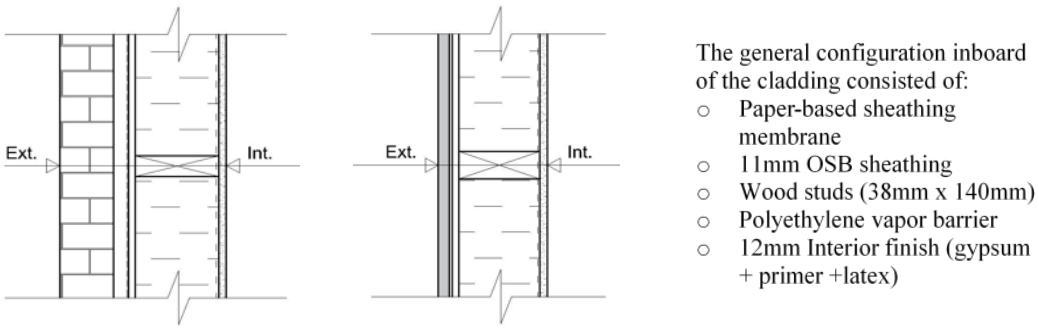

Figure 2. Wall assemblies' configuration for brick (a) and stucco (b).

2.3 Wall Orientation

This study was carried out for two wall orientations for each location: the orientation with the least annual solar radiation – meaning on a North-facing wall (N), and the orientation with the highest amount of annual wind-driven rain, calculated according to ASHRAE (ANSI/ASHRAE, 2016). The critical orientation (WDR) is presented in Table 2 for each city.

Table 2. Characteristis and wall orientation for selected Canadian cities.

City	Lat.	Long.	Climate zone	Time zone	Critical orientation (WDR)
Ottawa	45.25°	75.42°	6	-5	202.5° (SSW)
Vancouver	49.28°	123.12°	5	-8	157.5° (SSE)
Calgary	51.05°	114.07°	7A	-7	337.5° (NNW)

2.4 Boundary Conditions

2.4.1 Indoor Boundary Conditions

The indoor temperature and relative humidity conditions were selected as constants and set to 21°C and 50%, respectively. For the indoor vapour diffusion and the heat conduction, the transfer coefficients were assumed as $1.52*10^{-8}$ s/m and 8 W/m^{2}K, respectively.

2.4.2 Outdoor Boundary Conditions

Outdoor boundary conditions include heat conduction, vapor diffusion, wind driven rain, short wave radiation and long wave radiation. To compute the longwave radiation, the boundary layer method was selected in Delphin. The required longwave emission coefficient of the building surface was set to 0.9, whereas the convective heat transfer coefficient was calculated based on Equation (6):

$$h_{ce} = 4 + 4.v \quad (6)$$

Where, v is the wind speed. The reflection coefficient of the surrounding ground (albedo) was 0.2 and the absorptance coefficient of the cladding surface was equal to 0.6 for brick and 0.3 for stucco.

2.4.3 Wind-Driven Rain

WDR was calculated using the ASHRAE method (ANSI/ASHRAE, 2016) for a 3.5 storey building located in the suburban area. Assuming a medium exposure factor, the rain exposure factor (F_E) and the rain deposition factor (F_D) were set to 1.0 and 0.5, respectively.

2.5 Initial Conditions

The wall was first condionned with suitable climate and simulations were performed for a period of 7 successive years using the average year (based on MI ranking). Once a steady cyclical pattern was observed at the exterior side of OSB, the average temperature and relative humidity for each material were exported and used as initial conditions.

2.6 Performance Attributes for Assessing Wall Performance

One important performance attribute for wood-based building elements is the resistance to mould growth. Under favourable conditions of temperature and relative humidity, mould fungi can grow on building component surfaces and this is often regarded as problematic in respect to indoor air quality (Wang *et al*., 2018). OSB is susceptible to mould growth if subjected to these favourable conditions. The outward layer of the OSB sheathing (~ 0.1 mm) was selected as the critical location for this study. The mould growth index was calculated using Viitanen's model implemented in DELPHIN (Viitanen *et al.,* 2000).

Several trials were made to select the air change per hour (ACH) value in drainage cavities, in a way that the mold index stabilizes around a value of 3 during the long-term simulation. Different values of ACH were set based on the cladding type and the location (Table 3).

Table 3. ACH values selected according to different cladding and locations for North and WDR orientations.

Ottawa		**Vancouver**		**Calgary**	
Brick	Stucco	Brick	Stucco	Brick	Stucco
6	*10*	*12*	*40*	*3*	*5*

2.7 Simulations

Manual discretization was adopted; for the sheathing membrane and the vapour barrier, an equidistant mesh of 3 elements was assumed. Other materials were divided into three sections – with first and last sections of equal thicknesses. A fine and variable mesh was used for the latter, while an equidistant mesh was opted for the middle section.

A moisture source of 1% of the WDR was assumed and applied on the exterior wythe of the sheathing membrane – on the first layer of the membrane (ANSI/ASHRAE, 2016).

Each selected MRY was repeated 5 times; however, evaluation was made only for the 5th year. These results were compared to those of a long-term simulation of 31 consecutive years.

3 Results and Discussion

Figure 3 shows the predicted risk to mold growth on the outer layer of OSB for different types of walls under different climate loads, which were selected based on different reference year methods, i.e., MI and Isev. Results are compared to that of a long-term simulation (31-Y) in three Canadian cities. The 31-Y results were selected for the year having the second highest mold index value. In general, the differences amongst the mold indices vary with the cladding type, the location (climate) and the wall orientation. Comparing the impact of MRY selection method, in most of the cases, the mold index is found higher based on Isev selection – meaning that MRYs selected according to Isev predicted a higher damage risk than years selected based on MI. Moreover, results of the 31-Y seem more in accordance with Isev.

For a brick wall (Figure 3a), mold index values are found higher for Isev and 31-Y, and in some events, especially in Ottawa, results for Isev seem to overestimate the risk. This may be due to the difference between the MRYs selected by Isev and the years corresponding to the 2nd highest mold index value for the 31-Y. It seems that the climate selected based on Isev is more favorable for mold growth. However, for stucco (Figure 3b), results are found to be more consistent; with 31-Y estimating highest mold index values. Moreover, the difference between the methods had a greater impact on the wall performance. For instance, both 31-Y and Isev

estimated a considerable risk to mold growth compared to results given by MI. For a wall facing North in Ottawa, a maximum mold index value of 4.5 and 5 was attained for historical and future climate, respectively for 31-Y. Using the Isev method, values of 4 and 4.8 were reached. However, using MI, maximum values of 1 and 2.8 were attained for different climates. Likewise in Calgary, the difference in mold prediction risk varried considerably between the methods.

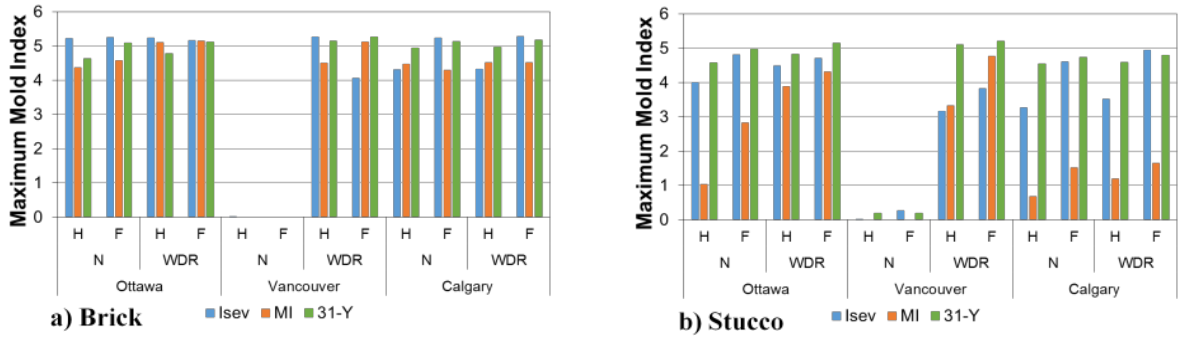

Figure 3. Summary of maximum mold index predicted through a long-term study (31-Y) and using MRYs given by Isev and MI for historical (H) and future (F) climatic loads, for walls facing North (N) and WDR.

It can be also observed that in Vancouver, when the wall is facing North, all three methods predicted no risk of mould growth. This can be explained due to a low amount of WDR impiging on a North facing wall in that city. It is also important to note the effect of the selection method on the assessment of the climate change impact on the hygrothermal response of walls. Mold index values increased under future climate loads in most of the cases, to the exception of a brick wall facing towards the WDR in Ottawa and Vancouver using Isev. Results showed a slight decrease in mold index for Ottawa but a considerable decrease for Vancouver (Figure 3a). The severity index calculated was based on the correlations developed for a North-facing orientation. Discrepancy may exist when the same year is used to evaluate walls oriented towards the prevailing WDR direction for cities with WDR direction distinctly different from the North and for absorptive cladding that is more sensitive to WDR. Further investigation is required on the aspect of wall orientation. The impact of climate change is more consistent for the stucco wall (Figure 3b), where the difference of mold index is increased by up to 2 indices (for the case of a north oriented wall in Ottawa and Calgary).

4 Conclusions

In this study, the effect of selecting MRYs on the expected long-term moisture performance and durability is investigated from results derived from hygrothermal simulations of typical wood-frame wall assemblies in three Canadian cities. The durability performance was assessed based on the potential to mold growth on the OSB sheathing incorporated in stucco and brick veneer clad wall assemblies. Results showed that the use of different climate load indices (*i.e.* MI or Isev) can lead to different conclusions on the moisture performance of these types of wood-frame walls. In general, higher mold index values were obtained from the long-term simulation and MRYs using Isev for both walls in all three locations. Comparing the results of different models under future climates, the three methods were in good agreement, except for a brick wall facing WDR in Ottawa and Vancouver. This might be due to the fact that the Isev correlations were developed based on a North-facing stucco wall (ASHRAE, 2010). In addition,

for a north-facing wall, an extremely low mold index was predicted for Vancouver, compared to the value of the mould index as was attained from simulations when the prevailing WDR direction was used as input to the climate loads. Thus, considering a North-facing wall as a criterion for performance evaluation might misrepresent the actual moisture behavior in some locations. Hence, for each location, both WDR and North orientations should be considered. A further study will be carried out to investigate the performance evaluation of Isev method for different types of wall systems and orientations.

ORCID

Sahar Sahyoun: https://orcid.org/0000-0001-5131-6134
Hua Ge: http://orcid.org/0000-0003-1368-4301
Chetan Aggarwal: http://orcid.org/0000-0002-7224-9740
Maurice Defo: http://orcid.org/0000-0001-9212-6599
Travis Moore: http://orcid.org/0000-0002-4920-9193

References

ANSI/ASHRAE. (2016). *Criteria for Moisture Control Design Analysis in Buildings.* Atlanta.

ASHRAE. (2010). *Environmental weather loads for hygro- thermal analysis and design of buildings. RP-1325, American Society of Heating, Refrigerating and Air- Conditioning Engineers, Inc.* Atlanta.

ASHRAE. (2009). *ASHRAE handbook: Fundamentals*. Atlanta.

Cornick, S., Djebbar, R. and Dalgliesh A.W. (2003). Selecting moisture reference years using a Moisture Index approach. *Building and Environment*, *38*(12), 1367–1379.

Delgado, J.M., Barreira, E., Ramos, N.M. and De Freitas, V.P. (2012). *Hygrothermal numerical simulation tools applied to building physics*. Springer Science & Business Media.

Environment and Climate Change Canada. (2018). *Memorandum of Understanding between National Research Council and Environment and Climate Change Canada….* Government of Canada: Ottawa, ON, Canada.

Gaur, A., Lacasse, M. and Armstrong, M. (2019). Climate Data to Undertake Hygrothermal and Whole Building Simulations Under Projected Climate Change Influences for 11 Canadian Cities. *Data*, *4*(2), 72.

Geving, S. (1997). *Moisture Design of Building Constructions: Hygrothermal Analysis Using Simulation Models-Part I and II,* PhD thesis, Norwegian University of Science and Technology.

Hagentoft, C. E. and Harderup, E. (1993). Reference for moisture calculations. Report T2-S-93/01, IEA Annex 24, HAMTIE.

Harderup, E. (1994). Durability reference year: Using the π-factor method to find the DRY for three locations in Sweden. Report T2-S-94/01, IEA Annex 24, HAMTIE.

Kalamees, T. and Vinha, J. (2004). Estonian climate analysis for selecting moisture reference years for hygrothermal calculations. *Journal of Thermal Envelope and Building Science 27*:199-220.

Salonvaara, M., Sedlbauer, K., Holm, A. and Pazera, M. (2010). Effect of selected weather year for hygrothermal analyses. *Proceedings of thermal performance of the exterior envelopes of whole buildings XI. ASHRAE.*

Viitanen, H., Hanhijärvi, A., Hukka, A. and Koskela, K. (2000). Modelling mould growth and decay damages. *Healthy Buildings*, 341-346.

Wang, J., Stirling, R., Morris, P., Taylor, A., Lloyd, J. and al. (2018). Durability of mass timber structures: A review of the biological risks. *Wood and Fiber Science 50,*(Special Issue), 110-127.

Zhou, X., Derome, D. and Carmeliet, J. (2016). A new procedure for selecting moisture reference years for hygrothermal simulations. *Bauphysik, 38,* 361-365.

XV International Conference on Durability of Building Materials and Components
DBMC 2020, Barcelona
C. Serrat, J.R. Casas and V. Gibert (Eds)

Freeze-Thaw Risk in Solid Masonry: Are 'Hygrothermal Response Based' Analyses Mandatory when Studying the Sensitivity of Building Envelopes to Climate Change?

Isabeau Vandemeulebroucke[1], Steven Caluwaerts[2] and Nathan Van Den Bossche[1]

[1] Building Physics Group, Department of Architecture and Urban Planning, Ghent University, Belgium, isabeau.vandemeulebroucke@ugent.be.

[2] Atmospheric Physics Group, Department of Physics and Astronomy, Ghent University, Belgium, steven.caluwaerts@ugent.be.

Abstract. *The 5th Assessment Report of the Intergovernmental Panel on Climate Change (IPCC) reports important evolutions in the climate system. These changes are likely to affect the durability of the built environment. Although many contemporary studies investigate the future energy efficiency of buildings, research on the impact of climate change on the hygrothermal behaviour and degradation of building envelopes is rather scarce. Using climate projections, we studied the advantage of 'hygrothermal response based' analyses over 'climate based' analyses when assessing the impact climate change on façades. This paper presents a sensitivity study on solid masonry wall assemblies, before and after internal retrofitting, using three RCP (Representative Concentration Pathways) projections of the ALARO-0 Regional Climate Model at the grid point of Brussels (BE). The findings suggest the necessity of a 'hygrothermal response based' analysis to study the sensitivity of the building envelope to climate change. Moreover, the largest sensitivity is observed for RCP 8.5, the scenario having the highest projected greenhouse gas concentrations by the end of the century.*

Keywords: *Hygrothermal Response, Building Envelope, Climate Change, HAM Simulation, Masonry.*

1 Introduction

The Fifth Assessment Report of the Intergovernmental Panel on Climate Change reports significant changes in the climate system (IPCC, 2014). Since pre-industrial times the global surface temperature has increased ca. 1°C, and is projected to rise further during the 21st century. Along with that, extreme events are influenced by the increased greenhouse gas (GHG) emission in our atmosphere. Across Europe, heat waves and extreme precipitation are likely to become more frequent, more intense and separated by longer periods of drought, and the number of freezing days is likely to decrease (IPCC, 2014).

The built environment will be significantly affected by climate change (de Wilde and Coley, 2012; Fatorić and Seekamp, 2017). Many studies focus on the energy efficiency of our building stock regarding climate change. This study investigates the climate sensitivity of retrofitting strategies of historical buildings to increase their thermal resistance and airtightness. As exterior retrofitting of heritage buildings is often not allowed due to the façade's historical value, interior retrofits may be the only solution to improve the energy efficiency of the building envelope (Straube and Schumacher, 2010). Studies on the durability of internally retrofitted solid masonry show that this strategy might increase the risk of moisture-related damages, as freeze-thaw action. However, few studies investigate the impact of climate change on the long term

durability of these retrofits, and there is no sound methodology to implement climate projections in Heat Air Moisture (HAM) simulations.

This paper aims to study the difference between a 'climate based' and 'hygrothermal response based' analysis when assessing the freeze-thaw risk in solid masonry, before and after internal retrofit, with regards to climate change.

2 Methodology

The 1-dimensional HAM simulations in this study are performed in Delphin 5.9.5, which has been successfully benchmarked in the past by the HAMSTAD Benchmark exercises a.o. (Nicolai, Grunewald and Zhang, 2007).

2.1 Climatological Conditions

This work applies the 4-km resolution ALARO-0 Regional Climate Model (RCM) data of the CORDEX.be project (Termonia *et al.,* 2018) to investigate the climate impact. Climate data for the period 1950-2100 are selected for the Uccle gridpoint. For the period 1950-2005 the historical run will be used, while for the 2006-2100 timeframe different climate projections forced by scenarios for future GHG emissions are considered to investigate the climate sensitivity. The Representative Concentration Pathways used in this study are RCP 2.6, RCP 4.5 and RCP 8.5, representing respectively a low, intermediate and high radiative forcing (IPCC, 2014).

The modelled meteorological parameters, used in this study, are air temperature (T_{air}), relative humidity, wind direction and velocity, precipitation, direct and diffuse shortwave radiation and downward longwave radiation. Climate model data are known to be subject to systematic biases. As this manuscript is focussed on the sensitivity (and no absolute values) of the HAM simulations to climate scenarios, no bias correction has been applied on the data.

The indoor T_{air} and relative humidity are calculated based on the standard ISO 13788, and range between 20-25°C and 35-65% respectively, depending on the outdoor T_{air}.

The HAM model is pre-conditioned by repeating the 1st year of the dataset four times, given this year does not represent extremes. The conditioning years are not part of the evaluation.

2.2 Wall Assemblies

Two variants of a solid masonry wall assembly are considered. In both cases the masonry has a width of 300 mm, and is selected from the Delphin Material Library, i.e. 'Historical Brick Cluster 4'. The original wall assembly is finished with 12 mm of gypsum plaster (interior). The second masonry wall (without plaster) is retrofitted at the interior with mineral wool (150 mm), open vapour barrier (sd = 2.3 m) and gypsum board (12 mm). The masonry is assumed homogenous brick, as this simplification is found acceptable by Vereecken and Roels (2013).

The critical degree of moisture saturation for freeze-thaw damage to occur, is not known for the selected brick material. Therefore, the arbitrary value of 25% ice volume rate is used (Straube, Schumacher, & Mensinga, 2010). The critical moisture content (MC_{crit}) for the masonry is 82.5 kg/m³. Note that this is a conservative value, considered as worst-case scenario.

2.3 HAM Simulations

Five situations are analysed: i) the original solid masonry wall facing the south-west (SW) (225°), the prevailing wind-driven rain (WDR) direction in Uccle, for RCP 8.5, ii-iv) the retrofitted wall facing SW for RCP 2.6, 4.5 and 8.5, and v) the retrofitted wall facing the north-west (NW) (315°) for RCP 8.5, to study an orientation receiving less solar radiation and a smaller WDR load.

The climate data and simulation results are analysed using the moving average per period of 30 years. All simulation results are analysed at a depth of 5 mm in the masonry (exterior side), as this is generally a critical depth for freeze-thaw action (Vandemeulebroucke *et al.* 2019).

3 Results

3.1 'Climate Based' Analysis

The moving average of the annual mean air temperature ($T_{air,mean,annual}$) confirms the warming trend over the 21st century especially for RCP 4.5 and 8.5, illustrated by the dotted lines in Figure 1 (IPCC, 2014). For the RCP 2.6 scenario which assumes strong mitigation measures, the temperature reaches a maximum around 2050. The warming over the whole period is ca. 1°C, 1.5°C and 3°C for RCP 2.6, 4.5 and 8.5 respectively. $T_{air,mean,winter}$, i.e. the average temperature during the period December-January-February, confirms the temperature trends. Analysed frost indices are the annual hours of frost and the number of freeze-thaw cycles based on temperature ($FTC_{T,air}$), considering freezing at -5°C and thawing at 0°C. These threshold values are selected anticipating the 'response based' analysis, as Straube and Schumacher (2006) suggest that no significant freeze-thaw damage occurs between 0°C and -5°C. Both the hours of frost (T_{air}) and the number of $FTC_{T,air}$ decrease by one third for RCP 4.5 and two thirds for RCP 8.5. The climate change signal for RCP 2.6 is less clear.

Furthermore, the annual precipitation amount is increasing for RCP 4.5 (7-10%) and 8.5 (9-12%). Again the climate change signal for RCP 2.6 is less clear (Figure 2). Changes are not as uniform as for $T_{air,mean}$, since precipitation has stronger year-to-year variability. The fraction of annual precipitation occurring in winter is ca. 25% and increases by 0-4% for RCP 4.5 and 8.5.

The other climate variables, e.g. as wind direction and velocity, show only small changes over the course of the 21st century (not illustrated here).

3.2 'Response Based' Analysis

The 'response based' analysis indicates that the mean temperature at 5 mm in the masonry ($T_{5mm,mean}$), illustrated by the solid lines in Figure 1, follows the same trend as the $T_{air,mean}$. However, the offset between the climate data and the simulated response of the masonry differs per season, wall assembly and orientation, ranging between -0.3°C–2.2°C. The offset slightly decreases towards the end of the 21st century. Except for the retrofitted walls in winter, $T_{5mm,mean}$ is higher than $T_{air,mean}$. The highest values are observed for the original wall for RCP 8.5 due to the lack of thermal insulation. The differences between the climate and response data are smaller in winter compared to the rest of the year. Whereas wall surfaces can heat up to temperatures higher than 40°C due to shortwave radiation, these surfaces are cooled down below T_{air} due to longwave radiation exchange with the sky hemisphere. Besides, the heat capacity of the brick masonry and embedded moisture both influence the $T_{5mm.}$ Therefore, the

hours of frost (threshold of 0°C) and the number of FTC_T (freezing at -5°C and thawing at 0°C) differ between the climate data (based on T_{air}) and simulation results (based on T_{5mm}), but also between the individual situations (Figure 1).

The hours of frost and FTC_T at 5 mm depth in the masonry follow the decreasing trend of the climate data for RCP 4.5 and 8.5 (Figure 1). Here, the offset between the climate and simulated results ranges between -25% – 20%, and -57% – 6%, respectively for both indices. The hours of frost (T_{5mm}) is the highest for the retrofitted SW-wall, whereas the retrofitted NW-wall entails almost equal values compared to the climate data. The hours of frost (T_{5mm}) is the lowest in the original wall. Moreover, the number of $FTC_{T,5mm}$ is the highest for the retrofitted NW-wall during the historical period. Whereas later on, the retrofitted NW-wall is similar to the retrofitted SW-wall, for RCP 8.5. The number of $FTC_{T,5mm}$ is the lowest for the original wall. Differences become smaller towards the end of the century.

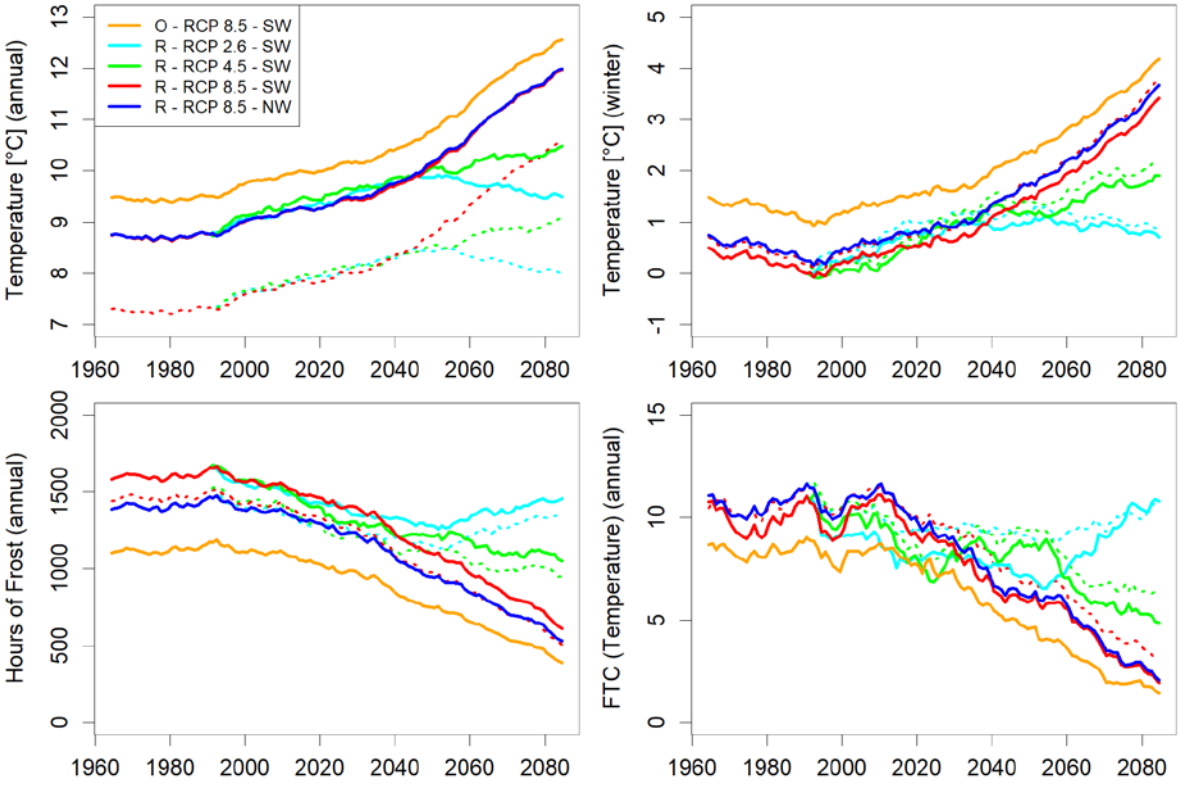

Figure 1. Moving average of the annual mean temperature (top, left), the mean temperature in winter (top, right), the annual hours of frost (bottom, left) and the annual number of FTC (freezing -5°C/ thawing 0°C) (bottom, right) at 5 mm depth in the masonry (O: original, R: retrofitted). The dotted lines present the air temperature climate data (cyan: RCP 2.6, green: RCP 4.5 and red: RCP 8.5).

To analyse the moisture management, WDR load and moisture content at 5 mm depth (MC_{5mm}) are evaluated. The drying potential is outside the scope of this paper. The WDR load depends on a complex relation between precipitation, wind velocity and wind direction, but also on catch ratio, height and wall orientation a.o. (Blocken and Carmeliet, 2010). As expected, the order of magnitude between the precipitation ('climate based') and WDR load ('response based') differs significantly (Figure 2). Besides, there is a large difference in WDR load

between the two orientations. As there is no significant climate change signal for wind direction and velocity, the increase in annual WDR load for the SW-orientation can be related to the increasing precipitation. For the NW-orientation, the WDR load remains low and there is no clear climate change signal. Analysing the percentage of precipitation and WDR load in winter, there can be observed that the percentage is significantly higher for the SW-WDR load (+-40%), than the precipitation amount (+-25%) (Figure 2). For a given precipitation amount, the percentage SW-WDR load in winter is higher because of higher wind velocities during this season. Both the precipitation and WDR load illustrate an increase in percentage during the winter, meaning that the climate change signal is not constant over the year.

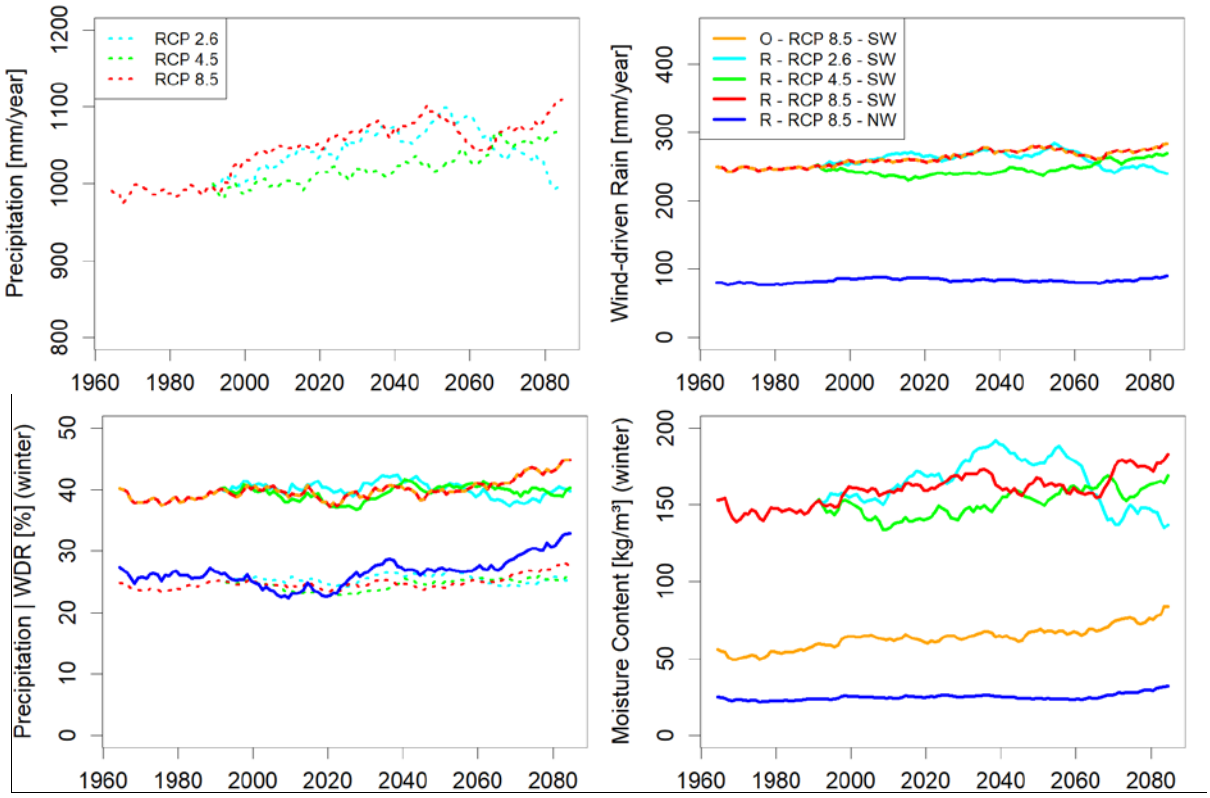

Figure 2. Moving average of the annual precipitation (top, left), the annual wind-driven rain load (top, right), the fraction of annual precipitation or WDR occurring in winter (bottom, left) and the moisture content in winter at 5 mm depth in the masonry (bottom, right) (O: original, R: retrofitted). The dotted lines illustrate the climate data (cyan: RCP 2.6, green: RCP 4.5 and red: RCP 8.5).

The $MC_{5mm,mean,winter}$ increases towards the end of the 21st century for RCP 8.5 (Figure 2). Especially for the original wall, which is SW orientated, and the retrofitted SW-wall, there is a clear climate change signal. The difference between the wall assemblies is significant. The $MC_{5mm,mean,winter}$ of the retrofitted SW-wall is ca. 3 times larger than the original wall, and ca. 6 times larger than the retrofitted NW-wall. The $MC_{5mm,mean,winter}$ in the retrofitted SW-wall exceeds the MC_{crit} for all three RCP projections.

Please note that the differences between the individual RCP projections for the WDR load and MC, considering the retrofitted SW-wall, are smaller than the differences between the wall assemblies and orientations (Figure 2). This means that the uncertainty about the WDR load

and MC induced by the variation in wall assembly and orientation is significantly larger than the uncertainty induced by the RCP projections.

Furthermore, the number of $FTC_{T,5mm}$ cannot be directly compared to the $FTC_{crit,5mm}$ in the masonry, as the latter is related to both the temperature and moisture saturation degree in the pore matrix. However, the trend lines of both indices are analysed. As for the hours of frost (T_{5mm}) and $FTC_{T,5mm}$, a decreasing trend in number of $FTC_{crit,5mm}$ is observed for RCP 4.5 and 8.5, but this trend is less pronounced (Figure 1 and 3). Although the number of $FTC_{T,5mm}$ in the retrofitted NW-wall (RCP 8.5) is the highest in comparison to the other situations (Figure 1), the number of $FTC_{crit,5mm}$ is the lowest for that wall and remains close to zero (Figure 3). The number of $FTC_{crit,5mm}$ for the retrofitted SW-wall in RCP 8.5, on the other hand, is the highest amongst the different situations for the three RCP's. The climate change signal shows a decrease of 20% and 45% for RCP 4.5 and 8.5, respectively. The original wall (RCP 8.5) displays a significantly lower number of $FTC_{crit,5mm}$, but higher than the retrofitted NW-wall. No clear climate signal is observed for the original wall. Additionally, Figure 2 illustrates the number of $FTC_{crit,5mm}$ per year. Please note that the annual variation is very large, even for the original wall assembly.

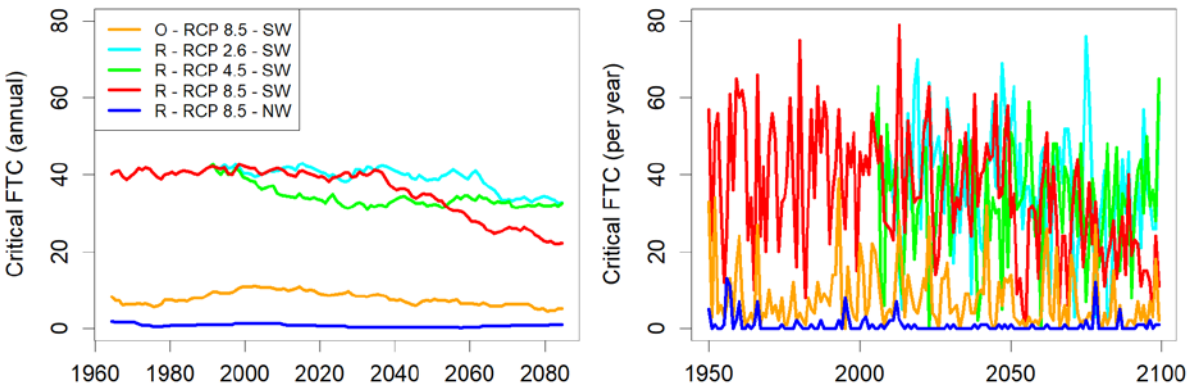

Figure 3. Moving average of the annual number of critical freeze-thaw cycles (FTC) (left) and the number of critical FTC per year (right) (O: original, R: retrofitted).

4 Discussion

The 'climate based' analysis illustrates that there is an increase in T_{air}, leading to a decrease in hours of frost (T_{air}) and $FTC_{T,air}$ by 33% for RCP 4.5 and 66% for RCP 8.5. This suggest that there might be a future decrease in freeze-thaw action in the brick masonry. The precipitation amount, on the other hand, is increasing over the course of the 21st century by about 10% for RCP 4.5 and 8.5. Besides, the percentage of precipitation in winter increases, and so does the precipitation amount during that season. This means that the moisture load is distributed more towards the cold season. An increase in moisture load may increase the likelihood of the MC_{crit} to be exceeded in the masonry upon freezing, potentially increasing the number of FTC_{crit}.

The 'hygrothermal response based' analysis assesses the combined effect of the climate data with a particular wall assembly for a given orientation. Although the T_{5mm} follows a similar trend compared to the climate data, there is an offset between the different trend lines depending on the wall assembly and orientation, but also on the season. As freeze-thaw action is sensitive

to small changes in temperature, this may lead to a different number of FTC_T in the masonry (Grossi *et al.*, 2007). Therefore, also the hours of frost (T_{5mm}) and $FTC_{T,5mm}$ display a significant offset per simulated case, respectively between -25% and 20%, and between -57% and 6%.

The WDR load increases by ca. 10% for RCP 4.5 and 8.5 over the 21st century as for precipitation, and the WDR percentage and load during winter increases. However, whereas the percentage in winter is ca. 25% for the precipitation amount and slightly higher for the NW-WDR load, the percentage SW-WDR load is ca. 40%. The increase in percentage over the century is larger for the WDR load than precipitation amount. Thus, the distribution of moisture load in winter is underestimated by the 'climate based' analysis.

In porous materials, no freeze-thaw damage will occur regardless the number of $FTC_{T,5mm}$ if the critical degree of moisture saturation is not exceeded (Fagerlund, 1973). Therefore, the moisture management of the building envelope is a key factor when assessing freeze-thaw risk. The $MC_{mean,winter}$ cannot be estimated based on only the climate data. The 'hygrothermal response based' results suggest increasing values of $MC_{mean,winter}$ throughout the 21st century, and large deviations between the simulated cases. The order of magnitude of $MC_{mean,winter}$ differs with a factor up to 6 between the combinations of wall assembly and orientation.

The retrofitted SW-wall for RCP 8.5 results in 20-35% more $FTC_{crit,5mm}$ than the original wall (same orientation). The number of $FTC_{crit,5mm}$ remains close to zero for the retrofitted NW-wall throughout the 21st century. Considering the number of $FTC_{crit,5mm}$, the climate change signal ranges between a decrease of 0% and 45%, depending on wall assembly and orientation. This means that the decrease of 66% in freeze-thaw action based on T_{air} (RPC 8.5), is mitigated by the increase in moisture load. Besides, it illustrates that the presence of interior retrofit and orientation induce a large uncertainty about the future freeze-thaw behaviour in solid masonry.

Future research should focus on the influence of biases in the RCM on the climate change signal when performing HAM simulations, especially when considering damage mechanisms at exact threshold values such as the freezing point. Whereas bias correction might seem an appropriate solution, this practice is not evident when dealing with the climate data for HAM modelling. The climate variables are related in a complex, non-linear manner, e.g. temperature and relative humidity. Correcting the variables without altering the correlations as well as maintaining physical laws is a difficult and non-trivial practice. As an alternative to bias correction, climate model ensembles, i.e. combining data from different RCM's, are used to estimate uncertainties and manage biases. Therefore, the results presented in this paper, which only consider one RCM, will be complemented with results from different high-resolution RCM's across Belgium in future studies.

5 Conclusion

Frost indices based on air temperature (T_{air}), i.e. considering the 'climate based' analysis, suggest that there is a decrease in frost action towards the end of the 21st century based on the ALARO-0 RCM. Both the hours of frost (T_{air}) and freeze-thaw cycles ($FTC_{T,air}$) are decreasing by 33% for RCP 4.5 and 66% for RPC 8.5. Precipitation amounts are increasing by about 10% for both RCP projections, and the fraction of annual precipitation occurring in winter is increasing as well. This may lead to higher future moisture loads, increasing the likelihood for the critical moisture content to be exceeded in the masonry upon freezing. The number of critical freeze-thaw cycles at 5 mm depth in the masonry ($FTC_{crit,5mm}$), resulting from the

'hygrothermal response based' analysis, is decreasing between 0-45% depending on wall orientation and the presence of interior retrofit. It is concluded that although freeze-thaw action is reduced, the increase in moisture load could counteract this and lead to an increase in frost related damages. Besides, orientation and presence of interior retrofitting entail large uncertainties about the future freeze-thaw risk of solid masonry. Therefore, HAM simulations, i.e. 'hygrothermal response based' analyses, are required when assessing the freeze-thaw behaviour of solid masonry, before and after retrofitting, with regards to climate change.

Acknowledgements

The authors would like to thank the Belgian Royal Meteorological Institute for providing climate projections. Isabeau Vandemeulebroucke acknowledges the support of Research Foundation – Flanders (FWO) (1S90420N).

ORCID

Isabeau Vandemeulebroucke: https://orcid.org/0000-0002-7718-144X
Steven Caluwaerts: https://orcid.org/0000-0001-7456-3891
Nathan Van Den Bossche: https://orcid.org/0000-0002-8738-7249

References

Blocken, B. and Carmeliet, J. (2010). Overview of three state-of-the-art wind-driven rain assessment models and comparison based on model theory. *Building and Environment, 45(3), 691–*703. doi: 10.1016/j.buildenv.2009.08.007.

de Wilde, P. and Coley, D. (2012). The implications of a changing climate for buildings. *Building and Environment, 55,* 1–7. doi: 10.1016/j.buildenv.2012.03.014.

Fagerlund, G. (1973). Critical degrees of saturation at freezing of porous and brittle materials. Tid. Institutionen för byggnadsteknik, Tekniska högskolani Lund, Lund.

Fatorić, S. and Seekamp, E. (2017). Are cultural heritage and resources threatened by climate change? A systematic literature review. *Climatic Change, 142(1–2),* 227–254. doi: 10.1007/s10584-017-1929-9.

Grossi, C.M., Brimblecombe, P. and Harris, I. (2007). Predicting long term freeze-thaw risks on Europe built heritage and archaeological sites in a changing climate. *Science of the Total Environment 377(2-3),* 273–281. doi: 10.1016/j.scitotenv.2007.02.014.

IPCC. (2014). Climate Change 2014: Synthesis Report. Contribution of Working Groups I, II and III to the Fifth Assessment Report of the Intergovernmental Panel on Climate Change [Core Writing Team, R.K. Pachauri and L.A. Meyer (eds.)]. Geneva, Switzerland: IPCC.

Nicolai, A., Grunewald, J. and Zhang, J. J. (2007). Recent improvements in HAM simulation tools: Delphin 5 / CHAMPS-BES. In *Proceedings of 12th Symposium of Building Physics*, Dresden, Germany, 28-30 March 2007, 866–876.

Straube, J. and Schumacher, C. (2006). Assessing the durability impacts of energy efficient enclosure upgrades using hygrothermal modeling. *Journal of the International Association for Science and Technology of Building Maintenance and Monuments Preservation, 2,* 197–222.

Straube, J., Schumacher, C. and Mensinga, P. (2010). Assessing the freeze–thaw resistance of clay brick for interior insulation retrofit projects. In *Proceedings of the Conference on Performances of Envelopes of Whole Buildings XI,* Clearwater Beach, Florida, 5–9 December 2010. ASHRAE.

Termonia, P., Fischer, C., Bazile, E., Bouyssel, F., Brožková, R., Bénard, P. and Bochenek, B. et al. (2018). The ALADIN system and its canonical model configurations AROME CY41T1 and ALARO CY40T1. *Geoscientific Model Development, 11(1),* 257–281. doi: 10.5194/gmd-11-257-2018.

Vandemeulebroucke, I., Calle, K., Caluwaerts, S., De Kock, T. and Van Den Bossche, N. (2019). Does historic construction suffer or benefit from the urban heat island effect in Ghent and global warming across Europe? *Canadian Journal of Civil Engineering, 46(11),* 1032-1042. doi: 10.1139/cjce-2018-0594.

Vereecken, E. and Roels, S. (2013). Hygric performance of a massive masonry wall: How do the mortar joints influence the moisture flux? *Construction and Building Materials, 41(4),* 697–707. doi: 10.1016/j.conbuildmat.2012.12.024.

Impact of Climate Change in Building Envelope Design: The Performance to Withstand Mould Growth

Klodian Gradeci, Alessandro Nocente, Nathalie Labonnote and Petra Rüther

SINTEF Community, Høgskoleringen 7B, 7034, Trondheim, Norway, klodian.gradeci@sintef.no

Abstract. *Mould growth is a biodeterioration phenomenon that jeopardizes the integrity, functionality and durability of building envelopes. The performance to withstand biodeterioration depends on the critical hygrothermal conditions inside the envelope. These conditions are subject to the configuration of building envelopes, and climate exposure, accounting for both the outdoor weather and indoor environments' conditions. These critical conditions are likely to intensify in response to the changing climate, and hence, modification and adaptation of the envelopes' configuration will be required. An understanding of the implications of envelope configurations' choices is required to set up guidelines for forthcoming building envelope design. Parametric analyses are a potent source of insight to investigate how the input parameters influence the desired outcome. In light of this, a parametric analysis is carried out to investigate the performance of three building envelopes to withstand mould growth. The impact of climate change in the performance evaluation is accounted for by employing both historic and future climate change scenarios in which the global climate temperature change is forecast to be 3.5°C. Input parameters related to the simulation of mould growth are also investigated. Recommendations to current building envelope design guidelines are drawn for the performance evaluation to withstand mould growth.*

Keywords: *Building Envelope, Climate Change, Mould Growth, Performance Evaluation.*

1 Introduction

1.1 Context

Mould growth is a biodeterioration phenomenon that jeopardizes the integrity, functionality and durability of building envelopes. The performance to withstand biodeterioration depends on the critical hygrothermal conditions, on the investigated material within or outside the building envelope, and also on the chosen approach to assess these conditions. The hygrothermal conditions are subject to the configuration of building envelopes on the one hand, and climate exposure, accounting for both the outdoor weather and indoor environments' conditions on the other hand. These critical conditions are likely to intensify in response to the changing climate, and hence, the exposure and strains will increase suggesting that the performance of building envelopes will have to accommodate new exposure. As a consequence, modification and adaptation of the envelopes' configuration will be required. Design approaches to performance evaluation to withstand mould growth available in current guidelines are more qualitative rather than quantitative. In most cases it is stated that mould growth should be avoided; a common criterion is based on a combination of threshold values of maximum relative humidity and a range of temperature values. However, mould growth is a complex biological phenomenon and studies show that its mathematical representation should simultaneously account for at least four factors: temperature, relative humidity, time, and substrate (Gradeci, Labonnote, Time, & Köhler, 2017). Many mould models, mathematical representations of the mould growth process, have been proposed during the past decades, but very few of them have been implemented in standards. ASHRAE 160 is indeed the only norm to base their guidelines on a mould model (VTT), and it suggests the growth not to exceed VTT index 3. Meanwhile, new guidelines which account for the performance to withstand mould growth are being developed

for the design of building envelopes (Lacasse *et al.*, 2018). In light of this, two research question are raised: (i) What are the implications of climate change in the hygrothermal conditions within the building envelopes and how is this reflected in the performance evaluation to withstand mould growth?, and (ii) How can current building envelope design guidelines be improved when considering the performance evaluation to withstand mould growth?

1.2 Aim and Objectives of the Study

The aim of this study is twofold: (i) to understand the implications of climate change in the performance evaluation to withstand mould growth; (ii) to provide recommendation to current building envelope design guidelines regarding the performance evaluation to withstand mould growth. The objectives that address the aforementioned aims are:

- to analyse the variations of the hygrothermal conditions within the building envelope by comparing historical and future climates,
- to investigate the changes of simulated mould growth within the building envelope by comparing historical and future climates.
- to investigate the impact of the selection of input in the simulated mould growth, including the choice of sensitivity and material class, simulation runtime, and performance criteria.

2 Material and Methods

2.1 Building Envelopes

Three North American wall assembly configurations are chosen and shown in Figure 1.

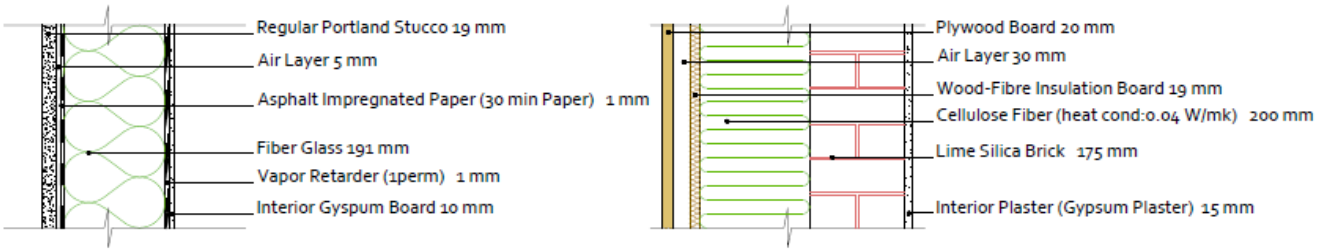

a) Wall Configuration 1(left) and 2 (right)

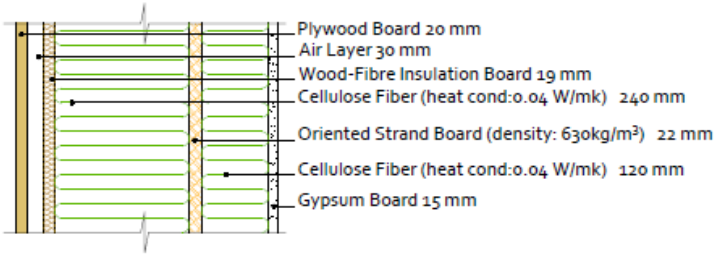

b) Wall Configuration 3

Figure 1. Three different wall assembly configurations.

2.2 Simulation and Evaluation of Mould Growth

2.1.1 Hygrothermal Simulations

The hygrothermal simulations are performed by WUFI 6.3 ® (Hartwig Michael Künzel, 1995), which has been validated by experimental studies for similar constructions (Mundt Petersen and Harderup, 2011). The initial conditions within the wall are set at RH = 80% and T = 20 ºC. Accounting for wind-driven rain falls out of scope of this study. The applicability of current available models for accounting for and determining the exposure for wind-driven rain may be

questionable for ventilated structures (Tietze *et al.*, 2017). The hygrothermal conditions between the wind barrier layer and insulation layer are investigated since they offer most favourable conditions for microbial growth. A monitor is placed in the asphalt impregnated paper for first case study or wood-fibre insulation board for the second case study. A schematic overview of the simulation process is provided in Figure 2. The selected location is Calgary, Canada. Two sets of climate data are implemented. They were generated in (Gaur, Lacasse, and Armstrong, 2019) and include the following: a) 15 historical climate data set, and b)15 climate data set for a climate change scenario in which the global climate temperature change is forecast to be 3.5 ºC. The indoor climate is set up as Medium Moisture Load +5% according to EN 15026 (15026, 2007) for each of the case studies.

2.1.2 Performance Evaluation

The hygrothermal conditions are retrieved for each case study and then processed in WUFI Model Index VTT 2.1 (WUFI-VTT, 2018), which is an add-on developed within a collaboration between the Finnish research institute VTT and Fraunhofer IBP. This add-on allows for calculation according to the VTT model. Three parameters are investigated from the model: the material class and sensitivity class that account for different building materials and the decline rate when mould is exposed to unfavourable conditions (see Appendix).

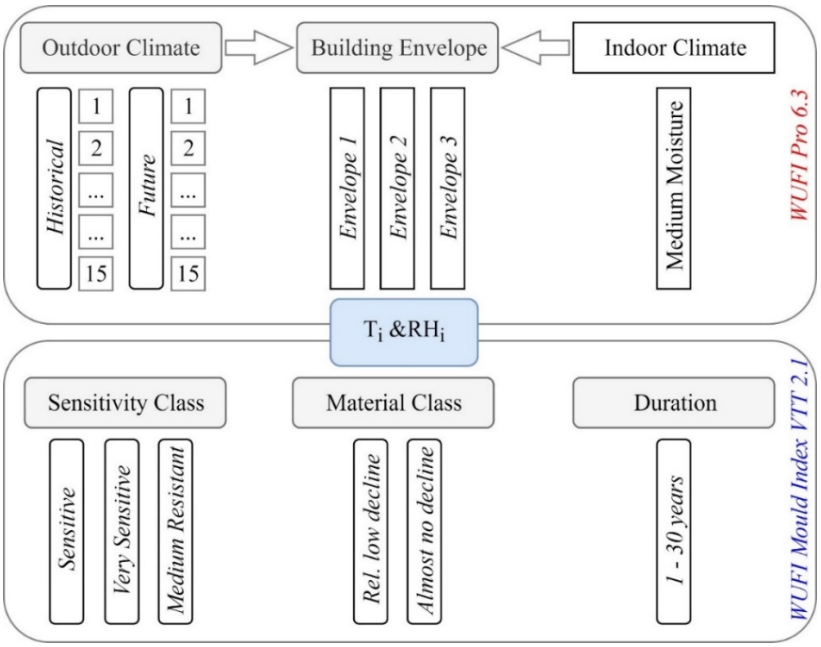

Figure 2. Schematic overview of the simulation process and its parameters.

3 Results

3.1 Implication of Climate Change in the Hygrothermal Performance of the Selected Building Envelopes

3.1.1 Implication in the hygrothermal conditions within the building envelopes

Table 1 shows the number of occurrences in hours of relative humidity and temperature that are usually favourable for the conditions of mould growth. The results are depicted for the three wall assembly configurations for the average of occurrences of the set of 15 historical and future climates. The results show that the effect of climate change is different for the three walls. For

the first wall, it can be observed higher levels of temperature and relative humidity compared to the historic exposure in the investigated layer, asphalt impregnated paper. In the other two walls the difference of hygrothermal conditions between the historic and future climates appears insignificant in the investigated layer, wood fibre insulation board, which lies a bit further away from the outdoor climate exposure, and hence its hygrothermal conditions may be highly dependent on the indoor climate.

Table 1. Comparison of occurrences in hours of higher levels of temperature and relative humidity between historical and future climate files for 30 years simulations.

			Historical				**Future**			
			Temperature							
			15-20	20-25	25-30	30-35	15-20	20-25	25-30	30-35
Wall 1	Relative Humidity [%]	80-85	1	5	8	3	46	223	308	260
		85-90	567	504	284	67	1022	1594	1278	685
		90-95	13316	5155	1282	88	17117	11985	5307	1314
		95-100	12825	3935	441	5	19840	11064	3336	309
Wall 2		80-85	539	183	22	1	359	187	28	1
		85-90	274	65	6	0	216	61	3	0
		90-95	106	25	2	0	94	14	0	0
		95-100	26	4	0	0	12	3	0	0
Wall 3		80-85	448	102	11	0	449	141	18	0
		85-90	124	23	1	0	110	13	1	0
		90-95	33	2	0	0	17	0	0	0
		95-100	0	0	0	0	0	0	0	0

3.1.2 Implications in the performance to withstand mould growth

The simulated mould growth results for the three wall assembly configurations exposed to 15 different outdoor climate files (both for historic and future) are plotted in Figure 3 and Table 4. The maximum simulated mould growth in a period of 30 years has been selected for each case study. For the first wall, the mould growth is simulated for the asphalt impregnated paper with the assumed sensitivity class '*medium resistant - relatively low decline*'. For the second and third wall, the mould growth is simulated for the wood-fibre insulation board with the assumed sensitivity class '*sensitive - low decline*'. As expected from the previous results, the difference between the simulated mould growth under future climate and historic climate is emphasised only for the first wall assembly configuration. Moreover, the results show that the simulated mould growth is sensitive to the uncertainties of outdoor climate for the first wall configuration assembly. Contrarily, the other two walls do not appear to be sensitive to the uncertainties of the outdoor climate, which may be justified from the fact that the hygrothermal conditions at the monitor position are highly dependent on the indoor climate.

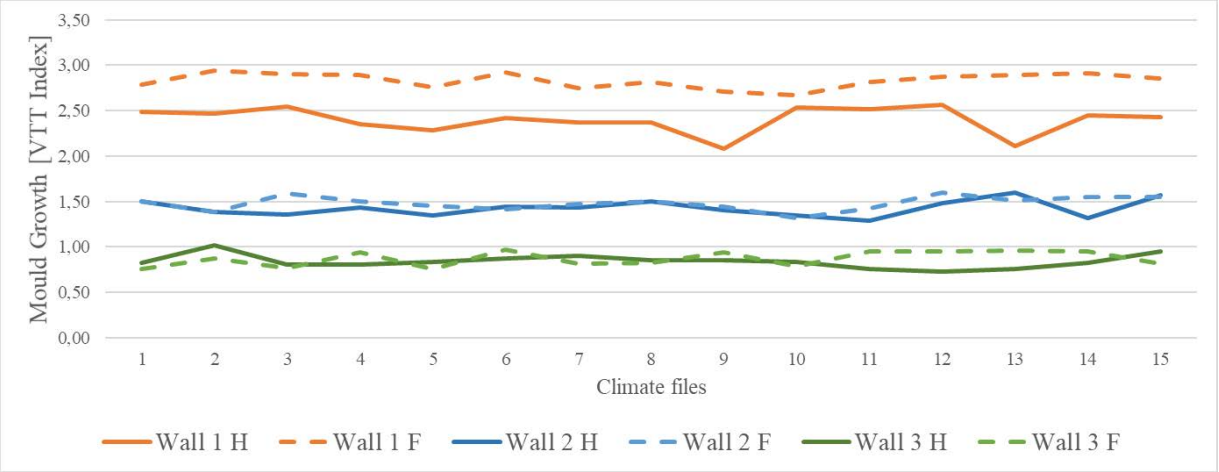

Figure 3. Results of mould growth for three wall assembly configurations simulated under historical and future climate files.

Table 2. Results of mould growth for three wall assembly configurations simulated under historical and future climate files.

Climate File	Wall 1		Wall 2		Wall 3	
	Historic	Future	Historic	Future	Historic	Future
Mean	2,4	2,83	1,43	1,48	0,84	0,87
Standard Deviation	0,15	0,18	0,09	0,08	0,08	0,08

3.2 Implications of Input Parameters in the Mould Growth Calculation

The results of mould growth for wall assembly one and two are shown in the tables below[1] for different selection of the sensitivity classes. For both cases it is also provided the amount of time in years until the peak simulated mould growth is reached. The results show that in both cases, the simulated mould growth and subsequently, the performance to withstand mould growth, are very sensitive to the selection of the material class and the sensitivity class. For example, in the first wall, the mould growth was simulated for the layer asphalt impregnated paper. According to the recommendation in the help guide (WUFI-VTT, 2018), this layer may fall under both sensitivity classes, *medium resistant* or *sensitive* with *relatively low decline* or *almost no decline*. This choice would shift the performance evaluating from acceptable (Mould Index lower than 3) to unacceptable (Mould Index greater than 3). This sensitivity is even more apparent for the second and third wall. Moreover, this sensitivity of the input parameters in the mould model is also reflected in the amount of time the simulated mould growth peak is reached. However, the latter is not the case for the other two walls where the maximum mould growth is reached within the first months, as expected considering the materials that were used in this simulation and that the initial conditions within these materials were assumed RH=80%.

4 Discussion and Recommendations

4.1 Implications of Climate change in Building Envelope Design

The results show that the implication of climate change, as accounted for by the generated climate files, can vary depending on the configuration of the wall assembly and numerical simulations. While the difference in the outdoor historic and future climate files is significant,

[1] The results of the third wall were similar to the second wall and were not shown to save space. In addition, the results are provided only for the first 5 historic climate.

its implications in the simulated mould growth were not. It was observed that mould growth results were intensified for only one among the three selected walls. This implies a potential future case scenario for building materials present in wall assemblies that is different from the current state, and hence underlies the need for a more detailed investigation of the hygrothermal conditions of different wall configurations. The latter can be exploited by carrying out multiple parametric analysis of simulated walls exposed to generated future climate. The results can be useful for direction and ideas of the properties that future building materials should have.

Table 3. Results of mould growth depening on different selection of input parameters of VTT model for wall configuration 1.

Climate	**Max Mould Growth [*VTT Index*] in 30 years**			**Years until peak**	
	S-ND	*S-LD*	*MR-LD*	*S*	*MR*
1	4,65	4,55	2,49	4	20
2	4,70	4,65	2,47	7	21
3	4,70	4,70	2,55	5	20
4	4,70	4,60	2,35	5	22
5	4,60	4,60	2,28	4	26

S- Sensitive, MR – Medium Resistant, ND – Almost no decline, LD- Relatively low decline

Table 4. Results of mould growth depening on different selection of input parameters of VTT model for wall configuration 2.

Climate	Max Mould Growth [*VTT Index*] in 30 years				Years until peak
	S-ND	*S-LD*	*VS-ND*	*VS-LD*	
1	1,5	1,480	4,250	4,150	1
2	1,380	1,290	4,100	3,900	1
3	1,360	1,280	4,100	4,000	1
4	1,430	1,350	4,300	4,180	1
5	1,350	1,300	3,800	3,750	1

S- Sensitive, VS – Very Resistant, ND – Almost no decline, LD- Relatively low decline

4.2 Recommendations about Building Design Guidelines

Choice of sensitivity class and material class: The study demonstrated that the simulated mould growth is very dependent on the selection of the sensitivity class and material. Shifting from one class to another can change the (un)acceptable performance of the building envelope. Current materials classes and sensitivity classes may not provide the required detailing that can accommodate current materials used in building envelopes. Therefore, the study underlies the need for the provision of a more detailed guideline recommending the categorization of common building materials into the respective sensitivity class of the mould model.

Simulation runtime: This study demonstrated that peak of mould growth can vary depending on wall configuration. In many mould models, the growth is represented as cumulative, with few ones considering optionable decline when unfavorable conditions are met. This underlies the need for connecting the performance criteria to runtime simulation. In other words, if the simulation runtime is short, then the performance criteria should be relative and conservative enough to accommodate the designated service life, otherwise, if the simulation runtime is as long as the designated service life, then the performance criteria should reflect the maximum absolute amount of tolerable mould growth.

Performance criteria: Currently, the only available performance criteria specifying the maximum acceptable level of mould growth is provided in ASHRAE 160, suggesting an amount of mould growth not to exceed VTT Index 3. The World Health Organization (2007) claims that there exists an association between health consequences and occurrence of mould growth; even though, there is no clear evidence that relates the microbial growth and mortality. This would imply that the threshold value should be depending on the case being investigated. For example, the same threshold may not be acceptable as in a hospital or other environments with higher exposure. Hence, the development of performance criteria to withstand mould growth can be approached by merging the following categories:

1. *Mould Index levels.* The mould index can have values from 0 to 6, as in the VTT model.
2. *Direct consequences*. The direct consequences of the mould growth are related to Indoor Air Quality (IAQ) and aesthetics.
3. *Exposure and extension*. Different levels of microbial growth can be associated with different levels of indirect consequences depending on several extents and exposure. They can be categorised based on: the depth of the wall (outer part of the wall, within the wall and inner part or contact with the indoor environment); the height of the building (i.e. underground, first floor, upper floors); part of the building (close to risk spots, the front part of the building); and typology of the building (i.e. hospital, museum, residential, office).
4. *Simulation runtime*. The design criteria should also consider the reference period as argued before.

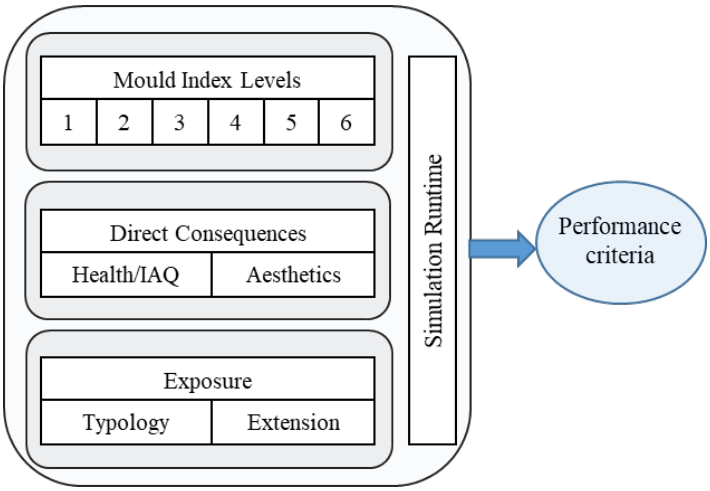

Figure 4. Schematic overview of developing performance criteria for the evaluation to withstand mould growth.

Acknowledgements

This study was funded by the project 'TightEN - Durable adhesive airtight solutions for energy efficient building envelopes'. Research Council of Norway; Country: Norway; Grant number: 294894.

ORCID

Klodian Gradeci: https://orcid.org/0000-0002-9837-3512

References

15026, E. (2007). Hygrothermal performance of building components and building elements–assessment of moisture transfer by numerical simulation. In: International Organization for Standardization Geneva.

Gaur, A., Lacasse, M., and Armstrong, M. (2019). Climate Data to Undertake Hygrothermal and Whole Building Simulations Under Projected Climate Change Influences for 11 Canadian Cities. *Data, 4*(2), 72.

Gradeci, K., Labonnote, N., Time, B., and Köhler, J. (2017). Mould growth criteria and design avoidance approaches in wood-based materials – A systematic review. *Construction and Building Materials, 150*(Supplement C), 77-88. doi:https://doi.org/10.1016/j.conbuildmat.2017.05.204

Hartwig Michael Künzel. (1995). Simultaneous heat and moisture transport in building components, One-and two-dimensional calculation using simple parameters. IRB-Verlag Stuttgart

Lacasse, M., Ge, H., Hegel, M., Jutras, R., Laouadi, A., Sturgeon, G., and Wells, J. (2018). Guideline on Design of Durability of Building Envelopes. *National Research Council of Canada, March*.

Mundt Petersen, S., and Harderup, L.-E. (2011). *Control of moisture safety design by comparison between calculations and measurements in passive house walls made of wood.* Paper presented at the XII DBMC-XII International Conference on Durability of Building Materials and Components.

Organization, W. H. (2007). Development of WHO guidelines for indoor air quality: Dampness and mould. *Germany: WHO*.

Tietze, A., Ott, S., Boulet, S., Gradeci, K., Labonnote, N., Grynning, S., . . . Pousette, A. (2017). *Tall Timber Facades – Identification of Cost-effective and Resilient Envelopes for Wood Constructions*. Retrieved from Munich:

WUFI-VTT. (2018). *WUFI® Mould Index VTT Help*. Retrieved from

Appendix: Details of input for VTT mould model

Table 5. Mould sensitivity classess and their respective materials according to the VTT mould model.

Mould sensitivity class	Materials
Very sensitive	Untreated wood, includes lots of nutrients for biological growth
Sensitive	Planed wood, paper coated products, wood based boards
Medium resistant	Cement or plastic based materials, mineral fibres
Resistant	Glass and metal products, materials with efficient protective compound treatments

Table 6. VTT index and performance criteria according to ASHRAE 160.

VTT Index	Description of the growth rate	Interior	Interfaces
0	No growth	Acceptable/ Green light	Acceptable/ Green light
1	Small amounts of mould surface (microscope), initial stages of local growth		
2	Several local mould growth colonies on surface (microscope)	Yellow traffic light	
	Visual findings of mould on surface, <10% coverage, or <50% coverage of mould (microscope)	Unacceptable/ Red light	Yellow traffic light
4	Visual findings of mould on surface, 10 - 50 % coverage, or >50% coverage of mould (microscope)		Unacceptable/ Red light
5	Plenty of growth on surface, > 50% coverage (visual)		
6	Heavy and tight growth, coverage about 100%		

XV International Conference on Durability of Building Materials and Components
DBMC 2020, Barcelona
C. Serrat, J.R. Casas and V. Gibert (Eds)

The Future Climate Moisture Susceptibility of Wall Assemblies: Analysis Based on Monte Carlo Simulation Using a Simplified Deterministic Hygrothermal Simulation Model

Carl-Eric Hagentoft[1] **and Pär Johansson**[1]

[1] Chalmers University of Technology, Department of Architecture and Civil Engineering,

SE-412 96 Göteborg, Sweden, carl-eric.hagentoft@chalmers.se

Abstract. *A newly developed generic algorithm to assess moisture susceptibility of simplified wall assemblies has been developed within the CIB-W080 WG 2. This group is focusing on guidelines for design for durability of building envelopes. The algorithm is implemented in a publicly available Matlab code. A simplified wall assembly consisting of up to four material elements is considered. Optional vapor retarder and thermal resistances are located between the elements. In this paper modelling of a ventilated cladding is implemented. Using the simplified numerical model, a probability-based risk analysis using the Monte Carlo method is demonstrated. The risk assessment of the wall assembly considers the interior and exterior climatic load. The moisture transport mechanism accounted for in the analysis is diffusion. The rain load is assumed to be transferred directly to a chosen outer susceptible material element in the construction. An insulated wooden wall structure is analyzed and the probability distribution of the time of wetness is presented for cases using sequence of 31 consecutive climatic years, randomly varying indoor moisture excess, indoor temperature and driving rain leakages.*

Keywords: *Climate, Driving Rain, Simplified Model, Risk Analysis, Monte Carlo Simulation.*

1 Introduction

The performances of buildings can vary quite a lot even if the design look identical in the drawings. The uncertainties are manifold and originate from the selection of the initial condition of materials, dimensions, and material properties. Also, the operation of the building causes uncertainties originating from the actual indoor moisture excess, internal heat gains, air infiltration, and ventilation. Obviously, weather conditions and the exposure to the external environment are also sources of uncertainties; this is illustrated in Figure 1. Because of all the uncertainties and possible variations, the total life cycle cost for the operation and maintenance of a stock of buildings will vary randomly due to the spread in factors such as initial investment, energy use, hygrothermal performances, and performance failures. To make balanced and sound choices of design strategies and investment decisions, all these factors should be included. The results from the IEA EBC project RAP-RETRO (Annex 55) (Hagentoft, 2017; Bednar and Hagentoft, 2015; Hagentoft *et al*., 2015a; 2015b; 2015c; 2015d) are intended to improve methods and tools for the integrated evaluation and optimization of retrofitting measures, including energy efficiency, life cycle cost, and durability.

doi:10.23967/dbmc.2020.197

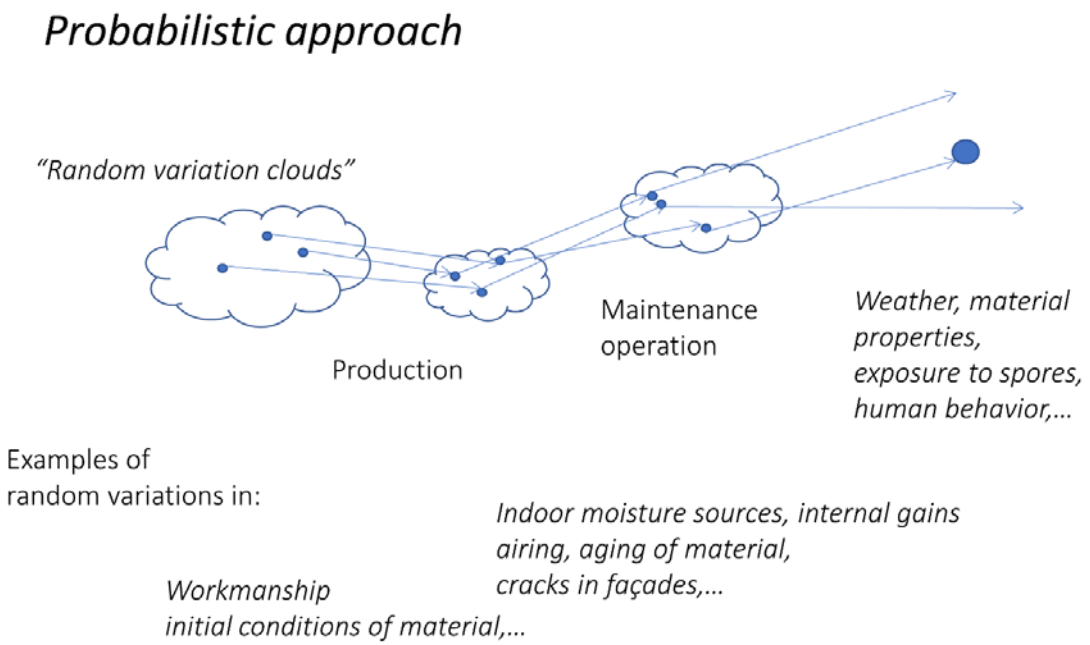

Figure 1. Random variation of cloud type representing variability and uncertainties.

One part of the annex 55 project was to develop and validate probabilistic methods and tools for energy use, lifecycle cost, and functional performance. The scope of this paper is to investigate the possibility to use a simplified numerical model for the heat and moisture transfer in a wall assembly. This model, intended to be used to assess moisture susceptibility of wall assemblies, is based on four material elements, each having resistances for vapor and heat between and at the surfaces, and includes rain intrusion. This approach represents several steps forward in terms of precision compared with the older and more traditional Glaser method and other later proposed models (Sanders, 1996; Hagentoft and Harderup, 1996). It is expected to be well in line with modern detailed moisture calculation models. With the proposed model, a probabilistic assessment of the risk for failure of various performances such as time of wetness, mould growth, and heat loss can be investigated. Also, sensitivity analysis can be performed on different calculation parameters.

The mathematics of the model is explained in detail (Hagentoft and Johansson, 2019) and can be implemented on various platforms such as Matlab or Python.

This work is a part of CIB W080, WG2, for the guidelines on design for durability of building envelopes for use by engineers and designers who are unlikely to have tools at their disposal to determine model inputs. It will provide background knowledge for hygrothermal simulations and long term durability risk assessments considering climate change. Within this work, the National Research Council (Conseil national de recherches Canada), NRC, provides climate data sets for historic and future scenarios.

2 Case Study

The investigated construction in this paper is an insulated wooden wall with an exterior air gap, see Figure 2. The insulation layer, outside the wooden layer, has a thickness of 300 mm and a thermal conductivity of 0.033 W/(m·K) while the wooden boards are 128 mm thick with a thermal conductivity of 0.14 W/(m·K). The material properties for the insulation and the wood are presented in Table 1 and Table 2.

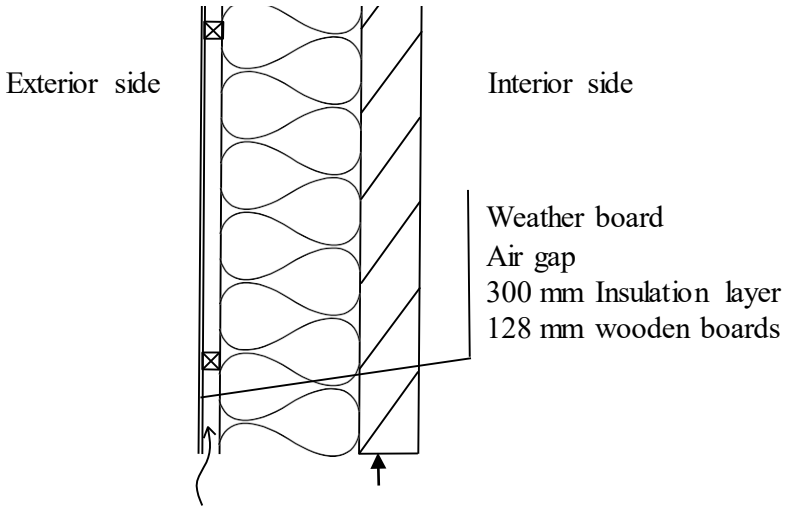

Figure 2. Insulated wooden wall that is investigated. The monitoring position is marked by the arrow.

Table 1. Material data for insulation and wood.

Material	Density (kg/m^3)	Thermal conductivity (W(mK)	Spec. heat capacity (J/kgK)	Diffusion resistance factor (-)
Insulation	200	0.033	800	2
Wood	430	0.14	1,600	30

Table 2. Moisture sorption isotherms.

Relative humidity	Insulation (kg/m^3)	Wood (kg/m^3)
0	0	0
35	0.25	37.5
50	0.40	47.5
70	0.47	65.0
80	0.53	77.5
90	0.60	100
95	1.0	117.5
99.9	10	140
100	100	1000

3 Weather Data

The historical and future climate data for the Canadian cities Toronto and Vancouver, see Table 3, were selected. The data was provided by (Gaur *et al*., 2019) who produced time-series of 30 consecutive years with hourly climate data corresponding to historical time-period (1986-2016) and future time-series corresponding to 2°C and 3.5°C increase in global temperature. In this paper the former climate scenario was selected.

Table 3. Data for Toronto and Vancouver.

City	Latitude (°C)	Longitude (°E)	Population in 2016 (1000s)	Climate zone
Toronto	43.7	-79.4	3731.6	Great lakes/St. Lawrence lowlands
Vancouver	49.3	-123.1	2463.4	Pacific coast/South British Columbia Mountains

3.1 Driving Rain Model

The rather simple and straight forward (Lacy, 1965) model is used to estimate the driving rain intensity, r_v (mm/(m^{2}h)), hitting the façade.

$$r_v = 0.208 \cdot \cos(\theta) \cdot v \cdot r_h \qquad r_v = 0 \; if \; |\theta| > 90° \tag{1}$$

Here, v (m/s) is the average wind velocity. The angle θ (-) is the angle between the wind direction and the normal of the considered wall. The formula relates the intensity of the rain hitting a horizontal surface, r_h (mm/(m^{2}h)), to a vertical one.

The modelling of the rain intrusion, bypassing the insulation layer, into the outer part of the wood, is based on 1% of the driving rain intensity. The leakage is based on a uniform random distribution, meaning that only one tenth of the rain events result in leakage corresponding to an intensity of 1% of the actual driving rain at that event. Table 4 presents the direction dependent driving rain intensity in each 30-year period in Toronto and Vancouver.

Table 4. Toronto and Vancouver driving rain intensity, the total summation of each 30-year period (tonnes/m^2).

Direction	Toronto (historical)	Toronto (+2°C)	Vancouver (historical)	Vancouver (+2°C)
North	6.64	7.97	1.19	1.61
East	7.68	9.41	18.5	19.9
South	9.15	8.65	26.5	26.8
West	7.09	6.25	4.32	4.53

The calculations show that direction South was the dominant direction for driving rain in Toronto, but in the future, this will change to East. In Vancouver, South is the dominant

direction for driving rain, both historically and in the future. In this study, for simplicity, only main compass directions were used and a South facing façade was chosen for both cities and for all the climate time-series.

3.2. Solar Radiation

Direct solar radiation and diffuse solar radiation on a vertical surface was given in the climate files. This was recalculated to hourly solar radiation for an inclined surface facing South based on angle of incidence, horizontal shadow angle and vertical shadow angle on inclined surface evaluated in middle of hour from reference year with hourly radiation data (Duffie and Beckman, 1991). The albedo of the ground was assumed to be 0.2.

4 Simulation Model

In the simplified model, a wall assembly consisting of four material elements is considered. Optional thin elements (zero thickness) with heat and vapor resistances are included in the model that for instance can be used for the representation of a vapor retarder. The risk assessment of the wall assembly considers the interior and exterior climates. The use of an equivalent external temperature permits consideration not only of the air temperature, but also of the effects of the long- and short-wave radiation. A prescribed driving rain intrusion function must be included that accounts for the effect of water leakage to the interior of the wall assembly. Prescribed outdoor and indoor water vapor concentrations are assumed where the moisture transport mechanism accounted for in the analysis is diffusion. The heat transfer is based on heat conduction. Heat and moisture convection are not accounted for. The moisture transfer is assumed to be driven by the gradient in humidity by volume.

The moisture transfer coefficient is treated as a constant, based on an average expected relative humidity in the material being considered. The heat is transferred by conduction, the thermal conductivity of the material is considered constant. The moisture content depends on the relative humidity only, and hysteresis is neglected. The latent heat due to evaporation and condensation is neglected. Many of these restrictions might be added in new coming versions of the model.

4.1 Ventilated Cavity

The following parameters are of importance: $R_{out}, R_a, \alpha_{c,cd}, \alpha_r, Z_{cladding}$. They are the total thermal resistance from the interior cladding surface to the outdoors including external surface resistance, air flow rate of the gap behind the cladding, the combined conductive and convective heat transfer coefficient of the air gap, the radiant heat transfer coefficient across the air gap, and finally the total vapor resistance of the cladding.

$$\begin{aligned} \alpha_c &= 2 \cdot \alpha_{c,cd} \\ \alpha_r &= 4\varepsilon_{12}\sigma T^3 \quad 1/\varepsilon_{12} = 1/\varepsilon_1 + 1/\varepsilon_2 - 1 \end{aligned} \tag{2}$$

In the last formula the emissivity of the surfaces surrounding the air gap is used together with the Stefan-Boltzmann constant. The temperature is in Kelvin.

Network analysis (Hagentoft, 2001) is used to reduce it all to effective resistances and external temperatures. The following expressions for the resistance of the analyzed structure to

the external environment is used, and replaces those used in (Hagentoft and Johansson, 2019):

$$R_0 = \frac{1}{K_a + K_b} + \frac{1}{K_2},\ Z_0 = \frac{1}{R_a + 1/Z_{cladding}},\ T^{eq}_{out,new} = \frac{K_a \cdot T^{eq} + K_b \cdot T_{out}}{K_a + K_b} \tag{3}$$

The humidity by volume, v_{out} (kg/m³), used in the model remains the same. The following parameters are used in the expression.

$$K_a = \frac{1}{R_{out} + 1/K_1} \quad K_b = \frac{1}{1/(R_a \cdot \rho c_{pa}) + 1/K_3}$$
$$K_1 = K_2 = \frac{\alpha_r \cdot \alpha_c}{\tilde{K}} \quad K_3 = \frac{\alpha_c^2}{\tilde{K}} \quad \tilde{K} = \frac{1}{2/\alpha_c + 1/\alpha_r} \tag{4}$$

Here, the volumetric heat capacity of air, ρc_{pa} (J/(m³K)), at atmospheric pressure is used.

4.2 Indoor Climate

In respect to the indoor conditions, the indoor temperature was varied around 20°C with a normal distribution and standard deviation of 1.5°C. The indoor moisture excess was always controlled to be greater than zero and varied with a normal distribution around 2 g/m³ and standard deviation of 1 g/m³.

5 Results

For simplicity in this study, the time of wetness was used as an indicator for the durability. This is the total time over the year that RH exceeds 80% for a specific susceptible element of the construction. Based on the previous study (Hagentoft, Johansson, 2019), the Monte Carlo simulations are run for a total of 600 31-consecutive-year simulations using the simplified model. One 30-year simulation period takes 17 minutes on a PC with a 1.9 GHz Intel® Core™ i7-8650U CPU. The results for Toronto and Vancouver are presented in Figure 3, 4 and 5.

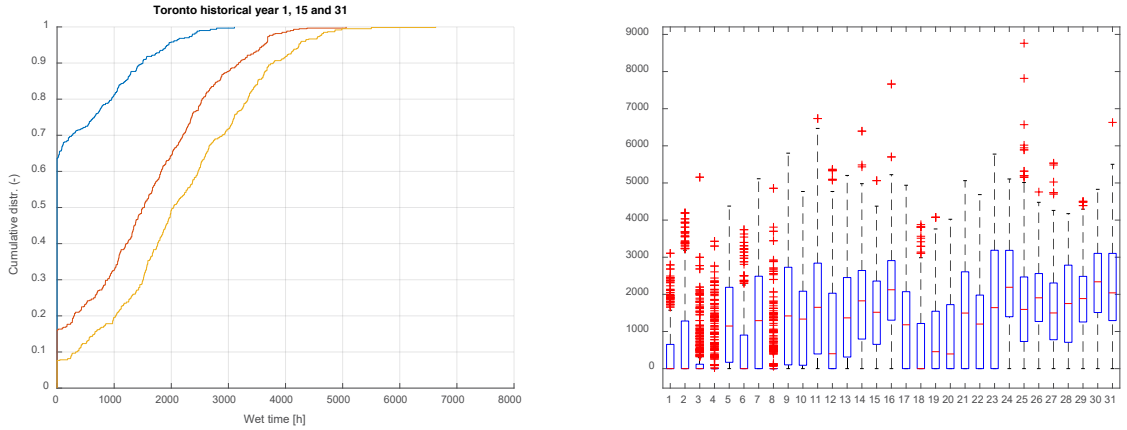

Figure 3. Results for the time of wetness for Toronto historical time-series.

There is a clear trend, visible both in the cumulative distribution and histogram, for Toronto

that the time of wetness was increasing the last 30 years. The average time of wetness for year 1 was 392 hours, while it was 1566 and 2146 hours for year 15 and 31 respectively. The continuing trend can also be found in the future scenarios, where the time of wetness is 2611 hours the first year while it is 2899 and 3831 hours respectively for year 15 and 31.

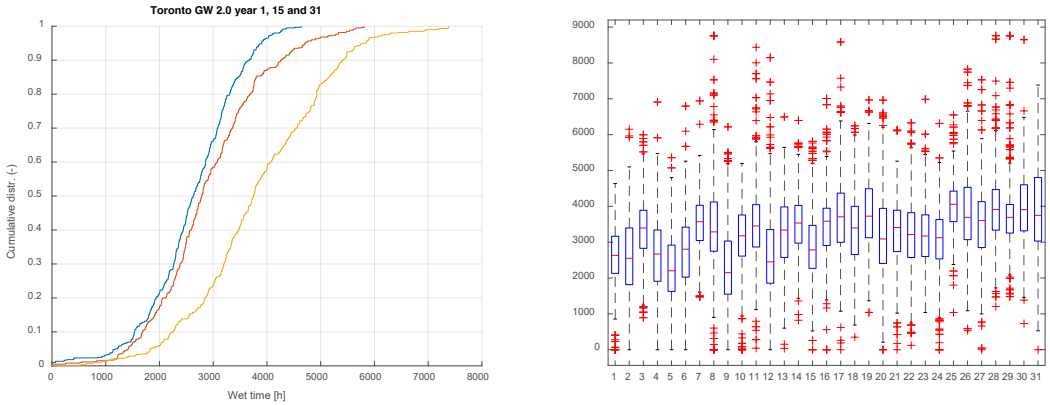

Figure 4. Results for the time of wetness for Toronto future scenario +2.0°C time-series.

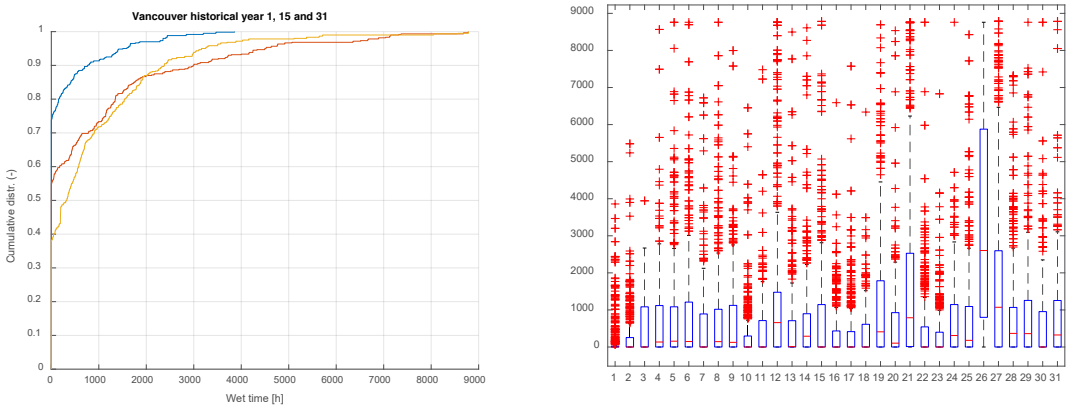

Figure 5. Results for the time of wetness for Vancouver historical time-series.

Also for Vancouver there is a clear trend in the cumulative distribution and histogram, that the time of wetness was increasing the last 30 years. The average time of wetness for year 1 was 219 hours, while it was 853 and 838 hours for year 15 and 31 respectively. It is also interesting to note the significantly larger number of outliers in Vancouver compared to in Toronto.

6 Conclusions

A previously developed simplified model for heat and mass transfer across walls, based on a four-element discretization of a wall assembly has been used in the paper. The simplified model offers good flexibility for representing multi-layer wall constructions with various barriers and

for moisture and heat transfer in between layers. As such, it is suitable to be used for the risk assessment of wall assemblies and similar constructions. In this paper additions to the model are presented that make it possible to analyze structures with a ventilated cladding.

For the case presented in this paper, the impact of rain leakage on the outermost part of the external wood layer of an insulated wooden wall was demonstrated. The risk analysis is based on Monte Carlo simulations of 600 runs of 31-consecutive-year historical and future climate scenarios for Toronto and Vancouver. The expected time of wetness is 5 times higher in Toronto in 2016 compared to in 1986, and 1.5 times higher in 2064 compared to in 2034. In Vancouver the expected time of wetness is 4 times higher in 2016 compared to in 1986. However, for Toronto this may not be the most extreme case considering that south is not the predominant direction of wind driven rain in the future.

ORCID

C-E. Hagentoft: http://orcid.org/0000-0002-1616-3619
P. Johansson: http://orcid.org/0000-0003-0935-7703

References

Bednar, T. and Hagentoft, C.-E. (2015). *IEA-EBC Annex 55. Reliability of energy efficient building retrofitting – probability assessment of performance and cost (RAP-RETRO): risk management by probabilistic assessment. Development of guidelines for practice*. Chalmers University of Technology, Gothenburg, Sweden.

Duffie, J.A. and Beckman, W. A. (1991). *Solar Engineering of Thermal Processes*. John Wiley & Sons, 2. ed.

Gaur, A., Lacasse, M. and Armstrong, M. (2019). Climate Data to Undertake Hygrothermal and Whole Building Simulations Under Projected Climate Change Influences for 11 Canadian Cities. Data, 4, 72.

Hagentoft, C.-E. (2001). *Introduction to building physics*. Studentlitteratur, Lund, Sweden.

Hagentoft, C.-E. (2017). Reliability of energy efficient building retrofitting – probability assessment of performance and cost (Annex 55, RAP-RETRO). *Energy and Buildings*, 155: 166–171. doi: 10.1016/j.enbuild.2017.09.007.

Hagentoft, C.-E. and Harderup, E. 1996. Climatic influences on the building envelope using the -factor. *Proceedings of the 4th Symposium on Building Physics in the Nordic Countries*, Finland.

Hagentoft, C.-E., Fink, M., Holm, A. and Antretter, F. (2015a). *IEA-EBC Annex 55, Reliability of energy efficient building retrofitting- probability assessment of performance and cost (RAP-RETRO): practice and guidelines*. Chalmers University of Technology, Gothenburg, Sweden.

Hagentoft, C.-E., Janssen, H., Roels, S., Gelder van, L. and Das, P. 2015b. *IEA-EBC Annex 55, Reliability of energy efficient building retrofitting - probability assessment of performance and cost, (RAP-RETRO): probabilistic tools*. Chalmers University of Technology, Gothenburg, Sweden.

Hagentoft, C.-E. and Johansson, P. (2019). Generic algorithm to assess moisture susceptibility of simplified wall assemblies. *Canadian Journal of Civil Engineering, special issue Durability and Climate Change*. doi: 10.1139/cjce-2018-0592.

Hagentoft, C.-E., Ramos, N. and Grunewald, J.(2015c). *IEA-EBC Annex 55, Reliability of energy efficient building retrofitting - probability assessment of performance and cost, (RAP-RETRO): stochastic data*. Chalmers University of Technology, Gothenburg, Sweden.

Hagentoft, C.-E., Sasic Kalagasidis, A. and Rode, C. (2015d). *IEA-EBC Annex 55, Reliability of energy efficient building retrofitting - probability assessment of performance and cost (RAP-RETRO): framework for probabilistic assessment of performance of retrofitted building envelopes*. Chalmers University of Technology, Gothenburg, Sweden.

Lacy, R.E. (1965). Driving-Rain Maps and the Onslaught of Rain on Buildings. *Proceedings of RILEM/CIB Symposium on Moisture Problems in Buildings,* Helsinki, Finland.

Sanders, C.H. (1996). IEA-EBC Annex 24, Design parameter used to avoid interstitial condensation for a range of climates: Task 2: environmental condition (HAMTIE).

XV International Conference on Durability of Building Materials and Components
DBMC 2020, Barcelona
C. Serrat, J.R. Casas and V. Gibert (Eds)

Validation of Three Methods of Selecting Moisture Reference Years for Hygrothermal Simulations

Chetan Aggarwal[1], Maurice Defo[2], Travis Moore[3], Michael A. Lacasse[4], Sahar Sahyoun[5] and Hua Ge[6]

[1] Ph.D. Student, Concordia University, Montreal, Quebec, Canada; c_agga@encs.concordia.ca

[2] Construction Research Centre, NRCC, Ottawa, Ontario, Canada; maurice.defo@nrc-cnrc.gc.ca

[3] Construction Research Centre, NRCC, Ottawa, Ontario, Canada; travis.moore@nrc-cnrc.gc.ca

[4] Construction Research Centre, NRCC, Ottawa, Ontario, Canada; michael.lacasse@nrc-cnrc.gc.ca

[5] Ph.D. Student, Concordia University, Montreal, Quebec, Canada; s_sahyo@live.concordia.ca

[6] Associate Professor, Concordia University, Montreal, Quebec, Canada; hua.ge@concordia.ca

Abstract. *Hygrothermal simulations are necessary to permit analyzing moisture performance when designing building envelopes. Owing to the high computing time and cost of the long term simulations, a common approach is to select representative year(s), the Moisture Reference Year(s), from a long-term series of climate data. It is assumed that the use of Moisture Reference Year(s) (MRYs) provides equivalent results as those provided using long-term series. The selection of MRY(s) is by itself based on the one of the methods available in the literature. In the present study, three methods of selecting the MRYs were evaluated i.e. the moisture index (MI), severity index (Isev) and climatic index (CI). Simulations were performed using individual years of historical climate data extending from 1986 to 2016 and projected future climate data representing the scenario with a 3.5°C increase in average temperature which is expected to occur from 2062 to 2092. Brick cladding installed on a wood frame wall assembly subjected to the climate of three different Canadian cities was selected for analysis. The cities selected were Vancouver (BC), Calgary (AB) and Ottawa (ON). These cities have differing levels of moisture loads. The year having the mould index value more than 3 for highest number of hours among the individual years was compared with the MRY given by three selected methods. A method was considered to be accurate in terms of the prediction if the year selected by that method gives the number of hours with mould index more than 3 which lies in the same class as that of year having maximum corresponding value. In general, it was observed that none of the methods provides the worst year with 100% accuracy, however for most of the cases, Isev method performs better than other two methods in terms of MRY selection.*

Keywords: *Moisture Performance, Climate Change, Hygrothermal Simulation, Moisture Reference Year(s) Selection Method.*

1 Introduction

One of the parameters that influences the moisture performance of the wall is the outdoor climate. However, having large number of climate parameters and estimating the effects of these parameters over the entire service life would result in a large simulation effort. One of the approaches to cut down the simulation time and cost is to select a year or combination of years called Moisture Reference Year(s) (MRYs) which is assumed to represent the entire set of long term climate data.

The π-factor method suggested by Hagentoft and Harderup (1996) compares the absolute humidity at the external wall surface with the absolute humidity of the outside air in order to compute the drying potential of the wall surface. They suggested that drying out potential is higher for a higher value of π-factor. Kalamees and Vinha (2004) used a method similar to π-factor method for selecting the MRY in terms of evaluating the risk of water vapor condensation. Carsten Rode (1993) proposed a construction dependent method, which compares the integral moisture content values for different wall constructions and orientations. He suggested that the higher the value of moisture content for a particular year, the more severe the year is in terms of moisture performance of the wall. Cornick *et al.* (2003) used an index called Moisture Index (MI) to categorize the years in terms of the severity. MI method uses wetting and drying function to compute MI and then further categorizes the year as dry, average and wet based on lowest, average and highest MI value respectively. From a dataset of years, the years having MI value in the range of more than one standard deviation (+/-) from the mean MI value are considered as dry and wet years, while those years having a value within (+/-) one standard deviation are referred to as average years. A method suggested by (ASHRAE, 2010) combines the climate load and durability to choose the "severe" weather years and provides a more representative ranking of the climate data. This approach, called the Severity Index (Isev), uses an equation to predict the RHT value as a damage function. Salonvaara *et al.* (2010) suggested the Isev equation as a reliable method of selecting representative years. A regression equation used for computing RHT value considers different climate parameters. The yearly average value of each climate parameter is used in the equation and the years are arranged in the descending order of the RHT values. The year with the third highest (top 10% years among 31 years) RHT value is selected as MRY for the hygrothermal simulations. The authors further compared their method with three other existing methods and concluded that their method performs better in predicting the severe years than other methods. The Climatic Index method suggested by Zhou *et al.* (2016) comprises wetting and drying components. The wetting component depends on the annual wind-driven rain and the drying component depends on the annual potential evaporation. Unlike MI method, this index takes into consideration the effect of many climate parameters such as net radiation, temperature, humidity, wind speed, wind direction and orientation of the façade. The authors made a comparison with MI method in terms of accuracy in predicting the MRY and suggested that the year predicted using climate index gives better result than MI method. However, based on the past research findings, none of the methods can be considered as a universal method for the selection of MRY.

The objective of this study is to investigate three MRY selection methods *i.e.* Moisture Index (MI), Severity Index (Isev) and Climatic Index (CI) in terms of their accuracy in predicting the worst year in terms of moisture performance among a series of long-term climate data. For all the methods, the year corresponding to the 97th percentile, (ranked second out of the 31 years) for each climate scenario was chosen as the MRY and is further compared with the individual year simulations to determine their capability in predicting the extreme year.

2 Methods

2.1 Description of MRY Selection Methods

Cornick *et al.* (2003) suggested the calculation of MI for every hour (MI_h) based on hourly

wetness (WI_h) and dryness (DI_h) indices. Here, WI_h corresponds to the normalized hourly rainfall and DI_h corresponds to Δp_v *i.e.* the difference between the saturation vapor pressure and vapor pressure of the ambient air. The saturation vapor pressure, p_{vs}, as a function of ambient temperature (T), was calculated as suggested by ASHRAE (2009).

The magnitude of Δp_v is calculated using Equation (1):

$$\Delta p_v = p_{vs} - p_v \tag{1}$$

Both the indices are further normalized as per the Equation (2):

$$I_{normalized} = (I - I_{min})/(I_{max} - I_{min}) \tag{2}$$

Where, I is the Index of interest.

Normalized values of Δp_v and accumulated hourly rainfall were used as DI_h and WI_h magnitudes respectively and equal weights are assigned for both the indices.

$$MI_h = \sqrt{(1 - DI_{h,norm})^2 + {WI_{h,norm}}^2} \tag{3}$$

Based on ASHRAE (2010), the severity index (Isev) for each year is calculated according to Equation (4):

$$\begin{aligned} I_{sev} = 108307 - 241.E_v - 1391.I_{cl} - 312326.\phi + 183308.r_{wd} + 15.2.p_v + 27.3.T^2 \\ + 261079.\phi^2 - 0.00972.p_v^2 \end{aligned} \tag{4}$$

Where, E_v is the solar radiation (W/m^2) incident on the wall; I_{cl} is the cloud index; ϕ is the relative humidity; r_{wd} is the wind-driven rain ($kg/(m^2.h)$ on the wall; p_v is vapor pressure (Pa), and T is the ambient temperature (°C). The method is explicitly valid for the orientation with highest amount of yearly Wind-driven-rain (WDR) and least solar radiation *i.e.* North orientation. A yearly average value is used for each climate parameter for each year.

Zhou *et al.* (2016) suggested calculation of CI based on annual wetting and drying. The wetting component includes annual wind-driven rain and drying component is based on the potential evaporation calculation based on Penman equation shown below:

$$E = \frac{\Delta}{\Delta + \gamma}\frac{K + L - A}{I} + \frac{\gamma}{\Delta + \gamma}h_m(e_a - e) \tag{5}$$

Where, $\frac{\Delta}{\Delta+\gamma}\frac{K+L-A}{I}$ represents the radiation term and $\frac{\gamma}{\Delta+\gamma}h_m(e_a - e)$ represents the turbulence term. E is the drying Index, K is the net short-wave radiation (Wm^{-2}), L is the net Longwave radiation (Wm^{-2}), A is the conductive heat flux to the porous material (Wm^{-2}), I is latent heat of vaporization (Jkg^{-1}), γ is the psychometric constant (PaK^{-1}), Δ is the slope of the relationship between saturation vapor partial pressure and air temperature, e_a is the saturated partial vapor pressure of the air, e is the vapor partial pressure in the air (Pa) and h_m is the convective vapor transfer coefficient (sm^{-1}). In the calculation of drying index, the conduction heat flux and long wave radiation were neglected since their values are much smaller in comparison to short wave radiation. Finally, the yearly sum values were taken and the CI was calculated as the ratio of Wetting Index and Drying Index.

2.2 Cities Selected & Wall Orientation

For the analysis, three cities were chosen from 3 different provinces of Canada: Ottawa (ON), Vancouver (BC), and Calgary (AB). Furthermore, the selected cities vary significantly in terms of their climate conditions. Amongst these cities, based on MI value; Vancouver and Calgary are the wettest and driest cities respectively and Ottawa being the city with an intermediate value of MI. The study was made for the orientation receiving least annual solar radiation *i.e.* a North-facing wall (N) for each city. Further details for these cities are listed in the Table 1.

Table 1. Characteristics of the selected cities.

City (Province)	Latitude	Longitude	HDD18	MI	Annual rain (mm)
Ottawa (ON)	45.25°	-75.42°	4440	0.84	750
Vancouver (BC)	49.28°	-123.12°	3100	1.93	1850
Calgary (AB)	51.05°	-114.07°	5000	0.37	325
HDD18 – heating degree days below 18ºC			MI – moisture index		

2.3 Wall Configuration

The modeled building was assumed to be a 3.5 storey type located in a suburban setting. Light weight wood frame wall assembly with brick cladding was simulated and the wall was assumed to be perfectly air tight. A detailed description of chosen wall assembly is shown in Figure 1.

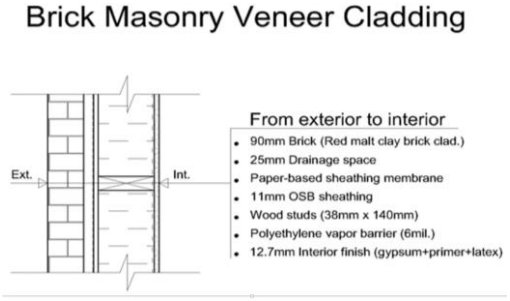

Figure 1. Description of the wall assembly.

The material properties were obtained from NRC material property database (Kumaran *et al.* 2002). For the air cavity, same value of Air Changes per Hour (ACH) was used for each city and climate scenario. Table 2 illustrates ACH values for different claddings and locations.

Table 2. Selected ACH values for different claddings and locations.

Ottawa		Vancouver		Calgary	
Brick	Stucco	Brick	Stucco	Brick	Stucco
6	10	12	40	3	5

Extensive trials were made for selecting an appropriate ACH value. For this purpose, simulations were made by repeating the average year (based on MI ranking) for 7 times and mould index value was computed at the exterior layer of the OSB. The aim was to choose a

value of ACH that results in having mould index stabilizes around a value of 3.

2.4 Climate Data and Wind Driven Rain

The climate data used for the present study includes hourly climate for a consecutive 31 years: from 1986-2016 for historical scenario; and, similarly 31 years when the global temperature will increase by 3.5°C. (Gaur *et al.* 2019). An increase of 3.5ºC global increase is expected to transpire between the years 2062-2092 as per the projections made by Environment and Climate Change Canada (2018). It was observed that, there is a minimal variation in RH value and an increase of approximately 5°C (annual average) in temperature from historical to future climate conditions for each city. Wind Driven Rain (WDR) was calculated using the ASHRAE method (ANSI/ASHRAE, 2016) assuming a medium exposure with the rain exposure factor (FE) and the rain deposition factor (FD) set to 1.0 and 0.5, respectively.

2.5 Boundary Conditions and Initial Conditions

Indoor temperature and relative humidity were assumed constant and set to 21ºC and 50% respectively. The indoor exchange coefficient for heat conduction was set to 8 W/m^{2}K and the indoor vapor diffusion coefficient was set to 1.52*10^{-8} s/m. As per the EN ISO 6946 standard, the convective heat transfer coefficient is $h_{ce} = 4 + 4v$, where v is the wind velocity at 10 m height. The convective vapor transfer coefficient is related to the convective heat transfer by the use of the Lewis analogy $\beta_v = 2.44 * 10^{-8} + 2.44 * 10^{-8}\ v$. The reflection coefficient of the surrounding ground (albedo) was 0.1 and the absorption coefficient for the brick cladding was equal to 0.6. The wall was conditioned with suitable climate by completing a consecutive seven (7) year simulation, repeating the average year (based on Moisture index ranking). At the end of simulation, the average value of temperature and RH for all the layers in the wall configuration were noted and used as initial conditions.

2.6 Simulations

Simulations were run over the individual years spanning a period of 31 years for historical and future climate using the Heat, Air and Moisture (HAM) simulation tool DELPHIN V5.9. For this study, only one-dimensional horizontal configuration of the wall was simulated. The water infiltration through the assembly was assumed to be 1% of the wind-driven rain and was applied to the exterior side of the sheathing membrane, as per ASHRAE 160 (2016). Manual meshing was opted for all the layers except sheathing membrane and vapor barrier. For these two layers, an equidistant mesh of 3 elements was assumed. For other layers, they were divided into 3 sections with first and last sections having equal thicknesses. For these two sections, a fine and variable mesh was used and an equidistant mesh was opted for the middle section.

2.7 Performance Indicator

For analyzing the moisture performance of the wall assembly, the mould index was computed at the exterior of the OSB layer (0.1mm thick element size) using the method proposed by Ojanen *et al.* (2010). The calculations were made assuming the sensitive class for material and surface and a decline factor of 0.5 (assuming significant decline) when the conditions become unfavorable for mould growth. Furthermore, for performance analysis, one way is to use the

maximum mould index value to compare different results. However, this can be misleading, especially in a situation when there is only one peak followed by set of low values. To tackle this situation and capture the trend, a better idea would be to count the number of hours when mould index value is above a threshold value and use that value as a performance indicator.

3 Results and Discussion

The accumulated number of hours when mould index (MoI) value is more than 3 was calculated for each year of the 31-year series. Figure 2 shows the results obtained for the brick cladding wall in Calgary exposed to future climate. It shows the total number of hours throughout the year when the MoI value was above 3. On the secondary axis, the maximum MoI for a particular year is shown. Furthermore, the year selected by each MRY selection method is marked on the chart. For this particular case, it was observed that Isev method predicts the year which performs the worst when simulated for moisture performance analysis. The years predicted by the other two methods are far away from the extreme year (based on simulation) in that dataset.

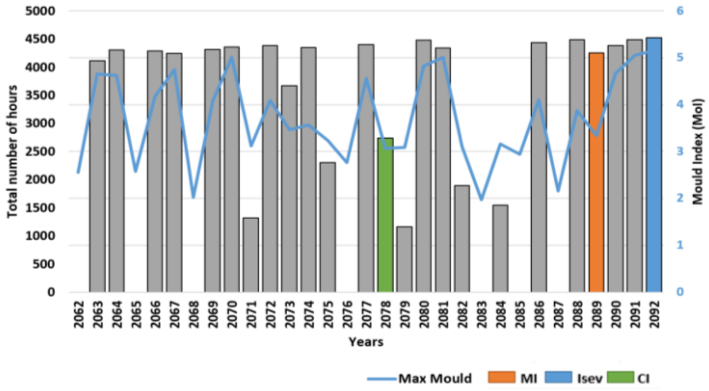

Figure 2. Total number of hours with MoI>3 for Brick wall in Calgary for future climate. Secondary axis shows the maximum value of MoI for each year.

To analyze the results in a more lucid way, further grouping was made wherein the hours were divided into classes having a range of 200 hours starting from 0 and ending with hours above 5000. The reason behind choosing a nominal value of 200 hours is to distinguish the years selected by different selection methods.

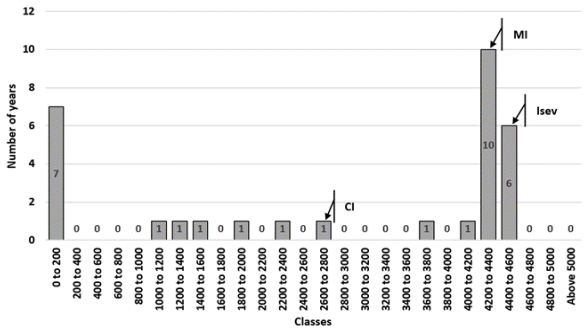

Figure 3. Grouping of years in terms of number of hours when MoI>3 for Brick wall in Calgary for future climate. Year given by three methods lies in one of the classes and are marked in with arrow in the chart.

Figure 3 shows the distribution of the 31 years among the different classes for brick cladding wall in Calgary exposed to the future climate. It is clear from Figure 3 that the year predicted by the Isev method falls in the same class as that of the year with maximum number of accumulated hours using simulation. For this case, the worst year is more in accordance with the year suggested by Isev method.

Similar analysis was made for different cities considered for historical and future climate scenarios. As a general trend, it was observed that the selection of year based on severity index method always lies closer to the class belonging to the worst year among the series of the years. It was observed that in Vancouver for a North facing wall, there is no risk of mould growth. This could be explained by the fact that in Vancouver, there was a very low amount of WDR falling on a North facing wall which in turn imposes almost no risk of mould growth.

Table 3. Summary of all the simulated cases. Year shows the year predicted by the method and class shows the range in which the corresponding year lies. (*Ott: Ottawa, Van: Vancouver, Cal: Calgary, H: Historical, F: Future).*

Case	Simulation		MI		Isev		CI	
	Year	Class (in 100s)	Year	Class (in 100s)	Year	Class (in 100s)	Year	Class (in 100s)
Ott_H	2009	42-44	2010	0-2	2009	42-44	2004	30-32
Ott_F	2081	>50	2085	0-2	2069	38-40	2070	46-48
Van_H	--	--	--	--	--	--	--	--
Van_F	--	--	--	--	--	--	--	--
Cal_H	1999	40-42	2005	34-36	1995	40-42	2014	40-42
Cal_F	2092	44-46	2089	42-44	2092	44-46	2078	26-28

Table 3 represents the results for all the considered cases. It shows the year selected by various methods and the year which actually performs the worst. Moreover, the table illustrates the class in which each method lies. Closer the class of each method to the simulation results, better the method is in its prediction. From the table it is clear that 3 out of 4 times, the year predicted by the Isev method lies in the same class as that of extreme year using simulations.

4 Summary and Conclusions

For analyzing the moisture performance of the wall assembly, 3 different Canadian cities were selected based on the different climate conditions. Number of hours when the mould index was more than 3 were calculated for each year and were then compared with the corresponding values for the MRY predicted using different methods. Different classes were made based on the number of hours and the years falling in the same class were grouped together. None of the three methods predicts the worst year with 100% accuracy when compared with the results from the simulation over the individual year for the 31 year data set. Furthermore, when the methods were compared against each other, it was observed that the severity index method was better in predicting the extreme year than the other two methods for both set of climate data *i.e.* historical as well as future climate scenario.

The study is limited to only 3 Canadian cities and it is of utmost importance to test more cities with varying climatic conditions. Furthermore, among the three MRY selection methods

chosen for the study, Isev method is limited to only North facing walls. Finally, the study uses total number of hours when MoI>3 as the damage criteria for one set of historical and future climate. The study could be further extended to analyze other damage functions for different sets of historical and future climate scenarios. Future work will be to incorporate the abovementioned limitations along with developing the moisture performance data for different wall systems obtained by completing hygrothermal simulations over a consecutive 31-year series of historical and future climate data. Later step will be to validate the (MRY), or a series of MRYs using the results from the consecutive year simulations.

ORCID

Chetan Aggarwal: https://orcid.org/0000-0002-7224-9740
Maurice Defo: https://orcid.org/0000-0001-9212-6599
Travis Moore: https://orcid.org/0000-0002-4920-9193
Michael Lacasse: https://orcid.org/0000-0001-7640-3701
Sahar Sahyoun: https://orcid.org/0000-0001-5131-6134
Hua Ge: http://orcid.org/0000-0003-1368-4301

References

ASHRAE. (2016). ASHRAE 160 (Criteria for Moisture-Control Design Analysis in Buildings). ASHRAE Standards Committe, Atlanta, GA.

ASHRAE. (2010). Environmental weather loads for hygro- thermal analysis and design of buildings. RP-1325, American Society of Heating, Refrigerating and Air- Conditioning Engineers, Inc. Atlanta.

ASHRAE. (2009). ASHRAE handbook: Fundamentals. Atlanta.

Cornick, S., Djebbar, R. and Dalgliesh, W. A. (2003). Selecting moisture reference years using a Moisture Index approach. Building and Environment, 38(12), 1367–1379. https://doi.org/10.1016/S0360-1323(03)00139-2.

Environment and Climate Change Canada. (2018). Memorandum of Understanding between National Research Council and Environment and Climate Change Canada…. Government of Canada: Ottawa, ON, Canada.

Gaur, A., Lacasse, M. and Armstrong, M. (2019). Climate Data to Undertake Hygrothermal and Whole Building Simulations Under Projected Climate Change Influences for 11 Canadian Cities. Data, 4(2), 72. https://doi.org/10.3390/data4020072.

Hagentoft CE, Harderup E. Climatic infuences on the building envelope using the π factor. IEA-Annex 24 Hamtie Task 2, Environmental Conditions. Closing Seminar, Finland, 1996.

ISO, 2017. ISO 06946 (Building components and building elements-Thermal resistance and thermal transmittance-Calculation methods), ISO, Switzerland

Kalamees, T. and Vinha, J. (2004). Estonian Climate Analysis for Selecting Moisture Reference Years for Hygrothermal Calculations. Journal of Building Physics, 27(3), 199–220.

Kumaran, M.K., Lackey, J. Normandin, N., Tariku, F. and van Reenen, D. (2002). A thermal and moisture transport property database for commom building and insulation materials (No. 1018- RP). ASHRAE.

Ojanen, T., Viitanen, H., Peuhkuri, R., Lähdesmäki, K., Vinha, J. and Salminen, K. (2010). Mold Growth Modeling of Building Structures Using Sensitivity Classes of Materials. Eleventh International Conference on Thermal Performance of the Exterior Envelopes of Whole Buildings, 10. Clearwater Beach, FL, US.

Rode C. Reference years for moisture calculations. Denmark. Report T2-DK-93/02, International Energy Agency, Energy Conservation in Buildings and Community Systems Program, Annex 24 Heat, Air, and Moisture Transfer in Insulated Building Parts (HAMTIE).

Salonvaara, M., Sedlbauer, K., Holm, A. and Pazera, M. (2010). Effect of selected weather year for hygrothermal analyses. Proceedings of thermal performance of the exterior envelopes of whole buildings XI. ASHRAE.

Zhou, X., Derome, D. and Carmeliet, J. (2016). Robust moisture reference year methodology for hygrothermal simulations. Building and Environment, 110, 23–35. https://doi.org/10.1016/j.buildenv.2016.09.021

XV International Conference on Durability of Building Materials and Components
DBMC 2020, Barcelona
C. Serrat, J.R. Casas and V. Gibert (Eds)

Biodegradable Polymers on Cementitious Materials

Julia García-González[1], Paulo C. Lemos[2], Alice S. Pereira[3], Julia Mª. Morán-del Pozo[1], M. Ignacio Guerra-Romero[1], Andrés Juan-Valdés[1] and Paulina Faria[4]

1 Escuela de Ingeniería Agraria y Forestal, University of Leon, León, Spain, jgarcg@unileon.es, jmmorp@unileon.es, miguer@unileon.es, ajuav@unileon.es

2 LAQV-REQUIMTE, Dep. of Chemistry, Faculdade de Ciências e Tecnologia, Universidade NOVA de Lisboa, Caparica, Portugal, paulo.lemos@fct.unl.pt

3 UCIBIO-REQUIMTE, Dep. of Chemistry, Faculdade de Ciências e Tecnologia, Universidade NOVA de Lisboa, Caparica, Portugal, masp@fct.unl.pt

4 CERIS and Dep. Civil Engineering, Faculdade de Ciências e Tecnologia, Universidade NOVA de Lisboa, Caparica, Portugal, mpr@fct.unl.pt

Abstract. *Nowadays the sustainability and safety requirements of structures inspire the study of new self-healing materials and preventive repair methods on cementitious elements. To achieve this undertaking, this research replaces widely employed synthetic polymers by biodegradable ones as consolidants and water-repellents, and assesses the protection and consolidation effect of biopolymers (obtained by using waste biomass of mixed microbial cultures from polyhydroxyalkanoates production processes) as eco-friendly healing agents by analysing the water absorption of two kind of materials. The first group of samples are cement mortar specimens whose external surface has been treated with biopolymer products and subsequently evaluated by water drop absorption test. The second group of samples are cement mortar specimens formulated with biopolymer products included in its mixing water and later the waterproofing efficiency is analysed by capillary water absorption tests. The water absorption behaviour of both kind of samples shows a potential improvement of cementitious elements durability, since water absorption results have decreased for treated samples in comparison with untreated ones.*

Keywords: *Repair Methods, Self-Healing, Polyhydroxyalknoates, Durability, Cement Mortar.*

1 Introduction

During historic and prehistoric period, the use of biopolymers from plants and natural sources was a common technique in the manufacture of construction materials. They developed suitable behaviour in terms of reducing the water content of the binding materials, accelerating the hardening process of the binders and achieving a compaction desirable in the production of compacted hardened structures with appropriate durability. Thereby a suitable binder to keep the structural integrity of aggregate-based materials used in ancient structures is reaching. In addition, these natural biopolymers can exhibit biocidal and insecticidal properties leading to resistance of the constructed structure to bio-corrosion as well as termite resistance (Karandikar *et al*., 2014). However, nowadays the usage of biopolymers has disappeared in the most of developed countries around the world, only in some rural areas of underdeveloped countries these eco-friendly techniques are still practised, where the knowledge has been inherited from one generation to another.

Demand for construction materials has been rising in recent decades in many countries, with

the intense industrialisation and urban development induced by economic and demographic growth, then self-healing materials and repair methods are required in construction sector.

Cement-based materials are inert, however, currently a number of chemical products are generally added to mortar and concrete mixes to control several parameters (plasticity, pumpability, setting time, water content, freeze-thaw resistance, strength, colour, etc.) Because of these chemical admixtures, today cement-based materials could become more harmful to the environment. They require more energy to be produced and more raw materials. The use of various synthetic admixtures in cement-based materials has been proved to have contributed to the emission of toxic species into the atmosphere (Hazarika *et al*., 2016).

The replacement of synthetic admixtures by natural polymers would pave the way for more green construction. The use of natural materials as opposed to non-renewable and petroleum-based products has been identified as a potential means for reducing the embodied energy and carbon footprint of buildings, as well as helping to create healthy and comfortable indoor environments (Dove, 2014; Felton *et al.*, 2013). Natural polymers are polymers synthesized by living organisms (plant, animal, algae, fungus or bacteria) and consist of long chains made of repeating, covalently bonded units, such as nucleotides, amino acids or monosaccharides. Biopolymers have the potential to reduce carbon emissions since the CO_2 released when they degrade can be reabsorbed by crops grown to replace them, making them close to carbon neutral.

Several publications have studied the usage of these natural products in the production of earthen buildings: vegetable oils (Ogacho *et al*, 2003; Balo and Yucel, 2013), plant gums and resins (Ruskulis, 2002), molasses (Vilane, 2010) or animal products (Ruskulis, 2002; Eires *et al*.,2013; Beas, 1991). However, there are few studies where this kind of additions are used on cement-based materials. In this study, the potential of a novel biopolymer from biodiesel by-product is evaluated to realize self-sealing of cement-based materials, on one hand, and surface repairing development of cement mortar samples, on the other hand.

2 Material and Methods

The bioproducts used as surface repairing agents were eco-friendly, being obtained by waste biomass from a microbial mixed culture (MMC) for polyhydroxyalkanoates production using crude glycerol (biodiesel by-product). MMC cell walls were disrupted by sonication (Sonicated bioproduct, B-S) or not (Non-sonicated bioproduct, B-NS). For comparison, different control samples were prepared: i) untreated; ii) specimens in which the bioproduct was replaced by the same volume of tap water. Table 1 shows the different treatments for external addition of biopolymers.

Table 1. Description and short names of bioproducts/biotreatments and controls.

Surface treatments		Short name
Controls	Control (no treatment)	Control
	Reference (tap water)	H_2O
MMC-glycerol bioproducts	MMC grown with crude glycerol	B-NS
	MMC grown with crude glycerol after sonication	B-S

Cement mortar to test the surface repair effect was produced with a cement CEM II/A-L-32.5 N (EN 197-1, 2011), from Secil Group, Portugal, with a loose bulk density of 1.18 kg/dm^3. The mortar was formulated with a cement:sand mass proportion of 1:1.9, that corresponds to a volumetric proportion of 1:3.

Triplicate specimens were prepared and tested. Bioproducts were applied onto the surface of mortar samples by dropping into a 3 x 3 grid of 9 addition points in a surface of 40 mm x 40 mm in a total of 2 cm^3 of each bioproduct suspensions using a pipette. To simulate degraded surfaces, a cut surface of samples was treated. Samples were located on a test room one week before biotreatments to establish uniform laboratory conditions (20 ± 2 °C and 40 ± 5% relative humidity).

Five days after the treatment, the repairing effect was assessed by a water-drop absorption test. This test allows evaluating the permeability variation of biotreated surfaces by monitoring the rate of absorption of a 0.1 cm^3 drop of water, that is, the time required for a material to fully absorb a water drop under open air conditions (Figure 1). The absorption period of time was video-recorded.

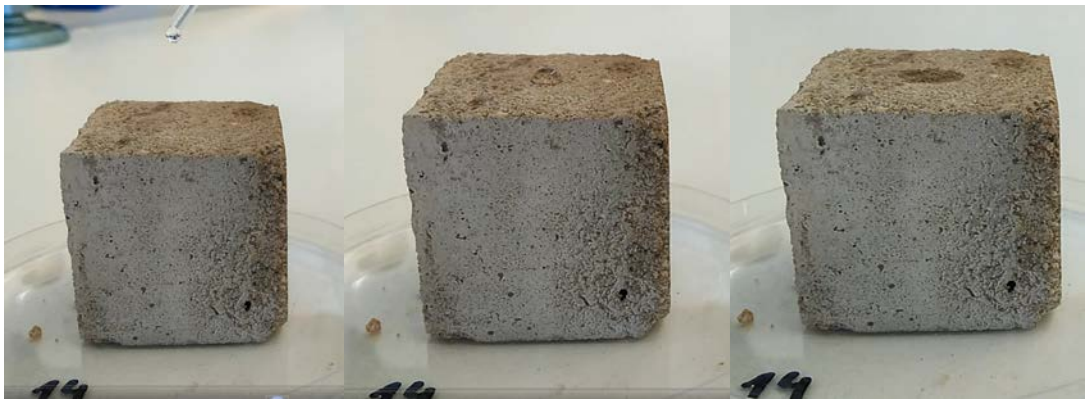

Figure 1.Steps of water drop absorption test.

Regarding internal addition of bioproducts, the cement mortar samples to test the self-healing effect of the biopolymer at different ages was bioformulated with the composition shown in Table 2.

Table 2. Composition and code of the cement mortar samples.

Sample	Code	Sand (g)	C (g)	Water(ml)	B1 (ml)	B2 (ml)
Control (Cement mortar with water formulation)	CW	4	627.13	530	0	0
B1 (Cement mortar with bioproduct formulation)	CB1	4	627.13	0	530	0
B2 (Cement mortar with older bioproduct-3 days old formulation)	CB2	4	627.13	0	0	530

Six months after the cement mortar manufacture, the healing effect was assessed by a water-drop absorption test, following the same steps explained previously for the surface treatment

samples. Triplicate specimens were tested, which were located on a test room one week before measurements to establish uniform laboratory conditions (20 ± 2 °C and 40 ± 5% relative humidity).

3 Results and Discussion

The results of the water drop absorption time of surface biotreated samples are represented in Figure 2, which showed that the samples exposed to only water (H_2O sample) reduced the time until water drop absorption, being a negative effect on the mortar durability, as expected. However, when the cement mortar was treated with non-sonicated bioproduct (B-NS), a waterproof effect was observed, since the water drop absorption time increased 601% in comparison with control sample. If the mortar surface is treated with the sonicated bioproduct (B-S), the waterproof response is even greater, since B-S sample showed a water absorption time 912% higher than the control sample. The development of a waterproof film in the external part of the sample (surface and external cracks), due to the biopolymer deposition is the reason of the better performance of treated samples in comparison with Control and H_2O samples.

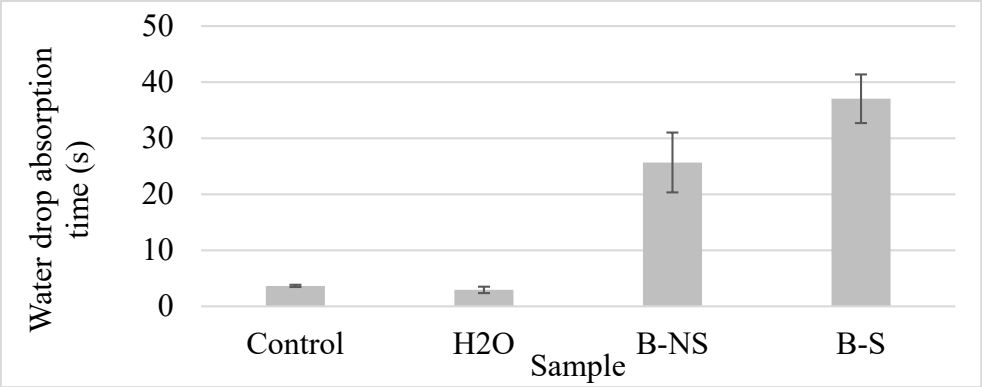

Figure 2. Water drop absorption time of surface treated cement mortar samples.

Authors as Subbiah *et al*. (2018) used silane enriched with nanomaterials as water-repellent on cement mortar, obtaining a 10% water absorption decrease. Treatment of cement mortars with nano-silica was tested by Hou *et al*. (2014) and they observed a water permeability decrease, by reducing the volume of pores larger than 50 nm and the threshold value of the pore network. Other authors as Chandra *et al*. (1998) applied water extracts of cactus to biotreat the surface of Portland cement mortar samples, achieving up to 83% improvement in water resistance.

The Figure 3 shows the water drop absorption time for the cement mortar with water (CW) and the bioformulated cement mortar with the biopolymer at different ages (CB1 and CB2). Although, deeper studies should be developed to decrease the standard deviation in the data, the results of this test state that the self-healing effect of biopolymer presence, since CB1 samples spend 12,5% more time to absorb the water drop than the CW sample. When the age of the biopolymer is increased (CB2 sample), the self-healing effect is even greater, raising the water drop absorption time until 16,7% in comparison with the control sample (CW). The better performance of bioformulated cement mortar than the conventional mortar in water drop

absorption test can be related with the low water accessible porosity on bioformulated samples due to the polyhydroxyalkanoates production on cement paste, which apparently increased over time, considering short periods of time.

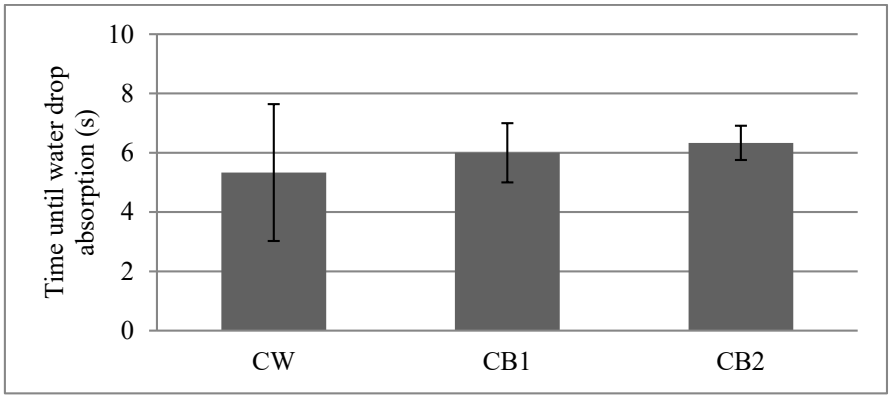

Figure 3. Time until water drop absorption of CW, CB1 and CB2 samples.

Previous results have already shown that addition of ecofriendly polymers on cement-based materials generated positive findings on material durability, such as Chandra et al (1998), who used the water extract of cactus in preparation of Portland cement mortar and this natural polymer improved water absorption and freeze-salt resistance. Also Chandra and Aavik (1983) used black gram as binder in cement mortar and stated that it worked like air entraining agent, improving the hydrophobicity of cement mortar. They also tested the addition of oil along with black gram, which worked as a defoaming agent and substantially improved the hydrophobic property of cement mortar. Hazarika *et al*. (2018) used a plant based polymeric material as a low cost chemical admixture in cement mortar and concrete preparations. The addition of this bio-admixture decreased the water absorption capacity as well as the porosity of the mortar samples.

In addition, the two approaches tested on this study showed that external treatment of mortar samples with biopolymers are more effective than when bioproducts are incorporated like mixture addition (bioformulation).

4 Conclusions

- The treatments with MMC bioproduct from glycerol showed a significant decrease of the permeability on the surface biotreated samples. The sonicated biopolymer exhibited a greater repairing effect than the non-sonicated one.
- Addition of MMC bioproduct on the formulation of cement mortars implied a positive effect on its durability and this result was greater when the bioproduct solution was older, involving a relatively short period of time (few days).

Acknowledgements

This work was supported by a STSM Grant from the COST Action CA15202. (http://www.sarcos.enq.cam.ac.uk), project BIA2017-83526-R supported by the Spanish Ministry of Science, Innovation and Universities, project DB-

Heritage - Database of building materials with historical and heritage interest (PTDC/EPH-PAT/4684/2014), project IF/01054/2014/CP1224/CT0005, the Associate Laboratory for Green Chemistry-LAQV and Applied Molecular Biosciences Unit-UCIBIO which are financed by national funds from FCT/MCTES (UID/QUI/50006/2019; UID/Multi/04378/2019) and co-financed by the ERDF under the PT2020 Partnership Agreement (POCI-01-0145-FEDER-007728).

ORCID

Julia García-González: http://orcid.org/0000-0002-8972-1861
Paulo C. Lemos: https://orcid.org/0000-0001-6094-0107
Alice S. Pereira: https://orcid.org/0000-0001-5567-6073
Julia Mª. Morán-del Pozo: http://orcid.org/0000-0001-8768-5898
M. Ignacio Guerra-Romero: http://orcid.org/ 000-0003-0244-6885
Andrés Juan-Valdés: http://orcid.org/ 0000-0003-0902-6429
Paulina Faria: https://orcid.org/0000-0003-0372-949X

References

Balo, F. and Yucel, H.L. (2013). Assessment of Thermal Performance of Green Building Materials Produced with Plant Oils. *International Journal of Materials Science*, 3(3), 118-129.

Beas, M. I. G. (1991). *Traditional architectural renders on earthen surfaces*, MSc Thesis, University of Pennsylvania. US.

Chandra, S. and Aavik, J. (1983). Influence of black gram (natural organic material) addition as admixture in cement mortar and concrete. *Cement and Concrete Research*, 13(3), 423-430. doi: 10.1016/0008-8846(83)90043-1

Chandra, S., Eklund, L. and Villarreal, R.R. (1998). Use of Cactus in Mortars and Concrete. *Cement and Concrete Research,* 28(1), 41-51. doi: 10.1016/S0008-8846(97)00254-8

Dove, C. (2014). The development of unfired earth bricks using seaweed biopolymers. *WIT Transactions on Ecology on The Built Environment*, 142(1), 219-230. doi:10.2495/ARC140201

Eires, R., Camões, A. and Jalali, S. (2013). Earth architecture: ancient and new methods for durability improvement. *Structures and Architecture: Concepts, Applications and Challenges*, P. J. S. Cruz, Ed. London: Taylor and Francis Group.

Felton, D., Fuller, R. and Crawford, R.H. (2013). The potential for renewable materials to reduce the embodied energy and associated greenhouse gas emissions of medium-rise buildings, *Architectural Science Review*, 57(1), 31–38. doi: 10.1080/00038628.2013.829022.

Hazarika, A., Hazarika, I. and Saikia, N. (2016). The effect of a plant based polymeric material on the fresh and hardened states properties of cement mortar. *1st International Conference on Civil Engineering for Sustainable Development-Opportunities and Challenges*, At Guwahati, India.

Hazarika, A., Hazarika, I., Gogoi, M., Bora, S.S., Borah, R.R., Goutam, P. J. and Saikia, N. (2018). Use of a plant based polymeric material as a low cost chemical admixture in cement mortar and concrete preparations *Journal of Building Engineering*, 15(1), 194-202. doi: 10.1016/j.jobe.2017.11.017

Hou, P., Cheng, X., Qian, J. and Shah, S.P. (2014). Effects and mechanisms of surface treatment of hardened cement-based materials with colloidal nanoSiO_2 and its precursor. *Construction and Building Materials*, 53 (1), 66-73. doi: 10.1016/j.conbuildmat.2013.11.062

Karandikar, M.V., Sarase S.B., Lele P.G. and Khadaikar S.A. (2014). Use of natural bio-polymers for improved mortar and concrete properties of cement – A review. *Indian Concrete Journal*, 88(7), 84-109.

Ogacho, A., Aduda, B. and Nyongesa, F. (2003). Thermal conductivity of a kaolinite refractory: effect of a plant-derived organic binder. *Journal of Materials Science*, 38(11), 2293-2297. doi: 10.1023/A:1023916009846.

Ruskulis, O. (2002). Additives to Clay: Organic Additives. *Practical Action, Technical Brief.*

Subbiah, K., Park, D.J., Lee, Y.S., Velu, S., Lee, H.S., Jang, H.O. and Choi, H.J. (2018). Development of water-repellent cement mortar using silane enriched with nanomaterials. *Progress in Organic Coatings*, 125(1), 48-60. doi: 10.1016/j.porgcoat.2018.08.021

Vilane, B. (2010). Assessment of stabilisation of adobes by confined compression tests. *Biosystems Engineering*, 106(4), 551–558. doi: 10.1016/j.biosystemseng.2010.06.008

XV International Conference on Durability of Building Materials and Components
DBMC 2020, Barcelona
C. Serrat, J.R. Casas and V. Gibert (Eds)

Biomimetic Antifreeze Polymers: A Natural Solution to Freeze-Thaw Damage in Cement and Concrete

Mohammad Matar[1], Shane Frazier[2] and Wil V. Srubar III[3]

[1] Department of Civil, Environmental, and Architectural Engineering, University of Colorado Boulder, ECOT 441 UCB 428, Boulder, Colorado 80309 USA, mohammad.matar@colorado.edu

[2] Materials Science and Engineering Program, University of Colorado Boulder, UCB 027, Boulder, Colorado 80303 USA, shane.frazier@colorado.edu

[3] Department of Civil, Environmental, and Architectural Engineering, University of Colorado Boulder, ECOT 441 UCB 428, Boulder, Colorado 80309 USA

Materials Science and Engineering Program, University of Colorado Boulder, UCB 027, Boulder, Colorado 80303 USA wsrubar@colorado.edu

Abstract. *Ice is one of the few substances on Earth that expands when it freezes. Consequently, this phase change causes damage to porous cementitious materials that absorb water and undergo freeze-thaw cycling. Inspired by nature, the objective of this work is to characterize biomimetic antifreeze polymers (BAPs) that explicitly mimic the behavior of antifreeze proteins (AFPs) and antifreeze glycoproteins (AFGPs) naturally found in plants, fish, insects, and bacteria for use as a concrete additive. The ultimate goal of this work is to enhance the freeze-thaw durability of ordinary portland cement (OPC) concrete without the use of traditional air entraining agents (AEAs). This work will highlight recent research that has shown that small additions, less than 0.1% by wt. of cement, of BAPs that exhibit ice recrystallization inhibition (IRI) activity can mitigate freeze-thaw damage in OPC paste and concrete while entraining less than 3% air.*

Keywords: *Biomimetic Antifreeze Polymer, Freeze-Thaw Durability.*

1 Introduction

1.1 Freeze-Thaw Damage

Concrete exposed to cyclic freezing and thawing temperatures is susceptible to damage. It is commonly accepted that hydraulic, osmotic, and crystallization pressures develop when ice forms in the pore structure of concrete leading to internal micro-cracking (Powers, 1975; Scherer *et al*., 2005). The internal damage reduces the durability by decreasing overall compressive strength, increasing susceptibility to water and ion ingress, and increasing susceptibility to additional freeze-thaw damage.

1.2 Mitigation of Freeze-Thaw Damage in Concrete

The default method used to mitigate freeze-thaw damage in OPC concrete since the 1930s has been through the creation of an entrained air void system via the addition of air entraining agents (AEAs). Research into other methods include super absorbent polymers to create properly sized and spaced voids (Lausten, *et al*., 2015), supplementary cementitious materials (Sabir, 1997; Duan, *et al*., 2013) and nanoparticles (Behfarnia, Salemi, 2013; Gonzalez, *et al*., 2016) for reducing porosity, hydrophobic materials to reduce water ingress (Liu, Hansen, 2016), and polymeric fibers for containment of crack propagation (Nam, *et al*., 2016).

doi:10.23967/dbmc.2020.176

1.2.1 Air entraining agents

AEAs stabilize air voids during the mixing process through a surfactant mechanism. The air voids provide pressure relief sites and preferred locations for ice formation in hardened concrete. In the field it is commonplace to only measure fresh state air content to predict the effectiveness air entrainment, with prescribed values being 3-7.5% by volume of concrete (ACI Committee 201, 2016). However, much research has shown that a proper pore size and pore size distribution, spacing factor, and minimum water saturation level (<86%) must be met for the air void system to be effective (Li, W, *et al*., 2012; T. C. Powers, *et al*. 1954; L. Du, *et al*., 2005; S. Chatterji, *et al*., 2003). AEAs can be highly effective when properly used but notable drawbacks include a reduction in mechanical strength, increased permeability, and retardation of set time (X. Chen *et al*., 2013; H. S. Wong *et al*., 2011). Additionally, it is difficult in the field to obtain a proper size distribution and spacing factor. Recent research has indicated that even when an air void system is properly created, that after a minimum water saturation level is met damage is inevitable (Li, W *et al*., 2012).

1.3 Biomimetic Antifreeze Polymers

Nature produces antifreeze proteins (AFPs) and antifreeze glycoproteins (AFGPs) to allow a variety of cold climate species to survive. Although AFPs display excellent antifreeze properties, they are currently not an economical option due to limitations in production and they are known to lose functionality in the highly basic and ionic environment of concrete (E. Delesky *et al*. 2019). There are a variety of polymeric materials that have shown similar behavior to AFPs and AFGPs, primarily ice recrystallization inhibition (IRI) activity, with PVA being the most widely studied (T. Congdon *et al*. 2013). IRI activity results in the reduction or even prevention of ice crystal grain growth over time (*i.e*., Ostwald ripening). The chemical functionality of PVA mimics the highly hydroxylated carbohydrates of AFGPs. Although PVA is soluble in water, it requires mild heat to go into solution. To this end, a more soluble polymer like polyvinyl alcohol-polyethylene glycol graft copolymer (PEG-PVA) is of interest. Recent work (Frazier *et al*., in review) showed that PEG-PVA displays IRI activity which was expected due to the fact that it is composed of 75% PVA (E. A. Fouad *et al*. 2011).

2 Experimental Methods

2.1 Specimen Preparation

Specimens were prepared using the mix compositions described in Table 1. Specimens were divided into three test groups and labeled according to their PEG-PVA content. One test group, AEA in Table 1, contained a commercially available liquid AEA.

The components of each test group were mixed and poured into cylindrical and prismatic molds. Three 4”x8” cylinders were made for compression testing. Four 3”x3”x16” prisms were made for each test group where three were subjected to freeze-thaw cycles and one kept at ambient conditions for the duration of the freeze-thaw testing. All specimens were stored at room temperature in a vibration-free environment and covered to prevent evaporation of

water. After 48 hours, specimens were removed from the molds and transferred to a saturated $Ca(OH)_2$ solution for the remainder of the curing process. Water was saturated with calcium hydroxide per ASTM C511 (ASTM 2003) to prevent leaching of calcium hydroxide. Cylindrical specimens were cured for twenty-eight days per ASTM C 192 (ASTM 2006) and prismatic specimens for 14 days per ASTM C 666 (ASTM 2008).

Table 1. Mix compositions used for all analysis.

Material (per cubic yard)	Test Group		
	Control	PEG-PVA	AEA
Cement (Type I/II) (lb.)	521	521	521
Fine aggregate (lb.)	1011	1011	1011
Coarse aggregate (lb.)	2040	2040	2040
Water/cement ratio (%)	50	50	50
PEG-PVA/cement ratio (%)	0	0.066	0
Air entraining agent (mL/100 kg cement)	0	0	15

2.2 Fresh State Concrete Properties

Slump and fresh state air content of mixed concrete were measured according to ASTM C143 (ASTM 2011) and C231 (ASTM 2010), respectively. The slump test was performed using a slump test set (Humboldt H-3645). Fresh state air content was determined using a concrete air meter (Humboldt H-2783).

2.3 Hardened State Concrete Properties

The hardened state air content was estimated by measuring the volume of all voids with a diameter greater than 15 μm from micro X-ray computed tomography (MXCT, ZEISS Xradia 520 Versa) scans. The diameter of 15 μm was chosen based on the accepted size range of air voids (P. K. Mehta *et al*., 2006), previous research (Kim, K.Y., *et al*., 2012), and resolution capabilities of MXCT. Cubes with a volume of ~1 in^3 were cut from samples before exposure to freeze-thaw cycles and used for the scans. The MXCT source voltage was set to 140 kV and the power to 10 W. The source and detector locations were varied to obtain a desired resolution of ~ 6 μm. Dragonfly 3.1 software (Object Research Systems) was used to identify voids and calculate their cumulative volume within the scanned volume.

To determine the compressive strength of samples, three cylindrical samples per test group were used in accordance to ASTM C39 (ASTM 2016b). Samples were tested using an ELE International compressive strength testing machine with 10 ksi capacity at a rate of 110 lb./sec.

2.4 Freeze-Thaw Resistance

Rapid freeze-thaw cycling was performed according to ASTM C666 Procedure A (ASTM 2008). Three prismatic specimens per test group were tested for 300 cycles. The freezing portion of the cycle had a duration of three hours and reached a minimum of -18 °C ± 2 °C. The thawing portion of the cycle had a duration of one hours and reached a maximum of 4 °C ± 2 °C. Freeze-thaw resistance was evaluated by measuring the fundamental transverse

frequency and length change of specimens every 36 cycles for up to 300 cycles. Fundamental transverse frequency was determined using forced resonance method in accordance to ASTM C215 (ASTM 2014). The length change was also measured every 36 cycles for the duration of testing.

3 Results and Discussion

3.1 Fresh State Properties

Table 2 provides the fresh state air content (%) and slump (in.) values that were measured at the time of mixing for each test group. Both the slump and fresh state air content increased with the addition of PEG-PVA. It was observed during mixing that the workability improved and concrete was easier to finish with PEG-PVA addition, relative to unmodified concrete. Air bubbles within PEG-PVA modified concrete in the fresh state were visually observed (data not shown) during mixing and finishing processes. It can be concluded that the addition of PEG-PVA entrains some air in the fresh state but less than the AEA dosage used indicating that PEG-PVA has mild surfactant properties. The stability of entrained air in PEG-PVA-modified concrete was investigated in this research and discussed in section 3.2. It is worth noting that the fresh state air content for PEG-PVA modified concrete is less than the 6% recommended for extreme conditions and a nominal maximum aggregate size of 1 in. per ACI Guide to Durable Concrete (ACI Committee 201, 2016).

Table 2. Fresh and hardened state properties of each test group.

Test Group	Slump (in.)	Fresh State Air Content (%)	Hardened State Air Content (%)	Compressive Strength (psi)	Unit Weight (pcf)
Control	0.375	2.1	2.7	5,229	146.13
PEG-PVA	1.625	4.2	2.3	5,086	145.98
AEA	0.625	7.0	4.0	4,902	145.50

3.2 Hardened State Properties

Table 2 presents hardened state properties of samples tested in this research. The air content of PEG-PVA-modified samples decreased from 4.2% in the fresh state to 2.3% in the hardened state which indicated that not all air voids generated by the addition PEG-PVA were stable. The reduction further indicates that the polymer only has a mild surfactant effect. In a similar fashion the samples containing air entraining agent saw a reduction in air content of 7.0% in the fresh state to 4.0% in the hardened state.

Compressive strength was tested for three 4”x8” cylinders per test group after 28 days of curing. The addition of PEG-PVA at an addition 0.066% by weight of cement was found to slightly reduce the average compressive strength by 2.73% compared to unmodified concrete. The addition of AEA at 15mL per 100 kg of cement was found to reduce average compressive strength by 6.25% compared to unmodified concrete. Unit weight at hardened state was found to not be impacted by the addition of PEG-PVA or air entraining agent with reductions of 0.10% and 0.43% compared to the unmodified samples respectively.

3.3 Freeze-Thaw Resistance

3.3.1 Relative dynamic modulus of elasticity

Three specimens per test group went through freeze and thaw cycles (P1, P2, and P3) while one stayed at room temperature (P4) for the duration of testing. Figures 1 shows the relative dynamic modulus of elasticity (P_c) with respect to the increasing number of cycles. Also shown is a constant horizontal line at 60% P_c which signifies failure as specified by ASTM C666. Figure 1a shows that the value of P_c for the unmodified specimens started to significantly decrease after around 75 cycles until failure at 125 cycles indicated by a reduction below 60%. As expected, the P_c for sample P4 maintained 80-90% of the initial measurement indicating that the performance of sample P4 has not changed. Figure 1b and 1c show that the behaviour of PEG-PVA and AEA modified both maintain a Pc above 80% for samples exposed to freeze-thaw cycling (P1-P3) and above 90% for the sample exposed to ambient conditions (P4). These results indicate excellent freeze-thaw resistance for both PEG-PVA and AEA. The fluctuations observed between each data point is likely due to variation in moisture content of each sample.

3.3.2 Durability factor

Figure 2a shows the average durability factor for each test group. Durability factor is a measure that indicates the performance of concrete exposed to freeze-thaw conditions. It is a function of the relative dynamic modulus of elasticity and the number of cycles at which freeze-thaw cycles are terminated as specified in ASTM C666. The average durability factors were 19.1%, 88.6%, and 86.2% for unmodified concrete, 0.066% PEG-PVA, and AEA test groups respectively. The durability factor of unmodified concrete indicates poor performance, which was visually apparent by the loss of paste and aggregate and general loss of structural

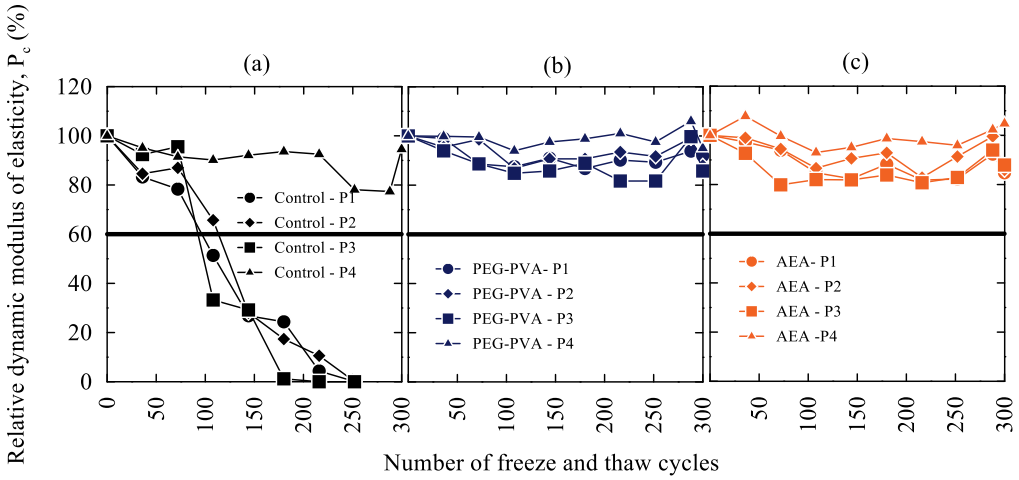

Figure 1. The relative dynamic modulus of elasticity (P_c) for each test group studied up to 300 freeze-thaw cycles. For each test group, samples P1-P3 were exposed to cyclic freeze-thaw temperature while P4 was kept at ambient temperature for the duration of testing. (**a**) 0% PEG-PVA/cement ratio addition (Control). (**b**) 0.066% PEG-PVA/cement ratio addition (PEG-PVA). **(c)** Air entraining agent addition (AEA). The line at P_c equal to 60% represents failure.

integrity of specimens with each subsequent set of cycles. On the other hand, durability factor values for 0.066% PEG-PVA and AEA modified concrete indicate excellent performance, which was also visually observed.

3.3.3 Length change

Measurement of length change during freeze-thaw cycling is described in ASTM C666 as an optional measurement to indicate performance. A length change of 0.1% maybe used as a trigger to stop freeze-thaw cycles and terminate testing. The greater the length change in concrete the more degradation it has experienced and the lower the performance. Figure 2b shows the change in length with increasing number of cycles. The figure indicates that unmodified samples experienced large expansion at the time of failure. 0.066% PEG-PVA and AEA modified samples experienced significantly less length change, less than 0.1%. According to ASTM C666 the unmodified concrete samples have failed while modified samples have passed.

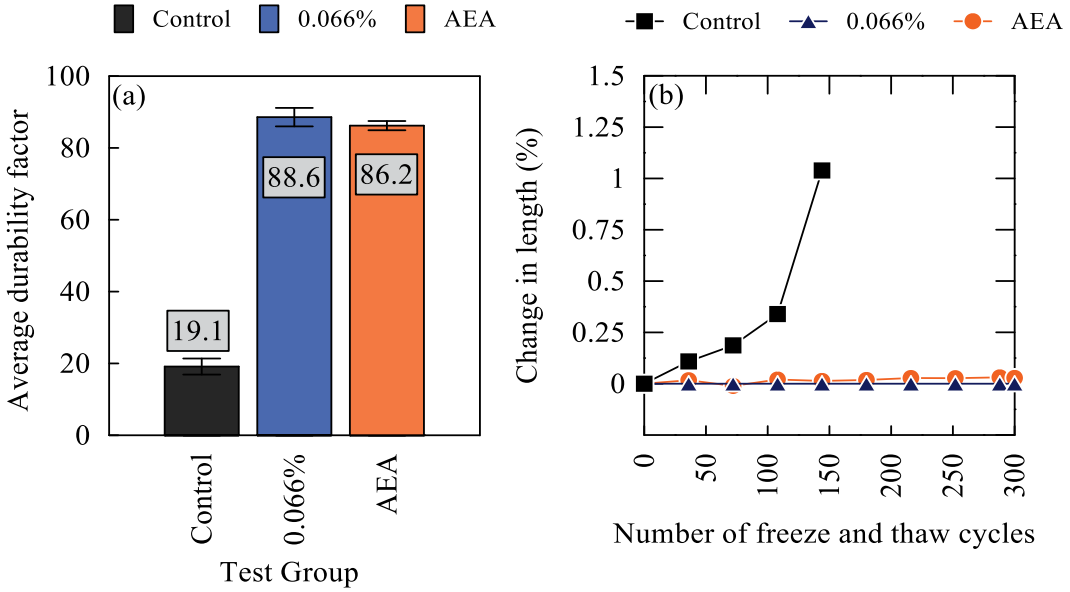

Figure 2. (**a**) Average durability factor for each test group. Error bars indicate standard deviation for n=3. (**b**) Average length change for each test group up to 300 freeze-thaw cycles. Average for n=3 samples per test group.

4 Conclusions

PEG-PVA was found to be as effective as a commercially available AEA at mitigating freeze-thaw damage while entraining minimal air. The addition of PEG-PVA was found to increase fresh state air content and slump compared to unmodified concrete. Although the fresh state air content increased with the addition of PEG-PVA, micro X-ray computed tomography has shown that hardened state air content was less than that of unmodified concrete, 2.3% for PEG-PVA addition. We can conclude that air entrained in the fresh state due to PEG-PVA addition is not stable and the air voids collapse during concrete consolidation and hardening. PEG-PVA-modified and AEA samples were proven to improve freeze and thaw resistance as

indicated by relative dynamic modulus (greater than 80%), durability factor (greater than 85%), and length change (less than 0.1%). Addition of PEG-PVA at a concentration of 0.066% was found to have no influence on compressive strength compared to AEA which experienced a 6.25% reduction.

ORCID

Wil Srubar: http://**orcid**.org/0000-0001-8226-2458

References

ACI Committee 201, Guide to Durable Concrete (American Concrete Institute, 2016)

ASTM. (2003). "Standard Specification for Mixing Rooms, Moist Cabinets, Moist Rooms, and Water Storage Tanks Used in the Testing of Hydraulic Cements and Concretes." Standard C511, *ASTM International,* West Conshohocken, PA.

ASTM. (2006). "Standard practice for making and curing concrete test specimens in the laboratory." Standard C192, *ASTM International,* West Conshohocken, PA.

ASTM. (2008). "Test method for resistance of concrete to rapid freezing and thawing." Standard C666, *ASTM International*, West Conshohocken, PA

ASTM. (2010). "Standard Test Method for Air Content of Freshly Mixed Concrete by the Pressure Method." Standard C231, *ASTM International,* West Conshohocken, PA.

ASTM. (2011). "Slump of Hydraulic Cement Concrete." Standard C143, *ASTM International,* West Conshohocken, PA.

ASTM. (2014). "Standard test method for fundamental transverse longitudinal, and torsional resonant frequencies of concrete specimens." Standard C215, *ASTM International,* West Conshohocken, PA.

ASTM. (2016). "Standard test method for compressive strength of cylindrical concrete specimens." Standard ASTM C39, *ASTM International,* West Conshohocken, PA.

Behfarnia, K. and Salemi, N. (2013). The effects of nano-silica and nano-alumina on frost resistance of normal concrete. *Constr. Build. Mater.*, *48*, 580-584. doi.org/10.1016/j.conbuildmat.2013.07.088

Chatterji, S. (2003). Freezing of air-entrained cement-based materials and specific actions of air-entraining agents. *Cem. Concr. Compos.* 25, 759-765.

Chen, X., Wu, S. and Zhou, J. (2013). Influence of porosity on compressive and tensile strength of cement mortar. *Constr. Build. Mater.* 40, 869-874.

Congdon, T. Notman, R. and Gibson, M.I. (2013). Antifreeze (Glyco)protein Mimetic Behavior of Poly(vinyl alcohol): Detailed Structure Ice Recrystallization Inhibition Activity Study. *Biomacromolecules* 14, 1578-1586.

Delesky, E.A., Frazier, S.D., Wallat, J.D., Bannister, K.L., Heveran, C.M. and Srubar III, W.V. (2019). Ice-Binding Protein from Shewanella frigidimarinas Inhibits Ice Crystal Growth in Highly Alkaline Solutions. *Polymers* 11, 299.

Du, L. and Folliard, K.J. (2015) Mechanisms of air entrainment in concrete. *Cem. Concr. Res*. 35, 1463-1471.

Duan, P., Shui, Z., Chen, W. and Shen, C. (2013). Enhancing microstructure and durability of concrete from ground granulated blast furnace slag and metakaolin as cement replacement materials. *J. Mater. Res. Technol.*, *2*(1), 52-59.

Fouad, E.A., El-Badry, M., Neau, S.H., Alanazi, F.K. and Alsarra, I.A. (2011). Technology evaluation: Kollicoat IR. Expert Opin. *Drug Deliv.* 8, 693-703.

Frazier, S. D., Matar, M. G., Osio-Norgaard, J., Aday, A. N., Delesky, E. A. and Srubar III, W. V. (2020). Inhibiting Freeze-Thaw Damage in Cement Paste and Concrete by Mimicking Nature's Antifreeze. *Cell Reports Physical Science*, 100060.

Gonzalez, M., Tighe, S. L., Hui, K., Rahman, S. and Lima, A. O. (2016). Evaluation of freeze/thaw and scaling response of nanoconcrete for Portland Cement Concrete (PCC) pavements. *Constr. Build. Mater.*, *120*(1), 465-472.

Laustsen, S.; Hasholt, M. T. and Jensen, O. M. (2015). Void Structure of Concrete with Superabsorbent Polymers and Its Relation to Frost Resistance of Concrete. *Mater. Struct.*, *48*(1–2), 357–368.

Li, W., Pour-Ghaz, M., Castro, J. and Weiss, J. (2012). Water Absorption and Critical Degree of Saturation Relating to Freeze-Thaw Damage in Concrete Pavement Joints. *J. Mater. Civil Eng.,* 24(3), 299–307.

Mehta, P.K. and Monteiro, P.J.M. Concrete: Microstructure, Properties, and Materials (McGraw-Hill, 2006).

Powers, T.C. (1954). Void Spacing as a Basis for Producing Air-Entrained Concrete. *J. Am. Concr. Inst.* 25, 741-760.

Powers, T. C. (1975). Freezing Effects in Concrete. In: *Durability of concrete*, American Concrete Institute, Special Publication 47, 1-12.

Sabir, B. B. (1997). Mechanical properties and frost resistance of silica fume concrete. *Cem. Concr. Compos.*, *19*(4), 285-294.

Scherer, G. W. and Valenza, J. J. (2005). Mechanism of frost damage. *Mater. Sci. of Concr. (VII)*, *7*, 209-246.

Wong, H.S., A. M. Pappas, A.M., Zimmerman, R.W., and Buenfeld, N.R. (2011). Effect of entrained air voids on the microstructure and mass transport properties of concrete. *Cem. Concr. Res*. 41, 1067-1077.

XV International Conference on Durability of Building Materials and Components
DBMC 2020, Barcelona
C. Serrat, J.R. Casas and V. Gibert (Eds)

Compressive Strength Improvement and Water Permeability of Self-Healing Concrete Using *Bacillus Subtilis* Natto

Nguyen Ngoc Tri Huynh[1], Kei-ichi Imamoto[2], and Chizuru Kiyohara[3]

[1] Department of Architecture, Tokyo University of Science (TUS), Japan, nnthuynh@hcmut.edu.vn
Department of Silicate Materials, Viet Nam National University Ho Chi Minh City (VNUHCM), Ho Chi Minh City University of Technology (HCMUT), Vietnam

[2] Department of Architecture, Tokyo University of Science (TUS), Japan, imamoto@rs.kagu.tus.ac.jp

[3] Department of Architecture, Tokyo University of Science (TUS), Japan, ckiyo@rs.tus.ac.jp

Abstract. *In recent years, many projects have been carried out to enhance the durability of concrete structure from the influence of cracks. Generally, managing cracks should be a rather preventative method for sustainable development. Based on that, Bacillus subtilis natto - a local bacterium in Japan was found to have the ability to form $CaCO_3$, which can be used as healing materials for cracks in the concrete structure. The bacterial biomineralization immobilized in lightweight aggregate was studied to improve the compressive strength by healing the cracks and densifying the structure. Moreover, as an essential parameter for durability enhancement, the water permeability of self-healing concrete through a water-flow system was carried out. Experimental results on the behavior of the materials indicate that Bacillus subtilis natto could lead the compressive strength to 40 % higher than the controls. Promising result in preventing the water through the cracks confirmed the self-healing effect with more potential in larger-scale.*

Keywords: *Self-Healing Concrete, Calcium Carbonate, Crack, Bacteria, Bacillus Subtilis Natto.*

1 Introduction

Although concrete is probably the most commonly used construction material, cracking in concrete structure has been experienced by both the research community and the industrial engineers. Cracking can lead to many problems, such as water leakage and reinforcement corrosion. For many years, although various repairing methods have been developed with deliberate external intervention, it is difficult in the case of the micro-cracks or cracks embedded deep in concrete structures. Therefore, an automated method to repair cracks is necessary for sustainable concrete infrastructure. Hence, bacteria-based self-healing concrete can be a promising solution to extend the service life and durability of concrete structures. According to previous studies, limited strains of bacteria can be used for self-healing concrete, such as *Bacillus cohnii* (Jonkers, 2007), *Bacillus pasteurii* (Ramachandran et al., 2001), *Bacillus pseudofirmus* (Jonkers and Schlangen, 2008), *Bacillus subtilis* (Matsushita et al., 2010; Huynh et al., 2017).

In this study, *Bacillus subtilis* natto - Japanese microorganism was selected and applied with a suitable proportion of nutrients to form $CaCO_3$ and prevent adverse effects on concrete durability. Based on the urea hydrolysis, bacteria become negatively charged, leading to the rapid attraction of surrounding calcium ions for the biomineralization. Also, bacteria can degrade organic compounds included lactose, as a carbon source for growth and activation.

doi:10.23967/dbmc.2020.024

These processes controlled the adverse effects of nutrients on the properties of fresh and hardened concrete. Moreover, the cement matrix and concrete structure can be enhanced by the densifying process with the generation of $CaCO_3$ and bacterial bioproducts, associated with the high mechanical resistance and high ability of water permeability. Besides, *Bacillus subtilis* natto does not cause disease (Brenner and Miller, 2014), and almost safe to work within the laboratory. Moreover, *Bacillus subtilis* natto would be an economical solution because of the low cost of bacteria spores, compared to the other microorganisms. We aimed to evaluate the strength improvement as well as the self-healing ability of concrete specimens with the bacteria immobilized in lightweight aggregate as a mixture component. This technique was expected to improve the self-healing capacity and extend the life span of bacteria. In addition, the water permeability of self-healing concrete was also investigated by a water-flow testing system.

2 Materials and Experiments

2.1 Compressive Strength Improvement Using Bacterial Lightweight Aggregate

Table 1. Mixture proportion and materials properties for 1 m^3 of concrete.

Group	W/C	Water (kg)	Cement (kg)	Sand (kg)	LWA (kg)	Bacteria (kg)	Flow Upper:no falling motion (mm)	Air content (%)	T (°C)
Natto	0.4	147	370	953	618	0.163	100.8x97.9 119.2x110.8	11	22.3
Controls	0.4	147	370	953	618	-	104.5x102.9 153.4x144.0	3.9	19.3
Particle size distribution of lightweight aggregate									
Particle Size (mm)			20		15		10		5
Percent passing (%)			100		99		47		8

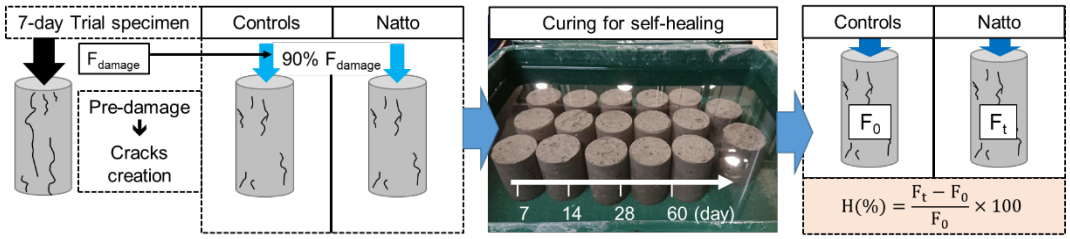

Figure 1. Flow chart for the preparation of lightweight aggregate immobilized bacteria and the continuous strength recovery test.

Table 1 shows the mixture proportion for concrete specimens (Φ = 50 mm, H = 100 mm). The lightweight aggregate (ρ = 1.68 g/cm^3, water absorption = 29.5 %,) immoblized bacteria was prepared as following steps: (i) mixed and stirred the bacterial solution (m_{urea} = 0.45 %m_{cement}, $m_{bacteria} \leq$ 0.5 %m_{cement}, m_{CaCl2} = 0.45%mc_{ement}); (ii) immersed the LWA in solution

for 24 hours; (iii) dried the LWA at 40 ºC for 24 hours. Based on the bacterial concentration in the mixture for 1 m^3 of concrete ($1.1x10^{12}$ CFU/m^3), the bacterial concentration for each specimen was calculated and estimated to $3x10^7$ CFU. Also, the dosage of urea and $CaCl_2$ was controlled with a safety limit according to ACI 318 for maximum chloride ion content in concrete to prevent the corrosion of reinforcement. For the group "Controls", the lightweight aggregate without bacteria was used as the reference. Figure 1 describes the flow chart of the continuous compressive strength improvement test. The load was defined based on the 7-day compressive strength of the "trial-specimen" with the mixture as the controlled. We used the value of 90 % of this value (F_{Damage} = 11 N/mm^2, loading rate = 1.17 kN/s) to create the crack for all of the specimens. The self-healing effect was expected to occur over curing time. The compressive strength was measured after each curing period of 7 days, 14 days, 28 days, and 60 days to compare with the controls for healing capacity calculation. The recovery of the compressive strength of concrete specimens can translate into the self-healing efficiency, and then gives information about the relation between self-healing capacity and curing time.

2.2 Water Permeability of Concrete Using Bacterial Lightweight Aggregate

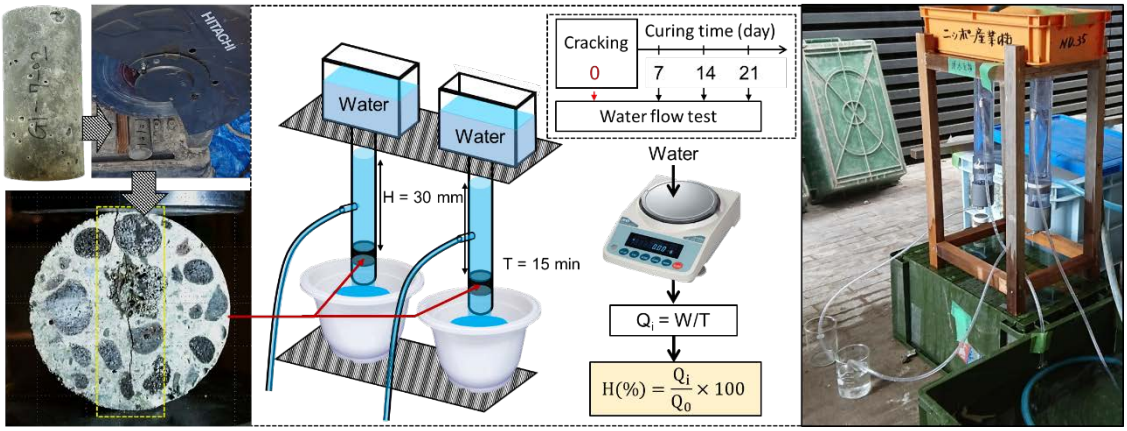

Figure 2. Flow chart for the water-flow test.

In both the cases of using capsule/microcapsule or vascular-based systems, capillary flow through discrete cracks is the primary mechanism (Gardner et al., 2017) for healing agents transporting in cement/mortar to damaged position and create the self-healing effect. Besides, the interaction between the healing fluid, in this case, is $CaCO_3$, and the matrix is rough and more complex than the fluid mechanical theoretical behavior. Therefore, as the description in Figure 2, the test system for evaluating the self-healing effect on water permeability was investigated. The 14-day concrete specimens (mixture as Table 1) were cut into slices (Φ = 50 mm, T = 30 mm) and then cracked under the splitting test. The crack width was measured by using an optical microscope. In the testing system, a continuous water flow with the water head of 30 mm was applied in 15 minutes. The water flow was measured after 7, 14, and 21 days of curing. The Hagen-Poiseuille's law was also used to compare and analyze the change of water flow and crack width under the healing effect. Based on the Hagen-Poiseuille's law, we calculated the water flow after 7 days and 28 days with the crack width by microscope observation. Then, we made the ratio of these values to the initial water flow (Q_T). With the

same method, we made the ratio of measurement value (Q_M). A comparison between the theoretical value and measured value in the experiment was expected to show the structural changes within the cracks, including crack width and crack depth. Also, one group of 1 mm-crack concrete slice was prepared to clarify the mechanism of the effect of biomineralization on the crack healing and reinforcing ability. These specimens were injected by commercial $CaCO_3$ paste ($CaCO_3$ powder and water) and then measured the water flow. The difference between the bonding of concrete substrates and minerals provided from outside and forming in the cracks can demonstrate the bacterial self-healing ability.

3 Results and Discussion

3.1 Compressive Strength Improvement Using Bacterial Lightweight Aggregate

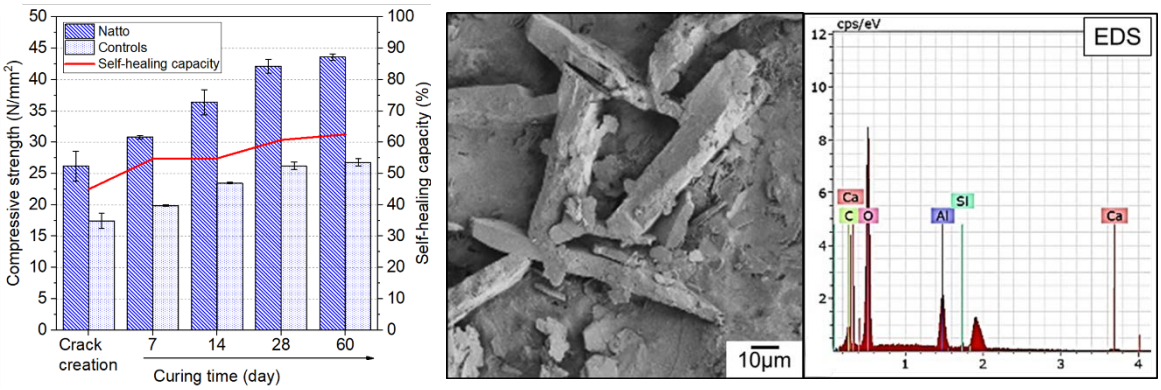

Figure 3. Compressive strength of concrete specimens in the continuous strength recovery test (a), and SEM/EDS result of precipitated $CaCO_3$ inside the crack (b).

Figure 3(a) shows that the longer the curing time, the higher the compressive strength. Also, the compressive strength of the group "Natto" was significantly higher than the "Controls" at every period. This difference could be caused by the self-healing effect with the capacity of over 40 % just after 7 days curing before the cracking day. This result is higher than the previous study in 2017 (20 %) when using *Bacillus subtilis* JC3 (Rao et al., 2017) directly with a concentration of 10^5 CFU/ml as mixing water; and the study in 2015 (Sarkar et al., 2015) using *Bacillus subtilis* with tryptone (16.6 %). Therefore, the immobilization of bacteria and nutrients in lightweight aggregate could not only prevent the disruption of concrete with the presence of organic matter but also fill the cracks and densify the pore structure. Besides, with this technique, the higher initial concentration of bacteria can be used for a longer duration and higher healing capacity. Moreover, from the 14-day curing period, the gap of compressive strength between the group "Natto" and "Controls" became higher. This result was relevant in the self-healing process with the increasing of $CaCO_3$ over time.

As expected, Figure 3(b) shows a massive amount of $CaCO_3$ formed inside the cracks by the biomineralization of *Bacillus subtilis* natto after 28 days. According to SEM observation, the shape of $CaCO_3$ crystals was similar to the finding of the study using *Sporosarcina pasteurrii* bacteria (Ameri et al., 2019). These rod-shaped crystals could be a reinforced component in

cracks, similar to the strength improvement mechanism of cementitious composite through whisker $CaCO_3$ (Cao et al., 2019). Also, the forming of $CaCO_3$ in the pores of concrete structure could densify the matrix contributes to the high compressive strength.

3.2 Water Permeability of Concrete Using Bacterial Lightweight Aggregate

Figure 4 shows the decrease of water flow with a decrease of crack width after three measurements. Under microscopic observation, the crack width range became smaller and smaller since the first test (Figure 4(a)). In contrast, the controlled specimens show a nearly constant result of water flow (Figure 4(b)) and a slightly reduced crack width. Note that the 0.10 mm or smaller cracks in the controlled specimens can be regarded as smooth and can be closed by the natural self-healing process by late hydration and the reaction of $Ca(OH)_2$ with CO_2. These results can be observed in both cases of test specimens with high correspond between Q_T and Q_M. For the large-sized cracks, it can be seen the increase of crack closing by the decrease of water flow over curing time by the biomineralization (Figure 5(a)). In contrast, the controls show the higher value of Q_M than Q_T after 28 days as a result of the opening inside the cracks with damage by water flow (Figure 5(b)). Also, the significant reduction of measured water flow in the case of bacterial specimens (Figure 5(c)) indicated that the cracks were healed from the internal subsurface. This result was confirmed by the optical microscopic analysis of the crack depth (Figure 5(d)).

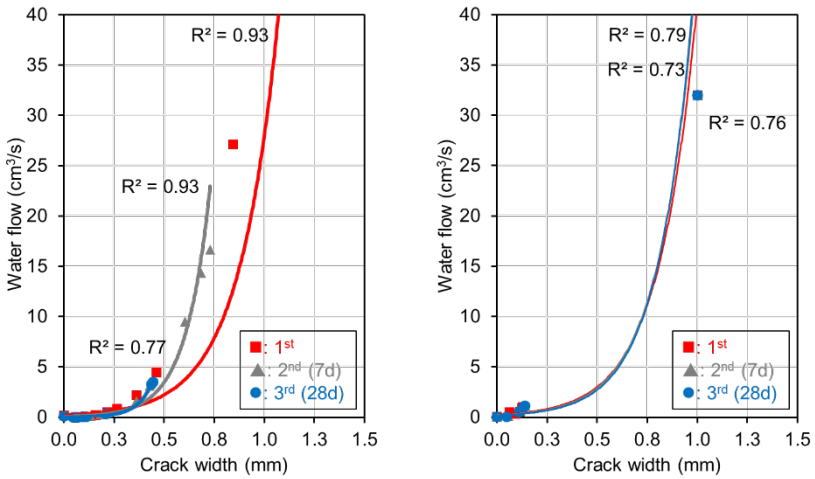

(a) (b)

Figure 4. Water flow-crack width relationship after curing time of bacterial specimens (a), and the controls (b).

It can be seen that although water could pass through the specimen, the microscopic images (Figure 6(a)) show that surface crack over 1.5 mm could be healed almost 100 % after 21 days of curing. Note that in the case of controlled specimens, cracks could only be healed within the maximum width of 0.1 mm by the late hydration effect. This result demonstrates that not only the internal subsurface but also the surface cracks could be healed with a high capacity over curing time.

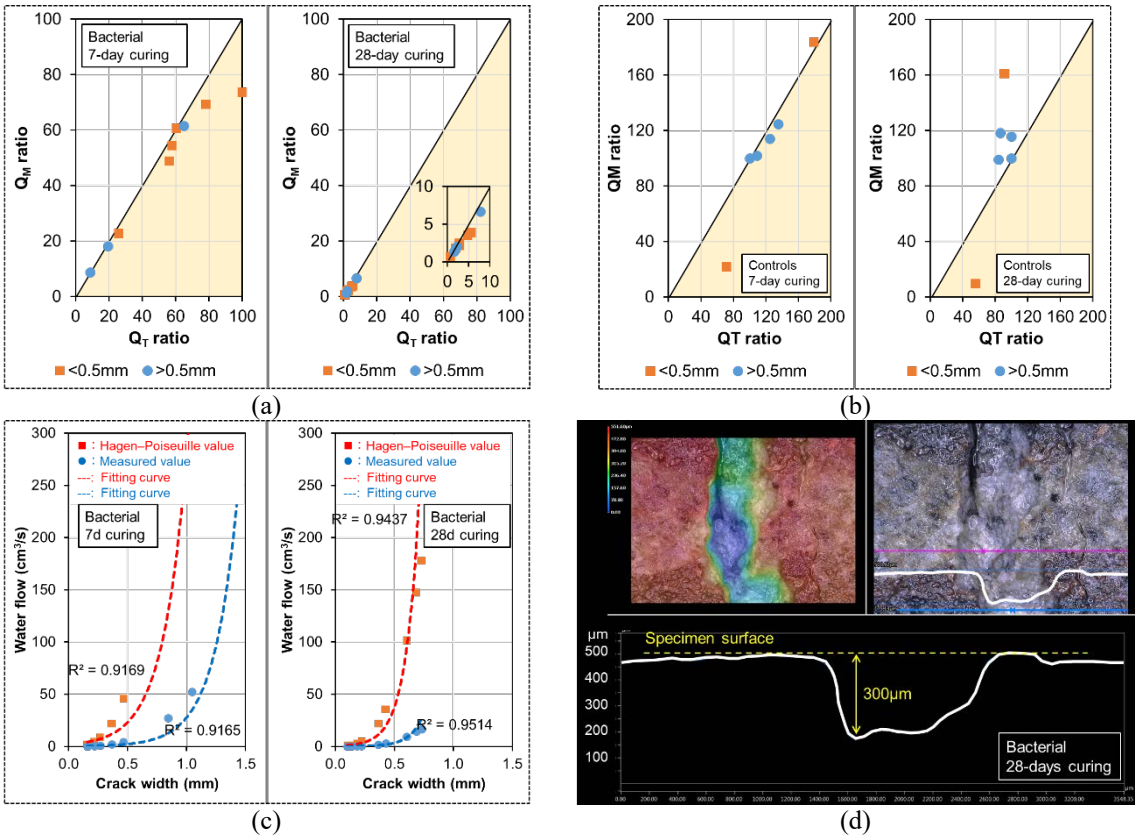

Figure 5. The relationship between the water flow by Hagen Hagen–Poiseuille's law (Q_T) and the measured water flow (Q_M) in the case of bacterial specimens (a), and the controls (b). The change of water flow-crack width over time (c) and the depth of healing crack by optical microscopic analysis (d).

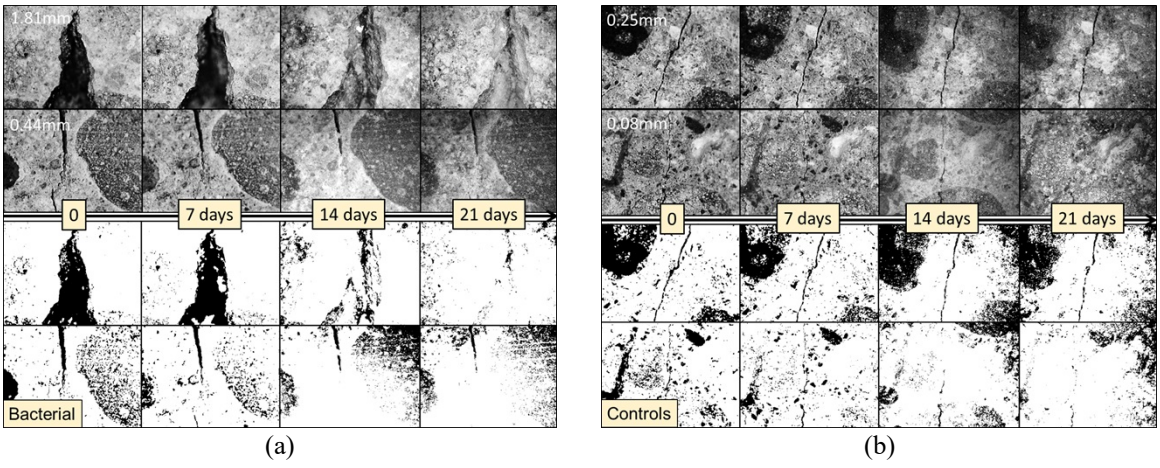

Figure 6. Crack width reduction over curing time in the case of bacterial specimens (a), and the controls (b).

Focus on the 1 mm-crack case; it can be seen the mechanism of $CaCO_3$ forming inside the crack by the activation of bacteria. The result of injected-$CaCO_3$ into the crack shows the significant low effectiveness on prevention water from passing to the upper face of the concrete

slice. This consequence is closely related to the bond between the concrete substrate and the $CaCO_3$ inserted into the crack. Harden concrete after setting period apparently cannot connect paste of $CaCO_3$ by chemical reaction. In this case, only physical force as friction played the role of glue the two surfaces. This temporary cohesiveness decease with the removing of water in the paste. Hence, after natural drying, concrete substrate and injected-$CaCO_3$ separated almost, and immediately be washed away from the crack. Note that a small part of $CaCO_3$ could be adhesive, particularly on the rough surface of the concrete crack. Although this phenomenon occurred nearly in the volume of 40 % of the total crack volume, a considerable amount of water was interrupted from continuously flowing (Figure 7(b)). This result indicates that large amounts of $CaCO_3$, especially rod-like crystals, as well as strong bonding to the concrete surface, can be an effective healing agent for waterproofing targets. Overall, therefore, the reducing of water flow over curing time in the case of using bacteria could be demonstrated clearly. The continuous water flows with 20 mm in height helped to remove the dust, sand, or broken piece of the concrete specimen from the crack position. Also, water pressure was enough to break down any weak bonding between concrete broken surfaces, and organic or inorganic matter potentially appeared. Rod-like $CaCO_3$ crystals precipitated layer by layer under the biomineralization of *Bacillus subtilis* natto may not only fill out the crack but also reinforce the damaged structure.

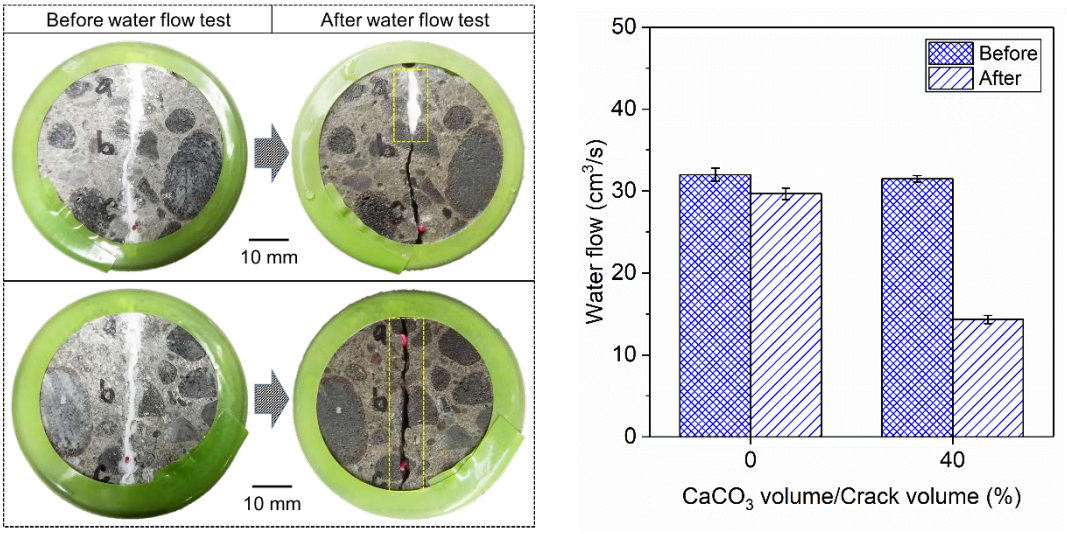

(a) (b)

Figure 7. The camera photos of injected-$CaCO_3$ specimens surface before and after the water flow test (a). The relation between the water flow of injected-$CaCO_3$ specimen and the estimating volume ratio (b).

4 Conclusion

Experimental results in this study indicate the following concluding remarks:

- Compressive strength after cracking could be improved in the case of using lightweight aggregate immobilized bacteria in the mixture. The healing capacity increased over curing time with the increasing of compressive strength.
- The massive amount of self-healing products could be observed by using SEM/EDS, and optical microscopic images played an essential role in closing the cracks and

densifying the concrete structure.
- The water permeability of specimens using lightweight aggregate immobilized bacteria was significant lower than the controls. Healing capacity increased with the decrease of water flow through cracks over curing time.
- Surface cracks around 1.5 mm could be healed after 21 days, while the internal cracks were closed little by little over curing time.

Acknowledgements (optional)

The authors would like to appreciate the Japanese Government through the MEXT Scholarship and Building Material Science IMAMOTO LAB, Biology Science SHIMIZU LAB – Tokyo University of Science for financial supporting, materials and technical equipment.

ORCID

Ngoc Tri Huynh Nguyen: https://orcid.org/0000-0003-2085-3564

References

Ameri, F., Shoaei, P., Bahrami, N., Vaezi, M. and Ozbakkaloglu, T. (2019). Optimum rice husk ash content and bacterial concentration in self-compacting concrete. *Construction and Building Materials*, *222*, 796–813.

Brenner, S. and Miller, J. H. (2014). *Brenner's encyclopedia of genetics*. Elsevier Science.

Cao, M., Li, L., Yin, H. and Ming, X. (2019). Microstructure and Strength of Calcium Carbonate (CaCO3) Whisker Reinforced Cement Paste After Exposed to High Temperatures. *Fire Technology*, 1–21.

Gardner, D., Herbert, D., Jayaprakash, M., Jefferson, A. and Paul, A. (2017). Capillary flow characteristics of an autogenic and autonomic healing agent for self-healing concrete. *Journal of Materials in Civil Engineering*, *29*(11), 04017228.

Huynh, N. N. T., Phuong, N. M., Toan, N. P. A. and Son, N. K. (2017). Bacillus subtilis HU58 Immobilized in micropores of diatomite for using in self-healing concrete. *Procedia Engineering*, *171*, 598–605.

Jonkers, H. M. (2007). Self healing concrete: A biological approach. In *Self healing materials* (pp. 195–204). Springer.

Jonkers, H. M. and Schlangen, E. (2008). Development of a bacteria-based self healing concrete. *Proc. Int. FIB Symposium*, *1*, 425–430.

Matsushita, Y., Shinichiro, O., Yasuhara, H. and Ujike, I. (2010). *Development of crack repairing method of concrete using microbial metabolism*. *Vol.32*(No.1).

Ramachandran, S. K., Ramakrishnan, V. and Bang, S. S. (2001). Remediation of concrete using micro-organisms. *ACI Materials Journal-American Concrete Institute*, *98*(1), 3–9.

Rao, M. S., Reddy, V. S. and Sasikala, C. (2017). Performance of Microbial Concrete Developed Using Bacillus Subtilus JC3. *Journal of The Institution of Engineers (India): Series A*, *98*(4), 501–510.

Sarkar, M., Adak, D., Tamang, A., Chattopadhyay, B. and Mandal, S. (2015). Genetically-enriched microbe-facilitated self-healing concrete–a sustainable material for a new generation of construction technology. *RSC Advances*, *5*(127), 105363–105371.

XVInternational Conference on Durability of Building Materials and Components
DBMC 2020, Barcelona
C. Serrat, J.R. Casas and V. Gibert (Eds)

Implication of Microbial Biofilm in the Biodeterioration of Cementitious Materials in the specific context of Anaerobic Digestion Conditions

Cédric Perez[1], Christine Lors[2], and Benjamin Erable[1]

[1] Laboratoire de Génie Chimique (LGC), CNRS, Université de Toulouse, 31432 Toulouse, France, cedric.perez@ensiacet.fr

[2] Laboratoire de Génie Civil et Géoenvironnement (LGCgE), IMT Lille Douai, Université de Lille, EA 4515, CERI Matériaux & Procédés, 59500 Douai, France

Abstract. *Anaerobic digestion is a renewable energy production process based on the fermentation of biodegradable biomass. The industrial digesters are usually made of cementitious materials. However, the microbial production of several aggressive compounds (CO_2, NH_4^+ and volatile fatty acids) during the digestion leads to the deterioration of the concrete structure. The growth of microbial biofilm on the surface of concrete is suspected to generate an even more severe biodeterioration. The goal of this study is to provide a better understanding of the biofilm involvement in the biodeterioration of cementitious materials during an anaerobic digestion process. More precisely, this study is focused on the biofilm heterogeneity and its development on cementitious materials in anaerobic digestion. Lab scale anaerobic bioreactors mimicking industrial anaerobic digestion medium were carried out to immerge CEM I cement pastes in this medium during 2, 3, 4 and 5 weeks. The deterioration of cement pastes was evaluated by using a scanning electron microscope to determine the deteriorated thickness and to quantify the volatile fatty acids in the medium. Biofilm attached on the surface of cement pastes was analyzed through molecular biology techniques, such as 16s rRNA gene sequencing analysis and qPCR.To assess the biofilm heterogeneity, successive stalls of the layers of the biofilm were realized using physical biofilm removal techniques. Three microbial fractions are defined: the planktonic microorganisms, the lousy attached and the strongly attached ones. Results showed that the methanogenic Archaea are found mainly in the medium while around half of the microbial population strongly attached is made of acidogenic bacteria. These results suggest that the biofilm could increase the biodétérioration of concrete since the fatty acids are massively produced at the proximity of the surface of the cementitious samples.*

Keywords: *Biodeterioration, Cementitious Material, Biofouling, Biofilm, Bacteria, Anaerobic Digestion.*

1 Introduction

Anaerobic digestion is a renewable energy production process based on the fermentation of biomass. It consists in the succession of four microbial reactions: hydrolysis, acidogenesis, acetogenesis and methanogenesis, leading to the transformation of the biomass into two valuable interest products: the biogas and the digestate. The biogas is mainly constituted of CH_4 and CO_2 at a concentration of about 40-75% of CH_4. The digestate can be used as a fertilizer for agronomic purposes (Bharathiraja *et al.*, 2018).

In the current period of energy transition towards non fossil renewable energies, the anaerobic digestion process shows a growing interest (Salvador *et al.*, 2019), especially on aspects of improving production performance and enriching CH_4 level. In this respect, the focus is on tracks that could increase its durability and thus its performance. One of those tracks could be the durability of the anaerobic digestion tanks (digesters) since it is linked to their lifetime and costs of maintenance. Industrials anaerobic digestion tanks are usually made out of concrete as it is a low cost material, easy to use and adapted to several m^3 tanks. However, anaerobic digestion media is known for being aggressive towards the cementitious materials. The microbial metabolism produces aggressive compounds (CO_2, NH_4, volatile fatty acids), which deteriorate the cementitious matrix. In addition, the formation of microbial biofilms on the concrete surface is highly suspected to increase the kinetics of this deterioration (Voegel *et al.*, 2015, 2016). Microbial biofilms can be described as an aggregation of microorganisms on solid surfaces embedded in a self-produced extracellular matrix; called EPS (extracellular polymeric substances). This microbial organization in biofilms allows the formation of micro-environments locally within the biofilm, as a result of the heterogenic repartition of the different microbial communities, their metabolisms and the diffusion properties of biofilm. Even though the deterioration mechanisms behind the biofilm fouling effects on concrete are not yet clearly identified, there is a strong hypothesis that it is linked to the existence of hyper-aggressive conditions locally on the concrete surface, i.e. at the scale of micro-environments located at the interface between the microbial biofilm and the external surface of the concrete (Bertron, 2014; Magniont *et al.*, 2011).

The present work aims at giving more insights in the biofilm implication in the biodeterioration process of concrete in the specific context of anaerobic digestion tanks. More precisely, this study is focused on the visualization and kinetics monitoring of the development of anaerobic digestion biofilms on cementitious materials, and the exploration of bacterial population heterogeneity in the different biofilm layers.

2 Material and Methods

2.1 Cement Paste Pellets Fabrication

Ordinary CEM I cement pastes were made with a water/cement mass ratio of 0.30. Cylindrical moulds of 2.8 cm of diameter and 6.5 cm height were used. A plastic straw was inserted inside the cement paste at the cylinder central axis, in order to leave an empty space necessary to suspend the paste in the medium during the biodeterioration assays. The cement pastes were then cured for 28 days at 20°C inside their closed moulds. After curing, cement paste pellets with a thickness of about 2.5 mm were obtained by cutting under water the cylindrical cement paste with a circular saw (Prezi, Mecatom 180). The pellets were then polished with a silicon carbide polishing wheel (ESCIL, P800-22 µm).

2.2 Microbial Inoculum and Anaerobic Digestion Culture Medium

Both microbial inoculum and culture medium were chosen to mimic industrial anaerobic digestion, according to the protocol and methods already described by (Voegel *et al.*, 2016). The medium was a synthetic biowaste made up of different organic fractions which have been blended for 5 min at 20°C (Table 1). The inoculum used was an activated sludge sampled from a municipal wastewater treatment plant in Toulouse (France). The volumic ratio microbial inoculum/medium was 2.5/1.

Table 1. Composition of the synthetic biowaste.

Organic fractions	Mass (%)
Water	75.6
potatoes	8.1
tomatoes	3.4
Minced meat	8.1
Milk powder	0.7
Crackers	4.1

2.3 Anaerobic Biodeterioration Assays

The protocol of the cement paste immersion in the culture medium is made to mimic the operating conditions of anaerobic digestion (Voegel *et al.*, 2016). The immersion of the cements pastes pellets were tested in two types of reactors: type A and type B reactors containing respectively eight pellets and one single pellet of cement paste (Figure 1). Type A and type B reactors contained 525 and 66 mL respectively. Therefore, the ratio of the surface of solid cement paste and the volume of the liquid phase was 220 $cm^2.L^{-1}$ in the two types of reactor. These reactors were carried out in the same conditions, at 37°C during 5 weeks for the type A

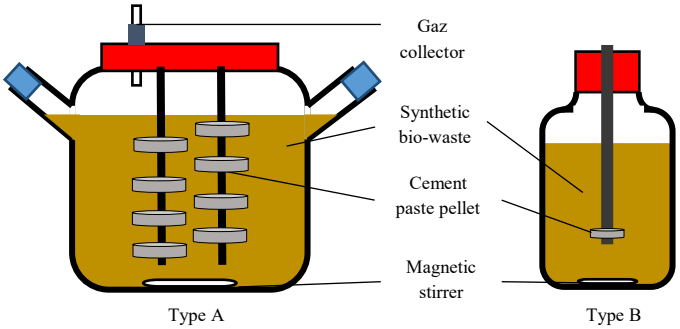

Figure 1. Experimental designs of the anaerobic digestion cultures.

reactor and 2, 3, 4 and 5 weeks for the type B reactor (triplicates for each duration tested). The gas phase (biogas) was collected continuously in the type A reactor and every day in the type B reactor with a collection bag connected to a needle.

2.4 Chemical Analysis

Samples of the medium were taken at the end of each culture and then filtered at 0.2 µm. Ammonium ions concentration was measured using Hach kit LCK 304, following manufacturer instructions. Dissolved organic carbon was determined with a TOC analyzer (TOC-SHIMADZU Combustion). Acetic, butyric and propionic acids concentrations were measured through high performance liquid chromatography (Thermo Scientific, Accela system, column Rezex ROA H^+ 8%, eluent H_2SO_4 10 mM, flow rate 170 $\mu L.min^{-1}$).

2.5 Microbial Populations Analysis

Concerning the biofilm sampling on the surface of cement paste pellets, two types of biofilm layers were defined: the “lousy attached” biomass and the “strongly attached” biomass. The “lousy attached” biomass was removed from a biocolonized cement paste pellet through an immersion of the pellet in 3 mL of phosphate buffered saline (PBS, 0.1M, pH 7.4) for 15 minutes. The “strongly attached” biomass was removed from a biocolonized cement paste pellet with a sonication treatment of 3 minutes in 5 mL of PBS. Removing treatments were not done successively, thus the “strongly attached” biomass should also contain the “lousy attached” one. 2 mL of the culture medium were as well sampled in triplicate. The samples of biocolonized cement paste originated from a type A reactor after 5 weeks of culture. Each removal protocol has been performed in triplicate, i.e. starting from three different biocolonized cement pellets. DNA extraction was performed on the three types of samples (liquid, strongly “attached and lousy attached” biomass) obtained using a DNeasy power biofilm kit, according to manufacturer instructions. Sequencing of the 16S SSU RNA was done using 515F and 806R primers targeting both bacteria and *Archaea*. The sequencing and its statistical analysis were performed by RTlab (USA).

2.6 Physical Analysis

Cement paste pellets from the type A reactor were taken out after 2, 3, 4 and 5 weeks. A cut of the cement paste pellets was realized with a circular saw, in order to divide the cylindrical sample into two identical parts. A part of the pellet was then impregnated under vacuum with epoxy resin (Araldite, 2020) in circular molds (diameter = 2.6 cm). After hardening of the epoxy resin, the surface was polished under water using several polishing disks having decreasing particle sizes of 200, 68, 27 and 15 µm. A thinner polishing was then done using several diamond-covered polishing disks with a decreasing particle sizes (6, 3 and 1 µm). Samples were carbon coated before observation under a scanning electron microscope (Hitachi S-4300 SE/N) coupled with a EDX detector (Thermo Scientific Ultradry) running at 15 kV.

3 Results and Discussion

3.1 Deterioration Profile of the Cement Paste

The evolution of the concentrations of volatile fatty acids (VFAs), ammonium ions and inorganic carbon from 2 to 5 weeks of anaerobic digestion process are shown on (Figure 2).

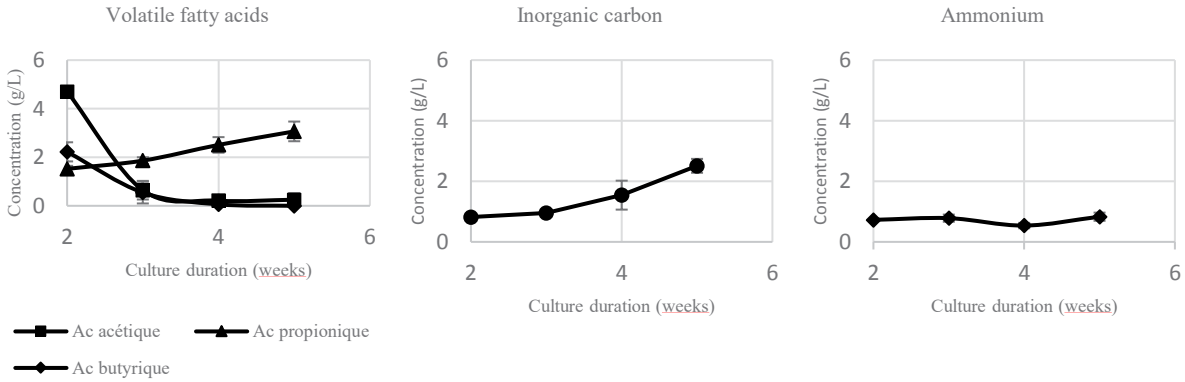

Figure 2. Evolution of concentrations of the aggressive metabolic compounds for a period of 5 weeks of anaerobic digestion process.

After two weeks of anaerobic digestion, the concentration of acetic and butyric acids were of 4.7 $g.L^{-1}$ and 2.2 $g.L^{-1}$ respectively. Their concentrations strongly decreased between week 2 and week 3 to finally stabilize around 0 g/L at end of the fourth week of anaerobic digestion. The propionic acid concentration evolved differently, since it was still increasing constantly from 1.5 to 3.0 $g.L^{-1}$ in the period of time between the 2nd and the 5th week (Voegel *et al.*, 2016). After 2 weeks, both acetic and butyric acids were consumed. This result corroborates those of Voegel *et al.* (2016), who showed that volatile fatty acids are accumulated during the first two weeks of the anaerobic digestion of biowaste, and finally consumed in the following weeks. More curiously, the propionic acid concentration did not drop in the weeks following the 2nd week, suggesting that this VFA has not been reused or metabolized by acetogenic microbial populations or that its production rate was seriously higher than the consumption rate. The dissolved carbon dioxide production increased from 0.8 $g.L^{-1}$, measured at the end of the week 2, to 2.5 $g.L^{-1}$ after 5 weeks. The concentration of ammonium has remained very stable, around 0.7 $g.L^{-1}$, from week 2 to week 5. Since ammonium ions are byproducts of amino acid fermentation (Ramsay and Pullammanappallil, 2001), it should be produced only during the acidogenesis stage occurring mainly during the first two weeks. In this way, we can make the hypothesis that the aggressive nature of the anaerobic digestion environment was at its maximum during the first two weeks of the experiment, since the concentration of aggressive compounds should be at its peak during this period.

Figure 3 allows the localization of the biodeteriorated zones in the depth of a cement paste sample exposed for 5 weeks in an anaerobic digestion medium.

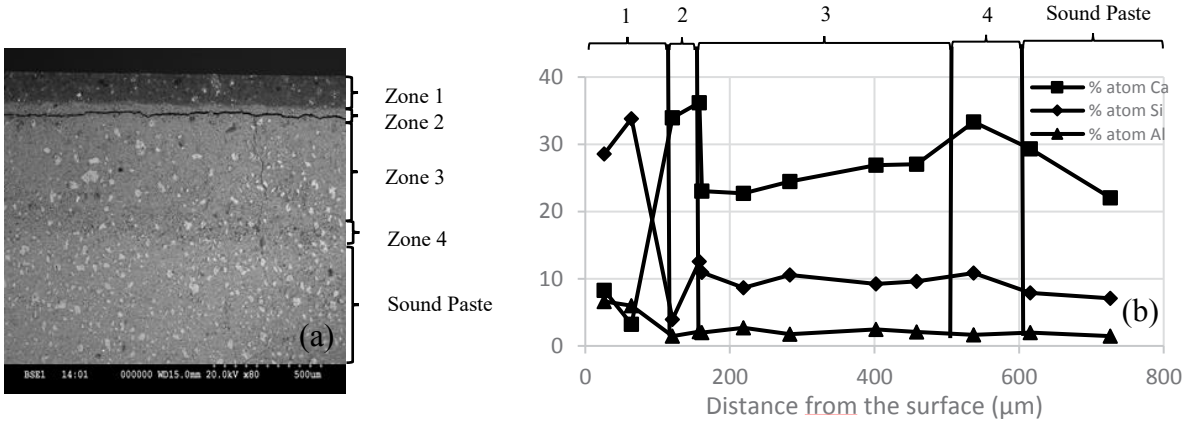

Figure 3. Repartition of the deteriorated zones within the depth of a cement paste (a) and the deterioration profile of a cement paste immerged for 5 weeks in an anaerobic digestion medium (b).

Four zones can be identified (Figure 3): a first layer darker than the others, of about 100 µm. A second zone, about 20-30 µm, can be identified around the crack. The third zone has a variable thickness among the different duration tested from 150 to 400 µm. A fourth zone darker than the third one is also observed, its thickness also changes from a duration to another from 150 to 430 µm, and finally at the heart of the cement paste there is a last zone corresponding to the sound paste. Figure 3(b) shows the evolution of the relative proportion of calcium (Ca), silicium (Si) and aluminum (Al) from the outer surface to 800 µm in the depth of biodeteriorated cement paste sample. The composition in Ca, Si and Al completely changes from a zone to another. All of those zones were found in every duration of exposition tested with the same global composition in each zone. The zone 1, the closest to the cement surface, had a low Ca proportion, around 10 %, a high Si proportion, around 30 %, and a high proportion of Al, about 7 %, in regard to the other zones. The zone 2 had a particularly specific composition: the Ca proportion was significantly higher than in any other zone, up to 70-76 % in both the samples immerged 3 and 4 weeks (data not shown), and a lower proportion of Al and Si around 1 and 5 % respectively. The presence of Phosphor was also observed in the first two zones (data not shown). In the three other zones (zones 2, 4 and 5), only a very small divergence in composition was detected: between 20 and 30 % of Ca, around 10 % in average of Si and 1.5 to 2 % of Al. Those results are representative of a Ca leaching and a P enrichment in the layers close to the surface. However, chemical element proportion analysis can not precisely show every change in mineral composition, as proportion could remain the same while the quantity could change.

Analysis with other techniques, such as X-Ray Diffraction, could give more information, particularly on the residual anhydrous grains. Those results are in accordance with the observations already reported by (Voegel *et al.*, 2016), who studied also cement paste biodeterioration after exposition to digested biowastes. These authors identified Ca leaching as part of the biodeterioration mechanisms.

Table 2 shows the evolution of the thickness of the total biodeteriorated zone for increasing time of cement paste exposition to anaerobic digestion environment. The thickness of the total biodeteriorated zone was determined by the Ca cartography obtained by SEM.

Table 2. Evolution thickness of the total biodeteriorated zone with the exposition time in anaerobic digestion medium.

Exposition time (weeks)	2	3	5
Thickness of the total biodeteriorated zone (µm)	554	594	619

The thickness of the total biodeteriorated zone increases from 2 weeks to 5 weeks of exposition time, from respectively 554 µm to 619 µm. The same kind of observations on cement pastes exposed for longer period, 10 and 15 weeks, should in the future make it possible to confirm this pattern.

3.2 Microbial Populations of the Biofilm

Figure 4 shows the repartition of the different bacterial phyla within the liquid fraction and in the "lousy attached" biomass and the "strongly attached" biomass collected on the surface of a cement paste after 5 weeks in type B reactor. Planktonic and sessile (attached) bacterial populations were different. Indeed, the proportion of *Archaea* was fairly higher in the liquid fraction, *i.e.* 22.0 % against 3.4 % in the attached biomass.

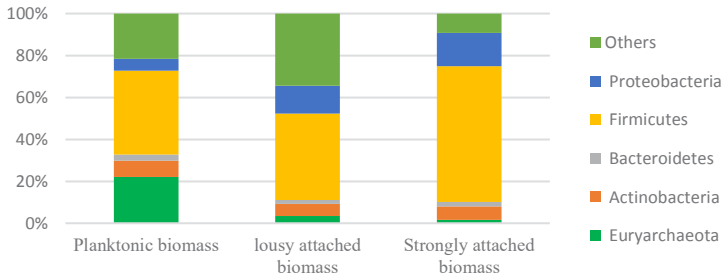

Figure 4. Relative repartition of the bacterial population in the planktonic biomass and in the cement paste attached biomass of a 5 weeks aged anaerobic digestion culture.

Among the *Archaea* highlighted in the liquid fraction, 17.7% belonged to the *methanosarcina* genus, which are anaerobic methanogens found in a multitude of environments and capable of producing methane by the three metabolic modes of methanogenesis (hydrogenotrophs, acetotrophs, methylotrophs) (De Vrieze *et al.*, 2012). The biofilm developed on the surface of the cement paste, and more specifically the "strongly attached" biomass, was rich in *Firmicutes*. Around 50% of the DNA sequences from the "strongly attached" biomass belonged to acidogenic populations. Among them, *Clostridium butyricum* (5.4%), is known to specifically produce butyric acid and *Megasphaera eldesnii* (29.5%), is described as able to produce acetic, propionic and butyric acids (Marounek *et al.*, 1989). Those results suggest that the acidogenesis step of the anaerobic digestion may mainly occur in the biofilm, while the methanogenesis step would take place in the liquid fraction. Beyond these considerations based essentially on the physical organization of communities (biofilms vs. suspended/planktonic populations), would not there be a major effect of pH behind this whole phenomenon? If the pH at the surface is too alkaline for bacteria to easily grow on it, perhaps only acidogens are able to lower the pH through the acids they produce to allow a biocolonization of the surface of material.

4 Conclusion

The SEM analysis of the cement pastes exposed from 2 to 5 weeks to an anaerobic digestion medium showed a biodeterioration of the cement paste characterized by a depth up to 700 µm with calcium leaching and phosphor enrichment in the first 100 µm. Bacteria present in the biofilm colonizing the cement paste are mainly acidogens, which may confirm the hypothesis that the microbial fouling of the cement paste is caused by the local production of aggressive compounds, such as organic acids acting on reducting the surface pH of cementitious materials. The use of fluorescent dyes could help measure the pH both in the biofilm and on the surface of the cement paste through fluorescence microscopy observation techniques.

ORCID

Cédric Perez: https://orcid.org/0000-0002-2057-5958
Christine Lors: https://orcid.org/0000-0002-2222-5556
Benjamin Erable: https://orcid.org/0000-0002-5332-9622

References

Bertron, A. (2014). Understanding interactions between cementitious materials and microorganisms: a key to sustainable and safe concrete structures in various contexts. *Materials and Structures*, *47*(11), 1787–1806. https://doi.org/10.1617/s11527-014-0433-1

Bharathiraja, B., Sudharsana, T., Jayamuthunagai, J., Praveenkumar, R., Chozhavendhan, S. and Iyyappan, J. (2018). Biogas production – A review on composition, fuel properties, feed stock and principles of anaerobic digestion. *Renewable and Sustainable Energy Reviews*, *90*, 570–582. https://doi.org/10.1016/j.rser.2018.03.093

De Vrieze, J., Hennebel, T., Boon, N. and Verstraete, W. (2012). Methanosarcina: The rediscovered methanogen for heavy duty biomethanation. *Bioresource Technology*, *112*, 1–9. https://doi.org/10.1016/j.biortech.2012.02.079

Magniont, C., Coutand, M., Bertron, A., Cameleyre, X., Lafforgue, C., Beaufort, S. and Escadeillas, G. (2011). A new test method to assess the bacterial deterioration of cementitious materials. *Cement and Concrete Research*, *41*(4), 429–438. https://doi.org/10.1016/j.cemconres.2011.01.014

Marounek, M., Fliegrova, K. and Bartos, S. (1989). *Metabolism and Some Characteristics of Ruminal Strains of Megasphaera elsdenii*. *55*, 4.

Ramsay, I. R. and Pullammanappallil, P. C. (2001). Protein degradation during anaerobic wastewater treatment: derivation of stoichiometry. *Biodegradation*, *12*(4), 247–256.

Salvador, R., Barros, M. V., Rosário, J. G. D. P. D., Piekarski, C. M., Luz, L. M. da, and Francisco, A. C. de. (2019). Life cycle assessment of electricity from biogas: A systematic literature review. *Environmental Progress & Sustainable Energy*, *38*(4). https://doi.org/10.1002/ep.13133

Voegel, C., Bertron, A. and Erable, B. (2015). Biodeterioration of cementitious materials in biogas digester. *Matériaux & Techniques*, *103*(2), 202. https://doi.org/10.1051/mattech/2015023

Voegel, C., Bertron, A. and Erable, B. (2016). Mechanisms of cementitious material deterioration in biogas digester. *Science of The Total Environment*, *571*, 892–901. https://doi.org/10.1016/j.scitotenv.2016.07.072

XV International Conference on Durability of Building Materials and Components
DBMC 2020, Barcelona
C. Serrat, J.R. Casas and V. Gibert (Eds)

Integrating Self-Sensing in Self-Healing Concrete: Towards a Biomimetic Approach to Repair

Kevin Paine[1], Bianca Reeksting[2], Hussameldin Taha[1] and Susanne Gebhard[2]

[1] BRE Centre for Innovative Construction Materials, University of Bath, United Kingdom,
k.paine@bath.ac.uk; h.m.taha.abdalgadir@bath.ac.uk

[2] Department of Biology and Biochemistry, University of Bath, United Kingdom,
b.j.reeksting@bath.ac.uk; s.gebhard@bath.ac.uk

Abstract. *Material degradation of our civil infrastructure is inevitable, and regular maintenance is required to mitigate against failure during the service-life. However, understanding and knowledge of composites is now leading to the creation of concretes with autonomic self-healing capabilities. This development will transform our infrastructure by embedding self-immunity and resilience so that structures evolve over their lifespan enhancing durability and serviceability, improving safety and reducing maintenance costs. Research in the UK under the auspices of Resilient Materials for Life (RM4L) has developed a suite of multiple-scale biomimetic self-healing concretes that can adapt and respond to damage without external intervention. This paper discusses the development of bacteria to precipitate calcite in cracks in concrete. Whilst bacteria-based healing is possible through several pathways, it is only now that a better understanding is permitting the optimization of the process. There are two key technologies for including bacteria healing in concrete: (i) encapsulation and (ii) vascular flow networks. Vascular flow networks permit continuous unlimited delivery of healing agents to internal areas of damage, facilitating repair on a reoccurring basis. However, in order to use them effectively human intervention is required to identify cracking and trigger healing processes. A more biomimetic approach is to provide the concrete with a form of self-sensing capability to enable it to initiate crack healing itself. Research using PZT sensors to detect cracking is described.*

Keywords: *Bacteria, Self-Healing, Self-Sensing, Flow Networks, PZT, Electromechanical Impedance.*

1 Introduction

Concrete remains the principal construction material used in buildings and infrastructure worldwide. However, it is susceptible to degradation which, given current design guidance, is nearly always inevitable over its lifetime. This means that intervention and mitigation, in the form of maintenance and repair, is necessary to retain and recover high levels of performance and durability. However, in recent years a range of 'smart' concretes has been developed, including those with autogenous and autonomic self-healing and self-repairing capabilities. Consequently, it is now possible to embed self-immunity and resilience in our concrete buildings and structures such that they evolve over their lifespan. This has significant implications for enhancing durability and serviceability, improving safety and reducing maintenance costs.

Research to develop a biomimetic approach to the repair of concrete is being undertaken in the United Kingdom as part of the £5M multi-disciplinary research project, Resilient Materials for Life (RM4L), a collaboration between Cardiff University, and the Universities of Bath, Bradford and Cambridge (Al-Tabbaa *et al*., 2018). RM4L has a broad remit to focus on tailoring

self-healing cementitious systems for use in specific applications and to address different damage scenarios and conditions. Furthermore, important damage scenarios have been identified, including time-related and cyclic damage as well as chemical damage, including corrosion. In addition to self-healing attributes, RM4L is initiating novel research aimed at embedding self-sensing, self-diagnosing, self-immunisation and self-reporting capabilities into cementitious systems in order to develop truly biomimetic responses in our infrastructure materials and structures.

This paper reports on current research being undertaken within RM4L by the University of Bath in the areas of bacteria-based self-healing concrete (BBSHC) and self-sensing concrete. We also introduce the concept of a smart biomimetic self-healing concrete formed from the integration of three technologies: (i) bacteria-mediated calcium carbonate precipitation, (ii) vascular flow networks (VFN) and (iii) electromechanical impedance (EMI) that could deliver long-term maintenance and repair of concrete buildings and structures without the need for human intervention.

2 Bacteria-Based Self-Healing

In order to achieve autonomic healing in concrete, a wide range of healing agents have been studied over the last 20 years. These healing agents need to be compatible with the cementitious matrix and their speed of reaction has to be appropriate to eliminate ingress of harmful pollutants (chlorides, sulfates etc.). In general, healing agents with low viscosity and high sorptivity have been preferred. Whilst cyanoacrylates and epoxy resins have these required properties, they are generally incompatible with the cementitious matrix. Consequently, there is a search for a suitable cement-like material. Research at the University of Cambridge is having some success with sodium silicate (Giannaros *et al.*, 2016) .

However, an alternative is to use of bacteria to aid with the precipitation of calcium carbonate within the crack. Calcium carbonate occurs naturally in concrete as it ages, and consequently its use as a healing compound is entirely appropriate.

Bacteria-based self-healing is achieved by embedding bacterial spores within the concrete and providing them with the nutrients that they need to grow. Whilst the bacteria are in their spore form, they are inactive. However, when conditions become favourable, they germinate into active cells and these multiply. These more favourable conditions occur when a crack forms in the concrete and water and oxygen ingress.

The presence of bacteria near a crack will aid the formation of calcium carbonate should the local environment be rich in dissolved inorganic carbon (DIC) and Ca^{2+} ions (Figure 1). For this reason, growth media containing both carbon and calcium sources are normally used simultaneously with the spores as healing agents. In general, bacteria-based self-healing of concrete can occur because of either ureolytic or non-ureolytic metabolism.

Research at Bath has performed a comparison between how ureolytic and non-ureolytic environmental bacteria precipitate calcium carbonate in order to understand how these mechanisms differ and how we can apply this knowledge to the improvement of self-healing concrete (Reeksting *et al.*, 2020). In this study, environmental bacteria were surveyed for their ability to precipitate calcium carbonate and both the mechanism and resulting precipitates were examined. It was shown that while ureolytic bacteria cause the most rapid precipitation, non-ureolytic bacteria were capable of producing similar amounts of calcium carbonate. In addition,

the crystals resulting from non-ureolytic carbonate precipitation appeared to have more organic components and subsequently occupy larger volumes (Figure 2, left), this is likely beneficial for crack sealing application as for the same amount of calcium a larger precipitate can be formed. Indeed, non-ureolytic bacteria caused a more consistent crack healing and subsequent recovery of water tightness (Figure 2, right).

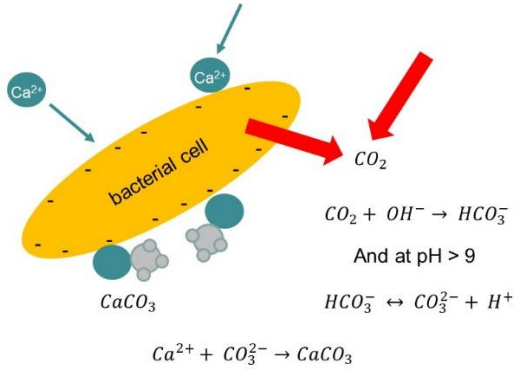

Figure 1. Process of calcium carbonate precipitation in a concrete crack (adapted from Dhami *et al.*, 2013).

To date, self-healing of cementitious composites at Bath has focused on non-ureolytic bacteria, *e.g.*, *Bacillus pseudofirmus* and *Bacillus cohnii* (Sharma *et al.*, 2017). The spores of the bacteria have been encapsulated under vacuum in a lightweight fine aggregate (*e.g.* perlite). The growth media, yeast extract and a calcium salt (calcium acetate or calcium nitrate) have been added either directly to the concrete, or encapsulated in lightweight fine aggregates, depending on the application.

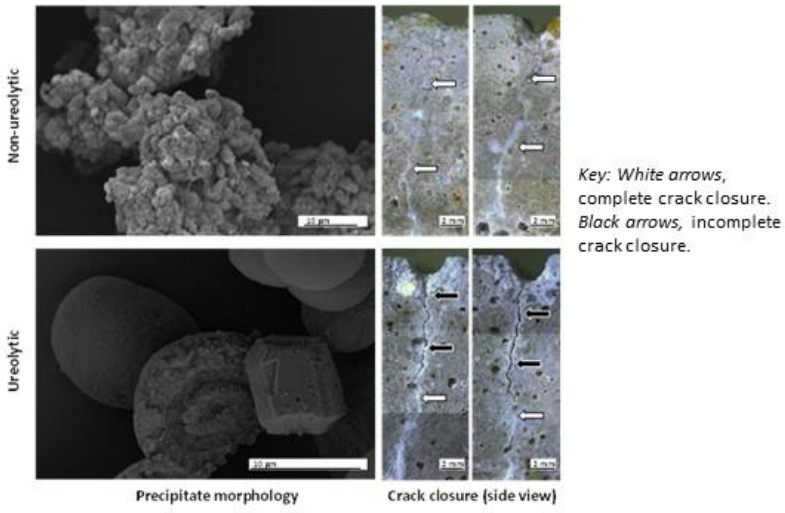

Figure 2. Crystal morphology and crack sealing in mortars containing either non-ureolytic or ureolytic bacteria. *Left*, electron micrographs of representative precipitate produced by non-ureolytic (top) and ureolytic (bottom) bacteria. *Right,* crack healing down the side of cement mortars at 8 weeks healing.

It has been shown that the lightweight fine aggregates rupture on cracking releasing the healing agents in a form that enables calcium carbonate precipitation and healing to take place and that the concrete recovers its water tightness (Alazhari *et al.*, 2018).

However, a concern with the use of lightweight aggregates is that they may not distribute homogeneously throughout the matrix. Consequently, there are some concerns (although not to date replicated in laboratory tests) that cracks may entirely miss the aggregates. For this reason, research at Bath has also considered supplying the spores and/or the growth media in microcapsules (Paine *et al.*, 2019). We have shown that the encapsulation of spores by, for example, the complex coacervation technique, creates few technical issues and that high yields of spores can be obtained in small microcapsules (180 μm). However, encapsulation of growth media is more difficult and only low loadings could be obtained and the microcapsules were much larger (~ 609 μm). In both cases, however, it was shown that the microcapsules rupture upon cracking of the concrete and that crack closure and recovery of water tightness occurs. That said, whilst the encapsulation of bacteria and growth media in concrete has proven successful there are some elements of this technique that could still be improved upon.

Firstly, the use of encapsulation means that the quantity of growth media in the concrete is fixed, limiting the amount of bacterial growth and the volumes of calcium carbonate precipitated. The addition of further growth media, such as yeast extract, directly into the concrete will substantially retard the cement hydration; whilst the calcium source is likely to carbonate and be unusable by the bacteria. The encapsulation of these growth media in lightweight aggregates will lead to unreasonable losses in strength.

Furthermore, recent research has shown that the degree of bacteria-based calcium carbonate precipitation in concrete is limited by the availability of oxygen (Nielsen *et al.*, 2019). Whilst researchers have attempted to overcome this by encapsulating calcium peroxide in the concrete (Zhang *et al.*, 2016). this has had limited success and creates additional complexity.

Consequently, it has been considered that there may be some benefit in providing a vascular flow network (VFN) within the concrete that can supply oxygen and nutrients to the crack when healing is required. Furthermore, this VFN could be used to resupply the concrete with further spores and nutrients to permit it to self-heal again should the crack reoccur at the same place.

3 Vascular Flow Networks

VFN systems have been considered as a viable technique for providing self-healing in materials as they more readily simulate the way flora and fauna heal themselves (White *et al.*, 2001). A wide range of healing agents or supplies can be pumped through a VFN to the site of damage as and when required. The reservoir of healing agent can be readily topped up allowing for multiple healing events and the healing agent can be varied to suit the type of damage.

However, until recently the use of VFN for concrete had created problems; primarily because the glass used to create the channels tended to break during casting. For this reason, a novel approach has been developed at Cardiff University (Davies *et al.*, 2015). Here, shrinkable polyurethane tubes are embedded in the concrete that can easily be removed after the concrete has hardened around them. This leaves a hollow network within the concrete. When healing is required, air can be removed from the VFN and the healing agents then added remotely and pumped through under pressure.

The addition of a 2-dimensional VFN to a bacteria-based self-healing concrete wall was trialled as part of a large-scale demonstration of self-healing techniques carried out as a forerunner to the RM4L project (Paine *et al.*, 2018). The wall consisted of both bacteria-based self-healing concrete and conventional concrete as shown in Figure 3. Bacteria-based self-healing concrete was only added to the wall at the section where cracking was designed to occur (Figure 3b). A vascular flow network consisting of 4 mm diameter channels was placed in the zone most susceptible to cracking. The network was created using polypropylene tubes which were removed from the concrete once it had hardened. The network channels were joined using 3D printed joints made from polylactic acid. Whilst the VFN was included to permit later addition of further growth media, bacteria or oxygen as required it was never actually used in this way and bacterial healing was allowed to progress without interference

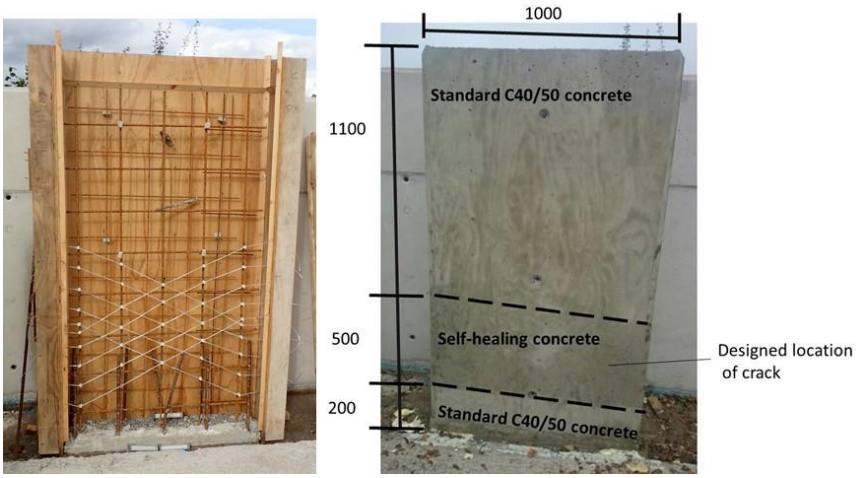

Figure 3. Large-scale demonstration of a bacteria-based self-healing concrete with: (a) VFN installed prior to casting of the concrete, (b) finished wall (dimensions in mm) (Paine *et al.*, 2018).

However, a principal problem with a VFN is that the release of the healing agents is not initiated by the cracking of the concrete. In general, it requires some form of monitoring system, often just visual observation, to detect the cracking and then human intervention is required to upload the healing agents and pressurize the system to pump the those healing agents through the network. However, recent research at Bath has been investigating the suitability of self-sensing systems that may detect and diagnose the formation of cracks, and their repair, within concrete. This sensing could potentially be used to trigger the healing system.

4 Triggering Healing Systems

Whilst there has been much research into the use of sensors for structural health monitoring, as far as we are aware there has been no research where autonomic self-healing responses have been triggered by sensors embedded within concrete. This is therefore a novel area of research.

Piezoelectric materials are popular sensors due to their ability to detect a wide range of parameters (stress, temperature, cracks and damage) and due to their high sensitivity, stability

and low cost. There has been significant research with lead zirconate titanate (PZT) transducers. Of note is the use of electromechanical impedance (EMI) in which the PZT transducer works as both an actuator and detector simultaneously. Damage in a structure can be observed from fluctuations in the admittance/impedance signature which are caused by changes in the intrinsic material properties such as mass, stiffness and damping.

To better understand how a sensing system could be used to trigger healing once damage occurs and deactivate after repair, research has been carried out at Bath to understand how the EMI response of a PZT responds in both damage and repair scenarios (Taha *et al.*, 2019).

This research has shown that localized damage in mortar beams, can be detected by a surface mounted PZT transducer located up to 220 mm away from where the damage has occurred. It was further observed that as the damage level increased, and approached the PZT, that the difference between the initial admittance signature and subsequent signatures increased, see Figure 4(a). This behavior was quantified by the root mean square (RMSD) response shown in Figure 4(b). On the other hand, when the damage was repaired, using a cement paste, it was observed that the RMSD gradually decreased (Figure 5). This indicated at least a partial recovery of properties due to the repair.

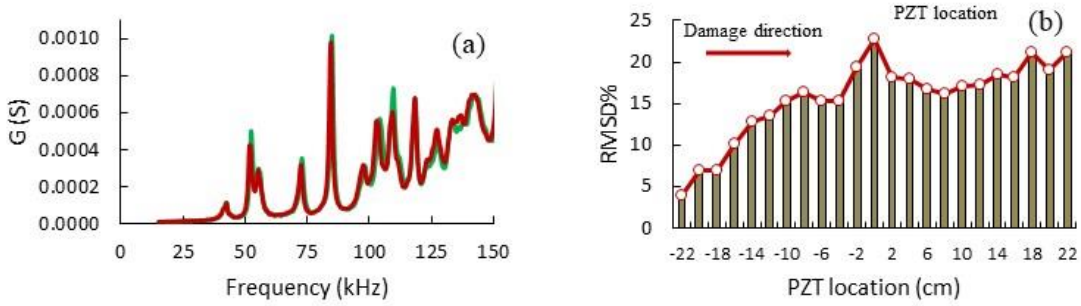

Figure 4. (a) Admittance signature for PZT before and after damage, (b) RMSD% as the damage approaches and distances from the PZT sensor.

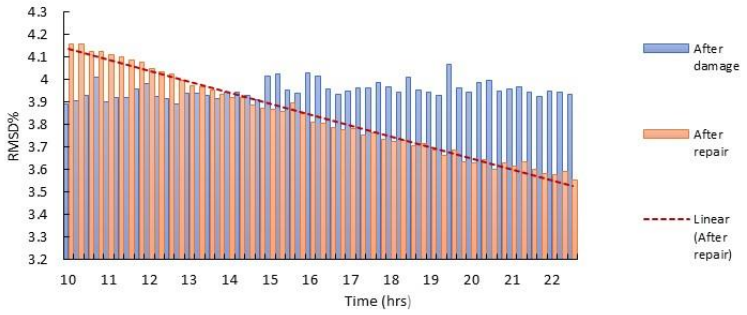

Figure 5. RMSD behavior 10 hours after repair as compared with the RMSD after damage.

5 Integration of Technologies

As described above research is being undertaken at the University of Bath and partner universities within the RM4L programme grant to develop these three technologies. Whilst these developments are primarily taking place individually, there is a proposition that they could be integrated to form a smart biomimetic self-healing concrete, as shown schematically in Figure 6. Here a concrete building or structure can be cast using BBSHC around an embedded VFN, with PZT sensors, or some other form of sensing, strategically placed within or on the surface of the concrete. When a crack occurs the bacterial activity autonomically heals the cracks by precipitating calcium carbonate. However, simultaneously, a sensor detects that cracking has occurred. If it detects, after a given period, that the degree of healing is insufficient it triggers through an interface the activation of the VFN. Consequently, oxygen and/or further growth media are pumped through the VFN to the site of the crack from an external reservoir. Once the sensors have identified that healing is sufficient, they stop supplying oxygen and/or growth media. It is possible that at this point further spores and nutrients could be pumped to the site of the crack to permit further autonomous healing and for the cycle to recommence should a crack reappear at the same location at some further point in time.

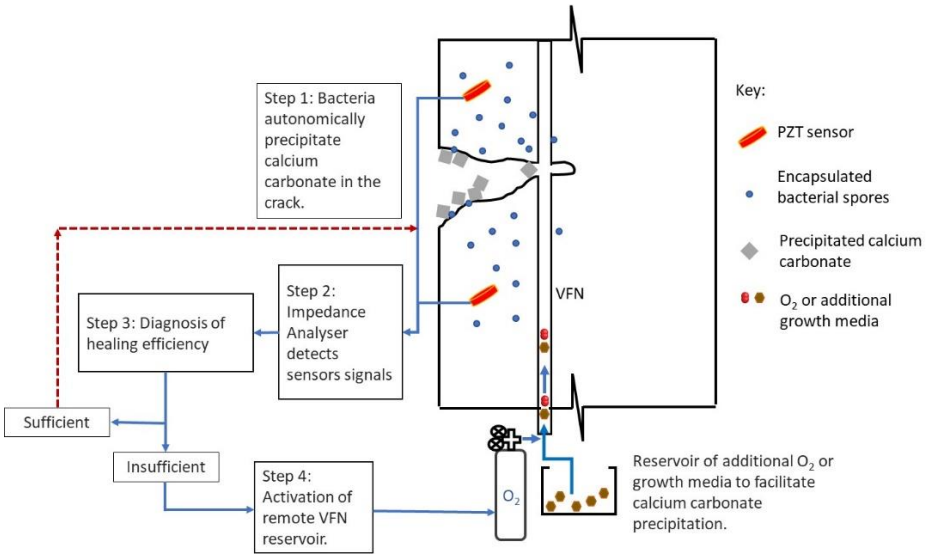

Figure 6. Schematic showing the integration of BBSHC, VFN and sensing technologies for biomimetic smart self-healing concrete.

6 Conclusions

- BBSHC, consisting of encapsulated spores and growth media, can be used to autonomically self-heal cracks in concrete as soon as they occur by precipitating calcium carbonate. However, the quantities of calcium carbonate precipitated may be limited by the availability of the growth media and oxygen.
- VFN can be formed in concrete and they permit remote healing agents and supplies to be pumped to the site of cracks to assist with bacteria-mediated calcium carbonate precipitation.

- EMI has potential as a sensing technology to identify the degree of healing (quantity of calcium carbonate precipitated) in cracks. When interfaced with appropriate software it can be used to trigger the supply of healing agents through the VFN.

Acknowledgements

The authors wish to thank the EPSRC for their funding of the Resilient Materials for Life (RM4L) programme grant (EP/P02081X/1).

ORCID

Kevin Paine: http://orcid.org/0000-0001-7455-7002
Bianca Reeksting: https://orcid.org/0000-0003-1219-9574
Hussameldin Taha: https://orcid.org/0000-0002-6167-7598
Susanne Gebhard: http://orcid.org/0000-0003-4783-6115

References

Al-Tabbaa, A., Lark, B., Paine, K., Jefferson, T., Litina, C., Gardner, D. and Embley, T. (2018). Biomimetic cementitious construction materials for next-generation infrastructure. *Proceedings of the Institution of Civil Engineers - Smart Infrastructure and Construction*, 171(2), 67-76. doi: 10.1680/jsmic.18.00005

Alazhari, M., Sharma, T., Heath, A., Cooper, R. and Paine, K. (2018). Application of expanded perlite encapsulated bacteria and growth media for self-healing concrete. *Construction and Building Materials*, 160, 610–619. doi: 10.1016/j.conbuildmat.2017.11.086

Davies, R.E., Jefferson, A., Lark, R. and Gardner, D. (2015). A novel 2D vascular network in cementitious materials. *fib Symposium,* Copenhagen, Denmark.

Dhami, N.K., Reddy, M.S. and Mukherjee, M.S. (2013). Biomineralization of calcium carbonates and their engineered applications: A review. *Frontiers in Microbiology*, 4, 1–13. doi: 10.3389/fmicb.2013.00314

Giannaros, P., Kanellopoulos, A. and Al-Tabbaa, A. (2016). Sealing of cracks in cement using microencapsulated sodium silicate. *Smart Materials and Structures*, 25(8), p.084005.

Nielsen, S.D., Koren, K., Löbmann, K., Hinge, M., Scoma, A., Kjeldsen, K.U. and Røy, H. (2019). Constraints on $CaCO_3$ precipitation in superabsorbent polymer by aerobic bacteria. *Applied Microbiology and Biotechnology*, 104, 365-375. doi: 10.1007/s00253-019-10215-4

Paine, K., Horne, I., Tan, L., Sharma, T., Heath, A., Cooper, R., Virgoe, J., Palmer, D. and Kerr, A. (2019). Microencapsulated spores and growth media for self-healing mortars. *Life-Cycle Analysis and Assessment in Civil Engineering: Towards an Integrated Vision*. Taylor & Francis Group.

Paine, K., Sharma, T., Alazhari, M., Heath, A. and Cooper, R. (2018). Application and performance of bacteria-based self-healing concrete. In: A. Bertron and H.M. Jonkers, eds. *Microorganisms-Cementitious Materials Interactions*. Toulouse, pp.387–394.

Reeksting, B.J., Hoffmann, T.D., Tan, L., Paine, K. and Gebhard, S. (2020). In-depth profiling of calcite precipitation by environmental bacteria reveals fundamental mechanistic differences with relevance to application. *Applied and Environmental Microbiology*. 86(7). doi: 10.1128/AEM.02739-19

Sharma, T.K., Alazhari, M., Heath, A., Paine, K. and Cooper, R.M. (2017). Alkaliphilic Bacillus species show potential application in concrete crack repair by virtue of rapid spore production and germination then extracellular calcite formation. *Journal of Applied Microbiology*, 122(5), 1233–1244. doi: 10.1111/jam.13421

Taha, H., Ball, R.J. and Paine, K. (2019). Sensing of Damage and Repair of Cement Mortar Using Electromechanical Impedance. *Materials*, 12(23), doi: 10.3390/ma12233925

White, S.R., Sottos, N.R., Geubelle, P.H., Moore, J.S., Kessler, M.R., Sriram, S.R., Brown, E.N. and Viswanathan, S. (2001). Autonomic healing of polymer composites. *Nature*, 409(6822), 794–797. doi: 10.1038/35057232

Zhang, J.L., Wang, C.G., Wang, Q.L., Feng, J.L., Pan, W., Zheng, X.C., Liu, B., Han, N.X., Xing, F. and Deng, X. (2016). A binary concrete crack self-healing system containing oxygen-releasing tablet and bacteria and its Ca^{2+}-precipitation performance. *Applied Microbiology and Biotechnology*, 100(24), 10295–10306.

XV International Conference on Durability of Building Materials and Components
DBMC 2020, Barcelona
C. Serrat, J.R. Casas and V. Gibert (Eds)

Two-Part Bio-Based Self-Healing Repair Agent for Cement-Based Mortar

Mustafa Mert Tezer[1] **and Zeynep Başaran Bundur**[1]

1 Department of Civil Engineering, Ozyegin University, Cekmeköy, 34987, Istanbul, Turkey
zeynep.basaran@ozyegin.edu.tr

Abstract. *Factors affecting durability of concrete structures are generally associated with each other. Due to its brittle nature, concrete can crack under stress and these cracks are one of the main reasons for a decrease in service life in concrete structures. Therefore, it is crucial to detect and recover microcracks, then to repair them as they were developed to wider cracks. Recent research in the field of concrete materials suggested that it might be possible to develop a smart cement-based material that is capable of remediate cracks by triggering biogenic calcium carbonate ($CaCO_3$) precipitaton. This paper summarizes a study undertaken to investigate the self-healing efficiency of Sporosarcina pasteurii (S. pasteurii) cells immobilized on both diatomaceous earth and pumice, to remediate flexural cracks on mortar in early ages (28 days after mixing). To obtain a two-phase bio additive, half of the minerals were saturated with a nutrient medium consisting of urea, corn-steep liqueur(CSL) and calcium acetate and the cells with immobilized to the other half without nutrients. Screening of the healing process was done with ultrasonic pulse velocity (UPV) testing and stereomicroscopy. With this approach, the cracks on mortar surface were sealed and the water absorption capacity of the so-called self-healed mortar decreased compared to its counterpart cracked mortar samples.*

Keywords: *Self-Healing, Biomineralization, Diatomaceous Earth, Pumice, Mortar.*

1 Introduction

Concrete is the most widely used material in the construction industry due to its high compressive strength, durability and cost efficiency compared to the alternative building materials. Nevertheless, early age cracks occurring in concrete can decrease the strength of the materials and limit the service life of the concrete structures. These cracks can create pathways for hazardous chemicals and excessive water and increasing permeability of concrete. Conventional repair methods like, epoxy sealing or grouting are applied from the outside and expected to penetrate into the cracks. While this approach is feasible for repairing large cracks, penetration of the abovementioned sealants to the inner parts of small and deep cracks is very limited. Therefore, for narrow microcracks, there is a need for an alternative repair method by mostly means of self-healing.

Recent studies in the field showed that it might be possible to develop a bio-based self-healing system where bacterial cells are being used to remediate cracks by triggering microbial induced calcium carbonate precipitation (MICP) (De Muynck *et al*. 2010; Wang *et al*. 2016; Zhang *et al*. 2015). MICP is a biochemical process in which microorganisms stimulate the formation of calcium carbonate ($CaCO_3$) (Mann 2001) . With this approach, tensile or flexural cracks as wide as 0.7 mm was remediated and the water permeability of mortar was reduced (Jonkers and Schlangen 2007; Wang *et al.* 2012c, 2014b; Wiktor and Jonkers 2011). Crack healing through MICP requires a suitable bacterial culture and the nutrients to support metabolic activity and create the proper environment for crack closure. The main challenge of the application is to find a microorganism that can tolerate highly alkaline conditions of cement

paste, can survive the mixing process, and can remain viable with limited access to nutrients (Tiago *et al.* 2004) . A simple approach by means of limiting the labor work in processing is adding the vegetative bacterial cells directly to the mix Previously, Bundur *et al.* (2017) showed that vegetative *S. pasteurii* cells could survive in mortar up to 11 months when they were added to the mix without any encapsulations. These remaining cells were found to be effective in remediation of the microstructure when internal microcracks (Liu *et al*. 2016) and flexural surface cracks in 7 day old samples (Amiri *et al.* 2018). However, limited viability and lack of O_2 decreased the performance of $CaCO_3$ yield through all crack the depth. Instead, the precipitation was found to be limited to the crack mouth in microscale cracks (Amiri *et al.* 2018). However, considering the larger surface cracks, the amount of retained viable cells may not be able to precipitate sufficient biogenic $CaCO_3$ to seal the cracks. Thus, it is crucial to develop a simpler and natural protection system to improve the robustness of the bacterial cells against the restrictive environment.

Concerns regarding the viability of the cells and limited crack healing led researchers to propose various encapsulation methodologies, particularly for dormant state endospores. The encapsulation methods consist of embedding the endospores in a protective covering, e.g. inorganic lightweight porous aggregates (LWAs) (Wiktor and Jonkers 2011), polymeric membrane (Bang *et al*. 2010; Wang *et al*. 2012a), microcapsules (Wang *et al.* 2014b), hydrogels (Wang *et al.* 2014a) and natural minerals (Alazhari *et al.* 2018; Wang *et al.* 2012b). Amongst all these approaches, LWAs and hydrogels have shown the most promising developments regarding the viability. The methods were promising in terms of healing cracks at various ages of concrete, but to-date most of the studies revealed that cracks could be healed in samples as old as 28 days.

Instead of using synthetic encapsulation covering, a more sustainable approach could be achieved by using natural additives or natural lightweight aggregates. Throughout the literature, studies showed that among several alternatives such as diatomaceous earth (DE), metakaolin, zeolites and expanded clay could be suitable for protection of the bacteria based on their effects on compressive strength and setting, in particular DE was found to be effective in self-healing of cracks (Erşan *et al*. 2015; Wang *et al*. 2012b). Nevertheless, considering the natural resources, the list of these natural protective barriers could be extended. A correct choice of the protection barrier and application methodology are of crucial for further development of self-healing concrete. This study presents a comparative study on the possible use of a mineral additive (DE) and a porous lightweight aggregate (pumice) as a protective barrier for bacterial cells.

2 Materials and Methods

2.1 Microorganism Selection and Growth

Leibniz Institute- German Collection of Microorganisms and Cell Cultures: S. pasteurii (DSMZ 33) cells were selected and used as a self-healing agent in cement-based materials. *S. pasteurii* cells were grown in a Urea-corn steep liqueur (CSL)-sodium acetate nutrient medium (UCSL) which includes tris base (0.13M), CSL (15 g), sodium acetate (10g) and urea (20 g) per liter of distilled (DI) water. The pH of the medium was adjusted to 9. First, the nutrient medium was sterilized at 121°C for 45 minutes. The cells were incubated aerobically in sterilized liquid

medium with shaking conditions (175 rpm) at 30°C until the stationary phase (10^9 CFU/mL) was reached. Then, the cells were collected from the culture by centrifuging at 6300g for 15 min. The cells were washed twice by PBS (Phosphate buffered solution) and stored at 4°C until immobilizing.

2.2 Material Composition

DE (Diatomaceous Earth), and pumice were used to immobilize bacterial cells. DE was provided regionally from a source in Turkey. DE particles used in the experiments were raw materials without any further treatment and having irregular shapes. A Mastersizer 2000 particle size analyzer with a Hydro MU 2000 (Malvern, Worcestershire, United Kingdom) wet dispersion unit was used to measure the particle size distributions of cement and DE. To prevent hydration of the cement particles, the cement particles were dispersed in ethanol. The average particle sizes of DE and cement were determined as 19.20 and 23.2 μm, respectively. The particle size was ranging from 0.375 to 90 μm for DE and it was ranging from 5 to 90 μm for OPC. DE was used as an addition to the mix by 5% of cement weight. The absorption capacity of DE was found to be almost 100% by its weight. Pumice was used as aggregate replacement such that 5% of the sand used in mortar mixes. The particle size of light weight pumice aggregate was in between 0.3 to 2.5 mm, while the absorption capacity was 45% by its weight.

Besides the additions or replacements, mortar samples were prepared using OPC CEM I 42.5R and standard sand accordingly to the norm EN 196-1. A polycarbooxylate superplasticizer was used to maintain the same workability criterion for all samples. The water to cement ratio (w/c) was kept at 0.45.

2.3 Immobilization Procedure

The immobilization was achieved by simply submerging the DE or pumice to a bacterial suspension. To immobilize the cells on DE, 2 grams of viable *S. pasteurii* cells were collected as it was stated in Section 2.1, and they were resuspended in a sterilized 50 mL PBS solution. Then, 22.5 g of DE was added to the suspension. Sixty-seven grams of pumice was added to the 6 grams of cell suspension in 80 mL PBS. Immobilization for both materials was achieved with shaking conditions (175 rpm) at 30°C for 24 hours. Then, the slurry was removed from incubation and kept at 40°C in an oved for an additional 12 hours. Excess PBS content on DE and pumice was calculated by subtracting the known weight of DE/pumice, bacterial cells and theoretical absorbed PBS from the final weight of oven dry slurry. This value was subtracted from the mixing water content. To ensure the immobilization was achieved, the morphology of the DE and pumice was evaluated before and after treatment by a FEI-Philips XL30 Environmental Scanning Electron Microscope with Field Emission Gun (FEG). Figure 1 and 2 show the SEM images obtained before and after immobilization procedure, respectively.

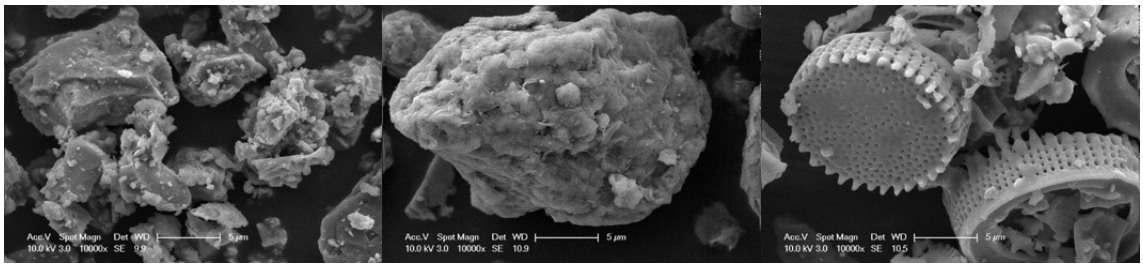

(a) (b) (c)

Figure 1. Morphology of (a) cement (b) pumice and (c) diatomaceous earth before immobilization. Scale: 5 µm.

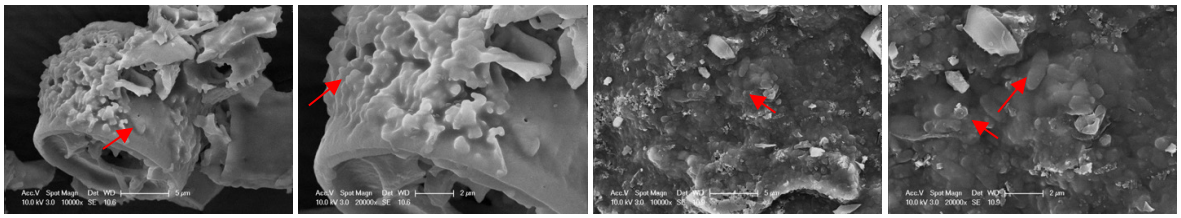

(a) (b) (c) (d)

Figure 2. Immobilization of bacterial cells on (a), (b) diatomaceous earth (c), (d) pumice. Scale: 2 and 5 µm.

2.3 Experimental Planning

2.3.1 Preparation of mortar samples

Mortar samples were prepared by ASTM C305-14. Samples were made with a water- to-cement ratio of 0.45 and a sand-to-cement ratio of 3. The mortar samples were then cast into 40 x 40 x 160 mm molds and kept in humid environment at 21°C for 24 h. Then the molds were removed, and the samples were further cured in moist environment until testing (22°C). To provide flexural resistance during crack initiation, 12-mm micro synthetic fibers were added to mortar (4 g/m^3 of mortar). A polycarboxylate ether (PCE)-based superplasticizer (BASF) was used to maintain the required workability of mortars in terms of flow table diameter based on ASTM C1437-15. To quantify the workability, a flow table test was conducted based on ASTM C1437-15 (ASTM International 2015). The workability of pastes was adjusted using PCE superplasticizer when necessary. PCE was added into mortar mixes until the desired flow reached (±10% of the control neat mortar). Average flow values were calculated from triplicates of samples from 5 batches (15 samples in total). Table 1 summarizes the composition and flow behavior of different mixes used in this study.

Table 1. Summary of mixing ingredients and flow (%). PBS: Phosphate buffes solution; SP: Superplasticizer; DE: Diatomaceous earth; Pum: Pumice. C: Only includes air dry minerals; Bac: all mineral content was saturated with bacterial cells and PBS; 2P: Two-phase bio additive containing bacterial cells and nutrients. Flow values were given average ± standard deviation.

Sample	*Cement*	*Sand*	*S. pasteurii cells*	*Mineral content*	*PBS*	*Nutrient solution*	*SP*	*Flow (%)*
Kontrol	450 g	1350 g	-	-	-	-	3 g	21 ± 0.4
DE-C	450 g	1350 g	-	22.5 g	-	-	4.5 g	30 ± 0.4
Pum-C	450 g	1282.5 g	-	67.5 g	-	-		15 ± 0.4
DE-Bac	450 g	1350 g	2 g	22.5 g	90 g	-	3 g	36 ± 0.4
Pum-Bac	450 g	1282.5 g	6 g	67.5 g	90 g	-		25 ± 0.4
DE-2P	450 g	1350 g	2 g	22.5 g	45 g	45 g	1.5 g	34 ± 0.4
Pum-2P	450 g	1282.5 g	6 g	67.5 g	45 g	45 g		32 ± 0.4

2.3.2 Crack formation, curing and evaluation of crack healing

At the end of the 28th day of mixing, the samples were removed from the curing environment and cracked under flexural loading using a servo hydraulic displacement-controlled device (0.05 mm/sec). The sample was unloaded once the crack was formed visually, which corresponded to 50 ± 3% of the ultimate flexural strength of samples. Upon unloading, the remaining crack width ranged from 0.30 mm to 0.35 mm. A set (3 samples) of control samples were not cracked for further analysis. Once the cracks were formed a set of cracked samples were cured in water and another set was cured in nutrient medium. Curing process was done by submerging the samples into curing solutions for 2-days and then, subsequently leaving them at ambient conditions for 2 days. This 2- day period curing process was applied until at least 90% crack sealing was observed. To investigate the self-healing in cement-based mortar, cracked beams were periodically observed under NIKON Inc. SMZ745T Stereomicroscope and analyzed with CLEMAX visual analysis system. Air dried samples were analyzed weekly for $CaCO_3$ crystal formation within cracks. Complementary quantification was done by Ultrasonic Pulse Velocity (UPV) test.

3 Results and Discussion

Upon 14 to 28 days of curing, the cracks were visually sealed in specimens containing bacterial cells (*DE-Bac; Pum-Bac; DE-2P and Pum-2P*) when additional nutrients were provided with curing. There was not any visual crack closure or any crystal precipitation in control samples without any bacterial cells regardless of the sample age and type of curing (within the 28-day observation period). From each set, triplicates of samples were cast and the specimens in the same sets showed similar crack- filling trend. Since the visual crack healing was almost the same for each set, one representative image of series with 28-day old samples containing bacterial cells is shown in Figure 3 and Figure 4.

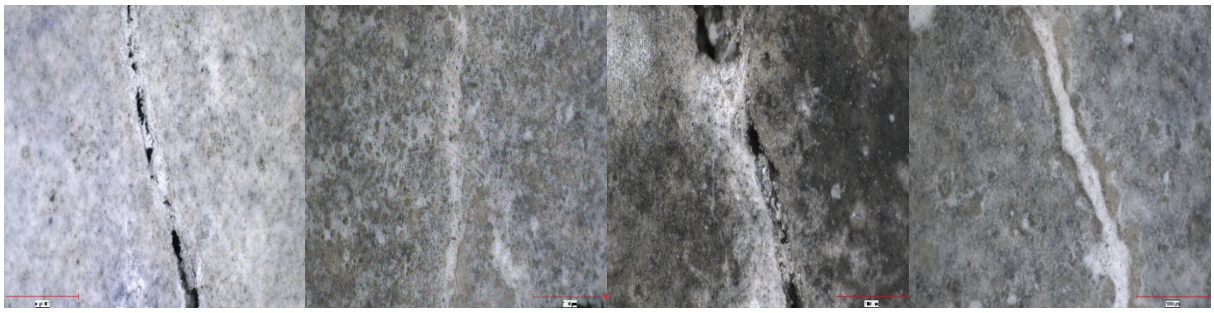

(a) (b) (c) (d)

Figure 3. Stereomicroscopy images of the cracks (0.3 to 0.4 μm) in 28-day old specimens containing diatomaceous earth (a) DE-Bac after 28-days of water curing (b) DE-Bac after 28-days nutrient curing (c) DE-2P after 14 days of water curing and (d) DE-2P after 14 days nutrient curing.

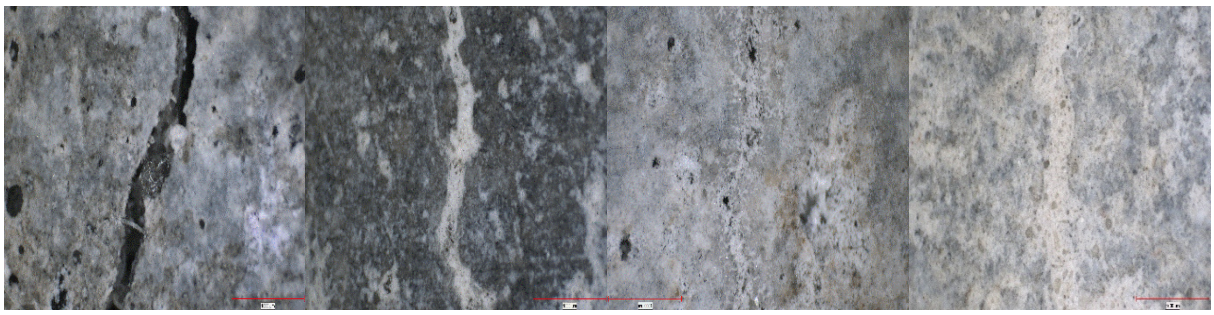

(a) (b) (c) (d)

Figure 4. Stereomicroscopy images of the cracks (0.3 to 0.4 μm) in 28-day old specimens containing pumice (a) Pum-Bac after 28-days of water curing (c) Pum-Bac after 28-days of nutrient curing (c) Pum-2P after 14-days of water curing and (d) Pum-2P after 14-days of nutrient curing.

Based on the visual crack evaluation, both DE and pumice was found to be effective in terms of immobilizing the bacterial cells and trigger self-healing. The possible mechanism of these minerals could be attributed to their relatively high capacity to absorb and hold bacterial cells on the surfaces. In addition, it could also be noted that additional nutrients as urea and [Ca^{+2}] source should be provided either during the mixing or in the curing solution. DE was already known to be a good mineral agent to immobilize and protect the cells from high pH environment of cement paste. This could be attributed to its relatively higher absorption capacity and high specific surface area which could enable a more homogenous. Since DE is also a microbiological formation, it could also provide a more suitable microenvironment for the bacterial cells compared to cementitious environment and thus bacteria could still decompose urea (Wang *et al*. 2012c). Even though, both minerals were effective in terms of remediating the cracks, however pumice was slightly more efficient compared to DE in terms of crack closure, particularly in samples containing 2-phase mineral additives. This could be directly related to the number of bacterial cells added to the mix. Since pumice have larger particle size, it was used as a sand replacement which was 3 times more than DE addition. Relatedly, the amount of bacterial cells and nutrient solution was also tripled. This might lead to a more efficient crack healing in pumice containing samples compared to DE modified samples.

UPV test results also confirmed that healing was occurred in cracks. Figure 5 shows the UPV test results for mortar samples cured in different conditions after crack initiation. There was a full crack closure in Pum-2P and DE-2P samples in 14 days, thus the evaluation of the sample was further done by water absorption test. Similar to the visual inspection, healing was observed in almost all samples containing bacterial cells. In particular, for samples containing DE, a higher self-healing was only observed in *DE-Bac* and *DE*-2P samples when they were cured in nutrient medium. However, there was also a change in UPV reading in DE-Bac and DE-2P samples cured in water. This might indicate that there might be an internal crack healing process occurred in the samples rather than crack mouth sealing, which might not be detected via visual inspection. Similar results were also obtained with *Pum-Bac* sample in which a higher UPV reading was observed without any visual crack sealing. Further investigations are being done in terms of quantifying self-healing through water absorption.

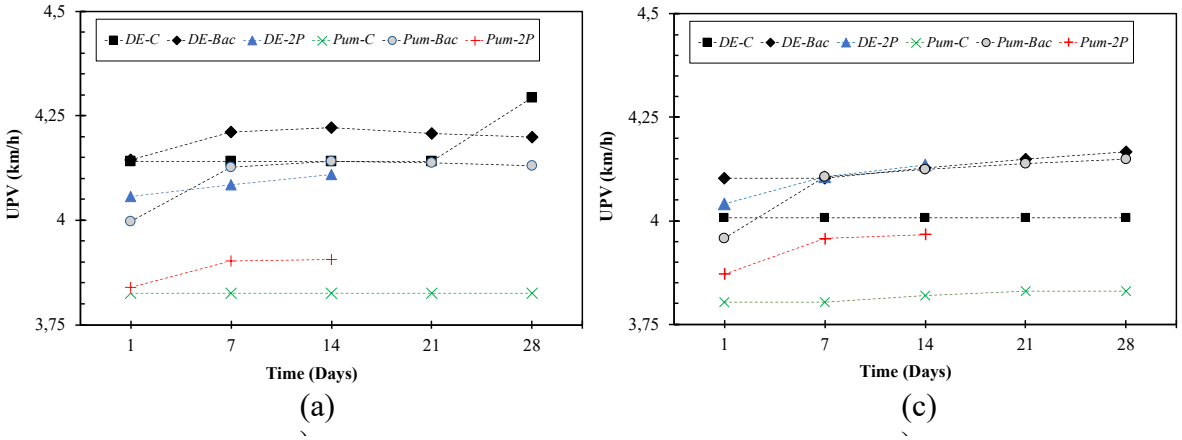

Figure 5. UPV record after crack healing (a) 28-days of water curing (b) 28-days of nutrient curing

4 Conclusion

This study was undertaken to investigate the possible use of diatomaceous earth and pumice as an immobilization barrier for bacterial cells to trigger crack remediation in mortar. Cracks with an average width of 0.4 mm in 28-day old mortar specimens were almost completely filled by bio-based precipitate depending on the curing regime. Results showed that cells require additional nutrient source as urea and calcium acetate either in the mix or as curing regardless of type of the immobilization barrier. Cracks were sealed even in sample including relatively smaller dosage of nutrients and bacterial cells in presence of moisture. Moreover, the duration of crack healing was approximately 21 days, which was almost half of the duration to remediate the cracks when cells were directly incorporated to the mix. Further investigation has to be done to characterize the precipitate and evaluate the influence of crack sealing on permeability.

Acknowledgements

This research was conducted by financial assistance of the Scientific and Technical Research Council (TUBITAK) of Turkey Project: MAG-118M327. SEM analysis was conducted in Advanced Technologies Research and Development Center facilities of Bogazici University, Istanbul. The authors graciously acknowledge Dr.Bilge Gedik Uluocak for her assistance during the analysis.

ORCID

Mustafa Mert Tezer https://orcid.org/0000-0001-9799-8871
Zeynep Başaran Bundur http://orcid.org/0000-0003-1398-4021

References

Alazhari, M., Sharma, T., Heath, A., Cooper, R. and Paine, K. (2018). "Application of expanded perlite encapsulated bacteria and growth media for self-healing concrete." *Construction and Building Materials*, The Authors, 160, 610–619.

Amiri, A., Azima, M. and Bundur, Z. B. (2018). "Crack remediation in mortar via biomineralization : Effects of chemical admixtures on biogenic calcium carbonate." 190, 317–325.

Bang, S. S., Lippert, J. J., Yerra, U., Mulukutla, S. and Ramakrishnan, V. (2010). "Microbial calcite, a bio-based smart nanomaterial in concrete remediation." *International Journal of Smart and Nano Materials*, 1(1), 28–39.

Bundur, Z. B., Bae, S., Kirisits, M. J. and Ferron, R. D. (2017). "Biomineralization in self-healing cement-based materials: Investigating the temporal evolution of microbial metabolic state and material porosity." *Journal of Materials in Civil Engineering*, American Society of Civil Engineers, 29(6).

Erşan, Y. Ç., Da Silva, F. B., Boon, N., Verstraete, W. and De Belie, N. (2015). "Screening of bacteria and concrete compatible protection materials." *Construction and Building Materials*, 88, 196–203.

Jonkers, H. M. and Schlangen, E. (2007). "Crack Repair By Concrete-Immobilized Bacteria." *Civil Engineering*, (April), 1–7.

Liu, S., Bundur, Z. B., Zhu, J.and Ferron, R. D. (2016). "Evaluation of self-healing of internal cracks in biomimetic mortar using coda wave interferometry." *Cement and Concrete Research*, 83.

Mann, S. (2001). *Biomineralization: Principles and Concepts in Bioinorganic Materials Chemistry*. Oxford, New York.

De Muynck, W., De Belie, N. and Verstraete, W. (2010). "Microbial carbonate precipitation in construction materials : A review." *Ecological Engineering*, 36, 118–136.

Tiago, I., Chung, A. P. and Verissimo, A. (2004). "Bacterial Diversity in a Nonsaline Alkaline Environment: Heterotrophic Aerobic Populations." *Applied and Environmental Microbiology*, 70(12), 7378–7387.

Wang, J., Ersan, Y. C., Boon, N. and De Belie, N. (2016). "Application of microorganisms in concrete: a promising sustainable strategy to improve concrete durability." *Applied Microbiology and Biotechnology*.

Wang, J., Van Tittelboom, K., De Belie, N. and Verstraete, W. (2012a). "Use of silica gel or polyurethane immobilized bacteria for self-healing concrete." *Construction and Building Materials*, Elsevier Ltd, 26(1), 532–540.

Wang, J. Y., De Belie, N.and Verstraete, W. (2012b). "Diatomaceous earth as a protective vehicle for bacteria applied for self-healing concrete." *Journal of Industrial Microbiology and Biotechnology*, 39(4), 567–577.

Wang, J. Y., De Belie, N. and Verstraete, W. (2012c). "Diatomaceous earth as a protective vehicle for bacteria applied for self-healing concrete." *Journal of industrial microbiology & biotechnology*, 39(4), 567–77.

Wang, J. Y., Snoeck, D., Van Vlierberghe, S., Verstraete, W. and De Belie, N. (2014a). "Application of hydrogel encapsulated carbonate precipitating bacteria for approaching a realistic self-healing in concrete." *Construction and Building Materials*, Elsevier Ltd, 68, 110–119.

Wang, J. Y., Soens, H., Verstraete, W. and De Belie, N. (2014b). "Self-healing concrete by use of microencapsulated bacterial spores." *Cement and Concrete Research*, Elsevier Ltd, 56, 139–152.

Wiktor, V. and Jonkers, H. M. (2011). "Quantification of crack-healing in novel bacteria-based self-healing concrete." *Cement and Concrete Composites*, 33, 763–770.

Zhang, B., Bundur, Z. B., Mondal, P. and Ferron, R. D. (2015). "Use of biomineralisation in developing smart concrete inspired by nature." *International Journal of Materials and Structural Integrity*, 9(1–3).

XV International Conference on Durability of Building Materials and Components
DBMC 2020, Barcelona
C. Serrat, J.R. Casas and V. Gibert (Eds)

Analysis of Change of Physical Properties of Organic Repair Products due to Fire Exposition

Menéndez, Esperanza[1], Imamoto, Kei-ichi[2], Gettu, Ravindra[3], Noguchi, Takafumi[4] and Recino Hairon[1]

[1]Institute Eduardo Torroja of Construction Science, Spanish National Research Council (IETcc-CSIC), Serrano Galvache street 4, 28033-Madrid, Spain, emm@ietcc.csic.es

[2]Tokyo University of Science, Faculty of Engineering, Department of Architecture, 113-8656-Tokyo, Japan, imamoto@rs.kagu.tus.ac.jp

[3]Indian Institute of Technology Madras, Department of Civil Engineering, Alumni Ave, 600036-Chennai, Tamil Nadu, India, gettu@iitm.ac.in

[4]Tokyo University, Faculty of Engineering and Graduate School of Engineering, 7-3-1 Hongo, Bunkyo-ku, 113-8656 Tokyo, Japan, noguchi@bme.arch.t.u-tokyo.ac.jp

Abstract. *Organic repair products for concrete can be exposed to accidental incidents, like fire. The increase of temperature produces a modification in some of their properties. In general, these types of repair products have organic fibers to increase their tixotropic properties, but they are more sensible to the high temperature than the Portland cement or aggregates. In order to analyze the behavior of organic repair mortars with temperature three types of repair mortars are studied. These repair products have the organic components composed by acetate fiber of polyvinyl like Vinyl Acetate Acrylate (VAA), Copolymer of Vinyl Acetate Vinyl Versatate (VeoVA) and Acrylic polymers fibres. The repair products are tested increasing the temperature from 1.7ºC /min until 200ºC, 400ºC or 600ºC respectively during 20 minutes. After that, the samples are cooled in four different cooling conditions two of them slow and two others fast, and with and without oxygen. These conditions are used in order to simulate the different conditions that can occur during the cooling after fire. After the testing the visual aspect, the color and brightness and the open porosity is analyzed in each condition of test. In this work the relationship between the temperature of exposition, the cooling conditions and the change in some physical properties are studied.*

Keywords: *Organic Repair Mortar, Fire Resistance Test, Color Change, Open Porosity.*

1 Introduction

The progression of the temperatures in the interior of the fire area is greatly conditioned by a series of very varied parameters, such as the type and density of the fire, the capacity for thermal dispersion of the epidermis, the level and disposition of the ventilation, etc. Kucera, P. (2007). Although it is possible to model or predict the thermal evolution of the gas in the affected area to a greater or lesser degree during the project, and from there and design sufficiently safe structures (with viable criteria for its use). The evaluation of the residual capacity of existing structures affected by a fire usually require a more realistic determination of the distribution of the temperatures in the different elements of the structure, Kodur, V.K.R. and Phan, L. (2007). It must be borne in mind that the real conditions of the fire (strength of the fire, ventilation, etc.) are difficult to determine precisely and a theoretical prediction not contrasted with real data

could give rise to significant deviations in areas relative to the thermal analysis of the structure and hence the mechanical evaluation.

The distribution of the temperatures in the interior of the area affected by the fire is not homogeneous, which is why the determination of the number of testing points, their distribution, etc., so that the results are representative and constitute a sound basis for the structural analysis is a relevant question. However, when samples taken from a real fire are analysed it is not always possible to have the suitable number or disposition samples available.

On the other hand, in order to determine the residual resistant capacity of the elements of the structural concrete affected by the fire, it is important to find out not only the distribution of the temperatures in the elements, but also how the effect on other relevant mechanical properties come about from exposure to fire, such as the steel-concrete adhesion. Within the series of temperatures that are produced in the interior of the section, there is an important significance from the mechanical point of view, as are 500ºC. On the one hand, the average value of the resistance to compression losses of the concrete (with lime aggregate) contemplated at a regulatory level is in the order of 40%, which would correspond approximately to the admissible loss in a residential or administrative building in a strict reinforced position (EN-1992 – Eurocode 2: Design of concrete Structures). It is the basis for one of the most used simplified calculation methods in the verification of concrete structures in the case of fire, which is known as the simplified 500ºC isothermal method, Ashely, E. (2007).

The cement based materials have a low thermal conductivity and an elevated specific heat, which is why ambient temperature constitutes a suitable protection for the reinforcement. However, when it becomes subject to higher temperatures it goes through a series of physical-thermal transformations that bring about a modification in the products of the hydration of the cement. From 300ºC, a loss of water comes about as a result of the decomposition of the CSH gel, which brings about a contraction as a result of this loss, even though it is necessary to exceed 900ºC in order to bring about a complete decomposition. Likewise, a decomposition of the portlandite comes about at between 450 – 550ºC, as does a loss of CO_2 of the carbonates from 600ºC. For its part, the siliceous aggregates also go through a physical-thermal transformation from 573ºC, while the lime experiences a decarbonisation at temperatures greater than 600ºC. Although it is important to indicate the possible changes in the aggregate as an effect of the temperature, it also depends on other factors such as size, porosity permeability, etc. – the less porous the aggregate, the less susceptible it is to the action of the fire, Charreau, G.L., Luna, F. (2000). The decomposition of portlandite in cement based materials can be used as an indicator of progression of temperature inside of the material and situate the isotherm 500 in the material, Menéndez, E., Vega, L. (2012).

The physical-thermal transformations undergone by the concrete as an effect of the temperature are translated into a loss of performance, especially when the material exceeds 600ºC. As the temperature increases, a modification in the creep comes about, which can also be seen as a strong dependency on its resistance and elasticity, Schneider, U. (1976). On the other hand, the conditions of putting out the fire must be taken into account, as the speed of cooling or the contact with the water has a significant influence on the physical-mechanical conditions present in the concrete once the fire is extinguished, Nassil, A. (2006). Specifically, the physical-thermal transformations that the components of the concrete go through serve to characterise it after it has been subject to the fire Colombo, M. and Felicetti, R. (2007). In this case, X-ray diffraction, thermal analysis and scanning electron microscopy techniques have

been used with the aim of analysing the behaviour of the concrete exposed to a real fire. Some of these instrumental techniques, such as thermal analysis, are usually used to study the behaviour of certain materials when exposed to the action of fire and high temperatures. As a rule, the fundamental objective of these analyses is to look at the possible improvements that could come about through the use of certain materials that could substitute or complement others, Zhong, H., Wei, P., Jiang, P. and Wang, G. (2006).

Polymer-modified mortar (PCM) contains synthetic resins and/or combustible polymers such as rubber. Hence, the combustibility of PCM is strongly affected by the type and amount of combustible polymer, S. Akihama, *et.al* (1973). The combustible properties of several types of PCMs at high temperatures can be tested using JIS A 1321 (a testing method for incombustibility of internal finish material and procedure of buildings), Y. Oham, S. Suzuki and H. Ozawa (1980). The influence of a polymer admixture on the fire resistance of PCC and analysis of peeling and explosion of PCMs by fire tests are carried out Chandra, S., Berntsson, L., and Anderberg, Y. (1980). On the other hand, the incombustibility of polymer-modified mortars is strongly affected by the polymer type rather than the polymer-cement ratio or polymer content. Some authors have been performed tests about heat release of PCMs Ohama, Y., Shirai, A., and Imamoto, K. (2011).

In the present work, studies of different polymer-modified mortars have been done. The repair mortars have exposed at 200ºC, 400ºC and 600ºC during 20 minutes and are cooling quickly or slowly. The visual aspect, open porosity and colorimetry is analysed in the different samples tested to take conclusions on their behaviour at different temperatures.

2 Raw Materials

Repair mortars were made from three products that were previously selected. Repair mortars, suppliers, characteristics, visual appearance, as well as the organic components that make up the fibers (main components), are shown below in Table 1.

Table 1. Information of repair mortars.

Product	Codification	Type of polymer	Visual Aspect
PLANITOP HDM MAXI	PHM	Acrylic polymer	
MAPEGROUT EASY FLOW GF	MEF	Copolymer of Vinyl Acetate Vinyl Versatate (VeoVA)	
MASTER EMACO S 5400	S5400	Vinyl Acetate Acrylate (VAA)	

3 Manufacturing, Curing Process of Repair Mortars and Test Procedure

Repair mortars were manufactured following the procedure described in the manufacturer's instructions, the mixture is kneaded, poured into the molds and the specimens are cured at 20° C and 60% humidity. Next, in Figure 1, the general appearance of the cured specimens is shown. Samples were tested at temperatures of 200 ° C, 400 ° C and 600 ° C. The exposure time as well as the thermal gradient of the test is shown in Figure 2 below. Four samples of each product

were tested, two in the presence of oxygen and another two in the absence of oxygen respectively. The cooling conditions are shown below:

- Slow cooling: Condition that allows the sample to cool inside the oven until it reaches room temperature (20ºC).
- Fast cooling: Condition that consists of suddenly removing the sample from the oven, so that it loses temperature quickly, while the sample is reserved in a desiccator.

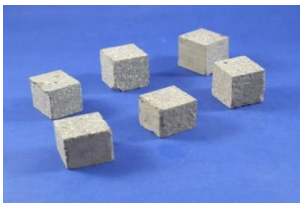

Figure 1. Visual Aspect of the repair mortar.

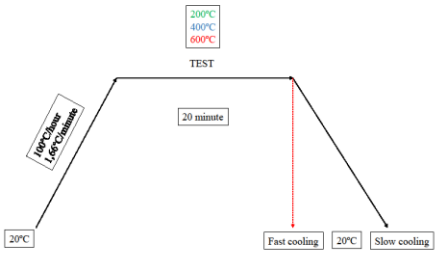

Figure 2. Heating curve proposed for the test.

4 Porosity Accessible to Water

The porosity of the mortars that have been made with the repair products is determined. For this, the porosity of samples that have not been subjected to heat treatment (reference) is determined, and the porosity of the samples subjected to the fire resistance test is determined. Procedure that allows to study the behavior of the porosity as the test conditions change.

The methodology described in the UNE EN 1936 standard is used to determine the porosity accessible to water. Next, Table 1 shows the test conditions that the samples are subjected to.

Table 2. Test conditions.

Temperatures	**200ºC**	**400ºC**	**600ºC**
Test conditions	Slow cooling without O_2 **(SC)**		
	Slow cooling with O_2 **(SCO)**		
	Fast cooling without O_2 **(FC)**		
	Fast cooling with O_2 **(FCO)**		

4.1 Porosity of Mortars as a Function of the Product Used

Next, Figures 3 shows the porosity values obtained from this test are plotted. Some dispersion in the porosity values is observed for each of the mortars tested. Porosity increases as the test temperature increases; the apparent increasing of cracking in mortars can causes this effect.

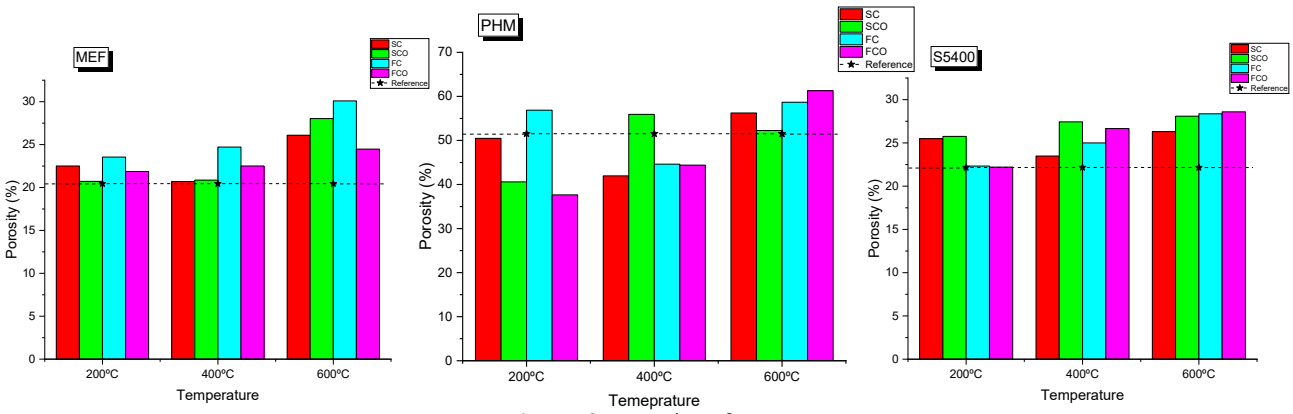

Figure 3. Porosity of mortars.

4.2 Porosity Variation as Function of the Test Temperature

In order to study the behavior of the products tested, at each test temperature, the variation of the porosity as a function of the study temperature is shown below (Figures 4).

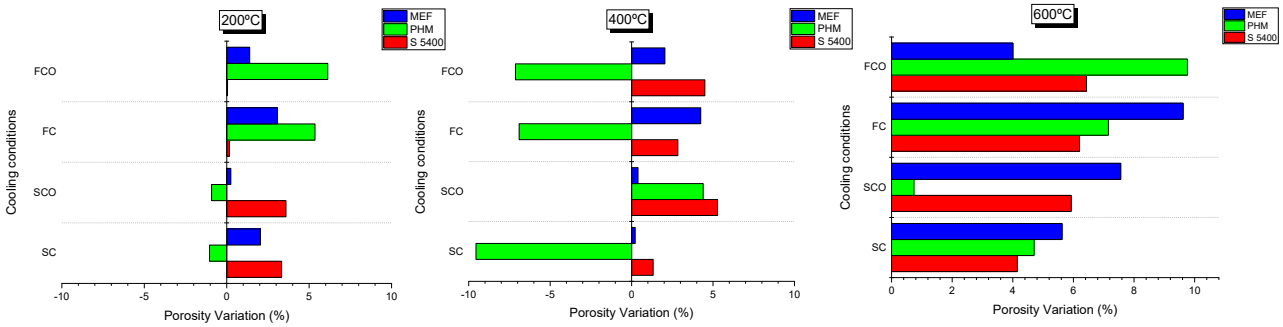

Figure 4. Porosity variation of mortars tested at **2**00, 400 and 600 ºC.

In general, an increase in porosity is observed as the test temperature increases. Samples subjected to 600°C contain fibers composed of polymers that decompose at temperatures above 500°C, forming gases such as methane, carbon dioxide and carbon monoxide among others. These gases increase the pressure inside the mortar, causing tensions in the areas where the pressure is higher, this effect can cause cracking, increasing the porosity of the mortar.

On the other hand, a decrease in the porosity in the PHM mortar is observed, at 400°C, caused by the fusion and diffusion of the fibers through the pores, filling the air pores, an effect that would explain this behavior.

4.3 Porosity Variation as Function of the Cooling Conditions

The increment of the porosity is shown depending on the test condition, it should be noted that the values shown below are values that reflect the increase in porosity with respect to the reference porosity values for each mortar tested. In any case, the most favorable scenario (least increase in porosity) is in which the mortar tested is cooled slowly. Although between the two scenarios in which it cools slowly, the one performed without oxygen shows less increase in porosity.

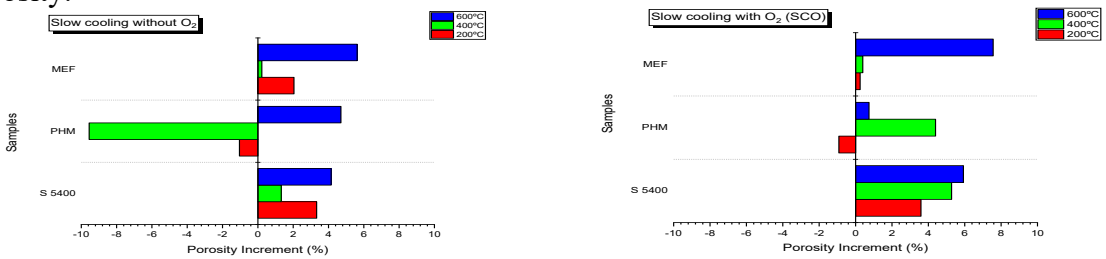

Figure 5. Porosity increment of mortars that were cooled slowly with and without O_2.

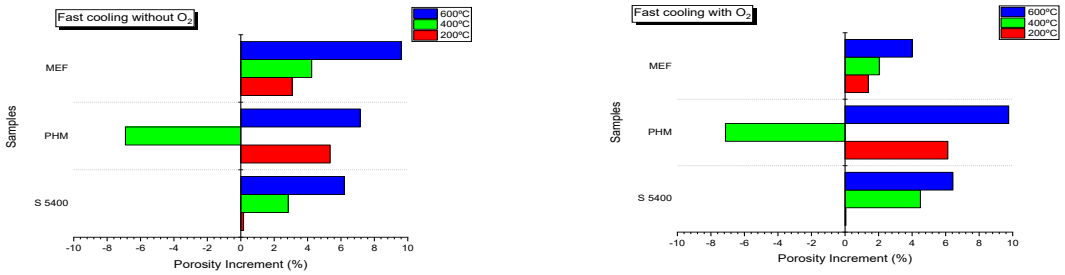

Figure 6. Porosity increment of mortars that were cooled suddenly with and without O_2.

5 Colorimetry

Colorimetric techniques are based on the measurement of radiation absorption in the visible area by colored substances. All systems that quantify color from three variables have colorimetric aspects: Luminance, Length and Purity.

With this technique, the color behavior of the mortars tested is studied, the color is measured in the mortars that have not been subjected to the test conditions, and then the color is measured in those mortars that have been analyzed in the test conditions shown in Table 3.

Table 3. Test conditions.

Temperature	**200ºC**	**400ºC**	**600ºC**
Test conditions	Slow cooling without O_2 **(SC)**		
	Slow cooling with O_2 **(SCO)**		
	Fast cooling without O_2 **(FC)**		
	Fast cooling with O_2 **(FCO)**		

5.2 Colorimetric Variation as Function of Test Temperature

Next, a data processing is carried out. The color variation of the tested products is determined, compared with the color tones of the reference (product without heat treatment).

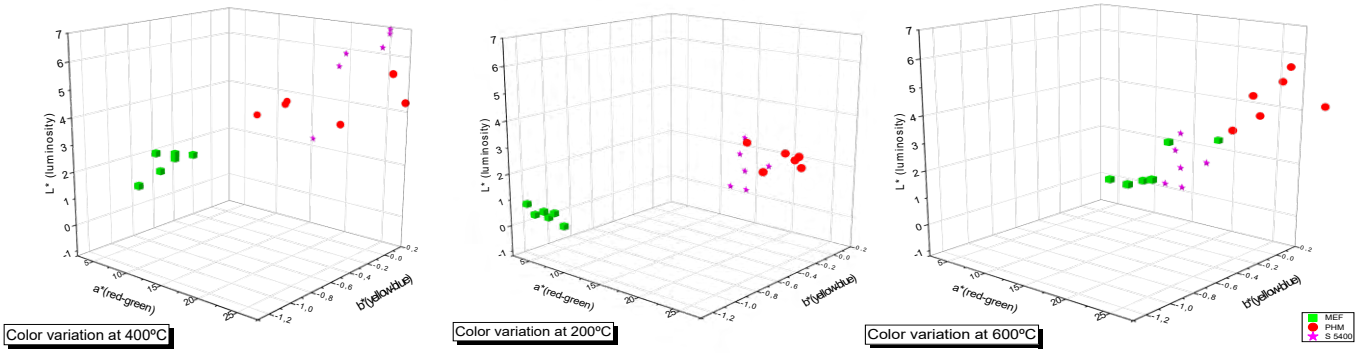

Figure 7. Color variation of the mortars tested at 200, 400 and 600°C.

At 200ºC and 400ºC, it is observed that the MEF product does not show variation around the

reference colorimetric values. As for the temperature of 600 ° C, the color variation of the products tested show a linear trend around the blue color when the brightness increases.

6 Conclusions

The following conclusions are obtained from the tests performed:

- The repair mortar that has the lowest porosity is MEF; on the other hand, the product that has the highest porosity is the PHM.
- In temperatures, at 200ºC and at 400ºC a good behavior is observed in the materials tested, while at 600ºC the behavior is very unfavorable in all cases, because at 600ºC, the increase in porosity is significant and it can cause reduction of mechanical strength. On the other hand, the PHM mortar is the one that shows the highest porosity, but it is the only one in which the porosity decreases when tested at temperatures between 200ºC-400ºC. This behavior may be caused by the composition of the fibers. The melting temperature of fibers is in the range 200° C - 400°C, causing diffusion of the fibers through the pores of the cementitious paste, filling capillary pores, and decreasing the porosity.
  In general, a linearity is observed between the increase in temperature and the decrease in brightness, approaching darker tones as the test temperature increases.

Acknowledgements

E. Menéndez would like to express their gratitude to the funding of the project *CSIC 201460E067 Analysis of systems of diagnosis, decision making in structures of concreter with non-directional cracking*.

ORCID
Esperanza Menéndez: http://orcid.org/0000-0001-6461-4798
Takafumi Noguchi: https://orcid.org/0000-0001-6115-2292
Kei-ichi Imamoto: https://orcid.org/0000-0001-8174-8827
Hairon Recino: https://orcid.org/0000-0002-4831-7790

References

Ashely, E. (2007). *The Role of Performance-Based Design in Concrete Fire Resistance.* Fire Resistance of Concrete Structures. Concrete in Focus, Fall.

Background document on parametric temperature-time curves according to Annex A of prEN1991-1-2. Profil Arbed. (2001). Centre de recherches. CEN/TC250/SC1/N298A. Document Nº EC1-1-2/72.

Chandra, S., Berntsson, L. and Anderberg, Y. (1980). *Some Effects of Polymer Addition on the Fire Resistance of Concrete*, Cement and Concrete Research, V.10, No.3, pp.367-375.

Charreau, G.L. and Luna, F. (2000). *Efecto del fuego sobre los hormigones. Alteraciones sufridas por los agregados.* Instituto Nacional de Tecnología Industrial. INTI – CECON. Jornadas de Desarrollo e Innovación.

Colombo, M. and Felicetti, R. (2007). New NDT techniques for the assessment of fire-damaged concrete structures. *Fire Safety Journal*, 42, pp. 461-472.

Concrete Masonry Fire Resistance.(2005). Northwest Concrete Masonry Association. Tek note.

Design of concrete structures for fire resistance. (1981). Bulletin d´information nº 145. Comite euro-international du beton.

Documento Básico DB-SI: Seguridad en caso de incendio.(2005). Código Técnico de la Edificación. Ministerio de Vivienda – Gobierno de España.

EN-1992 – Eurocode 2 (1992). Design of concrete Structures – Part 1.2: General rules – Structural fire design.

Ercolani, G.D., Ortega, N.F. and Señas, L. (2007). *Empleo de Ultrasonidos y Esclerometría en el diagnóstico de estructuras de hormigón afectadas por elevadas temperatura.* Asociación Argentina de Ensayos no Destructivos y Estructurales. IV Conferencia Panamericana de END. Buenos Aires.

Fletcher, I.A., Welch, S., Torero, J.L., Carvel, R.O. and Usmani, A. (2007). Behaviour of Concrete Structures in Fire. *Thermal Science*, 11, no.2, pp. 37-52.

Hajpál, M. Monuments Exposed to Fire or High Temperature. *Fire Technology*, 38, 2002, pp. 373-382.

K. Kishitani, et.al. (1982). *A study on fire resistance of polymer-modified mortar*, Summaries of technical papers of annual meeting Architectural Institute of Japan, pp.169-170.

Kodur, V.K.R. and Phan, L. (2007). Critical factors governing the fire performance of high strength concrete systems. *Fire Safety Journal*, 42, pp. 482-488

Kucera, P. (2007). *Thermal-mechanical Analysis of Concrete Structure Exposed to High Temperature.* Except from the Proceedings of the COMSOL Users Conference. Grenoble.

Lottman, B.B.G. (2007). Fire in bored tunnels. Structural behavior, during fire conditions, of bored tunnels made with a concrete segmental lining. Delf University of Technology. Netherlands.

Mehta, P.K. (1986). *Concrete. Structure, properties and materials*. Ed. Prentice-Hall, Inc. USA.

Menéndez, E. and Vega, L. (2012). Use of decomposition of portlandite in concrete fire as indicator of temperature progression into the material. JTAC, Vol. 110, N. 1. DOI:10.1007/s10973-011-2159-4

Menéndez, E. and Vega, L. Study of dehydration and rehydration processes of portlandite in mature and young cement pastes. JTAC, Vol. 110, N. 1. DOI:10.1007/s10973-011-2167-4

Menéndez, E. and Vega, L. (2010). Analysis of the behaviour of the structural concrete after the fire at the Windsord Building in Madrid. Fire & Materials, Vol. 34: 94-107. DOI:10.1002/fam.1013

Nassil, A. (2006). Postfire full stress-strain response of fire-damaged concrete. *Fire and Materials,*30: 323-332.

Ohama, Y., Shirai, A., and Imamoto, K. (2011). *Fire-Protecting Performance of Polymer-Modified Mortars Using Redispersible Polymer Powders*, European Symposium on Polymers in Sustainable Construction, Czarnecki Symposium (ESPSC 2011), Warsaw, Poland, pp.1/7-7/7.

Sarvaranta, L., Elomaam, M. and Järvelä, E. (1993). A study of spalling behaviour of PAN fibre-reinforced concrete by thermal analysis. *Fire and Materials,*17: 225-230.

Schneider, U. (1976). Behaviour of concrete under thermal steady state and non-steady state conditions. *Fire and Materials,* 1: 103-115.

Shirai, A., Ohama, Y. and Kokubun, Y. (2009). *Fire-Protecting Performance of Polymer-Modified Mortars for Buildings*, Proceedings of the 6th Asian Symposium on Polymers in Concrete, Shanghai, China, pp.507-513.

S. Akihama, et.al. (1973). A Study on shear wall using polymer-modified mortar （Part. 2) ― Mechanical properties, heat and fire resistance of concrete, Kajima Technical Research Report, Vol.21, pp.565-574.

Taylor, H.F.W. (1997). *Cement Chemistry*. Ed. Thomas Telford. USA.

UNE-EN-1991- Eurocódigo 1. (1991). Acciones en las estructuras. Parte 1-2: Acciones en estructuras expuestas al fuego.

Y. Ohama, Y. Kokubun and A. Shirai. (2008). Fire-protecting performance of polymer-modified mortar for buildings and proposal for fire-protecting performance test methods for them. J. Struc. Constr. Eng. AIJ, Vol.73, No.631, 1449-1457.

Y. Ohama, S. Suzuki and H. Ozawa. (1980). Incombustibility of polymer-modified mortar, Proceeding of JCI 2nd Conference, pp.253-256.

Zhong, H., Wei, P., Jiang, P. and Wang, G. (2006). Thermal degradation behaviours and flame retardancy of PC/ABS with novel silicon-containing flame retardant. *Fire and Materials*, 31: 411-423.

XV International Conference on Durability of Building Materials and Components
DBMC 2020, Barcelona
C. Serrat, J.R. Casas and V. Gibert (Eds)

Comparative Life-Cycle Analysis of Two Repair Measures for Chloride Contaminated Concrete Structures

Sylvia Keßler

Helmut-Schmidt-University/ University of the Federal Armed Forces Hamburg, Chair of Engineering Materials and Building Preservation, Holstenhofweg 85, Hamburg, 22043, Germany, sylvia.kessler@hsu-hh.de

Abstract. *Often the mere mention of the word "Sustainability" leads to the reflection of the effect of our actions on environment and future generations. Especially the application of reinforced concrete as the most used construction material has a huge impact on a society being sustainable. Thus, the construction industry focuses on the design of environmentally- and resource-friendly buildings. However, due to our aging infrastructure and expected high demand of maintenance and repair in future, a further look on the sustainability of different repair measures for reinforced concrete structures has been neglected in the past. This paper presents a comparative case study of the life-cycle analysis of two different repair measures for reinforced concrete affected by chloride-induced corrosion. The selected repair measures – removal of the chloride-contaminated concrete and cathodic protection – are the most common repair measures in Germany. In future way concrete repair measure could be selected not only by the costs but as well by their environmental impact. This paper provides first information to achieve this target.*

Keywords: *Reinforced Concrete Structures, Repair Measure, Life-Cycle-Analysis, Reinforcement Corrosion.*

1 Introduction

Our infrastructure is the backbone of our society and economy. Bridges and tunnels maintain our mobility and enable the transportation of constantly increasing number of goods. Additionally, in dense inner city areas multi-storey and underground car parks are of greatest importance to provide space keeping the traffic flowing. However, most of these reinforced concrete structures have achieved already their designed service life or the designed service life is shorten due to durability issues. Consequently, these structures need repair measures.

Especially, chloride-induced corrosion require maintenance actions as major reason for structures deterioration. Chlorides from sources such as de-icing salt or marine environment penetrate into the porous concrete and as soon as a critical chloride concentration accumulates at the reinforcement, corrosion initiation becomes likely. Consequences of reinforcement corrosion are the loss of rebar cross section and in an advanced stage cracking and spalling of the concrete cover. Thus, this deterioration process impairs the serviceability and the load bearing capacity of our infrastructure.

The standard, EN 1504-9 provides several repair principles for chloride-contaminated concrete structures with the aim to stop and to prevent reinforcement corrosion. The most commonly applied repair principles are:

- Principle 7: Preservation or restitution of the coat passive layer (RP)
- Principle 8: Increase of concrete resistance (IR)

doi:10.23967/dbmc.2020.021

- Principle 10: Cathodic protection (CP)

The principles 9 (cathode control) and 11 (anodic areas control) have no conceptual meaning in Germany since their effectiveness have not been proven yet.

The approach achieving corrosion control of each repair measure is different. For preserving and restoring the reinforcement's passivity, the chloride-contaminated concrete is removed and replaced by new, alkaline and chloride-free concrete. The high alkalinity of the fresh concrete leads to the repassivation of the former anodic areas and reinforcement corrosion is impaired. The repair measure is by far the most common one even though it is a significant intervention in the structure's integrity.

The increase of concrete resistance aims to dry out the concrete, *e.g.* by application of a concrete coating, until the electrolytic corrosion process is no longer possible and the corrosion velocity comes to a negligible rate.

In recent years, cathodic protection systems gain more and more attention and one standard (EN ISO 12696) focuses exclusively on this repair measure. Cathodic protection suppresses the anodic reaction by applying an electric potential. The polarization of the reinforcement forces the reinforcement to act electrochemically as a cathode. Consequently, no anodic reaction – no loss of cross section – can take place even though the chloride concentration is on a critical level. In addition, cathodic protection diminishes the driving potential between former anodic and cathodic rebar areas providing supplementary protection against corrosion.

Each repair principle can be pursued by different repair procedures/ methods that vary in the execution following the same objective.

The demand of maintenance and repair of reinforced concrete structures will increase tremendously in the upcoming year. We need a further look on their sustainability to support the decision-making of choosing an adequate repair principles and corresponding repair method. Thus, this paper presents a first approach comparing the life cycle analysis of two repair methods for a specific case study. The aim is to evaluate the category indicators (a) global warming potential, (b) abiotic depletion and (c) ozone layer depletion when applying cathodic protection and concrete replacement as repair measure.

2 Life Cycle Assessment

The Paris Agreement from the United Nations urges especially the developed countries to deliver an overall mitigation in global emissions. This goal is only achievable, if we are aware of our environmental impacts. This applies in particular to the construction industry as one of the major emitters due to e.g. the energy-intensive production of cement/ concrete and steel. One option to identify the most sustainable repair measures of reinforced concrete structures is the implementation of a life cycles assessment (LCA) according to DIN EN ISO 14040 and DIN EN ISO 14044.

The LCA study consists of several steps starting with the definition of the scope followed by the inventory analysis and impact assessment and ends with the interpretation of the results. The scope of the LCA should be described as precise as possible including all considered boundary conditions to ensure consistency. The inventory analysis collects all data involved such as the quantification of the relevant inputs and outputs of the repair action during the defined life cycle. The inputs and outputs should be broken down to the elementary level.

During the impact assessment phase, the impact of the repair measure on the environmental is estimated based on category indicators. Impact categories are the consumption of primary raw materials; water consumption, primary energy consumption, global warming potential, acidification potential, photochemical ozone creation potential and material recyclability. The final step is the discussion of the outcome taken into account the objective of the study.

Conclusions and recommendations complement the LCA study leading to a clear decision-making basis for more sustainable rehabilitation of concrete structures.

3 Case Study

The objective of the life-cycle assessment of two different repair measure is to support future decision-making for the most sustainable repair measure. Secondly, the study aims to identify missing data we need to collect in future to enable comprehensive sustainability analysis of repair measures.

3.1 Functional Unit

The functional unit for this sustainability assessment of repair measures is a very common constructive element: one square meter of reinforced concrete plate. This plate could be e.g. part of a bridge superstructure or part of a multi-storey car park. Consequently, the functional unit is assigned to exposure class XD3 (DIN EN 206), which considers chloride exposure from de-icing salts in combination with cyclic wetting and drying. Since the element is part of an aged, deteriorated structure the used cement type is Portland cement. The concrete cover is about 55 mm and therefore in compliance with the current standards. The same applies to the water-to-binder ratio of 0.45 and the cement content of 320 kg/m³. The designed service life is 75 years with a target reliability index of 0.5 (DAfStb, 2008). This target reliability corresponds to a corrosion probability of 30 %. No additional protection such as polymer concrete coatings are applied and possible cracking of the concrete cover, respectively crack repair is neglected.

3.2 Service-Life Assessment

First, a probabilistic service life prediction assists the decision making to estimate when and how often the functional unit requires repair actions. Figure 1 shows the results of the initial probabilistic service life prediction according to fib Model Code for Service Life Design (fib bulletins 34 and 76).

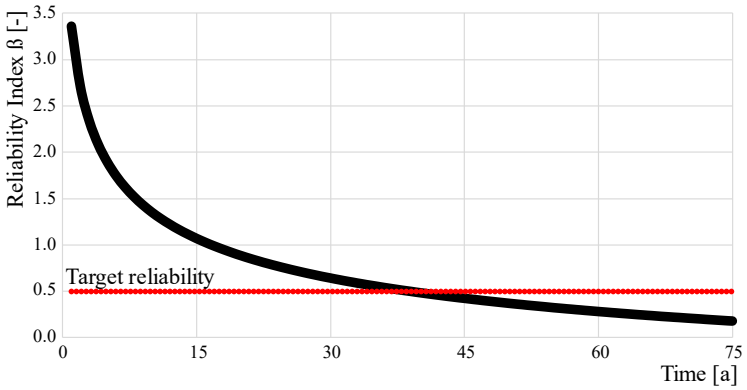

Figure 1. Service life assessment of the case study.

Even though, the durability design of the functional unit complies with the standards the target reliability of $\beta = 0.5$ is achieved after around 40 years. This result is in line with literature data (fib bulletin 76), which revealed that the durability design rules cannot ensure consequently a design service life of normally 50 years without the need of repair actions. However, the presented case study requires repair action within the designed service life of 75 years.

3.3 Repair Measures

As mentioned above the most common repair measures of chloride-contaminated concrete are based on the Principles 7 and 10 (EN 1504-9). Therefore, the life-cycle assessment includes one repair method from both principles:

- 7.2: Substitution of the chloride-contaminated concrete
- 10.1: Application of an electric potential

3.3.1 Repair measure 7.2

Roughly, the application of the repair method 7.2 consists of the mechanical removal of the chloride-contaminated concrete and the refill with fresh and alkaline concrete until the former or newly requested concrete cover is achieved. This procedure can be an intrusive intervention in the structure's integrity. On the other hand, it is an effective method to inhibit reinforcement corrosion.

However, very little information is available on the service life of this repair measure. Tilly and Jacobs (Tilly et Jacobs 2007) analyzed 230 case studies of concrete repair measures. Concrete replacement were effective only in rd. 50 % of the investigated use cases. The authors listed several reasons for the failure: inappropriate measure or material, execution error, non-conformance of the specifications etc.. After 5 years in service, 20 % of the repair measure needed repair measure, 55 % within 10 years and 90 % within 25 years. Polder et al. (Polder et al. 2016) confirmed the results of Tilly and Jacobs with data of a Dutch study.

3.3.2 Repair measure 10.1

Here, the application of the electric potential is implemented through an impressed current cathodic protection (ICCP) system, where an external power supply generates large potential

differences to enable the current flow needed for corrosion protection. In the electric circuit, the reinforcement acts as a cathode whereas the anode system is applied on the concrete surface layer. Several anode systems are on the market. The most common anode systems for plate elements are mixed metal oxide/titanium (MMO/Ti) anodes in shape of ribbons or meshes, which must be embedded in cementitious material to enable the electrolytic contact to the concrete. The application require several working steps, however, it maintains the structures integrity since the chloride-contaminated concrete remains in the structure.

The whole ICCP system needs to be applied only once and the effectiveness of the corrosion protection is monitored. Nevertheless, the systems includes many electrical components such a power supplies or electrical transformers with limited service life under continuous use. Their replacement is easy to handle and need to be considered for the life-cycle analysis.

The ISO 12696 indicates a service life of the NMO/Ti anodes in the range of 25 to 100 years in dependence of the range of the current density. Polder et al. (Polder et al. 2016) estimated the service life of a CP system of about 50 years and Wilson et al. (Wilson et al. 2013) of about 10 to 120 years, excluding the electric components, which need replacement at least every 20 years. Nevertheless, it is important to mention that cathodic protection systems on concrete structures is a relatively new repair measure (started in the 90's) and current experiences are based on the early, more vulnerable cathodic protection systems.

3.3.3 Repair measure cycles

It appears that very little information is available on the durability of repair measures itself. Based on the literature it is very likely that repair measure needs repair action due to the use of inadequate material or poor execution. These effects are very hard to predict and therefore, the estimation of repair cycles during a service life of a concrete structure is subject to assumptions.

The installation of the CP systems with ribbon anodes takes place earlier in a service life than the replacement of the chloride-contaminated concrete. The reason for that is that the CP system can only be applied when the corrosion damage is not in an advanced stage showing cracks and spalling of the concrete cover. Therefore, the timing of the CP installation is set when the reliability index is 1.3 (corrosion probability 10 %) after 11 years, see Figure 1. Every 20 years, in total for two times, all electronic components will be renewed. In contrast, the time of the concrete replacement corresponds to the time when the target reliability is reached after 40 years. It is assumed that the new concrete shows the same chloride penetration resistance as the former one. Therefore, the repair measure takes place only once until the end of the designed service life of the structure.

3.4 The Inventory Analysis

The objective of the inventory analysis is the collection of all relevant environmental information on the used material and the execution process for each repair measure. Each step includes if necessary the consumption of energy and water and the consideration of the transport (fuel, distance) of the needed material.

3.4.1 Relevant information of repair measure 7.2

The execution of the repair measure 7.2 consists of the following steps, which need to be considered for the LCA:

- Removal of concrete with ultra-high water pressure jetting
- Production of concrete
- Processing of the fresh concrete
- Disposal of concrete

3.4.2 Relevant information of repair measure 10.2

The following inputs and outputs are part of the installation of a cathodic protection system on reinforced concrete with ribbon anodes:

- Production of the titanium anodes
- Production of the embedding mortar
- Production of reference electrodes
- Production of the Electronic components (e.g. power supply, transformer and rectifier, control devices, data management systems and connection boxes, cables)
- Concrete milling
- Installation of the ribbon anodes
- Installation of the reference electrodes
- Installation of the electric contact to the reinforcement
- Processing of the embedding mortar
- Disposal of concrete
- Disposal of electronic waste

It is obvious, that the installation of a cathodic protection system requires much more working steps that the concrete removal. However, the quantity of the processed concrete is much higher for the concrete replacement, whereas only the cathodic protection system needs electric components.

Sometimes, during a concrete removal the structural element (functional unit) needs additional support for static reasons. This step is not included in this analysis.

3.5 Results

The software package SimaPro (Version 8.4.0.0) with the underlying databases of ecoinvent (Version 3) supported the evaluation of this LCA study using the CML-IA baseline method. The following results show the comparison of both repair measures for selected impact categories considering a service life of 75 years, see Figure 2.

In all three categories, the cathodic protection system shows greater impact on the environment than the concrete replacement measure. The greatest difference between both repair measures is in the global warming potential. Here, the impact of the CP systems is more than twice the level of the concrete replacement. The reason for this difference is the impact of the replacement (production and disposal) of the electronic components for the cathodic protection system with a value of 158 $kgCO_2eq$. The highest impact on the global warming potential within the concrete replacement has the removal of the old concrete using ultra-high water pressure jetting with a value of rd. 62 $kgCO_2eq$.

The same dependencies apply for the abiotic depletion. Here, the impact of the CP systems is much greater due to the production of the electronic components with a value of 586 MJ. Again, the ultra-high water pressure jetting during concrete removal has major impact on the

abiotic depletion of the concrete replacement. The difference between both repair measures is less pronounced considering the ozone layer depletion.

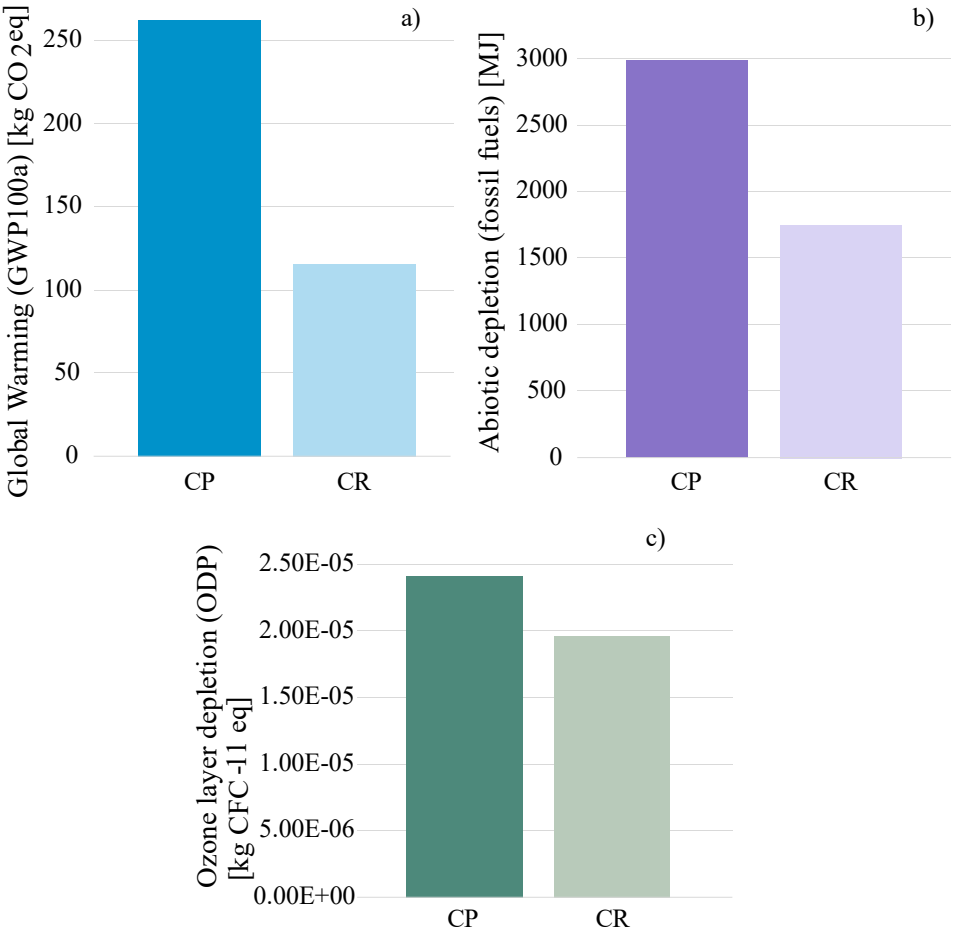

Figure 2. The comparison of the (a) global warming potential, (b) abiotic depletion and (c) ozone layer depletion of the two repair measures CP (cathodic protection) and CR (concrete replacement) on a reinforced concrete plate after a service life of 75 years.

However, the presented results are only of preliminary nature and do not provide a comprehensive study. Very often, the concrete surface needs an additional protection against ingress of chlorides such as polymer coatings if no CP system is installed. These coatings need also replacement in certain intervals. Thus, the consideration of a polymer concrete coating would lead to different LCA results. Furthermore, the service life of the concrete structure and the service life of the repair measure itself have a huge effect in the LCA outcome.

Nevertheless, this study provides a preliminary insight on the environmental impact on repair measures. Even though, the concrete replacement requires the removal and refill of great volume of concrete it is probably in a lot of use cases the most sustainable repair measure. The impact of electronic components or presumably the impact of polymer concrete coatings is much higher than the pure concrete.

Nowadays, the determination of the adequate repair measure depends mainly on other factors

such as costs, applicability, remaining service life, and many more. However, in future we should also be aware of the environmental impact of the chosen repair measure as well.

4 Conclusions

The following conclusions can be drawn from this specific comparative LCA of the concrete repair measures concrete replacement and cathodic protection.

- The environmental impact of the cathodic protection system is greater than the impact of the concrete replacement when comparing the category indicators global warming potential, abiotic depletion and ozone layer depletion.
- Even though, the concrete replacement consumes much higher quantity of energy-intensive concrete it is not necessarily the repair measures with the greatest impact on the environment.
- The high environmental impact of the cathodic protection system is the result of its demand of multiple electronic components.
- The service life of the electronic components is the determining factor of the sustainability of the cathodic protection system.

More generally, more field data on the durability of concrete replacement is required to enable reliable assumptions on repair intervals.

ORCID

Sylvia Keßler: http://orcid.org/0000-0002-1335-1104

References

DAfStb Positionspapier (2008), *Positionspapier des Deutschen Ausschusses für Stahlbeton zur Umsetzung des Konzepts von leistungsbezogenen Entwurfsverfahren unter Berücksichtigung von DIN EN 206-1*, Anhang J. Beton- und Stahlbetonbau 103, Heft 12.

DIN EN 206:2014 (2013) *Beton – Festlegung, Eigenschaften, Herstellung und Konformität*, Deutsche Fassung EN 206:2013.

DIN EN ISO 1269 (2017). *Cathodic protection of steel in concrete (ISO 12696:2016)*; German version EN ISO 12696:2016.

DIN EN 1504-9 (2008). *Products and systems for the protection and repair of concrete structures - Definitions, requirements, quality control and evaluation of conformity - Part 9: General principles for the use of products and systems*; German version EN 1504-9:2008. https://dx.doi.org/10.31030/1471480.

DIN EN ISO 14040 (2009) *Umweltmanagement – Ökobilanz – Grundsätze und Rahmenbedingungen,* Deutsche und Englische Fassung EN ISO 14040:2006.

DIN EN ISO 14044 (2006) *Umweltmanagement – Ökobilanz – Anforderungen und Anleitungen,* Deutsche und Englische Fassung EN ISO 14044:2006.

Fédération international du béton (fib). fib Bulletin No. 34 (2006) *Model Code for Service Life Design*.

Fédération international du béton (fib). fib Bulletin No. 76 (2015) *Benchmarking of deemed-to-statisfy provisions in standards: Durability of reinforced concrete structures exposed to chlorides*.

Polder, R., Pan, Y., Courage, W. and Peelen, W. (2016) *Preliminary study of life cycle cost of preventive measures and repair options for corrosion in concrete infrastructure*. HERON Vol. 61 No.1.

Tilly, G. P. and Jacobs, J. (2007) *Concrete Repairs – Performance in service and current practice*. IHS BRE Press, Backnell.

Wilson, K., Jawed, M. and Ngala, V. (2013) *The selection and use of cathodic protection systems for the repair of reinforced concrete structures*. Construction and Building Materials 39 19-25.

XV International Conference on Durability of Building Materials and Components
DBMC 2020, Barcelona
C. Serrat, J.R. Casas and V. Gibert (Eds)

Deterioration Prediction Model of Multi-Layer Coating Material and its Reference Service Life Evaluation in Terms of Carbonation Control Effect

Kotaro Etchuya [1], Keiichi Imamoto [2] and Chizuru Kiyohara [2]

[1]Japan Building Coating Materials Association, ecchuya@nsk-web.org

[2] Tokyo University of Science, Dr.Eng, imamoto@rs.tus.ac.jp

Abstract. *In this paper, authors propose a method to predict deterioration of exterior finishes using Markov Chain Model based on field survey results on cracks of exterior finishes of existing RC buildings. There existed correlation between degradation of finishing and carbonation progress. Authors propose the service life prediction approach to focus on the carbonation suppression effect into the concrete considering progress of exterior finish deterioration.*

Keywords: *Masonry Coating, Visual Survey, Markov Chain Model, Service Life Prediction Method.*

1 Introduction

Carbonation of concrete is one of the factors that determines the life of reinforced concrete buildings. In general, it is possible to prevent the carbonation and extend the life by applying an exterior coating material to the outer wall.

It is difficult to predict the degradation of finishing coatings because type of material, parts used, construction level and maintenance level interactively affect the degradation of coating material.

On the other hand, since the exterior finishing coatings is required to have protection performance against reinforced concrete, its end would be evaluated as a time when the carbonation suppression effect decreases a certain value. However, there are many unknown points about the relationship between the deterioration of the exterior coating material and the reduction of the carbonation suppression effect.

In this study, authors investigate the deterioration state of actual buildings throughout field survey, and propose a deterioration prediction method of exterior coating materials by using the Markov chain model, which is one of the comprehensive probabilistic models based on the results of the survey. In addition, focusing on change of carbonation suppression effect with deterioration of the exterior coating material, authors propose a method for evaluating the service life of the coating material.

2 Development of Deterioration Prediction Method for Exterior Coating Material

2.1 Collection of Deterioration Data of Exterior Coating Materials in Real BSuildings

Four reinforced concrete buildings shown in Table1 were surveyed from 2012 to 2016. It should be noted that "Age from Repaint" means the age of the exterior coating material from renovation year to 2016. In addition, since the four buildings locate in the neighborhood, it would be a

doi:10.23967/dbmc.2020.031

close environmental condition. The number of renovations of the exterior coating material is one, but years of the renovation is different.

Table 1. Surveyed Buildings.

	Survey Buildings			
	A	B	C	D
Construction	reinforced concrete construction			
Stories	4	4	4	12
Design Strength	18 N/mm^2	18 N/mm^2	21 N/mm^2	21 N/mm^2
Year of construction	1978	1977	1977	1977
Year of Repaint	2010	2008	2001	1997
Age from Repaint	6 old	8 old	15 old	19 old
Coating Material (construction)	Multi-layer Coating Material (E Type)			
Coating Material (repaint)	Synthetic Resin Emulsion Paint			
Color of finish	white			

Table 2. Classification of Crack Degradation.

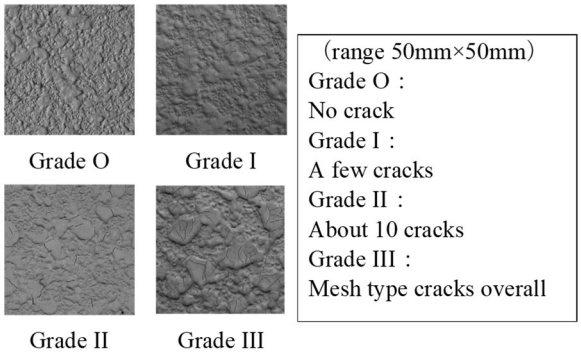

Survey items are as follows.

(1) Cracks: Visual cracks in the outer wall were classified into four grades. About 100 to 200 points with each point of 50mm x 50mm area for each building were surveyed. Grade detection was performed using a standard sample shown in Table 2.
(2) Carbonation: Carbonation depth was measured by phenolphthalein solution method with core specimens.

Fig. 1 shows relationship between elapsed years after the repair of the surveyed buildings and average crack grade of each surveyed location. As an overall trend, it was confirmed that cracking progressed with the passage of time since the renovation.
Fig. 2 shows relationship between elapsed years since renovation and depth of carbonation. It can be seen that the progress of carbonation is delayed as the passage of time from the renovation increases. Since age of each surveyed building is almost the same and the number of repaints is one, it would be thought that not only the aging from the renovation to the time of the survey, but also the aging from the new construction to the renovation affected the progress of carbonation. Furthermore, the carbonation progressed in the buildings where the renovation time was significantly delayed.

Figure 1. Crack Degradation.

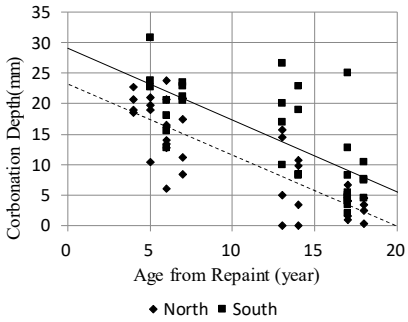

Figure 2. Carbonation.

2.2 Deterioration Prediction of Exterior Coating Materials

The Markov chain model is a probabilistic model for future condition prediction, and it is a

macro model that is used when it is difficult to predict by the accumulation of each affecting factor. Here, in the degradation grades from O to III as shown in Fig.3, the transition probability Xn is assumed to transit from certain degradation grade to the next grade after a certain time t. It is assumed that the distribution of the deterioration grade at any time can be simulated. This model has irreversible features, and its equation is represented in Fig.4.

As shown in Fig. 1, cracking phenomenon, which is the degradation phenomenon of exterior coating, tends to progress with time, and is consistent with the irreversible characteristics of the Markov chain model used in this study.

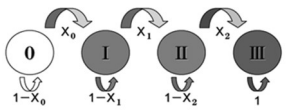

Figure 3. Conceptual Diagram of Markov Chain Model.

$$\begin{pmatrix} O \\ I \\ II \\ III \end{pmatrix} = \begin{pmatrix} 1-x_0 & 0 & 0 & 0 \\ x_0 & 1-x_1 & 0 & 0 \\ 0 & x_1 & 1-x_2 & 0 \\ 0 & 0 & x_2 & 1 \end{pmatrix}^t \begin{pmatrix} 1 \\ 0 \\ 0 \\ 0 \end{pmatrix}$$

Figure 4. Determinant .epresentation of Markov Chain Model.

Average values of the transition probability based on the results of the crack survey from 2012 to 2016 are shown in Table3. In addition, the results of prediction of deterioration of cracks by Markov chain model using the transition probability are shown in Fig.5.

Feature of this model is as follows. At the time of "0 years", crack grade 0 occupies the entire building, but the proportion of crack grade I increases as the age progresses, and the crack grade 0 decreases accordingly. Furthermore, the proportion of crack grade II increases as years progress, and crack grade 0 and I decrease. In the end, the ratio of crack grade III, which is the most significant degradation, increases.

Table 3. Degradation Probability.

	x0	x1	x2
Max	0.384	0.396	0.400
Min	0.016	0.015	0.004
Average	0.108	0.116	0.178

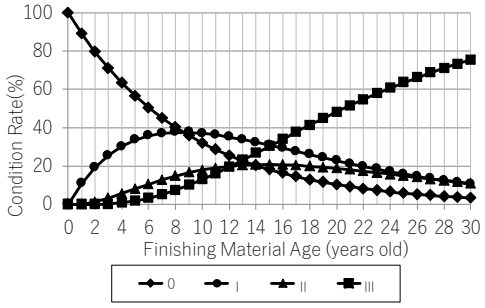

Figure 5. Prediction of Cracking.

3 Relationship between Cracking and Carbonation Suppression Effect

3.1 Decrease in Carbonation Suppression Effect by Cracking

Authors examine relationship between cracking and carbonation suppression effect.

Akio, T. (2013) showed that there is a certain correlation between surface air permeability coefficient and carbonation rate coefficient of existing RC buildings. In this study, time change of carbonation suppression effect of a multi-layer coating coating material was evaluated by the

air permeability test. Crack of the coating material is degradation phenomenon as shown in table 2 and CO_2 induced carbonation would occur at the cracks which strongly affects air permeability of the coating. Hence, the deterioration of the coating material and its relation to carbonation would be evaluated with surface air permeability.

3.2 Verification at Laboratory

Multi-layer coating materials for exterior finishing used in reinforced concrete buildings often composed of three layers that are a top coating layer that protects the outer wall from solar radiation and rain, a main material layer that provides texture and a primer layer that improves adhesion to the frame. Here, in order to confirm the possibility that the protective effect of the coating material would be reduced by cracking of the top coating material, the change of air permeability of the surface layer was measured at laboratory.

An outline of test specimen is shown in Fig.6. First, sewing thread is laid down at different intervals on calcium plate. Next, an acrylic resin emulsion paint as an overcoat layer for the exterior coating material was applied to the calcium plate with a roller. After 60 minutes, the sewing thread was pulled out to reproduce pseudo crack.

Surface permeability was evaluated using a double chamber method (1992) before the sewing machine was laid down.

Fig. 7 shows the ratios of the air permeability coefficient of the test specimen before and after crack initiation.

Here, “crack length” represents the total length of pseudo cracks in the range of the chamber of the measuring apparatus.

It can be seen that the air permeability coefficient increases with the increase of the length of the pseudo crack, and finally the air permeability coefficient approached to that of the calcium carbonate plate before coating.

This might indicate that when the cracks in the top coat layer increase, the air permeation becomes easier and the carbonation suppressing effect decreases. And the close air permeability to the substrate calcium carbonate plate at significant crack state might be same as no overcoat layer applied.

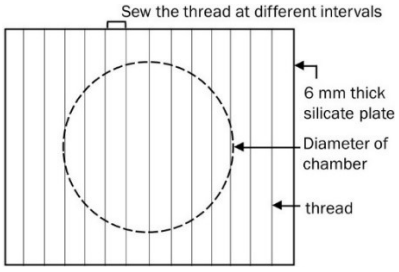

Figure 6. Test Models.

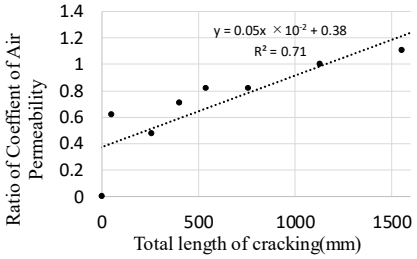

Figure 7. Relation of cracking and Coefficient of Air Permeability.

3.3 Survey of Actual Buildings

Crack and air permeability of actual buildings were surveyed. Nine reinforced concrete buildings estates shown in Table4 were surveyed at a position of about 1.5m height above the ground and a visual inspection of the cracks and surface air permeability tests were conducted

at the same location. As a feature of these buildings, each building is under almost same environmental conditions and age of construction and types of coating materials are same.
Fig. 8 shows secular change of crack grade and surface air permeability. As the years progress, the crack grade and air permeability coefficient tend to increase. As a result, there was a possibility that there was a temporary correlation between the cracks and air permeability of the coating material.

Table 4. Survey Buildings.

Buildings	Building Age	Finishing Material
A	11, 14, 18	Sprayed Tile
B	13, 16, 18	Multi-layer Finish Material (Thick E Type Treated Protrusion)
C	7, 9, 11	Sprayed Tile Thick E Type

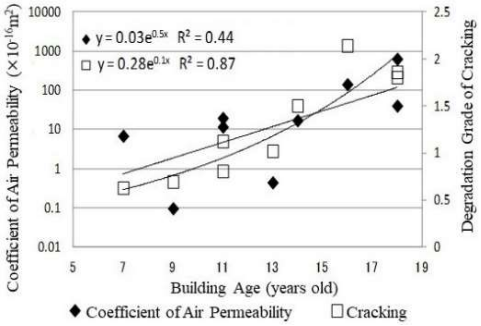

Figure 8. Aging Effect on cracking and Coefficient of Air Permeability.

3.4 Verification Using a Markov Chain Model for Deterioration Prediction Simulation

Kei.M (2013) evaluated period when carbonation rate coefficient of finished concrete became equal to that of exposed concrete due to deterioration of the coating film as the service life of the coating material. It was 13 years according to his study. Here, based on the fact that cracking of the coating material progresses with time in Fig. 1 and that carbonation tends to progress according to time from new construction to renovation, a damage of coating material was assumed to be critical. Hence, "Accumulation of degradation" was set in consideration of the relationship between years that exceeded the limit years and the degree of limit excess of deterioration as shown in the following equation (2). And the relationship between "Accumulation of degradation" and carbonation depth (Kotaro.E(2016)) was examined. Fig. 9 shows a conceptual diagram.

$$D_a = \sum_{n=1}^{N} \sum_{t=1}^{T(n)-L} \left(d_n(L+t) - d_n(L) \right) \tag{2}$$

Here,
Da: Accumulation of degradation", N(times): Number of paintings including when building exterior coating materials, T(n)(year): Number of years from the time of painting to the time of renovation (when n = N, from the time of painting to the time of survey), L(year): Marginal years for exterior coating materials, dn(x): Represents the ratio of degradation grade III (0 <dn (x) <1) of Markov simulation at the time of n times of coating n times, and is considered only when the age exceeds the limit years (x> L).

Based on previous research (2011), the relationship between "Accumulation of degradation" and the mean of the carbonation depth of each building assuming the limit of 13 years is shown in Fig.10 for the surveyed building shown in Table1. It can be seen that the average of the carbonation depth of the building increases as "Accumulation of degradation" increases, and there is a possibility that there is a certain relationship between the crack and the carbonation suppression effect.

Table 5 shows list of the all surveyed buildings. Although these buildings are different specification and subjected to different environmental conditions, design standard strength was close to each other. Hence, "(1) Crack" and "(2) Carbonation depth" using the methods described in chapter 2 were investigated. Fig. 11 shows relationship between "Accumulation of degradation" and carbonation depth for each survey target. Although the correlation of Fig.11 was lower than that of Fig. 10, a certain degree of correlation was kept. Thus, there would be correlation between the cracking and carbonation inhibitory effect of the multi-layer coating material.

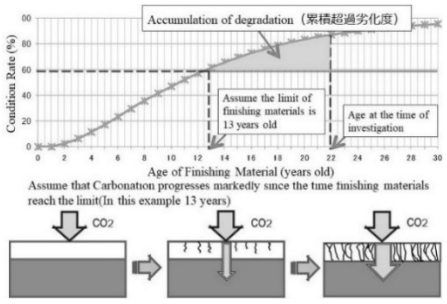

Figure 9. Models of Accumulation of degradation.

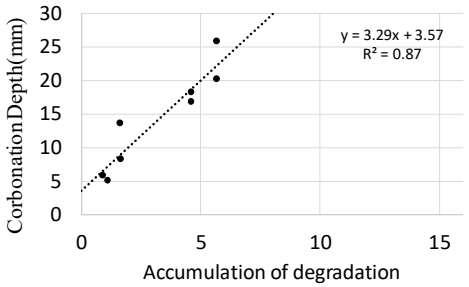

Figure 10. Relation of Accumulation of degradation and Carbonation depth.

Table 5. Survey Buildings

	Year of Const-ruction	Year of Re-paint (1)	Year of Re-paint (2)	Year of Sur-vey	Design Stren-gth (N/mm^2)	Sto-ries	Region
A	1978	2010		2012 ~ 2016	18	4	Ibaraki
B	1979	2008			18	4	Ibaraki
C	1979	2001			21	6	Ibaraki
D	1979	1997			21	10	Ibaraki
E	1967	1993		2015	18	2	Hyogo
F	1962	1992		2015	18	2	Ibaraki
G	1967	1992		2016	18	2	Shiga
H	1964	1981		2013	18	5	Tokyo
I	1977	1995	2013	2016	21	15	Saitama
J	1978	2010		2016	24	14	Tokyo
K	1977	2010		2015	24	14	Tokyo
L	1988			2015	unknown	6	Tokyo
RC Buildings, Multi-layer Coating Material (E Type)							

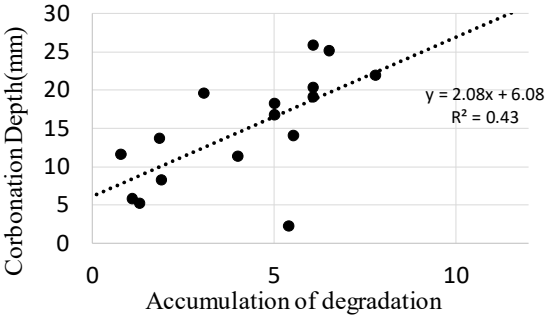

Figure 11. Relation of Accumulation of degradation and Carbonation depth.

4 A proposal for Service Life

In Fig. 10, it would be clear that carbonation depth would be 0, if "Accumulation of degradation" is 0. That means that the regression line should pass through the origin. At this that the regression line passed a bit other point of the figure because the limit age of the coating materials was assumed to be 13 years. Therefore, authors set the new limit years so that the regression line approaches the origin. In the subject of this survey, the regression straight line passed the origin when the limit age was 10 years. Fig. 12 shows the relationship between "Accumulation of degradation" and the carbonation depth with the critical age of 10 years.
When the limit service life is assumed to be 10 years, the deterioration rate shown in Fig. 5 (the

ratio of deterioration grade III) would be 16.0% with transition probabilities shown in Table 3. It would be possible to consider the time when this deterioration rate is reached based on carbonation of concrete.

As described above, the exterior coating materials can be used to minimize or control the carbonation of concrete by repainting within a range that does not cause "Accumulation of degradation" within 10 years. In this sense, it can be situated as a way of service life consideration.

The relationship between age and "Accumulation of degradation" is shown in Fig. 13 by Equation (2) for the survey target in Table 1.

In addition, the relationship between age and carbonation depth is shown in Fig. 14 by using the approximate expression of the relationship between "Accumulation of degradation" when the limit years as 10 years. On the other hands, if the cover thickness of reinforced concrete is 30 mm, this building will face to the end of life in 36 years unless it is repainted. Here, assuming that the required service life of the building is 100 years and the repainting interval at which carbonation does not reach 30 mm within 100 years, life cycle assessment of finishing coating in terms of carbonation would be possible. Table6 shows the prediction of the carbonation depth of buildings when the exterior coating materials are refurbished and the age reaches 100 years. It would be calculated that if the exterior coating material used in this building is repainted every 22 years (Fig.15), carbonation does not reach the reinforcing bars within 100 years.

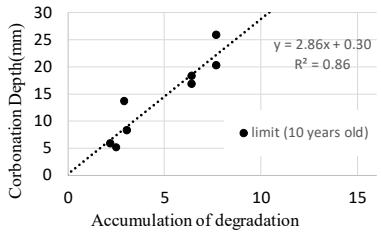

Figure 12. Relation of Accumulation of degradation and Carbonation depth.

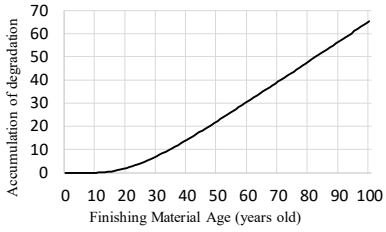

Figure 13. Prediction of Accumulation of degradation.

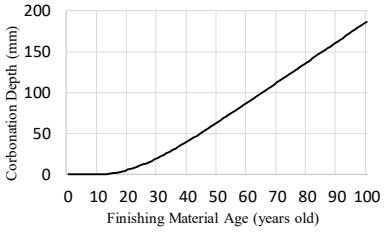

Figure 14. Prediction of Carbonation depth.

Table 6. Relation of Repaint interval and Prediction of Carbonation Depth in 100 years.

Repaint interval (year)	Prediction of Carbonation (mm)	Repaint interval (year)	Prediction of Carbonation (mm)
30	55. 21	25	41. 80
29	50. 60	24	36. 33
28	47. 11	23	31. 19
27	44. 75	22	26. 69
26	43. 49	21	24. 05

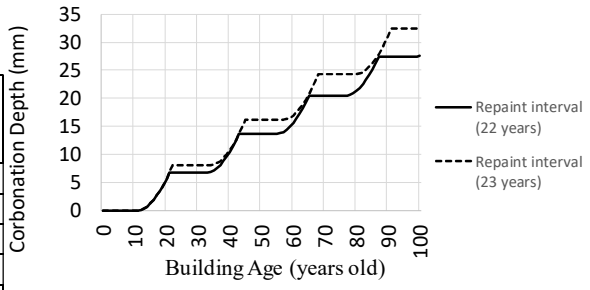

Figure 15. Prediction of Carbonation depth. (repaint interval 22years and 23years)

5 Summary

The findings obtained in this study are shown below.

- Authors investigated four buildings that were close environmental condition, focusing on cracking of multi-layer coating. As an overall trend, Cracking was confirmed that cracking progressed with the passage of time since the renovation.
- Based on the survey results on cracks in multi-layer coating materials applied to reinforced concrete buildings, authors presented a method for predicting crack degradation using a Markov chain model.
- Authors showed a possibility that there was a correlation between the cracks and air permeability of the coating materials by laboratory experiments and surveys of real buildings. In addition, by considering along with the report that there was a correlation between surface air permeability and carbonation rate coefficient of existing RC buildings, authors showed a possibility that there was a correlation between the cracking and carbonation inhibitory effect of the multi-layer coating materials.
- Authors proposed “Accumulation of degradation” considering the time and grade when the crack exceeded a certain value. And Authors confirmed that there is a certain correlation between the "Accumulation of degradation" and the carbonation depth of the buildings.
- By using the relationship between "Accumulation of degradation" and the carbonation depth of the buildings, Authors suggested the service life for the coating materials to use the buildings for the longest years and the required years.

ORCID

Kotaro Etchuya: https://orcid.org/0000-0002-7858-9420
Kei-ichi Imamoto: https://orcid.org/0000-0001-8174-8827
Chizuru Kiyohara: https://orcid.org/0000-0003-1286-9056

References

Akio Tanaka and Kei-ichi Imamoto (2013). Evaluation of carbonation progress of existing concrete structure based on air permeability of cover concrete, Journal of Structural and Construction Engineering (Transactions of AIJ), No. 691, pp.1539-1545.

Torrent R (1992). A two-chamber vacuum cell for measuring the coefficient of permeability to air of the concrete cover on site, Mater. & Struct., Vol.25, No.150, pp.358-365.

Masanori Kono, Yoshihiro Masuda, Ryota Ochiai and Tomoyuki Karasawa (2004). Study on the carbonation suppressive effects of concrete considering the aging of coating materials for textured finishes, Journal of Structural and Construction Engineering (Transactions of AIJ), Vol.69, No.584, pp.15-21.

Masanori Kono and Yoshihiro Masuda (2006). Verification of the carbonation suppressive effects evaluation method of concrete considering the aging of coating materials or textured finishes using the exposure data, Journal of Structural and Construction Engineering (Transactions of AIJ), Vol.71, No.609, pp.9-14.

Tomoyuki Karasawa and Yoshihiro Masuda (2011). Carbonation suppressive effects of coating materials for textured finishes based on the research of air permeability coefficient and carbonation depth of coating materials for textured finishes of the existing structure, Journal of Structural and Construction Engineering (Transactions of AIJ), Vol.76, No.661, pp.449-454.

Kei Matsuda, Kei-ichi Imamoto, Hiroshi Jinnai and Akiyuki Shimizu (2011). The evaluation of degradation of exterior finishes and its relation to concrete carbonation progress with combination of Markov Chain Model and in-situ non-destructive air permeability test for concrete cover, Journal of Structural and Construction Engineering (Transactions of AIJ), Vol.78, No.683, pp.27-33.

Kotaro Etchuya, Kei-ichi Imamoto, Kenji Motohashi and Chizuru Kiyohara (2016). Estimation of deterioration of exterior finishes and evaluation of carbonation progress of concrete by Markov chain model, Proceedings of the Japan Concrete Institute, pp.729-734.

XV International Conference on Durability of Building Materials and Components
DBMC 2020, Barcelona
C. Serrat, J.R. Casas and V. Gibert (Eds)

Effects of Finishing Materials against Carbonation and Corrosion Condition of Model Building Exposed to Outdoor Conditions for 30 Years

Koichi Matsuzawa[1], Osamu Senbu[2], Kei-ichi Imamoto[3], Chizuru Kiyohara[4], Kotaro Etchuya[5] and Kaori Nemoto[6]

[1] Dept. of Building Materials and Components, Building Research Institute, Japan, matsu@kenken.go.jp

[2] Faculty of Engineering, Hokkaido University, Japan, senbu@eng.hokudai.ac.jp

[3] Faculty of Engineering, Tokyo University of Science, Japan, imamoto@rs.kagu.tus.ac.jp

[4] Faculty of Engineering, Tokyo University of Science, Japan, ckiyo@rs.tus.ac.jp

[5] Japan Building Coating Material Association, Japan, ecchuya@nsk-web.org

[6] Housing Dept., National Institute for Land and Infrastructure Management, Japan, nemoto-k92ta@mlit.go.jp

Abstract. *A model building made out of concrete block specimens whose surfaces were coated with various finishing materials was constructed for the outdoor exposure test. After 30 years of outdoor exposure, the deterioration of finishes and their carbonation and corrosion inhibition effects were investigated. As a result, the following conclusions were obtained: Though the deterioration levels differed depending on their types and thickness, all finishing materials showed some kind of deterioration after 30 years' long-term outdoor exposure. The progress of carbonation and corrosion are prevented when the surface is coated with finishing materials of sufficient thickness or waterproof effect. Regarding the relationship between corrosion depth and carbonation depth, corrosion is initiated after the carbonation front reaches the area. It usually takes a while to initiate corrosion in the carbonated area, not immediately after the carbonation reaction. When the concrete surface is properly coated with finishing material, corrosion may not be initiated in non-carbonated area in concrete where the pH level is not lowered.*

Keywords: *Finishing Materials, Outdoor Exposure, Carbonation, Corrosion.*

1 Introduction

The durability of Reinforced concrete (RC) buildings are basically determined by the presence or absence of steel corrosion. In order to prevent corrosion of steel in concrete, degradation factors such as carbon dioxide (CO_2) and chloride ions need to be prevented from penetrating into concrete. In many RC buildings, finishes are applied to concrete surfaces, which prevent the penetration of degradation factors. While many studies have been reported on the preventive effects of finishing materials based on accelerated testing, little is based on the long-term exposure to the outdoor conditions (Hasegawa *et al.*, 2002, 2017).

In this study, a model building made out of concrete block specimens whose surfaces were coated with various finishing materials was constructed for the outdoor exposure test. After 30 years of outdoor exposure, the deterioration of finishes and their carbonation and corrosion inhibition effects were investigated.

doi:10.23967/dbmc.2020.059

2 Experiment Overview

2.1 Outline of Specimens

Table 1 shows the materials used for concrete, and Table 2 shows the mix proportion and properties. The water cement ratio (w/c) is 0.55 and 0.70, and unit water content was 176 kg/m^3. To measure corrosion depth by the corrosion indicator method (Senbu *et al.*, 1987), iron particles were mixed to some concrete specimens before casting to make them serve as corrosion indicators. Chloride ions were also premixed in some specimens of w/c ratio 0.70 at the concentrations of 0.3, 0.6, and 1.2kg/m^3 by dissolving NaCl in water to examine the effect of chloride on concrete. The iron particles had diameters of 0.15 to less than 2.5 mm, used as a partial replacement of fine aggregate at 20%. Concrete specimens of 100×100×400mm in size, whose shapes were designed to be piled up to build the model building, were prepared (Figure 1). After demolding, the specimens were cured in 20℃ water for 28 days, followed by an atmospheric curing period of 42 days at 20℃, 60% R.H. Surface finishing materials were then applied to the specimens.

Table 1. Materials.

Material	Mark	Detail
Cement	C	Ordinary Portland cement, Gravity=3.16g/cm^3
Fine aggregate	S	River sand, Specific gravity=2.60g/cm^3
Coarse aggregate	G	Gravel, Specific gravity=2.64g/cm^3
Iron particle	CI	0.15-2.5mm, Gravity=6.9g/cm^3
Admixture	Ad	Air entrained and reducing agent

Table 2. Mix proportion and properties.

Mark	W/C (%)	s/a (%)	Mass content (kg/m^3)						Ad (cc)	Slump (cm)	Air (%)	Compressive strength (N/mm^2)
			W	C	S	G	CI	Cl$^-$				
A	55	44.5	176	320	790	1000	-	-	800.0	18.5	3.7	38.2
B	70	47.5	176	251	871	977	-	-	628.6	18.5	4.0	22.9
C	55	44.5	176	320	632	1000	420	-	800.0	15.5	3.4	40.5
D	70	47.5	176	251	697	977	461	-	628.6	15.5	3.7	27.4
E	70	47.5	176	251	697	977	461	0.3	628.6	15.5	3.6	29.5
F	70	47.5	176	251	697	977	461	0.6	628.6	16.0	3.6	27.6
G	70	47.5	176	251	697	977	461	1.2	628.6	15.5	3.5	29.1

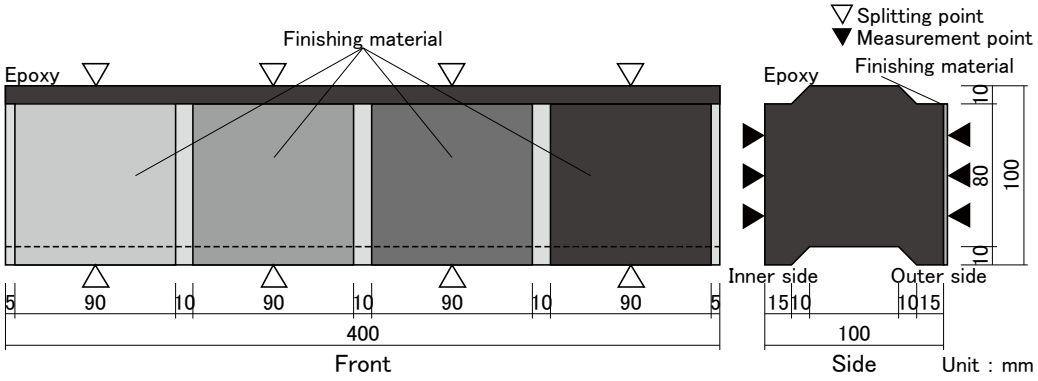

Figure 1. A schematic illustration of the specimen and measuring point of carbonation and corrosion depth.

Table 3 shows the types and amount of finishing materials used in this study. White color finishes (finishing coatings and paint), which are commonly used for the surface coating of RC buildings, were applied to the specimens, with a standard technique. A total of 7 types of finishing materials including penetrant (impregnation) were used. Four different finishes were applied to a 90×400mm surface of each one specimen, in the shapes of 90×100mm rectangular (Figure 1). This made a pair of concrete block specimens covered with 7 types of finishes including one surface area without a finish (fair-faced concrete). The specimens were then coated with epoxy resin, except for the surfaces covered with finishing materials and their opposite sides without finishes. The surface finishes were applied by experts.

Before the application of surface finishes, some specimens were subjected to accelerated carbonation curing for 8 weeks under the conditions of 20℃, 60% R.H. and 5% CO_2, to be examined the iron corrosion in carbonated areas. The prepared specimens were used for constructing the model building and were subjected to outdoor exposure test.

Table 3. Finishing materials.

Mark	Finishing material	Species and dosage (kg/m^2)			Luster
		Sealer	Main material	Top coating	
a	Thin coating material E	0.08	1.1 Spray	-	N
b	Multi-layer coating material E	Water-based 0.08	2.35	Acrylic 0.22	Y
c	Acrylic resin enamel	-	-	0.29	Y
d	Waterproof thin coating material E	Water-based 0.08	1.43	-	Y
e	Silane-type surface penetrants	0.20	-	-	-
f	Waterproof thin coating material E (Air permeability type)	-	1.52	-	Y
g	Thick coating material E	Water-based 0.08	3.65 Spray	-	N

2.2 Outline of Model Building

Figure 2 shows a photo of the model building. It was constructed on a premise of the Building Research Institute (BRI) in Tsukuba City, Ibaraki Prefecture. The model building was constructed with concrete specimens piled up in a boxy shape, whose outer surfaces were coated with various types of finishing materials. It had a box-shaped metal roof inclined to the north side. Inside of the building was sheltered from rain, and its room air temperature and humidity were not controlled.

Figure 2. A photo of the model building.

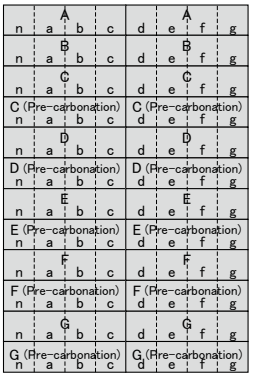

Figure 3. A layout of surface finishes.

Figure 3 shows the layout of surface finishes. The specimens on the south side of the model building were used for the study. From heights of 460mm above the ground, the specimens were piled up in 12 layers. The gap between the top of the wall and the metal roof was covered with plywood. A pair of concrete specimens with the same mix proportions were placed horizontally next to each other. A total of 7 different finishes were applied to the pair of specimens in the same layer. The capital letters in Figure 3 indicate the marks of concrete specimens (Table 2), and the lower-case letters indicate the types of finishes applied to the specimens (Table 3). The lower-case letter "n" indicates the specimens without finishes.

2.3 Test Methods

2.3.1 Evaluation of the surface finish deterioration

The deterioration of finishing materials was evaluated by peeling, cracking, dirt, and chalking. It was graded by multiple experts, using a 6-degree scale from 0 (no deterioration) to 5 (severe deterioration).

2.3.2 Measurement of carbonation depth

As shown in Figure 1, the carbonation depth was measured by splitting a concrete specimen evenly at the center of each finishing material, and then spraying 1% phenolphthalein solution over a freshly exposed surface of the specimen. It was measured at two sets of three points, each of inner and outer side of the model building.

2.3.3 Measurement of corrosion depth

Corrosion depth was measured by the corrosion indicator method. In this method, materials to detect corrosion (iron particles) are mixed to concrete before casting so that the depth of rust can be measured by splitting the hardened concrete specimens. Since the rusted iron particles indicate a condition that may cause rust on reinforcing steel, the corrosion indicator method enables us relatively easily to observe the variation of steel corrosion potential over time. The corrosion depth was measured at the same points as those of the carbonation depth measurement (Figure 1).

3 Results and Discussion

3.1 Deterioration of Finishing Materials

The finishing materials that are the type to form coating film on the surface, except silane-type surface penetrants (e), were evaluated for deterioration in Figure 4.

Acrylic resin enamel (c) shows the highest degree of peeling. One possible reason is that there was a loss of adhesion between the paint and the surface it's placed on due to long-term outdoor exposure, because a paint finish such as acrylic resin enamel has a thickness from several tens to hundred microns, while other ordinary finishes have thickness of 1-5 mm.

Multi-layer coating material E (b), acrylic resin enamel (c), waterproof thin coating material E (d) and waterproof thin coating material E (air permeability type) (f) showed high degrees of cracking. Though small in width (hairline crack), cracks in the specimens are often caused by the degradation of resin contained in finishing materials due to ultraviolet ray.

All finishes showed the deterioration degrees from 2 to 3, except that waterproof thin coating material E (d) remained lower levels of dirt. The adhesion of dirt is affected by the nature of surface finishing materials such as hydrophilicity, hydrophobicity, water absorbability, and water repellency. The smoothness and fineness of surface finishing materials are considered to be lost due to long-term outdoor exposure.

Multi-layer coating material E (b), acrylic resin enamel (c), waterproof thin coating material E (d) and waterproof thin coating material E (air permeability type) (f) showed high degree of chalking. Surface finishing material is usually a composite material containing aggregates and admixture that add thickness to surface, coloring agent to add color, and bonding material to bind them together. Degradation of bonding material and coloring agent is one of the reasons that cause chalking, which refers to the formation of fine powder on the surface of the paint film.

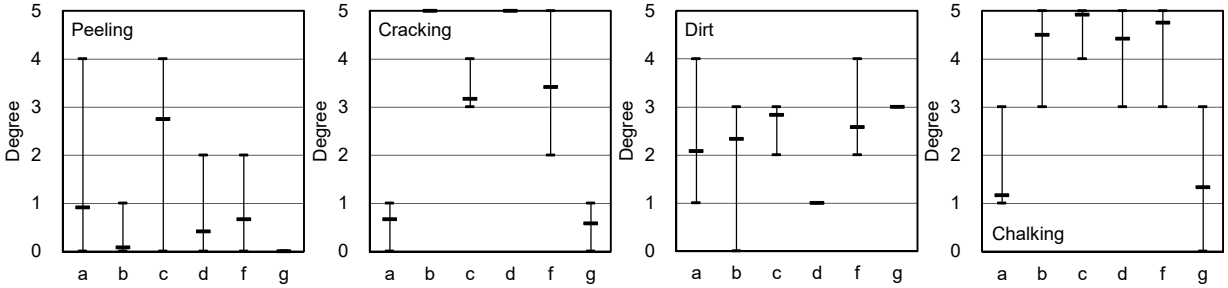

Figure 4. Deterioration degree of finishing materials.

3.2 Carbonation Depth

Figure 5 shows the carbonation depth measured from the outer surfaces of the specimens with different w/c ratios (A, B). The plain specimens without finishing materials (n) were measured from both inner (nI) and outer (nO) surfaces. As a whole, the specimens with higher w/c ratio showed deeper carbonation depth than those of lower w/c ratio. Regarding the plain specimen (n), inner surface (nI) had deeper carbonation depth compared to that of outer surface (nO). This is because the water content of outer surface was increased to some extent due to rainfall, while inner surface tended to dry and were more likely to be carbonated.

Among the carbonation depths measured from outer surfaces, thin coating material E (a), multi-layer coating material E (b), acrylic resin enamel (c), and waterproof thin coating material E (d) showed smaller carbonation depths, while silane-type surface penetrants (e) and waterproof thin coating material E (air permeability type) (f) showed deeper carbonation depths, compared to that of the plain specimen (nO). Having water repellency and air permeability, silane-type surface penetrants (e) and waterproof thin coating material E (air permeability type) (f) prevented water penetration into concrete and allowed evaporation at the same time. It can be assumed that these properties caused lower water content of concrete and deeper carbonation depth than the plain specimens (nO). The graph also shows that thick coating material E (g) with w/c of 0.55 had high carbonation inhibition effect, while that of w/c 0.70 did not. The presumed cause is delamination of the surface layer occurred in w/c 0.70 specimen during outdoor exposure, which allowed carbon dioxide to diffuse more easily from the surrounding environment.

Assume the ratio of carbonation depth of a specimen covered with finishing material to that of a plain specimen not covered with finishing material shows constant value. $S(t)$ is the carbonation rate representing the carbonation inhibition effect, and can be expressed by the following formula (1) (Nagase *et al.*, 2007).

$$S(t) = \frac{C_C(t)}{C_B(t)} \tag{1}$$

Here, $S(t)$ is carbonation rate at the time of exposure (time), $C_C(t)$ and $C_B(t)$ are carbonation depth of concrete covered with and without finishing material, respectively (mm).

Figure 6 shows the carbonation rate of finishing materials at the age of 30 years applied to the model building. Among them, multi-layer coating material E (b) and waterproof thin coating material E (d) showed particularly low rates, suggesting they have high carbonation inhibition effects. In addition, thick coating material E (g) would also have high carbonation inhibition effect, if it demonstrated its potential efficacy.

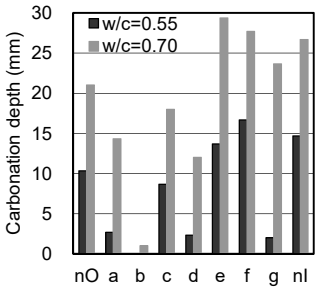

Figure 5. Carbonation depth.

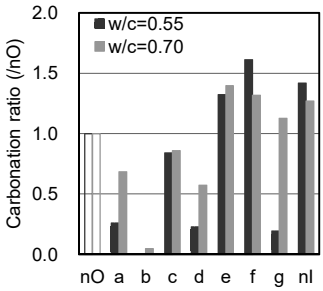

Figure 6. Carbonation rate.

3.3 Corrosion Depth

Figure 7 shows the corrosion depth measured from the outer surface (covered with finishing materials) of the concrete specimens (C, D) in which iron particles were mixed before casting. The plain specimens without finishing materials (n) were also measured from both inner (nI) and outer (nO) surfaces. As with the carbonation depth, specimens with higher w/c ratio showed deeper corrosion depth than those with lower w/c ratio. This indicates that higher w/c ratio make reinforcing steel more prone to corrosion. The graph also shows that the plain specimens (n) showed deeper corrosion depth, when measured from inner surface (nI) than from outer surface (nO).

Comparing the corrosion depth measured from outer surfaces, multi-layer coating material E (b), waterproof thin coating material E (d), and thick coating material E (g) had a smaller depth of corrosion than that of plain specimen (nO). Multi-layer coating material E (b) and waterproof thin coating material E (d) are considered to have relatively higher water repellent effect than other finishing materials. Though carbon dioxide may have permeated concrete from the delaminated surface, thick coating material E (g) is considered to have been effective in preventing water penetration.

The pre-carbonated specimens tended to have deeper corrosion depth, which was especially true for those with w/c 0.70. This indicates that reinforcing steel is more likely to corrode in carbonated area.

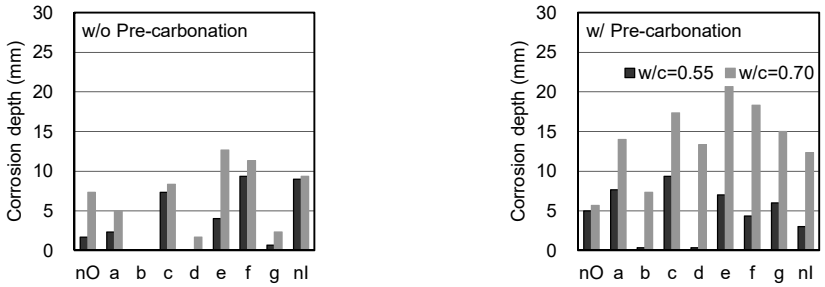

Figure 7. Corrosion depth.

Figure 8 shows the relationship of the corrosion depth to the amount of chloride ions in the specimens of w/c 0.70 (D, E, F, G), in which iron particles and chloride ions had been added before casting. Again, the pre-carbonated specimens tended to have deeper corrosion depth compared to those without pre-carbonation. However, the amount of chloride ions, including its presence or absence, did not show significant effects on the corrosion depth.

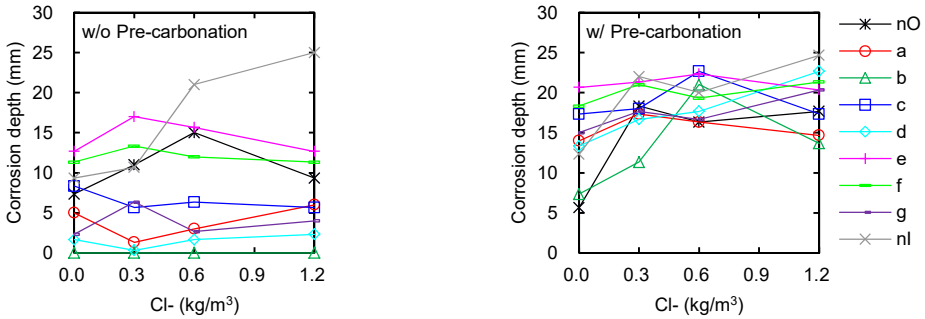

Figure 8. Relationship between corrosion depth and chloride ions.

3.4 Relation between Corrosion Depth and Carbonation Depth

Figure 9 shows the relationship between the corrosion depth and carbonation depth measured from the outer surfaces of the concrete specimens (C, D) in which iron particles had been mixed before casting. The depths measured at 3 points on each finishing material are plotted on the graph. The progress of corrosion is preceded by that of carbonation. This suggests that the corrosion is not initiated immediately after the carbonation front reaches reinforcing steel. It can be assumed that when the concrete surface is properly coated by finishing material, corrosion may not be initiated in non-carbonated area where the pH level is not lowered.

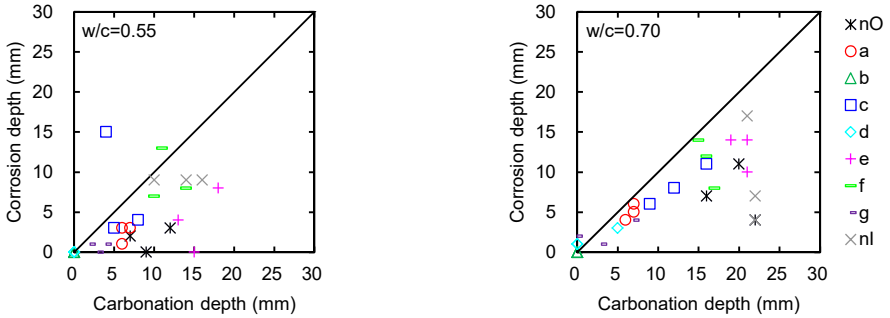

Figure 9. Relationship between corrosion depth and carbonation depth.

4 Conclusion

In this study, a model building made out of concrete block specimens whose surfaces were coated with various finishing materials was constructed for the outdoor exposure test. After 30 years of outdoor exposure, the deterioration of the finishing materials and their carbonation and corrosion inhibition effects were investigated. As a result, the following conclusions were obtained.

- Though the deterioration levels differed depending on their types and thickness, all finishing materials showed some kind of deterioration after 30 years' long-term outdoor exposure.
- The progress of carbonation is prevented when the surface is coated with finishing materials of sufficient thickness or waterproof effect. However, the carbonation inhibition effect cannot be obtained when using air-permeable finishing materials or there is a peeling finish on the surface.
- The progress of corrosion is prevented when the surface is coated with finishing materials of sufficient thickness or waterproof effect.
- Regarding the relationship between corrosion depth and carbonation depth, corrosion is initiated after the carbonation front reaches the area. It usually takes a while to initiate corrosion in the carbonated area, not immediately after the carbonation reaction.
- When the concrete surface is properly coated with finishing material, corrosion may not be initiated in non-carbonated area in concrete where the pH level is not lowered.

ORCID

Koichi Matsuzawa: http://orcid.org/0000-0003-1547-8368
Osamu Senbu: https://orcid.org/0000-0002-6952-342X
Kei-ichi Imamoto: https://orcid.org/0000-0001-8174-8827
Chizuru Kiyohara: https://orcid.org/0000-0003-1286-9056
Kotaro Etchuya: https://orcid.org/0000-0002-7858-9420
Kaori Nemoto: https://orcid.org/0000-0002-1177-9959

References

Hasegawa, T. *et al.* (2002). A study on the corrosion protection effects of surface finishing materials using a model building at the afe of eleven years. *J. Struct. Constr. Eng.*, *AIJ*, No.560, 27-33. (in Japanese)

Hasegawa, T. *et al.* (2017). Detarioration and preventitive effect of finishing materials against carbonation and corrosion of reinforcing bars in concrete based on twenty year outdoor exposure test using model building. *J. Struct. Constr. Eng.*, *AIJ*, No.733, 337-346. (in Japanese)

Senbu, O. *et al.* (1987). A proposal of corrosivity test for reinforced concrete. *Summaries of Technical Papers of Annual Meeting*, *AIJ*, 289-290. (in Japanese)

Nagase, K. *et al.* (2007). Evaluation of various finishing materials contributing to carbonation suppressive of concrete in structures Part1-Part8. *Summaries of Technical Papers of Annual Meeting*, *AIJ*, 1123-138. (in Japanese)

XV International Conference on Durability of Building Materials and Components
DBMC 2020, Barcelona
C. Serrat, J.R. Casas and V. Gibert (Eds)

Morphology Changes and Fillers Migration in Urethane Composites during Thermal Degradation

Atsuki Tanifuji[1], Takato Ishida[2] and Ryoma Kitagaki[1]

[1] Graduate School of Engineering, Division of Human Environmental Systems, Hokkaido University, Kita 13-Nishi 8, Kita-ku, Sapporo, Hokkaido 060-8628, Japan, atsuki_123@eis.hokudai.ac.jp

[2] Graduate School of Engineering, Division of Human Environmental Systems, Hokkaido University, Kita 13-Nishi 8, Kita-ku, Sapporo, Hokkaido 060-8628, Japan, takato.matphysichem@gmail.com

[3] Graduate School of Engineering, Division of Human Environmental Systems, Hokkaido University, Kita 13-Nishi 8, Kita-ku, Sapporo, Hokkaido 060-8628, Japan, ryoma@eng.hokudai.ac.jp

Abstract. *Polyurethane composite coatings are frequently applied to strengthen the barrier properties of various construction materials such as wood, metal and concrete. The changes of color and glossiness of the composite coatings for building materials proceeds more slowly than that of polyurethane because of containing fillers and several types of additives. However, the most critical barrier properties have not been studied directly based on the difference from the degradation mechanism of polyurethane coatings. Additionally, the difference in thermal and UV degradation mechanisms of coatings is not clear in the existing studies dealing with conventional accelerated weathering tests and outdoor exposure tests. Therefore, the behavior of the filler contained in the coatings was observed using an oven to accelerate thermal degradation. The chemical analysis of the coating surface by XPS and the analysis of the images and elemental mappings by SEM-EDS were carried out, and the mechanism of degradation progress was investigated. In addition, the temperature dependency of the degradation was studied in changing the heating temperature. It was suggested that polymer and fillers interact in promoting mass transfer at the same time as the thermal degradation reaction consequently.*

Keywords: *Building Material, Coating, Filler, Polymer, Thermal Degradation.*

1 Introduction

Building material products used for topcoat contain so many chemical materials and consist of chemically complex systems. The products contain polyurethane, polyacrylic, modified silicone, and hybrid polymers. Furthermore, their products contain plasticizers, additives, and inorganic fillers in order to ensure performance and durability (Annamalai Pratheep Kumar *et. al.* (2009), D.K. Chattopadhyay (2006), Ivan S. Stefanović *et. al.* (2019), Jun Liu *et. al.* (2017), Li Bin (2014), M.Sabzi *et. al.* (2008) and S.M. Mirabedini (2013)).

In the present circumstances, the degradation process of coating materials containing polymers and inorganic substances has not been discussed. Even manufacturing companies have difficulty in elucidating their degradation mechanism, because such companies purchase raw materials from other companies and mix them to make products in many cases. In addition, there are few studies that separate thermal degradation from UV degradation through accelerated weathering tests and outdoor exposure tests. Therefore, this paper examines thermal degradation mechanism of coatings based on the result of the chemical analysis of the coating surface by XPS and the analysis of the images and elemental mappings by SEM-EDS.

doi:10.23967/dbmc.2020.100

2 Methods

2.1 Samples

In this study, both thermally-degraded and non thermally-degraded samples were prepared. The Conventional two-component type urethane coating including TiO_2, $CaCO_3$, and $BaSO_4$ as fillers was coated on a slide glass with a spin coater to control film thickness. After the surfaces of the samples were sufficiently dried, they were cured for 120 days at 20°C and 60% relative humidity, and cut to 7mmX7mm for fitting measuring instruments.

Subsequently, the samples after cutting were heat-degraded at 30°C, 50°C, and 70°C. The periods of the degradation are 0, 1, 3, and 7 days, and XPS measurement and SEM-EDS measurement were conducted respectively. The features of the measurements are briefly shown in Table 1.

2.2 XPS Measurement

X-ray photoelectron spectroscopy (XPS) was used to evaluate the chemical properties of urethane resin coatings. This technique is applied to analyze the type, concentration, and chemical state of elements on sample surfaces. Each sample is irradiated with an X-ray source using Mg-Kα rays, and wide spectrums with a binding energy in the range of 10 to 1000 eV and narrow spectrums around the peak of each detected element was obtained at a measurement area of 1.0 mmX1.0mm. The shift of the peak due to charging is corrected by setting the C1s spectrum to 284.0 eV, and correction using a neutralizing electron gun is not performed.

2.3 SEM-EDS Observation

A scanning electron microscope (SEM) equipped with an energy dispersive X-ray analyzer (EDS) was applied due to analyze the elemental information of the cross section of the samples. The samples were preliminary processed with a cross section polisher (CP) using argon ion beam for cross sectional observation.

In addition, the surfaces of the samples were coated with Au by ion sputtering to avoid thermal degradation of the samples.

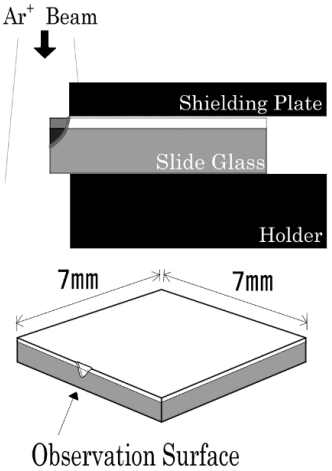

Figure 1. Processing before sample observation.

Table 1. Survey contents in each method.

XPS	・History of elemental type and chemical bonding state of coating surface layer	
SEM-EDS	SEM image	・Cross section thickness of coating ・Filler particle size
	Elemental mapping	・Distribution of elements in the cross section of coating film and its history

3 Results

3.1 XPS Scans

Figure 2 shows XPS narrow scan spectra of the urethane resin coatings that were thermally degraded at 70°C for 0, 1, 3, and 7 days. The peak of O 1s, N 1s, and Si-O increased as thermal degradation treatment continued. This result could be explained that the polymer such as urethane and siloxane was decomposed and appeared on the surface layer of the coatings due to low molecular weight and low density. On the other hand, the Ca peak was hardly detected on the surface layer. This result indicates that the substance in the coating may move up and down dramatically before the surface of the coating is cracked while the coating is thermally degraded. The fillers such as $CaCO_3$ originally floating on the surface of the coating film could be sunk as the polymers were scattered and float by heat.

Figure 3 shows O spectra of the samples that were thermally degraded at 30°C and 50°C for the same period. The graph shows that the peak increase on the 1st to 7th days at 30°C, however at 50°C, it increases on the 1st and 3rd days and decreases on the 7th day. These tendencies suggest the possibility of different thermal oxidation reactions on the coating surface, such as increases in C—O and C═O bonds and a decrease in O due to the progress of C crosslinking. Furthermore, each thermal oxidation reaction takes place at different times during the process of thermal degradation.

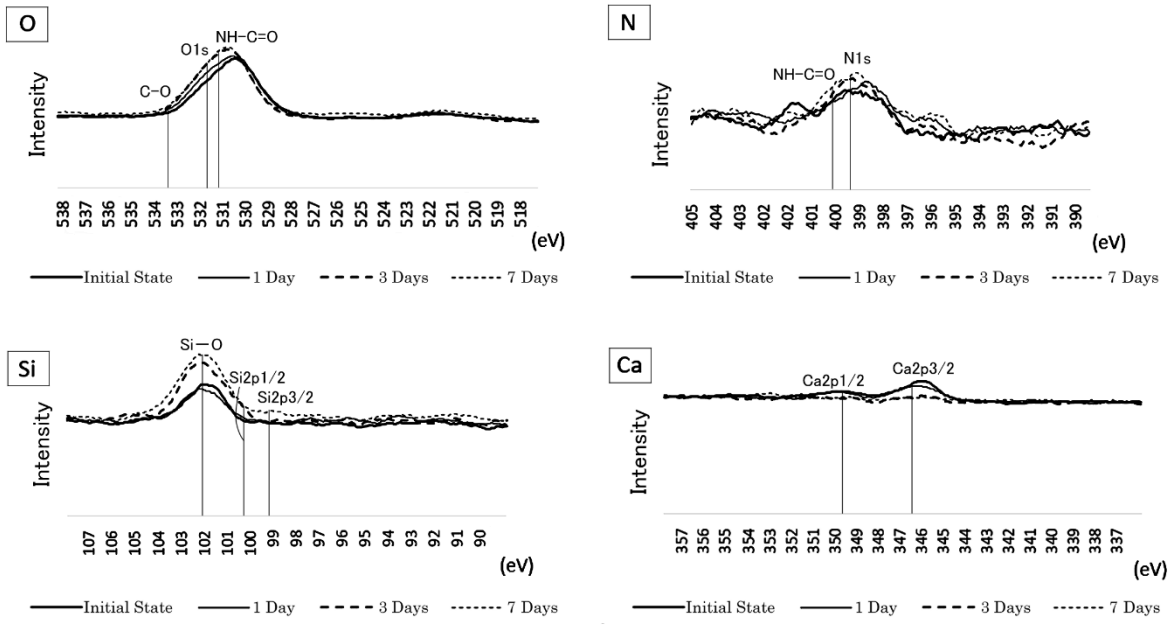

Figure 2. Narrow scan spectra of the urethane resin coatings that were thermally degraded at 70°C.

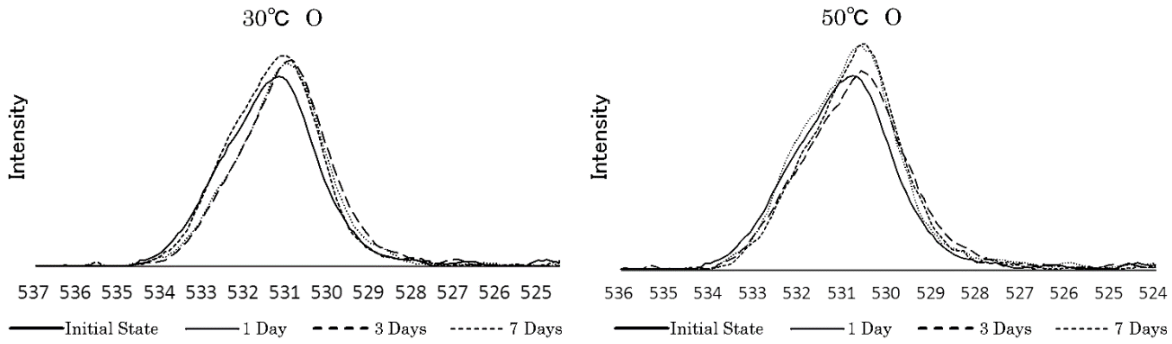

Figure 3. O spectra of the urethane resin coatings that were thermally degraded at 30°C and 50°C.

3.2 SEM Images

Figure 4 shows the film thickness history of each sample obtained from SEM image of the sample thermally degraded for 0, 1, 3, and 7days, respectively, at 30°C, 50°C, and 70°C. However, it should also be noted that samples exposed at 70°C and samples at 30°C or 50°C are different in initial states. In the non thermally-degraded sample, the thickness of the coating was approximately 60 mm. The thickness of coating gradually decreased due to heat degradation at 70°C, and was 38 mm on 1st day, 18 mm on 3rd day, and 10 mm on 7th day. The coating thickness decreased due to thermal decomposition and volatilization of components such as plasticizers in the coating (Wei, X. (2019)). In contrast, at 30°C, the film thickness increased slightly, and at 50°C, it appeared to decrease on the 7th day. The dimensional change of the coating could be caused not only due to reduction of components in coating but also due to changes of gel structure in cross-linking and scission (Petrović *et. al.* (2000) and Y. Nawab, *et. al.* (2017)).

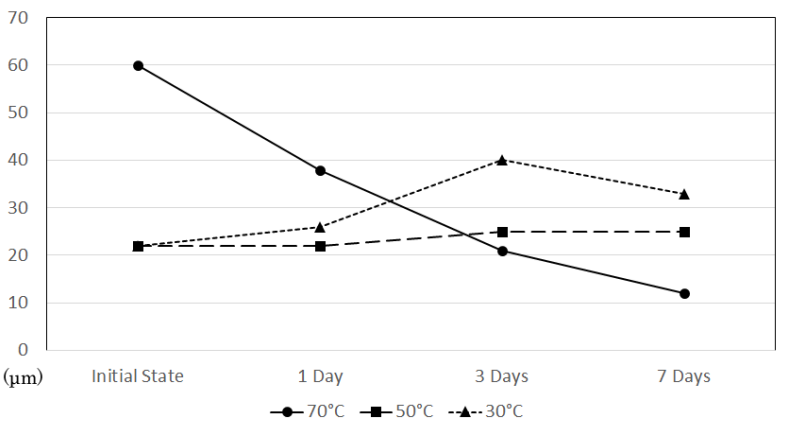

Figure 4. Changes in film thickness of each sample.

3.3 Elemental Mappings

Figure 5 shows the history of element mapping of Ti. Ti was homogeneous in the initial state, increased at the bottom on the first day, and gradually increased on the surface over time by heating at 50°C. On the first day, fillers move to the bottom of the coating as polymers become

smaller and less dense due to thermal decomposition. From the third day, filler have been pushed up from the bottom due to polymer cross-linking and polymerization reaction (Wei, X., *et. al.* (2019)).

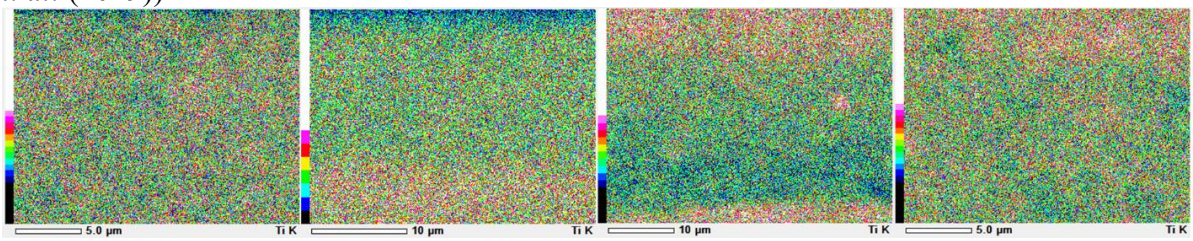

Figure 5. Sectional elemental mapping of Ti in urethane composite coatings at 50°C.

4 Discussion

4.1 Temperature Dependence of Coating Durability

The coating thickness increased initially at lower temperatures and decreased at higher temperatures, accompanied by the movement of the filler. Since fillers such as titanium dioxide have a role to protect the coating from UV degradation, the durability of the construction coating could vary greatly due to differences in temperature history.

4.2 Movement of the Filler

Why does the position of the inorganic filler in the coating fluctuate greatly due to thermal degradation? The movements of each filler of $CaCO_3$, TiO_2, and $BaSO_4$ were analyzed as follows.

4.2.1 $CaCO_3$

In elemental mapping, Ca is always homogeneous, whereas in XPS, the Ca peak increases and decreases depending on the temperature. There was no significant movement of $CaCO_3$ contained in the coating as a filler, and the XPS Ca peak changed due to a change in the state of the surface layer of the coating. The decrease in the Ca peak at 70 ° C could indicate that the surface layer became smoother and covered with polymer as the temperature of the coating approached the glass transition temperature (L.S De Bernarde, *et. al.* (1984)).

4.2.2 TiO_2 and $BaSO_4$

XPS peaks of titanium and barium were not detected, however in elemental mapping by SEM-EDS, there were dramatic movements in the coating as shown in Figure 5. Moreover, the movement tendency of the position of the two elements is very similar and corresponds to the movement of TiO_2 and $BaSO_4$ in the coating as fillers. These fillers could move shrinkage stress due to polymerization, expansion stress due to heating, and stress due to movement of the polymer having a low molecular weight. The positions of these fillers are inhomogeneous unlike CaSO4, because the stress from the polymer may differ depending on the particle size of the filler (Nabil Hayeemasae *et. al.* (2018)). However, understanding these mechanisms require further studies.

5 Conclusions

- The position of the fillers contained in the organic composite coating are inhomogeneous due to thermal degradation.
- Polymerization, scission and cross-linking of the polymers can be accelerated by the action of heat, which can affect the thickness of the coating.
- The cross-sectional morphology of the coating changes depending on the temperature of thermal degradation.
- Changes in thickness and inhomogeneous distribution of materials due to thermal degradation of architectural composite coatings could affect their barrier performance because of the movements of the fillers and changes of the thickness.

ORCID

Atsuki Tanifuji: http://orcid.org/0000-0003-4363-5834
Takato Ishida: http://orcid.org/0000-0003-3919-2348
Ryoma Kitagaki: http://orcid.org/0000-0001-6001-3688

References

Annamalai Pratheep Kumar, Dilip Depan, Namrata Singh Tomer and Raj Pal Singh (2009). Nanoscale particles for polymer degradation and stabilization—Trends and future perspectives*, Progress in Polymer Science, Volume 34, Issue 6, June 2009, Pages 479-515*

D.K. Chattopadhyay and K.V.S.N. Raju (2006). Structural engineering of polyurethane coatings for high performance application*s, Progress in Polymer Science, Volume 32, Issue 3, March 2007, Pages 352-418*

Ivan S. Stefanović, Jasmina Dostanić, Davor Lončarević, Dana Vasiljević-Radović, Sanja Ostojić, Smilja Marković and Marija V. Pergal (2019). Preparation and characterization of poly(urethane-siloxane)/titanium-dioxide nanocomposites*, SCIENTIFIC PAPER UDC: 620.3: 549.514.6: 62-97 Hem. Ind. 73 (1) 13-24*

Jun Liu, Youyuan Wang, Kun Xiao and Zhanxi Zhang (2017). Research on the Thermal Aging Behaviors of LDPE/TiO2 Nanocomposite*s, Journal of Nanomaterials, Volume 2017, Article ID 5048382, 11 pages*

Li Bin, Li Song-Mei, Liu Jian-Hua and Yu Mei (2014). The heat resistance of a polyurethane coating filled with modified nano-CaCO3*, Applied Surface Science, Volume 315, 1 October 2014, Pages 241-246*

L.S De Bernarde, J. Ferrón, E.C. Goldberg and R.H. Buitrago (1984). The effect of surface roughness on XPS and AES*, Volume 139, Issues 2–3, 2 April 1984, Pages 541-548*

M.Sabzi, S.M.Mirabedini, J.Zohuriaan-Mehr and M.Atai (2008). Surface modification of TiO2 nano-particles with silane coupling agent and investigation of its effect on the properties of polyurethane composite coating*, Progress in Organic Coatings, Volume 65, Issue 2, June 2009, Pages 222-228*

Nabil Hayeemasae, Hanafi Ismail, Suradet Matchawet and Abdulhakim Masa (2018). Kinetic of thermal degradation and thermal stability of natural rubber filled with titanium dioxide nanoparticle*s, Polymer Composites, Volume40, Issue8, August 2019, Pages 3149-3155*

S.M. Mirabedini and A. Kiamanesh (2013). The effect of micro and nano-sized particles on mechanical and adhesion properties of a clear polyester powder coating*, Progress in Organic Coatings, Volume 76, Issue 11, November 2013, Pages 1625-1632*

Wei, X., Linde, E. and Hedenqvist and M.S. (2019). Plasticiser loss from plastic or rubber products through diffusion and evaporation, *npj Mater Degradation, 3, Article number: 18*

Yasir Nawab, Pascal Casari, Nicolas Boyard and Frédéric Jacquemin (2017). Determination and modelling of the cure shrinkage of epoxy vinylester resin and associated composites by considering thermal gradients, *Composites Science and Technology, Volume 73, 23 November 2012, Pages 81-87*

Zoran S. Petrović, Ivan Javni, Alan Waddon and György Bánhegyi (2000). Structure and properties of polyurethane–silica nanocomposites, *Journal of Applied Polymer Science, Volume76, Issue2, 11 April 2000, Pages 133-151*

XV International Conference on Durability of Building Materials and Components
DBMC 2020, Barcelona
C. Serrat, J.R. Casas and V. Gibert (Eds)

Study on a Proper Repair Cycle of Finishing Materials in Condominiums

Tomotaka Ide[1], Hitoshi Hamasaki[2] and Yuki Soga[3]

[1] Shibaura Institute of Technology, Graduate school of Eng. and Sci., 3-7-5 Toyosu, Koto, Tokyo, Japan, me19007@shibaura-it.ac.jp

[2] Shibaura Institute of Technology, School of Arch., 3-7-5 Toyosu, Koto, Tokyo, Japan, hamasaki@shibaura-it.ac.jp

[3] Shibaura Institute of Technology, Graduate School of Eng. and Sci., 3-7-5 Toyosu, Koto, Tokyo, Japan, me18070@shibaura-it.ac.jp

Abstract. *In this paper, we discussed the concept for appropriate repair period for finishing materials of reinforced concrete structures. We investigated the actual building repair cycle, the progress of carbonation of concrete, and the adhesion strength of various finishing coating. In addition, we carried out 10-years exposure test of concrete with various finishing to evaluate the progress of carbonation and the degree of deterioration of the finish coating material. From these results, we showed the possibility of extending beyond the current repair cycle.*

Keywords: *Concrete, Finishing Materials, Repair Cycle, Carbonation and Appearance Change.*

1 Introduction

In order to use reinforced concrete buildings for a long term, it is necessary to regularly repair finishing materials in addition to appropriate daily maintenance. Therefore, in Japan, it is required to make a long-term repair plan for condominiums by law, and the repair plan is designed and executed according to the guidelines[1)] issued by the Ministry of Land, Infrastructure, Transport and Tourism. However, repair work, especially the recoating of exterior finish materials, has a uniform repair cycle in any condominiums regardless of their age, surrounding environment or type of finishing materials. Previous studies[2)-4)] pointed out that deterioration speed is different in each material or environment. In other words, in the current repair work may have problems such as deterioration in performance due to leaving the deteriorated part or an increase in extra cost due to the repair of the healthy part. Therefore, in order to efficiently repair work and reduce Life Cycle Cost, it is necessary to set an appropriate repair cycle corresponding to the type of materials, environment and deterioration status.

In this study, we evaluated the current repair cycle by analysing the relationship between the cycle and the deterioration state of existing RC condominiums. Then, we examine the idea of an appropriate repair cycle in terms of performance by verifying the carbonation preventive effects of the finishing materials using the specimen exposed outdoors for 10 years.

2 Materials and Method

2.1 Analysis of Current Repair Cycle and Deterioration State

In this study, we examined the actual status of finishing materials repair cycle and deterioration states before repair in 222 condominiums around Tokyo, Japan. Based on the deterioration

diagnosis report, we focused three deterioration index: carbonation of concrete and decrease in adhesion strength of finishing materials and cracks, and examined the actual deterioration state of exterior walls due to differences in factors affecting deterioration (especially age, repair period and directions). For these deterioration phenomena, we calculated the average value, maximum value and standard deviation for each building. In this report, we will report the results of carbonation and adhesion strength.

As shown in Table 1, we classified the finishing materials into three types: mastic, multi-layer and single-layer coating, and further classified into eight types by kind of materials.

Table 1. The types of finishing materials and number of condominiums.

Type	Number	Materials type	Number
Mastic (without substrate mortar)	53	Cement	39
		Acrylic	14
Multi-layer coating	112	Acrylic	41
		Acrylic Silicon	6
		Silicon	8
		Urethane	10
		Unknown	47
Single-layer coating (with substrate mortar)	57	Cement	50
		Synthetic resin	7

2.2 Performance Evaluation of Various Finishing Materials Using Exposure Specimens

Table 2 shows the Factors and levels of the exposed specimens. The finishing material was applied to the side of a concrete specimen having a water cement ratio of 65% and a size of 100 mm × 100 mm × 400 mm. We experimented six types of coating materials, three types of mortar and three types of tile finishing at exposure test site in Building Research Institute, Tsukuba, Ibaraki, Japan (N36°7’38”, E140°4′39″, sea level +29m).

Exposure environment were three types, indoors, outdoors and outdoors under eaves. We measured the carbonation depth and color difference of finishing materials. The color difference (ΔE) was measured by L*a*b* color coordinates using a colorimeter, and expressed by equation (1) as the difference from the indoor exposure test specimen that seems to be less deteriorated.

$$\Delta E = \sqrt{(L_o - L_i)^2 + (a_o - a_i)^2 + (b_o - b_i)^2} \qquad (1)$$

where L is Lightness, a and b are Chromaticity indicating hue and saturation, Subscript o is Measured value of outdoor exposure test specimen and Subscript i is Measured value of indoor exposure test specimen.

Table 2. Factors and levels of exposure specimens.

Factor	Level	
Exposure environment	Indoors, Outdoors (rain / no rain) Directions (North, East, South and West)	
Finishing material type	Coating	Synthetic resin (Multi / single) Waterproof synthetic resin (multi / single) Gloss paint
	Mortar	Cement mortar t=10 / 20 mm Polymer cement mortar t=10 mm
	Tile	Mortar t=2.0~3.0 / 10mm, Adhesive

3 Results and Analysis

3.1 Analysis of Current Repair Cycle and Deterioration State

3.1.1 Analysis of current repair cycle

Figure 1 shows the cycle and number of exterior walls repair carried out in 222 condominiums that were analyzed in this study. The cycle was an average of 12 years, with a minimum of 9 years and a maximum of 17 years. More than 70% of the first repairs were done by the 12th year. Most of the second repairs were carried out after the 12th year, and the cycle was longer than the first repair. Among the targeted apartment houses, there were only a few them that over 30 years old and the third large-scale repair work was carried out.

Table 4 shows the results of comparing the average repair cycle for each finishing materials. Looking at the types of finishing materials, the repair cycle of thin coating materials was slightly longer. Among them, the single-layer coating had the longest cycle, and the silicon multi-layer coating materials had the shortest cycle. However, although multi-layer coating generally has high durability, repair cycle has almost no change regardless of the difference in finishing materials. Accordingly, it indicates that the repair cycle was not set by the type of finishing materials or the degree of deterioration. In other words, it was set by the uniform repair plan.

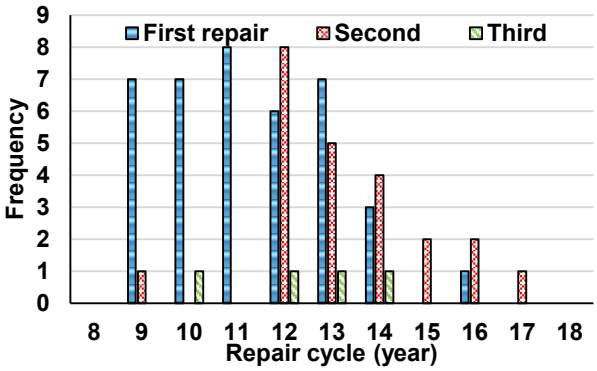

Figure 1. Cycle and number of exterior repairs.

Table 3. Repair cycle for each finishing materials.

Type	Cycle (year)	Materials type	Cycle (year)
Mastic	11.4	Cement	11.3
		Acrylic	12.0
Multi-layer	11.4	Acrylic	11.3
		Acrylic Silicon	11.3
		Silicon	10.5
		Urethane	12.5
Single-layer	12.5	Cement	12.3
		Emulsion	13.0

3.1.2 Analysis of carbonation preventive effect in existing condominiums

The following equation can express carbonation coefficient:

$$A = \frac{C}{\sqrt{t}} \tag{2}$$

where A is the carbonation coefficient (mm/years$^{0.5}$); C is the carbonation depth(mm); t is the time(years). In this study, we used this A as an index of performance against carbonation.

3.1.2.1 Relationship between carbonation and building age (repair cycle)

Figure 2 shows the carbonation coefficient for condominiums with different ages. Although it shows a few relatively large numbers after approximately 10 years, most of numbers are less than 1.50 after 20-30 years. Previous studies have revealed the relationship between carbonation coefficient and compressive strength in unfinished concrete.[5)] Assuming that the carbonation coefficient of targeted condominiums is estimated to be about 3.00 mm/years$^{0.5}$. Therefore, since the carbonation coefficient was kept low, the carbonation preventive effect has been maintained by repair work for more than 30 years.

Figure 3 shows the carbonation coefficient for each time of repair work. The average carbonation coefficient is about 0.5 to 1.0 mm/year$^{0.5}$. On the other hand, the maximum value for the first repair can be confirmed similar value to that of the unfinished concrete. However, in both the second and third repair, the maximum value is significantly lower than the first repair. This is an effect of recoating that the defective part at the time of construction such as pinhole was repaired.

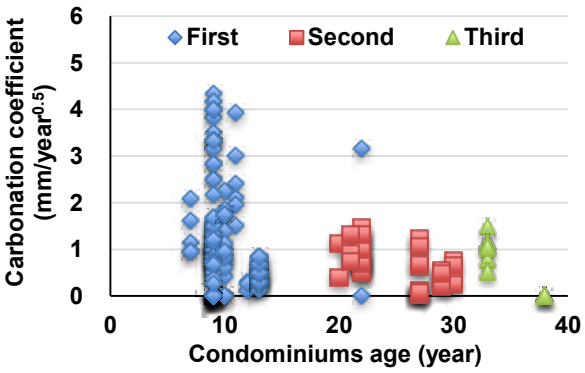

Figure 2. The carbonation speed coefficients for different ages.

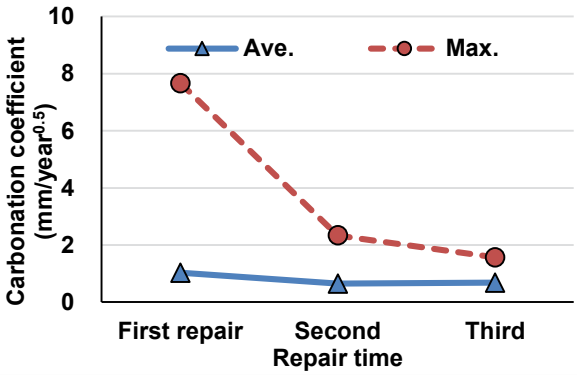

Figure 3. The carbonation coefficients for each repair time.

3.1.2.2 Relationship between carbonation and directions

Figure 4 shows the average of the carbonation speed coefficients for each orientation. The norther and southern sides show slightly larger values than the eastern and western surfaces, especially with thin coating materials. The southern surface has the highest amount of solar radiation, so it is possible that it is more susceptible to UV degradation than other surfaces. In addition, it is known that neutralization is more likely to proceed with dry concrete. In other words, the southern side was in an environment where it was easy to carbonate due to the prolonged dryness caused by solar radiation. According to this result, there is an orientation in

which the deterioration of the finishing material tends to proceed. On the other hand, the reason for the high numerical value on the north surface is unclear, so we analyzed further about relationship between carbonation and orientation in the exposure test conducted in 3.2.

3.1.2.3 Relationship between adhesion strength and repair cycle

Figure 5 shows the average adhesion strength for repair cycle. Mastic and multi-layer adhesion strength almost did not deteriorate. However, single-layer coating strength deteriorate, and seem to decline below 0.3-0.5 N/mm^2 that is established as quality standards of single-layer coating in Japanese Industrial Standards[6] after about 17 years. On the other hand, their strengths were maintained above quality standards in JIS until around 15 years.

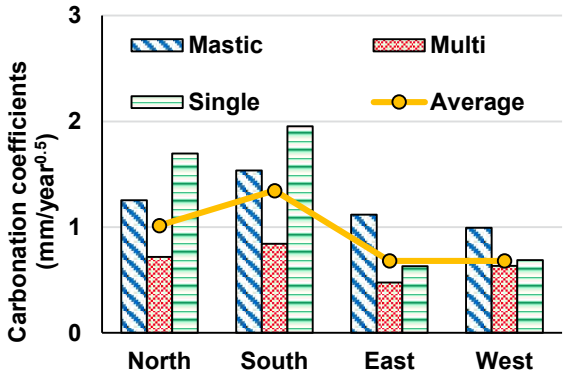

Figure 4. The carbonation coefficients for each direction.

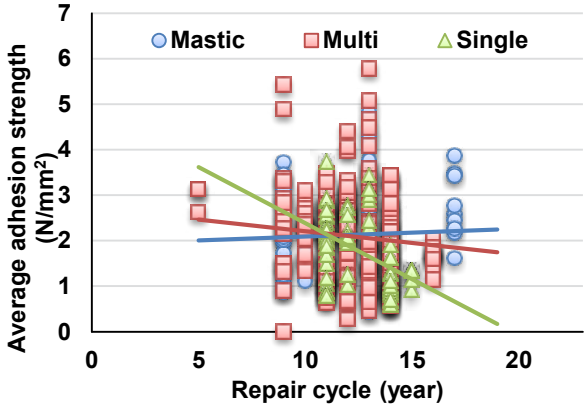

Figure 5. Adhesion strength for each repair times.

3.2 Performance Evaluation of Various Finishing Materials Using Exposure Specimens

3.2.1 Carbonation preventive effect after 10 years of each finishing materials

Figure 6-8 shows the carbonation coefficients for each finishing materials in each environment (left side) and each direction (right side). The carbonation coefficients of None finishing concrete was 4.56 mm/years$^{0.5}$ indoor, 1.95 mm/years$^{0.5}$ outdoor with rain, and 5.00 mm/years$^{0.5}$ outdoor under eaves. Therefore, we considered these values as each evaluation standard for the carbonation preventive effect of the finishing materials.

In the case of outdoors with rain, the single-layer coating is 1.89 mm/years$^{0.5}$, which is almost same value as none finishing one. This is because the single-layer coating has almost no carbonation suppressing effect, rather than due to deterioration. On the other hand, even with the synthetic resin type materials, multi-layer coatings and waterproof ones had a certain preventive effect. Similarly, even in the case of no rain, the single-layer coating shows a higher value than other finishing materials.

In other materials, mortar 10 mm and tile on substrate 2.0-3.0 mm mortar showed relatively high values outdoors without rain. However, the mortar 10 mm has low value outdoors with rain. This is because the specimen outdoor with rain was supplied with water by rain. It caused a high moist state in a specimen and the mortar became denser because the hydration reaction of the cement progressed. Therefore, the high carbonation coefficient of 10 mm mortar outdoors

without rain did not cause by deterioration.

Outdoors with rain, the carbonation preventive effect of most finishing materials was maintained except for the single-layer coating, so they had no deterioration of performance for coating materials, mortars and tiles by 10 years. From these results, it is possible to extend the repair cycle because the current cycle is not at the limit of performance in about 12 years. However, as the data for 10 years cannot mention how long we extend it, further exposure testing is necessary. Moreover, since we handled only synthetic resin type in the coating materials this time, we have to evaluate other coating materials.

Further, although the finishing materials are hardly deteriorated indoors, the tendency that the carbonation of the thin coating E was high, and the others were low is the same in this case.

3.2.2 Relationship between carbonation and orientation

The high values on the northern and southern sides of thin coating material E was similar to the survey results in 3.1. Especially on the northern side, it was much larger than the value of none finishing concrete. On the other hand, other materials had the small variation in each orientation and the deterioration has not been promoted by direction.

3.2.3 Analysis of color difference

Figure 9 shows the color difference of coating material specimens exposed outdoors. In an environment with rain, the color difference is large overall, especially in the single-layer coating. In general, the evaluation standards of color difference, people cannot identify color difference when it is lower than 3.2, can recognize a color difference when it over 6.5 and can recognize as a different color when it over 13.0. In these results, the single and multi-layer in an environment with rain coating have deteriorated in design. On the other hand, all finishing materials under eaves were lower than 13.0. However, because the carbonation of single-layer coating progress in under eaves, the change in appearance did not necessarily match the carbonation preventive effect depending on the type of finishing materials or environment. We need to consider changes in appearance and carbonation preventive effects as separate factors.

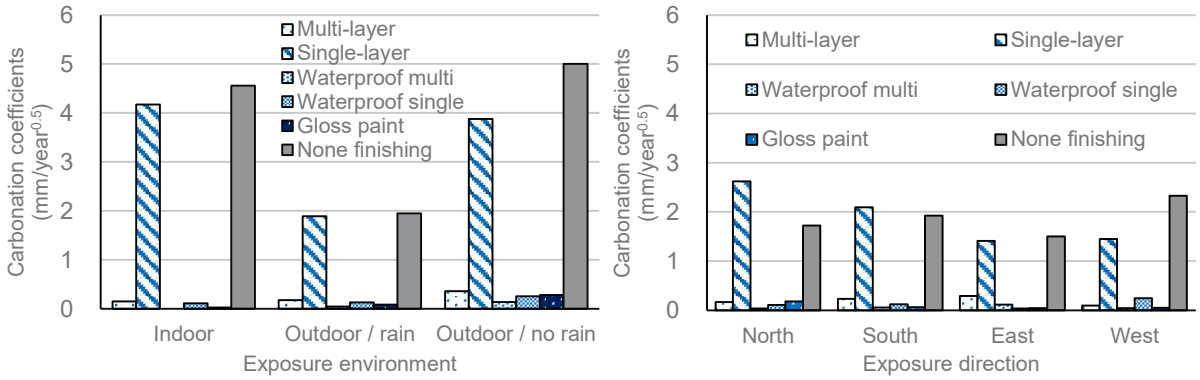

Figure 6. The carbonation coefficients after 10 years (Coating material).

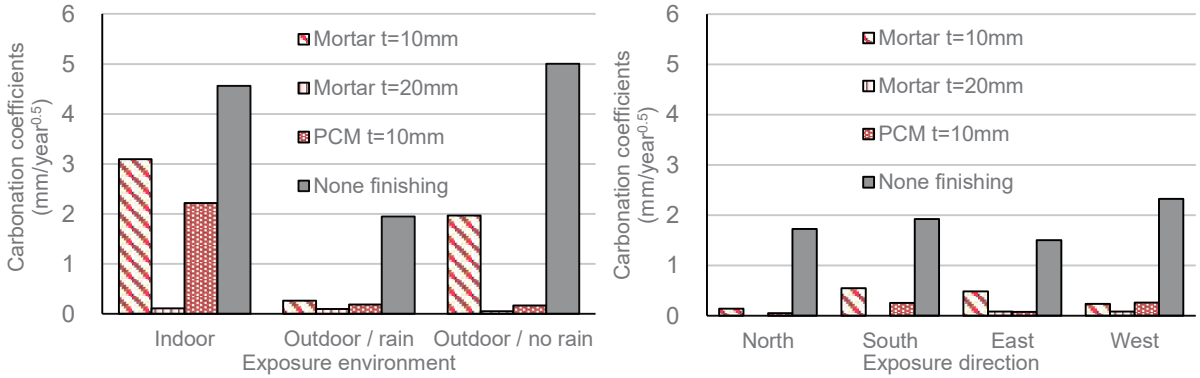

Figure 7. The carbonation coefficients after 10 years (Mortar).

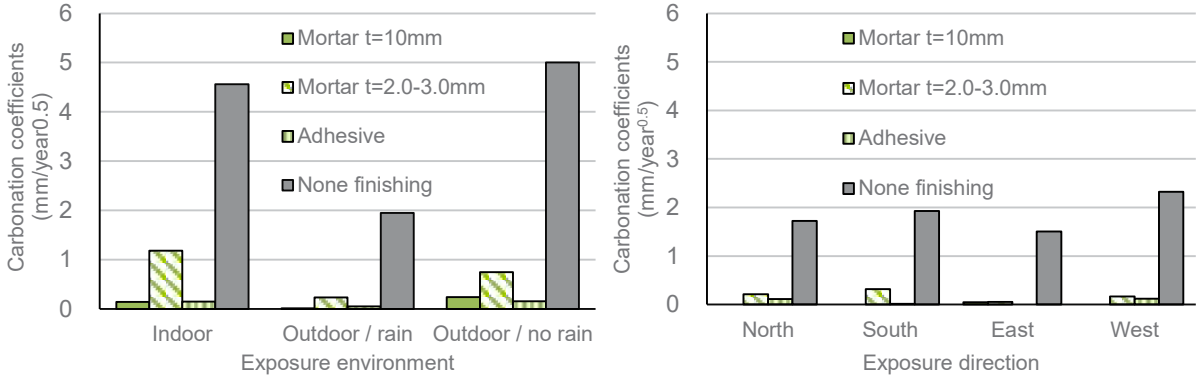

Figure 8. The carbonation coefficients after 10 years (Tile).

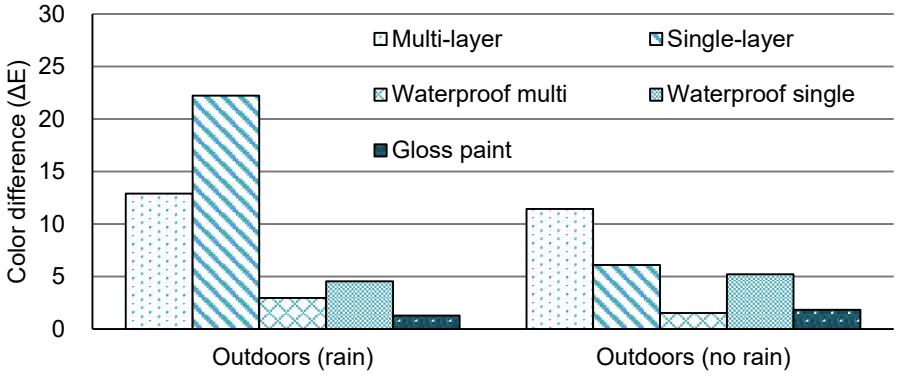

Figure 9. The color difference after 10 years (Coating material).

4 Conclusion

In this study, in order to examine the appropriate repair cycle of exterior finishing materials, we investigated and analyzed the current repair cycle and deterioration state, and second we evaluated the carbonation preventive effect of the finishing materials by using specimens exposed for 10 years. As a result of the survey, the current repair cycle was about 12 years, but since the carbonation preventive effect was sufficiently maintained at the time of repair, the repair cycle may be longer than the current cycle in terms of performance. Furthermore, in the exposed specimens, the single-layer coating had no carbonation preventive effect, but other materials still have the carbonation preventive effects at 10 years, and almost no difference of carbonation in each direction. In the previous study that conducted an outdoor exposure test for 20 years in model building[7)], the multi-layer coating had had the carbonation preventive effect even after 20 years.

While the finishing materials had not reached their performance limit, repairs may be done from an aesthetic point of view. In particular, appearance of coating materials in an environment with rain relatively changed more than under eaves them after 10 years. Therefore, we need to consider changes in appearance and carbonation preventive effects as separate factors. We will continue the exposure test for more long term to confirm the performance (the carbonation preventive effect, deterioration of coating itself and aesthetics) of each material at various environment.

References

Ministry of Land, Infrastructure and Transport (2008). *The guidlines for creation long-term repair plan*

Takuya Hasegawa et al. (2002). *A study on the corrosion protection effects of surface finishing materials using a model building at the age of eleven years* (in Japanese), Journal of structural and construction engineearing, Architectural Institute of Japan, No.555, 27-33

Takuya Hasegawa et al. (2002). *A study on the carbonation protection effects of surface finishing materials using a model building at the age of eleven years* (in Japanese), Journal of structural and construction engineearing, Architectural Institute of Japan, No.555, 37-43

Takuya Hasegawa et al. (2006). *A study on the carbonation preventive effects of coating materials for textured finishes of buildings* (in Japanese), Journal of structural and construction engineearing, Architectural Institute of Japan, No.609, 23-30

Taichiro Kawanishi et al. (2006). *Analysis on the carbonation of concrete based on investigation of exisiting buldings* (in Japanese), Journal of structural and construction engineearing, Architectural Institute of Japan, No.608, 9-14

JIS: Japanese Industrial Standards (2010).*JIS A 6909: Coating materials for textured finishes of buildings*

Takuya Hasegawa et al. (2017). *Deterioration and preventive effects of finishing materials against carbonation and corrosion of reinforcing bars in concrete based on twenty year outdoor exposure test using model building* (in Japanese), Journal of structural and construction engineearing, Architectural Institute of Japan, No.733, 337-346

XV International Conference on Durability of Building Materials and Components
DBMC 2020, Barcelona
C. Serrat, J.R. Casas and V. Gibert (Eds)

Assessing Water Resistance and Surface Properties of ETICS

Giovanni Borsoi[1], João Luís Parracha[2], Pedro Caiado[1], Inês Flores-Colen[1], Amélia Dionísio[3] and Rosário Veiga[2]

[1] CERIS, Civil Engineering Research and Innovation for Sustainability, Instituto Superior Técnico, University of Lisbon, 1049-001, Lisbon, Portugal, giovanni.borsoi@tecnico.ulisboa.pt, ines.flores.colen@tecnico.ulisboa.pt, pedrocpcaiado@gmail.com

[2] LNEC, National Laboratory for Civil Engineering, Av. do Brasil 101, Lisbon, Portugal, jparracha@lnec.pt, rveiga@lnec.pt

[3] CERENA, Centro de Recursos Naturais e Ambiente, Instituto Superior Técnico, University of Lisbon, 1049-001, Lisbon, Portugal, amelia.dionisio@tecnico.ulisboa.pt

Abstract. *External Thermal Insulation Composite Systems (ETICS) contribute significantly to building energy efficiency by increasing thermal insulation, correcting thermal bridges and reducing interior water condensation. Additionally, these solutions protect the structure and thus enhance the durability of the building. The use of ETICS remarkably increased in the last three decades also due to the introduction of new international and national regulations on building energy efficiency (e.g. EU Directive on the Energy Performance of Buildings). ETICS are constantly exposed to weathering (e.g. wind, rain, sun light) and anthropic factors (e.g. graffiti, environmental pollutants), which can lead to cracks, biocolonization and stains and thus affect ETICS durability. However, international technical documents on the evaluation of the effectiveness and durability of ETICS do not consider the possible synergies between these factors, which can trigger and speed up multiple biological, mechanical and chemical degradation processes. With the aim of filling this gap, this paper focused on the water resistance and surface properties of several ETICS surface coatings, verifying possible connections between these factors. The moisture transport properties (capillary water absorption, water vapour permeability, and drying kinetics) and surface properties (colour, brightness and roughness) of some commercially available ETICS were tested. This study is part of a wider research project (WGB_Shield: resistance for water, graffiti and biocolonization of external thermal insulation systems) that aims at the development of ETICS with improved durability in urban environment.*

Keywords: *ETICS, Durability, Water Behaviour, Surface Properties*.

1 Introduction

The implementation of long-term building renovation strategies is a key challenge in modern society. As a matter of fact, 40% of energy in EU is used for buildings (producing 36% of total CO_2 emission) and 2/3 of this energy consumption is used for heating and cooling. For these reasons, EU has set new rules also for energy efficiency, both in new and retrofitted buildings, with the objective of achieving a nearly zero energy built environment by 2050 (EPBD 2010).

In this context, External Thermal Insulation Composite Systems (ETICS), sometimes also identified as External Wall Insulation (EWI, in UK) or Exterior insulation finishing system (EIFS, in the US), can significantly improve the thermal performance and energetic efficiency of buildings. In fact, these systems can improve thermal insulation, reduce thermal bridges and avoid water

condensation within masonry. Additionally, these systems can increase occupants' health and wellbeing, by improved air quality, and thermal comfort (Barreira and P. de Freitas, 2013).

Hence, ETICS have been established in the last three decades among the most used solution to improve the energy efficiency of buildings, with a wide variety of system configurations and design. It is estimated that more than 2 billion m^2 have already been installed in Europe (Pasker, 2017).

These systems are generally composed of a variety of materials, which include insulation materials (Schiavoni *et al*., 2016), basecoats with mineral binders (*e.g.* air or hydraulic lime, cement), finishing coatings (*e.g.* silicate, acrylates, siloxanes and additives (*e.g.* aggregates, pigments, biocides). The compatibility among these components is a crucial factor to achieve an efficient and durable system.

According to the European Technical Approval Guideline (ETAG 004), which gather the technical approval requirements of ETICS in the EU zone, service life of ETICS should be over 25 years. It is thus necessary to plan a careful maintenance of these systems.

As a matter of fact, ETICS are constantly exposed to weathering agents (*e.g.* wind, rain, sun light, etc.) as well as to direct (*e.g.* vandalism) and indirect (*e.g.* environmental pollutants) anthropic factors. These factors have often a synergic effect on the affected surface, triggering and speeding up multiple biological, mechanical and chemical degradation processes.

Degradation patterns are typically identified in the alteration of the physical-chemical, aesthetical and mechanical properties of ETICS, with formation of *e.g.* cracks and stains.

In this paper, the moisture transport properties (water capillary absorption, drying kinetics, water vapour permeability) and superficial properties (colour, brightness, surface roughness) of several commercially available ETICS were studied. The main aim was the identification of the possible connection between these properties and, ultimately, a deeper comprehension of the dynamics behind the durability of ETICS surface coatings in urban environment.

2 Materials and Methods

2.1 Materials

Several ETICS were analysed, as resumed in Table 1. It has to be pointed out that 3 different ETICS producers were considered (systems 1 to 3; systems 4 to 8; systems 9 to 12). Specimens with 15x15 cm were considered for the absorption and drying kinetics, whereas cylindrical specimens (8 cm diameter) were used for the water vapour permeability test. Specimens 5x5 cm were used for the evaluation of the surface properties (colour, brightness, roughness). The specimens have thickness varying between 3.9 and 6.5 cm.

2.2 Methods

2.2.1 Absorption and drying kinetics

Capillary absorption tests were performed according to ETAG 004 (EOTA, 2013) in a conditioned room (at T=23 ± 2ºC and 65 ± 5% RH). A total of four cycles (with measurements at 3 min, 1h, 4h, 8h and 24h) of capillary absorption were conducted. Capillary water absorption coefficient was obtained by the slope of the initial phase of the curve that expresses the water absorption as a function of the square root of time.

Table 1. ETICS identification and composition (EPS = Expanded polystyrene; ICB: Insulation cork Board; MW = Mineral wool).

Systems	Thermal Insulation	Base Coat	Finishing coat
1	EPS	2 layers of cement-based mortar + mesh	*Primary:* water-based dispersions of acrylic co-polymer *Finishing:* acrylic paint + quartz aggregate
2	EPS	Cement-based mortar + mesh	*Primary:* water-based acrylic dispersion *Finishing:* a) water-based acrylic co-polymer + pigment + marble powder b) water-based acrylic paint
3	EPS		*Primary:* water-based acrylic dispersion *Finishing:* water-based acrylic co-polymer + pigment + marble powder
4	ICB	Hydraulic lime and cement mortar + mesh	*Mortar:* air lime + hydraulic binder + organic additives
5	ICB		*Primary:* acrylic co-polymer + mineral additives *Finishing:* acrylic paint + mineral aggregate + pigments
6	EPS		
7	EPS	Cement-based mortar + mesh	*Primary:* acrylic co-polymer + mineral aggregate *Finishing:* acrylic paint + organic additives + pigments
8	MW		*Primary:* acrylic co-polymer + mineral aggregate *Finishing:* acrylic paint+ mineral aggregate + pigments
9	ICB	Hydraulic lime and cork aggregate mortar + mesh	*Primary:* water-based dispersions of silicate *Finishing:* water-based silicate paint + organic additives + pigments
10	ICB		
11	EPS	Hydraulic lime and cement mortar + mesh	*Primary:* acrylic dispersion + mineral aggregate *Finishing:* acrylic paint + siloxane resin + marble powder
12	MW		

Drying test was performed following the recommendations of EN 16322 (2013) and started immediately after the capillarity test. The test was performed in a conditioned room (23 ± 2ºC and 65 ± 5% RH). Specimens were weighted after determined periods of time until the variation of mass was constant for all specimens. Two drying phases were determined: DR1 – the first drying phase, obtained by the negative slope of the initial linear section of the drying curve plotted with time in abscissa; and DR2 – the second drying phase, calculated by the negative slope of the linear section of the drying curve, plotted against the square root of time in abscissa. Drying index (DI) was obtained by Equation (1), in which M_x is the mass of the specimen registered during the drying process (g), M_1 is the mass of the specimen in a dry state (g), M_3 is the mass of the specimen in a saturated state (this mass corresponds to the mass at the beginning of the drying process (t_0), t_f is the time at the end of the drying process.

$$DI = \frac{\int_{t_0}^{t_f} f\left(\frac{M_x - M_1}{M_1}\right) dt}{\left(\frac{M_3 - M_1}{M_1}\right) \times t_f} \quad (1)$$

2.2.2 Water vapour permeability

Water vapour permeability (WVP) tests were performed according to ETAG 004 (EOTA, 2013), adopting the dry cup method, i.e. sealing the lateral and bottom side of ETICS specimens within a recipient which contains a dryer substance ($CaCl_2$) than the external

conditions. The lateral sides are sealed with paraffin, whereas the superficial finishing of the ETICS is exposed to the external environment. The cup is filled with a dessicant ($CaCl_2$), which keeps the relative humidity (RH) inside the cup fixed at ≈20%. All specimens are then stored within a climatic chamber at T=23 ± 2ºC and 50 ± 5% RH. Hence, water vapour is forced from the external environment (50% RH) to the interior of the cup (≈20% RH), fluxing through the layers of the ETICS. Specimens were weighted over time, till stabilization of the specimens' weights. The change in the mass of the cup's content is used to quantify the water vapour permeability of the ETICS.

Based on the obtained results, the following parameters can be obtained by using the following equations:

$$\Lambda = \frac{m}{A \times \Delta_p} \quad (2)$$

$$\mu = \frac{1.94 \times 10^{-10}}{\Lambda \times e} \quad (3)$$

$$S_d = \mu \times e \quad (4)$$

where Λ is the water vapour permeance (kg/m^2.s.Pa), which defines the Wvp; m is the slope of the linear relation between mass variation and time (kg/s), A the specimen area, Δp is the vapour pressure difference between the exterior and interior (Pa), referred to the thickness of the specimen (m), μ the water vapour diffusion resistance factor, Sd the diffusion-equivalent air-layer thickness (m).

Furthermore, the thermal insulation and complete systems (as in Table 1) were tested separately, in order to verify the requirements of the ETAG004 (EOTA, 2013). In fact, the WVP of the complete system (base and finishing coat) was analysed with the diffusion-equivalent air-layer thickness (S_d), whereas the WVP of the thermal insulation with the water vapour diffusion resistance factor (μ).

2.2.3 Colour and brightness

Colour was assessed with a colorimeter Minolta CR-410 Chroma Meter, by measuring the three colour coordinates (L^*, a^*, b^*) of the CieLAB colour system. L^* is the the lightness, which varies from 0 (black) to 100 (white), whereas a^* and b^* identify the colour, i.e. the chromatic coordinates of red-greed ($+a^*$ refers to red, $-a^*$ to green) and yellow-blue (($+b^*$ refers to yellow, $-b^*$ to blue). The chroma or colour saturation is calculated based on the values of a* and b*:

$$C = \sqrt{a^2 + b^2} \quad (5)$$

The total colour difference (ΔE^*), which takes into account the differences between the L, a, b of the specimens and a standard/reference specimen, can be calculated as follows:

$$\Delta E^* = \sqrt{\Delta L^{*2} + \Delta a^{*2} + \Delta b^{*2}} \quad (6)$$

Each specimen was analysed in 4 different spots, using a standard illuminant D65 (which

corresponds to average daylight, including Uv wavelength region, with a correlated colour temperature of 6504K). The colorimeter was set to measure 3 repeated times in each spot. The relative average values and standard deviations were considered.

Brightness test was performed according to ASTM D6578 (ASTM, 1987). A Rhopoint Novo- Gloss Lite equipment was used, measuring the brightness with a light source angle of 60º (suitable for matte specimens). The brightness (Gloss Unit – GU) was tested in 9 different spots in each specimen, considering the average value and relative standard deviation.

2.2.4 Surface roughness

An Elcometer 223digital surface profile gauge was used to measure the peak-to-valley height (surface roughness) of the specimens. This equipment can measure up to 2mm, with a resolution of 0,001 mm. Surface roughness was tested in 9 different spots in each specimen, considering the average value and relative standard deviation.

3 Results and Discussion

3.1 Capillary Absorption and Drying Tests

Results obtained for capillary absorption and drying kinetics are presented in Figure 1 and Table 2. It can be observed that the systems 4 and 5, from the same producers and both with ICB, have the higher capillary absorption values at 1h, as well as the higher capillarity coefficient (Table 2). However, those values are < 1kg/m^2, thus meeting the requirements of ETAG 004 for the technical approval of ETICS. Systems 7 and 8, which present the same cement-based base coat, present the higher capillary absorption at 24h (respectively, 1.36 and 1.46 kg/m^2). On the other hand, system 2 have the slower capillary absorption at 24h (0.24 kg/m^2). This latter system, similarly to systems 1, 3, 9 and 11, has capillary absorption < 0,5 kg/m^2, and, thus, according to ETAG 004, those systems are resistant to freeze-thaw cycles. It has to be pointed out that system 9, which presents a ICB thermal insulation, a base coat with NHL and cork aggregate and a silicate-based finishing coat, has lower capillary absorption values, when compared to system 10, which differs only for its acrylic-based finishing coat. This confirms that this silicate-based finishing coat has lower capillary absorption, when compared to the referred acrylic-based finishing coat.

Additionally, if comparing systems 2 and 3, which have the same base coat, it can be concluded that the combination of an acrylic-based and co-polymeric acrylic finishing coat (system 2) plays an important role in the reduction of the water absorption, which is considerably lower (44%) compared to system 3, which has only one layer of finishing coat.

Finally, it can be observed a significant difference between the capillary coefficient of systems 6 and 8, which differ only for their thermal insulation material (EPS and MW, respectively), as well as for systems 11 and 12, which again differ only for their thermal insulation materials (EPS and MW).

This can indicate that liquid water reaches the insulation layer and that there is an influence of the thermal insulation material on the capillary absorption, *i.e.* a higher and faster absorption of MW, when compared to EPS.

When observing drying kinetics, it can be noted that system 7 has the highest DR1 (which corresponds to water transport in the liquid phase), DR2 (which corresponds to water vapour

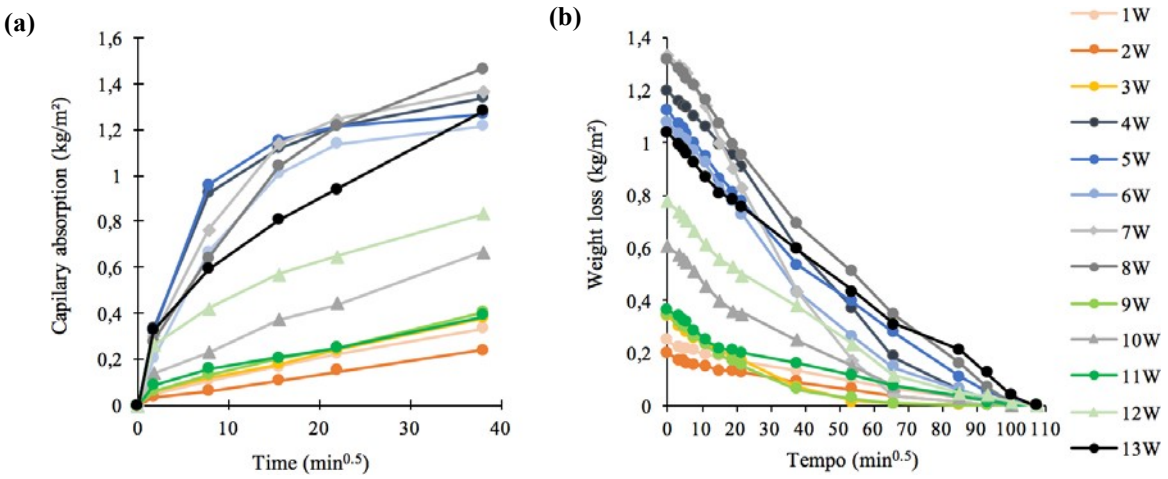

Figure 1. Capillary absorption (a) and drying curves (b) of the ETICS specimens.

diffusion) and drying index (0.94). Similar trends were observed for systems 4, 5, 6 and 8 (all from the same producers), which are also the systems with higher capillary absorption values. Conversely, ETICS 1, 2, 3 and 11 have the highest DR1 and DR2. It can be concluded that, generally, the systems that absorbed more water by capillarity, are those with faster drying, which allows for some compensation and a possible adequate global behaviour.

3.2 Water Vapour Permeability

Results are presented in Table 2. The highest values of water vapour diffusion resistance were registered for ETICS 1 (65.75) and 2 (65.22), followed by systems and 11 (48.94) and 3 (44.27). As a matter of a fact, these systems were those with lower capillary absorption and lower water transport in the liquid phase (DR1).

Conversely, systems 4, 5 and 8, those with higher capillary absorption, present lower values of water vapour diffusion resistance, with higher WVP and thus faster drying. A different trend was observed for systems 6 and 7, which have both a higher water vapour diffusion resistance and water absorption when compared to ETICS 8. This behaviour can hinder a suitable drying of this system.

However, when verifying the diffusion-equivalent air-layer thickness of the base and finishing coat of the systems (by subtracting the S_d of the whole system to that of the thermal insulation), these values are < 2m in all cases. Thus, all systems are in agreement with the requirements of the ETAG 004, which define S_d values limits of 2 m for EPS systems (specimens 1,2,3,6,7,11) and 1m for MW systems (specimens 8,12).

3.3 Colour and Brightness

Results presented in Figure 2 indicate a low chroma for all systems (minimum L* at 71.71, for ETICS 5), with shades of grey and a tendency to yellow (positive b* values). More specifically, systems 8 and 12, those with MW thermal insulation, have the higher b* values. In all systems, the a* values are close to zero, *i.e.* to an ideal white colour.

Table 2. Capillary water absorption, drying and water vapour permeability test results.

Systems	Capillary absorption		Drying				WVP	
	Capillary absorption 1h (kg/m²)	Cc (kg/m².min$^{0.5}$)	DR1 (kg/m².min$^{0.5}$)	DR2 (kg/m².min$^{0.5}$)	DI	μ ETICS	μ Thermal Insulation	Sd finishing (m)
1	0.10	0.027	0.000053	0.0027711	1.05	65.75		1.12
2	0.06	0.019	0.000050	0.0025406	1.05	65.22	42.45	1.15
3	0.12	0.034	0.000113	0.0051086	1.02	44.27		0.29
4	0.92	0.193	0.000287	0.0154256	1.02	16.28	8.86	0.54
5	0.96	0.184	0.000252	0.0127771	1.01	16.78		0.54
6	0.67	0.115	0.000283	0.0141846	0.98	32.63	35.81	-
7	0.77	0.172	0.000403	0.019722	0.94	42.20		0.58
8	0.64	0.160	0.000280	0.0146646	0.98	6.73	1.90	0.31
9	0.13	0.034	0.000110	0.0051607	1.03	12.06	14.07	-
10	0.23	0.081	0.000158	0.0079991	1.00	25.49		0.54
11	0.15	0.049	0.000086	0.0043290	1.00	48.94	39.83	0.59
12	0.42	0.151	0.000186	0.0099738	0.98	24.43	2.74	0.99

When comparing the different systems, it can be noted that ETICS 1 and 3 have similar chroma, even if system 1 is closer to an ideal white (lower C*). On the other hand, system 2 have higher L* and lower C*, being thus slightly brighter and more whitish than systems 1 and 3. Those systems are the only ones with –a* values (green component).

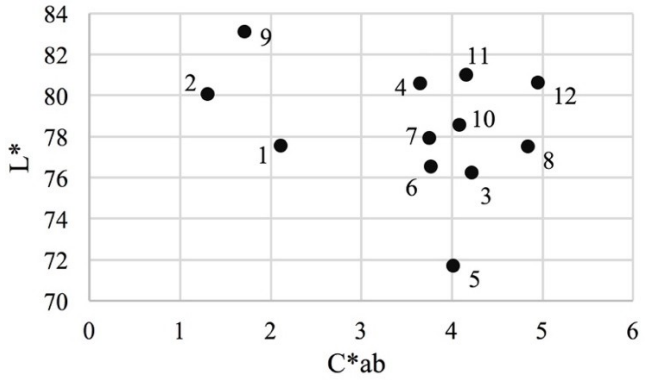

Figure 2. Comparison of the CieLAB values of the different ETICS.

When comparing systems 4 and 5, from the same producers and with the same thermal insulation (ICB), it can be noted a difference in L* and C*, attributed to the difference in their finishing coating (lime-based and acrylic-based, respectively). Systems 6 to 8, although with different compositions, have similar chromatic coordinates. ETICS 10 to 12 (from the same producers, and with the same acrylic-based finishing coat) have similar colour, although system 10 has lower chroma, which might be related to the use of ICB as thermal insulation. On the other hand, system 9 (finished with a silicate- based coating), has even higher L* and lower C*, being thus more close to an ideal white colour.

When considering brightness, it can be noted that those values are in agreement with colour values. In fact, systems 1 and 2 have similar brightness, whereas ETICS 3 (with co-polymeric

acrylic finishing coat) has significantly lower values, when compared to 1 and 2 (both with 100% acrylic- based finishing coat). Systems 6 to 8 have similar GU values, whereas ETICS 5 (which differs for its ICB thermal insulation, when compared to systems 6 to 8) have lower values. Conversely, system 4, finished with a (aerial and hydraulic) lime-based mortar, has brightness value which doubles that of system 5. Ultimately, systems 10 to 13 have similar brightness values, however, system 10 slightly differs from these systems, possibly due to its ICB thermal insulation. In agreement with colour values (Figure 2), system 9, is the only system with a silicate-based finishing coat, that has a considerably higher values when compared to systems 10 to 12 (all with acrylic-based finishing).

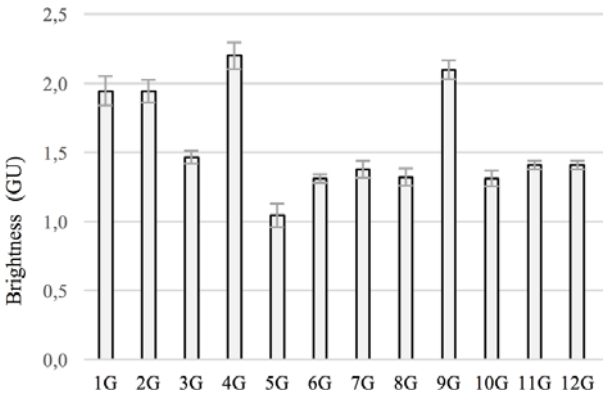

Figure 3. Brightness (average value and standard deviation) of the ETICS specimens**.**

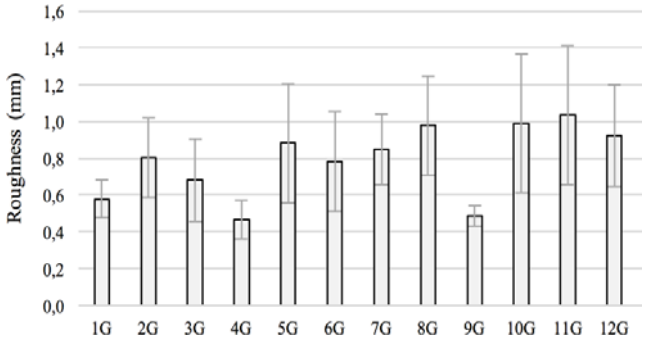

Figure 4. Surface roughness (average value and standard deviation) of the ETICS specimens.

3.4 Surface Roughness

Results show that systems 1, 4 and 9 (one for each producer) present the lower roughness values (467 µm to 580 µm) (Figure 4). When comparing systems 1 to 3, from the same producers, it can be noted that systems 2 and 3 have higher values, when compared to ETICS 1, due to the use of a coarser (co- polymeric-based) finishing coat. Systems 5 to 7, although with different compositions, have similar roughness values, whereas system 8 (with MW thermal insulation) have slightly higher (15%) values. The significant lower values of ETICS 4 can be attributed to the use of a thin lime-based layer as finishing coat, when compared to the systems 5 to 8 (784 µm to 978 µm), which present coarser mineral aggregates in their finishing coat. Ultimately, systems 10 to 12, which have the same acrylic- based finishing coat, have similar roughness (874 µm to 1035 µm), with slightly lower values in system 12. On the

other hand, ETICS 9, which is finished with a silicate-based coat, has remarkably lower surface roughness, comparable to that of systems 1 and 4.

When comparing the moisture transport properties and roughness of the 3 different producers, it is worth highlighting that systems 1 to 3, with relatively low roughness (0,575 μm 0,761 μm), have also low water capillary absorption. Conversely, ETICS 5 to 8 have slightly higher roughness (0,704 μm to 0,978 μm) and significantly higher water capillary absorption. A trend similar to the latter systems is observed with ETICS 10 and 12. Interestingly Systems 4 show both low roughness and capillary absorption, whereas systems 11 have low roughness and considerably high water absorption (and drying rate). This can be explained again by the composition of these systems (lime-based finishing for ETICS 4, silicate-based coating for ETICS 9).

4 Conclusions

The aim of this paper is the evaluation of the moisture transport properties and surface properties of commercially available external thermal insulation composite systems (ETICS).

Results showed that all systems respected the hygric requirements of ETAG for the technical approval of ETICS, *i.e.* all have capillary absorption lower than 1kg/m^2 at 1h and a suitable water vapour permeability (diffusion-equivalent air-layer thickness < 2m). It was observed that, generally, systems that absorb more water are those that have higher dry rates and higher water vapour permeability (as in the case of systems 4 to 8, from the same producer).Conversely, systems 1 to 3 (again, from the same producers) show an opposite behaviour. Furthermore, it can be concluded that the system with silicate-based finishing coat (system 9) has lower absorption and faster drying (however, slightly higher WVP) when compared to other systems (10 to 12) from the same producer. In general, an influence of the thermal insulation on moisture transport properties of the systems can be observed only in systems 11 (EPS) and 12 (MW), i.e. a higher capillary absorption, faster drying and higher WVP of the system with MW, when compared to that with EPS. Moreover, a significant difference in the moisture transport properties is given mostly by the composition of the finishing render (base and finishing coats), rather than the surface properties (*e.g.* roughness).

When observing results of the optical surface tests, it can be seen that the systems with acrylate- based finishing coat are generally less whitish and less bright, when compared to systems finished with silicate-based (ETICS 9) or lime-based (ETICS 4) systems.

Ultimately, it was observed that systems 1, 4 and 9 (one of each producer), the ones with the highest colour and brightness values, have also the lowest roughness values. The higher values of the other systems are attributed to the addition of mineral loads (aggregate) in the finishing coat.

It should be noted that all systems were tested in ideal conditions (no exposure to external weathering). For this reason, further tests are ongoing to assess the moisture transport properties and surface properties of ETICS before and after natural and artificial aging.

Acknowledgements

The authors acknowledge the Portuguese Foundation for Science and Technology (FCT) for the financial support of the research project PTDC/ECI-EGC/30681/2017 (WGB_Shield – Shielding building' facades on cities revitalization. Triple resistance for water, graffiti and biocolonization of external thermal insulation systems).

ORCID

Giovanni Borsoi: https://orcid.org/0000-0002-2194-4620
João Luís Parracha: https://orcid.org/0000-0001-6214-3400
Inês Flores-Colen: https://orcid.org/0000-0003-4038-6748
Amélia Dionísio: https://orcid.org/0000-0001-8016-4029
Maria do Rosário Veiga: https://orcid.org/0000-0002-7135-8603

References

ASTM D6578-00, 2000. Standard Practice for Determination of Graffiti Resistance. ASTM International, Pennsylvania, USA.

Barreira, E. and P. de Freitas, V. (2013). Experimental study of the hygrothermal behaviour of External Thermal Insulation Composite Systems (ETICS). *Building and Environment, 63*, 31-39.

Energy Performance of Building Directive (EPBD) (2010). Directive 2010-31-EU of the European Parliament and of the Council, Official Journal of the European.

EN 16322 (2013). *Conservation of Cultural Heritage – Test methods – Determination of drying properties.* European Committee for Standardization, Brussels, Belgium.

EOTA (2013). *Guideline for European Technical Approval of External Thermal Insulation Composite Systems with Rendering.* ETAG 004, Brussels.

Pasker, R. (2017). The European ETICS market – Do ETICS sufficiently contribute to meet political objectives?, in *4th European ETICS Forum*, Warsaw, Poland.

Schiavoni, S., D'Alessandro, F., Bianchi, F. and Asdrubali, F. (2016). Insulation materials for the building sector: A review and comparative analysis, *Renewable and Sustainable Energy Reviews*, 62, 988–1011.

XV International Conference on Durability of Building Materials and Components
DBMC 2020, Barcelona
C. Serrat, J.R. Casas and V. Gibert (Eds)

Development of an Integrated Durability Assessment Methodology of Thermal Mortars Applied in Multi-layer Systems

Joana Maia[1a], **Nuno M. M. Ramos**[1b] **and Rosário Veiga**[2]

[1] CONSTRUCT (LFC), Faculty of Engineering of University of Porto, R. Dr. Roberto Frias, s/n 4200-465 Porto, Portugal, [a]joanamaia@fe.up.pt, [b]nuno.ramos@fe.up.pt

[2] National Laboratory for Civil Engineering (LNEC), Av. do Brasil, 101 1700-066 Lisboa, Portugal, rveiga@lnec.pt

Abstract. *A gap in the durability assessment of thermal mortars applied in multi-layer systems was observed. The existing standardisation for the durability assessment of hardened mortars does not include a consistent evaluation of thermal coatings applied in multilayer systems, which motivated the development of a new durability assessment methodology. The determination of the physical, hygrothermal and mechanical properties allowed deepening the knowledge of thermal mortars, contributing to develop more reliable simulations. The existing durability methodologies applicable to one-coat mortars and those applicable to thermal multilayer systems (such as ETICS – External Thermal Insulation Composite Systems) are suitable to be adapted to thermal rendering and plastering systems since they present some similar characteristics. The methodology takes into account the material characteristics and specific requirements, such as the application and climatic conditions. The knowledge of these parameters allows the definition of representative accelerated ageing cycles of the relevant degradation mechanisms. The combination of existing procedures with hygrothermal simulation allowed the development of accelerated ageing cycles, taking into account the European climatic context. The existing procedures allowed analysing several degradation mechanisms, but the fixed parameters are not transversal to different climates. The developed methodology allows a realistic durability evaluation since the ageing cycles are adapted to thermal mortars and real climate conditions, contrary to the existing standardised procedures.*

Keywords: *Thermal Mortars, Durability, Accelerated Ageing, Experimental Tests, Methodology.*

1 Introduction

One of the seven objectives defined by the European Mortar Industry Organization (EMO) is to "raise awareness for sustainability", emphasizing the ecology of mineral mortars and the need to promote the advantages of using this type of products, their durability and lack of hazardous substances in comparison with other materials on the market (EMO, 2013). However, the concept of eco-design should relate to not only the environmental ecology issue but also the quality of life of the users of such products or services. According to Erhorn, Hansen, Kaan, and Barker (2007), eco-buildings can reduce energy consumption and enhance the use of renewable energies, bio-climatically designed. This reduction could be achieved taking into account sun exposure, architectural requirements, increase of the thermal insulation and tightness of the building, throughout new products, constructive solutions and viable technologies.

The use of thermal mortars in multi-layer façade systems influences several aspects of the sustainability of buildings as the fulfilment of several basic principles stated above. As such,

the continuous interest in the development of sustainable solutions with thermal enhanced properties, incorporating different types of wastes (industrial or plant origin), allows the development of new solutions with less harmful impact to environment than traditional construction materials (Matias, Faria, and Torres, 2014; Skoczylas and Rucińska, 2018; Torres and Matias, 2016). To improve the thermal behaviour of buildings, different products incorporating lightweight aggregates with low density and thermal conductivity have appeared on the market. Thermal renders and plasters continue to awaken the interest of the researchers (Borges, Flores-Colen, and de Brito, 2018; Nosrati and Berardi, 2018; Soares, de Fátima Júlio, Flores-Colen, Ilharco, and Brito, 2018; Westgate, Paine, and Ball, 2018).

Thermal mortars applied in multi-layer systems frequently have at least two different layers: thermal mortar and finishing coating. Thermal mortars are addressed in EN 998-1 (CEN, 2010), which refers to EN 1015-21 for durability test methods in mortars (CEN, 2002). However, this standard is only applicable to one-coat renders, not taking into account the different material layers (i.e. the system as a whole). The durability assessment methodologies preconized in the ETAG 004 (EOTA, 2013), are directly applied to ETICS. Consequently, the existing procedures, such as the ones provided by EN 1015-21 and ETAG 004, do not allow a feasible durability assessment of thermal rendering and plastering systems (see Figure 1).

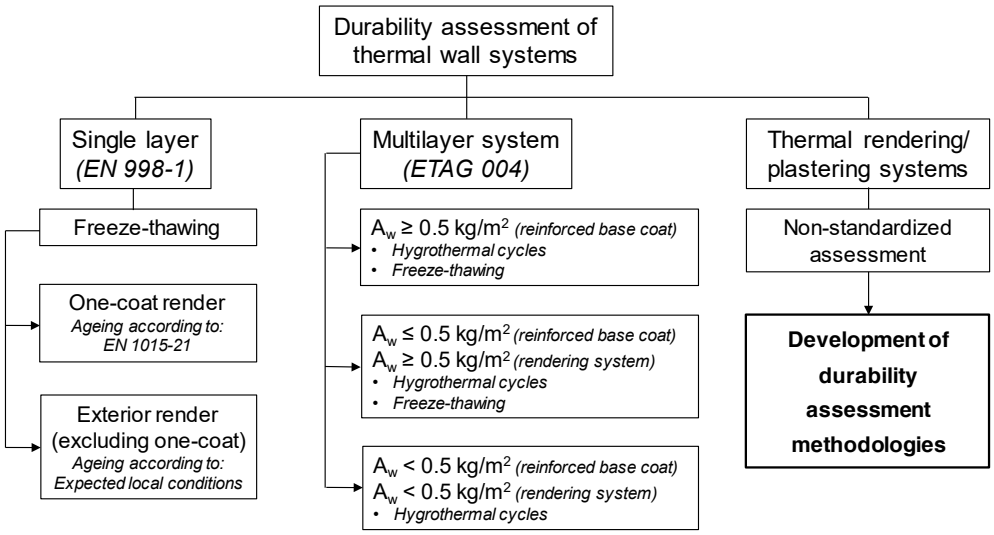

Figure 1. Framework of existing durability assessment methodologies, applicable to renders and thermal multilayer systems.

In order to obtain more durable building envelopes, the durability assessment should focus on the required performance, especially the climatic conditions (Pedro Júlio, Paiva, and Dominguez, 2013). Since construction materials are subjected to several degradation agents, which promote different degradation levels, their selection presents an important role in the durability of the system (ABCB, 2006; Gaspar and Brito, 2008). In that way, the objective of this paper consists of presenting an integrated proposal of a new durability assessment methodology applicable to thermal mortars in multilayer systems.

2 A New Durability Assessment Methodology – Methodological Process

Being the EN 1015-21 and ETAG 004 methodologies applicable to renders and thermal multilayer systems (ETICS), they may be adapted to thermal rendering and plastering systems, since they present some similar characteristics. This adaptation could give reliable data and inputs to the development of durability assessment methodologies directly applicable to thermal rendering and plastering systems. As such, a methodological process for the durability assessment of the systems in study was developed, as explained in Figure 2.

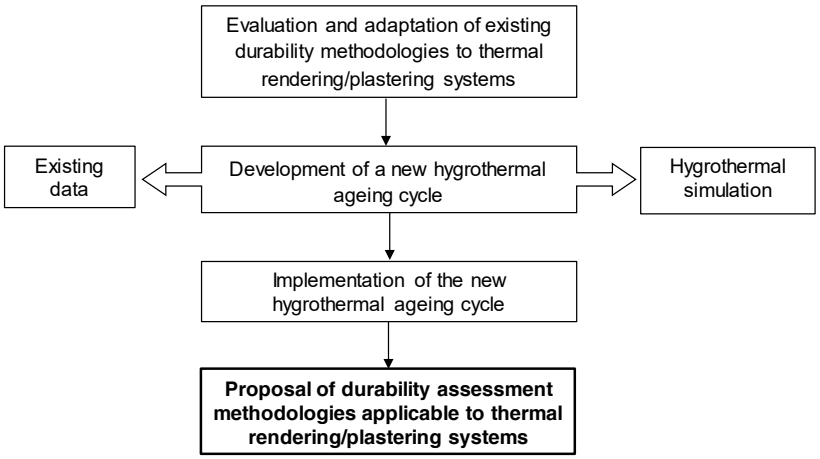

Figure 2. Methodological process for the durability assessment of thermal rendering/plastering systems.

The methodology combines several stages, being the first one the evaluation and adaptation of the referred existing methodologies (EN 1015-21 and ETAG 004). The analysis of existing ageing procedures combined with hygrothermal simulation and existing data resulted in the development of a new hygrothermal accelerated ageing cycle. The development of the hygrothermal cycle focus the South European climate context, using a representative Portuguese climate of the most severe conditions, in terms of temperature fluctuation. After the implementation of the new hygrothermal ageing cycle, it was possible extrapolating this methodology to the development of a theoretical algorithm. The developed algorithm is capable of defining accelerated heat-cold ageing cycles representative of several European climates (Maia, Ramos, and Veiga, 2019).

3 Durability Assessment of Thermal Mortars – Experimental Methodology

Figure 3 presents the adopted experimental methodology to evaluate the durability assessment of thermal rendering and plastering systems. The first step consists in the adaptation of existing methodologies, such as the envisaged in EN 1015-21 and ETAG 004, using small-scale specimens. The EN 1015-21 methodology includes heating-freezing and humidification-freezing ageing cycles and the ETAG 004 freeze-thawing cycles. The evaluation of the existing procedures allowed understanding the gaps, disadvantages and advantages of implementing such methodologies to thermal rendering and plastering systems. The second step consists in the implementation of a new accelerated ageing hygrothermal cycle adapted to thermal rendering systems, through hygrothermal simulation and previous knowledge of the existing

methodologies. Being the location where the system is intended to be applied, one of the main aspects to take into consideration in the durability assessment, the wide range of existing climates should be considered (Juaristi, Gómez-Acebo, and Monge-Barrio, 2018; Perino and Serra, 2015). In the present work, the European climatic context, which combines very different conditions, was analysed. Köppen-Geiger climate classification is one of the most used and well-known and classifies according to the main climate, precipitation and temperature (Kottek, Grieser, Beck, Rudolf, and Rubel, 2006). Focusing on the European context, the EOTA (1999) Guidance Document classifies the climatic zones according to the air temperature and the solar energy intensity. Analysing different European climates, a tendency from the lower to the higher latitudes was observed, being more representative of zones C to A, respectively. In that way, freeze-thaw may have a more relevant impact in northern climates, while thermal shock, originated by the incidence of cold rain in warm surfaces, in southern climates. In terms of internal environment, EOTA (1999) groups four sub-divisions, due to specific conditions to which the buildings are subjected: a) Temperature: heating, non-heating, refrigerating, localised radiation, etc.; b) Humidity: dry or wet conditions; c) Liquid water: permanently wet (*e.g.* bathrooms); and d) Chemicals: cleaning, cooking and special conditions in laboratories, hospitals, etc.. Figure 4 summarises the different stages of the durability assessment methodology and the sequencing between them.

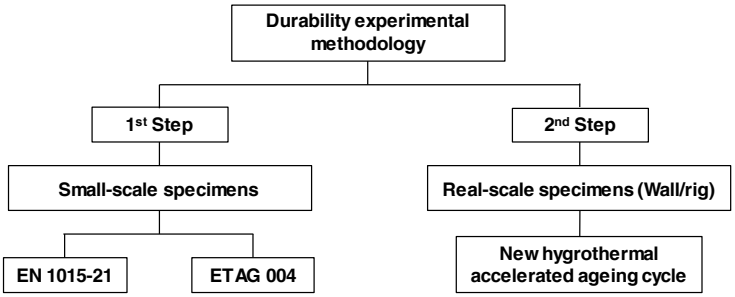

Figure 3. Durability experimental methodology.

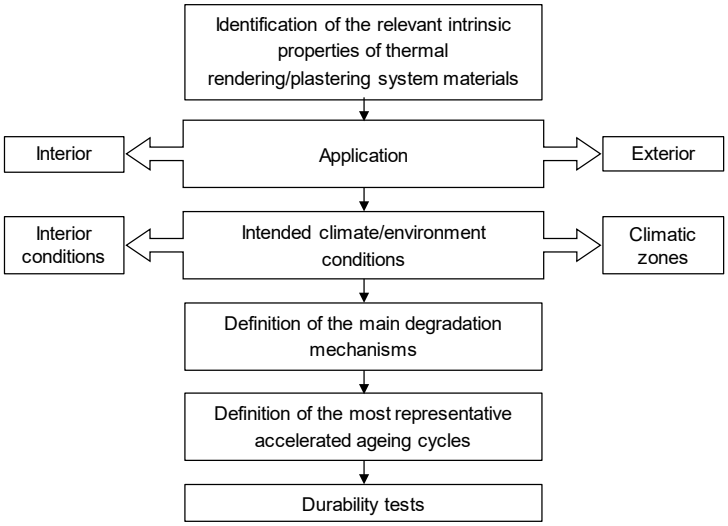

Figure 4. Durability assessment methodology.

4 An Integrated Durability Assessment Methodology Applicable to Thermal Mortars in Multi-layer Systems

4.1 General Methodology

The development of methodologies that reproduce the most relevant degradation mechanisms in thermal rendering and plastering systems were performed. According to the requirements applicable to thermal mortars and considering their relevant properties, a methodology regarding the application of the thermal mortars in multi-layer systems is presented in Figure 5. The knowledge of the physical and hygrothermal behaviour of the referred systems is based on the work developed in Maia, Ramos, and Veiga (2018).

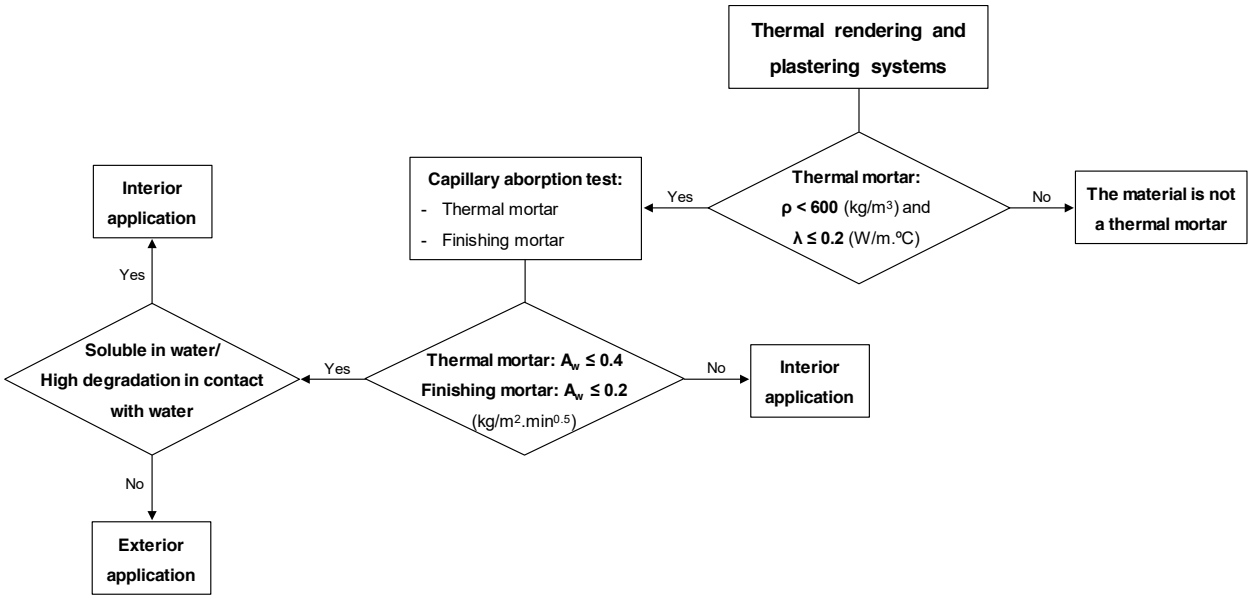

Figure 5. Methodology of application of thermal rendering and plastering systems.

4.2 Durability Assessment Methodology Applicable to Thermal Plastering Systems

Despite the little development of the durability assessment of thermal plastering systems, the implementation of EN 1015-21 ageing cycles allows observing the degradation of the system performance. As such, a preliminary proposal of a durability assessment methodology applicable to thermal plastering systems, regarding the interior application, is presented in Figure 6. The capillary absorption requirement is supported by the capillary classes defined in EN 998-1 (CEN, 2010). The heating (60 ºC)-freezing (-15 ºC) procedure (defined according to EN 1015-21 (CEN 2002a)), allows analysing the effect of the temperature fluctuation, regarding high-temperature variations. The application tof freezing conditions may be too severe for plastering systems applied in interior layers and may therefore be replaced by a higher minimum value adequately justified. However, the effect of humid environments, at high or low temperatures, was not evaluated and is a crucial aspect concerning the durability of plasters. In short, the application of thermal plastering systems requires an accurate analysis, regarding the environmental conditions where the system is intended to be applied, and the definition of the

related ageing cycles (that should represent the environment as accurately as possible).

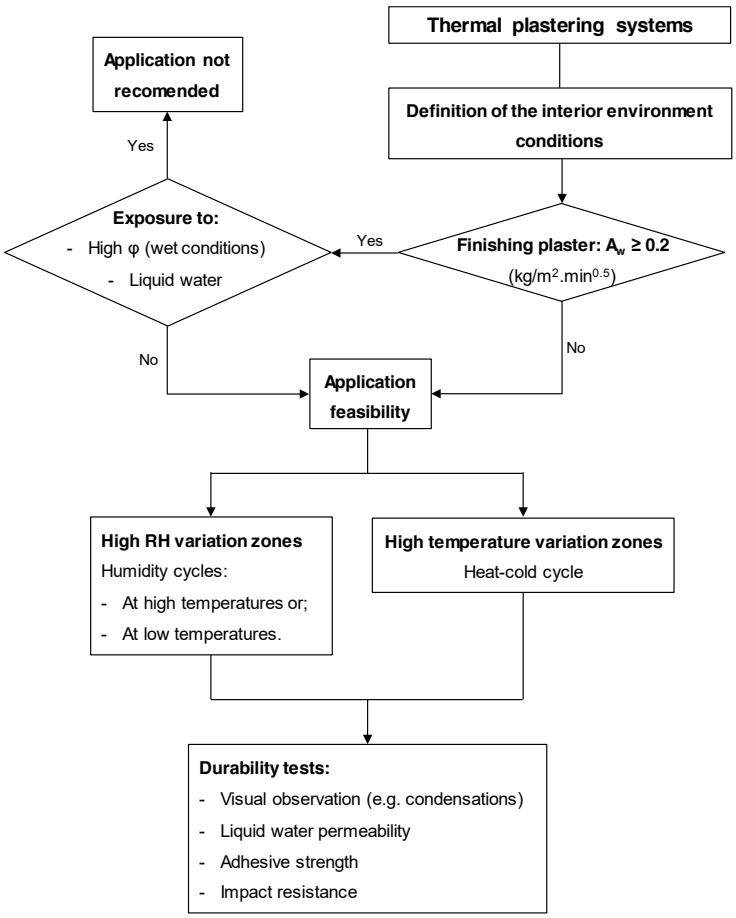

Figure 6. Preliminary durability assessment methodology applicable to thermal plastering systems.

4.3 Durability Assessment Methodology Applicable to Thermal Rendering Systems

The characteristics and durability of thermal rendering systems, suitable for the exterior application, were already presented in the previous work of Maia et al. (2019). The developed methodology, applicable to thermal rendering systems, combines the previous knowledge of the requirements and material properties (obtained by experimental tests and numerical simulation) with a detailed durability experimental campaign. This campaign preconizes the implementation of several accelerated ageing tests, taking into account the relevant degradation mechanisms. To a better adequacy of the durability assessment to thermal rendering systems, a new hygrothermal ageing cycle, which combines heat-cold and heat-rain cycles regarding the Portuguese climatic, was developed through climate analysis and hygrothermal simulation, with WUFI Pro software (IBP, 2018). The heat-cold cycle comprises a cold period (-5 ºC for 11h), a warm period (65 ºC for 7h) and the transitions between the 2 stages, resulting in a 24h cycle. The heat-rain cycle comprises a warm period (70 ºC for 2h), a rain period (15 ºC and 1l/m^2.min. of water spraying, for 1h) and the transitions between the 2 stages, resulting in a 6h cycle, repeated 80 times. This first approach allowed the development of a theoretical

methodology for the definition of heat-cold cycles in the European context (Maia *et al.*, 2019).

5 Conclusions

The existing durability assessment procedures of thermal mortars showed to be insufficient to a precise and realistic evaluation. In that way, the authors developed a new durability assessment methodology, based on real material characteristics and the performance of the system as a whole. The developed methodology highlighted the importance of combining different evaluation methods, such as numerical simulation and experimental tests (existing and new procedures). The previous knowledge of the application requirements allowed the definition of different paths regarding the main degradation mechanisms and, consequently, the most representative accelerated ageing cycles. The main degradation mechanisms include high temperature variations, high relative humidity variations, exposure to high relative humidity, exposure to liquid water and freeze-thaw. The presence of liquid water and high relative humidity is a key factor for the decision on the applicability conditions of thermal mortars. A high water absorption of both the thermal mortar and the finishing layers, in multilayer systems, will define the limitation to interior applications only.

In summary, the implementation of the standard procedures to different thermal rendering and plastering systems allowed understanding the deterioration caused by each degradation mechanism. The acquired knowledge contributed to the development of the hygrothermal ageing cycles since the relevant gaps were identified and bridged. The several experimental tests, performed before and after the different ageing procedures, deepened the knowledge of thermal renders/plasters and the respective systems, giving valuable information about their properties and performance. This knowledge is fundamental to develop the durability assessment methodology, applicable to thermal rendering and plastering systems, together with the developed hygrothermal cycle.

Acknowledgements

The first author would like to acknowledge the funding of the Doctoral Grant PD/BD/52659/2014, through the Doctoral Programme EcoCoRe of FCT – Fundação para a Ciência e a Tecnologia. This work was financially supported by Project PTDC/ECICON/28766/2017 – POCI-01-0145-FEDER-028766 funded by FEDER funds through COMPETE2020 - Programa Operacional Competitividade e Internacionalização (POCI) and by national funds (PIDDAC) through FCT/MCTES and the Project Reuse – Rehabilitation and Sustainability, supported by LNEC. This work was financially supported by: UID/ECI/04708/2019- CONSTRUCT – Instituto de I&D em Estruturas e Construções funded by national funds through the FCT/MCTES (PIDDAC). The authors also acknowledge to Saint-Gobain Weber, Secil Argamassas and Sival – Gessos Especiais to the materials supply.

ORCID

Joana Maia: https://orcid.org/0000-0001-5036-8581
Nuno M. M. Ramos: https://orcid.org/0000-0002-5331-7429
Rosário Veiga: https://orcid.org/0000-0002-7135-8603

References

ABCB. (2006). *Durability in Buildings. Handbook*.

Borges, A., Flores-Colen, I. and de Brito, J. (2018). Physical and mechanical performance of cement-based renders with different contents of fly ash, expanded cork granules and expanded clay. *Construction and Building Materials, 191*, 535-543. doi:10.1016/j.conbuildmat.2018.10.043

CEN. (2002). EN 1015 Methods of test for mortar for masonry. In *Part 21: Determination of the compatibility of one-coat rendering mortars with substrates*. Brussels: European Commitee for Standardization.

CEN. (2010). EN 998 Specification for mortar for masonry. In *Part 1: Rendering and plastering mortar*. Brussels: European Commitee for Standardization.

EMO. (2013). Goal 6. Retrieved from http://www.euromortar.com/7-goals/6-creating-awareness-for-sustainability/

EOTA. (1999). Assessment of working life of products. In *Guidance Document 003*. Brussels: European Organisation for Technical Approvals.

EOTA. (2013). ETAG 004. In *Guideline for European Technical Approval of External Thermal Insulation Composite Systems with Rendering*. Brussels: European Organisation for Technical Approvals.

Erhorn, H., Hansen, J. O., Kaan, H. and Barker, M. (2007). *What are Eco-Buildings and are they needed in the Seventh Framework Programme (FP7)?* : BRITA in PUBs.

Gaspar, P. L. and Brito, J. d. (2008). Quantifying environmental effects on cement-rendered facades: A comparison between different degradation indicators. *Building and Environment, 43*(11), 1818-1828. doi:https://doi.org/10.1016/j.buildenv.2007.10.022

IBP. (2018). WUFI Postptocessor: Thermal conductivity. *WUFI Pro Manual.*

Juaristi, M., Gómez-Acebo, T. and Monge-Barrio, A. (2018). Qualitative analysis of promising materials and technologies for the design and evaluation of Climate Adaptive Opaque Façades. *Building and Environment, 144*, 482-501. doi:https://doi.org/10.1016/j.buildenv.2018.08.028

Kottek, M., Grieser, J., Beck, C., Rudolf, B. and Rubel, F. (2006). World Map of the Köppen-Geiger climate classification updated. *Meteorologische Zeitschrift, 15*(No.3), 259-263. doi:10.1127/0941-2948/2006/0130

Maia, J., Ramos, N. M. M. and Veiga, R. (2018). Evaluation of the hygrothermal properties of thermal rendering systems. *Building and Environment, 144*, 437-449. doi:https://doi.org/10.1016/j.buildenv.2018.08.055

Maia, J., Ramos, N. M. M. and Veiga, R. (2019). A new durability assessment methodology of thermal mortars applied in multilayer rendering systems. *Construction and Building Materials, 222*, 654-663. doi:10.1016/j.conbuildmat.2019.06.178

Matias, G., Faria, P. and Torres, I. (2014). Lime mortars with ceramic wastes: Characterization of components and their influence on the mechanical behaviour. *Construction and Building Materials, 73*, 523-534. doi:http://dx.doi.org/10.1016/j.conbuildmat.2014.09.108

Nosrati, R. H. and Berardi, U. (2018). Hygrothermal characteristics of aerogel-enhanced insulating materials under different humidity and temperature conditions. *Energy and Buildings, 158*, 698-711. doi:10.1016/j.enbuild.2017.09.079

Pedro Júlio, J., Paiva, A. and Dominguez, C. (2013). *Aspects for the evaluation of Portuguese dwellings' quality and sustainability* (Vol. 5).

Perino, M. and Serra, V. (2015). Switching from static to adaptable and dynamic building envelopes: A paradigm shift for the energy efficiency in buildings. *Journal of Facade Design and Engineering*(2), 143-163%V 143. doi:10.7480/jfde.2015.2.1015

Skoczylas, K. and Rucińska, T. (2018). The effects of waste glass cullets and nanosilica on the long-term properties of cement mortars. *E3S Web Conf., 49*, 00102.

Soares, A., de Fátima Júlio, M., Flores-Colen, I., Ilharco, L. M. and Brito, J. D. (2018). EN 998-1 performance requirements for thermal aerogel-based renders. *Construction and Building Materials, 179*, 453-460. doi:10.1016/j.conbuildmat.2018.05.197

Torres, I. and Matias, G. (2016, 16-17 June). *Waste recovery to integration in renders.* Paper presented at the Argamassas 2016 - Symposium on Mortars and Thermal Coating Solutions, Coimbra, Portugal.

Westgate, P., Paine, K. and Ball, R. J. (2018). Physical and mechanical properties of plasters incorporating aerogel granules and polypropylene monofilament fibres. *Construction and Building Materials, 158*, 472-480. doi:10.1016/j.conbuildmat.2017.09.177

XV International Conference on Durability of Building Materials and Components
DBMC 2020, Barcelona
C. Serrat, J.R. Casas and V. Gibert (Eds)

Evaluation of ETICS Characteristics that Affect Surface Mould Development

João L. Parracha[1,2], Armand Cortay[1,3], Giovanni Borsoi[2], Rosário Veiga[1] and Lina Nunes[1,4]

[1] National Laboratory for Civil Engineering, LNEC, Av. do Brasil 101, Lisbon, Portugal, jparracha@lnec.pt, rveiga@lnec.pt, linanunes@lnec.pt

[2] Civil Engineering Research and Innovation for Sustainability, CERIS, Instituto Superior Técnico, University of Lisbon, 1049-001, Lisbon, Portugal, giovanni.borsoi@tecnico.ulisboa.pt

[3] École Nationale D´Ingénieurs de Saint-Étienne, ENISE, Rue Jean Parot 58, Saint-Étienne, France armand.cortay@enise.fr

[4] Centre for Ecology, Evolution and Environmental Changes, CE3C, Rua Capitão João d'Ávilla, Azores, Portugal

Abstract. *External Thermal Insulation Composite Systems (ETICS) are nowadays often used in new constructions but are also one of the most frequently used thermal retrofitting solutions for buildings. These systems have several advantages such as low installation cost, ease of application and increased thermal efficiency. Nevertheless, a number of questions have been raised on their long-time durability particularly related to biodeterioration. Biological growth is strongly influenced by several parameters, such as water content, temperature, pH but also by the type and hygroscopic properties of the building materials. It is therefore essential to understand and correlate those properties with biological growth. This paper aims at evaluating some ETICS characteristics that might influence surface mould development which is recognized as one of the major groups of deteriorating organisms. The susceptibility of the surface finishing layer and thermal insulation to biological growth was assessed through natural inocula and selected fungi and, whenever possible, correlated with water absorption and drying capacity. This study is part of a wider research project: WGB_Shield (Shielding building' facades on cities revitalization. Triple-resistance for water, graffiti and biocolonization of external thermal insulation systems) that aims at the development of ETICS with improved durability in the urban environment. Further development on this issue are ongoing.*

Keywords: *ETICS, Durability, Mould Growth, Water Performance, ETAG 004.*

1 Introduction

The External Thermal Insulation Composite Systems (ETICS) are nowadays often used in Europe for new constructions and for thermal refurbishment of building facades (Barreira and Freitas, 2013). These systems present several advantages in comparison with other insulation solutions, such as the correction of thermal bridges, reduction of interior water condensation and increase of thermal efficiency, while maintaining the aesthetic appearance of the building, with relatively low installation cost and ease of application (Simona *et al*., 2017). Nevertheless, biological growth has been identified as one of ETICS main disadvantages, with several ETICS facades showing this problem only few years after the building construction/intervention (Johansson *et al*., 2010). Over time, biological growth causes cladding defacement, though it might not have major influence on the thermal performance of the system itself, however,

altering the aesthetic appearance of the building. This situation commonly leads to a disapproval of the building owner, ending up with several economic and social consequences, that limit the full implementation and a wider diffusion of ETICS (Johansson *et al*., 2010).

Factors influencing mould growth on ETICS include nutrient availability, temperature, pH and moisture which seems to be the key factor (Johansson *et al*., 2012). Extensive fungal development is linked to high levels of surface moisture content, resulting from the combined effect of surface condensation, drying process as well as from the finishing render composition. When the drying process is slow, the surface moisture content remains high for long periods, increasing the risk of biocolonization (Barreira and de Freitas, 2013). Thus, the main parameters affecting biological colonization on ETICS are thought to be the composition of the different elements (insulation material, base coat mortar and finishing coat) and the behaviour of the system concerning water absorption and drying. It is therefore essential to understand the hygrometric properties of ETICS and their composition in order to correlate them with biological growth.

2 Materials and Methods

2.1 Materials

Seven different ETICS solutions from three different manufactures were tested for mould growth and water behavior (capillary absorption and drying capacity). Table 1 briefly describes the selected materials. Detailed information about the formulation of each solution is not available due to industrial confidentiality.

Table 1. Characteristics of each system.

System (S) / Manufacturer (M)	Thermal insulation (TI)	Finishing render (FR)*				S thickness (mm) = TI thickness + FR thickness
		Base coat (+ mesh)			Finishing coat	
		Binder	Aggregates	Admixtures and additives	Coating	
S1 / M1	EPS-1	Cement	Mineral fillers and resins	Not identified	Acrylic paint	S: 40.57 TI: 35.29
S2 / M1	EPS-1	Cement				S: 40.44 TI: 35.29
S3 / M2	ICB	Lime + hydraulic binders	Mineral fillers		Acrylic paint + pigment	S: 63.61 TI: 59.73
S4 / M2	EPS-2	Cement	Mineral fillers, resins, and synthetic fibres			S: 65.45 TI: 59.99
S5 / M3	ICB	Natural hydraulic lime +	Acrylic resins and mineral		Acrylic with siloxane resins	S: 41.91 TI: 37.91

		Mixed binders	fillers			
S6 / M3	EPS-2	Cement + Mixed binders				S: 43.30 TI: 38.30
S7 / M3	MW					S: 44.80 TI: 39.80
EPS: expanded polystyrene; ICB: expanded cork; MW: mineral wool. EPS-1 and EPS-2 were produced by different manufactures. *The FR includes a biocide						

Two types of samples were cut from the original ETICS panels of each system: the first was a set of 3 samples of each system with dimensions of 40 mm × 40 mm × S thickness (Tab. 1), which was used to assess mould growth; the other is described in Table 2 and was used to assess capillary absorption and drying capacity of each system. The total thickness of each system ranges between 40.44 mm and 65.45 mm and is presented in Table 1. The thermal insulation materials of each solution were also individually tested for mould growth. There are four types of insulation materials, including mineral wool (MW), expanded polystyrene from two different manufactures (EPS-1 and EPS-2) and expended cork (ICB). The dimensions of these samples are 40 mm × 40 mm × TI thickness (Tab. 1).

Table 2. Materials, samples and laboratory tests for water behavior assessment.

Test	Reference	Sampling [Samples × S]	Dimensions [mm]
Capillary absorption	ETAG 004 (2013)	2 × 7	150 × 150 × TI thickness
Drying	EN 16322 (2013)	2 × 7	150 × 150 × TI thickness

2.2 Mould Growth Tests

The resistance of the different ETICS and insulation materials to mould growth was assessed using a method adapted from ASTM D 5590-17 (2017) and ASTM C1338-19 (2019) and previously described by Santos *et al*. (2017). Three replicates of each ETICS solutions and corresponding thermal insulation were tested.

Three fungal species were used in this study: spore suspensions of *Aspergillus niger and Penicillium funiculosum*, applied together, and *Aureobasidium pullulans*, applied alone. These species were chosen due to their widespread presence in interior and outdoor environments and commonly referenced in the literature and standards (Hoang *et al*., 2010; ASTM D 5590-17, 2017; Verdier *et al*., 2014). A volume of 2 ml of each spore suspension was uniformly distributed on the surface of the previously sterilized specimens and controls and the surrounding culturing media (4% malt, 2% agar). The controls were 3 replicates of Whatman nº 1 filter paper (45 mm diameter) and 3 wood samples (*Pinus pinaster*) with dimensions 40 mm × 40 mm × 10 mm, that allowed the validation of the test (ASTM C1138-19, 2019). After inoculation, the test flasks were incubated at a temperature of 22 ± 1ºC and 70 ± 5% RH for a period of four weeks. A third group of test specimens was exposed in the same conditions but without any sterilization or inoculation thus allowing their natural inocula to potentially develop. Each week, the samples were visually rated for mould growth using the scale defined in Table 3. At the end of the exposure period the samples were removed from the flasks and the final percentage of contaminated surface (Table 3) was evaluated with the help of a stereo microscope.

Table 3. Rate of fungal (mould) development as defined in ASTM D 5590-17 (2017).

Rating	Description	Percentage of contaminated surface
0	None	0%
1	Traces of growth	<10%
2	Light growth	10 to 30%
3	Moderate growth	30 to 60%
4	Heavy growth	>60%

2.3 Capillary Absorption and Drying Tests

Water performance of ETICS was assessed through capillary absorption and drying capacity.

Capillary absorption tests were performed according to ETAG 004 (EOTA, 2013) in a conditioned room (T = 23 ± 2ºC and 65 ± 5% RH). A total of four cycles (each cycle has 24h with measurements at 3 min, 1, 4, 8 and 24h) of capillary absorption were conducted. Capillary water absorption coefficient was obtained by the slope of the initial phase of the curve that expresses the water absorption as a function of square root of time.

Drying test was performed following the recommendations of EN 16322 (2013) and started immediately after the capillarity test. The test was performed in a conditioned room (23 ± 2ºC and 65 ± 5% RH). Samples were weighted after determined periods of time until the variation of mass was constant for all samples. Two drying phases were determined: DR1 – the first drying phase, obtained by the negative slope of the initial linear section of the drying curve plotted with time in abscissa; and DR2 – the second drying phase, calculated by the negative slope of the linear section of the drying curve, plotted against the square root of time in abscissa. Drying index (DI) was obtained by Equation (1), in which M_x is the mass of the sample registered during the drying process (g), M_1 is the mass of the sample in a dry state (g), M_3 is the mass of the sample in a saturated state (this mass corresponds to the mass at the beginning of the drying process (t_0)), t_f is the time at the end of the drying process.

$$DI = \frac{\int_{t_0}^{t_f} f\left(\frac{M_x - M_1}{M_1}\right) dt}{\left(\frac{M_3 - M_1}{M_1}\right) \times t_f} \quad (1)$$

3 Results and Discussion

3.1 Resistance to Mould Growth

The results of the average rate of mould growth for ETICS surface finishing layer considering all type of inoculation were the same during or at the end of the test: zero (no growth). All controls (Whatman nº 1 filter paper and wood) were rated as 4 at the end of the 4-week testing which confirms the validity of the procedure. The fact that no growth occurs for any ETICS surface after 4 weeks of testing can be explained by the presence of biocide on the finishing render. Nevertheless, these are newly produced, unaltered sound systems, which were not subjected to any kind of aging or weathering procedures.

The results of the average rate of mould growth for the insulation materials are shown in Figure 1. After 4 weeks of incubation, significant mould growth was observed on the ICB samples, rated as 2 or more for every type of inocula (natural or artificial). For EPS-1 samples,

no growth was reported at any time during the test, however, for EPS-2, some samples presented traces of growth, especially with natural inocula. MW samples presented no growth for the *A. pullulans* inoculation and traces of growth since the first week of observations for the *A. niger* and *P. funiculosum* inoculation. Only one of the three MW tested samples showed traces of growth (rated as 1) after 4 weeks testing for natural inocula.

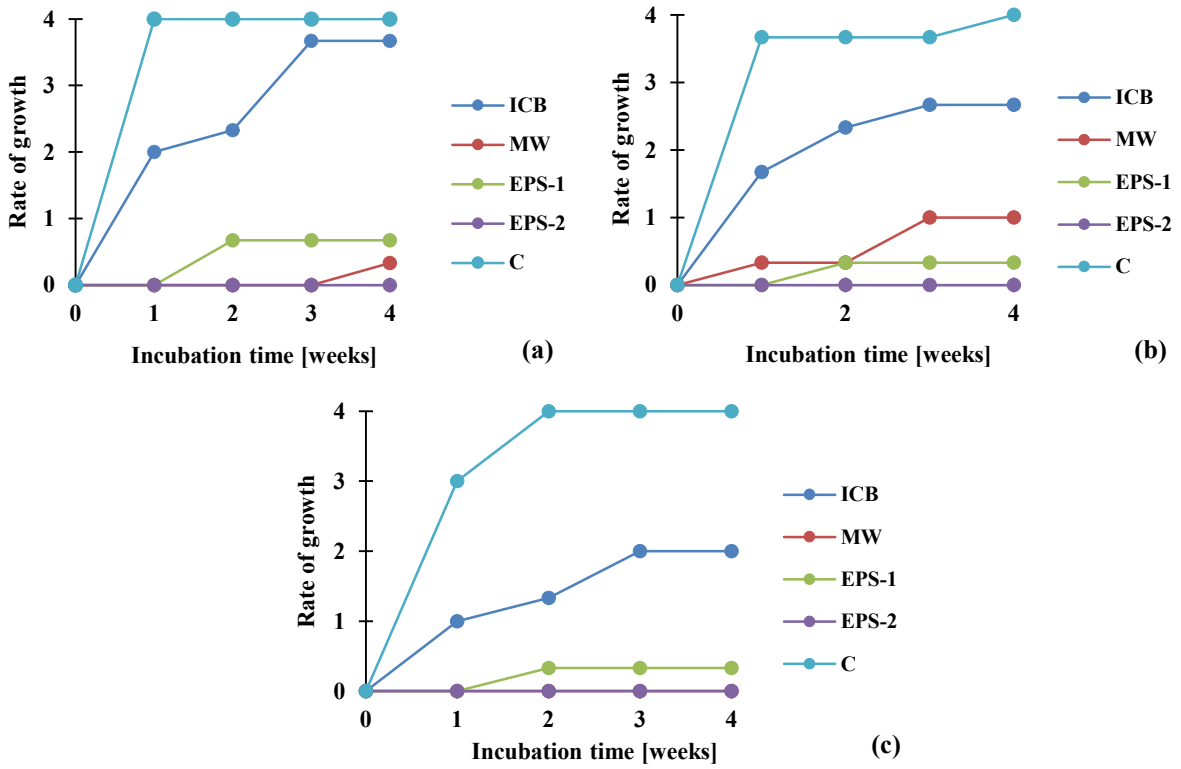

Figure 1. Results of the average rate of mould growth for the insulation materials considering: (a) natural inocula (b) artificial inoculation with *A. niger* and *P. funiculosum* (c) artificial inoculation with *A. pullulans*.

Amongst the insulation materials, ICB samples presented the most intense mould growth. In fact, cork is a natural organic material with suberin, lignin and polysaccharides (cellulose and hemicellulose) in its composition (Knapic *et al*., 2016). Organic or organic-based materials are more vulnerable to fungal deterioration since they provide ample nutrients, through their composition, contributing to fungal growth (Klamer *et al*., 2004; Hoang *et al*., 2010). Additionally, the results of rate of growth for ICB were significantly higher when inoculated with *A. niger* and *P. funiculosum* rather than *A. pullulans*.

In general, MW and EPS samples present a good resistance to mould attack, always presenting a rate of growth lower or equal to 1. Concerning MW, as an inorganic material, the susceptibility to mould growth is naturally lower than that of organic materials. The only sample rated as 1 for natural inocula could have been previously contaminated with some organic dust particles, that contributed to the increase of mould growth susceptibility (Jerábková and Tesarová, 2018). Regarding EPS, the resistance to fungal growth is noteworthy, which is in accordance with the results obtained by Jerábková and Tesarová (2018).

All insulation materials presented higher mould growth for natural inocula than for artificial inoculation. If, on the one hand, natural inocula can be more representative of real conditions (Hoang *et al*., 2010), artificial inoculation significantly accelerates the test while improving repeatability and comparison between materials (Johansson *et al*., 2012, 2014).

3.2 Capillary Water Absorption and Drying

The results obtained for capillary absorption and drying are shown in Table 4 and Figure 2. Sample S3 presents the highest value of capillary absorption at 1h and 24h, whereas sample S1 presents the lowest values. In fact, samples S1 and S2, both with cement-based matrix in the base coat and from the same manufacturer, presented lowest capillary water absorption, and, as a consequence of low water content, also the fastest drying capacity. Sample S1 presented not only the lowest values of capillary absorption at 1h and 24h but also the lowest value of capillary water absorption coefficient.

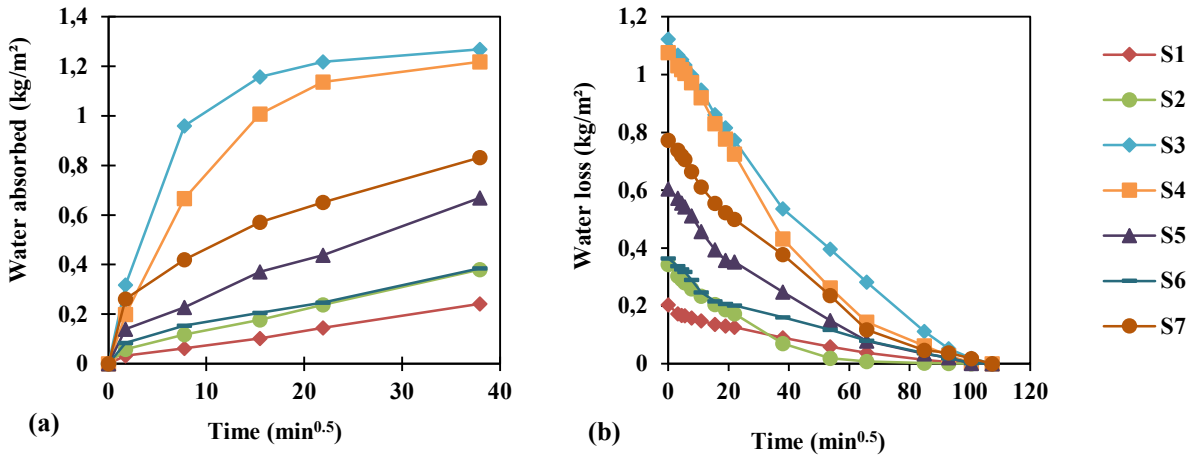

Figure 2. Capillary absorption curves (a) and drying curves (b).

By comparing the capillary water absorption coefficient (C) obtained for sample S5 and S6, it was noticed an increase of 65% of the value of C for S5 in relation to S6. These samples present the same composition of finishing render with exception of the binder (S5 has natural hydraulic lime and mixed binders while S6 is composed of cement and mixed binders).

All samples achieved values of capillary absorption after 1h testing that are lower than 1 kg/m^2, which is the value required by ETAG 004 (EOTA, 2013). In fact, for all tested solutions, the highest level of capillary absorption happens in the first hour of test (even in the first 3 min), followed by a stabilization of the capillary water absorption. Therefore, all solutions have an adequate performance with regards to capillary absorption and drying, presenting low values of capillary absorption.

The results obtained for drying test are in line with those obtained for capillary water absorption, since samples that generally absorb more water are those that present higher drying rates, allowing fast removal of absorbed water. Additionally, a high correlation was obtained between the capillary absorption coefficient and drying rate 2 ($R^2 = 0.77$).

Table 4. Capillary absorption and drying test results.

System (S)	Capillary absorption				Drying		
	Capillary absorption 1h (kg/m^2)	ETAG 004 (≤ 1 kg/m^2 at 1h)	Capillary absorption 24h (kg/m^2)	C ($kg/m^2.min^{0.5}$)	DR1 ($kg/m^2.h$)	DR2 ($kg/m^2.h^{0.5}$)	DI
S1	0.062	√	0.242	0.019	0.0030	0.0197	1.05
S2	0.118	√	0.379	0.034	0.0068	0.0396	1.02
S3	0.959	√	1.268	0.184	0.0151	0.0989	1.01
S4	0.667	√	1.217	0.115	0.0169	0.1099	0.94
S5	0.227	√	0.669	0.081	0.0095	0.0619	1.00
S6	0.154	√	0.385	0.049	0.0051	0.0335	1.00
S7	0.419	√	0.832	0.151	0.0111	0.0773	0.98

4 Conclusions

With the aim of evaluating the resistance of different ETICS surface finishing layer and insulation materials to mould growth under laboratory conditions, 7 different ETICS solutions were tested considering three different types of inoculation. The thermal insulation materials of each solution were also individually tested for mould growth. Additionally, capillary water absorption and drying capacity of each ETICS were assessed.

The main conclusions of this study are the following:

- No mould growth was detected on any ETICS surface finishing layer after 4-week testing though it should be noticed that the materials were tested without previous aging or weathering procedures.
- Considering the thermal insulation materials tested individually for mould growth, ICB samples were the ones obtaining the highest level of mould growth after 4-week of incubation. For EPS-1 samples, no growth was reported at any time during the test. However, this is not the case for the EPS-2, where some samples presented traces of growth, especially when considering the natural inocula. MW samples presented no growth for the *A. pullulans* inoculation but traces of growth for the mixed spore suspension. However, as stated in the previous point, these differences in the insulation materials didn't visibly affect the full system behavior.
- All insulation materials presented higher mould growth for natural inocula than for artificial inoculation with either of the spore suspensions.
- All tested ETICS solutions showed good performance regarding capillary water absorption and drying capacity, with all solutions accomplishing the ETAG 004 requirements. Such good characteristics could be one of the reasons why, at this stage, the susceptibility of some insulation materials to mould growth didn't affect the performance of the full system. However, further tests are necessary to assess the moisture transport properties of ETICS after natural and artificial aging and compare those values with the ones presented in this study.

The results obtained in the present study give an overview on ETICS characteristics (capillary absorption, drying capacity and composition of ETICS layers) that might affect surface mould development. The next step in the research will consist on verifying ETICS durability by natural and artificial aging tests, which will affect ETICS finishing coat, possibly

leading to a higher susceptibility of the system to mould growth.

Acknowledgements

The authors gratefully acknowledge the support given by Portuguese Foundation for Science and Technology (FCT) within research project PTDC/ECI-EGC/30681/2017 (WGB_Shield – Shielding building' facades on cities revitalization. Triple resistance for water, graffiti and biocolonization of external thermal insulation systems).

ORCID

João Luís Parracha: https://orcid.org/0000-0001-6214-3400
Giovanni Borsoi: https://orcid.org/0000-0002-2194-4620
Maria do Rosário Veiga: https://orcid.org/0000-0002-7135-8603
Lina Nunes: https://orcid.org/0000-0001-6849-3241

References

ASTM D 5590-17 (2017). Determining the resistance of paint films and related coatings to fungal defacement by accelerated four-week agar plate assay. ASTM International, Pennsylvania, USA

ASTM C1338-19 (2019). Standard test method for determinig fungi resistance of insulation materials and facings. ASTM International, Pennsylvania, USA

Barreira, E. and Freitas, V.P. (2013). Experimental study of the hygrothermal behaviour of External Thermal Insulation Composite Systems (ETICS). *Building and Environment, 63*, 31-39. doi: 10.1016/j.buildenv.2013.02.001

EN 16322 (2013). Conservation of Cultural Heritage – Test methods – Determination of drying properties. European Committee for Standardization, Brussels, Belgium

EOTA (2013). Guideline for european technical approval of external thermal insulation composite systems with rendering. ETAG 004. Brussels, Belgium

Hoang, C.P., Kinney, K.A., Corsi, R.L. and Szaniszlo, P.J. (2010). Resistance of green building materials to fungal growth. *International Biodeterioration & Biodegradation, 64,* 104-113. doi: 10.1016/j.ibiod.2009.11.001

Jerábková, E. and Tesarová, D. (2018). Resistance of various materials and coatings used in wood constructions to growth of microorganisms. *Wood Research, 63,* 993-1002.

Johansson, S., Wadsö, L. and Sandin, K. (2010). Estimation of mould growth levels on rendered façades based on surface relative humidity and surface temperature measurements. *Building and Environment, 45,* 1153-1160. doi: 10.1016/j.buildenv.2009.10.022

Johansson, P., Ekstrand-Tobin, A., Svensson, T. and Bok, G. (2012). Laboratory study to determine the critical moisture level for mould growth on building materials. *International Biodeterioration & Biodegradation, 73,* 23-32. doi: 10.1016/j.ibiod.2012.05.014

Johansson, P., Ekstrand-Tobin, A. and Bok, G. (2014). An innovative test method for evaluating the critical moisture level for mould growth on building materials. *Building and Environment, 81,* 404-409. doi: 10.1016/j.buildenv.2014.07.002

Klamer, M., Morsing, E. and Husemoen, T. (2004). Fungal growth on different insulation materials exposed to different moisture regimes. *International Biodeterioration & Biodegradation, 54,* 277-282. doi: 10.1016/j.ibiod.2004.03.016

Knapic, S., Oliveira, V., Machado J.S. and Pereira H. (2016). Cork as a building material: a review. *European Journal of Wood and Wood Products, 74,* 775-791. doi: 10.1007/s00107-016-1076-4

Santos, T., Nunes, L. and Faria P. (2017). Production of eco-efficient earth-based plasters: Influence of composition on physical performance and bio-susceptibility. *Journal of Cleaner Production, 167,* 55-67. doi: 10.1016/j.jclepro.2017.08.131

Simona, P.L., Spiru, P. and Ion, I.V. (2017). Increasing the energy efficiency of buildings thermal insulation. *Energy Procedia, 128,* 393-399. doi: 10.1016/J.EGYPRO.2017.09.044

Verdier, T., Coutand, M., Bertron, A. and Roques, C. (2014). A review of indoor microbial growth across building materials and sampling and analysis methods. *Building and Environment, 80,* 136-149. doi: 10.1016/j.buildenv.2014.05.030

XV International Conference on Durability of Building Materials and Components
DBMC 2020, Barcelona
C. Serrat, J R Casas and V. Gibert (Eds)

In-Situ Tests on Silica Aerogel-Based Rendering Walls

Inês Flores-Colen[1], Marco Pedroso[2], António Soares[3], Maria da Glória Gomes[4], Nuno M. M. Ramos[5], Joana Maia[6], Rui Sousa[7], Hipólito Sousa[8] and Luís Silva[9]

[1] Associate Professor, CERIS, Instituto Superior Técnico, Universidade de Lisboa, Av. Rovisco Pais, 1049-001 Lisbon, Portugal, ines.flores.colen@tecnico.ulisboa.pt
[2] PhD student, CERIS, Instituto Superior Técnico, Universidade de Lisboa, Av. Rovisco Pais, 1049-001 Lisbon, Portugal, marco.pedroso@tecnico.ulisboa.pt
[3] Post-doc researcher, CERIS, Instituto Superior Técnico, Universidade de Lisboa, Av. Rovisco Pais, 1049-001 Lisbon, Portugal, ortiz.soares@gmail.com
[4] Assistant Professor, CERIS, Instituto Superior Técnico, Universidade de Lisboa, Av. Rovisco Pais, 1049-001 Lisbon, Portugal, maria.gloria.gomes@tecnico.ulisboa.pt
[5] Assistant Professor, CONSTRUCT, Faculdade de Engenharia, Universidade do Porto, Rua Dr. Roberto Frias, 4200-465 Porto, Portugal, nuno.ramos@fe.up.pt
[6] Researcher, CONSTRUCT, Faculdade de Engenharia, Universidade do Porto, Rua Dr. Roberto Frias, 4200-465 Porto, Portugal, joanamaia@fe.up.pt
[7] Researcher, CONSTRUCT, Faculdade de Engenharia, Universidade do Porto, Rua Dr. Roberto Frias, 4200-465 Porto, Portugal, ruysousa@fe.up.pt
[8] Associate Professor, CONSTRUCT, Faculdade de Engenharia, Universidade do Porto, Rua Dr. Roberto Frias, 4200-465 Porto, Portugal, hipolito@fe.up.pt

Abstract. *In this paper, two aerogel-based renders are characterized based on in-situ testing of walls prototypes. The in-situ tests to assess the mechanical performance are: pull-off, surface impact tests and compressive strength on collected samples. The physical performance includes the water resistance and thermal conductivity coefficient. The tests carried out to assess water-resistance are: Karsten tube, moisture meter and capillary water absorption of collected samples. The thermal performance was tested based on infrared thermography and thermal conductivity transient method.*
The combination of these in-situ tests allowed a better performance characterization of the aerogel-based renders and characterized the applied renders. These results were carried out under two national research projects (Nanorender and P2020 PEP).

Keywords: *In-Situ Tests, Renders, Aerogel, Walls, Performance.*

1 Introduction

On-site performance testing of renders avoids subjective diagnosis and contribute to a better understanding of render behavior under natural exposure conditions. In-situ techniques on conventional renders have been applied on several studies (Flores-Colen *et al.*, 2011; Duarte *et al.*, 2020; Menezes *et al*., 2015; Santos *et al*., 2013) such as ultra-sound; pull-off; surface impact test; Karsten tube; moisture meter; and infrared thermography. Also, compressive strength and capillary water absorption have been carried out on render samples collected from on-site. The study of aerogel (Garrido *et al.*, 2019) and aerogel-based renders is increasing due to their excellent thermal performance and application on thermal rehabilitation of walls, with decreased thicknesses solutions when compared with other conventional thermal renders. In the literature there are already a few number of studies that focus on in-situ testing of aerogel-based

renders, but mainly on the hygrothermal behavior of these renders based on numerical simulations (Fantucci *et al.*, 2020; Fenoglio *et al.*, 2018; Ibrahim *et al.*, 2014; Stahl *et al.*, 2017).

In this paper, several in-situ techniques are applied on wall prototypes with different formulations of aerogel-based renders, in order to discuss the mechanical, water resistance, and thermal performance. The tested formulations (renders A and B) were developed in two national research projects. In Nanorender project (2012-2015), funded by FCT (Foundation for Science and Technology) PTDC/ECM/118262/2010 ("Nanorender: Performance of nanoaerogel silica-based renders" 2015), a cement-based aerogel render, with fly ash and lightweight co-aggregates was developed reaching a good balance between thermal conductivity (0.088 W/m.K) and compressive strength (1.03 MPa). In PEP project (2016-2019), funded by COMPETE 2020/Portugal P2020-POCI-01-0247-FEDER-017417, a new aerogel-based render was developed (thermal conductivity of 0.028 W/m.K) with compressive strength above 0.2 MPa and water vapour diffusion resistance coefficient below 15. Only some results are discussed for two specific aerogel-based renders formulations in order to discuss the potential of in-situ techniques to assess in-service performance.

2 Experimental Program

2.1 Materials

The render $A^{Aero+EC}$ has in its composition: cement CEM II B/L 32.5 N, 1% of surfactant agent and 0.075 % cellulose ether, in weight relative to the total mixture mass. The mixing procedure was initially manual and with slow rotation at the final part of the mixing procedure, following the EN 1015-11, and the water/binder ratio was 1.25. The aggregates include, in volume, 60% of commercial supercritical hybrid silica aerogel and 40% of expanded clay. The aerogel-based render showed problems in the application of a composition with 100% aerogel in volume of aggregates. Thus, the incorporation of the expanded clay (40% in volume) as a co-aggregate improved the mortar consistency and allowed a quick and easy application of the render. A render with only expanded clay (A^{EC}), with 0.05% of air-entraining agent instead of 1%, and with water/cement ratio of 0.78, was also produced and applied for comparative purpose (Lazera *et al.*, 2016).

The render B^{Aero} is composed by a blend of mineral binders, rheological agents, resins, hydrophobic agents, lightweight fillers, containing a commercial supercritical hydrophobic hybrid silica aerogel as a lightweight and thermal insulation aggregate. The silica aerogel granules represent around 58% in volume or a total of 37 % (m/m) in the weight, both for the mixture powder. The water/binder ratio was 1.33 (Pedroso *et al.*, 2019; Sousa *et al.*, 2019). This render has also a multilayer coating composed by a basecoat layer, fibreglass mesh, key coat, and an acrylic finishing coat (Pedroso *et al.*, 2019).

2.2 Wall Prototypes

The renders $A^{Aero+EC}$ and A^{EC} (Figure 1, a) were manually applied with 4 cm thickness on an opening of a brick wall, with 15 cm of thickness and 40x45 cm^2 dimensions. The curing conditions were at ambient air temperature (average of 15 ºC) during 28 days. The surface of the render was periodically moistened in the first days of curing, a plastic sheet covered the wall (Figure 1, b). The render B^{Aero} was mechanically applied with 5.5 cm of thickness on a lightweight concrete masonry wall with 3 x 3.6 m^2 (Figure 1, c and d). The curing conditions were at ambient air temperature

(average of 20 ºC) during 28 days without any humidification of the render surface.

2.3 Testing Procedures

Several techniques were carried out on the wall prototypes: adhesive strength on substrates (EN 1015-12 - pull-off; water permeability under low pressure (LNEC FE Pa 39.1/RILEM nº II.4) Figure 2 a; pendulum hammer index (RILEM MS-D.7), Figure 2 b; hardness impact (LNEC Fe Pa 25), Figure 2 c; thermal conductivity coefficient (ASTM D5930) and also following the test recommendations by Gomes *et al.* (2018), Figure 2 a; Tramex moisture meter (Figure 2 d), and FLIR infrared camera.

a) b) c) d)

Figure 1. a) Render $A^{Aero+EC}$; b) curing condition at early stages of renders $A^{Aero+EC}$ and A^{EC}; c) lightweight concrete block wall to receive render B^{Aero}; d) render B^{Aero}.

a) b) c) d)

Figure 2. a) Thermal conductivity, Karsten tube in render $A^{Aero+EC}$; b) pendulum hammer, c) impact test with Martinet Baronnie device; d) moisture meter in render B^{Aero}.

The prototypes were installed in climatic chambers with an internal controlled environment. Some samples were collected and prepared for compressive strength and capillary water absorption tests, with and without the multilayer finishing system (when applicable). All the renders were tested at 28 days of curing.

3 Results

Table 1 presents some of the experimental results obtained for aerogel-based renders A and B. These results showed that the applied thermal renders have good thermal performance. The incorporation of aerogel improves the thermal characteristics (for example compare A^{EC} and $A^{Aero+EC}$ with the same formulations, 0.1359 for A^{EC} and 0.1200 for $A^{Aero+EC}$)).

Furthermore, the thin coating of the multilayer coating system misleading the in-situ measurement of the thermal conductivity (0.034 for B^{Aero} and 0.120 W/m.K for the mortar with finish coating, respectively). The latter measurement should not be consider because two requirements of this technique are not accomplished: the measurements on a homogeneous material and the minimum thickness. Aerogel-based renders have low compressive strength values and low compacity. However, they have higher deformability, lower pendulum hammer index and higher notch diameter in the Martinet-Baronnie device. If necessary, depending on the surface requirements, a protective multilayer coating system could improve or maintain acceptable values of surface resistance (*e.g.* B^{Aero} has the same surface resistance than the $A^{Aero+EC}$ without a finish layer).

Table 1. Results aerogel-based renders A and B.

Render	Bulk density (kg/m^3)	R_c (MPa)	IE	$Ø_{notch}$ (mm)	*Pull-Off* (KN/m^2)	$H_{superficial}$ (%)	λ_{Isomet} (W/m.K)	*C* ($kg/m^2.min^{0,5}$)	*Volume of water at 60 min (ml)*	C_A ($kg/m^2.min^{0,5}$)
A^{EC}	721.8	2,879	91,1	14	x	27.67**	0.1359	x	10.37	x
$A^{Aero+EC}$	651.6	0.910	77.1	20.6	x	62.67**	0.1200	0.62	2.67	0.70
B^{Aero}	178	0.147	69.7*	20.67*	0.04 cohesive	nil	0.0340	0.02* 0.85	0.083	0.02

Caption: V_{US} – pulse velocity; R_c – compressive strength; IE. – pendulum hammer index; $Ø_{mossa}$ – notch diameter (superficial resistance) from *Martinet Baronnie*; $H_{superficial}$ – surface moisture; λ – thermal conductivity; C – initial slope of the graph with the water absorbed per area over time; C_A – water absorption under low pressure from Karsten tube (Equation 1), where Q = volume of water absorbed (ml), D is the surface diameter, which is 25 mm; t is the period test (min); x - nil tests due to several reasons: impossible to have reliable readings; reduced thickness of the collected samples from the walls; * with multilayer finishing system: ** with 41% of relative air humidity.

$$CA = \frac{Q \cdot 10^{-3}}{D^2 \cdot \left(\frac{\pi}{4} 10^{-6} \cdot \sqrt{t}\right)} \qquad (1)$$

The presence of expanded clay guarantees values of mechanical strength above the minimum of 0.4 MPa from EN 998-1, for thermal renders however significantly increases the thermal conductivity coefficient (from 0.034 of B^{Aero} for 0.12 for $A^{Aero+EC}$) (Júlio *et al.*, 2016). Therefore, both lightweight aggregates and paste formulation contribute to the balance between compressive strength and thermal conductivity.

In terms of water resistance, aerogel-based renders tend to have high water absorption (capillary suction or under low pressure) due to their high porosity, despite the hydrophobic nature of the aerogel and the introduction of more entraining agents (from 2.67 to 10.37 ml in $A^{Aero+EC}$ to A^{EC}. The water absorption due to capillary requirements for renders to be applied to external walls is not accomplished (0.85 and 0.62 $kg/m^2.min^{0.5}$, in table 2, for aerogel-based renders) according to EN 998-1 (CEN, 2010). However, a compatible multilayer coating reduces the water absorption of the render system (from 0.85 to 0.02 $kg/m^2.min^{0.5}$ in B^{Aero}).

The experimental results also showed that aerogel-based renders have drawbacks in adhesive strength. The majority of the results were nil, or the values were too low (0.04 MPa with cohesive rupture). Because of the low weight of these renders and low susceptibility to thermal gradients, the low adhesion values can be accepted. However, some admixtures could be added with this purpose). The results also showed that less intrusive pull-off technique should be adapted in the future to have a more reliable test to assess the adhesion of these renders and other lightweight thermal mortars. Furthermore, the moisture meter confirmed the presence of surface moisture on the render $A^{Aero+EC}$ after 28 days of curing in laboratory conditions. In render B^{Aero}, the values were nil due to the multilayer coating system. In addition, in this render, the infrared thermography was used and no significant differences of the superficial temperature was found, therefore concluding that there is a uniformity of the thermal render, without the presence of moist areas.

4 Conclusions and Future Developments

This paper contributes to the discussion of the performance of aerogel-based renders on walls prototypes. The results showed that these renders have excellent thermal behaviour but with specific characteristics in terms of compressive strength and water resistance.

The in-situ testing and lab testing on the collected samples confirm the mechanical, water-resistance and thermal performance of the applied aerogel-based renders. These renders tend to have lower compressive strength, low compactness but high surface deformability. Because of the low weight of these renders and low susceptibility to thermal gradients (lower values of thermal conductivity), the solutions are stable after application, despite of having reduced adhesion values.

The water resistance of these renders depends on the paste formulation notwithstanding the hydrophobic nature of the aerogel. However, the common application of a compatible multilayer coating system improves the water behavior of the complete render system (thermal render + multilayer coating system).

In-situ tests are relevant techniques to monitor the performance of aerogel-based renders and to give additional information to numerical simulations of these renders. However, some drawbacks can be highlighted, specially when multilayers systems are applied. For example, in-situ measurements of thermal conductivity with ISOMET technique are reliable only on aerogel-based renders without thin coating systems. Further research should discuss the thermal performance of these multilayer systems based on the thermal resistance.

Acknowledgements

The authors gratefully acknowledge the support of CERIS Research Centre, IST - University of Lisbon, Portuguese FCT - Foundation for Science and Technology, Saint-Gobain Weber Portugal, and COMPETE 2020 project POCI-01-0247-FEDER-017417. The second author also wants to thank FCT for PhD grant SFRH/BD/132239/2017.

ORCID

Inês Flores-Colen: https://orcid.org/0000-0003-4038-6748
Marco Pedroso: https://orcid.org/0000-0002-8119-6847
António Soares: https://orcid.org/0000-0002-0377-1295
Maria da Glória Gomes: https://orcid.org/0000-0003-1499-1370
Nuno M. M. Ramos: https://orcid.org/0000-0002-5331-7429

Joana Maia: https://orcid.org/0000-0001-5036-8581
Hipólito Sousa: http://orcid.org/0000-0001-8335-0898
Rui Sousa: http://orcid.org/0000-0003-3855-3252

References

Duarte, R., Flores-Colen, I., de Brito, J. and Hawreen, A. (2020). Variability of in-situ testing in wall coating systems - Karsten tube and moisture meter techniques. *Journal of Building Engineering*, 27, 100998. doi: 10.1016/j.jobe.2019.100998

Fantucci, S., Fenoglio, E., Serra, V., Perino, M., Dutto, M. and Marino, V. (2020). Hygrothermal Characterization of High-Performance Aerogel-Based Internal Plaster. In J. Littlewood, R. Howlett, i A. Capozzol, & L. Jain (Eds.), *Sustainability in Energy and Buildings*. Smart Innovation, Systems and Technologies (pp. 259–268). doi: 10.1007/978-981-32-9868-2_22

Fenoglio, E., Fantucci, S., Serra, V., Carbonaro, C. and Pollo, R. (2018). Hygrothermal and environmental performance of a perlite-based insulating plaster for the energy retrofit of buildings. *Energy and Buildings*, 179, 26–38. doi: 10.1016/j.enbuild.2018.08.017

Flores-Colen, I., Manuel Caliço Lopes de Brito, J. and Peixoto de Freitas, V. (2011). On-site performance assessment of rendering façades for predictive maintenance. *Structural Survey*, 29(2), 133–146. doi: 10.1108/02630801111132812

Garrido, R., Silvestre, J. D., Flores-Colen, I., Júlio, M. de F. and Pedroso, M. (2019). Economic assessment of the production of subcritically dried silica-based aerogels. J*ournal of Non-Crystalline Solids*, 516(January), 26–34. doi: 10.1016/j.jnoncrysol.2019.04.016

Gomes, M. G., Flores-Colen, I., da Silva, F. and Pedroso, M. (2018). Thermal conductivity measurement of thermal insulating mortars with EPS and silica aerogel by steady-state and transient methods. *Construction and Building Materials*, 172, 696–705. doi: 10.1016/j.conbuildmat.2018.03.162

Ibrahim, M., Wurtz, E., Biwole, P. H., Achard, P., and Sallee, H. (2014). Hygrothermal performance of exterior walls covered with aerogel-based insulating rendering. *Energy and Buildings*, 84, 241–251. doi: 10.1016/j.enbuild.2014.07.039

Júlio, M. F., Soares, A., Ilharco, L. M., Flores-Colen, I. and de Brito, J. (2016). Aerogel-based renders with lightweight aggregates: Correlation between molecular/pore structure and performance. *Construction and Building Materials*, 124, 485–495. doi: 10.1016/j.conbuildmat.2016.07.103

Lazera, R., Santos, A. R., Flores-Colen, I., Gomes, M. G. and Moret Rodrigues, A. (2016). Experimental study of mechanical and physical performance of thermal mortars. In L. Villegas, I. Lombillo, H. Blanco, & Y. Boffill (Eds.), *Rehabend 2016 Euro-American Congress,* Burgos - Spain.

Menezes, A., Glória Gomes, M. and Flores-Colen, I. (2015). In-situ assessment of physical performance and degradation analysis of rendering walls. *Construction and Building Materials*, 75, 283–292. doi: 10.1016/j.conbuildmat.2014.11.039

Pedroso, M., Flores-Colen, I., Dinis Silvestre, J., Gomes, M. G., Silva, L. and Ilharco, L. (2019). Physical, mechanical and microstructural characterization of a thermal insulating render incorporating silica aerogel: nanoSIR. *Energy and Buildings*, 211, 109793: doi.org/10.1016/j.enbuild.2020.109793

Santos, L. A., Flores-Colen, I. and Gomes, M. G. (2013). In-situ Techniques for Mechanical Performance and Degradation Analysis of Rendering Walls. *Restoration of Buildings and Monuments*, 19(4). doi: 10.1515/rbm-2013-6606

Sousa, R., Sousa, H., Silva, L., Flores-Colen, I. and Pedroso, M. (2019). Development of a wall system made with thermally optimized masonry and super insulation mortar render. *Masonry International*, 32(1), 3–14. https://www.scopus.com

Stahl, T., Ghazi Wakili, K., Hartmeier, S., Franov, E., Niederberger, W. and Zimmermann, M. (2017). Temperature and moisture evolution beneath an aerogel based rendering applied to a historic building. *Journal of Building Engineering*, 12, 140–146. doi: 10.1016/j.jobe.2017.05.016/

XV International Conference on Durability of Building Materials and Components
DBMC 2020, Barcelona
C. Serrat, J.R. Casas and V. Gibert (Eds)

Laboratory Vs Field Performance of Innovative Thermal Insulating Plasters

Stefano Fantucci, Elisa Fenoglio and Valentina Serra

Politecnico di Torino - Department of Energy, C.so Duca degli Abruzzi 24 Torino, Italy.
stefano.fantucci@polito.it

Abstract. *Thermal insulating plasters and renders are becoming a popular solution for the energy retrofit of existing and historic buildings because of their suitability/compatibility with the existing masonry supports. However, as for most of the insulating products, the actual performance of these materials might significantly differ from the one determined with simplified methods (EN ISO 6946 standard) that are commonly adopted by the designers. In this study, an overview of the latest Authors researches that involve three different thermal insulating plasters, containing respectively perlite, vegetal and aerogel aggregates, are presented. The developed plasters were characterized in the laboratory and successively applied in three demonstration buildings. From the in-field thermal monitoring activities, all the analysed thermal insulating plasters showed a decrease in the thermal performance between 25 and 30% if compared to the laboratory measurements.*

Keywords: *Plaster, Render, Aerogel, Retrofit, Historical Buildings.*

1 Introduction

In the last years the energy demand reduction, and hence, the reduction of greenhouse gas emission has become a crucial global strategy. Building sector can play a key role in this process. Since the largest part of the EU existing buildings is old and thus weak from the thermal point of view, retrofit strategies should be adopted for improving the thermal insulations level. Nevertheless, a big challenge is to identify suitable insulating solutions able to guarantee the proper compatibility with the existing masonries, considering that ~39% of the EU residential buildings were built before the 1960'. Recently, different retrofit strategies for existing buildings have been developed. Among all the different solutions one of the most promising is represented by the thermal insulating plasters and renders. These materials are similar to the traditional plasters, but the sand is replaced by lightweight thermal insulating aggregates (LWA) to reduce density and thermal conductivity. Key-features of these materials are the ease of application on irregular surface, the higher hygrothermal compatibility, the minimum space reduction (indoor application) and the good thermal performance improvement. Several studies have demonstrated that good thermal performance can nowadays be achieved by using different LWA typologies e.g. vegetal (Cherki A *et al.,* 2014, Mazhoud B. *et al.,* 2016, Brása A. *et al.,* 2013), mineral (Barbero-Barrera M. *et al.,* 2015, Osman G. 2016, Konakova D. *et al.,* 2017), polymeric (Mayor P. *et al.,* 2012, Šeputytė-Jucikė J. *et al.,* 2014) or silica aerogel (Ibrahim M. *et al.,* 2014, Stahl T. *et al.,* 2012, Buratti C. *et al.,* 2014, Fantucci S. *et al.,* 2020).

Nevertheless, despite the interesting potentials of thermal insulating plasters, some aspects are currently under investigation. Actually, during their service life, these materials might be exposed to variable boundary conditions *e.g.* temperature and relative humidity variations,

that can strongly affect the expected thermal performance. It seems evident that, in addition to the laboratory nominal thermal conductivity measurements, an in-field monitoring activity can be useful.

The aim of this paper is to present a comparison between the laboratory performance and the actual in-field monitored performance, in real case studies. For this sake, an overview of the latest Authors researches that involve the monitoring of three different historical case study buildings in northern Italy in which three different thermal insulating plasters containing different LWA were applied (vegetal, mineral and aerogel) is here presented.

1.1 The Developed Materials

The materials hereafter presented were developed adopting different LWA typologies (vegetal, mineral, and aerogel). The plasters were measured in the laboratory to determine the nominal thermal conductivity and then applied and monitored to different case study buildings in north Italy. The first formulation presented (VGT 04) is made by natural hydraulic lime as a binder with addition of vegetal and mineral aggregate, respectively corncobs (33% in weight) and perlite (10% in weight); the product was then applied to a historical building located in Turin (Ex Albergo della Virtù, 1580). The second analysed plaster typology (P_30) is made by mineral LWA. The Natural Hydraulic Lime (NHL2) was mixed with cement (<7.5% in weight) and perlite was used as aggregate (30% in weight); the product was applied to a XIX - XX century rural house located in Dogliani (CN).

The last plaster typology was made by a mineral-based binder with the addition of ~50% in weight of granular aerogel (Sample G). The product after the laboratory test was applied to a 1920 building located in Turin (ATC social house). More exhaustive analyses performed on the different materials were presented in (Bianco L. *et al.,* 2015, Fenoglio E. *et al.,* 2018, Fantucci S. *et al.,* 2019).

2 Laboratory Assessment

Accordingly, to the EN 998-1 standard, the thermal plaster to be classified as "T1" must achieve a λ-value lower than 0.10 W/mK. So for this classification, it is essential to experimentally assess the thermal conductivity in laboratory conditions.

2.1 The Laboratory Analysis

The procedure to perform the thermal conductivity measurement is reported in EN 12667:2001. The apparatus adopted for the plaster samples presented in this paper is the Heat Flux Meter (HFM Figure 1a). It is made by two flat parallel plates in which the plaster specimen is placed in between. It is possible to set different temperatures of the plates to establish a constant temperature difference ΔT, then the generated specific heat flux φ is measured. In this case, a temperature difference between the plates of 10°C was set. The HFM collects the surface temperature difference and the heat fluxes until constant conditions are reached, then for known specimen thickness t it is possible to determine the thermal conductivity as follow:

$$\lambda_{eq} = t \cdot \frac{\varphi}{\Delta T} \; [W \cdot m^{-1} K^{-1}] \tag{1}$$

The tested samples are characterized by a size of 60 x 60 x 10 cm (VGT 04) and of 40 x 40 x 5 cm (P_30 and G). Before to start the test, the samples were dried in a climatic chamber (ACS DM 340 Figure 1b) until a constant mass was reached. Then to avoid any vapour migration between the samples and the environment, they were sealed in a vapour-tight envelope.

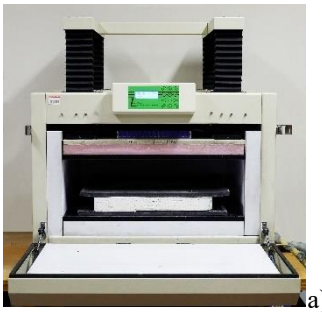
a)

b)

Figure 1. a) the heat flux meter adopted for the measurements (picture from Fantucci et al. 2020); b) the climatic chamber adopted for the material drying.

2.2 Results

The thermal conductivity of the thermal plaster formulations is reported in Table 1. Results show that the lower is the thermal conductivity of the LWA added in the formulations, the lower is the density of plaster, and hence, their thermal conductivity. Nevertheless, adopting non super-insulating LWA (perlite and corncob), a quite low thermal conductivity (below 0.1 W/mK) can be achieved to be classified as T1 plaster according to the EN 998-1 standard.

Table 1. Thermal conductivity results of the thermal plasters.

Code	Sample	ρ [kg/m^3]	$\lambda_{10,dry}$ [W/mK]	Results from
A	VGT_04 (vegetal)	400	0.090	Bianco L. et al., 2015
B	P_30 (perlite)	394	0.084	Fenoglio E. et al., 2018
C	Sample G (aerogel)	134	0.027	Fantucci S. et al., 2020

3 In-situ Monitoring

In addition to the laboratory thermal conductivity measurement, an in-field monitoring campaign was carried out for the three different thermal plaster formulations.

3.1 Demonstration Buildings

For each formulation, a different case study building was selected for the material installation. The monitoring phase aims at analysing the actual in-field thermal performance and to compare it with the laboratory measurements. For each case study, two identical walls with the same orientation were selected: one was kept as reference wall while the other was retrofitted with the thermal insulating plasters applied on the internal side of the wall.

The plaster A (vegetal-based) was applied at “Ex Albergo di Virtù” (1580), a historic

building located in Turin (Figure 2a). The south-east oriented external wall was selected for the application of 6 cm thick layer of thermal plaster from the interior side. The existing walls are made of a ~50 cm thick layer of stones and bricks.
The plaster B (perlite-based) was applied in a 5 cm thick layer for the energy retrofit of a rural building located in Dogliani (CN) (Figure 2b). The selected walls are north-east oriented, and the structure is made up of about 50 cm layer of solid bricks with an external lime plaster layer.

Finally, a 1920 social house building, located in Turin, and managed by ATC (Agenzia Territoriale Per La Casa del Piemonte Centrale) was chosen as reference building for the application and monitoring of the plaster C (aerogel-based) (Figure 2c). Two identical solid brick cavity walls south-east oriented were selected, the retrofitted one was coated with ~4.5 cm plaster layer.


a) b) c)

Figure 2. a) Ex Albergo di Virtù case study selected for plaster A (picture from Bianco *et al.,* 2015); b) the building during the refurbishment and selected for plaster B (picture from Fenoglio *et al.,* 2018); c) the ATC building selected for the plaster C (picture from Fantucci *et al.,* 2019).

3.2 Monitoring Procedures

The standard procedure for the in-field measurement of the thermal transmittance (U-value) and thermal resistance is reported in the ISO 9896:2014. In order to compare the U-values of the retrofitted and the non-retrofitted walls, the measurements were carried out simultaneously. A preliminary thermographic survey was performed to assure that the wall portion selected for the monitoring was sufficiently uniform and not affected by thermal bridges (Figure 3a). The internal and external air temperature values were measured by means of Type-T thermocouples. Moreover, heat flux plates (HFP01), glued on the inner side of the walls,were used to measure the heat flux densities and then, after at least 72 h of measurements, to assess the U-value by using the average method described in the ISO 9869 standard. The comparison of the U-values measured in the reference and in the retrofitted walls allowed determining the thermal performance improvement achievable by adopting the thermal insulating plaster. Furthermore, the equivalent thermal conductivity of the thermal insulating plaster layer was calculated according to Eq. (1).

$$\lambda_{eq} = t/\left(\frac{1}{U_{plt}} - \frac{1}{U_{ref}}\right) \left[{}^{W}/_{mK}\right] \quad (1)$$

Where: t is the plaster layer thickness [m]; U_{plt} is the thermal transmittance of the plastered wall [W/m^{2}K]; U_{ref} is the thermal transmittance of the reference wall [W/m^{2}K];

In the different case studies, the measurements were carried out for a period longer than those required by the standard. Moreover, since some façades are south-east oriented, the data adopted for the calculation correspond to the period with low solar radiation and external temperature.

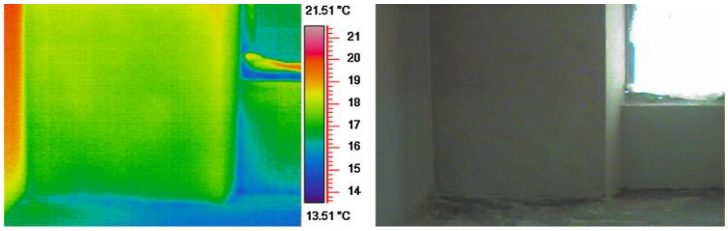

a)

Figure 3. a) a thermographic survey carried out on the Ex Albergo di Virtù (picture from Bianco et al. 2015).

3.3 Results

3.3.1 Results of Plaster A

Figure 4 report the data of the U-value for the wall retrofitted with the plaster A (vegetal-based). The measurement was performed for 19 consecutive days. The thermal transmittance value achieved at the end of the monitoring period was 0.56 W/m^{2}K. Considering a U-value of about 0.8 W/m^{2}K (estimated by EN ISO 6946 standard) for the reference wall, a reduction of about 30% can be underlined. Moreover, the equivalent thermal conductivity of the thermal plaster layer was determined according to eq. (1), so the estimated in-field actual conductivity (~0.116 W/mK) showed an increase of ~30% if compared to the laboratory value (0.09 W/mK). This thermal performance reduction can due to higher moisture content in the installed plaster compared to the one tested in the laboratory. Indeed, for this case study, it is worth to be highlighted that the drying process was still in progress during the testing phase and the wall U-value was slightly still decreasing.

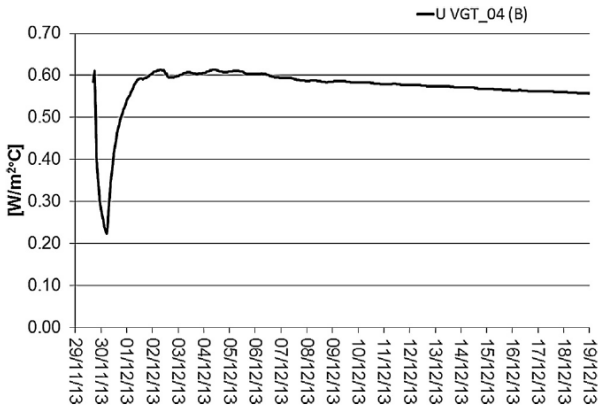

Figure 4. Thermal transmittance measured for the wall retrofitted with the plaster A.

3.3.2 Results of plaster B

The plastered and bare walls used for the thermal transmittance assessment of plaster B were monitored for 4 days and the results of the monitoring campaign are reported in Figure 5.

The plastered wall reached a U-value of ~0.80 W/m^{2}K that is the 45% lower than the value achieved by the bare wall (~1.43 W/m^{2}K).

The equivalent thermal conductivity calculated for the perlite-based thermal plaster reached a value ~0.092 W/mK that is ~10% higher than the values measured in the laboratory.

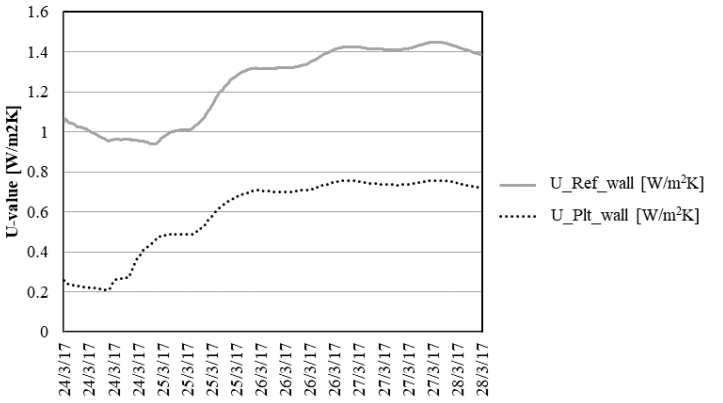

Figure 5. Thermal transmittance measured for the wall retrofitted with the plaster B.

3.3.3 Results of Plaster C

The aerogel-based plaster was monitored for more than one month. However, only one reference week was selected for the analysis because of the more suitable boundary conditions. Thermal transmittance values for both the bare and retrofitted wall were measured and reported in Figure 6. It is noticeable a thermal transmittance reduction of ~60%, indeed the reference wall shows a U-value of ~0.99 W/m^{2}K while the retrofitted wall reached a U-value of 0.42 W/m^{2}K. The thermal conductivity of the plaster layer that was calculated from the U-values of the two walls, was ~0.033 W/mK, that was about 17% higher than the value measured in laboratory conditions.

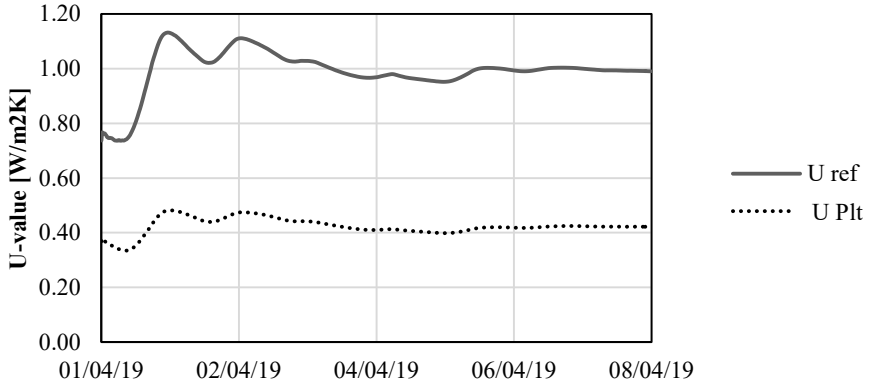

Figure 6. Thermal transmittance measured for the wall retrofitted with the plaster C.

4 Discussion

The laboratory tests performed on different thermal insulating plaster samples highlighted, as expected, a decrease of the thermal conductivity due to the addition of lightweight (vegetal, perlite and aerogel) aggregates in the formulations.

The in-situ measurements performed for the vegetal based plaster (~60 mm thick layer) have shown a decreasing of the U-value of about 30% respect to the non-retrofitted wall. Nevertheless, for this case study, it should be highlighted that the measurement was carried out when the material was still losing moisture. The perlite-based plaster shows a reduction of the U-value of about 45% (~50 mm thick layer). As expected, the plasters with a lower thermal conductivity (aerogel-based) allowed the achievement of the higher thermal transmittance reduction, up to 60% with a thinner layer (~45 mm). Comparing the nominal thermal conductivity values measured in the laboratory with the actual equivalent thermal conductivity determined through the monitoring campaign, an increment between 10% and 30% was highlighted a slight decrease in the thermal performance.

This performance decrease can be mainly related to different reasons: i) the high in-field measurement uncertainty; ii) the different drying stage of the three analysed plasters; iii) the different temperature and the higher moisture content of the in-field monitored plaster compared to the laboratory measurements. The latter reason can be explained since the material tested in the laboratory were dried before the test and the measurements were carried out at 10°C (mean temperature). Nevertheless, the results demonstrate that the adoption of the thermal insulating plasters are a suitable solution for the energy retrofit of existing buildings.

5 Conclusions

The thermal plaster formulations tested in this study were made up of different mineral (perlite), vegetal and super-insulating (aerogel) lightweight aggregates. The thermal conductivity measurements carried out in the laboratory have shown a significant decrease in the thermal conductivity by adding these LWA. Thermal conductivity values between 0.09 W/mK to 0.027 W/mK were achieved; as expected the lower is the thermal conductivity of the LWA adopted, the lower is the final thermal conductivity of the plaster.

The in-field applications and measurements, on three demonstration buildings, were performed for each plaster formulations to determine the benefit achievable in terms of thermal transmittance reduction. The promising results, that were achieved in the laboratory, were confirmed by the monitoring campaign: a reduction of thermal transmittance between 30% to 60% was measured for the different plaster.

Comparing the nominal thermal conductivity values measured in the laboratory with the actual equivalent thermal conductivity determined through the monitoring campaign, an increment between 10% and 30% were highlighted. This decrease of performance was mainly due to higher moisture content and different temperature at which the plasters were exposed.

From these analyses, it is possible to underline that the characterisation of the thermal conductivity at different temperatures and moisture content are necessary to properly evaluate the actual thermal performance and allow more conscious evaluation among different retrofit alternatives.

Acknowledgements

The research activities have received funding from the project “Wall-ACE” in the framework of EU Horizon 2020 research and innovation programme under the Grant Agreement No. 723574, and SI² - SISTEMI ISOLANTI INNOVATIVI. The authors would also thanks the Italian manufacturer Vimark for provide the materials and the installation on the pilot site, Pollo R., Grosso G., Lubrano F., Bianco L. and Carbonaro. C.

ORCID

Stefano Fantucci: http://orcid.org/0000-0001-8535-549X
Elisa Fenoglio: https://orcid.org/0000-0001-8142-6705
Valentina Serra: http://orcid.org/0000-0001-6341-5762

References

EN 12667 (2001). *Thermal performance of building materials and products - Determination of thermal resistance by means of guarded hot plate and heat flow meter methods*.

EN 998-1 (2010). Specification for mortar for masonry Part 1: Rendering and plastering mortar

Barbero-Barrera M., García-Santos A. and Neila-González F. (2014). *Thermal conductivity of lime mortars and calcined diatoms. Parameters influencing their performance and comparison with the traditional lime and mortars containing crushed marble used as render*s, Energy and Buildings.

Bianco, L., Serra, V., Fantucci, S., Dutto, M. and Massolino, M. (2015). *Thermal insulating plaster as a solution for refurbishing historic building envelopes: First experimental results*, Energy Build. 95 (2015).

Brása A., Goncalves F. and Faustino P. (2013). *Cork-based mortars for thermal bridges correction in a dwelling:Thermal performance and cost evaluation*, Energy and Buildings.

Buratti C., Moretti E., Belloni E. and Agosti F. (2014). *Development of Innovative Aerogel Based Plasters: Preliminary Thermal and Acoustic Performance Evaluation*, Sustainability.

Carbonaro C., Tedesco S., Thiebat F., Fantucci S., Serra V. and Dutto M. (2015). *An integrated design approach to the development of a vegetal-based thermal plaster for the energy retrofit of buildings*, Energy and Buildings.

Cherki A., Remy B., Khabbazi A., Jannot Y. and Baillis D. (2014) *Experimental thermal properties characterization of insulating cork–gypsum composite*, Construction and Building Materials.

Fantucci S., Fenoglio E., Grosso G., Serra V., Perino M., Marino V. and Dutto M. (2019). *Development of an aerogel-based thermal coating for the energy retrofit and the prevention of condensation risk in existing buildings*, Science and Technology for the Built Environment vol 25. Taylor and Francis.

Fantucci, S., Fenoglio, E., Serra, V., Perino, M., Dutto, M. and Marino, V. (2020). *Hygrothermal Characterization of High-Performance Aerogel-Based Internal Plaster*. In: Littlewood J., Howlett R., Capozzoli A., Jain L. (eds) Sustainability in Energy and Buildings. Smart Innovation, Systems and Technologies, 163. Springer.

Fenoglio, E., Fantucci, S., Serra, V., Carbonaro, C. and Pollo, R. (2018). *Hygrothermal and environmental performance of a perlite-based insulating plaster for the energy retrofit of buildings*, Energy and Buildings.

Herrero, S., Mayor, P. and Hernández-Olivares, F. (2012). *Influence of proportion and particle size gradation of rubber from end-of-life tires on mechanical, thermal and acoustic properties of plaster–rubber mortars*, Construction and Building Materials.

Ibrahim, M., Wurtz, E., Achard, P. and Biwole, P. H. (2014). *Aerogel-based coating for energy efficient building envelopes.* 9th International Energy Forum on Advanced Building Skins, Oct 2014, Bressanone, Italy, Proceedings of Energy Forum on Advanced Building Skins, 753-774.

ISO 9869-1 (2014). *Thermal insulation - Building elements - in situ measurement of thermal resistance and thermal transmittance - Part 1: Heat flow meter method.*

Konakova, D., Cachova, M., Vejmelkova, E., Keppert, M., Jerman, M., Bayer, P., Rovnaníkova, P. and Cerný, R. (2017). *Lime-based plasters with combined expanded clay-silica aggregate: Microstructure, texture and engineering properties*, Cement and Concrete Composites 83.

Mazhoud, B., Collet, F., Pretot, S. and Chamoin J. (2016). *Hygric and thermal properties of hemp-lime plasters*, Building and Environment.

Osman, G., Juan Jose, C. D, Mucahit, S., Fuat, K. and Felipe Pedro, Á. R. (2016). *A novel lightweight gypsum composite with diatomite and polypropylene fibers*, Construction and Building Materials.

Šeputytė-Jucikė, J., Sezeman, G. A., Sinica, M. and Modestas, M. (2014). *Impact of granules from crushed expanded polystyrene package on properties of thermoinsulating plaster*, Journal of Civil Engineering and Management.

Stahl, T., Brunner, S., Zimmermann, M. and Ghazi Wakili, K. (2012). *Thermo-hygric properties of a newly developed aerogel-based insulation rendering for both exterior and interior applications*, Energy and Buildings.

XV International Conference on Durability of Building Materials and Components
DBMC 2020, Barcelona
C. Serrat, J.R. Casas and V. Gibert (Eds)

Large Scale Laboratory and Field Tests of Aerogel Renders

Jürgen Frick[1], **Nayara R. M. Sakiyama**[1,2], **Marina Stipetic**[1] **and Harald Garrecht**[1]

[1] Materials Testing Institute (MPA), University of Stuttgart, Pfaffenwaldring 2b, 70569 Stuttgart, Germany, juergen.frick@mpa.uni-stuttgart.de

[2] Institute for Science, Engineering and Technology (ICET), Federal University of the Jeq. and Muc. Valleys (UFVJM), R. Cruzeiro, 01 -Jardim São Paulo, 39803-371 Teófilo Otoni, Brazil, nayara.sakiyama@ufvjm.edu.br

Abstract. *Within the framework of the European project Wall-ACE a large-scale laboratory test (EOTA-Wall Test) was performed. Additional a test field in Switzerland was equipped with six different aerogel renders by the project partner AGITEC. Laboratory walls and test field were equipped with sensors to monitor in real-time climate, heat flux, temperature, relative humidity, and at the laboratory tests additional material moisture. The data allow calculating U-values and material parameters as well as drying behaviour of render and substrate. During and after the artificial weathering in laboratory the renders were subjected to visual inspection and mechanical adhesion tests. The performance of the aerogel renders will be assessed and compared with results on conventional insulation renders.*

Keywords: *Aerogel, External Insulation.*

1 Introduction

As the European Union (EU) requires an improvement of 27% regarding the buildings energy efficiency by 2030 (European Commission), the development of innovative technologies to improve the performance levels of the building envelop is encouraged. In this sense, the Horizon 2020 project (Wall-ACE, 2016) aimed to develop a package of new advanced aerogel-based insulation products and systems that could be used to strengthen the competitiveness of Europe through innovation and excellence. Among the developed products was an external high performance insulating render, which had as goals providing a long lasting, breathable continuous insulation layer where its thickness could be adjusted depending on the climate, on the geographic orientation of the wall and on architectural or specific local needs (thermal bridges, uneven walls, windows reveals, architectural constraints such as in semidetached housing, etc.).

Within the framework of the project there were included tests to assess the efficiency and behaviour of the different insulation systems in extreme conditions in large-scale tests and real conditions on building scale.

2 Experimental

2.1 EOTA-Wall Test

To assess the durability of the external insulation render developed by the Wall-ACE project partner Quick-Mix, a large-scale laboratory test (EOTA-Wall test) was performed according to (EN 16383:2016).

doi:10.23967/dbmc.2020.089

2.1.1 Test set-up

The test chamber consists of two opposing walls spaced one meter apart, with the render system facing each other, forming an inner room that characterizes the outside conditions. On one of the chamber sidewalls, the Quick-mix external render, an aerogel-based exterior insulation render was applied, while on the other side a commercially available, regular perlite-based insulation render, TRI-O-THERM, was used as a reference material. Each wall was split vertically and was made up of bricks on one side and concrete blocks on the other, measuring in total 4.0 x 2.1 m (length x high). Therefore, it can be considered that four walls were under investigation, named here from A to D, see Figure 1.

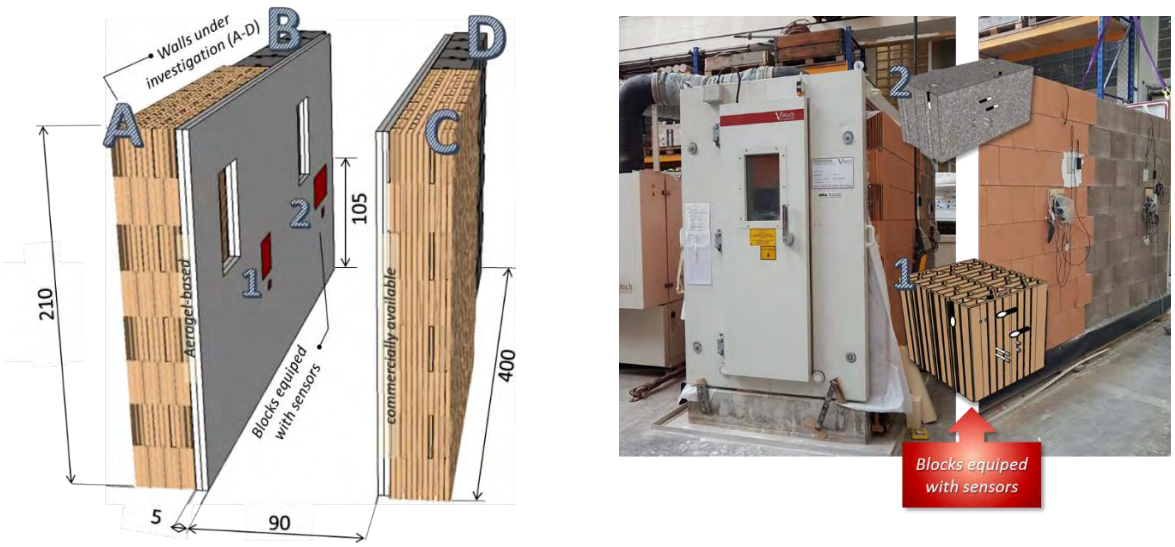

Figure 1. Left: Aerogel render wall (A, B), perlite render wall (C, D). Right: EOTA test rig and monitoring system.

The set-up of both walls are as following: 1 Substrate: bricks or concrete blocks, 2 adhesion layer (concrete blocks), 3 exterior insulation render: two layers of around 3 cm of aerogel or perlite render, 4 two layers of supporting plaster together with a reinforced mesh in the first layer, 5 hydrophobic final coting. Such solution is necessary to ensure both mechanically stability and protection from weathering and mechanical impact.

2.1.2 Durability test – weathering cycles

The large-scale test walls were exposed to weathering cycles according to (EN 16383:2016), which are grouped into heat-rain, heat-cold and heat-rain-cold cycles, see Figure 2. Lasting on average 84 days, the ageing test offers harsh conditions with a 90°C temperature range and 1.5 l/m²min amount of water during the rain cycles.

2.1.3 Material moisture and temperature monitoring

On each of the four monitored walls, one concrete or brick block equipped with impedance and hygro-thermal sensors was placed among the layered blocks (Figure 1). Impedance sensors, which consist of two probes (screws or thread rod) surrounded with a conduction rubber at a

proximity distance of 1.5 cm were incorporated in the bricks, joints and exterior render layers. Additional, hygro-thermal sensors were installed as well and covered with a porous tube or with a glass fibre tape. The used hygro-thermal sensors (Sensirion SHT25) have a small size (3x3x1.1 mm) and a resolution of ±0.2 K and ±1.8% RH.

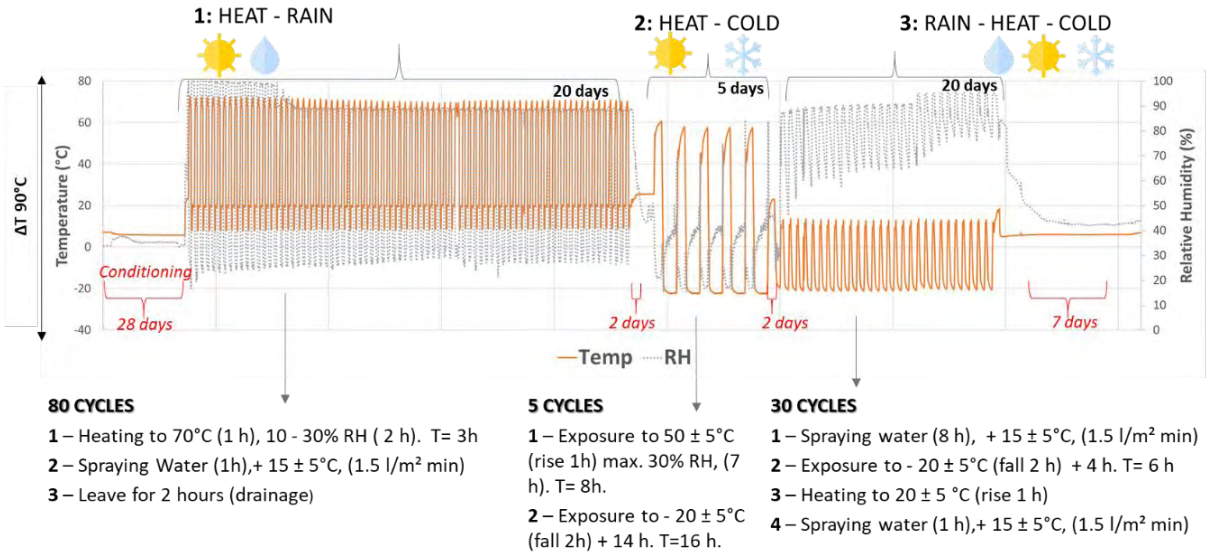

Figure 2. EOTA weathering cycles.

A cross-section of the walls with their corresponding materials and thickness as well as the positioning of the different sensors is shown in Figure 3. Furthermore, heat flux sensors (Ahlborn, FQA018C, type 118) were added at the tested walls. Together with the surface temperature measurements, the wall thermal resistance or U-value, according to (ISO 9869-1:2014) was determined before and after the weathering cycles.

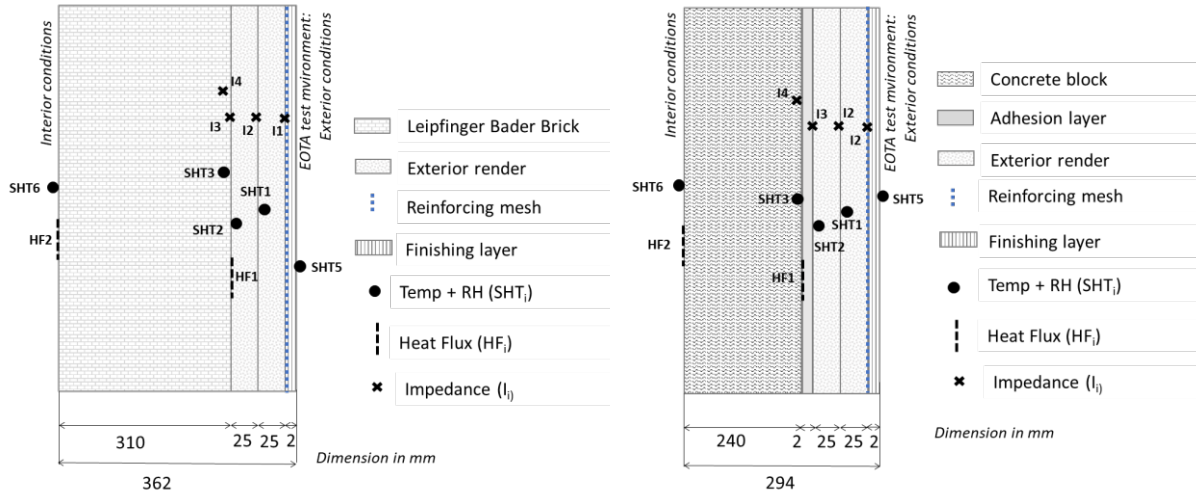

a) Brick walls (A and C) b) Concrete block walls (B and D)

Figure 3. EOTA test – walls sections (A-D).

2.1.4 Adhesive strength

Adhesive strength between insulation render and substrate was tested according to (ETAG 004:2013, Section 5.1.4.1.1, Paragraph 2). Adhesive strength was tested after the weathering cycles for both renders: developed aerogel-based and commercially available TRI-O-THERM.

Results of adhesive strength before weathering cycles represent initial adhesive strength. For testing of adhesive strength, square test surfaces with 50 mm edge length was chosen. The edges of the test surfaces (50 mm edge length) were dry-cut through the insulation render until substrate surface. A metal plate with an edge length of 50 mm was glued to each test surface using a 2-component adhesive based on epoxy resin. After sufficient hardening of the adhesive, the metal plate was pulled off using a pull-out testing device, see Figure 4.

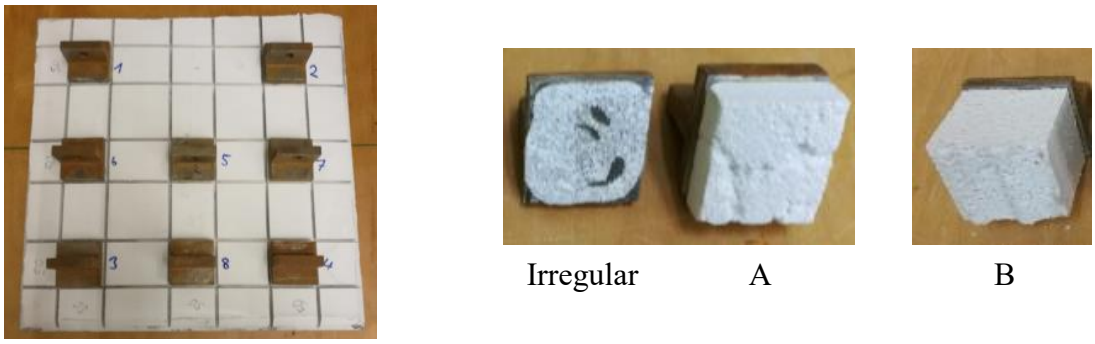

Figure 4. Testing of adhesion to the substrate: Glued tension plates on specimen surface and possible failure modes (from left to right): (Irregular) failure along glued Surface, (B) specimen failure, (A) adhesion failure.

2.2 Test Field

2.2.1 Case description

Different aerogel based exterior renders were spread over a south-oriented wall at storage and office building to both monitor their behaviour at a real building site and to pursue a comparison study to evaluate its performance. The wall under investigation stand to the left of the main entrance of AGITEC industrial shed building, located in Dällikon - Switzerland, close to the Zurich (47°26'44.3"N 8°26'26.2"E).

In details, the industrial shed area is the ground floor of the building with a total height of 7.07 m, and gross external dimensions of 15.20 m x 39.32 m. It has a prefabricated concrete structure, composed of pillars spaced every 6.5 m. Moreover, the warehouse has MDF and plasterboard partitions, both vertical (internal walls) and horizontal (floor slabs), thus creating small deposits in its interior space. These deposits have an average height of 3.10 m.

Regarding the analysed materials, four commercially available aerogel renders (anonymized data: A to D), and Quick-Mix Wall-ACE renders 1&2 (Figure 6) are studied. Firstly, the four commercially available aerogel renders (A-D) were applied to the industrial shed south façade with an area of 5.5 m² each. Later on, Quick-Mix Wall-ACE renders 1&2 were applied alongside the others, having an area of respectively 23 m² and 10 m². The application followed the following scheme: 1 cleaning, primer and roughcast for adhesion, 2 two layers of aerogel insulation render by machine spraying, 3 two layers of supporting plaster (the same for all walls) together with a reinforced mesh in the first layer, 4 final coting.

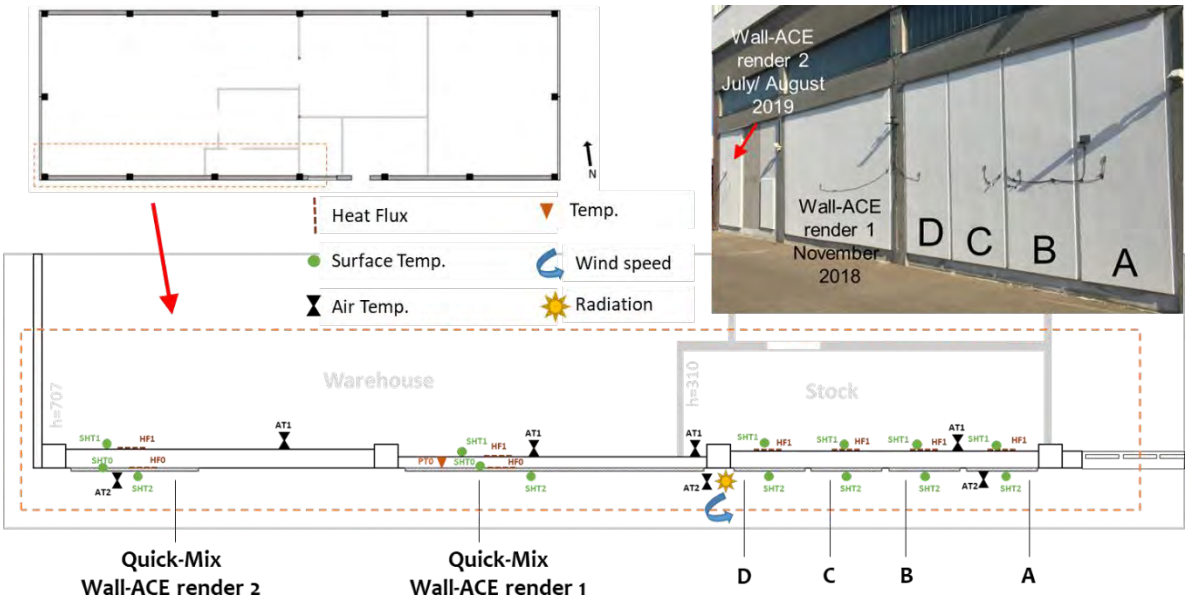

Figure 5. Floor plan: AGITEC storehouse. Feature test walls, sensors and installation.

2.2.2 Monitoring

Both environment/boundary conditions and walls elements were equipped with sensors to allow, through on-site measurements, an in situ thermal characterization and consequently, a performance analysis of the different aerogel render products under investigation.

For this, air temperature and relative humidity sensors were installed outside, inside the warehouse and stock (Sensirion STH25), and at both interior and exterior wall surfaces (Sensirion SHT31). Heat flux sensors (Ahlborn, FQA018C, type 118) were also installed at the inner side for all tested materials, and additionally between the Quick-Mix Wall-Ace exterior renders and the substrate wall. Besides that, sensors to measure global solar radiation (W/m²) and wind speed (m/s) were installed to assess the outside weather conditions. All sensors were placed approximately at 1.5m high (see Figure 6). However, the presence of outdoor weather conditions configures a challenge to estimate a stationary parameter such as thermal resistance. Moreover, the average method, described in ISO 9869-1:2014, requires walls not exposed to direct solar radiation, which is not the case here.

Furthermore, it is emphasized that the composition of the storehouse walls differ from each other, presenting distinct thicknesses and materials, according to their location (Figure 1), which also has different heights (warehouse= 7.07 m and stock=3.10 m). All these factors make an instant comparison between the renders difficult.

3 Results and Discussion

3.1 EOTA-Wall Test

3.1.1 Material moisture and temperature monitoring

The temperature difference across the brick and concrete block walls (ΔT=°C), as well as both heat flux (W/m²) and Impedance (MΩ) measured at the exterior insulation render layer are

shown in Figure 6. After certain weathering cycles the plasters showed a moisture uptake in the impedance measurements. Such behaviour should be omitted in the final product development due to the risk of frost cracking.

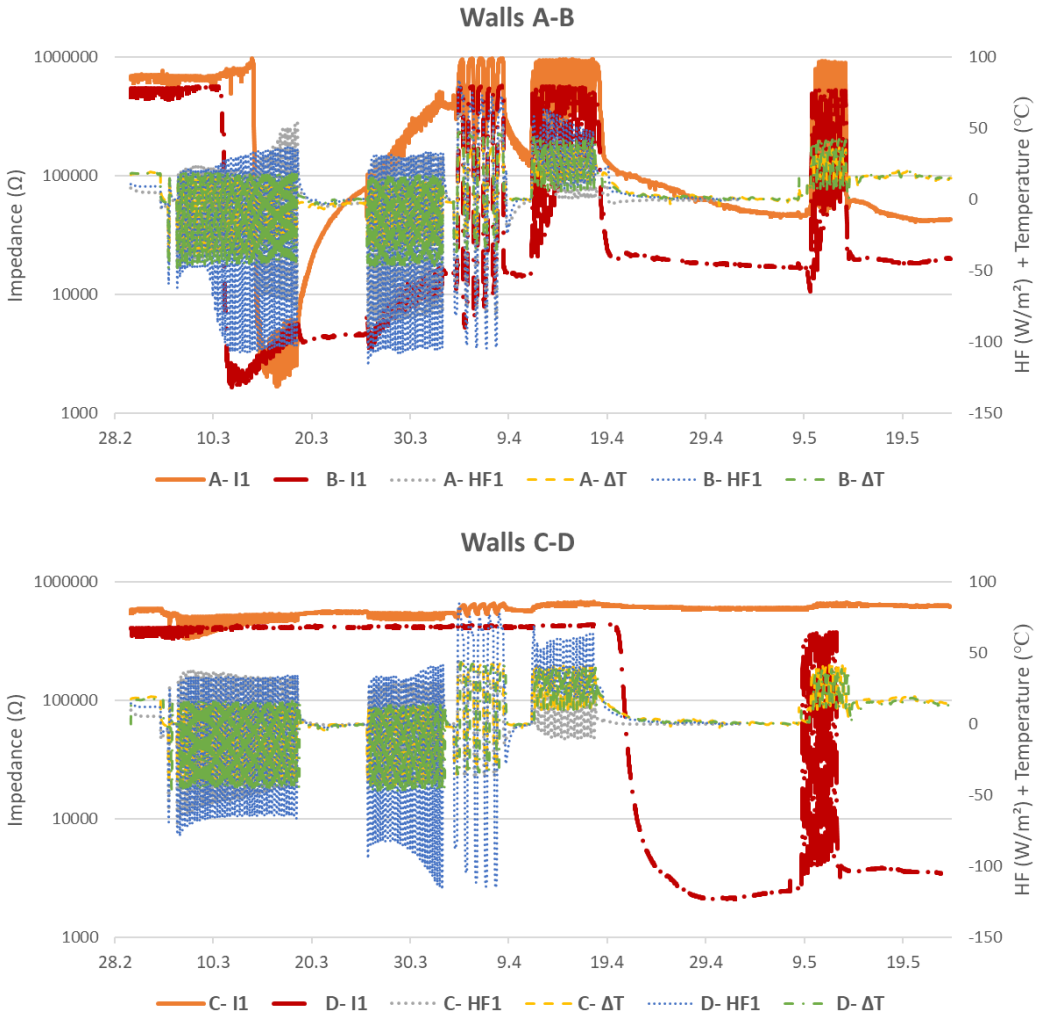

Figure 6. Temperature difference (°C), heat flux (W/m²) and Impedance (MΩ) measured during the EOTA test: (a) Wall A and B (Wall-ACE Quick-Mix Aerogel render); (b) Wall C and D (TRI-O-THERM render).

3.1.2 Adhesive strength

Results of adhesive strength (determined from the maximum load and the area of 2500 mm² subjected to tensile stress) are given in Table 1. It can be seen that average adhesive tensile strength of aerogel-based exterior insulation render was 33-60% lower after ageing compared to initial adhesive strength. These values (strength after ageing) are comparable with adhesive strength of TRI-O-THERM after ageing. The failure was 100% in the insulation render in all tests.

Before the start of the EOTA-Wall Test, the test wall was checked for its initial condition. No defects were found during the initial inspection.

Table 1. Results of adhesive strength

Substrate	Render type	Testing time	Adhesive strength [N/mm²]	Failure mode
Hollow brick	QUICK-MIX WALL-ACE	Before ageing	0.009	Specimen failure
Light weight concrete		Before ageing	0.005	Specimen failure
Hollow brick		After ageing	0.003	Specimen failure
Light weight concrete		After ageing	0.003	Specimen failure
Hollow brick	TRI-O-THERM	After ageing	0.004	Specimen failure
Light weight concrete		After ageing	0.004	Specimen failure

The test wall surface was observed during the EOTA test for changes such as cracks, chipping of surface, etc. Only minor chipping of surface was present after EOTA test. Furthermore, crack propagation (crack length/crack width) was observed for each window. Crack propagation is similar for both renders. Crack width is never bigger than 0.15 mm which is a sign for positive behaviour of tested systems.

3.2 Test Field

The weather data obtained from the experimental campaign (20/05/19 – 20/09/19) are shown in Figure 6. External conditions or outside environment measured by the sensors presented an average 26.5°C of air temperature, 52% of air relative humidity and 743 W/m² of global radiation since the analysed walls face south.

The completion of the Quick-Mix Wall-ACE render 2 applications is highlighted in the chart. Furthermore, in Figure 8 it is possible to follow the drying process of the material by reading the humidity between the brick and the render layer. By mid-September it is clear that the material is still damp. A U-value estimation is foreseen for the winter season 2019/2020.

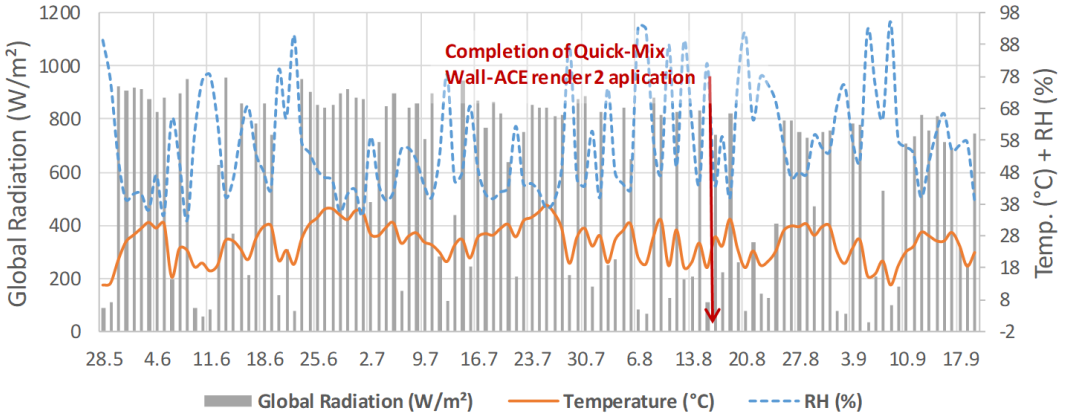

Figure 7. Environmental data at test side.

4 Conclusions

The large scale EOTA-Wall Test, originally developed for ETICS systems, is a valuable method to assess new developed insulation render systems. It provides a harsh environment and acts therefore as acceleration benchmark. Additional monitoring of certain parameters (moisture,

climate, heat flux) within the material helps to assess energy performance under such conditions. First experiences (Frick *et al.*, 2016) were further developed.

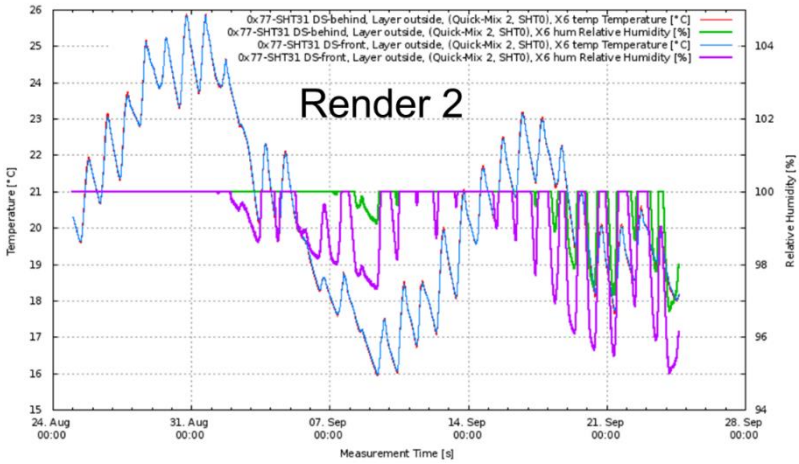

Figure 8. Temperature and relative humidity measured in the Quick-Mix render 2.

The field tests serve as benchmark in real conditions. The installation at the south side results in harsher conditions with higher temperature gradients. On the other side the estimation on energy performance parameters like U-values will be more difficult. Certain methodologies will be tested with the monitoring data from the upcoming winter season (Nocentini *et al.*, 2018).

Acknowledgements

The research project Wall-ACE has received funding from the EU Horizon 2020 research and innovation programme under the Grant Agreement No. 723574. The authors wish to thank the project partner AGITEC that installed the different aerogel materials and made available the building for the field tests, and Quick-mix that provided/installed the developed material in the experimental chamber.

ORCID

Jürgen Frick: https://orcid.org/0000-0002-2010-4830
Nayara R. M. Sakiyama: https://orcid.org/0000-0002-1928-4950
Harald Garrecht: https://orcid.org/0000-0002-7080-3197

References

CEN/TC 88 (2016). *EN 16383: Thermal insulation products for building applications – Determination of the hygrothermal behaviour of external thermal insulation composite systems with renders (ETICS)*

EOTA (2013). *ETAG 004: Guidline for European Technical Approval of External Thermal Insulation Composite Systems (ETICS) with Rendering.*

Frick, J., Reichert, M., Lehmann, F., Stegmaier, M. and Herter, K. (2016). *Moisture Monitoring during an Artificial Weathering Test of a Cultural Heritage Compatible Insulation Plaster*. In *Proceedings of the 19th World Conference on Non-Destructive Testing*, Munich, Germany, paper Mo2C3, 1-7. https://www.wcndt2016.com/portals/wcndt/bb/Mo2C3.pdf [acc. 18-12-2019]

ISO/TC 163/SC 1 (2014). *ISO 9869-1: Thermal insulation — Building elements — In-situ measurement of thermal resistance and thermal transmittance — Part 1: Heat flow meter method.*

Nocentini, K., Achard, P. and Biwolé, P. (2018). *Thermal performances of an innovative super-insulating material based on silica aerogel*. In *Proc. of 13th Conference on Advanced Building Skins*, Bern, Switzerland, 519-529.

Wall-ACE (2016). *Wall-ACE - WALL Insulation NOvel Nanomaterials Efficient systems,* EU Horizon 2020 project, Grant Agreement number: 723574, duration 2016-2019, https://www.wall-ace.eu/ [acc. 18-12-2109]

XV International Conference on Durability of Building Materials and Components
DBMC 2020, Barcelona
C. Serrat, J.R. Casas and V. Gibert (Eds)

Bio-Based Building Materials – How to Unravel the Role of Material Characteristics on Fungal Susceptibility?

Liselotte C. De Ligne[1,2], Jan B.B. Van den Bulcke[1], Jan M. Baetens[2], Bernard De Baets[2] and Joris C.M. Van Acker[1]

[1] Ghent University (UGent), Laboratory of Wood Technology (UGent-Woodlab), Coupure links 653, 9000 Ghent, Belgium, liselotte.deligne@ugent.be

[2] Ghent University (UGent), Research Unit Knowledge-based Systems (KERMIT), Coupure links 653, 9000 Ghent, Belgium, liselotte.deligne@ugent.be

Abstract. *Bio-based materials are gaining importance in the building industry, as the focus on sustainability and life-cycle-assessment has increased substantially over the last decade. Wood and wood-engineered products as well as insulation materials made from cellulose, wood, flax, hemp, etc. are increasingly used. These materials are made from renewable resources and with considerably lower energy consumption than various other building materials, such as insulation polymers, steel and concrete. As steel can corrode and concrete can rot, so can bio-based building materials degrade over time when exposed to those conditions that favour decay. Since fungi cause not only aesthetical degradation, but can also severely compromise the structural integrity of a building component this is critical for any service life approach. Consequently, a proper understanding of the fungal susceptibility of bio-based materials is needed, both for optimal application of bio-based materials as for the design of new materials. Based on a combination of tests we try to unravel the role of the material's chemical components, structure and moisture dynamics on its fungal susceptibility, as well as the interaction between those material characteristics. In a first test set-up, the 'paste test', the material's structure is removed and fungal growth is assessed over time in 2D, with only the material's chemical components playing a role. In the second test set-up, the 'X-ray CT test', fungal development is assessed non-destructively in 3D with X-ray CT, giving an indication of moisture production and distribution over time, in relation to the material's structure. By comparing the results, we have a better idea of how much each material characteristic influences fungal susceptibility. This knowledge can then be used for optimising fungal testing of bio-based materials, ensuring optimal application and providing the building industry with the confidence they need to pave the way to a more sustainable future.*

Keywords: *Bio-Based Building Materials, Material Characteristics, Fungal Degradation, X-Ray CT.*

1 Introduction

The construction sector has a considerable impact on the environment as it consumes large quantities of energy, water and raw materials (Melchert, 2007). In Europe, around 65% of all aggregates (sand, gravel and crushed rock) and approximately 20% of all metals are used in this sector (Herczeg *et al.*, 2014). There is, however, a clear trend towards sustainable building projects, both in the residential and industrial construction sector (Jones and Brischke, 2017). Bio-based materials, *in casu* wood, wood-engineered products and insulation materials made from cellulose, wood, flax, hemp, etc. are key in the sustainable building context. These materials originate from renewable resources and hence have several advantages. They constitute a significant carbon sink when managed sustainably and are produced by consuming considerable less energy than aluminium, steel and concrete (Sathre and O'Connor, 2008; Jones

and Brischke, 2017). As they are often biodegradable, they are easy to process at the end of their service life (Ganotopoulou, 2014). The latter characteristic is, however, most unwanted while in service. When an organic material is exposed to favourable moisture and temperature conditions as well as to degrading organisms, its functional and aesthetic service life can decrease. Fungi can also cause structural damage and lead to degradation of building materials (Bertron, 2014; Dedesko and Siegel, 2015). It is, for example, well known that most wood products used in outdoor environments must be protected against deterioration by decay fungi (Goodell *et al.*, 2003).

It is widely agreed that the proliferation and growth of fungi on building materials are controlled by the presence of nutrients and sufficiently available water. Moisture problems in buildings can for instance occur when building materials get moist during the construction phase, due to infiltration of rain water or because of condensation (Adan and Samson, 2011). When the environment provides a high relative humidity, porous materials can become sources of water for microorganisms (Hoang et al, 2010; Verdier *et al.*, 2014). Next to spatial structure and the closely related moisture dynamics (Verdier *et al.*, 2014), the chemical composition of a material plays an important role in fungal susceptibility as well. For example, there are several wood species of which the heartwood contains natural fungicidal extractives (Jebrane, 2014; Goodell, 2003). Other less durable materials are either modified or treated with protection products to increase their durability. For instance, solid wood and fibre products are subjected to heat treatment, hydrophobation with oils or resins and chemical modification such as acetylation and furfurylation to increase durability (Homan and Jorissen, 2004).

There is little detailed data available on the fungal susceptibility of bio-based materials, except for solid wood (CEN EN 350: 2016). The most widely used laboratory method for determining the natural durability of solid wood against wood-destroying fungi is the CEN TS 15083-1 test method (CEN TS 15083-1: 2015). Resistance of preservative-treated wood against basidiomycetes is assessed according to the standard EN 113 (CEN EN 113: 1996). Both tests subject wood samples (5 x 2.5 x 1.5 cm^3) for 16 weeks to pure cultures of white rot and brown rot fungi selected for their strong ability to degrade wood (CEN TS 15083-1: 2015). The samples are weighed before and after exposure to the test fungus and the amount of mass loss due to degradation is calculated. These standards for the assessment of the efficacy of wood preservatives and of the inherent resistance of wood species are generally regarded to be sufficient and adequate (Kutnik, 2013). However, these standards are typically inadequate for the qualification of new wood products, whose durability is not enhanced with biocides but by new technologies, such as chemically modified wood (acetylation, furfurylation, etc.), thermally treated wood, glue-laminated wood, wood-based panels and wood treated with water repellents (Candelier *et al.*, 2016; Jones and Brischke, 2017; Kutnik *et al.*, 2014; Ringman *et al.*, 2014; Ormondroyd *et al.*, 2015). For example, laboratory tests are performed using conditions optimal for the test fungus. A growth medium is used and serves two purposes: one being nutritional support for the fungus, the other to maintain a high enough moisture content for fungal activity. If the wood does not reach the required moisture content, the test may be declared invalid according to the strict interpretation of the standard (CEN EN 113: 1996, CEN TS 15083-1: 2015). However, thermal and chemical modifications change the wood-water interactions in such a way that the resulting equilibrium moisture content (EMC) of modified woods is lower than the equivalent non-modified wood (Candelier *et al.*, 2016; Mai *et al.*, 2010; Ormondroyd *et al.*, 2015; Ringman *et al.*, 2014). The modified wood samples might not moisten

fast enough during the 16 weeks testing period for the fungus to reach significant degradation. It does not mean, however, that these materials cannot eventually become wet enough for degradation. Kamden *et al.* (2002), confirmed that after a period of six weeks exposure, the modified wood samples did become wet and noted moisture contents varying between 72% and 156%. We therefore need to contemplate whether the set-up of the standard needs to be adapted, for instance by prolonging the test duration or increasing the initial moisture content of the modified wood, or whether fungal degradation of modified wood needs to be observed under the same humidity conditions as for the non-modified wood (Ormondroyd *et al.*,2015). This example illustrates the importance of understanding certain material characteristics and their influence on fungal resistance as well as the test methodology, in order to properly interpret experimental data derived from standard tests. Consequently, further research is needed on the intricate material-fungal relationship to gain the necessary insights for adequate adaptation of the standard tests, both for optimal application of bio-based materials as for the design of new materials. This is especially pressing given the lack of experience with these new materials compared to the traditional building practice.

In this paper, we propose two tests to unravel the role of the material's chemical components, structure and moisture dynamics on its fungal susceptibility, as well as the interaction between those material characteristics. In a first test set-up, the 'paste test', the material structure is removed and fungal growth is assessed over time in 2D, with only the material's chemical components playing a role. In the second test set-up, the 'X-ray CT test', fungal development is assessed non-destructively in 3D with X-ray CT, giving an indication of moisture production and distribution over time, in relation to the material's structure. By comparing the results, we have a better idea of how much each material characteristic influences the fungal susceptibility.

2 Assessing the Role of Material Chemistry on Fungal Susceptibility

In the paste test, a bio-based material is grinded to a fine powder with a particle size smaller than 0.1 mm, thus eliminating the influence of the material's structure on fungal growth. By mixing the powder with agar and water, we ensure that the powder is water saturated, thereby also limiting the influence of hydrophobic components. The resulting paste is inoculated with a wood degrading fungus and mycelial growth is assessed over time with a flatbed scanner. The paste test thus gives an indication of how the overall chemistry, consisting of the nutritional value and the presence of toxic components, influences the fungal susceptibility of a bio-based material.

Figure 1 shows the mycelial development of *Coniophora puteana,* a common wood-rotting basidiomycete, on four bio-based materials. A material with a low natural durability, such as untreated beech wood, does not inhibit mycelial growth (Fig. 1 a). In contrast, a wood species containing toxic components typically limits fungal growth, as is the case for the heartwood of European cherry (Fig. 1 b). The paste test provides additional insights when combined with other tests, for instance assessing the degradation of the material with the structure still intact or of the material with its toxic components removed. In that way, we can find out the influence of the chemistry, and to what extent the durability is due to the material's density or hygroscopic properties. An interesting example is thermally modified wood and derived products, which have been chemically changed because of the wood being heated at high temperatures (Homan

and Jorissen, 2004). Thermal modification reduces the amount of hydroxyl groups in the wood cellulose and hemicellulose (Mazela *et al.*, 2004). The wood-water interactions of thermally modified wood therefore change in such a way that the resulting EMC is lower than that of the equivalent non-modified wood (Candelier *et al.*, 2016; Mai *et al.*, 2010; Ormondroyd *et al.*, 2015; Ringman *et al.*, 2014). Mazela *et al.* (2004) determined the fungal resistance of blocks of Scots pine sapwood (*Pinus sylvestris* L.) subjected to different thermal and hydrothermal treatments. They found that wood blocks exposed to thermal treatments of 190°C and 220°C were resistant to the test fungi. They hypothesized that besides the thermal effects on wood hygroscopicity, thermal treatment also generates toxins that could affect fungal growth. With the paste test, we can easily verify whether the amount of toxins that are possibly formed, such as furfural or trace quantities of lignin phenol derivates (Mazela *et al.*, 2004), are sufficiently present to inhibit or slow down fungal growth. Figure 1 shows an example of the paste test performed on non-modified (c) and thermally modified (d) three-layer-plywood of spruce. In this case, we can state that the applied modification process did not generate meaningful amounts of toxins, as the mycelial development is not inhibited. The fungal resistance of this particular product therefore stems from its acquired hygroscopic properties.

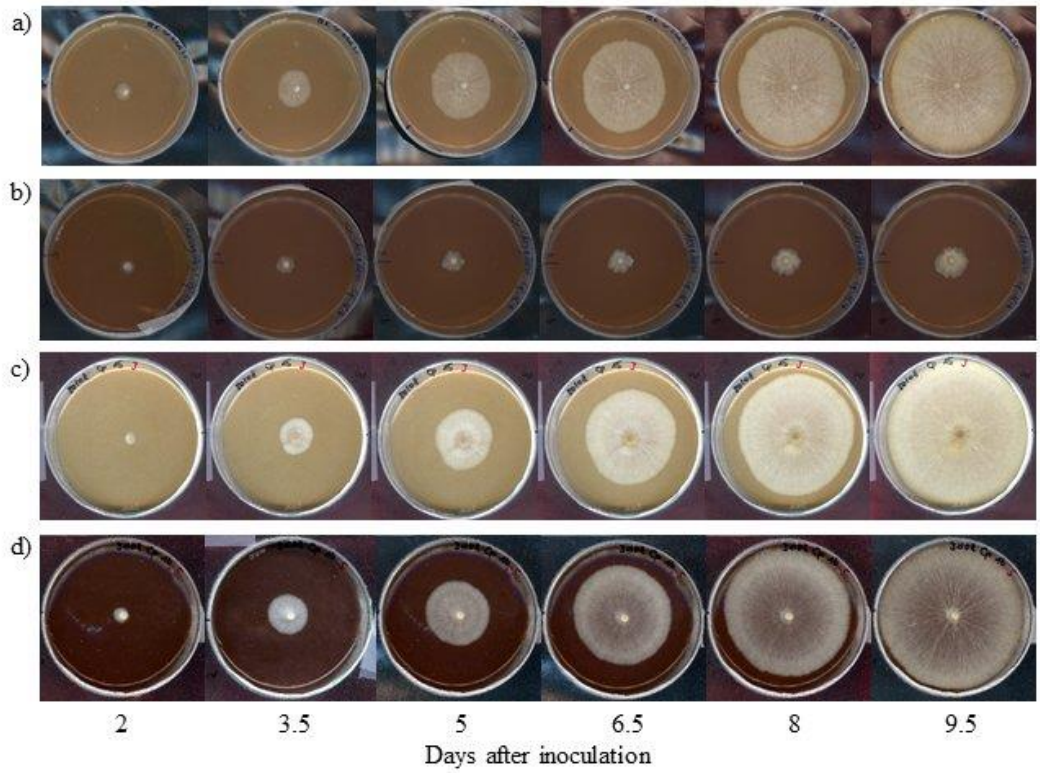

Figure 1. *C. puteana* growing on a paste of a) beech heartwood b) heartwood of European cherry c) three-layer-plywood of spruce and d) thermally modified three-layer-plywood of spruce.

3 Assessing the Role of the Material's Structure and Moisture Dynamics on Fungal Susceptibility

Degradation of (treated) solid wood is usually assessed by measuring the mass loss caused by decay fungi after sixteen weeks (CEN EN 113: 1996, CEN TS 15083-1: 2015). This is an excellent method for testing the durability of a certain wood species or the efficacy of a preservation product, but does not offer much information on what is going on inside the wood structure during degradation. To gain more insight into how the material's structure and moisture properties affect the degradation process, we propose X-ray CT to provide additional information. X-ray CT scanning is a technology that uses X-ray projections to produce tomographic images (slices) of specific areas of a scanned object, allowing the user to inspect the inside of the scanned object in a non-destructive way (Li, 2016). Due to the different attenuation coefficients between material and air, X-ray CT scanning can reveal the internal spatial structure and density distribution of a material (Bergsten *et al.*, 2001; Chen *et al.*, 2010; Freyburger *et al.*, 2009). It therefore enables us to obtain localized information inside wood during degradation, without disrupting the degradation process. The set-up we designed is able to automatically scan a stack of Petri dishes, one after the other, allowing extensive testing of the degradation process (Fig. 2).

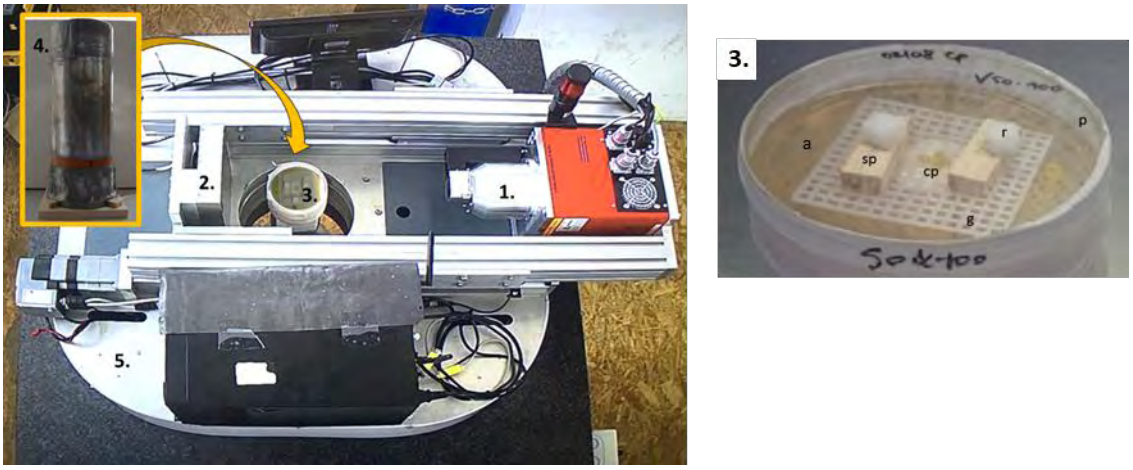

Figure 2: X-ray CT set-up. 1) X-ray source 2) Detector 3) Stack of Petri dishes 4) PVC tube with lead cladding 5) Rotation table. a= agar medium, cp= *C. puteana,* p = Petri dish, g = plastic grid, r = reference material, sp = Scots pine

A first test was performed on mini-blocks of Scots pine sapwood under degradation by *C. puteana*, scanned at weekly intervals with X-ray micro CT (De Ligne *et al.*, 2019). We were able to assess the weekly change in density for each wood block. The results are not straightforward to interpret as a consequence of confounding effects, as several factors affect the assessed density: moisture uptake from the agar medium and moisture production by the fungus increase the average density profile, while water evaporation and mass loss due to degradation decrease it. However, we were able to link increasing density to increasing moisture content, which in turn is linked to increasing fungal activity, as fungi metabolise sugars into carbon dioxide and water (Schmidt, 2006). To assess how the material's structure and density influence the fungal degradation process, we are currently performing a test on

mini-blocks (0.5 x 1 x 3 cm³) of four wood species with differing densities: beech (*Fagus sylvatica* L.) (a), gaboon (*Aucoumea klaineana* Pierre) (b), Scots pine sapwood (*Pinus sylvestris* L.) (c) and Norway spruce (*Picea abies* (L.) Karst) (d). Figure 3 gives a snapshot of the degradation process over time. Darker pixels indicate regions with low density, such as air. White pixels show regions with high density. The white stripes in beech (a), Scots pine sapwood (c) and spruce (d) indicate the latewood zones of the growth rings, which are denser than the earlywood. At the start of the experiment (week 0), no degradation had taken place. White blotches start appearing as degradation progresses over time. These regions with high density are an indication of liquid water production by the fungus, and demonstrate an increasing fungal activity. For Scots pine (c) and spruce (d), degradation is clearly starting from the sides of the mini-blocks (week 1) and progressing towards the center of the mini-blocks (week 4 to 8). This is to be expected, since the mini-blocks were cut in such a way that the transverse plane is one the side, providing ample tracheid openings through which hyphae and water can enter the wood.

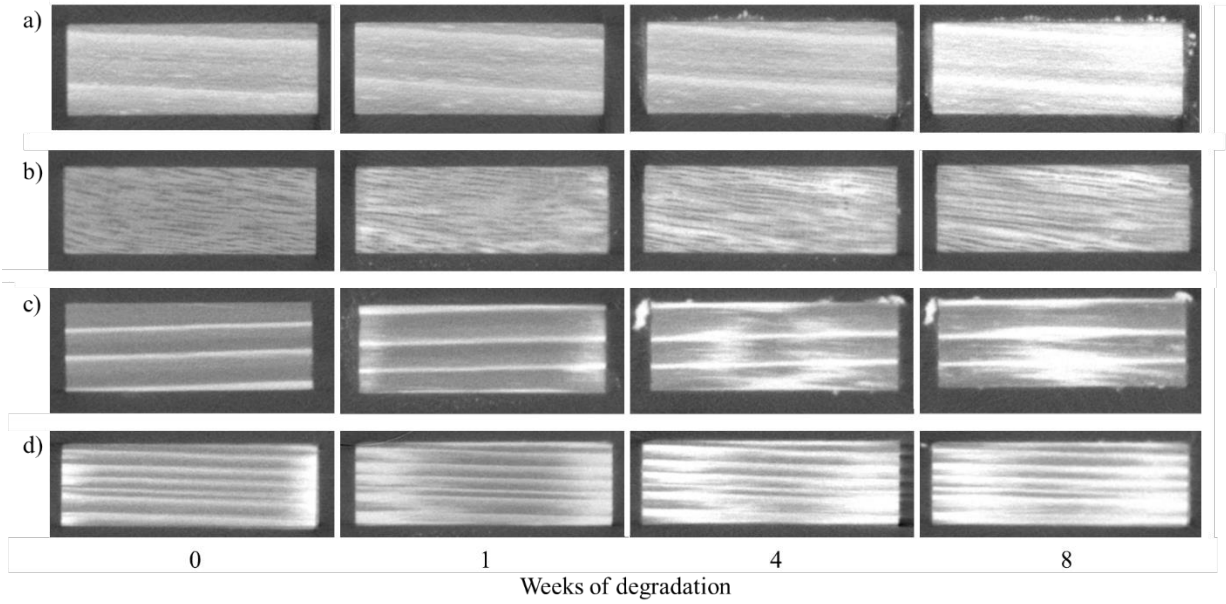

Figure 3. CT slices showing the fungal degradation of beech (*Fagus sylvatica* L.) (a), gaboon (*Aucoumea klaineana* Pierre) (b), Scots pine sapwood (*Pinus sylvestris* L.) (c) and Norway spruce (*Picea abies* (L.) Karst) (d) mini-blocks over time by *C. puteana.* The whiter the pixels, the higher the density.

4 Conclusions and Future Perspectives

- In the paste test, the influence of the material's structure and hygroscopic components on fungal growth is eliminated. It thus provides insight into the role of only the material chemistry on the overall fungal susceptibility of a material. It is currently being applied to a wide range of bio-based materials and will provide useful insights, especially in combination with other test methods.
- The X-ray CT test is useful to gain insight into the influence of material's structure and moisture dynamics on its fungal susceptibility. It allows us to gather localized

information on fungal activity during the entire degradation process, without disrupting it.

Acknowledgements

The authors gratefully acknowledge the financial support of the Research Foundation Flanders (FWO SB grant 1S53417N).

ORCID

Liselotte De Ligne: http://orcid.org/0000-0002-2202-42208
Jan Van den Bulcke: http://orcid.org/0000-0003-2939-5408
Jan M. Baetens: http://orcid.org/0000-0003-4084-9992
Bernard De Baets: http://orcid.org/0000-0002-3876-620X
Joris Van Acker: https://orcid.org/0000-0002-8961-0176

References

Adan, O.C. and Samson, R.A. (2011). *Fundamentals of Mold Growth in Indoor Environments and Strategies for Healthy Living.* Wageningen, Wageningen Academic Publishers.

Bergsten, U., Lindeberg, J., Rindby, A. and Evans, R. (2001). Batch measurements of wood density on intact or prepared drill cores using x-ray microdensitometry. *Wood Science and Technology, 35, 435–452.* doi: 10.1007/s002260100106

Bertron, A. (2014). Understanding interactions between cementitious materials and microorganisms: a key to sustainable and safe concrete structures in various contexts. *Materials and Structures, 47, 1787–1806*. doi: 10.1617/s11527-014-0433-1

Candelier, K., Thevenon, M.-F., Petrissans, A., Dumarcay, S., Gerardin, P. and Petrissans, M. (2016). Control of wood thermal treatment and its effiects on decay resistance: a review. *Annals of Forest Science,73, 571–583.* doi: 10.1007/s13595-016-0541-x

CEN (1996). *EN 113: Wood preservatives method of test for determining the protective effiectiveness against wood destroying basidiomycetes determination of the toxic values.*

CEN (2016). EN 350: *Durability of wood and wood-based products - Testing and classification of the durability to biological agents of wood and wood-based materials.*

CEN/TS (2015). *CEN/TS 15083-1: Durability of wood and wood-based products - determination of the natural durability of solid wood against wood-destroying fungi. Test methods - part 1, Basidiomycetes.*

Chen, S.G., Liu, X.H., Fang, L.M. and Wellwood, R. (2010). Digital X-ray analysis of density distribution characteristics of wood-based panels. *Wood Science and Technology, 44, 85-93*. doi: 10.1007/s00226-009-0256-3

De Ligne, L., Van den Bulcke, J., De Muynck, A., Baetens, J., De Baets, B., Van Hoorebeke, L. and Van Acker, J. (2019). Exploring the use of X-ray micro CT as a tool for the monitoring of moisture production and mass loss during lab-based fungal degradation testing. In *Proceedings of the 50th Annual Meeting of the International Research Group on Wood Protection,* Quebec city, Canada, IRG/WP 19-20654.

Dedesko, S. and Siegel, J.A. (2015). Moisture parameters and fungal communities associated with gypsum drywall in buildings*. Microbiome, 3, 1.* doi: 10.1186/s40168-015-0137-y

Freyburger, C., Longuetaud, F., Mothe, F., Constant, T. and Leban, J.M. (2009). Measuring wood density by means of X-ray computer tomography. *Annals of Forest Science, 66, 804.* doi: 10.1051/forest/2009071

Ganotopoulou, E. (2014). *Biodegradable materials: A research and design handbook; enhancing the use of biodegradable materials on building's envelopes in the Netherlands*(in English), PhD thesis, Delft University, Delft, The Netherlands.

Goodell, B., Nicholas, D.D. and Schultz, T.P. (2003). *Wood deterioration and preservation: Advances in our changing world.* Oxford, Oxford University Press.

Herczeg, M., McKinnon, D., Milios, L., Bakas, I., Klaassens, E., Svatikova, K. and Widerberg, O. (2014). *Resource efficiency in the building sector*, Final report prepared for the European Commission, ECORYS and Copenhagen Resource Institute, Rotterdam, the Netherlands.

Hoang, C.P., Kinney, K.A., Corsi, R.L. and Szaniszlo, P.J. (2010). Resistance of green building materials to fungal

growth. *International Biodeterioration & Biodegradation, 64, 104–113.* doi: 10.1016/j.ibiod.2009.11.001

Homan, W.J. and Jorissen, A.J. (2004). Wood modification developments. *Heron, 49, 360–369.*

Jebrane, M., Pockrandt, M. and Terziev, N. (2014). Natural durability of selected larch and Scots pine heartwoods in laboratory and field tests. *International Biodeterioration & Biodegradation, 91, 88–96.* doi: 10.1016/j.ibiod.2014.03.018

Jones D. and Brischke C. (2017). *Performance of Bio-Based Building Materials*. Duxford, Woodhead Publishing: Elsevier.

Kamdem, D., Pizzi, A. and Jermannaud, A. (2002). Durability of heat-treated wood. *Holz als Roh-und Werkstoff, 60, 1–6*. doi: 10.1007/s00107-001-0261-1

Kutnik, M. (2013). Focus on the european standardization - towards a revision of the en 350 natural durability standard: a diffierent approach to the inherent resistance and performance of wood and wood-based materials. In *Proceedings of the 44th Annual Meeting of the International Research Group on Wood Protection,* Stockholm, Sweden, IRG/WP 13-10811.

Kutnik, M., Suttie, E. and Brischke, C. (2014). European standards on durability and performance of wood and wood-based products-trends and challenges. *Wood Material Science and Engineering, 9, 122-133*. doi: 10.1080/17480272.2014.894574

Li, W. (2016). *Experimental investigation of the relation between structure and moisture behaviour of wood-based panels* (in English), PhD Thesis, Ghent University, Ghent, Belgium.

Mai, C., Verma, P., YanJun, X., Dyckmans, J. and Militz, H. (2010). Protection mechanisms of modified wood against decay by white and brown rot fungi. In *Proceedings of the 41st Annual Meeting of the International Research Group on Wood Protection,* Biarritz, France, IRG/WP 10-10713.

Mazela, B., Zakrzewski, R., Grze'skowiak, W., Cofta, G. and Bartkowiak, M. (2004). Resistance of thermally modified wood to basidiomycetes. *Electronic Journal of Polish Agricultural Universities, 7, 1505–0297*.

Melchert, L. (2007). The Dutch sustainable building policy: A model for developing countries? *Building and Environment, 42, 893–901.* doi: 10.1016/j.buildenv.2005.10.007

Ormondroyd, G., Spear, M. and Curling, S. (2015). Modified wood: review of efficacy and service life testing. *Proceedings of the Institution of Civil Engineers-Construction Materials, 168, 187-203.* doi: 10.1680/coma.14.00072

Ringman, R., Pilgffiard, A., Brischke and C., Richter, K. (2014). Mode of action of brown rot decay resistance in modified wood: a review. *Holzforschung, 68, 239-246*. doi: 10.1515/hf-2013-0057

Sathre, R. and O'Connor, J. (2008). *A synthesis of research on wood products and greenhouse gas impacts*, Technical report TR-19R, FPInnovations, Vancouver, Canada.

Schmidt, O. (2006). *Wood and Tree Fungi: Biology, Damage, Protection and Use.* Berlin, Springer-Verlag.

Verdier, T., Coutand, M., Bertron, A. and Roques, C. (2014). A review of indoor microbial growth across building materials and sampling and analysis methods. *Building and Environment, 80, 136–149.* doi: 10.1016/j.buildenv.2014.05.030

XV International Conference on Durability of Building Materials and Components
DBMC 2020, Barcelona
C. Serrat, J.R. Casas and V. Gibert (Eds)

Implementing a Framework for Qualitative Assessment of New Technical Solutions: A Case Study on CLT

Charlotte Svensson Tengberg[1] and Carl-Eric Hagentoft[2]

[1] Department of Architecture and Civil Engineering, Chalmers University of Technology, 412 96 Gothenburg Sweden and Skanska Sverige AB, Sweden, charlotte.tengberg@chalmers.se

[2] Department of Architecture and Civil Engineering, Chalmers University of Technology, 412 96 Gothenburg, Sweden, carl-eric.hagentoft@chalmers.se

Abstract. *New technical solutions are introduced at a fast pace in the Swedish construction industry, mainly driven by issues concerning costs and productivity. These new technical solutions can comprise new materials, new goods, new designs but also new processes. The record of accomplishment when introducing new technical solutions in the industry is not unproblematic and serial failures of different new technical solution have occurred. In an earlier interview study exploring introduction of new technical solutions in the Swedish construction industry, a common lack of thorough methods for evaluation of new solutions was identified. To address this issue, a case study was performed, exploring a method of evaluation with respect to building physics while implementing a cross laminated timber frame in a multifamily building. The case study uses a framework of assessment with focus on building physics. This paper presents the findings from the case study focusing on how evaluation of a new technical solution with respect to building physics is performed, together with an evaluation of the method, using the experiences of the participants in the case study.*

Keywords: *Serial Failure, Hygrothermal Performance, New Technical Solutions, Risk Assessment.*

1 Introduction

Introducing new technical solutions in the construction industry is a challenge. Examples exist in the Swedish construction industry of both too slow adaptation of new technical solutions, i.e. loss of competitiveness or not reducing emissions of greenhouse gases, and too fast adaptation, i.e. poor quality and failure as the functional requirements are not sustained. Building physics failures, mainly moisture related, have been reported as a significant contributor to poor quality and related costs in the Swedish construction industry (Boverket, 2018). To systematically address the specific problems related to introduction of new technical solutions, the term *Serial failures* has been introduced defined as "Multiple cases of failure where a specific technical solution fails to sustain the functional requirement due to reasons in the design or production phases that could have been predicted by calculations or other assessment in the design stage." (Svensson Tengberg and Hagentoft, 2019)

In an interview study exploring introduction of new technical solutions in the Swedish construction industry, a common lack of (use of) thorough methods for evaluation of new solutions was identified (Svensson Tengberg and Hagentoft, 2019). It was also noted new technical solutions are usually introduced and evaluated at construction project level, with the supplier as a strong actor, providing the solution as well as related documentation.

Risk can be defined as the effect of uncertainty on objectives. Risk can be described by risk sources and potential events as well as consequences and likelihood (ISO 31000:2018, 2018).

Risk management in the construction industry typically focuses on risks in the specific construction project. Although risk management in the construction industry complies with relevant standards (ISO 31000:2018, 2018) (ISO Guide 73:2009, 2009) (Project Management Institute, 2017), there is a lack of guidelines and systematic approach for selecting appropriate risk identification techniques according to (Siraj and Robinson Fayek, 2019). In a construction project there is a wide array of risks handled, *e.g.* risks related to management, commercial or technical issues. Specifically to address risks related to building physics/moisture performance, there is an Industry Standard, ByggaF (Mjörnell, Arfvidsson and Sikander, 2012), suggesting a common risk identification in the design stage where all actors in the design group should conduct a moisture risk analysis based on a checklist for each building part as a starting point. The checklist starts from applying relevant moisture sources to the designs and assess the (unwanted) effects on the design. A more elaborate framework for testing, evaluating and documenting variations in performance of building envelopes was suggested in a research project focusing on reliability through probability assessment of performance and cost (Bednar and Hagentoft, 2015) and (Sasic Kalagasidis and Rode , 2015), see Figure 1.

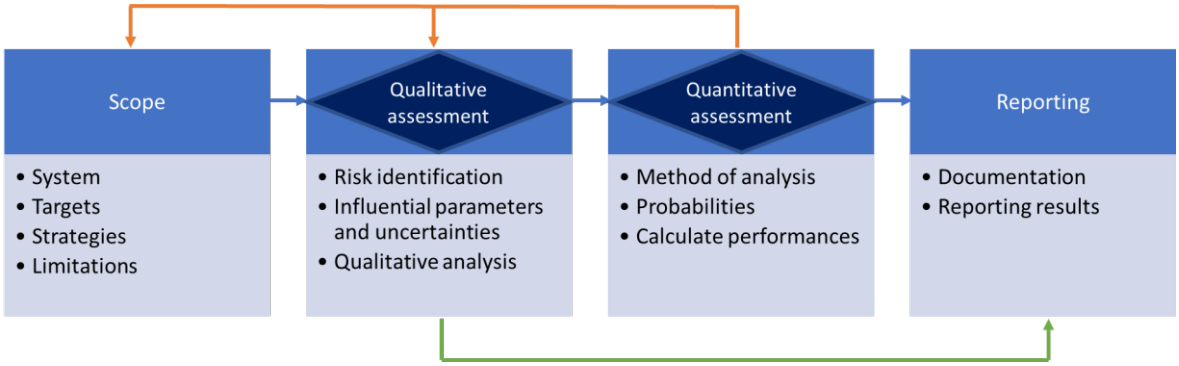

Figure 1. Work Flow adapted from Annex 55 (Bednar and Hagentoft, 2015).

This framework suggests involving a team of experts, not exclusively the project team, to perform the risk assessment and to perform the assessment methodically and transparently i.e. well documented. In (Pallin, 2013) it is suggested to perform the risk identification using common tools, *e.g.* ETA, FTA or VMEA. However, although there are suggestions of the format of the workshop and possible risk identification tool this is not further defined.

The objective of this paper is twofold, firstly to investigate the potential of the framework for qualitative assessment in a case study and secondly to collect data on risks associated to the case study. This paper is a part of a research project initiated with the aim of reducing risk of serial failure related to building physics when introducing new technical solutions in the construction industry.

2 A Case Study

To investigate the potential of the framework for qualitative assessment, a case study was designed. The case chosen for investigating the framework was *Fulfilment of functional requirements related to building physics using a technical solution of cross-laminated timber in a multi-dwelling building*. Cross-laminated timber was chosen as it is a relatively new technical solution, based on a material, wood, that historically has been associated with moisture issues. (Svenskt Trä, 2017) (Olsson, 2019). The outline of the work was performed

according to the first two parts of the framework in **Figure *1***: The scope and the Qualitative risk assessment including an expert workshop. :

- **Defining the scope.** The scope is described by *The system*, *The targets*, *The strategies* as well as *The limitations*. As the case study is not a retrofit, the existing conditions are not relevant and therefore omitted. This material was prepared before the workshop.
- **Qualitative assessment, Risk identification. Preparing the expert workshop.** To prepare for the expert workshop, a three-hour pre-workshop was performed with six participants representing the competences project management, designing engineer, moisture expert, and building physics. The objective of the pre-workshop was to try out the format and classifications before preparing material to the final workshop. The agenda was divided into Introduction, Theory and objectives, followed by Risk identification firstly on a general level and then in more detail, while discussing likelihood and consequences. As a result, a preparation material for the expert workshop was compiled and distributed.
- **Qualitative assessment, Risk identification. Expert workshop.** An expert workshop constituted the core of the qualitative risk assessment, as suggested in the framework. A four-hour expert workshop was designed , with the scope to identify and assess risks related to building physics for the technical solution. More specific, the focus was on “Not to exceed the critical moisture condition in the CLT structure” during production or operation of the building. The workshop started with a presentation of the participants, introduction to the background including an overview on risk management and objectives of the workshop. The risk assessment was divided into two sub workshops: risk identification (risk sources and potential events) and risk analysis (focus on uncertainties) respectively. The two parts were summarised at the end of the day. The participants were selected to represent key actors with different perspectives of the building process, Table 1. As researchers, the two authors took the part of workshop leaders.

Table 1. Workshop participants.

Profession	Gender	Profession	Gender
Project manager	M	Supplier, CLT	M
Design manager	F	Supplier, CLT	M
Construction manager	M	Supplier, CLT	M
Architect	F	Estimator	M
Designing engineer	M	Academia	M
Designing engineer	M	Academia	F
Building physics	M		

- **Evaluating the framework.** After the workshop, notes from the workshop were sent out to the participants together with a questionnaire with a few questions concerning their experience of the workshop, including the preparations, the different sections of the workshop and new insights.

3 Results and Discussion

3.1 Defining the Scope

One of the results was the scope definition according to the framework. It was summarised before the workshop and presented to the participants.

System. The system is defined as a five-storey multi-dwelling building with 18 apartments in a point block, using a cross-laminated timber structure situated in the metropolitan area of Stockholm. The building was chosen to be representative in size and type for a new Swedish multi-dwelling building. Point blocks represents more than a third of new built multi-dwelling buildings and four to six storeys are most common (SCB, 2019).

Targets. The target of the case study was defined as fulfilment of the building physics requirements described as "Not to exceed critical moisture condition in the CLT structure", addressing both construction phase and operation of the building. Other functional requirements according to building regulations (Boverket, 2018) should also be met.

Strategies. The anticipated design of the building is a cross laminated timber structure, including a timber structure in exterior walls and intermediate floors as well as balconies. The roof is assumed to be a timber frame construction. Energy performance of the building is assumed to be according to Swedish Building Regulations with U-values for walls, roof and windows in the range of 0.14/0.13/0.8 W/m^2/K respectively (average U-value of 0.34 W/m^2/K). A wooden façade is chosen. The building is heated to 22°C. The building is heated by district heating and an exhaust air heat pump. Air tightness of the building is expected to be 0.3 l/s/m^2 at 50 Pa.

Limitations. The assessment is made on basis of the prerequisites above. If changes are made, an update of the assessment should be performed.

3.2 Risk Identification During Expert Workshop

One of the results from the workshop was the thorough risk identification concerning building physics. At the workshop, the main risk categories as compiled from the hand-ins were presented and the participants were asked to supplement and adjust the risk list. In a summary of the risk identification, the participants were asked to vote on top-5 risks of interest. The issue that was given far most relevance was moisture during the construction phase, specifically

Precipitation during construction. Other risks of high relevance were noted: *Hygrothermal performance of external wall (including façade)*, *Window connections*, *Balconies* and *Walls with membranes on both sides*. It can also be noted, *Water leakage from pipes* was lifted as the effects were considered highly unknown. The results from the risk identification and the voting are shown in Table 2.

Table 2. Risk identification "To exceed critical moisture conditions in the CLT structure". Phase and location in the building are used as categories. Constr= Construction phase, Op= Operation phase.

Phase/location	General description	Votes
Constr/General	Precipitation during construction	18
Constr/General	Material moist/damaged by other materials/construction at site	4
Constr/General	Material moist/damaged before construction	1
Constr/General	Inferior air and moisture tightness between elements	8
Op/Wall	Hygrothermal performance of external wall design (incl. facade)	6
Op/Roof	Hygrothermal performance of external roof design	n.a.*
Op/Details	Bushings in wall	1
Op/Details	Connection wall/base	1
Op/Details	Connection wall/window	4
Op/Details	Balconies and connection wall/balcony	5
Op/Details	Connection wall/roof	0
Op/Details	Bushings in roof	n.a.*
Op/Details	Fastenings in roof	n.a.*
Op/Wet room	Walls with membranes on two sides	3
Op/Wet room	Bushings in wet room walls	0
Op/Wet room	Fastenings in wet room walls	0
Op/Wet room	Indoor climate exceeds critical conditions	0
Op/HVAC	Condensation at pipes	0
Op/HVAC	Leakage through deformations	0
Op/HVAC	Unknows effects of water leakage	1

* The roof in the case study is assumed to be a timber frame construction, not a CLT construction.

3.3 Risk Assessment During Expert Workshop: Precipitation During Production

Another result from the workshop was the risk assessment of a selected risk: *Precipitation during the production phase*. This risk was chosen as the participants identified it by far the most relevant risk. For the assessment, the participants were asked to identify relevant influential parameters and related available data/documentation as well as different types of uncertainties. The identified influencing parameters referred to *Design and material*, *Loads*, *Production methods* or to *Organisational issues* and were compiled in a table together with relevant influential parameters, uncertainties and correlations. An illustrated summary of the table with influencing parameters and a suggestion of which type of uncertainty associated with them is shown in Figure 2. Similar tables and illustrations were also developed for the other top-3 risks: *Hygrothermal performance of exterior wall* and *Balconies.* However, these are not presented in this paper.

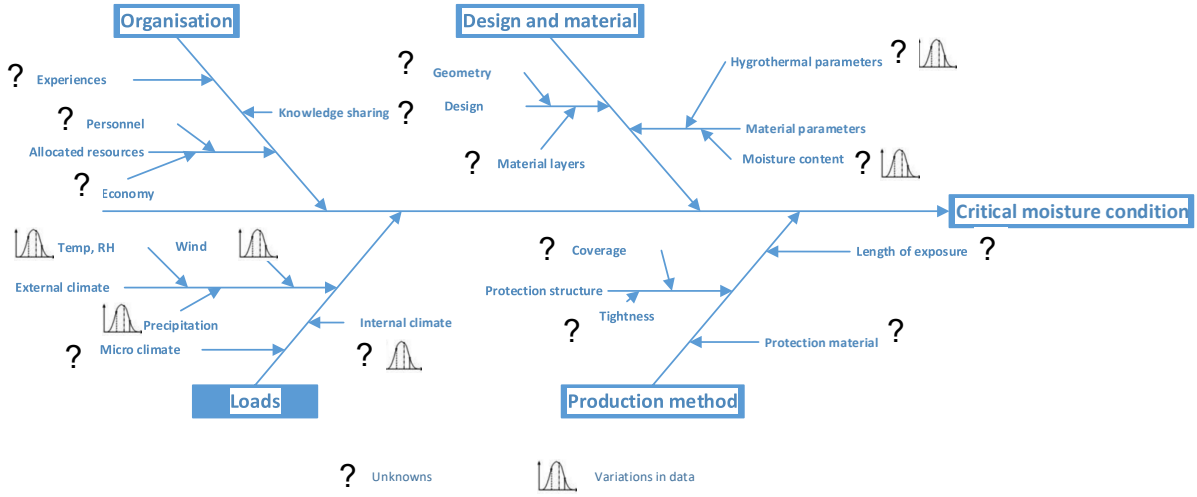

Figure 2. Precipitation during the production phase: Ishikawa graph showing identified influencing parameters for the risk of exceeding the critical moisture conditions. Also, anticipated type of uncertainties, unknowns and variations in data, are noted.

3.4 Risk Assessment During Expert Workshop: Important Uncertainties/Unknowns

The third result of the workshop is the identification of important uncertainties/unknowns for the case. After the top-3 risks with relevant influential parameters, uncertainties and correlations had been presented, the uncertainties perceived to have the most importance were identified by the participants:

- Unknown hygrothermal behaviour of wall (lack of data/variations)
- Unknown performance of material (lack of data/variations)
- Unknown moisture exposure and loads during construction (lack of data/variations)
- Unknown effects of water leakage during construction phase (lack of data/variations)
- Compliance to design and moisture routines (lack of data)
- Knowledge in the organisation (lack of data)
- Responsibility of different actors (lack of data)

3.5 Workshop Experiences

In the pre-workshop, valuable reflections were made. The suggested agenda was slightly changed, as the introduction was extended to create common understanding. The grouping of risks was added as an activity and thus, the continued risk description was left with less time for estimation of likelihood and consequences of identified risks. Also, the participants perceived the ranking of likeliness and consequences as difficult. Another experience was that several issues were lifted by the participants, where the level of uncertainty was low, but solutions had impact on other objectives (primarily costs but also other functional requirements). The insights from the pre-workshop resulted in a more thorough preparation material including a hand-in of three to five risks. The material was distributed to the participants two weeks in advance. The objective of the preparation material was to reduce time spent on these issues at the workshop.

At the main workshop the participant expressed their expectations. More than half of the expectations were oriented towards possibilities and finding solutions in general or to find a solution for a specific issue, i.e. the issue of moisture during the construction phase: “Is there need for weather protection?”. Other expectations on the workshop were to know more about the uncertainties of the technical solution in general or to be able to quantify the costs related to risks. One of the participants expressed a wish to be able to “…follow the risks from design to production.” At the end of the workshop, the participants agreed on that many of the expectations were met and that the workshop had provided a greater understanding and awareness of risks in general, and of the three selected risks specifically.

Eight out of eleven answered the survey after the workshop. The answers indicate a strongly positive experience of the workshop. The participants valued the overall experience of the workshop as good or very good (3 and 5 respectively), and most participants indicated that the workshop gave a lot of new insights in the subject. There were different opinions on the length of different parts of the workshop, with a slight tendency to experiencing the risk assessment and the summary as too short. The preparation material was perceived as helpful or very helpful, but a few of the participants had not had the time to use it.

4 Conclusions

The general perception of the workshop format was positive, and the expert workshop was perceived to give a lot of new insights to the participants.

Setting up appropriate boundary conditions of the workshop is important. The scope of the initiated workshop was broad, aiming at identifying relevant issues for multi-dwelling buildings using a cross-laminated timber structure. A broad topic will give results on a “landscape level”, while a targeted topic will give more developed and detailed results. In our case, we only analysed part of the material at the workshop, leaving part of the material for later analysis. Preferably, the workshop is repeated on increasingly more detailed level throughout the process.

A well-prepared workshop with preparation material and hand-ins will help the process, starting from a more advanced level, spending less time on background or trivia.

Likeliness and consequences of different events are perceived difficult when introducing new technical solutions. This was handled at the workshop with focusing on establishing a thorough list of relevant uncertainties.

The different competences at the workshop were perceived as a prerequisite to enable a fruitful risk identification.

4.1 Future Work

Future work will take two main paths:

- Continued analysis of the case study. Analysis of the data collected will result in a thorough qualitative assessment and in a quantitative assessment in line with the qualitative assessment, with the aim to address and reduce risks in multi-dwelling buildings with CLT.
- Continue to the adaption of the framework to the scope of introducing new technical solutions in the Swedish construction industry, by continuing the case study of multi-dwelling buildings with CLT and possibly extend with other case studies.

Acknowledgements
Support from the Development Fund of the Swedish Construction Industry (SBUF) is gratefully acknowledged.

ORCID

Charlotte Svensson Tengberg: https://orcid.org/0000-0002-8648-0871
Carl-Eric Hagentoft: https://orcid.org/0000-0002-1616-361

References

Bednar, T. and Hagentoft, C.-E. (2015). *Risk management by probabilistic assessment. Development of guidelines for practice, IEA Annex 55, RAP-RETRO.* Göteborg, Sweden: Department of Civil and Enivronmental Engineering, Chalmers University of Technology.

Boverket. (2018). *Boverkets byggregler - föreskrifter och allmänna råd, BBR. BFS 2011:6 med ändringar till och med BFS 2018:4 (Boverket's Building regulations).* Karlskrona, Sweden: Boverket.

Boverket. (2018). *Kartläggning av fel, brister och skador inom byggsektorn. Rapport 2018:36 (Survey on faults, defects and damage in the building sector).* ISBN: 978-91-7563-612-2: The Swedish National Board of Housing, Building and Planning, Karlskrona, Sweden.

Fuktcentrum. (2013). *Industrial standard - ByggaF*. Retrieved from http://www.fuktcentrum.lth.se/verktyg-och-hjaelpmedel/fuktsaekert-byggande/byggaf-metoden/

ISO 31000:2018. (2018). Risk management - Guidelines. *ISO 31000:2018, IDT*. Geneva, Switzerland: International Organization for Standardization.

ISO Guide 73:2009. (2009). Risk management - Vocabulary. *Guide 73*. Geneva, Switzerland: International Organization for Standardization.

Mjörnell, K., Arfvidsson, J. and Sikander, E. (2012). A Method for Including Moisture Safety in the Building Process. *Indoor Built Environment 21*, p583-594.

Olsson, L. (2019). *Fuktsäkerhet vid KL-träbyggande utan väderskydd (Moisture safety of CLT-construction without weather protection).* Stockholm, Sweden: RISE / SBUF ID 13548 www.sbuf.se .

Pallin, S. (2013). *Risk Assessment of Hygrothermal Performance - Building Envelope Retrofit.* Department of Civil and Environmental Engingeering. Gothenburg, Sweden: Chalmers university of Technology.

Project Management Institute. (2017). *Guide to the Project Management Body of Knowledge.* Project Management Institute, Inc.

Sasic Kalagasidis , A. and Rode , C. (2015). *Annex 55 RAP-RETRO. Framework for probabilistic assessment of performance of retrofitted building envelopes.* ISSN 1652-9162: Department of Civil and Environmental Engineering, Chalmers University of Technology, Göteborg, Sweden.

SCB. (2019, 10 10). *Statistical database*. Retrieved from Dwellings in newly constructed conventional multi-dwelling buildings by number of storeys in the building 2007-2017: http://www.statistikdatabasen.scb.se/pxweb/en/ssd/

Siraj, N. B. and Robinson Fayek, A. (2019). Risk Identification and Common Risks in Construction: Literature Review and Content Analysis. *Journal of Construction Engineering and Management*, 145/9 DOI: 10.1061/(ASCE)CO.1943-7862.0001685.

Svenskt Trä. (2017). *KL-trähandboken. Fakta och projektering av KL-träkonstruktioner (CLT hand book).* Stockholm, Sweden: Svenskt Trä.

Svensson Tengberg, C. and Hagentoft, C.-E. (2019). Introducing New Technical Solutions in the Swedish Construction Industry - Interviews with Key Actors. *ASHRAE Thermal Performance of the Exterior Envelopes of Whole Buildings XIV International Conference*, (pp. 810-817). Clearwater, Florida, USA.

XV International Conference on Durability of Building Materials and Components
DBMC 2020, Barcelona
C. Serrat, J.R. Casas and V. Gibert (Eds)

Influence of Grid Presence in the Characteristics of Applied Mortars

Isabel Torres[1], Inês F. Colen[2], Dora Silveira[3] and Rafael T. Pinto[4]

[1] DECivil, University of Coimbra/ADAI-LAETA/Itecons, itorres@dec.uc.pt

[2] CERIS, DECivil, IST, University of Lisbon, ines.flores.colen@tecnico.ulisboa.pt

[3] Itecons, dora.silveira@itecons.uc.pt

[4] PhD student, DECivil, University of Coimbra, Research fellow, IST, rafaeltravincas@gmail.com

Abstract. *The most commonly used wall coverings are still, undoubtedly, plasters and renders, whether lime-based or cement-based, whether traditional and prepared in-situ or pre-dosed. In accordance with the available standards, the characterization of these mortars is made on laboratory test specimens, with dimensions, curing conditions and test procedures according to the prescribed. However, when applying these mortars to the real substrates, their behaviour will not be the same. After application of the mortar to the substrate, an interface will be formed, and the interactions that occur after the contact of the mortar, still in the plastic state, with the substrate will change over time due to the hydration kinetics and absorption of the substrate. It is very important to know the real behaviour of mortars after application, in order to ensure their durability. A research project is being developed to analyse the proper behaviour of mortars after application to the substrates. In order to characterize a mortar after application to a substrate, it is necessary to detach it. The introduction of a fiberglass grid in the mortar-substrate interface makes the detachment easier. The purpose of this study is to determine if the placement of this grid will influence the characteristics of the applied mortar. For this, an experimental campaign was carried out, comparing the characteristics of two mortar formulations, applied to different types of substrate (without introduction of the fiberglass grid), with the characteristics of these mortars applied to the same substrates, but with the introduction of a fiberglass grid at the interface mortar-substrate. In this paper, we present the results obtained for some of the physical and mechanical characteristics of cement and hydraulic lime mortars.*

Keywords: *Mortars, Substrates, Interface, Durability, Fiberglass Grid.*

1 Introduction

Mortar based coverings are widely used in all types of constructions, whether new or old, in need of rehabilitation or requalification. When we talk about exterior coverings, we are talking about the outermost layer of protection of these constructions, i.e. the layer that will contribute most strongly to their durability. There is an increasing variety of available solutions, and it is very important to ensure the quality of the applied mortars, since they must contribute to the habitability, comfort and durability of buildings. In recent years, much research has been conducted to increase knowledge on the behaviour of different types of mortars and to develop new formulations incorporating new products, so that one can always make the best choices, regarding the type of mortar to be used, its composition and characteristics.

The choice of the mortar that is best suited to the real situation is based on its various properties, which are determined in laboratory, following all applicable standards, particularly with respect to the dimensions of the test specimens, curing conditions and test methodology.

After the mortar has been selected, it is applied to the real substrate — and there are various

types of substrates, such as hollow brick, solid brick, pre-cast concrete, concrete blocks, natural stone, among others. It is known that inter-layer adhesion is one of the key performance indicators of multi-layer systems. The behaviour of mortars depends on the adhesion between the substrate and the mortar itself. This is one of the characteristics that will influence the properties and behaviour of the mortar (Moropoulou *et al*., 2000).

When applying a mortar to a real substrate, which will always have some porosity — unlike the laboratory moulds where the specimens that are used to characterize mortars are made, which have virtually no porosity —, an interaction will occur between the two surfaces. The contact between these two elements occurs with the mortar still in the plastic state. When this contact occurs, part of the mixing water, containing dissolved components of the binder, is absorbed by the substrate and penetrates its pores and/or discontinuities. Inside the pores of the substrate, hydration phenomena of cement/lime occur. After this penetration into the substrate and during the subsequent mortar hardening phases, the mortar is subjected to real climatic conditions, which may be quite different from the curing conditions recommended by the mortar characterization standards.

From the foregoing, it can be concluded that the same mortar moulded into specimens and hardened in the laboratory, under standard curing conditions, when applied to real substrates subjected to real climatic conditions, will not acquire equal characteristics. Thus, in order to choose a mortar more rigorously, it is very important to predict the behaviour of the mortar after application to the substrate.

With the objective of being able to estimate the characteristics of the mortars applied to a substrate, using the mortar characteristics determined in laboratory conditions, a research project funded is under development: IF MORTAR.

The aim is to compare, for the same mortar, the characteristics analysed in laboratory specimens with the characteristics determined after application to the substrates. For this, it is necessary to apply the mortars to the substrates and, after hardening, to detach and analyse them. To facilitate the detachment of these mortars, a fiberglass grid has been introduced between the mortar and the substrate. However, a question arises: will the introduction of the grid change the characteristics of the applied mortars? To answer this question, a preliminary experimental campaign was carried out, comparing the characteristics of the mortars applied to the substrates, with and without the application of the grid. Until now only two prescribe mortars were analysed, but the intention is to also analyse design mortars.

2 Experimental Campaign

2.1 Introduction

The experimental campaign developed aimed to analyse the behaviour of cement and hydraulic lime mortars applied to hollow ceramic brick substrates, in two different conditions: with and without the introduction of a fiberglass grid between the mortar and the substrate.

For this, a fiberglass grid was applied to half of the hollow brick substrates. Then, all the brick substrates were moistened and a 1.5 cm mortar layer was applied (Figure 1).

The following mortars were selected for the experimental campaign:

- Cement mortar, with a 1:4 cement to sand ratio, by volume;
- Hydraulic lime mortar, with a 1:3 lime to sand ratio, by volume.

Both mortars were formulated in the laboratory.

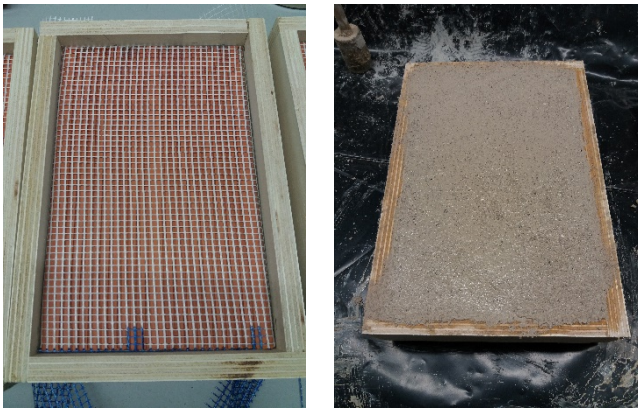

Figure 1. Application of the mortar to the substrate.

2.2 Specimens and Tests

The experimental campaign began with the execution of 40x40x160 mm3 prismatic specimens, for the determination of the bulk density, open porosity (NP EN 1936:2008), capillary water absorption (ISO 15148:2002) and compressive strength (EN 1015-11:1999), and cylindrical specimens (100 mm diameter and 15 mm thickness) for the determination of water vapour permeability (NP EN 1015-19:2008 and ISO 12572:2016) (Figure 2).

After the detachment of all mortars from the substrates, specimens of appropriate dimensions for the respective tests were cut. Given the thickness of the applied mortars (1.5 cm), it was not possible to obtain specimens with the exact dimensions indicated in the standards. Therefore, instead of 40x40x160 mm3 specimens, 40x40x15 mm3 specimens were used for the determination of bulk density, open porosity, capillary water absorption and compressive strength. For the determination of water vapour permeability, cylindrical specimens with 100 mm diameter and 15 mm thickness were used.

After the execution of the laboratory specimens and application of the mortar layer on the substrates, all specimens were subjected to the following standard curing conditions: 20ºC and 95% RH, for 7 days, and 20ºC and 65% RH, for another 21 days.

Figure 2. Test specimens.

The results of the tests carried out are presented and commented in the following section. Even though the main objective is to compare the behaviour of the mortars applied to the substrate, the results obtained for the mortars hardened in the laboratory moulds are also presented.

2.3 Presentation and Analysis of Results

2.3.1 Bulk density and open porosity

The determination of the bulk density by the geometric method, which translates the simple direct relationship between the dry mass of a specimen and its apparent volume (volume limited by the outer surface of the specimens, including all voids) and the determination of the open porosity, which represents the relationship between the open pores volume and the apparent volume of the specimen, was conducted according to the standard. Figures 3 and 4 show the medium values and standard deviation obtained for bulk density and open porosity, respectively, for the specimens hardened in the moulds and for the specimens hardened on the substrates (with and without grid). It can be seen that the open porosity of the mortars decreased and the bulk density increased, after application to the substrates, as was expected.

When comparing the results of the mortars applied with the grid with those of the mortars applied without grid, it can be seen that they are very similar, i.e. the presence of the grid does not affect the results obtained.

2.3.2 Capillary water absorption

The water absorption coefficient gives an indication of the water absorption capacity of a mortar when placed in contact with a water film. The results obtained for the water absorption coefficient, for all the mortars, are presented in Figure 5. Once again, it can be seen that the application of the mortars to the substrate changed this parameter, causing it to decrease. It is also possible to observe that the difference between the results corresponding to the two conditions of application (with and without grid) is small.

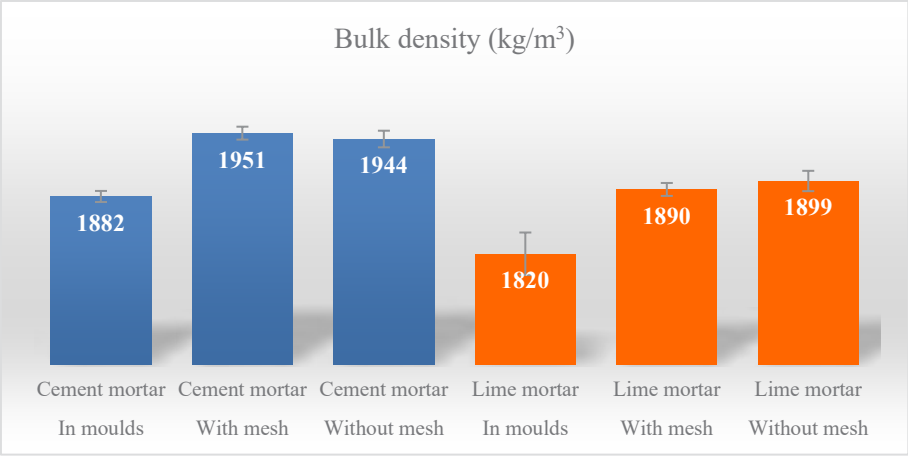

Figure 3. Bulk density.

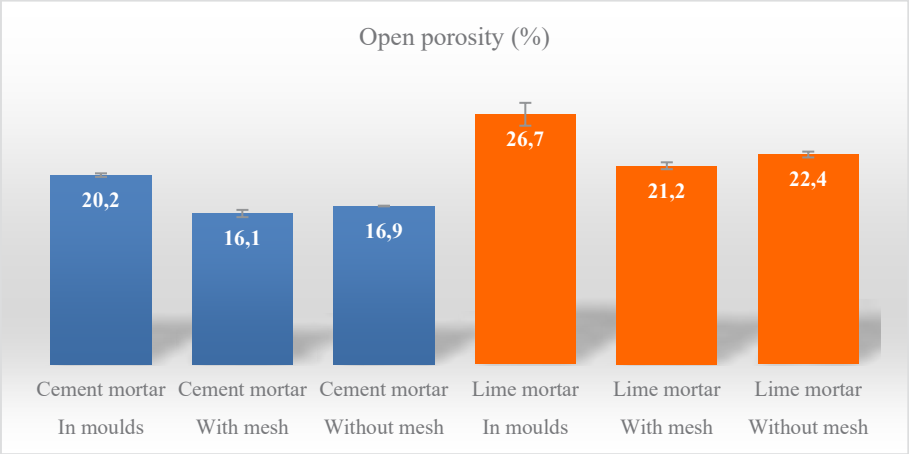

Figure 4. Open porosity.

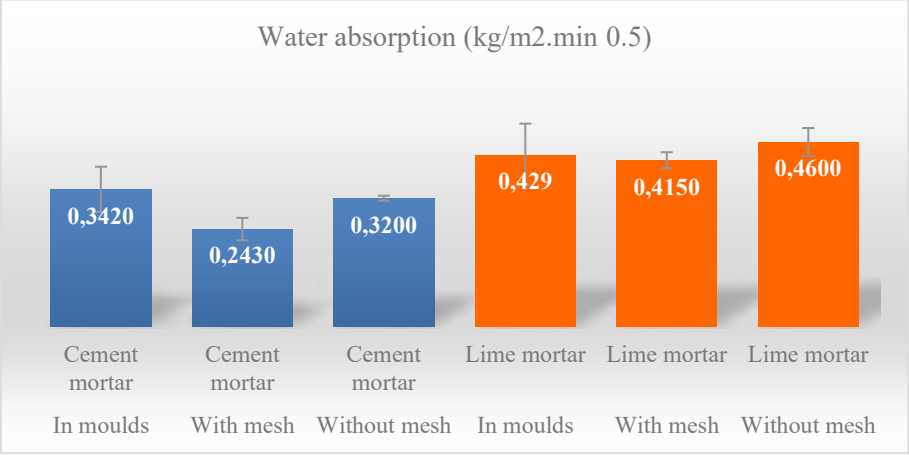

Figure 5. Water absorption coefficient.

2.3.3 Water vapour permeability

The water vapour permeability coefficient, which reflects the ability of a material to be traversed by water vapour, was determined using the wet cup method.

Figure 6 shows the water vapour permeability coefficient results obtained for all the mortars.

The application of the cement mortar to the substrate led to a decrease in its water vapour permeability, while the application of the hydraulic lime mortar led to an increase of this parameter. In the case of the cement mortar applied to the substrate without grid, it was not possible to detach specimens for this test due to the high cohesion of the mortar to the substrate. For the hydraulic lime mortar, it was verified, once again, that the difference between the results of the detached specimens with and without grid were not significant.

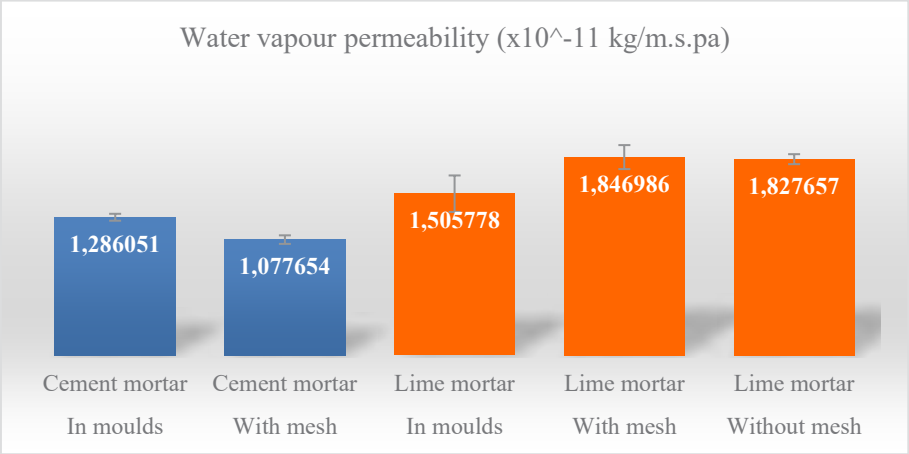

Figure 6. Water vapour permeability.

2.3.4 Compressive strength

As it is not possible to cut specimens of sufficient size for the flexural test from the mortar layer applied to the substrates, only the results obtained for the compressive strength are presented here. The compressive strength is obtained by applying a compressive force (until failure) centred on the application area of 40x40 mm^2.

The compressive strength was determined on specimens measuring 40x40x15 mm^3, both for the mortars hardened in the laboratory moulds and for the mortars applied to the substrates. Figure 7 presents the results obtained. It can be seen that the application to the substrates increased this property and that the introduction of the grid does not have great influence on the results.

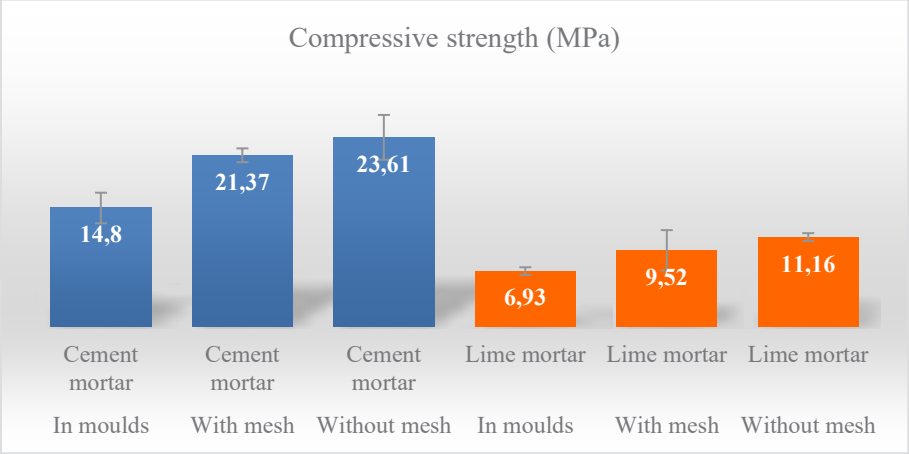

Figure 7. Compressive strength.

3 Conclusions

In order to choose a mortar in a more sustained way, regardless of its intended purpose, it is essential to know its behaviour, *i.e.* to know all its properties. These properties are determined

on mortars hardened in moulds, in the laboratory, in accordance with the applicable standards.

The mortar in service, i.e. after application to the substrate, will acquire different properties from those determined in the laboratory, because the application conditions, interface characteristics, curing conditions, etc., are different from those considered in the laboratory.

To have knowledge of the in-service characteristics of mortars, it is necessary to apply them to the substrates, wait for them to harden, detach them from the substrates and, finally, analyse them.

Mortars are applied to the substrate in the plastic state and, when hardened, will adhere to it. The greater their adherence to the substrate, the more difficult their detachment will be. To facilitate this detachment, a grid can be introduced between the substrate and the mortar, but it is important to know whether this grid will affect the final properties of the mortar. The main objective of this work was thus to analyse the influence of the presence of a fiberglass grid, placed between the mortar and the substrate, on the properties of the applied mortars.

The experimental campaign conducted, which included the analysis of the influence of the presence of the fiberglass grid in the behaviour of cement and hydraulic lime mortars, concluded that the properties of the mortars do not change significantly due to the presence of this grid.

In fact, it was observed that the presence of the gird caused a slight increase in open porosity which also slightly increased water absorption and vapour permeability.

Although it was not the main objective of this work, the behaviour of the two mortars moulded in the laboratory moulds was also analysed and compared with the behaviour of the mortars applied to the brick support. Observing the obtained results, it was possible to conclude that the application of the mortars in the support caused the increase of the bulk density and the decrease of the open porosity. The behaviour face to the presence of water was also affected. The water absorption coefficient also decreased. This behaviour is in line with what was expected because when the mortar of the fluid state comes into contact with the brick support, which is a porous material, part of its mixing water with the finer particles dissolved are absorbed and penetrate into its pores. This decrease in the amount of water causes lower porosity with the consequent increase in bulk density and decrease in water absorption.

Acknowledgements

The work presented was carried out within the framework of the IF MORTAR project (POCI-01-0145-FEDER-032223/PTDC/ECI-EGC/32223/2017,), within the scope of the Portugal 2020 program, financed by FEDER through the POCI program. The funding provided is kindly acknowledged. The authors also thank CERIS and CERENA, research units from IST.

ORCID

Isabel Torres: http://orcid.org/0000-0002-0515-1743
Inês Flores-Colen: http://orcid.org/0000-0003-4038-6748
Rafael Travincas Pinto: http://orcid.org/0000-0002-9059-1232
Dora Silveira: http://orcid.org/0000-0002-0063-2556

References

CEN (European Committee for Standardization). (1999). *Methods of test for mortar for masonry. Part 11: Determination of flexural and compressive strength of hardened mortar*. EN 1015–11. Brussels, Belgium: CEN.

CEN (European Committee for Standardization). (1998). *Methods of test for mortar for masonry. Part 19: Determination of water vapour permeability of hardened rendering and plastering mortars*. EN 1015–19. Brussels, Belgium: CEN.

CEN (European Committee for Standardization). (2001). *Hygrothermal performance of building materials and products—Determination of water vapour transmission properties.* EN ISO 12572. Brussels, Belgium: CEN.

CEN (European Committee for Standardization). (2002). *Methods of test for mortar for masonry. Determination of water absorption coefficient due to capillary action of hardened mortar.* EN 1015–18. Brussels, Belgium: CEN.

CEN (European Committee for Standardization). (2006). *Natural stone test methods. Determination of real density and apparent density, and of total and open porosity*. EN 1936. Brussels, Belgium: CEN.

CEN (European Committee for Standardization). (1998). *Methods of test for mortar for masonry. Part 2: Bulk samplingof mortars and preparation of test mortars.* EN 1015–2. Brussels, Belgium: CEN.

Moropoulou, A., A. Bakolas, and K. Bisbikou. (2000). *Physico-chemical adhesion and cohesion bonds in joint mortars imparting durability to the historic structures.* Constr. Build. Mater. 14 (1): 35–46. https://doi.org/10.1016/S0950-0618(99)00045-8.

Silva, C. M., Flores-Colen, I. and Gaspar, S. (2013). *Numerical analysis of renders' adhesión using an interface model*, Construction and Building Materials, 2013, 38, 292-305

XV International Conference on Durability of Building Materials and Components
DBMC 2020, Barcelona
C. Serrat, J.R. Casas and V. Gibert (Eds)

Influence of Lightweight Concrete Block Support on Physical and Mechanical Characteristics of Applied Mortars

Dora Silveira[1], **Isabel Torres**[2], **Inês F. Colen**[3] **and Rafael T. Pinto**[4]

[1] Itecons, ADAI-LAETA, dora.silveira@itecons.uc.pt

[2] DECivil, ADAI-LAETA, Itecons/University of Coimbra, itorres@dec.uc.pt

[3] CERIS, DECivil, IST, University of Lisbon, ines.flores.colen@tecnico.ulisboa.pt

[4] PhD student, DECivil, University of Coimbra, Research fellow, IST, rafaeltravincas@gmail.com

Abstract. *The objective of the present work is to analyze the influence of the lightweight concrete block support on the physical and mechanical characteristics of the applied mortar. This work aims to understand how the physical and mechanical properties of the mortar are modified by the support. The methodology used consisted of conducting laboratory experimental tests to compare the behavior of mortar molded in standard moulds with the behavior of mortar applied to lightweight concrete block supports. Open porosity, bulk density, capillary water absorption, water vapor permeability and compressive strength were studied. These results have shown how the support influences the characteristics of the mortar, improving the understanding of the performance of the applied mortar. This study provides a global approach to the assessment of mortar characteristics, considering the analysis and comparison of mortar applied to the support and molded in the laboratory, according to current standards. Such understanding may contribute to the reassessment of the way mortars are produced, seeking to optimize their characteristics and compatibility with the support.*

Keywords: *Mortar, Support, Performance, Lightweight Concrete Block.*

1 Introduction

Coating mortars have an important role in protecting buildings from degradation agents (Flores-Colen, 2016). One of the most important in-service degradation agents is water, which can lead to physical, chemical and, in some cases, mechanical deterioration (Addleson, 1991). Thus, the performance of coating mortars is influenced by water capillary absorption, hygroscopic moisture content, water permeability, diffusion of water vapor, porosity, soluble salts content and propensity for the growth of microorganisms (Flores-Colen, 2013).

Therefore, it is very important to ensure the quality of the applied mortars, as they contribute significantly to the durability of buildings. For this, it is important to use mortars that are compatible with the supports and that will ensure adequate protection to the building. Thus, low water permeability, good water vapor permeability, good adhesion to the substrate, deformation capacity, among others, are sought (LNEC, 1968; Flores-Colen, 2009; Martins, 2008; Arromba, 2011).

The influence of different factors on the behavior of mortars, such as the quality of the binder, aggregate particle size, water-binder ratio, application conditions, and dosage, have been extensively studied (Torres, 2014; Veiga, 2005; Veiga, 1998; Valente, 1996). However, there are still few studies on the influence of the support on mortar characteristics (Torres, 2014). This work aims to contribute to this knowledge.

doi:10.23967/dbmc.2020.083

This research intends to identify how the lightweight concrete block support influences the performance of the applied mortar, considering that the applied mortar is in different conditions than those of mortars hardened in laboratory molds. Thus, the understanding of the characteristics of the applied mortar and the possibility of creating a correlation with the characteristics of the mortar hardened in laboratory molds, may enable a greater compatibility of the mortar with the support and provide data for the optimization of mortar composition. Such understanding may help to increase the in-service durability of mortars.

2 Materials and Methods

2.1 Materials

In this experimental campaign, the following materials were used: lightweight concrete blocks, with Leca expanded clay aggregates, with dimensions of 50 x 20 x 10 cm³, CEM II / BL 32.5N cement and sand with well-distributed granulometry. For the cement mortar preparation, a cement/sand ratio of 1:4, in volume, and a water/cement ratio of 1:1, in weight, were used.

2.2 Methodology

A laboratory experimental campaign was carried out, for the comparison of the characteristics of the cement mortar hardened in standard laboratory metallic molds and the characteristics of the cement mortar applied to (and later detached from) lightweight concrete block supports.

For the execution of the tests and comparison of the results, the mortars hardened in the standard molds (with dimensions of 40 x 40 x 160 mm³) were cut into slices of 40 x 40 x 15 mm³, thus having the same dimensions of the mortar samples applied to the support and later detached.

To prepare the applied mortars, wooden molds were made in order to ensure a constant thickness (1.5 cm) of the mortar applied to the lightweight concrete block support, according to figure 1.

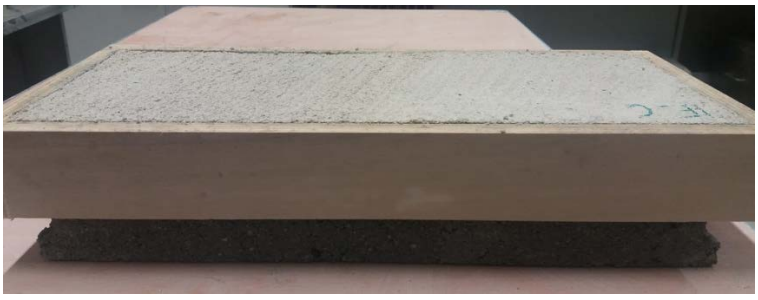

Figure 1. Lightweight concrete block with wooden frame and applied mortar.

As an initial step, the bricks were dried until mass stabilization, and, before applying the cement mortar, each support was wetted by spraying 100 ml of water.

The tests were performed after 28 days of curing. The curing was carried out according to the indications of EN 1015-11: 1999, both for the mortar hardened in the molds and for the mortar applied to the supports. The curing conditions were as follows:

• First 2 days: temperature of 20ºC +/- 2ºC, inside of a polyethylene bag (in the mold);
• Next 5 days: temperature of 20ºC +/- 2ºC, inside of a polyethylene bag (demolded);
• 21 days remaining: temperature of 20ºC +/- 2ºC, relative humidity of 65% +/- 5% (without the mold).

The tests carried out in this experimental campaign are listed in table 1. The results presented in the following sections refer to the average of results obtained in tests carried out on three specimens.

Table 1. Tests conducted and standards followed.

Test	Standard
Water absorption by capillarity	ISO 15148:2002
Open porosity	NP EN 1936:2008
Bulk density	NP EN 1936:2008
Water vapor permeability	ISO 12572:2016
Mechanical strengths	EN 1015-11:1999

3 Results and Discussion

3.1 Open Porosity

Open porosity represents the relationship between the volume of open pores and the apparent volume of the sample. Figure 2 presents the mean open porosity results and indicates a slight reduction in the open porosity of the detached mortar in relation to the mortar hardened in the mold. This can demonstrate a greater compactness of the applied mortar. In fact, when a mortar in the fresh state comes into contact with a porous support as is the case with lightweight concrete blocks, its mixing water together with the smaller particles is absorbed and as a consequence there will be a decrease in its pores and its open porosity.

3.2 Bulk Density

The determination of bulk density by the geometric method reflects the simple relationship between the dry mass and the apparent volume (including all voids) of a sample. Figure 3 shows a slight increase in the mean density of the mortar detached from the support in relation to the mortar hardened in the mold, which is consistent with the reduction of the open porosity.

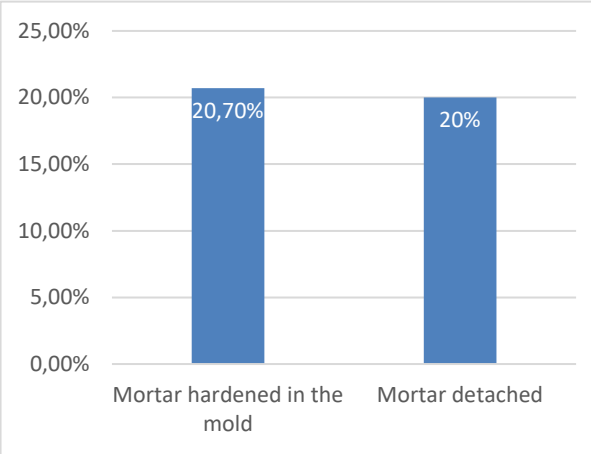

Figure 2. Open porosity.

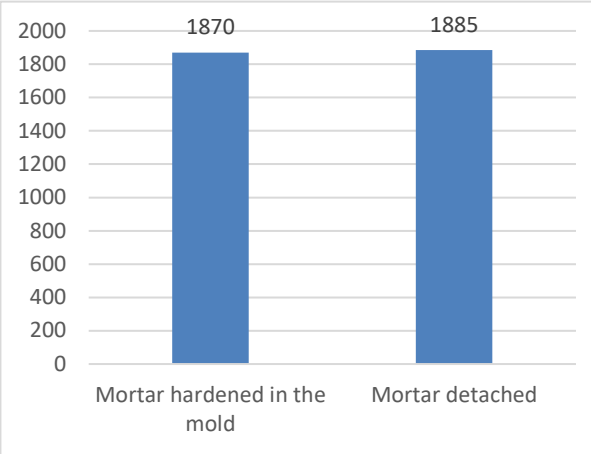

Figure 3. Bulk density (kg/m³).

3.3 Capillary Water Absorption

The water absorption coefficient provides an indication of the water-absorbing capacity of a mortar when placed in contact with a water film.

It can be seen, in figure 4, that the mortar hardened in the mold has a higher coefficient than the mortar detached from the lightweight concrete block support. These results confirm a slight increase in the compactness of the mortar applied to the lightweight concrete block, as mentioned in the discussion of the open porosity results.

3.4 Water Vapor Permeability

The water vapor permeability coefficient reflects the ability of a material to be traversed by water vapor. It can be seen, in Figure 5, that the mean water vapor permeability coefficient of the detached mortar is lower than that of the mortar hardened in the mold — such a result demonstrates a greater resistance to the passage of water vapor by the detached mortar in relation to the mortar hardened in the mold.

3.5 Compressive Strength

Figure 5 shows the mean results obtained in the compression test and indicates that the mortar hardened in the mold presented a slightly higher compressive strength in relation to the detached mortar. Although the decrease in open porosity could lead one to think that the mechanical strength would increase, it is possible that this decrease may be due to some weakening that may have occurred when detaching the mortar from the substrate.

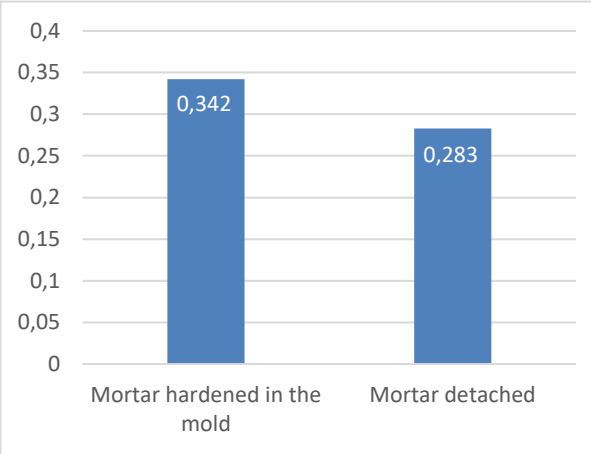

Figure 4. Capillary water absorption coefficient (kg / ($m^2.s^{0.5}$).

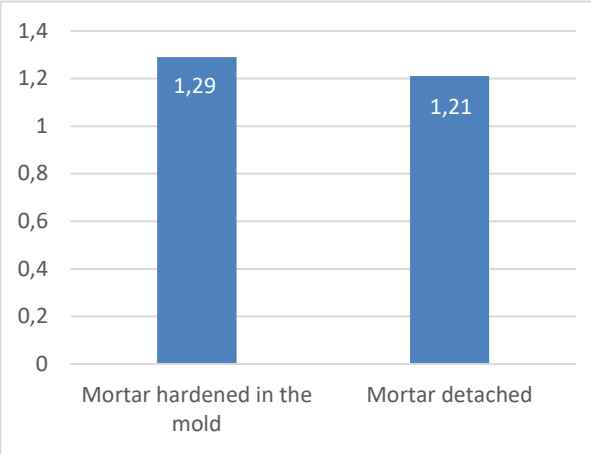

Figure 5. Water vapor permeability coefficient [(kg/(m.s.Pa).10^{-11}].

An expected result face to the obtained results for the characteristics already mentioned.

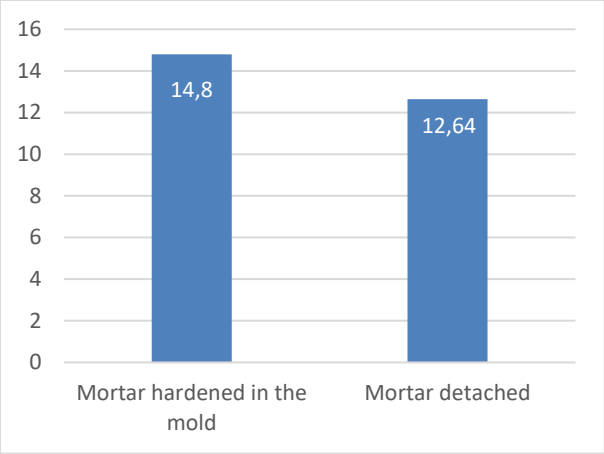

Figure 6. Compressive strength (MPa).

4 Conclusions

As a conclusion, it can be observed that the mortar detached from the support has slightly different characteristics in relation to the mortar hardened in the molds; however, it is not clear that these differences are due to the support. The support can influence the characteristics of the applied mortar, as already seen in previous works using the ceramic brick support (e.g. Torres, 2014), however this influence was not significant for the lightweight concrete block.

It can be seen that the mortar applied to the lightweight concrete block is slightly more compact, with less open porosity. Consistently, the lower water absorption and lower water vapor permeability occurred for the mortar applied to the support. Conversely, the compressive strength of the applied mortar is lower than that of the mortar hardened in the mold.

The influence of the support on the physical and mechanical characteristics of the applied mortar is a relevant issue in relation to performance and durability, and extensive studies on different types of supports and different types of mortar may increase the compatibility of the mortar/support interface.

Acknowledgements

The work presented was carried out within the framework of the IF MORTAR project (POCI-01-0145-FEDER-032223, PTDC/ECI-EGC/32223/2017,), within the scope of the Portugal 2020 program, financed by FEDER through the POCI program. The funding provided is kindly acknowledged. The authors also thank CERIS and CERENA, research units from IST.

ORCID

Dora Silveira: http://orcid.org/0000-0002-0063-2556
Isabel Torres: http://orcid.org/0000-0002-0515-1743
Inês F. Colen: http://orcid.org/0000-0003-4038-6748
Rafael T. Pinto: http://orcid.org/0000-0002-9059-1232

References

Arromba, J. (2011). “Influência do suporte no desempenho de rebocos aplicados em suportes de tijolo e betão recorrendo a técnicas de ensaio in-situ”. Dissertação para obtenção do grau de Mestre em Construção, Lisboa, Instituto Superior Técnico,

Flores-Colen, I. (2009). "Metodologia de avaliação do desempenho em serviço de fachadas rebocadas na óptica da manutenção predictiva". Tese de Doutoramento em Engenharia Civil, Lisboa, Instituto Superior Técnico.

Flores-Colen, I., Silva, L., de Brito, J. and de Freitas, V. P. (2016). Drying index for in-service physical performance assessment of renders. Construction and Building Materials, 112, 1101-1109.

I Flores-Colen, J de Brito and V. Freitas (2013). Assessment of in-use performance parameters of rendering façades CIB W86 Report. Publication 393, in: V.P. Freitas (Ed.), A State-of-the-art Report on Building Pathology, 2013. Rotterdam.

L Addleson and C Rice , (1991). Performance of Materials in Buildings – A Study of the Principles and Agencies of Change, Butterworth-Heinemann, UK, Oxford, p. 588.

LNEC (1968). “Recomendações para execução de revestimentos exteriores de argamassa”. Lisboa, Laboratório Nacional de Engenharia Civil.

Martins, A. (2008). "Estudo da influência da dosagem de cimento no desempenho de argamassas de reboco". Dissertação para obtenção do grau de Mestre em Construção, Lisboa, Instituto Superior Técnico,

Torres, I. (2014). “Influência da absorção do suporte na argamassa de revestimento” - Relatório de pós doutoramento

Valente, V. (1996). “Caracterização da aderência de argamassas tradicionais em paramentos exteriores constituídos por blocos de betão de argila expandida”. Dissertação submetida para satisfação parcial dos requisitos do grau de mestre em Construção de Edifícios, Porto, Faculdade de Engenharia da Universidade do Porto.

Veiga, R. (1998). "Comportamento de argamassas de revestimento de paredes – Contribuição para o estudo da sua resistência à fendilhação". Dissertação para a obtenção do grau de Doutor em Engenharia Civil pela Faculdade de Engenharia da Universidade do Porto, Teses e programas de investigação do Laboratório Nacional de Engenharia Civil Lisboa.

Veiga, R. (2005). "Comportamento de revestimentos de fachadas com base em ligante mineral. Exigências funcionais e avaliação do desempenho". 1o Congresso Nacional de Argamassas de Construção, Lisboa, LNEC.

XV International Conference on Durability of Building Materials and Components
DBMC 2020, Barcelona
C. Serrat, J.R. Casas and V. Gibert (Eds)

Performance and Durability of Adhesive Tapes for Building Applications. From Product Documentation to Scientific Knowledge (and Back Again)

Malin Sletnes[1] **and Susanne Frank**[2]

[1] SINTEF Community, Høgskoleringen 7B, 7034, Trondheim, Norway, malin.sletnes@sintef.no

[2] SINTEF Community, Høgskoleringen 7B, 7034, Trondheim, Norway, susanne.frank@sintef.no

Abstract. *Adhesive tapes are used extensively in both new buildings and renovation projects in order to achieve airtight building envelopes and energy efficient buildings. It is important to be able to reliably predict whether these adhesive solutions are durable. In our roles as both a research institute and a national approval body for building materials, SINTEF have been performing product evaluations and testing of adhesive tapes for 10 years. During this time, we have tested the durability of more than 30 different tapes on a variety of substrates commonly used in the building industry. After systemising and analysing this data, we have gained valuable insight into the factors governing the durability of adhesive tapes for the construction market. In this paper we share our findings and discuss how we intend to utilise the new knowledge in the design of further scientific experiments in the field.*

Keywords: *Adhesive Tape, Construction, Durability, Accelerated Ageing.*

1 Introduction

Air-tightening systems, such as vapour barriers and wind barriers are essential for energy efficient buildings. In order to achieve high air-tightness performance, the overlaps and connections of the air-tightening systems to other building components like foundations, roof constructions, windows, and air and electric ducts, are today frequently sealed by self-adhesive tapes. However, there is little knowledge on the durability of the adhesive tapes used in construction, partly because it is a relatively new application, and partly because it is a very complex system to study systematically in laboratory conditions (Leprince *et al.*, 2017) due to the many variables in the properties of adhesives and substrates, as well as the effect of initial conditions of the bond formation and climatic exposure.

In response to this knowledge gap several research groups have recently studied the durability of air-tightness systems including adhesive products. (Antonsen, 2017; Fufa *et al.*, 2018; Langmans *et al.*, 2017; Litvak *et al.*, 2019) The referenced papers all include well-defined, systematic studies, many of them focusing on full- or reduced-scale airtightness system testing before and after artificial ageing. However, the small number of adhesive tapes included in each study restricts the possibility to draw general conclusions. Often no more than two tapes are tested per system. This is a necessary limitation, due to the extensive experimental matrix that would otherwise arise if tapes should also be tested on several different substrates and under different exposure conditions.

The main objective of the research project TightEN (2019 – 2023) is to develop robust test and evaluation methodology for ensuring durable adhesive airtight solutions for energy efficient building envelopes. The experimental design at the starting phase of a project will be

important for the outcome, and prior knowledge of important parameters can result in a better design of the experimental matrix. Thus, we have systemised and analysed our existing data on adhesive tape durability in order to gain a better understanding of the importance of different parameters. In our roles as both a research institute and a national approval body for building materials, SINTEF have been performing product evaluations and testing of adhesive tapes for 10 years, testing more than 30 tapes. The data we have available is mostly from small-scale adhesive bond testing, such as peel and shear resistance of the joint. The correlation of these properties with the actual air-tightness performance is not well established and will be investigated more thoroughly in the TightEN project. Nevertheless, we believe that adhesive joint testing will in all probability still have a role in the evaluation of adhesive tapes for airtightness application because it is simple, cost-effective and standardised.

2 Data and Methodology

The data subject to analysis was collected from standardised peel and shear resistance testing of adhesive joints before and after artificial ageing, over a course of 10 years. Data from both product certification and previous research projects have been included. Some tapes have been tested several times, as a part of the control procedures for product certifications. An overview of the test methods, number of tapes and associated data points included in the study are given in Table 1.

Material testing and sample preparation was performed according to the European test standards for peel and shear resistance of joints for plastic and rubber sheets for roof waterproofing, EN 12316-2 and EN 12317-2. The joints were created by manually sticking the materials together and applying hand force. The resulting joint area was 50 x 100 mm. (This is not specified in the test standards and may have varied for the testing performed at the earliest dates in the 10-year time period.) Peel resistance was tested in the configuration of 180° peel for tapes adhered to rigid substrates, whereas a T-peel configuration was used for flexible substrates, such as vapour and wind barrier membranes. The test configurations for the two peel tests, as well as the shear test are shown in Figure 1.

The test specimens were exposed to artificial ageing according to one of the three different ageing programs shown in Table 1. The climate carousel refers to ageing in a vertical climate simulator according to NT Build 495. In the climate carousel, the samples are subjected in turn to four different climate exposure conditions; ultraviolet (UV) and infrared irradiation (black panel temperature of 63 °C), water spray, freezing (-20 °C) and ambient laboratory conditions. The exposure time is 1 h for each climate condition.

Table 1. Key information on the dataset subject to analysis.

Evaluation parameter	Test method	No. of unique tapes	No. of data points*
Average peel resistance	EN 12316-2	37 (30 acrylic, 7 butyl)	143
Shear resistance	EN 12317-2	38 (30 acrylic, 8 butyl)	132

* One data point includes the measurement values from both aged and non-aged samples. Each value represents the average of measurements on 5 individual samples (excluding outliers).

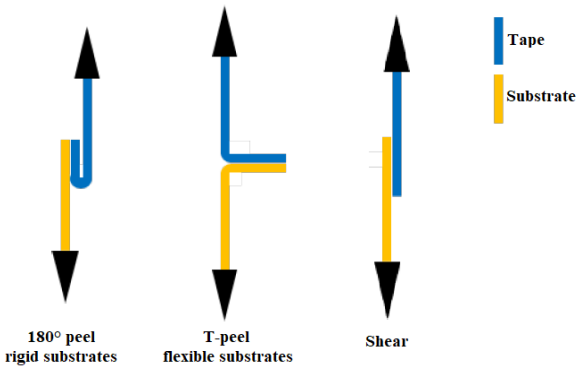

Figure 1. Configurations for testing peel and shear resistance.

Table 2. Ageing programs.

Ageing program	Climate carousel	UV light	Heat chamber at 70 °C
Climate simulator + heat	2 or 4 weeks	-	12, 22 or 24 weeks
UV fluorescent lamps + heat		2 days	12 weeks
Only heat ageing	-	-	24 weeks

The tapes have been anonymised and categorised based on adhesive type, backing material, intended application temperature range etc. whereas the different substrates have been broadly grouped into different material classes. Standardised substrates have not been used, and in general the choice of substrates have been individually chosen in each case, based on the intended application range of the tapes in question. If an adhesive tape was a part of a specific product range, for instance as part of an airtightness system, it would typically have been tested against a wind barrier in the same product range, as well as rigid substrates of typical construction materials, such as wood or steel. Therefore, we do not have a complete experimental matrix to analyse, and any attempts at performing rigid statistical analysis have been hampered by confounding variables and missing data points. Hence, the analysis is based on plotting and visualisation techniques.

3 Results and Discussion

3.1 Repeatability of the Data

The European test methods do not specify how the joint should be made, other than stating that the pieces should be joined by the methods to be used for installation in the end use application. *I.e.* application pressure and speed were not controlled. Nevertheless, the repeatability of the measurements was generally acceptable. The pooled standard deviation of measurement values within one test series (5 measurements on test specimens prepared from the same tape and substrates, undergoing identical ageing programs and conditioning, tested on the same day) was 2 N/50 mm before ageing and 4 N/50 mm after ageing for peel resistance, and 19 N/50 mm before ageing and 23 N/mm after ageing for shear resistance.

3.2 Correlation Between Measurements on Aged and Non-Aged Specimens

Peel resistance for aged specimens are plotted as a function of the peel resistance for the corresponding non-aged specimens in Figure 2a. The equivalent plot for shear resistance is shown in 2b. The light grey fields mark the regions where the peel or shear resistance decreased with ageing, whereas the darker grey fields mark the region where the said properties decreased more than 50 % relative to non-aged samples.

The purpose of the plots was to see if a correlation could be found between measurement values before and after ageing, *i.e.* if a high measurement value before ageing increased the probability of getting a high measurement value after aging. To some extent, this correlation is present, because large increases in joint strength after ageing were rarely observed. However, it is clear from Figure 2a, that peel resistance for non-aged samples is a poor predictor of peel resistance after ageing. In comparison, a much stronger correlation is observed for shear resistance (2b). In fact, shear resistance appears to have changed very little with ageing for a large portion of the test specimens.

The peel resistance is often seen as a measurement of the adhesion force between the adhesive and the substrate (presuming the failure mode is interfacial), whereas the shear resistance is considered to to a larger degree reflect the cohesive strength of the adhesive. Although this is a great simplification, the results can nevertheless be an indication that the degradation caused by the artificial ageing is more detrimental to the interfacial bond than to the bulk properties of the adhesive.

Another observation worthy of mention is that the lowest peel resistance values after ageing were from tapes adhered to flexible membranes, such as vapour or wind barriers, rather than rigid substrates. This could be due to interaction effects between the adhesive and substrate, but more likely it is an indication that it is also important to consider the effect of the ageing of the substrate as well as the adhesive tape.

For the design of experiments to investigate the durability of adhesive bonds, these findings highlight that peel resistance is a much more sensitive evaluation parameter than shear strength to assess changes caused by artificial ageing. However, more knowledge is needed on both correlation between natural and artificial ageing for adhesive tapes, as well as the acting forces in in-use condition to assess whether peel or shear resistance are good indicators for long-term performance.

3.3 Difference in Ageing Properties Across Adhesive Tape Products

Several attempts were made to group the available test results based on substrate types and surface materials, properties of the adhesive tape products (e.g. adhesive, backing material etc.) and investigate the effect on adhesive properties, however the result was always that the range of measurement values within the groups was considerably larger than the observed difference between the groups. The difference from one unique tape to another proved to be a confounding variable for all other attempted groupings. Thus, the conclusion was drawn that the effect of ageing and substrates had to be analysed on an individual tape basis. Because this could not easily and clearly be presented for all tapes in the dataset, a selection was done according to the following criteria:

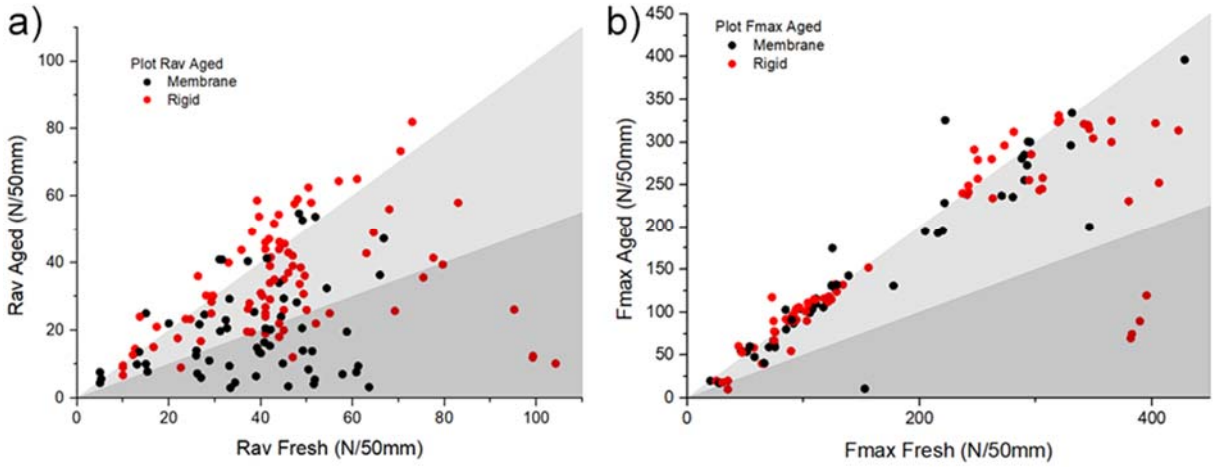

Figure 2. a) Peel resistance for aged specimens as a function of peel resistance for non-aged specimens b) Shear resistance for aged specimens as a function of shear resistance for non-aged specimens. The light and dark grey fields mark the regions where the shear resistance decreased 0 – 50 % and 50 – 100 %, respectively

- Only specimens subjected to 2 weeks climate carousel + 24 weeks heat ageing
- Only single-sided tapes
- Only tapes tested on at least two different substrates
- Excluding data points from substrates that could not be confidently categorized

The resulting plots are presented in Figures 3 and 4 for peel and shear resistance, respectively. In the plots, each row contains data points from one tape product, labelled A1 – A8 for acrylic tapes and B1 – B3 for butyl rubber tapes. The height of each row represents the full range of values for the peel/shear resistance in the dataset (0 – 110 N/50mm for peel and 0 – 450 N/50mm for shear resistance). A more detailed view of the data points for tapes A2, A3 and A4 are presented in Figure 5. Some important observations are:

- Both initial values and change with ageing differ greatly between tapes. This can be exemplified by studying the peel resistance of tapes A2, A3 and A4. Both A2 and A3 start out at medium peel resistance for all tested substrates before ageing. After ageing, the peel resistance for A2 is largely unchanged for all substrates, wheras the values for A3 drop somewhat for all substrates, and the drop is distinctly larger for the joint to the vapour barrier than to the other substrates. A4, on the other hand starts out with peel values at the very top of the range, but degrade dramatically upon ageing for all substrates.
- The trends in initial values and degradation upon ageing are in many cases similar for peel and shear resistance. For instance A4 displays a similar drop in shear resistance upon ageing as in peel resistance.
- The effect from testing on different substrates is less pronounced. With few exceptions, all values from one tape on different substrates are in the same range. This applies to both peel and shear resistance, and both before and after ageing, however the variation from substrate to substrate appears to be slightly higher after ageing.

All these tapes have been subjected to the same ageing program, yet they display completely different responses to the accelerated ageing. Thus, when designing experiments to learn more about the ageing mechanisms of adhesive tapes it is important to include enough different tape products to get the full picture. Furthermore, it is necessary to gain a better understanding of the differences between the tapes, and what properties are significant for the durability.

The number of substrates may be kept smaller to limit the size of the experimental matrix. However, it is important to do the ageing on stable, rigid substrates as well as membranes to account for the fact that membranes themselves are also subject to changing properties during the ageing process. If fact, membrane properties should possibly also be checked seperately, in order to correct for this.

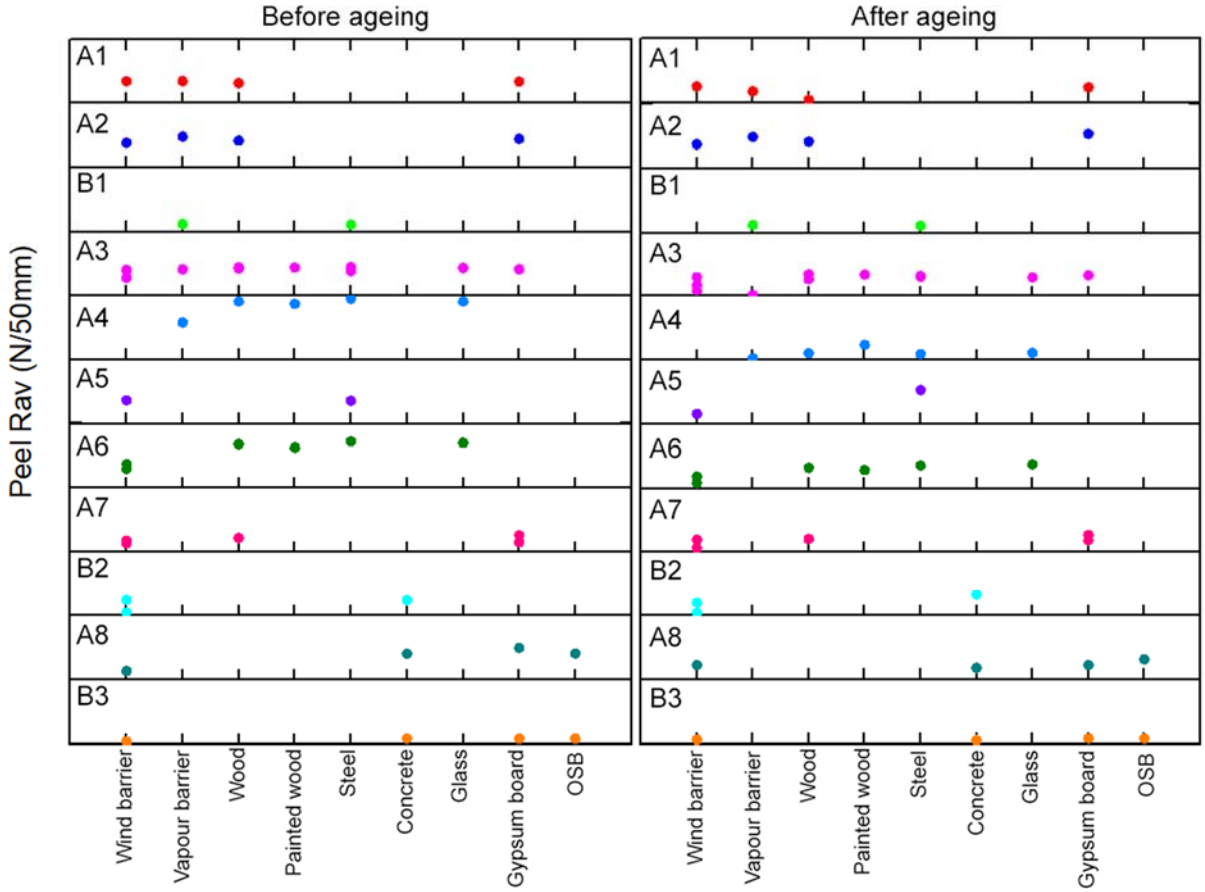

Figure 3. Stacked plot of peel resistance for 11 different adhesive tapes on various substrates. Each row contains data points from one tape product, labelled A1 – A8 for acrylic tapes and B1 – B3 for butyl rubber tapes. The y-axis for each row starts at 0 N/50mm and ends at 110 N/50 mm.

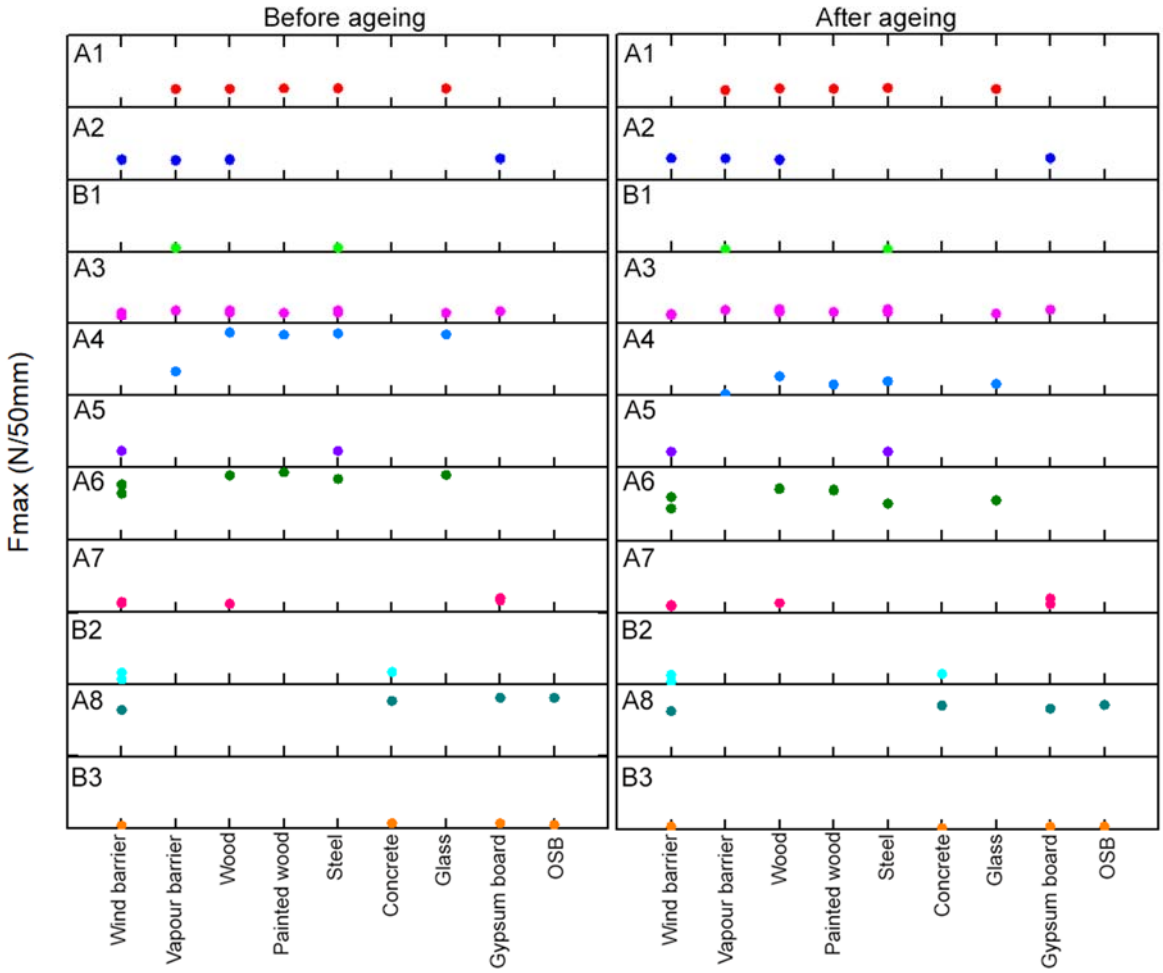

Figure 4. Stacked plot of shear resistance for 11 different adhesive tapes on various substrates. Each row contains data points from one tape product, labelled A1 – A8 for acrylic tapes and B1 – B3 for butyl rubber tapes. The y-axis for each row starts at 0 N/50mm and ends at 450 N/50 mm.

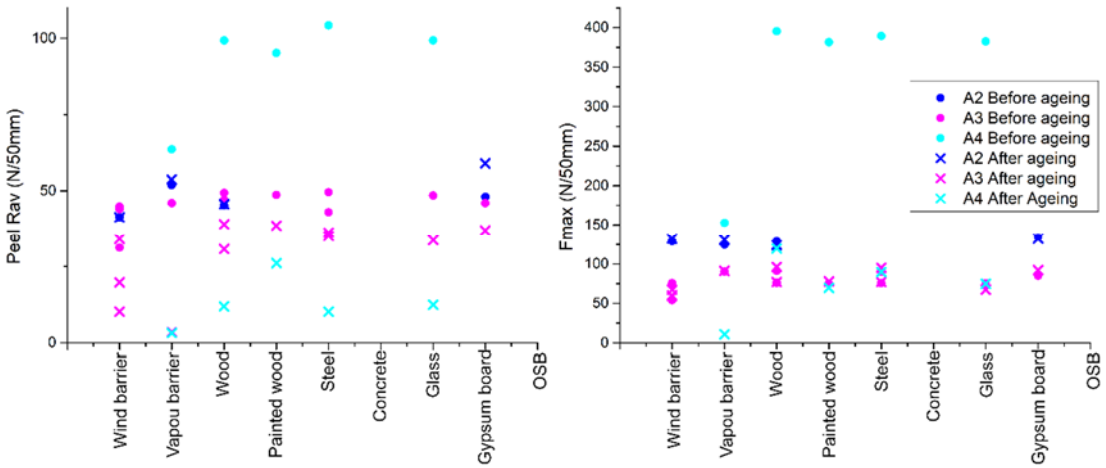

Figure 5. Peel and shear resistance before and after ageing for tapes A2, A3 and A4.

4 Conclusions

- Peel resistance for non-aged samples was a poor predictor of peel resistance after ageing.
- There was a clear correlation between shear resistance for aged and non-aged samples.
- Peel resistance was a more sensitive evaluation parameter than shear strength to assess changes caused by artificial ageing.
- The measurement values for peel and shear resistance varied considerably more between different tapes than between different substrates. This was true for both non-aged and aged test specimens.
- More consideration should be made to include several different tapes in the experimental matrix when planning experiments to study the durability of adhesive tapes for building air-tightness systems.

Acknowledgements

This study was funded by the project 'TightEN - Durable adhesive airtight solutions for energy efficient building envelopes'. Research Council of Norway; Country: Norway; Grant number: 294894.

ORCID

Malin Sletnes: https://orcid.org/0000-0001-8458-4653
Susanne Frank: https://orcid.org/0000-0002-4542-1402

References

Antonsen, U. (2017). *Slutrapport: Lufttäta klimatskal under verkliga förhållanden (In Swedish, Final report: Airtight building envelopes under real-life conditions)* (E2B2 Rapport 1:2017). Retrieved from

Fufa, S. M., Labonnote, N., Frank, S., Rüther, P., and Jelle, B. P. (2018). Durability evaluation of adhesive tapes for building applications. *Construction and Building Materials, 161*, 528-538. doi:https://doi.org/10.1016/j.conbuildmat.2017.11.056

Langmans, J., Desta, T. Z., Alderweireldt, L. and Roels, S. (2017). Durability of self-adhesive tapes for exterior air barrier applications: a laboratory investigation. *International Journal of Ventilation, 16*(1), 30-41. doi:10.1080/14733315.2016.1252154

Leprince, V., Moujalled, B. and Litvak, A. (2017). *Durability of building airtightness , review and analysis of existing studies*. Paper presented at the AIVC TightVent, Brussels.

Litvak, A., Allègre, F., Moujalled, B. and Leprince, V. (2019). *Assessment of the durability of airtightness products in laboratory controlled conditions: development and presentation of the experimental protocol.* Paper presented at the 40th AIVC Conference - From energy crisis to sustainable indoor climate - 40 years of AIVC, Ghent, Belgium. https://hal.archives-ouvertes.fr/hal-02335791

XV International Conference on Durability of Building Materials and Components
DBMC 2020, Barcelona
C. Serrat, J.R. Casas and V. Gibert (Eds)

Predominant Climate Exposure Strains - Thermal Degradation Testing Compared to Historical and Future Climate Scenarios

Petra Rüther, Klodian Gradeci and Malin Sletnes

SINTEF Community. Department for architecture, building materials and constructions, Høgskoleringen 7A, 7461 Trondheim, Norway, petra.ruther@sintef.no

Abstract. *The service life of a building or structure is often presumed to be 60 years. Products used in the building envelope are often covered by a facade material on the exterior side. Hence, the failure of these products is not easily observable, and the repair or replacement is normally not technically nor economically feasible. Thus, these products are expected to endure the entire estimated lifetime of the building. Service life prediction of these products is based on accelerated ageing tests, whose aim is to measure future possibilities of materials' durability under their expected service life. Preliminary calculations of acceleration factors are discussed and related to historical and future climate scenarios for a dataset from Calgary, Canada. The changes in temperature threshold values for this dataset is significant. Relating the measured values to a duration of a typical accelerated durability test indicates that the test duration is sufficient for a service life of 102 years according to historical climate, but only 52 years taking into account an assumed climate change.*

Keywords: *Durability Testing, Accelerated Ageing, Future Climate Scenarios, Exterior Applications.*

1 Introduction

The service life of buildings and building products is presumed to be 60 years. Wall membrane and roofing products, including adhesive products, are widely used in modern building assemblies and the service life of these products that play an important role in ensuring the air and rain tightness of the buildings has to reach 60 years. Furthermore, the inspection of these products, that are often hidden from visual inspection by cladding material mounted on the outermost layer of a building, is difficult.

Wall membrane and roofing products are usually subjected to an accelerated ageing procedure (see Table 1), depending on the use of the product in question. The test standards are designed with regards to the product in question and the prevailing climate condition in the use area of the product.

The ageing procedures are often, but not always a combination of what is believed to be a realistic climatic condition: elevated temperatures, (UV) radiation, water spray, freeze-thaw cycles, to mention the most common ones. Studies on material degradation usually involve a very detailed study of the degradation mechanism. The common ground for building products is usually their application area and not the type of material. Hence, test procedures should preferably account for the climatic strains, and attempt to reproduce the climatic conditions in service (Riahinezhad *et al.,* 2019) as correctly as possible.

While many test procedures are cycling several climatic agents, *e.g.* solar radiation and humidity, or humidity and elevated temperatures, this study will discuss implications for the testing in elevated temperatures, and discuss whether the effects of climate change, hence increased temperatures, need to be taken into account when designing accelerated ageing procedures.

doi:10.23967/dbmc.2020.226

2 Brief Review of Accelerated Weathering Methods

In order to be able to link the weather conditions to accelerated ageing methods, the temperatures are compared to the elevated temperatures of some European and international test standards for products used on the exterior of wall and roof assemblies.

Table 1. Summary of the most relevant ageing procedures for building envelope materials.

Standard	Temperature	RH	Test duration	Acceleration	Application
EN 1296:2000	70 ^{O}C	Not stated	24 weeks	not stated	Roofing membranes
EN 1297:2004	60 ^{O}C	10 ±5 %[1]	not stated	not stated	Roofing membranes [2]
NT BUILD 495	63 ±5 ^{O}C	not stated	not stated	not stated	Materials and components used in the building envelope [3]
NS 8140:1985	75 ±5 ^{O}C BPT	not stated	not stated	not stated	See footnote [4]
ETAG 004	(1) 70 ^{O}C (2) 50 ^{O}C /-20 ^{O}C	(1) 10-30% (2) 30%	(1) 80 cycles, 3h+1h spray and 2h rest (2) 7 h/16 h	not stated	External Thermal Insulation Composite Systems (Etics) with Rendering[5]
EOTA TR 010: 2004	M[6] 60 ± ^{O}C (BST) S[6] 70 ±3 ^{O}C	65 ± 5% (drying conditions)	5000 hours	5000 h = 5 years[7]	Liquid applied waterproofing kit
CAN/ULC – S741 (2008)	50ºC		32 days	not stated	Air barrier materials[8]

1 The relative humidity shall be (10 ±-5) % after 30 min of the dry period.
2 In addition to heat and humidity the standard requires UV radiation and cyclic water spraying
3 The test method is based on cycling radiation, water spray, frost and laboratory climate.
4 The test method resembles the Nordtest NT Build 495 method with minor adjustments.
5 The systems must pass a series of tests regarding the performance of the rendering after the cycles
6 Distinguishes between M (moderate climate) and S (severe climate). Weathering cycles include water spray. Focus on radiation exposure.
7 The AF refers to the radiation exposure.
8 CAN/ULC-S741 conditioning includes UV exposure followed by extended heat exposure. UV exposure includes 210 hours (10 hr for 21 days) of UV radiation according to ASTM G154. Heat exposure includes placing the specimens in an air circulation oven for either 772 hours at 50±2°C for non-accessible air barrier material or 336 hours at 50±2°C for accessible air barrier materials.

The above summary shows that most products for exterior applications in the building envelope are tested under elevated temperatures between 50°C and 70°C for between 32 days and 24 weeks. The acceleration factors stated are usually connected to the radiation exposure and not the thermal degradation.

3 Historical and Future Temperature Values

The selected location is Calgary, Canada. Two sets of climate data generated in Gaur *et.al.* (2019) that include the following:

- 15 historical climate data set, and
- 15 climate data set for a climate change scenario in which the global climate temperature change is forecast to be 3.5ºC.

The reader is referred to Gaur *et al.* (2019) for more in-depth understanding of the methodology used, while a short description follows. A merged observational climate time-series (1986–2016) for the city of Calgary was prepared from the hourly observations (surface global horizontal irradiance, total cloud cover, rainfall, relative humidity, air temperature, station pressure, 10 m wind-speed and wind-direction), and daily observations of the snow-depth from the collection of all of the Environment and Climate Change Canada (ECCC) climate gauging stations located within the domains of Calgary and containing more than one year of data between the time-period: 1986–2016. The database of climatic projections from

CanRCM4 LE, Global Climate Model (GCM), was used to extract climatic projections for Calgary spanning the historical and future time-periods. In total, 15 members of the hourly CanESM2 LE projections covering the historical and the future time-periods were extracted for the grids covering the Calgary for the generation of 15 historical and 15 projected time-series of the climate variables.

Data was analysed to find the time periods where temperatures lie above a distinct temperature threshold. Temperature steps of 10°C between a range of -45°C and +45°C. Results are presented below for historical data and for the chosen climate scenario, together with averages, standard deviations and differences.

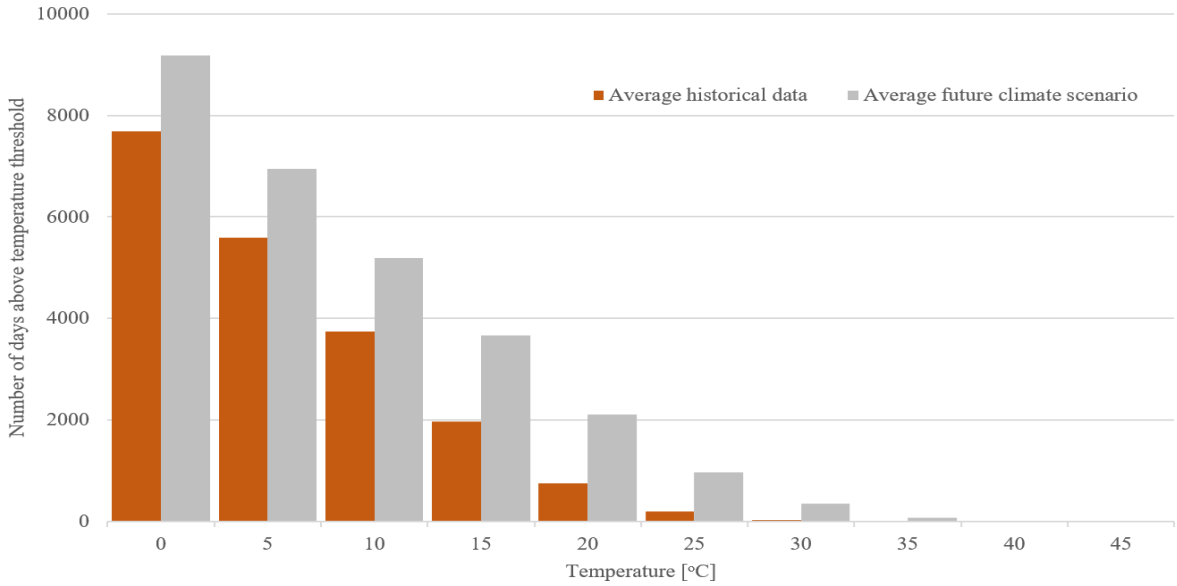

Figure 1. Number of days above temperature threshold for historical and future climate, temperatures above 0°C.

The analysis of the climate data presented in Figure 1 shows a significant deferral of the average temperatures towards higher temperature levels. The number of days where the temperature exceeds 0°C increases for example by 1490 in the course of a 30-year period, or by an average of 50 days per year. For elevated temperatures the relative increase in days above the threshold value is significant: The accumulated period where the average temperature exceeds 30°C increased 3.52 times from 30 days to 352 days in a 30-year period. Correspondingly, the amount of time accumulated at lower temperatures decrease

4 Investigation of Acceleration Factors

In order to ensure that building materials exposed to outdoor conditions have the quality to endure the desired service life, accelerated laboratory testing is conducted. A brief review of some common test methods is presented in Table 1. The tests commonly include amongst others solar radiation and elevated temperatures between 50°C and 70°C, for some test methods the temperatures are cycled and/or alternated with water spray.

The service life of buildings and building parts that are not to be replaced is often set to between 50 and 60 years (Byggforsk, 2017), for materials and components in the building envelope that are accessible for replacement between 25 and 30 years.

Hence, the durability test should aim for testing a service life of 25-30 years or 50-60 years, respectively. The common dilemma with durability testing is to keep the test duration as short

as possible, *i.e.* to accelerate the test as much as possible, without generating degradation effects caused by elevated temperatures not present in a real application.

The following sections explore and discuss acceleration factors along with respective test durations for thermal degradation processes based on the above presented historical and future climate scenarios.

4.1 Methodology

Polymeric materials used in building materials are subject to degradation mainly caused by photoirradiation and thermal degradation. The dependence of the rate of thermal degradation on the temperature can be described by the Arrhenius law:

$$\boldsymbol{k = A \cdot e^{\left(\frac{-E_a}{R \cdot T}\right)}} \tag{1}$$

where A is a pre-exponential factor, E_a [J/(mol K)] is the activation energy, R = 8.314 J/mol is the gas constant, and T [K] is the temperature. A temperature acceleration factor AF_{temp} may then be calculated as the ratio between the reaction rate in the accelerated weathering test k_1 and the natural outdoor weathering k_2, leading to the following equation for the acceleration factor AF_{temp}:

$$\boldsymbol{AF_{temp} = \frac{k_1}{k_2} = e^{\left(\left(\frac{E_a}{R}\right)\left(\frac{1}{T_1} - \frac{1}{T_2}\right)\right)}} \tag{2}$$

where T_1 and T_2 denote the temperature in the accelerated weathering test and the natural outdoor weathering, respectively. Given that the pre-exponential factor A is temperature independent, the calculation of the acceleration factor is only dependent on the value of the activation energy E_a and the two temperatures T_1 and T_2 (Meeker et al). The activation energy is strongly dependent on the material composition, the interaction between different chemical agents, the presence of catalysts, and hence very challenging to estimate for a complex material. However, for the purpose of this study four different activation energies have been used for the calculations: 72 kJ/(mol K) (as suggested by Riahinezhad *et al.,* 2019), 90 kJ/(mol K), 60 kJ/(mol K) and 50 kJ/(mol K).

The following assumptions and approximations are taken in the investigation of the acceleration factor:

- The pre-exponential factor A in Equation 1 does not vary during the degradation process.
- The calculations are solely based on thermal degradation.
- The reaction mechanism, and hence the activation energy, does not vary during the degradation process.
- The chosen values for E_a are either chosen from literature (72 kJ/(mol K) from Riahinezhad *et al.,* 2019) or parametrically assumed in order to explore the influence of the activation energy on the overall result.
- The temperature values for the outdoor exposure is based on average hourly values.

Acceleration factors are calculated based on Equation 2 for four different laboratory test temperatures T_1= 60°C, 70°C and 80°C and an effective outdoor temperature T_2, where the lowest included temperature is 0ºC, assuming that thermal degradation processes below 0ºC might be neglected for the purpose of this study.

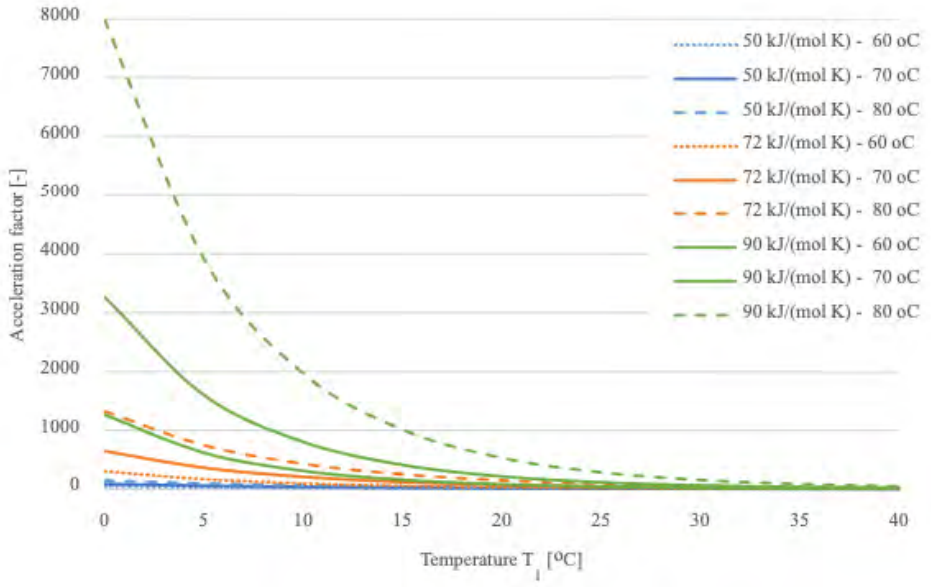

Figure 2. Acceleration factors plotted against average outdoor temperature for 80°C (dashed line), 70°C (solid line) and 60°C (dotted line) laboratory test temperature for different activation energies.

The value of the acceleration factor AF depends (given the assumptions and approximations stated in section 4.1) solely on the activation energy E_a and the two temperatures T_1 and T_2. Table 2 shows the acceleration factors calculated for an activation energy of 72 J/(mol K) for different temperatures T_1 and T_2. Figure 2 shows acceleration factors AF for different values of E_a.

In the further course of the calculations the focus will be on an activation energy of E_a= 72 kJ/(mol K), as shown in Figure 3 with a more detailed plot. With all assumptions considered, the acceleration factor varies between 23 and 1325 for a test temperature of 80°C, 11 and 648 for a test temperature of 70°C and between 5 and 304 for a test temperature of 60°C. Basing the calculation of the test duration on annual average values leads to an acceleration factor of 379 for historic (T_2 = 4,7°C) and 225 (T_2 = 9,4°C) for future climate scenarios (for E_a=72 kJ/(mol K) and 70°C test temperature), leading again to a laboratory test duration of 28 days and 48 days.

Table 2. Acceleration factors AF for E_a = 72 J/(mol K).

T_2 [°C]	**T_1** [°C]		
	60	**70**	**80**
0	304	648	1325
5	172	366	749
10	99	211	432
15	58	124	254
20	35	74	152
25	21	45	93
30	13	28	57
35	8	18	36
40	5	11	23

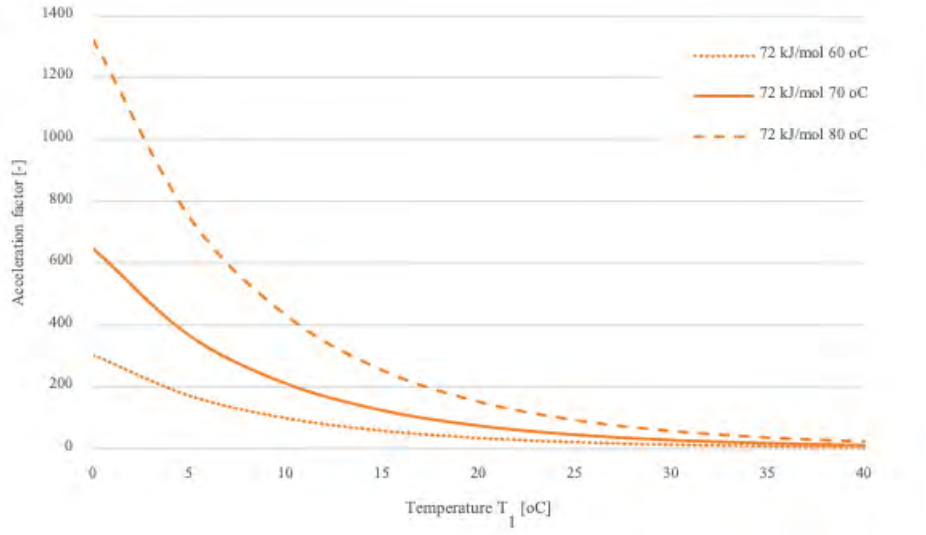

Figure 3. Acceleration factor plotted for E_a = 72 kJ/(mol K) for three different laboratory test temperatures for average outdoor temperatures between 0ºC and 40ºC.

5 Laboratory Test Duration

In order to estimate a laboratory test duration, an average temperature representing the outdoor temperature during the test period is to be calculated. The temperature data is divided into temperature ranges of 5ºC between 0ºC and 40ºC (assuming that the thermal degradation processes below 0ºC might be neglected). Further, the average temperature for each interval and the according duration is derived from the climate data. For the calculation of the acceleration factor for the respective temperature range, T_2 is set to the average temperature of the respective interval.

The results of the calculation are shown in Figure 5 for three different laboratory test temperatures for historical and future climate. For a laboratory test temperature T_1 the laboratory test duration (for a simulation of a 30-year outdoor test period) is 49 days based in historical climate scenarios and increased to 94 days based on future climate scenarios.

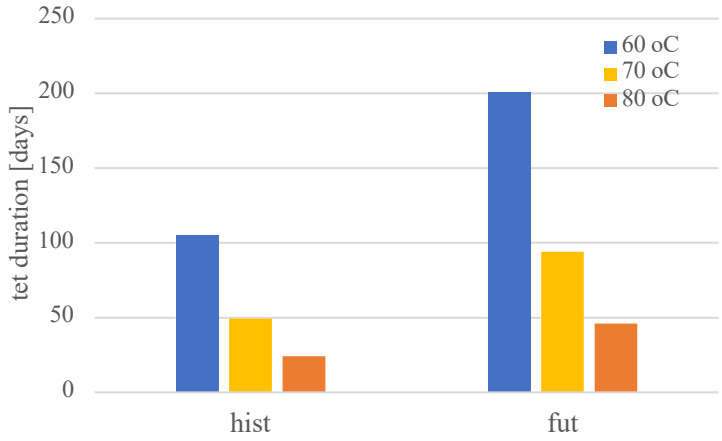

Figure 4. Laboratory test duration [days] for three different laboratory test temperatures T_1 based on historic and future climate scenarios.

With a calculation of the outdoor temperature T_2 in the above described way, the duration of the accelerated test is based on shorter time intervals with their respective duration based on hourly mean values. This contributes to a more accurate calculation, compared to *e.g.* using and average monthly or annual values, where the calculated test duration is considerably shorter (see section 4.1).

Due to the uncertainty in estimations of acceleration factors, test procedures for durability evaluation in product standards or for certification purposes normally specify longer test periods than those calculated from the Arrhenius equation. Thus, these tests have an inherent error margin to be on the safe side with regards to durability. This is known as stress testing, and the goal of the test is to assess whether it is probable that a product will have sufficient durability in the end use environment rather than specifying a particular service life. The error margin of durability testing may become smaller in the future due to climate change. For instance, in a common test method for roofing membranes (EN 1296, 2000), the temperature during the laboratory test is set to 70°C and the test duration is 24 weeks (168 days). Assuming an activation energy of 72 kJ/(mol K) this test roughly corresponds to an outdoor exposure period of 102 years based on historical climate data. Based on the future climate scenario, however, the laboratory testing would only correspond to 53 years of outdoor exposure.

6 Conclusions

The results show a significant influence of the increasing temperature on the accumulated amount of time where certain temperature threshold values are exceeded. For the Calgary data, where the historic average temperature is 4.7°C and the future average temperature over a 30-year time period is 9.4°C, the increase in amount of days where the threshold value exceeds 30°C is from 30 to 352.

In a durability test, based on the calculated acceleration factors, given a number of assumptions, based on thermal degradation and on historic climate data for Calgary, 49 days account for an outdoor test period of 30 years. Based on future climate data, the test duration must be increased to 94 days.

Compared to a commonly used laboratory durability test for roofing membranes (EN 1296, 2000), the test duration of 24 weeks (168 days) accounts for an outdoor test period of 102 years for historical climate and 53 years for future climate.

This calculation shows that future climate scenarios should be considered when designing laboratory experiments.

7 Future Work

This work is based on temperature data measured at a meteorological station. In order to account for microclimate at the exact location where the material in question is applied, it would be interesting to study the differences for temperature values. Also, different geographical locations and their future climate scenarios need to be explored to take into account different climate zones. The further exploration of degradation processes in order to deepen the understanding of thermal degradation and possible interactions between thermal degradation and other climatic strains needs to be further explored.

Ackowledgements

This study was funded by the project 'TightEN - Durable adhesive airtight solutions for energyefficient building envelopes' (www.tighten.no), the aim of developing robust test, evaluation and prediction methodologies for to ensuring durable adhesive airtight solutions for energy efficient building envelopes. Research Council of Norway; Country: Norway; Grant number: 294894.

ORCID
Petra Rüther: https://orcid.org/0000-0003-0245-6813
Klodian Gradeci: https://orcid.org/0000-0002-9837-3512
Malin Sletnes: https://orcid.org/0000-0001-8458-4653

References

ASTM E632-82(1996). Standard Practice for Developing Accelerated Tests to Aid Prediction of the Service Life of Building Components and Materials (Withdrawn 2005), ASTM International, West Conshohocken, PA, 1988, www.astm.org.

Byggforsk 700.320 (2017). Intervaller for vedlikehold og utskifting av bygningsdeler (Invervals for maintenance and replacement of building parts), SINTEF Community, Trondheim, Norway (in Norwegian).

CAN/ULC-S741 (2008). Standard for Air Barrier Materials – Specification.

EN 1296 (2000). Flexible sheets for waterproofing - Bitumen, plastic and rubber sheets for roofing - Method of artificial ageing by long term exposure to elevated temperature. The European Standardization Organization.

EN 1297 (2004). Flexible sheets for waterproofing - Bitumen, plastic and rubber sheets for roof waterproofing - Method of artificial ageing by long term exposure to the combination of UV radiation, elevated temperature and water. The European Standardization Organization.

EOTA TR 010 (2004). Exposure procedure for artificial weathering. EOTA European Organisation for Technical Approvals.

ETAG 004 (2013). External Thermal Insulation Composite Systems (Etics) with Rendering, EOTA. European Organisation for Technical Approvals.

Gaur, A., Lacasse, M. and Armstrong, M. (2019). Climate Data to Undertake Hygrothermal and Whole Building Simulations Under Projected Climate Change Influences for 11 Canadian Cities. *Data, 4*(2), 72.

Meeker, W.Q., Escobar, L.A. and Chan, V. (2002). Using accelerated tests to predict service life in highly variable environments. In Jonathan W. Martin and David R. Bauer, Editors, Service life Prediction. *Methodology and Metrologies, 805* of ACS Symposium Series, 396-412. American Chemical Society, Oxford University Press.

NS 8140:1985 (1985). Method of exposure of building components and building materials to accelerated climatic strains in a vertical position. The Norwegian Standardization Organization.

NT BUILD 495 (2000). Building materials and components in the vertical position: Exposure to accelerated climatic strains, Nordtest.

Riahinezhad, M., Eve, A., Armstrong, M., Collins, P. and Masson, J.F. (2019). Field temperature and moisture loads from a building envelope as the basis for accelerated aging of barrier membranes. *Canadian Journal of Civil Engineering, 46*, 969-978. https://doi.org/10.1139/cjce-2018-0757.

XV International Conference on Durability of Building Materials and Components
DBMC 2020, Barcelona
C. Serrat, J.R. Casas and V. Gibert (Eds)

Assessment of Moisture Performance of National Building Code Canada Compliant Wall Assemblies under Climate Change

Max Junginger[1], Maurice Defo[2], Travis Moore[3], Michael A. Lacasse[4] and Vanderley M. John[5]

[1] Polytechnic School, University of São Paulo, São Paulo, SP, Brazil. Maxjgg@gmail.com

[2] Construction Research Centre, NRCC, Ottawa, ON, Canada, Maurice.Defo@nrc-cnrc.gc.ca

[3] Construction Research Centre, NRCC, Ottawa, ON, Canada, Travis.Moore@nrc-cnrc.gc.ca

[4] Construction Research Centre, NRCC, Ottawa, ON, Canada, Michael.Lacasse@nrc-cnrc.gc.ca

[5] Polytechnic School, University of São Paulo, São Paulo, SP, Brazil, Vanderley.John@lme.pcc.usp.br

Abstract: *Due to climate change, higher temperatures and rainfalls are expected to happen in some areas of Canada, which might increase the climate loads on buildings and lead to premature degradation of moisture-sensitive materials in wall assemblies. To investigate potential durability issues in three cities across Canada (Ottawa, Vancouver and Calgary), code-compliant wood-frame walls with two types of claddings, stucco and brick, were simulated using Delphin 5.9. Two different climate data sets, historical and future when a global warming of 3.5ºC is expected to be reached were used. The hygrothermal performance in terms of mold growth risk was analysed with respect to cladding types, considering air leakage. All the three cities are similarly warmer in the future. However, wind-driven rain (WDR) is higher in Vancouver than in Ottawa and Calgary. With brick cladding the relative humidity is kept below the threshold for mould development only in Ottawa and Calgary. With stucco in future, while Ottawa shows greater mould indices than historical, Calgary shows opposite behavior. The results suggest that the risk of mould growth due to air leakage may decrease in the future.*

Keywords: *Code Compliant Walls, Moisture Performance, Climate Resilience, Air Leakage, Stucco Wall, Brick Cavity Wall.*

1 Introduction

Climate change has received increasing attention globally due to many possible consequences, including building long-term performance issues from temperature increases and more severe and frequent rainfall events. The Intergovernmental Panel on Climate Change (IPCC, 2014) has indicated that climate changes has resulted from anthropogenic action and, whereas temperature changes arising from human influence is indeed a global concern, it is known that in Canada annual average temperatures will rise about twice the global average.

It is also expected that weather extremes will intensify in the future from a warming climate and, even though rainfall events might decrease in some areas, these are likely to increase for over most of Canada (Bush and Lemmen, 2019). In some regions, increases in precipitation as high as 40% are expected and this will have significant effects on buildings: water infiltration, related mostly to wind-driven rain, will increase accordingly and might pose a higher risk to the premature degradation of moisture-sensitive materials in wall assemblies (Lacasse, Defo, *et al*., 2018).

To address these issues of moisture accumulation in wall assemblies due to condensation or

water ingress, the National Building Code (NRC, 2015) set prescriptive requirements for all the walls separating conditioned from unconditioned spaces. These include: i) minimum thermal insulation according to the climate zone; ii) an air barrier system with an air leakage rate not greater than 0.1 L/(s.m^2) at 75 Pa; iii) a vapor barrier with permeance not greater than 60 ng/(Pa.s.m^2); and iv) position of low permeance material in the wall. As well, in case where an exterior insulation is added, NBC might also require a minimum ratio between outboard and inboard thermal resistance (NRC, 2015, p. B-9.159). All these technical requirements are intended to minimize the chance of moisture accumulation in wall assemblies, which can lead to deterioration of wood and wood-based building products.

Although the requirements were set based on historical climate loads, item 5.1.4.2 of NBC says that "… assemblies exposed to the exterior shall be resistant to any mechanism of deterioration that may reasonably be expected". As such, the impacts of climate change on moisture performance of code-compliant walls need to be assessed.

The primary objective of this study is to evaluate the moisture performance of code-compliant wall assemblies in both historical and future climate. The approach followed is the one provided in the "Guideline for the Design for Durability of the Building Envelope" (Lacasse *et al*., 2018).

2 Methods

The methodology for the assessment of moisture performance of code-compliant wall assemblies as described in this paper follows the approach given in the "Guideline for the Design for Durability of the Building Envelope" (Lacasse, Ge, *et al*., 2018). This approach essentially uses hygrothermal modelling as means to assess the response of wall components to climate loads acting on the exterior and environmental conditions on the interior of the assembly; so, the moisture performance of the wall can be determined on the basis of the risk of mould growth or wood decay in wood based components.

The simulation tool is first described and, thereafter, details in respect to input data for simulation are provided: wall configuration, which is dependent on the geographic location for which simulations will be completed; weather data, and the reference years to be used in simulations; boundary conditions, in which boundary parameters are defined; air leakage; and material properties.

2.1 Geographic Location

Three cities were selected across Canada: Calgary (AB), Ottawa (ON) and Vancouver (BC), with low, medium and high moisture indices respectively. The main characteristics of the cities are shown in Table 1.

Table 1. Geographic location and climate details about the cities.

City (Province)	Latitude (°)	Longitude (°)	HDD	Zone	RSI_{min} (W/m^{2}K)	MI	Annual rain (mm)
Ottawa (ON)	45.25	-75.42	4440	6	2.97	0.84	750
Vancouver (BC)	49.28	-123.12	3100	4	2.78	1.93	1850
Calgary (AB)	51.05	-114.07	5000	7A	2.97	0.37	325

HDD - heating degree days below 18ºC
RSI - Effective thermal resistance
Zone - climatic zone
MI - moisture index

2.2 Simulation Tool

A state-of-the-art hygrothermal modelling software, Delphin 5.9, was used to undertake the hygrothermal simulations. The solver parameters were adjusted to 0.01 s initial time step, 60 s maximum time step, 10^{-6} relative tolerance and 10^{-7} moisture mass balance.

2.3 Wall Configuration

A wood frame wall of a 3.5-storey (10-m high) residential building located in suburban areas was considered. For each city, two cladding types were simulated: brick and stucco. Figure 1 shows the composition of the brick wall.

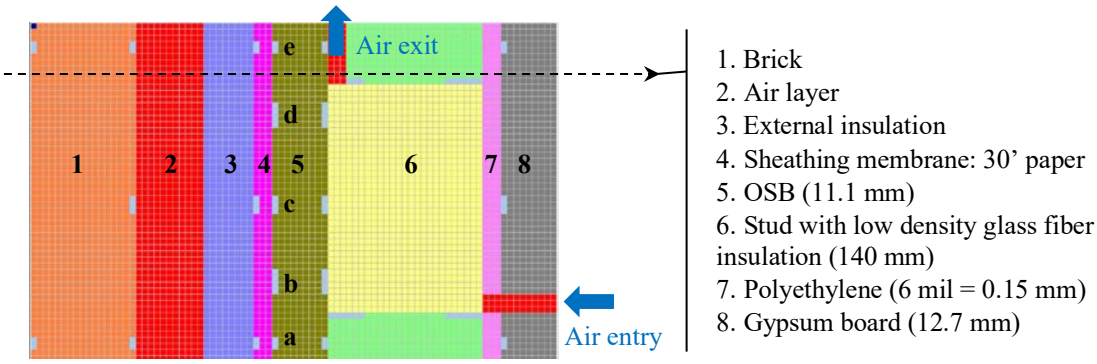

Figure 1. Layers of the brick wall and the locations for reading Relative Humidity and Temperature.

From the sheathing membrane to the interior side of the wall (from layer 4 to layer 8), all the layers are the same for all walls. The height of the wall was 2440 mm: 36 mm for the single bottom plate (spruce), 2332 mm for the insulation (low density glass fiber insulation) placed within the vertical wood studs, and 72 mm for the double top plate (spruce). For the outer part of the walls, complete details for each city are given in Table 2.

Table 2. Cladding details.

City	Cladding		Drainage cavity (mm)	External insulation	Air change (/h)	Air leakage
	Type	Thick (mm)				
Ottawa	Brick; Stucco	90; 19	25; None	EPS (6.5; 12.7 mm)	10; None	With and Without
Vancouver	Brick; Stucco	90; 19	25; 10	None; None	10; 10	
Calgary	Brick; Stucco	90; 19	25; None	EPS (6.5; 12.7 mm)	10; None	

In Calgary and Ottawa it was necessary to incorporate an external insulation to reach the minimum energy requirement (RSI ≥ 2.97 W/m^{2}K) whereas in the warmer climate of Vancouver (RSI ≥ 2.78 W/m^{2}K) the stud cavity insulation alone was enough.

2.4 Weather Data

Two sets of climate data were used: historical and future (when a global warming of 3.5ºC is expected to be reached). Both sets were prepared according to Gaur *et al*. (2019) and encompass a 31-year time period, from 1986 to 2016 and from 2062 to 2092. From each set, the median and the wettest years were selected based on the moisture index (Cornick *et al*., 2003) and were used as moisture reference years for simulations. Those years and the wall orientation with the

highest wind-driven rain load are summarized in Table 3. In all cases there is an increase in the temperature in the future; RH levels vary quite the same way in Calgary and Vancouver, but are higher in the future climate for Ottawa.

Table 3. Moisture reference years and wall orientation for each city.

City	H - Historical data (year)			Wall orientation (°)	F - Future data (year)			Wall orientation (°)
	Period	Median	Wet		Period	Median	Wet	
Ottawa	1986 to 2016	1989	1991	180	2062 to 2092	2074	2070	180
Vancouver		1988	1994	145		2091	2066	180
Calgary		2015	2016	292		2069	2063	315

2.5 Boundary conditions

2.5.1 Air Leakage

All the walls were simulated with and without air leakage and the exfiltration path (Figure 1) is one of the worst cases in terms of moisture accumulation suggested by Ojanen and Kumaran (1992; 1996). This path is also the same as the one used by Saber (2014). An air leakage rate of 0.1 L/(s.m^2) at 75 Pa was tested, which is the maximum rate prescribed by the NBC (NRC, 2015, p. B-5.27) when the indoor relative humidity ranges between 27 and 55%. An equivalent air leakage area was computed assuming a discharge coefficient of 0.6 and air density of 1.2 kg/m^3. For a 2.4 m high wall, the area of the orifice is around 35mm^2 at 75Pa, but since the real pressure difference between outdoors and indoors is roughly 10 Pa, this area was converted to 26 mm^2 (ASHRAE, 2017, p. 16.16). Indoor and outdoor air pressures were derived from the combination of wind and stack pressures and applied to the bottom and top openings of the wall respectively (Figure 1). Since the simulation was run in 2D, the opening was assumed to have a circular shape and its diameter was used as the width of the opening.

2.5.2 Wind-driven rain

Wind-driven rain (WDR), used as an imposed moisture flux on the exterior surface of the wall, was calculated according to ASHRAE 160 (ASHRAE, 2016, p. 6,7), assuming a 3.5 storey building (10-m high) located in a suburban area. The exposure (FE) and deposition (FD) factors were set to 1.0 and 0.5 respectively. Figure 2 shows the accumulated wind-driven rain for all cities, historical and future.

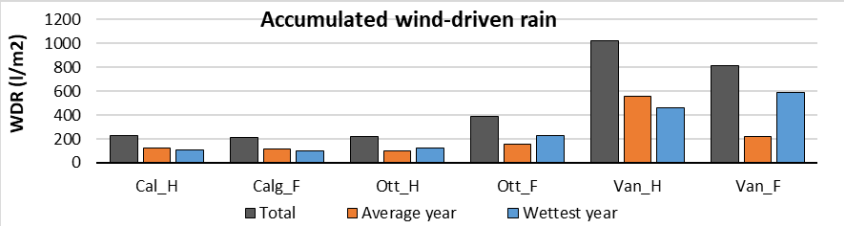

Figure 2. Accumulated wind-driven rain (ASHRAE) for all cities, historical and future.

Calgary has quite the same amount of rain in both scenarios for the two years together; Ottawa shows an increase in the rain in the future for both average and wettest years; Vancouver is less rainy in the future, but there is an important difference between the two years: in the

future, the average year is about 65% dryer and the wettest year is about 30% rainier.

2.5.3 Other parameters and conditions

Initial conditions for all layers were set to 21°C and 50%, respectively for temperature (T) and relative humidity (RH).

Indoor conditions were calculated using the ASHRAE method, heating only (ASHRAE, 2016, p. 4), which means $T \geq 21.1$°C (no upper limit) and $40\% \leq RH \leq 70\%$.

Other coefficients were adopted as follows: outdoor heat transfer coefficient: 4+4v W/m^{2}K (v is wind speed) (ISO, 2017); indoor heat transfer coefficient: 8 W/m^{2}K; outdoor vapor transfer coefficient: $2.44*10^{-8} + 2.44*10^{-8}$v s/m; indoor vapor transfer coefficient: $1.52*10^{-8}$ s/m; ground shortwave reflection = 0.1; shortwave surface absorption = 0.6; ground longwave emission coefficient = 0.9; surface longwave emission coefficient = 0.9.

For wall assemblies having a drainage cavity, the air change per hour (ACH) was set to 10.

2.6 Discretization of the Walls

Preliminary tests simulations with different number of elements were undertaken to select the optimal scheme in terms of accuracy and simulation time. The final mesh used in this paper was composed of 3465 elements for stucco and 4345 for brick.

2.7 Material Properties

Table 4 shows some basic properties of the materials for each of the two wall assemblies.

Table 4. Properties of the main materials according to Kumaran *et al*. (2002).

Material	Thickness (mm)	Dry density (kg/m^3)	Specific heat capacity (J/kg.K)	Thermal conductivity (W/m.K)	Vapor permeance[1] (ng/m^2.s.Pa)
Brick (Br)	90	1900	800	0.500	19
Stucco (Stu)	19	1960	840	0.407	94
OSB	11	600	1880	0.094	101
Glass fiber batt	140	11.5	840	0.043	990
Vapor barrier[2]	0.15	1256	840	0.159	60
Sheathing membrane[3]	0.22	909	1256	0.159	907

1. Values at 50% RH **2**. 0.15 mm polyethylene **3**. 30' asphalt impregnated paper

2.8 Performance Assessment

The performance assessment focused on the mould index calculated according to the VTT model described in Ojanen *et al.* (2010). It is known that mould growth is a highly complex mechanism which is mostly influenced by relative humidity, temperature, material susceptibility, surface quality (Vereecken and Roels, 2012). Different models use different parameters, and not necessarily the same way and, then, distinct outcomes are expected; a deeper discussion about this is out of the scope of this paper and can be found elsewhere, as in Sedlbauer (2001), Vereecken *et al*. (2011), Viitanen *et al*. (2015), Gradeci *et al*. (2017). In this study, the VTT model was adopted because it is recognized by ASHRAE 160 (ASHRAE, 2016, p. 7).

The index was calculated for many different locations of OSB, bottom plate and top plate,

assuming a sensitive class for both material and surface, and 0.1 as decline factor (there is no suggestion in ASHRAE for OSB and then 0.1 was adopted as a conservative value). The highlighted squares in Figure 1 show all the locations in the assembly where values of RH and T were acquired. However, the focus of this paper is in the worst position, identified with the letter "c" in Figure 1 (exterior layer of OSB at mid-height); RH and T values used to compute mould index were acquired on a portion with the dimensions of 0.5 mm x 500 mm.

3 Results and Discussion

Figure 3 shows the mould index profiles for stucco and brick claddings. Solid lines represent situations with no air leakage and dashed lines with air leakage.

Brick cladding in Vancouver (Figure 3a) develops mould, while in Ottawa and Calgary there is no mould growth. This may be explained by the higher amount of WDR in Vancouver compared to Ottawa and Calgary (Figure 2). In Vancouver, mould index profile is consistently greater for historical than future. In fact, the first year (average year) in the future has a lower amount of WDR, which may explain the fact that there is no mould growth, while the second year has more WDR in future than in historical.

In the case of stucco, mould index profiles were quite similar in Vancouver for both climate scenarios (Figure 3b), which is different to the observations for brick. This may be explained by the fact that stucco cladding has higher liquid diffusivity, smaller thickness, and a drainage cavity of only 10 mm. As such, the liquid water reaches the drainage cavity quickly and maintains high RH levels. These factors together with higher temperatures along the year led to high mould indices. Ottawa (Figure 3c) shows higher mould index profile in the future than historical. This may be explained by the fact that WDR is higher in future than historical; in the historical climate, however, the first year is dry and there is no mold growth. Unlike Ottawa, Calgary (Figure 3d) shows lower mould index profile in the future than historical. As shown in Figure 3, the WDR in Calgary is quite similar for historical and future climates, but the temperature is higher and therefore might have increased the drying potential of the whole assembly, decreasing the mould indices.

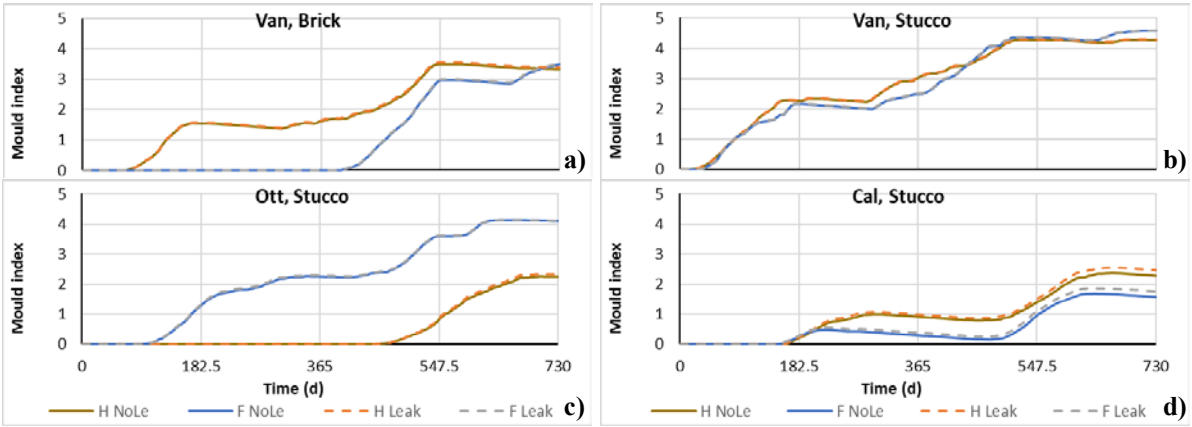

Figure 3. Mould index profiles in the worst position of OSB for both claddings, historical (H) and future (F) scenarios, with (Leak) and without (NoLe) air leakage.

In an attempt to assess the effect of future climate on the risk of mould growth, the difference between the maximum mould index for the cases with and without air leakage was calculated

for both historical and future periods. Table 5 shows the maximum mould values and the difference between historical and future scenarios, with and without air leakage. Those values are labeled as “Leak - NoLe” in the shaded columns.

Table 5. Maximum mould index in the worst position of OSB for each case.

City	Brick						Stucco					
	NoLe		Leak		Leak - NoLe		NoLe		Leak		Leak - NoLe	
	H	F	H	F	H	F	H	F	H	F	H	F
Ottawa	0	0	0	0	0	0	2.25	4.13	2.57	4.13	0.32	0
Vancouver	3.49	3.49	3.56	3.52	0.07	0.03	4.28	4.48	4.40	4.59	0.12	0.11
Calgary	0	0	0	0	0	0	2.36	1.68	2.55	1.86	0.19	0.18
H - Historical			F - Future				Leak - air leakage			NoLe - no air leakage		

Although this calculation is not exactly true because hygrothermal behavior is a combination of all the factors, it gives an idea of the influence of the air leakage itself. It can be seen that air leakage led to higher mould indices in all cases since the exfiltration process brings more humid air to the cavity. Also, the lower values of “Leak - NoLe” in the future suggest that there might be a decrease in the risk of mould growth due to air leakage in the future.

As a general observation of Figure 3 and Table 5, air leakage has a greater impact when the mould index is low, since the major factor responsible for mould growth is the moisture coming from brick and stucco layers. If this amount of moisture is already high, the contribution of the moisture brought to the cavity by the air leakage is very low when compared to the total, which means low impact over the mould indices.

4 Conclusions

Hygrothermal performance of two wall assemblies, stucco and brick cladding, has been assessed in three cities under historical and future climate with and without air leakage to see their response to a possible climate change. Mould index was used as a measurement of performance and the main findings for the cities and the wall configuration considered are:

- Future climate in Ottawa presents higher amount of WDR when comparing with historical, which means the moisture content of the assembly is higher and so is the risk of mould growth. In Calgary, the amount of rain is similar in both climates but the temperature is higher in the future, which means more drying potential and less mould development. Vancouver is rainy in both scenarios and the mould indices are similarly high.
- Brick cladding is safer than stucco in any case in future climate. The higher moisture capacity of the brick, the wider drainage cavity and the higher air temperature all together increase the drying capacity of the assembly, which helps on keeping lower levels of relative humidity and lower mould indices. This situation is more evident in Ottawa and Calgary, which have no mould with this cladding.
- Air leakage increases the mould development in all cases, but the differences are small and cannot be blamed for major changes in the indices. The results suggest risk to mould growth may decrease in the future climate.

ORCID

Max Junginger: 0000-0002-7112-8584
Maurice Defo: 0000-0001-9212-6599
Travis Moore: 0000-0002-4920-9193
Michael Lacasse: 0000-0001-7640-3701
Vanderley John: 0000-0002-0588-8382

References

ASHRAE. (2016). *ASHRAE 160* [Criteria for Moisture-Control Design Analysis in Buildings]. ASHRAE Standards Committe.

ASHRAE. (2017). *ASHRAE Handbook of fundamentals*. ASHRAE Standards Committe.

Bush, E. and Lemmen, D. S. (Eds.). (2019). *Canada's changing climate report.* Government of Canada. http://publications.gc.ca/collections/collection_2019/eccc/En4-368-2019-eng.pdf

Cornick, S., Djebbar, R. and Dalgliesh, W. A. (2003). Selecting moisture reference years using a Moisture Index approach. *Building and Environment*, *38*(12), 1367–1379. https://doi.org/10.1016/S0360-1323(03)00139-2

Gaur, A., Lacasse, M. and Armstrong, M. (2019). Climate Data to Undertake Hygrothermal and Whole Building Simulations Under Projected Climate Change Influences for 11 Canadian Cities. *Data*, *4*(2), 72. https://doi.org/10.3390/data4020072

Gradeci, K., Labonnote, N., Time, B. and Köhler, J. (2017). Mould growth criteria and design avoidance approaches in wood-based materials – A systematic review. *Construction and Building Materials*, *150*, 77–88. https://doi.org/10.1016/j.conbuildmat.2017.05.204

IPCC. (2014). *Climate change 2014: Synthesis report. Contribution of Working Groups I, II and III to the Fifth Assessment Report of the Intergovernmental Panel on Climate Change [Core Writing Team, R.K. Pachauri and L.A. Meyer (eds.)]* (p. 151). IPCC.

ISO. (2017). *ISO 6946* [Building components and building elements - Thermal resistance and thermal transmittance - Calculation methods]. ISO.

Kumaran, M. K., Lackey, J., Normandin, N., Tariku, F. and van Reenen, D. (2002). *A thermal and moisture transport property database for commom building and insulation materials* (No. 1018-RP). ASHRAE.

Lacasse, M. A., Defo, M., Gaur, A., Moore, T. and Sahyoun, S. (2018). *Approach for assessing the climate resilience of buildings to the effects of hygrothermal loads* (CRB-CPI-Y2-R18; p. 44). NRCC. http://nparc.nrc-cnrc.gc.ca/eng/view/object/?id=757e8bd5-90f3-4656-997f-3ac547fa66ec

Lacasse, M. A., Ge, H., Hegel, M., Jutras, R., Laouadi, A., Sturgeon, G. and Wells, J. (2018). *Guideline on design for durability of building envelopes* (CRBCPI-Y2-R19). http://nparc.nrc-cnrc.gc.ca/eng/view/ object/?id= 45b6a70c-e5a7-419a-bb1a-4687435c7895.

NRC. (2015). *National Building Code of Canada*. National Research Council.

Ojanen, T. and Kumaran, M. K. (1992). Air Exfiltration and Moisture Accumulation in Residential Wall Cavities. *Thermal Performance of the Exterior Envelopes of Buildings V*, 491–500.

Ojanen, T. and Kumaran, K. (1996). Effect of Exfiltration on the Hygrothermal Behaviour of a Residential Wall Assembly. *Journal of Thermal Insulation and Building Envelopes*, *19*(3), 215–227. https://doi.org/ 10.1177/ 109719639601900303.

Ojanen, T., Viitanen, H., Peuhkuri, R., Lähdesmäki, K., Vinha, J. and Salminen, K. (2010). Mold Growth Modeling of Building Structures Using Sensitivity Classes of Materials. *Eleventh International Conference on Thermal Performance of the Exterior Envelopes of Whole Buildings*, 10.

Saber, H. H. (2014). *Report on Properties and Position of Materials in the Building Envelope for Housing and Small Buildings* (No. A1-004615; p. 108). NRC-CNRC.

Sedlbauer, K. (2001). *Prediction of mould fungus formation on the surface of and inside building components* [Thesis (Doctorate)]. Sttutgart Universitat.

Vereecken, E. and Roels, S. (2012). Review of mould prediction models and their influence on mould risk evaluation. *Building and Environment*, *51*, 296–310. https://doi.org/10.1016/j.buildenv.2011.11.003.

Vereecken, E., Saelens, D. and Roels, S. (2011). A comparison of different mould prediction models. *12th Conference of International Building Performance Simulation Association*, 8.

Viitanen, H., Krus, M., Ojanen, T., Eitner, V. and Zirkelbach, D. (2015). Mold Risk Classification Based on Comparative Evaluation of Two Established Growth Models. *Energy Procedia*, *78*, 1425–1430. https://doi.org/10.1016/j.egypro.2015.11.165.

XV International Conference on Durability of Building Materials and Components
DBMC 2020, Barcelona
C. Serrat, J.R. Casas and V. Gibert (Eds)

Assessment of Moisture Response and Expected Durability of a Heritage Masonry Building Subjected to Projected Future Climate Loads of Ottawa, Canada

John A. Wells[1], Michael A. Lacasse[2] and Gary Sturgeon[3]

[1]Crosier Kilgour & Partners Ltd., Consulting Structural Engineers, Winnipeg, Manitoba, Canada
[2]Facade Systems and Products Group, Construction Research Centre, National Research Council of Canada, Ottawa, Ontario, Canada
[3]BBSTEK Ltd., Consultant & Structural Engineer, Millarville, Alberta, Canada

Abstract. *As part of the Canadian government's recent drive to the "on Greening Government initiative, heritage buildings forming part of the parliamentary precinct in Ottawa, Canada are to be retrofitted in the coming years to help reduce energy usage and decrease greenhouse gas emissions associated with heating and cooling. Increasing levels of GHG concentrations over time has the potential to raise the mean global temperature by +3.5 degrees. The predicted impact on Ottawa's climate will be significant, increasing precipitation annually by 14.4% and decreasing the January winter design temperature from -25°C to -11.7°C or 53%. In this paper, the moisture response of a heritage building located in Ottawa, Canada is determined from results of numerical simulations when subjected to both historical and projected future climate loads. Various insulation strategies for masonry wall systems were assessed. The objective was to decrease the energy demand associated with heating and cooling by applying insulation on the interior face of the masonry. Using future climate loads, results from hygrothermal modeling showed that although the climate change model produces higher volumes of annual precipitation, no deleterious levels of moisture build-up were observed in the wall system. In fact, moisture levels remained relatively consistent, irrespective of the insulation type applied to the interior face of the walls. Moisture content for all scenarios was well below critical saturation of the masonry materials. The warming climate has a dramatic effect by reducing the number of hours below freezing experienced by the interior brick wythe when interior insulation is applied. From the hygrothermal analysis, it was concluded that the warming temperatures will substantially reduce the number of hours the interior wythe of masonry experiences freezing temperatures which in turn, reduces the potential for freeze-thaw damage to the masonry. The interior application of moderate levels of insulation should therefore be considered for retrofit measures for this heritage building, located in Ottawa, Canada, without increasing the risk of damage to the wall.*

Keywords: *Climate Change, Durability, Historic Building, Hygrothermal Simulation, Masonry Walls, Moisture Response.*

1 Introduction

There is overwhelming evidence that continued increases in world greenhouse gas (GHG) generation is impacting climate change on a global scale. Although Canada's contribution to world GHG's has been trending downward from 1.8% to 1.6% over the last 10 years, it remains 9th overall in contribution to world GHG generation. Buildings in Canada contribute 12% of its overall GHG annual total and this number has remained relatively unchanged between 1990 and 2017[2]. Thus, significant room for improvement exists in Canada to decrease GHG's for both new and existing building stock.

The introduction of the National Energy Code of Canada for Buildings has initiated significant enhancements to reducing the GHG's of new buildings and additions to existing buildings; however, many existing buildings, and particularly heritage buildings are presently exempt from implementing the Code required changes to the building envelope to reduce the contribution of greenhouse gas generation associated with heating and cooling loads.

As part of the Canadian government's recent drive to the "Greening Government" initiative, heritage buildings forming part of the parliamentary precinct district in Ottawa are to be retrofitted in the coming years to help reduce energy use for heating and cooling loads and ultimately decrease greenhouse gas emissions. Such measures may require intensive remediation and for heritage restoration projects may also involve changes to the building envelope, including but not limited to, increased thermal resistance of the wall system, enhanced precipitation managements strategies, and introduction of an air barrier. However, sufficient number of case studies exist to conclude that caution is required when introducing insulation to masonry wall systems on heritage buildings because of the changes in thermal and moisture loads can induce damage, (Wilkenson, De Rose; Wojcik, Bomberg) principally by freeze-thaw degradation.

Hygrothermal modeling is often used to assess the impact changes to materials and assemblies in the building envelope may have on the durability of the exterior walls, primarily due to cumulative moisture effects and the associated degradation actions. Hygrothermal modeling for heritage buildings present a unique challenge for analysis, primarily because owners of these buildings understandably have an entrenched expectation of a long Design Service Life for mass masonry wall systems. The impact of climate change creates a potential confounding error in the analysis if historical weather databases are used in the hygrothermal model rather than databases for the predicted future climate.

The purpose of this paper is to present the results of the predicted durability analysis of one of the several Parliamentary precinct buildings, specifically, the Wellington Building located at 180 Wellington Street in downtown Ottawa, Canada. A comparative study is completed on the hygrothermal analysis for the typical masonry wall system of the building using both the present climatic data and a revised climatic data base that incorporates changes to climate associated with increasing levels of GHG's. The impact of various insulation strategies on cumulative moisture within wall materials and assemblies is also presented for discussion for both the existing and predicted changes in climatic load files.

2 Problem Background

Many historical buildings have performed well for decades (Mario D. Gonçalves 2007) when perimeter steam was used to heat the building and no forced air ventilation systems, or humidification were implemented. The warmer masonry increased the moisture storage capacity of the masonry, reducing condensation potential. Unfortunately, many multi-wythe clay brick buildings have experienced significant degradation after the introduction of interior insulation, forced air ventilation, and humidification (Mario D. Gonçalves 2007).

The presence of exterior Character Defining Elements in historical buildings prohibits the introduction of exterior insulation; thus, insulation is typically applied over the interior surfaces of the masonry to increase the thermal resistance of the wall section and decrease conductive heat loss. However, during the heating season, the low temperatures on the interior face of the brick masonry fluctuates in cold exterior temperatures and when combined with higher moisture levels in the air promote the formation of condensation within the wall system. In order to rationalize the introduction, location, and type of insulation to heritage buildings, a systematic approach is needed, as for example that provided in NRC's "Guideline for design for durability of building envelopes" (Lacasse, *et al.*).

Ottawa is qualitatively considered to have a cold, wet winter. However, climate change associated with increases in GHG's is expected to create overall higher ambient temperatures and rain fall. The Ottawa, Ontario historical (current) climate design values from Appendix C of the National Building Code of Canada are summarized in Table 1, and changes in the design parameters associated with global mean temperature increases of +2.0^{o} C and +3.5^{o}C are also provided for comparison purposes (source ECCC).

Table 1. Current National Building Code environmental loads and predicted loads based on mean global temperature increases of +2.0C and +3.5C. (Gaur, Lacasse, Armstrong)

Scenario	2.5% Jan. Degrees C	2.5% July Degrees C	Degree Days below 18C	Annual Rain mm	Snow Load kPa	Hourly Wind Press., kPa
Current	-25.0	+30.0	4440	750	2.4	0.41
@ +2.0ºC	-17.4	32.7	3609	857	1.66	0.41
@+3.5ºC	-11.7	34.4	3097	933	1.23	0.41

Current models suggest that in addition to rising mean temperatures, the climate will become wetter with estimated increases in annual precipitation of 8.1% and 14.4% for global temperature increases of 2.0º and 3.5ºC, respectively.

The primary goal of the broader investigation is to reduce the heating and cooling loads for heritage buildings and thus, decrease the contribution of building operations to global GHG's. The application of insulation to increase the thermal resistance of exterior walls was therefore analyzed using hygrothermal modeling to reveal deleterious moisture build-up, based on both the existing historical climate loads and predicted changes in climate from increases in GHG's.

3 Methodology

The commercial hygrothermal modeling program, WUFI6.3Pro was utilized for the analysis. The material property input data for WUFI requires the bulk density, porosity, heat capacity, thermal conductivity, and Water Vapour Resistance Factor. Bulk density, porosity, specific heat capacity, and heat conductivity value approximations do not significantly influence the hygrothermal analysis and estimates are generally sufficient (WUFI User Manual). A common problem when undertaking hygrothermal modeling is obtaining the necessary material properties for each of the components in the wall system (Wells, *et al.*). Material testing for all parameters is time consuming and expensive and thus, alternative techniques have been utilized to permit estimating the material properties required for the analysis, including the process of clustering (de Place Hansen and Moller). The following summarizes the known properties and assumptions made determining the material properties used in the present study while Figure 1 shows the plane of each material in the wall system.

- Indiana Limestone (exterior): Quarrier provided data on all properties with the exception of Water Vapour Resistance Factor. WUFI Data base on Krensheimer Shelly Limestone has similar properties; therefore, the vapour resistance for Krensheimer Limestone provided by the WUFI data base was used
- Clay brick (e): Brick hygrothermal data available for red clay brick from Ottawa, tested at NRC. Comparative analysis made to WUFI's material data base on Red Matt Clay Brick.
- Parging(d): Historic Lime and Pozzolana from WUFI data base; largely based on permeability.
- Cork(c), Plaster (a), Paint, etc. from North American WUFI Data base

The Wellington Building was designed and substantially complete in 1927. Figure 1 shows the existing building and interior cross-section; the painted plaster, air space, parging over two wythes of red clay brick, faced by exterior Indiana Limestone veneer. The black spots on the parging are the remnants of mastic that was used to bond one-inch cork insulation to the interior face of the parging.

Figure 1. General elevation view and cross section of exterior wall showing parging and interior red brick behind Indiana limestone veneer. Black spots are mastic used to bond one-inch cork insulation (Interior photo courtesy of JM Carriere of Adjeleian Allen Rubeli Ltd.).

For the hygrothermal analysis, the National Research Council of Canada created WUFI compatible hourly climate data files with assistance from Environment and Climate Change Canada (ECCC). Access to both historical and future projected climate data permits, on the basis of results derived from simulation, estimating the durability response for the exterior walls due to changing climatic exposure conditions. Two climate files were provided; NRC1989, representative of the historical climate loads over 31 years (1985-2016), and NRC2074, characteristic of the predicted climate loads associated with global mean temperature increase of +3.5C due to increasing levels of GHG's. A second set of runs were completed as the base case using the WUFI embedded ASHRAE RP1325 climatic data file for Ottawa.

A primary component of the overall investigation concerns the reduction in GHG generation associated with heating and cooling loads and thus, we assessed the impact on the application of insulation to the interior face of the parging (Figure 1 d.) which is bonded to the inner wythe of brick.The assumption was that the existing interior plaster and cork insulation would be removed to accommodate the new insulation. In total, three insulations were evaluated; open cell polyurethane foam, closed-cell polyurethane foam, and mineral wool insulation. Open cell was chosen to provide air leakage control, and thus an air barrier component on the interior face to reduce interstitial condensation due to its air permeance well below 0.02l/(s-m^2). Closed-cell foam was chosen to provide both air and vapour diffusion control. Finally, mineral wool was also evaluated because of its reversibility and non-combustibility. Each insulation was covered with painted drywall.

With respect to the level of thermal resistance considered for the retrofit, the energy consultant to the project suggested that economics would likely negate a cost-benefit ratio if more than RSI 1.75 to 2.11 were applied. Thus, the hygrothermal models were based on 75 mm of open-cell foam, 50 mm closed-cell foam, and 65 mm of mineral wool such that all levels of thermal resistance were within close agreement.

4 Results

To rationalize the number of hygrothermal model runs to be completed, the existing wall performance, without added insulation was examined based on the climatic data file for ASHRAE 160 embedded into the WUFI program. The ASHRAE 160 - RP1325 historical climate file was found to be generally colder and wetter than that provided in the NRC1989 data and was therefore used as the base or existing case. Four models were run, one for each face of the building, upper elevation to establish the governing case with respect to the largest

moisture build-up. Based on the building's size and geometry, it was confirmed that the upper north face of the building produced the greatest moisture accumulation for both the existing and projected climate change models, NRC2074. Thus, the focus of the investigation centred on the north face. In total, 24 individual hygrothermal model runs were completed for the analysis using an exposure period of five years. Model results were based on with and without the 1% retained moisture, as specified in the ASHRAE 160. In addition to modelling the performance of the existing wall cross-section, the impact of introducing three types of insulation was examined, each applied to the thickness required to increase the thermal resistance of the wall section to approximately RSI2.5.

The following table summarizes the results obtained for the existing ASHRAE Year 1 historical climatic load file, and the predicted performance, based on the 3.5°C mean increase in global temperature, NRC2074. The results show that conditions tend to stabilize seasonally in years three to five; thus, where relevant, the minimum and maximum moisture content is provided. Where moisture levels continue to increase over time, a "∧" has been added to show that the moisture content is generally increasing and not remaining stable over time.

Table 2. Five- year moisture content layer based on existing historical climatic data file and projected climate change model (NRC2074) for base case and insulated wall options.

Scenario	Total Water Content (kg/m^3)	Limestone M.C. (%)		Brick Layer M.C. (%)	Parging M.C. (%)	
		Max.	Min.		Max.	Min.
Exist. Wall	6.0 ∧	0.37	0.24	2.7	0.63	0.45
Exist. + NRC2074	6.0	0.37	0.25	2.90	0.55	0.38
Mineral Wool	6.5 ∧	0.36	0.23	2.80	1.8	0.40
M.W. + NRC2074	6.5	0.39	0.25	2.90	1.5	0.32
Open Cell Foam	6.5 ∧	0.36	0.22	2.80	1.8	0.40
OCF+ NRC2074	6.5	0.42	0.26	2.90	1.4	0.32
Closed Cell Foam	6.2 ∧	0.36	0.22	2.80	0.85	0.50
CCF+ NRC2074	6.5	0.42	0.26	2.90	0.77	0.40
M.W.+Infilt + NRC2074	6.5	0.37	0.23	2.90	2.3	0.40

From the information provided in Table 2, it may be seen that although the climate change model produces higher volumes of annual precipitation, no deleterious levels of moisture build-up were observed in the wall system. In fact, moisture levels remained relatively consistent, irrespective of the insulation type applied to the interior face of the walls. Moisture content for all scenarios is well below critical saturation of the masonry materials as the moisture storage capacity for the limestone, brick, and parging is over 70 kg/m^3, 50 kg/m^3, and 30 kg/m^3, respectively (WUFI Material Data Base).

The ASHRAE 160 recommendation of 1% retained moisture is observed to be the primary driver for increasing moisture content in the walls and based on the results for the existing, wall section (with and without insulation), the model results are indicative of continuing increases in moisture with time of exposure. The climate change model, NRC2074 appears however, to stabilize the moisture accumulation in the walls, regardless of the insulation type applied. The information provided in Figures 2 and 3 show the total water content for the mineral wool insulated wall section based on the current historical ASHRAE 160 climate data file, and the predicted climatic file based on the 3.5°C mean increase in global temperatures, NRC2074.

From the figures, the total moisture content quickly reaches a semi-asymptotic value for the climate change model whereas the historical data file creates a continuing increase in moisture within the wall system. We postulate that the increasing temperatures, as projected in the future under a warming climate, are facilitating a drying process of the walls.

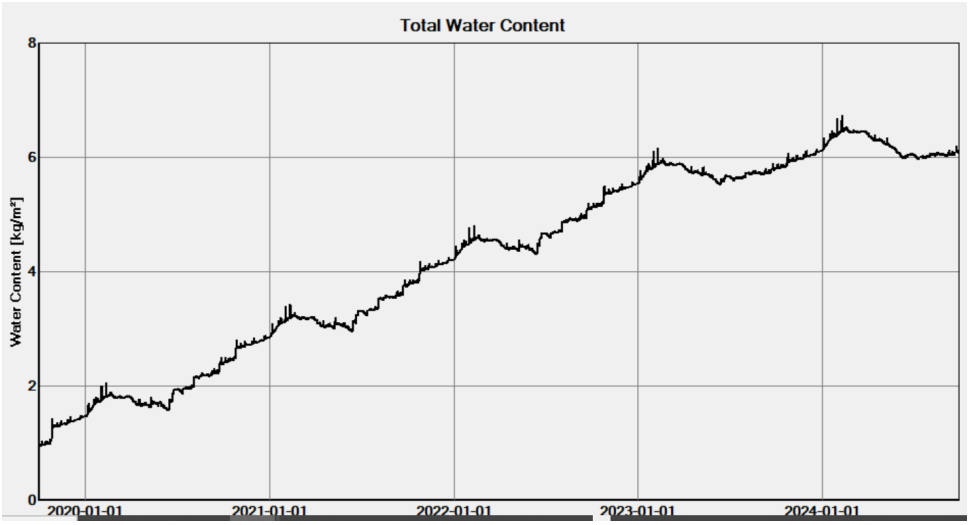

Figure 2. Total moisture content for mineral wool case based on historical ASHRAE 160 climatic data file.

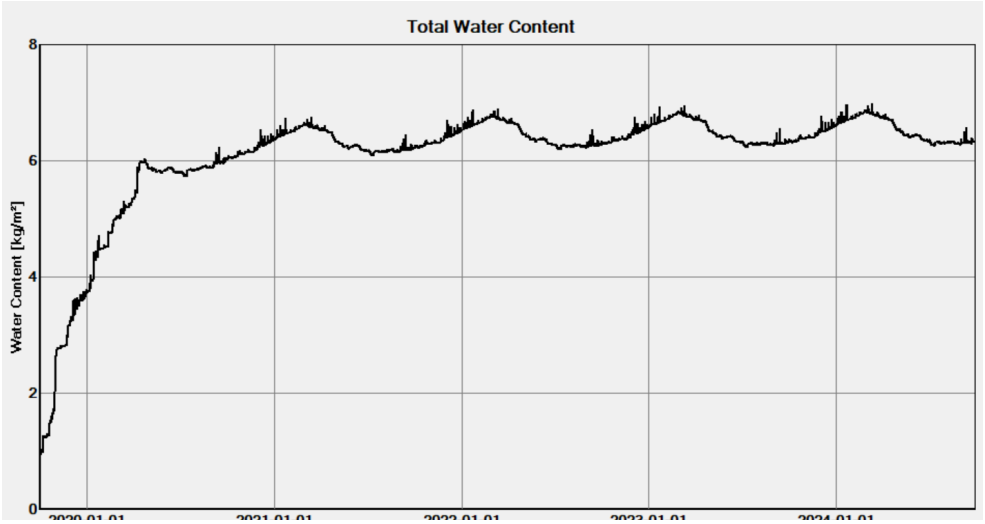

Figure 3. Total moisture content for mineral wool case based on NRC 2074 climate change data file.

One of the principal concerns about the durability of heritage buildings with the inclusion of interior insulation is the potential to reduce masonry wall temperatures below freezing, and to increase the likelihood of freeze-thaw degradation. For the NRC2074 climate file, we introduced air infiltration as a moisture source through the mineral wool insulation model to enable assessing the impact that condensation may have on increasing wall moisture levels. From Table 2, the simulation scenario labelled "M.W. +Infilt. + NRC2074" shows that the moisture levels of the parging and inner wythe of brick predictably increase; however, moisture content remains well below any reasonable limit that might initiate freeze-thaw degradation.

The number of hours per year that the interior face of the parging is below freezing was also found as a simple comparison to evaluate the impact that the different types of insulation have on keeping the interior parging below freezing. A summary of the results of the analysis are given in Table 3; these have been extracted from the WUFI data file in which the mean number of hours per year are provided for the interior parging. It shows the number of hours that the interior parging will be below freezing based on the future projected data (NRC2074) and the same for the historical climate data.

Table 3. Mean number of hours per year interior parging (bonded to inner brick) is below freezing based on existing and projected climate temperatures for existing wall and insulation options.

Climate File	Existing Wall	Mineral Wool	Open Cell Foam	Closed Cell Foam
Historic Climate	718 hrs	1514 hrs	1640 hrs	1733 hrs
Predicted Climate, NRC 2074	0 hrs	604 hrs	740 hrs	830 hrs

The differences in the number of hours per year below freezing amongst the different types of insulation used to retrofit the walls is a function of the type of material and minor differences in the thermal resistances provided by the various insulation types. Regardless, from the information provided in Table 3, the warming climate predicted with the 3.5°C mean global temperature increase will have a dramatic effect by reducing the number of hours the interior parging and inner wythe of brick experiences temperatures below freezing. The warming temperatures may therefore reduce the concern of installing insulation on the interior face of the masonry.

5 Summary and Conclusion

Hygrothermal modeling was utilized to establish if projected changes in temperature and precipitation loads predicted by climate change models from a warming climate will impact the durability of a masonry heritage building, located in Ottawa, Canada having insulation introduced on its interior wall face. The significant findings are summarized below.

- Increasing levels of GHG concentrations has the potential to raise the mean global temperature by +3.5°C degrees. The predicted impact on Ottawa's climate will be significant, increasing precipitation annually by 14.4% and decreasing the January winter design temperature from -25.0°C to -11.7°C or by 53%.
- Results show that although the climate change model produces higher volumes of annual precipitation, no deleterious levels of moisture build-up were observed in the masonry wall systems studied. In fact, moisture levels remained relatively consistent, irrespective of the insulation type applied to the interior face of the walls. Accumulated moisture content for all scenarios is well below critical saturation of the masonry materials.
- Total predicted moisture content in the wall system quickly reaches a semi-asymptotic value for the climate change model whereas the historical data file creates a continuing increase in moisture within the wall system. The increasing temperatures appear to facilitate drying of the walls.
- The warming climate has a dramatic effect by reducing the number of hours below freezing experienced by the interior parging and wythe of brick. The existing wall section, without insulation was predicted to have no hours below freezing along the interior wythe under future climate change loads versus 718 hours under historic loads. With the inclusion of insulation, the reduction in hours below freezing varies from 60%, 55%, and 52% for mineral wool, open-cell foam, and closed-cell foam, respectively, under exposure to future climate loads versus historic climate loads.

The placement of insulation on the interior face of masonry walls in heritage buildings is a proposed solution to reducing heating and cooling loads, and thus, to reducing GHG generation. Using hygrothermal analysis, the study shows that the warming temperatures resulting from climate change potentially will substantially reduce the number hours of freezing temperatures experienced by the interior wythe of masonry, maintain the moisture content of the masonry below a damage threshold, and therefore may reduce the potential for freeze-thaw damage to the masonry. The interior application of moderate levels of insulation should therefore be considered for retrofit measures for this heritage building, located in Ottawa, Canada, without increasing the

risk of damage to the wall. Future studies are proposed which will include a comparative analysis of the hygrothermal results based on testing the actual masonry materials in the Wellington Building in order to validate the material assumptions made in the present study.

Acknowledgements

The authors sincerely appreciate the contribution of Environment and Climate Change Canada (ECCC) for their contribution to the climate data files, Adjeleian Allen Rubeli for the Wellington Building interior photograph, and Mr. Brennan Sperl, E.I.T. of Crosier Kilgour & Partners Ltd. for running of the WUFI models.

References

DePlace Hansen and Moller (2018). How to estimate properties for external walls in historic buildings before applying internal insulation, *Energy Efficiency in Buildings.*

Environment and Climate Change Canada (2019). *Canadian Environmental Sustainability Indicators: Greenhouse Gas Emissions.*

Robert Wojcik and Mark Bomberg (2016). Journal of Building Physics, *On interior rehabilitation of buildings with historic facades*,*40*(2), 141-161.

Little, Ferraro, and Arregi. Historic Environment. *Assessing risks in insulation retrofits using hygrothermal software tools*., Scotland Technical Paper 15.

National Building Code of Canada (2015).

Lacasse, Michael, et al, (2018). National Research Council of Canada, *Guideline on Design of Durability of Building Envelopes*.

Gaur, Lacasse, Armstrong, (2019). *Climate data to undertake hygrothermal and whole building simulations under projected climate change influences for 11 Canadian Cities*.

Wells, Spewak, (2019). NRC Press/Canadian Journal of Civil Engineering, *The use of hygrothermal modeling to validate the application of an open-cell spray-foam insulation application to a high-rise heritage building in Winnipeg, MB*.

Wilkinson, DeRose and Sullivan, (2009). Journal of Building Enclosure Design *Measuring the impact of interior insulation on solid masonry walls in a cold climate*.

XV International Conference on Durability of Building Materials and Components
DBMC 2020, Barcelona
C. Serrat, J.R. Casas and V. Gibert (Eds)

Do We Need Hygrothermal Simulations to Evaluate the Design for Durability?

Martin Morelli[1] **and Erik Brandt**[2]

[1] Department of the Built Environment, Aalborg University, A.C. Meyers Vænge 15, 2450 Copenhagen, Denmark, marmo@build.aau.dk

[2] Department of the Built Environment, Aalborg University, A.C. Meyers Vænge 15, 2450 Copenhagen, Denmark, ebra@build.aau.dk

Abstract. *The Danish Building regulations are function based and describe in broad terms which requirements must be fulfilled. The main message is that buildings and their structures must be built in such a way that they have a satisfactory functionality and durability i.e. that materials and constructions used can resist the stresses they are exposed to under use. However, there are no Danish guidelines on how to document fulfillment of the requirements. Durability largely depends on moisture related problems, and many failure modes/mechanisms are linked to moisture conditions. It is a prerequisite that the hygrothermal performance of a building component is satisfactory if a long service life shall be obtained. The paper will demonstrate how the risk of moisture problems is assessed in Denmark by using a stud wall as an example. However, simulations can be used for documenting the expected performance of wall assemblies, under in use conditions, however is not a conditional necessity. Even though an evaluation or simulation of moisture conditions show satisfactory results problems can occur e.g. if unsuited materials are used or if materials or building elements are used in another way than foreseen. A few examples are shown how simulations could and could not be used to determine whether a structure would have a long service life or not. Finally, a comparison of simulations, calculations and measurements are performed to illustrate the difference in results from moisture assessment that can be achieved based on assessment methodology.*

Keywords: *Performance Criteria, Assessment of Durability, Documentation, Function-Based, Moisture Simulation.*

1 Introduction

Durability of building materials, components or elements is a crucial parameter in the design of buildings with a long service life. To design for durability, it is necessary to consider which environment the building element is located in, the agents that can degrade the materials and in case of degradation how to maintain or repair the building element (ISO, 2008; Morelli and Lacasse, 2019). Moisture damage is perhaps one of the most critical agents limiting the building's service life causing premature degradation of building elements (Nevalainen *et al.*, 2010; Becher *et al.*, 2017) and contamination of indoor environment (Hägerhed-Engman, Bornehag and Sundell, 2009). A too high moisture content for too long can cause degradation of components inside building elements and/or biological growth of *e.g.* mould. Consequently, studying the coupled heat and moisture transport in structures is essential to improve or document the performance of the building envelope.

This paper presents a number of methods that might be applicable to document the service life as required in the Danish Building regulations (BR, 2019) related to moisture problems.

Furthermore, the paper will discuss if hygrothermal simulations are needed for evaluating the durability of the design of structures. Using an exterior wooden-stud wall as example, the paper discusses how the risk of moisture problems can be assessed applying different methodologies. Furthermore, calculations/simulations are compared to measurements conducted in the stud wall, to illustrate how the documentation of the expected performance can be conducted. Finally, two examples are presented on failure mechanisms, where unsuited materials or design is used for a given outdoor climate.

1.1 Prescriptive or Performance-Based Building Regulations

During the past decades, the Danish building regulations have amended from prescriptive building regulations towards performance-based regulations. Gottlieb and Frederiksen (2019) mention the accelerating development of new products and materials as contributing to change the building regulations towards performance-based requirements. The development from prescriptive to performance-based regulations are seen in the building style of older apartment buildings in Copenhagen. Many old buildings constructed around 1900 have similar façade appearance because the building regulations had prescriptive requirements related to the building design; whereas the appearance of today's building stock is more varying. The performance-based regulations describe the functional attributes that *e.g.* building components must fulfill. These requirements can be achieved with several designs; *i.e.* the regulations do not any more describe how to build but rather what performance the finished buildings shall have.

The chapter of the building regulations related to energy consumption set out a maximum allowable energy consumption for the entire building (BR, 2019, §259-260) and an upper threshold for the U-values of the structures (BR, 2019, §257). In the chapter related to moisture, the regulations only describe that buildings and their structures must be built in such a way that they have a satisfactory functionality and durability, and that materials used can resist the environment they are exposed to (BR, 2019, §334). The energy and moisture examples illustrate the variation in details of the Danish building regulations, that consulting engineers and architects faces (hereafter referred to as designers). On the one hand, exact energy requirements are given (and there exist a tool to use for documentation); however, on the other hand there is no methodology to document that moisture will not result in moisture problems in the structure or indoor climate. Regarding documentation of moisture related properties, the designer can perform, *e.g.* Glaser method calculation (Glaser, 1958) or detailed hygrothermal simulations in 1D or 2D; however, it is up to the designers to decide on the level of documentation for whether the structures comply with the building regulations. A random check is performed in 10% of building projects with occupation permit, however, the random check does not necessary include an evaluation of the moisture documentation.

2 Methods for Assessing Moisture Problems

Designers of structures can use a variety of methods to support or document that the structure is durable regarding moisture exposure under in use conditions. However, the different methods all have limitations. The authors understand that the methods described below are those most commonly used in Denmark. The approaches are ranked from simple to complex, and can be used to evaluate the risk of moisture problems, where mould growth is considered the first

indication of a mediocre structure design, which can contribute to health problems indoors.

1. *"Common best practice" or learn from experience.* This is normally supported by guidelines (*e.g.* www.anvisninger.dk) and experience documents (*e.g.* Building defect sheets, www.byg-erfa.dk) made on basis of experience from the use in practice. Normally, materials and building elements described in this literature function satisfactory under the given climate condition etc. No calculations or further documentation for properties is needed.
2. *Simulation of isotherms combined with determination of the point where the relative humidity exceed 75% or condensation.* This is used in more complex structures of 2D problems. Combined with considerations of the indoor environment and temperatures in the construction this is a simple evaluation method. The designer has to decide on the evaluation criteria of a given relative humidity, which normally is set to 75%.
3. *Glaser calculation according to EN 13788 (EN ISO, 2012).* This includes calculation of surface and interstitial condensation including drying out of the structure or evaluation of critical points exceeding 75% relative humidity. Glaser is used on 1D problems.
4. *Hygrothermal simulations in 1D or 2D.* In more complex structures simulation programs can be used to determine the conditions in the structure and on all internal surfaces. This method is the most comprehensive approach for assessing moisture conditions in building elements. However, the results are to be post-processed with another evaluation tool.

Depending on the chosen approach (1-4), the simplest evaluation is to check if the relative humidity exceed a threshold value of 75%. Post-processing methods that are more sophisticated are developed to evaluate for example the performance of exterior walls with respect to exposure of high moisture load for too long. In these methods both time, temperature, moisture level and material are considered. For organic materials, this would especially be with respect to evaluating the risk of mould growth and/or wood rot, whereas for inorganic porous materials it could be evaluating the risk for freeze-thaw damages. Other types of environmental actions could be subterranean termites, drying and shrinkage as well as alkali-aggregate reactions.

3 Example of Measurements, Calculation and Simulation

In this example, we consider an exterior wood-stud wall constructed with 465 mm glass-fiber insulation as shown in Figure 1 and installed in a single-family house. The vapour barrier was mounted behind the first inside insulation layer. In the wall, measuring devices were installed to measure temperature and relative humidity. The measuring points were located in the interior insulation against the vapour barrier and in the exterior insulation against the plywood board. The measurements were conducted from October 2013 to March 2014.

3.1 Boundary Conditions

The Glaser calculation used boundary conditions from October to March; *i.e.* monthly average values of temperature and relative humidity for Denmark and internal humidity class 2 (EN ISO, 2012) for the interior climate, see Table 1.

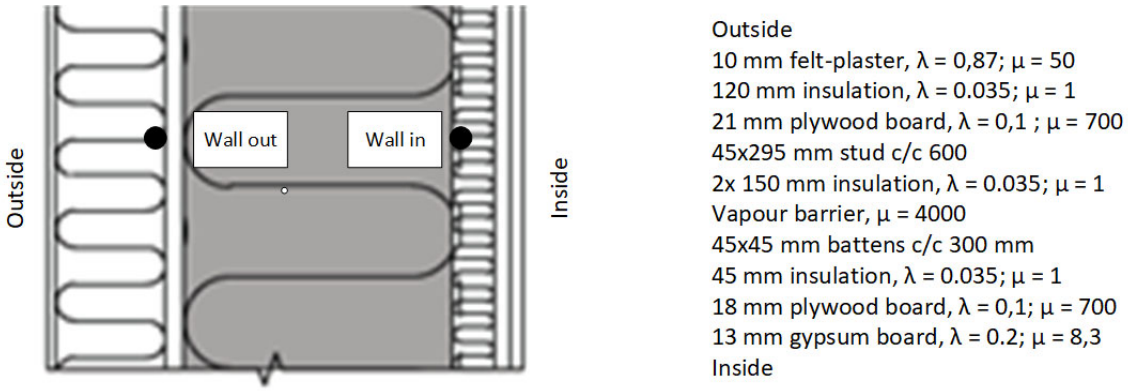

Figure 1. Exterior wood-stud wall with 465 mm insulation.

Table 1. Climate data for Glaser calculation. Temperature in ºC and relative humidity in %.

	October	November	December	January	February	March
T_{in}	20	20	20	20	20	20
RH_{in}	57	53	49	46	46	49
T_{out}	9.2	5.0	1.6	-0.6	-1.1	2.6
RH_{out}	87	91	88	94	91	91

In the hygrothermal simulations, weather data from Lund in southern Sweden (close to Denmark) was used as exterior boundary conditions, and the indoor climate was set according to the internal humidity class 2. Based on the results from the simulations the risk of mould growth was evaluated on the outside of the plywood and the inside of the vapour barrier, which then are comparable with the measurements and Glaser calculation.

3.2 Results from Measurements, Calculations and Simulations

Figure 2 show the results from WUFI simulations (Künzel, 1995), Glaser calculations and measurements for the period October to March. The results are not a validation of the three methods but only a way of illustrating how different approaches can bring different results.

4 Discussion

Designing for durability requires that designers consider several aspects where some information is difficult to predict *e.g.* climate changes and some are unknown *e.g.* material properties of new products. de Place Hansen *et al.* (2020) present a systematic review of new products used in building envelope structures, aiming at reducing the risk of using unsuited materials.

Using common best practice documents for design is based on many years of experience. However, the conditions under which the building elements perform is retrospective and the used materials and components are well known. Therefore, one might question how these structures will perform in the future with expected climate changes. These common best practice designs of the building envelope, further presume that built-in moisture is very limited, and that eaves protect the walls. The common best practice designs do not require documentation of the long-term performance, as this is implicit in the documents published.

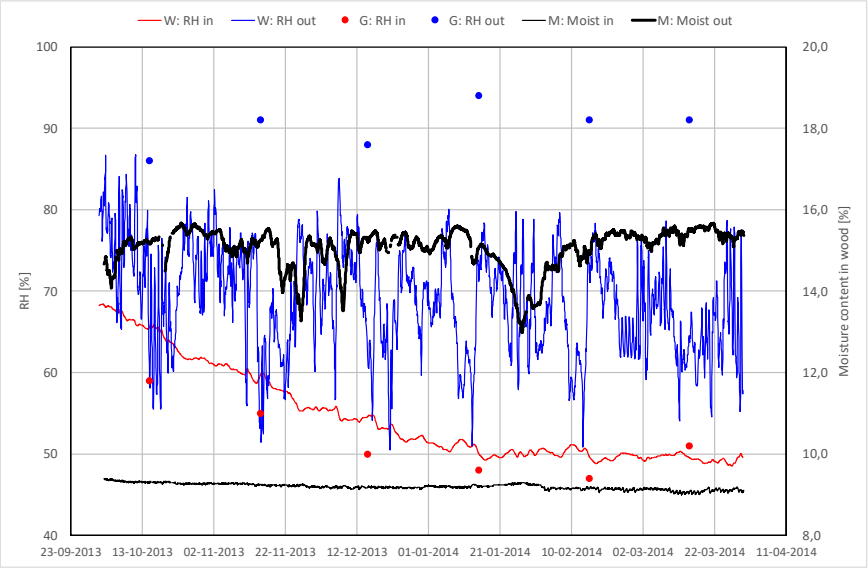

Figure 2. Results from WUFI simulations, Glaser calculations and Measurements from October to March.

Considering the other three methods (isotherm -, Glaser calculations and hygrothermal simulations) presented for assessing moisture problems in structures, all take into account interior and exterior boundary conditions differently. In a Danish context, the different methods are challenged by the different outdoor climate used, *e.g.*, that Glaser calculation uses monthly average values of temperature for a Danish reference year. Danish weather data does not exist for hygrothermal simulations where rain data are included. Therefore, weather data for either Sweden or Germany are used, as these are the closest data that is available. Finally, isotherm calculations only consider temperature.

The climate that the building envelope is exposed to – and especially moisture as an agent that might reduce the durability – is perhaps the most important. Therefore, moisture exposure during the construction phase should be limited as far as possible, thus increasing the durability.

The application of the four approaches are presented as methodologies for assessing the moisture durability of building envelope structure. Depending on the complexity of the structure or (un)known materials, one of the four approaches could be used for documenting the moisture durability, see Figure 3.

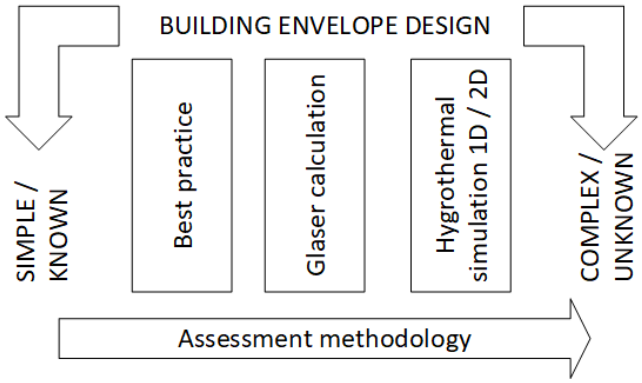

Figure 3. Example of an approach on how to document the moisture durability depending on complexity or (un)known materials.

Hygrothermal simulations are highly relevant in the toolbox of the designer when assessing the durability of building envelope structures. Therefore, it is important to investigate how the building envelope perform under future climate conditions. Performing simulations with a varying climate *e.g.*, as in Canada using cycles of wet-wet-dry years, future climates as can be found under Climate for Culture (a project that investigating the potential impact of climate change on Europe's cultural heritage assets) or weather data with 50 years of occurrence might be needed. Nevertheless, investigating the structure with a retrospective outdoor climate file for several continuous years seems to be insufficient.

In Denmark, the use of hygrothermal simulations become more popular in the design of new structures. However, there exist no guidelines on how to approach such a task and how to assess the output from the simulations. Therefore, the documentation of the requirements in the building regulations depends on the individual designer. The authors suggest that a guideline for design for durability is developed in Denmark. Such a guideline could be inspired by the "Guideline on design for durability of building envelopes" (Lacasse *et al.*, 2018) that is suggested to be implemented in the Canadian building codes. The guideline seems to be reasonable when having known materials that are built together in a different way as described in the common best practice documents. However, the application of the methodology is a challenge when new products are brought to the market that are not already incorporated in hygrothermal simulation programs or for which relevant material properties are not available – here a best estimation must be performed based on the known properties. New materials could be developed for a specific function in a stud wall, however the designer or contractor might suggest to use this new product instead of another product. In such cases, the product might be misused leading to major problems for the building owner. Such cases do not seem to be able to detect using hygrothermal simulation programs.

Performing assessment of the building envelope design also requires post-processing that are anchored in the national building regulations, thus a uniform assessment of the building envelope design for durability can be performed by different designers across the country, such an approach was presented by Overton (2019) for New Zealand.

4.1 Example of Problems Despite Good Results of Moisture Assessment

Even though an evaluation or simulation of moisture conditions show satisfactory results problems can occur e.g. if unsuited materials are used or if materials or building elements are used in another way than foreseen. A couple of examples are given below to illustrate the problems that may be encountered.

4.1.1 Use of MgO boards as wind barrier

MgO boards were introduced in Denmark for use as wind barriers in facades etc. around 2009-2010. Several different suppliers described the material as well suited for the use. The boards had many good properties including permeability, strength, weight, fire properties, workability and price. Due to the price and workability, the boards quickly became popular and gained a good market share even though there was not sufficient impartial documentation. After about five years problems started to occur. The use of boards as wind barrier meant that the boards were exposed to high relative humidity in longer periods of the year. This caused problems as the boards contains salt, which absorbs moisture until the boards start to "cry", *i.e.* salty water

was running from the boards. This caused problems with increased moisture levels in the neighboring materials, corrosion of fastener, screws etc. and mould growth.

The main problem here was that the degradation mechanisms for the material were not identified before the products was used. In this case, an identification of the properties of the board could have revealed that it was not able to withstand the environment in which it was envisaged to be used. A simulation of the moisture content on the wind barrier could have been used to identify the conditions the product would be exposed to.

4.1.2 Use of building elements in harsher environment

In Denmark moisture simulations and full scale tests have shown that wooden facades under certain conditions may be used without ventilation behind the outer cladding.

Recently, the Danish Building Research Institute was asked if the construction also were suited for use in a summer cottage near a coastline exposed to a lot of severe wind (and consequently a lot of driving rain). In this case, a construction tested under conditions simulating a heated house exposed to "normal" wind was proposed to be used under quite different conditions, *i.e.* no heating in winter time and therefore no vapour pressure to remove moisture from the wall, and at the same time risk of more water penetrating through the cladding due to the increased driving rain exposure.

The main problem here is that a correct assessment or simulation is not used – the result of the assessment might be quite different in the less favourable environment. Of importance is that one must understand the context of simulation results and the assumptions/limitations on those results before applying to new scenarios.

4.1.3 Degradation mechanisms must be identified

In order to make a good overall evaluation of the durability of a product it is a necessary condition that an assessment/simulation of the hygrothermal conditions is performed.

However, this is not a sufficient condition as it is also necessary to identify the degradation mechanism of the material or building component and the anticipated assemblies these are envisioned to be used in. The degradation mechanism may be identified partly based on knowledge about the material(s) used. Further, it should be investigated what the functions are of the product, which environment it will be used in (what is the product exposed to) and which properties are necessary.

To ensure long service life materials or building elements should be chosen so they have the sufficient properties. Proof of this should be documented by testing/evaluation of an impartial body.

In case the use conditions are changed as mentioned in the above example (4.1.2) or if the product is envisaged to be used for quite other purposes – *i.e.* with new functions – a new investigation of degradation mechanisms has to be performed as, exposure to another environment must be expected and the necessary properties therefore may be different.

5 Conclusion

To conclude, the authors do not believe that hygrothermal simulations always is the way of documenting building envelope design for its durability. However, the simulations are a strong tool to support the documentation and investigation of new structures that consist of known

materials and components. In any case, the designer must first determine the agents effecting the durability, and then decide how this can be documented *e.g.* applying hygrothermal simulations. Using new materials, the authors do not believe that environmental actions such as agents causing corrosion or decay always are identified as this depends on the designer knowledge. Furthermore, action effects are not necessary made visible through the simulations as new materials are not tested and available in hygrothermal simulation programs. In such cases, the simulations can be used to determine the microclimate that the new product is placed in and its required properties to secure a long service life.

The authors suggest, that in the Danish context, a Guideline on design for durability of building envelope is developed and guidelines for assessing results from hygrothermal simulations. Such two guidelines will be a valuable support for designers when they have to document the durability of structures according to the requirements in the performance-based building regulation. The authors outlined a framework for an approach on how to combine moisture assessment methodologies to the complexity of building envelope structures.

ORCID

Martin Morelli: https://orcid.org/0000-0002-1013-3136
Erik Brandt: https://orcid.org/0000-0003-1485-5600

References

Becher, R., Høie, A.H., Bakke, J.V., Holøs, S.B. and Øvrevik, J. (2017). Dampness and Moisture Problems in Norwegian Homes. *J. Environ. Res. Public Health*, 14(10): 1241.

BR (2019). *Danish Building Regulations*, Chapter 14 §334-338. www.bygningsreglementet.dk

EN ISO (2012). *EN ISO 13788: Hygrothermal performance of building components and building elements – Internal surface temperature to avoid critical surface humidity and interstitial condensation – Calculation methods.*

Glaser, H. (1958). Vereinfachte Berechnung der Dampfdiffusion durch geschichtete Wände bei Ausscheidung von Wasser und Eis. *Kältetechnik* 10, H. 11, S. 358-364 (part 1) and H. 12, S. 386-390 (part 2).

Gottlieb, S.C. and Frederiksen, N. (2019). Deregulation as socio-spatial transformation: Dimensions and consequences of shifting governmentalities in the Danish construction industry. *Environment and Planning C: Politics and Space*.

Hägerhed-Engman, L., Bornehag, C.-G. and Sundell, J. (2009). Building characteristics associated with moisture related problems in 8,918 Swedish dwellings. *International Journal of Environmental Health Research*, 19(4): 251-265.

de Place Hansen, E.J., Nielsen, J., Møller, E.B. and. Peuhkuri, R.H. (2020). How to Determine when a New Building Product is Suitable – Certifications and Experience. In *Proceedings of XV International Conference on Durability of Building Materials and Compponents*, Barcelona, Spain.

ISO (2008). *ISO 13823 General principles on the design of structures for durability.*

Künzel, H.M. (1995). *Simultaneous heat and moisture transport in building components. One- and two-dimensional calculation using simple parameters*. Fraunhofer IRB Verlag, Stuttgart

Lacasse, M.A., Ge, H., Hegel, M., Jutras, R., Laouadi, A., Sturgeon, G. and Wells, J. (2018). Guideline on design for durability of building envelopes. Report CRBCPI-Y2-R19. NRC, Construction.

Morelli, M. and Lacasse, M.A. (2019). A Systematic methodology for design of retrofit actions with longevity. *Journal of Building Physics*, 42(4): 585-604.

Nevalainen, A., Partanen, P., Jääskeläinen, E., Hyvärinen, A., Koskinen, O., Meklin, T., Vahteristo, M., Koivisto, J. and Husman, T. (2010). Prevalence of Moisture Problems in Finnish Houses. *Indoor Air*, 8(S4): pp-pp.

Overton G. (2019). Hygrothermal performance of New Zealand wall constructions – meeting the durability requirements of the New Zealand Building Code. *Canadian Journal of Civil Engineering*, 46(11).

XV International Conference on Durability of Building Materials and Components
DBMC 2020, Barcelona
C. Serrat, J.R. Casas and V. Gibert (Eds)

Hygrothermal Performance Difference of Wooden Beam Embedded in an Internally Insulated Masonry Wall in 2D and 3D Models

Xiaohai Zhou[1,2], Jan Carmeliet[2] and Dominique Derome[3]

[1] Laboratory of Multiscale Studies in Building Physics, Empa, Dübendorf, Switzerland, xiaohai.zhou@empa.ch

[2] Chair of Building Physics, ETH Zürich, Zürich, Switzerland, cajan@ethz.ch

[3] Department of Civil and Building Engineering, Université de Sherbrooke, Sherbrooke, Canada, dominique.derome@USherbrooke.ca

Abstract. *Internal insulation of masonry walls may significantly increase the decay risk of embedded wooden beams due to lower temperature and consequently lower drying potential in the existing wall. Since high moisture contents will affect the performance and service life of wood, the study of moisture-related damage problems in wooden beam-ends in internally insulated masonry walls is of great importance. In the previous studies, the numerical study of hygrothermal performance of wooden beam-ends is performed only with 2D models. In this paper, we study whether a 2D numerical model can represent accurately the 3D hygrothermal behavior of wooden beam-ends. Therefore, the difference between 2D and 3D model results of the hygrothermal performance of wooden beam-ends embedded in an internally insulated masonry wall is analyzed. The difference of temperature and relative humidity in wooden beam-end between 2D and 3D models is in general small. However, 2D hygrothermal models show much lower relative humidities and thus lower moisture risk at some locations in the wooden beam-end. We find that a 3D hygrothermal model more accurately simulates the hygrothermal behavior.*

Keywords: *Interior Thermal Insulation, Wooden Beam, 2D Modeling, 3D Modeling.*

1 Introduction

Many historical buildings are built with solid brick walls and wooden beam constructions. These buildings are mostly not energy efficient and represent a significant energy-saving potential. For some historical buildings with a worth-preserving facade, the only possible energy renovation measure is internal wall insulation. Internal insulation of masonry walls may significantly increase the moisture-related damage risk of building materials and components due to lower temperature and consequently lower drying potential in the existing wall (Morelli and Svendsen, 2013; Harrestrup and Svendsen, 2016; Zhou *et al.*, 2017; Zhou *et al.*, 2018). The floors in old masonry buildings are often carried by wooden beams embedded in the brick. The study of moisture-related problems in wooden beam-ends in internally insulated masonry walls is of high practical and scientific importance (Kehl *et al.*, 2013).

Field investigation and numerical study both indicate that exterior render affects water uptake by external walls during wind driving rain events (Künzel *et al.*, 2004; Pazera and Bomberg, 2010; Guizzardi *et al.*, 2015; Zhou *et al.*, 2018). Exterior renders with high liquid water permeability tend to lead to high moisture contents in the masonry. It is important to study the hygrothermal behavior and durability risk of wooden beam-ends after internal

insulation for renders with different rain protection.

Moisture and heat transport in masonry wall with wooden beam is in reality a three-dimensional problem. However, many studies use only 2D hygrothermal models to study the moisture risk of wooden beam-ends in internally insulated masonry (Johansson *et al.*, 2014; Guizzardi *et al.*, 2015; Harrestrup and Svendsen, 2016). In a 2D model, wooden beam is assumed to have the same width as the wall envelope. However, in reality, the width of wooden beam is much smaller compared to that of wall envelope. It is still an open question whether a simplified 2D numerical model can represent accurately the hygrothermal conditions as modelled in 3D. The aim of this paper is to compare 2D and 3D hygrothermal modelling of the hygrothermal performance of wooden beam-ends embedded in an internally insulated masonry wall.

2 Modelling

2.1 Methodology

Because of modelling restriction, it is hardly feasible to model all bricks and mortar joints of a masonry wall in 3D, since it would lead to very large meshes and high computational costs. Therefore, some simplifications are needed to model the masonry wall in 3D. First, a 2D model with a detailed distribution of bricks and mortar joints is built. Then a 2D model with simplified distribution of bricks and mortar joints is built and compared with the detailed 2D model. The simulated results from these two 2D models are compared and discussed. Finally, based on results of the simplified 2D model, a simplified 3D model is developed.

A typical masonry wall structure of Switzerland is considered for this analysis. The geometry of the 2D model with detailed distribution of bricks and mortar joints is shown in Figure 1. The 2D model comprises from exterior to interior in an exterior render, a masonry wall (three wythes of brick), an original interior plaster, an aerogel-based insulation layer and a new interior plaster layer. In the geometry, there is a 1-cm thick air gap at the wooden beam-end, which prevents direct contact between the wooden beam and the masonry and functions capillary break. A simplified 2D model of this wall is shown in Fig. 2, where the horizontal mortar joints are neglected. The horizontal mortar joints have much smaller liquid permeability compared to brick. Liquid water bypasses the horizontal mortar joints and transports to the inside mainly through brick. The vertical joints are however barriers to liquid transport and have to be considered. The 3D model follows the geometry of the simplified 2D model (Figure 3). In 3D, the width of masonry wall is 100 cm and the width of wooden beam is 20 cm.

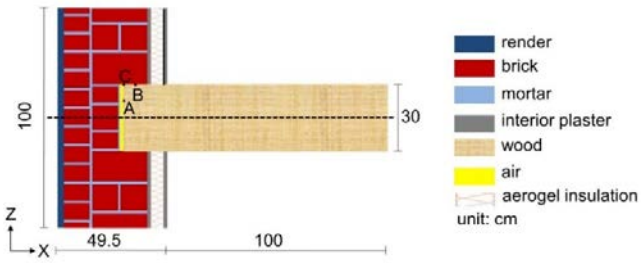

Figure 1. A detailed 2D schematic representation of wooden beam in an internally insulated masonry wall.

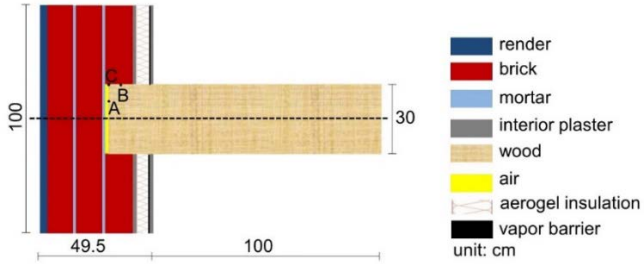

Figure 2. A simplified 2D schematic representation of wooden beam in an internally insulated masonry wall.

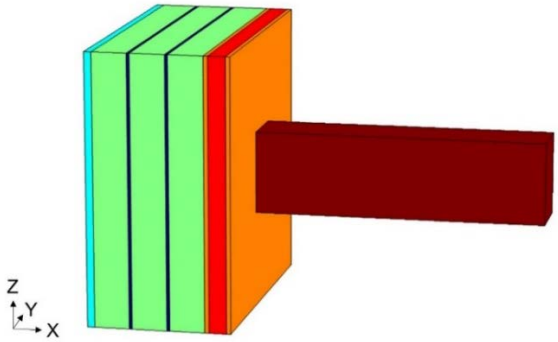

Figure 3. A 3D schematic representation of wooden beam in an internally insulated masonry wall.

2.2 Material Properties

Three types of exterior render are considered: cement lime plaster, lime cement plaster and mineral plaster, which are used to study the influence of the rain protection by the render on moisture-related damage risk of wooden beam-ends embedded in an internally insulated masonry wall. The properties of renders are taken from the WUFI material database (Künzel, 1995). The cement lime plaster shows the highest liquid permeability, followed by the lime cement plaster and the mineral plaster shows the lowest liquid permeability and thus the highest rain protection. No hydraulic interface resistance is considered between brick and mortar. The material properties of brick and interior plaster is from Hagentoft *et al.*, 2004. The material properties of mortar and aerogel plaster are from Guizzardi *et al.*, 2015. The wood of the beam is spruce. Its material properties are obtained from the WUFI database (Künzel, 1995). The wood is considered anisotropic, with longitudinal direction along the beam orientation. Vapor permeability, liquid permeability and thermal conductivity along longitudinal direction are different from those of radial and tangential directions.

2.3 Initial and Boundary Conditions

The hygrothermal performance analysis is based on the moisture reference year of 1999 for Zurich (Zhou *et al.*, 2016). This year is a wet year with a return period of 10 years. The selected wall orientation is 240 degrees from north (WSW), which shows the highest risk for moisture-related problems. This orientation is selected based on the procedure proposed in Zhou *et al.,* 2016. The exterior conditions consists in hourly values of meteorological data from the MeteoSwiss meteorological station. The exterior convective heat transfer coefficient

is calculated according to European standard EN15026. The exterior mass transfer coefficient is related to the exterior convective heat transfer by use of the Lewis analogy. The wind-driven rain load on wall surface is calculated according to ASHRAE Standard 160 - Criteria for Moisture Control Design Analysis in Buildings (TenWolde, 2008). According to Künzel and Kiessl (1996), 70% of the wind-driven rain hitting the façade stays there; the rest splashes off the surface and falls to the ground. The interior conditions are determined according to the European standard EN15026, in which the indoor air temperature and relative humidity depend linearly on the outdoor temperature. The building components have an initial temperature of 20.0 °C and relative humidity of 60%. The simulation is started from October 1st, and repeated for 8 years. The results of the 8th year, which are found to be independent from the initial conditions, are used for further analysis.

2.4 Governing Equation for Moisture and Heat Transport

The three-dimensional governing equations for coupled moisture and heat transport in the building wall envelopes are the following [17]:

$$\frac{\partial w}{\partial p_c}\frac{\partial p_c}{\partial t} + \nabla \cdot (\mathrm{g}_l + \mathrm{g}_v) = 0 \tag{1}$$

with

$$\text{liquid flow: } g_l = -K_{lx} \cdot \nabla p_c - K_{ly} \cdot \nabla p_c - K_{lz} \cdot \nabla p_c \tag{2}$$

Vapor flow:

$$\begin{aligned} g_v = &-\delta_{vx} \cdot \frac{p_v}{\rho_l \cdot R_v \cdot T} \cdot \nabla p_c - \delta_{vy} \cdot \frac{p_v}{\rho_l \cdot R_v \cdot T} \cdot \nabla p_c - \delta_{vz} \cdot \frac{p_v}{\rho_l \cdot R_v \cdot T} \cdot \nabla p_c \\ &-\delta_{vx} \cdot \frac{p_v}{\rho_l \cdot R_v \cdot T^2}(\rho_l \cdot L_v) \cdot \nabla T - \delta_{vy} \cdot \frac{p_v}{\rho_l \cdot R_v \cdot T^2}(\rho_l \cdot L_v) \cdot \nabla T - \delta_{vz} \cdot \frac{p_v}{\rho_l \cdot R_v \cdot T^2}(\rho_l \cdot L_v) \cdot \nabla T \end{aligned} \tag{3}$$

$$(c_0 \cdot \rho_0 + c_l \cdot w) \cdot \frac{\partial T}{\partial t} + \nabla \cdot (c_l \cdot (\mathrm{T} - \mathrm{T}_{ref}) \cdot g_l + (c_v \cdot (\mathrm{T} - \mathrm{T}_{ref}) + L_v) \cdot g_v = -\nabla(\lambda_x \nabla T + \lambda_y \nabla T + \lambda_z \nabla T) \tag{4}$$

where w is the moisture content (kg/m^3), p_c is the capillary pressure (Pa), g_l and g_v are the liquid and vapor flow (kg/m^{2}s), K_{lx}, K_{ly} and K_{lz} are the liquid permeability in the x, y and z direction (s), δ_{vx}, δ_{vy} and δ_{vz} are the water vapor permeability in the x, y and z direction (s), p_v is the vapor pressure (Pa), ρ_l is the density of water (kg/m^3), R_v is the gas constant of water (J/kg K), T is the temperature (K), c_0 is the specific heat capacity of solids (J/kg K), c_l is the specific heat capacity of water (J/kg K), c_v is the specific heat capacity of vapor (J/kg K), ρ_0 is the density of solids (kg/m^3), T_{ref} is the reference temperature (273.15 K), L_v is the latent heat of vaporization (J/kg), λ_x, λ_y and λ_z are the thermal conductivity in the x, y and z direction (W/mK). For two-dimensional model, the variables in the Y direction is neglected.

3 Results

3.1 Comparison of Results Between Detailed and Simplified 2D Model

The simulated results are given for three selected positions at the wooden beam of the 2D detailed and simplified models. The three positions are points A, B and C shown in Fig. 1 and 2. Point A is located next to the air gap in front of the wooden beam. Points B and C are located on the top of the wooden beam in contact with the masonry wall. Point B is located slightly more to the inside compared to Point C. Although the distribution of bricks and mortar joints is different between the detailed and simplified 2D models, the relative humidities are very close between these two models (Figure 4). For render of cement lime plaster and mineral plaster, the largest difference in relative humidity between the two models is less than 0.01. For render of lime cement plaster, the largest difference of relative humidity is less than 0.02. For all the three renders, the relative humidities are almost the same between the two models at Point C. In general, the relative humidity from the simplified 2D model is slightly higher during the cold period, whereas it is slightly lower during the warm period. As the moisture-related damage such as mould growth occurs in the cold period, the result from simplified 2D model will be slightly conservative compared to the detailed model. The difference of temperature between different points is very small. The largest difference in temperature is less than 0.1 K. Considering the small difference of relative humidity and temperature between the simplified and detailed 2D model, simplification of the detailed distribution of brick and mortar joint is reasonable and justified and the simplified 2D model can well represent the detailed 2D model.

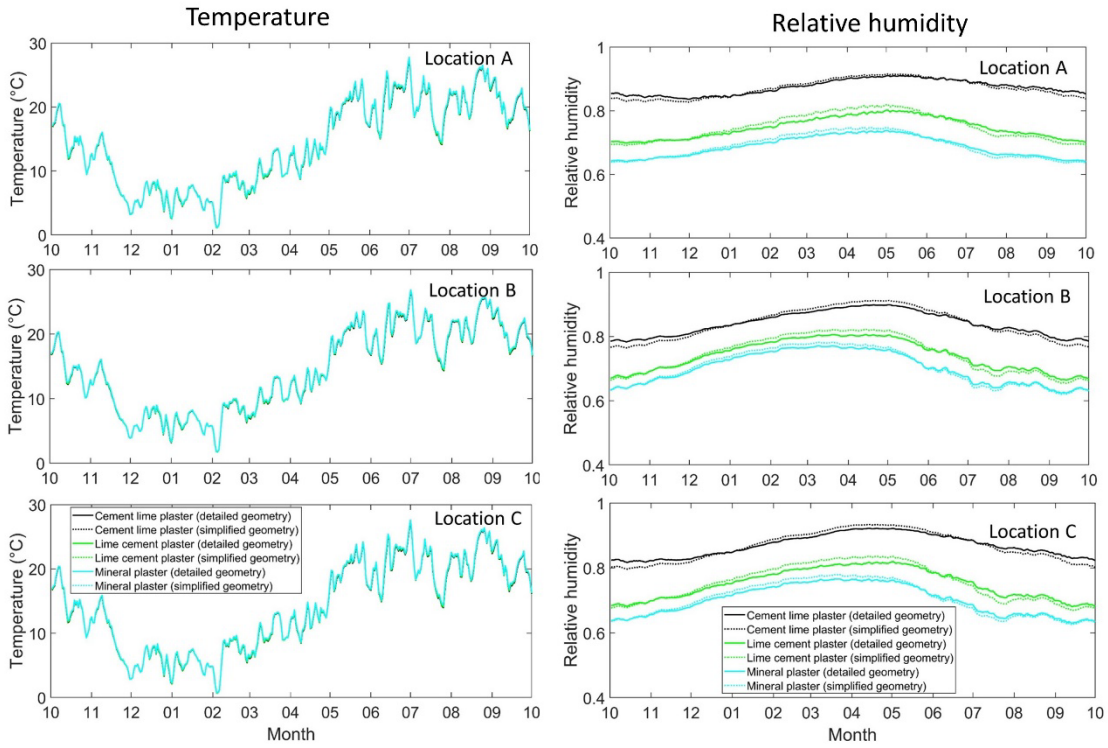

Figure 4. Temperature and relative humidity at Point A, B and C in detailed and simplified 2D model.

3.2 Comparison of Results Between 2D and 3D Model

3.2.1 Comparison of Temperature

In 3D we consider the real width of the wooden beam of 20 cm, while in 2D the wooden beam covers the total width of the wall. Although wood has rather low thermal conductivity, it is still much larger than that of aerogel plaster. Therefore, the wooden beam works as a kind of thermal bridge in the internally insulated masonry wall. Due to the higher heat flux in the beam, the middle cross section of the wooden beam embedded in masonry wall will be warmest cross section of the wooden beam during winter period, while the outermost surface in contact with masonry wall will be the coldest one. So, we consider the temperature in the points A, B and C in the middle section and in the surface in contact with the masonry (called outermost cross section). In general, there are some differences of temperature between the 2D and 3D models (Fig. 5). The temperature in the 2D cross section is the highest. The higher temperature in the 2D cross section is due to larger width of wooden beam and thus larger thermal bridge effect in the 2D model. The largest temperature difference at points A, B and C between the 2D and 3D cross sections is 1.08 K, while the smallest one is 0.02 K. In the 3D model, the temperature from the center cross section is higher than that in the outermost cross section. The largest temperature difference at points A, B and C between the 3D middle and 3D outermost cross sections is 0.46 K, while the smallest one is 0.02 K.

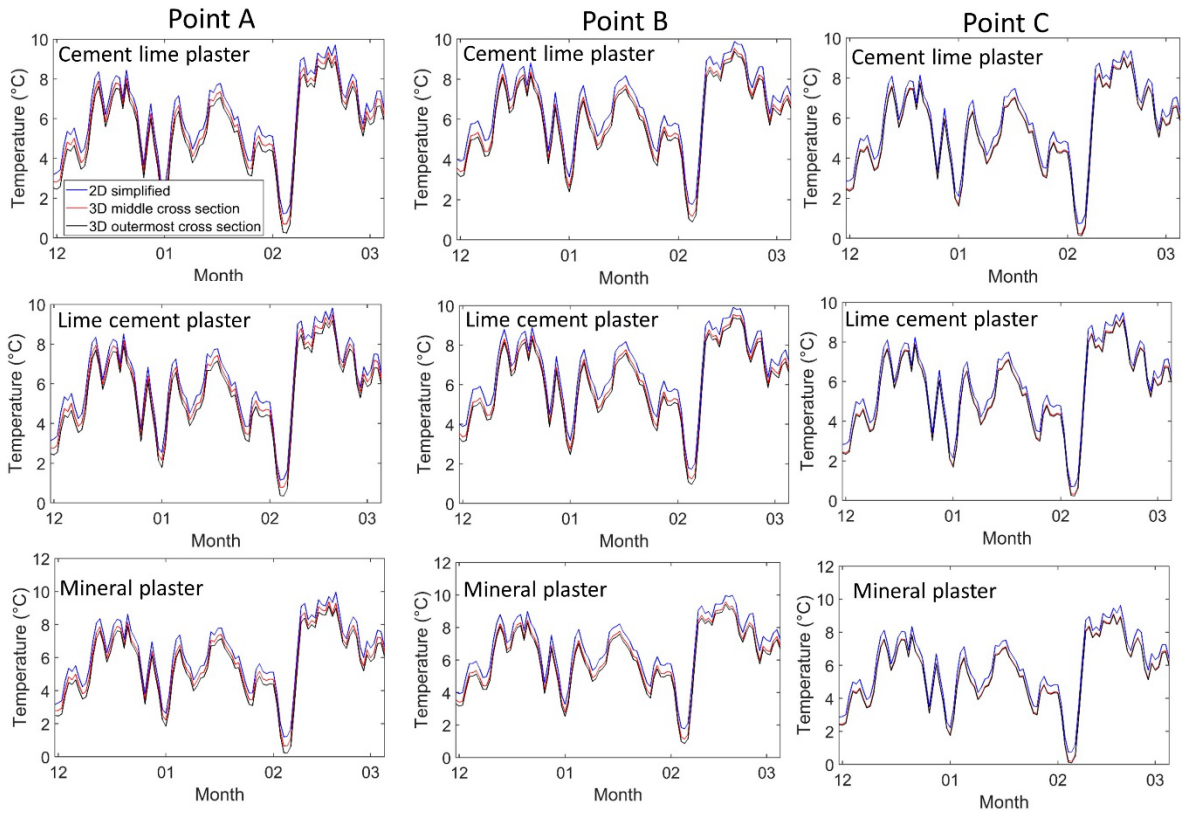

Figure 5. Temperature at Points A, B and C in simplified 2D model and middle and outermost cross section of the 3D model in winter period.

3.2.2 Comparison of relative humidity

The differences in relative humidity among different cross sections is large at point A (Figure 6). The largest difference is in the wall envelope with mineral plaster (low liquid permeability), which can reach 0.06. In general, the fluctuation of relative humidity at the outermost cross section of the 3D model is larger than at the central cross sections, especially during the cold periods. Relative humidity at point A at the central and outermost cross sections is quite different whereas relative humidity at points B and C at the central and outermost cross sections is very close. For the wall envelope with mineral plaster, relative humidity at point A is continuously below 0.8 in the 2D model while it can be above 0.8 continuously from February to June at the outermost cross section in the 3D model. The 2D model will in general underestimate to some extent the moisture risk compared to 3D model. If the study is to have accurate relative humidity in the wooden beam-end, it is not appropriate to replace a 3D model with a 2D one.

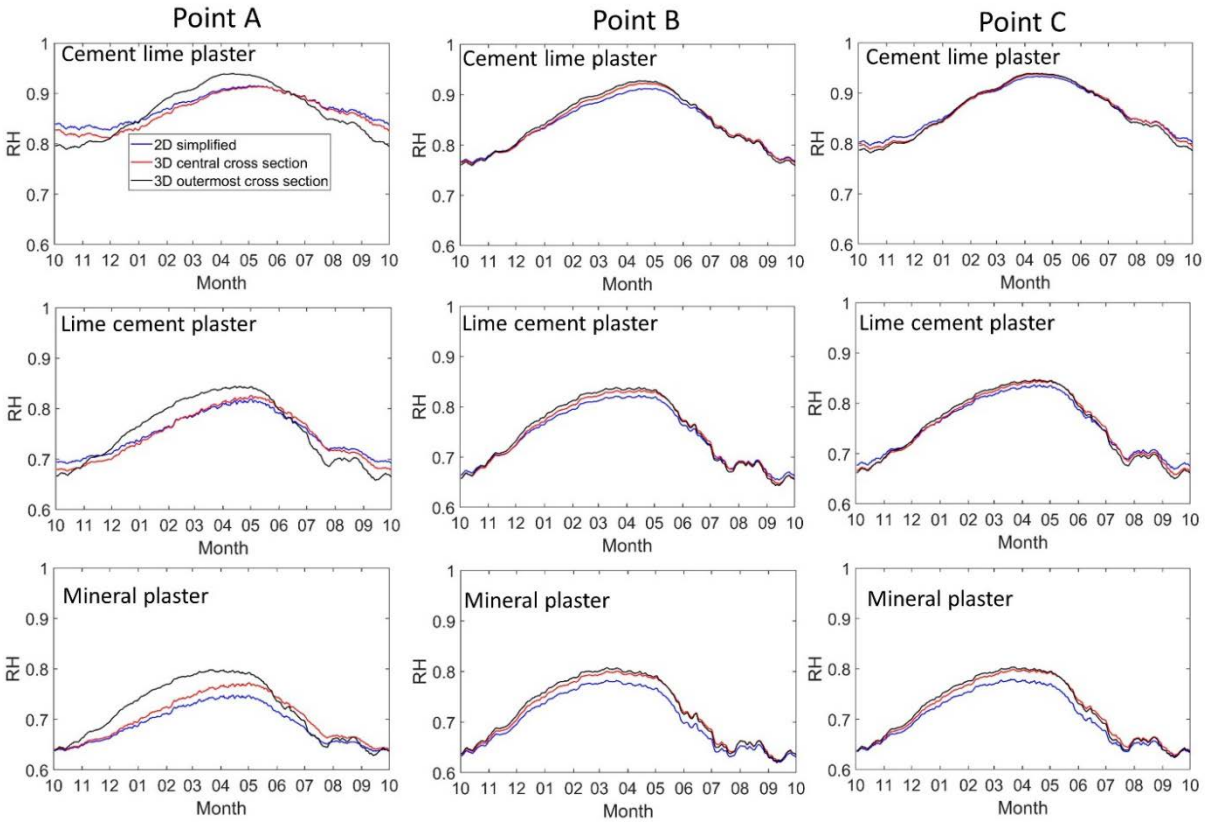

Figure 6. Relative humidity at Points A, B and C in simplified 2D model and central and outermost cross section of the 3D model.

13 Conclusions

- The hygrothermal performance of a wooden beam-end embedded in an internally insulated masonry wall is analyzed using 2D and 3D hygrothermal models.
- The difference of temperature and relative humidity in wooden beam-end between 2D

and 3D models is in general small. However, 2D hygrothermal models show much lower relative humidities and thus lower moisture risk at some locations in the wooden beam-end. In general, a 3D hygrothermal model can more accurately represent the hygrothermal condition than the 2D one.

Acknowledgements

This research project is part of the Swiss Competence Center for Energy Research SCCER FEEB&D of the Swiss Innovation Agency Innosuisse. The meteorological data have been provided by MeteoSwiss, the Swiss Federal Office of Meteorology and Climatology.

ORCID

Xiaohai Zhou: https://orcid.org/0000-0002-8291-250X
Jan Carmeliet: https://orcid.org/0000-0003-2186-963X
Dominique Derome: https://orcid.org/0000-0002-8018-1133

References

Guizzardi, M., Carmeliet, J. and Derome, D. (2015). Risk analysis of biodeterioration of wooden beams embedded in internally insulated masonry walls. *Construction and Building Materials*, *99*, 159–168.

Guizzardi, M., Derome, D., Vonbank, R. and Carmeliet, J. (2015). Hygrothermal behavior of a massive wall with interior insulation during wetting, *Building and Environment,* 89, 59-71.

Hagentoft, C.-E., Kalagasidis, A.S., Adl-Zarrabi, B., Roels, S., Carmeliet, J. and Hens, H., et al., (2004). Assessment method of numerical prediction models for combined heat, air and moisture transfer in building components: benchmarks for one-dimensional cases, *J Therm Envel Build Sci*, 27, 327–352.

Harrestrup, M., and Svendsen, S. (2016). Internal insulation applied in heritage multi-storey buildings with wooden beams embedded in solid masonry brick façades. *Building and Environment*, *99*, 59–72.

Johansson, P., Geving, S., Hagentoft, C. E., Jelle, B. P., Rognvik, E., Kalagasidis, A. S. and Time, B. (2014). Interior insulation retrofit of a historical brick wall using vacuum insulation panels: Hygrothermal numerical simulations and laboratory investigations. *Building and Environment*, *79*, 31–45.

Kehl, D., Ruisinger, U., Plagge, R. and Grunewald, J. (2013). Wooden beam ends in masonry with interior insulation–A literature review and simulation on causes and assessment of decay. In *Proceedings of the Central European Symposium on Building Physics*, Vienna, Austria, 299–304.

Künzel, H.M. Simultaneous Heat and Moisture Transport in Building Components, [PhD thesis] 1995 University of Stuttgart.

Künzel, H. M. and Kiessl, K. (1996). Calculation of heat and moisture transfer in exposed building components. *International Journal of Heat and Mass Transfer*, *40*(1), 159–167.

Künzel, H. M., Künzel, H. and Holm, A. (2004). Rain protection of stucco facades. In *Proceedings of the Thermal Performance of the Exterior Envelopes of Whole Buildings IX–International Conference*, Florida, USA, 1-7

Morelli, M. and Svendsen, S. (2013). Investigation of interior post-insulated masonry walls with wooden beam ends. *Journal of Building Physics*, *36*(3), 265–273.

Pazera, M. and Bomberg, M. (2010). Applying Lessons from Clay-Brick Veneer to Design a Stucco Mix. In *Proceedings of the BEST Conference Building Enclosure Science and Technology*, Portland, USA, 1-17.

TenWolde, A. (2008). *ASHRAE Standard 160P--criteria for moisture control design analysis in buildings*.

Zhou, X., Carmeliet, J. and Derome, D. (2018). Influence of envelope properties on interior insulation solutions for masonry walls. *Building and Environment*, *135*, 246–256.

Zhou, X., Derome, D. and Carmeliet, J. (2016). Robust moisture reference year methodology for hygrothermal simulations. *Building and Environment*, *110*, 23–35.

Zhou, X., Derome, D. and Carmeliet, J. (2017). Hygrothermal modeling and evaluation of freeze-thaw damage risk of masonry walls retrofitted with internal insulation. *Building and Environment*, *125*, 285–298

XV International Conference on Durability of Building Materials and Components
DBMC 2020, Barcelona
C. Serrat, J.R. Casas and V. Gibert (Eds)

Preventing Damage by Updating Moisture Control Standards

Hartwig M. Künzel

Fraunhofer Institute for Building Physics, 83626 Valley, Germany,
Hartwig.Kuenzel@ibp.fraunhofer.de

Abstract. *Despite progress in moisture control analysis, repairing moisture damage is still a considerable cost factor in the building sector. While there are many reasons for the lack of improvement during the last decades, inadequate moisture control standards are certainly also to blame. In many countries, interstitial condensation calculations according to Glaser are the sole means for assessing moisture control design, neglecting other important moisture loads such as driving rain, construction moisture and air infiltration. To overcome this lopsided focus on vapour diffusion, the update of the German moisture control standard has restricted the applicability of the Glaser method and introduced a normative Annex on performance evaluation by hygrothermal simulation. Recently, a new project has started to develop advanced models helping to evaluate the simulation results. Currently, it is already possible to assess the risk of mould growth, rot, and critical moisture accumulation by methods referred to in this standards. Also addressed in the standard is the selection of critical indoor and outdoor boundary conditions. Thus, it is officially encouraged to perform hygrothermal simulation, giving architects and engineers the chance to design more moisture tolerant and ultimately more durable constructions. Considering the necessity to reduce the carbon footprint of buildings, the application of hygrothermal simulation provides the opportunity to use more innovative renewable and recycled materials that could not adequately be judged by the Glaser method. Another benefit presents the analysis of construction resilience in case of natural disaster such as flooding or extreme rain events.*

Keywords: *Moisture Control Standard, Hygrothermal Simulation, Moisture Tolerance, Building Resilience, Damage Prevention.*

1 Introduction

Moisture in the building structure impairs thermal performance and accelerates ageing and degradation. Therefore, moisture control has always been an issue for architects and engineers. Despite an improvement in construction quality, moisture problems have not diminished accordingly. This may partly be due to increasing energy savings requirements. More insulation and better air-tightness have resulted in lower temperatures at the exterior layers of the building envelope and higher indoor humidity. This increases the risk of interstitial condensation and reduces the drying potential. The high number of moisture related building failure also demonstrates that traditional condensation control and the steady-state tools to evaluate vapour diffusion are not sufficient to account for all relevant moisture loads. Additionally, natural disaster with torrential rain and flooding will become more frequent which means more risk for moisture susceptible but environmental friendly renewable materials. However, adequate moisture control design can help to prevent problems even in the most energy efficient structures. The necessary design tools are there, but they have to be applied the right way. While it is fair to assume that a building has been erected according to best practice, a perfect seal against water, vapour or air entry is difficult to achieve. Therefore, the consideration of

imperfections should be part of moisture control assessments.

Hygrothermal simulation offers an opportunity to meet the current challenges if the underlying models allow for the fact that no building component is perfectly sealed and envelope leaks and other flaws are always built-in or may eventually occur during the building's service life. New approaches have been developed to account for rainwater penetration and indoor air infiltration. This paper summarizes these approaches and shows examples of standards and guidelines that have started to integrate them into the moisture control assessment process.

2 Moisture Control Design Standards and Guidelines

In the past, moisture control meant for most practitioners steady state vapour diffusion calculations – often called dew-point or "Glaser" calculations – that were performed to determine whether there is a risk of harmful interstitial condensation in the building assembly during the heating season. However, due to numerous simplifications the results of these calculations may be misleading especially when short-term loads such as solar vapour drive or rainwater absorption may have an impact. A steady-state calculation also means that all storage effects are neglected. This penalizes materials with moisture storage capacity, such as renewable insulation materials, because it assumes the formation of condensation where in real life only the sorption moisture content is slightly increased. There are actually many more drawbacks of employing dew-point calculations for moisture control design which lead to the following statement in the ASHRAE Handbook of Fundamentals (2017): *"The dew-point method is not recommended as a sole basis for hygrothermal design of building envelope assemblies. ASHRAE Standard 160 is recommended to assist in hygrothermal analysis for design purposes."* ASHRAE Standard 160 (2016) specifies the application of hygrothermal simulation tools.

To arrive at comparable results pertinent application standards for hygrothermal simulations have been developed which are under continuous revision in order to accommodate new approaches and feed-back from users. The first guideline on moisture control analysis by hygrothermal simulation was issued in 2002 by the WTA, an association dealing with preservation and renovation of heritage constructions and rehabilitation of the building stock (WTA 6-2 2002). Five years later the European Standard EN 15026 (2007) which is largely based on the WTA guideline was published. However, both documents did not contain any information on how to deal with small defects in the building envelope. Parallel to the standard work in Europe a slightly more comprehensive standard on moisture control design has been developed in North-America (ANSI/ASHRAE Standard 160 from 2009). As a result of numerous damage cases linked to rainwater penetration into constructions with rendered facades (Cheple and Huelman 2000), this standard has been the first that proposed the consideration of the effects of small leaks in the exterior finish of exposed walls.

2.1 Updated Version of the Hygrothermal Simulation Guideline WTA 6-2

Since the original version of the WTA 6-2 guideline served as blueprint for the European Standard 15026 (2007) and the updated version from 2014 has been referenced by the German Standard on moisture control design DIN 4108-3 (2018), the new items in this guideline will be described here briefly. Compared to the version from 2002 the WTA 6-2 (2014) allows the

consideration of imperfections in the building envelope by simplified models. It also shows a way of dealing with ventilated cavities in a one-dimensional way and contains some new information concerning boundary conditions. The new version recognizes the problem of determining the material properties as accurately as possible for the intended use by a chart that recommends the test method as function of moisture range. This issue has come up in the context of capillary active insulation materials. These materials are rather vapour permeable, however, they are supposed to prevent condensation at the cold side by compensating the diffusion flux with an opposed liquid flux. This means, liquid transport in capillary active insulation materials has to achieve a considerable magnitude well below 100% RH. Most of the currently employed methods have been designed to determine liquid transport properties in the high moisture range, i.e. when the majority of capillaries are filled with water. However, these methods turned out to be inappropriate for the accurate determination of liquid transport in the hygroscopic range. Therefore, a new method has been developed by Binder *et al.* (2013) that determines the properties of interior insulation materials under the boundary conditions close to the real situation in practice application.

From a moisture safety point of view, however, the most important improvement is the introduction of simplified models to account for unavoidable rainwater and indoor air leakage into the building assembly. These models have been designed for one-dimensional simulations with the aim to quantify the moisture impacts of imperfections in the building envelope without dealing with the complex 3D phenomena that are assumed to happen in reality. Thus, these models are of limited validity and may work well for some construction types but may not be transferable to others. This may seem unfortunate; however, not employing the models described below, may be even more risky. Numerous failures have proven that perfectly installed building assemblies without any leaks belongs to the realm of fiction. Nevertheless, it is absolutely feasible to reduce the potential leaks to a level that will not do any harm to a moisture tolerant construction. The application of the following model assumptions will help to design such moisture tolerant building assemblies.

2.1.1 Rainwater penetration through imperfection in the exterior finish

As already mentioned the American moisture control standard ANSI/ASHRAE 160 (2016) proposes the consideration of small rainwater leaks through the exterior finish which may result from gaps or cracks at joints and connections. It states: *"In the absence of specific fullscale test methods and data for the as-built exterior wall system being considered, the default value for water penetration through the exterior surface shall be 1% of the water reaching that exterior surface. The deposit site for the water shall be the exterior surface of the water-resistive barrier. If a water-resistive barrier is not provided, then the deposit site shall be described and a technical rationale for its selection shall be provided."* In the case of ETICS (external wall insulation systems) on load bearing masonry walls the rainwater deposit site is likely to be the surface of the masonry beneath the insulation (see Figure 1).

It is obvious that neither the leaks nor the wind driven rain exposure are evenly distributed over the building envelope. But the standard committee chose this simple one-dimensional approach as a method to consider the effects of complex bulk water penetration phenomena observed in practice. The rainwater leakage rate proposed in the standard is not meant to be a worst case scenario. It is not based on field test results but on hygrothermal simulations

(Desjarlais *et al.* 2001) that showed that more than 1% of rainwater penetration may be detrimental for a large portion of existing wooden wall structures. A recent literature review (Van Den Bossche *et al.* 2011), analysing data of leakage rates measured on different wall structures, confirmed the appropriateness of the "1% leakage" in ANSI/ASHRAE Standard 160. Therefore the rationale of this standard was also adopted for the new WTA 6-2 (2014) guideline.

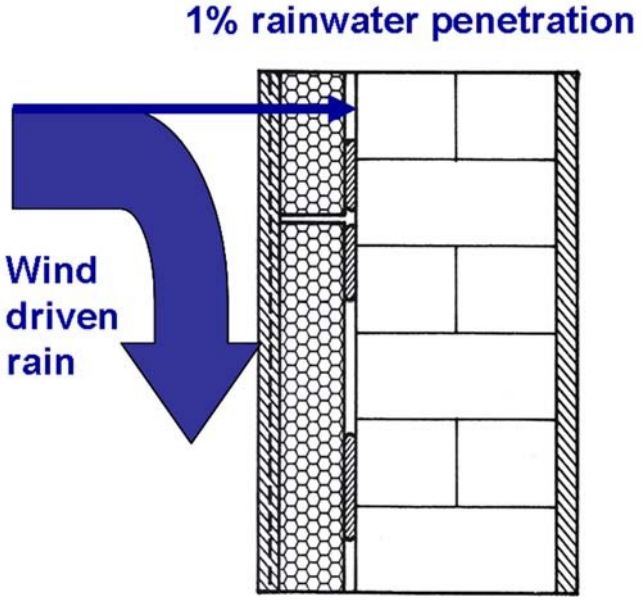

Figure 1. Exposed wall example showing the most likely deposit location for rainwater penetrating through leaks at joints and connections of masonry with external insulation system.

2.1.2 Moisture sources due to air flow through the building envelope

The convective moisture entry due to defects in the vapour respectively air control layer is a multidimensional effect, which cannot be captured directly by one-dimensional calculation. However, also the application of multidimensional simulation tools hardly solves the problem, because the exact configuration of leakages is generally unknown and the complexity of relevant flow paths is exceeding the capacity of most models. Therefore it has been decided to choose an approach that doesn't simulate the flow itself, but concentrates on the effects of vapour convection and subsequent condensation by introducing a moisture source inside the construction.

Based on experimental results from TenWolde *et al.* (1989), a simplified model to quantify the moisture sources due to vapour flow through the building envelope has been developed and checked for plausibility (*e.g.* Künzel *et al.* 2011). The model assumes that vapour contained in the indoor air, penetrating the envelope via so-called moisture leaks, condenses at the cold side of the insulation (see Figure 2). In contrast to energy leaks where the air remains warm because it flows in a short way from the room towards the outside, moisture leaks are small and tortuous channels where the air flow is slow and cools down within the flow path. These "moisture leaks" probably represent less than 10% of all leaks in the building envelope. The position of the condensation plane has to be selected by the user. Its temperature, governed by the transient

boundary conditions, is simulated without taking the latent heat of condensation into account. The right choice of this position depends on the construction. It must be cold enough for condensation to occur and it must be easily accessible for the indoor air that has penetrated the interior lining or air barrier. Examples are the exterior sheathing of wood frame walls or roofs and the interface between the interior insulation and the original wall after thermal retrofits of plastered masonry structures. The convective moisture source is equal to the amount of condensate that forms when the indoor air temperature is cooled down to the temperature of the selected condensation plane in the building assembly. Any increase in sorption water content that could occur in reality by the temperature drop is neglected. In order to remain on the safe side convective drying is excluded, i.e. the moisture accumulated by air convection can only dry out by vapour diffusion or liquid transport.

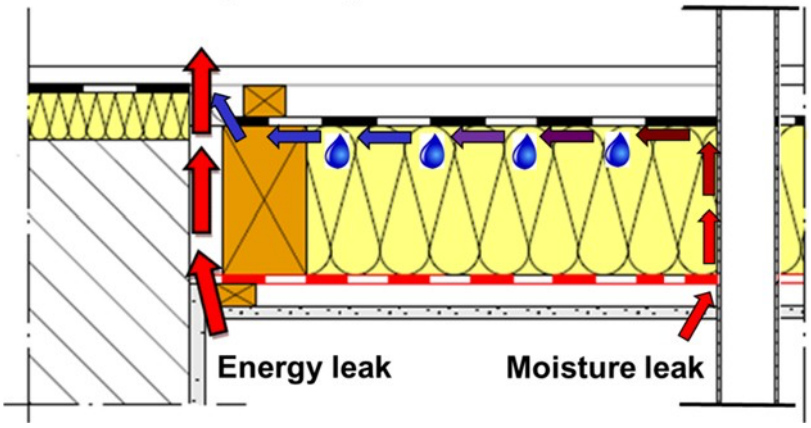

Figure 2. Indoor air leaking through a roof at joints and connections. If the flow path is short, it will be heated up by the air flow and only energy is lost. If the air flow creeps along the cold side of the structure before it finds its way out, its temperature may drop below the dew-point of the indoor air and cause condensation.

Thus the amount of condensation (moisture source S_{CL}), which results from vapour convection at the selected condensation plane p, is determined for each time step according to the following equation:

$$S_{CL} = k_{CL} \cdot \left(c_i - c_{sat,p}\right) \cdot (P_i - P_e) \tag{1}$$

where
S_{CL} moisture source due to vapour convection through the component (kg/(m²h))
k_{CL} air permeance of the "moisture leaks" of the component (m³/(m²·h·Pa))
c_i water vapour concentration of the indoor air (kg/m³)
$c_{sat,p}$ water vapour saturation concentration at predefined plane p (kg/m³)
$P_i - P_e$ air pressure difference over the considered envelope component (Pa)

The air pressure difference is assumed to be due to buoyancy effects and pressure differentials generated by ventilation systems. Wind pressure effects are disregarded because they are difficult to determine and do not act on the building envelope in a continuous manner. Based on investigations in Künzel *et al.* (2011) the air permeance of the moisture leaks is set to 1,9·10-6 m³/(m²s·Pa) [0,007 m³/(m²h·Pa)] for envelope components installed according to best practice. Buildings with higher k_{CL} would represent malpractice. Building components that can handle the moisture loads due to air convection are well-designed. Those that fail under these

circumstances should either be redesigned or special care must be taken during installation which may include continuous moisture monitoring.

2.2 New German Moisture Control Standard DIN 4108-3

The current German moisture control standard for building envelope components DIN 4108-3 (2018) includes three assessment options. As first option, a designer may select a wall or roof assembly from a list of deemed to satisfy (DTS) constructions included in the standard. The second option, which may be applied, if the assembly to be designed, is not part of the DTS list represents the assessment by a steady-state dew-point calculation with fixed boundary conditions. However, there are a number of restrictions that have to be observed, *e.g.* green roofs, unvented metal roofs, capillary active interior insulation systems or basement assemblies must not be assessed.

Most importantly, options one and two may only be applied for envelope components of residential buildings or those that have a similar indoor climate (*e.g.* offices) without air-conditioning. In all other cases option three applies, *i.e.* the designer has to perform a hygrothermal simulation according to appendix D of the standard. This appendix references EN 15026 and WTA 6-2 mentioned above as well as some other standards and guidelines dealing with the evaluation of hygrothermal simulation results, *e.g.* mould risk evaluation. A detailed flow chart showing the preconditions for selecting one of the options is depicted in figure 3.

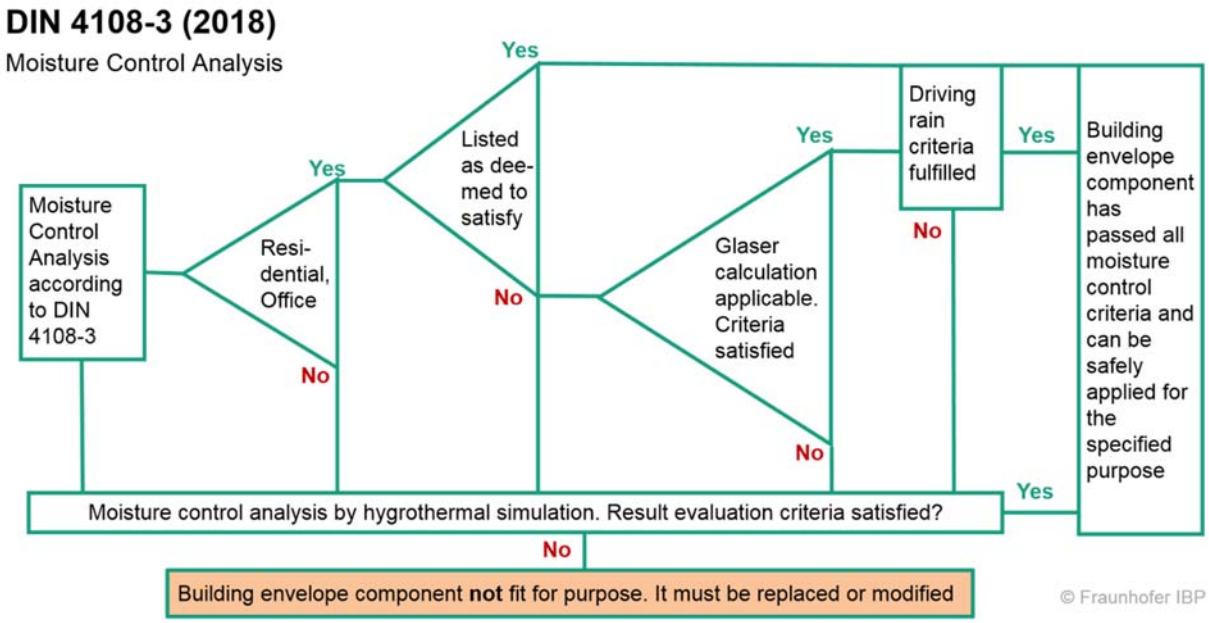

Figure 3. Flow chart explaining the preconditions for the moisture control assessment options in DIN 4108-3.

3 Conclusions and Outlook

Hygrothermal simulation models have become essential to advance our skills in sustainable and resilient building design. Practical experience has proven repeatedly that imperfections and small leakages in the building envelope are unavoidable and have to be accounted for. The same is true for material ageing and unexpected loads due to extreme weather conditions which will

probably occur more frequently in the wake of climate change. The development of hygrothermal design models has to respond to these factors by searching for new approaches that are able to represent real life impacts and effects. This won't be possible without increased research efforts looking at the effects of leaks and other imperfections with the aim to quantify them for different construction types. Most importantly however, there has to be widespread discussions on what kind of flaws are acceptable in order to define what best practice workmanship actually means. Ultimately, the definition of unavoidable moisture sources will result in a clear discrimination between design and installation failures.

This task is far from being easy and may be very controversial because there is a lot of money involved in litigation cases. However, it also represents a great opportunity to arrive at better and more durable constructions and it is preferable, as well as much more sustainable to spend money on improving design instead of wasting money and resources on repair and excessive maintenance. International moisture control standards are slowly moving in the right direction by emphasizing the importance of hygrothermal simulation for realistic building component assessments. However, the next important step represents the integration of moisture control considerations already at the beginning of the design process. Until now, this is mostly done in the end when all components and HVAC systems are already specified leaving only minor options for modifications – *e.g.* selecting the permeance of vapour control or insulation layers.

In the future, the building dynamics (hygrothermal storage capacities of envelope components including HVAC systems) will become quintessential because of the more fluctuating renewable energy supply. This requires new building operation concepts and more integral design of the interdependent building envelope and HVAC systems. Combinations of both, such as thermally activated components or radiant interior surface heating and cooling systems may be part of the response to the new challenges (see figure 4). Moisture control design of such systems is way beyond simple dew-point calculations and may even require new approaches for hygrothermal simulation models.

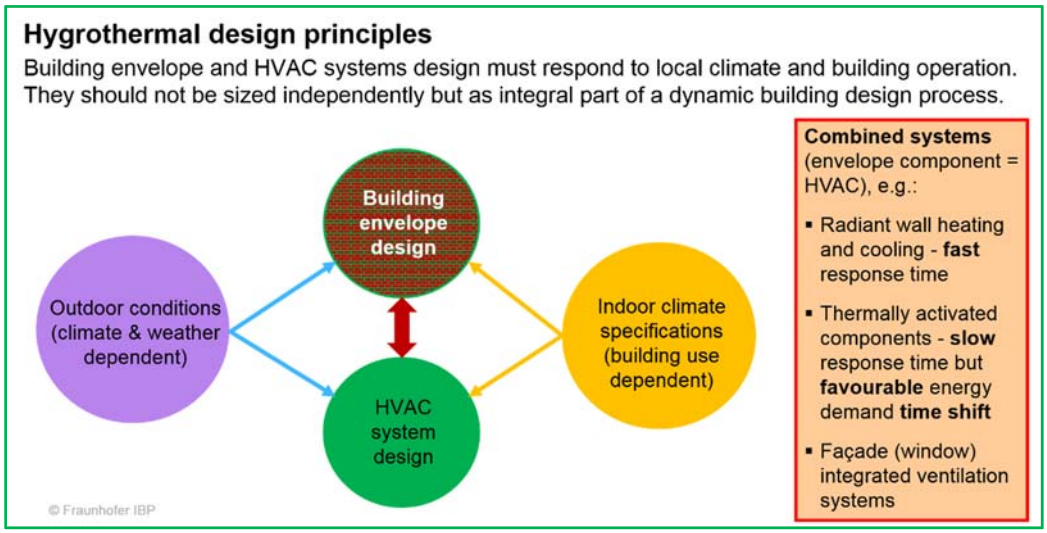

Figure 4. Appropriate design of building envelope and HVAC depends heavily on outdoor and indoor climate. Their performance is interdependent and increasingly both functions are combined in one system.

References

ANSI/ASHRAE Standard 160 (2016). *Criteria for Moisture Control Design Analysis in Buildings.*

ASHRAE Handbook of Fundamentals (2017). *Chapter 27 Heat, Air and Moisture Control in Building Assemblies - Examples.*

Binder, A., Künzel, H.M. and Zirkelbach, D. (2013). A new approach to measure liquid transport in capillary active interior insulation. *Proceedings 2nd Central European Symp. on Building Physics, TU Vienna, 393-400.*

Cheple, M. and Huelman, P. (2000). Literature Review of Exterior Insulation Finish. Systems and Stucco Finishes*, Report MNDC/RP B80-0130, University of Minnesota.*

Desjarlais, A.O., Karagiozis, A.N. and Aoki-Kramer, M. (2001). Wall Moisture Problems in Seattle. *Buildings VIII proceedings, ASHRAE, 8.*

DIN 4108-3 2018-10*. Protection against moisture subject to climate conditions - Part 3: Requirements and directions for design and construction.*

EN 15026 (2007). *Hygrothermal performance of building components and building elements - Assessment of moisture transfer by numerical simulation.*

Künzel, H.M., Zirkelbach, D. and Schafaczek, B. (2011). Vapour control design of wooden structures including moisture sources due to air exfiltration*. Proceedings 9th Nordic Symposium on Building Physics (NSB), Tampere, 189-196.*

TenWolde, A., Carll, C.G. and Malinauskas, V. (1998). Air Pressures in Wood Frame Walls*. Thermal Performance of the Exterior Envelopes of Buildings VII. Clearwater, Florida, USA.*

Van Den Bossche, N., Lacasse, M. and Janssens, A. (2011). Watertightness of Masonry Walls: An Overview*. Proccedings 12dbmc Porto, 8.*

WTA Guideline 6-2 (2014). *Simulation of heat and moisture transfer.*

XV International Conference on Durability of Building Materials and Components
DBMC 2020, Barcelona
C. Serrat, J.R. Casas and V. Gibert (Eds)

The Impact of Climate Change on Material Degradation: Finding a Feasible Approach for Climate Model Evaluation

Hamed Hedayatnia and Nathan Van Den Bossche

Building physics Group, Faculty of Engineering and Architecture Ghent University, 9000-Gent, Belgium,
hamed.hedayatnia@ugent.be

Abstract. *Understanding how climate change accelerates or slows down the process of material deterioration is the first step towards assessing adaptive approaches for the preservation of historical heritage. Analysis of the climate change effects on the degradation risk assessment parameters like freeze-thaw cycles and salt crystallization is also a key parameter when considering mitigating actions. Due to the vulnerability of cultural heritage in Iran to climate change, the impact of this phenomenon on basic parameters like temperature was analyzed. Choosing an appropriate regional climate model is the first and most crucial step in the analysis of climate change effects on heritage. The outputs of two different regional climate models: the ALARO-0-SURFEX model (Ghent University, Belgium) and the REMO model (HZG-GERICS, Germany) were analyzed to find out which model is more adapted to the region. So the focus of this research is mainly on the evaluation process to find a feasible approach for validation study to determine the reliability of each model. For model validation, a comparison between model data and observations was performed for 30 yearsfrom 1980-2017. Besides, some climatic parameters which are likely critical for heritage like freeze-thaw cycles were studied to find out how reliable these models are in the field of building pathology.*

Keywords: *Iran, Climate Change, Degradation Criteria, Heritage.*

1 Introduction

The Iranian plateau hosts one of the world's oldest civilizations. The country's rich cultural heritage is reflected in part by its 22 UNESCO world heritage sites. The Iranian Plateau is one of the world's most mountainous countries, with a landscape dominated by rugged mountain ranges.

Having 11 climates (Figure 1) out of the world's 13, Iran's climate is diverse, ranging from arid and semi-arid, to subtropical along the Caspian coast and the northern forests.

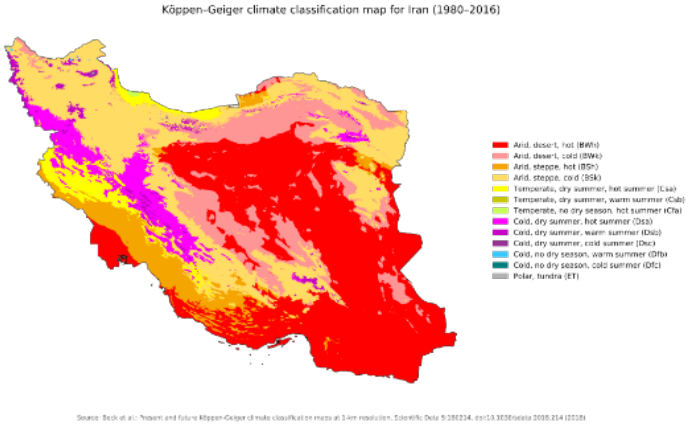

Figure 1.Climate map of Iran (Köppen-Geiger).

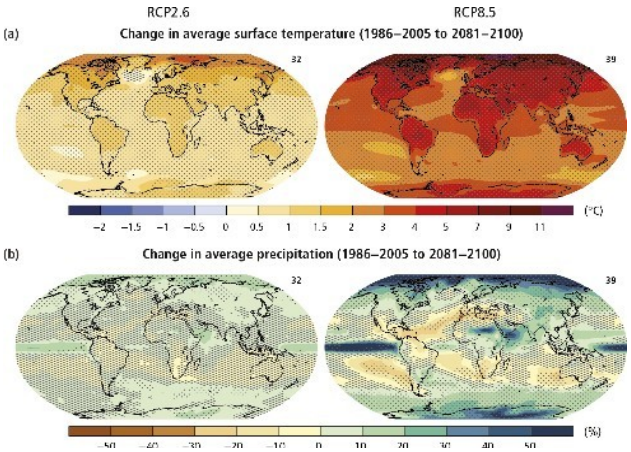

Figure 2.Change map during 1986-2100.

The Fifth Assessment Report of the Intergovernmental Panel on Climate Change suggests significant changes in climate conditions during the twenty-first century, such as drier and hotter summers over the middle East. Moreover, studies with different scenarios show that climate changes in Mediterranean Bassin are anticipated to exceed global mean values significantly (Giorgi 2006), and Iran is located in this region (Figure 2). Climate models are typically based on a top-down approach as a function of spatial and temporal resolution (Termonia, Schaeybroeck, De Cruz and De Troch *et al*. 2018). Therefore High-resolution regional climate models are needed to provide accurate climate change scenarios accounting for this region.

Today there are only low-resolution data available over this domain. Thus in this paper, high-resolution (*e.g*. 25 km) regional climate projections over Central Asia, including Iran, have been analyzed. For more accuracy, two different climate models have been evaluated to find a feasible approach for validating climate models as a non-meteorologist researcher. ALARO-0 model (Ghent University, Belgium) and REMO (HZG-GERICS, Germany). Both models provide climate projections for the "21st" century following different RCP scenarios. These models need to be evaluated first. The RCM data in this analysis originates from the ALARO-0 and REMO models at a spatial resolution of 25 km across the central Asia domain and time-frequency of 1-hour. The analyzed type of model run for both models is the evaluation run. This means that the lateral boundary conditions of the model*, i.e.* the Asian boundaries, are forced by reanalysis data. The evaluation run enables the possibility to evaluate whether the model is able to reproduce the weather conditions within the imposed boundaries conditions at given grid points.

To analyze the evaluation run of the models over the domain, four grid points located in different climate zones, were studied. A comparison is made with historical observations at the same locations using MATLAB. The discussed parameters are outdoor air temperature and relative humidity and precipitation. For each parameter, scatterplots of the observations and modelled data are produced, as well as distribution functions both based on hourly, daily, and monthly values. Through the validation study, some climatic parameters which are likely critical for heritage like freeze-thaw cycles and salt crystallization index were evaluated for both models in comparison with the historical data to find out how reliable these models are in the field of building pathology.

In the case of temperature, relative humidity, and wind velocity, daily values represent daily averages, whereas, for precipitation, total daily values are considered. Furthermore, the root means square error (RMSE), correlations, adjusted R-squared, and regression are computed to find out the reliability of the models. The studied grid points are listed below:

Mashhad**,** which is located in the northeastern corner of Iran, features a steppe climate (Köppen*/BSk*) with hot summers and cold winters.

Shiraz is located in the south of Iran. Shiraz's climate is overall classified as a hot semi-arid climate (Köppen climate classification *BSh*).

Tabriz is located in the northwest of Iran has a humid continental climate with regular seasons (Köppen *Dsa*) bordering Cold semi-arid climate (Köppen *BSk).*

Rasht is located on Iran's Caspian Sea coast, depending on the precipitation, Rasht either has a humid subtropical climate (*Cfa*) or a Mediterranean climate (*Csa*).

2 Methodology

2.1 Model Analysis

Given that Iran has an extended range of climate regions, and models are not often used for such a climatic zone, these models need to be evaluated first. The RCM data in this analysis originates from the ALARO-0 and REMO models at a spatial resolution of 25 km across the central Asia domain and time-frequency of 1-hour. The analyzed type of model run for both models is the evaluation run. This means that the lateral boundary conditions of the model, i.e., the Asian boundaries, are forced by reanalysis data. The evaluation run enables the possibility to evaluate whether the model can reproduce the weather conditions within the imposed boundaries conditions at given grid points.

To analyze the evaluation run of the models over the domain, Mashhad which is located in the northeastern corner of Iran and features a steppe climate (Köppen*/BSk*) with hot summers and cold winters were picked.

A comparison is made with historical observations at this location employing MATLAB. Since there is no full overlap between datasets, only the period 1980-2017 is analyzed. Tofind out which approach should be followed, temperature parameter was picked, and scatterplotsof the observations and modelled data are produced, as well as distribution functions both based on hourly, daily, and monthly values plus comparison plots based on daily, monthly and yearly values. Through the validation study, some climatic parameters which are likely critical for heritage like freeze-thaw cycles were evaluated for both models in comparison with the historical data to find out how reliable these models are in the field of buildingpathology.

In the case of temperature, daily values represent daily averages. Furthermore, the evaluation metrics comprise of correlations, adjusted R-squared, and regression are computed to find out the reliability of the models. In this paper, climate models have been evaluated.

2.1.1 Temperature Analysis

The scatterplot of both models during the studied period (Figure 3 and 4) indicates that there is a good overall representation of the observed hourly outdoor air temperature (T) by both models. The linear fit (red) of the hourly temperature almost follows the diagonal (perfect fit). The hourly temperature distribution of both datasets, i.e., the observations and the modeled data, confirms this statement. However, there is a slight bias towards colder temperatures by the ALARO-0 modelled data, and almost the same bias towards warmer temperatures by the REMO modelled data (Figure 5 and 6). In mid-range temperatures, models have different behaviours where ALARO-0 has an underestimation of mid-range temperatures, and REMO has an overestimation.

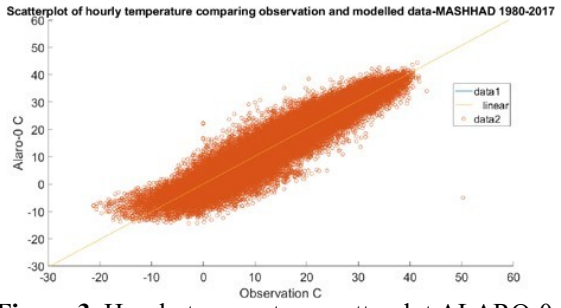

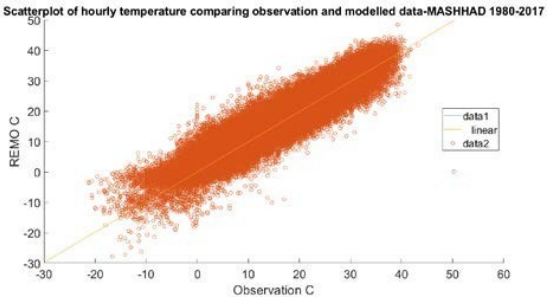

Figure 3. Hourly temperature scatterplot ALARO-0 model. **Figure 4**. scatterplot -Remo model(1980-2017).

In extreme maximum temperatures, both models follow a similar pattern. A small overestimation of extreme maximum temperatures where REMO has a bigger overestimation. In extreme minimum temperatures, REMO has a slight underestimation, and ALARO-0 has a slight overestimation. Please note that missing values in the observations are removed before calculating the distribution and statistics of the temperature dataset.

The observed T_{mean} over the whole dataset is 15.03° C. For the ALARO-0, the T_{mean} is 15.1°C, and for REMO is 15.6°C. There is a 0.6°C bias in T_{mean} across the entire 36 years dataset for REMO. T_{min} and T_{max} for the observations and modelled data are respectively -21.2°C and 43.2°C, and -14.5°C and 44.5°C (ALARO-0) and -28.8°C and 48.5°C(REMO). These values are not in line with the conclusions based on the distribution, i.e., the underestimation of extreme minimum temperatures by REMO modelled data towards colder temperatures. However, as these values are outliers, they are not expected to represent the temperature distribution.

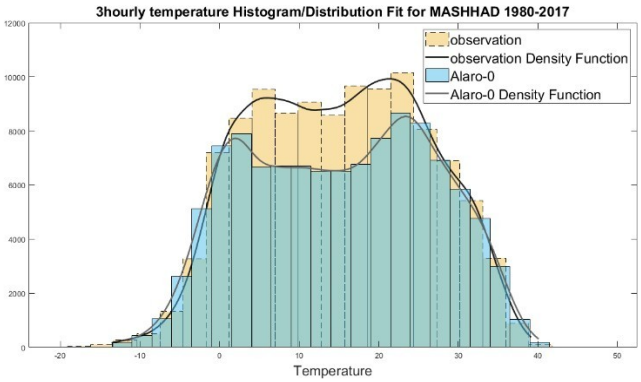

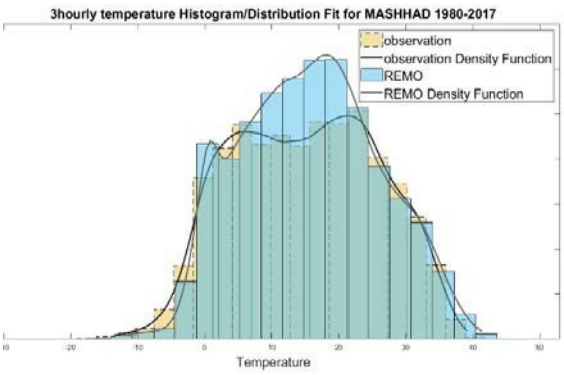

Figure 5.Hourly temperature Histogram ALARO-0. **Figure 6**.Hourly temperature Histogram REMO.

By analysis of the monthly statistics (Figure 7), it can be observed that the monthly T_{mean}, except the observation of summer months (higher temperatures), is lower than the REMO T_{mean} in all months. On the other hand, except winter months, the monthly T_{mean} of the observations is lower than the T_{mean} of the ALARO-0 model. Moreover, the absolute T_{max} of the observations, every month except for August is lower than T_{max} of the REMO. Whereas the observations and ALARO-0 model in this value are very consistent almost every month, the observed absolute T_{min} is lower than the ALARO-0 modeled temperature when the T_{min} is below 0^{o} C.

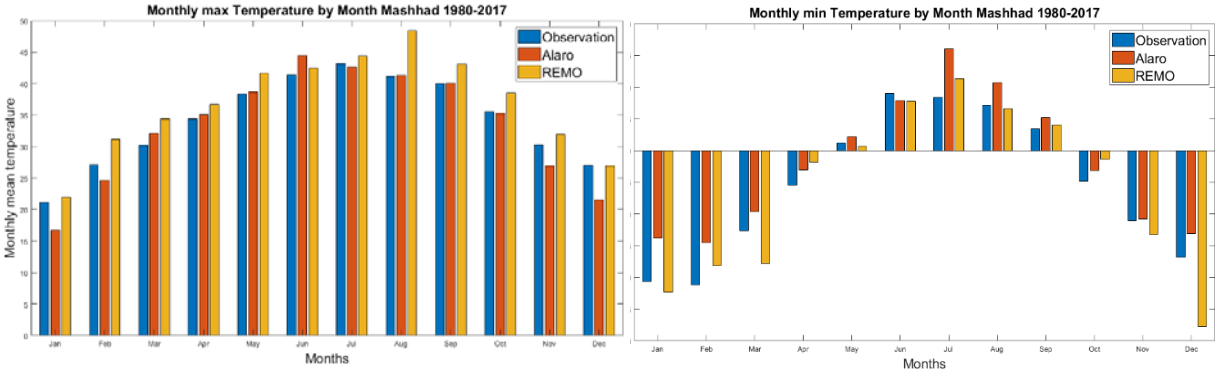

Figure 7. Comparison between monthly min and max temperature of observation and model data.

Figure 8 illustrates the average daily temperature across the entire period based on hourly data and the difference in temperature between the observed and modeled dataset. Note that the ALARO-0 modelled average day is significantly consistent with the observation. The bias range

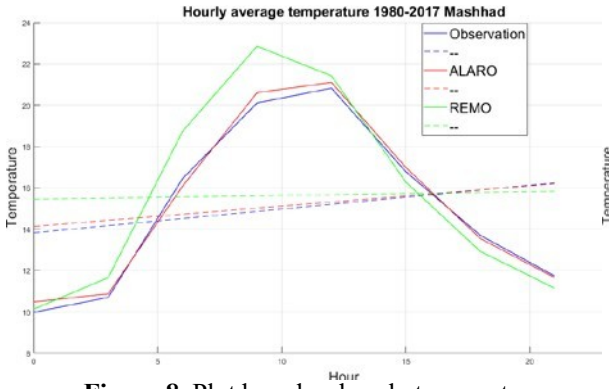

Figure 8. Plot based on hourly temperature.

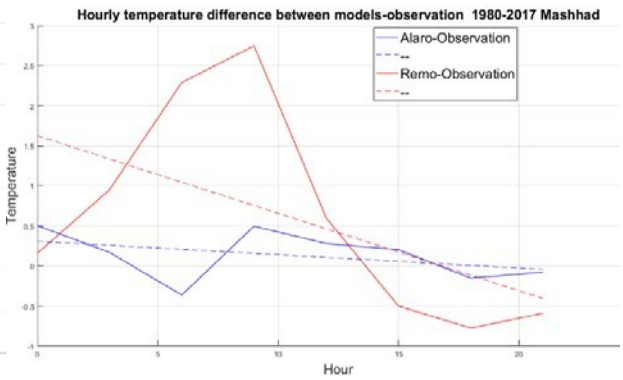

Figure 9. Difference between the datasets temperature.

is between -0.3 and +0.5 °C(Figure 9), respectively, at 6 am, and 9 am, whereas, in the REMO model, more bias is observed mainly during the first hours of the day before 10 am. Biased for every hour, ranging between -0.7 and +2.7 °C, respectively, at 6 pm and 9 am. The most substantial temperature difference is observed in the morning for both models. This could be related to the location of the station, which is located in a semi-arid area, and an essential specification of this climate area is a vast difference between temperature in day and night, and perhaps the REMO model does not capture this effect accurately.

The distributions of daily T_{mean} is provided per season (Figure10). Interestingly, both models show the same results. The most significant difference in distribution between the observations and both models is found in summer, whereas smaller differences characterize spring.

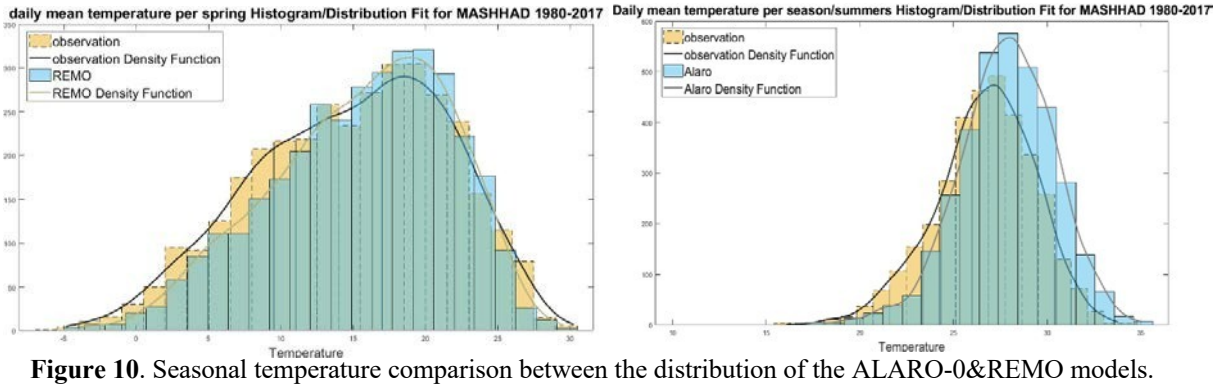

Figure 10. Seasonal temperature comparison between the distribution of the ALARO-0&REMO models.

Besides statistics on hourly and daily T_{mean}, some unusual indices are useful in the field of building physics, such as indices on frost. The first discussed index is the number of freeze-thaw cycles (FTC) as described by Grossi *et al*. (2007), referred to as criterion 1.

Based on daily T_{mean}, one cycle is counted each time the temperature drops below 0°C, given that the previous day was a non-freezing day. Following, the difference in the annual number of FTC between the observations and the modeled data is computed. It can be noted that unlike the observations, both models follow an increasing trend (Figure 11).

The hours of frost index, illustrated in Figure 12, indicate the annual duration of freezing temperatures. The REMO model has predicted considerably fewer frost hours in comparison with the ALARO-0 model and observations. Please note that unlike the observation, both models follow an increasing trend.

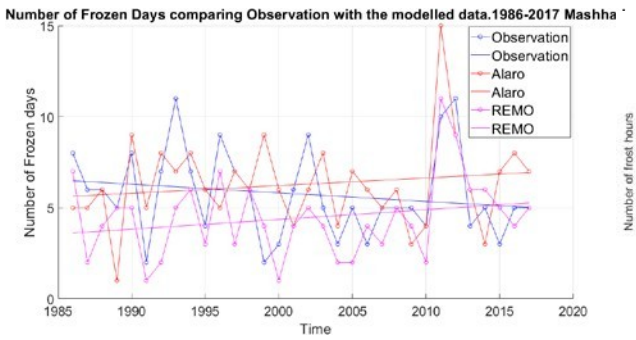

Figure 11. Number of FTC in models and observation.

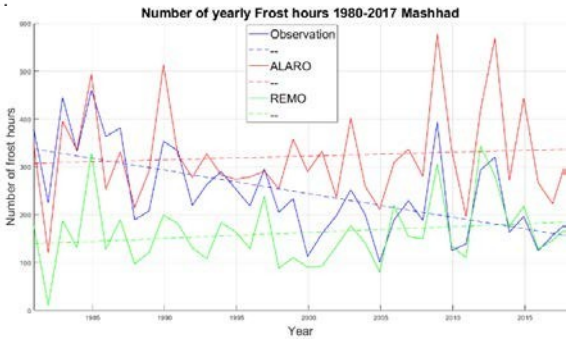

Figure 12. The number of frost hours per year.

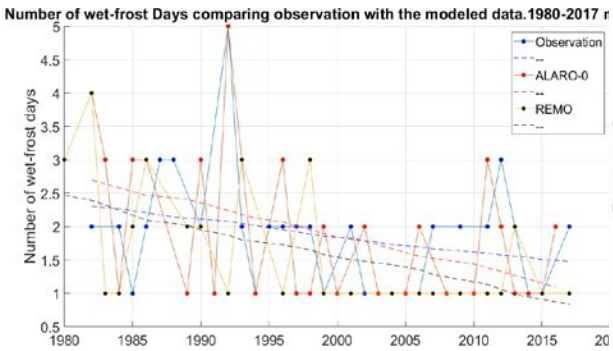

Figure 13. The number of wet-frost cycles. Mashhad.

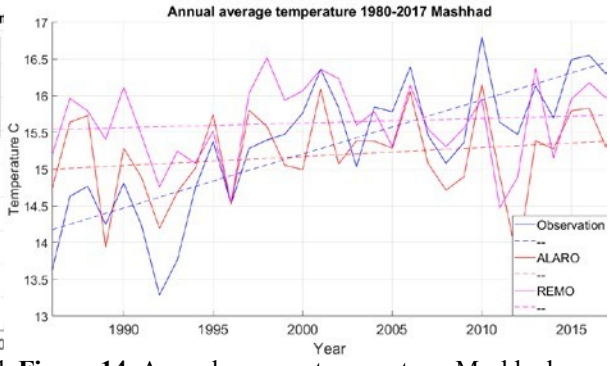

Figure 14. Annual average temperature, Mashhad.

Previous indices are only based on temperature. However, frost damage in building envelopes is highly related to the moisture content in the porous media. The wet frost index considers the annual number of rainy days, i.e., the total daily precipitation exceeding 2 mm and temperatures higher than 0°C, immediately followed by days having a T_{mean} below -1°C (Brimblecombe *et al*. 2006).

The wet frost index is generally higher for the ALARO-0 model compared to the REMO model and more consistent with the observation (Figure 13).

During the analysis of timetables, based on the yearly T_{mean} (Figure 14) regarding the trendlines, it can be observed that the slope of both models similar to observation is incremental, but the real temperature rises at a higher rate. The studied city is the second biggest city in Iran, a dense metropolitan area. Given the existence of the well-known urban heat island phenomenon(UHI), this strong urbanization might Contribute to additional warming at this location, and models cannot catch it.

The evaluation metrics, which are essential in the model validation analysis, are computed (Table.1) and explained in the final part. The adjusted R-squared is a modified version of R-squared that has been adjusted for the number of predictors in the model. An adjusted R-squared of 1 means that the model ultimately predicts the studied parameter. Based on the above descriptions, the correlation, RMSE, and Adjusted R-Squared coefficient of both models indicate high accuracy, but the ALARO-0 model seems more reliable.

Table 1. Validation metrics computed for the temperature parameter.

Mashhad						
Interval/Metrics	Correlation	Adjusted R-Squared	Regression	Correlation	Adjusted R-Squared	Regression
3hourly Temperature	0.9588	0.919	0.9554	0.9386	0.881	0.9674
Daily mean Temperature	0.9676	0.936	0.9558	0.9596	0.921	0.9848
Monthlymean Temperature	0.9882	0.977	0.9600	0.9886	0.977	0.9961

3 Conclusions

Regarding previous analysis and construing the figures and table of statistics, there can be concluded that the best approach for model validation is using the evaluation run of the model and comparing the model dataset with the historical observations in different parametersbased on hourly, daily and yearly time interval. Another critical issue that should be analyzed in each model validation study is considering relevant indexes to the research, i.e., freeze-thaw cycles, which are detrimental in building pathology in the current paper, should be analyzed. This method for our case study proved that both models based on temperature parameter are surprisingly accurate. Based on graphs construing and computed coefficients like correlation and adjusted R-squared, ALARO-0 model is a little more realistic and is suitable to use it as a reliable regional climate model over the target area.

Acknowledgement

The RCM runs used in this paper have performed in the context of the AFTER project, which is granted by the ERA.Net RUS Plus Initiative, ID 166. The computational resources and services for the ALARO-0-0 regional climate simulations were provided by the Flemish Supercomputer Center (VSC), funded by the Research Foundation-Flanders(FWO) and the Flemish Government department EWI. The CORDEX-CORE REMO simulations were performed under the GERICS/HZG share at the German Climate Computing Centre (DKRZ). We would like to thank Steven Caluwaerts (UGent), Lola Kotova (GERICS), and Sara Top (UGent) for providing climate data.

ORCID

Nathan Van Den Bossche: https://orcid.org/0000-0002-8738-7249
Hamed Hedayatnia: https://orcid.org/0000-0002-9894-1217

References

Brimblecombe, P., Grossi, C.M. and Harris, I.(2006). *Climate change critical to cultural heritage*. In: Fort R, Álvarez de Buergo M, Gómez-HerasC, Vázquez-Calvo C, editors. Heritage, Weathering and Conservation. Rotterdam: Balkema, 387–93

Grossi, C.M., Brimblecombe, P. and Harris, I. (2007). Predicting Long Term Freeze-thaw Risks on Europe Built. Heritage and Archaeological sites in a Changing Climate. *Science of the Total Environment,* 377, 273-281. Brimblecombe P, *"The NOAH's ARK Project: The Impact of Future Climate Change on Cultural Heritage*, The Eggs.Newsletter and Information Service of the EGU, no. 12, available at http://www.the-eggs.org/articles.php?id=70.

Giorgi, F.(2006). *Climate change hot-spots*. Geophys. Res. Lett., 33**,** L08707.

Termonia, P., Van Schaeybroeck, B., De Cruz, L. and De Troch, R. (2018). The CORDEX.be initiative as a foundation for climate services in Belgium. *Climate Services,* 11, 49-61.

XV International Conference on Durability of Building Materials and Components
DBMC 2020, Barcelona
C. Serrat, J.R. Casas and V. Gibert (Eds)

Various Factors of Water Entry and Penetration Through Water Proofing Layer in Wooden Wall Assembly

Hiroaki Saito [1] **and Masashi Miyamura** [2]

[1] Ashikaga University, Ashikaga, Japan 3268558,
Phone +81 284 22 5674, Fax +81 284 62 0976, hsaito@ashitech.ac.jp

[2] National Institute for Land and Infrastructure Management, Tsukuba, Japan 3050802,
Phone +81 29 864 4339, Fax +81 29 864 6774, miyamura-m92ta@mlit.go.jp

Abstract. *Rainwater entry and penetration through a waterproofing layer, such as external finishing and sheathing membrane, should be avoided to prevent moisture damage to a wooden wall assembly. However, housing warranty insurance organizations in Japan have reported that deterioration in some wall assemblies was caused by rain penetration, and severely damaged walls were detected in airtight and insulated building envelopes. This paper presents various factors of water entry and penetration of the waterproofing layers in wooden wall assemblies in terms of practical situations, as a part of a research project to reveal the risk of water and moisture accumulation in collaboration with government and industries in Japan. Several experimental works using mock-up specimens replicating a part of the wall assembly were carried out. As for external finishing, the water intrusion was observed not only at the joints but also at the bottom of vented cavities. Although these minor defects must be prevented by proper design and site work, it is difficult to avoid them completely through the construction process and period of use. Indeed, the extent of water entry was affected by various factors such as wall configuration, exposure conditions and so on. Experimental results suggested that various factors, including detail of interface and quality of materials, should be considered to assess service life prediction by hygrothermal analysis.*

Keywords: *Rainwater, Wall Assembly, Waterproofing Layer, Field Survey, Penetration Rate.*

1 Introduction

Global warming has a significant impact on exposure conditions related to the long-term durability of building envelopes. In humid climate regions, such as coastal areas in East Asia, the frequency of heavy rain tends to increase in recent years. Based on the trends in meteorological data issued by Japan Meteorological Agency, the annual number of days with heavy rain of more than 200 mm per day increased by 1.5 times in the past decade in comparison with the rate of increase 40 years ago (Japan Meteorological Agency, 2019).

Although the energy-efficient house has recently been required to reduce CO_2 emissions even in humid climate regions, a building envelope with higher insulation performance is potentially a concern for a decrease in drying performance (CMHC, 1996; Finch, 2007). An increase in heavy precipitation events might give excessive moisture load to wall and roof assemblies. The housing warranty insurance organizations (HWIO) in Japan reported that more than 90% in 550,000 cases of insurable contingencies was water leakage and its total number has gradually increased (HWIO, 2017). This investigation for the insurable contingency indicated that 80% of water leakage occurred in the wall and wall-roof interface (Figure 1a), and that 44% of it was detected in houses with a shedroof (Figure 1b). Additionally, the percentage of shedroofs

doi:10.23967/dbmc.2020.147

with short eaves and verges is higher than other types of roof in the insurable contingencies. This finding suggests that short eaves and verges are among the factors causing rain penetration through the waterproofing layer, and this phenomenon should be clarified and also quantified to assess the service life of building envelopes.

With these points in mind, this paper describes an experimental study regarding water penetration through primary and secondary waterproofing layers in wooden wall assemblies in consideration of practical situations. Water spray tests for several types of siding panels and wall-roof interfaces were implemented, and their details were selected from the insurable contingencies in HWIO. Water penetration through the fastener interface of the secondary waterproofing layer was also examined. Based on these results, the importance of the clarification of the water penetration rate as a boundary condition for hygrothermal analysis was discussed.

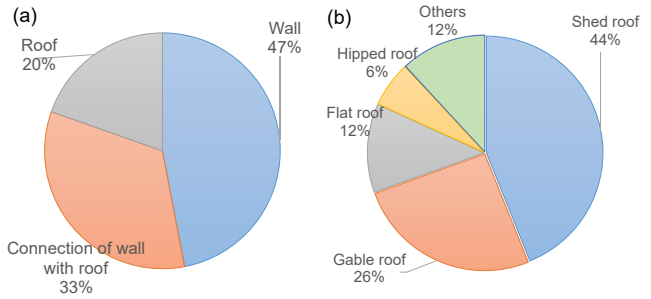

Figure 1. Percentage of water leakage location (a) and type of roof (b).

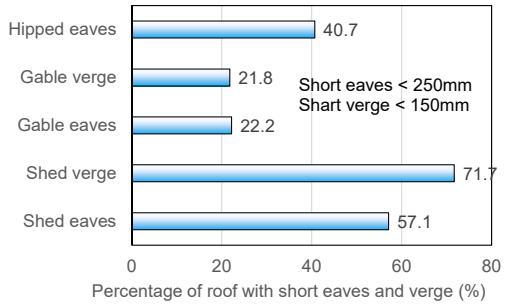

Figure 2. Percentage of roof with short eaves and verge.

2 Water Penetration Through Siding Joints

2.1 Outline of Water Spray Test

To compare watertightness of exterior systems using ceramic sidings, water spray tests (JIS A 1517: Watertightness test under dynamic pressure) with static and dynamic loading were implemented. The ceramic sidings of six products (Sp1 ~Sp6) were selected to understand the performance of representative products in the siding industry of Japan. All sidings employed a two-way shiplap joint between the top and the bottom, and a metal panel clip to fasten it to the substrate of the wall. The thickness and width of the panel were between 15 and 18 mm and 300 and 450 mm, respectively. The heights of the shiplap were between 11 and 15 mm.

Since the outside dimensions of the opening of an airtight box with water spray nozzles were 1.98 m by 1.98 m, two types of siding panel measuring 0.91 m by 1.98 m were fixed to a wood frame, side by side, as specimens (Figure 3). The sprayed water was uniformly applied at a rate of 4 L/[m^2min] across the exterior of the specimens in Case 1 and Case 2, as shown in Figure 4. A rate of 0.3 L/[m^2min] of the sprayed water was applied in Case 3. Static pressure differences through the siding panel were increased stepwise by 150 Pa, 240 Pa, 350 Pa, and 470 Pa with static loading. In addition, dynamic loading tests were implemented in Case 2 and Case 3. Water penetrating the inner plane through the shiplap joints was collected at the bottom of the specimen, and weighed to quantify the overall penetration rate.

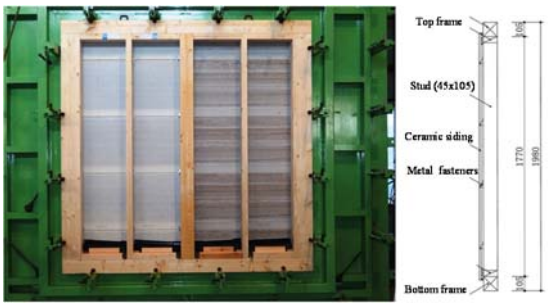

Figure 3. Specimens fixed to airtight box.

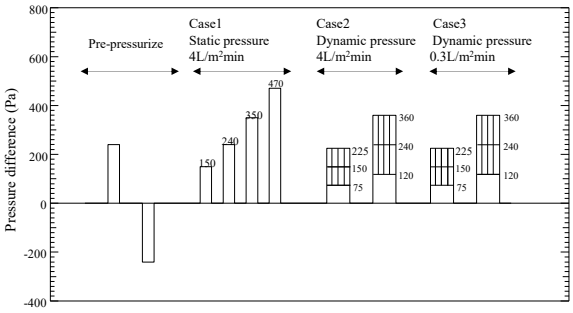

Figure 4. Pressurize process in water spray tests.

2.2 Water Penetration Rate from Siding Joints

The quantity of penetrating water and the water penetration ratio in Case 1 are shown in Figure 5 and Figure 6, respectively. The water penetration ratio means the ratio of the penetrating water and sprayed water. The quantity of the penetrating water in Sp1 and Sp2 exceeded 0.3 L/min m^2 in the range beyond 240 Pa. This value is approximately equivalent to 8% of the water penetration ratio in Figure 6. These values of the other specimens were less than 0.1 L/min m^2 and 3%. Figure 7 shows the water penetration ratio in dynamic presure conditions (Case 2, Case 3). Although the values in Case 2 are less than in Case1, in the event of an equivalent average pressure difference, those in Case 3 are larger than in Case 1. It is speculated that accumulated water in the shiplap joint played a role in stopping the water when the sprayed water was 4 L/min m^2.

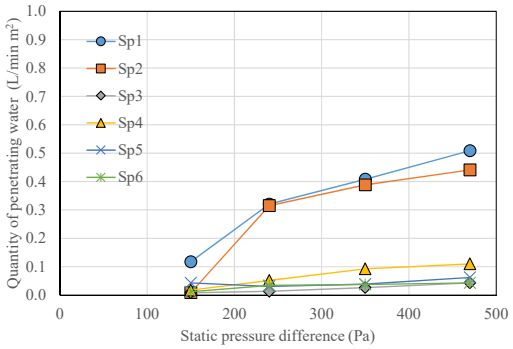

Figure 5. Quantity of penetrating water in Case 1.

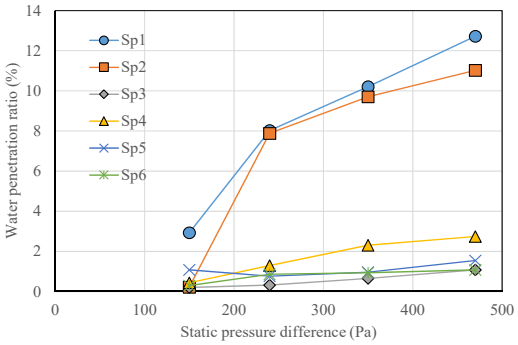

Figure 6. Water penetration ratio in Case 1.

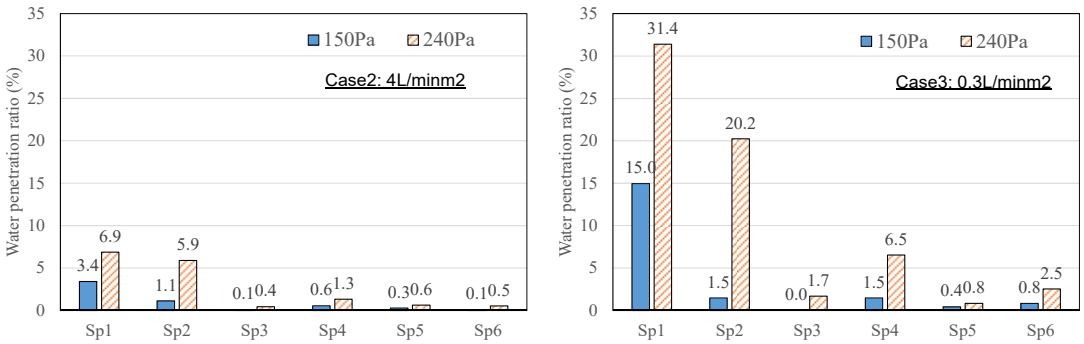

Figure 7. Water penetration ratio in dynamic test (left: Case2, Right: Case3).

According to past research (Sahal and Lacasse, 2005) regarding rainwater penetration through basic components of wall assembly, the quantity of water penetration through electrical outlets and vent ducts was approximately less than 0.25 L/min at 300 Pa of static pressure difference. However, water penetration from these shiplap joints in Sp1 and Sp2 reached 0.4 L/min m^2, meaning that 12 L/min of rainwater enters into the vented cavity when the wall area is 30 m^2. This result indicates that dispersion of the water entry in siding products cannot be neglected in determining the proper configuration of vented cavity in terms of drainage and drying performance.

3 Water Entry at the Top and Bottom of an Exterior with Short Eaves

3.1 Outline of Wind and Rain Blowing Test

In this section, a wind and rain blowing test was implemented to verify the risk of water leakage at the roof-wall interface and the bottom of the vented cavity, as shown in Figure 8. Four types of mock-up specimens incorporating the roof-wall interface were assembled in consideration of actual detail of the insurable contingencies. The width of the specimen was 1820 mm, and the length of the eaves from the center of the beam was 95 mm. A vented cavity connected the attic of the specimen with the top of the wall. Sheathing board such as plywood was not installed in the inner layer of the housewrap, in order to confirm water penetration through an overlap of the housewrap due to water splashing from the bottom of the vented cavity. Airtightness inside the wall was secured by a polyethylene sheet. Type 1, Type 2, and Type 3 shown in Figure 9 differ in details around the eaves. The top edge of the siding in Type 1 butted against the plywood, and additional fascia board or secondary flashing under the roof sheathing was attached in Type 2 or Type 3. The target of the test in Type 4 is the water leakage at the verge, and a bargeboard was attached to the butting of the siding. The specimens were mounted in front of a blowing device, and the roof-wall interface with eaves or verge was directed to the center of the air outlet of the blower. The levels of wind velocity were 5, 10, 15, 20 m/s, which correspond to wind pressure of 15, 60, 135, 240 Pa. The spray rate of water was 32 L/min, and duration time of the test was 15 min.

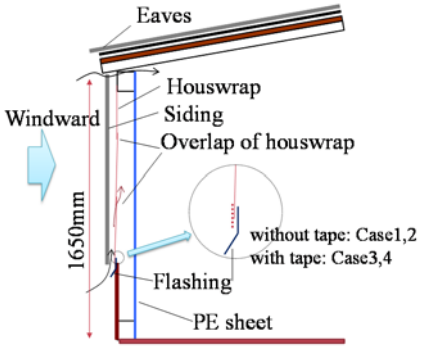

Figure 8. Mock-up specimen for blowing test.

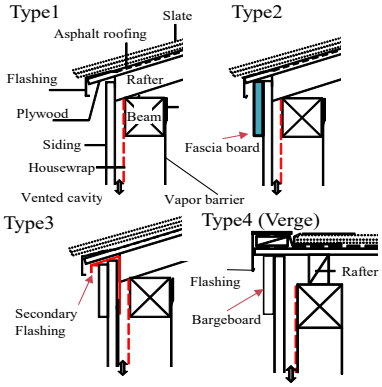

Figure 9. Detail around the eaves and verge.

3.2 Wind Velocity for Onset of Water Leakage and Wetting

Water leakage through the exterior layer in the wind - rain blowing test was confirmed by visual

observation from inside the specimen. Table 1 shows wind velocity for the onset of water leakage. Water splashing into the bottom of the cavity was observed on all specimens with a wind velocity of 5 m/s and above. Continuous splashing through the roof-wall interface was observed in Type 1. Type 1 carries the risk that rainwater penetrates into the thermal insulation layer. Although Type 2 presented better waterproof performance than Type 1 due to the addition of a fascia board at the roof-wall interface, water penetration into the rear face of the housewrap was observed from 15 m/s. Secondary flashing at the top of the siding in Type 3 prevented the water penetration even in 20 m/s. The result on the verge of the roof in Type 4 was approximately equivalent to Type 2.

Table 2 shows the relation between wetting location and wind velocity. Wetting at the ground sill was observed from 5 m/s in Type 1 and Type 2, because of a lack of tape at the bottom of the housewrap. Splashing water reached the overlap of the housewrap at 15 m/s, where the height was 1 m above the bottom of the vented cavity. Although such excess wind pressure at the bottom of the wall generally does not occur in urban areas, a vented cavity above a lean-to roof has the potential to cause pressurization.

These results indicate that imperfect detail for waterproofing at the roof-wall interface causes water penetration not only into the vented cavity but also into the rear of a secondary waterproofing layer, such as the housewrap. In addition, strong winds exceeding 20 m/s increase the water penetration that accelerates water absorption at the surface of sheathing board in wall assemblies. It is necessary for roofs with short eaves to assess safe detail against wind-driven rain.

Table 1. Wind velocity for onset of water leakage.

Observation of water leakage	Eaves			Verge
	Type1	Type2	Type3	Type4
Leakage from top of cavity	5 m/s	5 m/s	none	5 m/s
Splashing from bottom of cavity	5 m/s	5 m/s	5 m/s	5 m/s
Penetration into the rear of the housewrap from the top	5 m/s	15 m/s	none	15 m/s
Splashing into the rear of the housewrap from the bottom	5 m/s	5 m/s	15 m/s*	15 m/s*

*From the overlap above 1 m of floor

Table 2. Relation between wetting location and wind velocity.

Wetting location	Eaves			Verge
	Type1	Type2	Type3	Type4
Ground sill*	5 m/s	5 m/s	none	none
Sheathing roof board	5 m/s	5 m/s	none	5 m/s
Rafter	5 m/s	5 m/s	none	-
Pole plate	5 m/s	15 m/s	none	5 m/s
Purlin	-	-	-	10 m/s

* due to splashing water from the bottom of cavity

4 Water Penetration through Secondary Waterproofing Material

4.1 Water Penetration through a Pinhole in a Water-Resistant Barrier

Nails and staples are generally applied to secure secondary waterproofing material, such as permeable polymer houswrap and asphalt-impregnated felt. However, the fastener interface

carries a risk of water penetration, and past research (Saito, 2015) has tried to quantify water penetration rate through pinholes in roof underlayments after exposure to cyclic temperature variation. To clarify the dispersion of the risk, water penetration tests for representative products were conducted, and reported in this section.

4.2 Outline of Water Penetration Test for Fastener Interface

4.2.1 Case 1 (Without Outdoor Exposure)

The test protocol for the water penetration test was in accordance with Japanese Architectural Standard Specification JASS 12 [Roof construction] (2005, AIJ). Seven products of asphalt-impregnated felt (AF), two products of modified asphalt-impregnated felt (MF), and three products of permeable polymer housewrap (HS) for secondary waterproofing material of wall assembly were selected as the test samples. The AF and MF were immersed in calcium hydroxide for 168 hours before fastening on the substrates, while this alkali treatment was not performed on HS. These test samples were set on substrate and fastened by staples. Two products of staples with 13 mm and 19 mm leg lengths were employed as the fastener for AF and MF, and those with 13 mm leg length were used with HS. Water column containers were placed on the fasteners of the specimen, and colored water was injected into them, as shown in Figure 10. The potential of the hydraulic pressure was set at 30, 50, 100, 150 mm of height, and water penetration was confirmed by visual observation of the colored water leaking after 24 hours. Three spots for test target with the water column container were prepared for each combination of the sample and the staple, and consequently, the number of fasteners was 21 for AF, 6 for MF, and 9 for HS, respectively. Table 3 shows test cases and exposure conditions.

4.2.2 Case 2 (After Outdoor Exposure)

Water penetration tests in Case 2 were performed on three products of HS and one product each of AF and MF. Each sample was fastened to the substrate of plywood using the staple, and the target was nine spots per substrate. Figure 11 shows the configuration of the specimen. To consider the impact of exposure conditions on an actual construction site before installation of the exterior finish, the specimens were exposed to an outdoor environment on a 30-degree angle from the horizontal. The water penetration test was performed after the exposure for 2 weeks in winter. The water level for the water penetration test in Case 2 was only 30 mm.

Table 3. Test cases for water penetration test.

Case	Sample	Leg length of staple (mm)	The number of pinholes [The number of products]	Exposure condition before the test
1	AF	13	21 [7]	Alkalin for 168 hour
		19	21 [7]	
	MF	13	6 [2]	
		19	6 [2]	
	HS	13	9 [3]	-
2	AF	19	9 [1]	Outdoor environment for 7days
	MF	13	9 [1]	
	HS	13	27 [3]	

AF: Asphalt-impregnated felt 430, MF: Modified asphalt-impregnated felt, HS: Permeable polymer housewrap

4.3 Rate of Fastener Interface Securing Watertightness

4.3.1 Case 1 (Without Outdoor Exposure)

Figure 12 shows the relationship between the rate of the fastener interface securing watertightness and the water level. Water leakage was observed at 30 mm of the water level in HS, and all points of HS allowed water penetration through the fastener interface. Contrarily, AF and MF indicated higher performance for watertightness. However, water leakage in AF and MF was detected from 50 mm of water level, and half of the test spots allowed water penetration at 150 mm. Although this experiment in Case 1 showed the vulnerability of HS, it could not indicate a difference between AF and MF in terms of seal performance at fastener interface.

4.3.2 Case 2 (After Outdoor Exposure)

Table 4 shows the rate of watertightness after exposing the specimens in an outdoor environment for two weeks. Dispersion in the difference of the spots was not indicated in each waterproofing material. Although water penetration was detected on AF and HS, MF secured watertightness on all spots of the fastener interface even after outdoor exposure. In general, it takes more than a week for the installation of exterior finishing after fastening the waterproofing material in construction sites. The differing results between Case 1 and Case 2 suggested not only vulnerability in AF but also durability in MF against outdoor exposure, taking into account the construction schedule. Additionally, it can be said that durability against outdoor exposure is important in terms of assessing the performance of the secondary waterproofing layer.

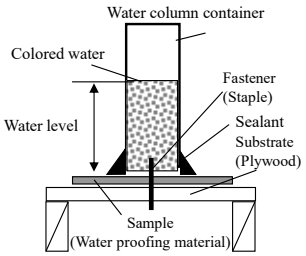

Figure 10. Setup for water penetration test.

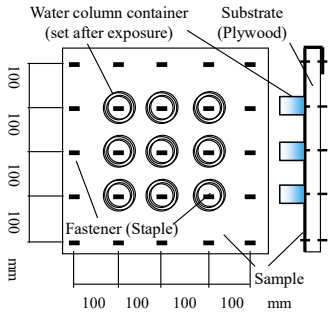

Figure 11. Configuration of specimen (Case 2).

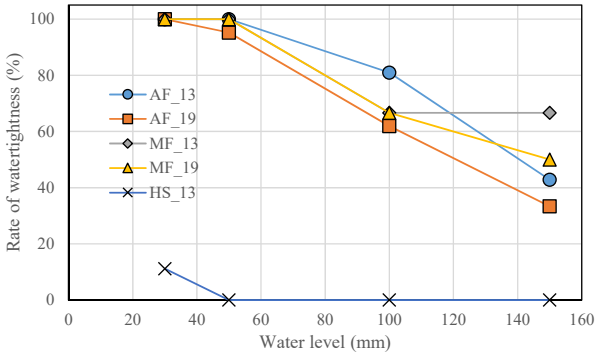

Figure 12. Rate of fastener interface securing watertightness in Case 1.

Table 4. Rate of watertightness in Case 2.

Waterproofing material	Rate of watertightness (%)
AF	0 [0/9]
MF	100 [9/9]
HS	0 (0/9)

5 Conclusions

To confirm the vulnerability of the primary and secondary waterproofing layer to water entry, water penetration tests were implemented on vulnerable parts, such as siding joints, wall-roof interfaces and fastener interfaces. The quantity of penetrated water in the worst specimens exceeded 0.3 L/min m^2 at 240 Pa of pressure difference, and this value is greater than water penetration from electrical outlets and vent ducts in past research (Sahal and Laccase, 2005). The significance in this experiment is that products with vulnerable watertightness occasionally exist, even though there was no remarkable difference in the specification. As for water entry at a wall-roof interface with short eaves, wind and rain blowing tests indicated that conventional details, using fasciaboard and bargeboard, are not useful in preventing water entry into the rear of the siding. Additionally, splashing water reached the pole plate and accumulated on it, when the wind pressure increased. Water penetration through permeable polymer housewrap was confirmed at the fastener interface. The watertightness of AF significantly decreased in outdoor exposure of just 2 weeks.

Although this paper merely addressed a few phenomena relating to water leakage, the results suggest that various factors, such as detail of interface and quality of materials, have significant impact on the extent of water leakage. Lately, consideration of rain penetration in hygrothermal analysis has been recommended in evaluation methods such as the ASHRAE Standard 160 (ASHRAE 2009), and a certain rain penetration ratio is provided. However, results in this paper imply that this value should be modified by the various factors discussed in order to assess the service life of building envelopes in practical use.

ORCID

Hiroaki Saito: https://orcid.org/0000-0003-3633-7679
Masashi Miyamura: https://orcid.org/0000-0002-5606-9117

References

Japan Meteorological Agency (2018). 2017 edition of Climate Change Monitoring Report

Canada Mortgage and Housing Corporation (1996). Survey of building envelope failures in the coastal climate of British Columbia, Columbia, Report prepared by Morrison Hershfield Limited

Finch, G. and Straube, J. (2007). Hygrothermal Performance and Drying Potential of Wood Frame Rainscreen Walls in Vancouver's Coastal Climate, *Proceedings of 11th Canadian Conference on Building Science and Technology*, Banff, Alberta

Japanese Standard Association (1996). *JIS A 1517: Windows and doorsets - Watertightness test under dynamic pressure.* (in Japanese)

Sahala, N. and Lacasse, M. (2005). Water entry function of a hardboard siding-clad wood stud wall, Building and Environment, 40, 1479–1491. doi:10.1016/j.buildenv.2004.11.019

Saito, H., (2015). Hygrothermal Analysis for Pitched Roof in Consideration of Water Penetration through Pinholes of Roofing Underlayment Assemblies, Roofing Research and Standards Development: 8th Volume, ASTM STP 1590, 206–222

Architectural Institute of Japan (2005). Japanese Architectural Specification Standard JASS 12 (in Japanese)

ASHRAE (2009). Criteria for Moisture-Control Design Analysis in Buildings. ASHRAE Standard 160.

XV International Conference on Durability of Building Materials and Components
DBMC 2020, Barcelona
C. Serrat, J.R. Casas and V. Gibert (Eds)

A Probabilistic Model for the Evolution of Porous Structure Caused by Solid-Phase Precipitation/Dissolution within Building Materials

Xiong Qing Xiang[1, a] and Meftah Fekri[1, b]

[1]Laboratory of Civil and Mechanical Engineering (LGCGM), National Institute for Applied Sciences, Campus Beaulieu, 35700 Rennes, France
[a]qingxiang.xiong@insa-rennes.fr, [b]fekri.meftah@insa-rennes.fr

Abstract. *Saline intrusion is a critical issue in building material because of the severe damages caused by the salt precipitation/dissolution process, especially for the porous material, which has good connectivity. When porous material is exposed to aggressive ambient, the pore structure, not only porosity but also pore size distribution, will be altered by salt precipitation/dissolution. As one of the most significant characteristics in the porous material, pore size distribution is always paid much attention in many literatures. However, a quantitative and practical determination method is still absent. This work aims to establish a probabilistic model to investigate the pore size distribution induced by solid-phase precipitation/dissolution. First, a lognormal distribution is proposed for the simulation of initial pore size distribution tested by the MIP method. Then we develop a probabilistic-based porous network to represent the evolution of microstructure due to precipitation/dissolution. To this end, two different transformation models are constructed to interpret the relation between initial pore radius and modified pore radius before and after precipitation/dissolution. With this probabilistic-based porous network, we could illustrate the precipitated profiles that evolve near the capillary interface during the salt precipitation/dissolution process for a given porosity and water saturation degree. Such a method could be used to interpret the mechanism of the local precipitation/dissolution process in pore scales, which cannot be implemented by experimental measurements.*

Keywords: *Pore Size Distribution, Precipitation/dissolution, Capillary Interface, Probabilistic Methods, Transformation Models.*

1 Introduction

The durability of construction material is always prevalently focused research since it is strictly relevant to the long and durable service life of building structures. As is generally accepted, salt precipitation/dissolution is one of the main factors for the deterioration of construction material, especially for the porous construction material, which has highly connected cavity facilitating the transport of moisture, ions, and chemical fluxes (Huang *et al.,* 2015). Salt precipitation/dissolution strongly influences the pore structure, which governs the most important properties of porous material, notably compressive strength for cement-based media (Cristina *et al.,* 2012). For example, salt dissolution induces high porosity, which accelerates the permeability of gases and liquids within the pore structure, thus affects the compatibility and durability of the construction materials. As a result, it brings about high maintenance and repair costs. (Fenaux *et al.,* 2019; Kumar *et al.,* 2003). Therefore, the porous structure directly impacts the durability and resistance of construction material and components. More specifically speaking, research on the processes involved in salt-induced corrosion is of utmost benefit for assessing the durability of construction material.

Apart from the porosity, the pore size distribution (PSD) also plays a vital role in

characterizing pore structure within porous media (Aligizaki *et al.,* 2005). However, the porosity does not give any information about pore size, shape, distribution, and connectivity; thus, the PSD should be employed to give a precise depiction of pore structure. The PSD, which is so complicated that covers several orders of magnitude of pore size, is principally influenced by several aspects, for instance, water, air, chemical reactions, and other fluids. (JR Nimmo, 2013) It is essential to recognize that many efforts of experimental measurements have been devoted to the description of PSD by previous researchers (D.N. Winslow, 1968; S. Roels *et al.,* 2001; E.Gallucci *et al.,* 2007; Yanbin Yao *et al.,* 2012; Gong Fuyuan *et al.,* 2014). However, a quantitative and practical determination method is still absent. Since the pore structure is heterogeneous and anomalous morphology in pore sizes, it is hard to describe it in full detail by experimental measurements. Therefore, the most reasonable method is to assess it by probabilistic models.

In this work, we adopted a lognormal distribution to approach the initial PSD before solid-phase precipitation occurred. Two representative models for pore radius were constructed by employing a monotonic transformation model and a non-monotonic transformation model. After several times of solid-phase precipitation, the new PSD was described by two different probabilistic methods. According to the comparison and parametric investigations, the proposed methods could provide us with an estimated prediction of the modified PSD, filling rate, and water saturation degree.

2 Methodologies

2.1 Transformation Models for Pore Radius

During the process of solid-phase precipitation/dissolution, the initial pore radius goes through a multi-step of transformation with the evolution $r_0 \to r_1 \to \cdots \to r_n \to r_{n+1}$, which is corresponding to the evolution of total porosity $\phi_0 \to \phi_1 \to \cdots \to \phi_n \to \phi_{n+1}$. According to the superposition principle, the new pore radius $r_{n+1}$is the superimposed of the current pore radius r_n and the increment term denoted as $\varepsilon_{n+1}(r_n)$, which is expressed as equation (1). As is mentioned above, precipitation/dissolution occurs near the capillary interface. Thus, the waterfront r_c is introduced into the transformation models of the pore radius. For the sake of simplification, it is assumed that the waterfront keeps constant as the evolution of pore structure. That is to say, the proposed pore system is open to the atmosphere to induce the water to evaporate into the ambient, which makes the waterfront be equilibrium. In this way, the capillary interface keeps constant for each time of transformation.

$$r_{n+1} = f_{n+1}(r_n) = r_n + \varepsilon_{n+1}(r_n) \tag{1}$$

Let us consider two different cases for the increment function $\varepsilon_{n+1}(r_n)$. For the monotonic model (see Figure 1a), water is filled in all the pores with the radius less than r_c. Solid-phase condenses inside the pores with the radius ranging from $r_c - \beta$ to $r_c + \beta$. When pore radius is large enough (*i.e.,* more than $r_c + \beta$), the accumulated solid-phase is assumed to be constant as $\bar{\varepsilon}_{n+1}$. For the non-monotonic model (see Figure 1b), the precipitated solid only occurs near the waterfront with the range from$r_c - \beta$ to $r_c + \beta$; for large pores with radius more than $r_c + \beta$, solid mass is supposed to be small enough to be neglected when compared to the large pore space.

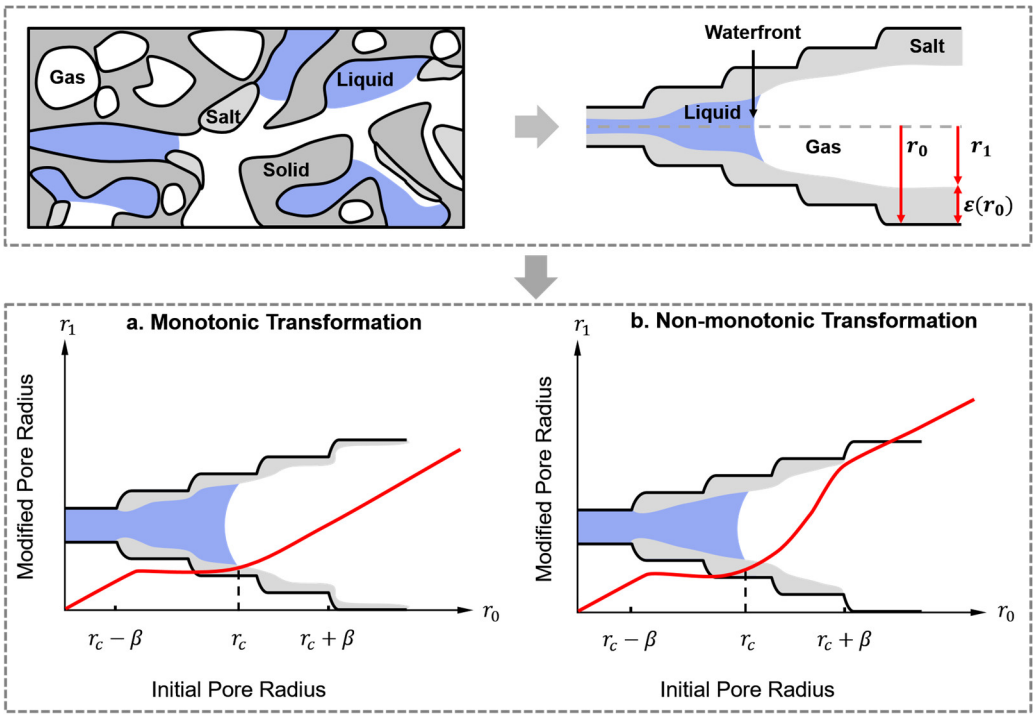

Figure 1. Schematic of the porous model for one single transformation (r_c is the maximum aperture filled with water, the so-called waterfront or capillary interface; β is the opening zone, indicating the range of solid precipitation/dissolution, $\varepsilon(r_0)$ is the increment term for the first time of transformation.).

Table 1. The monotonic transformation model and non-monotonic transformation model for new pore radius.

Function	Monotonic transformation model	Non-monotonic transformation model
$\varepsilon_{n+1}(r_n)$	$\begin{cases} 0 & r_n < r_c-\beta \\ \bar{\varepsilon}_{n+1}H(r_n) & r_c-\beta \le r_n \le r_c+\beta \\ \bar{\varepsilon}_{n+1} & r_n > r_c+\beta \end{cases}$	$\begin{cases} 0 & r_n < r_c-\beta \\ \bar{\varepsilon}_{n+1}H(r_n) & r_c-\beta \le r_n \le r_c \\ \bar{\varepsilon}_{n+1}G(r_n) & r_c \le r_n \le r_c+\beta \\ 0 & r_n > r_c+\beta \end{cases}$
$H(r_n)$	$\frac{3}{4}\left(\frac{r_n-r_c}{\beta}-\frac{(r_n-r_c)^3}{3\beta^3}\right)+\frac{1}{2}$	$\frac{3}{4}\left(\frac{2r_n+\beta-2r_c}{\beta}-\frac{(2r_n+\beta-2r_c)^3}{3\beta^3}\right)+\frac{1}{2}$
$G(r_n)$		$-\frac{3}{4}\left(\frac{2r_n-\beta-2r_c}{\beta}-\frac{(2r_n-\beta-2r_c)^3}{3\beta^3}\right)+\frac{1}{2}$
Remarks	The derived function should satisfy $H'(r_n) > 0$ in the case of salt precipitation, that is, $\bar{\varepsilon}_{n+1}$ is constrained in the range of $[0, -4/3\beta]$	

Table 1 shows the details of two different transformation functions. It should be noted if parameter $\bar{\varepsilon}_{n+1} > 0$, salt dissolution occurs; if $\bar{\varepsilon}_{n+1} < 0$, salt precipitation occurs. For the monotonic transformation model, the derived function $H'(r_n)$ should be positive to make sure the transformation function is one-to-one.

2.2 Probabilistic Methods for Modified Pore Size Distribution

The initial PSD for gel pores and capillary pores is presented in the form of lognormal probability density function that is expressed as:

$$P_0(r_0) = \frac{1}{\sigma_r\sqrt{2\pi}\, r_0} \exp\left(-\frac{(\ln r_0 - \mu_r)^2}{2\sigma_r^2}\right) \tag{2}$$

where μ_r, the location parameter, is the arithmetic mean of the representative pore size and σ_r, the standard deviation, is a measure of the dispersion of these pore size.

The total porosity for n+1th transformation is defined as:

$$\phi_{n+1}(r_{n+1}) = \phi_{n+1} \int_0^{r_{n+1}} P_{n+1}(t)dt \tag{3}$$

As we have the initial PDF $P_0(r_0)$ and two transformation models for pore radius, the new probability density function $P_{n+1}(r_{n+1})$ for n+1th transformation could be determined by the following two methods, which are presented in Table 2.

Table 2. Two probabilistic methods and their properties.

	Method one	Method two
Theoretical foundation	It is based on the assumption that porosity is proportionally distributed to each pore, the ratio of local porosity before and after transformation is equal to that of the ratio of global porosity: $\frac{\phi_{n+1}}{\phi_n} = \frac{d\phi_{n+1}}{d\phi_n}$	Let us consider the cylindrical form of the pores as to the end that the ratio of local porosity before and after transformation is equal to the ratio of pore volume, which could be represented by the following equation: $\frac{d\phi_{n+1}}{d\phi_n} = \frac{r_{n+1}dr_{n+1}}{r_n dr_n}$
P_{n+1}	$\left\lvert\left(\frac{dr_{n+1}(r_n)}{dr_n}\right)^{-1}\right\rvert P_n(r_n)$	$\frac{\phi_n}{\phi_{n+1}}\frac{r_{n+1}(r_n)}{r_n} P_n(r_n)$

According to Figure 1, the capillary condensation occurs in pores with radii smaller than r_c, thus the water saturation degree S_l (SD) can be obtained by the integration of the volume pores with sizes smaller than r_c.

$$S_l = \int_0^{r_c} P_{n+1} dr_n \tag{4}$$

3 Implementation and Parametric Study

The inputs parameters of initial pore size distribution were completed by experimental test mercury intrusion porosimetry (MIP) on masonry cement (see in Table 3 for more properties).

As the limitation of space, only the process of solid precipitation ($\bar{\varepsilon}_{n+1} < 0$) will be discussed in this work. The waterfront could occur in any position of capillary pores, ranging from 0.0025μm to 5μm (Huang et al., 2015), thus, the opening zone β could be any value that

is smaller than r_c.

Table 3. Characteristic parameters of lognormal distribution for the initial pore radius.

Initial porosity ϕ_0	Standard deviation σ_r	Mean Value μ_r	r_{min} (μm)	r_{max} (μm)
0.20	1.2	-1.8788	0.0015	165

3.1 One Transformation for the Monotonic Model

Let us study one monotonic transformation of PSD evolves with four different capillary interfaces both by method one and method two. When solid-phase precipitation occurs, the porosity is assumed to decrease from 0.2 to 0.18, and the opening zone is fixed at 0.05μm. Then we can get the new PSD for the single transformation according to the equations in Table 1 and Table 2.

Figure 2 indicates that significant and sharp salt precipitation occurs near the waterfront for method one (see in Figure 2a). For method two (see in Figure 2b), the variation of pore radius is much smoother than method one. Moreover, the modification was distributed evenly to the whole range of pore size in method two. Thus, it can be concluded that for the porous materials sensitive to the capillary effect, such as the porous material with a large number of fine pores and high permeability, method one is more appropriate to describe the slight salt deposition process than method two. Of course, the extent of salt precipitation also depends on the type of salts, temperature, concentration, and saturation degree of salt solution.

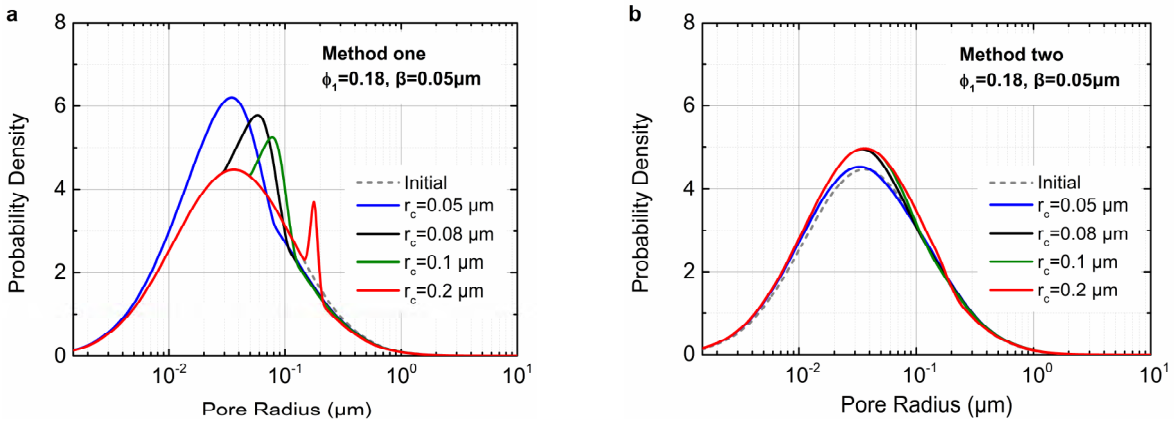

Figure 2. Pore size distribution with different waterfront for single transformation.

3.2 Successive Transformations for the Non-Monotonic Model

For the case of non-monotonic transformation models, we focus on five times of successive transformations with the porosity decreasing from 0.20 to 0.18 in the step of 0.004. The waterfront is fixed at 0.1 μm, and the opening zone is valued at 0.08μm. For non-monotonic transformation, there is no constraint to new porosity, and all we should concern about is that the critical parameter $\bar{\varepsilon}_{n+1}$cannot make the new pore radius negative.

From Figure 3, we can find that both method one and method two generate a bimodal probability density as the porosity decreasing to a specific value. As is similar to the single transformation, the probability density presented by method one shows a noticeable increment

of the peak value. In contrast, the probability density curve implemented by method two shows a slight shift to the left side, indicating produced more fine pores with the effect of precipitation.

As to the filling rate of pore radius due to the solid-phase precipitation presented in Figure 4, by dividing $\varepsilon_{n+1}(r_0)$ with r_0, after one time of transformation, that of the method one is up to 30% while that of the method two accomplishes around 10%. After five times of transformation, when the porosity decreases to 0.18, the porous material described by method one has the filling rate of almost reaching 70%, while method two only achieves over 30%. Thus, at the same porosity, method one presents a more efficient filling rate of pore radius than method two.

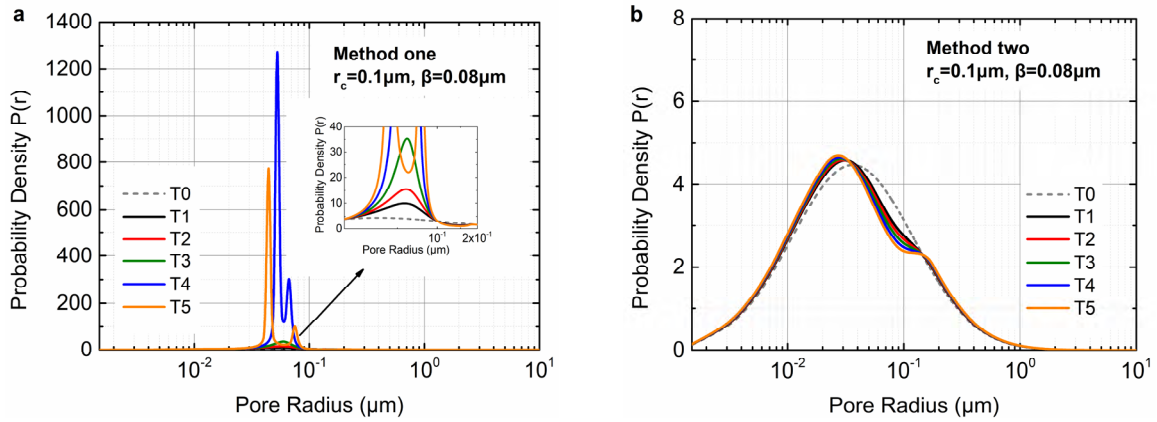

Figure 3. Pore size distribution for successive non-monotonic transformations by two different methods (According to Table 2, method one is related to the reciprocal of the derivative function of the non-monotonic transformation model, which induces the singularity points at the positions where the derivative function is equal to zero. As a result, the PDF tends to infinity at these singularity points. Herein the unbounded PDF is allowed because the integral of the modified PDF from 0 to ∞ is equal to 1.).

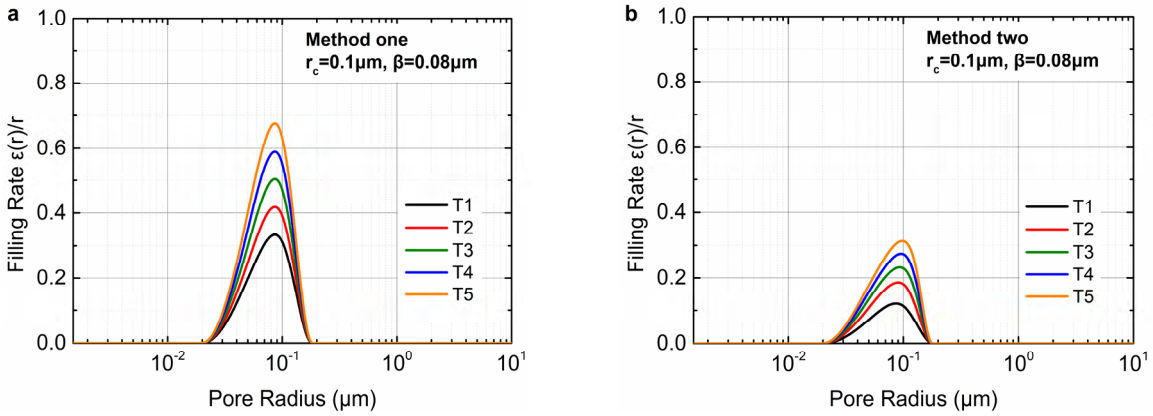

Figure 4. Filling rate of pore radius by two different methods during the process of salt precipitation.

To investigate the evolution of water saturation degree for successive transformations, we consider a case that porosity decreases from 0.2 to 0.185 by 30 steps, as is shown in Table 4.

Table 4. Parameter configurations for the investigation of the water saturation degree in non-monotonic successive transformations.

Initial porosity ϕ_0	Final porosity ϕ_{30}	Transformation Times	Transformation Steps of Porosity	Waterfront r_c (μm)	Opening Zone β (μm)
0.2	0.185	30	0.0005	0.1	0.08

Figure 5 shows the evolution of the water saturation degree with the porosity. It is observed that the water saturation degree calculated by method one shows a slight reduction while that is described by method two increases tremendously with the porosity decreasing. Besides, the incremental trend is more and more evident as the decreased porosity. It may be ascribed to the different filling rates of the two methods. For method two, the reduction rate of the pore volume is lower than that of water volume, leading to the increment of the water saturation degree. However, for method one, the reduction rate of the pore volume is fast enough to catch that of the water volume, and the two rates are almost the same. Consequently, the water saturation degree by method two almost keeps constant.

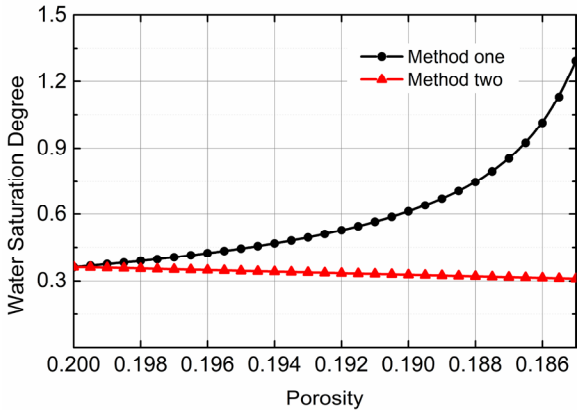

Figure 5. Water saturation degree implemented by two methods in the case of salt precipitation.

4 Conclusions

- When the waterfront moves to large pores, method one shows more evident modification than method two for PSD in the process of salt precipitation. Moreover, method one is more appropriate to the porous material that is sensitive to the capillary effect than method two. Besides, the monotonic model is very limited used, which is only applicable to the slight salt precipitation.
- The existing two probabilistic methods could estimate the filling rate caused by salt precipitation. According to the simulated results of non-monotonic transformation models after five times of transformations, method one has a higher filling rate than method two, which indirectly leads to the stable water saturation degree in method one. Such an approach of method one allows the water condensation in the open system that does not depend on the evolution of the pore structure.
- For further investigation, proper consideration for the mobilization of waterfront in a closed system should be taken into account to fully understand the evolution of

microstructure in the durability research for a porous material.

Acknowledgement

The author acknowledges Professor Ouali. Amiri of his generous providing experimental tested results for the reference of our work.

ORCID

Amiri, O: https://doi.org/10.1680/adcr.2005.17.1.39
Baroghel-Bouny Véronique: https://doi.org/10.1016/j.cemconres.2006.11.019
Fenaux, M : https://doi.org/10.1016/j.cemconcomp.2018.12.009
Gallucci Emmanuel: https://doi.org/10.1016/j.cemconres.2006.10.012
Gentilini Cristina : https://doi.org/10.1016/j.conbuildmat.2012.07.086
Gong Fuyuan: https://doi.org/10.1061/(ASCE)MT.1943-5533.0000945
Huang Qinghua: https://doi.org/10.1016/j.cemconres.2014.08.003
Kumar Rakesh: https://doi.org/10.1016/S0008-8846(02)00942-0
Nimmo, J: https://doi.org/10.1016/B978-0-12-409548-9.05265-9
Roels Staf: https://doi.org/10.1007/BF02481555
Windslow, D.N: https://doi.org/10.5703/1288284313747
YanbinYao: https://doi.org/10.1016/j.fuel.2011.12.039

References

Amiri, O., Aït-Mokhtar, A. and Sarhani, M. (2005). Tri-dimensional modelling of cementitious materials permeability from polymodal pore size distribution obtained by mercury intrusion porosimetry tests. Advances in Cement Research, 17(1), 39–45.

Aligizaki, K. K. (2005). Pore Structure of Cement-Based Materials: Testing, Interpretation and Requirements. CRC Press.

Fenaux, M., Reyes, E., Gálvez, J. C. and Moragues, A. (2019). Modelling the transport of chloride and other ions in cement-based materials. Cement and Concrete Composites, 97, 33–42.

Gallucci, E., Scrivener, K., Groso, A., Stampanoni, M. and Margaritondo, G. (2007). 3D Experimental Investigation of the Microstructure of Cement Paste Using Synchrotron X-Ray Microtomography (mu CT). Cement and Concrete Research, 37, 360–368.

Gentilini, C., Franzoni, E., Bandini, S. and Nobile, L. (2012). Effect of salt crystallisation on the shear behaviour of masonry walls: An experimental study. Construction and Building Materials, 37, 181–189.

Gong Fuyuan, Zhang Dawei, Sicat Evdon, and Ueda Tamon. (2014). Empirical Estimation of Pore Size Distribution in Cement, Mortar, and Concrete. Journal of Materials in Civil Engineering, 26(7), 04014023.

Huang, Q., Jiang, Z., Gu, X., Zhang, W. and Guo, B. (2015). Numerical simulation of moisture transport in concrete based on a pore size distribution model. Cement and Concrete Research, 67, 31–43.

Kumar, R. and Bhattacharjee, B. (2003). Porosity, pore size distribution and in situ strength of concrete. Cement and Concrete Research, 33(1), 155–164.

Nimmo, J. (2013). Porosity and Pore Size Distribution. Reference Module in Earth Systems and Environmental Sciences.

Roels, S., Elsen, J., Carmeliet, J. and Hens, H. (2001). Characterisation of pore structure by combining mercury porosimetry and micrography. Materials and Structures, 34(2), 76–82.

Windslow, D.N. (1968). The Pore Size Distribution of Portland Cement Paste. JTRP Technical Reports.

Yao, Y. and Liu, D. (2012). Comparison of low-field NMR and mercury intrusion porosimetry in characterizing pore size distributions of coals. Fuel, 95, 152–158.

XV International Conference on Durability of Building Materials and Components
DBMC 2020, Barcelona
C. Serrat, J.R. Casas and V. Gibert (Eds)

Assessment of Reasons behind and Level of Destruction of Aquatic Supports in a Hydraulic Ash Removal Bridge

Tomasz Błaszczyński[1] **and Aldona Łowińska-Kluge**[2]

[1] Professor emeritus, Poznan University of Technology, tomasz.blaszczynski@opal.info.pl

[2] Professor emeritus, Poznan University of Technology, lowinska-kluge@wp.pl

Abstract. *The presented article describes a case of damage to concrete in the aquatic supports of a hydraulic ash removal bridge in a power plant. Carrying out an assessment of the causes of concrete damage, as well as determining the possibility of the occurrence of corrosive phenomena within it, and thus, consequently, predicting the durability of the building structure and selecting, on its basis, a proper repair-renovation procedure, required a series of essential studies and analyses to be carried out. Therefore, in the analyzed case, a complex study was carried out on the structure as well as tests on samples of concrete cut out, in the form of core drillings, from the damaged structure (among others: macroscopic, microscopic SEM, XRD, DTA, chemical analyses). Based on these studies, the types of corrosion responsible for the analyzed damage were determined.*

Keywords: *RC Aquatic Supports, Durability, Destruction, SEM, XRD, DTA, Chemical Analyses.*

1 Introduction

For years now, not much attention has been given to industrial reinforced concrete structures. Unfortunately, the consequences of this are progressing phenomena of various types of corrosion, especially when the structures are under conditions posing a risk of corrosion. It is known that the corrosion of materials which buildings are made from is of fundamental importance to their durability (*Błaszczyński et al., 2008*). The reasons behind the corrosion of concrete, and therefore reinforced concrete, can be manifold. Such corrosion usually takes place under the influence of external effects. In the recent years, a frequent phenomenon in building practice is the occurrence of cracking of reinforced concrete structures across their entire width as early as at the stage of their realization. The reason behind such a state of things, as proven in works (*Błaszczyński et al., 2008, Łowińska-Kluge et al., 2012*), is internal corrosion in concrete. Concrete, as a structural material, is subjected to the corrosive effects of the outside environment. One type of corrosion that this material undergoes, frequently neglected by designers, is biological corrosion – a specific case of chemical corrosion. It ought to be pointed out that numerous physical and chemical transformations taking place in concrete are the result of the activity of metabolic organisms, i.e. bacteria, fungi or algae. The destruction of material caused by these living organisms takes place, among others, under the influence of biogeophysical processes, such as the changes in the porosity of material as a result of the development of a biological membrane on the surface of the concrete (*Horbik et al., 2013, Łowińska-Kluge et al., 2016, Mejíaa et al., 2019*).

2 Short Description of Analyzed Structure

Aquatic supports of a hydraulic ash-removal bridge are found in the area of a power plant, or,

doi:10.23967/dbmc.2020.013

more precisely, over the waters of a lake surrounding the actual plant. The lake serves to naturally cool off turbines. The supports are monolithic reinforced concrete structures in the form of reinforced concrete footings, found on a steel grated structure supporting structure, the construction of which is based mainly on channels or I sections.

After many years of service, the supports of the hydraulic ash-removal bridge are in a bad technical condition. Corroded and spalling concrete can be seen, as well as the progressing corrosion of reinforcing steel (Fig. 1, 2).

Figure 1, 2. Damages to pillars in the form of spalling corroded concrete and corroded reinforcing steel.

Centres of biological corrosion are also visible (Fig. 3 and 4).

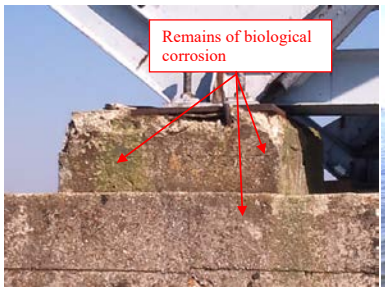

Figure 3. Reinforced concrete support with corrosion Centres.

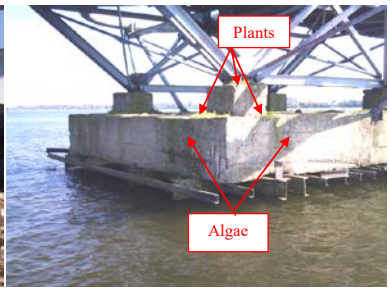

Figure 4. Reinforced concrete support along with the covering vegetation and algae.

3 Performed Laboratory Tests

Laboratory tests were carried out on the collected samples from the objects, which covered: concrete core drillings of ∅ 4.5 mm, defined as Concrete A (Fig. 5) as well as concrete piece samples from areas near reinforcing bars and labelled as Concrete B (Fig. 6).

Figure 5. View of collected samples in the form of core drillings.

Figure 6. View of collected pieces.

3.1 Macroscopic Studies

Based on macroscopic observations, the occurrence of natural aggregate of a similar

granulation as well as certain amounts of carbonate aggregate was determined in the analyzed types of concrete. Concrete samples are characterized by a porous structure and varying dimensions of pores, with the remains of corroded reinforcement bars (Fig. 7a) and carbonate aggregate (Fig. 7b) determined on the majority of the samples.).

The presence of biotic factors in the form of algae and mosses, which can cause biological corrosion, is confirmed on the outer side of samples A and B (Fig. 8).

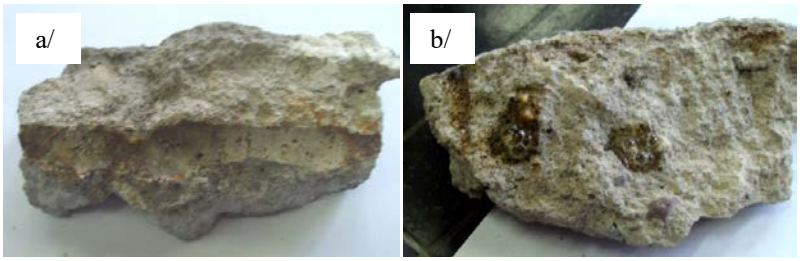

Figure 7. Piece samples of concrete: a/ porous structure and remains of corroded reinforcement bars, b/carbonate aggregate reacting with 10% HCl.

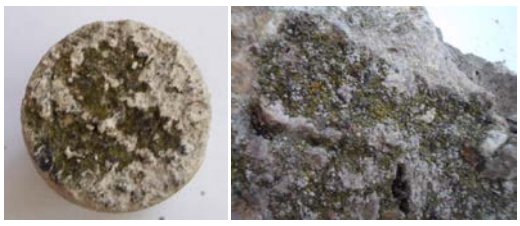

Figure 8. Concrete samples with visible biotic factors.

In order to assess the estimated course of carbonization in the analyzed concretes, the cross sections of concrete samples were sprayed with 1% phenolphthalein solution. Piece samples (Concrete B) are completely carbonized (Fig. 9), whereas in the samples from the core drillings (Concrete A), the carbonized layer is 1-3 cm in thickness (Fig. 10). Carbonization is not noted deeper within.

Figure 9. Pieces of Concrete B; completely carbonized concrete (all the way to the reinforcement bars) with visible remains of corroded reinforcement (pH>9).

Figure 10. Pieces of Concrete A; visible layer into concrete with an alkaline pH, carbonized 1-3 cm in thickness.

3.2 Determining Absorbability

Determining the absorbability of the collected concrete (serving the function of a cement

finish) was carried out using the desiccators - gravimetric method. The moisture content was determined in [%] from Formula (1):

$$n = (m\text{-}m_s)/m_s \cdot 100 \qquad [\%] \tag{1}$$

where:

n – absorbability [%],
m – mass of sample saturated with water to a constant mass [g],
m_s – mass of sample dried to a constant mass [g].

The results obtained for the analyzed concrete are given in Table 1.

Table 1. Absorbability of tested concretes.

Concrete type	Concrete A	Concrete B
absorbability [%]	6.77	7.84

The results presented in the above table are the average from three indications for each type of concrete.

All determined absorbability values exceed 5%. In accordance with p. 5.2 of the PH-88/B-06250 standard: absorbability of concrete should not be higher than 5% in the case of concrete directly exposed to the effects of atmospheric factors, as was the case in the concretes analyzed here.

3.3 Determining the pH Value of Concrete

The pH of aqueous extracts of ground concrete samples taken from different locations was measured. The measurements were carried out using a N5170E Ph-meter. A combined glass electrode was used for the studies. Each of the results is the average from three readings

Table 2. pH value of analyzed concretes.

Concrete type	Concrete A	Concrete B
pH value	10.28	7.29

A typical pH for normal concretes is a pH = 12.3 to 12.7. A pH value = 11.8 is the limiting value at which the C-S-H (tobermorite) and aluminosilicate phases in the cement rock are stable. Concrete at a PH < 11.8 ceases provide protection for steel. All collected samples were characterized by a pH < 11.8, which confirms the corrosion processes of steel taking place within the concretes. The pH of Concrete B points to extensive processes of corrosion.

3.4 Determining Concrete Strength

Studies on the compressive strength were carried out on a universal durometer for static samples. The machine has a electrohydraulic drive with a hydraulic control system. In accordance with the calibration certificate and with p. 4.2.2 of PN-EN 12390-4:2001: *Concrete tests. Part 4: Compressive strength. Requirements for durometers,* the machines ought to be categorized in Class 0.5. The maximum load of the machine was 300 kN.

The tests were carried out in accordance with the PN-EN 12390-3:2002: *Concrete tests. Part 3: Compressive strength of samples for testing.* Compressive strength tests were carried out on samples cut out from the provided drillings. In connection with the small diameters of the boreholes, only samples with a surface of < 225000 mm^2 were obtained, and thus all results should be lowered by a value of 10 to 15%. The carried out tests provided results of compressive strength with values ranging from 11.81 MPa to 27.19 MPa. The obtained average strengths, with a large range of values, allow only for qualifying the analyzed concretes in classes from 10 to 20 MPa, depending on the level of damage.

4 Selected Structural-Chemical Tests

The collected samples were also subjected to necessary structural-chemical tests, such as:

- microscopic examinations,
- necessary chemical analyses.

4.1 Microscopic Tests

In order to determine the structure and type of created compounds, as well as to assess the possibilities as well as directions of further reactions in the analyzed Concretes A and B, microscopic examinations were carried out.

Microscopic examinations were also to serve the purpose of assessing the potential possibilities and directions of further reactions taking place in the analyzed concrete (*Łowińska-Kluge et al., 2006*). The studies were carried out in accordance with the assumed guidelines of microscopic analyses, using a type VEGA TS 5135 MM scanning microscope, at a low vacuum in electrons reflected on non-sputter-coated samples. Over the course of the tests, photographs of characteristic areas of the analyzed samples were taken. Example result has been shown in Fig. 11.

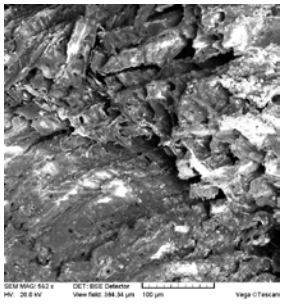

Figure 11. Microscopic SEM image of Concrete B surfaces contaminated with biotical factors (mosses, algae, fungi); very porous structure of cement matrix; visible "fibrous etchings" caused by the activity of biotic factors present in the gel phase.

Non-model microanalyses of EDS using an x-ray microanalysis system of characteristic products of reactions observed in the concrete of the finish and on eave sheet metals were also carried out.

The presence of carbon, calcium, oxygen, silicone, phosphorus, iron, sulphur, small amounts of nitrogen as well as trace amounts of potassium, zinc and aluminium is confirmed on the surface of the carried out non-model EDS x-ray microanalysis of the surface of

Concrete B contaminated with biotic factors (Fig. 11). Calcium silicates and aluminates had probably already undergone decomposition.

4.2 Necessary Chemical Analyses

In an effort to precisely specify the amount of compounds which can influence the properties of the analyzed concretes, chemical analyses of samples of these concretes were carried out.

Chemical analyses were carried out on adequately-sized samples of ground concretes A and B in accordance with the standards (*PN-EN 196-2:1996, PN-EN 196-21:1997, PN-EN 197-1:2002*) as well as the method of classical chemical analysis. The obtained results [%] have been presented in Tables 3 and 4.

Table 3. Determined $SO_{3\ total.}$, MgO, CaO, Na_2O, K_2O and Na_2Oeq contents in the entire concrete.

Concrete	Content of compounds in mean concrete sample [%]*					
	SO_{3total}	CaO	MgO	Na_2O	K_2O	$Na_2Oeq.$
A	2.44	29.53	1.03	0.14	0.387	0.39
B	0.96	32.87	1.53	0.11	0.70	0.57

* The results are the means of three recordings.

In Concrete A, a significantly higher content of SO_3, higher content of Na_2O and lower contents of MgO, K_2O and CaO occur as compared to Concrete B.

Estimated calculations of the amount of indicated compounds for concretes in [kg] and a comparison of the obtained results for the cement only [%] have been presented in Table 4.

An experimentally determined amount of cement was assumed for calculations due to not being familiar with the actual amount of cement used to create the tested concretes. In doing so, 306 kg cement per m^3 were assumed for Concrete A m^3, and 302 kg cement per m^3 for Concrete B. Concrete A has a relative density of 2446 kg/m^3, whereas that of concrete B is 2391 kg/m^3.

Table 4. Estimated amounts of $SO_{3całk.}$, MgO, Na_2Oeq in concrete.

Concrete type	In relation to:	Amount of indicated compounds in concrete		
		SO_{3total}	MgO	Na_2Oeq
Concrete A: - relative density = 2446 kg/m^3, - cement = 306 kg/m^3,	Concrete mass [kg]	(2.44·2446/100) = 59.68 kg/m^3	(1.03·2446/100) = 25.19 kg/m^3	(0.39·2446/100) = 9.53 kg/m^3
	Cement mass [kg]	(59.68·100/306) = 19.50 %	(25.19·100/306) = 8.23 %	(9.53·100/306) = 3.11 %
Concrete B: - relative density = 2391 kg/m^3, - cement = 302 kg/m^3,	Concrete mass [kg]	(0.96·2391/100) = 22,95 kg/m^3	(1.53·2391/100) = 36.58 kg/m^3	(0.57·2391/100) = 13.63 kg/m^3
	Cement mass[kg]	(22.95·100/302) = 7.60 %	(36.58·100/302) = 12.11 %	(13.63·100/302) = 4.51 %

The indicated amounts of SO_{3total} for the analyzed concretes range between 19.50% (A) to 7.60% (B) in relation to the estimated cement mass. The obtained amounts do not fulfil the requirement from Table 3 of the standards (*PN-EN 197-1:2002*) for Portland cement and Portland cements with additives, which, according to the standard, cannot exceed the value of 3.5%.

The indicated amounts of MgO, *i.e.* 8.23% in Concrete A and 12.11% in Concrete B, in reference to cement mass, exceed (according to *Peukert, 2000*), the permissible value of 4%. Over many years, MgO content of 5% in cement was permitted in the standards of most countries. However, cases of the destruction of many structures in the USA and other countries, as well as results of long-term studies, showed that additional safety measures are necessary.

The indicated amounts of alkalis (Na_2Oeq), *i.e.* 3.11% (A) and 4.51% (B) in relation to the cement mass exceed, according to (*Peukert, 2000*), the permissible value of 0.6%.

Sulphur compounds recalculated for total sulphur, MgO and Na_2Oeq in the tested concretes may come from the applied aggregates and their contaminants, as well as from cement.

5 Analysis Along with Assessment

Based on the description of the existing state, carried out tests and earlier analyses, it can be stated that the observed phenomena are mainly caused by leaching, carbon and biotic corrosion. Signs of sulphuric corrosion were not noted, though the use carbon aggregate and small amounts of fly ashes were confirmed in the concrete.

Unfortunately, the contractor refused to provide data on water and air contamination, making it much more difficult to search for reasons behind the occurrence of the present phenomena. The lack of adequate tightness of the surface layer caused constant dampening of the remaining layers of the analyzed concretes. Therefore, the moisture contained and persisting in the concrete led to the slow dissolvent of calcium compounds from the cement stone. This moisture, being the result of precipitation waters, that is soft waters with low carbonate hardness as well as water evaporating from the surrounding lake, leads to the emergence of leaching corrosion. Leaching is a diffusion process, the course of which is significantly influenced by water flow speed and pressure. The aggressiveness of soft water increases in lower temperatures. The leaching of calcium hydroxide begins in the surface layers. Over the course of time, $Ca(OH)_2$ from increasingly deeper layers is leached into the environment. First, $Ca(OH)_2$ (so-called free calcium) is dissolved, and along with the lowering of pH, also the calcium from hydrated silicates and calcium aluminates. These calcium compounds settled on the steel reinforcement bars and, in the presence of moisture, reacted with carbon dioxide (CO_2) that got through from the atmosphere. These gases, along with moisture, also entered the inside of the cement stone with the leaching of Ca compounds. The occurring reactions resulted in the formation of, among others, calcium carbonate and iron carbonate. These products are clearly identified during microscopic studies and over the course of EDS microanalysis. Steel reinforcement bars, in places of contact with concrete, were in a constantly moist environment.

Non-model EDS microanalysis revealed, above all, the presence of products from the cement matrix “interspersed” with products of rebar corrosion, as well as showing the

occurrence of products of the decomposition of the cement matrix and reinforcement bars (in the form of mainly calcium carbonates, iron and zinc). The probable distribution of calcium silicates and aluminates was determined on the basis of the carried out non-model x-ray EDS microanalysis of a zone of Concrete B surface contaminated with biotic factors. The lack of portlandite (significantly lower amount of C-S-H phases), very high amount of calcite (3.5 times higher) and decreased amount of quartz (twice lower), as compared to Concrete A, point to the extensive corrosion of the cement matrix in Concrete B. Sulphur compounds recalculated for total sulphur, MgO and Na_2Oeq content in the assessed concretes may come from the applied aggregates and their contaminants, as well as from cement.

As indicated by the results of the carried out laboratory studies and conducted analyses, the corroded surface layer of the concrete ought to be removed all the way to the reinforcement bars, with the uncovering and cleaning of the rebars. Next, new layers ought to be made in accordance with one of the systemic repair technologies.

ORCID

Tomasz Błaszczyński: https://orcid.org/0000-0003-3177-9654

References

Błaszczyński T. and Łowińska-Kluge A. (2008). *Durability assessment of RC floors based on concrete properties*, 6th International Conference AMCM'2008, Łódź, Poland, 371-372 + CD.

Horbik D., Łowińska-Kluge A., Górski Z., Stanisz E. and Zgoła-Grześkowiak A. (2013). *Microwave-Assisted Extraction Combined with HPLC-MS/MS for Diagnosis of Fungal Contamination in Building Materials*, J. Braz. Chem. Soc., Vol. 24, No. 9, 1478-1486.

Łowińska-Kluge A. and Błaszczyński T. (2012). *The influence of internal corrosion on the durability of concrete*, Archives of Civil and Mechanical Engineering, vol. XII, No 2, 219-227.

Łowińska-Kluge D., Horbik D., ZgoŁa-Grześkowiak A., Stanisz E. and Górski Z. (2016). *A comprehensive study on the risk of biocorrosion of building materials,* Corrosion Engineering, Science and Technology, DOI: 10.1080/1478422X.2016.1174326.

Łowińska-Kluge A. and Jóźwiak K (2006). *A study of the resistance of concrete to corrosion using SEM and microanalysis*, Microscopy and Analysis, 20, 1, 2006, 19-21.

Mejíaa E., Tobónb J.T. and Osorioc W. (2019). *Urban structure degradation caused by growth of plants and microbial activity*, Materiales de Construcción, Vol. 69, Issue 333, January-March, DOI.10.3989/mc.2019.09517.

Peukert S. (2000). *Cementy powszechnego użytku i specjalne* (in Polish), Polski Cement, Kraków.

PN-EN 196-2:(1996). *Methods of cement investigations. The chemical analysis of cement*.

PN-EN 196-21:(1997). *Methods of cement investigations*. *Designation of chlorides, carbon dioxide and alkalies content in the cement.*

PN-EN 197-1:(2002). *Cement*. *Part 1. Composition, requirements and conformities criteria concerning of general use cements.*

XV International Conference on Durability of Building Materials and Components
DBMC 2020, Barcelona
C. Serrat, J.R. Casas and V. Gibert (Eds)

Grain Size Analysis of Class C Fly ash Used for Aluminium-Silicate Binders Production

Tomasz Z. Błaszczyński[1] **and Maciej R. Król**[2]

[1] 62-002 Złotniki, Poland, tomasz.blaszczynski@opal.info.pl

[2] Koszalin University of Technology, Śniadeckich 2, 75-453 Koszalin, krol@wilsig.tu.koszalin.pl

Abstract. *Concrete structures are constantly moving in the direction of improving the durability. Durability depends on many factors, which are the composition of concrete mix, the usage of additives and admixtures and also the place, where material will work and carry the load. Taking into account that the consumption of cement on the globe gives way only to the consumption of drinking water, the issue of concrete technology begins to take on an economic and ecological aspect. Mentioned above the aspect of durability is strictly connected to economy. Due to huge amount of greenhouse gasses produced in the process of calcination, the ordinary Portland cements are responsible for even 8% of anthropogenic carbon dioxide production. This paper is focused on properties of materials known as green binders. They can be used to produce aluminium-siliceous binders and green concretes which can also be known as geopolymer concretes. Often used in construction industry, class F fly ashes are also good substratum also for aluminium- siliceous binders. Nevertheless amount of available class F fly ashes do not give the possibility to replace ordinary cements by aluminium-silicate one produced from this type of ash. This raises the need to look for replacement solutions for the substrate of the new green adhesive. As the substrate of new eco-binders there were used fly ash which came from coal and high calcium ash from the burning of lignite, called class C fly ashes. However not processed one, cannot compete with Portland cements due to durability. It surely depends on many aspects of polymerization process, which are for example maturation environment, concentration and type of alkaline activator, but the most important are parameters of fly ash substrate. This is because main attention was paid to granulation of examined class C fly ashes which have been subjected to a grinding process involving milling in a magnetic mill and subjected to ultrasonic waves. The analysis of grain change was presented in the aspect of the possibility of increasing the strength and durability of the cement material.*

Keywords: *Aluminium-Silcate Cements, Green Cements, Type C Fly Ash.*

1 Introduction

In recent years, many different kinds of cementiious materials have been developed. Many of them were alkali-activated cementiious materials. It is mostly because of their high strength and durability. Moreover they have got very low environmental impact due to emissions of greenhouse gasses which was subject in some papers (Błaszczyński *et al.* 2014, 2015; Juenger *et al.* 2011 and Barbosa *et al.* 2000). Most of used in civil-engineering and infrastructural construction fly ashes are type F. The reason of that is because of their excellent properties and wide spectrum of application. Much worse properties, especially in use as additives to cements and mortars gives usage of type C fly ash. According to Yang (Yang *et al.* 2008),

aluminosilicate materials obtained from alkali-activated class F fly ash have main binding phase as the amorphous hydrated alkali-aluminosilicate (Krizana *et al.* 2002; Haha *et al.* 2011 and Guo *et al.* 2010) proved that the major binding phase in alkali-activated ground granulated blast furnace slag similarly like in type C fly ash is calcium silicate hydrate (C-S-H). Because of this fact, main goal of this paper is to present future possibilities of treatment which could increase application range and utilization of C type fly ash.

Alkali-activated slag cements show good mechanical strength. Their strength, compressive and flexural can be even better than in ordinary cements which were shown by Hardjito and others (Hardjito *et al.* 2005; Wallah *et al.* 2006 and Cheng *et al.* 2003). The classical cements set owing to the special phenomenon of solvation, *i.e.* hydration. It is a compound process due to overlapping and a mutual influence of individual clinker phases that react with water. The total hydration process consists of three basic stages. The dissolution of soluble compounds in water, that is the proper hydration, which consists in the creation of the primary phase in a colloidal state (the formation of the plastic mass) and the crystallization of the hydration products (hardening of the plastic mass) what was presented by Błaszczyński and Król (Błaszczyński *et al.* 2015). The initial stage of the proper hydration of cement was presented by Kurdowski (Kurdowski, 2010). It is connected first of all with the C_3A phase. As a result of a fast reaction of this phase, large crystals of hydrated calcium aluminates are produced (Figure 1a). All the stages of hydration, as compared with the setting of the polymeric blend, are presented in Figure. 1.

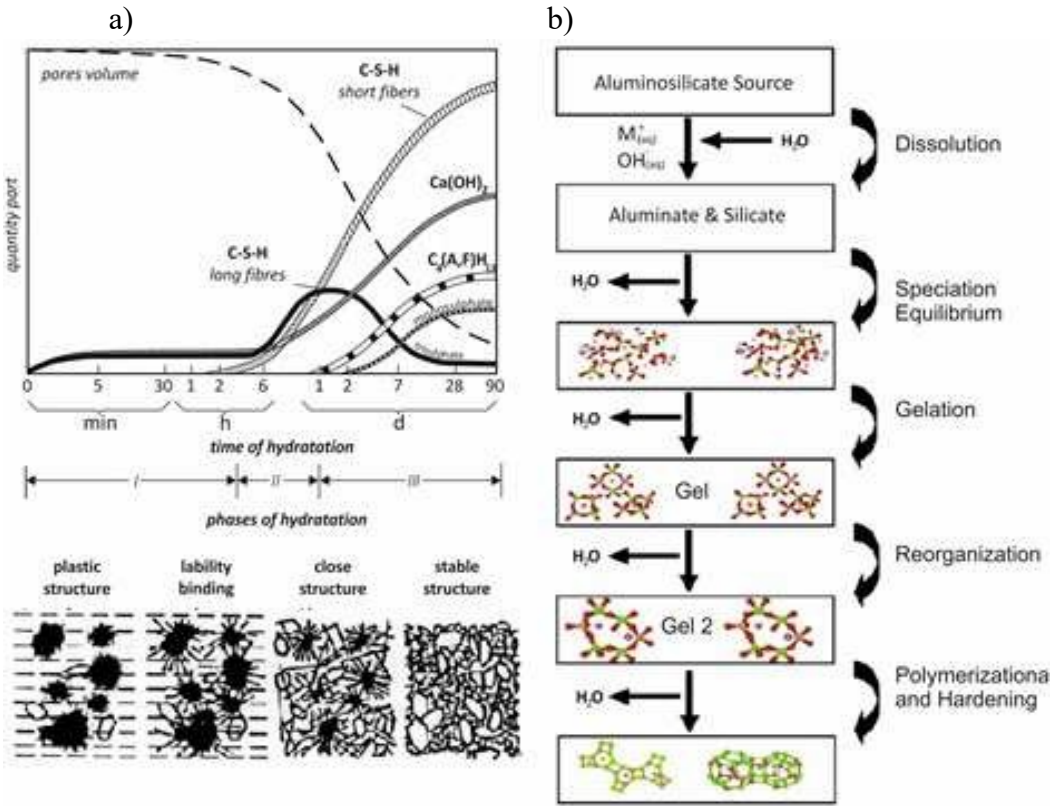

Figure 1. Comparison of phases: a) hydration of the Portland cement, b) polymerization.

The present state of knowledge was collated by Skvara (Skvara, 2007). It gives the possibility to present that a geopolymer based on fly ash is characterized by following properties:

- is built by structure similar to vitreous bodies what was presented by Barbosa and Mackenzie (Barbosa *et al.*, 2000),
- in structure of geopolymers there is presence of sodium and potassium cations (Na^+, K^+), which are not bonded so strong as it is in zeolite, it is a reason of potential efflorescence occurrence,
- structure of material is represented by a porous body,
- porous body of geopolymers contain water,
- the water is used in geopolymerization process as a transport of alkali activator,
- amorphous hydrates and crystalline can be noticed in structure only if material containing calcium are present (*i.e.* blast furnace slag, calcium fly ash).

A number of characteristics and properties of materials that are by-products in various processing processes are strictly conditioned by the technological cycle. Whether in the case of fly ash or blast furnace slag, temperature plays a major role in the quality of the products obtained, in addition to the properties and composition of the substrate. The higher it is, the cleaner the product is, the more finely divided it is, and the more extensive it can be used. What's more, the implication of binders in open atmosphere conditions is also possible, without the need for high-temperature ripening conditions. This situation occurs in the case of both fly ash and blast furnace slag what was topic of Małolepszy and Deja (Małolepszy *et al.,* 1999). The substrate used in the reactions in which the above by-products are formed determines the use of temperatures appropriate for the given reaction and technology. Małolepszy and Deja (Małolepszy *et al.,* 1999) suggest in their work, where the photos taken by scanning microscopes of fly ash samples from power plants and combined heat and power plants, in which various technologies of coal combustion differing among other temperatures of this process were used, that there is possible to systematize the composition of the sample together with the increase of the combustion temperature. Fly ash is artificial pozzolana, which is formed during the combustion of shredded coal in power plants equipped with dust boilers. Pozzolans do not self-harden after mixing with water. However, when they are finely ground after the addition of water, they react with calcium hydroxide, forming a mixture of aluminium silicates and calcium silicates with increasing strength and that has been proven by Barbosa and others (Barbosa *et al*., 2000; Duxson *et al.*, 2007 and Caijum *et al,.* 2011). The pozzolanic activity of ashes is significantly affected by their particle size. As the grain increases, the pozzolanic activity decreases. Fractions smaller than 45 [μm] can characterize pozzolanic activity significant for building materials

2 Experimental Program

2.1 Materials

Fly ash from brown coal combustion with a significant content of calcium compounds was used for the research. In the determined samples, the CaO content ranged from 15 to 24%. The samples were not cleaned of unburned coal, which was present in the composition in the size of approx. 3 to 5%. The chemical composition of tested fly ash is given bellow (Table 1).

As the activator, an aqueous solution of potassium hydroxide with a given molar ratio was used (Table 2). Aggregate was not added to the mix.

Table 1. Summary of the chemical composition used for testing fly ash.

Type of fly ash	SiO_2	Al_2O_3	Fe_2O_3	TiO_2	MgO	CaO	Na_2O	K_20	Ignition losses
TYPE C	44,17	21,79	4,58	1,85	1,49	21,06	0,23	0,19	4,64

Table 2. Properties of used alkaline activator.

Name	Molar mass [g/mol]	Density [g/cm^3]	Viscosity cP
potassium hydroxide	56,11*	2,12	-

2.2 Mixes Design and Specimens Preparation

For the first 12 h, the samples were kept at 80°C, and then were reaching their final proporties in air-dry conditions. After 24 hours of implementation, they were demoulded and successively tested for strength.

The selection of such temperature and treatment time was the result of previous tests. At 80°C, the tested binders obtained relatively the highest compressive strength. Samples made of calcium fly ash had a decrease in strength as the temperature increased to 95°C. Hence, the ideal ripening conditions were a temperature of 80°C and a ripening time of 12 hours in its surroundings. As the alkaline activator, the strongest available bases of potassium hydroxide were used in the concentration of 12M. The influence of activator concentration on the tested samples was not tested.

2.3 Methods

The treatment impact study was carried out on calcium fly ash. They have been checked for grain size. The material was then milled in an electromagnetic mill distinguishing samples in terms of milling time. After milling, the samples were examined for granulation and subjected to ultrasonic waves. After this treatment, the grain size of the material was again tested. This was to break down any agglomerates formed during grinding. Due to the limited amount of substrate that can be tested and the large number of millings, the test was carried out for times of 15, 30, 60, 120, 180 and 240 s, respectively.

Research related to determining the basic mechanical properties of geopolymer binders from treated ash in the form of milling was carried out on 40x40x40 mm cubic samples.

This allowed achieving additional volumes using less ash used. Two series of tests were obtained in this way:

- I - testing the efficiency of grinding substrates in the form of calcareous fly ashes by checking the difference in compressive strength of the ground substrate,
- II - testing the efficiency of grinding substrates in the form of calcareous fly ashes by checking the difference in tensile strength when splitting the ground substrate (Figure 2-3).

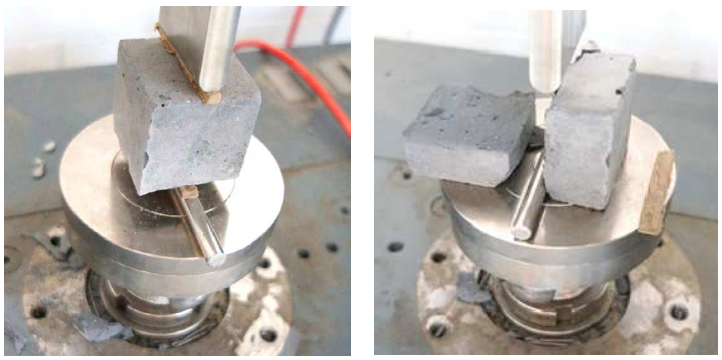

Figure 2-3. View of the sample before and after the splitting test

3 Results and Discussion

First obtained result was the effect of grinding and ultrasound treatment on grain size of tested samples. Grain size after grinding in times of 15, 30, 60, 120, 180 and 240 s, compared to samples additional subjected to ultrasound treatment is shown below (Figure 4-10).

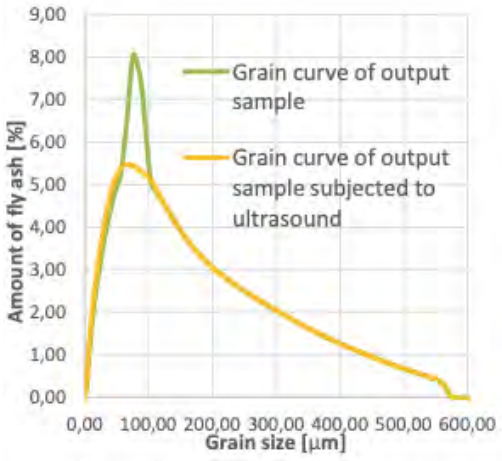

Figure 4. Grain size of output sample.

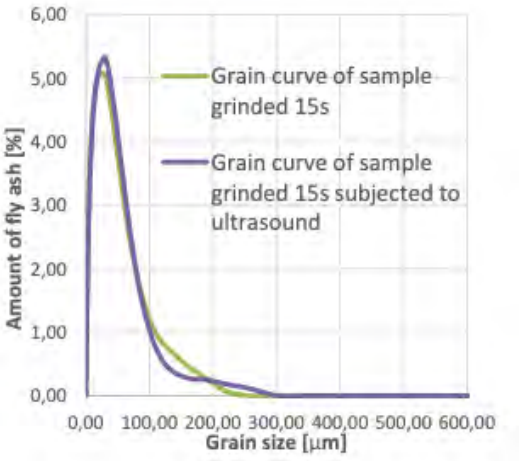

Figure 5. Grain size of sample grinded for 15s.

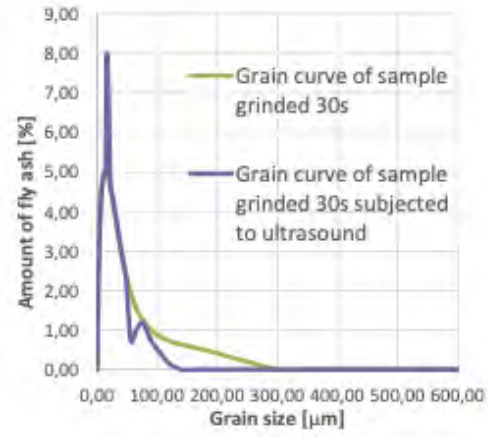

Figure 6. Grain size of sample grinded for 30s.

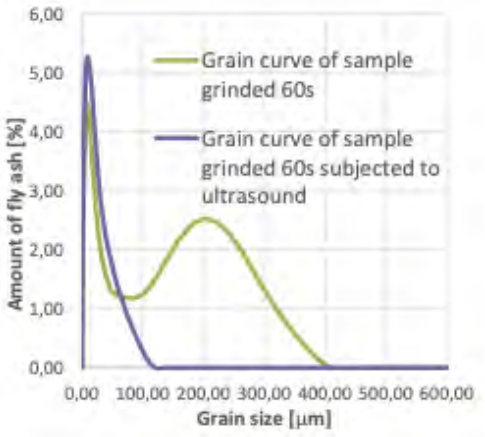

Figure 7. Grain size of sample grinded for 60s.

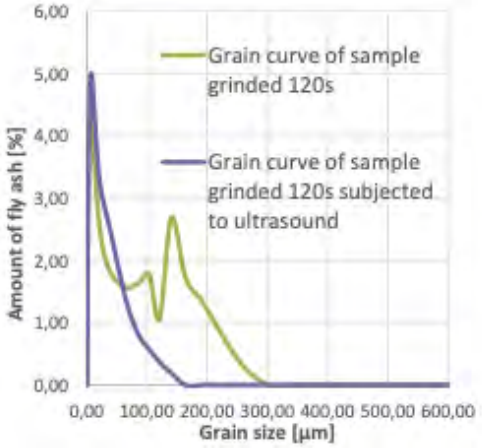

Figure 8. Grain size of sample grinded for 120s.

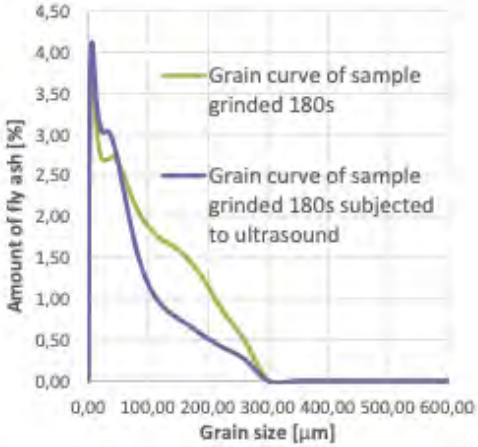

Figure 9. Grain size of sample grinded for 180s.

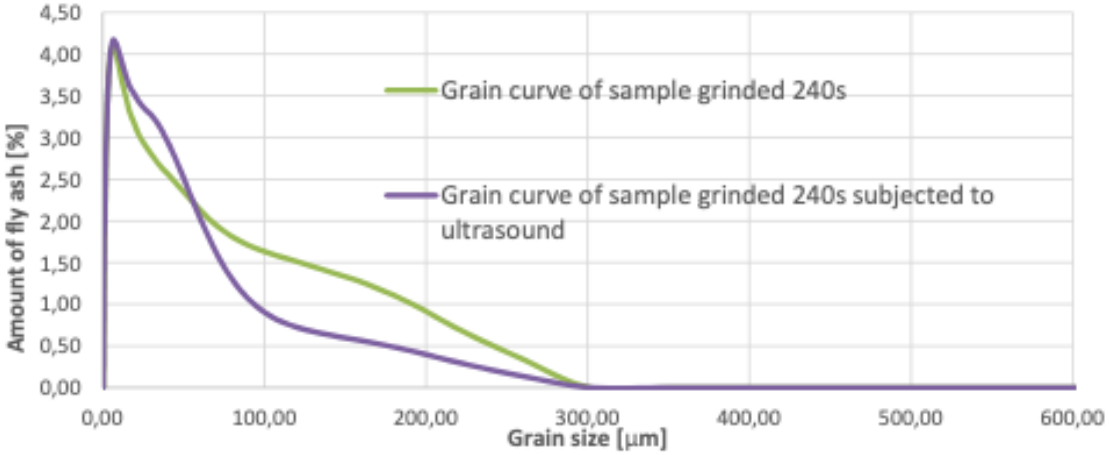

Figure 10. Grain size of sample grinded for 240s.

The most favourable in terms of maximum fragmentation turned out to be grinding time of 60s. During it, the highest ash content below 45 µm was obtained. Further increase in grinding time caused the opposite effect agglomerates began to form in the material. This happened because smaller particles of ash under the influence of fragmentation obtained greater pozzolanic reactivity, due to which under the influence of a small amount of moisture and heat generated during grinding they merged into larger particles. The next stage of treatment was subjecting the material to an ultrasonic wave, which broke the agglomerates formed, making the sample with the largest fragmentation become a milled sample for 120 [s]. The degree of comminution described by the specific surface in this case corresponded to the obtained compressive strength of the tested samples. The increase in tensile strength for the reference sample, which was a mixture constituting 50% of the ground material for 120 s and 25% of the value of the ground material for 30 and 240 [s], respectively, should be considered significant. The material obtained after mixing these components was characterized by the relatively largest amount of the finest material, with a grain size less than 10 [µm] in relation to the amount of material less than 45 [µm], and the most even distribution of grain size in the range of 10-45 [µm] (Figure 11-12).

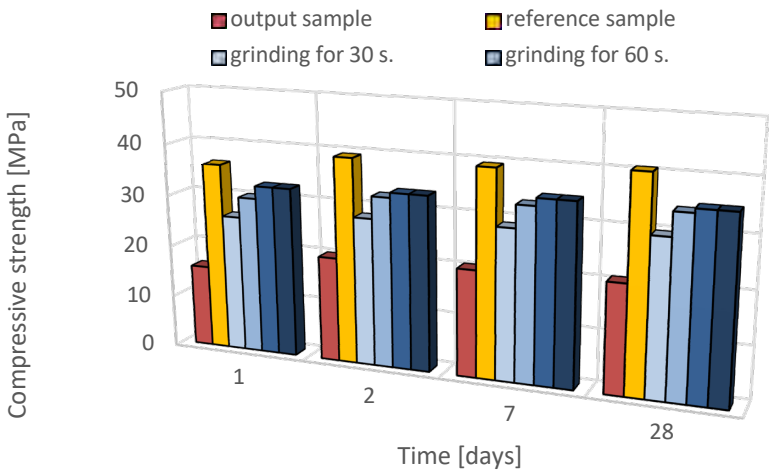

Figure 11. Compressive strength of samples made of treatment fly ash.

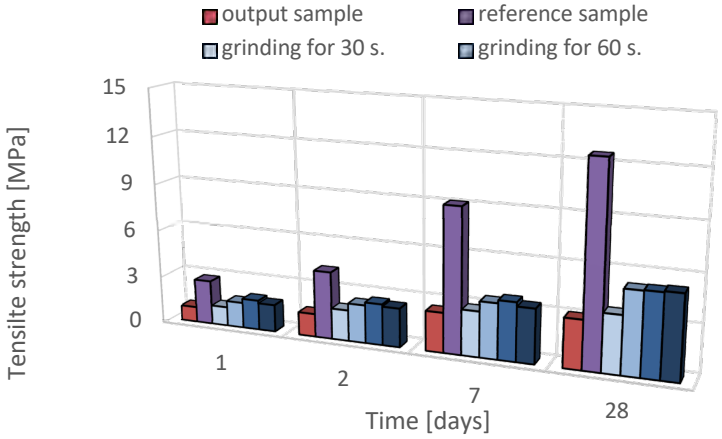

Figure 12. Tensile strength of samples made of treatment fly ash.

4 Conclusions

The strength results of binders made on the basis of calcium fly ash subjected to treatment in the form of ash milling show three basic relationships. First of all, milling of ashes has a significant impact on the achieved compressive and tensile strength of the tested samples. The most effective in terms of strength parameters of samples obtained from the tested ashes is the milling time of 120 s. Its increase did not cause a significant increase in compressive strength and in the case of tensile strength even a decrease in strength. The use of a mix of ashes with different grinding times had a positive effect on the increase of compressive and tensile strength as well as the ratio of these strengths. This was probably caused by a change in the form of granulometric distribution, which has a major impact on the rate and degree of geopolymerization.

ORCID

Tomasz Z. Błaszczyński: https://orcid.org/0000-0003-3177-9654
Maciej R. Król https:// orcid.org/0000-0002-8459-2837

References

Barbosa, V.F.F. and Mackenzie, K.J.D. (2000). *Synthesis and characterization of materials based on inorganic polymers of alumina and silica: sodium polysialate polymers. Int. J. Inorg. Mater, 2*(4), 309-317.

Błaszczyński, T. and Król, M. (2014). *Durability of Green-Concretes*, Proceedings of 8th International Conference AMCM 2014, Wrocław, Poland, 530-540.

Błaszczyński, T. and Król, M. (2015). Usage of green concrete technology in civil engineering. *Procedia Engineering, 122*, 296 – 301.

Błaszczyński, T. and Król, M. (2015). *Durability of cement and geopolymer composites*, 18th International Conference on Composite Structures ICCS18, Lisbona, 15-18.06.2015.

Błaszczyński, T. and Król, M. (2015). Geopolimers in construction. *Civil and Environmental Engineering Reports, 16*(1), 25-40.

Caijum, S., Fernandez-Jimenez, A.M. and Palomo A. (2011). New cements for the 21st century: The pursuit of an alternative to Portland cement. *Cement and Concrete Research,* 750-763.

Cheng, T. W. and Chiu J.P. (2003). Fire-resistant Geopolymer Produced by Granulated Blast Furnace Slag. *Minerals Engineering, 3*, 205-210.

Duxson, P., Fernandez-Jimenez, A.M., Provis, J.L., Lukey, G.C., Palomo, A. and van Deventer, J.S.J. (2007). *Geopolymer technology: the current state of the art, Advances in geopolymer science & technology,* J Mater Sci 2007, 2917-2933.

Guo, X., Shi, H. and Dick, W.A. (2010). Compressive strength and microstructural characteristics of class C fly ash geopolymer. *Cement Concrete Composites, 32*(2), 142–147.

Haha, M.B., Saout, G.L., Winnefeld, F. and Lothenbach B. (2011). Influence of activator type on hydration kinetics, hydrate assemblage and microstructural development of alkali activated blast-furnace slags. *Cement and Concrete Research, 41*, 301-310.

Hardjito, D. and Rangan, B. V. (2005). *Development and Properties of Low-Calcium Fly Ash-based Geopolymer Concrete,* Research Report GC-1, Faculty of Engineering, Curtin University of Technology, Perth, Australia.

Juenger, M.C.G., Winnefeld, F., Provis, J.L. and Ideker J. (2011). *Advances in alternative cementitious binders. Cement and Concrete Research, 41,* 1232-1243.

Krizana, D. and Zivanovic, B. (2002). Effects of dosage and modulus of water glass on early hydration of alkali–slag cements. *Cement and Concrete Research, 32,* 1181–1188.

Kurdowski, W. (2010). *Chemistry of cement and concrete,* Polish Cement Sp. z o.o., PWN (in Polish).

Małolepszy, J. and Deja J. (1999). Durability of alkali activated slag mortars and concretes, *2nd International Conference of Alkaline Cements and Concretes*, Kiev, 685-697.

Yang, X., Ni, W., Zhang, X. and Wang, Y. (2008). Effect of alkali-activation on aluminosilicate-based cementitious materials. *Journal of Beijing University of Science and Technology, 15*(6),796-801.

Skvara F. (2007). *Alkali activated materials of geopolymers?,* Ceramics – Silikaty 51 (3), 173-177.

Wallah S.E., Rangan, B.V. (2006). *Low-Calcium Fly Ash-Based Geopolymer Concrete: Long-Term Properties,* Research Report GC2, Faculty of Engineering. Curtin University of Technology, Perth, Australia.

XV International Conference on Durability of Building Materials and Components
DBMC 2020, Barcelona
C. Serrat, J.R. Casas and V. Gibert (Eds)

Hygrothermal Regulation of Brick Masonry of Nanjing City Wall by Plants

Changchang Xia[1], Zhenyi Kong[2], Shuichi Hokoi[3], Bo Ding[4], Tianwen Wang[5] and Yonghui Li[6]

[1]School of Architecture, Southeast University, Nanjing, China, xia_2017@seu.edu.cn
[2]School of Architecture, Southeast University, Nanjing, China, kongzhenyi@seu.edu.cn
[3]School of Architecture Internationalization Demonstration, Southeast University, Nanjing, China, hokoi@seu.edu.cn
[4]Nanjing Bureau of Culture and Tourism, Nanjing, China, 347464717@qq.com
[5]Nanjing City Wall Protection and Management Center, Nanjing, China, 77930380@qq.com
[6]School of Architecture, Southeast University, Nanjing, China, liyonghui@seu.edu.cn

Abstract. *Nanjing City Wall, one of the most important cultural heritages in China, has been damaged in a natural environment for centuries. Plants can be a candidate to regulate the micro-environment and mitigate the influence of local climates, which cannot be easily controlled by human efforts. Therefore, we examined the potential of the roadside trees along the City Wall to buffer the hygrothermal cycles that can deteriorate the City Wall. We surveyed the deteriorated state and measured the temperature and moisture content of the City Wall. Measured results showed smaller temperature fluctuation at shaded surface than the unshaded with a maximum temperature difference of 10.9 ℃ in summer. The measured water content decreased with height. A coupled two–dimensional hygrothermal 'City Wall–plant' model was proposed to clarify the influence of the roadside trees on the hygrothermal distribution of the City Wall. The proposed city wall-plant hygrothermal model could predict the surface temperature and water content well.*

Keywords: *Heritage Conservation, City Wall, Plant Regulation, Hygrothermal Distribution, Deterioration.*

1 Introduction

Nanjing City Wall, one of the most important cultural heritages in China, has a long history that can be traced back over 600 years. It is an ancient structure with abundant cultural heritage values, among which are inscriptions (Nanjing City Wall Protection and Management Centre, 2016) (Figure 1) that contain information about responsible organizations and persons on bricks. Nanjing City Wall was deteriorated due to efflorescence, peeling and cracking which damage surface inscriptions.

Related to conservation of cultural heritages, one key consideration is how to mitigate the effects of environmental fluctuations on wall materials. Nanjing City Wall has been exposed to climatic variations such as solar radiation, temperature, relative humidity, and rainfall. The humidity is strongly correlated with formation of the fungal communities that causes biodeterioration (Li*, et al*. 2020). Different ambient relative humidity conditions would result in various degrees of damage by the crystallization pressure of sodium sulphate (Rodriguez-Navarro and Eric, 1999). Moisture significantly reduces the compression strength of the bricks

(Foraboschi and Vanin, 2014) and determines the degree of freeze–thaw damage based on temperature (Feng, *et al*. 2019).

With respect to green urban development, coverage with vegetation offers a potential solution. English ivy has been found to reduce the range and variability of wall-surface microclimates over diurnal, seasonal and annual timescales (Sternberg, *et al*. 2011) and reduce the frequency, duration, and severity of freezing events (Coombes, *et al*. 2018) at historic sites in England. Araoka, *et al*. (2017) investigated the deterioration pattern of the Nanjing City Wall and found that shaded brick walls with trees on their side were relatively well-preserved.

This study aims at evaluating the potential of the roadside trees along the wall to buffer the microclimate of Nanjing City Wall. First, the situation of Nanjing City Wall was investigated and the temperature and moisture content of the wall were measured. Second, a two–dimensional hygrothermal 'City Wall–plant' model was developed to evaluate the influence of trees.

Figure 1. Inscriptions on the City Wall.

Figure 2. Vegetation status at monitoring points.

2 Method

2.1 Measurement

The measurements have been conducted around Jiefang gate(one gate at the northern part of City Wall). Two shaded walls (Sites 1and Site 2) and two unshaded wall (Site 3 and Site 4) were selected and been monitored from April 2019 to December 2019 (Figure 2). Air temperature and relative humidity under the canopy, surface temperature and water content of the City Wall were measured (Figure 3). The meteorological station was 800m apart from the monitored sites. The monitored weather data included the air temperature, relative humidity, rainfall, and horizontal solar radiation.

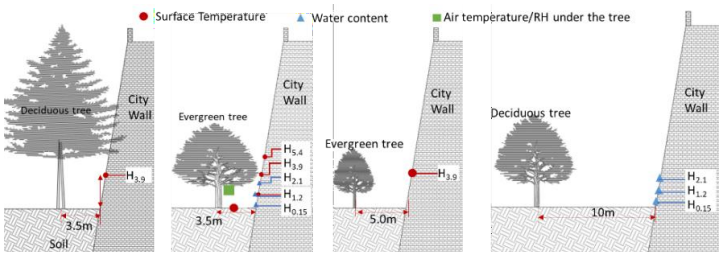

Figure 3. Outline of monitoring at each site. Monitoring period: Jun.- Dec. 2019 (temperature); Apr. - Dec. 2019 (water content). The heights of measured points are denoted as $H_{0.15}$ (0.15m), $H_{1.2}$ (1.2m), etc.

2.2 Simulation Model

2.2.1 City Wall

The simultaneous transfer model of heat and water by Matsumoto. (1978) was adopted in this paper. The water chemical potential μ is used to express moisture state in this paper. The relationship between μ and temperature and relative humidity is as follows:

$$\mu = R_v T In(h) \tag{1}$$

Heat balance equation:

$$c\rho \cdot \frac{\partial T}{\partial t} = \nabla[(\lambda + \lambda'_{Tg})\nabla T + r\lambda'_{Tg}\nabla\mu] \tag{2}$$

Moisture balance equation:

$$\rho_w \left(\frac{\partial \Psi}{\partial \mu}\right)\left(\frac{\partial \mu}{\partial t}\right) = \nabla[\lambda'_\mu(\nabla\mu - g\boldsymbol{n}) + \lambda'_T \nabla T] \tag{3}$$

2.2.2 Plant model

In our model, trees can reduce incident solar radiation to and the nocturnal radiation from the wall, and intercept the rainfall that dropped to vertical projection region (the ground and wall). Furthermore, the rainwater trapped by trees evaporated and removed heat from the plants. The model was based on the plant model by Kondou (1996). Figure 4 shows the thermal and moisture network model of the plant.

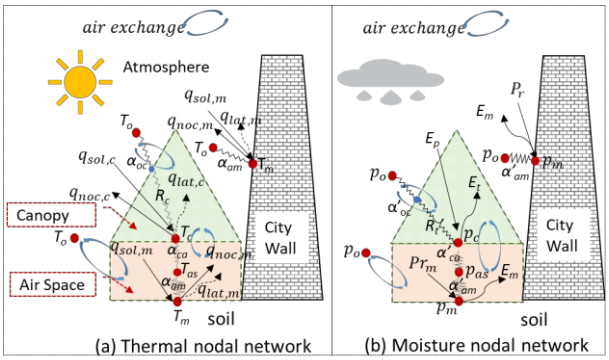

Figure 4. Thermal (a) and moisture (b) nodal networks of the plant-ground model.

3 Results and Discussion

3.1 Measured Results

3.1.1 Weather data

Figure 5 shows the weather data from Jan. 2019 to Dec. 2019. The temperature fluctuation was 42.6 °C (–2.6 °C~ 40 °C), and the annual average temperature was 18.1 °C. The relative humidity fluctuated between 15.8% and 100%, and exceeded 90% for 1369 hours (Figure 5a). It rained more in the summer, followed by winter (Figure 5c). The annual rainfall was 486.5

mm, much less than the average rainfall of 1206 mm for the last 10 years (Nanjing Bureau of Statistics. 2007-2017)).

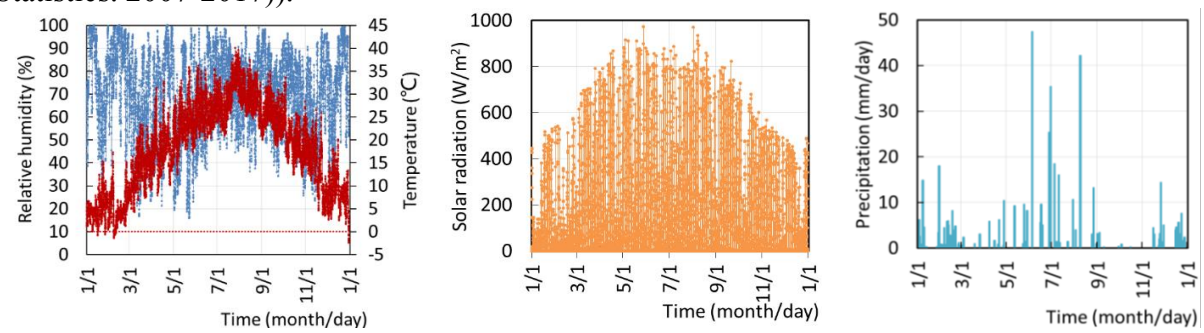

(a) Temperature and relative humidity (b) Solar radiation (c) Precipitation

Figure 5. Weather data (Jan. 2019-Dec. 2019).

3.1.2 Air temperature and relative humidity under the canopy

Figure 6 shows the measured air temperature and relative humidity under the canopy at Site 1 along with the meteorological (outdoor) data. During the monitoring period (Jun. 2019 - Dec. 2019), the temperature fluctuation of the air under the canopy and the outdoor air were 35.9 °C (1.8 °C~ 37.7 °C) and 38.4 °C (1.6 °C~ 40 °C), respectively. In summer, the temperature under the canopy was lower than the outdoor temperature for most time, with a 6.1 °C difference of maximum temperature. On the contrary, the relative humidity under the canopy was higher than that of the outdoor values for the most time. The relative humidity difference was usually between -27%~8%.

3.1.3 Surface temperature and water content of City Wall

Figure 7 shows the measured surface temperatures at Site 1 (shaded $H_{3.9}$) and Site 3 (unshaded $H_{3.9}$). Part of the temperature data was missing when the temperature recorder equipment was not powered. The temperature fluctuation at shaded $H_{3.9}$ was 33.2℃ (3.2℃~36.4℃), which was smaller than the temperature fluctuation of 43.7℃ (3.6℃~47.3℃) at shaded $H_{3.9}$. In summer, almost the same daily minimum temperatures and large differences in the maximum values were seen on shaded and unshaded points. In winter, due to the low solar altitude, the unshaded $H_{3.9}$ (Site 3) was partly shaded by trees. Then and the similar temperature fluctuation can be seen at shaded (Site 1) and unshaded $H_{3.9}$ (Site 3).

Figure 8 shows the average water content of 10 bricks at Site 2 and Site 4. Due to lawns on the south side of Site 4 with regular irrigation in summer, this may result in increased water content of the wall. Therefore, this paper compares the water content fluctuation in two cases, separately. The results show the water content decreased with height, while the water content at $H_{2.1}$ was higher than at $H_{1.2}$ in Site 4. It may be due to different water absorption and storage capacity of bricks and reduction of the evaporation rate by herbaceous plant at $H_{2.1}$, and needed to be further studied. During the monitoring period, the water content of each height was obviously affected by rainfall. The water content was higher in rainy season (July and August), while lower in arid season (September and October).

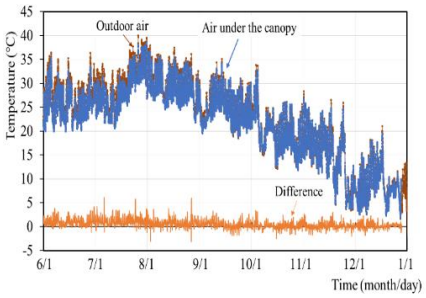

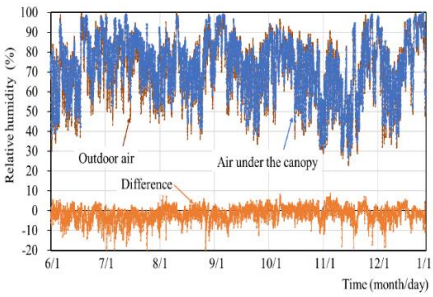

(a) Temperature (b) Relative humidity

Figure 6. Temperature (a) and relative humidity (b) under tree and at meteorological station (Jun. 2019 - Dec. 2019) (Difference = Outdoor air –Air under the tree).

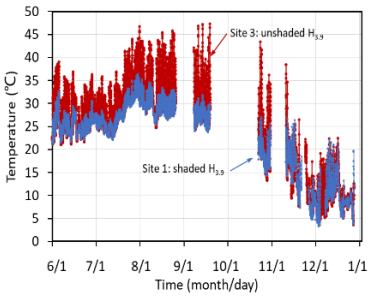

Figure 7. Measured surface temperatures on shaded and unshaded surfaces (Jun. 2019 - Dec. 2019).

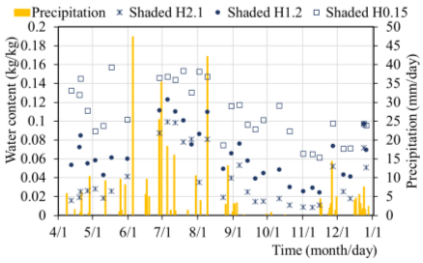

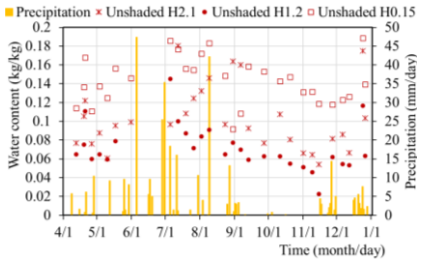

(a) Site 2 (shaded) (b) Site 4 (unshaded)

Figure 8. Average water content of 10 bricks located at Site 2 and Site 4.

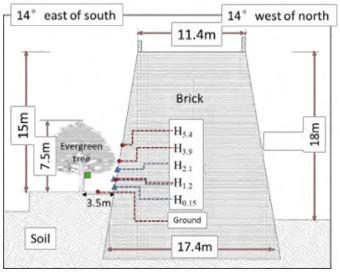

Figure 9. Schematic diagram of calculation model at Site 2.

3.2 Validation of Proposed Model (Comparison between measured and calculated results)

Figure 9 shows schematic diagram of a two-dimensional 'City Wall–plant' model. It is set up in FORTRAN language to simulate the Site 2. The tree is evergreen with a height of 7.5m and a distance of 3.5m to the city wall (Figure 9). The weather data (Jan. 2018 to Dec. 2018) was repeatedly used for 10- years calculation as the boundary condition. Then the calculation was conducted with meteorological data in 2019 for one year, and the calculated results were analysed.

Figure 10 shows the measured and simulated surface temperatures at three points $H_{1.2}$, $H_{3.9}$, and $H_{5.4}$ on the south facade at Site 2. A linear regression analysis was performed with the measured and simulated results, and a good correlation was obtained with slopes 1.00, 0.98, and 0.97 and goodness-of-fit 0.99, 0.98, and 0.96 at $H_{1.2}$, $H_{3.9}$, and $H_{5.4}$, respectively. Figure 11 shows the measured and simulated water content at three heights ($H_{0.15}$, $H_{1.2}$, and $H_{2.1}$). The calculated water content reproduced the time profile of the measured results. The water content assumed a peak value during rainfall, then gradually decreased probably due to evaporation and water movement in the wall. The mean absolute error (MAE) was used to analyse the consistency of measured and simulated values. The MAE at three heights $H_{0.15}$, $H_{1.2}$, and $H_{2.1}$ was 0.029m³/m³, 0.036m³/m³, 0.035m³/m³, respectively.

It can be concluded that the simulated temperatures and water content agreed well with the measured results in unshaded case. Thus, the proposed 'City Wall–plant' model can be used to examine the influence of the surrounding trees on the hygrothermal fluctuations and weathering of City Wall.

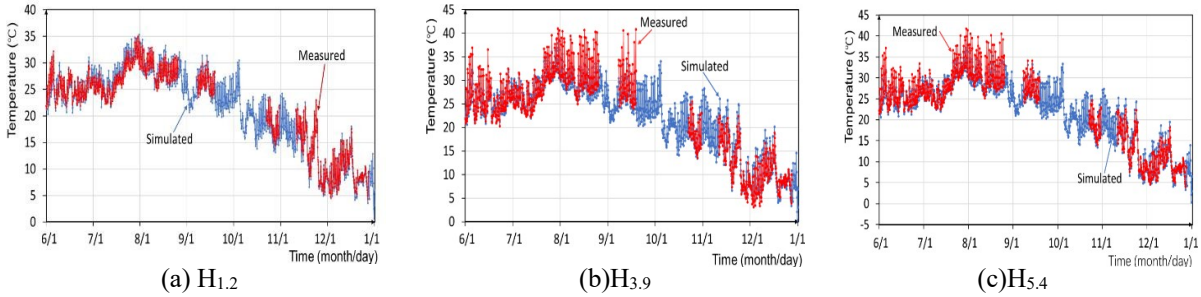

(a) $H_{1.2}$ (b)$H_{3.9}$ (c)$H_{5.4}$

Figure 10. Comparison of the measured and simulated surface temperatures at three heights.

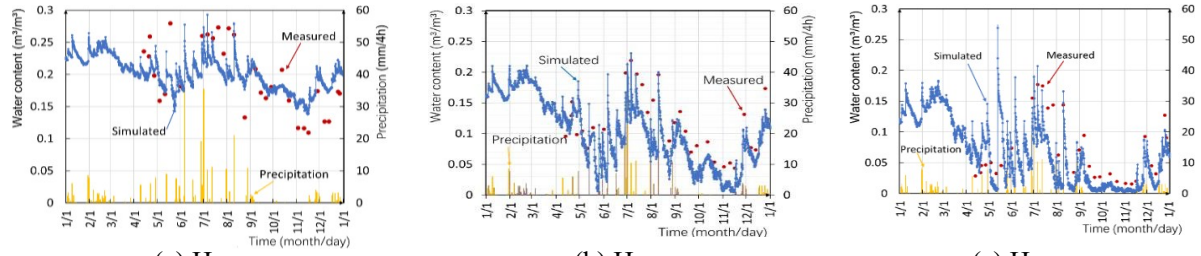

(a) $H_{0.15}$ (b) $H_{1.2}$ (c) $H_{2.1}$

Figure 11. Comparison of measured and simulated water content at three heights.

4 Conclusion

This study investigated the influence of trees on hygrothermal performance of Nanjing City Wall. The measured results showed that the air temperature under the canopy was lower than the outdoor air. The temperature fluctuation at shaded surface was smaller than the unshaded one, and the maximum temperature in shaded case was 6.1 ℃ lower than the unshaded in summer. The measured water content decreased with height.

The proposed 'City Wall–plant' model was validated through the comparison between measured and calculated results. Then the model can be used to analyse the trees' impact on the microclimate and surface weathering of Nanjing City Wall.

Acknowledgement

This research has been funded by the National Nature Science Foundation of China (Grant No. 51878140); the China National Key R&D Program during the 13th Five-year Plan Period (Grant No. 2019YFC1520901); Jiangsu Provincial Cultural Research Project (2017SK01). This work was also supported by Nanjing City Wall Protection and Management Canter.

ORCID

Changchang Xia: https://orcid.org/0000-0002-5104-0307
Zhenyi Kong: https://orcid.org/0000-0002-7121-7085

Shuichi Hokoi: https://orcid.org/0000-0002-3372-000X
Bo Ding: https://orcid.org/0000-0003-2356-9286
Tianwen Wang: https://orcid.org/0000-0003-3018-0762
Yonghui Li: https://orcid.org/0000-0001-9030-5358

References

Araoka, W., Hokoi, S., Ogura, D., Iba, C., Li, Y. and Hu, S. (2017). Deterioration and Preservation of City Wall in Nanjing. *Energy Procedia, 132,* 945-950. 10.1016/j.egypro.2017.09.734

Coombes, M.A., Viles, H.A. and Zhang, H. (2018). Thermal blanketing by ivy (Hedera helix L.) can protect building stone from damaging frosts. *Scientific Reports*, *8*(1), 9834. 10.1038/s41598-018-28276-2

Feng, C., Roels, S. and Janssen, H. (2019). Towards a more representative assessment of frost damage to porous building materials. *Building and Environment*, *164,* 106343. https://doi.org/10.1016/j.buildenv.2019.106343

Foraboschi, P. and Vanin, A. (2014). Experimental investigation on bricks from historical Venetian buildings subjected to moisture and salt crystallization. *Engineering Failure Analysis, 45,* 185-203. https://doi.org/10.1016/j.engfailanal.2014.06.019

Li, Y., Feng, Y., Kong, Z. and Hokoi, S. (2020). Optimization and Assessment of the Protective Shed of the Eastern Wu Tomb. *Energies, 13,* 1652.

Matsumoto, M. (1978). Simultaneous Heat and Moisture Transfer and Moisture Accumulation in Building Materials. Kyoto, Japan: Kyoto University.

Nanjing Bureau of Statistics http://tjj.nanjing.gov.cn/. 2007-2017

Nanjing City Wall Protection and Management Centre. (2016). *Inscription world Nanjing city wall brick (in Chinese)*. Nanjing: Nanjing Press.

Rodriguez-Navarro, C. and Eric, D. (1999). Salt Weathering: Influence of Evaporation Rate, Supersaturation and Crystallization Pattern. *Earth Surface Processes and Landforms, 24*(3), 191–209.

Sternberg, T., Viles, H. and Cathersides, A. (2011). Evaluating the role of ivy (Hedera helix) in moderating wall surface microclimates and contributing to the bioprotection of historic buildings. *Building and Environment*, *46*(2), 293-297. https://doi.org/10.1016/j.buildenv.2010.07.017

Kondou, S. (1996). *Meteorology of the water environment - heat and moisture equilibrium on the ground surface (in Japanese)*: Asakura bookstore.

Appendix A. Nomenclature

R_v	the gas constant of water ($R_v = R/M_v$)	I_n	nocturnal radiation [W/m^2]
R	the universal gas constant [Pa·m^3/kmol·K]	P_r	precipitation [kg/(m^{2}s)]
M_v	molar weight of water [kg/kmol]	$P_{r\,m}$	the rainfall to ground [kg/m^{2}s]
h	the relative humidity.	R	thermal resistance [(m^{2}K)/W]
ρ_w	water density [kg/m^3]	R'	moisture resistance [(m^2·K·Pa) / kg]
Ψ	the volumetric water content [m^3/m^3]	$c\rho$	specific heat capacity [J/(m^{3}K)]
$\boldsymbol{n}$	unit vector in the direction of gravity	c_a'	moisture capacity of the air [kg/(m^{3}Pa)]
q	heat flux [W/m^2]	V	volume [m^3]
j	total (liquid and vapor) water flux [kg/(m^2 · s)]	ρ	density [kg/m^3]
T	temperature [K]	β	evaporation efficiency of vegetation [-]
p	vapor pressure [Pa]	C_h	coefficient of volume movement [-]
p_{sat}	saturation vapor pressure [Pa]	U	wind speed [m/s]
μ	water chemical potential [J/kg]	S_h	specific humidity [kg/kg]
γ	transmission coefficient of solar radiation by canopy [-]	S	area[m^2]
γ'	transmittance of plants to rainwater [-]	r	heat of phase change of water [J/kg]
A	absorption coefficient of solar radiation [-]	g	gravitational acceleration [=9.8m/s^2]
ε	longwave emissivity [-]	E_p	rainfall trapped by trees [kg/(m^{2}s)]
α	heat transfer coefficient [W/(m^2 · K)]	E_t	evapotranspiration of plants [kg/m^{2}s]

α'	water vapor transfer coefficient [kg/m²sPa]
α'_μ	water vapor transfer coefficient under the gradient of water chemical potential [kg/m²·s·(J/kg)]
α'_T	water vapor transfer coefficient under the gradient of temperature [kg/m²·s·K]
λ	thermal conductivity [W/m·K]
λ'_μ	water (liquid and vapor) conductivity under the gradient of water chemical potential [kg/m· s·(J/kg)]
λ'_T	water (liquid and vapor) conductivity under the gradient of temperature [kg/m· s· K]
λ'_{Tg}	Water vapor conductivity of the solid material under the gradient of temperature [kg/(m · s · K)]
$\lambda'_{\mu g}$	Water vapor conductivity under the gradient of water chemical potential [kg/(m · s · (J/kg))]
I_s	solar radiation [W/m²]
E_m	evaporation from material (wall or ground) surface [kg/m²s]

Subscripts

a	air
o	outdoor
s	surface
c	canopy
as	air space
m	material (wall or ground)
sol	solar radiation
noc	nocturnal radiation
lat	latent heat
ex	air exchange
oc	the outdoor air -canopy surface
ca	the canopy-air space surface
am	the air space-material (wall or ground) surface

Appendix B. Plant model

The plant model was based on the plant model by Kondou (1996). The equations of heat and moisture balance in plant model are as follows.

1. Heat balance of the canopy cell：

$$(c\rho)_a \cdot V_c \cdot \frac{\partial T}{\partial t} = \{\frac{(T_o - T_c)}{(1/\alpha_{oc} + R_c)} + q_{sol,c} - q_{noc,c} - q_{lat,c} - \alpha_{ca} \cdot (T_c - T_{as})\} \cdot S + q_{ex,c} \quad \text{(B.1)}$$

Where, $q_{sol,c}$ is the solar radiation absorbed by trees($= I_s \cdot (1-\gamma) \cdot A_c$) [W/m²]; $q_{lat,c}$ is latent heat of evapotranspiration ($= r \cdot (E_t + E_p)$) [W/m²] ; $q_{noc,c}$ is the nocturnal radiation of trees ($= \varepsilon_c \cdot I_n$) [W/m²].

2. Heat balance of the air space under the canopy:

$$(c\rho)_a \cdot V_{as} \cdot \frac{\partial T}{\partial t} = \alpha_{ca} \cdot (T_c - T_{as}) \cdot S - \sum_1^{m1} \alpha_{am} \cdot (T_{as} - T_{m,i}) \cdot S_i + q_{ex,as} \quad \text{(B.2)}$$

3. Heat balance of the cell at material surface:

$$\alpha_{am}(T_{as} - T_m) + q_{sol,m} - q_{lat,m} - q_{noc,m} = -\left(\lambda + r\lambda'_{Tg}\right)\frac{\partial T}{\partial x} - r\lambda'_{\mu g}\frac{\partial \mu}{\partial x} \quad \text{(B.3)}$$

Where, $q_{sol,m}$ is the solar radiation absorbed by material (wall or ground) surface ($= I_s \cdot \gamma \cdot A_m$) [W/m²]; $q_{lat,m}$ is latent heat of evaporation from material (wall or ground) surface ($= r \cdot E_m$) [W/m²]; $q_{noc,m}$ is nocturnal radiation of material (wall or ground) surface ($= \varepsilon_m \cdot I_n$) [W/m²].

4. Moisture balance of the canopy cell:

$$C'_a \cdot V_c \frac{\partial p}{\partial t} = \{\frac{(p_o - p_c)}{(1/\alpha'_{oc} + R'_c)} + E_p + E_t - \alpha'_{ca} \cdot (p_c - p_{as})\} \cdot S + j_{ex,c} \quad \text{(B.4)}$$

5. Moisture balance of the air space under the canopy:

$$C'_a \cdot V_{as} \frac{\partial p}{\partial t} = \sum_1^{m2} E_{m,i} \cdot S_i + j_{ex,as} \quad \text{(B.5)}$$

6. Moisture balance of the cell at material surface：

$$\gamma' \cdot P_r - E_m = -\lambda'_\mu \cdot \left(\frac{\partial \mu}{\partial x} - g\right) - \lambda'_T \frac{\partial T}{\partial x} \quad \text{(B.6)}$$

Where,

$$E_t = \rho\beta C_h U \cdot \left(\frac{\partial S_h}{\partial P}\right) \cdot \left(p_{sat}(T_c) - p_o\right) \quad \text{(B.7)}$$

$$E_P = (1-\gamma') \cdot P_r \quad \text{(B.8)}$$

$$E_m = \alpha'_\mu(\mu_m - \mu_{as}) + \alpha'_T(T_m - T_{as}) \quad \text{(B.9)}$$

XV International Conference on Durability of Building Materials and Components
DBMC 2020, Barcelona
C. Serrat, J.R. Casas and V. Gibert (Eds)

Numerical Strategy to Simulate Seawater Ingress in RC Concrete Blocks Exposed to Wetting-Drying Cycles in Field Conditions During 19 years

Anthony Soive[1], Véronique Baroghel-Bouny[2] and Francis Lavergne[3]

[1] Cerema, UMR 7329 GEOAZUR, Pôle d'activités, avenue Albert Einstein CS 70499, 13593 Aix-en-Provence cedex 3, France, anthony.soive@cerema.fr

[2] Paris-Est University, IFSTTAR, MaSt/FM2D, F-77447 Marne-la-Vallée Cedex 2, France, veronique.baroghel-bouny@ifsttar.fr

[3] Centre Technique Ouvrage d'Art, CEREMA ITM, Provins Cedex BP214 77487, France, francis.lavergne@cerema.fr

Abstract. *Numerical results are compared to experimental data on concretes exposed in field conditions for 19 years and subjected to wetting/drying cycles in seawater after a couple of curing days. They were obtained thanks to a hydration model assuming fully hydrated concretes (19 years of curing time) and a reactive transport model in saturated conditions taking into account precipitation/dissolution of minerals and their kinetics and adsorption of ionic species on C-S-H. Numerical results show surprisingly rather good results, especially for concretes with fly ash. For OPC, although model considers average bulk porosity modifications, the experimental apparent diffusion coefficient increases much more. For concretes with silica fume, numerical results also show underestimations of total chloride content also experimental apparent diffusion coefficients are constant. Analysis of hydration calculations show that concretes are not fully hydrated after 19 years. Additional chloride content from reactions between anhydrous phases and chloride ingress may appear.*

Keywords: *Concrete, Chloride Binding, Seawater, Long-Term Exposure, Field Condition.*

1 Introduction

Numerical study of reinforced concrete durability exposed to seawater in field conditions is difficult in several aspects. Environmental conditions can play a significant role in the chloride ingress (temperature, RH, wetting-drying cycles, orientation, wind). Curing time is also important because of possible interactions between concrete and seawater as well as initial presence of chloride in mixing water (Suryavanshi and Swamy, 1996; Caré, 2008 to cite a few).
Previously reactive transport model taking into account precipitation and dissolution of mineral species with their kinetics as well as adsorption of ionic species on C-S-H were successfully used in order to simulate chloride ingress in laboratory concrete specimens (fully hydrated, controlled exposure conditions, saturated conditions) (Tran *et al.*, 2018). However, in field conditions, concrete is not fully hydrated when they are exposed to seawater. Influence of hydration degree on chloride binding capacity of concrete is interesting.

Numerical simulations were done and compared to experimental data on concretes exposed in field conditions for 19 years and subjected to wet- ting/drying cycles in seawater after a couple of curing days. A hydration model following by a reactive transport model taking into account precipita- tion/dissolution of mineral species with their kinetics as well as adsorption of ionic species on C-S-H were used. Regarding all the phenomena to take into account, severe hypotheses were done such as saturated materials and 19 curing years. The aim of this study is

doi:10.23967/dbmc.2020.196

to identify if such a severe hypothesis is sufficient in order to give a good approximation of chloride ingress.

2 Experimental Study and Numerical Approach

2.1 Experimental Study

Several concretes from the French project BHP2000 are exposed to sea- water and wetting-drying cycles in La Rochelle harbor (western French coast) since 19 years after 1 curing day (Baroghel-Bouny *et al.,* 2013). 4 HPCs with or without silica fume (SF) and 3 normal-strength FA concretes which can appear as interesting mixtures with respect to current sustainable-de- velopment considerations were studied. All concretes described in this article were casted with the same cement (CEM I 52.5 PM ES CP2, see Table 1). Concrete mix-design are described in Table 2.

Table 1. Chemical and mineralogical composition of the binder (%).

	SiO_2	Al_2O_3	Fe_2O_3	CaO	MgO	SO_3	K_2O	Na_2O
CEMI	21.39	3.49	4.16	65.12	0.82	2.86	0.30	0.12
Fly Ash	55.86	25.40	6.05	1.83	0.63	0.11	4.77	0.24
Silica Fume	94.75	0.07	0.08	0.34	0.28	0.05	0.28	0.18

Table 2. Mix-design, along with average 28 days cylinder compressive strength and 90 days porosity accessible to water (measured after water curing).

Concrete	Gravel/sand	Cement	FA	SF	Water	W/binder	σ_c	Porosity
M25FA	992/905	195	48	-	187	0.77	23.5	0.157
M30FA	986/879	223	95	-	166	0.52	48.5	0.141
M50FA	956/809	325	79	-	181	0.45	53.0	0.150
M50	937/806	410	-	-	197	0.48	55.5	0.145
M75	1025/808	461	-	-	146	0.32	75.0	0.114
M75SF	1044/877	360	-	22	136	0.36	85.5	0.100
M100SF	1049/871	377	-	38	124	0.30	109.0	0.084

3.2 Numerical Approach

A physically and chemically based model was developed to simulate ionic ingress in the materials. Calculations are managed with TOUGHREACT software (Xu *et al.*, 2012). The chemical part uses the thermodynamical database Cemdata18 (Lothenbach *et al.*, 2019). Hydration and interstitial solution calculations precede this reactive transport simulation (see Figure 1 for the description of the simulation steps). Input data are limited to chemical and mineralogical composition of the binder, concrete mix-design, average bulk porosity and effective diffusion coefficient of concrete.

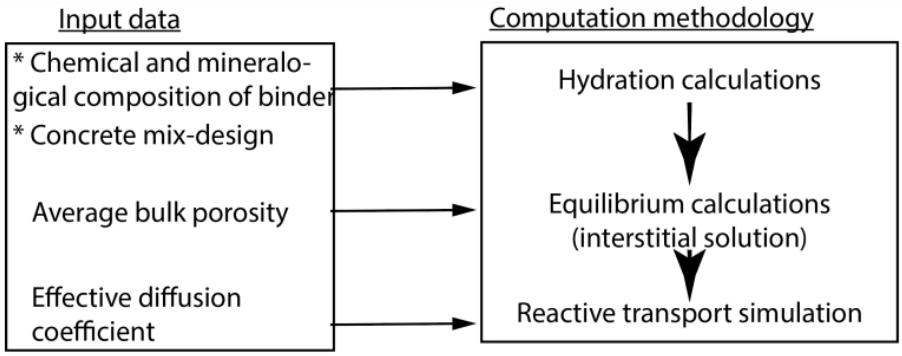

Figure 1. Flow chart of the reactive transport model.

The reactive transport model considers precipitation and dissolution of mineral species and their kinetics and adsorption of several ionic species on C-S-H (Cl^-, Na^+, K^+, Ca^{2+}, SO_4^{2-}). It has been validated on different experimental data such as laboratory concretes exposed to different solutions containing chloride (Tran *et al.*, 2018). Nevertheless, ingress of seawater in concrete exposed to field conditions after only few curing days is a difficult subject. In the case studied here, hydration was not complete when concretes were exposed to seawater leading to interactions between ionic species contained in seawater and anhydrous phases.

Although concretes are exposed to wetting-drying cycles, the present numerical model assumes that concrete is saturated by adopting a pure fickian approach (see Equation below). In fact, the wetting-drying cycle period is short (12 hours) and the mean value of the relative humidity in La Rochelle harbor is high (close to 67% (Baroghel-Bouny *et al.*, 2013)). Except for the first millimeters where carbonation can occur, this hypothesis seems to be reasonable (Soive *et al.*, 2018).

$$\frac{\partial \phi c_j}{\partial t} = div\left(D_e \vec{\nabla} c_j\right) + q_j \quad (1)$$

where φ is the average bulk porosity, c_j the concentration of species j [mol.m^{-3} of solution], D_e the effective diffusion coefficient [m^2.s^{-1}] (supposed to be equal for all species) and q_j source or sink term [mol.m^{-3}.s^{-1}]. Ions can chemically react with the matrix to precipitate minerals (*e.g.* ettringite, brucite, Kuzel and Friedel's salts) or to dissolve others (portlandite, monosulfate). They also can be bound (adsorbed or absorbed) to the surface of the matrix. As described in previous studies (Baroghel-Bouny *et al.*, 2013; Soive *et al.*, 2018), all mineral precipitation/dissolution kinetics also need to be taken into account. In addition, the effective diffusion coefficient D_e can evolve with average bulk porosity value change as follows:

$$D_e = \phi \tau D_W \quad (2)$$

where τ and D_w are the tortuosity and the diffusion coefficient of ionic species in water.

A 1D diffusion model is adopted. 250 elements are used to simulate ionic species ingress in 10cm structural depth. By sake of simplicity and to avoid complex calculations of ionic species ingress during hydration, hydration duration is supposed to be equal to the greater exposition duration (19 years). Of course, this is a very first approximation owing to the competition between hydration and seawater ingress at first time exposure. Chemical reactions between seawater and anhydrous species are not considered.

4 Results and Discussion

Total chloride content profiles were measured after 2, 4, 10, 16 and 19 years of exposure. Comparison between experimental data and numerical results with 19 curing years is exposed in Figure 2. Knowing the limited number of input data and the difficulty to catch all the phenomena, the numerical simulations show hopeful results.

Three aspects can be underlined: the "convection zone", the evolution of apparent diffusion coefficient as a function of time and possible chemical reactions between chloride and anhydrous phases.

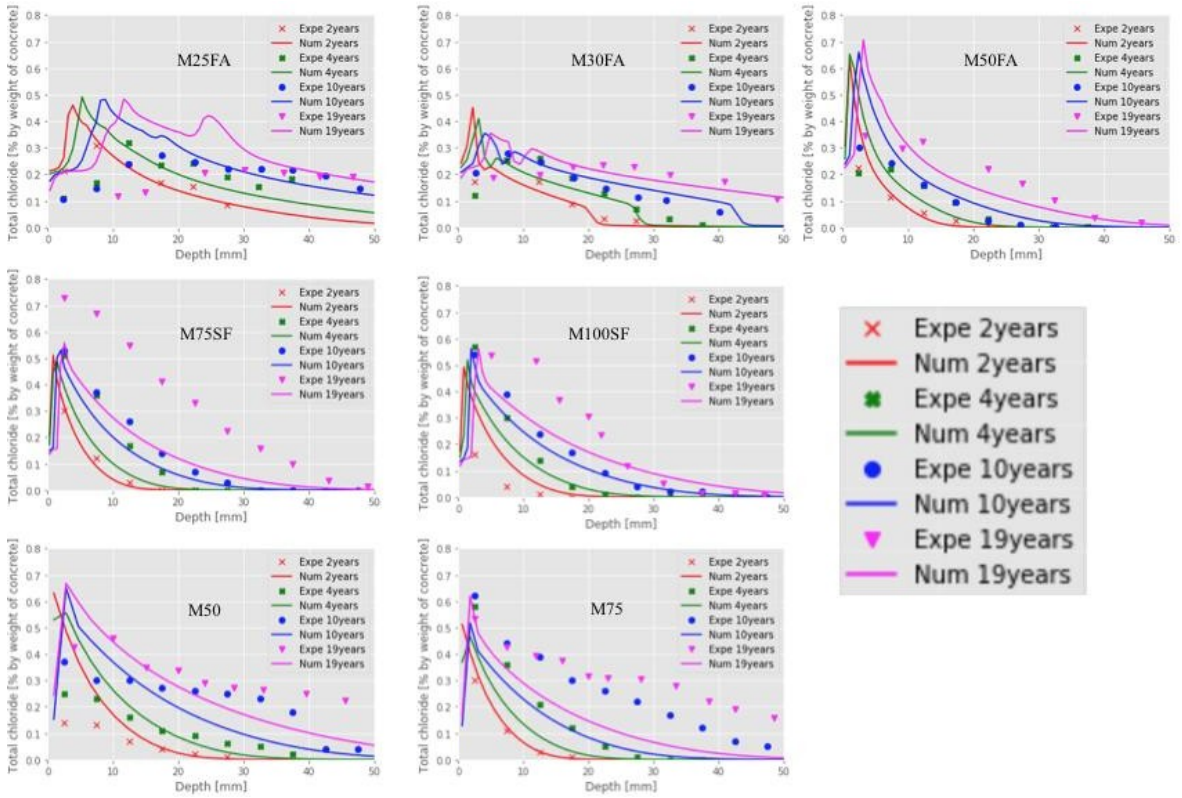

Figure 2. Comparison between experimental data and numerical results for total chloride profiles for 2, 4, 10, 16 and 20 years of exposure (19 curing years).

4.1 The « Convection Zone »

For concretes with fly ash (M25FA, M30FA, M50FA), results are rather good except in the first millimeters and although numerical model does not consider wetting/drying cycles. The depth at which total chloride content is maximum is to underline. This zone is often associated with the "convection zone". Nevertheless, even with a model that simulate the ingress of ionic species in saturated concrete such as the present one, this phenomenon is observed. As reported by Jakobsen *et al.* (2016), chemical and mineral zonation appear. Three zones (magnesium, sulfur and chloride-rich zones) are found irrespective of the age, location or binder composition. Figure 3 show that the model can qualitatively simulate these zones. However, in this "convection zone", results are very different from experimental data. The use of a model considering wetting-drying cycles is necessary in order to catch phenomena in this zone (convection, local chloride concentration increase).

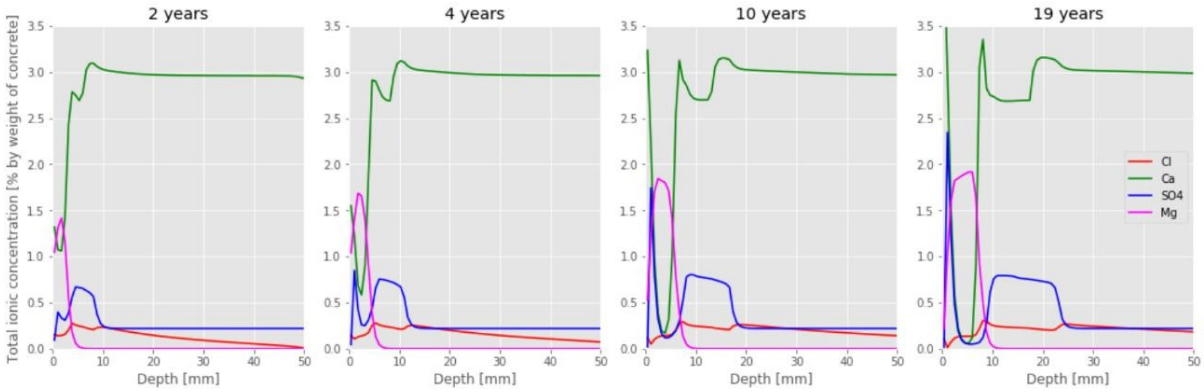

Figure 3. Ionic species ingress after 2, 4, 10, 16 and 20 years of exposure for M25FA (19 curing years)

4.2 The Evolution of Apparent Diffusion Coefficient with Time

For OPC (M50, M75), whereas profiles are close to experimental data after 2-year exposure, total chloride contents are underestimated for greater exposure durations. These differences can be partly explained by the fact that apparent diffusion coefficient (which includes both effective diffusion and binding) for M50 and M75 increases with time (by inverse analysis calculations on experimental data) from 1.6 10^{-13} to 2 10^{-13} $m^2.s^{-1}$ and 3.6 10^{-13} to 1.6 10^{-12} $m^2.s^{-1}$, respectively (see Figure 4). The present model considers microstructure evolution (average bulk porosity) due to mineral dissolution or precipitation (see Equation 2). It is also able to compute the evolution of chloride binding. However, the apparent coefficient increase is much greater than the one computed. Deeper experimental data investigations must be done in order to determine if other phenomena that are not modeled can appear, such as cracks, properties differences between concrete first millimeters and deeper.

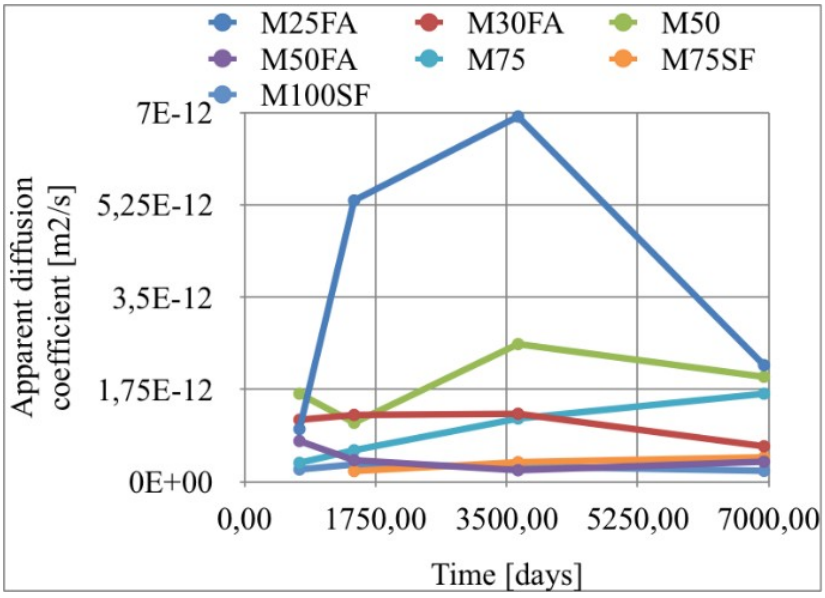

Figure 4. Apparent diffusion coefficient calculations by inverse analysis.

4.3 Possible Chemical Reactions between Chloride and Anhydrous Phases

For concretes with silica fume (M75SF, M100SF), underestimations ap- pear after 2-year exposure. Nevertheless, as can be seen in Figure 4 and contrary to M50 and M75, the apparent diffusion coefficients are constant. By analyzing hydration results of M75SF thanks to a hydration model developed at Cerema (Lavergne *et al.*, 2018) (see Figure 5), results show that anhydrous phases are still present after 19 curing years (6500 days) as well as a lack of monosulfate. These results confirm that hydration is slower for these concretes. However, presence of seawater can affect the hydration process by accelerating hydration or precipitating minerals containing chloride (Friedel's salt) (Li *et al.*, 2018). Unfortunately, the present model is not able to calculate chloride ingress in concretes that continue to hydrate.

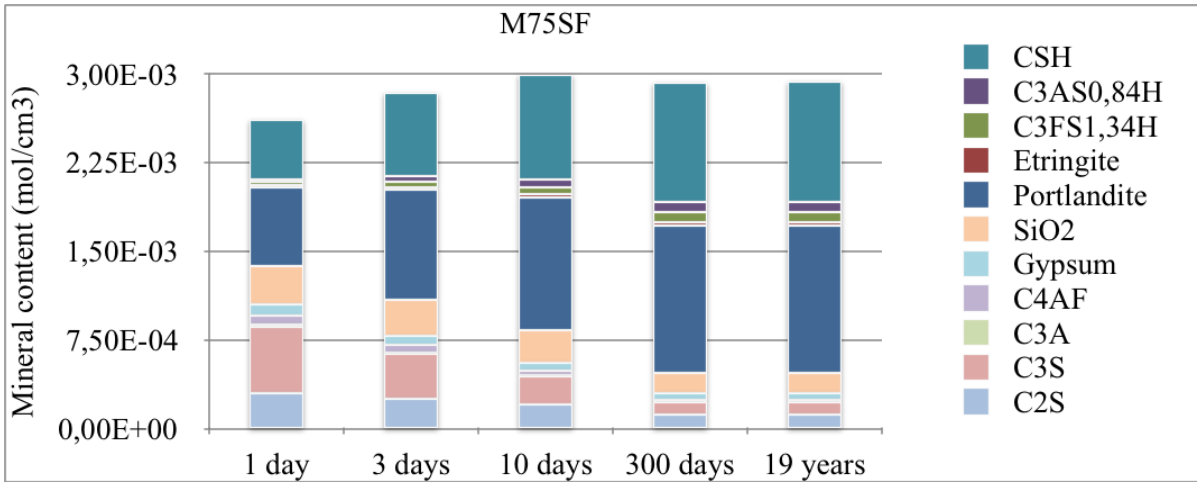

Figure 5. Hydration results after 1, 3, 10, 300 and 6500 curing days.

5 Conclusion

Experimental data on concretes exposed to tidal zone in field conditions for 19 years and subjected to wetting-drying cycles in seawater after a couple of curing days were compared to numerical results. Two OPCs, three concretes with fly ash and two concretes with silica fume with the same cement were studied. The numerical results were obtained thanks to a hydration model and a reactive transport model considering precipitation/dissolution of minerals and their kinetics and adsorption of ionic species on C-S-H.

A pure fickian approach in saturated materials is assumed. In addition, due to difficulties to model interactions between ingress of ionic species and hydration, numerical model assumes that hydration lasts for 19 years (last measurement value).

Knowing the limited number of input data and the difficulty to catch all the phenomena, the numerical simulations show hopeful results, especially for concrete with fly ash. In addition, the model can qualitatively simulate chemical and mineral zonation (magnesium, sulfur and chloride-rich zones) as reported in the literature. For OPC and concretes with silica fume, numerical results underestimate chloride content. For OPC, although numerical model considers porosity change due to mineral precipitation/dissolution, it is not able to simulate increase of apparent diffusion coefficient as observed on experimental data. Further investigations must be done in order to observe if cracks are visible. For concretes with silica fume, underestimation cannot be fully explained yet. One explanation can be the lack of additional chloride content coming from reactions between chloride and remaining anhydrous phases. Indeed, by analyzing results of hydration calculations, results show that anhydrous phases are still present even after 19 years and that additional chloride content can exist.

ORCID

Previous the references list, the authors' ORCID must be provided, in 10pt Times New Roman, as in the example:
Anthony Soive: https://orcid.org/0000-0002-2368-6848
Véronique Baroghle-Bouny:
Francis Lavergne: https://orcid.org/0000-0001-6984-3784

References

Baroghel-Bouny, V., Dierkens, M., Wang, X., Soive, A., Saillio, M., Thiery, M. and Thauvin, B. (2013). Ageing and durability of concrete in lab and in field conditions: Investigation of chloride penetration. *Journal of Sustainable Cement-Based Materials*, *2*(2), 67–110.

Caré, S. (2008). Effect of temperature on porosity and on chloride diffusion in cement pastes. *Construction and Building Materials*, *22*(7), 1560–1573. https://doi.org/10.1016/j.conbuildmat.2007.03.018

Jakobsen, U. H., De Weerdt, K. and Geiker, M. R. (2016). Elemental zonation in marine concrete. *Cement and Concrete Research*, *85*, 12–27. https://doi.org/10.1016/j.cemconres.2016.02.006

Lavergne, F., Ben Fraj, A., Bayane, I. and Barthélémy, J. F. (2018). Estimating the mechanical properties of hydrating blended cementitious materials: An investigation based on micromechanics. *Cement and Concrete Research*, *104*(April 2017), 37–60. https://doi.org/10.1016/j.cemconres.2017.10.018

Li, H., Farzadnia, N. and Shi, C. (2018). The role of seawater in interaction of slag and silica fume with cement in low water-to-binder ratio pastes at the early age of hydration. *Construction and Building Materials*. https://doi.org/10.1016/j.conbuildmat.2018.07.091

Lothenbach, B., Kulik, D. A., Matschei, T., Balonis, M., Baquerizo, L., Dilnesa, B. and Myers, R. J. (2019). Cemdata18: A chemical thermodynamic database for hydrated Portland cements and alkali-activated materials. *Cement and Concrete Research*, *115*(October 2018), 472–506. https://doi.org/10.1016/j.cemconres.2018.04.018

Soive, A., Tran, V.-Q. and Baroghel-bouny, V. (2018). Requirements and possible simplifications for multi-ionic transport models - Case of concrete subjected to wetting-drying cycles in marine environment. *Construction and Building Materials*, *164*.

Suryavanshi, A. K. and Swamy, R. N. (1996). Stability of Friedel's salt in carbonated concrete structural elements. *Cement and Concrete Research*, *26*(5), 729–741.

Tran, V.-Q., Soive, A. and Baroghel-bouny, V. (2018). Modelisation of chloride reactive transport in concrete including thermodynamic equilibrium, kinetic control and surface complexation. *Cement and Concrete Research*, *110*(January 2017), 70–85.

Xu, T., Spycher, N. and Sonnenthal, E. (2012). *TOUGHREACT User's Guide: A Simulation Program for Non-isothermal Multiphase Reactive Transport in Variably Saturated Geologic Media, version 2.0*. *Lawrence Berkeley …*.

XV International Conference on Durability of Building Materials and Components
DBMC 2020, Barcelona
C. Serrat, J.R. Casas and V. Gibert(Eds)

The Influence of Injection Agents Applied for Carrying out Secondary Horizontal Damp Proof Courses on Masonry Mortar Properties

Tomasz Błaszczyński[1], Barbara Ksit[2] and Bartłomiej Monczyński[3]

[1] 62-002 Złotniki, Poland, tomasz.blaszczynski@opal.info.pl

[2]Poznan University of Technology, 60-965 Poznań, Poland, barbara.ksit@put.poznan.pl

[3] Poznan University of Technology, 60-965 Poznań, Poland, bartlomiej@monczynski.pl

Abstract.*In the article, a comparative analysis of the effects of selected substances applied to create secondary horizontal damp proof courses of masonry walls by means of the chemical injection method on the properties of masonry mortar was carried out. Particular attention was given to the influence of impregnation on the hygric properties of mortar. The resistance to destructive factors accompanying the dampening of masonry wall structures was also subjected to observation.*

Keywords: *Injection, Damp Proof Course, Renovation, Dampening.*

1 Introduction

The problem of the excessive moisture content of brick walls in historical objects is present in many European countries because of their rich cultural heritage and dense accumulation of historical buildings (Hoła, 2017).The masonry walls of historical buildings - made of ceramic brick or stone - are often characterized by a high thickness and a lack of damp insulations. It refers primarily to horizontal insulations, which began to be executed in a modern way at the beginning of the twentieth century. The lack of damp insulations causes direct and prolonged contact of a wall with the ground (Adamowski, in., 2005; Franzoni 2014). As a result, water molecules that are contained in the substrate along with salts dissolved in them penetrate elements of the masonry wall making it damp. These elements are both ceramic brick and mortar from joints, and in walls made of stone these joints are usually of a large width. Capillarity, the process of which was described inter alia in (Camino *et al.* 2014; Raimondo *et al*. 2009, Hoła *et al.* 2017), causes water molecules to be transported into the wall and into its higher parts. In the case of a masonry wall with a large thickness, from which evaporation of moisture is naturally difficult, the degree of moisture content gradually increases with time (Goetzke-Pala *et al.* 2016; Gutarowska *et al.* 2007).

Groundwater together with the salts contained in it rises due to capillary action to ever higher parts of the walls made of capillary-porous materials, such as burnt clay brick, brickwork joint mortar and plaster. Also the concentration of salts in the brickwork and plaster components increases by the year (Rirsch *et al.* 2010; Torres *et al.* 2010; Espinosa;i in.,2008). The negative effects of the excessive build-up of moisture in the wall include: a decrease in brickwork strength, susceptibility to frost damage, falling off plaster, spalling mortar in the joints between bricks, an increase in the heat transfer coefficient of the building envelope and susceptibility to fungal decay and mouldiness(Franzoni *et al.* 2011; Gentillini *et al.* 2012 Solymez,1999; Blaszczynski, 2007).

The dampening of walls as a result of the capillary transport of water is one of the main

reasons behind damage in buildings, whereas the drying out of a wall by carrying out a secondary horizontal damp proof course in the wall is the most important element of renovation (Venzmer, 2008). One of the means of recreating horizontal insulation in a wall are injection (chemical) methods. Although the injection membrane, by assumption, is formed in the entire cross-section of the wall, in practice, the injection agent migrates mainly in the masonry mortar (Hölzen, 2006), especially in cases when injection openings are created (when using pressure injection as well as when applying injection creams) horizontally, in the supporting joint of the masonry wall.

2 Capillary Transport of Moisture in Mineral Construction Materials

The vast majority of materials applied in the inside walls of buildings are those described as capillary-porous, and thus characterized by a porous structure, with the pores connected with each other by a system of capillaries or partially separated by walls. The properties of capillary-porous bodies depend largely on the total volume of pores, the volume distribution of pores depending on their diameter (porosity structure), as well as the specific surface area of the pores. Although various criteria can be found in literature as far as the division of pores occurring in a material is concerned, the division given by the International Union of Pure and Applied Chemistry (UPEC) has been generally accepted, which, depending on the so-called effective pore radius (assuming for the sake of simplification their spherical shape) ref, distinguishes three groups:

- micropores: $r_{ef} \leq 2$ nm,
- mezopores: 2 nm $< r_{ef} \leq 50$ nm,
- macropores: $r_{ef} > 50$ nm.

It ought to be noticed, however, that capillary absorption and the transport of water is possible only in pores with a radius from 10-7 to 10-4 m (from 100 nm to 0.1 mm), also referred to as capillary pores. Pores with a diameter of less than 10-7 m, (gel pores), can fill up with water only as a result of capillary condensation, whereas pores greater than 10-4 m (air pores) can fill up with water only under pressure.

In addition to the structure and distribution of pores in a material, capillary transport of moisture is determined by the wetting properties of a liquid in relation to the material, or in other words – by the properties of the material in relation to water penetrating into the capillaries (Bonk, 2006; Balak, 2007). As a result of the surface tension forces of water, the surface of a liquid, upon contact with a solid body, creates the so-called contact angle, or the angle between the surface of the solid body and that contacting the surface of the liquid drawn at the point of contact (on the border of three phases). The value of angle θ is a measure of wettability:

- $0 < \theta < \pi/2$ – liquid wets, hydrophilic material
- $\pi/2 < \theta < \pi$ – liquid does not wet, hydrophobic material.

In the capillaries of a body characterized by good wettability, the surface of the liquid forms a concave meniscus (slightly rises when making contact with a solid body), whereas in the case of bodies with inadequate wettability – the meniscus is convex (falls).

It is very difficult to construct a model describing the capillary transport of moisture in porous materials, mainly due to the complex geometry of pores – seeing as how the network is formed from pores of various shapes (cylindrical, wedge-shaped, crevicular, spherical) as well as a diverse system of connections (open pores, pocket pores, closed pores). Capillaries also

create discontinuous systems, as well as systems of complex shapes.

Attempts at investigating the mechanism of the capillary movement of moisture are described by Pogorzelski (Pogorzelski, 2004), using a simplified model of a capillary body in the form of a bundle of parallel capillaries of an identical radius for this purpose. In accordance with the Young-Laplace equation, a difference in the pressures Δp will occur on both sides of the meniscus causing a rise of liquid in the capillary, up to the differences in the pressure evening out by the forces of inertia, friction (resulting from the Hagen-Poiseuille Law) as well as gravitational force. Basing on these assumptions, formulas for the rate of capillary movement (at vertical movement) were indicated:

$$\upsilon = \frac{dl}{d\tau} = \frac{r^2}{8\eta l}\left(\frac{2\sigma\cos\Theta}{r} - g\rho l\right) \tag{1}$$

As well as maximum capillary rise (determined by Washburn's equation):

$$H = l_{\max} = \frac{2\sigma\cos\Theta}{r\rho g} \tag{2}$$

where:l – length of capillary, τ – time of rise, r – capillary radius, η – dynamic density of liquid, σ – surface tension, Θ – contact angle, g – Earth's pressure, ρ – liquid viscosity.

Formulas (1) and (2) express two basic laws describing the capillary absorption of water. The first states that the rate of the capillary rise is higher in materials with "thick" capillaries than those with thin capillaries. In materials with thin capillaries, the level of rise is significantly higher. At a very small or very large radius of a capillary, the rates as well as the maximum level of rise are reduced to zero (in other words, capillary transport does not take place). In reality, although capillary-porous materials have a significantly more complex structure than that described by the model of a bundle of identical parallel capillaries (Pogorzelski,2004), in the case of capillaries with a radius of less than 0.1 μm, the rate of absorption vanishes, whereas in the case of capillaries with a radius exceeding 100 μm, the maximum possible rise falls to zero.

3 Materials and Methods

A cement-lime mortar with a volumetric composition of 2:0, 5:8 (hydrated lime: CEM I 32.5 Portland cement: sand with a granulation of 0-2 mm). The fresh mortar was placed in a mould made from PVC pipes 200 mm in diameter, cut in 300 mm sections. After the initial hardening of the mortar, that is two days after preparing the moulds, the samples were placed in polyethylene bags for another five days. After a period necessary for the mortar to reach full strength, it was subjected to dampening, placing the moulds in a tray with water (on a grate) so that the samples were constantly submerged in approximately 10 mm. After two days, the moulds were taken out of the water, wrapped in foil and left for two weeks in order to ensure even distribution of moisture in the mortar (Monczynski, 2019) (Figure 1).

Holes were made in the samples and gravitational injection, using an injection cream, and pressure injection (under a pressure of 0.2 MPa increased after 30 s to 0.5 MPa) using methyl silicates as well as silicone microemulsion (SMK), carried out. After a further four weeks, the mortar was taken out of its moulds and cut using a circular saw into cubic samples with sides

measuring approx. 45 mm.

Figure 1. Mortar samples during moulding, dampening and carrying out injections.

4 Results

Studies on absorbability were carried out on twenty-four cubic samples which, after drying at a temperature of 105±5°C and weighing, were placed in a tub, on a grate, and then submerged in water to approximately a quarter of their height (Wójcik, 2008). After 24 hours, that is after the completion of sample dampening as a result of capillary rise the samples were submerged to half their height and, following another 3 hours, to three-quarters of their height. The complete submersion of samples (minimum of 20 mm above the upper edge of the samples) took place 30 h after the commencement of the experiment. After complete impregnation, the samples were removed from water, dried with a rag and weighed (WTA, 2015). Absorbability in relation to the dry mass of the mortar was described according to the formula:

$$n_m = \frac{m_m - m_s}{m_s} \cdot 100\% \tag{3}$$

where: n_m – absorbability in relation to mortar mass [%], m_m – mass of sample saturated with water [g], m_s – mass of sample dried to a constant mass [g].

Studies on the phenomenon of capillary rise carried out on twenty-four cubic samples of a mortar dried to a constant mass, which, upon weighing, were placed on a grate in a flat tray which was then filled with water so that they would be submerged in water at a depth of approx. 10 mm. The measurement of capillary rise was carried out 1, 3, 6 and 24 h after submersion, weighing the samples (after first drying them with a rag). The increase in the mass of samples during individual measurements was calculated according to the formula:

$$m_i = \frac{m_c - m_s}{m_s} \cdot 100\% \tag{4}$$

where: m_i – increase in sample mass [%], m_c – mass of sample dampened by capillary rise of water, after 1, 3, 6 and 24 h respectively [g], m_s – mass of dried sample [g].

The water absorption coefficient was indicated according to the expression:

$$w_{24} = \frac{m}{A \cdot \sqrt{t}} \tag{5}$$

where: w_{24} – water absorption coefficient after 24 hours following submersion [kg/m^2·h^{0,5}], m – mass of absorbed water [kg], A- absorption surface [m^2],t – absorption time [h].

The results of studies on absorbability and capillary rise have been presented in Table 1.The compression test was carried out in an Instron 8500 Plus testing machine. Forty cubic samples

were used for the tests. The applied load was controlled by a force of 50 N/s – this value was selected so that the compression test of an individual sample would fell in the range of 30 to 90s. Due to the irregular shape of the samples, they underwent evening/smoothing with 220 grit sanding mesh (Gutarowska *et al.* 2004). Determining the resistance to frost is carried out by determining the mass loss caused by periodic freezing and thawing. Twenty-four samples were prepared for the test.

The samples were marked as follows:

- MKA – mortar impregnated with alkaline methyl silicate, ,
- SMK – mortar impregnated with silicone microemulsion,
- KI – mortar impregnated with injection cream,
- 0 – mortar lacking impregnation (controls).

Table 1. Results of studies on capillary rise and absorbability.

	m_1	m_3	m_6	m_{24}	w_{24}	n_m
0	11.7%	11.8%	11.8%	11.9%	1.89	11.8%
MKA	12.0%	12.1%	12.2%	12.3%	1.93	12.0%
SMK	11.5%	11.7%	11.7%	11.9%	1.87	12.0%
KI	7.8%	8.0%	8.1%	8.4%	1.35	10.2%

The compressive load (including breaking load), as well as movement under compression, were measured. The average compressive strength is presented in Figure 2.

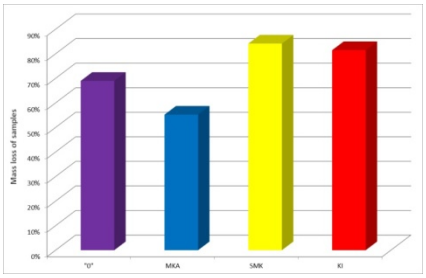

Figure 2. Average loss (percent) in mortar mass after freeze/thaw cycles.

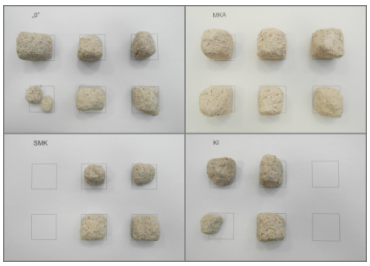

Figure 3. Mortar samples after 25 freeze/thaw cycles.

All were dried to a constant mass and next weighed. Next, the samples were submerged in water in order to completely dampen them. The saturated samples were removed from the water and placed for 4 h in a freezer, at a temperature of −20±2°C.Upon freezing, they were transferred to a tub with water at a temperature of 20±2°C for at least 4 h. Twenty-five freeze–thaw cycles were carried out, and next the sample was dried to a constant mass and weighed once again. The freeze-thaw resistance was indicated based on the formula:

$$\Delta m = \frac{m_d - m_f}{m_d} \cdot 100\% \tag{5}$$

where:Δm – the difference in the mass of the sample prior to testing and after testing [%], m_d– the mass of the sample dried to a constant mass prior to the first cycle [g], m_f – mass of sample dried to a constant mass following the last cycle [g].

Average losses in mass expressed as percentages are presented in Figure 2. Figure 3 shows the appearance of the samples upon the completion of the test. Testing the resistance to the crystallization of salts was carried out on twenty-four cubic samples which, after drying and weighing, were placed for 2 h in 14% solution of sodium sulphatedecahydrate (Na2SO4·10 H2O). Next, the samples were dried at a temperature of 105 ±5°C for a minimum of 16 h. In order to ensure high air humidity at the first stage of drying, a tray containing water was placed in the dryer prior to its initiation. After completion of the drying process, the samples were cooled for approx. 2 h to room temperature and once again submerged in a saline solution.

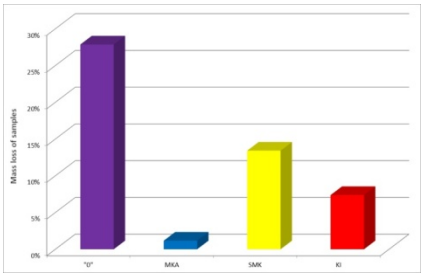

Figure 4. Average percentage loss of mass after testing the resistance to the crystallization of salts.

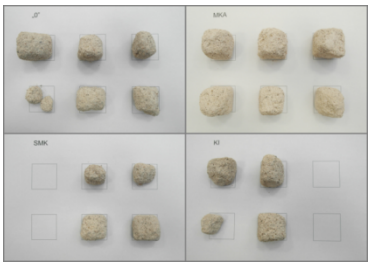

Figure 5. Mortar samples after 15 cycles of testing resistance to salinification.

Upon carrying out 15 such cycles, the samples were stored in water at room temperature for 24 h and next dried to a constant mass and weighed. The resistance to the crystallization of salts was indicated analogously to freeze-thaw resistance. Figure 4 shows the average percentage loss in mass, whereas Figure 5 presents the appearance of the samples after testing.

5 Conclusions

Impregnation of mortar was carried out with dampness resulting from close to maximal capillary rise of water. The results of studies on the capillary rise of water and total absorbability confirm that a high level of dampness makes it difficult or even impossible to apply agents based on alkaline methyl silicates and silicone micro emulsion. Injection creams, on the other hand, work very well in such cases (an over 13% reduction in total absorbability and nearly 29% decrease the capillary absorption coefficient were observed). All analyzed injection agents had a beneficial effect on the compressive strength as well as resistance to the harmful effects of construction salts. Alkaline Methyl silicates caused an increase in freeze-thaw resistance of the mortar. Due to the fact that the mortar subjected to the effects of agents based solely on hydrophobisation (silicone microemulsion and injection creams) caused a decrease in resistance to freezing and thawing, these substances should not be applied if there is no possibility to dry the wall before winter and it is not protected against freezing.

The results of the carried out studies also confirm that chemical injection treatment of the wall should not be carried out without accounting for specific conditions, such as the level of dampness, the location of the wall, conditions of the surroundings, etc. It should also be kept in mind that walls are conglomerates comprising materials characterized by various technical parameters.

ORCID

Tomasz Błaszczynski: https://orcid.org/0000-0003-3177-9654
Barbara Ksit: https://orcid.org/0000-0001-6459-8783
Bartłomiej Monczynski:https://orcid.org/0000-0002-6847-3854

References:

Adamowski J. Hoła J. and Matkowski Z. (2005). *Probleme und Losungen beim Feuchtigkeitsschutz des Mauerwerks von Baudenkmalern am Beispiel zweier grosser Barockbauten in Wroclaw*, Bautechnik, 82, issue 7**,** 426-33.

Balak, M.S.C.(2007). *Nachträglische Horizontalabdichtung von Mauerwerk mittels Injektionsverfahren - neueste Erkenntnisse*, Feuchtenschutz, Beuth, Berlin-Wien-Zürich, Beuth, 129-140.

Blaszczynski T. Zgola B. Kukurenda K. and Bazela C. (2007). *Durability and repairs efficiency in case of more than hundred years historical building*, in: M. Kaminski, J. Jasiczak, W. Buczkowski, T. Blaszczynski (Eds.), *Durability and Construction Repairs Efficiency*, DWE, Wroclaw.

Bonk M. (2006).*Sanierung von Abdichtungen*, Lufsky Bauwerkabdichtung, Wiesbaden, Teubner, 369-422.

Camino M. S. Leon F.J. Llorente A. and Olivar J. M. (2014). Evaluation of the behavior of brick tile masonry and mortar due to capillary rise of moisture, *Materiales de Construccion, 64*(31). doi:org/10.39899/mc.2014.02513.

Espinosa R.M. Franke L. and Deckelmann G. (2008). Phase changes of salts in porous materials: Crystallization, hydration and deliquescence, *Construction and Building Materials, 22*, 1758–1773.

Franzoni E. (2014). Rising damp removal from historical masonries: a still open challenge, *Construction and Building* Materials, *54*, 123–136.

Franzoni E. Sandrolini F. and Bandini S. (2011). An experimental fixture for continuous monitoring of electrical effects in moist masonry walls, *Construction and Building Materials, 25*, 2023–2029.

Gentillini C. Franzoni E. Bandini S. and Nobile L. (2012). Effect of salt crystallisation on the shear behaviour of masonry walls: an experimental study, *Construction and Building Materials, 37,* 181–189.

Goetzke-Pala and A. Hoła, J.(2016). Influence of burnt clay brick salinity on moisture content evaluated by non-destructive electric methods, *Archives of Civil and Mechanical Engineering, 16*(1), 101–111.

Goetzke-Pala A. Hoła A. and Sadowski Ł. (2018). A non-destructive method of the evaluation of the moisture in saline brick walls using artificial neural networks, *Archives of Civil and Mechanical Engineering, 18,* 1729–1742.

Gutarowska B. and Piotrowska M. (2007). Methods of mycological analysis in buildings, *Building and Environment, 42*, 1843–1850.

Hoła A. Matkowski Z. and Hoła J. (2017). Analysis of the moisture content of masonry walls in historical buildings using the basement of a medieval town hall as an example*, Procedia Engineering, 172*, 363 – 368.

Hoła A. (2017). *Measuring of the moisture content in brick walls of historical buildings – the overview of methods, IOP Conf. Series: Materials Science and Engineering*, doi:10.1088/1757-899X/251/1/012067.

Hölzen F.-J. (2006). *Zur Wirksamkeit von Injektionsmitteln an Fallbeispielen*, Injektionsmittelabdichtung, Stuttgard, Fraunhofer IRB, 117-131.

Monczynski B. Ksit B. and Szymczak-Graczyk A. (2019). *Assessment of The Effectiveness of Secondary Horizontal Insulation. Against Rising Damp Performed by Chemical Injection*doi.org/**10.1088/1757-899X/471/5/052063**.

Pogorzelski J. A. (2004). *The humidity state of building partitions (Part 2)*, Construction Materials, No 5, 80-83 (in Polish).

Pogorzelski J. A. (2004). *The humidity state of building partitions (Part 1)*, Construction Materials, No 4, 63-66 (in Polish).

Raimondo M. Dondi M. Guardini G. and Mazzanti F. (2009). Predicting the initial rate of water absorption in clay brick, *Construction and Building Materials, 23,* 2623–2630.

Rirsch E. and Zhang, Z. (2010). Rising damp in masonry walls and the importance of mortar properties, *Construction and Building Materials, 24*, 1815–1820.

Solymez M. (1999). On the effective thermal conductivity of building bricks, *Building and Environment, 34,* 1–5.

Torres I. and Peixoto de Freitas V. (2010). The influence of the thickness of the walls and their properties on the treatment of rising damp in historic buildings*, Construction and Building Materials, 24,* 1331–1339.

Venzmer H. Ryschtchenko M. Lesnych N. Fedorenko E. and Koss L. (2008). *Zur Prüfung der Effizienz von Injektionsmittel-Horizontalabdichtungen*, Europäischer Sanierungskalender, Berlin-Wien- Zürich, Beuth, 7-40.

Wójcik R. (2008). The reproduction of horizontal isolations in existing buildings with the method of the thermohermetic paraffin-injection, *Construction Materials, 3*, 7-8 (in Polish).

WTA Merkblatt 4-10-15/D.(2015). *Injektionsverfahren mit zertifizierten Injektionsstoffen gegen kapillaren Feuchtetransport. München:Wissenschaftlich-Technische Arbeitsgemeinschaft für Bauwerkserhaltung und Denkmalpflege e.V*.

XV International Conference on Durability of Building Materials and Components
DBMC 2020, Barcelona
C. Serrat, J.R. Casas and V. Gibert (Eds)

Client's Expectations vs Contractor's Pricing. Fair Prices or Bid Rigging

Hubert Anysz and Andrzej Foremny

Warsaw University of Technology (WUT), Civil Engineering Department, Al. Armii Ludowej 16, 00-637 Warsaw, Poland, h.anysz@il.pw.edu.pl, a.foremny@il.pw.edu.pl

Abstract. *The road construction sector is a specific part of the construction industry. It happens very rarely that a section of a road is financed also by a private entity. The other factor distinguishing it – is a significant value of road construction contracts. The Client's estimates of the value of the prospective contracts have to be based on the market prices in case of public procurement. However, this market is dominated by public orders. There is no comparison to the value of works ordered on the private part of the construction market, which is found more efficient by economists. Widely applied the "design and build" type of orders make the comparisons of the unit prices more difficult. The huge differences between the Client's estimates and the winning prices in the road construction public tender procedures are the bases of speculations about the fairness of the procedures. These differences can have a varied origin. There are several reasons for them e.g. varied contractor's risk, the size of the structure, type of order, the dynamics of the road construction market. Nevertheless, fraudulent practices can make the winning price much higher than the Client's estimate. The article is an attempt to finding the limit i.e. what part of these differences can be explained by fair, market reasons. If the found limit is exceeded, it should make the Client carefully consider the offers placed. The analysis is based on collected data concerning almost 400 tender procedures for the sections of roads in Poland in 2014-2017.*

Keywords: *Bid Rigging, Collusion, Road Construction Market, Bid Price, Client's Estimation.*

1 Introduction

Exceptionally high values of the construction contracts are observed in the road construction branch in Poland, Rynekinfrastruktury.pl (2019). Public procurements in the construction industry are specific. The Code (2004) enforced preparing a client's estimation of the contract value, before the announcement of a tender to enable a client to decide which type of tender procedure should be applied (as it is price dependent). Based on the ordinance (2004), that estimation should be based on market prices of construction works. The same base should be used for the "design and build" type of orders. The amount estimated by a client is announced together with disclosing the contractors' offers – not before. The extreme relation of the winner's price to the client's estimation (exceptionally low or high) usually becomes a base for suspicions and gossips about forbidden practices of offerors (dumping prices or collusion, bid rigging). The process of choosing the most attractive offer may lead to refusing the offer with exceptionally low price, not allowing – in the client's opinion – for executing all works on the subject, in the planned period. There is no such strong client's right for the case of exceptionally high prices given by all offerors. When the client's budget is short, insufficient to finance an unexpectedly expensive project, the tender procedure can be cancelled. This postpones the execution of the planned project for many months. If the prosecutor's office is informed, they can investigate if any illegal practice has accompanied certain tender procedure, OECD (2012). The choice of the most attractive offer (*i.e.* signing the contract with a contractor) with a very high price means indirectly acceptance of the offered price level. The paper concentrates on the

doi:10.23967/dbmc.2020.020

problem: how to distinguish high market offer prices in the tender for road construction works, from unrealistic high offer prices – pointing the illegal, collusive practices among offerors.

There are two opposite trends observed on contractors' offer prices. During economic growth, when the demand is increasing *(i.e.* the number of tenders being announced by clients increases), the contractors' means of production are fully utilized. Any new contract requires engaging the external forces on a much higher level. The new suppliers should be agreed to match this increasing demand. That makes offer prices higher. Oppositely, after the period of economic prosperity, the number of the tender procedures announced decreases. Partly, the contractors' means of production – after completing a contract – have no place of engagement. To manage them efficiently, contractors search for some new contracts by lowering the offer prices to make the chance of the win higher. The average number of contractors placing their offers in certain procedure increases then.

As every project is unique, to compare the price level between tender procedures the following – winner price to client's estimation (PtE) – ratio is defined (Anysz, 2019):

$$PtE = \frac{bid\ price\ chosen\ by\ a\ client\ as\ the\ best\ one}{client's\ estimation * 1{,}23} \quad (1)$$

It is required by Polish law to give the bid price including VAT but it is required to prepare a client's estimation in net values (excluding value-added tax) (code, 2004; ordinance, 2004). So, the denominator is corrected by the present Polish VAT rate for this type of construction works.

2 Price Level in Polish Road Construction Sector (2014-2017)

2.1 Database

Tender procedures completed by the choice of contractor for building or modernizing sections of roads are analysed. There were 388 tender procedures ended between Jun 2014 and Jul 2017 found, with winning bid price exceeding 10 million PLN. The following set of information about them is collected:

- bid prices of all (valid) tenders,
- names of clients and offerors,
- bid prices chosen by clients as the winning ones,
- the clients' estimated values of prospective contracts
- the dates of clients' decisions about choosing the contractors.

It was possible to collect the complete database concerning 382 tender procedures.

2.2 Price Level – PtE Distribution

The values of PtE ratio are calculated. Its basic statistics are presented in Table 1.

Table 1. Basic statistics of PtE.

Number of procedures	Mean average	Median value	Min	Max	St. dev.
382	0,607	0,578	0,195	1,793	0,216

It has occurred that in more than 82 % of tender procedures PtE value is over 0,4 and below 1,0. In approximately 14 % tender procedures winning bid price was very low ($PtE \leq 0{,}4$) and the chosen tender had the price over clients' estimates ($PtE \geq 1$) in 4 % of analysed procedures. The histogram of PtE values is presented in Figure 1.

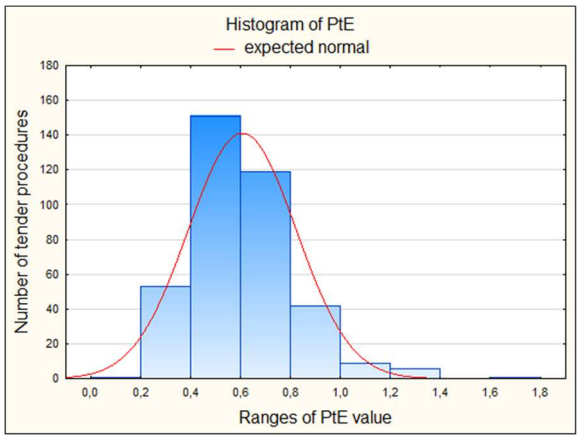

Figure 1. Histogram of PtE values in 382 tender procedures (Anysz, 2019).

2.3 Reasons for PtE Variations

The main reason for such significant variations of PtE value is the different aim of evaluations done by a client and a contractor. A client is obliged to apply market prices of different kinds of construction works i.e. average prices observed on the market. It is aimed to assess, which procedure of public procurement should be applied. Secondly, a client based on that can prepare a budget for the planned construction. A contractor calculates their bid price based on their costs, efficiencies of their brigades, etc. It is aimed at finding the price allowing for winning the contract, and for achieving the profit, which is necessary for a company to survive and business development. Taking into consideration the aims of evaluation, the contractor's bid price is unique, precisely adjusted to the company and market conditions. A client's evaluation is adjusted to the market conditions and based on average prices. Another reason also making PtE spectrum so wide is the fact that a client's estimation is prepared before the announcement of the tender procedure. The law limits the validity of such evaluation to six months. During this period, in a dynamically changing market, even average prices can change much. The next reason is an error of estimation. Finally – the standing of a national economy, and dynamics of the construction market influences the bid prices. Another group of reasons for PtE variations are illegal, collusive practices which makes bid prices vary from not abused market trends.

3 Market Phenomena Influencing the Bid Prices

Polish National Statistical Office (GUS) publishes on a monthly, quarterly or yearly basis much information collected on the market. One of the groups of published indicators is tendencies. The group of tendencies searched for this paper is "Business tendency survey in construction - current database - monthly data" (GUS, 2019). For 36 months analysed, the mean average of PtE in each month was calculated. Then, Pearson's correlations (Aczel, 1992) were checked

with different indicators of business tendencies (month to month; without any time shift). It has occurred that it is a quite high correlation coefficient – equals to 0,659 – between average PtE and the indicator "expected prices" assessed based on opinions of companies employing over 250 employees. It is the highest correlation among indicators published by GUS concerning the construction industry . Shifting the time of expectations one or two months haven't produced a higher correlation coefficient (see Figure 2).

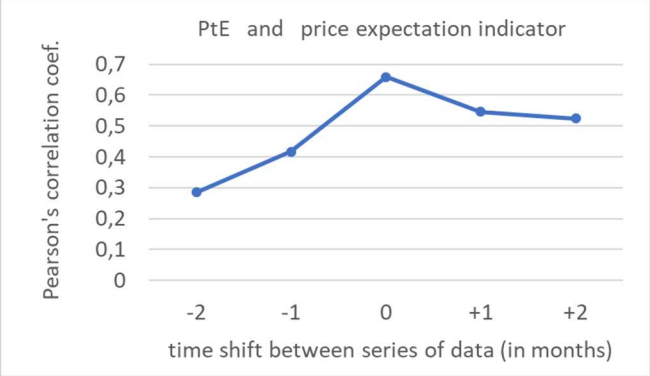

Figure 2. Pearson's correlation between PtE and price expectation indicator with time shifts.

As prices rise during the market growth, it can be said that PtE partly, positively reflects the trends on the market. Analysis of data collected does confirm findings of the number of tenders and their dependence on market prosperity proves that there are more tender procedures with the higher number of offerors when the market does not develop ($PtE \leq 0{,}4$). Procedures with more than 8 tenders almost don't appear (except 1 case) during the market growth – high bid prices dominate ($PtE \geq 1{,}0$). It can be observed in Figure 3.

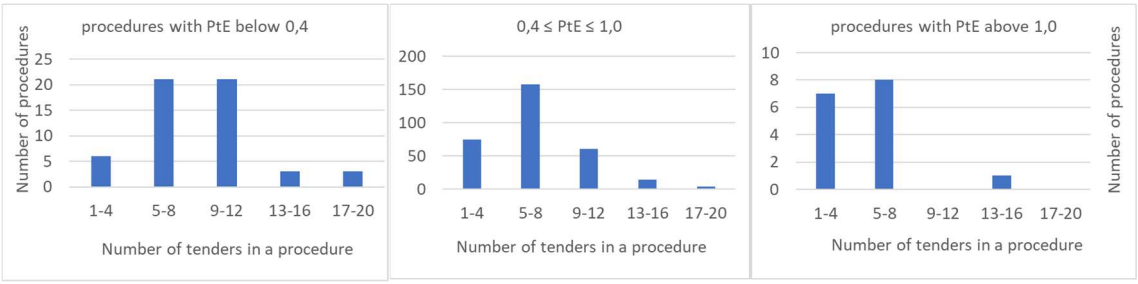

Figure 3. Histograms of the number of tenders for the procedures with different ranges of PtE (Anysz, 2019).

Moreover, the average PtE calculated monthly has the strong negative Pearson's correlation (-0,691) with an average number of tenders in a procedure. Described above dependencies are based on officially published (GUS, 2019) "expected prices" in the construction industry indicator (collected opinions of companies employing 250 and more persons) and collected real data concerning the tender procedures in the road construction sector. This is proof, that contractors observe the market tendencies and they adjust the bid price level to the market situation.

4 Fair Price or Bid Rigging

4.1 Fair Prices

As described above, differences between clients' estimation and the bid prices of the winners are natural. Clients are obliged to use market prices which are created in the cycle presented below – in Figure 4.

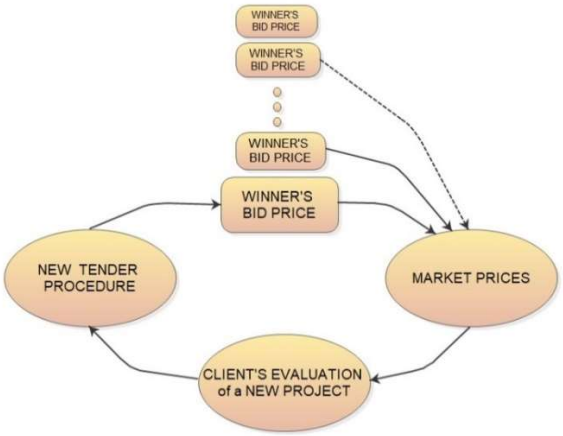

Figure 4. The mechanism of creating market prices.

As the winner of the tender procedure is chosen by a client, it can be understood, that the chosen contractor has fulfilled all formal criteria and their offer is the best (according to the criteria set by a client). The same refers to the price given by a winner – it creates one of the market prices. A certain client's estimation of a new project is based on unit market prices e.g. of 1 m3 of an embankment, 1 m3 of a concrete structure, etc.

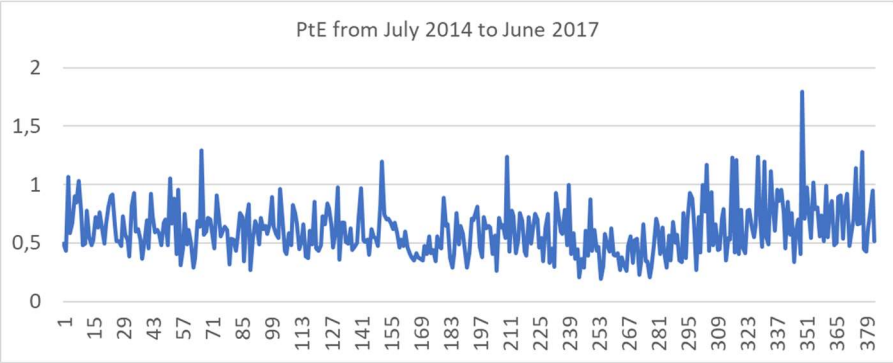

Figure 5. PtE values. Procedures from the year 2015 start from procedure No 71, 2016 from procedure No 163. 2017 from procedure No 311 (Anysz, 2019).

However, the market unit prices are created by previous orders. So, if any tendency could be observed on the market, the bid prices have to differ from the client's evaluations. Collected data allows presenting PtE for all examined 382 tender procedures. They are sorted by date

starting from July 2014 (see Figure 5).

4.2 Indicators of Collusive Practices

4.2.1 Low number of the tenders

Many sources are pointing the low number of tenders as an indicator of possible collusion (OECD, 2012; UOKiK, 2017; Huber and Imhof, 2018). It is also consistent with common sense, as it is much easier to keep the secret – illegal collusive agreement – among a few its participants that among several of them.

4.2.2 Narrow range of the bid prices

Another important factor that can pay a client's attention to the possibility of bid rigging is the range of the prices offered. The range R was defined (Foremny and Anysz, 2018) as:

$$R_{\mathrm{i}} = \frac{(V_{\mathrm{av\,i}} - V_{\mathrm{min\,i}})}{V_{\mathrm{av\,i}}} * 100\ \% \tag{2}$$

where:

R_i – the range for procedure i

$V_{min\,i}$ – the lowest value of an offer in procedure i

$V_{av\,i}$ – the mean average value of offers in procedure i

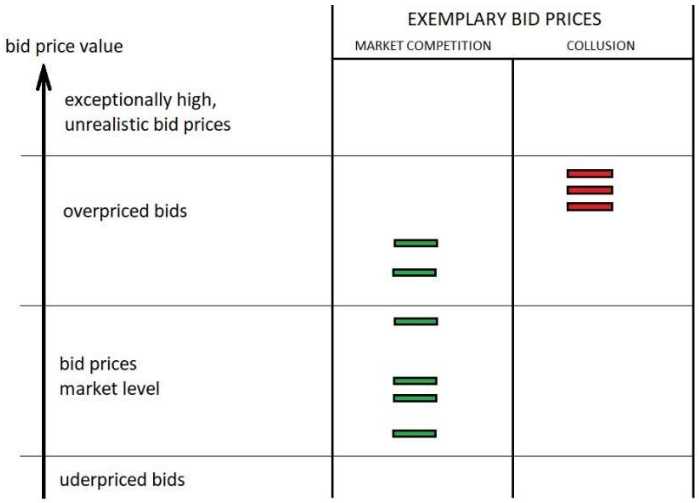

Figure 6. Exemplary bid price levels in case of market competition and collusion

The average R for examined 382 procedures is 13,5 %. In the case of collusion, where every bid price is over the market level, involved offerors increase their bid prices over the market level. However, their prices can't be recognized irrationally high. That makes the space for their bid prices much more narrow than in the case of market competition (see Figure 6). The range R is low then.

4.2.3 Other indicators

There are many more indicators (Ferwerda *et al.*, 2017; OECD, 2013; International Competition Network, 2010) of possible collusion, bid rigging (*e.g.* location distance of an offeror's enterprise vs location of offered services, simultaneous attendance in procedures of the same set of offerors, frequency of interaction through trade associations, staff moving between companies, market transparency, e.g. in bid rigging where openness makes it easier to monitor for cheating, excess capacity and inventories, ending of a price war and/or concerted moves to "discipline the market", existence of joint ventures etc.). Nevertheless, they are not so obvious, intuitive as indicators presented in the two previous sub-chapters. Moreover, they are more dependent on the specifics of a certain branch or market sector. Then the result of a tender in the road construction industry are announced, and the winner's price is high, it becomes the subject of many newspaper articles, controversies and speculations if the price is fair. These were an inspiration to verify what level of extremely high prices (chosen by clients as the best ones) can indicate the possibility of collusion or bid rigging.

5 Extremely High PtE as Collusion Indicator

5.1 Proposed model

It is, hereby, proposed to observe extreme deviation of PtE from its average value – especially in a case where – in a certain procedure – PtE is extremally high. As it was described above (*i.e.* in chapter 3), the state of the market influences the bid prices level. Thus, referring PtE to its average based on a long time is irrelevant. The simple moving average (SMA) (Gençay and Stengos, 1998; Elder, 1992) is presented in Figure 7 (yellow line) based on the following formula:

$$SMA(PtE) = \frac{\sum_{i=1}^{n} PtE_i}{n} \tag{3}$$

where:

PtE_i - the value of PtE in i tender procedure (one of the procedures completed in 30 predeceasing days),

n - the number of procedures completed in 30 predeceasing days.

Within random 30 days periods (chosen from July 2014 – June 2017) the number of completed procedures varies, so n varies for SMA calculated for different days. The 30 days period is chosen to calculate SMA according to the fact – described above, in chapter 3 – that the highest Pearson's correlation (PtE and "expected prices") was achieved for 30 days period (from 30, 60 and 90 days periods). Similarly to analysis of stock exchange prices with Bollinger bands (Baiynd, 2011; Lento *et al.*, 2007), the band around SMA is created by upper (L_U) and lower limit (L_L) defined as:

$$L_U = SMA + k \tag{4}$$

$$L_L = SMA - k \tag{5}$$

where: k - constant, greater than 0

When it is assumed that if for the chosen (by a client) bid price

$$PtE > L_U \tag{6}$$

in a given tender procedure, that may imply collusion existence, then there is a problem of choosing the value of the constant k. When it is set too small (close to 0), collusion can be expected in almost every tender procedure where

$$PtE > SMA \tag{7}$$

When k is too high, in none of bidding procedures PtE exceeds the upper limit – it means that the market is perfectly competitive.

Let's analyze one of the reasons, why bid prices differ from a clients' estimations – mistakes in contractors calculations of their bid prices. If the lowest bid price (mistakenly calculated so low) is chosen by a client as the best one and it is below SMA, the mistake can be done in only one offer. When a client chooses the bid price for which PtE is high above SMA, and it is the lowest bid price in a certain procedure, it means that all offerors made mistakes in their bid price calculation (if a mistake caused exceptionally high bid price). Moreover, the reasonable assumption can be made that the size of underpricing and overpricing made by mistakes in the bid prices calculations are statistically the same.

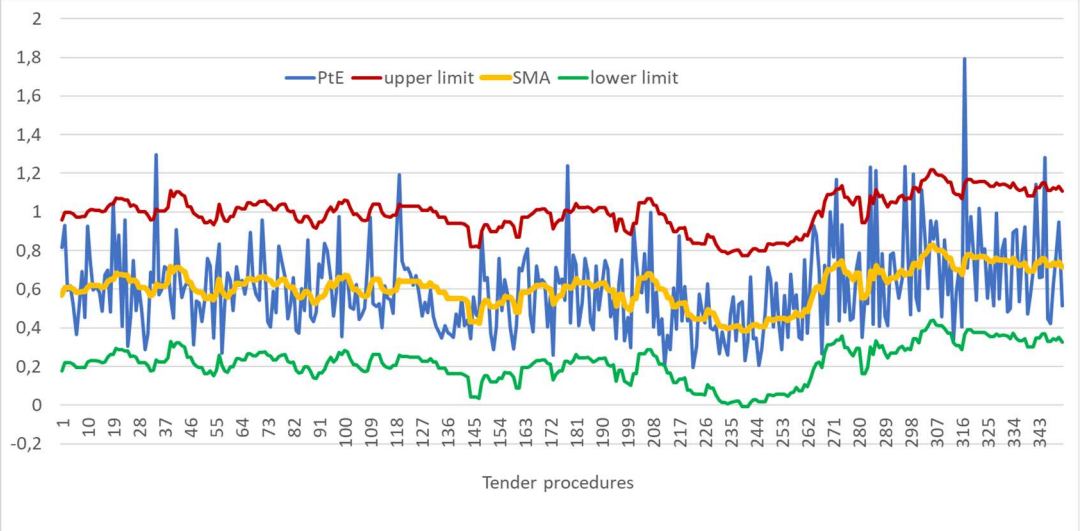

Figure 7. SMA, symmetric SMA band for $k = 0{,}39$ with PtE on the band

Making a mistake by one offeror is much more probable than by all offerors. As the mistake of only one offeror can push the bid price to the very low level, the following value of k can be set:

$$k\colon\ \forall SMA(PtE)\ \ L_L < PtE \tag{8}$$

For the data collected $k = 0{,}39$ made inequation (8) satisfied. Four lines are simultaneously presented in Figure 7, PtE, SMA and its band limits for $k = 0{,}39$.

It can be expected that the peaks of PtE exceeding the upper limit haven't been caused by mistakes in offerors' price calculations. The band is symmetric around SMA. The cases where

all bids are mistakenly highly overpriced (the lowest bid price, chosen by a client creates PtE) are very rare or even don't exist. Therefore, the collusion can be expected in all these PtE peaking tender procedures.

5.2 Verification of the Model

The best possible verification – the sentence of a court punishing collusive behaviors – is unavailable. There are 4 tender procedures found (among the analyzed set) which were a subject of such court procedure but all investigations dropped due to lack of collusion evidence. There are 11 tender procedures peaking above the upper limit – constructed from SMA increased by 0,39 (see Figure 7). It is possible to check, if other indicators of possible collusion i.e. low range of bid prices (calculated according to (2)) and the low number of offerors, confirm the possible non-concurrent character of offerors' behaviors in these procedures.

Table 2. Tender procedures with PtE exceeding the upper limit.

PtE peaking procedures	PtE	Number of offerors	Range R [%]	Possibility of collusion
1	1,295	8	13,4	low
2	1,195	1	0,0	high
3	1,239	15	20,9	low
4	1,168	5	4,5	high
5	1,233	6	16,8	low
6	1,213	6	25,0	low
7	1,236	1	0,0	high
8	1,196	4	6,7	high
9	1,793	5	3,8	high
10	1,143	1	0,0	high
11	1,281	5	15,5	moderate

Taking into consideration the average range R for all analyzed tender procedures (equal to 13,5 %) and the average number of participants in a tender procedure (6,9), the level of possibility of a collusion is assigned. The assessment is "high" for less than six offerors and the range R lower than 7 %. If there is only one offeror, there is no range of bid price values but the range equal to 0,0 is presented in Table 2. There are 6 tender procedures where collusion possibility is high, out of 11 tender procedures pointed by the model. There is no such an upper limit other than $1{,}295 < L_U < 1{,}793$ above which, all tender procedures would have a high level of possibility of collusion. Even for so high upper limit, there is only one tender procedure and its level of possibility of collusion is high – procedure labeled as 9 in Table 2. Nevertheless, as it is the only case, it can't be named the rule.

6 Conclusions

The model built for the real database of Polish tender procedures in the road construction industry, aimed at collusion finding, couldn't be verified directly. The indirect verification – through other indicators that usually accompany bid rigging, shows that comparison of PtE ratio with upper limit L_U (based on SMA) can't be the single collusion indicator. None of the

described bid rigging cases in the literature support the statement that in case of collusion all indicators have to point the collusion existence. The very high bid price level, defined here as PtE exceeding a single moving average of PtE increased by 0,39, is a separate indicator of unusually bid prices. One of the possible reasons can be collusion or bid rigging. It is proposed to observe it along with other factors i.e. the number of offerors and bid price range in each tender procedure. These three indicators are easily obtainable i.e. they don't require any advanced analytics (as other indicators). So, they can be applied easily by clients, who make decisions about spending public financial resources. The road construction contract values are one of the biggest and the type of construction works comprised by them is homogenous. The proposed model can be applied in other branches. However, it is to remember, that the data – the base for SMA calculation - should be collected within one branch to provide relevant information. A client's analysis done before the choice of a contractor may lead to successful price negotiations and finally to lowering the price. This means higher efficiency of spending public financial resources.

ORCID

Hubert Anysz: http://orcid.org/0000-0002-3804-5859
Andrzej Foremny: http://orcid.org/0000-0002-9425-353X

References

Aczel, A. D. (1992). *Complete Business Statistics*, Boston, MA, IRWIN

Anysz, H. (2019). *Relacja ceny najkorzystniejszej oferty do wartości oszacowania zamawiającego jednym z detektorów nieprawidłowości w postępowaniach przetargowych* (in Polish), Ceny, Zamawianie i Kosztorysowanie Robót Budowlanych, Zeszyt 9, WACETOB, Warsaw, Poland

Baiynd, A.-M. (2011). *The Trading Book: A Complete Solution to Mastering Technical Systems and Trading Psychology*, McGraw Hill

Ekder, A. (1992). *Trading for a Liiving. Psychology, Trading Tactics, Money Management*, New York, NY, John Wiley &Sons, Inc.

Ferwerda, J., Deleanu, I., and Unger, B. (2017). *Corruption in Public Procurement: Finding the Right Indicators*. European Journal on Criminal Policy&Research, 23(2), 245–267. https://doi.org/10.1007/s10610-016-9312-3

Foremny, A. and Anysz, H. (2018). *The collusion detection in public procurements–selected methods applied for the road construction industry in Poland*, MATEC Web of Conferences 219:04002. doi: 10.1051/matecconf/201821904002

Gençay, R. and Stegos, T. (1998). *Moving average rules, Volume and the Predictability of Security Returns with Feedforward Networks*, Journal of Forecasting, J. Forecast. 17, 401-414. doi: 10.1002/(sici)1099-131x(1998090)17:5/6<401::aid-for704>3.3.co;2-3

GUS (2019), https://stat.gov.pl/obszary-tematyczne/koniunktura/koniunktura-w-przetworstwie-przemyslowym-budownictwie-handlu-i-uslugach-2000-2019-pazdziernik-2019,4,30.html, (in Polish) access: Oct 2019

Huber, M., and Imhof, D. (2018). *Machine Learning with Screens for Detecting Bid-Rigging Cartels*

International Competition Network. (2010). *Anti-cartel enforcement manual*

Lento C., Gradojevic N., and Write C.S. (2007). *Investment Information Content in Bollinger Bands?*, Applied Financial Economoics Letters 3(4): 263-267. doi: 10.1080/17446540701206576

Office of Competition and Consumer Protection (UOKiK). (2017). *Zmowy przetargowe* (in Polish)

Ordinance of Minister of Infrastructure (2004*).* (in Polish) *Dz. U. 2004 Nr 130 poz. 1389*, Poland

OECD. (2013). *Ex Officio Cartel Investigations And The Use Of Screens to Detect Cartels*

OECD. (2012), *OECD recommendation of the council on fighting bid rigging in public procurement*

Pałys E. (2019). *Kto dokończy S5 po Toto? Pierwszy przetarg unieważniony.* Rynek Infrastruktury. (in Polish) https://www.rynekinfrastruktury.pl/wiadomosci/drogi/kto-dokonczy-s5-po-toto-pierwszy-przetarg-uniewazniony-68174.html acces: Nov 2019

Public Procurement Code (2004*).* (in Polish) *Dz. U. 2004 Nr 19 poz. 177*, Poland

XV International Conference on Durability of Building Materials and Components
DBMC 2020, Barcelona
C. Serrat, J.R. Casas and V. Gibert (Eds)

Evaluation of Economic Efficiency of Territory Development

Jana Korytárová[1], Vít Hromádka[2], Martin Marek[3], Svatopluk Pelčák[4] and Jiří Rouzek[5]

[1] Brno University of Technology, Faculty of Civil Engineering, Veveří 331/95, 602 00 Brno, Czech Republic, korytarova.j@fce.vutbr.cz

[2] Brno University of Technology, Faculty of Civil Engineering, Veveří 331/95, 602 00 Brno, Czech Republic, hromadka.v@fce.vutbr.cz

[3] Brno University of Technology, Faculty of Civil Engineering, Veveří 331/95, 602 00 Brno, Czech Republic, Martin.Marek3@vutbr.cz

[4] Brno University of Technology, Faculty of Civil Engineering, Veveří 331/95, 602 00 Brno, Czech Republic, 167293@vutbr.cz

[5] Brno University of Technology, Faculty of Civil Engineering, Veveří 331/95, 602 00 Brno, Czech Republic, 156940@vutbr.cz

Abstract. *The article deals with the analysis of background resources for the evaluation of socio-economic impact methodology elaboration of the territory development in the field of commercial, service and residential properties, mixed constructions and multifunctional buildings in the first phase of their life cycle. The research team investigated the possibilities of using the information and procedures for the evaluation of socio-economic impacts of the territory development. Relevant data for the evaluation was identified and analysed on the research sample of 12 major urban districts of the city of Brno. Technical and social parameters that appeared relevant for the economic evaluation of the surveyed location development were identified based on the available data on individual territories. The first identification step was their description. Subsequently, suitable metrics for their evaluation were examined. Findings about what socio-economic impacts these locations create in the field of interest and whether these impacts are efficient in terms of their functioning represent the output of the paper. This includes determining the overall economic efficiency of the implementation phase of their life cycle. This output then forms base for the future research focusing on the possibility of including other variables that shall focus on the operational phase of the life cycle and extend the assessment to a wider timeframe.*

Keywords: *Territory Development, Socio-Economic Evaluation, Multicriteria Analysis.*

1 Introduction

The method of assessing the economic efficiency of the territory development depends on the extent and specifications of the technical determination of the change in the current situation. From the development point of view, it can be a specific large-scale development project, for which the basic project documentation has already been elaborated at the architectural study level; furthermore, one of the stages of the project documentation can be processed for a particular sub-project. At the level of information provided by the specific technical documentation, it is possible to evaluate their economic efficiency with a certain amount of experience and knowledge, e.g. using the CBA method (projects of road and highway sections, railway corridors, waterways, specific buildings for civil or commercial purposes (Guide, 2014)). The authors of this article focus on a more general view of the territory development and its future potential use, already at the land use plan level. At this level, no specific

development projects are defined, however the territory is being prepared for a specific use or combination of uses. The land use plan sets out the urban concept, the concept of landscape arrangement and the concept of public infrastructure, it defines the built-up area, areas and corridors and sets the conditions for the use of these areas.

The research is aimed at finding suitable criteria that can be used to assess the socio-economic efficiency of the territories that are defined as areas or sets of areas, or parts of areas, defined on the basis of the prevailing character. The individual areas constituting the territory may be areas for housing, recreation, civic amenities, mixed residential, transport infrastructure, technical infrastructure, production and storage, mixed production, public areas, green areas, water and water management, agricultural, forest, natural, mixed undeveloped areas, mineral extraction and specific. The research question is whether the territories formed by the combination of the above-mentioned areas can be expressed by economic quantity that would prove their efficiency level. The municipality, in which cadastral the territory is located has to incur certain expenditures on preparation for its intended use. The question is whether there may be any revenues and/or socio-economic benefits that the new territory can bring to the municipality/society.

2 Analysis of the Current Situation

Urban sustainability is a multi-dimensional concept that includes environmental, economic, social and political dimensions (Huang *et al.*, 2009; Olewiler, 2006). The strategic plan towards sustainable development is fundamentally based on knowledge of the local economic opportunities, the local environmental conditions, and cultural and social characteristics (Scipioni *et al.*, 2009). Many authors describe the territory in various detail views. Moussiopoulos (2010*)* develops this concept in a framework of 13 discrete thematic areas, namely: (I) Economy–Population, (II) Land and Urban Planning, (III) Energy, (IV) Transportation, (V) Agriculture–Livestock–Fishery, (VI) Industry, (VII) Tourism, (VIII) Air Pollution–Climate Change, (IX) Water Resources and Sea Environment, (X) Solid Waste, (XI) Biodiversity, (XII) Health, (XIII) Education–Research and Technology.

(Nijkamp, 1995*)* sets main criteria and sub-criteria following A. Functional restructuring of the area (residential, tertiary and cultural function), B. Economic valorisation of the area (property value of real estate, commercial value, socio-economic value), C. Common utility (public recreational and supporting services) and D. Historic – environmental value (conservation and restoration value, aesthetic aspect of urban assets, integration with the historical city center).

For deciding on effective activities in the area it is sometimes necessary to quantify these variables. Research of the authors in the first phase focused only on a part of economic and socio-economic aspects, where it was able to define technical and socio-economic input variables, create their aggregation and produce relevant outputs.

3 Methodology

Changing the location purpose from the current prevailing use to another entails certain costs that the municipality has to incur in order to implement the new use of the location. These are mainly requirements for the construction of roads and backbone networks. At the same time, changes in the use of locations, depending on their character of the usable areas, can bring a

certain capacity of new residents and new jobs.

In order to work effectively with the technical-economic data, the characteristics of the locations were primarily defined. The basic attribute for their determination was the structure of the layout of the individual areas of the location, which may be residential (r), compact (c), empty (e), construction limited (l) or zoned (z). Average lengths of roads and backbone networks in m/ha were determined for each structure. Furthermore, possible incremental capacities of permanent residents and incremental capacities of new jobs were determined for each location. These data, which create important inputs into analysis presented in this paper, were taken from the results of the relevant scientific research oriented on evaluation of development opportunities prepared and proposed for the land use plan.

Based on the average length of roads and backbone networks in m/ha (water, sewerage, gas, electricity, central heating), including their average technical parameters together and their average unit prices according to national price databases, the cost in €/ha was determined for each location and the cost in €/m2 was derived from them. The total cost of the change in the use of the location (Criterion K1) is the sum of the costs of the areas that the location contains.

$$K1 = \sum_{i=1}^{n} CA_i \tag{1}$$

Where

K1… Total costs of the location in €

CA… Cost of i-th area in €

n… Number of areas in the location

Based on the incremental capacity of residents and the tax revenues of the municipality per capita, the potential revenue of the municipality (Criterion K2) can be determined according to the following relation:

$$K2 = I \times R_T \tag{2}$$

Where

K2… Total revenue of the location in €

I… Incremental capacity of residents

R_T… Tax revenue of the municipality per capita in €/cap.

The potential social benefit (Criterion K3) was determined on the basis of the incremental capacity of the new jobs in the location, where the unit of benefit is the socio-economic benefit arising for the company in creating one new job.

$$K3 = L \times B_J \tag{3}$$

Where

K3… Total socio-economic benefits of the site in €
L… Incremental capacity of jobs
B_J… Benefit of the society from one created job in €/job

The output of the economic model is the determination of the overall location efficiency (E), which is defined as the sum of the product of the location classification values in a given criterion (K) and its weight (w).

$$E = \sum_{i=1}^{n} K_i \times w_i \tag{4}$$

The rating scale for each criterion values are listed below. The criteria weights were expertly chosen as follows:
Criterion K1 weight $w_1 = 0.60$,
Criterion K2 weight $w_2 = 0.20$,
Criterion K3 weight $w_3 = 0.20$.

According to the fact that this is a "yield" criterion, higher value of overall efficiency E represents higher efficiency of the territory.

4 Results

Interim research results are presented on a case study. The case study includes the evaluation of 12 locations boroughs of the Statutory City of Brno.

4.1 Values of Input Variables

Based on the above-mentioned procedure, the costs for backbone networks were determined for individual representatives of the location structures. The values are given in Table 1.

Table 1. Model costs of the backbone network in €/ha.

Type of structure	Cost of Water [€/ha]	Cost of-Sewerage [€/ha]	Cost of Gas [€/ha]	Cost of Electricity [€/ha]	Cost of Central Heating [€/ha]
r	141,438	100,836	67,140	36,633	391,744
c	118,206	84,273	56,112	30,616	327,397
e	157,267	112,120	74,653	40,733	435,583
l	61,882	44,118	29,375	16,028	171,396
z	120,436	85,863	57,170	31,194	333,575

The costs of roads by length per hectare were further divided into groups according to the

assumed width of the road, considering the widths of 8, 12 and 24 m. The values obtained are shown in Table 2.

Table 2. Model costs of roads in the territory according to their widths in €/ha.

Type of structure	Width 8 m [€/ha]	Width 12 m [€/ha]	Width 24 m [€/ha]
r	228,275	342,413	684,826
c	190,779	286,169	572,338
e	253,821	380,732	761,464
l	99,875	149,813	299,625
z	194,379	291,569	583,137

The value of revenue per capita used is based on the statistical data of the set municipality, in the case of the mentioned case study - the final account of the Statutory City of Brno (SCB, 2018) in the current value of € 1,020/resident.

The average value of a socio-economic benefit arising for a society in creating one job without considering specific job positions is assumed for the Czech Republic at the current value of € 12,401/job (SEI, 2019).

4.2 Values of the Individual Criteria

The case study deals with 12 considered locations located in the cadastral territories of the individual city districts of the Statutory City of Brno. The location is described in the Table 3 below.

Table 3. Values of criteria K1, K2, K3 v €/m2.

Location in the cadastral area	Area ha	Incremental capacity of residents	Incremental capacity of jobs	K1 - costs €/m²	K2 - revenues €/ m²	K3 – benefits €/ m²
Prizrenice 1	62.52207	2,736	3,871	55.47	106.88	76.80
Prizrenice 2	58.32664	3,215	4,272	57.70	125.59	90.82
Cernovice 1	39.97897	458	4,668	65.20	1.17	144.80
Bosonohy 1	39.72692	1,407	874	45.00	3.63	27.27
Reckovice	38.96985	4,033	1,959	55.63	10.55	62.34
Styrice	38.76289	883	674	87.77	10.86	261.56
Bosonohy 2	34.87699	28	2,030	53.32	5.43	187.89
Komin	32.67942	982	573	47.34	3.09	21.76
Bohunice	31.46935	3,031	1,966	59.61	9.84	77.46
Dolni Herspice	30.93395	90	1,807	55.31	0.31	72.46
Prizrenice 3	30.68411	3,612	944	61.33	12.03	38.16
Cernovice 2	28.72383	380	3,191	62.42	1.37	137.77

4.3 Description of Classification Grades to Calculate the Overall Location Efficiency

For all the above-mentioned evaluation criteria, the following tables show the methods of their evaluation based on the classification according to the selected categorisation.

Criterion K1 – classification scale for cost value intervals per m^2

In terms of their cost per m^2, the assessed locations were divided into 5 classification grades (1 - least expensive, 5 - most expensive) according to the cost intervals given in the following Table 4.

Table 4. Classification grades for the cost interval per m2 of the designed location area.

Cost interval per m^2 [€/m^2]	Descriptor	Classification grade
< 39.06	Low cost	1
39.06 – 58.58	Lower cost	2
58.59 – 78.13	Average cost	3
78.14 – 97.66	Highest cost	4
> 97.66	High cost	5

Criterion K2 – classification scale for revenue value intervals per m^2

In terms of their revenue per m^2, the assessed locations were divided into 5 classification grades (I - highest revenue, V - lowest revenue) according to the revenue intervals given in the Table 5.

Table 5. Classification grades for the revenue interval per m2 of the designed location area.

Revenue interval per m^2 [€/m^2]	Descriptor	Classification grade
> 23.44	High revenue	I
20.35 – 23.44	Higher revenue	II
9.78 – 20.34	Average revenue	III
3.91 – 9.77	Lower revenue	IV
< 3.91	Low revenue	V

Note: For the calculation of the overall efficiency for this yield criterion, the classification grade "I" = 5 points, the classification grade "V" = 1 point (higher revenue is preferred).

Classification scale for the social benefits value interval

The assessed locations were divided into 5 classification grades (A to E, A - highest social benefit, E - lowest social benefit) according to their societal benefit intervals given in Table 6.

Table 6. Classification scale for social benefits interval per m2 of the designed location area.

Social benefit interval per m² €/m²	Descriptor	Classification grade
> 97.66	High benefit	A
58.65 – 97.66	Higher benefit	B
19.54 – 58.64	Average benefit	C
3.90 – 19.53	Lower benefit	D
< 3.90	Low benefit	E

Note: For the calculation of the overall efficiency for this yield criterion, the classification grade "A" = 5 points, the classification grade "E" = 1 point (higher benefit is preferred).

4.4 Resulting Ranking of the Locations According to Overall Efficiency

Table 7 shows the evaluation of locations according to individual classification grades and the overall efficiency of the location E according to the above-listed relation is determined as the sum of the products of the classification grade values in the relevant criterion and its weight.

Table 7. Overall efficiency of the locations, sorted by the value of the overall efficiency E descending.

Location in the cadastral area	K1 (cost per m2)	K2 (revenue per m2)	K3 (benefit per m2)	E (overall efficiency)
Prizrenice 1	4	V	A	4.20
Prizrenice 2	4	III	C	4.20
Cernovice 1	4	III	A	3.60
Bosonohy 1	3	V	A	3.40
Reckovice	3	V	A	3.20
Styrice	3	V	B	2,60
Bosonohy 2	2	I	B	2.40
Komin	2	V	C	2.40
Bohunice	2	III	B	2.40
Dolni Herspice	2	V	C	2.20
Prizrenice 3	2	I	B	2.20
Cernovice 2	2	V	B	2.00

Locations are sorted according to values of efficiency, according to the values of individual criteria is also clear how the individual criteria for overall efficiency involved. The overall efficiency ranges from 2 to 4.2 points of the 5-point scale.

5 Conclusion

The article deals with determination of the procedure for the evaluation of the economic efficiency of designed locations. The economic evaluation is made to compare the extent of economic intensity, potential revenue and socio-economic benefit of individual development

locations among themselves and to determine the possible succession for their implementation - a change in their use. For this reason, an economic model of costs, revenues and benefits related to the transformation of the current location into its proposed use was developed. The economic model is designed for the basic economic awareness of the costs, revenues and benefits of the areas under consideration at the level of detailed technical data that are part of the land use plan. For this reason, it works with the average values of the territory representatives. Value analysis procedures were chosen for comparison of designed locations. Future research will focus on another part of the life cycle of the municipal property thus created, namely the cost of repairing and maintaining in the operational phase, where it will be necessary, among others, to examine its average lifetime.

Acknowledgements

This paper has been worked out under the project of the specific research at Brno University of Technology no. FAST-S-20-6383 Selected Economic and Managerial Aspects in Construction Engineering.

ORCID

Jana Korytárová: http://orcid.org/0000-0002-0046-0141

Vít Hromádka: http://orcid.org/0000-0002-9590-9828

References

Huang, S. L., Yen, C. T., Budd, W. and Chen, L. L. (2009). *A Sensitivity Model (SM) approach to analyze urban development in Taiwan based on sustainability indicators*. Environ. Impact Asses. Rev. 29(2), 116–125.

Olewiler, N. (2006) *Environmental sustainability for urban areas: the role of natural capital indicators*. Cities 23(3), 184–195.

Scipioni, A., Mazzi, A., Mason, M. and Manzardo, A. (2009). *The dashboard of sustainability to measure the local urban sustainable development: the case study of Padua Municipality*. Ecol. Indic. 9(2), 364–380.

Nijkamp, P. and Artuso, L. (1995). *Methodology and Application of Sustainable Environment Concepts for the Built Environment*, Cerie Research Memoranda, 1995-48, VRIJE Universiteit, Amsterdam.

Moussiopoulosa, N., Achillasa, Ch., Vlachokostasa, Ch., Spyridia D. and Nikolaoub, K. (2010). *Environmental, social and economic information management for the evaluation of sustainability in urban areas: A system of indicators for Thessaloniki*, Greece , Cities, Volume 27, Issue 5, October 2010, Pages 377-384. https://doi.org/10.1016/j.cities.2010.06.001

Statutory City of Brno (SCB, 2018). *The final account of the Statutory City of Brno*, Brno City Hall, Budget and Finance Department.

Database of socio - economic impacts of OPEI (SEI, 2019). Available from https://www.agentura-api.org/cs/metodika/ekonomicke-hodnoceni/

Guide to Cost-Benefit Analysis of Investment Projects (Guide, 2014). *Economic Appraisal Tool for Cohesion Policy 2014-2020*, European Commission, Directorate-General for Regional and Urban Policy.

XV International Conference on Durability of Building Materials and Components
DBMC 2020, Barcelona
C. Serrat, J.R. Casas and V. Gibert (Eds)

Evaluation of Socio-economic Impacts of Incidents on the Railway Infrastructure

Vít Hromádka[1], Jana Korytárová[2], Eva Vítková[3], Tomáš Funk[4] and Herbert Seelmann[5]

[1] Brno University of Technology, Faculty of Civil Engineering, Veveří 331/95, 602 00 Brno, Czech Republic, hromadka.v@fce.vutbr.cz

[2] Brno University of Technology, Faculty of Civil Engineering, Veveří 331/95, 602 00 Brno, Czech Republic, korytarova.j@fce.vutbr.cz

[3] Brno University of Technology, Faculty of Civil Engineering, Veveří 331/95, 602 00 Brno, Czech Republic, vitkova.e@fce.vutbr.cz

[4] Brno University of Technology, Faculty of Civil Engineering, Veveří 331/95, 602 00 Brno, Czech Republic, funk.t@fce.vutbr.cz

[5] Brno University of Technology, Faculty of Civil Engineering, Veveří 331/95, 602 00 Brno, Czech Republic, seelmann.h@fce.vutbr.cz

Abstract. *Evaluation of the economic efficiency of investment projects in transport infrastructure in the Czech Republic is methodically based on the Departmental Methodology of the Ministry of Transport. Economic cash flows, generated in accordance with the CBA principles, are modelled within this methodology on the basis of the evaluation of socio-economic impact of individual projects. In the case of the railway infrastructure constructions, the socio-economic impacts used by the methodology do not include benefits associated with increasing safety and reliability of the railway infrastructure network due to new security systems implementation. Determination of socio-economic impacts associated with specific types of incidents on the railway which are caused by insufficient railway infrastructure security and which could be eliminated by the implementation of the higher-level signaling equipment forms the subject of the research. The research is based on the analysis of a database of incidents occurring on the railway in the Czech Republic in the 2009 – 2018 period, which describes the basic impacts associated with a particular incident. Statistical data on the railway infrastructure is also used to determine the impact of incidents in addition to the database. The key outcomes of the research are the determination of methodological steps for the evaluation of the impacts of incidents on the railway and a case study for their verification. Future research will focus on making evaluation of the above-mentioned benefits more detailed. Research outcomes will improve decision-making process on selection and financing of the projects related to railway infrastructure safety for their future implementation.*

Keywords: *Socio-Economic Impacts, Investment Project, Railways, Incidents, Evaluation.*

1 Introduction

The paper focuses on presentation of partial results of the research concentrating on the evaluation of benefits associated with increasing safety and reliability of the railway infrastructure. Improvement of safety and reliability is anticipated in particular by the implementation of suitable safety systems into the railway infrastructure to prevent the occurrence of incidents. The research outputs presented in this paper are mainly focused on the evaluation of economic impacts of the incidents. The research is based on the analysis of the database of incidents (RIA, 2018) provided for the purpose of the research by the Railway

Infrastructure Administration (SŽDC), within which the incidents registered for the period 2011–2018 are divided into various sub-categories. Within the framework of the paper, the number of relevant categories is reduced solely to those categories of incidents which occur on the railway infrastructure and for which it can be assumed that they can possibly be prevented by previous implementation of suitable track or station signalling systems. The research does not take into the account the accidents at the level crossings.

2 Present State References

The research can be based on the conclusions of a number of scientific and scholarly texts. A key basis for assessing the economic efficiency of investment projects in the public sector is the Guide to Cost-Benefit Analysis of Investment Projects (Sartori, 2014), published by the European Commission in 2014, which includes general rules for economic evaluation of public investment projects as well as framework methodologies for economic evaluation of public investment projects in particular areas of public investment; for these areas are also presented illustrative case studies. National methodology for evaluating the efficiency of investment projects in the area of transport infrastructure, called the Departmental Methodology (MoT CZ, 2017) is based on this methodology. The Departmental Methodology is focused primarily on assessing the financial and economic efficiency as well as risks of investment projects in transport infrastructure in the specific conditions of the Czech Republic. The issue of evaluation of impacts of incidents has not been dealt with in more detail in scientific literature, however, topics related to it definitely form the subject of the research. The issue of the relationship of incidents and human factor is dealt with in the research of (Baysari, McIntosh, Wilson, 2008), (Madigan, Golightly, Madders, 2016), the view of engine drivers has been more closely addressed in the Swedish study (Forsberg, 2016). The socio-economic aspects of incidents on the railway infrastructure are the subject of the following research articles (Klockner, Toft, 2018) and (Read, Lenné, Moss, 2012). Latent and active errors leading to railway incidents are dealt with in the paper by (Zhou, Lei, 2018).

3 Methodology

The subject of the research presented in this paper is to define methodological steps for evaluating the impacts of incidents on the railway infrastructure.

In particular, the following data from the information provided by the “Incident Statistics” (RIA, 2018) is considered within the research project:

- Impact on health
  - Death,
  - Serious injury,
  - Minor injury,
- Material damage,
- Costs,
- Number of delayed passenger trains,
- Total delay of passenger trains,
- Number of delayed freight trains,
- Total delay of freight trains,
- Cause of incident emergence

- Technical,
- Human factor,
- Others.

This paper evaluates especially the following characteristics of incidents:

- Impacts on health,
- Delay of passenger trains; and
- Delay of freight trains.

3.1 Impacts on Health

Incident impacts on health are based on the average number of casualties (dead, injured) and the unit cost associated with death, serious or minor injuries. Unit costs associated with traffic accidents are taken from the Departmental methodology of the Ministry of Transport and are described in more detail in Table 1.

Table 1. Cost associated with traffic accidents.

Traffic accident	Unit cost €/person
With death	839,306
With serious injury	202,968
With minor injury	26,202

Source: Departmental Methodology of the Ministry of Transport (MoT CZ, 2018)

3.2 Delay of Passenger Trains

Determination of the impacts associated with the delay of passenger trains is based on the average overall delay of passenger trains due to incident occurrence. The total delay of passengers travelling on delayed trains is then determined using the average train delay taking in account the average train occupancy. The total cost associated with the train delay resulting from the incident is then derived using the data from the Departmental Methodology which shows the passenger time values.

The average train occupancy for the whole railway network was determined using the data from the Czech Railways Statistical Yearbook of 2018 (CRG, 2018). In particular, information on the total transport performance of 2018 (assumed at 8,224.9 passenger-kilometres) and on the running of passenger trains for 2018 (123,596 train-kilometres in total) were used. The resulting average train occupancy for the entire railway network was set at 66.55 persons per train based on the above-mentioned data.

For the subsequent research, planned refinement of the average train occupancy calculation in terms of the division of the railway network into national and regional lines has been planned; where the national train lines are expected to have a higher average train occupancy than the regional train lines.

Passenger time values are taken from the Departmental Methodology and are shown in Table 2.

Table 2. Time values of passengers on the railway infrastructure.

Passenger transport		**€/person-hour**
Working time		24.21
Non-working time	Short transport	9.43
	Long transport	12.11
	Other – short distance	7.91
	Other – long distance	10.14

Source: Departmental Methodology of the Ministry of Transport (MoT CZ, 2018)

In accordance with the Departmental Methodology, it is generally assumed that in the case of non-working time, the ratio between commuting and other transport is balanced. Likewise, it is assumed that the ratio between long and short transport is also balanced. The ratio between business travel and non-business travel is considered to be 10/90. Based on the information provided, the average value of the passengers' time can be estimated at € 11.33 /person-hours. This value was taken in the account in the case study. In the follow-up research, it is possible to focus on a more precise ratio between the individual reasons for transport (commuting, other), depending on whether the transport is situated on the regional or national line.

3.3 Delay of Freight Trains

The determination of the impacts associated with the delay of freight trains is based on the average overall delay of freight trains due to the incident occurrence. From the total average delay of a freight train, the total delay of freight transported on delayed trains together with considering the average weight of the freight is subsequently determined. Using the data from the Departmental Methodology on the values of freight transport time, the total costs associated with the train delay due to incidents, has been subsequently derived.

The average weight of freight carried by train was determined for the entire railway network using data from the Statistical Yearbook of the Czech Railways Group in 2018 (CRG, 2018). Specifically, information on the total transport performance of 2018 (assumed at 11,085.9 million tkm (tariff tonne-kilometres) and on the running of freight trains also for 2018 (a total of 24,348 million train-kilometres) was used. The resulting average train freight weight for the whole rail network in relation to this data was set at 455 tonnes/train.

The values of freight transport time have been taken from the Departmental Methodology and are given in Table 3.

Table 3. Time values of freight traffic on the railway route.

Commodity	**€/tonne-hour**
Commodities with low added value	0.013
Normal cargo	0.248
Commodities with high added value	0.742

Source: Departmental Methodology of the Ministry of Transport (MoT CZ, 2018)

The percentage representation of the above-mentioned commodities can be derived from information on freight transport by commodity groups of goods from the Statistical Yearbook of the Czech Railways Group from 2018 (CRG, 2018, p. 8). Total weights of goods transported by individual commodity in 2018 are shown in Table 4.

Table 4. Freight transport by commodities in 2018.

Commodity	ths. tonnes
Iron and engineering products	7,979.7
Construction material	7,569.2
Lignite	6,637.1
Black coal and coke	7,352.9
Other building materials and ceramics	2,470.9
Chemical products and liquid fuels	4,764.6
Wood and paper products	4,733.2
Food and agricultural products	1,454.6
Combined transport	571.8
Automotive	1,589.6

Source: (CRG, 2018)

By assigning the commodities listed in Table 4 to one of the following groups:

- Commodities with low added value (e.g. bulk substrates),
- Normal cargo,
- Commodities with high added value (perishable goods by means of transport),

it is possible to determine the average share of the listed categories of commodities on the transport performance and thus the average value of the freight time in case of a freight train delay. The average value of freight transport time value was set at € 0.246/tonne-hour.

The quantities stated in the methodology are then used to determine the average economic impact of an incident of a given type. Within the research, only those incidents that may arise in connection with the insufficient security of the railway infrastructure in the area of the railway station or the railway line between the stations are considered. At the same time, only those incidents resulting from a human factor error are considered for the calculation of the average impacts of incidents. The following categories of incidents are therefore taken into account for this research:

A1 Collision of railway vehicles resulting in death or injury to at least 5 persons or large-scale damage,
A2 Derailment of a rail vehicle resulting in death or injury to at least 5 persons or large-scale damage,
A3 Collision of a rail vehicle with an obstacle in the passage resulting in death or injury to at least 5 persons or large-scale damage,
B1 Collision of railway vehicles resulting in consequences minor than in a serious accident,
B2 Derailment of a rail vehicle resulting in consequences minor than in a serious accident,
B3 Collision of a rail vehicle with an obstacle in the passage resulting in consequences minor than in a serious accident,
C1 Collision of railway vehicles resulting in consequences minor than in a serious accident or accident
C2 Derailment of a rail vehicle resulting in consequences minor than in a serious accident or accident,
C3 Collision of a rail vehicle with an obstacle in the passage resulting in consequences minor than in a serious accident or accident,
C6 Unauthorized movement of the rail vehicle behind a signalling device prohibiting

driving resulting in consequences minor than in an accident,
C12 Unsecured movement of a rail vehicle resulting in consequences minor than in an accident,
C16 Failure of signalling systems resulting in consequences minor than in an accident,
C19 Unspecified incident, arising in connection with the movement of the rail vehicle resulting in consequences minor than in an accident.

4 Results

Interim research results can be presented on a case study. The case study includes the determination of the average impact of an incident of a defined category on the railway infrastructure. The basic characteristics of the assessed incident are as follows:

Category:	A1 Collision of railway vehicles resulting in death or injury to at least 5 persons or large-scale damage
Number of incidents included in the analysis:	15
Nature of the cause:	human factor
Average number of deaths:	0.2
Average number of seriously injured:	0.33
Average number of minor injured:	3.8
Average delay of passenger trains:	941.82 min. (15.70 hours)
Average delay of freight trains:	83 min. (1.38 hours)
Average financial impact at 2018 prices:	436,162 €
Average occupancy of passenger trains:	66.55 person/train
Average freight weight of freight trains:	455 t/train

Table 5 contains the calculation of the total average impact of category A1 incident. Data for the calculation are taken from the methodology chapter.

Table 5. Average impact of category A1 emergency.

The nature of the incident impact	Unit impact	Number of units	Impact per item (€)
Killed persons	839,306 €/pers.	0.20 pers.	167,661.29
Seriously injured persons	202,968 €/pers.	0.33 pers.	66,979.35
Minor injured persons	26,202 €/pers.	3.80 pers.	99,566.13
Delay of passenger trains	11.33 €/pershr.	1,044.84 pershr.	11,834.50
Delay of freight trains	0.246 €/tonnehr.	627.90 tonnehr.	155.20
Financial impact at 2018 prices	436,162 €/inc.	1 inc.	436,162
Total economic impact			**782,358.93**

Source: own elaboration

The case study shows the procedure for determining the average economic impact of an incident occurring on the railway infrastructure. It is evident from the results that the average economic impact of one A1 incident is € 782,358.93. This procedure can be applied at other cases of incidents listed in the Methodology chapter. The subject of further research is supposed to be the calculation of the average economic impacts of other categories of incidents, this

calculation will be further refined by dividing the railway infrastructure into regional or national lines, where the average economic impacts of incidents on a regional line may be different from those on the national lines especially with regard to train occupancy or the level of security on the railway line.

4 Conclusions

The paper has been elaborated within the research project focused on taking into account the benefits resulting from increasing safety and reliability of the railway infrastructure in the economic evaluation of railway infrastructure projects. Specifically, the paper deals with identification of methodology for the evaluation of impacts caused by the occurrence of incidents on the railway infrastructure. The evaluation methodology is based on common principles of economic analysis of public investment projects and is based on data provided by the Departmental Methodology and data from the database of incidents. The proposed methodology includes, in particular, impacts on the health or lives of casualties involved in an incident, impacts in the form of delays of passenger and freight trains and impacts in the form of material damage and costs. The proposed methodology has subsequently been verified on a case study of the category A1 emergency. Follow-up research is supposed to include also an evaluation of other incidents that may potentially arise in the context of a lack of security and which could be prevented by the possible prior implementation of the new security systems.

Acknowledgements

This paper has been worked out under the project of the Technology Agency of the Czech Republic "TL02000278 Evaluation of increased safety and reliability of railway infrastructure after its modernization or reconstruction".

ORCID

Vít Hromádka: http://orcid.org/0000-0002-9590-9828
Jana Korytárová: http://orcid.org/0000-0002-0046-0141
Eva Vítková: http://orcid.org/0000-0002-2028-953X
Herbert Seelmann: http://orcid.org/0000-0003-0849-2495

References

Baysari, M., Mcintosh, A. and Wilson, J. (2008). Understanding the human factors contribution to railway accidents and incidents in Australia. *Accident Analysis and Prevention [online]*, Elsevier, 2008, 40(5), 1750-1757 [cit. 2019-02-18]. DOI: 10.1016/j.aap.2008.06.013. ISSN 0001-4575.

Czech Railways Group (CRG) (2018). *Statistical Yearbook of the Czech Railways Group*, 2018

Forsberg, R. (2016). Conditions affecting safety on the Swedish railway – Train drivers' experiences and perceptions. *Safety Science*, Volume 85, 2016, Pages 53-59, ISSN 0925-7535, https://doi.org/10.1016/j.ssci.2015.12.015.

Klockner, K. and Toft, Y. (2018). Railway accidents and incidents: Complex socio-technical system accident modelling comes of age. *Safety Science [online]*. Elsevier, 2018, 110, 59-66 [cit. 2019-02-18]. DOI: 10.1016/j.ssci.2017.11.022. ISSN 0925-7535.

Madigan, R., Golightly, D. and Madders, R. (2016). Application of Human Factors Analysis and Classification System (HFACS) to UK rail safety of the line incidents. *Accident Analysis & Prevention*, Volume 97, 2016, Pages 122-131, ISSN 0001-4575, DOI: 10.1016/j.aap.2016.08.023.

Ministry of Transport of the Czech Republic (MoT CZ) (2017). *Departmental Guideline for the Evaluation of Economic Effectiveness of Transport Construction Projects*. 2017. Retrieved from http://www.sfdi.cz/pravidla-metodiky-a-ceniky/metodiky/

Read, G. J. M., Lenné M. G. and Moss S. A. (2012). Associations between task, training and social environmental

factors and error types involved in rail incidents and accidents. *Accident Analysis & Prevention*, Volume 48, 2012, Pages 416-422, ISSN 00014575, DOI: 10.1016/j.aap.2012.02.014.

Railway Infrastructure Administration (RIA) (2018). *Statistics of Occurences 2009 – 2018*.

Sartori, D. (2014). *Guide to Cost-benefit Analysis of Investment Projects, Economic appraisal tool for Cohesion Policy 2014-2020*. European Commission, Directorate-General for Regional and Urban policy. 2014. ISBN 978-92-79-34796-2.

Zhou, J.-L. and Lei, Y. (2018). Paths between latent and active errors: Analysis of 407 railway accidents/incidents' causes in China. *Safety Science*, Volume 110, Part B, 2018, Pages 47-58, ISSN 0925-7535, DOI: 10.1016/j.ssci.2017.12.027.

XV International Conference on Durability of Building Materials and Components
DBMC 2020, Barcelona
C. Serrat, J.R. Casas and V. Gibert (Eds)

Identifying the Possibility of Using Unmanned Aerial Vehicles in the Process of Construction Projects Implementation

Dariusz Skorupka[1], Artur Duchaczek[2], Agnieszka Waniewska[3], Magdalena Kowacka[4] and Grzegorz Debita[5]

[1] Faculty of Management, General Tadeusz Kosciuszko Military University of Land Forces, 51-147 Wroclaw, ul. Czajkowskiego 109, Poland, dariusz.skorupka@awl.edu.pl

[2] Faculty of Management, General Tadeusz Kosciuszko Military University of Land Forces, 51-147 Wroclaw, ul. Czajkowskiego 109, Poland, artur.duchaczek@awl.edu.pl

[3] Faculty of Management, General Tadeusz Kosciuszko Military University of Land Forces, 51-147 Wroclaw, ul. Czajkowskiego 109, Poland, agnieszka.waniewska@awl.edu.pl

[4] Faculty of Management, General Tadeusz Kosciuszko Military University of Land Forces, 51-147 Wroclaw, ul. Czajkowskiego 109, Poland, magdalena.kowacka@awl.edu.pl

[5] Faculty of Management, General Tadeusz Kosciuszko Military University of Land Forces, 51-147 Wroclaw, ul. Czajkowskiego 109, Poland, grzegorz.debita@awl.edu.pl

Abstract. *Nowadays, dynamic progress in the field of modern technologies influences the development of unmanned aerial vehicles. The potential application area of this type of technology is constantly growing. The equipment is available to almost everyone and its use is becoming ever easier. The aim of the article is to present the possibility of using unmanned aerial vehicles in construction projects, for economic and time reasons, as well as to perform work in places that are inaccessible or too dangerous for humans. The article is the result of literature research, expert opinions and author's own analyses. The article draws attention to the fact that unmanned aerial vehicles may have a number of applications and unlimited possibilities. The use of modern technologies enables the flight at different heights and within a radius of many kilometers. Due to the fact that they are equipped with various types of cameras, they constitute a useful observation tool in various projects. The article presents thermal imaging tests in the area of construction and indicates that the value of energy consumption depends mainly on the effectiveness of insulation - increase in thermal insulation, while the effective way of their diagnosis is the use of thermal imaging camera. The authors of the article conduct research on a wide range of applications of unmanned aerial vehicles in construction projects.*

Keywords: *Unmanned Aerial Vehicles, Thermal Imaging, Modern Technology, Construction.*

1 Introduction

Unmanned aerial vehicles have been used in recent years in the civil market in a variety of economic sectors. They usually support aerial photography or filming. The equipment is available for almost everyone. In most cases, it is necessary to have ground-based staff to install or operate the platform itself and its systems. It should be noted that unmanned aerial vehicles combined with appropriate detectors and sensors are an excellent method of diagnosing and controlling the technical condition of objects. The combination of a thermal imaging camera and an unmanned aerial vehicle provides a useful tool for thermal imaging tests that can detect areas such as heat escapes from a building, thus preventing heat loss and significantly reducing building operating costs.

2 Unmanned Aerial Vehicles

Unmanned Aerial Vehicles (UAVs) is a generally accepted and used in engineering and science term. This term is also used by EUROCONTROL, the European Organisation for the Safety of Air Navigation, of which Poland has been a member since 2004 (Maj-Marjanska and Pietrzak, 2011). Unmanned aerial vehicles are defined by the U.S. Department of Defense as "powered, aerial vehicles that do not carry a human operator, use aerodynamic forces to provide vehicle lift, can fly autonomously or be piloted remotely, can be expendable or recoverable. It can carry a lethal or nonlethal payload" (Maj-Marjanska and Pietrzak, 2011). Unmanned aerial vehicles fly thanks to the use of two basic principles: lifting force and reactive torque. In this type of devices, counter-rotating propellers are used, which stabilise the fuselage during spinning. An unmanned aerial vehicle may be remotely piloted beyond visual line of sight (by an operator), or fly autonomously (by itself using an autopilot or another on-board system). However, most of them are piloted within their operators' line of sight. In both cases, ground-based staff are needed to install and operate the systems and the platform. The most important interface between the machine and the user is the radio system, the range of which is measured in kilometres. Many types of materials are used to construct modern unmanned aerial vehicles. The most popular include glass fibre, carbon fibre, as well as various types of plastics or metals. The materials listed above are characterised by a very good weight to strength ratio, but they are also very expensive. Modern aerial vehicles (military, civil ones) are the objects (systems) of very complex technical construction. They are usually built of many on board devices and subsystems, some of which make flying possible, while others provide the performance of specific functions within the combat mission. Their multifunctionality makes it possible, among other things, to perform aerial reconnaissance (Becmer and Romanek, 2011). The UAVs adopt different configurations and sizes - usually quadrocopters and octocopters, which are equipped with four or eight propellers respectively. The main propulsion systems include propellers and engines, which play a significant role here. The size of the propellers (blades) determines the lifting force, as well as the flight stability. The UAVs fuselage is stabilised by the counter- rotating propeller movement (Audronis, 2015). The selection of the right engines, which have to cope with the aerodynamic resistance, is an extremely important task. Thanks to them, UAVs can hover in the air for up to several dozen hours, uninterrupted.

UAVs can be equipped with various types of detectors, e.g. hazardous substances, automatic data analysis and transmission devices, as well as thermal imaging cameras. These devices are mostly used for filming and photographing. Real-time video playback makes unmanned aerial vehicles an ideal tool for, among other things, monitoring of dangerous goods transport routes or supervision of mass events (Audronis, 2015). The combination of UAV with such devices as digital cameras, directional microphones, thermal imaging sensors and network transmitters creates a number of new possibilities. They can be used both in site protection and in investment

control or logistics. They may be considered a tool that extends the range of offered services, but also significantly reduces operating costs. The potential for the use of aerial vehicles is being increased by the constantly developing structures of unmanned aerial vehicles and their resistance to atmospheric phenomena, greater range, as well as easier and more precise control. The dynamically developing market of telemetry and CCTV surveillance systems, with which unmanned aerial vehicles can be equipped, also contributes to the extended possibilities of using such devices (Bartkowiak, 2017).

3 Concept and Application of Thermal Imaging Testing

Thermal imaging, also called thermography, is a process of registering thermal radiation, emitted by physical bodies. The aim of the thermal imaging testing is, first of all, to present the image of heat emitted by physical objects in the Medium Wavelength Infrared (wavelength from about 900 to 1400 nm). This process makes it possible to record the thermal radiation emitted by all physical bodies in the temperature range typical of everyday conditions. It should be emphasised that objects do not need to be illuminated by an external light source. Such operation allows for a very accurate temperature measurement of objects in the places that interest us. Generally, thermal imaging testing is carried out in order to determine the level of emission and loss of thermal energy in, among others, industrial or residential buildings. This type of testing contributes to the determination of the object's thermal state. In addition, this method makes it possible to search for various inconsistencies and irregularities. Observation of heat emitted by objects in the field of vision is possible thanks to the use of a thermal imaging camera. It should be noted that all bodies whose temperature is higher than absolute zero are sources of radiation in the Medium Wavelength Infrared, i.e. infrared radiation with a wavelength of about 0.9 to 14 μm. Therefore, the functioning of a thermal imaging camera is based on a physical phenomenon concerning electromagnetic waves emitted by every body whose temperature is higher than absolute zero. Moreover, the intensity of infrared radiation is proportional to the body temperature.

The use of infrared has many advantages, especially when it is difficult to predict the temperature field distribution. Infrared has the advantage of producing accurate images of a thermal field in a non-contact manner. Even if it is difficult to determine where the problem is, it will appear in an easy to interpret thermal image.

4 Author's Own Research

Thermal imaging is more and more often used in various areas of life, including heat engineering, construction, power industry and medicine. A professional high-resolution thermal imaging camera should be used in order to obtain reliable results. Thermal imaging testing is common in the construction sector. The most frequently performed thermal imaging services during the year are, for example, detection of water leaks from the central heating system, leak detection and assessment of walls and ceilings dampness degree. Thermal imaging also makes it possible to search for leaks in underground pipe heating systems or to conduct testing. However, such projects require appropriate conditions and experience of the camera operator. Companies and individuals who own buildings control the water-tightness of facades and roofs to minimise heat loss. Improper construction may lead to significant financial losses over time, especially in winter. A tool that enables easy measurement in individual places is a thermal imaging camera. Using this type of camera, it is possible to determine the temperature in a place that may be leaky, *e.g.* between a window and a frame.

Thermal imaging may be considered one of the best ways to evaluate the quality of renovation work, such as thermal efficiency improvement of a building. Thanks to the combination of UAV and thermal imaging camera, this type of measurement can be performed even at considerable heights and in places not easily accessible to people. The advantage of this method is, first of all, accuracy, economy and a fast performance of measurements, thanks to which it is possible to rectify defects quickly (Kowalski and Bielecki, 2014). For this type of measurements it is also recommended to use radiometric cameras, thanks to which one may read the temperature in the given point of the registered infrared image.

The essential element during thermal imaging testing is the thermal transmittance, so the rate of transfer of heat through a structure, also known as U-value, calculated on the basis of thermographic measurements. Using the formula below we can calculate the heat transfer coefficient:

$$U_i = \frac{h_{si}(T_i - T_{si})}{T_i - T_e} \tag{1}$$

$$U_e = \frac{h_{se}(T_{se} - T_e)}{T_i - T_e} \tag{2}$$

$$U_{ie} = \frac{h_{si}\, h_{se}(T_i - T_{si})}{h_{se}(T_i - T_e) + h_{si}(T_i - T_{si})} \tag{3}$$

U- heat transfer coefficient
h_{si} - internal surface heat transfer coefficient
h_{se} - external surface heat transfer coefficient
T_i - temperature inside the building
T_e - temperature outside the building
T_{si} - internal surface temperature for partitions
T_{se} - external surface temperature for partitions (Kisilewicz and Wróbel, 2008).

Testing with the use of thermal imaging in open field may be subject to errors resulting from the so-called environmental factors. Direct sunlight strongly affects the readouts from the thermal imaging camera. Both sunlight and shade can affect the distribution of surface temperatures of the building for hours after the sun has stopped shining. Therefore, differences in thermal conductivity can lead to major temperature differences. Rain, which lowers the surface temperature of the material, is an equally dangerous factor. The evaporation of rainwater cools the material, which leads to a disturbed temperature distribution (Cwojdzinski, 2014)

When using a thermal imaging camera to detect insulation gaps or energy losses, it is best if the temperature difference between the inside of the building and the outside is at least +10 °C. With a high-resolution camera of high temperature sensitivity, the temperature difference can be smaller. Therefore, building inspections are often carried out in winter.

Currently, the authors are also conducting research on the application of UAV in the following areas:
- drawing up three-dimensional, detailed maps of the buildable lands, containing relevant data and information that may be of particular importance for the study phase and during conceptual preparation;

Testing with the use of thermal imaging in open field may be subject to errors resulting from the so-called environmental factors. Direct sunlight strongly affects the readouts from the thermal imaging camera. Both sunlight and shade can affect the distribution of surface temperatures of the building for hours after the sun has stopped shining. Therefore, differences in thermal conductivity can lead to major temperature differences. Rain, which lowers the surface temperature of the material, is an equally dangerous factor. The evaporation of rainwater cools the material, which leads to a disturbed temperature distribution (Cwojdzinski, 2014)

When using a thermal imaging camera to detect insulation gaps or energy losses, it is best if the temperature difference between the inside of the building and the outside is at least +10 °C. With a high-resolution camera of high temperature sensitivity, the temperature difference can be smaller. Therefore, building inspections are often carried out in winter.

Currently, the authors are also conducting research on the application of UAV in the following areas:
- drawing up three-dimensional, detailed maps of the buildable lands, containing relevant data and information that may be of particular importance for the study phase and during conceptual preparation;
- ongoing monitoring of the construction site and work in progress;
- controlling and supervising the works performed by the contractor, as well as supporting persons responsible for supervision;
- control over the supply of building materials and specialist equipment to the construction site;
- simulations that will provide the client with information on the topography and suggest what the best place for foundations excavation would be;
- monitoring the location of construction equipment that changes its position on the site, as well as supervising employees, properly performing their assigned duties and complying with occupational health and safety rules.

The authors' preliminary research shows that the application of UAV in the above mentioned projects will improve the effectiveness of their implementation.

5 Conclusions

Decreasing prices and increasing availability result in growing popularity of UAV. Thanks to the autopilot function, the device is easy to operate for almost every user. Determining parameters such as flight speed and altitude, flight course, monitoring of objects or phenomena in hard to reach locations is not a major problem. The possibility of using UAV with thermal imaging or HD cameras makes unmanned aerial vehicles a useful tool for conducting various types of tests. The conducted tests indicate that it is possible to identify areas of heat loss in the building and assess the temperature distribution. Moreover, the result is fast, accurate and non-invasive thanks to the use of an unmanned aerial vehicle combined with a thermal imaging camera. It allows, among other things, to identify defects in buildings, such as missing insulation, mortar flaking, dampness problems, and to assess the condition of heating, ventilation and air-conditioning systems. Such measurements are not only accurate, but also very cost-effective. Regular autonomous UAV flights may provide in a short period of time current and detailed data concerning the implemented construction projects.

ORCID

Agnieszka Waniewska https://orcid.org/0000-0002-6386-6579
Dariusz Skorupka https://orcid.org/0000-0002-6347-6562
Artur Duchaczek https://orcid.org/0000-0002-6263-5322
Magdalena Kowacka https://orcid.org/0000-0002-3553-9853
Grzegorz Debita https://orcid.org/0000-0003-1984-4740

References

Audronis, T. (2015). Drony: wprowadzenie: genialne ujecia z lotu ptaka. Gliwice: Wydawnictwo Helion.

Bartkowiak, N. (2017). Drony – wykorzystanie bezzałogowych statków powietrznych w systemach bezpieczenstwa.

Becmer, D. and Romanek, A. (2011). Bezzałogowe platformy latajace. Wrocław: WSOWL.

Cwojdzinski, L. (2014). Zadania wykonywane przez systemy platform bezzałogowych i powody ich stosowania.

Kisilewicz, T. and Wróbel, A. (2008). Inwentaryzacja rzeczywistych strat ciepła przez przegrody budynków z wykorzystaniem termografii. Archiwum Fotogrametrii, Kartografii i Teledetekcji, 18.

Kowalski, P. and Bielecki, K. (2014). Zastosowanie termowizji z wykorzystaniem dronów w budownictwie, 7730.

Maj-Marjanska, J. and Pietrzak, P. (2011). Prawne aspekty uzytkowania bezzałogowych statków powietrznych. *Bezpieczenstwo Narodowe, l8,* 197-204.

XV International Conference on Durability of Building Materials and Components
DBMC 2020, Barcelona
C. Serrat, J.R. Casas and V. Gibert (Eds)

Multiple-Criteria Cost Analysis for Simulated Life Cycle of Office Building

Michał Krzemiński

Department of Production Engineering and Construction Management, Institute of Building Engineering, Faculty of Civil Engineering, Warsaw University of Technology,
Al. Armii Ludowej 16, 00-637 Warsaw, Poland, m.krzeminski@il.pw.edu.pl

Abstract. *The article presents an office building life-cycle estimating possibility with the use of multiple-criteria evaluation and simulations modeling techniques. The first part describes the life cycle of an office building with a focus on the places where it is necessary to make strategic decisions. These decisions are most often associated with (the incurring of) high financial costs. It is, therefore, necessary to choose a tool supporting the decision-making process. Presents for evaluation several criteria were developed, a number of which concern office buildings. It should be remembered that the multiple-criteria assessment means not only the criteria but also weights which are assigned to them. The article discusses different ways of assigning weights to criteria, e.g. the Simos method. The use of several different methods of multiple-criteria evaluation was suggested, for example the method of weighted sum, the ideal point method and the entropy method. The analysis was based on simulation models. The full cost model was built in MS Excel. For modeling the Crystal Ball software was used. The software applied allowed not only to determine confidence in the selected scenarios, but also to point to the criterion or factor which has the greatest impact on the final result. Such information can be obtained through the use of sensitivity analysis.*

Keywords: *Office Building, Life-Cycle, Multiple-Criteria Analysis, Crystal Ball.*

1 Introduction

The definition of the life cycle of an office building can be fully based on the definition of the life cycle of a building as such. According to the definitions in ISO 15686-5: 2008, the life cycle of a building can be described as successive, interrelated periods of time between the selected time and the time of withdrawal or disposal of the building, in which certain criteria are assessed (*e.g.* costs, energy consumption, etc.).This period can be specified in the analysis, *e.g.* as a period equal to the time of renting or owning, or may cover the entire life cycle of a building, while the life cycle period is subject to the definition of the scope and specificity of operational requirements for a given building component. The definition includes a reference to the criteria of assessing the life cycle of an existing building. In the article, the author approaches the topic through the prism of strategic decisions accompanying the entire period in which an office building project is considered. These decisions are made throughout the entire life cycle of the project, at the initial, design, implementation and operational stages.

2 Strategic Decision Points

The most important points of strategic decisions, according to the author, are listed below. They have also been briefly characterized.

- Location Selection - different types of places: best, good, average, cheap, dedicated office buildings (*e.g.* near/in logistics centers ...).

doi:10.23967/dbmc.2020.202

- Widely understood construction technology that often affects the initial cost of the object. The cost is associated with the standard, which in many cases is the result of the location in which the object is designed.
- Permanent/Short-term tenants. There are various office buildings. In many cases, the assumption is that they are built for long-term tenants who are also strategic tenants and who often attract smaller ones. However, there are more and more advertisements of objects in which space is sublet for short periods of time, sometimes even for days.
- Renovations/Modernizations. The aims of renovation / modernization are an important issue. The existence of an office object is only justifiable when it brings profit. It is known that in time a building ceases to be as attractive as it was at the beginning. The aim of renovation, as it is understood by the author, is mainly to maintain the standard and output functionality. The aim of modernization, however, is to change the object in a way which makes it possible to place it at the top of the list of attractive objects in a given environment, which is its reference environment.

3 Renovations/Modernizations

According to the author, the scope of renovation and modernization works can be divided into four basic types, which are listed below. A set of criteria was also developed to evaluate these variants.

- basic renovation - aimed only at maintaining the object in working condition,
- full renovation - aimed at restoring the building to its original condition,
- inexpensive modernization - aimed at making the facility slightly more attractive,
- expensive modernization - aimed at restoring the facility's full attractiveness.

4 Criteria for Variants Assessement

The set of criteria includes four elements. The first three measurable criteria, which do not require any special ranking scale, are: cost, given in relation to a square meter of rentable space, time - given in days, and forecasted rental income, also given in relation to a square meter of rentable space. For the last criterion, which is the scope of works, a four-point scale was adopted. A description of the scale is presented below. It should be noted here that the increasement of scope may result in entering more and more serious construction works. With proper planning, the permit obtaining process and the design process should not pose a problem, but the construction process itself may already be problematic as unplanned delays, like on any construction site, may occur.

- 1 - the smallest scope of renovation and modernization works understood as the exchange of those elements only which are necessary to be replaced in order to meet the requirements, more technical than aesthetic. In this case, there is rather no risk of delays.
- 2 - is the scope of renovation which is characterized by incurring the expenditure necessary to restore the object to the condition of commissioning. It assumes greater work effort than in the first case as well as the probability of greater costs generated by the need to replace elements that admittedly meet the technical requirements but no longer meet the aesthetic requirements. Sometimes in the case of, *e.g.* facades, this can already be a high cost within the meaning of a significant range. Slight delays are

possible here.

- 3 - this note corresponds to renovation / modernization in which, apart from bringing the object to its full technical and aesthetic usability, minor changes are also made to the object. Such changes are, for example, a slight reconstruction of the facade including the modernization of the entrance portal. Changes can also be carried out inside the building and may involve, for example, the rearrangement of partition walls. In this case there is a risk of delay, which in extreme situations may become perceptible.
- 4 - such a note should be attributed to the renovation / modernization, which in principle will carry a significant scope of construction works. It may include works related to the complete reconstruction of the façade or to the modernization of communication routes, *e.g.* the addition of subsequent elevators. Such renovation/modernization can be considered as a reconstruction of the facility which carries a significant risk of delays.

5 Weight Scenarios, Assigning Weights Using the Simos Method

The original Simos method is based on the following three steps. First step is when the Decision Maker (DM) gives a set of cards with the name of one criterion the names of various criateria and a set of white cards. The number of white cards depends on the DM. In the next step the DM is asked to rank the cards from the most to the least important. If two cards are of the same importance they should be placed in the same line. In the last step the white cards are placed between the cards with the names of criteria. The assumption is that if two white cards are placed between criteria A and B, it means that A is three times more important than B. Basing on this we can describe Siomos algorithm in four steps. The first is the creation of the rank. Next, the distance between criteria is established by using the white cards. Step three is the calculation of non-normalized weights. In the last step normalized weights are calculated. The most important card should be placed at the bottom and the least important on the top of the table. In figure 1 below we can see the example of the usage of this method based on previously described criteria.

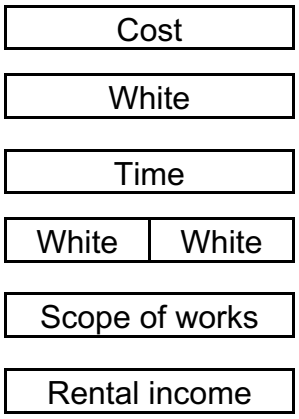

Figure 1. Cards order according to Simos method.

Table 1 below shows the results of calculations done with the use of Simos method.

Table 1. Criteria weight calculations with the use of Simos method.

	Cards number	Position	Non-normalized Weights	Normalized weights
Cost	1	1	1	0,06
White card	1	2	...	...
Time	1	3	3	0,18
White card	2	4;5	...	...
Scope of works	1	6	6	0,35
Rental income	1	7	7	0,41

In the fourth line of the table we can find two white cards. The author's assumption was that these two cards make bigger span between the criteria.

6 Multi-Criteria Assessment Methods

Weighted sum and ideal point methods are among the most basic methods of multi-criteria assessment. They are widely known and, according to the author, there is no need to quote their definitions and descriptions. The entropy method described below is more interesting.

The entropy is a thermodynamic parameter of the state of a system. However, in the statistical interpretation, it determines the degree of not ordering the harvest (or the degree of uniqueness). According to the Polish language dictionary, entropy in thermodynamics means the amount equal to the sum of the quotients of the heat portion taken by the system in a reversible process. In information theory it is the measure of indefiniteness, chaos, a degree of disorderness. The Entropy method allows us to estimate the validity of the analysed criteria describing the options in question based on the discrepancies in each. In theory, the information was first applied by Claude Shann and later refined by B. McMillana and L. Breiman. Based formula in entropy method is:

$$E_j = -\frac{1}{\ln n}\sum_{i=1}^{n} p_{ij} * \ln p_{ij} \tag{1}$$

where:
j - number of criterion,
i - number of assessed variant (from 1 to n),
p - assessment value.

It is easy to notice that if all the criteria have the same value of assessment, the entropy equals 1. For weights vector modification we use volatility level z based on following formula:

$$z_j = 1 - E_j \tag{2}$$

Criteria weights vector is modified by using:

$$w_j^0 = \frac{\frac{z_j}{\sum_{j=1}^{m} z_j} * \bar{w}_j}{\sum_{j=1}^{m}\left(\frac{z_j}{\sum_{j=1}^{m} z_j} * \bar{w}_j\right)} \tag{3}$$

where: $\bar{w}_j$ – weights established by DM, w_j^0 – new weights.

7 Example

Analyzed example concerns medium class office building located in Warsaw in range of 5 km from Palace of Culture and Science. Unnecessary data was collected in table below.

Table 2. Assessed investment options matrix.

	Variant 1	Variant 2	Variant 3
Cost	180	210	270
Time	15	40	60
Scope of works	1	2	3
Rental income [monthly]	50	55	75

Standarized grades used for assessment are in below table number 3.

Table 3. Standardized grades matrix.

	Variant 1	Variant 2	Variant 3
Cost	0,47	0,54	0,70
Time	0,20	0,54	0,81
Scope of works	0,27	0,53	0,80
Rental income [monthly]	0,66	0,60	0,44

The rental income were variated with Crystal Ball software use. On below figure there is example for rental income in third variant. Author made assumption that the best will be triangular distribution I range -10% to +5%.

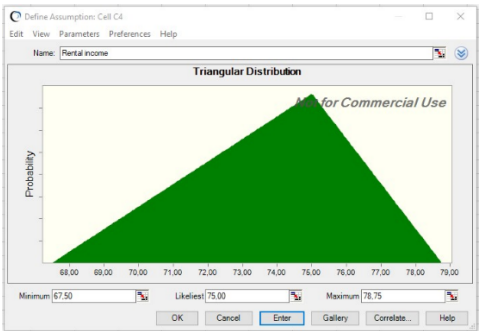

Figure 1. Triangular distribution for rental income variant 3

Calculation results were collect in below table 4. As it was previously mentioned calculation were made with three method use. Weighed sum, ideal point and entropy method. With accordance to all of this three method order was the same. The best was investment variant number one(minimum was looking for). Probably because cost of renovation and rental cost were going together proportionally, but the risk of delay grow quickly in meaning scope of works criterion. The result also shows how important this criterion actually is.

Table 3. Standardized grades matrix.

	Variant 1	Variant 2	Variant 3
Wighted sum	0,43	0,56	0,65
Ideal point	0,29	0,54	0,71
Entropy method	0,17	0,34	0,48

8 Conclusions

The article defines the life cycle of a building object together with the definition of strategic decision points. The assessment of the points regarding the decision on renovation or modernization was mainly considered.

A set of criteria have been developed to make the choice of the right option easier. In addition to the criteria, a weighting scenario was created with the use of Simos method. The entropy method used in the assessment was also described. During calculation, the expected rental income was established with the use of CrystalBall software.

The calculations made for the presented example show that this approach to the subject, in which various advanced methods are combined in multi-criteria assessment, gives good results and can be used assessing renovation and modernization options for office buildings.

ORCID

Michał Krzemiński: http://orcid.org/0000-0002-6352-5942

References

Biruk, S., Jaśkowski, P. and Krzemiński, M. (2019). Model of construction subcontractors selection with time windows for their availability. *Archives of Civil Engineering, 64(4),* 295-307. doi: 10.2478/ace-2019-0061

Figueiraa, J. and Roy, B. (2017). Determining the weights of criteria in the ELECTRE type methods with a revised Simos' procedure. *European Journal of Operational Research 139*, 317–326.

ISO/TC 59/SC 14 (2008). *ISO 15686-5: Buildings and constructed assets – Service life planning – Part 5: Life cycle costing.*

Juszczyk, M. and Leśniak, A. (2019). Modelling Construction Site Cost Index Based on Neural Network Ensembles. *Symmetry-Basel 11(3),* 411. doi:10.3390/sym11030411

Krzemiński, M. (2016). Comparison of selected multi-criteria assessment methods. *AIP Conference Proceedings 1738*, 200004. https://doi.org/10.1063/1.4951976

Krzemiński, M. (2016). Construction scheduling and stability of the resulting schedules. *Archives of Civil Engineering, 57(2)*, 89-100. doi: J0.1515/ace-2015-0067

Nowak, K. (2019). The Elasticity of the Office Space Market in Poland: Looking for the London Effect. World of Real Estate Journal, 5-18. doi: 10.14659/WOREJ.2019.108.01

Olszewski, K., Decyk, P. and Gołaszewska, K., (2018). Hedonic analysis of office and retail rents in three major cities in Poland. *Recent trends in the real estate market and its analysis, SGH Warsaw School of Economics* 383-392.

Siskos, E. and Tsotsolas N. (2015). Elicitation of criteria importance weights through the Simos method: Arobustness concern. *European Journal of Operational Research 246,* 543–553.

Syed, A. I. H. and Mandal U. K. (2016). Entropy based MCDM approach for Selection of material. *National Level Conference on Engineering Problems and Application of mathematics pp.1-7*, Agartala, Tipura, India

Wieczorek, D., Plebankiewicz, E. and Zima, K. (2019). Model estimation of the whole life cost of a building with respect to risk factors. *Technological and Economic Development of Economy 25(1),* 20-38. doi.org/10.3846/tede.2019.7455

XV International Conference on Durability of Building Materials and Components
DBMC 2020, Barcelona
C. Serrat, J.R. Casas and V. Gibert (Eds)

Possibilities of Reducing Energy Costs in the Life Cycle of Office Buildings

Edyta Plebankiewicz, Krzysztof Zima and Damian Wieczorek

Department of Construction Management, Faculty of Civil Engineering, Cracow University of Technology, Warszawska 24 St., 31-155 Kraków, Poland, eplebank@L3.pk.edu.pl

Abstract. *Buildings absorb energy at every stage of the life cycle. The paper analyses the phases of the life cycle of an office building indicating the possibilities of reducing energy consumption. In particular, attention was paid to the most energy-intensive phase, that is the use phase. Both simple actions and more advanced solutions allowing to reduce the energy demand of a building during the use phase are characterized. For an exemplary office building, life cycle costs were calculated taking into account selected solutions improving energy efficiency.*

Keywords: *Life Cycle Cost, Office Buildings, Energy.*

1 Introduction

Buildings are the largest energy consumer in Europe, utilizing about 40% of final energy, of which more than 55% is used for room heating and cooling. At the same time, it is estimated that about one third of the world's energy consumption is related to the use of office and residential buildings. An additional problem is that most of this energy is supplied from non-renewable sources, which contributes to environmental degradation and significant heating/cooling costs (Arendt *et al.*, 2015). It should also be remembered that oil and gas resources are limited and no longer so readily available (Firląg, 2018).

The aim of the paper is to analyse the possibility of reducing energy consumption in office buildings in all phases of their life cycle.

2 Energy Consumption of Buildings in the Various Life Cycle Phases

From the point of view of energy consumption and environmental impact, the life cycle of a building involves the following phases:

- the manufacturing the products necessary for the construction of the building,
- the construction of the building,
- the use of the building,
- the end of the life cycle.

Each of these phases entails energy demand. Detailed modules related to energy demand, being part of particular phases of the building life cycle are depicted in Table 1.

The energy consumption in the different phases of a building's life cycle depends on many factors. However, in general, when analysing the energy consumption of buildings in Poland, it is estimated that at the stage of construction of a building the energy consumption amounts to about 10%, at the stage of use (with implementation performed according to the current standards) – to about 72%, for the needs of renovation – to about 15% and for the demolition of the building – from 1 to 3% of the total accumulated energy demand in relation to the life cycle of the building, as illustrated in Figure 1.

doi:10.23967/dbmc.2020.111

Table 1. Phases of the building life cycle.

Life cycle phase	Life cycle modules
A – Product phase	A1 – Extraction and manufacture of raw materials
	A2 – Transport
	A3 – Manufacturing the product
B – Construction phase	B1 – Transport
	B2 – Construction
C – Operation phase	C1 – Usage
	C2 – Maintenance
	C3 – Repair
	C4 – Replacement
	C5 – Renovation
D – End of life cycle phase	D1 – Demolition
	D2 - Transport
	D3 – Recycling/reuse
	D4 – Stockpiling

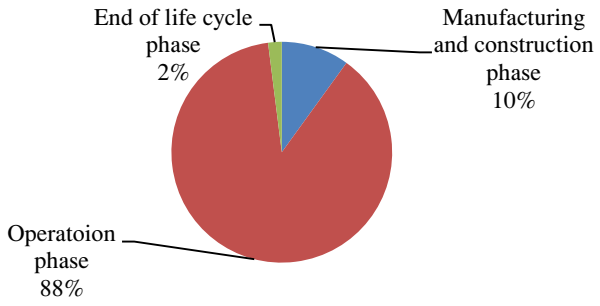

Figure 1. The energy consumption of buildings.

Since the greatest amount of energy is consumed in the operation phase of the building, therefore this issue is addressed mainly in the present paper.

However, the other phases cannot be ignored. In general, the energy consumed by the building include the following:

- embedded energy, that is energy accumulated in the building during its construction in the form of energy used for the production of materials, transport (A – product phase), building-in processes (B – construction phase) and energy necessary to perform repairs and maintenance (C – operation phase);
- operational energy, namely energy used for heating, ventilation, air conditioning, lighting and energy (C – operation phase);
- processing energy, meaning energy necessary for the demolition of the facility and waste management (D – end of life cycle phase).

The first phase of the building life cycle is related to the manufacturing building materials and products necessary for the construction of the building. According to the Guide of the Building Research Institute (Adamus, 2014), approximately three billion tonnes of raw

materials are used each year for the production of building materials, which accounts for 40-50% of global production. Characteristically of the construction industry, it is estimated that it uses more than 10 000 different types of materials, many of which are obtained through the exploitation of non-renewable resources. Table 2 shows the amount of embedded energy for common building materials, as revealed by European and US sources.

Table 2. The amount of embedded energy for common building materials.

Material	Embedded energy in MJ/kg, according to:	
	European sources	US sources
naturally dried wood	0.5	0.3 ÷ 1.1
processed wood	8 ÷ 24	8 ÷ 24
plastic materials	80 ÷ 110	55 ÷ 120
local stone	5 ÷ 6	0.8
prefabricated concrete	2	2
ceramics	2.5 ÷ 8	2.5 ÷ 7
glass	12 ÷ 26	14 ÷ 30

Table 3 depicts the amount of energy associated with the transport of building materials. As can be seen from this summary, the largest energy consumption is in road transport.

Table 3. The amount of energy associated with the transport of building materials.

Type of transport	Energy consumption in MJ/t:	
	Canada	Great Britain
road transport	1.18	4.50
rail transport	0.49	0.60
water transport	0.12	0.25

It should be emphasized that the proper selection of construction materials and products has an impact not only on the energy consumption during their manufacture and transport, but also on the energy demand in the operation phase, related to the need for repairs and renovations which are largely dependent on the characteristics of the material itself.

In general, the amount of the embedded energy of a building can be minimised by applying the following principles:

- design of objects with a long service life, made of durable materials and not requiring repair or overhaul;
- ensuring that the different materials can be easily separated from each other for repair and demolition;
- the use of locally available materials;
- the use of materials with a high recycling rate;
- avoidance of materials generating troublesome waste;
- minimising the use of highly energy-intensive materials;
- preference for renewable energy materials,
- the use of materials that reduce energy consumption during the operation of the building, which indicates the choice of sustainable materials.

3 Energy Consumption in Office Buildings at the Operation Stage

In every building, by far the highest energy consumption occurs during the operation phase. A specific feature of such buildings as commercial facilities is that their energy consumption per square metre is on average 40 % higher than that of residential buildings. Their electricity consumption is particularly high, due to complex lighting, air conditioning or ventilation systems. Also, the climate in countries such as Poland, for example, means that in standard buildings the heating season lasts 220-240 days a year, hence 70% of energy in buildings is used for heating and cooling.

Moreover, in comparison to other buildings, modern office facilities have a specific consumption of electricity associated with their high demand for energy needed to power computer and other office equipment. Figure 2. illustrates the energy consumption of an average office building in 2012. The data comes from the research conducted by an institution established in the USA, dealing with the collection and analysis of data on energy issues: the U.S. Energy Information Administration.

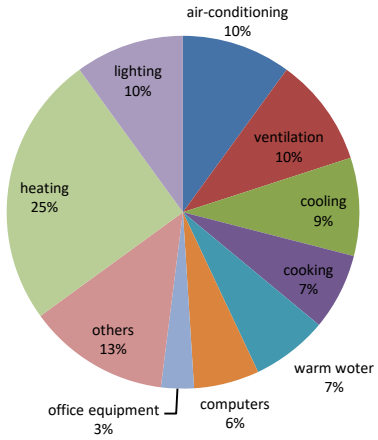

Figure 2. Energy consumption of a commercial building in 2012.

As Figure 2. reveals, the highest energy consumption in 2012 was due to the demand for heating of the building, while the power supply of office equipment and computers accounted for less than 9% of its total consumption. Moreover, forecasts for 2050 show that although demand for energy for heating and lighting in office buildings, for example, will decrease significantly, energy demand for computer hardware and other office equipment will increase by more than 20% (Figure 3).

Such specificity of office buildings should probably be one of the important factors when considering the possibility of reducing energy consumption. This does not mean, however, that no action should be taken to reduce the energy required for heating, cooling or ventilation.

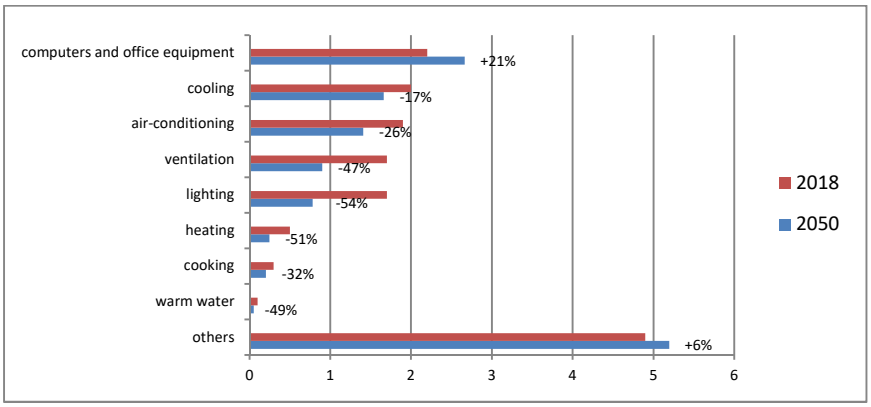

Figure 3. Current and planned energy consumption in office buildings (kilowatt hours per 1square foot).

4 Opportunities for the Reduction of Energy Consumption

Research results indicate that almost 75% of buildings are low energy efficient, which means that there is still significant potential for rational energy savings in buildings. According to the European Commission, a statistical building in the European Union countries consumes 15-25% more energy than it needs. In Poland, on the other hand, energy consumption in buildings is more than twice as high as in other EU countries. The Polish economy is also about 2.7 times more energy-intensive than in the European Union and 5 times more so than in Japan. Improvement of energy performance of buildings is therefore the biggest challenge for the coming decades (Skanska Property Poland, 2016).

Actions reducing energy consumption in buildings can be linked both to relatively simple as well as more advanced solutions aiming at decreasing heat loss in a building.

It can be observed that the largest heat losses in a building are related to the heat transfer through the building envelope, where the largest losses are those through glass envelope, such as windows and doors, amounting to about 60-70% of the total energy balance. Ventilation, on the other hand, causes losses of 30-40%. Therefore, it is necessary to minimize heat losses, while maximizing the use of energy gains.

Heat losses can be reduced by the following improvements in (Ministry of Investment and Economic Development in Poland, 2018):

- ventilation - application of mechanical ventilation with heat recovery (recuperation) and high tightness of the building,
- windows and doors - use of energy-saving woodwork,
- external walls - appropriate wall insulation,
- roof - appropriate roof insulation,
- floors on the ground - adequate insulation of the floor on the ground,
- thermal bridges - use of solutions minimizing the occurrence of thermal bridges.

In the case of existing buildings, this will involve thermal upgrading, such as replacing window frames, replacing central heating systems, or optimising heating by insulating hot water pipes, heat and small heat pump systems in the radiator. A simple change in habits can also lead to a reduction in energy consumption, such as (Kopietz-Unger, 2012):

- appropriate setting of air temperature in rooms, up to approx. 10%,

- exposing the radiators, about 10%,
- lowering the temperature of domestic hot water to approx. 6.6%,
- use of aerators, approx. 8%,
- the change from rib radiators to convection heaters, about 14%.

More complex solutions include the use of alternative solutions for heating water or building interiors. The increased use of alternative energy sources contributes to the development of low-carbon energy sources. Such solutions include the efficient use of solar collectors to heat water. Studies on the benefits of using natural energy sources, in particular solar panels, are presented in (Kale *et al*., 2018). The following conclusions can be drawn from the project:

- energy-saving approach to the solar collector system requires an initial investment of 1.3-16%,
- with minimal initial investment in solar panels, one can save 4.3% of the total cost within 30 years,
- with the proposed solar panel, 54 - 64% of the total cost can be saved within 25 years.

The use of solar systems can be effectively used to cool rooms. The solar system absorbs solar radiation and converts it into heat energy, which is subsequently transferred to a cooling exchanger and then to a central heating system for cooling.

An interesting solution is the use of photovoltaic cells to produce electricity. In Poland, from 1 m2 of solar cells it is possible to obtain up to 100 kWh of electricity. The condition is that the generated energy will not be used for water heating and heating purposes.

The solution used increasingly more often is the use of cooling and heating ceilings. Such ceilings use the thermal mass of the building to act. Pipes are placed in the concrete ceiling to transport cold and hot water. At night, the system brings coolness to the ceilings, and during the day, the cooled surfaces take heat from the building and thus lower the room temperature. This solution not only ensures comfort and healthy microclimate in rooms, but it also allows to reduce energy consumption. Unlike traditional air-conditioning systems, they operate in temperatures close to the environment, which contributes to increasing the efficiency of the source of heat and cold. An analysis performed on the example of a London office building with a total area of 1000 m2 showed that this type of ceiling provides annual savings of between 12 and 31% compared to conventional installations in the form of fan coil units, displacement ventilation or chilled beams of similar capacity. Manufacturers assure that the investment costs are low, with savings of 10-30% compared to conventional air conditioning systems and low maintenance and service costs up to 30%, compared to conventional air conditioning systems.

Modern office buildings contain rooms of a different character, such as: halls and reception areas, atria, server rooms, engine rooms, garages, offices, conference rooms, restaurants, retail and service premises. Each of them requires a separate system to guarantee different levels of comfort and safety. In order for all these elements to constitute a coherent and well-functioning whole, advanced automatic control and regulation systems, BMS (Building Management System), should be applied in office buildings, which in some cases are supplemented with functionalities allowing for energy consumption management, that is BEMS (Building Energy Management Systems). Their basic function is to ensure proper indoor environment parameters (user comfort) with rational energy consumption. According to the data from Distech Controls Inc., the manufacturer of building automation systems,

Building management systems never cost more than 1% of their value. However, on average 45% of energy consumption depends on their quality, that is 25% of the value of the investment over the 30 years of the life cycle of the building. Depending on the type of the building, lighting consumes 30-40% of the electricity, of which 10-58% can be saved. Over 65% of energy costs is absorbed by heating and air conditioning, and potential savings amount to 8-45%.

5 Cost-Benefit Analysis of Solutions that Improve the Energy Efficiency Standard of an Office Building

Simulations concerning analyses and benefits resulting from energy-saving construction were performed by the Polish National Energy Conservation Agency on the example of buildings of different purpose (Węglarz, 2017). One of the buildings under analysis was an office building. The model office facility selected for the analysis was a 6-storey building with a usable area of 2 124 m^2. On the basis of simulations and additional own analyses, the authors performed calculations which enabled the assessment of costs and benefits resulting from the application of solutions that increase the energy efficiency of the office building.

For standard buildings, the classic and most frequently used installation solutions were adopted, that is water heating systems with convector heaters and boilers for coal, natural gas, fuel oil, LPG or the application of a heat substation with a connection to a district heating network. In a high standard building, it was assumed that, in comparison to a standard building, the insulation thickness of the envelope was increased by 20 cm and that windows with a penetration coefficient of 0.5 W/(m^2·K) were used.

In addition, for the model building with energy-saving standards, the following were applied: higher thickness of pipeline thermal insulation, better quality control valves and thermo-valves, water-saving fittings in the hot water installation and mechanical ventilation with heat recovery of 85%. For the building with collectors, the use of flat solar collectors with an area of 32 m^2 was predicted.

Table 4. presents the costs of energy depending on its source, accepted for analysis.

Table 4. Energy costs depending on the source of energy (Węglarz, 2017).

Source of energy	External costs	
	EUR/MWH	EUR/GJ
Coal	11.00	3.06
GZ50	0.42	0.12
Electricity	57.00	15.83
Fuel oil	1.54	0.43
LPG	1.54	0.43
Network heat	10.40	2.89

The results of simulation analyses for an office building and coal heating are presented in Table 5.

Table 5. Results of simulation analyses for an office building for coal heating

	construction cost [EUR]	Annual energy cost [EUR/year]	LCC [EUR] (30 year; r=5%)
Standard building	1 373 692	8 428	1 915 361
High-standard building with cooling and heating ceilings	1 432 377	6 730	1 900 120
High standard building with collectors	1 506 222	1 966	1 868 795
High standard building with heat pump	1 536 054	2 096	1 731 453

6 Conclusions

Buildings absorb energy to varying degrees at every stage of their life cycle. By far the greatest demand for energy occurs during the operation phase of a building. Reducing energy consumption during this phase is necessary for both economic and environmental reasons.

The life cycle cost analysis of an office building conducted in the present paper showed the effectiveness of the use of cooling and heating ceilings, solar collectors and heat pumps.

ORCID

Edyta Plebankiewicz: http://orcid.org/0000-0003-0892-5027
Krzysztof Zima: http://orcid.org/0000-0001-5563-5482
Damian Wieczorek: http://orcid.org/0000- 0002-3191-2438

References

Adamus, Ł. (2014). *Zrównoważone budownictwo w UE Informator – cz . LVIII* (in Polish). Instytut Techniki Budowlanej.

Arendt, K., Krzaczek, M., Antczak, R. and Tejchman, J. (2015). Wpływ systemu ogrzewania na zużycie energii i koszty eksploatacyjne budynku (in Polish). *Przegląd Budowlany, 4*, 46–50.

Firląg, S. (2018). *Zrównoważone budynki biurowe* (in Polish). PWN.

Kale, N.N., Joshi, D. and Menon, R. (2016). Life cycle cost analysis of commercial buildings with energy efficient approach. *Perspectives in Science*, *8*, 452–454. DOI:https://doi.org/10.1016/j.pisc.2016.04.102.

Kopietz-Unger, J. (2012). Zmniejszenie zapotrzebowania na energię poprzez wzrost efektywości energetycznej budynku i działania prosumenckie (in Polish). *Przegląd Budowlany,* 12.

Ministry of Investment and Economic Development in Poland (in Polish). (2018). *Poradnik w zakresie poprawy charakterystyki energetycznej budynków*, Warszawa

Royal Institution of Chartered Surveyors (RICS). (2016). *Life cycle costing: RICS professional guidance*.

Skanska Property Poland , report (in Polish). , (2016). *Zużycie energii w budynkach biurowych*.

US Energy Information Administration https://www.eia.gov/

Węglarz, A. (2017). *Nakłady finansowe i korzyści wynikające z budowy różnych typów budynków energooszczędnych* (in Polish). Krajowa Agencja Poszanowania Energii S.A.

www.argox.com.pl/budownictwo_zrownowazone.php

www.instalacjebudowlane.pl/7894-23-53-stropy-chlodzace-grzewcze-uponor.html

XV International Conference on Durability of Building Materials and Components
DBMC 2020, Barcelona
C. Serrat, J.R. Casas and V. Gibert (Eds)

Application of Pro-Ecological Building Technologies in Contemporary Architecture

Jerzy Górski[1], **Joanna Klimowicz**[2] **and Anna Nowak**[3]

[1] Warsaw University of Technology, Faculty of Architecture, Department of Structure Design, Construction and Technical Infrastructure, Koszykowa 55, 00-661 Warsaw, Poland, jerzy.gorski@pw.edu.pl
[2] Warsaw University of Technology, Faculty of Architecture, Department of Urban Design and Spatial Planning, Koszykowa 55, 00-661 Warsaw, Poland, joanna.klimowicz@pw.edu.pl klijo@poczta.onet.pl
[3] Warsaw University of Technology, Faculty of Architecture, Department of Structure Design, Construction and Technical Infrastructure, Koszykowa 55, 00-661 Warsaw, Poland, anna.patrycja.nowak@gmail.com

Abstract. *Structural and material solutions of modern buildings are an important element of considerations in accordance with the idea of sustainable design, in which the aim is to minimize their negative impact on the environment. These searches turn towards low-tech technology, which uses natural and low-processed materials, which are possible to obtain in selected locations. Construction in the raw earth technology is a modernization of the traditional technology, in which it is possible to apply pro-ecological values associated with the used material. The paper presents research on insulation properties of walls in an experimental earth building located in Pasłęk in Poland. The aim of the research was to determine the potential of the applied raw earth technology in a local climate. The accepted design assumptions were verified due to the effects achieved in the empirical research on the thermo-humidity conditions in an experimental building. On the basis of the conducted research with the use of specialized tools, the positive and negative sides of the selected technology and building material were determined.*

Keywords: *Raw Earth Technology, Sustainable Design, Energy Efficiency.*

1 Introduction

In modern pro-ecological architecture, many trends can be identified, which lead to the design of architecture in accordance with the idea of sustainable development. One of them is circular design. The main assumption in this design approach is to use materials that can be obtained in close proximity to the design area, with the possibility of their reuse, or using bio-materials. According to this, structural and material solutions of modern buildings are an important element of considerations in accordance with the idea of sustainable design, in which the aim is to minimize their negative impact on the environment. These searches turn towards low-tech technology, which uses natural and low-processed materials, which are possible to obtain in selected locations. Construction in the raw earth technology is a modernization of the traditional technology, in which it is possible to apply pro-ecological values associated with the used material. The use of earth as "waste" from the excavated material after excavation of the foundations of the building, for the construction of external and internal walls of the designed object is an important element inscribing the project in the idea of circular design. The paper presents research on insulation properties of walls in an experimental earth building located in

Pasłęk in Poland. The aim of the research was to determine the potential of the applied raw earth technology in a local climate. The accepted design assumptions for the veranda design were verified due to the effects achieved in the empirical research on the thermo-humidity conditions in an experimental building. On the basis of the conducted research with the use of specialized tools, the positive and negative sides of the selected technology and building material were determined within the scope of a veranda designed as a heat accumulating element.

One of the trends of contemporary architecture is the use of traditional technologies and among them diverse raw earth solutions, wooden structures supplemented with straw bale walls, and use of various recycled materials.

In an experimental building described below located in the Ecological Park in Paslek in Poland the following types of raw earth technologies were used: rammed earth in formwork, earth pressed blocks, strew clay blocks and clay render. The project was carried out at the Faculty of Architecture of the Warsaw University of Technology by the team: prof. Teresa Kelm, arch. Jerzy Górski PhD, arch. Marek Kołłątaj, Dorota Długosz-Nowicka PhD, who cooperated on technological issues and carried out laboratory tests. Structures and installations designers participated in the preparation of the Construction Design.

Preparation of the project and construction of the building became possible thanks to the grant from the Ministry of Science and Higher Education in the years 2005 – 2008, involvement of the city authorities of Pasłęk and with the help of sponsors. The municipality of Pasłęk, had been interested in ecology for many years, made the plot available for construction to promote the idea of ecological construction in its area. The building was commissioned in 2012. and handed to the city. The building is administered by the management of the Ecological Park and used as an information, educational and exhibition centre.

The construction of the building was used for didactic programme on ecological construction with the use of raw earth technology, carried out in the form of seminars, practical classes, workshops and local inspections on the construction site. Also finished building is an object of further research and observation on the behavior of the structure during its exploitation. The results of such examinations will be shown in this paper.

2 Design Assumptions and Implementation Details

2.1 Spatial and Functional Characteristics of the Building

The building is detached, one-storey, without basement and is roofed by a single pitched, north-facing roof covered with extensive greenery. It is located in the south-eastern corner of a plot of land with an area of about 1 ha. It is flat meadow at a side of local lake, used by the Ecological Park to organize in summer outdoor events. In order to achieve the energy-optimal surface area of the facades, the longer axis of the building is located in the east-west direction. The facade with the largest surface area and the largest number of glazing is on the southern side, the facade on the northern side is smaller and has no openings. The main entrance to the building is located on the western side. It leads through the vestibule to the one-spatial didactic and exhibition hall located in the eastern part of the building and connected through two glass doors with a large fully glazed veranda located within the southern facade. The main room is connected with the external terrace located along the eastern elevation of the building and with the utility part

(kitchenette, toilet) located in the western part. The development area of the whole building is 105 m^2, usable area 75.5 m^2 and cubic capacity 250 m^3.

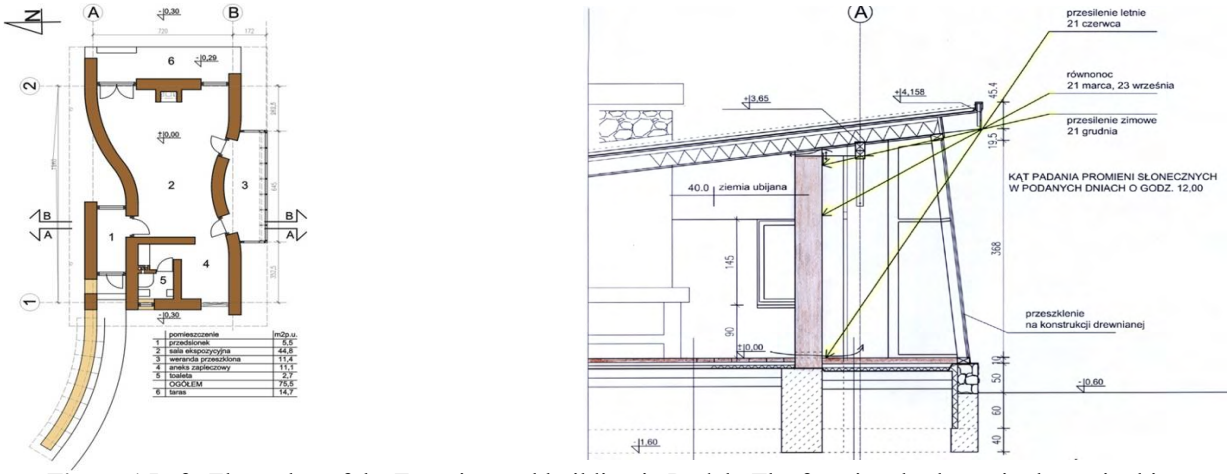

Figure 1. Left: Floor plan of the Experimental building in Pasłęk. The functional scheme is shown in this drawing 1. Vestibule, 2. Exhibition hall, 3. Veranda, 4. Back room annex, 5. Toilet, 6. Terrace; Right: Section through the veranda and the accumulation wall. The eaves is designed to shade the accumulation wall in summer. (accumulation wall not thermally insulated).

2.2 Construction Solutions

In the project, energy-efficient solutions were applied during both the implementation and the operational phases. The technology of rammed earth in the formwork was applied to the structural and external walls using the soil from the excavations on the plot (reduction of the costs of transport of construction materials). They are supplemented with an internal layer built of straw-clay blocks and thermal insulation. The partition walls are made of pressed earth blocks.

The foundations of the building are benches and foundation walls made of reinforced concrete and thermally insulated with foamed polystyrene inserts, and damp-proof with bitumen membrane. Taking into account the necessity of protecting the earth mass of the walls against water and ground dampness, the aboveground wall is elevated about 50 cm above the ground level and supported by a concrete foundation finished with natural stone.

The external walls are designed and constructed as three-layer partitions. The load-bearing layer is situated outside in form of rammed earth monolithic walls compacted in formwork using a pneumatic compactor. The raw material (soil from site) was supplemented - in order to obtain a mixture meeting the technical requirements for this type of elements - with modification additives like sand or gravel. Moreover, due to the contact of the walls with the air moisture, a stabiliser - 6 to 8 % by weight of cement - was added to the earth's mass. The load-bearing layer is topped off with a reinforced concrete ring beam with anchors for fixing the wall plates (roof structure). The internal layer of the partition was made of blocks made of clay and straw compacted mass, and the gap between the layers was to be filled with cellulose backfill (Ecofiber) replaced by mineral wool due to the price. Mineral wool is also used to insulate the roof. The inner blocks are finished with earth plaster to regulate the humidity of the interior or have a natural surface impregnated with varnish in order to stop the material from

chipping. Partition walls are made of blocks made of pressed earth without any additional finishing. The floors on the ground were damp insulated with bitumen membrane laid on the underlay concrete and thermally with polystyrene. A broken stone slab floor with concrete subfloor is a thermal accumulation mass.

The unconventional order of external wall layers (rammed earth load-bearing layer as external one) was dictated by research considerations - verification of the influence of climatic factors (humidity from the air) on the earth mass and of water vapour permeation through the partition layers, determination of the dew-point, etc. It was assumed that the external surface of the compacted earth wall would be left without any finishing, as a natural illustration of an unusual technology. External walls above the window openings are made as wooden frame walls, insulated with mineral wool with internal vapour-barrier insulation, external wind-barrier insulation and wooden boarding on both sides. The roof is a single pitched, with wooden wall plates, purlins and rafters. A layer of weather-resistant tundra greenery was laid on the roof. In order to protect the rammed earth walls from direct rainwater, the roof eaves were extended from the wall line at a distance of not less than 80 cm.

The fully glazed veranda with wooden construction has a southern sloping wall. It is separated from the main room by a thick, non-thermally insulated accumulation wall made of rammed earth and room is connected with veranda by two glass doors. The windows and exterior doors are made of wood. The building has a sewerage system, cold and hot water, and electricity. The main source of heating is a freestanding wood-burning cast iron fireplace.

Figure 2. Left and in middle: View of the experimental earth building located in the Ecological Park in Pasłęk. Right: The inside of the veranda. Wooden structure glazed with low-emission composite panes. On the right there is an accumulation wall made of compacted raw earth and a door connecting with the main hall.

2.3 Energy Performance of Building Components Using Raw Earth Technologies

The experimental building in Pasłęk was designed in terms of space and materials so that the assumed construction solutions could be used for later analysis and research. At the design stage, theoretical calculations were carried out, which can later be compared with the achieved effects .

The characteristics of the basic earth and insulating materials of external walls are presented below.

The thermal conductivity coefficients of λ [W/mK] of the materials used in the walls were as follows:

- Heavy earth (for rammed earth in formwork) – 0,870
- Light weight (straw and clay blocks) – 0,350

- Cellulose insulation (Eco-fibre)/(Mineral wool) -0,040

Building material solutions of the other elements (ceilings, floor, glazing) complement the design's assumptions concerning energy efficiency. The coefficient of heat transfer through the partition for the external wall - U0 (1/Rt) - was 0.34 W/m^{2}K. The designed building was classified as a public utility building, so the expected heat transfer coefficient through the partition complied with the regulations of that time. A significant role in the energy management of the object is the passive use of solar energy. This is achieved by using a glass veranda on the south side, glazed terrace doors and windows. The amount of solar energy penetrating into the room in the form of short wave radiation depends on the size of the glazing and the type of glass in the set, especially the type of external glass. Solar energy is stored in the compacted earth wall (without thermal insulation) between the veranda and the main room and in floors made of materials that well store heat - stone and in partition walls made of pressed blocks. The stored heat is retained in the interior by the use of double glazing with low-emission internal glazing and insulating properties of the external partitions.

2.4 Inspections and Technical Examinations

The building was subject to local inspections during its execution and operation by the design team and other persons from the Faculty of Architecture of the Warsaw University of Technology.

The building has been used in various ways for over 7 years and direct feedback from users was important and it shows that the internal climate is very comfortable. During the heating period, a wood-burning stove was sufficient as a source of heat. Solid walls and flooring were a good heat accumulator and the heat buffer in the glass veranda accumulated heat on sunny days in cold period and supplemented the overall heat balance. Multi-layered external walls and roof containing thermal insulation assured even internal temperature both in hot and cold periods.

During inspections also the structural and construction problems were observed. There are no signs of uneven settling, i.e. the dimensions and structure of the foundations are correct. The visible, stone-covered plinth is in a very good condition. Above the plinth a wall made of compacted earth does not show any negative effects of climatic factors. The principle of protecting the rammed earth from moisture by raising the walls above the stone plinth and protecting them from direct rainfall by roof eaves has proved its worth.

Site inspections in 2018 apart from construction problems, also took into account the issues of internal microclimate, insulating quality of partitions and energy management. In 2019 we repeat measurements incorporating some modifications as the result of previous experiences.

The measurements were carried out at different times of the year (spring, summer, late autumn). Field tests were carried out in the following methods:

- examination of heat transfer through external partitions with thermal imagine camera for identification of possible thermal bridges,
- outside the building, measuring air temperature, wall surface temperature, humidity, insolation, wind speed,
- inside - measuring air temperature and humidity, wall surface temperature and humidity.

The building has been used in various ways for over 7 years. Direct feedback from users is important, as it shows that the internal climate is very comfortable. During the heating period,

a wood-burning stove was sufficient as a source of heat. Solid walls and flooring were a good heat accumulator and the heat buffer in the glass veranda accumulated heat on sunny days and supplemented the overall heat balance.

Researches were divided into three parts: measurement of wall moisture (using TROTEC BM 22) in summer and in autumn, measurements of room temperature and humidity (using Testo 410-2) in summer and in autumn, and research with thermal camera (using SeeK Thermal) in autumn.

2.4.1 Measurements of Wall Moisture Using TROTEC BM 22

The first research of moisture took place on 1st August 2018. The temperature outside was 30°C and humidity outside the building was 45%. In the case of a veranda, the humidity of the partition wall from the outside decreased for 0,1%, which is caused by the relation between the southern exhibition and the positions of the points inside the veranda, which is heated by the sun during the summer period. Since the differences between the individual measurement points outside and inside the building are of the order of several decimals, it can be concluded that the walls will retain their stability.

The second research of moisture took place on 29 October 2018. The temperature outside was 5,46°C and humidity outside the building was 75%. In the case of a veranda, the humidity of partition wall from outside decreased for 0,2-0,3%. The wall moisture was higher in summer than in autumn. The amplitude of the moisture behind the accumulating wall inside the building about 0,1% and in veranda 0,2-0,3%. The difference probably depends on heating system in autumn.

2.4.2 Measurements of Room Temperature and Humidity Using Testo 410-2

The first research of temperature and humidity took place on 1st August 2018. The temperature outside was 30°C and humidity outside was 45%. The collected measurement results show higher humidity values inside than outside the building. Using this device, the humidity on the veranda was analysed, where the lowest percentage values of humidity were noted. The humidity in point 7 on the veranda was even up to 19.8% lower than in other points inside the building. It follows that a veranda with a glass wall reduces the humidity inside the building. The veranda also recorded the highest temperatures of 39°C and 40.5°C, while in other rooms the temperature ranged from 28.5°C to 29.8°C.

The second research of temperature and humidity took place on 29 October 2019. The temperature outside was 5,46°C and humidity outside the building was 75%. The humidity in veranda was the same or lower (about 1,3%) than in inside the building behind the partition wall. The temperature in veranda was lower than in inside of the building about 0,4-0,6°C.

The amplitude of temperature in summer and in autumn in veranda was 23,6°C, but delta of humidity was 5,5%. The amplitude of temperature behind the partition wall (accumulating wall) was 12,3°C and delta of humidity was 11,4%.

2.4.3 Research with Using Thermal Camera SeeK Thermal

During the visit on 29 November 2018 the SeeK Thermal thermal camera was used. Temperature measurements with the thermographic camera were taken between 14:00-15:00. During the analysis, the object was heated by a fireplace for about 2 hours.

Figure 3. Measurements with a thermal camera in the interior near the accumulation wall and the glass part of the southern wall.

The wall accumulation analysis from the inside showed the temperature difference depending on the finishing materials used. On the veranda side, in three measurement points of the wall, the same result of 17°C was obtained. From the main room side the temperature varies from 23°C towards the eastern elevation, through 22°C to 20°C from the western elevation side. In case of covering the wall with wooden cladding, the temperature was higher and constant, regardless of the measurement point, and it was 25°C.

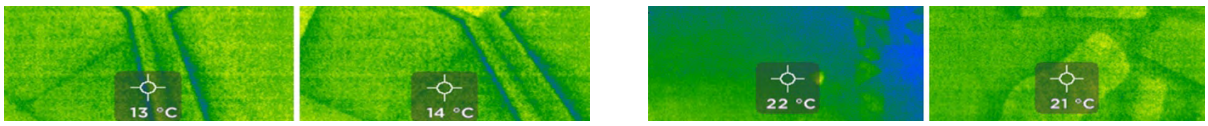

Figure 4. Measurements with a thermal camera of a glazed curtain wall on a veranda and a floor in the interior of the main utility part and veranda.

The difference in temperature in the veranda room and the main utility room is noticeable, which is caused by the adopted technical and material solutions of the external partitions. Measurements with a thermal camera show lower thermal insulation of the veranda external partitions made as a glazed curtain wall. The glazing temperature was 14°C, and the structural elements were 13°C. The temperature of the floor, finished with stone, in the part of the veranda and the main utility room was comparable. The temperature of the floor on the veranda was 21°C. The purpose of this floor is to accumulate heat generated by solar radiation penetrating through the glass wall of the veranda. The temperature of the floor in the main heated usable part was higher and amounted to 22°C. Despite the temperature difference in the rooms and external partitions, the floor temperature is similar in both rooms. It can be assumed that the stone flooring accumulates the heat generated by solar radiation, as assumed at the design concept stage.

3 Conclusions

Research has shown that there is no significant heat transfer from the veranda space, because no openings were introduced to allow ventilation and the doors, which were proposed in the design to perform this function, were closed during the use by users. Due to financial reasons external shading roller shutters, which were proposed in design, were abandoned. The research has shown that despite the fact that the object is located at the border of the forest at the southern orientation, the height of the trees crowns does not provide adequate shade. As a result, the veranda is overheated. The introduction of external roller shutters would improve the quality of the microclimate inside. At the same time, it should be emphasized that the designed accumulation wall fulfils its function and constitutes a barrier that stores heat and constitutes a thermal barrier between the veranda and other rooms. Openings in the accumulation wall should be added to allow for a correct flow of heated air from the veranda to the inside of the building. The wall made with the use of rammed earth technology meets the conditions of thermal insulation, maintaining proper temperature both in winter and in summer. The material is characterized by appropriate thermal capacity, ensuring thermal and humidity stability of the building. The rammed earth technology can be implemented in Poland in the temperate climate zone. The construction of the experimental building in Pasłęk met with interest in the scientific and architectural environment related to ecological construction. The building was awarded by an international jury of the European Union's Terra (In)cognita programme for design and innovative implementation and received the Outstanding Earthen Architecture in Europe Award in the year 2011.

ORCID

Jerzy Górski: http://orcid.org/0000-0002-4583-8144
Joanna Klimowicz: http://orcid.org/0000-0003-4950-3250
Anna Nowak: http://orcid.org/0000-0003-2952-904X

References

Ashour T., Heiko G. and Wei W. (2011). An experimental investigation on equilibrium moisture content of earth plaster with natural reinforcement fibres for straw bale buildings. *Applied Thermal Engineering, 31*(2-3), 293-303.

Dobson S. (2000). *Continuity of Tradition*: New Earth Building Terra.

Ford M., Griffiths R. and Watson L. (2005). The Sandford Inventory of Earth Buildings constructed using *a GIS Building and Environment, 40*(7), 964-972.

Górski J., Klimowicz J., Kołłątaj M. and Nowak A. (2018). *Mikroklimat obiektów jako efekt zastosowania proekologicznych technologii budowlanych* (in Polish), statutory work at the Faculty of Architecture in the Warsaw University of Technology, Warsaw, Poland.

Górski J., Kelm T., Klimowicz J. and Kołłątaj M. (2017). *Architektura ziemi i zielona infrastruktura* (in Polish), statutory work at the Faculty of Architecture in the Warsaw University of Technology, Warsaw, Poland.

Kelm T. (1996). *Architektura ziemi – tradycja i współczesność*. (in Polish) Oficyna Wydawnicza Politechniki Warszawskiej, Warsaw, Poland.

Niroumand H., Zain M. F M and Jamil M. (2013). A guideline for assessing of criticalparameters on Earth architecture and Earth buildings as a sustainablearchitecture in various countries. *Renewable and Sustainable Eneregy Reviews, 28*, 130-165. doi: 10.1016/j.rser.2013.07.020

Nother B. (1996). *Looking after earth buildingsContext,* (49), 22-23.

Thiers S. and Peuportier B. (2008). *Thermal and environmental assessment of a passive building equipped with an earth-to-air heat exchanger in France Solar Energy, 82*(9), 820-831.

Wallis R.K. (2012). *Modern Earth Buildings Elsevier,* 688-711.

XV International Conference on Durability of Building Materials and Components
DBMC 2020, Barcelona
C. Serrat, J.R. Casas and V. Gibert(Eds)

Fire Properties of Novel Cellulosic Material Modified with Expandable Graphite

Anielkis S.R. Batista, Wojciech Ł. Grześkowiak and Bartłomiej Mazela

Faculty of Wood Technology, Poznan University of Life Sciences, Wojska Polskiego 38/42, 60637 Poznan, Poland, e-mail: anielkis.batista@up.poznan.pl, wojciech.grzeskowiak@up.poznan.pl, bartlomiej.mazela@up.poznan.pl

Abstract. *Expandable graphite (EG) is an intumescent additive known to improve fire properties of various materials. Intumescent fire retardant (IFR) based on EG is a protection method for flammable materials taking the attention of researchers in the past few years (Xie et al., 2000). New studies indicate that EG is a good source of carbonization agent for effective and environmentally friendly intumescent systems (Feng et al. 2013). Although EG is used in a growing number of IFR systems as a blowing agent that will suppress flammable gases up to 75%, while reducing the flame spread index, its application to cellulosic material is not so popular in the cellulose industry today (Krassowski et al., 2012). The current study focuses on flammability, concerning cellulose modified material (CMM). The objective of this work was CMM encrusted with EG. The general aim of the research was to determine its basic fire resistance properties. The scope of the research included measurement of the following parameters: time to ignition (T_i), time to flame out (T_f), total heat peak (THR) and mass loss (ML). Samples of CMM sheets were manufactured with the use of hydropulper and rapid-koethen devices. Two types of EG (i.e. ES20 C200 and ES100 C10) were used. Sodra Black Cellulose fibres (700 kg/N^3) was used in this experiment. Cellulose milling time was 30 min. and drying time of 40 min. The drying temperature of the final sheets was controlled and kept at 93^0C to avoid graphite activation. Final sheets were conditioned at room temperature at 20^0C and relative humidity 60%. With heat flux of 35 kW/m², all samples were tested on MLC apparatus. The addition of EG was found to increase the flame retardant effectiveness of cellulosic material. Although T_i for all CMM species were lower than that of control samples, this fact actually favored the promotion of char forming, which led to a longer combustion process for all CMM.*

Keywords: *Mass Loss Calorimeter, Char, Expandable Graphite Cellulose, Flammability.*

1 Introduction

Fire retardant formulation (FRF) based on expandable graphite (EG) is a fire reinforcement method for flammable materials taking the attention of researchers in the past few years (Xie and Qu, 2000). As a carbon-layered crystal, EG consists of sheets of carbon atoms strongly bound to each other (Kruger, 2017). The literature indicates that EG is a good source of carbonization agent for effective design of environmentally friendly intumescent systems (Feng *et al.,* 2013). There are insufficient detailed reports in literature on the behaviour of EG-intumescent fire retardants (IFR) systems concerning cellulosic materials. Although EG is used in a growing number of IFR systems as a blowing agent that will suppress flammable gases up to 75%, while reducing the flame spread index, its application to cellulosic material is not so popular in the cellulose industry today. Depending on the processing methods, fire retardants (FR) are often categorized as: Additive or non-inert compounds. Additive FRs are often mixed inside the matrix of the polymer during its processing. These FR are usually inert

to de polymer. Reactive FRs are dose polymerized with a resin during processing of cellulosic material to become integrated into its molecular network structure. These FRs are also known as chemically modified FRs (Jesbains *et al.,* 2011). The footprints of fire retardants points to an effective ideal fire retardant that should be thermo-stable, compact with the protected polymer, should not change the physical-chemical properties of the protected polymer, and have low toxicity under heat exposure or during burning (Camino and Costa, 1987). In order to understand the dynamics of fire retardants it is required to have detailed knowledge of the mechanism of the thermal-degradation progress related to the polymer.

Inventions related to EG are usually linked to its thermal properties, therefore related to reducing the flammability and/or combustibility. In fact, the use of expandable graphite as part of flame retardant agents and fire protection is being promoted by laws and regulations that push the prohibitions of halogenated based fire retardants due to environmental concerns related to the emission of toxic gases from the thermal degradation of halogenated base flame retardants. The European Union is one of the organizations promoting the development of new halogen-free flame retardants (Acuna *et al.,* 2019). EG is a novel product in use in various inventions. Many patents claim that EG properties can be used for diverse of applications. Not only in the field of fire retardants where EG is used to protect fibrous materials, but also in electrical applications. As solid composite, EG was used in lithium/Sulphur batteries as cathode; the solid composite comprised of up to 75wt-% of expanded graphite (Schmidt *et al.,* 2017). Rubber melded body material with enhanced fire resistance. In this rubber composition, one of the main components was EG (Sakai and Nakano, 2019). EG is also used in devices of heat recovery unit, on this invention due to its heat resistance, EG was installed as a retention membrane (Murata and Koga 2019). EG is a multi-porous material with an average pore size distribution of about ~2 nm, this structure allows EG to accommodate other chemical espies in between is sheets to form other composites, it has been found to improve the conductivity properties of the polymer structure. From the exfoliation process of expandable graphite, we can obtain a good electrically conductive material, this is leading to several study of the electrical conductivity of some EG composites (Celzard, *et al.,* 2000). In solar energy storage researches, EG is one of the materials that can enhance the thermal conductivity of solar cell. In the works of Xiao *et al.,* (2013), sodium nitrate, potassium nitrate and their solution were used as the base material. The conductivity of the based material was of about 10 wt.%. With the addition of expanded graphite that has high thermal conductivity, the conductivity of the final material increased at about 40%. In his work, Xiao *et al.,* (2013) agreed that the theoretical results and the experimental results are in agreement. It is clear that the novel product has a diversity of fields/research areas to contribute with its property in this literature review we consider that the thermal conductivity properties and the potentially electrical conductivity properties are at the top potential characteristics that researchers at observing. Most articles do not address the aesthetic aspect of their final product. When combining EG with other additives the appearance of the final product is not so attractive the final application, especially when it is related to coatings fire retardants formulations. Other concern is related to cost of EG. The market to this product is growing at a fast speed. According to the Markets and Markets (2019), the global graphite market is projected to reach 29.05 billion dollars by 2022. This is a considerable amount that indicates that the global market is interested on these eco-friendly products. In the academy it is conclusive that the use of EG will increase as novel products

are developed.

To achieve this goal, the present preliminary experiment will use Mass Loss Calorimeter (MLC) infer the thermal stability of the CMM. MLC is frequently used to explore flammability properties of different type of materials, delivering a suitable sort of technical data (Krassowski *et al.,* 2012). Recent analysis of thermal stability of lingo-cellulosic materials under controlled conditions showed the decomposition temperatures (T_d) for lignin, hemicelluloses and cellulose. This last component, with $T_d = 320^0$C, char 6% by mass (Mazela *et al.,* 2018; Fox *et al.,* 2012). The current study focuses on flammability concerning cellulose component only.

The objective of this work was cellulose-based model material (CMM) encrusted with expandable graphite (EG). The general aim of the research was to determine its basic fire resistance properties. The scope of the research involved measurement of the following parameters: time to ignition (Ti), time to flame out (Tf), total heat release peak (THR) and mass loss (ML).

2 Methods

Samples of cellulose sheets were manufactured with the use of hydropulper and Rapid-Koethen devices. Cellulose sheets were encrusted with two types of EG (ES100 C10 and ES20 C200). EG was dispersed in a cellulose pulp at the preparation stage. ES20 C200 had higher amount of fine-grained fraction (90% <75µm) and thus was characterized by lower expansion volume (20 ml/g) in comparison to ES100 C10 type. Three variants of cellulose sheets were prepared: control sheets (pure cellulose) and sheets encrusted with graphite ES200 C20 or ES100 C10. Sodra Black Cellulose fibres (700 kg/m^3), with the following dimensions of fibers: 2.05 mm length, 30.0 µm width, were used for the process of cellulose sheets manufacture. The cellulose milling time was 30 minutes and the drying time 40 minutes. The drying temperature of the final sheets was maintained at 93^{0}C to avoid graphite activation notwithstanding the manufacture of EG advises that activation temperature is at about 320^{0}C. The final sheets were conditioned at room temperature at 200^{0}C and relative humidity 60%. All the samples were subjected to MLC measurements (Fig. 1). Heat flux at 35 kW/m^2 was estimated as suitable level for all tested samples. This work inferred conclusions on flammability properties of CMM by measuring time to ignition (Ti), time to flame out (Tf), total heat release peak (THR) and mass loss (ML). It was possible to account for all important aspect mentioned above however it was not possible to account for repeatability the samples. This led to some discrepancy in some sample properties (i.e. thickness) as shown on table 1. bellow.

Table 1. Characterization of samples.

Samples	Thickness	THR (MJ/m^2)	T_i (s)	T_f (s)	THR peak (MJ/m)
Cellulose 01	0.89	9	25	94	230.72
Cellulose 02	0.88	7.2	21	79	222.41
Cellulose 03	0.89	8.3	24	89	236.05
EG200-01	1.45	6.7	22	100	98.03
EG200-02	1.4	6	21	102	89.55
EG200-03	1.4	6	20	99	97.61
EG100-01	1.4	4.4	19	108	73.32
EG100-02	1.5	4.4	19	107	75.42
EG100-03	1.4	4.8	19	123	74.96

It is clear that the mass (g) of each sample are not the same. With the standard deviation calculated to be 0.1 for cellulose samples, 0.5 for EG200 and 0.3 for EG100.

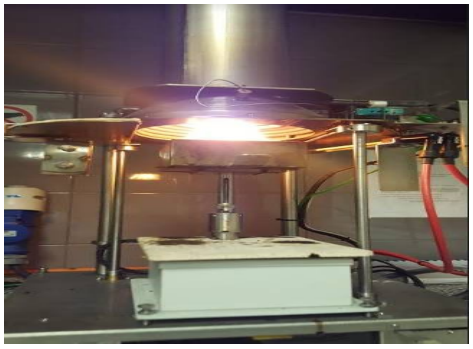

Figure 1. MLC apparatus set at 35kW/m^2.

3 Results

T_i for CMM encrusted with ES100 C10 and ES20 C200 was estimated at the average on 19.0 and 21.0s respectively. This corresponds to T_i of ES100 C10 2s faster than that of ES20 C200, while for control samples it was estimated on 23.3 s, control samples resisted 22% more time than the more "fragile" sample (ES100 C10). As we can confirm in the figure 2. In average, T_i for CMM encrusted with ES100 C10 and ES20 C200 were observed to ignite 4.3 s and 2.3 s, respectively faster than control samples.

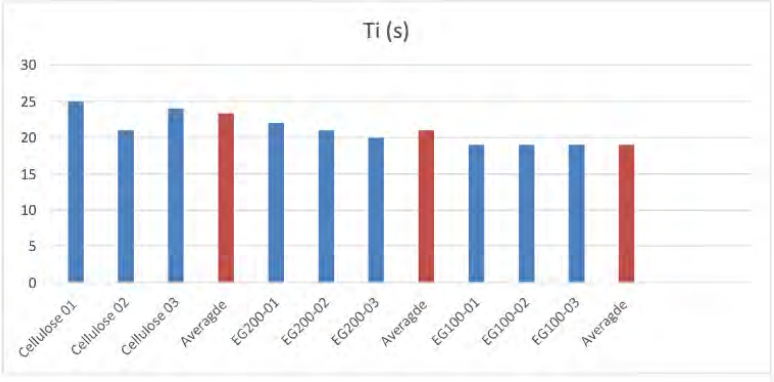

Figure 2. Time to ignition of all samples.

Figure 3. shows among others, the average T_f value for CMM encrusted with ES100 C10 was112.7 s, while pure cellulose and CMM with ES20 C200 did register an average of 87.7 and 108.0 s, respectively. In this case however, ES100 C10 showed a resilient behaviour, taking 28% more time to terminate its combustion process. ES100 C10 showed earlier char formation, this fact can help on fire protection properties.

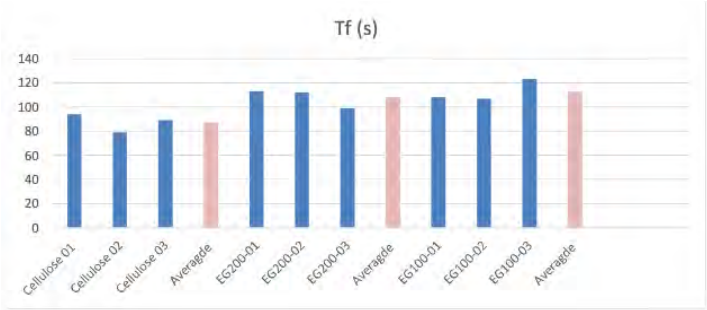

Figure 3. Time to flame out of all samples.

Maximum THR was observe to be 229.72 kW/m^2 for pure cellulose, 91.87 kW/m^2 for CMM with ES20 C200 and 71.51 kW/m^2 for CMM with ES100 C10, as presented in the in figure 4. ES100 C10 is a material that burns with a resilient behaviour. That is, this material suppresses better the refuel of the combustion process. Less heat released from the combustion process is redirect to the fire feed. One can observe that ES100 C10 have a more attractive fire property.

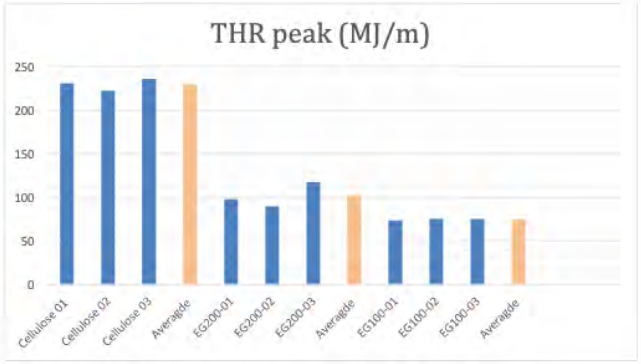

Figure 4. Time to flame out of all samples.

4 Conclusions

- The addition of EG was found to increase the flame-retardant effectiveness of cellulosic material.
- Although T_i for all CMM species were lower than for control samples, this fact actually favored the promotion of char forming. The improved physical characteristics of char is achieved by increasing the amount of the insulated layer and reducing crack formation. This aspect allowed the combustion process of CMM with ES100C10, to be 25s longer than combustion process of pure cellulose and almost 5 s longer than that of CMM with ES20 C200. In addition, the maximum HRR for CMM with ES100C10 was 69% smaller than its compared value for pure cellulose and 22% smaller than its compared value for CMM with ES20 C200.
- CMM with ES100 C10 is consequently the best performing system in terms of the observed parameters.

Acknowledgements

The work was financially supported by the Ministry of Science and Higher Education as the Project No 507.423.09. with subsidies for maintaining the research capacity and the paper was partially financed within the framework of Ministry of Science and Higher Education programme "Regional Initiative of Excellence' in years 2019-2022, Project NO. 005/RID/2018/19". Part of the above mentioned results were also presented on two scientific conferences in year 2019: INPAP 2019 - The future of papermaking, 10-12th of June, Augustów Poland and Wood Science Economy – International scientific conference, 21-22nd of October Poznan, Poland.

ORCID

Anielkis S.R. Batista: https://orcid.org/0000-0003-1765-1072
Wojciech Ł. Grześkowiak: https://orcid.org/0000-0002-6781-8187
Bartłomiej Mazela: https://orcid.org/0000-0003-0138-3034

References

Acuña, P., Li, Z., Santiago-Calvo, M., Villafañe, F., Rodríguez-Perez, M.Á. and Wang, D.Y. (2019). Influence of the Characteristics of Expandable Graphite on the Morphology, Thermal Properties, Fire Behaviour and Compression Performance of a Rigid Polyurethane Foam. *Polymers, 11*(1), 168. doi:10.3390/polym11010168.

Camino, G. and Costa, L. (1987). Performance and Mechanism of Fire Retardants in Polymers-A Review. *Polymer degradation and stability*, *20*, 271-294.

Celzard, A., Marêché, J., Furdin, G. and Puricelli, S. (2000). Electrical conductivity of anisotropic expanded graphite-based monoliths, *Journal of Physics D*: Applied Physics. doi: 33. 3094. 10.1088/0022-3727/33/23/313.

Feng, C., Zhang, Y., Lang, D., Liu, S., Chi, Z. and Xu, J. (2013). Flame Retardant Mechanism of a Novel Intumescent Flame Retardant Polypropylene. *Procedia Engineering, 52,* 97–104.

Fox, D.M., Lee, J., Zammarano, J., Katsoulis, D., Eldred, D.V., Haverhals, M.L., Trulove, P.C., DeLong, H.C. and Gilman, J.W. (2012). Char-forming behavior of nanofibrillated cellulose treated with glycidyl phenyl POSS. *Carbohydrate Polymers, 88*(3), 847–858.

Jesbains, K., Faiz, A., Megat-Yusoff, P. and Ullah, S. (2011). The Study of Bonding Mechanism of Expandable Graphite based Intumescent Coating 15. *Research Journal Of Chemistry And Environment*.

Krassowski, D.W., Hutchings, D.A. and Qureshi, S.P. (2012). Expandable Graphite Flake as an Additive for a New Flame Retardant Resin. GrafTech International Holdings Inc.

Kruger, H.J. (2017*). Characterization of expandable graphite and its flame retardant abilities in flame retardant systems for polyethylene*. PhD thesis Pretoria University.

Mazela, B., Perdoch, W., Grześkowiak, W. and Batista, A. (2018). Selection of heat flux value for wood fire retardants testing using MLC, IRG-WP doc. No.18-40846.

Murata, T. and Koga, Y. (2019). US2019/0093599 A1.

Sakai, T. and Nakano, S. (2019). US 2019/0225785A1.

Schmidt, R., Panchenko, A., Ewald, B., Hanefeld, P., Sorin, I., Moehwald, H. and Kovalev I., (2017). US 9,577,243 B2.

Xiao, X., Zhang, P. and Li, M. (2013). Thermal characterization of nitrates and nitrates/expanded graphite mixture phase change materials for solar energy storage. *Energy Conversion and Management,* ISSN 0196- 8904, doi.org/10.1016/j.enconman.2013.04.007.

Xie, R. and Qu, B. (2000). Synergistic effects of expandable graphite with some halogen-free flame-retardants in polyolefin blends. *Polymer Degradation and Stability, 71*(3), 375–380.

XV International Conference on Durability of Building Materials and Components
DBMC 2020, Barcelona
C. Serrat, J.R. Casas and V. Gibert (Eds)

Fundamental Properties and Durability of Concrete with Gasification Molten Slag as Fine Aggregate

Takafumi Watanabe, Hiromi Fujiwara, Masanori Maruoka and Koji Satori

Graduate School of Regional Development and Creativity, Utsunomiya University,

7-1-2 Yoto, Utsunomiya City, Tochigi Prefecture, Japan, mc196264@cc.utsunomiya-u.ac.jp

Abstract. *The proportion of electricity generated by coal-fired thermal power plants has been rising in Japan as a result of the nuclear plant accident caused by the Great East Japan Earthquake of 2011. Coal-fired electricity generation has a large environment impact, so the commercial application of integrated coal gasification combined cycle (IGCC) has been promoted. IGCC is an efficient generating method combining a steam turbine and a gas turbine. However, IGCC plants generate coal gasification molten slag (CGMS) and it is necessary to establish effective utilization methods for this slag for further promotion of IGCC technology. In this paper, the fresh properties, hardened properties and durability of concrete containing CGMS as fine aggregate are investigated. The results show that, in comparison with concrete using conventional fine aggregate, the air content introduced by an air-entraining agent is lower and bleeding is increased when CGMS is used as a fine aggregate. As for the hardened properties, compressive strength is slightly lower, while freeze-thaw resistance is significantly reduced. In additional tests, it is found possible to improve freeze-thaw resistance by increasing the air content.*

Keywords: *Coal Gasification Molten Slag, Fine Aggregate, Freeze-Thaw Resistance, Integrated Coal Gasification Combined Cycle (IGCC).*

1 Introduction

With environmental concerns restricting the extraction of natural aggregate, Japan's concrete industry is finding it difficult to secure supplies and is pursuing research to develop substitute aggregates. On the other hand, following the Great East Japan Earthquake and tsunami of 2011, the composition of Japan's electricity supply has tilted toward thermal power generation in place of the nuclear power that was predominant. Currently coal-fired power generation accounts for approximately 32.3% of all electricity generated in Japan. Conventional coal-fired power stations emit tremendous quantities of CO_2, so technology to reduce CO_2 emissions is needed. For this reason, the use of the highly efficient Integrated Gasification Combined Cycle (IGCC) has been promoted. With IGCC technology, impurities from coal that has been heated in a gasification furnace are melted and discharged as coal gasification molten slag (CGMS). CGMS is an amorphous material formed by rapid granulation in water. Establishing a method for effective use of this CGMS is essential to expansion of IGCC utilization. It is thought that using CGMS as concrete aggregate could make a major contribution to society. However, no standards have yet been established for such use of CGMS. This study investigates the potential for use of CGMS as a concrete aggregate. The fundamental properties of concrete incorporating CGMS are estimated and problems that must be resolved are isolated in order to provide data for the establishment of standards for the use of CGMS aggregate.

doi:10.23967/dbmc.2020.071

2 Characteristics of CGMS Fine Aggregate

The characteristics of the CGMS and crushed sand used as fine aggregates in this study were measured and compared. Figure 1 shows electron microscope pictures of the CGMS fine aggregate (symbol: Sg) and crushed sand (symbol: Sc) used in this study.

Table 1 gives the chemical composition of CGMS. The main components are silicon dioxide, aluminum oxide, calcium oxide and iron trioxide, which account for more than 90% by weight, with trace amounts of other minerals. These are all oxides of naturally existing elements.

Figure 1. (a) Coal gasification molten slag and (b) Crushed sand.

Table 1. Chemical composition of CGMS.

Detection component	Quantitative value (%)	Detection component	Quantitative value (%)
SiO_2 (Silicon dioxide)	30.4	K_2O (Potassium oxide)	1.2
Al_2O_3 (Aluminum oxide)	11.1	TiO_2 (titanium dioxide)	0.8
CaO (Calcium oxide)	23.1	MgO (Magnesium oxide)	11.5
Fe_2O_3 (Iron trioxide)	21.5	SO_3 (Sulfur trioxide)	0.0

2.1 Test Items

Density, water absorption, particle size distribution, bulk density and solid content, content under 75μm sieve, and solid volume percentage for shape determination were measured according to ISO, ASTM and EN.

In order to estimate strength and elastic deformation for use as aggregate, an aggregate strength indicator test was developed and used to characterize the CGMS and crushed sand aggregates. A steel container with an inner diameter of 33 mm and a height of 88 mm was used for this test. Figure 2 outlines this aggregate strength indicator test. The test is carried out as follows.

Under fully dried condition, aggregate with particles in the range 1.2–2.5 mm is separated by screening. Then 60 g of the separated particles are placed in the steel container and the upper surface is smoothed using the finger. A round steel loading bar is then inserted and a precision universal testing machine used to apply a compressive load P (kN) while at the same time measuring the displacement d (mm) using a laser displacement gauge. Loading continues up to a maximum of 90kN. A load-displacement curve is drawn from the measurements and the gradient of the proportional section of the curve is calculated as the aggregate strength index using Equation (1) below.

$$I(kN / mm) = P(kN) / d(mm) \quad (1)$$

where: I is the aggregate strength index value;
P is the compressive load; and
d is the displacement.

After the test, the particles are screened through a 0.30 mm sieve and then a 0.15 mm sieve, and the 0.30 crushing value (%) and 0.15 crushing value (%) are calculated from the quantity passing each sieve. These crushing values are calculated using the following equations (2) and (3).

$$0.30 \text{ crushing value} = B(g) / A(g) \times 100 \ (\%) \quad (2)$$

$$0.30 \text{ crushing value} = C(g) / A(g) \times 100 \ (\%) \quad (3)$$

Where: A is the weight of crushed aggregate;
B is the weight of aggregate passing the 0.30mm sieve; and
C is the weight of aggregate passing the 0.15mm sieve.

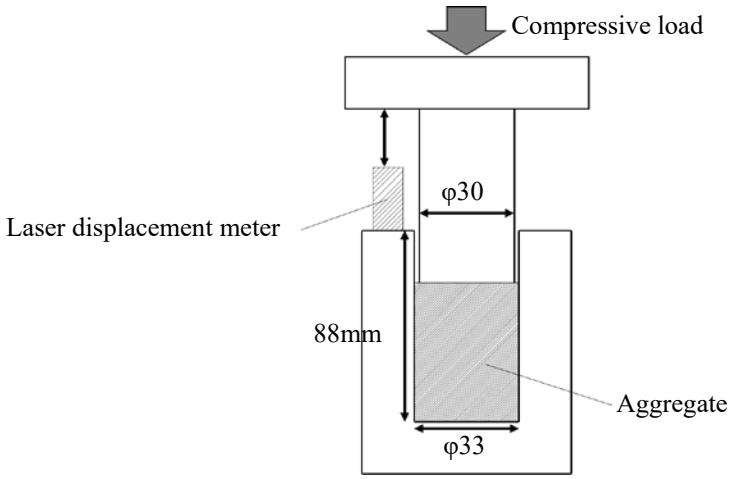

Figure 2. Outline of aggregate crushing test for strength index value.

2.2 Test Results

Table 2 shows the standard test results for the CGMS fine aggregate and crushed sand. Figure 3 shows the particle size distributions of the two fine aggregates as determined by sifting. The CGMS fine aggregate used in this study had a larger density of 3.08g/cm^3 in saturated surface-dry condition compared with crushed sand. Its water absorption rate is 0.70%, which is lower than that of crushed sand.

From these results, it is inferred that CGMS fine aggregate has a smooth surface and it is possible to reduce the restrained water volume on the surface of the aggregate. This leads to the expectation that the unit volume of water needed for a given slump can be reduced as compared to crushed sand. As the solid content and the solid volume percentage for shape determination are almost the same as the crushed sand values, it is thought that CGMS fine aggregate has appropriate particle shapes and sizes. From these data, improved fluidity can be expected for fresh concrete made with CGMS fine aggregate.

Figure 4 shows the relationships between compressive load and displacement in the aggregate strength indicator test. The resulting strength index values are shown in Table 3. These results show that CGMS fine aggregate has a higher strength index value than crushed

sand, resulting in greater resistance to deformation under external force. Moreover, the crushing values indicate that CGMS fine aggregate is more brittle than crushed sand.

Table 2. Characteristics of CGMS fine aggregate and crushed sand.

		Test method	Test value	
			Sg	Sc
Density in saturated surface-dry condition	g/cm^3	ISO 7033:1987	3.08	2.64
Absolute dry density	g/cm^3		3.06	2.60
Water absorption rate	%		0.70	1.33
Bulk density	kg/L	ISO 6782:1982	2.05	1.75
Solid content	%		66.9	67.3
Content of materials finer than 75μm sieve	%	ASTM C117	4.7	2.7
Solid volume percentage for shape determination	%	EN 933-3	57.1	56.7
Fineness modulus		ISO 6274:1982	2.50	2.73

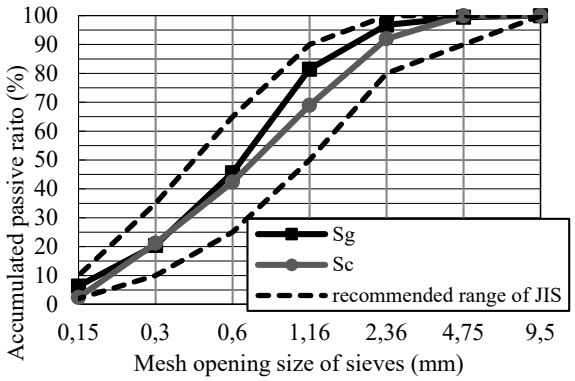

Figure 3. Particle size distribution of fine aggregates.

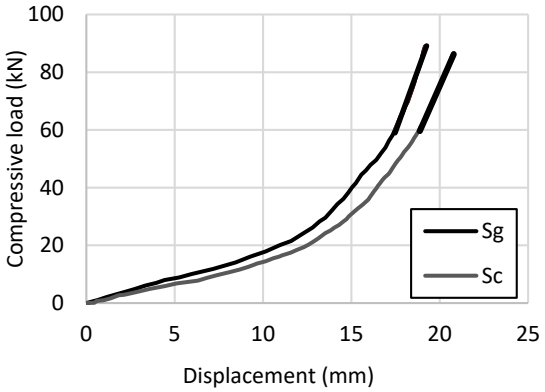

Figure 4. Relationship between compressive load and displacement.

Table 3. Aggregate strength index value and aggregate crushing test results.

	Sg	Sc
Aggregate strength index value: I	16.9	13.9
Crushing value 0.30 (%)	27.6	21.7
Crushing value 0.15 (%)	21.7	13.0

3 Fundamental Properties of Concrete Using CGMS as Fine Aggregate

3.1 Materials

Ordinary portland cement (symbol: C, density: 3.16 g/cm^3) was used as binder. Crushed sand (Sc) and CGMS fine aggregate (Sg) were used as fine aggregates. Crushed stone (symbol: G; density in saturated surface-dry condition: 2.61 g/cm^3) was used as the coarse aggregate.

Additionally, a high-performance water reducing admixture (symbol: SP), an air-entraining admixture (symbol: AE) and a deformer (symbol: DF) were included as admixtures.

3.2 Mixture Proportions

Table 4 shows the mixture proportions of the concrete used to cast specimens. The water-cement ratio was fixed at 50%. Sand fine aggregate was replaced by CGMS at volume ratios of 0%, 50% and 100%; the replacement ratio is expressed as Sg/S. The target values of fresh properties were 12.0±1.5 (cm) for slump and 4.5% ± 1.5% for air content. The rate of high-performance water reducing admixture addition was also fixed to 0.75% by mass, after an initial study in which the target values of fresh properties were obtained at this addition rate with Sg/S=100%. In order to obtain the target values at Sg/S=0% and Sg/S=50%, the unit volume of water was adjusted so as to carry out evaluations based on the unit volume of water that satisfied the target values, while keeping the SP addition rate constant.

Table 4. Mixture proportioning of concrete for fresh property testing.

W/C (%)	s/a (%)	Sg/S (%)	Unit content (kg/m^3)					Admixture addition rate (C×%)		
			W	C	Sc	Sg	G	SP	AE	DF
50	47	0	178	356	824	0	926	0.75	0.05	0.05
		50	180	360	410	478	921		1.40	0.05
		100	174	348	0	971	935		2.40	0.05

Table 5. Results of fresh properties tests.

W/C (%)	Sg/S (%)	Unit water (kg/m^3)	Slump (cm)	Air content (%)	Temperature (°C)	Bleeding rate (%)
50	0	178	12.0	4.0	20	7.00
	50	180	12.0	4.7	27	6.97
	100	174	11.5	3.9	27	9.24

3.3 Test Methods

The fresh properties measured were concrete slump, air content, concrete temperature, and bleeding ratio. The hardened concrete was tested for compressive strength. Durability was investigated by carrying out freeze-thaw tests, drying shrinkage tests and accelerated carbonation tests. These were all in accordance with ISO and ASTM.

3.4 Test Results

Table 5 shows the results of the fresh properties tests. The bleeding rate was found to increase at higher Sg/S ratios. With Sg/S = 100%, the unit water volume was lower but the bleeding rate increased. This is thought to be because the CGMS fine aggregate has a smooth surface and low water absorption rate, so there is a greater surplus of water when the mix includes more CGMS. And also, it is considered that water content increased. Then the same slump value could be obtained at lower unit water amount.

Figure 5 shows the results of the compressive strength tests. Concrete with CGMS fine aggregate has a slightly lower strength compared with concrete without it. This is considered to be because CGMS itself is not as strong as crushed sand, noting that the crushing values of CGMS fine aggregate are larger. Further, with the increased bleeding, it is also considered that voids in the interfaces with coarse aggregate particles increased, resulting in weaker interface bonding between coarse aggregate and cement paste.

Figure 6 shows the results of the freeze-thaw tests. Concrete including CGMS fine aggregate

showed very poor frost resistance. It is thought that this is because of the weaker interface bonding between paste and coarse aggregate particles, resulting from the high bleed rate. The expansion pressure of freezing water in the voids causes this reduced resistance. There is a need for studies aimed at improving the freeze-thaw resistance of concretes containing CGMS fine aggregate.

Figure 7 shows the results of the drying shrinkage tests. With higher Sg/S, drying shrinkage strain decreased. The reason for this is considered to be that, since the aggregate strength index of CGMS fine aggregate is larger, its deformation resistance is larger. With a higher Sg/S ratio, the unit water content decreased. As a result, drying shrinkage was reduced.

Figure 8 shows the results of the accelerated carbonation test. With a higher Sg/S ratio, the carbonation rate increased. More bleeding occurred at higher Sg/S, so a coarser microstructure formed in the concrete, allowing CO2 to enter the concrete more easily.

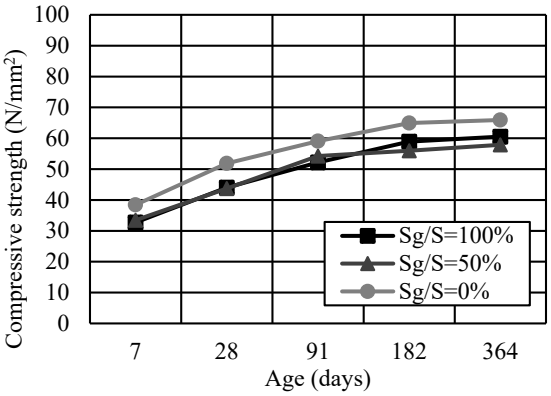

Figure 5. Results of compressive strength test.

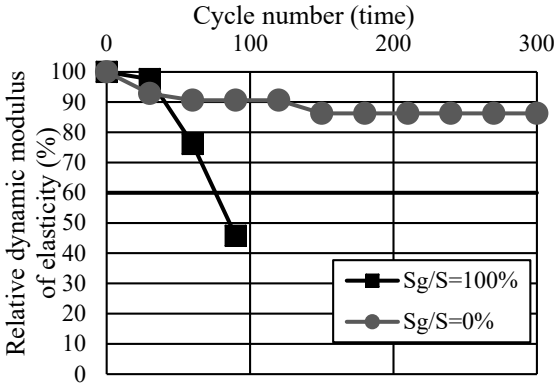

Figure 6. Results of freeze-thaw test.

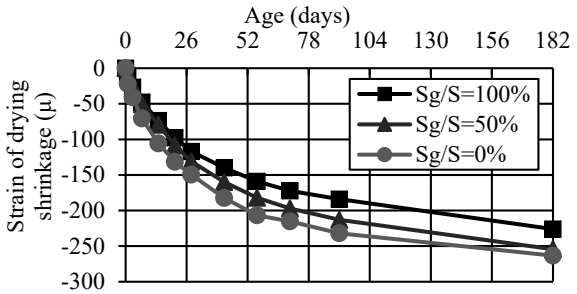

Figure 7. Results of drying shrinkage test.

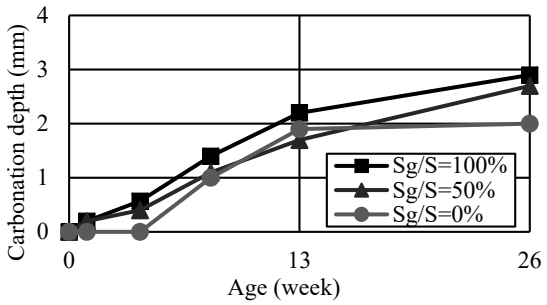

Figure 8. Results of accelerated carbonation test.

4 Experiment to Improve the Frost Resistance of Concrete Including CGMS Fine Aggregate

The results of the freeze-thaw test show that the resistance of concrete made with CGMS fine aggregate is significantly reduced. A possible method of improving freeze-thaw resistance by increasing the air content was examined.

Table 6 shows the mix proportions of the concrete used in this experiment and the results of the fresh properties tests.

The water-cement ratio was fixed at 50%. Sand fine aggregate was replaced by CGMS at a volume ratio (Sg/S) of 100%. The target values of fresh properties were 12.0 ± 1.5 (cm) for slump and the three values of air content: 4.5 ± 1.5%, 6.0 ± 0.5% and 7.5 ± 0.5%. As an additional test, the air-void spacing factor was measured by the linear-traverse method. This test was implemented in accordance with ASTM C 457-98.

Table 6. Mixture proportioning of concrete for freeze-thaw testing and results of fresh property tests.

Symbol	W/C (%)	Unit content (kg/m^3)				Admixture addition rate (C×%)			Air content (%)	Slump (cm)	Temperature (°C)
		W	C	Sg	G	SP	AE	DF			
Sg-4.5	50	174	348	971	935	0.75	2.40	0.05	3.9	11.5	27
Sg-6.0		171	342	978	942		1.40	0.05	5.5	10.5	27
Sg-7.5		169	338	983	947		2.20	0.05	7.7	13.0	28

4.1 Test Results

Figure 9 shows the results of the freeze-thaw test and Figure 10 shows the relationship between air-void spacing factor and durability factor. As can be seen in these results, freeze-thaw resistance was greatly improved by increasing the air content.

The experiment demonstrated that the entrainment of air in concrete containing CGMS fine aggregate is low during mixing. In order to obtain the target air content, it was necessary to add a large amount of AE admixture. These results indicate that CGMS contains a large amount of non-combustion carbon and this will require further study.

The air-void spacing factor was lower when the target air content was adjusted to 6.0% and 7.5% than when it was adjusted to 4.5%. This is because the number of air voids increased as the amount of air increased. And it is thought that bleeding rate was suppressed by increasing air content.

These results demonstrate that the freeze-thaw resistance of concrete containing CGMS fine aggregate can be improved, but further study is needed.

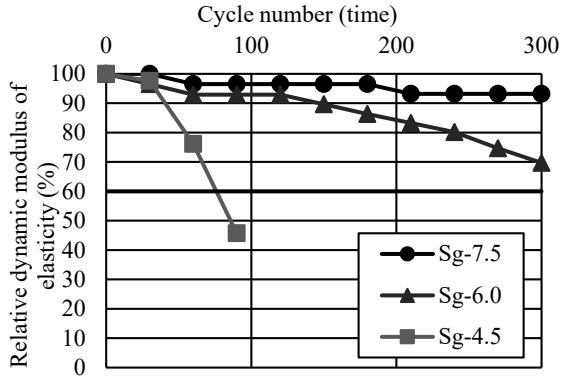

Figure 9. Results of freeze-thaw test.

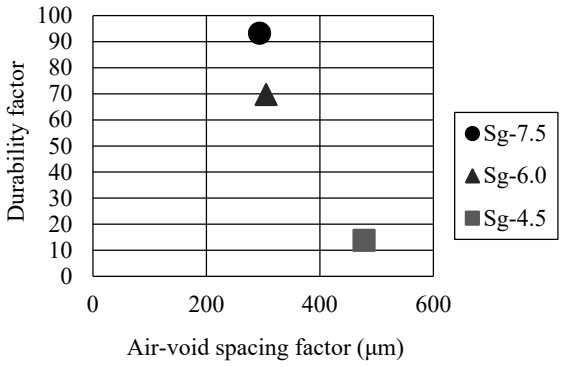

Figure 10. Relationship between air-void spacing factor and durability factor.

5 Conclusions

Experiments to determine the basic properties of concrete containing CGMS as fine aggregate showed that fluidity improved while compressive strength decreased slightly. In other results, drying shrinkage strain was reduced while carbonation resistance decreased.
In terms of durability, tests of freeze-thaw resistance were not very good. However, freeze-thaw resistance was shown to be improved by increasing the air content of the fresh concrete.

Acknowledgements

In this research project, Coal Energy Center of the General Foundation provided us with slag, adjusted its granularity and offered opportunities for testing. The research was entrusted to us by New Energy and Industrial Technology Development Organization (NEDO). The authors thank these organizations for their cooperation.

References

Ministry of Economy, Trade and Industry. (2019). Agency for Natural Resources and Energy: Outline of the Energy White Paper; https://www.enecho.meti.go.jp/about/whitepaper/2019pdf/whitepaper2019pdf_2_1.pdf

Yuto Yamanaka, Hiromi Fujiwara, Masanori Maruoka and Ryosuke Otsuka (2018). “Experimental Study on Properties of Mortar Containing Molten Slag from Integrated Coal Gasification Combined Cycle as Fine Aggregate”, Proceeding of 2nd International Workshop on Durability and Sustainable of Concrete Structures, USB

Ryotaro Kobayashi, Hiromi Fujiwara, Masanori Maruoka and Yuto Yamanaka (2019). “Experimental study on properties of concrete containing molten slag integrated coal gasification combined cycle as fine aggregate”, Proceedings of International Conference on Sustainable Materials, Systems and Structures (SMSS2019), 264-271

XV International Conference on Durability of Building Materials and Components
DBMC 2020, Barcelona
C. Serrat, J.R. Casas and V. Gibert (Eds)

Performance Based Specification of Wood – Project CLICKdesign

Ed Suttie[1], Christian Brischke[2], Eva Frühwald Hansson[3], Stefania Fortino[4], Jakub Sandak[5], Magdalena Kutnik[6], GryAlfredsen[7], Christophe Lucas[8] and Eric Vieillemard[9]

[1] BRE, Garston, Watford, WD25 9XX, United Kingdom Ed.Suttie@bregroup.com

[2] Abt. Holzbiologie und Holzprodukte, University of Göttingen, Büsgenweg 4, D-37077 Göttingen, Germany christian.brischke@uni-goettingen.de

[3] Structural Engineering, Lund University, Faculty of Engineering LTH, Box 118, SE-221 00 Lund, Sweden eva.fruhwald_hansson@kstr.lth.se

[4] Material Modeling and Ecodesign, VTT Ltd, PL 1000, FI-02044 Finland Stefania.Fortino@vtt.fi

[5] InnoRenew CoE, Livade 6, 6310 Izola, Slovenia jakub.sandak@innorenew.eu

[6] Technological Institute FCBA, Allées de Boutaut – BP 227, 33028 Bordeaux, France Magdalena.Kutnik@fcba.fr

[7] NIBIO, Norwegian Institute of Bioeconomy Research, Pb 115, NO-1431 Ås, Norway Gry.Alfredsen@nibio.no

[8] IRBI Institut de Recherche sur la Biologie de l'Insecte, Faculté des Sciences et Techniques, Avenue Monge, Parc Grandmont, 37200 TOURS (France)France christophe.lucas@univ-tours.fr

[9] Hygiene Office, 4 Rue Pelletier, 91320 Wissous, France ines.vieillemard@hygiene-office.fr

Abstract. *This paper introduces the ForestValue research project CLICKdesign – delivering fingertip knowledge to enable service life performance specification of wood. The consortium is working on a primary innovation to move from the complex, fragmented and general to the easy-to-use, consolidated and specific by provision of a digital tool for specifiers. Other materials tackle this and provide designers and architects with software. The specification of performance of wood products is complex and fraught with inconsistency and requires use of multiple platforms for data, experience, standards and national recommendations. CLICKdesign will provide a tool that has within it the decades of research, the complexity of the standards specification systems and the variation of approach due to tradition, materials and culture across Europe and beyond. A simple tool for nonexpert public users will be available as well as a tool accessible to professional users that will be refined with industry to ensure relevancy and accelerate uptake and use.*

Keywords: *Durability-Based Design, Knowledge Transfer, Modelling, Performance, Service Life Planning.*

1 Introduction

Concrete, steel and polymeric sectors deliver software to architects and students enabling easy performance-based specification and design. It also enables easy teaching of design best practice and informs learning gathered by product manufacturers. This does not happen for wood comprehensively in Europe, though specific initiatives e.g. UK Structural Timber

Association guidance (www.structuraltimber.co.uk) and the German Carpenter Association's Guideline on Building Facades, Terrace decking, and Balconies (BDZ 2011, 2016) do exist. In addition, technical specifications are integrated into increasingly used Building Information Modelling (BIM) and life cycle analysis (LCA) which includes service life data. Service life planning and performance classification are thus core issues in the building sector underpinning material/product specification and use. The absence of durability performance-based specification for wood is currently a limit of opportunity. Well-functioning 'performance models' are essential to predict the service life and functionality of buildings.

2 Project CLICKdesign Context

2.1 Analysis of the Problem

The established specification of wood is not performance based, historically standards refer to ineffectual terms to bridge the performance gap such as "a reasonable working life". Wood engineers utilising Eurocode 5 find the ineffectual language doesn't stand scrutiny and is of little value. Awareness of the cultural legacy of wood in construction around us, traditional uses and skills are constant reminders of the enduring possibility of wood if knowledge is applied, including knowledge of species and material qualities, knowledge of design details and construction skills, knowledge of local conditions, climatic or other challenges. This knowledge is fragmented, localised and in some cases difficult to analyse and use especially by non-wood experts. This is the problem. The solution is to put this knowledge at the fingertips of the specifier, in their language so more can meet their ambitions to deliver low carbon construction, through performance based design with wood.

The existing decision logic of specification of durability, and implied performance, considers first the suitability of a timber species for use in construction. This first considers the natural durability of the chosen timber species (EN 350: 2016) and notes the intended end use (EN 335: 2013), *e.g.* Use Class 4 for a fence post. EN 460: 1994 compares the requirements of Use Class with the natural durability and indicates whether natural durability is sufficient for the end use or whether preservative treatment is required. The European Standards related to specifying preservative treated timber, EN 351-1: 2007 and EN 351-2: 2007 require the specification to be written in terms of the end results of the treatment process i.e. penetration and retention in the wood of a preservative formulation found to be effective in a series of standard biological test methods laid down in EN 599-1: 2013. The specification of service life has evolved around the end results achieved following preservative treatment with service life referred to in an unquantified and ambiguous way using terms such as "reasonable working life" or "satisfactory performance". Standards that started to define desired service lives were a step in the right direction as the desire for information on performance of wood products grew in part buoyed by the application of LCA for construction products that pivots on their service life requirements. In Germany, France and UK there are national documents that set out frameworks for performance. In the UK the British Standard BS 8417: 2011 sets out a framework for specifiers to interpret the European standards and to base specifications on penetration and retention requirements linked to treated products and 'desired service life'.

The established wood species and treatment combination for a specific use class works well but has gaps that miss many additional opportunities for timber in construction through good

design detailing, the aesthetic performance, other tools to enhance natural properties, the impact of surface cracks on performance, surface roughness and the more subtle moisture dynamic of the wood material.

Different types of performance models have been established for various building materials but cannot be transferred to wood-based materials. For performance modelling of wood products biological agents need to be considered with particular attention for mould, decay fungi, termites and other insects as well as the strong societal values of regional vernacular, skills and traditions that only wood as a material brings. Different approaches to adequately reflect the influence of biotic and abiotic factors on the performance of wood have been reviewed and evaluated (Brischke and Thelandersson 2014) with respect to their usability in the building trade. They found that efforts in developing performance models for both fungal decay and mould growth have been intensified in recent years (*e.g.* MacKenzie *et al.*, 2007, de Freitas et al. 2010, Viitanen *et al.*, 2010, Isaksson *et al.*, 2013, Niklewski *et al.*, 2016). A high heterogeneity among the numerous attempts became visible, different strategies have been followed, and were roughly distinguished according to the respective objectives, governing variables (*e.g.* mass loss, strength loss, remaining strength, decay ratings, service life, aesthetic appearance), data sources and the resulting level of accuracy.

A framework of how exposure, dimension, design details, and the material-intrinsic ability to take up and release water can be linked to model the moisture risk in wood products and thus performance is the central need. First attempts prepared using various dosimeter models were made in previous European research projects, namely the WoodWisdom-Net projects WoodExter and DuraTB, the Swedish WoodBuild program, and the FP7 project PerformWOOD. Good progress has been made during recent years in service life planning and performance prediction of wood-based components and structures, but as repeatedly became evident, the complexity of performance is still not captured in these processes.

The cross-links and interactions between exposure models, different decay and degradation models, and material resistance models need to be deeply elaborated to allow their utilization for comprehensive performance prediction. Furthermore, the degradation processes described and forecasted with the help of models need to be assessed for the respective purpose. Hence, one needs to distinguish between aesthetic performance, functional performance, mechanical performance and other aspects of performance (Jones and Brischke 2017). In particular, the effect of fungal, bacterial or insect damage on the overall mechanical stability of wooden structures is still neither fully understood nor adequately modelled for engineering purposes.

2.2 Beyond the State-of-the-Art

Project CLICKdesign is shown schematically in Figure 1 and includes:

- Forecasting surface aesthetic changes developing the kinetic and/or intensity of such changes due to location, microclimate, architectural design and materials used.
- Development of damage spatial distribution significance on mechanical performance. Studying spatial distribution of fungal decay and its interaction with moisture transport and resulting gradients in buildings.
- Development of a termite/insect performance measure for the first time in Europe.

- Robust integrated performance classification based on the whole set of external parameters for the first time the foundation established for decay, material and integrity aspects, aesthetic limits and performance and termite/insect performance aspects.
- Providing a CLICKdesign tool that utilises European standards, the latest research findings and wood databases such as the IRG Durability Database (http://www.irg-wp.com/durability) and puts it at the fingertips of specifiers and users. This will increase market confidence with users for selecting wood as a reliable product and enhance an optimised performance of timber in the built environment.
- Features wholly not integrated into specification now. The significant variations due to climate change present changes to exposure dose for wood products and the distribution and locations of wood destroying organisms e.g. termite risk zones in Europe.
- Inspiring new wood and wood-based products using the tool, supported by training outreach, and creating business opportunities for industries to innovate.

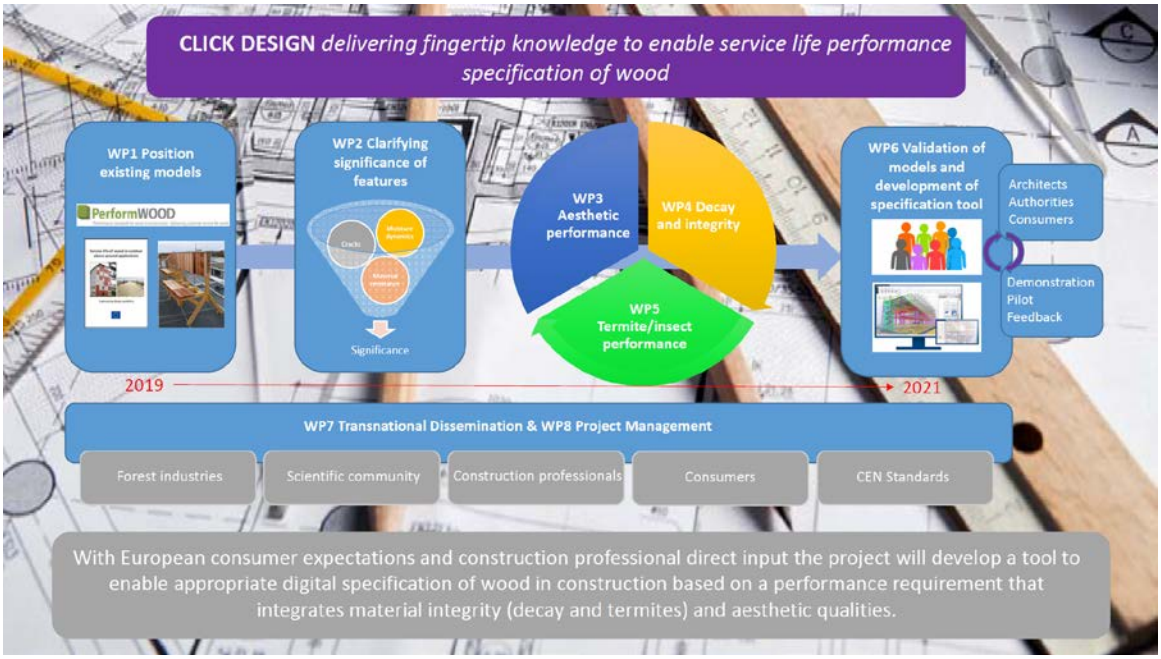

Figure 1. CLICKdesign project schematic showing proposed work packages.

The project builds on the foundations of the basic models and previous research work that comprise the existing knowledge landscape (Figure 2). Existing performance classification research has drawn together aspects of design detailing, climate and material and looked at forecasting performance compared to performance observed for construction products in buildings across Europe (PerformWOOD, WoodExter). Whilst this worked well as a rule of thumb it was missing two key features: aesthetics and insects.

In addition, modelling the effect of fungal decay on mechanical properties of wooden structures is being made, going beyond the simple limit states of previous work e.g. ‘onset of decay’ or ‘failure’. Including these features has never been done before alongside the relatively mature model position that we have established in Europe for materials, strength, decay, design and performance.

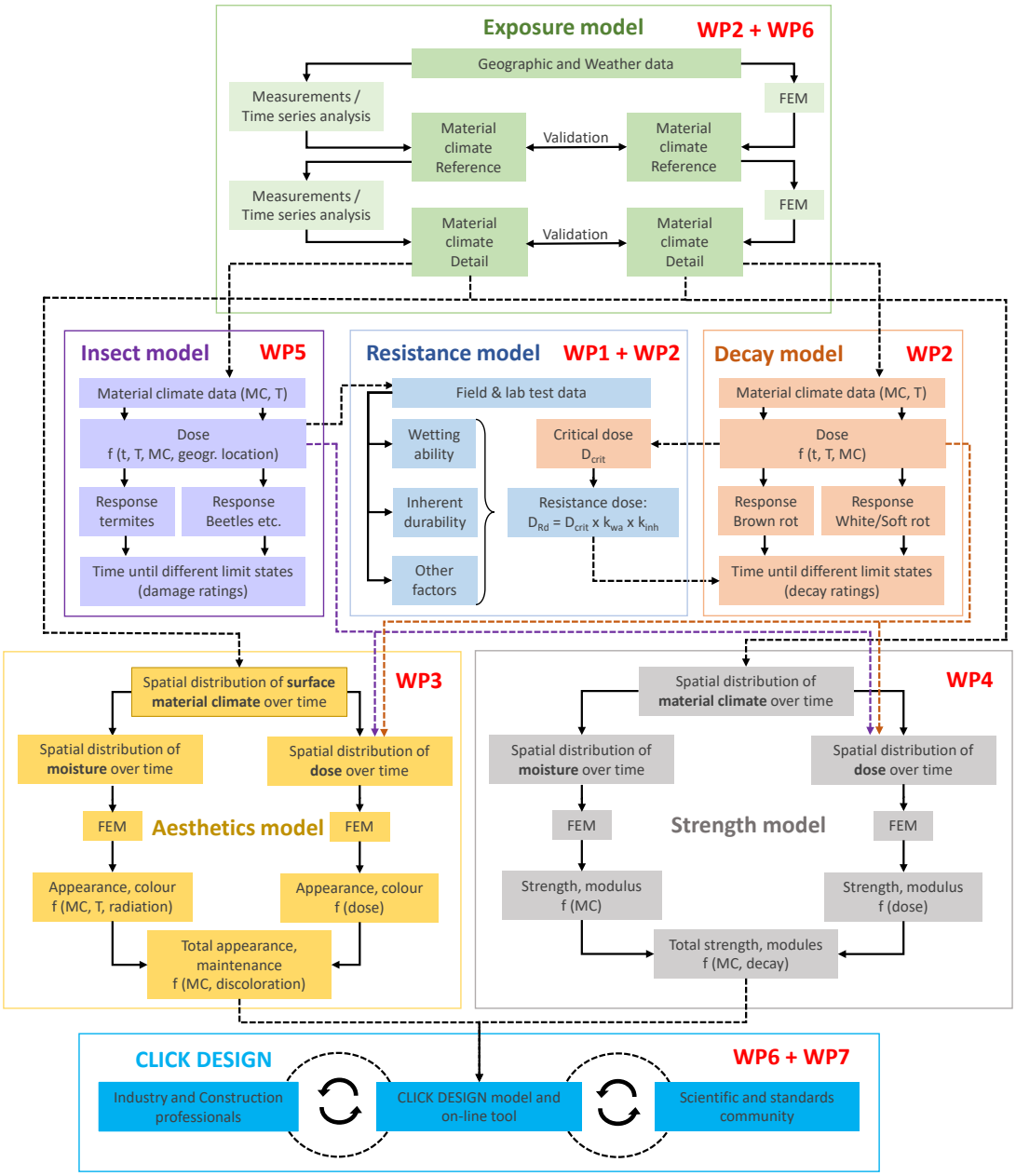

Figure 2. Different elements of performance modelling addressed in CLICKdesign.

For exterior cladding and other applications of wood and wood-based products the acceptance of changes in aesthetics (weathering, colour change, mould) is the key customer parameter (Gobakken 2009, Gellerich *et al.*, 2017). Forecasting of surface changes in terms of discoloration, roughness, overall appearance is therefore indispensable and needs to be linked with other performance models. This is especially critical for Use Class 3 (outdoor above-ground) wood performance classification and for pan-European uptake.

Different parameters need to be taken into account in order to define the risk for a wooden element of being degraded by biological agents, including termites and other insects. Subterranean termites are widely distributed in warm climates across the countries of southern Europe, both in rural and in urban areas. The most serious harm caused by subterranean termites to buildings is the degradation of the wooden elements, in particular those ensuring the integrity of the building such as the timber frame, load-bearing elements and structural panels.

Key to the success for CLICKdesign is that the tool finds application across Europe's rich diversity of geographic, climatic and cultural regions. The integration of climatic conditions (meso, macro and micro) into the models is fundamental and one approach where this is being tackled. The weather through experiences in projects such as DuraTB and Woodlife are translatable into microclimate in the wood and its response. A relationship connecting climate parameters to the material climate makes it possible to analyse a wide range of regional climates through use of open meteorological databases such as ECMWF www.ecmwf.int. Dosimeter approaches developed to describe the interrelationship between material-climatic parameters (exposure dose), material-specific resistance (resistance dose) and wood degradation (response) can then be used to study the regional-specific performance. The same methodology is also be employed for predicting degradation by termites and other insects. For that purpose, input variables need to be different and will be sought from existing field test data and short-term resistance tests performed within CLICKdesign. Success will be possible using a structured approach that couples models and enables direct localisation for the user. In addition, factors that differ between countries and regions of Europe we are cognisant of fostering the different traditions of use of wood, differences in expectations on service life and warranties, differences in cultural aspects towards product maintenance and language accessibility.

2.3 Project Facts

Project CLICKdesign started 1 March 2019 and runs for 3 years. A consortium of 8 European organisations is delivering the core research components of the project comprising building physics, wood science, BIM, service life modelling and entomology. It also has a direct link to the expert research team in FPI Innovations, Canada to look at global application and a diverse pan-European industry group of 18 members who will help pilot and bring together the modelled components of performance of wood in use to develop an open source tool.

2.4 Project Highlights to Date

Whilst additional DBMC papers (*e.g.* Digital transformation of biological processes and building design theory) are reporting on some of the detail a summary of highlights against work package (WP) are shown in Table 1.

3 Conclusions

The specification of performance of wood products is complex and fraught with inconsistency and requires use of multiple platforms for data, experience, standards and national recommendations. CLICKdesign will provide a tool that has within it the decades of excellent research, the complexity of the standards specification systems and the variation of approach due to tradition, materials and culture across Europe. The tool will be accessible to professional

users and will be refined with industry to ensure relevancy and accelerate its uptake and use. The project supports “fit for purpose” product specification and enables specifiers and users to understand the impact of their choices on performance.

Table 1. Summary of project CLICKdesign highlights up to November 2019.

Work Package	Achievements
1 Position existing models	A full review of existing models has been completed and an analysis extracting useful features completed.
2 Clarifying missing features	Research on missing features from existing models and testing of these features that impact on performance is underway including splash water effects, cracking, microclimate, vegetation and driving rain.
3 Aesthetic performance	Definition of a numerical parameter for aesthetic quality is underway alongside limit state definitions. A tool is ready that can be used to simulate changes in visual appearance due to weathering for facades.
4 Decay and Integrity	Hygrothermal models are being refined to include aspects of the spatial distribution of decay in wood to understand impact on structural integrity and enable deeper finite element analysis.
5 Termite/insect performance	A measure of the performance of relevant construction materials with regards to insect degradation is being laboratory tested to help define the performance measure.
6 Validation of models and specification tool	A specification tool has been developed to enable focus on its adaption and the inclusion of aesthetic and insect models.
7 Dissemination	Through conferences and articles over 15,000 construction professionals, regulators and product manufacturers have been reached.
8 Project management	A new self-funding partner the University of Vigo has joined the project which brings new expertise and includes Spain into our European reach.

Acknowledgement

Project CLICKdesign is supported under the umbrella of ERA-NET Cofund ForestValue by the Ministry of Education, Science and Sport (MIZS) - Slovenia; The Ministry of the Environment (YM) - Finland; The Forestry Commissioners (FC) - UK; Research Council of Norway (RCN) -Norway; The French Environment & Energy Management Agency (ADEME) and The French National Research Agency (ANR) - France; The Swedish Research Council for Environment, Agricultural Sciences and Spatial Planning (FORMAS), Swedish Energy Agency (SWEA), Swedish Governmental Agency for Innovation Systems (Vinnova) - Sweden; Federal Ministry of Food and Agriculture (BMEL) and Agency for Renewable Resources (FNR) - Germany. ForestValue has received funding from the European Union's Horizon 2020 research and innovation programme under grant agreement N° 773324.

ORCID
Ed Suttie: https://orcid.org/0000-0002-0938-3728
Christian Brischke: https://orcid.org/0000-0003-4652-825X
Eva Frühwald Hansson: https://orcid.org/0000-0003-2357-2135
Stefania Fortino: https://orcid.org/0000-0002-1613-6493
Jakub Sandak: https://orcid.org/0000-0001-9190-677X
Magdalena Kutnik: https://orcid.org/0000-0002-5522-5413
Gry Alfredsen: https://orcid.org/0000-0002-4560-9499

Christophe Lucas: https://orcid.org/0000-0003-2839-7583

References

Brischke, C. and Thelandersson, S. (2014). Modelling the outdoor performance of wood products –A review on existing approaches. *Constr. Build. Mat.* 66:384-397.

Brischke, C. and Meyer-Veltrup, L. (2016). Modelling timber decay caused by brown rot fungi. *Mat. Struct.* 49:3281-3291.

de Freitas, R.R., Molina, J.C. and Júnior, C.C. (2010). Mathematical model for timber decay in contact with the ground contact adjusted for the state of São Paulo, *Brazil. Mat. Res.* 13:151-158.

Foliente, G.C., Leicester, R.H., Wang, C.H., Mackenzie, C. and Cole, I. (2002). Durability design for wood construction. *For. Prod. J.* 52:10-19.

Fortino, S. (2017). Hygro-thermal models. In: Jones D, Brischke C (eds) Performance of Bio-based Building Materials. Elsevier:495-502.

Fortino, S., Genoese, A., Genoese, A., Nunes, L. and Palma, P. (2013). Numerical modelling of the hygro-thermal response of timber bridges during their service life: A monitoring case-study. Constr. Build. Mat. 47:1225-1234.

Fragiacomo, M., Fortino, S., Tononi, D., Usardi, I. and Toratti, T. (2011). Moisture-induced stresses perpendicular to grain in timber sections exposed to European climates. *Eng. Struct.* 33:3071–3078.

Gellerich, A., Emmerich, L., Brischke, C., Meyer-Veltrup, L. and Kaudewitz, P. (2017). Evaluation of surface cracks on wood – physical assessment versus subjective sensation. Proc. IRG Ann. Meeting, IRG/WP 17-20617.

Gobakken, L.R. (2009). Surface mould growth on painted and unpainted wood: influencing factors, modelling and aesthetic service life. PhD Thesis no. 2009:32. Norwegian University of Life Sciences.

Gobakken, L.R., Mattsson, J. and Alfredsen, G. (2008). In-service Performance of Wood Depends upon the Critical In-situ Conditions. Case Studies. Proc. IRG Ann. Meeting, IRG/WP 08-20382.

Hradil, P., Fortino, S., Salokangas, L., Musci, A. and Metelli, G. (2016). Effect of moisture induced stresses on the mechanical performance of glulam beams of Vihantasalmi bridge. WCTE 22-25 Aug. 2016, Vienna, Austria

Humar, M., De Angelis, M., Romagnoli, M., Vek, V., Poljanšek, I., Oven, P., Thaler, N., Lesar, B. and Kržišnik, D. (2018). Material Resistance and Chemical Composition of Italian Stone Pine (Pinus pinea). Proc. IRG Ann. Meeting, IRG/WP 18-20645.

Isaksson, T., Brischke, C. and Thelandersson, S. (2013). Development of decay performance models for outdoor timber structures. *Mat. Struct.* 46:1209-1225.

Leicester, R.H., Wanga, C.-H. and Cookson, L.-J. (2008). A reliability model for assessing the risk of termite attack on housing in Australia. *Reliab. Eng. Syst. Safety* 93:468–475

MacKenzie, C.E., Wang, C.-H., Leicester, R.H., Foliente, G.C. and Nguyen, M.N. (2007). Timber service life guide. Forest and Wood Products Limited, Victoria.

Meyer-Veltrup, L., Brischke, C., Alfredsen, G., Humar, M., Flæte, P.O., Isaksson, T. and Jermer, J. (2017). The combined effect of wetting ability and durability on outdoor performance of wood: development and verification of a new prediction approach. *Wood Sci. Technol.* 51:615-637.

Niklewski, J., Fredriksson, M. and Isaksson, T. (2016). Moisture content prediction of rain-exposed wood: Test and evaluation of a simple numerical model for durability applications. *Build. Environ.* 97:126-136.

Pousette, A., Malo, K., Thelandersson, S., Fortino, S., Salokangas, L. and Wacker, J. (2017). Durable Timber Bridges - Final Report & Guidelines. SP Report 25. RISE, Skellefteå, Sweden.

Sandak, A., Sandak, J., Dimitrou, A., Burud, I., Thiis, T., Gobakken, L.R., Ormondroyd, G.A. and Kraniotis, D. (2017). Assessment and monitoring of aesthetic appearance of building biomaterials along the service life. *WIT Transactions on Ecology & The Environment; Sustainable Development & Planning* 226:527-536

Sandak, J., Sandak, A. and Burud, I. (2017). Chapter 8.4. Modelling of weathering. In: Jones D, Brischke C (eds) Performance of Bio-based Building Materials. Elsevier: 502-510.

Tonini, F., Hochmair, H., Scheffrahn, R. and Deangelis, D. (2013). Simulating the Spread of an Invasive Termite in an Urban Environment Using a Stochastic Individual-Based Model. *Environ. Entomol.* 42:412

Viitanen, H., Toratti, T., Makkonen, L., Peuhkuri, R., Ojanen, T., Ruokolainen, L. and Räisänen, J. (2010). Towards modelling of decay risk of wooden materials. *Eur. J. Wood Wood Prod.* 68:303-313.

XV International Conference on Durability of Building Materials and Components
DBMC 2020, Barcelona
C. Serrat, J.R. Casas and V. Gibert (Eds)

Permeability of Ultra-Fine Reactive Fly Ash applied to Cement-Based Composites

Wei-Ting Lin[1], An Cheng[1], Wei-Chung Yeih[2], Kinga Korniejenko[3], Marek Hebda[3] and Michał Łach[3]

[1] Department of Civil Engineering, National Ilan University, No.1, Sec. 1, Shennong Rd., I-Lan 260, Taiwan, wtlin@niu.edu.tw
[2] Department of Harbor and River Engineering, National Taiwan Ocean University, No. 2, Beining Rd., Keelung City 20224, Taiwan, wcyeih@mail.ntou.edu.tw
[3] Institute of Materials Engineering, Faculty of Materials Engineering and Physics, Cracow University of Technology, Warszawska 24, 31-155 Kraków, Poland, kkorniej@gmail.com

Abstract. *This study explores the permeability of the partial replacement of cement using ultra-fine reactive fly ash (URFA) and silica fume. URFA is an industrial by-product from thermal power plants and it has a smaller spherical particle size (0.1 μm to 10 μm) than the general fly ash. The fixed water-to-binder ratio was 0.45 and the replacement of cement was used as 5% and 10%. The combinations of URFA and silica fume in composites were used as 5% URFA plus 5% silica fume and 8% URFA plus 2% silica fume. The results show that the inclusion of URFA was enhanced to increase the workability, and help to produce pozzolanic reaction and C-S-H colloids. The colloids were filling the pore structures to increase the compactness of specimen, which is consistency with the increased the compressive strength and reduction of the dry shrinkage. It also was reduced the chloride ion penetration and non-steady state migration coefficient, which is helpful for improving the mechanical properties and permeability. The composites with 10% URFA had a better performance. For blending specimen, it was also a tendency to improve mechanical properties and permeability; and the combination of 5% URFA and 5% silica fume in composites enhanced better performances.*

Keywords: *Ultra-Fine Reactive Fly Ash, Chloride Diffusion, Durability, Pore Structures.*

1 Introduction

Fly ash is a popular pozzolanic material with high SiO_2 and Al_2O_3 content. When cemented with water, the cementing performance is relatively low (Yang et al., 2018), but it will be activated by hydroxide ions (OH^-). Fly ash is usually added to cement as a pozzolana because it can be cured in wet conditions or underwater and further protect hardened materials from chemical attack. In most cases, fly ash is obtained from thermal power stations and is recycled as a pollution control measure, usually blended with ordinary cement to improve cement performance (Li *et al.*, 2014).

Fly ash is sufficiently reactive when it reacts with water and CaO in the cement (Telesca *et al.*, 2017). At room temperature, C–S–H gels are formed in the internal structure of the mixture, thereby forming hydraulic cementitious materials (Temuujin *et al.*, 2009; Duan *et al.*, 2017). Fly ash is also used to improve the performance of concrete in the fresh and hardened state, for improving workability, attaining high compressive strength at the early age, achieving long-term compressive strength, low drying-shrinkage and creep coupled with

excellent durability properties (Zuquan *et al.*, 2007; Xu *et al.*, 2017; Ahmad *et al.*, 2019; Tan *et al.*, 2019).

Several prominent researchers have devoted time to exploring the characteristics and application of fly ash in cementitious materials over the years and the general categories in which fly ash can be grouped regarding its effect on concrete includes morphological, active and micro-aggregate effects (Aiqin *et al.*, 2003; Aiqin *et al.*, 2004; Li *et al.*, 2013; Gardner *et al.*, 2015; Xu *et al.*, 2017). In concrete, fly ash has several functions as the concrete ages. In the early age stage, fly ash can act have a physical effect in that it fills up spaces in the microstructure of the concrete and it is also involved in the formation of ettringite. In the long term, they mainly participate in the hydration reaction in the form of silicon-aluminum binders (Shi *et al.*, 2006). At a later age, fly ash has two effects: it enhances the cohesion between molecules within the particle structure, and also absorbs the $Ca(OH)_2$, reducing its effect (Kolias *et al.*, 2005; Brostow *et al.*, 2016). However, Most of the molecules of the fly ash remain un-reacted even after a long period of curing, so fly ash may also be considered as a composite material with the ash particles serving as reactive micro-aggregates (Nadesan *et al.*, 2018). Structurally, fly ash is composed of lots of fine spherical micro-spheres, which are large glassy particles existing in a crystalline internal structure of fly ash. Due to density difference, the internal molecules of fly ash which are also called micro-beads or micro-spheres, are classified as sinking beads and floating beads (Li *et al.*, 2014). These micro-spheres are obtained from pulverized fuel ash (also called pulverized fly ash in some countries).

In the past decade, ultra-fine reactive fly ash (URFA) having very fine particles have been extracted by processing conventional fly ash, and it is becoming increasingly popular in the construction industry (Bagheri *et al.*, 2013). These fine particles often have a similar chemical composition with the conventional fly ash, but it has reduced surface area per particle. Recent research has shown that URFA exhibited better pozzolanic activity and more desirable performance in concrete than normal fly ash (Elsayed *et al.*, 2011; Duan *et al.*, 2018; Han *et al.*, 2019). When heated, micro-spheres heat up and crackle until they burst at about 260°C; their shells start to splinter at about 1100°C and finally collapse at about 1300°C. The superfine particles obtained can then be used to partially replace Portland cement in cementing material systems and their particulate structures. This study aims to determine its suitability as a pozzolanic additive to improve the performance of cement-based materials.

2 Experiments

2.1 Materials

Type I Portland cement was used in this study and it had a specific gravity of 3.15 and fineness of 3310 cm^2/g. The fine aggregates are natural river sand, it has an SSD specific gravity of 2.69, an absorption of 1.45% and a fineness modulus of 2.73. The specific gravity and specific surface area of silica fume is 2.20 and 22500 m^2/kg, respectively. Silica fume having an average content of 94.1% silicon dioxide was used in powder form. URFA was provided by TRIAXIS Corporation from a power plant in Inner Mongolia. The specific gravity and specific surface area of URFA is 2.20 and 3380 m^2/kg, respectively. URFA has an average content of 49.11% silicon dioxide, 28.07% aluminum oxide and 8.84% calcium oxide.

The SEM photo of URFA particles is shown in Fig. 1 and the average particle size was between 0.1 μm to 10 μm.

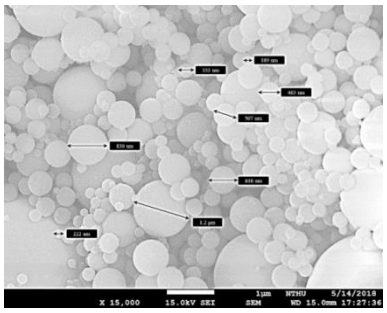

Figure 1. SEM photo of URFA.

2.2 Mix Design and Test Methods

According to the ASTM C109 specification, the water/cementitious ratio (w/c) of the mortar specimens was kept constant at 0.45, while the mass ratio of the cementitious /fine aggregates was 1: 2.75. Table 1 lists the mix designs for all mixes. The specimens were numbered using the letters and numbers to indicate the kind of replaced materials and dosage of the replaced materials. OPC, F, S denotes ordinary Portland mortar, URFA and silica fume; 5 and 10 refers to specimens containing 5% and 10% replaced materials. Table 2 presents the tests performed, the dimensions of the specimens and the standards.

Table 1. Mix design (kg/m^3).

Mix no.	Water	Cement	URFA	Silica fume	Fine aggregates	SP
OPC	242.6	547.9	0	0	1506.7	4.0
F5	243.0	520.5	27.4	0	1496.6	3.6
F10	244.0	493.1	54.8	0	1486.5	2.5
S5	241.9	520.5	0	27.4	1496.6	4.7
S10	240.9	493.1	0	54.8	1486.5	5.7
F5S5	242.1	493.1	27.4	27.4	1486.5	4.5
F8S2	243.4	493.1	43.8	11.0	1486.5	3.2

Table 2. Test methods.

Test Target		Specimen Dimensions (mm)	Referenced Standard
Fresh properties	Flow test	-	ASTM C230
Mechanical properties	Compressive strength test	50 × 50 × 50	ASTM C109
Durability	Drying shrinkage test	285 × 25 × 25	ASTM C596
	Rapid chloride penetration test	ϕ100 × 50	ASTM C1202

Micro-structure observations	Mercury intrusion porosimetry test	10 × 10 × 1	ASTM D4404
	SEM observation	10 × 10 × 1	ASTM C1723

3 Results and Discussion

3.1 Flowability

The results of flow test for all mixes are summarized in Table 3. The fluidity of the mortar specimens was controlled at 110±3% using appropriate amount of superplasticizer. The results indicated that the dosages of superplasticizer had a decrease trend with the increase in the replacement of URFA due to the due to its perfect spherical shape and micro-sized particles. However, the flowability had a decrease trend with the increase in the inclusion of silica fume due to its larger surface area. The desired flow and rheological properties will determine the optimal design mix that 10% URFA in mortar specimens should be used. The combination of silica fume and URFA in mortar specimens still had great flowability and F8S2 specimens had lowest dosages of superplasticizer at the desired flow.

Table 3. Example of the construction of a table.

Mix no.	Flowability (%)	Superplasticizer dosages (wt.% of cement)
OPC	112.3	0.73
F5	111.8	0.65
F10	110.0	0.46
S5	109.8	0.85
S10	108.3	1.04
F5S5	110.8	0.82
F8S2	109.8	0.58

3.2 Compressive Strength

The results of compressive strength test for all mixes are illustrated in Figure 2. As expected, the specimens containing 10% silica fume had highest compressive strength for all ages. The strength development trend of F10 specimens was closed to that of the S5 specimens. Compared with silica fume, URFA has a much smaller specific surface area, so it can increase bulk density without excessively increasing the total solid surface area. It is able to fill the voids in cement to increase the packing density of the cementitious materials. The compressive strengths of the F5S5 specimens were higher than that of the S5 specimens and F8S2 specimens; and the compressive strengths were lower that of the S10 specimens. URFA is considered to be a good filler for increasing parking density without excessively increasing surface area. It has a particle size of micrometer-scale and is spherical in shape. It is finer than cement and ordinary fly ash. Inclusion of URFA showed improved properties in compressive strength due to the active pozzolan reaction and filling effect.

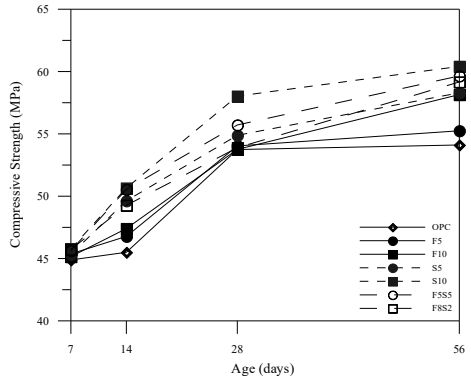

Figure 2. Compressive strength development curves.

3.3 Drying Shrinkage

The results of drying shrinkage test for all mixes are summarized in Figure 3. It indicated that drying shrinkage of the specimens containing URFA was lower than that of the specimens containing silica fume and control specimens. URFA can efficiently inhibit the dry shrinkage of mortar specimens due to the smaller specific surface area. URFA has a late hydration reaction and the dispersion effect on the cement particles can reduce the total hydration heat of the paste, and improve the drying shrinking performance.

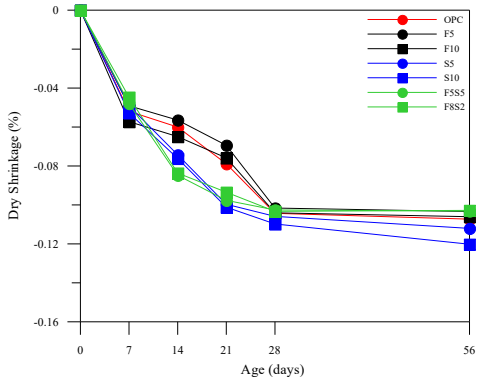

Figure 3. Dry shrinkage curves.

3.4 Chloride Penetration

The results of rapid chloride penetration test for all mixes are illustrated in Figure 4. The results indicated that the total charge passed of control specimens was higher than 10000 coulombs and the operated temperature of control specimens was higher than 90 ˚C. The test of control specimens has been stop because the temperature of the solutions should not be allowed to exceed 90 ˚C in order to avoid damage to the cell and to avoid boiling off the solutions. As expected, the specimens containing 10% silica fume had lowest total charge passed due to the finer particles. The trend of F5S5 specimens is closed to that of S5 specimens, which is due to the pore structure modification. Finer silica fume and URFA particles mixed into the mortar specimens improved the compactness through pozzolanic reactivity and pore filling effect. It may be as mainly hydrated reaction that $Ca(OH)_2$ reacted

with SiO_2 or Al_2O_3 to form C-S-H or C-A-S-H colloids.

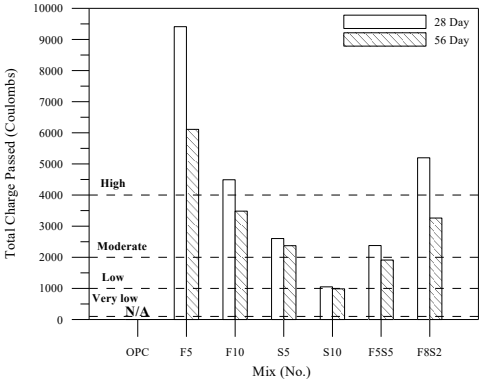

Figure 4. Total charge passed histograms.

3.5 Pore Structures

The MIP test results of the specimens containing URFA and control specimens are shown in Fig. 5. It indicated that the cumulative intrusion of specimens containing URFA significantly decreased that the control specimens. It was confirmed that the finer particles of URFA was useful to the pore structure modification, which is in agreement with the results of chloride penetration tests and compressive strength tests.

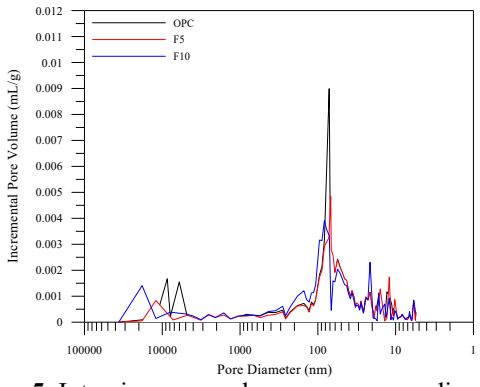

Figure 5. Intrusion pore volume versus pore diameter.

3.6 SEM Observations

It took SEM images of the various specimens at 28 days at 5000x magnification as illustrated in Figure 6. The results showed small porosity and smooth surface in the URFA or silica fume specimens than in the control specimens. Many pores in the URFA or silica fume specimens were filled with ettringite and C-S-H gel. C-S-H gel is the product of the hydrated reaction between water and tricalcium silicate or dicalcium silicate. Finer particles are needed to fill these pores. As shown, most of the pores have been filled with ettringite and C-S-H gel, which presents a dense appearance and reduces the chance of penetration of harmful substances. However, an increased amount of URFA may cause a partial reaction in the hydration process. Non-react particles of URFA can be seeing in the surface of the micro-structures. URFA is excellent cementitious filler for improving the flowability and strength of

cement pastes as shown in SEM photos and it needs more curing age to keep a continued hydration reaction.

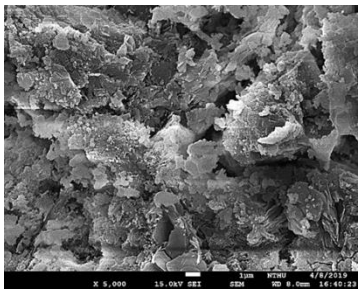
(a) control specimens

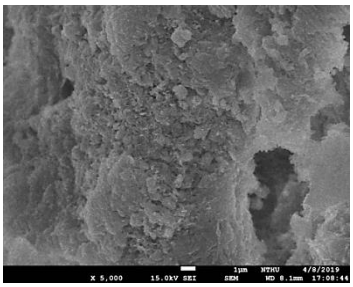
(b) S10 specimens

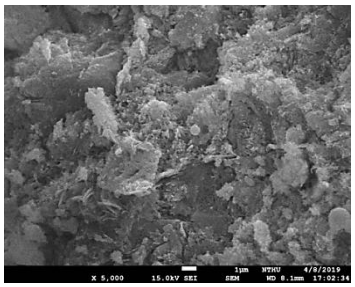
(c) F10 specimens

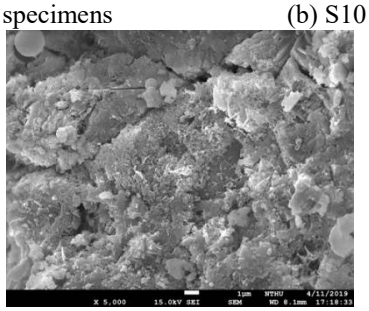
(d) F5S5 specimens

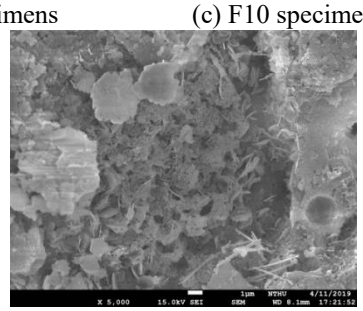
(e) F8S2 specimens

Figure 6. SEM photos for each mixtures (x5000).

4 Conclusions

- In order to produce a balance with a desired increase in packing density and suppression of an increase in undesired surface area, URFA microspheres thinner than cement but thicker than silica fume would be a better choice.
- URFA has a particle size of micrometer scale and is spherical in shape. It is finer than cement and ordinary fly ash. The specimens containing URFA can increase the packing density so as to enhance the performance of mortar specimens. It also can significantly decrease the dry shrinkage.
- SEM observations and MIP analysis confirmed that the finer particles of URFA were useful to the pore structure modification, which is in agreement with the results of chloride penetration tests and compressive strength tests.
- Environmental friendly and helps to reduce the carbon footprint produced in cement production, since it can be used to replace cement in cement mixtures, and from a life cycle assessment perspective. It is feasible to consider URFA as a relatively CO_2 free resource.

Acknowledgements

This support of the Ministry of Science and Technology (MOST) under the grant MOST 108-2221-E-197-006 in Taiwan is gratefully acknowledged. This work has been financed by the by Polish National Agency for Academic Exchange w under the International Academic Partnership Programme within the framework of the grant: E-mobility and sustainable materials and technologies EMMAT.

ORCID

Wei-Ting Lin: https://orcid.org/0000-0003-4792-4457

Kinga Korniejenko: https://orcid.org/0000-0002-8265-3982
Marek Hebda: https://orcid.org/0000-0002-8583-9459
Michał Łach: https://orcid.org/0000-0001-5713-9415

References

Aiqin, W. Chengzhi, Z. and Wei, S. (2003). Fly ash effects: I. The morphological effect of fly ash. *Cement and Concrete Research*, *33*(12), 2023-2029.

Aiqin, W. Chengzhi, Z. and Wei, S. (2004). Fly ash effects: II. The active effect of fly ash. *Cement and Concrete Research*, *34*(11), 2057-2060.

Ahmad, M.R. Chen, B. and Yu, J. (2019). A comprehensive study of basalt fiber reinforced magnesium phosphate cement incorporating ultrafine fly ash. *Composites Part B: Engineering*, *168*, 204-217.

Bagheri, A. Zanganeh, H. Alizadeh, H. Shakerinia, M. and Marian, M.A.S. (2013). Comparing the performance of fine fly ash and silica fume in enhancing the properties of concretes containing fly ash. *Construction and Building Materials*, *47*, 1402-1408.

Brostow, W. Chetuya, N. Hnatchuk, N. and Uygunoglu, T. (2016). Reinforcing concrete: comparison of filler effects. *Journal of Cleaner Production*, *112*, 2243-2248.

Duan, P. Yan, C. and Zhou, W. (2017). Compressive strength and microstructure of fly ash based geopolymer blended with silica fume under thermal cycle. *Cement and Concrete Composites*, *78*, 108-119.

Duan, S. Liao, H. Ma, Z. Cheng, F. and Yang, H. (2018). The relevance of ultrafine fly ash properties and mechanical properties in its fly ash-cement gelation blocks via static pressure forming. *Construction and Building Materials*, *186*, 1064-1071.

Elsayed AA. (2011). Influence of silica fume, fly ash, super pozz and high slag cement on water permeability and strength of concrete. *Jordan Journal of Civil Engineering*, *5*(2), 245-257.

Han, X. Yang, J. Feng, J. Zhou, C. and Wang, X. (2019). Research on hydration mechanism of ultrafine fly ash and cement composite. *Construction and Building Materials*, *227*, Article 116697.

Gardner, L.J. Bernal, S.A. Walling, S.A. Corkhill, C.L. Provis, J.L. and Hyatt, N.C. (2015). Characterisation of magnesium potassium phosphate cements blended with fly ash and ground granulated blast furnace slag. *Cement and Concrete Research*, *74*, 78-87.

Kolias, S. Kasselouri-Rigopoulou, V. and Karahalios, A. (2005). Stabilisation of clayey soils with high calcium fly ash and cement. *Cement and Concrete Composites*, *27*, 301-313.

Li, H. Xu, D. Feng, S. and Shang, B. (2014). Microstructure and performance of fly ash micro-beads in cementitious material system. *Construction and Building Materials*, *52*, 422–427.

Li, Y. and Che, B. (2013). Factors that affect the properties of magnesium phosphate cement. *Construction and Building Materials*, *47*, 977–983.

Nadesan, M.S. and Dinakar, P. (2018). Micro-structural behavior of interfacial transition zone of the porous sintered fly ash aggregate. *Journal of Building Engineering*, *16*, 31-38.

Shi, C. Krivenko, P.V. and Roy, D.M. (2006). *Alkali-activated Cements and Concretes*. Taylor & Francis, London, New York.

Tan, H. Nie, K. He, X. Deng, X. Zhang, X. Su, Y. and Yang, J. Compressive strength and hydration of high-volume wet-grinded coal fly ash cementitious materials. *Construction and Building Materials*, *206*, 248-260.

Telesca, A. Marroccoli, M. Ibris, N. Lupiáñez, C. Díez, L.I. Romeo, L.M. and Montagnaro, F. (2017). Use of oxyfuel combustion ash for the production of blended cements: a synergetic solution toward reduction of CO_2 emissions. *Fuel Processing Technology*, *156*, 211-220

Temuujin, J. van Riessen, A. and Williams, R. (2009). Influence of calcium compounds on the mechanical properties of fly ash geopolymer pastes. *Journal of Hazardous Materials*, *167*(1-3), 82-88.

Xu, B. Ma, H. Shao, H. Li, Z. and Lothenbach, B. (2017). Influence of fly ash on compressive strength and micro-characteristics of magnesium potassium phosphate cement mortars. *Cement and Concrete Research*, *99*, 86-94.

Yang, J. Su, Y. He, X. Tan, H. Jiang, Y. Zeng, L. and Strnadel, B. (2018). Pore structure evaluation of cementing composites blended with coal by-products: calcined coal gangue and coal fly ash. *Fuel Processing Technology*, *181*(1), 75-90

Zuquan, J. Wei, S. Yunsheng, Z. Jinyang, J. and Jianzhong, L. (2007). Interaction between sulfate and chloride solution attack of concretes with and without fly ash. *Cement and Concrete Research*, *37*(8), 1223-1232.

XV International Conference on Durability of Building Materials and Components
DBMC 2020, Barcelona
C. Serrat, J.R. Casas and V. Gibert (Eds)

Selecting Criteria for Assessing "Environmentally-Friendly" Material Options in Construction: Part I

Robert Bucoń[1] **and Agata Czarnigowska**[2]

[1] Dpt. Of Construction Methods and Management, Faculty of Civil Engineering and Architecture, Politechnika Lubelska, Nadbystrzycka 40, 20-618 Lublin, Poland, r.bucon@pollub.pl

[2] Dpt. Of Construction Methods and Management, Faculty of Civil Engineering and Architecture, Politechnika Lubelska, Nadbystrzycka 40, 20-618 Lublin, Poland, a.czarnigowska@pollub.pl

Abstract. *One of the design team's tasks is assuring that their project has a low negative impact on the environment. This comes from regulations as well as expectations of direct benefits (reduction of operating cost, the project's improved image in the eyes of the public, etc.). To fulfill this task, one needs to define criteria for assessing the design options. These are to correspond to the individual qualities of the project, and they should be significant and possible to assess. The paper, divided into two parts, presents a review of the literature concerning the criteria for the assessment of design solutions defined as "green" or "environmentally friendly". Part I presents the method of the analysis and investigates into the number and type of criteria adopted in the sample of papers being the object of analysis. Part II focuses on the ways of defining criteria values, weights, and methods of multicriteria assessment.*

Keywords: *Sustainable Construction, Component Selection, LCA, Literature Review.*

1 Introduction

It becomes apparent that humanity's appetite for resources became too much for the planet Earth to bear (Meadows *et al.*, 1972; Turner, 2008). Exponential population build-up combined with the global pursuit of economic growth results in the exponential growth of the demand for housing and infrastructure as well as production facilities. Construction means consuming a lot of energy, water, land, and minerals for creating millions of tons of materials, moving them to the destination and installing, followed by dismantling and relocating with the amount of effort comparable with that during erection. Technological progress makes construction components increasingly complex and sophisticated, which adds to the problem: highly processed products consume even more resources and are difficult to recycle. In the face of resource depletion and the likely suffocation with its own refuse within decades, humanity is dragged (Komatsu *et al*., 2019) towards the sustainable economy (D'Amato *et al*., 2019) and, in particular, sustainable construction (Goh *et al.*, 2020).

One of the aspects of construction sustainability is reducing the project's and the resulting built facility's negative impact on the environment. This impact is typically assessed in the course of some form of Life Cycle Analysis (LCA) (Ortiz *et al.*, 2009). The LCA has become an established practice in optimizing designs and assessing the quality of the built environment. The idea, described among others by ISO 14040 standard, evolved into a plethora of methodologies, tools and individual reports on analyses for estimating the impact of built assets on the environment from the perspective of:

- particular construction materials/products (*e.g.* Häfliger et al., 2017),
- functional components of particular buildings (*e.g*. Kellenberger and Althaus, 2009),

doi:10.23967/dbmc.2020.177

- whole buildings in the context of the way of use and building maintenance scenarios (Bucoń, 2019; Häfliger *et al*., 2017; Hasik *et al*., 2019),
- neighborhoods/cities (Bak *et al.*, 2019; Goldstein et al., 2013; Jeong and Ramirez-Gomez, 2018; Nematchoua *et al.*, 2020).

They typically share the element of assessing the environmental consequences of using particular construction materials in the building's fabric, so the materials' contribution to the overall environmental impact. However, even in this narrow aspect, the scope, criteria, and measures used in the analyses are not identical (Doan *et al.*, 2017; Park *et al.*, 2017).

On the one hand, there exist standards on reporting the environmental impact of products, (ecolabelling). As for the construction products, the European EN 15804 standard that sets requirements for voluntary Environmental Product Declarations (EPDs) (Kuittinen and Linkosalmi, 2015; Piasecki, 2014). On the other hand, the standards and methodologies evolve (Allacker *et al.*, 2017). Due to the proliferation of LCA methodologies, the comparability of information on a product's environmental qualities becomes an issue (European Commission, 2013; Galatola and Pant, 2014; Passer *et al.*, 2015). Many researchers and practitioners compare the environmental qualities of construction products using their own criteria and measures.

The paper is the first part of a review of the most recent literature on the comparison or assessment of construction products and components to select the "environmentally friendly" ones. The authors provide a classification of research problems covered by the sample, discuss papers devoted to designing "green" materials and selecting sustainability criteria for construction materials, products, or components. Finally, they investigate into the number and type of criteria in use, thus into how the authors understand the environmental impact of construction products or built facilities.

2 Materials and Methods

2.1 Benchmark Set of Criteria and the Scope of Analysis

The standards on EPDs are in use for some time, and the number of declarations in the databases is growing: this idea of standardized communication of environmental product properties seems to establish itself in practice. For this reason, the authors expect that the presentation of solutions to problems directly or indirectly related to construction material, component, or construction method selection in the field of architecture, building, and civil engineering are likely to draw from the methods elaborated by the environmental scientists.

Table 1. Classification of life cycle stages for assessing environmental impact of construction products, based on EPD (ITB, 2013).

Product stage	Construction process	Use stage	End of life	Benefits and loads beyond the system boundary
A1. Raw material supply A2. Transport A3. Manufacturing	A4. Transport to site A5. Installation	B1. Use B2. Maintenance B3. Repair B4. Replacement B5. Refurbishment B6. Operational energy use B7. Operational water use	C1. Deconstruction C2. Transport C3. Waste processing C4. Disposal	D. Reuse-recovery-recycling potential

Table 2. Indicators of environmental impacts, aspects of resource use and waste, based on EPD (ITB, 2013).

Environmental impacts	Environmental aspects of resource use (modified)	Environmental information of waste categories
Global warming potential	Total use of renewable primary energy (as raw mat. or energy)	Hazardous waste disposed
Depletion potential of the stratospheric ozone layer	Total use of non-renewable primary energy (as raw mat. or energy)	Non-hazardous waste disposed
Acidification potential of soil and water)	Use of secondary material	Radioactive waste disposed
Eutrophication potential	Use of renewable second. fuels	Components for re-use
Formation potential of tropospheric ozone	Use of non-renewable second. fuels	Materials for recycling
Abiotic depletion potential (ADP-elements) for non-fossil resources	Net use of fresh water	Materials for energy recovery
Abiotic depletion potential (ADP-fossil fuels) for fossil resources	-	Exported energy

Therefore, in the literature review process, the sources' approach to the life cycle phases was juxtaposed to life cycle phases used in LCA and adopted for EPDs (Table 1). In this paper, the "environmentally friendly" aspects were considered only those covered by the scope of the environmental impacts, aspects of resource use, and generation of waste as defined in EPDs (Table 2) prepared according to EN 15804:2012 before its amendment in 2019 (ITB, 2013).

2.2 The Sample

The query was arbitrarily limited to one database (Web of Science), publications from the years 2016-2020, and the following structure of search terms to identify within the title, abstract and author-specified keywords:

criteria AND construction AND (material OR product) AND (select* OR choice OR choose) AND ("environmentally friendly" OR green OR sustainable) (1)

The query produced a reasonable number of 110 publications. The selection was manually refined, on the basis of content analysis, to find papers that focused explicitly on:

- analyzing criteria for selecting materials or component options or options of construction methods based on their environmental impact,
- presenting methods or tools for assessing the environmental impact of materials or components or construction methods to justify their selection or ranking,
- individual presentations of selection/ranking problems as above (case studies),
- arguments for "green" properties" of new materials if juxtaposed with "traditional" materials.

For this reason, a considerable number of papers were excluded as proposals of new certification systems for whole buildings, general-purpose multicriteria methods where "green" features served only as examples of possible criteria, and papers focused on ecology (impact of built structures on particular species). One paper was excluded for not being available in English, and four proved unreachable (no access to full text). Therefore, the final sample comprised only 43 publications.

2.3 The Method

The sample of papers was analyzed in terms of aspects of sustainability covered by the analysis, scope of life cycle stages, sources of input, and mathematical methods used for selecting the best option (if applicable).

3 Results and Discussion

3.1 Topics of the Sample

The papers of the sample were classified into four groups according to their research problem (some paper dealt with more than one):

- designing environmentally-friendly materials (9 papers),
- selecting a set of sustainability criteria for comparing construction products or components of built structures (7 papers),
- assessing the sustainability of alternative solutions (materials, material supply chains, component design) (33 papers),
- optimizing construction components (2 papers).

3.2 Type and Number of Environmental Criteria

Nine papers from the sample focused on introducing environmental criteria into the design of materials themselves (Table 3). One of them (Imron *et al.*, 2017a) argued for eco-friendly properties of a new drywall material containing waste from food production, though, at the early stage of research, the argument was based only on intuitive SWOT analysis with two arbitrarily selected environmental criteria. Nevertheless, the advantages were utilizing waste and thus reducing the consumption of non-renewable resources.

Table 3. Papers devoted to material design (selecting components for a mix).

Paper	Aspects	Life cycle	Criteria list	Weights, method of calculation	Env. criteria	Criteria values:	Method
(Imron *et al.*, 2017b)	En	A	Arbitrary	-	2	-	SWOT
(Ahmed *et al.*, 2019)	T,Ec, En, S	not explicit	Team of experts	Team of experts, AHP; sensitivity analysis	6	T. of experts (pairwise comp.)	AHP, TOPSIS
(Falqi *et al.*, 2019)	T,Ec, En, S	not explicit	Arbitrary	M. experts, arithmetic mean of fuzzy ratings	5	M. experts, arithmetic mean of fuzzy ratings	fuzzy TOPSIS
(Kurda *et al.*, 2019)	T, Ec, En	A1-A3	Arbitrary (LCA)	Arbitrary (no. of scenarios)	2	Databases & calculations	SAW
(Rashid *et al.*, 2018)	T, En	A1-A3	Arbitrary	Arbitrary	2	Databases & calculations	AHP, TOPSIS
(Reddy *et al.*, 2020)	T, Ec, En, S	not explicit	Arbitrary	Not applicable	1	Databases & calculations	PSI
(Reddy *et al.*, 2019b)	Ec, En, S	A-D	Arbitrary	M. experts, relative importance index	5	M. experts	AHP
(Reddy *et al.*, 2019a)	Ec, En, S	A-D	Arbitrary	M. experts, AHP	5	M. experts	AHP
(Suarez Silgado *et al.*, 2018)	Ec, En	A1-A3	LCA	Arbitrary; sensitivity analysis	11	Databases & calculations	VIKOR

The remaining papers from this group presented a multicriteria selection of components (such as recycled aggregates or supplementary cementing materials made of waste) for concrete or asphalt mixes. All authors proposed a combined index to select the best mix out of the set of samples. However, the types of criteria incorporated in the indices were an individual selection of environmental (En), economic (Ec), social (S), and, in some cases, technological (T) properties of the mix and the hardened material. The number of environmental sub-criteria varied from one to eleven; the most common among them were: energy use and global warming potential. The authors did not agree on the life cycle stages included in the assessment.

In four papers out of seven, the authors decided to use criteria originating from some established LCA methodologies and calculate their values according to relevant life cycle inventory databases. Two papers (Kurda *et al.*, 2019; Suarez Silgado *et al.*, 2018) came from Europe, where such databases are available. One paper originated from Pakistan (Rashid *et al.*, 2018) and based on data found in the literature. The last one was from India (Reddy *et al.*, 2020); its only environmental criterion was service life estimate. Other authors resorted to expert ratings of criteria values expressed in some form of Likert scales or as pairwise comparisons.

Seven papers from the sample focused primarily on selecting sustainability criteria for comparing construction products or components of built structures. Khoshnava *et al.* (2018) observed that, in practice, the choice of ”green” criteria was done arbitrarily by the decision-makers. Therefore, the authors undertook a literature review and a broad survey among construction professionals to decide on a general-purpose set of criteria and their relative importance, as perceived by the experts from Malaysia. The product of their research was a list of 23 criteria (out of them, 14 related with environmental impact) and their ranking. Amer and Attia (2019) conducted a broad survey among European architects to define the set of criteria and their relative importance specifically for the sustainable design of vertical extensions of buildings. (Herda *et al.*, 2017), considering the problem of comparing construction products and switching to sustainable construction in Kenya, pointed to the lack of reliable databases of product properties that correspond to local conditions. Hoxha, Haugen and Bjorberg (2017), to propose a list of “green” criteria of material selection to appeal to the wider public, decided to investigate into the understanding of sustainability in Kosovo by means of a survey among non-professionals. Rashdan and Ashour (2018) reviewed the literature to define a list of aspects worth consideration in sustainability assessment of interior design products. Li *et al.* (2019) reviewed literature on factors incorporated into LCA and life cycle costing (LCC) related with assessing benefits of using solid waste for road pavement, finding that there is still no agreement on what properties and impacts should be included in such analyses. (Ishak *et al.*, 2017), to measure the self-assessed level of compliance of Malaysian construction products manufacturers with the rules of “green” production, compiled a list of as many as 33 environmental criteria based on the literature.

4 Summary and Conclusions

Judging by the analyzed sample of papers, there exists no agreed set of environmental criteria for comparing sustainability of alternative construction products, components and construction methods (Figure 1).

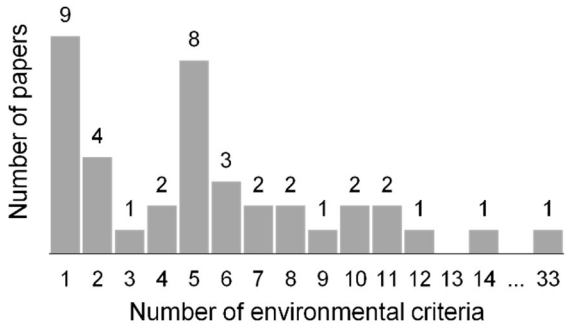

Figure 1. Frequency of selecting a particular number of criteria in the sample of papers.

Interestingly, even in the case of similar problems, the numbers and the type of criteria differed significantly. For instance, Potkany, Gejdos and Debnar (2018), Svajlenka and Kozlovska (2018), and Hassan and Johansson (2018) compared options of building frames basing on a set of sustainability measures without combining them into one index. They all did it within "cradle to gate" boundaries. Respectively, they used: six criteria known from EPD's (Table 1): primary energy input for production (PEI), global warming potential (GWP), acidification potential (AP), eutrophication potential (EP), ozone depletion potential (ODP), and photochemical ozone creation potential (POCP), three criteria (PEI, GWP, AP), and a single criterion (GWP).

Even the authors who decided on a single factor related to the environmental impact chose different criteria: energy embodied in the material used for a component, energy embodied up to the construction phase, potential for recycling, quantity of waste, GWP, or other. Moreover, most authors identified the criteria in the course of a literature review and interviews with experts to refine the list to suit a particular decision problem. Only 14 admitted drawing directly from particular LCA methodologies.

It is likely that the sample of papers analyzed above is not representative of the state-of-the-art in research on sustainability in construction. However, it indicates that this field is still in the stage of development.

Acknowledgements

The work was funded by the Polish Ministry of Science and Higher Education ILT 63. The authors gratefully acknowledge the support.

ORCID

Robert Bucoń: https://orcid.org/0000-0002-9397-639X
Agata Czarnigowska: https://orcid.org/0000-0003-3715-3521

References

Ahmed, M., Qureshi, M. N., Mallick, J. and Ben Kahla, N. (2019). Selection of Sustainable Supplementary Concrete Materials Using OSM-AHP-TOPSIS Approach. *Advances in Materials Science and Engineering*, *2019*. doi: 10.1155/2019/2850480

Allacker, K., Mathieux, F., Pennington, D. and Pant, R. (2017). The search for an appropriate end-of-life formula for the purpose of the European Commission Environmental Footprint initiative. *International Journal of Life Cycle Assessment*, *22*(9), 1441–1458. doi: 10.1007/s11367-016-1244-0

Amer, M. and Attia, S. (2019). Identification of sustainable criteria for decision-making on roof stacking

construction method. *Sustainable Cities and Society*, *47*(June 2018), 101456. doi: 10.1016/j.scs.2019.101456

Bak, J., Radziszewska-Zielina, E. and Zielina, M. (2019). Analysis of the Spatial Structure of Green Building in the Aspect of Selected Environmental Issues on the Example of the City of Cracow (Poland). *IOP Conference Series: Materials Science and Engineering*, *603*(4). doi: 10.1088/1757-899X/603/4/042099

Bucoń, R. (2019). Model supporting decisions on renovation and modernization of public utility buildings. *Open Engineering*, *9*(1), 178–185. doi: 10.1515/eng-2019-0022

D'Amato, D., Droste, N., Winkler, K. J. and Toppinen, A. (2019). Thinking green, circular or bio: Eliciting researchers' perspectives on a sustainable economy with Q method. *Journal of Cleaner Production*, *230*, 460–476. doi: 10.1016/J.JCLEPRO.2019.05.099

Doan, D. T., Ghaffarianhoseini, A., Naismith, N., Zhang, T., Ghaffarianhoseini, A. and Tookey, J. (2017). A critical comparison of green building rating systems. *Building and Environment*, *123*, 243–260. doi: 10.1016/J.BUILDENV.2017.07.007

European Commission. (2013). Recommendation 2013/179/EU on the use of common methods to measure and communicate the life cycle environmental performance of products and organisations. In *Official Journal of European Union* (Issue L 124). doi: doi:10.3000/19770677.L_2013.124.eng

Falqi, I. I., Ahmed, M. and Mallick, J. (2019). Siliceous Concrete Materials Management for Sustainability Using Fuzzy-TOPSIS Approach. *Applied Sciences*, *9*(17). doi: 10.3390/app9173457

Galatola, M. and Pant, R. (2014). Reply to the editorial "product environmental footprint - breakthrough or breakdown for policy implementation of life cycle assessment?" Written by Prof. Finkbeiner (Int J Life Cycle Assess 19(2):266-271). *International Journal of Life Cycle Assessment*, *19*(6), 1356–1360. doi: 10.1007/s11367-014-0740-3

Goh, C. S., Chong, H.-Y., Jack, L. and Mohd Faris, A. F. (2020). Revisiting triple bottom line within the context of sustainable construction: A systematic review. *Journal of Cleaner Production*, *252*, 119884. doi: 10.1016/J.JCLEPRO.2019.119884

Goldstein, B., Birkved, M., Quitzau, M.-B. and Hauschild, M. (2013). Quantification of urban metabolism through coupling with the life cycle assessment framework: concept development and case study. *Environmental Research Letters*, *8*(3), 035024. doi: 10.1088/1748-9326/8/3/035024

Häfliger, I.-F. F., John, V., Passer, A., Lasvaux, S., Hoxha, E., Saade, M. R. M. and Habert, G. (2017). Buildings environmental impacts' sensitivity related to LCA modelling choices of construction materials. *Journal of Cleaner Production*, *156*, 805–816.

Hasik, V., Ororbia, M., Warn, G. P. and Bilec, M. M. (2019). Whole building life cycle environmental impacts and costs: A sensitivity study of design and service decisions. *Building and Environment*, *163*, 106316. doi: 10.1016/J.BUILDENV.2019.106316

Hassan, O. A. B. and Johansson, C. (2018). Glued laminated timber and steel beams: A comparative study of structural design, economic and environmental consequences. *Journal of Engineering, Design and Technology*, *16*(3), 398–417. doi: 10.1108/JEDT-12-2017-0130

Herda, G., Sangori, R. and Bock, M. (2017). Low Cost, Low Carbon, but no Data: Kenya's Struggle to Develop the Availability of Performance Data for Building Products. *Procedia Environmental Sciences*, *38*, 452–460. doi: 10.1016/j.proenv.2017.03.136

Hoxha, V., Haugen, T. and Bjorberg, S. (2017). Measuring perception about sustainability of building materials in Kosovo. *Facilities*, *35*(7–8), 436–461. doi: 10.1108/F-04-2016-0040

Imron, M. A., Ahkam, D. N. I. and Hidayat, A. W. (2017a). DECO FRECASE (drywall eco-friendly from eggshell and cane bagasse) as an innovation of eco-friendly interior construction. *IOP Conference Series: Materials Science and Engineering*, *282*(1). doi: 10.1088/1757-899X/282/1/012009

Imron, M. A., Ahkam, D. N. I. and Hidayat, A. W. (2017b). DECO FRECASE (drywall eco-friendly from eggshell and cane bagasse) as an innovation of eco-friendly interior construction. *IOP Conference Series: Materials Science and Engineering*, *282*(1). doi: 10.1088/1757-899X/282/1/012009

Ishak, N. I., Kamal, E. M. and Yusof, N. (2017). The Green Manufacturer's Compliance With Green Criteria Throughout the Life Cycle of Building Material. *SAGE Open*, *7*(3). doi: 10.1177/2158244017725446

ITB. (2013). *LCA modules and indicators* (Issue Vii). https://www.itb.pl/epd.html

Jeong, J. S. and Ramirez-Gomez, A. (2018). Development of a web graphic model with fuzzy-decision-making Trial and Evaluation Laboratory/Multi-criteria-Spatial Decision Support System (F-DEMATEL/MC-SDSS) for sustainable planning and construction of rural housings. *JOURNAL OF CLEANER PRODUCTION*, *199*, 584–592. doi: 10.1016/j.jclepro.2018.07.227

Kellenberger, D. and Althaus, H.-J. (2009). Relevance of simplifications in LCA of building components. *Building and Environment*, *44*(4), 818–825. doi: 10.1016/J.BUILDENV.2008.06.002

Khoshnava, S. M., Rostami, R., Valipour, A., Ismail, M. and Rahmat, A. R. (2018). Rank of green building material criteria based on the three pillars of sustainability using the hybrid multi criteria decision making method. *Journal of Cleaner Production*, *173*, 82–99. doi: 10.1016/j.jclepro.2016.10.066

Komatsu, H., Rappleye, J. and Silova, I. (2019). Culture and the Independent Self: Obstacles to environmental sustainability? *Anthropocene*, *26*, 100198. doi: 10.1016/J.ANCENE.2019.100198

Kuittinen, M. and Linkosalmi, L. (2015). *Compiling environmental product declarations for wood-based construction products assessment and documentation* (Issue July).

Kurda, R., de Brito, J. and Silvestre, J. D. (2019). CONCRETop - A multi-criteria decision method for concrete optimization. *Environmental Impact Assesment Review*, *74*, 73–85. doi: 10.1016/j.eiar.2018.10.006

Li, J., Xiao, F., Zhang, L. and Amirkhanian, S. N. (2019). Life cycle assessment and life cycle cost analysis of recycled solid waste materials in highway pavement: A review. *Journal of Cleaner Production*, *233*, 1182–1206. doi: 10.1016/j.jclepro.2019.06.061

Meadows, D. H., Meadows, D. L., Randers, J. and Behren, W. W. (1972). *The Limits to growth: A report for the Club of Rome's project on the predicament of mankind*. Universe Books.

Nematchoua, M. K., Asadi, S. and Reiter, S. (2020). A study of life cycle assessment in two old neighbourhoods in Belgium. *Sustainable Cities and Society*, *52*, 101744. doi: 10.1016/J.SCS.2019.101744

Ortiz, O., Castells, F. and Sonnemann, G. (2009). Sustainability in the construction industry: A review of recent developments based on LCA. *Construction and Building Materials*, *23*(1), 28–39. doi: 10.1016/J.CONBUILDMAT.2007.11.012

Park, J., Yoon, J. and Kim, K.-H. (2017). Critical review of the material criteria of building sustainability assessment tools. *Sustainability (Switzerland)*, *9*(2). doi: 10.3390/su9020186

Passer, A., Lasvaux, S., Allacker, K., De Lathauwer, D., Spirinckx, C., Wittstock, B., Kellenberger, D., Gschösser, F., Wall, J. and Wallbaum, H. (2015). Environmental product declarations entering the building sector: critical reflections based on 5 to 10 years experience in different European countries. *International Journal of Life Cycle Assessment*, *20*(9), 1199–1212. doi: 10.1007/s11367-015-0926-3

Piasecki, M. (2014). Added value of the European Core EPD. *Proceedings of the World Sustainable Building Conference 2014*, 1–7.

Potkany, M., Gejdos, M. and Debnar, M. (2018). Sustainable Innovation Approach for Wood Quality Evaluation in Green Business. *Sustainability (Switzerland)*, *10*(9). doi: 10.3390/su10092984

Rashdan, W. and Ashour, A. F. (2018). Criteria for sustainable interir design solutions. In J. Brebbia, CA and Sendra (Ed.), *WIT Transactions on Ecology and The Environment* (Vol. 223, pp. 311–322). doi: 10.2495/SC170271

Rashid, K., Hameed, R., Ahmad, H. A., Razzaq, A., Ahmad, M. and Mahmood, A. (2018). Analytical framework for value added utilization of glass waste in concrete: Mechanical and environmental performance. *Waste Management*, *79*, 312–323. doi: 10.1016/j.wasman.2018.07.052

Reddy, A. S., Kumar, P. R. and Raj, P. A. (2019a). Developing a Material Sustainable Performance Score (MSPS) to select an alternative Cementitious Material. *Cement, Wapno, Beton*, *24*(1), 68+.

Reddy, A. S., Kumar, P. R. and Raj, P. A. (2019b). Preference based multi-criteria framework for developing a Sustainable Material Performance Index (SMPI). *International Journal of Sustainable Engineering*, *12*(6), 390–403. doi: 10.1080/19397038.2019.1581853

Reddy, A. S., Kumar, P. R. and Raj, P. A. (2020). Development of Sustainable Performance Index (SPI) for Self-Compacting Concretes. *Journal of Building Engineering*, *27*. doi: 10.1016/j.jobe.2019.100974

Suarez Silgado, S., Calderon Valdiviezo, L., Gasso Domingo, S. and Roca, X. (2018). Multi-criteria decision analysis to assess the environmental and economic performance of using recycled gypsum cement and recycled aggregate to produce concrete: The case of Catalonia (Spain). *Resources, Conservation & Recycling*, *133*, 120–131. doi: 10.1016/j.resconrec.2017.11.023

Svajlenka, J. and Kozlovska, M. (2018). Houses Based on Wood as an Ecological and Sustainable Housing Alternative-Case Study. *Sustainability (Switzerland)*, *10*(5). doi: 10.3390/su10051502

Turner, G. M. (2008). A comparison of The Limits to Growth with 30 years of reality. *Global Environmental Change*, *18*(3), 397–411. doi: 10.1016/J.GLOENVCHA.2008.05.001

XV International Conference on Durability of Building Materials and Components
DBMC 2020, Barcelona
C. Serrat, J.R. Casas and V. Gibert (Eds)

Selecting Criteria for Assessing "Environmentally-Friendly" Material Options in Construction: Part II

Robert Bucoń[1] **and Agata Czarnigowska**[2]

[1] Dpt. Of Construction Methods and Management, Faculty of Civil Engineering and Architecture, Politechnika Lubelska, Nadbystrzycka 40, 20-618 Lublin, Poland, r.bucon@pollub.pl

[2] Dpt. Of Construction Methods and Management, Faculty of Civil Engineering and Architecture, Politechnika Lubelska, Nadbystrzycka 40, 20-618 Lublin, Poland, a.czarnigowska@pollub.pl

Abstract. *One of the design team's tasks is assuring that their project has a low negative impact on the environment. This comes from regulations as well as expectations of direct benefits (reduction of operating cost, the project's improved image in the eyes of the public, etc.). To fulfill this task, one needs to define criteria for assessing the design options. These are to correspond to the individual qualities of the project, and they should be significant and possible to assess. The paper, divided into two parts, presents a review of the literature concerning the criteria for the assessment of design solutions defined as "green" or "environmentally friendly". Part I presented the method of the analysis and investigates into the number and type of criteria adopted in the sample of papers being the object of analysis. This part focuses on the ways of defining criteria values, weights, and methods of multicriteria assessment.*

Keywords: *Sustainable Construction, Component Selection, LCA, Literature Review.*

1 Introduction

In the face of resource depletion and the likely suffocation with its own refuse within decades, humanity is dragged towards a sustainable economy and, in particular, sustainable construction (Goh, Chong, Jack and Mohd Faris, 2020). One of the aspects of construction sustainability is reducing the project's and the resulting built facility's impact on the environment. This impact is typically assessed in the course of a Life Cycle Analysis (LCA) (Ortiz, Castells and Sonnemann, 2009). The idea of LCA evolved into many methodologies that share the element of assessing the consequences of using particular construction materials in the building's fabric. However, even in this narrow aspect, the analyses' scope, criteria, and measures are not identical (Park, Yoon and Kim, 2017). The standards and methodologies evolve (Allacker, Mathieux, Pennington and Pant, 2017). Due to the proliferation of LCA methodologies, the comparability of information on products' environmental qualities becomes an issue (European Union, 2013).

This paper is a second part of the review of the most recent literature on selecting the "environmentally friendly" material and component options in construction. The authors discuss a sample of papers devoted to assessing the sustainability of alternative solutions (materials, material supply chains, component design) and optimizing construction components, focusing on the ways of defining criteria values, the criteria's relative importance, and selecting the methods of multicriteria assessment.

2 Materials and Methods

The sources' approach to the life cycle phases was juxtaposed to the life cycle phases used in LCA and adopted for Environmental Product Declarations (EPDs). The "environmentally friendly" aspects were considered only those covered by the scope of environmental impacts, aspects of resource use, and generation of waste as defined in EPDs prepared according to EN 15804:2012. The query was limited to one database (Web of Science), publications from the years 2016-2020, and a particular structure of search terms, as presented in Part I. The selection was manually refined. The final sample comprised 43 publications. The sample was analyzed in terms of aspects of sustainability covered by the analysis, life cycle stages considered, sources of input, and mathematical methods used for selecting the best option (if applicable).

3 Results and Discussion

77% of papers of the sample focused on assessing the sustainability of alternative solutions. The problems differed much in terms of the object of the analysis: from comparing particular types of materials in the context of a local market, through types of complex components of buildings or civil engineering structures, to alternative ways of conducting whole projects or selecting supply chains to serve certain projects or regions.

Table 1 list the papers whose authors proposed some form of an integrated measure of sustainability with reference to alternative construction products (like bricks, windows, water pipes, paints) offered in a particular market.

Table 1. Works on ranking or selecting most sustainable construction products in a certain market/region (not adopting a project perspective).

Paper	Aspects	Life cycle	Criteria list	Weights, method of calculation	Env. criteria	Criteria values:	Method, output
(Govindan *et al.*, 2016)	Ec, En, S	not explicit	Arbitrary	M. experts, DEMATEL +ANP	10	Expert ratings: 1-5 scores used in example	TOPSIS,combined index
(Bissoli-Dalvi *et al.*, 2016)	En	A-D	Arbitrary	1 expert, ISMAS	7	Expert: ratings in 3-level scale	ISMAS, combined index
(Roy *et al.*, 2019)	Ec, En,S	not explicit	Arbitrary	M. experts, fuzzy pairwise comparisons, linear programming; sensitivity analysis	4	M. experts,, Fuzzy ratings	IVIF-CODAS. combined index
(Zhang *et al.*, 2017)	T, Ec, En	A1-A3+ disposal	Arbitrary	M. experts, DEMATEL +ANP; sensitivity analysis	5	Expert ratings in scale 1-5 in example	G-TOPSIS, combined index
(Mathiyazhagan *et al.*, 2019)	Ec, En,S	not explicit	team of experts /literature	M. experts, integrated by averaging; BWM	9	Expert ratings	fuzzy TOPSIS, combined index
(Rochikashvili and Bongaerts, 2016)	T, Ec, En, S	not explicit	Arbitrary	M. experts, ANP	1	Expert pairwise comparisons	ANP, combined index
(Maiolo *et al.*, 2018)	T, Ec, En	A1-A3	LCA (Impact 2002+)	Acc. to Impact 2002+	n/a	databases & calculations	multiplying two indices, combined index

A common feature of these papers is analyzing the options in abstraction from projects they might be used for. In this group, all papers but two presented analyses from the perspective of developing countries and based on criteria values rated by experts (though some methods were applicable also for measurable criteria).

For instance, Govindan, Madan Shankar, & Kannan (2016) used DEMATEL combined with ANP to establish the set of criteria and their relationships on the basis of opinions of multiple experts, and then TOPSIS for the assessment of options. They illustrated their approach on the example of selecting the "most sustainable" type of brick as perceived by the construction professionals (clients, architects, contractors) in UAE market. In this case, all 10 criteria related to the environmental impact would be possible to express as quantitative measures established in the course of LCA, but the authors were vague about the way of the source of their values; judging by the presentation of illustrative example, the values were expresses as arbitrary scores in a 1-5 scale. Bissoli-Dalvi *et al.* (2016) compared the sustainability of different types of windows used in Brazilian housing using an original ISMAS method. Due to the lack of databases of environmental product properties, they resorted to an individual set of "green" criteria and expressed their values by ratings in a unified 3-point scale (-1 for "worse than average requirements", 0 for "standard practice", 1 for qualities considered "better than acceptable"). The ratings were then treated as additive scores that, after being weighted, were combined into a quantitative index for direct comparison of options.

Rochikashvili and Bongaerts (2016) aimed at conducting the comparison of products to appeal to non-experts. For this reason, the authors did not use precise measures of environmental impact. Their criteria were selected arbitrarily and grouped into 4 categories: benefits, costs, opportunities, and risks. The sub-criteria related to the environmental impact belonged to the latter. Maiolo et al. (2018), to select the best type of water pipes applicable in particular soil conditions, conducted a thorough LCA (cradle to gate) of 10 products offered in the market using Impact 2002+ methodology, assuming Western European conditions. Then they combined its overall measure of environmental profile with the coefficient capturing mechanical properties. This was the only paper from this group resting upon precise measures of environmental impact.

Shipping large quantities of materials, as required in the case of construction projects, generates high cost, consumes fossil fuels and pollutes the natural environment. Therefore, the A2 and A4 phases of the lifecycle are a natural focus of construction sustainability researchers. In the sample, two papers were devoted to analyzing supply chains. Ahmadian *et al.* (2017) considered different sources, levels of prefabrication, modes and distances of transport. Designing their BIM-based supply chain management system, they argued that the environmental criteria should be project-specific and might be defined by experts, though they should refer at least to the material production, transport to the site and installation phase, as well as they should consider the potential of re-use and recycling. Basti (2018) analyzed the problem managing large quantities of earthquake debris, a current problem of Italian regions struck by natural disasters. He focused on environmental issues of deconstruction, transport, depositing, and reusing this material, as well as on constraints resulting from regulations. This was done not in a "per project" approach, but from the point of municipal strategies that consider the network of local enterprises to be engaged in the process, restrictions on road use for heavy transport, selection of means of transport with regard to location of debris processing, landfilling and reuse areas.

The biggest part of the sample of papers dealt with the problem of comparing alternative products of complex components from the perspective of a project (particular location, particular quantities, individual constraints due to the design of the building/civil engineering structure – Table 2).

Table 2. Works on comparing options of building components assuming perspective of a particular project.

Paper	Aspects	Life cycle	Criteria list	Weights, method of calculation	Env. criteria	Criteria values:	Method output
(Ananin *et al.*, 2018)	En	A1-A3	Arbitrary	-	1	databases & calculations	ranking acc. to energy embodied in materials
(Gomez-Soberon *et al.*, 2016)	En	A4-C?	Arbitrary	-	1	databases & calculations	calculation of the quantity of 5 types of waste for each option
(Potkany *et al.*, 2018)	Ec, En	A1-A3	LCA (EPD)	-	6	databases & calculations	calculation of a set of measures for each option
(Svajlenka and Kozlovska, 2018)	Ec, En	A1-A3	LCA	-	3	databases & calculations	calculation of a set of measures for each option
(Hassan and Johansson, 2018)	T, Ec, En	A1-A3?	Arbitrary	-	1	databases & calculations	calculation of a set of measures for each option
(Al-Nassar *et al.*, 2016)	Ec, En, S	A-C	LCA	Arbitrary; sensitivity analysis	8	databases & calculations	weighted sum combined index
(Chen *et al.*, 2019)	T,Ec, En, S	not explicit	Experts	M. experts BULI-based QFD; sensitivity analysis	5	M. experts	ELECTRE III combined index
(Casanovas-Rubio *et al.*, 2019)	Ec, En, S	A	Experts	T. of experts AHP; sensitivity analysis	5	databases & calculations	MIVES combined index
(Alberti *et al.*, 2018)	Ec, En, S	A-B	Experts	Arbitrary (literature);	5	databases & calculations	MIVES combined index
(Kripka *et al.*, 2019)	T, Ec, En, S	A	LCA (selected)	Arbitrary, AHP; sens analysis	1	databases & calculations	AHP, VIKOR combined index
(Kumanayake and Luo, 2017)	Ec, En	A-C	LCA (selected)	*not decided yet*	1	databases & calculations	*not decided yet* combined index
(Sarkkinen *et al.*, 2019)	T, Ec, En,S	not explicit	LCA	M. experts, AHP (geometric mean); sensitivity analysis	2	databases & calculations	AHP combined index
(J Santos *et al.*, 2019)	Ec, En, S	A-C	Arbitrary (selection justified)	3 approaches; sensitivity analysis	10	databases & calculations	PROMETHEE II combined index
(Joao Santos *et al.*, 2017)	Ec, En	A-C	LCA	Arbitrary (as in BEES); sensitivity analysis	8	databases & calculations	TOPSIS combined index
(Zheng *et al.*, 2019)	Ec, En,S	A-B	LCA	M. experts, AHP (geometric mean); sensitivity analysis	5	databases & calculations	VIKOR combined index
(Pavlovskis *et al.* 2016)	T, Ec, En	A-C	Arbitrary	M. experts WASPAS-G for aggregation	5	M. experts	WASPAS-G, combined index; Compared with results of o. methods

Five works produced sustainability measures without combining them into overall scores

(less convenient for comparison, but not affected by subjectivity in normalizing criteria values and setting weights). Among them, two papers considered a sole measure of the environmental impact. Among them, two papers considered sole measures of environmental impact: Ananin *et al.* (2018) looked for the best type for walls of a residential building in Russia with the lowest energy embodied in wall materials, while Gomez-Soberon *et al.* (2016) compared 3 options of floors according to the type and quantity of waste generated by replacement.

As the number of factors worth considering in the assessment may be large, some generalized measures to facilitate a clear distinction between options may be useful. 11 papers presented such measures. Among them, Chen *et al.* (2019) presented an interesting problem of designing components to the liking of various stakeholders by using Quality Function Deployment and ELECTRE III. They proposed a new group decision making method and illustrated its use on the example of selecting flooring for office space. With this approach, the set of criteria was individually defined for each case, expressing the stakeholders' point of view.

Casanovas-Rubio *et al.* (2019) assessed sustainability of trenching methods. Their method, MIVES, normalizes criteria scores by utility functions based on relative preferences expressed by experts. The values of criteria were expressed as precise numbers (e.g. water consumption in dm^3 per 1m of trench) or as scores (if the effort to estimate the precise measure was considered too great; however, justification for calculating the scores was provided). The analysis produced a single measure, Sustainability Index for Trenches, to compare the options. Alberti *et al.* (2018) used the same method to assess sustainability of two options of a structural component, namely a tunnel slab of reinforced concrete, that differed in the type of reinforcement. Interestingly, they based on the evidence on the components' performance over 3 years of use in the same conditions. This was a unique feature of this research.

Santos *et al.* (2019) presented a decision-support tool for ranking alternative pavement designs. The tool allows the user to define their own weights of criteria or to select the weights as found by the authors in a survey. All 10 sustainability indicators related with environmental impact were measurable, clearly defined in the literature, with the methods of calculation or sources of values of confirmed reliability. To exclude selection of options that compensate poor performance in some aspect by good performance in others, an outranking method with threshold values was selected as the core of the decision support tool. Out of the sample of papers, this one was considered to present the most convincing line of reasoning for selection of criteria (though the authors direct the reader to their subsequent publications for details) and methods for the ranking of options.

The remaining papers (not listed in Table 2) were not devoted to assessing predefined component options, but to solving multicriteria design problems. BuHamdan *et al.* (2019) presented a simulation model built to assess effects of combined design changes in a number of components (the size of glazed area, type of windows and thermal resistance of envelope) on the building's cost, measures of environmental impact in the construction, operation and demolition phase. Marti, Garcia-Segura and Yepes (2016) constructed an automated design optimization tool that prompts the best beam profile, concrete class and contents of prestressing and reinforcing steel of a prefabricated U-beam used in bridge construction. The model produces solutions that satisfy structural requirements at minimum cost and embodied energy in phase A of the lifecycle.

4 Summary and Conclusions

Values of the criteria related to the environmental impact were either calculated or rated arbitrarily by experts, in the latter case using a variety of rating scales or in the course pairwise comparisons. Among 35 papers that compared/ranked options or aimed at finding an optimal solution, a dependence was observed (p-value in χ^2 test of 0,00124) between the location of the object of analysis and the authors' method to define the criteria values (Figure 1). This observation is rather obvious: the geographical coverage of construction products' life cycle inventory databases is only slowly expanded on South America, Africa, and Asia.

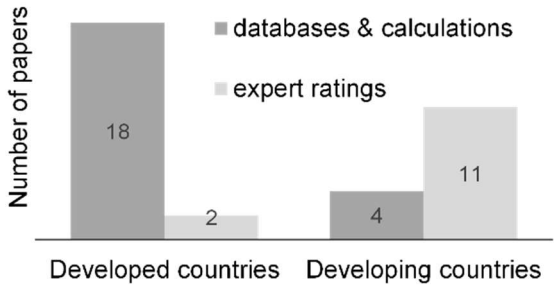

Figure 1. Methods of defining criteria values vs origin of the paper.

Nevertheless, a detailed and laborious calculation of criteria values in interval or ratio scales was not automatically an asset. As most of the authors who calculated criteria values this way (14 out of 22) aimed at providing an integrated index of sustainability to make the comparisons easier, they normalized the values in a way specific to the method of multicriteria analysis. Frequently, the precision of criteria measures was lost in this process, especially if measures were subject to pairwise comparisons. Four authors decided to directly account for the uncertainty of criteria ratings by expressing them by fuzzy or grey numbers.

Defining criteria weights, a key aspect of most multicriteria assessment methods, was most frequently done by collecting expert opinions. They were collected during panel meetings for direct consensus (10%) or independently, in interviews or questionnaire surveys (40%). Thus, 50% of authors based on weights prompted by the literature or decided to use arbitrary values, then check the sensitivity of their results to changes in criteria weights. Multiple opinions were aggregated in a number of ways: from mean scores to elaborate analysis in stakeholder groups.

As for the multicriteria assessment methods in use, the most popular of the established ones were TOPSIS (6 papers), AHP (5 papers), and VIKOR (3 papers). Some authors used a combination of methods or proposed their own to precisely account for the character of the problem. Nevertheless, out of 27 works that provided one combined measure for ranking options, 9 did not explicitly refer to any form of checking the sensitivity of the results to weights nor juxtaposed their ranking with rankings obtained by means of other methods.

The sample of papers analyzed above is certainly not representative of the state-of-the-art research on the environmental impact of construction. However, it indicates that this field is still in the stage of development. There is no agreement on the type of criteria, on their importance, nor the methods of assessment in analyzing the sustainability of construction products and components.

Acknowledgements

The work was funded by the Polish Ministry of Science and Higher Education ILT 63. The authors gratefully acknowledge the support.

ORCID

Robert Bucoń: https://orcid.org/0000-0002-9397-639X
Agata Czarnigowska: https://orcid.org/0000-0003-3715-3521

References

Ahmadian, A. F. F., Rashidi, T. H., Akbarnezhad, A. and Waller, S. T. (2017). BIM-enabled sustainability assessment of material supply decisions. *Engineering, Construction and Architectural Management*, *24*(4), 668–695. doi: 10.1108/ECAM-12-2015-0193

Al-Nassar, F., Ruparathna, R., Chhipi-Shrestha, G., Haider, H., Hewage, K. and Sadiq, R. (2016). Sustainability assessment framework for low rise commercial buildings: life cycle impact index-based approach. *Clean Technologies and Environmental Policy*, *18*(8, SI), 2579–2590. doi: 10.1007/s10098-016-1168-1

Alberti, M. G., Galvez, J. C., Enfedaque, A., Carmona, A., Valverde, C. and Pardo, G. (2018). Use of Steel and Polyolefin Fibres in the La Canda Tunnels: Applying MIVES for Assessing Sustainability Evaluation. *Sustainability (Switzerland)*, *10*(12). doi: 10.3390/su10124765

Allacker, K., Mathieux, F., Pennington, D. and Pant, R. (2017). The search for an appropriate end-of-life formula for the purpose of the European Commission Environmental Footprint initiative. *International Journal of Life Cycle Assessment*, *22*(9), 1441–1458. doi: 10.1007/s11367-016-1244-0

Ananin, M., Perfilyeva, N., Vedishcheva, I. and Vatin, N. (2018). Investigation of different materials usage expediency for a low-rise public building from the energy efficiency standpoint. *IOP Conference Series: Materials Science and Engineering*, *365*. doi: 10.1088/1757-899X/365/2/022014

Basti, A. (2018). Sustainable management of debris from the L'Aquilsearthquake: Environmental strategies and impact assessment. *Detritus*, *2*, 112–119. doi: 10.31025/2611-4135/2018.13661

Bissoli-Dalvi, M., Nico-Rodrigues, E. A., Alvarez, C. E. D., Saelzer Fuica, G. E. and Montarroyos, D. C. G. (2016). The sustainability of the materials under the approach of ISMAS. *Construction and Building Materials*, *106*, 357–363. doi: 10.1016/j.conbuildmat.2015.12.030

BuHamdan, S., Alwisy, A., Barkokebas, B., Bouferguene, A. and Al-Hussein, M. (2019). A multi-criteria lifecycle assessment framework for evaluating building systems design. *Journal of Building Engineering*, *23*, 388–402. doi: 10.1016/j.jobe.2019.02.010

Casanovas-Rubio, M. del M., Pujadas, P., Pardo-Bosch, F., Blanco, A. and Aguado, A. (2019). Sustainability assessment of trenches including the new eco-trench: A multi-criteria decision-making tool. *Journal of Cleaner Production*, *238*. doi: 10.1016/j.jclepro.2019.117957

Chen, Z.-S., Martínez, L., Chang, J.-P., Wang, X.-J., Xionge, S.-H. and Chin, K.-S. (2019). Sustainable building material selection: A QFD- and ELECTRE III-embedded hybrid MCGDM approach with consensus building. *Engineering Applications of Artificial Intelligence*, *85*(December 2018), 783–807. doi: 10.1016/j.engappai.2019.08.006

European Union. (2013). Council Directive 2013/59/Euratom. In *Official Journal of the European Union* (Vol. 56, Issue L 124). doi: 10.3000/19770677.L_2013.124.eng

Goh, C. S., Chong, H.-Y., Jack, L. and Mohd Faris, A. F. (2020). Revisiting triple bottom line within the context of sustainable construction: A systematic review. *Journal of Cleaner Production*, *252*, 119884. doi: 10.1016/J.JCLEPRO.2019.119884

Gomez-Soberon, J. M., Gomez-Soberon, M. C., Saldana-Marquez, H., Gamez-Garcia, D. C., Arredondo-Rea, S. P. and Corral-Higuera, R. (2016). Comparative by simulating the eventual waste generation of building indoor pavements construction. *2016 World Congress on Sustainable Technologies, WCST*, 117–121.

Govindan, K., Madan Shankar, K. and Kannan, D. (2016). Sustainable material selection for construction industry - A hybrid multi criteria decision making approach. *Renewable and Sustainable Energy Reviews*, *55*, 1274–1288. doi: 10.1016/j.rser.2015.07.100

Hassan, O. A. B. and Johansson, C. (2018). Glued laminated timber and steel beams: A comparative study of structural design, economic and environmental consequences. *Journal of Engineering, Design and Technology*,

16(3), 398–417. doi: 10.1108/JEDT-12-2017-0130
Kripka, M., Yepes, V. and Milani, C. J. (2019). Selection of sustainable short-span bridge design in Brazil. *Sustainability (Switzerland)*, *11*(5). doi: 10.3390/su11051307
Kumanayake, R. and Luo, H. (2017). Development of an automated tool for buildings' sustainability assessment in early design stage. *Procedia Engineering*, *196*, 903–910. doi: 10.1016/j.proeng.2017.08.023
Maiolo, M., Capano, G., Carini, M. and Pantusa, D. (2018). Sustainability criteria for the selection of water supply pipeline. *Cogent Engineering*, *5*(1). doi: 10.1080/23311916.2018.1491777
Marti, J. V, Garcia-Segura, T. and Yepes, V. (2016). Structural design of precast-prestressed concrete U-beam road bridges based on embodied energy. *Journal of Cleaner Production*, *120*, 231–240. doi: 10.1016/j.jclepro.2016.02.024
Mathiyazhagan, K., Gnanavelbabu, A. and Prabhuraj, B. L. (2019). A sustainable assessment model for material selection in construction industries perspective using hybrid MCDM approaches. *Journal of Advances in Management Research*, *16*(2), 234–259. doi: 10.1108/JAMR-09-2018-0085
Ortiz, O., Castells, F. and Sonnemann, G. (2009). Sustainability in the construction industry: A review of recent developments based on LCA. *Construction and Building Materials*, *23*(1), 28–39. doi: 10.1016/J.CONBUILDMAT.2007.11.012
Park, J., Yoon, J. and Kim, K.-H. (2017). Critical review of the material criteria of building sustainability assessment tools. *Sustainability (Switzerland)*, *9*(2). doi: 10.3390/su9020186
Pavlovskis, M., Antucheviciene, J. and Migilinskas, D. (2016). Application of MCDM and BIM for Evaluation of Asset Redevelopment Solutions. *Studies in Informatics and Control*, *25*(3), 293–302.
Potkany, M., Gejdos, M. and Debnar, M. (2018). Sustainable Innovation Approach for Wood Quality Evaluation in Green Business. *Sustainability (Switzerland)*, *10*(9). doi: 10.3390/su10092984
Rochikashvili, M. and Bongaerts, J. C. (2016). Multi-criteria decision-making for sustainable wall paints and coatings using Analytic Hierarchy Process. *Energy Procedia*, *96*, 923–933. doi: 10.1016/j.egypro.2016.09.167
Roy, J., Das, S., Kar, S. and Pamučar, D. (2019). An extension of the CODAS approach using interval-valued intuitionistic fuzzy set for sustainable material selection in construction projects with incomplete weight information. *Symmetry*, *11*(3). doi: 10.3390/sym11030393
Santos, J, Bressi, S., Cerezo, V. and Lo Presti, D. (2019). SUP&R DSS: A sustainability-based decision support system for road pavements. *Journal of Cleaner Production*, *206*, 524–540. doi: 10.1016/j.jclepro.2018.08.308
Santos, Joao, Flintsch, G. and Ferreira, A. (2017). Environmental and economic assessment of pavement construction and management practices for enhancing pavement sustainability. *Resources, Conservation & Recycling*, *116*, 15–31. doi: 10.1016/j.resconrec.2016.08.025
Sarkkinen, M., Kujala, K. and Gehör, S. (2019). Decision support framework for solid waste management based on sustainability criteria: A case study of tailings pond cover systems. *Journal of Cleaner Production*, *236*. doi: 10.1016/j.jclepro.2019.07.058
Svajlenka, J. and Kozlovska, M. (2018). Houses Based on Wood as an Ecological and Sustainable Housing Alternative-Case Study. *Sustainability (Switzerland)*, *10*(5). doi: 10.3390/su10051502
Zhang, H., Peng, Y., Tian, G., Wang, D. and Xie, P. (2017). Green material selection for sustainability: A hybrid MCDM approach. *PLOS ONE*, *12*(5). doi: 10.1371/journal.pone.0177578
Zheng, X., Easa, S. M., Yang, Z., Ji, T. and Jiang, Z. (2019). Life-cycle sustainability assessment of pavement maintenance alternatives: Methodology and case study. *Journal of Cleaner Production*, *213*, 659–672. doi: 10.1016/j.jclepro.2018.12.227

XV International Conference on Durability of Building Materials and Components
DBMC 2020, Barcelona
C. Serrat, J.R. Casas and V. Gibert (Eds)

Effects of Long-Term UV Exposure on the Performance of Cement Plasters Integrated with Thermochromic Paint and PCMs for Building Facade Applications

Shahrzad Soudian[1], Umberto Berardi[1] and Nadia O. Laschuk[2]

[1] Ryerson University, 350 Victoria St. Toronto, ON, Canada. shahrzad.soudian@ryerson.ca ; uberardi@ryerson.ca

[2] Ontario Tech University, 2000 Simcoe Street North, Oshawa, ON, Canada. nadia.laschuk@uoit.net

Abstract. *The exterior finish layer in building facades is exposed to considerable environmental loads, which can reduce the service life of the materials, increasing the need for replacement. New climate challenges impose to look more carefully at the long-term performance and durability of building components and materials. Thermal stresses due to daily temperature fluctuations and UV exposure can significantly damage facades and degrade their performance. This research measures the long-term performance of a responsive cementitious finish plaster. The developed cement plaster is combined with phase change materials (PCMs), and thermochromic (TC) pigments to control solar radiation and surface temperatures dynamically on the exterior façade year around. The main objective of the study is to quantify the effect of long-term UV exposure on the optical performance of the cement plasters. PCMs with three different melting temperatures of 18°C, 24°C, and 28°C were combined with two different colors of blue and red TC paint with a transition temperature of 31°C. Accelerated UV aging of the samples was performed using lab tests to simulate exposure to UV radiation for two years. The solar reflectance of the samples was characterized before and after the accelerated UV aging tests. The results of the aging tests revealed that UV exposure impacts the solar reflectance of the finish material based on the method of integrating the TC paint to the cement plaster. In the case of TC paint applied to the surface, the solar reflectance of the plasters with only the TC is reduced by 15% after aging, while the ones combined with PCMs have a similar solar reflectance value after aging.*

Keywords: *Durability, Building Façade, Thermal Energy Storage, Thermal Stress, Accelerated Aging, Urban Heat Island.*

1 Introduction

One of the main climate challenges in urban areas is the shifting weather patterns with increasing trends of temperature fluctuations in dense cities that can impact urban thermal comfort. The urban heat island (UHI) effect particularly is a known phenomenon that refers to the occurrence of higher ambient temperatures in cities compared to suburban areas (Santamouris *et al.*, 2016). This event is specifically due to higher solar absorption in urban surfaces such as building facades. In addition, the high surface temperatures of facades can lead to higher heat transfer through the building envelope leading to thermal comfort problems and higher energy demands. However, thermal stresses exposed to exterior building façade surfaces can critically impact the durability of the finish materials. The exterior finish layer in buildings is exposed to considerable environmental loads, namely thermal stresses and UV radiation, that over long-term exposure leads to degradation (Pisello, 2017). The temperature fluctuations experienced on the exterior surface of finish materials decrease the durability of the material (Hernandez-Perez *et al.*, 2014; Pisello, 2017).

doi:10.23967/dbmc.2020.163

Increasing the lifetime of the building façade by reducing exterior thermal stresses, therefore, becomes critical. By reviewing the literature, several strategies can be found that have been proposed for regulating external solar and thermal loads. The most prominent strategy is the application of cool/white or reflective coatings on exterior roof and façade surfaces. Such coatings have high solar reflectance and emittance, thus leading to lower surface temperature and better performance under UV exposure (Ascione *et al.*, 2018). With the growing application of cool coatings globally, the literature has mainly focused on their benefits in the cooling season. However, the heating penalty associated with lower solar gains on the surfaces with cool coatings could be comparable to their advantages in the cooling season (Ascione *et al.*, 2018; Garshasbi and Santamouris, 2019).

Several strategies to optimize the performance of reflective coatings have been evaluated, such as combining reflective coatings with phase change materials (PCMs) (Pisello *et al.*, 2017). This combination has been proposed to benefit from the large heat storage capacity of PCMs to buffer the peak temperatures and decrease the thermal fluctuations, which directly affect the durability of the finish materials (Pisello *et al.*, 2017). Another approach that is gaining attention is the use of dynamic coatings with variable optical properties using thermochromic (TC) coatings or paints (Karlessi *et al.*, 2011; Perez *et al.*, 2018). TC paint changes its colors in response to temperature, allowing a change in its optical properties at a specific transition temperature. The solar reflectance and emittance of the TC paint are increased with higher temperatures as it turns to whiter shades, and as the temperatures go down, the solar absorptivity of the paint is increased. Evaluating the key material properties of these smart materials is a crucial step to identify their potential in regulating solar and temperature loads in exterior finish applications. Several studies have focused primarily on this topic to identify the experimental methods to measure the characteristics of these materials (Zinzi, 2016). Additionally, to assess the impacts of environmental loads on the durability and performance of such smart materials, accelerated aging tests using lab equipment have been used extensively (Jelle, 2011; Karlessi *et al.*, 2015).

In this study, the application of TC paint and PCMs integrated into cement plasters is investigated in the climate context of Toronto, Canada. Cement plasters are a typical façade finish material used in different types of buildings in Toronto. The combination of the TC paint and PCMs in this study is used to address both thermal and solar exposure using different mechanisms of dynamic solar control and thermal energy storage. Different configurations of cement plasters with TC paint and PCMs have been developed and characterized for their optical and thermal properties. The aim of this paper is to evaluate how long-term exposure to solar radiation, particularly the negative impact of UV degradation impacts the optical performance of the samples. The objective is to compare the main optical property of the samples, namely solar reflectance in the primary stage to the post-aged stage using lab tests.

2 Methodology

2.1 Development of Cement Plaster Samples

The cement plaster was made based on the ASTM C926-18b standard for exterior plaster applications and mixed with microencapsulated PCMs and TC pigments. Three PCMs with different melting temperatures (T_{mp}) of 18ºC, 24ºC, and 28ºC were used. Blue and red Leuco

dye TC pigments with a transition temperature of 31°C were used in this study. Based on the dynamic properties of the TC paints selected, the color transition to white occurs above 31°C, and below 31°C, the paint turns back to its original color. The cement plaster samples were made into 10 cm x 10 cm tiles with a thickness of 1.2 cm. The PCMs and the TC paints were each added to the tiles based on a mass fraction of 2.5% of the base cement plaster tiles. Therefore, samples with both PCMs and the TC paint included a total of 5% of the materials and a 95% ratio of the cement plaster mixture. More detailed information on the sample production process can be found in Soudian and Berardi (2019).

One of the main variables in this study is two different types of cement plasters considering the integration of the TC paint in the plaster. Type 1 samples include the mixing of both the PCMs and the TC pigments inside the cement plaster mixture, as shown in Figure 1a. Type 2 samples include the mixing of PCMs inside the cement plaster mixture, while the TC paint is painted on the surface of the plaster tiles (Figure 1b). A total of twelve Type 1 samples and eight Type 2 samples were created.

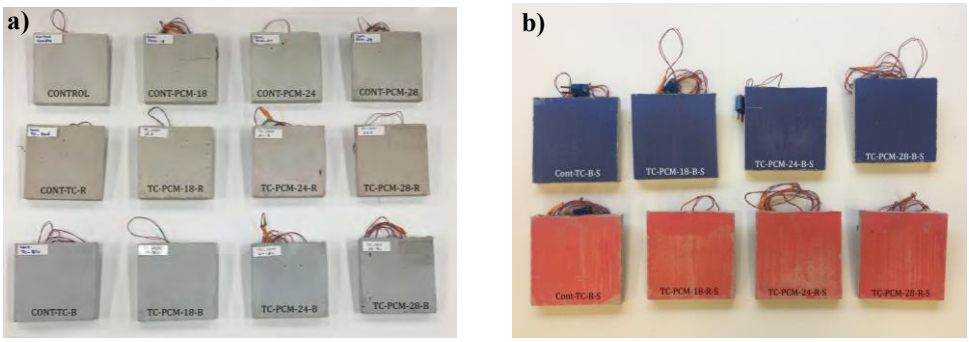

Figure 1. a) Type 1 samples; b) Type 2 samples.

2.2 Optical Characterization Tests

To measure the optical properties of the samples -considering their dynamic color change- the samples were subjected to one heating cycle and one cooling cycle prior to the measurements. The heating cycle was performed in an oven set to 45°C, which is above the transition temperature of the PCMs and the TC paints. In the cooling cycle, the samples were cooled to 8°C in a fridge. Figure 2 shows the color change of the Type 2 samples in both cycles. The spectral reflectance of the samples was measured according to the ASTM E903-12. The measurements were made using a Perkin Elmer's Lambda 750S UV-Vis/NIR spectrophotometer with 60 mm integrating spheres. The reflectance measurements were conducted in the range of 300-2500 nm with 10 nm steps (Soudian *et al.,* 2020).

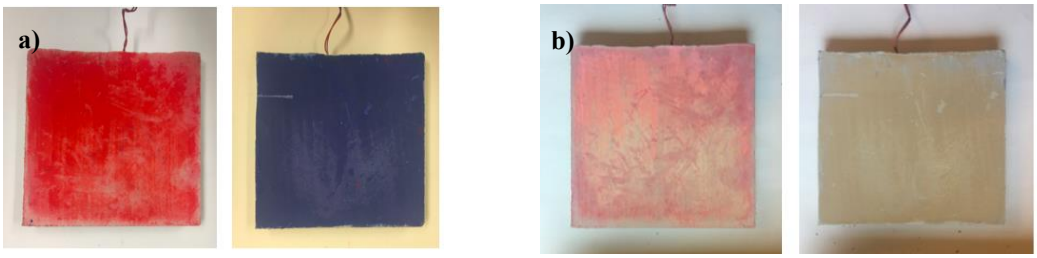

Figure 2. a) Type 2 samples at 8°C; b) Type 2 samples at 45°C.

2.3 Accelerated UV Aging

A QUV accelerated weather testing machine was used for the accelerated UV aging tests. The tests were performed according to ASTM G154-16. The UV acceleration factor (AF_{UV}) was calculated from Equation (1), where ϕ_{lab} indicates the total UV energy in the aging machine, and the ϕ_{nat} is the average natural outdoor energy for a given period.

$$AF_{UV} = \phi_{lab} / \phi_{nat} \quad (1)$$

The total UV intensity considered for the 340 nm UV lamps in the apparatus was set to 1.55 W/m^2, and the total energy calculated for one day of operation of the machine is 12.5 kWh/m^2. This setting represents the Cycle 6 configurations of the ASTM G154-16 standard. The average daily solar irradiance value for the city of Toronto is 126 Wh/m^2 obtained from Natural Resources Canada (2016). Therefore, the AF_{UV} calculated is 57. Based on the AF_{UV} and the exposure conditions determined by the standard, the samples were aged for seven days representing a two-year exposure to UV radiation. Figure 3 shows the testing apparatus and the cement plaster samples mounted on the QUV machine. The samples were subjected to an 8-hour cycle of UV exposure at 60ºC, followed by a 4-hour cycle of condensation at 50ºC.

Figure 3. Cement plaster samples in the QUV aging apparatus.

3 Results

3.1 Initial Characterization: Pre-Aging

All the samples showed a greater change in solar reflectance/absorptance in the near-infrared range (NIR) compared to the UV and the visible light (VIS) range, as shown in Figures 4 and 5. A distinct difference between the solar reflectance of Type 1 and Type 2 samples was observed in the heating and cooling cycles. At 45ºC, Type 2 samples with the TC paint on their surface showed an average of 13% higher range of solar reflectance in the NIR compared to Type 1 samples. The solar reflectance of all the eight Type 2 samples is higher than the control cement plaster sample, having a range of reflectance between 60%-80%, while the control sample has an average of 49.5% solar reflectance. In contrast, considering the importance of solar gain in colder temperatures, at 8ºC, Type 1 samples showed 12% higher solar absorptance in the NIR compared to the Type 2 samples. A much lower solar absorptance performance was observed in the case of Type 2 samples, as shown in Figure 8b, and all the samples have a lower percentage of solar absorptance in the NIR compared to the control sample.

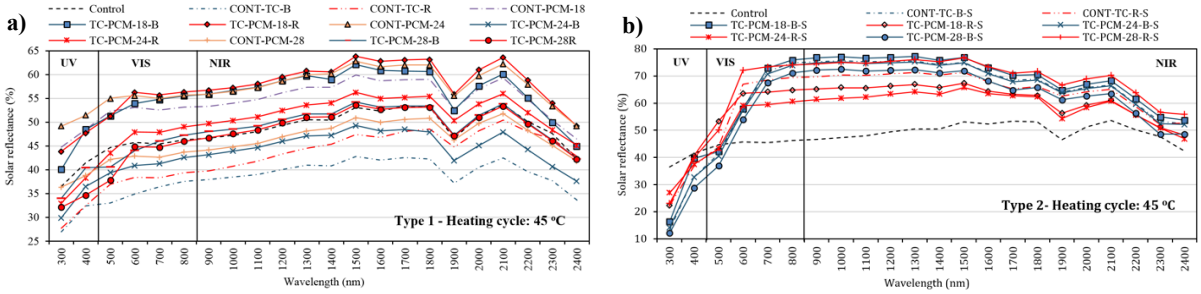

Figure 4. Solar reflectance at 45 °C: a) Type 1 samples; b) Type 2 samples.

The solar reflectance results of the samples with the blue and the red paint shows a higher solar reflectance recorded for the blue colored Type 2 samples. However, in Type 1 samples, all the mixed and control samples with the red TC paint showed a higher range of solar reflectance in the heating cycle. In Type 1 samples, the average solar reflectance of the control sample is higher than the control samples with only the TC paint. Considering the combination of the PCMs with TC paint, the best results are obtained by using the PCM- 18, as the combined samples show a 22% better performance than the CONT-PCM-18 sample, and 28% higher solar reflectance than the control samples with only the TC paint. In the cooling cycle, the overall solar absorption of Type 2 samples is considerably less than the control PCM samples, as well as the combined Type 1. This observation shows that applying the paint on the surface affects the potential to retain solar gains. It is observed that the total solar absorption range of the TC paints on the surface is much lower between 32% to 36%, which could pose challenges in the heating season for material durability and overall heat transfer through the envelope.

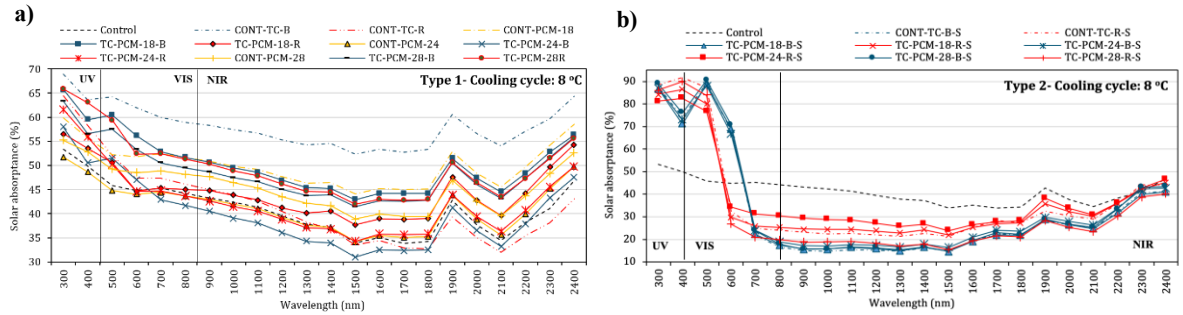

Figure 5. Solar absorptance at 8 °C: a) Type 1 samples; b) Type 2 samples.

3.2 Characterization- Post-Aging

The effect of the two-year accelerated UV aging on the visual appearance of the samples is shown in Figure 6. Compared to the initial images taken prior to the aging (Figure 1), the Type 2 samples have lost their colors, and in Type 1 samples, the slight color differences due to the TC paint is no longer visible. The performance of the samples is expected to be affected due to such considerable color variations.

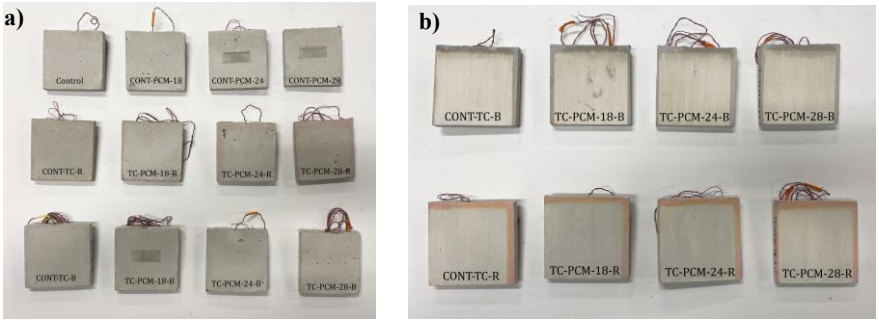

Figure 6. Visual changes to the samples a) Type 1 samples; b) Type 2 samples.

3.2.1 Solar reflectance measurements: Post-Aging

The same procedure to measure the solar reflectance of the samples was performed after the two-year aging tests. The results are shown in Figures 7 and 8 for the heating and the cooling cycles. Similar to the pre-aging results, the overall solar reflectance of the samples at 45ºC is higher in the Type 2 samples compared to Type 1 samples. However, the overall performance of the Type 1 samples in reflecting solar radiation is reduced considerably compared to the control sample. As shown in Figure 7a, the solar reflectance of the control sample in the NIR is higher than all the samples within the 1600-2500 nm wavelength. A general trend could be observed in both types of samples as the post-aging results show an increase in solar reflectance values in the UV and VIS range while the total reflectance in the NIR is reduced.

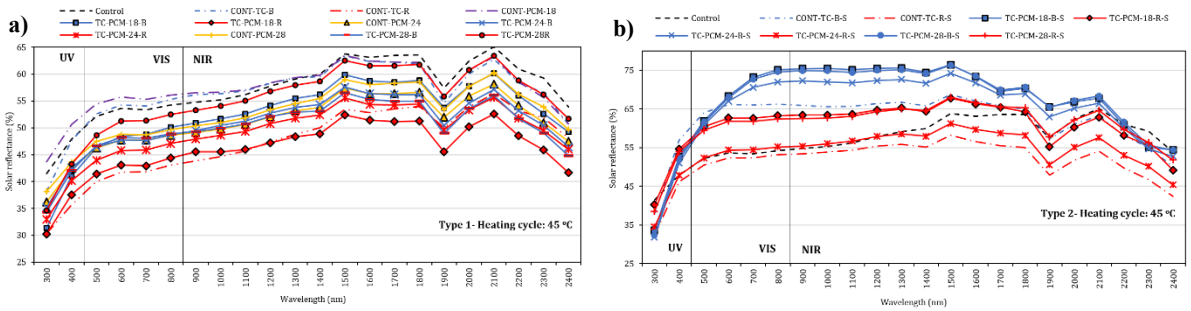

Figure 7. Solar reflectance at 45 ºC- Post-Aging: a) Type 1 samples; b) Type 2 samples.

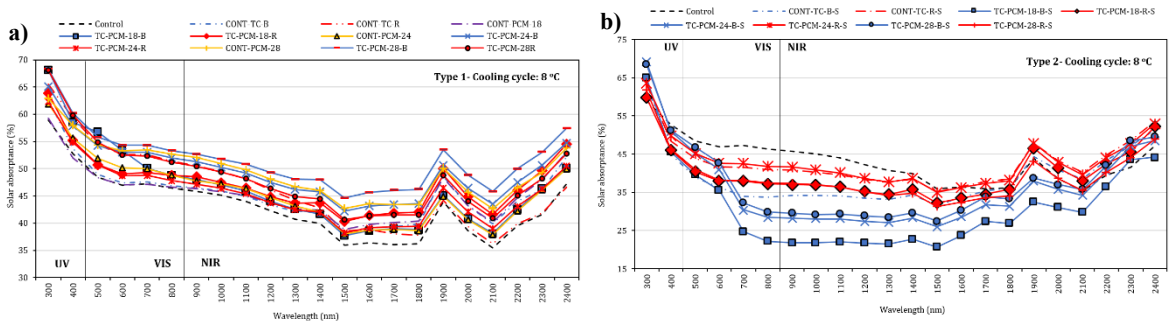

Figure 8. Solar absorptance at 8 ºC- Post-Aging: a) Type 1 samples; b) Type 2 samples.

In the cooling cycle, the aging did not significantly change the solar absorptance characteristic of the Type 1 samples, as shown in Figure 8a, and similar to Figure 5a, the control

sample holds the lowest rate of solar absorption at 8°C in the NIR. The total solar absorptance of the samples with the red paint in Type 2 samples is higher than the blue colored ones. The post-aging results show that the total solar absorptance of Type 2 samples have increased by 10% in the NIR.

3.3 Performance Change Comparison

By reviewing the pre and post aging results of solar reflectance values for all the samples, no specific trend could be established between the color of the TC paint and the T_{mp} of the PCMs. To better illustrate the effect of the two-year UV aging on the samples, Figure 9 shows the change in solar reflection characteristic of each sample in the heating cycle. As the figure shows, the impact of aging on the control samples with only the TC paint varies considerably between Type 1 and Type 2 samples. In Type 1 samples, the solar reflectance was increased after aging, in the Type 2 samples, solar reflectance decreased after the surface color faded.

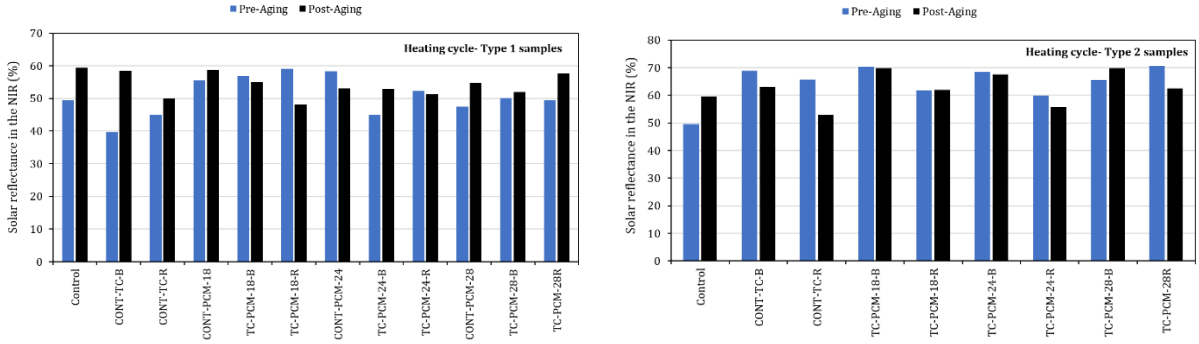

Figure 9. Rate of change in solar reflectance after the aging.

The impact of the PCMs in preserving the solar reflectance of the samples is more evident in the Type 2 samples, as the samples with both the TC and the PCM show the smallest percentage of change in solar reflectance in the NIR compared to the ones with only the TC paint. The results of the solar absorptance in the cooling cycle shows that in all Type 2 samples, the total solar absorptance is increased after the UV aging by an average of 30%.

4 Conclusions

This study evaluated the effect of accelerated UV aging on the optical performance of cementitious plasters integrated with TC paint and PCMs. This façade finish material intends to regulate thermal stresses exposed to exterior surfaces of building facades due to UV rays and temperature fluctuations. The dynamic properties of the TC paint to control solar radiation and the heat storage capacity of PCMs to control temperature on the surface could help increase the durability of the exterior façade finishing against thermal stresses. The results of the UV aging tests revealed that the impact of aging on the solar reflectance properties of the samples depends primarily on the method of TC paint integration in the cement plaster. Overall, at 45°C which is above the transition temperature of the selected TC and the PCMs, the solar reflectance of Type 1 samples with only the TC paint was increased, while the opposite occurs in the Type 2 samples. As the TC color fades on the surface of Type 2 samples, the total range of solar reflectance decreased in samples with only the TC paint. The solar reflectance properties of the

samples are primarily related to the TC paint. However, a lower rate of change in solar reflectance was observed in the combined PCM and TC scenarios, indicating the benefit of PCMs. A detailed analysis of the performance of the prototypes to regulate thermal stress is underway using temperature cycling tests to observe how the PCMs interact with the TC paints.

Acknowledgements

The authors wish to thank the Mitacs Organization for the financial support of this research project through the E-Accelerate fund. The authors are also grateful to Greg Labbe for his assistance in the experimental tests.

ORCID

Shahrzad Soudian: https://orcid.org/0000-0001-9838-7327
Umberto Berardi: https://orcid.org/0000-0002-0508-6195
Nadia O. Laschuk: https://orcid.org/0000-0001-6095-3522

References

Ascione, F., De Masi, R. F., Santamouris, M., Ruggiero, S. and Vanoli, G. P. (2018). Experimental and numerical evaluations on the energy penalty of reflective roofs during the heating season for Mediterranean climate. *Energy*, *144*, 178–199.

Garshasbi, S., and Santamouris, M. (2019). Using advanced thermochromic technologies in the built environment: Recent development and potential to decrease the energy consumption and fight urban overheating. *Solar Energy Materials and Solar Cells*, *191*(August 2018), 21–32.

Hernández-Pérez, I., Álvarez, G., Xamán, J., Zavala-Guillén, I., Arce, J., and Simá, E. (2014). Thermal performance of reflective materials applied to exterior building components - A review. *Energy and Buildings*, *80*, 81–105.

Jelle, B. P. (2012). Accelerated climate ageing of building materials, components and structures in the laboratory. *Journal of Materials Science*, *47*(18), 6475–6496.

Karlessi, T., Santamouris, M., Synnefa, A., Assimakopoulos, D., Didaskalopoulos, P., and Apostolakis, K. (2011). Development and testing of PCM doped cool colored coatings to mitigate urban heat island and cool buildings. *Building and Environment*, *46*(3), 570–576.

Karlessi, T., and Santamouris, M. (2015). Improving the performance of thermochromic coatings with the use of UV and optical filters tested under accelerated aging conditions. *International Journal of Low-Carbon Technologies*, *10*(1), 45–61.

Natural Resources Canada (NRC) (2016). Solar resource data available for Canada. Retrieved from:

Perez, G., Allegro, V. R., Corroto, M., Pons, A., and Guerrero, A. (2018). Smart reversible thermochromic mortar for improvement of energy efficiency in buildings. *Construction and Building Materials*, *186*, 884–891.

Pisello, A. L., Fortunati, E., Mattioli, S., Cabeza, L. F., Barreneche, C., Kenny, J. M., and Cotana, F. (2016). Innovative cool roofing membrane with integrated phase change materials: Experimental characterization of morphological, thermal and optic-energy behavior. *Energy and Buildings*, *112*, 40–48.

Pisello, A. L. (2017). State of the art on the development of cool coatings for buildings and cities. *Solar Energy*, *144*, 660–680.

Santamouris, M., Ding, L., Fiorito, F., Oldfield, P., Osmond, P., Paolini, R., … Synnefa, A. (2017). Passive and active cooling for the outdoor built environment – Analysis and assessment of the cooling potential of mitigation technologies using performance data from 220 large scale projects. *Solar Energy*, *154*, 14–33.

Soudian, S. Berardi, U. (2019). Cementitious plasters for façade finishing with phase change materials and thermochromic pigments, *IOP Conference Series: Materials Science and Engineering, 609*, 062023.

Soudian, S., Berardi, U. Laschuk, N. (2020). Development and thermo-optical characterization of a cementitious plaster with phase change materials and thermochromic paint, *Solar Energy, 205*,282-291.

Zinzi, M. (2016). Characterisation and assessment of near infrared reflective paintings for building facade applications. *Energy and Buildings*, *114*, 206–213.

XV International Conference on Durability of Building Materials and Components
DBMC 2020, Barcelona
C. Serrat, J.R. Casas and V. Gibert (Eds)

Experiences from Interior Super Insulation of a Brick Wall from the 1800s

Pär Johansson and Paula Wahlgren

Department of Architecture and Civil Engineering, Chalmers University of Technology, SE-412 96 Gothenburg, Sweden, par.johansson@chalmers.se

Abstract. *Many brick buildings in Sweden today face a large need for renovation measures to prolong their service life and make other uses possible. Conventional thermal insulation materials, such as fibre glass and EPS, demand a thick layer of insulation to reach the energy targets. Super insulation materials, such as vacuum insulation panels (VIP) and aerogel blankets (AB), are thermal insulation components with a 3-10 times higher thermal resistance than conventional insulation materials. In this study, the effect of interior insulation using super insulation materials is investigated, using experiences from a case study in a brick wall from the 1800s. Earlier research has shown that interior insulation decreases the drying-out capacity of an exterior wall and increases the risk for freeze-thaw damages in brick walls. The case study building is an industrial building from 1896 with 470 mm homogeneous brick masonry walls insulated with both aerogel insulation and with vacuum insulation panels. Six heat flux sensors were installed in the wall and used to evaluate the thermal resistance of the wall with and without insulation. The initial measurements showed that the rate of water flow in the bricks is approximately three times higher than that in modern bricks. The average calculated U-value was reduced by 70% for the AB and 81% for the VIP layers, while measurements at the three occasions gave a reduction of 72-83% for the AB and 72-84% for the VIP layers, i.e. in the same order of magnitude.*

Keywords: *Interior Insulation, Vacuum Insulation Panel, Aerogel, Thermal Inertia.*

1 Introduction

The construction sector is responsible for approximately 37% of the energy use in Sweden (Boverket, 2019). Around 78% of this energy is accounted to heating and cooling of buildings and the rest to construction, renovation and demolition activities. The amount of energy for heating has increased the last years and was 7% higher in 2016 than the average energy use in the preceding 10-year period and 8% higher than the previous year (Boverket, 2019). Around 25% of the energy for heating is used in the part of the building stock built before 1941 (Swedish Energy Agency, 2014). The focus on energy savings in society to mitigate carbon emissions, has led to implementations of several European directives on energy performance in buildings. The current intention is to enforce national renovation strategies of buildings to reach low or zero carbon dioxide emissions from the building industry by 2050. There is also an increased focus on embodied energy and life cycle assessment of materials that are used in the construction sector (Boverket, 2018).

There are several challenges associated with decreasing the energy use in existing buildings, especially in buildings located in areas of national interest for cultural heritage or listed buildings. The conflict between energy efficiency and heritage values in buildings have been touched upon on in several research projects and are common in everyday practice when renovating buildings for improved energy performance. Here, one of the challenges is to reduce the energy use while not tampering with the character defining elements of a building, such as the expression of the façade, the foundation, the volume of the building, the decoration of the

façade, the windows and the window frames. Generally, walls can be insulated either on the interior or exterior side. Concerning moisture performance, external insulation is beneficial as this increases the temperature of the original construction. Unfortunately, this is not allowed in many listed buildings. Therefore, interior insulation may be the only solution. Earlier research has shown that interior insulation decreases the drying-out capacity in the outer wall and increases the risk for freeze-thaw damages in brick walls (Johansson *et al.*, 2014). Interior insulation will also negatively affect the thermal storage capacity of the building and change the interior appearance of the walls, which is particularly important to consider for historical and/or listed buildings (Johansson *et al.*, 2019).

In this paper, a study based on a case study building of using super insulation materials in retrofitting of exterior walls is presented. The case study building, the background and planning of the study was presented in Johansson and Wahlgren (2018). In Johansson *et al.* (2019), the focus of the study was on the cultural heritage aspects and the conflict between energy efficiency and heritage values in buildings. Here, various parameters influencing the heat flux through the wall is discussed based on calculations and measurements from three separate occasions during the year. Two of these occasions were presented in Johansson *et al.* (2019) and in this paper measurements from the autumn season is added. These measurements add new information since the wall now has been heated for a longer time period while the average temperature is the same as in the spring season. The aim of the project is to propose practical guidelines and recommendations for using super insulation materials in listed buildings. This research is based on evaluation of vacuum insulation panels (VIP) and aerogel blankets (AB) in a case study building in Gothenburg, Sweden, where the thermal and moisture performance is monitored.

2 Super Insulation Materials

New materials and solutions are being developed that can contribute to improving the energy performance of historic buildings, without altering their character defining elements. Super insulation materials (SIM), such as VIP and AB, are thermal insulation components with a 3-10 times higher thermal resistance than conventional insulation materials, and thus thinner layers can be used. In the IEA Annex 65 'Long-Term Performance of Super-Insulating Materials in Building Components & Systems' several SIMs were investigated, and case studies were collected from all over the world. More information and conclusions are given by Adl-Zarrabi *et al.* (2020). In that project, SIMs were defined by having a thermal conductivity;

- below 25 mW/(m·K) if air filled such as aerogel,
- below 20 mW/(m·K) if gas filled such as gas filled panel (GFP), and
- below 15 mW/(m·K) if evacuated such as VIP.

As mentioned above, two examples of SIM are VIP and AB, see Figure 1. VIP are rigid panels which cannot be cut on site and are sensitive to puncturing. Therefore, attention must be paid in the design of details and envelope components. AB are more like conventional fibre-based insulation materials. They can be cut at the construction site and adapted to the specific measurements. VIP were first tested in buildings in the early 1990s which was later followed by several case studies both in laboratory and in the field while AB have been installed in various building assemblies since the early 2000s (Adl-Zarrabi *et al.*, 2020).

The long-term performance of SIMs must be determined based on case studies in field and laboratory. Full scale experiments provide knowledge of practical and technical difficulties as well as data for service life estimation. For certain conclusions to be drawn from the case studies, monitoring is essential. Unfortunately, monitoring is only performed in few case studies. These experiences are gathered and evaluated from a long-term performance perspective by Adl-Zarrabi *et al.* (2020).

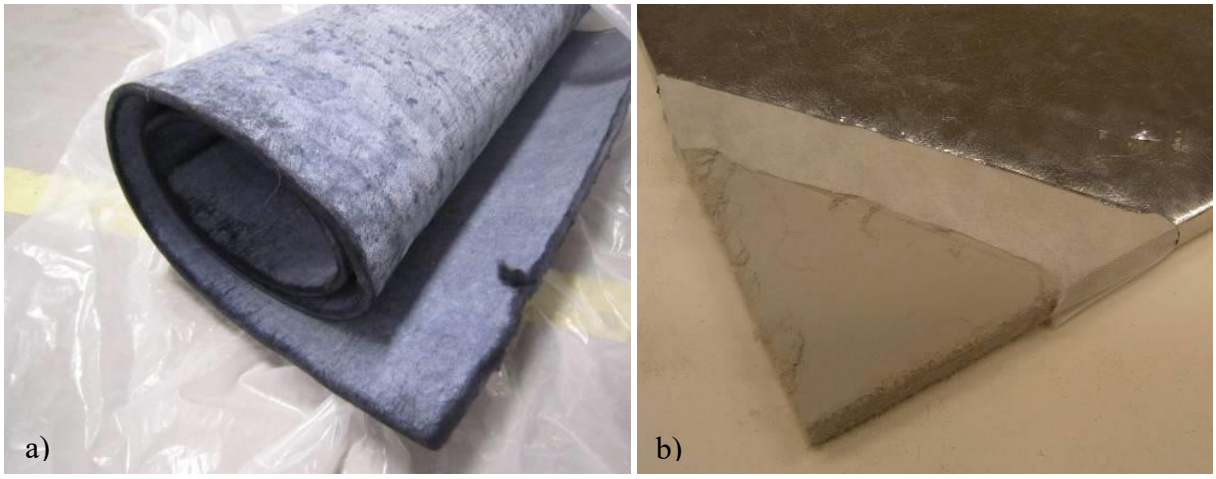

Figure 1. Super insulation materials; (a) aerogel blanket (AB), (b) vacuum insulation panel (VIP).

VIPs have different core materials (fumed silica, glass fibre, polyurethane, expanded polystyrene and others) and different envelopes (metalized film, aluminium laminate, stainless steel, woven glass fibre, or combinations). The thermal conductivity is 0.014-0.020 W/(m·K) for AB and 0.002-0.008 W/(m·K) for VIP (Heinemann *et al.*, 2020). The hygrothermal properties for ABs and VIPs differ substantially. The VIP envelope only allows a minimal amount of vapour and liquid water transfer at the edges between the VIPs (Johansson *et al.*, 2014), while the vapor diffusion resistance of AB is around μ=5 (-) which is a factor five higher than mineral wool. The blankets are coated with a water-repellent substance which reduce the liquid water transfer through the material.

3 Case Study Building

The case study building, the background and planning of the study is presented together with results from hygrothermal numerical simulations and a laboratory study of interior insulation of a brick wall in Johansson and Wahlgren (2018). The building where the tests are carried out is a long narrow brick and concrete building, once used as a paper machine hall, originally erected in 1896, see Figure 2. The building is one of the oldest in the area. For this case study the conservation officer at the city museum followed up on development of built heritage and monitor that appointed heritage values are being respected in transformation situations.

In the end it was difficult to predict all the uncertainties in the laboratory measurements using the hygrothermal numerical simulations (Johansson and Wahlgren, 2018). The first results from the case study building showed that there was a moisture excess of 0.8 g/m^3 in the building compared to outdoors. Inside a part of the building, a small room (2.1 x 2.6 x 4.0 m)

was constructed, consisting of floor, walls and roof insulated with 170 mm mineral wool, and the exposed brick wall with an interior mortar layer. Prior to the installation of the sensors, the existing plaster was removed from the interior brick surface. There was substantial capillary suction from the ground and from the exposure to driving rain from south-west, which is the dominant wind direction. The old plaster was loose up to approximately 1 meter above the concrete slab and came down easily, without applying force, while the upper part of the wall required demolition hammer to remove the plaster. The initial estimations showed that the rate of water flow in the bricks was approximately three times higher than that in modern bricks.

Figure 2. (a) The industrial building from 1896, photo from 1918, (b) the exterior of the tested external wall, (c) interior of the building when it was in operation as a paper mill.

The exterior wall is divided in three parts where AB and VIP are installed in 500 x 1,200 mm^2 panels, see Figure 3, and compared to a non-insulated reference. The air in the room is circulated by a fan to create homogenous temperature and moisture conditions in the entire room. It is heated to around 23°C and ventilated by natural ventilation with approximately 0.5 h^{-1} air exchange rate. The installation of the AB and the VIP was done in mid-June, 2018. The temperature and relative humidity of the air is measured by three sensors. The measurement accuracy is ± 2.5% for relative humidity in the range of 10 to 90% and ±0.5°C for temperature at 25°C. The temperature can be measured between -40 to 85°C. There were some initial problems with the equipment and electric power supply which made the indoor temperature vary more than planned.

The heat flux sensor Hukseflux HFP01 (thickness 5.4 mm, diameter 80 mm) was used to evaluate the thermal resistance of the wall with and without insulation. The heat flux in W/m^2 is calculated by dividing the voltage output by the sensor's sensitivity. The sensors were calibrated by the producer and delivered with a calibrated sensitivity and calibration uncertainty of 3% for each sensor.

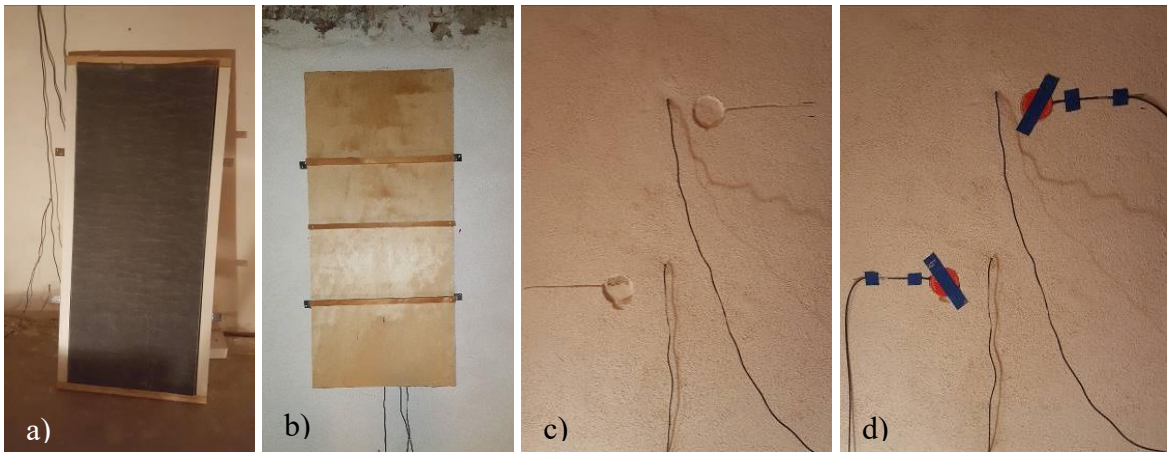

Figure 3. (a) AB insulated panel (removable for inspection), (b) installed AB and VIP panel, (c) before installation of two heat flux sensors inside the mortar layer, and (d) after installation of two heat flux sensors.

The sensor is a thermopile sensor which measures the temperature difference across the ceramic plastic composite body. Air gaps between the sensor and surface of the wall, and between the sensor and the surrounding environment could add additional resistances to the sensor thermal resistance. The sensor was placed in the mortar between the insulation and brick masonry in the wall panels with insulation, while the sensor was facing the indoor environment for the wall without insulation.

Each wall set-up (reference, AB, VIP) has two sensors, bottom and top and the heat flux was measured at three occasions (March, April and November) at all six locations. The first results from the heat flux measurements showed that the heat flux is substantially reduced in the wall with interior insulation (Johansson *et al.*, 2019). A difference between the top and bottom measurement locations was found, where the top location had a higher heat flux for the reference wall and the wall panel with VIP, while the wall panel with aerogel had a lower heat flux at the top location, compared to the bottom location. The higher heat flux closer to the bottom of the wall could be caused by the higher moisture content in the wall closer to the foundation and ground water. The deviation between the different parts of the wall could be explained by the difference in solar radiation between them, where the reference wall is less exposed to solar radiation than the parts with interior insulation. This part of the wall therefore has a higher temperature difference between the interior and exterior surfaces, and consequently a higher measured heat flux which results in a lower U-value (Johansson *et al.*, 2019).

4 Results from Heat Flux Measurements

The measured temperature difference between the indoor and outdoor air was averaged over the 3 preceding days due to the high thermal inertia of the brick wall. The thermal inertia was studied numerically by Johansson *et al.* (2019), where it was concluded that an outdoor air temperature measured for 3 days is enough for the estimation of the U-value from the heat flux measurements. The measurements were performed early in the morning before sunrise, after a cloudy night with stable outdoor temperature. The momentary U-value and percentage difference compared to the reference wall based on the measurements and calculations (following SS-EN ISO 6946:2017) are presented in Table 1.

Table 1. U-value and percentage difference compared to the reference wall based on heat flux measurements in the brick wall in the bottom and top of the wall. The average outdoor temperature was 5.1°C, 9,7°C and 4.5°C.

Location	March		April		November	
Aerogel bottom	0.310	77-84%	0.296	81-84%	0.357	70-72%
Aerogel top	0.292	78-85%	0.264	83-85%	0.339	71-73%
VIP bottom	0.308	77-84%	0.254	84-86%	0.341	71-73%
VIP top	0.323	74-84%	0.277	82-85%	0.358	70-72%
Reference bottom	1.331	-	1.549	-	1.188	-
Reference top	1.957	-	1.817	-	1.269	-

When calculating the U-value of the non-insulated wall based on the thermal conductivity of dry brick (λ=0.61 W/(m·K)) and wet brick (λ=1.0 W/(m·K)), this results in U-values ranging from 0.997 to 1.476 W/m^{2}K. Corresponding U-values for the part with 20 mm VIP are 0.264-0.286 W/m^{2}K and for the wall with 20 mm AB the range is 0.394-0.452 W/m^{2}K. The thermal conductivity is also influenced by the temperature. For this case, the influence is negligible as the dependency is typically around 0.0002 W/(m·K)/K for bricks.

The fact that the measured U-value of the non-insulated wall is lower in November than in March and April can be a result of the wall having dried out during spring and summertime. Since the interior insulation decreases the drying towards the interior side, drying is expected to be significantly slower for these cases, resulting in more moisture, which could explain the smaller variations in U-value for the insulated walls.

For the wall with VIP, the U-value based on heat flux measurements were more in line with the calculated U-value than for the non-insulated wall. The measured U-value for the wall with VIP was up to 35% higher than what was expected from the calculations. On the other hand, the measured U-value for the wall with AB was lower than what was expected from the calculations during all three measurement periods, for both the case with dry and wet brick. Cuce and Cuce (2016) experienced similar deviations in their study of interior insulation with AB. They developed a numerical statistical method to account for all effects by other factors.

In this case study, the different wall panels may be subjected to different amounts of solar radiation. The wall panel with AB is most exposed to solar radiation which may have influenced the measurements more here than for the other parts of the wall, resulting in a lower heat flux than expected due to the lower temperature difference (higher outdoor temperature). The other factors that could influence the measurements is the evaporation of water from the wall. This could increase the heat flux by around 5% which decreases the measured U-value for the reference wall but does not influence the parts of the wall with interior insulation.

One of the studied periods was unusually dry (summer 2018). For this case, the temperature difference between cooler lower parts and slightly warmer upper parts was smaller than other studied periods. This means that there might still be evaporation but that the source might not be rain but possibly evaporation of moisture from the ground. That moisture was rising from the ground was evident from the condition of the wall.

5 Conclusions

Many brick buildings in Sweden today face a large need for renovation measures to prolong their service life and make alternative uses possible. In a case study building, interior insulation

was proposed as a measure for combining energy efficiency and heritage preservation. The 470 mm homogenous brick masonry wall was investigated regarding the thermal performance of the wall with interior insulation. Earlier research has shown that interior insulation decreases the drying-out capacity of the exterior wall and increases the risk for freeze-thaw damages in brick walls. In this study the building was exposed to both heavy rain and rising ground water. No significant drying took place from the parts with interior insulation and water was added to the wall from the rain outside and through the foundation. Therefore, the owner has now planned to cover the building with an external rain protective envelope Measurements of the heat flux show that additional superinsulation substantially decreases the U-value of the wall. Assuming wet bricks, the average calculated U-value was reduced by 70% for the AB and 81% for the VIP layers, while the measurements gave a reduction of 72-83% for the AB and 72-84% for the VIP layers, i.e. the same order of magnitude. With planned measures to make the wall dryer, the interior insulation will be monitored continuously with the aim of contributing to the development of recommendations on how SIMs can be used in historic buildings

Acknowledgements

This study is supported by the Swedish Energy Agency through the project 42856-1. We would also like to thank MölnDala Fastighets AB and Pontus Johansson, Gabriella Josefsson, Maria Daoud Rajha and Mathis Gelot for performing the laboratory investigations.

ORCID

Pär Johansson: http://orcid.org/0000-0003-0935-7703
Paula Wahlgren: http://orcid.org/0000-0001-9645-8021

References

Adl-Zarrabi, B., Johansson, P., Batard, A., Brunner, S., Capozzoli, A., Galliano, R., Heinemann, U., Gudmundsson, K., Fantucci, S., Karami, P., Mukhopadhyaya, P., Lorenzati, A., Perino, M., Quenard, D., Sprengard, C., Treml, S. and Yrieix, B. (2020). *Annex 65, Long-Term Performance of Super-Insulating-Materials in Building Components and Systems. Report of Subtask III: Practical Applications – Retrofitting at the Building Scale – Field scale*.

Boverket. (2018). *Klimatdeklaration av byggnader: Förslag på metod och regler. Slutrapport. Rapport 2018:23*. Boverket (Karlskrona, Sweden).

Boverket. (2019). Bygg- och fastighetssektorns energianvändning uppdelat på förnybar energi, fossil energi och kärnkraft. Retrieved 7 January, 2020, from https://www.boverket.se/sv/byggande/hallbart-byggande-och-forvaltning/miljoindikatorer---aktuell-status/energianvandning.

Cuce, E. and Cuce, P. M. (2016). The impact of internal aerogel retrofitting on the thermal bridges of residential buildings: An experimental and statistical research. *Energy and Buildings*, 116, 449-454.

Heinemann, U, Adl-Zarrabi, B., Brunner, S., Foray, G., Johansson, P., Kono, J., Kücükpinar, E., Milow, B., Quenard, D., Sprengard, C., Wallbaum, H. and Yrieix, B. (2020). *Annex 65, Long-Term Performance of Super-Insulating-Materials in Building Components and Systems. Report of Subtask I: State of the Art and Case Studies*.

Johansson, P., Geving, S., Hagentoft, C.-E., Jelle, B. P., Rognvik, E., Kalagasidis, A. S. and Time, B. (2014). Interior insulation retrofit of a historical brick wall using vacuum insulation panels: Hygrothermal numerical simulations and laboratory investigations. *Building and Environment*, 79 (September 2014), 31-45.

Johansson, P. and Wahlgren, P. (2018). Interior insulation retrofit of a brick wall using super insulation materials: design of a field testing in an industrial brick building. In: *Proceedings of the 7th International Building Physics Conference, IBPC 2018*, Syracuse, NY, USA, September 23-26, 2018.

Johansson, P., Wahlgren, P. and Eriksson, P. (2019). Field Testing of Interior Super Insulation Materials on a Brick Wall in an Industrial Building. In: *Proceedings of the 13th International Conference on Thermal Performance of the Exterior Envelope of Whole Buildings*, Clearwater Beach, FL, USA, December 9-12, 2019.

Swedish Energy Agency. (2014). *Programbeskrivning för programmet Spara och bevara etapp 3, 2015-01-01 – 2018-12-31 (Programme Description for Save and Preserve Stage 3). [In Swedish]*. Swedish Energy Agency (Eskilstuna, Sweden).

Swedish Standards Institute. (2007). *SS-EN ISO 6946:2007. Building components and building elements - Thermal resistance and thermal transmittance - Calculation method*. Geneva, Switzerland: International Organization for Standardization (ISO).

XV International Conference on Durability of Building Materials and Components
DBMC 2020, Barcelona
C. Serrat, J.R. Casas and V. Gibert (Eds)

Experimental Verification of the Theoretical Aging of Vacuum Insulated Panels

Mahsa Nikafkar[1] **and Umberto Berardi**[2]

Dep. Architectural Science, Ryerson University, 350 Victoria Street, Toronto, M5B 2K3, ON, Canada
[1] mahsa.nikafkar@ryerson.ca [2] uberardi@ryerson.ca

Abstract. *Vacuum Insulation Panels (VIPs) encompass a higher thermal resistance per unit of thickness compared to any other kind of insulation. However, their aging has often shown some critical concerns among stakeholders. To support the broader use of VIPs in the building sector, a comprehensive analysis of the physical properties of VIPs and in particular of their thermal conductivity over long-periods is required. This research investigates the effect of the temperature and relative humidity on the service life and thermal conductivity of VIPs. The scope of this study is to validate existing aging models for VIPs. First, the experimental results of the thermal conductivity for five VIPs both in pristine and in laboratory-accelerated conditions are described. Then, an analytical aging method is employed to validate the collected data. Results show that the aging has a more significant impact on the performance of VIPs with a core of fiberglass-core than with VIPs with a core of fumed silica.*

Keywords: *Vacuum Insulation Panels, Durability, Service Life Prediction, Thermal Conductivity.*

1 Introduction

It is widely acknowledged that buildings account for more than 32% of total global energy consumption and contribute to 19% of the GHG emissions. The global energy-related CO_2 emissions from the building sector more than doubled between 1970 and 2010, and are projected to increase by another twofold by 2050 (Berardi, 2017). Several researches confirmed that the heat transfer (*i.e.* losses) through the building envelope is the most significant energy factor for building efficiency as such, significant attention exists for super-insulating materials. High-performance materials such as Vacuum Insulation Panels (VIPs) offer a high thermal resistance value with minimized thickness, thanks to their low thermal conductivity (0.003-0.005 W/mK) which is about five times lower than that of traditional insulation materials (Johansson *et al*., 2014; Karami *et al*., 2015). VIPs are non-homogeneous insulation materials consisting of a porous core which is evacuated from air and vapor, tightened, and then heat-sealed. VIPs materials are in the early market stages in the building sector and data about their thermal performance over the building lifetime is missing (Baetens *et al*., 2010; Kalnæs and Jelle, 2014).

Consequently, many international research efforts have focused on the thermal properties of VIPs over time (Wegger *et al*., 2011; Isaia *et al*., 2017; Mac Lean *et al*., 2017). Several works have proposed methods to predict the service life of VIPs with Fumed Silica (FS) core and on the development of models to determine their moisture content. Theoretical approaches to predict their long-term performances by means of interpreting accelerated aging tests done in laboratories have also been proposed (Table 1). The increase in pressure and humidity inside a VIP panel over time is often pointed as the main aging mechanism for VIPs (Schwab *et al*., 2005).

The objective of this paper is to evaluate experimentally the thermal conductivity of some VIP after several aging exposures and to assess the accuracy of existing thermal conductivity aging models through verification of collected results for different core materials of VIPs.

Table 1. Literature review summary of previous studies related to the topic of the present paper.

Study	Core type	Test type	Equivalent test period	Parameters of study results	Results
Simmler *et al*., 2005	-	laboratory work	5.5d at 23°C/80% RH, 9h at 30°C/90% RH, 65h at 65°C/75% RH, 152h at 80°C/80% RH	Ageing mechanism with results for different temperature and humidity	Pressure increase rate is about 2.1 mbar per year, while moisture accumulation rate is 0.18 mass% per year
Wegger *et al*., 2011	Va-q-VIPB 2009	laboratory work	25 years	Evaluating the accelerated ageing of VIPs for various procedures	Acceptable agreement with that of the accompanying theoretical analysis
Saber *et al*., 2015	fumed silica	in-situ test	a year	Effects of thickness and thermal conductivity on effective thermal resistance	The thermal resistance of the wall with VIP is higher than the wall with failed VIP or XPS
Kucukpinar *et al*., 2015	organic nano-foam	mock-up test	More than a year	Monitoring heat flow through the panels over months	Nanoporous foam VIPs are still effective
MacLean *et al*., 2017	VIP	pilot wall	-	long-term thermal performance of VIPs	Confirming the good performance of the VIPs compared to XPS
Batard *et al*., 2018	fumed silica	laboratory work	25 years at 23 °C for 80% RH	Comparison data of linear and dynamic model	Similar results for linear and dynamic models with a comparable increase of conductivity over time
Pons *et al*., 2018	fumed silica	laboratory work	10 years at 23 °C and 80% RH	Mild artificial aging of six VIPs samples	- The surface hydrophilicity of core aged VIPs is twice higher than the new one

2 Theoretical Background and Research Methodology

The thermal conductivity of VIPs is a critical characteristic to study. Solid conduction, air convection, and radiations determine the primary heat transfer mechanisms that control the insulation capacity of the panel. The thermal conductivity of VIPs has been proposed as a summation of different effects as reported in Eq. (1) (Wegger *et al*., 2010; Alotaibi *et al*., 2014):

$$\lambda_{tot} = \lambda_s + \lambda_g + \lambda_r + \lambda_{wv} + \lambda_w + \lambda_{cop} \quad (1)$$

where λ_s represents solid conduction through the material, λ_g shows gas conduction through the porous of material, λ_r presents radiation heat transfer between inner pore, λ_{wv} is the permeation of air and moisture through pores, λ_w is the thermal conduction over time based on adsorbed water within the core material, and λ_{cop} is the thermal conductivity accounting for second-order effects between the mentioned thermal conductivities. In Eq. (1), the λ_{wv} and λ_{cop} components have a lower value compared to other terms, and can often be neglected. The gas thermal conductivity is independent of the density, and its reduction provides a significant opportunity to improve the performance of the VIPs (Kwon *et al*., 2009).

A different way to express the thermal conductivity of VIP is by taking into account their aging, as described by Eq. 2 (Caps *et al*., 2008):

$$\lambda_{tot} = \lambda_{init} + \frac{\lambda_0}{1 + \frac{0.032}{p\Phi}} + bX_w(t) = \lambda_{init} + \frac{\lambda_0}{1 + \frac{0.032}{p\Phi}} + c\left(1 - exp\left(-\frac{t}{\tau_w}\right)\right) \quad (2)$$

where λ_{int} is a summation of solid and radiation thermal conductivities, λ_0 is the conductivity of air for atmospheric pressure, p is gas pressure, and Φ is the pore size of the pores.

As evident, to fully study the behaviour of Eg (2), long periods would be needed. Consequently, accelerated aging methods are often used to find failure modes in a shorter time, which is resulted after many years at a normal temperature. In this study, exposure of VIP to elevated temperature was used to age several VIP samples. The increase of temperature could grow the kinetic reaction rate within the molecules of materials which causes chemical deprivation. For this purpose, accelerated aging temperatures of building materials are often select around 70 ˚C (Jelle, 2012; Kunic, 2012). Arrhenius law was used to calculate the time equivalent to 25 years of aging. To determine the relationship between the aging test condition and the real condition, accelerated factor (AF_{temp}) was presented:

$$AF_{temp} = e^{-\frac{E_a}{K}\left(\frac{1}{T_A} - \frac{1}{T_U}\right)} \quad (3)$$

where AF_{temp} is the acceleration factor under stressed temperature, E_a is the activation energy of failure mechanism, K is the Boltzmann constant which equals 8.617×10^{-5} eV/K, T_A is the accelerated temperature, and T_U is the use condition temperature. The accelerated temperature of VIPs samples was 70˚C, and the constant use condition temperature was assumed at 15 ˚C. The thermal conductivity was measured, before and after the aging of each sample, in order to assess VIP thermal performance according to the ASTM C518 using heat flowmeter equipment HFM 436. The measurements were carried out in a temperature range of -10 ˚C to 30 ˚C with 5 ˚C temperature step. The temperature difference between the plates was kept at 10 ˚C.

3 Results

3.1 Pristine and Aged Thermal Conductivity

The thermal conductivity of various VIPs with different core panels including fiberglass, fumed silica, compressed microporous silica, and compressed microporous silica with celluloses fiber, were tested in this study. Different types of multilayer films which are common in the market were selected. The employed films include metal foils (AF), metalized films (MF) and polymer films (PF). The most common types can be described as follows:

- AF: In these ones, the thickness of the aluminum in the center is up to 5-10 μm and this layer is laminated by a polyethylene terephthalate (PET) as a protective layer in outer and polyethylene in the inner side of the layer (Wegger *et al*., 2011; Kalnæs *et al*., 2014).
- MFs: In these ones, there are three barrier layers of aluminum metalized PET and polyethylene (PE) sheets on the inner side with an aluminum coat of 20-100 nm thickness (Simmler *et al*., 2005; Ghazi Wakili *et al*., 2011; Alotaibi, 2014). This is a standard solution to make VIPs applicable in buildings because multiple aluminum layers provide a better impermeable layer in comparison to one-layer aluminum. However, MF type has a low thickness which is an issue as a low thickness results in higher gas and moisture permeance compared to the AF laminates. Table 2 reports the main characteristics of the selected VIPs.

Table 2. Experimentally characteristics of VIPs provided by manufacturers.

Sample type	Envelope type	Thermal conductivity (W/mK)	Company density (kg/m^3)	Core material	Pressure (mbar)	Size (cm x cm)
1	*NA*	0.0028	250	Fibreglass	≤ 5	30 x 30
2	MF3	0.0048	190	Fumed Silica	≤ 5	24 x 13.7
3	MF2	0.0037	208	Compressed microporous silica	≤ 5	30 x 30
4	MF2	0.0070	200	Compressed microporous silica + celluloses fibre	≤ 2	30 x 30
5	MF2	0.0070	250	Compressed microporous silica	≤ 5	30 x 30

The initial thermal conductivity of all samples is shown in Fig. 1. The experimental results validate that fiberglass provides the lowest thermal conductivity; in fact, the core of fiberglass, an open porous composite, allows easier air evacuation (Quenard and Salle, 2005; Kwon *et al.*, 2009). Pressed powder microporous silica would be the second option for high performing VIPs. The results in Fig. 1 shows a generally consistent behaviour of the VIPs and their lower thermal conductivity at lower temperatures (Berardi, 2019).

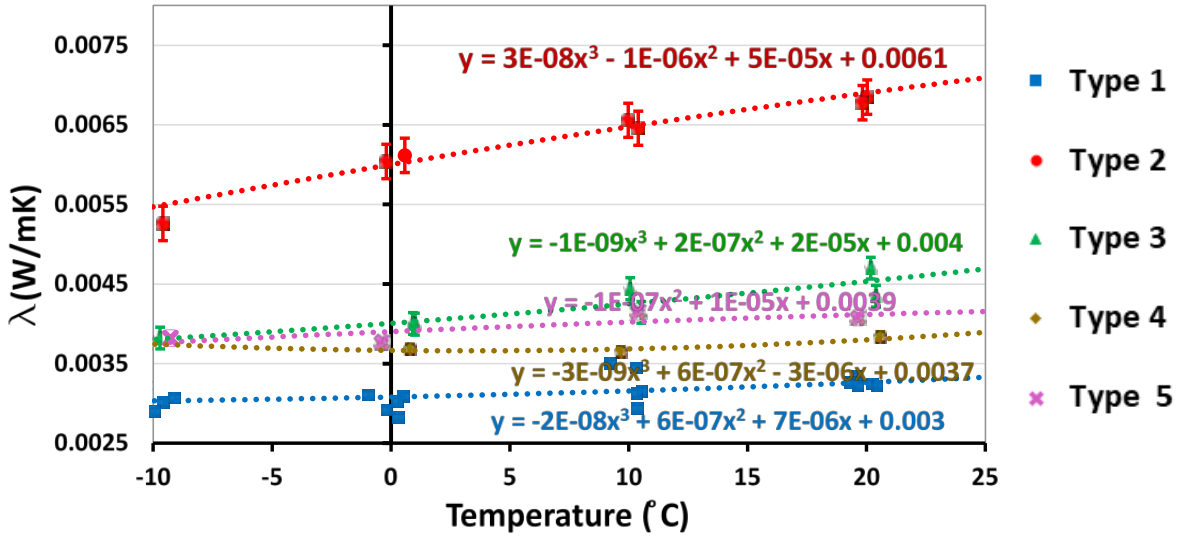

Figure 1. Value of pristine thermal conductivity for five types of VIP samples.

The induced changes in thermal conductivity of VIP samples with the exposure at high temperature, simulating their accelerated aging, are presented in Fig. 2. The results are shown for the average temperature between the two plates of the HFM of 18 ◦C. The thermal conductivity results were collected every five years of aging for each type of sample.

As can be seen in Fig. 2, Types 1 to 5 have a close initial thermal conductivity in the range from 0.003 W/mK to 0.0045 W/mK. While Type 1 with fiberglass core has the lowest initial thermal conductivity in comparison to the other samples, an increasing trend of thermal conductivity occurred compared to the other types in the same size. Types 3, 4 and 5 have an approximately constant thermal conductivity over 25 years. The type of the envelope and the thickness of the foil through the laminate affected the thermal conductivity. In fact, Type 5 which had an MF3 envelope showed minimal aging effects.

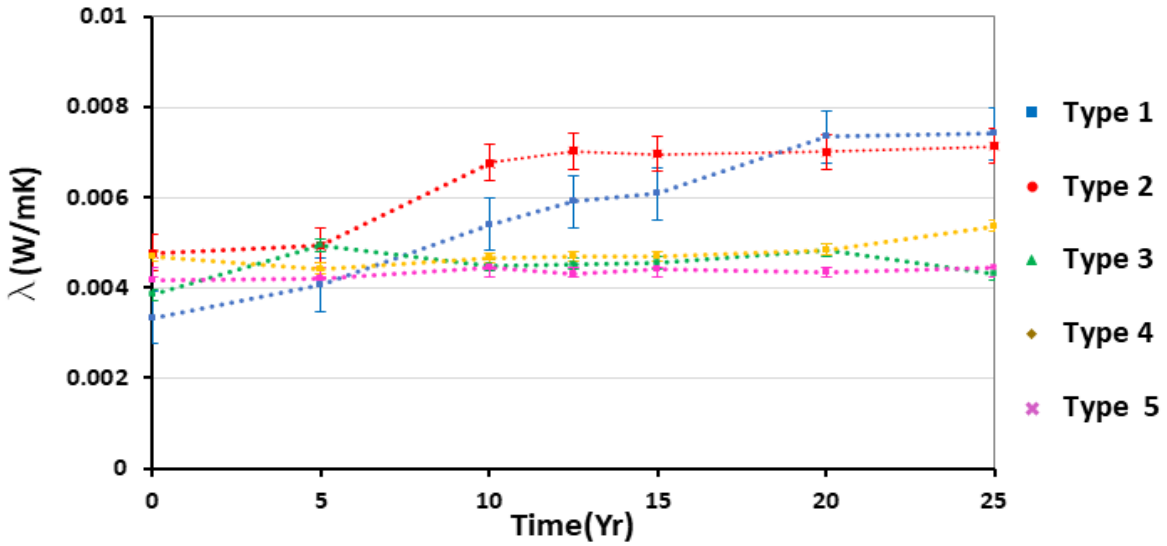

Figure 2. Dynamic variation with the accelerated aging of the thermal conductivity of the VIPs at 18 ºC.

3.2 Ageing Model Verification

Here, the studies in (Simmler *et al*. 2005b; Kim 2017, Mukhopadhyaya *et al*., 2011) are used as a reference model for evaluating the thermal conductivity trend. According to these papers, a simple version of the ageing thermal conductivity is:

$$\lambda_{tot} = \lambda_{init} + \lambda_p t + c\left(1 - exp\left(-\frac{t}{\tau_w}\right)\right) \tag{4}$$

where, λ_{init}, λ_p, c, and τ_w are regression parameters depending on the envelope and the core material. The parameters used in (Kim, 2017) are given in Table 3 as the reference model. In this research, the mentioned parameters (λ_{init}, λ_p, c, and τ_w) are derived from experimental result using Python curve fitting libraries. These unknown parameters are estimated such that the difference between the measured data and the model output is minimum. Table 3 lists these parameters for each sample and parameters in (Kim, 2017) as the reference.

Table 3. Parameters measured for samples under test and reference data proposed by Kim (2017).

Parameters	λ_{init} (mW/m K)	λ_p (mW/m.K.year)	c (mW/m K)	τ_w (year)
Reference Model (Kim 2017)	3.9 to 4.8	0.07	3.2	35.6
Type 1	3.20	0.17	1.30	35.6
Type 2	4.20	0.07	2.20	20.0
Type 3	4.00	0.05	0.66	35.6
Type 4	4.00	0.05	0.66	35.6
Type *5*	4.08	0.019	0.02	35.6

Figure 3 shows the thermal conductivity behaviour of these samples over 25 years. As it can be seen from this figure, overall, the thermal conductivity shows a linear trend over time for these samples. For Type 1, thermal conductivity measurements follow the reference model very well. The trend starts from 0.003 W/mK and uniformly increases to 0.008 W/mK, with a slope of 0.0002 W/mK per year. The thermal conductivity in this sample approximately increases by

160% over 25 years. In this type of sample, based on Table 3, the effect of λ_p is dominant. For Type 3, the thermal conductivity value increases by about 70% over 25 years, as thermal conductivity begins with 0.0041 W/mK and slowly reaches 0.0045 W/mK. Figure 3 shows a small increase for Type 4 thermal conductivity measurement over time, where thermal conductivity starts from 0.0041 W/mK and reaches to 0.0055 W/mK and it shows 34% of thermal conductivity increase. This thermal conductivity shows a linear trend with a slope of 0.00006 W/mK per year. Type 5 has a trend with a thermal conductivity raises up to 10%, and based on Table 3, it has a low gas thermal conductivity.

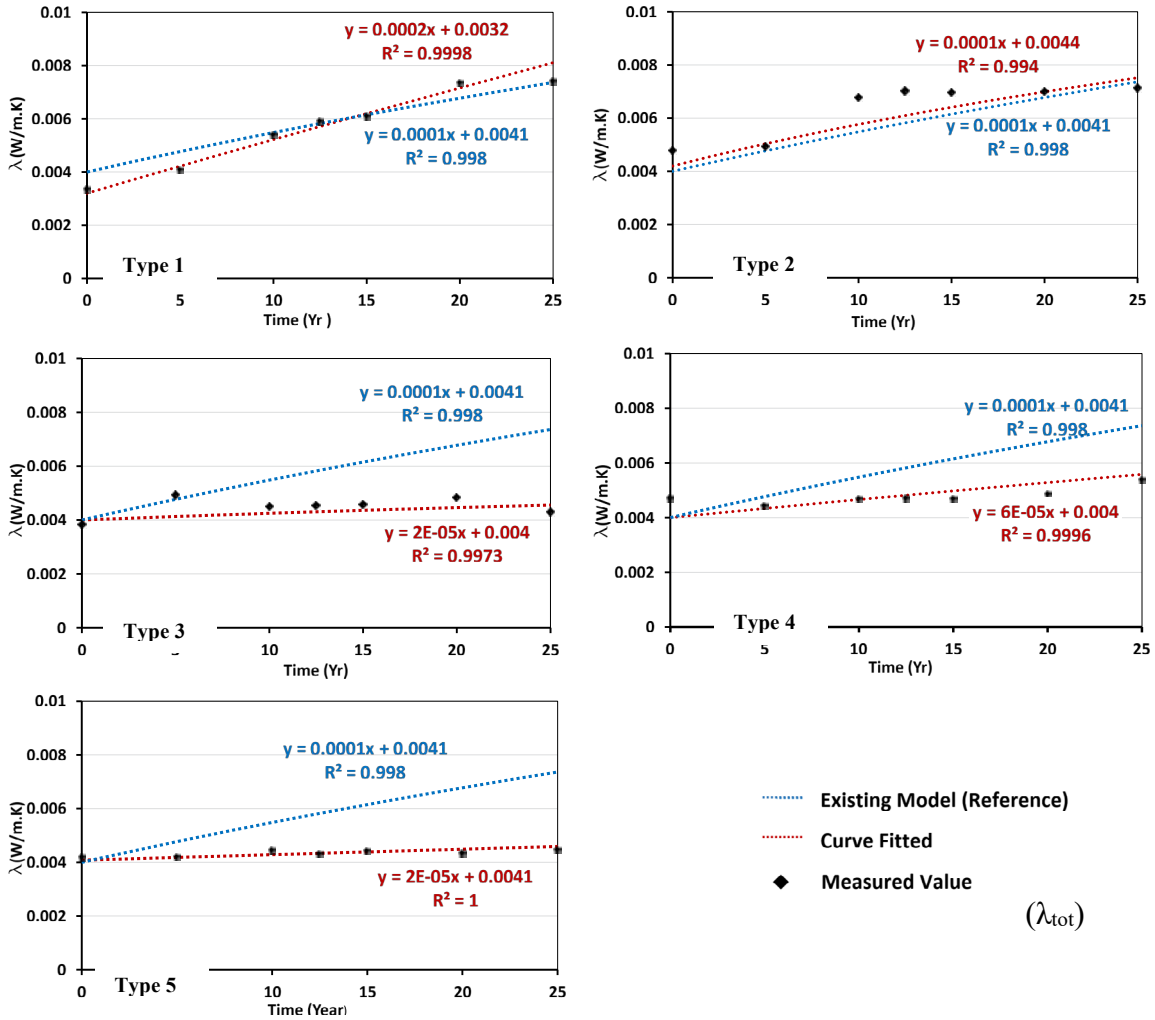

Figure 3. Thermal conductivity trend for different VIPs over time.

4 Discussion and Conclusions

Service life is one of the main characteristics of VIP assessment. The threshold value for the first definition of service life (ASTM C1484) is assumed to be 0.008 W/mK and 0.011 W/mK based on different references (Tenpierik *et al.*, 2010).

The threshold limitation and the service life of each specimen are reported in Table . Types 3 and 5 have the most extended service life among other types, formerly it followed by Types 4, 2, and 1 respectively.

Table 4. Service life of VIPs samples under test.

	Sample 1	Sample 2	Sample 3	Sample 4	Sample 5
Service life for 0.008 W/mK	25 years	30 years	> 100 years	70 years	> 100 years
Service life for 0.011 W/mK	40 years	65 years	> 100 years	> 100 years	> 100 years

The primary variables which define the quality of VIPs are the density of the core, the transmission rates of gas, and water vapor through the film barrier. Here, the test results collected from thermal conductivity measurements show that the thermal performance of the samples is mainly affected by temperature and, the amount of effect by moisture is minimal as they were also exposed to different levels of humidity without any appreciable results.

The analysis of the collected results represents that gas permeance is the factor that has the most considerable influence on VIP performance. The obtained results of Sample 1, 2 prove that the thermal resistance of the vacuum insulation panels reduces over time because of their higher gas and moisture transmittance. The thermal performances of Types 3, 4 and 5 are more stable. By comparing Types 1 and 3, it is obvious that the core materials with lower pore sizes have longer life spans due to less gas concentration. More results are reported in the paper Berardi *et al.*(2020).

Overall, the experimental analysis shows that:

- The thermal conductivity increases about 1%-2.5%, 2%, and 5%-11% a year, on average for compressed microporous silica-based, for compressed microporous silica with cellulose fiber, and for compressed microporous silica with cellulose fiber respectively.
- A small variation of thermal conductivity for compressed microporous silica and fiberglass-based cores was observed at temperatures below 0 ºC. However, since their core material porosity is dissimilar, they present different thermal conductivity behavior. The performance of the VIP microporous silica type is moderately better than that of the fiberglass over time.
- Although the initial thermal conductivity of VIP with fiberglass core is less than that of the compressed microporous silica one, fiberglass shows a significant increase in thermal conductivity after aging.
- The numerical reference model used by NRC is adapted for VIPs with fumed silica and fiberglass-based core material. However, a different mathematical model needs to be developed for compressed microporous silica and compressed microporous silica with cellulose. A significant mismatch is observed between the theoretical model plotted in Fig. 3, and the measurement results of these types.

ORCID

Umberto Berardi: https://orcid.org/0000-0002-0508-6195

References

Alotaibi, S.S. and Riffat, S. (2014). Vacuum insulated panels for sustainable buildings: a review of research and applications. *International Journal of Energy Research, 38*(1), 1-19, doi: 10.1002/er.3101

ASTM 1484 - American Society for Testing and Materials. (2018) Standard Specification for Vacuum Insulation Panels.

ASTM C518 - American Society for Testing and Materials. (2017). Standard Test Method for Steady-State Thermal Transmission Properties by Means of the Heat Flow Meter Apparatus.

Baetens, R., Jelle, B.P., Thue, J.V., Tenpierik, M.J., Grynning, S., Uvslokk, S. and Gustavsen, A. (2010). Vacuum insulation panels for building applications: A review and beyond. *Energy and Buildings, 42*(2), 147–172. doi: 10.1016/j.enbuild.2009.09.005

Batard, A., Duforestel, T., Flandin, L. and Yrieix, B. (2018). Modelling of long-term hygro-thermal behaviour of vacuum insulation panels. *Energy and Buildings, 173*, 252–267. doi: 10.1016/j.enbuild.2018.04.041

Berardi, U. Nikafkar, M. Wi, S. and Kim, S. (2020) Experimental verification of the theoretical aging of vacuum insulated panels, Journal of Industrial & Engineering Chemistry.

Berardi U. (2017). A cross country comparison of building energy consumption and their trends, *Resource Conservation and Recycling, 123,* 230-241, doi: 10.1016/j.resconrec.2016.03.014

Berardi U. (2019). The impact of aging and environmental conditions on the effective thermal conductivity of several foam materials, *Energy*, *182,* 777-794, doi: 10.1016/j.energy.2019.06.022

Caps, R., Beyrichen, H., Kraus, D. and Weismann, S. (2008). Quality control of vacuum insulation panels: Methods of measuring gas pressure. *Vacum 82,* 691–699. doi: 10.1016/j.vacuum.2007.10.015

Isaia, F., Fantucci, S., Capozzoli, A. and Perino, M. (2017). Thermal bridges in vacuum insulation panels at building scale. *Proceedings of the Institution of Civil Engineers: Engineering Sustainability*, *170*(1), 47–60. doi: 10.1680/jensu.15.00057

Jelle, P. (2012). Evaluation of Building Products by Conducting Accelerated Climate Ageing in the Laboratory, (7465), 1–9. https://www.irbnet.de/

Johansson, P., Geving, S., Hagentoft, C. E., Jelle, B. P., Rognvik, E., Kalagasidis, A. S. and Time, B. (2014). Interior insulation retrofit of a historical brick wall using vacuum insulation panels: Hygrothermal numerical simulations and laboratory investigations. *Building and Environment, 79,* 31–45. doi: 10.1016/j.buildenv.2014.04.014

Kalnæs, S. and Jelle, B. (2014). Vacuum insulation panel products: A state-of-the-art review and future research pathways. *Applied Energy, 116*(7465), 355–375. doi: 10.1016/j.apenergy.2013.11.032

Karami, P., Al-Ayish, N. and Gudmundsson, K. (2015). A comparative study of the environmental impact of Swedish residential buildings with vacuum insulation panels. *Energy and Buildings, 109,* 183–194. doi: 10.1016/j.enbuild.2015.10.031

Kim, J. H. (2017). Aging performance evaluation of vacuum insulation panel (VIP). *Case Studies in Construction Materials 7,* 329–335. doi: 10.1016/j.cscm.2017.09.003

Kucukpinar, E., Miesbauer, O., Carmi, Y., Fricke, M., Gullberg, L., Erkey, C., … Noller, K. (2015). Development of transparent and opaque vacuum insulation panels for energy efficient buildings. *Energy Procedia, 78,* 412–417. doi: 10.1016/j.egypro.2015.11.685

Kunic, R. (2012). Vacuum insulation panels - an assessment of the impact of accelerated ageing on service life. *Journal of Mechanical Engineering, 58*(10), 598–606. doi: 10.5545/sv-jme.2012.539

Kwon, J., Jang, C. H., Jung, H. and Song, T. (2009). Effective thermal conductivity of various filling materials for vacuum insulation panels. *International Journal of Heat and Mass Transfer, 52*(23–24), 5525–5532. doi: 10.1016/j.ijheatmasstransfer.2009.06.029

Lorenzati, A., Fantucci, S. Capozzoli, A. and Perino, M. (2017). The Effect of Temperature on Thermal Performance of Fumed Silica Based Vacuum Insulation Panels for Buildings. *Energy Procedia 111,* 490–99, doi: 10.1016/j.egypro.2017.03.211.

MacLean, D., Mukhopadhyaya, P., Korn, J. and Mooney, S. (2017). Design Details and Long-Term Performance of VIPs in Canada's North. *Energy Procedia 111,* 481–89, doi: 10.1016/j.egypro.2017.03.210.

Mukhopadhyaya P., M.K. Kumaran, G. Sherrer and D. Van Reenen (NRC-IRC).(2011) An Investigation on Long-Term Thermal Performance of Vacuum Insulation Panels.

Pons, E., Yrieix, B. and Brunner, S. (2018). Evaluation of VIPs after Mild Artificial Aging during 10 Years : Focus on the Core Behavior. *Energy and Buildings 162,* 198–207. doi: 10.1016/j.enbuild.2017.12.016

Quenard, D. and Sallee H. (2005) Micro-Nano Porous Materials for High Performance Thermal Insulation Micro-Nano Porous Materials for High Performance. *2nd International Symposium on Nanotechnology In Construction*.

Schwab, H., Heinemann, U., Beck, A., Ebert, H.P. and Fricke. J. (2005) Prediction of Service Life for Vacuum Insulation Panels with Fumed Silica Kernel and Foil Cover. *Journal of Thermal Envelope and Building Science, 28*(4), 357–74, doi: 10.1177/1097196305051894.

Simmler, H. and S. Brunner. (2005). Vacuum Insulation Panels for Building Application: Basic Properties, Aging Mechanisms and Service Life. *Energy and Buildings 37*(11), 1122–31, doi: 10.1016/j.enbuild.2005.06.015.

Wegger, E., Petter, B., Sveipe, E. and Grynning, S. (2010). Ageing Effects on Thermal Properties and Service Life of Vacuum Insulation Panels. *Building Physics 35*, 128–167, doi: 10.1177/1744259111398635.

XV International Conference on Durability of Building Materials and Components
DBMC 2020, Barcelona
C. Serrat, J.R. Casas and V. Gibert (Eds)

Failure Analysis of a Total Damage by Hail Impact of an External Thermal Insulation Composite Systems

Silvain Michel[1], Peter Flüeler[2], Martin Jordi[3] and Roger Welter[4]

[1] Mechanical Systems Engineering, Swiss Federal Laboratories for Materials Science and Technology (Empa), Überlandstrasse 129, CH-86000-Dübendorf, Switzerland, silvain.michel@empa.ch
[2] Flüeler Polymer Consulting GmbH, Robänkli 14, CH-8607-Aathal, Switzerland, info@fluelerpolymer.ch
[3] Natural Hazard Prevention, Association of Cantonal Fire Insurance Companies (ACFI), Bundesgasse 20, CH-3011-Bern, Switzerland, martin.jordi@vkf.ch
[4] Object Protection Consulting Natural Hazards, Building Insurance Canton of Zurich, Thurgauerstrasse 56, CH-8050-Zürich, Switzerland, roger.welter@gvz.ch

Abstract. *A hailstorm has heavily damaged a glass fibre mesh reinforced mineral render of an externally insulated composite system (ETICS) of a family house. While a neighbouring house of identical design and of the same age showed only minor defects, for the house under investigation it was a total failure of the render. Material probes were taken from the damaged façade and analysed physically and chemically. Before renovation, the hail resistance of the façade was determined with a unique artificial hail impact test method: Clear ice balls were shot against the façade with the help of a launcher, where the kinetic energy of the projectile can precisely be controlled. The type of damage due to natural hail could be reproduced. The impact energy needed to cause a damage similar to the one caused by the natural hail was determined. The hail impact damage was also identical to results from hail testing performed in the laboratory on similar systems. Since the amount of rendering material on the façade was not according to standards of the Swiss Society of Engineers and Architects - it was by far too thin - specific laboratory tests were performed with specimens not only made of similar materials but also with a comparable thin render layer. By systematic variation of the projectile size and its velocity, the impact parameters were studied and correlated to the type and extent of the hail impact damage. A threshold, associated with the first appearance of full circle cracks in the render, was found to be a kinetic energy of 2.5 J. The assessment of a supposed thickness effect and an effect of doubling the reinforcement on the hail impact resistance and the effect of the age of the façade however was a challenge. The methodological limitations given by the circumstances and the approach used are discussed in this paper.*

Keywords: *ETICS, Hail Damage, Impact, Ageing, Testing.*

1 Introduction

The effect of ageing on the durability of building elements, such as façades has been addressed in the last years by the scientific community of construction engineering and materials science (Bochen, 2009; Bochen and Gil, 2009; Daniotti *et al*., 2015; Daniotti, Paolini, and Re Cecconi, 2013; Griciute, Bliudzius, and Norvaisiene, 2013; Norvaišiene, Norvaišiene, GriciutĖ, Bliudzius, and Ramanauskas, 2013). Building insurances of Germany, Austria and Switzerland have established a register of products for building elements, which are certified for resistance against hail impact (ACFI, 2020). The certification is based on an artificial hail impact test,

which classifies the product in one of five hail resistance classes. A weakness of this certification is the fact, that products are tested and classified when they are new. The certification does not cover any deterioration of the hail resistance with the age of the product. It is an open question how much a product in service loses hail resistance with its age.

On first of August 2017 a heavy thunderstorm accompanied by hail passed the region of Winterthur, Eastern Switzerland. The building insurance of Zürich was informed by a house owner of a medium sized family house, that the façade oriented to northwest, from where the hailstorm came, has been heavily damaged. In the view of the building insurance, the ETICS on that façade should have resisted such a hailstorm and therefor the heavy damage was not expected. Swiss Federal Laboratories of Materials Science and Technology (Empa), Natural Hazard Prevention of the Association of Cantonal Fire Insurance Companies (ACFI) and the Building Insurance of Zürich (GVZ) have initiated thereafter a case study to get a deeper understanding of the cause of this damage.

2 Design of the Case Study

The idea of the study was that the façade, which was 17 years old, had a reduced hail resistance due to ageing. During the course of the study additional factors have been considered, such as the thickness of the render (amount of material applied) and the reinforcement. The case study had the following parts:

1) Description of the thunderstorm
2) Detailed description of the hail impact damage on the ETICS
3) Determination of the hail resistance of the ETICS on-site; measurement of the hail resistance in the aged condition
4) Fabrication of a representative peace of the façade in order to determine the hail resistance of a new façade of the same design
5) Comparison of the hail resistance of the new façade with the aged façade

3 The Thunderstorm of August 1st 2017 in Winterthur

August 1st 2017 was a typical high summer day with a flat atmospheric pressure distribution over Europe. In the meteorological forecast for Eastern Switzerland the development of thunderstorms was expected with hail of hailstones up to 4 cm in diameter. Observations of hail in the neighborhood of the house under investigation stated hailstones of as large as 32 mm, s. Fig 1.

Figure 1. Hailstones of the thunderstorm on August 1st 2017 in Winterthur.

These observations confirmed a hailstorm of class 3, which has an occurrence probability of one in in 5 to 20 years in this region. Therefore such a hailstorm as to be considered in the design of a building, because a building should last for 30 to 40 years, (Kempton, Chap, and Alani, 2002). According to CFIA standards, the façade should be class 3 hail resistant, which means, that this specific event should have been survived undamaged. The first conclusion was, that the façade was not as strong as it should be according to CFIA regulations.

4 Damage Description of the Affected Façade

The house was exposed to Northwest. An aerial view of the house with the affected façade from West is shown in Fig. 2. A detailed visual inspection showed 147 damage locations evenly distributed over the façade's area of 70 m^2. The damages found were classified in three categories: cracks (low level damage), full circle fracture (medium level damage) and breakout of the render with uncovering of the reinforcement (high level damage). Typical representations of these three types of damage are shown in Fig. 3. 71 locations showed a low level, 51 a medium level and 21 locations a high level damage. The morphology of these damages was similar to damages found in artificial hail tests on ETICS (Steinbauer, 2016).

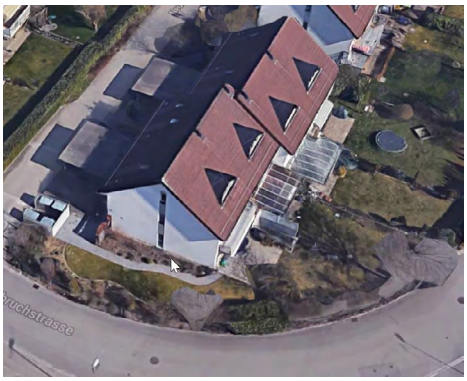

Figure 2. Aerial view of the façade from West.

Figure 3. Representations of the damage classes: crack (left), full circle fracture (center) and breakout (right).

5 Construction and Background of the Façade

The house was built in 2000. According to the drawings, the façade was based on a brick wall on which a thermal isolation of 10 cm thickness was bonded, covered by a rendering. This is a classical design of a modern ETICS. The originally used products could not be found out. Therefor 15 material probes were taken from the façade and analyzed physically and chemically.

The thermal isolation was a polystyrene foam with grain size of 2.8 mm and a density of 19.2 kg/m^3. The rendering was characterized with Thermal Gravimetric Analysis (TGA), Infrared Spectroscopy (IRS), and X-Ray Diffraction (XRD). The render was cement-bound. The main crystalline phase was calcite (aggregate, filler and carbonated binder). In addition, it contains dolomite, quartz and layer silicates as aggregates and filler. The calcium hydroxide was no longer visible from the cement, because it was carbonated (also not visible in the TGA). However, residues of the cement clinker phases were still visible. Mono-carbonate was seen as the hydration product. Some gypsum was also found. The chemical composition was as for a typical high strength mineral render bonded with Portland cement for thin layer application. The rendering was reinforced with a single or double layer of a mesh of glass fibers with an acrylic and polystyrene coating. The dimensions of the different layers were measured, s. Fig. 4. and table 1. Some those findings quality questions arose.

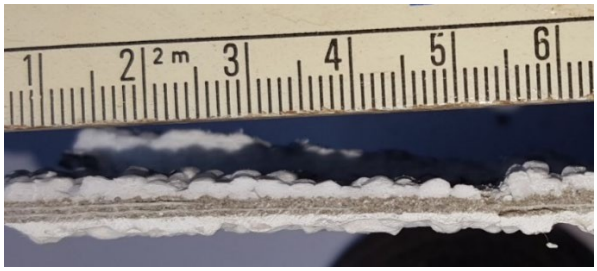

Figure 4. Cross section through the rendering (inside up – outside down): double reinforcement on the left, single reinforcement in the middle and on the right.

Table 1. Average and ranges of thickness of the different layers of the rendering of the façade.

Base coat, including the reinforcement	Finish coat, with sand grains	Paint coat	Total
mm	mm	mm	mm
1.5	1.4	0.2	3.1
1.4 – 1.6	0.4 – 1.6		2.5 – 4.5

For the strength of the rendering system, the paint coat and the finishing coat are of secondary importance. Therefore, in order to assess the quality of the rendering system, the focus was on the thickness of the base coat. According to the Swiss standard for Engineers and Architects SIA 243 (SIA, 1998), the base coat must have a thickness of 2 mm to 7 mm. Also the Austrian standard ÖNorm B 6410 specifies a minimum layer thickness of 2 mm. A new version of this standard requires an average layer thickness of 3.0 mm and a reinforcement mesh which must be covered with a minimum of 1.0 mm to a maximum of 3.0 mm of concealed render. Therefor we concluded, that the layer structure of the rendering of the façade under investigation was seriously defective and thus not carried out in accordance with the state of the art.

6 Determination of the Hail Resistance

6.1 Onsite Determination of the Hail Resistance of the Façade

6.1.1 Materials and Methods

The hail resistance was determined according to CFIA guidelines (ACFI, 2020). The test took place 8 month after the hailstorm in sunny weather (17°C / 40% r.h.). The facade was bombarded horizontally with clear ice balls at an angle of 45° with an ice ball launcher, see Fig. 5. This test equipment allows to precisely accelerating the projectiles.

Figure 5. On-site determination of the hail resistance with an ice ball launcher.

In total 19 ice balls, 15 with a diameters of 30 mm and four of 40 mm, were shot. The aim was on the one hand to determine the hail resistance class according to ACFI regulations and on the other hand to assess the energy required to provoke damage of the levels mentioned above. An energy threshold for a full circle fracture and the threshold for a breakout of the render could be determined.

6.1.2 Results

The damage caused by the artificial hail, e.g. the bombardment with ice balls, largely corresponded to the damage caused by the natural hailstorm of August 1st 2017. The shot with the lowest kinetic energy provoking a damage was 2.5 J, which corresponds to a natural hailstone of approx. 25 mm diameter in free fall. It resulted in a dent and a full circle fracture in the façade. When the façade was bombarded with 40 mm ice balls and with an energy beyond 10.0 J also breakout of the render was observed. The façade did not show a class 3 hail resistance according to the ACFI guidelines.

6.2 Determination of the Hail Resistance of Reference Specimens

6.2.1 Materials and methods

Two reference specimens representing the rendering with reinforcement built up on the thermal isolation plate were fabricated. The first was equipped with double reinforcement, as applied in the area of house edges and window cut-outs. The second reference specimen was fabricated with a single reinforcement only. Both specimen had two sections: The first section was fabricated with a base coat of only 1.5 mm thickness, representing the façade under investigation. The second section was fabricated according to SIA standards, e.g. with a base coat thickness of approx. 4 mm. For the production of the reference

specimens an equivalent rendering system was chosen which had similar chemical composition and mechanical properties. The specimens were put on the roof of the Empa laboratory for hardening under natural weathering condition for 2 and 7 month, respectively. The rendering of the reference specimens had the following dimensions:

Table 2. Average thickness of the different layers of the rendering of the reference specimens.

	Base coat, including the reinforcement	Finishing coat, with sand grains	Paint coat	Total
	mm	mm	mm	mm
Thin section 1	2.3	1.3	0.2	3.8
Standard section 1	3.8	1.8	0.2	5.8
Thin section 2	1.1	1.1	0.2	2.4
Standard section2	4.5	1.1	0.2	5.8

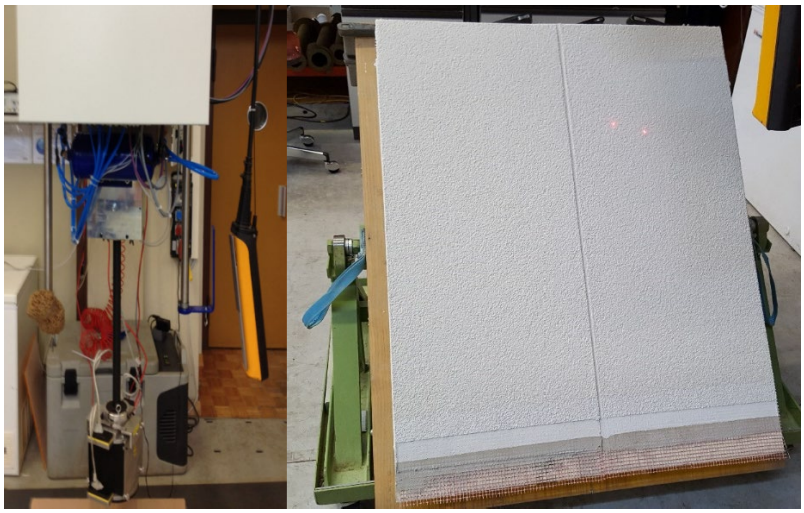

Figure 6. Air gun for artificial hail tests (left) - reference specimen before hail testing (right).

The hail tests were carried out with the Empa air gun for hail testing as well as with the ice ball launcher used onsite, see Fig. 6. The tests were carried out according to CFIA regulation No. 8 (ACFI, 2014). Both specimens were bombarded with 20 mm, 30 mm and 40 mm ice balls, which were made by the melting method from natural ice. The tests were performed at 23 °C / 50 % r.h. The aim was to reproduce the damage caused by the bombardment on the façade and to determine the threshold values for a crack, a full circle fracture and breakouts.

6.2.2 Results

A total of 67 shots were fired on the first specimen, 60 shots on the second specimen, evenly distributed over the two sections each. The results of the hail shots are summarized in table 3 and compared to the results of the shots on the façade. The façade was 17 years old and had a thin layer of base coat with a single layer of reinforcement. The reference specimens were new with a thick layer of base coat on one side and a thin layer of base coat on the other. One specimen had a single reinforcement and one a double reinforcement. Thus, the results can be analyzed with regard to a thickness effect, a reinforcement effect and an ageing effect by

comparing the values pairwise.

Table 3. Threshold for damage levels determined on the reference specimens and the façade.

base coat: reinforcement: age:	thick double new	thick single new	thin double new	thin single new	thin single aged
	J	J	J	J	J
Threshold for a crack	1.3	2.6	1.8	2.8	-
Threshold for a full circle fracture	1.9	2.9	3.3	2.8	2.5
Threshold for a breakout	15.4	11.7	12.4	11.6	10.0

No clear effect of the thickness can be seen: For double reinforcement, a thicker base coat may be favorable or unfavorable, depending on the damage level. For single reinforcement, the respective threshold values hardly differ. An effect of the reinforcement can also not be identify in the data: A double reinforcement is unfavorable for low damage level, but favorable for high damage level. An effect of ageing is weakly recognizable, both for a circle crack and a breakout: Both threshold values decrease with age, but only by approx. 15%.

7 Discussion and Conclusions

7.1 Discussion

The overlapping of three major influences makes it difficult to distinguish their individual impacts on hail resistance: For a complete investigation of all effects, not only a façade in the state "aged/too thin" would have had to be present, but also a façade "aged/standard layer". With the reference specimens the two states "new/too thin" and "new/standard layer" were available. Thus, on the one hand, the layer thickness effect could only be quantified in the "new" state and, on the other hand, the ageing effect could only be determined in the "too thin" state. The ageing effect of a rendering with standard layer thickness could not be determined with the available material. Since it was a classic mineral rendering, which was only discovered in the course of the investigation, a significant ageing effect could not have been expected. This result would probably be different if it was an organically bound rendering.

The results of the study leaves the possibility open that a thickness effect or an effect of the reinforcement only occurs in the aged state. A further possibility is that the ageing effect only occurs when the layer structure is correctly applied, but not when it is too thin. An indication that the first possibility applies is the comparison of the façade examined here with the façade of the neighboring house. Both houses have the same design and are of the same age. Assuming that the façade of the neighboring house was correctly manufactured, the thickness effect in the aged condition could be assessed by comparing these two façades. The façade of the neighboring house had only a few impact damages, which could be repaired locally. This indicates that it was not the advanced age that caused the massive damage to the façade, but the poor workmanship. The repair was a complete rebuilding of the rendering.

7.2 Conclusions

The damage to the façade by the natural hail event of August 1st 2017 could be reproduced by bombardments with ice balls of 30 mm in diameter and a kinetic energy of at least 2.5 J. Artificial hail impact with the ice ball launcher onsite as well as with the air gun in the laboratory gave similar results. Energy threshold values for typical damages were determined for a typical mineral rendering system. In the course of the study it became apparent that the structure of the façade did not meet the current standards. Thus, it had to be assumed that the damage to the façade was not only influenced by the age (17 years old), but also by a too thin rendering base coat (1.5 mm instead of at least 2.0 mm). An ageing effect is weakly discernible in the data, while an influence of the coating thickness could not be found.

Acknowledgements

The support of the company Dell'Elba Partner AG, which produced the reference specimens, the house owner Mr. Thomas Meier, who made the study possible are sincerely thanked.

ORCID

Silvain Michel: https://orcid.org/0000-0002-3337-2420
Peter Flüeler: https://orcid.org/0000-0002-2790-4128
Martin Jordi: https://orcid.org/0000-0002-6104-3085
Roger Welter: https://orcid.org/0000-0001-9854-3801

References

ACFI. (2014). CFIA Test Specification No. 08: Hail resistance of Exterior Insulation and Finish Systems (EIFS). In. Bern: Association of Cantonal Fire Insurences

ACFI. (2020). Hagelregister. Retrieved from https://www.hagelregister.ch/

Bochen, J. (2009). Study on the microstructure of thin-layer facade plasters of thermal insulating system during artificial weathering. *Constr. and Building Materials, 23.*

Bochen, J. and Gil, S. (2009). Properties of pore structure of thin layer external plasters under ageing in simulated environment. *Constr. and Building Materials, 23.*

Daniotti, B., Cecconi, F. R., Paolini, R., Cocchetti, G., Galliano, R. and Cornaggia, A. (2015). Multi-physics modelling for durability evaluation of ETICS. *Paper presented at the XIII Internation Conference on Durability of Building Materials and Components.*

Daniotti, B., Paolini, R. and Re Cecconi, F. (2013). *Effects of Ageing and Mositure on Thermal Performance of ETICS cladding* (Vol. 3): Springer.

Griciute, G., Bliudzius, R. and Norvaisiene, R. (2013). The Durability Test Method for External Thermal Insulation Composite System (ETICS) used in Cold and Wet Climate Couintries. *J of Sub Arch and Civil Eng,1*(2), 50.

Kempton, J., Chapman, K. and Alani, A. (2002). *Surveyor Element Lifetime Predictions and the Anchoring and Adjustment Heuristic,* Paper presented at the AR2002.

Norvaišiene, R., Griciutė, G., Bliudzius, R. and Ramanauskas, J. (2013). The Changes of Moisture Absorption Properties during the Service Life of External Thermal Insulation Composite System. *Medžiagotyra, 19*(1), 103-107.

SIA. (1998). *Verputzte Aussenwärmedämmung : Leistung und Ausmass : verlängerte Vernehmlassung* (Ausg. 1998 ed. Vol. V 243/2, Ed. 1998): Zürich : SIA.

Steinbauer, V. (2016). *Impact Resistance of External Thermal Insulation Composite Systems: Impact Process and Damage.* (PhD). University of Berne, Bern.

XV International Conference on Durability of Building Materials and Components
DBMC 2020, Barcelona
C. Serrat, J.R. Casas and V. Gibert (Eds)

Quantifying Thermal Performance of the Building Envelope - Beyond Common Practice

Simon Pallin[1], Jason W. DeGraw[1], Mahabir Bhandari[1] and Tyler Pilet[2]

[1] Oak Ridge National Laboratory, Building Envelope & Urban Systems Research Group, Energy and Transportation Division, 1 Bethel Valley Rd, Oak Ridge, TN 37830, USA, pallinsb@ornl.gov
[2] Georgia Institute of Technology, North Ave NW, Atlanta, GA 30332, USA, tpilet@gatech.edu

Abstract. *Performance metrics serve as useful tools and indicators for many applications. For the building industry, various metrics exist; typically, these metrics do not assess the whole building performance. Instead, these represent separate components or heat transfer mechanisms of a building like R-value, U-factor/value, and airtightness. The mechanisms defined under these metrics all contribute significantly to the overall thermal performance of a building but will rarely act independently. There are metrics that account for the overall energy performance of a building, such as Energy Use Intensity (EUI). However, these metrics tend to be highly influenced by how the building is operated and used. There are also metrics which provide assessment on a relative basis. These indices are based upon comparison to a baseline, which complicates meaningful metric-based energy analyses. This paper presents a performance metric developed to account for various thermal properties and behaviors of a building. The metric accounts for all the relevant mechanisms that influence heat losses and gains in buildings and is thus directly related to the energy performance. In addition, the metric is designed to comprise air infiltration and allows users to account for workmanship quality, and imperfections of the building thermal resistance due to penetrations and other installations. This paper will describe how the metric can be applied for various building types and in different climates.*

Keywords: *BEP, Energy, Demand, Thermal Mass, Whole-Building.*

1 Introduction

The thermal performance of a building depends on various building characteristics, including outdoor climate, building usage, HVAC equipment, occupants' indoor climate preferences, etc. Due to complex interaction between these variables, describing the thermal performance of a building is difficult. Many metrics exist to describe single variables, such as *R*-value, U-factor, airtightness (ACH50/75), Solar Heat Gain Coefficient (SHGC). However, none of these indicators can fully, or even realistically, solely describe the overall thermal performance.

Several attempts have been made to define metrics which account for most variables that possess a significant impact on the energy performance (Ferrari and Zanotto, 2016). Many of these efforts focus on the building envelope thermal mass, such as the TER (Reilly and Kinnane, 2017), the M-factor (Masonry Industry Committee, 1978; Yu, 1978), and the T-value (Alterman *et al.*, 2012). Typically, the greatest hurdle to overcome is to account for solar loads and the impact it has on exterior building envelope surface temperatures and interior heat loads. The sol-air temperature (O'Callaghan and Probert, 1977) defines a fictious ambient temperature that accounts for solar induced heat transfer through the opaque building envelope, but that does not reflect solar induced interior heat gains.

There are also various simplified methods to calculate heating and cooling loads in buildings from estimating the overall thermal performance of buildings, such as CLTD/CLF (Spitler,

doi:10.23967/dbmc.2020.204

McQuiston, and Lindsey, 1993) and the RTS method (ASHRAE, 2017). These methods include all variables relevant to the energy demand in buildings, including interior loads from solar radiation through windows. However, these methodologies do not result a single indicator that represents the whole building energy performance.

This paper proposes a simplified assessment that accounts for mechanisms relevant to the heat loss and gains through the building envelope and its impact on interior loads.

2 Method

This paper presents a methodology to assess the thermal performance of building using a single-valued metric. The metric is based on the following principle.

$$\frac{Q_{HVAC}}{\eta} = Q_{net}^{env}$$
$$Q_{net}^{env} = BEP \cdot A_{tot}^{env} \tag{1}$$

The HVAC energy demand (no internal loads), Q_{HVAC} (J[Btu]), will mainly depend on the efficiency of the HVAC system η (-) and the net building envelope heat transfer Q_{net}^{env} (J[Btu]). In Eq. (1), we introduce the Building Envelope Performance metric, BEP (J/m^2[Btu/ft^2]), which is defined by the overall building envelope thermal load per building envelope area, A_{tot}^{env}. For annual heating and cooling loads, BEP is a combination of the thermal resistance of all building envelope components, $\mathcal{R}$ ((m^2·K)/W [(°F·ft^2·hr)/Btu]), and the effective cooling (c) and heating (h) degree hours, as seen in Eq (3). $\mathcal{R}$ includes heat transfer from conduction, convection and radiation:

$$BEP = \frac{eCDH}{\mathcal{R}_c} + \frac{eHDH}{\mathcal{R}_h}$$
$$\mathcal{R} = \frac{1}{\frac{1}{\sigma \cdot R_{env}} + \frac{1}{R_{air}} + \frac{1}{R_{gain}}} \tag{2}$$

where

$eCDH$ = Effective cooling degree hours (K·hr [°F·hr]),
$eHDH$ = Effective heating degree hours (K·hr [°F·hr]),
R_{env} = Conductive thermal resistance, *R*-value ((m^2·K)/W [(°F·ft^2·hr)/Btu]),
R_{air} = Air leakage resistance ((m^2·K)/W [(°F·ft^2·hr)/Btu]),
R_{gain} = Window solar and internal heat gains resistance ((m^2·K)/W [(°F·ft^2·hr)/Btu]),
σ = Opaque envelope solar and thermal radiation correction factor (-).

$eCDH$ and $eHDH$ are calculated from average outdoor and indoor temperatures during cooling and heating mode respectively.

$$eCDH = (T_{out}^{avg,c} - T_{in,cool}) \cdot t_{cool}$$
$$eHDH = (T_{in,heat} - T_{out}^{avg,h}) \cdot t_{heat} \tag{3}$$

Here,

$T_{out}^{avg,c-h}$ = Average outdoor temperature during cooling (c) or heating (h) (K [°F]),

$T_{in,cool}$ = Indoor setpoint temperature for cooling (K [°F]),

$T_{in,heat}$ = Indoor setpoint temperature for heating (K [°F]),

t_{cool} = Time for which cooling occurs (hr),

t_{heat} = Time for which heating occurs (hr).

Note that the effective cooling and heating degree hours defined in Eq. (3) are not the same as regular cooling and heating degree hours (Erbs, Klein, and Beckman, 1984). For example, because of heat loads (solar and internal), cooling may occur when the ambient outdoor temperature is below the indoor cooling setpoint temperature. Defining effective degree hours are essential to account for all loads/sinks contributing to the HVAC running cycle.

2.1 Conductive Heat Transfer

The resulting building envelope *R*-value, R_{env}, is expressed as:

$$R_{env} = \frac{A_{tot}^{env}}{\frac{A_{wall}}{R_{wall} \cdot \phi_{wall}} + \frac{A_{roof}}{R_{roof} \cdot \phi_{roof}} + \frac{A_{slab}}{R_{slab} \cdot \phi_{slab}} + \frac{U_{wind} \cdot A_{wind}}{\phi_{wind}}} \quad . \tag{4}$$

$$A_{tot}^{env} = A_{wall} + A_{roof} + A_{slab} + A_{win}$$

where

R_k = Thermal resistance (*R*-value) of envelope component k ((m^2·K)/W [(°F·ft^2·hr)/Btu]),

ϕ_k = Conductive correction factor for envelope component k, due to thermal bridges, installation quality, etc. (-). (Not validated in this study)

The opaque envelope radiation correction factor, σ, accounts for increased surface temperatures due to solar radiation and is given by:

$$\sigma = \frac{T_{out}^{avg} - T_{in}}{T_{eq} - T_{in}} \quad , \tag{5}$$

where

$$T_{eq} = \frac{T_{eq}^{roof} \cdot A_{roof} + T_{eq}^{wall} \cdot A_{wall} + T_{out}^{avg} \left(A_{win} + A_{slab} \right)}{A_{tot}^{env}}, \tag{6}$$

In which,

$$T_{eq}^{wall} = T_{out}^{avg} + R_{se,wall}\left(\alpha_{wall}\left(\frac{I_{sol,E}^{avg}\cdot A_{wall,E} + I_{sol,S}^{avg}\cdot A_{wall,S} + I_{sol,W}^{avg}\cdot A_{wall,W} + I_{sol,N}^{avg}\cdot A_{wall,N}}{A_{wall}}\right)\right.$$
$$\left. + \frac{I_{sky,E}^{avg}\cdot A_{wall,E} + I_{sky,S}^{avg}\cdot A_{wall,S} + I_{sky,W}^{avg}\cdot A_{wall,W} + I_{sky,N}^{avg}\cdot A_{wall,N}}{A_{wall}}\right) \quad (7)$$
$$T_{eq}^{roof} = T_{out}^{avg} + R_{se,roof}\left(\alpha_{roof}\cdot I_{sol,hor}^{avg} + I_{sky,hor}^{avg}\right)$$

and

T_{eq} = Equivalent building envelope surface temperature (K [°F]),

T_{out}^{avg} = Average outdoor temperature when either cooling or heating occurs (K [°F]),

$I_{sol,j}^{avg}$ = Annual average incident solar radiation on vertical surface in direction j (W/m^2[Btu/(hr·ft^2)]),

$I_{sky,j}^{avg}$ = Annual average infrared radiation on vertical surface in direction j (W/m^2[Btu/(hr·ft^2)]),

$I_{sol,vert}^{avg}$ = Annual average incident solar radiation on vertical surfaces (W/m^2[Btu/(hr·ft^2)]),

$I_{sky,vert}^{avg}$ = Annual average infrared radiation on vertical surfaces (W/m^2[Btu/(hr·ft^2)]),

α_k = Material solar absorptivity of envelope component k (-),

ε_k = Material infrared emissivity of envelope component k (-),

R_{se} = Exterior surface transfer resistance ((m^2·K)/W [(°F·ft^2·hr)/Btu]),

$E / S / W / N$ = East, South, West and North respectively (-).

The opaque envelope solar and thermal radiation correction factor seen in Eq. (5) needs to be calculated for both heating ($t_{heat} > 0$) and cooling ($t_{cool} > 0$) since T_{eq} and T_{out}^{avg} varies accordingly.

$$\sigma^c = \frac{T_{out}^{avg,c} - T_{in,cool}}{T_{eq}^c - T_{in,cool}} \text{ and } \sigma^h = \frac{T_{out}^{avg,h} - T_{in,heat}}{T_{eq}^h - T_{in,heat}} . \quad (8)$$

2.2 Convective Heat Transfer

The effective thermal resistance due to air infiltration through the building envelope, R_{air}, is defined as:

$$R_{air} = \frac{A_{tot}^{env}}{\overline{\dot{V}}\cdot\rho_{air}\cdot c_{air}}. \quad (9)$$

$$\overline{\dot{V}} = C\cdot\left(\overline{\Delta P}\right)^n \quad (10)$$

Where

$\overline{\dot{V}}$ = Annual average air flow rate through the building envelope during either cooling or

heating (m^3/hr [ft^3/hr]),
ρ_{air} = Density of air (kg/m^3 [lb/ft^3]),
c_{air} = Specific heat of air (J/(kg·K) [Btu/(lb·°F)]),
C = Air flow coefficient (m^3/(s·Pa) [cfm/Pa]),
P = Air pressure (Pa),
n = Air leakage exponent (-).

The average air pressure difference is calculated during the time of either cooling or heating. Typically, the overall pressure gradient, ΔP, around the building envelope is the sum of three components; wind loads, ΔP_w, buoyancy effect (stack), ΔP_s, and ventilation, ΔP_v.

$$\Delta P = \Delta P_w + \Delta P_s + \Delta P_v \tag{11}$$

As for all variables in Eq. (2), R_{air} is defined for either cooling or heating.

2.3 Solar, Thermal and Internal Heat Gains

Finally, an effective thermal resistance is found, due to interior heat loads. These loads consist of solar and thermal radiation through windows and all interior loads from equipment, appliances, lighting, humans, etc. The heat gain resistance, R_{gain}, is written as

$$R_{gain} = \frac{\left(T_{out}^{avg,c-h} - T_{in}\right) \cdot A_{tot}^{env}}{Q_{load,in}}. \tag{12}$$

$$Q_{load,in} = SHGC \cdot \left(I_{sol,E}^{avg} \cdot A_{win,E} + I_{sol,S}^{avg} \cdot A_{win,S} + I_{sol,W}^{avg} \cdot A_{win,W} + I_{sol,N}^{avg} \cdot A_{win,N}\right) \tag{13}$$

where
$SHGC$ = Window solar heat gain coefficient (-),
R_{gain} is a fictitious thermal resistance based on the assumption of a given temperature gradient, $\left(T_{out}^{avg,c-h} - T_{in}\right)$, which allows all thermal resistances in Eq. (2) to be lumped together.

3 Result

The proposed BEP metric of this paper has been validated against transient energy modelling simulation tools (EnergyPlus, 2018). The simulated building was setup as a rectangular building and with characteristics described in Table 1.

The overall heating and cooling demands were computed for 16 different U.S. climate zones (IECC, 2015) and the indoor temperature was kept at 20°C [68°F]. As seen in Eq. (2), BEP relies on the effective heating and cooling degree hours. These hours are calculated based on all loads contributing to the indoor temperature. In general, cooling and heating degree hours are calculated under the following conditions:

$$\begin{aligned} &eCDH \ when \ Q_{net}^{cool} > 0 \\ &eHDH \ when \ Q_{net}^{heat} < 0 \end{aligned} \tag{14}$$

$$Q_{net}^{cool} = \mathcal{R} \cdot \left(T_{out}^{avg,c} - T_{in,cool} \right) \cdot A_{tot}^{env}$$
$$Q_{net}^{heat} = \mathcal{R} \cdot \left(T_{in,heat} - T_{out}^{avg,h} \right) \cdot A_{tot}^{env} \quad (15)$$

Table 1. Simulation model used to validate the BEP metric.

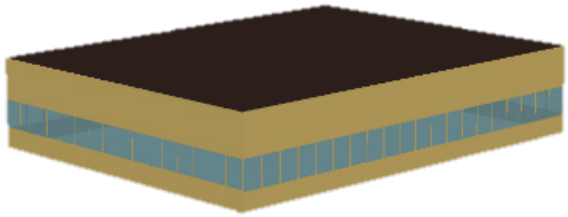

Length x Width x Height	20 x 15 x 4 m [65.6 x 49.2 x 13.1 ft]
Window Area	84 m^2 [275.6 ft^2]
SHGC	0.352 (-)
R-value Wall/Roof/Window/Slab	1.013/3.509/0.391/adiabatic (m^2·K)/W
Solar absorptance Wall/Roof	0.92/0.7
Surface heat transfer coefficient - Interior/Exterior	8/25 W/(m^2·K)
Air tightness	Not validated

Figure 1 reveals how the cooling and heating cycle varies in the simulations for warm (Miami, FL) and a cold (Minneapolis, MN) climate respectively.

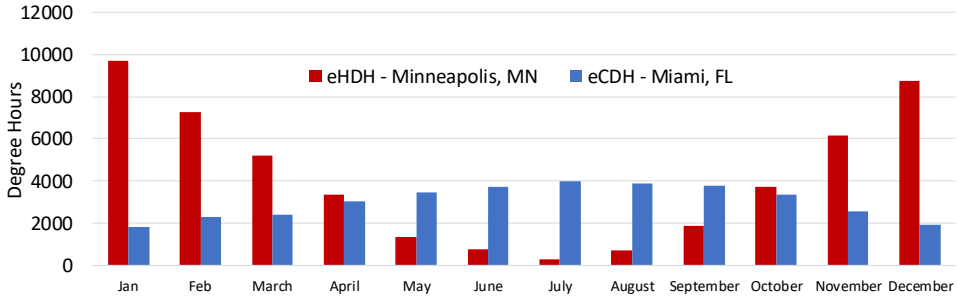

Figure 1. Variation in effective heating and cooling degree hours between a hot (Miami, FL) and cold (Minneapolis, MN) climate. $eCDH$ and $eHDH$ are calculated in accordance with Eq. (15).

A comparison was made for BEP between various comprehensive simulation models (EnergyPlus, 2018; IBP, 2019; van Dijk, Spiekman, and Hoes-van Oeffelen, 2016). Figure 2 depicts simulated cooling and heating demand for 16 locations in the U.S. According to this result, the BEP shows good agreement with more sophisticated simulation models. The main reason to the discrepancies depicted in Figure 2 for the simulated heating and cooling demand seems to be a result of dissimilar approaches to compute heat surface film coefficients.

As previously discussed, the BEP metric will account for various variables that are dependent on exterior climate conditions. **Figure 3** reveals the variation of BEP for various climates. According to the figure, colder climates tend to require an overall greater energy demand, thus a higher value of BEP.

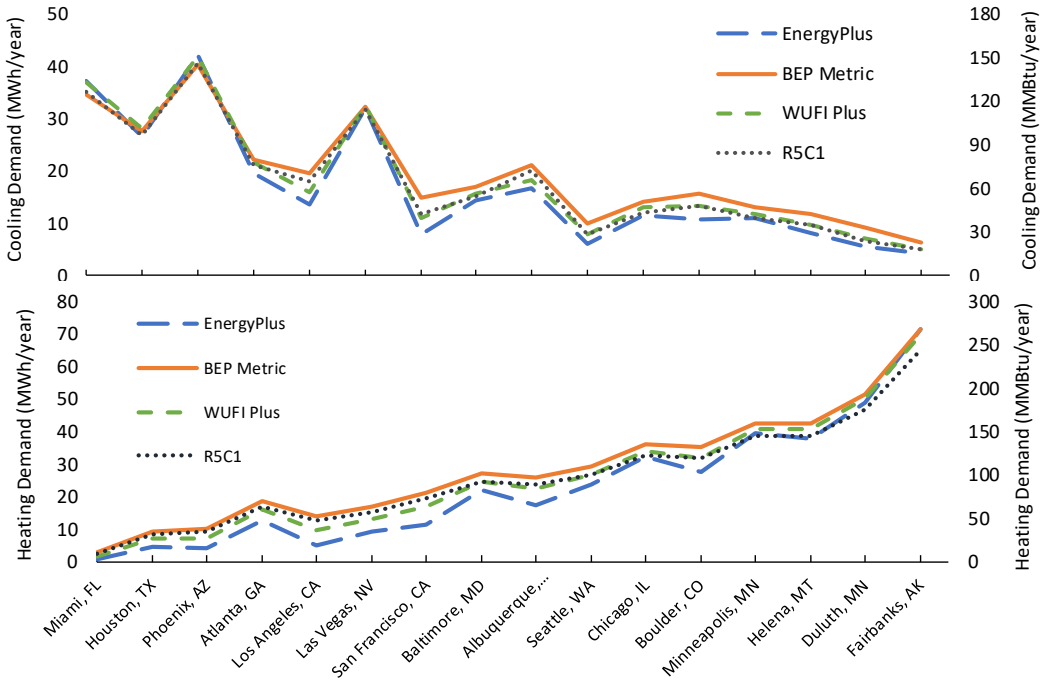

Figure 2. Validation between the proposed metric, EnergyPlus, R5C1, and finite element simulations. The proposed metric shows good agreement with more sophisticated simulation procedures.

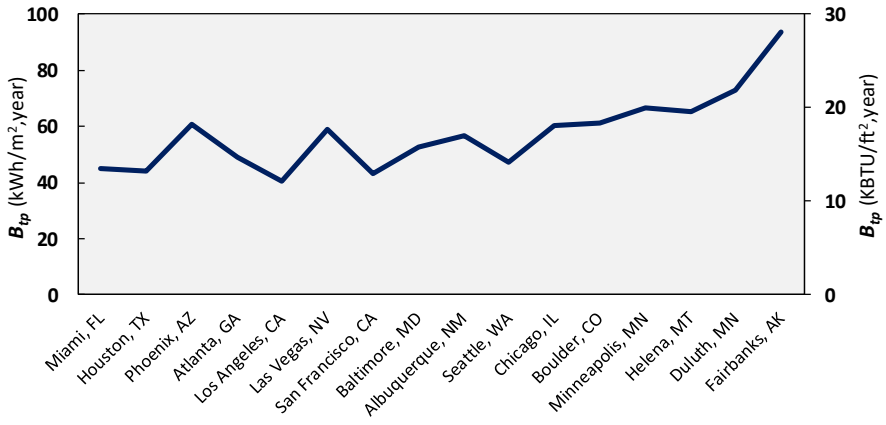

Figure 3. Variation in BEP between 16 different locations and U.S. climate zones for the validated building.

4 Conclusions

This paper introduces a new building envelope thermal performance metric, BEP. The metric accounts for all relevant heat transfer mechanisms affecting the energy demand of a building due to outdoor climate and interior thermal loads; conductive heat transfer, air infiltration, solar heat gains affecting opaque building envelope surface temperatures and indoor heat loads. This paper also presents an initial validation study by comparing simulation results from various whole building energy simulation tools. According to the comparison, BEP can predict overall energy performance similarly to existing simulation tools.

The purpose and advantage of BEP are that it does not require an iterative simulation

procedure. Instead, the proposed metric relies on input data given by the geometry of the building, thermal characteristics and outdoor climate date. This feature allows for a quick, yet accurate, thermal performance assessment of a building.

Lastly, BEP serves as an overall building envelope thermal performance metric. This allows for easy comparison of the thermal performance of buildings with varying building type, characteristics, and climate location. Additionally, the BEP allows for efficient comparison of the predicted energy performance of planned retrofits.

Acknowledgements

This manuscript has been authored by UT-Battelle LLC under contract DE-AC05-00OR22725 with the US Department of Energy (DOE). The US government retains and the publisher, by accepting the article for publication, acknowledges that the US government retains a nonexclusive, paid-up, irrevocable, worldwide license to publish or reproduce the published form of this manuscript, or allow others to do so, for US government purposes. DOE will provide public access to these results of federally sponsored research in accordance with the DOE Public Access Plan (http://energy.gov/ downloads/doe-public-access-plan).

ORCID

Simon Pallin: https://orcid.org/0000-0001-7197-6746
Mahabir Bhandari: https://orcid.org/0000-0003-1951-9876
Tyler Pilet: https://orcid.org/0000-0001-9680-6866

References

Alterman, D., Moffiet, T., Hands, S., Page, A., Luo, C. and Moghtaderi, B. (2012). A concept for a potential metric to characterise the dynamic thermal performance of walls. *Energy and Buildings, 54*, 52-60.

ASHRAE. (2017). ASHRAE handbook of fundamentals - Chapter 18 - Nonresidential Cooling and Heating Load Calculations. *American Society of Heating, Refrigerating and Air Conditioning Engineers, NY*.

EnergyPlus. (2018). EneryPlus Engineering Reference. Retrieved from https://energyplus.net/sites/all/modules/custom/nrel_custom/pdfs/pdfs_v8.9.0/EngineeringReference.pdf.

Erbs, D. G., Klein, S. A. and Beckman, W. A. (1984). Sol-air heating and cooling degree-days. *Solar Energy, 33*(6), 605-612. doi:https://doi.org/10.1016/0038-092X(84)90016-1

Ferrari, S. and Zanotto, V. (2016). Approximating Dynamic Thermal Behaviour of the Building Envelope. In S. Ferrari & V. Zanotto (Eds.), *Building Energy Performance Assessment in Southern Europe*, 21-33. Cham: Springer International Publishing.

IBP, F. (2019). Wufi Plus - Software for calculating three dimensional coupled heat and moisture transfer in building components. Retrieved from http://www.wufi.de/index_e.html

IECC. (2015). International Energy Conservation Code - Residential Energy Efficiency. In. Country Club Hills, IL, USA: International Code Council, Inc.

Masonry Industry Committee. (1978). *the "m" factor: The use of mass to save energy in heating and cooling of buildings*. Retrieved from Masonry Industry Committee:

O'Callaghan, P. W. and Probert, S. D. (1977). Sol-air temperature. *Applied Energy, 3*(4), 307-311. doi:https://doi.org/10.1016/0306-2619(77)90017-4

Reilly, A and Kinnane, O. (2017). The impact of thermal mass on building energy consumption. *Applied Energy, 198*, 108-121. doi:https://doi.org/10.1016/j.apenergy.2017.04.024

Spitler, J., McQuiston, F. and Lindsey, K. (1993). *CLTD/SCL/CLF cooling load calculation method.* Paper presented at the the 1993 Winter Meeting of ASHRAE Transactions. Part 1, Chicago, IL, USA, 01/23-27/93.

van Dijk, H., Spiekman, M. and Hoes-van Oeffelen, E. (2016). EPB standard EN ISO 52016: calculation of the building's energy needs for heating and cooling, internal temperatures and heating and cooling load.

Yu, H. C. (1978). The M Factor: A New Concept in Heat Transfer Calculations. *Consulting Engineer, 1978*.

XV International Conference on Durability of Building Materials and Components
DBMC 2020, Barcelona
C. Serrat, J.R. Casas and V. Gibert (Eds)

A 3D Model for Building Condition Assessment

Anna Banaszek[1], Sebastian Banaszek[1], Anna Cellmer[2], Vicenç Gibert[3] and Carles Serrat[4]

[1] Training and Research Center "DroneTechCamp", Ul. Jarocka 64/2, 10-699, Olsztyn, Poland, {anna.banaszek, sebastian.banaszek}@banaszekgroup.pl
[2] Dept. of Geoinformatics, The Faculty of Civil Engineering, Environmental Engineering and Geodesy, Koszalin University of Technology, Koszalin, Poland, anna.cellmer@tu.koszalin.pl
[3] LABEDI-EPSEB, Dept. of Architectural Technology, Universitat Politècnica de Catalunya-BarcelonaTECH, Av. Dr. Marañón, 44-50, 08028-Barcelona, Spain, vicenc.gibert@upc.edu
[4] IEMAE-EPSEB, Dept. of Mathematics, Universitat Politècnica de Catalunya-BarcelonaTECH, Av. Dr. Marañón, 44-50, 08028-Barcelona, Spain, carles.serrat@upc.edu

Abstract. *The aim of the paper is to analyze practical aspects with use of 3D Model for accurate building condition assessment. Use of fully interactive visualization methods from a technical condition assessment platform going to be, especially taking into consideration current COVID-19 scenarios, a very supportive tool for the massive inspection of building stocks, particularly in big residential areas. The authors present the approach based on high-performance images that were captured by Unmanned Aerial Vehicles (UAVs). The next step is the generation of a 3D model and orthophotos of building facades. The graphical information together with tables of attributes will allow the interactive geo-referenced management and assessment, that is proposed as a form of interactive cooperation. The idea of this approach corresponds widely with the Building Information Modeling aims. The authors introduce the methodology, stages of the inventory and follow-up process carried out within the platform requirements together with advantages of the visualization techniques, basing on a particular case study. Technical details about the information system and the analysis connected with the visualization utility will be presented and illustrated.*

Keywords: *Technical Condition, Assets Assessment, UAV, BIM, GIS.*

1 Introduction

The main aim of this paper is to introduce the further research and development of the utility previously presented by Banaszek *et al*. (2019) for the accurate assessment of the technical condition of buildings, as an efficient strategy and platform for the massive inspection of building stocks, in big residential areas. The approach is based on high-performance images captured by UAVs, and it is inspired by authors' previous works in the context of the Building Research Analysis and Information Network (Serrat *et al*., 2011, 2017).

The first successful ideas about using images taken from a model helicopter partly for the generation of a 3D-model of an historical mill we may find in Zischinsky *et al.* (2000). In recent years, there has been a growing demand in using UAVs for variety of purposes including monitoring, surveillance and information collection tasks. The application contexts and the objectives are different and diverse: natural disasters detection and monitoring, (Alexis *et al*., 2009, Neto *et al*., 2012, Popescu *et al*., 2015), marine-oceanic missions, (Rubio *et al*., 2004; Reineman *et al*., 2016; Schaub *et al*., 2018), surveillance of complex urban environments

(Semsch *et al*. 2009) among others. The specific use of multiple UAVs for a persistent surveillance aim has been also considered, and studied with optimized algorithms in (Nigam *et al*., 2012). Even taking into consideration all mentioned applications and research, the use of UAVs for collecting accurate information in a building, with purpose to assess and monitor its technical condition, has not been enough established. Few seminal studies have been developed (Eschmann *et al*., 2012; Hallerman *et al*., 2015; Banaszek *et al*., 2017) and by Serrat *et al*. (2018, 2019).

The idea presented in the article includes the full interactive visualization method for building condition assessment platform and may be considered as a part of the broadly understood Building Information Modeling (BIM). As a real-time capturing of data technology, UAV is used in the construction industry. In the recent years, the UAVs have been successfully used for different construction and operation applications of various types of construction projects (Asnafi *et al*., 2018). The topic of adapting the UAV technologies to efficiently collect information for an efficient BIM update, building management and documentation is being studied and considered in terms of systematic use by various authors (Vacanas *et al*., 2015; Chen *et al*., 2019; Grosso *et al*., 2020).

The paper is organized as follows. In Section 2 it will be presented the main methodology. Section 3 contains description of the case study and details of the procedure illustrated by a) the resulting 3D and 2D models for the building under assessment, and b) pictures of the elements, damages and severities identified by the methodology as a result of the inspection. The paper ends with a summary and the main conclusions of the conducted research.

2 Methodology

The new technologies in UAV data acquisition brings new opportunities in this field. In general, the method of visual building inspection using UAV is divided into two stages: data acquisition (in-flight) and digital post-processing (post-flight) (Eschmann *et al*., 2012). The quality and variety of data obtained from UAVs depends largely on installed sensors, the technical capabilities and good planning of photogrammetric flights. The flight mission of the UAVs has been technically protocolized in order to get the proper high-quality information about the real condition of the building. Based on that, the following methodology of a Fully Interactive Visualization is established and studied for building condition assessment.

Various research results (Mesas-Carrascosa *et al*., 2014.) proved that the UAVs orthophotos satisfactorily passed the spatial quality tests. The tested areas include urban, flat, agricultural and woods lands. Lately research have proposed building damage detection algorithms which use remote sensing technology. To estimate building damage detection and urban structural damage methods using UAV images and using 3D models' various authors described their possibilities (Torok *et al*., 2014; Fernandez *et al*., 2015; Maliki *et al*., 2016) The results shows that geometric parameters derived from the 3D point cloud can reveal damage indicators that are difficult to detect in the original imagery.

3 Case Study

The building was selected after taking into account the visible technical wear of the facade, the complicated shape and roof, and its location in a dense urban surrounding. The flight plan was established separately for each of the six facades and one for the whole roof, out in total there

were seven flights. The location in dense urban buildings required great caution during the flight. Usually during the flight there are variety of obstacles like the location of the sidewalks and the roadway next to the building caused the necessity of interrupting the flight when pedestrians or cars appeared, in particular the buses. Despite all these difficulties, the flight was carried out, which finally confirmed that the suggested solution can be used for the majority of buildings requiring a technical condition assessment.

For the experiment the DJI Inspire One lightweight quadcopter with the following specifications were used: weight: 2935g, vertical GPS accuracy: 0,5 m (accuracy determination), horizontal GPS accuracy: 2,5 m (accuracy of X, Y coordinates), Climb speed: 5 m/s, max. drop speed: 4 m s, max. cruising speed: 22m/s (ATTI mode, no wind), maximum flight height: 4500 m ASL (Above Sea Level), max. wind force:10 m/s, flight time: 18 minutes, operating temperature: -10 ° to 40 ° C, size: 438x451x301 mm. Digital camera (RGB sensor) has been used to obtain digital images with the following specifications: 12Mpix resolution (4000x3000), physical size 6.170mm x 4.628mm, focal length: 3.55mm. The flight weather condition was high humidity and transient slight rainfall, the temperature was about +5 degrees, wind at about 5 m/s (in gusts up to 10 m/s). As can be seen in Figure 1, despite the difficult weather conditions, vertical flight lines, including the assumed longitudinal and transverse overlap, have been preserved.

3.1 Digital Processing, Orthophoto Plans Generation and 3D Model

During the flight, 818 photos with a volume of 4.06 GB were made. As part of the inspection, no blurry photos were found and all of them were included in the processing process performed in the Pix4D software.

A desktop computer with the following parameters was used for processing: CPU: Intel (R) Core (TM) i7-2600 CPU @ 3.40GHz; RAM: 16GB; GPU: NVIDIA GeForce GTX 750 (Driver: 25.21.14.1694). The total processing time in the first iteration with standard processing settings was almost 7 hours:

Time for Point Cloud Densification - 3 hours. 44 min.

Time for 3D Textured Mesh Generation - 28 min.

Time for DSMGeneration - 42 min.

Time for Orthomosaic Generation - 1 hour. 42 min.

The following results of processing have been achieved:

GSD at the level of 0.36 cm / pix.

817 out of 817 images calibrated (100%), 1 image disabled.

1.93% relative difference between initial and optimized internal camera parameters.

Median of 13924.4 matches per calibrated image.

At this stage, it can be confirmed that the coating, despite the difficulties, was made correctly and the material can be used to generate the facade and roof elevation for the purpose of assessing the technical condition of the building. The final effect in the form of a 3D model generated in the 3rd iteration after cleaning the point cloud and recalculating the design is shown in Figure 2.

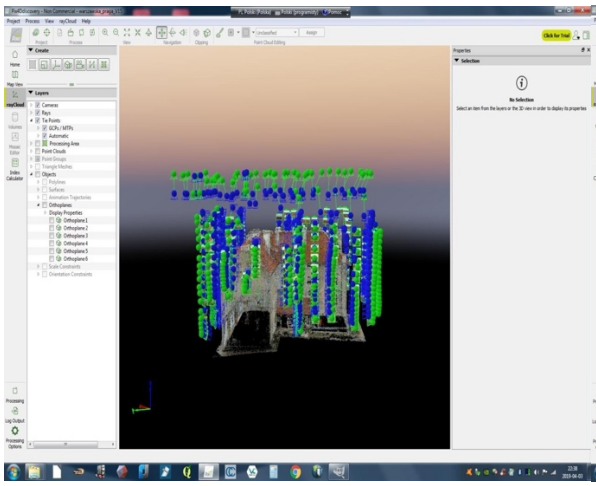

Figure 1. Location of images (view of the west facade).

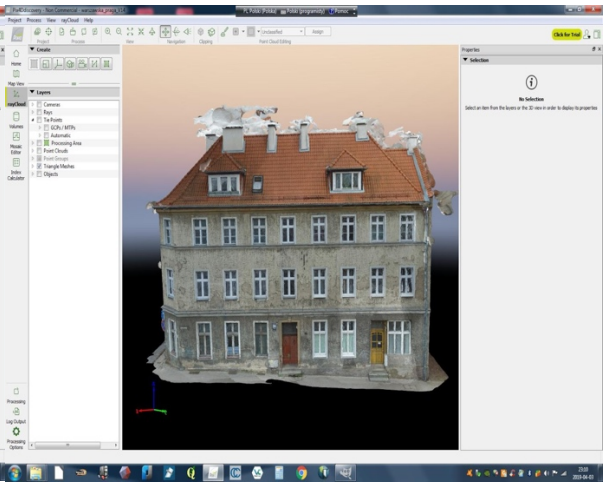

Figure 2. 3D model generated after three iterations.

Because of the GPS signal disturbances occurring during the raid, the data was processed in two blocks. Block I included the following elevations: south-west, west, north-west, north-east and a roof, and Block II included the south-eastern elevation.

On the one hand, it was necessary to enter the 11 manual tie point and reprocess the data to align the blocks. As a result, the cloud was generated in one block, and the inventoried object was characterized by the correct geometry, shape and proportions. Finally, the relative camera position and orientation of the uncertainties X, Y and Z was obtained at <0.025 for mean and <0.015 for sigma. On the other hand, it was also convenient to carry out manual cleaning and classification of the point cloud to generate a 3D model devoid of artifacts. (Figure 3 and Figure 4). This was long 6 hours process, but it resulted in the generation of a model practically free from contamination. The model allows it to be used for the visualization of selected, inventoried phenomena in 3D space in a natural way for the user. The carried-out process of cleaning the point cloud additionally influenced the quality of the generated orthophotoplanes of the facade and roof. In this stage, for each of the elevations an orthophotoplan separation was generated.

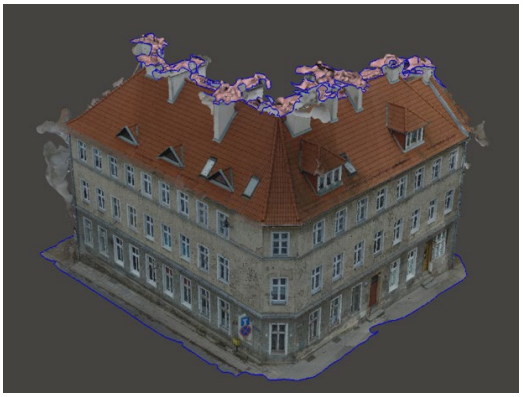

Figure 3. Visualization of the generated model in 3D space.

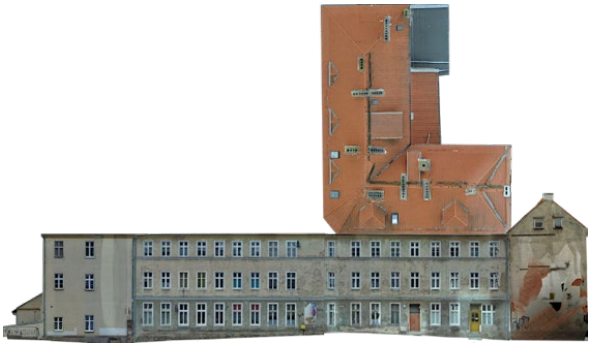

Figure 4. 3D model of an inventoried building in a flat projection.

3.2 A Square Grid and the Classification of Building Elements

In order to additionally view the selected image directly from the GIS application by indicating its center, the above-mentioned data should be enriched with the path to the directory in which the images will be ultimately stored. Good option for it is to use batch directory inventory software that saves data most often in a .txt file. Today's spreadsheets give us possibilities that can easily combine the contents of both files and generate a .txt or .csv file with the appropriate structure. The files prepared in such manner which are imported into the GIS software, after indicating columns containing the selected coordinates, enables visualization of image centers and preview of images directly from the application without the need to know their physical location. In case of image visualization in the orthophotomap area, we use the X and Y coordinates, in the case of orthophotos of elevations vertical Z and Y. During the. experiment it was generated a file consisting of 926 records, containing 5,556 attribute values. The next step to assign specific values of selected attributes for a previously defined part of the facade is to create a matrix of squares with an appropriate size. In our case study 40cm was chosen as a convenient.

The most required elements of the facade that are classified in the manual process include, parts of the geometry of the facade and the roof, window and the door joinery and architectural details. In further research with various assumed accuracy of the final inventory of all basic elements of the building one can be subjected to classic polygon vectorization (for the most accurate inventories) or indicated by assigning individual mesh squares a value corresponding to the inventoried elements (for the parts of inventory which requiring less accuracy). In case of this experiment, we used the second method and 5 classes of elements were defined: 1 - wall, 2 - molding, 3 - window, 4 - plinth, 5 - door (see Figure 5). Figure 6 shows the colorful identification of the elements.

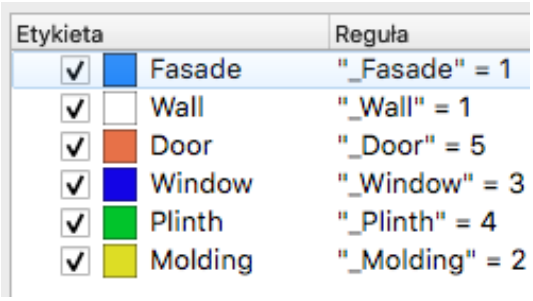

Figure 7. List of classes of identified facade elements.

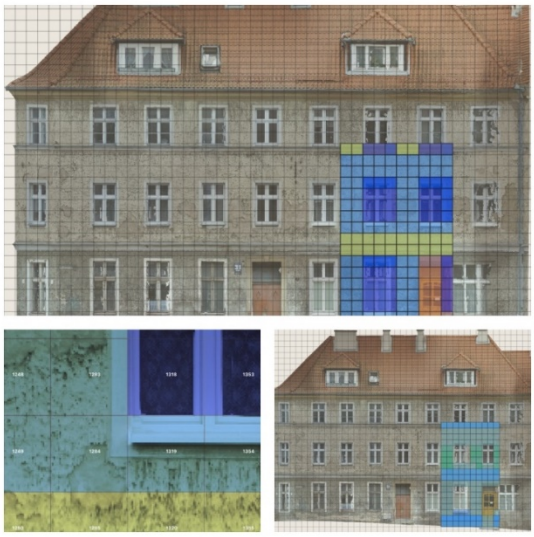

Figure 6. Ortophotoplan with completed qualification of inventoried elements.

3.3 The Visual Inventory of the Building

In the last stage, inspector carries out a visual assessment of the technical condition of the facade and determines the degree and type of damage on the basis of orthophotoplanes, looking at the square grid and classification table. Such implementation enables the automatic visualization of the technical condition in accordance with the indicated criteria and the determination of the area and position of each type of defects in the asset under inspection (Figure 7).

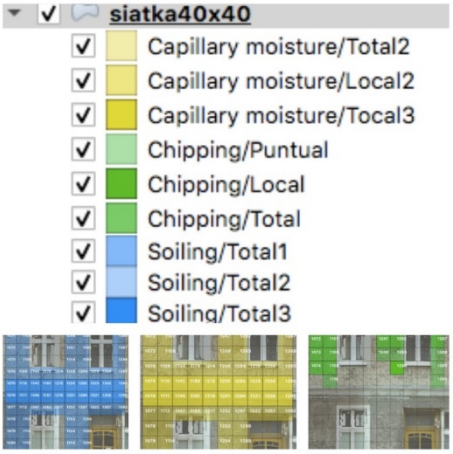

Figure 7. Visualization of different elements and damages identification.

4 Conclusions

The Full Interactive Visualization Method for Building Condition Assessment introduced in this paper, which is based primarily on high-quality digital information obtained from the deck of an unmanned aerial vehicle and good knowledge of inspector, proves to be the appropiate tool for the assessment of the technical condition of assets in residential areas. Digital images together with geoinformation data (photos, 3D model, orthophotos) with substantive data (facade element classification tables, damage classification tables) create a platform that allows intuitive access to view, to classificate, to edit and to perform the analysis of selected data, in two different modules:

- The 3D module enables the visualization of selected inventoried elements or characteristics of the asset under inspection in a 3D space in a natural way for the user and is most often used to carry out inspections and move around the model.
- The 2D module allows the technician to visualize selected inventoried elements or characteristics of the asset under inspection in a 2D space in a way that enables a more accurate and reliable identification, location, measurement and assessment.

The proposed platform provides to the users with a modern and efficient utility enabling full integration of the construction inventory process with BIM. In times when it is becoming difficult to arrange all work in a traditional form, due to the COVID-19 pandemic constraints, this tool optimizes the tasks of the different working groups. A proposal that makes feasible the situation in which the inspector's work can be efficiently carried out completely online.

Acknowledgements

This research has been partially supported by grants MTM2015-64465-C2-1-R (MINECO / FEDER) from the Ministerio de Economía y Competitividad (Spain) and 2017 SGR 622 from the Departament d'Economia i Coneixement de la Generalitat de Catalunya. Authors are grateful to the Laboratory of Photogrammetry and Remote Sensing (LFiT) Dron House S. A., Warsaw (Poland) its contribution in the technical part of using UAV technologies, as well as, to members of the IEMAE, LABEDI and GRASS-GRBIO groups their valuable comments and suggestions in the development of the work.

ORCID

Anna Banaszek: http://orcid.org/0000-0002-2744-2023
Sebastian Banaszek: http://orcid.org/0000-0001-6470-6270
Anna Cellmer: http://orcid.org/0000-0002-7872-6325
Vicenç Gibert: http://orcid.org/0000-0001-6341-5762
Carles Serrat: http://orcid.org/0000-0002-1504-5354

References

Alexis, K., Nikolakopoulos, G., Tzes, A. and Dritsas, L. (2009). Coordination of Helicopter UAVs for Aerial Forest-Fire Surveillance, in Valavanis K.P. (eds) Applications of Intelligent Control to Engineering Systems. *Intelligent Systems, Control, and Automation: Science and Engineering, 39*, 169–193, Springer, Dordrecht.

Asnafi, M. and Dastgheibifard, S. (2018). A Review on Potential Applications of Unmanned Aerial Vehicle for Construction Industry. *Sustainable Structures and Materials, An International Journal, 1*(2), 44–53.

Banaszek, A., Banaszek, S. and Cellmer, A. (2017) Possibilities of Use of UAVS for Technical Inspection of Buildings and Constructions. *IOP Conference Series: Earth and Environment Science, 95*, 032001, 1–6.

Banaszek, A., Banaszek, S., Cellmer. A., Gibert, V. and Serrat, C. (2019). A Fully Interactive Visualization Method for Building Condition Assessment. *IOP Conf. Ser.: Mater. Sci. Eng., 603*, 022011, 1–10.

Chen, Y., Zhang, J. and Min, B. (2019). Applications of BIM and UAV to construction safety. *CSCE Annual Conference*, 1-7.

Eschmann, C., Kuo, C.-M., Kuo, C.-H. and Boller, C. (2012). Unmanned Aircraft Systems for Remote Building Inspection and Monitoring, *6th European Workshop on Structural Health Monitoring, Th.2. B.1*, 1–8.

Fernandez Galarreta, J., Kerle, N. and Gerke, M. (2015). UAV-based urban structural damage assessment using object-based image analysis and semantic reasoning. *Nat. Hazards Earth Syst. Sci., 15*, 1087–1101.

Grosso, R., Mecca, U., Moglia, G., Prizzon, F. and Rebaudengo, M. (2020*).* Collecting Built Environment Information Using UAVs: Time and Applicability in Building Inspection Activities. *Sustainability*, *12*(11), 1–15.

Hallermann, N., Morgenthal, G. and Rodehorst, V. (2015). Unmanned Aerial Systems (UAS) – Case Studies of Vision Based Monitoring of Ageing Structures, *International Symposium Non-Destructive Testing in Civil Engineering (NDT-CE)*, Berlin, Germany.

Malihi, S., Valadan Zoej, M.J., Hahn, M., Mokhtarzade, M. and Arefi, H. (2016). 3D Building Reconstruction Using Dense Photogrammetric Point Cloud. *The International Archives of the Photogrammetry, Remote Sensing and Spatial Information Sciences, Volume XLI-B3*, 71–74.

Mesas-Carrascosa, F.J., Rumbao, I.C., Berrocal, J.A.B. and Porras, A.G.-F. (2014). Positional Quality Assessment of Orthophotos Obtained from Sensors Onboard Multi-Rotor UAV Platforms. *Sensors, 14,* 22394-22407.

Neto, J.M.M., da Paixo, R.A., Rodrigues, L.R.L., Moreira, E.M., dos Santos, J.C.J. and Rosa, P.F.F. (2012). A surveillance task for a UAV in a natural disaster scenario, in *2012 IEEE International Symposium on Industrial Electronics*, 1516–1522.

Nigam, N., Bieniawski, S., Kroo, I. and Vian, J. (2012). Control of Multiple UAVs for Persistent Surveillance: Algorithm and Flight Test Results, *IEEE Transactions on Control Systems Technology, 20*(5), 1236–1251.

Popescu, D., Ichim, L. and Caramihale, T. (2015). Flood areas detection based on UAV surveillance system. In *19th International Conference on System Theory, Control and Computing (ICSTCC),* 753–758.

Reineman, B.D., Lenain, L. and Melville, W.K., (2016). The use of ship-launched fixed-wing UAVs for measuring the marine atmospheric boundary layer and ocean surface processes, *Journal of Atmospheric and Oceanic Technology, 33*(9), 2029–2052.

Rubio, J.C., Vagners, J. and Rysdyk, R. (2004). Adaptive path planning for autonomous UAV oceanic search missions. In *American Institute of Aeronautics and Astronautics 1st Intelligent Systems Technical Conference, 6228*, 1–10.

Schaub, J., Hunt, B.P., Pakhomov, E.A., Holmes, K., Lu, Y. and Quayle, L. (2018). Using unmanned aerial vehicles (UAVs) to measure jellyfish aggregations. *Marine Ecology Progress Series, 591*, 29–36.

Semsch, E., Jakob, M. Pavlicek, D. and Pechoucek, M. (2009.) Autonomous UAV Surveillance in Complex Urban Environments. In *2009 IEEE/WIC/ACM International Joint Conference on Web Intelligence and Intelligent Agent Technology, 2*, 82–85

Serrat, C., Banaszek, A., Cellmer, A and Gibert, V, (2019). Use of UAVs for Technical Inspection of Buildings Within the BRAIN Massive Inspection Platform, *IOP Conference Series: Materials Science and Engineering, 471*, 022008, 1–9.

Serrat, C., Cellmer, A., Banaszek, A. and Gibert, V. (2019) Exploring Conditions and Usefulness of UAVs in the BRAIN Massive Inspections Protocol. *Open Engineering, 9*, 1–6.

Serrat, C. and Gibert, V. (2011). Survival analysis methodology for service live prediction and building maintenance. In *12th International Conference on Durability of Building Materials and Components, Porto, Portugal, vol. II,* 599–606.

Serrat, C., Gibert, V. Casas, J.R. and Rapinski, J. (2017). BRAIN: Building Research Analysis and Information Network. In *XIV International Conference on Durability of Building Materials and Components, Ghent, Belgium, 325*, 1–11.

Serrat, C., Gibert, V., Cellmer, A. and Banaszek, A. (2018). Quantitative comparison between visual UAV-based inspections for the assessment of the technical condition of building facades. In *Research and modelling in civil engineering*, J. Katzer, K. Cichocki and J. Domski (Eds), Koszalin University of Technology, 19–29.

Torok, M.M., Golparvar-Fard, M. and Kochersberger, K.B. (2014). Image-based automated 3D crack detection for post-disaster building assessment. *Journal of Computing in Civil Engineering, 28*(5).

Vacanas, Y., Themistocleous, K., Agapiou, A. and Hadjimitsis, D. (2015). Building Information Modelling (BIM) and Unmanned Aerial Vehicle (UAV) technologies in infrastructure construction project management and delay and disruption analysis. In *Proceedings of the Third International Conference on Remote Sensing and Geoinformation of the Environment*, 95350C.

Zischinsky, T., Dorffner, L. and Rottensteiner, F. (2000). Application of a new Model Helicopter System in Architectural Photogrammetry. *International Archives of Photogrammetry and Remote Sensing (IAPRS), 33*, B5/2.

XV International Conference on Durability of Building Materials and Components
DBMC 2020, Barcelona
C. Serrat, J.R. Casas and V. Gibert (Eds)

Identification of Defects and Hazards in Structures Based on the Point Cloud Using the OptD Method

Joanna Janicka and Wioleta Błaszczak-Bąk

University of Warmia and Mazury in Olsztyn, Institute of Geodesy, ul. Oczapowskiego 1, 10-719 Olsztyn, Poland, joanna.janicka@uwm.edu.pl, wioleta.blaszczak@uwm.edu.pl

Abstract. *Structural changes taking place in buildings and structures due to the passage of time are a normal phenomenon. However, the building objects are also adversely affected by atmospheric conditions or violent natural phenomena. Every year, our surroundings are increasingly attacked by extreme weather phenomena such as: floods, hurricanes, heavy storms with rain or extreme heat. Such phenomena are natural elements of nature, however they significantly interfere in the technical condition of the building. They often cause measurable economic losses: flooding, cracks, construction displacements and even their total destruction. At the time of estimating losses, calculating the costs of repair, and then making decisions about the method of restoration, a helpful tool can be laser scanning: terrestrial, airborne or mobile, depending on the character of the object and the size of the disaster. The paper presents an identification of defects and hazards in structures based on the point cloud using the OptD method.*

Keywords: *Buildings, TLS, OptD, Defects, Hazards.*

1 Introduction

Building objects are subject of the influence of various factors that affect their technical condition. Every day various types of atmospheric conditions and weather phenomena occurs (wind, snow, rain, sun) but there are also such as violent phenomena that are usually extreme (hurricanes, floods, earthquakes, etc.). Either way, when the technical condition deteriorates, engineering objects should be monitoring periodically or due to the impact of a sudden phenomenon.

Traditional methods of checking the condition of buildings are extensively time consuming, laborious, and expensive and pose health and safety threats to surveyors. They rely on the employment of building inspectors, who assess the technical condition. Inspections take a long time because they require many photos, drawings and notes. It sometimes happens that inspector has to return to the inspection site many times because not all relevant information has been registered. Therefore, further suggestions are being made to solve this problem, such as the use of wireless sensor networks or smartphone sensors (Noel A.B. *et al*.,2017), (Kong Q. *et al*., 2018). In addition, classic inventory may pose a threat to building inspectors, especially in hard to reach places or at heights (Perez H. Taha J.H.M and Mosavi A. 2019). Another factor that is important is the timing of inventory taking. In the manuscript authors (Perez H. Tahy J.H.M and Mosavi A. 2019) also noticed that clients are increasingly looking for fast and effective means to quickly and frequently survey and communicate the condition of their buildings. Therefore, the search for new ways to obtain a large amount of data in the shortest possible time is also a topic that appears in the area of conducting building monitoring.

Terrestrial laser scanning has been widely used for many years, especially when creating various types of architectural documentation. It can be also used to monitor various types of objects for example: buildings (Przyborski and Tysiąc 2018), forests (Liang X. *et al*., 2016), power lines (Maikainen, L. *et al*., 2016) etc.

It allows to collect a large dataset saved as a three-dimensional coordinates and intensity parameter. Having access to this type of data, one can conduct various types of analyses, simulations, calculations, etc. About effective use of both terrestrial laser scanning and the OptD method used to identify various defects in buildings one can read in manuscripts (Suchocki and Blaszczak-Bak 2019), (Sochocki *et al*., 2019).

2 OptD Method Description

TLS measurement technology is relatively simple, fast and effective technique for obtaining data, which one can then develop according to your preferences. The biggest problem for the operator is the size of the datasets. Many times, these are multi GB files. Data can be recorded with different resolutions ranging from tens of centimeters to single millimeters. The resolution and range of the measurement has an impact on the time of measurement but also on the final results.

Thus, obtaining data is only part of the task associated with the use of point clouds to identify defects and hazards in building constructions. If the object is scanned with high resolution, the acquired point cloud is a huge data set. Usually its original size is difficult to process because it requires high performance hardware. The solution to this problem is to reduce the point cloud by eliminating some points. Commercial programs usually contain basic methods of data reduction: random or with an assumed interval, etc. The disadvantage of doing so is that as a result of random reduction one can lose many valuable points associated with the geometrical features of the object. The proposal presented in this paper is to use the OptD method during data processing.

The OptD method has been already presented in papers (Błaszczak-Bąk 2016), (Błaszczak-Bąk *et al*., 2017), (Błaszczak-Bąk *et al*., 2018). This method was developed to reduce the dataset without losing the information that is necessary for the correct implementation of the planned task. It allows to reduce the dataset significantly, but preserving the characteristics of the object, and in particular, to obtain points representing the study object. The OptD method is carried out in the following stages by Suchocki and Błaszczak-Bąk (2019).

The diagram showing the principle of operation of the OptD method that was used during the tests is shown in Figure 1.

3 Description of Sample Objects

As it was mentioned at the beginning, one can distinguish construction objects that should be inventoried because they are deteriorating due to the passage of time or those whose technical condition has deteriorated due to an event related to the operation of nature. Regardless of the reason of the inventory, it happens that staying inside the inventoried object can be dangerous for the inspector, or there are uncomfortable conditions for longer staying. It may also happens that direct access to the defect is difficult or not available. The paper present selected cases that were the subject of measurement and with which the authors have personally encountered.

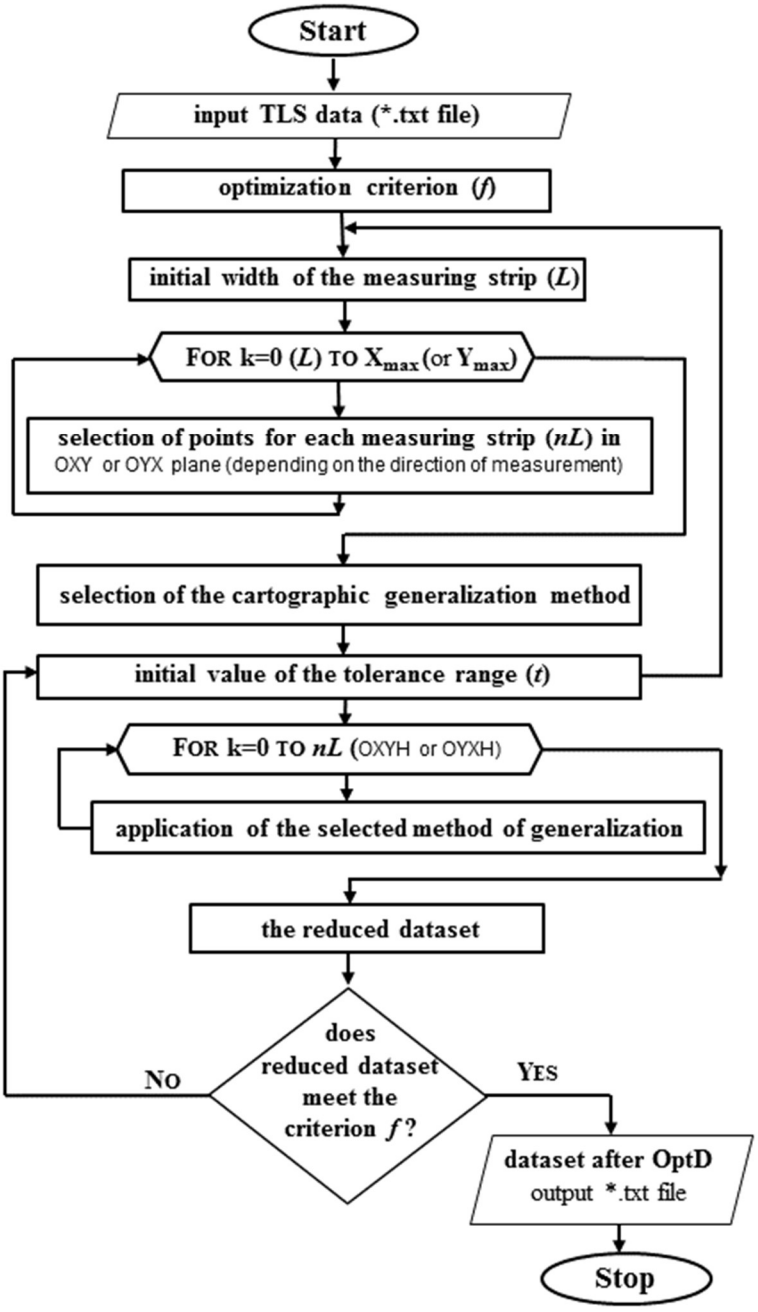

Figure 1. The scheme of the OptD reduction method.

Figure 2 presents the ruins of historic tower. In case of this tower's ruin important is to keep the fragments that are still in a quite good condition. Besides, in the underground of these

buildings there are also basements with no access to daylight. Due to the fact that there is no access to daylight or even artificial light and that the above ground remains of the tower are in a very poor condition, being in its underground is very dangerous. The technical condition of the basement is periodically checked and in this case, a terrestrial laser scanner can be a great tool because it doesn't require access to light during measurement**s.**

Figure 2. The ruins of historic tower.

The next object is a fragment of a retaining wall that supports the escarpment surrounding the primary school. The wall suffered because of a heavy downpour, therefore as a result of the natural phenomena The sudden and huge amount of water that fell on caused a lot of damage. Heavy rain eroded the area above the escarpment, and then the ground and water flowed down destroying the retaining wall. Figure 3 shows the fragments of the destroyed area.

Figure 3. Retaining wall destroyed as a result of heavy rain.

The last example is an object exposed to deformation due to subsidence. This is a church and monastery of Franciscan fathers in Barczewo, that was built in the 14th century. The Gothic church needs urgent renovation because its technical condition has deteriorated significantly.

The main reason is age and the unstable ground on which the church was built. As a result one of the church walls tilted significantly and cracked what is presented in Figure 4.

Figure. 4 Slanting church wall.

4 Results of the Processing Using OptD Method

Input point cloud is a very large dataset with the resolution of even single millimetres. Such a high resolution allows to present the tested object with high accuracy of details. However, it also happens that too densely distributed points on the scan, can hide some of the important information. The examples presented in this section show the advantages of reducing the output dataset using the OptD method. As a result of the reduction of the point cloud on selected objects, defects and hazards occurring on them were identified and presented in figures 5, 6 and 7.

Figure 5 shows detection of the basement brick wall defects using the OptD reduction. After the point cloud reduction with the proposed algorithm, those areas that have the greatest effects can be seen more clearly. OptD reduced the most points in areas that did not show significant changes in structure (in the middle of scanned object). In the area where the changes are larger, more points remain. This is visible at the bottom of the scan as a more intense green colour.

Figure 6 presents the second object and the result of the OptD reduction algorithm. The input point cloud (100 %) represents the measured object but it is difficult to observe this fragment of the wall that has been damaged. Reducing the data set by 95% allows to more accurately observe the area that is characterized by the largest defects in the wall.

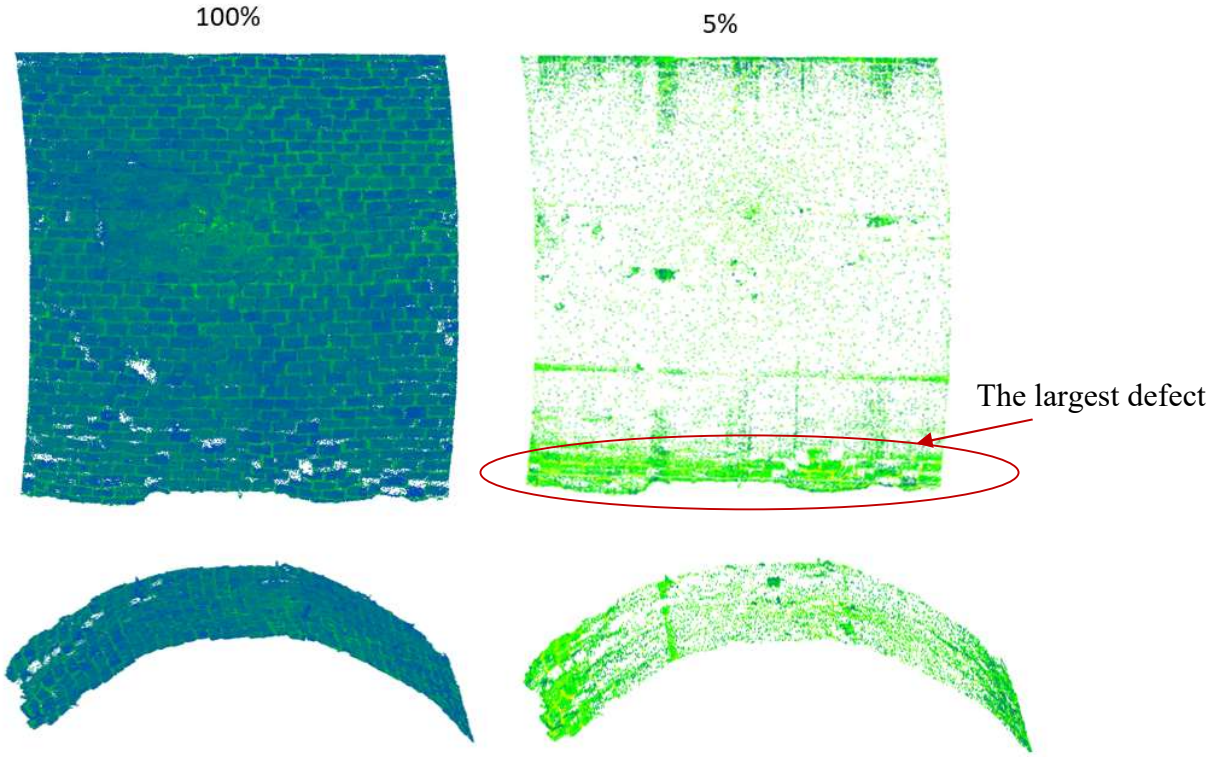

Figure 5. Detection of basement brick wall defects based on OptD: the input point cloud (100%) and the reduced dataset (5%).

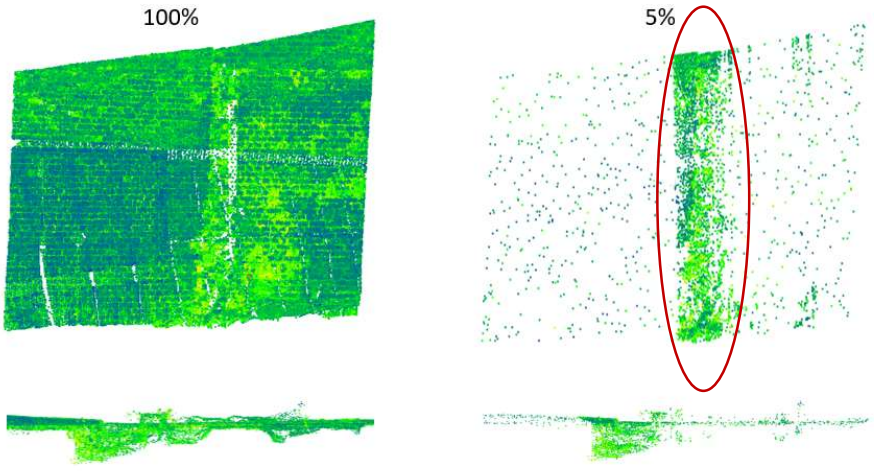

Figure 6. The retaining wall – input dataset and the reduced point cloud.

The last object is the wall of the church, which as a result of subsidence of the soil leaned out of the vertical and on its surface also formed cracks. Again, the reduction of points allowed to observe (in the form of a darker areas) the place of cracks (red line marked).

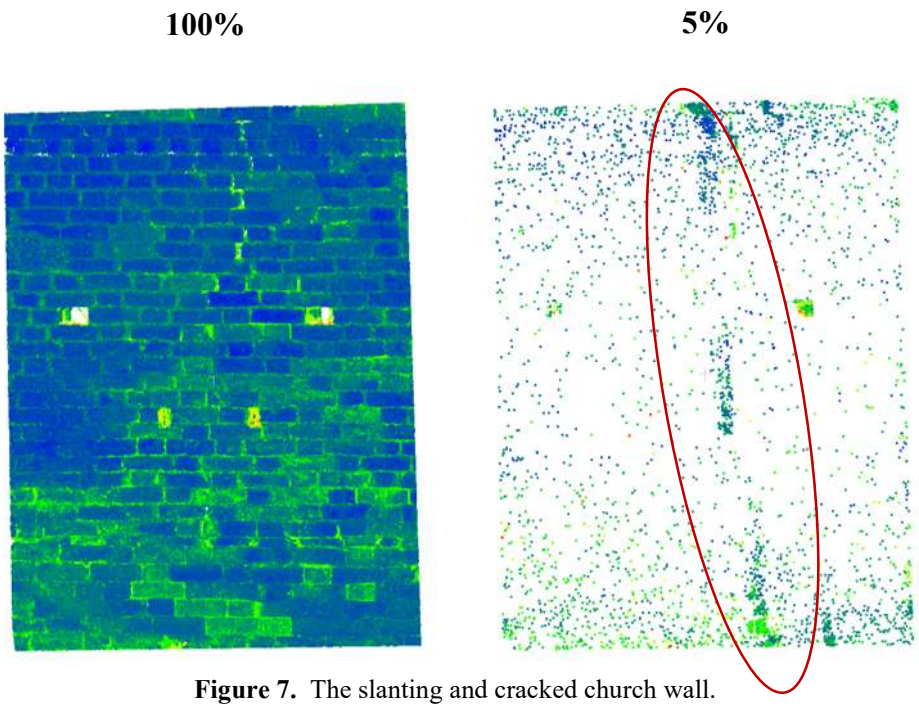

Figure 7. The slanting and cracked church wall.

5 Conclusions

Planning to measure using a terrestrial laser scanner, different approaches can be adopted. One can plan the measurement with lower resolution so that the distance between the measured points is several centimeters, and thus limit the data reduction process. Unfortunately, operator never knows exactly where the laser beam will reflect and which points will be measured and recorded. This may result in the necessity for re-measurements to udate missing information. One can also take measurements with high resolution but it takes more time, and the big dataset is obtained but a full set of information is available.

A good solution is to use the OptD reduction method in the processing of data obtained from laser scanning. The application of the OptD allows to keep more points of interest area where surface is imperfect (cracks and cavities) and reduce more points of the low interest homogeneous surface (redundant information).

ORCID

Joanna Janicka: http://orcid.org/ 0000-0002-1504-5354
Wioleta Błaszczak-Bąk: http://orcid.org/ 0000-0001-6169-1579

References

Błaszczak-Bąk, W. (2016). *New optimum dataset method in LiDAR processing*. Acta Geodyn. Geomater. 13, 381–388. doi:10.13168/AGG.2016.0020.

Błaszczak-Bąk, W. Koppanyi, Z. and Toth, C. (2018). *Reduction Method for Mobile Laser Scanning Data.* ISPRS Int. J. Geo-Information. 7, 1–13. doi:10.3390/ijgi7070285.

Błaszczak-Bąk,W., Sobieraj-Żłobińska, A. and Kowalik, M. (2017). *The OptD-multi method in LiDAR processing*. Meas. Sci. Technol. 28, 7500–7509. doi: 10.1088/1361-6501/aa7444.

Kong, Q., Allen, R., M. Kohler, M. D., Heaton, T. H. and Bunn, J. (2018). *Structural health monitoring of buildings using smartphone sensors*. Seismological Research Letters vol. 89, (2A), 594-602.

Liang, X. et al.,(2016). *Terretrial laser scanning in forest invetories*. ISPRS Journal of Photogrametry and Remote Sensing, Vol. 115. doi: 10.1016/j.isprsjprs.2016.01.006.

Matikainen L. (2016). *Remote sensing methods for power line corridor surveys*. ISPRS Journal of Photogrametry and Remote Sensing, Vol. 115. doi: 10.1016/j.isprsjprs.2016.01.006.

Noel, A. B. Abdaoui, A. Elfouly, T. Ahmed, M. H. Badawy, A. and Shehata, M. S. (2017). *Structural health monitoring using wireless sensor networks: A comprehensive survey.* IEEE Communications Surveys & Tutorials vol 19, (3), 1403-1423.

Perez, H., Tah, J.H.M. and Mosavi, A. (2019). *Deep Learning for Detecting Building Defects Using Convolutional Neural Networks*. Sensors 2019, 19, 3556.

Przyborski M. and Tysiac P. (2018). *As-built invenyory of the office building with the use of terrestrial laser scanning*. E3S Web of Conferences, Vol 26, doi: 10.1051/e3sconf/20182600011

Suchocki C. and Błaszczak-Bąk W. (2019). *Down-Sampling of Point Clouds for the Technical Diagnostics of Buildings and Structures*. Geosciences. 1–14. doi:10.3390/geosciences9020070.

Suchocki C., Błaszczak-Bąk W., Damięcka-Suchocka M., Jagoda M. and Masiero A. (2019). *An example of using the OptD method to optimization of point clouds in the buildings diagnostics*. 4th Jt. Int. Symp. Deform. Monit. (JISDM), Athens, Greece, 2019

Mobile Augmented Reality Application Supporting Building Facades Visualization

Michał Bednarczyk and Tomasz Templin

University of Warmia and Mazury in Olsztyn, Faculty of Geoengineering,
Institute of Geodesy and Civil Engineering

Abstract. *The use of mobile devices such as smartphones still increases over last years. Smartphone hardware capabilities are comparable with average personal computers. Thanks to the increasing computing power, their application is focused on more and more sophisticated and complex tasks. These includes among others augmented reality (AR) applications, which support precise GNSS localization and use signals from such devices like accelerometer or gyrocsope. They are able to create interactive, immersive real-time visualisation of any kind. The article presents a prototype Mobile Augmented Reality (MAR) Application for visualization of the building facades. It allows to support the original look of the building with the additional information from database. Software of this kind, can be used for overviewing, inspecting or work planning carried out on the facade of the building. As a part of the test, a prototype of the MAR application for Android has been prepared. Rest of the solution components have been presented in form of a concept, implementation of which is planned in near future. Basic technical assumptions are already developed, but details may change. The paper mentions also some important AR problems, especially positioning in urban environment and accurate registration of digital objects in the real world.*

Keywords: *Mobile Application, Augmented Reality, Technical Documentation of the Building, Spatial Information System of the Building.*

1 Introduction

The management of building maintenance is an important topic around the world, especially in recent decades, with the incorporation of tools to automate the tracking information and potential follow-up. From the social point of view it is illogical to leave the building stock without control. (Serrat, Gibert 2011) This is the reason why many companies and institutions invest in modern IT solutions to improve the process of ongoing buildings inspection. Data collected in this process are primarily: field data, cartographic data, cadastral data as well as plot building/facade data, architectural characteristics, existing elements and materials and the state of damages at the time of inspection. (Serrat, *et al*. 2016). Data collected reliably and systematically play a special role in monitoring and analyzing the degradation of building facades. In this way, the monitoring and maintenance of valuable historic buildings and the planning of ongoing renovations are significantly supported. (Gibert *et al.* 2014). The data analysis process is automated using various IT tools, including GIS systems, which are widely known and used in many fields. They allow to combine and process spatial data and non spatial data from many sources at the same time. This gives an ability to perform analysis, plan and undertake decisions in real world.

As observed in past years, there's been a new technology developed, which is called Augmented Reality (AR). It gives the ability to present data in a new way, not available before. AR means any system that “augments”, or overlays, the real world with digital

information that seems to co-exist with the real world. (Azuma 1997) Over the past few decades, this once theoretical field has matured into a mass medium (Ahonen 2012) with applications spanning countless industries. Speaking of AR, which is used in mobile devices, many authors (Höllerer, Feiner 2004; Henrysson 2007) use the term MAR (Mobile Augmented Reality), to clarify the scope of its application. AR technology, can be understood as a special video effect or real time digital image editing. It is similar to the techniques used in film editing or television. In this way, the illusion of "extending" or "augmenting" the observed reality with additional information and images can be obtained.

Generally, the combination of digital image with the real view is obtained by the use of the digital camera and the sensors like GPS/GNSS receiver, inclinometer, magnetometer, accelerometer, compass and other, which provide information about the location and orientation of the mobile device. Siltanen (Siltanen 2012) writes that AR technology connects two fields like:

- computer graphics needed for photorealistic rendering and interactive animations,
- computer vision used for marker and feature detection and tracking, motion detection and tracking, image analysis, gesture recognition and the construction of controlled environments containing a number of different sensors.
- Taking into account other technologies needed to develop a working AR application, also should be mentioned such fields as:
- GPS/GNSS and indoor navigation which is necessary in localization purposes. While GPS/GNSS navigation is quite accurate in open space, it doesn't work inside buildings nor under obstacles. Indoor should be used other navigation methods based on such technologies like *e.g.* WiFi or Bluetooth signal or image-based localization (Janowski, Bednarczyk 2016),
- digital cartography and mapping to provide spatial data presentation and georeference,
- WWW applications technologies, Service Oriented Architecture (SOA), Database Management Systems (DBMS) and other technologies for data storage, sharing and communication.

AR starts to be widely-used and ideas for its usage can be multiplied almost indefinitely. The most obvious and popular seems to be the usage in tourism, where tourist attractions, can be observed directly on the smartphone screen, giving additional information during the tour (Kounavis *et al.* 2012). Application of this technology can be found in many other fields, where presentation of spatial data is needed. For example in architecture AR is used to present the three-dimensional models of buildings, housing estates and cities, visualization of the construction details, including installation and equipment or interior designing and decoration (Broschart *et al.* 2013; Xiangyu 2009; VTT 2013). AR is also used in spatial designing and planning for presentation of three-dimensional scale models and visualizations of projects in a real environment. Augmented reality maps, the content of which is expanded with additional information, descriptions, graphics or 3D objects, also seems to be an interesting spatial data presentation form (Moloney, Bharat 2011).

Observing such a variety of applications, the hypothesis can be formulated, that AR technology can be helpful in the building inspection process. Generally, this process is based on a comparison of the current state of the object with the state from previous years. On this

basis, conclusions may be formulated regarding further actions. An important element here is the visualization of the current and historical state in the context of the building being under study.

2 How does Augmented Reality Work

AR Glossary, document published by the AR Community, mentions that augmentation means a relationship between the real world and a digital asset (AR Community 2017). It can be said that AR mixes virtual objects like graphics, sounds, videos,3D models etc. with the view of actual world. The effect of an augmentation is a composed scene. Augmentation may be formalized through an authoring and publishing process where the relationship between real and virtual is defined and made discoverable.

There are two primary techniques for image generation which lead to obtain the AR effect (Lechner 2015; AR Community 2017), they are:

1. Geospatial based Augmented Reality.
2. Computer-vision based Augmented Reality.

Figure 1. An example of geospatial based AR application supporting searching geodetic points in the field.

To compose a scene in geospatial based AR, algorithm needs the user's location and orientation in a geographic coordinate space. Determination of location is based on geo-positioning techniques such as GPS/GNSS, WiFi or other (e.g. Bluetooth). Sometimes, location can be determined by scanning specially prepared marker for that purpose. Device's orientation parameters like rotation, slope or direction are approximated, using sensors such as a digital compass, accelerometer or gyroscope. Once approximated device's orientation may be also refined by using computer vision techniques. The virtual object can be any digital object like image or icon. To place the virtual object in the right place on the screen and compose the AR scene, the real feature's location is also needed. The augmentation occurs when user is in the vicinity of real object and points on it with a device's camera. The software will automatically determine the location and orientation of the device and display respectively generated image (virtual object) on the screen (Lechner 2015). Figure 1 demonstrates the example of augmentation performed in described way. In this case there's a database of geodetic points, which are placed in the field. AR application connects to database of points and selects these, which are in the vicinity of the device. Then the augmentation process occurs and the searched point appears on the screen (Bednarczyk 2017(b)).

In computer-vision based AR, the computer vision algorithms are used to process the image viewed by the camera, and compare it with the reference images. Augmentation is obtained when application recognizes and identifies fragments of an image and displays on this place virtual objects. Figure 2 shows the example of augmentation performed this way. In this example, the reference images are created from raster image fragments of analog map. They represent each building on the map. Each building has it's individual virtual representation in a form of automatically generated icon with basic information acquired from GIS database. Furthermore each virtual icon has an interactive button "Details". When user directs the smartphone camera to the map, application recognizes the reference image and displays a virtual icon at this place. When user touches the “Details” button on the screen, application leeds him to additional information selected from database and displayed in a form of website (Bednarczyk 2017(a)).

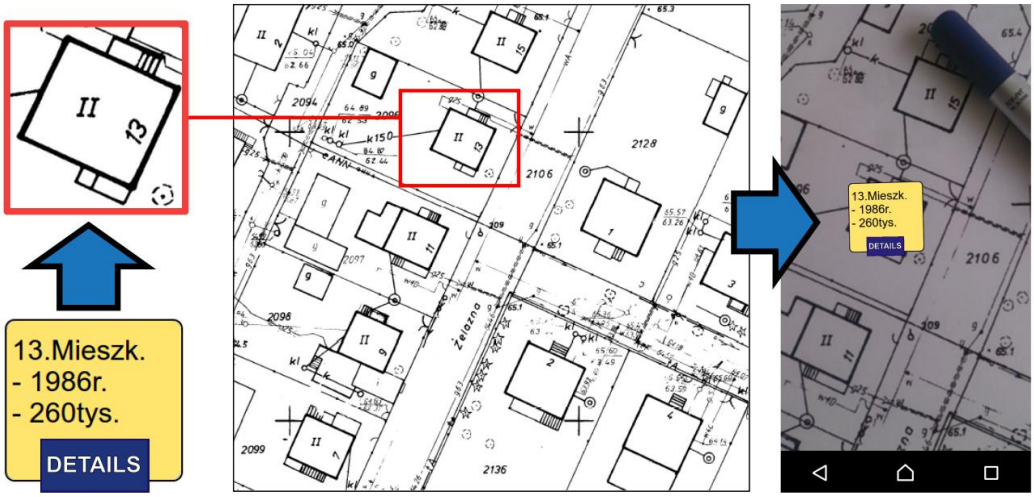

Figure 2. An example of computer-vision based AR on analog map.

3 Building Facade Visualization

As mentioned earlier, AR technology can be helpful in visualizing information about the state of the building facade during inspection. By mixing the real view of the object with the previously collected data, a direct comparison of the current and historical status can be obtained. A working prototype of the application, shown in fig. 3 uses computer-vision based AR to recognize the facade of a specific building. After that, an image (drawing) is overlayed that can contain any previously collected information related to the building, such as:

- descriptions and markings of construction elements
- descriptions and markings of defects and damages
- installation descriptions and markings
- interactive elements - to get additional information or perform an action in the application
- historical facade photos
- other useful information

Figure 3. Additional, sample information about building facade presented in AR mobile application.

At present, the application prototype is able to recognize the facade and display AR content. This software works in client-server architecture. Client application runs on a mobile device and is responsible for mixing and displaying the final image. Building the virtual "world" and sharing data is done on the server side. Further work will be focused on expanding the system's functionality.

First of all, it is needed to create an appropriate database of reference images like pictures of building facades. For the purposes of this experiment, a photo from Google Street View was used. It seems that in many cases this may be a sufficient source of images. However, this is a collection obtained automatically and, as a result, there is a risk that there may be photos taken at the wrong angle or some buildings may have been obstructed by obstacles (vegetation, people, vehicles, etc.). In addition, Street View vehicles do not visit every street or passage, but only the most important ones. Still, as of today, Street View appears to be the largest source of data of its kind.

Another important component is the inspections database of individual buildings. For testing purposes, the virtual image has been prepared manually in PNG format. It should be possible to save this data partially in vector format in a database. Thanks to this, it will be possible to generate virtual objects automatically.

To optimize performance and limit data transfer, the application should include an algorithm that allows selection of only those inspections that are closest to the observer. This can be solved by performing database queries taking into account GPS / GNSS location of the mobile device. If the proposed software is to be useful, in addition to viewing inspection data, it should be possible to edit it on site in real time. Thanks to this, inspection data could be supplemented based on the existing technical condition of the facade. All of proposed software should work under control, or be part of, more general system such as GIS or other

spatial information processing system of this kind. Schema of the conception of proposed AR system for building facades is presented in fig. 4.

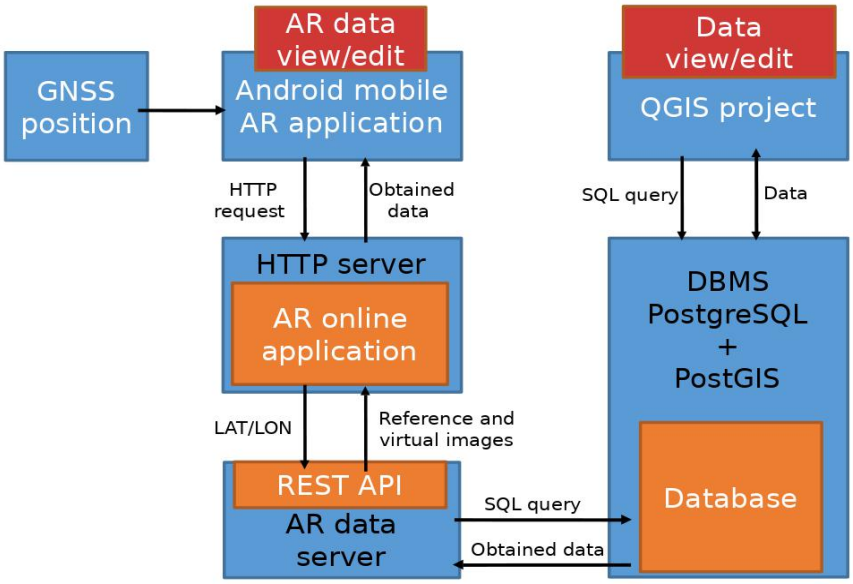

Figure 4. Components of proposed AR system for building facades.

4 Additional Observations and Results

In author's previous work on AR, some disadvantages have been observed in creating augmented reality scene (Bednarczyk 2017 (a,b)). In case of geospatial based AR, the problem is accuracy of GPS positioning, which influences quite significantly on AR virtual objects location displayed on the smartphone screen. If the GPS position error is small, AR marker indicates the destination with sufficient accuracy to identify the searched object - e.g. a geodetic point. For larger position errors, AR marker is positioned incorrectly in inappropriate place. Sometimes there is also a complete lack of GPS signal (e.g. in the forest, urban canion or while cloudy day), then the application does not work properly. This can be remedied by cutting off these observations that give too little accuracy in position determination. However, minor errors, if they occur frequently, will cause the effect of "swimming" or "jumping" virtual markers on the screen. In case of computer vision based AR, no such effects were found, but only point-oriented markers on small fragments of the analog map observed from a short distance - a few centimeters - were examined. In addition, their appearance was compact in form of an simple icon.

In this article, the virtual image covered larger area, the drawing was composed of many elements, and observation distance was several meters. In this case, it was observed that the position of the virtual image begins to deviate from the originally assumed, when changing view perspective or distance. Therefore, additional correction algorithms should be used to improve the generation of the AR scene in such cases, which will be considered in future work.

5 Conclusions

It can be assumed that visualization of building facades using AR can support the process of collecting data in the field. Using AR technology, one can display data from previous inspections, BIM, a database, or e.g. archival photos, overlaying them on the actual image of the building in real time in the field. Thanks to this, one can easily make a comparison with the existing state, make a quick view, take notes and decide whether to update the data.

However, in order to ultimately achieve the goal, further work needs to be done to refine the proposed solution. This applies above all to the system architecture, which should be expanded with appropriate components to ensure efficient and effective work, such as database of inspections and reference images. In addition, it is worth considering refining the algorithm responsible for generating the AR scene in case when observer changes the view perspective or approaches facade of the building.

Finally, considering the pros and cons of two different methods of generating an AR scene, it can be stated that, in case of facades visualization, computer vision based AR gives better results when creating an AR scene than geospatial based AR.

ORCID

Michał Bednarczyk: https://orcid.org/0000-0002-0450-5327
Tomasz Templin: https://orcid.org/0000-0003-2188-0097

References

Ahonen, T. (2012). Augmented Reality - the 8th Mass Medium: Tomi Ahonen at TEDxMongKok [online]. TEDx Talks [cited 20 November 2019]. Available from internet: http://www.youtube.com/watch?v=EvyfHuKZGXU&feature=youtube_gdata_player,

AR Community. (2017). AR Glossary [online]. AR Community for Open and Interoperable Augmented Reality Experiences [cited 20 November 2019]. Available from internet: http://www.perey.com/ARStandards/AR_Glossary_2.2_May_3.pdf

Azuma, R. (1997). A Survey of Augmented Reality. Presence: Teleoperators and Virtual Environments 6, no. 4 (1997): 355–385.

Bednarczyk M.(a), APPLICATION POSSIBILITIES OF AUGMENTED REALITY IN ANALOG MAPS, Geographic Information Systems Conference and Exhibition "GIS ODYSSEY 2017" Conference Proceedings, Italy 4th to 8th of September 2017, Trento, Vattaro, ISSN 2459-7627, http://gis.us.edu.pl/index.php/past-gis-conferences/24-gis-odyssey-2017

Bednarczyk M.(b), THE USE OF AUGMENTED REALITY IN GEOMATICS, 10th International Conference "Environmental Engineering", Vilnius, Lithuania, 27–28 April 2017, DOI: https://doi.org/10.3846/enviro.2017.162

Broschart, D. Zeile P. Streich B. (2013). Augmented Reality as a Communication Tool in Urban Design Processes, in REAL CORP 2013 Tagungsband Conference, 20-23 May 2013, Rome, Italy.

Gibert V., Serrat C. and Casas J.R. (2014). Determination of criteria for the exploration and for obtaining indicators in evolutional analysis of degradation in urban facades, in Proceeding of the 13th International Conference on Durability of Building Materials and Components, Sao Paulo, Brasil, 656-63.

Henrysson, A. (2007). Bringing Augmented Reality to Mobile Phones: Doctoral dissertation. Department of Science and Technology Linköpings Universitet, Norrköping.

Höllerer, T.; Feiner, S. (2004). Mobile Augmented Reality, Chapter 9 in Karimi, H.; Hammad, A. (Eds.). Telegeoinformatics: Location-Based, Computing and Services. Taylor and Francis Books Ltd., London, UK.

Janowski A., Bednarczyk M., (2016). Considerations on Indoor Navigation Based on Cheap Mobile Devices, 2016 Baltic Geodetic Congress (BGC Geomatics), At Gdańsk, Poland, DOI: 10.1109/BGC.Geomatics.2016.23

Kounavis, C. D. Kasimati, A. E.; Zamani, E. D. (2012). Enhancing the Tourism Experience through Mobile Augmented Reality: Challenges and Prospects. International Journal of Engineering Business Management, vol.4.

Lechner, M. (Ed.). (2015). OGC Augmented Reality Markup Language 2.0 (ARML 2.0). Open Geospatial Consortium.

Moloney, J.; Bharat, D. (2011). From Abstraction to Being There: Mixed Reality at the Early Stages of Design. International Journal of Architectural Computing 9, no. 1 (2011): 1–16.

Serrat C. and Gibert V. (2011). Survival analysis methodology for service live prediction and building maintenance, in Proceeding of the 12th International Conference on Durability of Building Materials and Components, vol. II, Porto, Portugal, 599-606.

Serrat C., Gibert V., Rapinski J., and Casas J.R., Followup and Decision (FAD) as a Strategic Tool for Building Stock Management, in Proceedings of the 2016 People, Buildings and Environment Conference, Luhacovice, Czech Republic, 2016.

Siltanen, S. (2012). Theory and applications of marker-based augmented reality. VTT Technical Research Centre of Finland.

Xiangyu, W. (2009). Augmented Reality in Architecture and Design: Potentials and Challenges for Application. International Journal of Architectural Computing, iss. 02, vol. 07, p.309-326.

XV International Conference on Durability of Building Materials and Components
DBMC 2020, Barcelona
C. Serrat, J.R. Casas and V. Gibert (Eds)

Out-Of-Plane Displacements Determination Based on the Analysis of Point Clouds from TLS Using the M-Split Estimation

Joanna Janicka[1], Jacek Rapiński[1], Wioleta Błaszczak-Bąk[1] and Czesław Suchocki[2]

[1]University of Warmia and Mazury in Olsztyn, Faculty of Geoengineering, ul. Oczapowskiego 1, 10-719 Olsztyn, Poland, joanna.janicka@uwm.edu.pl, jacek.rapinski@uwm.edu.pl, wioleta.blaszczak@uwm.edu.pl

[2]Koszalin University of Technology, Faculty of Civil Engineering Environmental and Geodetic Sciences, ul. Sniadeckich 2, 75-453 Koszalin, Poland

Abstract. *Building structures are exposed to the impact of various forces and natural phenomena. Earthquakes, heavy rains, displacements of land surrounding the building can have a significant and negative impact on the elements of buildings or entire construction objects. Terrestrial laser scanning technology can be successfully used to obtain data on changes in the structure of an object. This papier discusses the use of TLS as a measurement method for obtaining information on displacements and deformations that have occurred after heavy downpour. As a result of the rapid rain, the ground displacement occurred, which in effect led to damage to the retaining wall. The terrestrial laser scanning was used to measure the area covered by the displacements and the M-split method to model the obtained data.*

Keywords: *Buildings, TLS, M-split Estimation, Defects, Hazards.*

1 Introduction

Laser scanning technology allows to obtain a large amount of information about an object in a short time. For this reason, this technology is becoming increasingly popular also in buildings monitoring. Traditional methods of monitoring work require the involvement of building inspectors who assess the technical condition of the object. They take a series of measurements, drawings and photos and then the collected data are analysed. Sometimes it turns out that some information is missing or the inventory was not carried out correctly. In the classic approach to inventory, deficiencies in documentation require a re-visit to the site of inspection. Terrestrial laser scanning allows you to acquire data as a point cloud of varying accuracy. It is possible to measure an object with a resolution of 1 mm if such accuracy is required. Each measured point has three coordinates X, Y, Z and the intensity parameter. Thus, very detailed data about the object is obtained, that can be in the next step analyse.

Because some structures of building objects can be represented as vertices, lines, planes or others and can be described by a mathematical function. This gives the opportunity to automate the data processing what was discussed in many publication for example: Janowski and Rapiński (2013), Wang and Hsu (2007) and Zheng (2008). With this assumption it is possible to analyse for e.g. the building wall planarity, edge verticality or vertical and horizontal displacements. In the case of testing the displacement of two elements that constitute two

planes, the M_{split} estimation method can be used. The method developed by prof. Wisniewski (Wiśniewski, 2008), allows to split a functional model into two or more models, and thus identify for example two planes in the cloud of points. This paper presents the possibility of fitting planes into one cloud of points so that it is possible to identify fragments of two concrete slabs of the retaining wall that have been displaced due to ground displacement.

2 Msplit Estimation Description

The M_{split} estimation method assumes that every measurement result can be a realization of either of two or more different random variables. This estimation method was introduced by Wisniewski (Wiśniewski, 2008) and widely described in (Wiśniweski, 2009) and (Wiśniewski, 2010). Thus, based on the assumption that the functional model is split into two competitive model Y_α or Y_β each observation has its own "split potential"— the possibility to belong to one of the random variables. Therefore, the observation set $\mathbf{\Omega} = \{y_i : i = 1, 2, \ldots, n\}$ is a disordered mixture of the elements assigned to the random variables y_α or y_β in an unknown way. For that reason, each observation Y_i may have either of two competitive expected values $E_\alpha\{Y_i\} = E\{Y_\alpha\}$ or $E_\beta\{Y_i\} = E\{Y_\beta\}$. In this paper the functional model $\mathbf{V}=\mathbf{AX}+\mathbf{L}$ is split into two competitive ones which concern the same vector of observation $\mathbf{L}$:

$$\boldsymbol{split}\ (\boldsymbol{V} = \boldsymbol{AX} + \boldsymbol{L}) = \begin{cases} \boldsymbol{V_\alpha} = \boldsymbol{AX_\alpha} + \boldsymbol{L} \\ \boldsymbol{V_\beta} = \boldsymbol{AX_\beta} + \boldsymbol{L} \end{cases} \tag{1}$$

where $\mathbf{A}$ is a common coefficient matrix, $\mathbf{V}_\alpha$ and $\mathbf{V}_\beta$ are competitive vectors of random variables, $\mathbf{X}_\alpha$ and $\mathbf{X}_\beta$ are competitive parameter vectors. To achive this task the cross weighting procedure must be introduced. Estimation of competitive vectors ($\mathbf{X}_\alpha$ and $\mathbf{X}_\beta$) of parameters using the same observation vector L requires specially formulated of the objective function. The proposed method replaces function $\rho(v)$ with functions $\rho_\alpha(v_\alpha)$ and $\rho_\beta(v_\beta)$ according to the equation (2) and in compliance with the cross-weighting $\mathbf{V}_\alpha$ and $\mathbf{V}_\beta$. The weights of observations are modified according to the following equation:

$$\omega_\alpha(v_\beta) = \frac{\partial \rho_\alpha(v_\alpha)}{\partial(v_\alpha^2)}$$

$$\omega_\beta(v_\alpha) = \frac{\partial \rho_\beta(v_\beta)}{\partial(v_\beta^2)} \tag{2}$$

If $$\rho_\alpha(v_\alpha) = v_\alpha^2 v_\beta^2\,, \qquad \rho_\beta(v_\beta) = v_\beta^2 v_\alpha^2 \tag{3}$$

Then the weight functions can be written in the following form:

$$\omega_\alpha(v_\beta) = v_\beta^2, \qquad \omega_\beta(v_\alpha) = v_\alpha^2, \tag{4}$$

The idea of M_{split} estimation can be easily explained on the example presented in Figure 1.

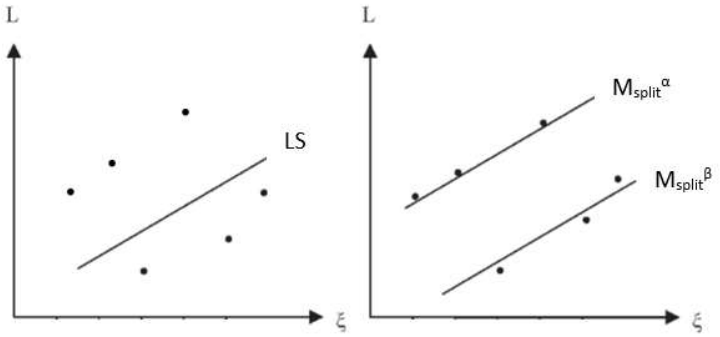

Figure 1. The idea of Msplit estimation and Least Square Method on the example of line fitting.

Figure 1 shows a line fitting using the least squares method and Msplit estimation. Similarly, one can fit two or more planes into a set of points by splitting the functional model into two or more respectively.

3 Application of M_{split} Estimation in Terrestrial Laser Scanning

Figure 2 shows the selected area of the retaining wall supporting the scarp. This scarp consists of several concrete slabs which as a result of the heavy rain were displaced and a crack was formed.

Figure 2. Two concrete slabs displaced due to ground washing.

The selected fragment shown in Figure 2 was measured using the terrestrial laser scanner. The scanning resolution set to 1mm /10 m. The crack, that formed as a result of the plates displacement is about 6-7 cm wide. The selected point cloud representing the displaced slabs and a crack is presented in Figure 3.

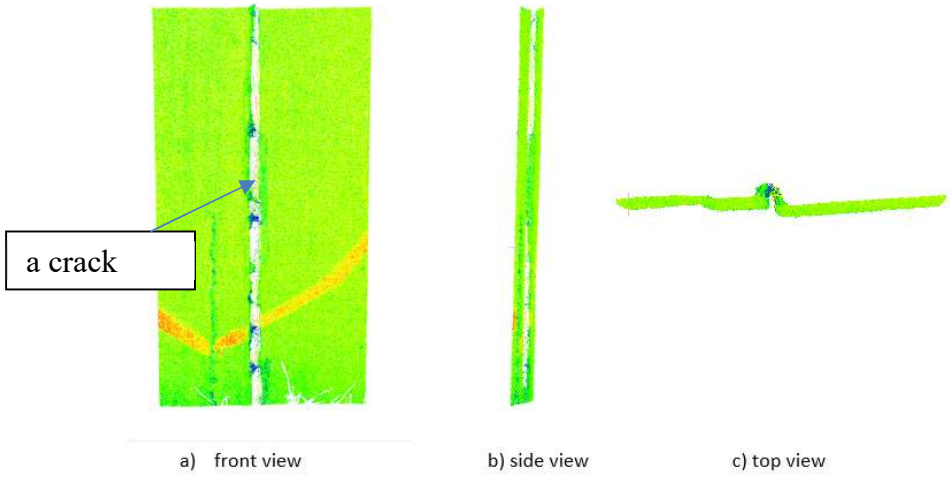

Figure 3. The selected point cloud representing two displaced slabs.

The classical approach would lead to fitting each plane separately with either manual selection of points or some search algorithm. To automate the process of fitting individual planes into the measured point cloud the M_{split} estimation method was used. The M_{split} estimation fitting results are presented in Figure 4 and Figure 5.

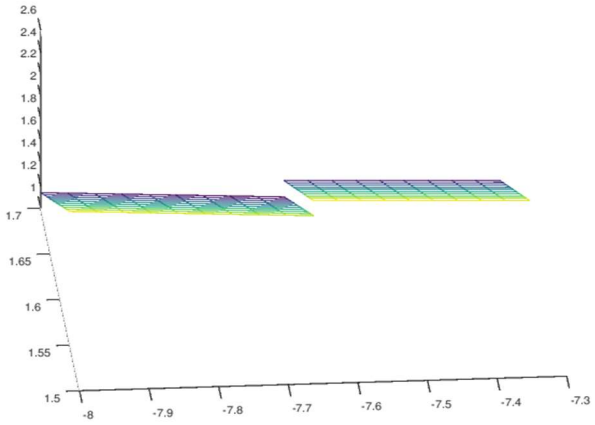

Figure 4. The result of fitting two planes into one cloud of points representing two concrete slabs of a retaining wall. Rotated view.

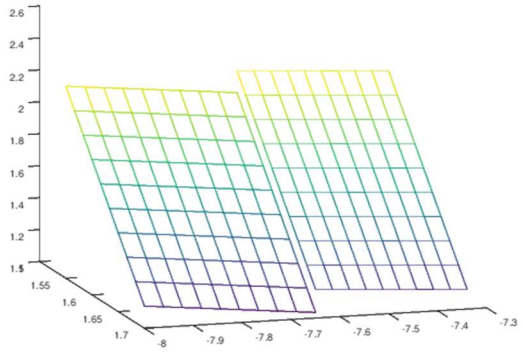

Figure 5. The result of fitting two planes into one cloud of points representing two concrete slabs of a retaining wall. Front view.

Figure 4 and Figure 5 present that the Msplit estimation can be successfully applied in two planes detection. As a result of the proposed algorithm two separate data sets were obtained. Thus, it was possible to automatically fit two planes representing displaced retaining wall slabs.

4 Conclusions

Displacements determination based on the analysis of point clouds from TLS using the M-split estimation can be successfully performed.

- The M_{split} estimation method can be successfully applied in detection of the adjacent planes.
- The M_{split} estimation method can be used assuming that the functional model is split into two models, thus it is possible to fit two planes into one point cloud.
- The possibility of fitting two planes allows for further analyzes, e.g. calculating the displacement of two plates, the distance between them and the angle of their inclination**.**

The proposed Msplit method has some disadvantages:

- as a result of TLS measuring a huge dataset (point cloud) is obtained, what affects the time-consuming data processing. So dataset should be reduced using an appropriate algorithm.
- the functional model must be selected very carefully in the terms of mathematical description of estimated model and data structure.

These topics will be the subject to further research and publications

ORCID

Joanna Janicka:http://orcid.org/ 0000-0002-1504-5354
Jacek Rapiński: http://orcid.org/ 0000-0002-8954-7963
Wioleta Błaczczak-Bąk: http://orcid.org/ 0000-0001-6169-1579
Czesław Suchocki: http://orcid.org/ 0000-0002-0121-5711

References

Janicka, J. and Rapinski, J. (2013). *Msplit transformation of coordinates*. Survey Review, Vol 45, No. 331, 269-274. doi: 10.1179/003962613X13726661625708 .

Wang, C. and Hsu, P. (2007). *Building detection and structure line extraction from airborne LiDAR data*. Journal of Photogrammetry and Remote Sensing, 12(4), 365– 379.

Wisniewski, Z. (2008). *Split estimation of parameters in Functional geodetic models*. Technical Sciences, 11, 202–212.

Wisniewski, Z. (2009). *Estimation of parameters in A split functional model of geodetic observations (Msplit estimation)*. Journal of Geodesy, 83, 105–120.

Wisniewski, Z. (2010). *Msplit(q)—estimation: Estimation of Parameters in a multi split functional model of geodetic Observations*. Journal of Geodesy, 84(6), 355–372.

Zheng, J., McCarthy, T., Fotheringham, A. S. and Yan, L. (2008*). Linear feature extraction of buildings from terrestrial LIDAR data with morphological techniques*. International Archives of the Photogrammetry Remote Sensing and Spatial Information Science, 37(part B1), 241–244.

XV International Conference on Durability of Building Materials and Components
DBMC 2020, Barcelona
C. Serrat, J.R. Casas and V. Gibert (Eds)

Verification of Building Constructions Surroundings Based on Airborne Laser Scanning Data

Maja Michałowska

University of Warmia and Mazury in Olsztyn, Institute of Geodesy, ul. Oczapowskiego 1, 10-719 Olsztyn, Poland, maja.michalowska@uwm.edu.pl

Abstract. *Light Detection and Ranging, as an active Remote Sensing Technology, enables gathering accurate, three-dimensional point cloud of scanned objects. Laser scanning might be provided on the terrestrial level for specific, defined constructions, as well as on the airborne level for aerial or linear objects. Using a laser sensor mounted on a moving platform is currently the most efficient way of obtaining in a short period, accurate positions of billions of points as a representation of a scanned area. Based on this kind of dataset it is possible to perform three-dimensional analysis of the safety of scanned objects without additional measurements in the field. This article presents the analysis performed in vMatic software on data from Airborne Laser Scanning for medium voltage power line verification of obstacles with the buildings. The analysis took less than 20 seconds for the detection of buildings points that are closer than 5m from conductors for seven spans wit a total length of almost 400m. Providing distance verification on 3D point cloud data is the fastest way to obtain a hazard awareness in a short time. Once acquired by LiDAR data can be used for other various analyses for any construction, depending on current, expected and future needs.*

Keywords: *Point Cloud, Laser Scanning, LiDAR, ALS, Remote Sensing, 3D Analysis, Hazards, Obstacles, Collisions, Power Lines.*

1 Introduction

Laser scanning is the most popular technology that enables obtaining accurate, three-dimensional point cloud of scanned objects in a short time. Scanning might be provided on the terrestrial level (Terrestrial Laser Scanning - TLS) for construction like architectural heritage (Pritchard *et al*., 2017), buildings (Karagianni, 2017), bridges (Truong-Hong and Laefer, 2015), and on the airborne level (Airborne Laser Scanning - ALS) using flying platform (airplane, helicopter, unmanned aerial vehicle - UAV), for aerial objects like forests (Hyyppä *et al*., 2012), environmental heritage, as well as for linear objects: power lines (Kwoczyńska and Dobek, 2016), roads, railways (Zhu and Hyyppä, 2014), etc.

Using a multi-sensors mounted on a moving platform, as a Mobile Mapping Technology (MMT), is currently the most efficient way of obtaining in a short time, accurate positions of billions of points as a representation of a scanned area (Tao and Li, 2020). MMT is using mostly in projects for aerial and linear objects reachable from a path of the mobile platform. Choosing a type of platform that carrying all technical equipment, have to be adjusted to the kind of object that have to be scanned and the purpose of the scanning. Using a car, as a mobile platform, for power line corridor scanning while there are no roads near the power lines, is not a good idea - it would be more propriety to choose a helicopter or a plane for this purpose. It has to be noticed that Airborne Mobile Mapping using airplanes or helicopters is much more expensive than using Terrestrial Mobile Mapping with a car as a moving platform.

doi:10.23967/dbmc.2020.148

1.1 Mobile Airborne Laser Scanning system

Mobile Mapping Systems (MMS) used in the ALS technique consist of among others laser scanner, Global Positioning System (GPS) receiver and Inertial Measurement Unit (IMU). The principle of the laser sensor is to release a pulse of infrared or near-infrared light, capture returned pulses and record the length of time the pulse reaches an object and is reflected to the sensor. Based on the recorded information distance to the reflected point from a laser scanner can be calculated. It's essential to record by GPS receiver using Global Navigation Satellite System (GNSS) a position of the flying platform and parallelly precise orientation of the laser scanner by IMU. This information is the key to calculate a highly accurate position in 3D dimensions of the laser scanner and all measured by scanner points during the acquisition.

2 Materials and Methods

2.1 Field Data

Vimap company, that provides MMT services for the energy sector, provided for research purposes a sample of a point cloud data acquired by Airborne Laser Scanning. Data was acquired in 2016, in Poland, near Ostróda city, for the MV power line corridor, as a test data for test flights before launching a commercial power lines ALS project. The sample test flight was done for about 400 m of power line in an urban area, which includes seven spans, from pole with a number of 14 to pole with a number of 19.

Vimap Mapping System was consisted of among other Riegl laser scanner, VUX1-UAV model, Trimble GPS receiver and IMU. All sensors were mounted on a helicopter. A mobile mapping platform with a mounted system presents Figure 2. The average flight altitude of the flying unit was approximately 40-50 m from ground level. Components of the system and flight parameters were set to fulfill requirements for the acquisition of 3D point cloud data of MV power line infrastructure and corridor of right-of-way.

Figure 2. Mobile platform with the measuring system.

Laser scanner that was used in the measuring system, Riegl VUX1-UAV, is dedicated to agriculture, forestry, archaeology, cultural heritage documentation, as well as corridor mapping for power lines, railway tracks, pipeline inspection, topography in open-cast mining and other.

Figure 3 presents Riegl VUX1-UAV laser scanner used in Airborne Laser Scanning (source: http://www.riegl.com/products/unmanned-scanning/riegl-vux-1uav/, 2020-04-13).

Figure 3. Laser scanner model used in ALS.

Technical parameters of the laser scanner, altitude and speed of the helicopter flight allow achievement of the density of 40 points per square meter. The technical specification of the laser scanner used in the Airborne Mobile Mapping System presents Table 1.

Table 1. Technical specification of the laser scanner used in the Airborne Mobile Mapping System.

Parameters	VUX1-UAV
Laser Pulse Repetition Rate	550 kHz
Max. Operating Flight Altitude	350m
Max. Effective Measurement Rate	500000 meas./s
Max. Scan Speed	200 ans/s

2.2 Point Cloud Data Elaboration

Acquired LiDAR data were processed in Riegl software. The accuracy of the measurement of horizontal coordinates (X, Y) RMSE = 0.05m, accuracy of point height measurement (Z) RMSE = 0.10m. The point cloud density equals 55 pts/m^2.

As the main reason for the Airborne Laser Scanning of MV power lines was to provide 3D analysis of the surroundings of the power line, two basic processes were needed - classification and power line modeling. In those steps, data was elaborated in TerraSoild and Microstation software.

2.2.1 Classification

Classifying of the LiDAR data into categorical object instances is the most critical step for further 3D analysis and modeling. It's a process of assigning a label to the points that represent a specified object, like the ground, building construction, power lines infrastructure, vegetation, etc. Classification allows us to group bunches of points into the specified representative of an object class, which helps to provide further 3D analysis. The correctness of classification has a big impact on the results of analyses that might be performed on classified data. Figure 4 presents a point cloud acquired by a laser scanner, as an input data for the classification process. Figure 5 presents the point cloud after classification.

Figure 4. Point cloud with no classification - color by point intensity.

Figure 5. Point cloud with classification.

Sample of acquired LiDAR data was classified semi-automatically - using an automatic segment-based classification strategy and manual corrections of segment-based classification. There were extracted objects of following classes: ground, building, vegetation, power line wires, power line pylons pipeline, paved road, unpaved road, water, railway and not classified. Figure 5 presents classified objects in the following colors: ground – light brown, building – red, vegetation – green, power line wires – yellow, power line pylons – blue, paved road – gray, not classified – white. Classified objects were set due to restrictions that have to be checked for a power line infrastructure on the point cloud data.

2.2.2 Objects Modeling

Poles and phase cables of the MV power line were digitized based on the point cloud and save to 3D ESRI shapefile. Visualization of the digitized 3D model in Google Earth Pro is presented in Figure 6.

Figure 6. Visualization of the digitized 3D model in Google Earth Pro.

2.3 vMatic Software

vMatic software, developed by Vimap company, enables point cloud presentation and automatic performance of three-dimensional analysis based on digitized 3D models. The user interface of vMatic software and visualization of point cloud and 3D model presents Figure 7.

Figure 7. vMatic software - visualization of ALS data.

vMatic software was designed mainly for the verification of the correctness of distances from power lines to nearby buildings, vegetation, ground and other objects that are close to the power line. The analysis in vMatic can be performed at the operating temperature of the power line, as well as at simulated, on any temperature conditions of the phase cables.

Classified LiDAR data and digitized 3D model of construction building - power line, are the basic inputs for 3D analysis in vMatic software. vMatic software allows detection of hazards to any 3D vector model. The collision searching mechanism is based on releasing a virtual cylinder with a radius specified by the user, along the course of the 3D model object and detecting whether the cylinder encounters points of the particular class.

3 Results

Based on acquired ALS data of the middle voltage power line corridor in an urban area, the detection of collisions with buildings was performed for digitized phase cables of the line for seven spans, from 14th pole to 19th pole (total length: 367m). Figure 8 shows the analyzed area on an orthophotomap, poles positions with their numbers are presented in yellow color.

Figure 8. Analyzed the MV power line corridor in the urban area.

The radius of a virtual cylinder was set at 5m. It means, that from each digitized phase cable detection of buildings point will be done in 5m distance and 360° range along the course of the conductor. The collision analysis for seven spans took 19 seconds in vMatic software.

Tool for automatic detection of building collision in 5m 3D range buffer from the power line conductors found in total 9 building obstacles. Two buildings were in a really close area to the power line, with the closest 3D distance equals 2.64m (span from 16th pole to 17th pole) and 2.77m (span from 17th a pole to 18th pole). One building was detected in 3.00 – 3.99m collision range, six buildings in a range from 4.00 m to 5.00m. The other fifteen buildings in the analyzed area weren't found due to 3D distance from power line wires to the building bigger than 5m. The results of the performed analysis with division into ranges of a 3D collision distance shows Table 2.

Figure 10 presents the visualization of buildings in the analyzed area highlighted in the range collision colors presented in Table 2. Buildings not treated as obstacles for the power line are presented in light green color.

Table 2. Results of performed buildings detections with a power line on LiDAR data.

Collision ranges distances	Found building collision	Span name with a distance of collision
0.00m - 1.99m	0	-
2.00m - 2.99m	2	16-17 2.64m 17a-18 2.77m
3.00m - 3.99m	1	15-16 3.85m
4.00m - 4.49m	2	18-19 4.12m 18-19 4.40m
4.50m - 5.00m	4	17a-18 4.56m 15-16 4.81m 15-16 4.84m 18-19 4.97m

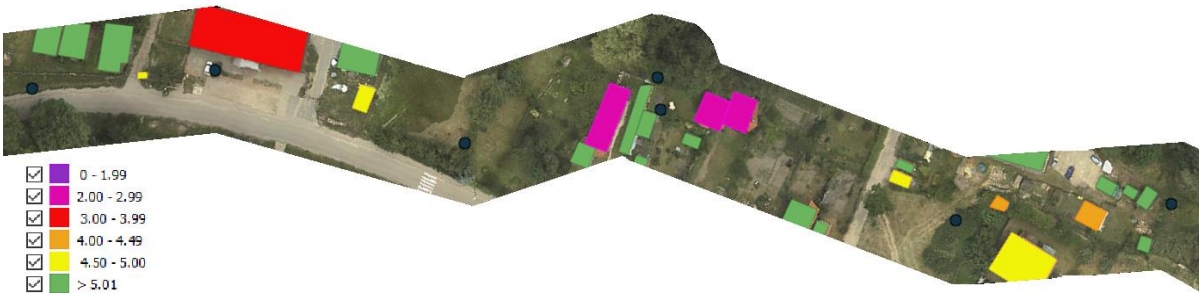

Figure 10. Buildings colored by a collision distance to the power line.

Figure 9 presents in vMatic software visualization of the closest collision from the power line wires to the building point with a distance of 2.64m (span from pole 16th to 17th). The point cloud is visualized in RGB colors, the area of collision of building points closer than 5m from power line wires is highlighted in red color.

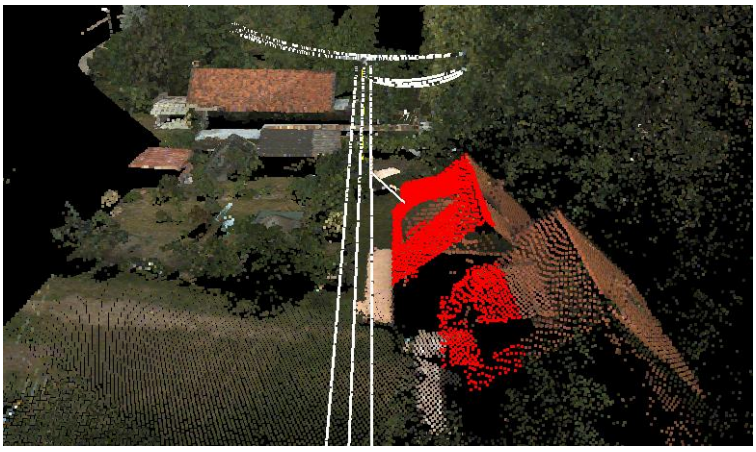

Figure 9. Found building close-up to the power line in vMatic software.

4 Conclusions

LiDAR data allows the performance of three-dimensional analysis for building constructions without any additional measurements in the field. Based on data gathered by remote sensing technology, verification of any construction surroundings can be performed in dedicated software to ensure the safety of the objects.

Performed in this article analysis of the power line obstacles were detected in vMatic software. The analysis took less than 20 seconds for the detection of buildings points (closer than 5m from conductors) for almost 400m length of the MV power line. vMatic software detected nine buildings that are too close to the power line.

Data from laser scanning, as a true representative of scanned objects/areas, might become a basic, complete product for providing 2D and 3D analysis. The results of the analysis performed on LiDAR data are reliable. Providing distance verification on 3D point cloud data is the fastest way to obtain a hazard awareness in a short time. Once acquired by LiDAR data can be used

for other various analyses for any construction, depending on current, expected and future needs.

ORCID
Maja Michałowska: http://orcid.org/0000-0002-5321-7946

References

Hyyppä, J., Yu X., Hyyppä, H., Vastaranta, M., Holopainen, M., Kukko, A., Kaartinen, H., Jaakkola, A., Vaaja, M. and Koskinen, J. (2012). *Advances in Forest Inventory Using Airborne Laser Scanning*. Remote Sensing 4 (1 December 2012), 1190–1207.

Karagianni, A. (2017). *Terrestrial Laser Scanning in Building Documentation.* Civil Engineering and Architecture 5.6 (2017) 215 - 221.

Kwoczyńska, B. and Dobek, J. (2016). *Elaboration of the 3d Model and Survey of the Power Lines Using Data from Airborne Laser Scanning*, Journal of Ecological Engineering 17 (1 September 2016): 65–74.

Pritchard, D., Sperner, J. Hoepner, S. and Tenschert, R., (2017). *Terrestrial Laser Scanning for Heritage Conservation: The Cologne Cathedral Documentation Project*, IV-2/W2:213–20.

Tao, V. C. and Li, J. (2020). *Advances in Mobile Mapping Technology*, 5 February 2020, Advances in Mobile Mapping Technology: ISPRS Series, volume 4.

Truong-Hong, L. and Laefer, D. F. (2015). *Documentation of Bridges by Terrestrial Laser Scanner*, IABSE Symposium Report, 105(19), 1–8.

Zhu, L. and Hyyppä, J. (2014). *The Use of Airborne and Mobile Laser Scanning for Modeling Railway Environments in 3D,* Remote Sensing 6 (4 April 2014): 3075–3100.

http://www.riegl.com/products/unmanned-scanning/riegl-vux-1uav/ 2020-04-13

XV International Conference on Durability of Building Materials and Components
DBMC 2020, Barcelona
C. Serrat, J.R. Casas and V. Gibert (Eds)

Durability in Marine Environment of High-performance Concrete with Electric arc Furnace Slags and Cupola Slag Admixture

Israel Sosa, Carlos Thomas, Juan Antonio Polanco, Jesús Setién and Pablo Tamayo

LADICIM (Laboratory of Materials Science and Engineering), University of Cantabria. E.T.S. de Ingenieros de Caminos, Canales y Puertos, Av.Los Castros 44, 39005 - Santander, Spain.
ladicim@unican.es

Abstract. *Obtaining new building materials that are more environmentally friendly than the traditional and that guarantee an optimal response to the most demanding conditions, is one of the greatest challenges in the science of materials. The use of electric arc furnaces slags (EAFS) and cupola slag (CS) to produce a structural self-compacting concrete (SCC), involves the valorization of industrial by-products that often end up in landfill and avoid the extraction of a natural resource. The potential qualities of these wastes make them desirable for the production of high quality concrete. High-performance concrete mixes are designed taking advantage of the high stiffness, the peculiar geometry and the high strength of the EAFS, as well as the high pozzolanicity of the cupola slag. There are great benefits at the mechanical level with its use, but it is necessary to know more about its durability. Different mixes using basalt aggregates and silica sand are used to compare the effects of using EAFS and cupola slag admixture in mixes that have been subjected to durability tests. These tests consist of the determination of chloride ion penetration and protection against reinforcement corrosion after 10 months of exposure in tidal race. The comparisons made after subjecting the different mixes to these tests allow to conclude that chloride ions penetrate almost twice with EAFS than with natural aggregates, while no corrosion of the bars has been shown in any of the mixes.*

Keywords: *Durability, EAFS, Cupola Slag, Chloride Ions Penetration, Corrosion.*

1 Introduction

Obtaining high-performance self-compacting concrete (SCC) with EAFS is a novelty, and its durability plays an important role in its application as a structural material. As a novelty as well, it is proposed to determine its response to the chlorides penetration in a marine environment, and to check the corrosion conditions of the rebar under the same conditions.

The durability of the concrete strongly depends on the fluid circulation capacity through its microstructure, being the capillarity of the material and the paste-aggregate interfacial transition zone, the main route of penetration of external agents. One of the main causes of the deterioration of concrete are the attacks by chlorides and sulfates, and the kinetics in which the degradation mechanisms act, are related to temperature, humidity and fluid transport capacity (Ministerio de Fomento de España, 2008). Before analyzing the response of the SCC against the causes of deterioration of concrete, it is important to take into account that the microstructure of the SCC depends on factors such as the water/fines ratio, the type and content of admixtures, the type and proportion of additives or the mixing procedure (De Schutter and Audenaert, 2007).

Chlorides in concrete can come from its components, because they are totally or partially submerged in seawater or by occasional contributions on the surface, in the form of salts for thawing on roads or through salty fog due to their proximity to the coastline.

The chloride ion penetrates the concrete pore network normally dissolved in water, one part is chemically bonded with the tricalcium aluminate of the cement to form the Friedel salt, another part is immobilized by physical bonds and the rest in the form of free chlorides in the pore solution (E. Medina, 2013). Depending on the concentration of free chlorides, pitting corrosion of the reinforcing steel rebars may occur. Additionally, when the water evaporates inside the pores, the salts crystallize generating, due to the increase in volume, internal tensions in the concrete and, consequently, cracks.

The response of the SSC against the penetration of chlorides depends on the pore structure and the ionic composition thereof. Zhu and Bartos (Zhu and Bartos, 2003) conclude that the diffusion of the chloride ion depends on the type of admixture used. Additionally, they comment that the penetration of chlorides is not less for the SCC with the same strength or manufactured with the same water/cement ratio as for a conventional vibrated concrete (CVC). Other authors have observed that chloride ion penetration decreases with the use of admixtures, especially those of a pozzolanic nature (Uysal and Yilmaz, 2011).

Thus, it is considered necessary to establish the behavior of these new SCC against aggressive environments, due to the variability on which their response depends. Four SCC mixes that incorporate natural and siderurgical aggregates will be tested, in addition to traditional and siderurgical admixtures. Reinforced concrete conical specimens of 28 days of age have been submerged for 10 months, then they were sectioned and the depth of the chlorine ion and the degree of corrosion in the reinforcement have been assessed.

2 Materials and Methods

2.1 Materials

Table 1. Concrete mix proportions (kg/m^3).

Concrete mix	SCC-DC-LF	SCC-DC-FA	SCC-DC-CS	SCC-SC-CS
Diabase coarse (DC)	896	896	896	-
Slag coarse (SC)	-	-	-	1101
Diabase sand (DS)	411	411	411	-
Silica sand (SIS)	386	386	386	605
Slag sand (SLS)	-	-	-	444
Limestone filler (LF)	100	-	-	-
Fly ash (FA)	-	80	-	-
Cupola slag filler (CS)	-	-	109	109
Cement	450	450	450	450
Water	180	180	180	174
Superplasticizer additive	9	9	9	9
w/c ratio	0.40	0.40	0.40	0.39

Four concrete mixes have been manufactured, using CEM I 52.5 R, sand 0/6 (diabase and EAFS), coarse 6/12 (diabase and EAFS) and silica sand 0/2, to compare the behavior of the siderurgical aggregate with the natural aggregate. In addition, three different filler materials (limestone, fly ash and cupola slag) have been used. A SCC has been designed according to the procedure described by Dinakar et al. (Dinakar et al., 2013) with a 2% (of the cement weight) of a superplasticizer additive, in a 120 l rotating drum mixer with a kneading time of 12 min. The concrete mix proportions appear in Table 1.

2.1 Methods

2.1.1 Preparation of the Specimens

The test campaign for the characterization of the durability of hardened concrete consists of exposure to seawater of conical specimens with embedded corrugated steel bars. For the manufacture of each specimen, an Abrams cone with the face of smaller diameter as a base, has been used to facilitate filling of the specimen, following the methodology described by C. Thomas *et al*. (Thomas *et al.*, 2013). In its interior two corrugated bars of diameter 10 mm have been placed vertically, arranged in such a way that the minimum covering of one of the bars at the base of the cone is 10 mm while, in the second bar, it is 30 mm, Figure 1.
This configuration has been designed with the objective of evaluating the protection against corrosion offered by self-compacting concrete made with coating thicknesses lower than those recommended. The conical geometry of the specimens and the vertical orientation of the bars allows the penetration of the chloride ion to different coating thicknesses.

In Figure 1 can be seen that, in addition to the corrugated bars, a black metal part has been embedded in order to facilitate the manipulation of the specimens, avoiding any kind of effort in the steel that can affect the adhesion between both materials.

The mixing time has been sufficient to guarantee the homogenization of the concrete, the filling of the molds and the specimens has been done in a single step and without external vibration. A total of 8 conical specimens were manufactured, corresponding to two specimens for each mix.

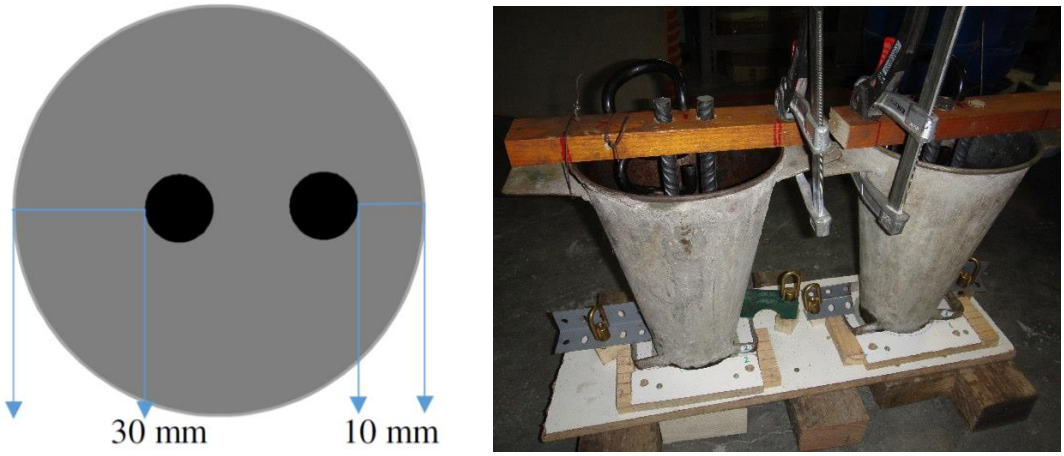

Figure 1. Arrangement of reinforcement bars on the underside of the cone and preparation of the truncated conical molds.

To ensure that the penetration of chlorides only occurs in the lateral surface of the cone, the upper and lower faces have been protected, as well as the sections of corrugated bars that protrude from the concrete with a thick layer of two-component epoxy coating, Figure 2.

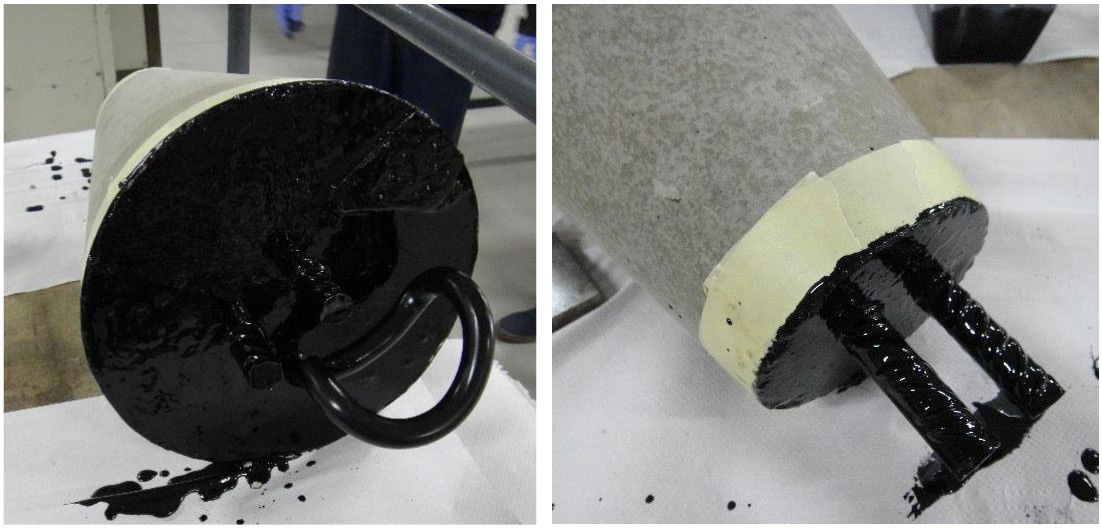

Figure 2. Detail of the application of the paint on the bases of the specimens and on the reinforcements.

After keeping the specimens in the humidity chamber for 28 days, one of each mix was transferred to the port of Bilbao. There they were distributed on two metal grids together with other specimens from other research centers (Figure 3 left). With the help of a crane, the grilles were suspended a few centimeters from the surface of the sea leaving the specimens exposed to tidal changes for 10 months, (Figure 3 right).

Figure 3. Arrangement and location of test samples in tidal race in the port of Bilbao.

2.1.2 Specimens Treatment

After 10 months, the specimens were removed and moved back to the laboratory. During the visual inspection, the abundant presence of mollusks adhered to the surface of the concrete specimens, the corrugated bars and the steel hook was observed (Figure 4). In the areas where

these colonies were not present, the formation of an organic greenish layer was observed.

Figure 4. Appearance of the specimens after exposure to the weather and tidal cycles.

With the help of a crowbar, the mollusks stuck in the concrete were removed, while those attached to the bars and the metal piece were crushed with a hammer. The surface was then rubbed with a scourer to remove the organic layer (Figure 5). Finally, they were rinsed and placed in the oven at 110 ± 5 °C until constant mass.

Figure 5. Appearance of samples before and after cleaning.

Finally, on each truncated conical specimen, two diametrically opposed longitudinal cuts were made with a radial cutter without the cutting disc reaching the corrugated bars.

2.1.3 Corrosion of the Bars and Penetration of Chlorine Ions

After breaking the truncated concrete cone into two halves, we first proceeded to observe the state of the bars mainly to assess the appearance of pitting along them. One of the halves was divided by a cross-section in order to extract a subsample with different coating thicknesses, which is used to determine, in the scanning electron microscope, the penetration depth of the chloride ion by dispersive spectroscopy of X-rays (EDX) techniques.

3 Results and Discussion

Figure 6 shows the appearance of the specimens after continued exposure to the marine environment and to the tidal race for 10 months, after cleaning the exterior faces and the longitudinal cut.

Figure 6. Exterior of conical specimens SCC-DC-LF, SCC-DC-CS, SCC-DC-FA and SCC-SC-CS after exposure to contact with seawater.

The absence of pathologies on the outside of the cone trunks can be verified as chipping or loss of material, while, in Figure 7, the intact state of the bars inside the concrete can be seen after making a longitudinal cut in the specimens. Direct exposure to seawater has not negatively affected embedded steel bars, with no deterioration observed. It should be noted that in the narrowest area of the specimens, the minimum coating thickness is only 10 mm.

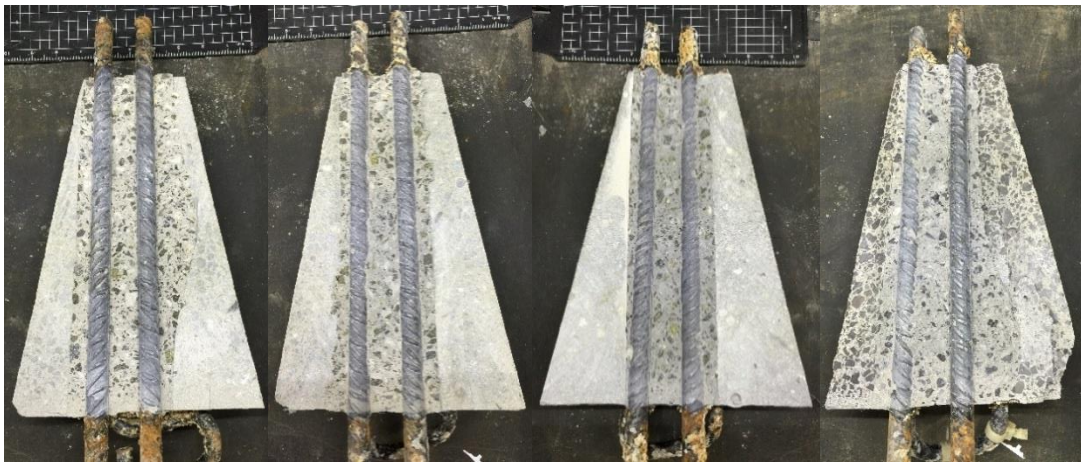

Figure 7. Inside of the SCC-DC-LF, SCC-DC-FA, SCC-DC-CS and SCC-SC-CS specimens after exposure to seawater.

Figure 8 shows in detail the appearance of the steel bars at the narrowest end of the conical specimens for the SCC-SC-CS mix. In some cases, pitting corrosion is observed in the bars, caused by the penetration of seawater from the top of the specimen as a result of the loss of the applied waterproofing paint.

Figure 8. Aspect of SCC-SC-CS and rebars after exposure to tidal race.

Due to the appearance of the steel bars inside the concrete, the cut was only made at the smaller diameter end of the cone to determine the penetration of the chloride ion in a scanning electron microscope.

Figure 9 shows the chloride concentration in the concrete obtained by microanalysis carried out from the outermost surface to the area where the steel bars are embbeded. It is observed, as expected, that the highest concentration is found on the surface. Of all the samples, the SCC-SC-CS has a much higher concentration of chlorides, while samples made with natural aggregates, despite containing different additions, have a very similar chloride content.

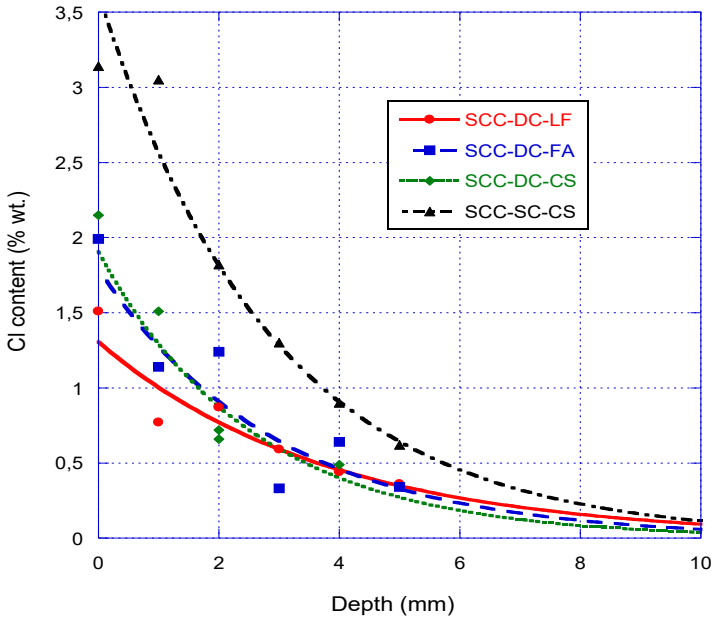

Figure 9. Penetration of chlorides in concrete.

These results agree with the oxygen permeability coefficients (Sosa et al., 2020), being able

to assume that the diffusion is carried out through the capillaries. In all the cases analyzed, it can be seen that, after 6 mm, the concentration of the Cl^- ion is less than 0.3%, which is at the limit of the detection capacity of the scanning electron microscope for this element. These results are markedly lower to those reported by C. Medina et al. for a CVC with recycled aggregates (Medina, Sánchez De Rojas, Thomas, Polanco & Frías, 2016).

4 Conclusions

In the present study, the durability of 4 concrete mixes incorporating aggregates and admixtures, both slag and natural, has been analyzed. This characterization has been carried out keeping the specimens in a tidal race, where both the marine environment and the submersion cycles can deteriorate the material prematurely. The main conclusion drawn is the following:

Exposure to seawater and the tidal race for 10 months has not affected the aesthetics, nor has it corroded steel reinforcements embedded in concrete. The concentration of chlorides in all cases is very small from 6 mm deep.

ORCID

Israel Sosa: https://orcid.org/0000-0003-1087-0838
Carlos Thomas: https://orcid.org/0000-0002-2641-9411
Juan Antonio Polanco: https://orcid.org/0000-0002-2649-9490
Jesús Setién: https://orcid.org/0000-0002-6285-8745
Pablo Tamayo: https://orcid.org/0000-0003-2195-7883

References

De Schutter, G. and Audenaert, K. (2007). *Durability of Self-Compacting Concrete - State-of-the-Art Report of RILEM Technical Committee 205-DSC* (S.A.R.L.). RILEM.

Dinakar, P., Sethy, K. P. and Sahoo, U. C. (2013). Design of self-compacting concrete with ground granulated blast furnace slag. *Materials & Design*, *43*(0), 161–169.

E. Medina, D. M. B. (2013). *Armaduras de acero inoxidable* (1st ed.). CEDINOX.

Medina, C., Sánchez De Rojas, M. I., Thomas, C., Polanco, J. A. and Frías, M. (2016). Durability of recycled concrete made with recycled ceramic sanitary ware aggregate. Inter-indicator relationships. *Construction and Building Materials*, *105*. https://doi.org/10.1016/j.conbuildmat.2015.12.176

Ministerio de Fomento de España, (2008). *EHE-08: Instrucción de Hormigón Estructural*. Retrieved from: http://www.fomento.gob.es/MFOM/LANG_CASTELLANO/ORGANOS_COLEGIADOS/CPH/instrucciones/EHE08INGLES/

Sosa, I., Thomas, C., Polanco, J. A., Setién, J. and Tamayo, P. (2020). High Performance Self-Compacting Concrete with Electric Arc Furnace Slag Aggregate and Cupola Slag Powder. *Applied Sciences*, *10*(3), 773.

Thomas, C., Cimentada, A., Polanco, J. a., Setién, J., Méndez, D. and Rico, J. (2013). Influence of recycled aggregates containing sulphur on properties of recycled aggregate mortar and concrete. *Composites Part B: Engineering*, *45*(1), 474–485. https://doi.org/10.1016/j.compositesb.2012.05.019

Uysal, M. and Yilmaz, K. (2011). Effect of mineral admixtures on properties of self-compacting concrete. *Cement and Concrete Composites*, *33*(7), 771–776. https://doi.org/10.1016/j.cemconcomp.2011.04.005

Zhu, W. and Bartos, P. J. M. (2003). Permeation properties of self-compacting concrete. *Cement and Concrete Research*, *33*(6), 921–926. https://doi.org/10.1016/S0008-8846(02)01090-6

XV International Conference on Durability of Building Materials and Components
DBMC 2020, Barcelona
C. Serrat, J.R. Casas and V. Gibert (Eds)

Durability Studies of Self-Compacting Concrete containing Electric Arc-Furnace Slag Aggregate

Amaia Santamaria[1], Marta Skaf[2], Vanesa Ortega-Lopez[3], Estibaliz Briz[4], José T. San José[5] and Javier J. González[6]

[1] Inter Department of Mechanical Engineering, University of the Basque Country UPV/EHU. Paseo Rafael Moreno Pitxitxi 2 - 48013 Bilbao, Spain amaia.santamaria@ehu.eus

2 Department of Construction, University of Burgos UBU. Calle Villadiego, s/n - 09001 Burgos, Spain mskaf@ubu.es

3 Department of Civil Engineering, University of Burgos UBU. Calle Villadiego, s/n - 09001 Burgos, Spain vortega@ubu.es

4 Department of Mechanical Engineering, University of the Basque Country UPV/EHU. Paseo Rafael Moreno Pitxitxi 2 - 48013 Bilbao, Spain estibaliz.briz@ehu.eus

5 Department of Metallurgical Engineering and Materials Science, University of the Basque Country UPV/EHU. Plaza Ingeniero Torres Quevedo, 1 - 48013 Bilbao, Spain josetomas.sanjose@ehu.eus

6 Department of Metallurgical Engineering and Materials Science, University of the Basque Country UPV/EHU. Plaza Ingeniero Torres Quevedo, 1 - 48013 Bilbao, Spain javierjesus.gonzalez@ehu.eus

Abstract. *The structure of self-compacting concretes containing electric arc-furnace slag, their mechanical behavior, and their durability are all studied in an extensive experimental campaign, to evaluate the suitability of three concrete mixes for use in real construction works. Specimens manufactured with self-compacting electric arc-furnace slag concrete are subjected to wetting-drying and freezing-thawing test procedures, for their study in aggressive environments, especially marine environments. In general, all the test results were quite encouraging. It was once again demonstrated that the use of electric arc-furnace slag in concrete represents an opportunity to reduce both the volume of siderurgical waste generated in our society, and the consumption of fresh raw materials.*

Keywords: *Self-Compacting Concrete, Electric Arc-Furnace Slag, Durability, Marine Environment.*

1 Introduction

The future of the environment is a source of growing concern in present-day society that is calling for increasingly sustainable development. The sustainability of production processes must be carefully studied and waste-streams must wherever possible be reutilized and recycled. However, waste reduction also implies the manufacture of products of greater durability. Sustainable production processes are already dynamizing the circular economy while maintaining relevant standards and properties. Concrete products that reuse waste must therefore at the very least equal those of conventional Portland mixes.

This study is focused on the reuse of Electric Arc-furnace Slag (EAFS), a residue from the steelmaking industry, as aggregate in concrete mixtures. The reuse of slag in cement-based

material has been a recurrent topic since Motz, Geiseler and Koros (Geiseler, 1996; Koros, 2003; Motz and Geiseler, 2001) published the first studies on the reuse of slag in the construction industry.

Since those first initial studies, the mechanical behavior and the hardened properties of concretes manufactured with EAFS as aggregate have been evaluated in several studies (Abu-Eishah, El-Dieb, and Bedir, 2012; Faleschini *et al.*, 2015; Manso, Gonzalez, and Polanco, 2004). Studies have also been performed on the durability of those types of concretes (Arribas, Vegas, San-José, and Manso, 2014; Manso, Polanco, Losañez, and González, 2006). In general, most of the tests on their mechanical behavior and durability have demonstrated that EAF concretes can at least equal the behavior of natural aggregate concrete.

In some of the above works, poorer workability than natural concrete aggregate has been identified as a disadvantage of EAFS concrete. In this work it will be demonstrated that with the correct mix design, self-compacting concrete can be made using EAFS as aggregate. Its durability will also be evaluated, lending special attention to the durability of EAFS self-compacting concretes in highly saline marine environments.

There are two principal reasons for this study: on the one hand, there are few studies on the evaluation of the behavior of EAFS concrete in marine environments and, on the other hand, the mechanical and the physical characteristics of EAFS concrete point to its suitability for the construction of dykes and blocks to form protective seawalls. In fact, work is underway with this type of concrete for that same purpose in coastal areas of the Basque Country, a region of northern Spain, where the evaluation of the durability of EAFS concrete in marine environments assumes special importance. In Bilbao, the port authority is pioneering the use of electric arc-furnace slag concrete in port construction works

2 Materials and Mixes

Two different cements were used: a Portland cement type I 52,5 R and a Portland cement type IV/B-V 32.5N, which included fly ash, as per standard EN 197-1.

Water was used from the urban mains supply of the city of Bilbao, free from additional particles that might adversely affect the mixes.

The commercial limestone aggregate was of three different sizes 0-1, 0-5, and 5-12. Likewise, the Electric Arc-furnace Slag (EAFS) had aggregate fractions of 0-4 and 4-12. Finally, a superplasticizer supplied by CHRYSO was selected to adjust the workability of the mix.

Three different mixes designs, shown in Table 1, were prepared with these materials:

- A reference mix, labeled NATI, manufactured with Portland cement type I and limestone aggregates,
- A mix labeled EAFSI, in which Portland cement-type I was used, although unlike in the reference mix, EAFS was used in partial substitution by volume of the limestone aggregates. Nevertheless, proportional amounts of the different aggregate fractions were not exactly the same. The higher density and the rougher surface of the EAFS particles require higher proportions of fines, to manufacture mixes with this type of aggregate (Santamaría *et al*., 2017).
- An EAFSIV mix, with exactly the same design as the EAFSI mix, except that Portland cement-type IV, rather than Portland cement-type I, was used.

Table 1. Mix design.

	NAT I	EAFSI	EAFSIV
Cement I	330	330	
Cement IV			330
Water	165	165	165
EAFS 4-12		760	760
EAFS 0-4		550	550
Limestone fines 0-1,2	690	900	900
Limestone 0-5	560		
Limestone 5-12	730		
Superplasticizer (% cement weight)	2%	2%	2%
Density (t/m^3)	2.41	2.69	2.58
Slump flow spread. Abrams Cone (mm)	630	680	700
L-box	1	1	1

The NATI mix was manufactured in a conventional laboratory mixer and cast in different molds. An industrial concrete mixer, depicted in Figure 1, was rented to prepare the mixes for the manufacture of EAFSI and EAFSIV. From the total batch of 600 lts., two beams of each mix and several molds were precast and their mechanical and durability properties were evaluated.

Figure 1. Concrete mixer.

3 Test Method

Two tests were used to evaluate the workability of the mixes, a slump flow cone in accordance with ASTM C1611 and the L-box test, in accordance with the EFNARC standard.

The bulk density of the mixes was measured as specified in the EN 1015-10 standard. The compressive strength of the mixes was evaluated at 7, 28, 90 and 180 days, as recommended in EN-12390-3.

The Fagerlund test described in the UNE 83982 standard, based on Darcy's law, was used to analyze water absorption by capillarity.

Mix durability was evaluated with wetting-drying and freezing-thawing tests. Both tests were performed on 2 different specimens of each mix, after 90 days of curing. 148 cycles were performed for each wetting-drying test. Each cycle involved leaving each specimen in water for 16 hours, in an oven at 60°C for 6 hours placed, and at room temperature for 2 hours, to prevent thermal shock. The freezing-thawing test involved 122 cycles, in which the specimens were kept in a freezer at -15°C for 24 hours and in water, at room temperature, over the following 24 hours. The mechanical properties of the specimens were evaluated both before and after the durability test.

Three batches of specimens (100x100x100mm^3) of each mix, as shown in Figure 2, were enclosed in cages suspended from a dock wall in Pasaia Donibane port, with the purpose of analyzing EAFS concrete durability in marine environments. The cages were suspended in an intertidal zone where they would be submerged under the seawater at high tide and exposed to the atmosphere at low tide. The specimens were left in the cages for one year. After their removal, chlorine and sulphate ion infiltration was evaluated, by cutting each specimen and placing it in a vacuum chamber that was filled with nitrogen at low pressure for Scanning Electron Microscopy (SEM) analysis. Energy-dispersive X-ray spectroscopy was used to obtain the chemical composition of the first 50mm of the fracture surface and to generate backscattered electron images.

Figure 2. Specimens placed in cages at Pasaia Port.

4 Results

4.1 Workability

The workability test results of the mixes are shown in Table 1. All the mixes could be classified as self-compacting mixes. The reference mix had a lower spread than the EAFS aggregate mixes, which was a somewhat surprising result, thought to be due to the different scale of the mixes. A large number of laboratory trials had been performed before manufacturing the 600 lt. of concrete used in the mixes. The workability of the mixes with the same dosages manufactured on a small scale was worse than in the larger mixes, due in all likelihood to the

skin effect. Nevertheless, such a slight difference in workability was marginal for the purposes of this research, alongside the key aspect: the self-compacting properties of the mixes.

4.2 Density and Mechanical Strength

As might be expected, the density of the concretes manufactured with EAFS was higher than the density of the concrete manufacture with natural aggregates, with increases of around 11% in the case of EAFSI and 7% in the case of EAFSIV.

Concrete strength over time is depicted in Figure 3. The behaviors of both concretes manufactured with Portland cement type I were very similar. The EAFSI mixes gained slightly higher strengths, compensating their higher density than the other mixes. The higher strength of EAFS concretes has been explained in a previous paper (Arribas, Santamaría, Ruiz, Ortega-López, and Manso, 2015), by the denser aggregate and cement-paste interface.

The hardened strength of EAFSIV was lower than its EAFSI counterpart, reflecting the characteristics of the Portland cement type IV.

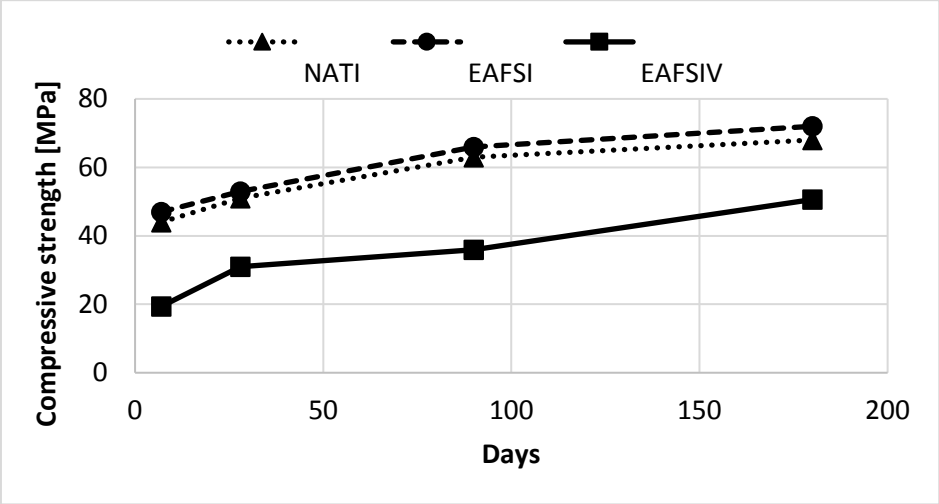

Figure 3. Compressive strength.

4.3 Capillarity Water Absorbtion

The results obtained in the capillarity water test are shown in Figure 4. The results for NATI and EAFSI were similar, unlike for EAFSIV. The curves can be divided into two zones: an initial rising zone; and, a second zone, where capillarity porosity was not evaluated as it involved other types of porosities. The less inclined slope (K coefficient 0,106 kg/m^{2}s$^{1/2}$) of the EAFSIV, in the first zone, represents low permeability. The value of the second zone shows us that the total porosity of the mix was high, which means that this mix may have a high number of single, unconnected spherical pores, which could also explain the lower density of the mix in comparison with the EAFSI mix. Both for NATI and for EAFSI, the slope of the curve was the same in the first zone (K coefficient 0,156 kg/m^{2}s$^{1/2}$), so the capillarity porosity was similar in both mixes, in the second zone, mix EAFSI achieved higher values, which might be explained by the higher porosity of the EAFS aggregate when compared with the limestone aggregate.

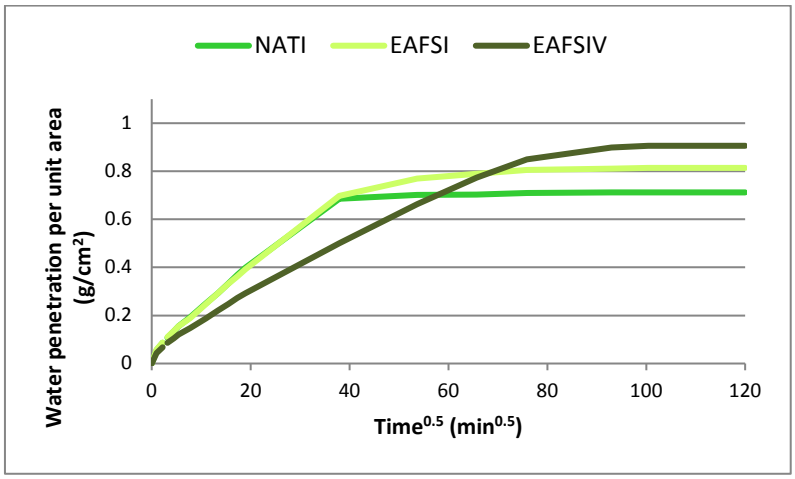

Figure 4. Capillarity test results.

4.4 Wetting-Drying and Freezing-Thawing Tests

The variation of the mechanical properties and weight of the mixes after performing durability tests are shown in Table 2. The mechanical properties of mixes NATI and EAFSI achieved similar levels. The mass loss of the EAFSI mix was higher than the mass loss of mix NATI, although if we take into account the different densities of both mixes, then their loss of volume was similar.

The behavior of mix EAFSIV during the durability test differed from the results obtained in mixes NATI and EAFSI. Strength gains were shown, rather than a loss of strength, due to the aggressive cycles. Results that are explained by the presence of fly ash associated with long-term pozzolanic reactions.

Table 2. Results of wetting-drying and freezing-thawing tests.

Mixture	Variation Strength frozen	Variation Stiffness frozen	Mass loss Frozen (g)/2500	Variation Strength wet	Variation Stiffness wet	Mass loss Wet (g)/2500
NATI	-21%	-2.8%	37.5	-2.1%	-0%	131
EAFSI	-25%	-5.1%	55.9	0%	-1.1%	158.5
EAFSIV	+6.5%	+9.4%	24	+7.5%	+13%	201.9

4.5 Marine Environment Test

In Figure 5, it is possible to see the specimens before and after exposure to a highly saline marine environment after one year. *I*t would appear, *a priori,* that this concrete has no compounds that could harm the marine ecosystem, as the specimens were teaming with mussels, oysters, and small crabs.

The behavior of EAFS concrete in marine environments was good, and even better than the behavior of natural aggregate concretes, showing slightly better strengths. The results of the analysis are in the Figure 6. No data on sulfate ions are included, as no ions of that type were found.

Figure 5. Specimens before and after the marine environment test.

Taking into account that 0.1% is a typical chlorine ion content of a cement paste, chlorine-ion penetration was around 35mm in NATI, and approximately 25mm and 15mm, in EAFSI and in EAFSIV, respectively. The higher resistance of EAFSIV to chlorine-ion penetration can be explained by looking at the results of the capillarity water test.

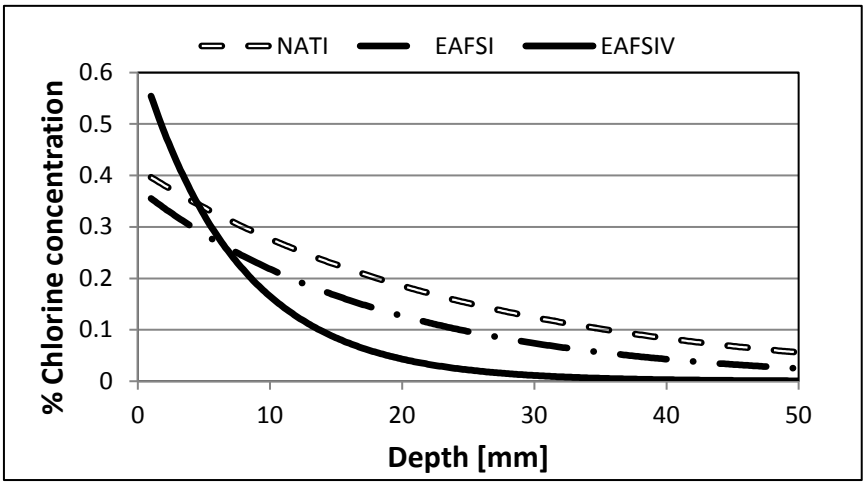

Figure 6. Specimens before and after the marine environment test.

5 Conclusion

Following the research campaign tests developed for this study, the following conclusions have been drawn:

- Mixes containing EAFS aggregate may be manufactured to the required workability, using the correct mix design. Self-compacting mixes have been successfully manufactured
- Both the mechanical behavior and the structure of the mixes manufactured with electric arc-furnace slag were fairly similar to the behavior and the structure of the mixes manufactured with natural aggregates. The main differences were observed when a different type of cement was used, in addition to the observably lower mechanical

strengths, as may be expected, in the cement type IV mixes, which also had different pore structures with larger pore volumes.

- The use of electric arc-furnace slag as a concrete aggregate was not detrimental to the durability of the concrete. The great similarities with no major differences between the natural and the EAFS aggregates were confirmed by the test results.

Acknowledgements

The authors wish to express their gratitude to the following institutions: the Spanish Ministry (MICINN) and FEDER (European Regional Development Funds) through contract RTI2018-097079-B-C31 (MCIU/AEI/FEDER, UE); the Basque Government research group (IT1314-19), and the UPV/EHU [PPGA19/029. Our thanks also go to the Vice-Rectorate of Investigation of the University of Burgos [SUCONS] and to the Junta de Castilla y León (Regional Government) for funding the UIC-231 group through project BU119P17 partially supported by FEDER funds Finally, our thanks likewise to HORMOR Zestoa for supplying the steelmaking slags and to the University of Burgos (EPS -LaMilanera) for their support at several experimental stages.

ORCID

Amaia Santamaria: https://orcid.org/0000-0002-4559-8734
Marta Skaf: https://orcid.org/0000-0001-7205-2692
Vanesa Ortega-Lopez: https://orcid.org/0000-0003-0212-355X
Estibaliz Briz: https://orcid.org/0000-0003-3933-3585
José Tomás San José: https://orcid.org/0000-0003-4904-6731
Javier Jesús González: https://orcid.org/0000-0002-0932-7937

References

Abu-Eishah, S. I., El-Dieb, A. S. and Bedir, M. S. (2012). Performance of concrete mixtures made with electric (EAF) steel slag aggregate produced in the Arabian Gulf region. Construction and Building Materials, 34, 249-256. doi:http://dx.doi.org/10.1016/j.conbuildmat.2012.02.012

Arribas, I., Santamaría, A., Ruiz, E., Ortega-López, V. and Manso, J. M. (2015). Electric arc furnace slag and its use in hydraulic concrete. Construction and Building Materials, 90, 68-79. doi:10.1016/j.conbuildmat.2015.05.003

Arribas, I., Vegas, I., San-José, J. T. and Manso, J. M. (2014). Durability studies on steelmaking slag concretes. Materials & Design, 63, 168-176. doi:http://dx.doi.org/10.1016/j.matdes.2014.06.002

Faleschini, F., Alejandro Fernández-Ruíz, M., Zanini, M. A., Brunelli, K., Pellegrino, C. and Hernández-Montes, E. (2015). High performance concrete with electric arc furnace slag as aggregate: Mechanical and durability properties. Construction and Building Materials, 101, 113-121. doi:10.1016/j.conbuildmat.2015.10.022

Geiseler, J. (1996). Use of steelworks slag in Europe doi:http://dx.doi.org/10.1016/S0956-053X(96)00070-0

Koros, P. J. (2003). Dusts, scale, slags, sludges... not wastes, but sources of profits. Metallurgical and Materials Transactions B, 34(6), 769-779. doi:10.1007/s11663-003-0083-0

Manso, J. M., Gonzalez, J. J. and Polanco, J. A. (2004). Electric arc furnace slag in concrete. Journal of Materials in Civil Engineering, 16(6), 639-645. doi:10.1061/(ASCE)0899-1561(2004)16:6(639)

Manso, J. M., Polanco, J. A., Losañez, M. and González, J. J. (2006). Durability of concrete made with EAF slag as aggregate. Cement and Concrete Composites, 28(6), 528-534. doi:10.1016/j.cemconcomp.2006.02.008

Motz, H. and Geiseler, J. (2001). Products of steel slags an opportunity to save natural resources. Waste Management, 21(3), 285-293.

Santamaría, A., Orbe, A., Losañez, M. M., Skaf, M., Ortega-Lopez, V. and González, J. J. (2017). Self-compacting concrete incorporating electric arc-furnace steelmaking slag as aggregate. Materials and Design, 115, 179-193. doi:10.1016/j.matdes.2016.11.048

XV International Conference on Durability of Building Materials and Components
DBMC 2020, Barcelona
C. Serrat, J.R. Casas and V. Gibert (Eds)

Durability Studies on Fiber-Reinforced Siderurgic Concrete

Vanesa Ortega-López[1], Víctor Revilla-Cuesta[2], Amaia Santamaría[3], Ana B. Espinosa[4], José A. Fuente-Alonso[5] and José A. Chica[6]

[1] University of Burgos. Escuela Politécnica Superior, 09001 Burgos, Spain. vortega@ubu.es

[2] University of Burgos. Escuela Politécnica Superior, 09001 Burgos, Spain. vrevilla@ubu.es

[3] University of Basque Country. Escuela de Ingeniería de Bilbao, 48013 Bilbao, Spain. amaia.santamaria@ehu.es

[4] University of Burgos. Escuela Politécnica Superior, 09001 Burgos, Spain. aespinosa@ubu.es

[5] University of Burgos. Escuela Politécnica Superior, 09001 Burgos, Spain. jafuente@ubu.es

[6] Fundación Tecnalia, Research & Innovation. Digital Construction Division, 48160 Derio, Vizcaya, Spain. joseantonio.chica@tecnalia.com

Abstract: The construction sector is clearly one of the most pollutant *at a global level and its consumption of natural resources is also enormous. Over recent years, heightened awareness of this issue within the construction sector has motivated changes within its working practice, seeking to reduce its environmental impacts and to mitigate the effects of climate change. The consumption of natural resources can be reduced in very different areas and special attention has been given to the substitution of Natural Aggregates (NA) in concrete design by replacing those aggregates with various waste co-products. Siderurgic concrete is the name given to concrete manufactured with siderurgical aggregate from the steel-making industry. In this paper, test results on fiber-reinforced siderurgical concrete are reported. The concrete is manufactured with approximately 50% Electric Arc Furnace Slag (EAFS) aggregate by volume, for use in pavement applications. Steel and polypropylene fibers, amounting to approximately 0.5% by volume of the concrete mass, are also added to the mix. The durability properties of this concrete type are analyzed through freeze/thaw and moist/dry tests. Furthermore, the long-term behavior of the concrete is explained through its internal structure, using Mercury Intrusion Porosity (MIP) and low-vacuum Scanning Electron Microscopy (SEM) analyses. The results add further weight to the feasibility of using EAFS in replacement of NA in fiber-reinforced concrete for pavement construction.*

Keywords: *EAFS, Freeze/Thaw, Moist/Dry, MIP, SEM.*

1 Introduction

The immense volumes of natural aggregates used for concrete production within the construction sector has motivated a search for feasible alternatives to natural resources. In consequence, several studies have over the past few decades examined the incorporation of slag from the steelmaking industry in construction and civil engineering applications (Akinmusuru, 1991; Faleschini *et al.*, 2015; Geiseler, 1996; Koros, 2003; Manso *et al.*, 2006; Motz and Geiseler, 2001; Pellegrino and Gaddo, 2009; Qasrawi, 2014; Santamaría *et al.*, 2017).

Although productive steel processes differ between plants, they may at present be divided into two types: Integral Siderurgy, in which the raw material, iron ore, is melted in a Blast Furnace, followed by a decarburization phase, usually in an Oxygen-Blow Converter, and the

Electric Cycle, in which scrap is melted in Electric Arc Furnaces (EAF). After this "primary metallurgy", a secondary refining phase usually takes place in a Ladle Furnace for carbon steels, and in a special converter for stainless steels.

Around 30% of European steel is produced with EAF technology. In the EU steel sector, a total of 47.8 Mt of steel slag were produced in 2018, of which Electric Arc Furnace Slag (EAFS) and secondary slags amounted to 7.9 Mt and 2.8 Mt, respectively, according to the EUROSLAG report "The European Association representing metallurgical slag producers and processors" (EUROSLAG, 2018), data from which are reproduced in Figure 1.

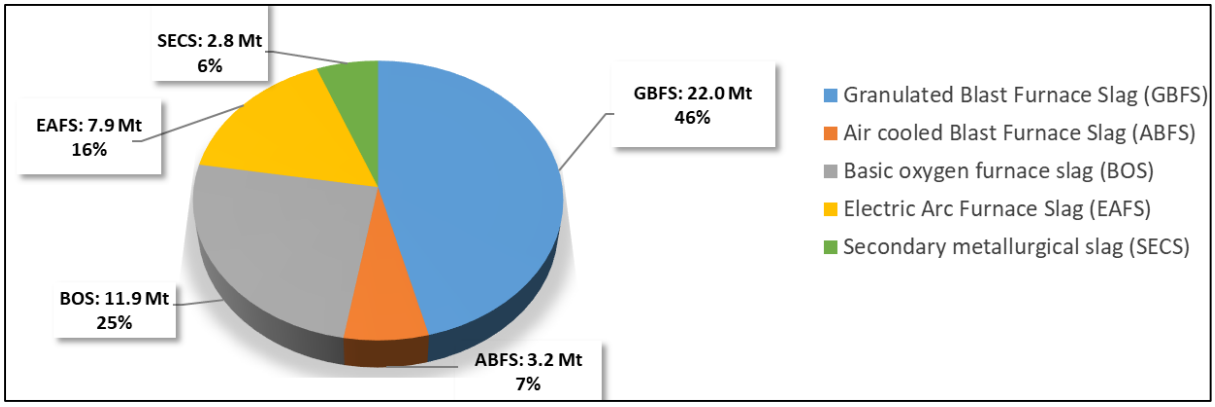

Figure 1. Slag production in the EU (% and Mt.).

Spain is the third largest producer of electric steel in the EU, after Germany and Italy, with production levels of around 10 MT of electric steel, together with more than 1 MT of EAFS and 0.5 MT of LFS by-products (Yearbook, 2019).

Taking into account the benefits of slag recycling, the viability of using Electric Arc Furnace Slags (EAFS) in fiber-reinforced concrete (FRC) is examined in this paper, for the subsequent manufacture of rigid pavements and industrial slabs. To do so, siderurgic concrete was prepared with approximately 50% EAFS and 0.5% (metallic or synthetic) fibers, in both cases by volume. The main mechanical properties of these siderurgic concretes will be analyzed and their long-term behavior examined in relation to their internal structure in the following sections, leading up to a discussion of the most significant results and relevant conclusions.

2 Materials and Methodology

The materials used in this research were: Ordinary Portland Cement (OPC) CEM I 42,5R, water, natural siliceous aggregates provided in three granulometric sizes of 0/4, 4/12 and 12/25 mm, superplasticizers (polycarboxylate modified with water), EAFS aggregates provided in three granulometric sizes of 0/4, 4/10 and 10/20 mm, metallic fibers (steel, RL-45/50-BN) and synthetic Fibers (polypropylene, M-48).

The main physical characteristics of the EAFS were: specific gravity of 3500 kg/m^3, high water absorption, low fines content, and 24% Los Angeles abrasion loss. The main chemical components were oxides of Fe, Ca and Si.

The methodology was based on the use of EAFS as coarse and medium aggregate in the concrete mix and the fine aggregate was prepared with 50% fine slag and 50% siliceous sand, in order to compensate for the lack of the fines in the EAFS.

Two reference mixtures were designed: mixture P, manufactured entirely with siliceous aggregates, and mixture E, manufactured with EAFS in coarse and medium gravel and 50%-50% of siliceous-EAFS in sand. Their mix design is shown in Table 1.

Taking the dosage of mixture E as a reference, two experimental mixtures reinforced with around 0.5% by volume of steel fibers identified as EM and with polypropylene fibers identified as ES were manufactured.

Table 1. Mix design of the reference mixtures (kg/m^3).

Mix design kg/m^3	Cement	Water	Siliceous aggregates			EAFS aggregates			Admixture
			0/4	4/12	12/20	0/4	4/10	10/20	
P	360	180	800	575	465	-	-	-	3.63
E	360	180	500	-	-	515	670	550	5.44

3 Results and Discussion

3.1 Mechanical Properties

The main mechanical properties of the siderurgic concretes are shown in Table 2.

Table 2. Mechanical properties of the experimental siderurgic concretes.

Property	standard	P	E	EM	ES
Compressive Strength at 28 days (MPa)	UNE 83507	46.3	66.1	72.6	74.0
Flexural Strength at 28 days (MPa)	UNE 83509	5.2	6.8	7.0	7.1
Splitting Tensile Strength at 28 days (MPa)	UNE 12390-6	4.3	4.2	5.5	5.2
Maximum depth of water penetration (mm)	UNE EN 12390-8	24.0	13.0	13.5	20.5
Flexural toughness (N·m)	UNE 83510	-	8.74	39.2	35.0
LOP (CMOD ≤ 0.05 mm) (MPa)	EN-14651	-	6.1	6.4	6.2
Blows until breakage in impact strength test	UNE 83514	-	13	155	88

The compressive strength of the siderurgic concrete E (66.1 MPa) was 43% higher than that of natural aggregates P (46.3 MPa), even reaching values of 72 and 74 MPa for mixtures EM and ES, respectively.

The flexural strength of the siderurgic concrete E (6.8 MPa) was also higher than that of conventional concrete P (5.2 MPa); mixtures EM and ES reaching values of around 7 MPa. This fact is attributable to the good (dense and not very porous) quality of the Interfacial Transition Zone (ITZ) of the siderurgic concretes (Arribas *et al.*, 2015) and to high adhesion between all the (aggregate, cement paste and fiber) components of the mixtures.

As regards the splitting tensile strength, little difference was observed between the reference concretes P (4.3 MPa, with fibers) and E (4.2 MPa, no fibers). An important improvement in the mixtures with fibers was once again observed, especially concretes EM (5.5 MPa) and ES (5.2 MPa).

All the mixes with EAFS showed better resistance to water penetration than the conventional concrete with natural aggregates. Likewise, they met the requirements of the EHE standard (2008), which specifies the maximum depth of water penetration under 30 mm. The impermeable nature of these concretes was therefore considered sufficient for pavement applications.

The toughness by flexion value of the fiber-reinforced mixes was close to 40 N.mm in the mix with steel fibers and was slightly lower in the mix with polypropylene fibers (35 N.mm), which in both cases are good values.

The Limit of Proportionality (LOP) tested in samples with a notch of 5 mm was similar in all the mixtures and was slightly higher in the mixtures with steel fibers (6.4 MPa).

Finally, the fiber-reinforced siderurgic concretes clearly had much a better impact strength until breakage (EM: 155 blows and ES: 88 blows) than the equivalent with non-reinforced concrete E (13 hits).

In view of these initial results, it can be concluded that the siderurgic concretes have the mechanical properties that are needed in industrial pavement slabs.

3.2 Long-Term Behavior and Durability

3.2.1 Freeze/thaw and moist/dry tests

The durability of a concrete pavement is determined by its permeability and its resistance to the very influential factors, such as the presence of water and temperature variance in its immediate environment. The freeze/thaw and moist/dry tests of the concretes under are especially interesting, given the very adverse climatic conditions of the Spanish region under study.

In this study, both the weight and the compressive strength of the mixes varied, following 56 freeze/thaw cycles and 30 moist/dry cycles, as per the UNE-CEN/TS 12390-9 and the ASTM D-559 standards("Annual Book of ASTM Standars, ASTM International, West Conshohocken, 19429-2959. PA, USA, 2008,"), respectively. The results are shown below, in Table 3.

Table 3. Freeze/thaw and moist/dry results of the siderurgic concretes.

Property	E	EM	ES
Weight variation after 56 freeze/thaw cycles (%)	-62.41	-2.92	-4.49
Variation of compressive strength after 56 freeze/thaw cycles (%)	-	-3.45	0.93
Weight variation after 30 moist/dry cycles (%)	0.23	0.14	0.34
Variation of compressive strength after 30 moist/dry cycles (%)	-15.2	-1.12	12.16

In the freeze/thaw test, cubic specimens, in duplicate, were introduced into a container filled with a solution of 3% sodium chloride (NaCl). These containers were placed in a freezer over 16 hours, at a temperature of -29ºC±1ºC, and in a container with water circulation at 20ºC±1ºC for 8 hours, and those test cycles were repeated 56 times throughout the duration of the test. Figure 2 shows the arrangement of the freeze/thaw test.

Figure 2. Arrangement of the freeze/thaw test: a) freezer at -29ºC; b) container with water at 20ºC.

After 56 freeze/thaw cycles, mix E lost a significant amount of material (-62.41%), while the results obtained for concrete mix ES (-4.49%) were good and even better for concrete mix EM (-2.92%), which maintained its cube shape. The compressive strength test at the end of all the cycles was only performed on the EM and ES specimens, due to the total deterioration of the E specimens during the freeze/thaw test. Slight damage to the EM specimens led to a decrease of 3.45% in their compressive strength, while the ES specimen showed a compressive strength that was slightly higher (+0.93 %) than before the freeze/thaw cycles. A fact also observed by other authors, which was probably caused by further hydration of the cement that came into direct contact with the water permeating through the frozen saturated surface due to its microporosity (Pellegrino and Gaddo, 2009).

The moist/dry test was also performed on cubic specimens, in duplicate. Each of the 24-hour cycles, repeated 30 times, consisted of 16 hours of immersion in fresh water at room temperature and 8 hours in an oven at 60 °C.

After the moist/dry test, all the concrete specimens showed good surface appearance and slight weight gains. The concrete with no fibers, E, showed an appreciable loss of compressive strength (-15.20%), unlike the concrete with metallic fibers, EM, that lost little strength (-1.12%) and the mix with synthetic fibers, ES, the strength of which increased (+12.16%). Similar results for concretes manufactured with EAFS were also found by other authors (Arribas *et al.*, 2014). These satisfactory results point to the good internal cohesiveness of the aggregates and fibers within the matrix of this fiber-reinforced slag concrete.

3.2.2 MIP analysis

Concrete-matrix porosity is a determining factor, in both the mechanical properties and the durability of cement-based materials, and was measured with Mercury Intrusion Porosimetry (MIP) analysis. The porosity values were as follows: 12.3% for mix E; 10.3 % for mix EM; and, 11.5% for mix ES; common values for well-performed concretes (Ortega-López *et al.*, 2018).

The lower porosity of the fiber-reinforced concretes with respect to the mix E, means that both the EM and the ES mixes were more compacted, which may also explain their higher compressive strength and the lower weight variation after the freeze/thaw and the moist/dry tests. The pore size frequency, shown in Figure 3, rises to an significant peak at around 100 nm,

higher in concrete E, with no fibers, which could be one cause of the worse behavior of this concrete against physical and chemical agents.

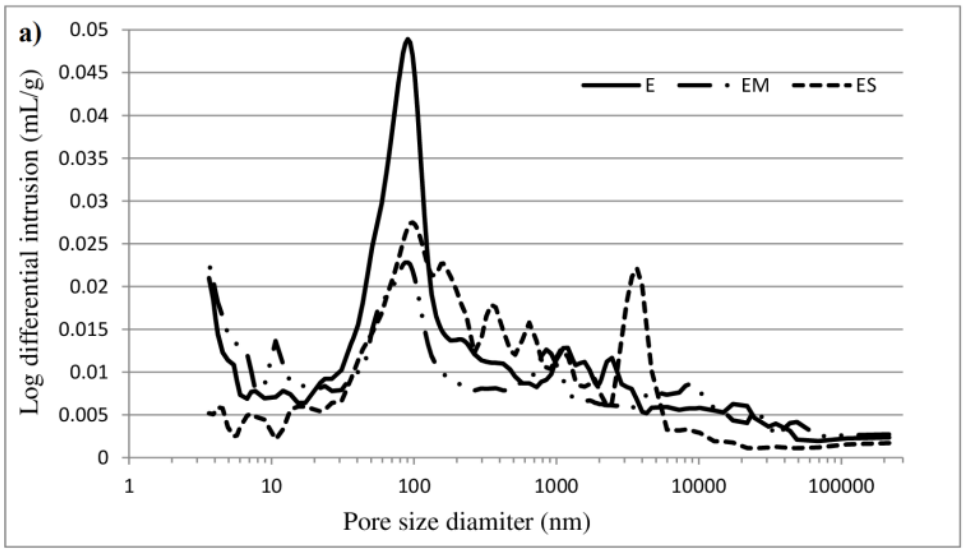

Figure 3. MIP analysis of siderurgic concretes: differential intrusion.

3.2.3 SEM observations

Low-vacuum scanning electron microscopy (SEM), with the backscattered electrons technique was used for analyzing the quality of the Interfacial Transition Zone (ITZ) and adherence between the concrete components.

Figure 4 shows three SEM images, one of each siderurgic concrete under study. In these images, it can be observed that the EAFS particles are of a lighter grey color, the siliceous particles are darker grey and, Figure 4b and Figure 4c clearly show the fibers, steel and polypropylene fibers, respectively.

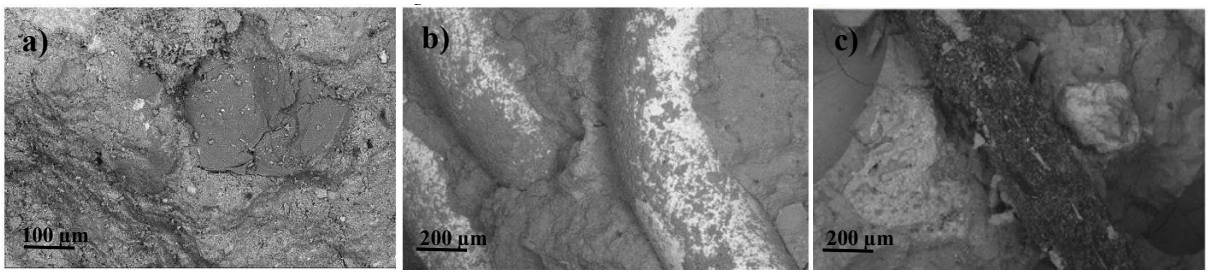

Figure 4. SEM images of concretes: a) concrete E; b) concrete EM; c) concrete ES.

All the SEM images support the conclusion that the cementitious matrices are of good quality, with excellent adherence of aggregates and fibers, which favors the durability of these concretes.

4 Conclusions

The conclusions of this work can be summarized as follows:

- The fiber-reinforced siderurgic concrete mixtures showed good mechanical properties. The results of the concretes reinforced with steel fibers were in general better than those for the concretes reinforced with polypropylene fibers.
- Durability tests delivered good results for the fiber-reinforced siderurgic concretes, yielding smaller variations of weight and strength after several conditions.
- MIP and SEM analyses revealed the good internal cohesiveness of both aggregates and fibers within the cement matrix, which favored their durability.

Acknowledgements

The authors wish to express their gratitude to: the Spanish Ministry MCIU, AEI, EU and ERDF [RTI2018-097079-B-C31; 10.13039/501100011033; FPU17/03374]; the Junta de Castilla y León (Regional Government) and ERDF [UIC-231, BU119P17]; Youth Employment Initiative (JCyL) and ESF [UBU05B_1274]; and finally, the funds from the university of The Basque Country [PPGA19/61] and the university of Burgos [grant SUCONS; Y135.GI]. Additionally, our thanks to the Basque Government research group [IT1314-19] and likewise to CHRYSO and HORMOR for supplying the materials used in this research.

ORCID

Vanesa Ortega-López: 0000-0003-0212-355x
Víctor Revilla-Cuesta: 0000-0003-3337-6250
Amaia Santamaría: 0000-0002-4559-8734
José Antonio de la Fuente Alonso: 0000-0002-3846-6047
José Antonio Chica: 0000-0002-3873-6086

References

Akinmusuru, J. O. (1991). Potential beneficial uses of steel slag wastes for civil engineering purposes. *Resources, Conservation and Recycling, 5*(1), 73-80. doi: 10.1016/0921-3449(91)90041-L

Arribas, I., Santamaría, A., Ruiz, E., Ortega-López, V. and Manso, J. M. (2015). Electric arc furnace slag and its use in hydraulic concrete. *Construction and Building Materials, 90*, 68-79. doi: 10.1016/j.conbuildmat.2015.05.003

Arribas, I., Vegas, I., San-José, J. T. and Manso, J. M. (2014). Durability studies on steelmaking slag concretes. *Materials and Design, 63*, 168-176. doi: 10.1016/j.matdes.2014.06.002

EUROSLAG. (2018). The European Slag Association. Position Paper on the Status of Ferrous Slag. https://www.euroslag.com/products/statistics/statistics-2018/.

Faleschini, F., Brunelli, K., Zanini, M. A., Dabalà, M. and Pellegrino, C. (2015). Electric Arc Furnace Slag as Coarse Recycled Aggregate for Concrete Production. *Journal of Sustainable Metallurgy*, 1-7.

Geiseler, J. (1996). Use of steelworks slag in Europe. *Waste Management, 16*(1-3), 59-63. doi: 10.1016/S0956-053X(96)00070-0

Koros, P. J. (2003). Dusts, Scale, Slags, Sludges. . . Not Wastes, but Sources of Profits. *Metallurgical and Materials Transactions B: Process Metallurgy and Materials Processing Science, 34*(6), 769-779.

Manso, J. M., Polanco, J. A., Losañez, M. and González, J. J. (2006). Durability of concrete made with EAF slag as aggregate. *Cement and Concrete Composites, 28*(6), 528-534. doi: 10.1016/j.cemconcomp.2006.02.008

Motz, H. and Geiseler, J. (2001). Products of steel slags an opportunity to save natural resources. *Waste Management, 21*(3), 285-293. doi: 10.1016/S0956-053X(00)00102-1

Ortega-López, V., Fuente-Alonso, J. A., Santamaría, A., San-José, J. T. and Aragón, Á. (2018). Durability studies on fiber-reinforced EAF slag concrete for pavements. *Construction and Building Materials, 163*, 471-481. doi: 10.1016/j.conbuildmat.2017.12.121

Pellegrino, C. and Gaddo, V. (2009). Mechanical and durability characteristics of concrete containing EAF slag as aggregate. *Cement and Concrete Composites, 31*(9), 663-671. doi: 10.1016/j.cemconcomp.2009.05.006

Qasrawi, H. (2014). The use of steel slag aggregate to enhance the mechanical properties of recycled aggregate concrete and retain the environment. *Construction and Building Materials, 54*, 298-304. doi: 10.1016/j.conbuildmat.2013.12.063

Santamaría, A., Ortega-López, V., Skaf, M., Marcos, I., San-José, J.-T. and González, J. J. (2017). Performance of Hydraulic Mixes Manufactured with Electric Arc Furnace Slag Aggregates. In M. A. Meyers, et al (Ed.), *Proceedings of the 3rd Pan American Materials Congress* (pp. 227-234). Cham: Springer International Publishing.

Yearbook. (2019). Steel Statistical Yearbook: World Steel Association.

XV International Conference on Durability of Building Materials and Components
DBMC 2020, Barcelona
C. Serrat, J.R. Casas and V. Gibert (Eds)

Mechanical and Environmental Behavior of Cement Mortars Containing Ladle Furnace Slag

Diego Aponte and Marilda Barra

Department of Civil and Environmental Engineering (DECA), Universitat Politècnica de Catalunya-BarcelonaTECH, Campus Nord UPC, 08034-Barcelona, Spain, diego.fernando.aponte@upc.edu

Abstract. *At present, steel production is mainly done in basic oxygen furnaces (BOF) and electric arc furnaces (EAF) (Pauliuk, S. et al, 2013, Morfeldt, J. et al, 2015). According to the statistics, it is expected that the use of electric arc furnaces to supply the demand for steel will prevail. In 2017, in Europe, 41% of steel was produced in electric arc furnaces, while in Spain, according to the Union of Steel Companies (UNESID, 2016), the percentage was almost 66% in 2016. In 2016 the European Union generated approximately 18.4 Mt of slag (black and white), of which 1.5 Mt was produced in Spain. In other words, the amount of white slag produced was about 286 thousand tons, approximately between 20 and 30 kg of slag per ton of steel (UNESID, 2016, Euroslag, 2016). Refining slag (white slag) is the second most abundant waste in steel production, and, to date, its final destination is still the landfill. This study has used ladle slag from refined steelworks, as a replacement for cement in different proportions (0, 25, 50 and 75%), for the manufacture of mortars. A broad characterization of the ladle slag has been carried out, as well as determining the mechanical, durable, and environmental properties of the manufactured mortars. The results show that using the ladle slag as a replacement for cement produces a decrease in compressive strength, but the expansion behavior remains below the stability limit. It also has been seen that the slag incorporated into mortars, evaluated by leaching test at 28 days, shows inert material behavior.*

Keywords: *Ladle Furnace Slag, Cement Mortars, Durability, and Environmental Impact.*

1 Introduction

Steel slag is waste that to date has no integral solution, since its properties depend on the raw materials, Steel manufacturing process and the recovery processes carried out. Slags from steel manufacturing can be either from melting or refining processes. The first ones have been subject to more research, as well as regulation. This is because, in 2016, more than 18 Mt of slag (black and white) was generated in the European Union, but they were mostly black slag (UNESID, 2016; Euroslag, 2016).

To date, different studies have been carried out on the possibility of the use of refining slag (white slag) in civil works. Some of the topics studied are: ladle slag as a filler in self-compacting concretes (Anastasiou, E. *et al.*, 2014, Sideris, K. K. *et al.*, 2018), ladle slag as a cementitious agent in concretes and mortars (Adolfsson, D. *et al.*, 2011, Herrero, T. *et al.*, 2016), ladle slag as a binder in soil stabilization (Manso, J. M. *et al.*, 2005, Ortega-López, V. *et al.*, 2014) and ladle slag as a filler in asphalt mixtures (Skaf, M. *et al.*, 2016). In the studies mentioned above, the durability problems due to the expansion of white slag are present, and it is an aspect that does not have an easy resolution. On the other hand, there are few works related to the environmental impact of slag in cement-based materials (Loncnar, M. *et al.*, 2016, Pantazopoulou, E. *et al.*, 2018).

doi:10.23967/dbmc.2020.191

Therefore, more research is still necessary to clarify the effect of ladle furnace slag when used in cement-based materials, due to its expansive behavior and its problems with the release of contaminant elements. In this context, the main goal of this study is to analyze the incorporation of fine ladle FURNACE slag in mortars in different rates (0, 25%, 50%, and 75%), and its influence in mechanical properties, expansion behavior and environmental impact (leaching test).

2 Materials and Testing Methods

The materials used for the experimental campaign are basically: (i) CEM I 52.5R Portland Cement, (ii) slag from the refining process of an electric arc furnace Steel plant, and (iii) limestone sand with a particle size between 0 to 5mm. Potable water is used for the manufacture of mortars, and MiliQ water (obtained by filtering distilled water through a Synergy water purification system-Merck) is used for all leaching tests.

Regarding the characterization tests, the size distribution of the sand is carried out in accordance with standard UNE EN 933-1, the determination of the apparent density of the cement and white slag is done in line with standard UNE EN 80103. The chemical composition is determined using the X-Ray fluorescent technique, using a Philips PW 2400 Spectrometer, and the Powder Diffraction technique for the mineralogical composition, using an Analytical X´pert PRO MPD Alpha 1 (diffractometer in Bragg Brentano $\theta/2\theta$ geometry of 240 mm of radius Cu Kα1 radiation λ = 1.5406 Å). Cement and slag size distribution is performed using a Beckman Coulter LS particle size analyzer, while a Scanning Electron Microscopy (SEM-EDS) is used to study the surface structure and perform microanalysis.

The mortars are manufactured in accordance with standard UNE EN 196-1, with a water to cement ratio of 0.5 in all cases. The nomenclature and dosage of the mortars are shown in Table 1.

Table 1. Dosage and nomenclature of mortars.

Mortar type	L. Slag (g)	Cement (g)	Sand (g)	Water (g)
Control	0	450	1350	225
M75/25	337.5	112.5	1350	225
M50/50	225	225	1350	225
M25/75	112.5	337.5	1350	225

At the ages of 7 and 28 days of curing, density and absorption are determined according to the standard ASTM C642, and the compressive strength according to standard UNE EN 196-1. A length comparator is used to measure the expansion/shrinkage of the mortars over time, which is fitted to the metal points that adhere to the mortars 24 hours after manufacture.

Finally, for the environmental impact tests, standard UNE EN 12457-2 is used for all mortars at the age of 28 days, as well as for white slag. In the case of mortars, they are dried in an oven at 40 ºC to a constant mass, at which point they are ground in a jaw crusher until all the material passes through the 4 mm sieve. It is then quartered to obtain representative samples. The results of this test are compared with the Decree on waste acceptance criteria in landfills (Council Decision 2003/33/EC of 19 December 2000) to classify mortars as an inert, non-hazardous, or

dangerous material.

3 Results and Discussion

In the following sections, the results obtained from the experimental campaign are analyzed, with emphasis on expansion behavior (durability) and environmental behavior (leaching).

3.1 Particle Size Distribution and Specific Gravity

White slag, used in this study, consists of particles between 0.1 microns to 75 microns approximately, granulometry obtained due to a process of grinding the material in a ball mill. Figure 1 shows the size distribution and compares it with the cement used (CEM I 52.5R). It can be seen that the cement has greater fineness from 2 microns to 60 microns, while the slag presents a slightly higher percentage of particles in the range 0.1 to 2 microns.

In Table 2, it can be seen that the density of the slag is lower than the density of the cement (approximately 9%). This situation will generate a change in the total volumes of mortars manufactured. But for this study, it is assumed that the influence will not change the behavioral trends if the dosage of the mortars is done in weight or volume. In Table 2, it is also observed that sand has an absorption of 1.65%, so it was decided to use this material in the condition of dry saturated surface at the time of manufacturing the mortars.

Table 2. Properties of raw materials.

Property	L. Slag	Cement	Sand
Apparent density (g/cm^3)	2.75	3.02	2.73
Dry density (g/cm^3)	--	--	2.55
Absorption (%)	--	--	1.65

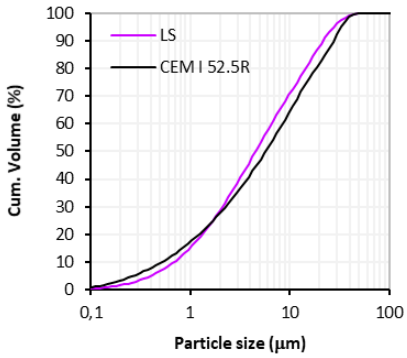

Figure 1. Particle size distribution for Ladle slag and Cement Portland.

3.2 Chemical and Mineralogical Composition

Slag and cement basically contain Calcium, Silica, Aluminium, and Iron. White slag has high magnesium content, and some of it may be present as Periclase, which will create expansion problems. Table 3 shows the compounds present in both the slag and the cement.

Table 3. Chemical composition for Ladle slag and Cement portland.

Element	Cement (%)	L. Slag (%)
CaO	63.21	46.78
SiO_2	18.65	18.60
Al_2O_3	3.98	6.62
Fe_2O_3	3.32	5.36
SO_3	2.94	1.51
MgO	1.42	10.85
Others	1.47	1.69
LOI	5.01	8.59

The phases identified in the cement used are: calcium silicates (C_3S, β-C_2S), calcium aluminate (C_3A), calcium ferroaluminate (C_4AF). Anhydrous gypsum ($CaSO_4$) and calcite ($CaCO_3$) have also been determined. It should be mentioned that the used slag contains a part of amorphous material, together with crystalline phases, such as: calcium silicates (α-C2S, β-C_2S), calcium aluminate (C_3A), gehlenite ($Ca_2Al((AlSi)O_7)$), wustite (FeO), and periclase (MgO). In addition, calcite ($CaCO_3$) and in low proportion portlandite ($Ca(OH)_2$) and lime (CaO) have been identified.

3.3 Particle Morphology and Microanalysis

Figure 2 and Figure 3 show different particles that make up the slag, and by performing micro-analysis, the compounds identified by XRD are confirmed. It is important to note that, for example, the calcium silicate compounds show a high variation in their proportions, so that it is not possible to speak of compounds with an exact composition. The presence of compounds from the gehlenite family has also been observed, which present greater or lesser amounts of aluminum in their composition.

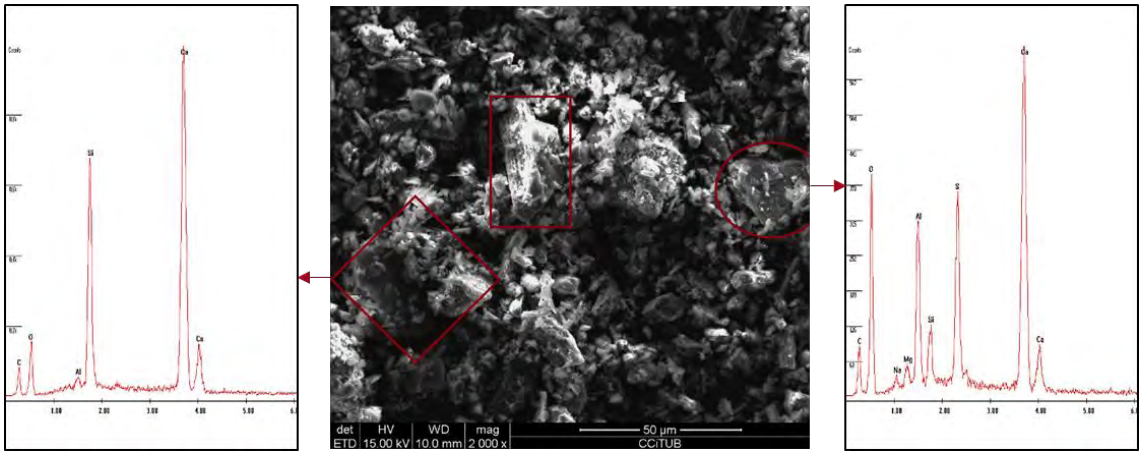

Figure 2. Chemical composition of different Calcium Silicates and Gehlenite of the particle of ladle slag.

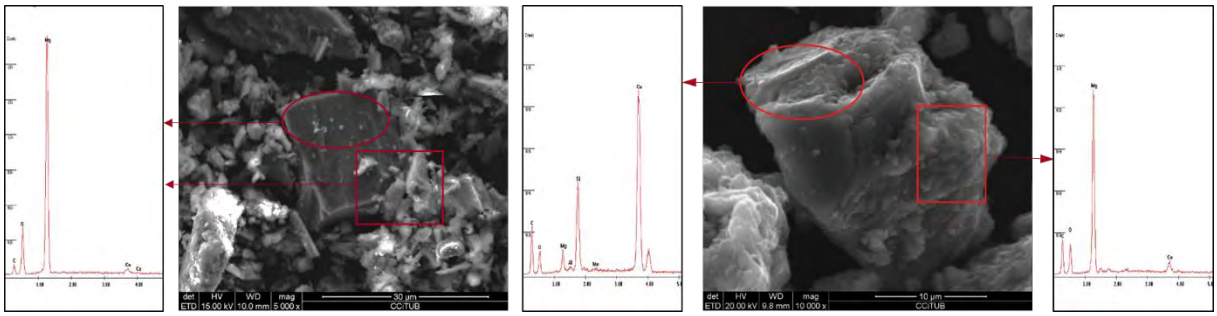

Figure 3. Periclase compound (left) and Calcium Silicate (right) in the Ladle slag.

In the samples analyzed by SEM-EDS, it was possible to find MgO particles, as shown in Figure 4. Again, the complexity of the mineralogical composition of the slag should be pointed out, since, as shown in Figure 4 right, in the same particle can be found compounds of calcium silicate and magnesium oxide.

3.4 Physical and Mechanical Properties of Mortars

As reported in the literature, fine slag has cementitious properties, but with low cementitious activity. This fact has been proved by XRD analyses, where the cementitious compounds are some slow reacting calcium silicates and possibly some gehlenites. Therefore, the particle size of the slag plays an important role in the development of mechanical properties, as it can act as a filler material.

Figure 4 shows the effect of incorporating slag into mortars and curing time (7 and 28 days) in compressive strength. It can be seen that as the amount of slag increases, the strength decreases, and this decrease is almost proportional. When 25% of the cement is replaced by slag, the strength falls by 20%, indicating that the material has a medium strength activity. However, when 50% is replaced, the compressive strength falls by 62%, and when 75% is replaced, the strength falls by 90%, clearly indicating that it is a material with medium-low cementing activity. It should be noted that with replacements from 50% cement, the strength achieved is almost 20 MPa, which means that there is a wide variety of materials that could be developed with these properties.

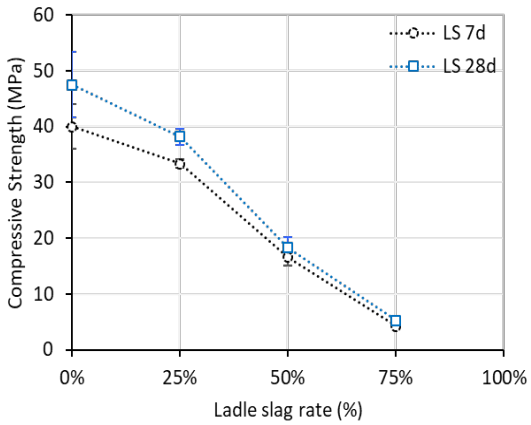

Figure 4. Compressive strength of mortar with different rates of ladle slag.

3.5 Expansion Behavior of Mortars

The volumetric stability behavior has been measured over time up to an age of approximately 400 days. The samples after manufacturing have been kept in a wet chamber (20°C and 95%R.H.), in order to have water availability and to facilitate the reactions of the expansive compounds.

Figure 5 shows the behavior for the different types of mortars (control = 0% L.S, M25/75 = 75% L.S, M50/50 = 50% L.S, and M75/25 = 75% L.S.). For the control mortar, a linear increase can be observed up to 100 days, and then the behavior is constant up to 0.02% linear expansion. For mortars containing slag, it can be seen that after 100 days, linear expansion continues to increase over time, possibly with greater expansion as the slag content increases.

The limit expansion value has been taken as 0.04%, which is used for aggregates with alkali-silica reactivity problems (Velasco, 2014). This is due to the fact that there is no regulation regarding the minimum or maximum expansion that can be accepted when using slags in rigid matrices.

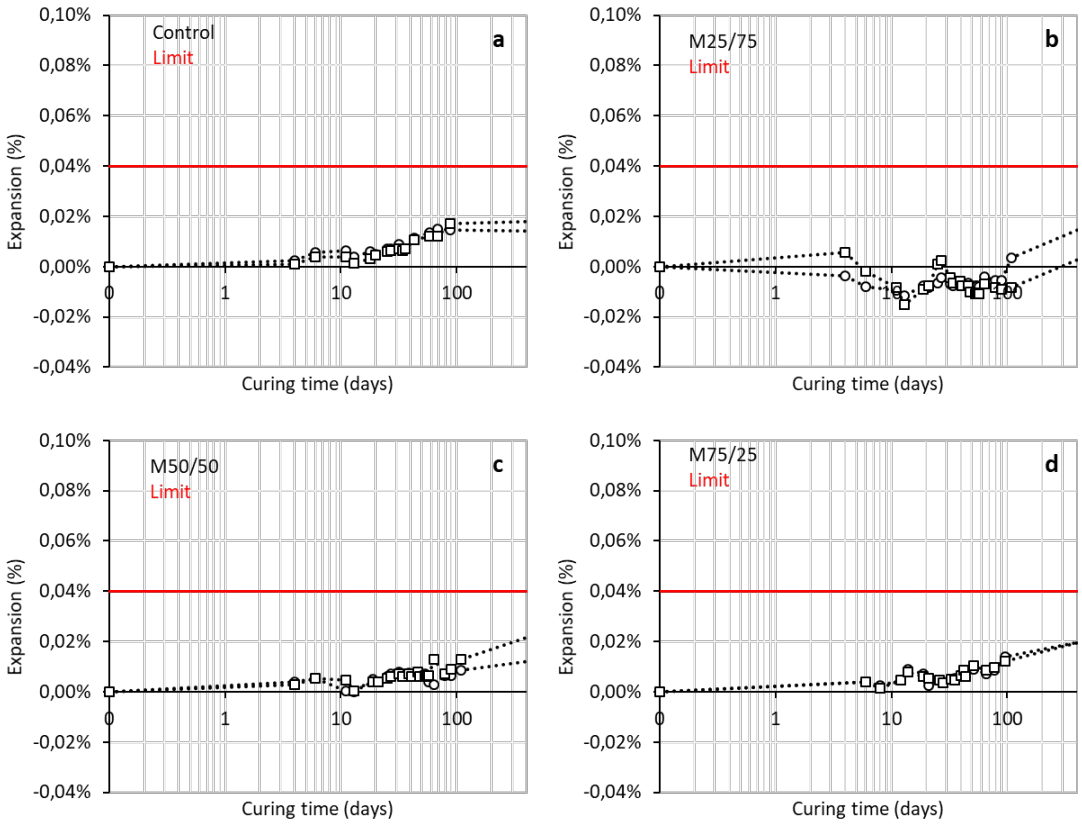

Figure 5. Expansion over time for control mortars (a), 25% ladle slag mortars(b), 50% ladle slag mortars (c) and 75% ladle slag mortars (d).

3.6 Environmental Behavior of Mortars with Ladle Slag

In general terms, in Spain and other European countries, slag is classified as an inert waste (REF). However, the classification is open and, in some cases, does not specify whether it is

black slag or white slag. In this context, some regulations have stated that the classification is only for black slag.

By carrying out leaching tests on the white slag, it can be verified that it is a material that can be in the range of non-hazardous material or hazardous material (Council Decision 2003/33/EC of 19 December 2000), depending on each manufacturing plant. In this study, the white slag analyzed present releases of some elements higher than those accepted for inert materials, such as Barium and Nickel (Fig. 7). However, it can be seen that once incorporated into the mortars, in all proportions, the release is below the limits. Figure 7 shows the quantities released for the elements Chromium, Copper, Molybdenum, Lead, and Zinc, which are below the limits for inert material.

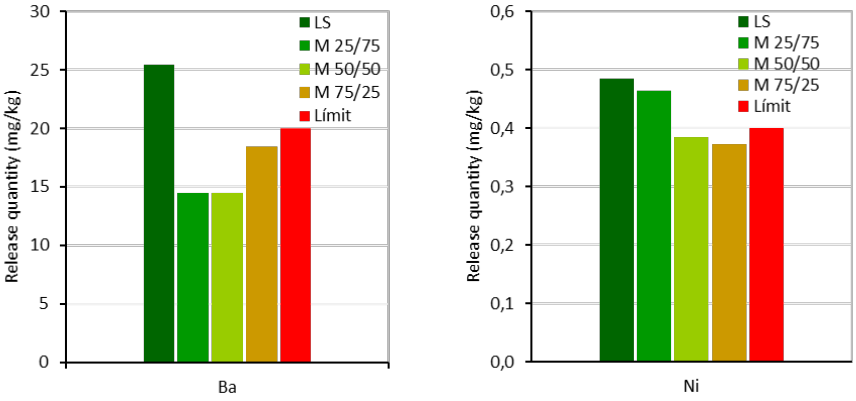

Figure 6. Release of Barium (left) and Niquel (right) of ladle slag and mortar.

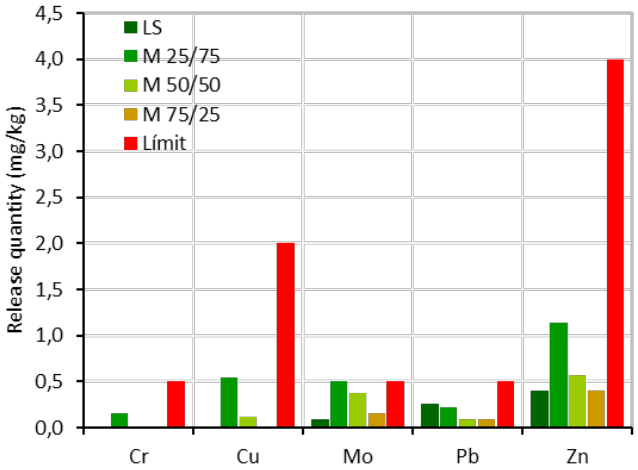

Figure 7. Release of Cr, Cu, Mo, Pb, and Zn of ladle slag and mortar.

4 Conclusions

According to the work done, the following conclusions can be drawn:

- The white slag studied presents phases that can generate cementing behavior. However, it is observed that its activity index is low (80%), and it is only working as a filler.

- Replacement of cement by slag in percentages from 50% generate materials with a compressive strength between 20 and 5 MPa. These values may be thought to be low, but they would allow the use of slag in a wide variety of applications, from low strength fluid fillers (< 2 MPa) to low mechanical stress pavement concretes (15 to 20 MPa).
- The expansive behavior of mortars has shown a tendency to increase over time, which can be a problem in terms of stability. However, linear expansions obtained up to 400 days of curing are below the 0.04% limit, which raises the possibility of their use in short-life materials.
- The white slag in this study is classified as non-hazardous materials, but when it is incorporated into mortars, it behaves like an inert material. Therefore, at the end of the lifespan of the material, it can be treated without further problems.

ORCID

Diego Aponte: http://orcid.org/0000-0001-5737-7819
Marilda Barra: http://orcid.org/0000-0002-1417-1615

References

A. Velasco Torres (2014). Estudio experimental sobre la reacción álcali-sílice en el hormigón producida por áridos de reacción lenta. PhD Thesis, Universidad Politécnica de Madrid. Madrid.

D. Adolfsson, F. Engström, R. Robinson, and B. Björkman (2011). Cementitious phases in ladle slag. Steel research Journal, No. 4, p, 398-403.

Eleftherios K. Anastasiou, Ioanna Papayianni, Michail Papachristoforou (2014). Behavior of self compacting concrete containing ladle furnace slag and steel fiber reinforcement. Materials and Design, vol. 59, p. 454-460.

E. Pantazopoulou, and A, Zouboulis (2018). Chemical toxicity and ecotoxicity of tannery stabilized with ladle furnace slag. Journal of Environmental Management, No. 216. P, 257-262.ISO/TC 59/SC 14 (2008). *ISO 15686-8: Buildings and constructed assets — Service-life planning — Part 8: Reference service life and service-life*

UNESID, "Unión de empresas siderúrgicas" On-line. Available: https://unesid.org/el-sector-el-sector-en-2016-producciones-basicas.php.

Euroslag. On-line. Available: ttps://www.euroslag.com/products/statistics/statistics-2016/

J. Morfeldt, W. Nijs, and S. Silveira (2015). "The impact of climate targets on the future steel production – an analysis based on a global energy system model". Journal of Cleaner Production, vol. 13, p. 469-482.

J. M. Manso, M. Losañez, J. A. Polanco, and J. González (2005). Ladle furnace slag in construction. Journal of Materials in Civil Engineering, vol. 17, p. 513-518.

K. K. Sideris, Ch. Tassos, A. Chatzopoulos, and P. Manita (2018). Mechanical characteristics and durability of self compacting concretes produced with ladle furnace slag. Construction and Building Materials, vol. 170, p. 660-667.

M. Loncnar, H. A. van der Sloot, A. Mladenovic, M. Zupancic, L. Kobal, and P. Bukovec (2016). Study of the leaching behaviour of ladle slags by means of leaching test combined with geochemical modelling and mineralogical investigations. Journal of Hazardous Materials, n. 317, p. 147-157.

M. Skaf, V. Ortega, J. A. Fuente-Alonso, A. Santamaría, and J. M. Manso (2016). Ladle furnace slag in asphalt mixes. Construction and Building Materials, vol. 122, p. 488-495.

S. Pauliuk, R. L. Milford, D. B. Múller and J. M. Allwood. "The steel scrap age" (2013). Environmental Science and Technology, Vol. 47, p. 3448-3454.

T. Herrero, I. Vegas, A. Santamaria, J. T. San-Jose, M. Skaf. Effect of high alumina ladle furnace slag as cement susbtitution in masonry mortars (2016). Construction and Building Materials, vol. 123, p. 404-413.

V. Ortega-López, J. M. Manso, I. I. Cuesta, and J. González (2014). The long term accelerated expansion of various ladle furnace basic slag and their soil stabilization applications. Construction and Building Materials, vol. 68, p. 455-464.

XV International Conference on Durability of Building Materials and Components
DBMC 2020, Barcelona
C. Serrat, J.R. Casas and V. Gibert (Eds)

Pore Refinement Action of GGBFS and Fly Ash on the Primary and Secondary Capillary Imbibition Rates of Concrete

Natalia M. Alderete[1], Yury A. Villagrán-Zaccardi[2] and Nele De Belie[1]

[1] Magnel Laboratory for Concrete Research, Ghent University, Technologiepark-Zwijnaarde 60, 9052-Gent, Belgium, nataliamariel.alderete@ugent.be, nele.debelie@ugent.be

[2] LEMIT, CONICET, Av. 52 entre 121 y 122 s/n, B1900AYA-La Plata, Argentina, yuryvillagran@conicet.gov.ar

Abstract. *Capillary imbibition is a transport phenomenon occurring in concrete structures exposed to weathering, frequently in direct connection with the resistance against different deterioration processes. This property depends on the volume and connectivity of pores. For ground granulated blast-furnace slag (GGBFS) and fly ash blended concrete mixes, the pore refining action of these supplementary cementitious materials plays a positive role in the disconnection of the capillary porosity and consequent reduction of the capillary imbibition rate. Moreover, for this particular transport process, primary and secondary transport rates can be defined in connection with different driving mechanisms. This allows a complementary description of the pore structure of concrete. In this paper, blended concrete mixes were prepared by substituting 20, 40 and 60 % of OPC by GGBFS, and 20, 30 and 40 % of OPC by fly ash. The pore structure of these concretes is assessed by water absorption under vacuum and mercury intrusion porosimetry after curing periods of 28 and 90 days. Long-term capillary imbibition tests were also performed and primary and secondary imbibition rates are computed by a novel approach that considers their linear evolution with the fourth root of time. Results show the refinement action of GGBFS and fly ash by a softening in the transition stage between the primary and secondary imbibition periods. A low water flow rate is consequently correlated with the increased tortuosity of samples.*

Keywords: *Sorptivity, Supplementary Cementitious Materials, Pore Structure, Imbibition.*

1 Introduction

Sorptivity is a widely used durability index of concrete. The quantification of the rate of water imbibition by capillarity in concrete describes the pore connectivity of cementitious materials. Previous work has shown that primary and secondary imbibition rates can be used for describing the pore structure on the basis of their corresponding driving mechanism.

The most usual assessment method considers the relation between water uptake and the square root of time, but it faces the significant difficulty of the lack of linearity of this relationship for the case of cementitious materials. This is usually referred as anomalous sorptivity (Hall, 2007; Küntz and Lavallée, 2001; Lockington and Parlange, 2003; Villagrán Zaccardi *et al.*, 2017). A comprehensive analysis of this analomaly led to the proposal of a new approach considering the fourth root of time, which was validated with experimental data in the short term (Villagrán Zaccardi *et al.*, 2017). The new model considers the swelling of the C-S-H gel as the main cause for the anomalous behaviour. Physical evidence of this swelling was recently presented in (Alderete *et al.*, 2019b), where the volumetric stability of mortar and concrete samples was registered using strain gauges.

During long-term exposure of samples, water uptake further continues at a very low rate even after the capillary rise has covered the full height of samples (Alderete *et al.*, 2019a; Bentz *et al.*, 2001; Castro *et al.*, 2011; Hall and Hoff, 2009; Kaufmann and Studer, 1995; Spragg *et al.*, 2011). A secondary imbibition period for the water ingress driven by diffusion into the finest pores of the cementitious matrix can be therefore defined. Allegedly, this process starts as soon as the material makes contact with water, but it is initially masked by the capillary action which dominates the water flow during the primary imbibition. The secondary capillary imbibition has been presented as a convenient complementary descriptor of the transport properties of cementitious materials (Henkensiefken *et al.*, 2009; Kurtis *et al.*, 2016; Liu and Hansen, 2016; Wei *et al.*, 2017). Both primary and secondary mechanisms should be considered for describing the whole moisture transport during imbibition.

In this paper, capillary imbibition tests were conducted for 17 weeks on concrete mixes with and without ground granulated blast furnace slag and fly ash to determine the primary and secondary capillary imbibition rates. These transport parameters are compared with the pore size distribution obtained by mercury intrusion porosimetry (MIP).

2 Materials and Methods

Concrete mixes were designed with a water to binder ratio (w/b) of 0.45. OPC type CEM I 42.5 N, ground granulated blast furnace slag (SB), and fly ash (FA) were used supplementary cementitious materials (SCMs) in partial replacement of OPC in proportions of 20, 40 and 60, and 20, 30 and 40%, respectively. A reference mix with only OPC as binder was also made. Table 1 displays the properties of the binders, including composition, density, and particle size distribution (obtained by laser diffractometry with optimal optical parameters chosen as suggested in (Alderete *et al.*, 2016)). Mix proportions, slump, air content, and compressive strength are provided in Table 2. The mixes were named based on the binder (OPC for control, SB, and FA for the blends) and the weight percentage of cement replacement. To improve the workability, a commercially available polycarboxylic ether-based superplasticiser was added to the concrete during mixing. In addition to five concrete cylinders with 10 cm in diameter, three 10 cm cubes for compressive strength were also cast for each mix and cured in a conditioned room at 20 °C ± 2 °C and 95 % ± 5 % RH for 28 and 90 days.

Table 1. Properties of OPC, SB, and FA.(nd = not determined, LOI = loss on ignition).

Properties	OPC				SB				FA			
Chemical composition (%)	CaO	64.67	S	nd	CaO	38.34	S	1.4	CaO	3.02	S	nd
	SiO_2	20.74	Fe_2O_3	1.52	SiO_2	33.7	Fe_2O_3	0.43	SiO_2	54.19	Fe_2O_3	7.92
	MgO	0.95	K_2O	0.77	MgO	8.18	K_2O	0.34	MgO	1.92	K_2O	3.38
	Al_2O_3	4.91	MnO	nd	Al_2O_3	11.36	MnO	8.18	Al_2O_3	23.5	MnO	nd
	Na_2O	0.27	Cl^-	0.07	Na_2O	0.35	Cl^-	0.01	Na_2O	0.39	Cl^-	<0.01
	SO_3	2.96	LOI	nd	SO_3	0.03	LOI	0.16	SO_3	0.94	LOI	1.84
Density (g/cm^3)	3.11				2.88				2.14			
Particle size dv10/50/90 (µm)	4.9/20.1/58.5				1.8/13.9/35.0				0.4/10/61.7			

Table 2. Nomenclature, mix composition, air content and slump of the studied concrete mixes.

	OPCc	SB20c	SB40c	SB60c	FA20c	FA30c	FA40c
Cement - CEM I 42.5 N (kg/m^3)	342	274	205	137	274	239	205
SCM (kg/m^3)	0	68	137	205	68	103	137
Water (kg/m^3)	154	154	154	154	154	154	154
Sand (kg/m^3)	865	860	860	860	860	860	855
Gravel 2/8 (kg/m^3)	500	497	495	493	497	493	490
Gravel 8/16 (kg/m^3)	540	535	535	535	535	535	530
Air content (%)	2.1	2.4	2.1	2.3	2.8	2.3	2.4
Slump (mm)	70	70	100	120	70	100	150
Compressive strength 28d (MPa)	50.6	42.6	32.6	32.2	50.1	50.8	48.8

The top halves of the five cylinders were used to determine water absorption by immersion. First, samples were submitted to vacuum for 2 h and then water was drawn into the vacuum chamber until the sample became fully immersed. After 24 h samples were removed and the saturated weight was registered. Then, samples were subjected to drying in an oven at 105 °C. Finally, water absorption was calculated from the difference between the saturated weight and the dry weight, relative to the dry weight.

The samples for MIP were approximately 125 mm^3, obtained from the core of one cylinder per mix. Microstructural damage during pre-conditioning was minimised by first drying samples at 40 °C for 24 h, and then vacuum-drying them at (20 ± 2) °C for two weeks at 0.1 bar (Snoeck *et al.*, 2014; Zhang and Scherer, 2011). The maximum applied pressure was 200 MPa in order to avoid massive cracking induced by the pressure (Beaudoin and Marchand, 2001). Measurements were corrected with a blank to disregard differential mercury compression. The intruding volume of mercury into the sample is a function of the pressure increase. Results are interpreted with the theoretical simplified model of cylindrical pores and translated into pore 'diameters' upon the application of the Lucas-Washburn equation. The surface tension and contact angle considered for these computations were 0.482 N/m and 142° (Ma, 2014), respectively. Qualitative contrasts are finally possible by comparing the threshold diameter (d_{th}) and intrudable pore volume (ϕ_{in}) (Ma, 2014). The calculation of d_{th} was made by the tangent method, and therefore denoted as d_{tg} (Liu and Winslow, 1995), corresponding to the intersection of tangent lines on the cumulative distribution curve at the smallest diameter that did not exhibit significant intrusion and the largest diameter that did. The range of the points to be fitted was determined by the analysis of the second derivative in the differential curve. Furthermore, according to the cumulative curve shape obtained, it is possible to make inferences about the presence of choke points.

The tested samples for the long-term capillary imbibition tests were obtained by sawing the section between 3 and 8 cm from the base of the five cylinders. Samples were laterally covered with aluminum-butyl tape to ensure one dimensional flow. The preconditioning procedure consisted in 72 h immersion in water and then drying in an oven at 50 °C until mass decrease was lower than a mass fraction of 0.1 % within 24 h. The capillary imbibition test consisted in putting the samples in contact with water, with an immersion depth of (3 ± 1) mm. Water evaporation was avoided by putting a lid on top of the water container. The water

level was checked regularly and the immersion depth was kept at (3 ± 1) mm during the whole testing period. Samples of OPCc and FA20c mixes with 28 days of curing were the first ones to be tested, with testing periods up to 10 weeks. Based on these results, it was decided to continue the measurements for the capillary imbibition tests on the rest of samples up to 17 weeks to obtain a larger amount of data for the secondary period than for the first data series. In this manner, a more complete description of the secondary period was achieved in those cases. Measurements were performed after exposure periods of 0.5 h, 1 h, 2 h, 3 h, 4 h, 5 h, 6 h, and 24 h and after that every 24 h during the first week, once a week during the first two months, and once a month until 4 months.

3 Results and Discussion

Figure 1 displays the results of relative water absorption of the mixes at 28 and 90 days. At 28 days, values of water absorption of all SB mixes are higher than the OPCc mix. However, at 90 days, mixes SB20c and SB40c had lower water absorption than OPCc at 90 days. Values of water absorption at 28 days increased slightly with the FA content. At 90 days, FA20c and FA30c show similar results as OPCc, but the higher replacement in FA40c does not allow to compensate the dilution effect.

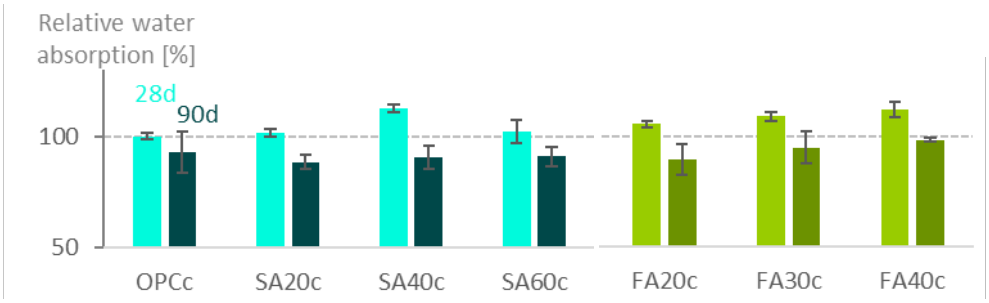

Figure 1. Relative open porosity and relative water absorption of OPCc, SB and FA concrete mixes at 28 and 90 days.

The cumulative mercury intruded volume curves of SB and FA mixes at 28 and 90 days are presented in Figure 2, with the indication of the ϕ_{in} and d_{tg} of each mix. Results reveal the refinement action of SB with time. All mixes had a reduction of ϕ_{in} between 16 % and 26 % after 90 days. Accordingly, d_{tg} values were reduced from 28 to 90 days. For FA mixes, results indicate the slower reaction of FA in comparison with SB, as indicated by reactivity tests (Alderete, 2018). Although all FA mixes have a lower ϕ_{in} at 90 days than at 28 days, the reduction is around half of that found for concrete mixes with SB. In fact, FA40c at 90 days displays a higher value than SB60c at 28 days. This shows that even with a lower amount of replacement ($40 < 60$) and with more time to react ($90 > 28$), FA does not compensate the clinker dilution as well as SB. Values of d_{tg} are in agreement with this as well, as they are higher for FA concrete mixes than SB mixes at 90 days.

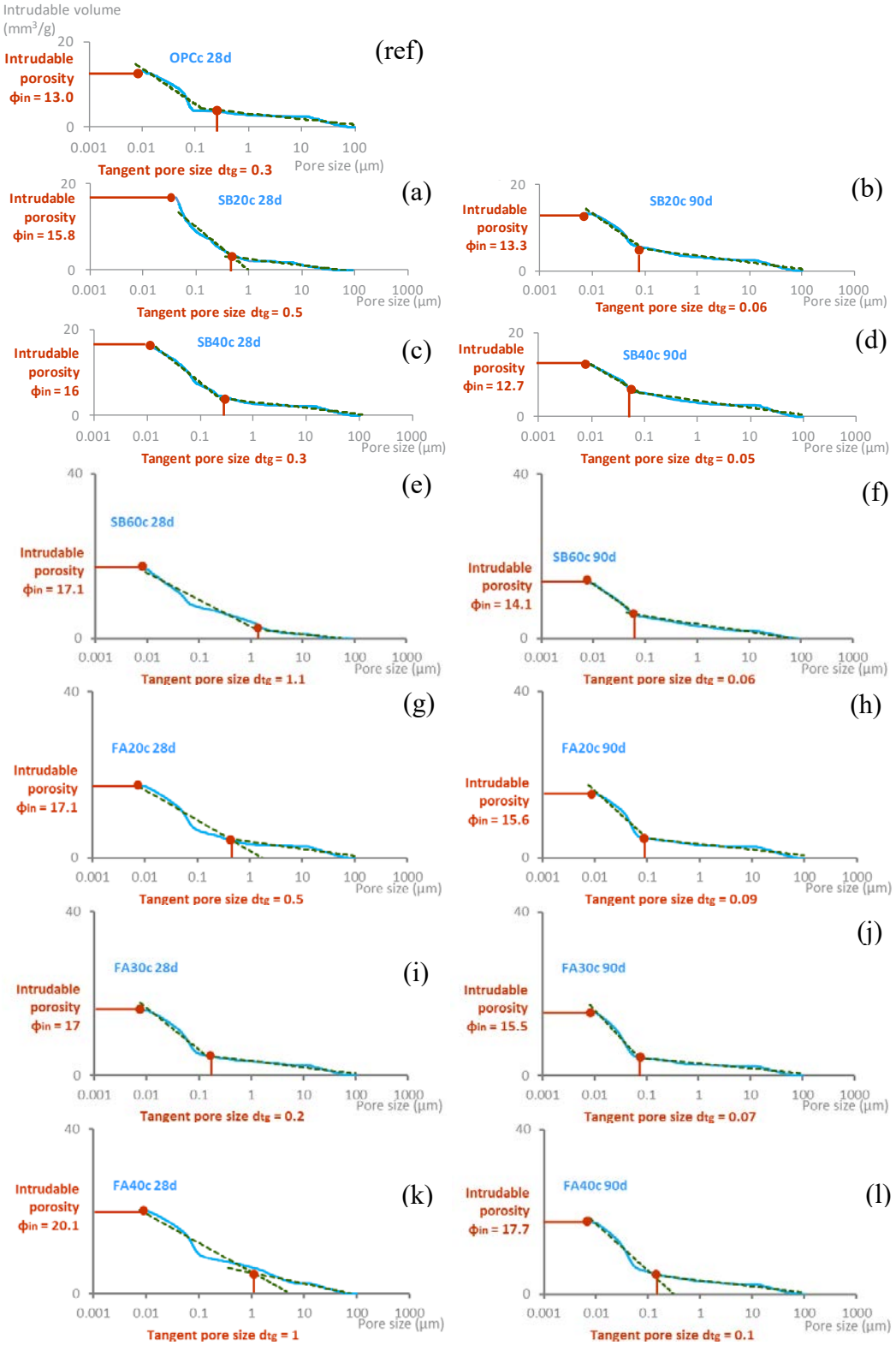

Figure 2. MIP curves of OPCc at 28 (ref), SB20c at 28 (a) and 90 (b), SB40c at 28 (c) and 90 (d), SB60c at 28 (e) and 90 (f), FA20c at 28 (g) and 90 (h), FA30c at 28 (i) and 90 (j), and FA40c at 28 (k) and 90 (l) days.

Results for the capillary imbibition of the mixes are shown in Figure 3. Two periods, primary and secondary, and a transition period in between, are observed. The primary imbibition period takes place within 1 and 3 weeks, for samples tested at 28 days and 90 days, respectively. Error bars represent the standard deviation (n = 5) and are marked in all graphs, but, as the variability was very small, some error bars are not visible because they are smaller than the marker. The capillary imbibition rate (CIR) is computed as the slope of the fitting line during the first week: CIR_{1w} (for 28 days); and during the first 3 weeks: CIR_{3w} (for 90 days). The secondary capillary imbibition rate is computed as the slope of the fitting line after the transition period: $sCIR_{1w}$ (for 28 days); and $sCIR_{3w}$ (for 90 days). The corresponding coefficients of determination are shown in the graphs. The transition period is highlighted in the graphs, where the difference between the primary and the secondary periods is less marked for blended than control concrete.

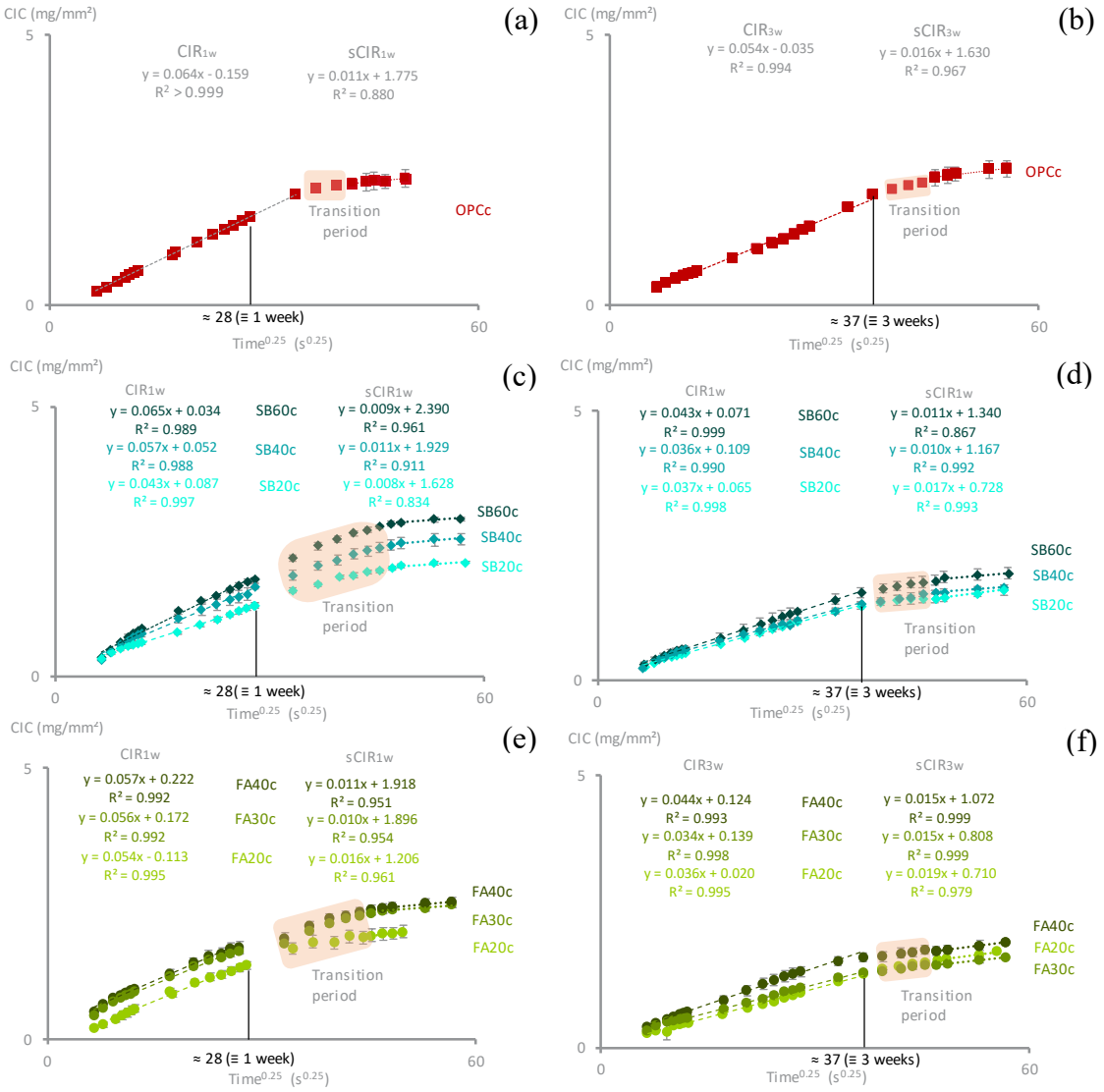

Figure 3. Long-term capillary water uptake results of OPCc at 28 (a) and 90 (b), SB at 28 (c) and 90 (d), and FA at 28 (e) and 90 (f) days.

Pore refinement due to the action of the SCMs led to a decrease in d_{tg} in the range of 0.2 to 1 μm at 28 days, to the range of 0.05 to 0.1 μm at 90 days, which corresponds to a decrease in the CIR from the range of 0.048 to 0.065 $mg \cdot mm^{-2} \cdot s^{-0.25}$ to the range of 0.034 to 0.044 $mg \cdot mm^{-2} \cdot s^{-0.25}$. This correlation is in contrast with the values of ϕ_{in}, which are not reflecting so well the refinement action of the SCMs. Contrarily, the sCIR does not show a clear connection with the MIP parameters, and this transport parameter is likely linked with the content of C-S-H in each mix and the gel pores. Additional research in this regard seems valuable. Furthermore, blended concrete mixes had a more marked transition period and lower imbibition rate at 90 days in comparison with 28 days, which indicates a lower flow rate due to their increased tortuosity.

4 Conclusions

The long-term exposure of unsaturated samples involves additional water uptake after the capillary rise has covered the total height of samples. This is a process that occurs at a much slower rate than the short-term capillary imbibition, and it can be related to a secondary transport through the finest range of pores. Long-term capillary imbibition tests in blended concretes manifested the existence of primary and secondary periods. Both periods display increasing water uptake proportional to $t^{0.25}$.

The pore refinement action of ground granulated blast-furnace slag and fly ash was reflected in the comparable reduction of the CIR and d_{tg} parameters. In second term, ϕ_{in} values were reduced from 28 to 90 days, but the correlation is not very good with the capillary imbibition. The likely reason is that pore refinement causes an increase in tortuosity more than a reduction in porosity. Lastly, sCIR does not reflect so well the refinement action of the SCMs. In this case, the transport parameter could be phenomelogically linked to the C-S-H content and its characteristic porosity.

Acknowledgements

Y. Villagrán-Zaccardi (MSCA - Seal of Excellence) and N. Alderete (12ZG820N) thank FWO-Vlaanderen for the financial support. Financial support from ANPCyT (PICT 2017-0091 Prest BID) is also appreciated.

ORCID

Natalia Alderete: https://orcid.org/0000-0001-7967-1955
Yury Villagrán-Zaccardi: https://orcid.org/0000-0002-0259-7213
Nele De Belie: https://orcid.org/0000-0002-0851-6242

References

Alderete, N. M. (2018). *Microstructure of mortar and concrete with supplementary cementitious materials: relation with the capillary imbibition phenomenon*, PhD Thesis, UGhent and UTN.

Alderete, N. M., Villagrán-Zaccardi, Y. A. and De Belie, N. (2019a). Mechanism of Long-Term Capillary Water Uptake in Cementitious Materials, *Cement & Concrete Composites*, submitted.

Alderete, N. M., Villagrán-Zaccardi, Y. A. and De Belie, N. (2019b). Physical evidence of swelling as the cause of anomalous capillary water uptake by cementitious materials, *Cement and Concrete Research*, 120, 256–266. https://doi.org/10.1016/j.cemconres.2019.04.001

Alderete, N. M., Villagrán Zaccardi, Y. A., Dos santos Coelho, G. S. and De Belie, N. (2016). Particle size distribution and specific surface area of SCMs compared through experimental techniques. In: *Proceedings of the International RILEM Conference on Materials, Systems and Structures in Civil Engineering*, Lyngby,

Denmark, 61–72.
Beaudoin, J. J. and Marchand, J. (2001). Pore Structure. In: *Handbook of Analytical Techniques in Concrete Science and Technology*, 528–628. https://doi.org/10.1016/B978-0-8155-1437-4.50017-5
Bentz, D. P., Ehlen, M. A., Ferraris, C. F. and Garboczi, E. J. (2001). Sorptivity-based service life predictions for concrete pavements. In: *Proc. of the 7th International Conference on Concrete Pavements*, Orlando (FL), 1, 9–13.
Castro, J., Bentz, D. and Weiss, J. (2011). Effect of sample conditioning on the water absorption of concrete. *Cement and Concrete Composites*, 33(8), 805–813. https://doi.org/10.1016/j.cemconcomp.2011.05.007
Hall, C. (2007). Anomalous diffusion in unsaturated flow : Fact or fiction? *Cement and Concrete Research*, 37, 378–385. https://doi.org/10.1016/j.cemconres.2006.10.004
Hall, C. and Hoff, W. (2009). Water transport in brick, stone and concrete. CRC Press, Boca Raton. https://doi.org/10.1520/CCA10518J
Henkensiefken, R., Castro, J., Bentz, D., Nantung, T. and Weiss, J. (2009). Water absorption in internally cured mortar made with water-filled lightweight aggregate. *Cement and Concrete Research*, 39(10), 883–892. https://doi.org/10.1016/j.cemconres.2009.06.009
Kaufmann, J. and Studer, W. (1995). One-dimensional water transport in covercrete - application of non-destructive methods. *Materials and Structures*, 28(2), 115–124.
Küntz, M. and Lavallée, P. (2001). Experimental evidence and theoretical analysis of anomalous diffusion during water infiltration in porous building materials. *Journal of Physics D: Applied Physics*, 34, 2547–2554.
Kurtis, K. E., Burris, L. and Alapati, P. (2016). Consider Functional Equivalence : A (Faster) Path to Upscaling Sustainable Infrastructure Materials Compositions. *In Proc. of the 1st International Conference on Grand Challenges in Construction Materials*, 8 p.
Liu, Z. and Hansen, W. (2016). A geometrical model for void saturation in air-entrained concrete under continuous water exposure. *Construction and Building Materials*, 124, 475–484. https://doi.org/10.1016/j.conbuildmat.2016.07.113
Liu, Z. and Winslow, D. (1995). Sub-distributions of pore size: A new approach to correlate pore structure with permeability. *Cement and Concrete Research*, 25(4), 769–778. https://doi.org/10.1016/0008-8846(95)00067-M
Lockington, D. A. and Parlange, J.-Y. (2003). Anomalous water absorption in porous materials. *Journal of Physics D: Applied Physics*, 36, 760–767. https://doi.org/10.1088/0022-3727/36/6/320
Ma, H. (2014). Mercury intrusion porosimetry in concrete technology: Tips in measurement, pore structure parameter acquisition and application. *Journal of Porous Materials*, 21(2), 207–215. https://doi.org/10.1007/s10934-013-9765-4
Snoeck, D., Velasco, L. F., Mignon, A., Van Vlierberghe, S., Dubruel, P., Lodewyckx, P. and De Belie, N. (2014). The influence of different drying techniques on the water sorption properties of cement-based materials. *Cement and Concrete Research*, 64, 54–62. https://doi.org/10.1016/j.cemconres.2014.06.009
Spragg, R. P., Castro, J., Li, W., Pour-Ghaz, M., Huang, P.-T. and Weiss, J. (2011). Wetting and drying of concrete using aqueous solutions containing deicing salts. *Cement and Concrete Composites*, 33(5), 535–542. https://doi.org/10.1016/J.CEMCONCOMP.2011.02.009
Villagrán Zaccardi, Y. A., Alderete, N. M. and De Belie, N. (2017). Improved model for capillary absorption in cementitious materials: Progress over the fourth root of time. *Cement and Concrete Research*, 100, 153–165. https://doi.org/10.1016/j.cemconres.2017.07.003
Wei, Z., Falzone, G., Wang, B., Thiele, A., Puerta-Falla, G., Pilon, L., Neithalath, N. and Sant, G. (2017). The durability of cementitious composites containing microencapsulated phase change materials. *Cement and Concrete Composites*, 81, 66–76. https://doi.org/10.1016/j.cemconcomp.2017.04.010
Zhang, J. and Scherer, G. W. (2011). Comparison of methods for arresting hydration of cement. *Cement and Concrete Research*, 41(10), 1024–1036. https://doi.org/10.1016/j.cemconres.2011.06.003

XV International Conference on Durability of Building Materials and Components
DBMC 2020, Barcelona
C. Serrat, J.R. Casas and V. Gibert (Eds)

Seismic Performance of RC Moment Frame Structures Made with EAF Slag Aggregates

Flora Faleschini, Mariano A. Zanini and Klajdi Toska

Dept. of Civil, Environmental and Architectural Engineering, University of Padova, Via Marzolo 9 35131-Padova, Italy, flora.faleschini@dicea.unipd.it, marianoangelo.zanini@dicea.unipd.it, klajdi.toska@dicea.unipd.it

Abstract. *Sustainability in the construction industry is becoming everyday more a major issue in todays world. To accomplish sustainability goals, adopted also by the Agenda 2030 of the United Nations, wide research has been carried out in the past years. Among this, the use of recycled aggregates has been proven to be promising both in terms of sustainability and material properties. Electric Arc Furnace (EAF) concrete has demonstrated a significant increase in mechanical properties when compared to natural aggregates (NA) ones. However, the mechanical properties enhancement is accompanied by an increase of its specific weight and the overall effects of its use in RC structures subjected to dynamic loads, has not been investigated yet. The present study aims to investigate the seismic reliability of reinforced concrete frame buildings made with EAF in comparison to the same structural configurations made with NA concrete, considering three different configurations (3-, 6- and 9- story building type) designed considering ordinary concretes made with natural aggregates.*

Keywords: *EAF Slag, Reinforced Concrete, Seismic Fragility, Seismic Reliability.*

1 Introduction

Sustainability is one of the global challenges that the construction industry must face in the near future. The 2030 Agenda of the United Nations sets as one of its main goals waste generation reduction and promotes policies of prevention, reduction, reuse, and recycling. Lately great effort has been made by the research community on the promotion of recycling and reuse opportunities of waste materials in the construction industry. One of the most remarkable cases of recycling is the Recycled Aggregates (RAs) production by Construction and Demolition Waste (C&DW) and their use is now regulated in most countries around the world (FHWA,1997; EN 12620:2008; NTC, 2018). More recently, waste originating from industrial processes, have been object of research to evaluate their possible use to produce RAs or so-called industrial aggregates. Among other industrial waste or by-products, those coming from steelmaking industry, particularly electric arc furnace (EAF) slag, offer great performance when used in structural concrete. In previous research has been observed that EAF slag use in concrete mixtures improves both mechanical strength (Pellegrino *et al.*, 2009; Arribas *et al.*, 2015; Rondi *et al*., 2016; Liapis *et al.*, 2018; Qasrawi, 2014) (i.e compressive strength, tensile strength and elastic properties) and durability (Faleschini *et al.*, 2015; Pellegrino *et al.*, 2012; Ortega-López *et al.*, 2018) when compared to concrete mixtures with ordinary ones. In addition, heavy-weight metals present in the EAF slag composition give to EAF concrete mixtures a higher specific weight with respect to NA mixtures.

Experimental work on the behavior of EAF concrete has been carried out also at the element scale. They have shown that reinforced concrete (RC) elements with EAF slag aggregates manifest better flexural and shear capacity with respect to ordinary RC when tested to

monotonic loading under four-point bending (Pellegrino *et al.*, 2013; De Domenico *et al.*, 2018). Axially loaded columns have shown a similar ductility to that of NA mixtures (Lee *et al.*, 2018) while a higher shear capacity of exterior beam-column joint is observed (Faleschini *et al.*, 2017). Laboratory tests on real scale EAF concrete joints under cyclic loading have shown gain with respect to NA ones in terms of ductility, dissipated energy and reduced cracking patter. Similar results were observed also for joints with lower cement content (Faleschini *et al.*, 2017). The use of EAF slag has shown enhanced ultimate and frictional bond strength with respect to conventional concrete (Faleschini *et al.*, 2017). Other beam-column joint conditions (i.e., strong beam – weak column and strong column – weak beam situations) have been numerically investigated (Faleschini *et al.*, 2017).

The results of the research work reported above have shown that EAF concrete can be suitably applied in gravity structures and in special facilities that require shielding from radiations where its high specific weight and high strength can be better exploited (Pomaro *et al.*, 2019). However, its efficiency is not so obvious when applied in elevation RC structures that are located in seismic regions where an important change of the building mass and stiffness can lead to a significant increase of the seismic loads in the structure. The present paper aims to study this topic, analyzing the seismic behavior of code conforming RC frame buildings built with ordinary concrete then replaced with three different classes of EAF concrete characterized by increasing aggregates replacement ratio. A dataset of experimental tests based on two previous research works of the same authors is used to define the mechanical properties of EAF concrete mixtures (Pellegrino *et al.*, 2016; Zanini, 2019). Via statistical analysis, ratios of variation of the main mechanical properties (i.e. compressive and tensile strength, and elastic moduli) and of the specific weight were defined for three EAF concrete classes (C1, C2, A) with respect to a benchmark mixture made with NAs. Three different geometrical configurations of regular RC frame structures with three, six and nine stories were designed according to the current Italian code for Constructions for a medium-to-high seismic hazard site. Fragility functions were then computed from the seismic responses of the analyzed configurations under a set of non-linear time history analysis (NLTHAs) and a seismic reliability assessment was carried out for all 12 resulting combinations (combining 3 structural configurations and 4 concrete mixes), investigating the variation of structural safety margins related to the use EAF concrete mixtures in replacement to a conventional NA concrete.

2 EAF Slag Concrete and RC Frame Case Studies

EAF slag is a by-product of the steelmaking industry which, after cooling from temperatures up to 1300 °C to ambient conditions, becomes a dark-grey stony material. EAF slag properties depend on the type of steel to be produced, scrap composition, slag cooling method and speed, and further weathering process. EAF aggregates present a rough texture and angular shape which influences bond development in the cement matrix since crushed stones present higher surface-to-volume ratio and require more cement paste to obtain a workable mixture in respect to NAs. The main physical properties of the slag for two size fractions, compared to a dolomitic aggregate, are reported in Table 1.

Generally, when used to replace NAs, EAF slag has a positive effect on the mechanical properties. However, the properties of the mixture strongly depend on type and amount of substitution. It has been experimentally proven that coarse aggregates have a beneficial effect,

while when fine fraction is used the beneficial effect is more limited (Pellegrino *et al.*, 2012). Compared to standard NA concrete, the EAF mixtures have higher specific weight about 3.3 – 4.0*t/m*3 against 2.7*t/m*3 of normal ones. Particular attention must be paid to the segregation phenomena. High specific weight can result in insufficient viscosity of the cement paste causing the migration of the two phases. Elastic modulus is also enhanced when using EAF slag. This is mainly because concrete elastic modulus depends mainly on the aggregates elastic modulus. The overall property improvements are also due to the interfacial transition zone (ITZ) between EAF aggregate and cementitious matrix that results denser and less porous than conventional concretes. However, if a bad quality cementitious matrix or a high water/cement ratio is employed property enhancements are less important.

Table 1. Physical properties of EAF slag compared to dolomitic aggregate (NA).

	Apparent density (kg/m^3)	Water absorption (%)	Porosity (%)	Shape
EAF slag 0-4 mm	3800	1.0 – 1.5	2.0	Crushed
EAF slag 4-16 mm	3950	<1.0	0.5 – 2-7	Crushed
NA 0-4 mm	2760	1.0 1.5	< 2.0	Roundish
NA 4-16 mm	2790	<0.5	0.9 – 1.8	Roundish

To analyze the structural response of buildings built with different concrete mixtures, three-moment frame RC structures with 3-, 6- and 9- stories were considered. The structures are characterized by a regular rectangular shape with five spans in the longitudinal direction and three in the transversal one. Spacing between consecutive bays is equal to 5 m.

The structures were supposed to be located in a moderate-to-high seismic hazard site (Municipality of Pordenone, Northeast Italy) and designed in accordance with the Italian Building Code considering a low ductility class (Class B). Seismic forces were computed from a dynamic linear analysis while beams and columns were sized accordingly, using Reference C25/30 strength class.

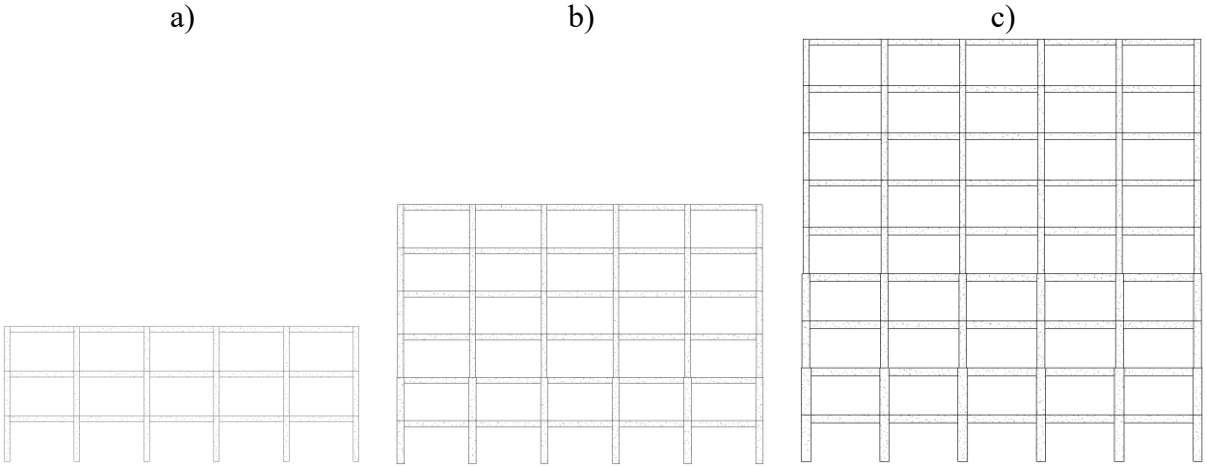

Figure 1. RC frame layouts analyzed: floor plan (a), 3- (b), 6- (c) and 9-story (d) building archetypes.

3 Seismic Reliability Analysis

For the Performance-Based Earthquake Engineering (PBEE) framework (Cornell *et al.*, 2000) the occurrence of mainshock events at a given site is assumed to be a Homogenous Poisson Process. Neglecting damage accumulation on structure, the process of events causing the structural failure is also represented by an HPP, whose unique parameter, the failure rate λ_f, can be used for computing the failure probability in any time interval. Particularly, it depends on the hazard curve (λ_{im}), representing the seismicity on a specific site, and on fragility curve ($P[f|im]$) being the probabilistic structural behavior of a specific structure. λ_f can be computed by applying the Total Probability Theorem in the following way:

$$\lambda_f = \int_{im} P[f|im] \cdot |d\lambda_{im}| \tag{1}$$

Once estimated the failure rate, based on the HPP assumption it is possible to quantify the probability of failure for a given time window of interest *t* due to earthquake occurrences:

$$P_{E,f} = 1 - e^{-\lambda_f t} \tag{2}$$

and further, derive the seismic reliability index ($\beta_{E,t}$) in accordance with the reliability analysis theory with the following transformation:

$$\beta_{E,t} = -\Phi^{-1}(P_{E,f}) \tag{3}$$

3.1 Seismic hazard and fragility estimation

To compute λ_{im}, seismic hazard map for Italy, provided by the National Institute of Geology and Volcanology (INGV), was used. To compute the failure rate a continuous hazard function is needed. Since INGV provides hazard data (values of the 16th, 50th and 84th percentile) only for nine return times, median values were fitted with a quadratic function in logarithmic space:

$$\lambda(s) = k_0\, e^{(-k_1 \ln(s) - k_2 ln^2(s))} \tag{4}$$

In assessing seismic reliability, instead of the median hazard curve, it is more suitable to refer to the mean one which is possible to derive with the following equation:

$$\bar{\lambda}(s) = \lambda(s)\, e^{(\frac{1}{2}\beta_H^2)} \tag{5}$$

Where β_H can be estimated as:

$$\beta_H = \frac{\ln(S_{84\%}) - \ln(S_{16\%})}{2} \tag{6}$$

The fragility function ($P[f|im]$) represents the probability to reach and exceed a certain damage state given a specific intensity im. In this work, Cloud Analysis method (Jalayer&Cornell, 2003) is adopted. The fragility parameters are estimated starting from a set of n natural ground motion records and the fragility function is computed as follows:

$$[f|im] = P\left[EDP > \overline{edp}|im\right] = 1 - P\left[EDP \leq \overline{edp}|im\right] = 1 - \Phi\left[\frac{ln(\overline{edp}) - ln(edp)}{\beta}\right] \tag{7}$$

$\overline{edp}$ is the median threshold value of the assumed structural limit state, and edp represents the median estimate of the demand that can be computed with a ln-linear regression model, as:

$$ln(edp) = a + b \cdot ln(im) \tag{8}$$

β is the standard deviation of the demand conditioned on im and can be estimated from the regression of the seismic demands as:

$$\beta_H = \frac{\ln(S_{84\%}) - \ln(S_{16\%})}{2} \tag{9}$$

4 Seismic Reliability Assessment of the EAF RC Frame Archetypes

For the NLTHAs a diffused plasticity model, using a fiber section discretization, was adopted to consider material non-linearities. Unconfined and confined concrete was modeled via the Mander *et al.* (1988) model whereas the Menegotto-Pinto (1973) steel model was used for the non-linear behavior of rebars. Simulations were carried out via SeismoStruct software and a set of 30 natural unscaled ground motion records were adopted using all three components of the seismic wave. EAF concrete characteristics are computed using the ratio coefficients in Table 2 and the reference concrete material (C25/30) characteristics.

Table 2. Ratios between EAF and Reference concrete properties.

	Class EAF-C1	Class EAF-C2	Class EAF-A
$\rho_{c,EAF} / \rho_{c,Ref}$	1.166	1.166	1.154
$f_{c,EAF} / f_{c,Ref}$	1.395	1.404	0.915
$f_{ct,EAF} / f_{ct,Ref}$	1.280	1.100	1.080
$E_{c,EAF} / E_{c,Ref}$	1.330	1.100	1.040

In the present paper, the chosen Engineering Demand Parameter (EDP) parameter is the maximum inter-story drift ratio (IDR) while the peak ground acceleration (PGA) is used as Intensity Measure (IM). Four damage states: Slight, Moderate, Extensive and Complete, with corresponding EPD threshold of 0.4%, 0.8%, 1.5% and 3%, were defined. Threshold values result similar to those proposed for ductile RC moment frame structures by Ghobarah (2004) and were defined from non-linear static analysis. For the mid-rise and high-rise buildings, a reduction factor of respectively 2/3 and 1/2 as proposed by FEMA (2012) was considered to account for higher mode effects and differences between average computed in non-linear static analysis and maximum individual IDR from NLTHAs.

5 Results and Discussion

Structural response was evaluated with respect to the four damage states previously defined, varying from Slight to Complete. Fragility functions were computed for each of the 12 cases, resulting from different geometrical and material combinations, using the Cloud Method described in Section 3.1 (Figure 2). A comparison of the seismic performance of structures built with the reference concrete and EAF concrete is given in Figure 2 with the fragility curves and the reliability index in Figure 3.

It can be noted that the overall performance of EAF concrete structures is close to the performance of the reference material one. The 6- story model has shown almost the same response for all considered materials, proven by overlapping fragility curves, while the 3- and 9- story curves tend to vary more when considering different materials.

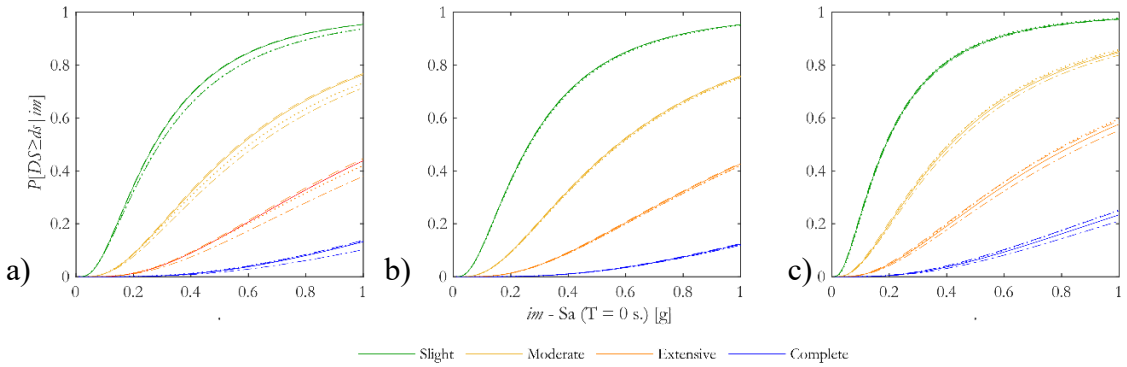

Figure 2. Slight, Moderate, Extensive and Complete DS fragility curves for 3- (a), 6- (b) and 9- (c) story RC frame archetypes (Solid - reference (C25/30); Dotted - EAF-C1; Dashed - EAF-C2; Dash-dot – EAF-A).

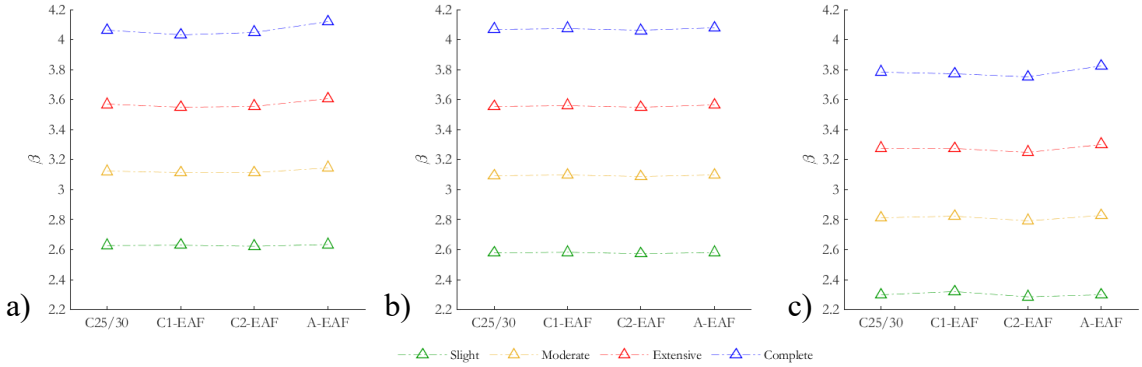

Figure 3. Reliability index for 3- (a), 6- (b) and 9- (c) story RC frame archetypes.

Mean failure rates and reliability indexes were also reported for all building frames (Table 3). When compared to the reference material, EAF concrete buildings report similar reliability indexes. This confirms that in terms of safety margins with respect to seismic actions, buildings designed with ordinary concrete but built with EAF aggregates are exposed to almost the same risk as those built with NAs ones.

This highlights that NAs replacement with EAF aggregates, in the same structural system, has a small impact in terms of seismic reliability levels achieved. The difference in the mean failure rate of the 9-story building and those of the 3- and 6-story ones may be due to the reduced damage states EDP threshold adopted for the 9- story by considering it a high-rise building. It also points out that current code recommendations do not guarantee building design characterized by the same level of seismic reliability but often some differences can be observed, especially when comparing different rise buildings.

Table 3. Comparison between mean failure rates and reliability indexes (β) derived for 3-, 6- and 9-story RC frame archetypes.

DS	Story	C25/30		C1-EAF		C2-EAF		A-EAF	
		λ_f	β	λ_f	β	λ_f	β	λ_f	β
Slight	3-	4.31E-03	2.63	4.28E-03	2.63	4.37E-03	2.62	4.22E-03	2.63
	6-	4.97E-03	2.58	4.91E-03	2.58	5.05E-03	2.57	4.94E-03	2.58
	9-	1.08E-02	2.30	1.02E-02	2.32	1.12E-02	2.29	1.08E-02	2.30

Moderate	3-	8.98E-04	3.12	9.23E-04	3.11	9.23E-04	3.11	8.27E-04	3.15
	6-	9.93E-04	3.09	9.77E-04	3.10	1.01E-03	3.09	9.76E-04	3.10
	9-	2.46E-03	2.81	2.39E-03	2.82	2.61E-03	2.79	2.34E-03	2.83
Extensive	3-	1.80E-04	3.57	1.93E-04	3.55	1.88E-04	3.56	1.55E-04	3.61
	6-	1.89E-04	3.56	1.85E-04	3.56	1.94E-04	3.55	1.83E-04	3.56
	9-	5.27E-04	3.28	5.30E-04	3.27	5.78E-04	3.25	4.80E-04	3.30
Complete	3-	2.43E-05	4.06	2.76E-05	4.03	2.58E-05	4.05	1.90E-05	4.12
	6-	2.36E-05	4.07	2.31E-05	4.07	2.45E-05	4.06	2.26E-05	4.08
	9-	7.71E-05	3.78	8.13E-05	3.77	8.80E-05	3.75	6.58E-05	3.82

6 Conclusions

The main goal of this paper was to investigate the effect of concrete mixtures with EAF slag in the seismic performance of different code conforming RC-frame structures (3-, 6- and 9-stories). The impact of EAG slag in mass and stiffness variation can lead to different seismic loads and global response of the building. A seismic reliability assessment was carried out and fragility functions, mean failure rates, and reliability indexes were computed for each combination of geometrical configuration and material. Based on the results of the present study the following conclusions can be highlighted:

- Using materials that were proved to have higher mechanical strength than the reference one, might not improve the global seismic behavior of the structure.
- When replacing NAs of ordinary concrete with EAF ones the seismic safety levels achieved are comparable to those of the same structural configuration built with ordinary concrete.
- For the low- and mid-rise buildings considered (3- and 6- stories) results showed similar reliability levels, while a more significant variation was observed for the high-rise case (9-story). This marks out how current building codes may not ensure the same seismic reliability level for all the designed structures.

ORCID

Flora Faleschini: https://orcid.org/0000-0003-2126-9300
Mariano A. Zanini: https://orcid.org/0000-0001-9326-802X
Klajdi Toska: https://orcid.org/0000-0002-4131-7683

References

Arribas I., Santamaría A., Ruiz E., Ortega-López V. and Manso J.M. (2015). Electric arc furnace slag and its use in hydraulic concrete. Constr Build Mater 90: 68-79. doi: 10.1016/j.conbuildmat.2015.05.003.

Cornell C.A. and Krawinkler H. (2000). Progress and challenges in seismic performance assessment. PEER Centre News, 3(2): 1-3.

De Domenico D., Faleschini F., Pellegrino C. and Ricciardi G. (2018). Structural behavior of RC beams containing EAF slag as recycled aggregate: Numerical versus experimental results. Constr Build Mater 171: 321-337. doi: 10.1016/j.conbuildmat.2018.03.128.

DM 17/01/2018 (2018). Aggiornamento delle Norme Tecniche per le Costruzioni, Roma, Italy. (in Italian)

EN 12620 (2008). Aggregates for concrete. Comité Européen de Normalisation, Brussels, Belgium.

Faleschini F., Alejandro Fernández-Ruíz M., Zanini M.A., Brunelli K., Pellegrino C. and Hernández-Montes E. (2015). High performance concrete with electric arc furnace slag as aggregate: mechanical and durability properties. Constr Build Mater 101, 113-121. doi: 10.1016/j.conbuildmat.2015.10.022

Faleschini F., Santamaria A., Zanini M.A., San José J.-T. and Pellegrino C. (2017). Bond between steel reinforcement bars and Electric Arc Furnace slag concrete. Mater Struct 50: 170. doi: 10.1617/s11527-017-

1038-2.
Faleschini F., Hofer L., Zanini M.A., Dalla Benetta M. and Pellegrino C. (2017). Experimental behavior of beam-column joints made with EAF concrete under cyclic loading. Eng Struct 139: 81-95. doi: 10.1016/j.engstruct.2017.02.038.
Faleschini F., Bragolusi P., Zanini M.A., Zampieri P. and Pellegrino C. (2017). Experimental and numerical investigation on the cyclic behavior of RC beam column joints with EAF slag concrete. Eng Struct 152: 335-347. doi: 10.1016/j.engstruct.2017.09.022.
FEMA (2012). Earthquake Model, Hazus-MH 2.1 Technical Manual. Federal Emergency Management Agency, Washington DC, US (available at: www.fema.gov/plan/prevent/hazus).
FHWA (1997). User Guidelines for Waste and Byproduct Materials in Pavement Construction. Federal Highway Administration Research and Technology Report no. FHWA-RD-97-148.
Ghobarah A. (2004). On drift limits associated with different damage levels. International workshop on Performance based design: concepts and implementations, 28 June- 1 July 2004.
INGV. Interactive Seismic Hazard Maps. Available at: http://esse1-gis.mi.ingv.it/s1_en.php (last access 04/03/2019).
Jalayer F. and Cornell C.A. (2003). Direct probabilistic seismic analysis: implementing non-linear dynamic assessments. Stanford University.
Liapis A., Anastasiou E.K., Papachristoforou M. and Papayianni I. (2018). Feasibility Study and Criteria for EAF Slag Utilization in Concrete Products. J Sustain Metall 4(1): 68-76. doi: 10.1007/s40831-017-0152-2.
Lee J.-M., Lee Y.-J., Jung Y.-J., Park J.-H., Lee B.-S. and Kim K.-H. (2018). Ductile capacity of reinforced concrete columns with electric arc furnace oxidizing slag aggregate. Constr Build Mater 162: 781-793. doi: 10.1016/j.conbuildmat.2017.12.045.
Mander J.B., Priestley M.J.N., and Park R. (1988). Theoretical stress-strain model for confined concrete. Journal of Structural Engineering, 114(8): 1804-1826.
Menegotto M. and Pinto P. E. (1973). Method of analysis for cyclically loaded reinforced concrete plane force and bending. In Proceedings, IABSE Symposium on Resistance and Ultimate Deformability of Structures Acted on by Well Defined Repeated Loads, Lisbon (pp. 15-22).
Ortega-López V., Fuente-Alonso J.A., Santamaría A., San-José J.T. and Aragón Á. (2018). Durability studies on fiber-reinforced EAF slag concrete for pavements. Constr Build Mater 163: 471-481. doi: 10.1016/j.conbuildmat.2017.12.121.
Pellegrino C. and Gaddo V. (2009). Mechanical and durability characteristics of concrete containing EAF slag as aggregate. Cem Concr Compos 31(9): 663-671. doi: 10.1016/j.cemconcomp.2009.05.006.
Pellegrino C., Cavagnis P., Faleschini F. and Brunelli K. (2012). Properties of concretes with black/oxidizing electric arc furnace slag aggregate. Cem Concr Compos 37: 232-240. doi: 10.1016/j.cemconcomp.2012.09.001.
Pellegrino C. and Faleschini F. (2013). Experimental behavior of reinforced concrete beams with electric arc furnace slag as recycled aggregate. ACI Mater. J. 110: 197-206.
Pellegrino C. and Faleschini F. (2016). Experimental Database of EAF Slag Use in Concrete. in: Sustainability Improvements in the Concrete Industry. Springer, Switzerland. doi: 10.1007/978-3-319-28540-5.
Pomaro B., Gramegna F., Cherubini R., De Nadal V., Salomoni V. and Faleschini F. (2019). Gamma-ray shielding properties of heavyweight concrete with Electric Arc Furnace slag as aggregate: An experimental and numerical study. Constr Build Mater 200: 188-197.
Qasrawi H. (2014). The use of steel slag aggregate to enhance the mechanical properties of recycled aggregate concrete and retain the environment. Constr Build Mater 54: 298-304. doi: 10.1016/j.conbuildmat.2013.12.063.
Rondi L., Bregoli G., Sorlini S., Cominoli L., Collivignarelli C. and Plizzari G. (2016). Concrete with EAF steel slag as aggregate: A comprehensive technical and environmental characterisation. Compos Part B 90: 195-202. doi: 10.1016/j.compositesb.2015.12.022.
SeismoSoft (2013). SeismoStruct – a computer program for static and dynamic nonlinear analysis of frames structures. Available at: http://www.seismosoft.com.
United Nations (2015). Resolution adopted by the General Assembly on 25 September 2015. 70/1. Transforming our world: the 2030 Agenda for Sustainable Development.
Zanini M.A. (2019). Structural reliability of bridges realized with reinforced concretes with electric arc furnace slag aggregates. Eng Struct *188*, 305-319.

XV International Conference on Durability of Building Materials and Components
DBMC 2020, Barcelona
C. Serrat, J.R. Casas and V. Gibert (Eds)

Application of Soft Computing Methods to Increase Sustainability in Construction

Silvana V. Petruseva[1] **and Valentina K. Zileska Pancovska**[2]

[1] University "Ss. Cyril and Methodius", Faculty of Civil Engineering, Skopje, Blvd. Partizanski Odredi 24, 1000 Skopje, North Macedonia, silvana@gf.ukim.edu.mk

[2] University "Ss. Cyril and Methodius", Faculty of Civil Engineering, Skopje, Blvd. Partizanski Odredi 24, 1000 Skopje, North Macedonia, valentinazp@gf.ukim.edu.mk

Abstract. *In the last three decades the soft computing methods were used by the research community in almost every branch of construction, providing successful and convenient solutions for different problems in civil engineering. This paper presents some of the applications of these methods – especially neural networks (NN) and support vector machine (SVM) - in sustainable construction, i.e. its economic, social and environmental aspects. Soft computing applications were made in the last several years by our research team at the Faculty of Civil Engineering in Skopje, N. Macedonia, in collaboration with other authors from our and other countries. Several predictive models were developed using: general regression neural network (GRNN), support vector machine (SVM) and radial basis function neural network (RBF NN), using predictive modelling software DTREG. Applications of these models cover most of the aspects of sustainability in construction. Models were focused on predicting: road structure construction costs, bidding price in construction, sustainability assessment at early facilities design phase, predicting construction cost and construction time and predicting consumption of energy in buildings. Some of the mentioned developed predictive models are hybrid, composed of process-based and data driven models which contributed very much to the improvement of the accuracy of the predicting. The general conclusion is that the soft computing methods are a useful tool for developing models in the area of all aspects of sustainability and their application can lead to increasing sustainability in construction.*

Keywords: *Sustainable Construction, Soft Computing Methods, Predictive Modelling.*

1 Introduction

The construction industry creates conditions for the whole development of the country, but it can have some negative impact on the sustainability aspects: environmental, social or economic aspect. In that regard, balancing society's needs with environmental and economical demands, the construction industry should fulfil the present society needs, but with respect to its future needs (Chendo, 2013; Rafandadi *et al.,* 2014).

The implementation of sustainable construction procedures is a slow process, mostly due to the widely spread opinion that they are time, effort and cost more demanding than traditional ones (Dobson *et al.,* 2013). Hence, meeting the sustainable aims has become a construction project participants' challenge and researches' focus worldwide. They have researched different sustainable aspects using various of techniques and methods. Some of them are soft computing methods (SCMs). SCMs are noted as useful for developing models for different sustainable problems in construction (Polat *et al.,* 2014; Ahmad *et al.,* 2014; Arida *et al.,* 2016). Therefore, the aim of this paper is to present a brief review of the authors' research on several construction

sustainability issues by using SCMs. The models were focused on predicting: sustainability assessment, bidding price, construction time, construction cost and energy consumption of buildings.

Sustainability assessment: Facilities construction is globally noted as having large consequences on sustainability aspects. Thus, in spite of the existence of numerous obstacles, balancing sustainable issues and their incorporating in facilities construction and maintaining is a challenge for all participants in the construction projects (Aksorn and Charoenngam, 2015). Therefore, the early design phase is seen as a phase with high impact on facilities sustainability due to its providing drawings and specifications for the facility in accordance with the clients' wishes and needs (Crawford, 2013). Facility design which integrates the sustainability issues provides benefits for the project participants, the facility users and the whole society (Adeyeye *et al.,* 2013). But that is a complex process which puts designers under pressure. Therefore, construction project managers can support the inclusion of sustainability aspects in the facility's design which will lead to increasing the money value of the facility, while providing satisfied customers and construction of eco-friendly facility.

Bidding price: Construction companies usually acquire their work by winning a tender. Hence, choosing the bidding price that will win the tender is of particular interest for each construction company. But the decision what price to bid is a responsible, time and effort-consuming process which is influenced by a set of factors (Watt *et al.,* 2009). Therefore, having a model for predicting the price in order to win the bid is useful and it facilitates the decision making process.

Construction time and cost are elements that are included in each contract regarding facilities construction. Hence, they have influence on the contract signer's work and reaching the contracted time and cost is signer's challenge. That leads to a number of investigations regarding construction cost and time, such as: their prediction, their overrun, the time-cost relation, their influencing factors, etc. (Abu Hammad *et al.,* 2008).

Energy consumption of buildings has an impact, not only on the comfort, costs and other social and economic aspects of users, but also on the environmental aspect. In fact, buildings are among the biggest users of energy, thus prediction of their energy consumption is of particular interest. During the stage of selecting the optimal design of the new building or old building reconstruction/renovation, numerous measures/solutions can be used for reducing the building's energy consumption. Some of them are: system with heat pump from ground source (Michopoulos *et al.,* 2016); renewable energy systems usage and their combination or combination of systems for heating, power and cooling; system installation for energy management, etc. (Farhat *et al.,* 2014; Rasool *et al.,* 2015; Kialashaki, 2018). Thus, of particular interest is to have models for energy consumption forecasting.

2 Literature Review

Sustainability outcomes and environment protection are in a significant positive relation (Smith and Rootman, 2013), so for owners the sustainability has impact on their portfolio (Warren-Myers, 2012). Rafindadi *et al.,* (2014) stated that there is no significant difference among project stakeholders on sustainable projects risks, so for Babawale and Oyalowo (2011) the real estate valuers should have more knowledge about sustainability aspects of properties in order to effectively assess their value. For Dobson *et al.,* (2013) there is perception that capital costs

for sustainability are high, which can be an obstacle for the construction.

Bidding price in construction – There are different categories of bidding-price models, such as: models that are directed towards maximization of the expected; models based on systems for decision support; models based on artificial intelligence, etc. (Polat *et al.,* 2014). For example: a bidding model that uses generic software for probability estimating of the success is presented by Kitchenham *et al.,* (2005).

Construction time and cost relation and their overruns are researched worldwide. Zhang and Ng (2012) solved time-cost optimization problems using evolutionary-based optimization algorithm. Similarly, Afshar and Fathi (2009) used Fuzzy-sets theory for accounting the uncertainness in each activity direct cost, in order to determine the financing cost and required credit. They developed a model for searching the solutions that are non-dominated for the construction objectives: total time, financing cost and required credit.

Energy consumption of buildings is among issues that are highly researched, from different aspects and using different methods and techniques. Widely used are: traditional numerical methods, statistical methods and intelligent methods. Promised results were given by: Ekici and Aksoy (2009) using backpropagation ANN; Holcomb *et al.,* (2009) with support vector regression, ANN and multilinear regression; Ahmad *et al*., (2014) with support vector machine and ANN concluding that hybridization of these methods is suitable for more accurate prediction; Arida *et al.,* (2016) using ANN, particular non-linear auto-regression ANN; Amber *et al.,* (2017) using the Multiple Regression technique; Li *et al.,* (2017) using extreme deep learning approach, etc.

3 Methods

There are generally two types of methods for analysing data: traditional hard-computing and modern soft computing methods. The hard computing methods use an accurately stated analytical model of the process that should be modelled, while the soft computing methods do not need analytical model of the process. The soft computing methods have been developed as an alternative solution for solving the contemporary problems. The two most important constituents of soft computing are learning from experimental data (neural networks and support vector machine) and fuzzy logic methods, but in recent years there are also other: probabilistic reasoning, genetic algorithms, chaos theories, fractals (Kecman, 2001). There are many different types of NNs developed for solving different problems, some of them being: GRNN, RBF NN, polynomial NN, probabilistic NN, multilayer perceptron (MLP), cascade correlation NN. In our research we have used only the first two.

3.1 Data-Driven Soft Computing Methods

Soft computing methods try to transfer the human knowledge into mathematical, analytical models by finding methods for learning from experimental data.

NNs and SVMs are mathematical computing models that implement the idea of learning from experimental data, and FL systems implement structured human knowledge into effective computing algorithms (Kecman, 2001).

3.1.1 Artificial neural networks (ANNs)

NNs implement the functioning of the human neurons. The three most important aspects of the NNs are: implementation of biological neural networks, the concept of parallel distributing processing and the concept of learning and self-organizing (Haykin, 2005). NNs can approximate multivariable nonlinear functions, identifying the interactions between input and output data easily, minimizing some error function which expresses the difference between actual output values and the predicted values by the NN. In our research most often used NNs were: GRNN and RBF NN.

Radial basis function neural network (RBF NN) is a 3 layered feed forward network (Figure 1 (Sherrod, 2013b)). The values from the input neurons are fed to the neurons from the next hidden layer, which has mutable number of neurons determined by the algorithm for the training process. RBF NN can have one or several outputs, depending on the task which is solved; if it is used for forecasting then RBF NN has only one output, but if it is used for classification, then it may have several outputs, equal to the number of categories of the target variable.

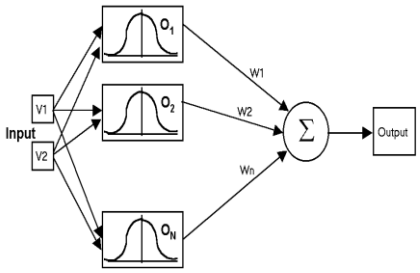

Figure 1. RBF NN architecture.

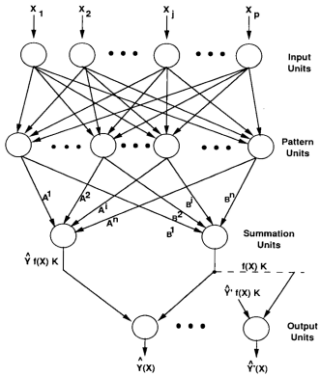

Figure 2. GRNN architecture.

General regression neural network (GRNN) is most often used NN in our research. This NN is in most of the cases very accurate and is used for forecasting, control problems, mapping (Specht, 1991). The most attractive characteristic of GRNN is its ability to converge to the optimal solution very quickly, requiring only several samples. GRNN has 4 layers (Figure 2) (Sherrod, 2013b).

3.1.2 Support vector machine (SVM)

SVM models have been developed to solve the contemporary problems that have appeared with the standard classical statistical modelling. SVMs can successfully work with standard contemporary multidimensional data sets and also with small training data sets (Kecman, 2001). SVMs have similar architecture as classical NNs. In fact, a two - layer feed forward NN is equivalent to a SVM model which uses sigmoid kernel function.

3.2 Bromilow Process-Based Model and Hybrid Modelling

The soft computing methods that were described above are *data-driven methods*, and they do not use any knowledge about the process which should be modelled in a form of some mathematical formula. *Process-based methods* describe the process by some mathematical formulae. The *hybrid modelling* is a relatively new field of investigation and very promising results have been reported.

The process-based model used in our research was the well-known Bromilow "time-cost" model which gives the relation between construction time and construction cost. This model is given by the equation (1):

$$T = aC^b \tag{1}$$

T is a construction time, C is a construction cost (price), *a* is a model parameter which expresses the average time needed for construction of a monetary value, and *b* is parameter which expresses the dependence of the time on cost change (Bromilow, 1969).

4 Results and Discussions

Using the methods described above, in the last several years predictive models applied for solving different problems in civil engineering have been developed by the research team from our country and also with collaboration with authors from other countries. The software used for developing the models was predictive modelling software DTREG (Sherrod, 2013a, 2013b). The developed models were applied for forecasting: sustainability assessment, bidding price, construction time, construction cost and energy consumption of buildings. Part of the available data for developing the models was used for training and part of them for validation of the model. The most used methods for validation were k-fold cross validation and random percent. The accuracy of the models has been estimated by the standard estimators: MAPE (mean absolute percentage error), and the coefficient of determination R^2 which measures the global fit of the model.

Sustainability assessment: 112 project managers from construction firms in R. Macedonia were participants in an anonymous survey, whose goal was to determine their opinion about the factors that mostly affect the sustainability assessment of the facilities' preliminary design. The questionnaire developed by the authors consisted of 72 questions, seen as factors that influence the sustainability of the facilities preliminary design. 27 of them were chosen as most representative for building the model. The participants were asked to answer the questions on a 6 point Likert scale (from 1 – unimportant, to 6 – extremely important). The questions were considered as predictors for the model. One of them was considered as target variable – the question: sustainability assessment of the preliminary design. GRNN from DTREG predictive modelling software was used for modelling. DTREG also computes the most important factors that impact the target variable, and the 6 most influential of them reported by DTREG were: 1) work experience, 2) work on several outline design proposals, 3) resolving issues between stakeholders, 4) prioritization of participants in the design phase, 5) procurement management and 6) defining project program and goals. The conclusion from this modelling is the finding that the project managers assessed the social aspects more influencing sustainability and economic and environmental issues less influential. The accuracy of the model was: MAPE= 2.6% and the coefficient of determination was R^2=0.84 (Zileska *et al*., 2017).

Bidding price: A model for forecasting bidding price was developed using SVM method for prediction. Data from 26 tenders were used for modelling out of 54 tenders that were collected from construction firms. Two variables were used as predictors (time for preparation and the price offered) and the target variable was price obtained. The accuracy of the model was with MAPE 2.5%, and $R^2 = 89.8\%$, (Petruseva *et al*., 2016).

Construction time: Several hybrid models were developed for predicting time of construction using Bromilow time-cost model (BTC model) as process-based model. One of them was hybrid, composed of BTC model and GRNN model and it was modelled with data for 116 different types of structures: road structures, petrol stations, bridges, education facilities, business buildings, and other. The data was about purpose of the structure, year of construction, region of location, contracted time and cost and also realized time and cost. Target variable was real time of construction, and as predictors were chosen: purpose of the structure, real and contracted cost and contracted time. The accuracy of the model was: MAPE=3.3% and $R^2 = 93.2\%$, using purpose of construction (as string variable), and contracted time, contracted cost and real cost of construction as predictors, and target variable was real time of construction. The input values of real and contracted time of construction and real and contracted cost of construction were not their actual values, but logarithm of their values, because of the application of the BTC model (eq. 1). This equation was applied for the relation of the real time and real cost of construction, and also for the contracted time and cost, and these two equations were logaritmized and summarized and the obtained equation was a relationship between their logarithmic values. We shall stress here the importance of the hybrid model which drastically improved the accuracy of the model, because without using BTC model as part of the hybrid model, the accuracy of the model was drastically decreased: MAPE = 31.8%, and R^2 =75,6% (Petruseva, Car-Pusic and Zileska, 2019).

Construction cost: One of the developed models for predicting construction cost was hybrid model, composed of RBF NN and BTC model with accuracy: MAPE = 0.64%, R^2=99.2%. The data were for 65 objects. Target variable was the real cost of construction, and predictors: contracted cost of construction and real and contracted time of construction, but here also as input values for these variables logarithms of their actual values were used because of the application of the BTC model. Without BTC model as part of the hybrid model, using only RBF NN, the accuracy of the model was: MAPE around 54% and R^2 around 44% (Zileska and Petruseva, 2017).

Energy consumption of buildings: The model developed for predicting building energy consumptions used data for real energy consumption for 55 residential buildings in R. Macedonia, constructed/reconstructed from 2013 to 2018. The accuracy of the model, using GRNN was: MAPE=3.12% and R^2=91.7%. The target variable was building energy consumption Q [kwh/m^2/year], and from all available data, 10 were chosen as most representative predictors, which were related to: 1) thermal transmittances (in W/m^2) of: walls, windows, floors, roofs, and also: 2) their corresponding geometries and areas (in m^2) – areas of the floors, walls and roofs (Zileska, Petruseva and Samardzioska, 2018).

5 Conclusions

Sustainability aspects are complex and inter-connected, so their researching and incorporating in construction is an effortful process. Furthermore, there are many sustainability influencing

factors, so it's useful to have prediction models for sustainable aspects. Recently, the most popular soft computing methods used for predictive modelling have been SVMs and NNs (GRNN, RBF NN, MLP, polynomial NN, cascade correlation NN, probabilistic NN). In the last several years we have developed several predictive models using mostly GRNN, SVM, RBF NN, and several hybrid models composed of data-driven and process-based model. The developed models gave a satisfied accuracy in prediction of: manager's assessment of the sustainability in early design phase for the facility, building energy usage, bidding price, construction time, construction cost, etc.

The models presented in this paper showed that the usage of SCMs facilitates the decision making process and leads to increasing the sustainability in construction.

ORCID

Silvana Petruseva: http://orcid.org/0000-0002-3752-513X
Valentina Zileska Pancovska: https://orcid.org/0000-0001-7620-4040.

References

Adeyeye, K., Piroozfar, P., Rosenkind, M., Winstanley, G. and Pegg, I. (2013). The impact of design decisions on post occupancy processes in school buildings. *Facilities, 31*(5/6), 255-278.

Afshar, A. and Fathi, H. (2009). Fuzzy multi-objective optimization of finance-based scheduling for construction projects with uncertainties in cost. *Engineering Optimization, 41*(11), 1063-1080, doi:10.1080/03052150902943004

Ahmad, S.A., Hassan, Y.M., Abdullah, P.M., Rahman, A.H., Hussin, F., Abdullah, H. and Saidur, R. (2014). A review on applications of ANN and SVM for building electrical energy consumption forecasting. *Renewable and Sustainable Energy Reviews, 33*. 102-109. https://doi.org/10.1016/j.rser.2014.01.069 194

Aksorn, P. and Charoenngam, C. (2015). Sustainability factors affecting local infrastructure project: the case of water resource, water supply, and local market projects in Thai communities. *Facilities, 33*(1/2), 119-143.

Amber, K.P., Aslam, M.W., Mahmood A., Kousar, A., Younis, M.Y., Akbar, B., Chaudhary, G.Q. and Hussain, S.K. (2017). Energy consumption forecasting for university sector buildings. *Energies*, *10*(1579), 1-18. doi:10.3390/en10101579

Arida, M., Nassif, N., Talib, R. and Abu-Lebdeh, T. (2016). Building energy modeling using artificial neural networks. *Energy Research Journal, 7*(2), 24-34. doi:10.3844/erjsp.2016.24.34

Babawale, G. K. and Oyalowo, B. A. (2011). Incorporating sustainability into real estate valuation: the perception of Nigerian valuers. *Journal of Sustainable Development, 4*(4), 236.

Bromilow, F.J. (1969). Contract time performance expectations and reality. *Building forum 1:* 70-80.

Chendo, N.A. (2013). Managers' perception of environmental sustainability in small and medium scale enterprises (SMEs): Implication for competitive marketing advantages for sachet water manufacturers in Anambra State, Nigeria. *European Journal of Business and Management*, 5(7), 186-195.

Crawford, L. (2013). *Sustainability Integration for Effective Project Management - Chapter 14: Leading sustainability through projects.* In Silvius, A.J.G. and Tharp, J. (Eds), IGI Global Publishing, Hershey, PA, 235-244.

Dobson, D. W., Sourani, A., Sertyesilisik, B. and Tunstall, A. (2013). Sustainable construction: analysis of its costs and benefits. *American Journal of Civil Engineering and Architecture, 1*(2), 32-38.

Ekici, B.B. and Aksoy, T.U. (2009). Prediction of building energy consumption by using artificial neural networks. *Advances in Engineering Software*. *40*(5). 356-362. https://doi.org/10.1016/j.advengsoft.2008.05.003

Farhat, R., Ghaddar, K.N. and Ghali. K. (2014). Investing in PV systems utilizing savings from building envelop replacement by sustainable local material: a case study in Lebanese inland region. *International Journal of Energy Economics and Policy. 4*(4), 554-567.

Hammad, A.A.A., Alhaj Ali, M.S., Ghaleb, S.J. and Bashir, A. (2008). Prediction model for construction cost and duration in Jordan. Jordan Journal of Civil Engineering*, 2,* 250–266.

Haykin, S. (2005). *Neural networks: a comprehensive foundation*, 2nd ed., Pearson Education Inc., Canada.

Holcomb, D., Li, W. and Seshia, A.S. (2009). Algorithms for green buildings: Learning-based techniques for energy prediction and fault diagnosis. *Electrical Engineering and Computer Sciences. University of California at Berkeley Technical Report No. UCB/EECS-2009-138 University of California at Berkeley.* http://www.eecs.berkeley.edu/Pubs/TechRpts/2009/EECS-2009-138.html

Kecman, V. (2001). *Learning and Soft Computing: support vector machines, neural networks and fuzzy logic models.* A Bradford Book. The MIT Press, Cambridge, Massachusetts, London, England.

Kialashaki, Y. (2018). A linear programming optimization model for optimal operation strategy design and sizing of the CCHP systems. *Energy Efficiency*, *11*(1), 225–238.

Kitchenham, B.A., Pickard, L., Linkman, S. and Jones, P. (2005). A framework for evaluating a software bidding model. *Information and Software Technology*, *47*(11), 747–760.

Li, C., Ding, Z., Zhao, D., Yi, J. and Zhang, G. (2017). Building energy consumption prediction: an extreme deep learning approach. *Energies. 10*(1525), 1-20. doi:10.3390/en10101525

Michopoulos, A., Voulgari, V., Tsikaloudaki, A. and Zachariadis, Th. (2016). Evaluation of ground source heat pump systems for residential buildings in warm Mediterranean regions: the example of Cyprus. *Energy Efficiency, 9*(6), 1421–1436.

Petruseva, S., Sherrod, P., Zileska Pancovska, V. and Petrovski, A. (2016). Predicting Bidding Price in Construction using Support Vector Machine. *Tem Journal, 5*(2), 143-151.

Petruseva, S., Zileska-Pancovska, V. and Car-Pusic, D. (2019). Implementation of process-based and data-driven models for early prediction of construction time. *Advances in Civil Engineering (HINDAWI),* Article ID 7405863, 12 pages, doi: 10.1155/2019/7405863

Polat, G., Bingol, B.N. and Uysalo, E. (2014). Modeling bid/no bid decision using adaptive neuro fuzzy inference system (ANFIS): a case study. *Construction Research Congress 2014, American Society of Civil Engineers,* 1083–1092. https://ascelibrary.org/doi/abs/10.1061/9780784413517.111 , (access7 Aug. 2019).

Rafindadi, A.D.U., Mikić, M., Kovačić, I. and Cekić, Z. (2014). Global perception of sustainable construction project risks. 27th IPMA World Congress, *Procedia-Social and Behavioural Sciences*, *119*, 456-465.

Rasool, Z., Tariq, W., Othman, L.M. and Jasni, J. (2015). What building management system can offer to reduce power wastage both social and economic: brief discussion by taking Malaysian power infrastructure as a sample. *The SIJ Transactions on Industrial, Financial & Business Management (IFBM), 3*(3), 27-31.

Smith, E.E. and Rootman, C. (2013). Assessing perceptions regarding the sustainability of contemporary organizations. *Business Management Dynamics, 3*(1), 1-16.

Sherrod, P. (2013a). *Predictive modelling software DTREG.* www.dtreg.com (Access on 16 February 2018).

Sherrod, P. (2013b). *Predictive modeling software DTREG - tutorial.* www.dtreg.com (acc.16 February 2018).

Specht, D.F.(1991). A general regression neural network. *IEEE Transactions on neural networks, 2*(6), 568- 576.

Watt DJ, Kayis B. and Willey K. (2009). Identifying key factors in the evaluation of tenders for projects and services. *International Journal of Project Management*, *27*(3), 250–260.

Warren-Myers, G. (2012). Sustainable management of real estate: is it really sustainability? *The Journal of Sustainable Real Estate*, *4(*1), 177-197.

Zhang, Y. and Ng, T.S. (2012). An ant colony system based decision support system for construction time-cost optimization. *Journal of Civil Engineering and Management*, *18*(4), 580–589.

Zileska Pancovska, V., Petruseva, S. and Petrovski, A. (2017). Predicting Sustainability assessment at early facilities design phase. *Facilities, 35*(5/6), 335-355.

Zileska-Pancovka, V. and Petruseva, S. (2017). Estimation of facilities construction cost using radial basis function neural network. In *Proceedings of CIRRE-2nd Conference of Interdisciplinary Research on Real Estate,* Cartagena, Spain, 88-98.

Zileska Pancovska, V., Petruseva, S. and Samardzioska,T. (2018). Building's energy consumption forecasting – a model based on general regression neural network. In *Book of Proceedings of the 3th Conference of Interdisciplinary Research on Real Estate (CIRRE 2018),* Groningen, Netherlands, 186-196.

XV International Conference on Durability of Building Materials and Components
DBMC 2020, Barcelona
C. Serrat, J.R. Casas and V. Gibert (Eds)

Decision Support to Identification of Road Infrastructure Segments With Poor Conditions

Nikša Jajac

Faculty of Civil Engineering, Architecture and Geodesy, University of Split, Matice hrvatske 15, 21214 Split, Croatia, niksa.jajac@gradst.hr

Abstract. *Planning of maintenance activities (an integral approach) on ever growing system such as urban road infrastructure requires decision makers to take into account large number of different data and usually conflicted criteria, derived from several aspects of analysed problem. This systematic approach to planning is based on the main three steps: identification of alternatives, their validation and selection for inclusion into a maintenance plan. Most of authors are dealing with the last two steps however, focus of this research is on the first step. This step is a critical phase of planning because it is important to identify road infrastructure segments that need to be improved. Meaning, those with poor condition. The condition of a segment must be expressed as simple as possible (by unique Condition Assessment Value) and by usage of few but most relevant criteria (such as level of service, safety, time period passed form the last renovation and stability). Another important issue is provision of relevant, relatively quick and consistent expert assessment of segment condition according to above mentioned criteria and for large number of segment. To insure such assessment with high quality of segments identification this paper propose an decision support concept/expert system based on combination of trained and tested Artificial Neural Networks (ANN) and Simple Additive Weighting (SAW) method. The concept is validated on urban road infrastructure of city centre of Split, Croatia and it proved to be useful for determining a set of road infrastructure segments where maintenance activities should be undertaken.*

Keywords: *Decision Support Concept, Road Infrastructure Segments, Planning, Artificial Neural Networks.*

1 Introduction

In the field of urban road infrastructure systems, planning process of maintenance activities is highly complex and ill structured problem. This complexity is defined by several factors: lots of stakeholders with different opinions, huge amount of information quantities, multidisciplinary character of the problem, conflicts among goals and criteria, budget restrictions, etc. These factors indicate that the decision-making to maintaining activities of the road infrastructure planning are burdened with complex and socially sensitive problems, especially for the long-term planning. For that reason, long-term planning tasks should be supported by decision making tools such are multicriteria methods that can contribute to a more efficient realization of the tasks. In order to manage such complexity, a decision support approach is proposed, aimed at improving decision making to planning of maintain activates at the road infrastructure system. This concept represents a multicriteria decision-making approach, and is based on multicriteria analysis. Three main steps are crucial for a realization of planning: identification of alternatives, their validation and selection for inclusion into a maintenance plan. In this research, focus is given to the first step where road infrastructure

segments are identified and need to be improved because of their poor condition. These conditions are express by Condition Assessment Value (CAV), using few the most relevant criteria (such as level of service, safety and time period passed form the last renovation, etc.).

Expert assessment of segments conditions according to defined criteria are given and to achieve the most precise assessment this paper propose an decision support concept and expert system based on combination of trained and tested Artificial Neural Networks (ANN) and Simple Additive Weighting (SAW) method. There are many studies dealing with possibilities of generating decision support tools for maintaining road infrastructure segments. Zavdskas, Liias and Turskis (2008) gave a review of international and national practices in investment decision support tools in bridges and road quality management. He, Song and Chaudhry (2013) in their paper, explored the integration problem of service-oriented system and intelligence technology through the use of a group decision support system, applied on transportation management. Petty and Mahoney (2008) gave enhancements and refinements associated with winter maintenance decisions that the United States Federal Highway Administration initiated in a project aimed at developing a winter road Maintenance Decision Support System (MDSS).

The goals of the MDSS project were to construct a functional prototype MDSS that can provide objective guidance to winter road maintenance decision makers concerning the appropriate treatment strategies These strategies are used to control roadway snow and ice during adverse winter weather events, and develop a prototype that will also serve as a catalyst for additional research and development by the private sector. Dunkel *et al*. (2011) proposed a reference architecture for event-driven traffic management systems, which enables the analysis and processing of complex event streams in real-time and is therefore well-suited for decision support in sensor-based traffic control systems. Zhou et al. (2010) presented a research effort undertaken to explore the applicability of data mining and knowledge discovery (DMKD) in combination with Geographic Information System (GIS) technology to pavement management to better decide maintenance strategies, set rehabilitation priorities, and make investment decisions. Bielli (1992) presented a decision support system to urban-traffic management to achieve maximum efficiency and productivity for the entire urban-traffic system, including the urban road infrastructure. Guisseppi and Forgione (2002) and Jajac, Knezić and Marović (2009) in their papers gave a cost and benefit aspect of potential infrastructure investments, showing that several decision-support models can be generated. Quintero, Konaré and Pierre (2005) described an improved decision support system named Intelligent Decision Support System that coordinates management of several urban infrastructure systems, such as the sewage and waterworks. Proposed Intelligent Decision Support System was a solution for the future urban infrastructure management. Similar approaches were given by Pomerol, Roy and Rosenthal-Sabroux (1996), Turban and Aronson (1995) and Leclerc *et al.* (2001). Sayers, Jessop and Hills (2003) used SAW method (Hwang and Yoon, 1981) to present a multicriteria evaluation of transport infrastructure for ranking transport investments. These investments aim was to improve infrastructure in small towns, analysing three solutions: minimum interventions on the existing network, upgrading the existing route, and building a bypass. A simplified transport project ranking methodology with an integrated multicriteria decision making process that prioritizes transport projects in cases when multiple stakeholders present various different opinions was given by Shelton and Medina (2010) and Jajac, Marovic and Baucic (2014). Jajac (2010) made a research on the development and maintenance of urban road infrastructure by implementing and using multicriteria analysis and ANN at strategic, tactical and operating

decision making levels, in urban areas. To improve a decision making process in such complex circumstances, it is important to develop new tools aimed at raising the level of transparency and objectivity in the solution-selection process (Jajac, 2010). This research is focused on decision support concept to maintenance activities panning of improving road infrastructure segments in urban areas. It is based on the multicriteria methods AHP and SAW, and expert systems, using ANN, to support project management. The concept is validated on the urban road infrastructure of the city centre of Split, Croatia, and proved to be useful for determining a set of road infrastructure segments where maintenance activities should be undertaken.

2 Decision Support to Improve Maintenance Planning of Road Infrastructure Segments

Using architecture of the DSS for urban-infrastructure management (Jajac, 2010), a decision support to planning of maintenance activates improvement of road infrastructure segments is developed. The model for improving urban road infrastructure segments maintenance planning is proposed in Figure 1. The process of decision-making starts at the strategic and tactical levels, where with the case study is determined and stakeholders are selected. The main characteristics of each segment of infrastructure are collected and stored in database, they are accessible for entering periodically new inputs at the operational level during the continuous maintenance process. These main characteristics of segments are important for defining criteria and their weights. Firstly, stakeholder are selected and gathered together through subjective assessment of their influence and legitimacy. They are divided into three groups:

Local government - deputy mayor who is responsible for utility affairs, and principals of several administrative offices (*e.g.* Office for Strategic Planning and Development, Office for Finance, Office for Physical Planning, etc.);

Experts - civil engineering, transport engineering, environmental, and economics experts of both academic and practical backgrounds;

Users - the representatives of city districts or similar city formations.

After the identification of stakeholders, goals, criteria, and weighting factors are defined. The goal analysis is given in the form of hierarchical structure of goals and criteria. The criteria are defined by local government and experts group, while criteria weights are determined by all stakeholder groups. Using the AHP method (Saaty, 1982) and interviewing all stakeholders, weights can easily be assigned through a group decision-making process. The decision-making process of each stakeholder group must be repeated until consistency of each group' criteria weights determination is achieved. Furthermore, having determined the hierarchy of goals and stakeholder groups, three scenarios are developed, while the final (fourth) scenario is determined as the compromise opinion of all groups. Values of the compromise opinion are introduced as weights for the SAW method, which is used to set priority of selected road segments according to their improvement requirements. After the goal hierarchy is defined, all segments are analyzed, and those with conditions that need to be improved are identified using ANN. This way the condition assessment for all segments is provided within the study area. Only those segments with the condition assessed as poor, unsuitable and worn-out are selected for further analysis and priority-setting. Moreover, the segments are then ranked according to defined criteria. The local-government representatives, as strategic decision-makers, assisted to the group of experts in selecting the most convenient solution based on the present policies and

multicriteria analysis. The selected solution establishes a strategic plan of the road infrastructure segments conditions improvement. The proposed concept was tested on the road infrastructure segments maintenance planning in the city of Split, Croatia.

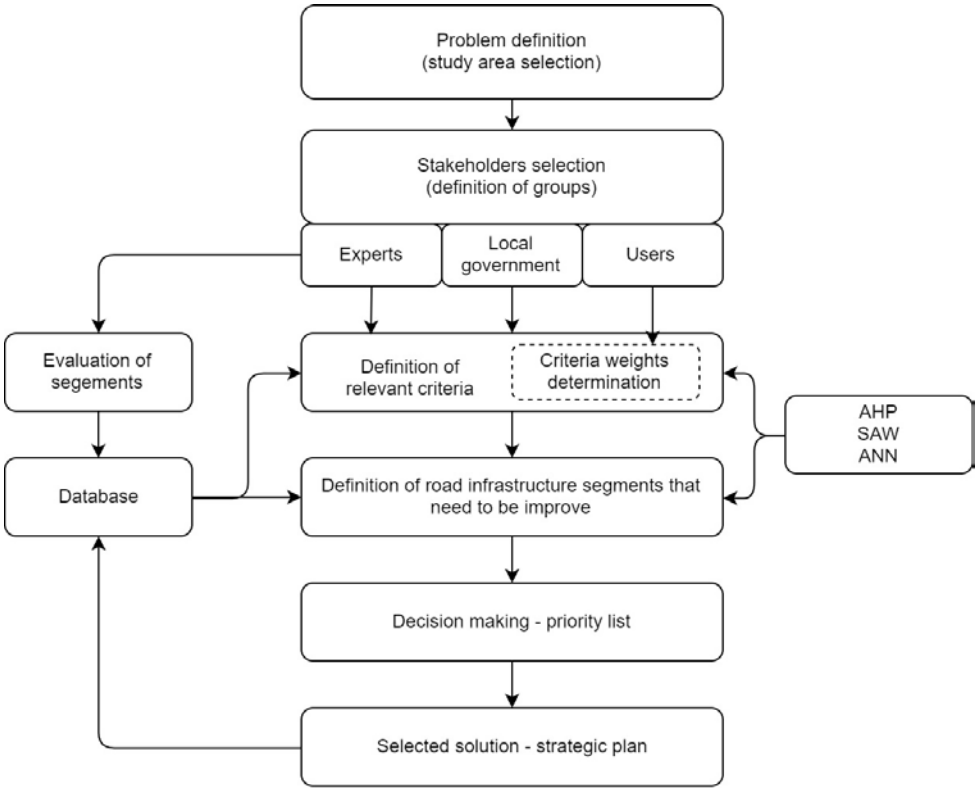

Figure 1. Decision support to road infrastructure segments improvement.

3 Road Infrastructure Segments Improvement Planning

The city of Split is taken as a study area. It has a high concentration of public facilities and pedestrian flows. There were 236 identified infrastructure segments, divided into 10 types: street, street section, crossroad, garage, parking, bus station, bus terminal, petrol station, overpass and tunnel. To evaluate each of the elements 13 criteria are defined. Each group of stakeholders defined criteria in their field of expertise. These criteria are grouped in social, technical, economic and ecologic group, as is shown in Table 1. Three scenarios are created, one for each stakeholders' groups and each for each scenario criteria weights are determined using AHP method. Compromise scenario is calculated as average value of each criterion weight by each scenario. Using compromise scenario, opinions of all three groups are equally taken into account.

Table 1. Criteria definition with weights and scenarios.

Group of criteria	Criteria name	Criteria label	Scenario 1	Scenario 2	Scenario 3	Compromise scenario
Social	Population density	C1	0.05	0.03	0.06	0.05
	Density of business facilities	C2	0.06	0.04	0.04	0.05
	Area of business facilities	C3	0.04	0.01	0.02	0.03
	Density of public facilities	C4	0.03	0.02	0.05	0.03
Technical	Constructability	C5	0.06	0.09	0.08	0.08
	Fitting into plans	C6	0.09	0.08	0.09	0.09
	Maintenance-segment improvement	C7	0.10	0.12	0.08	0.10
	Functionality improvement	C8	0.09	0.12	0.08	0.09
Economic	The amount of investment	C9	0.08	0.10	0.11	0.10
	The ability of land buying	C10	0.09	0.09	0.11	0.10
	The existence of investor	C11	0.09	0.09	0.10	0.09
Ecologic	The amount of noise	C12	0.10	0.11	0.08	0.10
	The amount of combustion gasses	C13	0.11	0.11	0.10	0.10

Criterion C7 (Maintenance – segment improvement) is divided into four subcriteria: level of service, safety, time period passed form the last renovation and stability. Using these four subcriteria and methodology of ANN, the unique Condition Assessment Value (CAV) is obtained. This value also presents an assessment of condition of segment.

4 Results

Using methodology of ANN, road-infrastructure segments in poor conditions are identified, by including four input variables and only one output variable. The four input variables are four criteria defined in previous section: level of service, safety, time period passed form the last renovation and stability. This ANN is trained by the back-propagation algorithm using the training set consisting of 200 cases, each case with four input variables (collected during the monitoring cycle), and 200 output variables, provided by experts' assessment. The output variable is CAV. Input values for 236 segments are collected during the second monitoring

cycle. Applying ANN methodology, conditions of segments are obtained. However, only segments assessed as inadequate and poor were selected for further analysis. If the CAV is less then 1, condition is classified as bad (0-worst condition, 1-the best condition). Segments with CAV values are shown in Table 2. There are 18 segments with poor condition, and the best one is segment Sg13 (crossroad), while the worst is Sg8 (street section).

Table 2. Road infrastructure segments with poor condition.

Infrastructure segment	Label of segment	CAV
Street section (Pojišanska1)	Sg1	0.458
Street section (Pojišanska 2)	Sg2	0.634
Crossroad (Pojišanska i Zvonimirova)	Sg3	0.556
Street (Put Stinica)	Sg4	0.543
Street section (Sukoišanska)	Sg5	0.687
Crossroad (Meštrovićeva, Sustipanskog P. and Ulica Dražanac)	Sg6	0.731
Crossroad (Spinčićeva, Zajčeva and Put Firula)	Sg7	0.476
Street section (Ulica slobode)	Sg8	0.437
Garage (Varoš 4)	Sg9	0.489
Crossroad (Hercegovačka, Put suplava and Put stinica)	Sg10	0.685
Crossroad (Sukoišanska and Starčevićeva)	Sg11	0.577
Street section (Domovinskog rata)	Sg12	0.496
Crossroad (Kavanjinova, Manđerova)	Sg13	0.832
Garage (Spinut North 4)	Sg14	0.747
Bus station (Pojišanska 2)	Sg15	0.659
Garage (Lovret North 1)	Sg16	0.671
Crossroad (Mažuranićevo Š., Dom. rata and Gundulićeva)	Sg17	0.681
Crossroad (Vukovarska, Bihaćka, Zagrebačka and Dom. rata)	Sg18	0.729

Table 3 shows the ranking of the infrastructure segments. Criteria weights values are calculate from the compromise scenario. These weight values are then used in the SAW method. Segments are evaluated by experts. Evaluations are normalized and transformed, and then SAW is included in further process. All of 13 criteria are used for evaluation of 18 infrastructure segments. Table 3 shows the ranking of 18 segments. The segment evaluation with higher score value means that the segment is considered as prior to improvement. In this case segment Sg10 (76.87) has the highest value, while the Sg8 (25.88) has the lowest.

Table 3. Ranking of segments.

Segment label	Score	Rank position	Segment label	Score	Rank position
Sg1	70.32	7.	Sg10	76.87	1.
Sg2	72.75	4.	Sg11	54.12	11.
Sg3	71.58	6.	Sg12	49.16	14.
Sg4	44.35	15.	Sg13	38.67	17.
Sg5	73.28	3.	Sg14	66.57	8.
Sg6	58.21	10.	Sg15	53.41	12.
Sg7	40.13	16.	Sg16	63.18	9.
Sg8	25.88	18.	Sg17	72.45	5.
Sg9	73.31	2.	Sg18	49.82	13.

With proposed model of decision support, ranking list for the priority of improvement of infrastructure segments is obtained as is shown in Table 3. Then local-government representatives selected the most appropriate solution, according to the results of the ranking and present policies. The selected solution must be in consent with financials available in the budget of city of Split. Finally, eight top-ranked segments are included in the maintenance plan, in the next investment period.

5 Conclusions

- In this paper an approach of decision support for the road infrastructure segments maintenance planning is proposed. With this approach, support to final decision maker, in this case to local government of city of Split, can be very useful and practical, especially in making decisions for the compound and ill-structured problem such is maintenance planning of the road infrastructure segments. One of the main characteristics of the approach is analysis of required data and selection of appropriate methods.
- The proposed approach is used for obtaining the priority ranking of the infrastructure segments. Relevant stakeholders are identified and gathered together to determined criteria that are used for segments evaluation. Stakeholders were divided into three groups: local government, experts, and users, and were directly involved in the decision-making process, expressing their opinions through criteria weights, using AHP and SAW method.
- This approach is a combination of multicriteria analysis and ANN. Monitoring the infrastructure segments using relevant criteria such are level of service, safety, time period passed form the last renovation and stability, data were collected that were further introduced into the ANN methodology. This way, condition evaluations of infrastructure segments are obtained as values of CAV. Involving ANN methodology as a knowledge-based system, substitution of experts can be achieved.
- The presented approach of decision support is an adequate tool for decision makers in the field of the improvement of maintenance planning of road-infrastructure segments.

Acknowledgements

This research is partially supported through project KK.01.1.1.02.0027, a project co-financed by the Croatian

Government and the European Union through the European Regional Development Fund–the Competitiveness and Cohesion Operational Programme**.**

ORCID

Nikša Jajac: https://orcid.org/0000-0003-2218-6507

References

Bielli, M. (1992). *A DSS approach to urban traffic management, European* Journal of Operational Research, 61(1-2), 106-113.

Deluka-Tibljaš, A., Karleuša, B., and Dragičević, N.(2013). *Review of multicriteria-analysis methods application in decision making about transport infrastructure*. Građevinar, 65(7), 619-631.

Dunkel, J., Fernandez, A., and Ortiz, R. et al. (2011). *Event-Driven Architecture for Decision Support in Traffic Management Systems.* Expert systems with applications , 38(6), 6530-6539.

Guisseppi, A., and Forgionne, G.A. (2002). *Selecting rail grade crossing investments with a decision supportsystem*. Information Sciences, 144(1-4), 75-90.

He, S., Song, R., and Chaudhry, S.S. (2014). *Service-oriented intelligent group decision support system:Application in transportation management.* Information Systems Frontiers, 16 (5), 939-951.

Hwang, C.-L., and Yoon, K. (1981). *Multiple Attribute Decision Making: Methods and Applications - A State-of the-Art Survey*. Springer-Verlag, New York.

Jajac, N. (2010). *Modeling of the decision support systems for urban road infrastructure development and maintenance.* Dissertation, University of Split, Faculty of Economics, Split, Croatia.

Jajac, N., Knezić, S., and Marović, I. (2009). *Decision support system to urban infrastructure maintenance management*. Organization, Technology and Management in Construction – An International Journal, 1(2), 72-79.

Jajac, N., Marovic, I., and Baucic, M. (2014). *Decicision support concept for managing the maintenance of city parking facilities.* Electronic journal of the Faculty of Civil Engineering Osijek-E-GFOS, 9, 60-69

Leclerc, G., Hmiya, S., Aïmeur, E., Quintero, A., Pierre, S., and Ochoa, G. (2001). *An intelligent decision support system (IDSS) for an urban infrastructure complaint management module*. World Multiconference on Systemics, Cybernetics and Informatics, ISAS/SCI 2001, Orlando, Florida, vol. XVIII, pp. 143–147.

Petty, K.R., and Mahoney, W.P. (2008). *The U.S. Federal Highway Administration winter road Maintenance Decision Support System (MDSS): Recent enhancements & refinements.* Sirwec, Prague, 14-16 May, 29: 1-12.

Pomerol, J., Roy, B., and Rosenthal-Sabroux, C. (1996). *Development of an "intelligent" system for the evaluation of railway timetables: Problems and issues*. Journal of Decision Systems, 5, 249–267.

Quintero, A., Konaré, D., and Pierre, S. (2005). *Prototyping an intelligent decision support system for improving urban infrastructures management*. European Journal of Operational Research, 162(3), 654–672.

Saaty, T.L.: Decision Making for Leaders, The Analytic Hierarchy Process for Decisions in a Complex World, Wadsworth, Belmont, 1982.

Sayers, T.M., Jessop, A.T., and Hills, P.J. (2003). *Multi-criteria evaluation of transport options-flexible, transparent and user-friendly?*, Transport Policy, 10(2), 95-105.

Shelton, J., and Medina, M. (2010). *Integrated multiple-criteria decision making method to prioritizetransportation projects*. Transportation Research Record: Journal of the Transportation Research Board, 2174,51-57.

Turban, E., and Aronson, J.E. (1995). *Decision Support Systems and Intelligent Systems*. 5th edition, Simon and Schuster Company, Upper Saddle River, NJ.

Zavadskas, E.K., Liias, R., and Turskis, Z. (2008). *Multi-attribute decision-making methods for assessment of quality in bridges and road construction: state-of-the-art surveys.* The Baltic journal of road and bridgeengineering, 3(3), 152–160.

Zhou, G., Wang, L., Wang,D., and Reichle, S. (2010). *Integration of GIS and Data Mining Technology to Enhance the Pavement Management Decision Making.* Journal of Transportation Engineering, 136(4), 136:332-341.

XV International Conference on Durability of Building Materials and Components
DBMC 2020, Barcelona
C. Serrat, J.R. Casas and V. Gibert (Eds)

Early Stage Construction Cost Prediction in Function of Project Sustainability

Diana Car-Pušić[1] **and Marko Mlađen**[2]

[1] Faculty of Civil Engineering, University of Rijeka, Radmile Matejčić 3, Rijeka, Croatia, diana.car.pusic@uniri.hr

[2] GT Trade Ltd., Spinčićeva 2d, Split, Croatia, marko.mladjen@gmail.com

Abstract. *Construction project costs often reach values higher than planned. Accuracy in project cost estimation is one of the most important criteria for project success, even for its sustainability.*
The main idea of this research is to examine the relationship between realized cost and contracted cost values for residential buildings. The aim of the research is to determine the mathematical relationship between realized and planned costs in the project implementation phase by using a few mathematical methods and some machine learning methods in comparison to linear regression. This would enable validation of methods themselves by comparing and evaluating the obtained relevant parameters. Comparison would be performed on two levels, based on its general characteristics, as well as on the results of their application on the basis of 24 building reconstructions and new buildings by comparing the mean absolute percentage error (MAPE) and the determination coefficient (R^2) using Predictive Modelling Software DTREG (pronounced D-T-Reg). The relationship of realized and planned costs will be determined for the building as a whole and for certain types of construction works. That relationship would enable more realistic budget planning of similar future projects. Cost overrun factors will be analysed for particular types of construction works, as well as the probability of their occurrence, and what measures should be undertaken to prevent or reduce them in similar future projects. The phenomenon known in project planning as "optimism bias" will be analysed in the context of research focus of exceeding the construction cost.

Keywords: *Building Construction, Contracted Cost, Realized Cost, Predictive Modelling Software, Machine Learning.*

1 Introduction

In the construction practice, the contracted construction cost overrun is a very common occurrence, which is a very frequent and undesired situation. The goal is to avoid or minimize cost overruns, which can be achieved by accurately estimating costs during project preparation, before signing a construction contract. This can be achieved by using scientifically based models obtained by applying adequate mathematical methods and by browsing the finished projects database. In contrast, experience shows that costs are usually calculated by method of unit price calculations and calculated quantities, but also estimated on a flat-rate basis, on the basis of experience, that is, without adequate scientifically or experientially based budgets. This often happens under deadline pressure as the cost information must be provided so that further project activities can continue. Thus, inherent uncertainties and risks, which are characteristic for all construction projects to a greater or lesser extent, are neglected, resulting in possible generation of higher costs of those estimated in the project.

Project cost estimation is a complex and challenging task, as evidenced by the cost overruns of numerous projects all over the world (Flyvbjerg *et al.*, 2002, Le-Hoai *et al.*, 2008; Žujo, 2008, Le-Hoai and Lee, 2009, Car-Pušić and Radujković, 2009; Žujo *et al*., 2010,). Scientific knowledge (Nikić, 1998, Radujković, 1999, Flyvbjerg *et al.*, 2002, Žujo, 2008; Le-Hoai *et.al.*, 2008, Žujo *et al.,* 2010; Car-Pušić and Radujković, 2009; Alshamrani, 2017, Petrusheva *et al.,* 2017, Juszczyk *et al.*, 2018) and experience show that the successful cost estimation requires:

1. Monitoring and registering data on constructed structures
2. Sufficient information about the new project
3. Application of multiple assessment methods and selection of the most accurate one.

Due to the diversity of projects, numerous risks involved and the complexity of cost estimation, researchers have often addressed this problem and developed a number of linear regression models to analyze costs depending on different variables, e.g. construction time (Žujo *et al.*, 2010) structure type, building area, number of floors, floor height (Alshamrani, 2017), geotechnical and construction variables (Petroutsatou *et al.*, 2006). Linear regression models using construction time, which is the most common independent variable, as a predictor (Žujo *et al.*, 2010) could be considered an inverse problem compared to the well-known "time-cost" ("TC") model used in the 1960s and founded by Bromilow (1969). Although this approach may be tempered by over-simplification because only one predictor is considered, numerous further studies have been conducted, which resulted in establishing of country-specific models, because the specific economic circumstances determine the parameters (Chan and Kumaraswamy, 1999; A.P.C. Chan, 1999; Car-Pušić, 2004). In some studies, this model has been used as the basis for the development of hybrid cost estimation models, which combine regression and neural networks (Petrusheva *et al*., 2017; Petrusheva *et al.*, 2019).

The application of artificial neural networks for cost estimation with one independent variable, the construction time, has been researched by some authors (Petrusheva *et al.,* 2017, Juszczyk *et al.*, 2018; Tijanić and Car-Pušić, 2019; Tijanić *et al*., 2019).

This research analyzes construction projects of building construction structures in a manner deviation from the usual one (Mlađen, 2017). The relationship between the realized and contracted costs is investigated. As these costs most often vary, the previous thesis is confirmed stating that often flat-rate and superficial assessment without applying scientifically proven methods and without considering the possible risks are employed. The difference in costs, expressed relatively, is known in the literature as "optimism bias". Available data are data on contracted and realized cost values and data on years of construction/reconstruction (Mlađen, 2017). Different methods seek to obtain the most accurate estimation model for this type of structure. Since these are the projects implemented in the territory of the Republic of Croatia in the County of Istria, the model is best applied for future projects in the area. This methodology can be applied to any type of facility and area. The cost difference obtained in this way can be considered a risk response measure.

2 The Main Research Goals

The main research goal is to define relation between the real and the contracted investment cost in building construction applying mathematical methods – linear regression and artificial neural

networks. The goal is to identify the model that provides the most accurate cost estimate and implementation guidelines.

3 Methodology

The set research hypothesis will be tested by applying linear regression and neural networks on data on constructed or reconstructed structures and by comparing the model accuracy.
The conditions of application for the most accurate cost estimation model will be analyzed.

3.1 Research Hypothesys

The value of construction works in building construction (reconstructions and new constructions) is not contracted in real terms, but usually below real values. The contracted value of works is the total value of works from the accepted best offer, which is usually obtained by method of unit price calculations and calculated quantities. The thesis is that the real value of the works most often exceeds the contracted value. There is a dependence between these values, which can be mathematically determined with satisfactory accuracy.

4 Research Methods, Data Base and Data Processing

Using the documentation review and analysis, data on contracted and realized prices of public and private building construction structures (new construction, reconstruction and rehabilitation), 24 in total, built on the territory of the County of Istria in the Republic of Croatia were obtained. (Mlađen, 2017).The investments were realized in the period from 2006 to 2017. The average overrun of the realized project values is 12.15%. The minimum overrun is 1.61% and the maximum is 41.49%. The standard deviation is 11.87%.

Predictive Modelling Software DTREG is used for data processing and modelling, which supports a wide range of models (regression models, decision trees for regression, neural networks, support vector machine, etc.). The database must be an ASCII file in Comma Separated Value (CSV) format with values for one case per row and one column for each variable. One of the variables is the target variable, while one or more other variables are predictors. DTREG analyzes the data and generates a model that gives the best estimate of the target variable based on the available predictor values. The software allows you to select model parameters from the multiple options offered. Moreover, the iteration offers the expected optimal parameters (Sherrod, 2014). In this research, the target variable is the value of the real construction cost C_R, and the predictor is the value of the expected, planned and contracted construction costs.

Considering the research goals and scientific hypothesis, the following methodological procedure is applied:

1. Application of linear regression
2. Application of neural networks and Support Vector Machine (SVM) model
3. Comparison of results for the validation data, discussion, application proposal.

4.1 Linear Regression

First, the simple regression analysis method was applied as a common and simple, well-understood, widely used method (Sherrod, 2014), and the adequacy and accuracy of the model

obtained was determined by appropriate indicators. The general form of the applied regression function is:

$$y = \beta_0 + \beta_1 x \tag{1}$$

4.1.1 Output generated for linear regression

The following parameters were obtained using simple regression analysis using DTREG software:

Table 1. Results for linear regression.

Variable	Coefficient	Std. Error	t	Prob.(t)
C_C	1.128	0.0137	82.22	<0.00001
Constant	14.877,5	1.532e+004	0.97	0.34209

The regression function is:

$$C_R = 1{,}128 C_C + 14877{,}5 \tag{2}$$

The t Statistic value is 82.22 with a probability <0.00001. The coefficient R^2 as a proportion of variance explained by the model is 0.98849 (98.849%). The correlation coefficient R between actual and predicted values is 0.99684 (99.684%). Mean Absolute Percentage Error (MAPE) is 13.824% for validation data.

4.2 Neural Networks and SVM Model

In an attempt to obtain a more accurate cost estimation model, i.e. a lower value of the MAPE parameter, the next step includes the application of General Regression Neural Network (GRNN), Radial Basis Function (RBF) and Support Vector Machine (SVM). These models were selected because they are suitable for continuous variables and for smaller databases. The Multilayer Perceptron (MLP) network has proven to be inappropriate due to too little data was excluded from further consideration.

4.2.1 Output generated for GRNN, SVM, RBF

For all models, the expected optimal initial parameters provided by the software were used.

For GRNN, the Gaussian kernel function was applied, σ values were calculated for each predictor variable (min σ 0,0001 and max σ 10, with 20 search steps) and Leave One Out (LOO) validation method of evaluating σ values during the optimization process was used. Each training model is built with all training rows except one and then, the error was evaluated. This was repeated for all rows, and the error was averaged (Sherrod, 2014).

The model has been reduced to 7 neurons when the minimum error occurred. Despite the small number of retained neurons, the reduction of neurons should be performed because it significantly contributes to the accuracy of the model. In this case, the MAPE was reduced from 75.488% to 35.130%. The coefficients R^2 and R are shown in Table 2.

The initially defined type of SVM model Epsilon-SVR model was used for the SVM. Another possible option is the V-SVR model. The differences that may arise are small and the other model has not been applied. Radial Basis Function (RBF) has been implemented as the kernel function, which in most cases produces the best results. Kernel function transforms the

input data into an n-dimensional space where a hyperplane can be constructed to partition the data (Sherrod, 2014). The optimal approximation linear function will be obtained in the new space (Petrusheva *et al.,* 2017).

Using the RBF, the SVM model generates the RBF network architecture. The difference is in the number and position of nodes. At SVM, their position is on the support vectors (Sherrod, 2014). 24 support vectors are used by the model.

Model validation is performed by Cross validation method with 10 cross-validation folds. At SVM, low values were obtained for R and R^2 as well as for MAPE 14.814% (Table 2).

After three iterations, the three-neuron RBF network gave the best result of 10.976% for MAPE, but lower values of R^2 and R (Table 2). The Cross validation method with 10 cross-validation folds was also applied as the validation method.

Table 2. Results for linear regression and neural networks for source data.

Parameter	LR	GRNN	SVM	RBF
R^2	0.988	0.605	0.345	0.556
R	0.997	0.919	0.644	0.796
MAPE /%/	13.824	35.130	14.814	10.976

4.3 Application of Input Variable Natural Algorithms

Following the time-cost model, the following model is assumed:

$$C_R = E \times C_C^F \tag{3}$$

$C_R =$ realized price
$C_C =$ contracted price
$E =$ model parameter that shows the average real price for monetary value construction
$F =$ model parameter that shows real cost dependence of contracted cost changes

The model can be expressed as a logarithm to obtain the following form:

$$lnC_R = lnE + FlnC_C \tag{4}$$

It means:

$$\left.\begin{array}{rcl} lnE & = & \beta_0 \\ E & = & e^{\beta_0} \end{array}\right\} \tag{5}$$

$$F = \beta_1 \tag{6}$$

4.3.1 Output generated for linear regression for logharitmized data

The natural logarithms of C_C predictors and the target variables C_R were calculated. Applying regression analysis on natural logarithms using DTREG software, the following parameters were obtained:

Table 3. Results for linear regression.

Variable	Coefficient β_1	Std. Error	t	Prob.(t)
lnC_C	1.03367	0.0165	62.64	<0.00001
Constant β_0	0.0700096	0.02752	2.54	0.01849

Using the information in the previous table (Table 3), the regression function reads:

$$lnC_R = 0{,}07 + 1{,}03367 lnC_C \tag{7}$$

$$lnE = 0{,}07$$

$$E = 1{,}07$$

$$F = 1{,}03367$$

The model which is obtained is:

$$C_R = 1{,}07 \cdot C_C^{1{,}03367} \tag{8}$$

The value of t Statistic is 62.64 with a probability of p (t) <0.00001. The values of R^2 and R are 0.993 and 0.997 respectively. These values confirm the regression dependence. The MAPE is 11.816%. (Table 4).

4.3.2 Output generated for GRNN, SVM, RBF for logharitmized data

The Gaussian kernel function was applied for GRNN, σ values were calculated for each predictor variable (min σ 0.0001 and max σ 10, with 20 search steps) and Leave one out (LOO) validation method was used. The model has been reduced to 18 neurons when the minimum error occurred. In this case, the MAPE is 12.291%. The coefficients R^2 and R are shown in Table 4.

After four iterations, the three-neuron RBF network earns the MAPE value of 23.810%, and the R^2 and R values shown in Table 4. As a validation method, the Cross validation method with 10 cross-validation folds was also applied.

The initially defined Epsilon-SVR model was used for the SVM. Radial Basis Function (RBF) was applied as the kernel function. 24 support vectors are used by the model. Model validation was performed by Cross validation method with 10 cross-validation folds.

Table 4. Results for linear regression and neural networks for logharitmized data.

Parameter	LR	GRNN	SVM	RBF
R^2	0.993	0.962	0.995	0.693
R	0.997	0.985	0.997	0.839
MAPE /%/	11.816	12.291	6.469	23.810

MAPE is 6.469 %, R^2 and R values are 0.995 and 0.997 respectively. By applying the SVM model to logarithmic values, the lowest model error value is obtained.

5 Discussion of Results

By applying the linear regression model to the original data, a MAPE of 13.824% was obtained. In order to obtain a more accurate cost estimation model, the neural network models GRNN and RBF and the SVM model were applied. RBF gives a more favorable MAPE of 10.976%.

By applying the linear regression and RBF, GRNN and SVM to the natural logarithms of the input data (following the Bromilow "time-cost" model), (Bromilow, 1969) the lowest MAPE was obtained using SVM. The MAPE is 6.469%. Compared to the lowest MAPE obtained by processing the original data, this one is lower by 4.507%.

6 Conclusions

- The real costs of new constructions and reconstructions of structures in building construction field often exceed contracted values. The accepted tender price, obtained from the bill of quantities and unit prices (C_C) is taken as the contracted price. The aim of the research was to obtain a model that accurately defines the functional dependence of the real price C_R and the planned price C_C. Thus obtained real price should be taken as the contract price. This would reduce the risk of the contract price being exceeded. Although the database consists of a relatively small amount of data, the possibility of applying linear regression models, neural networks and SVM models to estimate the real cost of construction and reconstruction of high-rise buildings is presented. These models were applied to the original values C_R and C_C as well as to the values of natural logarithms. Namely, following the Bromilow "time-cost" model, the model $C_R = E \times C_C^F$ was established and tested. By expressing it in logarithms, the linear regression function is obtained.
- By applying linear regression and neural networks to the values of the natural logarithms of the variables, it was found that more accurate results can be obtained compared to models with original data. The best results, i.e. the lowest MAPE of 6.469%, are obtained by the SVM model applied to natural logarithm values of the predictor and the target variable.
- Despite the small database, the obtained insight could be relevant to solving the real cost prediction problem when working with larger databases. The results should also be investigated for civil engineering databases.

Acknowledgements

This work has been fully supported by the University of Rijeka under the project uniri-tehnic-18-125.

ORCID

Diana Car-Pušić: https://orcid.org/0000-0003-2555-335X
Marko Mlađen: -

References

Alshamrani, O.S. (2017). Construction Cost Prediction Model for Conventional and Sustainable College Buildings in North America. *Journal of Taibah University of Science, 11(2),* 315-323. doi:10.1016/j.tusci.2016.01.004

Bromilow, F.J. (1969).Contract Time Performance Expectations and the Reality. *Building* Forum, *1(3),* 70-80.

Car-Pušić D. (2004). *Metodologija planiranja održivog vremena građenja* (in Croatian), PhD Thesis, Građevinski fakultet Sveučilišta u Zagrebu, Zagreb, Croatia.

Car-Pušić, D. and Radujković, M. (2009). Construction Time-Cost Model in Croatia. *International Journal for Engineering Modelling, 22(1–4),*63–70.

Chan, W.M.D. and Kumaraswamy, M.M. (1999). Forecasting Construction Durations for Public Housing Projects Hong Kong Perspective. *Building and Environment, 34(5),* 633-646. doi: 10.106/s0360-1323(98)00040-7

Chan, A.P.C. (1999). Time-cost Relationship of Public Sector Projects in Malaysia. *International Journal of Project Management, 19(4),* 223-229. doi:10.1016/S0263-7863(99)00072-1

Flyvbjerg, B., Holm, M.S. and Buhl, S.L. (2002). Underestimating Costs in Public Works Projects: Error or Lie? *Journal of the American Planning Association, 68(3),* 279–295. doi:10.1080/01944360208976273

Juszczyk, M., Leśniak, A. and Zima, K. (2018). ANN Based Approach for Estimation of Construction Costs of Sports Fields. *Complexity, Article ID 7952434, 11 pages*. doi:10.1155/2018/7952434

Le-Hoai L., Lee Y.D. and Lee, J.Y. (2008). Delay and Cost Overruns in Vietnam Large Construction Projects: a

Comparison with Other Selected Countries. *KSCE Journal of Civil Engineering, 12(6),*367–377. doi: 10.1007/s12205-008-0367-7

Le-Hoai L. and Lee Y.D. (2009). Time-Cost Relationships of Building Construction Project in Korea. *Facilities, 27 (13/14)*, 549–559. doi: 10.1108/02632770910996379

Mlađen, M. (2017). *Analiza uzroka i vjerojatnosti troškovnih odstupanja u projektima visokogradnje*, (in Croatian), Master's Thesis, Građevinski fakultet Sveučilišta u Rijeci, Rijeka, Croatia.

Nikić, R. (1998). *Upravljanje rizicima kod građevinskih projekata zemlje u tranziciji* (in Croatian), Master's Thesis, Građevinski fakultet Sveučilišta u Zagrebu, Zagreb, Croatia.

Tijanić, K., Car-Pušić, D. and Šperac, M. (2019). Cost Estimation in Road Construction Using Artificial Neural Network, *Neural Computing and Applications, accepted for publishing.* doi: 0.1007/s00521-019-04443-y

Petroutsatou, C., Lambropoulos, S. and Pantouvakis, J.P. (2006). Road Tunnel Early Cost Estimates Using Multiple Regression Analysis. *Operational Research 6(3),* 311-322. doi: 10.1007/BF02941259

Petrusheva S., Zileska-Pancovska, V., Žujo, V. and Brkan-Vejzović, A., (2017). Construction Costs Forecasting: Comparison of the Accuracy of Linear Regression and Support Vector Machine Models, *Technical Gazette, 24(5),* 1431-1438. doi:10.17559./TV-20150116001543

Petrusheva, S., Car-Pušić, D. and Zileska-Pancovska, V. (2019). Support Vector Machine Based Hybrid Model for Prediction of Road Structures Construction Costs. *IOP Conference Series: Earth and Environmental Science 222 (1755-1307)*. doi:10.1088/1755-1315/222/1/012010.

Radujković, M. (1999). Upravljanje rizikom i resursima kod građevinskih projekata, znanstveno istraživački project, MZITRH (Ministarstvo znanosti i tehnologije Republike Hrvatske) [Construction Project Risk and Resource Management, scientific research work of MST (Ministry of Science and Technology)], Građevinski fakultet, Sveučilište u Zagrebu, Faculty of Civil Engineering, University of Zagreb. (in Croatian)

Sherrod, P.H. (2014). Manual DTREG Predictive Modeling Software

Tijanić, K. and Car-Pušić, D. (2019).The Assessment of School Operational Costs by Using Artificial Neural Networks. In *Proceedings of the VII Gathering of Young Researchers in the Field of Civil Engineering and Related Technical Sciences Common found 2019*, Rijeka, Croatia, 126-131.

Žujo, V. (2008). *Upravljanje građevinskim projektima kroz planiranje vremena građenja* (in Bosnian), PhD Thesis, Građevinski fakultet Univerziteta Džemal Bijedić u Mostaru, Mostar, Federation of Bosnia and Herzegovina.

Žujo, V., Car-Pušić, D. and Brkan-Vejzović, A. (2010). Contracted price overrun as contracted construction time overrun function. *Technical Gazette, 17(1),* 23-29.

XV International Conference on Durability of Building Materials and Components
DBMC 2020, Barcelona
C. Serrat, J.R. Casas and V. Gibert (Eds)

Possible Applications of Neural Networks in Managing Urban Road Networks

Ivan Marović[1]

[1] Faculty of Civil Engineering, University of Rijeka, Radmile Matejčić 3, HR-51000 Rijeka, Croatia, ivan.marovic@uniri.hr

Abstract. *Life-cycle management of urban road networks as a part of an urban system is a very complex process from the management standpoint of social, technical and economic aspects. The complexity and multidisciplinarity of such a problem suggest the need for using soft computing tools as well as multi-criteria analysis and group decision-making. Recently, there is a significant increase in using various soft computing tools, especially neural networks, for different prediction purposes in the field of road construction planning and management. Along with known advantages of such a prediction method, yet some applications showed the shortcomings. In that sense, the focus of this research is on possible applications of neural networks related to the life-cycle phases during the management of urban road projects. This is done in both horizontal (projects' life-cycle phases) and vertical (hierarchical decision-making levels) approach. The final aim of the research is to compare and highlight the possible applications of neural networks as a prediction tool and support for decision-making in urban road management.*

Keywords: *Decision Support, Neural Networks, Project Management, Strategic Planning.*

1 Introduction

Urban development and management especially the management of urban road networks, as a part of the urban infrastructure system, is a highly complex process from the management standpoint of social, technical and economic aspects. The development of urban road infrastructure is an integral part of any urban expansion processes and often considered as a dominant transport asset. The World Road Association (2014) reported that the average length of public roads in OECD countries is more than 500,000 km with a strong tendency of increasing, and is often the largest publicly owned national asset. Therefore, in urban areas where road infrastructure covers over 20% of the whole city area (Deluka-Tibljaš *et al.*, 2013) it's quality and strategic development directly influence the citizens' quality of life (Hanak *et al.*, 2014). Developing management practices that effectively integrate the processes of urban infrastructure management is a challenging goal that many cities are struggling with nowadays, but is an important necessity to achieve desired long-term sustainability.

Public management of urban road networks is a highly complex and socially sensitive as the city governments encounter different problems during the decision-making phase when it is necessary to find a solution that would meet the requirements of all stakeholders. All solutions must be strategically aligned and be a part of the desired development concept. Initially, the different views are provided by stakeholders and experts regarding the scope, scale, and potential solutions. Such happens during the whole life-cycle of the urban road network as each municipality has a certain annual budget for its construction, maintenance, and remedial activities. Therefore, planning activities altogether with project prioritization emerges as one of

the most important and most difficult issues to be resolved.

The evaluation of such investments requires explicit consideration of multiple, conflicting and incommensurate criteria that have an important social, economic, and environmental influence on various stakeholders in different ways (Jajac et *al.*, 2015). The complexity and multidisciplinarity of such a problem suggest the need for using soft computing tools, such as artificial neural networks (ANN), as well as multi-criteria analysis and various decision-making methods. The use of ANNs in solving pavement engineering problems and road management has a long history as well. Since the 1990s, ANNs have been frequently used for solving various complex problems, mostly for operational purposes, such as automatic pavement evaluation (Kaseko and Ritchie, 1993), pavement performance prediction (Banan and Hjelmstad, 1996), rutting (Simpson *et al.*, 1995), and maintenance (Fwa and Chan, 1993). A very few stressed out the importance and possibilities of their application in decision-making processes as a part of a decision support system *i.e.* DSS (Turban, 1993; Turban and Aronson, 1995).

In the 2000s, researchers followed the scientific contribution from previous decade and enhance the efficacy of ANNs in assisting asphalt mixture design and evaluation (Sundin and Braban-Ledoux, 2002; Yang *et al.*, 2003; Tarefder *et al.*, 2005; Ceylan *et al.*, 2007; Terzi, 2007; Commuri and Zaman, 2008; Ozsahin and Oruc, 2008; Tapkin *et al.*, 2009; Tušar and Novič, 2009). All these aspects were evolved to efficiently solve technical problems that occur on the operational management levels. A very few gave another insight of ANNs to be used on higher management levels such as tactical and strategic. Researches such as Loia *et al.* (2000), Quintero *et al.* (2005), Šelih *et al.* (2008), and Jajac *et al.* (2009) can be highlighted as the one where ANNs were used for solving problems on both tactical and strategic management levels based upon Turban's DSS concept. Such approach bloomed in 2010s when more and more researchers very efficiently applied ANNs for solving structured problems that occur on operational level (Gesoglu *et al.*, 2010; Xiao *et al.*, 2010; Ozgan, 2011; Ciresan *et al.*, 2012; Singh *et al.*, 2013; Ozturk and Kutay, 2014; Zavratnik *et al.*, 2016; Androjić and Marović, 2017; Zhang *et al.*, 2018; Gong *et al.*, 2019) as well as for solving semi-structured and unstructured problems that occur on tactical and strategic levels as a part of various DSS'es (Durduran, 2010; Coutinho-Rodrigues *et al.*, 2011; Dahal *et al.*, 2013; Du *et al.*, 2014; Jajac *et al.*, 2014; Jajac *et al.*, 2015; Han *et al.*, 2016; Marović *et al.*, 2018).

The main objective of this paper is to summarize the findings of up-to-date research articles concerning the application of artificial intelligence, specifically neural networks, related to the life-cycle phases during the management of urban road networks as a part of an urban system. Some of the other objectives were also assessed, such as to: (i) identify specific problems that are solved by the aid of neural networks during life-cycle management of urban road networks, (ii) evaluate and highlight the possible applications of neural networks as a prediction tool and support for decision-making on different management levels.

2 Systematic Review

Studies about neural networks and urban infrastructure management, especially road networks, were surveyed. The review reflects on papers published in peer-reviewed journals preferably articles and review papers. Researches related to neural networks in managing urban road networks published from 2000 to 2019 was reviewed. The survey was conducted using selected keywords (artificial neural network, decision support, infrastructure, multi-criteria analysis, and

road management) that resulted in 1703 publications (1014 in Web of Science and 689 in Scopus) which were selected by the following criteria: year of publication (from year 2000); document type (only journal articles were taken into consideration); repetitions (duplicate between Web of Science and Scopus); and relevance and relation to the topic. This resulted in 73 selected articles. The number of publications considered in this paper and their corresponding year of publication is summarized in Figure 1. Only the papers that solely highlight the use of ANNs for solving various structured problems (operational level) and/or various semi-structured and unstructured problems (tactical and strategic level) are referred to.

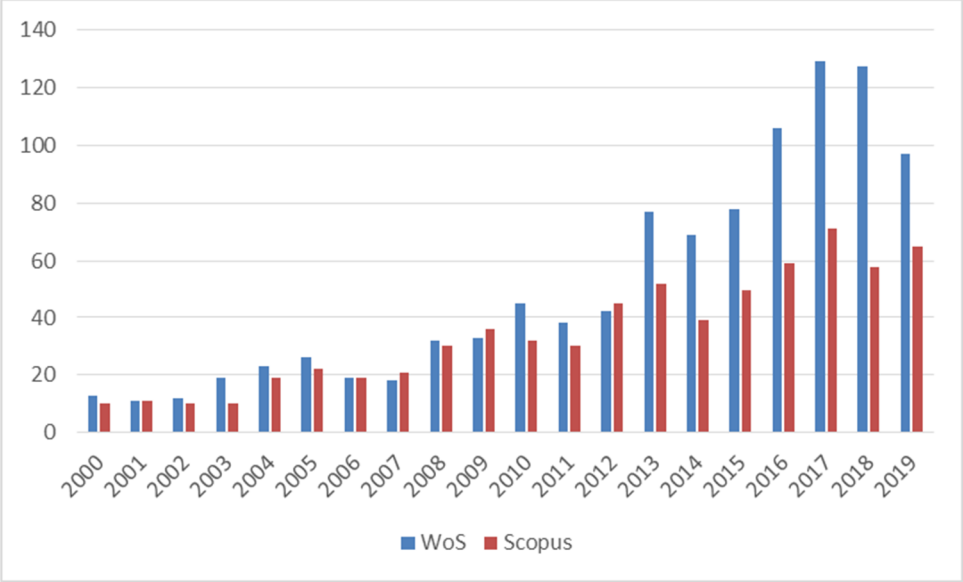

Figure 1. Number of publications and corresponding year of publication.

Collected data (Figure 1) shows the increasing interest and published papers on this topic by the research community from 2013 until now. Such is more evident regarding Web of Science than the Scopus database. For 2019, it should be noted that other papers may appear in the databases during October 2019 and later.

3 Urban Infrastructure Management

Life-cycle management of urban road networks, in general, can be seen through the interaction of horizontal and vertical aspects of urban road management (Figure 2) to achieve previously defined sustainable goals. The horizontal aspect takes into account the project management approach through four cyclically connected phases (*e.g.* initiation, planning, execution, and closure phase) thus represent the life-cycle phases. These phases do not change whether the project is managed traditionally or agile. Sure, it is obvious that projects do not appear and are not managed solely horizontally. Therefore, a vertical management component should not be forgotten and must be considered with all the difficulties that it brings. Such is observed throughout the vertical aspect of urban road management that takes into account the hierarchical management levels (operational, tactical and strategic).

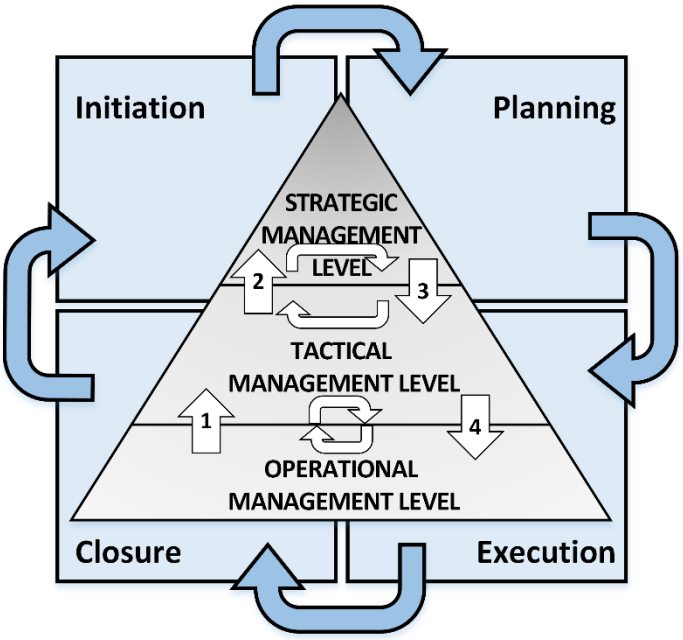

Figure 2. The horizontal and vertical aspects of urban road management.

The first management level supports decision-makers at the lowest operational management level. Besides its general function of supporting decision-making processes at the operational level, it is a meeting point of data and information where the problems are well defined and structured. This management level exclusively deals with structured problems that can be characterized as specified, detailed and narrow, clearly scheduled and internal. Additionally, it provides information flows towards higher decision levels (arrow 1 in Figure 2). A circular arrow between two management levels symbolizes interactions between the levels for purposes of solving specific problems. The decision-makers at the second management level (*i.e.,* tactical management level) deal with less-defined i.e. semi-structured problems and unstructured problems. At this level, tactical decisions are delivered, and it is a place where information basis and solutions are created. Problems that occur on this level can be characterized as broader than on lower level but still very focused and specified, clearly scheduled and internal. Based on applied models and methods, it gives alternatives and a basis for future decisions on the strategic management level (arrow 2 in Figure 2), which deals with even less-defined and unstructured problems. At the third management level, based on the expert deliverables from the tactical level, future development of the system is carried out. Strategies are formed, and they serve as frameworks for lower decision and management levels (arrows 3 and 4 in Figure 2). Problems that occur on this level are general and with a broad scope, both internal and external, and often ad hoc.

Depending on the management level and type of the occurred problem, various tools and methods could be used such as soft computing tools (for example, ANNs) as well as multi-criteria analysis and group decision-making. Many authors have studied possibilities for generating decision support tools for urban infrastructure management that convergence toward some type of decision framework is more or less similar to a basic DSS structure. According to Turban (1993; 1995), DSS's basic structure consists of three modules: database, model base, and dialog. In 2005, Quintero et al. introduced an improved DSS named IDSS (Intelligent

Decision Support System) as a solution for the future needs of urban infrastructure management. Later, Jajac *et al.* (2009) introduced the new architecture of DSS for urban infrastructure management that places the management levels in the core of the DSS structure. Such provided that the interactions between DSS modules are realized through decision-making processes at all management levels, which serve as meeting points of adequate models (from the model base) and data (from the database). The new architecture provided that complex and sensitive decision-making processes can be correctly supported if appropriate methods and data are properly organized and used. Gudac *et al.* (2014) highlighted the utter importance when decisions must be quickly made based upon real-time information, while Tijanić *et al.* (2019) proposed ANN based models to accurately estimate road construction costs.

3.1 Application of Neural Networks at the Operational Management Level

During the years various researches made a significant contribution with ANNs to efficiently solve technical problems that occur on the operational management levels in managing urban road networks. They were mostly focused on various asphalt mixtures and predictions of their properties during material production as well as during the exploitation period when the mixtures became part of the road network. In that sense, Xiao and Amirkhanian (2009) explored the application of ANN in predicting the stiffness behavior of asphalt mixtures and reported that the ANNs are more effective in predicting the fatigue life of the mixture than the traditional models. Ceylan *et al.* (2007) also reported the higher prediction accuracy of ANN compared to the existing regression models. Tušar and Novič (2009) analyzed the impact of various factors by using several models, multiple linear regression (MLR), partial least squares regression (PLS) and artificial neural networks (ANN), in the prediction process of the monitored hot mix asphalt properties. They reported that the use of MLR and PLS models show a better predictive ability that the ANN models. In 2016, Zavratnik *et al.* (2016) showed the application of ANN and MLR in the process of forecasting air void content with different used parameters on 5 types of asphalt mixtures. The authors concluded that the use of MLR models is better than ANN in the prediction of certain mixtures, but such is not the case for all asphalt mixtures together. In 2019, Androjić and Marović developed ANN and MLR models to predict the hot mix asphalt properties (air void and binder content) produced in a laboratory. The performed research on 6 types of asphalt mixtures indicates that it is possible and desirable to apply neural networks in the prediction process of the required properties of hot mix asphalt, wherein it is necessary to use a substantial set of input data. Gong *et al.* (2019) approach the fatigue cracking prediction problem in pavements by using the highly flexible ANNs through the deep learning framework. They reported that the difference between prediction performances of fatigue cracking transfer function concerning the proposed framework is 30% in favor of ANNs.

3.2 Application of Neural Networks at the Tactical Management Level

To improve conditions of road elements, as a part of sustainable development of the road infrastructure in the city of Split, Jajac *et al.* (2015) introduced the ANN that was trained and tested on road infrastructure data that come out of 236 city's road projects during the two years. Only road elements with insufficient conditions were assessed, while four network input variables were used: level of service (LOS), safety, savings on vehicle maintenance, and maintenance quality. In 2018, based on the decision support concept (Jajac *et al.*, 2009),

Marović et al. showed that complex and sensitive decision-making processes, such as the ones for road maintenance planning, can correctly be supported if appropriate methods and data are properly organized and used. They designed and developed an ANN model to achieve a successful prediction of road deterioration as a tool for maintenance planning activities. Recently with drastic improvements in computing capacity, fast optimization algorithms, and new network topology enabled researchers to explore considerably more complex models such as crack detection on asphalt surfaces (Zhang *et al.*, 2018) during maintenance phases, and to actively estimate and manage cost overruns (Tijanić *et al.*, 2019). Also, there is a strong tendency for optimizing ANNs for the evaluation of asphalt pavement structural performance (Bosurgi *et al.*, 2019) to improve the efficiency of pavement management systems.

3.3 Application of Neural Networks at the Strategic Management Level

The use of ANNs for solving problems at the strategic management level is closely connected with the ones previously stated at the tactical management level. It is important to note that at this management level ANN is used as one of the models out of the model base of the DSS for urban infrastructure management as a core management framework. This is the management level where all project phases are strategically managed. A specific decision support concept focused on the planning phase was proposed by Jajac *et al.* (2014), as a part of the decision support framework for the management of urban transport projects (Jajac *et al.*, 2015). Marović *et al.* (2018) highlighted the importance of the maintenance planning aspect of DSS that is based on real-time collected and processed data by the means of ANN. As road management is a spatial problem, Coutinho-Rodrigues *et al.* (2011) proposed a spatial DSS where they highlight the importance of implementing Geographic Information Systems (GIS) for planning and decision-making purposes. Such is helpful not only for a static view of road networks, such as planning and maintenance activities but also could provide additional dynamic benefits such as traffic accidents (Durduran, 2010), all as a part of sustainable urban infrastructure management framework (Torres-Machi *et al.*, 2018).

4 Conclusions

This paper has presented a literature review concerning the applications of neural networks in managing urban road networks. In recent years, an understanding and application of neural networks have been significantly increased as they have been applied in a variety of matters. The conducted literature review gave insight in ways that the neural networks have been used in different life-cycle phases during the management of urban road networks for solving structured, technical problems that occur on the operational management levels, but also as one of the methods for solving semi-structured and unstructured problems that occur on tactical and strategic levels as a part of various decision support systems.

At the operational level, neural networks are mostly used for predictions of various asphalt mixtures properties during material production as well as during the exploitation period when the mixtures became part of the road network. At tactical and strategic levels, neural networks are often used as one of the methods for improving conditions or road elements, maintenance planning activities, projects prioritization, all as a part of a decision support framework.

Acknowledgements

This research has been fully supported by the University of Rijeka under the project number uniri-pr-tehnic-19-18 and uniri-tehnic-18-125.

ORCID

Ivan Marović: https://orcid.org/0000-0003-1524-0333.

References

Androjić, I. and Marović, I. (2017). Development of artificial neural network and multiple linear regression models in the prediction process of the hot mix asphalt properties. *Canadian Journal of Civil Engineering*, 44(12), 994-1004. doi: 10.1139/cjce-2017-0300.

Banan, M.R. and Hjelmstad, K.D. (1996). Neural networks and AASHO road test. *Journal of Transportation Engineering*, 122(5), 358-366.

Bosurgi, G., Pellegrino, O. and Sollazzo, G. (2019). Optimizing artificial neural networks for the evaluation of asphalt pavement structural performance. *The Baltic Journal of Road and Bridge Engineering*, 14(1), 58-79.

Ceylan, H., Kin, S. and Gopalakrishnan, K. (2007). Hot mix asphalt dynamic modulus prediction models using neural networks approach. In *Proceeding of ANNIE 2007, ANNs in Engineering Conference*, St. Louis, Mo., 10-14 November.

Ciresan, D., Meier, U., Masci, J. and Schmidhuber, J. (2012). Multi-column deep neural network for traffic sign classification. *Neural Networks*, 32, 333-338. doi: 10.1016/j.neunet.2012.02.023.

Commuri, S. and Zaman, M. (2008). A novel neural network-based asphalt compaction analyzer. *International Journal of Pavement Engineering*, 9(3), 177-188.

Coutinho-Rodrigues, J., Simao, A. and Antunes, C.H. (2011). A GIS-based multicriteria spatial decision support system for plannign urban infrastructures. *Decision Support System*, 51(3), 720-726.

Dahal, K., Almejalli, K. and Alamgir Hossain, M. (2013). Decision support for coordinated road traffic control actions. *Decision Support Systems*, 54(2), 962-975. doi: 10.1016/j.dss.2012.10.022.

Deluka-Tibljaš, A., Karleuša, B. and Dragičević, N. (2013). Review of multicriteria-analysis methods application in decision making about transport infrastructure. *Gradevinar*, 65(7), 619-631.

Du, G., Safi, M., Perrersson, L. and Karoumi, R. (2014). Life cycle assessment as a decision support tool for bridge procurement: environmental impact comparison among five bridge designs. *The International Journal of Life Cycle Assessment*, 19(12), 1948-1954.

Durduran, S.S. (2010). A decision making system to automatic recognize of traffic accidents on the basis of a GIS platform. *Expert Systems with Applications*, 37(12), 7729-7736. doi: 10.1016/j.eswa.2010.04.068.

Fwa, T.F. and Chan, W.T. (1993). Priority rating of highway maintenance needs by neural networks. *Journal of Transportation Engineering*, 119(3), 419-432.

Gesoglu, M., Guneyisi, E., Ozturan, T. and Ozbay, E. (2010). Modeling the mechanical properties of rubbirized concretes by neural network and genetic programming. *Materials and Structures*, 43, 31-45.

Gong, H., Sun, Y., Hu, W. and Huang, B. (2019). Neural networks for fatigue cracking prediction using outputs from pavement mechanistic-empirical design. *International Journal of Pavement Engineering*, doi: 10.1080/10298436.2019.1580367.

Gudac, I., Marović, I., Hanak, T. (2014). Sustainable optimization of winter road maintenance services under real-time information. *Procedia Engineering*, 85, 183-192. doi: 10.1016/j.proeng.2014.10.543.

Han, D., Kaito, K., Kobayashi, K. and Aoki, K. (2016). Management scheme of road pavements considering heterogeneous multiple life cycles changed by repeated maintenance work. *KSCE Journal of Civil Engineering*, 21(5), 1747-1756.

Hanak, T., Marović, I. and Pavlović, S. (2014). Preliminary identification of residential environment assessment indicators for sustainable modelling of urban areas. *International Journal for Engineering Modelling*, 27(1-2), 61-68.

Jajac, N., Knezić, S. and Marović, I. (2009). Decision support system to urban infrastructure maintenance management. *Organization, Technology and Management in Construction*, 1(2), 72-79.

Jajac, N., Marović, I. and Hanak, T. (2015). Decision support for management of urban transport projects. *Gradevinar*, 67(2), 131-141. Doi: 10.14256/JCE.1160.2014.

Jajac, N., Marović, I. and Mladineo, M. (2014). Planning support concept to implementation of sustainable parking development projects in ancient Mediterranean cities. *Croatian Operational Research Review*, 5(2), 345-359.

Kaseko, M.S. and Ritchie, S.G. (1993). A neural network-based methodology for pavement crack detection and classification. *Transportation Research Part C: Emerging Technologies*, 1(4), 275-291.

Loia, V., Sessa, S., Staiano, A. and Tagliaferri, R. (2000). Merging fuzzy logic, neural networks, and gentic computation in the design of a decision support system. *International Journal of Intelligent Systems*, 15(7), 575-594.

Marović, I., Androjić, I., Jajac, N. and Hanak, T. (2018). Urban road infrastructure maintenance planning with application of neural networks. *Complexity*, vol. 2018, Article ID 5160417, 10 pages. doi: 10.1155/2018/5160417.

Ozgan, E. (2011). Artificial neural network based modelling of the Marshall Stability of asphalt concrete. *Expert Systems with Applications*, 38(5), 6025-6030. doi: 10.1016/j.eswa.2010.11.018.

Ozturk, H.I. and Kutay, M.E. (2014). An artificial neural network model for virtual Superpave asphalt mixture design. *International Journal of Pavement Engineering*, 15(2), 151-162. Doi: 10.1080/10298436.2013.808341.

Ozsahin, T.S. and Oruc, S. (2008). Neural network model for resilient modulus of emulsified asphalt mixtures. *Construction and Building Materials*, 22(7), 1436-1445.

Quintero, A., Konare, D., Pierre, S. (2005). Prototyping an intellingent decision support system for improving urban infrastructures management. *European Journal of Operation Research*, 162(3), 654-672.

Simpson, A.L., Daleiden, J.F. and Hadley, W.O. (1995). Rutting analysis from a different perspective. *Transportation Research Record*, 1473.

Singh, D., Zaman, M. and Commuri, S. (2013). Artificial neural network modeling for dynamic modulus of hot mix asphalt using aggregate shape properties. *Journal of Materials in Civil Engineering*, 25(1), 54-62.

Sundin, S. and Braban-Ledoux, C. (2002). Arfiticial intelligence-based decision support technologies in pavement management. *Computer-Aided Civil and Infrastructure Engineering*, 16(2), 143-157.

Šelih, J., Kne, A., Srdić, A. and Žura, M. (2008). Multiple-criteria decision support system in highway infrastructure management. *Transport*, 23(4), 299-305.

Tapkin, S, Cevik, A. and Usar, U. (2009). Accumulated strain prediction of polypropylene modified marshall specimens in repeated creep test using artificial neural networks. *Expert Systems with Applications*, 36(8), 11186-11197.

Tarefder, R.A., White, L. and Zaman, M. (2005). Neural network model for asphalt concrete permeability. *Journal of Materials in Civil Engineering*, 17(1), 19-27.

Terzi, S. (2007). Modeling the pavement serviceability ratio of flexible highway pavements by artificial neural networks. *Construction and Building Materials*, 21(3), 590-593. doi: 10.1016/j.conbuildmat.2005.11.001.

The World Road Association (PIARC), "The importance of road maintenance, The World Road Association (PIARC)," 2014, June 2019, http://www.erf.be/images/Importance_of_road_maintenance.pdf.

Tijanić, K., Car-Pušić, D. and Šperac, M. (2019). Cost estimation in road construction using artificial neural network. *Neural Computing and Applications*, doi: 10.1007/s00521-019-04443-y.

Torres-Machi, C., Osorio, A., Godoy, P., Chamorro, A., Mourgues, C. and Videla, C. (2018). Sustainable management framework for transportation assets: application to urban pavement networks. *KSCE Journal of Civil Engineering*, 22(10), 4095-4106. doi: 10.1007/s12205-018-1314-x.

Turban, E. (1993). *Decision Support and Expert Systems: Management Support Systems*, New York: Macmillan Publishing Company.

Turban, E. and Aronson, J.E. (1995). *Decision Support Systems and Intelligent Systems*, Upper Saddle River, NJ: Simon and Schuster Company.

Tušar, M. and Novič, M. (2009). Data exploration on standard asphalt mix analyses. *Journal of Chemometrics*, 23(6), 283-293. doi: 10.1002/cem.1229.

Xiao, F., Amirkhanian, S.N. and Juang, H.C. (2010). An artificial neural network approach to developing long-term aging models of asphalt binders. *Journal of Materials in Civil Engineering*, 21(6), 253-261.

Yang, J., Lu, J.J. and Gunaratne, M. 2003. *Application of neural network models for forecasting of pavement crack index and pavement condition rating*. Florida Department of Transportation, Tampa, Fl.

Zavratnik, N., Prosen, J., Tušar, M. and Turk, G. (2016). The use of artificial neural networks for modeling air void content in aggregate mixture. *Automation in Construction*, 63, 155-161. doi: 10.1016/j.autcon.2015.12.009.

Zhang, A., Wang, K.C.P., Fei, Y., Liu, Y., Tao, S., Chen, C., Li, J.Q. and Li, B. (2018). Deep learning – based fully automated pavement crack detention on 3D asphalt surfaces with an improved cracknet. *Journal of Computing in Civil Engineering*, 32(5), 04018041. doi: 10.1061/(ASCE)CP.1943-5487.0000775.

XV International Conference on Durability of Building Materials and Components
DBMC 2020, Barcelona
C. Serrat, J.R. Casas and V. Gibert (Eds)

Uncertainty and Sensitivity Analyses for Evaluating the Building Element's Replacement in Building LCA

Kyriaki Goulouti[1], Pierryves Padey[1], Alina Galimshina[2], Guillaume Habert[2] and Sébastien Lasvaux[1]

[1] Solar Energy and Building Physics Laboratory, Institute of Thermal Engineering, University of Applied Sciences of Western Switzerland (HES-SO), Yverdon-les-Bains, Switzerland, sebastien.lasvaux@hes-so.ch

[2] Chair of Sustainable Construction, Institute of Construction and Infrastructure Management, Swiss Federal Institute of Technology (ETH Zurich), Zurich, Switzerland

Abstract. *This paper presents a systematic way to consider the uncertainties of the building elements' service lives within a stochastic framework, by defining the corresponding probability density functions, based on a service life database. This methodology is appropriate for screening and detailed building LCA, since the service life database offers the possibility to define the probability density functions of the service lives, in different level of details.*

Keywords: *Service Life, Screening and Detailed LCA, Uncertainty, Global Sensitivity Analysis.*

1 Introduction

Designing sustainable buildings consists a key issue in order to reduce the environmental impacts of the building sector. It is important, thus, to identify the stages of the building life cycle and consequently the materials that are the main contributors to the building's *e.g.* greenhouse gas emissions. The evaluation of the environmental impacts is performed using the LCA methodology, which can successfully define the direct and indirect environmental impacts of products, goods, services and consequently buildings.

According to EN-15978:2011 (SN EN 15978:2011, 2011) the conventional life cycle stages of a building are the production and construction stage (A1-A3 and A4-A5, respectively), the use stage with the maintenance (B2), replacement (B4), operational energy (B6), water use (B7) and other processes, as well as the disposal at the end of life (C1-C4). Performing a building LCA is followed by many assumptions for several of the parameters included in the different LCA stages. Consequently, reliability and consistency issues derive from the uncertainty and variability of the input data, as already discussed in Huijebregts (Huijbregts, 1998).

One important parameter that contributes to the replacement stage (module B4) of a building LCA is the service life of the building elements. Different studies have shown that the service life calculation is governed by high uncertainty, as summarized in Grant (Grant, 2010), since it is influenced by a variety of uncertain factors, not necessarily technical, which cannot be defined objectively. Cooper (Cooper, 2004) summarizes different studies that identified parameters, such as *'the design, the technological change, the cost of repair and the availability of parts, the household affluence, the residual and resale values, the aesthetic and the functional quality, fashion, advertising and social pressure',* among the ones that influence the service life.

doi:10.23967/dbmc.2020.143

Furthermore, another uncertainty of the building elements' service life is linked to insufficient information, concerning the material choices, during the early design stages of the building process. The LCA in the early design stages can be used as a comparative tool for choosing the most sustainable building concept and lately, there is an increasing interest of the scientific community to conduct a building LCA in the early design stages (Azzouz *et al.*, 2017; Cavalliere *et al.*, 2018). However, the significant uncertainty in this design stage restricts the use of LCA calculations, (Röck *et al.*, 2018). Thus, LCA is generally applied in late design stages, when possible changes in the building design are not economically cost effective (Hollberg and Ruth, 2016).

A systematic way to consider the uncertainties (technical and other) in LCA is by using a stochastic approach. Hence, reliability issues in LCA calculations can be mitigated. Treating probabilistically the service lives has been already proposed by Aktas (Aktas and Bilec, 2012), Pannier (Pannier *et al.*, 2018) and Hoxha (Hoxha *et al.*, 2014). However, Aktas used only a limited number of materials, while the latter (Pannier and Hoxha) defined the probability density function, based on theoretical assumptions.

In this study, the service life of building elements is considered stochastically in order to include their uncertainty in the whole building LCA result and consequently enhance our confidence in the latter. The probability density functions of the service lives of building elements were defined with a consistent way, using input data from an international data collection. Finally, it was examined how the uncertainty of the LCA result can be allocated to the different sources (different building elements) of the input uncertainty using a sensitivity analysis (Saltelli, 2004).

2 Methodology

The general probabilistic framework, followed in the current study, has been already proposed by Padey (Padey *et al.*, 2013) and Cucurachi (Cucurachi *et al*, 2016). It consists of the following four steps: (1) definition of the LCA model, (2) determination of the probability density function (PDF) of the building elements' service life, (3) uncertainty analysis and (4) sensitivity analysis.

The building LCA model was calculated, using Eq. 1. The environmental impact of the materials and technical systems ($LCA_{Manufacturing}$ and $LCA_{disposal}$) were calculated for the greenhouse gas (GHG) emissions, using the *KBOB* database (Frischknecht and Büsser Knöpfel, 2013). The environmental impact of the operational energy was based on heating demand calculations according to SIA 380/1:2016 (SIA 380/1:2016, 2016), while the efficiency factor for heating and DHW was based on SIA 2040 (SIA 2040, 2017) and the impact values of the energy carrier were calculated using the KBOB database.

$$LCA_{tot}=LCA_{Manufacturing}+LCA_{Replacement}+LCA_{Disposal}+LCA_{Operational\ Energy} \quad (1)$$

The LCA of the replacement stage, was calculated, using Eq. 2,

$$LCA_{Replacement}=(LCA_{Manufacturing}+ LCA_{Disposal})*k \quad (2)$$

Where, k is the replacement rate that defines the number of replacements that occurs during the reference study period of the building. It was calculated for each building element, as a fractional number, according to SIA 2032 (SIA 2032, 2010), as shown in Eq. 3,

$$k=(RSP/SL)-1 \quad (3)$$

Where, RSP is the reference study period of the building, i.e. 60 years, according to SN EN 15978 (SN EN 15978:2011, 2011) and SL is the service life of the building element in years.

The probability density functions of the building elements were derived with a systematic way, from the DUREE Database, using a lognormal distribution (Goulouti *et al.*, 2020). This database includes international service life data from different sources. The database was structured, using the building decomposition of the Swiss construction costs, classified according to the Swiss Standard, *i.e.* eBKP-H – SN 506 511 (CRB, 2012). This building decomposition includes five main construction categories, *i.e.* structural work (C), technical systems (D), façade elements and coatings (E), roof elements (F) and internal layout (G). These main categories are further decomposed into two sub-categories, according to the SN 506511 nomenclature (*e.g.* the intermediate element level and the detailed element level). Five more sub-categories were added to this decomposition, in order to cover lower levels for more detailed components. Consequently, the service lives of the building elements can be assigned either to the main categories for screening LCA, or to the sub-categories in order to proceed to a detailed LCA. Table 1 presents the main categories and some of the subcategories of the database that were considered to the current study, as well.

Table 1. Building decomposition and building elements considered in the study.

SN 506511 element types considered in the study			**Screening LCA**	**Detailed LCA**
C. Structural work			60 years	60 years
D. Technical systems			X	
	D1. Electrical installations			X
	D5. Heating system			
		D5.2 Heat production		X
		D5.2d Solar collector system		X
		D5.3 Heat distribution		X
		D5.4 Heat emission		X
	D7. Ventilation and AC systems			X
	D8. Sanitary equipment			X
E. Facade elements and coatings			X	
	E2. External wall coatings			
		E2.2 Compact facade		X
		E2.3 Ventilated facade		X
	E3. Windows, doors			
		E3.1 Windows		X
F. Roof elements			X	
	F1. Covering			
		F1.2 Flat roof		X
		F1.3 Sloping roof		X
G. Interior layouts			X	
	G1. Partition walls, doors			X
	G2. Flooring			X
	G3. Wall coverings			X
	G4. Ceiling coverings			X

After the definition of the model and the identification of the input distributions, the uncertainty analysis followed and 40’000 Monte Carlo simulations were computed, in order to

achieve convergence. Based on these simulations, the Probability Density Function (PDF) of the LCA was calculated. In addition, a sensitivity analysis was conducted in order to define the building elements whose service life uncertainty mostly influences the LCA output. The variance-based global sensitivity analysis was chosen, which decomposes the variance of the model (LCA) into fractions, that can be attributed to the inputs, here the building elements (Saltelli, 2004). This method is used in order to rank variables, fix unessential variables and decrease problem dimensionality (Kucherenko and Song, 2017), (Sobol′, 2001). Hence, the first and the total Sobol' Indices (main and total effect, respectively) were calculated, which represent the unique contribution of the parameters or the joint one with other parameters, respectively.

3 Results

The methodology was applied to a building case study that represents a single family house (SFH) in Switzerland and its energy performance level complies with the SIA 380/1 Swiss Standard (SIA 380/1:2016, 2016). The case study was decomposed according to Table 1 for the screening LCA and the service lives of the building elements were attributed to the main group categories. The uncertainty analysis was conducted and the probabilistic LCA was calculated for the GHG emissions [expressed in $\mathrm{kg\,CO_{2-eq}\,/(m^2y)}$]. Figure 1(left) presents the PDF of the probabilistic LCA [$\mu = 23.20\ \mathrm{kg\,CO_{2-eq}\,/(m^2y)}$, $(\sigma^2 = 5.5^2)$], along with the deterministic LCA of the SIA 2032 [19.2 kg $CO_{2\text{-}eq}/(m^2y)$] and CRB [min=28.1 kg $CO_{2\text{-}eq}/(m^2y)$, mean=18.9 kg $CO_{2\text{-}eq}/(m^2y)$ and max= 15.1 kg $CO_{2\text{-}eq}/(m^2y)$]. The three CRB values (min – mean – max) correspond to the minimum, mean and maximum service lives, which mean maximum, mean and minimum replacement rates, respectively. Furthermore, the 95% confidence interval of the mean is narrow [$\mu = 23.22\ \mathrm{kg\,CO_{2-eq}\,/(m^2y)} \pm 0.05$], revealing the accuracy of the simulations. The most probable value of the LCA, *i.e.*, the mode of the distribution, *i.e.* $x_m = 20\ \mathrm{kg\,CO_{2-eq}\,/(m^2y)}$ is slightly higher than the deterministic SIA 2032 and CRB–mean (4% and 6% respectively).

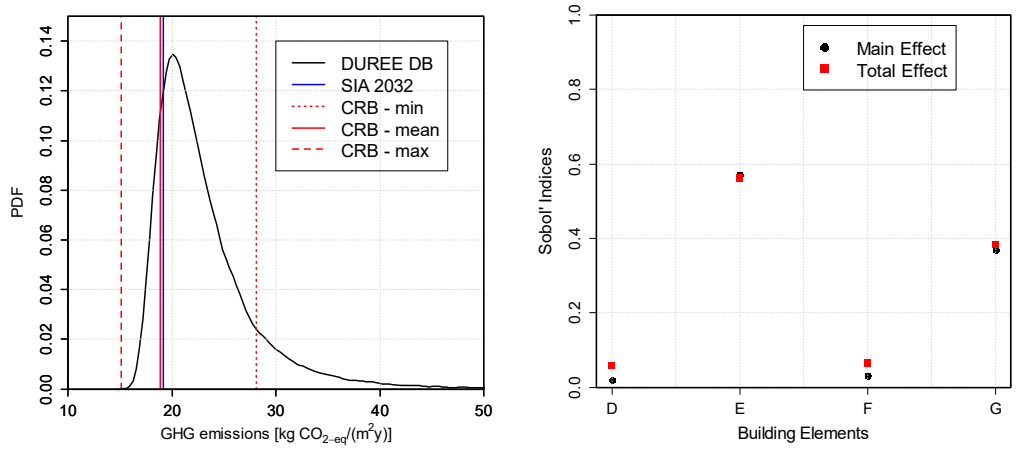

Figure 1. PDF of the probabilistic LCA (left) and Sobol' Indices for the screening LCA (right – *D: Technical systems, E: Façade coatings, F: Roof elements, G: Interior layout*).

Figure 1 (right) presents the sensitivity indices, which show the building elements whose uncertainty mostly influences the LCA uncertainty. Both the first order index (main effect) along with the total index (total effect, which includes the interactions between the parameters) are plotted. It is found that the individual effects and not the interactions among the building elements, explain the LCA uncertainty. This result proves that the initial hypothesis, according to which the replacement of a specific element does not interact with another element's replacement is valid. Furthermore, in order to verify the accuracy of the indices, a bootstrapping with 500 replicates was used (Archer, Saltelli and Sobol, 1997). The 95% confidence intervals of the indices remained narrow (*e.g.* for the G2 category, $S_{iG} = 0.38 \pm 0.05$) and of the same magnitude. Hence, we can be sure about their order, which determines the elements, with the highest impact on the LCA uncertainty (Cucurachi *et al.*, 2016). It can be concluded, that the E (façade) and G (interior finishes) building elements have the highest impact on the LCA uncertainty. The result is quite straightforward, since the LCA uncertainty is mostly influenced by the building elements that have the highest environmental impact (first the external façade – E and then the interior finishes – G) and the highest coefficients of variation, ($cv_E = \frac{sd}{mean} = 1.2$ and $cv_G = 1.4$) of the replacement rate probability distribution.

4 Discussion

As already mentioned the results of the sensitivity analysis can be used in order to rank the unimportant variables and thus simplify the model. The Sobol' Indices revealed that the service life uncertainty of the façade elements and the interior finishes have higher influence on the probabilistic LCA. On the contrary, the uncertainty on the service lives of the technical systems and the roof elements have no influence on the uncertainty of the building LCA. Thus, in further screening LCA, the service lives of the technical systems and the roof elements can be treated deterministically, by using current data from the standards. However, the prevailing Sobol' Indices of the façade elements and the interior finishes indicate that special attention is needed for determining their service life. This result derived, also, by the fact that different building components and layers are grouped together.

Hence, in order to explore the influence of the level of details of the building decomposition, a detailed LCA was conducted for which the service lives of the building elements were attributed in lower level of details, as it is shown in Table 1. Figure 2 presents the main and the total effects for this decomposition. The same validation procedure was followed, concerning the order of the indices, as already described. It is derived that, for this level of details too, the individual effects and not the interactions among the building elements explain the LCA uncertainty. The uncertainty of the LCA, expressed in GHG emissions can be mainly explained by five building elements, *i.e.* the E2.2 (compact façade), E3.1 (windows), F1.3 (sloping roof), G2 (flooring) and G3 (wall covering). Among the elements with the highest GHG emissions (first E2.2, followed by F1.3 and G2), it is the replacement rate of G2 that presents the highest coefficient of variation ($cv = 1.25$), followed by E2.2, ($cv = 1.01$), and F1.3 ($cv = 0.98$). The E3.1 and G3 building elements, present lower GHG emissions than F1.3, but the coefficient of variation of their replacement rate is more significant, which explains the higher relative sensitivity indices. The Sobol' Indices of the technical systems are found to be close to zero, proving that their service live uncertainty does not affect the GHG emissions uncertainty.

The same conclusions, concerning the service lives of the technical systems were derived

both by the screening and detailed LCA. However, as far as the roof elements are concerned, they exhibited a higher impact on the detailed LCA uncertainty, than in the screening LCA. In addition, by decomposing the building using a lower level of details, it can be seen that there is a prioritization concerning the façade elements and the interior finishes.

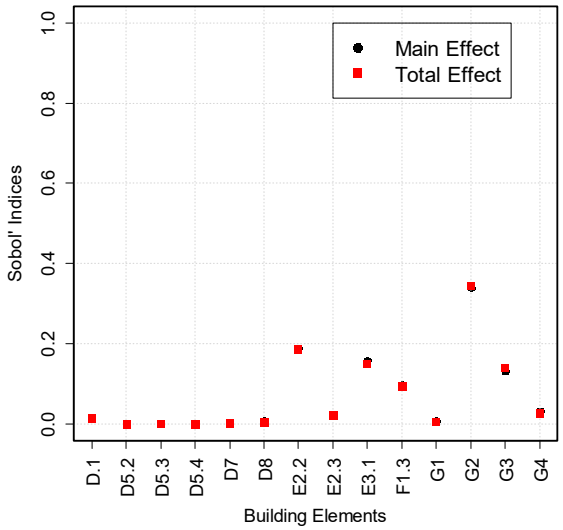

Names of building elements			
D1. Electrical installations	D7. Ventilation	E3.1 Windows	G3. Wall coverings
D5.2 Heat production	D8. Sanitary installations	F1.3 Sloping roof	G4. Ceiling coverings
D5.3 Heat distribution	E2.2 Compact façade	G1. Internal partitions	
D5.4 Heat diffusion	E2.3 Ventilated façade	G2. Flooring	

Figure 2. Sobol' Indices for the detailed LCA.

5 Conclusions

The current study presented a systematic way to treat probabilistically the replacement rate of the building elements and quantified the impact of the service lives' uncertainty on the LCA output. The main outcomes and recommendations derived are the following:

- A screening and a detailed LCA was conducted using the DUREE service life database. The results of the sensitivity analyses were similar. The façade elements and the interior layout explain mainly the LCA uncertainty;
- The screening and the detailed LCA revealed that the uncertainty of the technical systems service lives (D building element) present low impact on the LCA uncertainty. In further probabilistic LCA analysis, the LCA model could be simplified and conventional deterministic values from the standards (SIA 2032, CRB) could be used for this building element, instead;
- By conducting a detailed LCA, if a threshold is defined at 0.10 for the Sobol' Indices, only five building elements out of fourteen are the most influential on the LCA uncertainty, i.e. E2.2 (compact façade), the E3.1 (windows), the F1.3 (sloping roof), the G2 (flooring) and G3 (wall covering). This means that special attention should be given when defining the service lives for these element types in further LCA calculations.

Acknowledgements

The authors wish to acknowledge the support of this work by the Swiss Federal Office for Energy (SFOE, DUREE Project No. SI/501483-01) and the Swiss National Science Foundation (SNF, Grant No. 2-77059-17). This research study has been complemented with additional service life data, provided within the framework of the IEA-EBC Annex 72, which focuses on Assessing Life Cycle Related Environmental Impacts Caused by Buildings (http://annex72.iea-ebc.org). Finally, the authors are grateful to Alexander Hollberg from Chalmers University for the fruitful discussions during the early stage of this work.

ORCID

Kyriaki Goulouti : https://orcid.org/0000-0002-7165-6117
Pierryves Padey : https://orcid.org/0000-0003-0715-2149
Alina Galimshina : https://orcid.org/0000-0001-5281-7061
Guillaume Habert : https://orcid.org/0000-0003-3533-7896
Sébastien Lasvaux : https://orcid.org/0000-0002-8723-9676

References

Aktas, C. B. and Bilec, M. M. (2012). Impact of lifetime on US residential building LCA results. International Journal of Life Cycle Assessment, 17(3), 337–349. doi:10.1007/s11367-011-0363-x.

Archer, G. E. B., Saltelli, A.and Sobol, I. M. (1997). Sensitivity measures, anova-like techniques and the use of bootstrap. Journal of Statistical Computation and Simulation, 58(2), 99–120. doi:10.1080/00949659708811825.

Azzouz, A., Borchers, M., Moreira, J.and Mavrogianni, A. (2017). Life cycle assessment of energy conservation measures during early stage office building design: A case study in London, UK. Energy and Buildings, 139, 547–568. doi:10.1016/j.enbuild.2016.12.089.

Cahier Technique SIA 2040: “La voie vers l’efficacité énergétique.” , (2017).

Cavalliere C., Habert G., Dell’Osso R. and Hollberg A. (2018). Continuous BIM-based assessment of embodied environmental impacts throughout the design process. Journal of Cleaner Production.

Cooper, T. (2004). Inadequate Life?Evidence of Consumer Attitudes to Product Obsolescence. Journal of Consumer Policy, 27(4), 421–449. doi:10.1007/s10603-004-2284-6.

CRB. SN 506511, Code des coûts de construction Bâtiment. , (2012).

Cucurachi, S., Borgonovo, E. and Heijungs, R. (2016). A Protocol for the Global Sensitivity Analysis of Impact Assessment Models in Life Cycle Assessment. Risk Analysis, 36(2), 357–377. doi:10.1111/risa.12443.

Goulouti, K., Giorgi, M., Favre, D. and Lasvaux, S. (2020). Development of a Service Life Database of Building Elements Based on an International Data Collection. XV International Conferenceon Durability of Building Materials and Components, DBMC 2020 Barcelona.

Frischknecht, R. and Büsser Knöpfel, S. (2013). Swiss Eco-Factors 2013 according to the Ecological Scarcity Method. Methodological fundamentals and their application in Switzerland. Environmental studies no. 1330 (p. 254). p. 254. Bern: Federal Office for the Environment (FOEN).

Grant, A. (2010). The confluence of life cycle assessment and service life prediction: An analysis of the environmental impact of material longetivity in the building envelope, PhD Dissertation. University of Florida, Gainesville, FL USA.

Hollberg, A. and Ruth, J. (2016). LCA in architectural design—a parametric approach. International Journal of Life Cycle Assessment, 21(7), 943–960. doi:10.1007/s11367-016-1065-1.

Hoxha, E., Habert, G., Chevalier, J., Bazzana, M. and Le Roy, R. (2014). Method to analyse the contribution of material’s sensitivity in buildings’ environmental impact. Journal of Cleaner Production, 66, 54–64. doi:10.1016/j.jclepro.2013.10.056.

Huijbregts, M. A. J. (1998). Uncertainty in LCA LCA Methodology Application of Uncertainty and Variability in LCA. The International Journal of Life Cycle Assessment, 3(5), 273–280.

Kucherenko, S., and Song, S. (2017). Different numerical estimators for main effect global sensitivity indices. Reliability Engineering and System Safety, 165, 222–238. doi:10.1016/j.ress.2017.04.003

Padey, P., Beloin-Saint-Pierre, D., Girard, R., Le Boulch, D. and Blanc, I. (2013). Understanding LCA results variability : developing global sensitivity analysis with Sobol indices . A first application to photovoltaic

systems, International Symposium on Life Cycle Ssessment and Construction Civil Engineering and Buildings, 19–27.

Pannier, M. L., Schalbart, P. and Peuportier, B. (2018). Comprehensive assessment of sensitivity analysis methods for the identification of influential factors in building life cycle assessment. Journal of Cleaner Production, 199, 466–480. doi:10.1016/j.jclepro.2018.07.070.

Röck, M., Hollberg, A., Habert, G. and Passer, A. (2018). LCA and BIM: Integrated Assessment and Visualization of Building Elements' Embodied Impacts for Design Guidance in Early Stages. Procedia CIRP, 69(May), 218–223. doi:10.1016/j.procir.2017.11.087

Saltelli, A. (2004). Sensitivity analysis in practice: a guide to assessing scientific models (Google eBook). Retrieved from http://books.google.com/books?id=NsAVmohPNpQC&pgis=1.

SIA 2032. (2010). SIA 2032 - L'énergie grise des bâtiments. Zürich: Société Suisse des Ingénieurs et des Architectes (SIA).

SIA 380/1:2016 - Besoins de chaleur pour le chauffage (p. 60). (2016). Société Suisse des Ingénieurs et Architectes.

SN EN 15978:2011. Sustainability of construction works - Assessement of environemental performane of buildings-Calculation Methods. , (2011).

Sobol′, I. (2001). Global sensitivity indices for nonlinear mathematical models and their Monte Carlo estimates. Mathematics and Computers in Simulation, 55(1–3), 271–280, doi:10.1016/S0378-4754(00)00270-6.

XV International Conference on Durability of Building Materials and Components
DBMC 2020, Barcelona
C. Serrat, J.R. Casas and V. Gibert (Eds)

Use of Machine Learning in the Function of Sustainability of Wastewater Treatment Plants

Goran Volf

Faculty for Civil Engineering, University of Rijeka, Radmile Matejčić 3, 51000 Rijeka, Croatia, goran.volf@uniri.hr

Abstract. *Wastewater treatment plants (WWTP) are complex and dynamic systems whose management and sustainability can be improved by using different modelling and prediction approaches of their work. A machine learning tool for development of model trees was used in this paper in order to develop a model for chemical oxygen demand (COD) in the wastewater effluent from the WWTP with activated sludge to increase its sustainability and helps in its management purposes. Measured data, both in influent and effluent of the WWTP were used for modelling. For the COD model, machine learning tool Weka and algorithm for development of model trees M5P were used. Obtained model has a high descriptive power and correlation coefficient and thus can be used for prediction and modelling purposes, which can help in management and sustainability of the WWTP. Also, the purpose of this paper is to show the benefits of using machine learning tools for developing WWTP models.*

Keywords: *Wastewater Treatment Plant, Machine Learning, Model Trees, Function of Sustainability, Management.*

1 Introduction

There is a need for wastewater treatment plants (WWTP) to adapt to a rise in water and energy demands, prolonged periods of droughts, climate variability, and resource scarcity (Cornejo 2015).

As population increases, minimizing the carbon and energy footprints of wastewater treatment, while properly managing nutrients (mainly nitrogen and phosphorous) is crucial to improving the sustainability of WWTP. Integrated resource recovery can also mitigate the environmental impact of wastewater treatment systems, however, mitigation potentially depends on various factors such as: a) treatment technology, b) resource recovery strategy, and c) size of system (Cornejo 2015).

Today, the biological treatment of wastewater with activated sludge is one of the most widely used technological processes in WWTP, because of its capabilities, economy and efficiency. The two main components of this process are aeration basin, e.g. the bioreactor and the secondary clarifier (Henze *et al.*, 2002).

Biological treatment of wastewater consists of complex physical, chemical and biological processes through which organic matter, nitrogen and phosphorus are removed from the wastewater. Successful wastewater treatment requires appropriate concentrations and conditions for the growth of microorganisms that must be achieved in the bioreactor (Henze *et al.*, 2002).

Due to the complexity and sensitivity of the treatment process, it is difficult to continuously maintain optimal operating conditions within the WWTP. Because of this,

modelling becomes very useful tool that is often used to simulate and control the operation of the WWTP. Mathematical models (e.g, Activated Sludge Models (ASM), IWA task group, 2000) are commonly used to model WWTP. In this paper, machine learning tool Weka (Witten and Frank, 2000), e.g. the algorithm M5P for induction of model trees, is used to model the WWTP e.g. chemical oxygen demand (COD) concentration in the effluent of the WWTP.

Today, various tools and methods are used to model WWTP, such as, for example, statistical models (Čurlin *et al*., 2008; Dürrenmatt and Gujer 2011; Razifa *et al*., 2014), expert systems (Dürrenmatt and Gujer 2011; Baeza *et al*., 1999; Roda *et al*., 1999), knowledge-based approaches (Comas *et al*., 2003), neural networks (Dürrenmatt and Gujer 2011; Belanche *et al*., 1999; Zhao *et al*., 1999; Hong *et al*., 2015; Mjalli *et al*., 2007), hybrid approaches (Sànches-Marré *et al*., 1996; Grieu *et al*., 2005; Picioreanu *et al*., 2004; Picioreanu *et al*., 2003) and various types of machine learning (Dürrenmatt and Gujer 2011; Hong *et al*., 2015; Comas *et al*., 2001; Atanasova and Kompare 2002; Kompare *et al*., 2006; Manu *et al*., 2017).

The purpose of the model obtained with the use of machine learning tools in this paper is to model the concentration of COD in the effluent of the WWTP. The value of the COD in the effluent is considered as the best indicator for operation quality for the WWTP, i.e. residual organic loads, which also indicated the efficiency of the treatment process (Čurlin *et al*., 2008; Henze *et al*., 2002; Tchobanoglous *et al*., 2003). For this reason, the variable specified is defined as the observed parameter, which best indicates the state of the process in the WWTP, and also, the variable whose dynamics the machine learning tool wants to explain and predict. Using the given model, it would be possible to predict the values of the COD concentration, and if it is greater than the limit value prescribed by Ordinance on emission of limit values for wastewaters (2016), a rapid response would be possible which would then ensure its reduction to an acceptable level (Čurlin *et al*., 2008).

Except the modelling the COD concentration in the effluent from the WWTP with machine learning, the aim of this paper is to demonstrate also some of the advantages and capabilities of machine learning tools.

2 Materials and Methods

2.1 Description of the WWTP

Modeled WWTP is a second stage WWTP, with size of 9,500 population equivalent (PE). The WWTP on the water line consists of mechanical pretreatment and second stage treatment of wastewater (Figure 1). Mechanical pretreatment consists of a coarse, fine screens and aerated grit chamber. The second stage of treatment consists of selectors, aeration basins and secondary clarifiers.

The flow of water on the WWTP is: first, the wastewater enters a channel in which are located coarse and fine screens, after which the wastewater goes to the aerated grit chamber. The water is then transported to the selector, where the selection of microorganisms (contact of biomass with wastewater) takes place. After selector water is then transported to aeration basins (bioreactors), where biological treatment with activated sludge takes place. Finally, the mixture of water and activated sludge is transported to secondary clarifiers, where the activated sludge floccules are deposited and treated water is discharged into the recipient (sea)

through a submarine outlet. Part of the deposited sludge from secondary clarifiers is returned back to the selector or aeration basin in order to maintain the required concentration of activated sludge for successful biological treatment of the process in aeration basins.

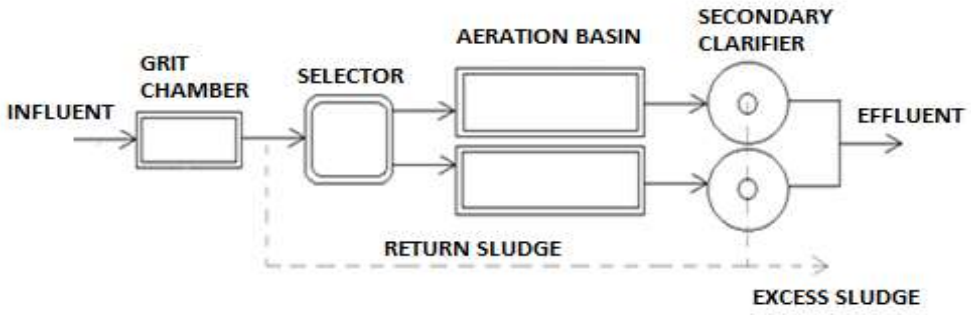

Figure 1. Water line for the WWTP.

2.2 Database

The data used for the modelling (see Table 1) were measured in influent and effluent of the WWTP. The data are presented as mean values through one day, that is, one record in the database represents the one-day situation of the WWTP operation. The database consists of total 718 situations (days).

To supplement the missing data in the total data set, the cubic spline method of interpolation between the measured values was used.

Table 1. Measured data at WWTP uded for modeling.

Data	Description	Unit
Q_{in}	Influent flow	m^3/s
Q_{out}	Effluent flow	m^3/s
T_{out}	Effluent temperature	^0C
COD_{in}	Influent Chemical Oxygen Demand	mg/l
COD_{out}	EffluentChemical Oxygen Demand	mg/l
NH_4-N_{in}	Influent Ammonium	mg/l

3 Machine Learning; Regression and Model Trees

While the simple linear regression calculates one equation (one weighing vector) for the entire data set, piecewise or tree-structured regression divides the data set into several subsets on which uniform class value or linear equation can be applied. The division to subsets is based on tests of the values of the input attributes which are put as nodes in a regression or model tree.

Thus, regression trees are hierarchical structures composed of nodes and branches, where the internal nodes contain tests on the input attributes. Each branch of an internal test corresponds to an outcome of the test and the predictions for the values of the target variable

(the class) are stored in the leaves which are the terminal nodes in the tree. If the leafs contain a single value for the class prediction, then we are talking about simple regression trees, while if a linear equation is used for prediction in the leaf, we are talking of model trees (Quinlan, 1992, Witten and Frank, 2000). Figure 2 illustrates the procedure of constructing regression and model trees.

For the experiment, a variation of the M5 algorithm was used, called M5P, implemented in the software package WEKA (Witten and Frank, 2000).

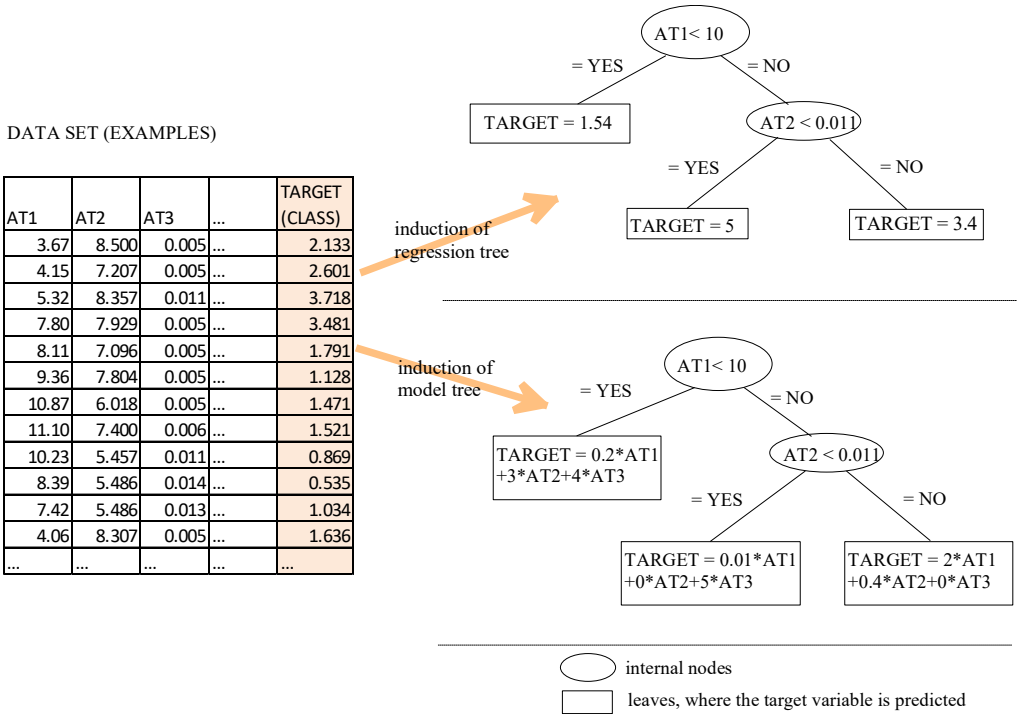

Figure 2. Induction of regression and model trees from given data set (examples).

4 Experiment Setup

The experiment was designed to produce a model of the COD concentration in the effluent of the WWTP. The COD concentration in the effluent was therefore set as the dependent variable, while the flow (Q), COD concentration, ammonium (NH_4-N) and total suspended solids (SS) in the influent of the WWTP were set as independent variables.

5 Results and Discussion

The purpose of the model obtained with machine learning tools, in this case model trees, is to predict the change in COD concentration in the effluent of the WWTP, using the measured variables in the influent of the WWTP. From the given data set (Table 1), a model of the COD concentration in the effluent of the WWTP was created (Figure 3). The model consists of a total 6 nodes and 7 leaves, which contains the values of the variables measured in the influent of the WWTP (see Table 1). Each leaf contains one equation to calculate the COD concentration in the effluent of the WWTP, depending on the structure of the tree itself. The

equations in the individual tree leaves are shown in Table 2. The correlation coefficient R for the obtained model using cross validation method is 0.64.

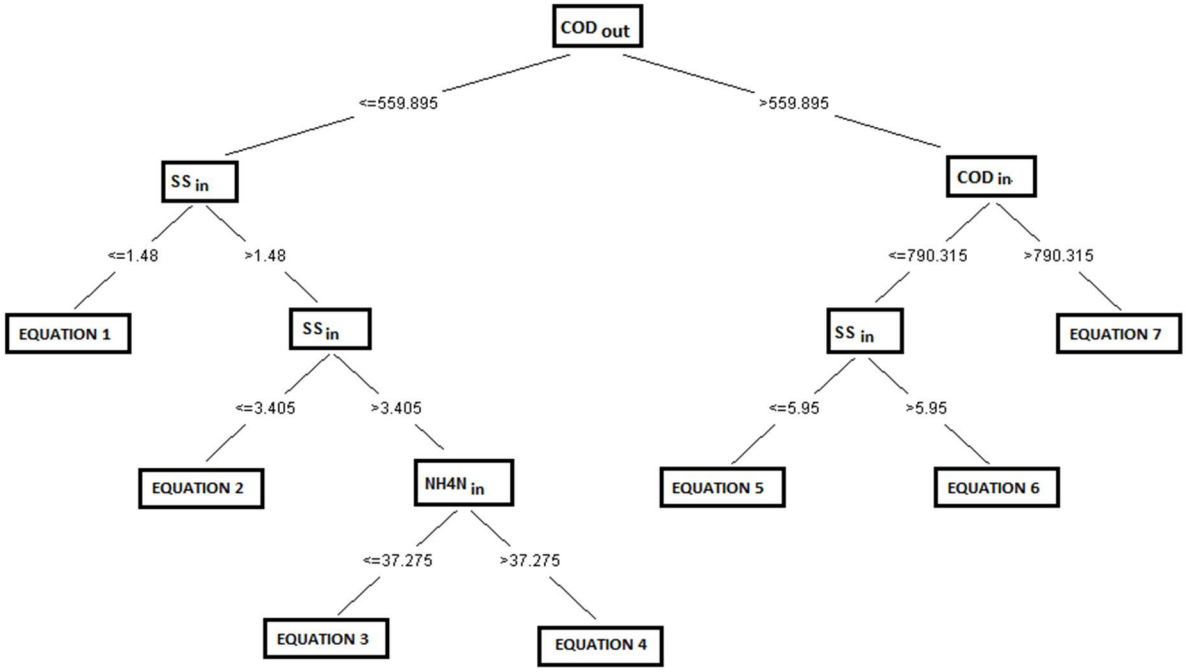

Figure 3. Obtained model for COD concentration.

Table 2. Model equations for COD concentration.

Equation number	Equation
1	COD_{out}=-0,0088*Q_{in} + 0,0954*COD_{in}-1,0529*NH_4N_{in}-0,0215*SS_{in}+45,669
2	COD_{out}=-0,0049*Q_{in}+0,038*COD_{in}-0,1132*NH_4N_{in}-0,0172*SS_{in}+20,0079
3	COD_{out}=-0,0006*Q_{in}+0,0016*COD_{in}-0,0016*NH_4N_{in}-0,0153*SS_{in}+20,1564
4	COD_{out}=-0,0006*Q_{in}+0,0016*COD_{in}-0,0034*NH_4N_{in}-0,0153*SS_{in}+23,1117
5	COD_{out}=-0,0009*Q_{in} +0,0046*COD_{in}+0,1559*NH_4N_{in}-0,0957*SS_{in}+24,0748
6	COD_{out} =-0,0009*Q_{in}+0,0046*COD_{in}+0,1559*NH_4N_{in}-0,0818*SS_{in}+17,0162
7	COD_{out}=-0,0009*Q_{in}+0,005*COD_{in}+1,3378*NH_4N_{in}-0,3479*SS_{in}-7,1299

To predict the COD concentration in the effluent of the WWTP, it is necessary to select from the model shown in Figure 3 the appropriate linear equation depending on the values of the individual attributes in the tree nodes. From Figure 3 can be seen that the COD concentration in the effluent depends mostly on the COD concentration at the inflow (initial

node), then SS and NH_4-N, while the flow (Q) do not appear in the tree at all, but only in single leaves equations. Interpreting the model results, the larger COD values in the effluent are given by the right side of the model tree, that is, the tree shown in Figure 3, and the smaller values by the left side of the model tree. Therefore, lower values of COD concentration in the effluent are associated with nodes in which SS and NH_4N are located, while the higher values are associated with nodes in which COD and SS are located.

A comparison of the time series of measured and modeled COD concentration values can be seen in Figure 5. From Figure 5, can also be seen a good adaptation of the measured and modeled COD concentration values, and also by visual inspection it can be concluded that the peak points values are satisfactorily matched.

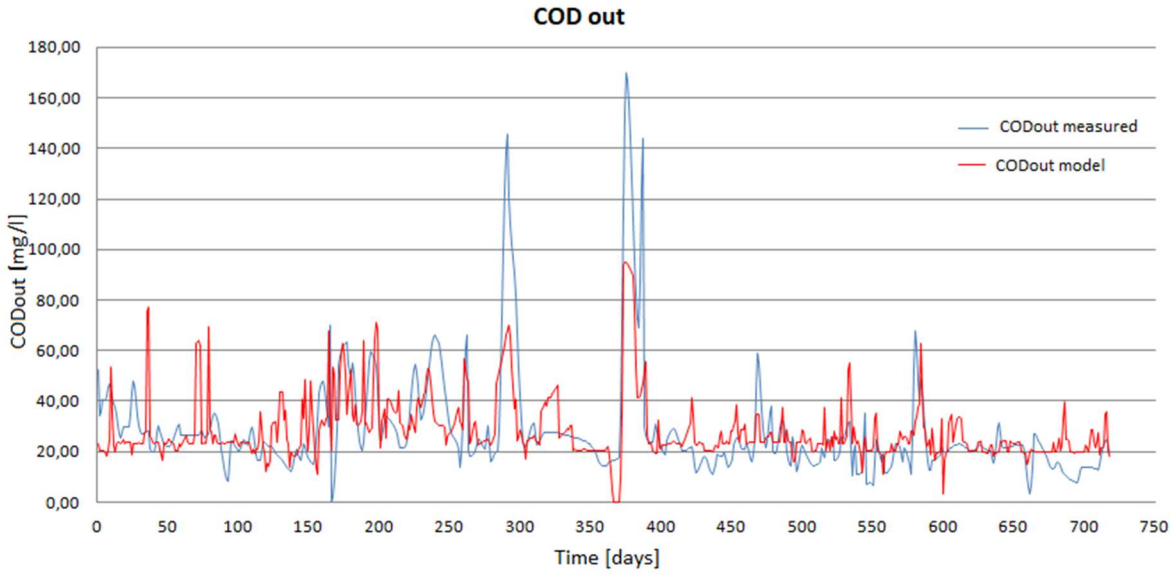

Figure 4. Time series comparison of measured and modeled values of COD concentrations in the effluent.

The results of the experiment show that it is useful to use different approaches when modeling WWTP. As for any method of modeling which use measured data, it is essential that the database consists of sufficiently different situations from which, in this case a machine learning algorithm can learn to predict a dependent variable. Also, for better model results, it would be useful to have more measured parameters in the influent of the WWTP affecting the dependent variable, such as water temperature, pH, chloride concentration (if it is a WWTP in the coastal area such as discussed in this paper), sludge age, sludge return, dissolved oxygen concentration in the aeration bioreactor, food to mass ratio (F/M), etc., which over a longer period can have a greater and significant impact on the COD concentrations (Henze *et al*., 2002). Therefore, as the database used in this paper contains relatively few input parameters, a more accurate prediction of the COD concentrations from the WWTP cannot be expected. However, the resulting model behaves as expected and produces satisfactory results.

7 Conclusions

Use of machine learning tools to create model from database, in this case model trees have been successfully applied to model WWTP, that is, the COD concentration in the effluent of the WWTP which can help in management and sustainability of the modeled WWTP. Obtained model is simple, understandable, and relatively accurate in predicting COD concentrations in the effluent of the WWTP. Before starting modelling procedure, it is important to note that the database contains the actual attribute values and that it has information about the time when the data was collected so that the dynamics of the system being modeled can be incorporated into the model.

Therefore, some of the advantages of using machine learning tools in modeling can be marked, firstly, the construction of descriptive, or white box models, which make it much easier to interpret the obtained models. Models are more comprehensible, thus providing insight into their functioning, that is, the functioning of the modeled system.

Also, it is especially important to emphasize the use of machine learning tools for simpler and more efficient management and sustainability of the WWTP, as shown in this paper.

Future work is recommended to focus on increasing the database so that model accuracy can be increased and other parameters such as nutrients, e.g. nitrogen and phosphorus can be modeled with the enlarged database, where properly managing of nutrients is crucial to improving the sustainability of the WWTP. Thus, new links and patterns among the data could be revealed.

Acknowledgements

This work has been supported by the University of Rijeka under the projects number 17.06.2.1.02 (River-Sea Interaction in the Context of Climate Change) and uniri-tehnic-18-129 5570 (Implementation of innovative methodologies, approaches and tools for sustainable river basin management). Also, this work is part of the project Influence of summer fire on soil and water quality founded by the Croatian Science Foundation.

ORCID

Goran Volf: https://orcid.org/0000-0002-7058-9012

References

Atanasova, N. and Kompare, B. (2002). Uporaba odločitvenih dreves pri modeliranju čistilne naprave za odpadno vodo. *Acta hydrotechnica*, 20, 33, 351-370.

Baeza, J., Gabriel, D. and Lafuente, J. (1999). An expert supervisory system for a pilot WWTP. *Environmental Modelling and Software,* 14, 383-390.

Belanche, L.I., Valdes, J.J., Comas, J., Roda, I.R. and Poch, M. (1999). Towards a Model of Input-Output Behaviour of Wastewater Treatment Plants using Soft Computing Techniques, *Environmental Modelling and Software,* 14, 409-419.

Cornejo, P.K. (2015). Environmental sustainabilita of wastewater treatment plants integrated with resource recovery: the impact of context and scale, *Graduate theses and disertations*, University of South Florida.

Comas, J., Dzeroski, S., Gibert, K., Roda, I.R. and Sanchez-Marre, M. (2001). Knowledge discovery by means of inductive methods in wastewater treatment data. *AI Communication*, 14, 45-62.

Comas, J., Rodríguez-Roda, I.R., Sànches-Marré, M., Cortés, U., Freixó, A., Arráez, J. and Poch, M. (2003). A knowledge-based approach to the defloculation problem: integrating on-line, off-line, and heuristic information, *Water Research,* 37, 2377-2387.

Čurlin, M., Bevetek, A., Ležajić, Z., Deverić-Meštrović, B. and Kurtanjek, Ž. (2008). Modeliranje procesa biološke obrade otpadne vode na komunalnom uređaju grada Velika Gorica. *Kemija u industriji,* 57, 2, 59-67.

Dürrenmatt, D.J. and Gujer, W. (2011). Data-driven modeling approaches to support wastewater treatment plant operation, *Environmental Modelling & Software*, 30, 47-56.

Grieu, S., Traoré, A., Polit, M. and Colprim, J. (2005). Prediction of parameters characterising the state of a pollution removal biologic process. *Engineering Applications of Artificial Intelligence*, 18, 559-573.

Henze, M., Herremoes, P., Jansen, JC. and Arvin E. (2002). *Wastewater Treatment-Biological and Chemical Processes*, Third edition. Springer. New York. US.

Hong, G., Kwanho, J., Jiyeon, L., Young M.K., Jong-pyo, P., Joon, H.K. and Kyung, H.C. (2015). Prediction of effluent concentration in a wastewater treatment plant using machine learning models, *Journal of Environmental Sciences*, 32, 90-101.

IWA Task group on mathematical modelling for design and operation of biological wastewater treatment, *Activated sludge models ASM1, ASM2, ASM2d and ASM3.* (2000). IWA Publishing. London. UK.

Kompare, B., Levstek, M. and Atanasova, N. (2006). Two approaches to wastewater treatment plant modelling. *Acta hydrotechnica,* 24, 40, 45-64.

Manu, D.S. and Thalla, A.K. (2017). Artificial intelligence models for predicting the performance of biological wastewater treatment plant in the removal of Kjeldahl Nitrogen from wastewater. *Applied Water Science*. doi 10.1007/s13201-017-0526-4.

Mjalli, F.S., Al-Asheh, S. and Alfadala, H.E. (2007). Use of artificial neural network black-box modeling for the prediction of wastewater treatment plants performance, *Journal of Environmental Management*, 83, 3, 329-338.

Ordinance on emission of limit values for wastewaters. Narodne novine br. 153/09, 63/11, 130/11 i 56/13, 2013, 80/13, 43/14, 27/15, 3/2016.

Picioreanu, C. and van Loosdrecht, M.C.M. (2003). *Use of mathematical modeling to study biofilm development and morphology.* IWA Publishing, University of Manchester (UK).

Picioreanu, C., Kreft J.U. and van Loosdrecht, M.C.M. (2004). Particle-based multidimensional multispecies biofilm model. *Microbiology,* 70, 5, 3024-3040.

Quinlan, J.R. (1992). *Learning with continuous classes.* Proc. AI'92, 5th Australian Joint Conference on Artificial Intelligence, Singapore. In: Adams & Sterling (Editors). World Scientific, 343-348.

Razifa, M., Bagyo Yanuwiadib, S., Rachmansyahb, A. and Belgiawanc, P.F. (2014). Implementation of Regression Linear Method to predict WWTP cost for EIA: case study of ten malls in Surabaya City, *Procedia Environmental Sciences*, 28, 158-165.

Roda, I.R., Comas, J., Sànches-Marré, M., Cortés, U., Lafuente, J. and Poch, M. (1999). Expert system development for a real wastewater treatment plant. *Chemical Industry and Environment III*, Proceedings. Kraków, Poland, 653-660.

Sànches-Marré, M., Cortés, U., Lafuente, J., Roda, I.R. and Poch, M. (1996). DAI-DEPUR: a distributed architecture for wastewater treatment plants supervision. *Artificial Intelligence in Engineering,* 10, 3, 379-423.

Tchobanoglous, G., Burton, FL. and Stensel, HD. (2003). *Wastewater Engineering-Treatment and Reuse.* Fourth edition. McGraw-Hill.

Witten, I.H. and Frank, E. (2000). *Data mining-Practical machine learning Tools and Techniques with Java implementations*. Academic Press.

Zhao, H., Hao, O.J. and McAvoy, T.J. (1999). Approaches to modeling nutrient dynamics: ASM2, simplified model and neural nets. *Water Science and Technology,* 39, 1, 227-234.

XV International Conference on Durability of Building Materials and Components
DBMC 2020, Barcelona
C. Serrat, J.R. Casas and V. Gibert (Eds)

A Comprehensive Description of a Low-Cost Wireless Dynamic Real-Time Data Acquisition and Monitoring System

Seyedmilad Komarizadehasl[1], Behnam Mobaraki[2], Jose A. Lozano-Galant[2], and Jose Turmo[1]

[1]Department of Civil and Environment Engineering, Universitat Politècnica de Catalunya, BarcelonaTech. C/ Jordi Girona 1-3, 08034, Barcelona, Spain. Seyedmilad.komarizadehasl@upc.edu, jose.turmo@upc.edu

[2]Department of Civil Engineering, Univesidad de Castilla-La Mancha. Av. Camilo Jose Cela s/n, Ciudad Real, 13071, Spain. behnam.mobaraki@uclm.es, Joseantonio.lozano@uclm.es

Abstract. *Nowadays, low-cost sensors and acquisition devices have been emerging as an obvious solution to many innovative applications such as Structural Health Monitoring (SHM) systems. In this paper, issues regarding dynamic data acquisition, as well as their respective solutions, are presented. Moreover, a comprehensive description through-out an inexpensive sensor network system using open-source hardware for a real-time acceleration data acquisition has been presented. The platform consists of an accelerometer, an Arduino board, and a computer as a data recorder and presenter. Data is recorded through an efficient microcontroller code that can provide a considerable reading frequency (up to 300Hz). Using Python, instant acceleration recording for all the three axes has been done. It is shown how the performance of the proposed system is efficient for the field of SHM systems.*

Keywords: *Arduino Due, Structural Health Monitoring (SHM), Mpu9250, Internet Of Things (IoT).*

1 Introduction

While low-cost sensors are getting significant attention from scientists, how to use them correctly is another matter. Here, by using an Arduino Due and an accelerometer and a raspberry pi, a wireless application has been presented. The nobility of this application would be the chance to observe data capturing in real-time from any place with any device. Firstly here, an introduction through Arduino due, raspberry pi, MPU9250 (the accelerometer) has been presented. Secondly, a brief presentation regarding the coding of the Arduino and the raspberry pi has been given. Finally, the methodology and the result of this application has been shown.

2 State of the Art

In this section, a brief review of the used sensors and a microcontroller in the project has been given together with their technical descriptions.

2.1 Arduino Due

Arduino is an open-source electronics platform based on easy-to-use hardware and software. The Arduino Due (Fig.1) is a microcontroller board based on the Atmel SAM3X8E ARM

doi:10.23967/dbmc.2020.200

Cortex-M3 CPU. It is the first Arduino board based on a 32-bit ARM core microcontroller. It has 54 digital input/output pins (of which 12 can be used as PWM outputs), 12 analog inputs, 4 UARTs (hardware serial ports), an 84 MHz clock, an USB OTG capable connection, 2 DAC (digital to analog), 2 TWI, a power jack, an SPI header, a JTAG header, a reset button and an erase button. Unlike most Arduino boards, the Arduino Due board runs at 3.3V. The maximum voltage that the I/O pins can tolerate is 3.3V. Applying voltages higher than 3.3V to any I/O pin could damage the board (Blum, 2013).

Figure 1. Schematic of an Arduino Due.

2.2 MPU9250

The MPU-9250 (Fig.2), delivered in a 3x3x1mm QFN package, is the world's smallest 9-axis MotionTracking device and incorporates the latest InvenSense design innovations, enabling dramatically reduced chip size and power consumption, while at the same time improving performance and cost. The MPU-9250 MotionTracking device sets a new benchmark for 9-axis performance with a power consumption of only 9.3μA and a size that is 44% smaller than the company's first-generation device. Gyro noise performance is three times better, and full-scale compass range is over four times better than competitive offerings. The MPU-9250 is a System in Package (SiP) that combines two chips: the MPU-6500, which contains a 3-axis gyroscope, a 3-axis accelerometer, and an onboard Digital Motion Processor™ (DMP™) capable of processing complex MotionFusion algorithms; and the AK8963, the market-leading 3-axis digital compass. Improvements include supporting the accelerometer low power mode with as little as 6.4μA of, and it provides improved compass data resolution of 16-bits (0.15 μT per LSB). (InvenSense, 2014).

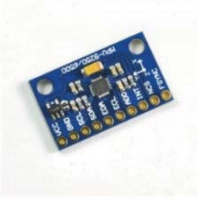

Figure2. Schematic of MPU9250 sensor.

3 Communication Ways

While many sensors use digital and Analog ports to provide the microcontroller the information which they have measured, some sensors use the inter-integrated circuit (I2C) protocol. This is a protocol that allows multiple "slave" digital integrated circuits (Sensors) to communicate with one or more "master" chips (Arduino). Like the Serial Peripheral Interface (SPI), which is only intended for short-distance communications within a single device(Ozdagli et al., 2018). The accelerometer sensor had to be connected to the I2C port (SCL, SDA) on the board. The code was written on the Arduino platform and uploaded to the board via a USB cable. For getting the main characteristics of these sensors, few tests have been done (Mobaraki et al., 2020) (Mobaraki and Vaghefi, 2016).

4 Methodology

After installing the last version of Python on the Computer. For communication of the computer with the Arduino, a library entitled pyserial had to be installed. With this done, the Arduino port could have been introduced to Python to show the captured data. With a python code, the received data were given their time of capture. For being able to use the exact time from the internet another library had to be added and used. The name of that library was DateTime.The given time to the received data had a resolution of 1 microsecond. For illustrating the data wirelessly, the computer had to be connected to the internet. The only power supply that this application needed was hocking up the computer. The Arduino gets its power from the USB port of the computer and initiates the accelerometer. In order to make this project wireless, another free application had to be installed on this computer (Komarizadehasl et al., 2020a) (Komarizadehasl et al., 2020b). The VNC is a remote application that lets users control their devices over the internet. By having the VCN application on any other internet-connected device, the functionality of this device would be observable. The written python code would save the data at the same time as it is illustrating them.

5 Experiment

For testing this sensor and its reliability, an experiment has been implemented. With a dynamic jack, a sinus signal has been programmed, and the vibrations had been saved by the accelerometer. In Fig.3, a picture of the jack can be seen. This jack can shake its bottom plate as was programmed. The instructions to the hydraulic jack were to make a wave with a fixed frequency of 5 hertz (5 complete waves in one second). The movement of the jack was to go up to 0.1 millimeters up and -0.1 millimeter down from its null axis to make a sinus wave. With a very simple two time differential, the acceleration equation could be calculated.

$$y = d * \sin(\omega * t + \varphi) \quad (1)$$

$$\omega = 2 * \pi * f \quad (2)$$

In the above equation, **y** is the displacement in time **t**, d is the maximum allowed movement of the jack in each cycle, $\boldsymbol{\omega}$ is the angular frequency, and $\boldsymbol{f}$ is the set frequency, which equals to 5Hz, and $\boldsymbol{\varphi}$ is the phase constant. On the equ.3, acceleration has been calculated from the Eq.1. This was done by getting the second-order derivative of the Eq.1. By putting all the data

in the Eq.3, the maximum acceleration was calculated as 10.4352 g*10^{-3} m/s^2.

$$a = \frac{d^2 * y}{dt^2} = \ddot{y} = -d * \omega^2 * \sin(\omega * t + \varphi) \quad (3)$$

Figure 3. The hydraulic jack subjected to the experiment.

6 Analysis

The very first faced problem in this experiment was that the sensor could not record data or, if recorded, the data were messy. It was deducted that the sensor had to be glued to the bottom plate of the jack for getting accurate information. The second problem was that the written python code could save only 120 data per second while the sensor was reporting more than 300 data per second. Although, by using serial port commercial software on the computer, it could have been possible to save data at the same speed as their production. Since here, getting the accurate time of capture was vital, it was obligatory to use Python to attach the provided data with their corresponding time. To tackle this problem, the speed of data capture had to be dialed down, so the Python could get and save them. To be on the safe side, the speed of capture had been set on 84Hz.

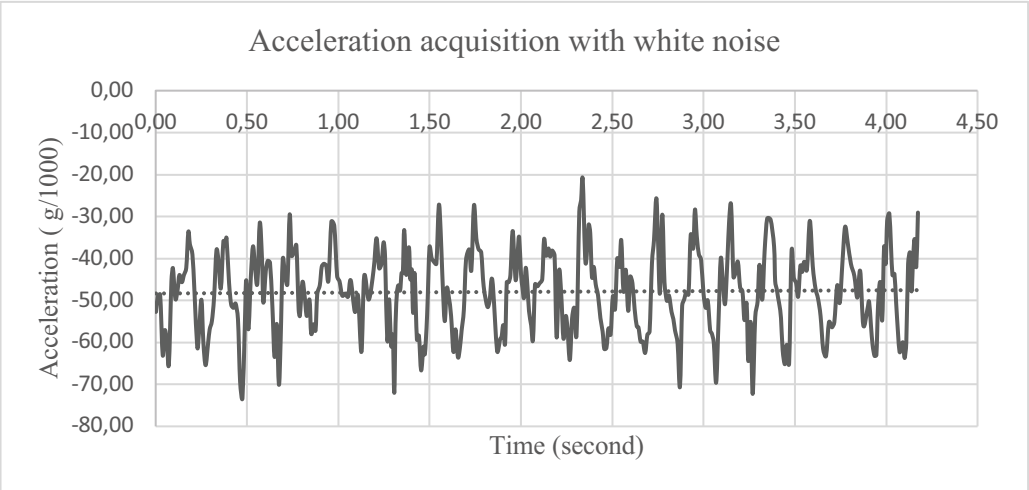

Figure 4. Acceleration, Time diagram with white noise.

The other unexpected issue that this project faced was that, though this sensor had been calibrated in the company, it had a constant number added to all provided data, which from nowhere it would be named as the white noise. As in the Fig.4, it has been illustrated, and the averaged data is around -50milli-g while they had to fluctuate around zero. This -50milli-g was considered as the white noise of this sensor. In order to measure this correctly, the average of 10000 sets of data in a vibration-free test has been calculated. For this sensor, the white noise had been calculated as -49.8535 milli-g.

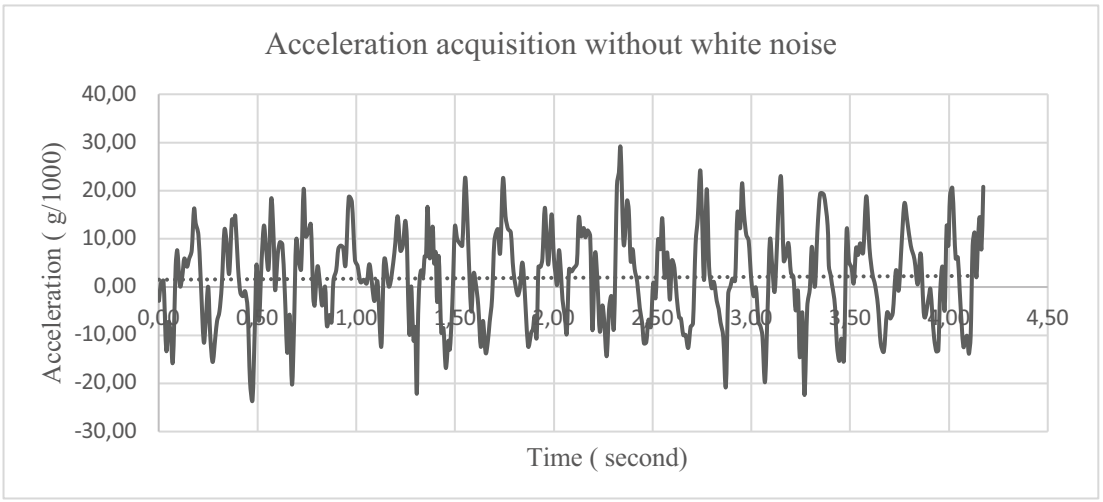

Figure 5. Acceleration, Time diagram without the white noise.

By removing this amount from the provided accelerations, the values had been pulled up where they needed to be. The data were clearer and more understandable when this white noise had been removed (Fig.5). Different accelerometer boards had been tested, and it was concluded that each circuit has its own different amount of white noise that must be dealt with. It should have been assured that this white noise is constant. Moreover, the circumstances and time

cannot change it. For this reason, the jack was programmed with many more different frequencies and displacements. In all of those experiments, the white noise stayed the same.

7 Conclusions

As in Fig.5, it is visible the sinus wave conducted from the accelerometer is quite close to the expected behavior. As it is observable, the sinus wave is fluctuating about 10.5 milli-g from its average as it was calculated in the last section, the graph should have had a 10.453 milli-g fluctuation. It is quite notable to see that they have worked out almost the same. In Fig.5, the filtered data from the 5Hz experiment has been shown. As can be seen, the result is not so accurate, for the fluctuation has other unexpected data or noises as well. In the future works, filters must be applied to delete the unwanted data and ambient noises that may have entered into this experiment unwantedly.

Acknowledgments

The authors are indebted to the Spanish Ministry of Economy and Competitiveness for the funding provided through the research project BIA2017-86811-C2-1-R directed by José Turmo and BIA2017-86811-C2-2-R, directed by Jose Antonio Lozano-Galant. All these projects are funded with FEDER funds. Authors are also indebted to the Secretaria d' Universitats i Recerca de la Generalitat de Catalunya for the funding provided through Agaur (2017 SGR 1481). It is also to be noted that funding for this research has been provided for MR. SEYEDMILAD KOMARIZADEHASL by Agencia Estatal de Investigación del Ministerio de Ciencia Innovación y Universidades grant and the Fondo Social Europeo grant (PRE2018-083238).

ORCID

Seyedmilad Komarizadehasl: https://orcid.org/0000-0002-9010-2611
Behnam Mobaraki: https://orcid.org/0000-0002-2924-643X
Jose Antonio Lozano Galant: http://orcid.org/0000-0003-0741-0566
Jose Turmo: https://orcid.org/0000-0001-5001-2438

References

Blum, J. (2013). Exploring Arduino: tools and techniques for engineering wizardry.

InvenSense, T., 2014. MPU-9250, Nine-Axis (Gyro+ Accelerometer+ Compass) MEMS MotionTracking™ Device.

Komarizadehasl, S., Mobaraki, B., Lozano-Galant, J.A., Turmo, J. (2020)a. Detailed evaluation of low-cost ranging sensors for structural health monitoring applications, in: International Conference of Recent Trends in Geotechnical and Geo-Environmental Engineering and Education. "RTCEE/RTGEE 2020, 8–12.

Komarizadehasl, S., Mobaraki, B., Lozano-Galant, J.A., Turmo, J., (2020)b. Evaluation of low-cost angular measuring sensors, in: International Conference of Recent Trends in Geotechnical and Geo-Environmental Engineering and Education. "RTCEE/RTGEE 2020, 17–21.

Mobaraki, B., Komarizadehasl, S., Castilla-Pascual, F.J., Lozano-Galant, J.A. (2020). Determination of Enviromental Parameters Based onArduino Based Low-Cost Sensors, in: International Conference of Recent Trends in Geotechnical and Geo-Environmental Engineering and Education. "RTCEE/RTGEE 2020.

Mobaraki, B., Vaghefi, M. (2016). Effect of the Soil Type on the Dynamic Response of a Tunnel under Surface Detonation. Combust. Explos. *Shock Waves 52,* 119–127. https://doi.org/10.1134/S0010508216030175

Ozdagli, A.I., Liu, B., and Moreu, F. (2018). Low-cost, efficient wireless intelligent sensors (LEWIS) measuring real-time reference-free dynamic displacements. Mech. Syst. *Signal Process. 107*, 343–356. https://doi.org/10.1016/j.ymssp.2018.01.034

XV International Conference on Durability of Building Materials and Components
DBMC 2020, Barcelona
C. Serrat, J.R. Casas and V. Gibert (Eds)

A Framework for Building Performance Analysis: Investment Return Approach for Energy Savings on Building Product Installation

Jalaycia O. Hughes[1], Simon Pallin[2] and Clayton J. Clark II[3]

[1] Department of Civil and Environmental Engineering, FAMU-FSU College of Engineering, Florida A&M University, Tallahassee, FL, jalaycia1.hughes@famu.edu
[2] Energy and Transportation Science Division, Building Envelope and Urban Systems Research, Oak Ridge National Lab, Oak Ridge, TN, pallinsb@ornl.gov
[3] Department of Civil and Environmental Engineering, FAMU-FSU College of Engineering, Florida A&M University, Tallahassee, FL, clayton.clarkii@famu.edu

Abstract. *Product installation during the construction process impacts the overall performance and durability of a building. However, when the building construction industry fails to address installation quality the product performance is affected. This research explores the importance of optimized product installation and how it affects product performance. During the installation period, standard product performance can be affected by the information known about the product and the amount of time put into the assembly of the product. The building products can vary from insulation, A/C units, water heaters, etc. An installers' workmanship can impact standard product performance if they have limited knowledge about the product and its operational functionality. The products' prescribed functionality could be altered due to less than standardized installation practices. Improper installation of a product can lead to major deviations in performance that can increase maintenance costs over the lifetime of the product in addition to adverse effects of the product during its normal life cycle. Labor sensitivity is an underrepresented aspect of building construction that contributes to the problem of energy inefficiency. The goal of this work is to develop a metric that can quantify how relatively sensitive a building product and overall building performance is to the efforts of time and knowledge, specifically during the installation process. From this metric, the impact of installation on performance for different products can be compared through numerical values, highlighting products that require special care during the installation process to ensure desired performance.*

Keywords: *Building Performance, Sustainability, Product Installation, Installation Cost.*

1 Introduction

In terms of product performance there are theoretical and practical benchmarks in place to evaluate standard operation and procedures. Manufacturers design a product with certain achievement expectations in mind during the product development process. Before production begins, prototypes are designed with the goal of meeting this desired performance set forth by the manufacturer. As Murthy and Rausand (2008) has classified that the prototype specifications are manipulated and changed until the desired performance is reached by the product. Essentially, the performance set by the manufacturer becomes the expected level of performance the product should reach after its usage. A perspective to consider when analyzing overall building performance, "achieving the expected performance requires that the factors
that the design concept is based on fulfils certain standards and are within expected ranges. Hagentoft (2017) suggest that these factors could for instance be workmanship, interior and exterior climate, maintenance and/or material properties.

There are several factors that contribute to inefficient building performance, we intend to focus on the impact of workmanship during the installation process. Individual product performance and energy usages contribute to the overall performance and efficiency of the building. Considering this approach to building performance leads us to focus on individual products and

how their performances measure on smaller scales within the performance gap. Frei (2017) considers the term "Performance Gap" used to denote deviations between a buildings' planned and actual performances. Comparatively so, the previous definition of a building performance gap is the framework for the gap between the actual and individual product performances; the expected performance would not be met if it varies from the actual performance. In this paper we focused on building products that are extremely sensitive to performance issues that occurred during the installation process as a result of workmanship.

Most specialized products and their installation within a building is dependent upon the workmanship of skilled laborers. Some of the products include HVAC systems and heat pumps, which are particularly susceptible to poor performance due to installation errors. Residential heat pump installations and the vocational education of technicians have a dynamic impact on the successfulness of the job completed by the installer. As Gleeson (2016) stated, the lack of broader educational content and deficiencies in engineering knowledge will have profound negative impacts on both the performance and market acceptance of heat pumps. Domanski (2014) conducted a sensitivity analysis on heap pump installation faults and its skewed performance as a result in five different climatic zones. Simulations were run for faults including duct leakage and refrigerant undercharge to determine the effects on energy performance. The study concluded that installation faults could be responsible for a 30% increase in energy usage. The findings in this study can be further validated by the energy reports from the American Council for Energy Efficient Economy. According to the ACEEE (2018), energy savings from high efficiency air conditioners and heat pumps can be negated by a 20-40% loss in energy efficiency due to poor installation. Additional performances of other building products were reviewed to contribute to the argument of unsatisfactory workmanship affecting standard functionality. According to Langmans (2017), the insulation installed in building cavity walls provides a thermal barrier for reducing energy consumption. A performance analysis of these building components illustrated that the thermal performance of especially rigid board insulated cavity walls were highly depending on the installation quality of the insulation layer.

The product used as an example throughout this framework is building insulation. Zero Carbon Hub (2014) acknowledged that faulty installation of insulation is the main contributor to the building performance gap. In their study, two groups of houses were constructed to simulate good and bad workmanship to measure the impacts. Some of the test houses were constructed carefully in a manner that could be described as good workmanship while others were constructed in such a way as to mimic poor workmanship…features associated with poor workmanship could in some cases cause the U-value to rise by as much as 310%. Other investigations related to similar issues performed by Doran (2008) included a thermographic test and visual inspection which found that the quality of installation of insulation can be very important. Essentially areas where insulation is poorly fitted can incur high levels of heat loss. From these results it can be concluded that the poor installation can be a contributor to poor product performance.

2 Methods

The proposed framework emphasizes the effects of installation and its importance for reducing energy consumption. Continual reduction of energy consumption will result in lower cost throughout the lifetime of the product. The overall goal of this paper is to produce a Probabilistic Investment Return (PIR) that includes cost and energy performance of any given product. Consumers can gain an understanding of how the installation cost of a product and its energy savings per year combined can provide information on how it will pay for itself over a span of time. The PIR is based on the installation and performance aspects of building products. In Figure 1, the development of this end goal is displayed in a concept map.

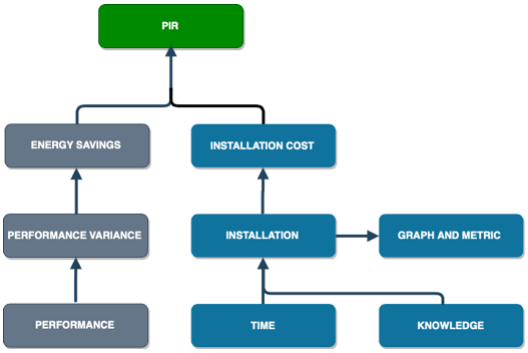

Figure 1. Probabilistic Investment Return Flow Map.

The proposed performance metric is based on the cost of installation and its potential energy savings. The Probabilistic Investment Return value is representative of the return on an investment of any given product in regard to its performance and installation cost. Apart from the installation process, this section will discuss how performance can be used to the estimate the returns on product investments. This figure is a representation of the developmental process and breakdown of each section in the overall framework.

The methods provided in this framework consider the difficulty of installation, variance in product performance, energy consumption as a result of performance, and a resulting probabilistic investment return. A conceptual map reflects the process of how each part within the developmental process of the PIR value was considered in the overall framework. A graphical representation of how an installer's performance is dependent on their contributions of time and knowledge is presented in Graph 1, representing a trade-off between an installer's knowledge and time spent on installation in relation to how a product performs.

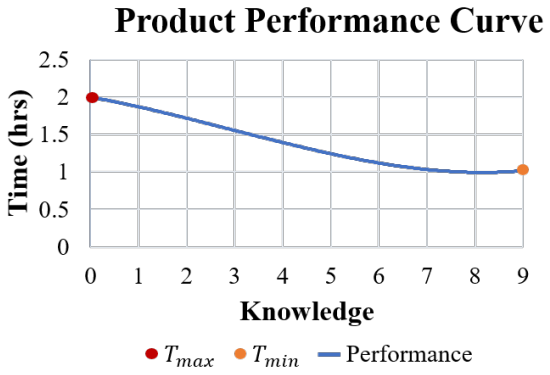

Figure 2. Product Performance Curve.

The above graphic is an example of the performance output of various products throughout a building system. Whether the product is a HVAC unit, heat pump, or roof/wall insulation there are apparent sensitivities to the installation process which require both time and knowledge. The time variable of this analysis was defined to be highly fluctuating due to the innate behavior of the installation process. There is no definite maximum on the time scale to measure the installation time. Depending on the installers' knowledge level different products will require varying time allotments to complete the installation. For this reason, time was treated as a relative variable that could be applied to all products. Knowledge proves to be more difficult to classify when

considering unskilled and skilled persons. This framework focuses on the comprehensive ability of an installer based on their knowledge and experience, so it requires a scale to measure that ability. In the UK, the NVQs, or national vocational qualifications, consists of a system for understanding vocational skill sets in terms of a ranking system. Gann and Senker (1998) suggest that different qualification levels can be met through performance-based assessments of vocational skills within specialized fields. A ranking system was developed in **Table 1** for an individual to place themselves on the knowledge scale. Intuitively, an installer would have a better gauge of their experience and to what extent it can be applied. The scale is also a rubric to help categorize and differentiate between areas of workmanship and understanding, which helps defines an individual's competency level.

Knowledge	
• Basic understanding of product and its functions	**+1**
• Read Installation Manual	**+1**
• Knowledge of required tools	**+1**
Training	
• Attended vocational training	**+1**
• Witnessed an installation/watched instructional video	**+1**
• Received certification	**+1**
Experience	
• Installed the product once	**+1**
• Has installed 50+ units	**+1**
• Has installed 100+ units	**+1**
Total Knowledge Score (0-9): *K*	

Table 1. Installer Knowledge Level Conditions.

Guo *et. al*., (2012) determined a knowledge worker's human capital scale to include the dimensions of education, work experience, learning ability, and training. The Knowledge Score (K) represents an individual's knowledge within a product installation context.

3 Installation Metric

The graphical representation presented above provides a visual understanding of the relationship between time, knowledge, and performance, but a metric is desired in order to fully understand the magnitude of the relationships. The metric proposed comes in two parts which together describe the installation effort and the variability in that effort.

$$\text{Metric} = \text{Area under Performance Curve} \tag{1}$$

$$\text{Area} = \frac{T_{max} - T_{min}}{T_{max}} \text{ X } 100\%$$

The first portion is determined from the area underneath the performance curve. Each unique product will have its own curve and therefore its own area. In this case, the area is a combination of time and knowledge which together are a representation of the effort required to reach expected performance. In order to perform the installation, the installer spends the necessary amount of time put forth time during the installation process. This time can be considered a portion of the effort required to install the product. The second contributor to this effort comes from the installer's knowledge level. To have met their current knowledge level, an installer must have invested in their understanding, training, and experience. Products which require the installation be completed by knowledgeable installers are considered effort intensive in terms of its underlying training and experience required to complete the process. The combination of time

and knowledge required to perform an installation describe the overall effort of installing the product.

The second portion of the metric intends to describe the variation in time and knowledge across the performance curve. A ratio is created by subtracting the minimum installation time from the maximum installation time and then dividing by the max installation time. This percentage gives an indicator of how much time and knowledge vary in relation to performance. From this percentage we can gain insight on the installation of a product. If this value is high, then the time required for a knowledgeable installer to perform the installation will be significantly less when compared to an unknowledgeable installer. If the percentage is low, then an installer with a high knowledge level will not receive a significant decrease in installation time when compared to unknowledgeable installer. This would indicate that the installation may take a similar amount of 'effort' in terms of time for all knowledge levels. This is particularly useful when determining who should install a product. Installers with greater knowledge levels typically have a higher hourly wage due to their experience and skill. An individual may choose to hire an installer with minimum knowledge if they can pay them less money but still have the job done correctly and on time. Generally, this percentage provides a depiction of the shape and steepness of the curve from start to finish. Both values can provide information on the visualization of the graph. For example, the area represents the space under the curve in units of time and knowledge combined (K-hrs). The percentage represents the time differential between the highest and lowest recorded times throughout the data. Both parameters are essential for providing the bounds of the graph. An example is provided below.

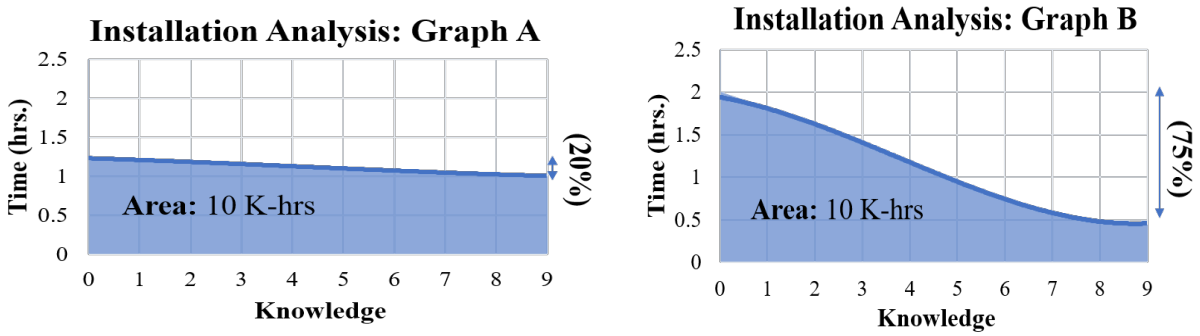

Figure 3. Installation Analysis of Two Performance Curves.

The two graphs shown in Figure 3 above represent possible curves for a product installation. Notably, both curves have a similar area meaning that on average, their installations require similar effort. However, the second graph has a 75% change in time while the first graph has a 20% change in time. This portion of the metric represents the variability of the installation effort across the performance curve. The graph with a 20% change in time is less variable across the curve. An installer with minimal knowledge would not spend a significant amount of time more on the installation than an installer with maximum knowledge. On the other hand, the graph with a 75% change in time has a greater variability in effort across the performance curve. An installer with maximum knowledge will take a significantly less amount of time to perform the installation than an installer with minimum knowledge.

4 Installation Cost

This framework also seeks to understand the costs associated with installation and performance; the installation analysis curve can be adapted to reflect installation costs. Because the knowledge and skills of a laborer are often reflected in their hourly pay, the knowledge scale on the x-axis is

adapted to represent hourly wages of installers. From this change, the cost of installation can be determined.

In Figure 3, the current performance curve is a representation of either the data collected through sampling installations or from the manufacturer questionnaire. The individual data points are a combination of the laborer's wage, W_n, and the installation time T_i. Together these can provide the total installation cost for each installation, C_i. Each individual installation will have its own cost depending on the labor hired to perform the installation. This cost adaptation can then be used to find the current average installation cost for the product being analyzed.

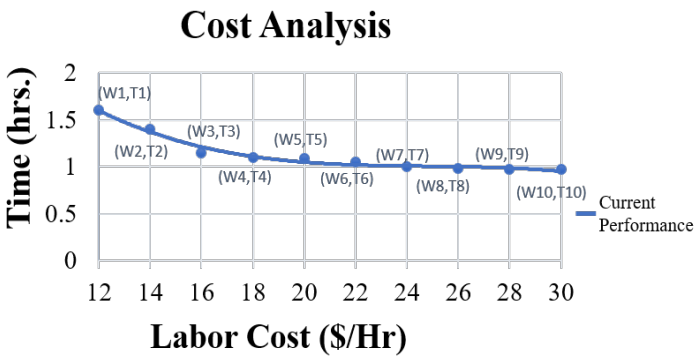

Figure 4. Cost Analysis of Installation.

Installation Cost ($) = Installation Time (hr) x Labor Wage ($\frac{\$}{hr}$)

$$C_i = T_i \text{ x } W_n \tag{2}$$

5 Probabilistic Investment Return

Together, the cost of installation, the cost of the product, and the energy savings for a performance level can provide a general return on investment in terms of years required for the product to pay for itself. We describe this in terms of Probabilistic Investment Return or PIR. The cost of each installation along with the product material cost is then divided by the yearly energy savings of each performance to determine the number of years required to break even on the investment. This is represented as

$$\text{PIR} = \frac{P(C_i) + C_P}{C_E \cdot P(\Delta\,\xi)} \tag{3}$$

where

$P(C_i) = P(T_i * C_w)$; $Probability\ of\ Installation\ Cost$ ($)

$T_i = Installation\ Time\ (hrs)$

$C_w = Installer\ Wage\ (\frac{\$}{hr})$

C_P: $Product\ Cost$ ($)

C_E: $Energy\ Cost\ (\frac{\$}{BTU \times yr})$

$P(\Delta\,\xi)$: $Probability\ of\ Change\ in\ Energy\ Consumption$ (BTU)

6 Conclusion

Throughout this research, we have provided evidence that specialized building products such as HVAC systems and heat pumps are impacted by installation. More specifically, the installers' knowledge is related to how well the product performs. Poor installation of products can result in energy waste in regard to the entire building and its envelope. We have provided a framework for analyzing the impact of installation building performance and its corresponding energy and cost factors. These methods have quantified the contributions of installers to performance levels, the extent of product performance gaps, and the probabilistic return on investment for installing a product. These efforts can then be considered a framework for a holistic understanding of the product installation process and its far-reaching effects on building performance. From this framework, products can be evaluated on an installation basis to determine their effects on building performance and to move toward overall reduced energy consumption in current buildings, retrofit projects, and future constructions.

Acknowledgements

Anna Danek: Oak Ridge National Laboratory
1 Bethel Valley Rd, Oak Ridge TN 37830

ORCID

Jalaycia Hughes: https://orcid.org/0000-0002-3278-7026
Simon Pallin: https://orcid.org/0000-0001-7197-6746

The authors from FAMU wish to thank the Capacity Competitiveness Enhancement Model (CCEM) Grant in the Minority Science and Engineering Improvement Program (MSEIP), Grant #:P120A160115, of the U.S. Department of Education for funding support.

References

Frei, B., C. Sagerschnig, and D. Gyalistras (2017). Performance gaps in Swiss buildings: an analysis of conflicting objectives and mitigation strategies. *Cisbat 2017 International Conference Future Buildings & Districts - Energy Efficiency from Nano to Urban Scale, 122*, 421-426.

Van den Brom, P., et al.(2019). Variances in residential heating consumption–Importance of building characteristics and occupants analysed by movers and stayers. *Applied Energy, 250,* 713-728.

Murthy, D.P., M. Rausand, and T. Østerås (2008). Product reliability: specification and performance. 2008: *Springer Science & Business Media*.

Hagentoft, C.E. (2017). Reliability of energy efficient building retrofitting - probability assessment of performance and cost *(Annex 55, RAP-RETRO). Energy and Buildings, 155,* 166-171.

Gleeson, C.P. (2016). Residential heat pump installations: the role of vocational education and training. *Building Research and Information, 44(4),* 394-406.

Domanski, P.A., H.I. Henderson, and W.V. Payne (2018). *Sensitivity analysis of installation faults on heat pump performance*. 2014: US Department of Commerce, National Institute of Standards and Technology.

ACEEE, (2019). Efficiency Programs: Promoting High-Efficiency Residential Air Conditioners and Heat Pumps in Energy Efficiency Programs, *American Council for an Energy Efficient Economy,* 1-5.

Langmans, J., M. Indekeu, and S. Roels (2017). The impact of workmanship on the thermal performance of cavity walls with rigid insulation boards: where are we today? *11th Nordic Symposium on Building Physics (Nsb2017), 132*, 255-260.

Hub, Z.C. (2008). *Closing the gap between design and as-built performance*. End of interim term progress report, 2014.

Doran, S. and B. Carr. *Thermal transmittance of walls of dwellings before and after application of insulation*. BRE

report, (222077).
Gann, D. and P. Senker (1998). Construction skills training for the next millennium. *Construction Management & Economics, 16*(5), 569-580.
Guo, W.C., H.J. Xiao, and X. Yang (2012). An Empirical Research on the Correlation between Human Capital and Career Success of Knowledge Workers in Enterprise. *International Conference on Solid State Devices and Materials Science, 25,* 715-725.

XV International Conference on Durability of Building Materials and Components
DBMC 2020, Barcelona
C. Serrat, J.R. Casas and V. Gibert (Eds)

A Maintenance Management Model. Upgrading and Experimentation

Maria Azzalin[1] **and Massimo Lauria**[2]

[1] Dipartimento dArTe, di Architettura e Territorio, Università degli studi *Mediterranea* di Reggio Calabria, via Melissari, Feo di Vito, 89124 Reggio Calabria, maria.azzalin@unirc.it

[2] Dipartimento dArTe, di Architettura e Territorio, Università degli studi Mediterranea di Reggio Calabria, via Melissari, Feo di Vito, 89124 Reggio Calabria, mlauria@unirc.it

Abstract. *The paper deals with the first results of the activities of BIG Building Innovative Governance srl, Academic Spin-Off and Innovative Start Up, which provides smart services for Building Maintenance and Facility Management also launching circular R&D actions in the relative reference areas. The contribution introduces some actions actually in progress geared to upgrading the Maintenance Management Model, M3, specifically aimed at managing the life cycle of buildings.*
The current stage of development corresponds to a TRL 4. TRL 8 is that expected by the end of 2020. Characterized by interconnectivity and scalability, the Maintenance Management Model is a dynamic, collaborative and implementable system, whose architecture consists of three separated but strongly interconnected devices: an information interface system, a collaborative platform, a remote cloud. An ICT network infrastructure able to activate using BIM models (IFC and COBie standards) circular information workflows between all operators and/or users involved in Maintenance and Facility Management processes. It allows the development and/or implementation of information management and sharing models based on Open Data and Semantic Web. Its use will also promote shared lexicons and the circulation of knowledge within a holistic process of managing information from and for Maintenance. The use of BIM models and the possibility of collecting and managing a large amount of data will be oriented to the structuring of information feedback databases according to ISO 15686 guidelines. In this way, available information can be usefully transferred in life cycle assessments and service life prediction of materials and components.

Keywords: *Facility Management, Information System, Maintenance Management Model, Operation&Maintenance, Service Life Planning.*

1 Introduction

BIG srl is a spin-off of the *Mediterranean* University of Reggio Calabria, as well as an enterprise registered in the list of innovative Startups.

It operates in the field of technological innovation exploiting, in line with the operational trend of Industry 4.0 and the potentials of Information Communication Technology, ICT; also provides Innovative Integrated Services characterized by technical-scientific nature and high technological value oriented to the construction market and in particular to the Facility Management, FM; develops R&D actions in the sectors focused on Smart Building and Smart Cities drivers. To implement its mission, it assumes as central the interactions between technological capital (infrastructure and technology), human capital (researchers, companies, professionals, users, etc.), administration (institutions, universities, managers, etc.) and real estate (public and/or private heritage).

BIG srl is currently engaged in the experimentation of an innovative governance system for real estate assets, *Maintenance Management Model*, M3.

The service offered through the proposed Maintenance Management Model answer for a primary need of the construction sector as well as of the research one: to increase the effectiveness, efficiency, circulation of information and communication between the operators involved in the management and operation & maintenance practices whose activities presuppose multidisciplinary approaches and great structured data availability.

This primary need is today perceived as immanent criticality for the construction sector. Its effects are felt with concern by technicians and workers, and at the same time, shape a crucial issue that manifests itself in all its severity due to the unexpectedly increasing costs - economic and social – connected with the lack of maintenance of infrastructures, buildings and plants. (World Economic Forum, 2016)

O&M operating and maintenance costs, which are generally neglected during the design phase, generally amount to more than half of the total costs of the building's life cycle (Becerik-Gerber *et al.*, 2012). However, more and more often they represent cost items linked to the inefficiency of choices in the design phase or to mistakes made during the construction phase.

The authors of the paper are among the founders of BIG srl and have been working on the issue for a long time in the scientific and academic field. (Lauria, 2003, Azzalin *et al*. 2005, Lauria and Azzalin, 2006, Azzalin, 2007, Lauria and Azzalin, 2007, Lauria *at al.* 2015, Lauria and Azzalin, 2019, Azzalin, 2019)

In addition to the skills of each founding members, BIG srl avails itself of the expertise recognized to the two industrial partners:

- ACCA software S.p.A. (Https://www.acca.it). Established in 1989, the company is today the Italian leader in the construction software market and a reference point for the sector. For BIG srl provides its expertise and its products with reference to the management of databases, information security, information systems through the implementation and use of collaborative platforms for maintenance and Facility Management purposes.
- BimCo (https://www.bim-co.com), an innovative Startup Enterprise specialized in the use of IT methods and tools for interoperability such as BIM, Building Information Modeling. For BIG srl, BimCo provides the skills related to the production, implementation and management of digital models.

2 Background

The service life and management of a building in its life cycle always combines the terms "costs", "efficiency", "maintainability" and "sustainability" with the planning activity. In this context, Facility Management is defined as an integrated approach oriented to the operation, maintenance, improvement and adaptation of real estate and infrastructure in order to meet the primary objectives of the occupants, owners and managers (Atkin and Brooks, 2009).

Its importance and relevance, assumed by BIG srl as a corporate policy, refers to and is framed, in numerous regulatory actions, scientific research, market trends, both internationally and nationally. The FM involves a relevant field of interest, requires numerous data and information and presupposes multidisciplinary approaches.

The available information and data, whether they concern new or existing construction, are almost never structured to be effectively used in the O&M activities, and not sufficient.

In practice, inefficiencies, disconnected processes and different degrees of dysfunction correspond to this gap.

In the recent past, and even today, data and information for FM are organized and managed by Computerized Maintenance Management System and Computer Aided Facility Management (CMMS and CAFM), Electronic Document Management Systems (EDMS), Building Automation Systems (BAS), etc.

However, these processes are subject to errors (Becerik-Gerber *et al*., 2012).

Today, in general, in the face of still limited use of open standards for structuring and transfer of information, the specific need for open systems and standardized data libraries and specifically declined is added (BIFM, 2012). The availability of open standards, Industrial Foundation Classes, IFC (ISO 16739-1:2018) and data specifications, Construction Operations Building information exchange (COBie-NBIMS-US-V3.4:2015), the diffusion of Building Information Modeling (BIM) methodologies and the adaptation of legacy systems represent the new frontier for the research and standardization challenges. (Kassem *et al.*, 2015a). Several countries, including the United Kingdom in the first place, have introduced and prescribed the use of interoperability tools based on open data, open standards (IFC) and data specifications (COBie) as formats and information exchange methods between the project delivery phases and the use phase of the building (Kassem et al., 2013).

As part of the aforementioned policies, in the United Kingdom the PAS 1192-3:2014 standard (BSI 2014a) is a reference for the structuring of data aimed at the management phase. It introduced an information management methodology based on openBIM standards and data specifications (COBie) connected with BS 8544:2013 (BSI 2013), relating to life cycle costs during the maintenance phase of buildings.

Currently, BuildingSMART deals with the open standards (BIM, IFC and COBie) with the aim of defining languages shared between the various operators and for each of the phases of the building process and the life cycle of the assets. (Atkin and Brooks, 2009).

Further research areas concern the COBie data exchange (Cabinet Office, 2012) for which the British industrial standard BS 1192-4:2014 (BSI 2014b) is the reference.

IFC and COBie are also employed in the context of standardization actions relating to Service Life Planning, ISO 15686 Series. In this sense ISO 15686-4:2014 is a specific reference. The standard proposes "IFC property sets" (IFC4) to support service life planning, including information on the durability of materials, semi-finished products and components. Moreover, the factors that affect durability as introduced in ISO 15686-2:2012, environmental impacts in ISO 15686-6:2004 (at now withdrawn), and Life Cycle Costing (LCC) according to the contents of ISO 15686-5:2017. This thus confirms a strong interrelationship between the LCC assessments, the costs in the usage phase of the building and the decision-making processes aimed at optimizing the Operation & Maintenance phase (Fu *et al.*, 2007, BSRIA, 2009). In other words, in a general context of life cycle management, the BIM based interoperability systems based on open data (IFC standards and COBie) can provide the information needed for planning, execution and management of maintenance actions allowing this information to be structured and kept in an organized management system (CIC, 2012). This system, which can be implemented and accessed over time, will be both a repository and a source of feedback information available at the design stage (Volk *et al.*, 2014).

In short, the essential background introduced above and, more specifically, OpenBIM for FM, the interactions between IFC and COBie and their applications for the management of FM processes and the service life planning (Maxwell, 2005, Kassem *et al.*, 2015b) configure the assumptions from which the R&D actions of BIG srl and the Upgrading of M3 start.

3 Upgrading M3

Currently the upgrade of the Maintenance Management Model, M3 specifically aimed at managing the life cycle of buildings is being implemented thanks to a public financing from the Calabria Region according to the Public Call of POR Calabria ERDF 2014/2020 Action 1.4.1 Support for the creation of innovative micro-enterprises Startup and Spinoff of research.

M3 is aimed at the assistance and smart accompaniment for building maintenance and real estate assets Facility Management activities.

Developed starting from a PhD research (Melchini, 2015), the subsequent definition and implementation of M3 has received significant validation resulting in being the winner and finalist of some contests for innovative business ideas (Coopstartup Calabria Ricomincio da T (r)E, 2016; StartcupCalabria, 2016, national finalist of Startup Europe Awards, 2017).

M3 is an ICT network infrastructure that will allow the development and/or implementation of information management and sharing models based on Open Data, as well as the definition and continuous verification of operational requirements (BSRIA, 2009) among the various operators involved in the whole cycle of life of a building. From the design phase (clients, designers, structural engineers, installers, etc.) and construction (companies and producers / suppliers of materials and components) to management (maintenance personnel, etc.) and disposal phases; and between all operators and the final users themselves (Figure 1).

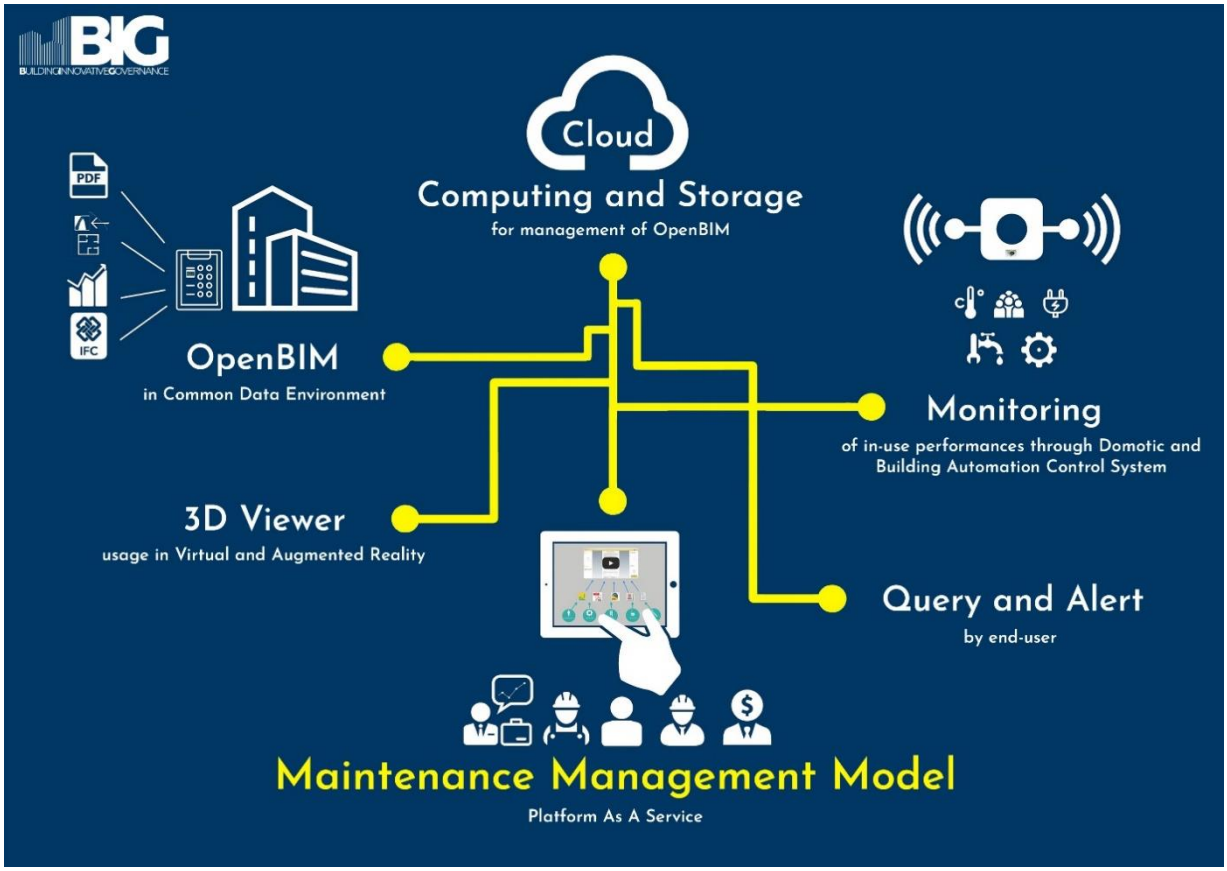

Figure 1. M3 Maintenance Management Model Architecture.

The objective is to support the decision-making process relating to the building management phase through an Information Modeling Asset (AIM) based on openBIM standards (IFC) and specifications on the data structure (COBie).

The structuring of the requirements that allow the definition of the AIM is based on the use of the ISO methodology, Information Delivery Manual (IDM) in ISO 29481-1:2016. A general methodology for defining the requirements of the FM format. In particular, IDM makes possible mapping and describing information processes throughout the life cycle of a building, maintaining links with each of the different phases in which information has been generated, exchanged, controlled and used.

Assumed as an initial development stage of the Management Model, a TRL 4 "low reliability prototype that can be built to demonstrate the technology and its function in the laboratory", a specific Business Development Plan and R&D is being implemented to allow:

- The realization of the engineering functioning model, corresponding to a TRL 6. In the specific case, the expected result is equivalent to an engineering prototype whose technology realizes a first connection level of the three apparatuses that make up the architecture of the Maintenance Management Model: an Information System (AIM); a collaborative platform (usBIM.platform by ACCA Software spa); a Cloud Computing.
- The upgrade to TRL 8 corresponding to a complete prototype system.
- Its experimentation, verification and validation (O.R.R., Operational Readness Review).
- Its marketing.

On a technical level, the availability of all the documentation, information and administrative management relating to the building/s appropriately collected and systematized in digital dossiers will allow, through an integrated system of alphanumeric and graphic databases (IFC and COBie format), the management of complex data concerning localization, use, security, accessibility, employment conditions, usability of spaces.

The availability of a digital twin in OpenBIM format will therefore allow, through a viewer and the interaction in Virtual and Augmented Reality modes, the following visualization:

- information on the current state of construction;
- the behavior of component and sistem transmitted by monitoring system (Building Automation home automation systems);
- the location and degree of severity of active fault and possible operational scenarios for the purpose of the intervention.

The partner ACCA spa, leader in the OpenBIM at national level, has made the usBIM.platform collaborative platform technology available for implementation in the direction described. With usBIM.platform is possible to manage the OpenBIM models (IFC standards and COBie specifications) of each type (architecture, plants, energy, structures, construction site and maintenance) in a single Data Sharing Environment (ACDat) or Common Data Environment (CDE). The related plug-in is being tested through a pilot application to the case study identified in a portion of the building asset of *Mediterranean* University of Reggio Calabria. In particular, the "usage scenario" of the system is the evaluation of IFC4 and COBie 2.4 and some of their enabling technologies.

The ongoing experimentation and the subsequent M3 implementation prefigure some main expected results. Evaluating IFC and COBie support in meeting the information requirements for the creation of the management activity register and proposing ways to implement and extract maintenance requirements respectively in and from BIM models.

The actions undertaken also promote shared lexicons and the circulation of knowledge within an interdisciplinary process of managing information from and for Maintenance.

The use of BIM models and the possibility of collecting and managing a large amount of data will be used as a source of information for service life planning. In particular, they will be oriented to the structuring of information feedback databases according to ISO 15686-7:2017 guidelines related to service life prediction of materials and components.

4 Conclusions

Although the results of the research in these areas refer to experiments that bring to the identification of some general OpenBIM requirements capable of supporting building maintenance activities (Hallberg and Tarandi, 2011, Becerik-Gerber *et al*., 2012, CIC, 2012, Motamedi *et al.*, 2014). To date, detailed studies and systematic evaluations of the IFC and COBie standards applied to FM are still lacking. In fact, it emerges from the literature that these, together with the available software support tools, are still inadequate for the management of the life cycle during the maintenance phase. (Kassem *et al.*, 2015a)

Furthermore, there are no widespread studies on the development of OpenBIM for FM and in particular research aimed at understanding "how" and "if" IFC and COBie can be effectively integrated to support FM processes.

Limits and criticalities that represent the areas of development and implementation of research in general and that related to the upgrade phase of M3 in particular but also of future commitments in the world of standardization and ICT.

In a perspective that embraces a holistic view of the life cycle of an artifact, which considers together: quality, duration, environmental, social and economic costs, the Maintenance Management Model, M3 takes on a dual meaning.

On the one hand, a tool to support the management of real estate assets through the activation of innovative information sharing processes (Open Data and Semantic Web).

On the other hand, it is evident that to effectively support decision-making processes in the development and execution of maintenance strategies, information on the useful life of building components is fundamental (Hovde and Moser, 2004) and should be taken into consideration from the earliest stages of planning (Marteinsson, 2005).

According to this vision M3 is beginning to look as a privileged "observatory" of the phenomena that characterize building systems over time, their operation and their use. Therefore, it appears functional for oriented collection of feedback data relating to the behavior of materials and components in specific contexts according to ISO 15686-7:2017 and as clearly expressed by the same ISO 15686-4:2014.

ORCID

Massimo Lauria: http://orcid.org/0000-0003-4363-6642
Maria Azzalin: http://orcid.org/0000-0002-4890-9251

References

Atkin, B. and Brooks, A. (2009). *Total Facilities Management*, 3rd edn, United Kingdom.

Azzalin, M., Nesi, A., Lannutti, C., Lauria, M., Nicosia, C. and Pastura, F., (2005). Standards and Tools for the Guarantee of the Reliability of the Intermediate Product in Building, *Proceeding of 10 International Conference on Durability of Building Materials and Components*.

Azzalin, Maria, (2007). "*Applicabilità del Factor Method per la valutazione della service life di materiali e componenti nel progetto dell'esistente. Manutenzione e Fattore manutentivo*", Tesi di Dottorato in Tecnologia dell'Architettura, XVIII ciclo 2003/2006 Università degli Studi Mediterranea di Reggio Calabria.

Azzalin, M., (2019). Manutenzione e valutazione della sostenibilità ambientale nelle costruzioni. Una sinergia possibile tra presente e futuro, in *Atti del Convegno Internazionale SBE19 - Sustainable Built Environment Conference*, May 16th – 17th 2019, Scilla (RC) Italia.

Becerik-Gerber, B., Jazizadeh, F., Li, N. and Calis, G. (2012). Application Areas and Data Requirements for BIM-Enabled Facilities Management*, Journal of Construction Engineering and Management*, vol. 138, no. 3.

BIFM (2012). BIM and FM: Bridging the gap for success, British Institute of Facilities Management, Bishop's Stortford, Hertfordshire, UK.

BSI (2014a). PAS 1192-3: *Specification for information management for the operational phase of assets using building information modelling*. BSI Standards Limited

BSI (2014b). BS 1192-4: *Collaborative production of information Part 4: Fulfilling employer's information exchange requirements using COBie – Code of practice*. BSI Standards Limited

BSI (2013). BS 8544: *Guide for life cycle costing of maintenance during the in-use phases of buildings*. BSI Standards Limited

BSRIA (2009). *The Soft Landings Framework*, BSRIA.

Cabinet Office (2012). *COBie Data Drops*.

CIC (2012). *Building Information Modeling Planning Guide for Facility Owners*.

Fu, C., Tah, J. and Aouad, G. (2007). The Life cycle Costing Simulation for Building Construction and Maintenance in nD Modelling, *Building Simulation 2007*, pp. 1580.

Hallberg, D. and Tarandi, V. (2011). On the use of 4D BIM and visualization in a predictive life cycle management system for construction works, *Journal of Information Technology in Construction* (ITcon), vol. 16, pp. 445.

Hovde, P. and Moser, K. 2004, *Performance Based Methods for Service Life Prediction, International Council for Research and Innovation in Building and Construction* (CIB).

ISO/TC 59/SC 14 (2004). 15686-6: *Buildings and constructed assets — Service life planning — Part 6: Procedures for considering environmental impacts*.

ISO/TC 59/SC 14 (2012). 15686-2: *Buildings and constructed assets — Service life planning — Part 2: Service life prediction procedures*.

ISO/TC 59/SC 14 (2014). ISO 15686-4: *Buildings and constructed assets — Service life planning — Part 4: Service life planning using Building Information Modelling*.

ISO/TC 59/SC 14 (2017). ISO 15686-5: *Buildings and constructed assets — Service life planning — Part 5: Life-cycle costing*.

ISO/TC 59/SC 14 (2017). ISO 15686-7: *Buildings and constructed assets — Service life planning — Part 7: Performance evaluation for feedback of service life data from practice*.

ISO/TC 59/SC 13 (2016). ISO 29481-1: *Building information models – Information delivery manual – Part 1: Methodology and format*.

ISO/TC 59/SC 13 (2018). 16739-1: *Industry Foundation Classes (IFC) for data sharing in the construction and facility management industries — Part 1: Data schema*.

Kassem, M., Succar, B. and Dawood N. (2013). A proposed approach to comparing the BIM maturity of countries, *Proceedings of the CIB W78 2013*: 30th International Conference, Beijing, China, 9-12 October

Kassem, M., Vukovic, V., Dawood N. and Patacas, J., (2015a). BIM for Facilities Management: evaluating BIM standards in asset register creation and service life planning*, Electronic Journal of Information Technology in Construction*.

Kassem, M., Kelly, K., Dawood, N., Serginson, M. and Lockley, S. (2015b), BIM in Facilities Management applications: a case study of a large university complex, *Built Environment Project and Asset Management*, Vol. 5(3).

Lauria, M., (2003). Evaluation of flat roofs reliability, in: Daniotti B., *Management of Durability in the Building Process*, Maggioli Editore, Rimini.

Lauria, M., Azzalin, M., (2006) Service Life Estimation and Maintenance in building design. A practical view on application of Factor Method, *Proceedings of 3rd World Congress of Maintenance 18th EuroMaintenance.*

Lauria, M. and Azzalin, M., (2007) Manutenzione e valutazione della service life nel progetto dell'esistente. Un'applicazione del Factor Method, in *La cultura della manutenzione nel progetto edilizio e urbano*, LetteraVentidue Edizioni, Siracusa.

Lauria, M., Milazzo and L., Modaffari, C., (2015). Operational tools for maintenance and renewal of school buildings patrimony, *Techne* n.9, FUP, Firenze.
Lauria M. and Azzalin M., (2019) Project and maintainability in the era of Industry 4.0, *Techne* n.18, FUP, Firenze
Maxwell, J.A. (2005) Qualitative research design: An interactive approach. 2nd edn. Thousand Oaks, CA: Sage Publications.
Marteinsson, B. (2005) Service life estimation in the design of buildings: A development of the factor method. PhD thesis. KTH Research School.
Melchini, T. (2015) *Il Building Information Modelling (BIM). Innovazione dei processi progettuali, realizzativi e gestionali nella governance del patrimonio residenziale pubblico*, PhD Thesis, Università *Mediterranea* di Reggio Calabria
Motamedi, A., Hammad, A. and Asen, Y. 2014, "Knowledge-assisted BIM-based visual analytics for failure root cause detection in facilities management", *Automation in Construction*, vol. 43.
World Economy Forum, Boston Consulting Group, (2016). *Shaping the Future of Construction. A Breakthrough in Mindset and Technology*
Volk, R., Stengel, J. and Schultmann, F. 2014, "Building Information Modeling (BIM) for existing buildings — Literature review and future needs", *Automation in Construction*, vol. 38.

XV International Conference on Durability of Building Materials and Components
DBMC 2020, Barcelona
C. Serrat, J.R. Casas and V. Gibert (Eds)

A Vector Scale of Severity of Damages in Buildings

Félix Ruiz[1], **Antonio Aguado**[1] **and Carles Serrat**[2]

[1] Dept. of Civil and Environmental Engineering, Universitat Politècnica de Catalunya-BarcelonaTECH, Jordi Girona, 1-3, 08034-Barcelona, Spain, felixruizgorrindo@gmail.com, antonio.aguado@upc.edu
[2] IEMAE-EPSEB, Dept. of Mathematics, Universitat Politècnica de Catalunya-BarcelonaTECH, Av. Dr. Marañón, 44-50, 08028-Barcelona, Spain, carles.serrat@upc.edu

Abstract. *In the context of the existing buildings, along the recent years the concept of maintenance has changed from corrective maintenance to preventive maintenance, which is based in part on periodic inspections. There is ample evidence that preventive maintenance is more efficient than corrective maintenance, since severe deteriorations that may represent danger to people are avoided, and also money is saved. To make periodic inspections of the buildings is useful to quantify the extent to which deficiencies are severe or not, in order to facilitate decision making and prioritize therapeutic interventions. To this purpose many scales have been used and are used to assess the degree of gravity of the damages in constructive elements. But it is important to say that there is no common consensus and these scales are different between them according to the study to which they belong. Thus, the main goal of this article is to propose a methodology for calculating the degree of severity of damages in buildings, which is of widespread use. This calculation method, which is in distribution and in scalar, lets to calculate the severity index of systems and of the entire building, and it is easy to use and flexible.*

Keywords: *Scale, Severity Index, Damages, Direct Assignment Method, Quartiles.*

1 Introduction

The rapid industrialization and population migration of the last 30 years, has led to a fast growing urbanization, doubling the building and partially the infrastructure stocks in very short periods (20-30 years) (Yang, 2006). In this context, the crucial indicator is the state of degradation of the different components of the stock (Kohler and Yang, 2007). Likewise, "What is not defined can not be measured. What is not measured can not be improved. What is not improved, it is always degraded". This phrase is from Sir William Thomson, Baron Kelvin of Largs. Although the phrase is from the nineteenth century, it is fully in force, and we are well aware of the importance of performing preventive maintenance in buildings in order to prevent their degradation and the appearance of severe deteriorations. In the framework of maintenance is true that to make periodic inspections of buildings, is useful to quantify the extent to which deteriorations are severe or not, in order to facilitate decision making and prioritize therapeutic interventions. In fact many scales have been used and are used to assess the degree of gravity of the constructive elements. But there is no common consensus and these scales are different from each other according to the study to which they belong (Ruiz, 2014).

All the referred shows the need to propose and validate a scale, in order to assess the severity index of constructive elements in buildings, which is of widespread use. Thus, the main goal of this article is to propose a calculation method, in distribution and in scalar, to calculate the degree of severity of systems and of the entire building, easy to use and flexible.

doi:10.23967/dbmc.2020.236

2 Methodology

In most of the known scales, there is not any method to calculate the degree of severity of a system or of the entire building. In the few scales where there is a method, the output values are scalars, which do not show the variability of the distribution of severities. The proposed methodology in this paper aims to add the variability of the distribution of severities in the resulting vector scale. It is also remarkable to highlight that unlike what happens in other areas of science where there are scales widely used and commonly accepted, in the field of the buildings there is not a common scale for assessing the degree of severity of the constructive elements, and there are many different scales. There is no doubt that in building engineering would be very useful to have a common scale and a methodology widely used to assess the degree of severity of the buildings.

2.1 Application Levels

In this section the proposed methodology for calculating the degree of severity of damages in buildings as a whole (biggest proposed unit) or parts thereof, which will be called systems (S) is introduced. It is considered appropriate to propose a reasonable division of building into systems, which is presented in Table 1. In order to provide flexibility to the methodology it allows that the total number of systems and the definition of them can be chosen by the technician that develops the study of the building, thus the proposed method is of general application. Therefore, the building as a whole is the sum of the systems that constitute it, as indicated in Equation (1):

$$Building\text{: } (B) = \sum_{i=1}^{n} (S)_i \tag{1}$$

Table 1. Proposal of building systems.

System	Description	Main constituent parts
1	Façades	Claddings, base material, cantilevers, cornices, windows and other practicable openings, railings, balustrades, ornamental elements, etc.
2	Vertical structure	Pillars, load walls, foundation, etc.
3	Horizontal structure	Beams, beam filling, vaults, arches, etc.
4	Roofs and inner courtyards	Roof tiles, pavements in flat roofs, waterproofing, thermal insulations, skylights, walls and practicable openings for inner courtyards, etc.
5	Interior building elements	Partitions, interior walls, practicable openings, pavements, interior claddings, etc.
6	Staircases	Walls, stair structure, steps, railings, etc.
7	Sewer facilities	Downpipes, drains, gutters, etc.
8	Other facilities	Electricity, water, gas, elevators, etc.

Each system can be divided into zones which constitute the last and smallest proposed unit to value. A zone is defined as a specific part of a constructive element, as for example an area of a wood beams floor, an area of a façade, an area of a reinforced concrete beam floor, an area of a balcony, etc. Figure 1 shows some images that represent what is named zone.

Figure 1. Images of four zones of construction elements.

Thus, the set of zones into which the system has been divided (p), constitutes the entire system, as shown in Equation (2):

$$System: (S)_i = \sum_{j=1}^{p} (Z)_j \tag{2}$$

One important point is that this methodology can be applied to any kind of existing scale of severity of damages in buildings, regardless they are based in direct assignment method (DA) or application of mathematical functions or algorithms method, or in both.

The proposed scale in this paper ranges from value 0 (zero gravity and the constructive element is in perfect condition) to value 10 (extreme gravity; it is not conceivable a greater gravity; pathology in terminal phase; collapse may occur at any time). Due to the scale is applicable to any type of constructive element (walls, beams, columns, bearing walls, façades, etc.), definitions are necessarily generic. These definitions can be seen in Ruiz *et al*. (2019).

2.2 A Vector Scale of Severity of Damages in Buildings

The proposed methodology, which is schematically presented in Figure 2, it is initiated by the direct assignment method (DA) based on the generic definitions of the reference scale, through which the grade or index of severity, G, is assigned to zones, j, of the building. In the variant called (a), the process ends at this level, which is in cases where the object of study is assessing the gravity of different zones of the building, but it is not necessary to evaluate the overall gravity of a system or of the whole building.

The next step of the methodology, when required, is to assess the severity of one or more systems, for which there are the variants called (b) and (c). In variant (b) DA method based on the generic definitions of the proposed scale is used, through which the degree of severity of

the considered system is assigned. In variant (c) the calculation method that it is proposed in the next subsection is used, applying it to the G_j values comprising the zones of the system, which allows to calculate the degree of severity of the considered system.

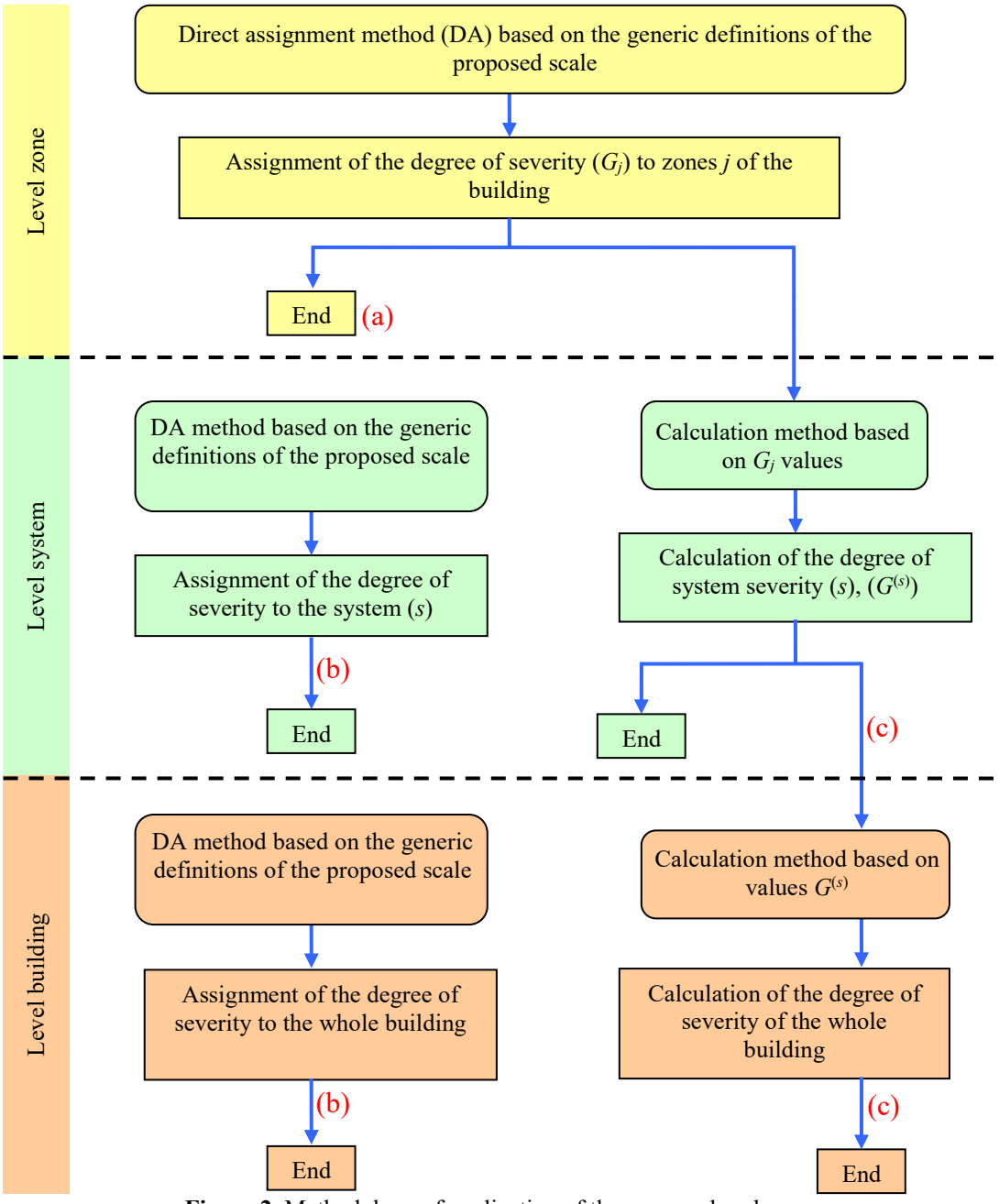

Figure 2. Methodology of application of the proposed scale

The variant (b) is of application in cases where the object of the study is such that it is necessary to spend a short time. Some of these cases may be the following: i) Global study of an urban area, in which it is necessary to assess the grade of gravity of hundreds or thousands of façades; ii) Emergency interventions, such as civil service technicians or firemen in cases of sever

deteriorations with potential risk for people. The variant (c) will be of application in the remaining cases in which is required to determine the grade of gravity of a system or building.

2.2.1 Definitions and computations at system level

Within the framework of variant (c) in Figure 2, first it should be said that to obtain the resultant severity of a system based on the summation of the G_j values of that system, applying a weight w_j that is based on the area or proportion of the zone j (A_j) regarding the area or whole unit (A_T) of the considered system, gives adequate results only for cases that severity of the system is homogeneous, for example if the entire system is heavily degraded or everything is in good condition. However, it gives inadequate results in cases where there is a significant variability of severity in the system, especially in cases of extreme dispersion.

For this reason, after discarding the previous method of calculation for being inadequate, in order to calculate the resulting severity of a system s it is proposed a method based on statistical quantiles. In this case quartiles are used as well as the minimum and maximum values of G_j of the analyzed system, allowing to define the distribution of severity of system s, $G_d^{(s)}$, as follows in Equation (3):

$$G_d^{(s)} = (q_0^{(s)} , q_{0.25}^{(s)} , q_{0.50}^{(s)} , q_{0.75}^{(s)} , q_{1.00}^{(s)}) \tag{3}$$

where, $q_0^{(s)}$ and $q_{1.00}^{(s)}$ are the minimum and maximum value, respectively, of G_j of the system s, and $q_{0.25}^{(s)}$, $q_{0.50}^{(s)}$ and $q_{0.75}^{(s)}$ are the maximum value of G_j corresponding to the 25%, 50%, 75% less degraded, respectively, of the system s.

With this methodology can be directly observed the highest value of G_j of each of the evaluated systems of the building ($q_{1.00}^{(s)}$). Similarly can be directly establish whether the extension of the pathologies is generalized or localized in function of the G_j values, which are derived from analyzing the 25%, 50% or 75% of the system.

The resulting vector of a system s allows to determine the priority of intervention of the system s, which is determined by the value of G_{max}, corresponding to the last value of the vector. $G_d^{(s)}$ also allows to establish the extension of the corresponding dysfunction to G_{max} , extension that it is denoted by $e(.,G_{\max})$, that evaluates the position of the minimum quartile in which the G_{max} value appears. Formally, it is defined in Equation (4):

$$e\left(G_d^{(s)}, G_{\max}\right) = q, \text{ where } q \text{ is the smallest } q_k \text{ such that } q_k = G_{max} \tag{4}$$

Thus, it should be emphasized that the proposed vector $G_d^{(s)} = \left(q_0^{(s)}, q_{0.2}^{(s)}, q_{0.5}^{(s)}, q_{0.7}^{(s)}, q_{1.0}^{(s)}\right)$ gives a lot of information about the severity of the system s, since besides it shows the minimum and maximum severity of the system, it shows the distribution of severities thereof. It must be said that while the vector $G_d^{(s)}$ describes numerically the grade of gravity of a system with sufficient accuracy, the distribution can be interesting to be summarized in a single value. To this end, we propose a method that transforms the vector $G_d^{(s)} \in \{0, \ldots, 10\}^5$ into a scalar $G_r^{(s)} \in [0, 10]$, which it is named resulting severity of the system, and it is denoted by $G_r^{(s)}$.

To estimate the mean value of the distribution and using the relationship $E(X) = \int R(g)dg$ that calculates the expectancy of a positive random variable X (in our case between 0 and 10) as the area under the complementary function of the distribution function ($R(g)$ = 1-$F(g)$), where F denotes the distribution function, it is proposed that $G_r^{(s)}$ is obtained as the first order approximation of the area under the empirical distribution of R from the distribution $G_d^{(s)}$. By construction it takes the values $R(q_0) = 1 - 0 = 1$; $R(q_{0.25}) = 1 - 0{,}25 = 0{,}75$; $R(q_{0.50}) = 1 - 0{,}50 = 0{,}50$; $R(q_{0.75}) = 1 - 0{,}75 = 0{,}25$ y $R(q_{1.00}) = 1 - 1 = 0$. Figure 3 illustrates this calculation for the numerical example $G_d^{(1)} = (0, 2, 5, 5, 8)$.

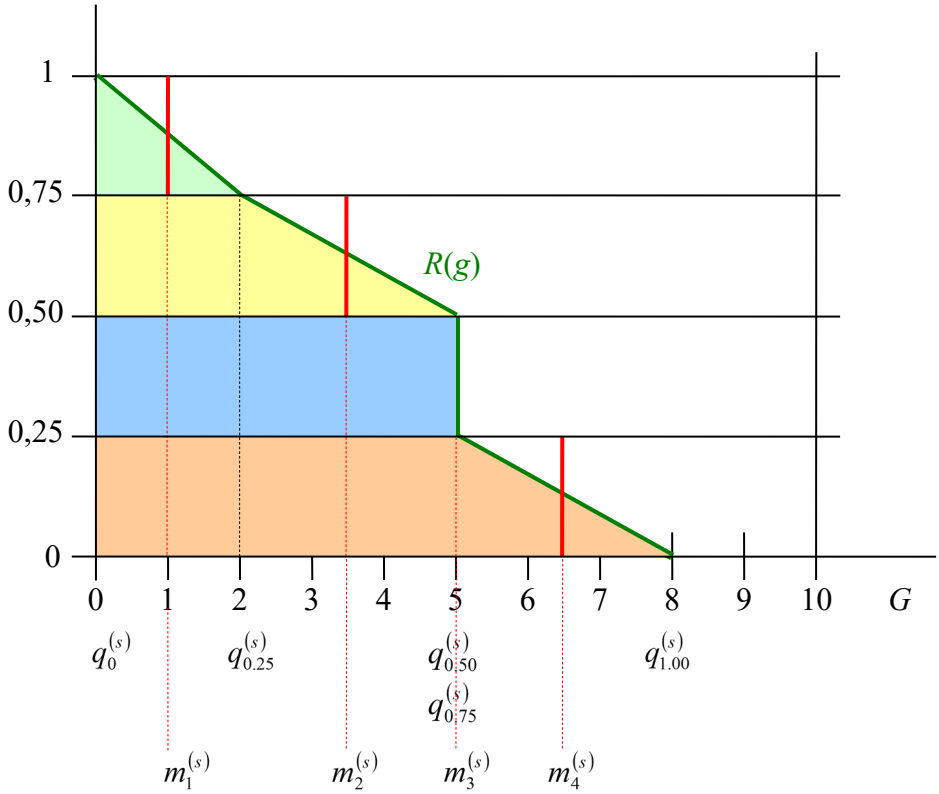

Figure 3. Function to determine the $G_r^{(s)}$ value.

So,

$$G_r^{(s)} = \left(\frac{q_0^{(s)} + q_{0.25}^{(s)}}{2}\right)\cdot 0{,}25 + \left(\frac{q_{0.25}^{(s)} + q_{0.50}^{(s)}}{2}\right)\cdot 0{,}25 + \left(\frac{q_{0.50}^{(s)} + q_{0.75}^{(s)}}{2}\right)\cdot 0{,}25 + \left(\frac{q_{0.75}^{(s)} + q_{1.00}^{(s)}}{2}\right)\cdot 0{,}25 =$$

$$= \frac{q_0^{(s)} + 2q_{0.25}^{(s)} + 2q_{0.50}^{(s)} + 2q_{0.75}^{(s)} + q_{1.00}^{(s)}}{8}, \quad (5)$$

or equivalently

$$G_r^{(s)} = \sum_{i=1}^{4} \frac{m_i^{(s)}}{4}, \quad (6)$$

where $m_i^{(s)}$ are the midpoints between the components of $G_d^{(s)}$.

In order to have a greater sensitivity over the parts of the building with greater severity, it is proposed to generalize the Equation (6), so it could be applied a set of coefficients $w_i^{(s)}$, which allows, among other possibilities, give more weight to the components on the right, which are those corresponding to the highest values G_j of the system. In order to provide flexibility to the methodology, it is proposed that the technician can determine the relative weights $w_i^{(s)}$ to give to each coefficient, under the condition that $\sum_{i=1}^{4} w_i^{(s)} = 1$. These coefficients act on the midpoints $m_i^{(s)}$ between components $q_k^{(s)}$, which allows to obtain $G_{rw}^{(s)}$ ($G_r^{(s)}$ weighted) defined as

$$G_{rw}^{(s)} = \sum_{i=1}^{4} w_i^{(s)} \cdot m_i^{(s)} \tag{7}$$

2.2.2 Definitions and computations at building level

After obtaining vectors $G_d^{(s)}$, s = 1,..., S, representing the distribution of the gravity of each system s, it is defined the distribution of severity of the building (G_d^*), as follows:

$$G_d^* = \begin{pmatrix} G_d^{(1)} \\ G_d^{(2)} \\ \dots \\ G_d^{(S)} \end{pmatrix} = \begin{pmatrix} q_0^{(1)} & q_{0.25}^{(1)} & q_{0.50}^{(1)} & q_{0.75}^{(1)} & q_{1.00}^{(1)} \\ q_0^{(2)} & q_{0.25}^{(2)} & q_{0.50}^{(2)} & q_{0.75}^{(2)} & q_{1.00}^{(2)} \\ \dots & \dots & \dots & \dots & \dots \\ q_0^{(S)} & q_{0.25}^{(S)} & q_{0.50}^{(S)} & q_{0.75}^{(S)} & q_{1.00}^{(S)} \end{pmatrix} \tag{8}$$

Therefore, G_d^* is a Sx5 matrix, stacking by rows the severity distributions of each system. Similarly than before, matrix G_d^* can be summarized to a single value $G^* \in [0,10]$ by defining

$$G_w^* = \frac{\sum_{s=1}^{S} w^{(s)} \cdot G_{rw}^{(s)} \cdot w_{(\tilde{s})}}{\sum_{s=1}^{S} w^{(s)} \cdot w_{(\tilde{s})}}, \tag{9}$$

where

- $w^{(s)}$: coefficient for each of the S systems of the building, in order to give more weight to the most important systems.
- $w_{(\tilde{s})}$: coefficient for each of the S systems of the building, in order to give more weight to those systems that are in worse condition, which numerically means to give more weight to those highest values $G_{rw}^{(s)}$.

3 Conclusion

It should be noted that the proposed methodology can be easy applied by a technician. Just determining the G_j severity (through DA method) and the A_j surfaces of different areas j, it is possible to obtain automatically the resulting severities of each system $G_{rw}^{(s)}$ and the resulting severity of the building, by using a spreadsheet. Likewise, when applying the methodology to real cases, consistent results have

been obtained, confirming the validation of the proposed methodology. Finally, it has been proven that this vector scale is an efficient tool as support to the technician in decision making.

Acknowledgements

This research has been partially supported by grants MTM2015-64465-C2-1-R (MINECO / FEDER) from the Ministerio de Economía y Competitividad (Spain) and 2017 SGR 622 from the Departament d'Economia i Coneixement de la Generalitat de Catalunya. Authors are grateful to members of the IEMAE, LABEDI and GRASS-GRBIO groups their valuable comments and suggestions in the development of the work.

ORCID

Felix Ruiz: http://orcid.org/0000-0002-7535-4490
Antonio Aguado: http://orcid.org/0000-0001-5542-6365
Carles Serrat: http://orcid.org/0000-0002-1504-5354

References

Kohler, N. and Yang, D. (2007). Long-term management of building stocks. *Building Research and Information*, *35*(4), 351–362.

Ruiz, F. (2014). *Escala de gravedad de daños en edificios: de la asignación directa a la constrastación estadística* (in spanish). Doctoral Thesis. School of Civil Engineering of Barcelona. Polytechnical University of Catalonia.

Ruiz, F., Aguado, A., Serrat, C. and Casas J.R. (2019). Optimal metric for condition rating of existing buildings: is five the right number? *Structure and Infrastructure Engineering, 15*(6), 740–753, doi: https://doi.org/10.1080/15732479.2018.1557702.

Yang, D. (2006). *International migration, remittances, and household investment: evidence from Philippine migrants exchange rate stocks.* National Bureau of Economic Research. Cambridge.

XV International Conference on Durability of Building Materials and Components
DBMC 2020, Barcelona
C. Serrat, J.R. Casas and V. Gibert (Eds)

Assessing the Condition of Reinforced Concrete Bridge Using Visual Inspection Ratings

Abdoul S. Bah[1], Thomas Sanchez[1], Yan Zhang[2], Kotaro Sasai[2], David Conciatori[1], Luc Chouinard[2], Gabriel J. Power[3] and Nicolas Zufferey[4]

[1] Research Center on Concrete Infrastructure (CRIB), Dept. of Civil and Water Engineering, Université Laval, Québec, QC, G1V 0A6, Canada, david.conciatori@gci.ulaval.ca

[2] Centre d'Études Interuniversitaire des Structures sous Charges Extrême (CEISCE), Dept. of Civil Engineering, McGill University, Montreal, QC, H3A OC3, Canada, luc.chouinard@mcgill.ca

[3] Research Center on Concrete Infrastructure (CRIB), Dept. of Finance, Insurance and Real Estate, Université Laval, Québec, QC, G1V 0A6, Canada, gabriel.power@fsa.ulaval.ca

[4] Geneva School of Economics and Management (GSEM), University of Geneva, 1211 Geneva 4, Switzerland, n.zufferey@unige.ch

Abstract. *The evolution of the state of a structure is characterized by deterioration. This is mainly due to corrosion of the steel reinforcement and damage from mechanical solicitations. The maintenance of existing infrastructures involves a good grasp of their condition and a high level of expertise on the part of the project managers. An accurate assessment of the bridge state condition is required to plan maintenance and repair activities for better durability, and to maintain the level of service of the road network. In this paper, an effective management framework for bridge is proposed using field observations from visual inspections. Each element of the bridge was evaluated separately by a visual inspection from which were derived ratings to quantify the structural performance and the material condition. The element ratings were also combined to obtain an overall rating for the bridge considering its defects and impact on the behavior of the complete structure. The modelling approach proposed in this work can better represent the deterioration of concrete-built bridges when the defect is visible. A representative structure in Quebec was studied to illustrate how to apply the methodology for the assessment of a real structure condition at specific times.*

Keywords: *Concrete, Bridge, State, Assessment, Durability.*

1 Introduction

The main cause of deterioration of road structures in cold regions is steel rebar corrosion in concrete with the presence of chloride ions (Conciatori, *et al.,* 2018; Roelfstra, *et al.,* 2004).

However, using de-icing salts during winter, due to the microclimate, problematic for the safety of structures (Angst, 2019). For example, there are 614,387 bridges in the USA, among which 56,007 were structurally deficient in 2016. Most bridges have been designed for a 50-year service life, but nearly 40% of them are more than 50 years old. Currently, the average age of those bridges is 43 years. Around 188 million users cross a structurally deficient bridge every day. The latest estimations bring the backlog of bridge rehabilitation needs in the USA to $123 billion (ASCE, 2017). In Canada, 60% of structures in the national highway network will be

more than 40 years old in 2020. The number of bridges built more than 50 years ago, has increased by 50% since 2010 (RRN, 2010). Usually, repair works are done each 30 years period.

For the next few years, maintenance and repair needs in Quebec, Canada will reach a high level. The setting of Quebec is interesting because it is a Nordic climate where the challenges of a cold, harsh winter, de-icing, etc. are significant.

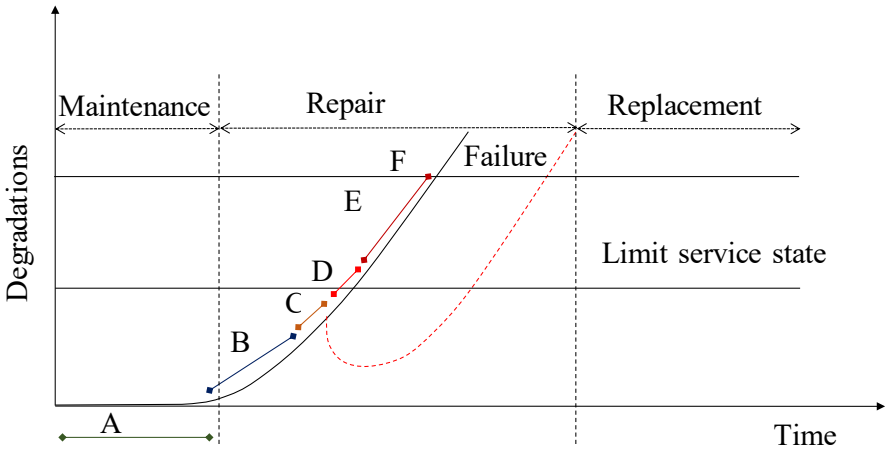

Figure 1. Evolution of the deterioration state of a reinforced concrete bridge: A: Very good; B: Good; C: Satisfactory; D: Bad; E: Very bad; F: Failure.

Monitoring the state condition of a bridge allows one to plan maintenance and repair activities. These activities, including replacement, have a considerable impact on the mobility of users and goods. Historical and current visual inspection data on bridge condition can be used to predict future bridge state conditions (Stewart, 2001). Inspectors are aware of the fast deterioration thanks to the visual inspection results and their follow-up is closer when degradation appears for the sensitive structural elements. Detailed historical inspection reports can be used to determine, during future inspections, the kinetics of degradation (CSA, 2014).

The evolution of the deterioration state of a reinforced concrete bridge and its rehabilitation can be represented with the state index indicator (Figure 1). A, B and C ratings mean very good, good and satisfactory conditions, respectively. D and E ratings are bad and very bad conditions, respectively (MTQ, 2018). The fundamental interest of a project manager is to understand perfectly the permissible service and failure limit states in order to plan appropriate repair activities (Ter Berg, *et al.,* 2019). Sustainability and resilience concepts for infrastructure systems are important for the community. Consequently, both of these concepts need to be integrated at the level of the infrastructure assessment to accurately determine the performance criteria of an infrastructure (Lounis and McAllister, 2016). This allows to consider the acceptable risk of service failure to minimize the consequences associated with the different limit states such as: accidents, interruptions of service to users and repair costs (Adey, *et al.,* 2003).

In this paper, a new approach to assess the condition of a typical structure is proposed. The methodology has been applied on a 60 year reinforced concrete bridge in Quebec (Figure 2).

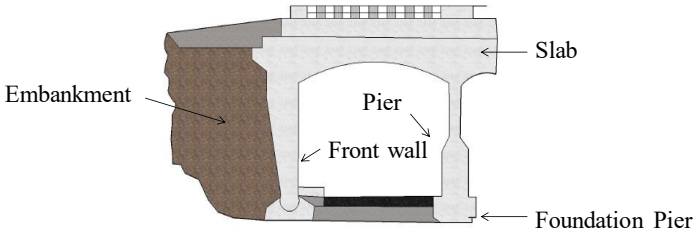

Figure 2. Half profile of the bridge (Quebec).

The bridge consists of a portico with two symmetrical spans (the free span is 11.4 m).The deck is a thick slab kind. Its thickness at the level of the supports is 1 m and its thickness at the centre is 0.60 m. The extremity supports and the central pier are continuous over the full width of the structure. It has four traffic lanes. The closure would cause significant inconvenience for the users which access to the lower four lanes under the bridge. This paper focuses on the degradation analysis process and the bridge assessment. This approach introduces a new management methodology for making an optimal and sustainable decision for bridge maintenance.

2 Degradation Analysis Process

A visual inspection of this bridge allowed us to evaluate its material and structural behavior state. The defects were identified during the visual inspection process, following the methodology in the inspection manual of the 'Ministère des Transports du Québec'(MTQ, 2017). The objective of the experimental procedure was to assess separately by the visual inspection method: (i) the material deterioration and (ii) the structural behavior of the bridge.

The purpose of material condition assessment is to provide with an assessment of the material defects detected on an element. To do this, four states ($\alpha, \beta, \gamma, \delta$) are defined, depending on the severity levels observed: no deterioration, moderate deterioration, significant deterioration, and very significant deterioration, respectively. The structural behavior evaluation rating of an element i (b_i rating) gives an indication of the impact of defects on its structural capacity, functionality, stability, user comfort and safety. The behavior rating for each bridge element is estimated with a four degradation scale: $1 \rightarrow 4$ (1 being the worst and 4 the best behavior).

Figure 3. Visual inspection of the front wall of the bridge.

The bridge was divided into elements, which were evaluated separately. As an example, the visual condition of the bridge front wall showed a reparation during the visual inspection (Figure 3).

Table 1. Visual inspection rating of material condition and behavior of the front wall of the bridge.

	Material (%)				Behavior
Ratings	α	β	γ	δ	b_i
Front wall	15	0	85	0	3

The inspection report for the front wall showed: α = 15% of the material has no deterioration and γ = 85 % has to be repaired, and the structural behavior reaches a rating of b_i = 3 because this defect affects appreciably the stability of the structure (Table 1). Similarly, the material and behavior defects for each element of the bridge were performed and presented in section 3 (Table 2).

The local rating on structural elements, as described above, allows one to identify the wrong behavior or a major deterioration on a part of the structure. This could provide the managers the idea to conduct some urgent local repair. However, structure managers are often interested to assess a global index of their structure. The global index allows managing the structure in the network scale and to plan its intervention agenda according to the whole network state, and with a minimum impact on the traffic. This global index gives an indication on the structural behavior and the material deterioration level of the entire structure, considering their impacts.

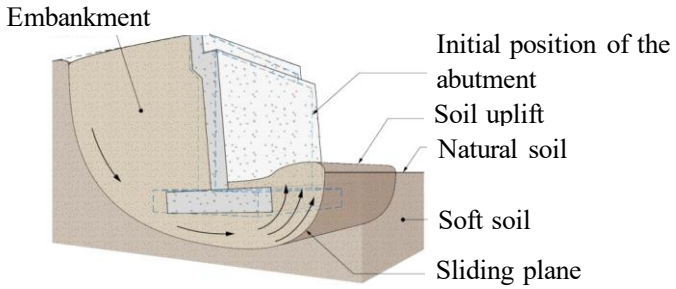

Figure 4. Example of abutment failure links (MTQ, 2017).

The following model proposes an evaluation of the global index as defects of each element (rating of each element) and the impact of the default on the structure by a decision tree analysis. The element ratings are merged considering failure assignment links to obtain the bridge global rating. For example, an abutment with a soil failure links has a repercussion on the abutment foundation (Figure 4). Additionally, the abutment foundation has a repercussion on the bridge seat, and the bridge seat has a repercussion on the slab. Let x_{ij} the defects affectation link between two elements *i* and *j*,

- x_{ij} = 1 when the degradation of an element i directly affects the adjacent element *j*;
- x_{ij} = 0 when there is no link between the defects of the adjacent elements i and *j*.

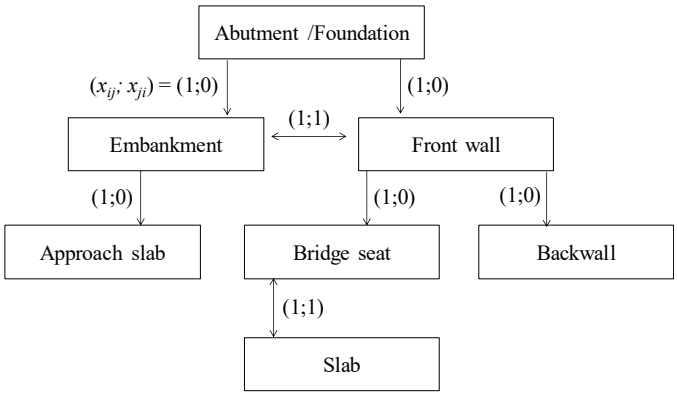

Figure 5. Failure links $(x_{ij}; x_{ji})$ for the abutment of the bridge.

In this way, $(x_{ij}; x_{ji}) = (1; 0)$ when element i is affected by element j but a defect of element j does not impact element i. Moreover, $(x_{ij}; x_{ji}) = (1; 1)$ when the defect of element i affects element j and, conversely, a defect of element j affects element i. The defect affectations of the bridge are given for the previous example with the abutment in Figure 5. This systematic approach is based on the qualitative and quantitative analysis of the visual inspection records. The parent-child principle, based on the decision tree analysis, enables to gradually identify the different links between the element failures at the local level. Thereafter, the bridge was assessed at the global level with different equations developed in the following section.

3 Bridge Assessment

For the bridge assessment, as initiated previously in section 2, two scales are developed: a local scale at the level of the structural element, and a global scale at the level of the structure. In this part, the rating of each element is calculated, and then a new model for assessing the material global index I_M and the behavior condition I_B of the bridge is proposed. A visual inspection was conducted in situ on the bridge to evaluate the material rating m_i and the behavior rating b_i of each element i. The visual inspection results for each bridge element are presented in Table 2. Some information is missing because the elements concerned were neither accessible nor visible.

Table 2. Visual inspection rating of material condition and behavior of the first span of the bridge.

Element	Material					Behavior
	α	β	σ	δ	m_i	b_i
Backfill Granular						4
Foundation Prefabricated concrete piles / abutment						4
Front Wall	15%	0	85%	0	2	3
Foundation Prefabricated concrete piles / Pier						4
Pier/Barrel	98%	0	2%	0	4	4

Running surface	80%	10%	10%	0	3	3
External side (North)	95%	0	5%	0	4	3
External side (South)	95%	0	5%	0	4	3
Deck Regular concrete slab	99%	0	1%	0	4	4
Sidewalk (North)	80%	20%	0	0	4	4
Sidewalk (South)	20%	0	80%	0	2	2
Guardrails Other Models	20%	80%	0	0	3	4

The four levels of material condition degradation (α to δ) were combined to obtain a single material rating m_i for each element i through equation (1):

$$m_i = \sum_{j=1}^{4} \frac{P_{j,i}}{P_{1,i}+\cdots+P_{4,i}}(5-j) \;\; with \;\; P_{1,i} = \alpha_i^{\exp n_{(\alpha)}}, \ldots, P_{4,i} = \delta_i^{\exp n_{(\delta)}} \tag{1}$$

P is the deterioration penalty of the bridge element i, n is the weight of the deterioration penalty, the exponential function represents a factor of the deterioration penalty, and j *is* the deterioration level. In this study, n is fixed for each level of degradation and defined such that the repair activities must be recommended for each element (Table 3) if at least one of the following conditions is true : $\delta > 1\%$; $\beta > 15\%$ and $\gamma > 13\%$; $\beta > 45\%$ and $\gamma = 13\%$; $\beta = 0$ and $\gamma \geq 15\%$. Such conditions allow to consider the moderate degradations β that are currently not considered by the traditional infrastructure managements.

Table 3. Weight of the penalty n assumed in this study.

Material state		$\boldsymbol{n}_{(.)}$
No deterioration	(α)	0
Moderate deterioration	(β)	0.15
Significant deterioration	(γ)	0.73
Very significant deterioration	(δ)	2.5

An example of the material rating calculation for the front wall of the bridge is illustrated by equation (2). m_i was evaluated using the extended visual inspection in Table 1:

$$m_i = \frac{15^{\exp 0}}{10{,}093}\cdot(5-1) + \frac{85^{\exp 0.73}}{10{,}093}\cdot(5-3) \approx 2 \tag{2}$$

Finally, the global index I_M and I_B are obtained from the rating m_i and b_i calculated for each element i and from the global assignment links (x_{ij}; x_{ji}). Intermediate equations R_M and R_B were defined to simplify the expression of I_M and I_B such as:

$$R_M = \sum_{i\epsilon W} A^{m_i} \sum_{j\epsilon W\setminus i} x_{ij} \text{ and } R_B = \sum_{i\epsilon W} A^{b_i} \sum_{j\epsilon W\setminus i} x_{ij} \tag{3}$$

where W is the global assignment links and A the factor of degradation evolution. A was assumed to be equal to 5 in this paper (W.R. de Sitter, 1984). Thus,

$$I_M(\%) = 100 * \left(1 - \left[\frac{R_M - R_{M_{best\,(\forall\, i,\ m_i=4)}}}{R_{M_{worst\,(\forall\, i,\ m_i=1)}} - R_{M_{best\,(\forall\, i,\ m_i=4)}}}\right]\right) \quad (4)$$

$$I_B\,(\%) = 100 * \left(1 - \left[\frac{R_B - R_{B_{best\,(\forall\, i,\ b_i=4)}}}{R_{B_{worse\,(\forall\, i,\ b_i=1)}} - R_{B_{best\,(\forall\, i,\ b_i=4)}}}\right]\right) \quad (5)$$

4 Results and Discussions

For the entire bridge, the results of the assessment model computations, based on the visual inspection, to assess its state condition are: I_M = 78.76 % and I_B = 79.97 % (Figure 6). The results of this model show that the deterioration level of the bridge, both in material and behavior is lower than the maximum accepted limit of 80 % defined by public sector managers. For structures in good condition, maintenance is recommended between 75 and 80 % as soon as possible. The present model allows one to provide advice for a maintenance to avoid further major repairs. However, using a model only based on visual inspection can only identified most obvious visible deteriorations (identified by C, D and E phases in Figure 1). The early signs of deteriorations, such as probable steel rebar corrosion (phase B), cannot be detected by the visual inspections to prevent the further deteriorations and anticipate preventive maintenance for cost efficiency.

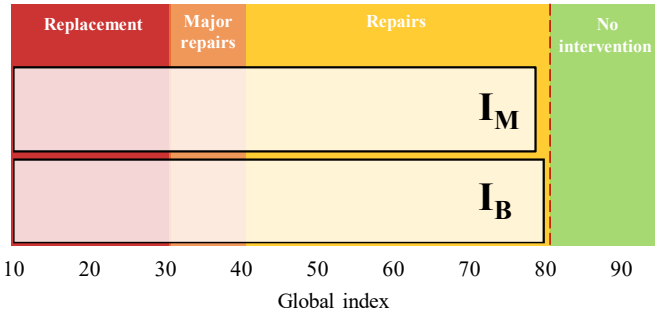

Figure 6. Bridge behavior and material condition by visual inspection.

5 Conclusion

The challenge for maintaining existing infrastructure plays an important role in a country's economical and social activities. This paper addresses the assessment of a bridge condition focusing on the resilience of each element at the local level to achieve a significant benefit at the global level of the bridge based on the visual inspection. The developed visual inspection model incorporates (in the assessment) the effects of moderate degradations, which are generally ignored by inspection managers. The consideration of those degradation levels revealed that the bridge needs maintenance. As a result, this assessment model based on visual

inspections allows to improve the degradation rating used by traditional public managers.

However, the uncertainty on the physical and chemical degradation observed by visual inspection have an important impact on the computation of the material and behavior indices. Further works in progress will improve the assessment of the bridge state condition by coupling the visual inspection model presented in this paper with a deterioration prediction model. This approach will refine the deterioration assessment to the early state phases (A and B phases in Figure 1) to forecast preventive maintenances.

Acknowledgements

The authors gratefully acknowledge the "Islamic Development Bank", "Fonds de recherche du Québec – Nature et technologies" for their financial support. The authors also want to thank "Service des infrastructures, de la voirie et des transports" of the city of Montreal and the "Quebec Ministry of Transportation" for their collaboration.

ORCID

Abdoul S. Bah: https://orcid.org/0000-0001-9245-9000
Thomas Shanchez: https://orcid.org/0000-0002-5929-7449
Yan Zhang: https://orcid.org/0000-0002-3222-2340
Kotaro Sasai: https://orcid.org/0000-0003-4483-5280
David Conciatori: https://orcid.org/0000-0002-1187-4868
Nicolas Zufferey: https://orcid.org/0000-0002-5500-010X

References

Adey, B., Hajdin, R. and Brühwiler, E. (2003). Supply and Demand System Approach to Development of Bridge Management Strategies. *Journal of Infrastructure Systems*, *9*(3), 117-131. doi.org/10.1061/(ASCE)1076-0342(2003)9:3(117)

Angst, U. M. (2019). Predicting the time to corrosion initiation in reinforced concrete structures exposed to chlorides. *Cement and Concrete Research*, *115*, 559-567.doi.org/10.1016/j.cemconres.2018.08.007

ASCE. (2017). Infrastructure Report Card. www.infrastructurereportcard.org/wpcontent/uploads/2016/10/2017-Infrastructure-Report Card.pdf

Conciatori, D., Brühwiler, E. and Linden, C. (2018). Numerical simulation of the probability of corrosion initiation of RC elements made of reinforcing steel with improved corrosion performance. *Structure and Infrastructure Engineering*, *0*(0), 1-9. doi:10.1080/15732479.2018.1446180

CSA. (2014). *S6-14 Code canadien sur le calcul des ponts routiers*. store.csagroup.org/

Lounis, Z. and McAllister, T. P. (2016). Risk-Based Decision Making for Sustainable and Resilient Infrastructure Systems. *Journal of Structural Engineering*, *142*(9), F4016005. doi.org/10.1061/(ASCE)ST.1943-541X.0001545

MTQ. (2017). Manuel d'inspection des structures. www3.publicationsduquebec.gouv.qc.ca › guides ›guide24.fr.

MTQ. (2018). Bilan de l'état des structures. www.transports.gouv.qc.ca/fr

Roelfstra, G., Hajdin, R., Adey, B. and Brühwiler, E. (2004). Condition Evolution in Bridge Management Systems and Corrosion-Induced Deterioration. *Journal of Bridge Engineering*, *9*(3), 268-277. doi.org/10.1061/(ASCE)1084-0702(2004)9:3(268)

RRN. (2010). Réseau Routier National du Canada. www.bv.transports.gouv.qc.ca/per/1018796/04_2010.pdf

Stewart, M. G. (2001). Effect of Construction and Service Loads on Reliability of Existing Rc Buildings. *Journal of Structural Engineering*, *127*(10), 1232. doi.org/10.1061/(ASCE)0733-9445(2001)127:10(1232)

Ter Berg, C. J. A., Leontaris, G., van den Boomen, M., Spaan, M. T. J. and Wolfert, A. R. M. (2019). Expert judgement based maintenance decision support method for structures with a long service-life. *Structure and Infrastructure Engineering*, 1-12. https://doi.org/10.1080/15732479.2018.1558270

W.R. de Sitter. (1984). Costs of service life optimization « The Law of Fives » CEB-RILEM Workshop on Durability of Concrete Structures (Copenhagen, Denmark, May 18-20, 1983).

XV International Conference on Durability of Building Materials and Components
DBMC 2020, Barcelona
C. Serrat, J.R. Casas and V. Gibert (Eds)

Condition-Based Maintenance Models for Stone Claddings

Cláudia Ferreira[1], Ana Silva[1], Jorge de Brito[1] and Luís C. Neves[2]

[1] CERIS, Instituto Superior Técnico, University of Lisbon, Av. Rovisco Pais, Lisbon, Portugal, claudiaarferreira@tecnico.ulisboa.pt, anasilva931@msn.com, jb@civil.ist.utl.pt

[2] Resilience Engineering Research Group, University of Nottingham, Nottingham, United Kingdom, luis.neves@nottingham.ac.uk

Abstract. *Most of the maintenance actions in the construction sector are still reactive and sporadic, based on subjective criteria. Usually, maintenance actions are performed when the building already presents unacceptable degradation levels, and the reactive maintenance actions carried out only correct the anomalies observed, not dealing with the causes, thus leading to additional costs and risks for owners. This study establishes a condition-based maintenance model applied to natural stone claddings. This model has a stochastic nature, in order to deal with the complexity of the degradation phenomena. For that purpose, Petri nets are used, providing an efficient tool to model the deterioration process and the maintenance decisions considered for stone claddings. The maintenance model is a full life-cycle model that encompasses: (i) the stochastic assessment of the degradation condition of the stone claddings, and their expected service life; (ii) and the inspections, maintenance and renewal processes. In this study, three maintenance strategies are considered: (i) major intervention only; (ii) combination of minor and major interventions; and (iii) combination of cleaning operations, minor and major interventions. The impact of the different maintenance strategies in the future performance and remaining service life of stone claddings is analysed, also evaluating the economic impact of each maintenance plan.*

Keywords: *Degradation, Service Life, Maintenance, Natural Stone Claddings, Petri Net.*

1 Introduction

The awareness of the building managers and/or owners about the need to maintain their assets more efficiently has increased over the last years (Silva and de Brito, 2019). The maintenance of buildings' envelope elements is not yet a first concern (Forster and Kayan, 2009; Thomsen and van der Flier, 2011). Usually, maintenance actions are carried out when the buildings' envelope elements are already severely degraded, or reactive maintenance actions are performed to react to failures and do not deal with the causes (Mobley, 2014), thus leading to additional costs and risks (Dann and Cantell, 2005). Furthermore, regular inspections to assess the condition and maintenance actions on these elements are not mandatory (Shohet *et al*., 2002). The definition of the end of their service life is subjective, based on the outward appearance, owners/users' demands and the funds available for maintenance works (Emídio *et al*., 2014).

Therefore, the development of more efficient methodologies for the implementation of strategic planning of maintenance actions is important (Lacasse and Vanier, 1996; Aikivuori, 1999). The existing tools have several limitations (Ashworth, 1996; Sherwin, 2000; Forster and Kayan, 2009): scarce data about maintenance protocols; poor or non-existent implementation of strategic procedures; lack of information regarding durability and performance of buildings; insufficiently accuracy of the existing maintenance policies; and lack of infor-

doi:10.23967/dbmc.2020.026

mation about global costs associated with repairs. This information is extremely relevant to managers, insurers, owners or users, and allows the adoption of more sustainable and durable solutions at the design stage and for the definition and implementation of reliable maintenance policies, enabling a more rational management of the building stock.

The main purpose of this study is the development and implementation of a condition-based maintenance model for Natural Stone Claddings (NSC). The proposed model is implemented using a stochastic Petri Nets (PN) framework. The case study selected is composed of 203 NSC, located in Portugal. The sample was established based on the diagnosis of the degradation condition of these claddings in-service performance, through *in situ* visual inspection. In the methodology developed, three maintenance strategies are assessed: (i) major intervention only; (ii) combination of minor and major interventions; and (iii) combination of cleaning operations, minor and major interventions. The first one represents the most common solution adopted by buildings' owners. The other two are analysed in order to evaluate the impact of the different alternatives in the claddings' service life and in the whole-life maintenance costs, for the period under analysis.

2 Petri Nets (PN)

PN are a mathematical and graphical modelling tool, introduced by Carl A. Petri in 1962 (Petri, 1962), suitable for description of systems whose dynamics are characterized as being concurrent, asynchronous, distributed, parallel, nondeterministic, and/or stochastic (Murata, 1989).

In a few words, PN can be defined as a bipartite directed graph that comprises two types of nodes, places (representing a state or condition of the system, drawn by circles) and transitions (representing an action, denoted by bars and/or boxes). Both nodes are linked by directed arcs. An arc connects a place with a transition, or vice-versa. Tokens (drawn by small black dots) are stored in places and its distribution (denoted by marking, M) represents the current state of the system. Transitions are responsible for the evolution of the system from one state to another (movement of the tokens between places). A transition is enabled to fire when, in all input places, there is at least one token. Furthermore, it is possible to assign to each transition a firing rate that can be deterministic or modelled by any probabilistic distribution. Figure 1 shows an example of PN composed of three places (p_1, p_2, p_3) and one transition (t_1). In this example, the transition is not enabled to fire since place p_2 is empty.

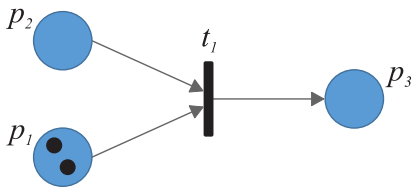

Figure 1. Example of a Petri net.

3 Maintenance Model

The maintenance model, based on the Petri nets methodology, proposed to assess the performance of NSC, is presented in Figure 2. Below, the meaning of each part of the model is briefly described. More information about the model can be seen in Ferreira *et al.* (2019).

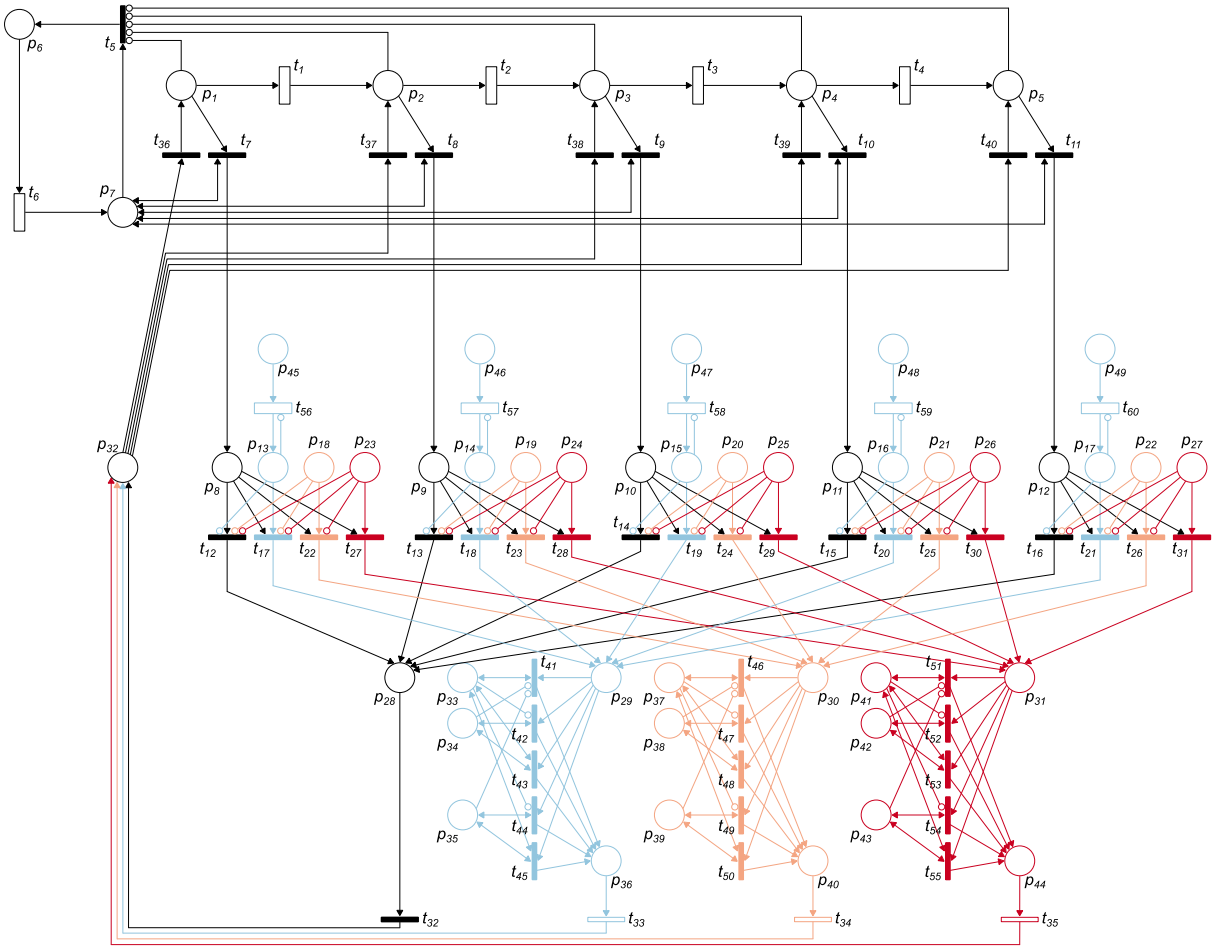

Figure 2. Petri net scheme of the maintenance model proposed.

The maintenance model implemented is a condition-based model, where it is assumed that maintenance actions are planned after the condition has been assessed through inspections. In other words, the need for a maintenance action is assessed during inspection, and then, according to the current observed degradation condition of the component under analysis, a decision on intervening is made. The model can be divided in several main parts: (i) degradation process; (ii) inspection process; (iii) maintenance process; (iv) modelling of the maintenance actions; and (v) periodicity of the cleaning operations.

In Figure 2, the degradation process is depicted by five places (p_1 to p_5) and four timed transitions (t_1 to t_4). Each place denotes a condition level defined in the classification system adopted, where places p_1 and p_5 represent, respectively, the best and worst condition level of the classification system. The timed transitions, located between places, model the transition times of moving between different condition levels. The transition times are samples from the appropriate distributions that can be obtained by studying the degradation characteristics of the NSC (Le and Andrews, 2016). The classification system adopted (Table 1), proposed by Silva *et al.* (2011), is based on visual inspections of the extent of the cladding area affected by the different anomalies. The severity of degradation index, S_w, is defined with the intent of expressing the overall degradation condition of these claddings, and is given by the ratio between the area affected by the defects

observed in a NSC, weighted according to their severity, and a reference area equivalent to the total cladding area with the highest possible level of degradation (Equation 1) (Silva *et al*., 2016).

$$S_w = \frac{\sum(A_n \times k_n \times k_{a,n})}{A \times \sum k} \quad (1)$$

where S_w represents the severity of degradation (in %), k the multiplying factor corresponding to the highest degradation condition level of the cladded area A, A_n the cladding area affected by any defect n (in m^2), k_n the multiplication factor for the defect n, in terms of their degradation condition, and A the total area of the NSC (in m^2). More information about the classification of defects and the determination of S_w can be found in Silva *et al*. (2016).

Table 1. Degradation conditions for natural stone cladding.

Degradation condition	Severity of degradation
Condition A: No visible degradation	$S_w \leq 1\%$
Condition B: Good	$1\% < S_w \leq 8\%$
Condition C: Slight degradation	$8\% < S_w \leq 20\%$
Condition D: Moderate degradation	$20\% < S_w \leq 45\%$
Condition E: Generalized degradation	$S_w \geq 45\%$

The inspection process is modelled through the cycle formed by nodes: p_6 - t_6 - p_7 - t_5 - p_6 (Andrews, 2013). A token in place p_6 means that an inspection should not be performed at that time and enables transitions t_6 that manages the time intervals between inspections, θ. A token in place p_7 means that it is time to perform an inspection, enabling several actions. First, it enables one of the transitions t_7 to t_{11}. The firing of one of these transitions allows revealing the true condition of the cladding. A token in places p_8, p_9, p_{10}, p_{11} or p_{12} means, respectively, that the true condition of the cladding is A, B, C, D or E. After that, transition t_5 is enabled, which causes the token in place p_7 to return to place p_6 to wait for the next inspection.

The maintenance process is represented by places p_{13} to p_{32} and by the transitions t_{12} to t_{40}. Here, the available types of interventions are analysed, according to the observed conditions. In the proposed methodology, three intervention levels are considered: cleaning operations, minor and major interventions. This information is introduced in the model through places p_{13} to p_{27}. Tokens in places p_{13} to p_{17} mean cleaning operations must be done, in p_{18} to p_{22} that a minor intervention is needed, and in p_{23} to p_{27} that a major intervention is required. If there is no token in these places, no interventions are performed. Otherwise, if, for the same condition, there is more than one type of intervention available, the highest impact intervention is performed. A token in places p_{28}, p_{29}, p_{30} or p_{31} indicates, respectively, that no intervention, cleaning operations, minor or major interventions are required. After that, the token returns to the degradation process by place p_{32} and transitions t_{36} to t_{40}.

In Figure 2, the cleaning operations is modelled by places p_{33} to p_{36} and by transitions t_{41} to t_{45}. The marking of places p_{33}, p_{34} or p_{35} means, respectively, that the cleaning operation, when applied, has the effect of improving the condition, supressing the degradation process or reducing the deterioration rate. Then, depending on the impact of the cleaning operation on the cladding, only one transition can be fired. For the minor (places p_{37} to p_{40} and transitions t_{46} to t_{50}) and major (places p_{41} to p_{44} and transitions t_{51} to t_{55}) interventions, the same methodology is implemented.

In this model, the periodicity of the cleaning operations is considered through places p_{45} to p_{49} and timed transitions t_{56} to t_{60}. The introduction of the information that this intervention is available in a given condition level is performed by placing tokens in places p_{45} to p_{49}. Transitions t_{56} to t_{60} are associated with a delay that allows, at the end of θ_{clean} time units, the tokens present in places p_{45} to p_{49} to be returned to places p_{13} to p_{17}, allowing cleaning operations to be performed at the next inspection time, if the imposed constrains are complied with.

4 Case Study: Natural Stone Claddings

The case study under examination is composed of 203 NSC directly adhered to the substrate, located in Portugal. The degradation condition of each cladding in the data set was analysed based on *in situ* visual inspections. The methodology described, was applied to analyse the degradation of NSC over their lifetime. A 150-year time horizon was considered and the cladding is expected to be in perfect conditions at the beginning of the analysis (in condition A).

4.1 Probabilistic Analysis of the Deterioration Process

To find the best distribution that describes the degradation characteristics of the NSC, the degradation process (without maintenance) is applied to the complete sample. Table 2 shows the optimized estimation parameters obtained for the three distribution functions (Exponential, Weibull and Lognormal) analysed, in terms of mean time in each degradation condition and standard deviation, as well as the respective log-likelihood value.

Table 2. Optimal parameters obtained using the three distributions analysed.

Distributions	Mean [years]				Standard deviation [years]				-log L
	T_A	T_B	T_C	T_D	T_A	T_B	T_C	T_D	
Exponential	5.8	51.6	84.9	1.67×10^7	5.8	51.6	84.9	1.67×10^7	161.89
Weibull	4.1	42.9	22.4	49.9	7.0	10.3	1.4	2.4	125.56
Lognormal	4.2	44.0	24.3	1.54×10^6	11.3	13.3	0.3	2.50×10^7	127.12

The parameters of the probability density function are fitted to the historic database based on the concept of maximum likelihood (Kalbfleisch and Lawless, 1985). The likelihood, L, is defined as the predicted probability of occurrence of the observed transitions (Equation 2).

$$L = \prod\prod\prod p_{ij} \Longrightarrow \log L = \sum\sum p_{ij} \tag{2}$$

where p_{ij} is the probability of transition from deterioration condition i to j.

The results allow concluding that two-parameter distributions (Weibull and Lognormal) show a better adjustment to the data set than the Exponential distribution. Since Weibull distribution is the one that shows a minor log-likelihood, log L, value and, consequently, a better fit to the historical data, this distribution is chosen to sample the transitions times that specify the movement between different conditions levels.

4.2 Maintenance Strategies and Costs

In this study, three Maintenance Strategies (MS) are considered: (i) major intervention only (MS1); (ii) combination of minor and major interventions (MS2); and (iii) combination of clean-

ing operations, minor and major interventions (MS3). The different strategies were defined based on previous works and on experts' judgement. Table 3 presents the fixed costs, application zones and impacts of the different types of interventions considered. It was assumed that an *Alpinina* marble cladding, directly adhered to the substrate, was used. For example, a cleaning operation of NSC has a cost of 31.37 €/m^2, is applied in condition B and improves it to condition A with a probability of 15% or causes no significant improvement with a probability of 85%. Regarding the inspections, a deterministic periodicity of 5 years is considered.

Table 3. Fixed costs, application zones and impacts of the different types of interventions considered.

Interventions	Cost [€/m^2]	Application zone	Impact of the maintenance actions [%]		
			P_A	P_B	P_c
Inspections	1.03	All	-	-	-
Cleaning operations	31.37	B	15.0	85.0	-
Minor interventions	68.80	C	-	80.4	19.6
Major interventions	149.51	D, E	100.0	-	-

4.3 Comparison of the Different Maintenance Strategies

Figure 3 compares the degradation curves obtained for the three MS and for the situation without interventions. The results show that the proposed MS have a significant impact on the mean severity of degradation. For all MS, the mean severity of degradation is less than 8% (condition B), with MS3 showing the greatest variation over time.

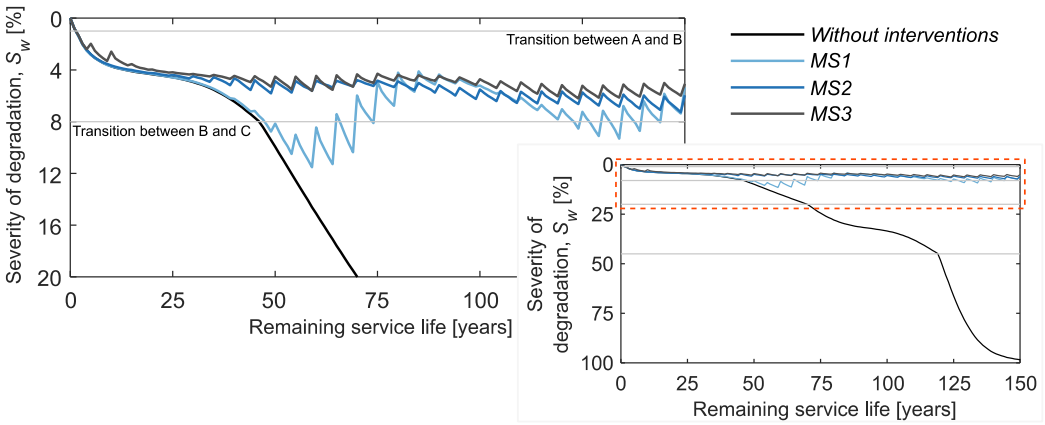

Figure 3. Comparison of the degradation curves over time for all maintenance strategies.

On the other hand, if the cumulative costs are analysed (Figure 4), MS2 has the lowest cumulative costs when the discount rate is 0% (Figure 4a) and MS1 for a discount rate of 6% (Figure 4b). For both rates, MS3 is the one with the highest cumulative maintenance costs.

The discount rate is used to balance the initial investment costs against the future maintenance cost. Since this parameter is difficult to predict, two extreme values were considered to assess the sensitivity of the results. Its choice is mainly a political decision, and the value usually ranges between 4% and 6% (van Noortwijk and Frangopol, 2004).

Finally, the number of interventions and the remaining service life for the three MS are analysed (Figure 5). According to Silva *et al*. (2016), the end of the service life of a NSC varies

between 68 and 90 years. The end of the service life occurs when a major intervention is performed. If the first major intervention is analysed (Figure 5a), for MS1, in year 85 there is a probability of 90% of NSC having been replaced at least once. The value agrees with the range suggested by Silva *et al*. (2016). On the other hand, for MS2, in year 150 there is only a 58% probability that the NSC has been replaced at least once, and, for EM3, this percentage in the same year is reduced to 28%. From this it results that combining major intervention with other intervention works, such as minor interventions and cleaning operations, increases the service life of NSC. Similar observations can be made for the minor intervention (Figure 5b). Considering cleaning operations in MS3 postpones the need of a minor intervention.

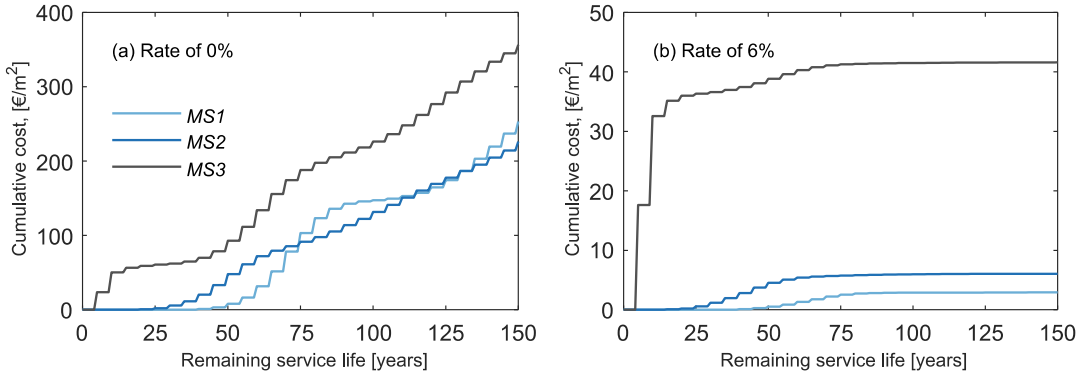

Figure 4. Comparison of the cumulative costs over time for all maintenance strategies.

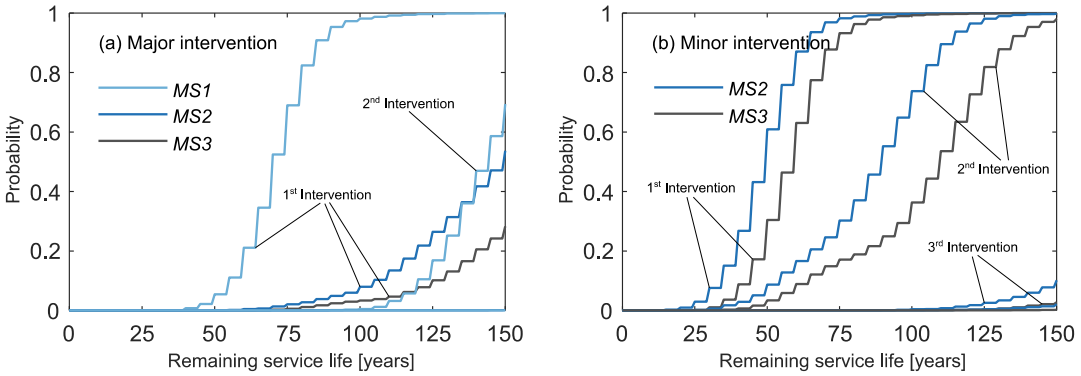

Figure 5. Comparison of the cumulative distribution function of the number of interventions.

5 Conclusions

In this study, a maintenance model, based on the PN formalism, is proposed to analyse the impact of different MS to control deterioration conditions of NSC. In the proposal methodology, three MS are analysed. These are composed by three different intervention levels: cleaning operations, minor and major interventions. The results reveal that: MS1 presents the lowest cumulative cost for a discount rate of 6%. In MS1, only replacement of the cladding is considered, which does not allow improving the condition over time, as well as its service life. MS3 shows the best degradation results but leads to the highest cumulative costs over the claddings' lifetime. MS2 seems to be the most rational and adequate solution, according to the model's assumptions, since it allows increasing the service life and the cumulative costs are competitive when compared with those of

MS1. However, in the end, the choice of the best MS is always assumed by the building managers and/or owners and depends on their budgets and target condition for the cladding.

Acknowledgements

The authors acknowledge the support of the Foundation for Science and Technology, CERIS Research Centre and Instituto Superior Técnico.

ORCID

Ana Silva: http://orcid.org/0000-0001-6715-474X
Jorge de Brito: http://orcid.org/0000-0001-6766-2736
Luís C. Neves: http://orcid.org/0000-0001-5034-8417

References

Aikivuori, A.M. (1999). Critical loss of performance - What fails before durability. Performance Based Methods for Service Life Prediction Reports compiled, CIB W80.

Andrews, J. (2013). A modelling approach to railway track asset management. *Journal of Rail and Rapid Transit*, *227*(1), 56-73.

Ashworth, A. (1996). Estimating the life expectancies of building components in life-cycle costing calculations. *Structural Survey*, *14*(2), 4-8.

Dann, N. and Cantell, T. (2005). Maintenance: from philosophy to practice. *Journal of Architectural Conservation*, *11*(1), 42-54.

Emídio, F., de Brito, J., Gaspar, P. L. and Silva, A. (2014). Application of the factor method to the estimation of the service life of natural stone cladding. *Construction and Building Materials*, *66*, 484-493.

Ferreira, C., Neves, L.C., Silva, A. and de Brito, J. (2019). Stochastic maintenance models for ceramic claddings. *Structure and Infrastructure Engineering, 16*(2), 247-265.

Forster, A.M. and Kayan, B. (2009). Maintenance for historic buildings: a current perspective. *Structural Survey*, *27*(3), 210-229.

Kalbfleisch, J.D. and Lawless, J.F. (1985). The analysis of the panel data under a Markov assumption. *Journal of the American Statistical Association*, *80*(392), 863–871.

Lacasse, M.A. and Vanier, D.J. (1996). A review of service life and durability issues. In *Proceedings of the VII International Conference on Durability of Building Materials and Components*, Stockholm, Sweden, Vol. 2, 857-866.

Le, B. and Andrews, J. (2016). Petri net modelling of bridge asset management using maintenance-related state conditions. *Structure and Infrastructure Engineering*, *12*(6), 730-751.

Mobley, R.K. (2014). *Maintenance Engineering Handbook*. New York, NY: MaGraw-Hill Education.

Murata, T. (1989). Petri nets: Properties analysis and applications. *Proceedings of the IEEE*, *77*(4), 541-580.

Petri, C.A. (1962). *Kommunikation mit automaten* (in German), PhD Thesis, Institut für Instrumentelle Mathematik an der Universität Bonn, Bonn, Germany.

Sherwin, D. (2000). A review of overall models for maintenance management. *Journal of Quality in Maintenance Engineering*, *6*(3), 138-164.

Shohet, I.M., Puterman, M. and Gilboa, E. (2002). Deterioration patterns of building cladding components for maintenance management. *Construction Management and Economics*, *20*(4), 305-314.

Silva, A., de Brito, J. and Gaspar, P.L. (2011). Service life prediction model applied to natural stone wall claddings (directly adhered to the substrate). *Construction and Building Materials*, *25*(9), 3674-3684.

Silva, A., de Brito, J. and Gaspar, P.L. (2016). *Methodologies for service life prediction of buildings: With a focus on façade claddings*. Switzerland: Springer International Publishing.

Silva, A. and de Brito, J. (2019). Do we need a buildings' inspection, diagnosis and service life prediction software?. *Journal of Building Engineering*, *22*, 335-348.

Thomsen, A. and van der Flier, K. (2011). Understanding obsolescence: a conceptual model for buildings. *Building Research & Information*, *39*(4), 352-362. doi: 10.1080/09613218.2011.576328

van Noortwijk, J.M. and Frangopol, D.M. (2004). Two probabilistic life-cycle maintenance models for deteriorating civil infrastructures. *Probabilistic Engineering Mechanics*, *19*(4), 345–359.

XV International Conference on Durability of Building Materials and Components
DBMC 2020, Barcelona
C. Serrat, J.R. Casas and V. Gibert (Eds)

Detection Sensitivity of Iron-Foil Corrosion Sensor in Simulated Concrete Solution

Akira Eriguchi[1], Hiromi Fujiwara[2], Hayato Itaya[3], Toru Wakabayashi[3], Shunsuke Otani[3] and Yukitoshi Isaka[1]

[1] Taiheiyo Cement Corporation Central Research Laboratory, Osaku, Sakura, Chiba, Japan, akira_eriguchi@taiheiyo-cement.co.jp

[2] Utsunomiya University, Yoto, Utsunomiya, Tochigi, Japan, fhiromi@cc.utsunomiya-u.ac.jp

[3] Nakabohtec Corroosion Protecting Corporation, Innovation and Technology Center, Nakaarai, Ageo, Saitama, Japan, h.itaya@nakabohtec.co.jp

Abstract. *This examined the performance of the iron-foil sensor in concrete and its relationship with the amount of chloride in the solution simulating concrete. The corrosion sensor reacted at a chloride ion concentration of 500 ppm. From the results, it was inferred that the sensor has a high sensitivity. Furthermore, to evaluate the performance of the sensor, it was built a wireless system using radio-frequency identification (RFID), embed it into an actual concrete structure, and subsequently initiate observation.*

Keywords: *Corrosion, Sensor, Chloride Ion, Monitoring, Solution Simulating Concrete.*

1 Introduction

Corrosion of the internal steel in reinforced concrete structures is a degradation phenomenon that causes cracks and significantly reduces structural strength. The ASTM C876-15 (2015) standard self-potential method and polarization resistance method of the CEB Working Group (1997) are widely used methods of confirming the soundness of the internal reinforcing steel. However, since those methods require running cable to the reinforcing steel, in practice they can require breaking parts of the structure. Even if the cables are installed in advance, it is difficult to ensure their long-term durability. Moreover, those methods represent a post hoc diagnostic approach that checks for corrosion for purposes of corrective maintenance. Once corrosion is confirmed, deterioration has likely already advanced.

For this reason, Lee and Shin (2003) and Takewaka and Yamamoto (2001) have been developing and studying sensors for monitoring corrosion in steel. In order to enable preventive maintenance by predicting the possibility of corrosion in advance, many of these sensors electrically identify corrosion, not in the reinforcing steel itself but in steel materials that act as a proxy for the reinforcing steel. Therefore, the sensors are able to identify corrosion with no damage to the structure. Furthermore, by identifying the risk of corrosion of the reinforcing steel at an early stage, the sensors enable a more efficient consideration of follow-up countermeasures.

We have developed a corrosion environment sensor that consists of a reinforced iron-foil. If the corrosion factors reach the sensor, the sensor itself will corrode and rupture. The sensor

doi:10.23967/dbmc.2020.029

is designed to detect the occurrence of corrosion by sensing the change in electrical resistance when the rupture occurs. To evaluate the performance of the corrosion environment sensor, we varied the concentration of chloride ions in a simulated concrete test solution and determined the point at which the sensor ruptured, thereby verifying the sensitivity of the corrosion environment sensor to the chloride concentration.

In order to develop the corrosion environment sensor into a practical system, we additionally designed a completely non-destructive monitoring system using passive radio-frequency identification (RFID), a close-proximity wireless technology, and installed it in an actual structure for use as a measurement and monitoring system.

2 Structure and Mechanism of the Corrosion Environment Sensor

The sensor consists of a circuit formed on an iron-foil positioned on top of a resin film as shown in Figure 1. The iron-foil is 0.01 mm thick and made of pure iron. The circuit is similar to a simple single conducting wire. When measured, the value of the electrical resistance between both ends is 15 Ω or less. However, if the sensor itself becomes corroded enough to disconnect, it will show a resistance of 100 Ω or more. Precious metals are deposited on the surface at the ends of the iron-foil to serve as cathode electrodes, making the film highly sensitive to corrosion. As shown in Figure 2, the iron-foil sensor is integrated into a ceramic housing and the surface is covered by mortar. This structure is designed to maintain an alkaline environment that prevents corrosion due to atmospheric factors, such as humidity.

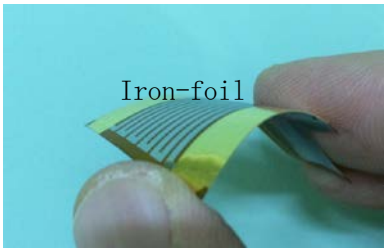

Figure 1. Appearance of the corrosion sensor.

3 Performance Testing of the Sensor

Since the sensor is made of iron, which is the main component of the reinforcing steel inside the concrete, it also suffers corrosion as corrosion factors from the environment penetrate into the concrete, increasing the risk of corrosion of the reinforcing steel. The sensor simply evaluates whether or not the iron has corroded, but cannot determine the cause of corrosion.

Although corrosion degradation of reinforcing steel is thought to occur due to multiple factors, the main factors include the rupture of the passive film due to salinity, reduction of alkali anti-corrosion protection due to carbonation, and penetration of moisture and oxygen. In Japan, the specifications of the Japan Society of Civil Engineers warn that steel corrosion occurs when the concentration of chloride ions in the concrete reaches 1.2 kg/m^3 or higher. There are also regulations in each country on the permissible chloride concentrations in the materials that make up concrete. In Japan, the concentration is generally capped at 0.30 kg/m^3.

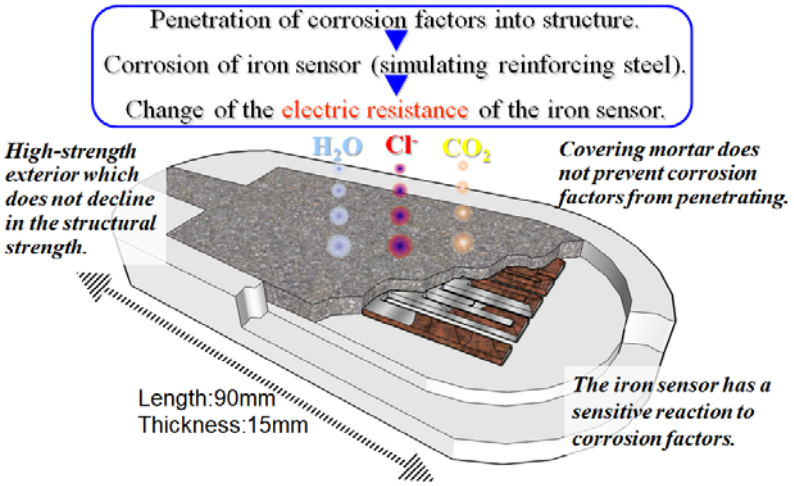

Figure 2. Overview of the corrosion sensor and its working.

From this perspective, we can evaluate the performance of the sensor by quantitatively capturing the penetration of chloride ions, which can cause degradation, and determining the relationship between the concentration of chloride ions and the detection performance of the sensor.

3.1 Overview of Performance Testing of the Corrosion Environment Sensor

Performance testing of the sensor was conducted in a saturated calcium hydroxide solution to mimic the internal environment concrete. This was done to maintain an environment of uniform pH and chloride content in the solution and to make it easy to retrieve the sensor as needed during testing to visually check the specimen (sensor) and the iron pieces used for comparison.

Figure 3 shows the configuration of the environment for performance testing of the sensor. An air pump was used to vent air into the saturated aqueous solution of calcium hydroxide. The carbon dioxide in the air reacted with the calcium hydroxide test solution, preventing the lowering of its pH, as indicated in Table 1. After the carbon dioxide was removed, the air was fed into the test tank. We periodically measured the pH of the test solution to ensure that its pH did not change.

If the sensor reached a resistance value of 100 Ω or more after the start of the test, it was considered ruptured. We tested five sensors per test level.

3.2 Verification of Corrosion Rate Using Steel

In order to understand the corrosion rate of each chloride ion concentration in the simulated concrete test solution, we immersed a sample of SS400 steel, of dimensions 20 × 80 × 2 mm, in the solution using the same test equipment configuration used to test the corrosion environment sensor.

To obtain the corrosion rate of the steel, we immersed a steel sample in each of the aqueous solutions shown in Table 1 and measured the reduction in the mass of the steel before and after the test. We tested five steel sheets per test level.

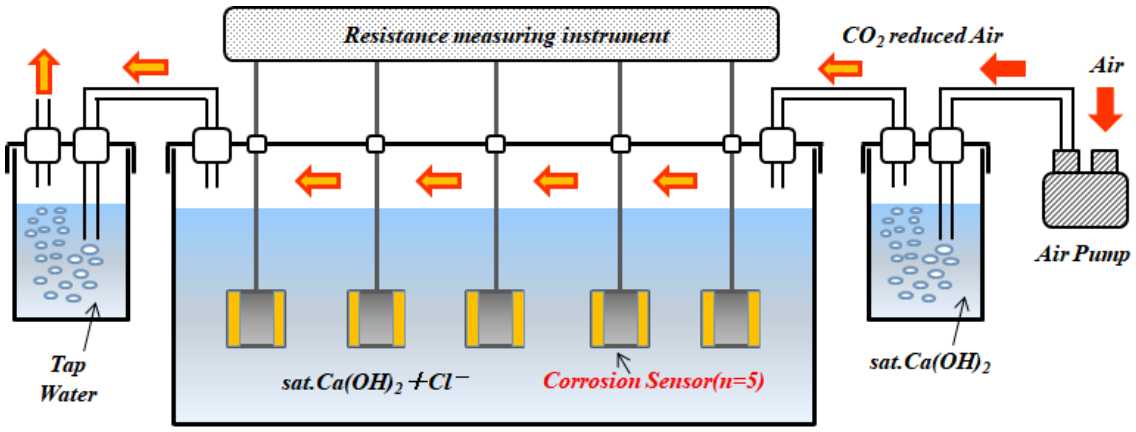

Figure 3. Configuration of the corrosion sensor evaluation experiment.

Table 1. List of aqueous solutions used to test the corrosion rate of the steel sample.

	Cl^- (ppm)
sat. $Ca(OH)_2$ pH 12.3 to 12.5	200
	500
	1000
	2000
	5000

To obtain the reduction in the mass of the steel after rust removal, we immersed the steel in a mixed solution of hydrochloric acid and corrosion inhibitors for a period of 36 days and then measured its mass. We subtracted this value from the mass of the steel measured before the test to obtain the reduction in mass.

4 Results of Performance Testing

4.1 Detection Performance of the Corrosion Environment Sensor

Figure 4 shows the time taken for each sensor to rupture. The earliest rupture occurred at the chloride ion concentration of 5000 ppm. At the chloride ion concentration of 200 ppm, no rupture was observed, even after 2500 hours. The graph shows that the sensor rupture time tends to increase as the concentration of chloride ions decreases. In particular, the chloride ion concentration of 500 ppm produced the longest rupture time, which was 1700 hours (about 70 days). The chloride ion concentrations of 500 ppm and 5000 ppm showed a difference in average rupture time of about 1000 hours.

Figure 5 shows the result of converting the horizontal axis of Figure 4 to represent the relative concentration between Cl^- and OH^- at a pH of 12.1. The sensors ruptured when Cl^-/OH^- was 0.71 or greater. There are various theories about steel corrosion thresholds based

on Cl^-/OH^-, but given that our test results are within the range of 0.6 to 1.0 reported of D. A. Hausmann (1967) in related literature, we can conclude that the sensor is able to rust and rupture with reasonable sensitivity.

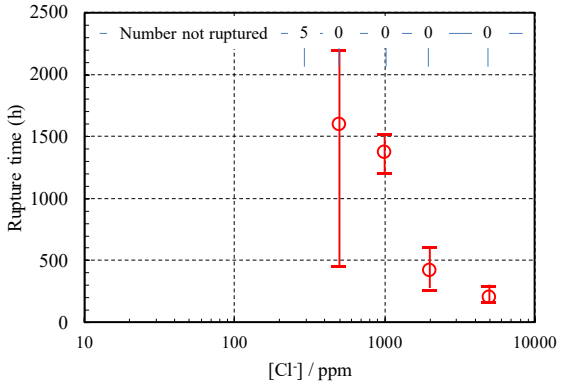

Figure 4. Rupture time of corrosion environment sensor at each chloride ion concentration.

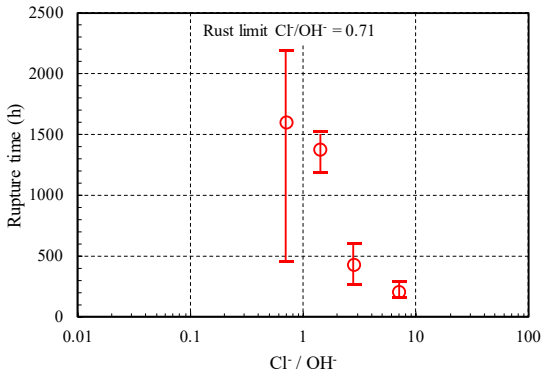

Figure 5. Relationship between sensor rupture time and Cl-/OH-.

4.2 Results of Steel Corrosion Rate Test

Figure 6 shows the corrosion rate of steel in the different aqueous solutions. In this test, the steel in the test solution with a chloride ion concentration of 200 ppm showed a corrosion rate of 0 mm/y, i.e. no corrosion. As the concentration increases from 500 ppm, the corrosion rate also increases. These results are similar to the differences in the rupture time of the sensors shown in Figure 4. At the chloride ion concentration of 500 ppm, a very small corrosion rate of 0.0001 mm/y was observed. Since the corrosion rate of steel in seawater is 0.1 mm/y, the fact that the sensor ruptures under conditions at which the corrosion rate of steel is approximately 0.001 mm/y suggests that the sensor has a highly sensitive reaction to the chloride ion concentration.

In alkaline environments, steel tends to form a passive film due to the supply of oxygen. In our testing environment, the air pump is used to inject oxygen partial pressure into the simulated concrete test solution under conditions that are close to natural. In evaluating the corrosion rate, it is important to prevent excessive increases in the oxygen partial pressure.

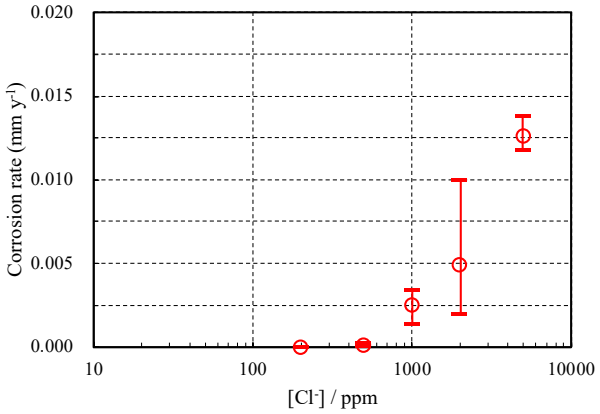

Figure 6. Corrosion rate of steel at each chloride ion concentration.

5 Measurement System of the Sensor

As explained above, the sensor detects whether the environment has become corrosive by measuring the electrical resistance in the sensor itself. This makes it easy to identify a corrosive environment by embedding the sensor in the structure and measuring the electrical resistance with a simple tester through a cable. However, to evaluate the corrosion environment inside an actual concrete structure, it is necessary to expose the cable to the outside environment for a long period of time, which may cause corrosion of the metal in the connectors or deterioration of the cable due to ultraviolet rays.

We therefore investigated ways to take sensor measurements wirelessly. We developed a wireless measurement system that uses passive RFID, a technology widely used for electronic money transfers. This system does not require a battery on the sensor itself. Figure 7 shows how the sensor is connected to the passive RFID.

The sensors and passive RFID units were connected by cable and embedded inside the structure. To measure the electrical resistance of the sensor, an electromagnetic wave was transmitted from the antenna of the RFID reader/writer to the RFID unit embedded in the concrete, and the measured output value was then returned to the RFID reader/writer. This system is powered by the electromotive force generated inside the RFID large-scale integration (LSI) chip.

This system enables completely non-destructive measurement with no need to expose the cables to the surface of the structure. To take a measurement, an electromagnetic wave is simply transmitted from the RFID reader/writer to the surface of the structure in which the RFID unit is embedded. The embedded sensors and RFID units do not require batteries, making them ideal for long-term maintenance without the hassle of battery replacement.

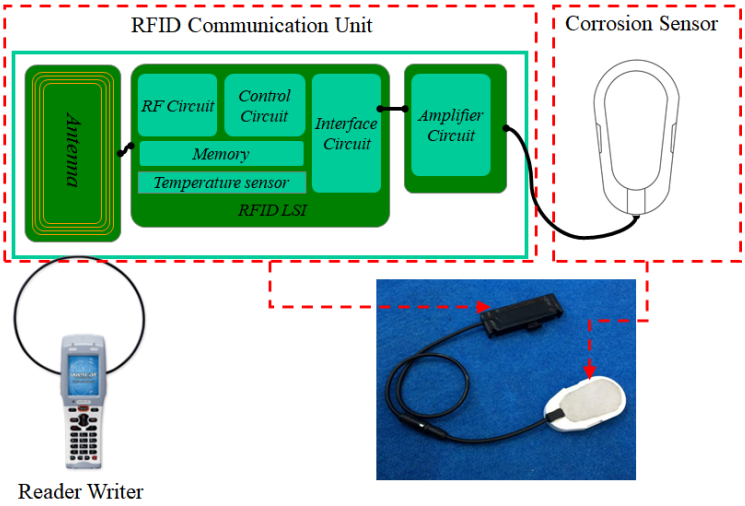

Figure 7. Configuration of the RFID corrosion sensor.

6 Examples of Application of the Sensor and Measurement System

The measurement system of the sensor is often used in concrete structures with high risk of steel corrosion. Major applications include port structures, such as lighthouses and piers, and road structures, including bridges where penetration of chloride ions from antifreeze agents is a concern.

The sensor has also been used to evaluate the repair effects of concrete structures. Figure 8 show the application of the sensor to bridge pier repairs. The subject bridge was constructed in 1973, in Hokkaido, Japan, and has undergone one round of repairs in 2007 following the occurrence of rebar corrosion-induced flaking. However, in just two years, the repaired area degraded. Therefore, we placed these sensors at six locations on the bridge following a second round of full-scale partial patching in 2011. Subsequently, corrosion was measured, once a year, for five years, followed by another measurement in the seventh year. One of the sensors detected salt-induced corrosion at a location, while the other five locations were observed to be stable. We confirmed that there was no issue with the measurement performance of the sensor, and established its durability and utility as an effective maintenance management system. Corrosion at the subject structure will be measured again in 2021 and subsequent repair plans will be made based on the measurements captured by the sensors.

Figure 8. Application of the system to bridge pier repairs.

7 Conclusions

We verified the performance of a corrosion environment sensor made of iron foil by measuring how long it took the sensor to identify corrosion under several different conditions corresponding to different chloride ion concentrations in a simulated concrete test solution. The following results were obtained:

- The corrosion environment sensor ruptured due to corrosion in environments with a chloride ion concentration of 500 ppm. The higher the chloride ion concentration, the shorter was the time to rupture.
- The fact that the sensor ruptures in an environment with a chloride ion concentration of 500 ppm, which corresponds to a corrosion rate of 0.001 mm/y, suggests that it has a highly sensitive reaction to the chloride ion concentration.
- By adopting passive RFID as the communication interface to the corrosion environment sensor, we were able to build a practical preventive maintenance system against steel corrosion.
- We were able to demonstrate the long-term durability of the sensor system based on passive RFID by applying it to repair work on real structures and maintaining it for seven years with no failures.

8 Future Work / Discussion

This sensor provides a simple way to determine whether the risk of corrosion increased in the environment around the sensor by detecting corrosion in iron as a proxy for corrosion in reinforcing steel. A variety of factors is involved in the corrosion of steel in actual structures, including the type of cement, formulation of the materials, and progress of carbonation. In this paper, we evaluated the performance of the sensor by focusing on the chloride ion concentration.

In the future, we plan to verify the performance of the sensor by focusing on other parameters, such as changes in the pH of the concrete, and to quantitatively evaluate the penetration of multiple corrosion factors into the concrete.

ORCID

Akira Eriguchi: https://orcid.org/0000-0001-7167-4019

References

ASTM C876-15. (2015). *Standard Test Method for Corrosion Potentials of Uncoated Reinforcing Steel in Concrete.*

CEB Working Party V/4.1. (Dec.1997). *Strategies for Testing and Assessment of Concrete Structures Affected by Reinforcement Corrosion (draft4)* BBRI-CSTC-WTCB.

Hausmann, D. A. (1967). *Materials Protection*, *6*(11), 19-23.

Lee, H. S., Shin, S., Ahn, J., Kim, Y. and Kho, Y. (2003). Development of corrosion sensors for monitoring steel-corroding agents in reinforced concrete structures. *Materials and Corrosion*, *54*(4), 229-234.

Takewaka, K. and Yamamoto, S. (2001). Development and research of non-destructive monitoring system for chloride penetration process in concrete. In *Proceedings of the Japan Concrete Institute*, *1*, 1183-1188.

XV International Conference on Durability of Building Materials and Components
DBMC 2020, Barcelona
C. Serrat, J.R. Casas and V. Gibert (Eds)

Development of an Apparatus for Measuring the Load Acting on Joint Sealant when Movement Occurs

Saori Ishihara[1], Hiroyuki Miyauchi[2], Akihiko Ito[3] and Kyoji Tanaka[4]

[1] Chiba Institute of Technology, 2-17-1 Tsudanuma Narashino-shi Chiba, Japan, saori.ishihara@it-chiba.ac.jp

[2] Building Research Institute, Ibaraki, Japan, miyauchi@kenken.go.jp

[3] Auto Chemical Industry, Co., Ltd., Ibaraki, Japan, akihiko.ito@autochem.co.jp

[4] Tokyo Institute of Technology, Yokohama, Japan, tanaka-kyoji@kme.biglobe.ne.jp

Abstract. *The sealant that fills the joints of an exterior walls of building is subjected to weather loads, such as sunlight, ambient temperature, and rain, as well as a movement of the joints. As a result, the sealant gradually deteriorates under the combined deterioration factors of weathering and movement. Meanwhile, the results of a 15-year outdoor dynamic exposure test conducted in Japan using the methodology of ISO 11617 showed that the progress of damage varies greatly depending on the type of sealant and the stress relaxation rate. However, the mechanism of damage progression is unclear. In the present study, we focused on the load when the sealant moves and developed a load-measuring apparatus as the first step in clarifying the relationship between the progress of damage and the load. The load was measured at −20, 23, and 40 °C for test specimens with different stress relaxation rates, and it was confirmed that the developed load-measuring apparatus was able to measure the load correctly. Furthermore, it was shown that it is difficult for the stress of the sealant with a high stress relaxation rate to relax over time at low temperature but easy at high temperature, and the load increases when switching from the compressed state to the extended state.*

Keywords: *Joint Sealant, Load Measuring Apparatus, Joint Movement, Deterioration, Durability.*

1 Introduction

The sealant used for a joint of an exterior wall is affected by various environmental factors, such as ultraviolet rays, the air temperature, and rain, and is gradually degraded by movement of the joint. In Japan, in the 15 years since 1992, dynamic outdoor exposure tests were carried out at three locations having warm, subtropical, and cold climates using a variable sealant as defined by ISO 2014: 11617. It was found that most sealants deteriorated remarkably at the subtropical location where irradiation by ultraviolet rays was strong. However, for some sealants (having a high stress relaxation rate), the damage depth (Df value) near the adherend was more remarkable at the warm and cold locations than at the subtropical location as shown in Fig. 1. It was believed that this was due to the load that the sealant received when movement occurred.

However, few studies have clarified the damage to sealants in terms of the load they are subjected to during service life. Further, commercially available accelerated testing machines are either accelerated weathering or fatigue testing machines, most studies have been limited to either of them. In the case of a material, such as a sealant, in which deterioration progresses due to the combined action of the weathering and the movement, it is desirable to verify the

durability by an acceleration test in which the weathering and the movement are simultaneously loaded.

In this study, as a first step to explain the mechanism by which deterioration is more intense in cold regions, we aim to develop an apparatus that measures the load applied to a sealant when both the weathering and the movement are combined. We fabricated prototype sealant with different stress relaxation rates and verified whether the load acting on the prototype sealant can be measured properly with a load-measuring apparatus.

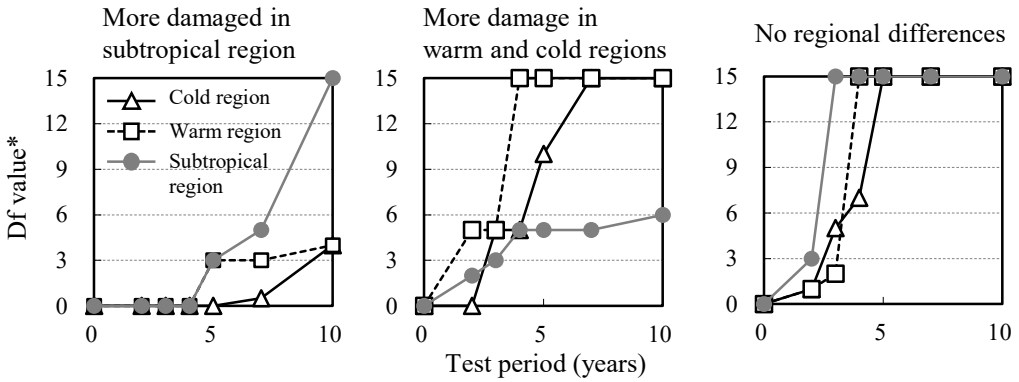

Figure 1. Example results of an outdoor dynamic exposure test.

2 Development of a Load-Measuring Apparatus

2.1 Load-Measuring Apparatus

To measure the load acting on the sealant when movement occurs, we developed a load-measuring apparatus as shown in Fig. 2. The ISO-type specimen shown in the figure is fixed to the load-measuring apparatus using a fixing jig. The portion of the specimen on the handle side is connected to a beam-type load cell, and the ball screw under the specimen portion is connected to the handle. When the handle is manually rotated, the specimen portion on the handle side moves horizontally, the sealant can be put into a compression or extension state, and the load generated in the sealant at that time can be measured by the load cell. A guide prevents displacement in the shear direction being applied to the specimen itself when movement is applied to the specimen. The dynamic outdoor exposure tests described above were carried out under various temperature conditions, and the temperature around the specimen could change. However, because the load cell is highly sensitive to temperature, the load cell is installed slightly away from the specimen so as not to be affected by temperature.

2.2 Prototype Sealant and its Stress Relaxation Ratio

As described above, sealants with high stress relaxation rates in the dynamic outdoor exposure test degraded greatly in a cold region. Two prototype sealants with different stress relaxation rates were therefore fabricated for testing in the present study.

The prototype sealants were two-component modified silicone sealants with different mixing ratios of the base material and curing agent. The sealants were intended to have almost the same moduli after standard curing but different stress relaxation rates.

To confirm that the intended sealants could be produced experimentally, test specimens of the

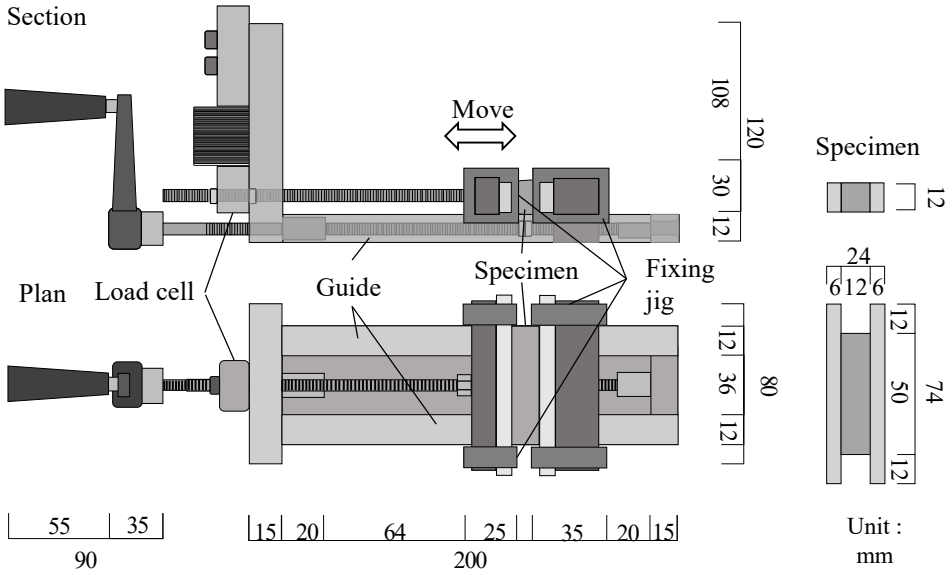

Figure 2. Load-measuring apparatus.

tensile adhesiveness test specified in JIS A 1439 were prepared using the prototype sealants (cured at 23 °C and 50% relative humidity for 7 days and at 50 °C and 50% relative humidity for 7 days, where the adherend was aluminum), and the stress relaxation rate was measured. Each specimen was attached to a tensile testing machine, the specimen width was extended by 30% (from 12 to 15.6 mm), and the stress was measured when the specimen was held for 18 hours in this state. The temperature was 23 °C and the tensile rate was 50 mm/min.

The temporal variation of stress is shown in Fig. 3 while physical properties, including the stress relaxation rate, are given in Table 1. The stress was a maximum when the specimen was extended by 30% and it lowered immediately afterwards. The stress did not decrease remarkably with time for specimen 1 having a low stress relaxation rate but lowered remarkably until 18 hours for specimen 2 having a high stress relaxation rate. Moreover, the moduli were almost the same, and it can be said that the aim of creating prototype sealants with almost the same initial modulus but different stress relaxation rates was achieved.

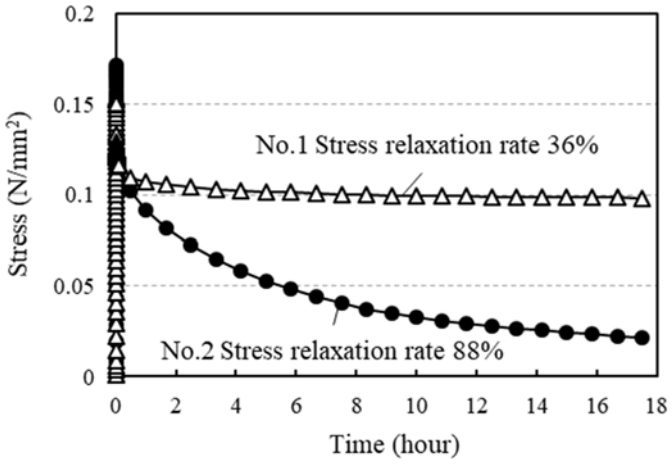

Figure 3. Temporal variation of stress.

Table 1. Physical properties of prototype sealant after standard curing.

Specimen	Stress relaxation rate*1(%)	Tensile adhesion*2		
		M_{50} (N/mm^2)	Tmax (N/mm^2)	Emax (%)
Specimen1	36	0.18	0.30	677
Specimen2	88	0.15	0.31	758

*1: Stress relaxation rate (%) = (Maximum stress -Stress after 18 hours) / MaximumStress × 100, Tensile speed 50 mm/min, Temperature of 23 ° C

*2: M 50: 50% modulus, Tmax: ultimate tensile stress, Emax: elongation at Tmax

2.3 Load-Measuring Procedure

To determine whether the load can be measured properly with the load-measuring apparatus, the joint width was compressed by 30% (from 12 to 8.4 mm) and held for 24 hours, and then extended by 30% (from 12 to 15.6 mm) and held for 24 hours, and the load was measured. The movement was realized manually as described above. The speed of movement was set to 50–100 mm/min with some variation.

As described above, there was more remarkable damage at the warm location and cold location than at the subtropical location in the dynamic outdoor exposure tests, and the present experiment was thus conducted taking the ambient temperature around the test specimen as a variable. The temperature conditions in the present experiment were set at three levels: a low temperature (−20 °C), normal temperature (23 °C), and high temperature (40 °C). The low-temperature condition was realized with a commercially available freezer, the normal-temperature condition with a constant-temperature and constant-humidity room, and the high-temperature condition with a box lined with insulating material and a planar heating element.

In cases of low and high temperature, only the temperature around the specimen was adjusted while the temperature of the load cell was kept constant. The test commenced after confirming that the internal temperature of the specimen was similar to the ambient temperature.

2.4 Test Results

Test results are shown in Fig. 4. For both specimens, the load peaked immediately upon movement but rapidly decreased immediately after and continued to decrease gradually with time. The decrease was remarkable for specimen 2 having a stress relaxation rate of 88% at normal and high temperatures. In other words, when the stress relaxation rate was high, the effect of temperature was strong, and the maximum load when switching to extension was large especially at high temperature. Furthermore, there was cohesive fracture during switching to extension at high temperature, and fracturing continued to progress even during holding in extension. The stress after 24 hours of compression had greatly relaxed, and it is thus considered that the sealant adapted to the compression state and the change due to the load generated in the next extension became large.

Table 2 shows the stress relaxation rate for extension. The stress relaxation rate at normal temperature (23 ° C) was slightly lower than that given in Table 1, which was measured by a tensile testing machine, because the specimen was extended after the compression state was

maintained. However, the difference in the stress relaxation rate was clearly well measured by Table 2 shows the stress relaxation rate for extension. The stress relaxation rate at normal temperature (23 ° C) was slightly lower than that given in Table 1, which was measured by a tensile testing machine, because the specimen was extended after the compression state was maintained. However, the difference in the stress relaxation rate was clearly well measured by the developed load-measuring apparatus, and it is considered that the change in stress with time can be appropriately measured even if the temperature of the environment changes.

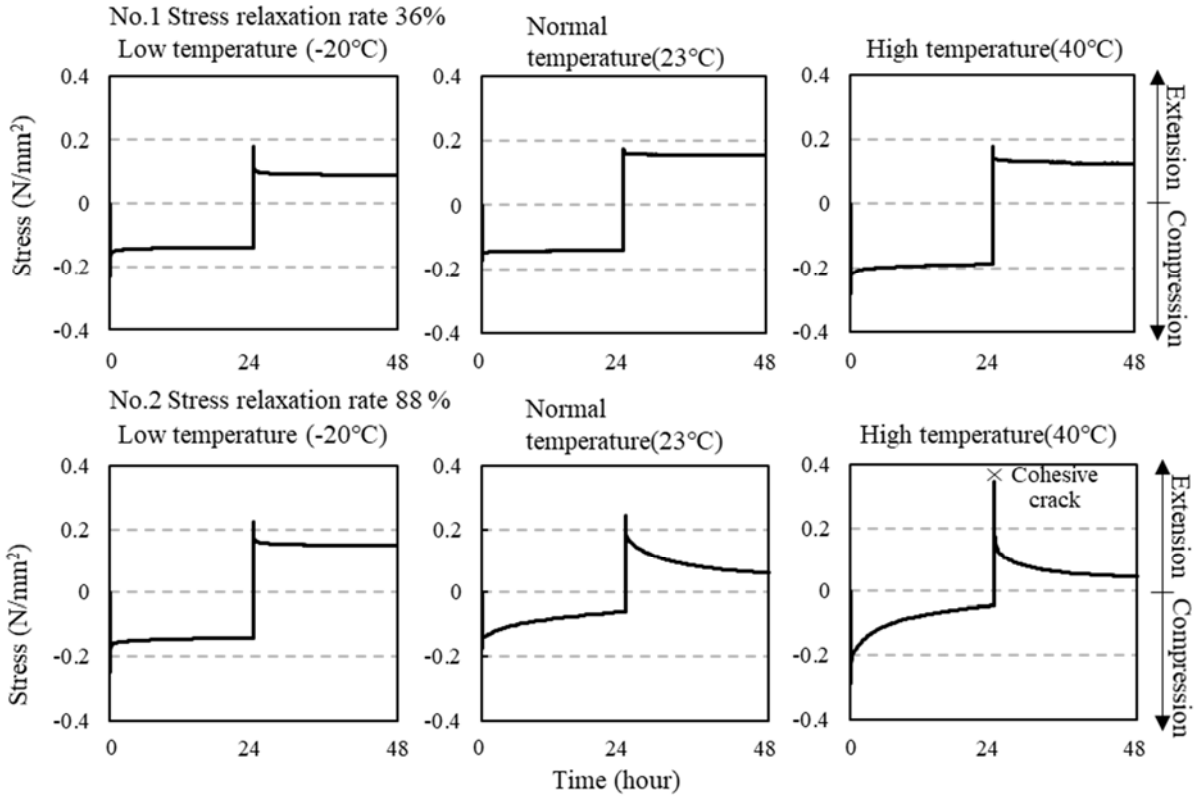

Figure 4. Temporal variation of stress.

Table 2. Stress relaxation rate measured by the load-measuring apparatus.

Specimen	Stress relaxation rate in extension as measured by the load-measuring apparatus [*1] (%)		
	Low temperature(-20℃)	Normal temperature(23℃)	High temperature(40℃)
Specimen1	50	11	30
Specimen2	61	72	92

3 Conclusion

The main contributions of the present study are as follows.

- We have developed an apparatus for measuring the load on a sealant during movement. Although an apparatus can handle any deformation rate, any temperature environment, any speed, and any movement period, it is difficult to perfectly match the movement speed each time because it is manually operated at present. Therefore, it is planned to

develop a load-measuring device for automatically generating a movement in the future.

- In order to verify the validity of the apparatus, we measured the load when 30% deformation was given at temperature (23 ° C), high temperature (40 ° C), and low temperature (-20 ° C) using two kinds of modified silicone sealants with different stress relaxation rates, it was found that the load gradually relaxed after compression and extension at normal temperature and high temperature but hardly relaxed at low temperature for prototype sealant with a stress relaxation rate of 88%. Meanwhile, the prototype sealant with a stress relaxation rate of 36% was hardly affected by temperature. The effect of temperature on the load can be measured using the load-measuring apparatus. It was shown that the effect of temperature on the load can be measured using the load-measuring apparatus.
- Although the purpose of this study was to develop of a load-measuring apparatus, our ultimate goal is to clarify the occurrence of sealant damage from the viewpoint of the load applied to the sealant. Therefore, in the future, it is planned to carry out repeated load measurement while applying other weathering such as ultraviolet rays by changing the type of sealant, stress relaxation rate, and deformation.

ORCID

Saori Ishihara: http://orcid.org/ 0000-0002-4990-5519

References

ISO 11617 (2014) (E) . *Buildings and civil engineering works — Sealants —Determination of changes in cohesion and appearance of elastic weatherproofing sealants after exposure of statically cured specimens to artificial weathering and mechanical cycling.*

JIS A 1439 (2004) . *Testing methods of sealants for sealing and glazing in buildings.*

ASTM STP 1453(2004) . *American Society for Testing and Materials*

Ramesh B. Malla, Matu R. Shrestha, Montgomery T. Shaw, and Smita B. Brijmohan(2011) . Temperature Aging, Compression Recovery, Creep, and Weathering of a Foam Silicone Sealant for Bridge Expansion Joints. *Journal of Materials in Civil Engineering* Volume 23 Issue 3

Andreas T. Wolf (2008) . RILEM TC190-SBJ: development of recommendations on novel durability test methods for wet-applied curtain-wall sealants. *Materials and Structures* 41 , 1473-1486. doi: 10.1617/s11527-008-9418-2

Noriyoshi Enomono and Kyoji Tanaka (2008). Quantification of Effect of Dynamic Movement for Weatherability of Construction Sealants. In *Proceedings of the 11th International Conference on Durability of Building Materials and Components*.

Hiroyuki Miyauchi, Noriyoshi Enomoto, Shigeki Sugiyama, and Kyoji Tanaka (2004). Artificial weathering and cyclicmovement test results based on RILEM TC 139 – DBS durability test method forconstruction sealants. In *Proceedings of the Symposium on Durability of Construction Sealants and Adhesives*

Su Hua Ding and Da Zhuang Liu(2006). Durability evaluation of building sealants by accelerated weathering and thermal analysis *Construction and Building Materials* Volume 20, Issue 10, 878-881.

Noriyoshi Enomono, Akihiko Ito, and Kyoji Tanaka (2009). Quantification of Effect of Enforced Cyclic Movement and Regional Exposure Factors on Weatherability of Construction Sealants *J. Struct. Constr. Eng., AIJ*, 73(633), 1907-1912. doi: 10.1520/JAI101949

Christopher C. White, Donald L. Hunston, Kar Tean Tan, James J. Filliben, Adam L. Pintar,and Greg Schueneman (2012). A Systematic Approach to the Study of Accelerated Weathering of Building Joint Sealants *Journal of ASTM International*, Vol. 9, No. 5.

Barbora Nečasováa, Pavel Liškaa, and Jiří Šlanhof (2017). Adhesion and Cohesion Testing of Joint Sealants after Artificial Weathering – New Test Method *Procedia Engineering* 190, 140-147.

XV International Conference on Durability of Building Materials and Components
DBMC 2020, Barcelona
C. Serrat, J.R. Casas and V. Gibert (Eds)

Financial Management of Construction Companies

Jiří Kusák[1] **and Eva Vítková**[2]

[1] Brno University of Technology, Faculty of Civil Engineering, Institute of Structural Economy and Management, Veveří 331/95, Brno, Czech Republic, jiri.kusak@vutbr.cz

[2] Brno University of Technology, Faculty of Civil Engineering, Institute of Structural Economy and Management, Veveří 331/95, Brno, Czech Republic, vitkova.e@fce.vutbr.cz

Abstract: *The objective of financial management of construction companies is to generate profit and provide financial stability. Financial stability is provided by managing the amount of both fixed and current assets, the amount of equity and external capital. Therefore, in order to reach the objective of financial management, it is necessary to comply with the basic financial rules. In the framework of nationwide analyses of economic indicators for different industries, there is data published on the website of the Ministry of Industry and Trade, which, however, apply to all construction companies. For this reason, the authors of the article focused on individual subcategories of construction companies (small, medium and large), which are defined by turnover, assets and number of employees. The research studied whether these subcategories fulfil all or part of the basic financial rules, including the following rules: golden rule of risk equalization: the ratio of own and external resources should be in the ratio of 1:1, golden balance rule: fixed assets should be covered by long-term resources; golden "pari" rule: fixed assets should be covered by equity. The research also monitored the structure of assets, i.e. the ratio between fixed and current assets and was based on elementary methods of financial analysis (vertical and horizontal methods). The outputs of the paper will be further used for the next step of the research, which will focus on tax optimization of individual categories of construction companies in relation to financial management of fixed assets.*

Keywords: *Financial Management, Construction Companies, Basic Financial Rules, Vertical and Horizontal Methods, Financial Analysis.*

1 Introduction

Financial management of companies, not exclusively construction companies, represent one component of important strategic management in terms of managing the entire economic development of the company. Financing is not only reflected in the indebtedness of the selected company and its liquidity, but also in providing cost-effectiveness, *i.e.* profitability. It is important to create a positive economic result for any viable company. This can be achieved by different financial resources. In general, the definition says that external sources of financing are always cheaper than own sources of financing (Srpová, Řehoř *et al.*, 2010). The Ministry of Industry and Trade publishes quarterly, semi-annual and annual statistics on financial indicators for individual sectors. Financial indicators relate not only to the percentage share of fixed assets on total assets, external resources of financing on total liabilities, and other indicators resulting from the vertical analysis of financial statements, but also ratios such as liquidity of all three levels, return on equity, indebtedness and others. In these statistical surveys, the above-mentioned indicators are kept by industrial sectors. This means that the closest sector to this research is construction industry, which is further divided in these statistics

into building construction, civil engineering and specialized construction activities. The total number of samples for the whole Czech Republic for these statistics was 85 companies. However, these statistics do not reflect the size of the company. The Accounting Act divides companies as accounting units into micro, small, medium and large according to their size, where the criteria for classification into a certain category are the amount of assets, the amount of turnover and the number of employees. For the above-mentioned reasons, the research was focused on the survey of selected financial indicators according to the categories corresponding to company sizes. The selected financial indicators for the research were mainly: the percentage share of fixed and current assets on total assets, percentage share of own and external capital (financial resources) on liabilities and other indicators that confirm basic financial rules for each size category of construction company doing business in the construction industry.

2 Present State References

Act No. 563/1991, on Accounting (1991) in Section 1b defines the categories of accounting unit sizes (companies) as micro, small, medium and large. This division is governed by the balance sheet data, at which the thresholds for the amount of assets, the total net annual turnover and the average annual number of employees are defined. EU Recommendation 2003/361/EC (2003) of 6 May 2003, published by the Ministry of Industry and Trade and the Office for the Protection of Competition, also defines the sizes of companies as micro, small and medium-sized companies. This definition, as well as the Accounting Act, deals with the amount of assets, the total net turnover and the average number of employees.

Srpová and Řehoř et al. (2010) in their book determine the basic rule of financing, which is related to time and states that fixed assets cannot be financed by short-term resources. From this definition it therefore applies that for proper financing, fixed assets should be covered by long-term resources.

Another financial rule is the risk equalization rule (Srpová, Řehoř et al. 2010), which states that the ratio of own and external resources should be 1:1, over time the ratio has changed to 1:2, and also to 1:3.

In her book, Kislinger (2007) defines the golden “pari” rule which states that fixed assets should be financed by company's own resource.

Biliavska, Mizunska and Yurii (2019) assessed the real financial status of both, identifying possible ways to improve the management of the existing assets of the two companies and the companies´ compliance with the golden rule of financing was analysed.

In the second paper, Biliavska, Mizunska and Kovalchuk (2019) assessed liquidity of two companies and the basic problems of the unstable financial condition of the companies determined with the help of calculated coefficients and the steps expedient for stabilization of the situation suggested.

Viszlai (2015) in his paper analysed structure of assets and capital structure in different forest companies and searched for differences between the model situation and real conditions. He used three basic financial rules for assessing and analysing assets and capital structure - golden rule of financing, current ratio and one to one rule.

Isik and Meric (2009) in their paper challenged the proposition that the golden rule of public sector borrowing its consistent with the principle of intertemporal allocative efficiency.

Groneck (2010) compared growth and welfare effects of various budget rules within an

endogenous growth model with productive public capital, utility enhancing public consumption and public debt. He found out that introducing a fixed deficit regime does not affect the long run growth rate compared to a balanced budget while establishing a golden rule results in higher growth.

Konečný (2013) in the paper studies whether the golden rules of financing are (or are not) respected depending on financial strategy in the sub-phases of the company life cycle.

3 Methodology

From a methodological point of view, the research was run on 17 samples for all categories of construction companies. The principle that at least 5 samples should fall within a given category has always been observed. In order to obtain input data from public sources, just the following categories were taken into account: small, medium and large. Financial statements from the website www.justice.cz, where financial statements for each accounting period are published, were used as input data. The period 2009–2017 was taken as the monitored period.

Individual categories of company sizes are defined by Act No. 563/1991 Coll., On Accounting, as follows:

- Small companies: total assets totalling at CZK 100,000,000, annual total net turnover of CZK 200,000,000, average number of employees 50; must not exceed at least 2 of the specified limits,
- Medium-sized companies: total assets totalling at CZK 500,000,000, annual total net turnover CZK 1,000,000,000, average number of employees 250; must not exceed at least 2 of the specified limits,
- Large companies: those that exceed at least 2 of the limits set out for medium-sized companies.

Financial indicators were processed using the basic method of financial analysis, namely vertical analysis. The principal of the vertical analysis is the ratio between the examined quantity and the basic quantity stated as a percentage.

$$Determination\ of\ percentage = \frac{researche\ quantity}{basic\ quantity} * 100 \quad (1)$$

The basic financial rules for efficient and sound company management are based on three pillars:

- 1st golden rule of risk equalization: the ratio of own and external resources should be 1:1,
- 2nd golden balance rule: fixed assets should be covered by long-term resources,
- 3rd golden "pari" rule: fixed assets should be covered by equity.

The Ministry of Industry and Trade (www.mpo.cz) in its statistical surveys and analytical materials lists only some indicators that can be used for the golden rules of financing. These are the indicators that assess the first golden rule of risk equalization and the third golden "pari" rule. It is necessary to note that the resulting values represent only the construction sector, the resulting values of the statistical survey do not reflect company size in any way. In the monitored years, according to analyses by the Ministry of Industry and Trade, the annual

percentages shares were as follows, see Tables 1 and 2.

Table 1. Ratio of own and external resources in the construction sector.

Year	2009	2010	2011	2012	2013	2014	2015	2016	2017	2018
Own resources (%)	35.20	37.31	38.56	40.96	40.68	40.53	40.12	45.30	45.49	44.23
External resources (%)	63.14	60.91	59.65	57.34	36.32	31.75	58.33	53.02	53.09	54.39

Table 2. Ratio of fixed and current assets in the construction sector.

Year	2009	2010	2011	2012	2013	2014	2015	2016	2017	2018
Fixed Assets (%)	27.93	30.44	32.17	29.93	33.04	33.61	34.37	33.78	33.71	32.78
Current assets (%)	71.21	68.93	67.09	69.12	66.17	65.80	65.08	65.74	65.71	66.75

The research therefore deals mainly with the differences in the individual golden rules of financing, which were researched according to the company size and, to a lesser extent, also the differences between the reported statistical surveys of the Ministry of Industry and Trade and values based on company sizes.

4 Results

Following financial indicators were monitored within the research using the vertical method, which is classified as an elementary method of financial analysis:

- own resources (equity)
- external resources
- fixed assets
- current assets
- long-term resources
- short-term resources

Within the individual golden rules, the research reached the following conclusions.

The first golden rule, which states that own resources of financing and external resources of financing should be in ratio of 1:1 and are evaluated by a nationwide statistical survey of the Ministry of Industry and Trade (see Table 1), was analysed according to the company size categories in the 2009-2017 period as follows, see Tables 3 and 4.

Table 3. Representation of own resources in individual categories of companies.

Year	2009	2010	2011	2012	2013	2014	2015	2016	2017	Average
Small	47.82	60.98	64.20	67.69	61.30	69.85	76.32	71.29	66.10	65.06
Medium	53.94	55.71	47.67	47.84	49.37	46.03	45.98	42.11	42.04	47.85
Large	28.33	29.15	29.84	29.79	29.08	29.18	29.24	26.25	30.28	29.02
Average	*43.36*	*48.61*	*47.24*	*48.44*	*46.58*	*48.35*	*50.51*	*46.55*	*46.14*	*47.31*

Table 4. Representation of external resources in individual categories of companies.

Year	2009	2010	2011	2012	2013	2014	2015	2016	2017	Average
Small	52.18	39.02	34.15	32.18	38.25	29.86	23.51	28.51	32.96	34.51
Medium	44.50	43.34	51.76	51.45	50.13	53.09	52.38	57.16	57.25	51.23
Large	69.71	68.82	68.74	68.78	69.87	69.49	69.58	72.54	68.37	69.54
Average	*55.41*	*50.40*	*51.55*	*50.80*	*52.75*	*50.81*	*48.49*	*52.74*	*52.86*	*51.76*

It is clear from the above-mentioned values that if we take into account the average values of own and external resources for all companies, they almost reach the ratio 1:1, which would confirm the first golden rule. However, if the average values of individual categories of company sizes were analysed, it was found out that the golden rule of financing was not exactly observed in any case. The analysis shows that small companies finance their activities more from their own resources, on average they were at 65%, and large companies, on the contrary, more from external resources, the average percentage share of external resources was about 70%. The medium-size companies were almost close to the 1:1 financing rule, where the difference was 2%, which is negligible. When comparing the resulting average values given in Table 3 and Table 4 with the average values calculated for the same period, i.e. 2009 - 2017 period by the Ministry of Industry and Trade listed in Table 1, it could be seen that within own resources the values differ by -7% and within external resources by +0.85%, which can be considered as insignificant deviations in both cases. These deviations can be caused by two factors, either a small sample for the research, or by several samples of one category of company size in the statistical survey of the Ministry of Industry and Trade, which affected the resulting values. It can be stated from the above analyses that the first golden rule of financing was almost observed for the medium-sized companies, however, not for small companies, where own resources are used more for financing and large companies, where external resources of financing are more used.

The second golden rule - the golden balance rule states that fixed assets should be covered by long-term resources (see Tables 5 and 7).

Table 5. Representation of fixed assets in individual categories of companies.

Year	2009	2010	2011	2012	2013	2014	2015	2016	2017	Average
Small	40.09	33.95	41.94	39.69	32.30	39.28	40.39	35.08	31.15	37.10
Medium	30.95	33.78	29.41	29.82	35.83	35.00	33.47	31.32	30.87	32.27
Large	15.98	16.96	16.43	16.41	15.72	15.78	14.52	16.55	18.40	16.31
Average	*29.00*	*28.23*	*29.26*	*28.64*	*27.95*	*30.02*	*29.46*	*27.65*	*26.81*	*28.56*

Table 6. Representation of current assets in individual categories of companies.

Year	2009	2010	2011	2012	2013	2014	2015	2016	2017	Average
Small	58.04	65.47	56.57	59.63	67.15	60.09	58.86	63.28	68.31	61.93
Medium	67.78	65.24	70.10	69.77	63.89	64.67	66.09	68.36	68.75	67.18
Large	84.26	84.90	86.19	86.51	87.14	86.35	86.53	86.67	84.63	85.91
Average	*70.03*	*71.87*	*70.95*	*71.97*	*72.72*	*70.37*	*70.49*	*72.77*	*73.90*	*71.67*

Table 7. Representation of long-term financial resources in individual categories of companies.

Year	2009	2010	2011	2012	2013	2014	2015	2016	2017	Average
Small	59.37	66.76	68.75	71.57	63.70	71.62	80.54	75.64	70.42	69.82
Medium	63.65	65.52	54.88	55.55	56.68	56.02	55.00	55.58	55.75	57.62
Large	39.22	41.98	41.79	42.38	40.80	41.67	43.99	46.11	46.69	42.74
Average	*54.08*	*58.09*	*55.14*	*56.50*	*53.73*	*56.44*	*59.85*	*59.11*	*57.62*	*56.73*

Table 8. Representation of short-term financial resources in individual categories of companies.

Year	2009	2010	2011	2012	2013	2014	2015	2016	2017	Average
Small	40.63	33.24	29.61	28.29	35.84	28.09	19.29	24.17	28.63	29.75
Medium	34.79	33.53	44.56	43.74	42.81	43.11	43.36	43.69	43.54	41.46
Large	58.83	55.99	56.78	56.18	58.15	57.01	54.82	52.68	51.96	55.82
Average	*44.75*	*40.92*	*43.65*	*42.73*	*45.60*	*42.73*	*39.16*	*40.18*	*41.38*	*42.34*

From the above-mentioned values (see Tables 5 and 7), it can be concluded that the second golden rule of financing was observed both in average values for all companies and for individual categories of company sizes.

In general, it can be stated that all companies had more current assets than long-term assets. A more significant difference in the share of fixed and current assets was in large companies, where it is clear that a larger financial volume is held in current assets, i.e. in inventories, receivables and cash, than in fixed assets. When comparing the resulting average values given in Table 5 and Table 6 with the average values calculated for the same period, i.e. 2009–2017 period by the Ministry of Industry and Trade from Table 2, it can be concluded that within fixed assets, the values differed by –3.55% and within current assets by +4.50%, which can be considered as insignificant deviations in both cases. These deviations can similarly be caused by two factors, either by a small sample used in the research, or by more samples of one category of company size in the statistical survey of the Ministry of Industry and Trade, which

would affect the resulting values.

Within the financial coverage of assets, long-term resources were used more in average values, which include share capital, profit or loss, funds, reserves, loans and liabilities with a maturity of more than 1 year. There was a more significant difference in small companies, where long-term resources were significantly more used, especially the positive economic result from previous years than short-term resources in the form of loans, credits or liabilities with a maturity of up to 1 year.

The third golden financing rule - golden "pari" rule states that fixed assets should be covered by equity (see Table 9).

Table 9. Average percentage share of fixed assets and equity for all analyzed companies.

Year	2009	2010	2011	2012	2013	2014	2015	2016	2017	Average
Fixed ass.	29.00	28.23	29.26	28.64	27.95	30.02	29.46	27.65	26.81	28.56
Own res.	43.36	48.61	47.24	48.44	46.58	48.35	50.51	46.55	46.14	47.31

It is clear from the values that the third golden rule of financing is fulfilled in all cases. This is mainly due to the low volume of fixed assets in individual categories of company sizes and, conversely, the greater share of own sources of financing. Items from the balance sheet such as share capital, funds, economic result were taken into account as own sources of financing.

5 Conclusions

The aim of the paper was to analyse the financial management of construction companies operating in the Czech Republic. Financial management of the companies was based on the confirmation or rejection of three basic financing rules, which include the share between own and external resources of financing, coverage of fixed assets by own and external long-term sources, and coverage of fixed assets only by own resources of financing. A financial analysis for individual industrial sectors published by the Ministry of Industry and Trade is published once a year within the framework of statistical surveys and analyses. The sector selected for the research corresponded to the basic activities of the companies analysed, namely construction industry. However, the size of company is neglected in these analyses. Therefore, the research was focused on examining financial management according to the company size. It was concluded from the overall research survey that the second and third financing rules were confirmed for all company sizes, unlike the first rule on company indebtedness was almost confirmed for medium-sized companies. The analysis of indebtedness showed that small companies use own resources more for financing their activities and, conversely, large companies use external resources more for financing their activities.

This article represents a basic input into the overall investigation into the financial management of companies according to their size. Further research will be based on the investigation into the financial management of only fixed assets of companies with an impact on the economic result and in the next step the impact on taxation. The size of the company will be reflected in the subsequent research as well.

ORCID

Jiří Kusák: https://orcid.org/0000-0002-1425-2001
Eva Vítková: http://orcid.org/0000-0002-2028-953X

References

Biliavska, A. V., Mizunska, I. R. and Kovalchuk, N. O. (2019). *The Analytical Aspects of Management of the Liquidity Level and Solvency of Enterprises in the Energy Industry*, Biznes Inform, Vol. 1(492), 255-261.

Biliavska, A. V., Mizunska, I. R. and Yurii, E. O. (2019). The *Comparative Analysis of the Financial Performance of the JSC «Chernivtsioblenergo» and JSC «Lvivoblenergo»,* Biznes Inform, Vol. 6(497), 169-176. doi: 10.32983/2222-4459-2019-6-169-176.

Doporučení 2003/361/ES ze dne 6. května 2003.

Groneck, M. (2010). *A golden rule of public finance or a fixed deficit regime?* Economic Modelling, Vol. 27(2), 523-534, doi: 10.1016/j.econmod.2009.11.005.

Isik and Meric (2009). *Public investment financing at European Union "Golden rule",* Ega Akademik bakis, Vol. 9(4), 1591-1603.

Kislingerová, E. (2007). *Manažerské finance.* Praha. C.H.Beck. ISBN 978-80-717-9903-0.

Konečný, Z. (2013). *Golden Rules of Financing Relating to the life Cycle of Czech Automotive Firms,* Journal of Competitiveness, Vol. 5(2),83-97, doi: 10.7441/joc.2013.02.06.

Srpová, J. and Řehoř, V. et al. (2010). *Základy podnikání.* Praha, Grada Publishing. ISBN 978-80-247-3339-5.

Vizslai, I. (2015). *Assessing the Assets and Capital Structure in Different Forest Companies,* Acta Facultatis Forestalis Zvolen.

Zákon č. 563/1991, Sb. o účetnictví.

XV International Conference on Durability of Building Materials and Components
DBMC 2020, Barcelona
C. Serrat, J.R. Casas and V. Gibert (Eds)

Neural Model of Projecting Compressive Strength of Cement Concrete Intended for Airfield Pavements

Małgorzata Linek

Kielce University of Technology, Faculty of Civil Engineering and Architecture, Department of Transportation Engineering, Aleja Państwa Polskiego Street 7,25-314 Kielce, Poland, tel.+48 41 3424844, e-mail: linekm@tu.kielce.pl

Abstract. *This work present to the mathematical model in the form of ANN, intended for projecting concrete compressive strength. Input data was classified according to the type of component material and its content in concrete mix (cement contents, coarse aggregate, fine aggregate, water and admixtures). In order to determine mathematical model, a multilayer, one-way perceptron network was used, recursion network with sigmoidal neurons. The model assumes that neurons are gathered in some layers (one input layer, hidden layers and one output layer). The conducted cross-section of the influence of variables parameters values (learning constant - α and momentum values - η) on the accuracy of representation of compressive strength was analyses. Assessment criterion was assumed taking into consideration the lowest mistake level and 100% compliance. According to the obtained analysis results ANN was assumed the best representing network for constant value of momentum 0,3, learning constant of 0,05 and 6 neurons in a hidden layer. Very good coincidence of component models with experiment results was achieved. At testing stage, the coincidence was achieved at the level of 99.74%, in case of the assumed network structure. During model verification by means of experimental results, the average coincidence was 99.83%.*

Keywords: *Compressive Strength, Cement Concrete, Airfield Pavements, Neural Model, Artificial Neural Networks.*

1 Introduction

The knowledge of mathematical model defining concrete resistance depending on the type of components and contribution thereto is interesting in terms of science and practice. Using Artificial Neural Networks (ANN) for this purpose and the opportunity to apply thereof for communications engineering and its particular applications are of the main interests of researchers of this field and construction branch in its general aspects. Potential capacities of ANN were proved, among others, in the following works (Bayrak *et al*., 2009; Bishop, 1995; Ceylan *et al*., 2007; Kasperkiewicz, 2004; Kim *et al*., Manerowski *et al*., 2006; Waszczyszyn, 2001). This work is an attempt to use ANN in order to design concrete mixtures intended for airfield pavements, define properties of hardened concrete and project the strength thereof. ANN provide the opportunity of structural dimensioning of susceptible and rigid pavements (*e.g*. Bilgehan *et al*., 2010; Ceylan *et al*., 1684; Ioannides *et al*., Noorzaei *et al*., 2007; Pożarycki, 2012; Thanoon *et al*., 2007; Urbańska *et al*., 2002). Using own collected database containing strength, laboratory test results, the mathematical model in the form of ANN, intended for projecting concrete strength, was presented. The essence of ANN is the selection of network structure (the number of layers and the number of neurons in particular layers) and defining the parameters thereof (constant values and weights).

2 Materials and Methods

This research paper concerns the issue of projecting the compressive strength of concrete intended for airfield pavements as far as structure durability is concerned. As a result of own laboratory and field tests (*e.g*. Linek *et al*., 2016; Linek, 2017; Linek *et al*., 2018), the strength of concrete containing various components of diversified contents were determined.

Consequently, the significant database was collected which enabled to prepare mathematical model allowing to determine concrete strength. Application of ANN resulted from the necessity to identify the diversification of compressive strength, which was the effect of changes in case of aggregate composition of concrete mix. One of the basic parameters of hardened concrete, which has the direct influence on the durability thereof in case of airfield pavement, is compressive strength (Glinicki, 2011; Nita, 2005; Szydło, 2004). This property depends on the diversified factors, among which there are the cement type and content, amount of coarse and fine aggregate and agents added to the mix aimed at the improvement of its parameters, and consequently also the parameters of hardened concrete. In case of each out of 6500 mixes, coarse and fine aggregate.

The aggregate should be distinguished by high durability and frost resistance, abrasion and polishing resistance and low absorbability. The designed aggregate compositions each time complied with (PN-EN 206-1:2003) and (NO 17A 204:2015). Mix composition included clean-clinker Portland cement in various amounts CEM I 42,5 (which fulfilled the requirements of (PN-EN 197-1)) and water (complied with (PN-EN 1008:2004)), designing diversified water-content ratio with reference to cement amount (w/c). Water-cement ratio significantly influences concrete durability. Limit content of individual mix components have been presented in the table 1.

Table 1. Limit component contents of the analyzed concrete mixes (content in kg/m^3).

Elements content	Cement	Coarse aggregate	Fine aggregate	Water	Admixtures
Min / Max	335 / 380	1149 / 1401	358 / 604	120 / 150	0.0 / 6.4

On the 28th day since concreting, each sample, prepared and cured in accordance with the requirements of (PN-EN 12390-2:2009), was subject to destructive tests by means of hydraulic press in compliance with (PN-EN 12390-4:2009). Maximum force destructing the sample, obtained according to the measurements, taking into consideration the assumed constant loading speed of 0,5MPa/s, was the basis for defining compressive strength of individual samples. The subject of further analyses included the samples which proved proper nature of destruction, after destructive test, according to (PN-EN 12309-3:2009). In case of each sample the compressive strength - f_c was determined, according to $f_c = F/A_c$, where F refers to maximum load registered in the course of sample destruction, while A_C refers to cross-sectional area of the sample which is influenced by the compressive force. The strength values obtained in this way were the input base to assess compressive strength of cement concrete intended for airfield pavements using ANN. All obtained test results concerning individual research series corresponded to the assumptions of the designed concrete classes and they were statistically essential. Therefore, they were the reliable source of input data for ANN identification, reflecting concrete strength in case of various compositions thereof.

3 Data Preparation

Operation of neural network depends on the type of neuron which will be accepted. Among the most commonly used, there are linear neurons, MLP, RBF, GRNN and Kohonen (Ossowski, 2006; Tadeusiewicz, 1993). Neuron used in the course of network designing process consists of output signal being the total of constant and relevant input signals multiplied by weight. Output signal structure in case of the analyzed network has been presented as follows (1):

$$y_i = S_i + \overline{X_\iota}(i,i)\,\overline{w^T}\,(i,i) \tag{1}$$

In case of equation (2) input signals take the form of $\overline{X_\iota} = [\,x_{i1}, x_{i2} \ldots x_{in}]$, while the corresponding weights $\overline{w_\iota} = [\,w_{i1}, w_{i2} \ldots w_{in}]$. The essence of the prepared network is to determine individual weights and constants S_i. Due to the fact that neurons have learning opportunities, synaptic scales were used, which can provide variable values and which are the basis for network learning. The applied activation function was presented by means of the following: $F(y_i) = 1 / (1+\exp(-2y_i))$. The assessment of representation accuracy of values from the experiment and coefficients generated by neural network was defined on the basis of two parameters. The first one is the average of the sum of squares of differences between the values of outputs from the real structure ($y_{rz\,i}$) and model (N) for experimental data (i = 1, 2, ..., N). The sum of squares of differences was determined according to the relationship (2).

$$\Delta\, y_{sr} = \frac{\sum_{i=1}^{N}(y_{SSN\,i} - y_{rz\,i})^2}{N} \tag{2}$$

However, the other parameter is the number of positive occurrences. Positive occurrences are understood, as the figure among all measurements which comply with the: $(y_{SNN\,i} - y_{rz\,i})^2 \leq \varepsilon$. Where y_i reflects output values of real measurements, i_i reflects output values from the model, while ε refers to the determined value of 0.01. The significant factor which influences the accuracy of projection of concrete strength by ANN is creating representative input dataset to determine thereof. Input data was classified according to the type of component material and its content in concrete mix. The following material types were considered: 9 types of cement, 17 types of coarse aggregate, 2 types of fine aggregate, 5 types of additives and 6 types of mix consistency as technological parameter, influencing proper structure performance related process. There were 6500 of diversified mix compositions collected, out of which 70% was assumed as input database for ANN, 15% was intended for testing purposes of the educated network, and the remaining 15% for network verification.

The selection of network structure is determined by the opportunity of feedback occurrence. These issues, among others, have been discussed in detail in the following work (Haykin, 1994), and their essence is the occurrence or absence of return connection (from latter to previous neurons), according to recursion and one-way structure. For the research paper purposes it was assumed that the feedbacks will not occur. Figure 1 presents schematic normalization process of input signals X and output signals y performed using ANN of the subject research paper. The results obtained as part of the conducted actual laboratory experiments were considered as the data. In case of the data which was subject to normalization, neural network was determined and then dimensional values thereof were calculated. In order to determine mathematical model, a multilayer, one-way perceptron

network was used, recursion network with sigmoidal neurons using JETNET 2.0 program (Lónnblad et al., 1992). The software used for network learning includes algorithm of moment method of backward mistake propagation (Rutkowski, 2005). ANN structure was presented in Figure 2. The data collected in the course of experiments was referred to as input layer of the prepared model. Input layer included 5 elements corresponding to individual cement contents (C), coarse aggregate (Kg), fine aggregate (Kd), water (W) and admixtures (D). The model assumes that neurons are gathered in some layers, among which there is one input layer, hidden layers and one output layer. It was assumed that input signals will be subject to normalization and have numeric values from 0 to 1. Among the available methods (among others min-max, Z-score, zero-mean, decimal calibration) normalization was selected in accordance with linear initial data transformation in compliance with: $\overline{x_l} = (x_i - x_{min})/\Delta x$, where $\overline{x_i}$ refers to normalized data, x_i – particular real values, x_{min} – minimum value of real values, while Δx refers to the difference between maximum and minimum value, i = 1, 2, ..., 5. Analogously for the output data in compliance with: $\overline{y_l} = (y_i - y_{min})/\Delta x$.

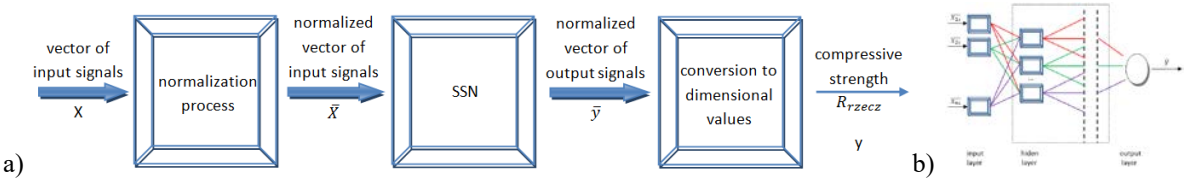

Figure 1. a) Diagram of using ANN in the model of compressive strength value estimation; b) graphic model of structure presenting the assumed multilayer artificial neural network.

4 Results

Analyses using artificial neural networks were conducted by means of NNair program creating regressive model, where it was expected to provide a specific numerical value being the solution to the problem. In case of the analyzed case this value was identified with the assumed compressive strength value. In order to conduct cross-section analysis of the influence of variables parameters values (α and η) on the accuracy of representation of compressive strength, analyses including matrix of 90x90 elements. According to the obtained results it was proved that the selection of α and η has significant influence on the extent of the obtained representation.

Table 2. Influence of learning constant value α on the accuracy of compressive strength representation (assuming constant value of momentum η = 0.3 and ε = 0.01).

No ANN	α	η	Number of inputs	Number of neurons	Number of outputs	Percentage of positive events	Δ y_{sr}
1-1	0.03	0.3	5	5	1	100	0.0034718
1-2	0.04	0.3	5	5	1	100	0.0031399
1-3	0.05	0.3	5	5	1	100	0.0028273
1-4	0.06	0.3	5	5	1	99.6	0.0025851
1-5	0.07	0.3	5	5	1	99.4	0.0024215

Table 3. Influence of momentum valueα (from 0.3 to 0.7) on the accuracy of compressive strength representation (assuming constant learning constant value of learning constant = 0.04 and ε = 0.01).

No ANN	α	η	Number of inputs	Number of neurons	Number of outputs	Percentage of positive events	Δ y_{sr}
2-1	0.04	0.30	5	4	1	99.6	0.0023666
2-2	0.04	0.40	5	4	1	99.4	0.0023475
2-3	0.04	0.50	5	4	1	99.4	0.0023339
2-4	0.04	0.60	5	4	1	98.2	0.0023255
2-5	0.04	0.70	5	4	1	97	0.0023281

Table 4. Influence of neurons number (5-10) in a hidden layer on the accuracy of representation of compressive strength at constant value of momentum 0.4, learning constant 0.03 and ε = 0.01.

percentage of positive events	the number of neurons in the hidden layer					
	5	6	7	8	9	10
	100	100	100	98,6	100	59,4
Δ y_{sr}	0.0028273	0.0022759	0.0031341	0.0022653	0.0027379	0.014378

Analyzing the data presented in table 2 and 3, the initial tolerance of learning constant was assumed at 0.05 and the initial tolerance of momentum was assumed at 0.3 for further analyses. In case of such assumed tolerance, the least value of the generated mistake, at the highest compliance of results was obtained.

Table 5. Influence of neurons number (1-5) in a hidden layer on the accuracy of representation of compressive strength at constant value of momentum 0.3, learning constant 0.05 and ε = 0.01.

No. ANN	α	η	number of inputs	Number of neurons in the hidden layer		number of outputs	percentage of positive events	Δ y_{sr}
				I	II			
3-1	0.05	0.30	5	6	1	1	87.0	0.004376
3-2	0.05	0.30	5	6	2	1	42.6	0.035561
3-3	0.05	0.30	5	6	3	1	46.2	0.029934
3-4	0.05	0.30	5	6	4	1	42.6	0.034757
3-5	0.05	0.30	5	6	5	1	46.2	0.028068
3-6	0.05	0.30	5	1	6	1	42.6	0.031157
3-7	0.05	0.30	5	2	6	1	46.2	0.028427
3-8	0.05	0.30	5	3	6	1	46.2	0.030317
3-9	0.05	0.30	5	4	6	1	87.0	0.004865
3-10	0.05	0.30	5	5	6	1	42.6	0.033186

According to the obtained analysis results ANN (tab. 4, 5) was assumed the best representing network for constant value of momentum 0.3, learning constant of 0.05, 6 neurons in a hidden layer and assumed ε = 0.01. In case of network of 5-6-1 structure, the first digit (5) refers to the number of inputs, next (6) the number of neurons in a hidden layer, and the last one (1) refers to one output identified with the assumed compressive strength value. This structure was assumed as a result of accuracy tests of representing real compressive strength values by the network. Assessment criterion was assumed taking into consideration the lowest mistake level and 100% compliance. Figure 3 presents the courses of learning in case of network of 6 neurons in a hidden layer. It can be observed that minimum values

$\Delta\, y_{sr}$ amount to 0.008, and maximum values amount to 0.520 in case of the assumed number of iterations. According to the obtained results of ANN analysis it was proved that the determined network can be recognized reliable for 38000 iterations.

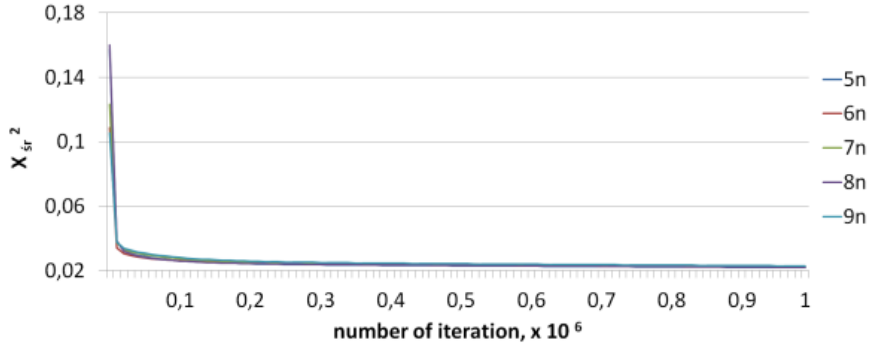

Figure 3. The course of learning process by ANN of diversified neurons number in a hidden layer.

Table 6 presents approximate contents of individual mix components intended for network testing. Figure 4(a) presents graphic summary of data determined at testing stage by the educated network. According to the obtained characteristics (Tab. 7 and Tab. 8) it was proved that the testing and verification of artificial neural network model reflects the values determined by the network. The obtained average value from 1300 events coincidence over 99% is very high. Average value of coincidence is 99.08 %. The obtained average value from 1300 events coincidence over 99% is very high. Average value of coincidence is 99.05 %.

Table 6. Limit component contents of the analyzed concrete mixes (content in kg/m^3).

Elements content	Cement	Coarse aggregate	Fine aggregate	Water	Admixtures
Min / Max	190 / 507	1000 / 1080	478 / 840	125 / 162	0 / 6.75

Table 7. Testing of ANN model (N- value determined from the network, T - value determined during testing).

No	Input data					Output data		
	C	Kg	Kd	W	D	N	T	accuracy
	[kg/m^3]	[kg/m^3]	[kg/m^3]	[kg/m^3]	[kg/m^3]	[MPa]	[MPa]	[%]
1.	324	1009	821	130	0.4	38.8	38.8	100.00
2.	386	1391	744	154	1.7	38.9	38.9	100.00
3.	424	1286	683	127	1.5	39.8	39.7	99.75
4.	350	1334	698	140	2.2	37.7	37.5	99.47
5.	434	1313	686	174	0.6	38.2	37.9	99.21
6.	437	1371	684	175	2.0	33.5	33.5	100.00
7.	390	1287	724	156	2.9	28.2	28.2	100.00
8.	400	1346	642	162	2.3	39.0	39.1	99.74
9.	368	1323	748	147	2.5	39.4	39.2	99.49
10.	356	1155	566	142	1.5	37.6	37.5	99.73

The educated and tested ANN network of 5-6-1 structure was intended for experimental verification. Figure 4(b) presents graphic summary of data determined at verification stage by the educated network. Table 8 includes the obtained selected analyses results.

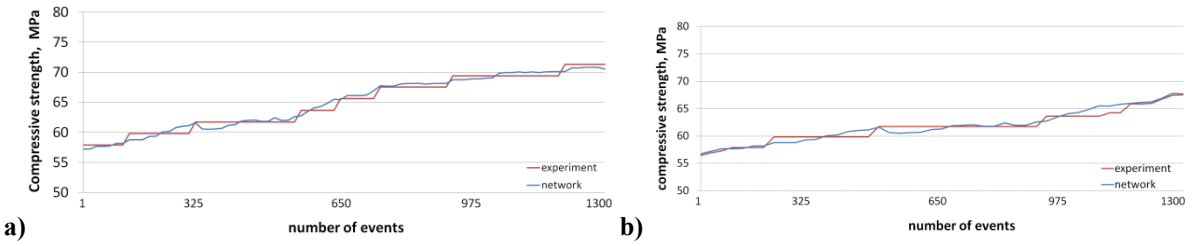

Figure 4. The course of (a) testing process and (b) verification neural networks of 5-6-1 structure.

Table 8. ANN model verification (N- value determined from the network, T - value determined during testing).

No	Input data					Output data		
	C	Kg	Kd	W	D	N	T	accuracy
	[kg/m^3]	[kg/m^3]	[kg/m^3]	[kg/m^3]	[kg/m^3]	[MPa]	[MPa]	[%]
1.	353	1096	675	141	0.4	34.1	34.2	99.75
2.	390	1402	667	156	0.7	37.6	37.5	99.54
3.	399	1199	733	159	0.8	26.8	26.7	99.63
4.	380	1305	677	152	0.8	34.2	34.2	100.00
5.	346	1242	771	138	1.3	38.0	37.9	99.77
6.	404	1244	699	161	1.5	36.4	36.4	100.00
7.	444	1182	795	178	2.2	37.5	37.4	99.77
8.	417	1318	743	166	2.4	33.0	33.0	100.00
9.	359	1207	591	143	2.7	37.9	37.8	99.77
10.	379	1402	692	151	2.8	36.2	36.2	100.00

5 Conclusions

It should be concluded that the assumptions concerning the construction of ANN model and the course of analysis can credibly anticipate parameters of composite material – concrete.

The results obtained as a result of the conducted analyses prove the purpose of application of the presented method in case of modeling the composition of concrete mix and projecting the strength obtained by concrete after 28 days of curing in standard conditions.

The analyzed structure 5-6-1 allows drawing the conclusions regarding material parameters even in case of limited number of elements. Based on the obtained results, the network structure has a large influence on the accuracy of mapping results from the experiment through the network. The network analyzing five neurons in an input layer, diversified in terms the selection of hidden neurons amount, complies with model assumptions. It was proved that 5-6-1 network, with learning constant of 0.05, momentum 0.3 and ε=0.01,is the most favorable structure for the assumed data. Very good coincidence of component models with experiment results was achieved. At testing stage, the coincidence was achieved at the level of 99.08%, in case of the assumed network structure. During model verification by means of experimental results, the average coincidence was 99.05%.

ORCID

Małgorzata Linek: http://orcid.org/0000-0003-1583-4377

References

Bayrak, M. and Ceylon, H. (2009). Neural Network-Based Approach for Analysis of Rigid Pavement Systems

Using Deflection Data, *Civil Construction and Environmental Engineering*, 5.
Bilgehan, M. and Turgut, P. (2010). The use of neural networks in concrete compressive strength estimation, *Computers and Concrete*, 7 (3), 271-283.
Bishop, C. M. (1995) *Neural Networks for pattern recognition*. Oxford University Press, Oxford;
Ceylan, H. and Gopalakrishnan, K.(2007). *Neural networksbased models for mechanistic-empirical design of rubblized concrete pavements*, Geotechnical/Materials Engineering.
Ceylan, H., Tutumluer, E. and Barenberg, E. J. Artificial Neural Networks for Analyzing Concrete Airfield Pavements Serving the Boeing B777 Aircraft, *Transportation Research* record 1684, Paper No. 99-1199.
Glinicki, M. A. (2011). *Durability of concrete in road surfaces. Effect of microstructure, materials design, diagnostics*. Road and Bridge Research Institute, Warsaw, vol. 66.
Haykin. (1994). *Neural Networks: A Comprehensive Foundation.*
Ioannides, A. M., Alexander, D. R., Hammons, I. and Davis, C. M. Application of Artificial Neural Networks to Concrete Pavement Joint Evaluation, *Transportation Research* record 1540.
Kasperkiewicz, J. (2004). On the possibilities of using artificial intelligence methods in civil engineering, *Roads and bridges*, 3, 15-37.
Kim, S., Gopalakrishnan, K. and Ceylan, H. (2009). Neural Networks Application in Pavement Infrastructure Materials, *Int. and Soft Comp. in Infrastr. Systems Eng., 259, Studies in Computational Intelligence*, 47-66.
Linek, M. (2017). Low-shrink airfield cement concrete with respect to thermal resistance, *MATEC Web of Conferences*, 133, 07002, DOI: 10.1051/matecconf/201713307002.
Linek, M. and Nita, P. (2016). Maintenance of Airfield Pavements Made of Cement Concrete with Respect to Their Durability, *Journal of KONES*, 1, DOI: 10.5604/12314005.1213570.
Linek, M., Nita, P., Wolka, P. and Żebrowski, W. (2018). Usefulness of porphyry and amphibolites as a component of concrete for airfield pavements, *MATEC WoC*, 163, 07002, DOI: 10.1051/matecconf/201816307002.
Lónnblad, L., Peterson, C. and Rógnvaldsson, T. (1992). *Pattern recognition in high physics with artificial neutral networks - JETNET 2.0 Computer Physics Communications 70*, Elsevier Science Publisher, 167-182.
Manerowski. J. and Zgrzywa F. (2006). Identification of a model of flight dynamics of a light turbo-prop, with artificial neural network employed, *Problems of Research and Operation of Aeronautics*, vol. 6, Publishing Air Force Institute of Technology, Warsaw.
Nita, P. (2005). *Concrete surface airport. Theory and structural dimensioning*, Publishing Air Force Institute of Technology, Warsaw.
Noorzaei, J., Hakim, S. J. S., Jaafar, M. and Thanoon, W. (2007). Development of Artificial Networks for predicting concrete compressive strength, *Int. J. of Engineering and Technology*, 4(2), 141-153.
Ossowski, S. (2006). *Neural networks for information processing* (in Polish), Warsaw University of Technology Publishing House, Warsaw.
Pożarycki A.(2012). Identification of the number and thickness of layers of the model of the new pavement of the test section by artificial intelligence methods (in Polish), *Roads and Bridges*, 2.
Rutkowski, L. (2005). *Artificial intelligence methods and techniques* (in Polish), PWN, Warsaw.
Szydło, A. (2004). *Road surfaces made of cement concrete* (in Polish), Polski Cement, Cracow.
Tadeusiewicz R.(1993). *Neural networks* (in Polish), Academic Publishing House RM, Warsaw.
Thanoon, W. A. M., J Noorzaei, SJS Hakim and MS Jaafar (2007). *Development of Artificial Neural Networks for predicting concrete compressive strength*, *Int. J. of Engineering and Technology*, 4, 141-153.
Urbańska A., Ligęza W. and Waszczyszyn Z. (2002). Analysis of concrete shrinkage using the RBF neural network (in Polish), *XLVIII Scientific Conference*, Krynica, 2002
Waszczyszyn, Z. (2001). Neural Networks in Structural Engineering. Some Recent Results and Prospects for Applications*, Computational Mechanics for the New Millenium*, Amsterdam, 1311-1320.
NO 17A 204 (2015).Airfield concrete pavements-Requirements and test methods for cement concrete pavements.
PN-EN 206-1 (2003). Concrete-Part 1: Specification, performance, production and conformity - Polish standard.
PN-EN 12390 (2009). Testing hardened concrete - Parts 2, 3 and 4 - Polish standard.
PN-EN 197-1 Cement part 1. Composition, specifications and conformity criteria for common cements.
PN-EN 1008 (2004). Mixing water for concrete-Specification for sampling, testing and assessing the suitability of water, including water recovered from processes in the concrete industry, as mixing water for concrete.

XV International Conference on Durability of Building Materials and Components
DBMC 2020, Barcelona
C. Serrat, J.R. Casas and V. Gibert (Eds)

Platform Development for Drone Utilization in the Architectural Field

Hiroyuki Miyauchi

Department of Building Materials and Components, Building Research Institute, 1 Tachihara, Tsukuba-shi, Ibaraki, 305-0802, Japan, miyauchi@kenken.go.jp

Abstract. *The utilization of drones is expected to streamline the process of building inspection in Japan; however, no known drone utilization platform exists in the region's architectural sector. Therefore, in this study we pioneered the development of a drone platform based on an industry–government–academia collaboration within Japan's architectural field. We first investigated drone-related trends, such as a utilization roadmap, flight rules, the drone market, new technologies and issues relating to the architecture field. Subsequently, we worked on solutions for drone utilization in the building sector, including methods for building inspection, determination of drone-flight risk factors relative to building inspection and the creation of a drone safety operation manual. Through field tests, we validated the effectiveness of the drone platform in building inspection, i.e., the determination of a cost–time relation during inspection, the merits of applying a high-resolution camera for inspection, the possibility of utilizing an infrared camera for exfoliation detection in exterior wall tiles and the development and efficiency of a built-in automatic inspection system. Furthermore, trial tests were conducted for the application of a drone-inspection system in disaster areas and a micro-drone in small building spaces. The findings of this study confirmed that the new drone platform achieved inspection- and disaster-related objectives within the architectural sector.*

Keywords: *Drone, Industrial Advances, Building Inspection, Risk Assessment, Field Test.*

1 Introduction

In Japan, the total number of pre-1980 housing stocks exceeds 13.69 million and is increasing every year. To ensure longevity, the assessment of buildings and their required maintenance has become an urgent issue. As such, efficient regular inspections are required as an important component of building maintenance. For example, periodic inspection reports according to Article 12 of the Building Standards Law are required for building health diagnosis. For the exterior wall inspection of buildings, a manual hammering test is required, especially for buildings that are more 10 years old. However, this test requires the setting up of temporary scaffolding for areas that cannot be reached by the investigator, making it costly for the building owner. There is an urgent need to develop a rational inspection method. In meeting this requirement, the use of drones is expected to play a significant role. An inspection technology for the maintenance of such buildings, the various potential uses of drones are being explored.

In 2016, the authors began research on (i) building inspection technology using drones and (ii) the construction of drone platforms. In the academic field, the Architectural Institute of Japan (AIJ) established a committee relating to the use drones and held the Architectural Drone Symposium to establish the current state of the art in drone usage. In the industrial field, the Japan Architectural Drone Association (JADA) was established in 2017 to address human resource development, technical support and standardization relating to the safe use of

doi:10.23967/dbmc.2020.110

drones. JADA has organized workshops and committees covering the safe operation of drones. In general, the use of drones in industry, government, and academia is gradually increasing.

Based on the above background, we herein report on (i) drone-related trends and levels of technology in the architectural field, (ii) demonstration experiments related to drone inspections and (iii) future prospects for drone usage.

2 Trends in the Use of Drones in the Architectural Field

2.1 Drone Technology Trends in Japan

As seen for Japan during 2018 (Figure 1), the use of drone services in sectors such as agriculture, surveying, aerial photography, inspection, crime prevention and logistics is expanding. Furthermore, by 2024 the infrastructure inspection sector is expected to outpace the agricultural sector. Figure 2 shows the roadmap for the utilization of drones according to the flight levels reported by the Ministry of Economy, Trade and Industry (METI). Level 1 corresponds to surveys such as those of a detached roof. Level 2 corresponds to a large area roof inspection or wall inspection. Level 4 is expected to be used for (i) the inspection of skyscrapers that are assumed to be non-visual flight in the 2022, (ii) logistics and security in cities and (iii) disaster-related issues. Therefore, in the architectural field, it is necessary to create a social infrastructure that assumes the use of drones in population-intensive areas. Table 1 shows the uses of drones in the architectural field. From all the papers submitted up to 2018, the importance of drone use follows the order: inspection, disaster, city/region, construction, environmental measurement, transportation and cultural heritage.

In particular, the use of drones for inspection is increasing, particularly in relation to the inspection of the outer walls of high-rise buildings, which would otherwise require scaffolding. These building inspection surveys are generally classified into primary to tertiary surveys according to the level of inspection, as shown in Table 2. Currently, primary and secondary surveys of a non-contact type are used for building inspection.

2.2 Drone Technology Development and Dissemination Efforts in the Architectural Academic Field

In April 2016, “WG on Application Guide of UAV to Building Performance Survey”

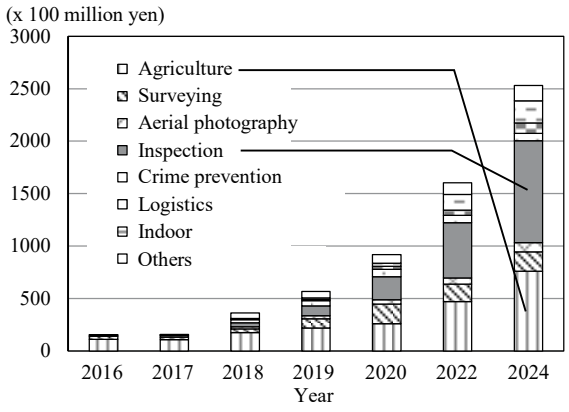

Figure 1. Drone service market in Japan.

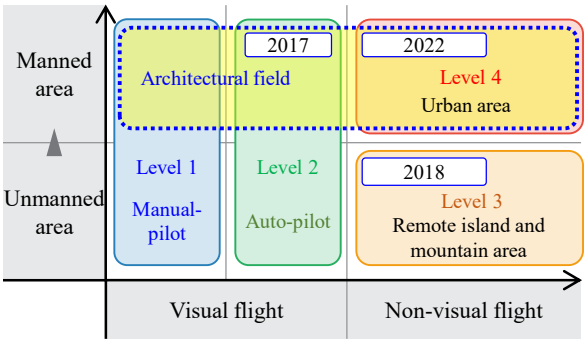

Figure 2. Utilization in architectural field at different flight levels.

(currently, Sub-committee for utilization of drone technology; Chairperson: H. Miyauchi) was established in the Durability and Maintenance Steering Committee, AIJ. The main foci of this WG were (i) the use of drones for the survey of building exterior walls, (ii) the collection of technical information, (iii) field trials and (iv) the examination of data collection and analysis methods. In May 2017, the first Architectural Drone Symposium was held with the aim of highlighting the advantages of drone technology across the entire architectural field. In 2019, a third symposium provided the latest information on the use of drones, covering regular use through to their use in disaster situations.

2.3 Challenges and Initiatives for the Utilization of Drones in the Construction Industry

The challenges facing the use of drones in the architectural field can be divided into (i) the damage caused by drone collisions and (ii) human issues. Regarding (i), Figure 3 shows the number of accidents caused by drones, based on information provided to Ministry of Land, Infrastructure, Transport and Tourism (MLIT). Compared with the 45 accidents for which no application for flight was required by the MLIT, 96 accidents (i.e., more than double) did require an application for flight. In particular, there are many population-intensive areas assumed during surveys of buildings and accidents when flying less than 30 m, and so sufficient safety measures are required when using drones in urban and architectural areas. Regarding (ii), there is a risk that video taken by drones may infringe privacy, as related to the

Table 1. Research topics with keyword "Drone and UAV" in AIJ annual paper.

Uses of drones in the architectural field	Year						Total
	2012		2015	2016	2017	2018	
Inspection	0		0	3	6	11	20
Disaster	0		0	0	3	3	6
City/Region	0		3	0	1	0	4
Construction	0		0	1	1	1	3
Environmental measurement	0		0	0	3	0	3
Transportation	0		0	0	1	1	2
Cultural heritage	1		0	0	0	0	1
Total	1		3	4	15	16	39

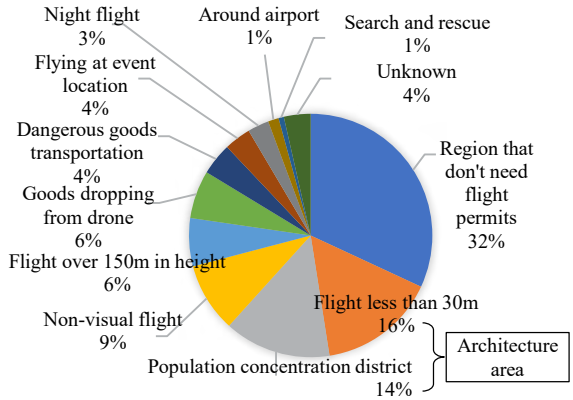

Year	2015	2016	2017
Number of accident	14	70	57

Figure 3. Number of accidents caused by drones (as of December 8, 2017).

Table 2. Technical levels for drone use in building inspection.

Inspection level	Inspection contents
Primary	Non-contact: Comprehensive inspection (Camera)
Secondary	Non-contact: Detailed inspection (High resolution camera, Infrared camera etc.)
	Proximity, Contact investigation (Hammering test etc.)
Tertiary	Contact investigation (Hole drilling etc.)

<Technical section>
Chapter 1: Basic drone utilization in the architectural field
Chapter 2: Architectural knowledge relating to use of drone
Chapter 3: Drone technology and safe operation
<Practical section>
Chapter 4: Construction management using drone
Chapter 5: Building inspection using drone

Figure 4. Safety Manual for Drone Utilization in Buildings and safety education workshop.

Personal Information Protection Law. There are also problems relating to noise during drone flight; therefore, it is necessary to give sufficient consideration to residents.

Against this background, JADA was established in September 2017 to develop human resources that can utilize drone technology across various applications in the architectural field. JADA also provides technical support and standardization. Activities were commenced with the aim of contributing to the realization of a safe, secure and sustainable society when conducting business. In particular, we are strengthening efforts relating to the safe operation of drones for building inspections. For example, as shown in Figure 4, the "Safety Manual for Drone Utilization in Buildings" was created, explaining basic knowledge relating to (i) drone utilization, (ii) drone technology and safe operation and (iii) construction management and inspection surveys for buildings. In addition, this manual is used in the "Building Drone Safety Education Workshop" to ensure thorough safety education.

3 Evaluation of Building Inspection using Drones

3.1 Effects of Cost and Time during Drone Inspection Surveys

Judgment criteria that show the superiority of drone usage over existing building inspections include (i) cost and time requirements from inspection to analysis and (ii) whether or not the level can be inspected under the same conditions as it can from the ground. From the above, using a six-story experimental wooden house at the Building Research Institute (BRI), the

(1) Inspection using a high work vehicle

(2) Inspection using ground photography

(3) Inspection using drone photography

Figure 5. Inspection methods.

Table 3. Visualization of buildings by drone.

	(2) Ground photography inspection			(3) Drone photography inspection		
Inspection area / Inspection ratio	Roof, Inspection impossible area; South, East, West, North			Roof; South, East, West, North		
	81% (Shooting distance: 7.5～17m)			100% (Shooting distance: 10m)		
	2F	4F	6F	2F	4F	6F
Visual performance						

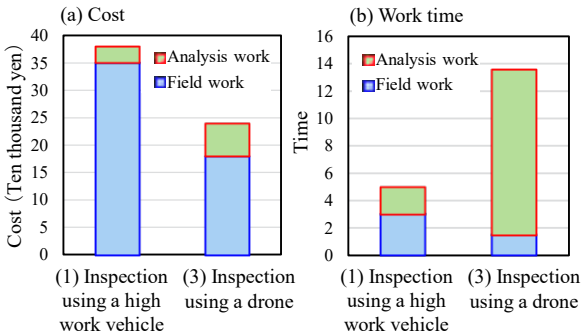

Figure 6. Comparison of cost and time requirements for high level manual inspection and drone photography inspection.

advantages of using a drone for building inspection were evaluated by comparison with a conventional inspection, as shown in Figure 5. Table 3 shows the results of comparing (2) ground photography and (3) drone photography. If a drone can secure a safe flight distance from a target object, it can photograph to the same accuracy as a visual inspection from the ground. For example, because the image size and image quality of the object can be kept constant during photographing by the drone, it is easy to subsequently analyze the image.

Figure 6 shows the results of comparing the cost and time requirements between (1) inspection using a high work vehicle and (3) inspection using a drone. Inspection by drone photography can be implemented at a lower price than that for a high work vehicle. On the other hand, the cost and time of image processing of drone images is higher; in particular, the analysis work is time consuming. These finding indicate the potential efficiency of on-site drone inspections but also suggest that image processing needs to be simplified and incorporate automated processing techniques.

3.2 Assessment of the Use of a High Resolution Camera

One of the important criteria that can be applied to building inspections is inspection accuracy in relation to specified requirements. Therefore, using a general-purpose 20-million pixel camera and a 100-million pixel camera (upper limit of resolution), we conducted a drone photographing experiment to evaluate the building inspection accuracy. Table 4 shows the performance values of the cameras used in the study. Figure 7 shows the visibility results of both cameras when a crack scale is attached to the outer wall and the drone flight shown in Figure 8 is taken. At a photographing distance of 5 m, it is difficult to see a 1.5-mm wide crack when using the 20-million pixel camera. However, at 100 million pixels, visual confirmation is possible down to a crack width of about 0.25 mm.

3.3 Assessment of the Applicability of using an Infrared Camera

When tiles are used for the exterior of a building, there is a risk of them peeling off due to a loss of adhesion between the base and the tiles. As an investigation method for this peeling, an expected inspection method is the use of a drone-mounted infrared ray camera. A demonstration experiment of this approach was conducted by MLIT in 2017–2018. At BRI,

Table 4. Specifications to satisfy 1-mm/pixel resolution

Performance	100-million pixel camera	20-million pixel camera
Distance	32.6 m	13.7 m
Photography area (H x W)	8.7 m x 11.6 m	5.3 m x 4.0 m
Viewing angle	15.2°	16.4°

Figure 7. Inspection test by drone.

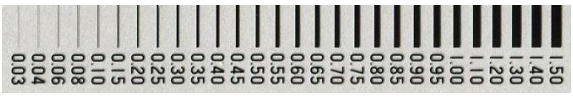

Original image of crack scale scanned by scanner

100-million pixel camera (Photographing distance:5m)

20-million pixel camera (Photographing distance:5m)

Figure 8. Images from different resolution cameras.

the test specimens included defect part between substrate and tile with 1m wide x 1m high were made as parameters with defect area and peeling depth. As shown in Figure 9, these specimens were placed on the roof of the building and aerial photographs were taken using two types of infrared camera mounted on a drone. An example of the detection of the defective part of a tiled specimen, as shown in the infrared image, is shown in Figure 10. When environmental conditions, such as solar radiation and temperature, and the performance of the applied infrared camera were appropriate, the detection rate of tile peeling was high. However, it was found that it is important to define the application range when using a drone-mounted infrared camera because the peeling conditions and photographic environment may differ in an actual building.

3.4 Development of Automatic Inspection and a Building Inspection System

Although drones are generally controlled by GPS, it is difficult to capture GPS signals in areas where buildings are densely packed, increasing the risk of crashing and potentially decreasing building inspection accuracy. In this study, we used SLAM (Simultaneous Localization and Mapping), as shown in Figure 11, which estimates the position of the camera based on the image information of the camera (i.e., independent of GPS signal). Figure 12 shows the results of a demonstration experiment of automatic drone inspection using an

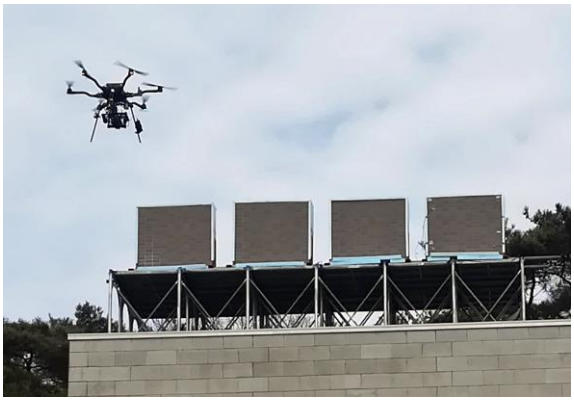

Figure 9. Inspection of tiled specimens using drone.

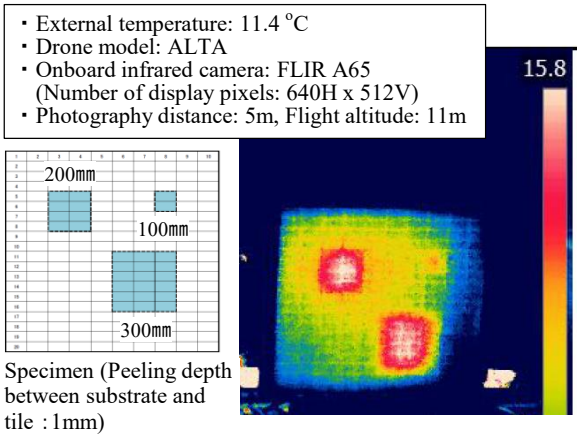

Figure 10. Inspection of defective parts of tile specimens by drone-mounted infrared camera.

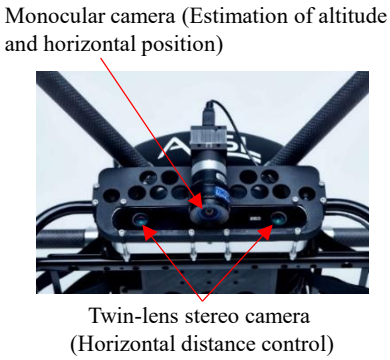

Figure 11. Visual SLAM type drone.

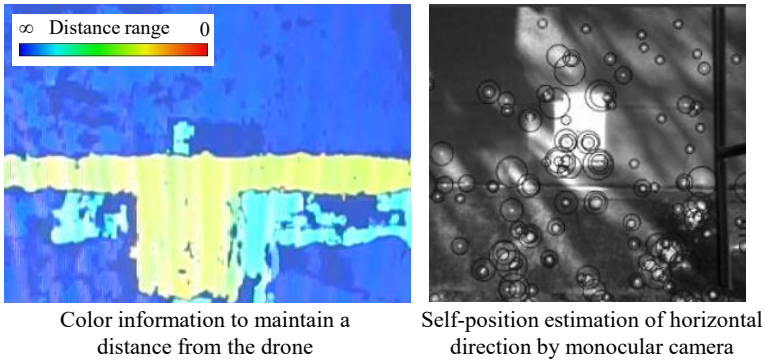

Figure 12. Test results for drone with Visual SLAM technology.

experimental building. The left of Figure 12 shows the use of a stereo camera to identify distance based on color information while maintaining a distance of 3 m from the drone. Furthermore, a downward camera was able to estimate self-position in the horizontal direction of the drone flight based on characteristic points on the asphalt pavement surface, as shown on the right of Figure 12.

3.5 Use for Data Recording and Analysis

It is important to record and measure building deterioration information on a regular basis. This information then needs to be stored and later used for building maintenance as required. Therefore, in Figure 13 we show an example of recording and storing deterioration information relating to a waterproof membrane sheet on the building roof. The resolution of the image was set to 1.2 mm/pixel and the altitude was set to 38 m from the roof. The entire roof surface was photographed during an automatic flight and a series of deterioration conditions for the roof were acquired. As shown in Figure 14 (m units), the flow of drainage on the waterproof sheet and the roof area could be measured. In cm units, the situation around the drain was able to confirm, in mm units, the crack and repair status of the waterproofing sheet. Therefore, it is possible to simultaneously record these states of degradation using a drone and archive them for use in future repairs.

3.6 New Methods for Building Inspection

Many natural disasters such as earthquakes, typhoons and floods occur in Japan and it is expected that drones will be used following such events to assess damage. A demonstration experiment using a drone was conducted on a three-story building damaged by the earthquake in Kumamoto Prefecture in 2016. The flow of the experiment is shown in Figure 15. Initially, the drone operator takes a picture of the building near the crack. The investigator wears VR goggles at a position away from the building and verifies whether the image information taken by the drone can be determined by extracting cracks that the investigator wants to confirm. Based on this assessment, it is considered possible to investigate damaged buildings via drone by remote control.

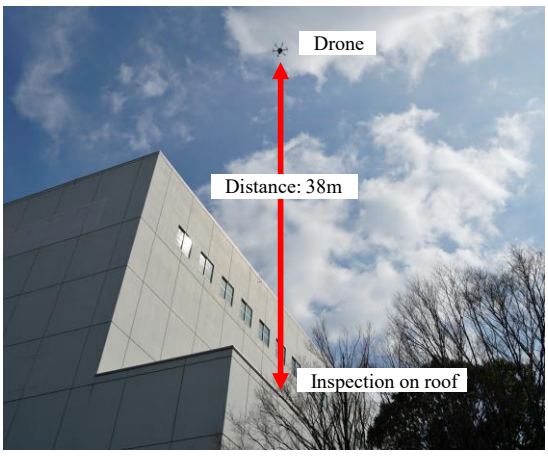

Figure 13. Flight test for checking degradation condition using drone.

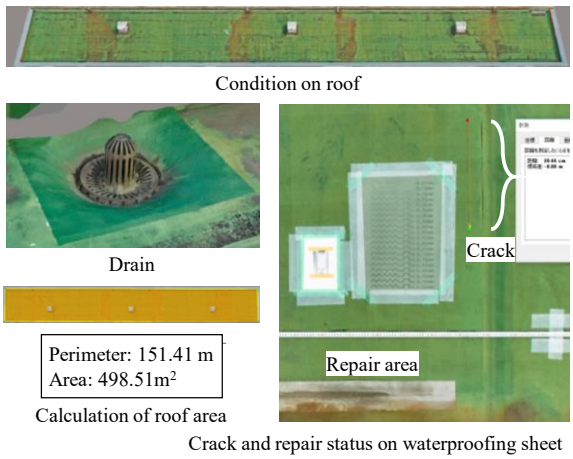

Figure 14. 3D model of degradation information (100-million pixels).

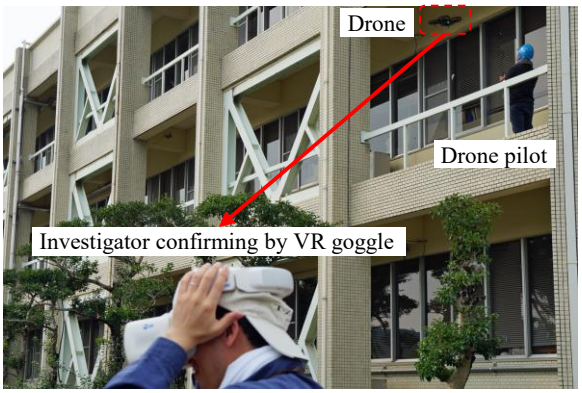

Figure 15. Remote investigation by drone in damaged building.

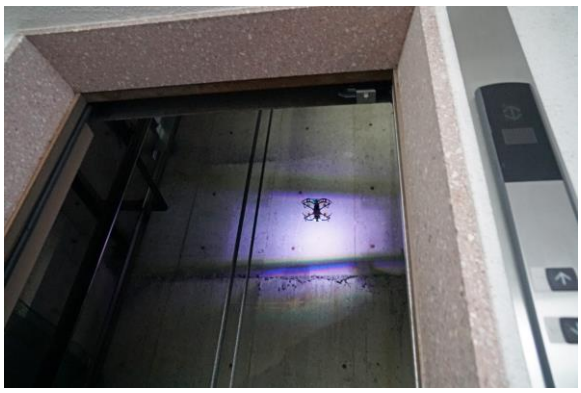

Figure 16. Drone inspection in confined space (elevator shaft).

Many external spaces related to buildings can be assessed using drones; however, drones are also highly usable in narrow spaces where human access is difficult, *e.g.*, behind ceilings and under floors. Therefore, in this study, we investigated the inner wall of an elevator shaft using a micro drone with a non-GPS control function that weighs less than 200 g, as shown in Figure 16. It was found that this approach can be used for inspection even in dark and confined spaces.

4 Conclusions

In this study, we investigated drone use trends in industry–government–academia for application to the architectural field. In addition, drone flight safety, cost reduction and labor-saving, inspection accuracy, application to archiving, and inspection automation were evaluated by field tests. Overall, the effectiveness of drone utilization was demonstrated. In addition to building inspection, drone technology is expected to be used across a wide range of fields, including disaster surveys, architectural education, information systems, facilities, design, urban planning, environmental engineering, architectural history, crime prevention and so on. It will be possible to create a new construction drone platform by strengthening the connected industries that link drones with various technologies (AI, AR, the cloud, etc.). For this purpose, it is very important to work with related parties so that the technology can effectively contribute to society.

ORCID

Hiroyuki Miyauchi: https://orcid.org/0000-0002-2391-4388

References

Impress (2018). Drone Business Survey Report 2018. Japan.

Japan Architectural Drone Association (2018). Safety Manual for Drone Utilization in Buildings. Japan.

Ministry of Economy, Trade and Industry (2017). Roadmap for utilization of the drone according to the flight level. Japan.

Ministry of Internal Affairs and Communications (2013). Housing and Land Survey. Japan.

Ministry of Land, Infrastructure, Transport and Tourism (2017-2018). Building standard maintenance promotion project T3. Japan.

Ishida, T. and Miyauchi, H. (2018). Verification of building inspection technology utilizing autopilot UAV by Visual SLAM: *Summaries of technical papers of annual meeting, Architectural Institute of Japan*. 561-562.

XV International Conference on Durability of Building Materials and Components
DBMC 2020, Barcelona
C. Serrat, J.R. Casas and V. Gibert (Eds)

Sustainability and Maintainability of High Rise Vertical Greenery Systems (VGS): its Lessons and Assessment Scoresheet

Sheila Conejos[1] **and Michael Y.L. Chew**[2]

[1] School of Science and Technology, Singapore University of Social Sciences,
sheilaconejos@suss.edu.sg
[2] Department of Building, National University of Singapore

Abstract. *Vertical Greenery Systems (VGS) applied on building has proven economic, environmental and social benefits which made it one of the widely accepted green building design strategies to support sustainable development. However, incorporating vertical greenery systems into innovative facades generates maintainability challenges. This paper highlights the best and good practices Design for Maintainability scoresheet, as well as the VGS defects and issues. The Design for Maintainability (DfM) assessment scoresheet will be beneficial in assessing and avoiding potential VGS defects leading to its maximum performance, longevity and sustainability. This research has established a list of best practice guidelines and measures with weighted scoring system for evaluating the maximum performance and efficient maintainability of VGS applications on facades while minimizing cost, risks, negative environmental impacts and consumption of matter/energy. The paper's contribution will be the improvement of the designers' decision making process, expanded library on vertical greenery systems defects as well as the importance of integrating maintainability of high-rise VGS facades in tropical conditions during its design inception.*

Keywords: *Building Maintainability, Green Building Technologies, Multi-Criteria Decision Assessment, Vertical Greenery Systems (VGS), Singapore.*

1 Introduction

Vertical Greenery Systems (VGS) applied on building has proven economic, environmental and social benefits (Chew and Conejos, 2016; Perini *et al.,* 2017) which made it one of the widely accepted green building design strategies to support sustainable development. However, incorporating vertical greenery systems into innovative facades generates maintainability challenges such as spoilt or falling leaves (Wong *et al.*, 2010), defective irrigation systems and inadequate installation methods which surges costs on operations and maintenance (Safikhani *et al.*, 2014), damaged surfaces due to plant roots infiltrating cracks (Manso and Castro-Gomes, 2015), lack/insufficient maintenance access (Behm and Poh, 2012; Köhler, 2008; Perini and Rosasco, 2013; Pérez *et al.,* 2014).

Chew and Conejos (2016) reports that less research has been undertaken concerning the maintainability of VGSs in tropical settings via design-based values, since this entails the vertical greenery system's sustainability (Emilsson, *et al.*, 2007). There is a need for the development of guidelines for VGS sustainability (Dvorak and Volder, 2010; Giordano *et al.,* 2017) which prompted the development of the Design for Maintainability guidelines for high rise vertical greenery systems in the tropics by Chew *et al.* (2019).

Chew and Conejos (2016) highlights various vertical greenery systems defects and issues in

Singapore and categorize them into technical and environmental defects based on previous research study and continually establishes more evidenced based issues and defects through qualitative approaches in this study in order to ascertain best practices as basis for a Design for Maintainability scoresheet in support for the design decision tool developed to assess the performance of vertical greenery systems.

2 Green Maintainability

The Green Maintainability concept (Chew, 2016; Conejos *et al.,* 2019) was established with the five green maintainability factors which incorporated facility management with sustainability right at the outset; such as: (1) maximizing performance – refers to the optimal competence of the building's function through design values, building science and engineering, efficient energy use and sustainability; (2) minimizing cost – pertains to the decrease in operations and maintenance costs and boosting savings throughout the entire building lifespan; (3) minimizing risk – denotes to the reduction of possible building defects occurrences and risks in the future; (4) minimizing negative environmental impact – concerns in the decrease of potential damaging effects caused by the discharge of a substance in the environment; and (5) minimizing consumption of matter and energy – indicates the conservation and management of the building's material, water and energy usage.

3 Research Methods

a) Qualitative Approach - The application of instrumental case study stipulates a comprehensive and in-depth interpretation of the cases, thereby in improving a theory (Stake, 1995), thus this approach was undertaken in the study to determine and establish evidence-based defects of high rise vertical greenery systems in the tropics. The selected instrumental case studies (Table 1) are physically accessible for field observation surveys and a wealth of recent data is on hand. The five green maintainability factors are used qualitatively in assessing the case studies' vertical greenery systems green maintainability potential via field observation survey and interview with expert and supported by stakeholders' via walkthrough interviews. b) Quantitative Approach – To provide an assessment scoresheet, a survey was conducted among practitioners and experts involved in designing and installing green facades. The Analytical Hierarchy Process (AHP) which is proven robust (Saaty, 1980) was used in analyzing the coded survey data in excel format.

Table 1. Instrumental Case Studies.

	Case Study (Year completed) and Awards Received	Vertical Greenery System (and Implementation)	Height
CS01	Commercial Bldg. (2014) BCA Green Mark Platinum Award	Support type system (Steel structure and high tensile steel cables)	5 storeys (M)
CS02	Mixed-use development (2016) BCA Green Mark Platinum Award	Support type system (Aluminum mesh)	30 storeys
CS03	Educational Bldg. A (2012) BCA UD Marks Platinum Award	Cassette system (Cassette)	6 storeys (M)
CS04	Educational Bldg. B (2015) BCA UD Marks Gold Plus Award	Support type system (Steel mesh)	11 storeys (M; S)
CS05	Educational Bldg. C (2013) BCA Green Mark Platinum Award	Support type system (Steel mesh)	7 storeys (M)
CS06	Residential Condo A (2015) BCA Green Mark Platinum Award	Cassette and planter box type systems (Tray)	22 storeys
CS07	Residential Condo B (2012) BCA Green Mark Platinum Award	Wire trellis support and planter box systems (Steel mesh)	25 storeys (S)
CS08	Residential Condo C (2013) BCA Green Mark Platinum Award	Support type system (Steel mesh)	24 storeys
CS09	Residential Condo D (2011) BCA Green Mark Gold Award	Support type system (High tensile steel cables)	6 storeys (M)
CS10	Residential Condo E (2014) BCA Green Mark Gold Award	Support type system (High tensile steel cables)	34 storeys (S)
CS11	Residential Condo F (2014) BCA Green Mark Platinum Award	Pocket type system (Substrate panel)	6 storeys

Source: Conejos et al. (2019).

4 Discussion of Findings

The identified critical high rise vertical greenery systems defects are due to lack of coordination among professionals lack of/insufficient coordination among building professionals which sometimes led to design oversights or inconsistencies. The following critical defects are:

- Lack of maintenance considerations such as insufficient/lack of maintenance access and safety issues/risks during cleaning and repairs. In some case studies, workers have to get through private balconies, pump rooms and air-conditioning units; climb over pool, parapet or glass enclosure; pass through pillars and traverse into narrow corridors that inhibits bulky maintenance equipment.
- VGS installation at the pool deck or over it which required frequent cleaning to preserve water quality.
- Lack/improper drainage system due to flat gradient or no screeding or lacking drains which causes water stagnation/ponding that will lead to pest infestation, mosquito breeding and algae/mould growth. In some instances, the drainage gutter has chokage issues due to falling leaves leading to water stagnation and possible mosquito breeding that will affect the health of residents and the public.
- Issues concerning infrequent/improper maintenance regimes due to the evident fallen leaves and dirt accumulation caused by heavy rainfall and strong winds. In some cases, the vines on the steel cable have thickened putting additional load to the support as it was not pruned or well maintained.
- Withering plants due to the suitability of plant species where in some cases where non-

tropical plants were installed which led to the drying and dying of plant species. The wrong choice of plant species can be considered a design oversight.
- Poor/faulty irrigation and water dripping issues caused by chokage or faulty components will lead to irregular plant growth or plants dying, rust of structural components, and high water consumption costs.
- Insufficient sunlight exposure also prevents plant growth and lead to plant dying or premature plant replacement regardless of proper irrigation regimes.
- Issues on maintenance cost (i.e. LCC) which entails a high cost of expenses when maintaining defective VGS.

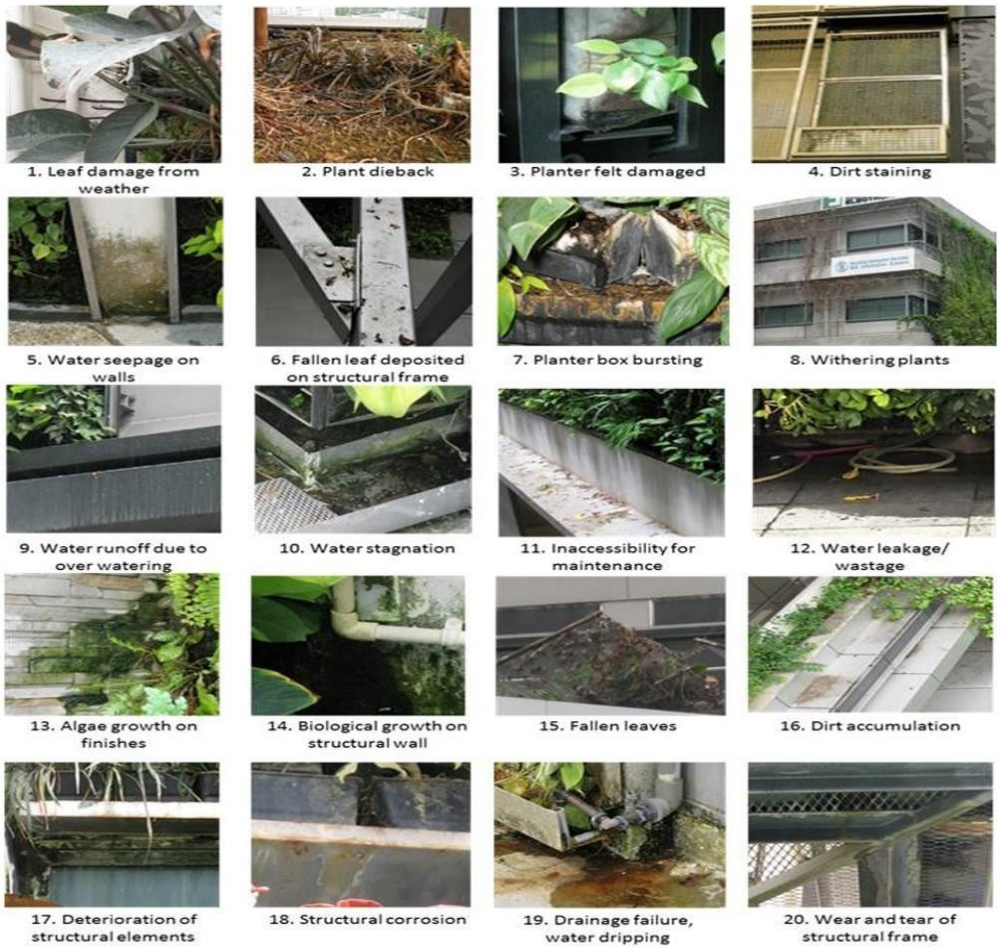

Figure 1. Some Defects of Vertical Greenery Systems.
(Source: Chew and Conejos, 2016).

5 Design for Maintainability (DfM) Scoresheet

In previous research studies, the *Design for Maintainability (DfM)* guidelines (Chew *et al.* 2019) and checklist (Conejos, *et al.* 2019) for vertical greenery systems has been established. In this study, the checklist is further developed into a graded scoring system which will assess

the vertical greenery systems' total performance according to the five green maintainability factors. The DfM scoresheet for high rise vertical greenery systems, highlights fourteen (14) design criteria with corresponding DfM good practice measures/guidelines and corresponding percentage scores with a total score of 100% when summed up (Table 2). The design criteria are grouped under the five green maintainability factors with corresponding percentages that totaled to 100% such as (1) maximizing performance – 21.47%; (2) minimizing cost – 17.45%; (3) minimizing risk – 30.81%; (4) minimizing negative environmental impact – 13.85%; and (5) minimizing consumption of matter and energy – 16.42%. Each design criterion is equally distributed according to the scoring percentage of each green maintainability factor. Based on the practitioner and expert survey results, the most critical green maintainability factor to be considered is minimizing risk which pertains to safety measures including fire safety and quality workmanship.

The importance of considering the green maintainability of a building throughout its life cycle will improve the sustainability and performance of high-rise vertical greenery systems in the tropics. The proposed checklist may aid in addressing the maximum performance and efficient maintainability of VGS applications on facades while minimizing cost, risks, negative environmental impacts and consumption of matter/energy.

6 Conclusions

This research has shown that considering maintainability right at the design inception is of great importance. Designing vertical greenery systems that are highly performing and easy to maintain guarantees long term sustainability. This paper highlights the evidence based defects and issues of vertical greenery systems under tropical conditions and through ascertaining best and good practices has introduced a set of Design for Maintainability (DfM) guidelines translated into a weighted scoresheet for assessment. The development of the Design for Maintainability (DfM) scoresheet for VGS is a valuable method in assessing the sustainability and maintainability potential of high-rise vertical greenery systems. The best practices and evidence based defects derived from these case studies and stakeholder insights will be useful in improving the decision making process for designers when it comes to the choice and design of VGS, as well as the expansion of the vertical greenery defects library. Lastly, one of the most important goals of VGS implementation is to promote a biophilic environment within high density areas as well as support climate change adaptation through the greening of the built environment.

ORCID

Sheila Conejos: https://orcid.org/0000-0001-6430-7042
Michael Y.L. Chew: https://orcid.org/0000-0002-3190-4315

References

Behm, M. and Poh, C.H. (2012). Safe design of skyrise greenery in Singapore, *Smart and Sustainable Built Environment*, *1* (2), 186–205. doi:10.1108/20466091211260677.

Chew, M.Y.L. (2016). *Maintainability of facilities: Green FM for building professionals (2nd ed.),* Singapore: World Scientific.

Chew, M.Y.L. and Conejos, S. (2016). Developing a green maintainability framework for green walls in

Singapore, *Structural Survey*, *34*(4/5), 379–406. doi:10.1108/SS-02-2016-0007.
Chew, M.Y.L., Conejos, S. and Azril, F.H.B. (2019). Design for maintainability of high-rise vertical green facades, *Building Research & Information*, *47* (4), 453-467. doi: 10.1080/09613218.2018.1440716.
Conejos, S., Chew, M.Y.L. and Azril, F.H.B. (2019). Green maintainability assessment of high-rise vertical greenery systems, Facilities, *37* (13/14), 1008-1047. doi: 10.1108/F-09-2018-0107.
Dvorak, B. and Volder, A. (2010). Green roof vegetation for North American ecoregions: A literature review, *Landscape and Urban Planning*, *96*(4), 197–213. doi:10.1016/j.landurbplan. 2010. 04. 009.
Emilsson, T., Berndtsson, J., Mattssona, J. and Rolfa, K. (2007). Effect of using conventional and controlled release fertilizer on nutrient runoff from various vegetated roof system, *Ecological Engineering*, *29*(4), 260–271. doi:10.1016/j.ecoleng.2006.01.001.
Giordano, R., Montacchini, E., Tedesco, S. and Perone, A. (2017). Living wall systems: A technical standard proposal, *Energy Procedia*, *111*, 298–307. doi:10.1016/j.egypro.2017.03.093.
Köhler, M. (2008). Green facades—a view back and some visions, *Urban Ecosystems*, *11*(4), 423–436. doi:10.1007/s11252-008-0063-x.
Manso, M. and Castro-Gomes, J. (2015). Green wall systems: A review of their characteristics, *Renewable and Sustainable Energy Reviews*, *41*, 863–871. doi:10.1016/j.rser.2014.07.203.
Pérez, G., Coma, J., Martorell, I. and Cabeza, L. F. (2014). Vertical greenery systems (VGS) for energy saving in buildings: A review, *Renewable and Sustainable Energy Reviews*, *39*, 139–165. doi:10.1016/j.rser.2014.07.055
Perini, K. and Rosasco, P. (2013). Cost–benefit analysis for green façades and living wall systems, *Building and Environment, 70,* 110–121. doi:10.1016/j.buildenv.2013.08.012.
Perini, K., Magliocco, A. and Giulini, S. (2017).Vertical greening systems evaporation measurements: Does plant species influence cooling performances? *International Journal of Ventilation*, *16*(2), 152–160. doi:10.1080/14733315.2016.1214388.
Saaty, T. L. (1980). *The analytic hierarchy process*, McGraw-Hill Inc., New York, US.
Safikhani, T., Abdullah, A. M., Ossen, D. R. and Baharvand, M. (2014). A review of energy characteristic of vertical greenery systems, *Renewable and Sustainable Energy Reviews*, *40*, 450–462. doi:10.1016/j.rser.2014.07.166.
Stake, R.E. (1995). *The Art of Case Study Research*, Sage, Thousand Oaks, CA.
Wong, N. H., Tan, A. Y. K., Tan, P. Y., Sia, A. and Wong, N. C. (2010). Perception studies of vertical greenery systems in Singapore, *Journal of Urban Planning and Development*, *136*(4), 330–338. doi:10.1061/(ASCE)UP.1943-5444.0000034.

Table 2. Design for Maintainability (DfM) Scoresheet for High Rise VGS.

Name of Building and Location:			
Building Profile:			
Instructions: Please refer to the following Guide Statements when assessing the Vertical Greenery Systems applied to high rise building. The scoring system is categorized ac corresponding total percentage at the leftmost column as reference. The Ranking result will be: Level 1 – 0% to 40% indicates low maintainability potential; Level 2 – 41% t – 61 to 100% indicates high maintainability potential.			
Design Categories		**Design Criteria**	**Good Practice Measures (incl. standards/guidelines/expert sourc**
Maximising performance	Climatic conditions	Availability of natural elements	Consider the proper orientation of the VGS, as well as the areas with strong winds due to location of the buildin altitudes. Provide sufficient soil depth for the roots to grow more freely (i.e. planter box size of 500w x 600d wi
			Consider alternative approaches such as hydroponics, light soil in skyrise greenery, as well as artificial lighting on VGS.
	Design considerations	Green wall systems	Consider VGS height, system capacity, lifespan and its replaceability.
		Plant suitability and sustainability	Specify the right plant species (e.g. native plants which are adapted to the local climate; plant appropriately for areas, etc.), as well as ensure that it considers the maintenance frequencies and cost issues.
			Avoid selecting plant species with excessive shedding of leaves and do not use some plant species (e.g. species require regular monitoring for signs of mosquito breeding.
			Recommend more than one species to ensure even coverage a and ensure the correct plant spacing for the desir
		Coordination among professions	Ensure that all involved stakeholders; design and construction professionals involved in the project are properly in from the design, construction, operations and maintenance aspects/process.
	Structural stability and material durability	Structural stability	Structural integrity of the green wall system should be certified by a professional structural engineer. Design th climber plants for high-rise VGS, as it can grow from ground level to the 10th storey.
		Material durability	Specify the use of quality materials (i.e. durable and stain-resistant materials) and ensure that the material selec cost issues.
Minimising cost	Maintenance considerations	Life cycle cost	LCC considerations include capital cost, ownership cost, operating cost and disposal cost.
		Maintenance Access	Provide easy and safe maintenance access (i.e. access via the front of green wall and access system considerati access provided) to all facade areas at every level. Each maintenance walkway level should have direct access worker movement during normal operations and emergencies. All designated access/inspection points shou maintenance access such as footpath leading to the tap. The greenery cascading down should not be encroachi water features. No unmaintained vegetation over private spaces.
			Provide permanent rear access and workspace (e.g. walkways and platforms) alongside the elevated greenery su parts of the green wall. The rear access must be designed with edge protection to prevent worker falling out d should have a minimum 600mm internal clearance width. Access should be designed via passive means as muc BMUs and other equipment required to facilitate accessibility but also to reduce instances of inconvenience to b
			For green wall no more than 2m in height, allow maintenance access from the front via suitable elevated wo scaffold, etc.), pole pruner and/or a combination of these equipment. For green wall more than 2m in height, p loading capacity in-front to allow safe and effective deployment of suitable elevated work platform and equipm landing with adequate load bearing capacity for safe deployment of elevated work platform such as MEWPs (mo wall more than 4m in height, the foreground when turfed/vegetated, should be designed, dimensioned and in provide adequate load bearing capacity for safe and effective deployment of MEWPs. Structural elements sho inspection.
		Frequency of Inspection and Maintenance	Put in place a regular maintenance schedule conducted by qualified workers to look out for potential risks, haza of supporting structures to ensure that structural integrity is maintained. Perform visual inspection for structural for plants' health status (i.e. pruning and ensure proper soil and irrigation, prevent unlikely planter bursting/ Install pre-planted panels safely and ensure quality workmanship. Provide a growing medium that is dense to nutrient needs. Follow and maintain a three-month pre-planting period for plant replacement so that plants will
	Drainage system	Drainage system management (e.g. gradient and water ponding)	Conform to BS 4428:1989 for proper drainage layout and system of landscape areas and ensure that planters sl towards the drain. Specify drains adjacent to planters at the base of the VGS. Drain gradient should be in the ra Consider using drainage trays at the base of the installation and provide metal drain covers. The width: depth ra

			facilitate ease of access. Provide anchor points or ladders to facilitate safety and access to drains and supporting maintenance.
			Drainage systems require regular maintenance and fixtures should be checked visually on a regular basis and th Test to ensure that during and after installation, the drainage systems effectively convey water to the storm wate systems, especially modular systems, for water ponding due to clogged drainage holes which allow mosquito br
Minimising risk	Installation and maintenance methods	Safety measures (incl. fire safety and quality of workmanship)	Safety and maintenance concerns must be thought of and addressed early during the design stage. Adhere to th the safe design, construction and maintenance of scaffolding, working platforms and gondolas (BS 6150:2006+ quality control during the installation of green wall components, installation of fixtures and fittings and vege performed by registered and specially trained workers to ensure quality workmanship. Ensure quality control du fixtures and fittings.
			Adequate site supervision should be performed to make sure that workers understand and comply with the esta work methods, including the proper usage of all personal protective equipment provided to avoid fall from heig SS CP 14:1996 and ensure the proper supervision of workers at heights. Implement a comprehensive safety plan fall prevention systems and personal fall arrest, and a permit-to-work system. Ensure that maintenance perso systems (BS EN 363:2008). Conform to ASME A120.1-2014 for the safe use of permanently installed building
			Considerations for fire-rated VGS materials to be specified as per SCDF requirements. Specify fire-rated VGS sufficient buffer between VGS and facade openings (e.g. balconies, windows) to prevent fire encroachment into biomass which contributes to fire risk. Ensure that chances of biomass contributing to fire risk should be reduce
Minimising negative environmental impact	Biological growth and animal management control	Algae and mould prevention	Choose plants that do not trap water and harbour pests and disease pathogens. During and after installation, pre algae) as much as possible. When necessary and not on regular basis, treat such growth with anti-algae/anti-fun growths with a stiff brush.
			Planters or modules should be designed to be sufficiently deep to contain the spread of roots. Roots should b encroaching onto building's facade walls. Keep the plants away from the building's walls by having a gap in be inspections to ensure that root growth are controlled to avoid penetration on walls. Waterproofing system at lan and made to be root resistant and/or alongside a suitable root barrier. Ensure good housekeeping practices waterproofing membrane.
		Pest and bird nesting control	Inspect systems, especially modular systems, for water ponding due to clogged drainage holes which allow mos contractors should include looking out for mosquito breeding sites (e.g. instances of water ponding) near VGS. pathogens should not be introduced into any new or existing planting areas, as eradication of pests and patho plants that do not trap water and harbour pests and disease pathogens. Inspect plants periodically for pest infesta and fungicides to prevent them from contaminating run-offs and eventually the groundwater. Fertilizers and inse & Veterinary Authority of Singapore.
			Conduct periodic inspections to ensure that branches have not thickened to avoid bird nesting. Conduct annual bird interaction with VGS for plant survival.
Minimising consumption of matter and energy	Water and irrigation and electrical and lighting systems	Water and energy efficiency	Specify a drip-based irrigation system complete with built-in rainwater harvesting and recycled water to min automatic-irrigation system with rain sensor. Recommend the use of an adjustable automated irrigation system of water. Energy efficiency considerations should include material selection, testing, fixing/ mounting/ installat
Total Score			

XV International Conference on Durability of Building Materials and Components
DBMC 2020, Barcelona
C. Serrat, J.R. Casas and V. Gibert (Eds)

Synthetic Resin Reinforcement of Timber Joints Deteriorated by Termites

Yamada Mikako[1,a], SawadaMasamitsu[2,b], Imamoto Kei-ichi[3,c] , Kiyohara Chizuru[4,d] and Ohtsuka Akiko[5,e]

[1] Tokyo University of Science, Tokyo, JAPAN, [a] sarusarumika0905@gmail.com

[2] Tokyo University of Science, Tokyo, JAPAN, [b] masayan.sawa.1120@gmail.com

[3] Tokyo University of Science, Tokyo, JAPAN, [c] imamoto@rs.tus.ac.jp

[4] Tokyo University of Science, Tokyo, JAPAN, [d] ckiyo@rs.tus.ac.jp

[5] Akita Prefectural University, Akita, JAPAN, [e] ohtsuka.akiko@gmail.com

Abstract. *Timber has been widely adopted as a global structural material. However, timber sometimes deteriorates due to various factors such as termite infestation, which may reduce its strength and durability. It is difficult to ascertain the degree of deterioration of timbers by visual inspection because deterioration by termites causes severe damage to the inner parts of the timber. Therefore, the damage is often discovered after the deterioration progresses. The restoration and refurbishment method currently implemented is removing the degraded parts and partially replacing them with new healthy wood. Although it is as desirable to reinforce the original part as it is to restore its strength, especially for historical timber structures, this approach has not yet been put into practical use. This study investigates the possibility of restoring timber deteriorated by termites with little changes in its appearance by using resin filling. Deterioration by termites occurs at the base of the timber. Therefore, the specimen is assumed to be the joint of a foundation and column. First, the deteriorated specimen was filled with epoxy resin, and then, the effectiveness of the filling was confirmed by a nondestructive test method using ultrasonic pulse velocity. Finally, shear strength test was performed for the joint. As a result, ultrasonic velocity significantly increased because of the resin filling. The strength of the specimen filled with epoxy resin was restored and was close to the strength of a healthy one. It was confirmed that this strengthening method with resin filling was useful for improving the structural performance of timber deteriorated by termites with little change in appearance.*

Keywords: *Strength, Termite Damage, Nondestructive Test, Epoxy Resin, Ultrasonic Pulse Velocity.*

1 Introduction

The damage caused by termites is one of the main degrading factors of timber structures. Termites are active in wet conditions; hence, they can cause damage to the base of timber that is close to the ground. In addition, in timber buildings, joint strength is very important. It is clear that the deformation and strength capacity of the joint strongly affects the deformation and structural capacity of the building. Therefore, in this study, the authors focus on the reinforcement of the base joint.

The authors examine the reinforcing method of injecting synthetic resin into the deteriorated parts of the timber. The reinforcing method is characterized by a little change in appearance, as shown in Figure 2.

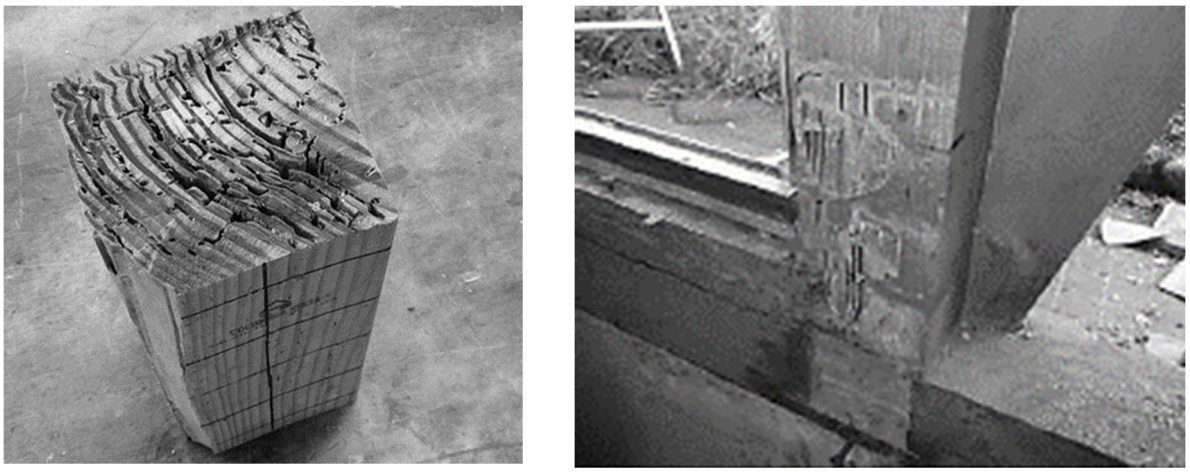

Figure 1. Timber damaged by termites. (Source: KAWATA Tasturo, 2017)

Figure 2. Timber filled with resin.

2 Shear Test of Pillar-Base Joints

2.1 Objective

The objective of this experiment was to examine the reinforcing effect of filling the synthetic resin on the restoration of timbers deteriorated by termites. The reinforcing method is as follows. First, the entire surface of the specimen is covered with tape. Next, the side of the specimen is drilled in a staggered manner at 100-mm intervals (Figure3). Finally, using a static mixer, the synthetic resin is injected through the hole into the specimen (Figure4).

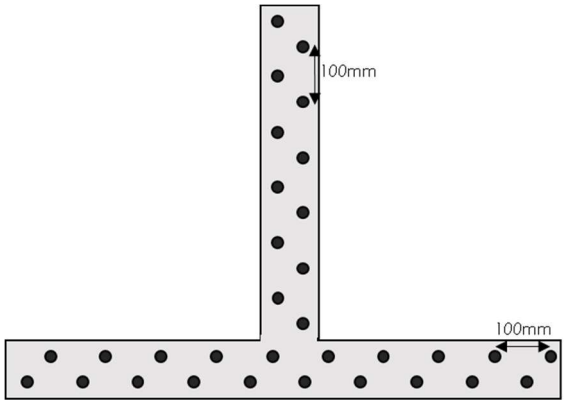

Figure 3. Image of filling hole.

Figure 4. Resin filling work.

2.2 Summary of Specimens

The specimen was prepared using Douglas fir. The dimensions of the column were 105 mm x 105 mm x 600 mm, and those of the base were 105 mm x 105 mm x 1000 mm. The joint was a stub tenon. The dimensions of the tenon were 30 mm x 75 mm x 50 mm, and those of the mortise were 30 mm x 75 mm x 80 mm. Ten sets of column and base specimens were prepared, and two of them were used as control. The deterioration was carried out for four months at a test site where termites live (Figure5). The degree of damage was evaluated by the mass reduction rate before and after the damage treatment. The specimens are listed in Table 1.

Regarding the resin filling, two types of synthetic resin, epoxy resin and polyamine resin, were used to examine the change in strength depending on the type of synthetic resin. In Table 1, “Resin A” is hard type, and “Resin B” is elastic type. Three specimens were prepared and filled with resin A, and two were filled with resin B. In this test, five restored specimens were used.

Figure 5. Soil exposure due to feeding damage caused by termites.

Table 1. Name of specimens and test parameters.

Name	Feeding damage rate[%]	Resin					
		Name	Materials	Fit ratio	Method	Tool	Feature
0-N①	0	None	-				
0-N②							
10-N	10						
15-N	15						
20-N	20						
10-A	10	A	epoxy resin +polyamine resin	2:1	filling	static mixer	hard
15-A	15						
20-A	20						
10-B	10	B	epoxy resin +polyamine resin	3:2	filling	static mixer	elasticity
15-B							

2.3 Loading Method and Loading Protocol

The experimental setup of a joint member with a column and base is shown in Figure 6. The base was fixed to the foundation steel member by passing bolts through the steel plate on the left and right sides and tightening each bolt with a strength of 20 N. In addition, by assuming the actual building weight, an axial load of 10 kN was applied to the column through a drop jig. Then, a positive and negative cyclic load testing was applied 500 mm height from the upper surface of the base portion. The applied rotation angle (θ) was 1/450, 1/300, 1/200, 1/150, 1/100, 1/75, and 1/50 [rad] in each three cycles, and then 1/30, 1/15, and 1/10 [rad].

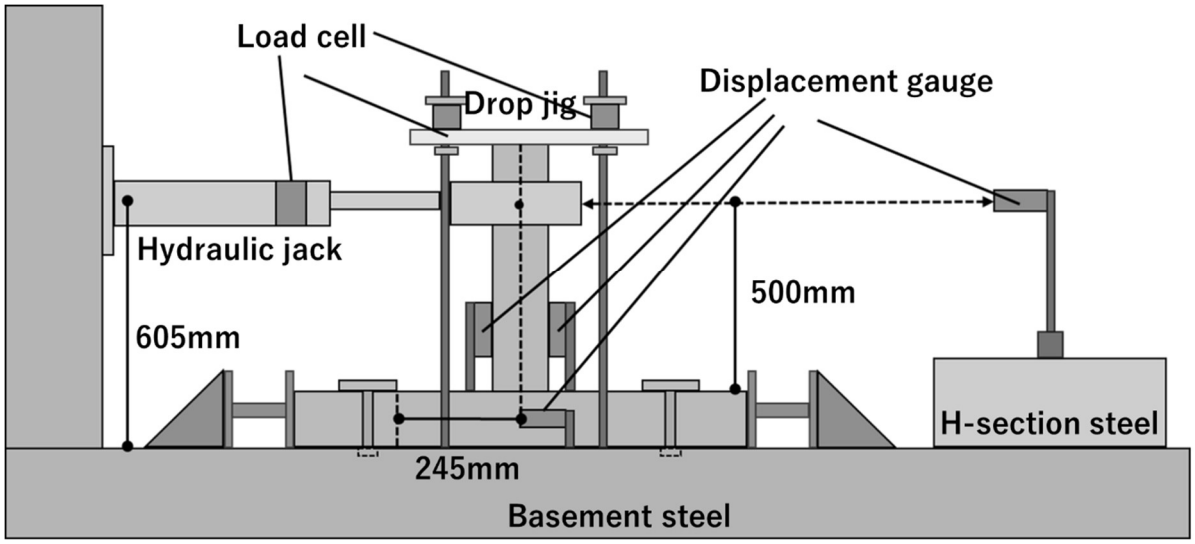

Figure 6. Experimental setup of flexural shear test.

2.4 Result of Experiment

Figure 7 shows the relationship between the moment and deformation angles of joint specimens. “0” means without termite damage. “10”, “15,” and “20” represent 10%, 15%, and 20% weight losses due to termite damage, respectively. For 0-N, 10-N, and 20-A, the bending moment was increased up to 1/30 rad (0.03 rad), and for the others, it was increased up to 1/50 rad (0.02 rad). It can be observed that the strength significantly decreased with an increase in damage rate. Furthermore, the decreased strength was significantly restored by resin reinforcement.

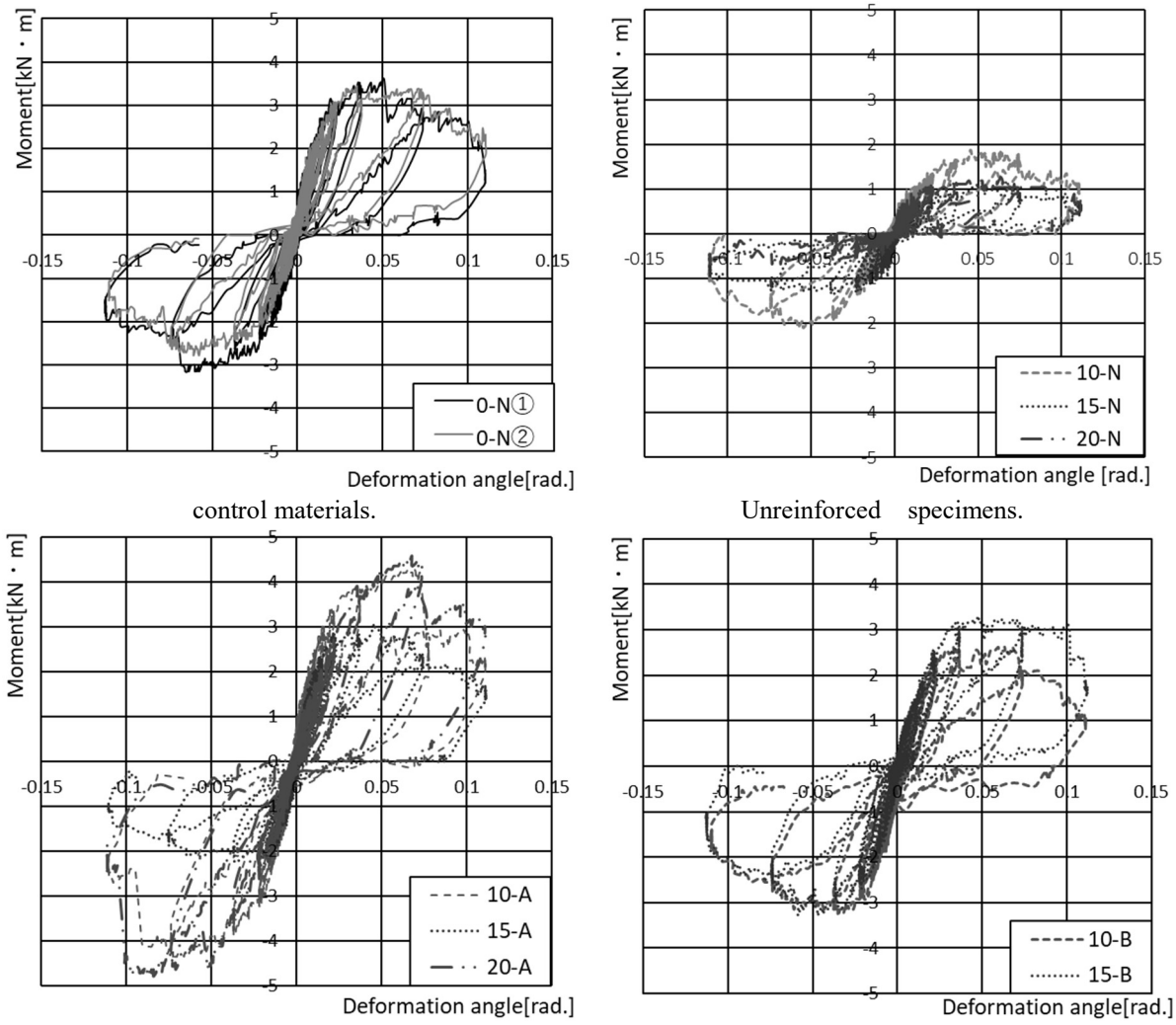

control materials. Unreinforced specimens.

Specimens filled with resin A. Specimens filled with resin B.

Figure 7. Relationship between the moment and deformation angle.

The volume ratio of the resin to be filled into the specimen was calculated by using its density information and the mass reduction rate of the deteriorated specimens, as shown in Figure 8. All specimens were filled with resin as described above, and a significant difference in the filling rate for each specimen was confirmed.

Figure 2 shows the skeletal curve between the moment and the deformation angle. Regarding the specimens without filling, the values of both rigidity and strength were lower than that of 0-N as a reference specimen. Regarding the specimens filled with resin A, a significant recovery in both rigidity and strength was observed. The rigidity and strength of 10-A and 20-A were higher than those of 0-N. The filling ratio of 15-A was about 10%. Therefore, it was observed that there would not be a considerable recovery of rigidity and strength because of insufficient filling. Overall, when the deteriorated timbers were filled with resin A, they exhibited a possibility of recovery in rigidity and strength. In contrast, the strength and rigidity of the specimens filled with resin B did not match that of 0-N. They exhibited higher strength and

rigidity than those without filling for the same feeding rate.

It was observed that the strength and rigidity of 10-B did not recover because of insufficient filling. In the case of 15-B, which had the highest filling rate, a complete recovery was not confirmed. This result might indicate that the low elasticity of resin was not effective for reinforcement. Despite the filling rate of approximately 40%, 10-A exhibited similar rigidity and strength to 0-N. If the filling level increased beyond a certain value, it might be unnecessary to fill the specimen completely. The variation in the filling rate was caused by bubbles generated due to the heat reaction of resin during curing. It will be necessary to evaluate the effect of the filling rate, filling position, and curing temperature of the resin on the mechanical properties of deteriorated timber members in the near future.

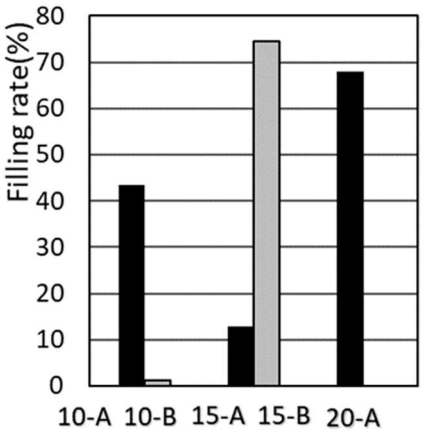

Figure 8. Filling rate.

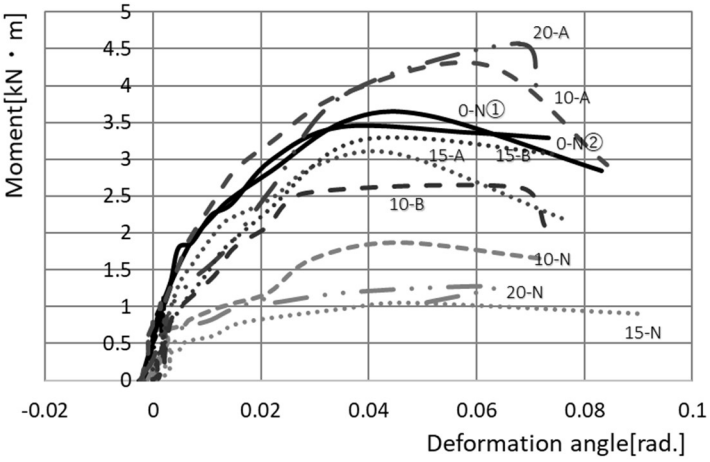

Figure 9. Relationship between moment and deformation angle

3 Ultrasonic Pulse Velocity Test

3.1 Aim

The damage caused by termites is significantly hidden inside the timber and often invisible. The ultrasonic testing machine (pundit) shown in Figure10, would be an effective method for detecting internal defects in timber. Ultrasonic pulse velocity can be measured by sandwiching both sides of the specimen. Filling conditions and restoration might be confirmed by evaluating the rate of change in ultrasonic velocity before and after resin filling.

3.2 Deterioration Detection

Figure11 shows the relationship between the mass reduction rate and the reduction in ultrasonic velocity before and after damage treatment. The reduction rate of ultrasonic pulse velocity is defined as the rate of the velocity to the velocity of the sound timber. A high correlation was observed between the mass loss rate and the reduction rate of ultrasonic velocity, as shown in Figure11. Hence, the mass loss rate can be identified by measuring the ultrasonic pulse velocity. As a result, it was suggested that the ultrasonic pulse velocity test might be effective in evaluating the deterioration by termites.

3.3 Check of Filling

The relationship between the filling rate and the increased rate of ultrasonic velocity is shown in Figure12, a high correlation was observed between them. Hence, the effectiveness of resin filling was confirmed by an increase in the ultrasonic pulse velocity

Figure 10. Ultrasonic testing machine. (pundit)

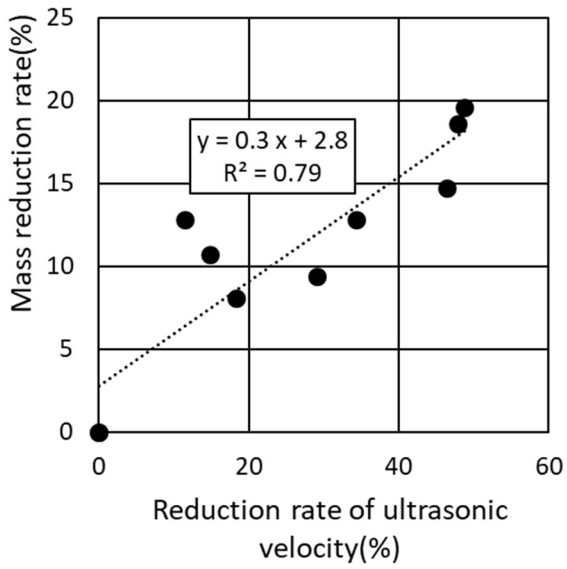

Figure 11. Relationship between mass reduction rate and reduction of ultrasonic velocity before and after feeding damage.

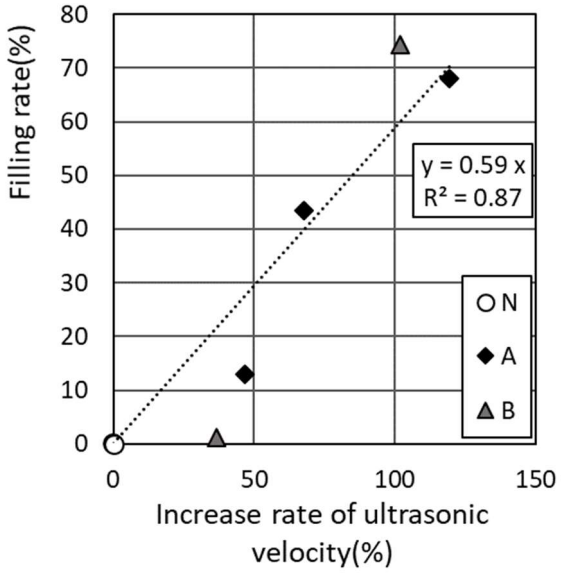

Figure 12. Relationship between filling rate and increase rate of ultrasonic velocity.

4 Conclusion

The following conclusion were obtained in this study:

- Throughout the shear test of pillar-base joints, filling the deteriorated timbers with the hard type resin led to the recovery of rigidity and strength. Hence, the effectiveness of resin filling as a reinforcement method was demonstrated.

- All test bodies were filled with resin in a staggered manner, and a significant variation in the filling rate for each specimen was confirmed. Even though the filling rate was approximately 40%, there was a specimen that showed rigidity and strength close to 0-N. If the filling level increases beyond a certain value, it might be unnecessary to completely fill the specimen. It will be necessary to examine the effect of the filling rate, filling position, and curing temperature of the resin on the mechanical properties of deteriorated timber members.
- A high correlation was confirmed between the mass loss rate and the reduction rate of ultrasonic velocity. Thus, it was suggested that the ultrasonic pulse velocity test might be effective in evaluating the deterioration by termites.
- A high correlation was observed between the filling rate and the increased rate of ultrasonic velocity. Therefore, the filling rate can be confirmed by an ultrasonic pulse velocity test in a non-destructive manner.

References

Architectural Institute of Japan (2018). Deformation and Fracture in Timber Structure, Maruzen Publishing Co., Ltd.

Goromaru Shuhei (2018). Proposal of reinforcement method by missing exploration and resin filling in deteriorated wooden buildings, Architectural Institute of Japan, Vol.88, pp.45-48

Higuchi Seiji (2003). A Retrospection: Early Examples of the Application of Synthetic Resins for the Conservation of Japanese Cultural Properties, Report of the National Museum of Ethnology, Vol.36, pp.53-91

Kawata Tatsuro (2017). Verification of termite and decay damages of wooden houses by dismantling survey, Architectural Institute of Japan, Vol.2017, pp.67-68

Takenouchi Yutaka (1998). Survey of Synthetic Resins Applied for the Conservation of Japanese Buildings, Science for conservation, Vol.37, pp.99-123

XV International Conference on Durability of Building Materials and Components
DBMC 2020, Barcelona
C. Serrat, J.R. Casas and V. Gibert (Eds)

Use of Steel Fiber Reinforced Concrete for the Protection of Buildings Against High Dynamic Actions

Vahan Zohrabyan, Thomas Braml, Tobias Zircher and Manfred Keuser

University of German Armed Forces, Chair for Concrete Construction,
Werner-Heisenberg-Weg 39, 85577 Neubiberg, Germany, vahan.zohrabyan@unibw.de

Abstract. *Nowadays ensuring the safety of people and the protection of infrastructure is a socially relevant topic, which requires a thorough investigation.*
The Institute of concrete construction at the University of the German Armed Forces in Munich is investigating the possibilities of using steel fiber concrete for the protection of military facilities and state-owned special buildings in Germany. In this research project steel fiber reinforced concrete is investigated under high dynamic loads specifically under contact detonation loading. Plates with varying reinforcement systems, different thicknesses, different fiber geometries, fiber contents and fiber types were produced.The following concrete compressive strengths C20/25, C40/50, C80/95 were used in this research project.The plates were loaded with 500 g, 750 g, 1000 g, 1500 g and 2000 g PETN explosive at the test facility of the German Armed Forces Technical centre for Protective and Special Technologies. An important property of construction material during ballistic threats and contact detonation is the concrete tensile strength. Through the addition of fibers, the post cracking behavior and the ductility of concrete components can be improved. All fiber-reinforced specimens showed less damage than the non-fiber reinforced elements. The aim of the study is to optimize the concrete mixture for the fiber concrete protection components considering the following factors: concrete quality, fiber content, fiber geometry, as well as aggregate size of the concrete. Another aim is to record and evaluate the damage parameters of the steel fiber reinforced concrete slabs after the highly dynamic load, and to investigate to offer suggestion for retrofitting. In this article, the test results of different steel framed concretes under highly dynamic conditions are presented.

Keywords: *High Dynamic Load, Protective Components, Contact Detonation, Steel Fiber Reinforced Concrete, Damage Crater.*

1 Introduction

As the number of people increases, the demand for both residential and public and state-owned buildings and infrastructures is increasing.

Taking into account the fact that mass influx of people to major cities is taking place lately, the demand for these buildings is increasing, resulting in higher prices for their construction, rent and service.

As the problem grows more serious and attracts a lot of construction space, it should be resolved as soon as possible by offering clear solutions. A solution to the problem for example can be the use of construction materials, structures and construction technologies that will make the structure more robust and durable (suitable for long-term use).

The resistance, security and durability of buildings for state and military facilities are set in completely different criteria such as embassies, military bases, nuclear power plants, chemical factories, government buildings, and so on.

doi:10.23967/dbmc.2020.145

Reconstruction or retrofitting work in these structures is always associated with high costs and high risks e.g.:

- the control should be increased during the construction works
- depending on the technological process, the production lines are partially or completely shifted which are associated with additional costs and effort
- auxiliary things, ammunition and workers should also be resettled

as a result, these buildings become more vulnerable and their normal operation is disrupted (one should not forget the fact that these facilities are the target of recent terrorist attacks).

In general, the protection of state-owned special buildings from possible terrorist attacks can be done in the following ways:

1. **newly constructed buildings:** depending on the significance of the building and the risks of the attack, the material must be defined and selected so that during the possible attack it ensures the safety of the objects and people (excluding of injuries and hazards in the shelter).
2. **already constructed buildings:** Depending on the significance of the building, the risks involved in the attack and the design, the protection can be implemented in the following ways:
   a) by reinforcing work
   b) by using an additional facade protection panel

2 Material and Constructions

The Institute of Concrete Construction at the Bundeswehr University Munich is investigating the possibilities of using steel fibre reinforced concrete for the protection of military facilities and state-owned federal buildings in Germany.

In this research project, reinforced concrete plates as well as steel fiber reinforced concrete plates made of different geometries and steel fiber content are produced and tested under different high dynamic loads (Zohrabyan *et al.*, 2019).

The impact on the components can consist of impact stress as well as contact detonation, near or far, from e.g. suicide bombers, vehicles loaded with explosives, etc.

For the construction of sensitive German Armed Forces infrastructure buildings and for buildings in out-of-area-operations, it is therefore necessary to consider these scenarios in design and service and to show to which extent the use of fiber reinforced concrete can lead to an improvement of the protective effect.

Within the framework of this research project, the protective wall and facing structures made of steel fiber reinforced concrete are investigated. Numerous experimental investigations are carried out.

The aim of the study is to make the panels as thin and light as possible in order to allow them to be attached to existing facades as a protective element. (Zircher *et al*., 2019)

Since in many buildings the panels cannot be fixed to the front of the building depending on the architectural solution, the protective wall would be used as a second alternative. The crash barrier panels should also be as light and thin as possible and must withstand both shock waves and impact loads. Here it is important that the panels can be produced in an economically favourable way and installed easily.

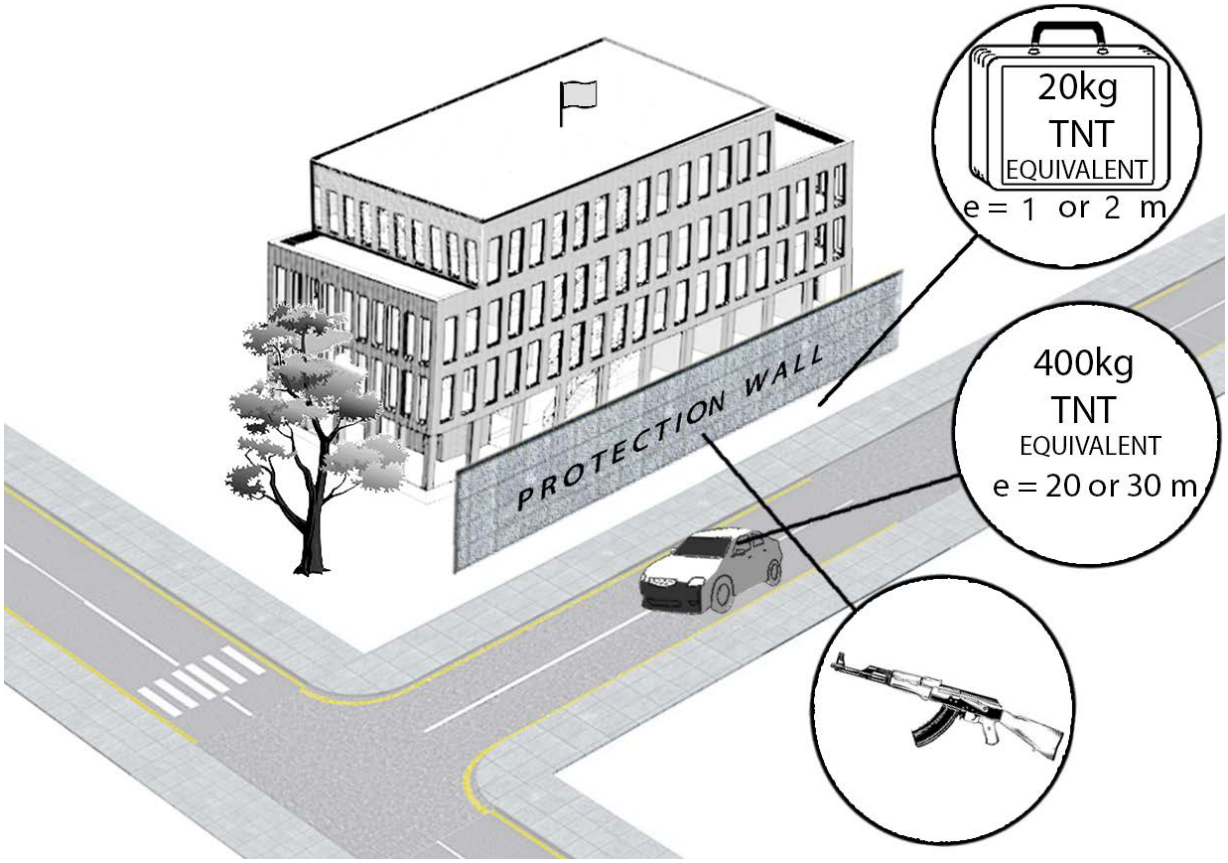

Figure 1. Scenarios of terroristic attacks on a building (Picture: V. Zohrabyan).

The hand gunshots represent a high risk for soldiers in action. If it were possible to eliminate this danger by using a protection system made of fiber concrete components with exclusion of secondary debris, part of the task would be solved. In order to slow down or completely intercept the secondary debris that flakes off as a result of the bombardment, the fiber reinforced concrete slabs will in future be equipped with a kind of steel grid curtain. In the following, the first test results of the fiber reinforced concrete slabs with high compressive strength concrete C80/95 under hand gunshot are presented.

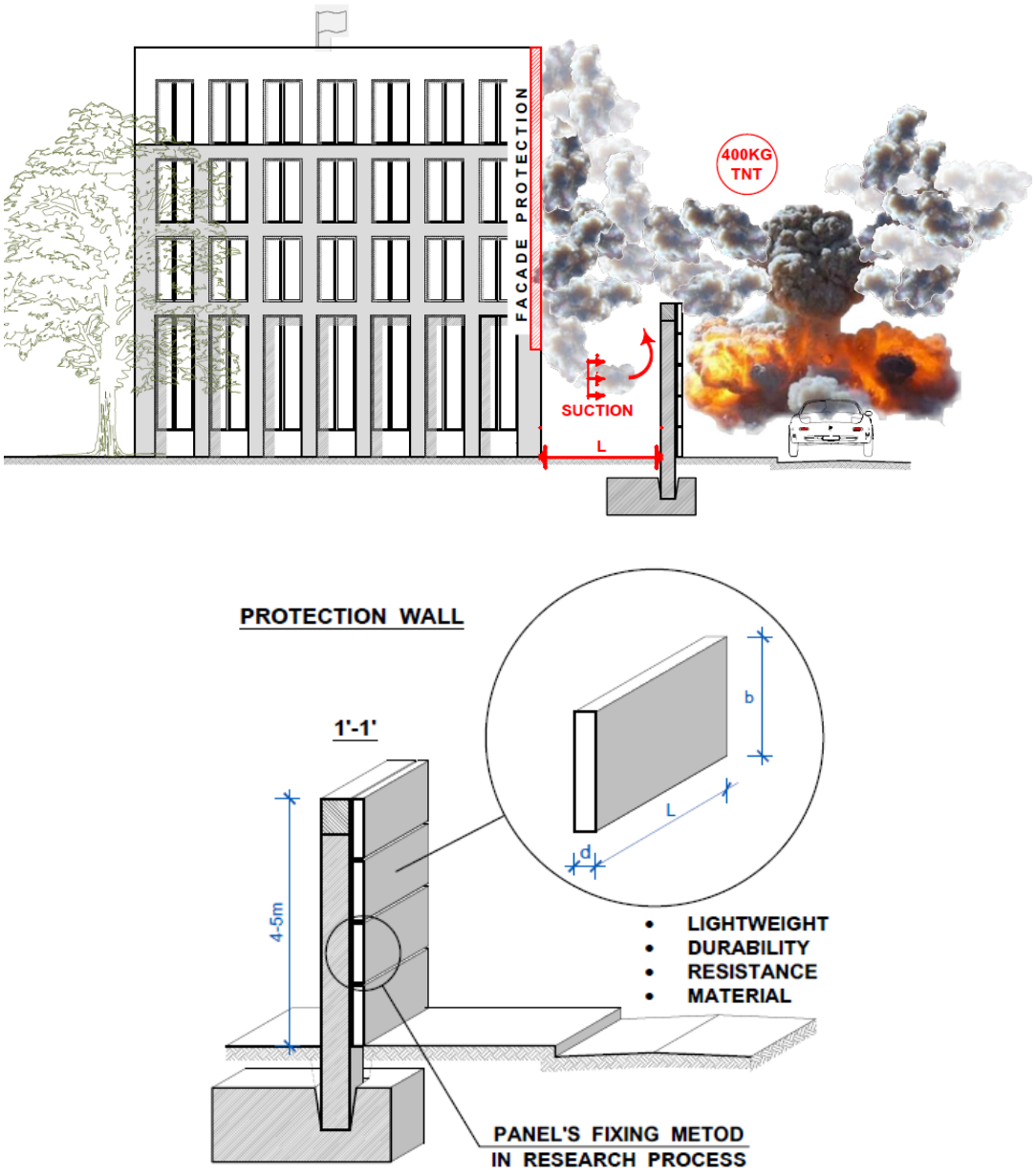

Figure 2. Attack with a car bomb with 400 kg TNT equivalent according to STANAG 2280 (Picture: V. Zohrabyan).

3 Concrete Mixtures and Plate Production for Hand Gunshot Tests

In this project there were produced four concrete mixtures, each consisting of 3 test specimens with different fiber types (polypropylene fibers and steel fibers). As steel fiber types, here it is used: Krampeharex KH DE35/0,55 N (length: 35 mm, diameter: 0,55 mm, tensile strength: 1350 N/mm²), (KRAMPEHAREX GmbH and Co. KG, 2017) BASFMF 254 (length: 54 mm, diameter: 0,81 mm, tensile strength: 552 N/mm²), BASFMF 249 (length: 48 mm, diameter:

0,85 mm, tensile strength: 400 N/mm²) and BASF MF 244 (length: 40 mm, diameter: 0,81 mm, tensile strength: 552 N/mm²) (BASF, 2017). The composition of the fiber concrete C80/95 is shown in Table 1.

Table 1.Concrete Composition Mix 1-4. (Kustermann *et al*., 2005) (Günter and Vollenschaar, 2011) (Richter, 2002) (Thienel and Kustermann, 2017)

Ingredients concrete mixture	**Mix 1-4**
Cement II/BM(S-D)52,5N	459 kg/m³
Stoneash	---
Aggregate 0/4 NfGK	784,9 kg/m³
Aggregate 4/8 NgGK	419,8 kg/m³
Aggregate 8/16 NgGK	620,6 kg/m³
Water	145 kg/m³
(W/C-ratio)	0,316
Superplasticizer	2,55 %
Fiber content	1 Vol % for Mix 1 to 4
Steel fiber KH DE35/0,55 N	78,5 kg/m³ (Mix 1)
Polypropylene fiber MF 244	9,1 kg/m³ (Mix 2)
Polypropylene fiber MF 249	9,1 kg/m³ (Mix 3)
Polypropylene fiber MF 254	9,1 kg/m³ (Mix 4)
Plate thickness	6 cm
Consistency	F4

The dimensions of the fiber reinforced plates are 300 x 300 x 60 mm.

Figure 3. Production of test specimens.

4 Hand Gunshot Test

The hand gunshot tests were carried out in the laboratory of the Institute of Ballistics Weapons and Munition at the Bundeswehr University Munich.

4.1 Test Setup and Execution

The 300 x 300 x 60 mm thick fiber concrete plates were shot with both soft- and hard-core shot caliber 7.62 mm x 51 308 Winchester. The projectiles have a weight of 9.5 g for soft core and 9.8 g for hard core. These were fired by the ammunition tester series 1055, which can be seen in the foreground in Figure 4.

The velocities of the projectiles were determined by measurement of two light barriers LS 23 F3/K2. These measure the speed with an accuracy of ± 0,1 %. An average bullet speed velocity is 842.75 m/s and an average projectile energy computed 3373.03 Joule. The camera was used in the bullet trap (Figure 4) which was triggered as soon as the projectile hit the plate.

Figure 4. Setup and execution of hand gunshot test.

4.2 Results

In order to measure the damage caused by the projectile, the 6 cm thick plates fired on were analyzed with regard to the crater volume (Figure 5).

The crater volume on the firing frontside and the opposite side as well as their mean values are given in Table 2 and compared Figure 6.

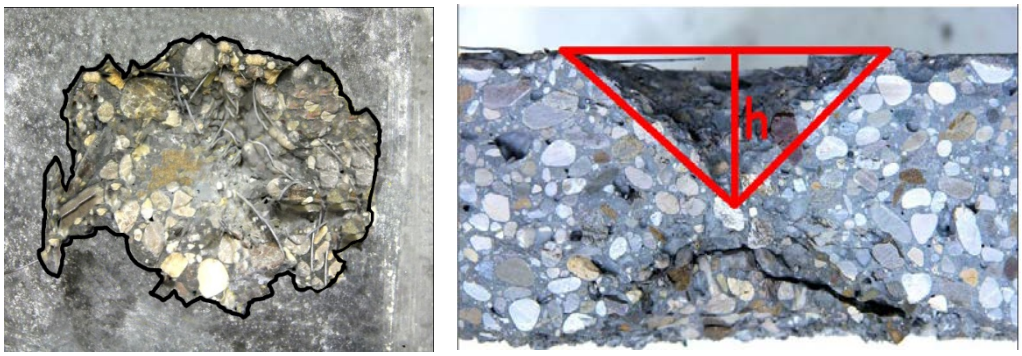

Figure 5. Crater volumes.

Table 2. Mean crater volume front and backside.

Steel Fiber Type	Munition	Crater vol. in front [cm ^{3}]	Crater vol. in backside [cm ^{3}]
MF 254	SC	59,93	148,58
MF 244	HC	65,71	68,33
MF 249	SC	130,74	239,66
KH DE35/0,55 N	SC	117,95	252,43

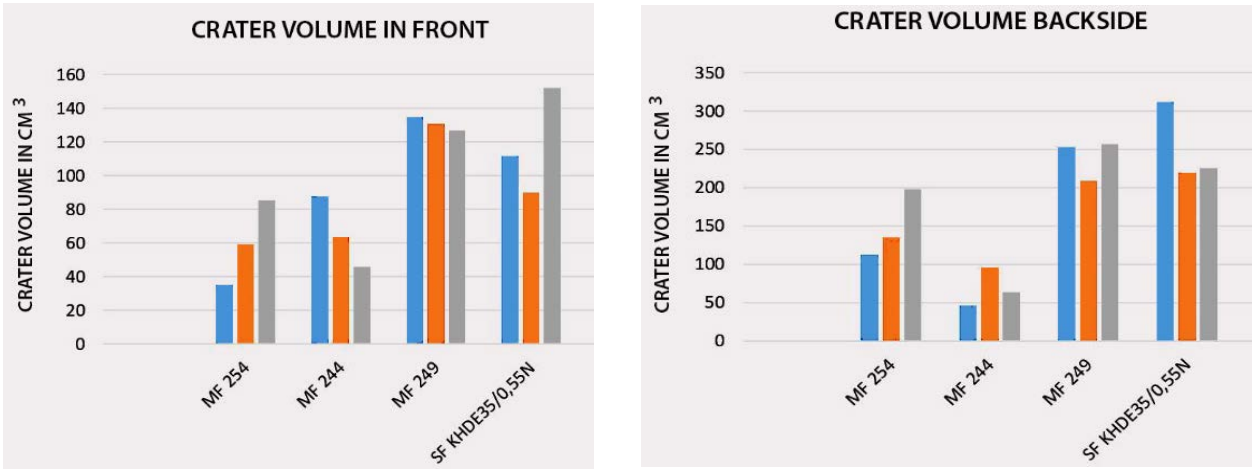

Figure 6. Evaluation of crater volumes.

5 Conclusions

The aim of the presented study was to develop a high-performance concrete mix of high – strength fiber concrete for the production of protective components, which was achieved.

- During the processing of the high-strength standard and fiber concrete, it turned out that a very high use of personnel compaction energy is required to ensure target-

oriented processing.

- The steel fibers KH DE35/0.55 N have the best effect in concrete in terms of increasing compressive strength and improving energy absorption when shot at with soft-core ammunition. The plates of this mixture showed a good protective capacity and withstood the shots well. (Michal *et al.*, 2014)
- It can be said that the specimens produced with fiber Masterfiber 249 also showed good results. It has to be said, however, that the fiber MF 249 only slowed down the projectile and did not stop it.

In conclusion, it can be said that it is possible to manufacture protective components from fiber reinforced, high-strength concrete.

Depending on the dimension and depth of damage after dynamic loading, the created cracks and voids in concrete components can be repaired and strengthened by impregnation and injection. The following variants are possible:

1) Closing the damage area: The aim is corrosion protection. It prevents the chloride entering the component.
2) Sealing the damaged area: The aim is to eliminate water-bearing cracks.
3) Frictional connection: The aim is to create a frictional connection between the two sides of the crack.

Acknowledgements

The authors thank the Institute of Ballistics Weapons and Munitions at the Bundeswehr University Munich for their supporting and providing their experimental facilities this project.

ORCID

Vahan Zohrabyan: http://orcid.org/0000-0003-3050-9687

References

BASF. (2017). *Broschüre MasterFiber-Lösungen für alternative Bewehrungen.*

Günter, N. and Vollenschaar, D. (2011). *Wendehorst Baustoffkunde: Grundlagen - Baustoffe - Oberflächenschutz ; mit 363 Tabellen.* Vieweg+Teubner Verlag / Springer Fachmedien Wiesbaden GmbH Wiesbaden, Wiesbaden, 27., vollständig überarbeitete Auflage Auflage.

KRAMPEHAREX GmbH and Co. KG. (2017). *Datenblatt Produkt Drahtfaser DE 35/0,55N.*

Kustermann, A., Keuser, M. and Grimm R. (2005). *Hochfeste Bindemittel und Zuschlagstoffe für hochfeste Betone unterschiedlicher Güte für Schutzanlagen der militärischenSonderinfrastruktur.* Universität der Bundeswehr München, Neubiberg: Doctorarbeit.

Michal, M., Keuser, M. and Frey, M. (2014). *Effects of a new Steel Fiber in Concrete under Small-Caliber Impact.* Universität der Bundeswehr München, Neubiberg: Doktorarbeit.

Richter, Th. (10.2002). *Zement Merkblatt Betontechnik Hochfester Beton / Hochleistungsbeton B16,.*

Thienel, K.-Ch. and Kustermann A. (2017). *Sonderbetone: Normalbeton, Hochfester Beton, Hochleistungsbeton, Ultrahochfester Beton.* Neubiberg.

Zircher, T., Keuser, M., Braml, Th., Berg, A. and Burbach, A. (2019). Investigations on the use of fiber concrete for infrastructure protection. *In Proceeding of the 18th International Symposium for the Interaction of Munitions with Structures*, Panama City Beach, FL, USA.

Zohrabyan, V., Braml, Th., Zircher, T. and Keuser, M. (2019). The residual load bearing capacity of reinforced concrete as well as steel fiber reinforced concrete components after contact detonation. In *Proceeding of the 18th International Symposium for the Interaction of Munitions with Structures*, Panama City Beach, FL, USA.

XV International Conference on Durability of Building Materials and Components
DBMC 2020, Barcelona
C. Serrat, J. R. Casas and V. Gibert (Eds)

Airborne Algal Growth on the Roofs of Membrane-Structured Residences in Cold Areas of Japan

Makiko Nakajima[1], Daisuke Masueda[1], Shuichi Hokoi[2] and Takayuki Matsushita[1]

[1] Department of Architecture, Graduate School of Engineering, Kobe University, 1-1 Nada-ku, Kobe, 657-8501, Japan, nakajima@gold.kobe-u.ac.jp

[2] Southeast University, Sipailou 2#, Nanjing, 210096, P. R. China, hokoi@seu.edu.cn

Abstract. *Discoloration of building facades due to airborne algae is observed in our surroundings. The growth conditions of these algae are not fully clear yet, and efficient preventive measures have not yet been determined. This study was aimed at investigating the influence of ambient environment and building structure on algal growth. A residential building in the cold region of Japan was surveyed. The roof was a multilayered structure consisting of a semi-transparent film, an air layer, an outside insulation layer, and was supported by rafters. The soiled state was visually observed and recorded through pictures, and seemed to be particularly increased in autumn. Several black stripes appeared on the northeast (NE) roof four months after its cleaning. The soiling first appeared on the film backed by the rafter, and then extended to the film backed by the air layer. It rarely appeared on the southeast roof. The roof-surface temperature was measured and a stripe-shaped distribution was observed. The temperature of the film with rafter was higher and lesser than that of the film with the air layer during the night and in the early morning, respectively. Although condensation occurred nightly, its frequency showed no orientational difference. Algae can die when exposed to a temperature higher than 40 °C. The southwest roof had the longest period of a surface temperature over 40 °C, while the northwest (NW) roof had the shortest period of this surface temperature. These measurements corresponded well to the survey results according to which soiling mainly occurred on the NE and NW sides of roofs. The time for algal growth was estimated assuming that algae can grow at surface temperatures between 0 and 40 °C.*

Keywords: *Roof Soiling, Airborne Algae, Surface Temperature, Condensation, Membrane Structure.*

1 Introduction

An observation of the exterior walls of building walls shows many black or/and green soiling. Some studies showed that this is caused by the adhesion and growth of airborne algae. Currently, the main countermeasures against the algal soling are cleaning and repainting of such walls; however, efficient preventive measures have not been developed yet.

Sharma et al. showed that airborne algae reported to date are species of 103 classes of the three divisions. Tsujimoto et al. investigated the algal soiling in Japan and showed that algal soiling could occur in all Japanese climatic zones. Häubner et al. showed that *Stichococcus* sp. and *Chlorella luteoviridis* could grow at 1–35 °C, and their growth rate increases with increasing temperature and reaches the maximum at 10–25 °C and is nonexistent at 30–35 °C. Agrawal et al. showed that the survival rate of algae is greatly reduced when algae are exposed to high temperatures over 40 °C for several tens of minutes. Nakajima et al. surveyed the soiling conditions of a building with respect to the surrounding environment and showed that algae could grow even on walls rarely exposed to rainwater when the humidity is high and if

temperatures remained below 40 °C. They thus proposed a predictive model of the algal growth and death on exterior walls as a function of the solar radiation, temperature, and humidity.

Although several studies have shown the qualitative relationship between airborne algal growth and the environment, their quantitative relationship has not been fully evaluated yet. This study was aimed at determining this relationship by focusing on a residential building with membrane-structured roofs in a cold region of Japan.

2 Method of Survey and Measurements

2.1 Overview of Measured Building and Climatic Conditions

The one-story residential building that was considered for this study is located in Taiki town, Hokkaido, Japan, and is surrounded by open grassland. It has a hipped roof structure, with rafters arranged at intervals of 40 cm and insulations packed between them (Figures 1a and 1b). The part with a thermal insulation layer has a cross section with a six-layer structure comprising an exterior film, an outside air layer, the thermal insulation, a vapor-barrier, an inside air layer, and the glass cloth, from the outside (Figure 1c). All the materials are semi-transparent. The exterior film is made of a vinyl chloride film and a polyester base fabric and coated by fluororesin.

Taiki town is located close to the sea and has subarctic climate. Figure 2 provides a graphical representation of the outdoor temperature, relative humidity, and precipitation. The daily average temperature falls below freezing point in winter but rises to approximately 20 °C in summer. The relative humidity is over 80% in summer.

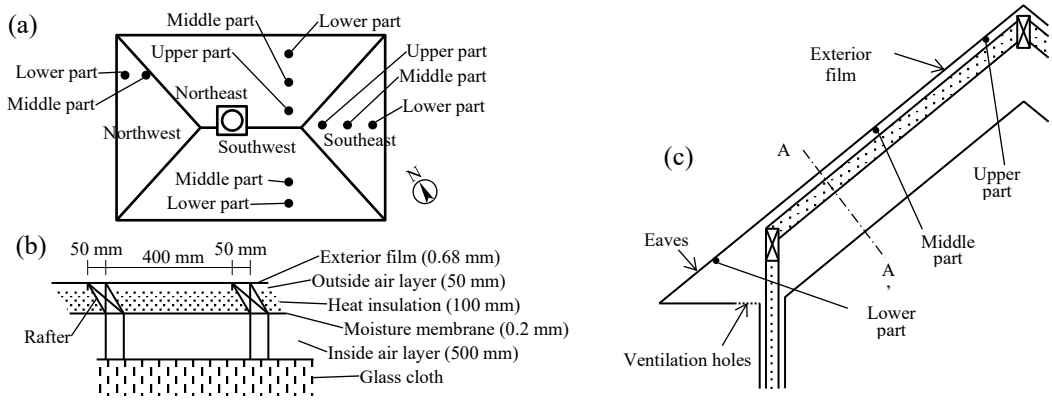

Figure 1. Overview of the measured house: (a) roof plan, (b) A–A' section of roof in (c), and (c) vertical section of the roof.

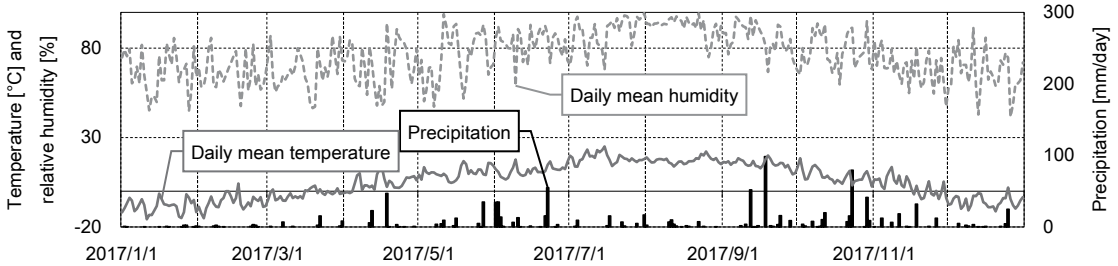

Figure 2. Outdoor temperature, relative humidity, and precipitation in Taiki Town, Hokkaido, Japan.

2.2 Measurement of Roof Surface Temperatures and Climatic Conditions

The surface temperatures of the roofs were measured through thermocouples and hygrothermal sensors. The thermocouples were fixed to the indoor side of the exterior film by tape, and the measured values were regarded as the surface temperatures because the film thickness was very thin at 0.68 mm. The surface temperature was measured at the upper, middle, and lower parts on the NE and southeast (SE) roofs, and at the middle and lower parts on the NW and southwest (SW) roofs, as shown in Figure 1a.

The outdoor temperature and humidity were measured by a thermometer and hygrometer (U23-002, Onset Computer Corporation), respectively, about 5-m NW to the building, where the vertical and horizontal global solar radiations were measured through pyrheliometers (ML-01, EKO Instruments).

2.3 Survey on Roof Soiling

The soiling of roofs was recorded through photographs captured by fixed-point cameras set around the building on September 2017; the NE, NW, and SE roofs were photographed every 4 h.

3 Surveyed and Measured Results

3.1 Soiling of Roof Surface

3.1.1 Soiling difference depending on roof orientation

The photos of each roof are shown in Figure 3. The stripe-shaped soiling extends vertically from the top to the bottom in the center of the NE roof. In the same manner, the stripe-shaped soiling is also generated in the center of the NW roof. The soiling cannot be seen on the SE and SW roofs.

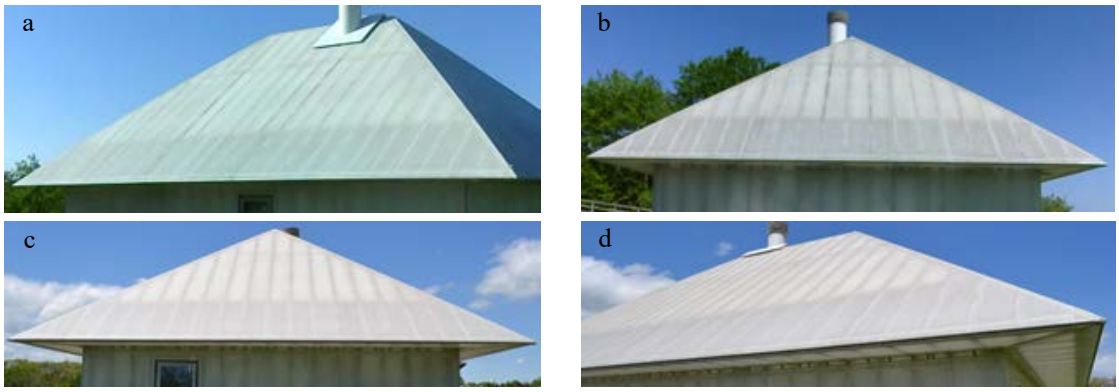

Figure 3. Photographs of (a) NE roof, (b) NW roof, (c) SE roof, and (d) SW roof on May 2018.

3.1.2 Time profiles of soiling on NE and NW roofs

The photos of the NE and NW roofs from September 19, 2017 to March 19, 2019 are shown in Figures 4 and 5, respectively. The roofs were cleaned by brushing and high-pressure washing

on April 4, 2017, after which soiling was not observed on July 5, 2017. The soiling occurred again at the mid-left part of the NE roof on September 19, 2017, and was observed on the roof part downward from the chimney on October 20, 2017. On November 18, 2017, the soiling darkened but did not show further change until December 15, 2017. The soiling on the eaves faded on May 27, 2018, then became darker between June 21 and July 26, 2018. On August 26, 2018, the soiled area increased, the color darkened more than that on July 26, and gradually darkened further from September 22 to October 15, 2018. The roofs were cleaned again on October 22, 2018, after which soiling occurred at the left part of the roof downward from the chimney on November 19, 2018; this remained unchanged from December 23, 2018 to January 23, 2019. The stripe-shaped soiling increased in the area downward from the chimney and darkened on March 19, 2019.

In summary, the soiling hardly increased in the summer (July and August) and winter (December, January, and February) but increased from March to June and from September to November. The NW and NE roofs showed the same soiling tendencies.

Figure 4. Photographs of NE roof from September 2017 to March 2019.

Figure 5. Photographs of NW roof from September 2017 to February 2019.

3.1 Surface Temperature of Roofs

3.2.1 Difference in film temperature between parts backed by rafter and air layer

The surface temperature of the NE roof in summer and winter is shown in Figure 6. In summer, the temperature of the film backed by the rafter (hereafter referred to as rafter part) was almost the same as that of the film backed by the air layer (air layer part) (Figure 6a). The temperature of the rafter part was approximately 1 °C higher than that of the air layer part during the daytime, and the temperatures of both were almost the same at night. In winter, the temperature of the air layer part was 3–5 °C higher than that of the rafter part in the daytime and 1–2 °C higher at night (Figure 7a).

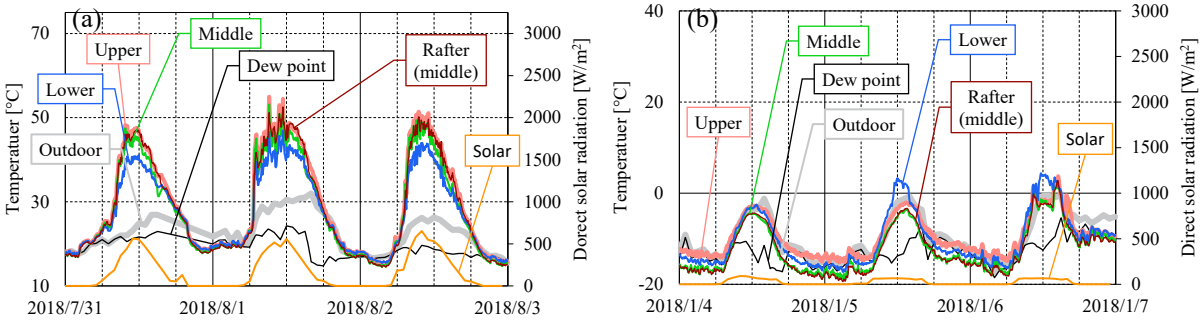

Figure 6. Direct solar radiation and surface temperatures of NE roof in (a) summer and (b) winter.

3.2.2 Annual change in surface temperature on each roof

The annual surface temperature on the NE and SW roofs is shown in Figure 7, where high temperatures of over 45 °C can be observed from June to August on the NE roof, and from February to December on the southwest roof. On the NE roof, where the incident direct solar radiation was the least, the frequency of temperature higher than 45 °C was least (Figure 7a). The daily fluctuation of the surface temperature was large on the SW roofs (Figure 7b).

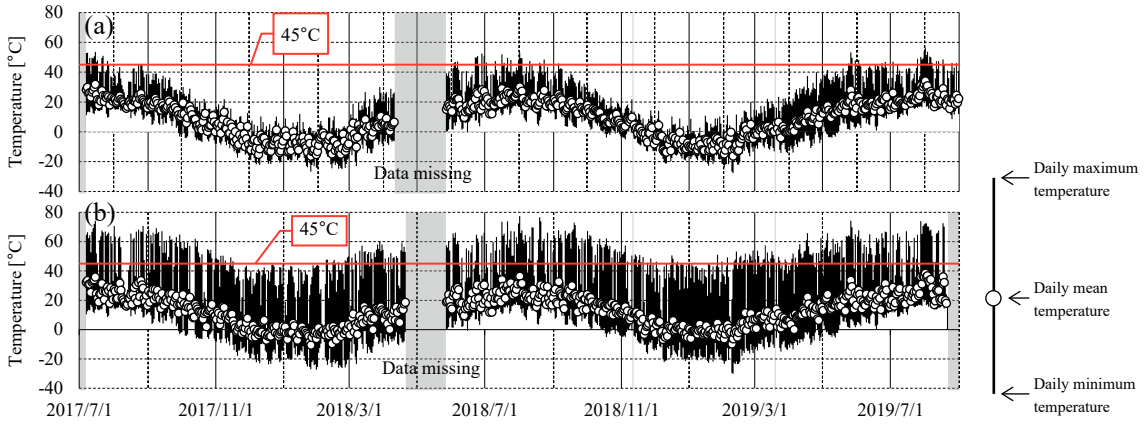

Figure 7. Annual surface-temperature change on (a) the NE and (b) SW roofs. The bar length and circles represent the daily-temperature difference and daily mean temperature, respectively.

3 Discussion

3.1 Relationship between Roof Surface Temperature and Roof Structure

In general, the roof surface temperature is higher at the upper part than at the lower parts (Figures 6). This is probably because the outside air layer was warmed by solar radiation, leading to thermal stratification. This stratification is likely to be accelerated by the nonuniform structure of the roof. The upper and middle parts comprise the air layer of 50-mm thickness and a 100-mm-thick insulating material, while the lower part does not have thermal insulation. Therefore, the air volume at the upper and middle parts was smaller than that at the lower part and their heat capacities were smaller.

4.2 Surface Condensation on Roof

Figure 8 shows the time when the surface temperature was below the dew-point temperature of the outdoor air. Frost was assumed to occur when the surface temperature was below 0 °C. As shown in Figures 6, the surface temperatures on all roofs decreased below the dew-point temperature of the outdoor air because of the nocturnal radiation, and they dropped below 0 °C at night from November to April. Condensation occurred from May to October, and condensation per day was long especially from September to October. This period of condensation differs depending on the roof orientation; however, the frequency of occurrence shows only a very small dependence on the orientation.

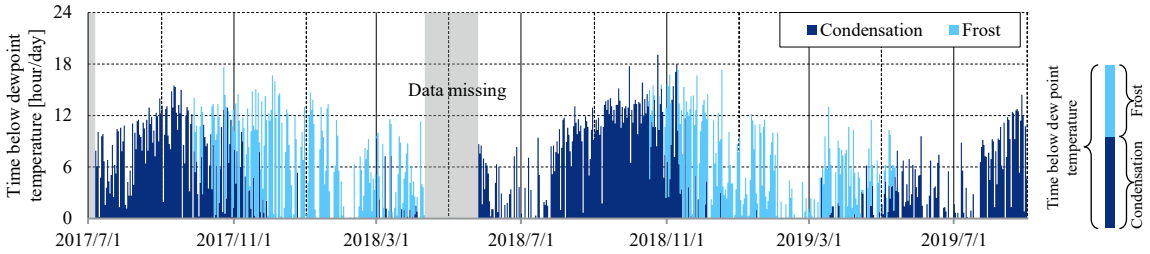

Figure 8. Time per day that the surface temperature was below the dew-point temperature of the outdoor air. Air-layer part at middle part of NE roof.

4.3 Dependence of Soiling on Roof Orientation

The soiling situation at the surveyed building was evaluated by focusing on the surface temperature and available water (condensation). Algae can grow in the temperature range of 1–30 °C, and they die when exposed to the high temperatures. Thus, we focused on the occurrence frequency of high temperatures of over 45°C.

On all the roofs, the surface condensation occurred (the source of water supply to the algae) at night from May to November. Therefore, the algae can grow from May to November.

The measured roof temperatures showed that the SW, SE, NW, and NE roofs, in this order, show high temperature frequency of over 45 °C. From May to November, the surface condensation on the SE and SW roofs occurred during the night but was over 45 °C almost every day. Therefore, the algae are considered to die because of high temperatures during daytime, and soiling did not occur despite sufficient water supply. Compared to all roofs, the frequency of the high temperature of over 45 °C was least on the NE roof when surface condensation occurred, and thus the algae grew most actively on this roof. These results correspond well to the surveyed results where soiling was observed to occur on the NE and NW roofs but not on the SE and SW roofs (Figure 3).

4.4 Difference between Soiling on Rafter and Air-Layer Parts

For the rafter and air-layer parts of the NE roof, the frequency of high temperatures of over 45 °C was almost same. However, the surface condensation on the rafter part occurred more frequently than on the air-layer part, and the condensation period per day was longer on the rafter part from March to November. Therefore, the algae are considered to grow more likely at the rafter part than at the air part (Figure 3).

4.5 Occurrence of Soiling Based on Time of Year

Considering the water supply and temperature suitable for algal growth, the estimated time of the year when the algae can survive is shown in Figure 9. For example, on the NE roof, the surface temperatures were from 0 to 45 °C and condensation occurred from August to September 2017, the middle of July 2018, and from September to October 2018. Thus, the algae are predicted to grow during these periods. This prediction corresponds well to the result that the soiling was observed from July to November 2017 and from June to November 2018, as shown in Figure 4.

On the SW roof, the high temperatures of over 45 °C occurred all year round. Therefore, it is predicted that the algae could grow only in a limited time in February 2017, from the end of November to the beginning of December 2017, and a part of January 2018. These predictions well correspond to the observed result that soiling did not occur on the SW roofs.

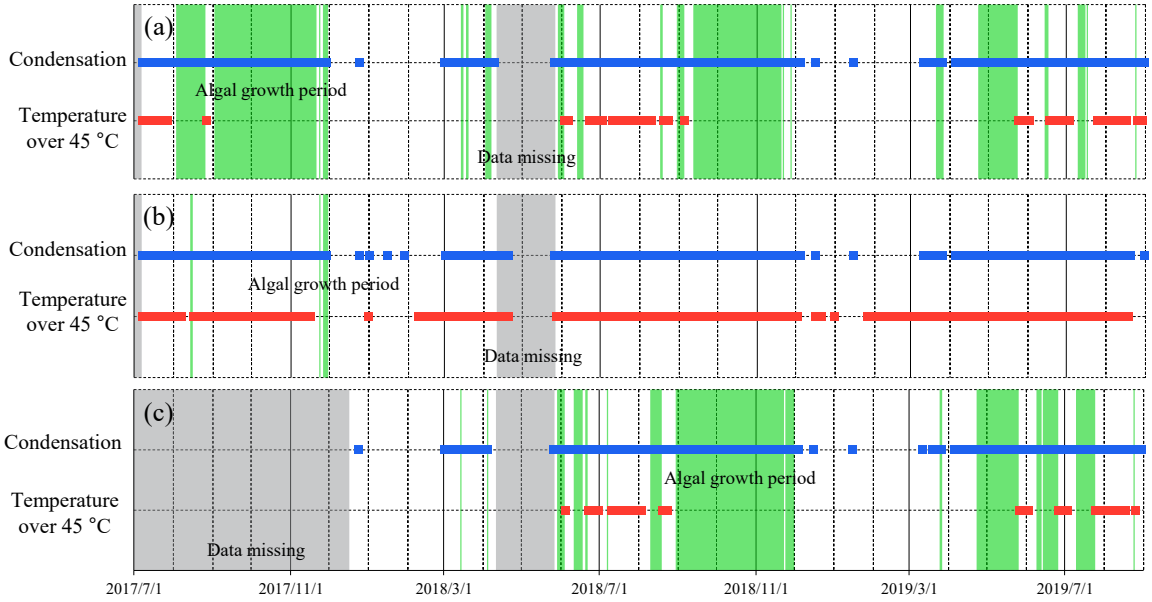

Figure 91. Estimated period for algal growth because of the occurrence of the condensation and high temperature. Air-layer part of middle part of the (a) NE and (b) SW roofs. (c) Rafter part of the middle part of the NE roof. Condensation: the day when the condensation occurred. Temperature over 45 °C: the day when the daily maximum temperature reached over 45 °C.

5 Conclusion

This study was aimed at clarifying the quantitative relationship between airborne algal growth and the surrounding environment. The following conclusions can be drawn.

- The stripe-shaped soiling extended vertically from top to bottom on the NE and NW roofs. In contrast, soiling did not occur on the SE and SW roofs. On the NE and NW roofs, the soiling hardly increased in the summer and winter but increased from March to June and from September to November.
- The SW, SE, NW, and NE roofs, in this order, showed the highest frequency of surface

temperatures of over 45 °C because of solar radiation.

- The surface condensation occurred on all roofs from May to October, and the daily condensation time was long, especially from September to October. The frequency and period of the condensation were almost the same for all roofs (orientation).
- The surface temperature of the SE and SW roofs was higher than 45 °C during the daytime from May to November. Therefore, despite the occurrence of the condensation, the algae died owing to the high temperature, and thus soiling did not occur.
- The comparison of the rafter and air-layer parts of the NE roof showed an almost same frequency of high temperatures of over 45 °C. However, the condensation time per day at the rafter part was longer than that at the air-layer part. Therefore, the algae could grow more on the rafter part, where the soiling was first observed to occur.

Acknowledgements

This work was supported by JSPS KAKENHI Grant Number 17K14772 and LIXIL Housing Foundation.

ORCID

Makiko Nakajima: https://orcid.org/0000-0001-7753-4113

References

Y. Tsujimoto, N. Ohba and T. Sudoh (1992). Identification of Fresh-water Algae of External Building Walls and Study on an Evaluation Method for the Soiling by Fresh-water Algae, J. Struct. Constr. Eng. (Transactions AIJ). 433 11–17. doi:10.3130/aijsx.433.0_11.

N. Ohba and Y. Tsujimoto (1996). Soiling of external materials by algae and its prevention 1. Situation of soiling and identification of algae, Mokuzai Gakkaishi. 42 589–595.

C.C. Gaylarde and P.M. Gaylarde (2005). A comparative study of the major microbial biomass of biofilms on exteriors of buildings in Europe and Latin America, Int. Biodeterior. Biodegradation. 55 131–139. doi:10.1016/J.IBIOD.2004.10.001.

A.Z. Miller, P. Sanmartín, L. Pereira-Pardo, A. Dionísio, C. Saiz-Jimenez, M.F. Macedo and B. Prieto, (2012). Bioreceptivity of building stones: A review, Sci. Total Environ. 426 1–12. doi:10.1016/j.scitotenv.2012.03.026.

N.K. Sharma, A.K. Rai, S. Singh and R.M. Brown (2007). Airborne algae: their present status and relevance1 doi:10.1111/j.1529-8817.2007.00373.x, J. Phycol. 43 615–627. http://www.blackwell-synergy.com/doi/abs/10.1111/j.1529-8817.2007.00373.x.

W.M. Darley (1982) Algal biology: a physiological approach, Blackwell Scientific Publications.

N. Häubner, R. Schumann and U. Karsten (2006). Aeroterrestrial microalgae growing in biofilms on facades - Response to temperature and water stress, Microb. Ecol. 51 285–293. doi:10.1007/s00248-006-9016-1.

S.C. Agrawal and V. Singh (2000). Vegetative survival, akinete formation and germination in three blue-green algae and one green alga in relation to light intensity, temperature, heat shock and UV exposure, Folia Microbiol. (Praha). 45 439–446. doi:10.1007/BF02817618.

M. Nakajima, S. Hokoi, D. Ogura and C. Iba (2015). Relationship between environmental conditions and algal growth on the exterior walls of the Ninna-ji Temple, Kyoto, in: Energy Procedia. doi:10.1016/j.egypro.2015.11.149.

M. Nakajima, S. Hokoi, D. Ogura and C. Iba (2015). Modeling of algal gorwth and death on exterior walls of buildings, J. Environ. Eng. 80. doi:10.3130/aije.80.1125.

T. Martinez, A. Bertron, G. Escadeillas and E. Ringot (2014). Algal growth inhibition on cement mortar: Efficiency of water repellent and photocatalytic treatments under UV/VIS illumination, Int. Biodeterior. Biodegradation. 89 115–125. doi:10.1016/J.IBIOD.2014.01.018.

F. Gladis and R. Schumann (2011). Influence of material properties and photocatalysis on phototrophic growth in multi-year roof weathering, Int. Biodeterior. Biodegradation. 65 36–44. doi:10.1016/J.IBIOD.2010.05.014.

XV International Conference on Durability of Building Materials and Components
DBMC 2020, Barcelona
C. Serrat, J.R. Casas and V. Gibert (Eds)

Analysis of the Degradation Condition of Elementary Schools

Sónia Raposo

Buildings Department, Laboratório Nacional de Engenharia Civil, Av. do Brasil 101, 1700-066 Lisboa, Portugal, sraposo@lnec.pt

Abstract. *Currently, there is still no information regarding the performance of public buildings after their construction and the relationship with the needs for carrying out maintenance activities. This paper presents some of the main anomalies detected in six schools, built between 1997 and 2003 in Lisbon. The analysis of the degradation condition of these schools was based on data obtained through detailed visual inspections, carried out in three distinct periods of their operation phase, 2007, 2013 and 2018. The highest level of severity mainly concerns defects on buildings structure and buildings envelope and results from bad decisions made during design and/or construction. Therefore, there are serious problems related to the premature deterioration of these educational buildings, requiring expensive, complex and unplanned major repairs to achieve their specified design service life. This work highlights the need for greater involvement of school building management entities, in the early stages of the building process, including design, tendering, construction and handover.*

Keywords: *Elementary School, Building Condition, Anomalies, Durability.*

1 Introduction

The building condition assessment (BCA) is a systematic inspection, review, and report on the state of a building's structure, construction elements and systems. The BCA provides an identification of elements anomalies and the expected costs to remedy those deficiencies. This is an important step for the management of buildings maintenance and should be applied to the existing elementary public school portfolio of Lisbon. This network of schools includes more than 100 buildings with construction ages ranging from the nineteenth century to the beginning of this century (Raposo, 2011). Despite the existence of schools operating in very old buildings, are the most recent schools, built after 1980, that present major problems of conservation and maintenance (Raposo *et al.*, 2008).

In the present paper, the results obtained through visual inspection of six school establishments, built between 1997 and 2003, are presented. Inspections were carried out in 2007, 2013 and 2018 and it was possible to identify some recurring anomalies and causes for the accelerated and premature degradation that occurs in these buildings.

2 Research Methodology

In 2007 Raposo, Fonseca and Brito (2008) carried out a preliminary research on six elementary school of recent construction in Lisbon. The work was developed in two phases: (i) collection and treatment of information from the design phase and from the use and operation phase, (ii) fieldwork with detailed visual inspection of the buildings. In 2013 an inspection and BCA was performed of the building's structural and envelope components and playgrounds and outdoor spaces (Luís, 2013), and of the building's interior elements, including finishes, walls, ceilings, doors and plumbing (Nogueira, 2013). In 2018, the National Laboratory for Civil Engineering

carry out an assessment of the maintenance condition of 55 kindergarten (k) and elementary schools (EB1), for the Municipality of Lisbon (Vilhena *et al.* 2019). Extensive and detailed photographic and written records were made about anomalies detected allowing its comparison over time.

Table 1 shows the building characteristics of Prista Monteiro School (PM), Vale de Alcântara School (VA), Alto da Faia School (AF), Padre Rocha e Melo School (PRM), Alta de Lisboa School (AL) and Vasco da Gama School (VG) integrating the kindergarten and three levels of basic education.

Table 1. School Buildings Characteristics.

Schools	Year	Pupils	Level	GA (m2)	Floors	Year of Inspection
PM	1997	110	EB1	2200	2	2007-2018
VG	1999	600	k+EB1/2/3	8800	3	2007-2018
VA	2001	130	k+EB1	1700	2	2007-2018
AF	2001	340	k+EB1	4000	3	2007-2013-2018
PRM	2002	330	k+EB1	3000	2	2007-2018
AL	2003	330	k+EB1	3300	2	2007-2013-2018

3 Results

3.1 Foundation and Structure

The structure of VA School building is a system of slabs, columns and beams in reinforced concrete. The inspection carried out at this school in 2018, revealed the existence of serious anomalies in the structure namely, the existence of extensive structural deformations and the existence of wide opening cracks in multiple walls and ceilings on the two floors of the building.

Figure 1 shows the result obtained through inspections carried out in 2007 and 2018, where it is possible to observe the degradation mechanism of the building's structure and interior and exterior partition walls. They were identified foundations settlement problems and water infiltration through the roof in several classrooms (Vilhena *et al.*, 2019). Following this inspection, the school was closed for further rehabilitation intervention.

Figure 1. VA School: deterioration process of the exterior partition wall in 2007 (a) and 2018 (b). Cracks in walls in 2007 (c) and 2018 (b).

The 2018 survey, carried out in AF school, revealed the existence of anomalies in the outdoor constructive elements. The most frequent anomalies in these elements are oriented cracking,

severe fracture, differential settlements and deteriorated expansion joints without sealant. Some of these defects were detected since 2007, when only six years had passed on handover of the building. Figure 2 shows the result obtained through inspections carried out in 2007, 2013 and 2018, on the supporting wall located in AF school's outdoor spaces. It is possible to observe the existence of settlements and structural movements that remain unsolved.

Figure 2. AF School-outdoor spaces: deformation and settlement of the supporting wall and the recurring appearance of cracks. Anomaly evolution in 2007 (a), 2013 (b) and 2018 (c).

AL School was implanted on a landfill site, which is very steep along the longitudinal and transversal development of the building. The building structure is in reinforced concrete and is made of two blocks connected by an access ramp and stairs. In 2007, the existence of several anomalies resulting from the differential settlement of the two blocks was already visible (cracking in walls and broken elements). Although several repairs have been carried out in the building, 2013 and 2018 surveys revealed that the settlement movement remains active and the cracks in the walls and floors continue to appear (Fig. 3a). In AL, AF and PRM Schools, deteriorated expansion joints without filling material and sealant was observed (Fig. 3b,c,d,e). Lack of repair of the joints exposes the building elements to water infiltration and mechanical actions.

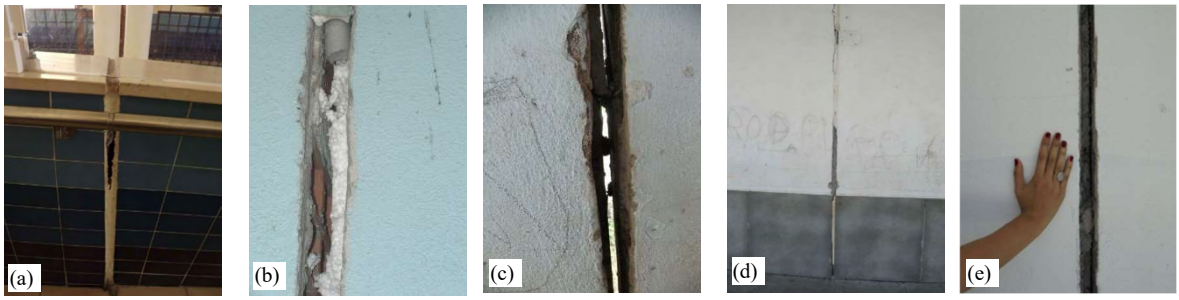

Figure 3. AL School: foundation settlement movement: broken stone and construction joint opening in 2013 (a). Expansion joints without sealant: AF School in 2007 (b) and 2018 (c); PRM School in 2007 (d) and 2018 (e).

3.2 Building Envelope

3.2.1 Roofs

Three of the six buildings have flat roofs (PRM, AL and VA schools), AF school presents a mixture of flat and sloping roofs in metal sheet, PM school present a sloping roof covered with

ceramic tiles, and VG School presents a non-traditional roof covering made of ceramic pellets. In PM School, infiltrations water problems continue to be observed since 2007 survey, in the area of the gymnasium affecting both the ceiling and the floor. The AF School continues to present problems between the several flat and sloped roofs boundary buildings (Fig. 4a). Skylights are the element that most frequently presents anomalies caused by water infiltration. It was possible to observe the degradation mechanism in ceilings, walls and floor coatings, caused by water infiltration through skylights in PMR School (Fig. 4b,c).

Figure 4. AF School: mixture of flat and sloping roofs in metal sheet (a). Water infiltration problems betewen the building´s roofs. PMR School skylights problems in 2018 (b), (c).

3.2.2 Exterior walls, windows and doors

Part of the exterior walls of AF School is made up of *Corten* steel panels and it was found that over the years, colour changed from orange-brown to dark brown as expected (the rust layer transforms into a patina layer) (Fig. 5a, 5b). However, aesthetically the overall wall covering did not result because there are panels with different colors, which may have been the result of localized repair work or replacement of some panels over the years. The wall facade presented serious problems of corrosion and lack of fixation, with risk for building users (Fig. 5c). In PRM School, the cladding of ventilated facades in wooden panels presented several anomalies related to acts of vandalism (scratches and graffiti), stains and non-uniforme darkening of the surface and unequal joint opening (with large local openings) without any filling (Fig. 5d,e) exposing the building elements to water infiltration.

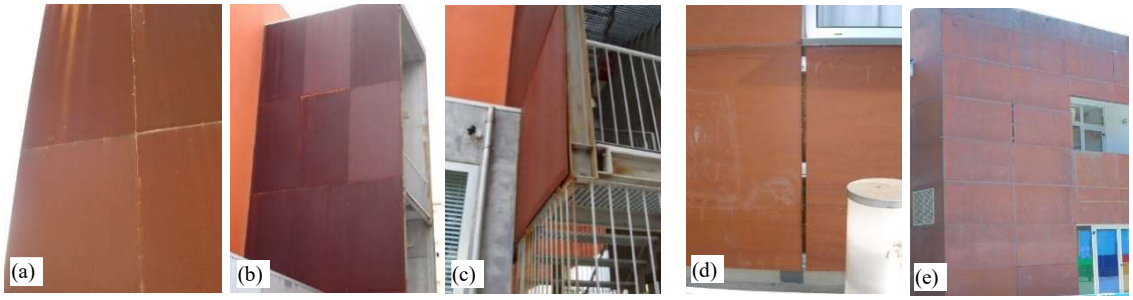

Figure 5. AF School – exterior walls in *Corten* steel panels: colour change from 2007 (a) to 2018 (b). Corrosion and fixation problems in panels in 2018 (c). PRM School wooden panels degradation in 2007 (d) and in 2018 (e) with 16 years of service life.

In PRM School, damaged or missing door locks and handles were observed in the surveys. These failures severely reduces the adequate serviceability of the exterior doors (Fig. 6a,b).

These anomalies were detected in 2007 in doors with 5 years of service life. In general, some problems with rain penetration were observed in windows and non-operational interior polystyrene blinds is a very frequent anomaly. In AF School the outdoors shading were broken and deformed caused by its proximity to the playing field (Fig. 6c,d).

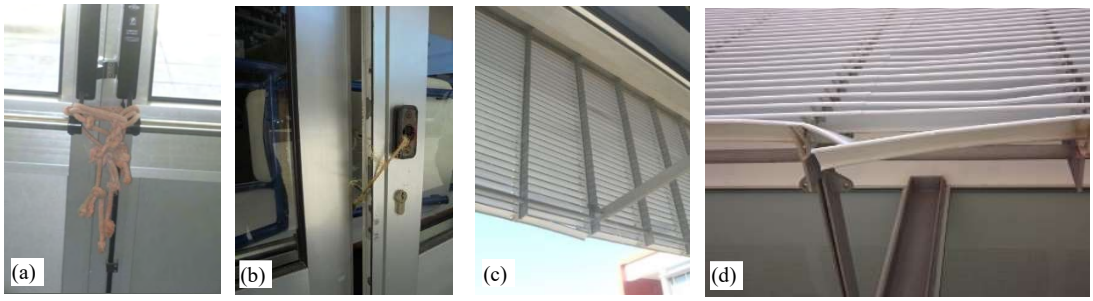

Figure 6. PRM School: missing door locks and handles 2007 (a) and 2018 (b). AF School: outdoors shading broken and deformed in 2007 (c) and 2018 (d).

3.3 Building Interior

3.3.1 Floors, walls, ceilings and doors

At PRM School, the degradation mechanism of the floor finishes, in the arts and crafts areas, next to the classrooms, caused by frequent water leakages from the washbasin siphons, has been observed since the 2007 inspection. In 2018, the placement of floor covering patches in this area was observed. Figure 7 (a,b,c) shows three stages of the vinyl floor covering degradation process caused by wet-dry cycles exposure conditions.

Figure 7. PRM School: vinyl floor degradation process caused by wet-dry cycles exposure conditions. Area in good condition and severely damaged area in 2007 (a,b); floor repaired in 2018 (c).

In the VA, AL, VG and PM Schools, cracks in interior to exterior walls and partitions walls were observed in 2018. In VA School, the severity and extent of the affected areas, indicates that the emergence of cracks is related to structural problems and differential settlements. In general, the most frequent anomalies in walls are related with deficient protection of corners and lack of adoption of wainscot/paneling elements in corridors and areas of intensive use.

Degradation in wall painting due to the use of adhesive tape for the exhibition of students' work was observed in the inspection carried out in 2007. In 2018 survey this anomaly was observed more frequently and over a larger area of walls (Fig. 8a).

In ceilings, moisture and water ingress are the most frequent anomalies. Figure 8 (b,c) shows the increased severity of this phenomenon in VA School, that may have resulted initially from lack or loss of waterproofing capacity of the building envelope (in 2007) and later resulted from the combination of several causes including building structural and foundations settlement problems (in 2018).

Figure 8. AF School: degradation in wall painting due to the use of adhesive tape for the exhibition of students' work in 2018 (a). VA School: water infiltrations in the ceilings in 2007 (b) and in 2018 (c).

The model of the sliding doors used to separate the classrooms from the arts and crafts areas and in bathrooms (PRM, PM and AF Schools) presented several functional problems related to unsuitable serviceability, vertical misalignment and deficient fixation tracks causing localized wear on the floors finishes (Fig. 9a). The use of large bellows doors to separate the gym from school cafeteria is a widely used solution in these recent buildings schools. This solution aims to open the spaces with an area for students to perform shows/theaters an area for the audience. Due to their characteristics, theses doors are large (length and height) and are heavy, which makes manual maneuvering difficult. These doors are now permanently closed and are not used because they require maintenance and repair actions without which their safe use is not guaranteed (Fig. 9b). At PRM School, door closer need to be repaired in interior fire doors. In 2007, these elements were damaged (Fig. 9c), while in the 2018 survey it was found that the element was not placed where it was supposed to be (Fig. 9d).

Figure 9. AF School: sliding door anomaly (a) non-operational bellows doors (b). PRM School: door closer anomaly in fire doors in 2007 (c) and 2018 (d).

3.3.2 Sanitary services

In 2018 survey, it was found that all schools continue to have recurrent problems and anomalies in the sanitary equipment and in the water supply and wastewater drainage networks. These installations are used intensively and not always in the most appropriate way. The most frequent

anomalies in these systems continue to be (i) the breakdown of the toilet flushes, (ii) fixing problems of water faucets and (iii) problems with the drainage capacity of the wastewater network. The lack of proper maintenance and misuse, results in nonfunctional equipment and sometimes in floods. Figure 10 (a) shows the poor fixing of the water tap and deficient drainage of the wastewater, (b) failure in the flushing system causing waste of water and (c) anomaly in the floor box of the wastewater network.

Figure 10. PRM School: anomalies on water tap and in the water flow, 2007 (a) failure in the flushing system, 2018 (b) and anomaly in the floor box covering finish of the wastewater network, 2018 (c).

4 Conclusions

This article presents the results of three inspections carried out in 2007, 2013 and 2018, on six school buildings built after 1997. The study revealed the existence of severe and unexpected degradation in these buildings. Anomalies related to the settlement of foundations and movements in the structure, are probable causes for the problems in other construction elements (cracking in interior and exterior walls and water infiltration). Observations made over the years showed that many of the structural problems are not stabilized what may have been caused by execution and/or design errors. It was found that one of the schools, with 19 years of service life, had to close, due to the existence of structural failures that endangered the health and safety of building users. Structural problems must be solved before carrying out many of the minor repairs, but they are complex, expensive, and so postponed.

Building schools should be designed to have a long service life, up from 50 years, so premature degradation of buildings is a problem with negative environmental, social and economic impacts. This work highlights the need for greater involvement of school building management entities, in the early stages of the building process, including design, tendering, construction and handover, to ensure that buildings and building elements fulfil their function for their specified design service lives.

ORCID

Sónia Raposo: https://orcid.org/0000-0002-7683-1391

References

Luís, J. (2013). *Characterization of the degradation condition of the exterior building elements and outdoor spaces of school establishments in service* (in Portuguese). Master Thesis, Universidade Técnica de Lisboa – Instituto Superior Técnico, Lisboa, Portugal.

Nogueira, W. (2013). *Characterization of the degradation condition of the interior building elements of school establishments in service* (in Portuguese). Master Thesis, Universidade Técnica de Lisboa – Instituto Superior Técnico, Lisboa, Portugal.

Raposo, S., Fonseca, M. and Brito, J. (2008). Survey of the state of degradation of the school buildings of the Lisbon region. In *Proceedings of the XI International Conference on Durability of Building Materials and Components*, Istambul, Turkey, 1789-1796.

Raposo, S. (2011). *The management of maintenance activity in public buildings. Model and strategies for a sustainable intervention* (in Portuguese). PhD Thesis, Universidade Técnica de Lisboa - Instituto Superior Técnico, Lisboa, Portugal.

S478-19 (2019). *Durability in buildings.* Ontario, Canada: Canadian Standards Association.

Sousa, L., Ferreira, M., Mota de Sá, F., Oliveira, C., Raposo, S., Sigbjornsson, R., Rupakhety, R., Zonno, G., Meroni, F., Bianco, F. and D'Amico, S. (2012). Quantitative seismic risk evaluation and mapping: cases of schools and residential facilities in Lisbon and Algarve. In *Proceedings of the 15th World Conference on Earthquake Engineering*, Lisbon, Portugal, 8836-8845.

Vilhena, A., Vasconcelos, A., Batista Coelho, A., Vicente, M. and Raposo, S. (2019). *Maintenance condition assessment of schools of the Municipality of Lisbon. Kindergarten and elementary schools* (in Portuguese). Scientific Report 259/2019 – Laboratório Nacional de Engenharia Civil. Lisboa, Portugal.

XV International Conference on Durability of Building Materials and Components
DBMC 2020, Barcelona
C. Serrat, J.R. Casas and V. Gibert (Eds)

Comparative Study on (Non-)Destructive Techniques for On-Site Strength and Durability Assessment of Limestone Based Concrete Slabs

Bart Craeye[1,2], Daan van Keijzerswaard[1] and Patricia Kara De Maeijer[1]

[1] Energy & Materials in Infrastructure & Buildings (EMIB), Faculty of Applied Engineering, University of Antwerp, Campus Groenenborger, 2020-Antwerp, Belgium, bart.craeye@uantwerpen.be

[2] Durable (re-)Building in Team (DuBiT Research Core), Department of Industrial Sciences & Technology, Odisee University College, Campus Aalst, 9300-Aalst, Belgium, bart.craeye@odisee.be

Abstract. *For rehabilitation of existing concrete structures, strength and durability related properties of the reinforced element are of high importance. Assessment of these properties of existing structures can be performed by (i) destructive testing of drilled cores and testing the extracted samples in lab environment and (ii) indirect methods by using non- or semi-destructive techniques on site. The use of core-drilling is a time-consuming and labour-intensive method that weakens the existing concrete structure, leaving a lasting impression on it. As an alternative, many different non and semi-destructive techniques are available for the in-situ determination of compressive strength and durability related properties. An experimental program is conducted on concrete slabs of different strength classes intended for various exposure classes (according to EN206), based on a limestone aggregate matrix, which is typically used for Belgian applications. The plates have an age of approximately 5 years, which were also characterized at younger stage (in 2014). Besides destructive core drilling and testing (compressive strength tests, chloride migration testing, and determination of carbonation rate), several non-destructive techniques were selected for this study: the rebound hammer, the ultrasonic pulse velocity tester, the Wenner probe for concrete resistivity and the air permeability tester. Best fit correlations between the output of these different techniques were established. The effect of age (e.g. carbonation) on the established predictive models is being evaluated.*

Keywords: *DT vs. NDT, Strength, Durability, Transport Properties, Age Effect.*

1 Introduction

For characterization of existing concrete structures, insight in the strength and durability related properties are necessary in order to come to an adequate rehabilitation or repair strategy (Hobbs *et al.* (2007)). Assessment of these properties can be performed by (i) time-consuming and labour-intensive destructive testing of drilled cores and testing the extracted samples in lab environment and/or (ii) indirect methods by using non- or semi-destructive techniques on site, as an alternative. In this study, an experimental program was conducted on concrete slabs with an approximate age of 5.5 years, intended for various exposure classes (variation in W/C-ratio, cement type and cement content), based on a limestone inert matrix, and frequently used for Belgian applications. These slabs were intensively investigated, both in 2014 and 2019, by means of destructive testing (compressive strength tests, chloride migration testing, and determination of carbonation rate), and non-destructive techniques: the rebound hammer, the ultrasonic pulse velocity tester, the Wenner probe for concrete resistivity and the air permeability tester. Best fit correlations between the output of these different techniques were

established. The effect of age (*e.g.* carbonation) on the established predictive models is being evaluated.

By measuring the propagation speed of ultrasound waves through the material, the concrete quality is investigated. A high pulse velocity will result in a good quality concrete and, therefore, a higher compressive strength and more durable material can be expected. In this study, only ultrasonic techniques were used to determine to ultrasonic pulse velocity (direct transmission), according to EN 12054-4. The main influencing parameters on the output of the UPV are the type, content and hardness of the aggregates, the presence of cracks/voids in the structure and the moisture content of the concrete (Breysse (2012)). The W/C-ratio also affects the readings in pulse velocity. Furthermore, relative humidity also influences the output. The pulse velocity might increase up to 5% between dry and saturated test specimens, according to Solís-Carcaño *et al.* (2008).

The rebound hammer measures the rebound of a spring-loaded mass impacting on the surface of a concrete sample or structure, generating the rebound number, according to EN 12504-2. The higher this number, the harder the surface, indicating a high concrete compressive strength. A correlation exists between the compressive strength of standard cubes and the rebound number obtained by the hammer. However, this correlation is not universal and has to be modified for different devices, different concrete mixes or different conditions of testing. The condition of the surface has a high influence on the readings. Furthermore the type and the hardness of the aggregate and the carbonation degree, as it increases the surface hardness of the concrete, will have a big influence on the rebound number (Kim *et al.* (2009)).

Measuring concrete resistivity on site can be performed in various ways. It is often measured with a Wenner probe consisting of four equally spaced point electrodes that are pressed onto the concrete surface. Results show that there is no appropriate relationship between surface resistivity and strength, generally due to different mechanisms support compressive strength and electrical resistivity. Consequently, it is not recommended to use surface resistivity as an indicator for evaluation of compressive strength (Ramezanianpour *et al.* (2011)). Nevertheless, the electrical resistivity of concrete is an important parameter, e.g. used to describe the corrosion rate of reinforced concrete elements for durability assessment. This parameter is related to the water content, the cement type, the W/C-ratio of concrete and the hydration degree. Environmental conditions such as relative humidity and temperature also affect the resistivity of the concrete matrix.

Several researches have shown that the coefficient of air permeability k_T correlates quite well with other standardized durability related tests (Jacobs *et al.*, 2009). For instance, carbonation depth of concretes after 500 days of natural exposure correlates well with their k_T values measured at 28 days: higher air permeability leads to higher carbonation rate. These concretes have W/C-ratios in the range 0.26-0.75 and are made with CEM I (except few mixes to which 5-8% silica fume was added). Torrent *et al.* (2012) also found a rather good correlation between k_T and results of the rapid chloride permeability test (ASTM C1202), with data originating from mixes with Portland cement, slags, fly-ashes and micro silica, and varying W/C-ratios (0.4-0.9).

2 Materials and Methods

2.1 Concrete Composition

The study was initiated in 2013, with the casting of 14 non-reinforced slabs using 7 concrete mixtures with strength classes varying from C12/15 up to C50/60. For each mix two slabs (600 x 100 x 100 mm³) were cast and tested (destructive compressive strength and various non- or semi-destructive techniques, as mentioned in (Craeye *et al.*, 2017)). The properties of these mixtures are given in Table 1. These concrete mixtures are frequently applied in Belgium for different exposure classes. Limestone aggregates are used (max. grain size 22 mm), except for mixture C25/30 (which used porphyry 8 mm). Blends of three different cement types are selected: Portland CEM I 52.5R and blast furnace slag CEM III/A 42.5N – CEM III/B 42.5N.

Once this research project was finished, the slabs were stored in an unconditioned but sheltered outside environment. For this research study, the slabs are tested with an approximate age of 5.5 years.

Table 1. Concrete composition in different strength classes.

Strength class	**Exposure Class**	**Slump W/C**	**Aggregates** Max. grain size	**Cement** Min. content
C12/15	X0	S4 1.00	Limestone 22 mm	CEM III/B 42.5N LH SR LA 260 kg/m³
C20/25	XC2	S3 0.60	Limestone 22 mm	CEM III/B 42.5N LH LA 280 kg/m³
C25/30	XC3-XF1	S3 0.55	Porphyry 8 mm	CEM III/B 42.5N LH LA 280 kg/m³
C30/37	XC4-XF1	S3 0.50	Limestone 22 mm	CEM I 52.5R + CEM III/B 42.5N LH LA 300 kg/m³
C35/45	XC4-XD3-XF4	S3 0.45	Limestone 22 mm	CEM III/A 42.5N LA 320 kg/m³
C40/50	XC4-XD3-XF4	S3 0.40	Limestone 22 mm	CEM I 52.5R + CEM III/A 42.5N LA 320 kg/m³
C50/60	XC4-XD3-XF4	S4 0.40	Limestone 22 mm	CEM I 52.5R + CEM III/A 42.5N LA 340 kg/³

2.2 Selection of (Non-)Destructive Methods

Out of each slab 7 cores (diameter 100 mm, height 100 mm) are drilled to perform compressive strength, chloride migration and carbonation tests. To determine the actual compressive strengths of the concrete slabs, 3 cores are tested per slab, according to EN 12504-1. The core strength is converted into the equivalent cube compressive strength ($f^*_{ccub150}$) by means of a shape factor (averaged value of 1.05, NBN B15-001).

Prior to the drilling the slabs are examined in a non-destructive way: ultrasonic pulse velocity (direct transmission), air-permeability, surface resistivity, and rebound hammer tests are executed, according to EN 12504-2, SIA 262/1, AASHTOT277 and 12504-4 respectively. The location of the tested area on the slab are identical for each test.

Chloride migration is determined in a non-stationary way, according to the NTBuild 492 regulations on 3 cores per slab. The depth of carbonation (or the carbonation coefficient) is determined on 1 core per slab, according to EN 14630, using 1% phenolphthalein solution.

3 Results and Discussion

3.1 Strength Assessment

In Figure 1a) the results of the individual tests on both slabs per strength class are given and compared to the results obtained in 2014. There is a time difference of 5.5 years in between the 2014 and 2019 results. In general, there is a slight decrease in strength, except for C20/25. Lower strength loss was observed for the lower strength classes: 1.3% and 4.9% for C12/15 and C20/25, while for C30/37-C35/45-C40/50-C50/60 the decrease is 20.9%-9.0%-4.4%-8.4% respectively.

The output of the equivalent cube compressive strength results is linked to the test results of the ultrasonic pulse velocity (direct transmission), the rebound hammer measurements and the air permeability measurements, as shown in Figure 1b), Figure 1c) and Figure 1d).

Linear regression analysis is performed the obtain the best fitting curve between destructive and non-destructive test, and the reliability of the correlation of one method specifically, is quantified by means of the coefficient of determination (R^2-value) and the standard deviation (shown in the graphs). A linear correlation exists between cube compressive strength and the ultrasonic pulse velocity and compressive strength and the rebound number, with comparable correlation R^2 of 0.701 and 0.726 respectively. Compared to the 2014 study, there is a noticeable drop in R^2 (0.957 for the rebound number, 0.886 for the ultrasonic pulse velocity): measurements on concrete surfaces that were subjected to environmental effects, have a significant lower linear coherence compared to tests performed on young concrete. It is known that carbonation has an effect on strength-hardness correlation (Kim *et al.*, 2009) which is also identified in this study. There is a noticeable shift in the correlation in between the 2014 and 2019 correlation curve (Figure 1a)). Furthermore, the difference in between the correlation provided by the provider of the supplier and the one obtained in this research is worth mentioning. For a given strength, the rebound number increases due to carbonation, and this effect is more prominent for higher strength classes. Comparable conclusions can be drawn regarding the correlation in between strength and ultrasonic pulse velocity. However, the effect of carbonation is less clear. Furthermore, the compressive strength is inversely proportional

with the air permeability (Figure 1c)): increasing the permeability of matrix leads to a decrease in strength. A good correlation is found in this project, R^2 equals 0.83.

As the resistivity meter is not designed for strength estimation, the measurements cannot be related to each other. In comparison with the 2014 study, it appears that the surface resistivity of the concrete slabs increased over a period of 5.5 years.

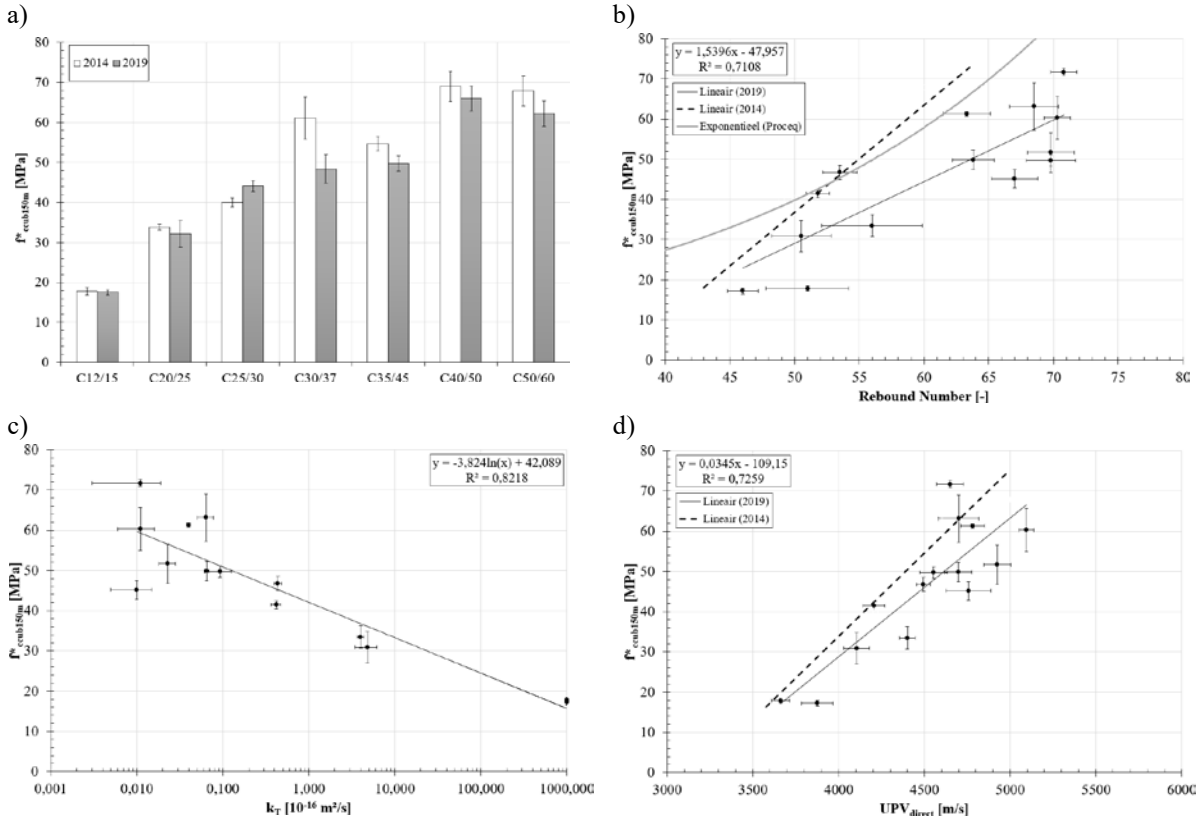

Figure 1. a) Equivalent cube compressive strength 2014-2019, b) correlation $f^*_{ccub150m}$-rebound number, c) correlation $f^*_{ccub150m}$-air permeability, d) correlation $f^*_{ccub150m}$-ultrasonic pulse velocity.

3.2 Durability Assessment

The depth of the carbonation and the chloride migration coefficient is determined destructively on the cores drilled out of the slabs. The results are presented in Figure 3a). The effect of the strength class is clearly noticeable. However, as the cement type has a decisive effect on durability and corrosion related properties such as carbonation and chloride migration (Hiemer *et al.* (2018)) a subdivision of the results is needed. The carbonation coefficient decreases with increased strength class for the slabs with a lower strength class concrete (C12/16 to C25/30) with blast furnace slag cement (CEM III/B) (Figure 3a)). For the higher concrete strength classes, using blends of Portland CEM I 52.5 and blast furnace slag CEM III, no effect of strength class on carbonation is found. The higher carbonation coefficient is noticed for the

slabs with strength class C35/45. This is due to the single use of blast furnace slag CEM III/A, which is more susceptive to carbonation. It is known that carbonation leads to precipitation of $CaCO_3$ which leads to an increase in hardness of the concrete surface and densification of the matrix, however without increasing the strength of the material. As carbonation of the concrete cover increases, the permeability of the matrix increases (Figure 3c)) and a decrease in pulse velocity can be identified (Figure 3b)). The permeability of concrete has an effect on the speed of propagation of the ultrasonic pulse, which is shown in Figure 3d). Elements with high permeability have a lower pulse velocity, mainly due to the scattering of the pulse through air present in the pores. It is important to note that the use of the air permeability meter can be a good alternative for the ultrasonic pulse velocity tester.

No trend is noticeable regarding effect of strength class on chloride migration (Figure 3a). The cement type has a decisive effect on transport of chlorides through concrete: using blast furnace slags has a more positive effect on chloride migration compared to the strength class. Finally, a higher chloride migration is found in case of higher air permeability or surface resistivity (Figure 3e), Figure 3f)), however the scatter on the results is quite high, and therefore a clear correlation cannot be established.

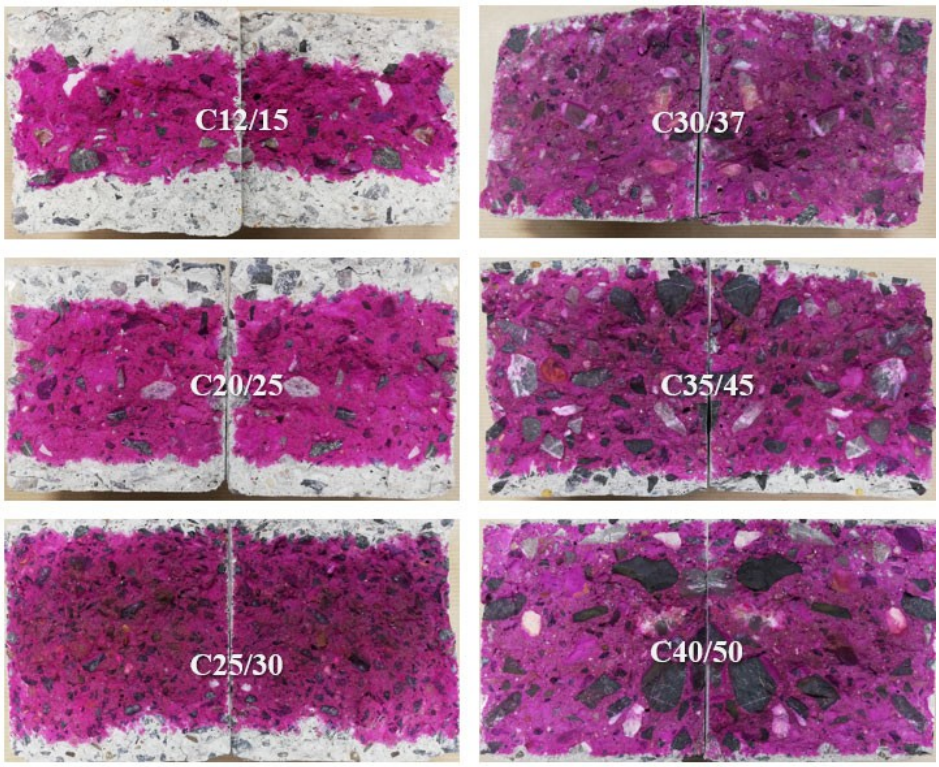

Figure 2. Carbonation depth of concrete with different strength classes.

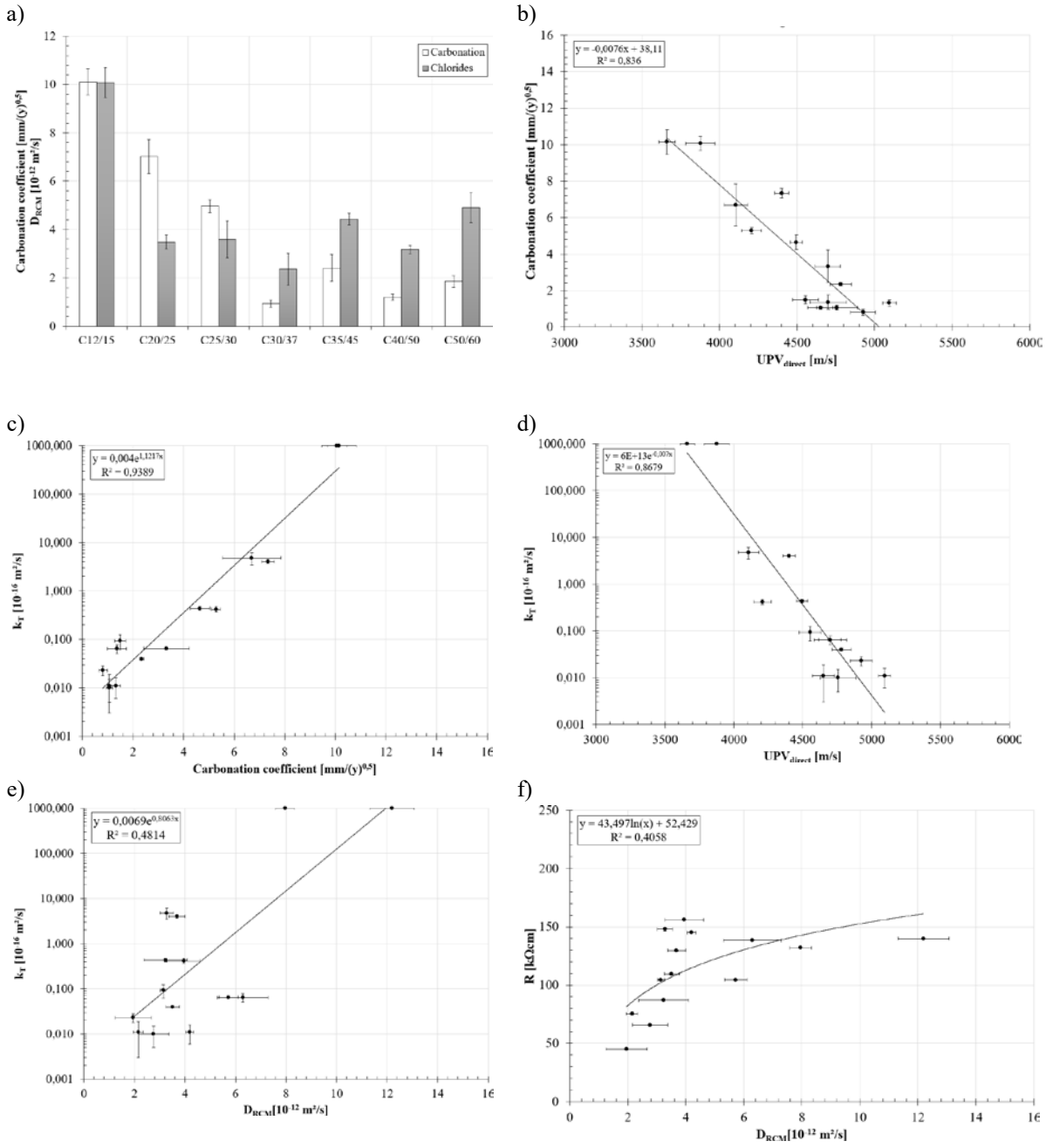

Figure 3. a) Results of carbonation coefficient and chloride migration D_{RCM}, b) correlation carbonation coefficient-ultrasonic pulse velocity, c) correlation air permeability-carbonation coefficient, d) correlation air permeability-ultrasonic pulse velocity, e) correlation air permeability-D_{RCM}, f) correlation surface resistivity-D_{RCM}.

4 Conclusions

In this study an experimental program is conducted on concrete slabs of different strength classes intended for various exposure classes, based on a limestone aggregate matrix. The plates have an age of 5.5 years, and are also characterized at younger stage (in 2014). Destructive core drilling and testing and several non-destructive techniques are used to assess strength and durability related properties of the slabs.

A slight strength decrease is found after 5.5 years with higher strength loss is for higher strength classes. Furthermore, the strength is linear proportional with surface hardness and ultrasonic pulse velocity and inversely proportional with air permeability. Compared to the results of 2014 (i) higher coefficient of determination on the obtained correlation curves is found and (ii) a shift on the correlation curves is noticeable, linked to the aging effect due to carbonation. This aging effect is more pronounced for the rebound hammer results. The effect of strength class on carbonation rate is clearly noticeable for slabs of lower strength classes (up to C25/30). For higher strength classes the effect of cement type is more pronounced.

A linear correlation with high coefficient of determination is found between carbonation coefficient, air permeability (directly proportional) and ultrasonic pulse velocity (inversely proportional). Note that the air permeability test is a good non-destructive alternative for the ultrasonic pulse velocity test: elements with high permeability have a lower pulse velocity, mainly due to the scattering of the pulse through air present in the pores.

Finally, no trend is noticeable regarding effect of strength class on chloride migration and a higher chloride migration is found in case of higher air permeability or surface resistivity, however a clear correlation cannot be established.

ORCID

Bart Craeye: http://orcid.org/0000-0003-4628-8057

References

Breysse, D. (2012). *Nondestructive evaluation of concrete strength: An historical review and a new perspective by combining NDT methods*, Construction and Building Materials, vol. 33, pp. 139–163.

Craeye, B., van de Laar, H., van der Eijk, J. and Lauriks, L. (2017). *On-site strength assessment of limestone based concrete slabs by combining non-destructive techniques*, Journal of Building Engineering, vol. 13, pp. 216-223.

Hiemer, F., Jakob, D., Kessler, S. and Gehlen, C. (2018). *Chloride induced corrosion in cracked and coated concrete: from experimental study to time-dependent modelling,* Materials and Corrosion, vol. 69, no. 11, pp. 1526-1538.

Hobbs, B. and Tchoketch Kebir, M. (2007). *Non-destructive testing techniques for the forensic engineering investigation of reinforced concrete buildings*, Forensic Science International, vol. 167, no. 2–3, pp. 167–72.

Jacobs, F., Denarié, E., Leemann, A. and Teruzzi, T. (2009). *VSS Report 641*, OFdR, Bern, Switzerland.

Kim, J.-K., Kim, C.-Y., Yi, S.-T. and Lee, Y.(2009). *Effect of carbonation on the rebound number and compressive strength of concrete*, Cement and Concrete Composites, vol. 31, no. 2, pp. 139–144.

Maierhofer, C., Reinhardt, H.-W. and Dobmaan, G. (2010). *Non-destructive evaluation of reinforced concrete structures*, Woodhead Publishing in Materials, CRC Press, UK.

Ramezanianpour, A.A., Pilvar, A., Mahdikhani, M. and Moodi, F. (2011). *Practical evaluation of relationship between concrete resistivity, water penetration, rapid chloride penetration and compressive strength*, Construction and Building Materials, vol. 25 , no.5, pp. 2472–2479.

Solís-Carcaño, R. and Moreno, E.I. (2008). *Evaluation of concrete made with crushed limestone aggregate based on ultrasonic pulse velocity*, Construction and Building Materials, vol. 22, no. 6, pp. 1225–1231.

Torrent, R., Denarié, E., Jacobs, F., Leemann, A. and Teruzzi, T. (2012). *Specification and site control of the permeability of the concrete cover*, Materials and Corrosion, vol. 63, no. 12, pp. 1127-1133.

XV International Conference on Durability of Building Materials and Components
DBMC 2020, Barcelona
C. Serrat, J.R. Casas and V. Gibert (Eds)

Concrete Durability Probed Using Compressive Strength, Chloride Penetration and Porosity Measurements on CEMII and CEMV Concretes Incorporating Mollusc Shell Spares in Artificial and Natural Seawaters

Marine D. Georges[1], Amel. Bourguiba[1], Nassim. Sebaibi[1], Daniel. Chateigner[2] and Mohamed. Boutouil[1]

[1]COMUE Normandie Université, Laboratoire ESITC - ESITC Caen, rue Pierre et Marie Curie 1, 14610 Epron, France, marine.georges@esitc-caen.fr

[2] Normandie Université, CRISMAT UMR CNRS n°6508, ENSICAEN, Université de Caen Normandie, 6 boulevard Maréchal Juin, 14050 Caen, France, daniel.chateigner@ensicaen.fr

Abstract. *The purpose of this study is to improve the recruitment of flat oyster larvae, an endangered species, by means of a specific marine infrastructure made of concrete. This work aims to develop and optimize concrete formulations by varying the type of cement and introducing shellfish by-products into their composition and determine which concrete formulation is the most sustainable to marine organism colonization. Indeed, it is essential to obtain a sustainable concrete submitted to aggressive marine environment (chloride ions diffusion and bio-colonisation). Four concrete formulations were tested with two types of cements (CEMII and CEMV) and with or without the incorporation of shell aggregates. The durability of these materials was tested after 3 months of immersion in the Rance of Dinard (France). It appears from this study that the CEMII concrete exhibits a good mechanical resistance independently of the presence of shell, after immersion in situ. This concrete also shows better resistance to chloride ions diffusion than CEMV. However, CEMV possess larger compressive strengths than CEMII, and mollusc shells incorporation does not decrease this strength as much as for CEMII. Shell incorporation in the concretes has an effect on strength, chloride penetration and porosity which depend on the used cement and seawater.*

Keywords: *Flat Oyster Larvae, Marine Infrastructure, Concrete, Bio-Colonisation, Durability.*

1 Introduction

Coastal areas play a crucial role in the economic, social and political development of most countries. As a result, the maritime coasts are increasingly urbanized. Indeed, human activities (ports, tourism, fishing ...) require maritime structures and infrastructures which are often made of concrete. These coastal developments are responsible for the loss of many marine species habitats (Firth *et al*., 2013, 2014).It is therefore important to offset the residual impacts by generating an equivalent gain in biodiversity.

This study is carried out within the framework of the European Marineff project, which is part of this context. One of this study‘s objectives is the design of maritime infrastructures for flat oysters (*Ostrea edulis* Linnaeus, 1758) restoration in the Channel. Indeed, the flat oyster is an endangered species.

Over the years, a new approach has emerged, in the aim of enhancing marine infrastructure (surface condition, structure and composition) to promote ecological succession (Firth *et al*.,

2014; Perkol-Finkel and Sella, 2014; Sella and Perkol-Finkel, 2015). Thus, the term "ecological engineering" emerged (Bergen *et al*., 2001; Dennis *et al*., 2018; Firth *et al*., 2014, 2016; Pioch *et al*., 2018; Strain *et al*., 2018). The effectiveness of eco-engineering interventions varies according to habitats and marine biological communities. Indeed, each marine organism has a different response depending on the infrastructure (Coombes *et al*., 2015; Hanlon *et al*., 2018; Jones *et al*., 1994).
One of the solutions could therefore be the design of bio-receptive and sustainable concrete for the implementation of these infrastructures. Concrete immersed in the marine environment will undergo chemical, physical and biological attacks that can lead to its deterioration (Bastidas-Arteaga *et al*., 2008; Sanchez-Silva and Rosowsky, 2008). It is therefore important to design concrete that is as durable as possible in order to ensure its sustainability in its immersion environment.

Using a combination of laboratory and field experiments, we aimed to: (1) develop and optimize concrete formulations by varying the type of cement and introducing shellfish by-products into their composition (2) determine which concrete formulation is the most sustainable following the colonization of marine organism.

2 Material and Methods

2.1 Concrete's Formulations

For this study, 4 concrete formulations were designed with 2 types of cement, Portland cement (Calcia), CEM II/A-LL 42.5 R CE PM-CP2 NF and CEM V/A (S-V) 32.5 N-LH CE PM-ES-CP1 NF. These two types of cement are suitable for use in sea waters. Siliceous alluvial sand was used in granular class 0/2. Alluvial aggregates were also used and are composed of two sizes, 4/10 and 10/20 (Figure 1). A substitution of 20% of the aggregates (D4/10) by oyster shell aggregates was made to study the effect of this biomineral by-product on the recruitment of oyster larvae. Indeed, the incorporation of mollusc shell aggregates can increase the bio-receptivity of concrete because they provide an ideal substrate for the settlement of marine organisms (Graham *et al*., 2017; Hanlon *et al*., 2018).

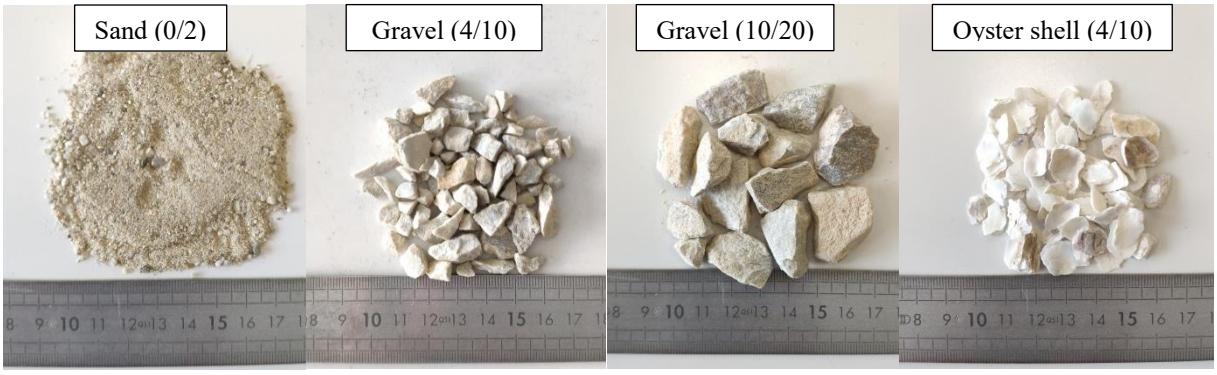

Figure 1. The various types of aggregates used to elaborate the concretes of this study.

After the characterization of the raw materials, concrete mix designs formulation was carried out in accordance with EN 206-1. The four studied concrete formulations are given in Table 1.

Table 1. Concrete's formulations (Proportions given in kg/m^3 of concrete).

Formulations / Components	F1 : CEM II without shell	F2 : CEM II with 20 % shell	F3 : CEM V without shell	F4 : CEM V with 20 % shell
Cement	350	350	350	350
Sand	800	800	800	800
Gravel 4/10	600	479	600	479
Gravel 10/20	500	500	500	500
Shell	-	121	-	121
Water	175	175	175	169
Superplastifiant	1.28 %	2%	1.28 %	2%

2.2 Concrete Durability Against Marine Environment

To study the sustainability of the concretes in marine environment, 11-cm diameter cylindrical samples with heights of either 22 cm or 5 cm were elaborated. Before their immersion in the Rance river of Dinard (France), the samples were placed in cages (iron grids). The immersion was carried out during 3 months to study marine organisms colonisation on the samples. After this period, mechanical and durability tests were carried out.

2.2.1 Compression test

The compression tests were carried out on the 11 cm × 22 cm cylindrical samples using a 3R press (4000 kN) after 90 days of curing (reference concrete) and after 90 days immersed in natural seawater. The test was operated in accordance within the NF EN 12390-3 standard.

2.2.2 Chloride ion diffusion tests

Ion chromatography was used to measure chloride ions concentrations for a total depth of 1 cm into the samples (using a 2 mm step). The powder produced by drilling was collected, filtered and diluted to 1/25th before being analyzed by a 883 Basic IC Ion Chromatograph using standard preparation procedures. The obtained leachate is also used to measure the pH of the material. This test was carried out on the samples immersed natural seawater and in artificial seawater.

2.2.3 Porosity accessible to water

Porosity is an important factor that influences the material's durability. This test was carried out on the immersed samples (natural seawater*)* and after 90 days of curing (reference concrete), according to the NF P18-459 standard.

The value of the porosity (p) is obtained by the equation (1):

$$p = \frac{M_{sds} - M_d}{M_{sds} - M_w} \times 100 \quad (1)$$

Where M_{sds} is the saturated dry surfaces sample mass, M_d the dry sample mass and M_w the mass in water.

3 Results and Discussion

In order to choose the best concrete formulation, several mechanical strength and durability tests were carried out. The 11x22 samples were colonised by sessile fauna and some macro-algae after 3 months of immersion in natural seawater. We could count some bryozoans, sponges, serpulid and spiral tubes of Spirorbs (Figure 2).

Figure 2. Concrete samples (11x22) after immersion for 3 months in natural seawater.

3.1 Compression Test

Mechanical strength results (Figure 3) show that, without shell incorporation, the compressive strength obtained after 90 days of curing is significantly higher for the CEMV type concrete (70.53 MPa) compared to CEMII (46.3 MPa) (Figure 3, A). A decrease in compressive strengths is noticed when adding shell aggregates, with values decreasing to 49 MPa and 32 MPa respectively. The compressive strength increases for all concretes except for CEMV without shells after 3 months of immersion in natural seawater compared to the reference concrete. This increase is larger for concretes containing shell aggregates, with approximately 35% larger strengths for CEMII with shells and 24% without (Figure 3, B). Interestingly, in CEMV concretes this latter tendancy is even increased, immersion in seawater inducing a decrease of compressive strength after 3 months without shell incorporations, while addition of shells increases the compressive response inside seawater. CEMV even exhibits the same compressive strength after 3 months of immersion with or without shells.

Rica *et al*., 2016 also studied the effect of colonisation on the mechanical strengths of several cementitious materials with and without shells at different timescales *in situ*. It was found that self-placing concrete with 40% of shells showed an increase in resistance (+8%) after an immersion of 22 weeks in seawater compared to 28 days of curing in the laboratory.

Shells are natural biominerals that do not modify intrinsically after immersion in seawater, even for long times after death. Consequently, if shell-cement interfaces are enough bounding them together, the resulting mechanical strength variations of the concrete over time are assumed to depend more on the cement behaviour. In our experiments bonding properties are not probed, but even after 90 days of curing, the cementing part of the concretes are not fully

matured and are potentially subjected to suffer some alteration in the aggressive seawater medium. This is at least the case for CEMV which exhibits a clear decrease in compressive strength after 3 months of immersion, and contraily to CEMII. But in shell-containing concretes compressive strength increase is observed for the two types of concretes. The effect of shell incorporation cannot be a simple steric effect with less deterioration thanks to shell additions, since this would only reduce the compressive strength decrease of CEMV comparing with and without shell.

We are then concluding that another effect occurs, beneficial to and not only buffering strength decrease. The mechanism for such an effect is not monitored by our experiments, and further investigations are needed to explain our results. A modification of the concrete microstructure due to calcium carbonates and organic species contained in the shells could be at the origin of the observed behaviour.

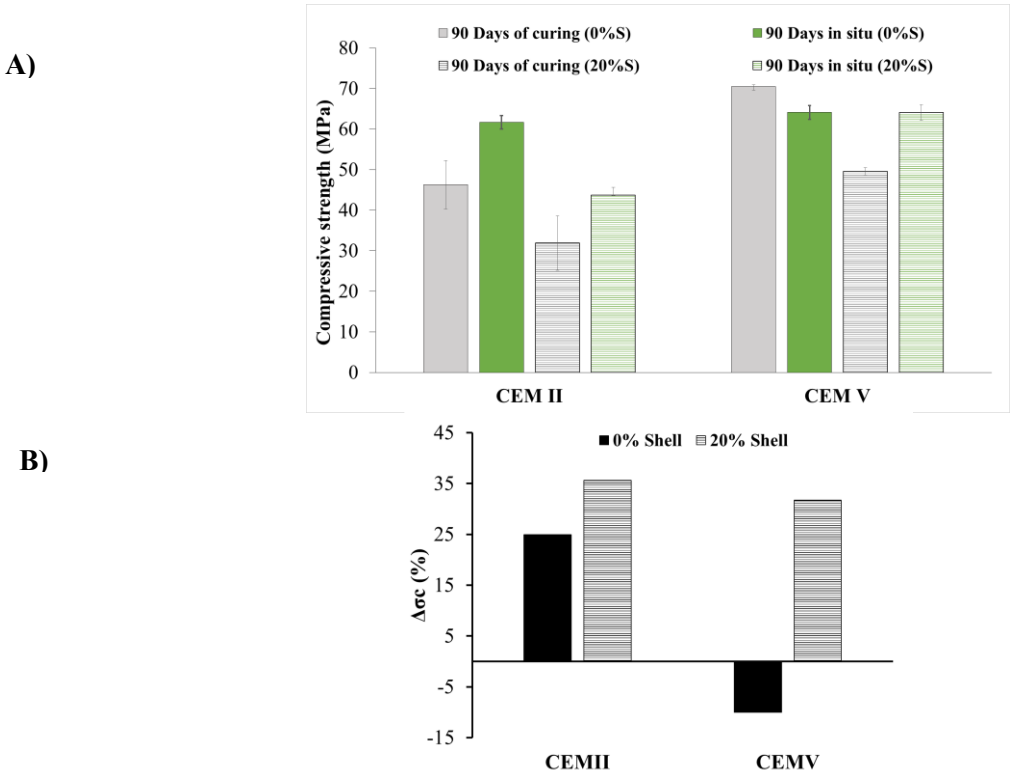

Figure 3. (A): Compressive strength of the different concrete formulations after 90 days of curing and after 90 days in natural seawater; (B) : Difference between the resistance of concretes immersed in seawater for 90 days vs. cured at 100% RH (90 days).

3.2 Chloride Ion Diffusion Tests

The durability of concrete mix designs against chloride ions diffusion were then studied after immersion in two different environments: artificial and natural seawaters. The evolution of the chloride ions content (as a function of depth and environment) is represented in Figure 4. We can also notice that after 3 months of immersion in natural seawater, we obtain higher chloride ions content between 0 and 6 mm for the concrete mix designs manufactured without shells

compared to those immersed in artificial seawater (Figure 4 A and C). This result can be explained by the fact that the bio-colonisation of samples facilitates the penetration of Cl^- ions.

In artificial seawater (ASW, Figure 4, solid lines), the presence of shells in the concrete (Figure 4B and D) tends to enhance chloride content by a factor of nearly 2 in the first millimeters compared to concretes without shells (Figure 4A and C). This tendancy is not observed for immersions in natural seawaters (NSW, dotted lines). The reason for such a behaviour could be seen in partial dissolution of shell pieces, which is more pronounced in artificial seawaters. Part of the molecules and macromolecules contained in shells are Water Soluble (WSM), and present in NSW but not in ASW. Consequently, immersing shells in ASW gives rise to larger chemical potentials than in NSW, tending to operate more dissolution and element infiltrations, the process being or not mediated by chloride ions.

The total chloride content in our concretes varies according to the cement type. In the first six millimetres, whatever the used conditions (with and without shells, seawater) the concretes made with CEMII are more sustainable from the point of view of chlorine penetration than those elaborated with CEMV. For CEMII, chloride content does not exceed 1500 ppm in the first millimetres (Figures 4A and B), while in CEMV (Figure 4C and D) this concentration is at least twice this amount (up to 3700 ppm).

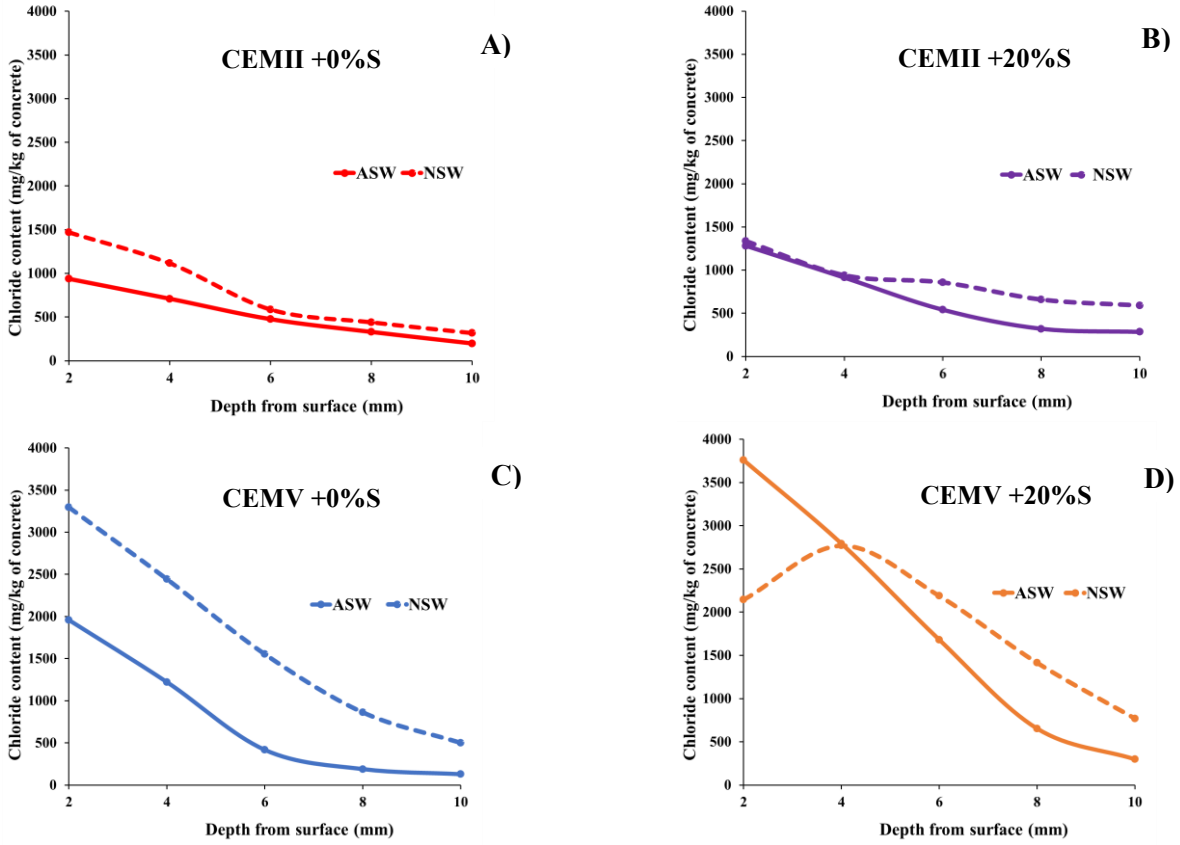

Figure 4. Chloride ions content after an immersion of 1 month in Artificial SeaWater (ASW) (solid line) and after 3 months in Natural SeaWater (NSW) (dotted line) for two different concrete composition CEMII and CEMV without Shells (S) (Respectively A et C) and CEMII and CEMV with Shells (Respectively B et D).

3.3 Porosity Accessible to Water

Measurements of porosity accessible to water (Figure 5) indicate that, except for a slight increase in porosity of around 0.1-0.2%, the two concrete formulations made with CEMII remain stable after immersion for 3 months in natural seawater. This is not the case for CEMV concretes for which we observe a decrease of porosity up to 4% after 3 months. The shell-containing CEMV concrete however exhibit less porosity decrease compared to such a concrete without shells. Such porosity decrease contributes undoubtfully to the compressive strength increase of the CEMV sample with shells.

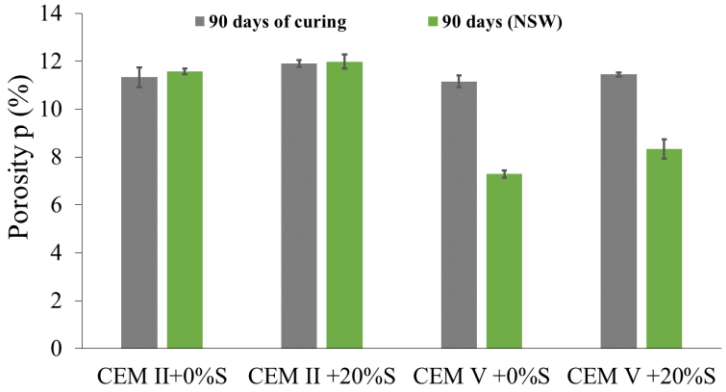

Figure 5. Porosity accessible to water after 90 days of curing and immersed after 90 days in NSW.

4 Conclusion

Our results indicate that the CEMII concrete formulations are the more resilient to chloride penetration in artificial and natural seawaters than CEMV concretes. The incorporation of shell aggregates does not significantly modify chloride penetration in natural seawater but increases it in artificial seawater. Porosities significantly decrease in CEMV concretes after 3 months of immersion, which partly explains the compressive strength increase of this material, while only slight porosity variations are observed in CEMII with aging in seawater. Calcium carbonates partial dissolution is more pronounced in artificial sea water, and combined with an increased chloride ion penetration inside the first millimeters of the materials. Longer term tests of durability are on-going (6 and 12 months), together with monitoring of colonisation by studying photosynthetic parameters.

Acknowledgements

We would like to thank the MNHN (Natural History National Museum) of Dinard for allowing us to immerse the concrete samples and have recover them after 3 months of immersion in the Rance of Dinard. Thanks to the Luc-sur-Mer Marine Station (Université de Caen Normandie) for allowing us to immerse our concrete samples for the long term tests.

ORCID

Nassim Sebaibi: http://orcid.org/0000-0002-1241-2745
Daniel Chateigner: http://orcid.org/0000-0001-7792-8702
Mohamed Boutouil: http://orcid.org/0000-0002-2752-8265

References

Bastidas-Arteaga, E., Sánchez-Silva, M., Chateauneuf, A., and Silva, M.R. (2008). Coupled reliability model of biodeterioration, chloride ingress and cracking for reinforced concrete structures. Struct. Saf. *30*, 110–129.

Bergen, S.D., Bolton, S.M. and L. Fridley, J. (2001). Design principles for ecological engineering. Ecol. Eng. *18*, 201–210.

Coombes, M.A., La Marca, E.C., Naylor, L.A. and Thompson, R.C. (2015). Getting into the groove: Opportunities to enhance the ecological value of hard coastal infrastructure using fine-scale surface textures. Ecol. Eng. *77*, 314–323.

Dennis, H.D., Evans, A.J., Banner, A.J. and Moore, P.J. (2018). Reefcrete: Reducing the environmental footprint of concretes for eco-engineering marine structures. Ecol. Eng. *120*, 668–678.

Firth, L.B., Mieszkowska, N., Thompson, R.C. and Hawkins, S.J. (2013). Climate change and adaptational impacts in coastal systems: the case of sea defences. Environ. Sci. Process. Impacts *15*, 1665–1670.

Firth, L.B., Thompson, R.C., Bohn, K., Abbiati, M., Airoldi, L., Bouma, T.J., Bozzeda, F., Ceccherelli, V.U., Colangelo, M.A., Evans, A., et al. (2014). Between a rock and a hard place: Environmental and engineering considerations when designing coastal defence structures. Coast. Eng. *87*, 122–135.

Firth, L.B., Browne, K.A., Knights, A.M., Hawkins, S.J. and Nash, R. (2016). Eco-engineered rock pools: a concrete solution to biodiversity loss and urban sprawl in the marine environment. Environ. Res. Lett. *11*, 094015.

Graham, P.M., Palmer, T.A. and Pollack, J.B. (2017). Oyster reef restoration: substrate suitability may depend on specific restoration goals. Restor. Ecol. *25*, 459–470.

Hanlon, N., Firth, L.B. and Knights, A.M. (2018). Time-dependent effects of orientation, heterogeneity and composition determines benthic biological community recruitment patterns on subtidal artificial structures. Ecol. Eng. *122*, 219–228.

Jones, C.G., Lawton, J.H. and Shachak, M. (1994). Organisms as Ecosystem Engineers. Oikos *69*, 373–386.

NF EN 206+A1, Concrete - Specification, performance, production and conformity, 2016.

NF EN 12390-3, Testing hardened concrete - Part 3 : compressive strength of test specimens, 2019.

NF P18-459, Concrete - Testing hardened concrete - Testing porosity and density, 2010.

Perkol-Finkel, S. and Sella, I. (2014). Ecologically Active Concrete for Coastal and Marine Infrastructure: Innovative Matrices and Designs. In From Sea to Shore ? Meeting the Challenges of the Sea, (ICE Publishing), pp. 1139–1149.

Pioch, S., Relini, G., Souche, J.C., Stive, M.J.F., De Monbrison, D., Nassif, S., Simard, F., Allemand, D., Saussol, P., Spieler, R., et al. (2018). Enhancing eco-engineering of coastal infrastructure with eco-design: Moving from mitigation to integration. Ecol. Eng. *120*, 574–584.

Rica, H.C., Boutouil, M., Boudart, B., Claquin, P. and Leroy, F. (2016). Colonisation et détérioration des bétons incorporant des coquilles pour récifs artificiels. Matér. Tech. *104*, 503.

Sanchez-Silva, M. and Rosowsky, D.V. (2008). Biodeterioration of Construction Materials: State of the Art and Future Challenges. J. Mater. Civ. Eng. *20*, 352–365.

Sella, I. and Perkol-Finkel, S. (2015). Blue is the new green – Ecological enhancement of concrete based coastal and marine infrastructure. Ecol. Eng. *84*, 260–272.

Strain, E.M.A., Olabarria, C., Mayer-Pinto, M., Cumbo, V., Morris, R.L., Bugnot, A.B., Dafforn, K.A., Heery, E., Firth, L.B., Brooks, P.R., et al. (2018). Eco-engineering urban infrastructure for marine and coastal biodiversity: Which interventions have the greatest ecological benefit? J. Appl. Ecol. *55*, 426–441.

XV International Conference on Durability of Building Materials and Components
DBMC 2020, Barcelona
C. Serrat, J.R. Casas and V. Gibert (Eds)

Development of a Damage Detecting Method for RC Slabs by Means of Machine Learning

Yutaka Tanaka and Takahiro Nishida

Port and Airport Research Institute, 3-1-1, Nagase, Yokosuka, 239-0826, JAPAN,
tanaka-yu@p.mpat.go.jp, nishida-ta@p.mpat.go.jp

Abstract. *It is beneficial to understand damage conditions of RC structural members by non-destructive methods. In this study, K-means clustering method was applied to the AE wave data in order to develop a damage detection method. From the result of this study, the damaged area had the relatively large number of AE hits and AE energy. In addition, from the result of the K-means clustering of the power spectral density of AE waves, the data could be separated into the obviously damaged area and other areas.*

Keywords: *AE, Non-Destructive Method, Machine Learning, Damage Detection, RC Slab.*

1 Introduction

It is beneficial to understand damage conditions of RC structural members by non-destructive methods for long term use of RC structures. Capturing AE signals is one of the effective methods to detect the damaged position and area in the structural member.

In the previous research, Nishida *et al*. (2019) developed an aggregation detector. The detector is equipped AE sensors to capture AE waves generated by the internal damage of the RC bridge deck. Nishida et al. focused on the AE energy in order to detect the damaged area and they proposed the method to decide the threshold value of AE energy to judge the damaged area.

In this study, authors applied a clustering method to the AE wave data that was obtained in previous research. The aim of this study is to develop a damage detecting method for RC slabs with machine learning.

2 Analysis of AE Waves

2.1 The Outline of Analysis of AE Waves

In this study, the AE wave data obtained in the previous research (Nishida *et al*., 2019) was analyzed. In the previous research, Nishida et al. focused on the total AE energy and did not focus on the number of AE hits. In general, the number of AE hits in damaged area is larger than that in sound area because the damaged area has a lot of AE source. Therefore, authors focused on not only the AE energy but also the number of AE hits. The AE wave data was separated into a group by 1.0 m for each measurement line, and then, the number of AE hits was counted in each group, and the average of AE energies was calculated in each group.

Authors also focused on the frequency domain of AE waves. The power spectral density (PSD) of each AE wave was calculated and averaged in each group. In this study, the averaged

doi:10.23967/dbmc.2020.034

PSDs were regarded as the representative values of each group and selected as the input data for the clustering method.

The K-means clustering method (MacQueen, 1967; Arthur and Vassilvitskii, 2007) was applied in this study. This method is a non-hierarchical clustering method and an unsupervised machine learning method. This method is used to divide automatically a data into k groups. The objective function of the K-means clustering that should be minimized is;

$$\mathrm{J} = \sum_{i=1}^{N} \sum_{k=1}^{K} w_{ik} \|x_i - c_k\|_2 \tag{1}$$

where N is the number of a data set, K is the number of the cluster, x_i is the i-th data in a data set, c_k is the centroid of the k-th cluster, $w_{ik} = 1$ if the data x_i belongs to cluster k, otherwise $w_{ik} = 0$ and $\|v\|_2$ is the Euclidean norm of a vector v.

The algorithm of the K-means is shown as follows.

1. Choose k initial centroids $\boldsymbol{C} = \{c_1, ..., c_k\}$.
2. For each $i \in \{1, ..., k\}$, set the cluster C_i to be the set of points in X that are closer to c_i than they are to c_j for all $i \neq j$.
3. For each $i \in \{1, ..., k\}$, set c_i to be the center of mass of all points in C_i.
4. Repeat Steps 2 and 3 until $\boldsymbol{C}$ no longer changes.

In this study, the number of the cluster k was changed to be from 2 to 5 due to find the optimal k for the clustering of the data.

The calculation of the K-means clustering and the power spectral density was conducted with Python, and the Scikit-learn (Pedregosa *et al*., 2011) was used for the K-means clustering and the SciPy (Virtanen *et al*., 2019) was used to calculate the power spectral density of the AE wave data.

3 Results and Discussions

Figure 1 shows the damaged area that was the result of the visual and the hammering inspection in the previous research. The red colored area is the damaged area where the crack or the delamination were observed.

3.1 The Number of AE Hits and the Average of AE Energies

Figure 2 and Figure 3 show contour maps of the number of AE hits and the average of AE energies in each group respectively. In Figure 2, the number of AE hits may have a close relation with the damaged area as shown in Figure 1, and the average of AE energies also have a relation with the damaged area.

In general, the defect such as the crack and the delamination become the source of AE signal. Therefore, the area where the number of AE hits is larger than the other areas has potential to be the damaged area.

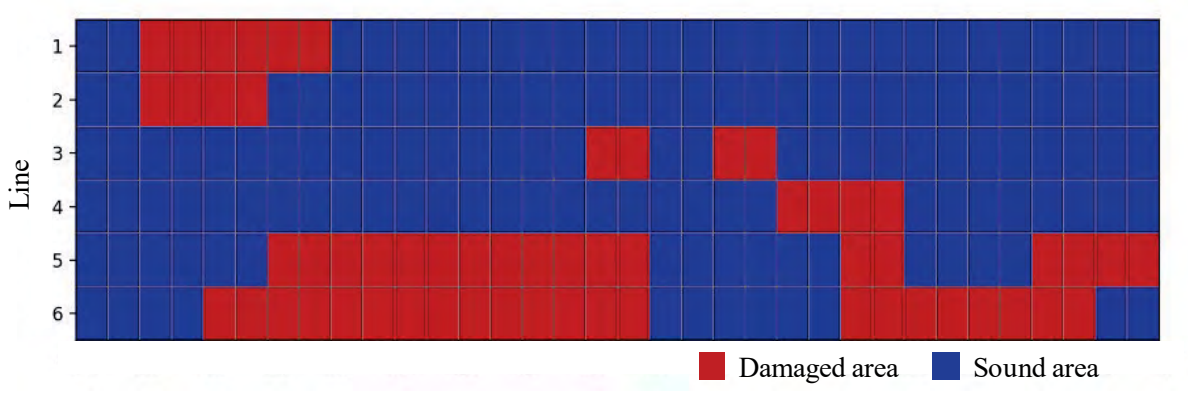

Figure 1. The result of the visual and the hammering inspection.

Figure 2. The number of AE hits in whole groups.

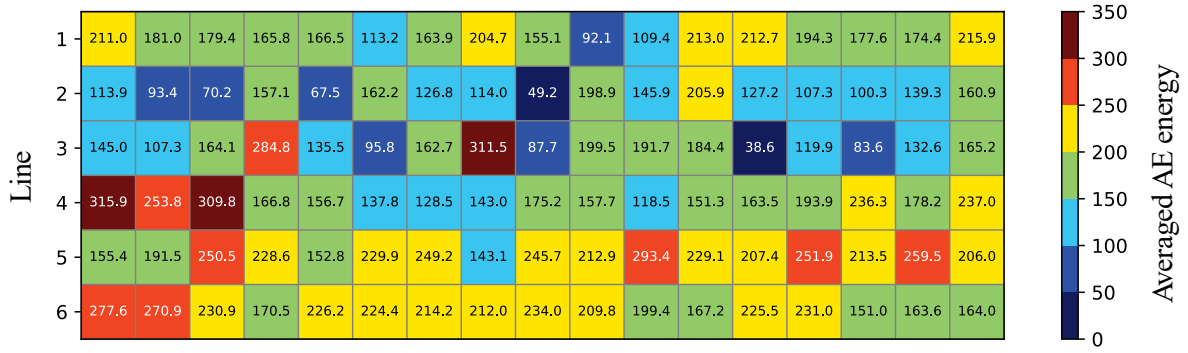

Figure 3. The average of AE energies in whole groups.

3.2 Clustering the PSD Data

Figure 4 (a) shows the PSD of the centroid of each cluster when the number of clusters was 2. The peak frequency and value of each PSD were different. Figure 4 (b) shows the scatter plot of each group. The number located beside each plot is the line number. In this figure, the all data belong to the cluster 2 was in the line 6 where a lot of defects were observed. From this result, the data was separated into the obviously damaged group and the other group, and the peak frequency of the PSD in the damaged area became lower than that in the other area.

Figure 5 (a) shows the PSD of the centroid of each cluster when the number of clusters was 3, and Figure 5 (b) shows the scatter plot of each group. From these figures, the cluster 1 in Figure 4 (b) was divided into two groups based on the average AE energy. In Figure 5 (a), the peaks of frequency and the forms of the PSD was also almost the same, but the peak values of the PSD were different in clusters 1 and 3.

Figure 6 (a) shows the PSD of the centroid of each cluster when the number of clusters was 4, and Figure 6 (b) shows the scatter plot of each group. From these figures, the cluster 1 in Figure 4 (b) was divided into three groups based on the average AE energy. In Figure 6 (a), the peaks of frequency and the forms of the PSD was also almost the same, but the peak values of the PSD were different in clusters 1, 3 and 4.

Figure 7 (a) shows the PSD of the centroid of each cluster when the number of clusters was 5, and Figure 7 (b) shows the scatter plot of each group. From these figures, the cluster 1 in Figure 4 (b) was divided into three groups and the cluster 2 in Figure 4 (b) divided into two groups based on the average AE energy. In Figure 7 (a), clusters 2, 3 and 4 were the same as clusters 2, 4, and 3 in Figure 6 (a) respectively. In addition, the peaks of frequency and the forms of the PSD was also almost the same, but the peak values of the PSD were different in clusters 1 and 5.

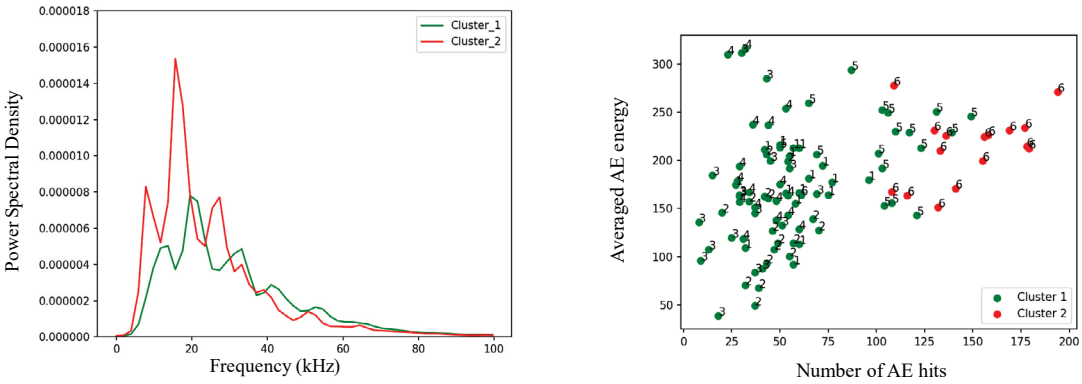

(a) PSD of each cluster centroid

(b) Scatter plot of each group

Figure 4. Clustering result of the data ($k = 2$).

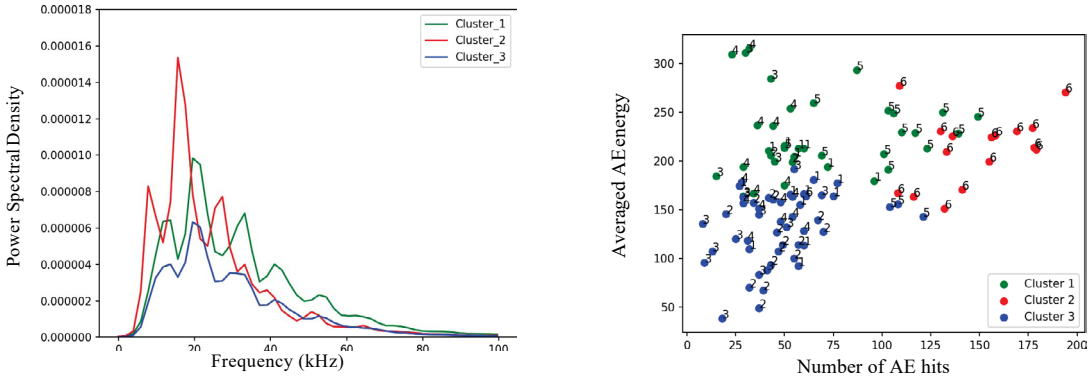

(a) PSD of each cluster centroid (b) Scatter plot of each group

Figure 5. Clustering result of the data (k = 3).

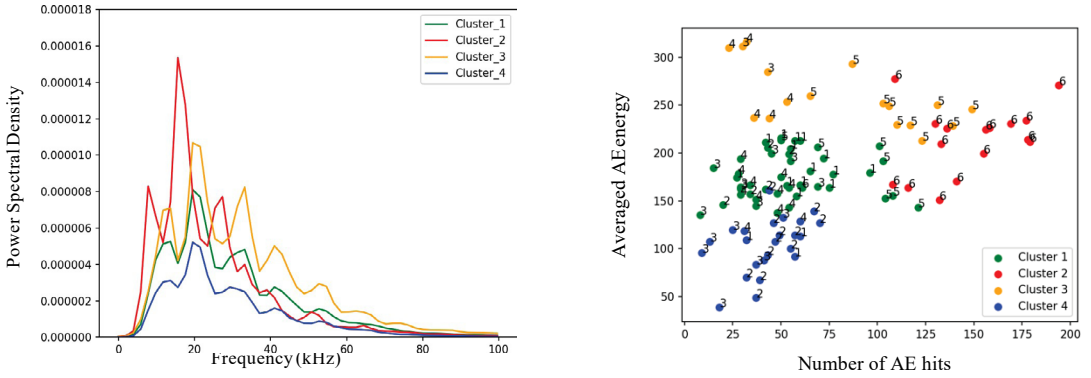

(a) PSD of each cluster centroid (b) Scatter plot of each group

Figure 6. Clustering result of the data (k = 4).

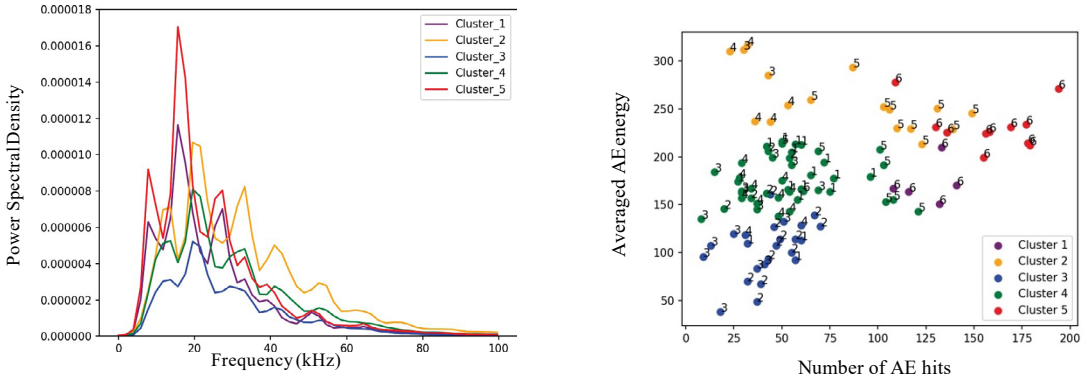

(a) PSD of each cluster centroid (b) Scatter plot of each group

Figure 7. Clustering result of the data (k = 5).

To evaluate the optimal k for the clustering, silhouette analysis (Rousseeuw, 1987) was conducted. The silhouette score of the data point i is:

$$s(i) = \frac{b(i) - a(i)}{max\{a(i), b(i)\}} \tag{2}$$

$$a(i) = \frac{1}{N_i - 1} \sum_{j \in C_i, i \neq j} d(i,j) \tag{3}$$

$$b(i) = \min_{k \neq i} \frac{1}{N_k} \sum_{j \in C_k} d(i,j) \tag{4}$$

where N_i is the number of data points in the cluster C_i, C_i is the cluster to whom the data point i belongs and $d(i, j)$ is the distance between data points i and j.
The range of the silhouette score is from -1 to +1, and a high value means that the data point is well matched to its cluster. From the plotting of the silhouette scores, the optimal number of the clusters can be determined graphically.

Figure 8 show the plotting of the silhouette score of each data. The black dotted line means the average of the whole silhouette score, and the thickness of the silhouette score of each cluster means the number of the data. In Figure 8 (a), the number of the data that belong to cluster 1 was larger than that to cluster 2, therefore, $k = 2$ may not be the optimal value for the clustering of the data. In Figures 8 (b) and 8 (d), some silhouette score was negative, therefore, $k = 3$ and 5 may not be also the optimal value for the clustering of the data. In Figure 8 (c), the thickness of the silhouette score of the cluster 1 was slightly thicker than those of other clusters, however, there was no negative silhouette score and many of silhouette scores exceeded the average silhouette score. Thus, $k = 4$ may be the optimal value for the clustering of the data.

The optimal k might be determined by the silhouette score, however, it is necessary to evaluate the accuracy of the clustered groups with the actual damage condition of the target structure. This is the future work for our study.

4 Conclusions

Following conclusions were derived from this study.

- The area where the number of AE hits and the average of AE energies were relatively lager than other areas might be the damaged area.
- From the result of the K-means clustering, the data was separated into the obviously damaged area and other areas. In addition, the characteristic of the power spectral density of the centroid of the damaged cluster was different from those of other clusters.
- As the increase of the number of centroids k, the data was separated into some groups based on the average of the AE energies.

ORCID

Yutaka Tanaka: https://orcid.org/0000-0002-9685-1330
Takahiro Nishida: https://orcid.org/0000-0002-2018-6928

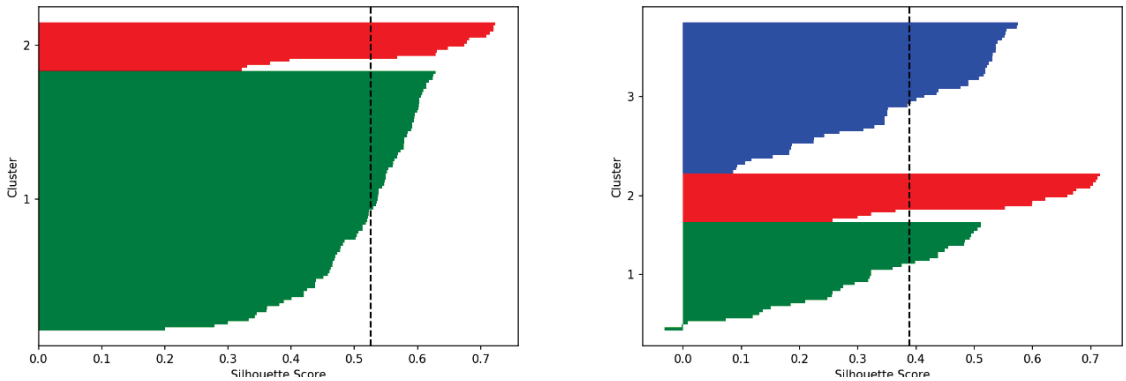

(a) $k = 2$ (b) $k = 3$

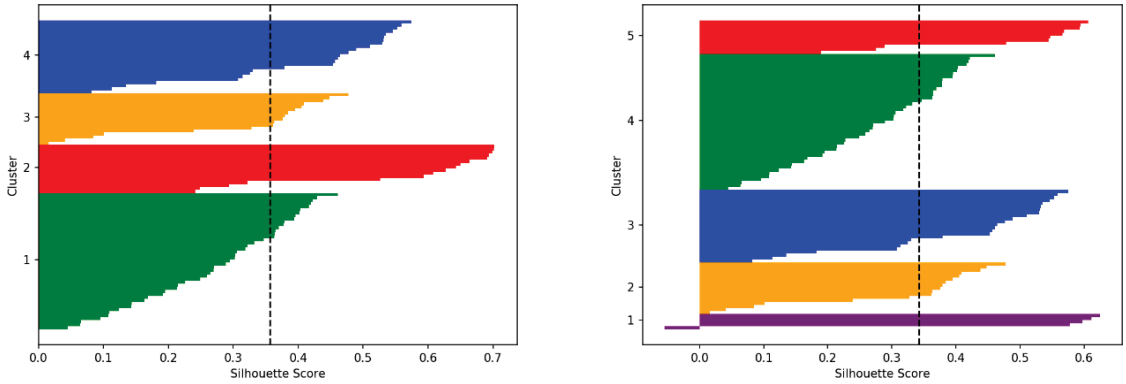

(c) $k = 4$ (d) $k = 5$

Figure 8. Silhouette score plots.

References

Arthur, D. and Vassilvitskii, S. (2007). *k*-means++: the advantages of careful seeding. *Proceedings of the eighteenth annual ACM-SIAM symposium on Discrete algorithms*, Society for Industrial and Applied Mathematics Philadelphia, PA, USA, 1027-1035.

MacQueen, J. B. (1967). Some Methods for classification and Analysis of Multivariate Observations. *Proceedings of 5th Berkeley Symposium on Mathematical Statistics and Probability*, University of California Press, 281-297.

Nishida, T., Hashimoto, K., Yasuzato, T. and Kawada, K. (2019). Data Analysis for Damage Area Detection of Reinforced Concrete Decks, *Proceedings of The 4th International Symposium on Concrete and Structures for Next Generation*, 371-376.

Pedregosa, F., Varoquaux, G., Gramfort, A., Michel, V., Thirion, B., Grisel, O., ... Duchesnay, E. (2011). Scikit-learn: Machine Learning in Python, *JMLR 12*, 2825-2830.

Rousseeuw J. P. (1987). Silhouettes: a graphical aid to the interpretation and validation of cluster analysis, *Journal of Computational and Applied Mathematics, 20*, 53-65.

Virtanen, P. *et al* (2019). SciPy 1.0 –Fundamental Algorithms for Scientific Computing in Python, arXiv:1907.10121.

XV International Conference on Durability of Building Materials and Components
DBMC 2020, Barcelona
C. Serrat, J.R. Casas and V. Gibert (Eds)

Dynamic Observability Method for Durability Assessment Considering Measurement Noise

Tian Peng, Juan R. Casas and Jose Turmo

Department of Civil and Environmental Engineering，Universitat Politècnica de Catalunya-BarcelonaTECH, Campus Nord UPC, 08034-Barcelona, Spain, {tian.peng, joan.ramon.casas, jose.turmo} @upc.edu

Abstract. *Due to the inevitable degradation of material properties in structures in daily use, such as stiffness degradation due to cracking in concrete elements, their durability will definitely be influenced, and their serviceability and safety could be in danger. Thus, understanding and identifying the change in the structural parameters provides new approaches to evaluate their durability. Structural system identification by dynamic observability method, which is using subsets of masses, natural frequencies and modal shapes, is a powerful tool to detect the change of structural parameters. Taking into account the presence of noise in the measurement data in real world structures, this method establishes the relative dynamic equation with the error separation items. The equation is solved by error minimization of an objective function combining the measured frequencies and mode shapes through the parameter MAC (Modal Assurance Criterion). Additionally, the algorithms and the steps are introduced based on the dynamic eigenvalue equation, which can fully demonstrate the performance of observability techniques. The present paper provides an example on how to successfully identify structural parameters. Its suitability for practical applications is demonstrated in a large frame structure. The result is a much more accurate identification of the parameters involved in the durability of the structure even in the case of noise-corrupted measurement signals*

Keywords: *Durability, Structural System Identification, Dynamic Observability Method, Frequencies，Mode Shapes.*

1 Introduction

Existing structures are inevitably exposed to the natural environment (wind, earthquake, temperature difference, or even some extreme climate) and human operationt (traffic, impact, daily degradation by use). Thus, the material properties are degraded such as the bending stiffness, axial stiffness, and mass. In this case, the durability of the structures may be influenced, leading them structures into a dangerous condition instead of the originally safe state.

Regarding the durability of structures, understanding and identifying the change in the structural parameters is a great way to estimate the structure condition and safety. Structural system identification (SSI) has become a powerful tool to help engineer decision making during the life cycle of civil and infrastructures systems. SSI can be classified as the static and dynamic analysis, as well as deterministic and probabilistic methods. The former research classification depends on the type of excitation and the latter is related to the uncertainty of the parameters involved.

It is worth mentioning that the development of Observability method (OM) makes relevant contributions to deal with the remaining problem of SSI, and has been used in several engineering fields, such as hydraulics, electrical and power networks, or transportation. The

SSI by OM under static conditions was proposed to identify 2-D beam element models in its plane, dealing with the partial observability problem and achieving an accurate assessment. While it is much easier to dynamically excite a large structure than statically, especially in large scale structures, the dynamic data are more difficult to deal with than the static one. As a result, the standard observability method used with dynamic data has shown deficient in identifying degradation processes endangering durability.

Thus, this paper proposes a new constrained dynamic observability SSI methodology, which allows the identification of a subset of characteristics of a structure, related to its durability parameters such as stiffness and mass. Subsets of natural frequencies and modal shapes are used. Firstly, the description of dynamic constrained OM method is demonstrated step by step. Secondly, the verification of this method is revealed by one example considering the measurement noise. Lastly, the potential of dynamic constrained OM when applied to large structures is shown.

2 Methodology

The dynamic equation of motion of a system with no damping and no external applied forces is shown in equation (1), expressing what is the eigenvalue or characteristic value problem.

The equation can be expressed for a two-dimensional structure with $\mathrm{N_N}$ nodes, $\mathrm{N_B}$ boundary conditions and R vibration modes as:

$$[K]^{[(3N_N-N_B)\times(3N_N-N_B)]}\{\emptyset_i\}^{[(3N_N-N_B)\times 1]} = \lambda_i\{M\}^{[(3N_N-N_B)\times(3N_N-N_B)]}\{\emptyset_i\}^{[(3N_N-N_B)\times 1]]} \quad (i = 1,2,3\ldots,R) \tag{1}$$

Where λ_i and $\emptyset_i$ are the eigenvalues and mode shapes of ith mode, and the $[K]$ and $[M]$ represent the stiffness matrix and mass matrix. $\emptyset_i$ includes the displacement in the x-direction (u_{ik}), y-direction (v_{ik}) and rotation (w_{ik}) at each node k for each vibration mode i.

The arrangement of equation (1) is done in a similar way to the static observability method, all the unknowns of the system are set up to one column vector and the known variables are joined into a vector $\{D\}$. In this way, the previous equation might be written as:

$$[B_i]\{z_i\} = \begin{bmatrix} K_{i,0}^{*(3N_N-N_B)\times rx} & -M_{i,0}^{*(3N_N-N_B)\times mx} \end{bmatrix} \begin{Bmatrix} \emptyset_{Ki,0}^{*rx\times 1} \\ \emptyset_{Mi,0}^{*mx\times 1} \end{Bmatrix} = \left\{ M_{i,1}^{*(3N_N-N_B)\times nx}\emptyset_{Mi,1}^{*nx\times 1} - K_{i,1}^{*(3N_N-N_B)\times sx}\emptyset_{Ki,1}^{*sx\times 1} \right\} = \{D_i\} \quad (i = 1,2,3\ldots,R) \tag{2}$$

Where z_i represents all the unknowns, B_i and D_i are the corresponding coefficient matrix and augmented matrix of ith mode.

Equation (2) is the description in ith mode. When multiple modes are considered together, the equation will be built by combining information of several modes. For example, the first R modal information is given by $[B]\{z\} = \{D\}$ shown as follows:

$$[B]\{z\} = \begin{bmatrix} B_1 & 0 & 0 & 0 \\ 0 & B_2 & 0 & 0 \\ 0 & 0 & \ddots & 0 \\ 0 & 0 & 0 & B_R \end{bmatrix} \begin{Bmatrix} z_1 \\ z_2 \\ \vdots \\ z_R \end{Bmatrix} = \begin{bmatrix} D_1 & 0 & 0 & 0 \\ 0 & D_2 & 0 & 0 \\ 0 & 0 & \ddots & 0 \\ 0 & 0 & 0 & D_R \end{bmatrix} = \{D\} \tag{3}$$

Expression in which $[B]$ is a matrix of constant coefficients, $\{D\}$ is a fully known vector and $\{z_i\}$ contains the full set of unknown variables. This system contains coupled and single variables. Thus, the identified coupled variables (*e.g.*, $EI_j w_{ik}$ that exist in Eq.(2)) are referred as observed variables. In other to uncouple the observed variables, e.g., $EI_j w_{ik} = EI_j * w_{ik}$, the dynamic COM (constrained observability method) is here proposed based on a similar procedure as in the static case. However, in this case, the objective function is defined as:

$$E = \sum_{i=1}^{R} (\Delta f_i)^2 + \sum_{i=1}^{R} \left(1 - \frac{\left[\emptyset_{mi}^T \overline{\emptyset_{mj}} \right]^2}{(\emptyset_{mi}^T \emptyset_{mi})(\overline{\emptyset_{mj}}^T \overline{\emptyset_{mj}})} \right) \tag{4}$$

The modal assurance criterion (MAC) is used in Eq. (4), which consists of computing the so-called MAC values as a measure for the correspondence between the calculated mode shape $\emptyset_{mi}$, obtained from the inverse analysis using the estimated stiffnesses and areas, and the measured shape $\overline{\emptyset_{mj}}$ as shown in Equation (5). Besides, Δf_i are the differences between the measured and estimated frequencies.

$$\text{MAC}\,(\emptyset_{mi}, \overline{\emptyset_{mj}}) = \frac{\left[\emptyset_{mi}^T \overline{\emptyset_{mj}} \right]^2}{(\emptyset_{mi}^T \emptyset_{mi})(\overline{\emptyset_{mj}}^T \overline{\emptyset_{mj}})} \tag{5}$$

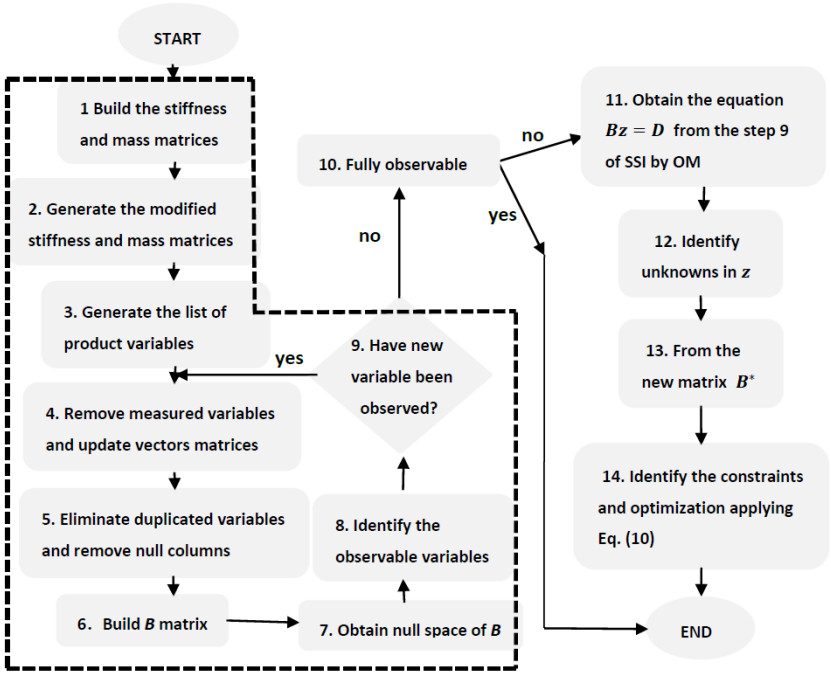

Figure 1. Flow-chart of algorithm of dynamic observability method.

The solution is obtained by minimizing equation (4) with the imposed constraints of the form: $EA_j u_{ik} = EA_j * u_{ik}$, $EI_j v_{ik} = EI_j * v_{ik}$, $EI_j w_{ik} = EI_j * w_{ik}$ present in equation (3), which is the so-called Constrained Observability Method .

The specific steps about the method are shown in Figure.1, which is developed on the base of the static COM method.

3 Example Analysis

3.1 Reinforced Concrete Beam

The dynamic constrained observability method is verified in a reinforced concrete beam. This beam is shown in Figure 2, with a length of 6m and equally divided into 30 elements, 10 parts, whose divisions can be seen minutely in Figure 2. The free vibration test of the beam was conducted by Ellen Simon, with the aim of obtaining its dynamic information, frequencies and mode shapes. The structure stiffnesses are estimated in the following way: $EI_i = x_i EI_{int}, i = 1{\sim}10, EI_{int} = 7.23 \times 10^6 \frac{N}{m^2}$, $x_i = [1.15, 1.04, 0.86, 0.90, 0.80, 0.54, 0.51, 0.57, 0.72, 0.86]$ by using the experimental data after some controlled damage was produced in the beam.

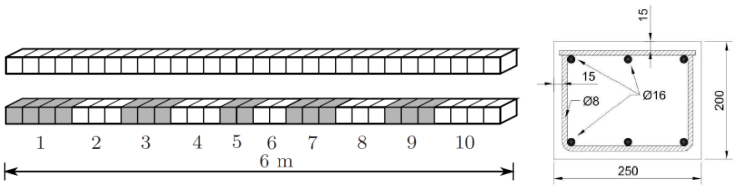

Figure 2. Set-up of static loading.

There is one way in using the estimated stiffnesses of EI_i as the input to do the direct analysis of the first four frequencies and mode shapes since the real experimental data is difficult to get from paper. Therefore, 100 samples of frequencies are generated for this set with an error of 2% while 100 samples of mode-shapes are obtained with an error of 10%, because frequency accuracy obtained from dynamic tests is normally higher than for mode. One sample for a given measurement set is the collection of the associated measurements generated by Eq. (6).

$$\tilde{\delta} = \delta(1 + E_{level} \cdot \S) \quad (\tilde{f} \text{ yielded in the same way}) \tag{6}$$

Here, the measurements $\tilde{\delta}$ are simulated by adding proportional errors to the theoretical values, δ are obtained by direct analysis. E_{level} is the error level in the measurement and § is a random number following a normal distribution with mean zero and standard deviation 0.51 to guarantee the 95% confidence interval. The samples of $\tilde{f}$ are yielded in the same way.

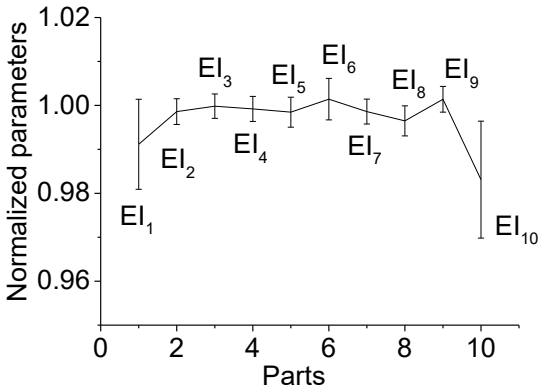

Figure 3. Mean and standard deviation of stiffness.

Figure 3 shows the estimated mean values of the 100 samples and their standard deviation for the estimated stiffness along the beam. It is shown how the errors in the mean values are less than 2% and the biggest standard deviations less than 1.5%, which is a reasonable range for parameter evaluation. However, it can be obviously observed that the standard deviations of EI_1 and EI_{10} are higher than other parameters, which may be due to the error accumulation from middle to the ends of the beam in the computational solution. Also the area of EI_1 and EI_{10} provides little information to the solution algorithm because of their free ends. This case can effectively explain the operability of the dynamic observability method to obtain the actual condition of the structure or its elements in relation to their durability.

3.2 Example of 13-Story Building

In order to show the possible applications and potential of the proposed methodology, a more complex example is presented in this section. The 13-story building shown in Figure 4 is taken under study. This structure was considered in Reference [16].

This frame is modeled using a total of 226 nodes and 273 elements and it is composed of a set of 8 different sections described in Figure 4, and the parameters are the same as in [16]. Therefore, the size of the system of equations is 678×678. The study will be performed for the first two vibration modes, which can provide relevant modal information. This structure is analyzed from a local perspective, using the constrained dynamic observability technique to only a part of the unknowns as shown in figure 4.

In fact, there are occasions in which there is interest of obtaining only the properties of one or a few members of the structure to check, for example, if it is locally damaged. This leads to a more economically efficient application of the technique. The normal procedure is to measure some of the displacements around this element or elements in order to activate its matrix components.

For this example, an assumption is made that the bending stiffnesses EI_1 and EI_2 of the structure are unknown and that the mechanical properties of the floor slab of the 12th floor are different from the theoretical one, because this part of the structure is damaged. Its modal frequency (only the first frequency is required) and mass are assumed to be known. Therefore, the properties to be observed are the bending stiffnesses of the elements between nodes 27 and 41.

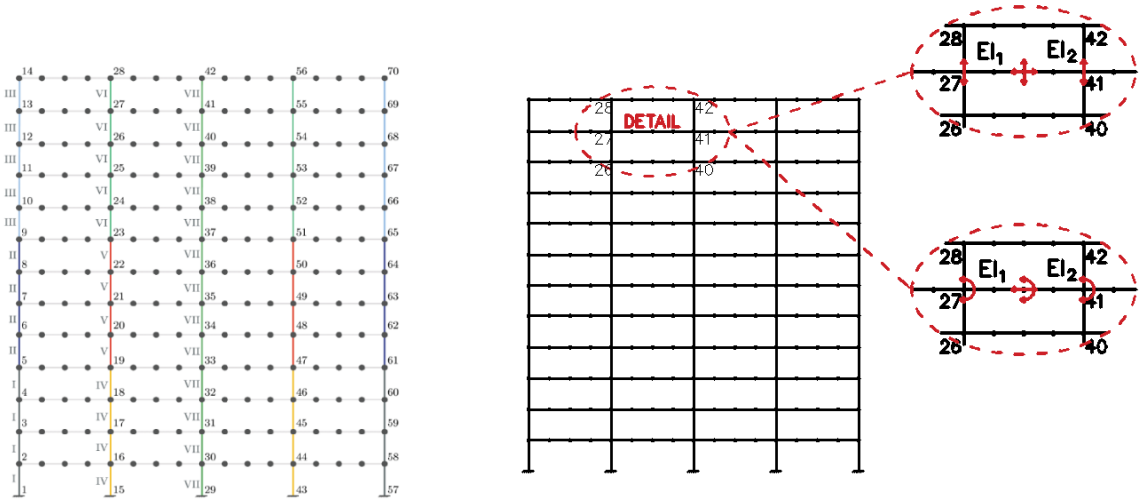

a) b)

Figure 4. a) Members with different characteristics are represented with different colors.
b) Sets of measurements used in the local analysis.

Two sets of measurements are proposed. The first one includes the vertical displacements in three nodes and the horizontal displacement in one node，which can be seen in the A detail in Figure 4(b) (4 measurements+ 1 frequency). The second one includes rotations in three nodes and horizontal displacements in one node, as shown in the B detail in Figure 4(b) (4 measurements+ 1 frequency).

After performing the analysis, the stiffnesses EI_1 and EI_2 can be identified by Constrained Observability assuming 2% and 5% errors in the frequencies and mode shapes respectively. The 100 samples are gained by Eq. (6). The estimated mean values and standard deviations of the 100 samples under the two measurement sets are illustrated in figure 5.

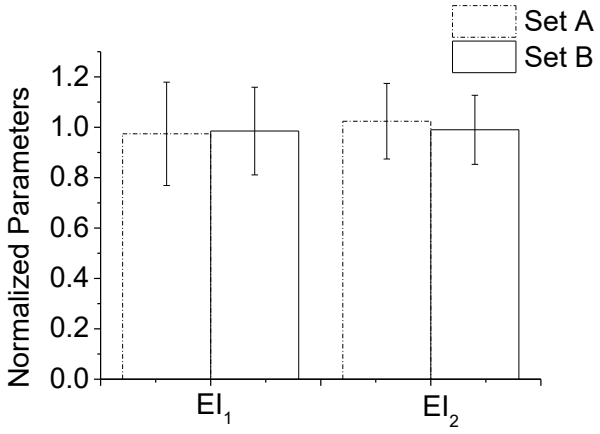

Figure 5. Mean and standard deviation of stiffness EI_1 and EI_2.

From figure 5, the maximum standard deviations are 2.0% and 1.7% for set A and set B

respectively, and the mean of EI_1 and EI_2 under both sets are very close to the true value, with a 2.3% error. No matter the set of A or B, the estimated value of EI_2 is a bit better than for EI_1 because of the slightly smaller standard deviations, which may be due to the stronger boundary conditions of node 41 than node 27. It has to be emphasized that these bending stiffnesses can be observed without knowing the surrounding ones, which shows the potential of the method when applied to large structures where only a small number of measurements can be obtained. The potential application of constrained dynamic observability method to large scale structures is then fully illustrated.

4 Conclusions

The main objective of this paper is the application of constrained observability techniques for parametric estimation of structures using dynamic information such as frequencies and mode-shapes. The final objective is to show the applicability of the method in efficiently identify the possible damages existing in the structure that may affect its durability (mainly cracking affecting the bending stiffness). A new algorithm is introduced based on the dynamic eigenvalue equation. The merit of the dynamic constrained observability analysis is demonstrated in the analysis of a RC beam and a large frame structure.

Acknowledgements

The authors are indebted to the Spanish Ministry of Economy and Competitiveness for the funding provided through the research projects BIA2013-47290-R and BIA2017-86811-C2-1-R founded with FEDER funds and directed by Professor José Turmo and through the research project BIA2017-86811-C2-2-R. It is also to be noted that the part of this work was done included an exchange of faculty financed by the Chinese government to Mrs.Peng thorough the program (No. 201808390083).

ORCID

Tian Peng: https://orcid.org/0000-0003-4592-6117
Joan R. Casas: http://orcid.org/0000-0003-4473-4308
Jose Turmo: https://orcid.org/0000-0001-5001-2438

References

Bakhtiari-Nejad, F. , Rahai, A. and Esfandiari, A. (2005). A structural damage detection method using static noisy data. *Engineering Structures*, 27(12), 1784-1793. doi: 10.1016/j.engstruct.2005.04.019.

Castillo, E., Lozano-Galant. JA., Nogal, M. and Turmo, J. (2015). New tool to help decision making in civil engineering. *Journal of Civil Engineering and Management*,21:689–97. doi: 10.3846/13923730.2014.893904.

Castillo, E. , Conejo, A. J. , Pruneda, R. E. and Solares, C. (2007). Observability in linear systems of equations and inequalities: applications. *Computers & operations research*, 34(6), p.1708-1720. doi:10.1016/j.cor.2005.05.035.

Castillo, E. , Nogal, M. , Antonio Lozano-Galant, J. and Turmo, J. (2016). Solving some special cases of monomial ratio equations appearing frequently in physical and engineering problems. *Mathematical Problems in Engineering*, 2016(pt.5), 9764913.1-9764913.25. doi: 10.1155/2016/9764913.

Ellen, S., Guido, D.R. and Geert, L. (2015). Dealing with uncertainty in model updating for damage assessment: a review. *Mechanical Systems & Signal Processing*, 56-57(may), 123-149. doi: 10.1016/j.ymssp.2014.11.001

Eskew, E. L. and Jang, S. (2017). Remaining stiffness estimation of buildings using incomplete measurements. *Structural Control and Health Monitoring*, 24:e1899. doi: 10.1002/stc.1899.

Gonzalez, Javier, Minguez, Roberto andDiaz and Sarai. (2016). Observability analysis in water transport networks: algebraic approach. *Journal of Water Resources Planning & Management*. 142:4015071.

doi:10.1061/(ASCE)WR.1943-5452.0000621.

Jin, S.S. and Jung. H.J. (2016). Sequential surrogate modeling for efficient finite element model updating. *Computer & Structures*, 168:30–45. doi: 10.1016/j.compstruc.2016.02.005

Jiang, X. , Mahadevan, S. and Adeli, H. (2010). Bayesian wavelet packet denoising for structural system identification. *Structural Control and Health Monitoring*, 14:333–56. doi: 10.1002/stc.161.

Lei, J., Xu, D. and Turmo, J. (2018). Static structural system identification for beam-like structures using compatibility conditions. *Structural Control and Health Monitoring*, 25, e2062. doi: 10.1002/stc.2062.

Lei, J., Nogal, M., Lozano-Galant. JA., Xu, D. and Turmo, J. (2018). Constrained observability method in static structural system identification, *Structural Control and Health Monitoring*, 25.1, e2040. doi:10.1002/stc.2040.

Li Z , Park H S and Adeli H. (2016). New method for modal identification of super high-rise building structures using discretized synchrosqueezed wavelet and Hilbert transforms. *The Structural Design of Tall and Special Buildings*, 1-16. doi: 10.1002/tal.1312.

Lozano-Galant, JA., Nogal, M. ,Castillo, E. and Turmo, J. (2015). Selection of measurement sets in static structural identification of bridges using observability trees. *Computers and Concrete*, 15 :771–794. doi: 10.12989/cac.2015.15.5.771.

Marano, G. C. , Quaranta, G. and Monti, G. (2011). Modified genetic algorithm for the dynamic identification of structural systems using incomplete measurements. *Computer Aided Civil & Infrastructure Engineering*, 26(2), p.92-110. doi: 10.1111/j.1467-8667.2010.00659.x.

Nogal, M. , Lozano-Galant, J. A. , Turmo, J. and Castillo, E. (2016). Numerical damage identification of structures by observability techniques based on static loading tests. *Structure & Infrastructure Engineering*, 12(9), 1216-1227. doi: 10.1080/15732479.2015.1101143.

Sanayei, M. and Scampoli, S. F. (1991). Structural element stiffness identification from static test data. *Journal of Engineering Mechanics*, 117(5). doi: 10.1061/(ASCE)0733-9399(1991)117:5(1021).

XV International Conference on Durability of Building Materials and Components
DBMC 2020, Barcelona
C. Serrat, J.R. Casas and V. Gibert (Eds)

Field Survey of Hygrothermal Behaviour within Wall Assembly Derived from Rain Penetration and Ventilation Performance of Exterior System

Sadaharu Osamura [1] **and Hiroaki Saito** [2]

[1] Misawa Homes Institute of Research and Development Co.Ltd, Tokyo, Japan 1680071,
Phone +81 3 3247 5647 Fax +81 3 5370 7323, Sadaharu_Osamura@home.misawa.co.jp

[2] Ashikaga University, Ashikaga, Japan 3268558,
Phone +81 284 22 5674, Fax +81 284 62 0976, hsaito@ashitech.ac.jp

Abstract. *Rainwater and moisture control are key factors for maintaining the durability of wooden houses. Wall assemblies with sidings are installed on vented cavities to build durable wooden houses. Moisture condensation does not occur generally behind a vapor retarder in walls assembled with a vented cavity; however, it is reported that the condensation mechanism which occurs in the wall assembly due to the high humidity of the vented cavity by rain penetration in Japan, there are only a few studies that investigate hygrothermal behaviour considering effects such as rain penetration in the exterior system. To unravel the mechanism of internal condensation derived from rain penetration, lab-experiments and field measurements were conducted. In the lab experiments, rain penetration from siding joints were quantitated using a water spray test. In the field measurements, for the exterior finishes of the experimental house, the sidings were installed on three types of vented cavities. To verify hygrothermal behavior within the wall assembly, intermittent long-term rain penetration into the vented cavity was reproduced for the experimental house. The measurements confirmed that internal condensation occurs with low ventilation performance, when moisture retained in the vented cavity is released into the wall assembly. This phenomenon is caused when the surface temperature on the sidings is increased because of solar radiation after rain. In conclusion, rain penetration through exterior finishes has a significant effect on the moisture behavior of wall assemblies. The obtained results verify that moisture condensation at the vapor retarder was caused by several factors including rain penetration, insufficient ventilation, and solar radiation. To maintain durability, it is important to ensure a ventilation performance and not retain moisture.*

Keywords: *Concealed Condensation, Vented Cavity, Rain Penetration, Absorption and Desorption, Field Survey, Siding.*

1 Introduction

Rainwater and moisture control are key factors for maintaining the durability of wooden houses. Wall assemblies with claddings are installed on vented cavities to build durable wooden houses (Figure. 1). In Japan, a fiber reinforced cement siding (hereinafter, called siding) is provided as an exterior system for outer walls in several houses. In this system, a vented cavity is provided between the siding of the primary waterproof layer and a water resistive barrier sheet of the secondary waterproof layer; the rainwater from the siding joints and the moisture from inside the house are discharged quickly (Figure. 2).

Recent years have seen an increase in houses designed with low eaves that experience rain penetration through the sidings under heavy rain; thus, the risk of rain penetration is increasing. It is difficult to completely prevent rain penetration into a vented cavity (Sahal, Lacasse and

Kimura). Technical note of National Institute for Land and Infrastructure Management of Japan has reported moisture condensation and structural decay of the wall assembly caused by rain penetration and insufficient ventilation. It is suggested that the condensation mechanism which occurs in the wall assembly due to the high humidity of the vented cavity by rain penetration (Umeno, 2011). Rain penetration have been considered evaluation methods such as ASHRAE Standard 160 in North America. However, there are only a few studies that investigate hygrothermal behavior considering effects such as rain penetration in the exterior system in Japan.

To maintain durability of wooden houses with the exterior system, this study confirmed the quantity of rain penetration from the siding joints using a water spray test, measured the temperature, humidity, and moisture content within the wall assembly during intermittent rain penetration into the vented cavity in the field survey. These results were used to clarify the mechanism of moisture accumulation in the wall assembly. Furthermore, the vented cavities of different cases were compared, the verification data on the ventilation performance of each case were verified. The impact of rain penetration on the exterior system of the hygrothermal behavior within wall assemblies was discussed.

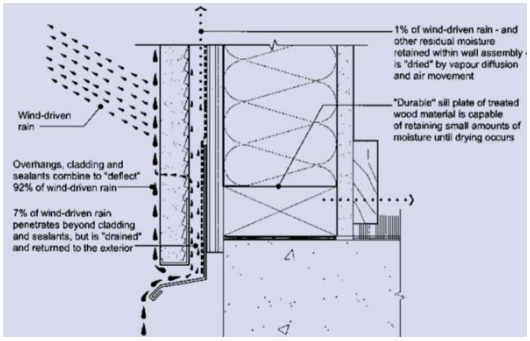

Figure 1. Four Line of Defense (Moisture Design for Wood-Frame Buildings, Canada).

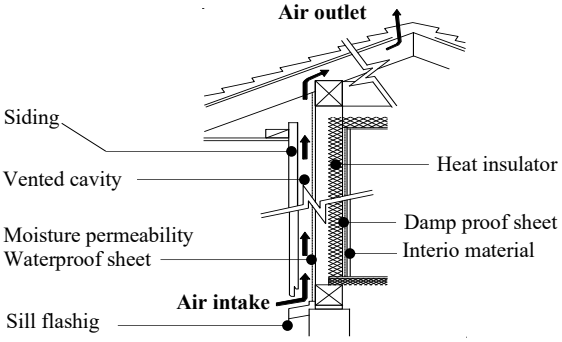

Figure 2. Siding standard installation method.

2 Quantification of Rain Penetration from the Siding Joints Using a Water Spray Test

To measure the quantity of rain penetration from the siding joints of an exterior system, the water spray test (JIS A 1517: Water tightness test under dynamic pressure) was performed.

As for the water penetration through the siding joint under strong wind, it is generally assumed that the rainwater flows over the shiplap joint and penetrates the vented cavity (Fig. 3(1)). When the wind is weak, the rainwater flows across the surface of the shiplap and penetrates into the vented cavity through the sealing area between the horizontal joints of sidings (Fig. 3(2)). The horizontal joint of the siding was placed at the center of the test specimen, and the quantity of rain penetration was measured with a plastic container. Figure 4 shows an outline of the experimental apparatus.

2.1 Experimental Conditions

General water spray tests are conducted under the conditions of high pressure difference (150–

350 Pa) and high water volume (4 l/min・m^2). However, frequency of these conditons are rare in real crimate data. To understand the quantity of rain penetration under the condition that may frequency occur in rainy day, this test was conducted at low pressure (0–250 Pa) and low water volume (0.2–0.8 l/min・m^2). The duration of the water spray test was 11 min; the pressure condition was not a pulsating pressure but a constant pressure.

To confirm the difference caused by the siding application method, test specimens were assembled using two application methods for a typical shiplap joint. Case A has a two-way shiplap with the top and the bottom; the left and right sides are joint using a sealant. Case B has a four-way shiplap with the top, bottom, left, and right. Figures 5 and 6 show the outline of specimen. In addition, the quantity of penetrated water and the water penetration rate in the water spray test were obtained from the following equation:

$$J_p = \frac{m_w}{t} \tag{1}$$

$$f = \frac{J_p}{R_w} \times 100 \tag{2}$$

where J_p is the quantity of penetration water (g/s), m_w is the measured total quantity of penetration water (g), t is the duration of the water spray test (s), f is the water penetration rate (%), and R_w is the quantity of water spray (g/s).

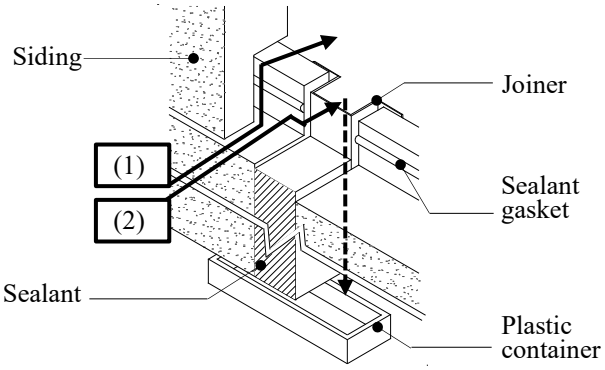

Figure 3. Water leakage path at two-way shiplap joint and Detail at the bottom of specimen.

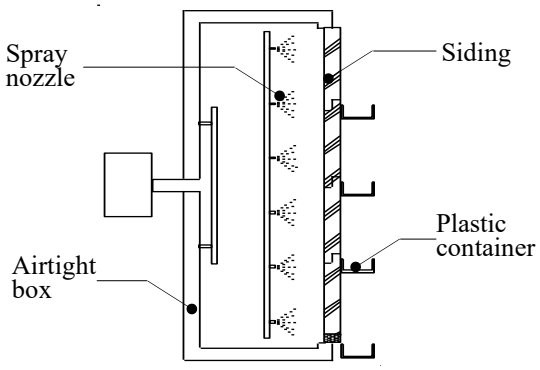

Figure 4. Apparatus for water spray test.

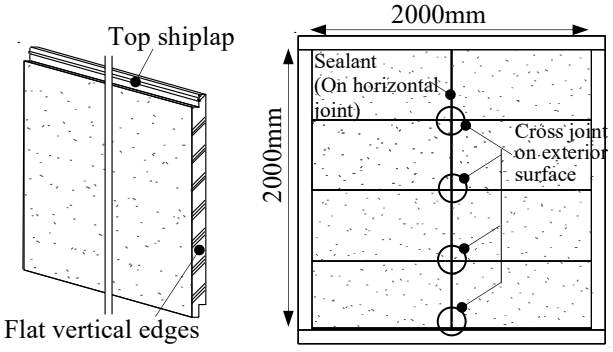

Figure 5. Siding shape of Two-way shiplap and Test specimen of Case A.

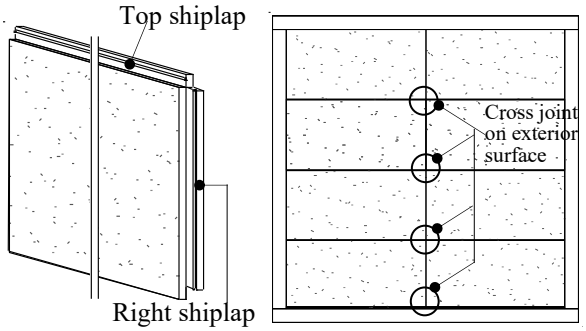

Figure 6. Siding shape of Four-way shiplap and Test specimen of Case B.

2.2 Relation Between Water Penetration Rate and Pressure Difference

Table 1 and Figure 7 show the experimental results. There are differences in the water penetration rate with the siding application.

For case A, under the conditions that rain penetration water was observed with a pressure difference of less than 150 Pa, the water that ran across the surface of the shiplap—the path shown in Fig. 3(2)—was transmitted to the sealant part of the horizontal joint, and it flowed down to the vented cavity. This water was accumulated in the plastic container at the bottom. When the pressure difference was 250 Pa, the water flowed over the sealant gasket of the shiplap joint shown in Fig. 3(1) and then flowed down the back of the siding. As a result, the water penetration rate increased significantly. For Case B, continuous flow occurred even in a pressure-equalized condition because there were pinholes at the cross joint on the exterior surface (Fig. 8). Thus, considerable penetration water that the water penetration rate was 5–11% was measured when the pressure difference was 0 Pa.

Owing to the difference in the siding application method, it is conceivable that there is no waterproofing performance criterion for driving rain. Furthermore, there is a possibility that the quantity of penetration water may increase because of the deterioration of sealants and the opening of the siding joint, which was caused by hardening shrinkage.

In consideration the above results, it is necessary for maintaining durability to consider the assumption that rainwater enters the vented cavity.

Table 1. Quantity of penetration water and water penetration rate.

Quantity of water spray (L/min・m²)	Pressure difference (Pa)	Case A			Case B		
		m_w (g)	Jp (g/s)	f (%)	m_w (g)	Jp (g/s)	f (%)
0.2	0	0	0.00	0.00	788	1.19	11.31
	15	0	0.00	0.00	812	1.23	11.65
	100	0	0.00	0.00	1177	1.78	16.90
	150	0	0.00	0.00	1497	2.27	21.49
	250	2245	3.40	32.22	2068	3.13	29.69
0.5	0	0	0.00	0.00	1200	1.82	6.91
	15	0	0.00	0.00	1408	2.13	8.11
	100	26	0.04	0.15	1941	2.94	11.18
	150	29	0.04	0.20	2472	3.74	14.23
	250	4805	7.28	27.67	3368	5.10	19.39
0.8	0	7	0.01	0.02	1385	2.10	4.80
	15	12	0.02	0.04	1594	2.42	5.52
	100	27	0.04	0.09	2197	3.33	7.61
	150	46	0.07	0.20	3082	4.67	10.67
	250	4859	7.36	16.83	4329	6.56	14.99

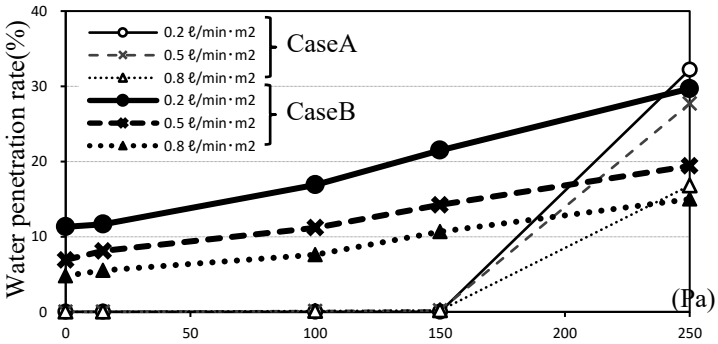

Figure 7. Relation between water penetration rate and pressure difference.

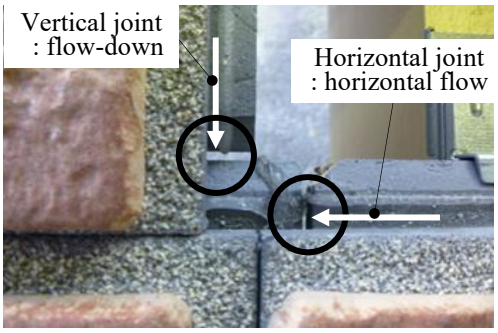

Figure 8. Leakage path (four-way shiplap joints).

3 Field Survey of Hygrothermal Behavior within Wall Assembly Derived from Rain Penetration

From the results in the previous section, it was suggested that wall assembly with a vented cavity using the siding has a risk of rain penetration from the shiplap joint. In this section, to unravel the mechanism behind internal condensation caused by moisture from the rainwater, an experimental house that reproduces intermittent long-term rain penetration into the vented cavity was constructed, and the hygrothermal behavior within the wall assembly was measured.

3.1 Outline of the Experimental House

The experimental house with a wood panel construction was constructed on the grounds of Ashikaga University in Tochigi (about 80km north of Tokyo). Three types of cavity configurations were installed in experimental house to compare the ventilation performance, Figure 10 shows the configuration of cavity. Case (1) is a horizontal furring strip (cavity depth: 12 mm), case (2) is a panel clip (cavity depth: 6 mm), and case (3) is a panel clip (cavity depth: 15 mm), horizontal furring strips is insufficient ventilation, while panel clips secure a ventilation path. The cavities are at 910 mm intervals.

The bottom of the vented cavity is open with a sill flashing. The upper end of the vented cavity is open to the outside by ridge ventilation through the attic space (Fig. 2).

For the quantity of rain penetration into the vented cavity, the rainwater collected with a pouring funnel attached to the eaves was injected directly into the vented cavity from the center of the wall surface using a tube. The diameters of the funnel were selected to reproduce the intermittent long-term rain penetration in proportion to the precipitation. For Case (1), 80mm funnel size was installed in three places, and water injection was divided into three parts: upper, middle, and lower areas of the horizontal furring strips. For Case (2) and (3), three times size of the funnel was installed respectively.

3.2 Measurement Item

Figures 9 and 10 show the measurement items and measurement positions in the wall. The temperature, humidity, and moisture content were set near the center height of the first floor (FL + 1300 mm). The temperature and humidity were measured outside the insulation and

inside the insulation; the moisture content was measured for the outer plywood facing the vented cavity. The measurement interval was 60 min, and the measurement period started from September 2018. Air conditioning in the room was not used.

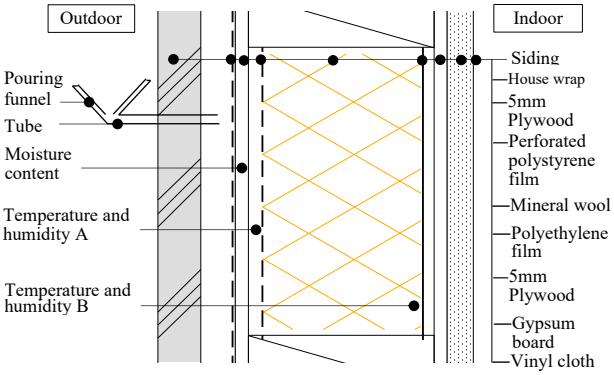

Figure 9. Wall configuration and sensor location.

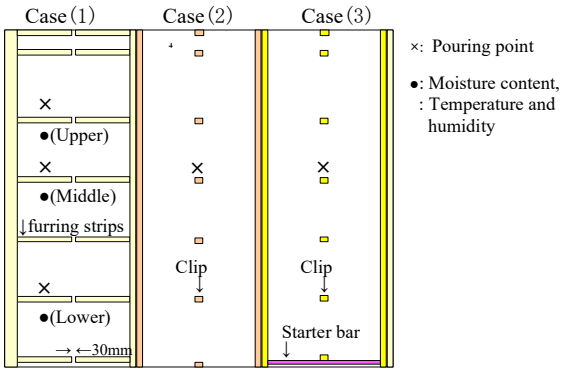

Figure 10. Configuration of cavity.

3.3 Results and Discussion

3.3.1 Increase in humidity and plywood moisture content due to rainfall in autumn

As an example of the measurement results in autumn, Fig. 11 shows the relative humidity between the insulation and vapor barrier. The outdoor temperature and precipitation are based on the weather data of the neighboring City. The relative humidity in the wall assembly increased after the rainy day, and moisture derived from rain penetration gradually accumulated in the wall due to repeating rainy and sunny days. Intermittent moisture condensation observed in some cases in early October.

The moisture in the wall assembly gradually decreased with reducing the quantity of precipitation since October 8. From this result, it can be indicated that rain penetration has a considerable impact on moisture accumulation in the wall assembly.

3.3.2 Process of hygrothermal behavior within wall assembly and the impact of ventilation performance.

Figures 12 and 13 show daily variations of relative humidity on the east side of wall on October 7, at location A (between outside plywood and perforated polystyrene film) and location B (between insulation and vapor barrier) were shown in Figure 9. Moisture condensation continues more than 9 hours at the location B with case (1) and (2), while it occurs less than 1 hour at the location A. In addition, relative humidity at location B increases with rising outdoor temperature.

From this result, it can be confirmed that moisture from rain penetration is accumulated on the indoor side. This phenomenon is thought to be the result that moisture retained in the sidings and the vented cavity was released by solar radiation; moisture that could not be discharged from the vented cavity moved to the wall assembly of the indoor side at a low temperature. Thus, temperature fluctuations due to solar radiation have a significant effect on hygrothermal behavior within a wall assembly. Temperature fluctuations release moisture retained in the

building materials, which forms water vapor and move through wall assembly and materials. Consequently, the moisture condenses on the indoor side of the low-temperature part.

Compare the ventilation performance with different cavity configurations. The rain penetration water in case (1) with 12 mm of the cavity depth tends to accumulate within the wall assembly, because it generally remains at the horizontal furring strips. Furthermore, insufficient ventilation performance extended duration of moisture condensation to more than 12 hours at the location B. Although the remained water in the vented cavity of case (2) is less than case (1), duration of moisture condensation reached 9 hours because of less ventilation performance due to thin cavity depth. As for case (3) with the panel clip and 15 mm of cavity depth, the moisture condensation did not occur because adequate ventilation and drainage performance was secured.

From the above results, the impact of ventilation performance on hygrothermal behavior within the wall assembly was confirmed. As in case (3), adequate ventilation performance tends to reduce moisture accumulation in the wall assembly. To maintain durability, it is important to ensure a ventilation performance and not retain moisture within the vented cavity.

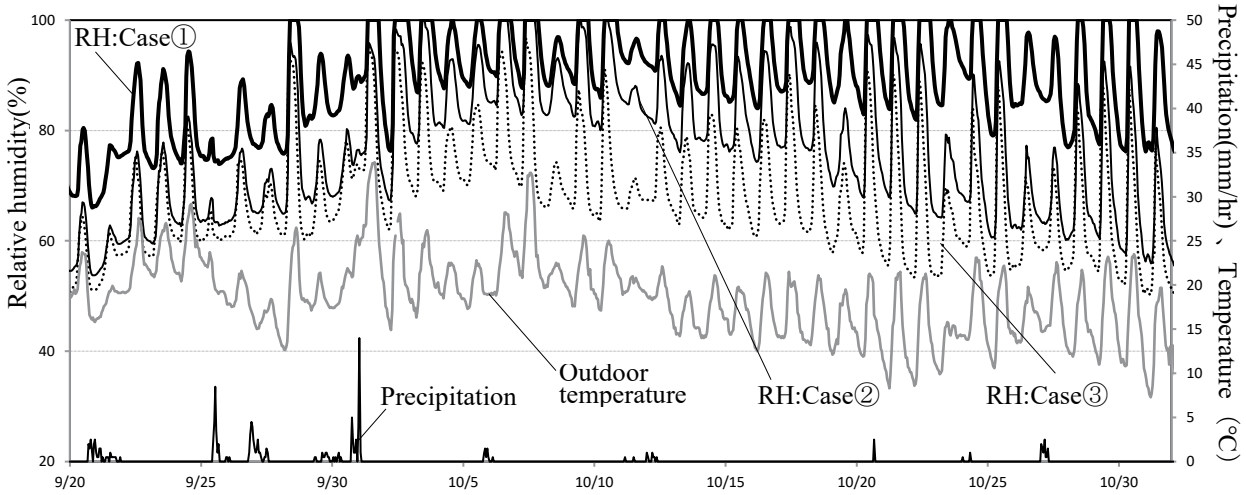

Figure 11. Relative humidity variation on the east wall location B.

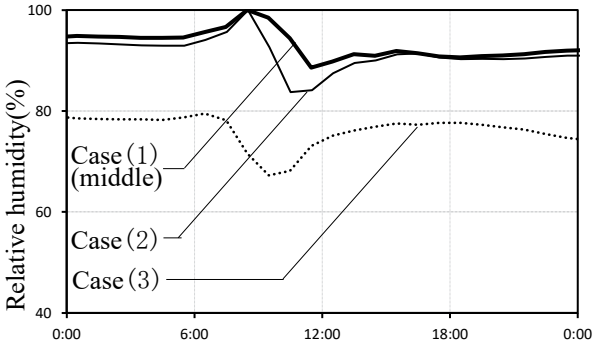

Figure 12. Relative humidity variation on east wall ocation A（10/7）.

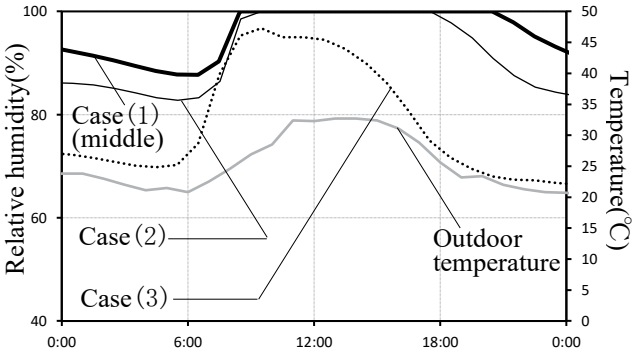

Figure 13. Relative humidity variation on east wall ocation B（10/7）.

4 Conclusion

This study was demonstrated the moisture accumulation in the wall assembly caused by rain penetration from the siding joints. In addition, the authors obtained an outline of the hygrothermal behavior within the wall assembly based on ventilation performance in the experimental house. The findings of the study are as follows:

- According to the quantity of rain penetration into the siding joints performing the water spray test, it was confirmed that there were significant differences in the water penetration rate between the application methods. For case B, continuous flow occurred even in a pressure-equalized condition because there were pinholes at the cross joint on the exterior surface. The rain penetration rate is 5–11% at low pressure difference (0–15 Pa) where the frequency is high. Thus, it is necessary for maintaining durability to consider the assumption that rainwater enters the vented cavity.
- According to the field survey of the experimental house, the relative humidity in the wall assembly increased after the rainy day, and moisture derived from rain penetration gradually accumulated in the wall. Intermittent moisture condensation observed in some cases. From this result, it can be indicated that rain penetration has a considerable impact on the moisture accumulation in the wall assembly.
- For the cases of low ventilation performance, the moisture condensation in the wall assembly observed more than for 9 hours in daytime. The case of high ventilation performance did not occur the moisture condensation. To maintain durability, it is important to ensure a good ventilation performance and not retain moisture.

Further studies are needed to develop a design method that can maintain the durability of wooden houses using the exterior system; in a future study, the authors expect to indicate the behavior of rain penetration water in the vented cavities and the ventilation characteristics.

ORCID

Sadaharu Osamura: 0000-0002-5473-1779 , Hiroaki Saito: 0000-0003-3633-7679

References

Cadada Wood Produits de bois canadien. Moisture and Wood-Frame Buildings, Moisture Design for Wood-Frame Buildings, https://canadawood.org/downloads/technical-publications/

National Institute for Land and Infrastructure Management Ministry of Land (2017), Research on construction method and its performance of external envelope of timber framed houses for durability upgrading, TECHNICAL NOTE of National Institute for Land and Infrastructure Management No.975

Nil, Sahal and Michael A, Lacasse. (2005). Water entry function of a hardboard siding-clab wood stud wall, Building and Environment, pp.1479-1491.

Michael A, Lacasse (2003). Recent studies on the control of rain penetration in exterior wood-frame walls, IRC Building Science Insight, pp.1-6.

Qian Mao *et al.* (2009) In-cavity evaporation allowance-A drying capacity indicator for wood-frame wall system, Building and Environment Vol.44, pp.2418-242.

ASHRAE (2009). Criteria for Moisture-Control Design Analysis in Buildings. ASHRAE Standard 160.

Umeno,T and Hokoi, S. (2011). Moisture damege in vented air space of exterior walls of woden houses, Journal of testing and evaluation, Vol 39, No.2, PP.243-249.

John Straube (2007). The role fo small gaps behind wall claddings on drainage and drying, 11th Canada Conderence on Building Science and Technolody Banff.

Japanese Industrial Standards(1996). Windows and doorsets- Watertightness test under dynamic pressure, Japanese Standards Association.

XV International Conference on Durability of Building Materials and Components
DBMC 2020, Barcelona
C. Serrat, J.R. Casas and V. Gibert (Eds)

Global Inspection, Diagnosis and Repair System for Buildings: Homogenising the Classification of Repair Techniques

Clara Pereira[1], Jorge de Brito[2] and José D. Silvestre[3]

[1] CERIS, Instituto Superior Técnico, Universidade de Lisboa, Av. Rovisco Pais, 1, 1049-001 Lisboa, Portugal, clareira@sapo.pt

[2] CERIS, Instituto Superior Técnico, Universidade de Lisboa, Av. Rovisco Pais, 1, 1049-001 Lisboa, Portugal, jb@civil.ist.utl.pt

[3] CERIS, Instituto Superior Técnico, Universidade de Lisboa, Av. Rovisco Pais, 1, 1049-001 Lisboa, Portugal, jose.silvestre@tecnico.ulisboa.pt

Abstract. *Building inspection systems are a useful tool for surveyors, standardising the collection of information. This research is framed within the development of a global inspection system based on twelve expert inspection systems for twelve types of building elements used in the envelope of current buildings. Homogenised classification lists replace the use of several records and unify designations used in fieldwork. A homogenised global classification list of repair techniques comprises, in a single component, all the techniques used to repair defects and eliminate their causes for different types of building elements. It includes curative and preventive repairs, as well as planned maintenance works. Well-defined criteria guided the harmonisation process of a large set of repair techniques in a user-friendly list. For instance, the association of different operations in a single repair technique took into account: similarities between procedures, applicability to one type of building element, solving identical defects and the use of similar repair materials. Considering data from the validation samples of the expert inspection systems, it is observed that techniques "R-A1 Cleaning" in painted façades and "R-A12 Application of a new (adequate) cladding/finishing coat over the existent/replacement" in wall renders are the most commonly prescribed. The provision of a homogenised classification list of repair techniques is expected to improve the quality of information collected on-site and give a comprehensive view of the most relevant repair techniques used in the envelope of current buildings.*

Keywords: *Building Pathology, Degradation, Inspection Systems, Maintenance, Repair Techniques.*

1 Introduction

Building inspection systems are useful for surveyors as they (i) help implementing uniform methodologies, (ii) guide the procedures through all the stages, and (iii) use standard designations. In this way, the collection of data on-site and inspection reports become methodic, hence standardising building inspections. This paper addresses the development of a global inspection system for the building envelope by a research team at Instituto Superior Técnico (IST), Universidade de Lisboa (UL), based on individual expert inspection systems (Pereira *et al.*, 2018).

The global inspection system under development at IST-UL is directed at current buildings. It is a broad tool including classification lists, correlation matrices, detailed information on degradation parameters, and an inspection form. It is based on existing expert inspection systems for individual building elements, which implies homogenising the system's components.

The homogenisation of classification lists simplifies the inspection process, replacing several lists with harmonised lists, more manageable to use. In this way, the identification of pathological phenomena in a painted façade or flat roof requires only one list of defects, for instance.

Additionally, standard designations may improve communication.

In this paper, the methodology of development of the harmonised list of repair techniques in the global inspection system is described, and the proposed classification list is presented. Then, using relative frequency results, the most common repair techniques are analysed. The paper ends summarising the research in concluding remarks.

2 Classification List of Repair Techniques

Following the structure of individual inspection systems, the global building inspection system includes a list of repair techniques. It contains techniques used to repair defects and eliminate their causes in the group of building elements taken into account in the inspection system. The particulars of each procedure are described in detail in files of repair techniques, out of the scope of this paper.

2.1 The Context of Developing a Global Inspection System

The development of the global building inspection system considered a well-defined range of building elements, corresponding to twelve expert inspection systems previously devised by researchers at IST-UL (Table 1). Those expert inspection systems have an identical structure and were all validated through the inspection of significant samples of building elements, hence providing a solid base for a new global system (Ferraz *et al.*, 2016).

All the selected individual expert inspection systems provide a classification list of repair techniques that may be recommended by surveyors following the detection and diagnosis of defects in visual and detailed building inspections. Those lists were based on the literature and experience, including curative and preventive techniques and planned maintenance works (Silvestre and de Brito, 2010). Curative repair techniques are those used to repair a defect directly, removing it. Preventive repair techniques refer to interventions on building elements that are not directly associated with a specific defect but, instead, act to eliminate the causes of potential issues. Curative and preventive repair techniques may include partial or complete replacement and changes in the characteristics of the building element (*e.g.* materials and geometry). Planned maintenance works are not intended to correct the behaviour of building elements, but to delay the natural ageing process and the resulting loss of performance and decrease of the service life.

2.2 Harmonisation Criteria

To achieve the goal of having a single list of repair techniques applying to different building elements within the global inspection system, all the expert classification lists had to be collected. Then, going through each list consecutively, the repair techniques referring to the same type of work were merged. For instance, ten out of twelve expert classification lists included cleaning works. Therefore, the global classification list comprises cleaning as one of the repair techniques. After that step, the list of repair techniques was still too long. So, similar techniques were grouped in a single repair technique considering equivalent scopes of intervention, identical procedures, and the resolution of the same kind of phenomena. For instance, different intervention techniques acting on the layers of cladding systems of flat roofs were gathered in a single and broader repair technique referring to the application, repair or replacement of the waterproofing system or separation layer in flat roofs (Conceição *et al.*, 2017). Despite the attempt of decreasing the extent of the global classification list of repair techniques, some specific techniques relating to only a type of building element were kept separately in the list, as no basis for merging applied.

Table 1. Expert inspection systems developed at IST-UL that were the basis of the global inspection system.

References	Building elements	Groups of repair techniques in the classification list	Validation sample	Average number of prescribed repair techniques per detected defect
(Garcez *et al.*, 2012b; a)	external claddings of pitched roofs (ECPR)	R-A Upper surface; R-B Inner surface; R-C Upper and inner surface; R-D Change of the ECPR; R-E Change of the bearing structure	207 surfaces 164 buildings	1.29
(Conceição *et al.*, 2017, 2019)	flat roofs (FL)	General; Specific	105 surfaces 105 buildings	0.63
(Silvestre and de Brito, 2010, 2011)	adhesive ceramic tiling (ACT) - walls and floorings	R-A ACT surface; R-B Tile bed; R-C Joints; R-D ACT; R-E Background; R-F Envelope	88 surfaces 46 buildings	2.26
(Neto and de Brito, 2011, 2012)	natural stone claddings (NSC) - walls and floorings	R-P Stone cladding surface (stone slab); R-A Bedding/anchoring/fixing material; R-J Joints; R-S Substrate; R-R Cladding system; R-E Envelope	128 surfaces 59 buildings	2.46
(Delgado *et al.*, 2013, 2018)	wood floorings (WF)	R-A WF covering; R-B WF surface; R-C WF substrate; R-D Joints between pieces of WF or with protruding elements	98 floorings 35 buildings	1.49
(Santos *et al.*, 2017a; b)	door and window frames (DWF)	R-A Accessories repair; R-F Fittings repair; R-P Profiles repair; R-V Glass repair	295 frames 96 buildings	1.11
(Garcia and de Brito, 2008)	epoxy resin industrial floor coatings (ERIFC)	R-A Current surface; R-B Flashings; R-C Joints	29 floorings 23 buildings	1.20
(Carvalho *et al.*, 2018, 2019)	vinyl and linoleum floorings (VLF)	R-A Superficial zones; R-B Whole flooring; R-C Substrate; R-D Flooring surrounding area	101 floorings 6 buildings	2.15
(Sá *et al.*, 2014, 2015)	wall renders (WR)	R-A Rendering surface; R-B Finishing layer; R-C Rendering system; R-D Envelope	150 surfaces 55 buildings	3.64
(Amaro *et al.*, 2013, 2014)	external thermal insulation composite systems (ETICS) - façades	TR-A Surface; TR-B Finishing coat; TR-C System	146 façades 14 buildings	1.61
(Pires *et al.*, 2015a; b)	painted façades (PF)	R-A Adherent pellicle cleaning; R-B Total/partial removal of existent pellicle; R-C Repainting	105 façades 41 buildings	3.09
(Silva *et al.*, 2017a; b)	architectural concrete surfaces (ACS) - walls	R-A Concrete surface; R-B Concrete; R-C Joints/discontinuities; R-D Periphery	110 surfaces 53 buildings	1.25

While merging and grouping repair techniques to obtain a more concise global list, balancing a simultaneously elaborate and succinct list is paramount for its broadness and user-friendliness. For instance, in the expert inspection system of wall renders (Sá *et al.*, 2014), five separate repair techniques were considered to express the idea of applying a new render with higher performance, namely: application of a reinforced rendering; execution of an external thermal insulation composite system (ETICS); execution of a reinforced render coating independent from the bearing wall; application of a render with higher thermal performance; and application of a drainage or corrective rendering. These five types of repair work refer to slightly different operations, but they are all based on the same concept: the existing render is not enough to prevent the occurrence of further defects and should be replaced or overlaid with a new one. Although separately considering each of these techniques may be reasonable in an inspection system only for wall renders, in a global building inspection system, it would hinder the ease of use of the classification list. For this reason, a single repair technique for the application of a higher performance render was proposed.

Still, other repair techniques could not be linked with any others, as they were too specific. For instance, executing a roof slab in pitched roofs is not comparable with other repairs. So, in the global classification list, it was considered separately, although not decreasing the list's complexity.

To guide the harmonisation of the global classification list of repair techniques, taking expert classification lists into account, a set of criteria was determined:

1. Building a **brief and concise** list of repair techniques without repetitions;

2. To decrease the extent of the list, coupling techniques in one repair technique considering:
    a. The **procedure** of the repair technique;
    b. The applicability of similar repair techniques to a **single type of building element**;
    c. Correcting **similar defects**;
    d. Using **repair materials** with **similar** properties;
3. Including all relevant repair techniques in the list, even though some may apply only to a single type of building element, so that the global classification list is **comprehensive**;
4. Grouping repair techniques into **categories** according to the intervention area within the cladding systems, namely: surface of the cladding, cladding system, change in the bearing structure/substrate and singularities.

2.3 Proposed Classification List of Repair Techniques

Table 2 presents the proposed classification list of repair techniques within a global inspection system. It is organised in four categories, according to the harmonisation criteria. Each technique is identified as constituting a curative (cr) or a preventive repair (pr) or planned maintenance work (pmw). Each category is linked to a code composed of letter R (for repair), a hyphen and a sequential capital letter (from A to D). Each repair technique also corresponds to a code, following that of its category, by adding a sequential number (*e.g.* R-A1, R-B2, R-C5 and R-D11).

Technique "R-D6 Application/repair/replacement/cleaning of drainage systems/plumbing" results from grouping similar repair techniques. R-D6 is a curative and preventive repair technique used in the drainage and plumbing equipment to eliminate or avoid clogging, accumulation of rainwater and leakages. In the expert system of flat roofs, the application, repair and replacement of the drainage system are mentioned (Conceição *et al.*, 2017), while the adhesive ceramic tiling expert system refers to the repair of defects in plumbing, separating embedded and exposed plumbing (Silvestre and de Brito, 2010). In turn, the classification list for natural stone claddings mentions the repair of defects in existing elements inside/outside the wall (Neto and de Brito, 2011). Plumbing is also mentioned for wood floorings (Delgado *et al.*, 2013), while, in door and window frames, the repair or execution of drains in the frames is pointed as a repair technique (Santos *et al.*, 2017b). In this context, technique R-D6 is an example of how conciseness influenced the development of the global classification list of repair techniques, as very similar techniques were harmonised in a single and broader repair technique.

Other techniques result from a direct transfer from the expert to the global classification lists. It is the case of "R-D9 Protecting or smoothing of protruding corners or edges", applying to adhesive ceramic tiling, natural stone claddings, wall renders, ETICS and architectural concrete surfaces.

3 Discussion

An analysis of the most frequently prescribed repair techniques may be performed using the data from the validation samples of the expert inspection systems (Table 1). To build Figure 1, the absolute frequency of recommendation of each repair technique was considered (Amaro *et al.*, 2014; Carvalho *et al.*, 2019; Conceição *et al.*, 2019; Delgado *et al.*, 2018; Garcez *et al.*, 2012a; Garcia and de Brito, 2008; Neto and de Brito, 2012; Pires *et al.*, 2015b; Sá *et al.*, 2015; Santos *et al.*, 2017a; Silva *et al.*, 2017b; Silvestre and de Brito, 2010), adapting the original repair techniques to the proposed global classification list. Then, those absolute frequencies were divided by the number of detected defects in each validation sample.

Table 2. Proposed classification list of repair techniques within a global inspection system.

Code	Category	Code	Repair technique
R-A	Surface of the cladding	R-A1	Cleaning (cr, pr, pmw)
		R-A2	Application of a protective coat (paint, varnish, water-repellent, antifungal, biocide) (cr, pr, pmw)
		R-A3	Corrosion removal and re-establishment of the anti-corrosion protection in metallic elements (cr)
		R-A4	Surface rehabilitation of the plastic external claddings of pitched roofs (cr)
		R-A5	Repair/execution of supplementary watertightness measures in pitched roofs (cr, pr)
		R-A6	Creation of pathways (pr)
		R-A7	Application of ventilation systems/accessories (cr, pr)
		R-A8	Encapsulation of asbestos-cement external claddings of pitched roofs (pr)
		R-A9	Application of spray polyurethane foam (SPF) on the external surface of pitched roofs (cr, pr)
		R-A10	Glazing repair in door and window frames (cr)
		R-A11	Replacement or reapplication of the cladding/glazing (partially or completely) (cr, pr)
		R-A12	Application of a new (adequate) cladding/finishing coat over the existent/replacement (cr, pr, pmw)
		R-A13	Application of another type of cladding (not epoxy) (cr)
		R-A14	Treatment of cracks or other holes in the cladding (cr)
		R-A15	Treatment of biodegradation in wood floorings (cr)
		R-A16	Complete/partial removal of the existing coat in painted façades (cr)
		R-A17	Correction of surface irregularities or evening an architectural concrete surface with mortar (cr)
R-B	Cladding system	R-B1	Application of underlayment in pitched roofs (pr)
		R-B2	*Flocage* in metallic claddings of pitched roofs (pr)
		R-B3	Application of spray polyurethane foam (SPF) on the interior surface of pitched roofs (cr, pr)
		R-B4	Application/repair/replacement of the vapour barrier (cr, pr, pmw)
		R-B5	Application/repair/replacement of the thermal insulation (cr, pr)
		R-B6	Application/repair/replacement of the waterproofing system or separation layer in flat roofs (cr, pr)
		R-B7	Injection of filling resins (bedding material) (cr)
		R-B8	Reinforcement of the bedding layer in localised areas (cr, pr)
		R-B9	Reinforcement with metallic elements or composite materials in wood floorings (cr)
		R-B10	Consolidation with concrete in wood floorings (cr)
		R-B11	Execution of prostheses or application of reinforcement profiles in door and window frames (cr, pr)
		R-B12	Deformation repair (distortion/shrinkage/warpage/expansion) in door and window frames (cr)
		R-B13	Change/replacement/repair of the fastening system or correction of holes in plates or substrate (cr, pr)
		R-B14	Application of a higher performance render (cr, pr)
		R-B15	Perforation/gap filling in ETICS (cr)
		R-B16	Repair of corroded reinforcement/concrete cover spalling in architectural concrete surfaces (cr)
		R-B17	Application of an additional concrete layer in architectural concrete surfaces (cr, pr)
R-C	Change in the bearing structure/substrate	R-C1	Execution of a roof slab in pitched roofs (cr)
		R-C2	Repair/reinforcement/replacement of the bearing structure in pitched roofs (cr, pr)
		R-C3	Application/replacement of the shaping or levelling layer (cr)
		R-C4	Repair of dead cracks in the substrate and reapplication of the cladding (cr, pr)
		R-C5	Pavement levelling in epoxy resin floor coatings (cr, pr)
R-D	Singularities	R-D1	Application/repair/replacement of expansion joints (cr, pr, pmw)
		R-D2	Replacement/repair of current joints' filling material and/or joints cleaning (cr, pr, pmw)
		R-D3	Application of fungicide, biocide or herbicide in joints (cr, pr)
		R-D4	Joint thickness increase or joint insertion (cr, pr)
		R-D5	Repair/application of tail-ends and associated protection elements (cr, pr, pmw)
		R-D6	Application/repair/replacement/cleaning of drainage systems/plumbing (cr, pr)
		R-D7	Removal of corroded or damaged metallic elements, with hole and notch filling (if applicable) (cr, pr, pmw)
		R-D8	Repair of water penetration spots (cr, pr)
		R-D9	Protecting or smoothing of protruding corners or edges (cr, pr)
		R-D10	Cleaning of façade's horizontal areas in adhesive ceramic tiling (pr, pmw)
		R-D11	Repair, insertion or replacement of sealants or insulation mastics in door and window frames (cr, pr)
		R-D12	Replacement of degraded, or missing, elements in door and window frames (cr, pr)
		R-D13	Adjustment, replacement or additional installation of hardware (hinges/locks/span-frame connections) in door and window frames (cr, pr)
		R-D14	Lowering of the tail-end area in epoxy resin floor coatings (cr, pr, pmw)
		R-D15	Execution of coves in epoxy resin floor coatings (cr, pr, pmw)
		R-D16	Correction of geometrical construction details (pr)

cr - curative repair; pr - preventive repair; pmw - planned maintenance works

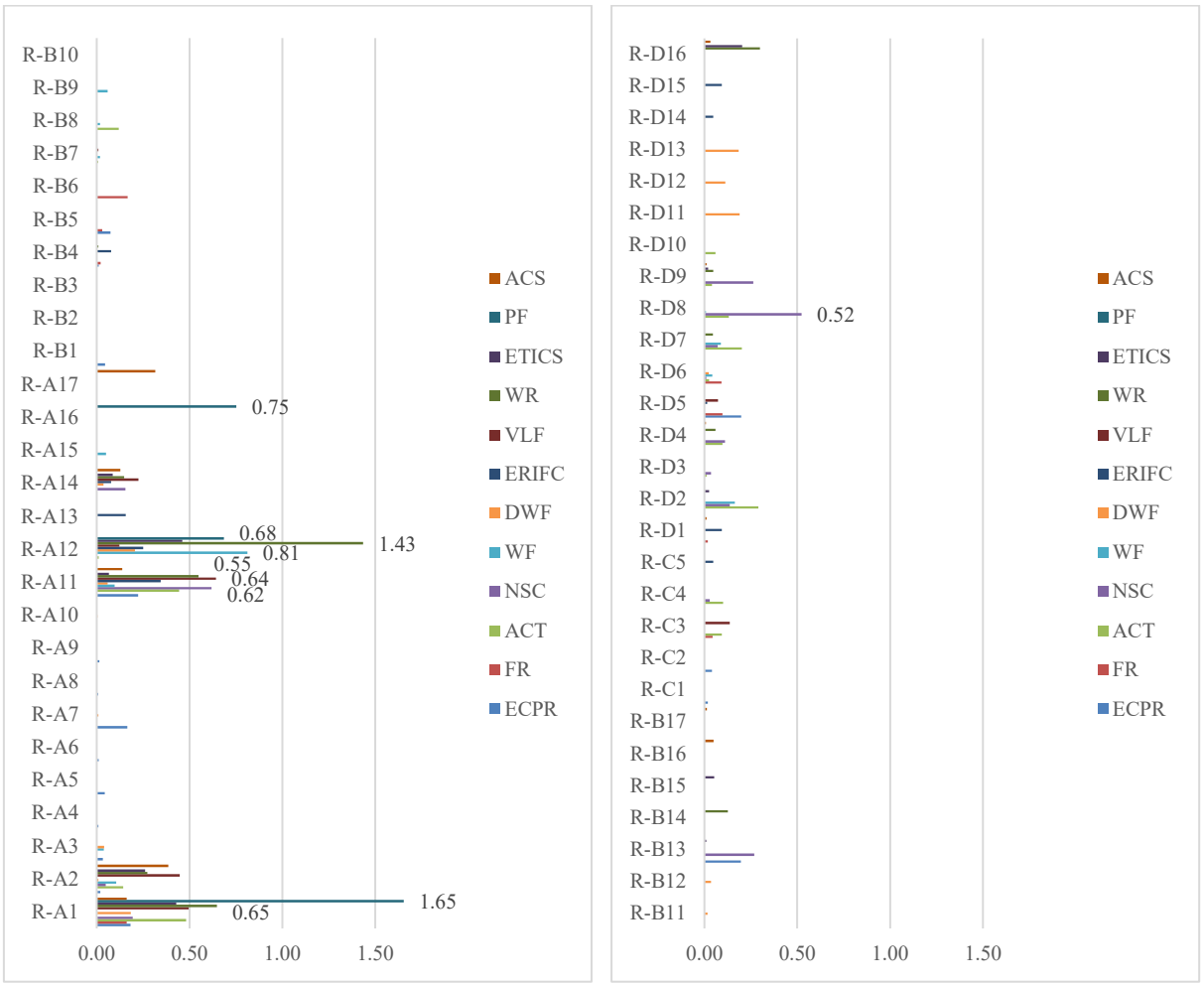

Figure 1. Relative frequency of prescribed repair techniques for detected defects in each expert inspection system.

Due to the adaptation to the global classification list, Figure 1 values may result from the sum of absolute frequencies, referring to the union of repair techniques from each expert classification list.

The highest relative frequency in Figure 1 refers to the prescription of "R-A1 Cleaning" in painted façades. R-A1 corresponds to four specific techniques in the expert inspection system of painted façades, which divide the act of cleaning in different operations, namely (Pires *et al.*, 2015a): scrubbing/dusting, manual washing with water and a sponge, washing with a low-pressure water jet, and chemical cleaning. As the result in Figure 1 (1.65) comes from the sum of four absolute frequencies, it exceeds the number of detected defects. It may be interpreted that, in many occurrences, more than one type of cleaning operation was prescribed considering (i) the combination of different activities for better results, or (ii) the prescription of different types of cleaning operations allowing the selection of the best method by decision-makers taking the available equipment and staff into account. Additionally, in the sample of Pires *et al.* (2015b), the category of anomalies referring to stains represents about 46% of all detected defects, partially explaining the recommendation of a high number of cleaning operations. Finally, cleaning a painted surface may frequently be considered as preliminary work to prepare the surface for further repairs.

"R-A12 Application of a new (adequate) cladding/finishing coat over the existent/replacement" is highly recommended in wall renders. Again, the value in Figure 1 (1.43) results from the sum of the absolute frequency of three repair techniques from the wall renders' expert classification list: full/partial replacement of the finishing coat, application of a new finish coat over the existing render, and application of cladding over the existing render (Sá *et al.*, 2014). Considering that inspected renders were protected with a paint coating, and the average age of the sample of buildings is 27 years (Sá *et al.*, 2015), many likely lacked maintenance or repainting according to the standard service life of paint coatings in façades—an average of 8.5 years, according to Chai *et al.* (2015). Additionally, in the sample of Sá *et al.* (2015), the cause referring to an irregular repainting periodicity was the most often identified among the group of wear and maintenance faults.

In general, observing Figure 1, it may be concluded that repair techniques in category "R-A Surface of the cladding" are the most commonly prescribed. The outer layer of a building element is the most exposed to aggressive agents. Furthermore, its integrity is of high importance to protect the conditions of the building element and the whole building.

4 Conclusions

The use of a single list of repair techniques in the context of building inspections is user-friendly for surveyors and contributes to the standardisation of inspection procedures and the improvement of communication between players in the construction sector. Such a single list of repair techniques may also be useful as it determines the general scope of repair techniques that should be expected within a maintenance plan, namely for this selection of twelve materials used in the building envelope. Additionally, analysing frequency data on the prescription of repair techniques allows building owners and maintenance managers to prepare the staff for the execution of the most common procedures, training workers and acquiring adequate equipment while balancing costs and benefits.

Acknowledgements

The authors gratefully acknowledge the support of CERIS, from IST-UL, and the *Fundação para a Ciência e a Tecnologia* (FCT) project PTDC/ECI-CON/29286/2017 "Buildings' Envelope SLP-based Maintenance: reducing the risks and costs for owners", as well as the FCT PhD Scholarship SFRH/BD/131113/2017.

ORCID

Clara Pereira: https://orcid.org/0000-0002-9535-1844
Jorge de Brito: https://orcid.org/0000-0001-6766-2736
José D. Silvestre: https://orcid.org/0000-0002-3330-2000

References

Amaro, B., Saraiva, D., de Brito, J. and Flores-Colen, I. (2013). Inspection and diagnosis system of ETICS on walls. *Construction and Building Materials*, *47*, 1257–1267. doi: 10.1016/j.conbuildmat.2013.06.024

Amaro, B., Saraiva, D., de Brito, J. and Flores-Colen, I. (2014). Statistical survey of the pathology, diagnosis and rehabilitation of ETICS in walls. *Journal of Civil Engineering and Management*, *20*(4), 511–526. doi: 10.3846/13923730.2013.801923

Carvalho, C., de Brito, J., Flores-Colen, I. and Pereira, C. (2018). Inspection, diagnosis, and rehabilitation system for vinyl and linoleum floorings in health infrastructures. *Journal of Performance of Constructed Facilities*, *32*(6), 04018078. doi: 10.1061/(ASCE)CF.1943-5509.0001229

Carvalho, C., de Brito, J., Flores-Colen, I. and Pereira, C. (2019). Pathology and rehabilitation of vinyl and linoleum floorings in health infrastructures: Statistical survey. *Buildings*, *9*(5), 116. doi: 10.3390/buildings9050116

Chai, C., de Brito, J., Gaspar, P.L. and Silva, A. (2015). Statistical modelling of the service life prediction of painted

surfaces. *International Journal of Strategic Property Management*, *19*(2), 173–185. doi: 10.3846/1648715X.2015.1031853

Conceição, J., Poça, B., de Brito, J., Flores-Colen, I. and Castelo, A. (2017). Inspection, diagnosis, and rehabilitation system for flat roofs. *Journal of Performance of Constructed Facilities*, *31*(6), 04017100. doi: 10.1061/(ASCE)CF.1943-5509.0001094.

Conceição, J., Poça, B., de Brito, J., Flores-Colen, I. and Castelo, A. (2019). Data analysis of inspection, diagnosis, and rehabilitation of flat roofs. *Journal of Performance of Constructed Facilities*, *33*(1), 04018100. doi: 10.1061/(ASCE)CF.1943-5509.0001252

Delgado, A., de Brito, J. and Silvestre, J.D. (2013). Inspection and diagnosis system for wood flooring. *Journal of Performance of Constructed Facilities*, *27*(5), 564–574. https://doi.org/10.1061/(ASCE)CF.1943-5509.0000342

Delgado, A., Pereira, C., de Brito, J. and Silvestre, J.D. (2018). Defect characterization, diagnosis and repair of wood flooring based on a field survey. *Materiales de Construcción*, *68*(329), 1–13. doi: 10.3989/mc.2018.01817

Ferraz, G.T., de Brito, J., de Freitas, V.P. and Silvestre, J.D. (2016). State-of-the-art review of building inspection systems. *Journal of Performance of Constructed Facilities*, *30*(5), 04016018. doi: 10.1061/(ASCE)CF.1943-5509.0000839

Garcez, N., Lopes, N., de Brito, J. and Sá, G. (2012). Pathology, diagnosis and repair of pitched roofs with ceramic tiles: Statistical characterisation and lessons learned from inspections. *Construction and Building Materials*, *36*, 807–819. doi: 10.1016/j.conbuildmat.2012.06.049

Garcez, N., Lopes, N., de Brito, J. and Silvestre, J. (2012). System of inspection, diagnosis and repair of external claddings of pitched roofs. *Construction and Building Materials*, *35*, 1034–1044. doi: 10.1016/j.conbuildmat.2012.06.047

Garcia, J. and de Brito, J. (2008). Inspection and diagnosis of epoxy resin industrial floor coatings. *Journal of Materials in Civil Engineering*, *20*(2), 128–136. doi: 10.10617(ASCE)0899-1561(2008)20:2(128)

Neto, N. and de Brito, J. (2011). Inspection and defect diagnosis system for natural stone cladding. *Journal of Materials in Civil Engineering*, *23*(10), 1433–1443. doi: 10.1061/(ASCE)MT.1943-5533.0000314.

Neto, N. and de Brito, J. (2012). Validation of an inspection and diagnosis system for anomalies in natural stone cladding (NSC). *Construction and Building Materials*, *30*, 224–236. doi: 10.1016/j.conbuildmat.2011.12.032

Pereira, C., de Brito, J. and Silvestre, J.D. (2018). Global inspection, diagnosis and repair system for buildings: managing the level of detail of the defects classification. In *Proceedings of the 7th Rehabend Congress - Construction Pathology, Rehabilitation Technology and Heritage Management*, Cáceres, Spain, pp. 572–579.

Pires, R., de Brito, J. and Amaro, B. (2015a). Inspection, diagnosis, and rehabilitation system of painted rendered façades. *Journal of Performance of Constructed Facilities*, *29*(2), 04014062. doi: 10.1061/(ASCE)CF.1943-5509.0000534

Pires, R., de Brito, J. and Amaro, B. (2015b). Statistical survey of the inspection, diagnosis and repair of painted rendered façades. *Structure and Infrastructure Engineering*, *11*(5), 605–618. doi: 10.1080/15732479.2014.890233

Sá, G., Sá, J., de Brito, J. and Amaro, B. (2014). Inspection and diagnosis system for rendered walls. *International Journal of Civil Engineering*, *12*(2 A), 279–290.

Sá, Gonçalo, Sá, J., de Brito, J. and Amaro, B. (2015). Statistical survey on inspection, diagnosis and repair of wall renderings. *Journal of Civil Engineering and Management*, *21*(5), 623–636. doi: 10.3846/13923730.2014.890666

Santos, A., Vicente, M., de Brito, J., Flores-Colen, I. and Castelo, A. (2017a). Analysis of the inspection, diagnosis, and repair of external door and window frames. *Journal of Performance of Constructed Facilities*, *31*(6), 04017098. doi: 10.1061/(ASCE)CF.1943-5509.0001095

Santos, A., Vicente, M., de Brito, J., Flores-Colen, I. and Castelo, A. (2017b). Inspection, diagnosis, and rehabilitation system of door and window frames. *Journal of Performance of Constructed Facilities*, *31*(3), 04016118. doi: 10.1061/(ASCE)CF.1943-5509.0000992

Silva, C. da, Coelho, F., de Brito, J., Silvestre, J. and Pereira, C. (2017a). Inspection, diagnosis, and repair system for architectural concrete surfaces. *Journal of Performance of Constructed Facilities*, *31*(5), 04017035. doi: 10.1061/(ASCE)CF.1943-5509.0001034

Silva, C. da, Coelho, F., de Brito, J., Silvestre, J. and Pereira, C. (2017b). Statistical survey on inspection, diagnosis and repair of architectural concrete surfaces. *Journal of Performance of Constructed Facilities*, *31*(6), 04017097. doi: 10.1061/(ASCE)CF.1943-5509.0001092

Silvestre, J.D. and de Brito, J. (2011). Ceramic tiling in building façades: Inspection and pathological characterization using an expert system. *Construction and Building Materials*, *25*(4), 1560–1571. doi: 10.1016/j.conbuildmat.2010.09.039

Silvestre, J. Dinis and de Brito, J. (2010). Inspection and repair of ceramic tiling within a building management system. *Journal of Materials in Civil Engineering*, *22*(1), 39–48. doi: 10.1061/(ASCE)0899-1561(2010)22:1(39)

XV International Conference on Durability of Building Materials and Components
DBMC 2020, Barcelona
C. Serrat, J.R. Casas and V. Gibert (Eds)

Higher Incidence Pathologies in Installations of Solar Energy, Gas, Cooling, Heating and Ventilation

Manuel J. Carretero-Ayuso

Musaat Foundation and University of Extremadura, Spain; *carreteroayuso@yahoo.es*

Abstract. *This paper focuses on the study and quantifications of pathologies in solar energy, gas, cooling, heating and ventilation installations, based on complaints filed in the courts by the owners of a large number of houses in which errors appeared in those installations. The relevant complaints filed across all of Spain were studied, in what is an important contribution to forensic engineering, given that access to the outcome of civil court cases is seldom obtained. The representativeness of the data is not partial but total, since the entirety of cases existing in the period under study was part of the sample, enabling us to consider this to be a general exposition on the epidemiology of construction pathologies in installations in houses in Spain. It should be noted that the Spanish construction sector is one of the most problematic ones, due to the dissatisfaction generated in homeowners, and as it is one of the ones leading to the highest number of complaints filed with consumer protection bureaus and in the courts. In the investigation, results have been obtained for each of the installations (183 cases in total), according to the type of anomaly (the most important are dysfunctions, leaks and humidity), the pathological origin (poorly arranged encounters, omissions of elements, among others) and the type of construction where it is produced (especially in block dwellings).*

Keywords: *Installations, Complaints, Construction Pathologies.*

1 Introduction

The purpose of an HVAC installation is to provide correct heating, ventilation and cooling, reliably maintaining comfortable values of humidity, temperature, and air quality, despite changes that might occur externally (Cohen *et al*. 2017). Accordingly, these installations (heating, ventilation and cooling) are key in air treatment, dehumidification, etc. Solar energy and gas supply installations further meet these needs, providing greater comfort. Indeed, in some context the set of these five types of installations are referred to as comfortability installations.

Recently, Yang *et al*. (2018) planned a fault detection mechanism for these installations, developing a method based of prognoses using synthetic data of temporal series through simulations in computer programmes. A year earlier, Turner *et al*. (2017) published a procedure for fault detection in buildings with some of these installations.

The scientific literature especially covers heating, ventilation, and cooling installations, from different perspectives. In 2018, a study was published identifying various factors affecting risk to cost and time in construction (Mosaad *et al*. 2018). In another perspective, Ruano *et al*. (2018) showed that half the energy consumption in residential and non-residential buildings was basically used by heating and cooling. It is for this reason that other authors (Wu and Sun 2011) consider it useful to develop methods of verification of certain parameters, through the use of energy flow models; including the study of air flow and the cooling/heating load (Cetin and Kallus 2016).

doi:10.23967/dbmc.2020.073

For Behfar *et al*. (2017), the detection and diagnosis of faults in buildings' installation systems (especially when those faults convert into pathology problems) is of interest given that they allow the reduction of consumptions and operating costs, thus being a useful work tool for all technicians (engineers as well as architects).

One of the main limitations for the ample and in-depth knowledge of problems in installations is that a part of the reviewed literature has relied on observation processes or on surveys more or less focused on buildings of a specific developer or builder. Moreover, the lower number of problems existing therein in relation to other units more prone to pathologies (such as roofs, facades and structures) lead to them being less known.

The purpose of this research is to identify the most important types of anomalies in these types of installations, as well as their recurrence, based on judicial complaints made across all of Spain by building owners. The knowledge of these anomalies will be useful to designers, construction managers, and maintenance supervisors.

2 Methodology

This research analysed the data corresponding to the policies dated 2014-2016 of the civil responsibility insurance of Spanish technical architects and building engineers (Musaat 2014 2016) that saw complaints by owners related to construction problems (Serjuteca 2014-2016). This data was sourced from the Musaat Foundation's study "National statistical analysis on construction anomalies" (Carretero-Ayuso and Moreno-Cansado 2016), that aimed to identify the most frequent anomalies in the Spanish construction sector.

When a building user experiences problems in the construction, and the developer and builder do not solve them, users often resort to the judicial route. At this point, they also file complaints against the technicians that participated in the construction process: the designer and construction managers. This is done mainly because these technicians should be covered by civil responsibility insurance, which, in turn, is not required in Spain for developer and builder companies.

Once the judicial process is initiated, expert reports are produced indicating the types of anomalies and in which construction elements or installations the problems occur. It is from this database, owned by the insurer of the technical architects and building engineers in question, that this study obtains all its resources and values. In this regard, it should be mentioned that, as a requirement to include the data in this research, it was determined that data points would only be considered when the respective court sentence was final and unappealable in any higher courts, often years after the complaint was first filed.

All the complaints filed in the country were analysed and protocolised, with 183 cases being found (number of times an anomaly was counted) related to the installations being study: 'Solar Energy' (I1), 'Gas' (I2), 'Cooling' (I3), 'Heating' (I4) and 'Ventilation' (I5).

The classes were classified into 4 groups, each representing a different type of anomaly that was the object of a complaint by owners, according to the conclusions of the relevant technical reports. The types of anomalies are: 'Fissures in the cladding' (A1), 'Deficient ventilation (A2), 'Leaks or humidities' (A3) and 'Dysfunctions' (A4).

The pathological origins leading to these anomalies were identified and catalogued into 4 types: 'Inadequate tail-ends' (OP1), 'Omission of elements' (OP2), 'Irregularities and deficiencies' (OP3), and 'Various' (OP4).

The types of construction studied were: 'Detached houses' (V1), 'Attached houses' (V2) and 'Block dwellings' (V3).

3 Results

3.1 General Values by Installation

The values obtained in the five installations were very different from one another. As shown in Figure 1, ventilation (I5=42%) accounts for the greatest percentage, followed by heating (I4=32%). In last place are solar energy installations (I1=2%).

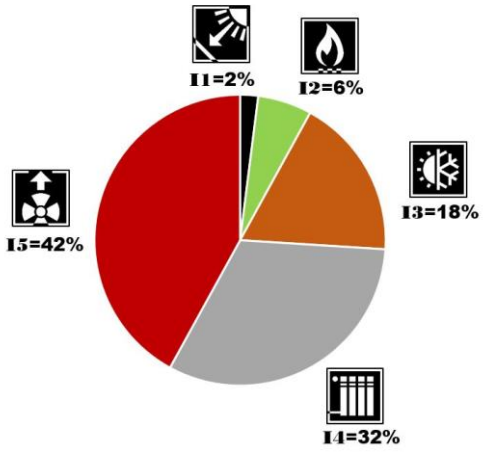

Figure 1. Percentages of cases existing in each installation.

3.2 Values by Type of Anomaly

As indicated above, each of the 4 types of anomalies that were the object of complaints were analysed. The one with the greatest prevalence was 'Dysfunctions' (A4=64%), a term that has grouped within it a series of anomalous and poorly functioning processes. As shown in Figure 2, 'Leaks or humidities' (A3=19%) are placed second.

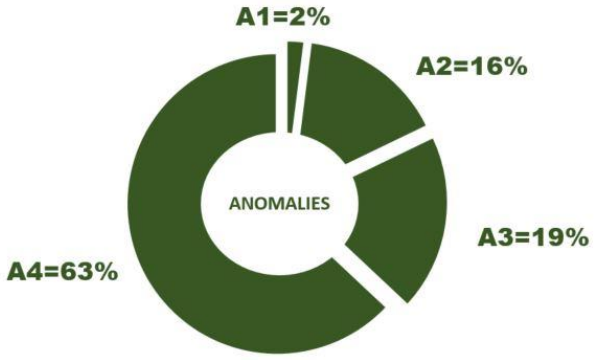

Figure 2. General percentages of the types of anomalies found in the research.

In order to further deepen and break down the information on the prevalence of the anomalies for each installation, Figure 3 was produced, showing the weight of each of them. It can be seen that heating and cooling have three types of anomalies each, while ventilation and gas installations have two types. Finally, we can observe that thermal solar energy installations concentrate all their anomalies in a single type ('dysfunctions').

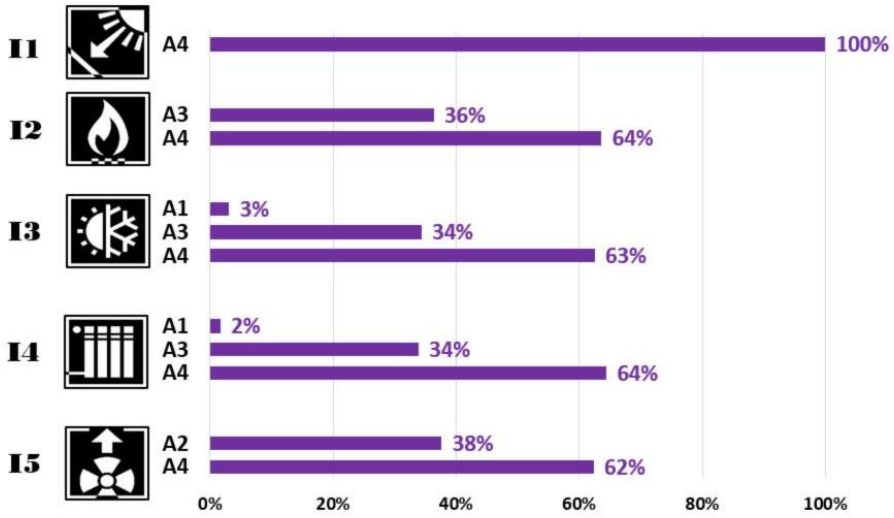

Figure 3. Distribution of the anomalies present in each of the installations.

It should be noted that in each of the installations there is clearly a dominant anomaly, aggregating approximately 2/3 of all cases (between 62% and 64%, except for I1, in which case it is 100%, as it is the sole anomaly). On the other hand, in those installations with three types of anomalies (I3 and I4), the anomaly with the lowest percentage always has a residual value (only 2% or 3% of the cases).

3.3 Values According to the Pathological Origin

The pathological origin (cause) with the greatest prevalence is OP4, with 35%, followed by OP3 with 34% (see Figure 4).

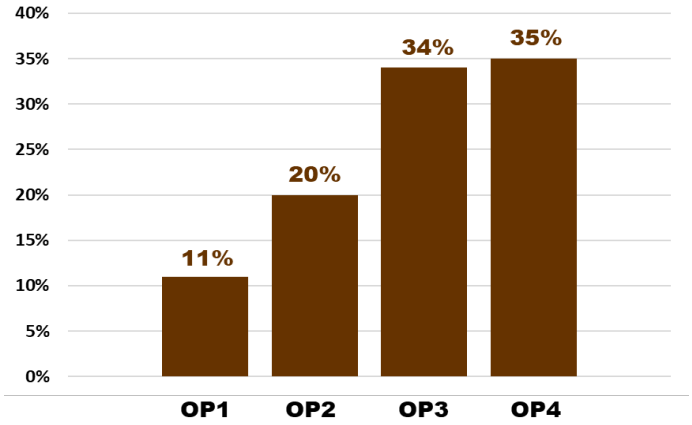

Figure 4. Values from smallest to largest of the different pathological origins found.

If the origins are broken down for each of the five installations, the following results are obtained:

-Solar energy (I1) = OP3(100%)
-Gas (I2) = OP1(45%) + OP3(36%) + OP4(18%)
-Cooling (I3) = OP1(16%) + OP2(13%) + OP3(31%) + OP4(41%)
-Heating (I4) = OP1(8%) + OP2(24%) + OP3(39%) + OP4(29%)
-Ventilation (I5) = OP1(8%) + OP2(25%) + OP3(27%) + OP4(40%)

It can be seen that the installations I3, I4, and I5 have 4 pathological origins each. In turn, I2 has 3 types of origins, and I1 has only 1 type.

3.4 Values According to Type of Construction and Type of Anomaly

One parameter that was also characterised by each of the anomalies was the type of construction in which they occurred. Based on Figure 5, they are most concentrated in 'block dwellings' (V3=60%), followed by 'attached houses' (V2= 26%). In all cases, the most frequent anomaly were 'dysfunctions' (A4 between 8% and 39%), with 'leaks or humidities' (A3 between 3% and 9%) in second place. Lastly, anomaly A1 is not present in the type of construction V2.

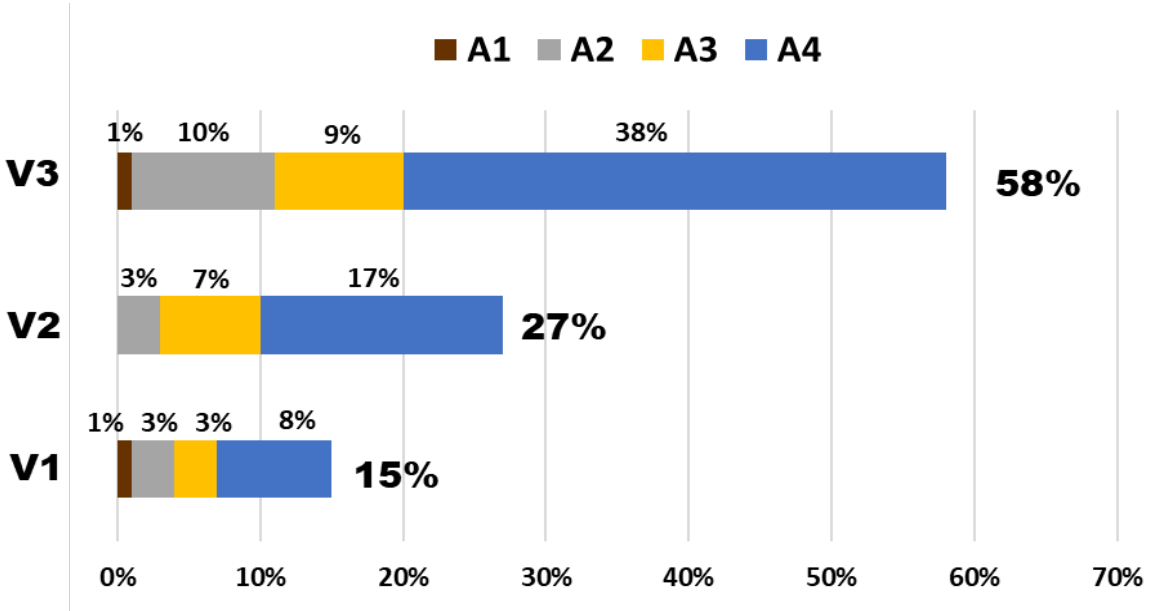

Figure 5. Relation between the type of anomaly and the type of construction.

3.5 Processes of Functional Deterioration

A 'process of functional deterioration' (p.f.d.) is the simultaneous and joint interrelation between each installation, its anomalies, and pathological origins; in this regard, each of the cases were studied and their anomalies were counted, differentiating them according to pathological origin.

A total of 30 different p.f.d. were detected in this study (see Table 1), demonstrating the variability of the situations that can take place. The ones with the most cases were I5-OP3-A4

and I5-OP4-A4 (18 cases each). They are followed by I4-OP2-A4 (14 cases).

With regard to installations, the one with the greatest percentage was I2, with two combinations: I2-OP1-A3 and I2-OP3-A4. Each represented 27% of anomalies found in gas installations. Solar energy (I1) has only one p.f.d., while cooling (I3) has the greatest variability: 9 p.f.d.

Table 1. Percentages of recurrence of each process of functional deterioration.

Installation		Pathological origin	Type of anomaly	% of the installations	% of the total
Icon	**Code**				
	I1	OP3	A4	100%	2%
	I2	OP1	A3	27%	2%
			A4	18%	1%
		OP3	A3	10%	1%
			A4	27%	2%
		OP4	A4	18%	1%
	I3	OP1	A3	13%	2%
			A4	3%	1%
		OP2	A3	3%	1%
			A4	9%	2%
		OP3	A3	6%	1%
			A4	25%	4%
		OP4	A1	3%	1%
			A3	13%	2%
			A4	25%	4%
	I4	OP1	A3	8%	3%
		OP2	A4	24%	8%
		OP3	A1	2%	1%
			A3	19%	5%
			A4	19%	5%
		OP4	A3	6%	2%
			A4	22%	7%
	I5	OP1	A2	1%	1%
			A4	6%	3%
		OP2	A2	16%	6%
			A4	10%	4%
		OP3	A2	4%	2%
			A4	23%	9%
		OP4	A2	17%	7%
			A4	23%	10%

The anomaly A4 (‘dysfunctions’) is present in all installations, being associated to three types of pathological origin: ‘inadequate tail-ends’ (OP1), ‘irregularities and deficiencies’ (OP3), and ‘various’ (OP4). The combinations occurring lest frequently (1 case) are: I2-OP3-A3, I3-OP1-A4, I3-OP2-A3, I3-OP4-A1, I4-OP3-A1 and I5-OP1-A4.

The determination and knowledge of each process of functional deterioration have not been identified nor calculated by any of the bibliographic references reviewed for this research. As such, this inclusion is considered to be a novel and important contribution to the technical-scientific knowledge on this type of installations, in addition to assisting technicians in focusing their attention on those combinations that are most problematic. In this manner, it will be possible to reduce anomalies in both the design and construction phases, as well as minimise non-quality costs.

4 Conclusions

- It was shown that the installations with the most cases are ‘Ventilation’ (I5=42%) and ‘Heating’ (I4=32%), representing practically 3/4 of the total. As such, efforts to reduce anomalies should be focused in these installations.
- The most frequent pathological origins were ‘Diverse’ (OP4=35%) and ‘Irregularities and deficiencies’ (OP3=34%), and most cases were concentrated in ‘block dwellings’ (V3=58%).
- Lastly, it was shown that the expert technical reports used as a basis for owners to be able to file their complaints were a very helpful procedure to determine the installations in which anomalies occur the most.

Acknowledgements

This work was carried out within the Musaat Foundation’s Action Plan, in line with the ‘Research project on pathologies in buildings in Spain’.

ORCID

Manuel J. Carretero-Ayuso. https://orcid.org/0000-0002-8082-8996

References

Behfar, A., Yuill, D. and Yu, Y. (2017). "Automated Fault Detection and Diagnosis Methods for Supermarket Equipment (RP-1615)". *Science and Technology for the Built Environment*, 23(8), 1253-1266.

Carretero-Ayuso, M. J. and Moreno-Cansado, A. (2016). National Statistical Analysis on Construction Anomalies. *MUSAAT Foundation*, Madrid.

Cetin, K. S. and Kallus, C. (2016). "Data-Driven Methodology for Energy and Peak Load Reduction of Residential HVAC Systems". *Procedia Engineering*, 145, 852-859.

Cohen, R., Austin, B., Bannister, P., Bordass, B. and Bunn, R. (2017). "How the Commitment to Disclose in-use Performance can Transform Energy Outcomes for New Buildings". *Building Services Engineering Research and Technology*, 38(6), 711-727.

Mosaad, S., Issa, U. and Hassan, M. S. (2018). "Risks Affecting the Delivery of HVAC Systems: Identifying and Analysis". *Journal of Building Engineering*, 16, 20-30.

MUSAAT (2014-2016). Expert Records and Reports if Accidents, *Mútua de Aparejadores y Arquitectos Técnicos*, Madrid.

Ruano, A., Silva, S., Duarte, H. and Ferreira, P. M. (2018). "Wireless Sensors and IoT Platform for Intelligent HVAC Control". *Applied Sciences*, 8(3), 370.

SERJUTECA (2014-2016). Reports and Documents on Accidents Involving Professional Civil Liability of Building Surveyors and Technical Architects, *Servicios Jurídicos Técnicos Aseguradores*, Madrid.

Turner, W., Staino, A. and Basu, B. (2017). "Residential HVAC Fault Detection using a System Identification Approach". *Energy Build*., 151, 1-17.

Wu, S. and Sun, J. (2011). "Cross-Level Fault Detection and Diagnosis of Building HVAC Systems". *Build. Environ.*, 46(8), 1558-1566.

Yang, C., Shen, W., Chen, Q. and Gunay, B. (2018). "A Practical Solution for HVAC Prognostics: Failure Mode and Effects Analysis in Building Maintenance". *Journal of Building Engineering*, 15, 26-32.

XV International Conference on Durability of Building Materials and Components
DBMC 2020, Barcelona
C. Serrat, J.R. Casas and V. Gibert (Eds)

Hydronium Detection in Hardened Concrete

Ana Martínez Ibernón[1], José M. Gandía Romero[1,2], Isabel Gasch[1] and Manuel Valcuende[2]

[1] Instituto Interuniversitario de Investigación de Reconocimiento Molecular y Desarrollo Tecnológico (IDM), Universitat Politècnica de València, Camino de Vera, s/n 46022 Valencia, Spain. E-mail: anmarib@arqt.upv.es

[2]Departamento de construcciones arquitectonicas. Universitat Politècnica de València, Camino de Vera s/n, 46022 Valencia, España. E-mail: mvalcuen@csa.upv.es

Abstract. *The monitoring of reinforced concrete structures allows us to detect the presence of aggressive agents into of the concrete matrix, on site and in a real time. These aggressive agents can produce the unexpected failure of the structures, thus discovering their presence is a fundamental aspect in the preservation of people safety and the durability of the structure. On the other hand, helps to reduce the cost of maintenance and repair operations, due to allow us to identify the problems faster, minimizing the intervention to be done. The present research paper was focused in the hydronium detection; the reduction of this species generates hydrogen, the hydrogen produces the embrittlement and cracking of the steel, which seriously compromises the right behaviour of the structure. The problem of hydrogen appears in industries such as ammonia processing or petrochemistry industries and nuclear power plants. All of them are industries in which a failure seriously compromises the welfare of people and the environment. Therefore, the detection of hydrogen penetration in reinforcement concrete structures in these cases are very interesting. In this study, with the purpose to detect the hydronium or hydrogen in the hardened concrete matrices is proposed the use of voltammetric sensor, which is part of a multisensory system called Electronic-Tongue. This is a preliminary study. The objective of these initial steps was to evaluate the detection capability of the sensor. Currently, have been designing a sequential test in order to evaluate the sensor in different partial hydrogen pressures with the purpose to develop mathematical models to the hydronium or hydrogen detection and quantification in hardened concrete matrix.*

Keywords: *Durability, Monitoring, Sensors, Hydrogen Embrittlement.*

1 Introduction

The detection of hydronium and hydrogen availability variations in the reinforcement concrete structures is interesting due to the presence of H^+/H_2 are involve in reactions that produce the durability loss of the structures.

The reaction and molecular recombination of the hydrogen with metals have a greatly impact on their mechanical properties (C A Zapfpe, Member, Sims, and Aime, 1941; Mansilla, Brandaleze, and Ines, 2018; Schroeder and Müller, 2003). In the case of the steels we can classify the damage produced by the hydrogen in:

- High-temperature Hydrogen Attack (Decarburization), in this process the high-temperature (<200˚C) reaction of absorbed hydrogen with carbides in the steel results in the decarburization forming methane which can not spread due to the size of its molecules producing intergranular fissuring (Ovejero,2009).

doi:10.23967/dbmc.2020.151

- Hydrogen-Induced Cracking (HIC), results from the penetration and molecular recombination of atomic hydrogen produced in the steel surface because of a corrosion process. This reaction generates high pressures which produce cracks or blisters in the steel (Ovejero,2009).
- Hydrogen Embrittlement (HE), produce the decrease of the metal ductility and load bering capability due to the absorption of hydrogen as atomic or molecular form by the metal. The hydrogen difuses to the metal grain boundaries producing pressure on the metal grains, this pressures can reach values that reduce the ductility and strength of the steel (Schroeder and Müller, 2003; Industrial Metallurgists, LLC).

In the case of reinforcement concrete structures these problems can produce the brittle failure of the structure (Ramón Zamora, 2018) which seriously threatens the people safety, also the failure generates high economical costs.

These phenomena affect in structures particularly in those industries that work with environments or substances that contain hydrogen. For instance: nuclear reactors, chemical industry, etc. Also, the hydrogen can be generated in structures where is used without any control of the potential the cathodic protection (impressed current) (Byrne, Norton, and Holmes, 2016; Enos, Williams, Clemeña, and Scully, 1998; Ishii, Seki, Fukute, and Ikawa, 1998).

There are other reactions where H_2/H^+ compromise the reinforcement durability such as the carbonation of the concrete and chlorides attack.

In the carbonation of the concrete the CO_2 penetrates reacting with the hydroxide ions and increasing (H_3O^+) activity. The pH drop of the concrete pore dissolution will produce the rebars passive layer destruction (Lee, Lee, Min, Lim, and Singh, 2018).

On the other hand, when the chlorides arrive to the rebar surface the following reaction take place (Neville, Wharf, Street, and The, 1995):

$$Fe^{2+} + 2Cl^- \rightarrow FeCl_2 \quad (1)$$

$$FeCl_2 + 2H_2O \rightarrow Fe(OH)_2 + 2HCl \quad (2)$$

This reaction produces a significant decrease of pH in the local solution inside the pits, so in this area the presence of H_2/H^+ increase (Andrade, Garcés, and Martínez, 2008).

As is widely known, concrete carbonation and chlorides attack produce the passive layer destruction and the active corrosion of reinforcements starts if thermodynamic conditions are favourable.

Therefore, the increase detection of the H_2/H^+ can help us to avoid the problems related to the absorption of the hydrogen or hydronium in the steel and also to prevent the corrosion of the rebars when the carbonation of the concrete or the chlorides attack is produced.

With the purpose of preventing or controlling these phenomena will be effective use monitoring systems to control the conditions of the rebars embedded in the concrete and also identify the presence of aggressive substance into of the concrete such as H_2/H^+.

In this study is proposed the use of a novelty and promising monitoring system formed by cross-sensitivity voltammetric sensor and named Electronic Tongue (e-Tongue). These systems are widely used in the food industry being very effective (Bataller, 2001; Ramón Zamora, 2018).

In this monitoring system, a potential signal vary over time is applied on the sensors, producing the reduction or oxidation over the sensors surfaces of different electroactive species presents in the electrolyte, being recorded an electrical current response from each sensor. The

reactions that produce these responses depend on the quantity of the electroactive species and the experimental conditions, such as the sensor material and the potential sweeping range. Therefore, depending on the agents of interest (oxygen, water, chlorides, H^+/H_2, etc.) the experimental conditions will be defined. Then, by means of multivariate analysis of the sensors response, can be developed forecasting and quantification mathematical models to modelling the presence of the interest substance in the hardened concrete matrix.

In this study was performed an initial evaluation of the Rh voltammetric sensors capability in order to detect variations in the couple hydronium/hydrogen inside of the hardened concrete.

These sensors form part of the novel multisensory system e-Tongue, which are currently under development. In a previous work was verified the capability of INOX voltammetric sensors to detect oxygen availability variations inside of the hardened concrete matrix (Martínez-Ibernón et al., 2020) which is going to form part of the e-Tongue.

2 Materials and Methods

Concrete sample (10 cm x10 cm x10 cm) of water/cement ratio 0.4 was made, the composition of the concrete is specified in Table 1.

Table 1. Composition of the concrete.

Materials	kg/m^3
Cement I 42.5 R-SR5	490
Water	196
Superplasticizer	3.4
Siliceous sand	1115
Aggregate	601

In the concrete sample was embedded one e-Tongue which is under development (Figure 1). This Electronic Tongue are made by a stainless-steel hollow cylinder filling with epoxi resin where are embedded the voltammetric sensors of the e-Tongue.

The purpose of this study is analysed the response of one of the sensors that forms the e-Tongue, this is the Rh voltammetric sensor, this are made with thread of this metal (1mm of diameter and 2mm of length).

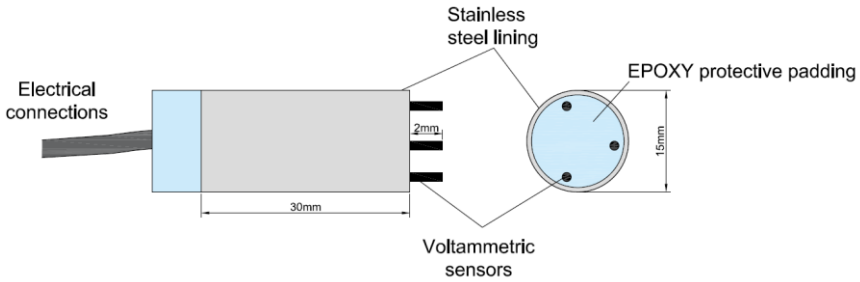

Figure 1. Electronic Tongue.

The samples were studied in two different conditions:

- State 1: Concrete in atmospheric conditions (dry conditions).

- State 2: Concrete saturated with water. In order to ensuring the higher quantity penetration of water inside of the concrete matrix, the samples were inserted in a deposit with an airtight lid. In this deposit was reached the vacuum conditions by means of a pump, these conditions were kept during three hours. Then was let the entrance of water until the samples were totally submerged. After two hours the vacuum was broken and the specimens were kept submerged in water as show the Figure 2.

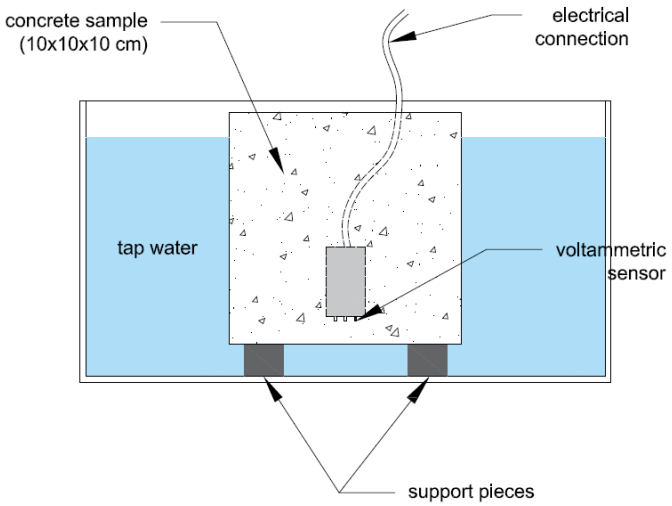

Figure 2. Test set-up, for submerged conditions (state 2).

Two different testing experiences were defined:

- Experience 1: First, the cyclic voltammetry (CV) technique was applied in the Rh sensor with the sample in state 1 (atmosphere conditions), then, the sample was saturated with water (state 2) and the voltammetry test was repeated in this condition. In the cyclic voltammetry test were applied three potential sweep signals with different potential ranges.
- Experience 2: In this experience, was used a high amplitude cathodic potential pulse (-1.6V amplitude signal), during 3 min, to ensure the generation of atomic and molecular hydrogen. The samples in this experience were in water saturated conditions (state 2). The test sequence was: Previously to apply the potential pulse was tested the sample with a CV, in order to define a baseline of the system conditions, then, the hydrogen generation pulse was applied, finally a cyclic voltammetry was applied. The experience was repeated for two different potential sweeps.

The electrochemical techniques were applied with three electrodes and Autolab PGSTAT10 equipment was used. Specifically, these three electrodes were:

- Reference electrode: a saturated calomel electrode (SCE).
- Counter electrode: Stainless steel lining (Figure 1).
- Working electrode: Rh voltammetric sensor.

The experiences defined allowed us to check the presence of peaks related to reactions associated with the hydronium and the hydrogen. It was possible through the comparation of

the results with the voltagrams for alkaline systems showed in the paper Jaksic, Johansen, and Tunold, (1994).

3 Results and Discussion

The Rh voltammetric sensors used in the Electronic Tongue are capable to detect the presence of hydronium and hydrogen in the concrete matrix. As we can see in the Figure 3, the morphology of the electric current density curve, obtained with the embedded sensor in the conditions of the state 2, is similar to the curve obtained in an alkaline system in dissolution (Jaksic, Johansen, and Tunold, 1994), we can identify the same peaks associated with reactions that involve H^+/H_2.

However, when the samples are in non-saturated conditions (state 1), meaning the water availability inside of the hardened concrete is very low, the peaks related to the hydronium and hydrogen do not appear (Figure 4).

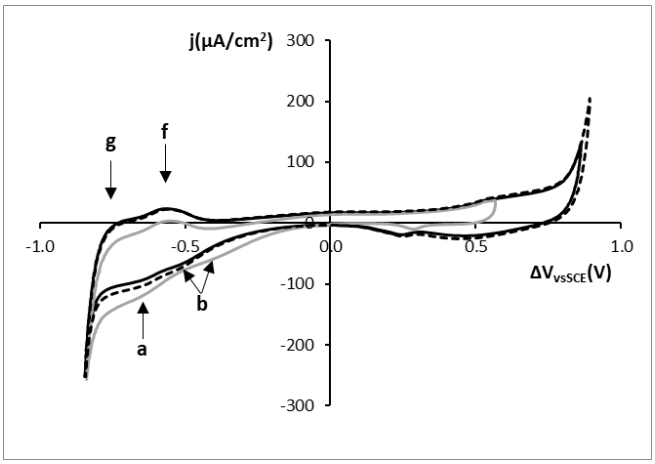

Figure 3. Results Experience 1: Successive cyclic voltagrams on the Rh electrode embedded in sample of w/c=0.4 concrete in saturated state (state 2). The points g, f, a and b are the peaks associated to the proton reactions as defined by Jaksic, Johansen, and Tunold, (1994).

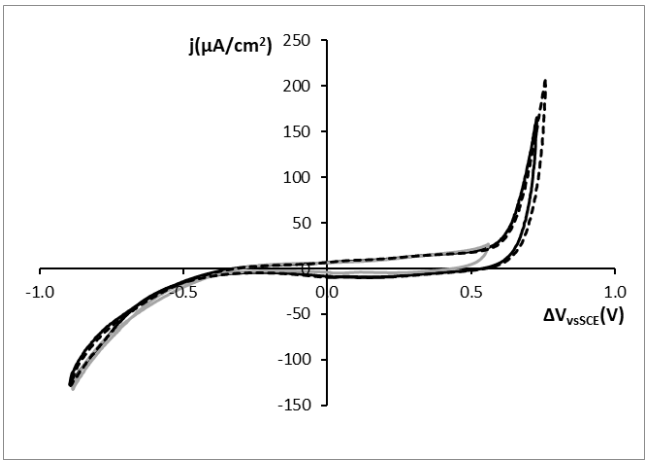

Figure 4. Results of Experience 1: Successive cyclic voltammograms on the Rh electrode embedded in sample of w/c=0.4 concrete in atmospheric state (state 1).

On the other hand, after to apply a high amplitude potential pulse with negative value, the generation of hydrogen was assured. The amplitude of the pulse was -1.6 V, at this potential and for pH similar to the concrete (pH≈12.5), water reduction is already taking place, in this reaction H_2 is generated.

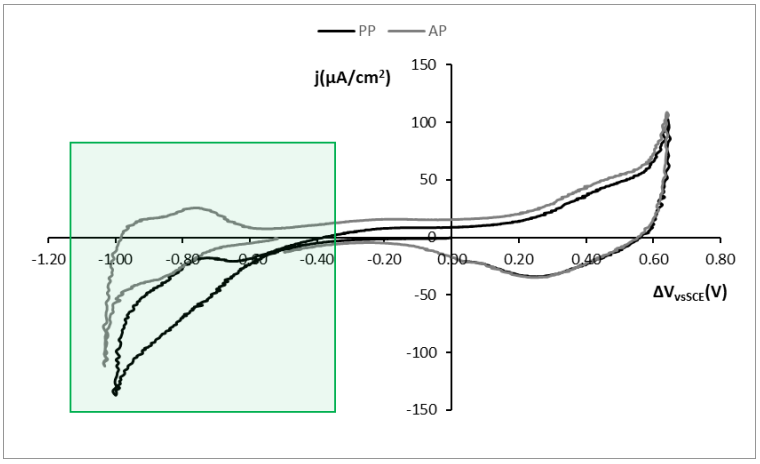

Figure 5. Results of Experience 2: Line black: Voltagram of the system previously cathodic pulse (PP). Line grey: Voltagram of the system after cathodic pulse (AP). Green square: Indicates the zone where the response is associated to reactions where are involved H+/H2.

The Figure 5 shows how after to apply the cathodic pulse (AP), the peaks associated with the desorption and adsorption of the H^+/H_2 risen. The increasement of the desorption peaks causes the upward movement of the curve, due to in this potential range the mainly reaction is with H^+/H_2, whereas previously to the potential pulse application the mainly reaction was the water reduction.

If the test is repeated doing several sweep cycles in each situation (AP and PP), we can see how in the PP situation (previously to the cathodic pulse application) (Figure 6 a) there are a negligible change from initial sweep. However the results obtained when the cathodic potential

pulse is applied (-1.6V) shows the increasement of the total electric density current as cycles are done (Figure 6 b).

This demonstrates that the Rh electrode has a region of potential sensitive to the generation and adsorption/desorption processes of H^+ / H_2. Therefore, this sensor could be used in hardened concrete matrix to detect the species involved in the redox couple.

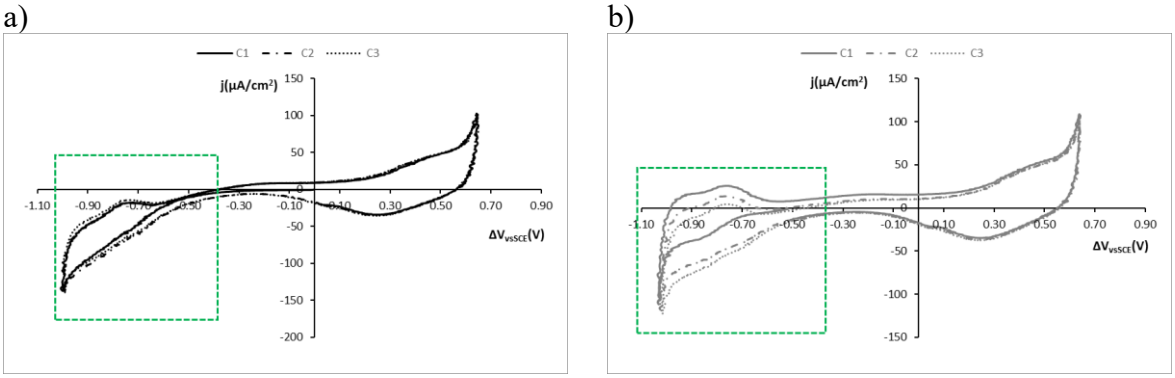

Figure 6. Results of Experience 2: a) Voltagram of the system previously cathodic pulse (PP). b) Voltagram of the system after cathodic pulse (AP). C1, C2 and C3 are successive cycles. The zone under examination are pointed with the green rectangle.

3 Conclusions

According to the results, the developing voltammetric sensors are capable to detect variations in the presence of the system hydronium/hydrogen inside of the hardened concrete matrix, and thus the Rh electrode could be useful to determine the pH or the hydrogen activity inside of the materials.

Acknowledgements

The authors would like to express their gratitude to the Spanish Ministry of Science and Innovation for the pre-doctoral scholarship granted to Ana Martínez Ibernón (FPU 16/00723). Also, to the Universitat Politècnica de València for the financial support in the project "Ayudas a Primeros Proyectos de Investigación (PAID-06-18)".

ORCID

A. Martínez Ibernón: https://orcid.org/0000-0003-2136-5650
J.M. Gandía Romero: https://orcid.org/0000-0003-0257-3286
I. Gasch: https://orcid.org/0000-0001-7036-4481
M. Valcuende: https://orcid.org/0000-0002-9967-1554

References

Andrade, C., Garcés, P. and Martínez, I. (2008). Galvanic currents and corrosion rates of reinforcements measured in cells simulating different pitting areas caused by chloride attack in sodium hydroxide. Corrosion Science, 50(10), 2959–2964. https://doi.org/10.1016/j.corsci.2008.07.013

Bataller, R. (2001). Fabricación y puesta a punto de una nariz electrónica húmeda para la detección de gases y vapores. P.h.D. Thesis, Universitat Politècnica de València, València, Spain,.

Byrne, A., Norton, B. and Holmes, N. (2016). State-of-the-art review of cathodic protection for reinforced concrete structures. Magazine of Concrete Research, 68(13), 664–677. https://doi.org/10.1680/jmacr.15.00083

C A Zapfpe, B. Y., Member, J., Sims, C. E. and Aime, M. (1941). Metals Technology, 1941, Vol. VIII - August 1941 - T.P. 1307 - Hydrogen Embrittlement, Internal Stress and Defects in Steel, 1307(1307). Retrieved from http://library.aimehq.org/library/books/Metals Technology, 1941, Vol. VIII/T.P. 1307.pdf

Enos, D. G., Williams, A. J., Clemeña, G. G. and Scully, J. R. (1998). Impressed-Current Cathodic Protection of Steel-Reinforced Concrete Pilings: Protection Criteria and the Threshold for Hydrogen Embrittlement. Corrosion, 54(5), 389–402. https://doi.org/10.5006/1.3284867

Hydrogen Embrittlement of Steel - Industrial Metallurgists. (2018, 9 julio). https://www.imetllc.com/training-article/hydrogen-embrittlement-steel/

Ishii, K., Seki, H., Fukute, T. and Ikawa, K. (1998). Cathodic protection for prestressed concrete structures. Construction and Building Materials, 12(2–4), 125–132.

Jaksic, M. M., Johansen, B. and Tunold, R. (1994). Electrochemical behaviour of rhodium in alkaline and acidic solutions of heavy and regular water. International Journal of Hydrogen Energy, 19(4), 35–51. https://doi.org/10.1016/0360-3199(94)90064-7

Lee, H. M., Lee, H. S., Min, S. H., Lim, S. and Singh, J. K. (2018). Carbonation-induced corrosion initiation probability of rebars in concretewith/without finishing materials. Sustainability (Switzerland), 10(10). https://doi.org/10.3390/su10103814

Mansilla, G. A., Brandaleze, E. and Ines, M. (2018). Interactions and effects of hydrogen on high strength steels I NTERACTIONS AND EFFECTS OF HYDROGEN ON HIGH STRENGTH STEELS Graciela A . Mansilla , Elena Brandaleze , Mariano N . Inés, (February 2019).

Martínez-Ibernón, A., Roig-Flores, M., Lliso-Ferrando, J., Mezquida-Alcaraz, E. J., Valcuende, M. and Serna, P. (2020). Influence of cracking on oxygen transport in UHPFRC using stainless steel sensors. Applied Sciences (Switzerland), 10(1). https://doi.org/10.3390/app10010239

Neville, A., Wharf, G., Street, H. and The, U. K. (1995). Chloride attack of reinforced concrete : an overview. pag_07_y_08_dano_por_hidrogeno-ovejero_garcia.pdf. (n.d.).

Ramón Zamora, J. E. (2018). Sistema de Sensores Embebidos para Monitorizar la Corrosión en Estructuras de Hormigón Armado . Fundamentos , Metodología y Aplicaciones. Ph.D. Thesis, Universitat Politècnica de València, València, Spain,.

Ovejero García, J. (2009). Una mirada a daño por hidrógeno en materiales metálicos. Recuperado de http://www.cab.cnea.gov.ar/ieds/images/extras/hojitas_conocimiento/materiales/pag_07_y_08_dano_por_hidrogeno-ovejero_garcia.pdf.

Schroeder, R. M. and Müller, I. L. (2003). Stress corrosion cracking and hydrogen embrittlement susceptibility of an eutectoid steel employed in prestressed concrete. Corrosion Science, 45(9), 1969–1983. https://doi.org/10.1016/S0010-938X(03)00035-0

XV International Conference on Durability of Building Materials and Components
DBMC 2020, Barcelona
C. Serrat, J.R. Casas and V. Gibert (Eds)

Implementation of an Embedded Sensor Based on Electrical Resistivity to Monitor Drying in Thick Concrete Structures

Joanna Badr[1,2], Géraldine Villain[2], Jean-Paul Balayssac[1], Sérgio Palma Lopes[2], Yannick Fargier[2], Fabrice Deby[1] and Sylvie Delepine-Lesoille[3]

[1] LMDC, Université de Toulouse, INSA/UPS Génie Civil, Toulouse 31077, France; badr@insa-toulouse.fr, balayssa@insa-toulouse.fr, f_deby@insa-toulouse.fr

[2] IFSTTAR, Site de Nantes, Bouguenais 44344, France; joanna.badr@ifsttar.fr, geraldine.villain@ifsttar.fr, sergio.lopes@ifsttar.fr, Site de Bron, Bron 69675, France; yannick.fargier@ifsttar.fr

[3] Andra, French National Radioactive Waste Management Agency, Chatenay-Malabry 92298, France; Sylvie.Lesoille@andra.fr

Abstract. *Electrical resistivity is a parameter sensitive to several properties of concrete, including water content, which is one of the key parameters governing concrete long-term durability. In this paper, the monitoring of the concrete water content profile throughout its entire thickness is discussed using an electrical approach as a measurement method. This is very relevant to applications requiring a centimeter resolution over a large thickness. The aim of this paper is to implement a multi-electrode embedded sensor in a concrete slab to determine the resistivity profile over concrete depth in order to monitor its drying. The sensor, designed as a printed circuit board (PCB), is integrated in two 30 cm thick concrete slabs. Different measurement configurations are presented. Following qualification in laboratory and controlled conditions, the study focuses on characterizing the sensor's response during the drying of the slabs. The results demonstrate the capability of the sensor to monitor concrete drying by measuring the resistivity profiles with a spatial centimetric resolution.*

Keywords: *Electrical Resistivity, Embedded Sensor, Monitoring, Thick Concrete Structures, Drying Process.*

1 Introduction

The durability of a concrete structure is characterized by its ability to keep the use functions for which it was designed. The main degradations of reinforced concrete structures are due to reinforcement corrosion, for which the parameter responsible for its development is the concrete water content.

The determination of the concrete water content using non-destructive testing (NDT) methods has been the subject of many studies (*e.g.* Balayssac and Garnier, 2017; Kaplanvural *et al*., 2018). Among these NDT methods, DC-electrical methods, which provide access to the electrical resistivity of the material, are particularly sensitive to the concrete water content (Millard, 1991; Andrade *et al*., 2007; Du Plooy *et al*., 2013; Fares *et al*., 2015). However, the electrical methods that are implemented on the surface have reduced resolutions with respect to the thickness of the concrete structures and the investigated depth does not generally exceed a few centimeters in the concrete cover. In addition, it is necessary to wet the surfaces of the electrodes to avoid high resistance contact. Hence, Badr *et al*. (2019) developed an embedded sensor based on a printed circuit board (PCB), which presents various advantages such as:

measuring profiles with a centimeter resolution through the whole thickness of a reinforced concrete structure, ensuring good and lasting electrical contact between the concrete and the electrodes, reducing invasiveness, allowing a high geometric accuracy together with a low fabrication cost and mitigating wiring problems. This new resistivity embedded sensor and the measurement chain were validated in various solutions and in small concrete specimens (Ø11x22 cm) but not in full scale concrete structures (Badr *et al*., 2019).

The main aim of this study is thus to characterize the PCB sensor in more realistic operational conditions, namely two 30 cm thick reinforced concrete slabs, one reinforced with carbon steel bars (HA), and the other one with fiberglass rebars (an electrically insulating material) (FV). The variability of the measurements and the impact of the reinforcements are evaluated in order to test the sensitivity of the sensors by determining the electrical resistivity profiles as a function of the depth. The evaluation of the water content profile requires a material-dependent calibration procedure which is not presented in this article.

The paper starts with a description of the experimental program carried out on the slabs HA and FV each instrumented with two embedded PCB sensors. Then the characterization of the embedded sensors is presented regarding the repeatability, reproducibility and influence of the reinforcement. Finally, we discuss the monitoring of the resistivity profiles during 372 days of drying at 45 °C and we conclude.

2 Experimental Program

The PCB sensors are embedded in the slabs HA and FV. The descriptions of the experimental program regarding the geometry and measurement configurations of the PCB sensors as well as the instrumentation of the slabs, are detailed in the following section.

2.1 Geometry of the PCB Embedded Sensor and Measurement Configurations

The PCB sensor has a ladder shape in order to improve the anchoring of the electrodes in the concrete. The number of electrodes in the PCB sensor used in this study was increased from 19 (Badr *et al*., 2019) to 28 electrodes, each having dimensions of 5x1.5 mm^2 staggered on either side of the circuit, to investigate the entire 30 cm thickness (Figure 1). The spacing between the electrodes is 2 cm on each side, hence 1 cm taking into account both sides.

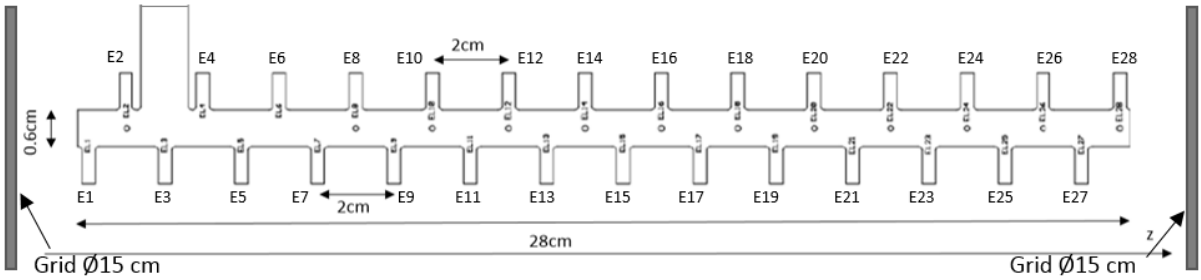

Figure 1. Schematic diagram of the PCB sensor with 28 electrodes.

The PCB sensor presents two measurement configuration modes: the Transmission configuration and the Wenner configuration. In the Transmission configuration mode, an electrical current of intensity *I* is transmitted through the two stainless steel grids (Ø = 15 cm)

placed on both sides of the PCB sensor and a potential drop (ΔV) is measured between all pairs of consecutive electrodes located on the same side of the PCB sensor (E1E3, E2E4, E3E5, …, E26E28) (Figure 1). In Wenner configuration mode, the quadrupole measurements C1C2P1P2 (where electrodes C1 and C2 are used for current injection and electrodes P1 and P2 are used for potential drop measurements) are successively E1E7E3E5, E2E8E4E6, E3E9E5E7, ..., E22E28E24E26 (Figure 1).

The apparent resistivity ρ_a is obtained for each configuration, using equation (1):

$$\rho_a = G\frac{\Delta V}{I} \tag{1}$$

where G (in meters) is a geometric factor which depends on the geometry of the structure and on the shape and positions of the electrodes. G is numerically determined in a homogeneous medium by a finite element calculation using COMSOL Multiphysics®.

2.2 Slabs Instrumentation

The concrete used in this study was based on cement type 1 (CEM I) with a water-cement ratio of 0.59 and a porosity of 15.0% ± 0.9%. Two concrete slabs measuring 75x75x30 cm^3, equipped with 12 mm diameter reinforcement, spaced 20 cm apart, were cast. The cover concrete thickness is equal to about 5 cm so the distance between the two rebar beds is about 20 cm. In one of the slabs the reinforcements are made of fiberglass (FV), and in the other the reinforcements are made of high-adhesion steel (HA), in order to check the possible influence of the reinforcement on the measurements with the embedded sensors.

Two PCB sensors of 28 electrodes are embedded in each slab, between two stainless steel grids of diameter 15 cm, and spaced by 29 cm. They are placed on the right (Ed) and on the left (Eg) hand side relative to the surface of the slab exposed to drying (Figure 2).

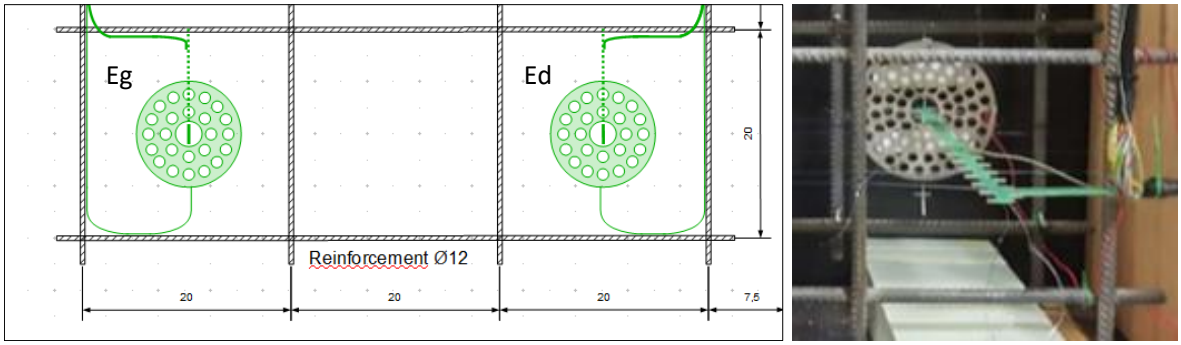

Figure 2. Instrumentation of the HA slab: (a) schematic diagram of the lower part of the slab where the PCB sensors Ed and Eg are placed (dimensions in cm), (b) close-up photo on the PCB sensor Ed in the mesh reinforcement (with only one of the grids).

The slabs were conditioned during 41 days in wet cure in a room at a temperature T = 20 ± 2 °C, and at a relative humidity HR = 95 ± 5%. The method of generating the water content profile consists in inducing a unidirectional drying by exposing a single face to drying and waterproofing the other five faces by coating them with aluminum foil. The FV slab was exposed to 5 months of drying at 20 °C and 1 year of drying at 45 °C in order to accelerate the

establishment of the resistivity profile. The HA slab was exposed to 13 months of drying at 20 °C and 3 months of drying at 45 °C.

3 Characterization of the PCB Sensors

This part of our work examines the characterization of the PCB sensors embedded in the two reinforced concrete slabs HA and FV. First, we check the repeatability and reproducibility of the measurements made with each sensor, then we show the influence of reinforcement (HA and FV) by comparing the response of the sensors in the two slabs.

3.1 Repeatability

The evaluation of the repeatability of the apparent resistivity measurement is obtained by performing three measurements, repeated with few minutes interval. These measurements are acquired, under both saturated conditions (Table 1) and unsaturated conditions (Table 2), for a chosen electrode configuration, in the middle of the slab ($z = 15 \pm 0.5$ cm), depending on the orientation of the sensor and the position associated with each configuration.

Table 1. Coefficient of variation (CV) of apparent resistivity measurements at the initial saturated state t0 with the PCB sensors in the slabs HA and FV for both Transmission and Wenner configurations.

ρ_a [Ω.m]	FV_Ed	FV_Eg	HA_Ed	HA_Eg
Transmission CV %	15.5 ± 1.5 9.6 %	9.5 ± 0.9 9.4 %	9.1 ± 0.3 3.3 %	17.7 ± 0.9 5.1 %
Wenner CV %	13.5 ± 0.1 0.7 %	13.8 ± 0.1 0.7 %	16.3 ± 0.1 0.6 %	16.1 ± 0.2 1.2 %

Table 2. Coefficient of variation (CV) of apparent resistivity measurements at an unsaturated state with the PCB sensors in the slabs HA and FV for both Transmission and Wenner configurations, where t'0 marks the beginning of concrete drying at 45 °C.

	t'0+268 days		t'0+62 days	
ρ_a [Ω.m]	FV_Ed	FV_Eg	HA_Ed	HA_Eg
Transmission CV %	71.9 ± 3.2 4.5 %	69.9 ± 4.1 5.9 %	24.1 ± 1.1 4.6 %	8.7 ± 0.8 9.2 %
Wenner CV. %	103.5 ± 0.6 0.6 %	82.7 ± 0.8 1.0 %	12.6 ± 0.2 1.6 %	19.9 ± 0.2 1.0 %

At the saturated state, the coefficient of variation CV for the repeatability ranged between 3.3% and 9.6% for the Transmission configuration and between 0.3% and 2.1% for the other configurations. At the unsaturated state, the CV varies between 4.5% and 9.2% for the Transmission configuration and between 0.5% and 2.1% for the other configurations. We note that the CV for the repeatability is consistently larger in the Transmission configuration. We recall that with this configuration, the current is injected through the metallic grids and the potential drop is measured between two consecutive electrodes of the PCB sensor. Therefore, a difference exists between the injection electrodes and the potential measurement electrodes concerning their size and the nature of the material that constitutes them. This may explain poorer repeatability compared to other configurations for which injection and potential

measurement electrodes are identical. We have also verified that these CVs do not increase with the drying of the concrete which is promising for our application.

3.2 Reproducibility Between PCB Sensors in the Right and Left Sides of Each Slab

In this section, our goal is to evaluate the difference in response between the PCB sensors located on the right and left side of each slab (respectively denoted Ed and Eg). The reproducibility between the sensors is associated here with both the sensor change and the variability of the concrete material. We present the results obtained in the FV slab where the drying is more advanced to show the extreme states (saturated and unsaturated), knowing that similar behaviors are observed in the HA slab. Figure 3 shows the apparent resistivity profiles measured with both PCB sensors, Ed and Eg, using the Transmission configuration.

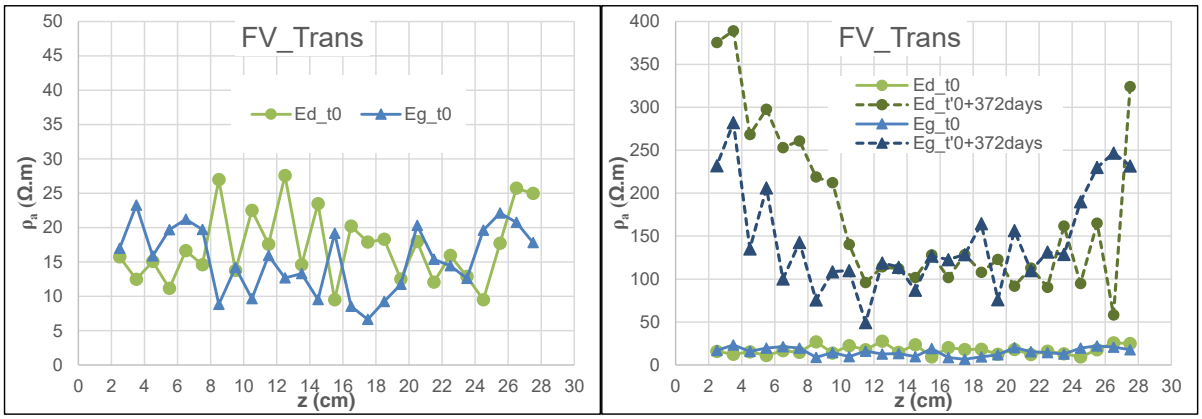

(a) (b)

Figure 3. Comparison of the apparent resistivity profiles measured with the PCB sensors on the right and left sides of the FV slab using the Transmission configuration: (a) at the saturated state, (b) at the saturated and unsaturated states (where t'0 marks the beginning of concrete drying at 45 °C).

The differences observed in Figure 3 can be related to the variability of the concrete. Indeed, a measurement is essentially sensitive to a restricted volume of material between (and around) the two electrodes where the potential is measured (Badr *et al*., 2019). This volume is less than the representative elementary volume (REV) of an electrical measurement in concrete, the dimensions of the REV having to be at least three times the maximum size of aggregates (Du Plooy *et al*., 2013), in this case 3Dmax = 36 mm. At the scale of these very local measurements, the material cannot be considered homogeneous. Measurements are therefore expected to be sensitive to the natural variability of the material, and, in particular, to the distribution of aggregates in the immediate vicinity of the electrodes.

On the other hand, from the point of view of the global trends, the measurements exhibit the same evolution of the concrete water content between t0 and t'0 + 372 days (Figure 3 (b)) on the left and right sides of the slab, which is also promising for our application. The reproducibility between both PCB sensors is therefore verified.

In the following, we only detail the results of the Ed sensors to simplify the presentation and interpretation. The measurements obtained from the Eg sensors are similar.

3.3 Influence of the Reinforcement

The presence of steel reinforcement can disturb the electrical resistivity measurements, due to the fact that steel is a much better electrical conductor than the liquid phase in concrete. Various authors have cited the importance of steel's influence on the electrical resistivity measurement in a reinforced concrete structure (Millard, 1991; Polder *et al*., 2000; Bungey *et al*. 2006, Reichling *et al*., 2015; Alhajj *et al.,* 2019; Villain *et al.,* 2020).

In this section, we compare the response of the PCB sensors between the HA and FV slabs to evaluate the influence of the reinforcement. At the saturated state, the slabs HA and FV are similar in all aspects except that of the reinforcement nature, it is therefore relevant to make this comparison at this state. Figure 4 shows a comparison of the measurements obtained with the PCB sensors in the slabs HA and FV using the Transmission configuration.

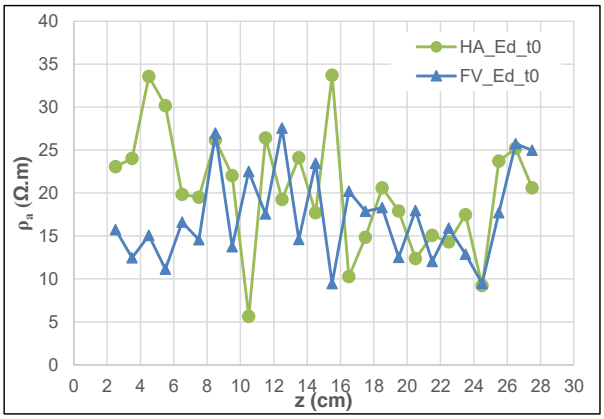

Figure 4. Comparison of apparent resistivity profiles measured with the PCB sensors in the saturated slabs HA and FV using the Transmission configuration.

Differences between the sensors' responses in the two slabs are observed in Figure 4. At the saturated state, a normalized mean root squared error (NRMSE) of 9.1% is obtained in Transmission configuration between HA and FV, comparable to 8.4% obtained, for the same configuration, between the PCB sensors on the right and on the left sides of the FV slab (section 3.2). Therefore, the difference in nature of the reinforcements (HA steel or FV fiberglass) has a small influence on the apparent resistivity measurements obtained by the PCB sensor placed in the center of the reinforcement mesh. Differences between the sensors' responses can be attributed to variations between the investigated materials in the two slabs.

Thus, in this study, the presence of steel reinforcements does not significantly affect the response of the PCB sensors.

4 Monitoring of the Resistivity Profiles

The purpose of this section is to study the apparent resistivity profiles of the PCB sensors during the drying of FV slab.

Due to the low resistivity gradient observed under drying at 20 °C, and in order to test the sensitivity of the sensors to a higher gradient with depth, we accelerated the drying of the slabs by exposing them to an increased temperature of 45 °C. The variation of the apparent resistivity profile with time for the FV slab, using Transmission and Wenner configurations, is illustrated

in Figure 5.

The monitoring carried out during the drying of the FV slab at 45 °C indicates a resistivity gradient between the surface exposed to drying (z = 0 cm) and the protected surface (z = 30 cm) revealing a lower saturation level at the surface, as we can observe in Figure 5. Near surface resistivity values (z = 3 ± 1 cm) increase gradually during the 372 days of drying.

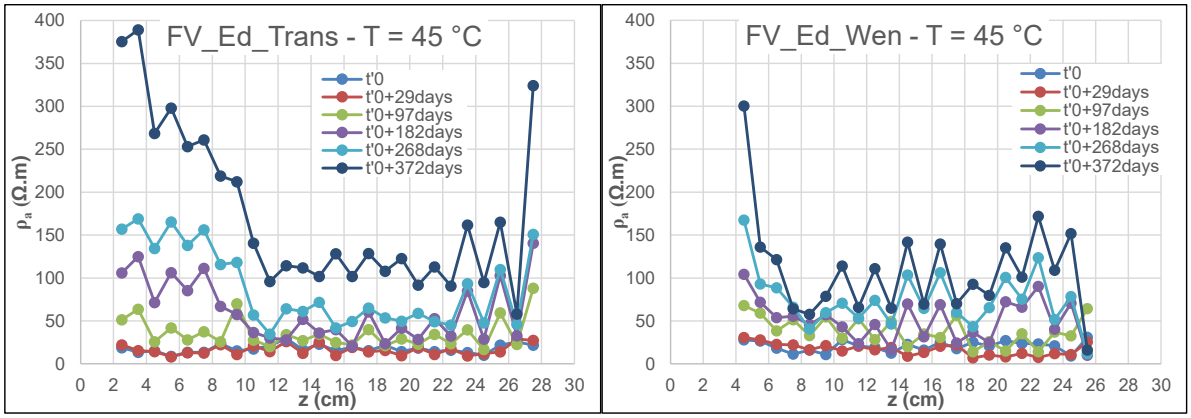

Figure 5. Monitoring of the apparent resistivity profiles measured with the PCB sensors during drying of the FV slab: (a) using the Transmission configuration, (b) using the Wenner configuration.

5 Conclusion

In this paper, a PCB sensor based on an electrical resistivity technique is used to evaluate the resistivity profile of two 30 cm thick reinforced concrete slabs, one reinforced with carbon steel bars (HA) and the other with fiberglass bars (FV). The repeatability and reproducibility of the measurements are checked in saturated and unsaturated conditions, confirming that the results measured with the PCB sensors are within an acceptable range of variability. A monitoring of the electrical resistivity profiles as a function of depth is carried out on the slabs at different times of drying. Resistivity measurements increase over time, showing the sensitivity of the sensors to the evolution of concrete during drying. Thus, this new embedded sensor is validated in a real size reinforced concrete structure and we showed that it reaches its monitoring requirement with a centimetric resolution. In perspective, it is expected that the developed PCB sensor will be used in concrete structures to monitor water content profiles by means of a specific calibration.

ORCID

Joanna Badr: https://orcid.org/0000-0003-2607-2662
Géraldine Villain: https://orcid.org/0000-0002-4478-034X
Jean-Paul Balayssac: https://orcid.org/0000-0003-3965-4709
Sérgio Palma Lopes: https://orcid.org/0000-0001-7022-389X
Yannick Fargier: https://orcid.org/0000-0003-1139-6461
Fabrice Deby: https://orcid.org/0000-0002-6246-9192
Sylvie Delepine-Lesoille: https://orcid.org/0000-0002-9717-639X

References

Alhajj, M-A., Palma-Lopes, S. and Villain, G. (2019). Accounting for steel rebar effect on resistivity profiles in view of reinforced concrete structure survey, *Construction and Building Materials*, *223*, 898-909. https://doi.org//10.1016/j.conbuildmat.2019.07.208.

Andrade, C., Polder, R. and Basheer, M. (2007). Non-destructive methods to measure ion migration. *RILEM TC*, 91–112.

Badr, J., Fargier, Y., Palma-Lopes, S., Deby, F., Balayssac, J.-P., Delepine-Lesoille, S. and Villain, G. (2019). Design and validation of a multi-electrode embedded sensor to monitor resistivity profiles over depth in concrete. *Construction and Building Materials*, *223*, 310-321. https://doi.org/10.1016/j.conbuildmat.2019.06.226.

Balayssac, J.-P. and Garnier, V. (Eds.) (2017). *Non-destructive testing and evaluation of civil engineering structures.* Elsevier, Amsterdam, The Netherlands.

Bungey, J. H., Millard, S. G. and Grantham, M. G. (2006). *Testing of concrete in structures (4th ed)*. Taylor & Francis, New York, United States.

Du Plooy, R., Palma-Lopes, S., Villain, G. and Derobert, X. (2013). Development of a multi-ring resistivity cell and multi-electrode resistivity probe for investigation of cover concrete condition. *NDT & E International, 54,* 27–36.

Fares, M., Villain, G., Fargier, Y., Thiery, M., Derobert, X. and Palma-Lopes, S. (2015). Estimation of water gradient and concrete durability indicators using capacitive and electrical probes. *International Symposium Non-Destructive Testing in Civil Engineering (NDT-CE 2015)*, 15-17 September 2015, Berlin, Germany, 9p.

Kaplanvural, İ., Pekşen, E. and Özkap, K. (2018). Volumetric water content estimation of C-30 concrete using GPR. *Construction and Building Materials, 166*, 141–146.

Millard, S. G. (1991). *Reinforced concrete resistivity measurement techniques*. Institution of Civil Engineers, March 1991, Liverpool, United Kingdom, 71-88.

Polder, R., Andrade, C., Elsener, B., Vennesland, Ø., Gulikers, J., Weidert, R. and Raupach, M. (2000). Test methods for on site measurement of resistivity of concrete. *Materials and Structures, 33(10)*, 603-611. https://doi.org/10.1007/BF02480599.

Reichling, K., Raupach, M. and Klitzsch, N. (2015). Determination of the distribution of electrical resistivity in reinforced concrete structures using electrical resistivity tomography. *Materials and Corrosion, 66(8)*, 763–771.

Villain, G., Alhajj, M.-A., Palma-Lopes, S. and Bouteiller, V. (2020). Towards the Determination of Chloride Profiles by means of Resistivity Measurements in Reinforced Concrete, In *Proceedings of the XV International Conference on Durability of Building Materials and Components DBMC 2020*, Barcelona, Spain, 8p.

XV International Conference on Durability of Building Materials and Components
DBMC 2020, Barcelona
C. Serrat, J.R. Casas and V. Gibert (Eds)

Macrocell Processes in Reinforced Concrete Structures

Josep R. Lliso-Ferrando, José E. Ramón Zamora, Román Bataller and Juan Soto

Instituto Interuniversitario de Investigación de Reconocimiento Molecular y Desarrollo Tecnológico (IDM), Universitat Politècnica de València, Camino de Vera, s/n 46022 Valencia, Spain. E-mail: jollife2@arq.upv.es

Abstract. *Corrosion of steel embedded in reinforced concrete is the phenomena that most affects the durability of this type of structures. The control and analysis of the rebars can help detect this problem beforehand, contributing to prevent costly repairs made when the damage is quite advanced. Currently, there are several techniques for measuring the corrosion rate of steel, but they have the disadvantage of being slow or requiring specialized tools. In addition, these techniques need direct connection to the rebars, so removing the concrete cover layer is necessary. This destructive technique is sometimes impossible to do because there are analysis zones which are inaccessible due to they are buried or submerged. Recently, using sensors embedded previously casting and external electrical connections let analyse the corrosion without using invasive techniques. This study presents the complementary technique of analysing macrocell currents in order to know the origin and direction of current in reinforcements. This technique requires less time and non-advanced material, only an ammeter and electrical connection to the rebars, executed before casting. In addition, this parameter provides information about the real corrosion of the different parts of the structure. In this study it is performed the laboratory analysis of this technique by the use of specimens containing one anode and one cathode inside them creating a macrocell. The influence of different environments on macrocell current intensities shall be studied and compared with other studied parameters as corrosion density.*

Keywords: *Macrocell Currents, Reinforced Concrete Durability, Corrosion Potential, Corrosion Density, Concrete Resistivity.*

1 Introduction

Reinforced concrete is the most used construction material worldwide due to its characteristics, mechanical properties, low-cost and durability. The durability concept is defined as the ability to withstand the mechanical actions, environmental conditions, chemical attack or any other kind of damage that affects the initial state and reduces the lifespan. Durability parameter became a key aspect during design process since nineties. (Tang *et al.,* 2015; Garcés *et al.,* 2008).

One of the most frequent problems that affects the durability of reinforced concrete structures is the corrosion of the rebars. High alkalinity generated by cement matrix (pH usually higher than 12.5) generates a passive layer on the reinforcements, which is transparent, continuous, compact and protects the rebars. In addition, the cement matrix entails a dense barrier between the rebars and the atmosphere where pieces are located. Nevertheless, the cover layer is porous and presents a certain permeability to gas and water, becoming an access path for aggressive agents. The aggressive agents, as chlorides or CO_2 are able to destroy the passive layer and trigger active corrosion, which is the main cause of reinforced concrete structures failure (Bertolini *et al.*, 2013; Garcés *et al*.,2008).

One of the greatest problems of steel corrosion in reinforced concrete is its difficult

detection. Corrosion phenomena develops itself internally and it is visible externally once the damage is quite advanced, through rust stains or cover layer cracks. As a result, corrosion generates expensive repairs due to the belated detection and the necessity of periodic reviews because it is not possible to eradicate the problem completely. Last reports and statistics show the great amount governments invest for repair of reinforced concrete structure (François *et al.*, 2018).

During the last twenty years, a lot of corrosion measurement techniques have emerged in order to help detecting corrosion beforehand. The main disadvantage of these techniques is the rebar connection necessity, so removing the concrete cover layer is required. Sometimes, this fact is impossible when the structural elements are submerged or buried. (Andrade *et al.,* 2001; Bertolini *et al*., 2013; Ramon Zamora, 2018; Ramón Zamora *et al*. 2016).

Using sensors embedded before casting has become an alternative during last years. Electrical connections executed previously casting let analyse the local corrosion without using invasive techniques. However, most of data collection require a lot of time or specific tools, which are really expensive (Ramón Zamora *et al*., 2016; Ramon Zamora, 2018).

The main inconvenient of using isolated sensors for corrosion monitoring is that it can be only measured the local corrosion. However, in structures, real corrosion is completely different to the local corrosion due to macrocell currents. Different parts of the reinforcements are electrically connected and macrocell currents generate currents becoming areas in anodes and cathodes.

This study shows the effectiveness of using macrocell current analysis as an important complementary measurement to the corrosion analysis. Macrocell analysis allows to observe the currents direction and to detect the zones shedding electrons (anodes) and demanding them (cathodes). In addition, using macrocell analysis, it is possible to know the general behaviour of the reinforcements and not just the local corrosion parameters.

2 Macrocell Currents Analysis

Galvanic macrocell is the most important electronic transference process in corrosion (Andrade *et al*., 1992). The macrocell is generated by the presence of great passive areas connected electrically to active areas, where corrosion phenomenon occurs. In this situation, active zones are the anodes (electrons source), while the rest of the passive rebars are the cathode, and the porous dissolution of the cement matrix serves as the electrolyte (Andrade *et al*., 2008; Bertolini *et al*., 2013).

Some authors highlight macrocell corrosion is produced together with microcell corrosion (Andrade *et al*., 1992; Ji *et al.,* 2013). The last one is due to heterogeneity of the material, creating small microcells between the different phases of the microstructure. In Figure 1, it is possible to see the difference between microcells and macrocells.

The macrocell current is measured with a Zero Resistance Ammeter (ZRA) (Andrade *et al*., 2008). Using ZRA in laboratory is possible due to specimens where anode and cathode have not electrical contact can be manufactured. However, measurements in real structures are impossible due to there are electrical contacts between rebars. In this case, it should be necessary to isolate one part of the reinforcements, becoming this measurement an invasive technique. Including isolated sensors and using electrical connections executed before casting would avoid destructive techniques and would facilitate the measurements.

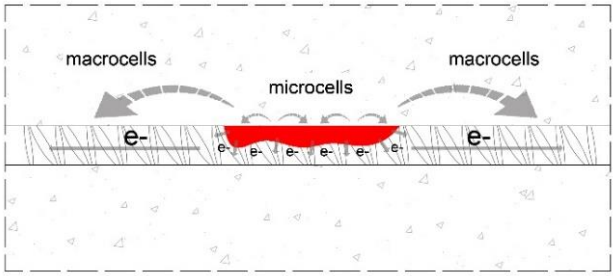

Figure 1. Macrocells and microcells.

2.1 Previous Work

Previously to this study, a macrocell analysis was performed using small specimens and different dosages (Lliso-Ferrando *et al*., 2019). During the first phase of this analysis, cylindrical test specimens where measured as it is shown in Figure 2. The corrosion process is slower than using impressed current, but it allows to observe the corrosion phenomena in a more natural way. The rebar works as anode and the stainless steel plates are the cathodes, which demand electrons to the carbon steel due to the oxygen availability in water.

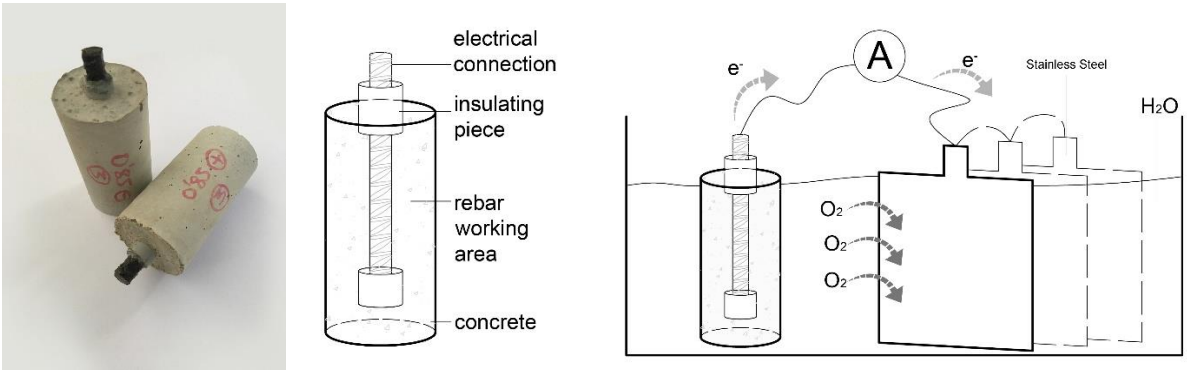

Figure 2. Test specimen and testing procedure.

The study allowed to analyse the influence between cathode-anode surface ratio in the corrosion intensities, as it is possible to see in Figure 3. Several specimens with different mixes were studied. The anode surface is always the same (specimen), and the cathode surface increase gradually (stainless steel plates). As shown in Figure 3, once the ratio between anode and cathode surface exceed 1/350, the macrocell intensity stabilizes because the anode is not able to provide more electrons. As it is possible to appreciate, depending on the concrete characteristics, the ratio can be lower if the concrete quality is better (lower water/cement ratio).

During the second phase of this study, the specimens were exposed in 24 hours' periods to different environments (Laboratory conditions (65% R.H. and 20ºC), Saturated, 100% R.H., dry (40ºC and 23% R.H.)). In every atmosphere, macrocell intensities were measured. It was found the cyclic tendency of this parameter. However, the cathode (stainless steel mesh) was joined to the specimen using a wet cloth. This situation simulated a hypothetic case.

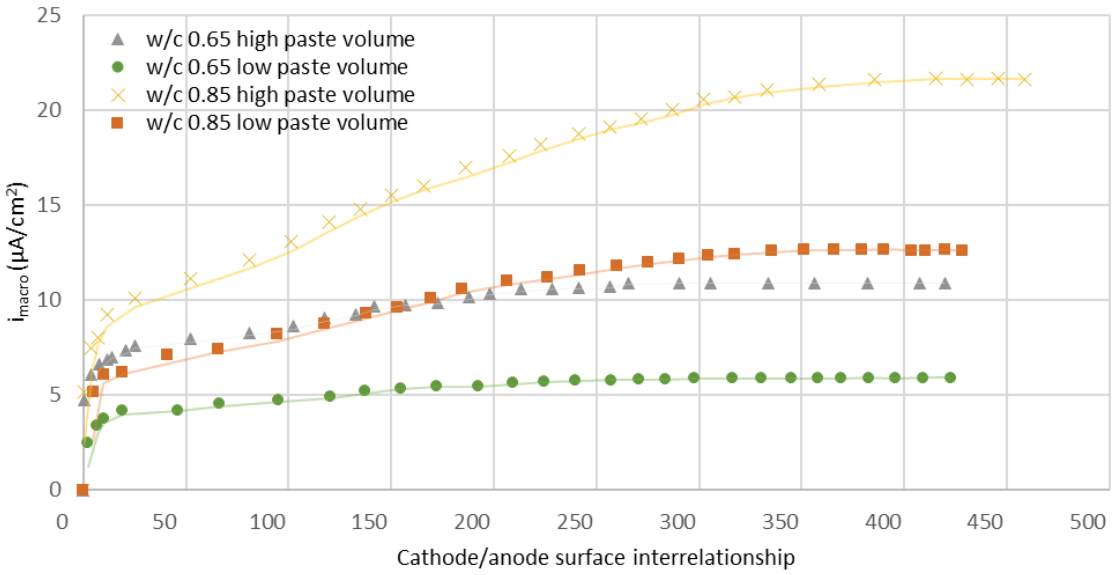

Figure 3. Cathode/anode surface ratio for several specimens with different W/C ratio.

In the present case study, the analysis is carried out on specimens where anode and cathode are embedded in concrete to simulate a real situation.

3 Experimental

3.1 Materials

Several concrete specimens were manufactured, using cement CEM I, and a water/cement ratio of 0.5. The table 1 shows the dosage and the compressive strength.

Table 1. Dosage of concrete per weight.

f_c	w/c	Cement*	Water	Superplasticizer	Sand
47.3 Mpa	0.5	360	180	1.1	1872

*CEM I 42.5.

3.2 Test Specimens

In Figure 4, test specimens' schemes and pictures are shown. The measurements were carried out on cylindrical specimens with a diameter of 100mm and a height of 200mm. Inside the specimen, a rebar was embedded (Ø1.2x16 cm) having electrical connection. A stainless steel mesh was embedded having a cable for electrical connection too. Using different steels, noblest metal is the cathode (stainless steel), while rebar is the anode (carbon steel), it is possible to create a macrocell when they are connected.

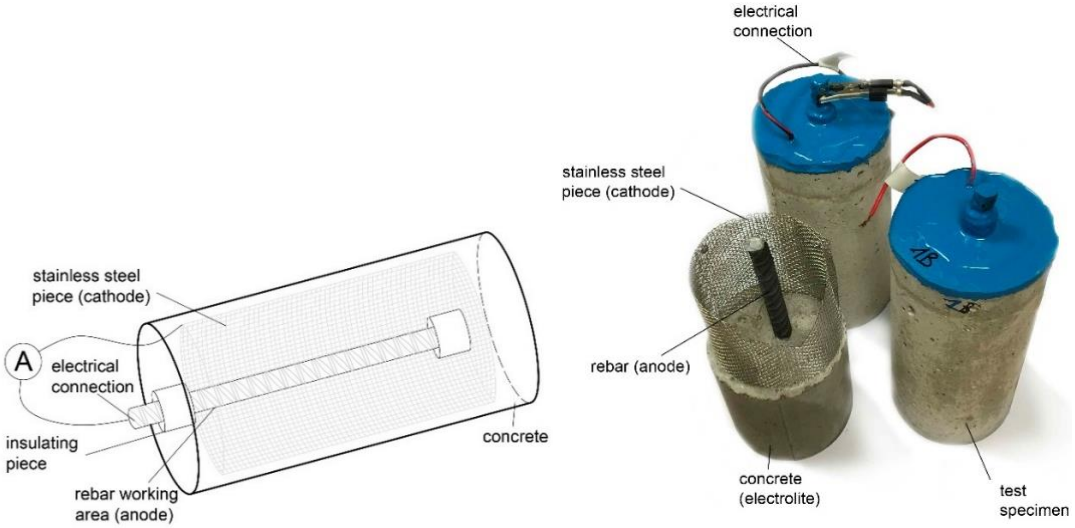

Figure 4. Test specimens.

3.3 Measurements

After 28 days of casting and curing, specimens were exposed to accelerated carbonation process. The chamber conditions were 20ºC, 65% R.H. and 30% CO_2. The specimens were located in the chamber until they were completely carbonated. This period lasted two months. This process allowed to work having higher macrocell and corrosion currents.

Once rebars were depassivated, the specimens were exposed to different atmospheres during 24 hours' periods. At the end of each cycle, resistivity, corrosion potential and macrocell and corrosion currents were measured. During all the process, anode and cathode were electrically connected and just for measuring they were disconnected.

The specimens were exposed to four different atmospheres: dry atmosphere (40ºC and 23% R.H.); saturated (3 hours in vacuum and 21 hours submerged); 100% Relative Humidity; and laboratory environment (approx. 65% R.H.).

Macrocell measurements were carried out with a ZRA.

4 Results

Figure 5 shows the macrocell and local corrosion currents evolution during the different cycles when concrete samples were exposed to different environments after carbonation process. As shown in Figure 5, macrocell currents have a cyclic tendency related to the changes in the environment where test specimens are located.

In addition, it is possible to appreciate how local corrosion intensity values also change depending on the atmosphere where specimens are located. This is due to the fact there are different humidity levels in each environment. On the one hand, when specimens are in a 40ºC and 23% R.H. atmospheres, there is barely enough humidity for let ionic transfer between anode and cathode, and intensities show lower values. Otherwise, when specimens are located in humid environments, presence of water allows the ionic transfer and intensity values doubled their previous ones.

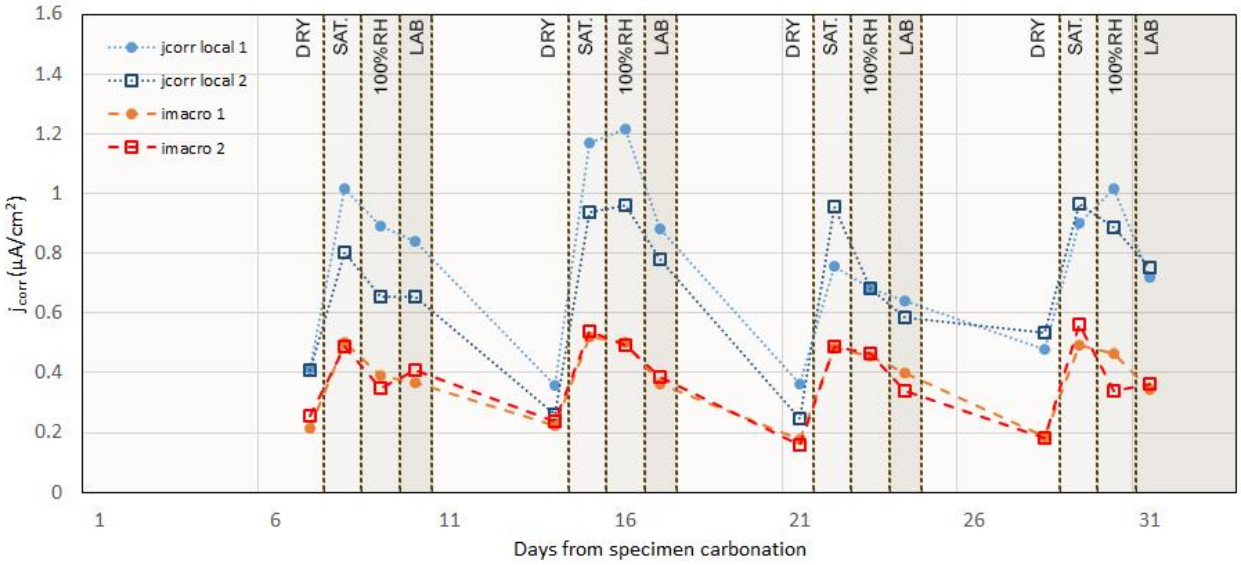

Figure 5. Macrocell current and local corrosion current cyclic variations.

Furthermore, we can appreciate there are not variations between macrocell intensities in specimens 1 and 2, despite having different cathode surfaces. As it was commented on Figure 3, depending on the concrete quality, the stabilization between cathode/anode surfaces can generate no differences between these currents. In this case, the ratio anode/cathode in specimen 1 was 1/10 and in specimen 2 was 1/20. However, as highlighted in Table 1, the concrete has a good quality (lower water/cement ratio) and these ratios are in the stabilized part.

Figure 6 shows the average values of macrocell and local corrosion intensities values. Also it is possible to appreciate the total corrosion intensity values.

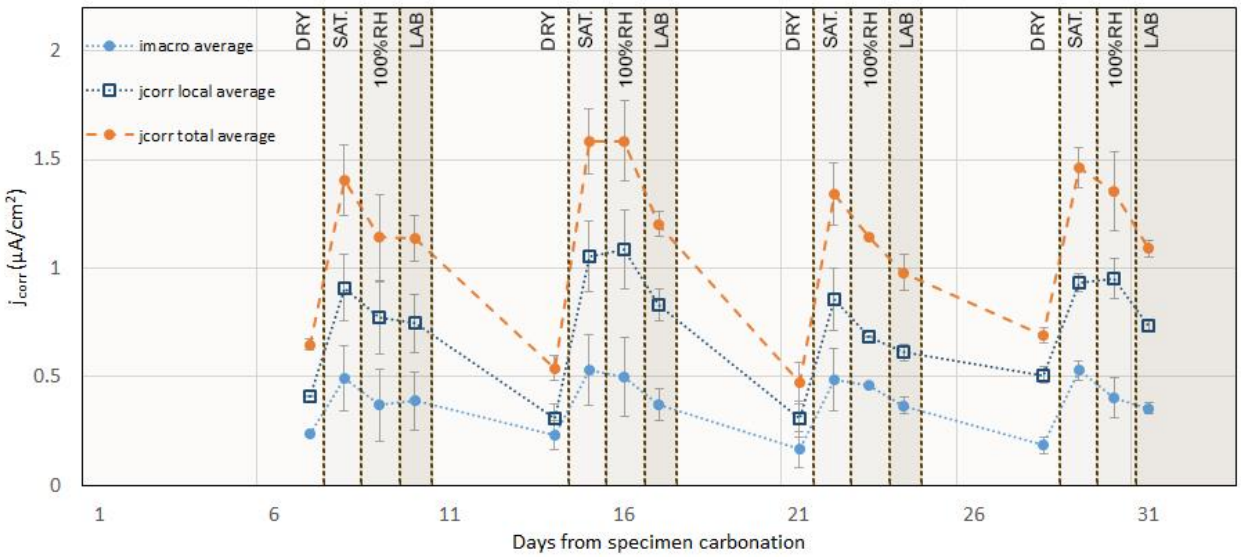

Figure 6. Macrocell and local corrosion intensities and the total corrosion intensity.

Total corrosion intensity has been obtained from the sum of macrocell intensity and local corrosion intensity. As shown in Figure 6, macrocell intensities ranged between 30%-40% from the total corrosion intensities. This fact highlights we mustn't underestimate the macrocell created in the reinforcements.

5 Conclusions

In this study, it has been shown the importance of analysing the macrocell currents in order to understand and know the real corrosion currents in rebars embedded in reinforced concrete structures. The experimental analysis has let to check the behaviour of macrocell and local corrosion intensities in different atmospheres. It has been possible to appreciate the relation of these parameters and the humidity/water presence in the cement matrix.

This study shows using sensors for analysing the local corrosion can lead to wrong results. Overlooking the macrocell currents it is possible to obtain corrosion values 30%-40% lower than the real corrosion intensities.

The main purpose of this study was understanding the macrocell currents in order to become possible the macrocell currents real-time monitoring in reinforced concrete structures. This fact can become an important tool in order to complement the corrosion analysis of the steel embedded in reinforced concrete structures.

6 Future Analysis

The next step for understanding better the macrocell current is the analysis using samples where rebars are not carbonated. This study was carried out using carbonated concrete specimens in order to get high corrosion and macrocell currents values. A variant of this study can be the analysis of corrosion and macrocell currents before the rebars depassivation and afterwards.
In addition, the analysis of macrocell currents in a real structure is an essential tool in order to understand the electrochemical processes and how they develop themselves in real cases. In the electrochemical laboratory of ETSIE, in UPV, a 20 meters long beam was manufactured two years ago. The beam is located in the campus gardens and it was exposed to the weather conditions. The piece includes several reinforcements embedded in order to observe the macrocell currents. The rebars are still passive and in a short-them period, the macrocell and corrosion intensities will be monitored and analysed in passive state and once they are depassivated.

Acknowledgements

The authors would like to express their gratitude to the Universitat Politècnica de València for the pre-doctoral scholarship granted to Josep Ramon Lliso Ferrando (FPI-UPV-2018). To the Spanish Ministry of Economy and Competitiveness for the financial support from the national program of oriented research, development and Innovation to societal challenges (ref. BIA2016-78460-C3-3-R).

ORCID

Josep Ramon Lliso Ferrando: https://orcid.org/0000-0002-2457-9024
José Enrique Ramón Zamora: https://orcid.org/0000-0002-6765-1735
Román Bataller Prats: https://orcid.org/0000-0003-2429-806X
Juan Soto Camino: https://orcid.org/0000-0001-5055-2768

References

Andrade, C., Garcés, P. and Martínez, I. (2008). Galvanic Currents and Corrosion Rates of Reinforcements Measured in Cells Simulating Different Pitting Areas Caused by Chloride Attack in Sodium Hydroxide. *Corrosion Science* 50 (10): 2959–64. https://doi.org/10.1016/j.corsci.2008.07.013.

Andrade, C., Maribona, I., Feliu, S. and González, J. A. (1992). The Effect of Macrocells between Active and Passive Areas of Steel Reinforcements. *Corrosion Science* 33: 237–49.

Andrade, C., Martínez, I., Alonso, C. and Fullea, J. (2001). New Advanced Electrochemical Techniques for on Site Measurements of Reinforcement Corrosion. *Materiales de Construccion* 2001 (263–264): 97–107. https://doi.org/10.3989/mc.2001.v51.i263-264.356.

Bertolini, L., Elsener, B., Pedeferri, P., Redaelli, E. and Polder, R. (2013). Corrosion of Stell in Concrete: Prevention, Diagnosis and Repair. Edited by Wiley VCH.

Raoul, F., Laurens, S. and Deby, F. (2018). Corrosion and Its Consequences for Reinforced Concrete Structures. *ISTE Press Ltd and Elsevier Ltd*. https://doi.org/10.1016/c2016-0-01228-7.

Garcés, P., Climent, M. A. and Zornoza, E. (2008). *Corrosión de Armaduras En Estructuras de Hormigón Armado* (in Spanish). *Editorial Club Universitario*.

Yong, J., Zhao, W., Zhou, M., Hui, M. and Zeng, P. (2013). Corrosion Current Distribution of Macrocell and Microcell of Steel Bar in Concrete Exposed to Chloride Environments. *Construction and Building Materials* 47: 104–10. https://doi.org/10.1016/j.conbuildmat.2013.05.003.

Lliso-Ferrando, J. R., Ramón, J. E., Bataller, R., Gasch, I. and Valcuende, M. (2019). Macrocell Processes Characterization in Reinforced Concrete Structures. *EUROCORR 2019 Proceedings*, no. Idm: 1–6.

Ramón, J. E., Gandía-Romero, J. M., Valcuende, M. and Bataller, R. (2016). Integrated Sensor Network for Monitoring Steel Corrosion in Concrete Structures. *VITRUVIO - International Journal of Architectural Technology and Sustainability* 1 (1): 65. https://doi.org/10.4995/vitruvio-ijats.2016.5191.

Ramon, J. E. (2018). *Sistema de Sensores Embebidos Para Monitorizar La Corrosión En Estructuras de Hormigón Armado. Fundamentos , Metodología y Aplicaciones* (in Spanish). PhD Thesis, Universitat Politècnica de València, Valencia, Spain.

Tang, S. W., Yao, Y, Andrade, C. and Li, Z. (2015). Recent Durability Studies on Concrete Structure. *Cement and Concrete Research* 78: 143–54. https://doi.org/10.1016/j.cemconres.2015.05.021.

XV International Conference on Durability of Building Materials and Components
DBMC 2020, Barcelona
C. Serrat, J.R. Casas and V. Gibert (Eds)

Mechanical Behaviour of ETICS in Presence of Water

Fulvio Re Cecconi[1], Giuseppe Cocchetti[2], Aram Cornaggia[3] and Tomaso Villa[4]

[1] Architecture, Built environment and Construction engineering – ABC Department, Politecnico di Milano, via Ponzio 31, 20133-Milano, Italy, fulvio.rececconi@polimi.it

[2] Civil and Environmental engineering – DICA Department, Politecnico di Milano, piazza Leonardo da Vinci 32, 20133-Milano, Italy, giuseppe.cocchetti@polimi.it

[3] Civil and Environmental engineering – DICA Department, Politecnico di Milano, piazza Leonardo da Vinci 32, 20133-Milano, Italy, aram.cornaggia@polimi.it

[4] Chemistry, Materials and Chemical Engineering "Giulio Natta" – DCMIC Department, Politecnico di Milano, piazza Leonardo da Vinci 32, 20133-Milano, Italy, tomaso.villa@polimi.it

Abstract. *Climate change and the request for better assets' energy performances are forcing the construction sector towards passive or even active buildings: assets with a positive balance between energy production and consumption. Building insulations play a crucial role in reducing energy demand. One of the most used technology to insulate new and refurbished buildings are the External Thermal Insulation Composite Systems (ETICS). Despite their thermal advantages, low cost, and ease of application, these systems may have serious problems if not well designed. Cracks on the coating layer are among the most common pathologies during ETICS service life. They have been studied using a Finite Element Method (FEM) analysis on two different types of ETICS in order to understand how cracks and the mechanical characteristics of materials used in the ETICS are related. The results show that errors during ETICS installation impacts on cracks occurrence as much as the mechanical performances of some layers. The FEM analysis have been complemented by the experimental study of the mechanical behavior of the coating layer under the effect of rainwater, in order to better understand ETICS behavior over their service life.*

Keywords: *External Thermal Insulation Composite Systems (ETCS), Finite Element Methods (FEM), Mechanical behavior, Durability.*

1 Introduction

Climate change and the request for better assets' energy performances given by the European Union (Directive EU 2018/844) are forcing the construction sector towards passive or even active buildings, *i.e.* assets with a positive balance between energy production and consumption. According to the (European Construction Sector Observatory, 2019) of the residential building stock in the EU Member States, on average 45.4% of the buildings were built before 1969 and 75.4% before 1990. This means that, not only designing and constructing energy efficient buildings should be targeted, but also retrofitting the building with energy efficient strategies to improve buildings performance through its lifespan should be considered (Sözer, 2019).

Building insulations play a crucial role in reducing energy demand. One of the most used technology to insulate new and refurbished buildings are the External Thermal Insulation Composite Systems (ETICS). According to (ETAG 004) an ETICS is "a system that comprises

a prefabricated insulation product bonded onto the wall, or mechanically fixed using anchors, profiles, special pieces, etc..., or a combination of adhesive and mechanical fixings. The insulation product is faced with a rendering consisting of one or more layers (site applied), one of which contains a reinforcement. The rendering is applied directly to the insulating panels, without any air gap or disconnecting layer".

ETICS, have often been used in Europe since the 1970s, both in new buildings and in retrofitting. The popularity of this technology grew due to its advantages regarding other techniques of insulation. ETICS guarantees the reduction of the thermal bridges and greater thermal comfort due to the preservation of interior thermal inertia, providing a finished appearance similar to the traditional rendering (Tavares, 2020).

The increasing and progressive use of ETICS has also resulted in a significant number of failure cases. Among these, the main defects found in literature can be classified into four main types (Tavares, 2020):

- staining/color or texture changes;
- joint defects;
- loss of continuity/integrity defects;
- loss of adhesion defects.

Examples of loss of continuity/integrity are oriented or mapped cracks and defects in corners that are usually caused by a combination of different causes. Cracks in ETICS are not only a serious aesthetic defect, they are also a weak point for the entry of rainwater into the facade. The consequences of the excessive presence of water inside an ETICS system are its accelerated degradation and a decay in the thermal resistance of the insulating layer. The latter compromises the performance of the entire system.

Thus, a study on the development of cracks in ETICS coatings is of utmost importance and understanding the causes may allow for better designed and longer life façades.

2 State of the Art

A research on the most common databases of scientific publications reveals how ETICS have been studied in relation to some of their characteristics and other performance of the building.

For example, Figure 1 shows a diagram obtained by searching SCOPUS and WebOfScience for the following research string: (ETICS OR "external thermal insulation composite systems") AND ("service life" OR durability OR (FEM OR "finite element method") OR crack* or "mechanical behavior"). This search string allows you to find articles that deal with ETICS and durability or service life, or ETICS and mechanical behavior, with attention to the occurrence of cracks.

It can be noted in Figure 1 (the biggest circle in picture) that ETICS have often been studied in relation to the thermal insulation requirement, which was easily foreseeable. For what is most relevant to the scope of this research, durability aspects of ETICS have been analyzed mainly in relation to moisture and, similarly, the keyword "degradation" has been often searched combined to "mold growth" and "biodegradation" especially on "housing". Nevertheless, some studies on cracks on ETICS can be found.

Durability of ETICS has been often associated to degradation of their coating layer due to mold growth (Kučeriková 2014, Stanaszek-Tomal, 2017). Although, ETICS generally perform satisfactorily if thoroughly designed and carefully erected, they are not very robust. Even minor

errors in design techniques and/or craftsmanship can lead to rendering defects (Kvande, 2018).

(Tavares, 2020) after a survey of 378 façade found that stains or aesthetic changes are the most common anomalies and were identified in practically all claddings. In contrast, anomalies associated with loss of adhesion were only identified in 10.5% of the sample set.

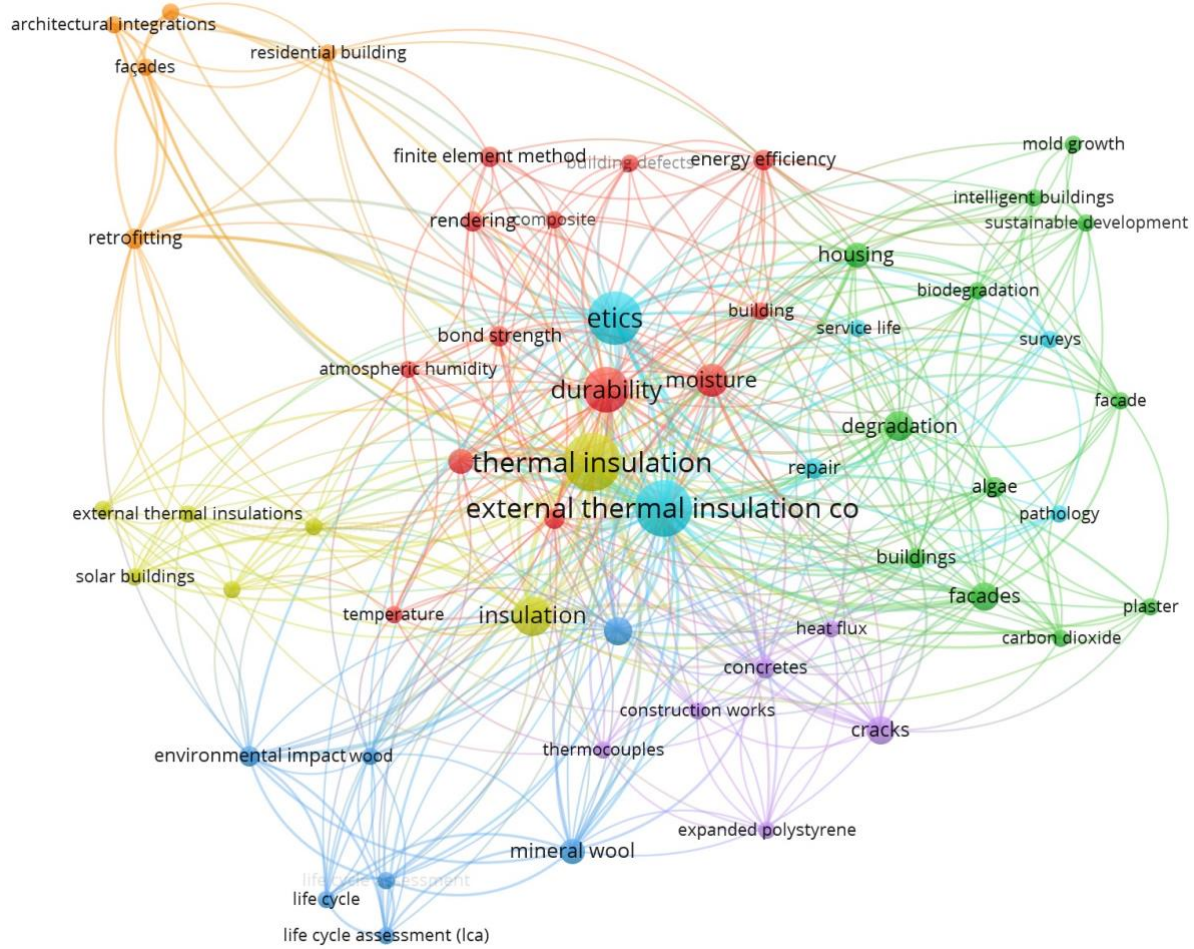

Figure 1. Network analysis of the keywords ETICS, external thermal insulation composite systems, service life, durability, FEM, finite element method, cracks, mechanical behavior.

In a survey of the facade defects with ETICS in a cold climate made by visual inspection (Liisma, 2016) found that most of the ETICS defects were material rupture (51%) and color/aesthetic defects (40%). Only a small proportion of defects were associated with flatness (9%).

3 Methods and Tools

The research is divided mainly into two great stages as pictured in Figure 2. The first one is dedicated to data gathering on both aging agents and materials' mechanical properties and to some pre-analysis needed to understand the behavior of the coating layer of ETICS. The second one is the actual FEM analysis and data post-processing for visualization.

Focusing on the first stage, an investigation of cracks in ETICS, conducted through

interviews with experts and some analyses of failure cases, has shown that temperature variations are one of the major stressing agents in this type of degradation. Noteworthy, researches (Künzel, 1999) prove that during the course of the day the surface of ETICS is exposed to thermal and hygric variations of up to 40 K and 80% RH.

Accordingly, the climate of some locations was analyzed in order to define the stress conditions to which the ETICS coat was subjected. In particular, when choosing the locations to be analyzed, attention was paid not only to the maximum air temperature but also to seasonal and day/night temperature variations. Eventually, the choice of locations was also influenced by the spread of ETICS on the market. Once the locations have been selected thermal stresses on ETICS have been computed using the model WUFI® (Künzel, 1994), which has been developed at Fraunhofer-IBP in Germany since mid of the 1990ies. In this model the relevant heat and moisture transport processes within hygroscopic porous media are described by two partial differential equations which are solved by the help of a finite volume procedure.

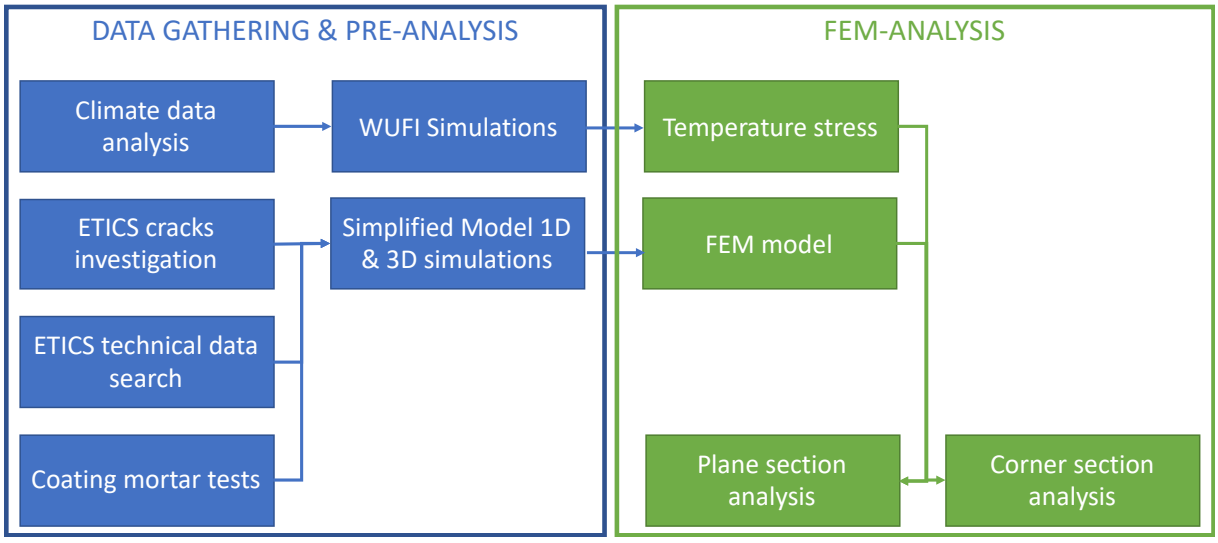

Figure 2. Research schema.

Alongside to the analysis of climate agents, simplified structural models have been created to better understand the phenomenon of the development of cracks on the external surface of ETICS. For example, a model was built by modelling the ETICS finishing layer as an elastic beam resting on a bed of springs whose rigidity is proportional to the compressive strength of the thermal insulation layer. These first analyses on simplified models have highlighted fundamental aspects for the prosecution of the research. It has emerged, for example, that in without imperfections in the installation phase or defects in the material such as the different thickness of the panels, the only thermal variations are not able to generate tension or compression stresses inside the coat that can cause the formation of cracks.

In the second stage of the research a nonlinear finite element model has been set-up for the mechanical analyses of ETICS. The model consists of seven insulating panels arranged in three rows so as to represent, considering the appropriate symmetries, the planar and central surface of the facade of a building. The chosen finite elements are of isoparametric kind, three-dimensional, with 8 nodes and incompatible shape modes. The total number of finite elements is about 70000, with about 75000 nodes.

On the ETICS bottom, *i.e.* where the system adheres to the supporting wall, fixed boundary conditions are imposed on surface parts physically glued. Boundary conditions, consistent with a periodic repetition of insulations panels, are set to the lateral surface.

FEM input is represented by the temperature distribution, along the ETICS thickness, computed by "WUFI" software in the first stage of the research. Non-linear kinematics has been adopted to perform the analyses.

Defects that may occur during the installation of the ETICS or imperfection in the thickness of the panels are modelled by a thickness reduction of the central panel. The onset of the fracture is checked by a Rankine criterion in the plaster.

In order to complete the finite element analysis and also to investigate particular configurations of the panels, different types of edge constraints have been imposed. The first stage of the research showed that in many cases the corners (edges of the facade, corners of doors and windows, corners in correspondence of balconies and loggias, ...) are places of frequent development of cracks. Thus, a second finite element model has been created to allow the analysis of these troublesome point in an ETICS façade.

Eventually, results FEM analyses were combined with some experimental investigation on the tensile strength of the coating made in the first stage of the research.

4 Results

The main research results are set out in this section. It should be noted that for all finite element models a double analysis has been made, one in the case of a polystyrene foam (EPS) insulation panel and another with the insulation panel made of mineral wool (MW).

The 1D preliminary analyses pointed out that a temperature increase cannot be the only cause of cracks (due to instability) on the base coat. If the coating is undamaged the critical (Eulerian) stress is σ_{cr} = 6.1 MPa and the corresponding critical temperature variation is ΔT_{cr} = 576 K. If the base coat is already cracked the same variables have the following values, σ_{cr} = 3.1 MPa, ΔT_{cr} = 288 K. On the other hand, a temperature drop may cause cracks on the base coat but only for a material with a medium to high Young modulus.

These preliminary results were confirmed by the 3D FEM analyses where a model made of seven insulation panel has been investigated using temperature distribution obtained from HMT analyses using weather data of the city of Milano. Even in FEM analyses, if the model has no imperfections, i.e. there are no errors in construction or insulation panels have no thick tolerances, then there are no signs of possible cracks. Otherwise, if errors or imperfection are modeled with one insulation panel (the central one in this case study) having a different thickness (1 mm thicker in this case study) then displacements are much bigger, as shown in Figure 3. Accordingly, in the coat significant stress concentrations at the joints of flanked insulation panels were found.

Figure 4 shows a comparison between stresses in the z direction, i.e. parallel to the longest side of the insulation panel, caused by a negative temperature variation may on ETICS made with two different materials for insulation layer: MS (a) and EPS (b).

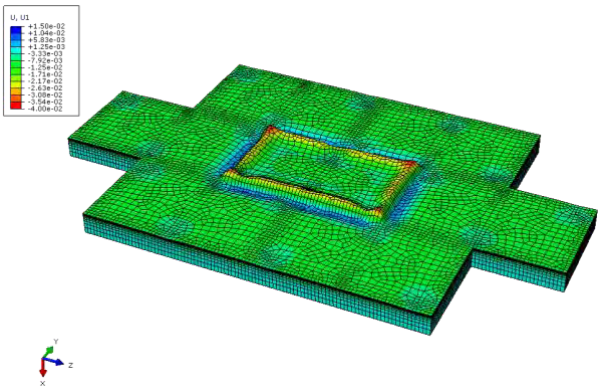

Figure 3. FEM Analysis results for the plane section of the MW ETICS. Displacements in x direction (thickness) [mm] for a positive temperature variation.

In both cases stresses in the coating layer were below the strength of the material. FEM analyses confirmed what had been found in the scientific literature and in the investigated fault cases: cracks on the coat of ETICS will develop if a) the external face of the insulation panels does not belong to a perfect plane; b) the coat has a high Young (elastic) modulus and c) there are high temperature variations.

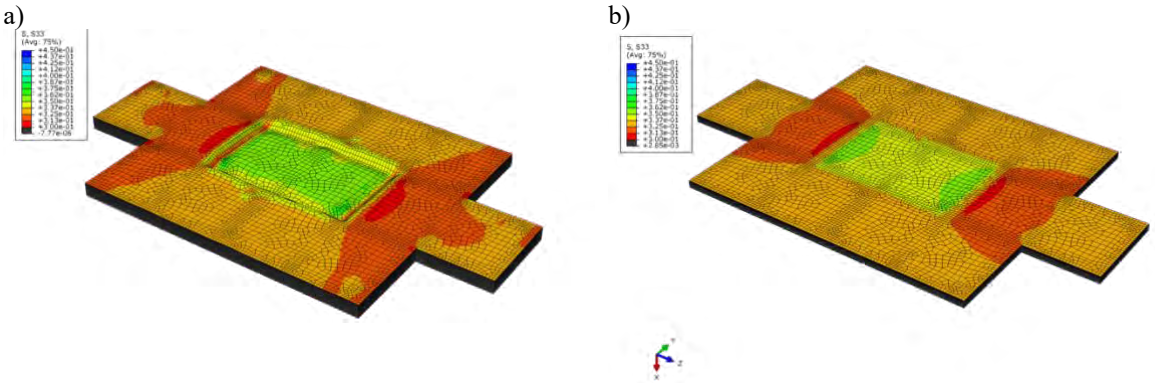

Figure 4. Comparison between mineral wool (a) and EPS (b). Stresses z direction [MPa] for a negative temperature variation.

In order to simulate the behavior of an ETICS near a corner some FEM analyses on a single insulation panel with two unconstrained edges have been done. An example of the results of these analyses is shown in Figure 5. The difference in the thermal expansion coefficient between the two insulation panel materials led to a huge difference in stresses in the coat layer, namely in the ETICS made of EPS stresses inside the coat are up to 6 times the stresses in ETICS made of mineral wool and with the given thermal stresses (city of Milano, medium dark color coat) are dangerously close to the strength of the coat.

Since the tensile strength of the coating play a crucial role in the development of cracks, 12 coat samples were tested to measure their tensile strength. Six of them were characterized by a high water content (immersed) and 6 with a standard water content (dry).

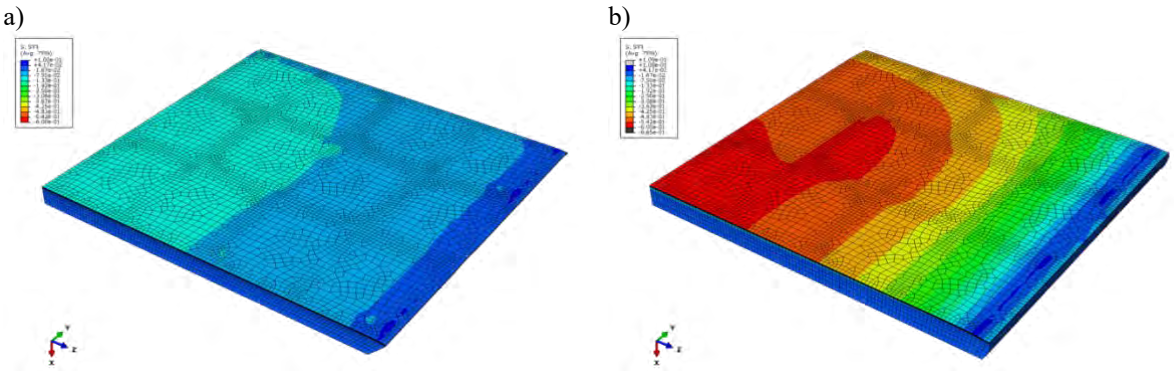

Figure 5. Comparison between mineral wool (a) and EPS (b). Stresses [MPa] when two edges of ETICS are unconstrained.

Experimental results proved that the average tensile strength applied to obtain a 2% strain varies significantly comparing the dry samples and the immersed ones with an average 42% reduction. By combining the results obtained in the two phases of the research, we can say that high water contents can easily halve the critical thermal variation, i.e. the thermal variation causing cracks on the ETICS coat. This high reduction is all the more dangerous as the elastic modulus of the insulating material increases.

5 Discussions and Conclusions

After a deep literature review performed to find the right values of material properties to be used in FEM simulation and some preliminary simplified analysis made to have a first feeling of the phenomena, two different kind of models were set up:

- one where ETICS is fully constrained to analyze the behavior of the system far from any singularity such as windows, doors, corner of buildings, etc…
- one where two side of the ETIC are unconstrained in order to investigate what happens away from the center of the façade (and of the ETICS)

In both cases thermal stresses were computed starting from a temperature distribution given by HMT simulations.

FEM simulations using the fully constrained model showed that cracks in the coat layer are mainly a consequences of steps in two near panels (a small step from one panel to the near one may be due even to a small tolerance in the thickness of the panel or to defects in the support layer and it's always present) and that a coat with high Young modulus suffers more than a rigid one high temperature variations. Simulations made with the unconstrained model highlighted that thermal expansion coefficient of the insulation panels and its compressive strength in the direction perpendicular to the main face are important factors for cracks development. An insulation panel with a low thermal expansion coefficient behave better in hot climate, the case studies showed, for example, that ETICS made with mineral wood insulation have stresses in the coat layer six times lower than the ones made with EPS. Some design principles can be deduced from FEM simulations:

- (if possible) always try to limit the thermal excursion of the coat layer of the ETICS using light colors in hot climate (or where there is a high sun radiation);

- use insulation panels with low tolerance in the thickness (small manufacturing errors) and fix them on a plaster layer (or be sure to have a very flat surface);
- in hot climate (or where there is a high sun radiation) use insulation panels with a low thermal expansion coefficient and a high compression resistance (in the direction perpendicular to the main surface);
- it is always better to protect ETICS from rainwater because the tensile strength of the coat decreases significantly in presence of water, thus lowering the threshold (temperature variation) of cracks.

Acknowledgements

The authors would like to acknowledge and thank PhD Riccardo Paolini for his invaluable contribution to this research. This research was partially founded by Rockwool International A/S, to which the authors express their deepest gratitude.

ORCID

Fulvio Re Cecconi: https://orcid.org/0000-0001-7716-8854
Giuseppe Cocchetti: http://orcid.org/0000-0002-9695-2967
Aram Cornaggia: http://orcid.org/0000-0001-7176-8664
Tomaso Villa: http://orcid.org/0000-0003-2663-6755

References

Directive (EU) 2018/844 of the European Parliament and of the Council of 30 May 2018 amending Directive 2010/31/EU on the energy performance of buildings and Directive 2012/27/EU on energy efficiency

ETAG 004 Guideline For European Technical Approval of External Thermal Insulation Composite Systems With Rendering edition March 2000, amended February 2013.

European Construction Sector Observatory (2019), Analytical report, Improving energy and resource efficiency

Liisma E., Sepri R., Raado L., Lill I., Witt E. Sulakatko V. and Põldaru M. (2016), *Defect analysis of renovated fcade walls with ETICS solutions in cold climate conditions*, Central Europe towards Sustainable Building (CESB16), Prague.

Kučeriková V., Kraus M. and Kubečková D. (2014). *Analysis of the Degradation of External Plasters in the Buildings with ETICS*, Advanced Materials Research, Vol. 1041, Pages 15-18, https://doi.org/10.4028/www.scientific.net/AMR.1041.15

Künzel, H.M. and Holm, A. (1999). *Praktische Beurteilung von Putzen durch moderne bauphysikalische Bewertung*. WTA-Schriftenreihe, Vol. 20, S.177-132.

Künzel, H.M. (1994). *Verfahren zur ein- und zweidimensionalen Berechnung des gekoppelten Wärme- und Feuchtetransports in Bauteilen mit einfachen Kennwerten*. Dissertation Universität Stuttgart

Kvande, T., Bakken, N., Bergheim, E., and Thue, J.V. (2018). Durability of ETICS with Rendering in Norway - Experimental and Field Investigations. Buildings, Vol. 8, 93, https://doi.org/10.3390/buildings8070093

Stanaszek-Tomal E. (2017). *The Problem of Biological Destruction of Façades of Insulated Buildings - Causes and Effects*, IOP Conf. Ser.: Mater. Sci. Eng. 245 032012, https://doi.org/10.1088/1757-899X/245/3/032012

Sözer H., Sözen H. (2019) *Energy saving, global warming and waste recovery potential of retrofitting process for a district*, Journal of Cleaner Production, Volume 238, ISSN 0959-6526.

Sulakatko, V., and Lill, I. (2019). *The economic relevance of on-site construction activities with the External Thermal Insulation Composite System (ETICS)*. International Journal of Strategic Property Management, 23(4), 213-226. https://doi.org/10.3846/ijspm.2019.7071

Tavares J., Silva A. and de Brito J. (2020). Computational models applied to the service life prediction of External Thermal Insulation Composite Systems (ETICS), Journal of Building Engineering, Volume 27, ISSN 2352-7102, https://doi.org/10.1016/j.jobe.2019.100944.

XV International Conference on Durability of Building Materials and Components
DBMC 2020, Barcelona
C. Serrat, J.R. Casas and V. Gibert (Eds)

Observations of Moisture Damages in Historic and Modern Wooden Constructions

Stephan Ott and Patrik Aondio

Department of Civil Geo and Environmental Engineering, Technical University of Munich, Arcisstrasse 21, 80333 Muenchen, Germany, ott@tum.de & aondio@tum.de

Abstract. *With the introduction of new building products made of planar glued board lamellas, the CLT, the restriction of load-bearing structures to linear and thus additively used load-bearing members was abolished. As a result, new, technically determined boundary conditions for moisture management in the interior of buildings have arisen. Due to the emergence of massive, planar wall and floor components as in concrete construction, the integration of building services technology in timber construction must now take place differently than was traditionally the case. In addition, it can be observed that the damage to building components is increasing, the detection of moisture damage is becoming more difficult and, ultimately, the consequences and risks are not yet foreseeable. The study focuses on the cause-effect relationship of increased water input and uses selected examples to reveal the problem of moisture exposure in the interior of buildings with planar load-bearing structures, the damage mechanisms and direct consequences set in motion. This paper shows the necessity for moisture protection measures in modern timber structures in comparison to traditional ways to construct with timber. It shows where moisture intake with modern structures must be considered and avoided from the engineering perspective in order to minimize the risk of moisture damage.*

Keywords: *Moisture Damage, Mass Timber Construction, CLT, Damage Mechanisms, Durability, Risk.*

1 Introduction

Wood is one of the oldest construction materials in our history. Due to its one-dimensional growth direction, it is mainly found in one-dimensional, linear components. This fact has significantly influenced the building with wood in the last centuries. Individual beams were used for load transfer, which worked alone or in combination with other beams. Only in the last decades a new building product has arisen by the emergence of the adhesive technology, which has created the breakthrough into our construction everyday life under the name *CLT*. In recent years, *CLT* has become one of the most popular building products for engineering timber construction. From today's point of view, its origins go back a very long way. In Central Europe, the first nailed *CLT* elements from the beginning of the 20th century are known under the name of construction method *Broda* (Kersten, 1926). In 1929 (Pohl, 1934), the Building Research Institute in Moscow had extensive investigations carried out on cylindrical shells made of nailed *CLT*. It was not until many years later (1992) that the company *Holzbau Merk*, *Aichach*, Germany, gained experience in the production of glued, large-format elements from crossed board lamellas. On this basis, the first general building authority approval (AbZ Z-9.1-354) was issued in 1998 under the name *Merk Dickholz*. Since this time, *CLT* production has shown a steady increase in production. According to the internet news portal *Holzkurier*, an annual

production output of 1.2 million cubic metres of cross-laminated timber is to be achieved in 2020 (Ebner, 2017).

The development of the cross-laminated timber construction product has massively changed the way walls and floor are designed. The once linear components of timber construction (beams) are increasingly being replaced by planar components made of cross-laminated timber. Construction times and construction heights can be reduced by constructing on the plane (see Figure 1), as the plane that encloses the room is combined with the load-bearing layer. The closed plane, which is formed by cross-laminated timber, is not only advantageous. If a building is to be constructed, different types of construction can be used for building floor. From a structural engineering point of view, the bending stiffness of the type of construction used is usually decisive, since it characterizes the serviceability limit state. If a 4-metre *CLT* floor is compared with a wooden beam floor, it can be seen that the *CLT* floor requires only 2/3 of the construction height of the beam floor with the same bending stiffness, cp. Figure 1.

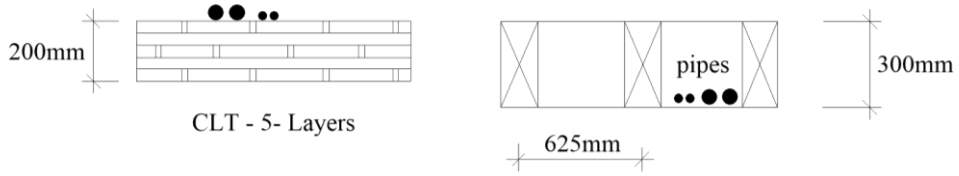

Figure 1. The two main different types of timber floor systems, a *CLT* plate with 2-axial structural span (left) and a traditional framed floor of joists with a 1-axial span (right). The installation of water pipes with respect of the type of construction is shown.

This article is intended to examine the problems of flat components with regard to their moisture resistance, special damage mechanisms as well as their causes and effects and the risks of repair, and to point out possible problem solutions and approaches for practical implementation.

Moisture damage generally poses a major problem in the construction industry and for wood components made of the renewable building material wood as well as most wood-based materials. Humidity usually does not destroy the building material suddenly, but slowly and gradually. What is the reason for this? On the one hand, wood itself has good resistance to short-term exposure to moisture. If the material can dry off quickly and the water content falls below 18% by mass again, then there are no concerns about durability. Even changing moisture contents of the material are in themselves harmless, although there are geometric changes in the cross-section due to shrinkage and swelling during moisture supply or removal. The geometrical changes are not to be classified as harmful if there are sufficient degrees of freedom of the component or a subcomponent. This shows examples, like wooden roof shingles from larch wood, which are to be found for example in the Alpine region frequently. Despite their constantly changing moisture content and additional exposure to wind and solar radiation, both of which promote drying, the material has a service life of 30 years or more in this application field.

In the case of moisture damage in the construction industry, most damage to wood only comes to light after a long period of time, apart from large and sudden damage events such as defects in water pipes. This type of defect is either concealed and is not noticed by anyone or the amount of moisture is small but constant and the damage mechanisms set in motion work slowly.

Damage mechanisms in wood and wood-based materials can be divided as follows: phenomena and damage mechanisms that do not damage the structure, directly damage the structure and indirectly damage it. Non-structural damaging mechanisms include the formation of mould on the material or component surface and blue stain fungi. These can be listed, however, as healthwise precarious and optically aesthetic lacks. The wood-destructive fungi (brown rot, dry rot) belong to the second damage-mechanism that leads to irreparable structure-damages in the material due to continuous high humidity. The last group of indirect damage mechanisms is triggered by moisture-dependent shrinkage and swelling and the reduction in strength due to high moisture. These two characteristics do not initially lead to damage to the material. However, shrinkage and swelling can lead to cracks in the cross-section along fibres and cause damage to entire components or adjacent components due to deformation of the cross-section, as the change in moisture can lead to large forces in the material. This can be observed in connection with internal stresses or settlement of components, but does not necessarily lead to damage to the material itself. By reducing the strength due to high humidity, deformations of the load-bearing component due to forces are possible and thus damage to the load-bearing or adjacent components is possible. The systematics of the damage mechanisms and their consequences are described in detail by (Ott *et al.*, 2017) in the report of TallFacades. The research project focused on moisture damage in the building envelope and the effects of weather and climate. It was already recognised that there are major risks of moisture damage inside buildings. The generally applicable damage mechanisms are not discussed in detail, nor are the direct consequences, since both can be read in the above-mentioned report on TallFacades. In principle, they also do not change in the event of damage inside buildings. In this article we get to the bottom of the following questions, following the damage and searching for the causal chain that leads to damp damage inside the building:

i) Which damage events can be observed inside buildings and how can the indirect consequences be linked with the overarching consequences of moisture damage?
ii) Which components are affected by moisture impacts and where have the damage mechanisms affected to what extent over time?
iii) How does the causal chain of damage mechanisms for the specific impact work?
iv) How much water and moisture has affected the wood.
v) Where does the impact (triggering event) come from?

Are there indications somewhere in the causal chain, either in the type of action or in the damage mechanisms or at the end in the direct and indirect consequences, which in particular are related to the aforementioned planar *CLT* structures?

In the discussion and summary, hints are given for the avoidance of impacts, elimination of damage mechanisms and minimization of consequences for the respective construction method (planar or linear). In addition, supplementary measures for the protection of the construction against excessive and continuous exposure to moisture are proposed through regular monitoring. Their final areas of application and application procedures, the testing and control of success are described in detail in a further paper.

2 Methods

2.1 Data

In order to analyse the relationships between the damage mechanisms and impacts, data from several damage surveys and expert opinions of the last five years are evaluated and compiled in Table 1. Specific information is taken from the sources in order to identify and further classify the damage to the construction methods and components.

Table 1. Data from evalutated multi-storey and mid-rise timber buildings.

Building and use	i) Construction type	ii) Structural part with damage	iii) Damage mechanism	iv) Water amount	v) Source of water
hotel	flat, 2-axial floor slab	top side *CLT* slab	top layers rotten	bathroom, leaking pipe	water on floor, below screed, not detectable
school	flat roof as warm roof, and beam structure	roof panelling, on bottom & top of beams	wood panels (OSB), rotten	construction moisture, no drying	tight roof top, vapour tight interior layer,
new office on top of existing parking, depot and heating plant	extension on RC-structure flat roof: beam flooring with timberframed panels	insulation inbetween beams, panelling	wet cellulose ins., beams, sills, and rotten panelling	construction moisture, high convective moisture input	neighbouring glass house, missing vapor barrier floor and edges, open shafts
daycare for children	nail laminated elements	nail laminated floor slabs and wall panels (1st floor and roof)	swelling of lamellas of elements, damage of connected elements	construction moisture, rain, high amount	missing protection during construction
pv-installation on tilted roof	beam structure	insulation inbetween beams, panelling	beams wet and dark coloured, wood panels rotten	rain water and convective moisture	small holes in roof cladding, penetration by pv-fixation

2.2 Procedure of Case Studies Analysis

The causal chain of the damage event and the damage mechanism, according to (Tietze et al. 2016), is evaluated and structured on the basis of the descriptions from the expert opinions and their categorization in Table 1. The following procedure is used: the primary influence of water damage on the position and size of the damage to the component is analyzed by the mutual investigation of the effect on the component and the damage resulting in the component. Information is evaluated to answer i) the general question about the occurrence of moisture damage in multi-story wooden buildings and ii) about the construction method and the affected

areas in the building components. The respective damage mechanism and the causal chain leading to the damage are determined in question iii) on the basis of the categorization of the damage patterns or according to the type of damage to the component. The trigger of too much moisture in the component is presented in question iv) according to the quantity and duration of the water impact. Finally, v) investigates the cause of excessive moisture ingress which leads to corresponding damage.

2.3 Systematization Results Case Studies

The systematization of damage mechanisms and their consequences is described in detail in the final report of the research project TallFacades (ibd.). The generally valid damage mechanisms are not discussed in detail, neither are the direct consequences, since both can be read in the report on TallFacades. In TallFacades the focus of the investigation was on moisture damage in the building envelope and the effects of the weather as a major cause and it has already been recognized in TallFacades that there are major risks for moisture damage inside buildings. These were only cursorily surveyed and the specific damage mechanisms were not dealt with either. As with the damage in the building envelope, the nature of the specific effects on internal components and the resulting indirect consequences in the building are explained in more detail. From this, initial findings on typical damage events will be summarized.

3 Results

3.1. Damage Incidents Inside

The evaluation of the results from the investigated case studies produces the following impact categories: Category of the size of the moisture input over time and the cause of the moisture input. The extracted subcategories are further specified in the explanations in the unexpected events in the interior of the building, mostly of great magnitude, which can be traced back to technical systems and which are paired with constructive characteristics. The primary damage mechanism is capillary water absorption. Another mechanism to be observed is the convective moisture input through unsealed components such as shafts or floor levels between different areas of use. The diffusive moisture input is hardly relevant. In addition, the loss of insulation properties and thus a building up effect of the humidity is not to be recognized in the present cases and unlikely, since the constructions lie predominantly in the interior and insulations are not necessary. With the few construction elements to the outside climate these are either completely unsealed or they show holes, which make the penetration of liquid water possible, which represents an unacceptable deficiency from the outset.

3.2 Construction Status (t=0)

As described in Chapter 1, *CLT* floors are becoming more and more popular as lower construction heights are required compared to beam floor with identical bending stiffness. However, with *CLT* floors, it is not possible to easily distort installations at the structural level. These must be installed in separate levels either above or below the *CLT* floor. This is different for beam floors, where pipes can also be routed between the beams, see Figure 1.

3.2 Unplanned Event = Damage (t=1 ... n)

Moisture damage is one of the most frequent types of damage in residential buildings. These are often caused by leaking pipes or design faults. In beam floor, the escaping water often migrates through the construction level and escapes at the underside and thus becomes visible quite quickly. Furthermore, the water inlet and outlet areas of beam floors are usually close to each other. If water is exposed to a closed surface such as *CLT*, the water moves to the deepest point of the structure where it collects, see Figure 2. Since the surface is usually closed and the water cannot pass unhindered through the construction level, it sometimes remains lying there for a long time and searches its way downwards along paths that are sometimes difficult to follow. Thus the place of the moisture entry and the place of the exit may be far apart. Furthermore, it can take a very long time until such moisture damage is detected. As an example the *CLT* floor of a hotel is shown here, where a damaged water connection was not found over 8 years, see Figure 3. From the once 220 mm thick *CLT* floor 100 mm have been decomposed by wood-destroying fungi. The floor structures originally did not suggest any damage, as the top of the floor and the underside of the floor were dry. In addition, the location of the maximum damage was several meters away from the cause of the damage (leaky water connection). Due to the very low construction height, the renovation was very costly. Auxiliary steel structures have to be used to replace the damaged *CLT* elements with new ones and to support the roof structure above.

Table 2. Categories of exposure and related reasons.

Scale & Time category	Reason	Explanation
large & suddenly	pipe burst, household applicance burst, sprinkler	- (unexpected event)
small & long-term (water source related)	pipe and fitting leakage, pipe connections	material damage, (quality management)
	complex and integrated installations	water leakage not detectable, continuous water supply (leakage)
small & long-term (construction technology related)	type of structures in mid-rise housing	large areas with flat slabs, thick slab dimensions, seldom beam structures
	ducts crossing different units without necessary barriers (air stops)	missing awareness & planning, expensive task, complex on-site work, no quality management, difficult maintenance
	type of indoor climate conditions	warm, humid, no or limited air-flow, no dry-out capacity

4 Discussion

4.1 Construction Technology Overview

The danger of moisture damage occurs wherever liquids are transported through pipe systems. Therefore, it is important to consider how structural measures can look like in order to avoid moisture damage as far as possible or to detect it as early as possible. If possible, pipes should be routed in such a way that they can be inspected. In addition, particularly vulnerable areas of

buildings such as wet rooms (bathrooms, toilets, washrooms, kitchens) should have special sealing systems that draw the user's attention to moisture damage and, for example, have overflows.

4.2 Outlook Repair (t=m)

If damage to the load-bearing structure is known, it must be repaired. In the case of the beam floor, the repair of damaged beams is relatively simple. In the simplest case, the damaged beams can be removed and replaced. Alternatively there are possibilities of lateral reinforcement by additional beams, construction materials or steel. As there is still space between the beams, this can be used for repair purposes. This is different for *CLT* constructions. Since the construction space is already completely occupied, *CLT* cannot simply be renovated or reinforced on the existing level. If a *CLT* floor cannot simply be replaced, complex constructions are often required to carry out the renovation. This is also reflected in the repair costs.

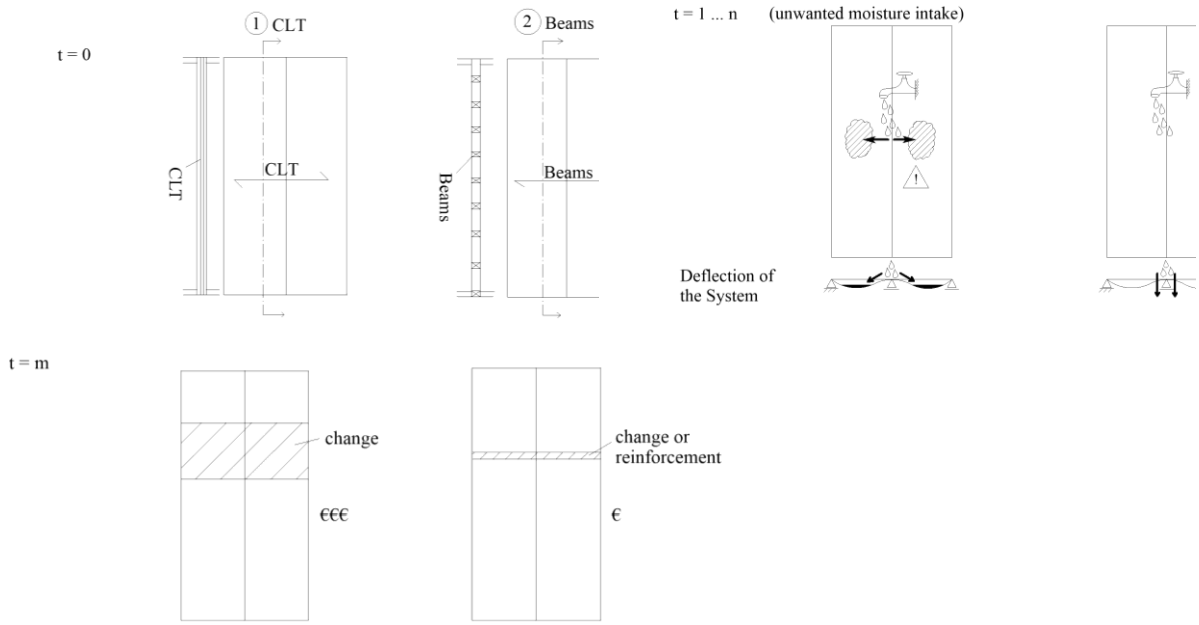

Figure 2. Timber floor systems 2-axial (left column) versus 1-axial during assembly t = 0, t = 1 …n with moisture intake and finally t = m with possible repair scenarios.

4.3 Outlook Monitoring

Since moisture leads to large damages in floor systems as discussed above, it is possible to set up appropriate monitoring systems. These can, for example, record the amount of water fed into and discharged from a building or room and issue a warning if the difference is too large. On the other hand, humidity sensors can also be installed directly at critical points. These humidity sensors would be particularly suitable for *CLT* floors, where water can wander along and is only discovered very late. This can be done by sensors placed close to the surface or in the wood.

5 Conclusion

The conclusions can be summarized as follows:

- Moisture damage with related wood decay inside buildings is a relevant problem,
- Such damages are difficult to detect because the damage mechanisms are acting slowly,
- Massive, planar structural components are particularly affected by slow decay mechanisms,
- Wood decay effects are mainly occurring due to defective water pipes on top of the floor.

In principle, the earlier an unexpected moisture penetration in timber constructions is detected, the smaller the damage and the lower the cost of restoration measures

Figure 3. Pictures of damaged *CLT* slab and wall elements in hotel room.

Acknowledgements

We want to acknowledge the support of T. Ihler and Dr. T. Linse who provided case studies from their professional expertise and additional we thank H. Bagehorn for the summary of the expert reports and the drawings.

ORCID

Stephan Ott, https://orcid.org/0000-0002-6760-869X
Patrik Aondio: https://orcid.org/0000-0002-7266-1292

References

Aondio, P. (2014). *Berechnung von Zylinderschalen aus Holz und Holzwerkstoffen unter Berücksichtigung der Spannungsrelaxation* [Dissertation]. Technische Universität München, München.

Ebner, G. (2017). Brettsperrholz in Europa: BSP-Produktion verdoppelt sich bis 2020. *Holzkurier*. https://www.holzkurier.com/holzprodukte/2017/06/brettsperrholz-produktion-in-europa---20162020.html (Dann werden 1,2 Mio. m3 in Europa produziert).

Kersten, C. (1926). *Freitragende Holzbauten: Ein Lehrbuch für Schule und Praxis* (2nd ed.). Springer Verlag.

Ott, S. Tietze, A. Boulet, S. Gradeci, K. Labonnote, N. Grynning, S. Noreen, J. and Pousette, A. (31.07.201´7). *Tall Timber Facades - Identification of Cost-effective and Resilient Envelopes for Wood Constructions (TallFacades): Final Project Report*. http://dx.doi.org/10.14459/2016md1422654

Ott, S. Tietze, A. and Winter, S. (2015). Wind driven rain and moisture safety of tall timber houses–Evaluation of simulation methods. *Wood Material Science & Engineering*, *10*(3), 300–311.

Pohl, K. A. (1934). Das Schalengewölbe als Holzkonstruktion. *Der Bauingenieur* (39/40), 381–384.

Tietze, A. Boulet, S. Ott, S. and Winter, S. (2016). Consideration of disturbances and deficiencies in the moisture safety design of tall timber facades. In J. Eberhardsteiner, W. Winter & A. Fadai (Chairs), *WCTE 2016 e-book: Containing all full papers submitted to the World Conference on Timber Engineering (WCTE 2016), August 22-25, 2016, Vienna, Austria*.

Z-9.1-354, Allgemeine bauaufsichtliche Zulassung AbZ Merk-Dickholz MDH, Dezember 1998.

XV International Conference on Durability of Building Materials and Components
DBMC 2020, Barcelona
C. Serrat, J.R. Casas and V. Gibert (Eds)

Pathologies of a Glass Building Envelope that Affect Durability and Comfort

Susana Santamaria-Fernandez[1], Arritokieta Eizaguirre-Iribar[2] and Xabier Olano-Azkune[3]

[1] Structural Safety Lab, Industry Area, Lab Services Division, TECNALIA, Basque Research and Technology Alliance (BRTA), Area Anardi 5, 20730-Azpeitia, Spain, susana.santamaria@tecnalia.com

[2] Fire Safety Lab, Industry Area, Lab Services Division, TECNALIA, Basque Research and Technology Alliance (BRTA), Area Anardi 5, 20730-Azpeitia, Spain, arritokieta.eizaguirre@tecnalia.com

[3] Fire Safety Lab, Industry Area, Lab Services Division, TECNALIA, Basque Research and Technology Alliance (BRTA), Area Anardi 5, 20730-Azpeitia, Spain, xabier.olano@tecnalia.com

Abstract. *The durability of materials used in buildings has been widely studied and, in many cases, there are standards to assess it. However, studies on how pathologies affect the durability and comfort of the building users are not so common. The aim of this article is to explain different pathologies of the building envelope, considering glass as its main element and to analyze the causes of those pathologies, agents involved, and how they have affected durability. For that purpose, different cases of pathologies were analyzed on-site, both during the construction process and during the final use of the building. The effects of the different pathologies were also assessed. In each case, the technical data sheets available of the materials involved and the information on the design and the expected performance of the constructive solution were compiled. In some cases, the pathologies had caused an irreversible damage, so, the solution had to be drastic; while in other cases, they were detected early enough to propose remedial actions without affecting the final durability of the building. After having analyzed the different cases, the agents causing the pathology or those responsible for it and the phase in which the pathology occurred were identified. As a result, remedial actions were proposed to avoid the generation of pathologies during the design, construction and maintenance processes that affect the durability of the building and their user's comfort.*

Keywords: *Glass, Pathology, Sealant, Coating, Durability.*

1 Introduction

Since the industrial breakthroughs that allowed massive, high-quality production of glass for building in the 1960s, large glazed buildings have proliferated and along with them their associated pathologies. Additionally, the improvement of thermal performance of insulated glass units (from now on IGU) due to the importance of energy efficiency have resulted in premature failures in several cases (Hubbs *et al.*, 2015). Accordingly, studies on failure cases have also increased in the literature in order to understand the reasons and effects of glass failures (Honfi *et al.*, 2014; Loughran, 2003).

The pathologies of a glazed envelope may be of different natures. Glass breakage is one of the most known failure and have been widely studied using qualitative and quantitative methods (Overend *et al.*, 2007). However, there are other pathologies (such as sealing failure, yellowness or delamination) that have a direct impact on the durability of the building, since they affect the

functionality of the building and/or the comfort of the users. It should be borne in mind that the pathologies in this building element usually have the added complexity that the number of materials and elements that form the envelope solution are many and of a very different nature and function.

The pathologies of a glass building envelope can occur due to the following causes: chemical incompatibility, manufacturing failure/error or because of a product is not suitable for its intended use.

In a building envelope there are a lot of different organic materials and it is complicated to verify the chemical compatibility between all of them. In extreme cases it is not even necessary that both materials are in physical contact for a failure to occur.

Manufacturing failures, such an incorrect choice of materials or unsuitable manufacturing times and conditions, may also create pathologies. They are common in innovative and unique products or solutions as there is no previous experience.

Finally, an unsuitable glass product can also cause pathologies. The product is correctly manufactured, but its intended use has not been taken into account and this leads to a pathology, i.e. not all glass products can be used in all situations. For example, the building envelope may be subject to adverse environmental conditions that were not considered at the design stage.

Therefore, a pathology can occur in any of the following stages of the building work: design, manufacturing, assembling, on-site execution and while it is in service. In this article, we will only focus on the failure mechanisms that appears in the service period. All these failures have a direct impact on the durability of the building envelope. On the one hand, directly on the durability of the materials and on the other hand, indirectly on the durability of the building since the thermal, acoustic and optical performance are affected.

In the following sections we will give notions and analyze each of them deeper through real case studies.

2 Sealing Failure

In this first case study, degradation in the form of a slump of one or both sealing barriers of a IGU is noted (Figure 1). This pathology occurs in an office building with a large glazed surface that is two years old. The construction of all the glazing in the building is unique, large-format double insulating glass units filled with argon gas formed both externally and internally by laminated glass.

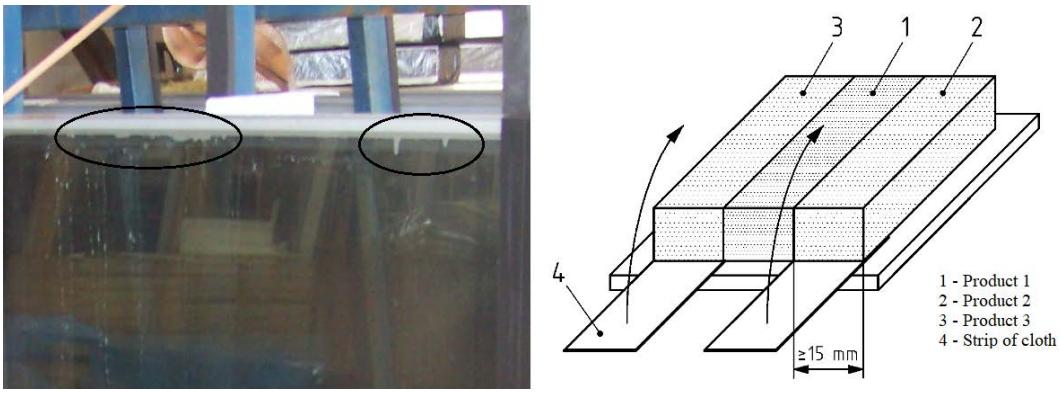

Figure 1. Sealant flowing (left) and test specimen for the chemical incompatibility test (right).

Degradation is detected in discrete areas of some of the IGUs. The concern with this pathology is firstly, the possible detachment of the outer sheet and its subsequent fall and secondly, if the property of thermal insulation is still preserved.

2.1 On-Site Inspection

When analyzing the units with pathology and their situation in the building, no pattern was detected due to their location in areas most exposed to solar radiation and therefore to a higher temperature. No water leakage was detected in the building envelope, i.e. the drainage system of the curtain wall seemed to be working correctly. All the glass units were exposed to equivalent UV radiation except for the differences due to the orientation of the building, however, no pattern showed that the failure was due to the orientation, height or degrees of exposure of those units and the pathology only appeared in some of them. Therefore, the influence of the environmental conditions such as temperature, humidity and radiation was dismissed early in the on-site inspection process.

When degradation of a sealant is observed, it is necessary to analyze which agents may be producing that degradation. Several IGUs were dismantled from the building and sent to the laboratory for a deep analysis, as only the on-site inspection couldn´t lead to a clear conclusion.

2.2 Laboratory Analysis

Once the samples were received in the laboratory, one of them was disassembled. Both sheets of glass were separated, and it was verified that the sealant was the one attacked. In this case, the degraded sealant was that of the first sealing barrier.

After this, all the polymeric products contained in the curtain wall were identified and gathered, such as sealants, adhesives, gaskets, supporting blocks... regardless of being in direct contact with each other or not. After this, sets of specimens containing adjacent materials were subjected to a chemical compatibility test using the UV method in accordance with section 7 of EN 15434:2007+A1:2010 Glass in building - Product standard for structural and/or ultra-violet resistant sealant (for use with structural sealant glazing and/or IGUs with exposed seals).

For performing the ageing, a laboratory weathering instrument ATLAS weather-ometer model Ci3000+ was used. The test specimens (Figure 1) were prepared with each two of the materials under study and they were exposed to UV solar radiation (by xenon lamps) for 504 hours and at 60 ºC temperature. After this UV exposure a peeling test was performed by means of strips of cloth or with cuts. A positive result in the test means that no visual discoloration appears and that no adhesive breakage occurs during the peeling tests.

After completing the compatibility test on the different combinations of adjacent materials, it was verified that the inner sealing barrier and the weathertightness gasket were highly incompatible.

Additionally, to this analysis, the building owner has made several measurements of the argon gas content of the glazing units, regardless degradation was present or not. Those measurements did not register a significant gas leakage on the units and a total detachment of the external glass pane has been dismissed up to now. The owner is performing regular controls to check the evolution of the pathology.

3 Luminous Transmittance Variation

The pathology studied in this second case occurred on two floors of a building that had not yet been occupied. There was no furniture or equipment that could alter human visual perception in any of the floors. However, a difference was noted by the owners in the perceived luminous radiation coming to the inside in each of the floors.

It was an office building with several floors where refurbishment was planned to be performed floor by floor. Refurbishment was integral, so affecting to the change of building envelope and interior furniture or equipment.

Refurbishment of the initial floor consisted in changing the carpentry and glazing of the complete envelope and after finishing there, works started in a new floor non adjacent to that first one.

First step of the pathology evaluation consisted in studying the type of glazing requested and checking delivery notes for the glazing of both floors. After that, an on-site visual inspection was carried out for a first approach. It was not so easy to visually quantify the difference in visual perception of the solar radiation, due to the great height gap between floors. This height gap means that shading due to adjacent buildings differs significantly and the influence on each floor is hard to quantify.

Therefore, the decision to remove two glazing units, one per each floor, and to measure their luminous and solar characteristics in the laboratory, was taken. IGUs were completely dismantled and luminous and solar transmittance and reflectance of all glazing panes were measured, in order to check whether those two glazing units were identical.

The IGU was composed by a laminated glazing (two annealed glass panes) on one side and a thermally toughened coated glass on the other side. For performing such measurements, a spectrophotometer UV-Vis-NIR Lambda 900 with a 150 mm integrating sphere was used.

As the laminated glass units were composed by annealed glass panes, they were cut into 100 mm x100 mm test specimens and transmittance and reflectance were measured from 280 to 2500 nm (Figure 2). In the case of thermally toughened coated glass though, it was not possible to prepare such test specimens and measurements were made with the equipment fully opened and the surrounding of the lab prepared to avoid external radiation getting inside.

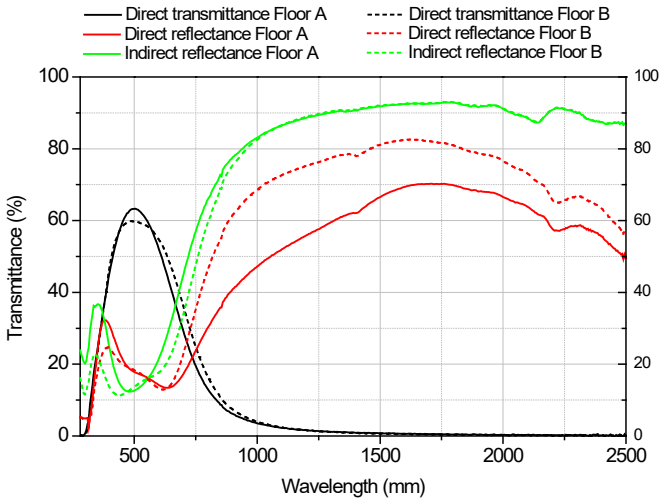

Figure 2. Transmittance and reflectance spectra of the coated glass.

After finishing the lab measurements, we noticed that laminated glass panes for both glazing units were the same but coated glass panes were not identical. Even though they were similar, differences were enough to be perceived by the human eye.

Considering manufacturing tolerances in the luminous/solar transmittance and/or reflectance, it could be concluded that both coated glass panes were not the same product.

Glass coatings are metallic oxides depositions that affect to the luminous, thermal or solar properties of the glass panes. Some coatings do not bear the thermal toughening process, so coatings are usually designed to provide similar properties, both for a toughened and a non-toughened version.

With the described measurements and collaboration from the manufacturer, we reached the conclusion that there was a manufacturing error, meaning that a coating not designed for the thermal toughening process, had been tempered by mistake.

4 Yellowness and Delamination

Pathologies are different for the sandwich products composed of glass and materials of different nature. An on-site inspection of the building of the third case showed colour change in glass products. Detachment of the exterior glass sheet was also detected in some cases. The inspection revealed that two types of glass solution with a similar external appearance had been used, one placed on the façade and the other on a sloping roof.

This case study refers to a semi-public building that has been in use for more than 10 years. For the study of pathologies, several affected units were disassembled and sent to the laboratory, along with stocked glass that had not been in use.

One of the solutions was a laminated glass unit consisting of an outer glass pane, an adhesive of an unknown nature, a marble pane, another adhesive similar to the previous one and an inner glass pane. The second solution was more complex and was composed of an exterior glass pane adhered to a pane of marble, which was in turn glued to an aluminium honeycomb panel.

Since the conditions of temperature and water presence are usually very different on the façade and the roof, it was concluded that ultraviolet radiation had been the main agent responsible for degradation. Nevertheless, the other agents –temperature and water in this case– had also played their role.

The durability of the material was evaluated by exposing two samples to ultraviolet radiation: a glass-marble-glass composition piece without defects and a glass-marble-honeycomb composition piece with colour degradation. Half of each piece was covered to avoid the degradation of that area. The test was carried out according to the procedure described in method A of section 7 of the standard EN ISO 12543-4:2011 Glass in building. Laminated glass and laminated safety glass. Part 4: Test methods for durability.

The test consisted in subjecting part of each panel to 2,000 hours of radiation. For this purpose, the panels were placed at 1,100 mm from 16 OSRAM ULTRAVITALUX lamps that formed an area of 1 m x 1 m. The radiation level on the panels was (900 ± 100) W/m^2. The radiation source used emits a spectrum similar to solar radiation and its spectral characteristics are as follows: UVB (280 - 315 nm) 3% ± 1%; UVA (315 - 380 nm) 8% ± 1%; Visible light (380 - 780 nm) 18% ± 1%; IRA (780 - 1400 nm) 24% ± 2%; IRB (1400 - 2600 nm) 27% ± 4%; and IRC (> 2600 nm) 20% ± 3%.

Three different areas of the exposed zone of each panel were selected and three luminous

reflectance measurements were made in each of them before and after the ageing. The luminous reflectance spectrum between 360 nm and 740 nm was measured using Minolta model CM2600d spectrocolorimeter in incidence d/8º. The colour coordinates L* a* b* for the observer at 10º and the illuminant D65 were calculated from the reflectance spectrum according to CIE76. Afterwards, the L* a* b* average colour coordinates of each area were determined and the ΔE*ab colour difference between the initial and final situation was calculated. The panels were also inspected for additional failures.

After 2,000 hours of exposure to simulated solar radiation, a considerable change in colour was observed between the exposed and unexposed areas of both panels (Figure 3). In the case of the glass-marble-glass composition, the difference in colour in the three selected areas before and after aging was less than 2.3 and in the case of the glass-marble-honeycomb composition the difference was greater than 2.3.

Figure 3. Exposed area of the panel (left) and unexposed area of the panel (right).

There is no requirement as to allowable colour difference after ultraviolet exposure for these innovative solutions. However, according to Sharma (2003) a colour difference ΔE*ab of approximately 2.3 is considered just noticeable difference. Therefore, in the case of the glass-marble-honeycomb composition the differences are clearly noticeable.

At the same time, the nature of the adhesives was analyzed by comparing the infrared spectra obtained by a Nicolet iS10 with the iD7 ATR accessory. Spectrum analysis was performed in transmittance mode, with 16 scans. Additionally, a thermogravimetric analysis was performed with a TG-DTA92 thermobalance in order to check the proportion of the different components. It is concluded that the nature of all adhesives used between glass and marble is the same regardless of the composition of the panel.

During the inspection of the building it was observed that the roof area was more degraded than the façade area. Even so, it is proved that in both cases the solution chosen was not suitable for the intended use. In order to avoid this pathology that directly affects durability, the suitability of both solutions should have been verified in the design implementation phase, considering the environmental conditions to which they would be exposed.

5 Interlayer Failures

In line with the latter case, bubbles, cloudiness, delamination or colour variations can be appeared in laminated glass compositions. The compositions of glass-glass with some other material embedded in the organic interlayer that joints both glasses are especially prone to failure. Therefore, those compositions are cases to be studied. In this regard, there are examples of the ageing behaviour of interlayer in the literature (Weller *et al.*, 2011).

The study of these kind of products should be carried out in the design implementation phase in order to validate the durability of the final product before being installed on site.

The procedures of the EN ISO 12543-4:2011 standard are used as a basis to assess the durability of this type of unique solution. This standard contemplates three possible exposures to attacks (high temperature, humidity and ultraviolet radiation) to which the laminated glass product must not present defects or must not vary its luminous transmittance.

5.1 High Temperature

In the case of high temperature exposure, test specimens are subjected to 100°C in an oven for 16 hours or by immersion in boiling water for 2 hours. In this way, it is checked whether the air between the two glasses was completely eliminated during the lamination process. It is not easy to eliminate this residual air when a metallic or plastic mesh type element is included in the interlayer and depending on its nature.

When this laminated glass is subjected to high temperatures, bubbles may appear in the mesh area. Different tests were carried out with different interlayers and it is easier to laminate this type of material with polyvinyl butyral intercalary. However, on certain occasions this type of interlayer is not suitable as it does not comply with certain mechanical aspects of the project and both the mechanical requirement and the durability must be assessed as a whole.

5.2 Humidity

In the case of exposure to moisture, the nature of the interlayers is decisive for studying the durability of the final product. Polyvinyl butyral and ionomer interlayers usually perform well in the presence of moisture, although this is not the case with liquid water. In the case of ethyl vinyl acetate interlayers, the humidity penetrates through the perimeter if this is not protected and, consequently, the interlayer become cloudier in the edges. If that laminated glass is no longer exposed to moisture, it migrates back to the outside and the laminated glass recovers its transparent appearance.

If there are embedded materials, special care must be taken if they reach the edge and how they react to moisture. The most obvious case is when the material placed between the two glasses is hygroscopic, since if the perimeter is not protected the moisture can migrate to the interior and produce a pathology that leads to lack of adhesion between materials, for example between marble and glass.

5.3 UV Exposure

The third attack on laminated glass to verify its durability refers to the ultraviolet exposure for 2,000 hours, after which the variation in luminous transmittance of the test specimens is limited. In this test, defects relating to delamination or bubbles do not usually occur, but the requirement for variation in luminous transmittance may not be met. The durability of laminated glass can also be verified by other standards, but the basis in all is similar. In the case of ANSI Z97.1-2015, for example, in addition to limiting the variation in luminous transmittance, the variation in yellowing index, the haze variation and the colour difference is also limited.

If there are additional embedded elements in the laminated glass, it must also be checked that there are no defects in that embedded material or in the interlayer, as it may happen that the two materials work well separately but not together.

Therefore, it is advisable to determine the variation of luminous reflectance or the variation of the colour coordinates of that embedded material –although the regulations do not contemplate it– in order to fully assess the degradation that the laminated glass is going to suffer.

6 Conclusions

- The pathologies of the glass building envelope may be different in nature and due to different causes, but they can be summed up in three main groups: chemical incompatibility, manufacturing failure/error or because of a product is not suitable for its intended use.
- After having analyzed the different cases, the design phase has been identified as the main stage of the building work in which the pathology could be avoided, followed by the product manufacturing phase. Accordingly, architects/project management or product manufacturers are the main agents causing the future pathology or those responsible for it. It should be added that a wrong assembly does not usually generate a pathology but contributes to its manifestation.
- As a result, two main remedial actions that can be implemented during the design, construction or maintenance processes are proposed to avoid the generation of pathologies that affect the durability of the building and their user's comfort. On the one hand, testing the selected products taking into account their intended use is the way to avoid failures before the construction of the building envelop. Most of the pathologies of the glass building envelope can be avoided if the durability of the chosen solution is verified during the design phase, considering the type of use and exposure to which the element will be placed. These previous checks are of particular interest in innovative or unique products or solutions, such as laminated glass products with organic interlayers. On the other hand, factory production controls became essential to avoid failures/errors that can occur in the product manufacturing stage.

ORCID

Susana Santamaria-Fernandez: https://orcid.org/0000-0002-0835-4757
Arritokieta Eizaguirre-Iribar: https://orcid.org/0000-0002-5651-9181
Xabier Olano: https://orcid.org/0000-0002-5647-1923

References

Honfi, D., Reith, A., Vigh, L.G. and Stocker, Gy. (2014). Why glass structures fail? – Learning from failures of glass structures. In Louter, Bos, Belis & Lebet (Eds), *Challenging Glass 4 & COST Action TU0905 Final Conference*. Taylor & Francis Group, London.

Hubbs, B. and Higgins, J. (2015). Glazing failures and ways to prevent them. In *30th RCI International Convention and Trade Show,* 149-160. San Antonio, Texas

Loughran, P. (2003). *Falling glass: Problems ans solutions in contemporary architecture*. Basel – Boston – Berlin: Birkhäuser – Publishers for Architecture.

Overend, M., De Gaetano, S. and Haldimann, M. (2007). Diagnostic Interpretation of Glass Failure. Structural Engineering International, 17 (2), 151-158.

Sharma, G. (2003). *Digital Color Imaging Handbook*. Boca Raton – London – New York – Washington, D.C.: CRC Press.

Weller, B. and Kothe, M. (2011). Ageing Behaviour of Polymeric Interlayer Materials and Laminates. In *Glass performance days, Conference Proceedings*. GDP, Tampere, Finland.

XV International Conference on Durability of Building Materials and Components
DBMC 2020, Barcelona
C. Serrat, J.R. Casas and V. Gibert (Eds)

Vinyl and Linoleum Floorings in Health Infrastructures: Maintenance Recommendations Based on Fieldwork Data

Cláudia Carvalho[1], Jorge de Brito[2], Inês Flores-Colen[3] and Clara Pereira[4]

[1] Civil Engineer, Instituto Superior Técnico, Universidade de Lisboa, Av. Rovisco Pais, 1049-001 Lisbon, Portugal, claudia.m.s.carvalho@ist.utl.pt

[2] Full Professor, CERIS, Instituto Superior Técnico, Universidade de Lisboa, Av. Rovisco Pais, 1049-001 Lisbon, Portugal, jb@civil.ist.utl.pt

[3] Associate Professor, CERIS, Instituto Superior Técnico, Universidade de Lisboa, Av. Rovisco Pais, 1049-001 Lisbon, Portugal, ines.flores.colen@tecnico.ulisboa.pt

[4] PhD Student, CERIS, Instituto Superior Técnico, Universidade de Lisboa, Av. Rovisco Pais, 1049-001 Lisbon, Portugal, clareira@sapo.pt

Abstract. *Resilient flooring is a popular choice in healthcare facilities, given its durability, comfort, low maintenance and cost. However, anomalies that occur in vinyl and linoleum floorings (VLF) often do not fulfil the expectations of a flooring with good performance and durability. In fact, studies show that pathological phenomena in VLF occur more often in the first years in service, indicating a probable connection with the design and execution stages. These stages are crucial to the quality of VLF, since, if not given adequate attention, pathological symptoms are likely to increase, hence decreasing service life. The authors developed an inspection, diagnosis and rehabilitation system for VLF in healthcare facilities, including: the classification of anomalies, their probable causes, in situ diagnosis methods and repair techniques; anomalies - causes, inter-anomalies, anomalies - diagnosis methods, and anomalies - repair techniques correlation matrices. The same system was validated through the visual inspection of 101 compartments in six health infrastructures in Lisbon, Portugal, and the respective descriptive statistics analysis of the collected data. That analysis showed, for instance, that the summed contribution of "design errors" and "execution errors" to "faulty welding joints" was 59%. Making an effort to change the situation diagnosed in the mentioned inspection sample, some design and application stages' recommendations are highlighted, according to the main sensitive issues of the flooring system during its service life. The sensitiveness of VLF highlights the importance of a suitable maintenance plan to minimise susceptibility to various degradation mechanisms.*

Keywords: *Building Pathology, Design and Execution Recommendations, Healthcare Infrastructures, Inspection System, Vinyl and Linoleum Floorings, Maintenance.*

1 Introduction

Apart from their durability, comfort, low maintenance and cost, vinyl and linoleum floorings (VLF) have ideal properties for health infrastructures, such as static control, slip resistance and antibacterial characteristics. However, without adequate maintenance of VLF, these properties can lose their effectiveness and anomalies may appear, hence decreasing performance levels and life expectancy.

With the recent rise of awareness towards decreasing the ecological footprint of the construction sector, recycling and using more environmental-friendly products have increased. In this context, considering life-cycle assessments, the expectation of extending the service life of the building elements brings new attention to maintenance programs (Ayçam *et al*., 2017; Harris and Fitzgerald,

2013). To avoid the development of pathological phenomena in VLF, an adequate maintenance program must be implemented from the beginning of their life-cycle, even before the application of the flooring. Therefore, it is of high importance to study the durability of VLF in sets of buildings in various locations, subject to different actions, in order to understand the pathology according to the characteristics of VLF. Inspections can be systematised and should be included in a maintenance plan, to prevent degradation of the flooring and its substrate.

Regarding the health sector, several studies emphasise the importance of adequate maintenance, in order to prevent hospital-acquired infections (Brito, 2017; Carling *et al.*, 2010; Harris *et al*., 2010; Harris and Detke, 2013; Harris, 2017). However, apart from maintenance manuals, there is hardly any literature regarding the maintenance of VLF.

An inspection, diagnosis and rehabilitation system for VLF in healthcare facilities (Carvalho *et al*., 2018) was developed, including: the classification of anomalies, their probable causes, in situ diagnosis methods and repair techniques; anomalies - causes, inter-anomalies, anomalies - diagnosis methods, and anomalies - repair techniques correlation matrices. This system was validated through the visual inspection of 101 compartments in six health infrastructures in Lisbon, Portugal, and the collected data were analysed with descriptive statistics (Carvalho *et al*., 2019).

The purpose of this paper is to gather the maximum of information available on "Maintenance Recommendations Guides" from several manufacturers, supporting the presented information with the statistical data acquired during the inspection and validation campaign of Carvalho *et al*. (2018, 2019). Regarding the design and execution stages of VLF, a complete analysis can be found in Carvalho *et al*. (2018, 2019).

2 Installation

Regarding the installation of VLF, the instructions given by the manufacturer must be strictly followed. However, there are some general preliminary actions that are necessary (Armstrong, 2019; Construction, 2013; Ovation, 2013; Polyflor, 2019; Tarkett, 2012), such as: (i) the materials must be kept in the room where they will be installed for at least 24 hours before application, at room temperature, to adapt to the ambient conditions; (ii) the layout should be designed for the lowest number of joints; (iii) the substrate must be dry, clean and level; (iv) if not level, a levelling screed must be applied; (v) before installation, the flooring must be unrolled, measured and pre-cut according to the areas to be coated to minimise waste; (vi) when cutting the material, extra 15-20 cm must be considered, depending on the length; (vii) after the installation of the flooring with adhesives, it will require a drying period, so it should not be walked on, washed or scrubbed within this period.

The preparation of the substrate is the same for vinyl and linoleum, whereas the application varies according to the type of adhesive and drying period. As for the preparation of the substrate, a 10 cm thick screed is usually applied. However, in rehabilitation works, due to ceiling height limitations, it is not always possible to ensure the minimum screed thickness. In such cases, a glass-fibre reinforced screed should be used. Also, on ground floors, a vapour barrier should be applied over the screed.

A levelling compound should be applied over the screed in two cross coats. Silica sand may be added to the second coat to improve adhesion. After drying, any loose sand is vacuumed, the floor is buffed and any dust is cleaned. Next, the coves, with varying heights, usually around 10 cm, are placed on the wall with contact glue. After drying, the pre-cut rolls are placed aligned

on the floor. The roll is folded in half and the adhesive is carefully applied on the floor (Figure 1a), with a specific comb, and on the coves, with a brush (Figure 1b). To avoid adhesive excess, it must be well spread. The drying period varies and depends on the weather, as humidity will delay drying. After drying, half the roll is placed on the adhesive and the press roller is used.

In order to be well laid, the VLF must be heated, to become flexible and follow the curve of the cove, and then compressed, to ensure adhesion. Therefore, a welding machine is used, without the welding tool, to make the vinyl more ductile (Figure 1c). If this step is skipped, detachment of the coving may occur. In the corners, 45º cuts must be made (Figure 1d) using a utility knife, which is also used to make straight cuts in vinyl. The curved-tip knife (banana knife) is used to remove excess vinyl on the cove, before fitting it to the upper housing.

Before welding the joints, a half-moon shaped tool is used to create the necessary spacing to place the string. The welding string is then applied using a welding machine or a robot. After the string has cooled, the excess must be removed either by using two tools separately (Figures 1e) or one tool, with a single cut. Then, a transition profile, made of PVC or aluminium, should be placed at each room entrance to ensure a smooth transition between different floorings of similar thickness. Optionally, a silicone string may be applied in the joint between the coving and the wall, to minimise the risk of possible water ingress.

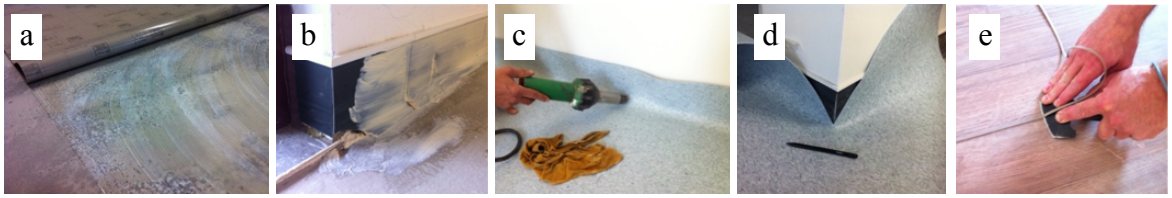

Figure 1. Installation of vinyl flooring: a) application of adhesive on the floor; b) application of adhesive on the footers; c) heating of the flooring; d) corner detail; e) removal of the string excess.

3 Maintenance

Floorings are selected for many reasons including colour, design and sometimes special properties, such as static control or slip resistance. Without regular maintenance, dust and soiling build up quickly, changing aesthetic properties and making special features practically useless. Moreover, dirt and soiling usually harbour bacteria, making the flooring a health hazard. Also, dust and grit underfoot can act as an abrasive, which, if left uncontrolled, will shorten the service life of the flooring, causing premature replacement.

Regular and well-planned maintenance keeps the flooring in pristine condition and can enhance its original appearance. It can also reduce wear and ultimately prolong the service life of the flooring. Adequate maintenance (daily/regular and periodic) may lead to high costs in the long run, but the lack of adequate maintenance means higher costs in the future with localised or total replacements. By defining a maintenance programme, real savings can be made without compromising appearance, hygiene and cleanliness requirements.

3.1 Factor Points to Consider

Before establishing a maintenance programme, some variables should be considered, as they affect the method, frequency and hence the cost of maintenance. So, the floor location, type and volume

of traffic, and the existence of dirt barriers should be taken into account. The location of the flooring in the building is one of the main factors, since entrance and reception areas will require more intensive and frequent cleaning than upper floors or low traffic corridors. The types of traffic, density and frequency in the given location also play an important part, since the density of traffic and type of footwear used in common corridors differs from the ones in operation rooms. The expectation of the client for a given location also plays an important part. If a high level of hygiene is required, like in the health department, the maintenance regime must be able to provide it. Finally, the type of cleaning equipment conditions the programme, since manual methods may be time-consuming in large areas and incompatible with the periodicity requirement. However, large machines used in confined spaces can take longer than manual methods (Polyflor, 2019). Additionally, the colour of the flooring is important, since, in general, light colours show soiling more easily and need more frequent cleaning, whereas dark colours more easily show loss of gloss.

3.1.1 Assessing the location

The first part of the maintenance programme process is to break down areas to be cleaned into a series of independent locations. Then, each one should be assessed before a particular maintenance strategy is employed to provide a clear indication as to where the effort and therefore the cost should be applied best.

The assessment should establish the following: type of cleaning; frequency of cleaning; cleaning products and equipment; the level of labour required; and time to be allocated. It is of high importance to regularly assess the different locations and be flexible about the planned maintenance. If the floor in a particular place needs more attention, then it must be ensured that it is addressed as soon as possible. On the other hand, if some areas seem over-maintained (*e.g.* with polish build-up in the non-walked on areas), then the maintenance level should be adjusted, but the situation must always be monitored to ensure it remains within control.

According to Carvalho *et al*. (2019), anomalies "staining/dirt/colour changes" and "brightness changes" resulted exclusively from causes in groups "environmental actions" and "maintenance errors", the latter represented only by "insufficient/incorrect cleaning of the flooring". In both "staining/dirt/colour changes" and "brightness changes", the predominant environmental causes were "biological action/chemically aggressive agents" (50% and 94%, respectively). Such frequencies were expected, as the use of inappropriate cleansers or spilling of aggressive substances, such as antiseptic drugs, causes blemishes, changes in brightness, or indelible stains.

3.1.2 Dirt barrier systems

The dirt barrier systems (DBS) play an essential role in VLF maintenance, as most dirt, grit and moisture are carried into a building by users. By reducing the amount of these elements that are brought in, not only would this cut the cost of its removal, but it would also cause less abrasive action on the flooring. Also, with less moisture, there would be less potential for slipping. An effective "passive" DBS has both scraping and absorbing qualities and is sufficiently large to perform these actions on both feet during normal walking (Polyflor, 2019).

An exterior and an interior mat should compose the DBS. The exterior scraper mat should be at least two paces long, set into a mat well and have enough height to allow grit to fall below. Inside the building, an interior grade combination of scraper and moisture mat of two to three metres long should be installed, as it removes most moisture and any fine abrasive particles.

However, to keep the effectiveness of DBS, they must also have adequate maintenance and be cleaned regularly; otherwise, they can increase the soil intake by creating a "soil reservoir" at the entrance of the building.

It is highly important to invest in high-quality floor mats for an extra layer of protection. The mats should be placed at entrances and exits to collect and trap corrosive substances that can be tracked in, such as dirt, sand, oil, grit, asphalt, among others.

3.2 Types of Maintenance

The best way to maintain the product characteristics for long-term use is to perform regular cleaning and proper maintenance. In this context, two factors contribute to the decrease of a VLF life-cycle: the lack of maintenance or an inadequate one. The first scenario includes the permanent accumulation of dust, loose dirt and other corrosive materials (such as hand disinfectant). The second scenario includes the use of aggressive cleaning agents, which remove the superficial protection barrier of these floorings, or excessive waxing.

According to Harris (2017), the most common resilient floorings used in patient rooms are rubber, linoleum and vinyl roll and tiles. Tiled vinyl is considered to be the most durable and cost-effective at initial costs, though it requires continuous maintenance at high long-term costs. As for vinyl roll, it is less stable and durable than tiles, but its welding joint mitigates the risk of contamination of the bedding layer. Finally, linoleum derives from natural resources, having antistatic and antimicrobial constituents. However, it is susceptible to water damage, usually requiring a surface protector that inhibits antimicrobial properties.

Before the flooring installation, the site must be adequately cleaned, otherwise some anomalies may arise immediately. Therefore, all loose dirt, dust and grit must be removed by mopping, sweeping or vacuuming. Also, all traces of adhesive on the surface of the flooring must be removed.

Harris and Fitzgerald (2015) identify the procedures for adequate maintenance of resilient floorings exposed to heavy traffic in healthcare facilities. Daily cleaning should be performed with a dry and wet mop; weekly, localised cleaning; quarterly, scrubbing and polishing cleaning; and semi-annually a surface protector should be applied.

According to Carvalho *et al*. (2019), anomalies "scratches/wear", "staining/dirt/colour changes" and "faulty welding joints" occurred in more than half of the inspected floorings. The most frequent anomaly was "scratches/wear", which was expected considering how easy it is to scratch a VLF (Douglas, 2011), since careless dragging of equipment is enough to leave a scratch, and the wheels of most trolleys have inadequate or worn-out material. The second most frequent anomaly is "faulty welding joint". The absence or deficiency of the welding joint, allied with inadequate cleaning, creates a singularity where water may enter, triggering detachment of the flooring. This shows the importance of timely maintenance interventions at welding joints to guarantee the expected service life of the VLF. In general, dirt can be eliminated by cleaning, whereas for indelible stains and colour changes in linoleum floorings, they can only be removed by stripping. In vinyl or recent linoleum floorings, they can be removed by polishing. In these cases, the VLF is only replaced when the affected area is of exceptional aesthetic value.

As for the location of anomalies, in some situations, a specific type of anomaly is predominant. For example, anomaly "scratches/wear" is often seen in poorly executed transition areas or at the rooms' entrance (Figure 3a and b). It is also the case of anomaly "brightness changes", which often occurs immediately below the alcohol-based disinfectant dispensers (Figure 3c).

According to Carvalho *et al*. (2019), there are some repair techniques that should be adopted in the maintenance program, according to the different types of anomalies detected in the regular flooring inspections. For example, the application of a surface protector is a technique widely used for scratches/wear, staining/dirt/colour changes and brightness changes, to reduce its aesthetic impact by smoothing the surface. When scratches exist, partial or total replacement of the flooring should only take place when the area has a high aesthetic value. Stripping is a technique exclusively used in linoleum floorings, being less associated with stains than with brightness changes. In some cases, the floorings are cleaned and waxed regularly, but stripping is only partial and not in the required timings, often resulting in alternated areas with different wax thicknesses, as seen in Figure 3d.

Figure 2. Anomalies: (a) scratches; (b) wear; (c) brightness changes; (d) brightness changes on a linoleum flooring due to inadequate maintenance.

Anomaly prickles/punctures was only not associated with repair techniques "glue injection" and "repair of anomalies in footers". The application of the repair techniques depends on the area affected by the anomaly. For small areas, cleaning and applying a sealant or a welding string is sufficient. For linoleum floorings, they can be stripped, or the punctures can be covered with a mixture of white glue and linoleum scraps.

3.2.1 Routine/regular/daily maintenance

The following recommendations are provided as guidelines. However, the periodicity of each operation depends on the amount and type of traffic, the provision of adequate DBS and the maintenance equipment available.

For daily vinyl cleaning, the flooring should be mopped, swept or vacuumed to remove dust and loose dirt. Stains can be easily removed with detergent and subsequently rinsed. If required, to remove persistent black marks, the floor may be damp mopped with a neutral cleanser—the label must always be read to ascertain suitability, and the manufacturer's instructions for application must be followed. It is highly important that the flooring is washed with nonabrasive cleaners. When rinsed, the floor must be allowed to dry. All smooth floorings can be slippery when wet. If necessary, the floor may be buffed with a dry soft mop or cloth. The appearance of the flooring should be assessed weekly.

Once a week or, if necessary, more often, the floor should be cleaned with a damp cloth or a mop soaked in warm water and a neutral cleaner. Light scuffing is executed with a buffing machine with a suitable dry and clean pad.

3.2.2 Periodic maintenance

The appearance of the floor should be periodically assessed. If the floor has dirt build–up, it should be machine scrubbed with a scrubber dryer fitted with a suitable clean pad, using neutral detergent.

Then, it should be rinsed thoroughly and allowed to dry. To restore the finish, it may be dry buffed.

Regarding the stripping and resealing of a linoleum floor, according to Gorrée *et al*. (2002), stripping should be done six times in 20 years (approximately every three years) in public buildings.

3.2.3 Preventive measures

To prevent damage, some precautions should be taken. For example, spills should be cleaned immediately, since the longer spilt materials are left on the floor, the higher the risk of irreversible staining. Regarding the furniture, it should always be lifted and carried, instead of pushed, pulled, or dragged over the floorings. According to Carvalho *et al*. (2019), cause "dragging of equipment" was the most frequent, being indicated in approximately 28% of anomalies, probably due to a close correlation with the occurrence of scratches. This cause represents the use of improper wheel material, which easily leaves a mark in VLF, or moving of furniture without adequate protections. Furthermore, heavy furniture or appliances that are not moved often should be equipped with flat, non-staining floor protectors, to avoid indentation from heavy furniture or sharp furniture feet. The heavier the furniture, the wider the protectors should be (Seeley, 1985). Vacuum cleaners with beater bars should be avoided, as they can damage the flooring. Black rubber wheels and rubber feet can cause discolouration. Strong detergents must be avoided, as they may wear the protective layer. Cleaning and maintenance training courses from manufacturers, including both practical and theory work, should help facilities maintenance staff get the best from vinyl floorings by using adequate cleaning methods and products (Polyflor, 2019; Tarkett, 2012).

4 Conclusions and Future Developments

Several difficulties were found during the research, mainly the scarce scientific literature about VLF, both in general and in health infrastructures. Therefore, the recommendations stem from different sources, namely supplier guidelines, site assessment and statistical evaluation from site assessments (Carvalho *et al*., 2018 and Carvalho *et al*., 2019).

This paper contributes to the dissemination of knowledge on the maintenance of VLF, specifically in health infrastructures, as the presented information may be used to improve and increase the effectiveness of maintenance plans. Additionally, it may also be useful at the application stage, as some defects with substrate origin, for instance, may be prevented with adequate cleaning of the substrate. Moreover, at the design stage, a maintenance manual or a concise user's manual of the flooring may be developed and delivered to the client. Furthermore, the consideration of efficient dirt barriers, with scraping and absorbing qualities, should take place early at the specification stage, and not afterwards, when there are rarely enough funds or space to do the job correctly.

To avoid defects at the application stage, several measures may be implemented, always starting with the use of specialised labour and better communication between contractors. Specialised labour is more likely to apply floorings according to the best practices, hence avoiding defects caused by execution errors. In terms of maintenance, regular cleaning is more beneficial and cost-effective to the flooring than occasional heavy cleaning.

Regarding future developments to increase the life cycle, cleaning and maintenance training courses given by the manufacturers should be mandatory. It is essential to train the cleaning staff since inadequate maintenance directly contributes to accelerating the degradation of VLF. Moreover, regular inspections are also necessary to ensure the quality control of the VLF application. It is

also expected that the efficiency and effectiveness of maintenance in VLF increase if the inspection system proposed by Carvalho *et al*. (2018) is used. In the future, to improve the system, a wider inspections campaign should be made.

Acknowledgements

The authors gratefully acknowledge the support of the CERIS Research Institute; IST, University of Lisbon; and FCT, Foundation for Science and Technology, through the BestMaintenance Project PTDC/ECI-CON/29286/2017.

ORCID

Cláudia Carvalho: https://orcid.org/0000-0002-0804-6594
Jorge de Brito: https://orcid.org/0000-0001-6766-2736
Inês Flores-Colen: https://orcid.org/0000-0003-4038-6748
Clara Pereira: https://orcid.org/0000-0002-9535-1844

References

Agence Qualité Construction (2013). Fiche no F1 - Décollement de revêtements de sols souples collés.

Armstrong: "Luxury Vinyl Tile a & plank maintenace recommendations" (website: https://www.armstrongflooring.com/pdbupimages-flr/205123.pdf, visited on October 2019);

Ayçam, Í. and Yazici, A. (2017). Evaluation of operating room units within the context of green design criteria. In *GU J. Sci.*, 30, 1–15.

Brito, F. (2017). Controlo da contaminação de superfícies no meio hospitalar (Contamination control of surfaces in the hospital environment). *TecnoHospital*, 79, 10–11 (in Portuguese).

Carling, P.C. and Bartley, J.M. (2010). Evaluating hygienic cleaning in health care settings: What you do not know can harm your patients. In *Am. J. Infect. Control*, 38, S41–S50, doi:10.1016/j.ajic.2010.03.004.

Carvalho, C., de Brito, J., Flores-Colen, I. and Pereira, C. (2018). Inspection, diagnosis and rehabilitation system for vinyl and linoleum floorings in health infrastructures. In *J. Perform. Constr. Facil*, 32, 04018078.

Carvalho, C., de Brito, J., Flores-Colen, I. and Pereira, C. (2019). Pathology and Rehabilitation of Vinyl and Linoleum Floorings in Health Infrastructures: Statistical Survey. In *Buildings*, 9 (5), 116, doi:10.3390/buildings9050116.

Douglas, J. and Noy, E.A. (2011). Building Surveys and Reports, 4th ed.; Wiley-Blackwell: Chichester, UK, 203–204.

Gorrée, M., Guinée, J.B., Huppes, G. and Oers, L.V. (2002). Environmental life cycle assessment of linoleum. *Int. J. Life Cycle Assess*, 7, 158–166, doi:10.1007/BF02994050.

Harris, D.D. (2017). A material world: A comparative study of flooring material influence on patient safety, satisfaction, and quality of care. *J. Interior Des*. 42, 85–104; doi:10.1111/joid.12100.

Harris, D.D., Pacheco, A. and Lindner, A.S. (2010). Detecting potential pathogens on hospital surfaces: An assessment of carpet tile flooring in the hospital patient environment. In *Indoor Built Environ*. 19, 239–249, doi:10.1177/1420326X09347050.

Harris, D.D. and Detke, L.A. (2013). The role of flooring as a design element affecting patient and healthcare worker safety. *HERD-Health Environ*. Res. 6, 95–119, doi:10.1177/193758671300600308.

Harris, D.D. and Fitzgerald, L. (2013). A life-cycle cost analysis for flooring materials for healthcare facilities. In *J. Hosp. Adm*., 4, 92–100, doi:10.5430/jha.v4n4p92.

Lent, T., Silas, J. and Vallete, J. (2010). Chemical hazards analysis of resilient flooring for healthcare. *HERD-Health Environ. Res*., 3, 97–117, doi:10.1177/193758671000300209.

Ovation Interior Flooring Design Limited: "Care and maintenance instructions for vinyl floors", 1 (4) 2013-01-01 (website:http://www.ovationflooring.com/wp-content/uploads/2015/11/Oceanic_Maintenance_Info.pdf, visited on October 2019);

Polyflor: "Floor Care and Maintenace", Section 14 (website: https://www.polyflor.ca/maintenance-guides, visited on October 2019);

Seeley, I. H. (1985). Building Surveys, Reports and Dilapidations. Macmillan;

Tarkett: "Cleaning and Maintenace Guides" for iQ Range, Homogeneous compact vinyl, April 2012.

XV International Conference on Durability of Building Materials and Components
DBMC 2020, Barcelona
C. Serrat, J.R. Casas and V. Gibert (Eds)

A New Alkali-Silica Reaction (ASR) Mitigation Technology – Part I: Comparing with Li, Ca, Al Salts, and Densified Silica Fume

Frank Ong[1], **Michael Myers**[2], **Thomas Vickers**[3], **Jacki Atienza**[4], **Lesley Ko**[5] **and Paul Seiler**[6]

[1] Master Builders Solutions – Admixture Systems N.A. 23700 Chagrin Blvd, Beachwood, Ohio, 44122, United States, frank.ong@mbcc-group.com

[2] Master Builders Solutions– Admixture Systems N.A. 23700 Chagrin Blvd, Beachwood, Ohio, 44122, United States, michael.myers@mbcc-group.com

[3] Master Builders Solutions – Admixture Systems N.A. 23700 Chagrin Blvd, Beachwood, Ohio, 44122, United States, thomas.vickers@mbcc-group.com

[4] Master Builders Solutions – Admixture Systems N.A. 23700 Chagrin Blvd, Beachwood, Ohio, 44122, United States, jacki.atienza@mbcc-group.com

[5] Master Builders Solutions – Admixture Systems N.A. 23700 Chagrin Blvd, Beachwood, Ohio, 44122, United States, lesley.ko@mbcc-group.com

[6] Master Builders Solutions – Admixture Systems N.A. 23700 Chagrin Blvd, Beachwood, Ohio, 44122, United States, paul.seiler@mbcc-group.com

Abstract. *Alkali–silica reaction (ASR) is a major concrete durability problem. The occurrence of ASR results in significant maintenance and reconstruction costs to concrete infrastructures all over the world. Ever since Stanton (1940) discovered the expansive characteristics of ASR in 1940, there has been much speculation as to the cause and actual mechanism of expansion. Current market solutions are not always sustainable, such as hauling non-reactive aggregates or fly ash from long distance; or use of Li-based chemical admixture that is facing challenge of raw material's availability. The current article will present a patent pending technology which provides a commercial solution for mitigating the ASR. The ASR mitigating effect of this technology is compared with lithium, calcium, and aluminum salts, and densified silica fume.*

Keywords: *Alkali–Silica Reaction (ASR), Durability, Silica Fume, Metakaolin, $LiNO_3$, $Ca(NO_3)_2$, $Ca(NO_2)_2$, $Al(NO_3)_3$, Expansion, Slurry, Solution.*

1 Introduction

Since Stanton (1940) demonstrated that reaction between high-alkali cements and certain aggregates could cause disintegration of concrete, a large amount of research has focused on the alkali aggregate reaction. An annotated bibliography containing over 1300 references pertinent to the phenomenon of alkali silica reaction (ASR), was compiled by Diamond (1992). ASR has remained a subject of much research and discussion because of the necessity of employing marginal aggregates in many areas, as well as the limited availability of low alkali cement, class F fly ash, slag, and lithium. Szeles *et al.* (2017) estimated that by 2030, the supply of fly ash in the United States will be approximately 14 million tons, but the demand will exceed 35 million tons. Lithium-based chemical admixtures face limited raw material availability and

rising price. Tesla and other electric-vehicle makers dominate lithium consumption, a lightweight element that some call "white petroleum" for its use in lithium-ion batteries that power electric cars. 'In order to produce half a million cars a year…we would basically need to absorb the entire world's lithium-ion production,' Elon Musk said in March 2016 according the Wall Street Journal (2016).

Densified silica fume has been used to increase ASR resistance. Due to low volume demand, concrete manufacturers do not normally install a silo for densified silica fume. The two main issues of densified silica fume are: (1) it might cause ASR due to agglomeration (Pettersson 1992), and (2) densified silica fume in bags are difficult use in concrete manufacturing. Clearly, the concrete industry is looking for alternative chemical admixtures, which are easily dispensed into a central mixer or concrete truck in ready mix concrete or precast plants, for mitigating ASR.

Six pumpable products, which are three salt solutions and three slurries were selected in this study. The three salt solutions are Calcium Nitrate ($Ca(NO_3)_2$), Calcium Nitite ($Ca(NO_2)_2$), and Aluminum Nitrate ($Al(NO_3)_3$). The three pumpable slurries are based on densified silica fume, metakaolin, and Z silica fume (a by product from zirconia oxide manufacture). The technology of manufacturing these slurries is patent pending. A screening test method was developed based on ASTM C1567 (2018) to evaluate the ASR mitigating effects of these six products.

2 Experimental

2.1 Materials and Test Method

An ASTM C150 Type I/II portland cement with alkali content of 0.93% equivalent Na_2O was used throughout the study. The reactive aggregates are recycled borosilicate glass granules from Vitro Minerals. Commercial Solutions of $LiNO_3$, $Ca(NO_3)_2$, and $Ca(NO_2)_2$ were used. The $Al(NO_3)_3$ solution was prepared from analytical reagent grade of $Al(NO_3)_3 \cdot 9H_2O$.

2.2 Accelerated ASR Test Method

To evaluate the ASR mitigation effects of the selected materials, an accelerated test method based on ASTM C1567 (2018) was developed. The key for developing an accelerated ASR test method is to determine the pessimum amount reactive aggregate (borosilicate granules) in the mortar mixture. The pessimum amount of borosilicate is about 25% of total fine aggregate, which caused the maximum ASR expansion under the current test condition. Therefore, the screening test for evaluating potential candidates for ASR mitigation was designed as follows:

- Mortar with pessimum amount of reactive aggregate (25% borosilicate).
- Follow the ASTM C1567 test procedure.
- The expansion results are an average of four measurements.

3 Results and Discussion

3.1 Effects of $LiNO_3$, $Ca(NO_3)_2$, $Ca(NO_2)_2$, and $Al(NO_3)_3$ on ASR

The alkali silica reaction (ASR) is primarily one of OH^- ions rather than of alkali cations; nevertheless, the latter are of critical importance. Both sodium and potassium ions cause distress; lithium apparently not, and its presence tends to inhibit distress. In an attempt to find

a compound that would effectively inhibit ASR, McCoy and Caldwell (1951) carried out a vast number of mortar tests with a representative selection of many types of possible additive materials. The most significant facts that emerged from this study was that lithium compounds (LiCl, Li_2CO_3, LiF, Li_2SiO_3, $LiNO_3$, and Li_2SO_4), in some unexplained way, reduced mortar expansion. Even almost insoluble lithium salts, such as LiF, seemed to be beneficial. Ong (1993) demonstrated that these insoluble lithium salts, such as LiF and Li_2CO_3 were quickly converted to LiOH in pore solution of cement paste. Due to its high solubility in water, $LiNO_3$ has been commercially used as a chemical admixture for mitigating ASR. The mechanisms of ASR mitigating by $LiNO_3$ was recently studied by Feng *et al.* (2010) and Guo *et al.* (2019). The formation of Li-Si crystal (Feng 2010) or Li-Si amorphous structure (Guo 2019) act as barrier surface on the reactive aggregate surface and prevent ASR.

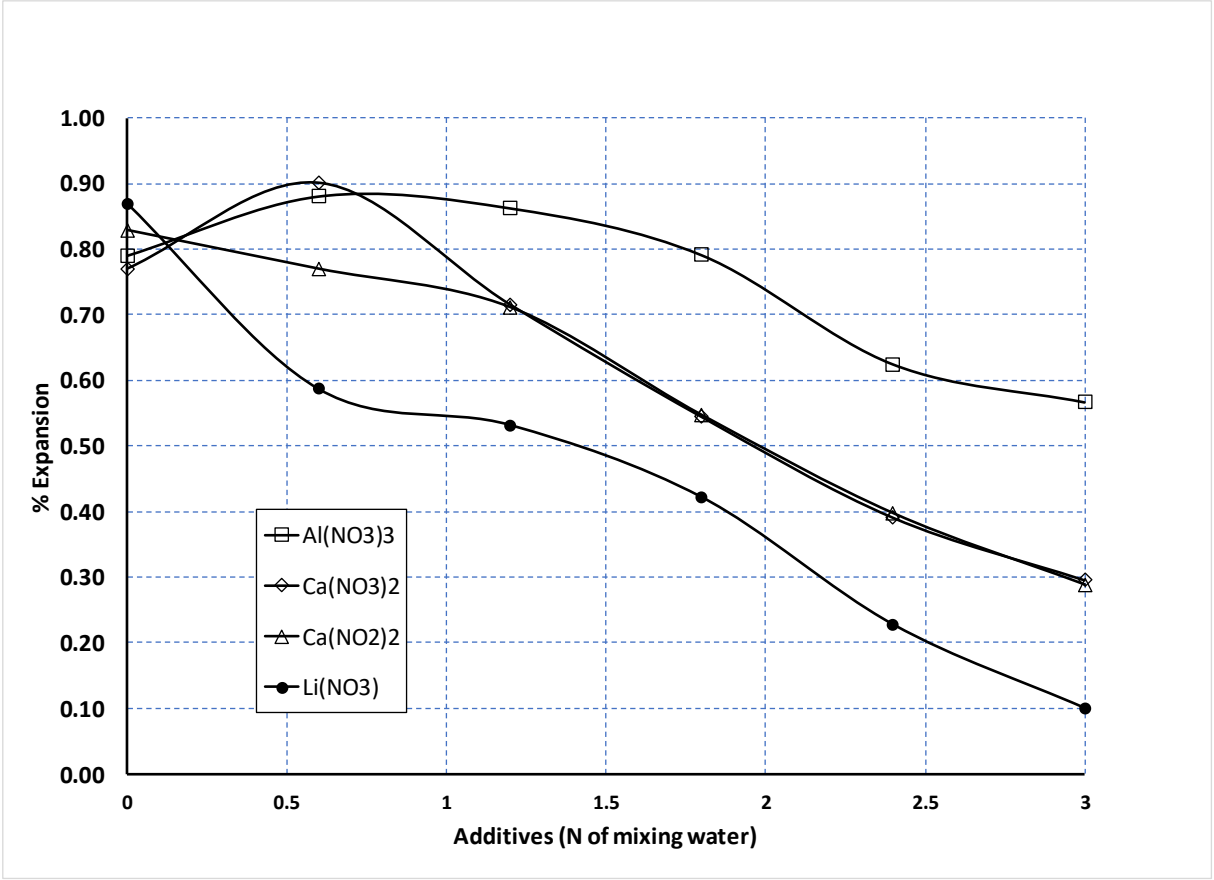

Figure 1. The comparison of ASR mitigating effects of $LiNO_3$, $Ca(NO_3)_2$, $Ca(NO_2)_2$, and $Al(NO_3)_3$.

The role of calcium ions in ASR have been investigated and debated for many years. Powers and Steinour (1955) suggested that ASR gel with a low-calcium content was expansive, while ASR gel with a high-calcium content was not expansive. Hudec and Banahene (1993) indicated that calcium ions mitigated ASR. Concrete with some free calcium ions in pore solution did not expand as much as one without. On the other side, many studies (Kawamura *et al.*, 1998, Aquino *et al.*, 2001, and Feng *et al.*, 2010) suggested that calcium ions are vital for

deleterious ASR expansion to occur. Without calcium ions, silica dissolves by OH^- and remains in solution (Thomas 1998).

Even though there are limited studies directly on the effect of aluminum on ASR, a good review on the beneficial effects of aluminum in mitigating ASR was provided by Rajabipour *et al.* (2015). The proposed explanations for Al benefits are:

- Reducing silica dissolution by Al adsorption on the surface of reactive aggregate.
- Removing OH^- ions by the formation of C-A-S-H.
- Removing $Ca(OH)_2$ to form calcium aluminate phase.

The above hypotheses were further investigated by studying the effect of $Al(OH)_3$ on ASR expansion with ASTM C1293 concrete prisms (Szeles *et al.*, 2017). It was found that the replacement of 20% cement with $Al(OH)_3$ significantly reduced silica dissolution and prevented ASR expansion.

The ASR mitigating effects of lithium, calcium and aluminum salt solutions were compared at five dosages: 0.6, 1.2, 1.8, 2.4, and 3.0 N of the initial mixing water. Figure 1 compares the ASR mitigating effects with different salts, at 14-day expansion as a function of additive normality of initial mixing water. The results in Figure 6 are summarized as following:

1. $LiNO_3$ solution has the most ASR mitigating effect in term of expansion reduction, among the four salt solutions tested. The addition of 0.6N of $LiNO_3$ significantly reduced ASR expansion, however this dosage was not enough to suppress the ASR. The 14-day expansion was still 0.59%. With increasing dosage of $LiNO_3$, ASR expansion was continuously reduced. At the highest test dosage of $LiNO_3$ investigated (3.0 N), the 14-day expansion was reduced to 0.10%.
2. At higher dosages (1.2N), the effectiveness of ASR mitigating with $Ca(NO_3)_2$ and $Ca(NO_2)_2$ are almost identical. With addition of 3N of Ca^{2+}, the 14-day expansion was still 0.3%, which is much higher than the 0.1% limit.
3. $Al(NO_3)_3$ solution has a slight ASR mitigating effect at dosages higher than 1.8N, and causes increased ASR expansion at lower dosages.

3.2 Effects of Silica Fume and Metakaolin Slurries on ASR

Silica fume is an ultrafine powder collected as a by-product of the silicon and ferrosilicon alloy production with a very light bulk density of 130 kg/m^3. Densified silica fume is produced by treating silica fume to increase the bulk density up to a maximum of about 400 to 720 kg/m^3. This increase in bulk density is usually accomplished by tumbling the silica fume particles in a silo, which causes surface charges to build up. One harmful consequence of the densification is that significant contents of undispersed grains of the order of several hundred microns are found in cementitious materials treated with densified silica fume (Diamond 1997). The grain can react with OH^- which may give rise to ASR distress. The agglomeration of silica fume particles is illustrated in the low and high magnification SEM images shown in Figure 2. At low magnifcation, the silica fume was clustered in grains of a few microns to several hundred microns, as shown in the left side image in Figure 2. The original size of the silica fume particles were in the range of a few nanometers to several hundred nanometers, as shown in the high magnification image on the right side of Figure 2.

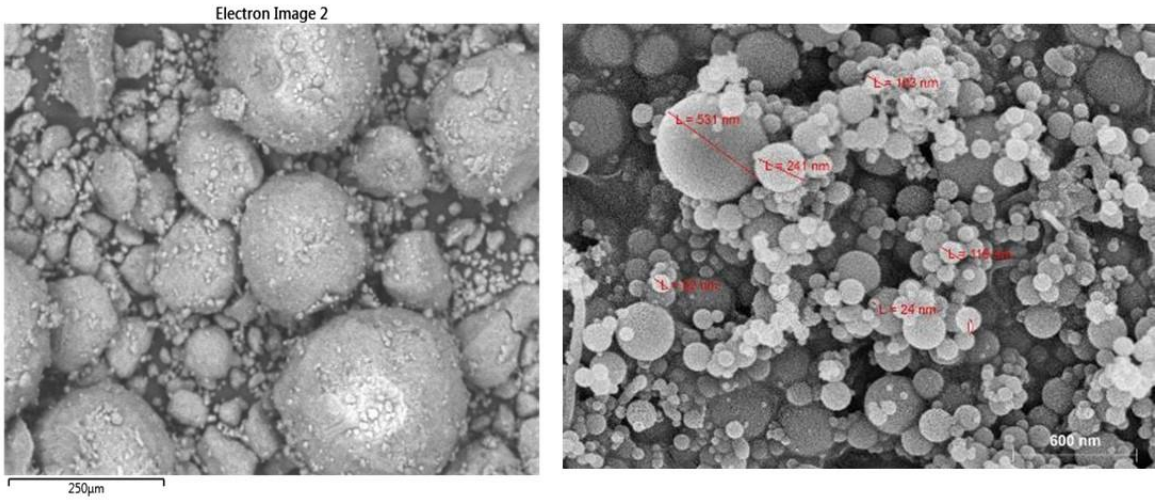

Figure 2. The SEM images of densified silica fume with low and high magnifications.

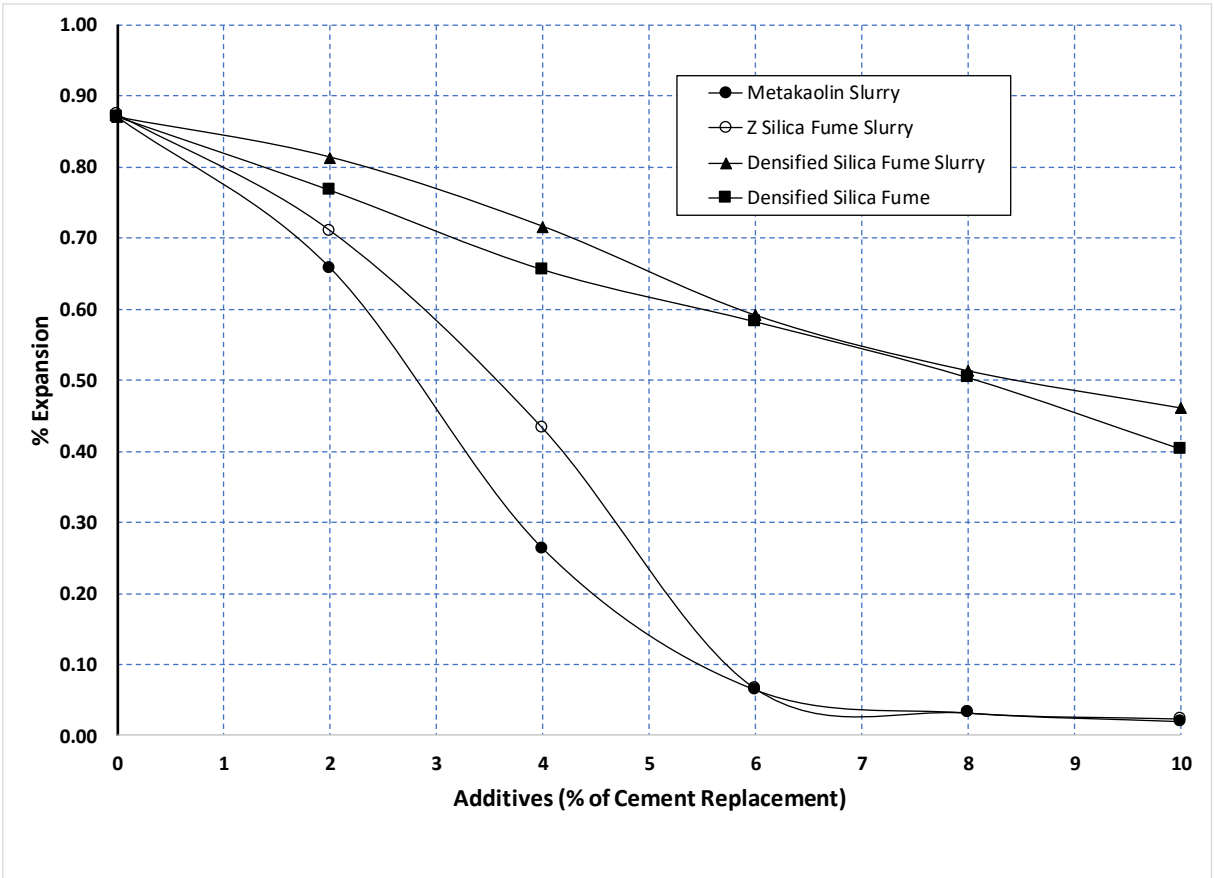

Figure 3. The comparison of ASR mitigating effects of different slurries and densified silica fume.

A direct comparison of the ASR mitigating effects of densified silica fume and the three slurries, at 14-day expansion, as a function of additive percentage by weight of cement replacement, are compiled in Figure 3. The results in Figure 3 are summarized as following:

1. Densified silica fume has the lowest ASR mitigating effect in term of expansion reduction, among the four products tested.
2. Converting densified silica fume to a slurry form only slightly improves the ASR mitigating effect.
3. Metakaolin and Z silica fume slurries have almost identical ASR mitigating effect. When the dosages of both slurries were increased to 6% (dry basis), the ASR was almost stopped, resulting in only 0.07% expansion at 14.

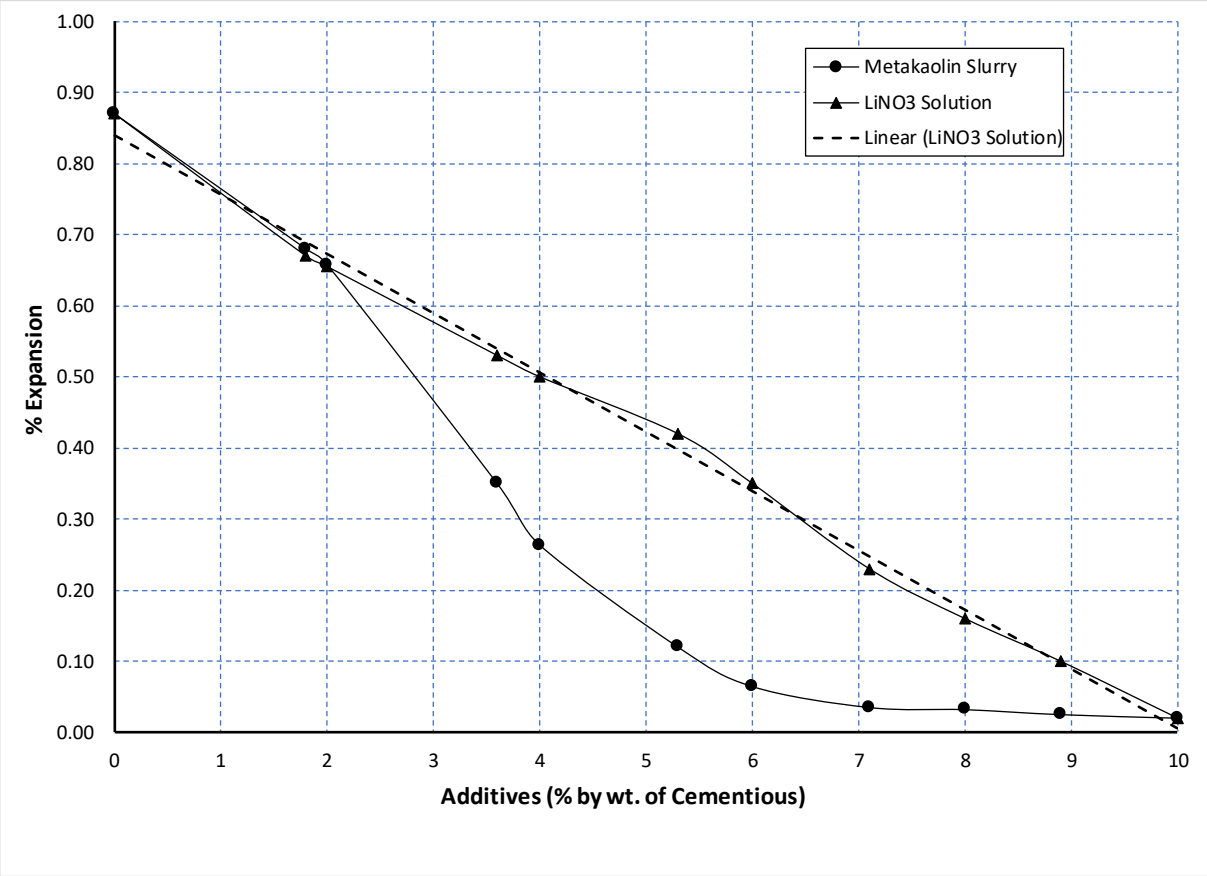

Figure 4. The comparison of ASR mitigating effects of $LiNO_3$ solution and metakaolin slurry.

The ASR mitigating effects of $LiNO_3$ solution and metakaolin slurry are compared in Figure 4. Dosages are expressed as percentage of total cementitious materials on a dry basis. The results in Figure 4 are summarized as following:

1. At low dosages (less than 2%), both $LiNO_3$ solution and metakaolin have similar ASR mitigating effect.
2. The reduction of ASR expansion by $LiNO_3$ solution is increased almost linearly with increasing dosage. To achieve a 14-day expansion less than 0.1%, the dosage of $LiNO_3$ exceeded 8.9% by weight of cement in the current testing condition, whose soak solution is not buffered with $LiNO_3$.

3. At a dosage greater than 2%, the reduction in ASR expansion by the metakaolin slurry is accelerated away from linear. A metakaolin dosage of 6% by weight of total cementitious materials is enough to suppress the ASR.

4 Conclusions

Due to a critical shortage of lithium raw material and difficulty with using densified silica fume, an effort was made to develop an alternative chemical admixture for mitigating ASR. Six dispensible materials were tested as potential candiates to replace $LiNO_3$ and densified silica fume. Based on the results of ASTM C 1567 expansions of mortar bars, the following conclusions can be made:

- For salt solutions, $LiNO_3$ is the best choice for ASR mitigating.
- Solutions of $Ca(NO_3)_2$ and $Ca(NO_2)_2$ have the same ASR mitigating effect, but are not effective enough to stop ASR. Therefore, $Ca(NO_3)_2$ or $Ca(NO_2)_2$ solution itself can't not be the candidate to replace $LiNO_3$ as chemical admixture for mitigating ASR.
- $Al(NO_3)_3$ solution has a weak ASR mitigating effect and a negative effect on workability. It will not be recommended as chemical admixture for mitigating ASR.
- The densified silica fume slurry has only slighly better ASR mitigating effect than densified silica fume. The slurry manufacturing procedure was unable to break-down clustered silica fume particles.
- Both pumpable slurries of metakaolin and Z silica fume have an excellent ASR mitigating effect.

ORCID

Frank Ong: http://orcid.org/0000-0003-4018-8346

References

Aquino, A., Lange, D.A. and Olek J. (2001). *The influence of mekakaolin and silica fume on the chemistry of alkali-silica reaction products*, Cement & Concrete Composites, 23, pp. 485-493, 2001.

ASTM C1567 (2018). *Standard test method for determining the potential alkali-silica reactivity of combinations of cementitious materials and aggregate (accelerated mortar-bar method),* Annual Book of ASTM Standards, Vol. 04.02, pp. 816-821, 2018.

Diamond, S. (1997). *Alkali silica reaction – some paradoxes*, Cement and Concrete Composites, pp. 391-401, 1997.

Diamond, S. (1992). *Alkali aggregate reactions in concrete: an annotated bibliography 1939-1991*, SHRP-C/UWP-92-601, 465 pages, 1992.

Feng, X., Thomas, M.D.A., Bremner, T.W., Folliard, K.J. and Fournier, B. (2010). *New onservations on the mechanism of lithium nitrate against alkali silica reaction (ASR)*, Cement and Concrete Research 40 pp. 94-101, 2010.

Guo, S., Dai, Q. and Si, R. (2019). *Effect of calcium and lithium on alkali-silica reaction kinetics and phase development*, Cement and Concrete Research 115, pp. 220-229, 2019.

Hudec, P.P. and Banahene, N.K. (1993). *Chemical treatments and additives for controlling alkali activity*, Cement & Concrete Composites 15, pp. 21-26, 1993.

Kawamura, M., Noriyuki, A. and Terashima, T. (1998). *Mechanisms of suppression of ASR expansion by fly ash from the view point of gel composition*, The Sidney Diamond Symposium, pp. 277-284, 1998.

McCoy, W.J. and Caldwell, A.G. (1951). *New approach to inhibiting alkali-aggregate expansion*, Journal of ACI, May 1951, Vol. 12, No. 1, pp. 96-103.

Ong, S. (1993). *Studies of steam curing and alkali hydroxide additions on pore solution chemistry, microstructure and alkali silica reations*, Ph.D. thesis, Purdue University, 1993.

Pettersson, K. (2017). *Effects of silica fume on alkali-silica expansion in mortar specimens*, Cement and Concrete Research, 22(1), pp. 15-22, 1992.

Powers, T.C. and Steinour, H.H. (1955). *An interpretation of some published researches on the alkali-aggregate reaction Part I, the chemical reactions and mechanism of expansion*, ACI Journal, Vol. 26, No. 6, pp. 497-516, 1955.

Rajabipour, F., Giannini, E., Dunant, C., Ideker J.H. and Thomas, M.D.A. (2015). *Alkali-silica reaction: current understanding of the reaction mechanisms and the knowledge gaps*, Cement and Concrete Research 76 pp. 130-146, 2015.

Stanton, T.E. (1940). *Expansion of concrete through reaction between cement and aggregate*, Proceedings, ASCE, Vol. 66, 1940, pp. 1781-1811.

Szeles, T., Wright, J., Rajabipour, F. and Stoffels, S. (2017). *Mitigation of alkali-silica reaction by hydrated alumina*, Journal of the Transportation Research Board, No. 2629, 2017, pp. 15-23.

Thomas, M.D.A. (1998). *The role of calcium in alkali-silica reaction*, The Sidney Diamond Symposium, pp. 325-331, 1998.

Wall Street Journal. (2016). https://www.wsj.com/articles/how-lithium-defied-the-global-commodities-rout-1462450790, 2016.

XV International Conference on Durability of Building Materials and Components
DBMC 2020, Barcelona
C. Serrat, J.R. Casas and V. Gibert (Eds)

An Experimental Evaluation of the Thermal Performance of Felt Type Vegetated Facade System

Elif Özer Yüksel[1] and Nil Türkeri[2]

[1] Department of Architecture, Faculty of Architecture, Gebze Technical University, Kocaeli, Turkey, e.yuksel@gtu.edu.tr

[2] Department of Architecture, Faculty of Architecture, İstanbul Technical University, Kocaeli, Turkey, sahal@itu.edu.tr

Abstract. *Vegetated facade systems (VFS) have been used as green building envelope systems in recent years. Using VFS for ecological strategies and evaluating thermal performance of these sytems are not a new concept. However, there is not any experimental study in literature which evaluates thermal performance of felt type VFS applied on an insulated existing building wall which is located in Csa climate during cooling and heating periods. Hence, an experimental study was conducted to measure thermal performance of felt type (type which used felt material as growing media) VFS in Kocaeli (under Csa climate). Test results indicate that in day time with high amount of solar radiation, felt type VFS decreased exterior surface temperatures of an insulated existing wall by maximum of 30°C. Also, interior surface temperatures of vegetated facade were lower than interior surface temperatures of reference facade with the maxiumum difference of 1.8°C. Although high differences between exterior surface temperatures of vegetated and reference walls were observed, there was no significant difference between interior surface temperatures of vegetated and reference walls. This is due to the fact that existing building exterior wall assembly includes 5 cm thickness expanded thermal insulation material which enchance thermal performance of brick wall. In addition, indoor air temperatures behind both facades were close to each other, and were not suitable according to ISO 7730 and ASHRAE 55 Standards comfort range for representative summer days with high ambient air temperatures. Nevertheless, indoor air temperatures behind vegetated facade were in the comfort range in the fall representative day which required cooling, while indoor air temperatures behind reference facade were not in the comfort range in summer representative day.*

Keywords: *Vegetated Facade System, Thermal Performance, Field Measurement, Surface Temperature, Sustainability.*

1 Introduction

Fourth Assessment Report of Intergovernmental Panel on Climate Change indicates that average temperature on earth has increased by 0.75 °C from the beginning of the 20th century until today (IPCC, n.d.). Additionally, it is predicted that average air temperature on earth will increase by 1.8-4°C at the end of 21th century (MCCAR, n.d.). Also it is claimed that annual average air temperature in Turkey will rise by 2.5-4°C in following years (Turkey's National Climate Change Adaptation Strategy, 2011). Urbanization causes reduction of huge amount of green areas and replaces them with buildings and surfaces with low albedo value (Cheng *et al*., 2010; Koyama *et al*., 2013; Wong *et al*., 2010). These changes cause a significant rise of urban temperature known as heat island effect, which is responsible for the increase of ambient air temperatures (Wong *et al*., 2010; Alexandri and Jones, 2008). Use of vegetated

surfaces and vegetated facade systems plays an important role to reduce urban heat island effect (Koyama *et al*., 2013; Alexandri and Jones, 2008; Olivieri *et al*., 2014). Greenhouse effect plays also an important role in the increase of ambient air temperatures. Building sector is responsible of 40% of the CO_2 and other greenhouse gases emissions. With improvements in economic development, energy use in building sector has increased (Perez *et al*., 2017; Technology Roadmap, 2013). In order to decrease greenhouse gases emissions it is essential to use renewable energy sources instead of fossil fuels and/or reduce energy consumptions. Energy consumption caused by building sector can be reduced by several sustainable design strategies. One of them is covering walls with vegetation, that is called as vegetated facade systems (VFS). "Greeney" is a common term in literature, hovewer in the present study it is prefered to nomenclature these systems as "vegetated facade systems" because of the reason that main components of these system are vegetation and growing media. Literature review reveals that vegetated facades minimize heat gain through building facade, decrease surface temperature and increase energy efficiency of buildings (Perez *et al*., 2017; Safikhani *et al*., 2014; Raji *et al*., 2015; Konteleon and Eumorfopoulou, 2010; Haggag *et al*., 2014; Feng and Hewage, 2014; Perini *et al*., 2011). Studies in Köppen subgroup "Csa" (mild with no dry and hot summer climate) indicate that vegetated facade systems reduce the maximum exterior surface temperature of reference building surface up to 25°C in cooling period (Olivieri *et al*., 2014; Akbari *et al*., 1997). Aim of the present paper is to evaluate thermal performance of felt type VFS in Csa climate conditions during cooling period in summer and fall seasons. Also, by means of the results of the present study it is aimed to fill the gap in literature regarding data of thermal performance of VFS applied on insulated wall and lack of data for thermal performance of felt type VFS. Initially, design of vegetated facade, instrumental setup and measurement parameters are presented. Subsequently, solar radiation and surface temperature results are given and values of both vegetated and reference facades are comparatively assessed.

2 Materials and Methods

Thermal performance monitoring was conducted at a building located in Gebze Technical University, Gebze, Kocaeli. Gebze Technical University is located at 40°48'41"N, 29°21'19"E (GTU, 2017). Kocaeli is classified as "Csa" (mild with dry and hot summer climate) according to Köppen climate classification. Vegetated facade system and instruments were installed in the first week of September 2016. Trial tests were done during 5 months after installation of experimental setup. Monitoring including whole parameters are started on 04 February 2017.

2.1 Experimental Building

An existing office building located on Gebze Technical University Campus was chosen as experimental building, two facade surfaces of the building were determined to be used as vegetated and reference facades. Both facades are oriented to the south. They are exposed to solar radiation for the majority of the day (especially hours when solar radiation reaches high values) and there are no obstructions in front of the facades. Also, there is no opening in the respective south oriented walls, both facades are fully opaque and have same dimensions. Window to wall ratio (WWR) of east oriented exterior wall of room which south wall was

fully vegetated is 20%, while WWR of east oriented exterior wall of room which south wall was non vegetated is 13%. Spaces behind both facades are office rooms which have approximately similar conditions. Both of them have the same heating and cooling systems, which is air conditioning. It operates between 08:00 and 17:00 during week days and doesn't operate during weekends. Existing wall system of the building is composed of the following components from inside to outside: 19 cm brick wall with 2 cm thickness interior plaster and 5 cm thickness expanded polystrene heat insulation material and 3 cm thickness exterior plaster. This wall system is considered to be reference wall system. Most widely used VFS in Turkey is "felt system" (Yüksel and Türkeri, 2016a). Additionally, there is no previous experimental study in literature in which the thermal performance of a felt type VFS under Csa climate region has been measured during neither cooling period nor heating period (Yüksel and Türkeri, 2016b; Yüksel and Türkeri, 2017). Therefore felt type was chosen as vegetated facade system. Also, "euonymus japonica" was selected due to its well adaptation to survive in temperate and mediterranean climates. The vegetated facade is composed of two main components: existing wall system and vegetated system. Vegetated system consists of following components from inside to outside: 40x40x2mm galvanized steel frame mounted on the wall, PVC panel of 1 cm thickness fixed on this frame, first and second layers of geotextile felt attached on it and vegetation layer embedded the felt pockets.

2.2 Instrumental Setup for Monitoring

An instrumental setup was designed and installed at the reference and vegetated facade systems to measure solar reflectance, surface and air temperatures (Figure 1a,b). Local meteorological data (air temperature and humidity, atmospheric pressure, wind direction and wind velocity) was measured by a weather station installed on the roof parapet of existing building (Figure 1c).


(a)

(b)

(c)

Figure 1. Image of VFS (left) and RFS (middle) and image of the weather station on the roof parapet (right).

Figure 2 designates sections of reference facade and vegetated facade test assemblies. Three pyranometers were used to measure solar radiation incident and solar reflectance. A pyranometer ("I" in Fig. 2b) was installed vertically in front of the vegetated facade to measure solar irradiance reflected from the vegetated facade. Two pyranometers were installed in front of the reference facade vertically and mounted back to back symmetrically. One of these pyranometers, ("D" in Fig. 2a) was used to measure solar radiation incident on reference and vegetated facades and the other ("E" in Fig. 2a) measures solar irradiance reflected from the reference facade. Only one pyranometer was decided to measure incident

solar radiation since solar radiation values reaching each both facades are accepted as identical. Infrared non-contact thermometers were used to measure surface temperatures of exterior wall of reference facade ("F" in Fig. 2a), exterior wall of vegetated facade ("N" in Fig. 2b), back ("M" in Fig. 2b) and front ("L" in Fig. 2b) side of the PVC panel, second layer of felt ("K" in Fig. 2b). Contact thermometers were used to measure surface temperatures of interior walls of reference ("G" in Fig. 2a) and vegetated ("O" in Fig. 2b) facades. Also, indoor temperature and humidity sensors were placed 20 cm in front of the interior wall surface of the reference ("H" in Fig. 2a) and vegetated ("P" in Fig. 2b) facades in order the measure indoor air temperature of the rooms behind the vegetated and reference walls. Additionally, a temperature sensor ("J" in Fig. 2b) was placed inside the leaves to measure the air temperature among leaves (Yüksel and Türkeri, 2017).

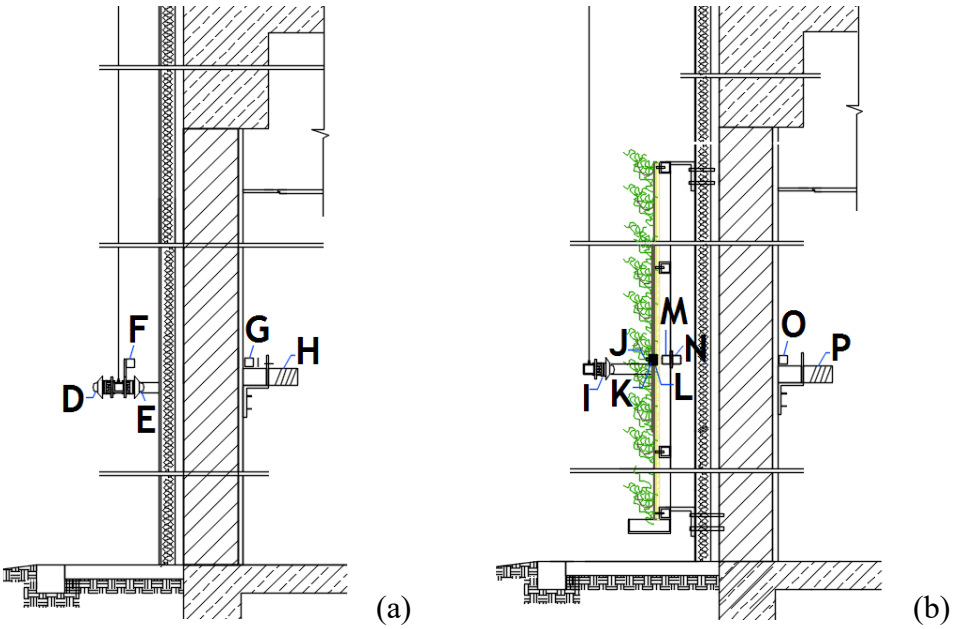

Figure 2. Section of reference facade (left) and vegetated facade (right) test assemblies.

Monitoring periods included months representing summer and fall seasons of the year 2017. Data regarding each parameter was recorded every 10 minutes during these periods. Nevertheless, user behaviours were found to be different in office rooms during weekdays behind vegetated and reference rooms. Hence, representative weekend days were selected for the summer and fall periods when high solar radiation was observed and exterior surface temperatures of reference facade reached maximum values.

3 Test Results

Exterior and interior surface temperatures and indoor air temperatures of vegetated and reference facades were compared with each other. Also, indoor air temperatures were evaluated according to comfort temperature range identified in ISO 7730 and ASHRAE 55 Standards. Additionally, solar reflectance ratio of reference facade and vegetated facades were compared with each other. Solar reflectance ratio were calculated according to ASTM E

1918:2006 (ASTM E1918:2006). For each representative day and for both facades, the ratio of reflected solar irradiance values to total solar irradiance values was calculated between 09:00-15:00. August 12, 2017 and September 24, 2017 were chosen as representative days for the summer and fall periods, respectively, because of the reason that high solar radiation values occured and exterior surface temperatures of reference facade reached maximum values in that hot days. Test results regarding that days such as microclimate values, solar reflectance values of reference and vegetated walls and maximum exterior surface temperatures of reference and vegetated facades are shown in Table 1.

Table 1. Microclimate, solar reflectance and maximum exterior surface temperature values observed on August 12, 2017 and September 24, 2017.

Ambient air temp. ranges	Relative humidity ranges	Max. solar radiation reaching to facades	Max. solar radiation reflecting from RFS	Max. solar radiation reflecting from VFS	Solar reflectance of RFS	Solar reflectance of VFS	Max. exterior surf. temp. of RFS	Max. exterior surf. temp. of VFS
22.4°C - 33.1°C	29% -93%	454W/m^2 (at 14:10)	364W/m^2	54W/m^2	0.88	0.12	53.2°C (at 14:40)	30°C (at 16:40)
13.1°C - 25.6°C	39% -93%	642W/m^2 (at 14:10)	448W/m^2	73W/m^2	0.80	0.10	53.3°C (at 15:00)	23.6°C (at 15:50)

Exterior surface temperatures of vegetated wall were extremely lower than exterior surface temperatures of reference wall for both periods during the day time (Figure 3 and Figure 4).

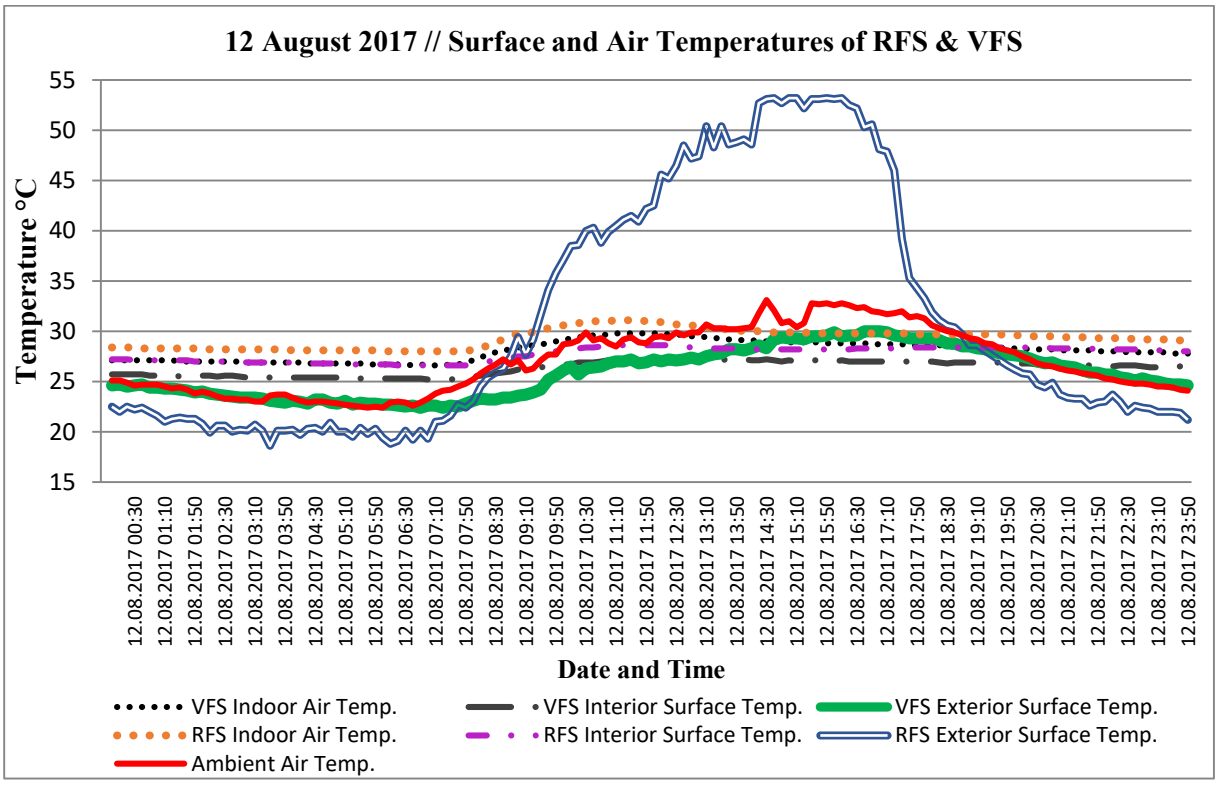

Figure 3. Exterior and interior surface and indoor air temperatures of RFS and VFS on August 12, 2017.

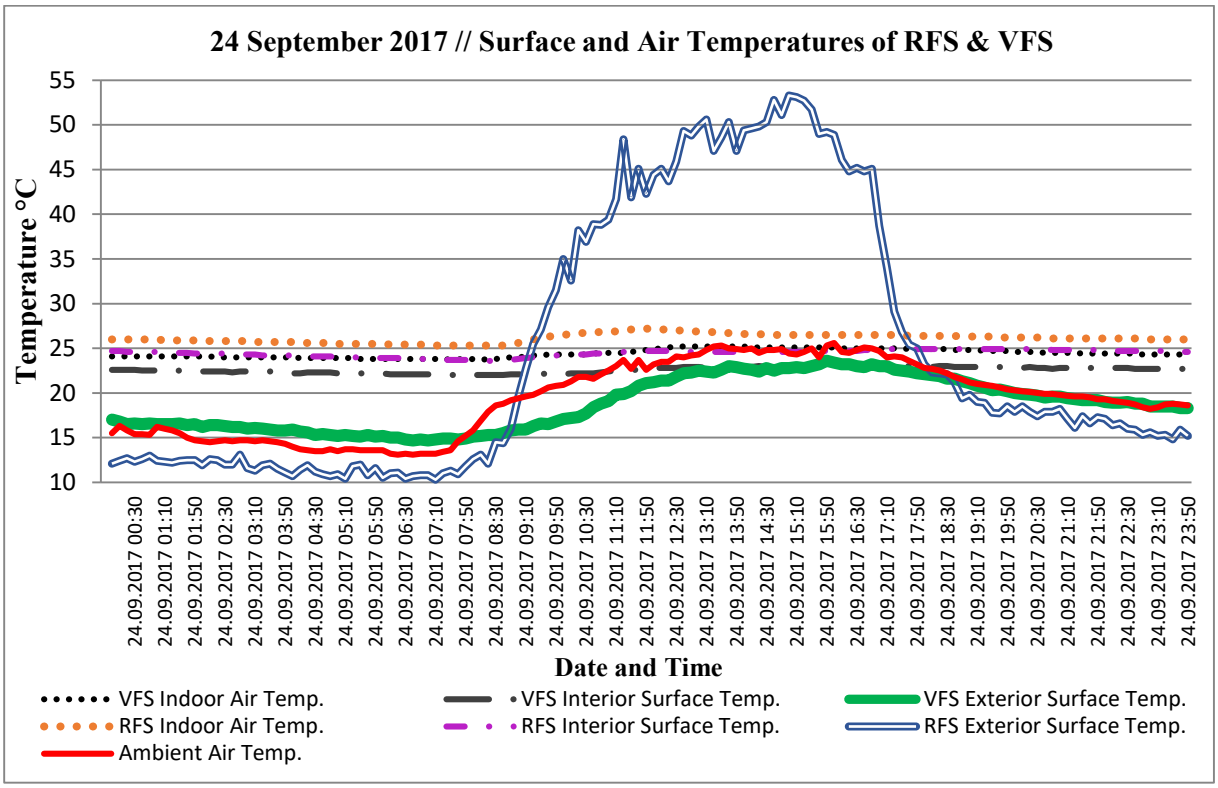

Figure 4. Exterior and interior surface and indoor air temperatures of RFS and VFS on September 24, 2017.

Differences between maximum exterior surface temperatures of reference and vegetated facades were 24°C and 30.5°C for representative days of summer and fall periods, respectively. Also, during the night time, exterior surface temperatures of vegetated wall are higher than exterior surface temperatures of reference walls for both periods. Interior surface temperatures of reference facade were also higher than interior surface temperatures of vegetated facade along the day time. Differences between maximum interior surface temperatures of reference and vegetated facades were 1.3°C and 1.8°C for representative days in summer and fall periods, respectively (Fig. 3 and Fig. 4). Additionally, Fig. 3 presents that on August 12, indoor air temperatures behind both facades were not in the range of 23-26°C which is recommended as a comfort range for cooling period in ISO 7730:2005 Standard and ASHRAE Standard 55-2010. Nevertheless, on September 24, max. indoor air temperature (25°C) behind vegetated facade is lower than upper limit value of 26°C, while maximum indoor air temperature (26.5°C) behind reference facade is higher than 26°C (Fig. 4).

4 Discussion

Although high differences between exterior surface temperatures of vegetated and reference walls were observed, there was no significant difference between interior surface temperatures of vegetated and reference walls. Also, there was no significant difference between indoor air temperatures behind vegetated and reference walls. The results regarding indoor air temperature differences between vegetated and reference facade showed similarities with the results of the study conducted under a different climate condition

(Cfa:humid subtropical climates) by Chen et al., (2013) which revealed that cooling effect of VFS on the indoor environment is relative small because of the high heat resistance of the wall. If the existing exterior wall was designed without any thermal insulation, it is obvious that the VFS would present greater passive cooling effect. In addition, indoor air temperatures behind both rooms were not suitable according to comfort temperature ranges indicated in standards for representative summer day. Nevertheless, indoor air temperatures behind VFS were in the comfort range in the fall representative day in day time which required cooling, while indoor air temperatures behind reference facade were not in the comfort range. Also, it can be claimed that indoor air temperatures of both rooms were not only affected by exterior surface temperatures of south oriented walls, but also by the surface temperatures of interior walls, ceeling, slab and east oriented exterior walls. Also, it can be assumed that vegetated room gained and lost more heat through windows due to higher WWR compared with reference room. It can be claimed that if east facades of both rooms had same WWR, vegetated room would show greater performance in terms of indoor air temperatures compared with reference room.

5 Conclusions

It can be concluded that felt type VFS decreases exterior surface temperatures of an insulated existing wall located in Csa climate. In addition, most remarkable results were observed in fall period, and in that period the differences between exterior surface temperatures of reference and vegetated facades reached to 30.5°C. These results suggest that VFS has a positive contribution on thermal performance of building wall during cooling period. In addition, solar reflectance of reference facade was 3-8 times higher than solar reflectance of VFS. Although solar reflectance of reference facade was higher than solar reflectance of VFS, exterior surface temperature of vegetated facade was significantly lower than exterior surface temperature of reference facade. That is because VFS transfers less energy to exterior wall of building even though VFS absorbs more solar radiation compared with reference facade system. Thus, it can be claimed that VFS uses most of energy reaching on its surface and so transfers less amount of energy to the exterior wall surface of building wall. Also, lower solar reflectance values of VFS indicate that these systems have positive impact on reducing urban heat island effect.

Acknowledgements

Authors gratefully acknowledge to Istanbul Technical University (ITU) Scientific Research Department for funding the research project.

ORCID

Elif Özer Yüksel: https://orcid.org/0000-0002-1041-8748
Nil Türkeri: https://orcid.org/0000-0003-4060-6528

References

Akbari, H., Kurn, D.M., Bretz, S.E. and Hanford, J.W. (1997). Peak Power and Cooling Energy Savings of Shade Trees. *Energy and Buildings,* 25, 139-148.

Alexandri, E. and Jones, P. (2008). Temperature Decreases inan Urban Canyon due to Green Walls and Green Roofs in Diverse Climates. *Building and Environment*, 43, 480-493.

ASHRAE, ANSI/ASHRAE Standard 55-2010. *Thermal environmental conditions for human occupancy, American Society of Heating, Ventilating and Air-conditioning Engineers.* Atlanta, GA, USA.

ASTM E1918 (2006). *Standard Test Method for Measuring Solar Reflectance of Horizontal and Low-Sloped Surfaces in the Field.* ASTM International. USA.

Chen, Q., Li, B. and Liu, X. (2013). An experimental evaluation of the living wall system in hot and humid climate. *Energy and Buildings*, 61, 298–307.

Cheng, C.Y., Cheung, K.K.S. and Chu, L.M. (2010). Thermal Performance of a Vegetated Cladding System on Facade Walls. *Building and Environment*, 45, 1779-1787.

Feng, H. and Hewage, K. (2014). Energy Saving Performance of Green Vegetation on LEED Certified Building. *Energy and Buildings*, 75, 281–289.

GTU. (2017). http://wikimapia.org/15049881/tr/Gebze-Teknik-%C3%9Cniversitesi-GT%C3%9C-%C3%87ay%C4%B1rova-Yerle%C5%9Fkesi (accessed 13 October 2017).

Haggag, M., Hassan, A. and Elmasry, S. (2014). Experimental Study on Reduced Heat Gain Through Green Facades in a Heat Load Climate. *Energy and Buildings,* 82, 668-674.

IPCC (Intergovernmental Panel on Climate Change). Working Group I: The Scientific Basis. (n.d.). http://www.ipcc.ch/ipccreports/tar/wg1/index.php?idp=5 (accessed 08.11.2017).

ISO 7730:2005. *Ergonomics of the thermal environment- Analytical determination and interpretation of thermal comfort using calculation of the PMV and PPD indices and local thermal comfort criteria*. International Organisation for Standardisation.

Kontoleon, K.J. and Eumorfopoulou, E.A. (2010). The Effect of the Orientation and Proportion of a Plant-Covered Wall Layer on the Thermal Performance of a Building Zone. *Building and Environment*, 45, 1287-1303.

Koyama, T., Yoshinaga, M., Hayashi, H., Maeda, K. and Yamauchi A. (2013). Identification Of Key Plant Traits Contributing to the Cooling Effects of Green Façades Using Freestanding Walls. *Building and Environment*, 66, 96-103.

MCCAR (Massachusetts Climate Change Adaptation Report). The Changing Climate and Its Impact. (n.d.). http://www.mass.gov/eea/docs/eea/energy/cca/eea-climate-adaptation-chapter-2.pdf (accessed 12.11.2015).

Olivieri, F., Olivieri, L. and Neila, J. (2014). Experimental Study of the Thermal-Energy Performance of an Insulated Vegetal Facade Under Summer Conditions in a Continental Mediterranean Climate. *Building and Environment*, 77, 61-76.

Perez, G., Coma, J., Sol, S. and Cabeza, L.F. (2017). Green Facade for Energy Savings in Buildings: The Influence of Leaf Area Index and Facade Orientation on the Shadow Effect. *Applied Energy*, 187, 424-437.

Perini, K., Ottele, M., Fraai, A.L.A., Haas, E.M. and Raiteri, R. (2011). Vertical Greening Systems and the Effect on Air Flow and Temperature on the Building Envelope. *Building and Environment*, 46, 2287-2294.

Raji, B., Tenpierik, M.J. and Dobbelsteen, A. (2015). The Impact of Greening Systems on Building Energy Performance: A Literature Review. *Renewable and Sustainable Energy Reviews*, 45, 610–623.

Safikhani, T., Abdullah, A.M., Ossen, D.R. and Baharvand, M.A. (2014). Review of Energy Characteristic of Vertical Greenery Systems. *Renewable and Sustainable Energy Reviews*, 40, 450-462.

Technology Roadmap, Energy Efficient Building Envelopes. (2013). https://www.iea.org/publications/freepublications/publication/TechnologyRoadmapEnergyEfficientBuildingEnvelopes.pdf (accessed 01.11.2017).

Turkey's National Climate Change Adaptation Strategy. (2011). http://www.csb.gov.tr/db/iklim/editordosya/Adaptation_Strategy.pdf (accessed 20.07.2014).

Wong, N.H., Tan, A.Y.K., Chen, Y., Sekar, K., Tan, P. Y., Chan, D., Chiang, K. and Wong, N.C. (2010). Thermal Evaluation of Vertical Greenery Systems for Buildings Wall. *Building and Environment*, 45, 663-672.

Yüksel, E. and Türkeri, A.N. (2016a). Sustainable Facade System: Types of Vegetated Facade Systems Designed and Constructed in Turkey, *In Proceedings of SBE 16 Istanbul – International Conference on Sustainable Built Environment*, 13-15 October 2016, Istanbul.

Yüksel, E. and Türkeri, A.N. (2016b). Bitkilendirilmiş Cephe Sistemlerinin Farklı İklim Bölgelerindeki Isıl Performanslarının Değerlendirilmesi, *2.Ulusal Yapı Fiziği ve Çevre Kontrolü Kongresi*, 04-06 May 2016, Istanbul Technical University, İstanbul.

Yüksel, E. and Türkeri, A.N. (2017). Litterature Review of Experimental Setups Monitoring Thermal Performance of Vegetated Facade Systems, *Journal of Facade Design & Engineering*, 5(2), 67-85.

XV International Conference on Durability of Building Materials and Components
DBMC 2020, Barcelona
C. Serrat, J.R. Casas and V. Gibert (Eds)

An Experimental Study on the Thermal Conductivity of Concrete Containing Coal Bottom Ash Aggregate

In-Hwan Yang, Jihun Park and Hoe-Won Jung

Kunsan National University, Department of Civil Engineering, Jeonbuk 54150, Kunsan, Republic of Korea, ihyang@kunsan.ac.kr

Abstract. *Thermal conductivity plays a significant role in efficient energy usage, especially in the construction field. Low thermal conductivity is preferable because lower thermal conductivity will increase the thermal insulation provided by the concrete and reduce the heating and cooling costs for residential and commercial buildings. To accomplish this goal, porous materials can be considered for use in concrete. Additionally, researchers have had challenges producing high-strength concrete with low thermal conductivity. Therefore, this study aims to investigate the effects of replacing crushed fine aggregates with coal bottom ash (CBA) on the thermal conductivity and mechanical properties of high-strength concrete. The concrete properties, including unit weight, compressive strength, and thermal conductivity, were measured. The experimental results revealed that the thermal conductivity of the CBA concrete decreased as the unit weight of the CBA concrete decreased, and the thermal conductivity also decreased as the compressive strength decreased. Finally, the relationships between the thermal conductivity, unit weight, and compressive strength of the CBA concrete were also examined.*

Keywords: *Coal Bottom Ash, Thermal Conductivity, High-Strength Concrete, Porosity.*

1 Introduction

Currently, the demand for energy-efficient buildings is increasing to optimize the internal temperature of buildings (Najjar *et al.,* 2019). One of the key factors for optimizing energy efficiency is thermal conductivity. When a building is constructed from materials with higher thermal conductivity, to ensure the internal temperature of the building, a greater amount of energy must be consumed for cooling and heating. To address this issue, materials with low thermal conductivity are recommended during construction. Thus, considering concrete with low thermal conductivity is the most suitable choice.

To produce concrete with low thermal conductivity, Aghdam *et al.* (2019) carried an experimental study to estimate the effects of carbon nanotubes on the thermal conductivity of steel fiber-reinforced concrete. Their test results indicated that the agglomeration of carbon nanotubes caused a decline in the concrete thermal conductivity. However, the use of carbon nanotubes is expensive, and high-strength concrete is not considered.

Currently, coal-fired thermal power plants create a substantial amount of bottom ash and fly ash. Bottom ash is industrial waste produced at the bottom of coal furnaces. To develop concrete

doi:10.23967/dbmc.2020.172

with low thermal conductivity for energy efficiency, an experimental study to investigate the effects of partial or total replacement of crushed fine aggregates with coal bottom ash (CBA) on the thermal properties of concrete is vitally necessary.

Therefore, in this experimental study, the thermal conductivity and mechanical properties of high-strength concrete specimens containing 25, 50, 75, and 100% replacement of crushed fine aggregates with CBA were investigated at a curing age of 28 days. The compressive strength, unit weight, and thermal conductivity of these specimens were measured. The relationships between the thermal conductivity, unit weight, and compressive strength of the CBA concrete were also examined.

2. Experimental Program

2.1 Materials

Figure 1. CBA aggregate.

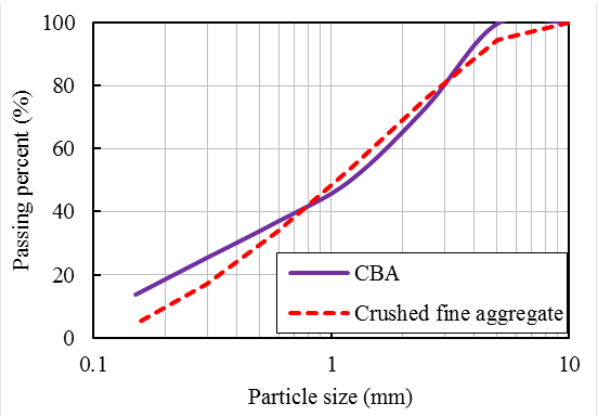

Figure 2. Grading curve of CBA and crushed fine aggregate.

Table 1. Physical properties of fine, coarse and coal bottom ash aggregate.

	Fineness modulus	Water absorption (%)	Unit weight (g/cm^3)
Crushed fine aggregate	3.17	0.69	2.60
Coarse aggregate	6.77	1.44	2.61
CBA	3.83	6.87	1.84

The coal bottom ash used in this study was collected from a thermal power plant company in Korea. The CBA aggregate was screened to remove particles greater than 5.0 mm and to retain the particles greater than 0.15 mm. The CBA used for this study is presented in Figure 1, and the particle size distribution of the CBA is also presented in Figure 2. The test results of the density and water absorption of the CBA are shown in Table 1. The particle size distribution of the crushed fine aggregates is illustrated in Figure 2. The unit weight, water

absorption and fineness modulus results of the crushed fine and coarse aggregates are also shown in Table 1.

2.2 Mix Proportions

A concrete mix was designed with a target compressive strength of 60 MPa at a curing age of 28 days. The mixing proportions of the control concrete and coal bottom ash concrete are indicated in Table 2. The crushed fine aggregate was replaced with five different volume fractions (0, 25, 50, 75, and 100%) of coal bottom ash in the concrete.

Table 2. Mixing proportions of the coal bottom ash concrete.

Mixtures	Replacements of CBA (%)	W/C	Water	Unit content (kg/m^3)				
				Cement (OPC)[a]	Coarse aggregate	Fine aggregate	Coal bottom ash	HWRA[b] (0.6% × cement)
CBA00	0	0.3	178.5	595	878.5	663	0	3.6
CBA25	25	0.3	178.5	595	878.5	497.2	117.7	3.6
CBA50	50	0.3	178.5	595	878.5	331.5	235.3	3.6
CBA75	75	0.3	178.5	595	878.5	165.7	353	3.6
CBA100	100	0.3	178.5	595	878.5	0	470.7	3.6

a: OPC: ordinary Portland cement.
b: HRWA: high water reducing agent.

2.3 Specimens and Test Procedures

Cylindrical specimens with dimensions of 100 mm × 200 mm were cast to measure the unit weight, compressive strength, and thermal conductivity of the different samples. The unit weight, compressive strength, and thermal conductivity of the CBA concrete were measured at a curing age of 28 days. The thermal conductivity of each specimen was measured using a transient plane source (TPS) measurement system, as shown in Figure 3.

3 Test Results and Discussion

3.1 Unit weight

The unit weight results of the concrete specimens with different coal bottom ash ratios are shown in Figure 4. The figure indicates that the unit weight of the CBA concrete decreased as the replacement of crushed fine aggregate with CBA increased in the concrete. At a curing age of 28 days, the unit weight of the control mixture was 2,370 kg/m^3, whereas the unit weights of the coal bottom ash concrete mixtures CBA25, CBA50, CBA75, and CBA100 were reduced by 2.1, 3.2, 5.3, and 7.6%, respectively. The decrease in the unit weight of the CBA concrete mixtures is due to the replacement of coal bottom ash, which is a lighter fine aggregate than crushed fine aggregate, as shown in Table 1.

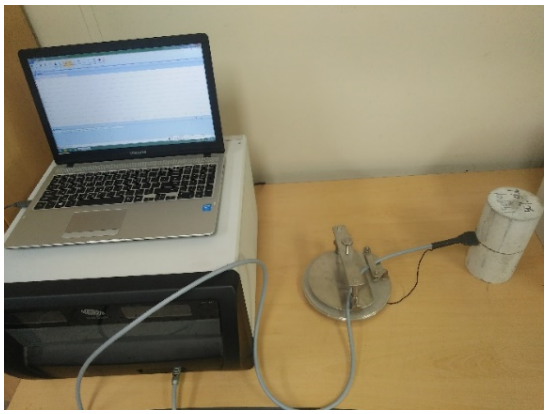

Figure 3. Test setup for thermal conductivity measurements.

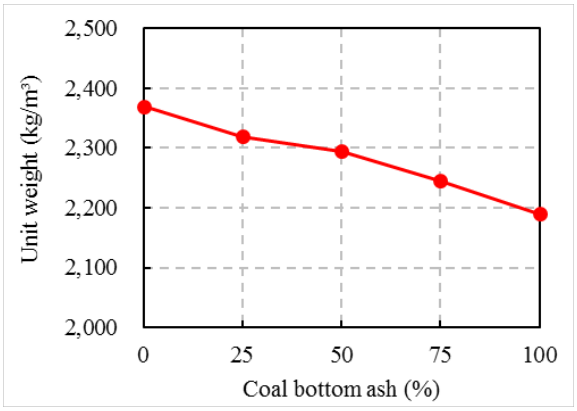

Figure 4. Effect of CBA replacements on unit weight of concrete.

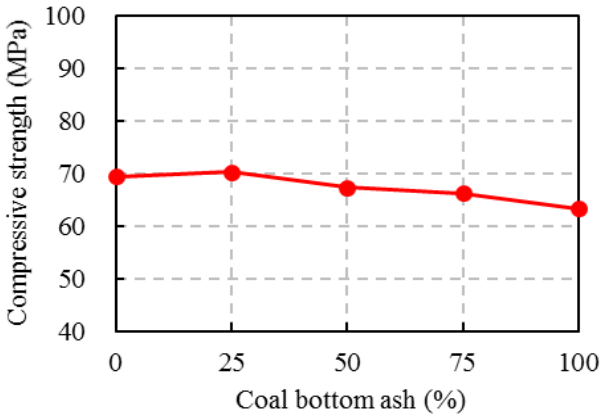

Figure 5. Effect of CBA replacement on compressive strength.

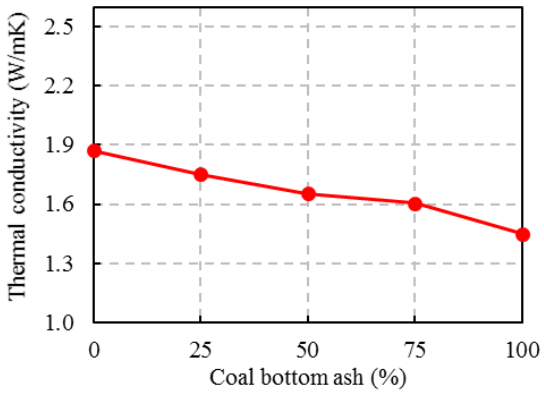

Figure 6. Effect of CBA replacement on thermal conductivity.

3.2 Compressive Strength

The test results of the compressive strength of the concrete specimens with different coal bottom ash contents are summarized in Figure 5. Generally, at a curing age of 28 days, the compressive strength of the CBA mixtures decreased as the CBA replacement increased. The compressive strength of the coal bottom ash concrete mixtures CBA50, CBA75, and CBA100 were 3.0, 4.6, and 8.8% less than that of the control concrete mixture (69.4 MPa), respectively. However, the compressive strength of the coal bottom ash concrete mixture CBA25 was insubstantially higher (1.2%) than that of the control concrete mixture. The compressive strength loss could be explained by the increase in the porosity of the concrete. These porosities cause negative impact on concrete matrix and reduce the compressive strength of the CBA concrete specimens [Singh *et al.,* 2014].

3.3 Thermal Conductivity

The thermal conductivities of the concrete specimens with different CBA contents are presented in Figure 6. At a 28-day curing age, the thermal conductivities of the CBA mixtures decreased as the CBA content increased. The thermal conductivities of the CBA concrete

mixtures CBA25, CBA50, CBA75 and CBA100 were 6.4, 11.7, 14.2, and 22.5% less than that of the control concrete mixture (1.87 W/m·K), respectively. The thermal conductivity of the CBA concrete with a 100% CBA content was significantly less than that of the control concrete mixture. It is known that thermal conductivity highly depends on the lightweight aggregate pore structure, the concrete density and the cement paste. Hence, the pore structure was one of the key elements affecting thermal conductivity (Tasdemir *et al.,* 2017). For that reason, the observed decline in thermal conductivity could be explained by the increase in the CBA concrete in the concrete. As the CBA content increased, the total volume of porosity of the concrete increased, and the thermal conductivities of the concrete decreased. Reducing the thermal conductivity would increase the thermal insulation provided by the concrete and reduce the heating and cooling costs for buildings.

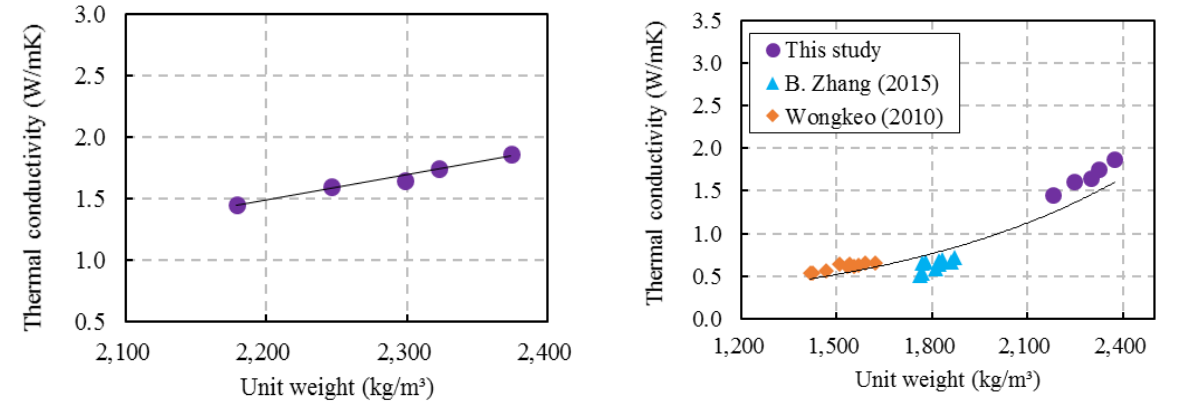

(a) Test results of this study

(b) Comparison between this study and previous studies

Figure 7. Relationship between the thermal conductivity and unit weight.

The relationship between the thermal conductivity and unit weight of the CBA concrete is demonstrated in Figure 7. As the unit weight of the CBA concrete increased, the thermal conductivity of the CBA concrete increased. Moreover, the thermal conductivity of the CBA concrete is nearly linearly proportional to the unit weight. Increasing the air voids or lightweight aggregate in concrete is a method to reduce unit weight and thermal conductivity. A similar trend was found when analyzing the test results of Wongkeo *et al.* (2010) and Zhang *et al.* (2015), in which the unit weights ranged from 1417 to 1621 kg/m^3 and from 1760 to 1870 kg/m^3, respectively, as shown in Figure 7(b).

The relationship between the thermal conductivity and the compressive strength is demonstrated in Figure 8. This relationship is similar to the relationship between the thermal conductivity and unit weight of the CBA concrete. Additionally, the thermal conductivity has a direct relationship with the compressive strength of the CBA concrete. Figure 8(b) shows a similar trend between the test results in the present research and those of other authors.

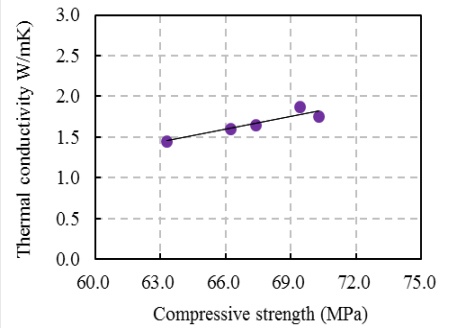

(a) Test results of this study

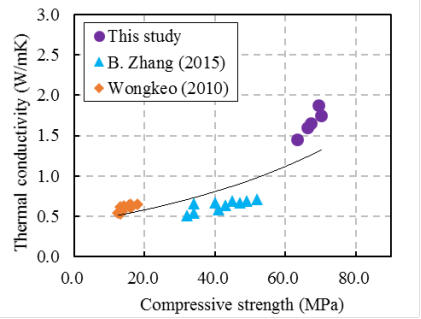

(b) Comparison between this study and previous studies

Figure 8. Relationship between the thermal conductivity and compressive strength.

4 Conclusions

In this research, an experimental study was performed on the low thermal conductivity of high-strength concrete specimens with different CBA replacement ratios. The research findings are summarized hereafter:

- The thermal conductivity of the CBA concrete is highly dependent on the porosity in the concrete specimens. For that reason, as the CBA content increased, the thermal conductivity of the CBA concrete decreased gradually. Remarkably, when replacing all the crushed fine aggregate with CBA, the thermal conductivity of the CBA concrete was 22.5% less than that of the control mixture.
- As the coal bottom ash content in the CBA concrete increased, the compressive strength of the CBA concrete decreased. In particular, the compressive strength of mixture CBA100 was 8.8% less than that of the control mixture CBA00.
- As the compressive strength of the CBA concrete decreased, the thermal conductivity of the CBA concrete also decreased.

Acknowledgments

This research was supported by a grant (19CTAP-C151889-01) from the Technology Advancement Research Program (TARP), which was funded by Ministry of Land, Infrastructure and Transport of Korean government.

References

Aghdam, M.K.H., Mahmoodi, M.J. and Safi, M. (2019). Effect of adding carbon nanotubes on the thermal conductivity of steel fiber-reinforced concrete. *Composites Part B*, *174*, 106972.

Najjar, M., Figueiredo, K., Hammad, A.W.A. and Haddad, A. (2019). Integrated optimization with building information modeling and life cycle assessment for generating energy efficient buildings. *Applied Energy*, *250*, 1366-1382.

Singh, M. and Siddique, R. (2014). Strength properties and micro-structural properties of concrete containing coal bottom ash as partial replacement of fine aggregate. *Construction and Building Materials*, *50*, 246–256.

Tasdemir, C., Sengul, O. and Tasdemir, M.A. (2017). A comparative study on the thermal conductivities and mechanical properties of lightweight concretes. *Energy and Buildings*, *151*, 469–475.

Wongkeo, W. and Chaipanich, A. (2010). Compressive strength, microstructure and thermal analysis of autoclaved and air cured structural lightweight concrete made with coal bottom ash and silica fume. *Materials Science and Engineering A, 527*, 3676-3684.

Zhang, B. and Poon, C.S. (2015). Use of furnace bottom ash for producing lightweight aggregate concrete with thermal insulation properties. *Journal of Cleaner Production, 99*, 94-100.

XV International Conference on Durability of Building Materials and Components
DBMC 2020, Barcelona
C. Serrat, J.R. Casas and V. Gibert (Eds)

Behaviour of Surface Chloride Concentration in Concretes Subjected to Field Exposure in Marine Atmosphere Zone

Gibson R. Meira[1], Pablo R. R. Ferreira[2], Maria S. Freitas[3] and Carmen Andrade[4]

[1] Paraíba Federal Institute, Civil and Environmental Eng. Post-graduate Program of UFPB, Av. João da Mata, 256, 58015-020, João Pessoa, Brazil, gibsonmeira@yahoo.com, gibson.meira@ifpb.edu.br

[2] Paraíba Federal Institute, Civil and Environmental Eng. Post-graduate Program of UFPB, Av. João da Mata, 256, 58015-020, João Pessoa, Brazil, pablo.r06@hotmail.com, pablo.ferreira@ifpb.edu.br

[3] Civil and Environmental Engineering Post-graduate Program of UFPB, Av. João da Mata, 256, 58015-020, João Pessoa, Brazil, mariasilvajn@gmail.com

[4] International Centre for Numerical Methods in Engineering (CIMNE), Campus Nord UPC C/ Gran Capità, S/N 08034, Barcelona, Spain, candrade@cimne.upc.edu

Abstract. *Surface chloride concentration (Cs) is one of the parameters that feed models used to simulate chloride ingress into concrete. Therefore, understanding its behaviour over time is important for a more accurate forecasting. This work is part of a larger researcher project that aims to analyse the transport of chlorides into concrete in marine atmosphere zone based on long-term field exposures. The present paper focuses on the behaviour of Cs along 12.5 years. Prismatic concrete specimens with three different mixtures were exposed at places located at four different distances from the sea. Climatic variables and chloride deposition on the wet candle were parameters used to characterise the environment. Periodically, samples from concrete surface were extracted from the specimens and chemically analysed. Results show that Cs increases along the years and suggests a tendency of stabilisation over time, although this level could not be reached in the present exposure period. The relationship between Cs and chloride deposition rate on the wet candle was analysed and it was observed that the function* $Cs = C_0 + k_{cs}.(Dac)^n$ *is the one that best fits to experimental data.*

Keywords: *Concrete, Corrosion, Marine Atmosphere Zone, Surface Chloride Concentration.*

1 Introduction

Surface chloride concentration (*Cs*) is one of the main parameters to feed models used to simulate chloride penetration into concrete structures. It has been observed that *Cs* tends to increase over the years (Costa and Appleton, 1999; Yang *et al.*, 2017). However, this increase tendency weakens along time reaching a stabilisation, which can be observed after about ten years of exposure time in some cases (Andrade *et al.*, 2000). This behaviour can be represented by some mathematical models, which are presented in Table 1, that shows functions proposed in literature to represent the behaviour of *Cs* in concrete structures exposed in marine atmosphere zone.

It can be observed that there are not many studies aimed on the behaviour of *Cs* and that most of functions are power or exponential functions, with a predominance of first one.

Analysing the results presented by the studies referenced in Table 1 it can be observed that, in general, *Cs* sharply increases in the first years and, in the following years of exposure, this trend gives way to a more understated increase. Depending on the function adopted to represent

data behaviour, its final part can assume a more asymptotic shape, which denotes a stabilisation trend along the years. Moreover, in some cases *Cs* presents some fluctuation, which can be a result of the environmental interaction (Andrade *et al.*, 2000; Meira, 2004).

Table 1. Literature models to represent surface chloride concentration behaviour in marine atmosphere zone.

Source of data	Exposure time (years)	Function	Authors	Year
Japan	23 - 58	$Cs=a.t^{0,5}$	Uji *et al.*	1990
Portugal	0.5 - 5.5	$Cs=a.t^{b}$	Costa and Appleton	1999
United States of America	2 - 16	$Cs=a.(1-e^{b.t})$	Kassir *et al.*	2002
South Corea	0.7 – 48.7	$Cs=a.Ln.(b.t+1)+c$	Pack *et al.*	2010
Data from literature	0 – 3	$Cs=a+b.t^{0,5}$	Zhou *et al.*	2016
Data from literature	0 - 5	$Cs=a.(1-e^{b.t})$	Yang *et al.*	2017

Cs = surface chloride concentration *t* = exposure time

Regarding the shape of *Cs* curve, the continuous cement paste hydration along time is one of the aspects that may influence its behaviour. As hydration of cement paste advances, the concrete surface becomes less porous and less chloride ions can be captured in this region (Maheswaram and Sanjayan, 2004; Pack *et al*., 2010). As a consequence, the rate of Cs increase weakens. Besides that, the concrete ability in capturing chlorides decreases with the chloride concentration increase, which also contributes in the same way.

Another aspect to be considered in this analysis is the aggressiveness of the environment to which concrete structure is subjected. At places with a higher availability of chlorides there is a stronger increase of *Cs* in the first years with a subsequent attenuation with time (Sandberg *et al*., 1998; Costa and Appleton, 1999). However, along the years, *Cs* may present some fluctuation, which can be related to the ions movement towards bulk concrete or to effects like surface chloride removal due to rainfall.

Although there are some proposals to represent *Cs* behaviour along time in marine atmosphere zone, they are still scarce and there is no consensus related to the best function to represent *Cs* behaviour. This work contributes to this discussion and analyses the behaviour of *Cs* in concretes exposed along 12.5 years at a marine atmosphere zone located in northeast of Brazil. This is part of a project that studies the long-term chloride transport into concrete under natural exposure in marine atmosphere zone.

2 Experimental Work

Experimental work was based on environmental characterisation and chloride concentration measurements in concrete surface.

2.1 Environmental Characterization

The environmental characterization was done on temperature, relative humidity, rainfall, wind characteristics and sea-salt data. Climatic data were collected by a Brazilian Government weather station located in the region where the research took place. Sea-salt data was collected

at places 10, 100, 200 and 500 m far from the sea (Figure 1 and Table 2) using the wet candle method, according to ASTM standard G140 (ASTM, 2014).

Figure 1. Region where wet candle devices and concrete specimens were exposed.

Table 2. Geographical coordinates of exposure sites in northeast of Brazil.

Distance from the sea (m)	Latitude	Longitude
10	7º1'42.9''	34º49'50.1''
100	7º1'42.2''	34º49'52.8''
200	7º1'41.0''	34º49'55.8''
500	7º1'47.2''	34º50'13.1''

2.2. Surface Chloride Concentration in Concrete

Prismatic concrete specimens (0.15 x 0.15 x 1.40 m) were cast using a filler-modified Portland Brazilian cement, which chemical and physical properties are presented in Table 3. Concrete mixtures, with w/b ratios between 0.65 to 0.50, and physical properties are presented in Table 4. They are identified as C65, C57 and C50. Considering that these mixtures were performed a long time ago, they considered w/b that are not usual nowadays.

Table 3. Chemical and physical properties of used cement.

Composition (%)	SO_3	SiO_2	Al_2O_3	Fe_2O_3	CaO	MgO	Na_2O	K_2O	Insoluble residue (IR)	Loss on ignition (LI)
	3.21	18.11	4.31	2.27	59.87	3.61	0.21	1.51	1.45	5.50
Property	Specific surface (cm^2/g)			Specific density (g/cm^3)						
	3650			3.06						

Table 4. Concrete mixtures and properties.

Concrete	C50	C57	C65
Mixture			
Cement (kg/m^3)	406	356	320
Sand (kg/m^3)	769	812	840
Coarse aggregate (kg/m^3)	947	947	947
Plasticiser (kg/m^3)	1.22	1.06	-
w/b	0.5	0.57	0.65
Property			
Slump (mm)	80	80	80
Compressive strength (MPa – 28 days)	31	27	20

The specimens were cured in a wet chamber for 7 days and afterwards they were painted with a waterproof film at those surfaces thorough which chloride penetration should be avoided. Then, the specimens were placed at the same monitoring stations used for wet candle devices. After 6, 10, 14, 18, 46, 78 and 150 months of exposure, samples were extracted from the specimens to obtain chloride profiles in concrete. Although chloride profiles were obtained at each sampling period, here only surface chloride contents are analysed. These samples were extracted in the first millimetre of the exposure surfaces of specimens. The total chloride content was determined by potentiometric titration, following the procedures of the International Union of Laboratories and Experts in Construction Materials, Systems and Structures (RILEM, 2002).

3 Results and Analysis

Climatic results show that temperature ranged between 16 and 33.6 ºC along this period, with an average value of 27 ºC. The relative humidity presented a fluctuation between 55 and 99 %, with an average value of 76.6 %. Higher values were reached during the winter (rainy season) that takes place mainly between May and August. Wind speed data ranged between 1.5 and 7.6 m/s, with average value in this period around 3 m/s. Predominant wind directions were south (S), southeast (SE) and East (E), with a preponderance of SE winds. This is a typical behaviour for the studied region (Meira *et al*., 2006).

Average chloride deposition data are presented in Figure 2. This figure shows a strong salinity decrease in the first meters far from the sea, which may affect reinforced concrete structures in different levels. This drop in salinity is a consequence of the removal of marine aerosol salt particles due to gravimetric effect joined with other removal mechanisms (obstacles, rain, etc.).

Results of the surface chloride concentration are presented in Figure 3, considering the three different concretes and the four exposure sites and their distances from shoreline. Regarding the general aspects of the data, they show some fluctuation in the first exposure months, followed by a period of significant increase and afterwards a tendency of increase at lower rates, which suggests a tendency of reaching a maximum along time, but that was not possible to be observed in these 12.5 years of exposure. The initial fluctuation of chloride concentration in concrete surface can be attributed to the environmental interaction, where the rainfall can play an important role, due to the wash-out effect [Meira 2004, Chen *et al.*, 2013].

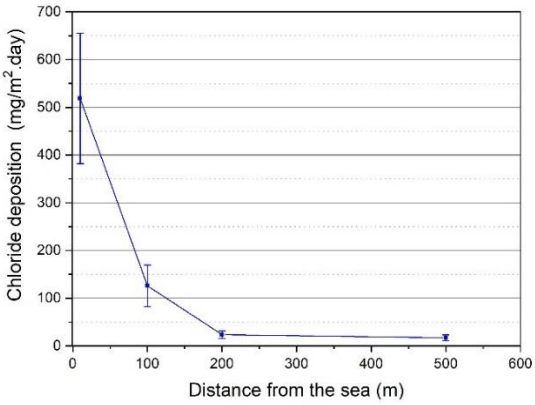

Figure 2. Average chloride deposition data during the research period.

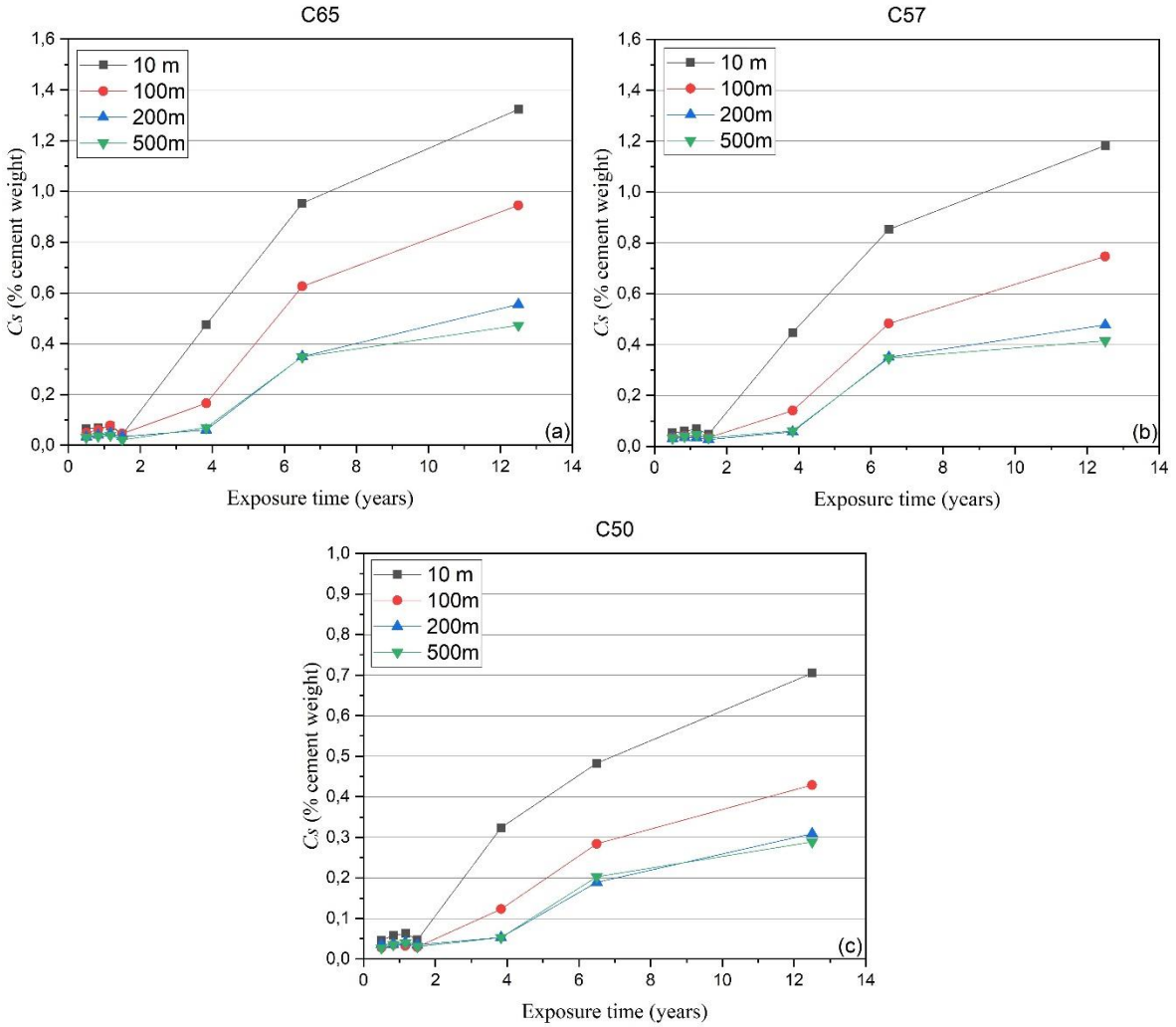

Figure 3. Behaviour of *Cs* along time for concretes C65 (a), C57 (b) and C50 (c).

Regarding the influence of concrete characteristics, it is clear the higher accumulation of chlorides in concrete surface as concrete porosity increases (higher w/b). Moreover, taking into account the distance from the sea, it is noticeable the chloride concentrations decay as going far from the sea, which is a consequence of the aggressiveness decrease at sites far from the shoreline due to the lower availability of chlorides in atmosphere.

Considering that the time is not the main variable that influences *Cs* increase, but the availability of chlorides in atmosphere, it seems quite reasonable to analyse the relationship between *Cs* and the accumulated deposition of chlorides on the wet candle (*Dac*), which is obtained summing month-to-month the chloride deposition on the wet candle (Figure 4).

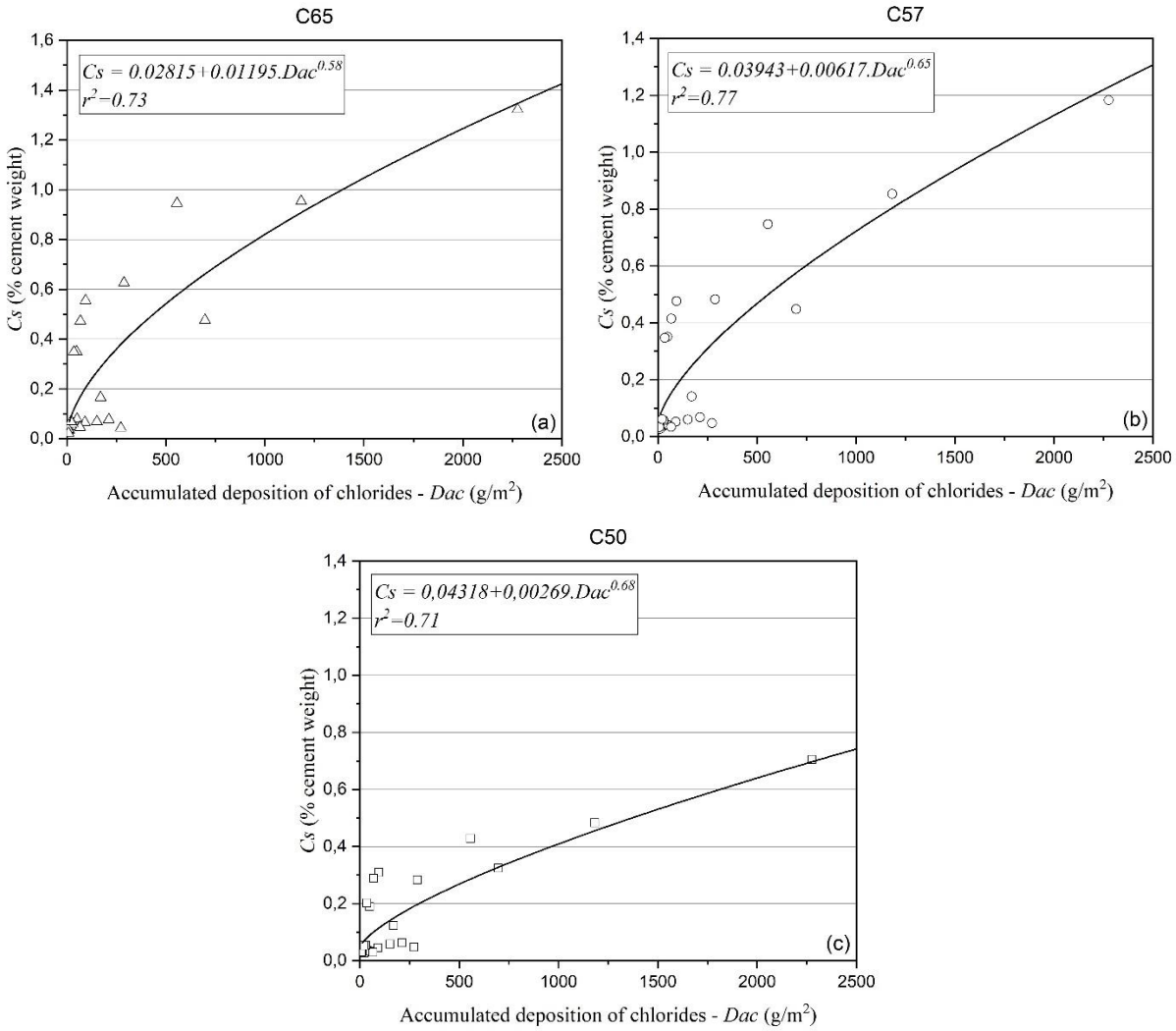

Figure 4. Relationship between *Cs* and accumulated deposition of chlorides (*Dac*) for concretes C65 (a), C57 (b) and C50 (c).

As can be seen in Figure 4, the relationship between *Cs* and *Dac* can be represented by the Equation (1), where *Cs* is the surface chloride concentration, C_0 is the initial chloride concentration in concrete, k_{cs} is a coefficient associated to the concrete ability in capturing

chlorides from atmosphere, *Dac* is the accumulated deposition of chlorides and *n* is a coefficient associated to the rate of *Dac* increase along time.

$$Cs = C_0 + k_{cs}.(Dac)^n \quad (1)$$

This Equation follows a similar way of some previous studies when considered the influence of time on *Cs* increase (Uji *et al*., 1990; Costa and Appleton, 1999; Zhou et al., 2016). However, it has the advantage of taking into account the direct relation between the chlorides present in atmosphere and those captured in concrete surface.

4 Conclusions

The main conclusion that can be drown up from the present analysis are:

- *Cs* increases along time and although tends to reach a maximum, this moment was not reached in 12.5 years of exposure time.
- Concrete porosity influences on *Cs* behaviour in a direct way. Concretes with higher w/b present a faster increase of *Cs* values.
- The availability of chlorides in atmosphere plays an important role in *Cs* behaviour. Higher availability of chlorides means higher *Cs* values. However, this relationship does not follow a linear function.
- The best function to represent the relationship between *Cs* and the availability of chlorides in atmosphere is $Cs = C_0 + k_{cs}.(Dac)^n$, where *Cs* is the surface chloride concentration, C_0 is the initial chloride concentration in concrete, k_{cs} is a coefficient associated to the concrete ability in capturing chlorides from atmosphere, *Dac* is the accumulated deposition of chlorides and *n* is a coefficient associated to the rate of *Dac* increase along time.

Acknowledgements

The authors thank CNPq (Brazilian National Council for Scientific and Technological Development) and the Research Laboratory on Building and Waste Materials of IFPB (Paraíba Federal Institute) for partially supporting this research. The authors also thank the Brazilian Institute of Meteorology for providing climatic data.

ORCID

Gibson R. Meira: http://orcid.org/0000-0002-2010-5315
Pablo R. R. Ferreira: http://orcid.org/0000-0002-4881-0737
Maria S. Freitas: http://orcid.org/0000-0002-9734-4242
Carmen Andrade: https://orcid.org/0000-0003-2374-0928

References

ASTM G-140-02 (2014). *Standard test method for determining atmospheric chloride deposition rate by wet candle method*.

Andrade, C., Sagrera, J. L. and Sanjuán, M. A. (2000). Several years study on chloride ion penetration into concrete exposed to Atlantic ocean water. In *Proceedings of the Second International RILEM Worshop on Testing and Modelling Chloride Ingress into Concrete*, Paris, France.

Chen, Y.S., Chiu, H.J., Chan, Y.W., Chang, Y.C. and Yang, C.C. (2013). The correlation between airborne salt

and chlorides cumulated on concrete surface in the marine atmosphere zone in north taiwan. Journal of Marine Science and Technology, (21), 24–34.

Costa, A. and Appleton, J. (1999). Chloride penetration into concrete in marine environment – part II: Prediction of long term chloride penetration. *Materials and Structures*, (32), 354-359.

Kassir, M. K. and Ghosn, M. (2002). Chloride-induced corrosion of reinforced concrete bridge decks. *Cement and Concrete Composites*, 32(1), 139-143.

Maheswaran, T. and Sanjayan, J. G. (2004). A semi-closed-form solution for chloride diffusion in concrete with time-varying parameters. *Cement and Concrete Research*, 56(6), 359–366.

Meira, G. R. (2004). *Chloride aggressiveness in marine atmosphere zone connected with corrosion problems in reinforced concrete structures* (in Portuguese). PhD. Thesis, Federal University of Santa Catarina, Florianópolis, Brazil.

Meira, G. R., Andrade, C., Padaratz, I. J., Alonso, C. and Borba Jr, J.C. (2006). Measurements and modelling of marine salt transportation and deposition in a tropical region in Brazil. *Atmospheric Environment*, (40), 5596–5607.

Pack, S., Jung, M., Song, H., Kim, S. H. and Ann, K. Y.(2010). Prediction of time dependent chloride transport in concrete structure exposed to a marine environment. *Cement and Concrete Research*, 40(2), 302–312.

RILEM TC 178-TMC (2002). Analysis of total chloride content in concrete. *Materials and Structures*, (35), 583–588.

Sandberg, P., Tang, L. and Andersen, A. (1998). Recurrent studies of chloride ingress in uncracked marine concrete at various exposure times and elevations. *Cement and Concrete Research*, 28 (10), 1489- 1503.

Uji, K., Matsuoka, Y. and Maruya, T. (1990). Formulation of equation for surface chloride conctent due to permeation of chloride. In *Proceedings of Corrosion of Reinforcement in Concrete*, Belfast, Ireland, 258 – 267.

Yang, L. F. Cai, R. and Yu, B. (2017). Investigation of computational model for surface chloride concentration of concrete in marine atmosphere zone. *Ocean Engineering*, (138), 105-111.

Zhou, S. (2016). Analytical model for square root increase of surface chloride concentration and decrease of chloride diffusivity. *Journal of Materials in Civil Engineering* (ASCE), 28(4), p.040151811-040151817.

XV International Conference on Durability of Building Materials and Components
DBMC 2020, Barcelona
C. Serrat, J.R. Casas and V. Gibert (Eds)

Carbonation Effect on the Chloride Profile

Carmen Andrade

International Center for Numerical Methods in Engineering (CIMNE), Universitat Politècnica de Catalunya - BarcelonaTECH, Campus Nord UPC, 08034-Barcelona, Spain, candrade@cimne.upc.edu

Abstract. *In natural marine exposures, the chloride profile may have a maximum in the concrete surface (surface concentration) or this maximum may appear some mm or even centimeters, in depth. This fact has been attributed to a) a "washing effect" due the continuous action of the sea water, b) the wet and dry "convection" induced by the action of the sea water waves c) the leaching of the hydroxide ions or d) the carbonation of the external layer of concrete. In a test in the laboratory, the profile resulting in a diffusion chloride test in most of the cases presents the maximum in the surface of the specimen but seldom has this maximum beyond the surface. This behaviour in natural and in laboratory conditions, although noticed, has not been satisfactorily explained. The author has addressed the problem in a previous communication. In present one shows evidences on the role of the carbonates/bicarbonates in the water of the testing solution. It can be deduced from the analysis of the profiles obtained with de-carbonated solutions that the carbonates/bicarbonates ions compete with the chlorides in the binding with the hydrated cement phases, which results in a modification of the chloride profile and a different diffusion coefficient. The maximum seems to be produced by the higher mobility of the chloride with respect to the carbonate/bicarbonate. The bound chlorides are displaced by the carbonation and the free chlorides move inside forward. In the external parts less total chlorides are noticed because the free chlorides are function of the bound chlorides.*

Keywords: *Concrete, Chlorides, Profile, Maximum, Carbonate.*

1 Introduction

In marine environments, chlorides penetrate trough the pore network of concrete. This ingress is usually modelled, through the so named "error function equation", assuming pure diffusion, a constant external chloride concentration and a constant diffusion coefficient, in spite that wet-dry cycles are produced in the atmospheric and tidal zones. The chloride profiles obtained can have a decreasing shape from the concrete surface or can present a maximum some mm inside the concrete (Andrade *et al*., 1997; Andrade *et al.,* 2015). This "anomalous" profile departing from the fickian behaviour has been attributed to four main causes (Baroghel *et al.,* 2012; Qiang *et al.,* 2011; Lianfang *et al.,* 1999; Ngala *et al.,* 1997; Galan *et al.*, 2015): a) convection due to wet and dry cycling b) leaching of calcium and hydroxides, c) carbonation of the concrete skin or d) that the concrete "skin" has a different microstructure than of the concrete bulk. All these processes may overlap with the pure diffusion. The reasons and the interaction of several of them remain without experimental confirmation. The consequence of this lack of description of the process is one of main limitations for the accuracy of the prediction of concrete service life because the error can be of decades.

Present work contributes to study the effect of carbonation in the production of the profile maximum and in particular, analyses the impact in the chloride testing by pure diffusion (ponding test), because it is studied the effect of de-carbonating the external salt solution by boiling the water. The results show that the carbon dioxide dissolved in the solution

influences the profile shape giving different diffusion coefficient that could explain part of the scatter in the testing. The results also show that the previous carbonation does not prevent completely the chloride binding, that also impacts in the value of the diffusion coefficient deduced from fitting of the error function equation.

2 Experimental

The cement used was an OPC of low C_{3A} content (CEM I 52.5 N-SR). Its chemical composition is shown in Table 1.

Table 1. Chemical composition (%) of CEM I 52.5 N-SR 5.

SiO_2	Al_2O_3	CaO	Fe_2O_3	K_2O	MgO	Na_2O	SrO
19.868	3.751	64.356	4.052	0.65	0.624	0.65	0.051

The specimens were of paste in order to avoid the influence of the aggregate proportion in the further analysis. The w/c ratio was of 0.4. Three cylindrical paste specimens of 200 mm height and 150 mm diameter were moulded. After setting and hardening for 24h, the specimens were cured in the humid chamber with humidity higher than 95% and temperature about 23^{o}C for 6 further days. After removing the specimens from the curing chamber, the three specimens were cut horizontally by its half, in order to have the tests by duplicate exposing the same surface (the cut one) to the salt solution.

The following conditions were tested:

1. Normal salt solution of 30 g/l of NaCl
2. De-carbonated: salt solution of 30 g/l de-carbonated by boiling the water before adding the salt in order to expel out the dissolved gases (air)
3. Pre-carbonated: the specimen was first carbonated and then submitted to the 30 g/l NaCl solution.

When the specimens were cut to have the duplicate samples, two of the set (1 and 2) were sealed on all faces except the exposure surface and a pond was placed on the top (cut surface): in set-1 non-de-carbonated and in set 2 the solution was previously de-carbonated.

The other two duplicates of the set-3 were introduced in a carbonation chamber at 100% CO_2 during 30 days. Then, the pond was placed on the cut surface with a normal solution of NaCl for 90 days. The pond was covered with a plastic film in order to minimize the progressive uptake of air by the solution during the exposure time.

Finally, when removing the pond, chloride profiles were made by grinding the specimens mm-per-mm and analysing the chlorides (total and water soluble) (Castellote *et al*., 2002; Castellote *et al.,* 2002a; Cen 12390-11 2009). In the powder samples it was also determined the portlandite and carbonate contents by Differential Thermal Analisys (DTA).

3 Results

The chloride profiles of the three set of specimens are given in Figure 1. The three profiles differ significantly, mainly when the sample was previously carbonated. Each profile is the average of the duplicate samples, which gave very similar ones. The symbols here and in the rest of Figures are: Set-1 (NaCl), set-2 (Cl+CO_2), set-3 (CO_2).

All the profiles of the three set show a maximum some mm far from the concrete surface. Contrary to what was expected the highest chloride concentration is shown by the set-2 with non-de-carbonated solution. The smallest chloride concentration is logically given by the sample previously carbonated, although the high difference between total and water-soluble chlorides indicates that there is significant amount of bound chlorides.

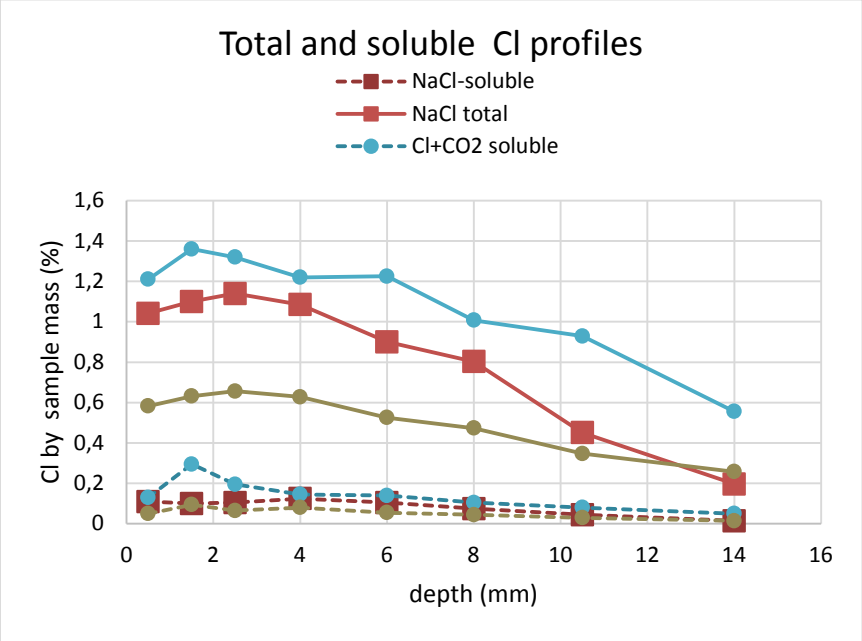

Figure 1. Chloride profiles of total and water soluble chlorides (average of the duplicated samples) of the three set of tests. The symbols here and in the rest of Figures are: Set-1 (NaCl), set-2 ($Cl+CO_2$), set-3 (CO_2).

In Figure 2 is given the relation between the soluble chlorides (named free in the Figures) and the total chlorides in function of the depth of penetration. All the relations are around 0.1% denoting very high binding ability of the cement, in spite of its low C_3A content. This binding is attributed to the chloride adsorption in the C-S-H gel and in the portlandite (Florea and Brouwers, 2012). It is interesting to notice that the relation is not constant because it decreases with the depth and it is a bit smaller in the case of the carbonated specimen. Finally, it is important also to notice that the highest value of soluble chlorides appear in the case of normal salt solution (non-decarbonated set-2) in the depth where the maximum appears and that, therefore, it is the reason of the higher total value.

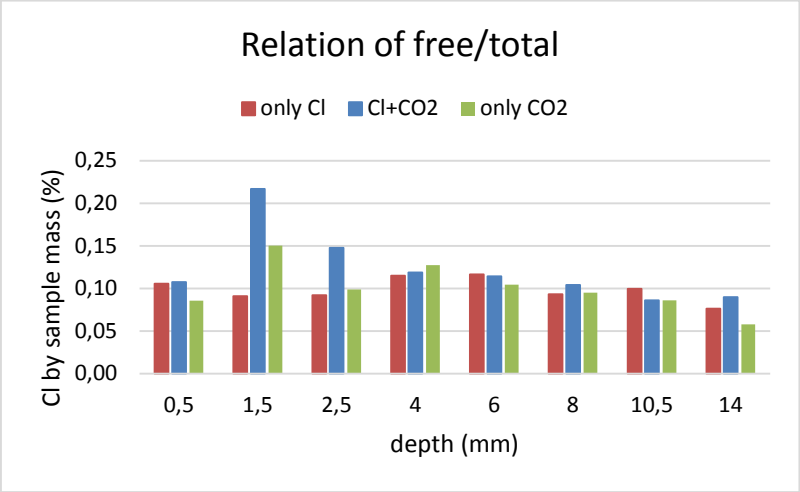

Figure 2. Ratios of free/ bound chlorides in the three set of specimens.

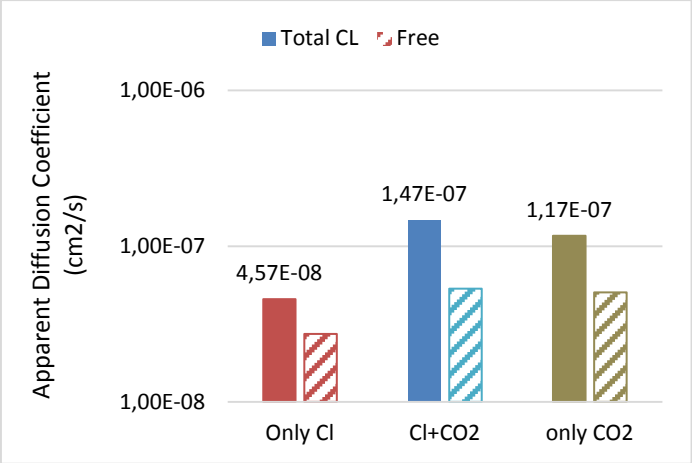

Figure 3. Apparent Diffusion Coefficient calculated through the fitting of the error function equation into the profiles of Figure 1.

The diffusion coefficient and the surface concentration deduced from the fitting of the error function equation into the profiles, are given in Figures 3 and 4 respectively. The diffusion coefficients, D_{ap}, differ between the three set and also between fitting into the soluble and total chloride profiles, being smaller if fitted into the soluble chloride profile. The highest value of both parameters is given by the normal salt solution (set-2) and the smallest surface concentration but highest D_{ap}, in the case of the pre-carbonated specimen (set-3).

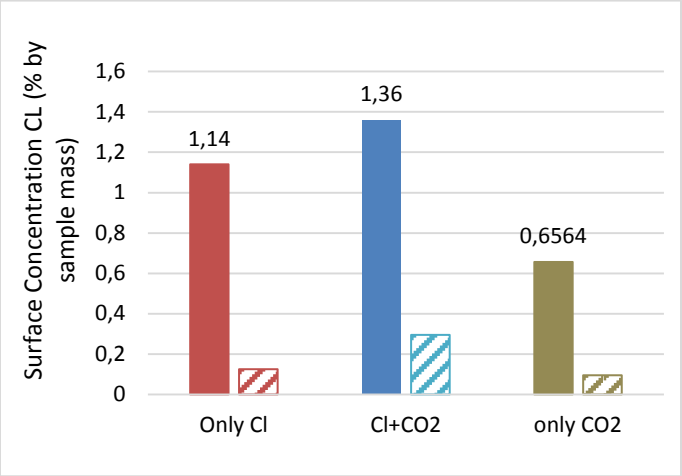

Figure 4. Chloride surface concentration calculated through the fitting of the error function equation into the profiles of Figure 1.

The results of the Portlandite and Calcite contents calculated from DTA analysis are shown in Figure 5 to 7 together with the chloride profiles. One first surprise is that the content of calcite in the surface of the concrete is a bit higher in the sample with de-carbonated solution, which indicates that the carbon dioxide has been uptake during the exposure of the 90 days in spite of the covering of the pond. Other observation is that the calcite profile is decreasing towards the interior and the portlandite, on the opposite, is increasing. Then, the carbon dioxide is reacting at least with the portlandite and carbonation is produced. The pre-carbonated specimen shows logically the highest proportion of calcite, but it is also decreasing towards the interior, which means that the specimen was not homogeneously pre-carbonated and it shows the maximum Calcite content (around 12%) in the surface.

The presence of calcite seems to have a direct relation to the production of the maximum in the chloride profile.

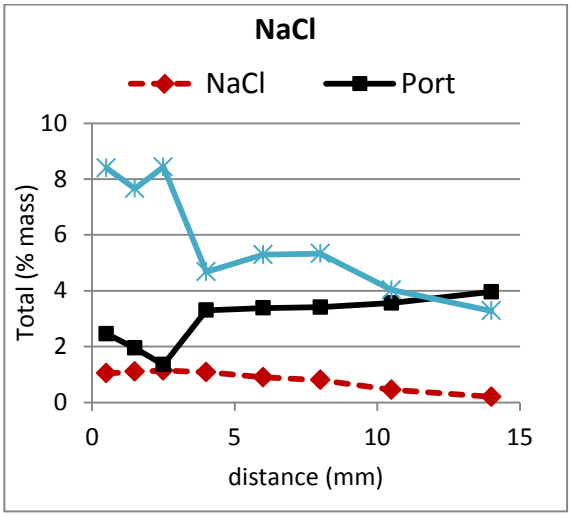

Figure 5. Profiles of calcite, portlandite and total chlorides in set-1.

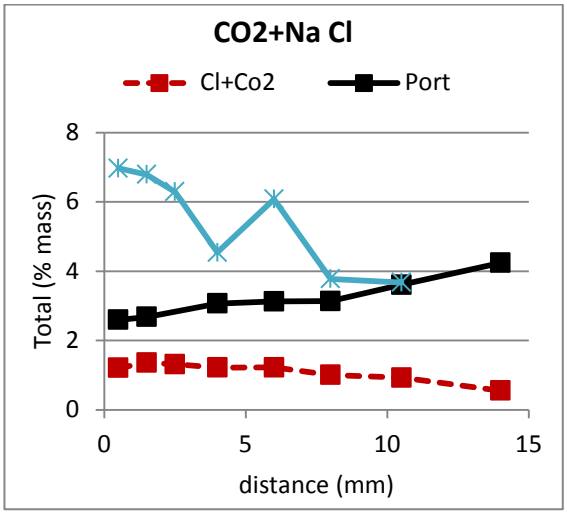

Figure 6. Profiles of calcite, portlandite and total chlorides in set-2.

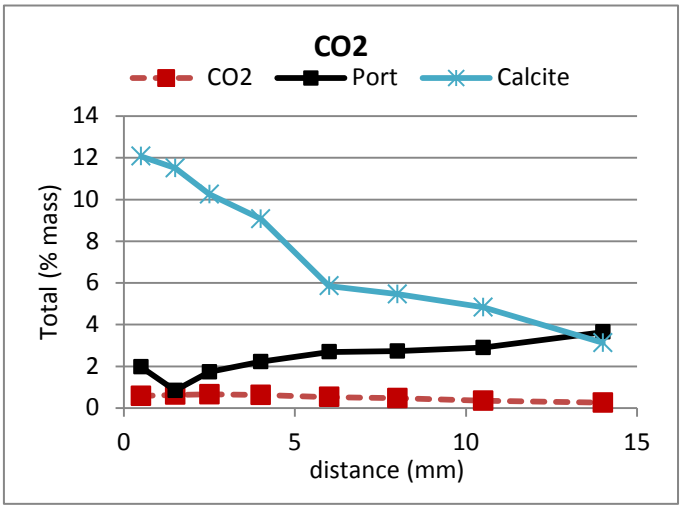

Figure 7. Profiles of calcite, portlandite and total chlorides in set-3.

4 Discussion

The results enable to emphasize that carbonation is not only produced in unsaturated conditions, but it is also produced by the air dissolved in the water in contact to a saturated concrete.

With respect to the mechanism of production of the maximum in the profile, there will be commented further the pre-carbonated sample (set-3) and first the other two cases (set 1 and 2). In set-2, the salt solution has "free" CO_2 gas and bicarbonates due to its neutral pH value. The bicarbonate will be transformed into carbonate ion as soon as it entries in contact to the high alkalinity of the pore solution leading into the precipitation of calcium carbonate, while the calcium bicarbonate is soluble and does not precipitate. There is a buffer of carbonate/bicarbonate at pH = 10.4. The bicarbonates can diffuse inside the sample producing again $CO_3^{=}$ ions. The pH value (OH^- content) simultaneously decreases, also because its leaching out due to the external pH value is neutral.

In set-2 with the standard salt solution, the chlorides and the bicarbonate entry simultaneously but the chlorides have higher ionic mobility. They penetrate first and bind with the hydrated phases (Afm phases, C-S-H gel and portlandite). The bicarbonate arriving later, on one hand, exchanges with the chloride in the hydrated phases releasing free chlorides to the pore solution, which move inwards again. They cannot move backwards due to the concentration gradient. On the other hand, the bicarbonates become carbonate ion due to the high alkalinity, precipitating $CaCO_3$. The $CaCO_3$ nucleation will physically cover the pore walls, decreasing the reactive sites for the chloride in the hydrated phases. Consequently. The total chloride decreases in the carbonated zone.

The maximum is produced because the pushing inside of the released Cl by the carbonation from the bound ones. The CO_2 in the salt solution acts as an intensifier of the chloride penetration. The profile advances due to the gradient between the maximum and its farther front inside the concrete. All the profile moves a step forward. New chlorides have to penetrate from outside to maintain the equilibrium with the bound chlorides to fulfil the so called chloride isotherm (Tang and Nilsson, 1993), all along the profile. That is, the

progressive carbonation of the skin decreases its bound and total chloride content, but does not stop the chloride penetration due to the need to maintain the Bound/ free chloride equilibrium, although this carbonation perhaps reduces with the time the amount of penetrating chlorides and it is one of the reasons of the "aging" effect (decrease with time of the diffusion coefficient). The external carbonated zone acts as a "filter" by the progressive decreasing the chloride flow.

In set-1 with the de-carbonated salt solution, the profile shape is similar than in set-2, but the total amount of chlorides is smaller. If the bicarbonates are in smaller amount, the carbonation will be less intense and the amount of exchanged chlorides in the interior of the pores will be smaller, and so the released free chlorides. The maximum in the profile is produced, but the total chlorides are smaller.

In the case of the pre-carbonated specimen (set-3), the profile shape is different than the other two set, because it is flatter. The total chloride is even smaller than in set-2 due to the reactive sites, from the beginning, are in much smaller amount. Also less chloride amount penetrate perhaps due to the smaller porosity produced by the carbonation. In addition, the pH of the pore solution is neutral, and then the bicarbonate will not be converted into carbonate when entering in the pore network. The neo-formed calcite will be in less amount. The specimens have more calcite due to the previous carbonation.

In this set-3, the pre-carbonation has not being complete enough to stop binding and then, it is remaining Afm, C-S-H and portlandite that are able to adsorb chlorides (Figure 1). This behaviour helps to conclude that the carbonation influences in a different manner the chloride penetration when it is produced previously, than when it is simultaneous to the chloride penetration. One main difference found is the pH value, because while the accelerated carbonation previously decreases the pH of the pore solution towards neutrality, similar to that of the salt solution, in the case of the CO_2 in the solution (set-2), the pH value of the pore solution is initially alkaline.

In summary, not only the carbonation itself, but the equilibrium carbonate/bicarbonate, which is pH dependent, seems to have a key role in the production of the maximum in the chloride profile. This evidence indicates the need to continue the understanding of the process by studying the diffusion of the bicarbonate ion into the pore network, because it seems that the HCO_3^- as being soluble, is a competitor of the chloride to be bound in the reactive sites and because it is evolving to carbonate at high pH level, inducing the precipitation of calcium carbonate, physically affecting the contact area of the pore solution and the reactive hydrated phases.

5 Conclusions

- The air (CO_2) content of the salt solution influences the chloride profile and in consequence, the calculated diffusion coefficient.
- The most aggressive condition (enabling higher chloride penetration) opposite to what was the hypothesis, is that of the standard salt solution (non-de-carbonated). This enables to confirm that present testing conditions for natural diffusion, are the most convenient ones.
- The pre-carbonation of the specimen leads into smaller amount of penetrated chlorides and a flatter profile.

- The production of the maximum in the chloride profile is attributed to the higher ionic mobility of the chlorides with respect to the carbonate/bicarbonates. Chloride binding is produced before the advance of the $CO_3^{=}/HCO_3^{=}$. When carbonation is produced behind the chloride penetration, chlorides are released that move forward making the profile to advance.
  - In the external layers of concrete the bound chlorides are smaller due to the carbonation. This mechanism may contribute to the known as "aging effect".
  - Bound chlorides have to be in equilibrium with the free chlorides given by the corresponding isotherm.
- Previous carbonation decreases the amount of reactive sites for the chlorides although may not fully exhaust them.
  - A maximum is also noticed in the pre-carbonated specimen attributed to the same mechanism than the non-carbonated, as in the material remain sites for chloride adsorption.

Acknowledgements

The author is grateful to Prof. A. Moragues of the Faculty of Civil Engineering of the Polytechnic University of Madrid for the fruitful discussions on the subject and the analysis made on the samples.

References

Andrade, C. Díez, J. and M. Alonso, C. (1997). Mathematical modelling of a concrete surface "skin effect" on Diffusion in chloride contaminated media. *Advances Cement Based Materials, 6,* 39-44.

Andrade, C. Climent, M.A. and de Vera, G. (2015). Procedure for calculating the chloride diffusion coefficient and surface concentration from a profile having a maximum beyond the concrete Surface. *Materials and Structures, 48*, 863–869.

Baroghel-Bouny, V., Wang, X., Thiery, M., Saillio, M. and Barberon, F. (2012). Prediction of chloride binding isotherms of cementitious materials by analytical model or numerical inverse analysis. *Cement and Concrete Research, 42,* 1207-1224.

Castellote, M. and Andrade, C. (2002). Analysis of total chloride content. RILEM Recommendation of TC-178-Testing and modelling chloride penetration in concrete. *Materials and Structures, 35,* 583-585.

Castellote, M. and Andrade, C. (2002a). Analysis of water soluble chloride content in concrete. RILEM Recommendation of TC-178. Testing and modelling chloride penetration in concrete. *Materials and Structures, 35,* 586-588.

CEN/TS 12390-11: 2009. Testing hardened concrete. Determination of the chloride resistance of concrete. Unidirectional diffusion.

Florea, M.V.A. and Brouwers, H.J.H. (2012). Chloride binding related to hydration products Part I: Ordinary Portland Cement and Concrete Research, 42, 282-290.

Galan, I. and Glasser, F.P. (2015). Chloride in Cement. *Advances in Cement Research, 27*(2), 63-97.

Lianfang, L. and Sagües A.A. (1999). Effect of chloride concentration on the pitting and repassivation potentials of reinforcing steel in alkaline solutions. *NACE Corrosion Paper, 567.*

Ngala, V.T. and Page, C.L (1997). Effects of carbonation on pore structure and diffusional properties of hydrated cement pastes. *Cement and Concrete Research, 27*(7), 95-1007.

Qiang, Y., Caijun, S., De Schutter, G., Dehua, D. and Fuqiang, H. (2011). Chloride Ion Concentration on the Surface of Cement-Based Materials in Chloride Solutions. *Journal of the Chinese Ceramic Society, 39*(3), 544-549.

Tang, L.P. and Nilsson, L.O. (1993). Chloride binding capacity and binding isotherms of OPC pastes and mortars. *Cement and Concrete Research, 23,* 247-253.

XV International Conference on Durability of Building Materials and Components
DBMC 2020, Barcelona
C. Serrat, J.R. Casas and V. Gibert (Eds)

Detailed Modelling of the Masonry Unit-Mortar Interface Using Hygrothermal Simulation

Michael Gutland, Scott Bucking and Mario Santana Quintero

Department of Civil and Environmental Engineering, Carleton University, Ottawa Ontario, Canada,
michaelgutland@cmail.carleton.ca

Abstract. *Hygrothermal models are important tool for assessing the risk of moisture-related decay mechanisms in historic masonry structures. However, there are significant uncertainties in the process related to material properties, boundary conditions and quality of construction that effect confidence in the model's predictions compared to measured values. This paper examines one potential source of uncertainty; the imperfect nature of mortar joints in masonry walls, exemplified by such things as open joints, hairline cracks and imperfect bonds at the interface between mortar and unit. These are rarely considered in hygrothermal modelling in detail, where perfect interfaces are typically inferred. The premise is that at this interface, liquid transport behaviour is more similar to that of a fracture than that of a bundle of capillaries. These fractures of varying heights (or aperture) can affect transport into and out of the plane of the wall (perpendicular plane) and impede the liquid transport between mortar and the masonry unit (in-plane). This could lead to the "effective" moisture transport being different than what would be predicted using measured bulk material properties. A more detailed method for modelling this interface, borrowing techniques from the field of geohydrology is presented which demonstrates the effect that detailed modelling of the mortar joint has on moisture transport in masonry. A brick wall with cement mortar is studied. A two-dimensional hygrothermal model was created to demonstrate the effect of increased liquid conductivity into the wall cause by fractures.*

Keywords: *Masonry, Hygrothermal Simulation, Moisture Transport, Calibration, Mortar.*

1 Introduction

Hygrothermal models are an important tool for assessing the risk of moisture-related decay such as biological growth (mould and wood rot fungi), corrosion and freeze-thaw action in building envelopes. There are several gaps in our understanding and application of hygrothermal modelling involving uncertainty of material properties, boundary conditions, two-dimensional interactions and quality of construction. This can make it difficult to calibrate hygrothermal models to in-situ measurements and without calibration, our confidence in a hygrothermal model's predictions is lessened.

This paper examines one potential source of uncertainty; namely, the imperfect interface between mortar and the masonry unit. Imperfections may take the form of open joints (mm range), hairline cracks (μm range), or an imperfect bond between the mortar and the unit (**Figure 1**). These can be caused by structural displacements, shrinkage, decay/maintenance or inherent from its construction. It is intuitive to assume that a large presence of these openings will increase moisture transfer into the wall caused by wind-driven rain. The question is how much

and how do we properly account for this in hygrothermal simulations?

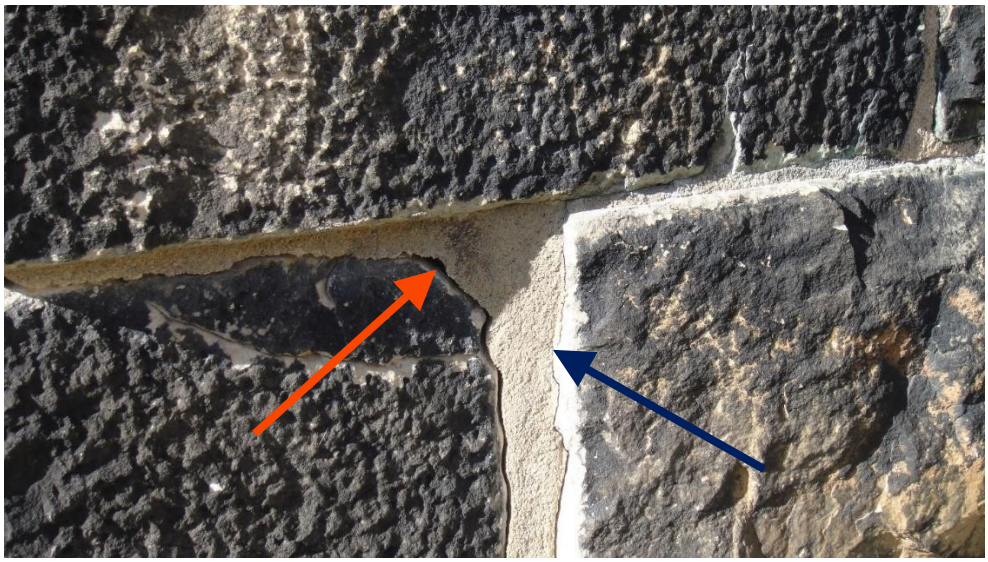

Figure 1. Sandstone masonry wall with open joint (Orange arrow) and hairline crack (dark blue arrow) between stone and mortar.

This paper proposes a methodology for explicitly modelling imperfections at the masonry interface by modelling this region as a fracture. The models assume a varying crack width (also called aperture). Material properties of the fracture are derived from fundamental principles for moisture retention and liquid conductivity.

2 Literature Review

Hygrothermal modelling software simulates the coupled heat and moisture flow (vapour and liquid) through building envelopes and assemblies using finite-element methods. The coupled heat and moisture equations are given in Equations 1 and 2:

$$\frac{\partial H}{\partial t} = -\nabla[\lambda \nabla T + h_v(k_v \nabla P_v) + h_l(k_l \nabla P_c)] \tag{1}$$

$$\frac{\partial w}{\partial t} = -\nabla(k_v \nabla P_v + k_l \nabla P_c) \tag{2}$$

Of particular interest to this paper is the term for liquid conductivity k_l. This controls the rate of liquid water ingress into a material by a capillary pressure gradient. Liquid conductivity is a function of moisture content and can be estimated from water absorption tests or pressure plate apparatus.

2.1 Masonry Interface

Previous studies have looked at moisture transfer at the interface and have shown that there is an interface resistance (R_{IF}) which inhibits transfer from one material to the other. This is analogous to contact resistances in the heat transfer of electronics. The presence of an interface resistance is caused by one of two reasons. The first is an imperfect contact between the two materials which forces water to travel across the interface through vapour diffusion instead of

the faster capillary method. The second reason is migration of fine particles toward the mortar joint during the curing stages (Brocken, 1998). The fine particles form smaller pores near the interface, and this reduces liquid flow.

Laboratory testing has measured the interface resistance between 1.0E08 and 1.0E12 m/s (Calle, De Kock, Cnudde, and Van den Bossche, 2019; Derluyn, Janssen, and Carmeliet, 2011; Qiu, Haghighat, and Kumaran, 2003). Simulations have demonstrated the effect that the interface resistance have on moisture uptake (Vereecken and Roels, 2013; Zhou, Desmarais, Vontobel, Carmeliet, and Derome, 2018). These methods only consider moisture transfer across the interface and not parallel to it.

2.2 Fractures in Masonry

There have been previous studies exploring water uptake in fractured building materials. Roels (2003) examined water uptake in a fractured brick sample and Rouchier (2012) modelled a detailed 2D crack network in a sample of concrete. Both studies required a detailed geometry of the fracture to be defined and meshed into a finite – element model. This is time and computationally expensive. It is also highly unfeasible to do on anything greater than a small sample. Modelling with an assumed fracture width will remove this need.

These simulations were also done on homogenous materials, meaning that the material was the same either side of the fracture. In a masonry interface that is not true as the material properties of the two adjacent materials may be quite different. These studies also looked primarily at water uptake and did not consider the drying phase.

2.3 Capillary Mechanics

Hygroscopic materials are often idealized as a bundle of round capillaries or pores of varying sizes. With knowledge of the pore size distribution though porosimetry or other means, it is possible to infer many of the important hygroscopic material properties required to model moisture transport. This includes the moisture retention, liquid conductivity and vapour diffusion curves. The Young-Laplace equation relates capillary pressure to pore radius:

$$\Delta P = \frac{2\gamma cos\theta}{r} \tag{3}$$

If the capillary suction pressure is greater than this, a capillary with this radius will not be filled. The Kelvin Equation describes the relationship between vapour pressure and condensation inside the capillary:

$$\mathrm{LN}\left(\frac{p}{p_{sat}}\right) = \frac{2\Gamma \mathrm{V_M}}{\mathrm{RRT}} \tag{4}$$

These equations combined with the pore size distribution allow for construction of the moisture retention curve, describing the relationship between saturation and capillary suction pressure. Narrower pores retain moisture longer and larger pores catch and release moisture more easily.

Moisture retention curves can be measured in the laboratory or estimated with the Van Genuchten equation, where α and n are material- specific parameters (van Genuchten, 1980).

$$P_c = \frac{1}{\alpha}\left[S_{eff}^{-\left(\frac{n}{n-1}\right)} - 1\right]^{\frac{1}{n}} \tag{5}$$

Liquid Conductivity is also a function of the capillary radius and can be calculated through the Hagen-Poiseuille equation:

$$k_l = \frac{\rho r^2}{8\eta_l} \tag{6}$$

Liquid transport only occurs when capillaries are filled. Therefore, liquid conductivity is a function of saturation and exponentially increases with saturation. The moisture-dependent conductivity $k_l(\theta_l)$ can be estimated by integrating the Hagen-Poiseuille over the range of active capillaries or by using the Burdine relative permeability approach (Burdine, 1953).

$$k_l(\theta_l) = \frac{\rho}{\tau} \int_{R_{min}}^{R} \frac{\pi r^4}{8\mu_l} \frac{dn}{dr} dr \tag{7}$$

The theoretical curve will not match the measured liquid conductivity curves (Scheffler, Grunewald, and Häupl, 2004). Tortuosity (τ) is included in this equation to account for the reduction in flow due to tortuosity, pore shape and the degree of interconnectivity of pores. Likewise, vapour diffusion can be estimated from fundamentals, but is not discussed here.

Determining the hygroscopic properties of a fracture is similar to the process for determining those of capillary materials. To begin, we need to determine the size of the aperture with which liquid is flowing, similar to what is learned from the pore size distribution. Aperture (h) is the distance between the boundary surfaces of the fracture. Apertures are not constant in real-world applications because it widens and contracts along its path and generally follows a tortuous path. There are two methods for determining an "effective" aperture. The first is to use the average aperture ($\overline{h}$), and the other is to use the hydraulic aperture (h_H) which is the value which would make the cubic law true (Zimmerman and Bodvarsson, 1994).

Typical apertures in subterranean rock are reported to be in the 0.001-0.1 mm range (Pyrack-Nolte, Myer, Cook, and Witherspoon, 1987). Fractures in building materials range are in a similar range ((Roels *et al*., 2003; Rouchier, 2012). Anything much smaller than this and liquid transport is greatly reduced.

The hygroscopic material properties of the fracture can be calculated with a few distinctions to that of capillary materials. The liquid conductivity is calculated with the cubic-law or Reynold's Equation, the difference being a change in the denominator.

$$k_l = \frac{\rho_h{}^2}{12\eta_l} \tag{8}$$

Fractures can also have a much higher porosity with few obstructions. A smooth moisture retention curve can be created if an aperture distribution is assumed. The larger the aperture the further to the left the curve will be.

3 Methodology

DELPHIN 6.0 was used for hygrothermal simulations (Bauklimatik Dresden, 2018). DELPHIN allows input of custom material properties including direction-dependent properties, detailed moisture retention curves, and moisture-dependent liquid and vapour transfer coefficients.

3.1 Material Properties

The first step was to define material properties of the masonry. Typical bulk material properties for brick and cement mortar were determined by the taking median values for all materials of its class in the DELPHIN library. The moisture retention curve for each material was estimated using a unimodal Van Genuchten with parameters n and α where calculated using least-squares regression.

Table 1. Bulk material properties used in hygrothermal simulations.

Position	Clay Brick	Cement Mortar
θ [--]	0.294	0.2296
λ [W/m-K]	0.682	0.723
μ [--]	20.2	25.6
$k_{l,\,eff}$ [s]	2.21E-09	9.053E-12
n [--]	1.55	1.48
α [1/Pa]	1.00	2.172

The approach for creating the liquid conductivity curve was to use the theoretical curve (Equation 7) below the capillary water content (θ) scaled by the tortuosity (**τ**).

$$\tau = \frac{k_l(\theta_{cap})}{k_{l,eff}} \tag{9}$$

The liquid conductivity above the capillary suction curve was held fixed at $k_{l,eff}$. For simplicity, sorption hysteresis, temperature or moisture-dependent thermal properties and air permeability were neglected for the purposes of this experiment.

The fracture material properties were calculated based on apertures in a range from 0.25μm to 10μm. The fractures were modelled as a normally distributed curve with standard deviation of (h/2). This was done to smooth the moisture retention curve and help the numerical calculations. At high degrees of saturation, the liquid conductivity of the fracture is several orders of magnitude greater than the brick and mortar. It is less pronounced at lower degrees of saturation. Even though the exposed area of the fracture is small it can contribute to an increase in overall moisture transport.

3.2 Finite-Element Model

There are three materials in the finite element model shown in Figure 2: unit, interface and mortar. The dimensions of the model (taking advantage of symmetry) are 5mm thick mortar, *x* mm aperture and 28mm brick. The width of the assembly is 92mm.

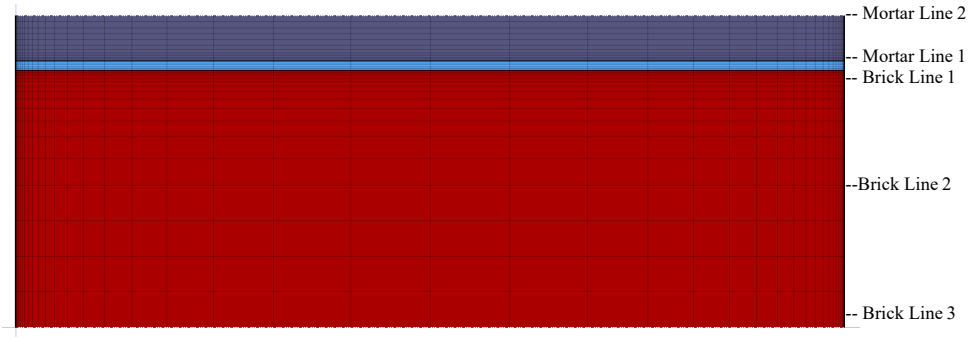

Figure 2. Finite Element Model (interface is not drawn to scale).

3.3 Boundary and Initial Conditions

The simulation was performed under the following boundary conditions:

1. Water Uptake – All materials set to 50%RH and exposed to a capillary pressure of -0.025m on one side only. This was done to mimic a water absorption experiment.
2. Drying – All materials are set to 99.99%RH and exposed to an RH of 30% on one side.

All other sides are adiabatic and there is no temperature gradient, sources/sinks in the model.

4 Results

A sample of the results are shown in **Figure 3** and **Figure 4** for the moisture content of the brick

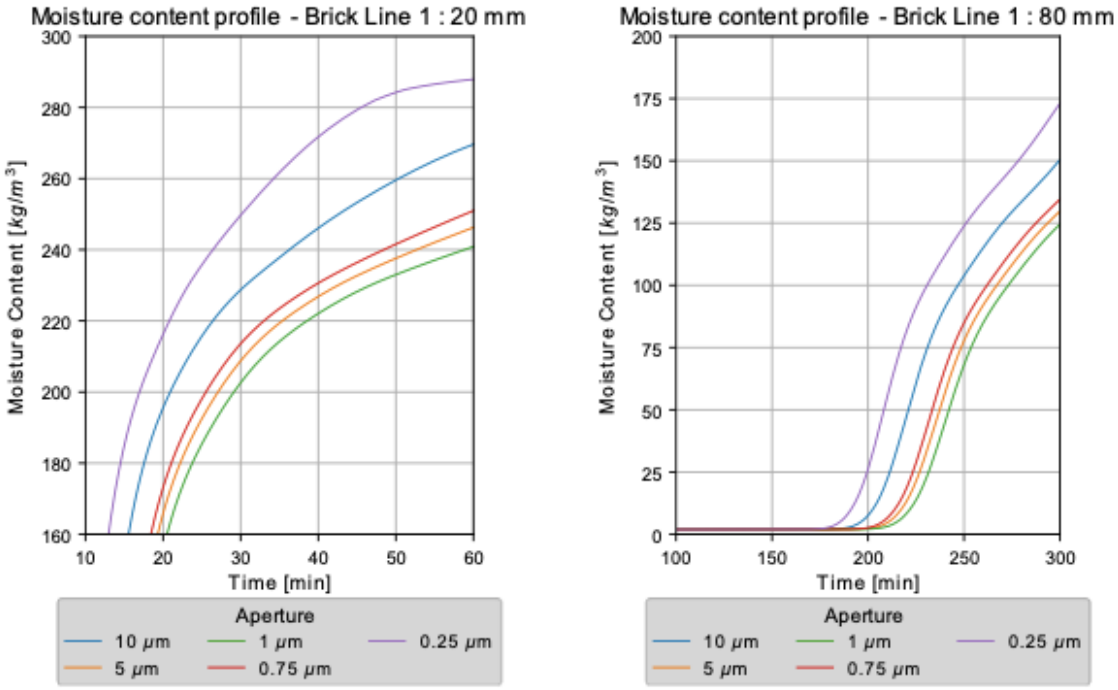

Figure 3. Moisture content of the brick adjacent to the fracture at 20mm depth (left) and 80 mm depth (right).

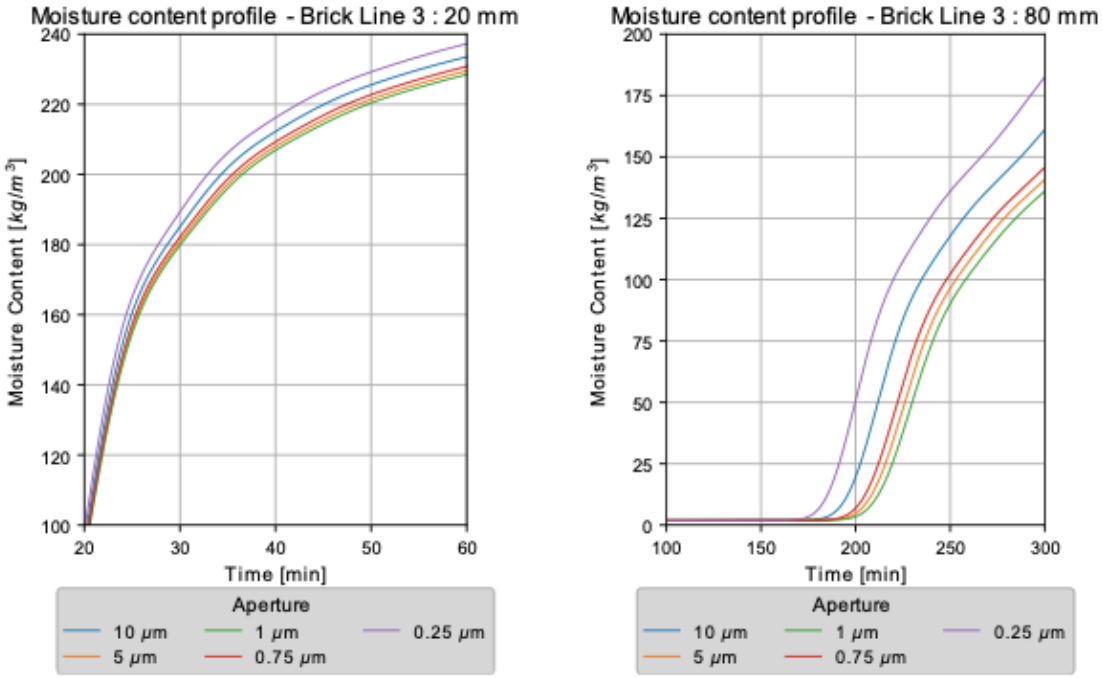

Figure 4. Moisture content of the brick at centreline of brick at 20mm depth (left) and 80 mm depth (right).

adjacent to the fracture and at the centreline of the brick. The results show that there is a significant change in moisture content depending on the aperture height. What is interesting to note is that there does not appear to be a linear relationship between moisture absorption and aperture, in fact it appears to be parabolic. Both sets of graphs show that a 1 µm aperture (green) has the minimum uptake while both smaller apertures (purple and red) and larger apertures (blue and orange) have increased absorption. The smaller apertures, while having a lower maximum flow rate are easier to fully wet and become active at higher capillary pressures. The larger apertures need extremely low (and in the reality of building walls, extremely rare) capillary pressures to become active and allow liquid to flow. The effect was noticeable adjacent to the fracture and the centre of the unit.

The simulation was performed on a sandstone/lime mortar combination with roughly twice the material dimensions. The results were not as pronounced as the case of brick/cement mortar combination. The impact of the fracture appears to be dependent on bulk material properties and the relative area density of the interfaces.

The drying simulation was performed over the course of one calendar year. The effect of the fracture was found to be minimal with a reduction in RH of less than 1% at the centre of the brick. It was determined that any enhancement to vapour diffusion out through the fracture was minimal.

5 Conclusion

The results of the DELPHIN simulations show that modelling imperfections at the masonry interface explicitly as fractures can affect simulation results compared to using only bulk material properties. The presence of fractures greatly increases the liquid conductivity locally

in a fashion similar to a thermal bridge. Future work will look at incorporating an anisotropic model into the fracture interface to account for interface resistances across the fractures as well as under more realistic boundary conditions such as typical meteorological years. Further research needs to be done to determine what the range of apertures are common in masonry walls and correlate the models to experimental data. The goal is to determine "effective" moisture transport coefficients which take into consideration imperfections and two-dimensional interactions which can be used by practitioners.

ORCID

Michael Gutland: https://orcid.org/0000-0001-8907-4046
Mario Santana Quintero: https://orcid.org/0000-0002-3836-9714
Scott Bucking: https://orcid.org/0000-0002-3237-183X

References

Bauklimatik Dresden. (2018). DELPHIN 6.0 (Version 6.0.18). Dresden.

Brocken, H.J.P. (1998). Moisture transport in brick masonry: The grey area between bricks (Dissertation). Technische Universiteit Eindhoven.

Burdine, N.T. (1953). Relative Permeability Calculations From Pore Size Distribution Data. SPE-225-G, 5(03), 71–78. https://doi.org/10.2118/225-G

Calle, K., De Kock, T., Cnudde, V. and Van den Bossche, N. (2019). Liquid moisture transport in combined ceramic brick and natural hydraulic lime mortar samples: Does the hygric interface resistance dominate the moisture transport? *Journal of Building Physics, 43*(3), 208–228. https://doi.org/10.1177/1744259119857762

Derluyn, H., Janssen, H. and Carmeliet, J. (2011). Influence of the nature of interfaces on the capillary transport in layered materials. *Construction and Building Materials, 25*(9), 3685–3693. https://doi.org/10.1016/j.conbuildmat.2011.03.063

Pyrack-Nolte, L.J., Myer, L.R., Cook, N.G.W. and Witherspoon, P.A. (1987). Hydraulic and mechanical properties of natural fractures in low-permeability rock. Presented at the Research Org.:Lawrence Berkeley Lab., CA (USA). Retrieved from https://www.osti.gov/servlets/purl/6406367

Qiu, X., Haghighat, F. and Kumaran, M. (2003). Moisture Transport Across Interfaces Between Autoclaved Aerated Concrete and Mortar. *Journal of Building Physics, 26*. https://doi.org/10.1177/109719603032804

Roels, S., Vandersteen, K. and Carmeliet, J. (2003). Measuring and simulating moisture uptake in a fractured porous medium. *Advances in Water Resources, 26*(3), 237–246. https://doi.org/10.1016/S0309 1708(02)00185-9

Rouchier, S. (2012). Hygrothermal performance assessment of damaged building materials (Doctorate, Université de Lyon). https://doi.org/10.13140/rg.2.1.1532.4561

Scheffler, G., Grunewald, J. and Häupl, P. (2004). Calibration of an engineering model of hygrothermal material characterisation. Council for Research and Innovation in Building and Construction W40 Meeting. Presented at the Glasgow, Scotland. Glasgow, Scotland: Council for Research and Innovation in Building and Construction.

Van Genuchten, Martinus. Th. (1980). A Closed-form Equation for Predicting the Hydraulic Conductivity of Unsaturated Soils1. *Soil Science Society of America Journal, 44*(5), 892. https://doi.org/10.2136/sssaj1980.03615995004400050002x

Vereecken, E. and Roels, S. (2013). Hygric performance of a massive masonry wall: How do the mortar joints influence the moisture flux? *Construction and Building Materials, 41,* 697–707. https://doi.org/10.1016/j.conbuildmat.2012.12.024

Zhou, X., Desmarais, G., Vontobel, P., Carmeliet, J. and Derome, D. (2018). Water uptake in masonry: Effect of brick/mortar interface. *7th International Building Physics Conference Proceedings*, 103–108. Syracuse.

Zimmerman, R.W. and Bodvarsson, G.S. (1994). Hydraulic Conductivity of Rock Fractures. Lawrence Berkley Laboratory.

XV International Conference on Durability of Building Materials and Components
DBMC 2020, Barcelona
C. Serrat, J. R. Casas and V. Gibert (Eds)

Drying Potential of Wood Frame Walls Subjected to Accidental Water Infiltration

Marijke Steeman, Nathan Van Den Bossche and Klaas Calle

Building Physics research group, Ghent University, J. Plateaustraat 22 B-9000 Ghent, Belgium, Marijke.Steeman@UGent.be

Abstract. *Wood frame construction is the most widespread building method. In Belgium the number of wood frame buildings has grown in the last years: in 2018 over 10% of all new built dwellings were wood frame buildings. This increase can be partly attributed to the growing attention for energy performant buildings with a low environmental impact. In contrary to masonry construction, wood frame is more vulnerable to moisture problems, mould growth and wood rot. An important risk is water infiltration through imperfections in the building envelope as a result of driving rain. Therefore it is important for the design to be resilient and allow drying without consequential damage. To analyze the drying potential, an experimental set-up with 8 wood frame compartments was built. The compartments differ in the type of insulation material (mineral wool or cellulose) and the type of vapour retarder (OSB or smart vapour retarder) that were used. In this way 4 types of compartments were obtained, each having a different combination of insulation and vapour retarder. Of each combination there are 2 identical compartments. This allows to insert water in one of both, to mimic rain water infiltration from the outside into the compartment. Temperature, relative humidity and moisture content were measured on different locations in the construction (in total 92 sensors). In this way, the hygrothermal performance of the compartments with and without water infiltration can be analyzed, as well as the drying rate.*

Keywords: *Wood Frame Construction, Measurements, Drying, Water Infiltration.*

1 Introduction

Though masonry is the most common construction method in Belgium, wood frame construction is gaining more popularity. On the one hand this can be attributed to the stricter energy requirements and the associated thicker insulation layers. On the other hand, there is also a growing attention for sustainable construction, *i.e.* CO_2 captured in wood. In 2018, over 10% of all new dwellings were wood frame buildings and that number has increased over the last years. Also for renovations and extensions to existing buildings, wood frame is interesting due to its limited weight (Houtinfobois, 2019).

Scandinavian countries or countries such as Canada where wood frame is the main construction type, are characterised by a cold climate that limits the conditions for mould growth. In contrast to that, Belgium has a moderate maritime climate with a dominant wind-driven rain from south-west orientation. It is therefore crucial to design constructions in a resilient way to guarantee drying without consequential damage in case of accidental water infiltration.

This paper therefore investigates the hygrothermal performance and the drying potential of different wood frame wall constructions subjected to water infiltration, using in-situ measurements on a test wall.

doi:10.23967/dbmc.2020.039

2 Experimental Set-up

2.1 Pavilion and Test Wall

A test pavilion (6,60m x 4,37m) called “STEAMlab21” was built in Kortrijk and consists of two adjacent rooms. Figure 1 shows the floor plan and a vertical section of the pavilion.

The exterior north-west facing wall is replaceable and used as a test wall. The test wall is a wood frame wall with 8 compartments. The compartments consist of I-joists filled with insulation material, wood fibre board and a ventilated wooden cladding at the outside. At the inside a service cavity with a gypsum fibreboard finishing is installed. All other exterior walls of the pavilion are constructed with SIP panels.

The test pavilion and the test wall were built about one year prior to the measurements described in this paper and therefore subjected to the outdoor climate.

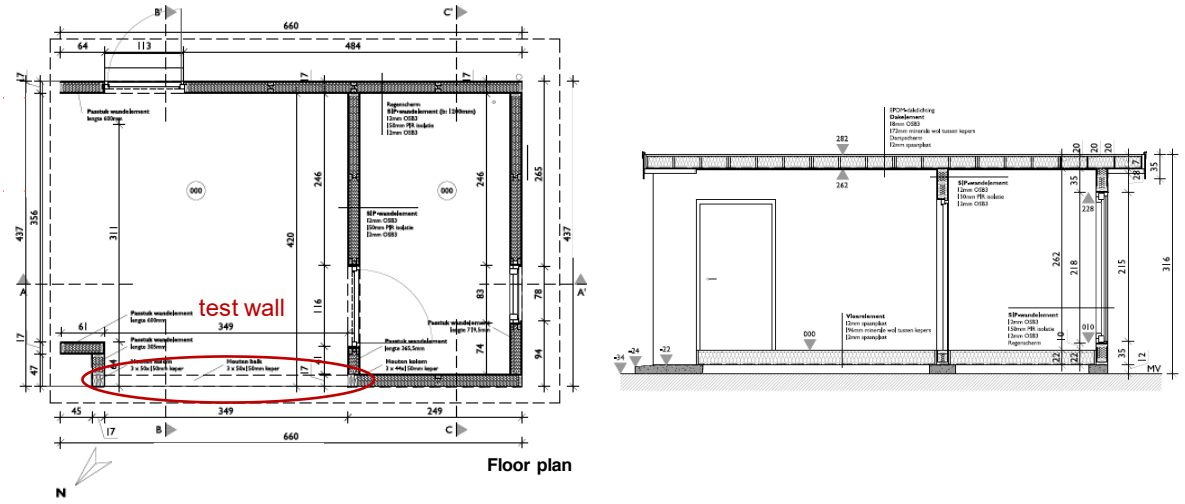

Figure 1. Floor plan (left) and section AA’ (right).

Each compartment of the test wall measures 34,4 cm width and 266 cm height. The compartments differ in the type of insulation material and the type of vapour retarder that were used. Two types of insulation material were used: mineral wool and cellulose; and two types of vapour retarder: a smart vapour retarder (SVR) and oriented strand board (OSB). In this way 4 types of compartments were obtained, each having a different combination of insulation and vapour retarder. Two identical compartments of each combination of insulation type and vapour retarder were available.

Water is added from the outside in one of the two identical compartments, mimicking rain water infiltration. In order to avoid mutual influence between the compartments, a vapour tight coating was applied to the I-joists between the compartments. Figure 2 lists the characteristics of each wall compartment, while Table 1 shows an overview of the most important material properties. The U-value of the test wall was 0,10 W/m²K for the compartments with mineral wool and 0,11 W/m²K for the compartments with cellulose.

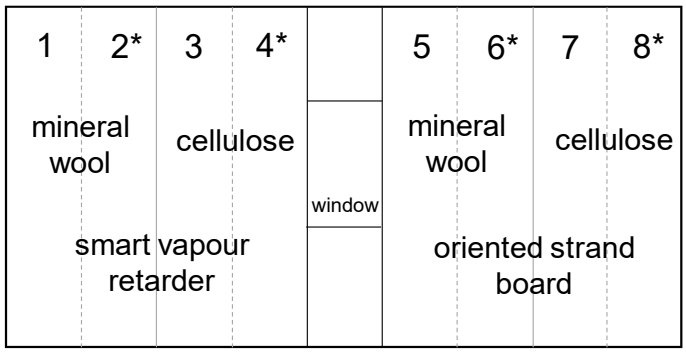

Figure 2. Schematic overview of the test wall with 8 compartments. Compartments with water injection are marked with *.

Table 1. Characteristics of the materials used in the test wall.

Material	Thickness (m)	Thermal conductivity (W/mK)	Vapour diffusion resistance factor (-)
Wooden cladding	0,026	0,090*	-
Ventilated cavity	0,022	-	-
Wood fibre board	0,022	0,048	5
Glass wool (blown in)	0,300	0,034	1
Cellulose (blown in)	0,300	0,038	1-2
Smart vapour retarder	0,0004	0,170	Sd 0.25 → 25 m
OSB3 board	0,015	0,130	175
Service cavity	0,06 - 0,072	-	1
Gypsum fibre board	0,0125	0,320	13

All data are based on technical specifications, (*) data based on the material database in WUFI.

2.2 Measurement Equipment

Temperature, relative humidity and moisture content were measured on different locations in the test wall. In total 92 sensors were installed. At the following locations, also indicated in Figure 3, thermocouples type K (accuracy ±0,1°C) and RH sensors (HIH-40000 Series Humidity Sensors, accuracy ±3,5% RH) were installed:

- On the inner surface of the wall at two locations: in the middle of the left and right wall side, at half height
- In the service cavity of each compartment at ± 1,80m height (illustrated in Figure 4, left photo)
- On the interior side of the insulation layer for each compartment, at two heights: at ± 0,80m and at ± 1,80 m height
- On the exterior side of the insulation layer for each compartment, at ± 1,80 m height
- In the ventilated cavity of the wall at two locations: in the middle of the left and right wall side, at ± 0,80m and at ± 1,80 m height (illustrated in Figure 4, photo on the right)

All sensors were connected to a data logger that registers the measurements every 15 minutes. Additionally, in each compartment of the test wall two moisture pins were installed and connected to the data logger: one in the bottom plate and one in the I-joist to measure the

moisture content of the wood. Unfortunately, the results of these moisture content measurements showed to be unreliable and therefore they are not included in this paper.

Furthermore the temperature and relative humidity of the indoor and outdoor climate were monitored. A HOBO U12-013 was used to monitor the indoor temperature (accuracy ± 0,21°C) and relative humidity (accuracy ± 2,5 % RH). A HOBO U23 Pro v2 logger was located outside shielded from direct sun irradiation and precipitation for measuring temperature (accuracy ± 0,21°C) and relative humidity (accuracy ± 2,5 %RH).

A convector was installed in the test room to control the indoor climate. The set point was 20°C. Furthermore, a fan was used to ensure well-mixed air conditions.

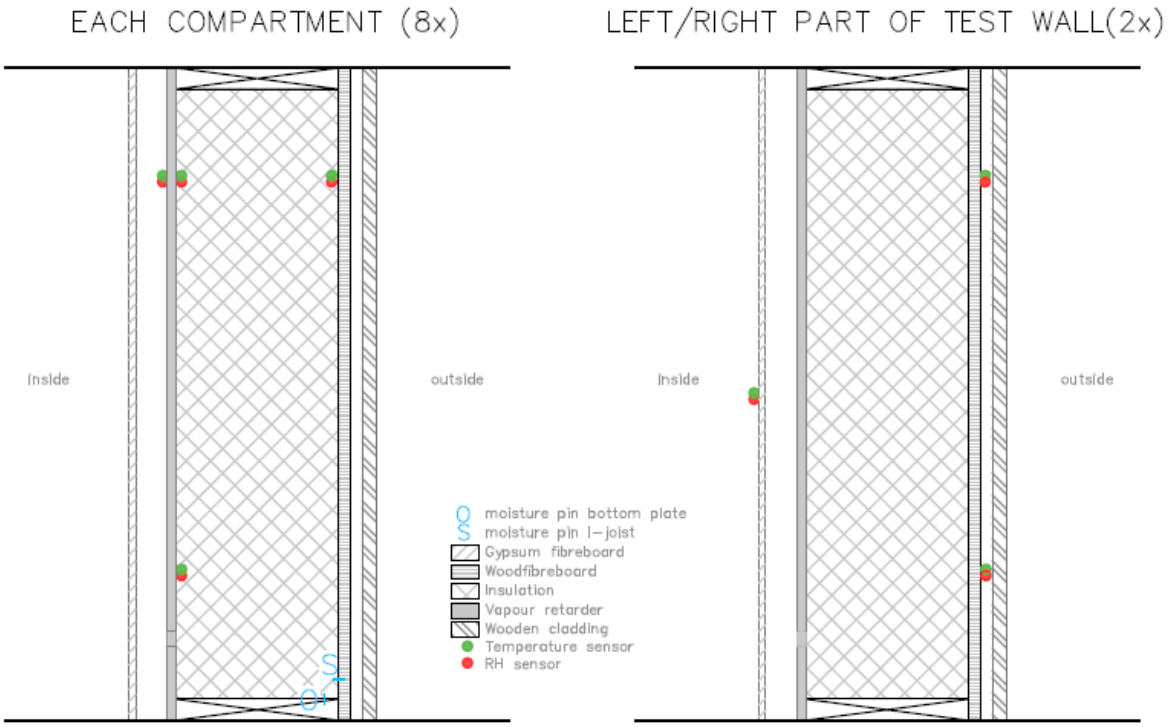

Figure 3. Scheme with location of the sensors in the test wall.

2.3 Water Infiltration

In 4 compartments (2, 4, 6 and 8) 0,2323 l water was injected into the insulation layer. Figure 4 (photo on the right) shows the outside of the test wall with the infiltration tubes at half height. The tubes were installed in such a way that the water is infiltrates between the wood fibre board and the insulation layer.

The amount of water was calculated based on the horizontal rain load during a heavy rain shower with a duration of 4 hours in Belgium (rain load 72,4 mm or 18,1 mm/h based on data from RMI), the measured wind speed during a realistic rain event (based on Van Goethem, 2014) and a worst case infiltration percentage of 0,6% of the incident rain that infiltrates in the construction. The latter was based on water infiltration measurements in a typical cavity wall construction (Geldof, 2016). In this way, a rather high amount of rain water infiltration was obtained, based on the maximum rain load.

Figure 4. View on the compartments from the inside (photo left) and view on the outside with water infiltration tubes, indicated with a red circle (photo right).

3 Measurement Results

Measurements were carried out for 30 days from April 28th to May 27th 2019 every 15 minutes. Water was injected on April 30th 2019 at 2 pm. After the water was injected, measurements ran for 27 days.

3.1 Moisture Buffering Effect

Figure 5 shows the course of the relative humidity in the insulation layer for a compartment filled with mineral wool (compartment 5) and a compartment filled with cellulose insulation (compartment 7). In both compartments, there was no water infiltration.

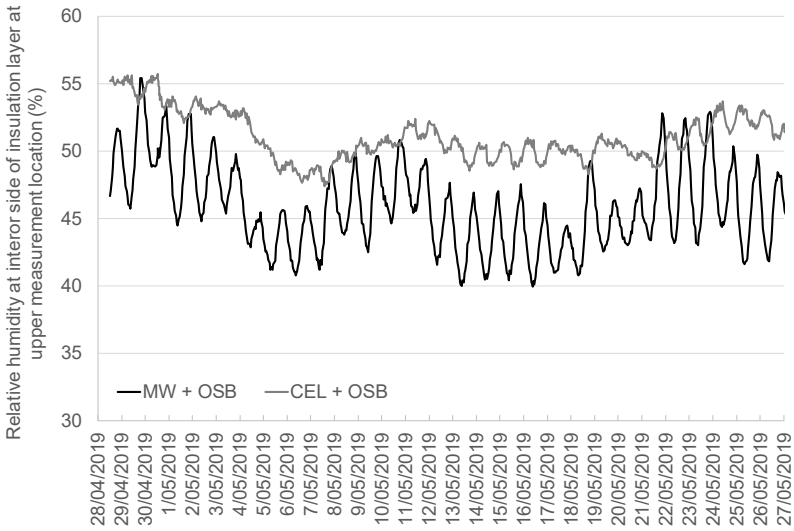

Figure 5. Course of the RH measured at the inside of the insulation layer (upper measurement location) for a compartment with mineral wool (comp. 5) and cellulose (comp. 7), both without water infiltration.

Figure 5 shows that the relative humidity fluctuates a lot more in the compartments filled with mineral wool compared to the compartments filled with cellulose insulation. This observation is expected and can be explained by the hygroscopic characteristics of cellulose. The oriented strand board has similar moisture buffering characteristics, but because the

thickness of the layer is limited (0,015m), this effect is rather small.

3.2 Moisture Increase and Drying Rate

When the measurement results were analyzed it was clear that the injection of water was mainly visible at the interior side of the insulation (lower measurement location). The relative humidity clearly increases when water is injected.

Figure 6 compares the relative humidity of the wall compartments with and without water infiltration for each combination of insulation and vapour retarder. The moment water is injected into the construction can be clearly read from the graphs (also indicated with a black arrow). The graphs show that the relative humidity increase is higher for the compartments with mineral wool than for the compartments with cellulose insulation. This can again be attributed to the hygroscopic characteristics of cellulose.

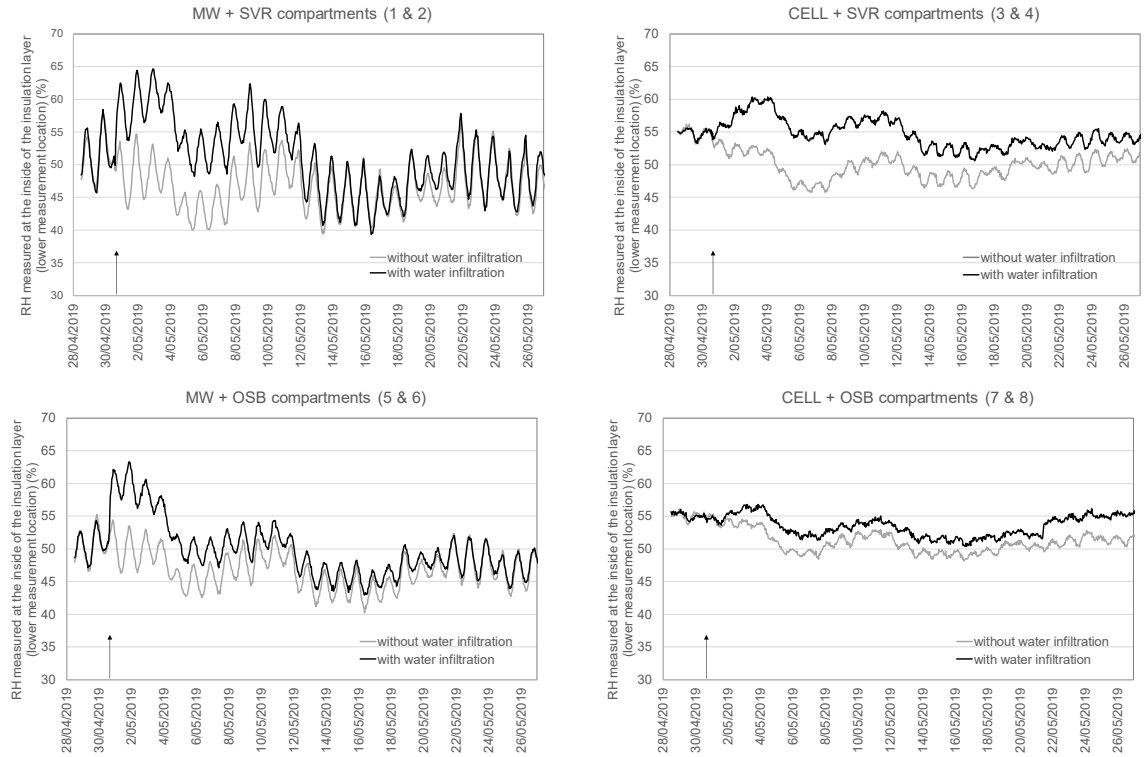

Figure 6. Course of the RH measured at the inside of the insulation layer (lower measurement location) for all compartments, with and without water infiltration.

Figures 7 and 8 show the relative humidity course measured at the interior side of the insulation (upper measurement location) and at the exterior side of the insulation for compartments 1 and 2, and 3 and 4 respectively. It is clear that the water injection is harder to observe from these measurement locations. For the compartments with mineral wool (Fig. 7) the relative humidity of the dry compartment is slightly higher than the relative humidity of the wet compartment, although the difference is still within the accuracy of the sensor. For the compartments with cellulose insulation (Fig. 8) the relative humidity of the wet compartment is slightly higher than the relative humidity of the dry compartment, but the difference is very

limited. For the other compartments, similar observations were made. This suggests that the injected water mainly runs down at the interior side of the insulation layer, especially for the compartments with mineral wool because the moisture buffering capacity of mineral wool is very low.

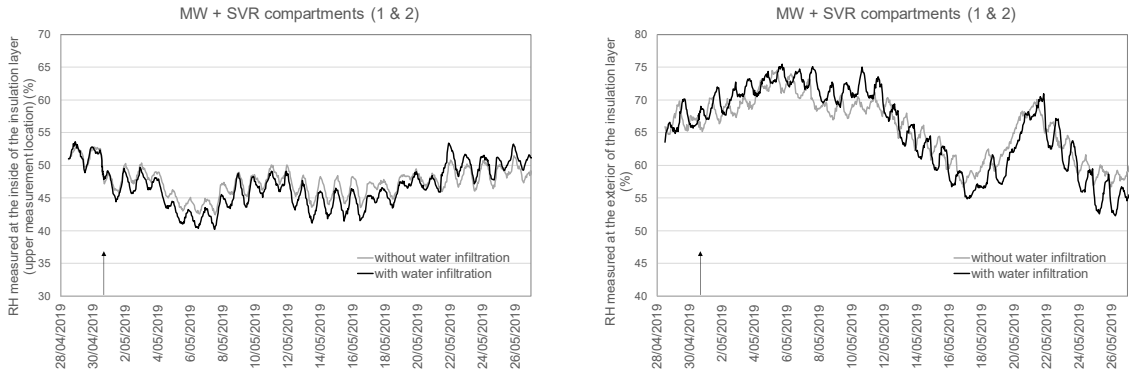

Figure 7. Course of the RH measured at the inside of the insulation layer (upper measurement location) (left) and at the exterior side of the insulation layer (right) for the compartments with mineral wool and SVR (1 & 2).

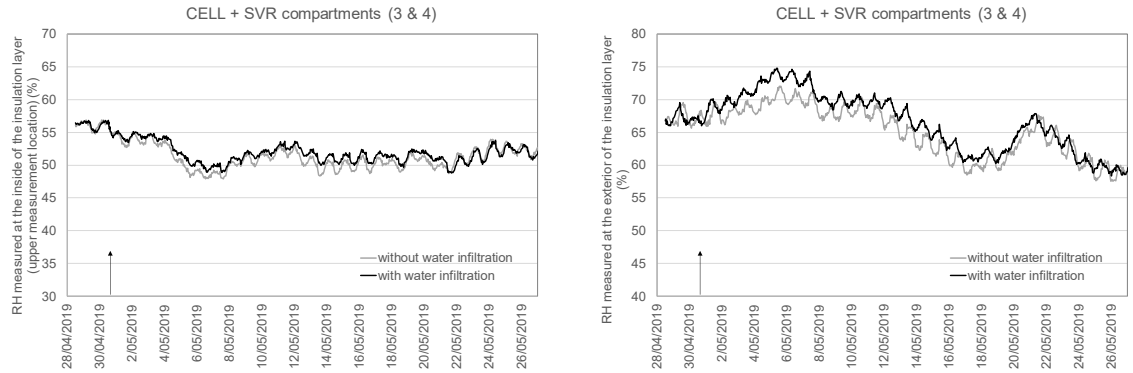

Figure 8. Course of the RH measured at the inside of the insulation layer (upper measurement location) (left) and at the exterior side of the insulation layer (right) for the compartments with cellulose and SVR (3 & 4).

In order to estimate the drying rate of the test compartments, the relative humidity of the wet and dry compartment of each construction type are compared (lower measurement location at interior side of insulation) in Figure 9 (graph left). The relative humidity difference increases faster in the compartments filled with mineral wool compared to the compartments filled with cellulose. Similarly, the drying rate of the compartments with cellulose is lower.

For the compartment with mineral wool and SVR (compartment 2) and with mineral wool and OSB (compartment 6), the drying period is ± 14 days and ± 21 days respectively. For the compartments with cellulose (compartments 4 and 8), the drying period is considered longer then the measurement period (> 27 days). For compartment 8 an increase in RH is noted after 21 days (May 21th), but no explanation for this observation could be found.

Drying out is considered mainly towards the inside of the construction. Figure 9 (right-hand graph) compares the measured vapour pressure in the insulation layer (interior side, lower measurement location) with the vapour pressure in the service cavity. For compartment 2 with mineral wool drying starts immediately after water infiltration, while for compartment 4 with

cellulose there is a time delay and drying starts later. During measuring, there were no internal moisture loads.

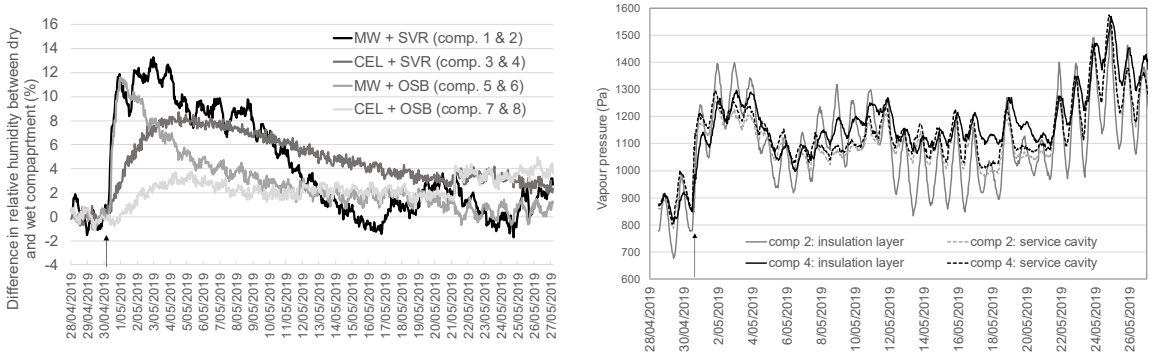

Figure 9. Difference in RH between wet compartment and the dry compartment (left) and vapour pressure in the insulation layer and service cavity for compartments 2 (MW + SVR) and 4 (CELL + SVR).

4 Conclusions

The aim of the study was to analyze the hygrothermal performance of wood frame construction subjected to accidental water infiltration. The results showed that the drying rate was faster for the compartments with mineral wool, and for the compartments where a smart vapour retarder was used. Also moisture buffering in the cellulose was clearly observed. In all cases, the construction dries out and no moisture damage is expected at first glance. However, further research should give insight in the moisture content of the wooden elements (bottom plate, I-joists) when water runs down. In the experiment water was injected at only one moment in time. In reality, water could leak into the construction in a more contentious way. This was not taken into account here. Also, parameters such as the moment of water injection, orientation of the test wall and boundary conditions (*e.g.* presence of internal moisture loads) will have an effect on the resulting drying rate and should be studied in more detail.

Acknowledgements

The test pavilion was built in cooperation with the VTI in Kortrijk, the authors highly appreciate the support of the staff. The authors also would like to thank MSc-students M. Veraeverbeke, J. Lagniau, B. Gryson and L. Dewachter for their help with the experiments in the context of their Master thesis.

ORCID

Marijke Steeman: https://orcid.org/0000-0002-6575-5389
Nathan Van Den Bossche: https://orcid.org/0000-0002-8738-7249
Klaas Calle: http://orcid.org/0000-0001-6736-6662

References

Houtinfobois. (2019). *Houtbouw in België 2017-2018* (in Dutch), Retrieved from https://houtinfobois.be/nl/
Royal Meteorological Insitute (RMI). Retrieved from https://www.meteo.be/en/belgium

Van Goethem, S. (2014). *Rainwater runoff on building facades: numerical simulations and analysis of wetting patterns.* Master dissertation. Ghent University.

Geldof L. (2016). *Kwantificatie van waterinfiltratie bij raamaansluitingen.* Master dissertation. Ghent University (in Dutch).

XV International Conference on Durability of Building Materials and Components
DBMC 2020, Barcelona
C. Serrat, J.R. Casas and V. Gibert (Eds)

Durability Evaluation of Hemp Fibers and Recycled Aggregates Concrete

Samer Ghosn[1] **and Bilal Hamad**[2]

[1] Department of Civil and Environmental Engineering, American University of Beirut, P.O. Box 11-0236 Riad El Solh 1107-2020, Beirut, Lebanon; ssg13@mail.aub.edu

[2] Department of Civil and Environmental Engineering, American University of Beirut, P.O. Box 11-0236 Riad El Solh 1107-2020, Beirut, Lebanon; bhamad@aub.edu.lb

Abstract. *Hemp and Recycled Aggregates Concrete (HRAC) is a sustainable concrete where coarse aggregates are partially replaced with industrial hemp fibers and recycled concrete aggregates (RCA). This replacement has two main benefits: it saves on natural resources and it recycles and reuses waste material. Previous studies showed that the mechanical performance of HRAC is satisfactory. On the other hand, concrete's durability is also an important criterion to evaluate concrete's performance and HRAC's durability can be affected by the presence of both RCA and hemp fibers in the concrete's alkaline environment. This paper aims at investigating the durability of HRAC concrete mixes by comparing the mechanical performance of HRAC specimens at the ages of 2 and 28 days. Furthermore, the performance of HRAC under freeze/thaw cycles is evaluated and compared to that of regular concrete. Results showed that the mechanical performance of HRAC improves at older age and the resistance of HRAC mixes to freeze-thaw cycles is similar to that of control mixes.*

Keywords: *Sustainable Concrete Materials, Recycled Aggregates, Hemp Fibers, Durability, Mechanical Properties.*

1 Introduction and Background

Sustainability has become an essential issue on a global scale in the recent years. Therefore, construction, among other sectors, is reviewing its practices to make them more environmentally friendly and reduce their negative effect on the planet as a whole.

Concrete production consumes large quantities of natural aggregates causing significant damage to the environment. To reduce the amount of natural aggregates used in concrete HRAC is proposed. This is a concrete mix where hemp fibers are incorporated in the mix, the amount of natural coarse aggregates (NCA) is reduced by 20%, and where 50% of NCA are replaced by RCA.

HRAC also helps in reducing the problem of construction and demolition wastes (CDW) which are a mixture of surplus materials generated during new construction, renovation, and demolition of buildings, roads, bridges, and other structures (Cheng *et al.,* 2013)

A sustainable concrete should be also durable; therefore, it is important to study the effect of the incorporation of hemp fibers and RCA on the durability properties of concrete.

Ramli *et al.* (2013) studied the durability of coconut-fiber-reinforced concrete in aggressive environments. Results showed that the damaging effects of aggressive environments on concrete can be lowered with fiber-reinforced concrete since the fibers play a role in restraining the development of cracks. Awwad *et al.* (2014) investigated the long-term behavior of concrete incorporating hemp fibers and concluded that at an age of 1.5 years

hemp fibers did not have a negative effect on concrete strength. Vázquez et al. (2014) found that the presence of RCA in concrete can improve the resistance to chloride penetration since C-S-H gels that exist in higher amounts in RCA assist in chloride binding. Also, the resistance of high-performance concrete with RCA to freezing can be similar to that of normal concrete (Ajdukiewicz *et al.,* 2002). The carbonation depth increases with the increase of RCA replacement ratio, but Lei *et al.* (2008) found that when the percentage replacement of NCA with RCA was higher than 70%, the carbonation depth decreased, which may be due to the adhered mortar on the RCA which increases the total cement content and slows down the carbonation rate.

In this paper, the durability of the proposed HRAC is investigated by evaluating its mechanical performance at the age of 2 years and by studying its resistance to freeze-thaw cycles.

2 Materials and Experimental Procedures

Sixteen different mixes were prepared and are identified in Table 1. The mixes are divided into two groups: Group 1 with MSA of 10 mm and Group 2 with MSA of 20 mm. The control mixes with no hemp fibers and no coarse aggregate reduction are referred to as N10 (NCA with MSA = 10 mm) and N20 (NCA with MSA = 20 mm), and were designed to achieve a concrete compressive strength of 30 MPa. R10 and R20 are two mixes with 50 percent replacement of NCA with RCA, no hemp fibers, and also no reduction of coarse aggregate content.

The other twelve mixes with hemp fibers are identified by a three-part notation. The first part is N (100% NCA) or R (50% replacement of NCA with RCA) and 10 or 20 mm are the MSA. The second part of the notation refers to the length of the hemp fibers (H20 is 20 mm and H30 is 30 mm). The third part is the type of fiber treatment where T1 is alkali treatment and T2 is acetyl treatment. A total of 7 HRAC mixes were used.

Based on the reported studies of Awwad *et al.* (2014), hemp fibers in mixes with fibers were added in a volumetric percentage of 0.75% of the volume of concrete. The weight of the fibers was then calculated based on the average density of the fibers determined to be 1,400 kg/m^3. The weight of the coarse aggregates for these mixes was also reduced by 20% of the concrete volume.

To study the long-term mechanical performance of HRAC, compressive strength tests, flexural strength tests and modulus of elasticity tests were performed at an age of 2 years for 14 of the 16 mixes and the results were compared to the results at 28 days presented in previous studies (Ghosn *et al.,* 2019). The tests were done according to ASTM C39 (2017), ASTM C78 (2016) and ASTM C469 (2014) respectively. For each test, 2 replicates were made for each mix.

The resistance to freeze-thaw cycles was conducted according to ASTM C666 (2015). For each mix, one prismatic specimen (75x100x405 mm) was cast and cured in water for 28 days. Each specimen was then brought to a temperature of -18 °C and tested for fundamental transverse frequency. Then, the specimens were exposed to 144 cycles of freezing and thawing. Each freezing-and-thawing cycle consisted of lowering the temperature of the specimens from 4 to -18 °C and raising it from -18 to 4 °C in a period of 4 hours and 40 minutes.

Table 1. Identification of the concrete mixes.

	Mix No.	Mix ID	MSA (mm)	% Replacement of NCA by RCA	Fiber Length (mm)	Fiber Treatment
Group 1 MSA = 10 mm	1	N10 (Control10)	10	0	-	-
	2	R10	10	50	-	-
	3	N10-H20-T1	10	0	20	Alkali
	4	R10-H20-T1	10	50	20	Alkali
	5	R10-H20-T2	10	50	20	Acetyl
	6	N10-H30-T1	10	0	30	Alkali
	7	R10-H30-T1	10	50	30	Alkali
Group 2 MSA = 20 mm	8	N20 (Control20)	20	0	-	-
	9	R20	20	50	-	-
	10	N20-H20-T1	20	0	20	Alkali
	11	R20-H20-T1	20	50	20	Alkali
	12	N20-H20-T2	20	0	20	Acetyl
	13	R20-H20-T2	20	50	20	Acetyl
	14	N20-H30-T1	20	0	30	Alkali
	15	R20-H30-T1	20	50	30	Alkali
	16	R20-H30-T2	20	50	30	Acetyl

The specimens were tested for their fundamental transverse frequency each 36 cycles. The fundamental transverse frequency (n) was determined according to ASTM C215 (2008) using Humboldt HC-3177 Resonance Test Gauge. The relative dynamic modulus of elasticity (RDME) was then calculated as follows:

$$P_c = \frac{n_1^2}{n^2} \times 100 \quad (1)$$

Where: P_c = Relative dynamic modulus of elasticity (RDME) after c cycles of freezing and thawing (%), n is the fundamental transverse frequency before proceeding freezing and thawing cycles, and n_1 is the fundamental transverse frequency after c cycles of freezing and thawing.

For each test two groups of specimens were tested: Group 1 with MSA of 10 mm and Group 2 with MSA of 20 mm. In each group, normal and recycled aggregate mixes (N and R mixes) with or without hemp fibers and with different fiber lengths and fiber treatments were tested and compared.

3 Results and Discussion

3.1 Long-Term Mechanical Performance

3.1.1 Compressive strength

The results of the compressive strength test are presented in Table 2.

Table 2. Compressive strength test results.

	Mix ID	28 days Compressive Strength Value (MPa)	28 days Compressive Strength Ratio*	2 years Compressive Strength Value (MPa)	2 years Compressive Strength Ratio*	Ratio (2 years /28 days)
Group 1; MSA = 10 mm	N10 (Control10)	38	-	42	1.00	1.11
	R10	34.25	0.9	37.75	0.90	1.10
	N10-H20-T1	23	0.61	29.5	0.70	1.28
	R10-H20-T1	24.5	0.64	29.25	0.70	1.19
	R10-H20-T2	24.5	0.64	26.5	0.63	1.08
	N10-H30-T1	24	0.63	26.25	0.63	1.09
	R10-H30-T1	24	0.63	27.5	0.65	1.15
Group 2; MSA = 20 mm	N20 (Control20)	39	-	44	1.00	1.13
	R20	35	0.9	38	0.86	1.09
	N20-H20-T1	28	0.72	34	0.77	1.21
	R20-H20-T1	25	0.64	31.5	0.72	1.26
	N20-H30-T1	32	0.82	34	0.77	1.06
	R20-H30-T1	26	0.67	31.25	0.71	1.20
	R20-H30-T2	25	0.64	32.75	0.74	1.31

**Ratio = Mechanical property value for the mix divided by that of the control mix N10 in Group 1 and by that of the control mix N20 in Group 2.*

In general, the results at the age of 2 years were consistent with results at the age of 28 days; when the hemp fibers are incorporated in the mix, the compressive strength decreases since aggregates which are the hardest elements in a concrete mix are replaced by fibers which are weak in compression. Furthermore, all mixes showed an improved compressive

strength at the age of 2 years as compared to those at the age of 28 days. This increase ranges from 6 up to 31% for the HRAC mix R20-H30-T2.

3.1.1 Flexural strength

The results of the flexural strength test are presented in Table 3.

Table 3. Flexural strength test results.

	Mix ID	28 days Modulus of Rupture Value (MPa)	Ratio*	2 years Modulus of Rupture Value (MPa)	Ratio*	Ratio (2 years /28 days)
Group 1; MSA = 10 mm	N10 (Control10)	5.1	-	6.87	-	1.35
	R10	4.8	0.94	6.78	0.99	1.41
	N10-H20-T1	4.95	0.97	5.75	0.84	1.16
	R10-H20-T1	4.35	0.85	5.43	0.79	1.25
	R10-H20-T2	4.2	0.82	6.07	0.88	1.45
	N10-H30-T1	4.8	0.94	6.71	0.98	1.40
	R10-H30-T1	4.2	0.82	6.43	0.94	1.53
Group 2; MSA = 20 mm	N20 (Control20)	5.25	-	7.71	-	1.47
	R20	4.57	0.87	7.30	0.95	1.60
	N20-H20-T1	5.1	0.97	6.05	0.78	1.19
	R20-H20-T1	4.65	0.89	5.77	0.75	1.24
	N20-H30-T1	4.95	0.94	6.71	0.87	1.35
	R20-H30-T1	4.5	0.86	6.68	0.87	1.48
	R20-H30-T2	4.5	0.86	6.19	0.80	1.38

**Ratio = Mechanical property value for the mix divided by that of the control mix N10 in Group 1 and by that of the control mix N20 in Group 2.*

The variation of the flexural strength at the age of 2 years is consistent with that at the 28 days; the incorporation of hemp fibers and recycled aggregates leads to lower flexural strength. However, this decrease is less significant as compared to that in the compressive strength as some HRAC mixes have a flexural strength of 94% compared to the that of the control mix at the age of 2 years. In addition, the flexural strength shows a significant increase at the age of 2 years with increases around 50% in some of the HRAC mixes.

3.1.1 Modulus of Elasticity

The results of the flexural strength test are presented in Table 4.

Table 4. Modulus of elasticity test results.

	Mix ID	28 days Modulus of Elasticity Value (MPa)	Ratio*	2 years Modulus of Elasticity Value (MPa)	Ratio*	Ratio (2 years /28 days)
Group 1; MSA = 10 mm	N10 (Control10)	34.2	1.00	30.8	1.00	1.11
	R10	34.1	0.94	28.8	1.00	1.18
	N10-H20-T1	28.6	0.72	22.2	0.84	1.29
	R10-H20-T1	27.7	0.74	22.8	0.81	1.21
	R10-H20-T2	26.8	0.74	22.9	0.78	1.17
	N10-H30-T1	28.3	0.74	22.7	0.83	1.25
	R10-H30-T1	28.8	0.73	22.5	0.84	1.28
Group 2; MSA = 20 mm	N20 (Control20)	36.3	1.00	33.2	1.00	1.09
	R20	34.5	0.95	31.4	0.95	1.10
	N20-H20-T1	30.3	0.78	26	0.83	1.17
	R20-H20-T1	28.9	0.71	23.7	0.80	1.22
	N20-H30-T1	28.6	0.82	27.2	0.79	1.05
	R20-H30-T1	25.5	0.73	24.3	0.70	1.05
	R20-H30-T2	25.7	0.71	23.7	0.71	1.08

**Ratio = Mechanical property value for the mix divided by that of the control mix N10 in Group 1 and by that of the control mix N20 in Group 2.*

Similar to the compressive strength, the MOE is also higher at the age of 2 years than at the age of 28 days. The increase ranges between 5 and 28% for HRAC mixes.

3.1 Resistance to Freeze/Thaw Cycles

Results of Pc or RDME after each 36 cycles of freezing and thawing are presented in Table 5. Group 1 with MSA of 10 mm, had a good resistance to freeze-thaw cycles for all tested specimens with Pc ranging from 77% to 90.4% after 144 cycles. While Pc for the recycled aggregate mix R10 was the lowest in the group (77%), mixes with hemp fibers had a Pc ranging between 77 and 90.4, a value which is even higher than the control mix (83.5%).

Group 2 mixes with MSA of 20 mm, had a lower resistance to freeze-thaw cycles than that of Group 1 mixes. Pc decreased more quickly to reach values ranging between 31% and 56.5% after 144 cycles. Similar to Group 1, 50% replacement of NCA with RCA but without hemp fibers incorporation (R20) led to the lowest value of Pc after 144 cycles (31%). This poor resistance of Group 2 to freeze-thaw cycles can be due to the fact that when the MSA increases from 10 to 20 mm, the cement matrix contains less entrapped air bubbles. During the freezing phase of a cycle, the water present in the matrix freezes and expands causing pressure that may lead to cracks and to the deterioration of the concrete. The more entrapped air bubbles present in the 10-mm matrix relieves the pressure by providing more space for water to expand into when it freezes. As for the effect of incorporating hemp fibers in the mix, the four mixes with hemp fibers had values ranging between 42 and 56.5% as compared with 51% for the control mix N20.

Table 5. Relative dynamic modulus of elasticity (RDME) values of all mixes after each 36 cycles.

	Mix ID	Relative Dynamic Modulus of Elasticity P_C (%)				
		c = 0	c = 36*	c = 72	c = 108	c = 144
Group 1 MSA = 10 mm	N10 (Control10)	100	94.1	90.2	86.2	83.5
	R10	100	98.2	89.5	87.5	77.0
	N10-H20-T1	100	93.8	87.2	81.6	77.0
	R10-H20-T1	100	90.5	90.5	90.5	88.5
	R10-H20-T2	100	90.2	88.5	83.7	79.5
	N10-H30-T1	100	95.2	93.0	93.0	90.4
	R10-H30-T1	100	95.2	93.0	90.4	90.4
Group 2 MSA = 20 mm	N20 (Control20)	100	93.2	79.2	62.4	51.0
	R20	100	92.7	70.2	57.8	31.0
	N20-H20-T1	100	88.1	79.2	70.8	42.0
	N20-H20-T2	100	83.2	75.3	63.7	55.5
	R20-H20-T2	100	85.8	78.3	69.5	53.2
	R20-H30-T1	100	87.7	77.2	70.5	56.5

**c = number of freeze-thaw cycles.*

4 Conclusion

This paper studies the durability and long-term performance of HRAC, a "green" concrete material where natural aggregates are partially replaced by recycled concrete aggregates and industrial hemp fibers. Results showed that at the age of 2 years, HRAC mixes have an improved mechanical performance as compared to the age of 28 days, The compressive strength, the flexural strength and the modulus of elasticity improved by up to 31%, 53% and 28%, respectively. The variation in the mechanical performance between HRAC mixes and control mixes was also consistent at the age of 28 days and the age of 2 years. Furthermore, the resistance to freeze-thaw cycles of HRAC was similar to that of normal concrete mixes after 144 cycles.

Based on these results, it can be concluded that HRAC is a durable concrete that has a reliable long-term mechanical performance and it can be used in cold climates as it has a freeze/thaw durability performance comparable to that of ordinary concrete mixes.

ORCID

Samer Ghosn: http://orcid.org/0000-0002-0829-1311
Bilal Hamad: http://orcid.org/0000-0001-7057-573X

References

Cheng, J.C. and Ma, L.Y. (2013). A BIM-based system for demolition and renovation waste estimation and planning. *Waste management*, 33(6), pp.1539-1551.

Ramli, M., Kwan, W.H. and Abas, N.F. (2013). Strength and durability of coconut-fiber-reinforced concrete in aggressive environments. *Construction and Building Materials*, 38, pp.554-566.

Awwad, E., Hamad, B., Mabsout, M. and Khatib, H. (2014). Long Term Strength Behavior of Hemp-Concrete.

Vázquez, E., Barra, M., Aponte, D., Jiménez, C. and Valls, S. (2014). Improvement of the durability of concrete with recycled aggregates in chloride exposed environment. *Construction and Building Materials*, 67, pp.61-67.

Ajdukiewicz, A. and Kliszczewicz, A. (2002). Influence of recycled aggregates on mechanical properties of HS/HPC. *Cement and concrete composites*, 24(2), pp.269-279.

Lei, B. and XIAO, J.Z. (2008). Research on carbonation resistance of recycled aggregate concrete. *Journal of Building Materials*, 5, pp. 605-611.

Awwad, E., Mabsout, M., Hamad, B., Farran, M.T. and Khatib, H. (2012). Studies on fiber-reinforced concrete using industrial hemp fibers. *Construction and Building Materials*, 35, pp.710-717.

Ghosn, S., Cherkawi, N. and Hamad, B. (2019). Preliminary studies of hemp and recycled aggregate concrete. Academic Journal of Civil Engineering, 37(2), 520-524.

ASTM C666/C666M-15: (2015). Standard test method for resistance of concrete to rapid freezing and thawing. ASTM International, West Conshohocken, PA.

ASTM C215 - 08: (2008). Standard test method for fundamental transverse, longitudinal, and torsional frequencies of concrete specimens. *ASTM International*, West Conshohocken, PA.

ASTM C39/C39M-18: (2018). Standard test method for compressive strength of cylindrical concrete specimens. *ASTM International*, West Conshohocken, PA.

ASTM C469/C469M-14: (2014). Standard test method for static modulus of elasticity and poisson's ratio of concrete in compression. *ASTM International*, West Conshohocken, PA.

ASTM C78/C78M-18: (2018). Standard test method for flexural strength of concrete (using simple beam with third-point loading). *ASTM International*, West Conshohocken, PA.

XV International Conference on Durability of Building Materials and Components
DBMC 2020, Barcelona
C. Serrat, J.R. Casas and V. Gibert (Eds)

Effect of Crack Repair by Bio-Based Materials Using Alginate and Bacillus Subtilis under Wet and Dry Environment Part-II

Takahiro Nishida[1], **Keiyu Kawaai**[2] **and Atsushi Saito**[3]

[1] National Research and Development Agency, National Institute of Maritime, Port and Aviation Technology, Port and Airport Research Institute, Japan, nishida-ta@p.mpat.go.jp

[2] Civil and Environmental Engineering, Ehime University, 3, Bunkyocho, Matsuyama, Ehime, Japan kkawaai@cee.ehime-u.ac.jp

[3] Reseach Center, Hazama Ando Corporation, Japan, atsushi.saito@ad-hzm.co.jp

Abstract. *This study examined durability of mortar after repairing crack using alginate gel films (1.5 wt.%) mixed with healing agents under seawater splayed condition. The healing agents consist of Bacillus subtilis (natto) as an aerobic microorganism and glucose as an organic carbon source, thereby producing insoluble calcium carbonate in the gel films in the presence of calcium ions. In this study, repaired mortar was dried under room condition for half year and exposed at seawater splayed condition for another half year. After that, surface condition, elastic wave velocity was measured. In addition, the inside situation in the crack was observed by X ray computed tomography. Based on the results of elastic wave velocity, the property of repair material in mortar was improved under the seawater splayed condition. Additionally the substance in crack derived from healing agents was remained even after seawater splayed exposure.*

Keywords: *Self-Healing, Aerobic Microorganisms, Bio-Composite, Seawater Splayed Exposure.*

1 Introduction

Recently, repair materials associated with microbial induced calcium carbonate precipitation (MICCP) have been intensively studied in the field of self-healing concrete *e.g.* (Jonkers et al., 2010). We proposed a liquid based repair system comprising dry yeast, organic carbon sources, calcium sources mixed with Tris alkali buffering solution (Kawaai *et al*., 2016; Putri *at el*., 2016). The grout used for repairing cracks in concrete is supposed to seep into deeper zones in cracks, joints and gaps spatially distributed in larger areas. Then, calcium carbonate precipitation mainly contributing to the sealing effect can be formed in the cracks well before 24 hours (Kawaai *et al*., 2016). It has been reported that the precipitation rate was largely dependent on the concentration of constituents, pH levels, and ambient environment such as temperature. The effect of temperature is significant in facilitating the precipitation process (Putri *et al.*, 2016), thus leading to a larger amount of precipitates formed compared to those tested in normal room conditions.

Apart from the grout system, the activity of Bacteria added to mixing water was observed to be limited owing to the pore solution with highly alkaline environment (Jonkers, 2011). In order to protect them from corrosive agents and the severe environment, much research has been carried out in the development of encapsulation techniques including expanded clay particles, glass tubes, superabsorbent polymer, more recently alginate-based systems (Jonkers, 2011; Tittleboom *et al.*, 2011; Wang *et al.*, 2014; Palin *et al.*, 2016).

doi:10.23967/dbmc.2020.053

According to past research reported by Kawaai *et al.*, (2017), precipitation of calcium carbonate in alkaline environment has been confirmed by precipitation tests using aerobic Bacillus subtilis (natto) encapsulated in calcium alginate capsules. Sodium alginate extracted from brown seaweed could provide viscosity in aqueous solution, which varies depending on the concentrations. When sodium alginate dissolved in a liquid is used for repairing cracks in concrete, there is a strong possibility that the alginate reacts with calcium ions available on the cracked surface, thus forming a polymer comprising calcium alginate via ion-link on the cracked surface. This could result in in-situ encapsulation for the microorganism and nutrients in the cracks. Generally, there are two types of microorganisms, anaerobic and aerobic microorganisms. The former can metabolize an organic carbon sources in an oxygen-free environment. On the other hand, the latter requires oxygen for the metabolic activity. In this study, we selected Bacillus subtilis (natto) as an aerobic microorganism. The liquid-based mixture is supposed to be applied to concrete structures in tidal zones under marine environment. Dissolved oxygen is expected to be available during the wet and dry cycles. Based on the above background, this study examines the durability of repaired mortar under seawater splayed environment.

2 Experimental Programs

2.1 Materials

First, culture solution of Bacillus subtilis (natto) containing sodium alginate is stirred using a stirrer for 30 minutes until the sodium alginate dissolves. Subsequently, Tris buffer solution or glucose is added. The concentrations of each constituent of the mixtures are shown in Table 1. The experimental parameters include the presence (N1 mixtures) and absence (W mixture) of Bacillus subtilis (natto), the concentration of sodium alginate is specified as 1.5 wt.% for all the mixtures tested. The use of Tris buffer solution with concentrations of 0.1 mol/L is also considered as a testing parameter. In this study, three mixtures were totally prepared.

Table 1. Concentrations of each constituent of mixtures.

	Mixtures	Sodium Alginate (%)	Glucose (mol/L)	Tris buffering solution (mol/L)
N1	N1-G1-T0	1.5	0.4	-
	N1-G1-T1	1.5	0.4	0.10
W	W -G0-T0	1.5	-	-

2.2 Cultivation of Bacillus Subtilis (Natto)

In this study, Bacillus subtilis (natto) was cultivated using culture media mainly comprising NH_4Cl, NH_4NO_3, Na_2SO_4, $MgSO_4$, $CaCl_2$, K_2HPO_4, KH_2PO_4 in this study. The round rod shape of Bacillus subtilis (natto) forms a spore per a bacterial cell in the bacterial body.

Spores are formed when it becomes an environment not suitable for growth such as oxygen, water and nutrient sources. And then, they become dormant and inactive. However, if the environment is set, the spore dormancy state ends, and germination begins. And then it becomes vegetative cell and the activity starts. Therefore, the Bacillus subtilis (natto) has higher resistance to environmental fluctuation compared to other microorganisms. In this study, the culture solution of the Bacillus subtilis (natto) after 24 hours was used as repair mixtures. Before preparing the mixtures, the dissolved oxygen concentration in the culture solution was measured to confirm the metabolic activity of Bacillus subtilis (natto) without an aeration apparatus.

2.3 Specimen Preparation and Exposure Tests

In this study, a mortar specimen with a water cement ratio of 0.5 and unit water content of 316 kg/m^3 and unit weight of crushed sand 1264 kg/m^3 was prepared using a cylindrical mold of ϕ 50×100 mm. Specimens were demolded after 24 hours and sealed curing was carried out until the age of 28 days. In order to simulate the cracks generated in the concrete member, split cracks were induced using a loading machine. The experimental set-up is similar to tensile strength test. The crack width was targeted around 0.5 mm. And then, the repair mixtures were poured into the cracks. After 1 week, exposure tests were carried out either through wet conditions (12 hours) and dry conditions (12 hours) or only wet conditions (24 hours). Wet cycles were executed using distilled water containing NaCl (3%) for both cases.

2.4 Measurement of Crack Width and Sealing Rate

The crack width and sealing rate by MICCP are measured using microscope (Dino-Lite Edge AM7915, ANMO) as shown in Figure 1. The five points highlighted in the figure are consistently measured using two specimens subjected to each exposure condition. The sealing rate is calculated based on the ratio of widths occupied with the precipitates over crack widths at each measurement point.

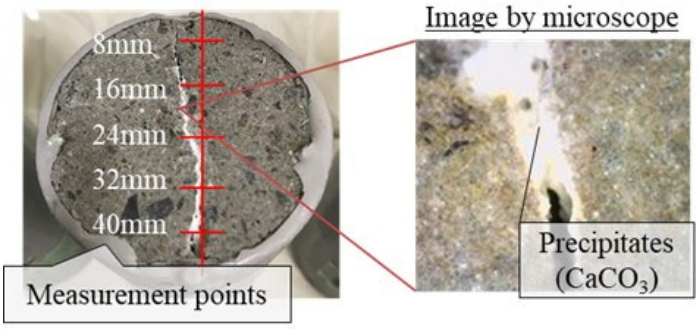

Figure 1. Measurement of crack width and sealing rate by microscope.

2.5 Exposure Condition after Repairing

The specimen after repairing was exposed to seawater splayed condition. The seawater was pumped up from Kurihama bay and splayed to specimens as shown in Figure 2. Seawater was splayed twice in a day and specimen was exposed for 6 months.

Figure 2. Seawater splayed environment.

2.5 Measurement of Elastic Wave Velocity

In order to evaluate the crack filling effect of self-healing material, the elastic wave velocity was measured every 1 month after exposure test. Elastic wave velocity can evaluate the connectivity of materials at crack part and the value increase with the crack filling due to deposition of healing materials produced by the metabolic activity of Bacillus subtilis. The schematic figure of measurement was illustrated in Figure 3. The sensors were set at the side surface of specimen and the elastic wave velocities against vertical direction along the crack were evaluated.

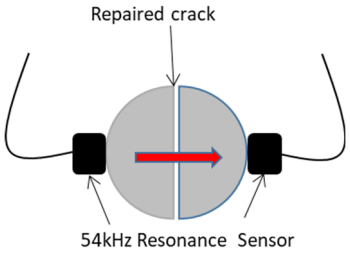

Figure 3. Measurement outline of elastic wave velocity.

3 Experimental Results and Discussion

3.1 Results of Elastic Wave Velocity

The elastic wave velocity of each specimen exposure to seawater splayed condition after 0, 30, 90, 180 days is shown in Figure 4. Before exposure to seawater splayed condition, the specimens were exposed to experimental room (20 degree centigrade and 60 % R.H.) and specimens were dried. Therefore the results of all of elastic wave velocity of specimens before exposure were equivalent to cracked mortar. After exposed to seawater splayed environment,

the elastic wave velocities of mortar with crack were increased. Especially in the cases of specimen with Bacillus subtilis, the elastic wave velocities of specimen were clearly increased.

It was assumed that the repair substance inside of crack remained and the elastic wave penetrate that part. Figure 5 show the result of X ray CT in crack after 180 days exposure. From this figure, it can be said that the substance produced by Bacillus subtilis were remained inside of crack even after exposed to seawater splayed condtion.

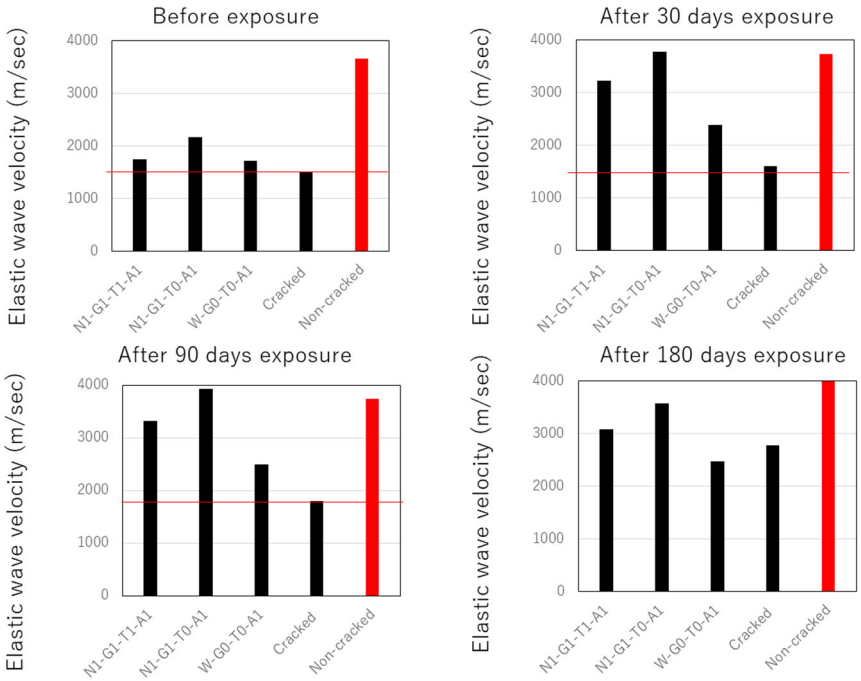

Figure 4. Elastic wave velocities before and after exposure.

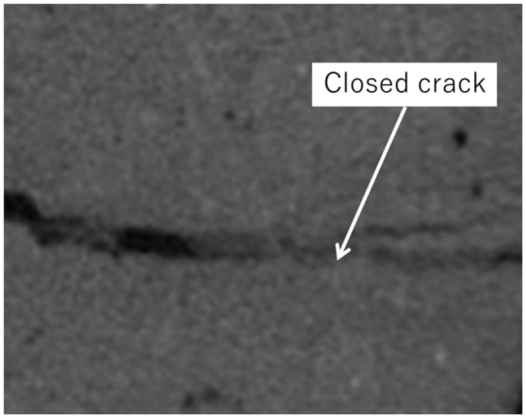

Figure 5. Crack closure situation after exposure for 6 months under seawater splayed condition.

4 Conclusions

- Based on the observations made on the sealing rate of crack repair, the presence of gel films remained intact on the cracked surface under exposure conditions could contribute to higher sealing effect in the cases of the N1 mixtures.
- The results suggest that the repair effect of crack produced by Bacillus subtilis would be kept even after exposed to seawater splayed condition.

Acknowledgements

This study is financially supported by JSPS KAKENHI Grant-in-Aid for Scientific Research (B), Grant numbers 19H02216.

ORCID

Takahiro Nishida: https://orcid.org/0000-0002-2018-6928
Keiyu Kawaai: https://orcid.org/0000-0003-4767-4355
Atsushi Saito: https://orcid.org/0000-0001-6866-1882

References

Jonkers, H.M., Thijssen, A., Muyzer, G., Copuroglu, O. and Schlangen, E. (2010). Application of bacteria as self-healing agent for the development of sustainable concrete, Ecological Engineering, 36, 230-235.

Kawaai, K., Ujike, I., Yamamoto, S. and Putri, P.Y. (2016). Some considerations on precipitation rate of calcium carbonate in bio-based materials used for concrete repair, Concrete Solutions 2016, 6th International Conference on Concrete Repair, 571-578.

Putri, P.Y., Kawaai, K., Ujike, I. and Yamamoto, S. (2016). Effect of Temperature on Precipitation Rate of Calcium Carbonate Produced through Microbial Metabolic Process of Bio Materials, Civil Engineering Dimension, 18(2), 103-108.

Jonkers, H.M. (2011). Bacteria-based self-healing concrete, Heron, 56 (1/2).

Tittelboom, K.V., Belie, N.D., Loo, D.V. and Jacobs, P. (2011). Self-healing efficiency of cementitious materials containing tubular capsules filled with healing agent, Cement and concrete Composites, 33, 497-505, 2011.

Wang, J., Snoeck, D., Vlierberghe, S.V., Verstraete, W. and Belie, N.D. (2014). Application of hydrogel encapsulated carbonate precipitating bacteria for approaching a realistic self-healing in concrete, Construction and Building Materials, 68, 110-119.

Palin, D., Wiktor, V. and Jonkers, H.M. (2016). A bacteria-based bead for possible self-healing marine concrete applications, Smart Materials and Structures, 25(8).

Kawaai, K., Nishida, T. and Saito, A. (2017). Calcite-alginate bio-composite formation in alginate gel films for self-healing concrete application, Proceedings of the 5th Seminar Workshop on the Utilization of Waste Materials in conjunction with the 2nd International Symposium on Concrete and Structure for the Next Generation, Manila Philippines, 5.

XV International Conference on Durability of Building Materials and Components
DBMC 2020, Barcelona
C. Serrat, J.R. Casas and V. Gibert (Eds)

Effect of Vapor Diffusion Port on Drying of Wood-Frame Walls

Ben Zegen Reich[1], **Hua Ge**[1] **and Jieying Wang**[2]

[1] Department of Building, Civil and Environmental Engineering, Concordia University, Montreal, Canada, hua.ge@concordia.ca

[2] FPInnovations, 2665 East Mall, Vancouver V6T 1Z4, Canada, Jieying.Wang@fpinnovations.ca

Abstract. *Vapor diffusion ports (VDP) that are drilled in the exterior sheathing of wood-frame walls are commonly used in wood-frame construction in the coastal region of British Columbia with the intention to improve the drying capacity of wood-frame exterior walls. This practice was originated following the systematic building envelope failures due to rain penetration that occurred in this region around 1985-1995. A previous laboratory study carried out by FPInnovations found that the diffusion ports provided substantial improvement in the drying rates of Oriented Strand Board (OSB) sheathed walls, but not for plywood sheathed walls (Hazleden and Morris, 2001). A more recent laboratory test (Wang, 2018) using wood-frame walls with higher insulation levels in compliance with the current more stringent energy code found that VDPs did not significantly improve the drying rates; On the other hand, the provision of VDPs may allow moisture ingress into the wall assembly instead in a damp environment. The difference in these two studies in terms of test wall sizes, moisture sources, and test conditions may have attributed to the different findings. To provide a more comprehensive and systematic evaluation of the effect of VDPs, hygrothermal simulations using Wufi-2D are carried out in this study. The Wufi-2D model is firstly validated by comparing simulation results to the test results provided by Wang (2018), which tested the effect of VDPs under laboratory conditions by using a wetted wood block installed inside each wall assembly as a simulated moisture source. The simulation results agree well with the measurements. The Model is then used for sensitivity analysis with different levels of rain leakage with and without VDPs using yearly weather data. The variables included are types of exterior insulation, types of sheathing (OSB versus Plywood), and types of sheathing membrane. This paper presents the validation of the model and simulation results under transient conditions with rain leakage. General conclusions on the effect of VDPs are provided.*

Keywords: *Vapor Diffusion Ports, Wood-Frame Walls, Hygrothermal Simulations, Durability.*

1 Introduction

Moisture content (MC) of various elements of a building's wall assembly greatly influences its durability. In areas with high seasonal wetting potential such as the coastal region of British Columbia (BC), a practice of providing vapor diffusion ports (VDP) in the exterior sheathing of wood-frame exterior walls to encourage drying was introduced in the late 1990's and gained popularity in the region. However, little research has been done to investigate the effect of VDPs on building assembly durability. There are mainly two laboratory experiments. Hazleden and Morris (2001) compared drying rates of larger wood-frame assemblies with framing wetted to high level of moisture contents initially using a large environmental chamber under laboratory conditions with the addition of VDPs. The moisture contents of sheathing were measured. It was found that for OSB sheathed walls, VDPs had a substantial effect on drying of sheathing, with typical MC levels in the sheathing being 34%-36% MC without a VDP and 22%-25% MC with a VDP after the drying process. For plywood sheathed walls, VDPs had

doi:10.23967/dbmc.2020.160

very little effect on drying performance. Wang (2018) tested the VDPs applied on more recent but smaller wall assemblies and materials, including deep cavity walls and exterior insulated assemblies under laboratory conditions. The moisture contents of an initially wetted wood blocked placed over the bottom plate were measured. The study concluded that VDPs had insignificant effects on drying of the wet wood block simulating a rain leakage scenario for assemblies sheathed in OSB or plywood.

These two previous studies focused on laboratory testing under simulated environmental conditions. This study aims to provide a more comprehensive and systematic evaluation of the effect of VDPs through transient hygrothermal simulations representing more realistic climatic weather conditions and moisture loads.

2 Methodology

The program chosen for hygrothermal simulation is Wufi-2D, a transient 2D heat and mass transfer program that is capable of simulating the effect of VDPs on the hygrothermal performance of the wall assemblies. The model is firstly validated by comparing simulation results with the measurements from the recent experiment conducted by Wang (2018) under laboratory conditions. The validated model is then used to evaluate the effect of VDP on the hygrothermal performance of a typical 2x6 wood-frame wall, defined as a baseline wall, under real weather conditions with rain leakage assumed to the exterior surface of sheathing as a moisture source. A parametric study is carried out on the baseline wall to investigate the effect of various parameters including wall orientation, sheathing materials, and exterior insulation.

2.1 Hygrothermal Model Setup

The experiment by Wang (2018) was carried out for a variety of wall assemblies and an initially wetted wood block placed above the bottom plate was used as the moisture source. The moisture content of the wet wood block was measured during the drying process at two depths, 5 mm and 12 mm, and 18 readings were taken on a weekly basis over the test period of 127 days. The hygrothermal model is set up to represent the test configuration as close as possible. The wet wood block is divided into two layers, surface and center, for a better comparison of measurements at two depths. The VDP has a diameter of 50 mm and placed 100 mm above the wet wood block. The VDP is represented by a 50 mm slot in the hygrothermal model. The initial MC of each layer is set to match the experiment readings on day 0, which vary among test assemblies. The experiment was conducted in an outside shed that was open to the environment but covered from solar radiation and rain events, and the simulation model uses temperature and relative humidity (RH) data measured on-site but no rain or solar inputs. Figure 1 shows the simulation model in Wufi-2D and the experiment test setup.

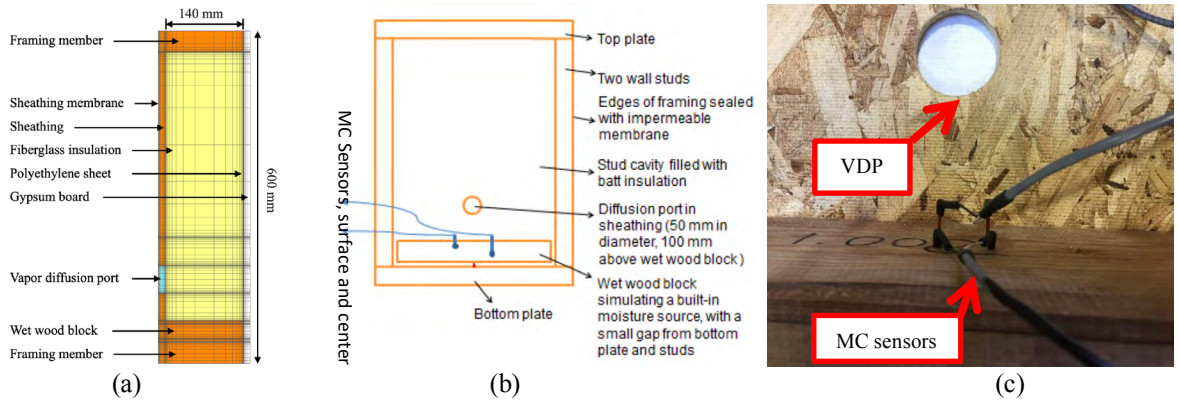

Figure 1. (a) Wufi-2D simulation model for validation (b, c) Experiment assembly (Wang, 2018).

2.2 Hygrothermal Model Validation

Sixteen of these wall assemblies are simulated, with OSB and plywood sheathing, with and without exterior insulation, with and without VDPs, and the MC of the wet wood block from the simulations are compared to the experiment results. As an example, Figure 2 shows the comparison between experimental and simulation results for the case of an OSB sheathed 2x6 wall with no VDP and the case of OSB sheathed wall with VDP. In general, the simulation results agree well with the measurements. The simulation results have a better agreement with the measurements for the center location than that for the surface layer. The main discrepancy occurs during the initial drying period. This may have attributed to the initial moisture content set in the model as only two measurements, at 5mm and 12mm depth, are available and also the model's limited capacity in modeling moisture transport in wood at moisture content level above its fiber saturation. The comparison between the simulation and experiment results is made by root-mean-square error (RMSE), which is the root of the sum of the differences squared, divided by the number of measurements. Of 16 simulation cases compared to the experiment, the RMSE ranges from 0.81 to 3.77 with a median value of 1.65 for the surface layer, and ranges from 0.38 to 4.72 with a median value of 1.30 for the center layer.

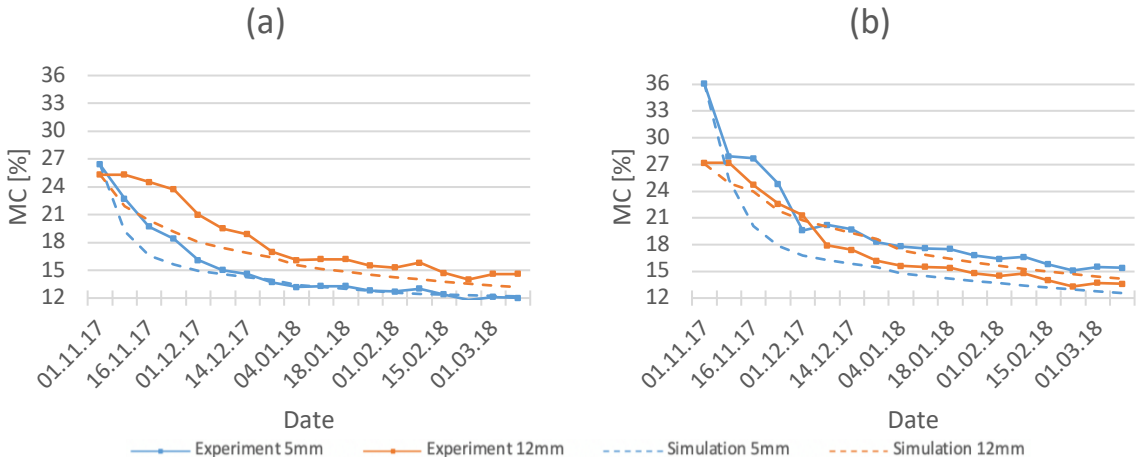

Figure 2. MC of wet wood block for an OSB sheathed 2x6 wall with no exterior insulation, surface and center layers, experiment and simulation results, without (a) and with (b) VDP.

2.3 Parametric Study

The baseline assembly is a 140 mm deep and 600 mm high wall cavity filled with fiber glass insulation, a polyethylene vapor barrier and gypsum board towards the interior, sheathed in OSB and protected with a spun bonded-polyolefin (SBPO) membrane. Cladding assumed is a 13 mm fiber cement layer with a 20 mm ventilated air space behind it with a 100 air changes per hour to the exterior air assumed. To evaluate the role of VDPs under more realistic conditions, the validated model is adapted with the removal of the wet wood block and the addition of rain penetration to the sheathing as an ongoing moisture source, aligned with the ASHRAE 160 standard. 1% fraction of driving rain is applied uniformly on the sheathing material. The initial MC of the sheathing and framing is set to 10%.

The weather data used is for Vancouver, BC. The baseline weather data corresponds to the most severe year concerning moisture damage to building envelopes out of a measured period of 10 years, as published in ASHRAE RP-1325 by Salonvaara, Zhang, and Karagiozis (2011). Orientation is East, the prevailing wind-driven rain direction. The rain model used is for buildings up to 10 meters in height. Interior conditions are set using ASHRAE-160 model, heating only. The simulation time period is two years, starting November 1st, 2017 at 1-hour intervals.

Following the baseline simulations, the effect of wall orientation is investigated by facing the wall to south instead of east for the maximum solar exposure instead of maximum rain deposition. Plywood sheathing is simulated to compare with the OSB baseline. Mineral wool exterior insulation is added and compared to the baseline with no exterior insulation.

3 Results and Discussion

3.1 MC Analysis

The simulated MC of the sheathing below the VDP and the bottom plate is used for a comparison of assemblies with and without VDPs.

3.1.1 Baseline case

3.1.1.1 Sheathing Figure 3 presents the MC of the OSB sheathing below the VDP and of the bottom plate for the baseline simulations. The simulation begins Nov. 1st, the beginning of the winter which is the rainy season in Vancouver, and so in the beginning of the simulation there is quick intake of MC from the environment and rain penetration. The moisture intake is slightly more rapid for the assembly with a VDP by a maximum difference of 0.63% MC that happens on Nov. 11th. Both assemblies reach a similar maximum MC after the first winter, with the VDP assembly reaching 27.5% MC on Feb. 28th and the assembly without the port reaching 28.3% MC on the same day. On following winters, when the starting MC is higher, the VDP assembly reaches 28.8% MC and the assembly without the port reaches 30.4% MC, also on Feb. 28th. Thus, the maximum MC value for the assembly without a VDP is 1.6% higher than that with VDP.

From beginning of the spring until end of the summer (beginning of Mar. until end of Aug.), the assemblies dry out to the exterior, and the assembly with the VDP has MC by up to 3.8% lower than the assembly without VDP at times.

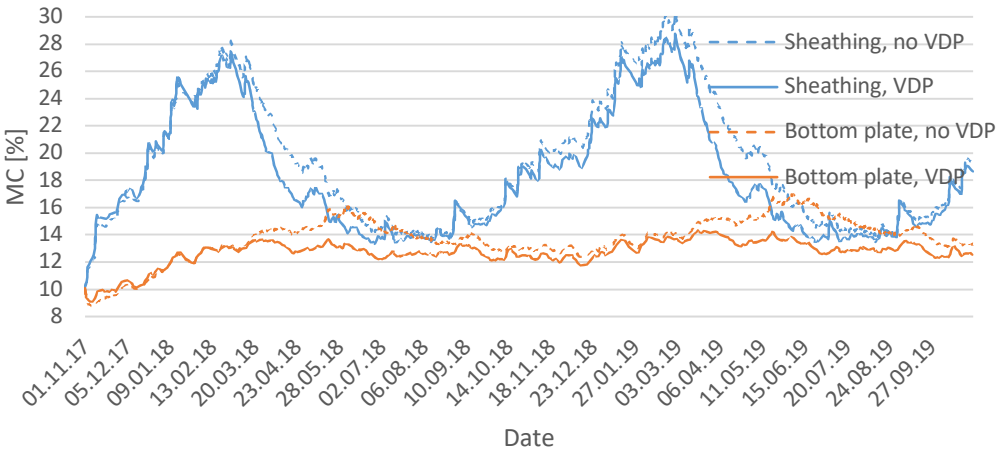

Figure 3. MC of OSB sheathing and bottom plate for the baseline rain infiltration simulations.

The time to dry from the maximum MC to under 20% MC is 34 days for the VDP assembly, occurring on April 4th, compared to 56 days for the assembly with no port, occurring on April 26th. The autumn period (Sep. to Nov.) is similar to the winter period with slightly decreased wetting.

Other than the beginning of the first winter, the assembly with the VDP has a lower value of MC for the rest of the simulation duration. During dryer periods the OSB sheathing MC with and without VDP is similar, and there is no observed effect of moisture intake from the environment due to the VDP.

3.1.1.2 Bottom plate. In order to investigate the effects of the VDP on other components in the wall assembly that are further away from the port, MC is displayed in Figure 3 for the top 5.3mm of the bottom plate, which is the portion of the bottom plate that would be more susceptible to durability issues including mold growth when conditions allow it.

After an initial phase of water intake from the environment and redistribution in the assembly, the bottom plate shows a relatively low variance in MC values throughout the year. During periods of wetting, which occurs to the sheathing, there is little difference between the MC with and without the VDP. Contrarily, during drying periods, the MC of the bottom plate for assemblies with a VDP is by up to 3.3% lower. This can be explained by the quick redistribution process within the assembly, which makes the MC difference in the bottom plate follow the MC difference in the sheathing.

For the bottom plate, similar to the sheathing, no undesired effects of the VDP are observed, except for the beginning portion of the simulation where the VDP allows for quicker moisture intake. Overall, it is found that the MC of other components in the assembly follows closely the differences in MC in the sheathing.

3.1.2 Effect of wall orientation

Two assemblies with the same parameters but facing south instead of east for maximum solar exposure instead of maximum rain deposition are simulated. Figure 4 presents these results compared to the baseline. Due to the lower rain exposure on south orientation, the MC values of sheathing are significantly lower, with a maximum value of below 20% MC as opposed to a

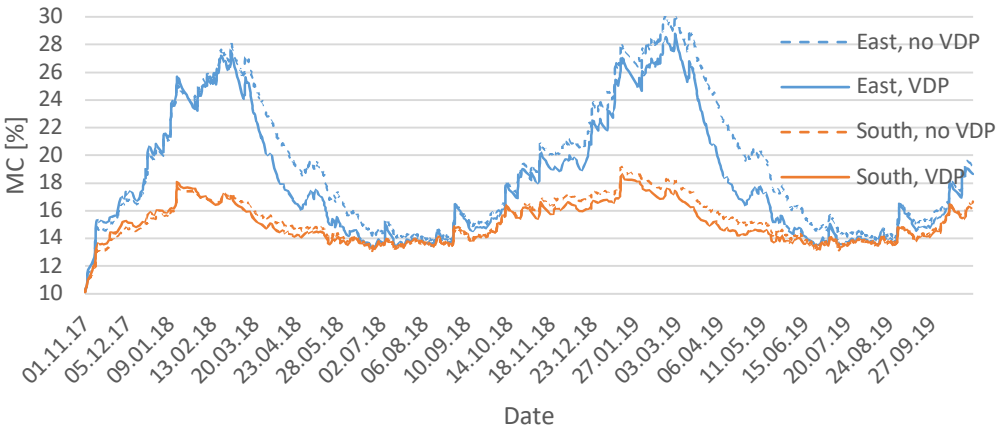

Figure 4. sheathing MC for east and south orientations, with and without a VDP.

value of 30% MC for the baseline simulation facing East. The effect of the orientation change is significant because it directly affects the amount of driving rain that is deposed on the sheathing. The VDP assembly compared to the one without shows a more moderate improvement of 1% lower MC facing south compared to 3.8% facing east at most. Same as with the baseline simulations, there are no adverse VDP effects except for a faster moisture intake during the first transient phase of moisture equilibration in the beginning of the simulation.

3.1.3 Effect of sheathing materials

Figure 5 shows the comparison in MC between plywood and OSB. Overall, MC behavior is similar to the OSB assemblies, as are drying times to reach under 20% MC. The maximum difference between values with and without a VDP is 4.8% MC for plywood compared to 3.8% in OSB, and occurs at the same time. This can be explained by the plywood assemblies reaching higher MC values and being able to dry further than the OSB assemblies, with or without the presence of a VDP. It shows that for high load of wetting, VDPs can be beneficial in plywood too.

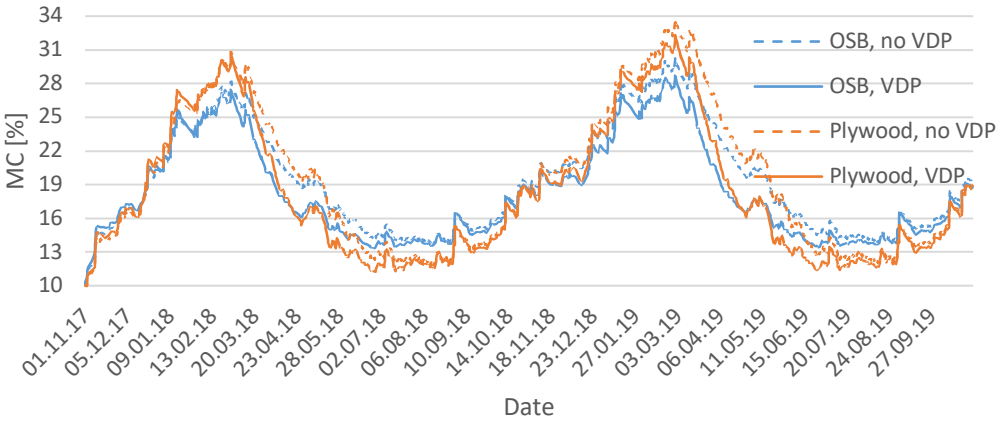

Figure 5. MC in sheathing (OSB vs. plywood), east orientation, with and without a VDP.

3.1.4 Effect of adding exterior insulation

An exterior insulation layer of 75 mm mineral wool is added to the baseline assembly. Figure 6 presents the sheathing MC for the assemblies with and without mineral wool exterior insulation, with and without a VDP. MC is significantly lowered and so the VDP effect is reduced. The MC behavior stays similar to the baseline simulation. For the baseline simulation with no VDP compared to the assembly with mineral wool exterior insulation and no VDP, the maximum MC is reduced by 7.5%, from 30.5% to 23%, while the minimum MC values do not change. The VDP maximal effect is reduced from maximum relative drying of 3.8% to 2.2% MC, and there is no moisture intake from the environment.

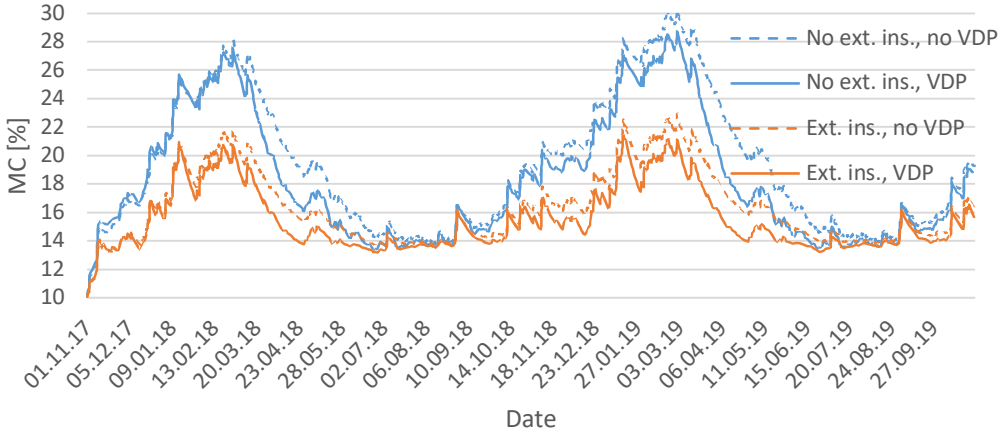

Figure 6. MC of OSB sheathing with and without mineral wool ext. insulation, with and without a VDP.

3.2 Mold Index

In addition to the examination of resulting MC in the assembly, mold index is calculated following ASHRAE standard 160-2016. Mold growth index is calculated and compared for two sensitivity classes: “Sensitive” class, corresponding to wood-based boards such as plywood and OSB, and “Very sensitive”, usually used for untreated wood and used here as a worst-case scenario for mold growth potential. The mold growth index calculation uses hourly temperature and relative humidity data extracted from the simulations following the procedure prescribed in ASHRAE 160. The standard states that in order to minimize problems related to mold growth, the mold growth index should not exceed a value of three.

The maximum mold growth index over the simulation period is summarized in Table 1. The mold growth index is slightly higher for the assemblies with a VDP, in spite of the lower MC values on the sheathing. The explanation for this phenomenon is that during the beginning of the simulation there is a short period during which the MC and RH are rising quicker in the assemblies with a VDP, and therefore a higher maximum mold growth index in the VDP assemblies. Later in the simulation RH levels are lower in the assemblies with the VDPs and the difference in mold index reduces, but the 2-year simulation period is not enough to close the initial gap in mold index for most simulations. For the assemblies examined, no improvement in mold index was found, even though MC values did show improvement. According to ASHRAE 160 criteria, there is mold growth risks only when “very sensitive” class is assumed for both OSB and Plywood sheathed wall assemblies.

Table 1. Maximum mold growth index over the simulation period.

Simulation inputs			Mold index, Sensitive		Mold index, Very sensitive	
Sheathing	Exterior insulation	Orientation	without VDP	with VDP	without VDP	with VDP
OSB		East	1.38	1.39	4.41	4.43
OSB		South	0.02	0.02	0.02	0.02
Plywood		East	1.00	1.12	3.47	3.84
OSB	Mineral wool	East	0.03	0.07	0.11	0.21

4 Conclusions and Discussions

Vapor diffusion ports have an ability to modestly improve the rate of drying for wall assemblies with an on-going moisture source of rain infiltration on the sheathing layer based on the hygrothermal simulations of this study. Table 2 summarizes the improvement due to VDP effects of MC (max and root mean square difference), mold index, and number of days to dry to under 20% MC. The higher the MC of the assembly, the greater the potential contribution of the VDP to drying. For the East-oriented wall, the maximum MC difference in OSB sheathing is 3.85% with an average difference of 1.5%, while for the south-oriented wall the maximum MC difference in OSB sheathing is 1% with an average difference of 0.4%. Similar trend is found for plywood-sheathed wall. With the addition of exterior insulation, the temperature of sheathing is elevated and therefore improved drying capacity. Consequently, the contribution of VDP to drying is reduced. The provision of VDP also reduces the time for OSB sheathing to dry to below 20% MC. For example, an OSB sheathed wall with no exterior insulation oriented to the east will take 22 less days to dry to under 20% MC due to the presence of a VDP. However, the effect of VDP on the mold growth risk is negligible.

Table 2. Summary of improvement in MC and mold index due to VDP effects (comparison between assemblies with VDP and without VDP).

Simulation inputs			MC - Max [%]	MC- RMSD [%]	Mold index	Time to dry under 20% MC [days]
Sheathing	Exterior insulation	Orientation				
OSB		East	-3.85	-1.50	0.02	-22
OSB		South	-1.09	-0.44	0.00	NA
Plywood		East	-4.85	-1.84	0.37	-38
OSB	Mineral wool	East	-2.19	-1.07	0.10	-17

ORCID

Ben Zegen Reich: http://orcid.org/0000-0003-1192-499X
Hua Ge: http://orcid.org/0000-0003-1368-4301
Jieying Wang: http://orcid.org/0000-0002-0895-1797

References

ASHRAE Standard 160, Criteria for Moisture-Control Design Analysis in Buildings, ASHRAE, Atlanta, 2009

Hazleden, D. G. and Morris, P. I. (2001). Evaluation of Vapor Diffusion Ports on Drying of Wood-frame Walls under Controlled Conditions. Forintek Canada Corp. report for project 3134. Vancouver, BC.

Salonvaara, M., Zhang, J. and Karagiozis, K. (2011). Environmental Weather Loads for Hygrothermal Analysis and Design of Buildings. ASHRAE RP-1325. Simulation studies and data analysis.

Wang, J. (2018). Evaluation of Effects of Vapor Diffusion Ports on Drying Performance of Modern Wood-Frame Walls. FPInnovations report to Forestry Innovation Investment and the CFS, NRC. Vancouver, BC.

XV International Conference on Durability of Building Materials and Components
DBMC 2020, Barcelona
C. Serrat, J.R. Casas and V. Gibert (Eds)

Evaluation of Pore Structure of Hardened Cement Paste Immersed in Sodium Sulfate Solution

Otsuka Sakata, H. Nicolas [1], Kennosuke Sato[2] and Shigehiko Saito[2]

[1] University of Yamanashi, Faculty of Engineering, Integrated Graduate School of Medicine, Engineering and Agricultural Sciences, 4-3-11, Takeda, Kofu, Yamanashi, 400-8511, Japan, g19tc003@yamanashi.ac.jp

[2] University of Yamanashi, Graduate School of Engineering, Department of Civil Engineering and Environmental Engineering, 4-3-11, Takeda, Kofu, Yamanashi, 400-8511, Japan, satok@yamanashi.ac.jp

Abstract. *The purpose of the present study is to evaluate pore structure of hardened cement paste immersed in sodium sulfate solutions and to experimentally examine the relation between the change of pore structure and hydration products. Cement paste specimens were immersed in sodium sulfate solutions and ion-exchanged water for two weeks. Since oxygen gas can pass through the pores having micro scale, it is possible to evaluate the effect of the pore structure on the oxygen transport in cement pastes. Thus, the oxygen diffusion coefficient (D_{O2}) of the specimens after immersion were measured, and the pore volume and the pore size distribution were also measured. In addition, the phase compositions of the specimens were acquired. As a result, D_{O2} of the specimens immersed in the sodium sulfate solutions decreased as compared to the specimens immersed in the ion-exchanged water. The tortuosity of the specimens immersed in the sodium sulfate solutions increased due to decreasing of the pore volume having a diameter larger than 20 nm. There was a correlation between the volume of ettringite and the pore volume having a diameter larger than 20 nm. According to the above results, it was considered that the decreasing of D_{O2} in the case of sulfate immersion can occur as a result of the complication of the pore structure owing to filling of the pores by ettringite.*

Keywords: *Sulfate Attack, Oxygen Diffusion Coefficient, Pore Structure, Tortuosity, Ettringite.*

1 Introduction

The sulfate attack is known as a chemical reaction caused by sulfate and causes the fragility and tissue fragility in hardened cement paste by generating a large amount of ettringite. Although there are not many cases of sulfate deterioration in Japan, there is a high potential risk of sulfate attack in Japan because it is revealed that the marine clay layer producing sulfates is widely distributed (Matsushita *et al.,* 2010). In addition, it is considered that cement-based materials are used for building of radioactive waste processing facilities.

Generally, in order to predict the deterioration phenomenon, it is necessary to grasp the ion transfer characteristics affecting the degradation of hardened cement paste. Furthermore, the ion transfer in the hardened cement paste is known to be greatly affected by the pore structure. Thus, in order to predict the progress of sulfate attack, it is necessary to grasp the pore structure as a transferring field of sulfate ions. However, the pore structure and mass transfer characteristics are significantly changed when the sulfate ions penetrate the hardened cement paste. Sulfate ions causes a reaction with cement hydrate constituting the solid phase and generates ettringite in large quantities, that is considered the cause of change, but there are few

examples of experimentally examined changes of pore structure and mass transfer characteristics when affected by sulfate attack.

Therefore, we evaluated the oxygen transfer characteristics affected solely by pore structure to clarify the change in the pore structure of the hardened cement paste immersed in sodium sulfate solutions.

2 Specimens and Methods

2.1 Preparation of Specimens

In this study, ordinary portland cement was used. Table 1 shows the chemical compositions of the cement, and Table 2 shows the density and specific surface area. The mineral compositions calculated by Bogue equation is shown in Table 3. Three types of cement paste specimens having water to cement ratio of 45%, 55% and 65% were prepared. The size of the specimens was 3 × 4 × 0.5 cm. It was demolded at 1 d, and it was wet-sealed curing until 28 d at 20 °C.

Table 1. Chemical compositions of cement (mass%).

Ig. loss	insol.	SiO_2	Al_2O_3	Fe_2O_3	CaO	MgO
0.71	0.08	20.89	5.44	2.94	65.11	1.54

Na_2O	K_2O	TiO_2	P_2O_5	MnO	Cl	Total
0.27	0.53	0.26	0.14	0.05	0.014	97.99

Table 2. Density and surface area of cement.

Density (g/cm^3)	Blaine specific surface area (cm^2/g)
3.16	3450

Table 3. Mineral compositions of cement (mass%).

C_3S	C_2S	C_3A	C_4AF	Gypsum	MgO
60.00	15.00	9.00	9.00	3.54	1.54

2.2 Sodium Sulfate Immersion and Ion-Exchanged Water Immersion

The specimens were immersed in sulfate solutions. Sodium sulfate and ion-exchanged water (electrical conductivity 0.055μS/cm) were used for sulfate solutions. The concentrations of sodium sulfate solutions were 0.5 and 5 mass%. The specimens were immersed in solutions with the liquid-to-solid ratio of 5.0 at 20 °C for 2 weeks. The specimens were also immersed in the ion-exchanged water for comparison with the case of sodium sulfate immersion.

2.3 Analysis

The pore volume of each specimen was measured by Archimedes method. Each specimen after immersion was crushed into small pieces, after which 3 pieces (about 3 g) were immersed in ion-exchanged water and reduced pressure for 30 min. The mass of the specimens under water and the mass of the surface-dried condition were subsequently measured. Thereafter, the specimens were dried at 50 °C in a drying oven until the specimens mass no longer changed. The pore volume was calculated by the following equation (1)

$$V = \frac{m_s - m_{50d}}{m_s - m_W} \tag{1}$$

where V is the pore volume (m^3/m^3), m_s is the mass of the surface-dried condition (g), m_{50d} is the mass of the dried condition at 50 °C (g), and m_w is the mass of the specimen under water(g).

Pore size distribution was measured by mercury-intrusion-porosimeter. The crushed samples (about 5 mm) were immersed in acetone for 2 d to prevent further hydration. These specimens were subsequently placed under vacuum to remove the acetone and stored in a desiccator in the presence of silica gel until the mass no longer changed. The pressure range was 0.1 kPa to 400MPa. The measurement range of the pore diameter is approximately 4 nm to 120 μm.

Kikuchi *et al*. (2010) was measured the oxygen diffusion coefficient of the hardened cement paste, which is capable of grasping the complexity of the pore structure. Therefore, in order to grasp the pore structure of the specimens immersed in sodium sulfate solutions, the oxygen diffusion test was performed. The specimens after immersion were dried in a desiccator containing silica gel until the mass no longer changed. The oxygen diffusion test was carried out with reference to the method of Shirakawa *et al*. (1999). The oxygen concentration was recorded, when the change in oxygen concentration in the nitrogen gas side cell became constant. The oxygen diffusion coefficient was determined using the formula (2)

$$D_{O_2} = \frac{R_N \cdot (C_N - C_b) \cdot (L + \delta_N + \delta_O)}{\left\{1 - \frac{R_N}{R_O} \cdot \left(\frac{M_O}{M_N}\right)^{\frac{1}{2}} \cdot (C_N - C_b) - C_N\right\} \cdot A_C} \tag{2}$$

where D_{O_2} is the oxygen diffusion coefficient (cm^2/s), C_N is the oxygen concentration in nitrogen gas (%), C_b is the oxygen concentration in nitrogen gas cylinder (%), R_N and R_O are the nitrogen and oxygen gas flow rates (cm^2/s), M_N and M_O are the nitrogen and oxygen molecular weight (g/mol), L is the specimen thickness (cm), A_C is the cross-sectional area of the specimen (cm^2), and δ_N and δ_O are the boundary film thickness of the nitrogen gas side and oxygen gas side (mm).

Phase composition of the crystal phase of the sample was quantified by XRD / Rietveld analysis. The samples after immersion were immersed in acetone for 2 d and subsequently placed under vacuum to remove the acetone for 2 d. The samples were crushed and dried at 20 °C and 11% RH until the sample mass no longer changed. In this study, corundum was used as a standard sample, and the amount of the amorphous phase was quantified by the external standard method (Sagawa *et al.,* 2014). The compositions of amorphous phase and CaO/SiO_2 molar ratio of C-S-H (C/S ratio) were calculated by mass balance calculation (Maruyama *et al*., 2010) using the composition of each hydrate in 11% RH reported by Suda *et al*. (2014).

3 Results and Discussion

3.1 Effect of Sodium Sulfate on Oxygen Diffusion Coefficient

Figure 1 shows the oxygen diffusion coefficient of the sample immersed in sodium sulfate and ion-exchanged water. The oxygen diffusion coefficients of the specimens immersed in sodium

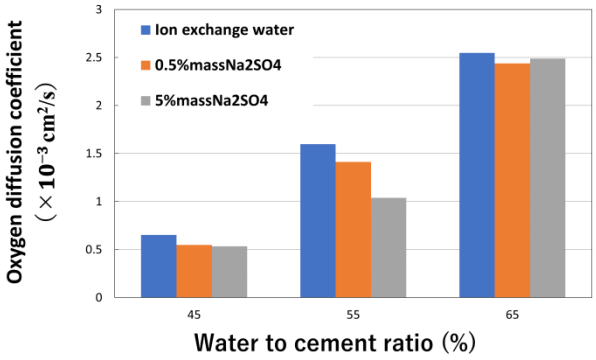

Figure 1. Oxygen diffusion coefficient of hardened cement pastes after immersion.

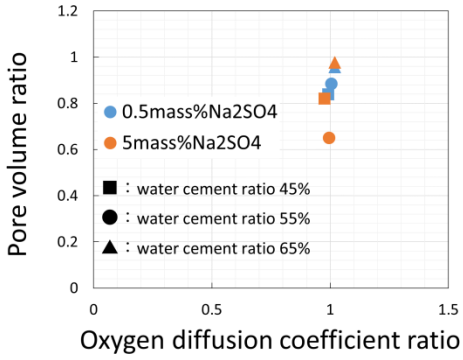

Figure 2. Relationship between oxygen diffusion coefficient ratio and pore volume ratio.

sulfate were reduced regardless of the water-to-cement ratio as compared with the case of ion-exchanged water. However, the degree of decreasing in the oxygen diffusion coefficient varies from water-to-cement ratio. The water-to-cement ratio 55% is large reduction degree, on the other hand, the degree of decreasing was reduced at the water-to-cement ratio 65%.

3.2 Change in Pore Structure by the Effects of Sodium Sulfate

The relationship between the decreasing in the oxygen diffusion coefficient affected by sodium sulfate and the change in the pore structure of the specimens was examined. First, the effect of the change in the pore volume was examined to quantify the change caused by the effect of sodium sulfate. The oxygen diffusion coefficient ratio R_{O_2} was calculated by the equation (3) using the value of the sample immersed in ion-exchanged water $D_{O_2\_water}$, which is not affected by sodium sulfate. Similarly, the pore ratio was calculated.

$$R_{O_2} = \frac{D_{O_2\_Na_2SO_4}}{D_{O_2\_water}} \tag{3}$$

Figure 2 shows the relationship between the oxygen diffusion coefficient ratio and the pore volume ratio. From the figure, the pore volume ratio is almost unchanged at 1.0 while the oxygen diffusion coefficient ratio is greatly changed in the range of 1.0 to 0.6. Thus, the decreasing in the oxygen diffusion coefficient caused by the effect of sodium sulfate could not be explained by a change in the pore volume.

Because it has been reported that the tortuosity is an index representing the complexity of the pore structure (Saeki *et al.*, 2014), the tortuosity of the oxygen diffusion in the hardened cement paste was calculated in this study. The tortuosity of the oxygen diffusion was calculated using the formula (4), with reference to the past studies (Kikuchi *et al.,* 2010; Saeki *et al., 2014*)

$$D_{O_2} = \frac{1}{{\tau_{O_2}}^2} \cdot D \tag{4}$$

where τ_{O_2} is the tortuosity of the oxygen diffusion, and D is the effective diffusion coefficient in the pore (cm^2/s).

In this study, the parallel pore model was adopted, and the effective diffusion coefficient in the pore was calculated by equation (5)

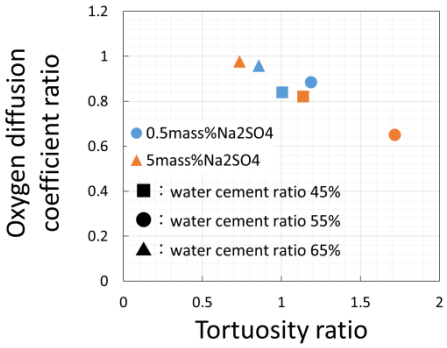

Figure 3. Relationship between oxygen diffusion coefficient ratio and tortuosity ratio.

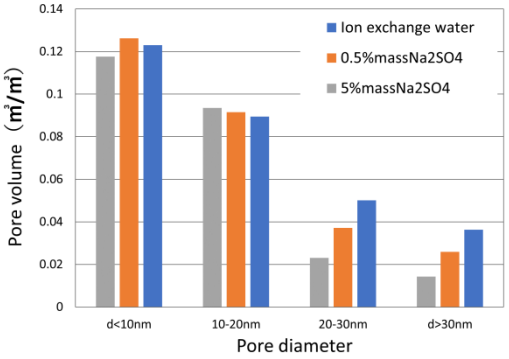

Figure 4. Pore volume of each pore diameter (water to cement ratio of 45%).

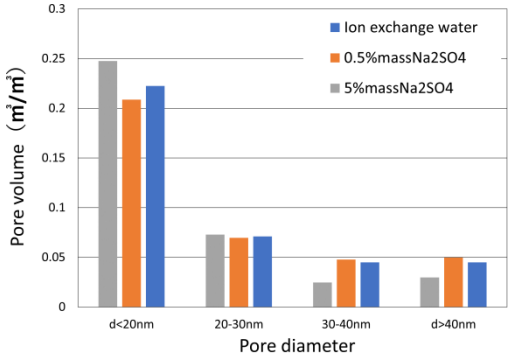

Figure 5. Pore volume of each pore diameter (water to cement ratio of 55%).

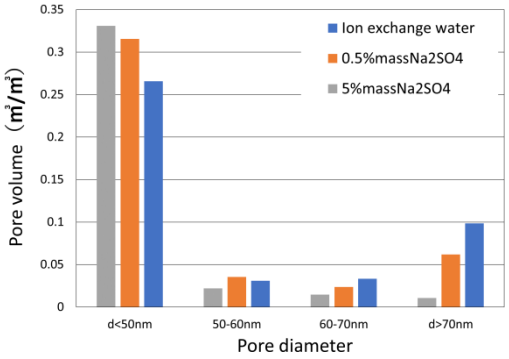

Figure 6. Pore volume of each pore diameter (water to cement ratio of 65%).

$$D = \left(\frac{\varepsilon_a}{\frac{1}{D_{Ka}} + \frac{1}{D_{ON}}} \right) + \left(\frac{\varepsilon_b}{\frac{1}{D_{Kb}} + \frac{1}{D_{ON}}} \right) \quad (5)$$

where ε_a is the pore volume having a diameter < 50 nm (cm^3/cm^3), ε_b is the pore volume having a diameter > 50 nm (cm^3/cm^3), D_{Ka} is the Knudsen diffusion coefficient of the average pore diameters < 50 nm (cm^2/s), D_{Kb} is the Knudsen diffusion coefficient of the average pore diameters > 50 nm (cm^2/s), D_{ON} is the molecular diffusion coefficient of nitrogen and oxygen (cm^2/s). The tortuosity ratio was calculated in the same manner as the oxygen diffusion coefficient ratio described above.

Figure 3 shows the relationship between the oxygen diffusion coefficient ratio and the tortuosity ratio. The oxygen diffusion coefficient ratio is reduced with increasing of the tortuosity ratio. These results suggest that the decreasing of the oxygen diffusion characteristics in the hardened cement paste affected sodium sulfate was caused by the increasing of the complexity of the pore structure due to sodium sulfate immersion.

Subsequently, in order to investigate the increasing of the pore structure complexity, we focused on changes in the pore size distribution. Figure 4 to 6 shows the pore volume of each

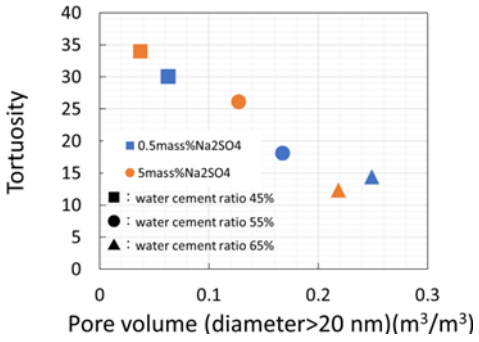

Figure 7. Relationship between tortuosity and pore volume (d > 20nm).

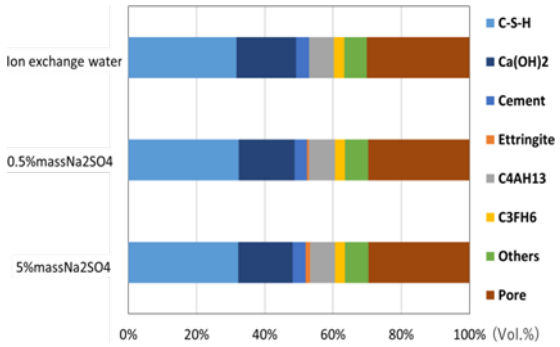

Figure 8. Phase compositions of the specimens after immersion (water-to-cement ratio of 45%)

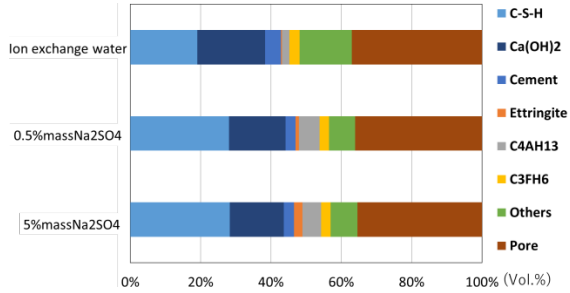

F igure 9. Phase compositions of the specimens after immersion (water-to-cement ratio of 55%)..

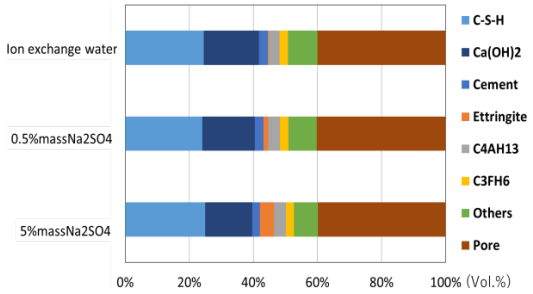

Figure 10. Phase compositions of the specimens after immersion (water-to-cement ratio of 65%).

pore diameter. From Figure 4, in the case of water-to-cement ratio of 45%, in the division of the diameter < 20nm, it was confirmed that the pore volume of the sodium sulfate immersion sample was slightly larger than that of the ion-exchanged water immersion sample. On the other hand, in the division of diameter > 20nm, the pore volume of the sodium sulfate immersion sample is reduced as compared to the ion-exchanged water immersion sample. It was confirmed that the diameter of 20 nm is the boundary of the trend change.

Figure 7 shows the relationship between the tortuosity and the pore volume having a diameter > 20 nm. From the figure, the tortuosity increased with decreasing of the pore volume having a diameter > 20nm. These results suggest that because the pore volume having a diameter > 20 nm in the specimen immersed in sodium sulfate decreased, the pore structure was complicated and the oxygen transfer was suppressed.

3.3 Effect of Hydration Products on the Change of Pore Structure

Figures 8 to 10 shows the phase compositions of the specimens after immersion having each water-to-cement ratio. In the case of the ion-exchanged water immersion, which is not affected by sodium sulfate, the C-S-H occupies most of the solid phases. In the case of sodium sulfate immersion, the C-S-H also occupies most of the solid phase at any water-to-cement ratio. Furthermore, the higher the water-to-cement ratio and the higher the sodium sulfate concentration, the amount of ettringite was increased. Therefore, we examined the relationship

between the pore volume having a diameter > 20 nm and the generation of C-S-H and ettringite.

In order to calculate the volume of C-S-H, which is affecting the pore volume, the amount of C-S-H was calculated using equation (6)

$$M_{C-S-H} = m_C \cdot \left(\frac{m'_{C-S-H}}{100}\right) \tag{6}$$

where M_{C-S-H} is the amount of C-S-H per unit volume (g/m^3), m_C is the amount of cement paste per unit volume (g/m^3), m'_{C-S-H} is the amount of C-S-H (cm^2/s). The volume of C-S-H V_I (m^3/m^3) was calculated by dividing the M_{C-S-H} by ρ_{C-S-H}, which is the density of C-S-H (g/m^3) as shown in equation (7).

$$V_I = \left(\frac{M_{C-S-H}}{\rho_{C-S-H}}\right) \tag{7}$$

Because the density of C-S-H changes depending on the C/S ratio, it was calculated from each C/S ratio using the equation (8) of Suda *et al*. (2014).

$$\rho_{C-S-H} = 0.45(C/S) + 1.36 \tag{8}$$

Furthermore, as shown in the equation (9), the volume of C-S-H was calculated

$$V_{C-S-H} = \frac{V_I}{P} \tag{9}$$

where V_{C-S-H} is the volume of C-S-H (m^3/m^3), P is the capillary pore volume (m^3/m^3).

Figure 11 shows the relationship between the C-S-H volume and the pore volume having a diameter > 20 nm. In both of the sodium sulfate solution concentration, the pore volume having a diameter > 20 nm decreased with the increasing of the volume of C-S-H. However, when a regression line was drawn for each sodium sulfate solution concentration, there was a slight error between the two lines. Since different linear relationships were shown for each solution concentration, it was considered that there were other factors besides the volume change of C-S-H in the change of the pore volume having a diameter > 20 nm. Therefore, the volume of ettringite was considered, in addition to C-S-H.

The volume of ettringite (V_{Ett}) was calculated using the same calculation as in equations (6), (7), and (9). The density of the ettringite was 1.78×10^6g/m^3 (Suda *et al*., 2014). As shown in equation (10), the total volume (V_{C-S-H_Ett}) was obtained by adding the V_{Ett} to the V_{C-S-H}.

$$V_{C-S-H\_Ett} = V_{C-S-H} + V_{Ett} \tag{10}$$

Figure 12 shows the relationship between the pore volume having a diameter > 20 nm and the volume of C-S-H and ettringite. In this case, the regression line drawn for each sodium sulfate solution concentration showed almost no error. These results suggest that the decreasing of the oxygen diffusion coefficient of the specimens affected by sodium sulfate was caused by the formation of ettringite, which is filling the pores having a diameter > 20 nm and the complication of the pore structure.

4 Conclusions

The purpose of this study was to investigate the effect of sodium sulfate on the oxygen transfer characteristics and the pore structure of hardened cement paste. The conclusions derived from this study can be summarized as follows.

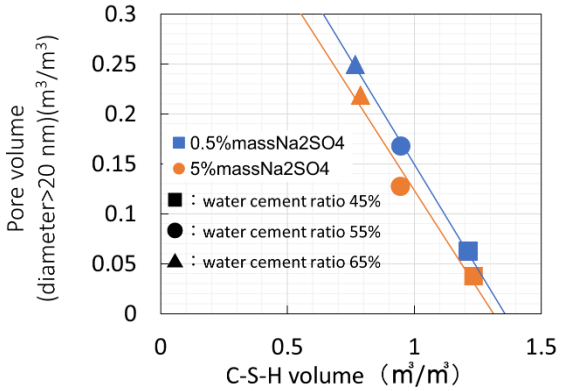

Figure 11. Relationship between pore volume (d > 20nm) and volume of C-S-H.

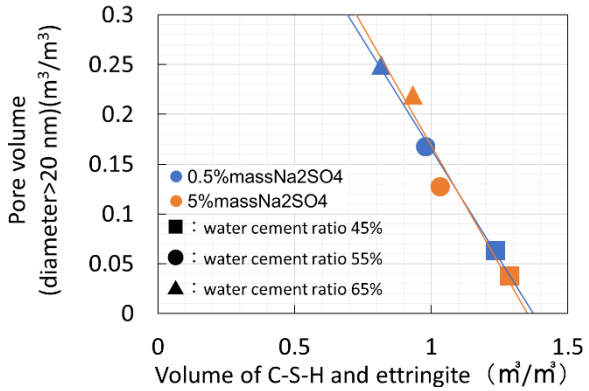

Figure 12. Relationship between pore volume (d > 20nm) and volume of C-S-H and ettringite.

When the cement paste was affected by sodium sulfate, the oxygen diffusion coefficient decreased compared to the case immersed in ion-exchanged water.

The decreasing of the oxygen diffusion coefficient affected by sodium sulfate was due to the increasing of the tortuosity owing to the decreasing of the pore volume having over 20 nm in diameter.

The decreasing of the oxygen diffusion coefficient of the specimens affected by sodium sulfate was caused by the formation of ettringite, which is filling the pores having over 20 nm in diameter and the complication of the pore structure.

ORCID

Herly Nicolas Otsuka Sakata: https://orcid.org/0000-0003-0434-9595
Kennosuke Sato: http://orcid.org/0000-0002-3456-4037
Shigehiko Saito: http://orcid.org/0000-0001-6789-3198

References

Maruyama, I., Matsushita T., Noguchi, Takafumi., Hosokawa, Y. and Yamada, K. (2010). *Rate of Hydration of Alite and Belite in Portland Cement -Hydration system of Portland cement Part 1-*. J. Struct. Constr. Eng., AIJ. 650, 681-688.

Matsushita, H., Sagawa, Y. and Sato, T. (2010). *Classification of probability of deterioration of concrete by sulfate arrack based on investigation results of sulfate content of ground.* Journal of Japan Society of Civil Engineers E, 66(4), 507-519.

Kikuchi, M., Suda, Y. and Saeki, T. (2010). *Evaluation for Ion Transport in Hardened Cementitious Paste by Oxygen Diffusion and Chloride Diffusion.* Cement Science and Concrete Technology, 64 346-353.

Shirakawa, T., Shimazoe, Y., Aso, M., Nagamatsu, S. and Sato, Y. (1999). *The Proposal of Testing Method for Determination of Gas Diffusion Coefficient in Hardenend Cement.* J. Struct. Constr. Eng., AIJ. 515, 15-21.

Sagawa, T. and Toyoharu, N. (2014). *Hydration Analysis and Phase Composition of Cement-based Materials by X-Ray Diffraction / Rietveld Method using an External Standard.* Cement Science and Concrete Technology, 68, 46-52.

Saeki, T., Mashima K., Kikuchi, M. and Saito, T. (2014). *Chroride Ion Diffusivity in Hardended Cementitious Materials using Various Silica Fume.* Cement Science and Concrete Technology, 68, 352-359.

Suda, Y., Saeki, T. and Saito, T. (2014). *Effect Chemical Composition of C-S-H on Volume and Pore Size Distribution of Gel Pore*. (2014). Journal of Japan Society of Civil Engineers E2, 70(2), 134-152.

XV International Conference on Durability of Building Materials and Components
DBMC 2020, Barcelona
C. Serrat, J.R. Casas and V. Gibert (Eds)

Evaluation of Tortuosity in Cemented Sand Using X-Ray Computed Microtomography

Junil Pae[1] **and Juhyuk Moon**[2]

[1] Department of Civil and Environmental Engineering, Seoul National University, 1 Gwanak-ro, Gwanak-gu, Seoul, 08826, Republic of Korea, sdc03055@snu.ac.kr

[2] Department of Civil and Environmental Engineering, Seoul National University, 1 Gwanak-ro, Gwanak-gu, Seoul, 08826, Republic of Korea, juhyukmoon@snu.ac.kr

Abstract. *Cemented sand is a common way for soil stabilization or ground improvement. Tortuosity is an important parameter that has a significant impact on flow and transport characteristics of porous media and related to permeability and diffusion coefficient. This study aims to quantitatively investigate the tortuosity of the cemented sand with different cement content using X-ray computed tomography (CT) based random walk simulation. The cemented samples were scanned using micro-CT and converted to 3D pore space through image processing. Random walk simulation was applied to the reconstructed 3D pore space to calculate the tortuosity. Higher cement content gave an increase in tortuosity and a decrease in porosity. This indicates that the addition of cement makes pore space more tortuous and decreases both permeability and diffusion coefficient which are being treated as important parameters for durability of construction materials.*

Keywords: *Cemented Sand, Tortuosity, X-Ray Microtomography, Random Walk Simulation.*

1 Introduction

Soil stabilization by cement mixing is one of the common methods to improve natural soil. Generally, cemented sand which is produced by mixing cement, sand, and water, has greater strength than natural soil. Ordinary Portland Cement is widely used in soil stabilization and many researches were carried out to investigate its mechanical (Consoli, Viana da Fonseca, Cruz, and Heineck, 2009; Wang and Leung, 2008). Pore network in cementitious material is an important factor that affects many mechanical properties including strength and stiffness as well as durability. However, it is difficult to quantitatively analyse due to its complexity thus several experimental parameters like porosity, permeability, and diffusivity are frequently being used to understand pore network and resulting durability, indirectly. Therefore, the knowledge of tortuosity for cemented sand is strongly required for designing not only the cement content for soil stabilization but also evaluating life span of cementitious materials under various environments.

X-ray Computed Tomography (CT) has been utilized to examine the microstructure of porous media. X-ray CT is a non-destructive technique that allows X-rays to pass through the material at different angles and measures the attenuation using the director. The key advantage of X-ray CT is that it is a unique way to obtain three-dimensional microstructure at specific resolution. This study aims to investigate the tortuosity of the cemented sand with different cement content from the X-ray CT based random walk simulation.

doi:10.23967/dbmc.2020.206

2 Background of Definition of Tortuosity

Tortuosity is a meaningful parameter that has a significant impact on flow and transport characteristics of porous media. The classic definition of tortuosity (τ) is given as the ratio of the average lengths of the actual paths that fluid or electric particles migrate from one point to the final point through the pore space of a porous medium to the corresponding straight and shortest distance between these points. In this regard, tortuosity is always greater than or equal to 1. The importance of tortuosity can be observed in various engineering applications (*e.g.*, diffusion, mass transfer and separation of mixtures) (Boudreau, 1996; Champoux and Allard, 1991; Thorat *et al.*, 2009).

In this study, tortuosity is treated as a property of the porous media which can be calculated from 3D micro-geometry of the pore structure. For instance, the tortuosity in cementitious materials has been evaluated by random walk simulation in the 3D pore structure obtained by X-ray microtomography (Promentilla, Sugiyama, Hitomi, and Takeda, 2009; Provis, Myers, White, Rose, and Van Deventer, 2012).

Diffusion tortuosity is defined as a ratio of the self-diffusion coefficient (D_0) of non-sorbing walkers in free space to the long-time self-diffusion coefficient (D_∞) of these walkers in pore space. The self-diffusion coefficient is estimated from mean square displacement (MSD) from the movement trajectories these random walkers as a function of time. The time-dependent diffusion coefficient D_t associated with the random Brownian motion of molecules in porous media. If diffusion time is great enough, it will be a non-zero value that can represent the entire pore characteristic because walkers can travel all of the pore space, but it approaches zero in a closed pore space. Thus, the long-time self-diffusion coefficient of molecule only in a connected pore structure divided by the one in the free space can be defined as the diffusion tortuosity.

The formation factor (F) can be calculated from the tortuosity and interconnecting porosity.

$$F = \frac{\tau_D}{\emptyset} \tag{1}$$

By Nernst–Einstein relation, the relative diffusibility, formation factor, porosity and tortuosity are related to each other.

$$\frac{D_e}{D_f} = \frac{1}{F} = \frac{\emptyset}{\tau_D} \tag{2}$$

where D_e is the intrinsic diffusion coefficient by using Fick's law, and D_f is the diffusion coefficient in the free fluid (Promentilla *et al.*, 2009).

3 Materials and Methods

3.1 Sample Preparations and Image Acquisition

The specimens of cemented sand used in this study were prepared by mixing Jumunjin standard sand and ordinary Portland cement Type 1. The sand/cement ratio of each specimen is 0%, 1%, 3%, 5%, 7% and water content which means the ratio of mass of water to solids (includes both sand and cement) is 0.1. The mix design is shown in Table 1. Samples are prepared in PVC molds and cured at 20℃ for 7days. One specimen per each mix was

analyzed by the CT and one volume of interest (VOI) per specimen was selected for image processing as described below.

Table 1. Mix design of cemented sand.

.

Sand (g)	Cement (g)	Water (g)	w/c ratio
1000	0	100	-
1000	10	101	10.1
1000	30	103	3.43
1000	50	105	2.10
1000	70	107	1.53

The X-ray imaging of specimens was performed by the Skyscan micro-CT (Skyscan1272, Bruker, Belgium). Acquired reconstructed image from tomographic data has 4904×4904 pixels and pixel size is 5 μm by 5 μm. 3280 layers of X-ray projection image are obtained with exposure time of 5000ms and an angle step of 0.1°.

3.2 Construct of 3D Pore Space

The VOI which is the portion of the full data set chosen for segmentation is necessary due to some limitations of memory during computation. The size of VOI should also be large enough to eliminate the introduction of errors resulting from the cropping images (i.e., the finite size). It has been suggested in previous literature that the minimum VOI should be at least 100 μm^3, or 3 to 5 times larger than the size of the largest distinct feature of the sample for hardened OPC pastes, to eliminate finite size error (Garboczi and Bentz, 2001; Provis *et al.*, 2012). In this study, 1000×1000 pixels of region of interest applied to each images and then it merged to 1000^3voxels of VOI which is equal to 3D pore space which satisfies the size requirement in image analysis. Hence, the raw images were cropped to 1000×1000 pixels in the center of the specimen (Figure 1).

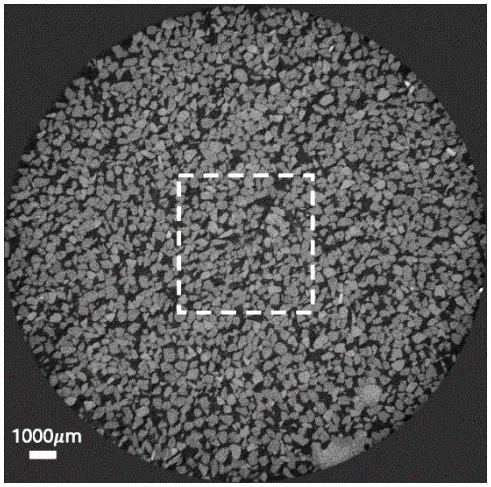

Figure 1. A slice through the full tomographic reconstruction of the 7-day 1% cemented sand specimen. White dotted area shows the size of the VOI selected.

First, Gaussian blur and anisotropic diffusion were adjusted in sequence in order to smooth the raw images while remaining the narrow pore space between sand particles. This procedure enhances the accuracy of watershed algorithm applied later. Then, segmentation is carried out to separate pore and solid due to the difficulty of distinguish sand phase and cement phase in X-ray image at a resolution lower than 1μm/pixel. Thresholding value in grayscale is selected as 5 greater than the value calculated by Otsu method in entire dataset due to eliminate the noises in pores space (Otsu, 1979). In addition, the narrow pores between sand particles containing lots of noises could be converted to pore after segmentation. Sand and pore phase are modified to white and black, respectively.

After pore segmentation, 1000 slices of 2D images are merged to 3D pore space to

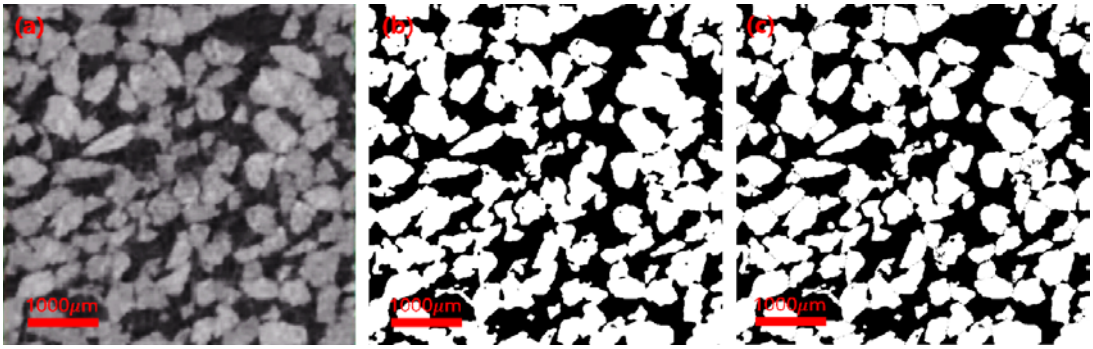

Figure 2. Application of watershed algorithm to separate the connected sand particles (2D images of 1% cement content): (a) filtered greyscale image, (b) binary segmented image, (c) binary image after applying watershed algorithm.

implement further processing at 3D pore space directly. The white closed particles of which size is smaller than the realistic sand particle is removed and the black closed particles that has smaller size than one that exists in the sand particles are also removed. In Figure 2(b), sand particles connected to each other in filtered greyscale image need to be separated because in actual cemented sand, sand particles cannot adhere completely to other due to roughness of surface. In addition, the narrow pores located near sand are transformed into solid phase. Eventually, watershed algorithm is applied to binary segmented image for severing connected sand fragments and restoring narrow pore surrounded by sand particles.

3.3 Particle Size Distribution of Sand

Particle size distribution (PSD) of sand is considered to verify the used image processing method. Sieve analysis was performed for the identical sand to gain PSD data following ASTM D422. In 3D pore space after applying watershed algorithm, all of the sand particles exist independently. It allows to calculate the volume of each separated sand particles by using cluster labeling. PSD is also obtained from these volume data by calculating equivalent diameter. Therefore, the accuracy of segmented 3D pore structure can be evaluated by the comparison of the PSDs obtained from the sieve analysis and image processing.

3.4 Tortuosity Calculation From Random Walk Simulation in 3D Pore Space

A 3D random walker simulation (Nakashima and Kamiya, 2007) implanted in MATLAB was used to compute the MSD of random walkers in the segmented pore space. Mirror image

boundary conditions were employed to the original pore space, resulting to an infinitely expanded pore structure where simulations are performed with preserving the continuity of inter-connected pore network. The average displacement of the walkers was plotted as a function of the number of the timesteps and the tortuosity was calculated from the inverse of the slope of this curve.

To execute the random walker simulation, a random pore voxel in the inter-connected pore network is chosen as the initial position of each walker. In each timesteps, the one was selected among the six voxels which are face-to-face connected with the random walker. Then the random walker migrates to the selected voxel when it has been identified as pore space. The diffusion tortuosity is defined as the ratio of the self-diffusion of a walker in free space to the self-diffusion of a walker in the pore space such that:

$$\tau_D = \frac{D_0}{D_\infty} = \left[\lim_{t\to\infty} \frac{\mathrm{d}\langle r^2(t)\rangle}{\mathrm{d}t}\right]^{-1} \tag{3}$$

where D_0 is the self-diffusion coefficient of a walker in free space, D_∞ is the self-diffusion coefficient of a walker in the pore space, and $\langle r^2(t)\rangle$ is the average of MSD as a function of a time. By using Eq. (3), restricted diffusion that reflects the geometry of the entire pore space can be defined as the diffusion tortuosity. On such time scales, the MSD starts to increase linearly with the number of timesteps due to an ample time for random walkers to travel the entire pore space, leading to constant calculated tortuosity.

4 Results and Discussion

An example of the results from image analysis of the VOI is shown in Fig. 4. Segmented solid phase is corresponding to the sand and cement particles including both hydrated and unhydrated

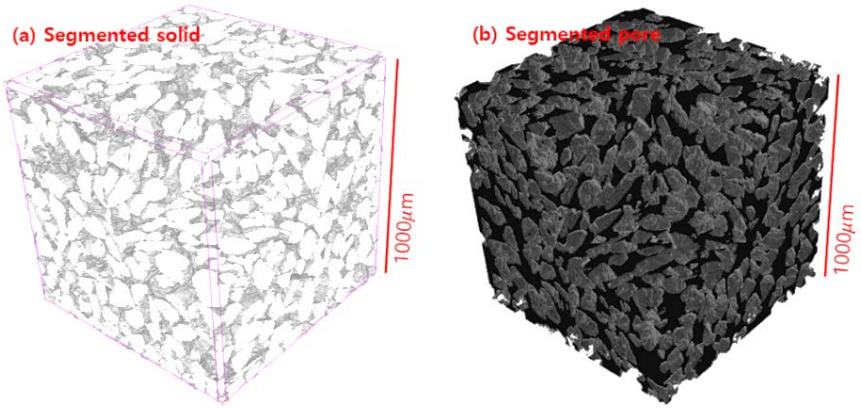

Figure 3. Visualization of pore space from microtomographic images of the 1% cemented sand sample ($\mathbf{1000^3}$ voxels). (a) binary image of segmented solid phase. (b) binary image of segmented pore phase.

4.1 Porosity

The data presented in Figure 4 shows that the segmented porosity decreases as the cement content increases. This trend holds for all samples with one exception of 0% cement sample. It showed a lower porosity than 1% cement sample. The 0% cement sample has only two phases which are sand and pore besides other samples have three phase including cement hydrate. This different number of phases can introduce the difference in overall shape of the greyscale histograms that affects to the threshold value selection in segmentation process and results underestimated porosity in the 0% cement sample. As cement content increases, porosity decreases because cement particles fill more pore space which are formed by packing of sand particles. The inter-connected porosity is completely equal to general porosity. This implies that all pores found in cemented sample are connected.

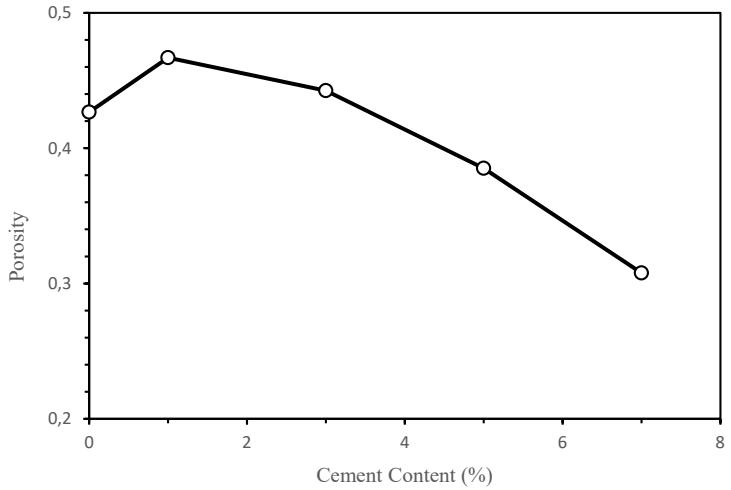

Figure 4. Relationship between the porosity and cement content for all samples.

4.2 Particle Size Distribution of Sand

Figure 5 compares the PSD of raw sand from sieve analysis and those of segmented solid obtained by image analysis. The 0% cement sample and sieve analysis are subject to investigate the accuracy of the microtomographic data in compare with actual data (*i.e.*, sieve result). There is a consistent horizontal shift between PSDs. The constant horizontal shift can be introduced due to the discrepancy of the diameter used to plot. For instance, volume-equivalent diameter was applied to generate PSDs for all cemented sand samples, whereas the diameter used for sieve analysis was a maximum diameter that a sand particle had to pass through the specific sieve.

For the 1%, 3%, 5%, and 7% cemented sand samples, the size of segmented solid particles increased as the cement content increased. This is expected because cement hydrate adheres to sand particles. The size of segmented particle size is the largest for 7% cemented sand sample because of the largest amount of cement used.

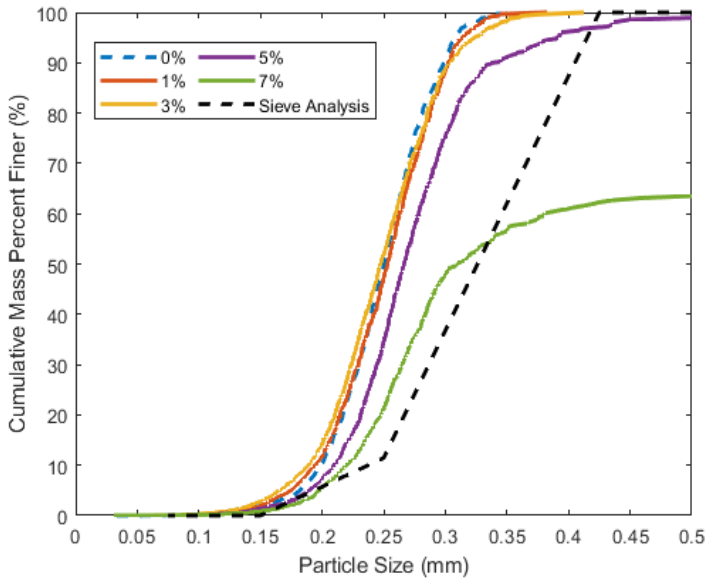

Figure 5. Particle size distribution of sand particles for all cemented sand sample and the data obtained by sieve analysis.

4.3 Tortuosity

Figure 6 shows the diffusion tortuosity of each sample calculated by random walker simulation on the segmented pore space (*i.e.*, interconnected pore). The diffusion tortuosity increased with cement content increased. This implies that the pore space is being more tortuous as cement added in the system. Cement hydration mainly occurs on the surface of the existing sand structure. Therefore, cement hydrates adhere to the surface of sand particles partially and make surface rough. At the same time, pores become narrower due to the adsorption of cement hydrates resulting the increase of tortuosity.

Figure 7 presents the formation factor as a function of cement content. The formation factor increased as cement content increased except for 0% cement sample which has intrinsically different solid system (*i.e.*, two phases vs. three phases) as previously discussed. Nevertheless, obtained trends of increasing tortuosity and formation factor clearly suggest that permeability and diffusion coefficient should decrease with cement addition. Thus, it can be quantitatively inferred that the addition of cement in cemented sand is an effective way for controlling permeability and diffusion.

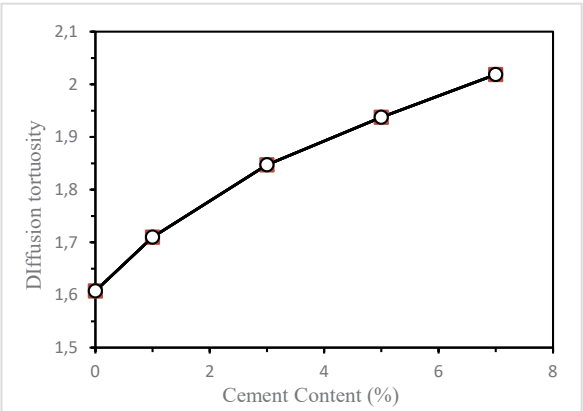

Figure 6. Relationship between the diffusion tortuosity and cement content for cemented sand sample.

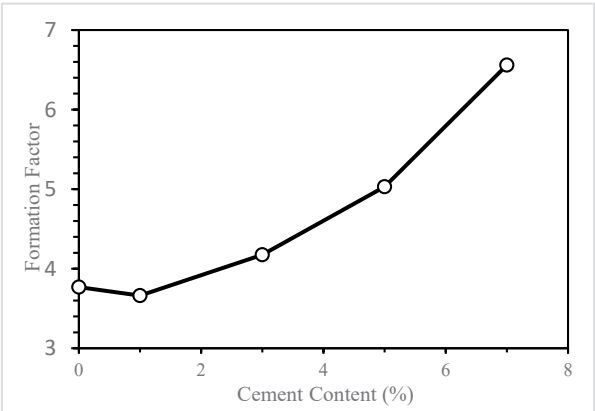

Figure 7. Relationship between the formation factor and cement content for cemented sand sample.

5 Conclusion

The porosity and tortuosity parameters obtained from the tomography data here provide an indication of the pore network geometry and microstructure of cemented sand. Higher cement content gave an increase in tortuosity and a decrease in porosity. This indicates that the small addition of cement hydrate in compacted sand, makes pore space more tortuous.

This study has provided the methodical three-dimensional analysis of cemented sand by X-ray microtomography. There remain difficulties in the accurate identification of pore and solid regions in cemented sand due to the low X-ray absorption. Phase contrast tomography proposes the potential in this area, but there is integral limitation due to microscale VOI which is small to represent intrinsic parameters of cemented sand. Nevertheless, the data presented in this study provide invaluable information regarding pore network, porosity and tortuosity, and suggest the novel method for future developments which can be led to further understanding on durability of solid materials.

Acknowledgement

This work was supported by the BK4 funded by the Ministry of Education, Republic of Korea.

ORCID

Junil Pae: http://orcid.org/0000-0002-1494-5270
Juhyuk Moon: http://orcid.org/0000-0003-4473-4308

References

Boudreau, B. P. (1996). The diffusive tortuosity of fine-grained unlithified sediments. *Geochimica et Cosmochimica Acta*, 60(16), 3139-3142.

Champoux, Y. and Allard, J. F. (1991). Dynamic tortuosity and bulk modulus in air-saturated porous media. *Journal of applied physics*, 70(4), 1975-1979.

Consoli, N. C., Viana da Fonseca, A., Cruz, R. C. and Heineck, K. S. (2009). Fundamental parameters for the stiffness and strength control of artificially cemented sand. *Journal of geotechnical and geoenvironmental engineering*, 135(9), 1347-1353.

Garboczi, E. J. and Bentz, D. P. (2001). The effect of statistical fluctuation, finite size error, and digital resolution on the phase percolation and transport properties of the NIST cement hydration model. *Cement and Concrete Research*, 31(10), 1501-1514.

Nakashima, Y. and Kamiya, S. (2007). Mathematica programs for the analysis of three-dimensional pore connectivity and anisotropic tortuosity of porous rocks using X-ray computed tomography image data. *Journal of Nuclear Science and Technology*, 44(9), 1233-1247.

Otsu, N. (1979). A threshold selection method from gray-level histograms. *IEEE transactions on systems, man, and cybernetics*, 9(1), 62-66.

Promentilla, M. A. B., Sugiyama, T., Hitomi, T. and Takeda, N. (2009). Quantification of tortuosity in hardened cement pastes using synchrotron-based X-ray computed microtomography. *Cement and Concrete Research*, 39(6), 548-557.

Provis, J. L., Myers, R. J., White, C. E., Rose, V. and Van Deventer, J. S. (2012). X-ray microtomography shows pore structure and tortuosity in alkali-activated binders. *Cement and Concrete Research*, 42(6), 855-864.

Thorat, I. V., Stephenson, D. E., Zacharias, N. A., Zaghib, K., Harb, J. N. and Wheeler, D. R. (2009). Quantifying tortuosity in porous Li-ion battery materials. *Journal of Power Sources*, 188(2), 592-600.

Wang, Y. and Leung, S. (2008). Characterization of cemented sand by experimental and numerical investigations. *Journal of geotechnical and geoenvironmental engineering*, 134(7), 992-1004.

XV International Conference on Durability of Building Materials and Components
DBMC 2020, Barcelona
C. Serrat, J.R. Casas and V. Gibert (Eds)

Examination of Optimum Construction Area for Appropriate Thickness in Polyurethane Waterproofing Construction

Yuji Hosshin [1], Saori Ishihara [2] and Kyoji Tanaka [3]

[1] Haseko Corporation, 32-1 Shiba 2-chome, Minato-ku, Tokyo, Japan 105-8507, Yuji_Hosshin@haseko.co.jp

[2] Chiba Institute of Technology, 2-17-1 Tsudanuma Narashino-shi Chiba, Japan 275-0016, saori.ishihara@it-chiba.ac.jp

[3] Tokyo Institute of Technology, 9-2 Nihonbashi hisamatsutyo chuo-ku Tokyo, Japan 103-0005, tanaka-kyoji@kme.biglobe.ne.jp

Abstract. *Polyurethane waterproofing membranes are constructed at building sites by applying liquid material to substrate. The membrane thickness is related to the durability of the waterproof material, so quality control during construction is important. However, the membrane thickness is likely to be unstable because it is affected by various factors, such as the environment, substrate conditions, method of waterproofing material application, and construction skills. Therefore, a reduction in thickness variation is extremely important to secure the quality of the waterproofing membrane.*
To examine which construction conditions can ensure a uniform and appropriate thickness, we examined the combination of allocation method of the suitable construction area and application tools as an example of process control during construction. The construction area width and length were important, and a comparatively uniform and appropriate thickness could be ensured, when construction was carried out over an area with a 1.4-m width and length of 5.15 m by using the trowel and squeegee.

Keywords: *Waterproofing Membrane, Polyurethane, Thickness of Membrane, Construction Area, Application Tool.*

1 Introduction

Waterproofing membranes that are generally used in Japan are a liquid material that is applied to a base in a construction site, and a waterproof layer is formed by its hardening. The most important quality control item is to ensure the appropriate membrane thickness, which is related directly to the performance and service life of the waterproof layer. However, the membrane thickness tends to become unequal, because it is affected by the construction environment, foundation conditions, material, application method, and skill. Standard Japanese specifications state that the thickness of the waterproof urethane coating membrane is confirmed by the quantity used per unit area. However, there is no more detailed description of the concrete construction method except for "In order to secure the thickness of membrane, the coating amount per set of waterproof material is divided." Therefore, in many cases, concrete construction is achieved by the judgment of the constructor, and as a result, waterproof layers do not always reach the prescribed membrane thickness.

In this study, waterproofing membrane formation during construction was studied, and the effect of area on the membrane thickness was examined as an example of the quality control technique. The waterproof layer construction must be carried out over an appropriate time, and this paper aims to show the optimum construction area by considering these. By using a

doi:10.23967/dbmc.2020.158

concrete repair site floor and indoor laboratory, we carried out experiments by combining the partition shape and sprinkling method of the waterproof material and construction equipment as factors.

2 Effect of Observation of Waterproofing Membrane Work and Construction Area on Membrane Thickness

2.1 Experimental Outline

The experiment was carried out by using the roof of a multiple-dwelling house to observe the work content during waterproofing membrane construction and the effect of construction area on the membrane thickness. The plain field with a comparatively small gradient was selected as the waterproofing underlayer, and the area was made to be 14.0 m^2 (4.0 m × 3.5 m) by converting 27 kg of waterproofing material in one set into a target membrane thickness of 1.5 mm for one layer. As shown in Figure 1, two areas were prepared: area A in which the area line was indicated clearly, and area B in which a mark was provided at each of four corners. The waterproof material used was a two-component hand-kneaded type for flat field based on the Japanese Industrial Standard.

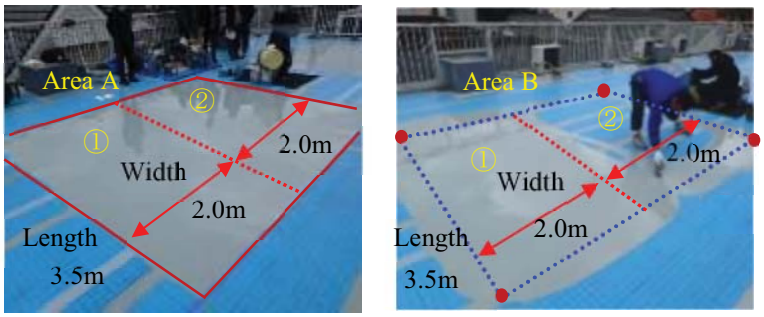

Figure 1. Application of polyurethane material in the two areas.

2.2 Experimental Methods

The construction procedure was as follows. A ventilation buffer sheet was attached to the entire roof. Then, three rows of 50-mm-wide aluminum tape were installed at 1.0-m intervals on the base surface because the membrane thickness is measured by a nondestructive inspection method (eddy current-type thickness membrane meter). The abovementioned area was prepared, and the waterproof layer was constructed with a target membrane thickness of 1.5 mm. The constructor was a technician with more than 20 years of experience, and a trowel was used as the construction application tool. The outside air temperature was 12 °C and the humidity was 45%.

2.3 Work Observation and Thickness of Membrane-Measurement Methods

During the experiment, moving image photography was carried out from the work start to the end, and the work content of the constructor was observed. After confirmation of the hardening of the waterproof layer on the following day, the membrane thickness was measured by using an eddy current-type thickness membrane meter. The measurement points were placed at 45 locations on the aluminum tape in each construction area.

2.4 Work Contents of Contractor

The waterproofing membrane was constructed as follows. The constructor divided the 4.0-m wide × 3.5-m long area into a 2.0-m width in which work was possible. A two-component waterproof material was kneaded with a main agent and a hardener in the field. The kneaded waterproof material was halved (13.5 kg) to fit the divided width of 2.0 m × 3.5 m length and poured using a container. The waterproofing material that was poured in the construction area was spread right and left by using a trowel. The other half of the plots was subjected to similar work. Observation indicated that the waterproofing membrane construction is composed of work where material was poured on the base and work where material was spread. The construction area in the field was divided by the width in which the spreading work was easy, and the amount of waterproof material poured was calculated in proportion.

2.5 Effect of Construction Area

The measured membrane thickness is shown in Figure 2 and it varied across both construction areas. In construction area A in which the area was strengthened, the average membrane thickness was 1.2 mm. In construction area B, which was constructed without much attention given to the area, the waterproof material protruded from the area. Therefore, the coating quantity in the area was insufficient compared with construction area A, and the average membrane thickness decreased to 0.9 mm.

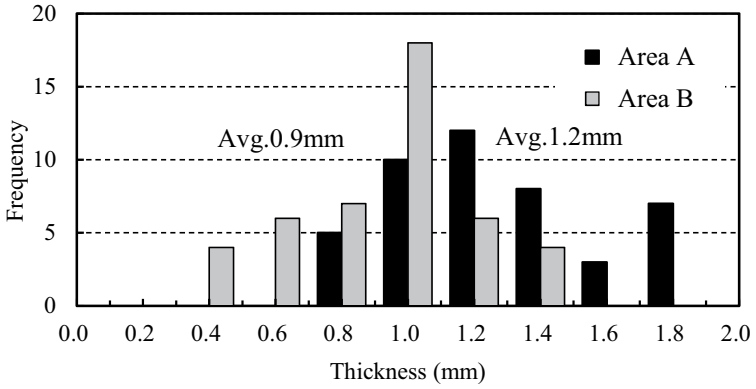

Figure 2. Measured thickness of areas A and B.

3 Effect of Pouring Waterproofing Membrane Material on Variation of Membrane Thickness

3.1 Experimental Outline

The work observation indicated that it is necessary for the constructor to pour waterproof material evenly from the container to the prescribed area, and to spread it uniformly by using the construction tool. The waterproofing membrane thickness, "Area Length" appears to be related to the pouring of the waterproof material, and the "Area Width" appears to be related to the work of pushing and spreading. Therefore, the experiment was carried out by using these as variables. A concrete floor (< 3/1000 accuracy) in an indoor laboratory was used as a base.

In the confirmation experiment of the preceding section, the partition width was divided into

2.0 m to facilitate the spreading. This experiment was carried out at three section-length levels of 9.0 m (0.8 m wide), 5.15 m (1.4 m wide), and 3.6 m (2.0 m wide), with a 7.2 m^2 construction area. To omit mixing in the field, the waterproof material of one component type for a flat field based on the Japanese Industrial Standard was used.

3.2 Experimental Methods

The construction procedure was as follows. First, a polyethylene film sheet was laid on the working surface because the waterproof material after curing was peeled from the base and the mass was measured. The division was carried out and waterproof material (14.0 kg) that was suitable for a target film thickness of 1.5 mm was poured linearly in the center of the division width by using a pail can as shown in Figure 3. These operations were carried out in an environment at a room temperature of ~23 °C and a 60% relative humidity by technicians with more than 20 years of experience. After confirming the hardening of the waterproof layers the following day, the spread waterproof material was cut into 10 pieces and its mass was measured.

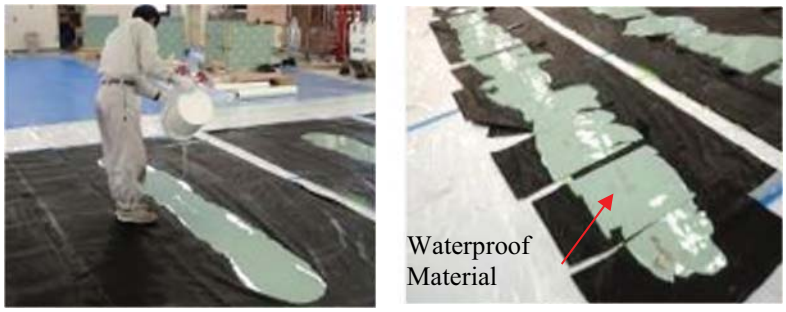

Figure 3. Pouring works (left) and cut membrane to measure their mass (right).

3.3 Area Length Effect

When the pouring work was observed, the waterproofing material appeared to flow out uniformly from the container. However, the variation after curing was large, wide, and narrow portions were intermingled. The mass standard deviation per unit length is shown in Figure 4.

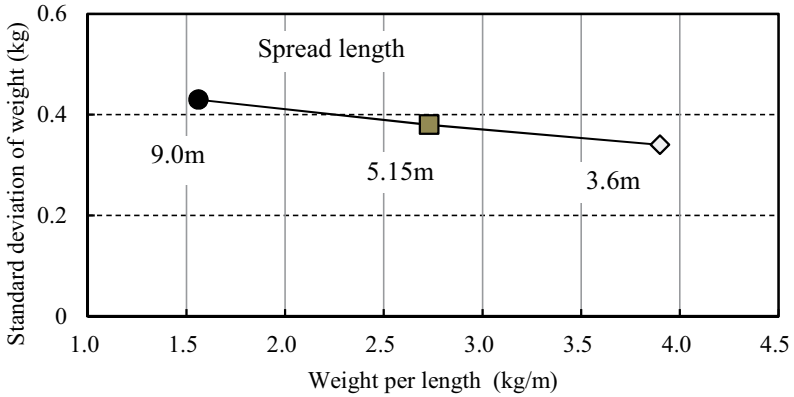

Figure 4. Relationship between material masses in three areas and their standard deviations
Polyurethane material and standard deviation of mass.

based on the measured mass of the waterproof material. The standard deviation of the area length of 9.0 m was 0.43 kg, that of 5.15 m was 0.38 kg, and that of 3.6 m was 0.34 kg. This information shows that the material tended to be poured unevenly, when the length from which the waterproof material was poured was lengthened.

4 Effect of Spreading Urethane Coating Waterproof Material on Membrane Thickness

4.1 Experimental Outline

To confirm the effect of the "Area Width" on the film thickness, the experiment was carried out with the same concrete base and construction area as used previously. The division width was made to be three levels of a width of: 1.4 m (5.1 m long), which allows for a natural trowel movement to the left and right; a narrower 0.8 m (9.0 m long); and a wider 2.0 m (3.6 m long).

As shown in Figure 5, the construction tool was a trowel, which was a standard construction tool, and a polyethylene patterned squeegee with a 5-mm groove depth and a 600-mm width. The target waterproof layer membrane thickness was 1.5 mm for the first layer and 1.5 mm for the second layer, which totaled 3.0 mm. The waterproofing material was used in a commercial one-component-type flat field, and the regulated quantity was measured for each construction area.

These tasks were performed by technicians with more than 20 years of experience in an environment of ~23 °C and a 60% relative humidity.

4.2 Experimental Methods

The construction procedure was as follows. At first, a ventilation buffer sheet that was treated with aluminum alloy thin film was laid on the entire surface of the base because the membrane thickness was measured in detail by using the eddy current-type thickness membrane meter.

The area was divided by the above-mentioned area width. To evaluate the effect of spreading the waterproof material accurately, a frame was made in the central part of the area by a 10-mm foamed polyethylene material, and a specified amount of waterproof material was poured uniformly into the frame. The waterproof material was spread with each construction tool. After confirming the hardening of the waterproof layer, the thickness of the first layer was measured.

The second layer was constructed by the same construction method, and the total membrane thickness was measured on the next day. The membrane thickness was measured at 105 positions

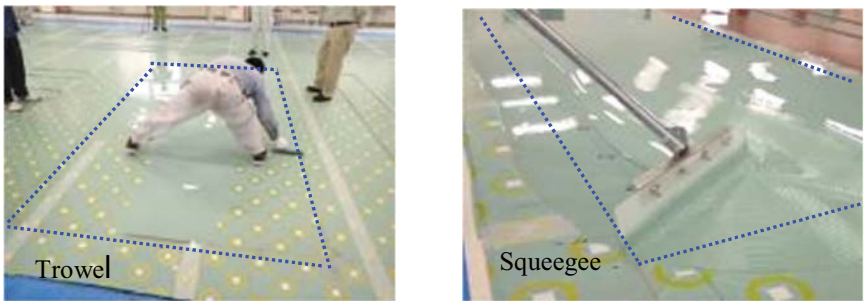

Figure 5. Spreading work using a trowel (left) and using a squeegee (right).

from the center of the partition width at 0.3-m intervals on the left and right sides, respectively. The time required from the start to the end of the spreading work was also measured.

4.3 Effects of Area Width and Application Tools on Membrane Thickness

The relationship between the mean membrane thickness and the standard deviation is shown in Figure 6. The membrane thickness distribution from the spreading work tends to be larger in the second layer. The average membrane thickness from the trowel was 1.3–1.4 mm in the first layer and 2.8 mm in the second layer. The value tended to be close to the target membrane thickness, which indicates that the target membrane thickness is approached regardless of the partition shape when the specified amount of waterproofing material is sprayed by specifying the partition. The membrane thickness distribution increased as the area width increased and was 1.1–1.9 mm in the first layer and 1.9–3.5 mm in the second layer. This occurs because, when the area widens, the distance required to move the trowel to the right and left increases, and it becomes difficult to push and expand the waterproof material uniformly. The average squeegee membrane thickness was 1.3 mm in the first layer, it became 2.7–2.5 mm in the second layer, and it decreased with an increase in area width.

When the construction area was observed, the waterproof material stuck out from the area by back and forth application by the tool. Therefore, the coating quantity in the construction area is believed to be insufficient, and the film thickness was affected. The membrane thickness dispersion decreased as the area width increased. The membrane thickness of the first layer was 0.9 mm and that of the second layer was 1.3–1.5 mm, which was more uniform than that achieved with the trowel.

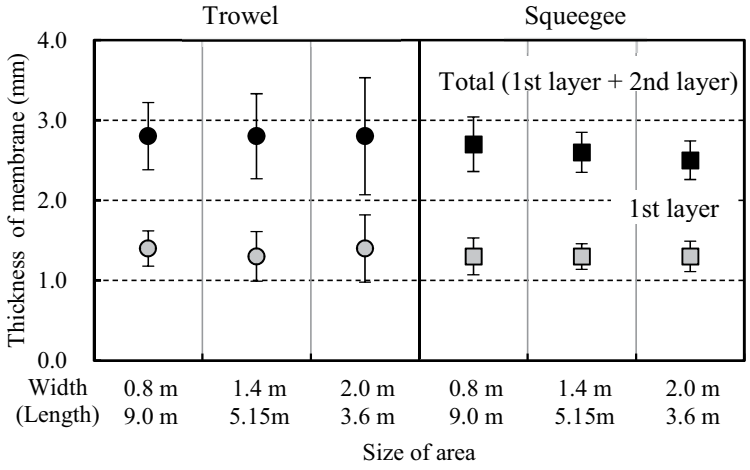

Figure 6. Average thickness of membrane and standard deviation of three.

4.4 Effect of Area Width and Application Tools on Work Time

Figure 7 shows the relationship between the shape of the construction areas and the work time for each construction application tool. The work time for the trowel decreased as the area width increased, especially in the second layer. For the squeegee, the work time lengthened as the area widened. This tendency is opposite to that for the trowel because a large amount of waterproofing materials can be pushed out at one time when the area width increased. The squeegee is efficient when the area length is long because it requires application tools to carry

out the spreading work while pulling in the advancing direction. However, it is necessary to turn the application tools back and forth at a considerable frequency, when the area width widens like this experiment, and these appear to affect the work time.

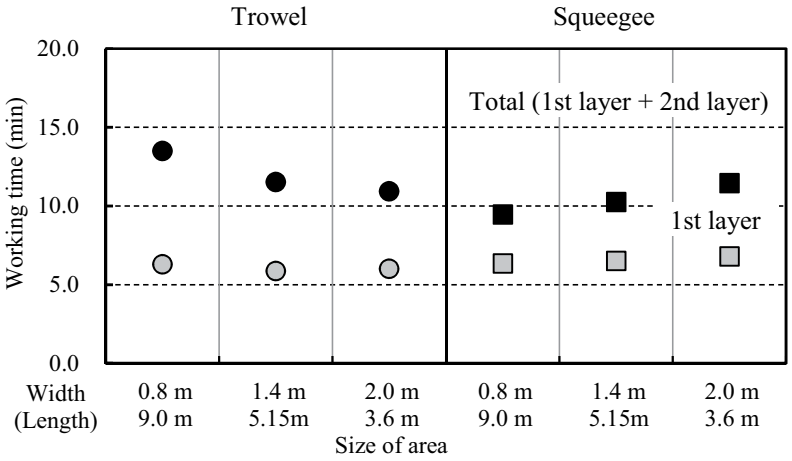

Figure 7. Working time in spreading work of three areas.

4.5 Consideration of Optimal Construction Area from the Viewpoint of Securing Membrane Thickness

The standard deviation of the membrane thickness for the trowel and squeegee area and the pouring and spreading work are shown in Figure 8. To ensure a stable membrane thickness, an area with a wide width and a short length should be used in the pouring work. On the other hand, the spreading work differs depending on the application tools and a narrow partition is desirable for the trowel. In a squeegee, the standard deviation tends to decrease as the area width increases and the area length shortens, and a trade-off relationship exists. The squeegee appears to be an effective application tool when the application quantity is easy to control compared with the trowel because the edge of the tip is a combed shape, and when the construction area is wide. The work time is reduced, and the productivity is improved when the area width increases. However, a reciprocal relationship exists with the quality, and the membrane thickness

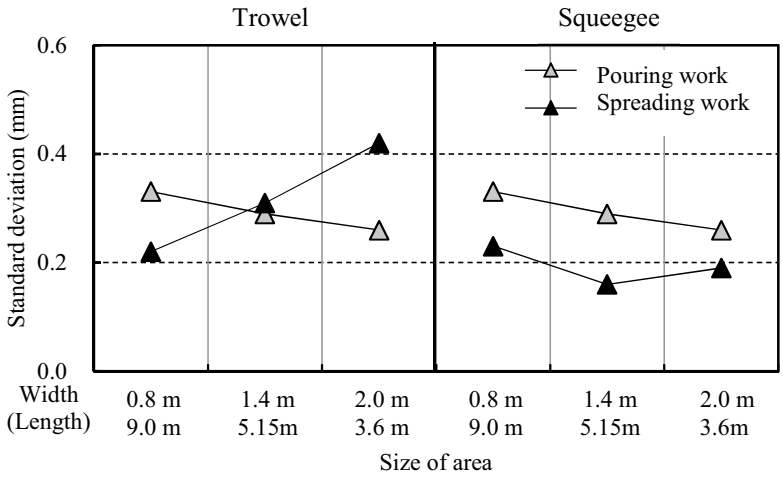

Figure 8. Standard deviation of membrane in pouring and spreading work.

distribution increases, when the time is shortened excessively. The area and cure time of materials at the construction area and the work quantity and productivity must be considered and judged synthetically.

Although this experiment was a prerequisite construction area of 7.2 m^2, it appeared to be a well-balanced construction area where the width of 1.4 m and the length of 5.15 m made it easy to prepare a suitable membrane thickness, when the time required for both application tools was considered.

5 Conclusion

We obtained the following conclusions from this study.

- To secure the waterproofing membrane thickness, a clarification of the construction area and the area shape are important in addition to the management of the application amount.
- During the waterproof material pour, the dispersion is smaller in the shorter area length. The length of the pouring waterproofing material increases and tends to be scattered unevenly.
- The area width of the spreading work differs according to the construction application tools. The membrane thickness distribution tended to be small; the partition width was narrow for the trowel and was widened with the squeegee.
- The work time differed significantly according to the construction application tool. The work time decreased when the area width widened with the trowel and became narrower for the squeegee.
- The partition width and length are important to ensure an appropriate membrane thickness. In this experiment, an area width of 1.4 m and a length of 5.15 m appeared to provide a comparatively well-balanced construction area shape for the trowel and squeegee.

Acknowledgements

This study was conducted as part of the activities of the Building Waterproofing Safety and Quality Council.
I would like to give heartful thanks to Dr. H. Nachi from Shimizu Corporation who provided carefully considered feedback and valuable comments.

ORCID

Yuji Hosshin: https://orcid.org/0000-0001-9591-2464

References

Hiroshi Nachi, Yuji Hosshin, Yoshiaki Takemoto, Saori Ishihara, Hikaru Watanabe, Kenji Kumagai, Yumiko Nakajima and Kyoji Tanaka (2018). *Quality Control of Polyurethane Waterproofing Membranes usingthe Process Management Methods* (in Japanese), AIJ Journal of Technology and Design, Vol. 24, No. 56, 23-27.

Japan Architectural Institute (2014). *Standard construction specifications for construction work and commentary,* JASS8 Waterproof construction.

Keiichi Nara, Saori Ishihara, Hayashi Kouichi, Nishimura Takeshi, Tanaka Hideo, Tsuruta Yutaka, and Kyoji Tanaka (2013). *Effect of Dilution of Material and Application Tool on Thickness of Fluid-Applied Polyurethane Membrane* (in Japanese), AIJ Journal of Technology and Design,Vol. 19, No. 42, 397-402.

Public Buildings Association (2016). *Public Building Construction Standard Specification (Construction Work).*

Saori Ishihara and Kyoji Tanaka (2014). *Effects of Polyurethane Dilution and Choice of Application Tool on the Workability and Thickness of Fluid-Applied Polyurethane Membranes* (in Germany),Proceedings of International Conference on Building Envelope Systems and Technologies.

XV International Conference on Durability of Building Materials and Components
DBMC 2020, Barcelona
C. Serrat, J.R. Casas and V. Gibert (Eds)

Field Study on Hydrophobised Internally Insulated Masonry Walls

Evy Vereecken, Daan Deckers, Hans Janssen and Staf Roels

KU Leuven, Department of Civil Engineering, Building Physics Section, Kasteelpark Arenberg 40, 3001 Leuven, Belgium, Evy.Vereecken@kuleuven.be

Abstract. *This paper presents a field study on the hygrothermal performance of hydrophobised masonry walls, provided with vapour tight or capillary active interior insulation. As a reference, also non-hydrophobised and non-insulated walls are analysed. To study the hygric performance, apart from traditional relative humidity sensors, in-house made moisture pins are embedded in the walls and are shown to yield valuable information in the high moisture range. Attention is given to the hygric performance of the wooden beam heads, the impact of wind-driven rain on the moisture conditions in the masonry wall, as well as to the impregnation depth of the water repellent agent. For the latter, the field study is supplemented with X-ray and liquid droplet measurements on a small semi-duplicate test wall. During the hydrophobisation process, an increased moisture level was induced. A drying period was needed to again reduce this level. After this period, a hydrophobic treatment showed a positive impact on the wall's hygric performance. The non-hydrophobised wall with a vapour tight interior insulation system showed the highest moisture level, especially deeper in the wall and thus where the wooden beam ends are located.*

Keywords: *Internally Insulated Masonry, Hydrophobisation, Hygrothermal Performance, Wooden Beams, Moisture Pins.*

1 Introduction

Driven by energy concerns and stricter energy regulations, wall insulation gains increasing importance. When dealing with renovation projects, three post-insulation techniques make a thermal upgrade of existing walls possible, i.e. cavity wall insulation, exterior insulation or interior insulation. For massive masonry walls with a valuable exterior facade, however, interior insulation remains as the only option. Unfortunately, interior insulation often leads to higher moisture contents in the wall, increasing the risk on wood rot of embedded wooden beam ends, frost damage, etc. (Vereecken *et al.*, 2015). These damage patterns are to a large extent caused by an exterior moisture source such as wind-driven rain (WDR), and therefore the application of a hydrophobic treatment is often pushed forward. To correctly estimate the effectiveness and potential side effects of a hydrophobic treatment, however, more insight on the moisture transport in hydrophobised walls is required. Thereto, this paper presents the results of a field study on the hygrothermal performance of hydrophobised internally insulated masonry walls.

Both walls with a vapour tight and with a capillary active interior insulation system are studied. As a reference, non-hydrophobised and non-insulated walls are analysed. The paper is organised as follows. Section 2 first describes the field test setup and the applied measurement techniques. Next, in Section 3 a selection of the logged data is presented and analysed. In Section 4, a special focus is put on the impregnation depth in the masonry. Finally, in Section 5 the main conclusions are drawn.

doi:10.23967/dbmc.2020.067

2 Field Test Setup

2.1 Test Walls

To study the impact of hydrophobisation on internally insulated walls, six 1.5-stone thick masonry test walls of approximately 32 cm thick, 0.6 m wide and 2.7 m high were constructed in two south-west oriented wall frames of the VLIET test building of KU Leuven (Figure 1a).

The masonry assemblies were masoned by use of Vandersanden Robusta bricks ($A_{cap} \approx 0.61$ kg/(m^2.s$^{0.5}$)) and lime mortar (ratio: 12.5 kg Saint-Astier NHL3.5, 50 kg River sand 0/2, 10 litres water; $A_{cap} \approx 0.26$ kg/(m^2.s$^{0.5}$) for mould cured mortar). Between the different test walls a barrier was provided, such that the hygrothermal behaviour of the test walls was not affected by the adjacent test walls. The construction of the test walls was finalised by the end of August 2017, after which a drying period took place. On October 23th 2018, three of the six test walls (Figure 1b) were hydrophobised by use of Silres® SMK2100 from Wacker Chemie AG. An impregnation depth of 3 cm in the bricks was pursued, for which per m^2 wall 6.9 litres of a 10 vol% hydrophobic agent solution was applied by spraying. The rain load on the test setup was measured via two wall-mounted WDR gauges (Figure 1b,c), with a collection area of 0.2 m x 0.2 m, as used by Blocken and Carmeliet (2006). To ease a comparison between the wall's hygrothermal performance and the WDR, the WDR load measured by the top WDR gauge is shown together with the results (Figure 4a).

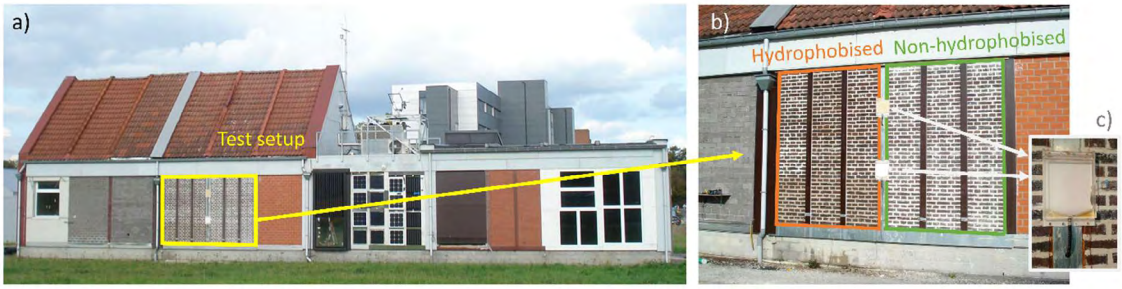

Figure 1. Outside view of the field test setup: (a) south-west oriented side of the VLIET-test building, (b) hydrophobised and non-hydrophobised masonry test walls with (c) wind-driven rain gauges.

On the inside, two test walls were provided with a vapour tight XPS interior insulation system, while two other test walls had a capillary active calcium silicate (CaSi) interior insulation system. Both systems were built up of a 10 cm thick insulation board which was fully adhered to the masonry by use of a glue mortar. As an interior finish, the XPS-system and the CaSi-system were provided with a gypsum board and plaster layer, respectively. The application of the interior insulation systems was performed in the second half of December 2018. The remaining two test walls had no interior insulation system, and thus acted as reference walls. An overview of the six test cases is given in Table 1. In each of the test walls, two wooden beam ends were embedded in the masonry (Figure 2). The upper wooden beam ends were in contact with a mortar layer, whereas for the lower wooden beam ends an air gap was present at all sides except for the bottom of the wooden beam end. At the room side, the end of the wooden beams were covered with bituminous paint, avoiding vapour diffusion via the longitudinal wood direction. To prevent convective moisture transport, as discussed in

(Vereecken and Roels, 2018), the gap between the wooden beam and the insulation system was sprayed up with flexible PUR-foam and the connection with the interior surface was sealed with an airtight tape. After all, also in hygrothermal studies including a wind-driven rain exposure (Kopecký *et al.*, 2019) an airtight sealing of the beam junction has been put forward.

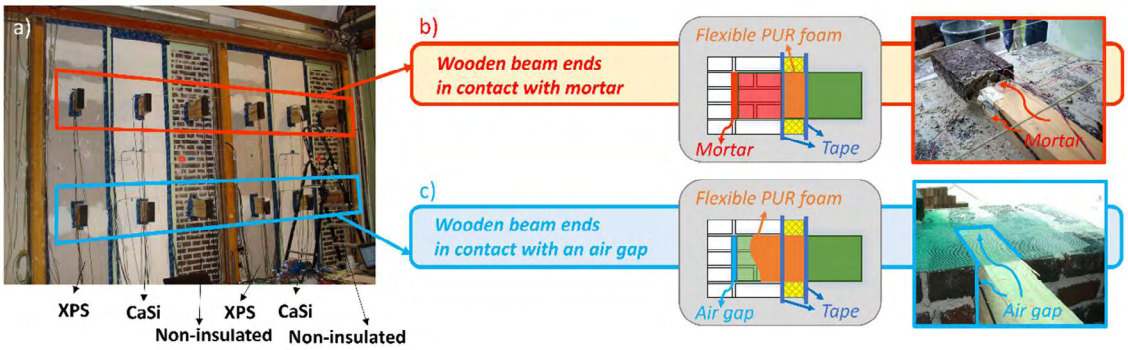

Figure 2. Inside view of the test walls: (a) global overview of the internally insulated and non-insulated test walls with embedded wooden beam ends, (b) wooden beam end in contact with mortar and (c) wooden beam end in contact with an air gap.

Table 1. Overview of the test walls.

Label	Hydrophobisation?	Interior insulation system
NH-XPS	No	XPS
NH-CaSi	No	CaSi
NH-Non	No	Non-insulated
H-XPS	Yes	XPS
H-CaSi	Yes	CaSi
H-Non	Yes	Non-insulated

2.2 Measurement Techniques

The temperature and the relative humidity in the test walls were measured by use of in-house calibrated Thermo Electric Type T (class 1) thermocouples and Honeywell HIH-4021 humidity sensors, with an accuracy of +/- 0.2°C and +/- 2% RH. Furthermore, in-house made moisture pins, measuring the electrical resistance, were used to analyse the moisture conditions at the back of the wooden beam ends, in the mortar in the masonry, in the glue mortar and in the calcium silicate. It is well known that the electrical resistance of a material depends on the material's moisture content, as moisture is a good electrical conductor. The lower the electrical resistance measured in a material, the higher the moisture content of the material. For a more in depth description on the electrical resistance method, the reader is referred to (Otten *et al.*, 2017). At half height of the test walls, additionally a heat flux sensor was glued at the warm side of the masonry. The position of the different sensors is shown in Figure 3. For the moisture pins a preliminary calibration took place, of which an example for the in-situ mortar moisture pins is given in Figure 3c.

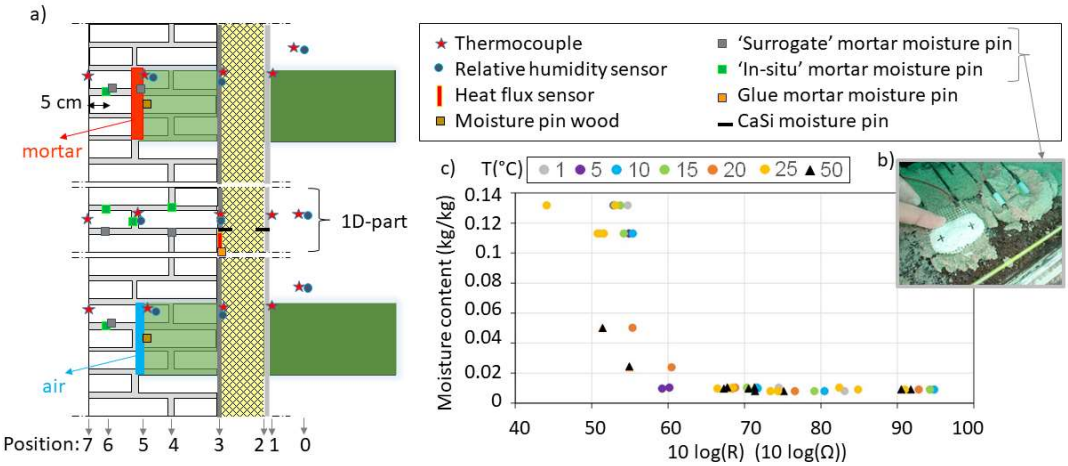

Figure 3. (a) Position of the thermocouples, humidity sensors, moisture pins and heat flow sensor indicated for the wall with CaSi, (b) in-house made surrogate (left) and in-situ (right) mortar moisture pins, (c) preliminary calibration curve for the in-situ mortar moisture pin.

3 Results

Hourly-averaged data are used for the analysis of the hygrothermal performance of the test walls. In what follows, the measurements achieved in the period from June 2018 till the end of October 2019 are shown. Thus, a period in which the walls were all non-hydrophobised and non-insulated is included, showing the similar initial moisture level for the six walls. In the legend of the graphs, from the start however, these walls are indicated by their final state of hydrophobisation and interior insulation system. Focus is put on the moisture conditions in the mortar layer in the 1D-part of the masonry, as measured by the in-situ mortar moisture pins, and on the moisture conditions of the wooden beam ends. To analyse the data measured by the moisture pins, it is important to keep in mind the inverse relation between electrical resistance and moisture content. A lower electrical resistance represents a higher moisture content.

Furthermore, a preliminary calibration of the in-situ mortar moisture pins (Figure 3c) showed an electrical resistance above 60 x 10 log(Ω) to correspond to a similar moisture content. The electrical resistance at which this phenomenon occurs can however slightly vary depending on the material the moisture pins are embedded in (Brischke *et al.*, 2008). Hence, at this point, the moisture pins don't allow an absolute comparison of the measurement data in the lower moisture range (above an electrical resistance in the range of 60 x 10 log(Ω)).

3.1 Moisture Conditions in the 1D-Masonry Part

Figure 4b, c and d show the electrical resistance as measured by the in-situ mortar moisture pins in the middle (1D) part of the test walls. Additionally, the relative humidity at Position 5 is shown (Figure 4e). Both the relative humidity and the electrical resistance show a drying behaviour in the period before the water repellent agent was applied. When applying the hydrophobisation, for the hydrophobised walls an abrupt drop in electrical resistance is shown at Position 6, which is closest to the outer surface. After this, the electrical resistance starts increasing again slowly, which indicates a drying of this outer masonry region. For Position 5,

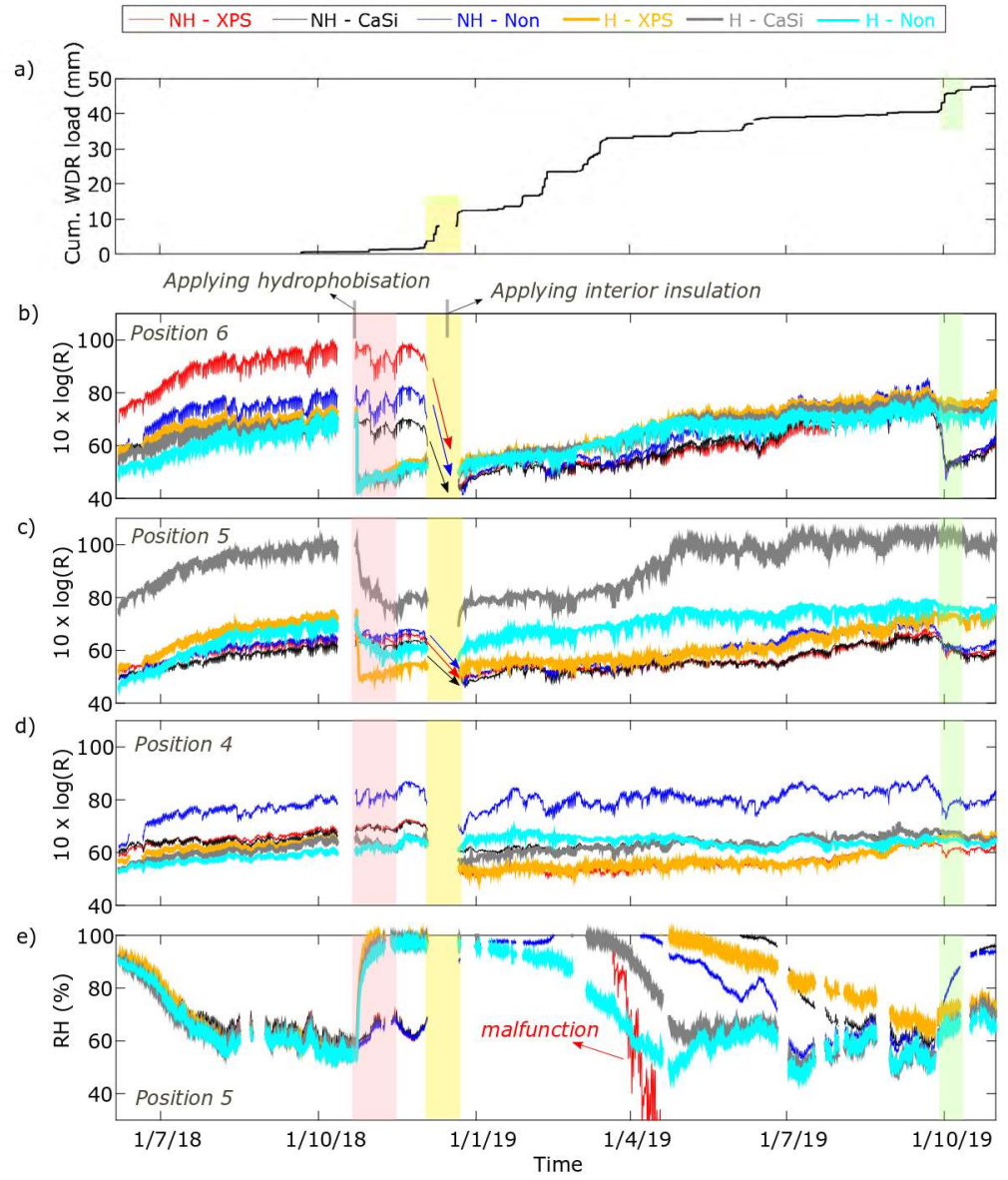

Figure 4. (a) Cumulative wind-driven rain load measured by the top WDR gauge, (b,c,d) electrical resistance measured by the moisture pins in the 1D-part of the walls for (b) Position 6, (c) Position 5 and (d) Position 4, (e) relative humidity measured in the 1D-part at Position 5 (see Figure 3 for an indication of the positions).

a decrease in electrical resistance occurs over a longer time period after the hydrophobisation (pink rectangle), which can be attributed to an inward redistribution of the water used for the water repellent solution. For the hydrophobised wall with a CaSi-interior insulation system, the measurement data seem to be shifted upward compared to the other walls. No explanation is found for this behaviour and a malfunctioning of the moisture pin is assumed; though the decreasing trend is also here visible. For the three hydrophobised walls, the inward redistribution indicated by the moisture pins is confirmed by the relative humidity sensor at

Position 5 (Figure 4e). Deeper in the wall (Position 4), no distinct changes are found during or shortly after the application of the hydrophobisation (Figure 4d).

In December 2018 (yellow rectangle), a reverse behaviour can be observed. In a part of this period the sensors were disconnected to install the interior insulation systems. Though, a comparison of the data before and after this interruption shows, especially for Position 6, a strong decrease in electrical resistance for the three non-hydrophobised walls. This can be attributed to wind-driven rain absorbed by the walls (see Figure 4a). The electrical resistance measured in the hydrophobised walls remains substantially the same. A similar behaviour is found in October 2019. Other WDR loads (*e.g.* in February/March 2019) are less visible, since the moisture level in the wall is already high at that time.

The impact of the interior insulation systems is visible in the relative humidity at Position 5 (Figure 4e). In spring and summer, a decrease in relative humidity is observed, which occurs first for the hydrophobised non-insulated wall, followed by the hydrophobised wall with the CaSi-system and the non-hydrophobised non-insulated wall. Next, the relative humidity in the hydrophobised wall with XPS starts decreasing, but this occurs slower than found for the non-hydrophobised wall with the CaSi-system. The relative humidity sensor in the non-hydrophobised wall with XPS showed some malfunctioning due to the high moisture load.

3.2 Moisture Conditions at the Wooden Beam Ends

Figure 5 shows the relative humidity at Position 5 on the wooden beam ends. For the beam ends in contact with mortar (Figure 5a) the relative humidity at the beginning of June 2018 is found to be above 90%. The test walls are at that moment still non-hydrophobised and non-insulated, and hence show a relative humidity that is in close agreement for the different walls. During the next half year, a drying out takes place until a quasi-equilibrium is found close above 60% RH. For the lower beam ends provided with an air gap between beam and masonry (Figure 5b), the relative humidity level is found to be between 40 and 65% during this entire period.

For the period after January 2019, for both the upper and lower wooden beam end an increase

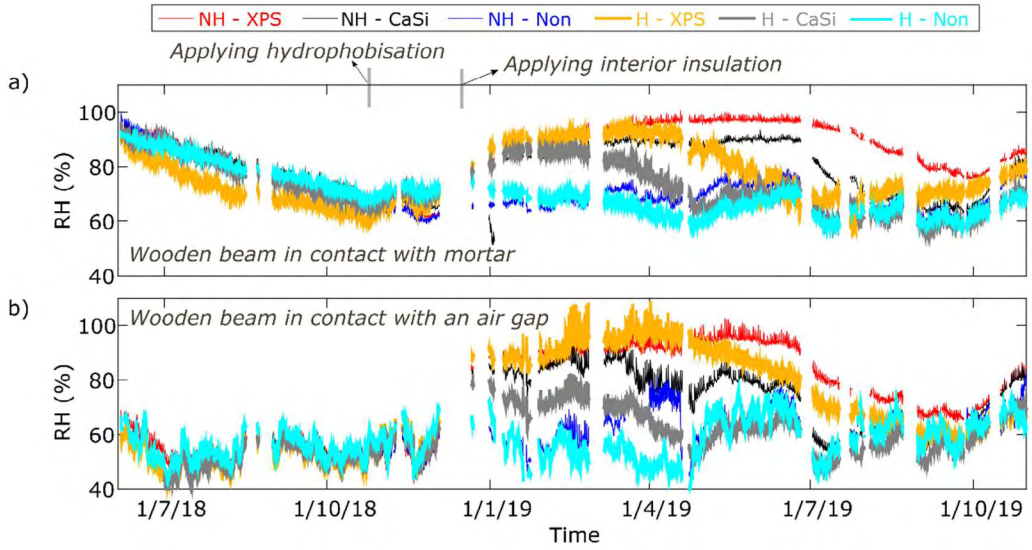

Figure 5. Relative humidity at Position 5 (see Figure 3) at (a) the upper and (b) the lower wooden beam end.

in relative humidity is measured for the walls with interior insulation. This can be partially explained by the lower wall temperature. Apart from this, also a higher moisture content in the wall as indicated by the moisture sensors (Figure 4d) can contribute to this, especially for the upper wooden beam which is in contact with mortar. During spring and summer, the relative humidity starts decreasing again. Also here, the slowest decrease is found for the non-hydrophobised wall with XPS and the fastest for the hydrophobised system with CaSi. The relative humidity level for the non-insulated walls remains rather stable over the entire period.

4 Analysis of the Impregnation Depth

In Section 3, the hydophobisation process was shown to induce a large increase in moisture content in the mortar at 5 cm from the outer surface of the masonry (Position 6). In order to achieve a view on the extent to which also the hydrophobic agent was transported in the wall, the impregnation depth was further analysed via an additional laboratory test setup. Thereto, a small test wall masoned with the same type of bricks and mortar as applied in the VLIET test setup and hydrophobised in a similar way (Figure 6a) was built. This wall was cut in half (Figure 6b) and tilt such that the center plane became a horizontal plane on which the penetration depth of the hydrophic agent could be analysed via the droplet method. Water droplets were dropped on the surface by use of a pipette and the contact angle of the droplet was analysed. For the bricks, three zones were detected (Figure 6c). In the zone closest to the outer (hydrophobised) surface a fully hydrophobised effect was observed. Droplets with a contact angle larger than 90° were clearly noticed (Figure 6e). The impregnation depth in the bricks seemed to be larger than the pursued 3 cm, which might be due to the dynamic way of spraying the hydrophobisation. This zone passed into a second zone where the droplets collapsed and were next absorbed slowly by the brick layer (Figure 6d). Deeper in the wall the bricks seemed not impregnated. After this droplet measurement, a small brick-mortar sample (Figure 6f) was sawn out of the middle surface of the smaller test wall. The non-hydrophobised surface was brought in contact with a water level, while the moisture content in the test sample was analysed by the X-ray projection technique (Roels and Carmeliet, 2006). At the end of this experiment, the moisture front had reached the boundary of the first impregnation zone (figure 6g). In the mortar layer, the impregnation depth was found to be much smaller (1 to 2 cm). Hence, the increase in moisture content observed in Section 3 is expected to be attributed to liquid transport only. The active ingredient is not transported with it to the position of the moisture pins in the mortar.

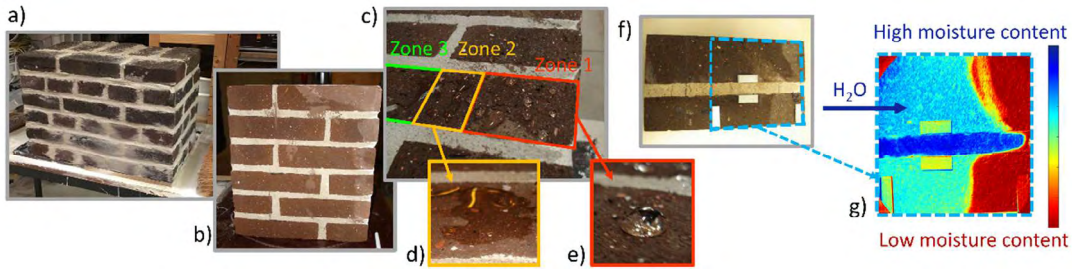

Figure 6. Study on the impregnation depth for a small semi-duplicate test wall: (a) the test wall, (b) test wall vertically cut in half, (c,d,e) droplets and collapsed droplets indicating different hydrophobised zones, (f) test sample sawn out the test wall for the X-ray test with metal dummy's as position references, (g) moisture content measured by the X-ray projection method after bringing the non-hydrophobised surface in contact with water.

5 Discussion and Conclusions

Preliminary results of a field study on the impact of interior insulation and hydrophobisation on the hygrothermal performance of massive masonry walls with embedded wooden beam ends has been presented. In-house made moisture pins yielded valuable information on the moisture transfer in the masonry during and after spraying the water repellent agent. After all, installing RH sensors in the wet mortar entails a risk on malfunction of the sensors and is not obvious in the high moisture range. A further calibration of the moisture pins is however required to make a conversion to the moisture content and a further analysis of the measurements possible.

In the current study, an increased moisture level was induced during the hydrophobisation process. A drying period was needed to again reduce the moisture level near the outer surface.

When disregarding the period shortly after applying the water repellent agent, hydrophobisation showed a positive impact on the wall's hygric performance. Deeper in the wall, near the wooden beams ends, the highest relative humidity was observed for the non-hydrophobised wall with a vapour tight interior insulation system. The non-insulated test walls showed the lowest relative humidity, regardless of the presence of a hydrophobisation. Further research will include an analysis over a longer time period, to exclude the initial influence of the application of the water repellent agent, and this for the total set of sensors and moisture pins embedded in the test walls.

Acknowledgements

The results within this paper have been partially obtained within the EU Horizon 2020 RiBuild project (Project ID 637268). Evy Vereecken is a postdoctoral fellow of the Research Foundation (FWO) - Flanders, Belgium (FWO project 12J5219N). These financial supports are gratefully acknowledged. The authors are very grateful to Wim Bertels, Patricia Elsen, Bernd Salaets and Jimmy Van Criekingen for their dedicated contributions in realising these measurements in practice.

ORCID

Evy Vereecken: https://orcid.org/0000-0003-2700-7969
Hans Janssen: https://orcid.org/0000-0002-8315-3955
Staf Roels: http://orcid.org/0000-0002-1156-8553

References

Blocken, B. and Carmeliet, J. (2006). On the accuracy of wind-driven rain measurements on buildings. *Building and Environment, 41(12)*, 1798-1810. doi: 10.1016/j.buildenv.2005.07.022

Otten, K., Brischke, C. and Meyer, C. (2017). Material moisture content of wood and cement mortars – electrical resistance-based measurements in the high ohmic range. *Construction and Building Materials, 153*, 640-646. doi: 10.1016/j.conbuildmat.2017.07.090

Kopecký, P., Staněk, K., Bureš. M., Richter, J., Ryparová, P. and Tywoniak, J. (2019). Experimental investigations of wooden beam ends in masonry with interior insulation: Measured data in real-scale experimental walls exposed to semi-continental climatic conditions. *Journal of Building Physics, 43(3)*, 147-170. doi: 10.1177/1744259119867461

Roels, S. and Carmeliet, J. (2006). Analysis of moisture flow in porous materials using microfocus X-ray radiography. *International Journal of Heath and Mass Transfer, 49*, 4762-4772. doi: 10.1016/j.ijheatmasstransfer.2006.06.035

Vereecken, E., Van Gelder, L., Janssen, H. and Roels, S. (2015). Interior insulation for wall retrofitting – A probabilistic analysis of energy savings and hygrothermal risks. *Energy and Buildings, 89,* 231-244. doi: 10.1016/j.enbuild.2014.12.031

Vereecken, E. and Roels, S. (2018). Wooden beam ends in combination with interior insulation: An experimental study on the impact of convective moisture transport. *Building and Environment*, *148*, 524-534. doi: 10.1016/j.buildenv.2018.10.060

XV International Conference on Durability of Building Materials and Components
DBMC 2020, Barcelona
C. Serrat, J.R. Casas and V. Gibert (Eds)

Hempcrete Buildings: Environmental Sustainability and Durability of Two Case-Studies in North and South Italy

Giovanni Dotelli[1], Chiara Moletti[1], Patrizia Aversa[2], Sergio Sabbadini[3], Anna Marzo[4], Concetta Tripepi[4], Pasqua Lauriola[5] and Vincenza A.M. Luprano[2]

[1] Politecnico di Milano, Dip. Chimica, Materiali e Ingegneria Chimica "G.Natta", p.zza L. da Vinci 32, 20133 Milano, Italy, giovanni.dotelli@polimi.it

[2]ENEA C.R. Brindisi - SS 7 km 706 – Brindisi, Italy

[3]Politecnico di Milano, Dip. Architettura e Studi Urbani, p.zza L. da Vinci 32, 20133 Milano, Italy 4

[4]ENEA C.R. Bologna - Via Martiri Monte Sole, 4 – Bologna, Italy

[5] Private Architecture Studio

Abstract. *In the framework of Circular Economy policies aimed at reducing the consumption of raw materials, shives, as an agricultural by-product of hemp cultivation, have gained a renovated life in the construction sector. Its excellent thermal insulating properties permitted the development of new building materials to be used in various executive technologies. When shives are mixed with a mineral binder such as lime or cement, the mixture is usually referred to as hempcrete. In Italy, the use of hempcrete and the development of new production chains and implementation techniques dates back only to about the last decade, while other European countries have more long-lasting experiences (90s). In order to assess the potential benefits of hempcrete in the construction sector, its environmental performances were evaluated using the LCA methodology, by comparing four non-loadbearing representative walls, one made with hempcrete blocks and the others with more "traditional" materials. This research constitutes a solid basis for the development of future guidelines and/or regulations at national and international level in order to guarantee the maximum diffusion of this type of product. Then, a study has been carried out regarding the functionality of hempcrete blocks in masonry, layered with finishing plaster made of fine hemp shives, to evaluate the in-situ hygrothermal building performance. In particular, measurement methods were developed and analysis were carried out on two houses, one in northern Italy and one in southern Italy, and precisely in Sicily, focusing the study on the performances of the walls subjected to warm Mediterranean climates. Indeed, the literature on masonry behavior in hot Mediterranean climates is much scarcer than in cold climates.*

Keywords: *Hempcrete, Hygrothermal Behaviour, Sustainable Materials, Mediterranean Climate, Durability.*

1 Introduction

The building sector has a major impact on the natural environment, so sustainable building materials have been developed to reduce the emission into the atmosphere of carbon dioxide and polluting gasses typical of the process of production of traditional building materials. Among sustainable materials, the nature-based solutions are carbon negative and characterized by low-embodied energy (Murphy and Norton, 2008; Ip and Miller, 2012); in addition, they are able to improve the performances of a building envelope because of their remarkable insulating properties.

Many bio-composite materials are produced introducing biomasses, residual of agricultural cultivation (e.g. hemp, straw, rice-husk), into traditional binders (e.g. lime, concrete). In this way, the new building materials exploit natural resources that would otherwise be wasted, being the by-product of agricultural activities (Liu *et al.*, 2017).

This study focusses on hempcrete which is produced introducing hemp shives into an hydraulic binder. The increasing utilization of this material is due to its characteristic hygroscopic properties which determine an improvement of the indoor environmental comfort as reported, for example, by Nordby and Shea (2013). The present research aims to investigate the performances of walls built using hempcrete blocks. The bio-blocks are not- loadbearing and they are used to insulate thermally external or internal walls or to divide internal spaces. The prefabricated blocks production developed in order to solve some issues typical of casting of hempcrete in situ; especially the hardening step which is critical as it significantly influences the homogeneity of the properties in the casted material. Hence, by producing blocks, it is possible to control the hardening phase and to improve the quality of the material (Elfordy *et al*., 2008).

A preliminary evaluation of the environmental performances of a wall made with hempcrete blocks has been performed through LCA (Life Cycle Assessment) methodology according to EN ISO 14040-14044:2006 standards. A comparative assessment with different wall systems was started, preliminarily only at A1-A3 stages, i.e. product stage (EN 15804:2012 +A2:2019).

Then, this research develops experimental methodologies to investigate the hygrothermal behaviour of hempcrete during its service life, so it would be possible to evaluate its durability in situ. The measurements have been performed on walls built using the same type of hempcrete blocks in two residential houses in Sicily (southern Italy) and in Veneto (northern Italy).

2 Durability of Hempcrete

Durability has a crucial importance for building materials, few data exist about the durability of hempcrete in real structures because its utilization is relatively recent, it has been used in France from 1990s and in Italy only from 2000s. The first data collected on buildings have given good results, comparable to the performances of traditional materials (Clarke, 2002). The aim of this project is to perform field test in the two selected buildings, both in Sicily and in Veneto, to obtain information about the behaviour of hempcrete blocks. This would support the users in the utilization of the material. The interesting results on the performances of the material presented in this paper will be implemented with periodical tests to study the evolution of the performances of the material and its durability in residential structures.

The main concern about the durability of hempcrete is determined by the presence of vegetal material because the variation of moisture conditions can cause its degradation. Thus, a decrease of the performances of hempcrete and, possibly, a reduction of the salubrity of the environment could occur.

Data about the durability of hempcrete can be collected carrying out laboratory tests, some studies have simulated possible critical situations, typical of the service life, but field tests are recommended to increase the knowledge about the material. The effects of biological attack by bacteria or fungi have been studied by inoculating microorganisms into the material. Periodic measurements along two years have been carried out by Walker *et al.* (2014) after the abundant introduction of bacteria; the results show that microorganisms, even those able to live in alkaline conditions, did not proliferate and degradation did not occur. Moreover, the alternating high and low values of humidity, typical of Mediterranean climate, further limit their permanence into the material. The alternation of wet and dry periods is fundamental to avoid the biological degradation: high humidity favours the spread of fungi or bacteria on the surface of hempcrete reducing the hygrometric performances of the wall while low humidity allows the penetration of microorganisms inside the material reducing the water vapour permeability (Arizzi *et al.,* 2016). The importance of testing even after several months is underlined by Marceau *et al.* (2017) who have found the conditions necessary for the mould growth: high relative humidity (around 98%) and pH lower than 10. The pH of hempcrete decreases due to the carbonation process, for this reason a long-term monitoring would allow to investigate the behaviour of the material in critical conditions. Some biocide treatments as γ irradiation of hemp shives, addition of anti-microbial or nanoparticles able to increase the resistance to bacteria or fungi have been proposed (Arizzi *et al.*, 2016).

Beside the growth of microorganisms, the moisture content influences also the density and, consequently, the thermal conductivity of the material. Hence, proper ventilation and correct selection of the protective coating, are crucial to preserve the properties of hempcrete besides to counter the biological degradation (Marceau *et al.*, 2017). The resistance to freeze-thaw cycles is good, no cracks or modification of the microstructure have been detected for a year on hempcrete blocks, characterized by different hemp-to-lime ratios, after 10 freeze-thaw cycles in conditions near saturation (RH around 90%). Carbonation reduces the vulnerability to freeze-thaw cycles because the formation of calcium carbonate reduces the porosity of hempcrete and hence the amount of water absorbed (Walker *et al.*, 2014). Furthermore, tests of exposure to salt (NaCl) performed by Walker *et al.* (2014) and Arizzi *et al.* (2016) did not provoke degradation of blocks and no effloresce was detected. If salt precipitates on the surface, it is easily removed by rainfall while, if absorbed, the hygroscopic behaviour helps in weathering through natural wet-dry cycles. Therefore, the weathering of salt is less aggressive in hempcrete than in other inorganic porous materials (*e.g.* stone, mortar).

3 Life Cycle Assessment

In recent years, the interest for hemp-based building materials has increased also due to their expected positive environmental performances (Ingrao *et al.*, 2015). However, few LCA

studies have evaluated different hempcrete wall technologies: spray (Boutin *et al.*, 2006; Pretot *et al.*, 2014) sprayed hempcrete with timber frame support (Ip and Miller, 2012; Pretot *et al.*, 2014) and blocks. A preliminary environmental assessment of the hempcrete technology is given here by evaluating a representative wall made with hempcrete blocks. Recently, the environmental performances of an Italian hempcrete block (Arrigoni *et al.*, 2017) as well as hemp cultivation (Zampori *et al.*, 2013) have been carried out.

In order to assess the environmental sustainability of hempcrete blocks used in non-load bearing walls, three additional alternatives have been selected and compared at the level of materials production (A1-A3, EN 15804:2012+A1:2019): masonry bricks, expanded clay bricks and aerated autoclaved concrete (AAC) blocks with cement-lime mortars. The comparison is based on 1 m^2 of vertical non-load-bearing wall (Functional Unit). Data for alternative bricks are taken from Environmental Product Declarations (EPDs) of selected producers (Aversa *et al.*, 2019; Margutti and Pennati, 2018). The impact categories selected are those reported in the EPDs and the method used to evaluate the environmental burden of the four walls is CML 2001 (Guinée and Lindeijer, 2002).

In Figure 1, the results of the four walls in seven impact categories are compared. The hempcrete wall solution has very positive performances in six out of seven impact categories. This preliminary LCA is highly promising, especially considering that only the first life cycle stages of the building are included in the analysis. Further benefits will certainly come from the use stage and end-of-life. Moreover, a detailed LCA study of hempcrete blocks is being carried out to take into account production improvements occurred in the last year.

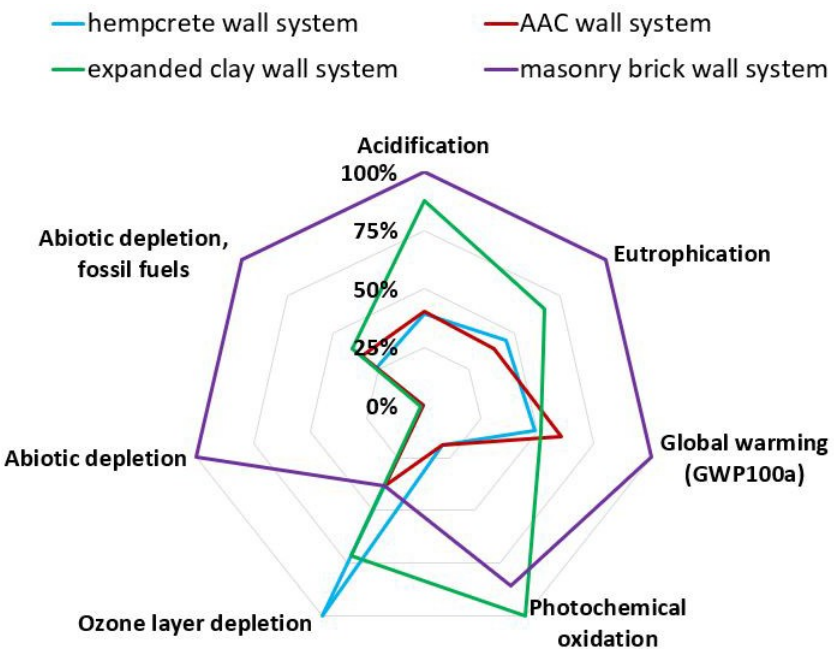

Figure 1. Wall system s comparative LCA assessment at the product stage A1-A3.

4 Case Study

The experimental methodology to perform the field measurements that allow to determine the hygrothermal performances of hempcrete walls has been tested in laboratory on a 1m^2 wall, built in hempcrete blocks, introduced in a climatic chamber. Known temperature cycles have been applied to simulate hot temperate climates (Aversa *et al*., 2019). The test wall had been built employing the same type of blocks used in the perimeter walls of the detached houses in Sicily (Serradifalco, CL).

Currently, the data collected in the Sicilian campaign have been elaborated, the reference standards are UNI EN 15026:2008 and UNI EN ISO 13788:2013. The measurements have been performed on the South-West, South-East and North-West walls for 13 days (in August) during which the inhabitants where not present to exclude the influence of the air conditioning system. The wall system is 400mm thick (Figure 2): the hempcrete blocks have a thickness of 360 mm, the ratio between dolomitic lime and hemp shives is 3:1; the plaster is premixed, constituted by hydraulic lime NHL 5 and it has thickness of 20 mm both on the internal and on the external face of the walls. The bedding mortar is characterized by a dolomitic lime-to- hemp shive ratio of 3:1.

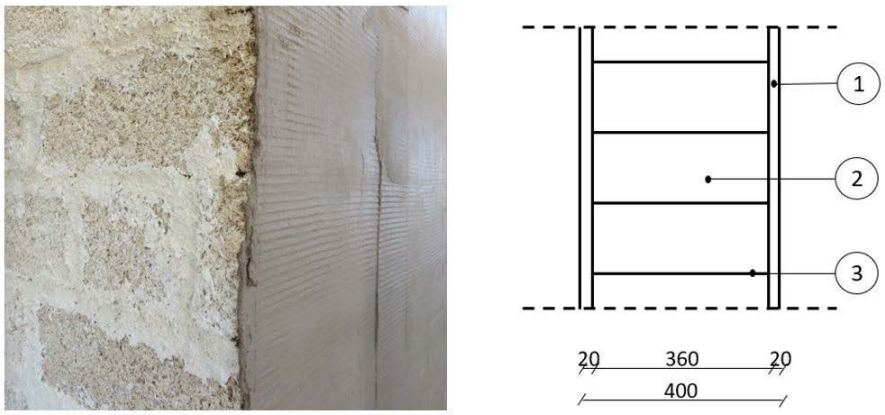

Figure 2. Wall system: 1-plaster (thickness: 20 mm); 2-hempcrete blocks (thickness:360mm); 3-bedding mortar.

Temperature and humidity sensors have been applied on the walls (see Aversa *et al*., 2019) while the outdoor weather conditions have been measured by a weather control unit. The temperature and humidity of internal and external surfaces of the North-West wall, detected during the period of analysis, are plotted in Figure 3.

Regarding the relative humidity, on the internal wall an average value of 67% has been measured while the external value shows variations in between 40% and 100%, due to some rainy days during the monitoring period. Hence, the behaviour of the wall is good, the damping has been higher than 80%. Also, the thermal response has been good, the average temperature measured on the internal wall has been 26°C (with variations of ± 1.5°C) in

response to the variations of external temperature between 15°C and 35°C. Likewise humidity, the damping is higher than 80%. The offset between internal and external humidity is of 6 hours, relatively to the maximum peak of humidity, while the offset was around 8 hours in laboratory tests (Aversa *et al.,* 2019).

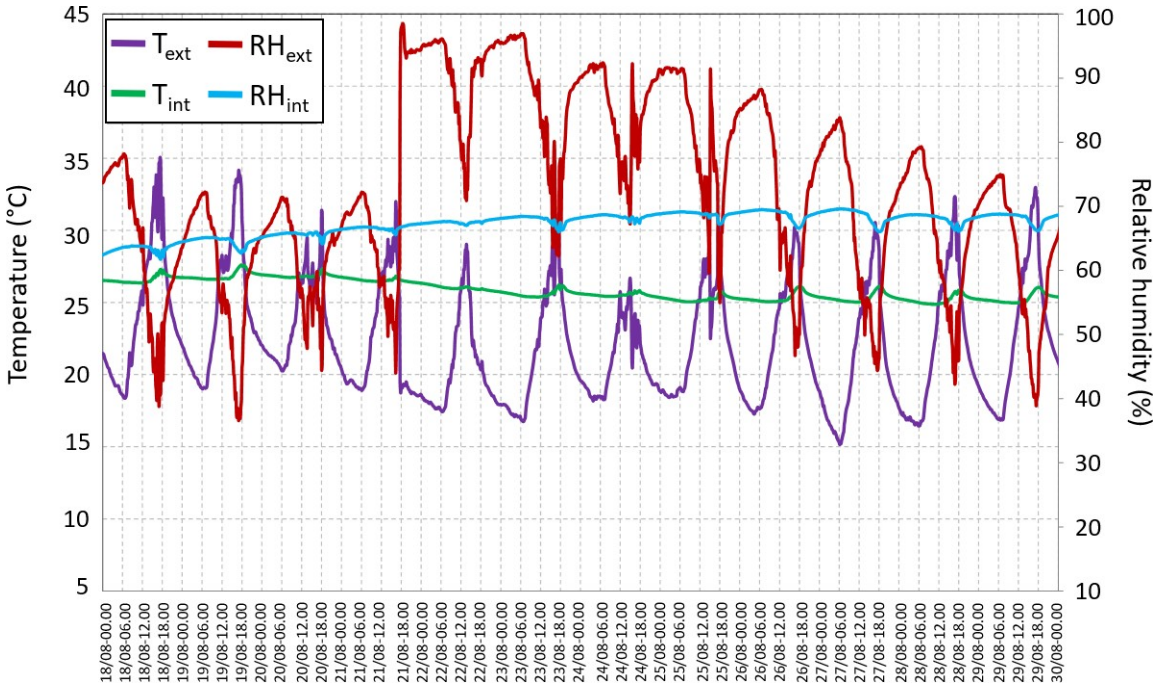

Figure 3. Temperature (T) and relative humidity (RH) measured on the internal (int) and external (ext) faces of the North-West wall of the house in Sicily during the 13 days of analysis.

The implementation of the results with the numerical simulations and the new experimental campaigns will enrich the knowledge about the behaviour of hempcrete in a detached house. This will be implemented by the measurements carried out in Veneto. The case-study in Sona (VR) is different from the Sicilian because hempcrete has been applied only in a room, during the renovation of the building. In this case, the data will provide information both on the performances of hempcrete into a different climate than the Sicilian one and on the behaviour of the material when installed in combination with other materials.

5 Conclusions

This study shows the promising performances of hempcrete blocks both in terms of environmental sustainability and hygrothermal properties. The preliminary environmental assessment through LCA is highly encouraging and seems to confirm what has been already

demonstrated in the recent literature, *i.e.* that the use of hempcrete blocks has a beneficial effect on relevant impact categories. Furthermore, some of the advantages of the hempcrete are not clearly evidenced in the first life cycle stages of a building, in terms of energy saving and recyclability at the end-of-life.

The first evaluation of the hygrothermal performances of hempcrete blocks in the Sicilian climate is positive. The indoor temperature and humidity were almost constant during the analysis period without the utilization of ventilation, air-conditioning systems or air exchange. Further measurement in situ will allow to understand the evolution of the material performances in time. Thus, the durability of hempcrete will be evaluated together with the possibility to install it in place of traditional materials, especially when sudden climatic variations occur, or higher humidity and continuous rain conditions verify.

Moreover, the availability of residential houses for in situ measurements will allow the evaluation of energetic behaviour of the buildings and the evaluation of the environmental performances of the material when applied in construction works. Also, the effects on the indoor comfort will be investigated *i.e.* humidity and temperature of the internal spaces will be measured.

Acknowledgements

This study is based on PAR2017 Project (D.2 Nearly zero energy buildings (nZEB)) funded by Italian Ministry of Economic Development.

ORCID

Giovanni Dotelli: https://orcid.org/0000-0003-1876-9881
Chiara Moletti: https://orcid.org/0000-0001-9737-9835
Patrizia Aversa: https://orcid.org/0000-0003-4734-3329
Sergio Sabbadini: https://orcid.org/0000-0002-5848-9756
Anna Marzo: http://orcid.org/0000-0002-1469-0626
Concetta Tripepi: https://orcid.org/0000-0003-0761-856X
Pasqua Lauriola: http://orcid.org/0000-0003-1275-7994
Vincenza A.M. Luprano: https://orcid.org/0000-0003-4942-3664

References

Arizzi, A., Viles, H., Martín-Sanchez, I. and Cultrone, G. (2016). Predicting the Long-Term Durability of Hemp- Lime Renders in Inland and Coastal Areas Using Mediterranean, Tropical and Semi-Arid Climatic Simulations. *Science of the Total Environment, 542,* 757-770. doi:10.1016/j.scitotenv.2015.10.141.

Arrigoni, A., Pelosato, R., Melià, P., Ruggieri, G., Sabbadini, S. and Dotelli, G. (2017). Life Cycle Assessment of Natural Building Materials: The Role of Carbonation, Mixture Components and Transport in the Environmental Impacts of Hempcrete Blocks. *Journal of Cleaner Production, 149,* 1051–1061. doi:10.1016/j.jclepro.2017.02.161.

Aversa, P., Daniotti, B., Dotelli, G., Marzo, A., Tripepi, C., Sabbadini, S., Lauriola, P. and Luprano, V. A.M. (2019). Thermo-Hygrometric Behavior of Hempcrete Walls for Sustainable Building Construction in the Mediterranean Area. *IOP Conference Series: Earth and Environmental Science, 296(1).* doi: 10.1088/1755-1315/296/1/012020.

Boutin, M.P., Flamin,C., Quinton, S. and Gosse, G. (2006). Study on the Environmental Characteristics of Hemp through the Analysis of its Life Cycle (in French). Ministry of Agriculture, Agrifood, and Forestry, Paris , France.

CEN (2019). *EN 15804:2012 + A2:2019 Sustainability of construction works - Environmental product declarations - Core rules for the product category of construction products.*

CEN (2006). *EN ISO 14040: Environmental Management – Life Cycle Assessment– Principles and Framework.*

CEN (2006). *EN ISO 14044: Environmental Management – Life Cycle Assessment- Requirements and Guidelines.* Clarke, S. (2002). Final Report on the Construction of the Hemp Houses at Haverhill, Suffolk. *Suffolk. Building Research Establishment, Watford,* (209), 209–717.

Elfordy, S., Lucas, F., Tancret, F., Scudeller, Y. and Goudet, L. (2008). Mechanical and Thermal Properties of Lime and Hemp Concrete ('hempcrete') Manufactured by a Projection Process. *Construction and Building Materials, 22* (10), 2116–2123. doi: 10.1016/j.conbuildmat.2007.07.016.

Guinée, J. B. and Lindeijer, E. (2002). *Handbook on life cycle assessment: operational guide to the ISO standards*. Netherlands: Springer Science & Business Media.

Ingrao, C., Lo Giudice, A., Bacenetti, J., Tricase, C., Dotelli, G., Fiala, M., Siracusa, V. and Mbohwa, C. (2015). Energy and Environmental Assessment of Industrial Hemp for Building Applications: A Review. *Renewable and Sustainable Energy Reviews, 51,* 29-42. doi:10.1016/j.rser.2015.06.002.

Ip, K. and Miller, A. (2012). Life Cycle Greenhouse Gas Emissions of Hemp-Lime Wall Constructions in the UK. *Resources, Conservation and Recycling, 69,* 1–9. doi: 10.1016/j.resconrec.2012.09.001.

Liu, L.F., Li, H. Q., Lazzaretto, A., Manente, G., Tong, C.Y., Liu, Q.B. and Li, N.P. (2017). The Development History and Prospects of Biomass-Based Insulation Materials for Buildings. *Renewableand Sustainable Energy Reviews, 69,* 912–932. doi:10.1016/j.rser.2016.11.140.

Marceau, S., Glé, P., Guéguen-Minerbe, M., Gourlay, E., Moscardelli, S., Nour, I. and Amziane, S. (2017). Influence of Accelerated Aging on the Properties of Hemp Concretes. *Construction and Building Materials, 139,* 524-530. doi:10.1016/j.conbuildmat.2016.11.129.

Margutti, M. and Pennati, A. (2018) *Definition ofmethods for the control of qualityand for the correct laying and management of hempcrete blocks*, MSc Thesis, Politecnico di Milano, Milan, Italy.

Murphy, R. J. and Norton, A. (2008). Life Cycle Assessments of Natural Fibre Insulation Materials Final Report. *11th International Conferenceon Non-Conventional Materials and Technologies, NOCMAT 2009, no. February: 79.*

Nordby, A.S. and Shea, A.D. (2013). Building Materials in the Operational Phase: Impacts of Direct Carbon Exchanges and Hygrothermal Effects. *Journal of Industrial Ecology, 17* (5), 763–776. doi: 10.1111/jiec.12046.

Pretot, S., Collet, F. and Garnier, C. (2014). Life Cycle Assessment of a Hemp Concrete Wall: Impact of Thickness and Coating. *Building and Environment, 72,* 223–31. doi:10.1016/j.buildenv.2013.11.010.

UNI/TS 11300-1 (2008). *UNI EN 15026: Hygrothermal performance of building components and building elements. Assessment ofmoisture transfer by numerical simulation.*

UNI/TS 11300-1 (2013). *UNI EN ISO 13788: Hygrothermal performance of building components and building elements. Internal surfacetemperature to avoid critical surfacehumidityand interstitial condensation.*

Walker, R., Pavia, S. and Mitchell, R. (2014). Mechanical Properties and Durability of Hemp-Lime Concretes. *Construction and Building Materials, 61,* 340-348. doi:10.1016/j.conbuildmat.2014.02.065.

Zampori, L., Dotelli, G. and Vernelli, V. (2013). Life Cycle Assessment of Hemp Cultivation and Use of Hemp- Based Thermal Insulator Materials in Buildings. *Environmental Science and Technology, 47* (13), 7413 – 20. doi:10.1021/es401326a.

XV International Conference on Durability of Building Materials and Components
DBMC 2020, Barcelona
C. Serrat, J.R. Casas and V. Gibert (Eds)

Improving Frost Durability Prediction based on Relationship between Pore Structure and Water Absorption

Mohamed A. Aldabibi[1], Michelle R. Nokken[2] and Hua Ge[3]

[1] Ph.D. Candidate, Dept. of Building, Civil & Environment Engineering, Concordia University, Montreal, Canada, M_aldabibi@yahoo.com

[2] Professor. Dept. of Building, Civil & Environmental Engineering, Concordia University, Montreal, Canada, m.nokken@concordia.ca

[3] Associate Professor, Dept. of Building, Civil & Environmental Engineering, Concordia University, Montreal, Canada, Hua.Ge@concordia.ca

Abstract. *In North America, clay bricks are qualified as durable if they meet either the ASTM C216 or CAN/CSA A82.1 standard. Although these standards are widely used in North America, they have not been linked with pore Structure (PS). Furthermore, moisture content and pore structure (PS) are two significant parameters that influence the performance of clay bricks during the freezing-thawing process. Thus, finding a relationship between them will lead to a quick assessment of water absorption (WA) and knowing their effect on frost resistance (FR). This work aims to investigate the relationship between PS and WA of clay bricks. Five different types of clay bricks were examined. WA of brick samples was determined according to the CAN/CSA A82.1 standard. Mercury Intrusion Porosimetry (MIP) was used to determine the total porosity and pore size distribution (PSD). The variation of 24-h cold water absorption (CWA) among samples of each type of brick was analyzed and each type of brick was divided into three groups according to their 24-h CWA: low – medium – high. The PSD of bricks was also divided into several ranges based on the pore size. The results indicated that some types of brick have a wide variation in 24-h CWA, which could affect the frost resistance evaluation. The strong relationship between WA and PSD was found, which could be used as a base for determining 24-h CWA.*

Keywords: *Clay Brick, Frost Resistance, Water Absorption, Pore Structure.*

1 Introduction

Numerous contributions in the literature have dealt with the frost durability problem regarding its mechanism and theories, influential factors, and evaluation methods (Stupart, 1989). Frost resistance (FR) is defined as the ability of materials to resist frost damage when exposed to climatic conditions (Mallidi and Reddy , 1996). Many researchers also have studied and determined the parameters that influence the FR of clay brick. They concluded that these parameters could be identified through the material characteristics and the physical state of water (ice). These studies indicated that water absorption (WA) and pore structure (PS) affect FR. Essential components of the PS of clay brick, which involve determining the FR, are its porosity and pore size distribution (PSD) (Stupart, 1989). Generally, the pores are the place where ice expansion occurs, resulting in pressure development inside porous materials.

Generated pressure typically depends upon the amount of pores and the degree of saturation of the material during the freezing process. Clay bricks typically are subjected to a wide range of water saturation levels during their service life. Hence, high levels of saturation sometimes cause durability problems, especially when it is accompanied with severe freeze/thaw (F/T)

conditions. Water absorption is defined as the ratio between the mass of absorbed water to the dry mass of the sample (De Rose *et al*., 2014). The relationship between capillary pores, *i.e*., pores are larger than 0.01μm according to (Gao *et al*., 2015) and adsorbed water is a positive relation, whereas increased capillary pores lead to increased WA, which in turn affects frost durability (Davison, 1980). Thus, appropriate evaluation of potential FR of bricks requires a sufficient understanding of the relationship between FR and brick properties (*i.e*., PS and WA).

Predicting the FR of bricks based on a physical property assessment is known as an indirect method. In North America, the clay brick is qualified as durable if it meets the criteria based on a physical property stated in the Canadian standard CAN/CSA A82.1. The CSA A82.1 standard depends on a direct determination of compressive strength and WA. In other words, three conditions should be met which are the minimum compressive strength, maximum water absorption (*i.e*., 24-h CWA), and maximum saturation coefficient (C/B) (CSA-A82.1, 2006). The 24-h CWA is defined as an amount of water that absorbed during a 24-hour divided by the sample's dry mass, while C/B is determined based on the ratio between 24-h CWA and 5-h boiling water absorption (5-h BWA). Besides, several indices have been used to evaluate potential FR such as (Maage, 1984), (Nakamura, 1988), and (Koroth *et al*., 1998). Maage's index (Maage, 1984) is a preferred indirect method (Davison, 1980) that is used for the evaluation of FR. The method depends on measuring the PSD of a brick using mercury intrusion porosimetry (MIP). Ultimately, the durability factor (Df) is calculated using Eq (1) (Maage, 1984).

$$DF = 3.2/PV + 2.4 * P3 \quad (1)$$

Where: DF is a durability factor; PV is maximum intruded pore volume of brick; P3 is the percentage of pores with diameters bigger than 3 μm (% of PV).

Although many previous studies have investigated the FR and material properties, there is no literature reporting the relationship between two essential properties of clay brick (*i.e*., pore system and water absorption). The aim of this paper is to investigate the relationship between pore properties and water absorption to provide the right prediction of the amount of absorbed water thus improving frost durability prediction. To achieve this goal, five different types of clay brick were examined using two approaches and their measurement results were analyzed.

2 Material and Methods

The determination of the relationship between PS and WA properties includes several consecutive procedures. These procedures involve selecting different types of clay bricks, determining their PSD, and measuring WA. Finally, data analysis is carried out to derive the relationship between the PS and WA. To obtain a wide range of properties, five sets of brick specimens from three different types (new exterior brick, reclaimed exterior brick, and reclaimed interior brick) were obtained from local vendors in Montreal, Quebec and examined. Table 1 shows the brick types that used in this research.

2.1 Water Absorption (WA)

Each type of brick was tested in accordance with CSA -A82.1 standard to determine WA. First, the dried weight is determined according to CSA -A82.1 at a temperature of 110 to 115 ºC for at least 24h.

Table 1. Different types of bricks used in this study.

Brick Type	Brick name	Samples number	Nomenclature
Reclaimed exterior brick	LAPRAIRIE	35	PO
	OUTREMONT	35	UO
New exterior brick	BRGG52	35	B52
	OLD ENGLAND	35	OE
Reclaimed interior brick	MOLLE	35	MO

2.1.1 The 24-h cold water absorption (CWA)

The 24-h CWA is determined according to CSA-A 82.1 following the drying and cooling procedure mentioned above. The dried full specimen was immersed completely in clean water at room temperature for 24h. The specimen was removed and wiped of excess water and then mass determined. The 24-h CWA is calculated based on Eq (2).

$$24\text{-}h\ CWA = (W_s - W_d)/ W_d * 100 \quad (2)$$

Where: W_d = dry weight of specimens; W_s = saturated weight of the specimen after 24h submersion in cold water.

2.1.2 The 5-h boiling water absorption (BWA)

The specimen, after being subjected to cold water absorption, was immersed in clean water and the water was heated to boiling for 5 hours. The specimen was cooled by natural loss of heat until reaching room temperature. The specimen was removed from the container and wiped, and then mass determined. The 5-h BWA is calculated based on Eq (3).

$$5\text{-}h\ BWA = (W_b - W_d)/ W_d * 100 \quad (3)$$

Where: W_d = dry weight of specimens; W_b = saturated weight of the specimen after 5h submersion in boiling water.

2.2 Mercury Intrusion Porosimetry (MIP)

MIP has been known as a suitable method to examine the PS of mineral building materials since 1970 (Rubner and Hoffmann, 2006) and used by many researchers to determine open porosity and the PSD (Maage, 1984). A set of pore parameters can be determined and derived by MIP such as pore volume, porosity, pore range, and median pore size. The width of the PSD is expressed using the Scatter coefficient (Cd), which is calculated from Eq (4).

$$Cd = (r20 - r80)/ r50 \quad (4)$$

Porosimetric determinations were performed by means of MIP (PoreSizer 9320). PSD was calculated from the mercury intrusion results by assuming a surface tension of mercury of 0.485 N/m and a contact angle of 124°. The relationship between pressure and size of the pore is given by the Washburn equation (5).

$$D = -4\gamma\cos\theta/\rho \quad (5)$$

Where: D is pore diameter; p = applied pressure; γ= surface tension; and θ = contact angle.

The results showed a wide range of 24-h CWA within the same brick type. To have a range of results, three samples were selected for MIP measurement from the 35 samples tested. Each type of brick was divided into three groups based on the variation in 24h CWA values (low, medium, and high). Eventually, MIP test was performed on small – cored samples taken out from the brick samples to characterize the pore system. Thirty small cores, 15 mm in diameter and 22 to 25 mm length, were derived from all brick types and then examined by the MIP test with two replicates per brick type and absorption value. The small cores were dried in an oven at 105 – 110 ºC for 24-h and stored in a sealed container until testing.

3 Results and Discussion

3.1 Water Absorption Properties

Thirty-five specimens of each brick type were subjected to the WA test to determine 24-h CWA, C/B, bulk density (BD), porosity (P), and apparent density (AD). Table 2 shows all brick properties that were determined based on the WA test. In general, the 24-h CWA values of the bricks as an average ranged from 4.42% (for new exterior brick OE) to about 16.68% (for reclaimed interior brick MO). Brick types PO, B52, and OE on average passed the CSA – A82.1 requirement; these are all bricks intended for exterior use. However, brick types MO and UO failed to meet CSA-A82 requirements of 24-h CWA (8%). This was somewhat surprising as UO was identified for exterior use, which is probably due to the effects of the service life. Table 2 shows the individual results of 24-h CWA test of all brick types. Table 2 also shows that all samples of brick MO did not meet the 24-h CWA criteria requirement, while brick types PO, UO, B52, and OE meet 24-h CWA criteria as percentage 59%, 12%, 86%, 95%, respectively. The results of 24-h CWA also show that there is a variation among 24-h CWA values of the sample from the same type of brick. This variation can be seen through the standard deviation of each brick type, where brick types MO, OE, B52, UO, and PO show standard deviation 1.86, 1.80, 1.65, 1.38, and 0.84, respectively.

Table 2. Brick properties based on water absorption test.

Brick type	24-h CWA %				5-h BWA %	C/B	BD	AD	P
	Ave	SD	Individual			Ave	kg / m^3	kg / m^3	m^3/ m^3
			Pass	Fail					
MO	16.68	1.86	0	35	19.62	0.85	1777	2725	0.35
PO	7.88	0.84	20	15	10.14	0.78	2085	2642	0.21
UO	9.57	1.38	5	30	12.28	0.78	1968	2596	0.24
B52	5.42	1.65	30	5	10.38	0.51	1904	2398	0.20
OE	4.42	1.80	33	2	6.25	0.69	2245	2610	0.14

The C/B values of the bricks as an average ranged from 0.51 (for new exterior brick B52) to about 0.85 (for reclaimed interior brick MO). The results show that on average brick types B52 and OE meet the CSA-A82 requirements for exterior brick. Brick type MO also meets the CSA-

A82 for interior brick. While brick types PO and UO exhibit the C/B at threshold 0.78 of the CSA-A82 standard as shown in Table 2. The porosity (P) of brick types is from 14% (for new exterior brick OE) to 35% (for reclaimed interior brick MO). The bulk density (BD) of brick types is between 1777 kg/m^3 (for reclaimed interior brick MO) to 2245 kg/m^3 (for new exterior brick OE) as shown in Table 2.

3.2 Pore System Properties

From the MIP test, curves of cumulative pore volume and diameter were derived. Based on the calculation from Maage's equation (1) and criteria (*i.e.*, durable DF>70; uncertain durability DF= 55-70; nondurable DF<55), most of brick types have good durability. They show (DF>70) except samples MO12 – H1 and MO9- H2 that show (DF<55) as shown in Table 3. Brick sample OE31-H1 has the lowest pore volume (PV) compared to other samples of brick types while brick sample MO12-H1 has the highest PV. Brick sample B52-27-H2 shows a high percentage, *i.e.* 76%, of pore volume with a diameter bigger than 3μm. In contrast, brick sample MO12-H1 shows a low value, *i.e*. 3%, of pore volume with a diameter bigger than 3μm.

According to Maage's principle, sample B52-27-H2 with a DF of 226 has low water absorption and better frost resistance. In contrast, the sample MO12-H1 with a DF of 20 has high water absorption and poor frost resistance. The scattering coefficient (Cd) of all brick types ranges between 0.52 and 36. If Cd is less than 1, it means the PSD is narrow. The samples MO9-H2 and MO12-H1 have narrow PSD thus most ice will form within a small temperature interval.

The rest of the samples PO, MO15, B52, UO, and OE have Cd bigger than 1, thus they have a wide PSD and ice formation will occur in wide temperature interval. It can be drawn from the data analysis that samples MO15 and MO12-2 of type MO (that exhibits a high WA) have a predominant pore size ranges between 0.1and 0.3 μm. While sample MO9 has a predominant pore size range between 0.3 and 1.0 μm. The Sample B52-27 of type B52 (that exhibits a low WA) has a dominant range of pore size, which is 10-20 μm. Sample OE31 of type OE with the lowest value of WA has a predominant pore size ranges between 7 and 20 μm.

3.3 Relationship Between 24-h CWA and PSD

As shown in Figure 1, a linear correlation between 24-h CWA and its PV (porosity) exists with a high correlation coefficient ($R^2 = 0.93$). With the increase of porosity, i.e., pore volume, the 24-h CWA increases. To obtain a better analysis of the effect of PSD on WA, some further analysis was undertaken. Three features were investigated: PSD of the samples that had the highest and lowest values of 24-h CWA among all brick types, PSD of three samples from the same type, and PSD of the sample have the same PV. The samples MO12-H1 and MO9-H2 have the highest 24-h CWA 19.81 and 15.36, respectively. It can be seen from PSD of these samples, as shown in Figure 2, that their PSD range between 0.03 and 2μm. The samples OE31-H1 and B52-27-H2 have the lowest 24-h CWA 1.57 and 3.24, respectively with pores larger than 2 μm. The samples with higher porosity had smaller pores.

The PSD of three samples of brick type B52 shows that they have a bimodal pore structure (*i.e*., two different ranges of median and large pores). Comparing their PSD with the change in 24-h CWA, it can be observed that increasing a percentage of pores with diameters bigger than 5 μm results in decreasing 24-h CWA and vice versa. The samples UO30-H2 and UO13-H1

have approximately constant PV, 0.0906 ml/g and 0.0909 ml/g, respectively. The samples PO14-H1 and OE2-H2 also have nearly the same PV, 0.1045 ml/g and 0.1039 ml/g, respectively. It can be seen from Figure 3 that 24-h CWA of these samples increases with pores having diameters smaller than 2 μm and vice versa. The empirical analysis of the relationship between 24-h CWA and PSD showed that 24-h CWA has a good correlation with the range of pores between 0.03 and 2 μm.

Table 3. Durability factor with 24-h CWA and C/B for all selected samples.

Brick Sample	MIP Method				WA Method	
	PV (ml/g)	P3 (%)	DF	Cd	24-h CWA %	C/B
PO-08-H1(low)	0.0893	72	209	2.74	6.03	0.74
PO-14-H1 (med)	0.1045	58	170	2.51	8.04	0.76
PO-09-H2 (high)	0.1186	48	141	12.38	9.19	0.77
UO-13-H1(low)	0.0909	73	211	7.24	6.28	0.64
UO-30 H2(med)	0.0906	46	146	8.15	8.94	0.80
UO-07-H1 (high)	0.1566	42	121	7.49	11.64	0.79
MO-15-H2 (low)	0.1485	25	82	36.88	10.62	0.68
MO-09-H2(med)	0.1735	5	32	0.52	15.36	0.87
MO-12-H1 (high)	0.2295	3	20	0.67	19.81	0.87
OE-31-H1 (low)	0.0325	48	215	3.94	1.57	0.48
OE-12-H1(med)	0.0607	39	146	4.32	5.89	0.76
OE-02-H2 (high)	0.1039	16	70	1.92	9.26	0.86
B52-27-H2 (low)	0.0729	76	226	1.57	3.24	0.39
B52-31-H2(med)	0.0681	73	213	1.56	5.87	0.53
B52-14-H2 (high)	0.1123	58	167	2.41	8.65	0.64

According to findings in previous studies, which indicated that larger pores are filled with water first, then water is delivered to smaller pores (Fagerlund, 1973). Furthermore, small pores have a greater suction stress due to their diameters, but a lower rate of uptake compared with large pores. The variation between the different pore sizes will result in sucking water from the large pores and delivery to small pores. When equilibrium is reached, the movement of water will be stopped. Hence, it can be observed that water absorption is also influenced by the relationship between the amount of pores volume in the range of 0.03 μm to 2 μm and the amount of pores volume bigger than 2 μm. Thus, the parameter (A) can be derived from the empirical analysis of the relationship between these pores, as shown in Eq (6).

$$A = (MP - LP)/LP \tag{6}$$

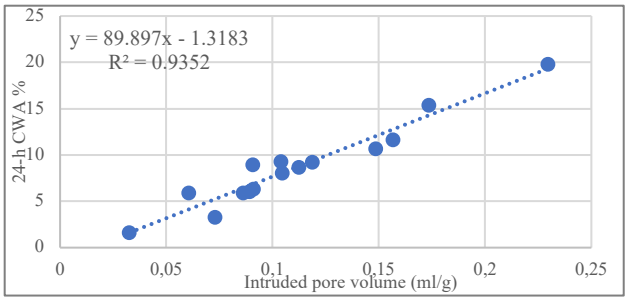

Figure 1. The correlation between 24-h CWA and intruded pore volume.

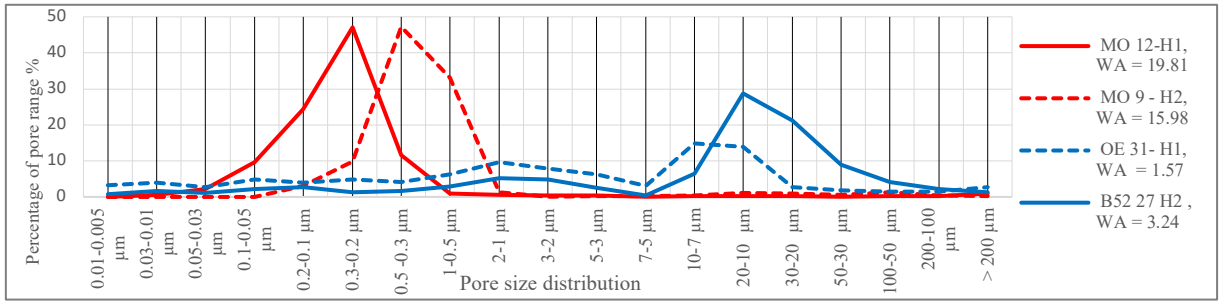

Figure 2. Pore size distribution of brick sample having maximum and minimum WA.

The ration between subtracting the percentage of pores bigger than 2µm (LP) of the percentage of pores in the range of 0.03 µm to 2 µm (MP) divided by (LP) shows a good correlation with WA. Eventually, the correlation between 24-h CWA, PV, the percentage of pores (0.03-2 µm), percentage of pores bigger than 2 µm, and the parameter (A) were input into regression analysis and the Eq (6) for determining 24-h CWA based on pore size was derived.

$$CWA_{24\text{-}h} = 59.68\,PV + 0.023MP - 1441.78/LP + 14.58A + 29.65 \quad (R^2=0.97) \tag{7}$$

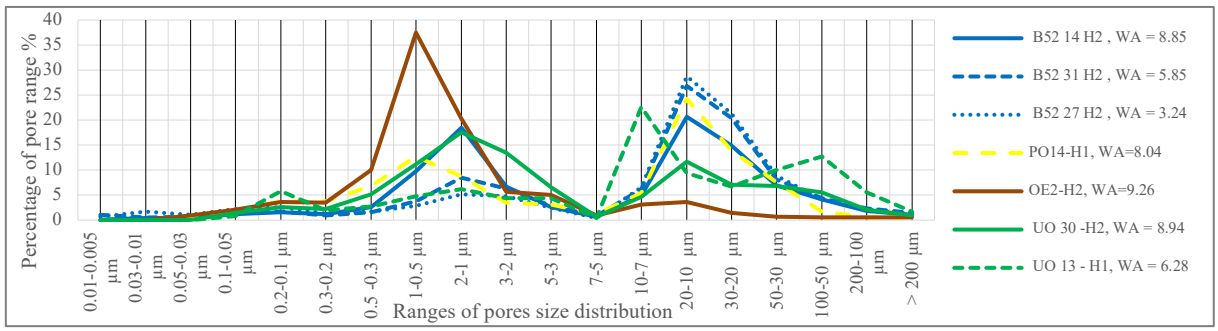

Figure 3. Pore size distribution of brick samples type B52 and other samples of different types having the same PV but with different levels of WA

4 Conclusions

The study investigates the relationship between WA and PS, as well as their effect on the prediction of FR. Main findings from this study are summarized as follows:

- All brick types show a variation in water absorption properties, which are essential

elements for the evaluation of frost durability using CSA and ASTM standards. The variation may attribute to manufacturing process control and conditions exposed through their service life for reclaimed bricks. Therefore, relying on 24-h CWA and C/B for predicting frost resistance could result in a misleading assessment.

- The WA of clay brick is considerably increased with the increase of pore volume having pore size ranging between 0.03- 2μm. Thus, decreasing the percentage of these pores will enhance the frost resistance of clay brick.
- Despite PSD is an important factor when evaluating the FR, it is not involved in the WA method. Hence, combining PSD with WA can give a good estimation of FR.

Maage's index deals with pores bigger than 3 μm as if they have uniform size and the same effect. But in fact, this contradicts several facts, namely, that pores have a different impact in terms of the size of their diameters when absorbing water. Consequently, further investigation of this issue will be required. Furthermore, a study about the relationship between the critical degree of saturation and PSD will be worthwhile to add a good contribution to the evaluation of frost resistance of clay brick.

ORCID

Mohamed A. Aldabibi: http://orcid.org/0000-0003-2146-9062
Michelle R. Nokken: http://orcid.org/0000-0002-5090-0248
Hua Ge: http://orcid.org/0000-0003-1368-4301

References

CSA-A82.1. (2006). *Fired Masonry Brick Made from Clay or Shale, Canadian Standards Association.* Canadian Standard Association.

Davison (1980). Liner Expansion due to Freezing and other Properties of Brick. *In Second Canadian Masonry Symposium,* 13-24. Ottawa : Carleton University .

De Rose et al. (2014). Towards a limit states approach to insulating solid masonry walls in a cold climate. *In 14th Canadian Conference on Building Science and Technology.*

Fagerlund. (1973). Critical degrees of saturation at freezing of porous and brittle materials. *Division of Building technology, Lund Institute of Technology*.

Gao et al. (2015). Multi-scale simulation of capillary pores and gel pores in Portland cement paste. *In 14th International Congress on the Chemistry of Cement*, 1-14.

Koroth et al . (1998). Development of new durability index for clay bricks. *Journal of architectural engineering*, 87-93.

Maage. (1984). Frost Resistance and Pore Size Distribution in Brick. Material and Structure . *Material Construction*, 345-350.

Mallidi and Reddy . (1996). Application of mercury intrusion porosimetry on Cay Bricks to Assess Freeze - Thaw Durability - A Bibiography with Abstract. *Construction and Building Materials* , 461-465.

Nakamura. (1988). Indirect evaluation of frost susceptibility of building materials. *American Ceramic Society bulletin*, 1964-1965.

Rubner and Hoffmann. (2006). Characterization of mineral building materials by mercury - intrusion porosimetry. *Particle systems characterization* , 20-28.

Stupart. (1989). A Survey of Literature Relation to Frot Damage in Bricks. *Masonry International* , 42-50.

XV International Conference on Durability of Building Materials and Components
DBMC 2020, Barcelona
C. Serrat, J.R. Casas and V. Gibert (Eds)

Intrinsic Differences on the Photodegradation Mechanisms between Pigmented and Non-Pigmented Coatings Determined by Multi-Scale Analysis

Takato Ishida[1], Ryoma Kitagaki[2], Hideaki Hagihara[3] and Yogarajah Elakneswaran[4]

[1] Ph.D. student, Graduate School of Engineering, Hokkaido University, Nishi-8-chome, Kita-13-jyo, Kita-ku, Sapporo-shi, Hokkaido, 060-8628, Japan, takato.matphysichem@gmail.com

[2] Graduate School of Engineering, Hokkaido University, Nishi-8-chome, Kita-13-jyo, Kita-ku, Sapporo-shi, Hokkaido, 060-8628, Japan, ryoma@eng.hokudai.ac.jp

[3] Research Institute for Sustainable Chemistry, National Institute of Advanced Industrial Science and Technology (AIST), Tsukuba, Ibaraki, 305-8565, Japan, h-hagihara@aist.go.jp

[4] Graduate School of Engineering, Hokkaido University, Nishi-8-chome, Kita-13-jyo, Kita-ku, Sapporo-shi, Hokkaido, 060-8628, Japan, elakneswaran@eng.hokudai.ac.jp

Abstract. *Multi-scale analysis of photodegradation are conducted for pigmented coating containing acrylic urethane + TiO_2 pigment and for non-pigmented coating containing only acrylic urethane. We discuss the intrinsic differences in the photodegradation mechanism between the pigmented and non-pigmented coatings and the effect of the interface between the pigment and the binder. Photo-aging tests are conducted using artificial ultraviolet (UV) irradiation under conditions of 60 °C and dry atmosphere. The results of Fourier transform infrared spectroscopy (FTIR), solvent swelling experiments, ultrasonic measurements of elastic moduli, and colourimetry used for material characterisation before and after photo-aging. Although the behaviour of E and the carbonyl index (CI) show common trends for both samples, the overall trends of yellowness index (YI) and swelling degree (Q) differ significantly between the pigmented and non-pigmented samples. The results reveal that changes in macroscopic properties may not necessarily correspond with the CI behaviour and that characteristic interfacial effects exist between the pigment and the binder. The onsets of coating erosion and chalking are observed in the pigmented coating as surface topological changes. The different behaviour of YI and Q between the sample types can be attributed to the interfacial effect at pigment/binder interface based on the photo-catalytic effect from TiO_2 pigment.*

Keywords: *Photodegradation, Coatings, Internal Morphology, Photo-Aging, Multi-Scale Analysis.*

1 Introduction

The durability of protective surface coatings is a critical factor for long-term quality with respect to buildings and infrastructures because these coatings act as gas barrier material and enhance the aesthetic qualities. Thus, improvement is needed in the long-term performance of these coatings, and an appropriate evaluation procedure should be established.

For assessing the degree of degradation in polymer-based materials, the carbonyl index (CI) is commonly applied because it reflects the macroscopic degradation occurring in barrier properties, elasticity, and surface colour and gloss in these materials. Although it is well accepted as a relevant criterion, CI may be not appropriate for evaluating the degradation level in all physical properties (Rouillon *et al*., 2016). CI could be applied to analyse the chemical oxidation level microscopically; however, it is not appropriate for evaluating some macroscopic

properties related to the material's internal morphology such as macromolecular architecture, pore structure, and configuration of fillers. Hence, recent multi-scale degradation research has been conducted to analyse microscale phenomena and macroscale properties with a focus on mesoscale alteration of materials (Courvoisier *et al.*, 2018; Richaud *et al*., 2010).

Two types of coatings are used for buildings and construction: pigmented and non-pigmented in coloured and clear coatings, respectively. Unfortunately, it can be difficult to evaluate the degradation level by applying only a single index to the durability of both coating types because they exhibit intrinsic differences in the photodegradation mechanisms such as the interfacial effect between the pigment and the binder, as evidenced by the differences in internal structures.

In this work, multi-scale analysis of photodegradation is conducted for both pigmented and non-pigmented coatings, as shown in Figure 1. We analyse the intrinsic differences noted in photodegradation between the two coatings and the effect of the interface between the pigment and the binder. Titanium dioxide (TiO_2) is most commonly used as white pigment for coatings of buildings owing to its good brightness and photo-catalytic effect. However, the photo-catalytic effect might be responsible for these differences because it produces hydroxyl radicals (·OH) under ultraviolet (UV) irradiation as part of the decomposition of surface contaminants (Pang *et al*. 2014).

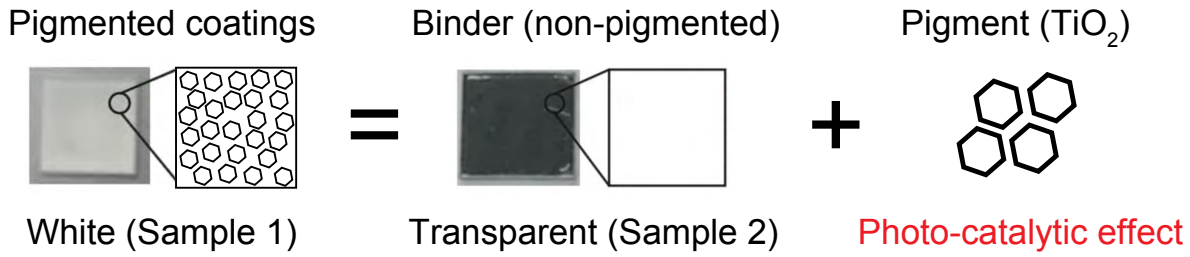

Figure 1. Composition of sample coatings.

2 Materials and Experimental Methods

2.1 Coating Sample Preparation

The coating was applied on Si substrates using the spin-coating technique at a speed of 2000 rpm for both the pigmented and non-pigmented coatings. The pigmented coating, which was purchased from Japanese industry, is a two-part-type urethane-based white paint (Sample 1). The main chemical component of the pigmented paint was analysed by pyrolysis gas chromatography mass spectroscopy, which detected acrylic polyol and hexamethylene diisocyanate (HDI) trimer. The elemental analysis revealed that the pigment particles are composed of TiO_2. The non-pigmented paint (Sample 2) was provided by Japanese industry. This paint had the similar chemical structure as that detected in the binder component of Sample 1—acrylic urethane—with no additives.

The curing process was the same as that discussed in our previous study (Ishida *et al*., 2019). The thickness of the coating film sample was approximately 30 um and 10 um for the pigmented and non-pigmented samples, respectively. The reason for using such thin film samples was to obtain homogeneously degraded samples with no obvious heterogeneous oxidation.

2.2 Artificial Photo-Aging

Ultraviolet irradiation was performed by simulating the aging conditions by UV irradiation in our lab (Ishida *et al*., 2019). This apparatus effectively controls the sample surface temperature under UV irradiation by blown air to eliminate radiation heat emitted by a metal halide lamp. The lamp was set with wavelengths below 295 nm and was filtered by using borosilicate glass; the light intensity was set at 180 W/m^2 (calculated λ = 300–400 nm). Photo-aging tests were conducted under a surface temperature of 60 °C and low relative humidity (RH) at <10%.

2.3 Characterisation Methods

We performed multi-scale analysis of photodegradation according to the combined results of Fourier transform infrared spectroscopy (FTIR), solvent swelling experiments, ultrasonic measurements of elastic moduli, and colourimetry. The FTIR and solvent swelling experiments were conducted to detect changes in the chemical structure and in the pore structure, respectively, by using the same method as that reported in an earlier study (Ishida *et al*., 2019). Ultrasonic measurements were conducted by using an ultrasonic device (38DL, Olympus, Japan, and the elastic moduli (E) were calculated on the basis of the ultrasonic speed in the materials (Göbel *et al.* 2018) as

$$E = 2\rho v_T^2 + \frac{v_L^2 - 2v_T^2}{v_L^2 - v_T^2}\rho v_T^2 \quad (1)$$

where ρ is the sample density, v_L is the longitudinal wave speed in the samples, and v_T is the transverse wave speed in the samples. Colour measurements were performed by using a spectrophotometer (CM-600d, Konica-Minolta, Japan) with the illuminant set to D65 and the observer set to 10°; the scale selected was L*a*b*. Colour data were illustrated as changes in the yellowness index (YI) according to the ASTM D1925 standard. For evaluating the changes in surface topology, tapping atomic force microscopy (AFM) and scanning electron microscopy (SEM) were applied to the pigmented coatings.

3 Results and Discussions

Firstly, we evaluated the CI change behaviour in the aging process, which is a widely accepted degradation indicator. The CI is calculated as the ratio of the peak areas (C=O vibration and C–H vibration) and is expressed as

$$CI = \frac{A_{C=O}}{A_{C-H}} = \frac{\text{Peak area } (1600\ cm^{-1} - 1850\ cm^{-1})}{\text{Peak area } (2800\ cm^{-1} - 3000\ cm^{-1})} \quad (2)$$

Figure 2 illustrates the CI behaviour for both pigmented and non-pigmented coating samples. Similar behaviours were shown, which indicates little difference in the chemical degradation (oxidation) rates between the two types. This result was expected because the chemical structures of their organic components are essentially the same. We then compared the CI and the macroscopic properties, E and YI. Figure 3 (a) illustrates the changes in E and YI values as a function of photo-aging time. For the pigmented sample, the E values roughly

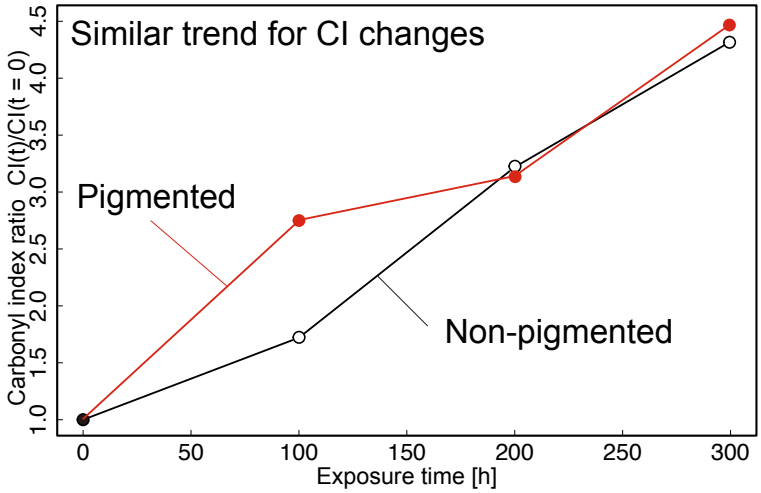

Figure 2. Carbonyl index (CI) as a function of exposure time for pigmented and non-pigmented coatings.

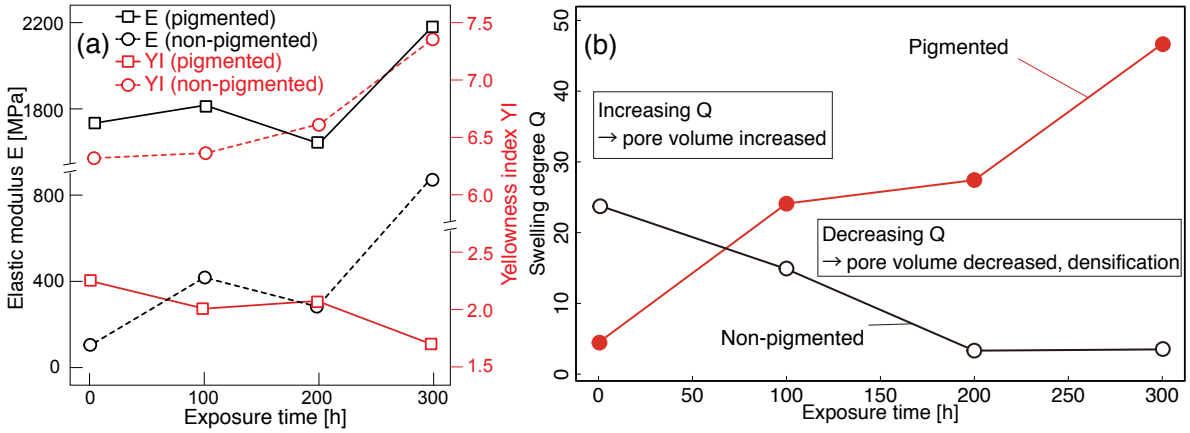

Figure 3. (a) Elastic modulus (E) and yellowness index (YI) as functions of exposure time for pigmented (solid lines) and non-pigmented coatings (dashed lines). (b) Swelling degree (Q) as a function of exposure time for pigmented and non-pigmented coatings.

increased and the YI values decreased with an increase in aging time. For the non-pigmented samples, the E value trend was similar to that in the pigmented samples; however, the YI values were decreased. Although the changes in E value behaviour corresponded with the CI behaviour for both coating types, those in the YI behaviour did not conform with the CI in the pigmented sample. In addition, a decrease in the b* value was observed in degraded pigmented samples, which implies a blue shift (Rosu *et al.*, 2009). Although carbonyl species are well known as typical coloured chemical products, carbonyl growth may not necessarily contribute to yellowing in all pigmented coatings. Figure 4 illustrates the relationship of colour with the absorption wavelength and number of conjugated double bonds for coloured chemical products (Bacaloglu and Stewen, 2001). The results imply differences in the chain length of degraded (oxidised) chemical products between pigmented and non-pigmented coatings, i.e. yellow chemical products from non-pigmented samples had longer conjugated

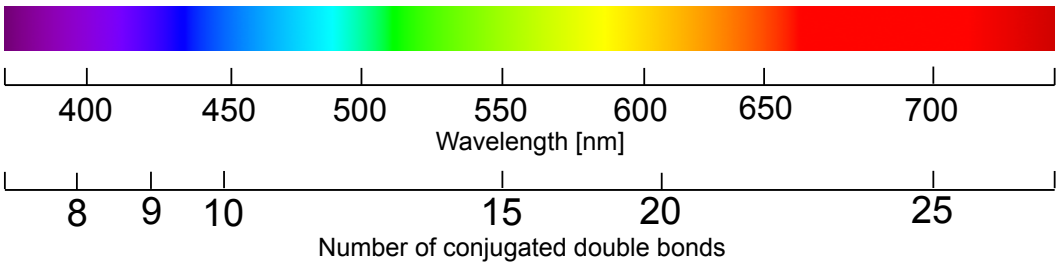

Figure 4. Continuous colour chart and its relationship with wavelength and number of conjugated double bonds.

double bonds than those from pigmented coatings. The photo-catalytic reaction of TiO_2 on pigmented coatings may have increased the efficiency of chain scission compared with that in the non-pigmented coatings. In addition, this effect appears to have influenced even the internal morphological changes in photo-aging. The behaviour of swelling degree showed differences between both coating types, as shown in Figure 3 (b). The swelling degree is derived as the sample volume change ratio before and after immersion in a solvent, which in this case was toluene (Ishida *et al*., 2019), and may be related to the internal total pore volume. The pigmented samples might have become porous because the total pore volume increased for the pigmented coating; however, the pore volume for the non-pigmented coating decreased. This occurred because the organic component (binder) hardened and shrank as a result of extensive cross-linking formation in the photo-aging process, which corresponds with our previous results using positron annihilation spectroscopy and FTIR (Ishida *et al*., 2019). In the pigmented coating, pore generation at the interfacial region between the pigment and the binder might be implied by considering the swelling behaviour combined with the changes in E value behaviour. As shown in Figure 5, surface topology alteration for the pigmented samples further substantiates this inference. We observed pigment particles exposed at the surface and an apparent increase in surface roughness, which correspond to the 'chalking' and 'coating erosion' described by Skaja *et al*. (2006) and Pang *et al*. (2014). Figure 6 summarises these intrinsic differences in the photodegradation mechanisms between the pigmented- and non-pigmented coatings, particularly the internal morphological changes. These apparent differences might be attributed to the two following mechanisms.

- Binder selective decomposition around pigments induced by photo-catalytic reaction, i.e. attacking of ·OH radicals generated from TiO_2 pigment (Pang *et al*., 2014).
- Binder shrinkage accompanied by the release of volatile degradation products (Skaja *et al*., 2006); approximately 10% shrinkage and 15 wt% mass loss were observed in the non-pigmented coating in this study after 300 h of photo-aging.

Neither chalking nor coating erosion occurred on the non-pigmented coatings because these are characteristics of pigmented coatings. Obviously, the interfacial effects occurring at pigment/binder under UV irradiation requires further investigation for better understanding of the photodegradation mechanisms.

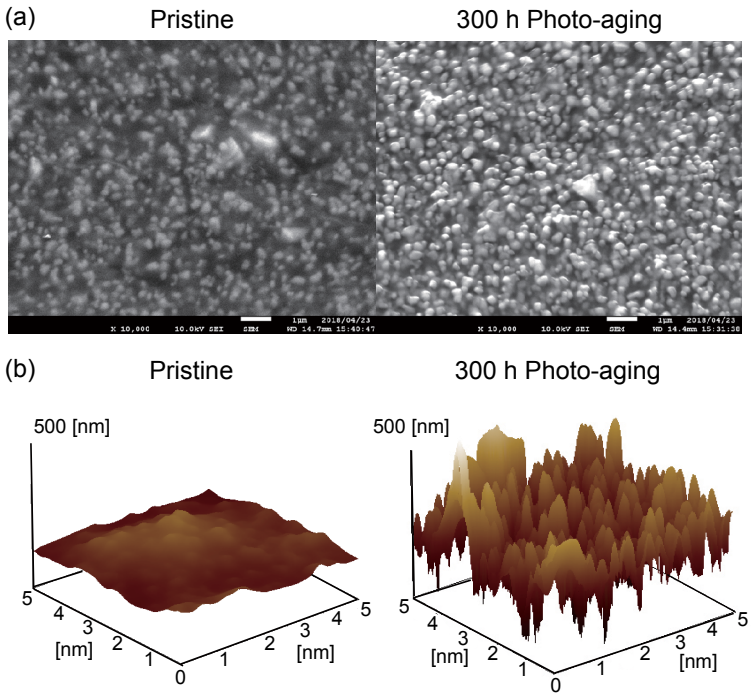

Figure 5. Surface topological changes in pigmented coating before and after photo-aging. (a) SEM images (x10000); (b) tapping AFM images.

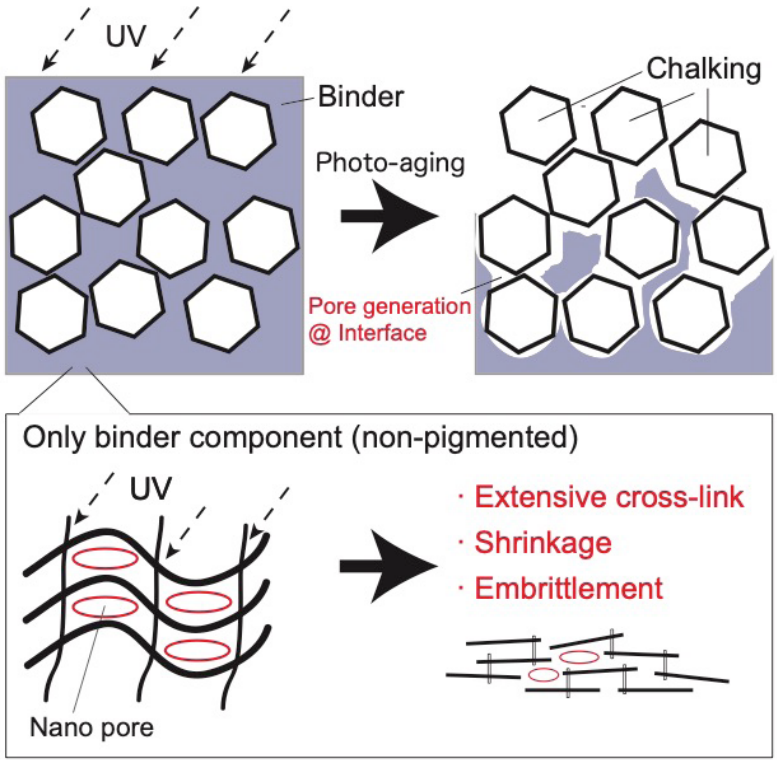

Figure 6. Schematic diagram of the intrinsic differences in the photodegradation mechanisms between pigmented- and non-pigmented coatings in terms of internal morphological changes.

4 Conclusions

Multi-scale analysis of photodegradation was conducted for both pigmented and non-pigmented coatings containing acrylic urethane + TiO_2 pigment and only acrylic-urethane, respectively. We discussed the differences in photodegradation between pigmented and non-pigmented coatings and the effect of the interface between the pigment and the binder.

The CI was increased for both coating types in photo-aging, which implies the progression of chemical degradation (oxidation). However, the changes in macroscopic properties did not necessarily correspond with the CI behaviour. Although the E value increased in accordance with the change in the CI, the YI increased for non-pigmented samples and decreased for pigmented samples, showing showed blue shift. It should be noted that although carbonyl species were produced, they were created by differences in the conjugated double bond length. This implies that the photo-catalytic effect of TiO_2 pigment might have an influence on the photo-oxidative degradation.

Internal morphological alterations were also studied by analysing the swelling behaviour of samples immersed in toluene. The pore volume of the organic component (binder) was decreased, which might be associated with hardening and shrinkage as the result of extensive cross-linking formation in the aging behaviour of the non-pigmented sample. On the contrary, pore generation at the interfacial region at pigment/binder interface was implied in the pigmented coating. In addition, we observed pigment particles exposed at the surface and an apparent increase in surface roughness. These two features, which are referred to as chalking and coating erosion, respectively, are characteristics of pigmented coating. The interfacial effects at the pigment/binder under UV irradiation involves complicated physicochemical processes. Therefore, further investigation and diversified experimental observation are needed for better understanding of the photodegradation mechanisms.

Acknowledgements

This work was supported by a Grant-in-Aid for the Japan Society for the Promotion of Science (JSPS) Fellows (Number 19J20126).

ORCID

Takato Ishida: https://orcid.org/0000-0003-3919-2348
Ryoma Kitagaki: https://orcid.org/0000-0001-6001-3688
Hideaki Hagihara: https://orcid.org/0000-0001-9790-8864
Yogarajah Elakneswaran: https://orcid.org/0000-0001-5496-5551

References

Bacaloglu, R. and Stewen, U. (2001). Study of PVC Degradation Using a Fast Computer Scanning Procedure. *Journal of Vinyl and Additive Technology*, *7*(3), 149–155. doi: 10.1002/vnl.10283

Courvoisier, E., Bicaba, Y. and Colin, X. (2018). Multi-scale and multi-technical analysis of the thermal degradation of poly(ether imide), *Polymer Degradation and Stability*, *147*, 177–186. doi: 10.1016/J.POLYMDEGRADSTAB.2017

Göbel, L., Bos, C., Schwaiger, A., Flohr, A. and Osburg, A. (2018). Micromechanics-based investigation of the elastic properties of polymer-modified cementitious materials using nanoindentation and semi-analytical modeling, *Cement and Concrete Composites*, *88*, 100–114. doi: 10.1016/j.cemconcomp.2018.01.010

Ishida, T., Kitagaki, R., Yamane, S. and Hagihara, H. (2019). Temperature dependence of structural alteration by ultraviolet irradiation in acrylic-urethane coatings studied by positron annihilation spectroscopy and solvent swelling behavior, *Polymer Degradation and Stability*, *162*, 85–93. doi:

10.1016/j.polymdegradstab.2019.02.00

Pang, Y., Watson, S.S. and Sung, L.P. (2014). Surface degradation process affected by heterogeneity in nano-titanium dioxide filled acrylic urethane coatings under accelerated UV exposure, *Polymer*, *55*(25), 6594–6603. doi: 10.1016/J.POLYMER.2014.10.030

Richaud, E., Ferreira, P., Audouin, L., Colin, X., Verdu, J. and Monchy-Leroy, C. (2010). Radiochemical ageing of poly (ether ether ketone), *European Polymer Journal*, *46*(4), 731–743. doi: 10.1016/J.EURPOLYMJ.2009.12.026

Rosu, D., Rosu, L. and Cascaval, C.N. (2009). IR-change and yellowing of polyurethane as a result of UV irradiation, *Polymer Degradation and Stability*, *94*(4), 591–596. doi: 10.1016/j.polymdegradstab.2009.01.01

Rouillon, C., Bussiere, P.O., Desnoux, E., Collin, S., Vial, C., Therias, S. and Gardette, J.L. (2016). Is carbonyl index a quantitative probe to monitor polypropylene photodegradation? *Polymer Degradation and Stability, 128*, 200–208. doi: 10.1016/J.POLYMDEGRADSTAB.2015

Skaja, A., Fernando, D. and Croll, S. (2006). Mechanical property changes and degradation during accelerated weathering of polyester-urethane coatings, *Journal of Coatings Technology and Research*, *3*(1), 41–51. doi: 10.1007/s11998-006-0004-7

XV International Conference on Durability of Building Materials and Components
DBMC 2020, Barcelona
C. Serrat, J.R. Casas and V. Gibert (Eds)

Ionic Diffusivity and Pore Structure of Hardened Cement Paste Exposed to High Temperature Environment for Long Period

Isao Kurashige

Nuclear Fuel Cycle Backend Research Center, Civil Engineering Research Laboratory,
Central Research Institute of Electric Power Industry, 1646 Abiko, Abiko-shi, Chiba, 270-1194, Japan,
kurasige@criepi.denken.or.jp

Abstract. *Ion diffusion through cement-based barrier is key to safe radionuclide transfer in intermediate radioactive waste disposal facilities. The purpose of this research is to elicit the behavior of ionic diffusivity and pore structure of hardened cement paste specimens for the barrier system when exposed to high temperatures (up to 80°C) for long periods (up to one year). The cement paste is made of an ordinary Portland cement base- and a low-heat Portland cement / fly ash / limestone filler (LF) system. The results of the adsorption isotherms of N_2 and water vapor of the specimens exposed to lime-saturated water of different temperatures, 20, 40, 50, 60, and 80°C, are presented, and their pore size distributions are analyzed by the Barrett-Joyner-Halenda method. The change of specific surface areas is measured and the influence of high temperature on the pore structure is discussed. Additionally, results of chloride ionic diffusivity test for the specimens after the high-temperature exposure are contrasted with the tendency of pore structure change. It is found that the LF system has much higher resistance to high-temperature exposure than ordinary Portland cement; however, temperatures greater than or equal to 60°C deteriorate the ionic diffusivity. These experimental results may indicate the ionic diffusivity of hardened cement paste can be influenced by the spatial electrical charge in micropores depending on the electrical charge of pore wall and the ion composition of pore solution.*

Keywords: *Radioactive Waste Disposal, Cement-Based Barrier, High Temperature, Ionic Diffusivity, Hardened Cement, Microstructure.*

1 Introduction

The microstructure of hardened cement with micro- and nano-sized hierarchical pore structure is not fully understood. The amorphous structure of calcium silicate hydrate (C-S-H), which is the main product of the hydration of cement, is considered one of the reasons for that.

The structure of C-S-H can change due to the hydration and polymerization reactions under the influence of temperature (Scrivener, *et al*., 2019). Consequently, changes in the microstructure influences the ionic diffusivity in the hardened cement. Evaluation of ionic diffusivity is also a key issue for the design and assessment of a radioactive waste disposal system with a cement-based barrier. Especially, for disposal of heat exothermic radioactive waste, the influence of high temperature on the performance of a cement-based barrier should be thoroughly examined to build a disposal system with high reliability and safety. The temperature of the action depends on the actual concentration of exothermic radionuclides such as cobalt-60 in nuclear waste, assumed to be around 60°C below the design temperature, to prevent excessive influence of temperature on the disposal system. The duration of the exposure to the high temperature can extend over several decades or hundred years. However, until now, few studies have reported on the influence of long-term high temperature on the ionic diffusivity of hardened cement.

doi:10.23967/dbmc.2020.088

Therefore, it is necessary to gain deeper understanding on the behavior of the hardened cement under the high temperature.

The purpose of this study is to investigate the ionic diffusivity of hardened cement exposed to high temperatures over a long period. From the results of the investigation, we discuss the effectiveness of a prime candidate material for the disposal system. The rest of the manuscript is structured as follows: Section 2 discusses the composition of the hardened cementitious specimens and the experimental methodology (adsorption tests and ion-diffusion test). Section 3 produces experimental results and discusses about the pore structure of the specimens exposed to various temperature levels for one year. It also compares the effect of temperature on Cl^- ion diffusivity with that of the pore structure of hardened cement paste.

2 Materials and Methods

2.1 Materials

The cement-based barrier for the nuclear waste disposal system should be durable and denser, experience little shrinkage, and have low hydration heat among others, for enhancing the barrier performance. In this context, two specimens of cement paste were prepared with a water-binder mass ratio (W/B) of 0.45, as shown in Table 1. The first specimen was made of ordinary Portland cement. The second specimen was made of low-heat Portland cement, which is a mix of siliceous fly ash and lime stone filler (fly ash binder mass ratio (FA/B) = 0.30: lime stone filler powder mass ratio (LS/P) = 0.38). LF30 is a prime candidate mix for the nuclear waste disposal system.

The specimens were cast in molds of 2 × 2 × 8 cm^3 volume. They were then demolded and subsequently stored in a saturated atmosphere at 20°C for one year, for an adequately mature hydration reaction. This is because the high temperature condition in a nuclear disposal facility occurs after the backfill closure of the disposal tunnel. After curing, the specimens were immersed in lime-saturated water at 20, 40, 50, 60, and 80°C for one year.

Table 1. Mix proportions of cement paste.

Mix code	W/B	W/P	FA/B	LS/P
OPC	0.45	0.45	-	-
LF30		0.28	0.30	0.38

2.2 Methods

2.2.1. Nitrogen gas and water vapor adsorption tests

For the adsorption test, the specimens were ground into particles of size 106-500 μm and degassed at 105°C in vacuum for 24 h. Adsorption tests with N_2 gas and water vapor were carried out using Quantachrome instruments autosorb iQ and VSTAR, respectively. The measurement temperatures were 77 K for N_2 adsorption and 293 K for H_2O vapor adsorption.

The pore size distribution (2 nm to 500 μm) was determined by the Barrett-Joyner-Halenda (BJH) method using the N_2 desorption isotherm data. In addition, from adsorption isotherms of N_2 and H_2O, based on the Brunauer-Emmett-Teller theory, under a relative pressure (P/P_0) of 0.05-0.30, the specific surface areas of the specimens were calculated.

2.2.2. Measurement of effective diffusion coefficient of Cl^- ions

The effective diffusion coefficient of Cl^- ions of the specimens after exposure was measured by the steady-state penetration-type diffusion test, with a concentration difference of 1,700 ppm of Cl in lime-saturated NaCl solution at 20°C. Samples for the diffusion test were cut to 2 × 2 × 0.5 cm^3 and saturated in lime water under vacuum for one day. The effective diffusion coefficient was determined when the diffusion was in steady sate. The test time to reach equilibrium was less than six months for OPC and more than one year for LF30.

3 Results and Discussion

3.1 Adsorption Isotherms and Microstructure of Cement Paste

3.1.1. Nitrogen adsorption isotherms

The measured N_2 adsorption isotherms of the OPC and LF30 specimens are shown in Figures 1 and 2, respectively. According to the classification of adsorption isotherms by IUPAC, these isotherms correspond to type IV(a), the type of hysteresis loop in their isotherms have characteristics of both H2(a) and H2(b) as pore blocking/percolation effects and evaporation via cavitation in a relative pressure range of 0.42 to 0.50 are indicated (Cychosz, *et al.*, 2017).

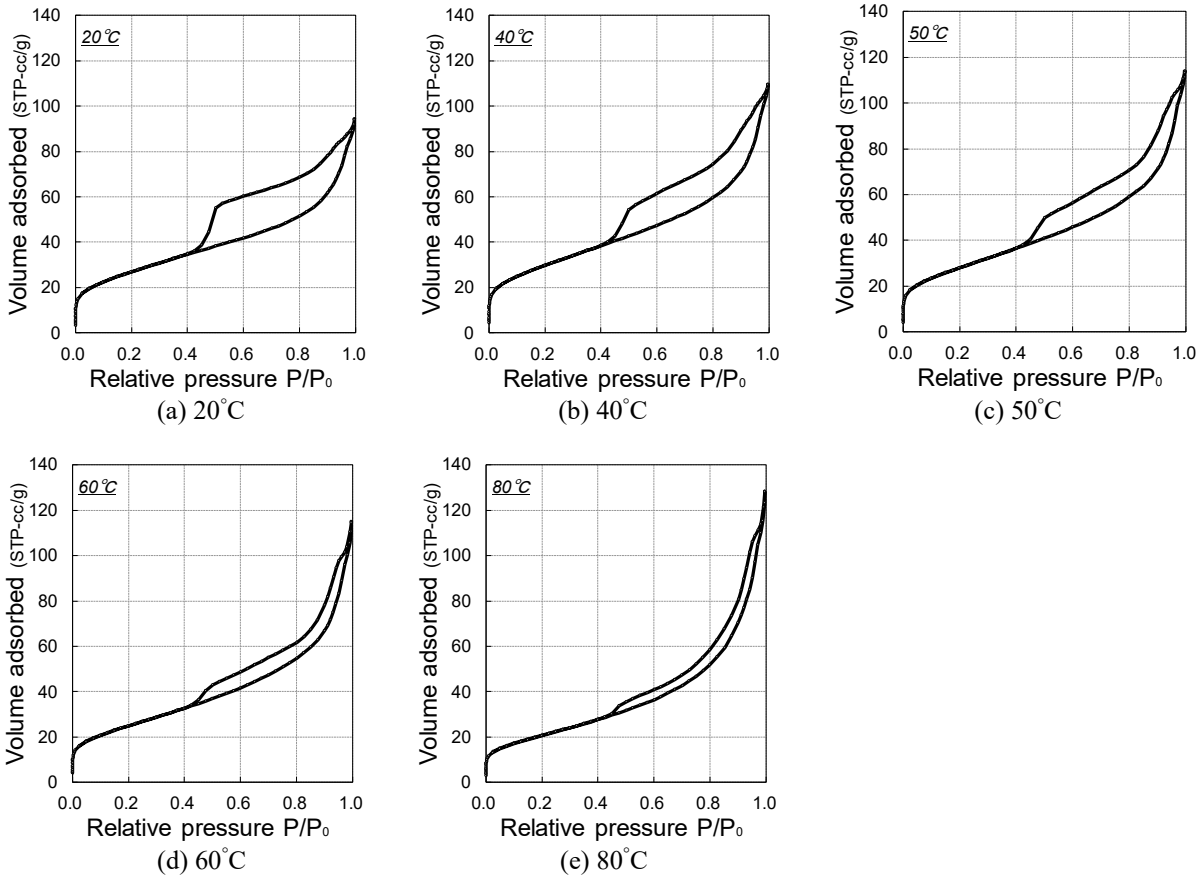

Figure 1. N_2 gas adsorption isotherms of OPC specimens exposed to various temperature conditions.

On the one hand, as shown in Figure 1, it is evident that the level of exposure temperature has a significant impact on the N_2 adsorption isotherms of OPC where higher temperature makes the hysteresis weak and remarkably reduces the desorption volume via cavitation. These changes are presumably due to the coarsening of the pore structure with expanded neck pores as well as a simplified pore network with ink-bottle-shaped pores (Gallucci, *et al.*, 2013). On the other hand, the isotherms of LF30 in Figure 2 are not influenced by the temperature so much as OPC, indicating the superiority of mix proportion of LF30 on resistance to high temperatures. Since solid-state ^{29}Si NMR detected the reaction progress of unreacted fly ash in LF30 during the high temperature exposure, the change for the worse in pore structure of LF30 could be reduced by the healing effect of fly ash.

Figure 3 illustrates pore size distributions determined for the different specimens and temperatures by the BJH method. A clear difference in the pore size distributions of OPC due to the exposure to high temperature can be seen Figure 3 (a), where higher temperature leads to an increase of gel pores around 10 to 50 nm. It should be noted that the sharp peaks at approximately 4 nm do not correspond to the actual pore in the specimens, which is an apparent peak calculated from the drastic evaporation via cavitation. The total pore volumes as well as the change in pore size distribution in LF30 are smaller than those in OPC.

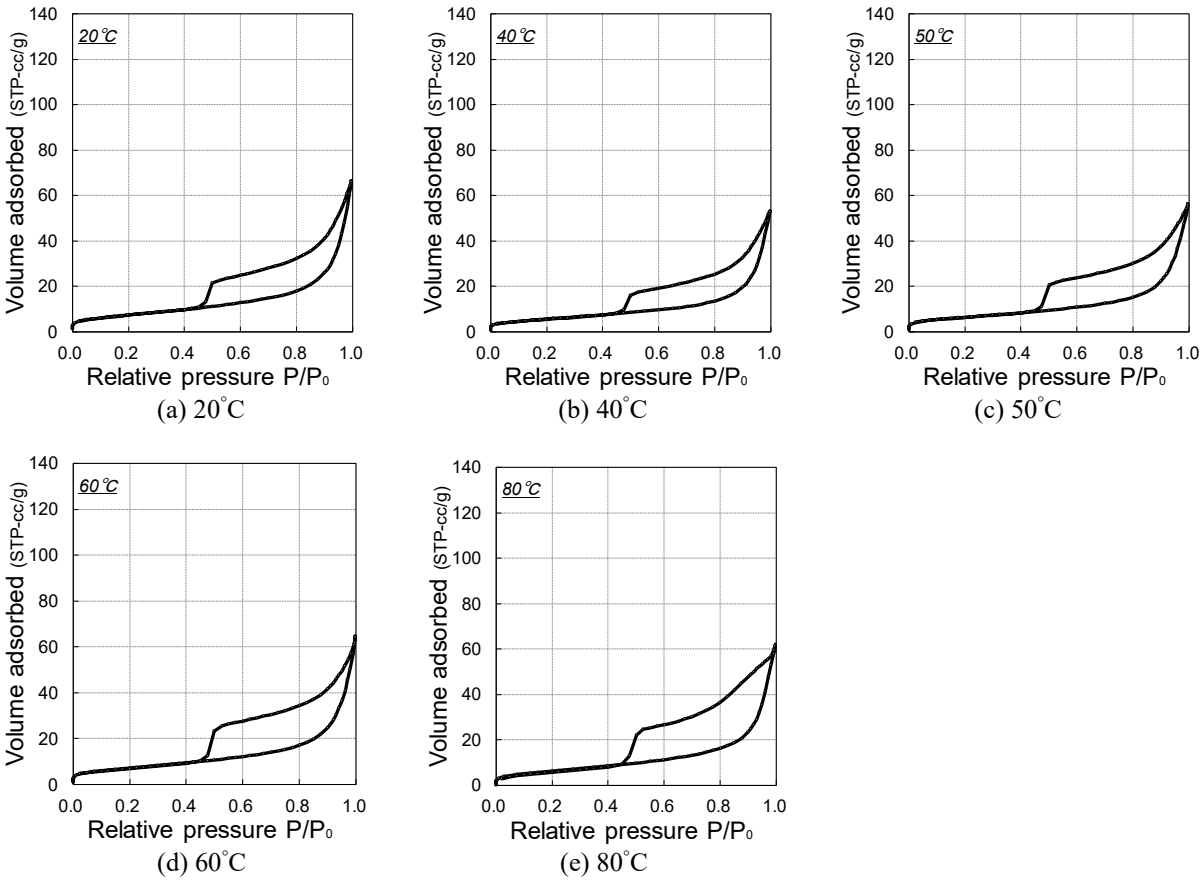

Figure 2. N_2 gas adsorption isotherms of LF30 specimens exposed to various temperature conditions.

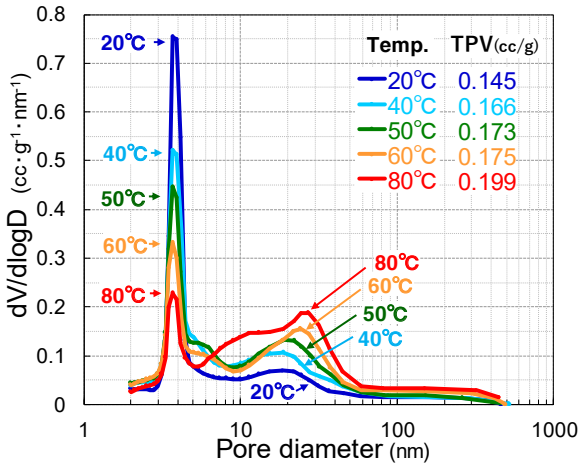

(a) OPC

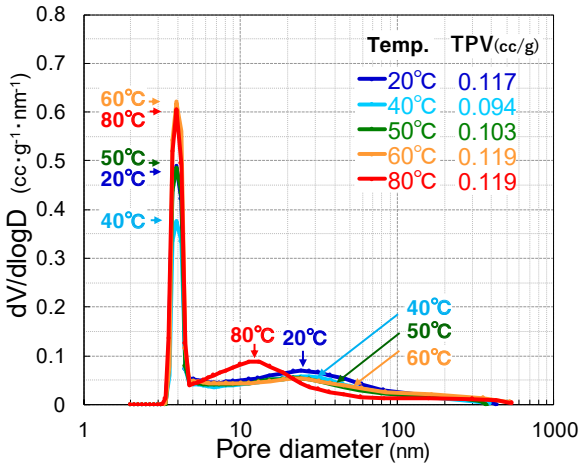

(b) LF30

Figure 3. Pore size distributions calculated from N_2 gas desorption isotherms.

3.1.2. Water vapor adsorption isotherms

Adsorption isotherms of water vapor in Figure 4 show a similar trend with those of the N_2 gas. In the case of OPC, volume of drastic desorption shown at P/P_0 = approximately 0.35 is found to be smaller at the higher temperature, which can be due to the cavitation of water (Maruyama, *et al.*, 2018). The difference in the isotherms of LF30 is found to be smaller than those of OPC. This trend is similar to that of the N_2 gas adsorption isotherms. The adsorption volume remained uniform at $P/P_0 = 0.05$ in the desorption branch of OPC is decreased with higher temperature level. This result indicates that the water retention capacity of the OPC specimens can be degraded by high temperature. By contrast, in the case of LF30, this trend is not clear except at 80°C.

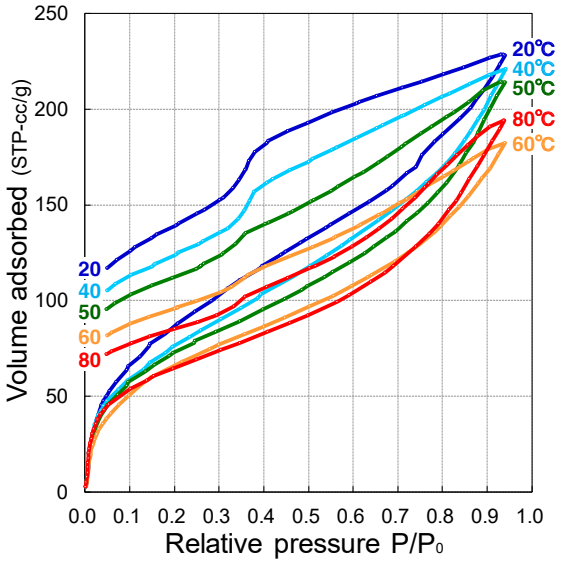

(a) OPC

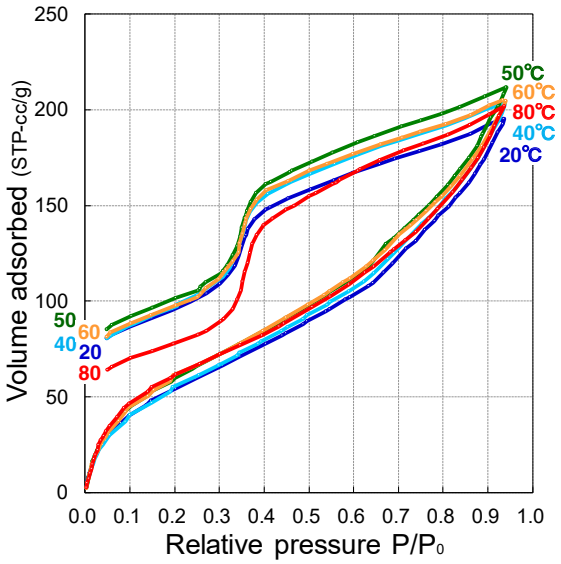

(b) LF30

Figure 4. Water vapor adsorption isotherms of specimens exposed to various temperature conditions.

3.1.3. Specific surface area

BET surface areas of N_2 and H_2O for all specimens can be compared in Figure 5. Water molecules smaller than N_2 molecules can access narrower pores than the accessible size (approximately 0.45 nm diameter calculated from the cross-section area of N_2 molecule). Therefore, from Figure 5, BET surface areas of H_2O for any specimens is larger than that of N_2. The decrease in the BET areas of N_2 and H_2O for OPC when exposed to high temperature was caused by polymerization of the silicate chains in C-S-H (Gallucci, *et al.*, 2013), which was

detected by the NMR measurement. In contrast, in the case of LF30, there were no significant changes in the BET surface areas. However, as with OPC, the NMR detected the polymerization of C-A-S-H under higer temperature.

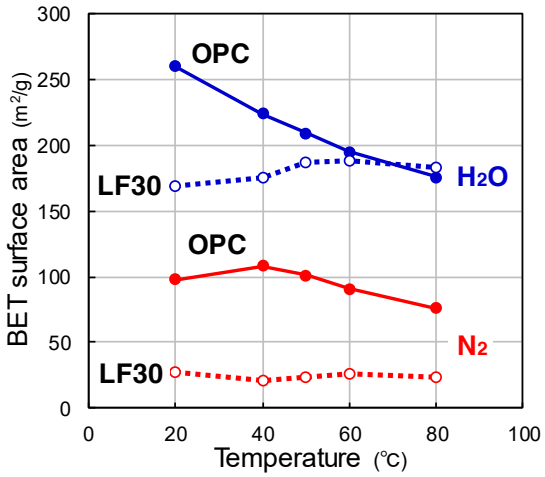

Figure 5. BET surface areas obtained from N_2 gas and water vapor adsorption isotherms.

3.2 Chloride Ionic Diffusivity

The effective diffusion coefficient of Cl^- ions, D_{cl} in the specimens are shown in Figure 6. The results revealed that D_{cl} of LF30 is nearly four orders of magnitude lower than that of OPC, when exposed to temperatures below 50°C. On the other hand, the influence of temperature varied with the specimen; higher the temperature, larger the D_{cl} of OPC. On the other hand, D_{cl} of LF30 slightly increased at 60°C and significantly at 80°C. This increase of does not agree with the trend of change in pore structure shown in subsection 3.1. Hence, a clear understanding about the mechanism of this phenomenon is needed. It is recognized that the incorporation of aluminum in fly ash modifies the structure of C-S-H (C-A-S-H) and also the surface charge (L'Hopital, *et al.*, 2015). Moreover, the surface charge and ionic composition in pore solution have a strong influence on the ionic diffusion through hardened cement, especially when the microstructure is very dense (Yang, *et al.*, 2019). Furthermore, the decomosition of AFt and AFm phases and its influence on the ionic compositon in pore solution and ionic diffusivity should be discussed for this mix proportion and materials.

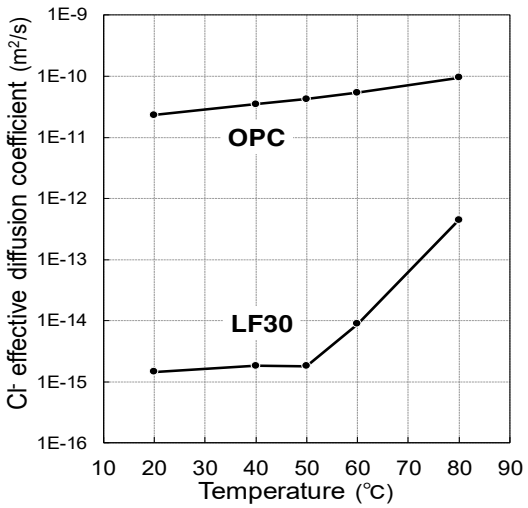

Figure 6. Effective diffusion coefficients of Cl^- ions.

4 Conclusions

- In the case of OPC, the pore size distribution determined from N_2 gas desorption isotherms using the BJH method shows obvious temperature-dependent coarsening of the microstructure of hardened cement. In the case of LF30, temperature had a negligible influence on the microstructure, except at 80°C.
- BET surface area of OPC calculated from N_2 gas and water vapor adsorption isotherms decreased with temperature. In contrast, the BET surface area of LF30 had low sensitivity to temperature.
- The Cl^- ionic diffusion coefficient of OPC increased with temperature. The coefficient of LF30 is nearly four orders of magnitude lower than that of OPC below 50°C. However, the value slightly increased at 60°C and significantly at 80°C.

ORCID

Isao Kurashige: http://orcid.org/0000-0002-2773-0885

References

Cychosz, K.A., Guillet-Nicolas, R., Garcia-Martinez, J. and Thommes, M. (2017). Recent advances in the textural characterization of hierarchically structured nanoporous materials. *Royal Society of Chemistry*, 46, 389-414.

Gallucci, E., Zhang, S. and Scriviner, K. (2013). Effect of temperature on the microstructure of calcium silicate hydrate (C-S-H), *Cement and Concrete Research*, 53, 185-195.

L'Hopital, E., Lothenbach, E., Le Saout, G., Kulik, D. and Scrivener, K. (2015). Incorporation of aluminium in calcium-silicate-hydrates, *Cement and Concrete Research*, 75, 91-103.

Maruyama, I., Rymes, J., Vandamme, M. and Coasne, B. (2018). Cavitation of water in hardened cement paste under short-term desorption measurements, *Materials and Structures*, 51, 159.

Scrivener, K., Ouzia, A., Juilland, P. and Mohamed, A.K. (2019). Advances in understanding cement hydration mechanisms, *Cement and Concrete Research*, 124, 105823.

Ynag, Y., Patel, R.A., Churakov, S.V., Prasianakis, N.I., Kosakowski, G. and Wang, M. (2019). Multiscale modeling of ion diffusion in cement paste: electrical double layer effects, *Cement and Concrete Composites*, 96, 55-65.

XV International Conference on Durability of Building Materials and Components
DBMC 2020, Barcelona
C. Serrat, J.R. Casas and V. Gibert (Eds)

Monitoring Durability of Limestone Cement Paste Stored at Conditions Promoting Thaumasite Formation

Konstantinos Sotiriadis[1], Michal Hlobil[1], Jaromír Toušek[2], Dita Machová[1], Petra Mácová[1], Michal Vopálenský[1] and Alberto Viani[1]

[1] Institute of Theoretical and Applied Mechanics of the Czech Academy of Sciences, Prosecká 809/76, 19000 Prague 9, Czechia, sotiriadis@itam.cas.cz

[2] CEITEC – Central European Institute of Technology, Masaryk University, Kamenice 5/A4, 62500 Brno, Czechia, tousek@chemi.muni.cz

Abstract. *The durability of Portland-limestone cement with high limestone content was monitored at conditions promoting thaumasite formation. Pore structure and deterioration characteristics were assessed with X-ray micro-computed tomography and correlated with material's strength. Changes in crystalline and amorphous phases of the cement paste were investigated with X-ray powder diffraction and solid state nuclear magnetic resonance spectroscopy. Rapid deterioration was observed, evolving as a front causing concentric crack patterns followed by detachment of the part of specimen in contact with the corrosive solution. This ultimately led to loss of structural integrity after 4 months of exposure. During sulfate attack, thaumasite, ettringite and gypsum formed at the expense of portlandite, calcite and monocarboaluminate hydrate. Furthermore, polymerization of silicate chains in C-S-H and deterioration of C-S-H also occurred.*

Keywords: *Limestone Cement, Thaumasite Sulfate Attack, Microstructure, Solid State NMR Spectroscopy, X-Ray Micro-Computed Tomography.*

1 Introduction

Portland-limestone cements (EN 197-1:2011), developed as alternative to ordinary Portland cement, are characterized by competitive properties and lower environmental impact (Tsivilis *et al.*, 2000; Worrell *et al.*, 2013). These features are in line with the global trend towards the reduction of CO_2 emissions and energy needs of the cement production process, and with the rationalization of raw materials usage as well. However, the high limestone content increases the risk for a specific type of sulfate attack, occurring at low temperature and excess humidity. Under such conditions, sulfate and carbonate ions react with calcium silicate hydrates (C─S─H), leading to the formation of thaumasite ($CaSiO_3 \cdot CaCO_3 \cdot CaSO_4 \cdot 15H_2O$) and, subsequently, to the deterioration of the hardened material (Irassar, 2009).

Long-term mechanical performance of limestone cement concrete exposed to conditions promoting this type of chemical attack is, thus, a crucial issue in real structures. A model able to predict the mechanical properties of cementitious materials in sulfate-bearing environments would allow for optimizing concrete composition both in terms of durability and environmental impact. Aiming at the development of a predictive mathematical model, this study is focused on obtaining necessary data concerning the microstructure and strength of the material.

Insights into the pore structure of Portland-limestone cement paste specimens were obtained with X-ray micro-computed tomography (XmCT), following an approach similar to previous studies (Yang *et al.*, 2018; Ma *et al.*, 2018). Paste compressive strength was correlated with the

damage observed in the specimens. Changes in phase composition were monitored with X-ray powder diffraction (XRPD) with the Rietveld method and solid state nuclear magnetic resonance spectroscopy (ssNMR); the usage of these techniques allowed for assessing both crystalline and amorphous fraction of the hardened cement paste (Álvarez-Pinazo *et al.*, 2012; Richardson *et al.*, 2010).

2 Experimental

2.1 Materials

Portland-limestone cement paste was produced (water-to-cement ratio of 0.45) employing a commercial CEM II/B-LL cement (Cement Hranice, a.s.), and casted in the form of cylinders (d=20 mm; h=50 mm). The paste remained in the molds for 24h. After demolding, the specimens were water-cured for 27 days, and then exposed to magnesium sulfate solution (S) of 20 g/L SO_4^{2-} content until loss of structural integrity, and in water (W) as reference, both at 5 °C.

2.2 Tests

Tests were performed after initial curing (at 28 days) and then regularly on specimens stored in magnesium sulfate solution and water.

Cylinders were scanned with the custom developed patented Twinned Orthogonal Adjustable Tomograph (TORATOM), made up of two imaging axes, each bearing an X-ray tube and a detector, with a shared rotational stage. In this study, the configuration involved a reflection-type cone-beam XWT-240-SE tube (X-ray WorX, Germany) (190 kV and 132 μA; power output of 25.1 W at the target), and a Dexela 1512 NDT detector (Perkin Elmer, USA) (active area of 1944 × 1536 pixels; 74.8 μm pixel size). Scans were performed on one specimen for each exposure environment and storage period. Aiming at sufficient magnification for providing pixel size between 12 and 17 μm, the source-to-sample distance and sample-to-detector distance were properly adjusted. A total number of 3200 projections were collected for each tomographic scan, which were flat-field corrected. VG Studio Max software was employed to obtain 3D models, using filtered back projection algorithm. Visualization of the data acquired was accomplished with ImageJ software. Quantitative image analysis of the cement matrix was carried out on volumes of interest, cut from the original volume and excluding large defects (pores, cracks), using Pore3D software which allowed for deriving porosity, specific surface area of pores (S_v), and integral of mean curvature of pores (M_v).

Compressive strength tests were performed on five specimens for each exposure environment and storage period. The results are the average values from five measurements.

Fractions from cylinders stored in water, and material obtained from the deteriorated surface of the specimens exposed to magnesium sulfate solution, were powdered (particle size below 63 μm) and employed for XRPD and ssNMR spectroscopy measurements. One specimen stored in water and eight specimens stored in sulfate solution, were used for each storage period.

XRPD data were collected with a Bruker D8 Advance diffractometer [CuKα radiation (λ = 1.5418 Å)] in the angular range 5–80° 2θ, at 40 kV and 40 mA. Rietveld refinements of the XRPD patterns were performed with the TOPAS 4.2 software (Bruker AXS), allowing for quantitative phase analysis (QPA). The internal standard method was applied for determining

the amorphous fraction.

One-pulse ^{29}Si MAS NMR spectra were collected at 25 °C with a Bruker Avance-Neo 500 spectrometer (magnetic field of 11.75 T), using a 4-mm CP/MAS probe at the Larmor frequency of 99.4 MHz. Samples were loaded into a zirconium oxide rotor (4 mm in diameter) spinning at 12.5 kHz. As external reference, 4,4-dimethyl-4-silapentane-1-sulfonic acid (DSS) (0.0 ppm) was used. 10000 scans were recorded during each measurement with 4.0 μs pulse length, and 20 s relaxation delay. Components of ^{29}Si MAS NMR spectra were deconvoluted with PeakFit 4.12 software (Systat Software).

3 Results and Discussion

Sulfate attack resulted in rapid disintegration of the specimens; structural integrity was lost already after 3.5─4 months, not allowing for performing further compressive strength tests. XRPD and ssNMR measurements on samples obtained from the deteriorated part of the specimens continued up to 5 months.

In Figure 1, cross sectional XmCT slices of specimens exposed for 3 (left) and 4 (right) months to magnesium sulfate solution, are illustrated. The deterioration proceeded through the formation of concentric cracks, as indicated by the white arrows, resulting in expansion of the specimen and, eventually, detachment of the damaged part. As the process evolved, concentric cracks formed closer to the center of the cylinder, pointing to a layer-type deterioration.

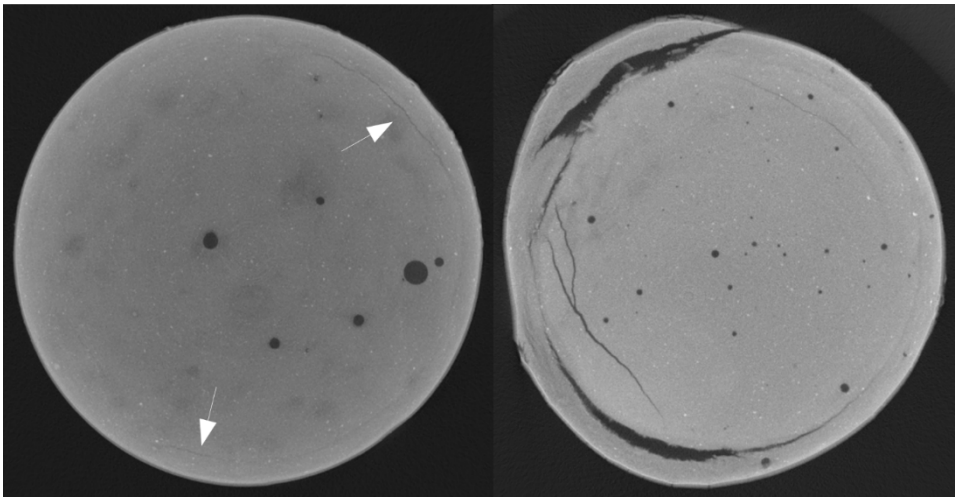

Figure 1. Cross sectional XmCT images of specimens exposed to magnesium sulfate solution for 3 months (left) and 4 months (right); white arrows indicate cracks formed due to sulfate attack.

Quantitative image analysis of the reconstructed volumes allowed for obtaining detailed information about the microstructure of the specimens. The values determined for porosity, S_v and M_v are summarized in Table 1. They indicate that the microstructure of the sound part of specimens exposed to S solution resembles to that of the specimens stored in W, supporting the assumption that sulfate attack proceeded as a deterioration front moving from the surface to the center of the specimen. Although attention was paid for excluding large defects during analysis, slightly higher average values were calculated for the specimens stored in S solution. Considering that entrapped air should be on average the same in all samples, random

irregularities in the matrix of the deteriorated specimens were most likely included in the reconstructed volumes processed, affecting the results.

Table 1. Numerical results derived from quantitative analysis of XmCT images relative to the sound part of the specimens (S_v: specific surface area of pores; M_v: integral of mean curvative of pores).

	Specimens exposed to W			Specimens exposed to S		
Exposure period (months)	Porosity (%)	S_v (mm^{-1})	M_v (mm^{-2})	Porosity (%)	S_v (mm^{-1})	M_v (mm^{-2})
REF	0.26	0.34	36.28	—	—	—
1	0.34	0.85	529.71	0.78	1.50	215.11
2	0.39	0.86	536.45	0.70	1.48	457.38
3	0.65	0.95	66.25	0.64	2.82	606.24
4	1.02	1.55	193.24	0.49	1.20	214.76
Average	0.53	0.91	272.39	0.65	1.75	373.37

In Figure 2, the compressive strength of the specimens exposed to sulfate solution relative to that measured for the specimens stored in water, is presented. Although the damage is not extensive at 3 months (Figure 1), the specimens had lost already 55% of their strength by this time, pointing to a rapid decline of compressive strength due to deterioration.

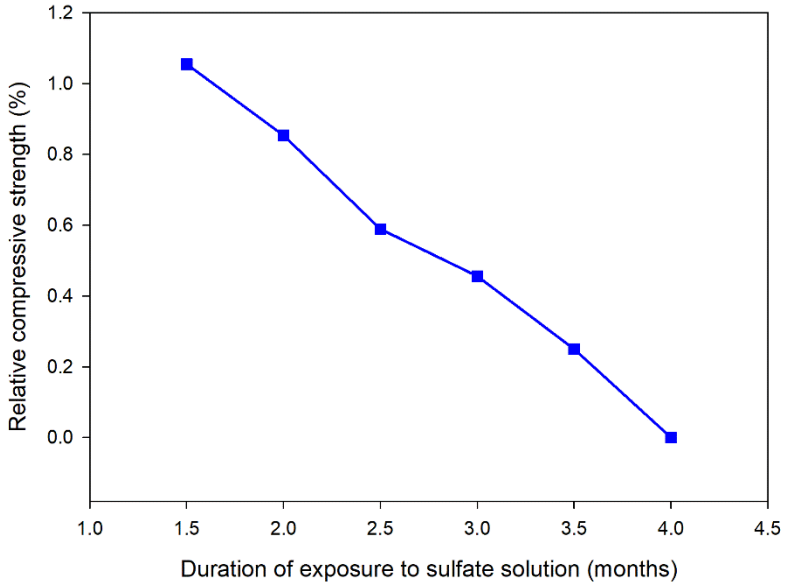

Figure 2. Relative compressive strength of specimens exposed to sulfate solution and water.

QPA results are summarized in Table 2. Decreasing amounts of belite were detected in the specimens stored in water, contrary to the other clinker phases which are absent already at 3 months. Large quantities of portlandite and traces of hydrogarnet were detected in these specimens. Gypsum was consumed towards ettringite formation. Reduction in calcite content and formation of carboaluminate hydrates indicated the participation of calcite in the hydration process of cement. During sulfate attack, ettringite content increased, whilst gypsum and thaumasite formed. The formation of these minerals is directly linked to the consumption of

portlandite and carboaluminates, and to the decrease in calcite content. Sulfate attack led to significant reduction of the amorphous fraction, pointing to severe degradation of calcium silicate hydrate phase, which is the main amorphous component of the hardened cement paste. The presence of brucite was inherited from the magnesium content of the corrosive solution.

Table 2. Quantitative phase analysis (wt.%) of the cement used, of the samples obtained from specimens exposed to W, and from the deterioated part of spesimens exposed to S.

Phase	Cement	Exposure period to W (months)			Exposure period to S (months)		
		3	4	5	3	4	5
Alite	32.5	–	–	–	–	–	–
Belite	6.0	1.0	1.4	0.7	–	–	–
C_3A	2.5	–	–	–	–	–	–
Brownmillerite	3.9	–	–	–	–	–	–
Hydrogarnet	–	<1.0	<1.0	<1.0	–	–	–
Monocarboaluminate	–	3.6	3.4	3.4	–	–	–
Hemicarboaluminate	–	<0.5	<0.5	<0.5	–	–	–
Portlandite	–	12.6	11.6	10.4	<0.5	<0.5	<0.5
Gypsum	3.2	–	–	–	26.8	38.3	39.3
Ettringite	–	6.1	5.5	5.8	7.6	7.2	9.2
Thaumasite	–	–	–	–	4.5	1.1	2.3
Calcite	22.7	13.4	16.0	16.8	7.1	8.8	9.5
Brucite	–	–	–	–	3.5	2.8	2.7
Amorphous	29.0	62.0	61.0	62.0	50.0	42.0	36.7

One-pulse ^{29}Si MAS NMR spectra are illustrated in Figure 3.

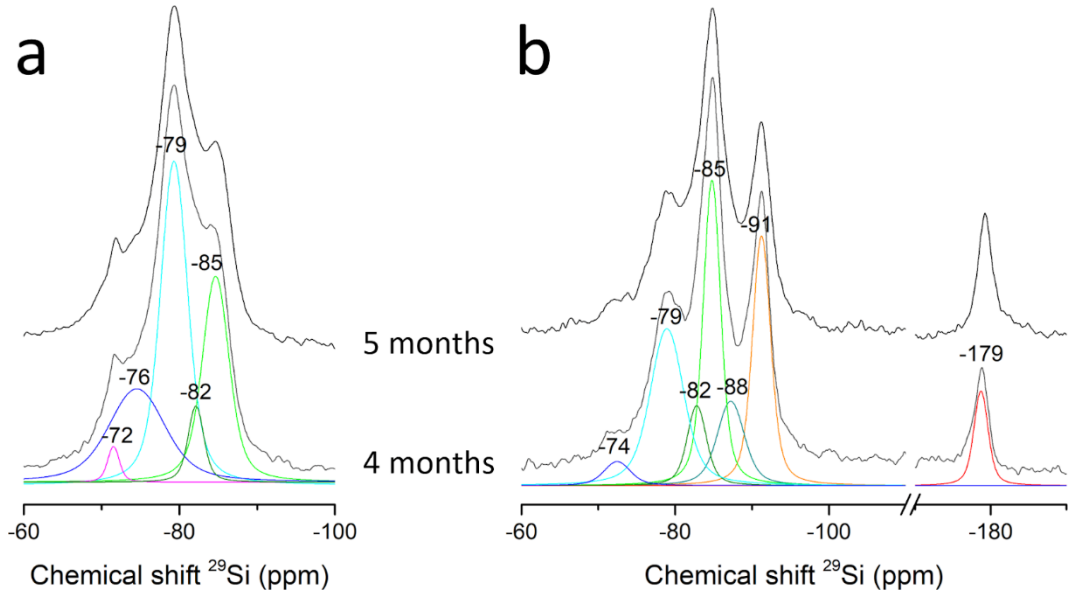

Figure 3. ^{29}Si MAS NMR spectra collected at 4 and 5 months for specimens stored in water (a) and for samples obtained from the deteriorated surface of specimens exposed to magnesium sulfate solution (b). Black curves: experimental spectra; Colored curves: deconvoluted spectra.

Five components were detected in the water-cured specimens with isotropic chemical shifts at around ─85 ppm, ─82 ppm, ─79 ppm, ─76 ppm and ─72 ppm. The first three values correspond to Q^2, Q^2(1Al) and Q^1 species, respectively, which are characteristic for the C─S─H phase (Walkley and Provis, 2019; Richardson *et al.*, 1993; Kunther *et al.*, 2015). The quite broad component at ─76 ppm is in close proximity to the isotropic chemical shift values assigned to anhydrated alite grains (Rawal *et al.*, 2010), indicating an amorphous environment which is related to hydrated clinker grains. The isotropic chemical shift at ─72 ppm is characteristic of unreacted belite (Andersen *et al.*, 2003), in agreement with XRPD results.

Q^2, Q^2(1Al) and Q^1 species were also identified in the samples obtained from the deteriorated surface of specimens exposed to S solution. Another component at around ─88 ppm, attributed to bridging SiO_4 tetrahedra in C─S─H connected to each other through hydrogen bonding (Q^2_u species) (L' Hôpital *et al.*, 2015), was identified in these samples. In addition, two more components were detected; one at ─179 ppm assigned to SiO_6 group, which is characteristic of the thaumasite structure (Grimmer *et al.*, 1986), and another at ─91 ppm which is attributed to Q^3(1Al) species in cross-linked aluminosilicate chains (Richardson *et al.*, 2010). The presence of both components points to deterioration of C─S─H phase during sulfate attack. The broad shape of the component at around ─73 ppm, most likely, corresponds to partially hydrated clinker phases, since there is no indication of anhydrated grains in the XRPD patterns. Quantitative results derived from the deconvolution of spectra are reported in Table 3.

Table 3. Intergrated area (%) derived from component deconvolution of ^{29}Si MAS NMR spectra.

		Exposure period to W		Exposure period to S	
Isotropic chemical shift (ppm)	Component	4 months	5 months	4 months	5 months
─179	SiO_6	─	─	6.6	10.0
─91	Q^3(1Al)	─	─	21.8	19.2
─88	Q^2_u	─	─	10.9	12.9
─85	Q^2	26.1	25.2	25.5	23.4
─82	Q^2(1Al)	5.7	5.1	7.4	7.9
─79	Q^1	41.4	39.4	24.9	22.8
─76	Q^1	24.9	28.6	─	─
─74	Q^1	─	─	3.0	3.7
─72	Q^0 (belite)	2.0	1.7	─	─

Minor differences were observed between samples obtained from specimens exposed for 4 and 5 months to the same environment. The main observation, regarding the water-cured specimens, is the increase of the component at ─76 ppm and the decrease of the one at ─72, indicating the ongoing hydration of clinker. In samples obtained from deteriorated specimens, the increase in the content of SiO_6 component with time is related to the increase of thaumasite content, as confirmed by XRPD (Table 2). Comparison of the sulfate-affected specimens with those stored in water reveals that, besides thaumasite formation, sulfate attack led to consumption of Q^0 phases and polymerization of silicate chains (formation Q^2, Q^2_u and Q^3(1Al) species at the expense of Q^1).

4 Conclusions

- The aggressive chemical environment employed in the study produced intense deterioration of the limestone cement paste specimens, which resulted in the rapid decline of compressive strength.
- Deterioration proceeded as a front that initiated through the formation of concentric crack patterns, followed by detachment of the sulfate-affected external part from the sound core.
- Thaumasite, ettringite and gypsum formed during sulfate attack at the expense of portlandite, calcite, monocarboaluminate hydrate and C─S─H; gypsum was the most abundant deterioration product, whose quantity increased with time.
- Sulfate attack promoted polymerization of silicate chains in C─S─H (increase of Q^2 and increase of Q^1 species), and extensive deterioration of C─S─H phase as indicated from the presence of Q^3(1Al) component.
- The collected quantitative data will be employed in the development of a micromechanical model for predicting mechanical properties of cementitious materials exposed to thaumasite sulfate attack.

Acknowledgements

The study was performed within the project "Experimental quantification and modelling of deterioration in Portland-limestone cement pastes affected by thaumasite sulfate attack" (grant number 18-26056Y), supported by the Czech Science Foundation (GAČR). CIISB research infrastructure project LM2015043 funded by Ministry of Education, Youth and Sports of the Czech Republic is gratefully acknowledged for the financial support of the measurements at the CF Josef Dadok National NMR Centre.

ORCID

Konstantinos Sotiriadis: http://orcid.org/0000-0002-9848-4028
Michal Hlobil: http://orcid.org/0000-0001-5818-7320
Jaromír Toušek: http://orcid.org/0000-0002-3231-2370
Dita Machová: http://orcid.org/0000-0001-9956-7282
Petra Mácová: http://orcid.org/0000-0002-8277-133X
Michal Vopálenský: http://orcid.org/0000-0002-9932-6486
Alberto Viani: http://orcid.org/0000-0002-6019-1094

References

Álvarez-Pinazo, G., Cuesta, A., Garcia-Maté, M., Santacruz, I., Losilla, E.R., La Torre, A.G.D., León-Reina, L. and Aranda, M.A.G. (2012). *A practical guide to microstructural analysis of cementitious materials.* Boca Raton, FL: CRC Press.

Andersen, M.D., Jakobsen, H.J. and Skibsted, J. (2004). Characterization of white Portland cement hydration and the C-S-H structure in the presence of sodium aluminate by ^{27}Al and ^{29}Si MAS NMR spectroscopy *Cement and Concrete Research*, *34*(5), 857–868. doi: 10.1016/j.cemconres.2003.10.009

EN/TC 51/WG 6 (2011). *EN 197-1: Cement — Part 1: Composition, specifications and conformity criteria for common cements*.

Grimmer, A.R., von Lampe, F. and Mägi, M. (1986). Solid-state high-resolution ^{29}Si MAS NMR of silicates with sixfold coordinated silicon *Chemical Physics Letters*, *132*(6), 549–553. doi: 10.1016/0009-2614(86)87122-6

Irassar, E.F. (2009). Sulfate attack on cementitious materials containing limestone filler – A review *Cement and Concrete Research*, *39*(3), 241–254. doi: 10.1016/j.cemconres.2008.11.007

Kunther, W., Lothenbach, B. and Skibsted, J. (2015). Influence of Ca/Si ratio of the C-S-H phase on the interaction with sulfate ions and its impact on the ettringite crystallization pressure *Cement and Concrete Research*, *69*,

37–49. doi: 10.1016/j.cemconres.2014.12.002

L' Hôpital, E., Lothenbach, B., Le Saout, G. and Kulik, D. (2015). Incorporation of aluminium in calcium-silicate-hydrates *Cement and Concrete Research*, *75*, 91–103. doi: doi:10.1016/j.cemconres.2015.04.007

Ma, X., Çopuroğlu, O., Schlangen, E., Han, N. and Xing, F. (2018). Expansion and degradation of cement paste in sodium sulfate solutions *Construction and Building Materials*, *158*, 410–422. doi: 10.1016/j.conbuildmat.2017.10.026

Rawal, A., Smith, B.J., Athens, G.L., Edwards, C.L., Roberts, L., Gupta, V. and Chmelka, B.F. (2010). Molecular silicate and aluminate species in anhydrous and hydrated cements *Journal of the American Chemical Society*, *132*(21), 7321–7337. doi: 10.1021/ja908146m

Richardson, I.G., Brough, A.R., Brydson, R., Groves, G.W. and Dobsont, C.M. (1993). Location of aluminum in substituted calcium silicate hydrate (C-S-H) gels as determined by ^{29}Si and ^{27}Al NMR and EELS *Journal of the American Ceramic Society*, *76*(9), 2285–2288. doi: 10.1111/j.1151-2916.1993.tb07765.x

Richardson, I.G., Skibsted, J., Black, L. and Kirkpatrick, R.J. (2010). Characterization of cement hydrate phases by TEM, NMR and Raman spectroscopy *Advances in Cement Research*, *22*(4), 233–248. doi: 10.1680/adcr.2010.22.4.233

Tsivilis, S., Batis, G., Chaniotakis, E., Grigoriadis, G. and Theodossis, D. (2000). Properties and behavior of limestone cement concrete and mortar *Cement and Concrete Research*, *30*(10), 1679–1683. doi: 10.1016/S0008-8846(00)00372-0

Walkley, B. and Provis, J.L. (2009). Solid-state nuclear magnetic resonance spectroscopy pf cements *Materials Today Advances*, *1*, 100007. doi: 10.1016/j.mtadv.2019.100007

Worrell, E., Kermeli, K. and Galitsky, C. (2013). *Energy efficiency improvement and cost saving opportunities for cement making: An ENERGY STAR ® guide for energy and plant managers*. Berkeley, CA: Lawrence Berkeley National Laboratory.

Yang, Y., Zhang, Y., She, W., Liu, N. and Liu, Zh. (2018). In situ observing the erosion process of cement pastes exposed to different sulfate solutions with X-ray computed tomography *Construction and Building Materials*, *176*, 556–565. doi: 10.1016/j.conbuildmat.2018.05.093

XV International Conference on Durability of Building Materials and Components
DBMC 2020, Barcelona
C. Serrat, J.R. Casas and V. Gibert (Eds)

Non-Destructive Evaluation of Micro-Cracked SCC by Ultrasonic Waves

Irene Palomar[1], Gonzalo Barluenga[1], Hugo Varela[1], Javier Puentes[2] and Ángel Rodríguez[3]

[1] Department of Architecture, University of Alcala, Madrid, Spain, irene.palomar@uah.es; gonzalo.barluenga@uah.es; hugo.varela@edu.uah.es

[2] Institute of Construction Sciences Eduardo Torroja, CSIC, Spain, javier.puentes@ietcc.csic.es

[3] Systems Engineering and Automation Dept., University Carlos III of Madrid, Spain, angrodri@ing.uc3m.es

Abstract. *Self-Compacting Concrete (SCC) is an effective, reliable and safer technology to cast-in-place concrete structures. However, the large amount of paste required to achieve its high flowability may increase drying shrinkage at early age, due to the undesirable effects of curing conditions, producing micro-cracking and damaging concrete members. When this happens, an evaluation of the hardened SCC is necessary and Non-destructive testing techniques (NDT) can be suitable. Among NDT, Ultrasonic pulses (US) have showed to be very useful due to its portability, easiness of application and sensitivity to changes in material microstructure, porosity and presence of defects. In order to evaluate the applicability of ultrasonic (US) waves to better understand the relations among composition, microstructure, properties, curing conditions and micro-cracking, an experimental program using transmission P- and S- waves was carried out on SCC with limestone filler (LF), microsilica (MS) and nanosilica (NS), set and hardened under different curing conditions: 10, 20 and 30 °C and 40 and 80 % relative humidity. Free shrinkage and double displacement restrained slabs were tested and cracking potential due to Early Age Shrinkage was assessed. Ultrasonic transmission time and wave amplitude of the raw US signal were measured and Ultrasonic pulse velocity (UPV) and attenuation coefficient were calculated. In addition, some physical and mechanical properties of cracked and un-cracked samples were measured. The aim of this study was to compare US parameters to hardened properties of cracked and un-cracked SCC. Correlations for SCC micro-cracking based on US parameters were identified, demonstrating the potential of using transmission US P- and S- waves as an evaluation technique for micro-damaged SCC.*

Keywords: *Ultrasonic, P and S Waves, Micro-Cracking, SCC, Hardened Properties.*

1 Introduction

Self-Compacting Concrete (SCC) is designed to improve cast-in-place structures by increasing paste phase and enhancing fresh rheology. However, larger paste volume makes SCC more sensitive to curing conditions, increasing early age (EA) drying shrinkage and micro-cracking potential (Puentes *et al.*, 2014). SCC usually incorporates supplementary cementitious materials (SCM) in its composition. The type and amount of SCM used has been identified to also affect cracking potential damage jointly with curing conditions on SCC with limestone filler, microsilica and nanosilica (Barluenga *et al.*, 2018). When EA cracking occurs, an evaluation of the hardened properties of SCC is necessary. Among the Non-destructive testing techniques (NDT) available, radar, electrical resistivity, capacitance measurements and ultrasound have been described to be suitable for estimating material properties (Garnier *et al.*, 2013). Ultrasonic

pulses (US) is often preferred due to its portability, easiness of application and sensitivity to changes in material microstructure, porosity and defect detection (Selleck *et al.*, 1998; Aggelis, 2013; Barluenga *et al.*, 2015; Palomar *et al.*, 2017). US parameters such as ultrasonic transmission times and wave amplitude of the raw US signal propagated through the material can be used to evaluate the relations among composition, microstructure, properties, curing conditions and micro-cracking (Yim *et al.*, 2012; Shiotani *et al.*, 2009). The most commonly used US wave type is compressive or P-wave, although there are transducers commercially available that combine P- and S-waves (shear pulses). Thus, the wave velocity propagation (UPV), the wave attenuation coefficient (AT) and Young modulus, Shear modulus and Poisson's coefficient ratio can be calculated (Palomar *et al.*, 2017). The combination of US parameters considering both UPV and AT can be used for concrete micro-cracking assessment (Shiotani *et al.*, 2009).

The aim of this study was to compare US parameters to hardened properties of cracked and un-cracked SCC with limestone filler (LF), microsilica (MS) and nanosilica (NS). An experimental program using transmission P- and S- waves was carried out on SCC set and hardened under different curing conditions. The applicability of ultrasonic (US) waves to better understand the relations among composition, microstructure, properties, curing conditions and micro-cracking was evaluated.

2 Experimental Program

2.1 Materials and Mixtures

SCC mixtures are summarized in Table 1. A reference SCC containing a CEM I 42.5 R cement, limestone filler; fine and coarse aggregates, water and 1% by weight of cement (bwoc) of a high range water reducing admixture (HRWRA) was designed (HCA). Afterwards, limestone filler was replaced by densified microsilica (HCAMS) and colloidal nanosilica (HCANS), 10 and 5% bwoc respectively (see Barluenga *et al.*, 2018 for further descriptions).

2.2 Experimental Methods and Preliminary Results

2.2.1 Early age cracking potential in different curing conditions

Early age (EA) cracking potential was measured using a double restrained slab test subjected to 10, 20 and 30 °C curing temperatures and 40 and 80 % relative humidity (RH) during the first 24 h. The test setup consisted of 400 x 300 x 45 mm slabs, with double displacement restricted by internal plugs attached to the mold, in order to maximize EA cracking potential (Barluenga *et al.*, 2018). The slabs were demolded at 24 h and stored in laboratory conditions until crack measurement at 7 days. The cracked area (A_c) summarized in Table 2 was calculated measuring cracks length (L) and width (W) (Puentes *et al.*, 2014). The results of the SCC mixes with filler (HCA) showed high A_c. It can also be observed that the L and W for HCA were higher, especially at 20°C and 40% RH. SCC with Microsilica (HCAMS) reduced significantly EA cracking, except for hot-dry conditions. In the case of SCC with nanosilica (HCANS) A_c was slightly lower, although the cracks were narrower than HCA and HCAMS. In general, silica based additions at hot-dry conditions showed a high EA cracking risk, whereas it was minimized

in hot-wet conditions. The increase of hydration speed and microstructure formation in hot-dry curing conditions may explain this effect on EA cracking (Barluenga *et al.*, 2018).

Table 1. SCC Compositions (kg/m^3).

	HCA	HCAMS	HCANS
Cement	350	350	350
Limestone Filler	350	315	332.5
Gravel (4–20 mm)	790	790	790
Sand (0–4 mm)	679	679	679
Microsilica	-	35	-
Nanosilica	-	-	79.5
Water*	179	179	117
HRWRA	3.5	3.5	3.5
w/c **	0.6	0.6	0.6
w/b **	0.3	0.3	0.3

* Liquid water added.
** The amount of water included in the components (sand humidity (4.3%), SP and NS) was also considered.

Table 2. Early age cracking parameters. Physical and mechanical properties at hardened state.

	A_c mm^2/m^2	L_{max} mm	W_m mm	AER* 10^3ml/s mm^2	WAR * 10^6ml/s mm^2	Po** %	CS** MPa
HCA	539	66	0.17	0.48	0.93	2.34	34
10-40	353	70	0.07	0.63	1.12	2.55	35
10-80	448	90	0.18	0.27	1.09	3.11	30
20-40	2139	145	0.66	0.45	1.25	1.85	35
20-80	0	0	0	0.73	1.29	3.21	31
30-40	42	25	0.05	0.67	0.32	-	34
30-80	253	65	0.06	0.13	0.50	0.97	37
HCAMS	122	17	0.05	0.18	1.02	1.88	33
10-40	91	25	0.09	0.18	1.03	2.47	37
10-80	0	0	0	0.12	1.52	1.28	36
20-40	0	0	0	0.09	0.67	2.22	32
20-80	0	0	0	0.17	0.83	2.33	37
30-40	641	75	0.21	0.47	1.37	2.06	29
30-80	0	0	0	0.07	0.67	0.92	30
HCANS	327	59	0.06	0.22	1.05	2.29	36
10-40	166	70	0.06	0.16	2.18	1.98	42
10-80	231	50	0.05	0.31	1.09	2.58	37
20-40	391	140	0.12	0.10	0.51	1.43	34
20-80	592	55	0.05	0.17	0.94	2.21	36
30-40	584	40	0.06	0.25	0.70	4.64	33
30-80	0	0	0	0.32	0.87	0.89	36

* Cracked samples. ** Un-cracked samples at 28 days.

2.2.2 NDT assessment by ultrasonic pulse propagation

Ultrasonic pulses (US) were applied on hardened samples of cracked and un-cracked SCC samples with dimensions of 400 x 300 x 45 mm and 60 x 50 x 100 mm, respectively. P- and S-

waves 250 kHz transducers were used. The amplitude (V) in time domain (μs) of the P- and S-wave raw signal through SCC samples were obtained. P-wave (Pw) and S-wave (Sw) pulse velocity were identified using the Hilbert transform algorithm (Birgül, 2009). In addition, attenuation coefficient (AT_{250}) was calculated (Palomar *et al.*, 2017), where the higher AT_{250}, the lower the US energy absorbed by the SCC sample.

2.2.3 SCC hardened properties

Table 2 also summarizes several hardened physical and mechanical properties measured on 400 x 300 x 45 mm cracked slabs or 100 x 100 x 100 mm un-cracked samples. Air and water permeability were measured on cracked SCC slabs with a Figg's method based apparatus (Porosiscope™). The measured time for air or water to permeate through the concrete was used to estimate Air Exclusion Rating (AER) and Water Absorption Rate (WAR), respectively (Barluenga *et al.*, 2017). Open porosity accessible to water (P_O) and compressive strength (CS) were measured on cubic un-cracked samples at 28 days. HCA showed higher air permeability than SCC with silica based additions, while water permeability values were similar for all SCC compositions. Regarding curing conditions, HCA and HCANS samples showed large AER values even when cracks were not observed on the slabs. In contrast, the most damaged HCAMS slab presented the highest AER value. WAR was larger for HCA and HCAMS slabs without visible damage. SCC with nanosilica (HCANS) produced large values of WAR at cold-dry conditions despite its higher CS. Some correlations among the composition parameters, hardened properties and curing conditions have been described in a previous work (Barluenga *et al.*, 2018). Regarding SCC compositions, HCAMS reduced open porosity and HCANS increased compressive strength. In general, hot-wet curing conditions produced lower P_O, independently to the SCC composition, and increased CS on HCA samples. Cold-dry environment on HCMS and HCANS produced higher CS.

Table 3. P- and S-wave velocity and attenuation coefficient of US signal for SCC un-cracked samples.

	Pw m/s	**Sw** m/s	**AT_{250}** dB/mm
HCA	3938	2472	0.36
HCAMS	3926	2342	0.53
HCANS	3684	2201	0.52

3 Experimental Results and Discussion

3.1 Ultrasonic Characterization of Un-Cracked SCC Samples

Table 3 summarizes the experimental results of P- and S-wave propagation velocities (Pw and Sw) and attenuation coefficient (AT_{250}) of un-cracked SCC samples. Pw and AT_{250} presented lower variability related to SCC compositions. In contrast, Sw was sensitive to SCC composition: the smaller the particle size, the slower S-wave propagation velocity. Figure 1 plots the experimental results of Pw and Sw and AT_{250} of un-cracked SCC samples in different curing conditions. Pw and AT250 presented a high variability, although they showed different trends, while Sw did not depend on curing conditions.

3.2 Ultrasonic Evaluation of Cracked SCC Samples

Figure 2 and 3 plot the experimental results of Pw and Sw and AT_{250} of cracked SCC samples.

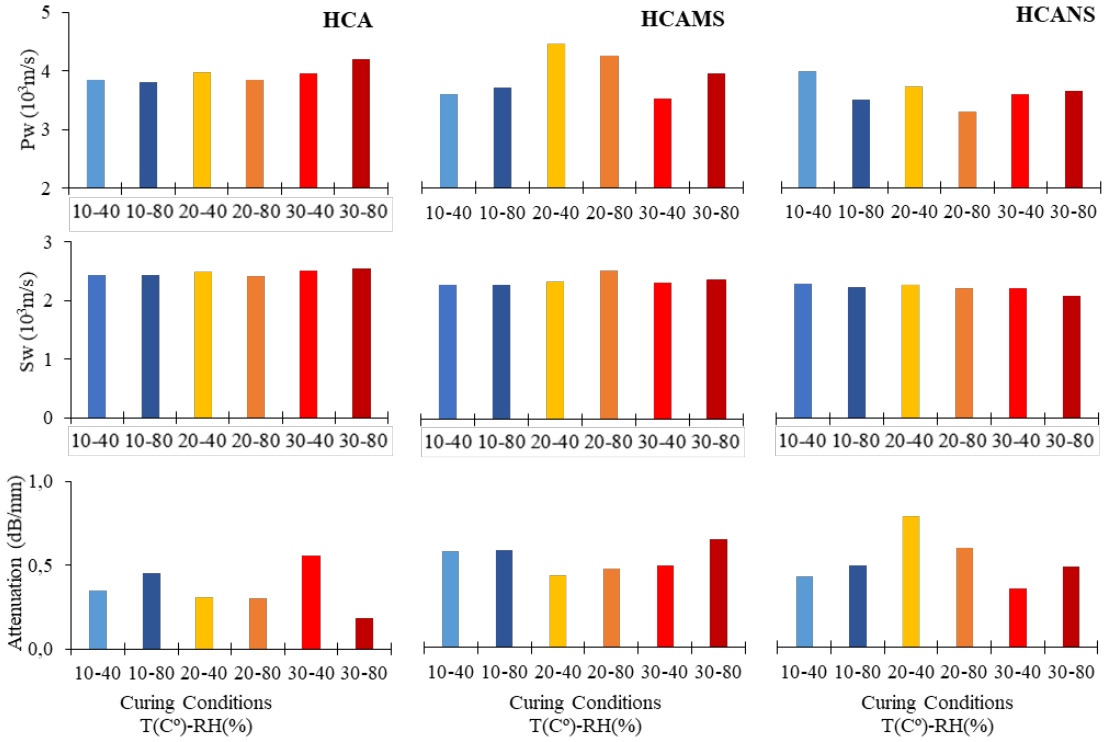

Figure 1. P- and S-wave velocity and attenuation coefficient of US signal for SCC un-cracked samples at different curing conditions.

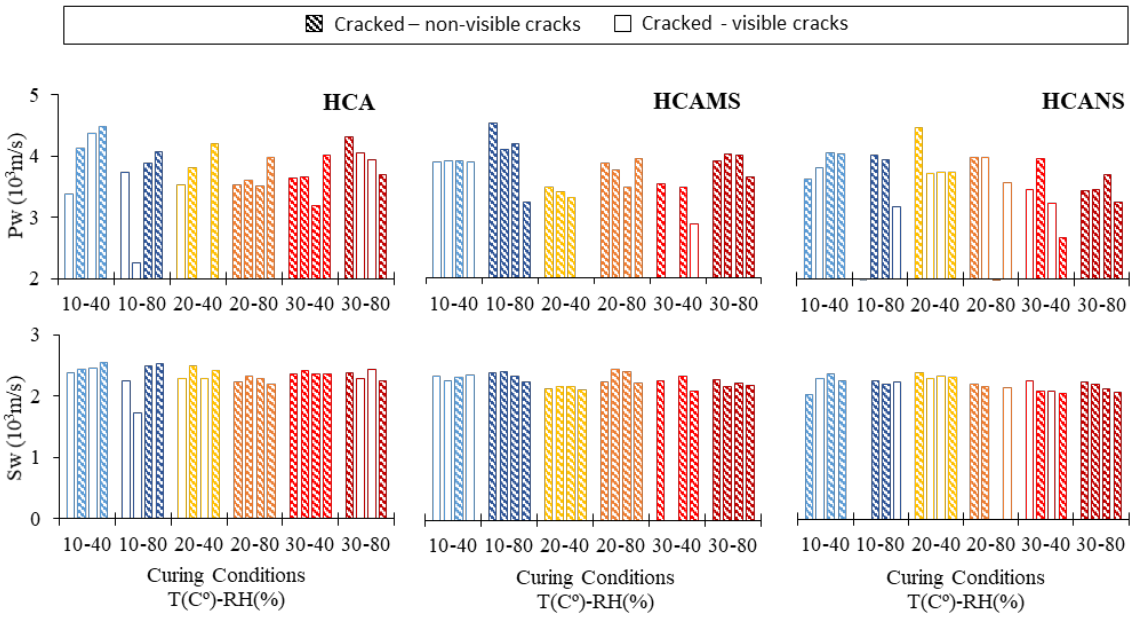

Figure 2. P- and S-wave velocity of US signal for SCC cracked samples at different curing conditions.

US propagation was measured on damaged slabs with visible (VC) and non-visible cracks (NVC). Regarding US velocities, Pw scatter was slightly higher in cracked samples than in un-cracked samples, although cracked values were lower than un-cracked. Pw on NVC was around 230 m/s faster than VC. Sw showed very low variability on cracked samples despite the effect of composition, curing conditions and NVC or VC. In addition, some damaged samples showed similar Pw and Sw values, with differences smaller than 1000 m/s. These values do not correspond to undamaged SCC and cannot be used to calculate mechanical properties of damaged slabs, as elastic modulus or Poisson Coefficient (Barluenga *et al.*, 2018).

A large dispersion of attenuation was recorded for cracked samples (Figure 3) and AT_{250} was higher for VC than NVC. The highest AT_{250} values (closely 1.00 dB/mm) corresponded to the widest cracks measured (HCA-1080 and 2040 and HCAMS-3040). Thus, cracks decreased the amplitude of the wave in damaged areas due to scattering and diffraction effects (Yim *et al.*, 2012). These results points out the sensitivity of AT_{250} to concentrated damage as visible cracks. However, some cracks produced by EA shrinkage of displacement restrained SCC members can progress from inside of the sample (Serpukhov *et al.*, 2010), producing AT_{250} values with little differences between VC and NVC areas. Accordingly, AT_{250} can detect both VC and NVC.

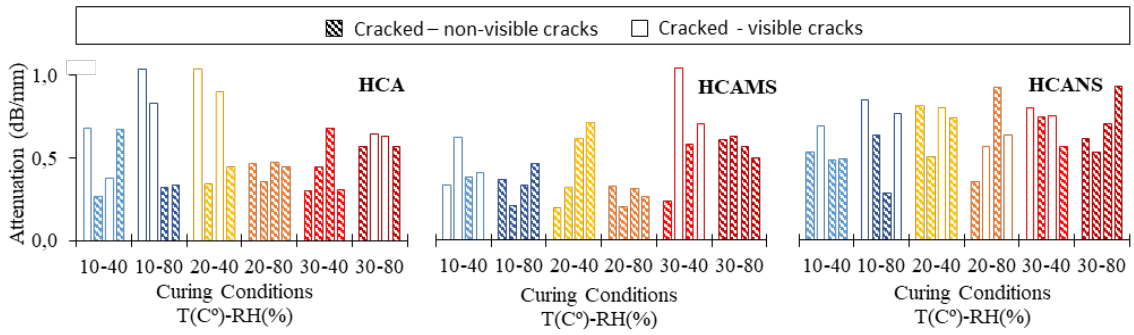

Figure 3. Attenuation coefficient of US signal for SCC cracked samples at different curing conditions.

3.3 Damage Evaluation of SCC Using NDT

An evaluation of damage and cracking potential by US analysis was carried out and is plotted in Figures 4 and 5, respectively. Regarding damage and US parameters, in general velocities of cracked samples were slower than on un-cracked samples (Selleck *et al.*, 1998), except HCA and HCAMS cured at 10º C. On the other hand, two behaviors were identified in AT_{250}: 1) HCA and HCANS; values of un-cracked samples were lower than cracked ones; 2) HCAMS AT_{250} values were higher for un-cracked than for cracked samples. These differences can be explained considering the effect of SCC composition on cracking potential. HCA and HCANS showed larger cracking potential, whereas HCAMS cracking potential was remarkably lower. There were two exceptions to this trends: HCAMS 3040 (visible damage) and HCANS-2040 (red labeled in the graph). This last case showed long and wide cracks and low AER and WAR, meaning concentrated damages that can explain its exceptionality.

As a predictive tool for EA cracking potential of SCC, cracked area (A_c) can be compared to the ratio between Pw and Sw (Pw/Sw) of un-cracked samples (Figure 5). The results showed an inverse relationship between Pw/Sw and A_c until a constant value of 1.60 or 1.80, which

depended on sample composition. A ratio of 1.80 means a Poisson's ratio (υ) around 0.28: the larger the ratio the lower the compressibility. Therefore, if the un-cracked sample reaches a certain Pw/Sw or compressibility, EA cracking potential will be minimized (HCAMS and HCANS). In the case of HCA, Pw/Sw showed littele cracking potential variability.

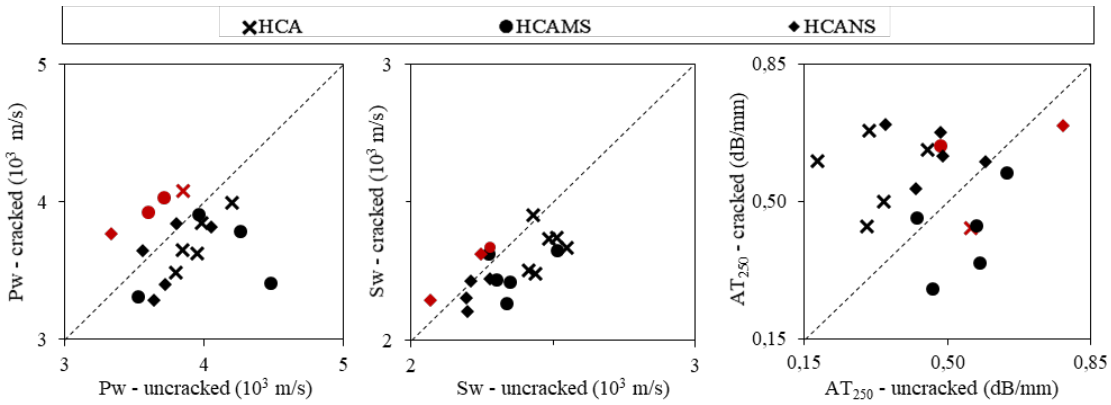

Figure 4. Ultrasonic pulse velocity and attenuation coefficient: un-cracked vs cracked values.

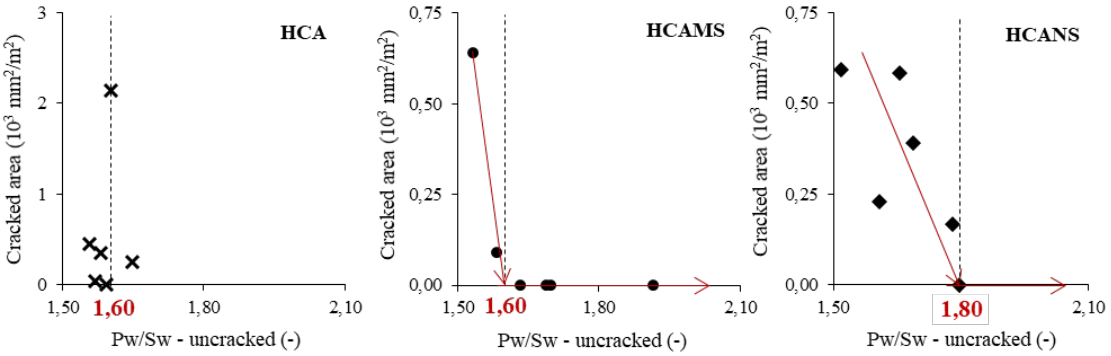

Figure 5. P- and S-wave velocity ratio (Pw/Sw) for un-cracked samples vs EA cracking parameters (A_c).

4 Conclusions

The applicability of ultrasonic (US) waves to better understand the relations among composition, microstructure, properties, curing conditions and early age cracking potential of SCC with limestone filler (LF), microsilica (MS) and nanosilica (NS) was assessed. The influence of composition, curing conditions and micro-damage on US parameters (P- and S-wave velocities and signal attenuation) were analyzed. The main conclusions were:

- Changes in SCC compositions and curing conditions modified early age (EA) cracking potential and hardened properties.
- SCC compositions and curing conditions had a significant effect on US velocity propagation and attenuation coefficient in un-cracked and cracked samples, although the effect on US parameters it is not linear.
- US parameters were identified as key parameters to assess the micro-damage or the EA cracking potential of SCC.
- US velocities of un-cracked samples were higher than those of cracked samples. The

attenuation coefficient of un-cracked SCC was lower than the damaged samples, either when the cracks were externally visible and when they were internal and non-visible.
- EA cracking potential was estimated for samples set and hardened under same curing conditions, using P- and S-wave velocity ratio (Pw/Sw) of un-cracked samples.

Acknowledgements

Financial support was provided by the Spanish Ministry of Economy & Competitiveness (NanoCompaC, BIA2016-77911-R) and UAH (postdoctoral fellowship - Ayuda Postdoctoral/Modalidad A/2017). Some of the components were supplied by BASF Spain S.L, Omya Clariana S.L, and Portland Cement Vaderrivas.

ORCID

Irene Palomar: https://orcid.org/0000-0003-2743-3618
Gonzalo Barluenga: https://orcid.org/0000-0002-2996-3412
Hugo Varela: https://orcid.org/0000-0001-8094-6071
Javier Puentes: https://orcid.org/0000-0001-8748-7664
Ángel Rodríguez: http://orcid.org/0000-0002-6897-2194

References

Aggelis, D.G. (2013). Wave propagation through engineering materials; assessment and monitoring of structures through non-destructive techniques. *Materials and Structures, 46*, 519-532. doi: 10.1617/s11527-013-0020-x

Barluenga, G., Guardia, C. and Puentes, J. (2018). Effect of curing temperature and relative humidity on early age and hardened properties of SCC. *Construction and Building Materials, 167*, 235-242. doi: 10.1016/j.conbuildmat.2018.02.029

Barluenga, G., Guardia, C. and Puentes, J. (2017). Effect of curing conditions on microstructure, cracking and durability of SCC. In *Proceedings of the 14th International Conference on Durability of Building Materials and Components (RILEM PRO 107)*, Ghent, Bélgica, 163 (DBMC-p163.pdf).

Barluenga, G., Palomar, I. and Puentes, J. (2015). Hardened properties and microstructure of SCC with mineral additions. *Construction and Building Materials, 94*, 728-736. doi: 10.1016/j.conbuildmat.2015.07.072

Birgül, R. (2009). Hilbert transformation of waveforms to determine shear wave velocity in concrete. *Cement and Concrete Research, 39(8),* 696-700. doi: 10.1016/j.cemconres.2009.05.003

Garnier, V., Piwakowski, B., Abraham, O., Villain, G., Payan, C. and Chaix, J.F. (2013). Acoustic techniques for concrete evaluation: Improvements, comparisons and consistency. *Construction and Building Materials*, *43*, 598-613. doi: 10.1016/j.conbuildmat.2013.01.035

Palomar, I. and Barluenga, G. (2017). Assessment of lime-cement mortar microstructure and properties by P- and S- ultrasonic waves. *Construction and Building Materials, 139*, 334-341. doi: 10.1016/j.conbuildmat.2017.02.083

Puentes, J., Barluenga, G. and Palomar, I. (2014). Effects of nano-components on early age cracking of self-compacting concretes. *Construction and Building Materials, 73*, 89-96. doi: 10.1016/j.conbuildmat.2014.09.061

Selleck, S.F., Landis, E.N., Peterson, M.L., Shah, S.P. and Achenbach, J.D. (1998). Ultrasonic Investigation of Concrete with Distributed Damage. *ACI Materials Journal*, *95-M4*, 27-36.

Serpukhov, I. and Mechtcherine, V. (2015). Early-age shrinkage of ordinary concrete and strain-hardening cement-based composite (SHCC) in conditions of hot-weather casting. In *Proceedings of the 10th International Conference on Mechanics and Physics of Creep, Shrinkage, and Durability of Concrete and Concrete Structures*, Vienna, Austria, 1504–1513. doi: 10.1061/9780784479346.176

Shiotani, T. and Aggelis, D.G. (2009). Wave propagation in cementitious material containing artificial distributed damage. *Materials and Structures, 42(3)*, 377–384. doi: 10.1617/s11527-008-9388-4

Yim, H.J., Kwak H.G. and Kim J.H. (2012). Wave attenuation measurement technique for nondestructive evaluation of concrete. *Nondestructive Testing and Evaluation*, *27(1)*, 81-94. doi: 10.1080/10589759.2011.606319

XV International Conference on Durability of Building Materials and Components
DBMC 2020, Barcelona
C. Serrat, J.R. Casas and V. Gibert (Eds)

On Bio-Deterioration of Solar Reflective Materials: An Innovative Experimental Procedure to Accelerate the Ageing Process of Surfaces

Giulia Santunione[1], Chiara Ferrari[1], Alberto Muscio[1] and Elisabetta Sgarbi[2]

[1] Department of Engineering "Enzo Ferrari", University of Modena and Reggio Emilia, Italy, giulia.santunione@unimore.it

[2] Department of Life Science, University of Modena and Reggio Emilia, Italy, elisabetta.sgarbi@unimore.it

Abstract. *Solar reflective materials are one of the most efficient solution to the urban heat island effect, according to which temperatures, in urban areas are significantly higher than those in the surrounding rural areas. Solar reflective materials (SRM) are characterized by the ability to reflect solar radiation in the whole wavelength spectrum remaining cooler under the sun. The importance of radiative properties focused the attention more on SRM subjected to aging processes instead of the new products. According to this, several standards are, nowadays, available to investigate natural (ASTM G7, ANSI CRRC/S100) and accelerated (ASTM D7897) aging. Unfortunately, these standards do not take into account the presence and the growth of microorganisms such as algae and cyanobacteria, which can be responsible not only for the decrease of radiative properties against time, but also for the decay of physical and chemical properties of SRM themselves. This study outlines an experimental procedure to accelerate natural bio-deterioration of building materials through a laboratory test. Two types of SRM have been involved, studying their thermal properties before and after the bio-deterioration accelerated treatment. The methodology involves the use of a Temporary Immersion System (TIS bioreactor), which is based on the temporized soaking of materials samples with a liquid growth medium inoculated by selected species of algae or cyanobacteria. The system promotes a homogeneous contact between the materials surfaces and these microorganisms blowing sterilized air into the medium inside the bioreactor chamber. Within three weeks into TIS bioreactor, materials samples have shown large areas of biofilm deposition on themselves. The experimental procedure, hence, confirms the capability of the system to optimize environment conditions where the growth of microorganism and their interactions with materials results accelerated. Very high attention is given to the aim to make the procedure repeatable. For this proposal, all the variable factors are minimized, maintaining constant the environmental condition and working on sterility in order to do not contaminate or alter the growth inside the bioreactor.*

Keywords: *Solar Reflectance, Colorimetry, Bio-Deterioration, Bioreactor.*

1 Introduction

Building materials are affected by several aesthetical and functional issues due to ageing processes which can be related to physical, chemical or biological factors (Sleiman *et al*. 2014). Among these factors, the biological growth represents a phenomenon in addition to physical and chemical problems due to weathering and soiling, which accelerates the fouling process of outdoor materials (Ferrari *et al*. 2015). The biofilm changes the aesthetical appearance of materials and can even compromise the durability of structures by corrosion and biodeterioration induced by the microorganisms (Maury-Ramirez *et al*., 2013).

Several studies on natural conditions suggests that bio colonization is primarily related to the physical characteristics of the stone surface (porosity, roughness, and permeability) and secondarily to the nature of substratum (Gaylarde *et al*., 2011). Microorganisms produce variously coloured patinas on the materials inducing aesthetical damage (Ortega-Calvo *et al.*, 1995). Biological growth also exerts a pressure inside the pores on the surface, resulting in biogeophysical deterioration, i.e. the surface detachment and superficial losses. Definitively, microorganisms play an important role in the deterioration of building materials, being responsible for aesthetic, biogeophysical and biogeochemical damage.

Considering Solar Reflective Materials (SRM), bio-deterioration process takes part to important performances losses in terms of surface thermal properties, such as solar reflectance and thermal emittance. Since studying microbial growth under natural conditions is too slow as an investigation approach to develop and to improve industrial products, several studies have been carried out on surface bio-ageing with the aim of analyse and to assess the energy impact on the buildings (Cheng *et al*., 2011; Cheng *et al*.,2012; Gaylarde and Gaylarde, 2005; Mastrapostoli *et al*., 2016). However, due to its the wide variability depending on environmental conditions and mainly by geographical position of the building, bio-deterioration is not yet being completely understood and quantify by the scientific community.

Thus, this study is aimed to study biological colonization on building materials in a repeatable and reproducible way, in order to quantify the changes on the surfaces properties due to biological growth. An innovative and laboratory protocol to accelerate biological colonization effects on building surfaces by different pioneering organisms (algae and cyanobacteria) is here presented. The goal was to provide a faster, reproducible and reliable test method to assess the long term behaviour of building surfaces relevant to, among the other, energy performance for cooling.

2 Material and Methods

A laboratory protocol to expose building material samples to biological colonization is here presented. The setup consists in a growth chamber (Figure 1), where all the environmental factors have been maintained constantly monitored and stable. The device chosen as growth chamber is a TIS (Temporary Immersion System) bioreactor (Welander *et al.*, 2014).

a.  b. 

Figure 1. (a) TIS bioreactor equipped with the samples; (b) couple of TIS bioreactors for different environmental microorganisms (*Chlorella mirabilis* and *Nostoc commune*), start time of the test (t0).

It is a sealing growth camera where the samples are placed on a tray and temporarily flooded by 500 ml of culture medium, inoculated by selected microorganisms according to 1:50 concentration rate. The submersion is induced by a pump (10 W), which inputs sterilized air inside the liquid medium in order to raise the level of that and submerge the samples on the tray. The level of the medium is subsequently lowered by stopping the air supply into the

medium and raising the air pressure inside the camera, through a second pump (5 W). These working conditions were turned on and off trough a complete automated system. A complete bio-ageing cycle lasts 3 weeks and two types of building material were involved in this preliminary work: single ply cool white membrane (WM) and asphalt shingle (AS). Two samples for each type of material were included for each bioreactor, and each bio-ageing cycle was performed in triplicate in order to get statistically significant results.

Two specie of different microorganisms were used separately to study biofilm formation on sample surfaces: the green microalga *Chlorella mirabilis* and the cyanobacteria *Nostoc commune*. They were chosen among the huge variability of environmental ubiquitous organisms (Ferrari *et al*. 2015) and different culture medium were used for each microorganism: Bold Basal Medium (BBM) (ref) was applied for *Chlorella m.* and Blue Green medium (BG-11) for *Nostoc c.* TIS bioreactors were put into the incubator (Biolog, AG-System) where the temperature and relative humidity level was stable (23°C and 50% respectively), and 14h light/10h dark periods are contemporarily alternated by a fluorescent lamp system.

Since the study is finalized to develop a repeatable and reproducible protocol for bio-ageing trial, TIS bioreactors and culture medium are therefore completely sterilized before use to minimize the variability of environmental factors and avoid contamination of the biological cultures on growth. Two different sample submersion times were investigated: 10 minutes/6 times a day every 4 hours (setup #1) and 30 minute /6 times a day every 4 hours (setup #2): each time condition has been tested three repeated times as abovementioned. The complete overview on experimental setup studied in this work are shown in Figure 2.

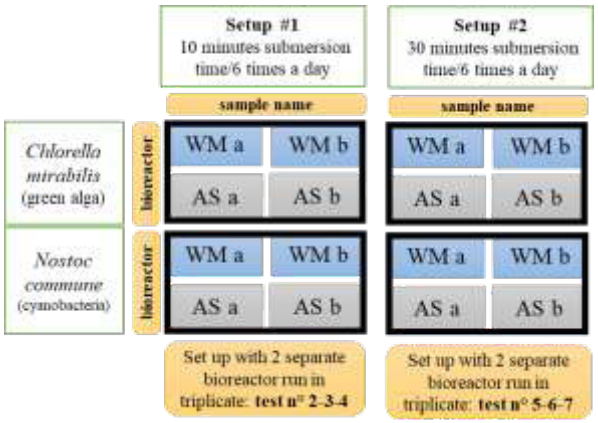

Figure 2. Bio-ageing experimental design: 2 bioreactors types were prepared for each trial; 4 samples were included into each bioreactor (double samples for each material); two setups were studied; the trials have been run in triplicate.

Such "*flood and dry*" approach tries to replicate the natural wetting and dry cycles that typically occur outdoor on the building surfaces. Reproducing a bio-deterioration phenomenon in laboratory allows to choose and set up stable environmental conditions, which are the optimum for biological growth, and to compress colonization time.

2.1 Material Characterization

Material characterization was performed on sample surface before and after the bio-ageing test through several analyses. Firstly, surface microstructure were investigated by Environmental Scanning Electron Microscope (ESEM, Quanta200) operating in low vacuum conditions; Solar Reflectance (ρ_{sol}) was analyzed by UV-Vis-Nir Spectrophotometer (Jasco V-670), according with ASTM Standard E903 (ASTM E903, 1996). To evaluate how the surface color was modified during the whole campaign L*a*b* values were calculated both on new and aged samples starting from solar reflectance values in visible region (λ range: 300-800 nm). ΔE values were calculated by means of $\Delta E = \sqrt{(L_1^* - L_2^*)^2 + (a_1^* - a_2^*)^2 + (b_1^* - b_2^*)^2}$ to quantify the difference in color between the two stages of aging. Statistical analysis by ANOVA (Past3 Software) has been run in order to evaluate the repeatability of the preliminary protocol.

3 Results and Discussion

The differences collected between setup#1 and setup #2 trials are visibly high as the example reported in Figure 3. The first set up trial, reported in triplicate, shows a weaker but more homogeneous growth on materials samples then the second set up trials, where the submersion time has been 30 minutes for 6 times a day.

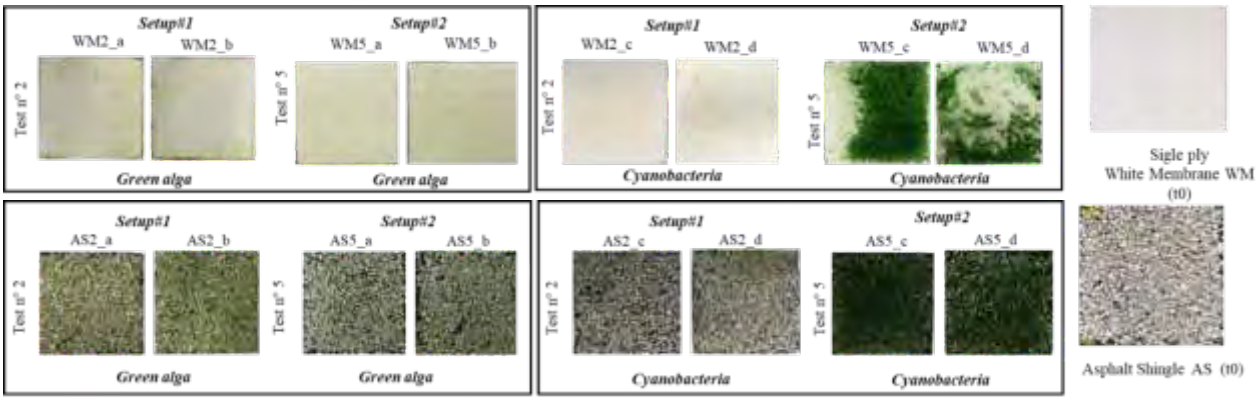

Figure 3. WM and AS aged samples are shown: *a* and *b* samples come from bioreactor run with green alga inoculum; *c* and *d* ones come from bioreactor run with cyanobacteria inoculum; the results from 1 (test n° 2 and test n° 5) of 3 repeated tests by both setups types are shown; on the right, new (t0) sample are shown.

3.1 Electron Microscopy

Micromorphology and chemical composition analysis through Electron Microscopy carried out on samples before colonization, additional analysis were performed on aged samples immediately after the end of the bio-ageing trials. This allow to check microorganisms while they were still alive. Figure 4 shows the two different colonies of organisms in separate TIS bioreactor on AS sample: green alga (*Chlorella m.*) build spherical shape colonies (Fig. 4a) and cyanobacteria (*Nostoc c.*) are set in filamentous colonies (Fig. 4b).

Roughness on AS samples is high due to the presence of grains: this create the presence of several niches on surfaces, which represents a suitable place for biological growth thanks the

longer staying of humidity. C is the most aboundant element in both AS (65.0% ± 22.7%) and WM (96.6% ± 4.4%) materials, but AS samples are richer in elemental diversity: traces of Mg, Al, Si, S, K, Ca, Ti, Fe compounds have been detected by ESEM.

a. 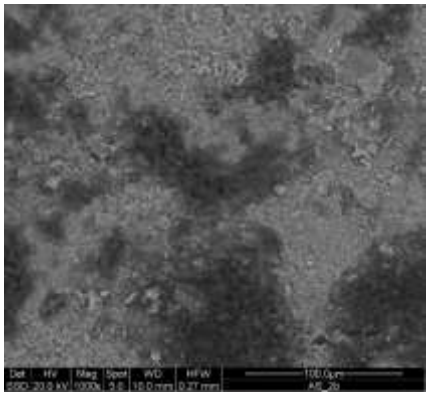 b. 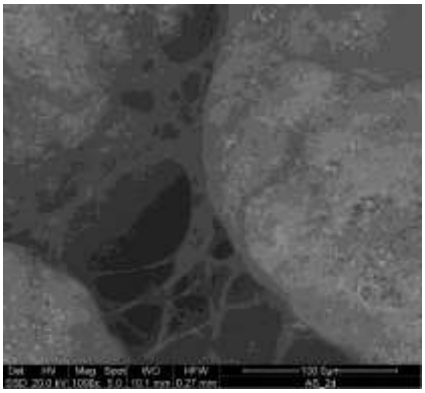

Figure 4. ESEM images from ESEM analysis: (a) *Chlorella m.* spherical cells colonies on AS sample; (b) *Nostoc c.* filamentous structure on AS sample. Mag. 1000X.

3.2 Solar Reflectance

Solar reflectance (ρ_{sol}) values and standard deviation calculated on average values between samples exposed to the same microorganism (*a* and *b* to *Chlorella m.* and *c* and *d* to *Nostoc c.*) have been reported in Table 1. New and aged values are shown. Results have been elaborated comparing the same material ρ_{sol} values between two different setup trials (#1 and #2) and within the same set up trial. The evaluation on sample surface colonized by two different microorganisms (green alga and cyanobacteria) have been kept separated.

Solar reflectance values got on aged surfaces through two different TIS bioreactor submersion time (setup #1 and #2) highlight significant differences on both types of material, rising the strong variability among setups. Moreover, the colonization level due to green alga (*Chlorella m.*) compared with the one due to cyanobacteria (*Nostoc c.*) are significantly distant: they have been evaluated separately.

Table 1 shows ρ_{sol} decrease considering only *a* and *b* samples, before and after bio-ageing process. Samples *a* and *b*, exposed to green alga, underline a lower ρ_{sol} decrease through setup #2 compared with setup #1. This is true for both WM and AS samples. A reverse situation was achieved on samples *c* and *d* for both material types, exposed to cyanobacteria: the ρ_{sol} decrease is higher through setup #2, where the submersion time is tripled compared with setup #1.

Statistical analysis among solar reflectance results obtained through repeated trials within the same setup type was performed. TIS bioreactor system, in particularly the case with green alga and setup#1 shows a good repeatability: the differences among ρ_{sol} on the same material type (AS or WM) from different trials are not significant (p-value >0.05). However, this not occurs on ρ_{sol} measured on aged samples *c* and *d* exposed to cyanobacteria colonization, neither for setup#1 and setup #2: in these cases, the statistical analysis highlight high significant differences among repeated trials (p-value<<0.05).

Table 1. Solar reflectance values by ASTM E903 are shown: AS and WM samples from both bioreactors with green alga (*a-b*) and cyanobacteria (*c-d*) inoculum; mean values on *a-b* and *c-d* samples are reported; $\Delta\ \rho_{sol}$ between new and aged samples are reported; SD among repeated ρ_{sol} measurements are considered.

	Sample name	ρ_{sol} (new)	Mean ρ_{sol} (aged)	$\Delta\ \rho_{sol}$	SD
set up#1	AS2_*a-b*	0.304	0.260	-0.045	0.011
	AS3_*a-b*	0.304	0.275	-0.029	0.021
	AS4_*a-b*	0.303	0.229	-0.071	0.030
set up #2	AS5_*a-b*	0.304	0.294	-0.010	0.014
	AS6_*a-b*	0.304	0.295	-0.008	0.005
	AS7_*a-b*	0.308	0.312	0.004	0.010

	Sample name	ρ_{sol} (new)	Mean ρ_{sol} (aged)	$\Delta\ \rho_{sol}$	SD
set up#1	AS2_*c-d*	0.305	0.281	-0.024	0.012
	AS3_*c-d*	0.305	0.280	-0.025	0.002
	AS4_*c-d*	0.298	0.232	-0.066	0.015
set up #2	AS5_*c-d*	0.303	0.218	-0.085	0.007
	AS6_*c-d*	0.306	0.203	-0.103	0.005
	AS7_*c-d*	0.293	0.249	-0.044	0.008

	Sample name	ρ_{sol} (new)	Mean ρ_{sol} (aged)	$\Delta\ \rho_{sol}$	SD
set up#1	WM2_*a-b*	0.837	0.801	-0.037	0.002
	WM3_*a-b*	0.837	0.759	-0.078	0.003
	WM4_*a-b*	0.837	0.804	-0.033	0.007
set up #2	WM5_*a-b*	0.836	0.760	-0.076	0.007
	WM6_*a-b*	0.827	0.769	-0.058	0.012
	WM7_*a-b*	0.822	0.787	-0.035	0.018

	Sample name	ρ_{sol} (new)	Mean ρ_{sol} (aged)	$\Delta\ \rho_{sol}$	SD
set up#1	WM2_*c-d*	0.837	0.788	-0.049	0.005
	WM3_*c-d*	0.837	0.753	-0.084	0.004
	WM4_*c-d*	0.837	0.775	-0.061	0.013
set up #2	WM5_*c-d*	0.832	0.600	-0.232	0.037
	WM6_*c-d*	0.828	0.705	-0.123	0.024
	WM7_*c-d*	0.819	0.574	-0.244	0.034

Since ASTM E903 spectral chart analysis (Figure 4) underlines how the main difference occurred within the Visible range of the complete solar reflectance spectrum, as showed in Figure 5, colorimetry analysis was deemed important to better evaluate the results of bio-ageing protocol.

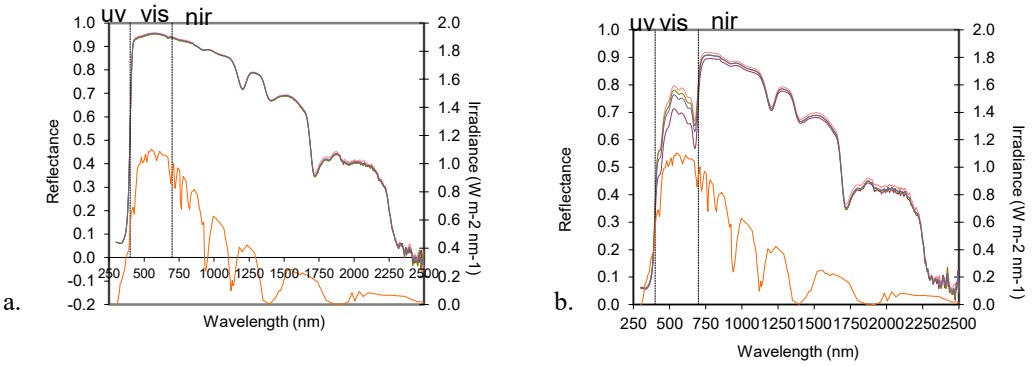

Figure 5. ASTM Solar Reflectance spectral chart on WM sample: (a) results on new sample; (b) results on bio-aged sample. 3 repeated measurements on the same sample have been performed.

3.2 Colorimetry

Figure 5 reports the colorimetric differences between new (L* values) and aged (ΔL* and ΔE) material types. Colorimetric differences have been calculated using the difference ρ_{sol} within 300-800-nm λ range (visible region). ΔL* and ΔE have been assessed comparing all the samples (*a,b,c,d*) coming from two different setup: again, the repeatability was described within the three trials with the same setup. These results confirm what noticed through solar reflectance:

while the colonization level and solar reflectance decrease showed a good repeatability within the trials of setup#1, this was not happened to setup #2, where sample submersion time was tripled compared with #1.

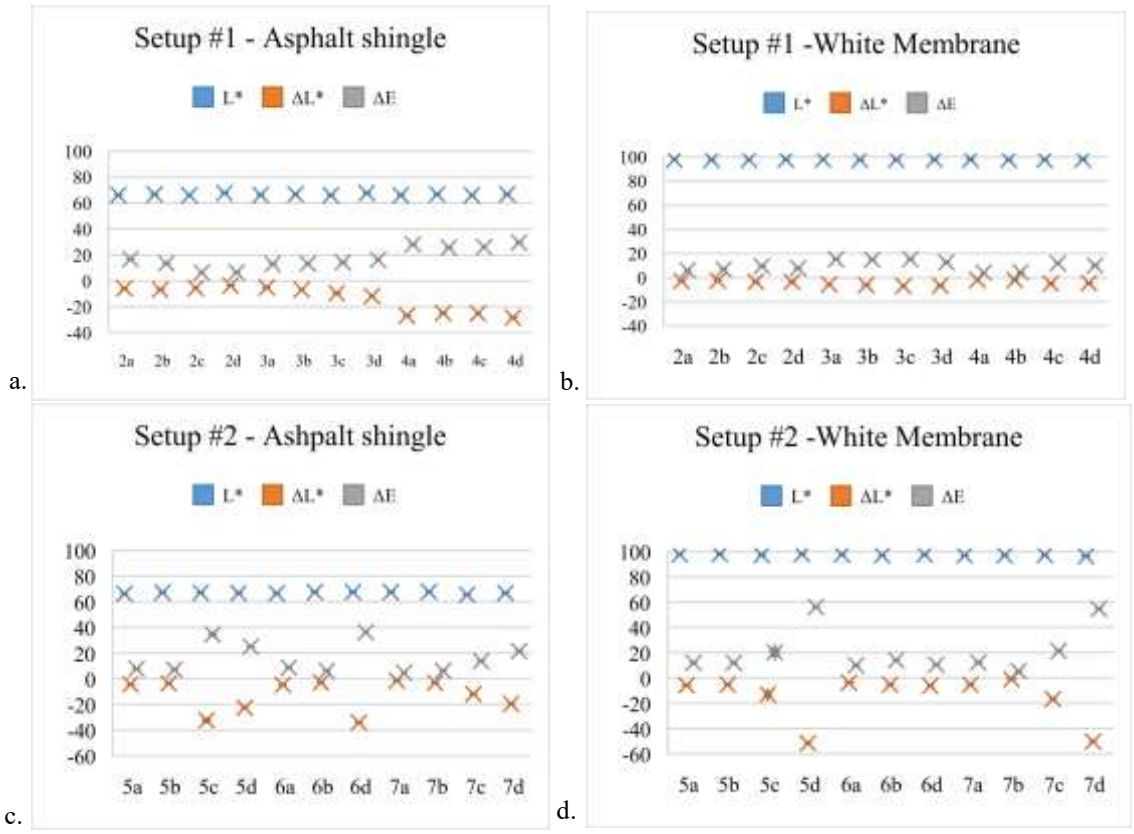

Figure 6. Colorimetry values among bio-ageing trials 2-3-4 run through setup#1 (*a, b*) and among bio-ageing trials 5-6-7 run through setup#2 (*c, d*). All sample values are shown.

Microorganisms pigments are the main responsible of aesthetical damage on surfaces and they sharply contribute to losses in solar reflectance, as observed in this study. As shown in Figure 5, ΔL* and ΔE are averagely higher on AS samples (mean ΔL* -13.4±1.3; mean ΔE 17.5±1.1) than in WM ones (mean ΔL* -4.3±0.5; mean ΔE 9.9±0.9) for setup #1. ΔL* and ΔE from setup #2 are similar to #1 for AS samples (mean ΔL* -14.4±1.5; mean ΔE 17.2±1.3), but the colorimetric distances from new and aged surfaces are deeper.

4 Conclusions

This work provides a preliminary laboratory bio-ageing protocol suitable to study the bio-deterioration dynamics on building materials surfaces, in particular solar reflective materials. Since biological growth variability that occurs on surfaces in natural environment is really high, the bio-ageing protocol here proposed has been thought in order to keep stable and monitored all the laboratory environmental factors. Two specie of microorganisms, *Chlorella m*. and *Nostoc c*., and two different laboratory setup have been investigated (setup#1 and setup#2) in

order to study the more repeatable experimental conditions. Solar reflectance and colorimetry analysis on repeated trials shows setup#1 (where 10 minutes of sample submersion time are repeated 6 times a day every 4 hours) as the most repeatable, and specifically when run with the green alga (*Chlorella m.*). All the other experimental conditions achieved differences among the same sample type statistically significant. Even though the challenge to make repeatable something that it is not for its meaning definition, the preliminary bio-ageing setup#1 confirms the capability of the system to optimize environment conditions where the growth of microorganisms and their interactions with materials results faster, providing a way to investigate bio-deterioration processes on materials.

ORCID

Giulia Santunione http://orcid.org/0000-0001-6133-108X
Chiara Ferrari http://orcid.org/0000-0003-2188-6464
Alberto Muscio http://orcid.org/0000-0002-3085-3958
Elisabetta Sgarbi http://orcid.org/0000-0003-4366-6956

References

Cheng, Meng-Dawn D., Susan M. Pfiffner, William A. Miller and Paul Berdahl. (2011). "Chemical and Microbial Effects of Atmospheric Particles on the Performance of Steep-Slope Roofing Materials." Building and Environment 46(5):999–1010.

Cheng, Meng Dawn, William Miller, Joshua New and Paul Berdahl. (2012). "Understanding the Long-Term Effects of Environmental Exposure on Roof Reflectance in California." Construction and Building Materials 26(1):516–26.

Ferrari, C., G. Santunione, A. Libbra, A. Muscio, E. Sgarbi, C. Siligardi and G. S. Barozzi. (2015). "Review on the Influence of Biological Deterioration on the Surface Properties of Building Materials: Organisms, Materials, and Methods." International Journal of Design and Nature and Ecodynamics 10(1):21–39.

Gaylarde, C. C. C., L. H. G. H. G. Morton, K. Loh and M. A. A. Shirakawa. (2011). "Biodeterioration of External Architectural Paint Films - A Review." International Biodeterioration and Biodegradation 65(8):1189–98.

Gaylarde, Christine C. and Peter M. Gaylarde. (2005). "A Comparative Study of the Major Microbial Biomass of Biofilms on Exteriors of Buildings in Europe and Latin America." International Biodeterioration & Biodegradation 55(2):131–39.

Mastrapostoli, Elena, Matthaios Santamouris, Dionysia Kolokotsa, Perdikatsis Vassilis, Danae Venieri and Kostas Gompakis. (2016). "On the Ageing of Cool Roofs: Measure of the Optical Degradation, Chemical and Biological Analysis and Assessment of the Energy Impact." Energy and Buildings 114:191–99.

Maury-Ramirez, Anibal, Willem De Muynck, Ruben Stevens, Kristof Demeestere and Nele De Belie. (2013). "Titanium Dioxide Based Strategies to Prevent Algal Fouling on Cementitious Materials." Cement and Concrete Composites 36(0):93–100.

Ortega-Calvo, J. J., X. Ariño, M. Hernandez-Marine and C. Saiz-Jimenez. (1995). "Factors Affecting the Weathering and Colonization of Monuments by Phototrophic Microorganisms." Science of The Total Environment 167(1–3):329–41.

Standard Test method for Solar Absorptance. ASTM E903, Performance, Measuring, Near Infrared Spectrophotom-, Air Mass, Zero Solar, Irradiance Tables, Sheet Materials, and Using Sunlight. (1996). "Standard Test Method for Solar Absorptance , Reflectance , and Transmittance of Materials Using Integrating Spheres 1." 03:1–9.

Sleiman, Mohamad, Thomas W. Kirchstetter, Paul Berdahl, Haley E. Gilbert, Sarah Quelen, Lea Marlot, Chelsea V. Preble, Sharon Chen, Amandine Montalbano, Olivier Rosseler, Hashem Akbari, Ronnen Levinson and Hugo Destaillats. (2014). "Soiling of Building Envelope Surfaces and Its Effect on Solar Reflectance - Part II: Development of an Accelerated Aging Method for Roofing Materials." Solar Energy Materials and Solar Cells 122:271–81.

Welander, M., J. Persson, H. Asp and L. H. Zhu. (2014). "Evaluation of a New Vessel System Based on Temporary Immersion System for Micropropagation." Scientia Horticulturae.

XV International Conference on Durability of Building Materials and Components
DBMC 2020, Barcelona
C. Serrat, J.R. Casas and V. Gibert (Eds)

Post Peak Behavior of Carbonated Concrete Structure - A Case Study of the Former Shime Mining Office Vertical Derrick in Japan

Kaiting Su[1], Kei-ichi Imamoto[2], Takafumi Noguchi[3], Manabu Kanematsu[4], Hitoshi Hamasaki[5], Kohji Teranishi[6], Chizuru Kiyohara[7]and Munenori Yamada[8]

1 Tokyo University of Science, viki417@gmail.com

2 Tokyo University of Science, imamoto@rs.kagu.tus.ac.jp

3 The University of Tokyo, noguchi@bme.arch.t.u-tokyo.ac.jp

4 Tokyo University of Science, manabu@rs.noda.tus.ac.jp

5 Shibaura Institute of Technology, hamasaki@shibaura-it-ac.jp

6 Meijo University, ktera@meijo-u.ac.jp

7 Tokyo University of Science, ckiyo@rs.tus.ac.jp

8 Center for Better Living, m-yamada@tbtl.org

Abstract. *This paper is a report on the investigation results of the Former Shime Mining Office Vertical Derrick, which was built in 1943 and was 75 years old at the time of the investigation. The building suffered from serious deterioration including rebar corrosion, which led to large area of concrete spalling. In this report, aggregation data of concrete spalling has been presented along with the investigation results of cover thickness. According to the investigation results, concrete spalling occurred in places where cover thickness was less than 25 mm. And According to the aggregation data, concrete spalling flakes increased by approximately 200 pieces per year, with the average size of 10 cm in diameter. Also, a possible relation between concrete spalling and rainfall was observed during the investigation. Equations using the proportion of wet area affected by rainfall to estimate the area of spalling are proposed, although the value of empirical coefficient α needs further discussion, including collecting data from other buildings where spalling occurs.*

Keywords: *Durability, Historical Buildings, Concrete Spalling, Concrete Moisture, Rebar Corrosion.*

1 Introduction

Concrete moisture is known to be a key parameter of rebar corrosion which leads to spalling and deterioration of the concrete structure. While reports on evolution of water content in real structures are still scarce, This paper is a report on the investigation results of the Former Shime Mining Office Vertical Derrick, which was 75 years old at the time of the investigation and had suffered from severe deterioration including rebar corrosion, which led to large area of concrete spalling. In addition, a possible relation between concrete spalling and rainfall was observed.

The introduction and the photo of the Former Shime Mining Office Vertical Derrick are shown in Table 1 and Figure 1.

2 Approach

To monitor the inner relative humidity evolution where the concrete cover was thin, from June 1st to July 25th, 2018, several thermo-hygrometers were implanted inside the concrete with cover thickness of 10mm and 40 mm. Concrete spalling had been observed and calculated every 3 months since February 2011. Cover thickness was measured with an electromagnetic radar method or a scale according to the condition of the cover.

Table 1. Introduction of the Former Shime Mining Office Vertical Derrick.

Location	Shime town, Fukuoka	Structure	RC
Owner	Shime town	Completion	May, 1943
Size (m)	height	47.6	
	length	15.3	
	width	12.3	

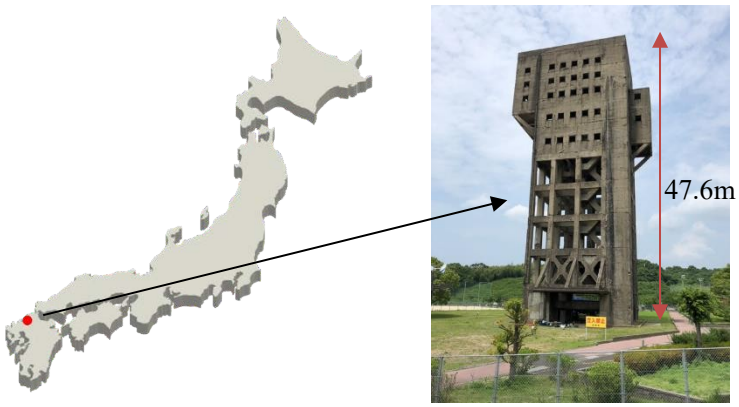

Figure 1. Photo of the Former Shime Mining Office Vertical Derrick.

3 Results

3.1 Results of Relative Humidity Monitoring

The results of relative humidity and temperature monitored during June 1st to July 25th, 2018, along with precipitation observed by Japan Meteorological Agency are shown in Figure 2. These results indicate that places with thinner cover thickness tend to be influenced by weather events such as rain.

3.2 Results of Concrete Spalling and Cover Thickness

Concrete spalling had been observed every 3 months since February 2011. The Figures used below are based on the observation record. Figure 3 shows the accumulated number of concrete flakes, which increased by the rate of approximately 200 pieces per year. However, the influence of weather events or earthquake was still unclear. Figure 5 shows the size and numbers of the flakes, which are around 5~10 cm in diameter. In addition, cover thickness

and level of rebar corrosion in relation to concrete spalling were also investigated. The subjects investigated included pillars and beams of 4 directions from 1st floor to 3rd floor. The aggregated results of cover thickness by are shown in Figure 6. According to the results, rebar exposure induced by concrete spalling occurred when cover thickness was less than 25 mm.

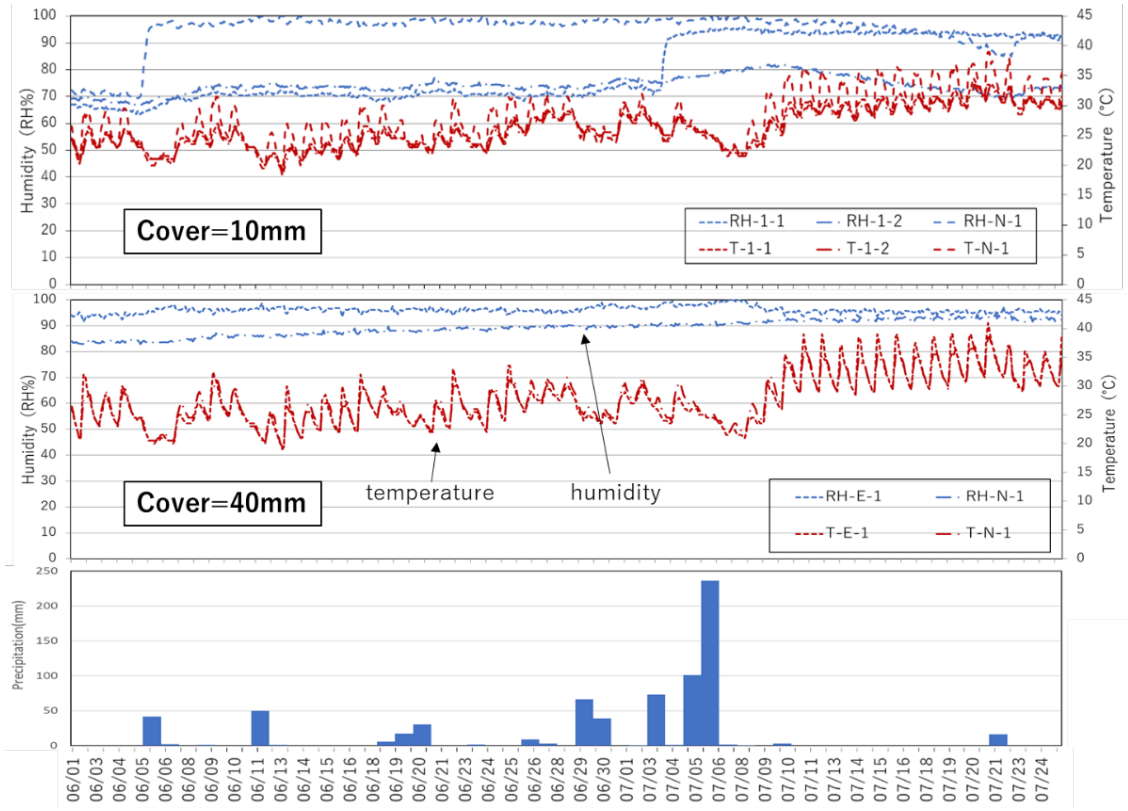

Figure 2. Evolution of Relative Humidity and Temperature (Upper: Cover=10mm, Middle: Cover=40mm) and Precipitation.

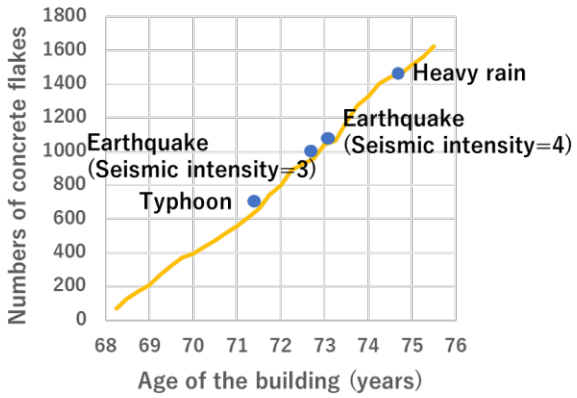

Figure 3. Accumulated number of concrete flakes.

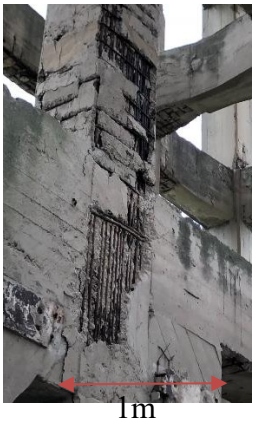

Figure 4. Rebar exposure due to spalling.

3.3 Results of Air Permeability Test and Carbonation

The results of the relation between the coefficient of carbonation and the coefficient of air permeability are shown in figure 7, along with previous investigation results of other buildings. The coefficient of carbonation is calculated by C/√t, where C stands for the depth of carbonation and t stands for years of use. The depth of carbonation is measured by applying phenolphthalein solution to concrete cores following the instructions in JIS A 1152. The coefficient of air permeability is calculated by the Torrent method (double chamber method). According to previous investigations, the coefficient of air permeability increases when the coefficient of carbonation increases. According to Figure 5, the results Vertical Derrick are within the range of previous results.

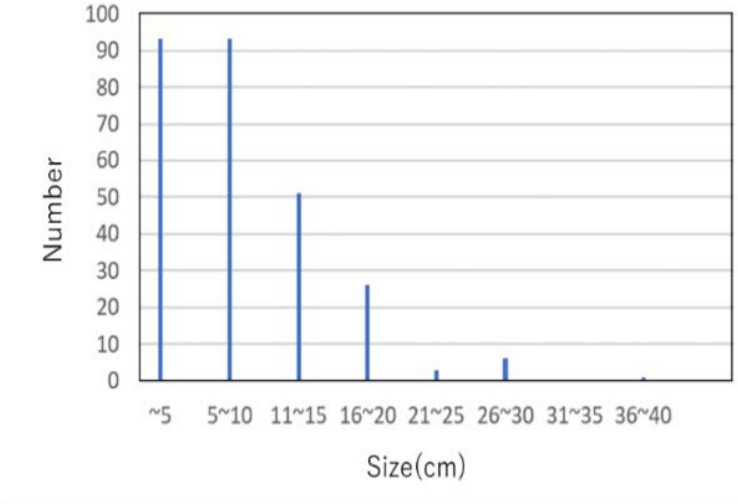

Figure 5. Size of concrete flakes.

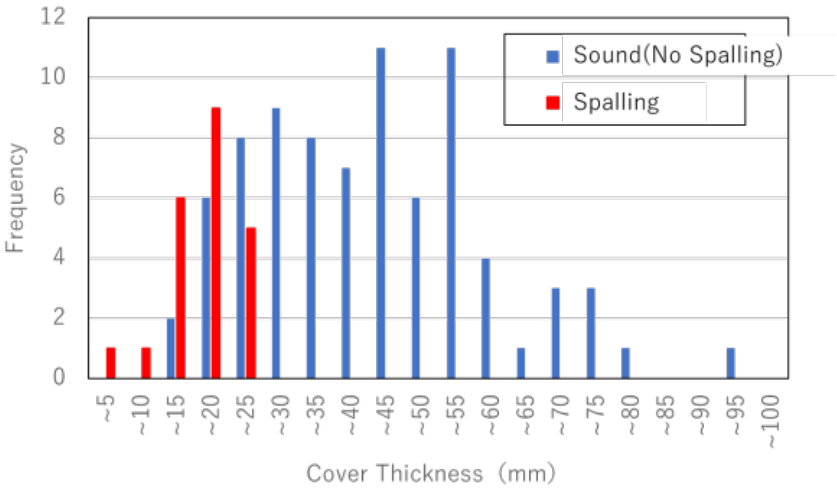

Figure 6. Cover thickness and rebar expose. (Tomotaka Ide, 2019)

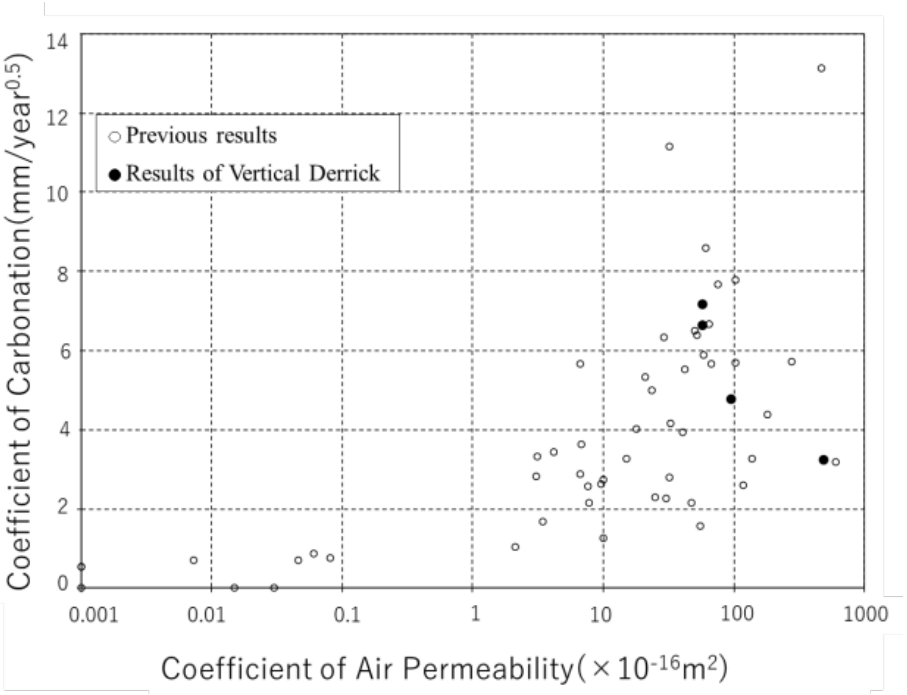

Figure 7. Relation between coefficient of air permeability and coefficient of carbonation. (Akio Tanaka; Kei-ichi Imomoto, 2013).

4 Discussion

4.1 Flying Distance of Flakes

Figure 8 shows the number and horizontal flying distance of flakes of each direction. According to Figure 8, concrete flakes mostly fell within the 7 meters range from the building. The height of the building was 47 meters. For the flying distance of 7 meters, the falling degree was 21.7° and the horizontal flying distance was 0.15 times the height of the building. Concrete flakes that fell out of this range needs further discussion concerning the windswept condition of this location. Table 2 shows the percentage of the spalling area of each direction. According to Table 2, the percentages of spalling area are between 5~10%.

Table 2. Spalling percentage of each direction. (spalling/total area of each side of the wall).

West	South	North	East
9.91%	5.20%	9.35%	3.71%

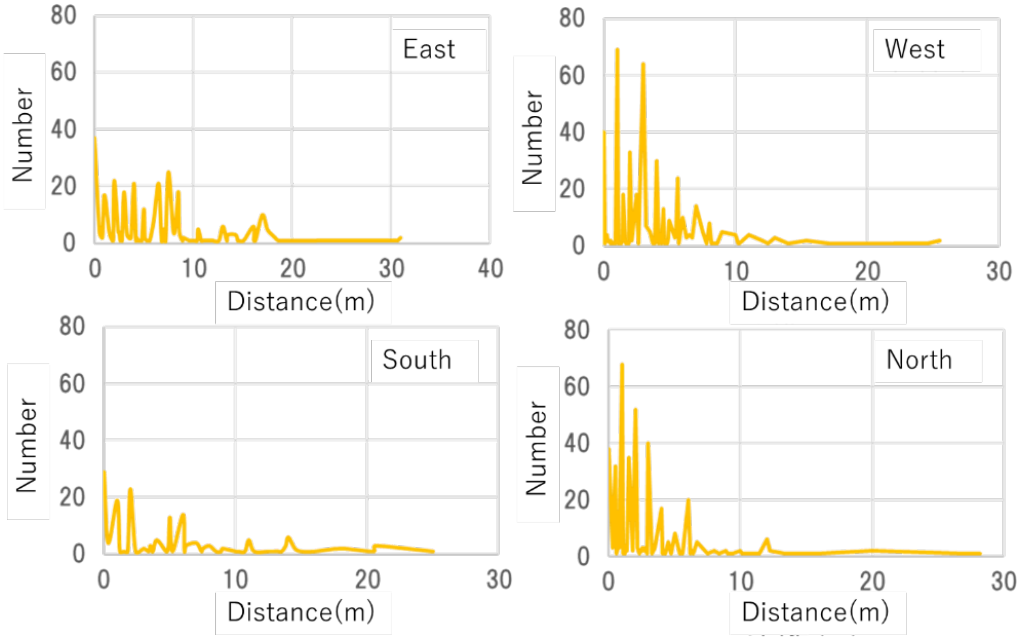

Figure 8. Number and horizontal flying distance of concrete flakes.

4.2 The Relation between Rainfall and Spalling

Figure 9 shows the percentage of wet area after rainfall. The percentages were calculated by wet /total area of each side of the wall. The calculation of wet areas from photos involved the image processing software, ImageJ. By circling the target areas, ImageJ automatically calculated the pixels of the selected areas. The manual selection of the wet areas brought an uncertainty to the results. To increase accuracy, image processing method should be further discussed in future researches. According to the results, the north and the west side with higher number of concrete flakes also showed higher percentage of the wet area. At this location, due to northwest wind blew throughout the year, the north and the west side of the building were more possible to be affected by rainfall than the south and the east side. This observation indicates that there might be a relation between spalling and rainfall. The following equations are proposed considering the relation between the two.

$$\textit{Coefficient of Rainfall} = \textit{Percentage of Wet Area} \times \textit{Number of Days with Precipitation over 10mm} \quad (1)$$

$$\textit{Percentage of Spalling Area} = \textit{Years after Carbonation reaches 25mm} \times \textit{Coefficient of Rainfall} \times \textit{Percentage of Cover Thickness Less than 25mm} \times \alpha \quad (2)$$

Table 3 shows the results of the *Coefficient of Rainfall* and the empirical coefficient α by applying equation (1) and (2) to the north and the south side. When the value of α is 0.006, according to the *Coefficient of Rainfall* in Table 3, the estimated values of spalling area along with measured spalling area are shown in Table 4.

Table 3. Results of the coefficient of rainfall and the empirical coefficient α of the south and the north side.

	South	North
Coefficient of Rainfall	1.231	4.537
α	0.0062	0.0012

West, 78% wet South, 19% wet North, 70% wet East, 36% wet

Figure 9. Percentage of wet area (wet/total area of each side) after rainfall.

Table 4. The estimated value and measured value of spalling area of the east and the west side.

Percentage of Spalling Area	East	West
Estimated Value	3.63%	5.45%
Measured Value	3.71%	9.91%

5 Conclusions

Post peak behaviors of carbonated concrete structures are as follows.

- Concrete spalling flakes increased by the rate of 200 pieces per year while the influence of climate events was still unclear. The sizes of the flakes were around 10 cm in diameter.
- The horizontal flying distance of concrete flakes were approximately 0.15 times the height of the building.
- The sides of the walls with higher proportion of concrete spalling also present higher proportion of wet area during rainfall.

Acknowledgements

Thanks to the board of education of Shime-Cho, who had given the chance for the investigation of Shime Mining Office Vertical Derrick and cooperated with the aggregation of concrete flakes and other deterioration investigations.

ORCID

Kaiting Su: https://orcid.org/0000-0003-2503-4154
Kei-ichi Imamoto: https://orcid.org/0000-0001-8174-8827
Takafumi Noguchi: https://orcid.org/0000-0001-6115-2292
Manabu Kanematsu: https://orcid.org/0000-0003-2473-0625
Hitoshi Hamasaki: https://orcid.org/0000-0002-1830-3734
Chizuru Kiyohara: https://orcid.org/0000-0003-1286-9056

References

Akio Tanaka and Kei-ichi Imomoto. (2013). Evaluation of Carbonation Progress of Existing Concrete Structure Based on Air Permeability of Cover Concrete J. *Struct. Constr. Eng., AIJ, 78*(691), 1539-1544.

Japan Meteorological Agency. *Earthquake information centered on the west off the Satsuma Peninsula.*

Kyushu Reginal Development Association. *Disaster History Information in Kyushu.*

Kyushu Sangyo University. *The possibility of Reservation of the Former Shime Mining Office Vertical Derrick.*

Shime Town. *Important Cultural Property Plan for Reservation and Utilization of the Former Shime Mining Office Vertical Derrick.*

Tomotaka Ide. (2019). Investigation of Shime Old Coal Mine Tower-Part 1 Result of the Cover Depth and Rebar Corrosion, and Humidity Change in Concrete. *Summaries of Technical Papers of Annual Meeting, 807- 808.*

XV International Conference on Durability of Building Materials and Components
DBMC 2020, Barcelona
C. Serrat, J.R. Casas and V. Gibert (Eds)

Proven Performance: Aged TPO Field Study

Jennifer Keegan[1], Thomas J. Taylor[2] and James R. Kirby[3]

[1] Director, Building and Roofing Science at GAF, 1 Campus Drive, Parsippany, NJ 07054, USA, jennifer.keegan@gaf.com
[2] Building and Roofing Science Advisor at GAF, 1 Campus Drive, Parsippany, NJ 07054, USA, thomas.taylor@gaf.com
[3] Building and Roofing Science Architect at GAF, 1 Campus Drive, Parsippany, NJ 07054, USA, james.kirby@gaf.com

Abstract. *New thermoplastic polyolefin (TPO) roof membranes have been extensively analyzed in laboratories, roof exposure farm fields, and under accelerated weathering conditions. The ASTM International material standard specification for TPO membranes has been regularly improved since its inception to incorporate more demanding tested-product performance, including requirements for accelerated weathering and aging. Industry data on the aged performance of TPO roof membranes to date has largely been based on laboratory work, regional studies, and anecdotal case studies of TPO roofs, predominantly those that have been improperly designed and/or installed, and membranes with retired formulations that resulted in premature failure. Today, there are TPO roofs in the United States that have been in service for nearly 20 years. This paper will review the long-term performance of a large sampling of TPO roof membranes installed throughout the United States by evaluating thickness, flexibility, inspection under 7X magnification, aged seam strength, and repair weld adhesion. The intent of this study was to evaluate 1) field-aged TPO roof membrane performance and 2) the ability to repair field-aged TPO roof membranes.*

Keywords: *TPO, FPO, Aged Performance, Field-Study, Long-Term Performance, Repairability.*

1 Introduction

Flexible Polyolefin (FPO) roof membranes have been part of the European roofing market since the late 1980's. In the early 1990's, this technology migrated to the United States as Thermoplastic Polyolefin (TPO). FPO and TPO are the same polymer that use different terminology in the European and United States markets, respectively, and will be referred to as TPO throughout this paper.

TPO roof membranes are the fastest growing commercial roof membrane on the market, and has grown significantly over the past 20 years. According to the European Single Ply Waterproofing Association (ESWA), TPO is growing in market share, and according to the Single Ply Roofing Institute, TPO represents almost half of the installed low-slope roofing in the United States. The global TPO roof membrane market is expected to reach $2.2 billion by 2024, with a compound annual growth rate (CAGR) of 3.7-percent from 2019 to 2024 (ResearchAndMarkets, 2019).

These membranes are now regarded as a mature technology with properties defined by the ASTM International material standard for TPO membranes, ASTM D6878. These standards have been improved since their inception to incorporate more demanding tested-product performance, including stronger requirements for accelerated weathering and aging.

Today, there are TPO roofs that have been in service for over 20 years (ASTM D573; Taylor and Xing, 2015). This paper reviews the long term performance of field-aged TPO roof membranes to assess performance and the ability to repair aged TPO roof membranes. Specifically addressed are known failure modes of some manufactured TPO membranes which include erosion of the cap (thickness over scrim) down to the scrim and surface cracking, as well as concerns surrounding the ability to repair aging TPO membranes.

2 Program

The intent of this study was to evaluate field-aged TPO roof membrane performance and the ability to repair membranes as they age. Membrane samples were collected from roofs around the United States that were at least 12 years in service. Roofs were selected to gain a general sense of typical performance in various locations across the country. Most of the roofs evaluated to date in this study were installed between 2005 and 2006; the oldest sample reviewed to date was installed 18 years ago. All samples were from the same manufacturer and were predominantly 45 and 60-mil (equivalent of 1.2 and 1.5 mm) smooth-back membranes. Samples were taken from mechanically attached, induction welded, and adhered roofs. Self-adhered membranes were excluded from this study.

2.1 Sample Selection

Each Samples approximately 60 cm by 90 cm (2-foot by 3-foot) and captured a field-welded seam, were taken from the field of the roof and in a location that resulted in increased heat exposure.

The large samples were cut into smaller pieces to evaluate membrane thickness, thickness over scrim, brittleness, heat aging and weather resistance, ply adhesion of existing welds, and ply adhesion of repair welds. Each test was conducted on five unique specimens from each location on the roof.

2.2 Test Program

The testing program was built around ASTM D6878-19, with modifications as needed for aged samples. The artificial aging tests were replaced with field aging for a minimum of 12 years. All tests were conducted in a commercial test laboratory. All data gathered was used in the analysis.

2.2.1 Membrane Thickness and Thickness of Coating Over Scrim

TPO membranes consist of two polymer layers of TPO, the cap and the core, which are laminated together with a polyester reinforcing scrim in-between. Following ASTM D751 and ASTMD7635/D7635M respectively, the overall membrane thickness and the thickness of the coating over the scrim (or cap layer) was measured. This measurement was compared to the current ASTM TPO standard requirements for new membranes to evaluate how they are weathering.

2.2.2 Heat Aging and Weather Resistance

ASTM D6878-19 requires 56 days of heat aging or a radiant exposure of 10,080 kJ/(m^2.nm) prior to the mandrel bend and inspection. As the membrane samples were already aged, the artificial UV and heat aging exposures were eliminated from the test protocol and the pass/fail requirements were applied to the field aged materials.

Heat aging and weather resistance are evaluated per ASTM D573 and ASTM G151/G155 respectively, which includes an inspection at 7X magnification when bent over a 3-inch diameter mandrel for surface cracking.

2.2.3 Low Temperature Flexibility

Low temperature flexibility or the brittleness point was evaluated per ASTM D2137, method B. The specimens were examined at 5X magnification for any visible fracture or crack in the cap layer after having bent the specimens to an angle of 180° in the same direction caused by the test impact.

2.2.4 Aged Ply Adhesion

ASTM D1876, also referred to as the T-Peel Test, was used to evaluate the welded seam ply adhesion. The ply adhesion values reported are the average of the maximum load values at the initial break.

Ply adhesion testing of a proper weld will fail cohesively within one of the plies, exposing the underlying scrim. This is called a “film tearing bond” and is also used to evaluate the integrity of the weld. For the purposes of this evaluation, anything over 70-percent film tearing bond was considered a proper weld.

2.2.5 Repair Ply Adhesion

New TPO membrane that was commensurate in type and thickness of the existing membrane, was welded to the aged membrane to evaluate the ability to repair aged materials. Repairs with new membrane welded to the cap of the aged membrane were evaluated, as well as new material welded to the core (the underside) of the aged membrane. Ply adhesion to the core was not evaluated for adhered membrane samples due to remnants of adhesive and/or facer

from the insulation or cover board. Given the remnants attached to the underside of adhered membranes, repairs to the core would not be reliable.

3 Data Analysis

Samples were taken from 20 different roofs across the United States (See Figure 1). Climatic conditions of the United States cities were matched up with their European counterparts, and are shown in Figure 2 to illustrate the approximate European climate equivalents captured in this study. These roofs were installed over office buildings, manufacturing facilities, retail outlets, libraries, automotive repair shops, warehouses, and a grocery store. All data gathered was used in the analysis.

Figure 1. To date, samples have been collected from 20 roofs across the United States.

Figure 2. European climatic equivalent locations to the samples collected across the United States.

On average, a typical roof membrane in this study was installed between 2005 and 2006 has been exposed to 20 hail storms, over 50 feet of rain, over 500 days of 32°C+ (90°F+) and wind gusts of up to 148 kph (92 mph). Specifically, the roof membrane from Orlando, Florida has been exposed to the elements for over 17 years. This roof has weathered 9 hurricanes, 13 hail storms, 56 feet of rain, 1,660 days of 32°C+ (90°F+) and wind gusts of up to 169 kph (105 mph). While the United States and European climates are somewhat comparable, the wind gusts are more aggressive than what is typical in Europe.

3.1 Membrane Thickness and Thickness of Coating over Scrim

Retention of the cap material, *i.e.* the thickness over scrim, is critical to the membrane's long-term performance as it provides the UV and heat stabilization properties of the membrane. As the cap erodes, the scrim can become exposed and the weather tightness of the membrane is then compromised.

The analysis of aged roof samples began with overall membrane thickness. ASTM standard D6878-19 requires the as-produced membrane to be within +15%, -10% of stated thickness, and not less than 39-mils. Even after 12 or more years of aging, all of the 45 and 60-mil (1.2mm and 1.5 mm equivalent) membrane samples complied with the current ASTM requirements for newly manufactured TPO membranes.

ASTM standard D6878-03, the active specification at the time the sampled roofs were installed, required 12-mil (0.30mm) thickness over scrim. The current version of this standard requires the thickness over scrim to be at least 30-percent of the overall membrane thickness and not less than 18-mils (0.45mm). Both the 45 and 60-mil (1.2mm and 1.5 mm equivalent) membranes analyzed in this study are still in compliance with the newly manufactured membrane requirements and are even in compliance with the current standard ASTM D6878-19, with the thickness over scrim exceeding ASTM minimums and averaging 37- to 40-percent of the nominal membrane thickness. The 45-mil (1.2mm) samples averaged 18-mils (0.45mm) over scrim and the 60-mils (1.5mm) samples averaged 22-mils (0.56mm) over scrim. It should be noted that the EN 13956-12 does not include thickness over scrim measurements.

3.2 Heat Aging and Weather Resistance

Surface cracking was evaluated by visual inspection of the roof membranes at the time the samples were collected, and through modified versions of heat aging and weather resistance testing. Both ASTM tests require inspection at 7X magnification when bent over a 7.6mm (3-inch) diameter mandrel. As the samples were field aged for a minimum of 12 years artificial heat aging and weathering were eliminated, and a focus placed on visual assessment. This evaluation is an important indicator of long term performance (Taylor and Xing, 2015). Surface cracking can lead to quick deterioration of the membrane and is a good indicator of long term performance concerns. All of the samples, both the 45 and 60-mil (1.2mm and 1.5mm equivalent) membranes, exhibited no signs of cracking when bent over the mandrel and viewed at 7X magnification.

3.3 Low Temperature Flexibility

The aged roof samples were evaluated for low temperature flexibility to determine if the membrane became more brittle and prone to cracking as it aged. ASTM standard D6878-19 requires new membranes to have a brittleness point of -40°C (-40°F) or lower. All of the 60-mil (1.5mm) samples tested to date still met this requirement after 12 or more years of field aging. The 45-mil (1.2mm) samples showed signs of cracking at -37°C (-35°F). While this is still good performance and aged membranes cannot be expected to perform at the same level as new membranes, the data does support the use of thicker membranes for longer term performance.

3.4 Aged Ply Adhesion and Repair Ply Adhesion

The ply adhesion of the aged samples averaged approximately 8.76 N/mm (50 lbf/in.) for both the 45 and 60-mil (1.2mm and 1.5mm equivalent) membranes, with a minimum of 70-percent film tearing bond. Representative data are shown in Figure 14. Ply adhesion of TPO membranes should be evaluated throughout the day during installation. The film tearing bond sample is evaluated to confirm the membrane is properly welded together. If the sample fails

and the scrim is not exposed, or the film tearing bond is not greater than 70-percent, the contractor must adjust the heat and/or speed at which the welding equipment is being used. While failures associated with welded seam delamination are not common, and poor welds are generally identified during routine inspections during installation, ply adhesion is used as a quality control tool in the field. However, there is not a clear industry consensus on the minimum strength requirement to evaluate ply adhesion.

New TPO membrane samples included in a broad TPO sampling study of all industry manufacturers conducted by Structural Research, Inc. (SRI) (Dupuis, 2019) averaged a ply adhesion (T-Peel) value of 7.01 N/mm (40 lbf/in.), with a minimum value of 5.13 N/mm (29.3 lbf/in.) However previously, (Simmons *et al*., 1999) found that the ply adhesion tests typically failed adhesively, meaning there was not a strong bond between the TPO layers, when the ply adhesion was 4.55 N/mm (26 lbf/in.) or less. Simmons findings supports SRI's minimum value threshold for ply adhesion. The ply adhesion values of the aged TPO membranes were 15-percent above the average ply adhesion value from the SRI study on new TPO membranes. Therefore, as expected, the aged welds appear to be performing well and are of adequate strength. To address questions around the ability to repair aged TPO membranes, this study examined the adhesion of new membrane to aged membrane. Two approaches were examined; welding the new membrane to the cap of the aged membrane, and new membrane welded to the core of the aged membrane.

The ply adhesion of the new membrane to the aged cap averaged 7.5 N/mm (43 lbf/in.) for 45-mil (1.2mm) membranes and 8.23 N/mm (47 lbf/in.) for 60-mil (1.5mm) membranes. For the new membrane welded to the aged core, the ply adhesion averaged 9.28 N/mm (53 lbf/in.) and 9.98 N/mm (57 lbf/in.) for the 45-mil and 60-mil (1.2mm and 1.5mm equivalent) membranes, respectively.

The ply adhesion values of new repair membrane to the aged TPO membrane are above the average ply adhesion value of 7.01 N/mm (40 lbf/in.) from the SRI study on new TPO membranes. This provides validity to the integrity of repairs to aged TPO membranes and the ongoing maintainability of these roofs.

4 Next Steps and Interim Conclusions

While this paper summarizes data from 20 different roofs from around the country, samples will continue to be collected and analyzed. It is noted that all data received to date has been included in this analysis. No data detrimental or otherwise has been excluded from the analysis or findings.

The findings to date, as summarized in Figure 3, illustrate the robust performance of TPO membranes as they age. Given the inherent flexibility and fungal resistance of TPO, and the UV and heat stabilizers, this comes as no surprise. However, the ability to repair aged TPO membranes has been undefined and anecdotal to date. The interim findings of this study clearly demonstrate the weld integrity of properly executed repairs.

While this study is focused on TPO membranes the United States, this evaluation only strengthens the findings of previous studies on the durability and repairability of TPO roof membranes in Europe.

60 mil (1.5mm) white TPO	Average	Performance	45 mil (1.2mm) white TPO	Average	Performance
Membrane Thickness	1.40mm (55 mils)	Exceeds ASTM D6878	Membrane Thickness	0.46mm (18 mils)	Exceeds ASTM D6878
Thickness over Scrim	0.56mm (22 mils)	Exceeds ASTM D6878	Thickness over Scrim	1.07mm (42 mils)	Exceeds ASTM D6878
Low Temperature Flexibility	-40°C (-40°F)	Meets ASTM D6878	Low Temperature Flexibility	-37°C (-35°F)	<ASTM D6878 (-40°F)
Heat Aging/Weather Resistance (7X Magnification mandrel bend)	Pass	Meets ASTM D6878	Heat Aging/Weather Resistance (7X Magnification mandrel bend)	Pass	Meets ASTM D6878
Aged Ply Adhesion	8.93 N/mm (51 lbf/in)	> Avg. ply adhesion for new TPO membrane[1]	Aged Ply Adhesion	8.58 N/mm (49 lbf/in)	> Avg. ply adhesion for new TPO membrane[1]
Repair Ply Adhesion to Cap	8.23 N/mm (47 lbf/in)		Repair Ply Adhesion to Cap	7.53 N/mm (43 lbf/in)	
Repair Ply Adhesion to Core	9.98 N/mm (57 lbf/in)		Repair Ply Adhesion to Core	9.28 N/mm (53 lbf/in)	

1. Dupuis, Rene M., "Final Report on 2013-2014 Broad Sampling TPO Test Program"

Figure 3. Average findings from study to date for 45 and 60-mil (1.2mm and 1.5mm equivalent) membranes as compared to ASTM D6878-19.

5 Conclusion

In summary, the aged TPO membrane roofs in this study are performing well and in most instances, meeting the current ASTM D6878-19 requirements for newly manufactured membranes.

- Even after 12 or more years of aging, both the 45 and 60-mil (1.2mm and 1.5mm equivalent) membranes analyzed in this study are still in compliance with these newly-manufactured membrane requirements, with the thickness over scrim averaging over 40-percent of the actual aged membrane thickness.
- All of the samples, both the 45 and 60-mil (1.2mm and 1.5mm equivalent) membranes, exhibited no signs of cracking when bent over the mandrel and viewed at 7X magnification.
- All of the 60-mil (1.5mm) samples tested to date still meet cold temperature flexibility requirements of -40°C (-40°F) after 12 or more years of aging. The 45-mil (1.2mm) samples showed signs of cracking at -37°C (-35°F).
- Ply adhesion values of new repair membrane to the aged TPO membrane are above the average for new TPO membranes. This provides some validity to the integrity of properly executed repairs to aged TPO membranes.

Acknowledgements

The authors would like to thank Christopher McGroarty, Greg Coletto, Jim Brikla, Mark Anderson, and Joshua Wilson for their assistance in this research initiative.

References

ASTM D573. *Standard Test Method for Rubber—Deterioration in an Air Oven.*
ASTM D751. *Test Methods for Coated Fabrics.*

ASTM D7635/D7635M. *Standard Test Method for Measurement of Thickness of Coatings Over Fabric Reinforcement.*

ASTM D1876 – 08. *Standard Test Method for Peel Resistance of Adhesives.*

ASTM D2137. *Standard Test Methods for Rubber Property—Brittleness Point of Flexible Polymers and Coated Fabrics.*

ASTM G151. *Standard Practice for Exposing Nonmetallic Materials in Accelerated Test Devices that Use Laboratory Light Sources.*

ASTM G155 *Standard Practice for Operating Xenon Arc Light Apparatus for Exposure of Non-Metallic Materials.*

Beer, H.R. *et al*. (2011). Longterm Field Studies and Residual Service Life Prediction of FPO Roofing Membranes, DBMC XII.

Croce, S. and Fiori, M. (2008). Polyolefin Roof Membranes On Site Durability Evaluation, *11th International Conference on Durability of Building Materials and Components*, Istanbul, Turkey, May 11th -14th.

Dupuis, R.M. (2019). Final Report on 2013-2014 Broad Sampling TPO Test Program, 2015, 1-7.

European Single ply Waterproofing Association Roofing, page: https://www.eswa.be/roofing.cfm as stated on website as seen on October 14, 2019.

Pierce, H.H. and Xing, L. (2017). Understanding Accelerated UV, Field and Thermal Aging of Thermoplastic Roofing Membranes, XIV DMBC 2017.

ResearchAndMarkets.com, TPO Roofing Membrane Market Report: Trends, Forecast and Competitive Analysis July 2019 .

Simmons, T.R., Runyan, D., Liu, K.K.Y., Paroli, R.M., Delgado, A.H. and Irwin, J.D. (1999). Effects of Welding Parameters on Seam Strength of Thermoplastic Polyolefin (TPO) Roofing Membranes, Proceedings of the North American Conference on Roofing Technology, 56–65.

Taylor, T.J. (2015). The History of TPO and How it Has Changed the Commercial Roofing Market, Florida Roofing, 10-11.

Taylor, T.J. and Xing, L. (2015). Accelerated Aging of Thermoplastic Polyolefin Membranes Prediction of Actual Performance, in *Roofing Research and Standards Development: 8th Volume*, ed. W. Rossiter and S. Molleti (West Conshohocken, PA: ASTM International), 139-152.

Western States Roofing Contractors Association (2011). TPO Roof Research and Testing Project - 10th Year Update Report, 1-18.

XV International Conference on Durability of Building Materials and Components
DBMC 2020, Barcelona
C. Serrat, J.R. Casas and V. Gibert (Eds)

Rainwater Management of Ventilated Facades: Impact of Joint Width and Cavity Size

Stéphanie Van Linden and Nathan Van Den Bossche

Ghent University, Faculty of Engineering and Architecture, Building Physics Group, Sint-Pietersnieuwstraat 41 B4, Ghent, Belgium, stephanie.vanlinden@ugent.be

Abstract. *During a rain event, most of the raindrops reaching the facade either splash back or run off the exterior surface of the facade. However, it is evident that also a portion of the water infiltrates through the open joints of a ventilated facade. The infiltrated water may either be drained in the cavity to the bottom of the wall or reach the insulation layer. If there are any deficiencies present in the insulation layer or at the connection of the brackets, the infiltrated water might introduce problems. Additionally, if the cavity is not able to drain all the infiltrated water or adhered droplets to one of the cavity surfaces do not dry out, moisture problems might occur. Experiments were conducted to determine the infiltration rate through ventilated facades with open joint widths of 5 mm, 10 mm and 15 mm and cavity widths ranging from 190 mm to 40 mm. It was observed that the amount of infiltrating water was larger for larger joints widths. Due to the larger kinetic energy of the drops flowing through the larger joint widths, the drops were able to reach the exterior surface of the insulation layer, even for large cavity widths. The results from the experimental assessment were used as input parameters for hygrothermal simulations to determine the risk of moisture problems.*

Keywords: *Water Infiltration, Drainage, Ventilated Facades, Moisture Loads.*

1 Introduction

Ventilated facades are usually designed according to the open rainscreen principle to control rainwater penetration (Garden, 1963). The external cladding, which usually consists of independent facade panels, is supposed to keep out most of the rain. Evidently, also a portion of the driving rain infiltrates through the open joints between the facade panels and reaches the air cavity behind the external cladding. This cavity acts as a capillary break and drains the infiltrated water to the bottom of the wall where it may flow back to the exterior through drainage holes. The air barrier at the interior side of the facade restricts the airflow through the wall. Combined with the open joints between the facade panels, the pressure difference over the cladding is minimized. This reduces the pressure difference acting as one of the main driving forces for water to infiltrate (Suresh Kumar, 2000). Other forces that may affect water infiltration through joints are surface tension, capillarity, kinetic energy and gravity. Experiments conducted by Mas *et al.,* (Mas, Gutiérrez, Gil, Gil, and Galvan, 2011) revealed that for joint widths larger than 8 mm, gravity and kinetic energy are the main forces driving rain through the joints, capillarity and surface tension having less importance.

For the same weather conditions, the amount of infiltrating water depends on the geometry of the joints and the material characteristics. When raindrops infiltrate, they are either drained to the bottom of the wall or they may reach the drainage layer at the back of the cavity dependent

on the cavity size and the geometry of the joints. If there are any deficiencies present at the drainage layer or at the connection of the brackets, the infiltrated water might introduce problems. Additionally, if the cavity is not able to drain all the infiltrated water or if adhered water drops to one of the cavity surfaces do not dry out, moisture problems might occur. However, the amount of experimental work that quantifies the portion of infiltrating water through ventilated facades and the portion of water reaching the drainage layer at the back of the cavity, is very limited.

Recatala *et al.,* (2017) assessed the watertightness performance of a full-scale ventilated facade specimen with joint widths of 10 mm. Laboratory experiments showed that the airtightness level of the wall did not have an impact on the infiltration rates as pressure moderation over the external cladding was achieved for both leaky and sealed constructions. The applied spray rate, however, did have a significant impact on the infiltration rate. A parabolic correlation was obtained between both parameters. It was observed that when a lot of water was running down the external cladding, the water runoff film prevented driving rain drops from infiltrating through the open joints and bounced and splashed off the surface instead. The results also showed that the infiltration rate of water through the horizontal joints was significantly larger than the infiltration rate through the vertical joints. Also the impact of the horizontal joints on the amount of water reaching the drainage layer at the back of the cavity was larger compared to the impact of vertical joints. The splattering effect of raindrops in the joints and onto the brackets caused additional raindrops to reach the drainage layer. However, most of the infiltrated water was drained to the bottom of the cavity. Only 0,54% of the impinging water on the external cladding averagely reached the drainage layer which was situated 10 cm behind the cladding panels. The ASHRAE standard 160 (2016), however, proposes a default penetration rate of 1% deposited on the water-resistive-barrier. It is clear that more research on the amount of rain that penetrates through various types of claddings and different wall configurations is necessary.

The objective of this study is to assess the impact of the joint width and cavity size of a ventilated facade specimen on the amount of water infiltrating through the joints and the amount of water reaching the drainage layer at the back of the cavity. Additionally, the impact of a panel installed out of plane of the exterior surface on the infiltration rate was assessed. The results from the experimental assessment were used as input parameters for hygrothermal simulations to determine the risk of moisture problems.

2 Test Setup and Methodology

2.1 Test Setup

The impact of joint width, cavity size and construction errors on the infiltration rates through ventilated facades was evaluated by means of five test specimens. Each test specimen was mounted in a steel frame with dimensions 2390 x 1070 mm and incorporated 24 fibre cement boards. These boards were screwed onto vertical timber studs with a cross-section of 38 x 90 mm. The vertical studs were positioned at the vertical joints between the facade panels. Flashing was applied between the studs and the facade panels as recommended by the manufacturer to avoid water being absorbed by the wood studs. The vertical studs were affixed to a wood frame, simulating the structural wall, by means of threaded rods. In between the vertical studs and the

wood frame a PMMA panel was installed, simulating the drainage layer which in case of ventilated facades usually is the insulation layer. The PMMA panel could be moved further away or closer to the facade panels in order to vary the cavity width. The fibre cement boards had a thickness of 8 mm and a width and length of 300 mm. The width of the boards at the sides of the specimens was dependent on the applied joint width.

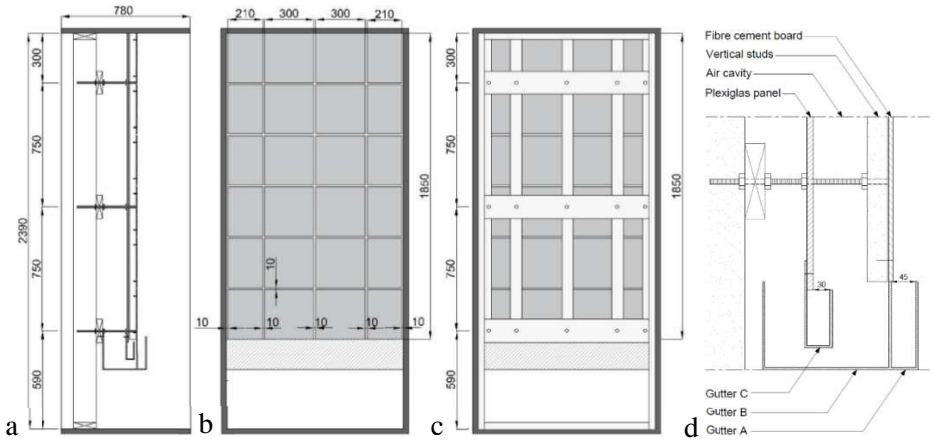

Figure 1. a) Cross section, b) Front view, c) Rear view of test setup 2, d) Detailed cross section gutter system.

The specimens evaluated by Recatala *et al.,* (2017) had a joint width of 10 mm. The same width was chosen as the standard joint width in this study. Additionally, a joint width of 5 mm was evaluated, as Mas *et al.,* (2011) stated that the impact of surface tension and capillarity increased for joint widths smaller than 8 mm. The largest evaluated joint width was 15 mm.

The smallest evaluated cavity width was 40 mm as this was the combined thickness of the vertical studs and the flashing. The largest evaluated cavity width was 190 mm as it was observed that no significant differences were measured for a cavity width of 160 mm and 190 mm.

Three gutters were installed at the bottom of each specimen: gutter A collected the water which flowed downward at the exterior side of the facade panels during the test or splashed back up to 45 mm in front of the panels, gutter B collected the water which flowed downward at the back of the facade panels, the vertical studs and in the drainage cavity, and gutter C collected the water which flowed downward at the PMMA panel and up to 30 mm in front of the panel. In case a cavity width of 40 mm was applied, gutter B only collected the water that ran off the interior side of the facade panels and gutter C collected the remaining portion of water that reached the cavity.

2.2 Test Procedure

Water was sprayed onto the test specimens by means of a spraying rack with full cone nozzles which were installed at the top of the specimens and at a horizontal distance of 250 mm. A constant spray rate of 120 l/h was applied. No pressure difference was applied to the external cladding as Recatala (2017) already observed that pressure equalization was achieved for both leaky and sealed specimens. The water collected by the gutters was weighed both during and after the test by means of weighing scales with an accuracy of ± 0,1 g. Water was sprayed for 400 seconds or until the infiltration rate for all gutters was constant for a significant amount of

time. The pattern of water droplets which adhered to the PMMA panel after the test was visually evaluated. The repeatability of the test procedure was evaluated by conducting the same experiment at least two times.

3 Experimental Results and Discussion

3.1 Impact of Joint and Cavity Width

Figure 2 shows the percentage of water collected by gutter A, B and C relative to the total amount of collected water. The tests were conducted for different cavity widths ranging from 4 cm to 19 cm and joint widths of 5 mm, 10 mm and 15 mm for respectively specimen 1, 2 and 3. As the timber studs were situated at the vertical joints, the collected water only infiltrated through the open horizontal joints.

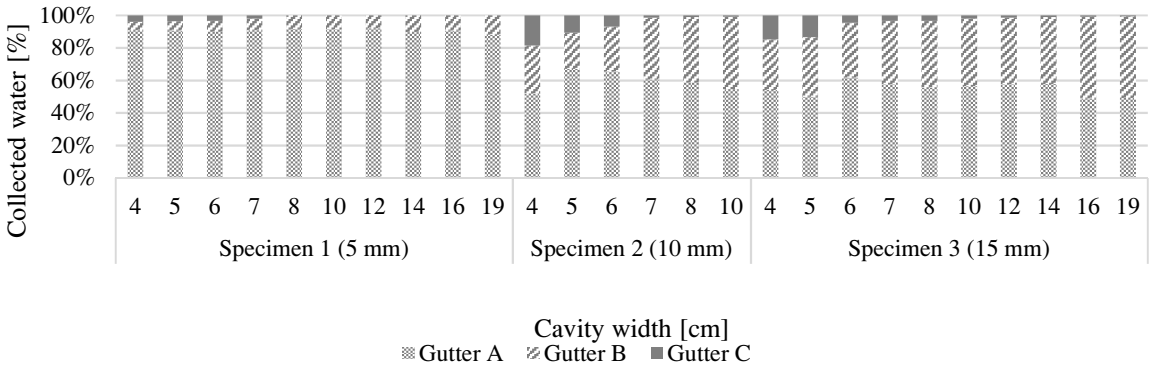

Figure 2. Percentage of water collected by gutter A, B and C for all specimens and different cavity widths.

The total amount of infiltrated water through the open joints is collected by gutter B and C at the bottom of each specimen for different cavity widths. Figure 2 shows that the percentage of infiltrated water through specimen 1 with a joint width of 5 mm (9,48% ± 1,13%) is significantly smaller than the percentage of infiltrated water through both specimen 2 (40,30% ± 5,89%) and 3 (45,15% ± 4,29%) with respective joint widths of 10 and 15 mm. Raindrops may either infiltrate due to kinetic energy, gravity, surface tension or capillarity. Also some drops might stagnate on top of the facade panels. In case other drops impinge on these stagnating drops, water may infiltrate due to splattering. Raindrops may also bounce on top of the facade panels or splash open. The larger percentage of infiltrated water through larger joint widths implies that more raindrops are able to flow freely through the larger joints and therefore the kinetic energy of the water drops has a larger impact on the infiltration rates. In case of smaller joint widths (5 mm) the effect of capillarity and surface tension becomes more important and water bridging of the joint is observed at some locations. Water drops are no longer able to flow freely through the joints and splatter onto the occluded joints, significantly reducing the infiltration rate. The increase in infiltration percentage from 10 mm joint widths to 15 mm joint widths, however, is not significant.

The reduced impact of kinetic energy on the infiltration rate for smaller joint widths is also apparent when the amount of water reaching the back of the cavity and collected by gutter C is compared for the different specimens. For specimen 1 with a joint width of 5 mm, water reaches the back of the drainage cavity for cavity widths of 7 cm and smaller (2,05% of collected

water). In contrast, water was already collected in gutter C for specimen 2 with a cavity width of 10 cm (0,88% of collected water) and for specimen 3 even for cavity widths of 19 cm (0,82% of total collected water). For a cavity width of 5 cm and 4 cm, a constant water runoff was visible at the PMMA panel for both specimen 2 and 3. In case of a cavity width of 4 cm, 18,71% and 14,80% of the total amount of collected water was collected by gutter C for respectively specimen 2 and 3. For specimen 1, no runoff was present for these cavity widths at the PMMA panel, only some drops reached the panel, in particular at the height of the spraying rack. The collected water in gutter C of specimen 1 was mainly attributed to water running off the vertical studs instead of water reaching the PMMA panel.

The results obtained by Recatala et al. (2017) are within the same order of magnitude as the results obtained in this study. For a cavity width of 10 cm and a joint width of 10 mm Recatala measured an infiltration rate at the drainage layer of 0,0029 l/min.m, compared to an infiltration rate of 0,0024 l/min.m in this study.

3.2 Impact of Construction Errors

Figure 3 shows the percentage of water collected by gutter A, B and C for specimens 2, 4 and 5. Specimen 4 and 5 incorporated one facade panel installed respectively 5 mm and 10 mm out of the exterior plane. The joint width applied to all specimens was 10 mm. The tests were conducted for cavity widths of 4, 8 and 12 cm.

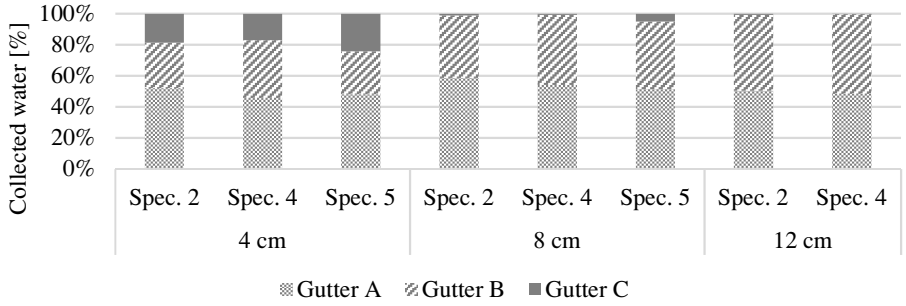

Figure 3. Percentage of water collected for specimen 2 (no error), specimen 4 (5 mm error) and specimen 5 (10 mm error) at different cavity widths.

Although a larger opening was present through which water could infiltrate freely due to the out of plane installed panels, only a small increase in the percentage of infiltrated water was measured. As the panel of specimen 4 was only installed 5 mm out of plane and the total thickness of the facade panels was 8 mm, there was still an overlap between the other panels and the panel out of plane. This prevented downward flowing drops from infiltrating due to gravity. Water drops instead bounced, splashed or stagnated on the top of the out of plane installed panel, with only a small increase of the infiltrated water as a result. When the panel was installed 10 mm out of plane (specimen 5), downward flowing water drops were able to infiltrate due to gravity. As the panels were installed vertically out of plane, however, these infiltrated drops were able to flow further down along the exterior surface of the underlying panel. Due to the larger horizontally oriented open joint, water drops could flow more freely through the opening and due to kinetic energy they were able to reach further into the cavity resulting in larger percentages of water collected in gutter C of specimen 5.

4 Hygrothermal Evaluation

As observed in the laboratory experiments, water drops are able to infiltrate through the open joints of ventilated facades and reach the insulation layer. In case a small cavity width is applied and deficiencies are present at the insulation layer, *e.g.* an open joint between two insulation panels, raindrops are able to flow through this open joint. These raindrops can either stagnate on top of the insulation panel and dry out again or flow further inward and reach the brick layer of the wall. This might cause mould growth or a reduced thermal performance of the insulation. The risk of both phenomena was assessed by means of the hygrothermal simulations. A common used ventilated facade construction in Belgium was modelled in WUFI PRO 5.3. A worst-case scenario was simulated, i.e. a small cavity width of 40 mm was applied and it was assumed that all infiltrating water reached the brick layer behind the insulation. The construction had a south-west orientation and a height up to 10 m. The material properties used in the simulations can be found in Table 1. The simulations start at October 1st and run for a period of 3 years. A time step of 1 hour was applied.

Table 1. Material properties (based on WUFI material database).

Material	t (mm)	ρ (kg/m^3)	C_p (J/kgK)	λ_{dry} (W/mK)	W_{sat} (kg/m^3)	w_{80} (kg/m^3)	Porosity
Eternit Duripanel A2	8	1326	1500	0,4	345	119,5	0,345
Air layer	40	1,3	1000	0,23	-	-	0,999
Isover GW Integra ZFK - 032	100	32,5	840	0,032	473	0,82	0,950
Solid Brick, extruded	140	1650	850	0,6	370	9,2	0,410
Interior Plaster (Gypsum Plaster)	10	850	850	0,2	400	6,3	0,650

4.1 Risk of Mould Growth

In case raindrops are able to reach the brick layer of the wall assembly, the raindrops will be absorbed by the brick. High infiltration rates combined with drying out to the inside of the wall can possibly cause mould growth at the interior surface of the wall assembly.
The risk of mould growth is assessed by means of the isopleth model by Sedlbauer which is implemented in WUFI. The isopleth curves separate favourable from unfavourable temperature and relative humidity conditions for mould growth for different substrate groups (Sedlbauer, 2001). A moisture source was implemented in the brick layer of the modelled wall assembly.

In case 15% of the driving rain reaches the brick layer and the air change rate in the air cavity is 10 h^{-1}, some data points are situated above the LIM I curve of Sedlbauer, meaning that there is a risk of mould growth for biologically recyclable materials. If the infiltration percentage is increased to 20% of the driving rain, the limiting isopleth for biologically adverse recyclable building materials (LIM II) is exceeded for a longer period and the risk of mould growth at the interior surface is significant. The results from the experimental study showed the highest infiltration percentages (collected by gutter C) for a ventilated facade with a joint width of 10 mm and a cavity width of 4 cm, i.e. 18,71%. However, in reality only a portion of the infiltrated water will reach the insulation layer and a small percentage will infiltrate toward the brick layer. It can therefore be stated that the risk of mould growth is limited for the assessed ventilated facade.

If the air change rate is increased from 10 h^{-1} to 1000 h-1, the limiting isopleth for biologically adverse recyclable building materials is still exceeded for an infiltration percentage of 20%. This implies that in case raindrops are able to reach the brick layer behind the insulation, increasing the air change rate only has a limited impact on the mould growth.

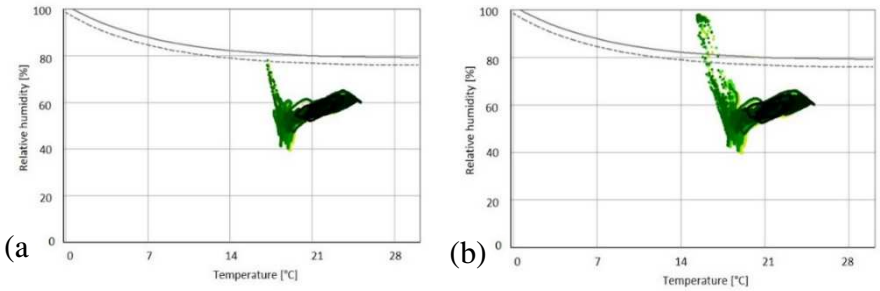

Figure 4. Isopleths on the interior surface, (a) infiltration percentage of 15% and (b) infiltration percentage of 20%.

4.2 Impact on Heat Flux

As the thermal conductivity of the insulation is moisture-dependent, infiltrating water in the wall assembly will have an impact on the heat losses through the wall assembly. As insulation is a non-hygroscopic material, raindrops infiltrating through deficiencies in the insulation layer, will either dry out or flow further inward. In case of a worst-case scenario, infiltrating raindrops might reach the brick layer behind the insulation. The drops will then be absorbed by the brick and accumulation of moisture can occur, increasing the relative humidity over the wall assembly. This may cause moisture to condensate at the cold side of the insulation which will reduce the thermal performance of the insulation.

Table 2. Impact of infiltration percentage in brick layer on air change rate on heat flux at interior surface.

Infiltration percentage [%]	**Heat flux [MJ/m²] per year**			**Increase relative to no moisture**		
ACH	10 h^{-1}	100 h^{-1}	500 h^{-1}	10 h^{-1}	100 h^{-1}	500 h^{-1}
No moisture source	96,56	97,68	99,23	0%	0%	0%
1	99,74	100,93	102,55	3,29%	4,00%	3,35%
5	112,30	114,22	116,14	16,66%	20,38%	17,04%
10	129,30	129,97	132,36	33,91%	39,79%	33,38%
15	149,60	144,00	147,05	54,93%	57,07%	48,19%
20	172,92	154,46	158,22	79,08%	69,97%	59,45%

In case a moisture source of 1% of the driving rain is implemented in the middle of the brick layer, an increase of 3,29% of the heat flux at the interior surface is measured compared to the case with no moisture source. This increase in total heat flux is primarily attributed to the increase of the latent heat flow associated with vapour diffusion at the surface. In case the latent heat flow is excluded, the increase in heat flux is 0,04% for a moisture source of 1% of the driving rain. In case a moisture source of 10% of the driving rain is applied, an increase of the total heat flux at the interior surface of 34,62% is measured. Excluding the latent heat flow, the moisture source causes an increase of the total heat flux of 3,41%. In case of a moisture source of 10% of the driving rain, the insulation layer still dries out over a period of one year. In case however, a moisture source of 15% of the driving rain is applied, i.e. all the infiltrating water

reaches the brick layer behind the insulation, the water in the insulation layer does not evaporate over a period of 1 year and instead accumulates. Increasing the air change rate in the air cavity in front of the insulation, increases the air velocity at the insulation layer, resulting in an improved drying of the wet insulation and therefore a reduction of the heat flux.

5 Conclusions

An experimental study was conducted to assess the impact of the joint width and the cavity size of a ventilated facade specimen on the amount of water infiltrating through the open joints and the amount of water reaching the drainage layer at the back of the cavity. Additionally, the impact of a panel installed out of plane of the exterior surface on the infiltration rate was assessed. The results from the experimental assessment were used as input parameters for hygrothermal simulations to determine the risk of moisture problems.

The experimental study showed that the infiltration percentage of raindrops through open joints of 5 mm (9,48% ± 1,13%) was significantly smaller compared to the infiltration percentage through joints of 10 mm (40,30% ± 5,89%). Raindrops infiltrating through the 5 mm joints of the ventilated facade reached the drainage layer and up to 3 cm in front of the drainage layer for cavity widths of 7 cm and smaller. For joint widths of 10 mm and 15 mm however, water was already collected 3 cm in front of the drainage layer for cavity widths of respectively 10 cm and 19 cm and a runoff film was present at the drainage layer for cavity widths of 4 and 5 cm. Hygrothermal simulations showed that the risk of mould growth at the interior surface of a ventilated wall assembly is limited for the measured infiltration percentages. The impact on the heat flux at the interior surface is however, significant, in case a cavity of 40 mm is assumed and all infiltrating water reaches the brick layer at the interior side of the wall through deficiencies in the insulation layer. An infiltration percentage of 1% of the driving rain in the brick layer and an air change rate of 10 h^{-1}, causes an increase of the heat flux of 3,29%. This increase in heat flux is primarily attributed to the latent heat flow associated with vapour diffusion at the surface. In case of an infiltration percentage of 10%, the increase in heat flux measures 34,62% and 3,41% excluding the latent heat flow.

ORCID

Stéphanie Van Linden: https://orcid.org/0000-0002-4102-2076
Nathan Van Den Bossche: https://orcid.org/0000-0002-8738-7249

References

Arce Recatala, M., Garcia Morales, S. and Van Den Bossche, N. (2017). Experimental assessment of rainwater management of a ventilated façade. *Journal of Building Physics*, 1-30.

ASHRAE. (2016). *Ashrae Standard 160-2016 - Criteria for moisture-control design analysis in buildings.* Atlanta.

Garden, G. (1963). Rain penetration and its control. *Canadian Building Digest, 40*, 401-404.

Mas, A., Gutiérrez, J., Gil, E., Gil, A. and Galvan, V. (2011). Design and construction recommendations to improve impermeability in rainscreen walls built with natural stone coverings. *Construction and Building Materials*, 1753-1761.

Sedlbauer, K. (2001). *Prediction of mould manifestation on and in buildings.* Stuttgart: University of Stuttgart.

Suresh Kumar, K. (2000). Pressure equalization of rainscreen walls: a critical review. *Building and Environment*, 161-179.

XV International Conference on Durability of Building Materials and Components
DBMC 2020, Barcelona
C. Serrat, J.R. Casas and V. Gibert (Eds)

Salt and Ice Crystallization Resistance of Lime Mortars with Natural Lightweight Aggregate

Martin Vyšvařil and Patrik Bayer

Brno University of Technology, Faculty of Civil Engineering, Veveří 331/95, 602 00 Brno, Czech Republic, vysvaril.m@fce.vutbr.cz

Abstract. *In this study, the comparison of lava sand, pumice, and natural zeolite as lightweight aggregate in air lime mortars, natural hydraulic lime mortars, and cement-lime mortars has been investigated with emphasis on the resistance of salt and ice crystallization. The lava sand and pumice improved frost resistance of the mortars while natural zeolite mortars remained without this effect due to their high water absorption. Salt crystallization resistance of the mortars was improved by using lava sand and natural pumice, while the mortars with natural zeolite were not resistant to crystallization of sodium chloride. The mortars have relatively little resistance to the reacting of Na_2SO_4, where gypsum and calcium sulfoaluminates were formed breaking the structure of the mortars. The best results were obtained using natural pumice.*

Keywords: *Lime Mortar, Natural Zeolite, Pumice, Lava Sand, Salt and Ice Crystallization Resistance.*

1 Introduction

The protection of historic buildings requires the use of traditional building materials compatible with the historical ones or as close to them as possible. Air lime mortars are not suitable for use in the moist environment because of their non-hydraulic properties and low frost resistance. The use of renders made of natural hydraulic lime (NHL) is therefore often preferred for renovation purposes, although lime–cement mortars are also accepted (Pacheco-Torgal *et al.*, 2012). Significant change of air lime mortars properties can be achieved by addition of pozzolanic admixtures or aggregates with pozzolanic properties. In the past, the most used ones were natural pozzolanic materials such as crushed bricks, ceramic, volcanic ash, scoria, pumice, which are still many times mentioned in conservation mortar works (Henry *et al.*, 2012; Matias *et al*., 2014; Moropoulou *et al.*, 2005; Sánchez-Moral *et al*., 2005; Silva *et al*., 2010). Porous aggregate with pozzolanic properties can improve not only the mechanical properties of mortars, but also their ability to salt accumulation from masonry, frost resistance, and liquid water transport to the mortar surface. The use of natural lightweight aggregates such as lava sand, pumice, or natural zeolite is quite common in concrete, however their utilization in lime mortars is still scarce (Barnat-Hunek *et al*., 2017; Ferraz *et al*., 2014; Lemougna *et al*., 2018).

In this study, the comparison of lava sand, pumice, and natural zeolite as lightweight aggregate in air lime mortars, natural hydraulic lime mortars, and cement-lime mortars has been investigated with emphasis on the resistance of salt and ice crystallization. The strength characteristics, pore structure and capillary water action of natural zeolite mortars and lava sand mortars, respectively, have already been investigated (Vyšvařil *et al*., 2019, Vyšvařil *et al*., 2019) with the conclusion that both natural aggregates positively affect the mortar strength, increase their porosity by forming coarse pores and facilitate water capillarity.

2 Materials and Methodology

A commercial hydrated lime CL90-S (Čertovy Schody, Inc., Lhoist group, Tmaň, Czech Republic), a natural hydraulic lime NHL 3.5 (Zement- und Kalkwerke Otterbein GmbH & Co. KG, Großenlüder, Germany), and a laboratory prepared blend of CL90-S and Portland cement CEM I 42.5 R (Českomoravský cement Inc., Mokrá, Czech Republic) were used as binders in prepared 3 groups of mortar mixes. Each mortars group consisted of reference samples made of quartz sand (Filtrační písky, Ltd., Chlum u Doks, CZ), and 3 types of samples with different natural lightweight aggregate (0/2 mm), fully replacing quartz sand, namely, natural zeolite (ACRE, Ltd., CZ), lava sand (Der Naturstein Garten, Hillscheid, DE), and natural pumice (Der Naturstein Garten, Hillscheid, DE). The chemical composition of all raw materials is given in Table 1. The phase compositions obtained by the X-ray diffraction analysis are presented in Table 2. Particle size distribution and loose bulk density of the aggregates are shown in author`s previous publication (Vyšvařil *et al*., 2019).

Table 1. Chemical composition of initial materials (mass%).

	SiO_2	Al_2O_3	Fe_2O_3	CaO	MgO	K_2O	Na_2O	MnO	TiO_2	SO_3	L.O.I.
Lime	0.92	0.71	0.39	68.09	1.33	0.48	0.11	0.03	0.10	0.19	27.94
NHL 3.5	12.76	4.12	1.47	59.87	2.79	1.13	0.09	0.04	0.05	0.15	15.28
Cement	21.26	5.08	3.64	61.48	0.86	0.91	0.12	0.44	0.29	2.42	4.17
Quartz sand	98.50	0.38	0.15	0.01	0.03	0.09	0.01	0.01	0.09	0.02	0.12
Natural zeolite	67.46	11.73	1.37	2.84	0.73	3.02	0.50	0.16	0.17	0.01	11.57
Lava sand	43.20	13.54	10.73	11.93	8.82	2.81	3.76	1.77	2.63	0.05	0.40
Pumice	62.13	17.50	4.45	1.57	0.99	3.90	5.97	2.54	0.65	0.08	0.72

Mortar mixtures were made using the correct amount of water required to obtain a normal consistency and a good workability of the mortars (160 ± 5 mm; measured by the flow table test). This consistency of lime mortars enables their easy application and good adhesion to the substrate. The proportioning of the mortar mixtures is given in Table 3. The composition of mortar mixtures considers constant binder:aggregate volume ratio of 1:1.15 based on a practical point of view supported by the results obtained by Lanas *et al*. (2003). Fresh mixtures were cast into prismatic moulds of size 40 × 40 × 160 mm. Standard conditions of sample storage were 22 ± 2 °C and relative humidity of 50 ± 5%.

The water absorption of mortars was measured according to EN 13755:2008 after curing times of 28 d. Three mortar specimens were used to conduct the test. The total porosity of the specimens was assessed using a mercury intrusion porosimetry (MIP). Frost resistance tests were carried out according to modified Czech standard ČSN 722452. The samples were tested after 28 curing days. The total test required 15 freeze-thaw cycles. One cycle consisted of 6 h freezing at −20 °C and 12 h thawing in a desiccator at constant relative humidity of 98 % and temperature of 20 °C. The frost resistance coefficient D_f was determined as the ratio of

flexural strength of specimens subjected to 15 freeze-thaw cycles to the flexural strength of reference specimens that did not undergo the frost resistance test. The salt crystallization resistance of mortars was determined using following solutions: 10% Na_2SO_4, 3% NaCl, and 3% NH_4NO_3. The dried samples were immersed into the solutions for 7 h and then dried for 16.5 h at 60 °C. The process was performed in the number of 10 cycles or till the partial disintegration of the samples. The procedure was performed according to the relevant European standard (EN 12370:1999). The state of the test specimens was monitored photographically, and detailed microstructure images were taken via a scanning electron microscope (SEM) equipped with EDX probe. The content of anions in aqueous leaches of the samples was determined by routine chemical analyses (10 g of mortar sample, 500 ml of deionized H_2O). Sulfates were set gravimetrically according to ISO 9280:1990, chlorides by mercurimetric method (ISO 5790:1979), and nitrates using Nitratax sc optical probe allowing the determination of nitrates directly in the medium.

Table 2. Mineralogical composition of initial materials (mass%).

Mineral	Lime	NHL 3.5	Cement	Quartz sand	Natural zeolite	Lava sand	Pumice
Alite	–	–	50.6	–	–	–	–
Aluminate	–	2.7	3.9	–	–	–	–
Albite	–	–	–	–	7.7	–	–
Anorthite	–	–	–	–	–	–	19.7
Larnite	–	22.5	4.9	–	–	–	–
Biotite	–	–	–	–	1.3	0.8	0.8
Brownmillerite	–	1.4	8.6	–	–	–	–
Brucite	0.5	–	–	–	–	–	–
Calcite	1.8	6.2	–	–	–	–	–
Chlorite	–	–	–	–	–	–	1.0
Clinoptilolite	–	–	–	–	50.0	–	–
Clinopyroxene	–	–	–	–	–	17.0	–
Cristobalite	–	–	–	–	17.5	–	–
Diopside	–	–	–	–	–	24.8	1.9
Ferroenstatite	–	–	–	–	–	–	4.7
Gypsum	–	–	3.8	–	–	–	–
Hematite	–	–	–	–	–	5.7	–
Hornblende	–	–	–	–	–	1.5	–
Magnetite	–	–	–	–	–	–	0.3
Microcline	–	–	–	0.4	–	–	–
Leucite	–	–	–	–	–	9.9	–
Nepheline	–	–	–	–	–	9.7	–
Portlandite	97.1	41.3	–	–	–	–	–
Quartz	–	–	–	97.9	–	1.9	22.5
Sanidine	–	–	–	–	–	11.2	–
Staurolite	–	–	–	1.1	–	–	–
Tridymite	–	–	–	–	1.9	–	–
Amorphous phases	–	25.1	28.4	–	20.4	17.1	48.5

Table 3. Composition of mortar mixtures.

Mixture	Lime (g)	NHL 3.5 (g)	Cement (g)	Quartz sand (g)	Natural zeolite (g)	Lava sand (g)	Pumice (g)	H_2O (ml)
L-ref	100	–	–	400	–	–	–	120
L-NZ	100	–	–	–	245	–	–	155
L-LS	100	–	–	–	–	340	–	115
L-Pu	100	–	–	–	–	–	235	135
NHL-ref	–	100	–	340	–	–	–	75
NHL-NZ	–	100	–	–	210	–	–	115
NHL-LS	–	100	–	–	–	285	–	80
NHL-Pu	–	100	–	–	–	–	200	105
LC-ref	50	–	50	280	–	–	–	70
LC-NZ	50	–	50	–	175	–	–	105
LC-LS	50	–	50	–	–	240	–	70
LC-Pu	50	–	50	–	–	–	165	95

3 Results and Discussion

3.1 Total Porosity and Water Absorption

Since the resistance and durability of lime mortars is very dependent on their pore structure, the total porosity of the mortars (obtained by MIP) and the water absorption has been determined before the resistance tests (Figure 1). The increasing total porosity of the mortars corresponds to the decreasing loose bulk density of the lightweight aggregate (Vyšvařil *et al*., 2019), therefore the mortars with the lightest pumice aggregate (-Pu) showed the highest total porosity, which can be potentially beneficial for salt and ice crystallization resistance of these mortars.

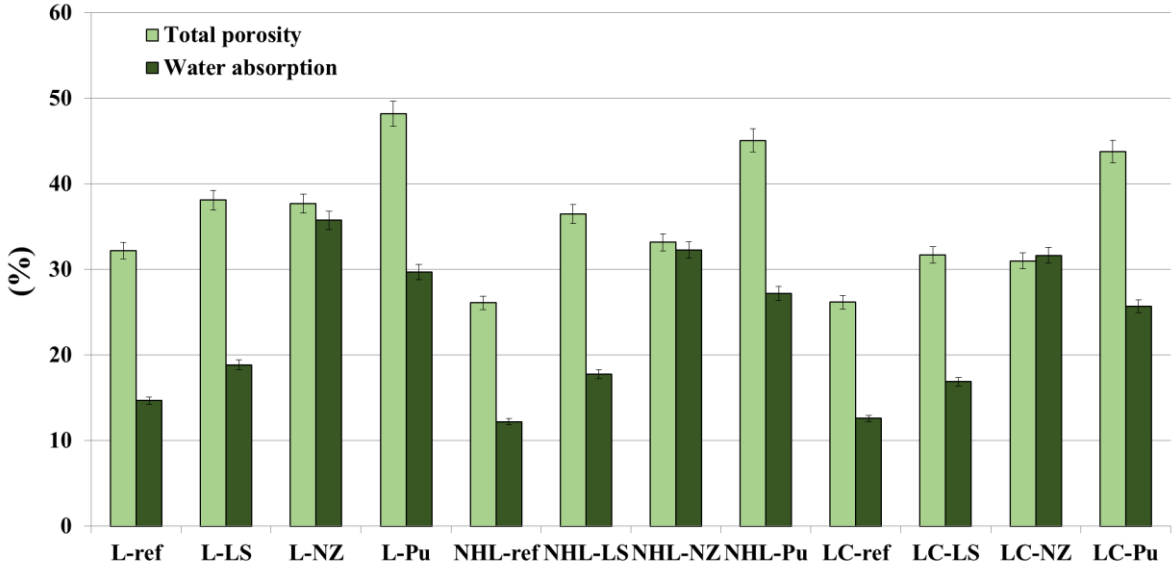

Figure 1. Total porosity and water absorption of mortar samples.

The type of lightweight aggregate had a great influence on the water absorption of mortars. Above all, the open porous structure of the aggregate and its water-binding capacity plays an important role in water absorption, which is especially evident when using natural zeolite. This is also obvious from the high dosages of mixing water required to achieve the desired consistency of these mortars (Table 3).

3.2 Frost Resistance

Determination of frost resistance of mortars according to ČSN 72 2452 is a test of alternating freezing and thawing of water-saturated mortar beams in the number of 15 cycles. Due to the saturation of the samples with water, air lime mortars usually break up in this test before the completed 15 cycles. In this study, all tested mixtures withstood 15 freeze-thaw cycles and it was possible to determine their flexural tensile strengths and subsequently evaluate the frost resistance coefficients, D_f (Figure 2). The frost resistance of mortars increased with increasing porosity of the samples, except for natural zeolite mortars, where the huge water-binding capacity led to a decrease in the frost resistance. Only NHL-Pu, LC-ref, LC-LS, and LC-Pu mortars exceeded the frost resistance coefficient of 0.75 and thus met the frost resistance criterion. In general, replacement of quartz sand with natural lightweight aggregate has led to a substantial improvement in the frost resistance of mortars (except natural zeolite); the best results were obtained using natural pumice.

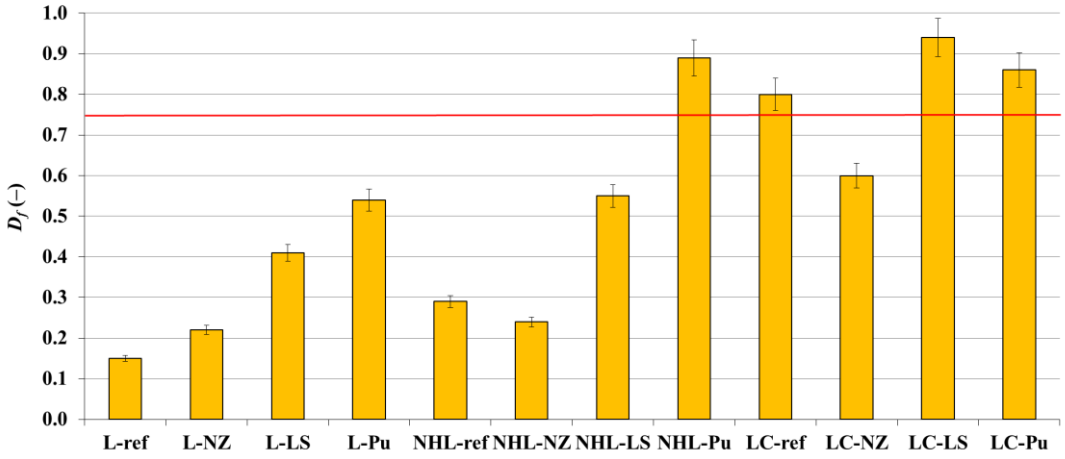

Figure 2. Frost resistance coefficient of mortar samples (red line – standard frost resistance criterion).

3.3 Salt Crystallization Resistance

The content of anions in aqueous leaches of the samples before and after salt crystallization resistance test is presented in Table 4 together with the sequence of the decay cycle. The results show that the concentration of the monitored anions in the samples after treatment with saline solutions increased more than 100 times; mostly in pumice samples, which also best resisted crystallization of the salts used. Thus, it has been confirmed that increased porosity is a good prerequisite for higher ability to salt accumulation and mortar resistance to salt crystallization. Table 4 shows that the mortars with NZ are not resistant to crystallization of sodium chloride. All mortar samples were also broken down after several crystallization

cycles of sodium sulfate, where gypsum with high molar volume are formed. The NHL and LC mortars break down in the sodium sulphate solution earlier due to the presence of the aluminate phase and the formation of bulkily calcium sulfoaluminates (monosulfate and ettringite) breaking the structure of the mortar.

Table 4. Concentrations of monitored anions in aqueous leaches of mortar samples before (c_{g0}) and after (c_g) salt crystallization resistance test, and number of test cycles to sample disintegration (10 = intact sample).

Mixture	c_{g0} SO_4^{2-} (g kg^{-1})	c_{g0} Cl^- (g kg^{-1})	c_{g0} NO_3^- (g kg^{-1})	c_g SO_4^{2-} (g kg^{-1})	c_g Cl^- (g kg^{-1})	c_g NO_3^- (g kg^{-1})	Cycle count in Na_2SO_4	Cycle count in NaCl	Cycle count in NH_4NO_3
L-ref	**0.103**	**0.055**	**0.487**	**21.04**	**7.73**	**19.85**	**6**	**10**	**10**
L-NZ	0.083	0.040	0.323	36.43	26.20	32.11	9	8	10
L-LS	0.089	0.054	0.445	24.88	22.81	36.18	7	10	10
L-Pu	0.084	0.099	0.550	33.57	31.42	39.38	8	10	10
NHL-ref	**0.087**	**0.049**	**0.408**	**36.44**	**9.85**	**10.43**	**4**	**10**	**10**
NHL-NZ	0.069	0.039	0.273	50.56	19.93	28.85	7	8	10
NHL-LS	0.074	0.047	0.373	40.73	14.28	31.76	4	10	10
NHL-Pu	0.063	0.079	0.466	44.79	23.64	38.16	6	10	10
LC-ref	**1.733**	**0.043**	**0.401**	**22.45**	**23.50**	**20.25**	**4**	**10**	**10**
LC-NZ	1.165	0.038	0.255	45.03	23.90	29.57	5	10	10
LC-LS	0.589	0.040	0.321	30.78	26.63	34.73	6	10	10
LC-Pu	0.658	0.069	0.440	36.37	25.39	41.52	7	10	10

The microstructure of mortar samples was determined before and after the salt crystallization resistance test. Microstructure images of NZ mortar samples were selected for presentation due to the largest differences between them (Figure 3). The images show that the structure of the L-NZ sample prior to the salt crystallization resistance test was relatively compact. After Na_2SO_4 treatment, the formation of crystalline neoplasms, namely plate-shaped hexagonal crystals of monosulfate and needle-like ettringite, was enormous, while the structure became more porous. Natural zeolite acted as an aluminum source for the formation of sulfoaluminate phases. Despite the higher aluminum content in the mortars with NZ aggregates compared to the reference samples and thus easier formation of the aluminate phases, the samples disintegrated later, probably due to higher porosity of these samples. In the case of NH_4NO_3, no products of relevant degradation reactions were observed in the microstructure of mortars, only calcite recrystallization occurred during each cycles of treatment, which is represented in the SEM image in the form of a large number of sharp-edged calcite crystals. The structure remained relatively close. Treatment with NaCl solution resulted in a very porous mortar structure for both the L-NZ sample (Figure 3, d) and the NHL-NZ sample (Figure 3, e). The poor resistance of lime mortars with natural zeolite to NaCl crystallization is likely due to leaching of the binder from the mortar structure, since no degradation reaction products have been observed in these mortars. For comparison, the microstructure of the LC-NZ sample, which is much more compact and characterized by the presence of amorphous CSH gel and ettringite needles, is also shown in Figure 3. This sample remained intact after NaCl treatment.

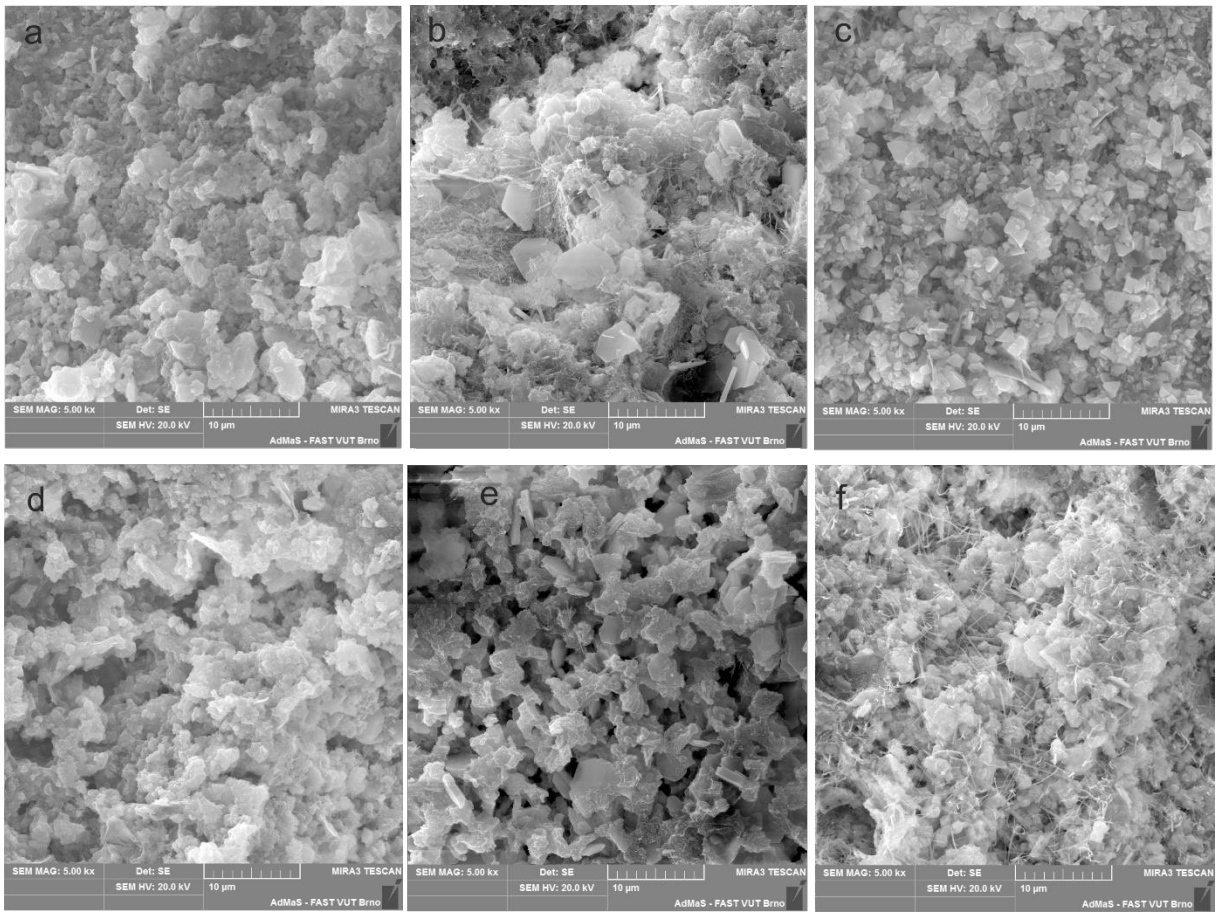

Figure 3. SEM images of L-NZ sample before salt crystallization resistance test (a), after 8 cycles in Na_2SO_4 (b), after 10 cycles in NH_4NO_3 (c), after 6 cycles in NaCl (d), NHL-NZ sample after 7 cycles in NaCl (e), LC-NZ sample after 10 cycles in NaCl (f).

4 Conclusions

- All lightweight aggregates increased the total porosity of mortars in accordance with their decreasing loose bulk density. Enhanced total porosity appears to be beneficial for salt and ice crystallization resistance of the mortars.
- Full replacement of quartz sand with natural lightweight aggregate has led to a considerable improvement in the frost resistance of mortars (except natural zeolite); the best results were obtained using natural pumice.
- Salt crystallization resistance of the mortars was improved by using lava sand and natural pumice, while the mortars with natural zeolite were not resistant to crystallization of sodium chloride. The mortars have relatively little resistance to the reacting of Na_2SO_4, where gypsum and calcium sulfoaluminates were formed breaking the structure of the mortars.
- In terms of salt and ice crystallization resistance, natural pumice seems to be the most suitable natural lightweight aggregate for lime mortars.

Acknowledgements

This work has been financially supported by The Czech Science Foundation (GA CR) project No. 18-07332S.

ORCID

Martin Vyšvařil: https://orcid.org/0000-0002-4325-6087
Patrik Bayer: https://orcid.org/0000-0001-7866-1085

References

Barnat-Hunek, D., Siddique, R., Klimek, B. and Franus, M. (2017). The use of zeolite, lightweight aggregate and boiler slag in restoration renders. *Construction and Building Materials*, 142, 162–174. doi: 10.1016/j.conbuildmat.2017.03.079

ÚNM (1970). ČSN 72 2452: *Testing of frost resistance of mortar*. In Czech

CEN/TC 246/WG 2 (2020). EN 12370: *Natural stone test methods – Determination of resistance to salt crystallisation.*

CEN/TC 246/WG 2 (2008). EN 13755: *Natural stone test methods – Determination of water absorption at atmospheric pressure*.

Ferraz, E., Andrejkovicová, S., Velosa, A.L., Silva, A.S. and Rocha, F. (2014). Synthetic zeolite pellets incorporated to air lime–metakaolin mortars: mechanical properties. Construction and Building Materials, 69, 243-252. doi: 10.1016/j.conbuildmat.2014.07.030

Henry, A. and Stewart, J. (2012). *Practical Building Conservation: Mortars Plasters and Renders*. Farnham, England: Ashgate Publishing.

ISO/TC 147/SC 2 (1990). *ISO 9280: Water quality – Determination of sulfate – Gravimetric method using barium chloride*.

ISO/TC 47 (1979). *ISO 5790: Inorganic chemical products for industrial use — General method for determination of chloride content — Mercurimetric method.*

Lanas, J. and Alvarez-Galindo, J.I. (2003). Masonry repair lime-based mortars: factors affecting the mechanical behaviour. *Cement and Concrete Research*, 33(11), 1867–1876. doi: 10.1016/s0008-8846(03)00210-2

Lemougna, P.N., Wang, K., Tang, Q., Nzeukou, A.N. and Billong, N. (2018). Review on the use of volcanic ashes for engineering applications. *Resources, Conservation & Recycling*, 137, 177–190. doi: 10.1016/j.resconrec.2018.05.031

Matias, G., Faria, P. and Torres, I. (2014) Lime mortars with heat treated clays and ceramic waste: a review. *Construction and Building Materials*, 73, 125-136. doi: 10.1016/j.conbuildmat.2014.09.028

Moropoulou, A., Bakolas, A. and Anagnostopoulou, S. (2005). Composite materials in ancient structures. *Cement and Concrete Composites*, 27(2), 295-300. doi: 10.1016/j.cemconcomp.2004.02.018

Pacheco-Torgal, F., Faria, J. and Jalali, S. (2012). Some considerations about the use of lime–cement mortars for building conservation purpose in Portugal: a reprehensible option or a lesser evil? *Construction and Building Materials*, 30, 488–94. doi: 10.1016/j.conbuildmat.2011.12.003

Sánchez-Moral, S., Luque, L., Canaveras, J.-C., Soler, V., Garcia-Guinea, J. and Aparicio, A. (2005). Lime pozzolana mortars in Roman catacombs: composition, structures and restoration. *Cement and Concrete Research*, 35(8), 1555-1565. doi: 10.1016/j.cemconres.2004.08.009

Silva, L.M., Ribeiro, R.A., Labrincha, J.A. and Ferreira, V.M. (2010). Role of lightweight fillers on the properties of a mixed-binder mortar. *Cement and Concrete Composites,* 32(1), 19–24. doi: 10.1016/j.cemconcomp.2009.07.003

Vyšvařil, M., Bayer, P., Žižlavský, T. and Rovnaníková, P. (2019). Use of natural zeolite aggregate in restoration lime renders. In *PRO 130: 5th Historic Mortars Conference*, Paris, France, 261–272.

Vyšvařil, M., Bayer, P. and Rovnaníková, P. (2019). Use of Lava Sand as an Alternative to Standard Quartz Aggregate in Lime Mortars. *Solid State Phenomena*, 296, 73–78. doi: 10.4028/www.scientific.net/SSP.296.73

Vyšvařil, M., Topolář, L. and Dvořák, R. (2019). Acoustic insulation properties of lime mortars with natural lightweight aggregate. *MATEC Web Conf.*, 282, 02075. doi: 10.1051/matecconf/201928202075

XV International Conference on Durability of Building Materials and Components
DBMC 2020, Barcelona
C. Serrat, J.R. Casas and V. Gibert (Eds)

Self-Compacting Concrete with Recycled Concrete Aggregate: Resistance against Aggressive External Agents

Víctor Revilla-Cuesta[1], Marta Skaf[2], Aratz García-Llona[3], Ignacio Piñero[3], Juan M. Manso[1] and Vanesa Ortega-López[1]

[1] Department of Civil Engineering, Higher Polytechnic School, University of Burgos, Villadiego St, 09001 Burgos, Spain, {vrevilla, jmmanso, vortega}@ubu.es. Víctor Revilla-Cuesta: Corresponding author

[2] Department of Construction, Higher Polytechnic School, University of Burgos, Villadiego St, 09001 Burgos, Spain, {mskaf}@ubu.es

[3] Fundación TECNALIA Research & Innovation. Parque Tecnológico de Bizkaia. C/Geldo, ed.700, E48160 Derio-Bizkaia, Spain, {aratz.garcia, ignacio.pinero}@tecnalia.com

Abstract. *The use of waste in civil-engineering products, such as concrete and asphalt mixes, is a very effective strategy for reducing high consumption levels of Natural Aggregates (NA) in the construction sector. In this research, rejected precast concrete elements of high compressive strength are studied, following their crushing for use as a high quality Recycled Concrete Aggregate (RCA) in the manufacture of Self-Compacting Concrete (SCC). High volumes of this waste stream are employed in the mixture, completely replacing the coarse fraction of the natural aggregate (100% replacement rate) and half of the fine fraction (50% replacement rate). Once hardened, samples of the recycled SCC are exposed to several aggressive external agents, in order to evaluate their performance and durability in aggressive environments. Behavioral tests on the concrete in the presence of the most frequent aggressive agents in the surrounding environment demonstrated that the SCC containing RCA was resistant to freeze/thaw and moist/dry cycles, and sulphate attack, according to the results obtained in 4, 3 and 2 samples respectively, and of sufficient durability for use in structural concrete components.*

Keywords: *Self-Compacting Concrete, Recycled Concrete Aggregate, Freeze/Thaw Test, Moist/Dry Test, Sulphate Attack Test.*

1 Introduction

Modern-day society currently faces two immense environmental problems: climate change and the lack of natural resources (IPCC, 2014). Climate change is mainly due to the emission of greenhouse gases, resulting from a wide range of collective human actions related to manufacturing, transport, and energy production. High consumption in some areas of natural resources has led to shortages over recent years, as expanding populations need continual development of technology and infrastructure.

The construction sector is a major contributor to these problems (Sandanayake *et al.*, 2019): the cement industry emits high volumes of CO_2 (Maddalena *et al.*, 2018) and many other construction activities have a high carbon footprint (Noh *et al.*, 2018). Aggregate consumption in asphalt mixes, and concretes is also very high, in the order of 80% and 95% by volume. (CESCE, 2018). According to the Asociación Nacional de Empresarios Fabricantes de Áridos (ANEFA) [National Association of Aggregate Manufacturers of Spain], in 2017, 112 million tons of aggregates were consumed in Spain (ANEFA, 2018). The sector therefore has some responsibility to contribute to the reduction of these problems.

Aggregate substitution in several materials, including concrete, by different types of waste, such as rubber, slag, and even Recycled Concrete Aggregate (RCA), is an area of study that has opened several research lines (Busic *et al.*, 2018; Safiuddin *et al.*, 2013; Verian *et al.*, 2018). Hence, the use of RCA in this study is evaluated for the manufacture of concrete.

The mechanical performance of vibrated concrete with RCA is well-known: RCA, especially the fine fraction, decreases compressive strength (Evangelista *et al.*, 2014; Silva *et al.*, 2015). Durability is also affected, because of the high porosity of the attached mortar, which raises permeability levels and the entry of external agents (Guo *et al.*, 2018).

Self-Compacting Concrete (SCC) is of greater fluidity, so its porosity is lower. RCA can even improve its durability and enhance some other properties (Boudali *et al.*, 2016; Pereira-De-Oliveira *et al.*, 2014). The RCA effect on mechanical properties will not change due to self-compactability (Fiol *et al.*, 2018; Grdic *et al.*, 2010). Nevertheless, there is a scarcity of studies on precise definitions of the RCA effect.

In line with the above, the durability of an SCC design consisting of 100% coarse RCA and 50% by volume of fine RCA will be evaluated in this research. This concrete underwent three tests: behavior during freeze/thaw and moist/dry cycles, and resistance to sulphate attack, demonstrating its performance when exposed to highly aggressive environmental agents.

2 Materials

Three types of materials were employed: RCA, natural aggregates (NA), and non-aggregate.

CEM I 52.5 R with a density of 3.1 kg/dm^3 was employed as a non-aggregate material. Water was obtained from the mains water supply system of Burgos. Two admixtures were also used: a viscosity adjuster (called admixture 1) and a superplasticizer (called admixture 2). Previous studies showed that, if the amount of water is optimal, the quantity of these admixtures will range between 0.5-1.5% of the cement weight (Fiol *et al.*, 2018).

Only the fine NA fractions were used. Siliceous sand with a density of 2.58 kg/dm^3 and a 24h water absorption of 0.25% was used. In addition, SCC requires a large fines content for acceptable flowability, so limestone sand 0/1.2mm (density of 2.62 kg/dm^3 and a 24h water absorption of 2.08%) and limestone filler <0.063 mm (density of 2.77 kg/dm^3) were used.

The RCA consisted of rejected precast elements with a characteristic compressive strength of 40-45 MPa prior to crushing. The crushed RCA was sized between 0 and 30 mm, for which reason it was screened to obtain the desired fractions: the fine fraction 0/4 mm (density of 2.37 kg/dm^3 and 24h water absorption of 7.36%) and the coarse fraction 4/12.5 mm (density of 2.42 kg/dm^3 and 24h water absorption of 6.25%). Particles larger than 12.5 mm were discarded, because they were considered too large to make an SCC.

The appearance of the aggregate and their granulometry are shown in Figure 1 and Figure 2.

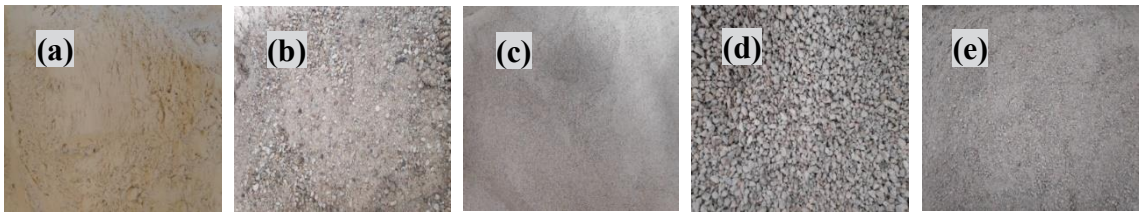

Figure 1. Appearance of the aggregates used for the manufacture of the SCC: a) Limestone filler <0.063 mm; b) Siliceous sand 0/4 mm; c) Limestone sand 0/1.2 mm; d) Coarse RCA 4/12.5 mm; e) Fine RCA 0/4 mm.

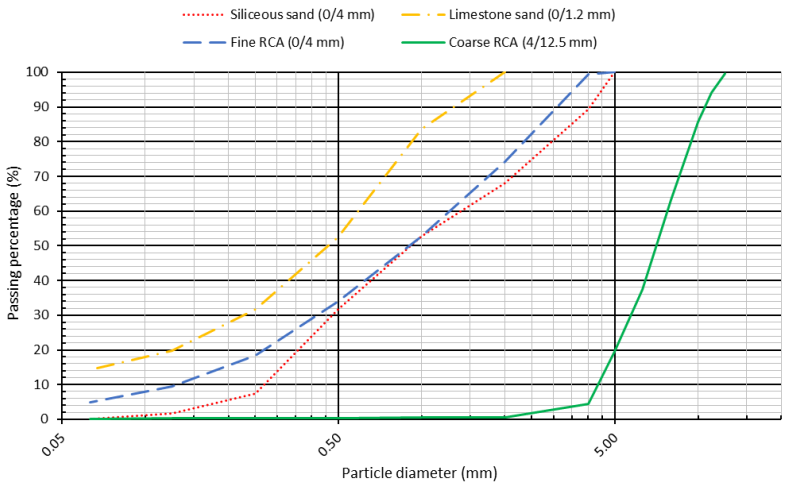

Figure 2. Aggregate granulometry.

3 Mix-Design

The SCC under evaluation was designed with the materials detailed in the preceding section and labelled SCC-I-50/100-D.

The dosage of the SCC was designed, so that neither segregation nor exudation would affect the final SCC and so that it would have an SF2 slump-flow class (maximum diameter between 650 and 750 mm). Design by trial and error began with a very common dosage in the precast cement component industry as the initial dosage. The results of a slump-flow test, norm EN 12350-8 (EN-Euronorm.), suggested adjustments to the proportions of the materials in a second stage. The process of trial and error was repeated several times (third dosage, forth one…) until the definitive optimal dosage was obtained: 296 kg/m^3 of cement, 122 kg/m^3 of filler, 183 kg/m^3 of water, 522 kg/m^3 of coarse RCA, 570 kg/m^3 of fine RCA, 343 kg/m^3 of siliceous sand 0/4 mm, 215 kg/m^3 of limestone sand 0/1.2 mm, 2.20 kg/m^3 of admixture 1, and 4.35 kg/m^3 of admixture 2. In Figure 3, some slump-flow trials during the design process can be observed.

Figure 3. Dosages by trial and error during the development of the SCC: a) Initial dosage; b) Dosage with high segregation in the central area: c) Dosage with minimal segregation in the central area; d) Optimal dosage.

4 In-Fresh State Behavior

The slump flow test is insufficient in itself to ensure optimal SCC flowability and further characterization of the in-fresh state behavior is necessary (EFNARC, 2002).

- The slump flow test was performed first (EN 12350-8). A diameter of 500 mm was

achieved in 4 s, being the maximum diameter 720 mm (SF2 slump-flow class).

- Viscosity was measured by the time it took the SCC mix to pass through a V-funnel (EN 12350-9), which took 7s (viscosity class VF1, time under 8s).
- The 2-bar L-box test (EN 12350-10) measured the passing ability of the SCC. The quotient between the maximum and the minimum height was 0.97 (passing-ability class PA1, quotient greater than 0.80 and 2-bar L-box).
- The sieve segregation test (EN 12350-11) assessed the segregation resistance. The result obtained was 0.41% (SR2 class, segregation lower than 15%).

5 Compressive Strength

Compressive strength at different ages was measured, to guarantee its structural suitability. Two specimens were tested at each age (1, 7 and 28 days),

At 1 day, the normalized sample already had a high compressive strength (28 MPa, 61.4% of 28-days strength). Increased strength over the first seven days was very fast (84.0% of the final strength was reached at 28 days, 38.3 MPa). After three weeks, the compressive strength increase slowed down, reaching 45.6 MPa at 28 days. The SCC could therefore be suitable for precast elements (compressive strength greater than 45MPa).

6 Durability

Three durability tests were performed as part of the analysis of the effects of aggressive external agents: freeze/thaw and moist/dry test cycles, and sulphate attack. All the tests began on the same day. 10 cm-side cubic samples cured over 30 days were used. On first day of the tests, the compressive strength, measured on two cubic samples, was 47.61 MPa on average, which subsequently became the reference for any quantifiable decrease in compressive strength.

6.1 Freeze/Thaw Test

Freeze/thaw tests were performed according to UNE-CEN/TS-12390-9-EX (2008) (CEN). Four 10 cm-side cubic samples were introduced into a container full of water with 3% by mass of NaCl and subjected to 56 freeze/thaw cycles. In each 24h cycle, the container was exposed to 16h of freezing at a temperature of -15ºC and to 8h of thawing in water at 20ºC. Any loose materials were removed every 10 cycles and the specimens were then dried and weighed. Figure 4 shows the loss of mass and, Figure 5, the initial and final state of the test specimens.

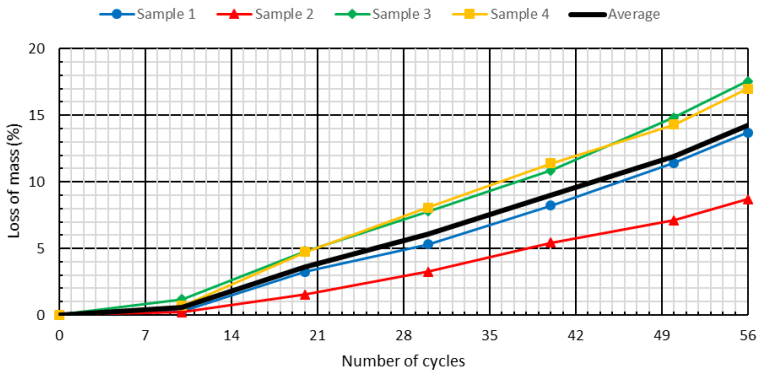

Figure 4. Loss of mass over freeze/thaw test. Average loss of mass at the end of the test: 14.23%.

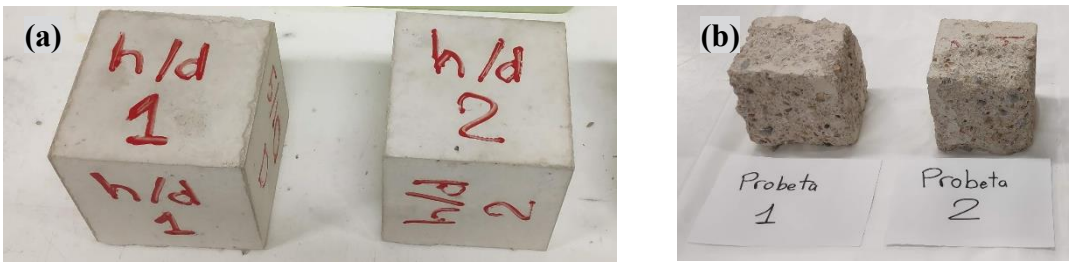

Figure 5. Freeze/thaw test: A) Initial state; B) Final state.

In addition to loss of mass, Ultrasonic Pulse Velocity (UPV), an indirect measure of compressive strength, was evaluated both before and after the test. The strength was also measured after the test. All the results are shown in Table 1.

Table 1. Freeze/thaw test. Results related to UPV and compressive strength.

Test/Sample	Sample 1	Sample 2	Sample 3	Sample 4	Average	Standard deviation
UPV before the test (km/s)	3.95	3.57	3.72	3.51	3.69	0.20
UPV after the test (km/s)	3.13	3.11	3.28	3.07	3.15	0.09
Comp. strength after the test (MPa)	37.06	20.94	32.62	34.46	31.27	7.12
UPV average variation (%): -14.67%		Comp. strength average variation (%): -34.32%				

The decrease in compressive strength was high, unlike the loss of mass. A decrease that could be due to the increased volume of water that expanded when frozen, opening internal micro-voids in the mortar that had adhered to the aggregate (a process that the mortar assists, because of its high porosity). It all caused a sharp decrease in compressive strength.

6.2 Moist/Dry Test

This test was performed by adapting the test in the ASTM D 559 standard (ASTM-International, 2008) that simulates the effects of rain and subsequent drying by solar radiation on concrete. Fundamentally, the thermal shock inflicted during the changeover from a wet to a dry situation. To do so, three 10 cm-side cubic specimens were subjected to 30 24-hour cycles, which consisted of full immersion in water at a temperature between 18ºC and 22ºC, over 16h, followed by oven drying for 8h at 60ºC.

The external appearance of each sample after the test is shown in Figure 6. Every 10 cycles, each specimen was weighed and its UPV was measured, a parameter that had also been measured before the beginning of the test. When the trial ended, the samples were tested to compressive strength. The results obtained can be seen in Table 2.

Figure 6. Moist/dry test. Final state of the samples.

Table 2. Results of moist/dry test.

Test/Sample	Sample 1	Sample 2	Sample 3	Average	Standard deviation
Initial mass (g)	2,068.8	2,189.1	2,094.1	2,117.33	63.42
Mass after 10 cycles (g)	2,043.5	2,152.0	2,047.1	2,080.87	61.63
Mass after 20 cycles (g)	2,022.2	2,146.3	2,044.8	2,071.10	66.10
Mass after the test, 30 cycles (g)	2015.8	2,140.0	2,043.9	2,066.57	65.13
UPV before the test (km/s)	3.72	3.79	3.64	3.71	0.08
UPV after the test (km/s)	2.60	2.65	2.56	2.60	0.04
Comp. strength after the test (MPa)	35.00	32.92	32.17	33.36	1.47
Mass average variation (%): -2.40%		UPV average variation (%): -29.87%			
Compressive strength average variation (%): -29.93%					

The external appearance (without appreciable changes except the increased number of external voids on sample Nª3) and the loss of mass showed no visible change in the concrete. However, the compressive strength and the UPV showed significant changes at a microscopic level. Both changes could be explained by the appearance of larger internal micro voids than in the freeze/thaw test. Nevertheless, the decrease in compressive strength was very similar in both the moist/dry test and the freeze/thaw test. It appears that the large number of micro voids in the moist/dry test was compensated by the negligible loss of mass.

6.3 Sulphate Attack Test

This test was performed according to the ASTM C 1012 standard (ASTM-International, 2008), in which the concrete is exposed to sodium sulphate decahydrate that crystallizes within the sample, thereby increasing its volume. Each of the 15 24-hours cycles consisted of a 5-hour immersion in water with 14% by mass of $Na_2SO_4 \cdot 10H_2O$, oven drying for 17h at 60ºC and cooling at room temperature (23ºC) for 2h.

The final appearance of the two specimens tested is shown in Figure 7. No visible change was detected, except discoloration in the form of darkening, due to sodium sulphate precipitation. Before and after the trial the samples were weighed, the length of their sides was measured (in order to determine the expansion of concrete by the absorption and crystallization of the salt) and the UPV was determined. In addition, both specimens were tested to compressive strength. All the results are indicated in Table 3.

Table 3. Sulphate attack test. Individual and average results.

Test/Sample	Sample 1	Sample 2	Average	Standard deviation
Initial mass (g)	2,098.8	2,199.2	2,149.0	70.99
Final mass (g)	2,083.9	2,193.3	2,138.6	77.36
Initial average side length (mm.)	100.11	100.33	100.22	0.16
Final average side length (mm.)	100.13	100.34	100.24	0.15
UPV before the test (km/s)	3.69	3.58	3.64	0.08
UPV after the test (km/s)	3.38	2.63	3.01	0.53
Compressive strength after the test (MPa)	41.44	35.68	38.56	4.07
Mass average variation (%): -0.48%	Side expansion (%): +0.02%			
UPV average variation (%): -16.62%	Comp. strength average variation (%): -19.01%			

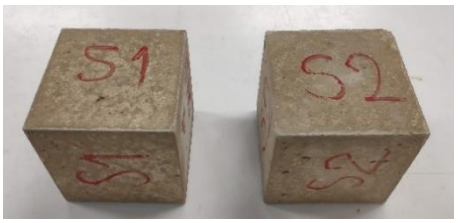

Figure 7. Sulphate attack test. Final state of the samples.

Neither the variation in either mass or length nor in the external appearance of the concrete samples showed relevant changes. The only noticeable effect was the reduction in compressive strength and the logical decrease in UPV. Nevertheless, compressive strength was less effected by the sulphates than by consequences of exposure to water in the moist/dry test. This difference can be explained by the high flowability of SCC, which implies that the concrete had a very low number of small-sized surface pores in the hardened state. Hence, the penetration of higher density solutions within the concrete was less likely, because water with no salt solutions penetrates with greater ease through surface pores than a sulphate solution, meaning that the sulphate effect would be lower towards the interior of the sample.

7 Conclusions

The following conclusions can be drawn from the study reported in this paper:

- Correct dosage design of an SCC with large amounts of both coarse and fine RCA will result in high flowability in the fresh state and a high compressive strength.
- A good design will mean that the SCC with RCA can be used in environments with aggressive external agents, with high precipitation and frequent frosts. These agents adversely affect the properties of the concrete, although the affections are not critical.
- The durability of the SCC exposed to aggressive external agents is linked to their external porosity. In other words, the greater the ease with which the external agent penetrates within the concrete, the worse the effect of those agents on the concrete.
- The concrete samples showed uniform behavior in all the tests, with similar results for all specimens, although those test results can vary depending on the surface finish. The homogeneity and workability of the mix was optimal when the specimens were manufactured, clearly demonstrating the uniform behavior and the durability of this SCC concrete for use in structural elements. This conclusion is based on the results obtained on four specimens in the freeze/thaw test, on three samples in the moist/dry test and two specimens in the sulphate attack test.

Acknowledgments

The authors want to express their gratitude to: the Vice Rectorate of Research of the University of Burgos (SUCONS grant); the Junta de Castilla y León for assistance to research group UIC-231 through project BU119P17 partially funded by FEDER funds; the Spanish Ministry MICIU and FEDER (European Regional Development Funds) for project funding FPU17/03374.

ORCID

Víctor Revilla-Cuesta: http://orcid.org/0000-0003-3337-6250
Marta Skaf: http://orcid.org/0000-0001-7205-2692
Aratz García-Llona: http://orcid.org/0000-0002-8202-1424
Ignacio Piñero: http://orcid.org/0000-0003-1987-1677
Juan M. Manso: http://orcid.org/0000-0003-4964-5128
Vanesa Ortega-López: http://orcid.org/0000-0003-0212-355x

References

ANEFA (2018). Informe de situación económica sectorial.

ASTM-International (2008). Book Annual of ASTM Standards, West Conshohocken, 19429–2959 2008 USA PA.

Boudali, S., Kerdal, D.E., Ayed, K., Abdulsalam, B. and Soliman, A.M. (2016). Performance of self-compacting concrete incorporating recycled concrete fines and aggregate exposed to sulphate attack. *Construction and Building Materials*, *124*, 705-713. doi: 10.1016/j.conbuildmat.2016.06.058.

Busic, R., Milicevic, I., Sipos, T.K. and Strukar, K. (2018). Recycled Rubber as an Aggregate Replacement in Self-Compacting Concrete-Literature Overview. *Materials*, *11(9)*. doi: 10.3390/ma11091729.

CEN Comité Europeo de Normalización, Comité Européen de Normalisation.

CESCE (2018). Informe sectorial de la economía española: Materiales de construcción.

EFNARC (2002). Specification Guidelines for Self-compacting Concrete, European Federation of National Associations Representing Producers and Applicators of Specialist Building Products for Concrete.

EN-Euronorm. Rue de stassart, 36. Belgium-1050 Brussels, European Committee for Standardization.

Evangelista, L. and De Brito, J. (2014). Concrete with fine recycled aggregates: A review. *European Journal of Environmental and Civil Engineering*, *18(2)*, 129-172. doi: 10.1080/19648189.2013.851038.

Fiol, F., Thomas, C., Muñoz, C., Ortega-López, V. and Manso, J.M. (2018). The influence of recycled aggregates from precast elements on the mechanical properties of structural self-compacting concrete. *Construction and Building Materials*, *182*, 309-323. doi: 10.1016/j.conbuildmat.2018.06.132.

Grdic, Z.J., Toplicic-Curcic, G.A., Despotovic, I.M. and Ristic, N.S. (2010). Properties of self-compacting concrete prepared with coarse recycled concrete aggregate. *Construction and Building Materials*, *24(7)*, 1129-1133. doi: 10.1016/j.conbuildmat.2009.12.029.

Guo, H., Shi, C., Guan, X., Zhu, J., Ding, Y., Ling, T.C., Zhang, H. and Wang, Y. (2018). Durability of recycled aggregate concrete – A review. *Cement and Concrete Composites*, *89*, 251-259. doi: 10.1016/j.cemconcomp.2018.03.008.

IPCC (2014). Climate Change 2014: Synthesis Report. 176.

Maddalena, R., Roberts, J.J. and Hamilton, A. (2018). Can Portland cement be replaced by low-carbon alternative materials? A study on the thermal properties and carbon emissions of innovative cements. *Journal of Cleaner Production*, *186*, 933-942. doi: 10.1016/j.jclepro.2018.02.138.

Noh, S., Son, Y. and Park, J. (2018). Life cycle carbon dioxide emissions for fill dams. *Journal of Cleaner Production*, *201*, 820-829. doi: 10.1016/j.jclepro.2018.08.099.

Pereira-De-Oliveira, L.A., Nepomuceno, M.C.S., Castro-Gomes, J.P. and Vila, M.F.C. (2014). Permeability properties of self-Compacting concrete with coarse recycled aggregates. *Construction and Building Materials*, *51*, 113-120. doi: 10.1016/j.conbuildmat.2013.10.061.

Safiuddin, M., Alengaram, U.J., Rahman, M.M., Salam, M.A. and Jumaat, M.Z. (2013). Use of recycled concrete aggregate in concrete: A review. *Journal of Civil Engineering and Management*, *19(6)*, 796-810. doi: 10.3846/13923730.2013.799093.

Sandanayake, M., Zhang, G. and Setunge, S. (2019). Estimation of environmental emissions and impacts of building construction - A decision making tool for contractors. *Journal of Building Engineering*, *21*, 173-185. doi: 10.1016/j.jobe.2018.10.023.

Silva, R.V., De Brito, J. and Dhir, R.K. (2015). The influence of the use of recycled aggregates on the compressive strength of concrete: A review. *European Journal of Environmental and Civil Engineering*, *19(7)*, 825-849. doi: 10.1080/19648189.2014.974831.

UNE-CEN/TS-12390-9-EX (2008). Testing hardened concrete. Part 9: Freeze-thaw resistance. Scaling.

Verian, K.P., Ashraf, W. and Cao, Y. (2018). Properties of recycled concrete aggregate and their influence in new concrete production. *Resources, Conservation and Recycling*, *133*, 30-49. doi: 10.1016/j.resconrec.2018.02.005.

XV International Conference on Durability of Building Materials and Components
DBMC 2020, Barcelona
C. Serrat, J.R. Casas and V. Gibert (Eds)

Statistical Analysis of Sulfate Attack Resistance of Reactive Powder Concrete

Umut Bektimirova[1], Eldar Sharafutdinov[2], Chang S. Shon[3], Dichuan Zhang[4], and Jong R. Kim[5]

[1] Department of Civil and Environmental Engineering, Nazarbayev University, 53 Kabanbay batyr avenue, Nur-Sultan, Kazakhstan, 010000, ubakhbergenova@nu.edu.kz

[2] Department of Civil and Environmental Engineering, Nazarbayev University, 53 Kabanbay batyr avenue, Nur-Sultan, Kazakhstan, 010000, esharafutdinov@nu.edu.kz

[3] Department of Civil and Environmental Engineering, Nazarbayev University, 53 Kabanbay batyr avenue, Nur-Sultan, Kazakhstan, 010000, chang.shon@nu.edu.kz

[4] Department of Civil and Environmental Engineering, Nazarbayev University, 53 Kabanbay batyr avenue, Nur-Sultan, Kazakhstan, 010000, dichuan.zhang@nu.edu.kz

[5] Department of Civil and Environmental Engineering, Nazarbayev University, 53 Kabanbay batyr avenue, Nur-Sultan, Kazakhstan, 010000, jong.kim@nu.edu.kz

Abstract. *This paper is the study of sulfate attack resistance of reactive powder concrete (RPC). RPC that is also known as ultra-high performance concrete is a special type of concrete material obtained when fine powders like silica fume (SF) are added into the concrete mortar along with very low water-to-binder ratio (w/b). SF is a pozzolanic material obtained as a by-product of silicon metal or ferrosilicon alloys production. In this study, total 6 different RPC mixtures with various w/b (0.18, 0.22 and 0.26) and various SF content were studied. SF was added into the concrete mixtures in the amount of 15%, 20% and 25% of cement by weight. The other testing parameter includes 3 different concentrations of sodium sulfate (Na_2SO_4) solutions (0.35 M, 0.7 M and 1.4 M concentrations). Broad laboratory investigations of behavior of the RPC mixtures were conducted in terms of compressive strength and mass gain of cubes (50×50×50 mm^3) and expansion and mass change as in accordance with ASTM C1012. Test results had been analyzed and assessed by Taguchi method. The significance level of experimental parameters was determined by using Analysis of variance (ANOVA) method. According to statistical and analytical results it was observed that RPC has high sulfate attack resistance. Moreover, addition of optimal amount of SF into the RPC mixtures as well as decreasing w/b can significantly improve Na_2SO_4 resistance of RPC.*

Keywords: *Reactive Powder Concrete, Taguchi Method, Silica Fume, Sulfate Attack Resistance.*

1 Introduction

Sustainable development concept has recently become one of the most important topics in the construction industry. Moreover, development of alternative sources of energy in the face of energy crisis due to limited natural resources is foremost issue of the industry. Compressed air energy storage system incorporated into pile foundation system of the apartment building is proposed as a viable alternative to accumulating excess energy from solar panels installed on the building during the off-peak hours to be able to use it during the increased demand periods (Tulebekova *et al.*, 2017, Zhang *et al.*, 2018). Hence, complex structural and internal loading conditions require the piles to be made of superior performance material such as ultra-high performance concrete (Tulebekova *et al.*, 2019). Reactive Powder Concrete (RPC) is a type of

ultra-high performance concrete that is obtained by removing coarse aggregates from and addition of pozzolanic materials like silica fume (SF) to the concrete along with very low water-to-binder ratio (w/b) (Sun *et al.,* 2015). RPC has a densified microstructure that is attributed to the removal of coarse aggregates and the pozzolanic reaction that lead to the formation of strong bonds in interfacial transition zone due to the increased formation of strong calcium silicate hydrate lattices (Beglarigale and Yazıcı, 2015). It was investigated that the optimization of SF content and w/b results in the RPC with very high compressive and tensile strength (Ahmad *et al.,* 2015; Bektimirova *et al.,* 2018). Moreover, compressive strength of RPC could be increased further by optimization of packing degree of small aggregate (Ji *et al.,* 2011, Bektimirova *et al.*, 2020). Nevertheless, RPC is a relatively new type of concrete material, and its durability properties is still an ongoing topic of research.

External sulfate attack (ESA) is a concrete durability issue arising from the migration of sulfate ions from surrounding soils into the concrete structure, resulting in the series of chemical reactions and physical processes that cause irrecoverable damage to material (Marchand *et al.,* 2003). Even though the exact mechanism of sulfate attack is still questionable, it is agreed that the physical damage in the material occurs through the formation of expansive products such as gypsum and ettringite (Tixier and Mobasher, 2003) that leads to dimensional expansion and mass gain of the specimen. Expansive products form in the cracks in the microstructure of concrete and exert pressures that could be sustained by the pore spaces in the material (Ikumi *et al.,* 2019). However, the extensive or prolonged formation of expansive products might lead to the irreclaimable damage to concrete microstructure causing material degradation, loss of cohesiveness and strength (Gu *et al.,* 2019). Although Haufe and Vollpracht (2019) reported that RPC has moderate to high resistance to ESA due to its improved microstructure and reduced porosity, little data are available on the ESA resistance of RPC.

In this study, the ESA resistance of different RPC mixtures was investigated. SF content w/b, and concentration of sodium sulfate (Na_2SO_4) solution were selected as primary factors to influence on the compressive strength and expansion of the RPC mixtures exposed to the ESA environment by Taguchi method. Analysis of variance (ANOVA) was used to assess the significance level of experimental parameters.

2 Experimental Program

2.1 Materials

Ordinary Portland cement (ASTM type I) and SF with specific gravities 3.15 and 2.22 correspondingly were used as binder materials in this study. The chemical composition of cement and SF is provided in Table 1. Locally available quartz sand with specific gravity 2.4, absorption capacity of 6.2% was used as a fine aggregate for the RPC mixtures.

Liquid superplasticizer (SP) Master Glenium ACE 430 with specific gravity 1.02, and ordinary tap water were used in RPC mixing.

Table 1. Chemical composition of binders.

Components	Cement	SF
CaO [%]	65.91	0.22
SiO_2 [%]	21.55	97.54
Al_2O_3 [%]	5.55	0.2
Fe_2O_3 [%]	4.7	0.06
SO_3 [%]	1.9	-
MgO [%]	1.46	-
K_2O [%]	0.35	-
Loss on Ignition [%]	0.49	2.08

2.2 Mixture Proportion and Levels of Evaluation Variables

The experiments were designed to analyze the influence of various w/b, SF content, and sulfate concentration on the compressive strength and expansion of RPC. Mixture proportioning of RPC mixtures was completed using the absolute volume method. The details of mixture proportion are provided in Table 2.

Table 2. Mixture proportion of RPC (kg/m^3).

No.	Mixture ID	WB	SF	Cement	SF	Sand	Water	SP [% of binder]
1	0.18WB-20SF	0.18	20	1000	200	903	216	2
2	0.22WB-20SF	0.22	20	1000	200	788	264	1.5
3	0.26WB-20SF	0.26	20	1000	200	673	312	1.5
4	0.22WB-15SF	0.22	15	1043	157	802	264	1.5
5	0.22WB-25SF	0.22	25	960	240	776	264	1.5

The Taguchi statistical analysis method was used to determine the optimal mixture that will have the maximum compressive strength and the highest ESA resistance which is determined by the lowest expansion and mass gain during the exposure. Taguchi analysis was performed for 3 factors at a time with 3 levels each. Thus, 2 sets of analyses were performed: first one for w/b, second one for SF content, while sulfate concentration and exposure time were factors of analysis for both sets. Factors and levels of Taguchi analysis are shown in Table 3.

Table 3. Levels of the variables in the experimental program.

Factors	Level 1	Level 2	Level 3
w/b	0.18	0.22	0.26
SF content	15	20	25
Na_2SO_4 concentration	0.35	0.7	1.4
Time of exposure	1 week	4 weeks	13 weeks

2.3 Casting, Curing and Maintaining the Samples

Mixing RPC was completed in pan type mixer with total mixing time of 9±1 min. Immediately after mixing was complete, RPC was placed into the molds: 50 x 50 x 50 mm cube mold as required in ASTM C109 for compressive strength test; and, 25 x 25 x 250 mm prism molds as required by ASTM C1012 for length and mass change test. RPC specimens were cured for 24 hours in molds covered by plastic sheets to avoid water evaporation, after which they were placed into the Na_2SO_4 solution where they were stored until the test date.

2.4 Test Methods

The length and mass change tests of RPC were performed in accordance with ASTM C 1012 and ASTM C490 on the same samples. Accuracy of digital length comparator and digital scales used for measurements of length and mass change are ±0.0001 mm and ±0.001 g correspondingly. The compressive strength test of RPC was conducted in accordance with ASTM C109.

A number of samples are varied from mixture to mixture: 4-8 samples. To achieve better statistical reliability, outliers had been removed from calculated data as in accordance with ASTM E178. The test set up is provided in Figures 1 (a) and 1 (b).

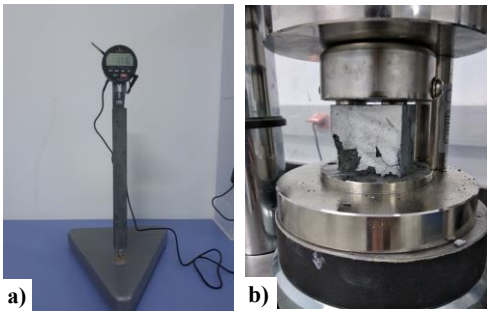

Figure 1. Test setup: (a) length change test; (b) compressive strength test.

3 Results and Discussion

3.1 Statistical Analysis

General Linear Model of analysis of variance (ANOVA) was used to observe statistically important parameters of experiments. Furthermore, to assess the contribution percentage of each parameter to the compressive strength, length and mass change, P-value was used: smaller P-value indicates more affective parameter in the concrete performance characteristics (Lin *et al., 2000*). The results of ANOVA for both sets of w/b-concentration-time and SF content-concentration-time are shown in Table 5.

Table 5. Results of ANOVA for w/b-concentration-time set and SF content-concentration-time set.

Source	SS	MS	F	P-Value	Source	SS	MS	F	P-Value
ANOVA for Compressive Strength of RPC									
w/b	48	24	0.31	0.735	SF	472.6	236.29	2.16	0.142
conc	329.4	164.7	2.15	0.143	conc	143.4	71.72	0.65	0.53
time	4731.02	2365.51	30.86	0	time	4090.2	2045.12	18.67	0
ANOVA for Length Change of RPC									
w/b	0.002954	0.001477	41.65	0	SF	0.001211	0.000605	19.76	0
conc	0.000478	0.000239	6.74	0.006	conc	0.000404	0.000202	6.59	0.006
time	0.000484	0.000242	6.82	0.006	time	0.000353	0.000177	5.77	0.011
ANOVA for Mass Change of RPC									
w/b	6.1525	3.07624	41.31	0	SF	0.3926	0.1963	7.22	0.004
conc	1.1562	0.57808	7.76	0.003	conc	2.604	1.302	47.89	0
time	0.8825	0.44127	5.93	0.01	time	1.0554	0.52768	19.41	0

According to Table 5, time is the most important parameter for compressive strength in both sets of experiments while length change is controlled by w/b and SF factors in w/b-concentration-time and SF content-concentration-time sets respectively. Mass change is also influenced mostly by w/b in w/b-concentration-time set; nevertheless, in SF content-concentration-time set it is affected by time and concentration factors. Hence, it is possible to suggest that time of exposure and RPC mixture content play more important role in ESA resistance of RPC.

3.2 Taguchi Analysis

The "smaller is better" Taguchi's quality loss function for compressive strength, length, and mass change of RPC was used to determine the optimal conditions for both w/b-concentration-time and SF content-concentration-time sets. The loss function is transferred further into utility function called Signal-to-Noise ratio (S/N) developed by Taguchi. S/N allows to identify performance characteristic deviating from desired value (Rahimi et al., 2016). Noise factor is any factor that causes deviation from targeted value for measurable product or process characteristics. Minitab statistical software was used for the statistical analysis of the results which are discussed in following sections.

3.2.1 Compressive strength

The main goal of every experiment is to determine the highest possible S/N value that will indicate that random effects of the noise factors are negligible compared to that of the signal. Fig. 2 shows the S/N ratio of compressive strength for w/b-concentration-time and SF-concentration-time sets.

As presented in Fig. 2, the minimum variation in compressive strength was obtained for the RPC containing w/b=0.26 and SF=25 %. Fig. 2 also shows that optimal values of concentration and curing time are 0.35M and 1-week in both w/b-concentration-time and SF content-concentration-time sets. In fact, compressive strength of RPC generally tends to decrease with

increasing the concentration of Na_2SO_4 solution: The higher concentration of Na_2SO_4 solution, the more deterioration of in RPC performance. It is possible to observe from Fig. 2 that 1.4M Na_2SO_4 solution not only has lower S/N ratio, but also has more damaging effect on compressive strength than 0.7M solution. This result may be attributed to stoichiometry of chemical reaction occurring during the sulfate attack exposure of concrete: As the concentration of Na_2SO_4 solution increases, more sulfate ions penetrate in to the specimen, consequently leading to more deteriorative cracks inside specimen and the reduction of the strength.

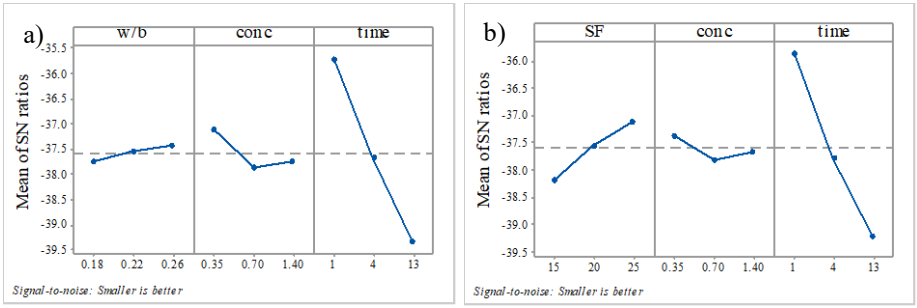

Figure 2. Main effects plots for SN ratios (Compressive strength): (a) w/b-concentration-time set; (b) SF content-concentration-time set.

3.2.2 Length and Mass change

Fig. 3 shows the S/N ratio of length change for two sets of experiments. According to Fig. 3 (a), the minimum variation of length change is created by w/b=0.18 at 0.35M Na_2SO_4 concentration at 1-week exposure. According to Fig. 2 (b) SF content=25 has the most stable reading.

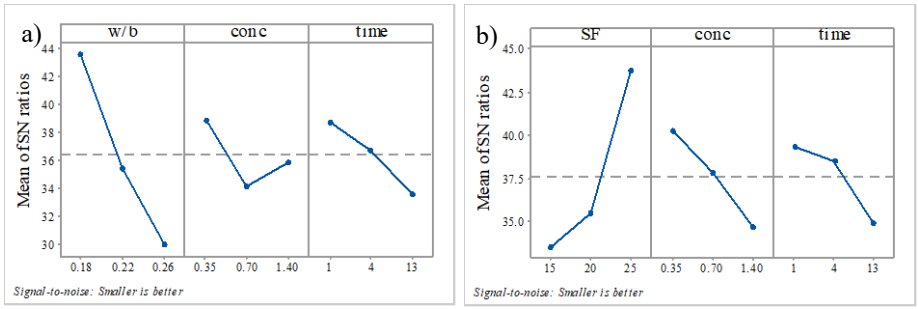

Figure 3. Main effects plots for SN ratios (Length change): (a) w/b-concentration-time set; (b) SF content-concentration-time set.

Fig. 4 shows the S/N ratio of mass change for two sets of experiments. Accordingly S/N ratios of mass change show the same trends as for length change for both sets of experiments. The reason is possibly that the same samples were used for both measurements. Furthermore, expansion of RPC exposed to sulfate attack result in both mass gain and elongation of the sample. Thus, formation and accommodation of expansive products in the RPC internal structure is indicated by the mass gain of the samples. Moreover, the process of accommodation of expansive products (ettringite formation) leads to internal cracking resulting in the expansion

of concrete. Hence, it appears to be logical that both length and mass change measurements show similar statistical behavior as it is observed by Taguchi analysis in this study.

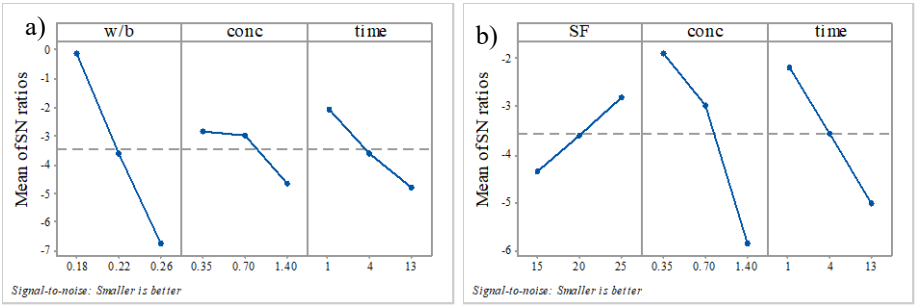

Figure 4. Main effects plots for SN ratios (Mass change): (a) w/b-concentration-time set; (b) SF content-concentration-time set.

4 Conclusion

Sulfate attack is an important durability problem of concrete structures exposed to groundwaters containing sulfate ions as in case of pile foundations. RPC is a relatively new type of material that has superior durability and mechanical characteristics. This study statistically analyzed sulfate attack resistance of RPC in two sets of influence factors. Accordingly, the following conclusions can be made:

- The ANOVA analysis showed that compressive strength of RPC exposed to Na_2SO_4 environment is influenced by time factor for both sets of experiment; while length and mass change are mostly affected by the RPC mixture content (w/b and SF content) and time of exposure.
- Based on Taguchi analysis, it is possible to suggest that optimal w/b=0.18 and optimal SF content=25 % for all three performance characteristics, namely compressive strength, length and mass change.

In conclusion, RPC appears to have high resistance to sulfate attack; however, this study is limited by the statistical analysis of standard test methods. Thus, more comprehensive study of sulfate attack resistance of RPC considering temperature effect and other types of sulfate solution may be needed to assess the resistance of RPC to sulfate attack incorporated with statistical analysis.

Acknowledgements

This research was supported by the Nazarbayev University Research Fund under Grant (#SOE2017001) “Development of a Renewable Energy Storage System Using Reinforced Concrete Foundations”. The authors are grateful for this supports. The authors would like to thank Nurdaulet Kutymbek, Kirill Kryzhanovskiy and Islam Mukhammedrakhym, laboratory assistant and undergraduate students of Nazarbayev University for their assistance in the laboratory work.

ORCID

Umut Bektimirova: https://orcid.org/0000-0002-8910-6631
Eldar Sharafutdinov: https://orcid.org/0000-0002-8320-3780
Chang S. Shon: https://orcid.org/0000-0003-4849-3206
Dichuan Zhang: https://orcid.org/0000-0002-9253-4178

Jong R. Kim: https://orcid.org/0000-0002-8796-3832

References

Ahmad, S., Zubair, A., and Maslehuddin, M. (2015). Effect of key mixture parameters on flow and mechanical properties of reactive powder concrete. *Construction and Building Materials*, *99*, 73-81.

American Society for Testing and Materials. (2016). Standard Test Method for Compressive Strength of Hydraulic Cement Mortars, ASTM C109, ASTM International, West Conshohocken, PA, USA.

American Society for Testing and Materials. (2015). Standard Practice for Use of Apparatus for the Determination of Length Change of Hardened Cement Paste, Mortar, and Concrete, ASTM C490, ASTM International, West Conshohocken, PA, USA.

American Society for Testing and Materials. (2015). Standard Test Method for Length Change of Hydraulic-Cement Mortars Exposed to a Sulfate Solution, ASTM C1012, ASTM International, West Conshohocken, PA, USA.

American Society for Testing and Materials. (2016). Standard Practice for Dealing with Outlying Observations; ASTM E178; ASTM International: West Conshohocken, PA, USA.

Beglarigale, A., and Yazıcı, H. (2015). Pull-out behavior of steel fiber embedded in flowable RPC and ordinary mortar. *Construction and building materials*, *75*, 255-265.

Bektimirova, U., Shon, C. S., Zhang, D., Sharafutdinov, E., and Kim, J. (2018). Proportioning and Characterization of Reactive Powder Concrete for an Energy Storage Pile Application. *Applied Sciences*, *8*(12), 2507.

Bektimirova, U., Mukhammedrakhym, I., Shon, C. S., Zhang, D. C., and Kim, J. (2020). Effect of Aggregate Packing on Strength of Reactive Powder Concrete: Modeling and Experimental Evaluation. *In Materials Science Forum* (in press.) Trans Tech Publications.

Gu, Y., Martin, R. P., Metalssi, O. O., Fen-Chong, T., and Dangla, P. (2019). Pore size analyses of cement paste exposed to external sulfate attack and delayed ettringite formation. *Cement and Concrete Research.*

Haufe, J., and Vollpracht, A. (2019). Tensile strength of concrete exposed to sulfate attack. *Cement and Concrete Research*, *116*, 81-88.

Ikumi, T., Cavalaro, S. H., and Segura, I. (2019). The role of porosity in external sulphate attack. *Cement and Concrete Composites*, *97*, 1-12.

Ji, T., Chen, B. C., Zhuang, Y. Z., Li, F., Huang, Z. B., and Liang, Y. N. (2011). Effects of sand particle size and gradation on strength of reactive powder concrete. In *Advanced Materials Research* (Vol. 261, pp. 208-211). Trans Tech Publications.

Lin, J. L., Wang, K. S., Yan, B. H., and Tarng, Y. S. (2000). An investigation into improving worn electrode reliability in the electrical discharge machining process. The International Journal of Advanced Manufacturing Technology, 16(2), 113-119.

Marchand, J., Odler, I., and Skalny, J. P. (2003). Sulfate attack on concrete. CRC Press.

Tixier, R., & Mobasher, B. (2003). Modeling of damage in cement-based materials subjected to external sulfate attack. I: formulation. *Journal of materials in civil engineering*, *15*(4), 305-313.

Tulebekova, S., Saliyev, D., Zhang, D., Kim, J. R., Karabay, A., Turlybek, A., and Kazybayeva, L. (2017, November). Preliminary analytical study on the feasibility of using reinforced concrete pile foundations for renewable energy storage by compressed air energy storage technology. In *Materials Science and Engineering Conference Series* (Vol. 271, No. 1, p. 012023).

Tulebekova, S., Zhang, D., Lee, D., Kim, J. R., Barissov, T., and Tsoy, V. (2019). Nonlinear responses of energy storage pile foundations with fiber reinforced concrete. Structural Engineering and Mechanics, 71(4), 363-375.

Rahimi, S., Nikbin, I. M., Allahyari, H., and Habibi, S. (2016). Sustainable approach for recycling waste tire rubber and polyethylene terephthalate (PET) to produce green concrete with resistance against sulfuric acid attack. Journal of Cleaner Production, 126, 166-177.

Sun, H., Li, Z., Memon, S., Zhang, Q., Wang, Y., Liu, B., and Xing, F. (2015). Influence of ultrafine 2CaO· SiO2 powder on hydration properties of reactive powder concrete. *Materials*, *8*(9), 6195-6207.

Zhang, D., Kim, J., Tulebekova, S., Saliyev, D., and Lee, D. (2018). Structural Responses of Reinforced Concrete Pile Foundations Subjected to Pressures from Compressed Air for Renewable Energy Storage. International Journal of Concrete Structures and Materials, 12(1), 74.

XV International Conference on Durability of Building Materials and Components
DBMC 2020, Barcelona
C. Serrat, J.R. Casas and V. Gibert (Eds)

Study on the Practical Use of Urea to Reduce Drying Shrinkage of Concrete by Spraying Urea Solution under Cold Environment

Takumi Sato, Hiromi Fujiwara, Masanori Maruoka and Liu Lingling

Graduate School of Regional Development and Creativity, Utsunomiya University,
7-1-2 Yoto, Utsunomiya City, Tochigi Prefecture, Japan, mc196256@cc.utsunomiya-u.ac.jp

Abstract. *Concrete cracking caused by drying shrinkage adversely affects the durability of a structure. The results of past research has shown that drying shrinkage can be reduced by adding urea as an admixture to the concrete. However, mixing various admixtures at the factory increases the costs for equipment and labor. To reduce drying shrinkage more easily and inexpensively, the urea solution can be applied to the concrete surface by soaking or brushing. However, urea solutions are not suitable for use in cold weather because urea in solution crystallizes at low temperatures. This study attempted to solve this problem by mixing antifreeze, which resists freezing, with a urea solution. It was found that the crystallization temperature of urea can be lowered by mixing the urea solution the antifreeze. Furthermore, it was confirmed that the antifreeze/urea solution reduced drying shrinkage for both mortar and concrete.*

Keywords: *Urea Solution, Drying Shrinkage, Soaking, Antifreeze, Cold Weather.*

1 Introduction

Concrete cracking caused by drying shrinkage adversely affects the durability of a structure. Adding urea to concrete is an effective method for reducing drying shrinkage[1)]. However, in ready-mixed concrete factories in Japan, adding various admixture materials to concrete will increase equipment and labor costs. Moreover, drying shrinkage occurs mainly on the surface of concrete, so applying an agent to the surface is more efficient and economical. This paper describes a method of applying urea solution to the surface of concrete after demolding that efficiently and economically reduces drying shrinkage.

2 Past Achievements

In previous studies, specimens soaked in a urea solution had less drying shrinkage than untreated specimens (Figure 1). Moreover, the amount of drying shrinkage continue to fall as the soaking time increased[2)]. However, soaking concrete in a urea solution of site is not practical, so an experiment was conducted in which urea solution was brushed onto the surface of the concrete. It was found that the brushing method provide an equal or greater effect on drying shrinkage as soaking[3)].

On the other hand, the specimens had higher compressive strength after soaking in a urea solution, as shown in Figure 2. Moreover, the strength increased as the soaking time increased. These results were likely due to the urea solution entering the concrete and the urea recrystallizing in the voids. The expansion pressure from the urea crystals helped to reduce the drying shrinkage and increase the compressive strength. The water retention effect of the urea crystals may also prevent the dissipation of moisture inside the concrete, which also helped to suppressing drying.

doi:10.23967/dbmc.2020.134

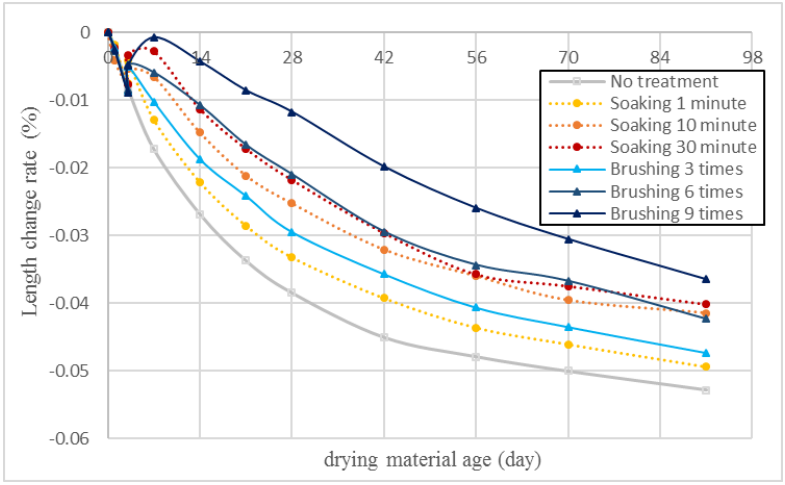

Figure 1. Drying shrinkage reduction.

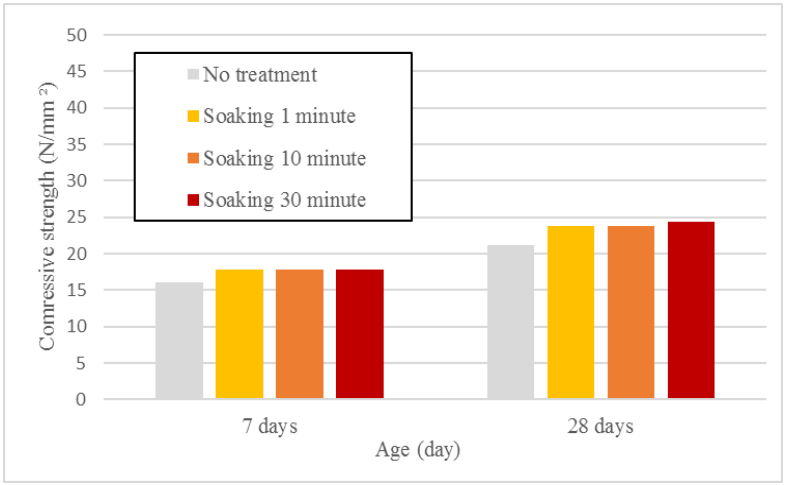

Figure 2. Result of compressive strength test.

3 Applying Antifreeze in Cold Weather

3.1 Outline

Previous studies have shown that applying a urea solution to concrete helps to reduce drying shrinkage. However, the solubility of urea decreases at lower temperatures, causing the urea in the water to crystallize and separate out. In cold weather, the urea crystallizes before the solution can be applied to the concrete, thereby reducing the solution's effect on drying shrinkage. To prevent the crystallization of the urea in the solution at low temperatures, antifreeze with freezing resistance was added to the solution. This lowered the crystallization temperature, allowing the urea solution to be used in cold weather.

3.2 Crystallization Temperature of Urea When Antifreeze is Mixed at Different Rates

The freezing resistance property of the antifreeze can be varied by adjusting its concentration

in the urea solution. Therefore, this study investigated the effect of different concentrations of antifreeze on the crystallization temperature of urea in a solution.

3.2.1 Antifreeze mix solution

In this test, a commercially available antifreeze used for air conditioner or refrigeration facility was used. The main component of this antifreeze is ethylene glycol. In order to produce different freezing temperatures, the ratio of antifreeze to water were set to 3:7, 4:6 and 5:5 (Figure 3). Moreover, in order to make comparisons with a urea solution containing the maximum amount of urea that can dissolve in water at 20 (°C), the maximum amount of urea that can dissolve at 20 (°C) was added to the antifreeze solution.

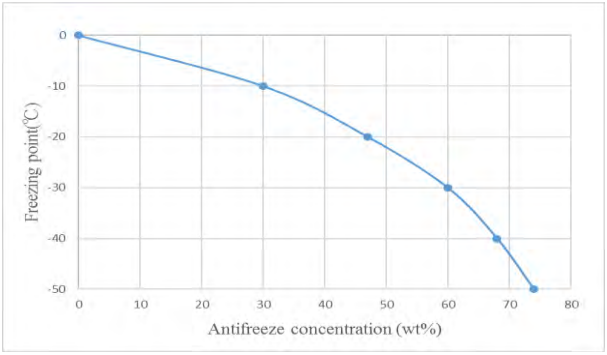

Figure 3. Freezing point of antifreeze.

Photo 1. Antifreeze concentrations in a solution.

3.2.2 Test method

Photograph 1 shows the different antifreeze concentrations in a urea solution. First, solutions with different antifreeze concentrations were placed in transparent containers. Next, the temperature of the solutions was lowered by immersing the containers in ice water. Using a thermometer, the crystallization temperature (the temperature at which urea crystals formed) was measured.

3.2.3 Test result

As shown in Table 1, the crystallization temperature decreased as the concentration of antifreeze increased. Therefore, it was considered that antifreeze solutions can be applied to concrete in cold weather to reduce drying shrinkage.

Table 1. Crystallization temperature of urea.

Name	Component (mass ratio) Antifreeze : Water : Urea	Crystallization temperature (°C)
Antifreeze 30%	3 : 7 : 8	5
Antifreeze 40%	4 : 6 : 7	4
Antifreeze 50%	5 : 5 : 6.5	1
Urea solution	0 : 1 : 1	8

3.3 Effect of a 30 % Antifreeze Solution on Shrinkage Reduction in Mortar

3.3.1 Materials

Table 2 shows the materials used in this test.

3.3.2 Mix condition

Table 3 shows the mixing conditions and the properties of the fresh mortar. The target values were 200 ± 20 mm for 15 strokes flow, 2.0 ± 1.5 % for the air volume.

3.3.3 Mixing method

For mixing, an omni type mixer with a nominal capacity of 10 liters was used. First, cement and sand were mixed for 15 seconds. Next, water was added and mixed for 60 seconds. Finally, the mortar was discharged.

Table 2. Materials.

Type	Name	Symbol	Density g/cm^3
Water	Tap water	W	1.00
Binder	Ordinary Portland cement	C	3.16
Sand	River sand (F.M.: 2.61,Warer absorption rate : 1.94)	S	2.61
Gravel	Crushed stone (F.M.: 2.62,Water absorption rate : 0.75)	G	2.62
Admixture	Poly-carboxylic acid-based high-performance air-entraining and water reducing admixture	SP	1.00
Chemical materials	Industrial urea	U	1.32
	Antifreeze	AF	1.03

Table 3. Mixing condition and properties of fresh mortar.

W/C (%)	S/C	Unit quantity(kg/m^3)			Air volume(%)	Flow (mm)
		W	C	S		
50	2.3	293	550	1247	2.4	220

3.3.4 Test items

(1) 15 strokes flow test
The 15 stroke flow test was carried out in accordance with ISO 679 2009.
(2) Air volume test
The air volume test was carried out in accordance with ISO 1920-2 2016.
(3) Drying shrinkage test
The drying shrinkage test was carried out in accordance with ISO 1920-8. Figure 4 shows the method used for this test. Prismatic specimens (40 × 40 × 160 mm) were made for this test. The specimens were demolded one day after mixing, and this day was taken as day 0 for the start of air curing. The specimens were cured in a room at a constant temperature of 20 ± 3 (°C) and 60

± 5 % relative humidity and changes in length and mass were measured. Next, some specimens were soaked in a 30% antifreeze solution for 1 minute, 10 minutes, and 30 minutes (Table 1). Other specimens were not soaked. Changes in the length and mass of all of the specimens were measured for 91 days.

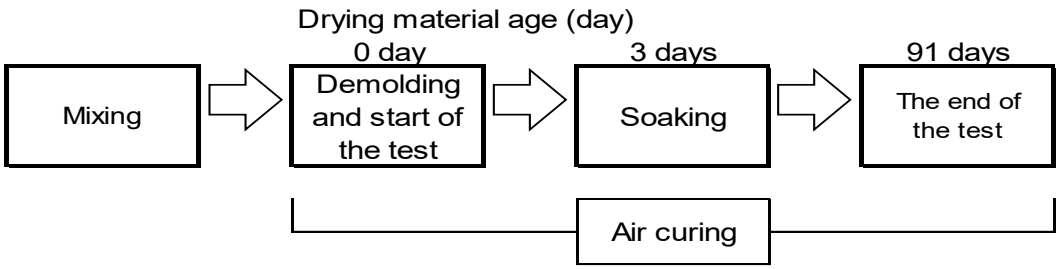

Figure 4. Method used for drying shrinkage test.

3.3.5 Test results

The results of the drying shrinkage test of mortar show that the specimens soaked in a 30% antifreeze solution exhibited a greater drying shrinkage effect than the specimens that were not soaked (Fig. 5). Moreover, the effect became larger as the soaking time increased.

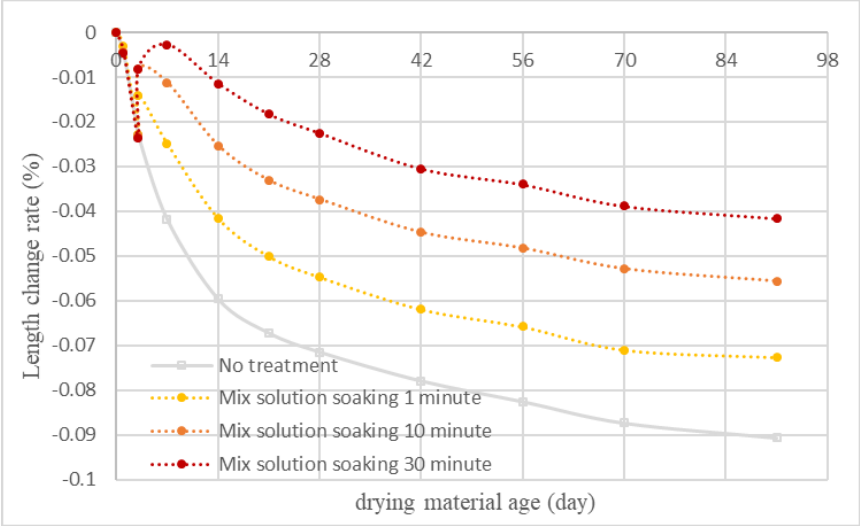

Figure 5. Drying shrinkage test of mortar.

3.4 Concrete Soaked in 30 % Antifreeze Solution

Since the 30% antifreeze solution clearly reduced drying shrinkage in mortar, the same experiment was conducted using concrete.

3.4.1 Materials

The materials used were the same as those described in section 3.3.1 above.

3.4.2 Mixing conditions

Table 4 shows the mixing conditions and properties of fresh concrete. The target values of the

freshness properties were 8.0 ± 1.5 cm for slump, 4.5 ± 1.5% for air volume.

Table 4. Mixing conditions and properties of fresh concrete.

W/C (%)	Unit quantity (kg/m³)				Addition rate (C×%)	Air volume (%)	Slump (cm)
	W	C	S	G	SP		
50	170	340	798	969	0.10	4.0	8.5

3.4.3 Mixing method

A pan type mixer with a nominal capacity of 55 (L) was used for mixing. First, cement, sand, and gravel were mixed for 15 seconds. Next, water mixed with SP was added and mixed for 60 seconds. Finally, the concrete was discharged.

3.4.4 Test items

(1) Concrete slump test
The concrete slump test was carried out in accordance with ISO 1920-2 2005.
(2) Air volume test
The air volume test was carried out in accordance with ISO 1920-2 2016.
(3) Drying shrinkage test
The drying shrinkage test was carried out using the same method and room conditions used for the mortar experiment, but with 100 × 100 × 400 mm prismatic specimens.
(4) Compressive strength test
The compressive strength test was carried out in accordance with ISO 1920-8. After demolding on day 1, the specimens were cured in a room at a constant temperature of 20 ± 3°C and 60 ± 5 % relative humidity. but soaked in antifreeze mix solution at 3rd day. Then the compressive strength tests were conducted at age of 7 and 28 days.

3.4.5 Test result

The test results confirmed that soaking concrete in a 30% antifreeze solution reduces drying shrinkage (Fig. 6). Previous studies have shown a drying shrinkage reduction effect when specimens are soaked in a urea solution. This study showed that antifreeze solutions also reduce drying shrinkage. Urea recrystallizes in the voids of concrete after soaking in an antifreeze solution also reduce drying shrinkage due to the recrystallization of urea in the voids of the concrete.

Figure 7 shows the results of the compressive strength test. As shown in previous studies, this study confirmed that soaking concrete in an antifreeze solution increased the compressive strength. Moreover, the strength increased as the soaking time increased. The urea crystals help improve compressive strength.

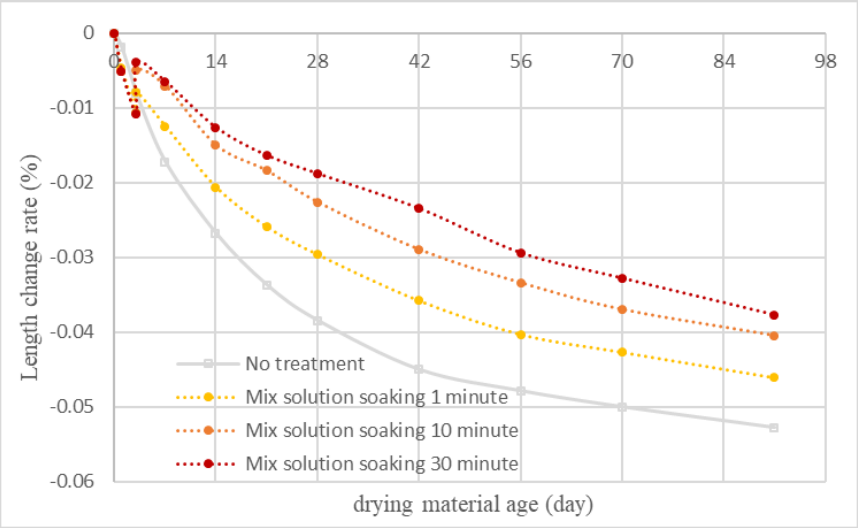

Figure 6. Drying shrinkage test of concrete.

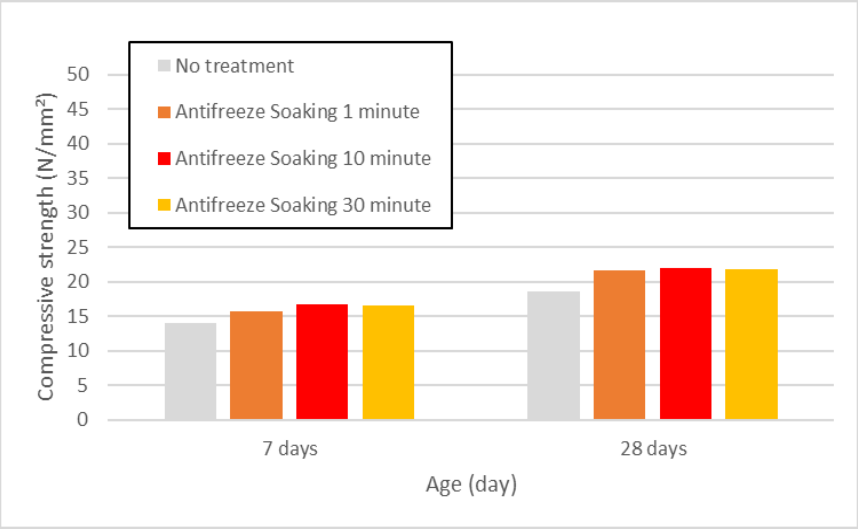

Figure 7. Compressive strength.

3.5 Conclusion

This study showed that the crystallization temperature of urea can be lowered by mixing it with antifreeze. Furthermore, soaking the concrete in an antifreeze solution reduces drying shrinkage, as indicated by the lower length change rate in the drying shrinkage test. These results confirm that an antifreeze solution can be used as a drying shrinkage reduction agent in cold weather. The practical application of this method in the field, however, requires further study.

ORCID

Takumi Sato: https://orcid.org/0000-0002-8181-3489
Hiromi Fujiwara: https://orcid.org/0000-0003-3032-480X
Masanori Maruoka: https://orcid.org/0000-0002-3041-0700
Liu Lingling: https://orcid.org/0000-0001-9450-7598

References

Kawai T and Sakata K. (2007). Properties of concrete incorporating urea. *Proceeding of the Japan Concrete Institute*, Volume 29, 639-644.

Liu L, Fujiwara H, and Maruoka M. (2017). Development of a new drying shrinkage reducing agent of concrete by spraying on surface of concrete. *Proceeding of the Japan Concrete Institute*, Volume 39, 415-420.

Liu L, Fujiwara H, Maruoka M, and Shirayama K. (2018). Development of a drying shrinkage reducing agent of concrete by spraying and brushing urea solution. *Proceeding of the Japan Concrete Institute*, Volume 41, 407-412.

XV International Conference on Durability of Building Materials and Components
DBMC 2020, Barcelona
C. Serrat, J.R. Casas and V. Gibert (Eds)

The Durability of Plant-Based Air Filtering Systems in Buildings: From an Air Quality and Energy Reduction Perspective

Ahu Aydogan

Bernard and Anne Spitzer School of Architecture, City College of New York, NY 10031, USA,
aaydogan@ccny.cuny.edu

Abstract. *After the oil crisis, all the commercial and residential buildings were designed with tightly sealed envelopes to minimize the air leakage through the building to save energy. Since buildings were no longer able to breathe naturally, indoor air quality problems started to occur. Currently, there is still a dilemma between these two parameters inside the buildings. To address IAQ issues and reduce the energy loads in mechanical conditioning systems, the plant-based air filtering system is designed. The proposed system is a hydroponic system (plants growing without soil) that is composed of a mixed bed of activated carbon adsorbents and porous glass stones that capture and filter the toxins in the air. HVAC-integrated plant walls that include growth media are designed to support the plants and capturing toxins. These toxins are then metabolized by the plants which can create a self-regenerating filtration system that requires less outdoor air being fed into the building, thereby reducing the conditioning costs associated with HVAC. This paper is focused on the durability of the design and fabrication of a plant-based air filtering system from an air quality and energy reduction perspective.*

Keywords: *Filter, Indoor Air Quality, Mechanical Conditioning Systems, HVAC, Hydroponics.*

1 Introduction

Buildings and construction operations are responsible for about 40% of the final energy consumption and generation of energy-related carbon dioxide (UN, 2017) In mechanically ventilated buildings, most of the energy consumption is related to the heating and cooling outdoor air and distributing it internally (Chan, 2010; Hughesa, 2011). The American Society of Heating, Refrigerating and Air-Conditioning Engineers (ASHRAE) has designated of the health of the occupants and energy consumption profiles of the buildings (Roth, 2002) as the two key contributing factors in assessing the indoor air quality (IAQ) in ASHRAE standards. However, after 40 years of research and practical experiments in the field, finding a satisfactory solution to reduce building energy consumption while mainlining high indoor air quality remains a challenge. Even though HVAC filtration systems seem to be among the best solution for IAQ, they are mostly ineffective for volatile organic compounds (VOCs) and mostly contaminate the air instead of filtering it by infrequently changed filters (Bluyssen, 2003; Schleibinger, 1999).

Indoor air can be more contaminated than outdoor air and may lead to serious health problems related to the length of exposure (Liu, 2007). People, particularly living in urban areas, spend up to 90% of their time in indoor environments (Klepeis N.E., 2001; Robinson, 1995; USEPA, 2002). In the US alone, the annual economic losses related to IAQ is between $40 billion and $160 billion (Fisk, 1997; Lomborj, 2002), the cost which is associated with the loss of productivity and medical costs for the individuals who suffer from asthma, sick building syndrome and allergies caused due to poor IAQ (Guo, 2009). Passive techniques like increasing ventilation in buildings can improve IAQ. However; they are not suitable for many climate

doi:10.23967/dbmc.2020.165

conditions due to the increasing energy expenditures of HVAC systems related to the heating and cooling loads (Kibert, 2008). Since filters are also not efficient to remove most of the cancerogenic pollutants like formaldehyde and benzene, efficient filters need to be designed to protect building occupants from indoor air pollutants. There is a clear need for the design of a system that can address the IAQ concerns in the buildings and reduce the energy load from the HVAC systems at the same time. The successful design of such a system would have significant impacts on the urban environment and sustainability.

Plants can improve IAQ by metabolizing airborne pollutants such as formaldehyde, benzene, and xylene (Wolverton, 1993; Yoo, 2006; Aydogan, 2011). The utilization of the root zone (rhizosphere) of the plant is paramount to achieving high purification ability. There have been numerous applications of plants in buildings and the most relevant to our work is the integration of the plants into buildings to improve the quality of life in the indoor environment (Blanc, 2012). However; this system does not take advantage of the full cleaning capacity of plants, especially the root zone. Therefore, they do not sufficiently remediate pollutants within an indoor environment, nor do they incorporate their performance with the commercial buildings HVAC systems. For that reason, air remediation capacity, maintenance, energy savings and the cost of the system is lower than building-integrated systems. Building-integrated botanical air filtration systems are integrated into the building's conventional air handling units to save energy and provide a filtration system for the entire building. These systems take advantage of root zone of the plants which were the direct agents of toxin removal (Wolverton, 1993; Wang, 2014; Wolverton, 1993; Wood, 2002; Orwell, 2006). Building-integrated botanical air filtration systems have been recommended by the U.S. Department of Energy's Building Technologies Program for industrial-scale research, development and demonstration to improve air quality, energy efficiency and public health (USDOE, 2010).

The proposed botanically-based air purifying system constitutes plant-based air remediation strategies. It is a hydroponic system (plants growing without soil) that is composed of adsorbents and porous glass stones to capture and filter the toxins in the air. Plant-associated microbes in the rootzone convert these toxins to nutrients, which are then consumed by the plants. Through this, a self-regenerating filtration system is created. Significant work in plant-based filtering systems has been completed (Aydogan et al., 2016; Aydogan and Tardos, 2017) In continuation of earlier works of the author, this paper is focusing on the durability of the prototype design, fabrication, and assembly of an alternative filtration system by utilizing plants to clean indoor air and reduce energy consumption.

The paper is outlined as follows. In section 2, a discussion on the methods and the material used for the design is presented. Section 3 presents the results of the analysis, and section 4, concludes the paper by discussing the potential future developments of the system.

2 Materials and Methods

2.1 Materials

The prototype of the plant-based air filtering system is composed of three main parts: *(1)* a cassette holding the mesh, *(2)* a mesh holding the plants and growing media, and *(3)* a structure holding the cassettes together. The system components are shown in the exploded diagram in Figure 1. The heaviest elements of the prototype are the base and water basins (for watering the plants), which provide structural stability when located on the bottom.

The design of the modular system utilizes a series of cassettes that are repetitive and arranged to form a wall system. Through this design, natural channels are created on the back of the cassettes

to allow the air pass through and circulate back to the environment by the fans on each side of the panel prototype (Figure 2a). Each cassette holds the mesh containing lightweight growing media and the plants, LED lighting and drip irrigation tools (hose and drippers) (Figure 2b). The LED lighting system, which aids photosynthesis, is designed to be hidden within the three sides of the cassettes' lids. The irrigation is a closed-loop system, where the water flow is controlled using a timer. This allows the exact amount of water to drip and reach to the plants' roots without excess water overflowing in the prototype system. Five 0.25 gallons per hour drip emitters are aligned to be used in each of the cassettes. The pumps are located at the bottom of the prototype inside the water basins and the hoses of the drippers are hidden (on the back) between the cassettes (Figure 3a).

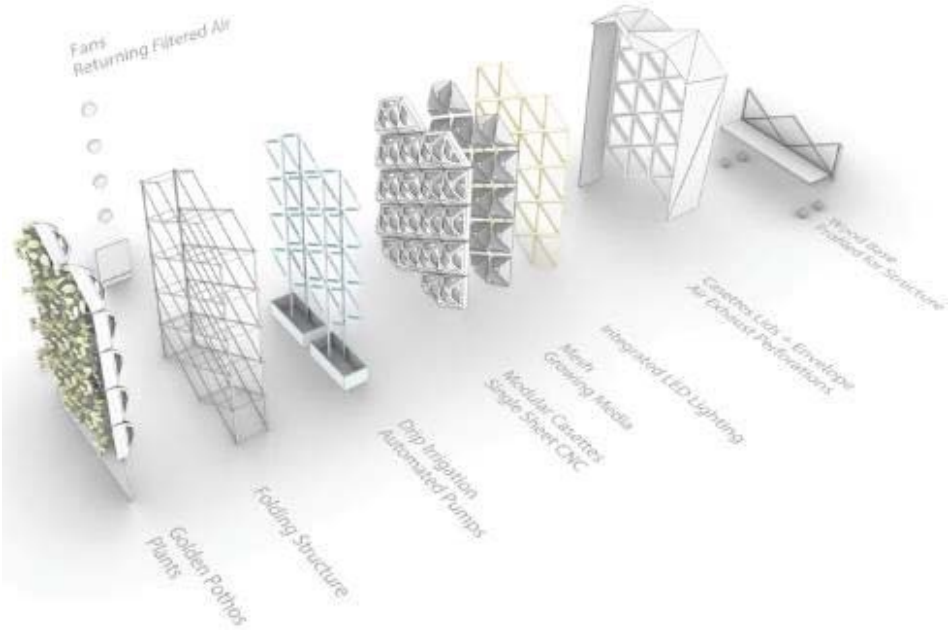

Figure 1. Exploded diagram of plant-based air filtering system.

In the design of the structure, steel bars with the dimension of 1/2" (width) x 1/8" (depth) are used. Since the prototype is double-sided (plant cassettes on both sides), the structure is designed to be versatile with easy and fast assembly by creating pockets that cassettes settle in. The bottom of the bars is embedded in the groves created in the wooden base that are profiled for the flat steel bars.

A mesh that holds the plants and growing media is designed by using a three-dimensional reinforcement mat (Enkamat7020), commonly used for erosion control on the slopes in the urban scale applications. This material is selected due to its performative features. It allows airflow to pass through the growing media and plants without creating additional pressure on the surface, it doesn't absorb moisture, it is UV resistant and holds the growing media with plants in place even it is installed vertically (Figure 3b).

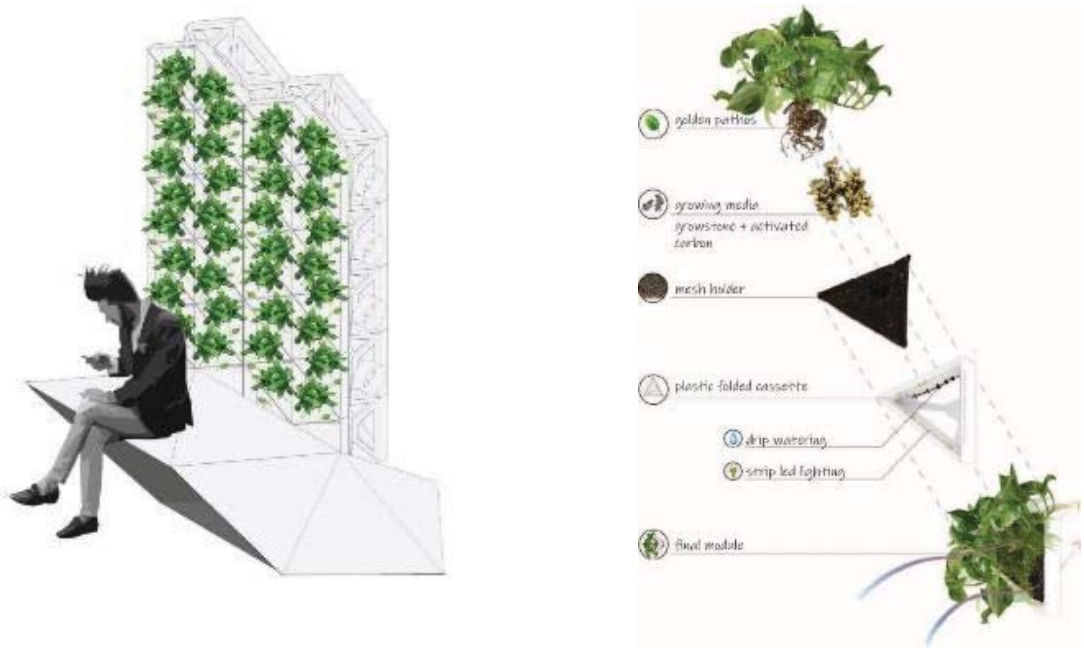

Figure 2. a. The double-sided prototype of plant-base air filtering system; b. Components of plant-based air filtering system.

Figure 3. a. Folded cassettes and dripper attachments**;** b. 3d mesh holding growing media and plants.

Growing media used in this system is composed of a mixed bed of activated carbon (4 × 8 Coconut Shell Granular) adsorbents and porous glass stones (GS2 Soil Aerator) that capture and filter the toxins in the air. The role of activated carbon in this mix is to capture toxins whereas porous glass stones are used for creating an environment for roots to grow. The porous surface on the glass stones makes it ideal for the roots to get water and climb.

Different kinds of plant species can be used in indoor environments and, essentially, depending on the specific functions that they can serve. Additional knowledge of the conditions that are required for their growth such as lighting requirements, watering, and maintenance are also vital factors. However, the most important principle for this project is their toxin degradation capacity through their rhizosphere. Golden Pothos (*Epipremnum aureum)* and English Ivy (*Hedera Helix*) are the two plants that are used in this prototype, based on the results of the toxin removal capacity that was discovered through our previous studies (Aydogan, 2011).

2.2 Methods

In this prototype, different materials and techniques of fabrication are investigated. Emphasis is placed on designing a lightweight and collapsible scissor structure, which allows the project to be easily transported and assembled. Subtractive manufacturing methods are selected to be used to conduct the base and the cassettes of the prototype. Computed-numerically-controlled (CNC) machine is used to cut the 1” wood base and sides. Precise 3/4” deep grooves are routered on the interior faces of the base so that the steel structure would snap into its designated shape. The structure’s geometry is designed to hold two abutting cassettes per one parallelogram (Figure 4a and Figure 4b). While the base’s hidden grooves and inserted cassettes hold the metal scissor structure’s geometry in place, it is the 1” plywood walls on both sides that provide support against shear stresses. These sidewalls are holding the fans that are used to distribute the air, which was cleaned by the plant cassettes.

Figure 4. a. Assembly of the prototype; b. Plant assembly of the prototype.

17 sheets of HDPE are used to CNC cut the cassettes of this prototype. A total of four cassettes are cut from a 49” × 96” sized sheet. The cassettes are designed and assembled by folding technique (Figure 5).

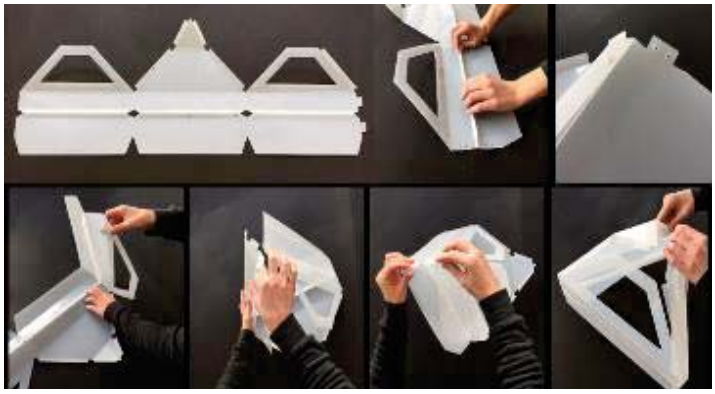

Figure 5. Cassette assembly by folding.

Cutout sheets are used to cut the mesh and create individual mesh holders. It is designed to fold and sewed a zipper in the seams, which makes planting easier. Three zippers are used in the mesh, two of them on the sides and one in the middle, which are preventing the growing media to fall and holding plants in place. In plant-based filtering systems, porous glass stones and activated carbon have different particle sizes and creates opportunities for settling in the planters. This creates a loss of active adsorption area in the cassettes. To prevent this problem two growth media are granulated (bonded together).

3 Results

In this project, a prototype containing 68 modules was designed and fabricated (Figure 6a and Figure 6b). Folding technique for the structure and cassettes seemed to be a practical solution, however; due to connection problems on the corners, the fabrication technique needs to be revisited for the cassettes. Using CNC for cutting the material was not the ideal solution due to time-inefficient and waste of material concerns. Two different solutions were generated to solve this problem.

Figure 6 a and b. The plant-based air filtering system prototype.

Those solutions are either using different fabrication techniques as traditional die cutting to cut the HDPE sheets for the cassettes or changing the folding technique to a different design so that more cassettes can be generated through one sheet of HDPE. 1/8" thick HDPE is also found not to be practical for reusing after disassembly of the cassettes and it can easily crack. Instead of HDPE, more flexible materials are recommended as Styrene, Vinyl or Polypyrene.

The structural scissor system is a practical technique to allow the ability to open and fold easily with lighter elements that carry the cassettes and growing media. The prototype generated valuable feedbacks on the structure by showing arising potential problems.

The mesh holding the plants worked very well with the media. Zippers around the perimeter of the mesh and sleeve create easiness for the assembly of the growing media and planting. Since the system is designed on the premise of flexibility and modularity, the mesh can be easily replaced for the maintenance without shutting the whole system, which allows the durability of the system in the long run.

4 Conclusion and Future Potentials

The durability of the plant-based filtration system is investigated by exploring the design, fabrication and installation properties of the materials. Most of the plant-based integrations in the field do not take advantage of the root zone (rhizosphere) cleaning capacity and have limited applicability in terms of modularity, scalability, flexibility, disassembly /reassembly and life cycle factors. In this paper, the project focused on the design and prototyping of the system to analyze the ways to minimize the maintenance cost and maximize the durability of the system by demonstrating the constructive feasibility of the modular, durable, easily transportable, flexible, adaptable approaches that can be efficiently mounted in indoor spaces. The conclusion of these investigations is showing that especially the structural scissors system and mesh holding (the growth media and plants) has a high potential to be applied to the plant-based filtration system.

Full-scale implementation of plant-based air filtering system is an alternative filtration solution that provides fresh air through the purification of recirculated air. In addition, by this system, end-use energy efficiency will be obtained due to the reduced outdoor air intake and recirculated indoor air. The proposed plant-based air filtering system would provide crucial support for building air handling systems.

Acknowledgments

I would like to thank all the research assistants at Spitzer School of Architecture, who participated on the design and fabrication of this system and Mahdieh Allahviranloo, Grove School of Engineering, City College of New York for her invaluable comments on this article.

ORCID
Ahu Aydogan: http://orcid.org/0000-0002-7523-8289

References

Aydogan, A. and Montoya, L.D. (2011). Formaldehyde removal by common indoor plant species and various growing media. *Atmospheric Environment, 45*(16), 2675-2682. doi:10.1016/j.atmosenv.2011.02.062

Aydogan, A. and Tardos, G. (2017). USA Patent No.: R. F. o. t. C. U. o. N. York.

Aydogan, A., Tardos, G. and Biddinger, E.J. (2016). *Granulation of Growth Media for Indoor Air Purification Utilizing Botanically-Based Systems* Paper presented at the Indoor Air 2016: The 14th International Conference on Indoor Air Quality and Climate, Ghent, Belgium.

Blanc, P. (2012). *The Vertical Garden: From Nature to the City*: W. W. Norton & Company.

Bluyssen, P.M., Cox, C., Seppänen, O., Oliveira Fernandes, E.d., Clausen, G., Müller, B. and Roulet, C.A. (2003). Why, when and how do HVAC-systems pollute the indoor environment and what to do about it? the European AIRLESS project. *Building and Environment, 38*(2), 209-225. doi:http://dx.doi.org/10.1016/S0360-1323(02)00058-6

Chan, H.Y., Riffat, S.B. and Zhu, J. (2010). Review of passive solar heating and cooling technologies. *Renewable and Sustainable Energy Reviews, 14,* 781-789.

Fisk, W.J. and Rosenfeld, A.H. (1997). Estimates of Improved Productivity and Health from Better Indoor Environments. *Indoor Air, 7*(3), 158-172.

Guo, H., Kwok, N.H., Cheng, H.R., Lee, S.C., Hung, W.T. and Li, Y.S. (2009). Formaldehyde and volatile organic compounds in Hong Kong homes: concentrations and impact factors. *Indoor Air, 19*(3), 206-217.

Hughesa, B.R., Chaudhrya H.N. and Ghanib, S.A. (2011). A review of sustainable cooling technologies in buildings. *Renewable and Sustainable Energy Reviews, 15*, 3112– 3120.

Kibert, J.C. (2008). *Sustainable Construction: Green Building Design and Delivery*. Hoboken, NJ: John Wiley & Sons, Inc.

Klepeis N.E., Nelson W.C., Ott W.R., Robinson J.P., Tsang A.M., Switzer.P, . . . Engelmann, W.H. (2001). The national human activity pattern survey (NHAPS): a resource for assessing exposure to environmental pollutants. *Journal of Exposure Analysis and Environmental Epidemiology, 11*, 231–252.

Liu, Y.J., Mu, Y.J., Zhu, Y.G., Ding, H. and Crystal Arens, N. (2007). Which ornamental plant species effectively remove benzene from indoor air? *Atmospheric Environment, 41*(3), 650-654. doi:DOI: 10.1016/j.atmosenv.2006.08.001

Lomborj, B. (2002). *The Skeptical Environmentalist*. Cambridge, MA: Cambridge University Press.

Orwell, L. R., Wood, L. R., Tarran, J., Torpy, F. and Burchett, D. M. (2006). *Water, Air, and Soil Pollution, 177*, 59-80.

Robinson, J. and Nelson, W.C. (1995). *The national human activity pattern survey data base*. Retrieved from NC: Roth, K.W., Westphalen, D., Dieckmann, J., Hamilton, S.D. and Goetzler, W. (2002). *Energy Consumption Characteristics of Commercial Building HVAC Systems Volume III: Energy Savings Potential.*

Schleibinger, H. and Ruden, H. (1999). Air filters from HVAC systems as possible source of volatile organic compounds (VOC) - laboratory and field assays. *Atmospheric Environment, 33*(28), 4571-4577. doi:10.1016/S1352-2310(99)00274-5

UN: Environment and International Energy Agency (2017). *Towards a zero-emission, efficient, and resilient buildings and construction sector*. Global Status Report 2017.

USDOE. (2010). *2010 Buildings Energy Data Book. "Table 1.1.9. Buildings Share of U.S. Electricity Consumption (Percent). State Energy Data 2008: Consumption, 2010.] and [U.S. Energy Information Administration. " Summary Reference Case Tables, Table A2, p. 3-5 for 2008-2035 consumption, Table A3, p. 4-6 for 2008 expenditures." Annual Energy Outlook 2011 Early Release, 2010.]*. Prepared by D&R International, Ltd, 2011. [U.S. Energy Information Administration.

USEPA. (2002). *Child-Specific Exposure Factors Handbook. EPA/600/P-00/002B.* Retrieved from Washington, DC: U.S.

Wang, Z., Pei, J. and Zhang, J.S. (2014). Experimental investigation of the formaldehyde removal mechanisms in a dynamic botanical filtration system for indoor air purification. *Journal of Hazardous Materials, 280*, 235-243. doi:http://dx.doi.org/10.1016/j.jhazmat.2014.07.059

Wolverton, B.C. and Wolverton, D.J. (1993). Plants and soil microorganisms: removal of formaldehyde, xylene, and ammonia from the indoor environment. *Journal of Mississippi Academy of Sciences, 32*(2), 11-15.

Wood, R.A., Orwell, R.L., Tarran, J., Torpy, F. and Burchett, M.D. (2002). Potted-plant/growth media interactions and capacities for removal of volatiles from indoor air. *Journal of Horticultural Science & Biotechnology, 77*(1), 120-129.

Yoo, M.H., Kwon, Y.J., Son, K. and Kays, S.J. (2006). Efficacy of indoor plants for the removal of single and mixed volatile organic pollutants and physiological effects of the volatiles on the plants. *Journal of the American Society for Horticultural Science, 131*, 452-458.

Yoo, M.H., Kwon, Y.J., Son, K. and Kays, S.J. (2006). Efficacy of indoor plants for the removal of single and mixed volatile organic pollutants and physiological effects of the volatiles on the plants. *Journal of the American Society for Horticultural Science, 131*, 452-458.

XV International Conference on Durability of Building Materials and Components
DBMC 2020, Barcelona
C. Serrat, J.R. Casas and V. Gibert (Eds)

Thermodynamic Processes in Nanostructured Thermocoatings

David Bozsaky

Department of Architecture and Building Construction, Faculty of Architecture, Civil Engineering and Transport Sciences, Széchenyi István University, H-9024 Győr, Hungary, Egyetem tér 1, bozsaky@gmail.com

Abstract. *In the 21st century, global climate change and the high level of fossil energy consumption have introduced changes affecting all sectors of the economy, including the building industry. This process has prompted EU members to create strict regulations in building energetics. It has become a serious task for architects to find more effective ways for thermal insulation. One of these options is the application of nanostructured materials. Among them nano-ceramic thermocoatings open a wide range of research fields, because complete agreement had not been already found about their insulating effect. In order to explore and describe the thermodynamic process inside nano-ceramic thermocoatings 6 series of heat transfer resistance experiments were performed in 2014-2018. Several building structure configurations with 12 different orders of layers were tested with a standard heat flow meter. On basis of these results it could be concluded that in case of nano-structured thermocoatings convective heat transfer coefficient might be taken account in different way than in case of traditional macro-structured thermal insulation materials. Based on research results, the limits of its applicability can also be concluded. It has also been found that the insulating effect of nanostructured thermocoatings depends on the material characteristics of the insulated surface.*

Keywords: *Thermal Insulation, Nanotechnology, Thermocoating, Thermodynamics, Building Physics.*

1 Introduction

In the 21st century, humanity has faced serious problems of energy and environmental aspects. Reducing energy consumption and preferring renewable materials with low environmental impact are fundamental tools in order to slow the degradation of our environment as well as early exhaustion of non-renewable fossil energy resources. Building sector represents over 40% of global energy consumption and 56.7% in carbon dioxide emissions, which is considerable (Shea *et al.*, 2012; Anestopoulou *et al.*, 2017). Because of these reasons regulations relating to thermal insulation performance of buildings are getting more and more rigorous nowadays. It has become a serious task for architects and civil engineers to find more and more effective ways for thermal insulation of buildings.

The appearance of nanotechnology-based thermal insulation materials in building industry opened several possibilities in the 1990s for designers because of their high-performance thermal insulating quality (Leydecker, 2008). A variety of nanotechnology-based thermal insulation materials could be found in building industry (*e.g.*, aerogel, VIPs), from which nano-ceramic thermocoatings are generally considered to be the most critical because of the contradictory technical data about their thermal insulating mechanism that could be founded in producers' handouts and also in special literature. Therefore, this material has become the focus of this paper.

2 Nano-Ceramic Thermocoatings

Synthetizing of nano-ceramic microspheres was developed in 1981 by S. Komarneni and R. Roy. This so-called 'sol-gel' process enabled researchers to test the properties of nano-ceramics (Hoffman *et al.*, 1984). To produce nano-ceramics at a more efficient way this process was later replaced by microwave sintering.

The most paint-on insulation products contain microscopic vacuum-hollow ceramic microspheres with a diameter of 20-120 μm and with a cellular wall thickness of 50-200 nm. Nano-ceramic thermocoatings are made of melted glass or ceramics on high gas-pressure and high temperature (1500 °C). After cooling down, the pressure ends, leaving vacuum inside the microspheres. A mixture of synthetic rubber and other polymers is used as binding materials. Its main components are styrene (20%) and acryl latex (80%). Styrene enhances mechanical strength and acryl latex makes nano-ceramic coating resistant against weather conditions and provides flexibility. Other additives (*e.g.,* biocides, anti-fouling and antifungal materials) make the final product durable and mold-proofed (Thermo-Shield Inc., 2017; Lan *et al.*, 2014).

Nano-ceramic coatings are typically used for exterior and interior wall insulation, but they are also suitable for pipe insulation and protection against fire and corrosion. They can be easily transmitted to hard-to-reach places. After mixing the ceramic microspheres with binding material, additives and water, a brush, roller or spray can be used to apply on the surface to be insulated. All surfaces must be clean and free from any contamination before painting. Generally two insulating layers are required, the first of which acts as a primer layer. The drying time of a layer depends on the temperature (at 20 °C, it takes 4-5 hours). The complete solidification takes 72 hours (Thermo-Shield Inc., 2017; Lan *et al.*, 2014).

3 Literature Summary

Special literature provides different data about thermal insulation quality and thermodynamic details about nano-ceramic thermocoatings (Paul *et al.*, 2010; Koniorczyk *et al.*, 2004). Some sources state that their thermal conductivity is around 0.001-0.003 W/mK based on measurements of university laboratories in Latvia, Russia (Volgograd) and Hungary (Debrecen) (Orbán, 2012; Thermo-Shield Inc., 2017). Other sources publish much higher values (from 0.014 W/mK to 0.140 W/mK) and talk about their effective thermal conductivity which contains the internal and external convective heat transfer coefficients (h_i and h_e) of the enclosed nanoscale pores inside the nanostructure. These details are often not confirmed by documented laboratory tests or refer to insufficiently introduced experiments (Orbán, 2015; Lakatos, 2016; Chukhlanov *et al.*, 2017). Others calculate thermal conductivity of nano-ceramic coatings from heat transfer coefficient (U-value) of a global building structure (Lakatos, 2016). Each method has the same problem that it tries to determine thermal conductivity by an indirect way using conventional data and calculation and it does not take in account that physical and chemical processes inside structures in range from 1 to 100 nanometers can occur differently than in traditional macro sizes.

In order to test thermal performance of nano-ceramic thermocoatings energy balance was investigated in periods of heating and also in the summer at external building surfaces using dynamic outdoor testing. Measurements demonstrated that coating consisting of hollow ceramic microspheres has the same thermodynamic properties as a standard facing coating

(Čekon, 2013; Čekon *et al.*, 2014). Spectral emissivity properties and reflective ability of nano-ceramic thermal insulation coatings were also tested and measured data demonstrated that coatings have the same radiant properties as standard building coatings (Čekon, 2012; Ádám *et al.*, 2016). Based on GOST 23630.2-79 (Russian standard) using an IT-λ-400 instrument thermal conductivity of nano-ceramic coatings consisted of hollow inorganic microspheres measured to be 0.10-0.18 W/mK and the effective thickness of the thin-film insulation coating was determined at least 5 mm (that requires application of 4 layers of material at each layer thickness of 1-1.5 mm) (Chukhlanov *et al.*, 2017).

Nano-ceramic thermocoating was applied on façade walls of an experimental building and the total energy consumption of the building was examined. It has been shown that there is an effective thermal insulating effect of the coating both in winter and summer. However, exact value of conductivity was not determined (Oda *et al.*, 2015). Similar conclusion was made after examining a 10 cm thick masonry wall with heat chamber method under summer climatic conditions (outside wall surface was covered with nano-ceramic thermocoating). It was found that thermal insulating ability is up to 25% more effective when the coating was applied in 2 or 3 layers (Esfandyari *et al.*, 2018).

Other researchers claim that thermal insulation coatings can highly increase heat transfer resistance of the insulated surface by reducing convective heat transfer coefficient (Orbán, 2015). Experiments have shown that they are able to improve the heat transfer coefficient of solid brick masonry (Lakatos, 2016). It has also been found that thermal insulation capacity of nano-ceramic thermocoatings is affected by its thermal inertia (thermal lag). During the review of heat transfer processes, a further discovery has been made that the physical equations used for atomic diffusion can be applied to heat diffusion (Lakatos, 2017).

4 Laboratory Experiments

The main research task was to clear and describe the thermphysical processes inside nano-ceramic thermocoatings. Based on the literature review, it was intended to perform series of laboratory tests that can provide clear information about the heat reflectivity, thermal conductivity and heat transfer resistance of nano-ceramic thermocoatings. After studying the special literature six experiments were made in the Laboratory of Building Materials and Building Physics at Széchenyi István University (Győr, Hungary) in 2014-2018.

4.1 Experiment 1 and Experiment 2

Experiment 1 and Experiment 2 were conducted to find out that the material really has heat reflective ability (heat mirror effect) and to check whether it has an extremely low thermal conductivity claimed by some special literature references and the manufacturer's handouts. Results of these experiments were published in 2015-2017 but in order for better understanding a brief summary is important (Bozsaky, 2015; Bozsaky, 2017).

In Experiment 1 five types (Type 1-5) of samples were made from different kind of traditional thermal insulation materials: expanded polystyrene (EPS), extruded polystyrene (XPS) and oriented strand board (OSB). Sample Type 1 was uncoated and homogeneous, other samples were sprayed with nano-ceramic thermocoating. According to EN 12667:2001 standard Taurus TCA 300 heat flow meter was used for measurements. Thermal conductivity of homogeneous samples and the effective thermal conductivity (λ_{eff}) of inhomogeneous

samples (Type 2-5) were compared and results seemed to show a minor negative effect of nano-ceramic coating to thermal insulation quality. Only XPS samples showed a small positive effect with an insignificant decreasing value (Bozsaky, 2015; Bozsaky, 2017).

During Experiment 2 thermal conductivity of the pure nano-ceramic coating was measured directly with a standard heat flow meter on samples with thicknesses of 25, 30 and 35 mm (However, this material is practically not used with such thickness, because they are applied as a 0.5-2.0 mm thin membrane). The average thermal conductivity in air-dry condition was 0.0690 W/mK. In addition each sample was measured 3 times in order to increase measuring accuracy (standard requires only one measurement). Analyzing the results the average thermal conductivity in air-dry condition was 0.0690 W/mK regardless of thickness. Due to the significantly increased measurement accuracy and the fact that there was no difference in thermal conductivity of samples with different thicknesses, it could be concluded that thickness has no significant effect on thermal conductivity. Therefore it could not be clearly declared that thermal conductivity of this material has the same thermal conductivity if it is used as a very thin membrane (Bozsaky, 2015; Bozsaky, 2017).

4.2 Experiments 3-6

Based on former experiments it was concluded that insulating effect of nano-ceramic thermocoatings is probably not caused by their extremely low thermal conductivity. As it was formerly mentioned, some sources claim that insulating effect of these materials is generated by not their extremely low thermal conductivity but their high surface heat transfer resistance. Considering it as a basic concept four more heat transfer resistance experiments were conducted in 2016-2018 (Experiments 3, 4, 5 and 6). For these experiments 6 different order of layers were constructed from 30x30 cm samples of thermal insulation materials. Moreover, an additional Air Gap (AG) was included into the construction with different sizes (Table 1). There were configurations (Figure 1), which contained nano-ceramic coated and uncoated samples as well (Type 1-6).

Table 1. Size of air gap in Experiments 3-6.

Experiment	Size of AG (cm)
3	10 x 10 x 2
	10 x 10 x 3
4	20 x 20 x 2
	20 x 20 x 3
5	20 x 20 x 5
6	20 x 20 x 8

Measurements were carried out by the same heat flow meter used in Experiments 1 and 2. Effective thermal conductivity of 3-3 pieces from each type of configurations was measured using 3 different kinds of thermal insulation materials (EPS, XPS, and OSB plates). Each sample was measured 3 times. Moreover, sample Types 1-4 were measured in two ways; firstly coating was on the warm side; secondly it was on the cold side. Consequently, a total number of 883 thermal conductivity measurements were conducted. Unfortunately, because of the measuring limits (120 mm maximum sample thickness) it was possible to test only 4 Types (Types 1-4) of configurations in Experiment 6. Sample Types 5-6 were too thick (16-

18 cm); therefore, they could not fit to the measurement chamber of the heat flow meter.

Because of the inhomogeneous, multi-layer structure heat flow meter was able to determine effective thermal conductivity (λ_{eff}). The main focus of experiments was the difference in effective thermal conductivity between coated and uncoated samples.

All of the samples contained air gap, the effect of convection and conduction inside it was included by the λ_{eff} value. Air gap has the same position and the same size in each sample so the conduction and convection inside air gap should be also the same in each case. This is why difference between effective thermal conductivity of coated and uncoated samples could be attributed only to the coating.

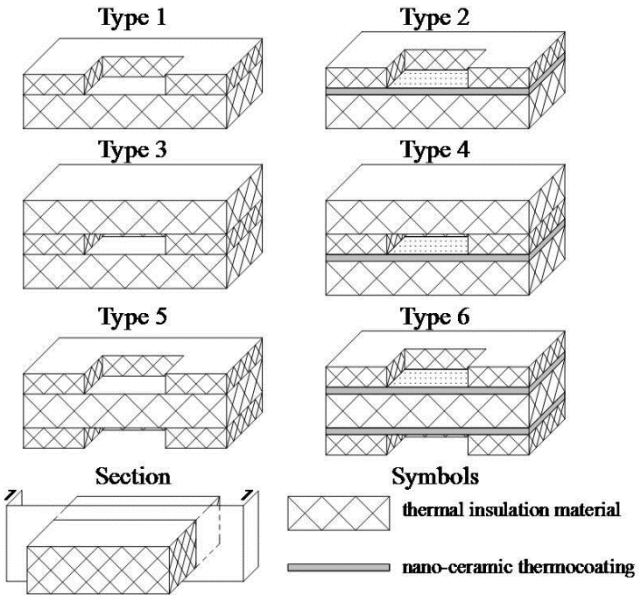

Figure 1. Sample types for Experiments 3-6.

From these tests is was expected that there will be significant differences in effective thermal conductivity between coated and uncoated samples and the increasing size of air gap should cause higher changes. It was supposed that in larger air gaps air particles should have more possibility for bulk movements; thereby surface heat transfer resistance can prevail much better and higher differences may arise between coated and uncoated samples. Results were correspondent for expectations.

Unfortunately, most of the test results showed lower differences than the measurement accuracy of Taurus TCA heat flow meter (5%). Due to the fact that measurement accuracy was increased by testing the samples in 3 times this problem was eliminated (Standard prescribes only one measurement). However; in 89% of the measurements there were no deviation between 3 test results of an individual sample and in 11% the difference was only ± 0.0002 W/mK which means also 0.1-0.4% accuracy instead of the theoretically 5% accuracy of the heat flow instrument. Therefore, the resulted changes in effective thermal conductivity could be considered to be relevant.

Table 2. Changes of effective thermal conductivity in Experiments 3-6.

Experiment	AG size (cm)		Change of λ_{eff} (%)								
			EPS			XPS			OSB		
			1/2	3/4	5/6	1/2	3/4	5/6	1/2	3/4	5/6
3	10x10x2	$\Delta\lambda_{eff, cold}$	-6,16	-4,69	-	-3,57	-3,64	-	+3,74	+2,57	-
		$\Delta\lambda_{eff, warm}$	-5,50	-4,80	-	-3,33	-3,34	-	+2,70	+3,08	-
		$\Delta_{\lambda eff}$	-5,83	-4,75	-8,66	-3,45	-3,49	-2,79	+3,22	+2,82	+2,29
	10x10x3	$\Delta\lambda_{eff, cold}$	-5,71	-4,96	-	-3,40	-3,53	-	+1,83	+3,04	-
		$\Delta\lambda_{eff, warm}$	-5,79	-4,94	-	-2,80	-3,16	-	+2,91	+2,63	-
		$\Delta_{\lambda eff}$	-5,75	-4,95	-8,19	-3,10	-3,35	-2,74	+2,37	+2,83	+1,21
4	20x20x2	$\Delta\lambda_{eff, cold}$	-6,84	-4,85	-	-5,44	-3,56	-	+4,72	+2,45	-
		$\Delta\lambda_{eff, warm}$	-6,40	-4,59	-	-4,95	-2,97	-	+3,03	+3,71	-
		$\Delta_{\lambda eff}$	-6,62	-4,72	-9,96	-5,19	-3,24	-3,71	+3,88	+3,08	+2,16
	20x20x3	$\Delta\lambda_{eff, cold}$	-6,50	-5,14	-	-5,06	-4,14	-	+2,98	+2,46	-
		$\Delta\lambda_{eff, warm}$	-5,52	-4,90	-	-4,82	-2,87	-	+4,51	+2,91	-
		$\Delta_{\lambda eff}$	-6,01	-5,02	-12,04	-4,94	-3,51	-4,92	+3,75	+2,68	-0,02
5	20x20x5	$\Delta\lambda_{eff, cold}$	-8,99	-5,97	-	-6,17	-3,73	-	+3,52	+1,63	-
		$\Delta\lambda_{eff, warm}$	-7,88	-5,00	-	-4,00	-2,38	-	+4,85	+2,12	-
		$\Delta_{\lambda eff}$	-8,43	-5,48	-12,84	-5,08	-2,87	-4,53	+4,19	+1,88	-1,04
6	20x20x8	$\Delta\lambda_{eff, cold}$	-14,70	-8,24	-	-8,91	-5,02	-	+2,06	+0,94	-
		$\Delta\lambda_{eff, warm}$	-10,78	-6,50	-	-8,90	-3,49	-	+2,45	+1,16	-
		$\Delta_{\lambda eff}$	-12,74	-7,37	-	-8,91	-4,26	-	+2,25	+1,05	-

Table 2 summarizes the analysis of measurement results. Looking at the data it could be stated that changes in EPS samples were the most apparent. The most significant differences (8.66% and 8.19% in Experiment 3, 9.96% and 12.04% in Experiment 4 and 12.84% in Experiment 5) were found in configuration Types 5-6. In case of configuration Types 1-2 change level was also high even if the coating was on the cold or warm side. The lowest changes were measured in case of Types 3-4. This phenomenon can be explained that if an air gap is closed inside two layers of thermal insulation air particles are less able to move and the effect of surface heat transfer resistance becomes smaller.

In case of XPS samples smaller changes can be observed (Table 2). Change of thermal conductivity was the most significant in configuration Types 1-2. Just like EPS samples, using the coating on the warm side the changes were lower, and the difference from samples with cold-side painting became more and more significant. In case of Types 5-6 lower changes were measured, and the lowest changes were measured in case of Types 3-4 (excepting Experiment 3). In case of XPS samples smaller changes can be observed than in case of EPS. This could be explained by the results of Experiment 1 where nano-ceramic coating itself had resulted reduction of thermal conductivity. This is why surface heat transfer resistance seems to have minor effect on thermal insulation quality

It was also a novelty that in Experiment 3 and Experiment 4 there were detectable but not enough significant differences between measurement results depending on the location of the coating (warm or cold side) in case of EPS and XPS samples. These differences became more and more significant by increasing the size of the air gap (see the results of Experiment 5 and Experiment 6 in Table 2) which showed that nano-ceramic coating has stronger effect on the

cold side.

In case of OSB boards insulating effect of nano-ceramic coating was undetectable in Experiment 3 and 4. All measurements showed that coating has a negative effect on thermal insulation quality. Except sample Types 5-6 in Experiment 5, all measurements showed that coating has a negative effect on thermal insulation quality. It can be observed that this negative effect is decreasing by increasing the size of the air gap. In Experiment 4 nearly zero (0.02%) change was measured and in in Experiment 5 a very small decreasing of effective thermal conductivity was detected (-1.04%).

However, it should be noted that the negative effect of nano-ceramic thermocoating was reducing by increasing the size of the air gap. Probably, not the same material quality and composition is suitable for all building structures and materials. Every time we need to find correct solution and the same material is not suitable for all surfaces. Presumably, insulating OSB plates needs different material quality, composition or application technology than EPS and XPS plates to achieve significant insulating effect.

5 Conclusions

Former laboratory tests showed that nano-ceramic thermocoatings do not have an extremely low thermal conductivity that was described by the available documents of producers and distributors. Moreover, thermal conductivity of nanostructured thermocoatings is independent from materials thickness.

Due to the fact that test results of EPS and XPS samples were consistent with preliminary expectations, Experiments 3-6 confirmed the previously raised theory that because of their special nanostructure, insulating effect of nano-ceramic thermocoatings lies in their significantly higher surface heat transfer resistance than traditional, macro-structured thermal insulation materials.

It can be declared that in case of using nano-structured thermocoatings on the surfaces of building structures convective heat transfer coefficient (h_i or h_e, according to the location of the coating) might be taken account in different way than in case of traditional macro-structured thermal insulation materials. New results also showed that the effectiveness of nano-ceramic thermocoatings is more intensive using them on the cold side of the structure (contrary to producers' claim that the effect is the same on warm and on cold side).

It can also be stated that the application of nano-ceramic thermocoatings between two structural layers is the least effective method from thermal insulating point of view.

Test results of OSB samples showed that the same material quality, composition and application technology may not be suitable for insulating different kind of surfaces.

Furthermore; it would be important to make in-situ heat transfer experiments with nano-ceramic thermocoatings in order to understand better the thermal insulation behavior of the material. In order to achieve this goal heat transfer coefficient of several sample buildings should be measured without any thermal insulation. These basic data should be compared with the heat transfer coefficient of structures with nanostructured thermocoating.

Acknowledgements

The author would like to acknowledge and thank the financial support of the project EFOP-3.6.1-16-2016-00017 - Internationalization, initiatives to establish a new source of researchers and graduates, and development of knowledge and technological transfer as instruments of intelligent specializations at Széchenyi István University.

ORCID

David Bozsaky: https://orcid.org/0000-0002-2099-9435

References

Ádám, L., Nagy, B. and Nemes, R. (2016). Sugárzás-visszaverő bevonatok laboratóriumi vizsgálata és fejlesztési lehetőségei (in Hungarian), *Megtérülő Épületenergetika*, 3(7), 35-39.

Anestopoulou, C., Efthymiou, C., Kokkonis, D. and Santamouris, M. (2017). On the development, testing and performance evaluation of energy efficient coatings for buildings, *International Journal of Low-Carbon Technologies*, *12*(3), 310-322. doi: 10.1093/ijlct/ctw023

Bozsaky D. (2015). Laboratory test with liquid nano-ceramic thermal insulation coating, *Procedia Engineering*, *123*, 68−75. doi: 10.1016/j.proeng.2015.10.059

Bozsaky, D. (2017). Thermodynamic Tests with Nano-Ceramic Thermal Insulation Coatings, Pollack Periodica, *12*(1), 135-145. doi: 10.1556/606.2017.12.1.11

Čekon, M. (2012). Spectral emissivity properties of reflective coatings, *Slovak Journal of Civil Engineering*, *20*(2), 1-7. doi: 10.2478/v10189-012-0007-6

Čekon, M. (2013). Thermodynamic Properties of Reflective Coatings, *Advanced Materials Research*, *649*, 179-182. doi: 10.4028/www.scientific.net/AMR.649.179

Čekon, M., Kalousek, M., Hraška, J. and Ingeli, R. (2014). Spectral optical properties and thermodynamic performance of reflective coatings in a Mild Climate Zone, *Energy and Buildings*, *77*, 343-354. doi: 10.1016/j.enbuild.2014.04.005

Chukhlanov, V. Y., Trifonova, T. A., Selivanov, O. G., Ilina, M. E. and Chukhlanova, N.V. (2017). Thin-Film Coatings Based on Hollow Inorganic Microsheres and Polyacrilic Binder, *International Journal of Applied Engineering Research*, *12*(7), 1194-1199. doi: 10.3311/ppci.12178

Hoffman, D., Roy R. and Komarneni S. (1984). Diphasic ceramic composites via a sol-gel method, *Materials Letters*, *2*(3), 245−247. doi: 10.1016/0167-577X(84)90035-1

Leydecker, S. (2008). *Nano Materials – in Architecture, Interior Architecture and Design*, Birkhäuser Verlag AG, Berlin (Germany), ISBN 978-3-7643-7995-7, 192 p.

Oda, T., Nakai, T., Toba, K. and Jianbo, H. (2015). Measurement of amenity in buildings interiors coated with ceramic insulating paint, *Procedia Manufacturing*, *3*, 1728-1733. doi: 10.1016/j.promfg.2015.07.488

Esfandyari, M., Salehi, H., Jafari, D., Koolivand-salooki, M. and Esfandyari, J. R. (2018). Experimental Study on Heat Insulation Performance of Ceramic Additives Paint (CAP) in an Indoor Closed Media, *Silicon*, *10* (3), 2341-2351. doi: 10.1007/s12633-018-9770-y

Koniorczyk, P., Zmywaczyk, J. and Kowalski, M. (2004). Experimental Studies of Thermal Conductivity of the Composite Coating Consisted of Hollow Ceramic Microspheres, In *1st Scientific International Coating Congress*, 4-5 November 2004, Berlin (Germany), 15 p.

Lakatos, Á. (2016). Nanotechnológiás hőszigetelő anyagok vizsgálata tömör tégla falazaton (in Hungarian), *Energiagazdálkodás*, *57*(3-4), 21-25.

Lakatos, Á. (2017). Thermophysical Investigations of Nanotechnological Insulation Materials, *AIP Conference Proceedings*, *1866*(1), Paper ID: 030003, 7 p. doi: 10.1063/1.4994479

Lan, W., Kexing F., Liang, Y. and Botao, W. (2014). The Application of Ceramic Coatings in Petroleum Chemical and Building Industries, In *International Conference on Material and Environmental Engineering*, 21-24 March 2014, Jiujiang (Jiangxi, China), Atlantis Press, pp. 146-149. doi: 10.2991/icmaee-14.2014.39

Orbán, J. (2012). A nanotechnológia építőanyagipari alkalmazásai – II. rész (in Hungarian), *Magyar Építéstechnika*, 50(2-3), 54-57.

Orbán, J. (2015). Épületek energiafelhasználásának csökkentése hővédő vékonybevonattal – II. rész (in Hungarian), *Magyar Építéstechnika*, *53*(9), 40-42.

Paul, G., Chopkar, M., Manna, I. and Das, P.K. (2010). Techniques for Measuring the Thermal Conductivity of Nanofluids - A Review, *Renewable and Sustainable Energy Reviews*, *14*(7), 1913-1924. doi: 10.1016/j.rser.2010.03.017

Shea, A., Lawrence, M. and Walker, P (2012). Hygrothrermal performance of an experimental hemp-lime building, *Construction and Building Materials*, *36*, 270-275. doi: 10.1016/j.conbuildmat.2012.04.123

Thermo-Shield Inc. (2017). Exterior Wall Coats, *SPM Thermo-Shield Inc.*, Naples (Florida, United States), http://www.thermoshield.com/index.html/thermoshieldexteriorwall.html (last visited 5 May 2017)

XV International Conference on Durability of Building Materials and Components
DBMC 2020, Barcelona
C. Serrat, J.R. Casas and V. Gibert (Eds)

Towards the Determination of Chloride Profiles by means of Resistivity Measurements in Reinforced Concrete

Géraldine Villain [1], Marie-Antoinette Alhajj [1], Sérgio Palma Lopes [2] and Véronique Bouteiller [3]

[1] MAST-LAMES, Université Gustave Eiffel, IFSTTAR, Campus de Nantes, Allée des Ponts et Chaussées, CS 5004, 44344 Bouguenais cedex France, geraldine.villain@univ-eiffel.fr, marie-antoinette.alhajj@univ-eiffel.fr

[2] GERS-GéoEND, Université Gustave Eiffel, IFSTTAR, Campus de Nantes, Allée des Ponts et Chaussées, CS 5004, 44344 Bouguenais cedex France, sergio.palma-lopes@ univ-eiffel.fr

[3] MAST-EMGCU, Université Gustave Eiffel, IFSTTAR, Cité Descartes, 14-20 boulevard Newton, Champs sur Marne, 77447 Marne la Vallée cedex 2 France, veronique.bouteiller@univ-eiffel.fr

Abstract. *Reinforced concrete (RC) structures, such wharfs or floating structures, are submitted to chloride ingress which can lead to rebar corrosion. Before the corrosion initiation, in a preventive point of view, engineers can be interested in non-destructive evaluation and inspection methods. In that way, electrical resistivity tomography is a promising tool to access to resistivity profiles then to chloride profiles in real RC structures in the future. We would like to present herein the advances in the necessary research developments to reach this goal, i.e. the resistivity profiles obtained in reinforced concrete slabs submitted to chloride ingress. The 4 slab dimensions are 90x70x13 cm. The specimens are cured, dried during 9 months then submitted to salted water imbibition during 4 months. Electrical resistivity tomography measurements are performed at short terms during 1 week of imbibition. The monitoring show that several phenomena influence the resistivity profiles such as the penetration of water and chloride ions. Meanwhile, steel rebar effect can be considered thus eliminated from electrical resistivity profiles following the method developed by (Alhajj et al. 2019).*

Keywords: *Electrical Resistivity Tomography, NDT, Inversion, Durability, Reinforcement.*

1 Introduction

The preservation of our civil engineering infrastructure heritage is part of sustainable development initiatives and programs. Reinforced concrete (RC) structures exposed to de-icing salts and the marine environment may corrode through the action of chloride ions, water and oxygen. It has been shown that the methods for measuring the electrical resistivity of concrete are effective in alerting the potential corrosion risk (Gowers *et al.* 1999, Andrade *et al.* 2009). They are particularly sensitive to the moisture and chloride contents in concrete (Saleem *et al.* 1996). Finally, electrical resistivity tomography methods also have the great advantage of investigating the concrete from the surface to the core in a non-destructive manner and of drawing as information the apparent resistivity. However, such data need to be inverted to obtain a resistivity profile with depth (Loke *et al.* 1996, Chouteau *et al.* 2002, Fares *et al.* 2018). The calibration determines the conversion function to obtain the desired indicator: either the water content or the chloride content (Villain *et al.*, Fares *et al.* 2018). But the presence of metal reinforcements disturbs the electric field and the measurement of apparent resistivities (Sengul

et al. 2009, Presuel-Moreno *et al.* 2013, Garzon *et al.* 2014) and can prevent the inversion process, which is why the RILEM recommends to place itself at a distance from the reinforcements (Polder, 2001). The work of Alhajj *et al.* (2019) showed that it was possible to reproduce by finite elements modelling the effect of the reinforcements on the measurement of apparent resistivities.

The objective of this paper is to present the first results of the inversion programmed by Alhajj *et al.* (2020) for reinforced and unreinforced slabs subjected to an imbibition of a saline solution in the laboratory. The first part presents the measurement method and summarizes the inversion procedure. The second part details the experimental program. The third one shows the measurement results and the monitoring of resistivity profiles over time in both reinforced and unreinforced slabs.

2 Method used for Non-Destructive Evaluation

The selected non-destructive evaluation (NDE) method is electrical resistivity tomography (ERT) because it is very sensitive to the water content and chloride content of concrete.

2.1 Electrical Resistivity Measurement Principle and Method

The electrical resistivity method used is based on the Wenner principle for 4 electrodes regularly spaced (spacing a). The current is injected by the 2 external electrodes and the potential difference measured between the 2 inner electrodes. The apparent resistivity is calculated from current and potential measurements and a geometric coefficient G (Marescot *et al.* 2006). G is calculated by finite element modelling taking into account the geometry of the test body and the position of the electrodes. If the medium is homogeneous the apparent resistivity is equal to the «true» resistivity of the medium.

The device used was developed by (Du Plooy *et al.* 2013). It consists of 14 inline electrodes, 2cm-spaced. This allows the implementation of 26 Wenner configurations with 4 different spacings a=2 cm, a=4 cm, a=6 cm and a=8 cm. The larger is the spacing, the larger the volume examined from the surface. The raw results correspond to apparent resistivities at each level of spacing. They give information about the presence of a gradient in concrete.

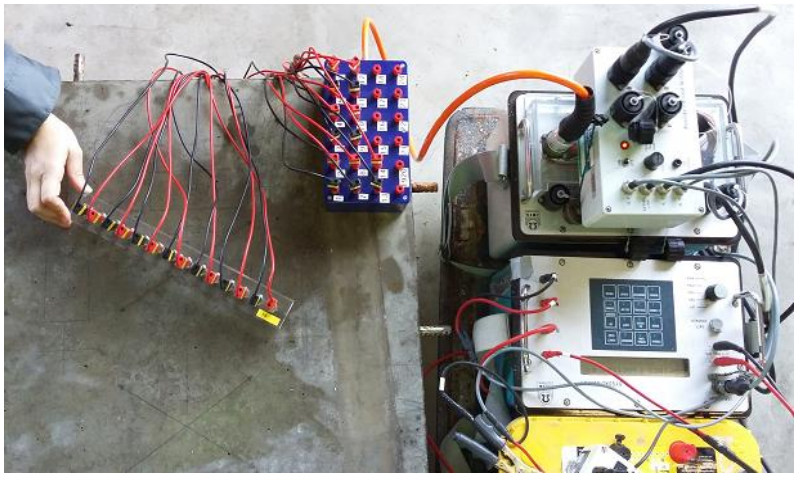

Figure 1. Picture of the ERT testing device.

2.2 Inversion Process

The inversion of these raw results allows to obtain a resistivity profile according to the depth. Loke *et al.* (1996) notably developed an inversion algorithm for a discrete, multi-layer material model. The resulting RES1D software is free of access and gives good results for unreinforced concrete slabs. However, the presence of metal reinforcements alters the current lines in the reinforced concrete slabs, thus influencing apparent resistivity measurements. This influence can be quantified by finite element modelling (Alhajj *et al.* 2019). It must be taken into account in the inversion process.

An inversion process has been developed and is presented at the DBMC 2020 Congress by Alhajj *et al.* (2020). In summary, the imposed initial true resistivity profile is continuous and follows a Weibull law with 4 parameters. The direct finite element model (Comsol Multiphysics®) calculates the modelled apparent resistivities. The least squares cost function between the modelled and the measured apparent resistivities is computed. A Levenberg-Marquardt algorithm minimizes this cost function in order to fit an estimated resistivity profile of the concrete. The iterative optimization algorithm is written in Matlab® linked with Comsol and is called "IFSTTAR inversion program" in the following. The finite element model may or may not take into account steel reinforcements present or not in concrete slabs. The resistivity profile obtained corresponds to the resistivity of the concrete material with a gradient of saline solution, independently of the conductive steel influence.

3 Experimental Program

A research project called APOS (Villain *et al.* 2015) aimed to compare embedded sensor results and non-destructive evaluations of reinforced concrete slabs submitted to chloride ingress in the initiation phase then in the corrosion phase (Bouteiller *et al.* 2018). The present study is limited to ERT in the initiation phase to evaluate chloride ingress in the cover concrete. The purpose of this section is to present the concrete formulation, the geometry of the slabs, their preconditioning and the chronology of the experimental program of this study.

3.1 Concrete and Slabs

Table 1. Concrete mix design and properties.

Aggregates 11.2/22.4	(kg/m^3)	760
Aggregates 6.3/10	(kg/m^3)	320
Sand 0-4	(kg/m^3)	860
Cement CEM I 52.5N CE CP2 NF St Pierre La Cour	(kg/m^3)	305
Total water	(kg/m^3)	190
Admixture AD Sika Prise SC2	(kg/m^3)	0.7
Water to cement ratio	W_{eff}/C (-)	0.58
Compressive strength at 28 days	Rcsat (MPa)	36.3 ± 0.9
Saturated mean density	ρ_{sat} (kg/m^3)	2332 ± 23
Porosity (water saturation under vacuum)	ϕ (%)	15.9 ± 0.7

Concrete is of type C30 containing ordinary Portland cement (Table 1). Its 28-day compressive strength equals 36.3±0.9 MPa and its porosity equals 15.9±0.7%. For this concrete, 10 slabs

were casted to study the penetration of a saline solution of concentration [NaCl] = 35 g/L, close to that of the Atlantic Ocean. Among these slabs, we will study here 1 non-reinforced slab placed in salt solution (noted 13-NS), 2 slabs reinforced with carbon steel placed in salt solution (noted 14-CS and 15-CS), and 1 reinforced slab with stainless steels (noted 18-SS).

The dimensions of all the slabs are 90x75x13 cm. The reinforced slabs contain 1 single bed of rebars placed at 3 cm of depth, forming 4 meshes of 20x30 cm (Figure 2).

After casting, the moulds were removed at the age of 3 days. Then, the slabs were placed in a room first not ventilated for 3 months and then ventilated with fans for 6 months to accelerate drying. The side faces are protected by 2 layers of epoxy resin to keep transfers along the depth.

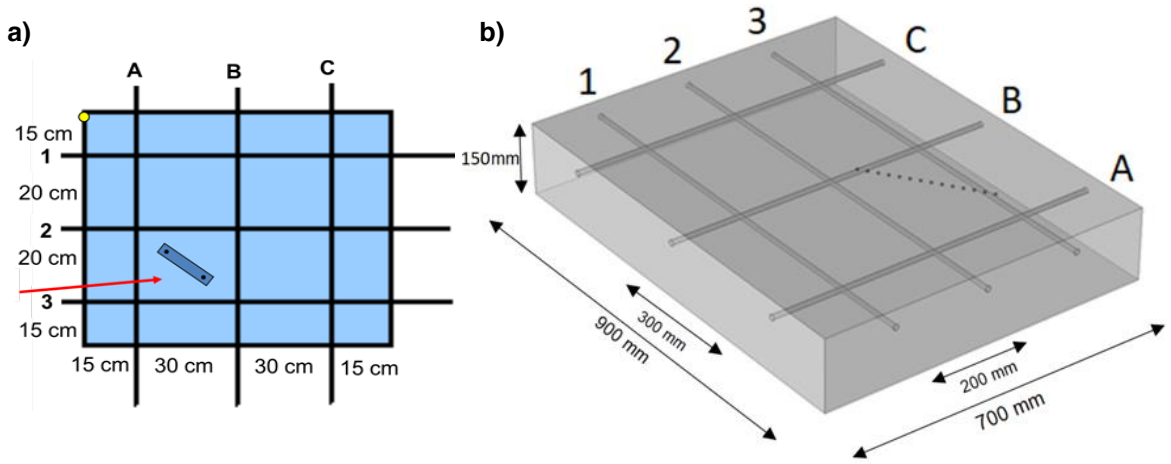

Figure 2. Scheme of the reinforced concrete slab -a- Position of the ERT testing device -b- FE model.

3.2 Imbibition Program

At the age of 9 months (T0 test time for imbibition process), the slabs were tested by non-destructive evaluation methods (NDT) and then placed in 1 to 2 cm of salt solution in pools, so that it can penetrate by imbibition on the reinforced side (Figure 3). At each test time, the slabs are removed from the salt solutions and subjected to NDT testing; then, they are put back in the pools. The chosen test times are about 1h, 4h, 1day, 2days, 7 days, 1 month, 4 months. Note that there can be differences between the slab for the out-of-water duration due to the numerous slabs and NDT methods. Here, we present the results of the first 4 test times (T1 to T4) which correspond to the imbibition of salt solution under temperature conditions of about 18-20°C. Moreover, at these early test times, the resistivity contrasts are higher and the ERT method gives thus the best results.

For each test time, the resistivity measurements were performed on the mesh AB23 along both diagonals (Figure 2), minimum twice, usually 3 or 4 times. The mean values are used for inversion.

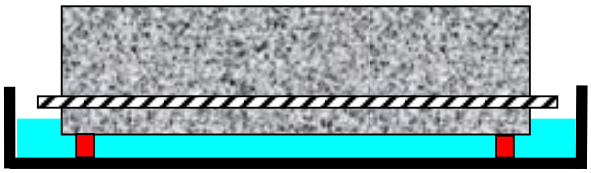

Figure 3. Scheme of the slab during the imbibition process in a pool filled with saline solution and showing the steel reinforcement.

4 Raw Results and Profiles of Resistivity versus Depth

The influence of the steel reinforcement on the apparent resistivity measurements is presented, first. Then, the inverted resistivity profiles are show in the 2nd and 3rd sub-sections.

4.1 Raw Results and Influence of Steel Rebars

Figure 4 shows the apparent resistivity measurements determined for 4 spacings of the Wenner configuration, for test times T1 to T4. The resistivity measurement was impossible at T0 because the slab surface was too dry. In Figure 4-a, corresponding to the non-reinforced slab 13-NS, at T1, the apparent resistivity is lower near the face in contact with the salt solution (a = 2 cm) than for larger spacings corresponding to higher volumes of investigation. Moreover, for later test times, the apparent resistivity decreases due to salt solution ingress into the concrete.

In Figure 4-b, corresponding to the reinforced slab 14-CS, for small spacing a = 2 cm, the apparent resistivity values are similar for both slabs, they decrease when the salt solution penetrates along time. But, for the other spacings, the larger are the spacings, the lower are the apparent resistivities. This is due to the steel rebar influence in accordance with literature results (Polder, 2001). This influence was quantified by a direct model using finite elements by Alhajj *et al.* (2019).

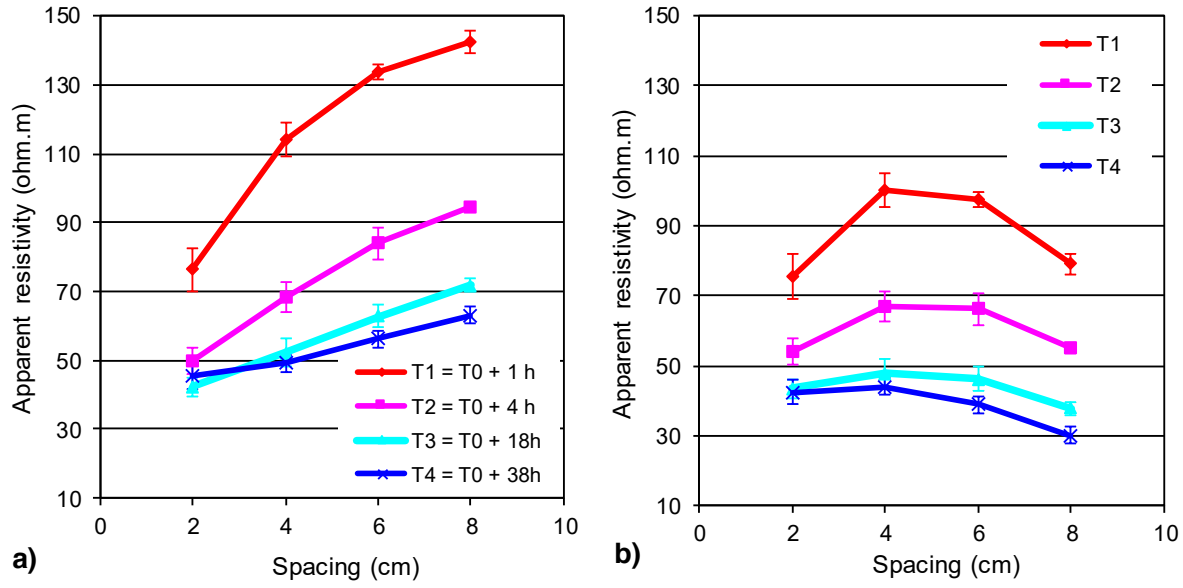

Figure 4. Apparent resistivity measurements for 4 Wenner configuration spacings -a- Unreinforced slab 13-NS - b- Reinforced slab 14-CS.

4.2 Resistivity Profiles versus Depth in the Unreinforced Concrete Slab

For each test time, the apparent resistivities obtained for the unreinforced slab (13-NS) are inverted:

- Firstly, by using the free-access software RES1D from Loke (2001); the resulting resistivity profiles are shown in Figure 5-a;
- Secondly, by using the ISTTAR Program; the resulting resistivity profiles are shown in

Figure 5-b and compared to the RES1D resistivity profiles.

In Figure 5, the resistivity profiles show the salt solution ingress. Concerning RES1D (Fig. 5-a), the inversion process is very fast. Figure 5-b presents the results of both inversion programs which are in a good agreement especially at the 2 first test times. This can be explained by the ERT method, more informative about shallower volumes, thus less accurate for deeper volumes.

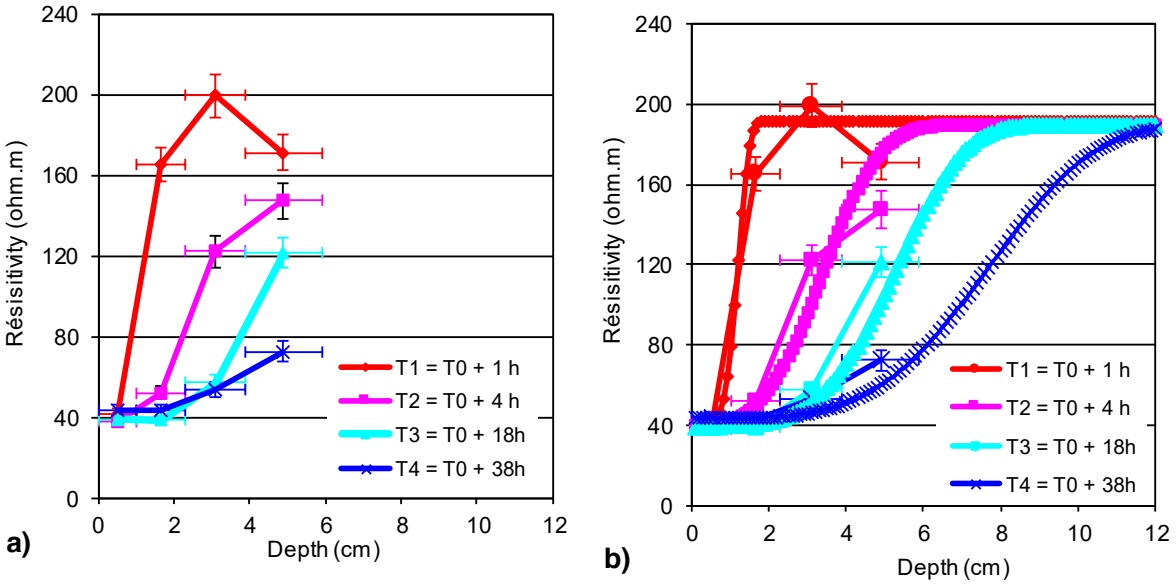

Figure 5. Inverted Resistivity profiles at test times T1 to T4, for the slab 13-NS -a- Inversion with RES1D -b- Inversion with "IFSTTAR program" (superimposed on the RES1D results).

4.3 Resistivity Profiles versus Depth in Reinforced Concrete Slab with HA Carbon Steel and Stainless Steel

Then, for each test time, the apparent resistivities obtained for the reinforced slabs (14-CS, 15-CS and 18-SS) are inverted by using the same initial parameters as those used for the slab 13-NS. The inversion is performed with IFSTTAR program because it is not possible with RES1D.

Figure 6-a makes it possible to compare the resistivity profile obtained for unreinforced slab (13-NS) and reinforced slab (14-CS). Figure 6-b presents the resistivity profiles obtained for the 3 reinforced slabs.

The profiles in non-reinforced and reinforced slabs are very similar for T1, T2 and T3 (Fig. 6-a). The discrepancies between the profiles are of the same order of magnitude as the ones between the profiles of the 3 reinforced slabs (Fig. 6-b). This uncertainty can be due to the concrete material variations which influence the kinetics of the penetration of the salt solution. For the later test times, the discrepancies between all the curves increase. The uncertainty of the measurement method for a higher spacing is higher.

Moreover, the resistivity profile of the slab reinforced with stainless steel rebars (18-SS) is similar to the profiles of the 2 other slabs reinforced with carbon steel rebars (14 and 15-CS). The reinforcement is indeed in passive conditions in this study.

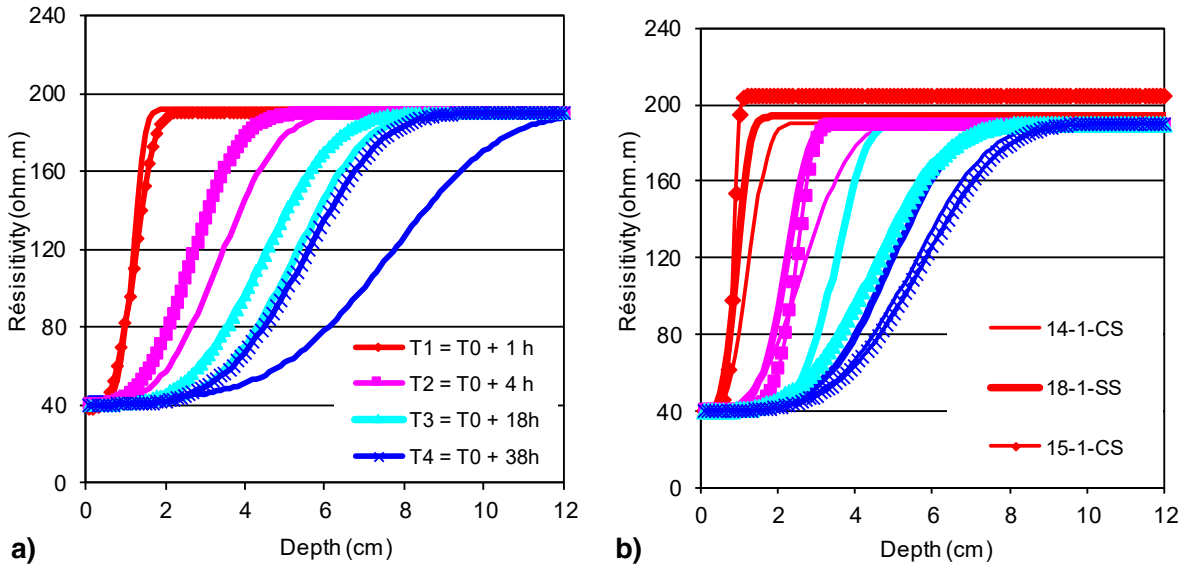

Figure 6. Comparison of resistivity profiles corresponding to salt solution ingress in non-reinforced and reinforced concrete slabs -a- Slabs 13-NS and 14-CS (line with marks) -b- Slabs 14-CS, 15-CS and 18-SS.

5 Conclusions and Further Developments

This paper presents the first results of an ERT inversion code tested on both reinforced and unreinforced slabs subjected to an imbibition of a saline solution in the laboratory. This study shows that it is possible to take into account the influence of steel reinforcement on the apparent resistivity measurements, to proceed to their inversion and obtain the "true" resistivity profiles. These profiles make it possible to monitor and evaluate the penetration of a salt solution (35 g/L) in the cover concrete.

Four slabs, either non-reinforced or reinforced with carbon or stainless steel rebars were submitted to the same imbibition process. The similar resistivity profiles obtained enable us to assess the uncertainty range due to both the concrete material variability and the ERT method itself. Indeed, the ERT uncertainty increases with high value of resistivity (it is higher for the dry core of slabs) and ERT give less information for larger volumes of investigation.

Note that carbon and stainless steel give similar resistivity results in passive conditions.

However, to convert resistivity profiles into free chloride content profiles, calibration curves are needed, but they are not available at various water contents. Imbibition is a rapid process but more complex than diffusion in saturated conditions. This point has to be developed.

In further developments, non-destructive evaluations by ERT will be compared to embedded sensors in the concrete slab in view of structural health monitoring.

Acknowledgements

The authors would like to thank all the team from the Regional Laboratory of de Saint-Brieuc (Cerema) in particular B. Thauvin, R. Queguiner, S. Pasquiet, P. Boulaire for the slab instrumentation and casting, as well as the slab survey during the experimental campaign. The authors are also grateful to the Ministry of Ecology MTES, IFSTTAR and Cerema for their financial support of the research project APOS.

ORCID

Géraldine Villain: https://orcid.org/0000-0002-4478-034X
Marie-Antoinette Alhajj: https://orcid.org/0000-0001-7711-5103
Sérgio Palma Lopes : https://orcid.org/0000-0001-7022-389X
Véronique Bouteiller: https://orcid.org/0000-0003-1467-0622

References

Alhajj M.A., Palma Lopes S. and Villain G. (2019). Accounting for steel rebar effect on resistivity profiles in view of reinforced concrete structure survey, *Constr. Build. Mat.*, 223, 898-909. /10.1016/j.conbuildmat.2019.07.208

Alhajj M.A., Villain G., Bourguignon S. and Palma-Lopes S. (2020). A joint inversion technique of electric and electromagnetic measurements for the determination of water saturation profiles in concrete structures, In *XV Int. Conference on Durability of Building Materials and Components DBMC 2020*, Barcelona, Spain, 6p.

Andrade C., D'Andréa R., Castillo A. and Castel M. (2009). The Use of Electrical Resistivity as NDT Method for the Specification of the durability of Reinforced Concrete. In *Proceedings of the Int. Symposium on Non-Destructive Testing in Civil Engineering NDTCE'09*. Nantes, France, 2009.

Badr J., Fargier Y., Palma-Lopes S., Deby F., Balayssac J.P., Delepine-Lesoille S., Cottineau L.M., and Villain G. (2019). Design and Validation of a Multi-Electrode Embedded Sensor to Monitor Resistivity Profiles over Depth in Concrete, *Constr. Build. Mat.*, 223, 310-321. /10.1016/j.conbuildmat.2019.06.226

Bouteiller V., Villain G., Thauvin B., Marie-Victoire E. and Bouichou M. (2019). Evaluation de la durabilité du beton armé vis-a-vis des ions chlorure à l'aide de capteurs noyés dans le beton versus des auscultations en parement, In *Proceedings of AFGC'2019*, Cachan, France, 20 et 21 mars 2019, 8p.

Chouteau M. and Beaulieu S. (2002). An investigation on application of the electrical resistivity tomography method to concrete structures., In: *2nd Annu. Conf. Appl. Geophys. NDT Methodol. to Transp.*, 2002.

Du Plooy R., Palma Lopes S., Villain G. and Dérobert X. (2013). Development of a multi-ring resistivity cell and multi-electrode resistivity probe for investigation of cover concrete condition. *NDT&E Int.*, 54:27-36

Fares M., Villain G., Bonnet S., Palma Lopes S., Thauvin B. and Thiéry M. (2018). Determining chloride content profiles in concrete using a resistivity probe, *Cem. Concr. Compos.* 94, 315-326 /10.1016/j.cemconcomp.2018.08.001

Loke M.H. and Barker R.D. (1996). Rapid least-squares inversion of apparent resistivity pseudosections by a quasi-Newton method, Geophysical Prospecting, 44, 131–152. /10.1111/j.1365-2478.1996.tb00142.x

Garzon A., Sanchez J., Andrade C., Rebolledo N., Menéndez E. and Fullea J. (2014). Modification of four point method to measure the concrete electrical resistivity in presence of reinforcing bars., *Cem. Concr. Compos.* 83 308–322.

Gowers K.R. and Millard S.G. (1999). Measurement of concrete resistivity for assessment of corrosion severity of steel using Wenner technique, *ACI Materials Journal,* 1999, 96(5)

Marescot L., Rigobert S., Palma Lopes S., Lagabrielle R. and Chapellier D. (2006). A general approach for DC apparent resistivity evaluation on arbitrarily shaped 3D structures, *Journal of Applied Geophysics*, 60, 55–67

Polder R.B. (2001) Test methods for on site measurement of resistivity of concrete- a RILEM TC-154 technical recommendation, *Constr. Build. Mater*, 2001, 15, 125-131

Presuel-Moreno F., Liu Y. and Wu Y. (2013). Numerical modeling of the effects of rebar presence and/or multilayered concrete resistivity on the apparent resistivity measured via the Wenner method., *Constr. Build. Mater.* 48: 16–25.

Saleem M., Shameemt M., Hussain S. and Maslehuddintf M. (1996). Effect of moisture, chloride and sulphate contamination on the electrical resistivity of Portland cement concrete., *Constr. Build. Mater*. 10: 209–214.

Sengul O. and Gjorv O. (2009). Effect of embedded steel on electrical resistivity measurements on concrete structures., *ACI Mater J.* 106: 11–18.

Villain G., Orcesi A., Gaillet L. and Thauvin B. (Eds) (2015). *Résultats des opérations de recherche APOS et MCV*, IFSTTAR & CEREMA, IFSTTAR, Marne-la-Vallée, 2015 Actes Interactifs, AII1. *website: Site internet APOS* : http://www.ifsttar.fr/collections/ActesInteractifs/AII1/index.html

Villain G., Garnier V., Sbartaï M., Dérobert X. and Balayssac J.P. (2018). Development of a calibration methodology to improve the on-site non-destructive evaluation of concrete durability indicators., *Mater. Struct.* 51–40.

XV International Conference on Durability of Building Materials and Components
DBMC 2020, Barcelona
C. Serrat, J.R. Casas and V. Gibert (Eds)

Understanding the Reactivity of Dicalcium Silicate by Density Functional Theory

Seungchan Kim[1], Juhyuk Moon[2] and Johann Plank[3]

[1] Dept. of Civil and Environmental Engineering, Seoul National University, 1 Gwanak-ro, Gwanak-gu, 08026-Seoul, Republic of Korea, matues00@snu.ac.kr

[2] Dept. of Civil and Environmental Engineering, Seoul National University, 1 Gwanak-ro, Gwanak-gu, 08026-Seoul, Republic of Korea, juhyukmoon@snu.ac.kr

[3] Chair for Construction Chemistry, Technische Universität München, Lichtenbergstraße 4, Garching 85748, Germany, johann.plank@bauchemie.ch.tum.de

Abstract. *Ordinary Portland Cement (OPC) is a mixture consisting of various phases. Because of mineralogical complexity, the relationship between chemical reactivity of the mixture and each individual phase is still unanswered question. In this study, computational method based on Density Functional Theory (DFT) was applied to investigate the chemical reactivity of different polymorphs of dicalcium silicate crystals. At first, computationally generated dicalcium silicate crystals were geometrically optimized to achieve targeted convergence criteria for computing the total internal energy, lattice parameters, and atomic arrangement at 0K. The simulations performed explain well the thermodynamic stability as well as the synthesis temperatures of the different polymorphs of dicalcium silicate.*

Keywords: *Ordinary Portland Cement, Dicalcium Silicate, Reactivity, Density Functional Theory.*

1 Introduction

Ordinary Portland Cement (OPC) is one of the most manufactured materials in the world. Cement presents a mixture of various minerals as the elevated temperature decreases during the cement manufacturing process (Taylor, 1997). Because of the mineralogical complexity of clinker materials and complicated chemistry at high temperature, the origin of different reactivity of various minerals or different polymorphs in cement is still an open question. For instance, the reactivity of dicalcium silicate, which accounts for the second largest portion in typical OPC can be a key issue to produce high performance cement or reduce carbon dioxide emissions in cement manufacturing. However, the origin of the different reactivity of the polymorphs of dicalcium silicate has not been studied yet. Dicalcium silicate forms five different polymorphs (α-C_2S, α'_H-C_2S, α'_L-C_2S, β-C_2S, γ-C_2S) depending on sintering temperatures (Balonis and Glasser, 2009; Cuberos *et al*., 2009; Taylor, 1997). It is well known that these polymorphs have identical chemical formula and mineral composition, albeit with slightly different ion substitution rates. They exhibit different crystal structures and reactivity characteristics which determine the entire chemical reaction kinetics of cement particles containing dicalcium silicate.

Several experimental methods have been conducted to study the reactivity of dicalcium silicate. Bensted (1978) found that γ-C_2S has significantly lower reactivity than β-C_2S by studying X-Ray Diffraction and Differential Thermal Analysis. The results of Cuberos et al.

(2009) and Fukuda and Taguchi (1999) suggest that the order of reactivity between the polymorphs of dicalcium silicate is α-C_2S > α'$_H$-C_2S > β-C_2S > α'$_L$-C_2S > γ-C_2S. These experimental methods, however, have limitations in terms of the difficulty of synthesizing pure polymorphs with and without ion substitution and the quantitative interpretation of the order of reactivity.

To accurately and quantitatively determine the reactivity among the different polymorphs of dicalcium silicate, the effect of foreign ion substitution should be eliminated. Recently, the reactivity of pure polymorph states has been studied through simulations. Among the simulation methods, DFT calculation has an advantage of high accuracy in simulating the crystal structures. Recent works on the reactivity of dicalcium silicate using the DFT calculation have been mainly conducted through identifying the Density of States (DOS). Wang et al. (2014) proposed the reactivity of α'$_H$-C_2S, β-C_2S and γ-C_2S in terms of Partial DOS (PDOS) and Local DOS (LDOS) based on data obtained using DFT calculation. Other results (Rejmak, Dolado, Aranda, and Ayuela, 2019; Tao, Zhang, Li, Wang, and Hu, 2019; Wang, Manzano, López-Arbeloa, and Shen, 2018) also show efforts to use DFT calculations in the reactivity studies of dicalcium silicate. However, as a result of the combined peak data from the PDOS, it is difficult to grasp the behavior of individual atoms, thus it is still difficult to find the origin of the difference in reactivity.

In this study, the relationship between the order of reactivity of different polymoprhs of dicalcium silicate and its total energy was investigated by DFT calculation. In addition, the effects of sintering temperature and the total energy of each polymorph are discussed.

2 Computational Methods

Quantum Espresso DFT package was used to perform the basic modeling and analysis of crystals of dicalcium silicates (Giannozzi *et al*., 2009). The initial model of dicalcium silicate was taken from the lattice parameters and crystal structures published for all cement phases by Balonis and Glasser (2009). In the two crystal structures of α-C_2S and α'$_H$-C_2S, the atoms with occupancies were removed due to the duplicate positions with other atoms. Figure 1 shows α-C_2S which has duplicate atoms in a unit cell. All of the crystal structures were relaxed by Quantum Espresso pw.x executable to obtain a basically stable crystal structure at 0K. The DFT calculations were performed by Perdew-Burke-Ernzerhof (PBE) Generalized-Gradient-Approximation (GGA) functionals. The pseudopotentials made out of ultrasoft-postprecessing (USPP) were used to obtain the electronical information of each atom. The force convergence threshold and energy convergent threshold were 10^{-4} Ry/au and 10^{-3} Ry, respectively. The plane-wave biases set was converged by the energy cutoff of 800 Ry. The crystal structures of all polymorphs were relaxed with Broyden-Fletcher-Goldfarb-Shannno (BFGS) algorithm. Due to the large scale of unit cell, gamma-point sampling was used.

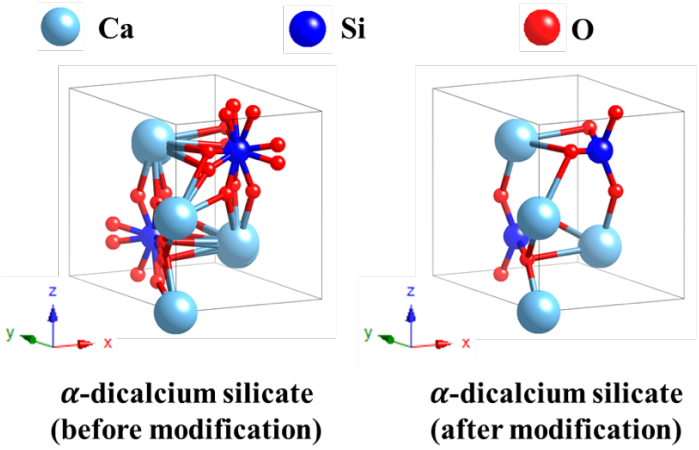

Figure 1. The crystal structure of α-C_2S before and after modification.

3 Results and Discussion

3.1 Relaxation of Polymorphs

The crystal structures of all polymorphs of dicalcium silicate were relaxed from the original crystal structure starting from the lattice parameters and positions taken from the data of cement phases as shown in Table 1 (Balonis and Glasser, 2009). Figure 2 shows the crystal structure viewed from (100), (010) and (001) planes and the standard orientation for the five relaxed dicalcium silicate crystal structures. Since the relaxation method was used which did not change the lattice parameter itself, the basic crystal shape did not change significantly.

Table 1. Cell parameters of dicalcium silicate unit cells.

Polymorphs	Crystal Structure	*a* (Å)	*b* (Å)	*c* (Å)	*α* (°)	*β* (°)	*γ* (°)	Z
α-C_2S	Hexagonal	5.579	5.579	7.15	90	90	120	2
α'$_H$-C_2S	Orthorhombic	6.85	5.49	9.49	90	90	90	4
α'$_L$-C_2S	Orthorhombic	20.871	9.496	5.6	90	90	90	12
β-C_2S	Monoclinic	5.502	6.745	9.297	90	85.45	90	4
γ-C_2S	Orthorhombic	5.081	11.224	6.778	90	90	90	4

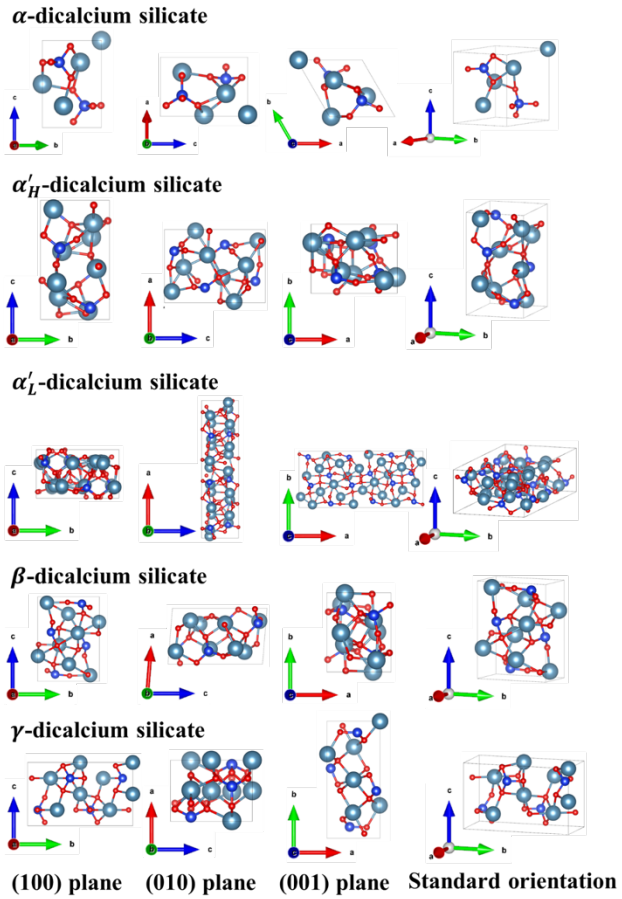

Figure 2. Relaxed crystal structures of the polymorphs of dicalcium silicate.

3.2 Total Energy

The total energy value from the DFT calculation was used to explain the origin of different reactivity among the five polymorphs of dicalcium silicate. A significant difference was found in the total energy values of the five polymorphs of dicalcium silicate. The total energy values of each crystal structure are shown in Table 2. The total energy values were divided by the Z values for comparison between each formula. Figure 3 shows that the higher the total energy value of the crystal structure, the higher the reactivity. This phenomenon can be explained by the high total energy possessed by the crystal structure which causes the instability of the structure, leading to higher reactivity.

Table 2. The total energy values of the polymorphs of dicalcium silicate.

Polymorphs	Crystal Structure	Total Energy/Z (Ry)	Reactivity Order
α-C_2S	Hexagonal	-288.31	1st
α'$_H$-C_2S	Orthorhombic	-288.33	2nd
α'$_L$-C_2S	Orthorhombic	-288.37	4th
β-C_2S	Monoclinic	-288.36	3rd
γ-C_2S	Orthorhombic	-288.41	5th

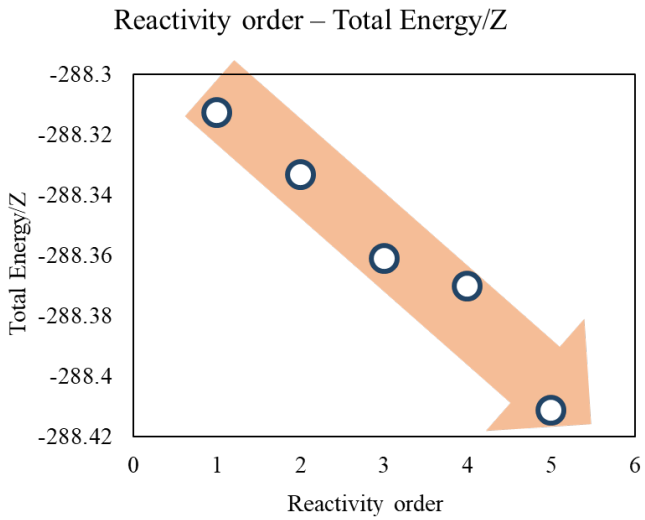

Figure 3. The relationship between the total energy and the order of reactivity.

3.3 Sintering Temperature

This can be also linked to the order of sintering temperature. It is well known that the polymorphs of dicalcium silicate forms at different sintering temperatures. Table 3 shows the relationship between the sintering temperature and the order of reactivity. As the sintering temperature required for the formation of each crystal structure increases, more unstable polymorphs are produced. This is observed for α'_H-C_2S, α'_L-C_2S and γ-C_2S. For these three polymorphs having the same orthorhombic structure, it can be inferred that the orders of sintering temperature, total energy, and reactivity match well. The reversed reactivity order of α'_L-C_2S and β-C_2S can be explained due to the different crystal structures.

Table 3. The sintering temperature and the order of reactivity of polymorphs of dicalcium silicate.

Polymorphs	Crystal Structure	Sintering Temperature (°C)	Reactivity Order
α-C_2S	Hexagonal	>1425	1st
α'_H-C_2S	Orthorhombic	1160-1425	2nd
α'_L-C_2S	Orthorhombic	680-1160	4th
β-C_2S	Monoclinic	500-680	3rd
γ-C_2S	Orthorhombic	<500	5th

4 Conclusion

- This study presents a new perspective to quantitatively explain the order of total energy, instability, and the reactivity of dicalcium silicate crystals in cement.
- In summary, the relationship between the total energy and the reactivity order of the five dicalcium silicate polymorphs was revealed by DFT calculation. The order of α-C_2S > α'_H-C_2S > β-C_2S > α'_L-C_2S > γ-C_2S, which is the well-known order of reactivity for dicalcium silicate, matches well with the order of the total internal energy calculated from the DFT. This indicates a C_2S polymorph with a higher total energy is more

unstable and thus shows higher reactivity.

- In addition, the order of sintering temperature which plays an important role in cement production was shown to be almost identical with the order of reactivity or the order of total internal energy. In particular, the sintering temperatures of α'_H-C_2S, α'_L-C_2S and γ-C_2S correspond exactly to the order of reactivity. Possible explanation is that materials which are stable at higher temperatures present a more unstable structure at lower temperature, thus resulting in higher reactivity.

Acknowledgement

This work was supported by the BK4 funded by the Ministry of Education, Republic of Korea.

ORCID

Seungchan Kim: https://orcid.org/0000-0001-9564-4367
Juhyuk Moon: https://orcid.org/0000-0002-7049-892X
Johann Plank: https://orcid.org/0000-0002-4129-4784

References

Balonis M. and Glasser F.P. (2009). The density of cement phases. *Cement and Concrete Research*, *39*(9), 733-739. doi:https://doi.org/10.1016/j.cemconres.2009.06.005

Bensted J. (1978). γ-dicalcium silicate and its hydraulicity. *Cement and Concrete Research, 8*(1), 73-76. doi:https://doi.org/10.1016/0008-8846(78)90059-5

Cuberos A.J.M., De la Torre Á.G., Martín-Sedeño M.C., Moreno-Real L., Merlini M., Ordónez L.M. and Aranda M.A.G. (2009). Phase development in conventional and active belite cement pastes by Rietveld analysis and chemical constraints. *Cement and Concrete Research, 39(*10), 833-842. doi:https://doi.org/10.1016/j.cemconres.2009.06.017

Fukuda K. and Taguchi H. (1999). Hydration of α′L- and β-dicalcium silicates with identical concentration of phosphorus oxide. *Cement and Concrete Research*, *29*(4), 503-506. doi:https://doi.org/10.1016/S0008-8846(98)00195-1

Giannozzi P., Baroni S., Bonini N., Calandra M., Car R., Cavazzoni C., . . . Wentzcovitch R.M. (2009). QUANTUM ESPRESSO: a modular and open-source software project for quantum simulations of materials. *Journal of Physics: Condensed Matter, 21*(39), 395502. doi:10.1088/0953-8984/21/39/395502

Rejmak P., Dolado J.S., Aranda M.A.G. and Ayuela A. (2019). First-Principles Calculations on Polymorphs of Dicalcium Silicate—Belite, a Main Component of Portland Cement. *The Journal of Physical Chemistry C*, *123*(11), 6768-6777. doi:10.1021/acs.jpcc.8b10045

Tao Y., Zhang W., Li N., Wang F. and Hu S. (2019). Predicting Hydration Reactivity of Cu-Doped Clinker Crystals by Capturing Electronic Structure Modification. *ACS Sustainable Chemistry & Engineering, 7*(6), 6412-6421. doi:10.1021/acssuschemeng.9b00327

Taylor H.F.W. (1997). Cement chemistry. London: Thomas Telford.

Wang Q., Li F., Shen X., Shi W., Li X., Guo Y., . . . Zhu Q. (2014). Relation between reactivity and electronic structure for α′L-, β- and γ-dicalcium silicate: A first-principles study. *Cement and Concrete Research*, *57*, 28-32. doi:https://doi.org/10.1016/j.cemconres.2013.12.004

Wang Q., Manzano H., López-Arbeloa I. and Shen X. (2018). Water Adsorption on the β-Dicalcium Silicate Surface from DFT Simulations. *Minerals, 8,* 386. doi:10.3390/min8090386

XV International Conference on Durability of Building Materials and Components
DBMC 2020, Barcelona
C. Serrat, J.R. Casas and V. Gibert (Eds)

Durability of Internally Insulated Historical Solid Masonry under Future Climates: A Stochastic Approach

Sahar Sahyoun[1], Lin Wang[2], Hua Ge[3], Maurice Defo[4] and Michael Lacasse[5]

[1] Ph.D. Student, Concordia University, Montreal, Canada; s_sahyo@concordia.live.ca

[2] Post-Doctoral Fellow, Concordia University, Montreal, Canada; forestwang2013@gmail.com

[3] Associate Professor, Concordia University, Montreal, Canada; hua.ge@concordia.ca

[4] Associate Research Officer, Construction Research Centre, National Research Council Canada, Ottawa, Canada; Maurice.Defo@nrc-cnrc.gc.ca

[5] Senior Research Officer and Team lead, Façade Systems and Products, Construction Research Centre, National Research Council Canada, Ottawa, Canada; Michael.Lacasse@nrc-cnrc.gc.ca

Abstract. *Today, it is globally known that climate change needs to be addressed to mitigate its harmful effects on our environment. It is also common knowledge that the contribution of historical buildings to the energy consumption of the existing Canadian building stock is severe. Buildings of historical identity are often poorly thermally insulated. Thus, to increase energy efficiency and occupant comfort in cold climates, the application of thermal insulation on the interior side of solid masonry walls offers a possibility to improve the historic buildings' energy performance, without compromising their identity and cultural heritage values. As a result, the historical masonry will be subjected to lower temperature during the heating season, which can increase the potential for condensation and frost within the wall. A balance must therefore be reached between durability measures and thermal performance objectives. This paper intends to achieve this balance through determining the impact of the interior insulation thickness on the durability of a typical historical masonry wall under the effect of climate change. A stochastic approach is used in hygrothermal simulations to account for the uncertainty in material properties. Results in Ottawa indicate a higher risk to frost damage after interior insulation is added to a brick wall having a moisture critical degree of saturation (Scrit) of 0.25 and 0.35. Moreover, both deterministic and the stochastic results were in good agreement. Also, both methods showed an increase risk to frost damage under a changing climate.*

Keywords: *Historical Buildings, Solid Masonry, Stochastic Approach, Future Climates, Durability.*

1 Introduction

One typical way to reduce a building's heating energy consumption is insulating its envelope. Generally, exterior insulation systems are considered the best alternative to retrofit existing buildings due to their ability to prevent thermal bridges (Straube *et al.,* 2012). However, in the case of historical buildings, exterior insulation is not possible due to architectural and aesthetical reasons. Thus, the only way to retrofit these buildings is through adding interior insulation. Straube *et al.* (2012) suggested spraying an airtight insulating foam directly to the interior side of the existing masonry. However, normally after insulation is installed, the moisture content of the masonry wall increases, which may lead to a higher potential for hygrothermal problems, such as frost damage.

Frost damage is one of the main reasons threatening durability of masonry structures in cold climates. Previous research has shown that under a changing climate, higher rainfall intensity, strong winds, and more frequent storms are expected, which may increase WDR loads on the façade and subsequently, risks for rain penetration (IPCC, 2001). On the other hand, increased solar radiation and air temperature may increase the drying potentials. It is therefore important to assess the effect of climate change on the potential risk to freeze-thaw (FT) damage.

The hygrothermal performance of masonry walls are usually assessed by means of deterministic approach. Though, the hygrothermal responses are influenced by stochastic factors, such as the variability of material properties, boundary conditions and environmental loads. The uncertainties of the input parameters may lead to a deviation between simulation results and the actual performance of the wall assemblies, consequently, leading to faulty designs.

The objective of this paper is to investigate the impact of the interior insulation thickness on the freeze-thaw damage risk of the existing masonry wall assemblies. A masonary basewall and three retrofit options having three different insulation thicknesses were tested. First, a deterministic approach was used to evaluate the hygrothermal performance of wall assemblies using Delphin. Second, a stochastic approach was used to take into account the uncertainties in brick masonry properties under different climate conditions and design configurations.

2 Methods

The methodology includes a deterministic and a stochastic modelling approaches. The latter was developed by Wang and Ge (2018) and applied to investigate the impact of insulation thickness on the FT risk of masonry walls.

2.1 Weather Data

Weather data for Ottawa were provided by the National Research Council of Canada (NRC). A continuous time-series[1] of hourly climate data was prepared for a baseline time-period spanning from 1986-2016 and 31-year long future time-period when global warming of 3.5°C is expected to be reached in the future (Gaur et al., 2019). Future data of 3.5ºC increase, will be reached between 2062-2092 (Environment and Climate Change Canada, 2018). Each data set includes 15 realizations; however, only the median realization based on MI was used.

2.1.1 Selection of reference years

The selection of reference years was made with the intention to test wall assemblies under more representative design weather years in the selected timelines. Annual average of the Moisture Index (MI) (Cornick *et al.,* 2003) and Severity Index (Isev) (ASHRAE, 2010) were computed for the chosen time-periods, and the years were ranked in ascending order. The year corresponding to the 97th percentile (ranked second out of the 31 years) in each time-period was chosen as the MRY. Table 1 summarizes the selection of MRYs under historical and future time-periods.

[1] The full dataset can be accessed from: 10.17605/OSF.IO/UPFXJ.

Table 1. Summary of selected moisture reference year and their values.

City	Data	MI – MRY	Isev_MRY
Ottawa	Historical	2010	2009
	Future	2085	2066

A comparison was then made between the selected MRYs weather data, as shown in Figure 1 for historical and future data. The temperature difference between the MI and Isev MRYs was not as significant as the difference of their rain amount. Monthly rain variation looked relatively uniform throughout the year for MRYs selected by the MI method (2010 and 2085) and considerably less than that found for the years selected using the Isev method (2009 and 2066). MRYs selected using Isev seem to be more severe than years selected by MI; therefore, 2009 and 2066 were selected as the MRYs for this study.

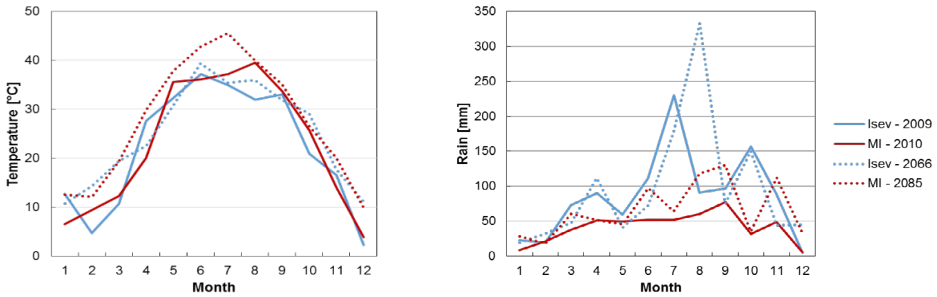

Figure 1. Comparison of monthly temperatures (a) and rain (b) for the years selected in historical data using MI (2010) and Isev (2009) and future data using MI (2085) and Isev (2066) for Ottawa.

2.2 Wall Assemblies

Four wall assemblies were evaluated in this study: a solid masonry wall assembly and three internally retrofitted solid masonry wall assemblies. The first configuration consists of 300mm historical brick (Old Building Brick Rote Kaserne Potsdam – outer brick 1) and 15mm of gypsum plaster. Retrofitted wall assemblies differ only by their insulation thickness: 50 mm (2 inches) and 100mm (4 inches) of polyurethane foam were added as recommended by Straube *et al.* (2012); the insulation thickness was increased to 200mm (8 inches) to satisfy the Passive House requirement (Straube, 2009). Figure 1 shows the configuration of the retrofitted wall assemblies. Material properties are from the Delphin Material Library.

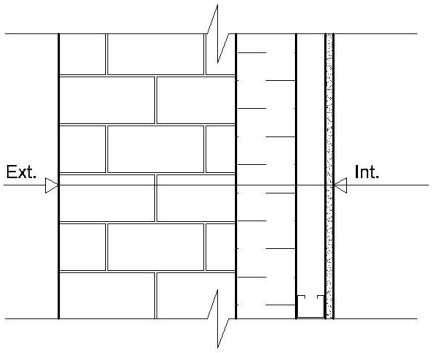

- Existing old brick (300mm)
- Added polyurethane foam
- Added (38mm x 50mm) steel stud
- Added gypsum board (12.7mm)

Figure 2. Solid masonry Wall retrofit solution.

2.3 Stochastic Model's Setup

The stochastic models were generated according to the stochastic hygric material properties of brick. The Latin Hypercube Sampling method was applied to generate the stochastic models (Wang and Ge, 2018). The basic material parameters such as effective saturation (θ_{eff}), water vapor diffusion resistance factor at dry state (μ) and liquid water conductivity at effective saturation (k_l) are considered as stochastic variables. Their mean values were based on DELPHIN material properties. Whereas, the standard deviation was calculated as a function of the coefficient of variance (CV). Values of CV were found for a similar type of brick in the literature (Zhao *et al.,* 2015). Descriptive statistics of material properties of the specific old brick material are presented in Tables 2 and 3.

Table 2. Deterministic parameters of brick.

Material property	Unit	Mean
ρ	[kg/m^3]	1842.47
c	[J/kgK]	772.224
λ	[W/mK]	0.7975
θ_{por}	[m^3/m^3]	0.304727
θ_{cap}	[m^3/m^3]	0.255
A_w	[kg/m^{2}s$^{0.5}$]	0.0668929

Table 3. Stochastic parameters of brick.

Material property	Unit	Mean	Std dev	CV (%)
θ_{eff}	[m^3/m^3]	0.28399	0.00954	3.36
μ	[-]	37.5558	9.8734	26.29
k_l	[s]	2E-8	5.248E-09	26.24

2.4 Wall Orientation

This study was carried out for the orientation with the highest amount of annual wind-driven rain calculated according to ASHRAE (ANSI/ASHRAE, 2016). In Ottawa, a wall facing South-South-West (202.5°) was considered. Note that a North-facing wall (receiving least solar radiation) was not included in this analyis; but will be further investigated.

2.5 Boundary Conditions

2.5.1 Indoor boundary conditions

The indoor relative humidity was computed using the ASHRAE 160 simple method (ANSI/ASHRAE, 2016). The indoor temperature was also calculated using the same model for heating only. As for the indoor vapour diffusion and the indoor heat conduction coefficients, they were assumed as $1.52*10^{-8}$ s/m and 8 W/m^{2}K, respectively.

2.5.2 Outdoor boundary conditions

Outdoor boundary conditions include heat conduction, vapor diffusion, wind driven rain, short wave radiation and long wave radiation. To compute the longwave radiation, the boundary layer method was selected in Delphin. The required longwave emission coefficient of the building surface was set to 0.9. And the convective heat transfer coefficient was calculated based on Equation (1):

$$h_{ce} = 4 + 4.v \quad (1)$$

Where, *v* is the wind speed. The reflection coefficient of the surrounding ground (albedo) was 0.2 and the absorptance coefficient of the brick cladding surface was equal to 0.6.

2.5.3 Wind-driven rain

WDR is calculated using ASHRAE method (ANSI/ASHRAE, 2016) for a 3.5 storey building located in the suburban area. Assuming a medium exposure factor, the rain exposure factor (F_E) and the rain deposition factor (F_D) were set to 1.0 and 0.5, respectively.

2.6 Initial Conditions

Initial temperature and relative humidity conditions were selected as constants and set to 21°C and 50%, respectively.

2.7 Performance Indicator for Assessing Wall Performance

One of the most important damage mechanisms in porous materials is caused by the action of freezing and thawing inside materials (K.R. Lisø *et al.,* 2007 G.; Wardeh and B. Perrin, 2008). The onset of freeze-thaw damage in porous materials requires that the value of moisture saturation is exceeded simultaneously with the occurrence of freezing temperatures. According to Straube *et al.* (2006), the critical degree of moisture saturation (Scrit) of masonry can vary considerably among different types of historical brick. For instance, following an experimental study using frost dilatometry, the Scrit of three brick stones found in Canada was found between 0.25 and 0.87 (Straube *et al.,* 2010). In this paper, values of (Scrit) equal to 0.25, 0.35, 0.5 and 0.8 were considered. Also, freezing is considered to occur at temperatures below -5°C within the material (Straube and Schumacher, 2006). The risk of freeze-thaw damage is computed using the critical number of freeze-thaw cycles (FTC). One cycle is counted when temperature decreases below the freezing temperature and moisture content exceeds its critical level.

2.8 Simulations

Simulations were performed for the base and retrofitted walls under historical and future loads, using hygrothermal simulation program Delphin 5, v5.9.4. No air and moisture leakage source were assumed. Simulations were executed over a period of five years using the reference year for each time-period; meaning that each selected year is repeated 5 times. However, only the results of the 5th year are evaluated.

A fine variable discretization, with a minimum element width of 0.5 mm and a stretch factor of 125 was used to set up the meshing of the materials. The point of investigation was placed at a depth of 5mm of the brick surface.

3 Results and Discussion

Figure 3 shows the impact of interior insulation thickness on the estimated number of freeze-thaw cycles (FTC) of an old brick masonry wall located in Ottawa and modelled for historical and future climatic loads. The brick was tested for different critical degree of saturation: 0.25, 0.35, 0.5 and 0.8. However, Figure 3 shows stochastic results for Scrit equals to 0.25 and 0.35 only. For higher saturation degrees, i.e., brick having higher resistance properties, the insulation thickness did not have any influence on the durability of the masonry wall. Estimated FTCs

indicated zero; therefore no potential risk to freeze-thaw damage to occur. Therefore, only results for a brick with Scrit equal 0.25 and 0.35 will be discussed.

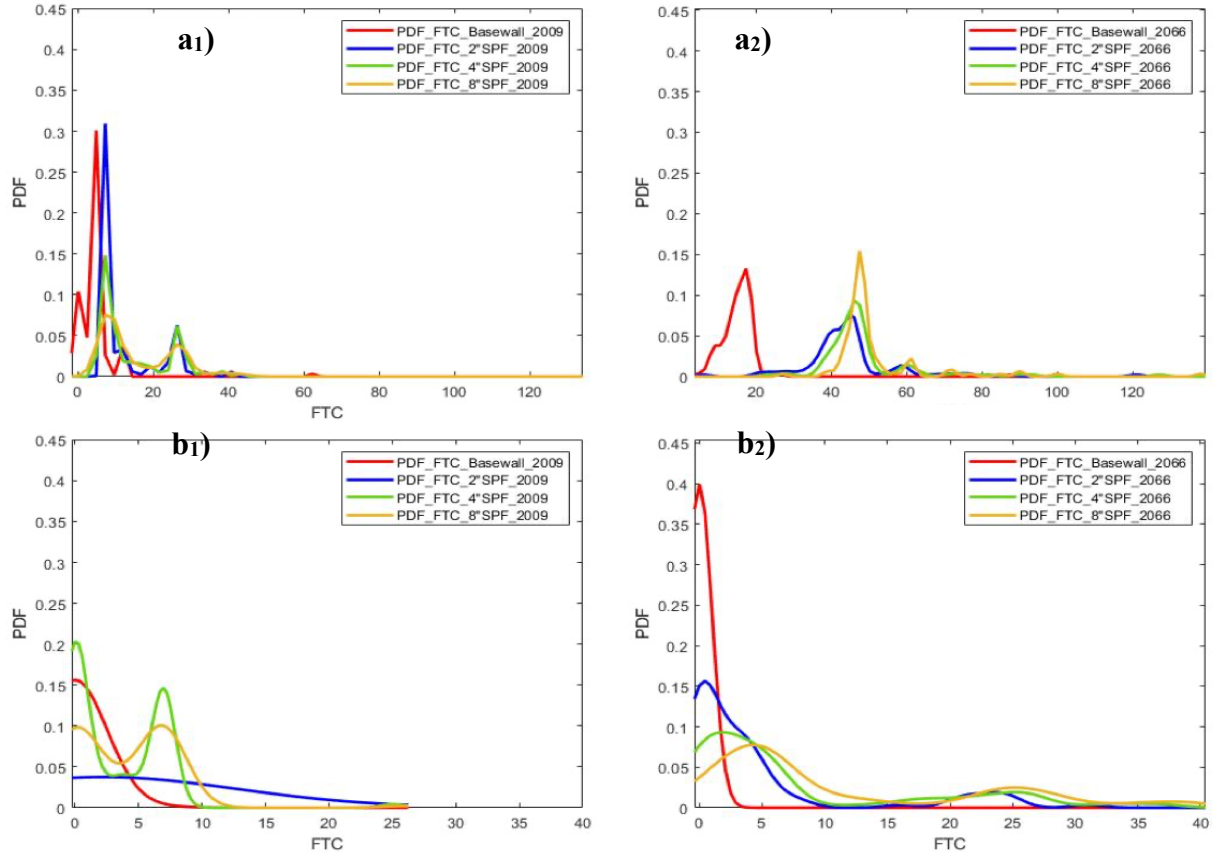

PDF = Probability density function; SPF = Spray polyurethane foam; [1]Historical year (2009); and [2]Future year (2066).

Figure 3. Stochastic results – the impact of insulation thickness on the estimated number of freeze-thaw cycles (FTC) for brick masonry having a critical degree of saturation of a) Scrit = 0.25; and b) Scrit = 0.35.

In general, after interior insulation was added, the number of FTCs increased, indicating a higher potential of freeze-thaw to occur. For instance, FTC values varied between 0 and 12 for a base wall with Scrit = 0.25. These values increased to range between 5 and 30 FTCs when 2" of insulation was added. When adding a larger insulation thickness of 4" and 8", the number of FTCs reached a range of [5 – 42] and [5 – 50], respectively (Figure 3-a_1). The probability distribution of FTCs for the same type of brick under future climate denoted a larger difference between the base wall and the retrofitted options. While values of FTC varied between 0 and 22 for a base wall, added insulation has caused the FTC to range between 0 and 100, with a higher probability around 50 cycles (Figure 3-a_2). When the Scrit is 0.35 (Figure 3-b_1 and Figure 3-b_2), adding insulation still has increased the number of FTC; however, with less discrepancies.

Table 4 represents the deterministic results of the predicted number of freeze-thaw cycles. Comparing results obtained by the deterministic and the stochastic methods, they seem in good agreement. Values of FTCs calculated using the deterministic approach corresponds in most of the cases to the FTC number having the highest density within the stochastic results range.

Table 4. Estimated number of FTC results for the deterministic method.

	Basewall			2" added insulation			4" added insulation			8" added insulation		
Scrit	0.25	0.35	0.5 – 0.8	0.25	0.35	0.5 – 0.8	0.25	0.35	0.5 – 0.8	0.25	0.35	0.5 – 0.8
2009	*5*	*0*	*0*	*24*	*2*	*0*	*29*	*6*	*0*	*32*	*7*	*0*
2066	*5*	*0*	*0*	*49*	*2*	*0*	*52*	*9*	*0*	*56*	*21*	*0*

Figure 4 illustrates the impact of climate change on the potential risk to freeze-thaw damage. Stochastic results clearly show that FTC increased in number and spread under future conditions. Deterministic results in Table 4 demonstrated the same as well.

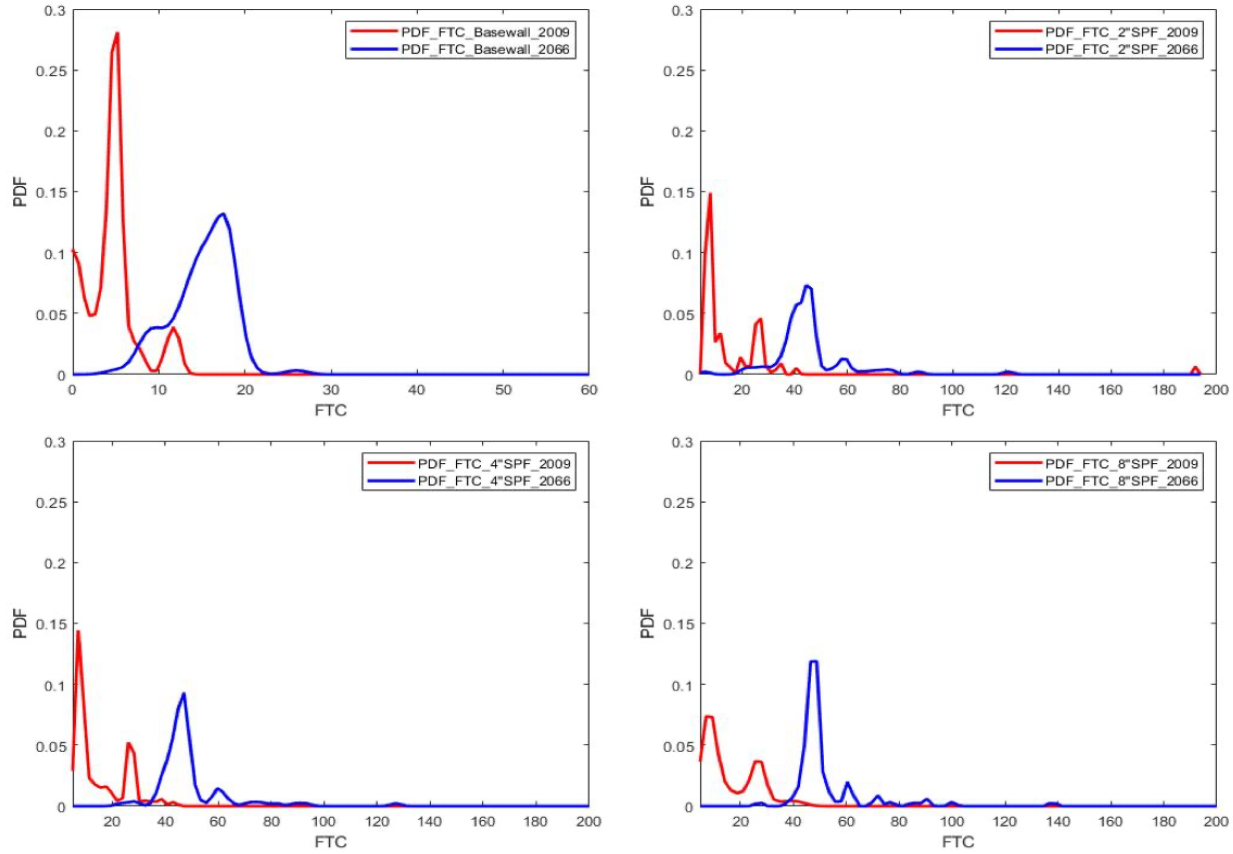

Figure 4. Stochastic results – the climate change effect on the estimated number of FTC for brick masonry having a Scrit of 0.25.

4 Conclusions

The durability performance of a masonary basewall and three retrofit alternatives of the same wall, having three different insulation thicknesses were evaluated using both a deterministic and a stochastic method. This study took into account the uncertainties in brick masonry properties under historical and future climate conditions. The brick was tested for different critical degree of saturation: 0.25, 0.35, 0.5 and 0.8. The insulation thickness did not have any influence on the durability of the masonry brick with better frost resistance, i.e. higher critical degree of saturation of 0.5 and 0.8. However, for a Scrit of 0.25 and 0.35, the number of FTCs

increased, indicating a higher potential of freeze-thaw to occur. Results obtained by the deterministic and the stochastic methods were in good agreement, as values of FTCs calculated using the deterministic approach correspond to the number of FTC having the highest probability within the stochastic results range. In addition, both methods showed an increase in FTCs' number and spread under future conditions; thus, a higher risk to frost damage. To provide a safe insulation type and thickness range for the retrofit of masonry walls and to account for the uncertainty of future climate, a study will be carried out later.

ORCID

Sahar Sahyoun: https://orcid.org/0000-0001-5131-6134
Lin Wang: https://orcid.org/0000-0002-6529-1123
Hua Ge: http://orcid.org/0000-0003-1368-4301
Maurice Defo: http://orcid.org/0000-0001-9212-6599
Michael Lacasse: https://orcid.org/0000-0001-7640-3701

References

ANSI/ASHRAE. (2016). *Criteria for Moisture Control Design Analysis in Buildings.* Atlanta.

ASHRAE. (2010). *Environmental weather loads for hygro- thermal analysis and design of buildings. RP-1325, American Society of Heating, Refrigerating and Air- Conditioning Engineers, Inc.* Atlanta.

Cornick, S., Djebbar, R. and Dalgliesh A.W. (2003). Selecting moisture reference years using a Moisture Index approach. *Building and Environment*, *38*(12), 1367–1379.

Environment and Climate Change Canada. (2018). *Memorandum of Understanding between National Research Council and Environment and Climate Change Canada….* Government of Canada: Ottawa, ON, Canada.

Gaur, A., Lacasse, M. and Armstrong, M. (2019). Climate Data to Undertake Hygrothermal and Whole Building Simulations Under Projected Climate Change Influences for 11 Canadian Cities. *Data*, *4*(2), 72.

IPCC. (2001). *Climate Change 2001: Impacts, Adaptation, and Vulnerability. Intergovernmental Panel on Climate Change Third Assessment Report*. Report of Working Group II, Geneva, Switzerland.

Lisø, K. R., Kvande, T., Hygen, H. O., Thue, J. V. and Harstveit, K. (2007). A frost decay exposure index for porous, mineral building materials. *Building and Environment*, *42*(10), 3547–3555.

Straube, J. and Schumacher, C. (2006). Assessing the durability impacts of energy efficient enclosure upgrades using hygrothermal modeling. *WTA-Journal: Internationales Journal Für Technologie Und Praxis Der Bauwerkserhaltung Und Denkmalpflege*, 197–222.

Straube, J. (2009). BSI-025: The Passive House (Passivhaus) Standard—A comparison to other cold climate low-energy houses. *Building Science Corporation, Somerville, Massachusetts, USA.*

Straube, J., Schumacher, C. and Mensinga, P. (2010). Assessing the freeze-thaw resistance of clay brick for interior insulation retrofit projects. *Proceedings of the Performances of Envelopes of Whole Buildings XI*, 1–8.

Straube, J. F., Ueno, K. and Schumacher, C. J. (2012). *Measure guideline: internal insulation of masonry walls* (No. DOE/GO-102012-3523). National Renewable Energy Lab. (NREL), Golden, CO (United States).

Wang, L. and Ge, H. (2018). Stochastic modelling of hygrothermal performance of highly insulated wood framed walls. *Building and Environment, 146,* 12–28.

Wardeh, G. and Perrin, B. (2008). Freezing-thawing phenomena in fired clay materials and consequences on their durability. *Construction and Building Materials*, *22*(5), 820–828.

Zhao, J., Plagge, R., Ramos, N. M., Simões, M. L. and Grunewald, J. (2015). Concept for development of stochastic databases for building performance simulation–A material database pilot project. *Building and environment*, *84*, 189-203.

XV International Conference on Durability of Building Materials and Components
DBMC 2020, Barcelona
C. Serrat, J.R. Casas and V. Gibert(Eds)

Earth Construction Durability: In-Service Deterioration of Compressed and Stabilized Earth Block (CSEB) Housing in Algeria

Adel. Benidir, M'hamed. Mahdad and Ahmed. Brara

National Center of Integrated Studies and Research on Building Engineering (CNERIB), 16201, Souidania, Algiers, Algeria, abenidir.cnerib@gmail.com

Abstract. *The present work deals with a unique in-service valuation of CSEB structures in Algeria. The inspection tries to bring out the impact of long time exposure under different and opposite climate and micro-seismic contexts. The diagnosis methodology is inspired by the approach largely adopted for the rehabilitation of traditional architecture. It involves the compilation of the previous survey reports, visual inspection of the structures, in-situ and laboratory tests to assess the residual CSEB mechanical properties. The CSEB constructions are located in the coastal north and the desertical south part of Algeria and were exposed respectively to a long-term Mediterranean and Saharian climate. The results of the investigation show that the CSEB in the construction located in the northern region is increasingly altered by the humidity. As the relative humidity rises, the fouling layers grow over some level. The surface pitting which is the consequence of long exposure to the wetting/drying cycles is also observed. The outer surfaces of the walls were honeycombed which reduce drastically the block resistance against the abrasion test. In some cases, differential erosion appears in the front of the walls, which indicates that the alteration does not proceed at the same rate from one area of the block to the other. However, owing to highly cementitious mortar used to join the earth blocks, the edges and corners remain unchipped. In the southern region where the arid climate dominating, the degradation of the CSEB is less prone to water attack but roughly exposed to the effect of the wind-dust frequent in this region and to the unawareness of the population. The paper presents also some recommendations to improve the earth construction durability with CSEB technique.*

Keywords: *Earth Blocks, Durability Valuation, Weather Exposure.*

1 Introduction

Among the eco-friendly building materials, the Stabilized and Compressed Earth Block (CSEB) is considered the most promising. Hence, improving the sustainability of this material deserves more attention and study. If the durability at the scale of the unit and the structural element in CSEB (Guettala *et al*., 2006), the scientific literature is prolific, it is not the same for constructions in the field with this material. Regular monitoring of CSEB building in the aim to assess the durability of the materials has received little formal research. The returns are generally based on a review or reported after a large building degradation or collapse. For instance, the document elaborated by Arandara and Jayasinghe (2007) on the durability of the CSEB construction gives prominent insight. The project focused on the report of the degradations observed on a group of 50 houses, 59 % of which were built in Matara (Sri Lanka) with stabilized earth blocks. This appraisal shows that the pathologies identified are mainly due to climatic factors, in particular, heavy rainfall and wind. It has been observed the appearance of water absorption by capillarity caused by the inappropriate stabilization of the

earth blocks. In addition, more erosion of the walls composed with the weakly stabilized block was noticed.

Based on previous experience, in 1949, India launched a program of construction of several hundred housing units (Bangalore), in which earth blocks manually compressed and stabilized with 5% of the cement was used. Some of these houses are still occupied to this day. Certain blocks from the demolished buildings were found to have a wet compressive strength of the order of 1.5 MPa. On the African continent, the survey reported by Oppong and Badu (2012) revealed that the walls (built with CSEB) exhibit considerable damages due to their exposure to high water absorption in Ghana. The recurring cycles of wetting/drying have inevitably caused their cracking alterations. Moreover, the blocks have been found to have low tensile strength and abrasion. In Uganda, where the projected housing backlog by the year 2000 was estimated at 3 million dwellings, an inventory of CSEB structures has been achieved by Kerali (2017). The author confirmed that in humid tropical areas, rainfall and temperature variations can adversely affect the performance of a block exposed to the elements. It was further related to the extensive appeal to this kind of construction in low income urban and rural areas.

2 Methods

The chosen diagnosis methodology is inspired by the one recommended by the Réhabimed guide (RéhabiMed, 2007) concerning the approach to be followed for the rehabilitation of traditional architecture. This guide is the work of a consortium of Mediterranean experts. In the present context, the investigation is sequenced in three stages: pre-diagnosis, multidisciplinary studies, and diagnosis. The first step ensures a brief location of the disorders and defines their nature and their extent. Herein, the classification of the construction according to the state of degradation could be partitioned into i) The building lost its structural stability or ii) The building suffers from structural disorders or other ageing pathologies. The second stage considers all historical and documentary studies that lead to the identification, the evolution and the transformation of the construction. Accordingly, that delimits and locates the factors of degradations. Finally, the diagnosis is developed following the analysis of the whole collected information to determine the causes of the disorders in order to define in fine the appropriate remedies. The diagnosis is supported by the analysis of the recorded climatic and seismic activity data of each region over the last decades.

Furthermore, laboratory and in situ tests have been performed to assess the block residual mechanical properties with both destructive (crushing) and non-destructive tests (mass rebound, abrasion). The compressive test using an universal press were extracted from the cornice and acroterion and replaced by new CSEBs in the building. The in situ tests rely on the use of pendulum sclerometer, consisting of the measurement the return of the rebound of a mass impacting a vertical surface. Abrasion tests has been performed on the block at different locations of the wall. Using a steel brush, the technique undertakes surface brushing along the entire length of the block for about a minute, which equals 30 round trips.

3 Location of the Sites, CSEB Buildings and Climate Environment

The figure 1 shows the geographic locations of the different sites assigned to the earth constructions studied throughout this investigation program.

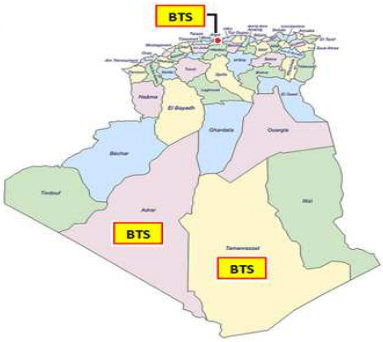

Figure 1. Geographic locations of sites.

The buildings are ground dwellings except in one residential site situated in the north region (see figure 2.c). The stabilisation of the earth blocs are both chemical and mechanical. The portion of cement exceeds 7 % and could be in some places more than 10 %. The second stage of stabilisation relies on reducing the pores volume by applying a compactive effort with at least 7 MPa of stress, using as a matter of fact a manual or a hydraulic semi-automatic press. This moulding pressure raises the bulk density of the block as it improves the block performance against the water runoff erosion phenomenon. The cure process involves a storage of the blocks under roofing or hat for 28 days. It requires also a light watering for a week with a wrap. The dimensions of the blocks used in these constructions are different from one site to another. For instance, the dimensions of the blocks manufactured and used to build the first bioclimatic prototype at Souidania in 1984 (Algiers, figure 2.a) are 250 mm in length, 125 mm in width and 70 mm in height. In 2007, blocks with the dimensions of 295 mm in length, 140 mm in width and 90 mm in height were prepared to construct the second bioclimatic prototype (figure 2.b). Over all the surveyed houses, the earth blocks are entire except in the site of Beni Messous where compressed earth hollow blocks were used.

a) Bioclimatic prototype Souidania (1984, Algiers)

b) Bioclimatic prototype Souidania (2007, Algiers)

c) Houses at Beni Messous (1987, Algiers)

Figure 2. Load bearing soil–cement block residential building in the northern region.

a) Adrar b) Sersouf (Tamanrasset) c) Mouflon (Tamanrasset)

Figure 3. Load bearing soil–cement block residential building in the northern region.

The appraisal concerns three departments (Wilaya): Algiers (Capital), Adrar and Tamanrasset. The temperature, the relative humidity and the accumulated rainfall amounts referring to these regions are respectively depicted in figure 4, 5 and 6. In summer, the maximum temperature (not the peak) reaches 44 °C in Tamanrasset and 33 °C in Algiers The relative humidity is up 78 % in the north and less than 40 % in the south. The maximum accumulated rainfall amounts in the coastal region is around 1000 mm where the value of this parameter is extensively in decrease in the south region.

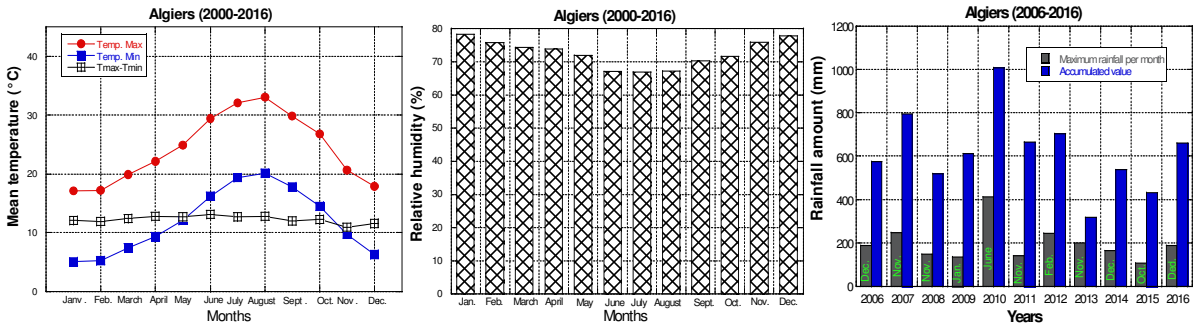

(a) (b) (c)

Figure 4. Climatic parameters in Algiers department, a) temperature, b) relative humidity c) rainfall amounts.

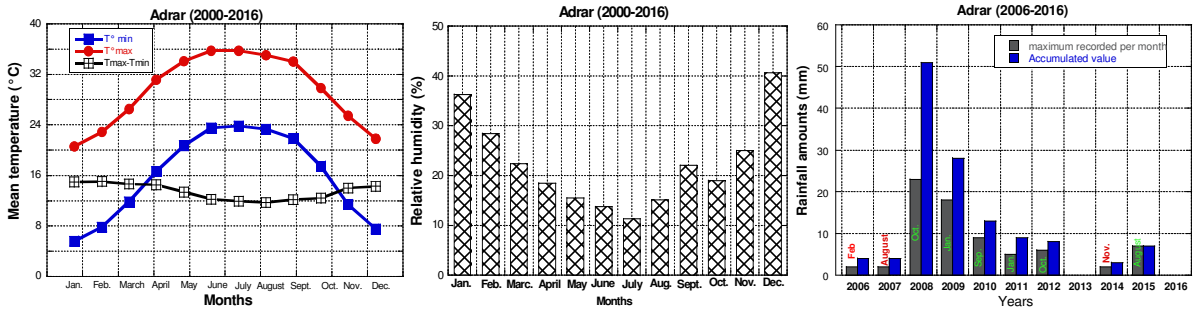

(a) (b) (c)

Figure 5. Climatic parameters in the department of Adrar, a) temperature, b) relative humidity c) rainfall amounts.

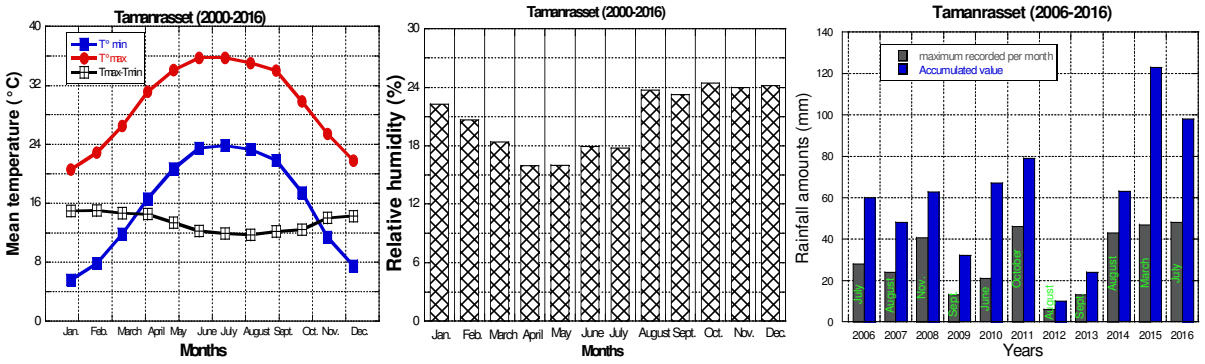

(a) (b) (c)

Figure 6. Climatic parameters in the department of Tamanrasset, a) temperature, b) relative humidity c) rainfall amounts.

4 Results

Ageing-related pathologies observed in stabilized earth constructions (CSEB) in the coastal northern region are mainly caused by weather element. Water (rain, humidity) is considered as the main cause of damage. For instance, the abundant rain in the northern region has three main effects:

i) The direct and repeated impact of the violent rain alters the surface of the external elements and causes a crumbling,

ii) The flow of rainwater on a surface (runoff phenomenon) causes surface erosion of the blocks which thereby provokes detachment of render,

iii) The splashing and infiltration generated by the indirect and repeated impact of rain on the ground, awning, exterior pavement, salient or re-entrant elements, followed by weathering, crumbling and digging.

As depicted on figure 7.a, the crumbling due to the impact of splashing attains generally the area close to the ground where the runoff phenomenon could provoke erosion in a large surface above the base (figure 7.b).

a) Splashing b) Surface erosion

Figure 7. Impact of the mechanical action of the rainwater.

The inattention on removing the element likely to cause seasonal variations in humidity in particular the vegetation near the building participate actively on the development of humid pathology (figure 8).

Figure 8. Degradation observed in the north region (humid pathology).

Furthermore, due to the high humidity rate, the pollution released in the air is fixed on the structures' external envelopes by dirtying the contact surfaces and favouring biological colonization (figure 9).

Figure 9 : Wall Pollution.

The structural degradation of the CSEB housing ascribed to the micro-seismic activity is not evident to distinguish. Although the coastal area is subjected to an important micro-seismic activity (about 60 micro-earthquakes per month), the noticed structural defects could be assigned to the differential settlement.

For the southern region, the investigation has ultimately identified very little pathologies due to exposure to climate, characterized by very low rainfall. On the other hand, the very frequent winds activity in this region has a stronger mechanical action when they carry suspended particles, such as the sands. The most common defects observed included: surface roughening, erosion and surface pitting. However, the inspection in the North and South regions has highlighted significant degradation resulting from poor design, production and implementation of the blocks, as well as others due to human intervention such as undertaking fitting out works or installation of air conditioning equipments.

Figure 10. Direct impact of the mechanical action of the wind.

5 Conclusions and Contribution

In this contribution, an evaluation of the in-service earth housing degradation in Algeria is reported. The investigation consists of an in-field visit including visual inspections supported by in situ and laboratory tests on CSEB. The visited earth constructions are long-time exposed to varied micro-seismic and climate contexts. In the coastal region where the high rainfall frequency and important humidity rate prevails, the CSEB constructions defects included: black fouling, due to pollution and biological colonization, efflorescence, detachment of render and erosions caused by the effects of whipping rains. On the one hand, the housing experiencing arid climate condition, the blocks are less prone to humid pathology. The observed defects concern surface roughening and pitting. On the other hand, the degradation caused by the inhabitant unawareness adversely affects the performance of the blocks. From the analysis of the degradations unveiled by the in-field investigation, some recommendations to improve the durability of the CSEB constructions are made:

Maintenance of the terraces according to the geographical situation and the climatic conditions.

Cleaning walls affected by fouling and biological colonization.

Checking the correct drainage of rainwater (avoid stagnation of water) to provide a good circulation and evacuation of the collected rainwater.

Removing the element likely to cause seasonal variations in humidity in particular the vegetation near the building.

Elevating the base, putting a sufficient roof overhang or installing an anti-capillary barrier especially in the North region.

Resorting to the earth construction guide in the selection of the soil nature and the process of stabilization.

Installing a windbreak and / or choosing an appropriate orientation of the structure minimizing the direct exposure to the winds.

ORCID

Adel Benidir : https://orcid.org/0000-0002-7645-1903
M'hamed Mahdad : https://orcid.org/0000-0002-6957-0648
Ahmed Brara : not available.

References

Arandara, K. P. and Jayasinghe, C. (2007). Identification of Durability Problem in Earth Building, *ENGINEER. Journal of the Institution of Engineers*, Sri Lanka, Vol. xxxx. no.04, Sri Lanka, pp.14-21. doi.org/10.4038/engineer.v52i2.7352

Guettala, A. Abibsi, A and H. Houari. (2006). Durability study of stabilized earth concrete under both laboratory and climatic conditions exposure, *Construction and Building Materials*, 20, 119-127. doi:org/10.1016/j.conbuildmat.2005.02.001

Kerali G.A. (2017). Exposure condition survey and measurement of defects in compressed stabilized earth block structures in uganda. *International Journal of Recent Innovation in Engineering and Research*. Volume: 02 Issue: 08.

Oppong, R. A. and Badu, E. (2012). Evaluation of stabilised-earth block for housing provision and construction Ghana. *Journal of Science and Technology*, Vol. 32, No. 2, pp 104-118. doi.org/10.4314/just.v32i2.12

XV International Conference on Durability of Building Materials and Components
DBMC 2020, Barcelona
C. Serrat, J.R. Casas and V. Gibert (Eds)

Effect of Mortar Age on the Textile-to-Mortar Bond Behavior

Ali Dalalbashi[1], Bahman Ghiassi[2], and Daniel V. Oliveira[3]

[1] PhD Student, ISISE, University of Minho, Department of Civil Engineering, Azurém, 4800-058 Guimarães, Portugal. E-mail: alidalalbashi@gmail.com

[2] Assistant Professor, Centre for Structural Engineering and Informatics, Faculty of Engineering, University of Nottingham, Nottingham, United Kingdom. E-mail: bahman.ghiassi@nottingham.ac.uk

[3] Associate Professor, ISISE & IB-S, University of Minho, Department of Civil Engineering, Azurém, 4800-058 Guimarães, Portugal. E-mail: danvco@civil.uminho.pt

Abstract. *Textile-reinforced mortar (TRM) composites have received extensive attention as a sustainable solution for seismic strengthening of masonry and historical structures. This new system is composed of textile fibers embedded in an inorganic matrix and is applied on the masonry and the concrete substrate surface as an externally bonded reinforcement (EBR) system. The bond at the textile-to-mortar interfaces is the main stress-transfer mechanism and, therefore, should be thoroughly investigated. Furthermore, the effectiveness of TRMs in improving the seismic performance of existing structures is highly dependent on the durability of its components, materials, textile-to-mortar bond, and their long-term behavior. Due to the novelty of these materials in application to masonry structures, several aspects related to the durability and long-term performance of them are still not clear. To that end, a new study has been launched that looks at the time effect on the mechanical properties and bond behavior between fiber and mortar. For this purpose, two different hydraulic lime-based mortars, as well as steel and glass fibers, are used to investigate the effect of mortar age on the TRM system after 180 days. The results show that at the early age of mortars, their mechanical properties, and the bond behavior of textile-to-mortar have been increased. Another critical point to remember is that by increasing the mortar age, textile-to-mortar bond and mortar strength are decreased.*

Keywords: *Textile-to-Mortar Bond Behavior, Durability, Long-Term Behavior, Degradation Mechanism.*

1 Introduction

The advantages of textile reinforced mortar (TRM) composites to fiber-reinforced polymers (FRPs) are the fire resistance, the vapor permeability, the removability, and the compatibility with masonry and concrete substrates (Carozzi and Poggi, 2015; Papanicolaou, Triantafillou, Papathanasiou, and Karlos, 2007). Thus, these advantages have made TRM composites very interesting for externally bonded reinforcement of masonry and reinforced concrete structures.

Mechanical properties of the TRMs and structural components strengthened with TRMs are strongly dependent on the properties of both the mortar and the fiber, the interfacial bond behavior of the fiber-to-mortar, and the interfacial bond behavior between the TRM composite and masonry substrate (Ghiassi, Oliveira, Marques, Soares, and Maljaee, 2016). Although mechanical characterization of TRMs (Leone *et al.*, 2017; Lignola *et al.*, 2017), or the bond between TRM and masonry substrate (Ascione, De Felice, and De Santis, 2015; Razavizadeh *et al.*, 2014) have been the subjects of several studies, the fiber-to-mortar bond

response has not received the attention (Dalalbashi, Ghiassi, Oliveira, and Freitas, 2018a; Ghiassi *et al.*, 2016). The fiber-to-mortar bond response of TRMs made of cementitious composites has been the subject of several studies, but this mechanism in case of lime-based TRMs that are usually used for strengthening of masonry structures is relatively unknown. The fundamental differences between the mechanical properties of lime-based and cementitious mortars indicates that a different bond behavior should be expected. Therefore, there is a clear need for understanding of this mechanism in lime-based TRMs and the parameters affecting that for fit-for-purpose design of TRMs, as well as, fully utilization of this strengthening system when application to masonry structures.

The age of mortar for performing pull-out tests (or any other mechanical characterization tests) on TRM composites seem to be a critical issue. Hydraulic lime-based mortars usually used in TRMs for application to masonry, and historical structures harden over prolonged periods. It means that probably the bond and mechanical properties of the TRM composite is also developed over longer periods, compared to the 30 days curing time commonly used for cementitious materials. In this study, to better understand the role of mortar age on the bond behavior of the fiber-to-mortar, pull-out tests are performed from 15 to 180 days of curing, and the results are compared and discussed.

2 Experimental Program

The experimental program consists of evaluating the role of mortar age on the pull-out response of single fibers embedded in lime-based mortars. For this purpose, two commonly used fiber types (steel and glass) with their counterpart mortars are used for these investigations.

2.1 Materials

Materials consisted of two commercial hydraulic lime-based mortars referred to as M1 and M2 throughout this paper. Mortar M1 is a high-ductility hydraulic lime mortar (Planitop HDM Restauro), and mortar M2 is a pure natural NHL 3.5 lime and mineral geo-binder base (GeoCalce).

The reinforcing materials are glass and steel fibers. The glass fiber is a woven biaxial fabric mesh (Mapegrid G220), and based on the technical datasheets, the elongation at breakage, modulus of elasticity, and tensile strength are 1.8 %, 72 GPa, and of 45 kN/m, respectively. The steel fiber is a unidirectional ultra-high tensile steel sheet (GeoSteel G600) and is made by twisting five individual wires together. The density and effective area of one cord (five wires) is equal to 670 g/m^2 and 0.538 mm^2, respectively. Additionally, its tensile strength and elastic modulus are equal to 2800 MPa and 190 GPa, respectively.

The fiber/mortar pairs are selected from the same provider in this study. It means that the glass fibers are used with the mortar M1 and the steel fibers with the mortar M2.

2.2 Material Characterization Tests

Mechanical characterization tests on mortar included compressive and flexural tests, according to ASTM C109 and EN 1015-11. The changes in the mechanical properties of mortar with curing age are evaluated by performing the tests at the ages of 14, 28, 60, 90, 180 days.

The compressive tests are performed on five cubics (50×50×50 mm^3) specimens at each age with a Lloyd testing machine under force-controlled conditions at a rate of 2.5 N/s. A pair of Teflon sheets with a layer of oil in between is placed between the specimens and the compression plates to reduce friction near the boundaries (Figure 1a). The flexural tests are performed on five prismatic (40×40×160 mm^3) specimens, at each age, following a three-point bending test scheme (Figure 1b). The tests are performed with a Lloyd testing machine under force-controlled conditions at a rate of 10 N/s.

(a) (b)

Figure 1. Mechanical characterization tests: (a) mortar compressive test; (b) mortar flexural test.

2.3 Pull-out Test

The single-sided pull-out test setup developed and presented by the authors in (Dalalbashi *et al.*, 2018a) is used in this study for investigating the fiber-to-mortar bond performance. The specimens consist of fibers embedded in disk-shaped mortars with a thickness of 16 mm (see Figure 2). The free length of the fiber is embedded in an epoxy resin block with a rectangular cross-sectional area of 10×16 mm^2, as shown in Figure 2. For detailed information on the procedure followed for the preparation of the specimens, the reader is referred to (Dalalbashi *et al.*, 2018a). The embedded lengths of steel and glass fibers are equal to 150 and 50 mm, respectively. These embedded lengths are corresponding to the sufficient embedded length of each composite system (Dalalbashi, Ghiassi, Oliveira, and Freitas, 2018b). The specimens are demolded after 24 hours of preparation and are stored in the lab environmental conditions (20°C, 60% RH) until the test day. Both glass and steel-based specimens are tested at the ages of 15, 30, 90, and 180 days ,to evaluate the role of mortar age on the fiber-to-mortar bond behavior.

U-shape steel support is utilized for supporting the specimens (Figure 2). A mechanical clamp is used to grip the epoxy resin from the top. Also, two LVDTs with a 20 mm range and 2-µm sensibility are located at the side and in front of the epoxy block, at the vicinity of the mortar edge, to record the slip. All the tests are carried out using a servo-hydraulic system with a maximum capacity of 25 kN at a displacement rate of 1.0 mm/min.

3 Experimental Results and Discussion

3.1 Material Properties

Table 1 presents the changes of mortars' mechanical properties with age. Although both mortars show similar value for the maximum compressive strength (8.31 MPa for M1 and

9.53 MPa for M2), the peak values are reached at different times. Mortar M2 shows the maximum gain of compressive strength in the first 30 days, and after that, a slight decrement of compressive strength is observed until 180 days. Meanwhile, mortar M1 reaches its peak compressive strength in 60 days, and after that, the changes in the compressive strength are negligible.

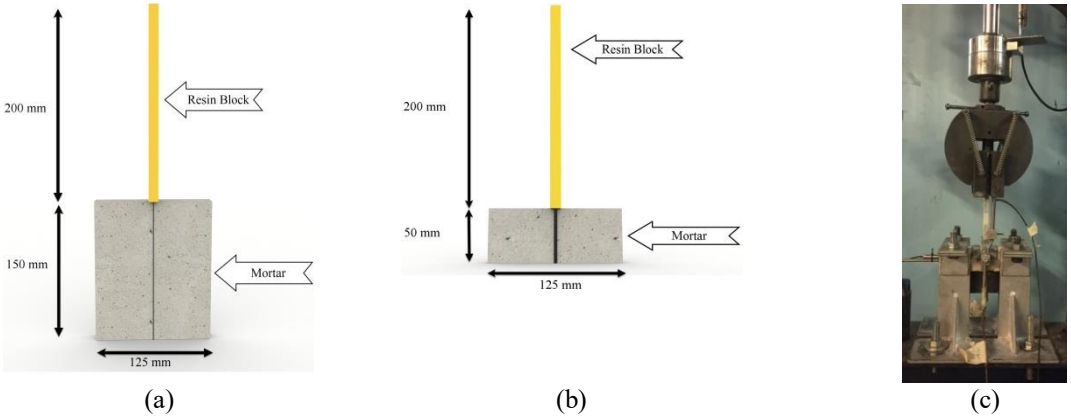

(a) (b) (c)

Figure 2. Details of pull-out specimens and test: (a) steel-based TRM; (b) glass-based TRM; (c) test setup.

Mortar M2 reaches its peak flexural strength in the first 30 days, but the flexural strength of mortar M1 increase until 180 days. As flexural strength is indirectly related to the tensile strength of the mortar, an evolutionary bond behavior should also be expected in the experimental pull-out curves until 180 days. Additionally, mortar M1 shows a higher flexural strength (6.0 MPa), in contrast to M2 (2.62 MPa), even if it has a smaller compressive strength that is an indication of a more ductile response of M1 mortar.

Table 1. Mortar mechanical properties with age.

Mortar	Test [MPa]	Mortar age [days]				
		14	28	60	90	180
M1	Compressive strength	5.91 (8)	7.07 (9)	8.31 (11)	7.84 (4)	7.46 (10)
M1	Flexural strength	4.03 (3)	4.71 (7)	5.10 (3)	4.66 (8)	6.0 (10)
M2	Compressive strength	8.76 (7)	9.53 (10)	8.81 (12)	8.89 (5)	7.48 (5)
M2	Flexural strength	1.79 (12)	2.54 (9)	2.09 (7)	2.33 (9)	2.62 (13)

Coefficients of variation (%) are provided in parentheses.

3.2 Pull-out Response

3.2.1 Steel-based TRM composite

Figure 3 and Table 2 present the evolution of the pull-out response of steel-based TRMs with time and the summary of the main characteristics of the pull-out curves of different ages.

A typical three-stage of the bond behavior of the fiber-to-mortar (linear, nonlinear, and dynamic stage) is shown by the pull-out response of steel-based TRM at all ages. The linear elastic range terminates with the first debonding at the interface occurs that leads to a concave-downward shape in the pull-put curves (D'Antino, Carrozzi, Colombi, and Poggi, 2017). Once the peak load is reached, which is corresponding to the full debonding along the embedded length, the pull-out load is dropped, because the bond force is larger than the frictional force in this system (Li, Wu, and Chan, 1995). The pull-out curves, then, show a strain hardening behavior (forming a second peak load) and then a softening response until the end of the tests.

By comparing the average curves, a slight increase in the pull-out response can be observed in the first 30 days, followed by a slight decrease until 180 days. A possible explanation for this phenomenon is due to the changes in the mechanical properties of the mortar M2 that followed a very similar trend with time. Table 2 shows the bond properties of steel-based TRM. While the toughness follows a similar trend as the peak load (increases initially and then a decrease), the slip corresponding to the first peak load is almost constant. At the same time, the initial stiffness of the pull-out curves seems to be decreasing with time.

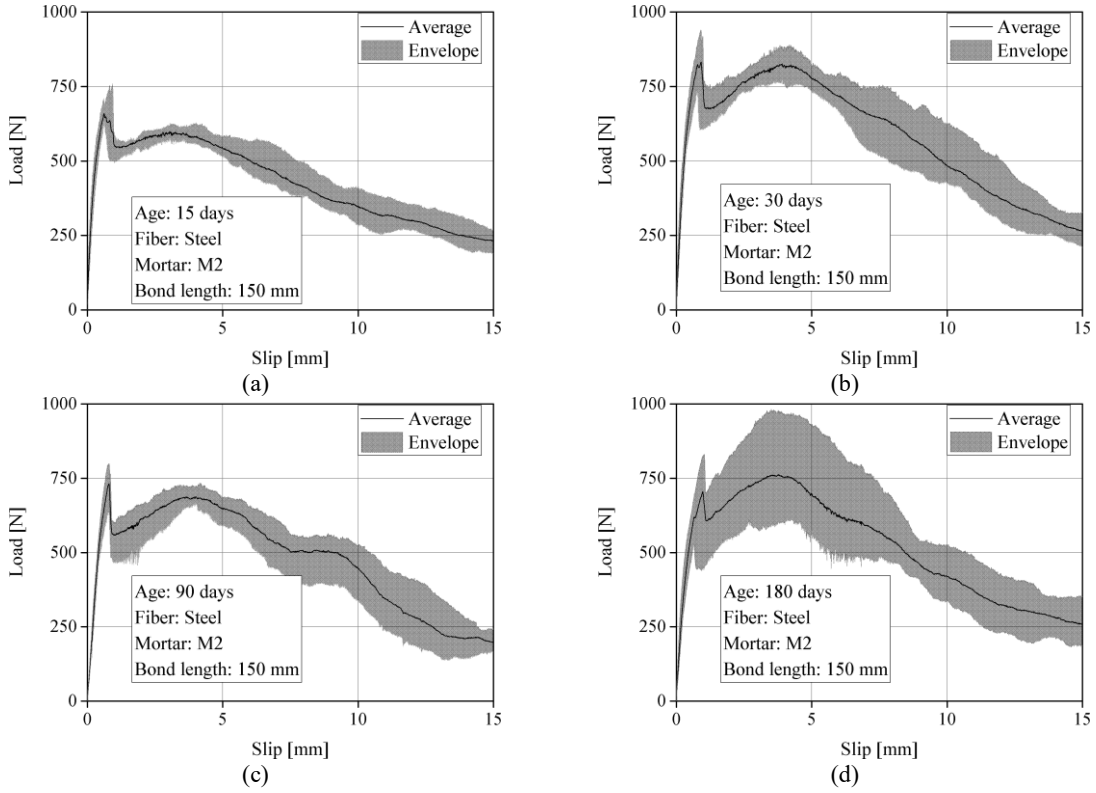

Figure 3. Envelope load-slip curves of steel-based TRM at different mortar ages: (a) 15 days; (b) 30 days; (c) 90 days; (d) 180 days .

Table 2. Effect of mortar age on the pull-out response of steel-based TRMs.

Age [days]	Slip corresponding to peak load [mm]	Peak load [N]	Toughness at a crack opening of [N.mm]			Initial stiffness [N/mm]
			1 mm	4 mm	8 mm	
15	0.8 (16)	711 (7)	511 (8)	2238 (4)	4236 (5)	1903 (19)
30	0.9 (9)	872 (9)	599 (10)	2861 (5)	5745 (6)	2076 (23)
90	0.8 (3)	741 (9)	474 (8)	2372 (7)	4747 (7)	1277 (10)
180	0.9 (16)	731 (17)	476 (16)	2581 (15)	5143 (17)	1360 (14)

Coefficients of variation (%) are provided in parentheses.

3.2.2 Glass-based TRM composite

It can be observed that the pull-out response of the glass-based TRMs shows a significant change with time, as shown in Figure 4. At the mortar ages of 15 and 30 days, after complete debonding (at peak load), a descending trend in the pull-out force can be observed. In contrast, at the age of 90 and 180 days, the pull-out force increases after complete debonding, showing a slip hardening behavior. This behavior, again, is in-line with the observed changes in the mechanical properties of mortar M1. The flexural strength of mortar M1 continuously increased until 180 days, and therefore increasing bond strength is also expected to be developed during this period.

The summary of the pull-out curves presented in Table 3 shows the slip corresponding to the peak load is relatively constant. In contrast, the peak load, toughness, and initial stiffness of the pull-out curves increase with time until 180 days.

Table 3. Effect of mortar age on the pull-out response of glass-based TRMs.

Age [days]	Slip corresponding to peak load [mm]	Peak load [N]	Toughness at a crack opening of [N.mm]			Initial stiffness [N/mm]
			1 mm	4 mm	8 mm	
15	2.6 (12)	285 (10)	154(11)	914 (10)	1778 (4)	456 (4)
30	1.9 (31)	251 (30)	156(18)	805(24)	1540(27)	815 (22)
90	2.3 (13)	379 (16)	227(9)	1727 (12)	2476 (16)	858 (22)
180	2.3 (27)	391 (12)	191 (17)	1252 (3)	2673 (9)	909 (35)

Coefficients of variation (%) are provided in parentheses.

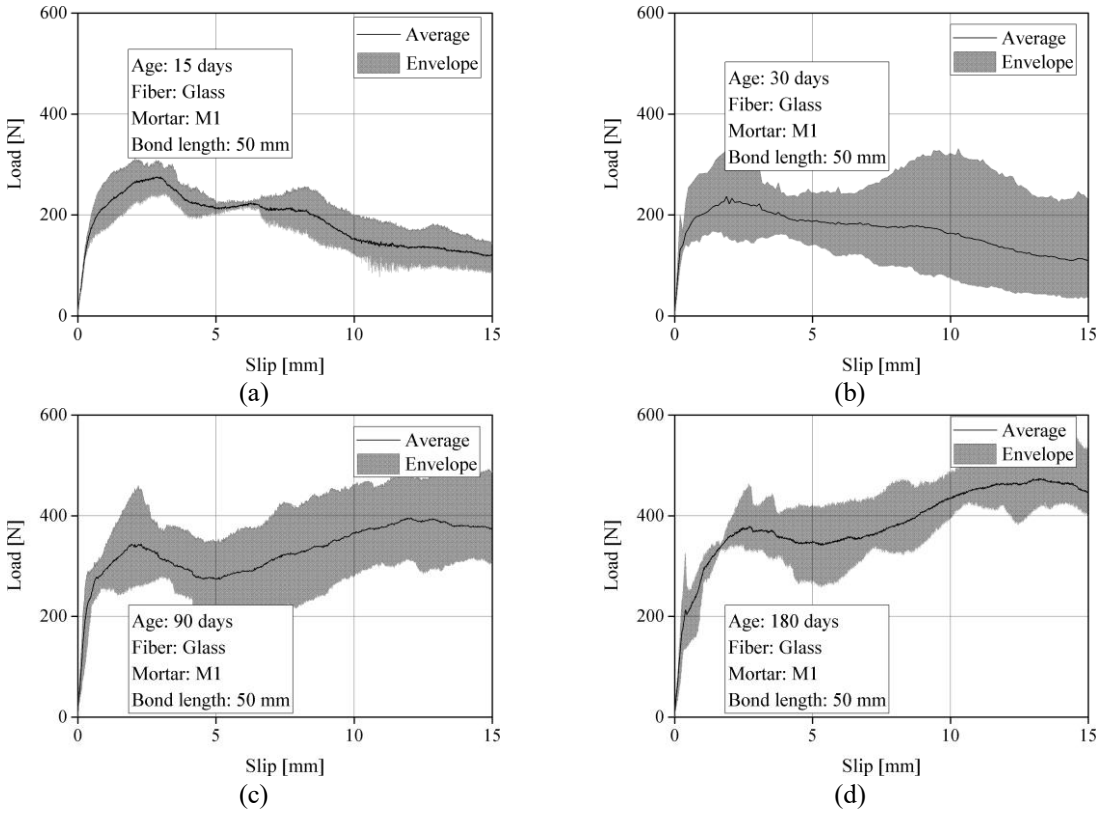

Figure 4. Envelope load-slip curves of glass-based TRM at different mortar ages: (a) 15 days; (b) 30 days; (c) 90 days; (d) 180 days .

4 Conclusions

A comprehensive experimental study is presented in this paper on the role of mortar age on the pull-out response of single fibers embedded in lime-based matrices. The following conclusions can be drawn from the obtained experimental results:

- The results show the significant effect of mortar age on the bond response. In particular, it seems that the 30 days curing period that is usually used for cementitious mortars is not suitable for lime-based mortars.
- It is difficult to propose a generic curing time for performing the pull-out tests when lime-based mortar is used as the matrix. In one of the studied mortars, 60 days of curing seemed to be sufficient for obtaining realistic bond behavior, while in the other mortar 90 days is found to be the minimum required aging time.
- The changes of flexural strength of the mortar seemed to be a good indication of the changes in the bond behavior and are suggested to be considered in investigations for estimating the suitable curing age for evaluating the mechanical properties and bond response of these systems.

Acknowledgements

This work was partly financed by FEDER funds through the Competitivity Factors Operational Programme (COMPETE) and by national funds through the Foundation for Science and Technology (FCT) within the scope of the project POCI-01-0145-FEDER-007633. The support to the first author through grant SFRH/BD/131282/2017 is acknowledged. Also, the authors would like to thank the Kerakoll Company for supplying the GeoCalce Fino mortar as well as GeoSteel G600 fibers.

ORCID

Ali Dalalbashi: https://orcid.org/0000-0003-0486-1433
Bahman Ghiassi: http://orcid.org/0000-0003-4212-8961
Daniel V. Oliveira: http://orcid.org/0000-0002-8547-3805

References

Ascione, L., De Felice, G. and De Santis, S. (2015). A qualification method for externally bonded Fibre Reinforced Cementitious Matrix (FRCM) strengthening systems. *Composites Part B: Engineering*, *78*, 497–506. doi: 10.1016/j.compositesb.2015.03.079

Carozzi, F. G. and Poggi, C. (2015). Mechanical properties and debonding strength of Fabric Reinforced Cementitious Matrix (FRCM) systems for masonry strengthening. *Composites Part B: Engineering*, *70*, 215–230. doi: 10.1016/j.compositesb.2014.10.056

D'Antino, T., Carrozzi, F. G., Colombi, P. and Poggi, C. (2017). A New Pull-Out Test to Study the Bond Behavior of Fiber Reinforced Cementitious Composites. *Key Engineering Materials*, *747*, 258–265. doi: 10.4028/www.scientific.net/KEM.747.258

Dalalbashi, A., Ghiassi, B., Oliveira, D. V. and Freitas, A. (2018a). Effect of test setup on the fiber-to-mortar pullout response in TRM composites: experimental and analytical modeling. *Composites Part B: Engineering*, *143*, 250–268. doi: 10.1016/j.compositesb.2018.02.010

Dalalbashi, A., Ghiassi, B., Oliveira, D. V. and Freitas, A. (2018b). Fiber-to-mortar bond behavior in TRM composites: effect of embedded length and fiber configuration. *Composites Part B: Engineering*, *152*, 43–57. doi: 10.1016/j.compositesb.2018.06.014

Ghiassi, B., Oliveira, D. V, Marques, V., Soares, E. and Maljaee, H. (2016). Multi-level characterization of steel reinforced mortars for strengthening of masonry structures. *Materials and Design*, *110*, 903–913. doi: 10.1016/j.matdes.2016.08.034

Leone, M., Aiello, M. A., Balsamo, A., Carozzi, F. G., Ceroni, F., Corradi, M. and Saenger, D. (2017). Glass fabric reinforced cementitious matrix: Tensile properties and bond performance on masonry substrate. *Composites Part B: Engineering*, *127*. doi: 10.1016/j.compositesb.2017.06.028

Li, V. C., Wu, H. C. and Chan, Y. W. (1995). Interfacial property tailoring for pseudo strain- hardening cementitious composites. *Adv Technol Des Fabr Compos Mater Struct Eng Appl Fract Mech, 14*. doi: 10.1007/978-94-015-8563-7_18.

Lignola, G. P., Caggegi, C., Ceroni, F., De Santis, S., Krajewski, P., Lourenço, P. B. and Zuccarino, L. (2017). Performance assessment of basalt FRCM for retrofit applications on masonry. *Composites Part B: Engineering*, *128*, 1–18. doi: 10.1016/j.compositesb.2017.05.003

Papanicolaou, C. G., Triantafillou, T. C., Papathanasiou, M. and Karlos, K. (2007). Textile-reinforced mortar (TRM) versus FRP as strengthening material of URM walls: in-plane cyclic loading. *Materials and Structures*, *40*(10), 1081–1097. doi: 10.1617/s11527-006-9207-8

Razavizadeh, A., Ghiassi, B. and Oliveira, D. V. (2014). Bond behavior of SRG-strengthened masonry units: Testing and numerical modeling. *Construction and Building Materials*, *64*, 387–397. doi: 10.1016/j.conbuildmat.2014.04.070

XV International Conference on Durability of Building Materials and Components
DBMC 2020, Barcelona
C. Serrat, J.R. Casas and V. Gibert (Eds)

Electro-Desalination of Sandstones With Cracks

Lisbeth M. Ottosen

Department of Civil Engineering, building 128, Technical University of Denmark, 2800 Lyngby, Denmark, LO@byg.dtu.dk

Abstract. *Historical stone monuments and buildings are lost due to salt induced decay. This paper deals with a method, electro-desalination (ED), in which an electric DC field is applied to the infected stones. The method utilizes that ions are transported (electromigrating) in the pore solution in the electric field. In the experimental work here, sandstone prisms were spiked with NaCl to high concentrations prior to ED. During the application of current, the Cl ions are electromigrating into a poultice at the anode, and Na ions into a poultice at the cathode. Damaged stones are often fragile and cracked, and the focus of this paper is to investigate experimentally if the salts are removed effectively from the stone parts next to a crack. In the lab experiments performed, a crack was cut half through the rectangular sandstone prisms perpendicular to the electric field. The results showed no delay on the ED process from the crack. All through the stone, very low concentrations of Na and Cl were reached. The concentration were even lower than the concentrations before the spiking. This finding of effective desalination around a crack is important, as it means that during ED, the poultice with electrodes can be placed around the cracked and fragile surfaces, and thus further damage from physical contact between poultice and fragile stone can be avoided.*

Keywords: *Salt Induced Decay, NaCl, Sandstone, Electro-Desalination, Historical Buildings.*

1 Introduction

Soluble salts cause damage to many historic stone buildings and monuments, and cultural heritage is lost. When water accesses the pore network of a stone, it may carry various salts in solution. Several mechanisms can subsequently cause crystal growth and crystallization-dissolution cycles, which can result in severe stone damage. The techniques to remove the damaging salts are few, and an overall effective method is lacking. The use of poultice materials to reduce the salt content of salt deteriorated objects is a long established technique in conservation (Sawdy-Heritage *et al.,* 2008). However, due to the complex nature of salt problems within historic structures the result of such interventions can be variable and unpredictable. The amount and depth to which salts are mobilised, and where they are transported to, is dependent on the inter-relationship between the poultice and the substrate, the drying conditions and also the initial salt distribution (Sawdy-Heritage *et al.,* 2008).

Another option is electro-desalination (ED), which is a method under development. ED is based on application of an electric DC potential gradient to the salt contaminated stone. The method utilizes that ions in the pore solution are transported by electromigration towards the electrode of opposite polarity when the electric field is applied. The electrodes are placed externally on the stone surface in electrode compartments with poultice, and the ions from the salts concentrate in the poultice during the treatment. When the poultices are removed after the ED, the ions of the salts are removed with them.

Electrolysis of water occurs at both metallic electrodes: at the anode $H_2O \rightarrow 2H^+ + ½\ O_2\,(g)$

doi:10.23967/dbmc.2020.210

+ $2e^-$ and at the cathode $2H_2O + 2e^- \rightarrow 2OH^- + H_2$ (g). As seen, pH decreases at the anode and increases at the cathode. It is necessary to neutralize the pH changes to prevent severe damage of the stone. The work by (Herinckx *et al*., 2011; Skibsted, 2013) underlined the importance of avoiding stone acidification, as in ED experiments without pH neutralization, the stones were severely damaged next to the anode. Use of a calcite rich clay poultice offers neutralization of the acidification from the anode (Rörig-Dalgaard, 2013). The calcite buffers the acid and the clay gives workability, so the poultice can have optimal contact to the stone surface during the treatment.

Previous research has shown that ED can be removed from high and damaging concentrations to very low concentrations in laboratory scale from different types of sandstones: Posta and Cotta sandstones (Ottosen and Christensen, 2012), Gotland Sandstone (Skibsted, 2013), Nexø sandstone (Pedersen *et al*., 2010), and granite (Feijoo *et al*., 2013). No limitation posed by the stone type has been reported. Also successful removal of different salts of chlorides (Ottosen and Christensen, 2012), nitrates (Skibsted *et al.,* 2013) and sulphates (Ottosen, 2016) have been obtained.

An advantage of ED over poultising is that whereas in poulticing the poultice needs to be covering the surface of the object, inclusive the most fragile parts, this is not necessary in ED. In ED, the poultice with electrodes can be placed around the fragile parts, and the electric field will distribute into the stone material. It has been shown experimentally that the salts can be removed from stone parts, which are not placed in the direct line between the electrodes, which means that e.g. carvings can be desalinated (Ottosen *et al.,* 2014 ; Feijoo *et al.,* 2017;Ottosen, 2017).

Damaged stones are often cracked, and thus it is relevant to investigate if the salts are removed efficiently around the cracks. The electric field can pass only through the moisture of the pores and in case the crack is air-filled, it acts as an insulator, which the electric field lines cannot pass. This work is an experimental investigation of the influence from a major crack on the ED process. Laboratory experiments are conducted with single sandstones, where a major crack is cut perpendicular to the electric field lines, and the salt concentration around the crack is measured after different durations of the desalination.

2 Materials and Methods

2.1 Experimental Stones

The experimental work was conducted with Gotland Sandstone. This type of stone was chosen, as it is relatively homogeneous and it is commonly used in Denmark. All sandstone pieces in this work were cut from the same block.

2.2 Measuring Techniques

For the measurement of pH, conductivity and concentration of soluble Cl and Na, the dried stone samples were grinded in a mechanical mortar. Following 10 g powder was suspended in 25 ml distilled water and agitated for 24 h. The samples settled for 10 min and pH was measured. The samples were filtered through 0.45 µm filter. Na concentrations were measured by ICP-OES. Cl concentrations were measured by ion chromatography (IC, Dionex DX-120). The concentrations for each segment was measured as single determination.

The open porosity and density of the Gotland Sandstone used in this work were determined (five replicates). Sanstone pieces of 170-190 g were dried (105 °C for 24 hours), weighed (m_{dry}), and placed in a desiccator under vacuum for approximately 3 h. After 3 h, distilled water at room temperature was led into the desiccator, so that the discs were completely submerged. Vacuum was maintained for 1 h. Hereafter, air was let into the desiccator and the submerged discs were left at atmospheric pressure overnight. The water-saturated pieces were weighed in water (m_{sw}) and in air after wiping excess water of the surface (m_{sa}). The open porosity was calculated as $(((m_{sa} - m_{dry})/(m_{sa} - m_{sw})) *100\%)$; and apparent density $(((m_{dry}*\rho_w)/(m_{sa} - m_{sw}))$, where ρ_w (970 kg/m3) is the density of water.

To have a uniform distribution of the salt prior to the experiments, the stone samples were contaminated with the salt in the lab: the stone prisms were dried at 105°C and vacuum saturated by 80 g/l solution of NaCl in a desiccator prior to the ED experiments. The dry weight of the stone prisms before vacuum saturation (m_d) and the stone weight after vacuum saturation (m_0) were measured and from these the initial water content was calculated as $(m_0 - m_d)/m_d)*100\%$.

2.3 Electro-Desalination Experiments

Four rectangular stone prisms were cut from the same stone block. The prisms were 13.5 cm x 7.5 cm x 5.5 cm. A crack was cut half way through each prism in the middle, perpendicular to the longest side (and the electric field lines) (Figure 1). The width of the void was about 1 mm.

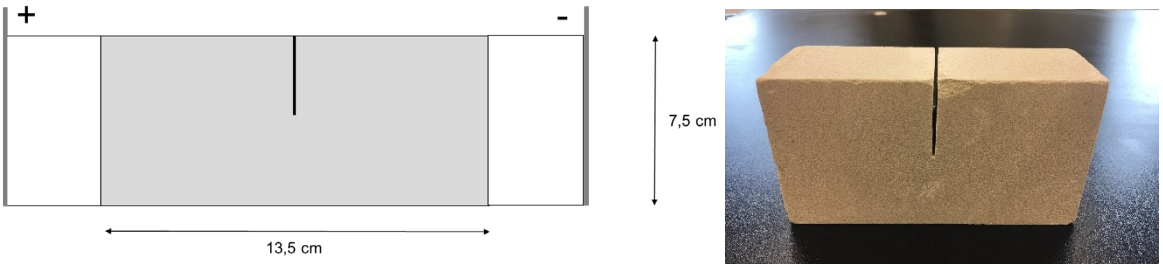

Figure 1. The setup for electro-desalination. The electrodes are placed in clay poultice on each end of the stone, and a crack is cut half into the stone perpendicular to the electric field.

Electrode compartments were placed at each end of the rectangular stone prism as illustrated in figure 1(a). For the electrode compartments a frame was folded in thin plastic to fit the surface of the stone at each side. The frames were filled with poultice; a mixture of kaolinite and CaCO3 [3] with an initial water content of 54%. Inert platinum coated electrode meshes were placed at the end of each electrode compartment. The sandstone and electrode compartments were wrapped in plastic film to hinder evaporation. A reference stone (REF) was made with no applied current. The REF stone was wrapped in plastic film for 14 days. Three ED experiments were made differing only in duration: 2, 4 and 5 weeks (ED_2, ED_4 and ED_5). A constant current of 10 mA was applied to the electrodes all through these experiments. Table 1 shows the dry weight (m_d) of the different stone prisms, the water content after the vacuum saturation and the duration of the experiments in weeks.

Table 1. REF and ED experiments. Dry weight of stone, initial water content after vacuum saturation and duration of experiment.

	Stone weight, m_d (g)	Initial water content (%)	Duration (weeks)
REF	1072	10.2	2 (no current)
ED_2	1056	10.4	2
ED_4	1084	10.5	4
ED_5	1079	9.4	5

After the REF and ED experiments, the stone prisms were segmented with hammer and chisel into 8 segments (Figure 2). The upper row of segments were named a-segments and the lower b-segments. All segments were weighed and dried (24 hours at 105°C), and the water content calculated. The dried segments were grinded in a mechanical mortar (FRITSCH – pulverisette 9) for 10 seconds. Following, 10 g powder was suspended in 25 ml distilled water and agitated for 24 h. The samples settled for 10 min and pH was measured. The samples were filtered through 0.45 µm filter. The Cl concentrations were analyzed by ion chromatography (IC, Dionex DX-120).

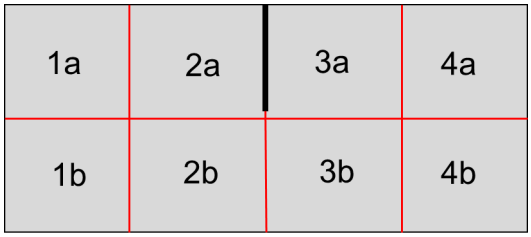

Figure 2. Segmentation of stone block after electro-desalination.

The poultices were changed every 7th day. The poultices were weighed. The Cl and Na concentrations, water content and pH were measured using the same methods as for the stone segments.

3 Results and Discussion

3.1 Characteristics of the Sandstone

The porosity of the Gotlandic sandstone used in the experimental work was 20.4% ± 0.03%, which is higher than previously reported (15%) by (Nord and Tronner, 1995). The difference shows a natural variation in the porosity of Gotlandic sandstone. Nord and Tronner (1995) reported that the grey, calcitic Gotland sandstone is composed of about 60 wt% quartz grains, cemented together by 7-10 wt% calcite, and with lower amounts of clay minerals, micas, feldspar minerals, pyrite, and glanuconite.

The concentrations of Cl and Na before and after spiking with NaCl is shown in table 2 together with pH and conductivity. The salt concentration is similar to previous investigations with the same type of sandstone and concentration of NaCl in the spiking solution (Ottosen *et al*. 2014).

Table 2. Concentrations of Na and Cl, pH and conductivity of the stone before and after spiking with NaCl.

	Na (mg/kg)	Cl (mg/kg)	Conductivity (mS/cm)	pH
Before spiking	23.3 ± 0.3	21.4 ± 4.2	0.46 ± 0.04	8.6 ± 0.04
After spiking	2520 ± 230	4200 ± 130	5.33 ± 0.16	9.1 ± 0.1

3.2 Electro-Desalination Results

The concentrations of Cl and Na in the different segments after the REF and the three ED experiments are shown in figure 3. The decrease in concentrations is clear and the average concentrations were already about halved after two weeks.

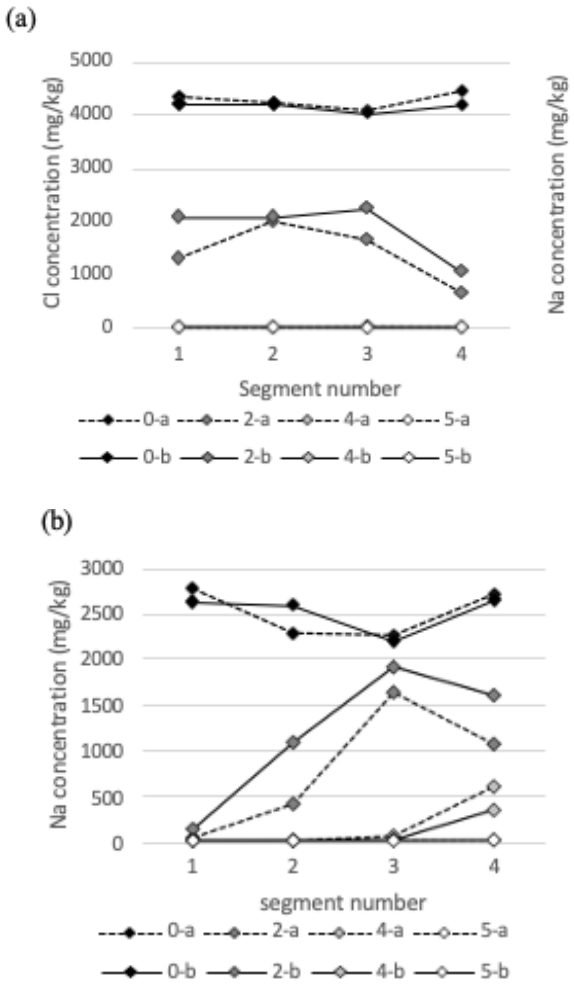

Figure 3. Concentration profiles of (a) Cl and (b) Na in the stone segments at the end of the experiments. The dotted lines are the profiles in the segment row with the crack (a-segments) and the full lines are the lower row of segments (b-segments).

The final Cl concentration in all segments in ED_4 was between 14 to 19 mg Cl/kg (figure 3), which corresponds to a reduction of more than 99.5% in comparison to the 4200 mg Cl/kg, which was the initial concentration in the ED experiments (Table 2, concentration after spiking). The final Cl concentrations were even lower than the concentration in the stone before the spiking (21.4 mg Cl/kg; table 2), and the Cl removal was successful all through the stone. Thus, the final Cl concentration in the segments next to the crack was not negatively influenced by the crack.

The Na removal was not finished in ED_4 since the concentration was still 340 and 600 mg Na/kg in the segments closest to the cathode, 4a and 4b, respectively (figure 3). Thus, the removal of Na was slightly slower than the removal of Cl. However, within one week longer treatment, the Na removal was successful, as in ED_5 the concentrations in the segments were between 7 and 11 mg Na/kg, which was also less than before the spiking (2520 mg Na/kg).

The successful desalination was supported by the conductivity, which in the segments after ED_5 was 0.096 ± 0.007 mS/cm was also less than the 0.46 ± 0.04 mS/cm prior to the spiking.

The pH in the segments after ED_5 was between 9.7 and 10.3. Since the initial pH was 9.1 (table 2), the pH was increased all through the stone, and the acidic front was thus prevented in developing into the stone by the poultice.

In summary, Na and Cl were removed to very low concentrations in all stone segments during the ED treatment and after 5 weeks, the concentrations were lower than before the stones were spiked. Thus, the crack did not prevent successful desalination.

Results from experiment ED_5 are in figure 4 as the accumulated moles of Cl removed into the poultice at the anode and Na into the poultice at the cathode. The number of moles were calculated from concentrations measured in the poultices when they were changed every 7 day. In figure 4, the electrical resistivity is shown as well (calculated as voltage divided by current). During the first approximately three weeks, the removed mass of Cl and Na is almost linear with the duration of the treatment, and in this period, the electrical resistivity is very low. After about 3 weeks, the removal rate decreased as result of a lower concentration of the ions in the stone. After a little more than 3 weeks of treatment, it is also seen that the electrical resistivity increases dramatically corresponding to the low level of removal indicating lower salt content left in the stone. Thus, the time for the desalination to be finished is indicated by an increase in electrical conductivity.

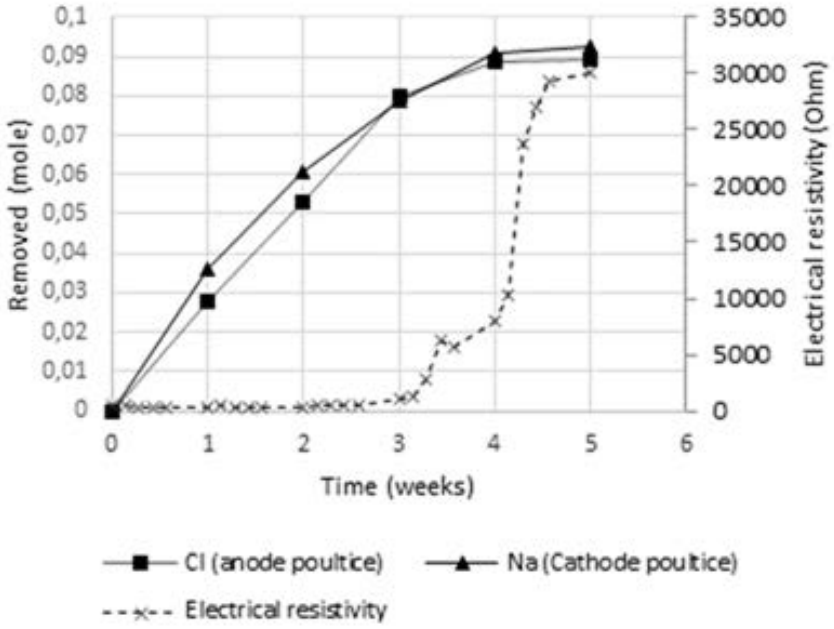

Figure 4. Number of moles Cl removed into in the anode poultice and Na into the cathode poultice over time in experiment ED_5. The electrical resistivity over time in ED_5 is shown as well.

4 Conclusions

Electro-desalination was experimentally shown to effectively remove Na and Cl from stone parts next to a crack. A crack was cut half through rectangular sandstone prisms (13.5 cm x 7.5 cm x 5.5 cm) and electrode compartments were placed in each end of the prism. The prisms were spiked with NaCl to high concentrations prior to the electro-desalination, and after 5 weeks of treatment, the salts were removed again and even to concentrations lower than present in the stone prior to the spiking. The concentrations in the stone next to the crack were as low as in the other parts of the stone, and thus the interference of the crack on the overall desalination is minor.

ORCID

Lisbeth M. Ottosen: https://orcid.org/0000-0001-7756-382X

References

Feijoo, J., Matycak, O., Ottosen, L.M., Rivas, T. and Nóvoa, X.R. (2017). Electrokinetic desalination of protruded areas of stone avoiding the direct contact with electrodes. *Materials and Structures*, 50(82), 15.

Feijoo, J., Nóvoa, X.R., Rivas, T., Mosquera, M.J., Taboada, J., Montojo, C. and Carrera, F. (2013). Granite desalination using electromigration. Influence of type of granite and saline contaminant. *Journal of Cultural Heritage,14,* 365–376.

Herinckx, S., Vanhellemont, Y., Hendrickx, R., Roels, S. and De Clercq, H. (2011). Salt removal from stone building materials using an electric field. In: *Proceedings from the international conference on salt weathering on building and stone sculptures,* I. Iannou & M. Theodoridou (eds.), Cyprus 19-22 October, 357-364.

Nord, A.G. and Tronner, K. (1995). Effect of acid rain on sandstone: The Royal Palace and the Riddarholm Church, Stockholm. *Water Air and Soil Pollution, 85*, 2719-2724.

Ottosen, L.M. (2016). Electro-desalination of sulfate contaminated carbonaceous sandstone – risk for salt induced decay during the process. In Science and Art: A Future for Stone: *Proceedings of the 13th International Congress on the Deterioration and Conservation of Stone.* Eds. John J. Hughes, Torsten Howind, 2, 897-904.

Ottosen, L.M. and Andersson, L.H. (2017). Electrode placement during electro-desalination of NaCl contaminated sandstone – simulating treatment of carved stones. SWBSS 2017, *4th International Conference on Salt Weathering of Buildings and Stone Sculptures.* Potsdam, Germany, 20-22, 150-157.

Ottosen, L.M. and Christensen, I.V. (2012). Electrokinetic desalination of sandstones for NaCl removal - Test of different clay poultices at the electrodes. *Electrochimica Acta. 86*, 192– 202.

Ottosen, L.M., Skibsted, G. and Præstholm, T. (2014). Electrodesalination of sandstones with irregular shapes and uneven distribution of salts. Proceedings from *SWBSS2014 3rd International Conference on Salt Weathering of Buildings and Stone Sculptures*. Ed. H. De Clercq, 405-420.

Petersen, G., Ottosen, L.M. and Jensen, P.E. (2010). The possibility for using electrokinetics for desalination of sandstone with low porosity. Proceedings from *8th fib International PhD Symposium in Civil Engineering.* Kgs. Lyngby, Denmark, June 20-23, 455-460.

Rörig-Dalgaard, I. (2013). Development of a poultice for electrochemical desalination of porous building materials: desalination effect and pH changes. *Materials and Structures, 46*(6), 959-970.

Sawdy-Heritage, A. M., Heritage, A. and Pel, L. (2008). A review of salt transport in porous media : assessment methods and salt reduction treatments. *In Salt weathering on buildings and stone sculptures* (SWBSS), 22 – 24, Copenhagen, Denmark.

Skibsted, G. (2013). Electrochemical desalination of limestone spiked with Na2SO4 – importance of buffering anode produced acid. Paper E in PhD thesis Matrix changes and side effects induced by electrokinetic treatment of porous and particulate materials, Technical University of Denmark.

Skibsted, G., Ottosen, L.M., Jensen, P.E. and Paz-Garcia, J.M. (2015). Electrochemical desalination of bricks - Experimental and modeling. *Electrochimica Acta, 181*, 24-30.

XV International Conference on Durability of Building Materials and Components
DBMC 2020, Barcelona
C. Serrat, J.R. Casas and V. Gibert (Eds)

Freeze-Thaw Deicing salt Attack on Concrete: Towards Engineering Modelling

Charlotte Thiel, Vadym Lomakovych and Christoph Gehlen

Centre for Building Materials, Technical University of Munich, Franz-Langinger-Str. 10, 81245 Muenchen, Germany, charlotte.thiel@tum.de

Abstract. *In order to reduce carbon dioxide emissions, the construction sector is increasingly using clinker-reduced concretes. Concrete with high amounts of ground granulated blast furnace slag (GGBFS) show increased durability performance in certain environmental conditions compared to concrete with Ordinary Portland cement (OPC). However, in laboratory studies, concrete with GGBFS show an increased initial scaling rate in comparison with OPC concrete. Changing weather conditions and high relative humidities > 70 % in field lead to less carbonation and thus, to a better freeze-thaw deicing salt resistance (FTDSR). Therefore, the current lab performance test penalizes GGBFS concrete. This contribution studied the impact of carbonation and intermittent dry periods on FTDSR of GGBFS concrete compared to that of OPC concrete. It could be shown that for concrete with OPC, intermittent dry periods lead to an accumulation of salt in the near surface, which causes a reduction of the scaling. GGBFS concrete, on the other hand, shows an opposite behavior: carbonation causes an increase in scaling after the dry period. GGBFS concrete samples with CO_2-free pre-storage show the lowest scaling of all samples investigated. A better simulation of the behavior of GGBFS concrete could lead to economical as well as optimized solutions for the local environment conditions and enable the large-scale use of more environmentally-friendly concretes. Therefore, by taking the effect of carbonation and intermittent dry periods into account in a simple engineering model, the prediction of concrete scaling under consideration of real climatic conditions is possible in an eco-efficient manner.*

Keywords: *Freeze-Thaw Deicing Salt Attack, Carbonation, Durability, Service Life Prediction, Combined Attack.*

1 Introduction

With the increased use of clinker-reduced concretes, the evaluation of durability design methods remains a topical issue. There are mainly three design strategies:

- Deemed to satisfy rules: Avoidance of damage by complying with the requirements from the exposure classes, and
- Lab-Performance concept: Compliance tests with accepted limit criteria provide a yes/no decision on the suitability of a material for a certain environment; see (Thiel and Gehlen, 2018).
- Performance based durability design: The condition of a structure remains with a certain reliability below selected limit states (Gehlen, Schießl and Schießl-Pecka, 2008.; fib, 2006).

Performance based durability design can be further divided into fully probabilistic approaches, and the partial safety approach derived from the probabilistic concept. Probabilistic service life design require deterioration-time-laws that account for statistical uncertainty. An important input parameter is the material resistance, which is usually determined in compliance tests in the laboratory, (Thiel and Gehlen, 2018). Those engineering models should be as simple as possible in order to promote acceptance. In addition, different attack intensities, i.e. different

climatic conditions should be realistically displayed. They should also be flexible so that new materials, new knowledge or new situations (*e.g.* climate change) can be accounted for. The use of performance based design concepts offer the following advantages

- Quantification of deviations between execution and planning
- Optimized maintenance strategies through service life prediction
- Optimized choice of material as well as curing time and type
- Simplified use of new building materials through proof of performance

Djuric successfully combined the critical saturation model from Fagerlund (Fagerlund, 2004) with the transport mechanism of the micro ice lens pump (Setzer, 1999) for pure freeze-thaw attack, thus developing a model for the evolution of internal structural damage (Djuric, 2017). For the durability assessment of structural components under combined freeze-thaw deicing salt attack (FTDSA), different approaches exist. For example, a simple performance concept based on the CDF method was proposed by Guse (Guse, 2009). The glue-spall model developed by Valenza (Valenza and Scherer, 2007) is able to explain most observations during FTDSA. An easy and structured factor approach was proposed by Sarja *et al.* (Sarja and Vesikari, 1996) and further developed by Lowke *et al.* (Lowke and Brandes, 2008). Currently, Müller *et al.* (Mueller; Ludwig and Erhardt, 2019) are combining the cryogenic suction model with frost suction in order to model the scaling evolution under FTDSA.

However, evidence of large-scale practical applications of these concepts is still missing. The aim of this contribution is to demonstrate, by means of practical experiments, how the strongly varying attack intensity under field conditions can be taken into account.

2 Materials and Methods

Two concrete mixes using quarzitic sand and gravel were produced, Table 1. C1 contained Ordinary Portland Cement (OPC) with the European label CEM I 42.5 R, while C2 labelled CEM III/B 42.5 N contained 75 % ground granulated blast furnace slag (GGBFS). For carbonation to occur, a rather high w/b-ratio of 0.55 was used. Therefore, the concrete composition is neither XF2 nor XF4 conform, see (DIN 1045-2:2008-08).

Table 1. Concrete composition, air content and compressive strength.

	C1	C2
Binder type	OPC	GGBFSC
Binder amount (kg/m³)	320	320
w/b-ratio	0.55	0.55
Sand + Gravel (kg/m³)	1732	1724
Air content	1.9	2.0
28d compressive strength	42.5	38.5

Entrained air is the dominant factor in ensuring high FTDSR for OPC based systems (Powers, 1949). However, Auberg showed that the FTDSR of concrete with GGBFS ≥ 58% in the cement was largely unaffected by entrained air voids (Auberg, 1999). Furthermore, entrained air is not required in the exposure class XF2. As this contribution intends to exploit the potential of non-entrained concrete more effectively, no air-entraining agent was used. Carbonation leads to increased initial scaling and is the dominant parameter for concrete with

GGBFS cement. Ludwig justified this observation with the coarsening of the pore structure due to the formation of metastable aragonite and vaterite, which are dissolved by FTDSA. 25 cubes (edge length 150 mm) were cast against PTFE slides, immediately covered with moist cloth and stored at 20±2°C. After demoulding at an age of 1 d, the samples were stored further 6 d under water. Then the samples were cut according to the CDF method (DIN CEN-TS 12390-9:2017-05) and divided in five different series of five samples each, Fig. 1.

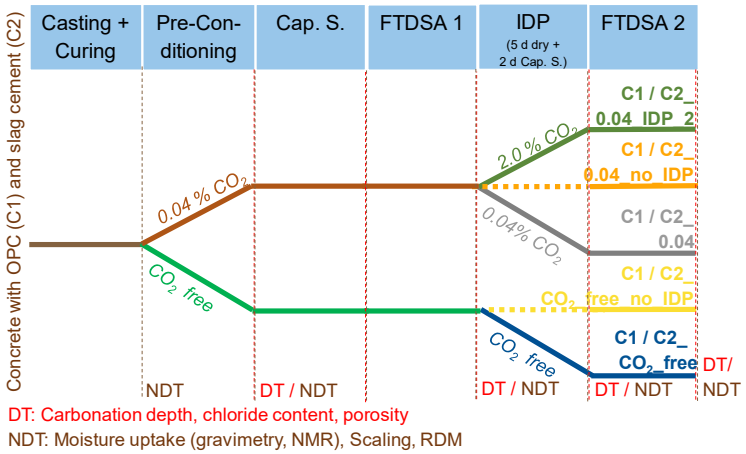

Figure 1. Overview of experimental program (FTDSA: Freeze-thaw deicing salt attack, Cap. S.: Capillary Suction; IDP: intermittent dry period, DT: destructive testing, NDT: non-destructive testing, RDM: relative Young's modulus).

Three series were stored according to the CDF method at 20±2°C and 65±2 % RH and natural CO_2 content of 0.04±0.005 % by vol. Two series were preconditioned under the same temperature and humidity conditions but in argon flooded chambers creating a CO_2 free atmosphere. All samples were exposed to a seven days period of capillary suction followed by freeze-thaw cycles in 3 % NaCl solution. The setup followed the guidelines of the CDF method, however the temperature cycle was changed. In order to reduce damage, the minimum temperature was increased to -10°C, which is closer to field situation in Germany, see (Siebel *et al.*, 2005). Here, the holding times remained constant but cooling and heating rate were lowered from 10 K/h to 7.5 K/h. Before, during and after FTDSA nondestructive tests as well as destructive tests characterized the evolution of damage, Table 2. For porosity measurements, the samples were manually broken, immediately exposed to isopropanol for 12 - 24 h and then oven dried at 40°C for 24 ± 2 h.

Table 2. Experimental methods.

Test	Goal	Device	Reference
Modified CDF (-10°C): Scaling, Relative Young's Modulus (RDM), solution uptake	Determination of scaling rate and possible relation to moisture uptake	Chamber, Balance, US-equipment (Pundit)	(DIN CEN-TS 12390-9:2017-05)
Carbonation depth (colour indicator spray test)	Determination of the effect of carbonation	Spray bottle with 1% phenolphthalein in 70% ethanol	(RILEM CPC-18, 1988)
Mercury Intrusion Porosimetry (MIP)	Determination the effect of carbonation and FTDSA on pore structure	AutoPore III, hammer for crushing	(Lomakovych, V., 2018)

3 Results and Discussion

Fig. 2 shows scaling, moisture uptake and RDM of the concretes. Especially the accelerated carbonation leads to a five times higher scaling rate for C2. The orange line (C1/2_0.04_no_IDP) represents the standardized procedure (DIN CEN-TS 12390-9:2017-05), which is quite in the middle of the different series. Despite the significant effect of the different storage conditions, the carbonation depth in general was very low. Thus, Table 3 shows only the carbonation depth of the series with which a color change occurred at all. For the C1 samples, for example, only the surface was usually uncolored, while the carbonation depth for the C2 was 0.1 mm, which disappeared in the course of the 14 freeze-thaw-cycles (FTCs). No carbonation was detected before the intermittent dry period (IDP) indicating that the carbonated layer scaled off.

Table 3. Carbonation depth (mm).

Series	Exposure time (d)			
	0 (before FTC)	7 (after 14 FTC)	14 (after either 28 FTC or after IDP)	21 (after 28 FTC
C1_0.04_IDP_2	0.0*	0.0	0.1	0.0
C2_0.04_IDP_2	0.1	0.0	0.4	0.0
C2_0.04	0.1	0.0	0.0*	0.0
C2_0.04%_no IDP	0.1	0.0	0.1	0.0

*Surface was colorless (carbonation depth < 0.1 mm)

The solution uptake shown in Fig. 2 middle correlates neither with the external damage nor with the drop of the RDM (bottom). After an IDP, the samples very quickly reabsorb moisture; however, for all series the total solution uptake remains below the level of the continuously exposed series. The RDM of the C1 only decreases for samples that have not been dried in the meantime ("no_IDP"). The high scatter of the reference series (C1/2_0.04_no_IDP) is most likely due to detaching of the sealing of two samples. This is also reflected in the RDM.
C2 did not show any significant changes in RDM. This could be due to the finer pore structure,

Fig. 3. C1 has a lower total porosity before and after the FTDSA compared to C2.

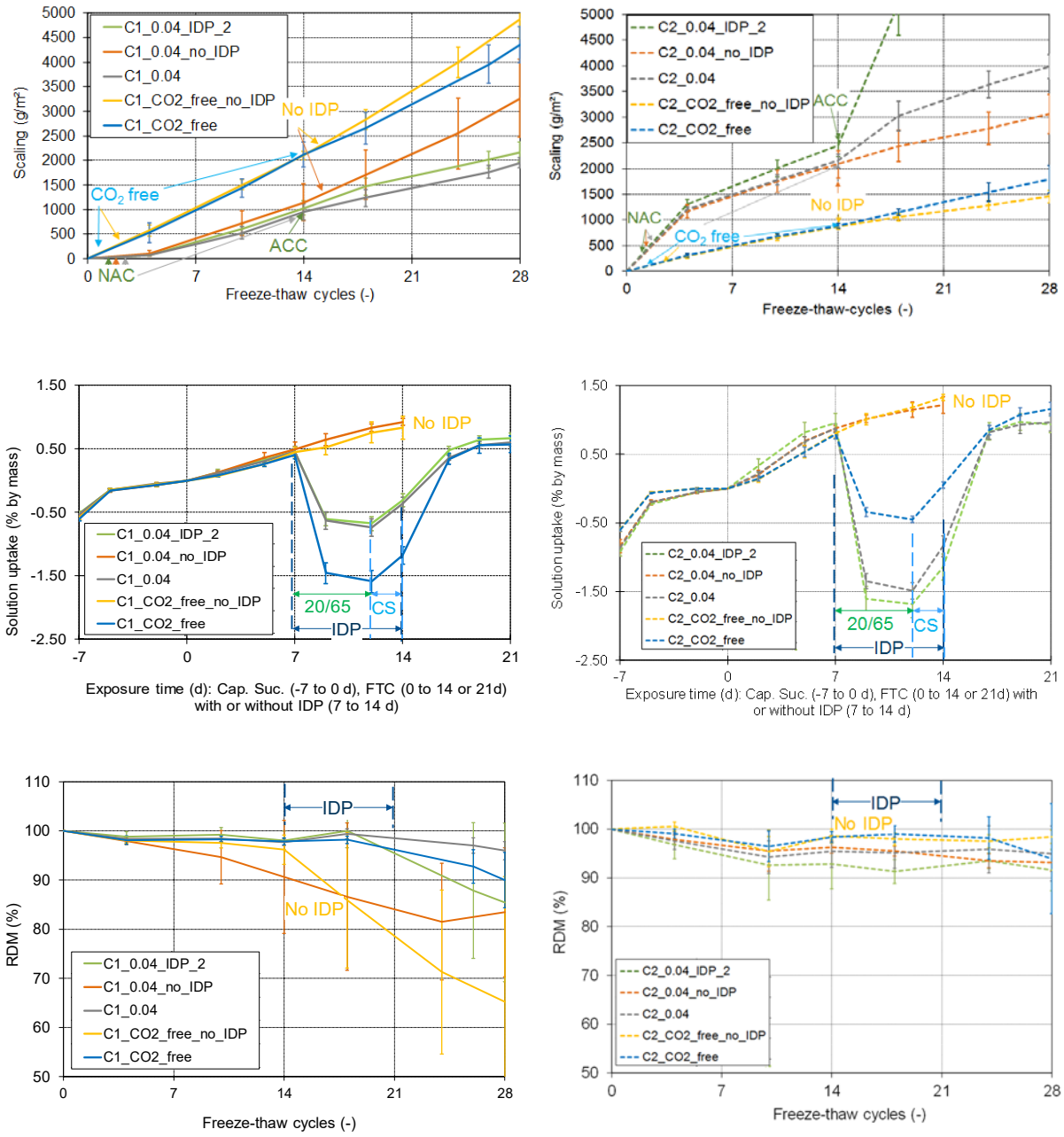

Figure 2. Top: Scaling of C1 (left) and C2 (right), middle: solution uptake of C1 (left) and C2 (right) (note: x-axis starts with dry state before capillary suction and represents the exposure time); bottom: Relative Young's modulus of C1 (left) and C2 (right). (NAC: Natural Carbonation; ACC: Accelerated Carbonation, CS: Capillary suction).

In all cases, FTDSA led to an increased total porosity. Note that only concrete exposed to three weeks of natural carbonation was measured as "before FTDSA". The carbonation front was already scaled off which explains why the well described coarsening of the pore structure

due to carbonation in C2 was not found here. C1_0.04_no_IDP had the highest total porosity and a clear increase in the capillary pore range. This clearly indicates micro-cracking which is also confirmed by the RDM (Fig. 2 middle left).While a coarsening of the pore structure occurred for C1, the pore structure became finer in all C2 series, Fig. 3. This is most likely due to ongoing hydration. To simplify matters, if the carbonated surface layer is scaled off, GGBFS concrete show higher FTDSR than OPC concretes with otherwise identical composition. However, IDPs can cause the exposed surface layer to carbonate again, resulting in high initial scaling, corresponding to the carbonation depth. With OPC the behaviour is reversed. This shows that a test according to 28d is not sufficient to describe the damage behaviour in practice and that it is absolutely necessary to consider the age and the degree of carbonation and hydration.

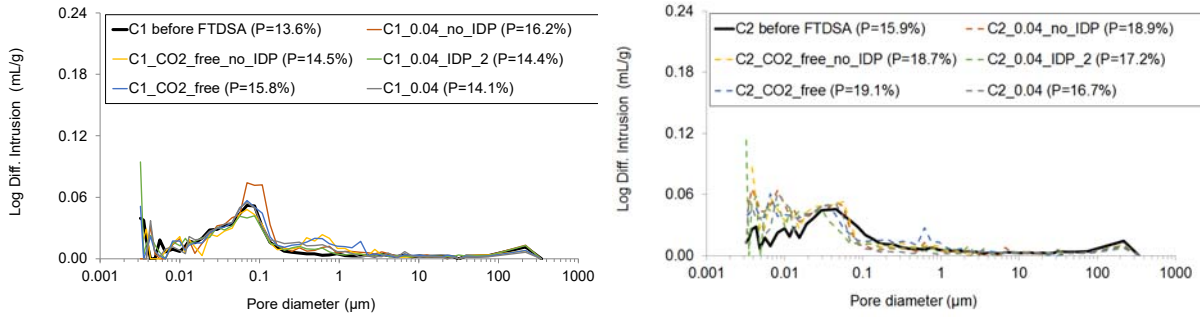

Figure 3. Pore size distribution and total porosity (P) of C1 (left) and C2 (right) before and after FTDSA.

The following options are available for considering our findings when designing or maintaining structural components exposed to FTDSA:

- Deemed to satisfy rules: Further subdivision of the exposure classes XF2 and XF4 according to the expected time in which a critical saturation occurs.
- Performance based durability design: Implementing the effect of IDPs and carbonation on scaling rate in an engineering models

4 Engineering Model

For chloride-induced corrosion as well as for carbonation validated probabilistic models exist (Gehlen, 2000). For carbonation induced corrosion, the effect of changing moisture conditions is taken into account by a parameter for considering the effect of micro-climatic conditions (relative humidity) and a parameter for considering the macro-climatic conditions (time of wetness and probability of wind-driven rain for vertical components. A similar procedure could be used for scaling due to FTDSA: The scaling rate over time $s_r(t)$ can be described by including the initial scaling rate and a later scaling rate determined in a lab performance test. The initial scaling rate $s_{r,ini}$ accounts for the effect of carbonation while the later scaling rate $s_{r,prog}$ represents the evolution of scaling of the uncarbonated material under damage-relevant environment. The environment only leads to scaling when sufficient moisture, rather low chloride content and a minimum Temperature below - 5°C are present at the same time. This is included in the environment factor f_e, which depends on the number of damage-relevant freeze-thaw-cycles in one winter period as well as on the outer salt concentration and the minimum

temperature. As the resistance of the concrete is affected by curing, the curing factor f_c is also introduced, Equation 1.

$$s_r(t) = (s_{r,ini} + t \cdot s_{r,prog}) \cdot f_c \cdot f_e \cdot f_a \quad (1)$$

This approach allows a weighting of the different scaling rates. The exact statistical distributions as well as dependencies need to be quantified in future. Moreover, suitable limit states need to be defined. Scaling not only leads to visual defects, it also reduces the concrete cover. Cracking reduces mechanical performance and might accelerate other mechanisms relevant to durability. Therefore, a much lower scaling depth than the concrete cover is certainly tolerable.

5 Conclusions and Outlook

FTDSA is very versatile. It strongly depends not only on the material resistance but also on the macro- and micro-climatic conditions. Recent investigations (Aßbrock *et al.*, 2019) showed that for most European locations, freeze-thaw deicing salt attack (FTDSA) is milder than displayed in laboratory tests. Consequently, there is a need for eco-efficient and economic methods to design and maintain structures under FTDSA despite the current deemed to satisfy rules. The most important findings of this contribution are summarized as follows:

- Damage evolution strongly depends on the climatic conditions. The scaling rate can change considerably for structural components that can dry in field during periods without precipitation.
- For concrete with OPC, the scaling rate was reduced by intermittent dry periods with and without carbonation. The main reason for the reduction of the scaling rate is probably salt crystallization, which should be further investigated.
- Carbonation was the dominant influencing parameter for concrete with GGBFS. Here, after an IDP concrete with GGBFS will always exhibit a new increased initial scaling rate until the carbonated layer is scaled off. Afterwards, the scaling rate is lower than for concrete with OPC. Concretes with high amount of GGBFS could be used in building components that are exposed to low carbonation (few dry periods, high relative humidity).
- Palecki (Palecki, 2005) and others found a correlation between inner damage and moisture uptake for freeze-thaw attack without deicing agents. This correlation could not be confirmed for FTDSA. Although concrete with GGBFS absorbed more solution than concrete with OPC, the finer pore structure caused only minor changes in the RDM while concrete with OPC showed a significant drop in RDM.
- IDPs significantly reduce the occurrence of inner damage.
- A new concept was proposed to consider the effect of real weather data and include the effect of carbonation. With the help of this, a weighting of the different scaling rates of the carbonated and non-carbonated layers would be possible.
- Taking into account the actual performance of the material as well as the actual expected intensity of attack would enable more economic and eco-efficient design of concrete structures.

ORCID

Charlotte Thiel: https://orcid.org/0000-0002-0092-468X
Vadym Lomakovych: -
Christoph Gehlen: https://orcid.org/0000-0002-1214-3960

References

Aßbrock, O. et al. (2019). Schlussbericht zum AiF-Forschungsvorhaben 15214 BG „Verbundforschung Frost- und Frost-Tausalz-Widerstand von Beton unter besonderer Berücksichtigung der verwendeten Gesteinskörnungen“. https://www.transportbeton.org/fileadmin/transportbeton-org/media/Branche/pdf/2019-05-21-Frostwiderstand_Gesteinskoernung_im_Beton_Schlussbericht_gesamt_15214_BG_online.pdf, downloaded on 11/20/2019.

Auberg R. (1999). *Zuverlässige Prüfung des Frost- und Frost-Tausalz-Widerstands von Beton mit dem CDF- und CIF-Test.* Doctoral thesis. Universität Essen. Shaker Verlag.

DIN 1045-2:2008-08 Concrete, reinforced and prestressed concrete structures - Part 2: Concrete - Specification, properties, production and conformity - Application rules for DIN EN 206-1. Beuth. dx.doi.org/10.31030/1453177

DIN CEN-TS 12390-9:2017-05. Testing hardened concrete - Part 9: Freeze-thaw resistance with de-icing salts - Scaling; German version CEN/TS 12390-9:2016. Beuth. dx.doi.org/10.31030/2649732

Đuric, Z. (2017). *Sättigungsverhalten und Schädigung von Zementstein bei Frostbeanspruchung*. KIT Karlsruhe. Institut für Massivbau und Baustofftechnologie (IMB). DOI: 10.5445/IR/1000079299

Fagerlund, G. (2004). A Service Life Model for International Frost Damage in concrete. TVBM-3119, Lund, Institute of Technology, Division of Building Materials.

Gehlen, C. (2000). *Probabilistische Lebensdauerbemessung von Stahlbetonbauwerken : Zuverlässigkeitsbetrachtungen zur wirksamen Vermeidung von Bewehrungskorrosion.* Doctoral thesis. Aachen, Technische Hochschule.

Gehlen, C., Schießl, P. and Schießl-Pecka, A. (2008). Hintergrundinformationen zum Positionspapier des DAfStb zur Umsetzung des Konzepts von leistungsbezogenen Entwurfsverfahren unter Berücksichtigung von DIN EN 206-1 , Anhang J , für dauerhaftigkeitsrelevante Problemstellungen. *Beton- und Stahlbetonbau,* 840 -851. doi.org/10.1002/best.200808230

Guse, U. (2009). Frost- und Frost-Taussalz-Prüfverfahren und ihre Übertragbarkeit. *Symposium Dauerhafter Beton - Grundlagen, Planung und Ausführung Bei Frost- und Frost-Taumittel-Beanspruchung*, 43–56. Karlsruhe: Universitätsverlag Karlsruhe.

fib (International Federation for Structural Concrete) (2006). MC-SLD:2006. Model Code for Service Life Design. In *model code Bulletin 34*.

Lomakovych, V. (2018). *Einfluss der Carbonatisierung und Trockenperio-den auf die Abwitterung von Beton unter Frost-Tausalz-Beanspruchung*. Technical University of Munich.

Lowke, D. and Brandes, C. (2008). Prognose der Schädigungsentwicklung von Betonen bei einem Frost-Tausalz-Angriff. *8. Münchner Baustoffseminar, cbm TU München*.

Ludwig, H.-M. (1996). *Zur Rolle von Phasenumwandlungen bei der Frost- und Frost-Tausalz-Belastung von Beton.* Doctoral thesis. Bauhaus-Universität Weimar.

Müller, M.; Ludwig, H.-M. and Ehrhardt, D. (2019). Frost-Tausalz-Angriff auf Beton: Mechanismen und Schadensmodelle. *Beton- und Stahlbetonbau 114(1)*. https://doi.org/10.1002/best.201800096

Palecki, S. (2005). *Hochleistungsbeton unter* Frost-*Tau-Wechselbelastung : Schädigungs- und Transportmechanismen.* Doctoral thesis. Universität Duisburg-Essen.

Powers, T. C. (1949). *The air requirements of frost-resistantconcrete.* Proceedings of the Twenty-Ninth Annual Meeting of the Highway Research Board Held at Washington, D.C.

RILEM CPC-18 (1988). Measurements of hardened concrete carbonation depth. *Materials and Structures, 21, 453-455.*

Sarja, A. and Vesikari, E. (1996). Durability Design of Concrete Structures, *Rilem Report 14*, Taylor and Francis, London and New York.

Setzer, M.J. (1999). Mikroeislinsenbildung und Frostschaden. *Werkstoffe im Bauwesen - Theorie und Praxis. Eligehausen (edts), Ibidem Verlag, Stuttgart.* 394-413.

Siebel *et al.* (2005). Sachstandbericht Übertragbarkeit von Frost-Laborprüfungen auf Praxisverhältnisse. Heft 560 der Schriftenreihe des Deutschen Ausschuss für Stahlbeton. Beuth. Berlin. 2005. ISBN 3-410-65760-6.

Thiel, C. and Gehlen, C. (2018). Compliance testing for probabilistic durability design purposes. Proceedings of The 6th International Symposium on Life-Cycle Civil Engineering (IALCCE), Ghent, Belgium.

Valenza, J.J., Scherer, G.W. (2007). A Review of Salt Scaling: II. Mechanisms. *Cement and Concrete Research, 37*, 1022-1034. doi.org/10.1016/j.cemconres.2007.03.003.

XV International Conference on Durability of Building Materials and Components
DBMC 2020, Barcelona
C. Serrat, J.R. Casas and V. Gibert (Eds)

FRP Reinforcement for Concrete Frame Buildings at Mexico City Around 1900 to 1960

Juan M. García Garduño[1], Perla R. Santa Ana Lozada[2] and Lucia G. Santa Ana Lozada[3]

[1] Faculty of Architecture, Universidad Nacional Autónoma de México, Av. Universidad 3000, Ciudad de México, México, manuel.tolentino@live.com

[2] Faculty of Architecture, Universidad Nacional Autónoma de México, Av. Universidad 3000, Ciudad de México, México, psal@unam.mx

[3] Faculty of Architecture, Universidad Nacional Autónoma de México, Av. Universidad 3000, Ciudad de México, México, lsl@unam.mx

Abstract. *Mexico City is located at a seismic region with a complex soil. That condition had an impact on buildings and their conservation; it requires to know their structural state to control strain and cracks that could cause severe damages. To accomplish that objective this research contemplates the evaluation of concrete elements to propose an alternative to restraint antique concrete deformations using FRP system.*

Keywords: *Architecture, Reinforced Concrete, Plastic Flow, Textile Composites, Carbon Fiber.*

1 Introduction

Construction has always been complicated as the city is located on a seismic region (Servicio Geológico Mexicano, 2017), which also has a subsistence ground (Marsal J. and Mazari, 2016); specially during 1940, when technical information about the city complex soil was starting to be studied, and new constructive methods were developed for skyscrapers. Specialized research on the geotechnical and seismic engineering started in 1955 and 1962, respectively; twelve years after the Mexico City building code was used for the construction, about 1942- 1966. Thus, all RC structures built before 1960 have a probability of exhibiting some damage. The aging of RC structures could be accelerated due to soil and seismic stresses. Permanent axial load causes plastic flow on RC (Park and Paulay, 1988), creating disbalance between the load/stress distribution of the structural system and producing fissures, structural cracks, or increasing the one that exists (Muñoz and Mendoza, 2012). Another critical factor for RC frames built on seismic areas is ductility of columns, which is provided by reinforcing bars (rebars), but buildings constructed before 1970 are considered as non-ductile (Al-Mahaidi and Kalfat, 2018) while their columns have not enough rebars to accomplish with current regulation codes (Moehle, 1997).

Today most of these 1940-1960 buildings are still operative. The aim of this project is to improve the structural performance of historic buildings without affecting their patrimonial integrity. To accomplish the last objective, this study proposes the use of Fiber Reinforced Polymers (FRP) as a rehabilitation/reinforcement system. This method is selected because if

doi:10.23967/dbmc.2020.220

its correctly applied, FRP could increase RC life-service by improving ductility and control plastic flow (Metha and Monteiro, 1998; Park and Paulay, 1988). The following variables will be analyzed to confirm the hypothesis:

a) The evaluation of FRP composites attached to a standard concrete mix will be made while analyzing the adherence between phases and the performance of FRP;

b) Analysis of the adherence between FRP composite and old concrete specimen;

c) Comparison between the previous data obtained with a weathering reinforced concrete specimen

2 Method and Materials

For this research FRP method refers to the use of a composite material made with carbon fiber impregnated with epoxy resin, applied to rehabilitate a structural member (American Concrete Institute, 2008). Carbon fiber CF) is the most commonly type of concrete reinforcement sections because its range of tensile properties allows an acceptable mechanical performance between phases (Hull, 2010; Park S.-J. , 2018), its semi crystalline microstructure exhibit an tensile strength over 1200-2250 MPa (Teng, Chen, Smith and Lam, 2002). Wet lay-up is the preferable method to applied CF because it has major advantages for *in situ* installation wherefor CF sheet can adapt to complex geometries (Teng, *et al*, 2002). Composites materials are based on mechanical adherence amid epoxy resin and concrete surface, so previous applied carbon FRP over the concrete section, it must be cleaned free of dust, oil or solvents. To increase phase adherence, it could be peel off the surface until it is removed, a thin layer with an average thickness from 0.5mm to 2mm. For the experimental campaign it selected 12K unidirectional carbon tow sheet thus one direction cloth has the strongest tensile resistance (Chanda, 2018). To attach the fiber, it is used an epoxy adhesive indicated by the manufacturer, Quintum ©. Their mechanical properties on Tables 1 and 2.

Table 1. Mechanical Properties of Carbon fiber.

Material	Ultimate Tensile Strength	Young Modulus	Weight
QuintumWrap-300©	875 MPa	34, 500 MPa	302 g/m^2

Mechanical properties of carbon fiber imbibed into epoxy resin. The cloth physical characteristics are: 0.5mm thickness, 500mm wide and 12K tow.

Table 2. Mechanical Properties of Epoxy Resin.

Material	Compressive Strength	Lap shear Adhesion Strength	Tensile Strength
Q102R ©	121 MPa	12 MPa	42 MPa

Epoxy adhesive is formed by two components: part A, bisphenol resin type and part B, ammonium adduct as hardener. Both shall mix in a 100g :10gr relation.

2.1 Manufacturing Specimens

Concrete specimens were designed considering a structural resistance of 25Mpa (CEMEX) using the standards C192/C192M (ASTM, 2002). For the experimental campaign they were made six concrete cylinders of 150mm radius and 300mm height, using Portland Composite Cement (IMCyC, s.f.). Three of them were selected for control of the mix and three more for FRP reinforcement.

2.2 Confined Concrete with Carbon Fiber

After 20 days of demolding concrete cylinders, three specimens were prepared to attach CF by scabbling a 2mm layer from the surface using an angle grinder. FRP method consisted of five steps that were made considering the combined action principle (Callister, 2009). The first step was applying a uniform layer of epoxy resin over the concrete surface. The second step was immersing the CF sheet ultimately into epoxy resin to reduce the air content and dry zones. The third step was wrapping to confining specimens with an impregnated fiber sheet with overlapping of 10 centimeters. The fourth step was removed the air trapped into the tows dragging a palette knife over the wrap. The fifth step was applied another uniform epoxy layer.

3 Compression Test

The compression test consists of applied a uniaxial increasing load on the material to deformed it until it's ultimate strain. If carbon fiber is correctly attached to concrete, it shall restring the lateral pressure and radial expansion, assuming that epoxy layer has the same thickness on both sides of fiber; tensile stress shall be equal in the hoop direction. Specimens were tested 28 days after manufacturing. Tests were made in an INTRON universal testing machine, screw-type UTM model MII 400WHVL with capacity for 200 tons.

4 Results

Control specimens showed average compression strength of 22MPa and for the FRP it was an average strength over 38 MPa. CF almost doubled the compressive strength of concrete. In Table 3 shown test results.

Table 3. Results of compression test for Control and FRP specimens.

Specimen	Maximal Load	Ultimate Compression Strength	Strain
Control 1	38,514 kgf	21 MPa	2.1 mm
Control 2	43,154 kgf	23.5 MPa	3.6 mm
Control 3	39,791 kgf	21.7 MPa	2.9 mm
FRP 1	65,914 kgf	36.5 MPa	5.1 mm
FRP 2	66,235 kgf	36.7 MPa	5.2 mm
FRP 3	73,090 kgf	40.5 MPa	5.5 mm

Table 3 shows the maximal values obtained from data bases of test machine.

Mechanical behavior of FRP specimens is shown in Figure 1. The three curves have a similar development with a semi-ductile trend, and all of them showed a small dropping when concrete reached its maximal compressive strength, as it is shown on figure 1 (left). All curves had the same geometrical composition, also, according with data in table 3: FRP 1-2 had a very similar mechanical behavior. On the other hand, FRP 3 continues growing asymmetric. The average FRP ratio was calculated using a sixth-grade polynomial trend line to correct each curve. After that, corrected data were put on the same base to define another trend line and made one more correction. The final result was the edited stress-strain curve, which had the average behavior of FRP specimens, it is shown in Figure 1 (right). Physical analysis shown in Figure 2-4.

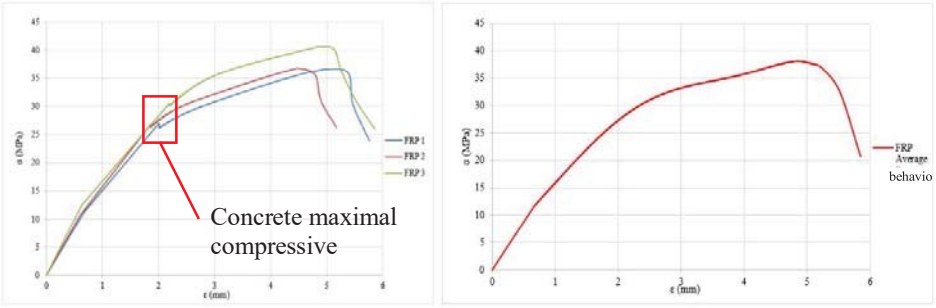

Figure 1. Stress-strain curves of FRP specimens and edited curve after statistical analysis.

On Figure 1, it is presented, from left to right, stress-strain curves of all FRP cylinders; stress-strain curve performed with edited compression data base.

Figure 2. FRP specimens after compression test.

On Figure 2 it is shown, from left to right, FRP 1 with total detachment of CF; FRP 2, total detachment of CF; FRP 3, partial detachment of CF.

Specimens FRP 1 -2 failed because a delamination from overlap section, it shown on Figure 3A. The revision of the pulled off carbon layer showed the presence of a considerable quantity of voids at overlapping area, Figure 3B. While the rest had concrete residuum, Figure 3C. For those two cases, the matrix layers were detached because the distribution of stress was discontinuous

due to voids. Internal stress at borders generated micro tangential tensions which broken the matrix, then shear produced by pressure delaminates the overlap. Concrete aggregate exposed refers to such good phase adhesion. According to the partial uniform state of the concrete section, specimens FRP 1-2 can not reached their ultimate compression strength; otherwise, residual concrete would be abundant cracks on the cylinder section; checking numerical data at Table 3, load stress was transmitted by both phases only before delamination of FRP, after that each phase was working by itself: CF jacket was just restrung cylinder bulge until epoxy matrix was completely broken.

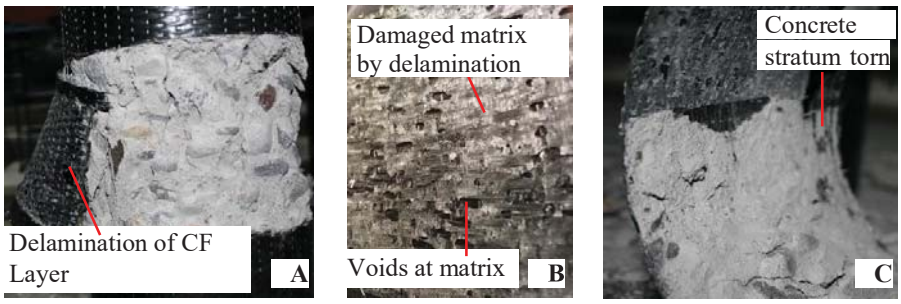

Figure 3. Detail of delamination in FRP at compression test.

On Figure 3 showed: (A) delamination of FRP matrix; (B) detail of voids at overlapping; (C) detail of adherence between phases.

FRP 3 reached its ultimate compressive strength. In this case, tangential tension was uniformly distributed over the cylinder's section until pressure shear the carbon layer causing an explosion. The tested specimen had small delamination on overlap area, Figure 4D. Then, it assumes less void contain at matrix and a uniformly epoxy coat on each side of layer. The explosion also produced the tearing of CF cloth, shown in Figure 4E; it observes parts from the concrete section who were torn by the adhesive and remained attached to the epoxy matrix, Figure 4F. In FRP 3, serious cracks were caused by stress distribution, which means that when the concrete reached its maximal compressive strength, it still transmitting load. That indicates the simultaneous transmission of stress from both phases; this specimen already worked as a composite material.

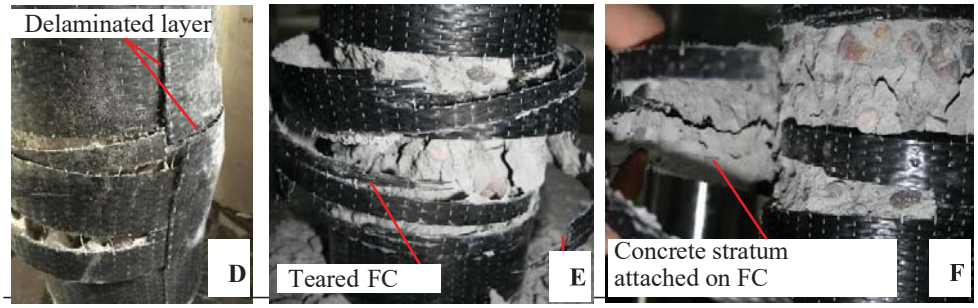

Figure 4. Detail of failure in FRP at compression test.

On Figure 4 it can be seen: (D) Partial delamination of FRP matrix; (E) detail of CF teared by shear strength; (F) detail of adherence between phases.

Below its presented, on Figure 5, the results of concrete and FRP cylinders to contrast the influence of CF cloth. On this figure observes that carbon fiber actually extend the plastic zone of concrete allowing it major load resistance.

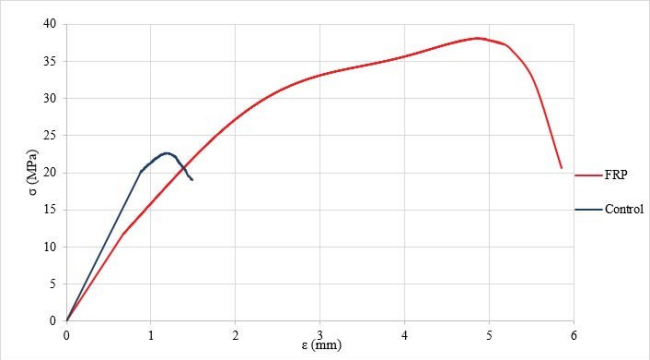

Figure 5. Comparation between FRP and pure concrete specimens.

Based on the current normative of the ACI (American Concrete Institute, 2008), the FRP manual of SIKA (SIKA, 2015) and current investigations about carbon fiber (Hernández Pérez, 2019), the theorical compressive strength results for FRP cylinders are compared with the practical test results. On Table 4 shown the results.

Table 4. Results of compression test for Control and FRP specimens.

Specimen	Theorical Confined Compressive Strength	Practical Confined Compressive Strength
FRP 1	30.92 MPa	36.5 MPa
FRP 2	30.92 MPa	36.7 MPa
FRP 3	30.92 MPa	40.5 MPa

Theorical confined compressive strength at table 4 only consider the design target compressive strength of 25 MPa for the three specimens.

Comparison of numerical results at table 4 expressed an increment of 40% in practical tests compared with the theorical calculation, even with the cylinders whose FRP was detached.

5 Conclusions

- Based on the numerical data provided by the mechanical test, the method of manufacture, and the physic analysis of the FRP concrete specimens it concludes that the fiber reinforcement polymer method increases the compressive strength of concrete even if FRP is not well attached. This condition means that quality control at FRP application

must be hardly supervised.

- The surface treatment had successful results on adherence between epoxy-concrete interphase. Mechanical adhesion between phases was strong to keep them together after radial pressure pull off the epoxy matrix. Considering that, significant attention must be put on overlapping while FRP method is applied. Delamination at this zone is the common cause of failure at confining, the matrix is easy to fracture by shear strength if there is a high void percent.
- The adherence range of service is such enough to control longitudinal and transversal deformation and consequently adding partial ductile properties. So then, carbon fiber is capable of retarding plastic deformation on concrete by full confining. The compression test is an accelerate process to deforming concrete until it is destroyed, then considering that plastic flow is a slow process it can conclude CF could stop deformation by aging.
- At service, FRP could produce some elasticity to concrete because its tensile resistance parallels to the axis. However, the characteristic of its materials still having a fragile trend. Under that premise, the porous matrix at the overlapping area is vulnerable to shear, torsion, impact, etc. As an optional experimental purpose to improve adherence in epoxy-epoxy interphase, it could use a compatible polymeric adherence bridge.

Acknowledgements

This work was supported by the Materials Mechanics Laboratory at Engineering Faculty from the UNAM. We are especially grateful to Eng. Juan Luis Cottier Caviedes, Master of engineering Miguel Angel Zúñiga Bravo and his technical team: Francisco J. Valencia Maqueda, Elia Camaño Cuevas, Ricardo Valencia Pérez; and Dr. Mikhail Zolotukhin. Also, thanks to PAPIIT IN404318 DGAPA UNAM for their support.

ORCID

Juan Manuel García Garduño: https://orcid.org/0000-0002-3652-0564
Perla Rafael Santa Ana Lozada: http://orcid.org/0000-0002-7631-0895

References

Administración Pública de la Ciudad de México (2017). *Gaseta oficial de la Ciudad de México: Título Sexto, de la Seguridad Estructural de las Construcciones, Capitulo 1, Generalidades.*

Al-Mahaidi, R. and Kalfat, R. (2018). *Rehabilitation of Concrete Structures with Fiber-Reinforced Polymer.* Butterworth-Heinemann.

American Concrete Institute (2008). *ACI 440.2R-08: Guide for the Design and Construction of Externally Bonded FRP Systems for Strengthening Concrete Structures.* USA: American Concrete Institute.

ASTM (2002). *C192/C192M-02 Srandard Practice for: Making and Curing Concrete Test Specimens in the Laboratory.* American Society for Testing and Materials.

Callister, W. (2009). *Introducción a la Ciencia e Ingeniería de Materiales.* Ciudad de México: Limusa Wiley.

CEDEX (2010). *http://www.cehopu.cedex.es/.*

CEMEX. *Manual del Constructor.* CEMEX concretos.

Chanda, M. (2018). *Plastics Technology Handbook.* Florida, USA: CRC Press, Taylor & Francis Group.

Hernández Pérez, M.E. (2019). *Refuerzo y rehabilitación de especímenes de concreto con polímeros reforzados con fibra.* Ciudad de México: UNAM.

Hull, D. (2010). *Materiales Compuestos.* España: Editorial Reverté.

IMCyC (2010). Especial Bicentenario. *Construcción y Tecnología en Concreto (271).* http://www.imcyc.com/revistacyt/dic10/especial2.htm

IMCyC. *http://imcyc.com*. Obtenido de Guía de productos: concreto: Holcim Apasco: http://imcyc.com/ct2009/guiadeproductosjun09/concreto/holcimapasco.htm

Marsal J.R. and Mazari, M. (2016). *El Subsuelo de la Ciudad de México.* Ciudad de México: Instituto de Ingeniería UNAM.

Metha, P.K. and Monteiro, J.P. (1998). *Concreto: Estructura, propiedades y materiales.* Ciudad de Mexico: Instituto Mexicano del Cemento y el Concreto, A.C.

Moehle, J. (1997). *State of research on seismic retrofit of concrete building structures in the US.* Obtenido de http://www.ironwarrior.org/ARE/Lateral_Forces/us-japan_rehab_paper%20Seismic%20Retrofit.pdf

Muñoz, S.F. and Mendoza, E.C. (2012). La Durabilidad en las Estructuras de Concreto Reforzado des de la Perspectiva de la Norma Española para Estructuras de Concreto. *Concreto y Cemento. Investigación y Desarrollo, 4*(1), 63-86. https://www.redalyc.org/pdf/3612/361233551004.pdf

Organo del Gobierno Constitucional de los Estados Unidos Mexicanos (1942). *http://www.smie.org.mx.* Información técnica/reglamentos de construcción/Distrito Federal: http://www.smie.org.mx/layout/reglamentos- construccion/distrito-federal-reglamento-construccion-estatal-1942.pdf

Park, R. and Paulay, T. (1988). *Estructuras de Concreto Reforzado.* Ciudad de México: Editorial Limusa. S.A. de C.V.

Park, S.J. (2018). *Carbon Fibers.* Korea: Springer.

Servicio Geológico Mexicano (2017). *www.sgm.gob.mx*. Sismología de México: https://www.sgm.gob.mx/Web/MuseoVirtual/Riesgos-geologicos/Sismologia-de-Mexico.html

SIKA. (2015). *Guía de Usuario, Software de diseño Sika CarboDur, Basado en ACI 440.2R-8.* Lima, Perú: SIKA.

Teng, J., Chen, J., Smith, S. and Lam, L. (2002). *FRP Strengthened RC Structures.* England: John Wiley & Sons.Ltd.

XV International Conference on Durability of Building Materials and Components
DBMC 2020, Barcelona
C. Serrat, J.R. Casas and V. Gibert (Eds)

Properties of Czech WW2 Concrete Fortifications after 80 Years

Ondřej Holčapek[1], **Pavel Reiterman**[2] **and Jiří Pazderka**[3]

[1] Experimental Centre, Faculty of Civil Engineering, Czech Technical University in Prague (CTU), Thákurova 7, 166 29 Prague 6, Czech Republic, ondrej.holcapek@fsv.cvut.cz

[2] Experimental Centre, Faculty of Civil Engineering, Czech Technical University in Prague (CTU), Thákurova 7, 166 29 Prague 6, Czech Republic, pavel.reiterman@fsv.cvut.cz

[3] Department of Building Structures, Faculty of Civil Engineering, Czech Technical University in Prague (CTU), Thákurova 7, 166 29 Prague 6, Czech Republic, jiri.pazderka@fsv.cvut.cz

Abstract. *This paper deals with the investigation of properties of Czech fortification concrete bunkers built before Second World War (WWII). The Czech defense system consisted mainly of light bunkers type No. 37. The vast numbers of these bunkers have been preserved in various conditions to nowadays. The light bunkers type No. 37 were designed to last limited lifetime of decades. According to the preserved test protocols, strength of used concrete varied from 40 to 50 MPa, measured on cube specimens with dimensions 200×200×200 mm. There is an information, in general public, about high quality and strength of used concrete. The non-destructive analysis of compressive strength, determined by Schmidt hammer was performed. This method was used to maintain a historical value of the structures. Three were analyzed different bunkers type No. 37 located in Western Bohemia – Pilsner region. Tested bunkers are preserved in various conditions with various quality of concrete. The measurements by Schmidt hammer took place in several locations especially in the interior part. The exterior was also investigated but only in the locations of surface which were not covered with camouflage plaster. Non-destructive testing had shown high quality of concrete older than 80 years old concrete, with compressive strength between 50 to 60 MPa. On the other hand, based on the visual assessment, the concrete showed very different characteristics, especially in compactness and the quality of surface layer. We can find places with insufficiently compacted concrete with exposed steel reinforcement.*

Keywords: *Concrete, Fortification, WW2, Non-Destructive Testing, Schmidt Hammer.*

1 Introduction

The European continent has a great historical, cultural and architectural heritage, which includes monuments dated back several centuries and even millennia. The architectural heritage contains relicts of ancient civilizations, medieval buildings, sacral and also profane buildings. In the terms of building monuments, materials used most frequently are bricks or stone masonry, timber and steel (traditional and proven materials). The field of architectural heritage is closely connected with the restoration, reconstruction and, if necessary, strengthening. The strengthening and conservation of widely used structural elements (column, pillar, vault, beam etc.) made with traditional materials is well described and mastered. Even modern materials with high utility properties are successfully implemented into the strengthening process – we can find the application of carbon rods or fabrics (Witzany *et al.,* 2016, Jongsung *et al*., 2005). Even very modern material – textile reinforced concrete can be used for stabilization or

strengthening of masonry structures (Garmendia *et al.,* 2014).

Even relatively new buildings and structures are in the center of interest of exploration and conservation. We can see a growing interest in exploring industrial heritage as a reflection of its time. This brings new challenges for historians, architects and engineers. A very good example of this phenomenon is the system of the Czech fortification system, built by former Czechoslovakian government in years before the WWII. This example of widespread use of concrete has been extensively preserved in various conditions till today. For general public, concrete is not the representative of historical material (Heinemann *et al.,* 2008).

1.1 Czech Fortification System

The system of fortification was built in relatively short time during 1930s by incurring high financial and material costs. The whole system consisted of several defensive lines of light bunkers for seven soldiers. In this way, the strategic disadvantage of defending very long borders with Germany, Poland and later with Austria and Hungary, with limited human capacity, had been solved. This system of light bunkers had been supplemented in certain places, usually in mountainous terrain by artillery fortresses. The support of the defense system contains large number of smaller fortresses, usually connected by system of underground corridors. Unlike the bunkers type No. 37, these fortresses were intended for long-term stay of military crews. The bunkers type No. 37 were designed for short stay of soldiers only at the time of threat. Due to their cramped space, longer stay of crews was not possible. In the event of war crash, bunkers No. 37 were designed for indirect firing, when individual fire fans of each bunker overlap with the fire fans of its neighbor. The front wall was the strongest part of fortification and it was also protected from exterior part by a stone flat with loam (also used as camouflage).

The vast majority of the preserved bunkers No. 37, according to cadastral information, are owned by the Army of Czech Republic. More extensive preserved complexes and artillery forts have a status of official cultural heritage and are open to the public. A large number of objects of varying size and technical conditions are also owned by private persons or group of WWII fans. These organizations or individualities usually try to restore the bunker to its original state, including camouflage, armament and equipment. However, with more intensive use and reconstruction works, there are many challenges that need to be solved. The bunkers were not designed for long-term stay of military crew. Various problems are connected with the actions of capillarity and moisture penetration. An extensive experiment and numerical simulation on this topic performed Pazderka *et al.,* 2016. The problem with massive water ingress can be solved by using modern crystallizing coating (Pazderka *et al.,*2019). On these two examples we can see that the issue of defensive structures gains its importance, therefore the theoretical investigation and field in-situ survey are also significant and important.

2 Performed Investigation and Observation

Three preserved examples of bunkers No. 37 located in the “Pilsner line” in West Bohemia region were chosen for the purpose of this contribution. The designations of investigated bunkers are D-19/22/A-160, D-19/47/A-160 and D-20/4/A-160. This number has its systems and contains the information about location and type of object. The first part “D-19” or “D-20” means the construction section, in this case “Nové Městečko” respectively “Blažim”. It was

usually named about the nearest important city or village. The next number, in our case “22”, “47” and “4” means the order of the bunker in the particular construction section. The last part, in this case “A-160” means the type of bunker. Letter “A” means, that the investigated bunkers represent the most commonly used type with ordinary ballistic resistance. There were also bunkers with letter “Z”, which describes the bunker with higher ballistic resistance with stronger front wall. The last number characterizes the angle of coverage with installed machine guns.

2.1 Testing by Schmidt Hammer

Testing by Schmidt hammer represents commonly used method for non-destructive testing of concrete´s mechanical properties. This method is standardized and allowed by standard systems of many countries. There have been cases where Schmidt hammer was used as representative of non-destructive method for measurement of compressive strength of masonry elements (Aliabdo *et al.,* 2012). However, the most widespread use still represent concrete, as a material usually supplemented by destructive testing if circumstances permit (Holčapek *et al.,* 2014). The standard Schmidt hammer type N was used, according to Czech standard (CSN EN 2013). Due to the preserved external plasters the investigation took place mainly in the interior part. The schematic cross-section of bunker No. 37 with marked location of performed measurements is shown on Figure 1. Minimum of 50 measurements were performed on each place (places in different heights). Also the quality of roof was investigated.

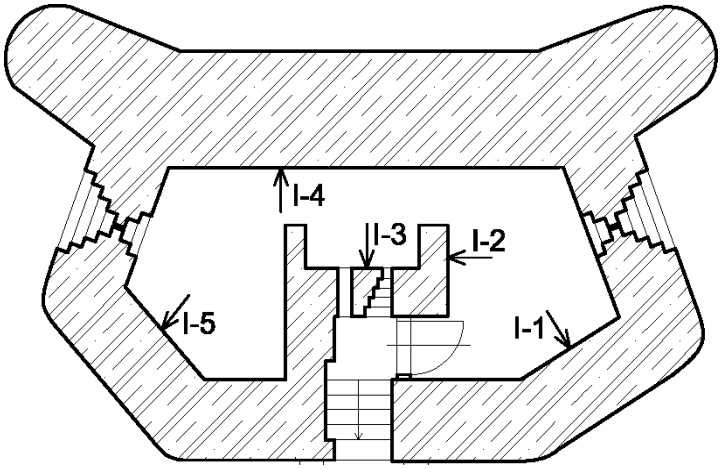

Figure 1. Schematic cross-section with marked places of performed measurements.

2.2 Visual Evaluation

Analyzed bunkers are situated in one location and were built in approximately in the same period of second half of 1937. Their entrances are not locked, which means that the bunkers are not protected against vandalism. We can still observe the residua of original timber cladding in the interior part, as shown on Figure 2 and also on Figure 3. These timber elements were exposed to moisture and the effects of fungi and microorganisms. An important finding is that the quality of concrete within a single object is variable. We can observe excellent quality of surface layer, without any cracks or cluster of aggregate. There are places with very poor quality

of compaction in the same bunker. We can see reinforcement uncoated by concrete, clusters of coarse aggregate and other imperfections. This surface was originally covered by timber cladding and the estimated designed lifetime was only about 20 years, bud if we want to preserved these objects to future generations, we have to deal also with these problems.

Figure 2. Residuum of internal timber cladding, poor quality of surface layer of concrete.

Figure 3. Insufficient compaction with uncovered steel reinforcement.

3 Results and Discussion

As mentioned above, totally six different locations in the interior part were investigated by Schmidt hammer. The investigation in exterior part is limited by the protective earth wall in the front part and also by the residues of masking plasters, but one location was also analyzed.

All results of performed measurements are summarized in Table 1. The first column describes the location according to Figure 1. Following three columns list the values of tentative

compressive strength of three different bunkers No. 37. The last row in the table contains the compressive strength calculated according to destructive test performed in 1937 on cube specimens with dimension 200×200×200 mm.

Table 1. Results of performed non-destructive measurements.

Designation	D-19/22/A-160	D-19/47/A-160	D-20/4/A-160
	[MPa]	[MPa]	[MPa]
Exterior	67.5	59.7	N/A
Interior (I-1)	58.1	54.3	57.8
Interior (I-2)	51.7	48.8	53.4
Interior (I-3)	56.3	63.4	59.6
Interior (I-4)	61.2	68.9	57.8
Interior (I-5)	53.9	59.9	64.7
Interior (roof)	59.4	58.6	53.1
Compressive strength (test performed in 1937	49.5	57.5	51.4

The strength in the exterior part of investigated bunker D-200/4/A-160 could not be measured due to well preserved camouflage plasters on the walls. There were several places on remaining two bunkers, where the plasters did not preserve and it was possible do a measurement of the concrete wall directly. The properties of concrete in the exterior part can be influenced by the carbonation process that caused increased strength of the surface layer, where the measurement took place. It is recommended to mechanically remove thin part of carbonated layer. Considering the non-invasive approach to testing, this recommendation was not chosen. Each value from interior part represents an average of at least 50 measurements. A relatively small spread of values can be observed.

4 Conclusions

Based on performed non-destructive testing of compressive strength, determined by Schmidt hammer, in different location of light bunkers knows as “Model No. 37” and also according to visual evaluation we can obtain following conclusions:

- The non-destructive testing of compressive strength of concrete plays its important role for determination tentative quality of concrete structures. The importance of non-destructive testing is increasing in the case of historically valuable structures that we do not want or cannot damage. Obtained values showed high strength of over 80 years old concrete and confirmed the strength determined in 1930s on specimens with dimension 200×200×200 mm (according to the army methodology used before WWII).
- The quality of concrete from investigated bunkers shows very different properties. On one object, we can find areas with excellent surface quality and well compacted concrete. These locations alternate areas with exposed reinforcement and insufficiently compacted concrete with large gaps. This phenomenon is caused by the originally used method of compaction with rammer in 1930s. The exposed and uncovered reinforcement is not a result of concrete´s degradation.
- Durability of concrete is very important and currently discussed parameter. In the case

of studied bunkers No. 37 the durability is closely connected with long-term properties of concrete and steel reinforcement. All these parameters are connected with the function of waterproofing (foundations and roof). According to performed in-situ investigations the biggest problems connected with durability are leaches of minerals from concrete. Due to the age of structures (over 80 years) extensive carbonation of concrete can be expected, which is also related to the corrosion of steel reinforcement with insufficient concrete cover layer. Based on the performed analysis (visual evaluation and the Schmidt hammer measurements) we can expect long service life and good durability of bunkers No. 37. At the same time is necessary to provide further moisture penetration into the structure - restoration of the waterproofing function of roof and insulation of foundations from moisture. Due to the age of bunkers, we can identify problems, that affect the overall service life and durability which can be solved by repairs and reconstruction works and precautions.

Acknowledgements

This research was supported by project NAKI II – DG18P02OVV063.

ORCID

Holčapek Ondřej: https://orcid.org/0000-0003-3795-1478
Pavel Reiterman: https://orcid.org/0000-0002-3918-3647
Jiří Pazderka: https://orcid.org/0000-0002-4611-8931

References

Aliabdo, A.A.E. and Elmoaty, A.E.M.A., (2012). *Reliability of using nondestructive tests to estimate compressive strength of building stones and bricks. Alexandria Engineering Journal(51). 193-203.* doi:https://doi.org/10.1016/j.aej.2012.004

CSN EN 73 13010 (2013). Testing concrete in structures – Part 2: Non-destructive testing – Determination of rebound number.

Garmendia, L., Larrinaga, P., García, D. and Marcos, I. (2014). *Textile-Reinforced Mortar as Strengthening Material for Masonry Arches. International Journal of Architectural Heritage: Conservation, Analysis, and Restoration (8), 627-648.* doi: https://doi.org/10.1080/15583058.2012.704480

Heinemann, H.A., Van Hees, R.P.J. and Nijland, T.G. (2008). *Concrete: Too young for conservation? Proceedings of 6th International Conference on Structural analysis of historical constructions: preserving safety and significance (1), 151-159.*

Holčapek, O., Litoš, J. and Zatloukal, J. (2014). *Destructive and Nondestructive Testing of Old Concrete. Advanced Materials Research (1054), Special Concrete and Composites 2014. 243-247.* doi:https//doi.org/10.4028/www.scientifi.net/AMR.1054.243.

Jongsung, S., Cheolwoo, P. and Do., Y.M. (2005). Characteristics of basalt fiber as a strengthening material for concrete structures. *Composites Part B: Engineering, (36). 504-512.* doi: https://doi.org/10.1016/j.compositesb.2005.02.002

Pazderka, J., Purkrtová, M. and Reiterman, P. (2016). *Moisture-related problems of historic concrete structure. Materials Science Forum (865). 219-226.* doi:10.4028/www.scientific.net/MSF.865.219.

Pazderka, J. and Reiterman, P. (2019). *Czech WWII Concrete Fortifications: Corrosion Process and Remediation Method Based on Crystallizing Coating. Acta Polytechnica (59). 359-371.* Doi:http://doi.org/10.14311/AP.2019.0359

Witzany, J., Zigler, R. and Kroftová K. (2016). Strengthening of compressed brick masonry walls with carbon composites. *Construction and Building Materials, (112), 1066-1079.* doi: https://doi.org/10.1016/j.conbuildmat.2016.03.026

XV International Conference on Durability of Building Materials and Components
DBMC 2020, Barcelona
C. Serrat, J.R. Casas and V. Gibert (Eds)

Stability Assessment of Historic Plaster Ceilings on Wood Lath

Helena M. Currie, Matthew B. Bronski, and Rachel M. Lynde

Simpson Gumpertz & Heger, Inc. (SGH), 480 Totten Pond Road, Waltham, Massachusetts 02451, United States of America, HMCurrie@sgh.com, MBBronski@sgh.com, RMLynde@sgh.com

Abstract. *Plaster (often lime plaster, reinforced with animal hair) installed on wood lath secured to wood framing was a common ceiling system for hundreds of years in the Americas, and for thousands of years in Europe. Despite having a relatively good record of stability, some ceilings of this type have collapsed. Given their overhead position, often above large groups of people, when cracks or localized areas of displacement or damage occur in these ceilings, the question often arises as to whether the ceiling is stable and safe. Because procedures for stability assessment of historic plaster ceilings on wood lath are not well quantified in building codes or technical literature, this article proposes key considerations and best practices for assessing these ceilings.*

Keywords: *Historic, Plaster Ceilings, Condition Assessment, Structural Stability, Vibration Monitoring.*

1 Typical Construction

Plaster ceilings on wood lath were a common ceiling system for hundreds of years in the Americas, and for thousands of years in Europe. European plaster ceilings typically consist of lime-based plaster (lime and sand) that is reinforced with animal hair, applied to a network of narrow, closely spaced wood members, that are secured to an overlying structural framework of larger wood members, either by tying in the earlier examples, or nailing in the later examples. Similar plaster ceilings applied to dried wood reeds (aka wattle, or wicker) were constructed over 2,000 years ago, as described by the Roman architect Vitruvius in the first century BCE in his treatise *De Architectura* [Vitruvius]. Multiple 500 year-old examples of this plaster ceiling construction survive from the Italian Renaissance.

Historic examples in the USA survive from as early as the mid-18th century, and were typically constructed of lime-based plaster with animal hair fibers (Fig. 1A), similar to earlier European examples; however, closely spaced wood members are lath (long slender wood pieces) rather than dried reeds. Prior to the early 19th century, the wood lath was typically riven (*i.e.*, hand-split), and from the early 19th to the early 20th century, the wood lath was typically sawn. In both cases, pieces of the wood lath were approximately 6 mm thick by 60 mm wide, with gaps approximately 6 mm wide between the long edges in sawn lath, and approximately 2-6 mm wide between the long edges of riven lath. The lath is secured to the overlying structural wood framing (*e.g.*, the floor framing of the roof or attic above) by smooth shank nails, installed from the underside. Prior to the late 19th century, the nails were either hand-forged wrought nails or cut nails, which both have a wedge-shaped profile, tapering from head to tip. After the late 19th century, the nails are typically wire nails, which have a uniform cylindrical shank and a point only at the tip.

In both European and US examples, the dense network of slender wood members (dried reeds or lath) are intentionally spaced with gaps between the long edges to provide space for the wet plaster to be forced between the gaps and create hardened plaster "keys" on the topside

of the lath or reeds, that are wider than the gaps, and thus form lines of mechanical interlock between the plaster and the topside of the reeds or lath. In both European and US examples, whether tied or nailed from below, the connection of the dried reeds or wood lath to the overlying structural wood framing is a tensile connection.

2 Typical Failure Modes

Failures of these historic plaster ceilings in the US typically fall into one of two primary failure modes: 1) failure of plaster keys (Fig. 1B), or 2) tensile failure or "pull-out" of the nailed connections of the lath to the overlying wood framing (Fig. 1C).

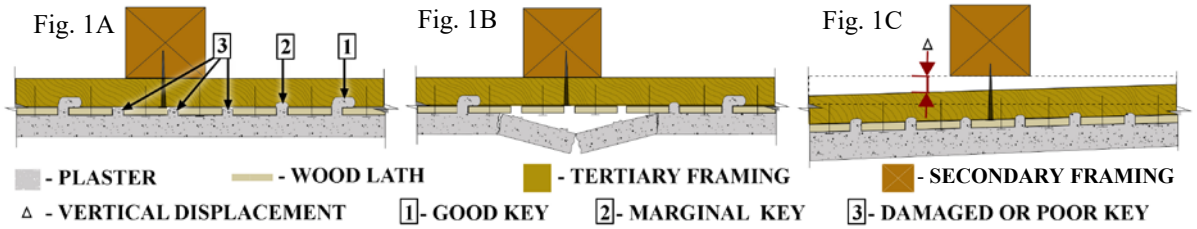

Figure 1. Typical historic plaster ceiling construction on wood lath (Fig. 1A) and two primary failure modes: plaster key failure (Fig. 1B) and fastener "pull-out" (tensile) failure of supporting framing connections (Fig.1C).

Multiple causes (*e.g.*, impact damage, structural over-loading, moisture-related deterioration, excessive deflection, or lateral movement, excessive vibration, etc.) can contribute to the two primary failure modes for historic plaster ceilings, failure of the plaster keys and tensile failure of nailed connections, which are described below in more detail.

2.1 Failure of Plaster Keying

Deteriorated, damaged, insufficient or otherwise failed keying of the plaster can lead to loss of mechanical interlock with the wood lath and localized failure of the plaster. However, this failure mode does not tend to lead to progressive widespread collapse of entire ceilings. Rather, this failure tends to be self-arresting. As unkeyed, debonded plaster starts to separate and displace downward from the wood lath, the self-weight of the debonded area may exceed the remaining interlock capacity of the remaining plaster keys, if any, and cause a relatively small (< 0.1 m^2) displaced piece to break off (as a result of the low shear strength and flexural strength of the plaster) before the displaced piece becomes relatively large (Fig. 1B). Generally, this failure mode tends to result in the falling of relatively small pieces of plaster alone (with no wood lath or framing). Given the light weight and friability of the lime plaster, plaster pieces of this size (< 0.1 m^2) generally do not pose a significant life safety risk when they fall. When evaluating the condition of plaster keys, it is helpful to distinguish between the original condition and current condition of the plaster keys, because the severity and extent of currently damaged keys, compared to the condition and performance of the original plaster keys, will inform to what extent one can or cannot rely on the track record of performance of the keying as testament to its current stability.

Original Adequacy of Plaster Keys: The adequacy of the plaster keying through the lath, as originally constructed, depends on how well-keyed (mechanically interlocked) it is with the topside of the wood lath to which it is applied. Substantially interlocked plaster keys are clearly

wider than the corresponding gap in the lath, and thick enough where they pass over the back edge of the lath to resist a shear or flexural failure within the plaster key. Keys that are at least twice the width of the gap, and with a thickness of plaster of at least 6 mm above the top edge of the lath, we consider to be "good" keys. By contrast, we consider "marginal" keys to be barely wider than their corresponding gap in the lath, with minimal thickness (less than 6 mm) where they pass over the top edge of the lath. We consider "poor" keys to be equal to or less than the width of their corresponding gap in the lath. In any ceiling installation, the best keys tend to occur at more vertical portions of the ceiling, where the wet plaster keys were applied with more ease and sagged down and over the topside/backside of the wood lath during the original installation. In the more horizontal portions of a plaster ceiling, where gravity does not aid in the formation of keys, good keying was achieved only when the workers forced sufficient plaster through the gaps in the lath with sufficient hand pressure on the trowel. Thus, the quality of the original keying in horizontal (overhead) conditions relied heavily on workmanship.

A common approach in evaluating ceilings is to conservatively consider marginal keys as not contributing to the reliability of the plaster ceiling attachment. However, in our experience, reviewing the performance of plaster ceilings a century or more old, good keys are quite reliable, and even marginal keys may perform well long-term. One historic ceiling we examined that is constructed primarily of marginal keys has performed relatively well for 200+ years, with only a few highly localized failures (*e.g.* locations where less than 0.1 m^2 pieces of plaster have fallen from the ceiling). While clearly not as strong or reliable as "good" plaster keys, marginal plaster keys likely still contribute to the reliability of the plaster ceiling attachment, unless there is evidence of marginal key failure or site-specific testing is performed. While there is no definitive research indicating whether "poor" plaster keys contribute to the load-carrying capacity of the ceiling attachment through friction between the sides of the plaster key and the wood lath, we conservatively consider "poor" plaster keys as not contributing to the overall reliability of the plaster ceiling attachment, regardless of whether displacement is evident, unless site-specific testing is performed.

Current Condition of Plaster Keys: Where keys are cracked, deteriorated, separated, or otherwise damaged, their current condition (*e.g.*, of good, marginal or poor) should be based on their remaining intact section, rather than their original width or thickness**.** In cases where relatively little damage has occurred to the keys since their original construction, one can more reasonably rely on the track record of performance of the keying as a testament to its current stability, since the adequacy of the keying has not been significantly diminished**.** Conversely, in cases where extensive damage has occurred to the keys since their original construction, one cannot reasonably rely on the track record of performance of the keying.

2.2 Failure of Supporting Wood Framing

Failure of the overlying structural wood framing, and/or its connections can potentially lead to progressive collapse of the entire plaster ceiling. Indications of this failure mode are often visible at the topside plaster framing and include gross withdrawal ("pull-out") of nailed wood-wood connections (often smooth shank or tapered nails), or gross displacement of wood members or connections (Fig. 1C). When an individual connection pulls out, the loads and stresses tend to redistribute to the adjacent connections, potentially causing them to become overstressed and more likely to pull out, which can cause a "domino effect" leading to

progressive collapse of the entire plaster ceiling (*i.e.*, the plaster, wood lath and wood framing, not just the plaster). As such, this failure mode presents a far more significant risk to life safety than the more common (and generally self-arresting) failure mode of inadequate plaster keying.

3 Stability Assessment: Current Common Practices

Numerous publications we reviewed emphasize that visual survey is the initial step for plaster evaluation. However, visual survey of plaster is subjective and damage is not consistently defined. Multiple publications also agree that damage visible at the underside of a plaster ceiling often correlates with damage on the topside of the plaster ceiling (Stewart H., 2011; Goeke, 2008). While some practitioners employ destructive tactile tests (*i.e.*, prying of plaster keys from the topside with light hand pressure to determine whether the plaster breaks) to evaluate topside conditions, in our opinion this test is problematic and ill-advised because it is destructive, non-qualitative and highly subjective. If deemed necessary, hands-on assessment, testing, and/or instrumented monitoring may supplement the initial visual assessment of plaster.

Current literature does not clearly define the condition of plaster keys (*e.g.*, "good", "fair", "poor"). While most publications agree that the percentages of damaged plaster keys are an *approximate* indicator of the overall condition of the plaster (Stewart. R, 2013), percentages that define plaster conditions vary widely in currently available literature, ranging anywhere from 30%-70% loss of plaster keys in a given area as meriting repair. Further, the pattern of plaster damage (*e.g.* whether plaster key loss is highly concentrated or uniformly distributed over a given area) that distinguishes "good" from "fair" or "poor" is not consistently considered as a factor in the overall condition or stability of plaster ceilings.

4 Recommended Best Practices for Stability Assessment

4.1 Three Step Approach to Initial Visual Assessment

Visual Assessment: An initial visual assessment of plaster ceilings is a generally accepted part of plaster evaluations. We recommend the visual assessment is best achieved using the following three step approach:

- Visual review of the underside plaster surface to document cracking and out-of-plane displacement (*e.g.*, sagging, vertical offsets) that may indicate damage or deterioration. This survey is best done first, so that areas of damage at the underside can be examined more closely and correlated with damage identified at the topside.
- Visual review of the topside wood framing to document any indications of gross withdrawal ("pull-out") of nailed wood-wood connections, or gross displacement or deterioration of wood members or connections.
- Visual review of the topside plaster keys to categorize the adequacy of mechanical keying of the plaster into the lath as good, marginal or poor (as previously defined).

Correlating Visual Review of Plaster keys with Tactile Assessment: The visual assessment of the topside plaster should include gentle, non-destructive tactile assessment of a localized area of plaster keys, after a visual-only assessment of the same area. The goal is to correlate the two methods in a representative area and confirm that the visual-only survey of

the plaster keys does not overlook concealed damage to plaster keys that was found in the tactile survey. If visual and tactile assessment of representative areas yield similar results, proceeding with a visual-only survey (with intermittent tactile testing) is appropriate.

Documenting Current Conditions: Clear, consistent documentation of the existing conditions is critical. Documentation should include clear definitions of each condition (*e.g.*, good, marginal, poor), and indicate the location and condition of keys or panels. Any imminent safety hazards should be identified on-site during the visual assessment, not postponed until synthesis.

4.2 Additional In-Situ Testing or Monitoring

In-situ "pull" testing (tensile testing conducted from the underside) of representative types of keys and derivative calculation to determine the actual factor of safety in representative areas can be used to refine the initial approximate criteria for critical percentages of plaster damage with respect to stability. If the ceiling is vaulted, it is preferable to conduct pull tests data on both horizontal and approximately vertical applications of each plaster condition type to get the full range of existing conditions. Pull-testing is most prudent when conservative assumptions and approaches would otherwise lead to invasive recommendations. If vibrations are suspected to be contributing to plaster damage, vibration monitoring may be prudent (Section 5).

4.3 Synthesis

Synthesis of the information gained from the in-situ assessment is needed to evaluate the overall stability of the plaster ceiling, to identify any potential risks, and to develop recommendations for repair. We divide the synthesis into the following steps:

Initial Categorization – As a first step, classify areas of plaster keys into condition categories (*e.g.*, "good", "marginal", "poor") based on the percentage of poor keys in a known area. Initial categorization should also include review of the overlying framing and connections. We often graphically depict condition categories as distinct colors on a ceiling plan, to help visualize patterns and areas of concern.

Review Performance History – Understand the performance history (*i.e.*, "track record") of how the plaster keying has performed over time (*e.g.*, few or many areas of previous repair or fallen plaster) to evaluate to what extent undamaged original keying can be relied upon, especially undamaged original "marginal" keys. Compare the current conditions to those of other plaster ceilings of similar construction and the track records of those ceilings.

Assess Sources of Deterioration – For areas where plaster and/or supporting framing is deteriorated or damaged, assess whether source(s) for deterioration are active (*e.g.*, a roof leak), and if so, whether they can be mitigated.

Calculate the Factor of Safety – To assess whether plaster keying conditions are at risk of failure, calculate the ceiling-specific factor of safety for the range of typical conditions and orientations present. The factor of safety (FS) under gravity-loading conditions (not seismic) consists of $FS = P_{fl}/P_{sw}$, where P_{fl} is the failure load applied to the plaster during the tensile "pull" test, and P_{sw} is the self-weight of the plaster for the same surface area. Standard structural engineering procedures and calculations can be used to evaluate the safety and stability of the supporting wood framing and connections.

5 Recommended Best Practices for Vibration Monitoring

5.1 Standards for Protection of Historic Buildings from Vibration Damage

There are numerous guidelines and publications for the protection of historic buildings from vibrations; however, various factors make it difficult to directly apply the criteria in these guidelines to evaluating the stability of historic plaster ceilings:

- Criteria for minimizing the probability of damage to existing buildings vary widely (*e.g.*, typical values for peak particle velocity range from 0.06 to 2.0 in./sec.).
- Criteria tend to be conservative, in that they are typically created to define low vibration levels at, or below, which damage almost certainly will NOT occur, to be relatively certain that vibrations from nearby construction will not damage an historic building. Thus, they are NOT intended to define a threshold at which damage WILL occur.
- Furthermore, these criteria tend to be based on vibration measurements taken at grade outside the historic building, closer to the external source of vibration, not inside the building or at a plaster ceiling itself (where the same external vibrations would measure at lower levels). Thus, these criteria are even more conservative when applied to internal vibration sources as measured at the interior.

Based on our review of various articles (Johnson, Hannen), as well as common vibration standards (*e.g.*, the British, German, and Swiss Standards), the vibration guideline values listed in the Swiss Standard for Building Class 4 (*i.e.*, the most sensitive class for historic and protected buildings) is often referred to as the most appropriate standard for evaluation of historic or sensitive materials. Further, the vibration criteria provided in the Swiss Standard are generally more conservative than other commonly referenced standards. Thus, by selecting the most conservative vibration criteria (*i.e.* 0.06 in./sec.), in one of the most conservative standards as the threshold vibration limit for monitoring and further review, it is highly unlikely that aesthetic or structural damage will occur if vibration levels in the plaster are less than 0.06 in./sec. Because the Swiss Standard and others are not directly applicable and likely highly conservative, these standard values should be treated as initial values that will likely require further evaluation and refinement. In some cases, ambient vibrations (*i.e.* vibrations experienced by the plaster ceiling regularly) or anticipated vibrations exceed these conservative limits. In these cases, project-specific vibration monitoring and/or testing may allow less-conservative project-specific threshold vibration criteria to be established for specific ceilings.

5.2 Continuous and Discrete Vibration Monitoring

A successful vibration monitoring program must achieve two primary objectives: 1) quantify the vibration levels experienced by the plaster over time and 2) evaluate specific vibration sources that pose a potential risk of damaging the plaster. Continuous vibration monitoring over an extended period of time, at the point of interest (*i.e.* at the topside of the plaster) quantifies both the ambient (typical) and atypical vibrations at the plaster ceiling. When ambient vibrations fall below the conservative industry thresholds, vibrations are highly unlikely to cause plaster damage. Where ambient vibrations levels are higher than these thresholds, however, vibrations will not necessarily cause damage to the ceiling. By contrast, this may confirm that the industry standard vibration criteria are not appropriate. Additionally, the type

and regularity of occurrence for each vibration source that coincides with high vibration levels should be taken into consideration (some standards do not account for these factors).

All potential vibration sources identified during continuous monitoring as exceeding the ambient or industry-standard threshold should be further assessed by discrete vibration testing of those specific sources, isolated to the greatest extent possible. Consider vibration monitoring information jointly with the plaster condition assessment to determine whether any of the plaster damage is likely associated with suspect vibrations sources. For example, where damaged plaster keys are highly concentrated adjacent to walkways at the topside of the ceiling, vibration monitoring can help to evaluate whether the damage is from accidental direct impact (*e.g.*, individuals bumping into the plaster) or transferred vibrations (*e.g.*, from footsteps on the walkway transmitted through rigid connections to the ceiling framing) (Fig. 2).

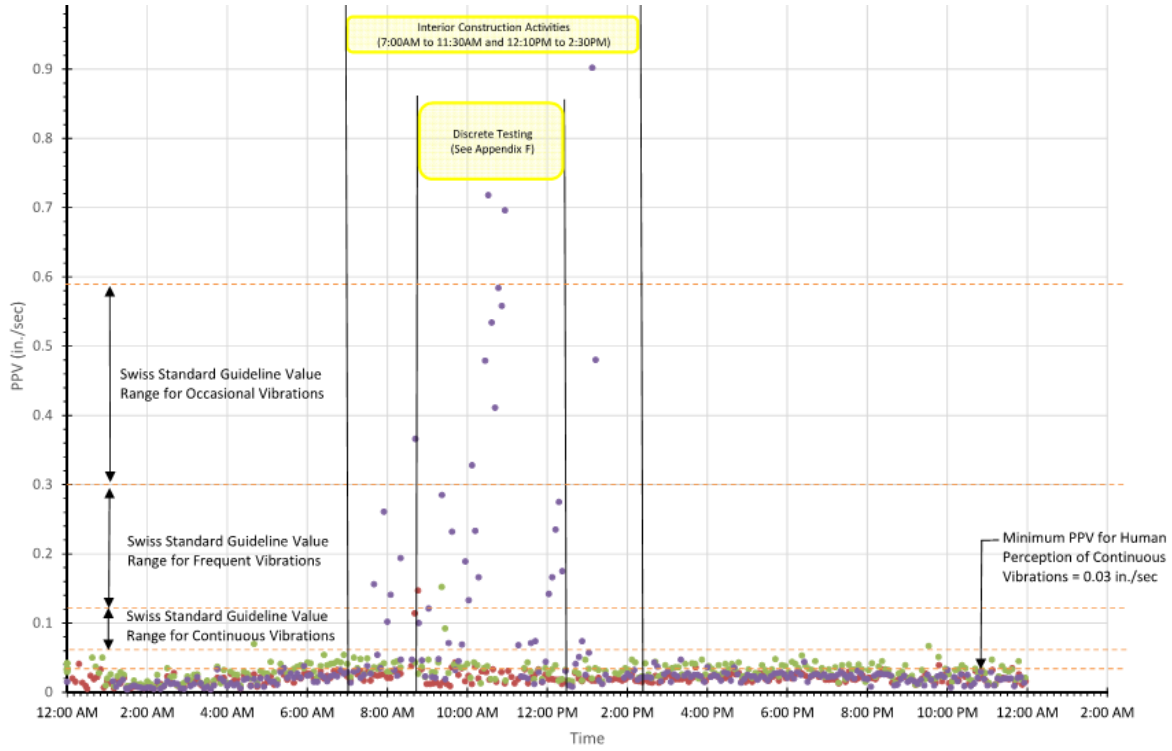

Figure 2. Example of vibration measurements collected at the topside of a plaster ceiling (where plaster damage was concentrated adjacent to attic walkways) during targeted vibration monitoring of an historic plaster ceiling.

In turn, this diagnosis should inform the recommendations to mitigate the problem (*e.g.*, implementing a protection system to mitigate accidental impact, or developing a dampening system to mitigate walkway vibrations, respectively).

6 Conclusion

Historic plaster ceilings on wood lath have been used for thousands of years, in many countries on multiple continents, and are a valuable historic resource well worth preserving. Despite some failures, plaster ceilings on wood lath generally have a reliable track record. The two most

common failure modes are failure of plaster keys and failure or "pull-out" of the supporting wood framing, the latter of which can result in progressive or whole-sale collapse. While vibrations are seldom the driving mechanism for failure, vibration monitoring is helpful in some cases where vibrations are a suspected cause of damage. In the US, the lack of guidelines or standards on how to evaluate historic plaster ceiling stability, and relatively little technical literature on the topic has been a hindrance to their proper evaluation of life safety/stability. Based on our experience, we utilize and recommend the condition and stability assessment procedure described herein, which includes documenting the original and current condition through visual assessment and correlation of visual observations with intermittent tactile assessment and empirical comparisons, in-situ testing and/or monitoring where prudent, and development of evaluation criteria and recommendations through post-processing and synthesis.

ORCID

Helena M. Currie: https://orcid.org/0000-0001-8991-7226
Matthew B. Bronski: https://orcid.org/0000-0002-6360-3226
Rachel M. Lynde: https://orcid.org/0000-0003-1639-8896

References

British Standard: *Evaluation and Measurement for Vibrations in Buildings, Part 2* (1993). BS 7385-2.

Deutsch Norm (German Standard) DIN 4150-3: *Erschutterungen im Bauwesen – Teil 3: Einworkungen auf bauliche Anlagen*, (*Structural Vibration - Part 3: Effects of vibration on structures*), (1999), English Translation. Berlin, Germany.

Giovanetti, F., ed. (1997). *Manuale del Rucupero del Comune di Roma*, secondo edizione (*Manual of the Recovery of the Municipality of Rome*, second edition).

Goeke, M. L. (2008). *Assessment and Analysis of the Plaster Exhibit Hall Ceiling at the Wagner Free Institue of Science*. Philadelphia, PA.

Johnson, A. and Hannen, W.R., (2015). "Vibration Limits for Historic Buildings and Art Collections", *Association for Preservation Technology (APT) Bulletin*, Vol. 46:2-3, pp.66-74.

Mednick, N. (2013). *Plaster Consolidation.* Clem Labine's Traditional Building.

Stewart, H. (2011). *Practical Building Conservation: Mortars, Renders, and Plasters*. English Heritage, Ashgate, Farnham, England.

Stewart, R (2013). *A systematic method for Assessing Wood Lath & Plaster Ceilings in Historic Churches and Heritage Buildings.* Conference for Catholic Facility Managment.

Swiss Association of Road and Transport Experts, Swiss Standard SN 640 312A, *Vibration Impacts on Structures*, (1992), English Translation. Zurich, Switzerland.

Vitruvius, (c. 25 BCE), *De Architectura*, English language translation by Morris Hicky Morgan, *Vitruvius: The Ten Books on Architecture*, Dover, 1960.

XV International Conference on Durability of Building Materials and Components
DBMC 2020, Barcelona
C. Serrat, J.R. Casas and V. Gibert (Eds)

The Stone Masonry Contribution in Greek Industrial Buildings' Typology and Construction Durability (Late 19th to Early 20th Century)

Georgia G. Cheirchanteri

Department of Civil Engineer, Faculty of Engineering, University of West Attica (UNIWA), Ag. Spyridonos 28 p.c. 12243 Egaleo, Athens, Greece, geoxeirr@gmail.com

Abstract. *Stone masonry is the oldest form of construction in the world until the beginning of the 20th century. The first stone walls were constructed by farmers and primitive people by piling loose field stones into a dry stone wall. Later, mortar and plaster were used, especially in the construction of city walls, castles, and other fortifications before and during the Middle Ages. These stone walls are spread throughout the world in different forms. Stone walls are usually made of local materials varying from limestone and flint to granite and sandstone. However, the quality of building stone varies greatly, both in its endurance to weathering, resistance to water penetration and in its ability to be worked into regular shapes before construction. Also, the majority of buildings in Greece at the end of 19th century up to the use of concrete in constructions are load-bearing stone masonry structures. Moreover, research shows that it is the most widely construction material in industrial buildings, that era. As it is known, stone masonry has high compression strength under vertical loads but has low tensile strength (against twisting or stretching) unless reinforced, while the tensile strength of masonry walls can be increased by thickening the wall. In general, industrial buildings constructed of stone masonry, from late 19th to early 20th century, have particularities in their typology because they were directly dependent on their mechanical equipment and production line. The aim of this study is to investigate the contribution of stone masonry as a construction material in the typology of these industrial buildings concerning their durability.*

Keywords: *Stone Masonry, Durability, Stone Masonry Properties, Traditional Constructions, Industrial Buildings' Typology.*

1 Introduction

Stone masonry is a traditional form of construction practiced for centuries in the regions where stone is locally available (Khan, Lemmen, 2013). Until the emergence and wide use of steel around the mid-20th century, load-bearing masonry was the only building material up to date in the construction of various works around the world. Exceptions were areas where wood was used exclusively for building. In countries with a tradition in using masonry constructions and where there was no strong seismicity such as Great Britain new buildings up to four floors using bearing masonry techniques are still constructed.

This type of masonry is still found in old historic centres, often in buildings of cultural and historical significance, and in developing countries where it represents affordable and cost-effective housing construction. This construction type is present in earthquake-prone regions of the world, such as Mediterranean Europe and North Africa, the Middle East, India, Nepal, and other parts of Asia.

Houses of this construction type are found both in urban and rural areas. There are broad variations in their shape and the number of storeys. Houses in rural areas are generally smaller in size and have smaller openings since they are typically used by a single family. Buildings in urban areas are often of mixed use, that is, with a commercial ground floor and a multifamily residential area above. Houses in the countryside are built as stand-alone

structures, while the neighboring houses in old town centers often share a common wall.

Moreover, research shows that it is the most widely construction material in industrial buildings, after the first Industrial Revolution. Between the end of the 19th and the beginning of the 20th century, industrial buildings constituted a large part of the cities' urban fabric, especially ports, such as Piraeus in Attica, Volos in Thessaly, Syros in the Cyclades etc., constituting an important chapter in the architectural development of each area. Therefore, their typological structures as well as their morphology, in relation to their structural construction system, which is bearing stone masonry and its durability, need special study.

2 Stone Masonry: Building Materials and Construction Technology

The main components of stone masonry are simple stones and synthetic mortar. Stones come mainly from sturdy rocks, which after a short or a long process get the proper shape to be suitable for the construction of the project. From a geological point of view, and depending on the way the rocks are formed, the natural stones used in building construction can be classified according to their origin as igneous, sedimentary and metamorphic.

The igneous stone principally used in building is granite, which was formed from the fusion of minerals under great heat below the earth's surface many thousands of years ago. Sedimentary stone was formed gradually over thousands of years from particles of calcium carbonate or sand deposited by settlement in bodies of water. Gradually layer upon layer of particles of lime or sand settled into depression in the earth's surface and in course of time these layers of lime or sand particles became compacted by the water or earth above them. Metamorphic stones have been changed from igneous or sedimentary stone or from earth into metamorphic stone by pressure, or heat, or both in the earth's crust. Examples are: a) marble which was formed from limestone and slate and b) shale formed from clay (Anmol, J.-10: 2019).

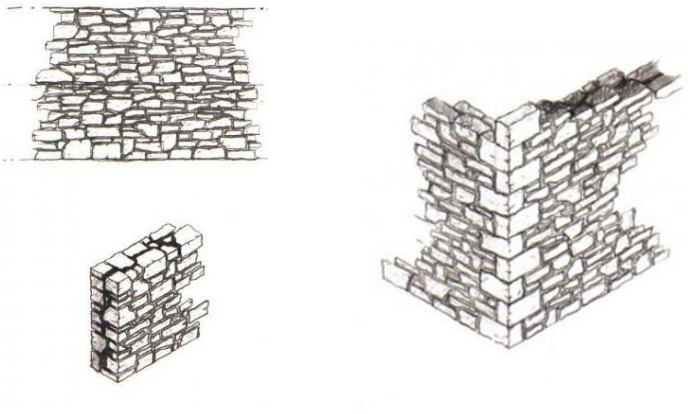

Figure 1. Stone masonry constructions.

Stone masonry is the most common type of masonry in Greek traditional architecture due to the abundance of stone in many places in Greece. They can be distinguished in coursed rubble masonry and uncoursed rubble masonry (Fig1.). The coursed rubble masonry walls have more durability due to the better fitting of the stones and homogeneity. However, they require larger and better quality of stones, in order to have quantity and quality material for achieving the best possible fitting. Furthermore, highly skilled craftsmen are required to carve

the stones properly. The highest level of coursed rubble and durability, was achieved by the creators of the marble buildings in the Acropolis rock, in Athens. The carved stones were so well fitted together that no mortar was needed and their interconnection was finalized with internal metal fasteners.

On the other hand, uncoursed rubble masonry has the disadvantage of less durability, due to the poor adhesion of the stones and the high proportion of mortar required to fill the gaps. Another factor of less strength is the heterogeneity of the stones, since their irregular shape requires the use of different sizes to fill the gaps. Typical traditional architecture adopts an intermediate state using the coursed rubble stones are in the most sensitive parts of the building (corners, base, crown), and the uncoursed rubble stones in the least sensitive or visible parts of the building. Although brick masonry is very common in lowland areas where stone is scarce, as well as in northern Europe, in areas where the stone is abundant, there are brick masonry constructions, because they have some advantages over stone masonry such as the light weight of the bricks compared to the stones and the standardization of their dimensions (Ravi *et al*., 2014; Francis *et al.,* 1971).

Mortar, the binder material between the stones in masonry, is called the mixture consisting of fine aggregates (maximum aggregate grain diameter 4mm), cements such as binder and treatment water, having a wide variety of compositions and strengths (ASTM C 270-10:1019). Generally, the use of mortars makes the stonewall a comprehensive body, carrying safely the loads it was designed for and remaining also unchanged over time. Mortar's mechanical properties have a catalytic effect on the masonry characteristics. An additional factor of diversity is the construction type or otherwise the "knitting" way of masonry construction, giving to the stone masonry a distinct character and some additional features, such as better bonding and stone durability.

Structural walls are supported either by stone masonry strip footings or not. Floor structures in towns and historic centers are vaulted brick masonry at the ground floor level and timber joists at the upper floor levels. Timber joists are usually placed on walls without any physical connection. The original floor structures in historic buildings have typically been replaced either by a precast joist system or by solid reinforced concrete slabs especially in Italy (WHE Report 28-8:1019) and Slovenia (WHE Report 58-8:1019).

3 The Structural Stone Masonry Mechanical Behavior and Durability Under Vertical and Seismic Loads

The mechanical behavior of masonry is characterized by:
-Relatively high compressive strength.
-Extremely low tensile strength.
-Relatively satisfactory shear strength.
-Strongly anisotropic behavior.

The high compression strength of the masonry compared to its other mechanical properties also determined its use as a mainly compressed load bearing component (Stylianidis *et al.*-10:2019). Both the strength and type of failure of compression masonry are strongly influenced by the angle of the compression force as to the direction of horizontal joints (anisotropy).

When a masonry construction is being pressed perpendicularly to the main horizontal joints, usually, fails due to transverse splitting of the stones, due to the development of tensile

strength in transverse directions. These tensile strengths are caused by the reconciliation of the large transverse deformations of the mortar joints with the smaller ones of the bricks, which causes corresponding transverse adhesion in the mortar. Thus, under axial compressive loading of the masonry, triaxial strength is developing on the stones and joint mortar. When using the term masonry strength refers to the compressive strength perpendicular to the horizontal joints (Tensing *et al.,* 2013).

The compressive strength of the masonry depends on:

1. The properties of stones, such as their strength, type and geometry.
2. The characteristics of the mortar such as its durability and composition.
3. The prevailing conditions in masonry i.e. the manner of engagement of masonry.
4. The material and the thickness of the joint.
5. How to apply and effect concentrated loads.
6. The quality of construction.

On the other hand, features of weaknesses in masonry are due to the behavior of the contact interface, mainly, along the repeated horizontal joints that have been characterized as "weak levels of masonry". The tensile strength of the masonry is clearly much lower than the compression, varying and depending on the angle of the tensile strength in the horizontal joints. In particular, the tensile strength of the bearing masonry is low, being perpendicularly to the horizontal joints and greater when is parallel to them. In case there is tensile strength on the joints, the mortar will be detached. Usually, the tensile strength being parallel to the joints is greater the tensile strength is greater, because of the resistance to sliding mortar or stone, as well as, the tensile strength of masonry.

Factors affecting tensile strength of masonry:

A. Joint resistance to detachment
B. Tensile strength mortar.
C. Mortar coherence.

Masonry's behavior in shear compression is more satisfactory, as the incurred structure passes through various stages, until reach the crash stage. Pressing under vertical loads is clearly defined, but it is not the same in case of seismic pressing. Even after the simplification of the earthquake action in the two main directions of the building, the size and distribution of the seismic intersection (also between the vertical load-bearing elements of each floor) depending on the geometric and dynamic mechanical characteristics of the bearing organism, remains unpredictable (Kaaki, 2013).

The most important factors affecting the seismic performance of these type of buildings are the strength of the stone and mortar, the quality of construction and the density, distribution of structural walls and wall intersections and floor/roof-wall connections (Costa *et al.,* 2011).

Stone masonry construction generally shows very poor seismic performance. Poor quality of mortar is the main reason for the low tensile strength of rubble stone masonry. Timber floor and roof structures are usually not heavy and therefore do not induce large seismic forces. However, typical timber floor structures are made of timber joists that are not properly connected to structural walls. These structures are rather flexible and are not able to act as rigid diaphragms. Due to their large thickness, stone masonry walls are rather heavy and induce significant seismic forces.

Typical damage patterns for built rubble stone masonry are delamination and disintegration, infilling in weak mud mortar with many air voids. Out-of-plane failure can occur when the connections between the exterior and interior walls are inadequate. When the

connections between the perpendicular walls are strong, the wall shear capacity can be exhausted, thus causing typical shear cracks can be developed.

Figure 2. Dracopoulos Textile House, Athens, Greece (1882). **Figure 3.** Politis Factory, Piraeus, Greece (1882).

Figures 4, 5, 6. Power Plant in Karditsa, Greece (1909).

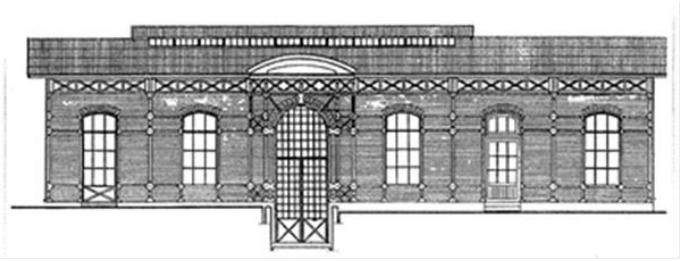

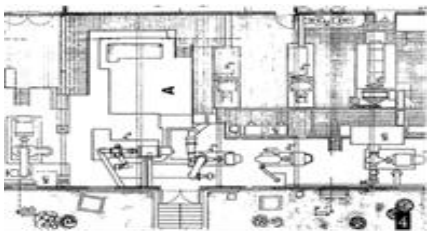

Figures 7, 8. Water Pumping Station building, Thessaloniki, Greece (1890-1892).

4 Typological and Material Characterization of Stone Masonry Durability in Industrial Buildings

Basic properties of stones for stone masonry are strength and durability, while economy and appearance are additional values. The main considerations for durability are the lasting qualities of stone itself and the locality where it is going to be used. Porous stones are unsuitable for areas prone to heavy rainfall and frost. Stones, e.g. marbles having low porosity and low coefficients of expansion and contraction should be used in areas subjected to large variations in rainfall and temperatures. Generally, lime and cement mortars are used for stone masonry, providing a workable matrix and ultimately a hard building material, which renders masonry into a monolithic unit.

As a matter of fact, the typology of traditional industrial buildings has been characterized by the elongated rectangular shape of the ground plan (Fig 8,9.), which contained the mechanical equipment for the production of the products. These elongated rectangular industrial buildings must have very thick walls (from 0,50 to approximately 1,00 meter, depending on the building's size: height and length) in order masonry durability to be increased. Also, this building's shape proves that the layout of the machines was not random, but was arranged in a linear layout to facilitate the production line. Using the perimetric bearing stone masonry, which was the structural construction system until the early 20th century, it was possible to construct most of the rectangular elongated buildings, or even having a square ground plan (Cheirchanteri, 2014).

The entrance of this type of buildings was most often located in the center of the narrow or longitudinal side, in such a way, that the production line was not interrupted. In this construction building system, although the openings were large, symmetrical, repetitive and sometimes arched, interior lighting was not sufficient in the middle of the building. As a result, elevated skylights were installed along the roof in order to enhance lighting (Fig 7,10,11.), (Cheirchanteri, 2014).

Masonry advantages, usually, include thermal insulation, fire safety, durability, ecological recycling materials of the building at the end of its lifetime and the elegant façade appearance. Among the disadvantages is the diversity of the stones, which makes its mechanical behavior unpredictable, contributing in the great difficulty of standardizing materials and methods (Phan *et al.,* 2003).

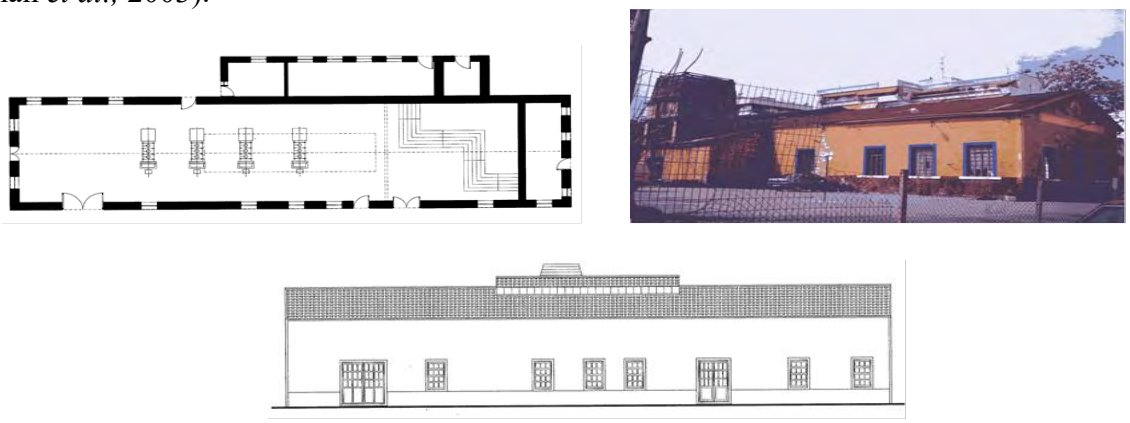

Figures 9, 10, 11. Power Plant building in Larisa, Greece (1913).

4.1 Stone Masonry Greek Industrial Buildings' Typology and Construction Durability

Until World War I, the typology of industrial buildings in Greece was the same as in Europe. The architectural volumes of these buildings were adapted to the shape and size of the mechanical equipment, as well as to the needs of the production cycle, unlike to other private and public buildings of that era, in which the shape, size, and layout were following strictly by the stereotypes, dictated by neoclassicism.

The basic type of these industrial buildings was the elongated rectangular shape, while the facilities were formed by the layout of many similar units. The machines were positioned across the production area, due to the motion transmission way and the side windows location, which were the only source of natural light for the workforce. Most of them were constructed using traditional techniques. It should be noted that industrial buildings were morphologically influenced by neoclassicism. According to their characteristics they were classified into three categories: the traditional industrial buildings, the monumental and the ragged in shape.

The industrial ground floor buildings constructed until 1900, were usually using in masonries stones cut and dressed to proper shapes, as well as, double incline roofed contractions, with small rectangular repeated openings. The stone masonry of these buildings was load-bearing, made of traditional materials such as wood, stone, tiles, and in many cases cast iron and steel. But their dominant feature was the incorporation of local architectural elements, achieved using traditional materials and construction methods. Concerning construction durability, bearing walls used to be very thick, about 1,00 meter, because of their very big height and length, which were demanded for their mechanical equipment.

A typical example of a traditional industrial ground floor building, built in 1882 in Athens, is the Drakopoulos Textile House (Fig 2.). It was one of the rare occasions among the first factories that the building was outstanding (variety of apertures, classic pediment on the façades, elaborate details, characteristic patterns), as opposed to the simple form of other factories in Greece. Also, the Politis factory in Piraeus (Fig3.), built between 1907 and 1916, had the same treatment as the first ground floor industrial buildings. The arched openings were dominant, while the consecutive double incline roofs had jagged architraves, with double skylights windows in the center, forming small, rectangular openings (Cheirchanteri, 2014).

The Turbine House of the Larissa's Power Plant in Thessaly (1913, Fig 9,10,11.), was a building with an oblong rectangular ground plan and a double incline tiled roof elevated on its central part, completing natural lighting and ventilation of the building. On the other hand, the Power Plant in Karditsa city, also in Thessaly area (1909, Fig 4,5,6.) was an industrial complex of two buildings, one and two-storey, correspondingly. Additionally, noteworthy is the monumental Water Pumping Station building in Thessaloniki (Fig 7,8.), built by Belgian engineers in 1890–1892. The metal elements in combination with the bricks in the prominent masonry of the building formed a radical façade appearance (Cheirchanteri, 2014).

5 Conclusions

- Stone masonry as the oldest traditional form construction in the world was also the most popular construction material in industrial buildings, after the first Industrial Revolution. The typology of industrial buildings in Greece was the same as in Europe, where the architectural volumes of these buildings were adapted to the shape and size

of their mechanical equipment and production needs.

- The typology of traditional industrial buildings in Greece was characterized by the elongated rectangular shape of the ground plan, which depended on the stone masonry load-bearing construction system and the mechanical production equipment.
- Stone masonry has high compressive strength under vertical loads, but has low tensile strength (against twisting or stretching) unless reinforced, while the tensile strength of masonry walls can be increased by thickening the wall.
- Concluding, the stone masonry contribution in Greek industrial buildings' typology and construction durability has been proved by the elongated rectangular shape ground plan, which includes the arranged linear machines layout, in order to facilitate the product line. Concerning the industrial buildings construction durability, it was achieved by the big thickness of bearing walls, despite their length and height. In many occasions they were big enough due to the requirements of the mechanical equipment, which was located inside the buildings.

Acknowledgments
The publication/registration fees were totally covered by the University of West Attica.

ORCID
Georgia Cheirchanteri: https://orcid.org/0000-0001-8099-7522

References

Anmol, J. (2019). Stone masonry, https://www.scribd.com/document/137931876/Lecture-No-11-Stone-Masonry (attached 15-10-2019)

ASTM C270, Specification of Mortars and Masonry Units.

Cheirchanteri, G. (2014). *Power plants' first buildings during the period 1889-1940/50: Founding Factors and Planning* (in Greek), PhD Thesis in NTUA, Athens.

Costa, C., Costa, P., Arêde, A. and Costa,A. (2011). Detailed FEM modelling of stone masonry arch bridges under road traffic moving loads, in: M. Papadrakakis, M. Fragiadakis, V. Plevris (Eds.), *3rd ECCOMAS Thematic Conference on Computational Methods in Structural Dynamics and Earthquake Engineering* - COMPDYN 2011, Corfu, Greece

Francis, A.J., Horman, C.B. and Jerems, L.E. (1971). The effect of Joint Thickness and other factors on ths Compressive Strength of Brickwork, *Proc. of the 2nd Inter. Brick – Masonry Conf*., G. Britain, pp 31-37.

Kaaki,T. (2013). *Behaviour and Strength of Masonry Prisms Loaded in Compression*, Dalhousie University

Khan, A. and Lemmen, C. (2013). Bricks and urbanism in the Indus valley, rise and decline, available at: https://arxiv.org/pdf/1303.1426.pdf (attached 20-10-2019)

Phan, L.T. and Carino, N.J. (2003). Code provisions for high strength concrete strength-temperature relationship at elevated temperatures, *Materials and Structures, Vol. 36, No. 2*, pp. 91-98, 2003

Ravi, S., Viswanathan, S., Nagarajan, T., Srinivas,V. and Narayanan, P. (2014). Experimental and Numerical Investigations on Material Behaviour of Brick Masonry, *2nd International Conference on Research in Science, Engineering and Technology*, Dubai, UAE, March 21-22-2014.

Stylianidis, K. and Ignadakis, C. (2019). Masonry load bearing constructions, Technical Chamber of Greece, Central Makedonia Sector, http://www.kxcivileng.gr/archive/technical/Katskeues_ferousas_toixopoiias.pdf (attached 15-10-2019)

Tensing, D., Freeda, C.C. and Mercy, S.R. (2013). Experimental study on axial compressive strength and elastic modulus of the clay and fly ash brick masonry, *Journal of Civil Engineering and Construction Technology, Vol. 4, No. 4*, pp. 134-141

World Housing Encyclopedia, Italy WHE Report 28 (attached 20-8-2019)

World Housing Encyclopedia, Slovenia WHE Report 58 (attached 20-8-2019)

XV International Conference on Durability of Building Materials and Components
DBMC 2020, Barcelona
C. Serrat, J.R. Casas and V. Gibert (Eds)

The Structural Strengthening of a Masonry Heritage Shop House using Glass Fibre Based Materials

Kribanandan Gurusamy Naidu

JTK Consult Sdn Bhd, Kuala Lumpur, Federal Territory, Malaysia, drkribangn@jtkconsult.com.my

Abstract. *A two-storey masonry pre-war shop house in Taiping, Malaysia was badly affected by construction being undertaken at an adjacent lot. The building was in a serious state of disrepair and on the verge of collapse at the time of the investigation and temporary propping and a stoppage of adjacent works had to be imposed. For the remedial intervention a rapid approach was critical with materials and methodologies selected to incur minimum additional impacts on the building in terms of physical works and with flexibility on site. Several innovative techniques developed for the structural intervention of masonry buildings was considered. In this case the masonry wall cracks were repaired by a stitching method using the glass fiber rod maperod g which was considered a suitable material due to the compatibility of modulus of elasticity (40,800N/mm2) to the lime mortar, having good tensile strength of 760 N/mm2 to help bridge the cracks in case of further movement and is also corrosion resistant and will remain protected in future even though it is embedded in a highly porous masonry substrate. The materials used were easily transportable, flexible (ie) could be prepared to requirements on site and could be delivered to site quickly despite this being imported. The approach taken resulted in a rapid reinstatement of the building, minimised the risk of losing heritage features and matched the client's overall objectives. The paper provides details of the approach taken and the basis for the remedial intervention.*

Keywords: *Masonry, Structural Cracking, Remedial Intervention, Glass Fibre Materials.*

1 Introduction

1.1 Project Background

A masonry shop house in Taiping, Perak in Malaysia was badly affected by construction being undertaken at an adjacent lot. There was significant evidence of settlement at the front and back of the building, leading to significant cracking of a party wall, front and rear walls and the main walkway Arch Supporting the upper floor and wall.

The building is a 2 storey pre-war shop house with an overall layout plan as shown in Figure 1. The building housed a family business until adjacent construction activity forced the owners to move from the premises due to an eviction order imposed by the local authority arising from the dangerous state of the building. The actual construction details of the adjacent building was not made available but the site visit confirmed that the original 2 storey building next door had been torn down to make way for a 3 storey structure on piled foundations with a lift at the rear.

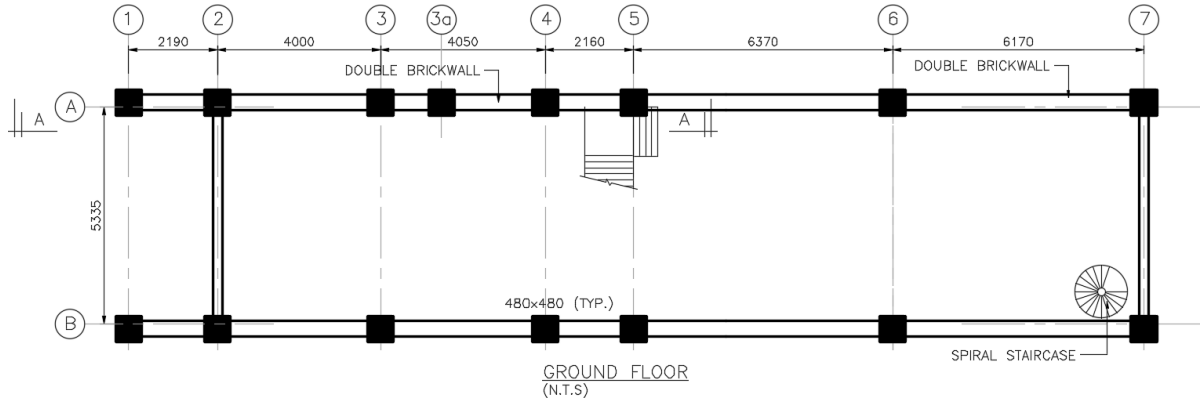

Figure 1. Plan View of Shop House.

The only precaution taken to protect the shop house was an attempt to support the common corridor arch at the front of the building with Timber Props which was totally inappropriate for a structural masonry arch and had potentially accentuated the serious damage caused by imposed stress concentrations due to the settlement and vibration. The structural Engineer who designed the new adjacent 3 storey shop house was asked by the local authority to provide a report and a basis for remedial intervention. The initial suggested approach to epoxy inject the cracks were considered wholly inadequate and not a serious measure of what was required to reinstate the shop house to its original design intent and to guard against long term settlement and cracking associated with the disturbed foundations. A site walk through was undertaken to view the condition of the structure and this is discussed below.

1.2 Condition Audit

There was considerable evidence of settlement of the columns in gridline A/1-3 as shown in Figure 2. This led to uneven loads on the masonry columns causing the characteristic structural cracking of the Arch, where cracks of up to 50 mm in width were noted. A closer examination of the party wall from the adjacent shop house confirmed that the structural cracking extended to this wall along Gridline A2- A5 where cracks of up to 30 mm were noted. In general the party wall away from the new development was structurally intact. An immediate intervention was proposed to structurally reinstate the front Arch, the common party wall along gridline A and other settlement and cracking points. It was noted that the building was not loaded with the full complement of live loads which can be expected. The cracking on the walls and the Corridor Arch were clearly to do with settlement and vibration loads associated with the adjacent construction, rendering the building unsafe to use at the time of the investigation. There was also a considerable amount of water ingress into the building particular at gridline A-B'/5-7 and also at the building corners at gridline A1 and A5 which had not been a problem previously. Based on the visual survey the key defects noted are summarised in Table1.

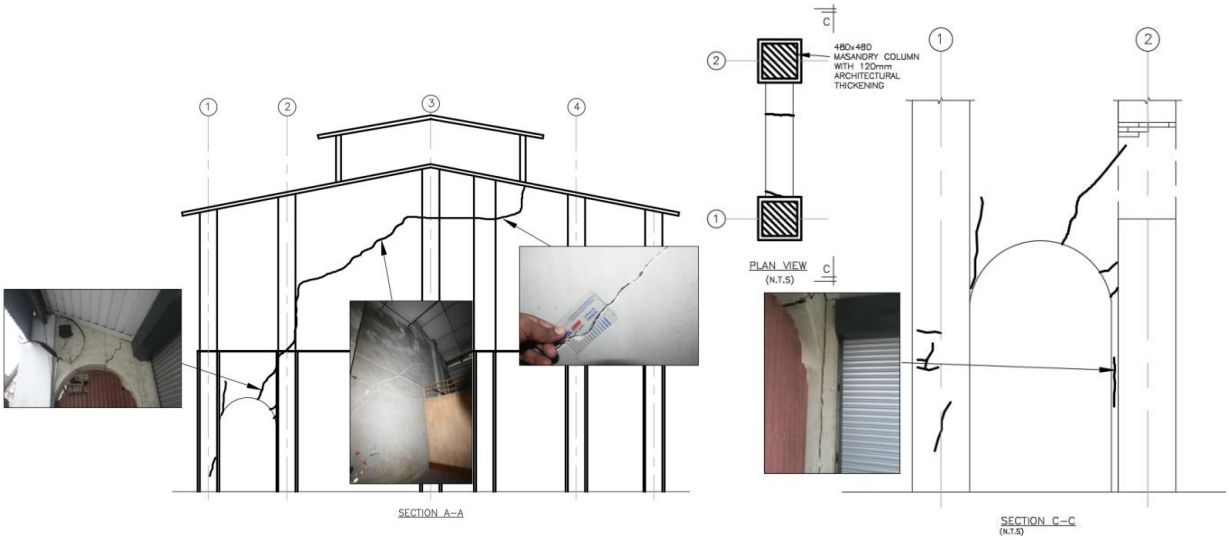

Figure 2. A Record of the defects at the Main Arch at the Shop House Front and at the Party Wall.

2 Engineering Features

2.1 Overview

Demolition of masonry shop houses and rebuilding is often considered the preferred option when such structures come into disrepair. Increasingly however repair and refurbishment is seen as a more sustainable option in terms of architectural value, materials use, neighbourhood disruption, waste disposal and overall cost. By avoiding expensive demolition and rebuild, the development of repair and refurbishment techniques retains the aesthetic and historic value of a building including its appearance and providing a sustainable structural solution. It also potentially reduces costs.

Where defects are related to settlement, it is necessary to repair or underpin the foundations before any stitching of the cracks on the brick masonry. In historic buildings, it is important to preserve as much of the original materials as possible and consider repair options which are relatively reversible and do not damage the original building fabric.

2.2 Options for Structural Reinstatement

The building was in a serious state of disrepair and on the verge of collapse. Temporary propping and a stoppage of adjacent works had to be imposed. A rapid approach was critical for the intervention, with materials and methodologies selected to incur minimum additional impacts on the building in terms of physical works and with flexibility on site.

Table 1. Summary of Condition Audit Findings.

Item	Type of Damage	Location of Damage	Options for Reinstatement
1	Damage to Footings Leading to Settlement	Party Wall between unit 150 and 152, Gridline A1-7	Compensation Grouting was done for all footings at the common Boundary between the Shop House 150 and 152 from Gridline A/1 to 7 to guard against future movement and settlement.
2	Structural Cracking of the Arch and associated Party Wall	At the Front Corridor Gridline A/1 - 3	The Arch was fully supported with a radial support structure and props to facilitate repairs. The remedial works involved reinforcing the whole span of the masonry arch across the crack with Carbon Fibre Rods and an appropriate mortar effectively introducing structural beams above the arch opening so that load shedding is directed to the columns. The remedial intervention also involved stitching of structural cracking which extended to the party wall and columns to cover the full extent of cracking
3	Wall Crack	Party wall between Gridline A/2 - 4	The remedial works consisted of stitching the cracks with Carbon Fibre Rods and a structural grade epoxy. The stitching was extended to the full extent of cracking
4	Window Lintol and wall Cracks	Gridline A-B/1	Epoxy Injection and Borehole Suspension' Grout used
5	Settlement Cracks at the Rear of Building	Gridline A-B/7	Epoxy Injection and Borehole Suspension' Grout used
6	Level 1 Cracks Leading to Water Ingress	A-B'/5-7	Flexible Acrylic Gel to Seal the Cracks with the Option of Reinjection if the problem is not resolved in the first instance
7	Other Areas of Water Ingress	A1 and A5	Further investigation was required at roof level to ascertain the source of the water leakage problems. Repair as per 6 was required and in this case replacement of damp plaster works was also necessary.
8	General		Replastering, Overall Repainting and Replacement of Internal fittings affected by moisture ingress adjacent to party wall was done.

Several innovative techniques have been developed for the structural intervention of masonry buildings. Among the key developments in this area includes the use of stainless steel helical ties and slim ties developed by Helifix (www.helifix.com). These form very strong axial ties to resist lateral forces, yet are flexible enough to accommodate natural building movement without introducing further stresses in the substrate. The associated concealed, non-disruptive installation techniques provide many outstanding benefits, from the simplicity of their design to ease of installation and their long term performance. At the time of the investigation the options for repair had been further advanced by Mapei using alternative materials with glass fibre as the base ie Maperod G and Mapewrap Foccio. Where masonry wall cracks are to be repaired by a stitching method, the glass fiber rod maperod G is a suitable material due to the compatibility of modulus of elasticity (40,800N/mm2) to the lime mortar. It also has a good tensile strength of 760 N/mm2 to help bridge the cracks in case of further movement. As glass fiber is also corrosion resistant it will be protected in future even though it is embedded in the highly porous masonry substrate. In the case of the Taiping shop house the latter approach *i.e* Mapei rod was used as the materials were easily transportable, flexible *i.e* could be prepared to requirements on site, and Mapei had the infrastructure to deliver the materials to site quickly despite this being imported.

2.3 Approach to Reinstatement

The extent of the remedial works was confirmed based on the visual examination and following hammer tapping and hacking to confirm the extent of the problem. The final remedial works undertaken between gridlines 1-5/A included the following:

a) Stabilization of six column foundations A/1, A/2, A/3, A/4, A/5 and A/6 with soil grouting using OPC and Intraplast –Z.
b) Stabilization of six column foundations A/1, A/2, A/3, A/4, A/5 and A/6 with soil grouting using OPC and Intraplast –Z.
c) Removal of wall plaster and re plastering using Mape-Antique MC a prebagged lime based plaster
d) The full reconstruction of one column at gridline A/3 by re-using the existing bricks which were carefully dismantled piece by piece.
e) The columns at gridline A/2 and A/5 were partially removed and the bricks reinstated and injected using Mape-Antique I by a low pressure injection method.
f) The Arch and wall cracks were repaired by a stitching method using Maperod G a glass fibre rod which is inert within the matrix but providing structural strength.
g) Mapewrap G Fiocco was used allowing stitching to be performed at one-side with minimum impact to the overall wall with the anchors planted deep into the masonry wall to provide the full anchorage.

In this case the stitching could only be performed at one-side and for this reason Mapewrap G Fiocco was selected as an appropriate method. Mapewrap G Fiocco is made into an L-shaped anchor using epoxy impregnator Mapewrap 31 SP and is bonded at both ends of the Maperod G.

The anchor is planted deep into the masonry wall, ie approximately to a depth of 140mm to provide the full anchorage. To structurally bond the Maperod G and Mapewrap Fiocco to the masonry wall, epoxy adhesive Adesilex PG2 TG was selected. Epoxy has high durability and good mechanical properties in terms of compressive, flexural, tensile and shear strength.

To enhance the bonding to the masonry wall, all contact surfaces of the masonry were primed with Mapewrap Primer 1 SP to consolidate the porous surface and eliminate dust. The crack lines were reinforced at every 4-5 brick intervals and inserted into the pointing layer for a minimal impact on the existing masonry wall. The full extent of the repairs is illustrated in Figure 3.

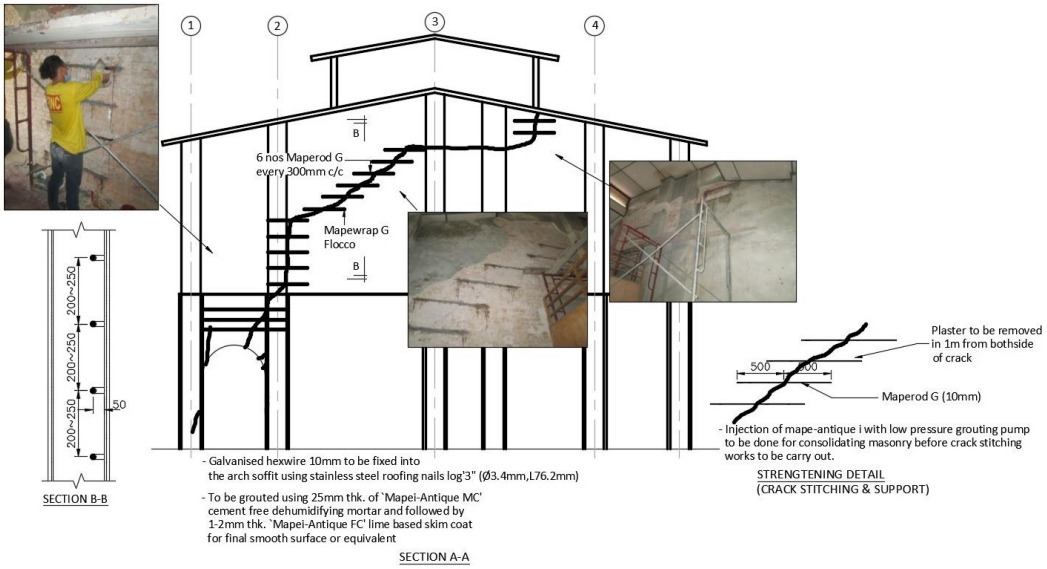

Figure 3. Significant Cracking of the Arch and Party Wall and the proposed approach to crack repair.

The remedial work was carried out by a specialist contractor and the repair materials were supplied by Mapei. The works were carried out successfully and the shop house was reinstated to its original condition within 3 weeks (see Figure 4).

Figure 4. Additional Illustrations of the Remedial works.

3 Project Accomplishment

3.1 Client Needs

The remedial works were undertaken rapidly and reduced the impact of the loss of access to the facility. The alternative which was on the cards was demolition and rebuilding. The engineering solution entailed using modern materials developed specifically for heritage upgrading which had never been used in a practical project application before for structural restoration. The work was done with little impact on the overall heritage value of the building.

3.2 Budget and Project Time Line

The project was successfully controlled with the implementation of proper documentation in the form of detailed method statements and pre-selection of materials to be used directly from a specialist supplier (Mapei). In conjunction with Mapei an off-site training was undertaken of key personnel involved in the project to minimise delay on site.

The arches and key structural components had been temporarily propped using specially designed timber props to guard against collapse and this was removed progressively. The stabilization of the foundation was undertaken within a week and as the injection works were completed in a particular area masonry strengthening works proceeded in the associated area. The crack repair works and stabilisation of the masonry walls proceeded over a 2 week period. The finishing works and painting was then undertaken by the main contractor.

The works were successfully undertaken at approximately a quarter of the cost and 1/3 of time compared to rebuilding of the structure which was the only other option. As this was the full responsibility of the adjacent works contractor as per the court order, the approach taken was a win-win for all parties (ie) in terms of time and cost. This met the client's requirements for speed and minimisation of the disruption after a lengthy delay due to the legal action.

3.3 Overview

This work demonstrated the validity of the use of modern materials for a non-invasive low maintenance reinstatement of a heritage building badly affected by settlement and structural movement with little impact on its heritage value. This was considered to be the most cost-effective solution and appropriate, where speed of reinstatement to manage structurally compromised masonry buildings are concerned. As the structural rods used in strengthening are made with glass fibre reinforcement these are not affected by corrosion which is a problem in porous Masonry structures particularly if rebars are used for strengthening. In this case life cycle issues outweighed initial capital expenditures particularly as a period building was concerned and the approach minimised the risk of any repeat intervention which would have in a rapid reinstatement of the building, minimised the risk of losing heritage features and matched the client's overall objectives.

3.4 Budget and Project Time Line

The project was successfully controlled with the implementation of proper documentation in the form of detailed method statements and pre-selection of materials to be used directly from a specialist supplier (Mapei). In conjunction with Mapei an off-site training was undertaken of key personnel involved in the project to minimise delay on site.

The arches and key structural components had been temporarily propped using specially designed timber props to guard against collapse and this was removed progressively. The stabilization of the foundation was undertaken within a week and as the injection works were completed in a particular area masonry strengthening works proceeded in the associated area. The crack repair works and stabilisation of the masonry walls proceeded over a 2 week period. The finishing works and painting was then undertaken by the main contractor.

The works were successfully undertaken at approximately a quarter of the cost and 1/3 of time compared to rebuilding of the structure which was the only other option. As this was the full responsibility of the adjacent works contractor as per the court order, the approach taken was a win-win for all parties (ie) in terms of time and cost. This met the client's requirements for speed and minimisation of the disruption after a lengthy delay due to the legal action.

3.5 Overview

This work demonstrated the validity of the use of modern materials for a non-invasive low maintenance reinstatement of a heritage building badly affected by settlement and structural movement with little impact on its heritage value. This was considered to be the most cost-effective solution and appropriate, where speed of reinstatement to manage structurally compromised masonry buildings are concerned. As the structural rods used in strengthening are made with glass fibre reinforcement these are not affected by corrosion which is a problem in porous Masonry structures particularly if rebars are used for strengthening. In this case life cycle issues outweighed initial capital expenditures particularly as a period building was concerned and the approach minimised the risk of any repeat intervention which would have in a rapid reinstatement of the building, minimised the risk of losing heritage features and matched the client's overall objectives.

ORCID

Kribanandan Gurusamy Naidu: https://orcid.org/0000-0002-6782-594

References

Avdeeva, A., Shlykova, I., Antonova, M., Baraanschikov, Y. and Belyaeva, S. (2016). *Reinforcement of concrete tructures by fiberglass rods*. (Russia), St. Persburg State Polytechnical University, St Petersburg, Russia.

Jarek, B. and Kubik, A. (2015). The Examination of the Glass Fiber Reinforced Polymer Composite Rods in Terms of the Application for Concrete Reinforcement. *Procedia Engineering, 108*, 394 - 401.

Sheppard, P. and Tercelj, S. (1980). The effect of repair and strengthenings method for masonry walls. *Proceedings 7th WCEE,*6, 255 Istanbul.

Plecnik, J.M., Corsins, T. and O'Conner, E. (1986). Strengthening of Unreinforced Masonry. *Journal of structural engineering ASCE, 112*(5), 1070-1087.

XV International Conference on Durability of Building Materials and Components
DBMC 2020, Barcelona
C. Serrat, J.R. Casas and V. Gibert (Eds)

Analysis of Steel Bars in Corrosion Process after 70 Years of Natural Aging

Francieli Schmoeller[1], Maryangela G. Lima[2] and Silvelene A. Silva[3]

[1] Instituto Tecnológico de Aeronáutica (ITA), Dept. of Civil Engineering, Marechal Eduardo Gomes Sq., 50, 12228-900, São José dos Campos-SP, Brazil, francieli.schmoeller@gmail.com

[2] Instituto Tecnológico de Aeronáutica (ITA), Dept. of Civil Engineering, Marechal Eduardo Gomes Sq., 50, 12228-900, São José dos Campos-SP, Brazil, magdlima@gmail.com

[3] Instituto de Estudos Avançados (IEAv), St. Coronel Aviador José Alberto Albano do Amarante, 01, 12228-001, São José dos Campos-SP, Brazil, lenisoni@uol.com.br

Abstract. *Reinforced concrete structures are commonly used in civil engineering. However, the number of deteriorations in these structures is increasing, especially problems related to steel corrosion. Also, according studies, corrosion is responsible for about 3.5 % of annual GDP with recovery costs in world. Thus, this study analyzed the corrosion of steel bars at 70-year-old, which are in corrosion process by natural aging. Tests were performed to analyze the bars microstructure, using SEM and EDS, as well as analysis of the current mechanical characteristics, with tensile test. Through SEM, it was possible to measure the layer of the corrosion products formed at the samples edge, and to observe the fragility of this region, with the presence of several microcracks. EDS test contributed to verify the oxygen difference from the nucleus until to the specimen edge. It was possible to notice that in the edge, presence of oxygen is much greater. In the mechanical tests, by the tensile test, the samples do not reach the minimum elongation and the limit of resistance prescribed in the standard. Thus, it is believed after 70 years of natural aging, the samples are in advanced process of corrosion, with edges worn out, and no comply with the minimum mechanical requirements.*

Keywords: *Corrosion, Steel Bars, Microstructure, Deterioration, Natural Aging.*

1 Introduction

Reinforced concrete is one of the structural elements most used in construction worldwide. Consequently, the incidence of pathological manifestations that deteriorate this type of structure is increasing, mainly problems related with corrosion. In addition, corrosion causes a lot of damage to the global economic sector, generating a high cost of recovery. It is estimated that around 3.5 % of world GDP is spent annually on corrosion (SCHMITT *et al*., 2009; KOCH *et al*., 2016).

Corrosion is considered a destructive interaction of a material with its environment, usually occurring in aqueous environment, known as electrochemical corrosion. In this degradation, oxidation and reduction reactions occur, forming an electric current and an ionic current. Insomuch, it is possible to form iron oxides and hydroxides, which deposit on rebar surface and are called corrosion products.

One of variables that favor corrosion is the pH of the environment, which is responsible for enhancing this degradation. As stated by Mehta and Monteiro (2006), from the moment the concrete pH becomes lower than 11.5, the passivation film on rebar is broken, which

allows the beginning of corrosion. After the steel depassivation, the corrosion propagation phase begins, with the development of the corrosive process, in which each material reacts and has a particular deterioration velocity (SOUZA and RIPPER, 1998).

Thus, there is a relation as pH function, which is represented in E-pH diagram, known as the Pourbaix diagram (1974). In this diagram, the pH conditions are established in relation to the potential that take the material to three distinct situations: the immunity region, which independent of pH, the steel has a very low corrosion potential, being protected; the passivation area, which the armor has the protective layer; and corrosion, located in circumstances of more acidic pH, which the reinforcement depassivation occurs and, consequently, its deterioration.

Also, there are two main aggressive agents helping in reinforcement depassivation: the carbonation of concrete and the presence of chloride ions. Carbonation involves the penetration of carbon dioxide (CO_2) into the concrete by diffusion, resulting in a gradual decrease of pH. It is ranging from 12.5-13.5 to a pH close 9, thus losing its high alkalinity (LIMA, 1996).

Other aggressive agent is chloride (Cl^-) ions, penetrating or embedded in the concrete, which reach the steel, resulting in the reinforcement depassivation even with the high pH (LIMA, 1996). Thereby, the presence of chlorides ions especially in marine exposure and the loss of alkalinity due to the carbonation of the concrete can destroy the passive film that protects the steel and induce its corrosion (BOSSIO *et al*., 2015).

Tuutti (1982) proposed what currently is considered the classical model of reinforcement concrete structure life cycle, which period of life cycle is considered as the sum of the corrosion initiation and propagation periods, until the moment the structure needs correction. Moreover, any loss of rebar protection affects significantly the durability and service life of reinforced concrete structures and may compromise and even induce to collapse.

Necessity to better understand this degradation process, in order to improve the quality and performance of structures, resulted in the microstructural study of steel bars at 70-year-old, which were in corrosion process by natural aging.

Scanning electron microscopy (SEM) was used to analyze the material's microstructure. Energy Dispersive X-Ray Spectroscopy (EDS) was utilized to examine the difference in chemical composition between the grains and the layer of corrosion products formed on the surface. In addition, the mechanical tensile test was performed to obtain the current mechanical state of the specimens.

2 Materials and Methods

This chapter will present the materials that composed the sample of the study, as well as the methodology used to achieve the intended tests.

2.1 Materials

Three bars composed the specimens, belonging to foundation block of ITA’s building. The bars were smooth, originally had a nominal diameter of 15.88 mm (5/8”), and were named B1, B2 and B6.

Figure 1. Specimen B2 before preparation and cutting.

These bars remained underground and unloaded for approximately a period 60 years, from their construction to 2008, when the samples were collected and stocked in the Materials Laboratory of the Civil Engineering Department. Currently, these bars have about 70 years of natural aging.

2.2 Methods

Methodology used in this study searched the analysis of steel bars with about 70 years of age, which were in corrosion process by natural aging. Figure shows the flowchart of the proposed analyses.

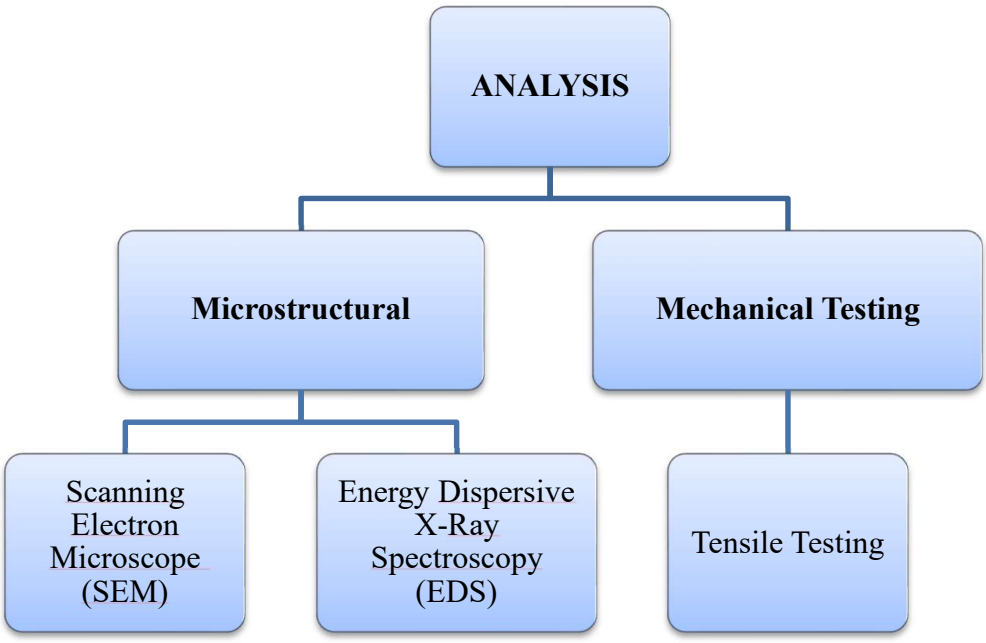

Figure 2. Flowchart with studies performed.

2.2.1 Microstructural Analysis

Scanning electron microscopy (SEM) was used to analyze the general structure of the samples, allowing the visualization of grains and grain boundaries. Thus, the bars were cut to 10 mm (0.39 in.) in length and metallographic preparation was performed to preserve the corroded edges.

Analysis by energy dispersive X-ray spectroscopy (EDS) using the Linescan technique allowed the comparison of samples chemical composition between the grains not corroded in relation to the layer of corrosion products. For this test, were used the same samples of the SEM.

2.2.2 Mechanical Testing

Tensile test was carried out on samples of 210 mm in length, seeking to analyze the behavior of the material during the test until its rupture. Therefore, it is possible to analyze the current resistance of the bars and compare with the minimum resistance required by the standard.

3 Results and Discussion

This chapter will present and analyze the results obtained from the methodology described in the previous chapter.

3.1 Microstructural Analysis

Scanning electron microscopy resulted in a more detailed study of the material, with verification of the structure formed by the grains and their boundaries. It was possible to observe the homogeneity in the grain structure of sample. Still, two distinct grain tones were observed, some grains are lighter than others, characteristic of different phases (PANDOLFO, 2006). The following image shows the result obtained by microscopy.

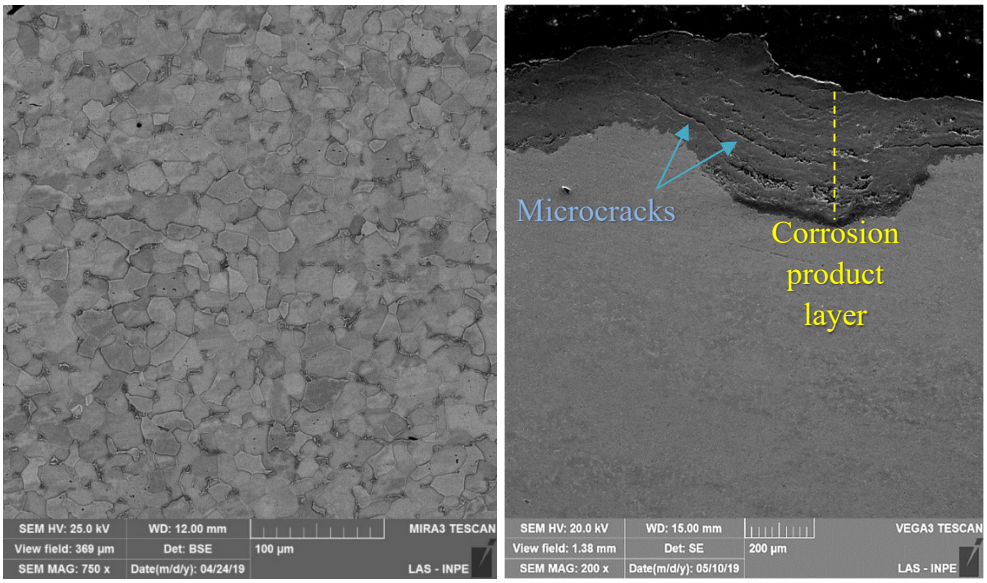

(a) (b)

Figure 3. SEM image (a) at center of the sample (b) of corrosion product layer.

Figure (a) was obtained through the backscattered detector, which allows verifying broadly the material configuration. SEM also showed the presence of the corrosion product layer formed on surface of the samples, as shown in (b). Corrosion product layer found in the bars showed irregular wear at the edges, as well as different corrosion depths. Thickness of corrosion layer ranged from 62.38 µm to 381.20 µm. Also, several microcracks and various micropores were visualized in this corrosion layer, showing fragility of this material.

Through X-ray dispersive energy spectroscopy analysis, using the Linescan technique, verified the variation in concentration of main chemical elements. For this, was defined in sample a line from the center to the corrosion layer, as shown in Figure .

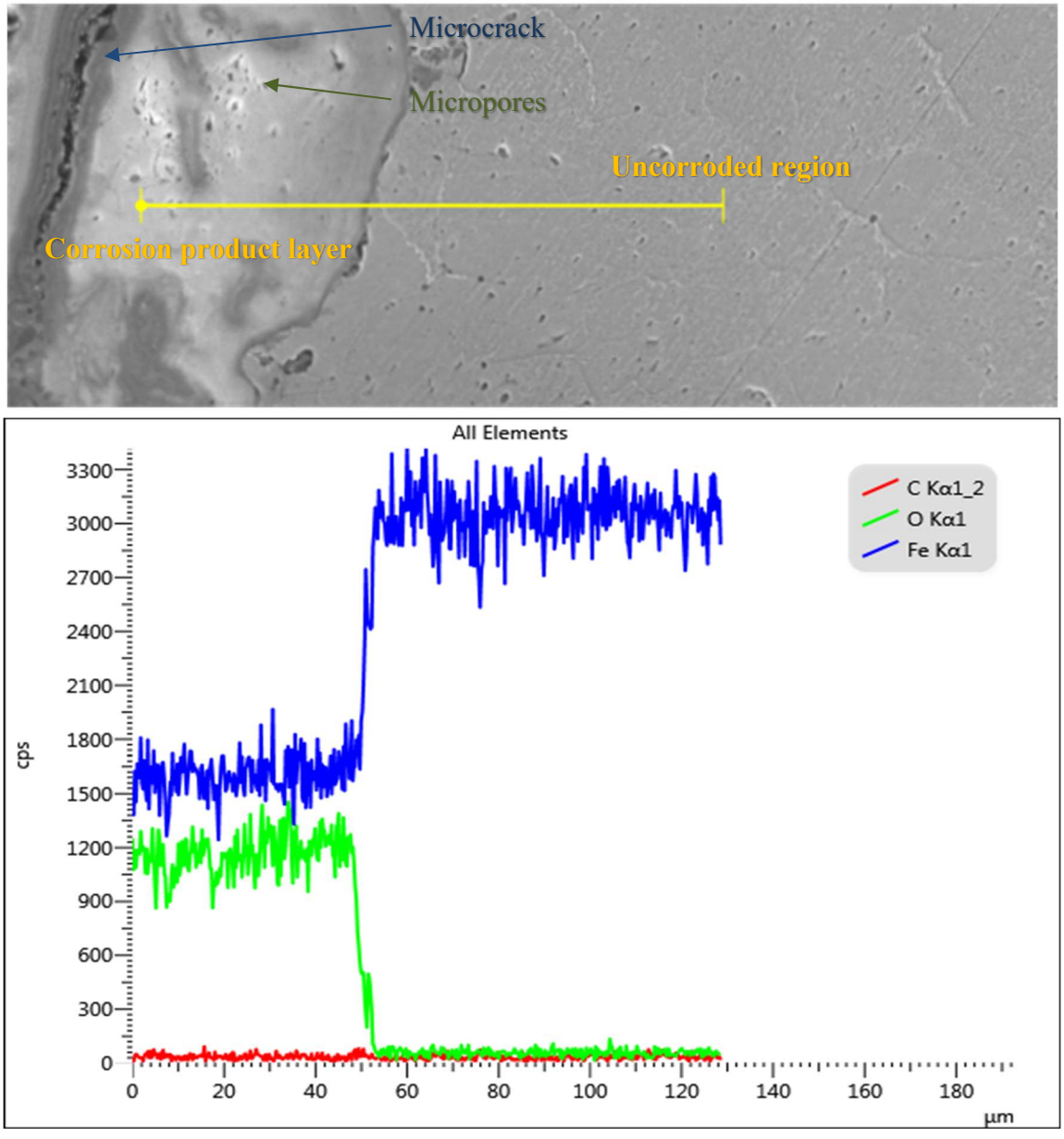

Figure 4. EDS Linescan image.

Linescan technique showed variation in concentration mainly of oxygen and iron. Non-corroded region of the three samples resulted in high iron concentration and insignificant amount of oxygen. Where the analysis reaches the corrosion layer, the iron concentration drops abruptly and the oxygen concentration rises, thus remaining throughout the corrosion product layer. As the corroded layer is formed by corrosion products, which are composed of different types of oxides and hydroxides, according Gomes and Barreto *apud* Helene (1993), this high presence of oxygen identifies the presence of these products in the corroded layer.

3.2 Mechanical Testing

To finalize the bars analysis, mechanical tensile test was performed, in order to obtain the bars strength limit. It was followed the criteria established by ASTM E8.E8M:2016, which resulted in the following data:

Table 1. Mechanical tensile test.

Sample	Tensile Strength (MPa)	Tensile Rupture (MPa)	Elongation (%)
B1	385	290	17,14
B2	355	352	19,18
B6	338	264	14,79

Comparing the results of the three samples obtained from tensile test, the strength values differed by about 12 %, ranging between 338 MPa and 385 MPa. Regarding the minimum elongation, a difference was greater, 23 %. Standard ABNT EB 3:1939 defines the minimum strength tensile of 370 MPa for these steel bars (37-CA class). Only the specimen B1 comply with the standard resistance. Still, this standard determines the minimum elongation of 18 %. In this parameter only the specimen B2 corresponds the value. Specimen B6 did not reached any of the standards requirements.

Therefore, in terms of mechanical characteristics according to tensile test performed, the steel bars are not presented in conformity to the current rules, given their state of degradation after about 70 years inside the concrete structure.

4 Conclusions

Through microstructural studies, it is possible to visualize the configuration of the material, which presented itself in a homogeneous way, with irregular grain size and shapes. In addition, the presence of grains with two different shades was observed, possibly presenting two distinct phases.

The microstructural analysis also allowed to observe a generalized corrosion process in the studied bars, with some more accentuated corrosion pits. As the corrosion occurred and progressed irregularly from the surface, points with very superficial corrosion depth and other more advanced points were found. This irregular wear can best be seen through the contrast caused by bakelite, showing that the corrosion front in this case did not act uniformly.

Another microstructural analysis was the layer of corrosion products formed on the surface of the bars. This layer presented with varied thickness, from 62.38 μm to 381.20 μm,

emphasizing that the corrosion does not occur in a uniform way. Still, the fragility of the corrosion products was observed on the surface of the bar, since the layer presented several microcracks and micropores. As shown by Zhang (1996), corrosion products may differ in their composition, structure, morphology and properties, and this will depend on the specific conditions under which the corrosion process occurs, and some are thicker, more voluminous and more porous than others.

Chemical evaluation by EDS, using the Linescan technique, it was clear the high presence of oxygen in the corroded layer, and the abrupt fall as soon as this barrier is overcome, reaching the steel that does not show signals of corrosion. This is justified because the oxygen penetration into the corroded layer is facilitated, due the presence of microcracks, differently of more conserved steel that has less porosity. Furthermore, the corrosion products formed on the surface of the steel bar are various oxides and hydroxides, which provides a high presence of oxygen in this region.

Through the tensile test, sample B1 meets the minimum strength and sample B2 corresponds to the minimum elongation indicated by the standard. However, none of the tested bars showed all results according to the established values.

Finally, all these results showed that, it was possible to notice their advanced corrosion process, after 70 years of the bars aging naturally and with no records of repair in the structures in which the bars were inserted.

Acknowledgements

Authors are grateful for the infrastructure and support of laboratory technicians from the Instituto Tecnológico de Aeronáutica (ITA), from the Instituto de Estudos Avançados (IEAv) and from the Instituto Nacional de Pesquisas Espaciais (INPE).

ORCID

Francieli Schmoeller: https://orcid.org/0000-0003-1384-1880
Maryangela Geimba de Lima: https://orcid.org/0000-0002-0046-3991
Silvelene Alessandra Silva: https://orcid.org/0000-0003-1601-5373

References

American Society for Testing and Materials. (2016). *E8/E8M. Standard test methods for tension testing of metallic materials.* Pensilvânia.

Associação Brasileira de Normas Técnicas (1939). EB-3. *Barras laminadas de aço comum para concreto armado*. Rio de Janeiro.

Bossio, A., Monetta, T., Bellucci, F., Lignola, G. P. and Prota, A. (2015). Modeling of concrete cracking due to corrosion process of reinforcement bars. *Cement and Concrete Research*, 71, 78–92. doi: 10.1016/j.cemconres.2015.01.010

Helene, P. R. L. (1993). *Contribuição ao estudo da corrosão em armaduras de concreto armado* (in portuguese), PhD Thesis. Escola Politécnica da Universidade de São Paulo (USP), São Paulo.

Koch, G., Varney, J., Thompson, N., Moghissi, O., Gould, M. and Payer, J. (2016). *International measures of prevention, application, and economics of corrosion technologies study*. Texas: NACE International.

Lima, M. G. (1996). *Inibidores de corrosão: avaliação da eficiência frente à corrosão de armaduras provocada por cloretos* (in portuguese), PhD Thesis. Escola Politécnica da Universidade de São Paulo (USP), São Paulo.

Mehta, P. K. and Monteiro, P. J. M. (2006). *Concrete: microstructure, properties, and materials*. New York, NY: McGraw-Hill.

Pandolfo, F. G. (2006). *Análise modal de materiais compósitos* (in portuguese), Dissertation. Universidade de Caxias do Sul, Rio Grande do Sul.

Pourbaix, M. (1974). *Atlas of electrochemical equilibria in aqueous solutions*. Brussels: CEBELCOR.

Schmitt, G., Schütze, M., Hays, G. F., Burns, W., Han, E. Pourbaix, A. and Jacobson, G. (2009). *Global needs for knowledge dissemination, research, and development in materials deterioration and corrosion control.* World Corrosion Organization, Worldwide.

Souza, V. C. M. and Ripper, T. (1998). *Patologia, recuperação e reforço de estruturas de concreto***.** São Paulo: PINI.

Tuutti, K. (1982). Corrosion of steel in concrete. *Swedish Cement and Concrete Research Institute*. Stockholm: CBI forskning research.

Zhang X. G. (1996). Corrosion Products. *Corrosion and Electrochemistry of Zinc*. Boston: Springer.

XV International Conference on Durability of Building Materials and Components
DBMC 2020, Barcelona
C. Serrat, J.R. Casas and V. Gibert (Eds)

Analysis of the Variation of Thermal Conductivity of Rigid Polyisocyanurate Foam (PIR) in The Context of Aging

Tomas Makaveckas, Raimondas Bliūdžius and Aurelija Levinskytė

Institute of Architecture and Construction, Kaunas University of Technology, Tunelio 60, LT-44405 Kaunas, Lithuania, asi@ktu.lt

Abstract. *For most building insulation materials, dependency of the thermal conductivity on temperature is close to linear, and it increases with rising materials temperature, but the thermal conductivity of the polyisocyanurate foam (PIR) increases in the lower temperature range, so the heat transfer through the partition insulated with this material is increased in the cold season. The thermal conductivity of PIR also increases during the aging process, especially during the later operating period, which is not covered by the standard aging procedure used to determine the declared thermal conductivity value. Also, there is a lack of information how PIR reacts to the certain temperatures and other climate conditions, and how fast it loses its thermal properties. The aim of this experimental research was to analyse the change of the thermal conductivity depending on aging temperature. 30, 50 mm thick PIR samples were prepared for the test, and the thermal conductivity of all specimens was measured at the standard conditions prior to the start of the test using the heat flow meter FOX 314, and again after each stage of aging, when the samples were kept at the certain temperature for 21 days. The results showed that the thermal conductivity of PIR increases more (up to 10 %) when kept at higher temperatures (+50 °C, and +70 °C), and after specimens undergo negative temperatures (-18 °C) it has a minor influence to the change of thermal conductivity of PIR.*

Keywords: *Polyisocyanurate Foam Insulation, Thermal Conductivity, Aging.*

1 Introduction

Thermal insulation for buildings is used to create indoor thermal comfort using as little thermal energy as possible. The thermal insulation in building envelope extends the periods of indoor thermal comfort, and by keeping buildings with smaller temperature fluctuations, it helps to preserve the integrity of building structures, increasing their lifetime (Berardi and Naldi, 2017). Long-term performance is an important consideration for choosing the best insulation material for each application (Alvey *et al.*, 2017). Change of thermal conductivity over time has been extensively studied for different thermal insulation materials such as mineral wool, expanded polystyrene foam (EPS), and extruded polystyrene foam (XPS) which are used in building insulation layer (Berardi, 2017; Khoukhi *et al.*, 2016). Current environmental issues require intensive research on energy efficiency and energy savings in buildings to reduce consumption of conventional fuel and CO_2 emissions that generate greenhouse effect (Paraschiv *et al*., 2017). Therefore, the use of rigid polyisocyanurate-polyurethane foam (PIR/PUR) in construction has recently significantly increased due to its excellent mechanical properties and low thermal conductivity (Jin *et al.*, 2014). However, changes in the thermal properties of this thermal insulation material due to environmental influences have not been sufficiently investigated.

Polyurethanes are urethane bonded polymers and are made by reacting diisocyanates with polyols, and some additional chemicals and catalysts. Polyurethane foams are one of the most effective thermal insulation materials because blowing agent gas with extremely low thermal

conductivity is trapped in the closed porous structure (Zhang *et al.*, 2017). Thermal conductivity of this material at its standard measurement temperature is low due to the blowing agent trapped in the insulation cells, which is more inert and has a lower thermal conductivity than air. This reduces heat transfer through the cells by thermal conduction and convection, however, if the temperature falls below the condensation point of the blowing agent, the gas condenses in the cell space, and since the liquid phase of the blowing agent is more conductive than its gaseous phase, the heat transfer increases (Berardi and Naldi, 2017). These phenomena result in a continuous reduction of thermal resistance (i.e. aging) of the foam over period of time, resting to a long-term equilibrium value (Mukhopadhyaya *et al.*, 2004) For a gas to function as an insulating gas in the cell of polyurethane and polyisocyanurate foam, it must be in a gaseous state (Bogdan *et al.*, 2005). Bogdan *et al.* (2005) gives few diagrams showing thermal conductivity of gases versus temperature. Few researchers showed that the thermal conductivity of porous insulating materials strongly depend on their moisture content (Berardi, 2019).

Tests have shown that the thermal resistance R, ($m^2 \cdot K/W$) of PIR decreases when the ambient temperature drops below 0 ^oC, reaching a peak when the material temperature is like the indoor air temperature (i.e. between 2.2 ^oC and 42.2 ^oC). During the winter, when the temperature falls below 0 ^oC and the time when a PIR-insulated roof is heated by the sun and the material temperature rises higher than 45 ^oC, the R-value of the thermal resistance decreases (Building Science Corporation, 2013). However, Finch *et al.* (2014) noted that in roof assembly using other insulation materials, such as mineral wool, together with PIR may significantly improve the effective R-value of the polyisocyanurate as it keeps it near optimum temperatures (near room temperature). Berardi (2019) performed an experiment with several foam materials showing that the aging of the foams and the operating temperatures have higher impacts on the polyisocyanurates than on polyurethanes. His study showed that different aging mechanisms impact mainly the polyisocyanurate which increased their effective thermal conductivity significantly.

Standard methods for predicting the change in thermal properties of polyurethane foam: aging at high temperature and thin PUR/PIR slice aging were found to be inconsistent with the actual material use conditions. Increased temperature changes the diffusion intensity of the gas trapped in the pores of the material in a non-uniform manner (pentane-foamed material gases are CO_2, air, and different pentane isomers) (Christian *et al.*, 1995; Stovall *et al.*, 2013). Thin slicing and weighing do not appreciate the fact that the surface layers of PIR with facing are denser than the inner layers (Singh *et al.*, 2003). The main standard for rigid polyurethane foam (PUR/PIR) products is EN 13165:2012+A2:2016, and the aged value can be determined in one of two ways according to this standard. The first is the thermal conductivity measured after 175 days aging at 70 °C, with the addition of safety factor which depends on the type of facing, the blowing agent of the foam and the thickness of the product. The safety factor may be adjusted on the basis of a comparison between the aged values at 23 °C and 70 °C. The second is the thermal conductivity measured after 21 days of exposure at 70 °C with addition of a fixed increment. Fixed increment depends mainly on the type of facing and is different for different blowing agents.

As PIR thermal insulation material is rapidly gaining popularity in the Northern Europe, which has a wide range of ambient air temperatures, it is important to investigate its thermal properties under operating conditions, and to predict the influence of temperature, and aging effects on the thermal properties of buildings insulated with PIR.

2 Research Methodology

2.1. Sampling and Sample Preparation for Testing

In this experiment, samples are aged like in the standard fixed increment procedure, but the samples are used at full thickness as fabricated, i.e. without cutting a 20 *mm* sample from the core of the product. This is done to find out how the entire product is aging at different temperatures and how the (non)presence of a facing affects the change in thermal conductivity. For this experimental study, PIR specimens were obtained from the producer. The dimensions of the specimens are 300x300 *mm*, thicknesses 30 and 50 *mm*. Samples of each thickness are taken from products of three different production dates. There are three types of specimens for each date of production: the first specimen is with a factory-made composite non-diffusion facing; the second sample is sealed with a diffusion-tight film from all sides; the third sample has its facing removed. Products are stored at (23±3) *°C* and (50±10) *%* relative humidity for at least 16 hours before cutting. Prior to thermal treatment, the value of the thermal conductivity of each sample is measured using FOX 314 Heat Flow Meter in conformity to ISO 8301. Two tests are performed in parallel: first - successive effects of temperature on specimens, maintaining the same specimens at different temperatures and measuring their thermal conductivity after each step corresponding to the temperature environment over the year; second - measuring different specimens after storing in different temperature environments, to determine certain temperature impact on thermal conductivity.

2.2 Influence of Successive Thermal Treatment on Thermal Conductivity of Specimens

The algorithm for this experiment is presented in Figure 1. The specimens are placed at (70±2) *°C* for a period of (21±1) days. After certain period, specimens are reconditioned for 16 *h* at (23±3) *°C* and (50±10) *%* relative humidity, then the aged values of thermal conductivity are determined using FOX 314 Heat Flow Meter. The measured value is compared with the value obtained from a standardized measurement (Fixed increment procedure). Later, using the same procedures the specimens are treated at (50±2), (23±2), (0±2), and (-18±2) *°C* for (21±1) day, and their thermal conductivity is measured after each stage. Table 1 shows the mean values of the measured thermal conductivity before and after each exposure at different temperature conditions.

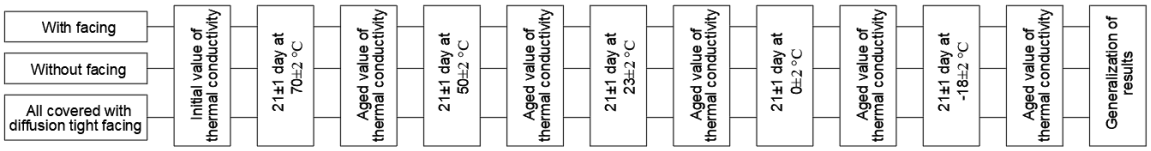

Figure 1. Algorithm of the experiment.

Table 1. Average thermal conductivity values after successive aging in different temperature conditions.

Thickness, *mm*	Type of facing	λ value, *W/m·K*					
		Initial	Aged at 70 °C	Aged at 50 °C	Aged at 23 °C	Aged at 0 °C	Aged at -18 °C
30	Diffusion tight/covered	0,0206	0,0224	0,0226	0,0228	0,0226	0,0219
	Diffusion tight	0,0204	0,0219	0,0220	0,0221	0,0221	0,0222
	Without facing	0,0208	0,0238	0,0243	0,0243	0,0241	0,0232
50	Diffusion tight/covered	0,0205	0,0219	0,0220	0,0219	0,0219	0,0222
	Diffusion tight	0,0206	0,0220	0,0220	0,0221	0,0221	0,0222
	Without facing	0,0207	0,0230	0,0232	0,0231	0,0230	0,0232

2.3 Influence of Particular Thermal Treatment on Thermal Conductivity of Specimens

This experiment is conducted to investigate the effect of ambient temperature conditions on the thermal conductivity of specimens. The specimens are kept at different temperature environments: (70±2), (50±2), (23±2) and (-18±2) °*C* for (21±1) days, after which the specimens are reconditioned for 16 *h* at (23±3) °*C* temperature and (50±10) *%* relative humidity, and the change in thermal conductivity is measured. The results of the measurements are given in Table 2.

Table 2. Thermal conductivity values after particular aging in different temperature conditions.

Thickness, *mm*	Date of production	Initial λ value, *W/m·K*	Aged at 70 °C λ value, *W/m·K*	Aged at 50 °C λ value, *W/m·K*	Aged at 23 °C λ value, *W/m·K*	Aged at -18 °C λ value, *W/m·K*
50	23.10.2018	0,0205	0,0222			
		0,0204	0,0222			
		0,0209	0,0231			
	15.02.2019	0,0201		0,0218		
		0,0206		0,0224		
		0,0207		0,0226		
	08.04.2019	0,0210			0,0214	
		0,0204			0,0210	
		0,0208			0,0210	
	18.06.2019	0,0205				0,0206
		0,0204				0,0204
		0,0208				0,0209
30	15.02.2019	0,0206	0,0226			
		0,0209	0,0239			
		0,0210	0,0242			
	22.10.2018	0,0213		0,0222		
		0,0207		0,0214		
		0,0208		0,0223		
	08.04.2019	0,0208			0,0216	
		0,0206			0,0214	
		0,0211			0,0220	
	20.06.2019	0,0204				0,0204
		0,0207				0,0206
		0,0211				0,0213

Specimens with facings
Covered specimens
Specimens without facings

3 Results and Discussion

The thermal conductivity values of PIR specimens measured in both experimental studies were

compared with the declared thermal conductivity value, which is determined by standard procedures, i.e. aging and measuring a 20 *mm* sample cut from the core of the product.

Figure 2 shows the thermal conductivity variation of 30 *mm* thick PIR specimens using a successive thermal treatment procedure. All types of specimens show a significant increase in thermal conductivity after heating at 70 *°C*. This change could be explained by the intense diffusion of gas out of the material pores into the surrounding environment. It can be noticed, that when the same specimens are kept at a lower positive temperatures, the increase in the thermal conductivity is insignificant, while for specimens with facing it is close to linear. This indicates that the emission of gas into the environment at this stage is largely dependent on their movement from the inner layers of the material to the superficial layers. The thermal conductivity of the unfaced samples ceases to increase earlier than that of the faced samples, and it depends on the diffusion possibilities, which are limited by the facings.

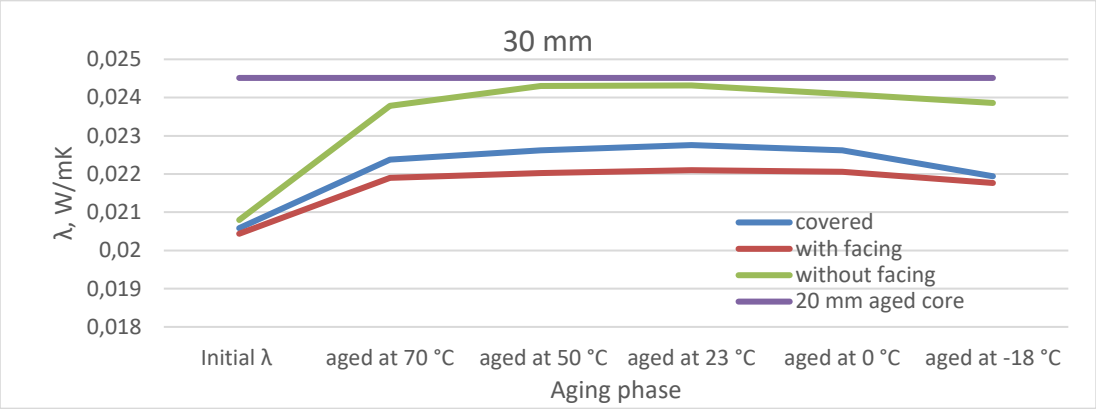

Figure 2. Variation of average thermal conductivity coefficient of 30 *mm* thick samples during successive aging.

The results of this experiment also show that the thermal conductivity of unfaced specimens at the average operating conditions is close to the declared thermal conductivity of the product, and significantly lower than that of the faced specimens. This shows that when standard procedure is applied, even for 30 *mm* thick products with facing thermal properties can be unreasonably degraded.

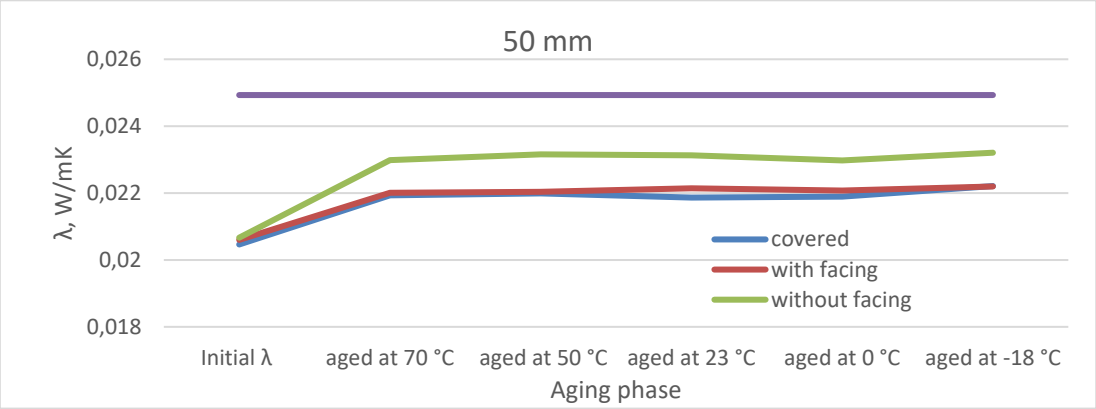

Figure 3. Variation of average thermal conductivity coefficient of 50 *mm* thick samples during successive aging.

The tendency of the PIR thermal conductivity change is similar for 50 *mm* thick specimens (Figure 3). In this case, it has been found that the post-production side facings of the specimen do not affect its thermal conductivity because they do not ensure a gas-tight permeability. It can also be seen in this graph that the increase in the thermal conductivity of the specimens stabilized earlier (already after heating at 70 °*C*), than that of the 30 *mm* thick specimens. This may be due to the larger lateral area of the test specimens, which could have released more gas during the same period. Examination of 50 *mm* thick specimens also showed that the thermal conductivity of the specimens with removed facing remains lower than that of the same 30 *mm* thick specimens during the successive aging. This difference may be due to the fact that the surface layers of the material are compacted to such an extent that they significantly stop the gas diffusion into the environment, and at the end of the experiment, the remaining gas concentrations in the pores of 50 *mm* thick specimens is higher than in the 30 *mm* thick specimens. Only further investigations could determine the effect of the thickness on the rate of gas diffusion and consequently on the increase in thermal conductivity for specimens with removed facing.

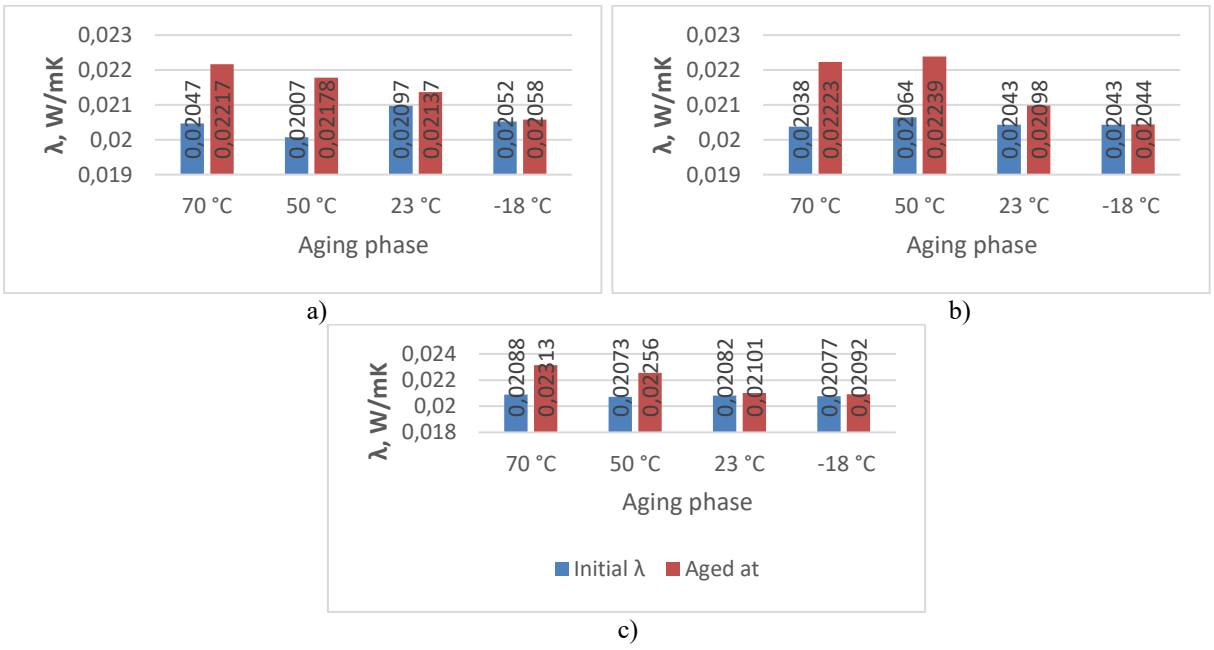

Figure 4. Influence of temperature conditions on the thermal conductivity of PIR (50 *mm* sample: a) covered, b) with facing, c) without facing).

The influence of specific temperature environmental conditions on the variation of PIR thermal conductivity is presented in Figures 4 and 5. Analysing changes in the thermal conductivity of 50 *mm* thick specimens showed that temperatures 70 °*C* and 50 °*C* has the greatest influence. For both types of specimens with diffusion-tight facing, the thermal conductivity increases by 8-9 *%* after exposure to higher temperatures (50 °*C,* 70 °*C*), and to 11 *%* for specimens with removed facings (Figure 4c). This confirms the effect of diffusion of the gases, present in the pores of the material, on the thermal conductivity of the material. Exposure to negative temperatures (-18 °*C*) does not alter the thermal insulation properties of all specimens.

Examination of 30 *mm* thick specimens showed that in all three cases aging at 70 °*C* had the greatest influence (up to 10-15 %) on their thermal conductivity (Figure 5). The influence of 50 °*C* on the thermal conductivity of the 30 *mm* samples with facings is smaller (only 3-4 %), while that of the samples without facings was slightly higher – 7 % (Figure 5c). As with 50 *mm* thick specimens, the change in the thermal conductivity of the 30 *mm* thick specimens is not affected by the negative temperature. This indicates that the gas condensation in the pores does not change the thermal properties of the material.

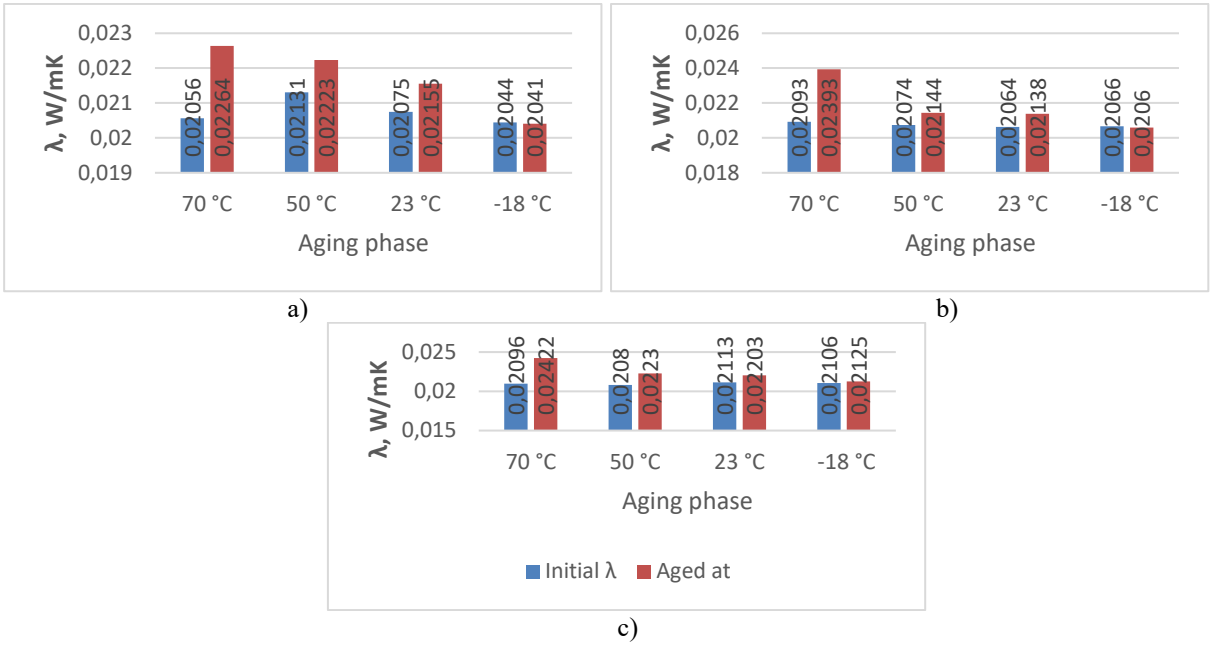

Figure 5. Influence of temperature conditions on the thermal conductivity of PIR (30 *mm* sample: a) covered, b) with facing, c) without facing).

4 Conclusions

- The standard methodology for determining the declared value of the thermal conductivity of PIR, when a specimen is cut from the core of a product, does not meet the conditions of use of products faced with diffusion tight facings, and must be adjusted providing aging and measurement of the specimens with such facings.
- The thermal conductivity of PIR is mostly changed after storage at 70 °*C*. The higher growth in thermal conductivity was measured for thinner specimens - 30 *mm*. Experiments showed that the 21 days aging period at the high temperature is enough for the samples to have a thermal conductivity settling down. After storage at -18 °*C*, the thermal conductivity of the material does not change under standard conditions. From the point of view of thermal insulation of structures, it is important to determine the thermal conductivity of PIR at negative temperatures, for which further studies are carried out.
- The removal of the facing results in up to 8 % greater change in thermal conductivity after exposure to high temperatures, compared to specimens faced with diffusion tight facings. The application of diffusion tight film to the sides of the specimens does not affect the change in thermal conductivity of the specimens after aging, because it is not as tightly pressed to the foam core as for factory made faced insulation boards.

- The results of this study are important to get knowledge about the aging of PIR insulation when it is installed in building envelope, so further research is being conducted on different facing materials on boards open ends to select a reliable technology to prevent thermal conductivity increase through the open ends (e.g. wall corners).

ORCID

Tomas Makaveckas: https://orcid.org/0000-0002-0643-7807
Raimondas Bliūdžius: https://orcid.org/0000-0003-4703-1106
Aurelija Levinskytė: https://orcid.org/0000-0002-7295-8045

References

Alvey, B. J., Patel, J. and Stephenson, D. L. (2017). Experimental study on the effects of humidity and temperature on aerogel composite and foam insulations. *Energy and Buildings*, 144, 358-371. doi: 10.1016/j.enbuild.2017.03.070

Berardi, U. and Naldi, M. (2017). The impact of the temperature dependent thermal conductivity of insulating materials on the effective building envelope performance. *Energy and Buildings,* 144, 262-275. doi: 10.1016/j.enbuild.2017.03.052

Berardi, U. (2017). The impact of temperature dependecy of the building insulation thermal conductivity in the Canadian climate. *Energy Procedia*, 132, 237-242. doi: 10.1016/j.egypro.2017.09.684

Berardi, U. (2019). The impact of aging and environmental conditions on the effective thermal conductivity of several foam materials. *Energy*, 182, 777-794. doi: 10.1016/j.energy.2019.06.022

Bogdan, M., Hoerter, J. and Moore, F. O. Jr. (2005). Meeting the Insulation Requirements of the Building Envelope with Polyurethane and Polyisocyanurate Foam. *Journal of Cellular Plastics*, 41, 41-56. doi: 10.1177/0021955X05049869

Building Science Corporation Information Sheet 502 (2013). *Understanding the Temperature Dependence of R-values for Polyisocyanurate Roof Insulation*.

Christian, J. E., Desjarlais, A., Graves, R. and Smith, T. L. (1995). Five-year Field Study Confirms the PIMA Standard for Estimating Polyisocyanurate Insulation Long-term Thermal Performance. *Proceedings of the 11th Conference on Roofing Technology*, 67-77.

EN 13165:2012+A2 (2016). Thermal insulation products for buildings – Factory made rigid polyurethane foam (PU) products – Specification.

Finch, G., Ricketts, L. and Dell, M. (2014). Conventional Roofs: Measuring Impacts of Insulation Strategy & Membrane Colour in Canada. *Proceedings of the 14th Canadian Conference on Building Science and Technology*

Jin, J., Dong, Q., Shu, Z., Wang, W. and He, K. (2014). Flame retardant Properties of Polyurethane/expandable Praphite Composites. *Procedia Engineering*, Nr. 71. 304-309. doi: 10.1016/j.proeng.2014.04.044

Khoukhi, M., Fezzioui, N., Draoui, B. and Salah, L. (2016). The impact of changes in thermal conductivity of polystyrene insulation material under different operating temperatures on the heat transfer through the building envelope. *Applied Thermal Engineering* 105, 669-674. doi: 10.1016/j.applthermaleng.2016.03.065

Mukhopadhyaya, P., Bomberg, M. T., Kumaran, M. K., Drouin, M., Lackey, J., Reenen, v. D. and Normandin, N. (2004). Long-Term Thermal Resistance of Polyisocyanurate Foam Insulation with Gas Barrier. *Proceedings of the Buildings IX* (ASHRAE)

Paraschiv, S. L., Paraschiv, S. and Ion, I. V. (2017). Increasing the energy efficiency of buildings by thermal insulation. *Energy Procedia* 128, 393-399. doi: 10.1016/j.egypro.2017.09.044

Singh, S. N., Ntiru, M. and Dedecker, K. (2003). Long Term Thermal Resistance of Pentane Blown Polyisocyanurate Laminate Boards. *Journal of Cellular Plastics*, Vol. 39, 265-280. doi: 10.1177/002195503035065

Stovall, T., Vanderlan, M. and Atchley, J. (2013). Evaluation of Experimental Parameters in the Accelerated Aging of Closed-Cell Foam Insulation: Results after Five Years of Full-Thickness Aging. *Proceedings of the Thermal Performance of the Exterior Envelopes of Whole Buildings XII International Conference* (ASHRAE)

Zhang, H., Fang, W., Li, Y. and Tao, W. (2017). Experimental study of the thermal conductivity of polyurethane foams. *Applied Thermal Engineering,* 115, 528-538. doi: 10.1016/j.applthermaleng.2016.12.057

XV International Conference on Durability of Building Materials and Components
DBMC 2020, Barcelona
C. Serrat, J.R. Casas and V. Gibert (Eds)

Are Mineral Toppings of Asphalt Roofing Sufficient to Protect Flat Roofs and Roofing Felt Alone?

Tomasz Szkuta[1] **and Maria Wesołowska**[2]

[1] Polish Association of Civil Engineers and Technicians (PZITB) Branch in Toruń,
Szeroka 34 Str., 87-100 Toruń, Poland, tomszkuta@gmail.com

[2] University of Technology and Life Sciences in Bydgoszcz,
Al. Prof. S. Kaliskiego 7, 85-796 Bydgoszcz, Poland, Wesolowska.Maria@utp.edu.pl

Abstract. *Mineral surfaces are an integral part of bituminous roofing felt. Their task is to protect less resistant elements from the destructive effects of the environment. Since the first application in 1897, they have been constantly improved in the direction of better functionality and aesthetics. It often turns out that the intended effect has not been achieved. During the first years of operation, there are signs of roof damages on most facilities. Due to the complex interaction of roofing elements, several causes of damages can be defined. A group of processes taking place in mineral roofing toppings is important for roofing felt. Mineral surfaces are exposed to physical, chemical and biological factors. They cause losses due to the unavoidable breaking of adhesion to the modified asphalt. Pulling out caused by factors occurring on the roof is a long-term process with more effects on the covering, in particular its durability and tightness. In the paper, the reasons for the release of mineral topping from the SBS modified asphalt layer were defined. The analysis shows that as a result of significant degradation and harmful impact of mineral coverage, this layer may lose the ability to protect the roofing paper, and long-term changes threaten the durability of roofing materials. Solutions have been proposed to significantly reduce the phenomenon caused by specific factors.*

Keywords: *Mineral-Surfaced Tar Board, Durability of Roofing Felt, Impact of Environment.*

1 Introduction

The subject of the work is the problem of top covering roofing felt. It is visible already in the first years of operation of the roofing felt. Depending on the quality of the roofing felt (price), this process takes place faster or slower, but inevitably occurs.

Figure.1 This is a comparison of mineral topping on new roofing paper and topping on the same roofing paper after several years of use in adverse conditions (on the right photo a drastic example of a significant loss of granules and exposure of asphalt in a roof depression - a periodic puddle).

doi:10.23967/dbmc.2020.166

Figure 2. This is the cross-section of an ordinary polymer-asphalt covering roofing felt, on polyester nonwovens using typical roofing felt.

Mineral surfaces protect the roof against atmospheric influences and to some extent against mechanical influences. They have been known, used, modified and improved for years. They are getting better and prettier really. They are absolutely necessary but do they fully fulfill their role on flat roofs? They were invented and began to be used a hundred years ago. Is the inertia of the solution justified and does it have to be continued?

Despite the objections of producers and some specialists outraged by such a suggestion, it must be made. Mineral surfaces are an ad hoc invention, an added element. They used to be a cheap and quick solution to the problem, but today they is not. Today we find improper cooperation with roofing felt and no cover durability guarantee. This is especially visible in the light of the changes that are taking place in the climate around us. Roof temperatures up to almost 90^{o}C is an examined fact. It turns out that the problem is not only the temperature, there are many more.

Due to the location of the place of work or residence, we rely on data from Poland. However, the principles of analysis are universal.

Roofing granules are released during the operation of roofs covered with roofing felt from polymer-modified asphalt (mainly SBS in Poland). The applicable European standard EN12039 from July 2016. regarding possible defects on up to 30% of the mineral topping, during tests, is significant. Such large roof defects are real, as shown in the above photos. The defect itself is one thing but the effects of the way they are formed are a much broader topic.

The purpose of the work is to analyze the reasons for the deterioration of roofing materials over time. Due to the possible volume of occurrence content, limited only to roofing granules.

Analyzes of other elements of cover materials on flat roofs should be expected in subsequent publications.

2 Method

To find out the reasons for the appearance of roofing defects and the effects on the roofing felt and roofs, an analysis of processes and phenomena occurring on the roofs is needed. For the purposes of the study, the processes were divided into groups depending on the seasons.

General description of processes, impact on roofs (roof granules):

Autumn, winter, spring: snow retention; melting and freezing of snow in contact with the covering surface and stands (!), deepening effect (increased hydrostatic pressure), penetration into asphalt cracks and between granules and disintegration; the bottom layer of thawed and frozen snow turns into ice, the top layer from thawed snow (sun) and frozen turns into ice, after freezing it in whole we have a thick layer of ice with a significant mechanical breaking strength (linear expansion of the ice when the temperature drops below $0^{o}C$) ; passing through "$0^{o}C$" up to 100 times per year (deepening effects).

Summer: rainfall on a hot roof (hydrophobization is less effective - Table 1, significant energy of falling drops - Figure 4), soaking of mineral topping; rapid temperature changes, water, hail falling on the roof heated to almost $90^{o}C$; chemical impact on toppings - decomposition, leaching, formation of chemical solutions; leaching of soluble components of roofing felt (*e.g.* sulfur), solutions effecting on roof granules and other cover elements; crystallization of water chemical contaminations in crevices and soaked granules, destruction of granule-asphalt adhesion and cohesion of granules, increasing the concentration of solutions at subsequent precipitation; wet and dry deposition of media enabling the development of living organisms (lichen, algae, other).

Regardless of the season: linear expansion of roof materials and their interactions affecting mineral toppings; additional impact, wind pressure and suction transporting loose material; capillary penetration into granules, theoretically reduced by hydrophobization, practically depends on temperature (Figure 3), water pollution (*e.g.* PH, Table1) and other phenomena associated with the shape and number of open pores may also occur.

Identification of the main physical phenomena generating the indicated processes:

Weather conditions and their changes together with climate changes: precipitation; humidity; winds; insolation; temperature changes; wet and dry deposition of mineral, chemical, organic and inorganic compounds and substances.

Physical properties of materials used to make coverage, precipitation and deposits, and their interactions: linear expansion (discontinuous linear expansion); adhesion and cohesion; humidity; solubility; hygroscopicity; surface tension; changes in physical state; density; melting and softening point; copolymer uncoupling temperature; viscosity stiffness; ductility; flexibility; thermal conductivity; brittleness; reflection; radiation absorption.

Chemical properties of materials used for covering, precipitation and deposits, and their interactions (as additional): PH; causing chemical corrosion; change in physical properties (*e.g.* surface tension).

Research and analysis carried out:

We focused primarily on long-term observations and research of flat roofs in situ. An important observation during the tests turned out to be the quality of roofing, often correlated with the quality of the materials used. It should be emphasized here, that perfectly made covers made of the best materials on the market are not often the subject of expertise. They are much less frequently and more slowly damaged and constitute a small part of the market. We focused on the greater part of the market where the important measure of the quality of materials used and the quality of workmanship is the criterion of a lower price.

Analysis of the impact of differences in linear expansion of polymer-asphalt layers reinforced with polyester nonwovens and mineral topping immersed in puddles formed in an improperly shaped roof surface: expansion of polymer-asphalt felt; ice expansion; thermal shock with rapid temperature changes (summer downpours, hail).

Analysis of the effect of crystallization of chemical compounds found in puddles on roofs: chemical compounds found on roofs; crystallization of chemical compounds between the granules; crystallization of chemical compounds in the joints of roofing felt sheets.

Analysis of weakening of roof paper sheets joints by the presence of granules embedded in joints in the context of linear expansion and crystallization in puddles: quality of joints and the way they are made; facilitating the possibility of water getting into the contacts areas; blasting through ice, the effect of temperature shrinkage of roofing felt.

Analysis of the impact of hydrophobization on the number of granules defects in real conditions on roofs: phenomena eliminating increased surface tension on hydrophobized materials (Table 1, Figure 3, Figure 4, Table 2), surfactants, the occurrence of these phenomena on roofs, the impact of these phenomena on defects of granules

Table 1. Surface tension values of sulfur-contaminated water PH dependant (Janocha, 2014) .

Surface tension [mN/m]	pH
74	6,5
52,6	6,8
49,2	7,2

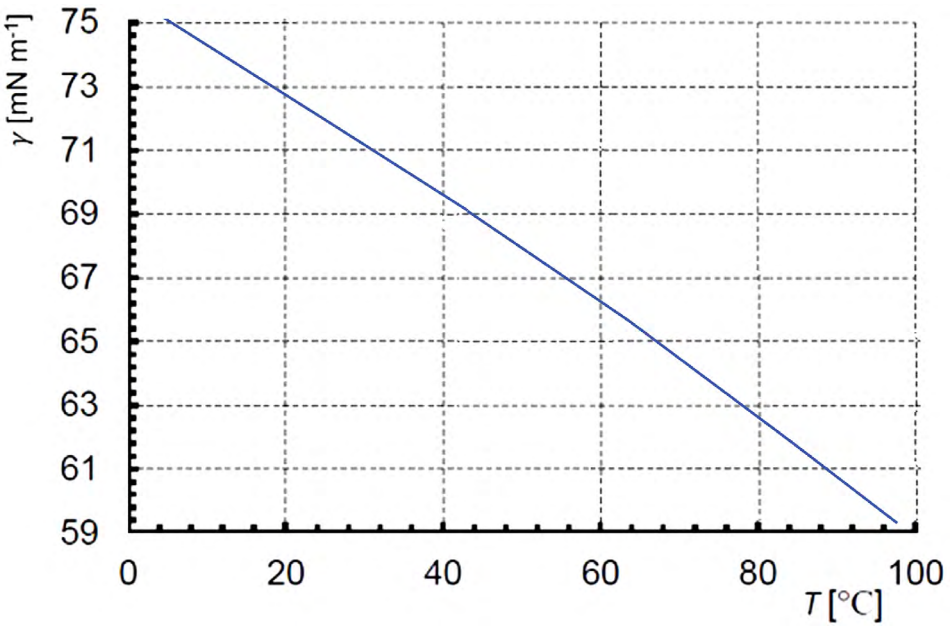

Figure 3. Surface tension of pure water as a function of temperature (at saturation pressure) (Vargaftik *at al*., 1983).

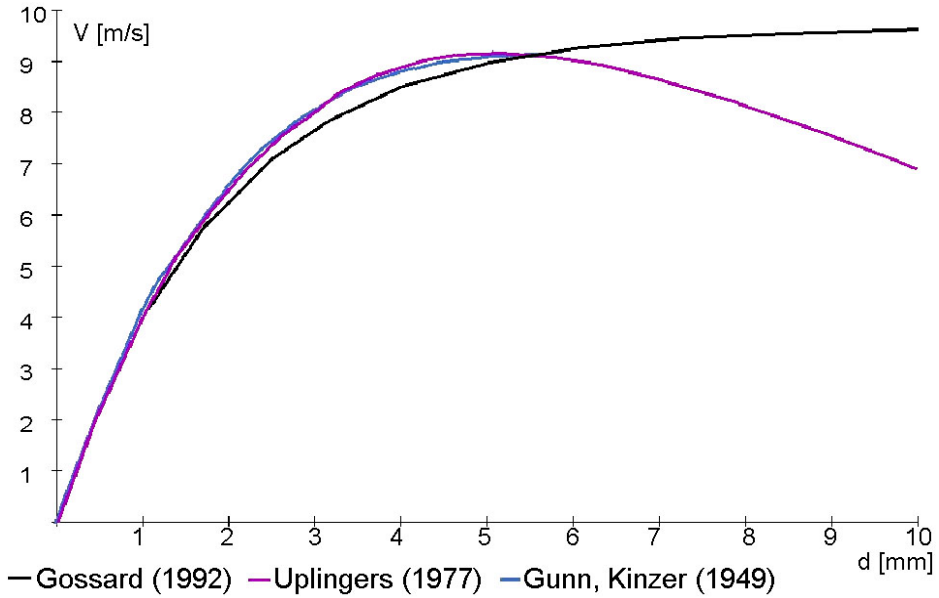

Figure 4. Water drop falling rates for ideal conditions (Van Boxel *et al.*, 1998).

Analysis of released granules accumulation places and the impact on the destruction of these places; location of accumulation of unbound granules; phenomena occurring at places where pellets accumulate; the impact of these phenomena on the durability of roofing felt and roof.

Figure 5. Accumulation of released granules (roof after one year of operation)

Analysis of the impact of granules accumulating in the gutters on gutter durability: transport for gutters - mechanical impact; transport in gutters - mechanical impact; slowing down the flow of water and prolonging the impact of chemical compounds present in the water flowing from the roof (influence of rainfall intensity on corrosion).

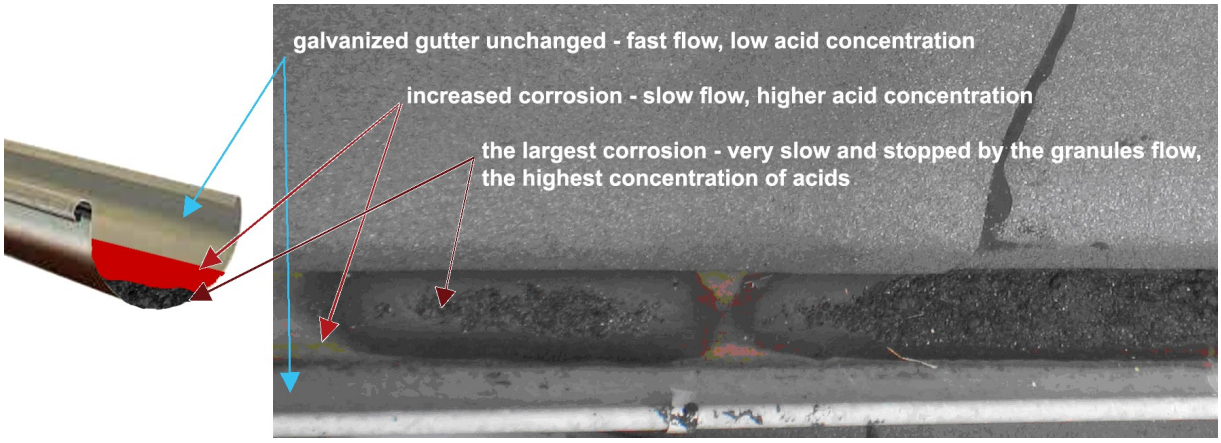

Figure 6. Accumulation of free granules in the gutter, retention of chemically polluted water and corrosion. The rust level determines the water flow rate at which the acid concentration is sufficient to cause rapid corrosion. The concentration of chemical pollution increases during low runoff from the roof surface.

Analysis of the impact of granules transported with water on the durability of downpipes: topping transport in downpipes; clogging of pipe inflows and outflows.

Analysis of the impact of hail rainfall on driving the topping into the polymer-asphalt layer at a significantly heated roof surface.

Table 2. Energy of falling hail (Heymsfield *at al*., 2014).

Diameter [cm]	Mass [g]	Speed [km/h]	Energy [J]
1	0,5	52	0,05
3	13	90	4
5	59	116	31
7	162	138	118
10	471	164	491

Effect analysis of contacts of polymer-asphalt felt with elements of different thermal expansion (flashings, batten protections ...) on defects in granules: way of contacts interact; resistance of roofing felt to contacts; increased granules defects at the contact points and consequences for exposed polymeric asphalt.

Analysis of the impact of roof loading elements (*e.g.* roof bases for lightning and ventilation systems) on indentation of granules in the places of contact edges at high temperatures: quality of loading elements - eccentricity for small elements, edge action and wind action for large elements; the effect of high temperatures on roofs for puncturing asphalt roofing felt with granules.

Analysis of the impact of exposing polymeric asphalt mass by tearing off the topping and releasing mainly sulfur compounds as a prolonged process: sulfur compounds as a component of polymer-asphalt mass; long-term release of sulfur compounds; the impact of sulfur compounds on roof elements (Figure 6).

Analysis of the influence of granules on the possibility of accumulation of deposits constituting the basis enabling the growth of living organisms: topping structure that holds deposits; collecting water.

Analysis of the impact of living organisms (algae, lichen, mosses, plants) on pulling out roofing powder: colonization by living organisms; method of long-term extraction of granules (growth of mosses, lichen, plants).

Analysis of the impact of temperatures on roofs on the possibility of sinking the granules in the top layer of roofing felt and the possibility of penetration into the layer of polyester nonwoven fabric: polymer decoupling temperature for lower quality roofing paper; impact on the decomposition temperature of polymers in roofing paper resulting from the lack of obligation to carry out direct tests and to specify the composition of polymer-asphalt; methods of kneading the granules (shoes, storage of renovation materials).

Analysis of the shape and size of the granules influence for possible damage to roofing felt: granules used by roofing felt producers and their most common shapes; size, thickness of topping; the possibility of causing damage.

3 Results

As a result of research and analysis we have determined:

The positive functions of roof granules – as the protective layer are: mechanical protection; UV protection; now also enabling, by means of adhesion, the use of additional roofing protection measures (*e.g.* expensive paints increasing the reflection of heat radiation); architectural and decorative functions.

Negative impacts of roof granules - the "protective layer" on the roof are: uncertainty of attachment in polymer-asphalt and protection losses; too high porosity of the layer and the possibility of retaining deposits and water in the layer; systematic and unavoidable release of pellets during roof operation; leaching of sulfur compounds from asphalt resulting from the method of releasing the granules (pulling out, UV exposure, slow destruction of the surface); too much heat radiation absorption; possibility of mechanical destructive impact on polymer-asphalt; making it possible to transfer the destructive effects of freezing water to polymer-asphalt (the protective layer is a tool of destruction); accumulation of released pellets in different areas of the roof increasing the amount of deposits and water retained on the roof; mechanical impact of granules transported by rain and wind on other roof elements; participation in clogging water outflows; weakening of torched joints between transverse joint of the roofing felt.

4 Conclusions

Elimination the negative effects of roof granules on existing roofing felt is possible by: coating with materials that reduce the porosity of the layer; covering with materials increasing the reflection of solar radiation; increasing resistance to the development of living organisms; coating with materials that reduce the release of primarily sulfur compounds. Such actions are effective but expensive and labor-intensive.

Elimination of the negative effects of granules layer is possible by replacing it in the production process with materials characterized by: inability to accumulate in the layer wet and dry deposits; reflection of a significant part of solar radiation; limiting or eliminating the possibility of harmful chemical compounds emission from modified asphalt, above all sulfur; high adhesion to asphalt; the possibility of periodic and cheap renovation - enabling the use of cheap spray paints; enabling the effects of texture and colors for small visible roofs; gives possibility of obtain flat and smooth self-cleaning surfaces for large-area roofs. Such actions are more beneficial, cost effective and introduce the possibility of cheaper and simpler systematic renovation of roof coverings, increasing their durability.

In connection with the climate change, there is an urgent need to redefine the territorial aapplication of cover materials and their required characteristics for these areas.

The authors team is in the process of developing and patenting a new material solution for the surface layer of asphalt felt for flat roofs. The solution should, basing on existing production technology, enable the production of a new generation of roofing felt.

ORCID

Tomasz Szkuta: http://orcid.org/ 0000-0003-2089-1106
Maria Wesołowska: http://orcid.org/ 0000-0001-7914-6077

References:

Barnat-Hunek D. (2016) Swobodna energia powierzchniowa jako czynnik kształtujący skuteczność hydrofobizacji w ochronie konstrukcji bud. (in Polish). *Politechnika Lubelska.* ISBN: 978-83-7947-216-1.

Boczkaj G. (2012) *Badania wpływu na środowisko technologii wytwarzania, dystrybucji i stosowania asfaltów naftowych* (in Polish). PHD dissertation, PG (Gdańsk University of Technology).

Cullen W. C. NIST various studies from the 70's, 80's,90's. *United States. National Bureau of Standards Report.*

Heymsfield A. J.,and Giammanco I. M. Wright R. (2014) Terminal velocities and kinetic energies of natural hailstones*. Geophys. Res. Lett.,41, 8666–8672,* doi:10.1002/2014 GL062324.

Janocha A. (2014) Zmiany napięcia powierzchniowego zasiarczonej wody złożowej na granicy z powietrzem (in Polish). *Nafta-Gaz* 6/14, p. 365 – 369.

Kałasa J. (1988) Biodegradacja przeciwwilgociowych materiałów izolacyjnych (in Polish). *Building Research Institute (ITB)* - Quarterly no 4 (108).

Porowska D. (2005) Ocena zanieczyszczenia opadów atmosferycznych w rejonie Warszawy na tle badań regionalnych (in Polish). *Przegląd Geologiczny 53*, p. 1060–1061.

Stefańczyk B. and Mieczkowski P. (2008*)* Wpływ czynników fizyczno-chemicznych na kształtowanie trwałych i skutecznych hydroizolacji papowych (in Polish). *Materiały Budowlane* 430/08, p. 12-13.

Szkuta T. and Wesołowska M. (2019) Skutki zjawisk fizycznych na dachach płaskich. Część I – Nieprawidłowości, analiza stanu (in Polish). *Przegląd Budowlany 7-8/19 p. 103-105. ISSN0033-2038, Indeks 37067.*

Trzaska E. (2011) Adhezja asfaltu do kruszywa (in Polish). *Nafta-Gaz* 6/11, p. 423 – 427.

Vargaftik N.B., Volkov B.N. and Voljak L.D. (1983) International tables of the surface tension of water. *J. Phys. Chem.* Ref. Data 12 p. 817-820.

Van Boxel J. (1998). Numerical model for the fall speed of raindrops in a rainfall simulator. *ICE Special Report*, 1998/1, p. 77-85

Żelazny M. (2005) Wpływ czasu trwania opadu atmosferycznego (mokrego) na średnią dynamikę zmian stężeń jonów w pojedynczym opadzie w zasięgu oddziaływania dużych ośrodków miejsko-przemysłowych Łazy k. Bochni (in Polish). *v.53 n. 11*, Indeks 370908, ISSN-0033-2151.

XV International Conference on Durability of Building Materials and Components
DBMC 2020, Barcelona
C. Serrat, J.R. Casas and V. Gibert (Eds)

Behavior of Mortars with Different Porosities in Front of Attack of Aggressive Agents

Alessandra M. Weber[1], Wellington Mazer[2], Daniela E. Pedroso[3] and Cleber Pedroso[4]

[1] Academic Department of Civil Construction, Federal and Technological University of Parana (UTFPR), Campus Ecoville, Curitiba, Brazil, alessandramoniqueweber@gmail.com

[2] Academic Department of Civil Construction, Federal and Technological University of Parana (UTFPR), Campus Ecoville, Curitiba, Brazil, wmazer@utfpr.edu.br

[3] Academic Department of Civil Construction, Federal and Technological University of Parana (UTFPR), Campus Ecoville, Curitiba, Brazil, danievaniki@hotmail.com

[4] Academic Department of Civil Construction, Federal and Technological University of Parana (UTFPR), Campus Ecoville, Curitiba, Brazil, cleber.ped@gmail.com

Abstract. *Chemical reactions that lead to decreased durability in concrete structures may result from chemical interactions between aggressive agents present in the external environment and cement paste compounds or may result from internal reactions. The chemical reactions are manifested by the physical properties of the concrete, such as porosity and permeability and the decrease of resistance and cracking. Among the several aggressive agents that attack the reinforced concrete structures it can be highlighted chloride ions, sulphate ions and carbon dioxide. In this context, the study presents the analysis of different traces of mortar executed with cement type CPII-F-32 (OPC Cement, in Brazil one of the most used cements) with w/c ratios of 0.4 and 0.7, when subjected to the attack of sulphates, chlorides and carbonation. The analyzes quantitatively evaluated the amount of ions present after exposure to the agents and demonstrate the importance of evaluating the dosage of water in the mortars to minimize future problems with durability.*

Keywords: *Mortars, Sulphate Attack, Chloride Attack, Carbonation, Porosity.*

1 Introduction

Chemical reactions leading to decreased durability in concrete structures may result from chemical interactions between aggressive agents present in the external environment and cement paste compounds or may result from internal reactions like alkali-aggregate reaction, or from reaction of delayed hydration CaO and MgO crystalline, if present in excessive amounts in Portland cement, or electrochemical corrosion of concrete reinforcement. Chemical reactions manifest themselves through the physical failures of concrete such as porosity and permeability, decreased strength and cracking.

Among the various aggressive agents that attack reinforced concrete structures, chloride ions, sulphate ions and carbon dioxide can be highlighted.

Sulphate can be found in soils such as landfills and is a major cause of degradation of cement-based materials. The attack by sulfate ions stands out especially when dealing with marine, underground or sewage handling structures (Mehta and Monteiro, 2014; Wei *et al.*, 2019).

When dissolved sulfate ions (SO_4) react with hydrated cement paste the two main means of

sulfate attack are: reaction with hydration products of unhydrated tricalcium aluminate (C_3A) producing ettringite and reaction with calcium hydroxide producing gypsum. Sulfate attack on concrete can manifest as expansion or cracking, leading to increased concrete permeability, structural problems and initiating corrosion processes of reinforcement (Mehta and Monteiro, 2014).

According Mangat and Ojedokun (2019) the chloride concentration of concrete exposed to a chloride environment is a parameter used to characterize the long term chloride resistance of concrete. The presence of chlorides is a cause of the corrosion process in reinforcement of reinforced concrete structures. The structure in an environment that has seawater, sea salt and thaw salts is subject to attack by chlorides. The rate of chloride penetration from the surface to the interior of the concrete depends on: the amount of chloride ions in the environment, the permeability of the concrete and the humidity of the environment (Aguiar, 2011).

Carbonation of concrete is directly linked to the CO_2 diffusion coefficient that is determined by Fick's first law, but there are limitations in some parameters, for example CO_2 diffusivity varies over time and strongly depends on the moisture content of the pores. concrete, as well as other variables that may also influence the microstructure of the concrete, such as cure condition, moisture content, location, elapsed time and mixing parameters (Yoon *et al.*, 2007).

In this context, the objective is to analyze different traces of mortars made with type CP II – F32 cement with w/c factors of 0.4 and 0.7 when subjected to the attack of sulfates, chlorides and carbonation.

2 Materials and Methods

To evaluate the durability, the specimens were exposed for 70 days to aggressive agents to verify their performance against the attack of sulfate ions, chlorides and carbonation. For the evaluation, quantitative tests were performed. The tested mortar has a 1:3 trait (cement: sand), varying the water/cement ratio in two levels, being 0.4 to obtain less porous mortar and w/c of 0.7 for a more porous mortar. In samples with w/c of 0.4, 1% hyperplasticizer was added to aid in the consistency of the mortar.

The binder used was Portland Cement CP II – F32, chosen for its wide availability in the market. The choice of producing mortars is due to the fact of ease in smaller samples, in this case it was decided to mold 10 x 5 cm cylindrical specimens. According to some authors such as Papadakis (2000), Kulakowski (2002), Gervais *et al.* (2004), Pauletti *et al.* (2007), Pauletti (2009) and Neville (2015) explain about better results that the use of mortar brings in the carbonation front analysis, such as the influence of the presence of coarse aggregate.

For durability analysis against the aggressive agents the specimens were submitted after cure of 28 days in a humid chamber, for the sulfate solution was used 10% magnesium sulfate ($MgSO_4$). For the accelerated chloride attack, 10% sodium chloride (NaCl) solution was added and for carbonation depth evaluation, the specimens were deposited in a carbonation chamber with 10% controlled CO_2 concentration, without the control of humidity and temperature.

2.1 Sulphate Content

The samples were fully submerged in magnesium sulphate ($MgSO_4$) solution of 10% for up to 70 days. The chemical test to determine the sulphate ions content in the samples was made according to an adaptation of the standard APHA Method 4500-SO_4^{2-} (1997). The procedure consists to submit the ground sample, whose diameter is less than 600 μm, to a solution of hydrochloric acid (HCl), shown in Figure 1, with barium chloride ($BaCl_2$), which will form a precipitate of barium sulphate ($BaSO_4$), which after calcination at 800°C is heavy ($M_{calcined}$).

Figure 1. On the left the sample mixture with hydrochloric acid and on the right the filtered solution.

To determine the percentage of sulphate in the sample, the equation is:

$$SO_3(\%) = \frac{34{,}3045 \cdot M_{calcined}}{M_{standard}} \quad (1)$$

Where the mass of the standard sample is weighed prior to the test in grams.

2.2 Chloride Concentration

The chloride concentration of the mortar powder sample was obtained Volhard's titration method. The procedure consists an indirect titration to determine the chloride ion that precipitates with silver ion (Figure 2).

The acid soluble chloride content was calculated as a percentage of chloride ions by weight of the binder, by the following equation:

$$Cl^-(\%) = 0{,}1773 \cdot \frac{V_2 - V_1}{m_1} \quad (2)$$

Where V1 is the volume of ammonium thiocyanate of a standard sample in ml, previously determined to be 0,07; V_2 is the volume of ammonia thiocyanate in the concrete sample in ml; and m_1 is the mass of the concrete sample in grams.

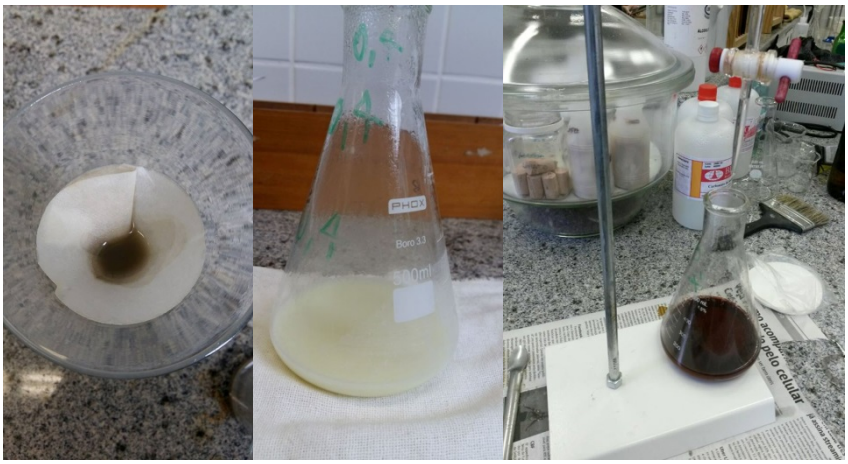

Figure 2. Silver chloride solution filtration and coagulation after boiling and then titanium ammonium titration.

2.3 Carbonation Penetration

Carbonation tests were performed by cylindrical mortar samples**.** Phenolphthalein was used as test to carbonation penetration. It is in the initiation phase that it was intended to verify the occurrence of carbonation, because generally the typical appearance of carbonation is the occurrence of light spots produced by refraction of calcium carbonate, it is necessary to verify the carbonation using colorimetric indicators that point the pH. The lower the pH, the lighter its appearance, tending to colorless in the less alkaline regions. A non-carbonated concrete in the most alkaline region turns purple when using this same indicator. The most commonly used carbonation or pH indicator is the phenolphthalein solution or equivalent, being successfully used for pH between 8 and 11.

Figure 3 shows the color of the specimen when the phenolphthalein solution is sprayed.

Figure 3. Specimens submitted to the phenolphthalein spray test.

3 Results

The average values of the analyzes of the three tests performed for the sample group, considering the w/c variations are presented in Table 1.

Table 1. Mean values for durability analyzes.

Specimens		Sulphate content (%)	Chloride content (%)	Carbonation Penetrarion (mm)
CP II – F32	w/c 0.4	6.28	0.55	-
	w/c 0.7	8.39	0.69	2.1

Sulphate content increased by more than 33% when the water factor used in the mortar was added.

CP II – F32 cement analysis for chloride determination by chloride submerged samples resulted in chloride content of 0.69% for samples with water/cement ratio of 0.7 and 0.55% for samples with water/cement ratio of 0.4. According to NBR 12655 (ABNT, 2015) the maximum chloride content for reinforced concrete exposed to chloride in the service conditions of the structure is 0.15% (considering aggressive classes III and IV, which includes marine and industrial environments with chemical agents). Therefore, all the samples exceeded this reference.

It was not possible to measure the carbonation depth for the samples with water/cement ratio of 0.4 because no sufficiently measurable points were observed for the caliper measurement. For the trace with w/c 0.7 the average carbonation point was 2.1 mm.

4 Conclusions

- OPC cement mortars using w/c fractions of 0.4 show better durability results when compared to 0.7 water dosing.
- The proposed tests serve as durability indicators for previous considerations due to the attack of sulfates, chlorides and carbonates.
- The service life of concrete structures depends mainly on the durability of the concrete. Concrete made from traditional Portland cement is considered a durable material for the non-aggressive environment, however water should be carefully considered as a direct influence on the durability of mortars and concretes, due to the increased porosity.

ORCID

Alessandra M. Weber: http://orcid.org/0000-0002-0991-1842
Wellington Mazer: http://orcid.org/0000-0002-9941-999X
Daniela E. Pedroso: http://orcid.org/0000-0003-3077-4544
Cleber Pedroso: http://orcid.org/0000-0002-8265-2920

References

ABNT (2015). *NBR 12655*: Concreto de cimento Portland - Preparo, controle, recebimento e aceitação – Procedimento, Rio de Janeiro, Brasil.

Aguiar, J.E. (2011). *Durabilidade, proteção e recuperação das estruturas*, Class Notes, Escola de Engenharia da

Universidade Federal de Minas Gerais, Belo Horizonte, Brasil.

APHA, (1997). *Method 4500-SO_4^{2-} - Sulfate*. Standard Methods for the Examination of Water and Wastewater. American Public Health Association.

Gervais, C., Garrabrants, A.C., Sanchez, F., Barna, R., Moszkowicz, P. and Kosson, D.S. (2004). The effects of carbonation and drying during intermittent leaching on the release of inorganic constituents from a cement-based matrix. *Cement and Concrete Research, 34* (1), 119-131. doi: 10.1016/S0008-8846(03)00248-5

Kulakowski, M.P. (2002). *Contribuição ao estudo da carbonatação em concretos e argamassas compostos com adição de sílica ativa*, PhD Thesis, Universidade Federal do Rio Grande do Sul, Porto Alegre, Brasil.

Mangat, P.S. and Ojedokun, O.O. (2019). Bound chloride ingress in alkali activated concrete. *Construction and Building Materials, 212*, 375–387. doi:10.1016/j.conbuildmat.2019.03.302

Mehta, P.K. and Monteiro, P.J. (2014). *Concreto: microestrutura, propriedades e materiais*. São Paulo: IBRACON.

Neville, A.M. (2015). *Propriedades do Concreto*. Brasil: Bookman Editora.

Papadakis, V. G. (2000). Effect of supplementary cementing materials on concrete resistance against carbonation and chloride ingress. *Cement and concrete research, 30*(2), 291-299. doi: 10.1016/S0008-8846(99)00249-5

Pauletti, C. (2009). *Estimate of natural carbonation of cement materials based on accelerated tests and prediction models,* PhD Thesis, Universidade Federal do Rio Grande do Sul, Porto Alegre, Brasil.

Pauletti, C., Possan, E. and Dal Molin, D.C.C. (2007). Carbonatação acelerada: estado da arte das pesquisas no Brasil. *Ambiente construído, 7* (4), 7-20.

Wei, L., Xiao-Guang, J. and Zhong-Ya, Z. (2019). Triaxial test on concrete material containing accelerators under physical sulphate attack. *Construction and Building Materials, 206*, 641-654. doi: 10.1016/j.conbuildmat.2019.01.186

Yoon, I.S., Çopuroğlu, O. and Park, K.B. (2007). Effect of global climatic change on carbonation progress of concrete. *Atmospheric environment, 41* (34), 7274-7285. doi: 10.1016/j.atmosenv.2007.05.028

XV International Conference on Durability of Building Materials and Components
DBMC 2020, Barcelona
C. Serrat, J.R. Casas and V. Gibert (Eds)

Behavior of Waterproofing Systems Exposed to Environmental Agents

Julie A. Braun[1], **Flávio L. Maranhão**[2] **and Renata Monte**[3]

[1] Department of Civil Engineering, Universidade de São Paulo (USP), Av. Prof. Almeida Prado-Trav. 2, 05508900-São Paulo, Brazil, julie.braun@usp.br

[2] Department of Civil Engineering, Universidade de São Paulo (USP), Av. Prof. Almeida Prado-Trav. 2, 05508900-São Paulo, Brazil, flavio.maranhao@usp.br

[3] Department of Civil Engineering, Universidade de São Paulo (USP), Av. Prof. Almeida Prado-Trav. 2, 05508900-São Paulo, Brazil, renata.monte@usp.br

Abstract. *The service life of buildings can be associated with the durability of enveloping the elements, e.g., the flat roofs that are constantly exposed to environmental agents. Waterproof membranes, produced with bituminous or polymeric materials, usually protect these elements. This paper presents an experimental study of waterproofing systems subjected to environmental agents of degradation. Four types of membranes were tested: bituminous, polyurethane, acrylic and acrylic with polyester mesh. All membranes were applied to concrete substrates and exposed to cycles of 48 hours in 70°C oven and 24 hours in immersion vats with 23°C water. The specimens were subjected to 0, 4, or 8 cycles and submitted to pull-off tests. The results demonstrated that the waterproof system behavior change when subjected to cycles of the temperature gradient. The tests show that the different thermal deformation between the membranes and the concrete substrate results in loss of adhesion.*

Keywords: *Waterproofing System, Durability, Environmental Agent, Adhesion.*

1 Introduction

The waterproofing layer of the roof system can be considered as a building protection system since it prevents damaging actions of water as well as aggressive elements of the atmosphere (Gonçalves *et al*., 2019). It is related to the building service life and it is the first principle of their durability (Henshell, 2000). The loss of properties of its materials can cause premature degradation in other building systems (Navratilova Rovenska, Jiránek, and Kačmaříková, 2015).

The roof is one of the building envelope part that requires the design of a system to predict the service life. The durability of the roofing system depends on several parameters (Cash, 2003) because it involves choosing proper design and materials considering the detrimental effects of natural agents (Henshell and Griffin, 2000).

The materials used in waterproofing systems, mainly those for flat roofs, are exposed to environmental agents like ultraviolet radiation, mechanical actions, contact of the organic solvents, moisture, and cycles of the oxygen, carbon and temperature (Bertolini, 2014; Marques, Lopes, and Correia, 2011; Pirondi, 1988). Due to these factors, the waterproofing systems are subject to natural and accelerated degradation processes of their mechanical water-tightness characteristics (Walter, De Brito, and Lopes, 2005).

The main factor for material degradation is temperature according to Patterson and Mehta (2001), the heat transference by radiation occurs because every object produces electromagnetic

waves by virtual temperature. The membranes and sheets of the weatherproof system are polymeric materials like polyurethane, polyvinyl chloride, bituminous, acrylic, polypropylene (Cash, 2003; Marques *et al*., 2011). This class of material is known for its temperature instability due to its thermoplastic characteristics. The internal energy of polymers rises with the increase in temperatures, reducing weak bonds between macromolecules (Callister and Rethwisch, 2001). It leads to lower elastic modulus and higher flexibility (Bertolini, 2014). However, at high temperatures, covalent bonds are broken, leading to irreversible chemical degradation of the material. With this regard, it is important to understand the behavior of these materials when working together with building as a system, not just as a material.

In this work, the main objective is to analyze the behavior of four waterproofing materials applied in a concrete substrate submitted to weathering actions by temperature, air and wetting.

2 Methodology

This work evaluated the behavior of waterproofing systems when submitted to wetting and drying cycles. In the experimental study, four waterproofing systems adhered to the substrate were evaluated: acrylic with and without polyester mesh, polyurethane, and bituminous. The substrate used was concrete with steel mesh, produced according to the Brazilian standard ABNT NBR 14081-2: 2015.

The specimens were submitted to the aging process by wetting and drying cycles, placed in a forced air circulation oven at a constant temperature of (70 ± 1) ºC for 48 hours and moved to a water vat at (23 ± 1) °C for 24 hours. So, each cycle corresponds to 72 hours. Four substrates were tested for each waterproofing system, varying the number of cycles: 0, 4, 8 and 16.

Visual analyses were performed at each cycle stage. After finishing the cycles, the membranes were submitted to pull-off tests, using 10 samples for each substrate.

2.1 Materials

The selection of the waterproofing materials for the experiment was based on their relevance and application in the Brazilian market, their adhesion to the substrate and their distinct chemical composition and mechanical behavior. Table 1 presents the Brazilian standard and manufactures characteristics of the materials to compose the waterproofing systems: acrylic membrane, polyurethane membrane and bituminous sheet adhered with heated asphalt.

Table 1. Characteristic of waterproofing materials tested.

Characteristics	Acrylic Membrane	Polyurethane	Bituminous sheet
Color	White	Green	Black
Density (g/cm³)	1.40	1.4-1.6	Undeclared
Elongation (%)	200	70	30
Touch drying (h)	4	6	-
Consumption (kg/m²)	1.2	1.7	1.15m²/m²
Thickness (mm)	0.50-1.00	Undeclared	4.00
Application state	One-component liquid	Two-component viscous	Solid

The Systems composed of acrylic membrane received structural reinforcement with polyester mesh, table 2 present its physical and mechanical properties.

Table 2. Physical and mechanical properties of polyester mesh.

Physical and mechanical properties	Unit	Standard	Specifications
Longitudinal tensile strength	kgf	EN-ISO 1421	25±5
Transverse tensile strength	kgf	EN-ISO 1421	25 ± 5
Stretching	%	EN-ISO 1421	Max. 25
Resistance to longitudinal tear	kgf	DIN 53.363	15 ± 5
Tear Resistance	kgf	DIN 53.363	15 ± 5
Grimace	g/m²	EN-ISO 2286	15 ± 5
Thickness	mm	EN-ISO 2286	0.25 ± 0.05

The structural reinforcing mesh has the function of resisting the tensile forces when it is requested from the system (Pirondi, 1988). The bituminous sheet is prefabricated, modified with SBS (styrene-butadiene-styrene), structured with nonwoven continuous filament and sand-finished on both sides, with a thickness of 4 mm.

2.2.2 Specimens Preparation

The waterproofing systems were applied to the previously prepared substrate. The application process differs when the material is prefabricated or molded on-site. The membranes were applied using a brush and the material quantity is controlled by weighing it on a precision scale (0.01 g). For thickness control, a measurement was performed using a wet layer thickness gauge (25 to 3000 µm). Figures 1 to 4 demonstrate the procedure for specimens preparation.

Figure 1. Preparation of Bituminous sheet.

Figure 2. Application of the Bituminous sheet adhered with heated cement asphalt.

Figure 3. Application of Polyurethane membrane and inspection the thickness.

Figure 4. Application of the Acrylic membrane with polyester mesh.

The wetting and drying cycle started with the specimens in an air circulation oven at (70 ± 1) ºC. After 48 hours at a constant temperature, the specimens were removed and submerged in a water vat at (23 ± 1) ºC.

3 Results and Analysis

The test results were analyzed qualitatively and quantitatively. The first was performed by visual observations of changes in the systems during each cycle and the second by pull-off tests. The analysis of variance method (ANOVA) was used to evaluate if differences between the cycles are statistically significant.

3.1 Visual Analysis

Figures 5 to 10 illustrate the visual observations made in the test specimens throughout the 16 cycles. The visual inspection shows the occurrence of microbubbles, air bubbles, apparent pores, melting and debonding.

Figure 5. Air bubble disrupted and microporous in the Acrylic membrane with mesh.

Figure 6. Microbubbles and microporous in the Acrylic membrane.

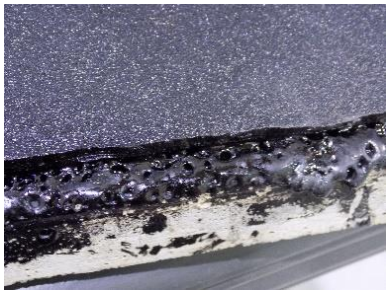

Figure 7. Increase in viscosity (melting) and microbubbles in the asphalt cement between the bituminous sheet and substrate.

Figure 8. Debonding of the bituminous sheet of the substrate with increase the temperature.

Figure 9. Air bubble in the Polyurethane system.

Figure 10. Microbubbles and apparent porous in the Polyurethane system.

3.2 Pull-off Analysis

The adhesion strength was measured using pull-off tests that were performed at the end of each wetting and drying cycle. Figures 11 to 12 demonstrate the preparation and performance of the test.

Figure 11. Preparation of the samples to the pull-off test.

Figure 12. Pull-off test in the polyurethane membrane.

The adhesion strength is given by the following equation:

$$Ra = \frac{F}{A} \tag{1}$$

Where *Ra* is the adhesion strength, expressed in Megapascal (MPa), *F* is the force, expressed in Newton (N), and *A* is the tested area, expressed in square millimeters (mm²).

In Figures 13 to 16 should be noticed that all waterproofing systems presented a decrease in adhesion strength when at least 4 wet-dry cycles were applied.

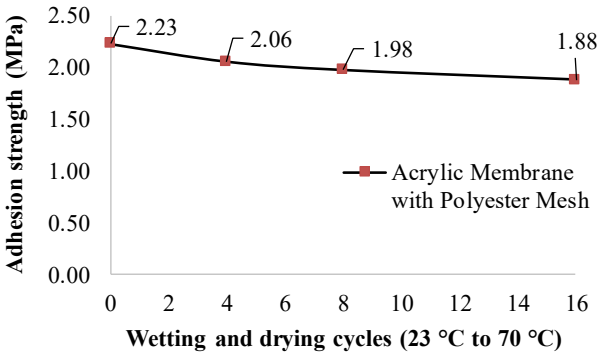

Figure 13. Adhesion Strength of Acrylic membrane with Polyester mesh.

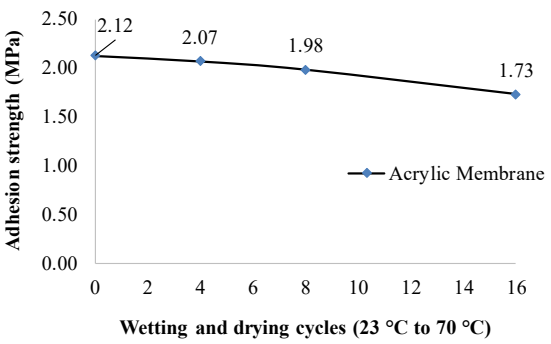

Figure 14. Adhesion Strength of Acrylic membrane.

Comparing Figures 13 and 14, it is can be seen that the reinforcement has no influence at the adhesion strength of acrylic membranes. Also, a decline of adherence with number of cycles is presented in both systems. Figures 15 and 16 indicates that the bituminous sheet and the polyurethane membrane show no significant decrease in adhesion strength after 4 cycles.

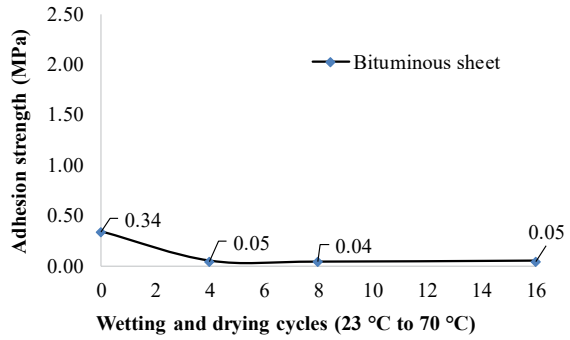

Figure 15. Adhesion Strength of Bituminous sheet.

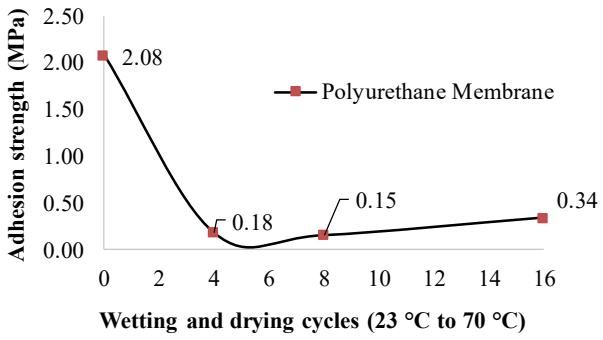

Figure 16. Adhesion Strength of Polyurethane membrane.

In Figure 17, the variability of the adhesion strength results is presented. Each result is an average of 10 specimens tested in each substrate plate. It is observed that polyurethane systems presented a larger deviation. It was observed that specimens located in points where air bubble formation results adhesion next to zero. Also, in the case of bituminous system, the penetration of fluids in the polymer-modified asphalt pores causes a debonding process.

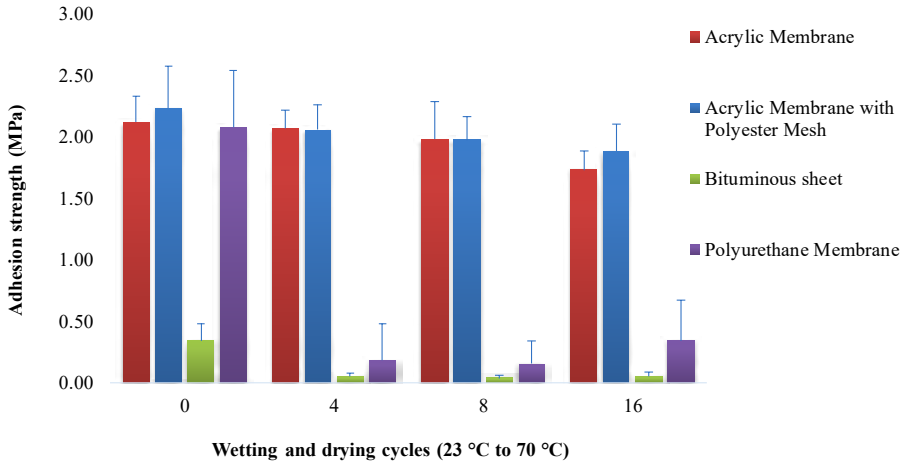

Figure 17. The Standard deviation of each waterproofing system.

It is noted that the behavior of the bituminous and polyurethane systems proved to be highly sensitive to temperature actions and wetting cycles. Additionally, it is noticeable that the adhesion strength of the bituminous sheet is the lowest, even in cycle 0. This factor is related to the adhesion shape, thickness, and type of material used to adhere the layers. The system consists of 3 layers: primer, polymer-modified asphalt cement and the bituminous sheet itself, resulting a 6 mm thickness. So, there is a larger area for energy dispersion when the system is stressed. In cycle 0, the adhesion strength of the polyurethane system was considerably high comparing to the other systems. However, the cycles of weathering result a loss of this initial behavior. As shown in Figure 9, during the wetting and drying cycle, air bubbles were formed between the substrate and the polyurethane system. In this process, the system had a loss of adhesion in some parts of the substrate.

Table 3 presents the comparison of adhesion strength of the tested systems using the analysis of variance (ANOVA), the level of significance considered is 5%.

Table 3. Analysis of variance and Tukey's paired comparisons of adherence strength.

System	Cycle	Value-P	Media	Group	
Acrylic Membrane	0	0.002	2.12	A	
	4		2.07	A	
	8		1.98	A	B
	16		1.73		B
Acrylic Membrane with Polyester Mesh	0	0.024	2.23	A	
	4		2.06	A	B
	8		1.98	A	B
	16		1.88		B
Bituminous sheet	0	0.000	0.34	A	
	4		0.05		B
	8		0.04		B
	16		0.05		B
Polyurethane Membrane	0	0.000	2.08	A	
	4		0.18		B
	8		0.15		B
	16		0.34		B

It can be seen that for all the systems the weathering cycle is significant for the decrease in adherence (value-P is less than 5%). Also, a Tukey's method is used to compare all possible pairs of results for each system. With this, it is possible to observe in the bituminous sheet and polyurethane membrane the cycle 0 and the others are significant different. Bur, the acrylic membranes do not show a significant difference in the adhesion strength up to the cycle 8.

4 Conclusions

Waterproofing systems as an integral part of the building need to provide weathering resistance. Through tests on wetting and drying cycles, it was possible to understand the behavior of waterproofing systems when adhered to the substrate. From the tests performed and materials used the following conclusions are drawn:

- The adherence of the acrylic membranes to the substrate is less influenced by weathering cycles than other systems. In addition, the use of reinforcement mesh does not influence significantly in this pattern.
- Despite the high adhesion strength of acrylic membranes, it was observed over the cycles the manifestation of air bubble disrupted and microporous. This may compromise the system in terms of watertightness.
- The polyurethane membrane system and the bituminous sheet system lost their bonding characteristic to the substrate after 4 cycles. In view of this behavior, it is necessary to evaluate previously the place where it will be applied; therefore, it is not indicated for regions susceptible to severe weather conditions, such as cycles of intensive rain and extremely high temperature.
- The results demonstrate the importance of the thermal protection layer in waterproofing systems that will be exposed to weather cycles. Moreover, a special attention should be taken in the design and execution of this layer.

ORCID

Julie Anne Braun: https://orcid.org/0000-0002-8254-644X
Renata Monte: https://orcid.org/0000-0003-3555-4655
Flavio Leal Maranhão: https://orcid.org/0000-0003-4941-8558

References

ABNT NBR 12171. (1992). *Waterproofing system with impermeable cement and polymers adhesion - Method of the test*.

ABNT NBR 13321. (2008). *Acrylic membrane for waterproofing*.

ABNT NBR 15487. (2007). *Polyurethane membrane for waterproofing*.

ABNT NBR 9952. (2014). *Asphaltic membrane for waterproofing*.

ABNT NBR 14081-2. (2015). *Adhesive mortars industrialized for the settlement of ceramic tiles Part 2: Execution of the standard substrate and application of the fresh mortar for test.*

Bertolini, L. (2014). *Materiais de Construção: Patologia, reabilitação, prevenção* (2 Ed.). São Paulo: Oficina de Textos.

Callister, W. D. and Rethwisch, D. G. (2001). *Fundamentals of Materials Science and Engineering An Introduction*.

Cash, C. G. (2003). *Roofing Failures* (1st Ed.). London: Spon Press.

Gonçalves, M., Silvestre, J. D., de Brito, J. and Gomes, R. (2019). Environmental and economic comparison of the life cycle of waterproofing solutions for flat roofs. *Journal of Building Engineering*. https://doi.org/10.1016/j.jobe.2019.02.002

Henshell, J. (2000). *The Manual of Below-Grade Waterproofing Systems* (2nd ed.). United States: John Wiley and Sons., Inc.

Henshell, J. and Griffin, C. W. Charles W. (2000). *Manual of below-grade waterproofing systems*. John Wiley and Sons.

Marques, J. A., Lopes, J. G. and Correia, J. R. (2011). Durability of the adhesion between bituminous coatings and self-protection mineral granules of waterproofing membranes. *Construction and Building Materials*. https://doi.org/10.1016/j.conbuildmat.2010.06.047

Navratilova Rovenska, K., Jiránek, M. and Kačmaříková, V. (2015). The influence of long-term degradation of waterproof membranes on mechanical properties and on the radon diffusion coefficient - Preliminary results. *Journal of Cleaner Production*. https://doi.org/10.1016/j.jclepro.2014.06.012

NRCA. (2007). *the NRCA Roofing Manual: Membrane Roof Systems* (National R).

Patterson, S. and Mehta, M. (2001). *Roofing Design and Practice* (1 ed). United States: Prentice Hall.

Pirondi, Z. (1988). *Manual Prático da Impermeabilização e de isolação térmica* (2nd ed.). São Paulo: PINI.

Walter, A., De Brito, J. and Lopes, J. G. (2005). Current flat roof bituminous membranes waterproofing systems - Inspection, diagnosis and pathology classification. *Construction and Building Materials*. https://doi.org/10.1016/j.conbuildmat.2004.05.008

XV International Conference on Durability of Building Materials and Components
DBMC 2020, Barcelona
C. Serrat, J.R. Casas and V. Gibert (Eds)

Carbonation Behavior of Powdered Cement-Based Materials Under Different Relative Humidities and CO_2 Concentrations

Kiyofumi Nakada[1], Katsuhito Komiya[2], Hikaru Fumino[2], Yuhei Nishio[2], Manabu Kanematsu[2] and Takafumi Noguchi[3]

[1] Department of Building Materials and Components, Building Research Institute, 1 Tachihara, Tsukuba-shi, Ibaraki-ken 305-0802, Japan, nakada@kenken.go.jp

[2] Department of Architecture, Graduate School of Science and Technology, Tokyo University of Science, 2641 Yamazaki, Noda-shi, Chiba-ken 278-8510, Japan, manabu@rs.tus.ac.jp

[3] Department of Architecture, Graduate School of Engineering, The University of Tokyo, 7-3-1 Hongo, Bunkyo-ku, Tokyo, Japan, noguchi@bme.arch.t.u-tokyo.ac.jp

Abstract. *The aim of the current study is to investigate the carbonation behavior of cement hydrates at different environments. Hardened cement pastes are prepared using OPC and BFS and crushed into ~90μm powder. The powder samples are carbonated at 5/20% CO_2 and at 60/85%RH. TGA, XRD and phenolphthalein tests are conducted before and after carbonation. The results show that CH remain uncarbonated even after CO_2 uptake apparently ended and that the amount of the residual CH affects the results of phenolphthalein test. External humidity strongly affects the carbonation behavior of both CH and other hydrates. The degree of CH carbonation is greater at higher humidity, while the degree of other hydrates carbonation is greater at lower humidity. This conflicting effect can occur at surface of bulk concretes and changes in its properties (coarsening of pore structure and cracking) can be caused without apparent carbonation detected by phenol phthalein test. The effect of relative humidity on CSH carbonation should be taken into consideration when estimating long-term performance of carbonated concretes.*

Keywords: *Carbonation, OPC, BFS, Relative Humidity, Phenolphthalein Test.*

1 Introduction

Carbonation of concrete leads to significant changes in its chemical and physical properties. During the process, gaseous CO_2 diffuses through pore network of concrete and react with cement hydrates. When Portlandite (CH) is carbonated and consumed, pH value of pore water decreases, which causes depassivation of steel bars embedded in RC structures. CH carbonation also contributes to reduction in concrete porosity because precipitated calcium carbonate ($C\hat{C}$) clogs up the pore space. The clogging of porosity results in a decrease of diffusion path, which improves weight transport resistance in general (Houst *et al*., 1994). In terms of porosity change, it has been reported that carbonation of calcium silicate hydrate (CSH) has greater impact than CH carbonation (Morandeau *et al*., 2014). CSH carbonation also alters pore size distribution of cement pastes, which can cause coarsening of pore structure (Auroy *et al*., 2014). Furthermore, it has been known that CSH carbonation is responsible for carbonation shrinkage and subsequent cracking (Chen *et al*., 2006).

Summarizing the above, carbonation reaction of cement hydrates governs the property changes of carbonated concrete. Better understanding on both the reaction behavior and the impacts can help us to estimate the long-term performance of carbonated concretes. Up to the

present, the impacts of cement hydrate carbonation has been widely investigated (Borges *et al*., 2010; Auroy *et al*., 2014), and the changes in physical properties can be related to the degree of carbonation (Morandeau *et al*., 2014). On the other hand, data on carbonation behavior of cement hydrates are lacking.

As has been already known, carbonation behavior of cement hydrates is strongly affected by external environment (Castellote *et al*., 2009; Galan *et al*., 2013). Thus, the aim of the current study is to investigate the carbonation behavior of cement pastes at different humidity and CO_2 concentration. Also, cement hydrates inside bulk concretes are carbonated under changing environments (humidity and CO_2 concentration), because concrete carbonation basically occurs during drying process. In order to estimate the carbonation degree at any environment, it is desirable to remove the bulk effect and to obtain direct relationship between the carbonation degree and external environments. Considering the above, powdered samples (hardened cement pastes) are employed in this study.

2 Materials and Experiments

3 types of cement pastes were prepared. 2 of them were made with OPC (LOI: 0.97%, SiO_2: 21.41%, Al_2O_3: 4.84%, Fe_2O_3: 3.20%, CaO: 65.01%, MgO: 1.08%, SO_3: 2.02%) and their water to cement ratio were 0.45 and 0.60 (N45 and N60). The other was made with OPC and BFS (50:50) and its water to cement ratio was 0.60 (BB60). The pastes were cast into prismatic molds (40×40×160mm) and demolded after 24 hours. They were cured until 91 days under water, and then crushed into powder. In order to uniform their particle size, crashed powders were sieved with 90μm mesh. The powder samples were dried in N2-purged desiccators, where temperature and humidity were controlled at 20℃ and 60/85%RH. After drying, the samples were carbonated at 4 different environments (Relative humidities were 60/85% and temperature was 20℃, CO_2 concentrations were 5/20%, and they are denoted as 6005, 6020, 8505 and 8520.). In order to monitor CO_2 uptake rate, sample weight was measured during carbonation, and the tests were finished after 24 hours at CO_2 concentration of 20% and 72 hours at CO_2 concentration of 5%.

After accelerated carbonation, TGA tests were performed on carbonated and non-carbonated samples. Measurement temperature ranged from 105℃ to 1050℃ at the heating rate of 10℃/min. The amount of CH and C$\hat{C}$ were calculated from TG curves and their decomposition was detected from inflection point of ΔTG curves around 400℃ to 550℃ and 550℃ to 800℃. Before the tests the samples were soaked in acetone for 48 hours and dried in vacuum desiccator. XRD tests were also performed on the same samples. Patterns were obtained from 2θ of 5° to 65°. In addition to TGA and XRD tests, phenolphthalein tests were carried out so as to compare apparent carbonation and the degree of carbonation. The powders are packed into sample holder (10×10×0.2mm), and phenolphthalein solution was dropped onto them. Sample color was measured by means of color difference meter before and after phenolphthalein was dropped.

3 Results

3.1 Weight Change and CO_2 Uptake

Figure 1. shows the results of monitoring of the sample weight during carbonation at 5% CO_2 concentration. Sample weight shapely increased in first 8 hours, but the change slowed down

quickly and was completed within 24 hours in most samples. The weight increase is mainly due to CO_2 uptake and evaporation of water generated through carbonation reaction. In the case of OPC system, larger amount of CO_2 was absorbed when water to cement ratio and external humidity is higher. On the other hand, little difference can be found in OPC-BFS system, although gentle weight increase continued after 24-hour carbonation at 60% RH. In Figure 2, influence of CO_2 concentration on the weight change is compared. As expected, increase in sample weight was higher when CO_2 concentration is higher. and the influence is more obvious in higher relative humidity.

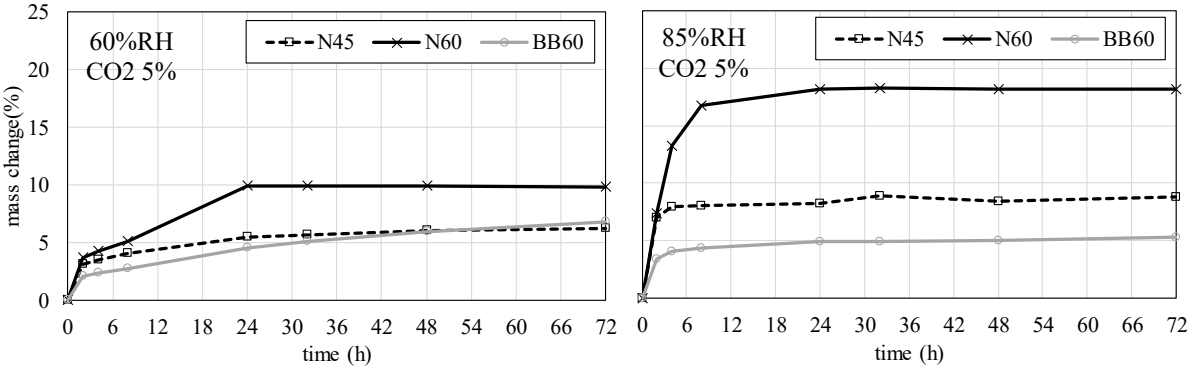

Figure 1. Sample weight monitored during carbonation (5%CO_2).

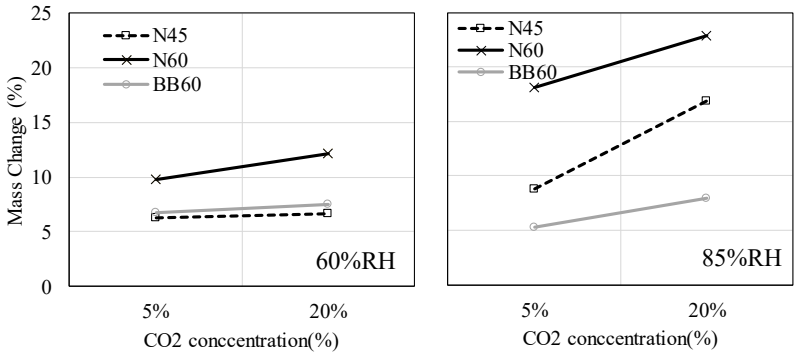

Figure 2. Weight change after carbonation. Carbonation time was 24 hours for 20 % CO_2 and 72 hours for 5% CO_2.

3.2 Carbonation Behavior of Cement Hydrates

Figure 3. shows the results of TGA tests before and after carbonation. In some cases, especially in lower relative humidity, CH dose not reach full carbonation even after CO_2 uptake apparently stopped (Figure 1.). It has been pointed out that degree of CH carbonation is strongly affected by external humidity and that larger amount of CH is carbonated in more humid environment (López-Arce *et al*., 2011; Galan *et al*., 2015). In Figure 3, the results of 5% CO_2 concentration are coincide with the reported behavior of CH carbonation, although little difference can be found in the residual CH of 20% CO_2 concentration.

In addition to the TGA results, the amount of $C\hat{C}$ generated from CH carbonation ($n_{C\hat{C}}^{CH}$) and other hydrates carbonation ($n_{C\hat{C}}^{others}$) is calculated using the following equations.

$$n_{C\hat{C}}^{CH} = n_{CH,nc} - n_{CH,c} \quad (1)$$

$$n_{C\hat{C}}^{others} = n_{C\hat{C},c} - n_{C\hat{C},nc} - n_{C\hat{C}}^{CH} \quad (2)$$

Where $n_{CH,nc}$ and $n_{CH,c}$ are the amount of CH contained in non-carbonated and carbonated samples respectively (mmol/g). $n_{C\hat{C},nc}$ and $n_{C\hat{C},c}$ are the amount of $C\hat{C}$ before and after carbonation (mmol/g).

The calculation results (grey and yellow lines in Figure 3.) illustrate that relative humidity also has impact on other hydrates carbonation. In most cases, larger amount of $C\hat{C}$ is generated from other hydrates at 60% RH than at 85% RH, and the amount of $C\hat{C}$ from other hydrates exceeds that from CH carbonation at 60% RH. This general tendency is similar to carbonation behavior of synthesized CSH reported elsewhere (Kim *et al*. 1995), where it has been pointed out that CSH carbonation continues longer and greater amount of CO_2 is absorbed at 60% RH than at 80%RH. In summary, higher humidity promotes CH carbonation and larger amount of CH is consumed. On the other hand, lower relative humidity contributes to other hydrate carbonation and larger amount of CH remain uncarbonated.

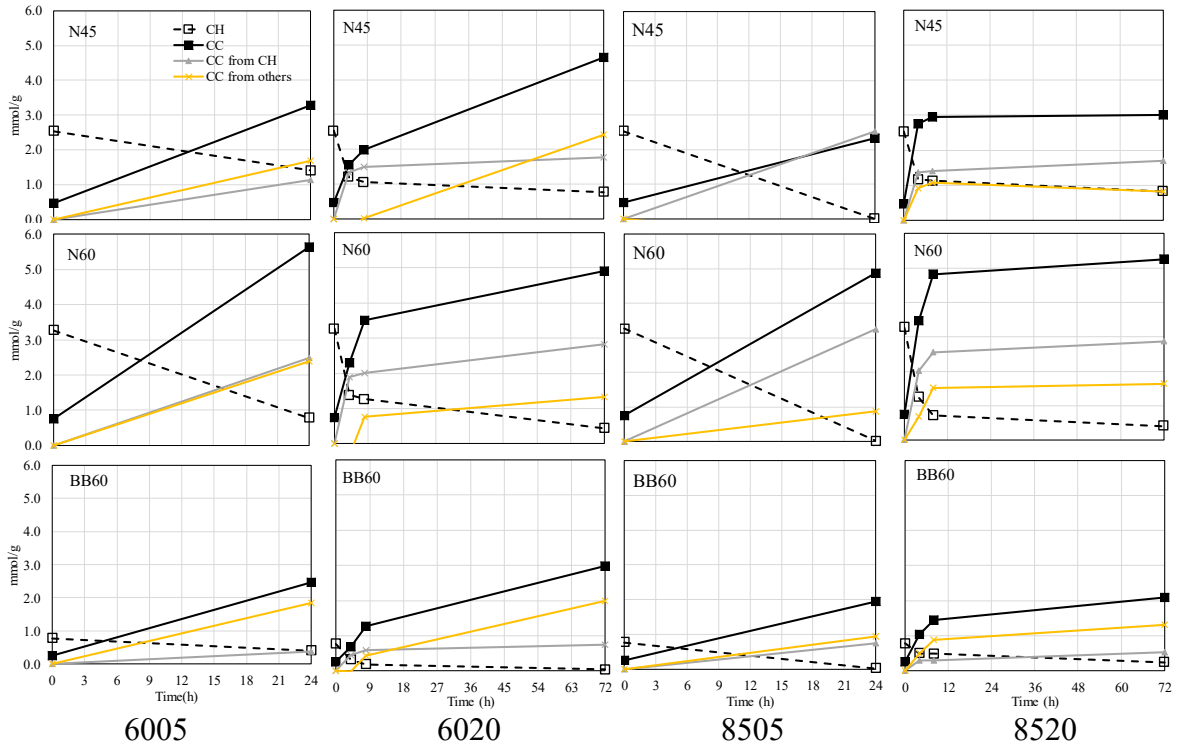

Figure 3. Changes in the amount CH and $C\hat{C}$. The amounts of $C\hat{C}$ coming from CH carbonation and other hydrates carbonation are also illustrated in grey and yellow lines.

3.3 Difference in Calcium Carbonate

Figure 4. shows XRD patterns for carbonated and non-carbonated samples. To compare the presence of CH and three polymorphs of CĈ, only the range from 25° to 35° is shown in the figure. In general, CH peaks do not disappear after carbonation and their peak height is higher when samples are carbonated at 60%RH, which agrees with TGA results. In regard to CĈ calcite and vaterite peaks are observed in every pattern, but their proportion of peak height is different depending on relative humidity. At Vaterite peak height of 60%RH (orange) is higher, whereas at calcite peak that of 85%RH (grey) is higher. Aragonite can be found only in 5% carbonation (N45_6005 and BB60_6005).

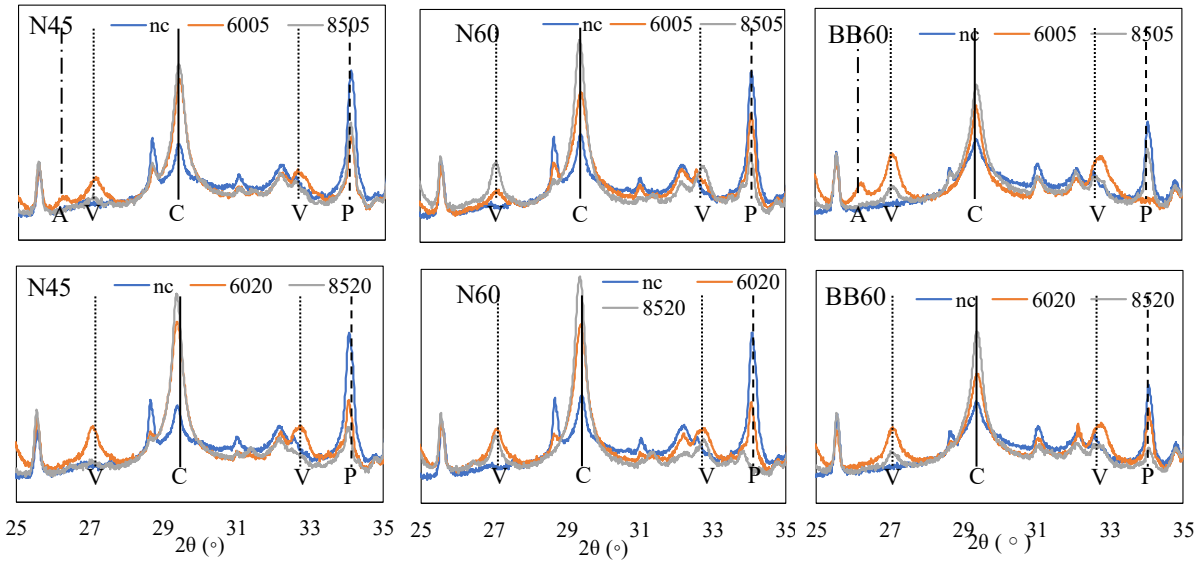

Figure 4. XRD patterns for carbonated (6005, 8505, 6020 and 8520) and non-carbonated (nc) samples. A, C, V and P denote aragonite, calcite vaterite and portlandite respectively.

3.4 Color Change During Phenolphthalein Test

Table 1. and Figure 5. show the results of the phenolphthalein tests. Here, the color difference before and after phenolphthalein addition is determined based on CIE L*a*b* color space, where a* coordinate indicates red (positive) or green (negative). The color of non-carbonated samples turns red immediately and Δa* value reach around 50 whereas, color change of carbonated samples is slower and their Δa* value is below that of non-carbonated. The results of carbonated samples also indicate that carbonation environment (both external humidity and CO_2 concentration) affects the sensitivity to the indicator, that is to say, Δa* value is smaller when relative humidity and CO_2 concentration are higher. In addition, the effect of relative humidity is greater than that of CO_2 concentration.

Table 1. Photographs of compacted samples 60 minutes after phenolphthalein indicator was dropped. Color difference index Δa* (positive: redder and negative: greener) is also shown below each photograph.

	Non-carbonation	carbonated 6005	6020	8505	8520
N45	 Δa*=49.8	 Δa*=46.6	 Δa*=44.5	 Δa*=26.6	 Δa*=24.6
N60	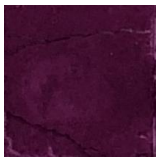 Δa*=51.2	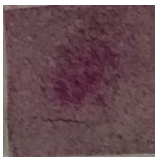 Δa*=18.9	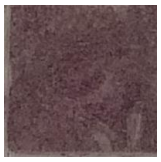 Δa*=14.0	 Δa*=2.93	 Δa*=2.64
BB60	 Δa*=48.4	 Δa*=3.58	 Δa*=18.4	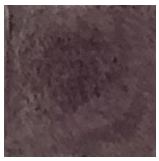 Δa*=13.6	 Δa*=12.1

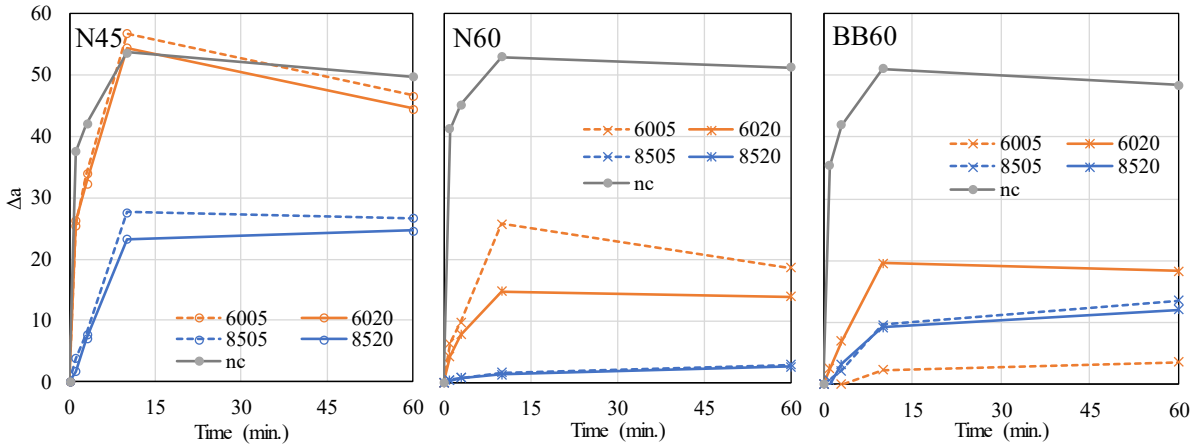

Figure 5. Changes in Δa* after phenolphthalein indicator was dropped. Non-carbonated (nc), carbonated at 60%RH and carbonated at 85%RH are illustrated as grey, orange and blue lines respectively.

4 Discussions

Based on the obtained results, carbonation behavior of cement hydrates and their impact on concrete properties are discussed. First of all, the results of weight increase (Figure 2.) do not agree with the increase in $C\hat{C}$ amount after carbonation (Figure 3.). In other words, TGA results indicate that less amount of CO_2 is absorbed at 85%RH, whereas the weight increase is greater at 85%RH. According to natural carbonation tests (Galan *et al*., 2012), larger amount of water is released from CSH when it is carbonated at lower relative humidity (about 38%RH and 58% are compared). Although the carbonation environment is different from that of the current study, this carbonation behavior of CSH can explain the reason for the disagreement in the figures 2 and 3. When the powder samples are carbonated at lower relative humidity, more H_2O can be released from CSH due to drying and weight increase due to CO_2 uptake is canceled.

Regarding to carbonation behavior of CH and other hydrates, the impact of relative humidity is clearly observed. As has been pointed out, CH carbonation is promoted at higher relative humidity (85%RH) and less amount of CH remain uncarbonated. Compared to the results of phenolphthalein test, the amount of residual CH can be related to color change of phenolphthalein. On the other hand, other hydrates carbonation is promoted at lower relative humidity (60%RH). As a result, at 60%RH, other hydrates carbonation proceeds without enough CH carbonation. Because other hydrates carbonation is more responsible for pore structure changes and carbonation shrinkage, changes in cement paste properties can occur without color change of phenolphthalein in such environments.

As mentioned in the first section, carbonation occurs during drying process. Especially around surface of bulk samples or in small samples, drying proceeds immediately. In such situation, carbonation reaction proceeds under lower relative humidity, which leads to other hydrate carbonation without CH carbonation. In the previous research, CO_2 concentration is main factor for CSH carbonation and decomposition (Castellote *et al.*, 2009). Relative humidity also affects CSH carbonation, and this factor should be taken into account when estimating long-term performance of carbonated concretes.

5 Conclusions

- Powdered cement pastes were carbonated in order to investigate the impact of external environment on carbonation behavior of CH and other hydrates.
- The results of weight increase do not agree with that of TGA tests. The disagreement can be related to the effect of relative humidity on stoichiometry coefficient of H_2O CSH carbonation reaction.
- CH remain uncarbonated even after CO_2 uptake apparently end and the amount of the residual CH affects the results of phenolphthalein test. External humidity strongly affects the carbonation behavior of both CH and other hydrates. The degree of CH carbonation is greater at higher humidity, while the degree of other hydrates carbonation is greater at lower humidity. The conflicting effect above can occur at surface of bulk concretes, and changes in its properties (especially coarsening of pore structure and cracking) can be induced without apparent carbonation detected by phenol phthalein test.
- Relative humidity, as well as CO_2 concentration, strongly affects CSH carbonation, and

this factor should be taken into account when estimating long-term performance of carbonated concretes.

ORCID

Kiyofumi Nakada: https://orcid.org/0000-0003-2744-1669
Katsuhito Komiya: https://orcid.org/0000-0001-8331-677X
Yuhei Nishio: https://orcid.org/0000-0002-9865-8606
Hikaru Fumino: https://orcid.org/0000-0001-9394-7372
Manabu Kanematsu: https://orcid.org/0000-0003-2473-0625
Takafumi Noguchi: https://orcid.org/0000-0001-6115-2292

References

Auroy, M. *et al*. (2015). 'Impact of carbonation on unsaturated water transport properties of cement-based materials', *Cement and Concrete Research. Elsevier Ltd, 74*, pp. 44–58. doi: 10.1016/j.cemconres.2015.04.002.

Borges, P. H. R. *et al*. (2010). 'Carbonation of CH and C-S-H in composite cement pastes containing high amounts of BFS', *Cement and Concrete Research, 40(2)*, pp. 284–292. doi: 10.1016/j.cemconres.2009.10.020.

Chen, J. J., Thomas, J. J. and Jennings, H. M. (2006). 'Decalcification shrinkage of cement paste', *Cement and Concrete Research, 36(5)*, pp. 801–809. doi: 10.1016/j.cemconres.2005.11.003.

Castellote, M. *et al*. (2009). 'Chemical changes and phase analysis of OPC pastes carbonated at different CO2 concentrations', *Materials and Structures, 42(4)*, 515–525. doi: 10.1617/s11527-008-9399-1.

Galan, I., Andrade, C. and Castellote, M. (2012). 'Thermogravimetrical analysis for monitoring carbonation of cementitious materials Uptake of CO2 and deepening in C–S–H knowledge', *J Therm Anal Calorim, 110*, 309-319. doi: 10.1007/s10973-012-2466-4

Galan, I., Andrade, C. and Castellote, M. (2013). 'Natural and accelerated CO2 binding kinetics in cement paste at different relative humidities', *Cement and Concrete Research. Elsevier Ltd, 49*, pp. 21–28. doi: 10.1016/j.cemconres.2013.03.009.

Galan, I. *et al*. (2015). 'Assessment of the protective effect of carbonation on portlandite crystals', *Cement and Concrete Research. Elsevier Ltd, 74*, 68–77. doi: 10.1016/j.cemconres.2015.04.001.

Houst, Y. F. and Wittmann, F. H. (1994). 'Influence of porosity and water content on the diffusivity of CO2 and O2 through hydrated cement paste', *Cement and Concrete Research, 24(6)*, 1165–1176. doi: 10.1016/0008-8846(94)90040-X.

Kim, S. *et al*. (1995). 'The Carbonation of Calcium Hydroxide and Calcium Silicate Hydrates', *Inorganic Materials, 2(254)*, 18-25. https://doi.org/10.11451/mukimate1994.2.18

López-Arce, P. et al. (2011). 'Influence of relative humidity on the carbonation of calcium hydroxide nanoparticles and the formation of calcium carbonate polymorphs', *Powder Technology. Elsevier B.V., 205(1–3)*, 263–269. doi: 10.1016/j.powtec.2010.09.026.

Morandeau, A., Thierry, M. and Dangla, P. (2014). 'Investigation of the carbonation mechanism of CH and C-S-H in terms of kinetics, microstructure changes and moisture properties', *Cement and Concrete Research. Elsevier Ltd, 56*, 153–170. doi: 10.1016/j.cemconres.2013.11.015.

XV International Conference on Durability of Building Materials and Components
DBMC 2020, Barcelona
C. Serrat, J.R. Casas and V. Gibert (Eds)

Case Study of Pathological Manifestations of Neoprene Support Devices in Infrastructure

Felipe R. Gonçalves[1a], Lais A. Alves[2], Assed N. Haddad [1b] and Elaine G. Vazquez[1c]

[1] Escola Politécnica, Department of Civil Construction, Universidade Federal do Rio de Janeiro (UFRJ), Technology Center, Av. Athos da Silveira, 149 CT – Sector A, 2º floor, 21941-909 – Cidade Universitária, Rio de Janeiro, Brazil, felipe.rezende@poli.ufrj.br, assed@poli.ufrj.br, elainevazquez@poli.ufrj.br

[2] Department of Civil Construction, Federal Center of Technological Education Celso Suckow da Fonseca, Av. Maracanã, 229 Sector E, 2º floor, 20271-110 - Maracanã, Brazil, lais.alves@cefet-rj.br

Abstract. *The so-called works of special arts, are constructions of high complexities that allow the advancement of widening gaps and overcoming obstacles previously unthinkable. With the increase in magnitude of these structures, in addition to greater investments, the maintenance of these structures becomes an increasingly important factor for engineering. Among the elements of bridge structures, the support devices are components with important structural functions, being essential for their proper functioning and especially the durability of the entire structure. This paper aims to evaluate the pathological manifestations in support devices so, according to inspections performed and the diagnosis of causes, define their best practices and treatments for the maintenance and mitigation of the pathologies found. In the practical study the following steps were performed: survey and selection of the structures currently under maintenance of MetrôRio; selection of criteria for the evaluation of pathologies; carrying out inspections; comparative analysis between the viaducts to determine the priority order for negotiations; and definition of conduct. The results obtained were the result of evaluation of the field analysis, diagnosis and comparison with tests performed in support devices. Having as input the tests in the support devices, the best treatments and suggestions to avoid new pathologies were proposed.*

Keywords: *Support Device, Infrastructure, Pathological Manifestation, Maintenance.*

1 Introduction

Throughout history, bridges have been built to exemplify the engineering prowess of a civilization, many enduring longer than the empires that built them (Wilson, 2009).

Bridges and infrastructures systems, due to their inherent vulnerability, are at risk from ageing, fatigue and deterioration process due to aggressive chemical attacks and other physical damage mechanisms (Biondini, 2015). The preventive and corrective maintenance should be part of a comprehensive management process, including periodic surveys aimed at identifying any existing structural anomalies and failures, diagnosing them and then defining recovery and treatment actions, if necessary (Kainuma *et al.*, 2014).

The culture of inspection and maintenance of road bridges, railroads and viaducts in Brazil is recent, being from the 80's the first studies of pathologies in the structures (Araujoa, 2017).

There is a specific standard for the inspection work on bridges, viaducts and concrete walkways, ABNT / NBR 9452/2016 (ABNT NBR 9452, 2016).

Support devices are components with structural functions essential for the proper functioning and durability of the structure, but not just a sample of the entire structure, the support device alone can already represent a maintenance point of the structure, so its monitoring continuous inspections are considered very important in the bridge maintenance management process (Freire *et al.*, 2015).

It can be said that knowledge of the state of the bearing apparatus is a good sign and well represents the state of the bridges in their entirety in structural terms. Therefore, the analysis of their pathologies, causes and origins is of great importance in defining the treatment and maintenance of bridges, elevations and viaducts. (Freire *et al.*, 2014).

Metal and concrete support devices expose some problems that discourage their use, either in terms of maintenance difficulty, poor property of materials or even the built-in cost. Therefore, over time, it was searched for elements that could cover all the needs of a support device, this way arose the support devices in elastomer, based on polychloroprene, whose widespread trade name is neoprene which as a product industrialized, it presents greater uniformity of physical characteristics, as well as exceptional resistance to light and ozone, thus providing durability significantly superior to that of other types of elastomers (Cordeiro,2014).

This paper aims to present approaches towards improving some specific infrastructure maintenance principles, strategies, models and practices, based on a recent study to evaluate the pathological manifestations in neoprene support devices, of the structures currently under maintenance of *MetrôRio*.

The novelty of this work is in proposing a systematic approach to condition assessment, deterioration forecasting, and maintenance decision making over the life-cycle of the built asset. Given the importance of *MetrôRio* to society in Rio de Janeiro, it is essential that the entire system works continuously as there is no margin to support major service disruptions.

2 Methods

In the methodology the following steps were used: survey of the viaducts, elevations and bridges existing in the subway railway; selection of structures to be inspected; selection of criteria used in the evaluation of pathological manifestations; conducting visual inspections based on ABNT NBR 9452/2016; and suggestions for future interventions.

2.1 Inspection of Bridges and Support Equipment

Inspections are paramount to characterize the bridge's constituent elements and, therefore, their classification according to criteria established in ABNT NBR 9452 (2016). Each element is evaluated according to specific visual aspects defined in the standard. According to the same standard, the following types of inspections are considered: cadastral, routine, special and extraordinary.

ABNT NBR9452 (2016) provides in Annex A, a basic roadmap for tokens and cadastral inspections, the proposed initial documents are described such as project data, execution record and changes in the construction phase, previous inspections, among other elements that may provide more inputs for the definition of the causes and better dealings.

Inspection of assistive devices may not be limited to the space in which they are positioned and to the element. It is necessary to identify the general functioning of the studied artwork and to verify the compatibility with the current behavior of the support devices.

Because of their location, support devices are structural elements that are difficult to inspect, but their behavior must be monitored by inspectors according to the following general procedures in Table 1 (DNIT, 2004).

Table 1. Items to be inspected on assistive devices (DNIT, 2004).

Visually inspect the accessible faces of the appliance; After a few years of service, small cracks 2 to 3mm deep and 2 to 3mm long are tolerable;	Check that the support device has been correctly vulcanized and that there are visible and oxidized charter steel sheets;
If there is displacement of the structure, measure the angles between the surfaces of the structures in contact with the support apparatus;	Check for defective expansion joints on the superstructure, very close to the support device or directly above the device.
Measure distortions of the support apparatus;	Check that the support device has been moved from its original position;
Check for the presence of oils, greases or any other substance harmful to the elastomer;	Measure the heights of the support apparatus at the edges and center points;

According to ABNT NBR9452 (2016), Table 2 can be considered as a parameter for evaluating support equipment, given its condition and the scenario to which it is exposed.

Table 2. Device Classification (ABNT NBR9452, 2016).

Condition	Description
Critical	Support devices and / or their surroundings present breakdowns at risk of structural collapse requiring repair intervention and / or immediate device replacement.
Bad	Support devices and / or their surroundings present damage that compromises structural safety without risk of collapse, requiring repair intervention and / or short-term device replacement. All devices with breakage with charter exposure fall into this classification. Follow-up is recommended and interventions may be needed in the short term.
Regular	Support devices and / or their surroundings present malfunctions that may generate some structural deficiency, but there are no signs of deterioration of the devices, nor compromise of the stability of the work. Follow-up is recommended and interventions may be necessary in the medium term.
Good	Support devices and / or surroundings are not malfunctioning. Interventions may be necessary in the long run.
Excellent	Support devices and / or their surroundings are not damaged and the devices were manufactured from 1987 following the recommendations of ABNT NBR 9783 (1987).

2.2 Pathological Manifestation in Neoprene Support Devices

Although it has excellent performance compared to other types of support equipment, especially when not in need of maintenance, the neoprene device also requires some care. Table 3 shows recurrent pathological manifestations in neoprene supports.

Table 3. Pathological Manifestations in Neoprene Apparatus (Cordeiro, 2014).

Most Common Pathological Manifestations - Neoprene Apparatus
High Neoprene Distortion
Neoprene cracking or creep
Frame contact zone shutdown
High compression on neoprene
Loss of serviceability and distortion
Variations in rubber layer thickness
Unsticking of vulcanization of inner sheets
Degradation of sliding plates, guides or stops
Oxidation of steel elements

The causes for the deterioration of structures can be as diverse as the natural "aging" of the structure to the irresponsibility of some professionals who choose to use materials that are out of specification (Souza and Ripper, 1998).

The causes of pathologies in structures have their origins in two groups: intrinsic causes - referring to the processes of deterioration inherent in the structure itself, *i.e.* its origin is in execution, use, human failures, etc. and extrinsic causes - external to the material body, can be understood as factors that attack the structures from the outside inwards, throughout the process of conception, execution or the useful life. The most common causes of decreased service life in assistive devices are listed in the Table 4 (DNER, 2006).

Table 4. Causes of Pathological Manifestations in Support Devices (DNER, 2006).

Most common causes of pathological manifestations	
Intrinsic damage not detected during installation	Irregular seating causing additional localized overload
Displacements, rotations and loads in service much higher than estimated	Unintended aggressiveness of the environment
Attack by chemicals	Badly nesting in the crib

The treatment of a pathological manifestation should be done according to the inspection report, condition and definition of the causes of the given manifestation.

As it is a synthetic structure, of specific manufacture, it is more common that if it presents anomalies, it will be replaced by a new device. Except in the case of incorrect positioning of support devices or displacement of a Teflon sliding plate, for example.

Table 5 presents some common types of repair methods according to each pathology in neoprene support devices (Cordeiro, 2014).

Table 5. Neoprene Support Devices Treatments – adapted (Cordeiro, 2014).

Damage to Support Devices	Repair Dealer
Corrosion, presence of dust and moisture	Cleaning and use of protective paint.
Massive corrosion leading to section loss	Replacement
Offset or misalignment	Component replacement or total
Neoprene deterioration or wear	Replacement
Fissures	Crack sealing or replacement
Fragmentation of concrete in support	Removal and execution of new concrete

3 Results – Case Study of Pathological Manifestations, Their Causes and Treatments in Neoprene

All *MetrôRio's* assets are cataloged according to an asset tree ABNT NBR ISO 55000 (2014), which aims to give an overview, keep all history of interventions, corrective or preventive, and maintenance plans in force combined with each group of systems and equipment. Thus, the support devices studied in this work are under the structures system.

The object of case study was the support devices and their surroundings. The elevations between São Cristóvão and the *MetrôRio* Maintenance Center and between the Triagem and Maria da Graça stations are the oldest in the system, and their construction dates back to the late 1970s, or about 35 years of operation.

The recommendations of DNIT inspections were followed (DNIT,2004). Field information has been posted in a specific form for this service. A specific inspection campaign was carried out for the support devices of each structure. As an input for maintenance decision-making, 1228 neoprene support devices were performed along the entire railway structure. The inspections were performed by specialized technicians using the visual method, with the naked eye, and the access was made by stairs with a reach of 9.00 meters in height. The fieldwork was accompanied by a professional specialized in occupational safety, all safety procedures were complied with in accordance with current legislation. No device has been classified in the Excellent Class because it is over 30 years old and has not been manufactured (ABNT NBR 9783, 1987).

The CNV - SCR Elevated is located between the Maintenance Center - MC and the São Cristóvão station (later, there was also the connection of the elevated with Cidade Nova station). The old elevation has a total length of 970m and consists of 30 spans, 4 spans with 4 beams, 1 span with 3 beam and 25 spans with 2 beams. The trays are seated on 28 pillars and two staked joints at the longitudinal ends, constituting isostatic spans. In the beam x pillar and beam x encounter interface there are chartered neoprene support devices with regular dimensions of 700 x 250 x 40 mm. In this elevation, 30 pillars and 138 support devices were evaluated, two of which were not inspected for being covered. It was found that most of the assistive devices (79 units) inspected at this stage were classified as being in a regular state of conservation (57%). Supporting devices fitted with poor condition total 57 units (42%), as shown in Fig. 1.

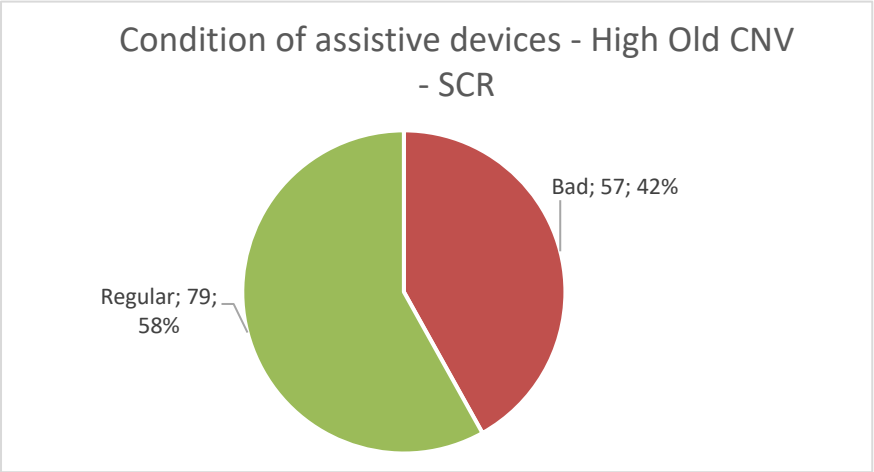

Figure 1. Support Device Conditions - CNV – SCR.

Elevated TRG -MGR is mostly located between the Triagem (TRG) and Maria da Graça (MGR) stations and starts after leaving the Bernold tunnel next to the Mangueira Olympic village. The Elevado has a total length of 2,925 meters and is formed by 84 spans, mostly with 4 precast beams each, with chartered neoprene appliances with dimensions 750 x 200 x 40 mm. In this elevation, 361 support devices were evaluated, and 37 pillars were not inspected because they were in a risk area where access could endanger the inspection team. It was found that most of the support devices (269 units) inspected at this stage were classified as being in a regular state of conservation (75%). Poorly classified support devices total 78 units (22%), 9 units (2%) were considered in good condition and 5 critical support devices (1%), as shown in Fig. 2.

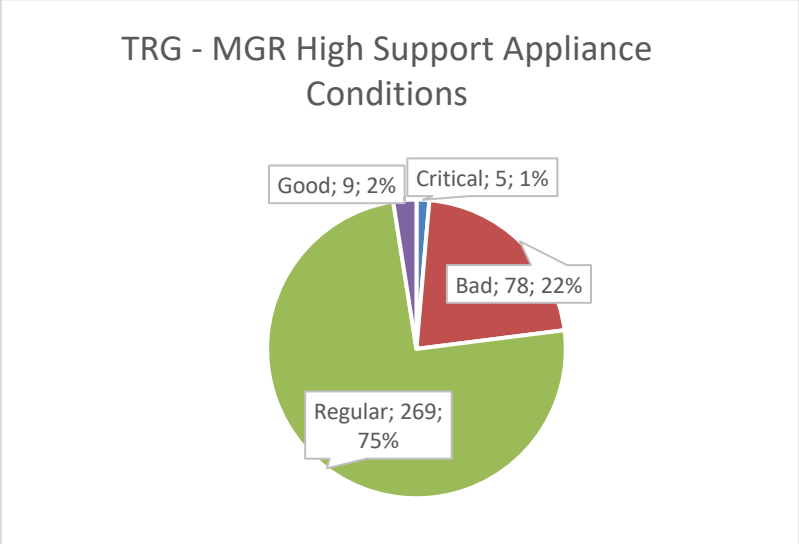

Figure 2. Support Device Conditions - TRG – MGR.

With the definition of the pillars that concentrated the largest number of critical devices, aiming at a better use of the operation, the decision was made to replace 12 units, from the perspective of urgent replacement. Tables 6 present this pathological manifestation, with the degree of risk, possible cause and the indicated treatment.

Table 6. Pathological manifestations in the devices and support.

Pathological Manifestation - Cradle Degradation (Plinth)	
Pathology	Anomaly around the support apparatus, but caused by malfunction of the element. 
Risk	Critical risk - severe pathological manifestation with compromised structural safety
Cause	From a malfunction of the supporting bond between the superstructure and the mesostructure of the elevation.
Treating	The treatment, in addition to the replacement of the support apparatus, should include reinforcement of the plinth with its recomposition at the bottom, called the cradle. As said, in neoprene support devices, it is not common to perform maintenance and treatment interventions on the element, but rather its immediate replacement.

4 Conclusions

The concern with the maintenance of structures such as those of special artworks was motivating for the work and allowed to relate the pathological manifestations in support devices with the pathological manifestations of the structures, the intrinsic and extrinsic causes as a whole, allowing an analysis, albeit superficial in the field of subject matter, sufficient for decision. The novelty was the proposal of a systematic approach to condition assessment, deterioration forecasting, and maintenance decision making over the life-cycle of the built asset.

Supporting devices are structural connecting elements which allow forces to be transmitted between the superstructure of the artwork and its support and are therefore essential elements for the proper functioning of the structure into which they are inserted.

The inspection processes took place exactly in accordance with all the literature found, allowing great inputs for subsequent decision making. Thus, the pathological manifestations were quite explicit.

As for the causes of the manifestations, it is a complex study and although there is literature, it is not trivial to understand the reason why two support devices, theoretically manufactured under the same process, of the same age, suppose stored in the same form, are adjacent to each other, exposed to very close loads and exhibit behaviors so distinct in terms of behavior in service.

Even with breakage and chartering exposed in the corrosion process, the devices can still perform satisfactorily without causing movement restriction of the part. But in these cases, annual monitoring is essential to follow up on a case-by-case basis to make sure that the performance and operation of the chartered neoprene parts is still adequate.

As for the process of negotiations, in cases where no substitution was considered, monitoring will take place in accordance with the first inspection. Thus, the big point of the issue of support devices is to understand their operation not individually but in conjunction with adjacent structures, as it is evident that despite some anomalies found, support devices, except those that had signs of degradation around them, they were still able to remain in service, provided they were well monitored.

ORCID

Lais Alves: https://orcid.org/0000-0003-0543-2374
Assed Haddad: https://orcid.org/0000-0002-4793-0905
Elaine Vazquez: https://orcid.org/0000-0002-7262-6753

References

Araujoa C. (2017). Main aspects covered in ABNT NBR 9452: 2016, the importance of maintenance activities in bridges and viaducts and the difficulties of the conditions of access to the inspections. *Revista IPT | Tecnologia e Inovação* 1(5), 1-12.

Associação Brasileira de Normas Técnicas (2014). *ABNT NBR ISO 55000:2014 Gestão de Ativos – Visão geral, princípios e terminologia.* Rio de Janeiro, Brazil.

Associação Brasileira de Normas Técnicas (2018). *ABNT NBR 9783:1987 - Inspeções em pontes e viadutos de concreto armado e protendido - Procedimento.* Rio de Janeiro, Brazil.

Associação Brasileira de Normas Técnicas (2016). *ABNT NBR 9452: 2016 Vistorias de pontes, viadutos e passarelas de concreto.* Rio de Janeiro, Brazil.

Biondini F. and Frangopol Dan M. (2015). *Design, assessment, monitoring and maintenance of bridges and infrastructurenetworks Structure and Infrastructure Engineering*, 11(4), 413-414.

Cordeiro J. (2014) *Aparelhos de Apoio em Pontes Vida Útil e Procedimentos de Substituição*. Dissertação de Mestrado. ISEL (Instituto Superior de Engenharia de Lisboa). Lisboa, Portugal.

Departamento de Estradas e Rodagem (DNER) (2006). *Substituição de aparelhos de apoio e juntas de dilatação – Código 020*. São Paulo, Brazil.

Departamento Nacional de Infra-Estrutura de Transportes (DNIT) (2004). *Manual de Inspeção de Pontes Rodoviárias*, 2ª Edição, Rio de Janeiro, Brazil.

Freire L., Brito J. de and Correia J. (2015). Inspection Survey of Support Bearings I Road Bridges. *Journal of Performance of Constructed Facilities*, Vol.29(4), 100-112.

Freire L., Brito J. de and Correia J. (2014). Management system for road bridge structural bearings Structure and Infrastructure Engineering, 10(8), 1068-1086.

Kainuma S., Ahn J-H., Jeong Y-S., Imamura T. and Matsuda T. (2014). Applicability and structural response for bearing system replacement in suspension bridge rehabilitation, *Journal of Constructional Steel Research*, 95(19), 172-192.

Souza V., Ripper T. (1998). *Patologia, Recuperação e Reforço de Estruturas de Concreto*. 1 ed. São Paulo, Brazil, Ed. Pini.

Wilson K. (2009). *Building bridges: from simple stone spans to complex constructions of iron and concrete*, Britain's abundance of bridges offers endless opportunities for photographic creativity. (GEO photo) Cengage Learning, Inc. Geographical, 81(9), 82 -97.

XV International Conference on Durability of Building Materials and Components
DBMC 2020, Barcelona
C. Serrat, J.R. Casas and V. Gibert (Eds)

Characteristics of the Changes in the Compressive and Tensile Stress of the Construction Sealant under Cyclic Movement

Kohei Yamashita[1], **Hiroyuki Miyauchi**[2], **Akihiko Ito**[3], **Tomomi Soeta**[4] **and Tohru Nakashima**[1]

[1] Performance Polymers (MS) Solutions Vehicle, KANEKA CORPORATION, 2-3-18, Nakanoshima, Kita-ku Osaka 530-8288, Japan, Kohei.Yamashita@kaneka.co.jp, Tohru.Nakashima@kaneka.co.jp
[2] Department of Building, Materials and Components, Building Research Institute, 1 Tachihara, Tsukuba-shi, Ibaraki, 305-0802, Japan, miyauchi@kenken.go.jp
[3] Production Division, Auto Chemical Industry Co.,LTD., 2044-6 Kamiinayoshi, Kasumigaura-Shi, Ibaraki 315-0056, Japan, akihiko.ito@autochem.co.jp
[4] Technology Development Division, Fujita Corporation, 2025-1, Ono, Atsugi City, Kanagawa 243-0125, Japan, soeta@fujita.co.jp

Abstract. *A compact fatigue testing machine to quantitatively evaluate the effects of this complex degradation of sealants and the load change of the sealant under dynamic fatigue has been developed. The developed fatigue testing machine is compact with dimensions of (width) 100 × (length) 135 × (height) 110 mm. It can be installed in an outdoor exposure test site or in a chamber. Thus, this machine can be used for performing various compounded accelerated degradation tests. We report the use of this testing machine to examine the effects of this complex degradation of sealants and the load change of the sealant under dynamic fatigue.*

Keywords: *Fatigue Testing Machine, Sealant, Joint, Fatigue Resistance.*

1 Introduction

The factors contributing to the degradation of the construction sealants used in exterior walls can be broadly classified into weathering (heat, ultraviolet rays, moisture, etc.) and joint movement and they work simultaneously in a complex manner. Especially, for dynamic joints, these factors work simultaneously and in a complex manner, and they continue to take effect from the moment that they are filled in the joint until the end of their life.

Current evaluation tests for the sealants mainly evaluate properties after curing in relation to a single degradation factor. No evaluation method for the effect of movement during curing process or one in which complex degradation can be applied had been established yet.

For this reason, we worked on developing a compact fatigue testing machine for the sealant to quantitatively evaluate the effect of complex degradation and load change in the sealants at the time of dynamic fatigue.

Using the developed compact fatigue testing machine the effects of the joint movement during curing on the physical characteristics and the shape of the sealant and the changes in physical properties of the cured sealants were evaluated. The changes in compression and tensile stress of the sealant when repetitive expansion/contraction fatigue (deformation) was applied to the sealing joints with variable fatigue cycle, displacement, and temperature were also measured and examined.

doi:10.23967/dbmc.2020.154

2 Overview of the Fatigue Test

2.1 Overview of the Fatigue Testing Machine

Conventional fatigue test machines are all large devices with low versatility and high price. When developing the current fatigue machine, the following points were paid attention to (a) compact size, lightweight, installable in a chamber; (b) easy mechanism; and (c) the price range is such that concerned parties can use the machine in round-robin fashion.

An overview of the developed testing machine is shown in Figure 1 and Table 1. It comprises of (1) fatigue testing machine unit, (2) load measurement device, and (3) PC for measurement purposes. It is capable of measuring the stress (load) on the sealants simultaneously while applying repetitive expansion/contraction deformation.

The dimensions of the fatigue testing machine are 100 mm (Width) × 135 mm (Length) × 110 mm (Height) mm and it weighs only 1.3 kg and can be held by one hand. The device runs on AC 100 V power source or a DC 12 V battery, so it can be installed for outdoor exposure test and can also be placed in a chamber.

Two types of machines with different fatigue cycles were made. One was a fixed-cycle (one cycle/24 hrs) type, in which the number of rotations was controlled only by the combination of a motor equipped with a decelerator and a worm gear. Another was a variable cycle type, in which the number of rotations could be electronically changed with a stepping motor which was combined with the reduction gear ratio of the worm gear. The main unit is separated into the test unit on the upper fixed platform and that on the lower control unit. A test specimen was fixed between the movable section jig and the fixed section jig in the test section, and the load generated by the reciprocal motion of the compression and tension displacement of the movable section was detected by a load cell. In the control unit, high torque is realized by the motor equipped with the decelerator or the combination of the stepping motor and the worm gear, and it rotated within the specified range controlled by a displacement control cam attached to a rotation axis. The load method is explained as follows. In the displacement mode we used, the compression and tension displacement were applied alternately in a sine wave. The displacement was set at ± 1.2 mm (± 10%), ± 2.4 mm (± 20%), and ± 3.6 mm (± 30%) in relation to the joint width of 12 mm. For joint movement cycle, with this machine two levels could be selected, i.e., once per day (24 hrs) and 5 cycles/min (approximately 12 s). The latter is the range specified in JIS A 1439.

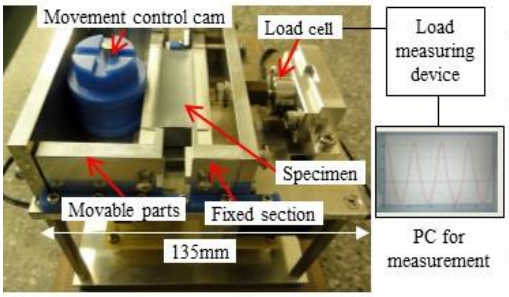

Figure 1. Compact Fatigue Testing Machine (Variable cycle type).

Table 1. Compact Fatigue Testing Machine Specification.

Testing machine type	Fixed Cycle type	Once per day: Decelerator-attached motor control
	Variable Cycle type	Once per day to 5 times/minute: Stepping motor + electric control
Load method	Drive method	Motor + worm gear
	Displacement mechanism	Displacement control by cam eccentric motion
	Displacement mode	Compressed tensile displacement: ±1.2, 2.4, 3.6mm
	Cycle	Once per day, 5 times/minute (sine wave)
Load	Load resistance	Maximum 100N
	Load measurement	Tensile compression load cell (Max.200N)
Environment used	Temperature	-10 to +50°C (depends on motor spec)
	Power	AC100V, DC12V battery (for low load)
Others	Dimensions/weight	Width 100 × length 135 × height 110mm, 1.3kg

2.2 Sealants Used in the Test

Silyl-terminated polyether (STPE) type sealants having a silylated polyether main chain with reactive silyl terminal groups as the main ingredient, which forms siloxane bonds through moisture-curing and thereby exhibits rubber elasticity, were selected. It has excellent weatherability, durability, heat resistance, workability, and good paintability on the surface and is widely used for construction sealing materials and elastic adhesives. General structural formula of STPE is shown in Figure 2.

In the test, the two types of sealants were used, i.e., 1-component type (MS-1) and 2-component type (MS-2, F-25LM-9030), with tensile properties and relaxation rate shown in Table 2. The tensile properties were measured according to JIS A 1439 (tensile velocity was 5.5 ± 0.7 mm/min). The stress relaxation rate was obtained from Equation 1. The larger the stress relaxation rate is, more is the reduction in tensile stress generated in the sealant with time.

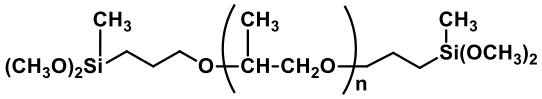

Figure 2. General structure of silyl-terminated polyether.

Table 2. Tensile test results and stress relaxation rate of the sealant used.

Sealant	M_{50} (N/mm^2)	T_{MAX} (N/mm^2)	E_{MAX} (%)	Stress relaxation rate (%)
MS-1	0.06	0.25	580	68
MS-2	0.12	0.25	410	28

$$Stress\ relaxation\ rate = Tensile\ stress\ immediately\ after\ 30\%\ tension - \frac{Tensile\ stress\ after\ 30\%\ tension\ being\ held\ for\ 15\ hrs}{Tensile\ stress\ immediately\ after\ 30\%\ tension} \quad (1)$$

2.3 Specimen Shape

As shown in Figure 3, the test specimen was an ISO type (W 12 mm × D 12 mm × L 50 mm) using anodic oxide coated aluminum as the substrate. The substrate was coated with a primer exclusive for sealants.

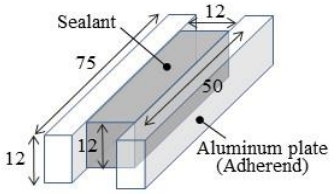

Figure 3. Specimen (ISO type) shape /dimensions (unit:mm).

3 Effect of Repetitive Deformation on Curing Sealants

3.1 Fatigue Test Method

Tests were carried out on two types of test specimens for MS-1 and MS-2, i.e., the cured test specimen in accordance with JIS A 1439 (also called specimen after curing) and the test specimen immediately after the sealants had been applied to the joints (also called specimen before curing). In order to measure the load change in the joint, backup material was not used in the specimen, and Teflon tape was attached to the bottom of the rear side so that the sealant could be peeled off. The deformation rate of the joint was set at ± 20%, and the test was started from the compression side. The cycle was set at once per day in accordance with the actual joint behavior. The test period was set to two weeks (total number of deformations: 14). Load (stress) changes in case of movement applied to sealants during curing were evaluated.

3.2 Fatigue Test Results

3.2.1 Load changes and damage state of the sealant

Figure 4 shows the load changes in each specimen related to the repetitive deformation. For both MS-1 and MS-2, we can see that the specimen before curing had a reduced load amplitude compared to the specimen after curing, and that it was affected by the movement during the curing. In particular, the MS-1 specimen before curing showed these tendencies prominently. The conditions of the front and rear face of each pre-cured specimen subjected to fatigue test did not show any change. Meanwhile, the front face of the specimen before curing swelled in a convex shape, as shown in Table 3. The MS-1 specimen before curing had a large hole in the center of the rear side. It was considered that the sealant was damaged due to significant effect of the movement applied during curing. Additionally, the rear face of the MS-2 specimen before curing was deformed to a convex shape.

Table 3. Surface/reverse for specimen before curing after

	MS-1 Specimen before curing	MS-2 Specimen before curing
Surface		
Side		

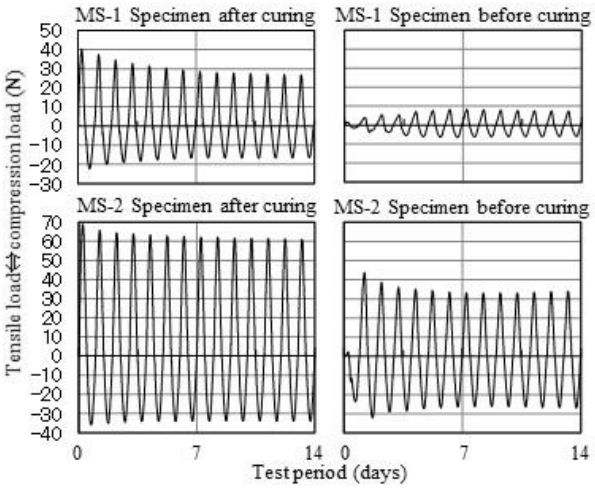

Figure 4. Changes in load against repetitive deformation.

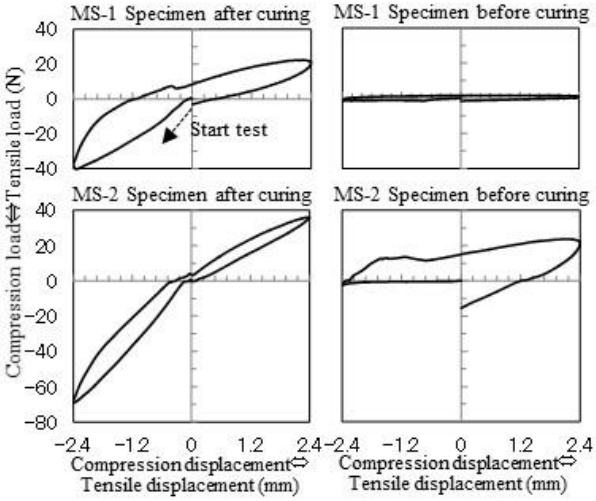

Figure 5. Displacement and load hysteresis curve for the first repetitive deformation.

3.2.2 Hysteresis curve of the displacement and load after first fatigue cycle

Figure 5 shows the hysteresis curve of the displacement and load of the sealants after first repetitive deformation cycle. The initially uncured specimens were slow in expressing the strength compared to the cured specimens, and the load zero value before and after one fatigue cycle did not match. This may be due to change in shape of the sealants or due to damage. Meanwhile, for the cured MS-1 specimen, the difference in the load before and after the tension/compression round-trip was greater compared to that of the cured MS-2 specimen, presumably due to fatigue.

3.3 Observations Concerning Fatigue Resistance

3.3.1 Effect of curing state due to repetitive deformation

In case of the uncured MS-1 specimen, the sealants hardened gradually from the surface (Figure 6). Since the shape coefficient D/W (D: joint depth, W: joint width) decreases in the initial

curing period, the sealant was rendered into a state being easily deformed outward, as shown in Figure, once the compression movement was incurred during the curing. Additionally, when the movement occurred during the curing of MS-2, the compression/tensile load ratio changed (Figure 7). This also suggests that the change occurred similarly in the joint cross-section. That is, when it receives the movement during the curing, the subsequent fatigue resistance would be affected.

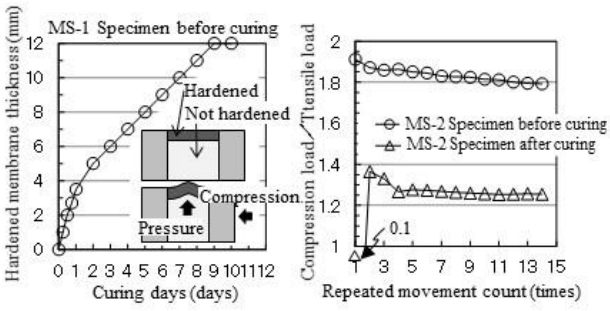

Figure 6. Changes in membrane thickness and joint cross-section change.

Figure 7. Changes in compression /tensile load (cycle day 1).

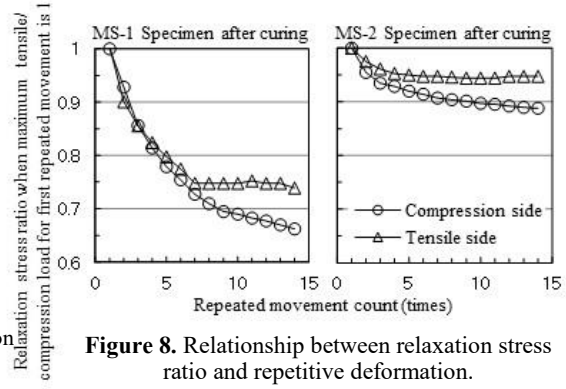

Figure 8. Relationship between relaxation stress ratio and repetitive deformation.

3.3.2 Effect of stress relaxation due to repetitive deformation

The relaxation stress ratio (fatigue stress ratio) has been defined as the ratio of the generated stress under the repetitive deformation to the maximum stress (load) at the first movement cycle expressed as the reference value 1. Its relationship with the number of repetitive deformations is shown in Figure 8 above. The reduction in relaxation stress ratio of the cured MS-1 specimen is larger, compared to the cured MS-2 specimen. Additionally, the relaxation stress rate greatly decreased after applying repetitive deformation. For both specimens, the decrease in the stress relaxation ratio on the compression side was greater than that on the tensile side, and it can be considered necessary to carry out repetitive fatigue tests to evaluate the effect of stress relaxation in the sealants.

4 Effect of Repetitive Deformation in Relation to Cured Sealant

Next, different repetitive deformation were applied to the cured sealant and the compression and tensile stress of the sealant were measured and observed.

4.1 Fatigue Test Method

MS-1 and MS-2 described in Section 2.2 were used. The compression and tension deformation rate of the joint was 20% of joint width, and the fatigue test started from the compression side. The cycle was 12 s, and the maximum number of the fatigue cycles were 10,000.

4.1.1 Viscoelasticity Properties of Sealant

The changes in the stress of the sealant at the first fatigue deformation is shown in Figure 9. For MS-1, maximum compression stress was 2.2 times greater than the maximum tensile stress, and this ratio was 2 times for MS-2. For MS-2, at the displacement zero point (at 6 s

where the joint changed from contraction to expansion), the stress became zero, indicating the elasticity. Meanwhile, for MS-1, the changes in the stress preceded the movement, and the tensile stress was generated at the displacement zero point, indicating the tendency to easily undergo compressive setting and the viscoelasticity.

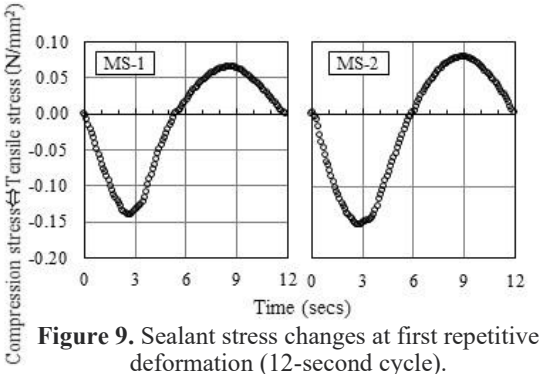

Figure 9. Sealant stress changes at first repetitive deformation (12-second cycle).

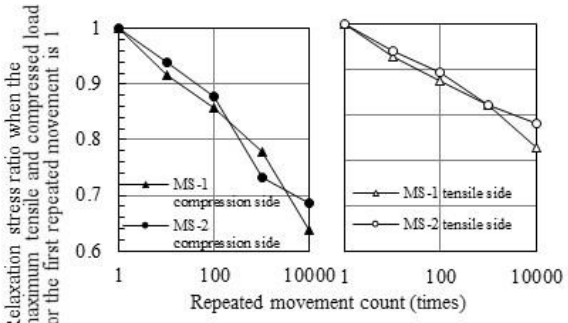

Figure 10. Relationship between relaxation stress ratio and the number of deformation (12-second cycle).

4.1.2 Sealant Stress Reduction Characteristics in Relation to Repetitive Deformation

The relationship between the relaxation stress ratio and the number of the repetitive deformation (when maximum tension and compression load for the first repetitive deformation cycle = 1) is shown in Figure 10. For both MS-1 and MS-2, the stress relaxation ratio in the compression side became smaller compared to that in the tensile side as the number of the repetitive deformations increased. This is particularly prominent in the case of MS-1. Figure 11 shows the hysteresis curve of the displacement quantity and stress for each fatigue cycle.

When the repetitive deformation was applied once, the phase differences for both displacement and stress for both MS-1 and MS-2 were large. The difference was particularly large in MS-1, compared to MS-2. Additionally, in terms of the effect of the joint displacement, the effect of the compression side is greater than that of the tensile side. Therefore, MS-1 has more viscous properties (dashpot) and less elastic properties (spring) than MS-2. However, as the number of the fatigue cycles increased, phase difference became smaller.

4.1.3 Effect of the Fatigue Cycle

Table 4 shows the relationship between the number of test days and total strain energy under test conditions. The 12-s cycle test had $1/10^{th}$ the duration compared to 1-d cycle test, but the total strain energy was five times greater. Figure 12 shows the relaxation stress ratio for the 12-s and 1 day fatigue cycle tests. For MS-2, the stress relaxation ratio at the 14th fatigue cycle in both cases was almost the same. This is because the number of repetitions of the joint deformation may be dominantly influencing the MS-2 stress reduction characteristics, as shown in Figure 10. Meanwhile, for MS-1, the stress relaxation ratio at the 14th fatigue cycle in the 1-d duration cycle test is small, compared to that of the 12-s cycle. This is assumed to be because the fatigue loading time exerts a dominant influence on the MS-1 stress reduction characteristics.

From the above, MS-2 was able to bear the effect of 1 cycle/day fatigue (the actual cycle) based on the test method using a fatigue cycle of 5-6 cycles/min specified in JIS A 1439 under temperature conditions of 23 ± 2ºC. However, for MS-1, it is may be necessary to execute fatigue tests in accordance with the actual cycle.

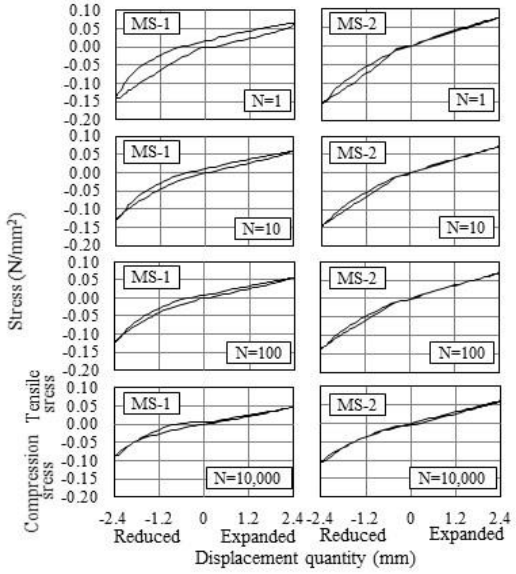

Figure 11. Hysteresis curve for displacement and stress (12-second cycle).

Table 4. Relationship between the number of test days and the strain energy under the load cycles and the maximum deformation cycle in this study.

Test conditions		Days (ratio)	Total strain energy
Cycle	Movement count (ratio)		
12 secs	10,000 (714 times)	1.4 (1)	5 times
1 day	14 (1)	14 (10 times)	1

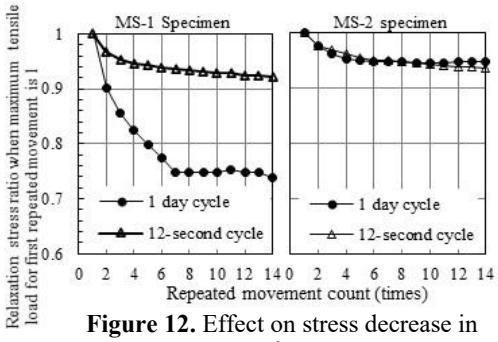

Figure 12. Effect on stress decrease in sealants

5 Effect of Displacement Quantity, Temperature Conditions and Repetitive Elongation/Reduction Deformation

Next, the changes in the compression and tensile stress of the sealant when the repetitive expansion/contraction reformation was applied to the cured sealants while changing the displacement and temperature were measured and examined.

5.1 Fatigue Test Method

After installing MS-2 specimen in the compact fatigue testing machine, it was kept for sufficient time under arbitrary temperature conditions (5, 23, 40°C). Then the repetitive expansion/contraction fatigue with a deformation rate of ± 10% or ± 20% in relation to the joint width was applied from the compression side. The repetition cycle was 12 s, and the maximum number of fatigue cycles were 8,000 to 10,000 (at 23°C, ± 20% 30,000 times maximum).

5.2 Fatigue Test Results and Discussion

5.2.1 Sealant Stress Reduction Characteristics in Relation to Repetitive deformation

The relationship between the relaxation stress ratio when the maximum tension stress (load) for the first repetitive deformation cycle was expressed as 1 and the number of the repetitive deformation is shown in Figure 13.

Under the deformation rates of both ± 10% and ± 20%, the relaxation stress ratio became lower for each repetition. Also, the deformation rate of ± 20% had a smaller relaxation stress rate compared to that of ± 10%. Meanwhile, no significant

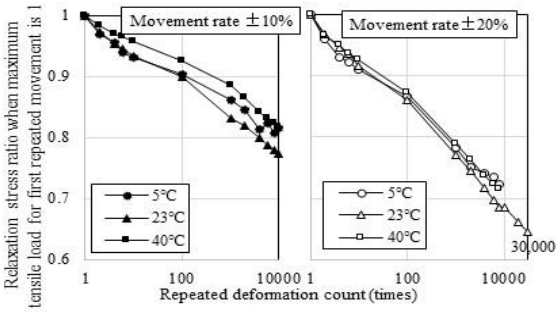

Figure 13. Relationship between relaxation stress rate and the number of deformation (12-second cycle).

temperature dependency was observed for the relaxation stress ratio.

5.2.2 Hysteresis Curve of Displacement Quantity and Load

The hysteresis curves of displacement and the load under various temperature conditions with the deformation rate of ± 20% are shown in Figure 14.

At 23°C, the displacement and the phase difference of the load were small up to a fatigue count of 8,000, whereas the phase difference became large at or above the fatigue count of 20,000. Meanwhile, at 5°C, the phase difference was large even at the fatigue count of 8,000, and it was larger than that at 23°C and 40°C.

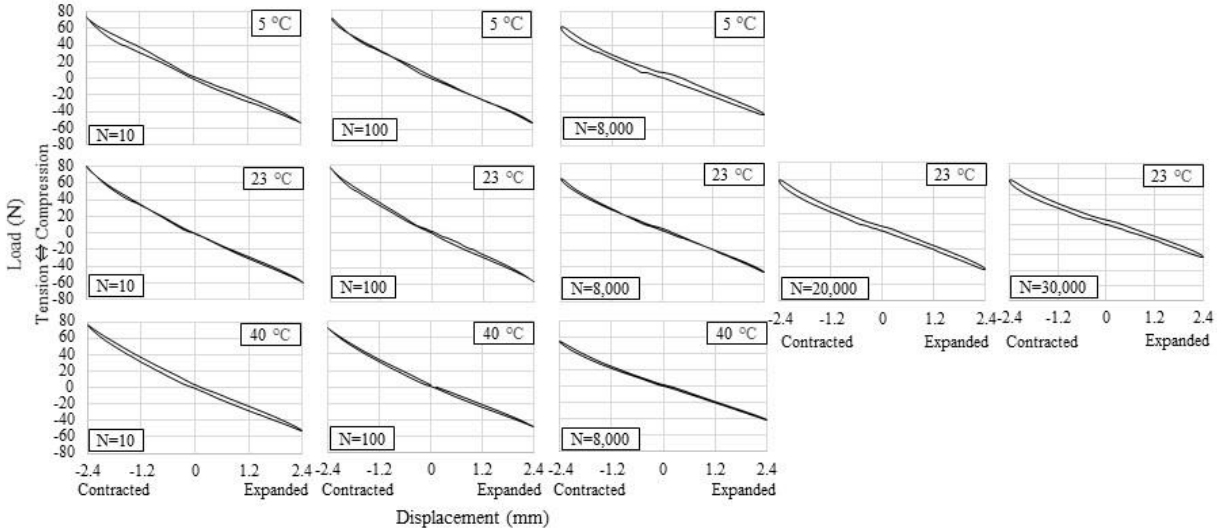

Figure 14. Hysteresis curve of displacement and load under various temperatures (deformation rate ± 20%).

6 Conclusions

This fatigue testing machine was developed to evaluate the durability of sealants against degradation under outdoor environment. Various methods of utilization can be sought according to the user objectives. For example, the testing machine we developed reproduces the movement of the sealants and can be used in combination with outdoor exposure or in an accelerated deterioration test device. This way It is possible to perform a variety of complex degradation tests and further utilization for future sealing technology can be sought.

ORCID

Kohei Yamashita: https://orcid.org/0000-0001-9144-4835

References

Hiroyuki Miyauchi et.al: Measurement of compression-tensile force of sealant when loading cyclic movement to sealed joint by handy-dynamic fatigue testing machine, A-1, Summary of Papers by the Architectural Institute of Japan, pp.1343-1344, 2016

Hitoshi Yamada et.al: Characteristic of compressive-tensile stress change when loading joint movement to sealed joint, Part 1, A-1, Summary of Papers by the Architectural Institute of Japan, pp.903-904, 2017

Kohei Yamashita et.al: Characteristics of compressive and tensile stress change of construction sealant under cyclic movement, Part2, A-1,Summary of Papers by the Architectural Institute of Japan, pp.1033-1034, 2019

XV International Conference on Durability of Building Materials and Components
DBMC 2020, Barcelona
C. Serrat, J.R. Casas and V. Gibert (Eds)

Composite Façade Elements with Self-Cleaning Surface made of Ultra-High-Performance Concrete (UHPC)

Julia von Werder[1], Patrick Fontana[2], Johannes Hoppe[1], Serdar Bilgin[3] and Birgit Meng[1]

[1] Bundesanstalt für Materialforschung und -prüfung (BAM), Unter den Eichen 87, 12205 Berlin, Germany, julia.von-werder@bam.de

[2] RISE Research Institutes of Sweden, Division Built Environment, Drottning Kristinas väg 26, 114 28 Stockholm, Sweden, Patrick.fontana@ri.se

[3] Deutscher Beton- und Bautechnik-Verein E.V., Kurfürstenstraße 129, 10785 Berlin, Bilgin@betonverein.de

Abstract. *In the framework of the European project H-House various concrete façade elements were developed with the aim to ensure a long service life by combining a very durable material with self-cleaning properties. The façade elements presented are made of a shell of UHPC filled with blocks of aerated autoclaved concrete as insulating material. Self-cleaning properties were realized amongst others by imprinting a microstructure into the surface during casting. The paper focuses on selected technological aspects of the manufacturing process of prototypes which had to be performed in two concreting sections. Furthermore the challenges faced when upscaling the self-cleaning properties are addressed and the strategy to assess the self-cleaning properties by measuring the contact and the roll-off angel is presented. The results show that a successfull upscalaing process requires detailed planning and that the best results can often be achieved with a moderate work effort or material use.*

Keywords: *Ultra-High-Performance Concrete, Façade Elements, Self-Cleaning Properties, Adhesive Pull-Strength, Microstructure, Architectural Concrete.*

1 Introduction

Highly automated production plants and design methods based on Building Information Modelling (BIM) make the prefabrication of building elements very efficient. Façade elements made from concrete can be produced regardless of weather conditions in variable shapes and at the highest quality and delivered just in time to the building site. Aim of the European project [H]house (Healthier Life with Eco-innovative Components for housing Constructions) was to develop a variety of new multifunctional and flexible building components which are characterized by long service life, reduced maintenance and a long-term improvement of energy efficiency. Within the project part the BAM was involved, self-supporting sandwich façade elements consisting of a thin shell of ultra-high performance concrete (UHPC) filled with an insulation of autoclaved aerated concrete (AAC) were designed (Miccoli *et al*., 2015, Fontana *et al.*, 2016). UHPC allows the manufacture of very filigree, lightweight and resource-efficient building components with high durability and is therefore optimally suited for pre-fabrication. Sustainability of the façade elements was further increased by the optimization of the binder and adding self-cleaning properties to the surface based on either the integration of photocatalytic TiO_2 into the bulk of the thin UHPC layer or by copying the Lotus® effect. Self-cleaning properties referred to as the Lotus® effect are based on the interaction of the specific micro texture and the water-repellent nature of the surface that makes a water droplet taking off

pollutions from the surface when it is rolling off (Barthlott *et al*., 2016, Si *et al*., 2018)

2 Materials and Methods

The concrete mixture specified in Table 1 was designed by the company Dyckerhoff which was one of the industrial project partners. While ensuring a minimum strength requirement of 100 MPa a binder composition named [H]house Compound 5941 based on the Nanodur® fine mix was developed which contains less than 55 % Portland cement clinker and results in a reduction of non-renewable energy and global warming potential (Deuse *et al.*, 2018).

Table 1. UHPC mixture.

Material	Content in kg/m³
[H]house Compound 5941 grey	1050
Aggregate (0-2 mm)	1150
PCE superplasticizer	17,85
Water	178,5

Due to its fineness and fine-tuned granulometry the mixture further allows to imprint a microstructure into the concrete surface with very high quality. Figure 1 shows confocal laser images of a technical fabric with a defined micro texture that was used as substrate for the UHPC cast (a) and the resulting UHPC surface (b), which demonstrate the very accurate and almost defect-free replication of the micro texture (as negative imprint). To achieve a hydrophobic surface a hydrophobing agent was applied to the substrate shortly before concreting and incorporated into the hardening concrete.

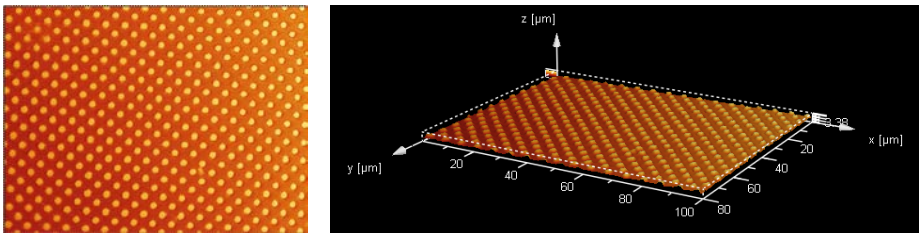

a. Substrate with ‘pimples’ (diameter: 3 µm)

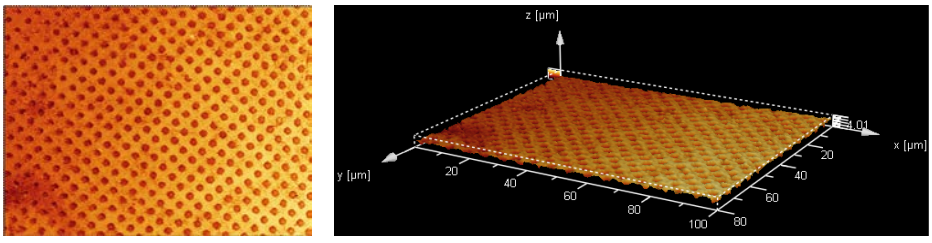

b. UHPC cast with holes (diameter: 3 µm)

Figure 1. Confocal laser images of substrate (a) and UHPC surface (b).

Based on structural and economic reasons the façade panels are designed as box shaped UHPC elements which are protecting the shock sensitive AAC insulation (Figure 2). Due to the

support from the edges of the box no shear forces are generated in the interface between load bearing structure and insulation during transport and service life so that additional connectors can be omitted. The frame further increases the stiffness of the box-shaped element so that the cross-section of the UHPC can be decreased. When casting the elements with a single concrete batch the floating body had to be protected against buoyancy which was discarded because of its proneness to errors. Therefore, the façade elements were manufactured in two steps. After initial hardening of the exterior layer a rigid frame was placed as internal formwork on top of the panel and the upturning edges of the box were cast in a second concreting section.

In the following sections selected tests regarding different technological aspects during the upscaling process are presented. They concern the analysis of the bond strength between the two concreting sections, the optimization of imprinting a microstructure with a hydrophobic surface and the assessment of the homogeneity of the self-cleaning surface.

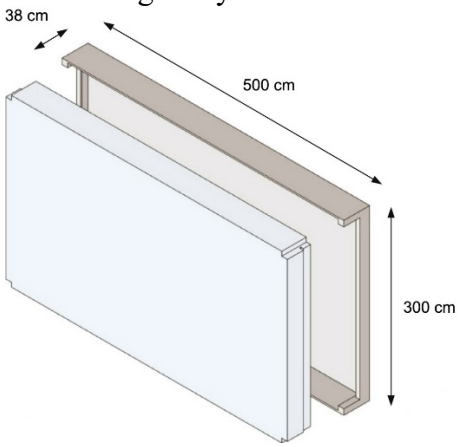

Figure 2. Façade panel consisting of box-shaped UHPC element and insulation of AAC.

3 Technological Aspects

3.1 Adhesive Pull Strength between the Two Concreting Sections

To identify the best surface treatment for an optimum bond between the two concreting sections adhesive pull strength tests were performed at samples sized 30 x 30 cm which were manufactured in wooden formwork coated with a plastic film. After the final setting of the first 2,5 cm thick concreting layer the surface was either left untouched, wetted or roughened using a wire brush (b) in one (1d) or two directions (2d) before the second layer with a thickness of 7,5 cm was poured (Figure 3). After an aeration time of 5 minutes the samples were covered until stripping after 18 hours. The samples were turned around so that the first thinner layer was on the top and the adhesive pull strength was tested according to DIN EN 1542. The surface tensile strength of the monolithic system served as reference. In addition, the effect of a bonding coat (BC) applied to the first layer before concreting the second layer was included into the examination.

The results of the adhesive pull strength (Figure 4) illustrate that without roughening the surface the bond strength between the two concreting sections is only about 12 % of the surface bond strength of the reference sample and wetting of the surface only has a negligible effect.

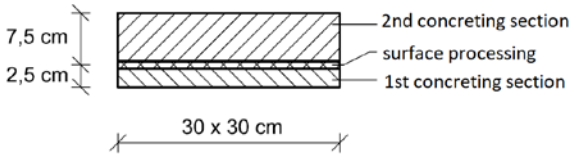

Figure 3. Sample for testing adhesive strength.

Within the "elephant skin" which formed on the first layer ventilation pores are trapped and weaken the cross section (Figure 5, left). After roughening the surface with a steel brush in one direction the loadbearing behavior corresponds to the monolithic reference so that no further measures are necessary. The system fails not in the joint but within the second layer, which was concreted several hours later than the first layer. The application of a bonding coat in contrast lead to an early cohesion failure within the bonding coat.

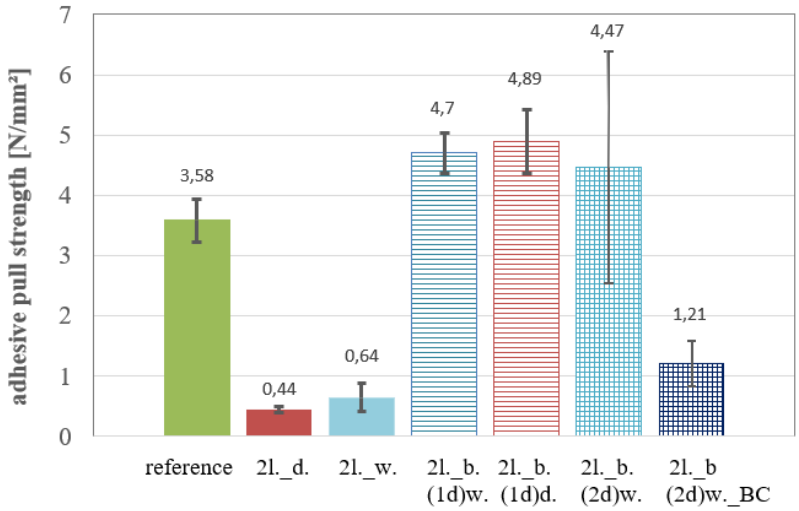

Figure 4. Surface (reference) and adhesive pull strength depending on the processing of the surface before concreting the second layer. 2l = two layers, b= brush, d = dry, w = wet, BC = bonding coat.

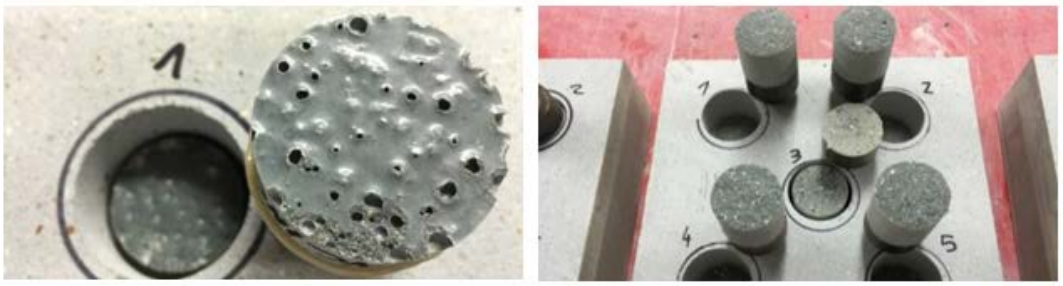

Figure 5. Failure in the joint due to "elephant skin" (left) and cohesion failure within the 2nd layer (right).

3.2 Upscaling of Micro Structured Self-Cleaning Surfaces

For the manufacture of the micro structured surfaces formliners covered with a hydrophobing or releasing agent were integrated into the formwork. In a first step different substrates were analyzed regarding the durability of the surface quality and the hydrophobic properties of the concrete specimens cast in them. For this, measurements of roughness, contact and roll-off angle, lightness and proportion of pores were performed over the course of ten consecutive pours using the same formwork. The root mean squared roughness was measured with a confocal laser microscope and the contact and roll-off angle were determined with a contact angle measuring system. The lightness and the proportion of pores were calculated using a color calibrated scanner whereby the value 255 corresponds to white. Best results were achieved for a substrate of polyurethane rubber to which 80g /m² of hydrophobing agent based on silane and siloxane were applied before the concreting.

All the parameters measured for evaluating the stability of the surface quality for both substrate and concrete exhibit only minor changes over the course of the pours (Figure 6). The contact angle measured on the formliner when using the hydrophobing agent as test liquid is always far below 90 ° ensuring a homogeneous wetting of the substrate. The contact angles of the concrete surfaces in contrast stay always over 140° and are thereby attaining super-hydrophobic properties. The slope angels of the concrete samples cast remain very small throughout the repeated use of the formwork ensuring very good self-cleaning properties. The lightness of the surface does not decrease and the proportion of pores is always below 0,9 % (Figure 6) thereby fulfilling the requirements for architectural concrete class 3 (DBV, 2004).

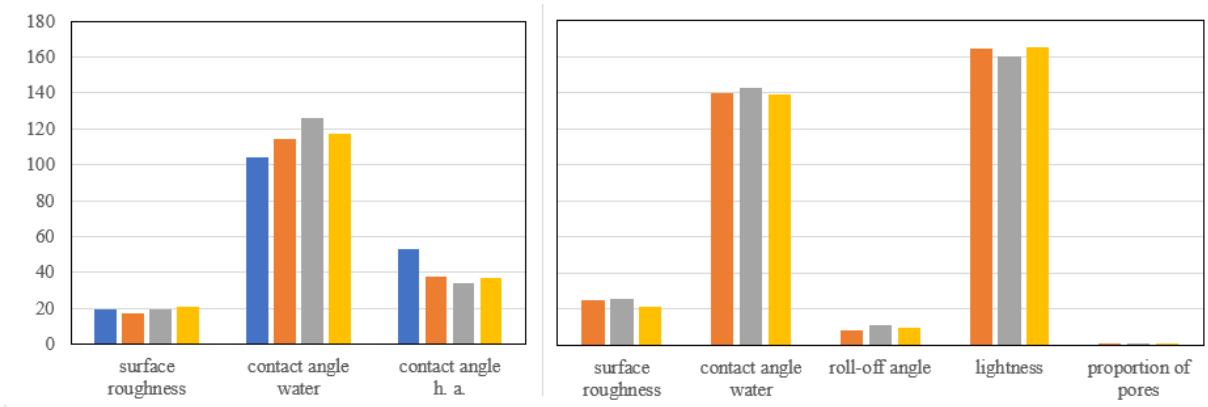

Figure 6. Parameters evaluated for the substrate and the UHPC sample during subsequent concreting.

In a second study the impact of the time span between application of the hydrophobing agent and the concreting was examined in detail using the following test set-up: Ten frame formworks sized 10 x 10 cm were positioned on a micro-structured silicone mat, to which 90 g /m² (45 g of active ingredient) of the hydrophobing agent was applied with a brush. After continuously increasing time intervals the formwork was filled with concrete and after 5 minutes of deaeration covered with plastic sheets for curing. To analyze the evaporated amount of hydrophobing agent in the time span between application and concreting a reference formwork consisting of frame and silicone mat with the equal amount of hydrophobing agent was weighed in the corresponding time intervals.

After stripping the formwork, the concrete surface was assessed visually and by measuring the contact and the roll-off angel (Figure 7).

The results show that even after a time span of 90 minutes between application of the hydrophobing agent and concreting the UHPC surface can be called superhydrophobic. While the contact angel remains on the original level, the slope angel after 30 minutes increases discontinuously from 5 to 37° (Figure 7). The quality of the architectural concrete however deteriorates when the time span between application of the hydrophobing agent and concreting exceeds 10 minutes (Figure 8).

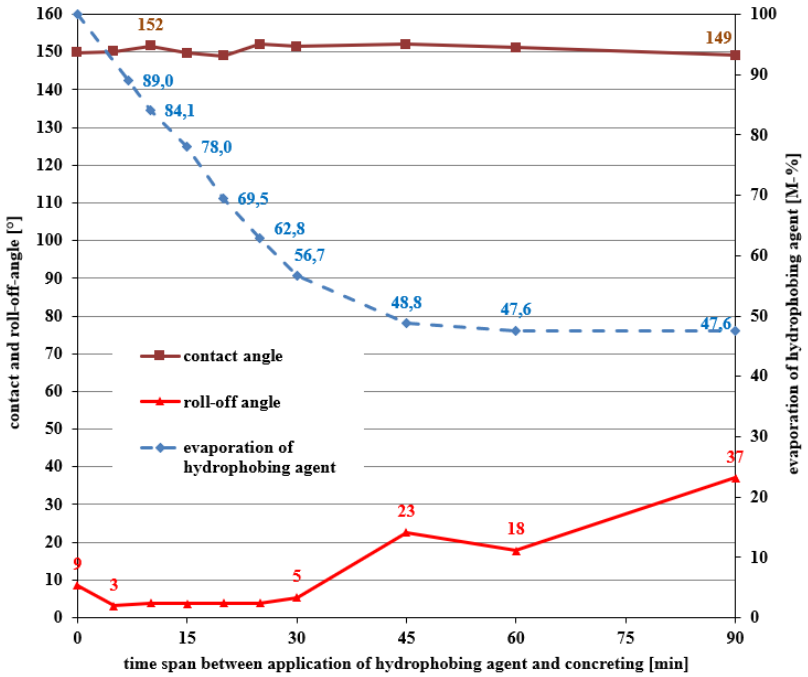

Figure 7. Development of the hydrophobic quality of the surface in dependence of the time interval between application of the hydrophobing agent and concreting.

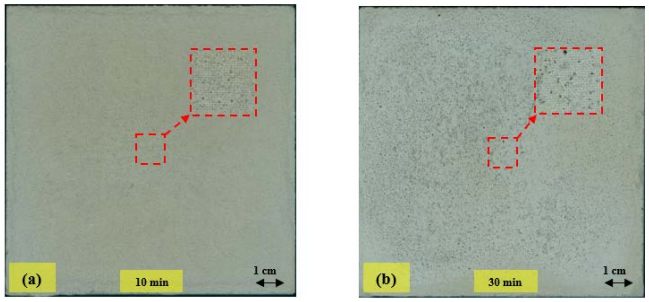

Figure 8. Quality of architectural concrete gained after (a) 10 min and (b) 30 min time span between application of the hydrophobing agent and concreting.

In a further step the impact of the application of the hydrophobing agent and the flow behavior on the hydrophobicity of the concrete surface was assessed by concreting samples sized 160 x 60 cm. Within the test series the hydrophobing agent was applied in different

amounts 160 g/m² and 80 g/m² (active ingredient content 80 g/m² and 40 g/m²) and dilution with water (1:1, none) to the silicon mat at the bottom of the formwork in two different ways (spray and roller application). Maximum 5 minutes after the application of the hydrophobing agent the concrete was cast using a conical discharge hopper positioned 40 cm from the rim of the formwork (Figure 9, left). The formwork was stripped after 24 hours and the elements were stored for 14 days at 23°C and 50 RH. Afterwards 11 cores with a diameter of 10 cm were drilled out of the element (Figure 9, right) and after cleaning with rinsing water stored for another week at 23 °C and 50 RH before the contact and slope angles were measured.

Figure 9. Concreting of test samples (left) and core extractions (right) to assess the self-cleaning properties.

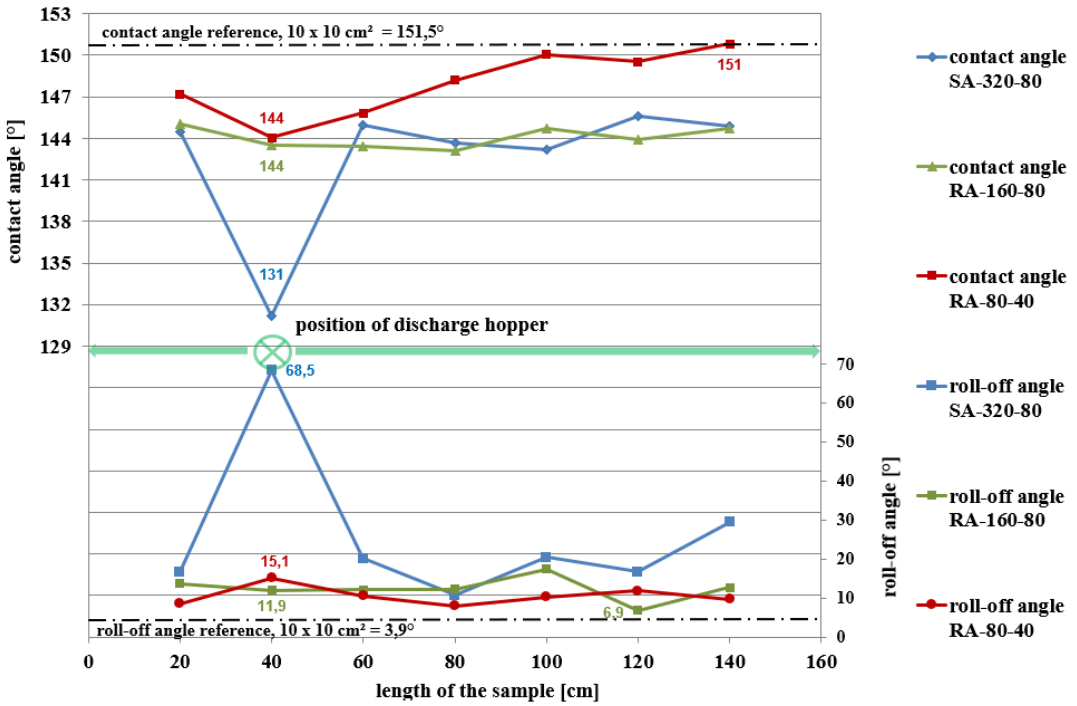

Figure 10. Hydrophobic quality of the surface depending on the distance from the discharge hopper. SA = spray application, RA = roller application; numbers define amount of application / active ingredient [g/m²].

The assessment of the hydrophobic quality (Figure 10) illustrates that the application of a bigger amount of hydrophobing agent diluted in the proportion of 1:1 with water leads to a strong increase of the hydrophobic surface quality at the discharge hopper (blue curve). For the small amount of hydrophobing agent applied undiluted to the silicon mat in contrast only a

small decrease of the contact angle was measured at the position of the discharge hopper (red curve). With increasing distance from the location of pouring the contact angle increased. The specimen further showed the smallest and most homogeneous sliding angels.

4 Conclusions

- The results show that upscaling the production of the façade elements needs detailed planning in order to achieve architectural concrete with self-cleaning properties. The highest bond strength between the two concreting sections is achieved by roughening the surface of the first section with a wire brush. An additional wetting of the surface deteriorates rather than improves the adhesive pull strength between the concreting sections. Also, for the application of the hydrophobing agent it turned out that less is more. The best results regarding the homogeneity of the self-cleaning properties were measured for the application of the smallest amount of hydrophobing agent using a brush.
- The time span between application of the hydrophobing agent and concreting is limited due to the decrease in quality of the architectural concrete.

Acknowledgements

The authors thank Paul Schwer for conducting some of the experiments and the European Union for the grant agreement no. 608893 (H-House) within the European Union's Seventh Framework Programme.

ORCID

Julia von Werder: https://orcid.org/0000-0002-1685-580X
Patrick Fontana: https://orcid.org/0000-0002-0356-8203
Johannes Hoppe: https://orcid.org/0000-0001-7724-0270
Serdar Bilgin: https://orcid.org/0000-0002-0771-2620
Birgit Meng: https://orcid.org/0000-0003-2445-6734

References

Barthlott W., Mail M. and Neinhuis C. (2016). Superhydrophobic Hierarchically Structured Surfaces in Biology: Evolution, Structural Principles and Biomimetic Applications. *Philos. Trans. R. Soc., A 2016, 374*, doi: 10.1098/rsta.2016.0191

Deuse, T., Mutke, S., Parker, F., Qvaeschning D. and Wulff, M. (2018). Nanotechnically optimized binders for the production of user-friendly high-performance concrete-part 1, *Cement International 1/18, Vol. 16, 59-69*

Deuse, T., Mutke, S., Parker, F., Qvaeschning D. and Wulff, M. (2018). Nanotechnically optimized binders for the production of user-friendly high-performance concrete-part 2, *Cement International 5/18, Vol. 16, 12-22*

Deutscher Beton- and Bautechnik-Verein E.V. (DBV), Verein Deutscher Zementwerke E.V. (VDZ) (2004). Merkblätter, Deutscher Beton- und Bautechnik-Verein E.V., Bauausführung, *Sichtbeton Exposed Concrete*, Berlin / Düsseldorf

DIN EN 1542: 1999-07: *Products and systems for the protection and repair of concrete structures - Test methods - Measurement of bond strength by pull-off*

Fontana, P., Miccoli, L., Kocadag, R., Silva, N., Qvaeschning, D., Kreft, O. and Cederquvist, C. (2016). Composite UHPC façade elements with functional surfaces, *HiPerMat 2016*, Kassel, Germany, March 9-11

Miccoli, L., Fontana, P, Silva, N., Klinge, A., Cederqvist, C., Kreft, O., Qvaeschning, D. and Sjöstrom, C. (2015). Composite UHPC-AAC/CLC facade elements with modified interior plaster for new buildings and refurbishment. *Materials and production technology, Journal of Facade Design and Engineering 3, 91-102*, doi: 10.3233/FDE-150029

Si, Y., Dong, Z. and Jiang, L. (2018) Bioinspired Designs of Superhydrophobic and Superhydrophilic Materials, *ACS Cent. Sci. 2018, 4, 9*, 1102-1112, doi: 10.1021/acscentsci.8b00504

XV International Conference on Durability of Building Materials and Components
DBMC 2020, Barcelona
C. Serrat, J.R. Casas and V. Gibert (Eds)

Concrete: Limit States and Sustainability

Kristýna Hrabová[1], Břetislav Teplý[2] and Tomáš Vymazal[1]

[1] Institute of Building Testing, Faculty of Civil Engineering, Brno University of Technology, Czech Republic, Veveří 331/95, Brno 602 00, kristyna.hrabova@vutbr.cz, tomas.vymazal@vutbr.cz

[2] Institute of Structural Mechanics, Faculty of Civil Engineering, Brno University of Technology, Czech Republic, Veveří 331/95, Brno 602 00, teply.b@fce.vutbr.cz

Abstract. *The structural design of concrete structures has to result in qualities ensuring ordinary structural safety and serviceability, together with durability. Recently, it has become necessary to pursue sustainability as well, and rather newly the issue of resilience has also appeared. It is now apparent that the effects of mechanical load, environmental load and even social coherence need to be reflected and included in the formulation of limit states. This is a complex matter involving the factors of time, service life, degradation effects, modelling, probability analyses, limit states, costs and other phenomena. It has not yet been completely understood, albeit several notions in this context are contained in different codes and regulations, e.g. EN 1990, EN 1992, ISO 13823:2008, ISO 16204:2012, fib MC2010 and fib MC2020 (currently under preparation by the fib committees). According to fib Model Code 2010, the design method most commonly used for concrete structures today is performance-based. Sustainable target value design can be briefly expressed as the comparison of sustainable capacity vs. sustainable impacts. This requires the formulation of a new class of limit states – apart from those of the engineering (or structural) type, also sustainability limit states now need to be specified. The presented contribution briefly mentions traditional and durability limit states, discussing their variants and context, and then concentrates specifically on the formulation of limit states for concrete sustainability at material level. It also presents some examples which apply a full probabilistic approach.*

Keywords: *Durability, Sustainability, Limit States, Concrete.*

1 Introduction

When designing or assessing a RC structure in all situations and/or at all levels, use should be made of the limit state concept and performance models included in ISO 2394 (2015). Generally, possible structural responses are divided into two domains consisting of desirable or undesirable states; the boundary between these domains is called a limit state (LS). The traditional ultimate limit state (ULS) and serviceability limit state (SLS) were initially utilized in engineering practice (ISO 2394:1998) either as part of the semi-probabilistic format (partial factor) or in the fully probabilistic approach, which was mainly applied during research activities. Both material and structural levels were applied.

Limit state design is a common approach in civil engineering practice today. It is described in several international documents, *e.g.* EN 1992-1-1 (2004), ISO 16204 (2012) and *fib* MC2010 (2012). At the turn of the present century, the issue of durability and service life started to be considered important and thus relevant limit states appeared; however, up to now this theme has not yet been fully explored and definitively dealt with. Also, completely new types of engineering tasks have emerged recently, such as the maximising of sustainability

and resilience, which may also need relevant definition and application in terms of limit states. A brief and effective overview of the LS context up to the current stage of progress with regard to sustainability LS can be found in Geiker *et al.* (2019).

Generally, structural assessment/analysis is governed by a LS probability condition which in its general form reads:

$$P_f = P\left[A(t) \geq B(t) \right] < P_d \tag{1}$$

P_d is the design probability (target, limiting, required), t is time, S is the effect of the action being analysed and R is the appropriate barrier (*e.g.* the resistance of the material or structure). Generally, both S and R are time-dependent and hence the probability of failure P_f is time-dependent as well. At the point in time associated with the limit $P_f = P_d$, a design service life t_D can be defined. The combined effect of both structural performance and ageing should be considered wherever relevant. Note that the index of reliability β frequently stands in for the probability of failure P_f in structural design practice (ISO 2394:2015). The present contribution briefly reviews the development of LS issues and concentrates on the formulation of material sustainability limit states, showing some examples.

2 Traditional LS

The traditional ultimate limit state (ULS) and serviceability limit state (SLS) were presented in the nineties in standards – see ISO 2394 (2015).

The ULS concerns the safety of people and/or structures. The ultimate limit state is defined for material deterioration resulting in failure due to loss of resistance when the resistance of the component or structure becomes equal to or less than the relevant internal force.

The SLS concerns the functioning of the structure, the comfort of people and the appearance of construction work. For material degradation, the serviceability limit state is defined by:

- Local damage (including cracking) or changes in appearance which affect the function or appearance of structural or non-structural components.
- Relative displacements which affect the function or appearance of structural or non-structural components.

An allowable value (target, design) P_d for the probability of failure was given in EN 1990, Annex C (EN 1990:2002/A1:2005/AC:2010), differentiating them according to LS type, three reliability classes and three consequence classes. A distinction must be made between the design of new structures and the assessment of existing structures. Note that at the beginning of limit state development the level of reliability in the context of durability was left to the client's decision, together with the definition of the target service life.

3 The Durability Concept

According to Tutti (1982), the durability of reinforced concrete components or structures was later included in the LS concept mainly in connection with the consideration of reinforcement corrosion – (i) an initiation period (reinforcement depassivation leading to corrosion initiation, usually due to carbonation or chloride ingress) and (ii) a propagation period (the

development of reinforcement corrosion with a decrease in the effective reinforcement area, crack formation and spalling). There are numerous research works dealing with the durability of concrete structures, of which only a few of the earliest of them shall be mentioned here, *e.g.* Mehta (1997), Rostam and Schiessl (1994), Keršner *et al.* (1996) and Gehlen (2000). The durability of concrete structures is influenced by degradation effects and exposure conditions, and using appropriate LS the service life L can be assessed as well. This can be performed with a suitable model analysis via the use of effective software tools, *e.g.* Matesová *et al.* (2008), Life 365 (effect of chloride ingress) or Novák *et al.* (2014), Teplý *et al.* (2018) (FReET-D, incorporating a number of different numerical degradation models in a probabilistic format, producing statistical, sensitivity and probability analyses). Broadly accepted models (carbonation, and chloride effect) were included in the Model Code for Service Life Design (2008) and later in fib Model Code 2010 (2012).

The time passing before the initiation of rebar corrosion is usually considered the most conservative limiting state. It is known as the durability limit state (DLS) or initial limit state – see ISO 13823 (2008). Note that this category of LS is referred to the SLS in ISO 2394 (2015). For such a probability condition the basic form (1) can be reformulated as follows:

$$P_f(t_D) = P\{a - x_c(t_D) \leq 0\} \leq P_d \tag{2}$$

The thickness of concrete cover a, x_c is the depth of the carbonated zone, t_D is the design (target) service life and P_d is the design (target) probability of "failure".

Evidently, during a structure's service life the SLS and ULS have to be fulfilled, so the DLS is a "prerequisite" in this respect. All this also has to be considered when determining the relevant failure probability value. To complete such considerations the standard ISO 2394 **(**2015) describes, apart from the SLS and ULS, another LS – the condition limit state (CLS), which corresponds to following situations:

- An approximation to the real LS that is either not well-defined or is difficult to calculate (examples include initiation limit states or LS associated with the propagation period - *i.e.* the corrosion of reinforcement (Matesová *et al.*, 2008)).
- Local damage (including cracking).
- Additional LS thresholds in the case of a continuously increasing loss of function.

The CLS has not yet been fully understood and utilized in practice; this kind of LS is expected to be presented and explained in more detail by the upcoming fib Model Code 2020. Moreover, when dealing with durability tasks this LS is often affected by a particular combination of actions (mechanical, environmental); see *e.g.* Vořechovská *et al.* (2008). Also, the eventual reversibility or irreversibility of the LS has to be taken into account.

4 The Limit State Concept from the Perspective of Sustainability

According to the *fib* Model Code 2010 (2012), the most commonly used method of designing concrete structures today is performance-based design. Sustainable target value design can be briefly expressed as the comparison of sustainable capacity vs. sustainable impacts. This requires a new class of limit state – apart from those of the engineering (or structural) type, sustainability limit states have to be specified as well. This was mentioned in the *fib* Model

Code 2010 (2012), and also in Geiker *et al.* (2019), which states that by means of Eq. (1) the environmental performance of a concrete structure shall be verified by confirming that the retained performance or barrier (R), defined by using appropriate indexes with regard to the environment, is larger (or smaller) than the set value or effect of the action (S) of the relevant performance requirement (Section 7.10) (*fib* Model Code 2010; 2012). Social performance is described in a similar way in this section. Note that in this respect, safety, serviceability and durability are also social aspects (Hájek, 2018), *i.e.* elements of social responsibility, and therefore SLS, ULS and *L* also fall into this category - usually being understood and utilized as basic safety and serviceability criteria as well. Details concerning this class of limit equations and their practical utilization have not yet been specified in the *fib* Model Code 2010 (2012) or anywhere else to the best knowledge of the authors; an overview of the equations and a short literature review can be found in Hrabová *et al.* (2019).

The new *fib* Model Code 2020, which is currently under development, will include an implementation of the sustainability approach (Matthews, 2017): "MC2020 will take sustainability as a fundamental requirement, based upon a holistic treatment of societal needs and impacts, lifecycle costs, and environmental impacts." The limit state approach is not yet commonly used for sustainability analysis and the relevant limit states are not being employed in practice at the present time. A recent paper discusses this without formulating relevant limit state equations. A new design limit state approach is needed, and it has to be based on the probabilistic approach combined with the life cycle approach. It is a highly complex matter, as besides the existing construction limit states, new sustainability LS (environmental and social) need to be addressed together with service life and/or financial factors. These LS have not yet been identified. However, some recent works deserve consideration in this respect and are briefly mentioned below.

Fantilli *et al.* (2019) presented a procedure for RC beam design called "global impact of the beam", which introduces the specific limit state of sustainability (in accordance with the ULS and SLS). It is based on a function relating the mass of CO_2 emitted by the production of a cubic meter of concrete to average compressive strength, while also considering partial substitution of the cement by fly ash. The procedure is an iterative one and deterministic, *i.e.* it does not result in a relevant probability level. The durability issue is not considered, so the LS presented in Fantilli *et al.* (2019) is not a true sustainability limit state.

Geiker *et al.* (2019): in their work a sustainability LS is advocated using a comparison of two potential design scenarios. Considering each scenario´s full design service life, a cumulative emissions envelope can be computed for both scenarios and the actual reduction target (global warming potential emission reduction) is assessed together with the probability of failing to meet a sustainability-focused goal. Reliable and valid models for the assessment of degradation (*e.g.* for corroding structures) are needed to check engineering LS; this also leads to an iterative process. Moreover, there are not yet any approved acceptable failure probability values for a sustainability LS.

Authors of the present contribution have developed a sustainability LS formulation at material level using the sustainability potential indicator k_{SB}, Eq. (3). This combined indicator was recently presented in, *e.g.* Hrabová *et al.* (2019), Teplý *et al.* (2018) and Konečný *et al.* (in revision). Indicator k_{SB} is a normalized form of the Building Material Sustainability Potential (BMSP) defined previously by Müller (2013). In order to transform the BMSP into a normalized form, the quantities *L* (service life), *R* (performance) and *E* (eco-cost) are divided

by the arbitrary reference values L_{ref}, R_{ref} and E_{ref}, thus leading to a dimensionless quantity (3) whose value approximates 1.0. The greater the value of k_{SB}, the higher the sustainability level within the group of studied mixes for concrete production; the ranking of k_{SB} values is the resulting information. It should be noted that the presented method is supposed to enable the comparison of concrete mixture sustainability levels within a group of analysed mixtures under a given degradation effect.

$$k_{SB} = \frac{\frac{R}{R_{ref}} \cdot \frac{L}{L_{ref}}}{\frac{E}{E_{ref}}} \tag{3}$$

Eq. (3) can be further enhanced by considering the costs, C, of concrete (material and production) leading to a modified indicator. More details can be found in, *e.g.* Konečný *et al.* (in revision). Additionally, for any individual concrete composition using k_{SB} as an action and the limiting value indicator $k_{SB,lim}$ as a barrier, the general limit state condition (1) may be rewritten into the sustainability LS form.

$$P_{SB} = \left[\left(k_{SB} - k_{SB,lim}\right) \leq 0\right] \geq P_{d.SB} \tag{4}$$

This equation enables the evaluation of the probability P_{SB}, with which a certain limit value $k_{SB,lim}$ can be exceeded for the concrete mixture in question. However, this value has not yet been discussed and no experience or recommendations are known in this respect. Note that $k_{SB,lim}$ depends on three involved factors, *R, L* and *E*, which makes its determination complex. A less complicated option can be formulated utilizing the individual limit values R_{lim}, L_{lim} and E_{lim} of quantities *R*, *L* and *E*, respectively, or in other words to determine the $k_{SB,lim}$ value as follows:

$$\boldsymbol{k_{SB,lim}} = \frac{\frac{\boldsymbol{R_{lim}}}{\boldsymbol{R_{ref}}} \cdot \frac{\boldsymbol{L_{lim}}}{\boldsymbol{L_{ref}}}}{\frac{\boldsymbol{E_{lim}}}{\boldsymbol{E_{ref}}}} \tag{5}$$

As can be expected, in a real situation factors *R, L* and *E* may often possess different level of dominance. In such a case a more fitting variant of Eq. (5) can be arranged using the weighting coefficients w_R, w_L and w_E:

$$\boldsymbol{k_{SB,lim}} = \frac{\boldsymbol{w_R}\frac{\boldsymbol{R_{lim}}}{\boldsymbol{R_{ref}}} \cdot \boldsymbol{w_L}\frac{\boldsymbol{L_{lim}}}{\boldsymbol{L_{ref}}}}{\boldsymbol{w_E}\frac{\boldsymbol{E_{lim}}}{\boldsymbol{E_{ref}}}} \tag{6}$$

Alternatively only one of the quantities R_{lim}, L_{lim}, or E_{lim} can be employed individually in (5) when $k_{SB,lim}$ is computed (case dependent).

A major obstacle for the effective utilization of the limit state condition (4) is the choice of a suitable value for target reliability $P_{d,SB}$, which is not yet available in any recommendation or standard. The following notes can provide a degree of help when deciding about the $P_{d,SB}$ value:

- in situations when material parameter *R* is dominant (*e.g.* considering requirements for the robustness of the structure or the resilience of its functionality), a $P_{d,SB}$ reliability similar to a relevant one from the ULS group, *i.e.* $3.7 \leq \beta \leq 4.4$ according to ISO 2394 (2015), may be acceptable;

- in cases where L is dominant (if durability is at the centre of interest) then a $P_{d,SB}$ value in the range of $0.8 < \beta_d \leq 1.6$ similar to the SLS or DLS could be relevant;
- if the environmental issue dominates, *e.g.* via the eco-costs E (expenditures on measures to be taken so as to reduce environmental impacts to a sustainable level), then it is not straightforward to decide on a relevant $P_{d,SB}$. Environmental impact targets and/or greenhouse gas reductions must be considered, and also associated human health consequences need to be thought about. In such cases, the involvement of policy-makers at a local or regional level is needed.

Unfortunately, there are no historical bases available for considering an acceptable failure probability for sustainability limit states. A brief discussion of this problem can be found in Geiker *et al.* (2019).

5 Numerical Demonstration of the Presented Approach

A simple example of the sustainability limit state assessment of concrete composition is presented below. The sample consists of 290 kg/m^3 CEM I 42.5 R, 812 kg/m^3 0-4 mm aggregate, 910 kg/m^3 8-16 mm aggregate, 194 kg/m^3 fly ash, and 182 kg/m^3 water. The concrete in question is supposed to suffer from carbonation, so the service life L is calculated according to the initiation period stage of reinforcement corrosion caused by concrete carbonation using an analytical model. The FReET-D tool with model Carb4b are used (Papadakis and Tsimas, 2002). The basic input values were: concrete cover 30 mm; atmospheric CO_2 concentration 820 [mg/m^3]; RH = 70 %; k–value concept k = 0.4 (as stated in EN 206-1, 2013). The strength of the concrete is considered to indicate the performance R in this example. It was gained via sample testing within the grant project GA ČR 103/07/0034 at the Faculty of Civil Engineering, Brno University of Technology. The eco-cost of each concrete mixture element has a unit price obtained from an established database (Eco Costs Data, 2019). Reference values (chosen arbitrarily) used: R_{lim} = 71.9 MPa, L_{lim} = 125 years and E_{lim} = 54.5 €/m^3.

Table 1. Concrete properties.

Property	Pdf	Mean	COV
60-day cube strength [MPa]	Normal	47.2	0.06
Service life [years]	Normal	73	0.16
Eco-costs [€/m^3]	Rectangular	54.3	0.20

Limit values were chosen for the purpose of this illustrative example via the authors' engineering judgement in order to represent the trend of the probability P_{SB} due to limit values R_{lim} while keeping L_{lim} and E_{lim} unchanged. Therefore, three cases (A, B and C) were analysed: A: R_{lim} = 95 % R_{ref}; L_{lim} = 0.66 L_{ref}; E_{lim} = 1.33 E_{ref}; B: R_{lim} = 90 % R_{ref}; L_{lim} = 0.66 L_{ref}; E_{lim} = 1.33 E_{ref}; C: R_{lim} = 85 % R_{ref}; L_{lim} = 0.66 L_{ref}; E_{lim} = 1.33 E_{ref}.

Table 2. Conclusions.

	A	B	C
k_{SB}	1.04	1.04	1.04
$k_{SB,lim}$	0.49	0.47	0.44
P_{SB}	0.04	0.03	0.03
β	1.74	1.84	1.95

The values obtained for k_{SB} and P_{SB} were analysed using a specialized version of FReET software and applying Eq. (3) and (4). As mentioned above, relevant values for the target reliability $P_{d,SB}$ are not available in any recommendation at present. The resulting probability values (and the associated index of reliability β) in the studied ad-hoc case (Table 2) fall into the range "between" usual ULS and SLS values.

6 Concluding Remarks

The paper discusses limit state variants in the context of concrete structures, reviews the current position with regard to traditional Ultimate Limit States and Serviceability Limit States, and mentions Durability LS (initiation and propagation stages) as well as Condition Limit States. It then concentrates on the description and formulation of limit states for material sustainability, noting relevant related documents and attempts at presenting this kind of LS. A general definition of a Sustainability Limit State has not yet been established officially.

This contribution presents a novel form of Sustainability Limit State which utilizes the sustainability potential indicator. This indicator represents an enhanced method for the simple, yet complete sustainability assessment of concrete mixtures, which involves concrete strength, durability measure and eco-costs. The full probabilistic approach is applied and the method illustrated on an ad-hoc case - concrete suffering from carbonation. The resulting probability values and associated values of index of reliability β for different limit values are shown. The study provides engineers and researchers with an emerging tool for effective decision-making concerning concrete mixes that gives consideration to sustainability.

Acknowledgements

This work was supported by Czech Science Foundation project No. 19-22708S.

ORCID
Kristyna Hrabova http://orcid.org/0000-0003-2078-1898
Bretislav Teply: http://orcid.org/0000-0001-9067-9122
Tomas Vymazal: http://orcid.org/0000-0002-3633-047X

References

Eco Costs Data, *Design-4-Sustainability: Inspiration and knowledge by designers for designers* [online] Available in: http://www.design-4-sustainability.com/ecocosts.

EN 1990:2002/A1:2005/AC:2010 (1990) Eurocode - *Basis of structural design*.

EN 1992-1-1 (2004). (English): Eurocode 2: *Design of concrete structures - Part 1-1: General rules and rules for buildings.*

EN 206 (2013). *Concrete Specification, performance, production and conformity*, Brussels: European Committee for Standardization – CEN.

Fantilli A.P., Tondolo P., Chiaia B. and Habert G. (2019). *Designing Reinforced Concrete Beams Containing Supplementary Cementitious Materials*. *Materials* 2019,1248; https://doi.org/10.3390/ma12081248.

fib bulletin 34 (2006). *Model Code for Service Life Design*, International Federation for Structural Concrete (fib), Lausanne Switzerland.

fib bulletin No. 65 and 66 *fib* Model Code 2010 (2012). *International Federation for Structural Concrete* (fib), Lausanne Switzerland.

Gehlen, Ch. (2000). *Probabilistishe Lebensdauerbemessung von Stahlbeton bauwerken*, Deutsher Ausschuss fuer Stahlbeton, Heft 510, Berlin.

Geiker M.R., Michel A., Stang H., Vikan and Lepech MD (2019). *Design and maintenance of concrete structures requires both engineering and sustainability limit states*. Life-Cycle Analysis and Assessment in Civil Engineering: Towards an Integrated Vision, London.

Geiker M.R., Michel A., Stang H. and Lepech M.D. (2019). *Limit states for sustainable reinforced concrete structures*. Cement and Concrete Research 122, 189-195.

Hájek P. (2018). *Contribution of concrete structures to sustainability – challenge for the future*. IOP Conference Series: Materials Science and Engineering, Volume 442.

Hrabová K., Teplý B. and Hájek P. (2019). *Concrete, sustainability and limit states.* IOP Conference Series: Earth and Environmental Science, vol. 290, no. 1, p. 1-9. ISSN: 1755-1315.

Chromá, M., Rovnaník, P. and Teplý, B. (2007). *Carbonation modelling and reliability analysis of RC structures made from blended cements*, Proc. of International RILEM Workshop on Performance Based Evaluation and Indicators for Concrete Durability, 19-21 March 2006, Madrid, Spain, 319-325.

ISO/TC 98/SC 2 (2008) ISO 13823: *General Principles on the Design of Structures for Durability*.

ISO/TC 71/SC 3 (2012) ISO 16204*: Durability – Service life design of concrete structures.*

ISO/TC 98/SC 2 (2015) ISO 2394: *General principles on reliability for structures*.

Keršner Z., Teplý B. and Novák D. (1996). Uncertainty in service life prediction based on carbonation of concrete. 7th International Conference on the Durability of Building Materials and Components (7DBMC), Stockholm, Sweden, 13–20.

Konečný P., Ghosh P. Hrabová K., Lehner P. and Teplý B. (2019). *Effective methodology of sustainability assessment of concrete mixtures*, Materials and Structures (in revision).

Matesová D., Chromá M. and Teplý B. (2008*). Durability Limit States of Concrete Structures: Probabilistic Modeling*. 11DBMC, Istanbul, Turkey.

Matthews S. (2017). *fib Model Code 2020 - A new development in structural codes*, Structural Concrete Journal of the fib, Volume 18, Issue 5, 651–652.

Müller H.S. (2013). *Sustainable structural concrete – from today´s approach to future challenge*. Structural Concrete 14 (4), 299-300.

Novák, D, Vořechovský, M and Teplý, B (2014). *FReET – Software for the statistical and reliability analysis of engineering problems and FReET-D: Degradation Module*, Advances in Engineering Software, 179-192.

Papadakis V.G. and Tsimas S. (2002) *Supplementary cementing materials in concrete,* Part I: Efficiency and design, Cement and Concrete Research 32 (10), 1525–1532.

Rostam S. and Schiessl P. (1994). *Service Life Design in Practice – Today and Tomorrow*, Proceedings, International Symposium "Concrete Across Borders", Odense, Denmark.

Teplý, B., Vořechovská, D. and Chromá, M. (2018). *Probabilistic based models for material degradation processes*. Chapter in fib Bulletin No. 86, The International Federation of Structural Concrete.

Teplý B, Rovnaníková P. and Vymazal T. (2018). *Sustainability Quantification of Concrete Structures.* Chapter in Advances in Environmental Research, Vol 63, NOVA Science Publishers, NY, USA, 231-248.

Tuutti, K. (1982). *Corrosion of steel in concrete*, Swedish Cement and Concrete Research Inst., 17-21.

Vořechovská D., Šomodíková M., Podroužek J., Lehký D. and Teplý B. (2008). *Concrete structures under combined mechanical and environmental actions: Modelling of durability and reliability*. Computers and Concrete, Vol. 20, No. 1, 99-106.

XV International Conference on Durability of Building Materials and Components
DBMC 2020, Barcelona
C. Serrat, J.R. Casas and V. Gibert (Eds)

Deformation Velocity Survey in Mortar and Cement Paste Specimens Subjected to External Aggressive Attacks

Cristina Tedeschi and Elsa Garavaglia

Department of Civil and Environmental Engineering, Politecnico di Milano, Milan, Italy.

cristina.tedeschi@polimi.it, elsa.garavaglia@polimi.it

Abstract. *The durability of concrete depends not only on the composition of the material and its resulting porosity, but also on the environmental conditions. Contact between concrete or cement mortars with water and soils containing sulphates, of a natural, biological origin or deriving from pollution, can activate chemical reactions in the cement paste inducing an expansion and degradation of the concrete. To evaluate the behaviour of the cementitious material subjected to various external aggressive attacks, prismatic samples of cement paste and mortar samples produced with the same binder (Portland cement) were immersed in demineralised water and in various solutions containing 5% and 10% sodium sulphates. Their expansion was monitored over time by a direct length measurement. This paper shows the results achieved in a rather long laboratory investigation and a first hypothesis has been formulated on the possible expansion rate in the first 56 test days and in the following 850 days.*

Keywords: *Cement Mortar, Aggressive Environment, Sodium Sulphate Attacks, Experimental Tests, Deformation Velocity.*

1 Introduction

The durability of a concrete structure represents the ability to withstand aggressive environmental stresses, therefore it depends not only on the composition of the material and the resulting porosity, but also on environmental conditions. The different causes of damage to concrete, can be divided into different types depending on whether the aggressive action involves one or more components of the conglomerate (cement paste, aggregate or metallic reinforcement).

In particular, when a concrete structure comes into contact with waters or soils rich in sulphates, a series of complex chemical reactions can occur the sulphates which propagate inside the material and aluminates of cement paste, leading to the formation of leading to the formation of gypsum, secondary ettringite, and in some cases, thaumasite with the consequent expansion and formation of cracks and expulsion of parts of concrete. These phenomena are collected in the general term of the external sulphate attack.

Various researches have been carried out on this subject, many of which were dedicated to the description of sulphate attack from an experimental point of view. There are numerous experimental campaigns carried out on cement paste, mortar and concrete samples, however the results depend strongly on the test conditions, the cement used and the aggregates and their particle size distribution.

On this topic there are researches in the literature that for the most part focus on the evaluation of durability and the evolution of damage (Anzani *et al.,* 2018, Garavaglia *et al.,* 2018, Garavaglia *et al.,* 2017, Garavaglia *et al*., 2016, Anzani *et al*, 2009, Garavaglia *et al*., 2008, Tedeschi and Garavaglia, 2019, Cefis *et al*. 2015, Tedeschi *et al.* 2017).

doi:10.23967/dbmc.2020.027

In this paper, the results of an ongoing experimental campaign are reported, carried out on prismatic samples of cement paste and mortar. An objective of this experimental program is also to highlight the role of the aggregate on the degradation phenomenon, for this reason samples of cement mortar were prepared with two different types of aggregate.

To evaluate the behaviour of the cement material subjected to various external aggressive attacks, laboratory tests were carried out during which cement paste samples (P-CEM), mortar samples with normalised sand (M-nor) and samples of mortar with aggregate (M-agg), were subjected to immersion cycles, thus simulating three different aggressive attacks: from demineralised water, from sodium sulphate at 5% salt concentration and from sodium sulphate at 10% concentration. The expansion was monitored over time by direct length measurements.

The tests were performed in accordance with the UNI EN 12617-4: 2003, but they lasted longer in time in order to verify any changes in behaviour over time.

The results obtained in the 889 days are shown as the variational behaviour of the deformation (shrinkage/expansion) recorded, but also in terms of deformation velocity, variable at each instant of the test process and function of the deformation value recorded.

There are not many approaches to this topic in the literature. The topic investigated is the transmission of waves in the material (Tseng *et al*., 1999, Boyd and Ferraro, 2005), not the deformation velocity of materials subject to degradation. A similar approach is present in Zhanga *et al*., 2012, which stimulates the authors to continue on this path.

Future research developments will be oriented towards probabilistic modelling of the detected behaviours.

2 Laboratory Test Procedure

2.1 Preparation of Specimens

The experimental campaign began 29 months ago and was conducted on prismatic samples of mortar and cement paste of 40mmx40mmx160mm size.

For all the samples a CEM I 52.5R (P_CEM)- type Portland binder cement was used, and for the two series of mortar samples two types of siliceous aggregate were used. The chemical composition of the cement is shown in Table 1.

Table 1. Chemical composition of cement.

Cement	C3A	C4AF	SO3
CEM I 52.5R	4.22%	5.16%	3.61%

The named samples (M_agg), were prepared with a siliceous aggregate for concrete, but used by eliminating the aggregates greater than 2mm by sieving, while the named prisms (M_nor), were prepared with standardised sand used for the certification of mortars (EN 1015-1).

To evaluate the behaviour of the cementitious material subjected to different external aggressive attacks, three prisms for each type of mixture were prepared, and laboratory tests were performed during which the prismatic samples were immersed respectively in deionized water and in a solution of 5 and 10% sodium sulphate. Once hardened, the samples were subjected to measurement to evaluate their variations in length, so as to be able to study their overall expansion, but above all to evaluate the trend and the degradation mechanisms over time.

2.2 Test Procedure

The determination of the expansion was determined according to the standard EN 12617-4: 2003, using an uncontrasted linear measurement method after the immersion in water of prismatic of 40mmx40mmx160 mm size specimens, from 24h after the casting.

The samples were prepared/made in a climatic chamber at temperature T = 20 ° C and relative humidity RH = 65% and subsequently placed in a climatic chamber at T = 20 ° C and relative humidity RH = 90%. After 24 hours from the preparation, the specimens were removed from the moulds and completely immersed in pure water (double-distilled) and in a solution with a concentration of 5% Na_2SO_4 and 10% sodium sulphate.

The prisms were periodically extracted from the solutions, in order to be able to measure the variations in weight and length. Before the initial measurement, the adhesion of the measuring pins was verified. Table 2 indicates the codes of the samples and their corresponding test conditions. In Figure 1, Samples during the measurement phase; b) Samples during the last curing period.

Table 2. Name of the individual specimens and seasoning conditions.

P_CEM Water	P_CEM 5% Na_2SO_4	P_CEM 10% Na_2SO_4	M_agg; water	M_agg; 5% Na_2SO_4	M_agg; 10% Na_2SO_4	M_nor water	M_nor 5% Na_2SO_4	M_nor 10% Na_2SO_4
2.1	2.4	2.7	1.1	1.4	1.7	3.1	3.4	3.7
2.2	2.5	2.8	1.2	1.5	1.8	3.2	3.5	3.8
2.3	2.6	2.9	1.3	1.6	1.9	3.3	3.6	3.9

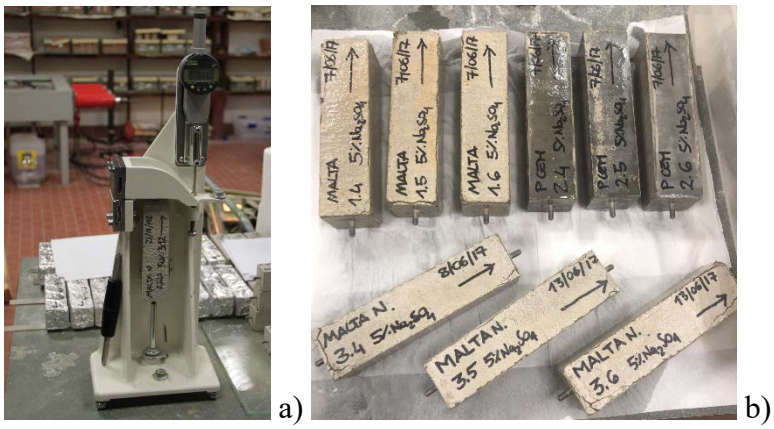

a) b)

Figure 1. a) Samples during the measurement phase; b) Samples during the last curing period.

3 Deformation Survey

3.1 Deformation Measurement

In compliance with the standards required in UNI EN 12617-4:2003 the variation in length was calculated in relation to L_0 length detected after 24 hours of immersion of the specimens in water:

$$\Delta L_i = \left(L_i - L_0\right) \quad (1)$$

where: ΔL_i is the variation of the length at time t_i; L_i is the length of the specimen at time t_i; L_0 is the initial length of the specimen after 4 hours of immersion.

The deformation ε_i at each instant of measurement, t_i, is thus expressed by the formula:

$$\varepsilon_i = \frac{\Delta L_i}{L_g} \qquad (2)$$

where ΔL_i is the variation of length expressed by (1) and L_g is the verified length of the specimen before immersion (in the case studied 160mm).

3.2 Observations on the Results Obtained

Figures 2 and 3 show the trend of the average deformations recorded for the tested specimens. In these figures, the deformation values are compared in the three aggressive situations imposed on the test: immersion in water, and immersion in a saline solution with a 5% and 10% concentration, for each type of mixture.

The deformation recorded in the first 56 days of testing shows an initial shrinkage (indicated with a negative numbering in figure 2) more evident in P-CEM specimens.

The continuation of the phenomenon seems to be more rapid for the P-CEM and slower and almost stationary in the M-agg and M-nor. In P-CEM the salt concentration of 5% seems to trigger a process of deformation greater than the processes caused by demineralised water and by the salt concentration of 10%. This is probably due to the porosity of the material. (Fig. 2 a), b) c)).

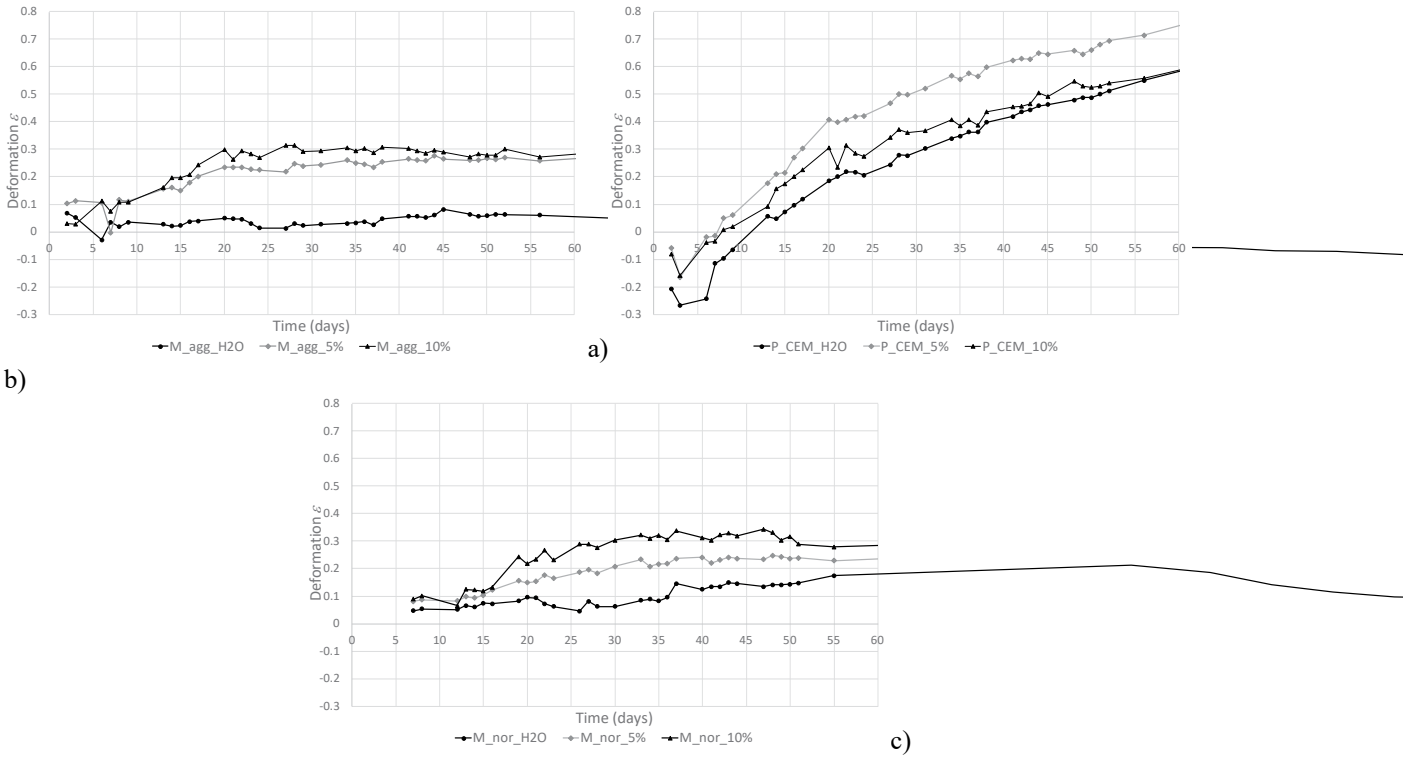

Figure 2. Comparison of the variation of deformation in the first 56 days of testing, referring to the three aggressive agents tested and the mixtures: a) M_agg, b) P_CEM and c) M_nor.

Figure 3 shows the same comparisons but for the entire testing period (889 days).

In this case it is interesting to note that after an initial rather rapid shrinkage of the P-CEM specimens, it stabilises and becomes constant for the entire testing period and for all three aggressive agents. It is not excluded that the continuation of the same test does not lead to different results that are for now unexpected.

Whereas for the M-agg and M-nor mixtures and for the salt concentrations at 5% and 10% after the 500th test day there is an increase in the deformation, perhaps as a consequence of initial cracking of the material for specimens immersed in water, instead, there is an almost constant behavior.

This result indicates that the formation of salt crystals inside of less consolidated pastes does not cause serious problems because they fill the pores and interstices without causing serious pressure on the surrounding material. Over time crystals deposit and during the subsequent immersions they do not have the time to melt, therefore the new attack increases the salt volume and the pressure on the material thus producing micro-fractures which accentuate the deformation, furthermore these results show how the addition of aggregate to the cement paste mixture changes the deformation behaviour of the material.

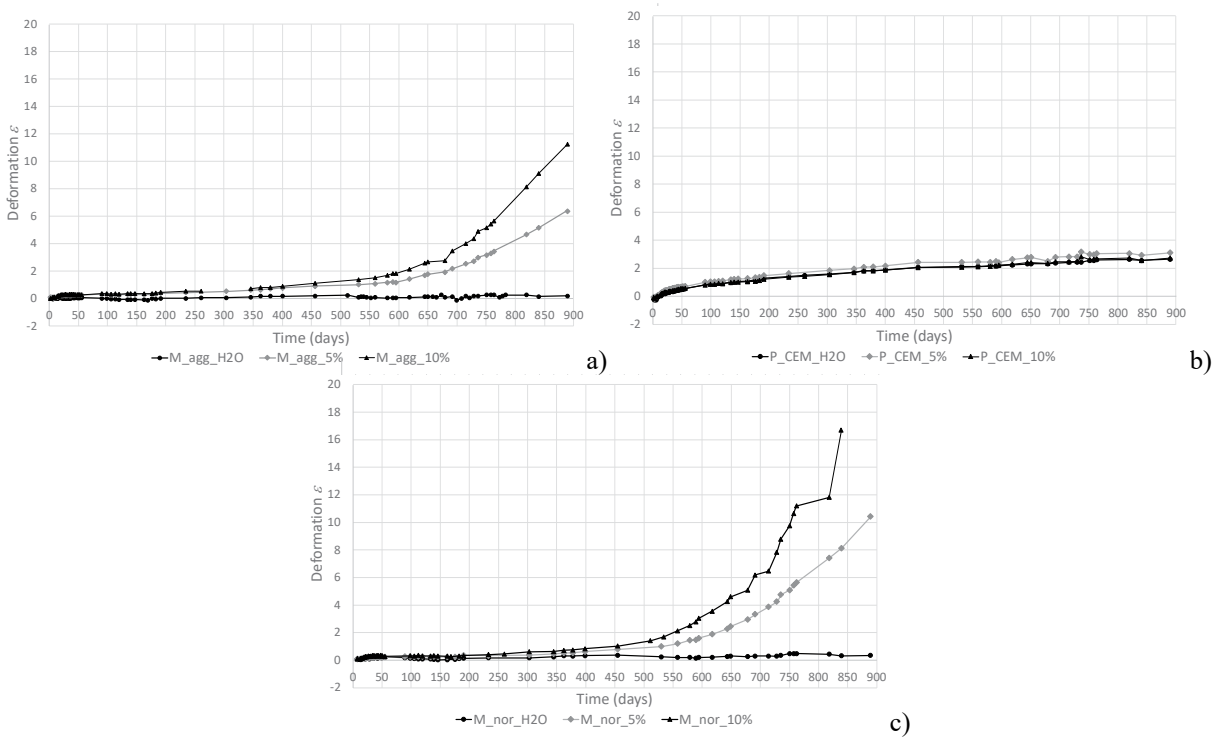

Figure 3. Comparison of the variation of deformation in the 889 testing days, referred to the three aggressive agents tested and the mixtures: a) M_ag: b) P_CEM and c) M_nor.

3.3 Deformation Velocity Survey

From the test procedure adopted and from the results obtained from the quantification of the deformation induced by sulphates attack dissolved in different concentration, the survey and the calculation of velocity were carried out and with which the deformation phenomenon occurred.

The quantification of velocity $\mathbf{v}_i$, relative to each testing cycle, follows the classical definition as reported below:

$$\mathbf{v}_i = \frac{\varepsilon_i}{\left(t_i - t_{(i-1)}\right)} \qquad (3)$$

where: ε_i is the deformation defined in (2); t_i is the instant of testing (measured in days) and $t_{i\text{-}1}$ is the previous instant.

Equation 3 allows to evaluate the variation of deformation velocity instant by instant and to formulate hypotheses on the future of the investigated phenomenon.

3.4. Observation of the Results Obtained.

The calculation of the variations in velocity was performed for all three mixtures investigated in the test (M_agg; P_CEM and M_nor), both for samples immersed in demineralised water (H2O) and for those with a salt concentration of 5% and 10%. The results obtained show interesting aspects that characterise the evolution of the deformation phenomenon.

At first the evolution of the phenomenon was considered in the first 56 days of tests. Figure 4 shows the comparison between the behaviour of the samples at the three different stresses for each type of mixture.

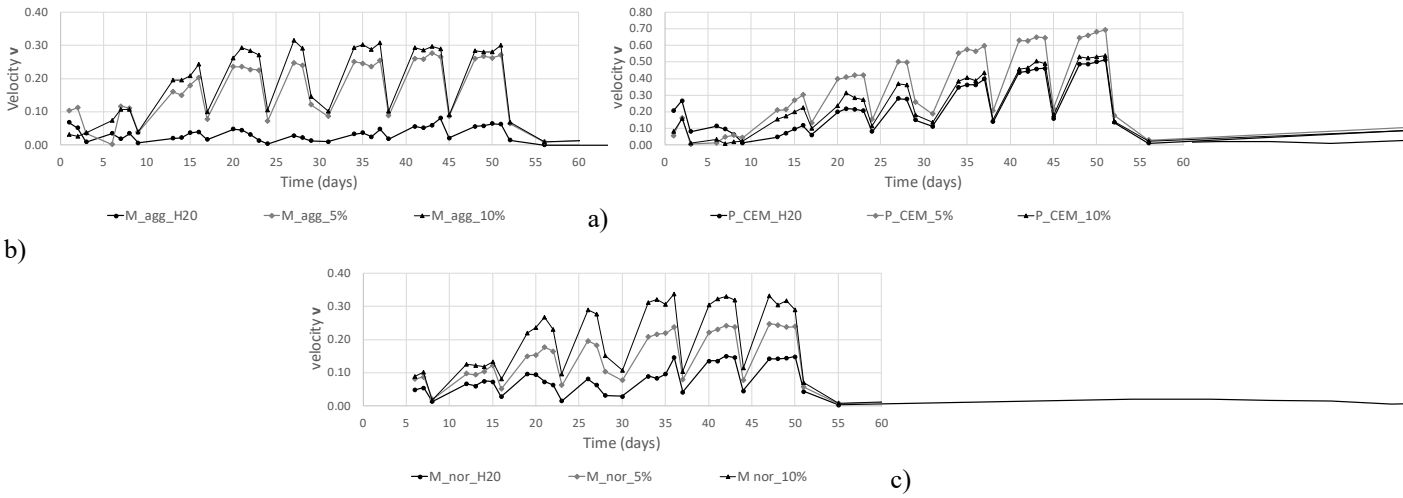

Figure 4. Deformation velocity comparison vs. time for the first 56 days of testing referring to the three aggressive agents tested and for the mixtures: a) M_agg, b) P_CEM and c) M_nor.

Figure 4 clearly shows that for all the mixtures there is a cyclic repetition of velocity increase followed by a stasis phase and subsequently by a velocity decrease phase. This trend seems to be associated with the deformation phases (Figure 2 and Figure 3): when the almost stationary deformation phase ends there is a slowing down of the process which then resumes decisively and with an increase in velocity in the next phase. This behaviour is more regular and marked for the P-CEM mixture.

Figure 5 shows, instead, the trend of the deformation velocity, **v**, for longer test periods.

Here there is a material compromise after 500 days. Test after test, for all the mixtures there is an increase in velocity, a more evident behaviour for the mixtures subjected to saline aggression.

These velocity increases are followed by decreases and subsequent increments. These variations appear to continue to occur every 30 to 70 days. This cyclicality occurs already after the 100th day of the testing.

From the comparison between Figure 4 and Figure 5, the relationship between the increase in deformation velocity and important changes in the deformation phase is even more evident.

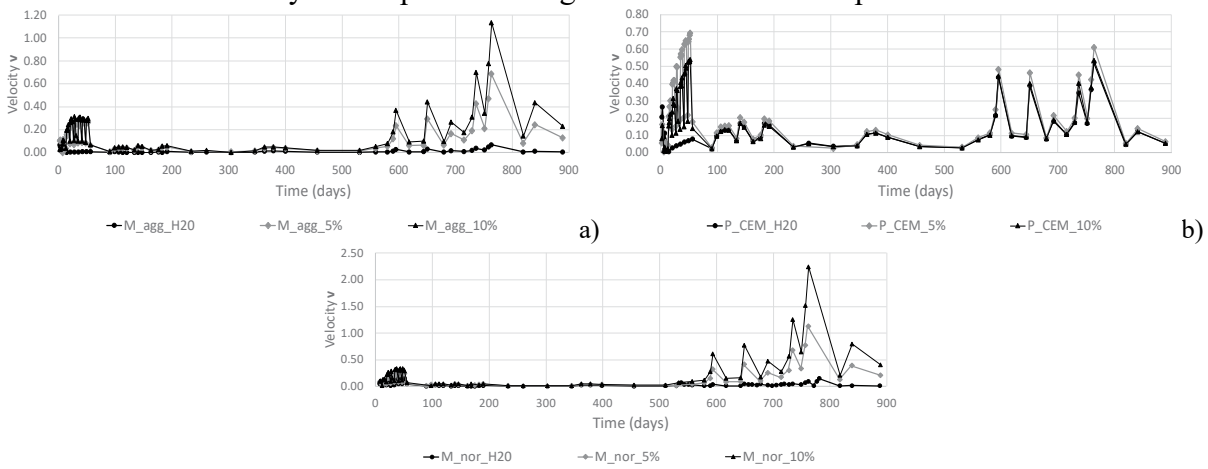

Figure 5. Comparison of deformation velocity vs. time for the 889 days of testing referred to three aggressive agents tested and for the mixtures: a) M_agg;, b) P_CEM and c) M_nor.

5 Conclusions

The laboratory tests applied to specimens of different mixtures and subjected to simulations of different aggressive attacks have shown a propensity to deformation that can be classified in three phases. The first phase takes place in the first 56 test days (test time limit recognised by the legislation). During this phase the velocity shows a periodicity of behaviour that seems to be correlated to the occurrence of a greater deformation after a phase of relative stability; this phase is weekly. The next phase shows a constant deformation behaviour. However, in this phase the velocity shows a certain periodicity and the frequency of the periodicity is in this case variable between 30 and 70 days.

The third phase takes place after the 500-day testing and is typical of the behaviour of saline attacks for M-agg and M-nor. It shows a rather variable deformation velocity (Figure 5a and c), but always with a certain cyclical behaviour, which is matched by a decisive increase in deformation behaviour (Figure 3a and c). Moreover, Figure 3 highlights the different deformation behaviour of P-CEM cement paste compared to M-agg and M-nor mixtures. It is possible that this behaviour is associated with the occurrence of a start of detachment of the material now stressed by the presence of salt crystals inside it. This aspect will be investigated. It is the intention of the authors to proceed with the development of a mechanical test that may monitor this phenomenon.

As for the P-CEM mixture the deformation velocity (Figure 5b) shows the same behaviour recorded for the other mixtures, but with lower values. This is certainly due to a more regular deformation behaviour (Figure 3b).

ORCID

Cristina Tedeschi: http://orcid.org/0000-0002-1718-1632
Elsa Garavaglia: http://orcid.org/0000-0002-7448-8374

References

Anzani A., Cardani G., Condoleo P., Garavaglia E., Saisi A., Tedeschi C., Tiraboschi C. and Valluzzi M.R. (2018). Understanding of historical masonry for conservation approaches: the contribution of Prof. Luigia Binda to research advancement, in Topical Collection 50 years of *Materials and Structures, Mater Struct*. (2018) 51:140, 1-27.

Anzani A., Garavaglia E. and Binda L. (2009). Long-term damage of historic masonry: a probabilistic model, *Construction and Building Materials, Elsevier*, 23(2), 713-724 ISSN 0950-0618 (Print).

Boyd A. J. and Ferraro C. C. (2005). Effect of Curing and Deterioration on Stress Wave Velocities in Concrete, *Journal of Materials in Civil Engineering*, 17(2), 153–158, ASCE, ISSN 0899-1561/2005/2.

Cefis N., Comi C. and Tedeschi C. (2015). Modellazione del degrado nel calcestruzzo dovuto a formazione di ettringite secondaria. In: Memorie estese XII Congresso dell'Associazione Italiana di Meccanica Teorica e Applicata. p. 488-497, ISBN: 978-88-97752-55-4, Genova, Italy, 14/9/2015-17/9/2015.

EN 1015-1:(2006). Methods of test for mortar for masonry - Part 1: Determination of particle size distribution (by sieve analysis).

EN 12617-4:(2003). Product and Systems for the protection and repair of concrete structures. Test Methods – Determination of shrinkage and expansion.

Garavaglia E., Anzani A., Binda L. and Cardani G. (2008). Fragility curve probabilistic model applied to durability and long term mechanical damages of masonry. *Materials and Structures/Matériaux et Constructions*, RILEM Pub. s.a.r.l., Springer Ed., 41(4), 733-749. ISSN 1359-5997 (Print).

Garavaglia E., Basso N. and Sgambi L. (2018). Probabilistic life-cycle assessment and rehabilitation strategies for deteriorating structures: a case study. *International Journal of Architectural Heritage*, 12(6), 2018, 981-996.

Garavaglia E., Tedeschi C. and Perego S. (2017). Probabilistic evaluation of concrete durability subject to accelerated decay by salt crystallization, Keynote Lecture, *Proc. of XIV DBMC 14th Int. Conf. on Durability of Building Materials and Components*. May, 29-31, 2017, Ghent, Belgium, De Schutter, et al. Editors, RILEM Publication S.A.R.L., Paris, PRO 107, USB, 225-236.

Garavaglia E., Tedeschi C., Perego S. and Valluzzi M. R. (2016). Probabilistic Modelling of the damage induced by salt crystallization in fiber reinforced clay brick masonry". *Proc. of* IB^{2}MAC, *16th International Brick and Block Masonry Conference*, *Trends, Innovations and Challenges*, Padova, Italy, June, 26-30, 2016, C. Modena, et al. Editors, CRC Press, Taylor & Francis Group, A. Balkema Book, 487-494.

Tedeschi C., Cefis N. and Comi C. (2017). The effect of external sulfate attack on concrete, mortar and cement paste, Proc. of XIV DBMC 14th Int. Conf. on Durability of Building Materials and Components. May, 29-31, 2017, Ghent, Belgium, De Schutter, et al. Editors, RILEM Publication S.A.R.L., Paris, PRO 107, USB, 225-236.

Tedeschi C. and Garavaglia E. (2019). A probabilistic approach to investigate the physical compatibility between bedding and re-pointing mortars, *Pro. of SMSS 2019 - RILEM International Conference Sustainable Materials, Systems and Structures,* 18-22 March, 2019, Rovinj, Croatia, Bričević et al. Editors, RILEM Publication S.A.R.L., PRO 128, Vol.3, CD-ROM, 700-707.

Tseng W.-T., Chin J.-H. and Kang L.-C. (1999). A Comparative Study on the Roles of Velocity in the Material Removal Rate during Chemical Mechanical Polishing, *Journal of The Electrochemical Society*, 146 (5), 1952-1959, S0013-4651(97)11-028-X CCC.

Zhanga Y., Abrahama O., Grondinb F., Loukilib A., Tournatc V., Le Duffd A., Lascoupe B. and Duranda O. (2012). Study of stress-induced velocity variation in concrete under direct tensile force and monitoring of the damage level by using thermally-compensated Coda Wave Interferometry, *Ultrasonics* 52(8), 1038-1045.

XV International Conference on Durability of Building Materials and Components
DBMC 2020, Barcelona
C. Serrat, J.R. Casas and V. Gibert (Eds)

Deterioration of CLT under Humid and Dry Cyclic Climate

Shiro Nakajima[1], Yoshihei Sakabe[2], Seiya Kimoto[3] and Yoshinori Ohashi[4]

[1] Department of Architecture and Urban Design, Faculty of Regional Design, Utsunomiya University, 7-1-2 Yoto, Utsunomiya City, Tochigi Pref., Japan, s-nakajima@cc.utsunomiya-u.ac.jp.

[2] Japan CLT Association, 2-15-5 Higashi-Nihonbashi, Chuo-ku, Tokyo Met. Japan, y.sakabe@clta.jp.

[3] Technology Research Institute, Mitsui Home Co.Ltd., 2-1-1 Nishi-Shinjuku, Sinjuku-ku, Tokyo Met., Japan, s-kimoto@mitsuihome.co.jp.

[4] Hokkaido Research Organization, Forest Products Research Institute, 1-10 Nishi-Kagura, Asahikawa City, Hokkaido, Japan, ohasi-yosinori@hro.or.jp.

Abstract. *Cross laminated timber (CLT) are composed of longitudinal layers and cross layers. And as the laminations of the adjoin layers are glued orthogonally deterioration of the laminations such as check and shake and delamination can be rather frequently come out when CLT is exposed to humid and dry cyclic climate. In Japan more than 100 CLT buildings have been constructed and the number of CLT building is increasing. In some buildings the CLT is designed as to be the exterior members and exposed to the outdoor climate. Several CLT buildings that have CLT as exterior members was investigated to make clear what was ongoing on the CLT panels exposed to outdoor climate. Remarkable check and shake, warp and delamination was observed for the CLT in some of the investigated buildings. To bring out the mechanism of the distortion of CLT under humid and dry cyclic climate and to give a solution to prevent deterioration of CLT a series of laboratory tests were conducted. The CLT panels were set in a climate chamber and exposed to a humid and dry cyclic climate. And the moisture content and the movement of the laminations of CLT were measured. The movement was affected by the species of the laminations and also by the direction of the surface, sap-side or heart-side. And the film forming type painting worked well as to prevent the deterioration and the penetrating type painting could slightly reduce the deterioration.*

Keywords: *CLT, Humid and Dry Cyclic Climate, Delamination, Movement, Species.*

1 Introduction

In Japan more than 100 CLT buildings have been constructed and the number of CLT buildings is increasing. In some buildings the CLT is designed as to be the exterior members and exposed to the outdoor climate. And even not exposed to the outdoor climate the surface of CLT in many buildings is exposed to the indoor climate.

Cross laminated timber (CLT) are composed of longitudinal layers and cross layers. And the laminations of the adjoin layers are glued orthogonally. Wood has different swelling and shrinkage ratio for tangential direction and radial direction. It is commonly known that the swelling and shrinkage ration of the tangential direction is approximately two times larger than that of the radial direction. The layer arrangement of CLT cause uneven swelling and shrinkage between the adjoin layers particularly under humid and dry cyclic climate. Oshima, A. (2017) indicated that this uneven swelling and shrinkage between the adjoin layers occasionally cause distortion or deformation of the laminations such as check and shake, warp and delamination.

Lepage, R.T.M. (2012) measured the response of CLT under changing moisture conditions and also simulated the response. CLT produced in Japan are in most cases composed of Japanese species. And there is limited knowledge for the distortion of CLT composed Japanese species. To find a solution to reduce the distortion of CLT the mechanism of the distortion of CLT laminations under humid and dry cyclic climate should be clarified. A series of tests were carried out to estimate the mechanism of distortion of the CLT and to evaluate the capability of surface coating or surface painting against the distortion prevention.

2 Distortion of CLT Exposed to Outdoor or Indoor Climate

Several CLT buildings was investigated to have knowledge of the conditions of the CLT panels exposed to the outdoor or indoor climate. The buildings were investigated 2 to 3 years after their completion. Remarkable check and shake, warp and delamination were observed in some of the CLT panels exposed to the outdoor climate and check and shake were also observed in some of the CLT panels exposed to the indoor climate.

Figure 1 shows a bicycle parking space constructed with CLT panels for their walls and roofs. To protect the CLT panels from the sunshine and rain the panels were painted by some impregnated paint designed to protect wood from the outdoor climate. A certain number of check and shake was observed at the bottom of the wall panels and at the roof panels. And warp and delamination were also observed at the edge of the roof panels. The moisture, rain drop and sunshine (i.e. ultra-violet wave) may have caused these distortions.

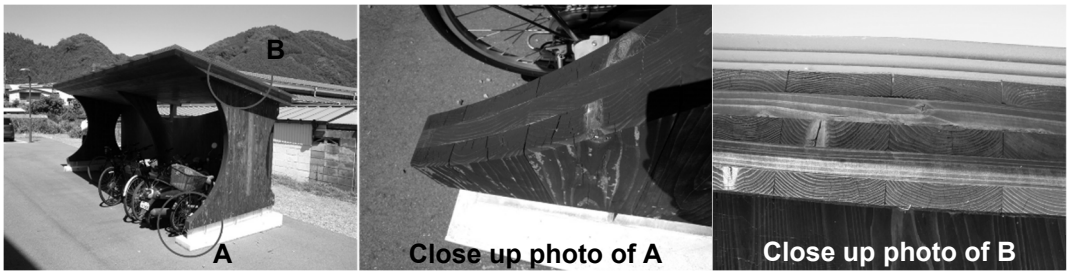

Figure 1. Deformation of CLT exposed to outdoor climate (Bicycle parking space).

Figure 2. Deformation of CLT exposed to outdoor climate (Eaves of CLT flat roof).

Figure 2 shows the eaves of the CLT flat roof. As the edge of the panels was not covered with weather protecting materials such as steel sheet materials or ceramic boards the edge of the panels was fully exposed to the weathering force. And the panels had damages such as check and shake, warp and delamination.

Figure 3(a) shows the delamination of the lamination of CLT panels used for the indoor partition wall. Figure 3(b) shows the check and shake and warp of the surface lamination of the CLT panels located close to the outlet of the air conditioner. The shrinkage of the surface of the CLT panels may have caused these types of distortion.

(a) Delamination of the surface lamination. (b) Check and shake of the surface lamination.

Figure 3. Distortion of the CLT panels under indoor climate.

3 Shrinkage and Swelling of CLT and Glue-Laminated Timber (GLT)

3.1 Assumption of the Deformation

CLT are supposed to shrink as illustrated in Figure 4(a) when it is exposed to a humid to dry climate and the moisture content of the material decreases. This deformation is caused by the composition of CLT (*i.e.* the laminations of the adjoin layers are glued orthogonally) and the shrinkage ratio of wood (*i.e.* the shrinkage ratio of the tangential direction is approximately 20 times larger than that of the axial direction and the shrinkage ratio of the radial direction is approximately 10 times larger than that of the axial direction). This type of deformation also occurs when CLT is exposed to a dry to humid climate.

On the other hand, the direction of the laminations of glue-laminated timbers (GLT) is same for all layers. For this lamination arrangement all the layers will deform in a similar way under humid and dry climate. And the shrinkage or swelling will be same for all layers as illustrated in Figure 4(b).

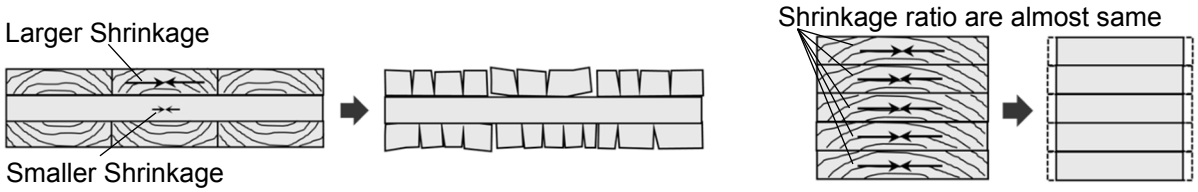

(a) CLT (b) GLT

Figure 4. Deformation of CLT and GLT under humid to dry climate (Cross section).

The response of CLT under its drying process can be modeled as shown in Figure 5. The different shrinkage ratio of the adjoining layers is supposed to be the reason for the check and shake, warp and delamination of the laminations.

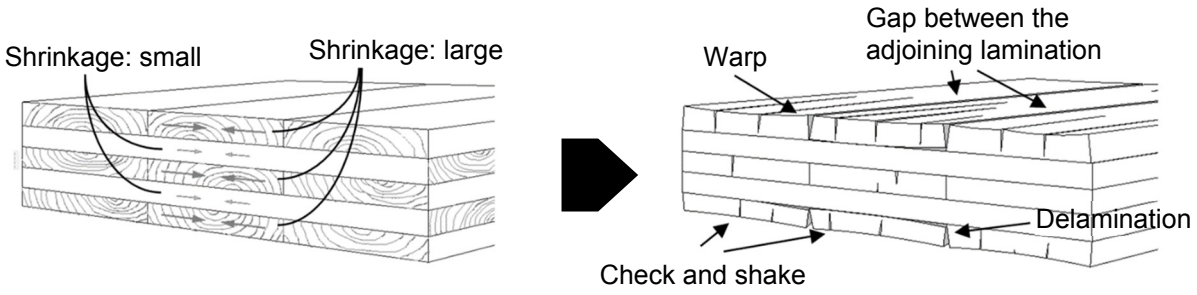

Figure 5. Assumption of the distortion of CLT under its drying process.

3.2 Testing to Verify the Deformation of CLT and GLT Under Humid and Dry Cyclic Climate

To verify the assumption that CLT and GLT deform differently when they shrink or swell the deformation of both materials were measured under humid and dry cyclic climate. Figure 6 shows the shape and size of the test specimens and the measuring points of the displacement and moisture content. The deformation of the surface and cross section of both materials were measured by displacement meters and the moisture content of both materials was measured by a moisture meter. The species of the test specimens was Japanese Cedar (*cryptomeria japonica*) the most popular species for CLT in Japan. The CLT test specimens had five layers and the thickness of each layer was 30mm. The GLT test specimens had 12 layers and thickness of each layer was 30mm. The test specimens were put in a conditioned chamber and conditioned for 10 days followed by 3 days' humidification, 7 days' drying, 10 days' humidification, 17 days' drying and 3 days' humidification. The relative humidity of chamber during the humidification process was 100% and that of the drying process was approximately 40%.

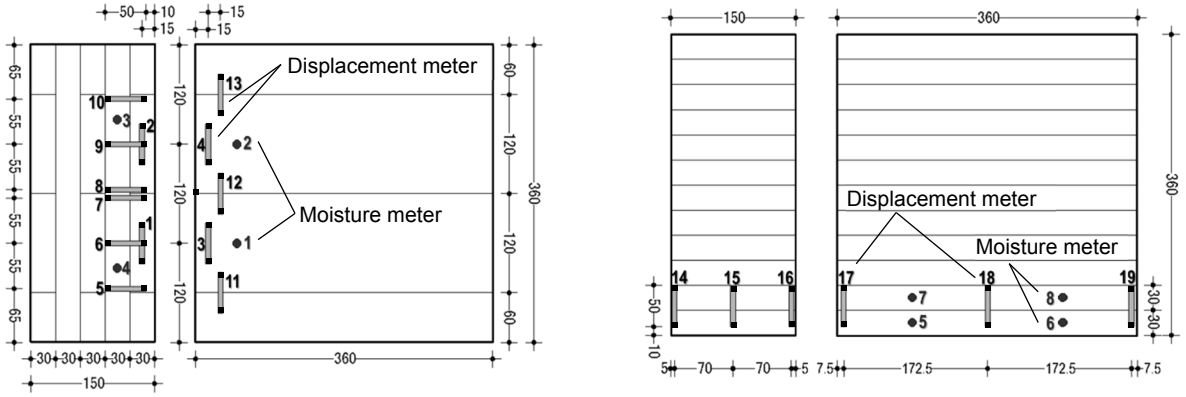

(a) CLT (b) GLT

Figure 6. Shape and size of the test specimens and configuration of the measuring points.

Note: The displacement of CLT was measured at 13 points (the gray bar) and moisture content was measured at 4 points (the gray circle). The local displacement of GLT was measured at 6 points and moisture content was measured at 4 points.

3.3 Results and Discussion

The measured deformation of the cross section of CLT and GLT under humid and dry cyclic climate was measured as shown in Figure 7(a). The narrow lines give the displacement of each measuring point and the thick lines give the average displacement of the measuring points. The deformation of CLT (solid line) is approximately 2 times larger than that of the GLT (broken line). CLT seem to have larger shrinkage and swelling than GLT. The damages of the cross section of CLT and GLT are given in Figure 7(b). Where GLT had only one standing out crack CLT had few cracks on its lamination and gaps between the adjoining laminations.

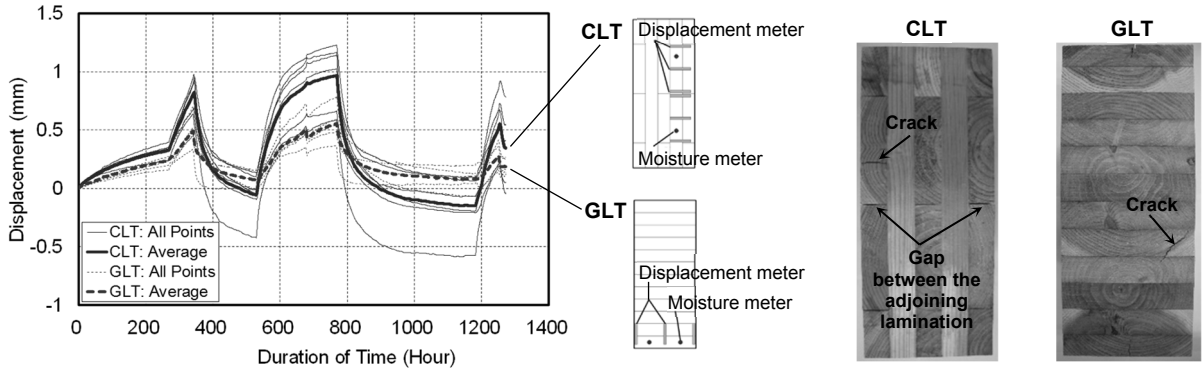

(a) Deformation under humid and dry cyclic climate (b) Damages of cross section

Figure 7. Deformation of cross section of CLT and GLT under humid and dry cyclic climate.

4 Effect of Weather Resistant Paint Against Distortion Prevention

4.1 Testing to Verify the Effect of Weather Resistant Paintings

To evaluate how the weather resistant paint can reduce the distortion of CLT under humid and dry cyclic climate test specimens painted by weather resistance paints were put in chamber under humid and dry cyclic climate. Four CLT test specimens were tested and three of them were painted by different types of weather resistance paint as shown in Table 1. The species of the test specimens was Japanese Cedar and the size of the test specimens was 1000mm in length, 1000mm in width and 150mm in depth. The density and initial moisture content of the test specimens are given in Table 1.

Table 1. Type of weather resistant paints and density and initial moisture content of CLT test specimens.

Name of test specimens	Type of paint	Density (kg/m3)	Moisture content (%)
Control	No painting	423.5	9.3
Painted-1	Penetrating type 1	415.2	10.6
Painted-2	Penetrating type 2	418.9	13.2
Painted-3	Film forming type	417.4	11.8

The displacement of the test specimens was measured for 8 points for each test specimen. The in-plane displacement and the out-plane displacement of the laminations were measured as

illustrated in Figure 8. The measuring points no.1, 2, 5 and 6 are to measure the out-plane deformation of the laminations and the measuring points no.3, 4, 7 and 8 are to measure the in-plane deformation of the laminations. And the measuring points no.1, 2, 3 and 4 are measuring the deformation of the laminations that have their sap-side on the surface side of CLT and the measuring points no.5, 6, 7 and 8 are measuring the deformation of the laminations that have their heart-side on the surface side of CLT.

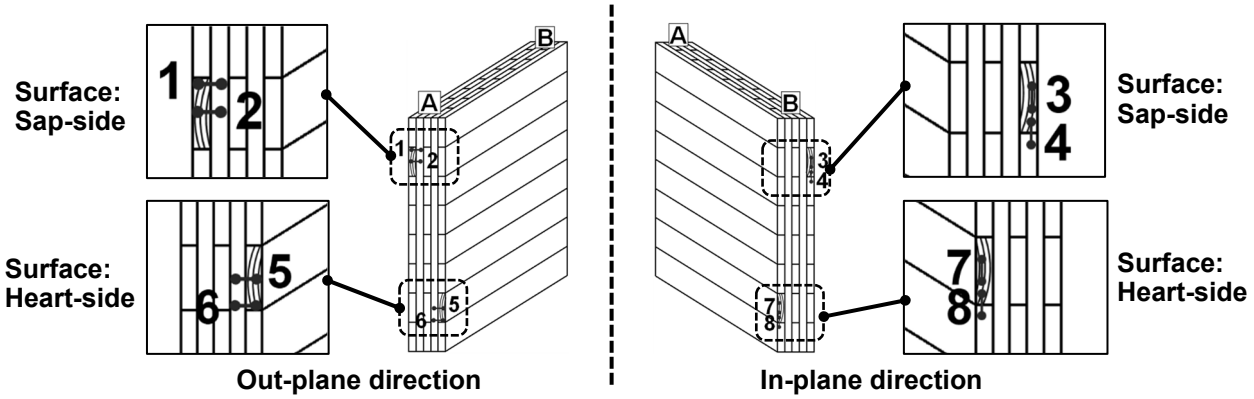

Figure 8. Location of the displacement meters set to measure the displacement of the laminations.

4.2 Results and Discussion

The movement of the laminations measured by the displacement meters no.1, 2, 5 and 6 are given in Figure 9. Figure 9 gives the maximum movement of the four measuring points. The movement of the CLT with no painting (control) was the largest and the movement of CLT painted with film forming type paint was the smallest. The movement of CLT painted with penetrating type paint was almost same to that of CLT with no painting.

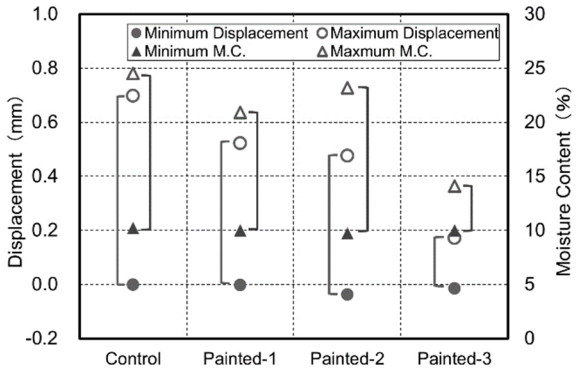

Figure 9. Movement of displacement and movement of moisture content.

Note: ○ gives maximum displacement measured by the displacement meters no.1, 2, 5 and 6 and ● gives minimum displacement. △ gives maximum moisture content of the CLTs and ▲ gives minimum moisture content.

The tendency of the moisture content was almost similar to that of the displacement. The moisture content of CLT with no painting had the largest variation and that of CLT painted with

film forming type paint had the smallest variation. The film forming type paint seems to work well as to reduce the deformation of CLT under humid and dry climate. And the penetrating type paint seem to not work well as to reduce the deformation of CLT.

5 Effect of the Surface Direction (Sap-Side or Heart-Side)

5.1 Testing to Verify the Effect of the Surface Direction

To verify the effect of the surface direction of the out most layer on the distortion of the laminations CLT composed of sap-side on its surface and CLT composed of heart-side on its surface were tested for their distortion. Figure 10 gives the size and shape of the test specimens and the location of the measuring points for deformation and moisture content. The test specimens were 800mm in length, 800mm in width and 90mm in thickness. And the species of the laminations were Larch (*larix kaempferi*) or Sakhalin fir (*abies sachalinensis*). These two species are the northern species in Japan and known as to have relatively high response for moisture content movement. The test specimens were set in a climate that was controlled as to have relative humidity 100% for 6 days followed by relative humidity 40% for 12 days and again relative humidity 100% for another 6 days. The response of the CLT under humid and dry cyclic climate was measured for two directions the out-plane direction and the in-plane direction as shown in Figure 10.

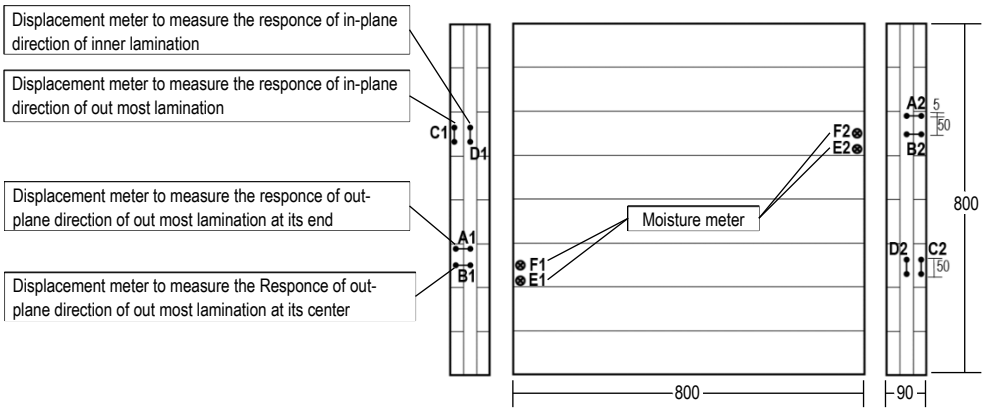

Figure 10. Size and shape of the test specimens, the location of displacement meters and moisture meter.

5.2 Test Results and Discussion

The out-plane movement of the out most laminations of Larch CLT under the humid and dry cyclic climate is given in Figure 11(a) and (b). And the in-plane movement of the out most laminations of Larch CLT under the humid and dry cyclic climate is given in Figure 11(c) and (d). The out-plane deformation of the out most laminations was larger than the in-plane deformation. And in general, CLT composed of laminations with heart wood side on the surface side had relatively larger deformation than CLT composed of laminations with sap wood side on the surface side. The test result for Sakhalin fir CLT was almost same to that of Larch CLT. These test results indicate that one solution to reduce the moisture related deformation of CLT is to arrange the out most laminations so as to cover the surface of CLT with the sap wood side of the laminations.

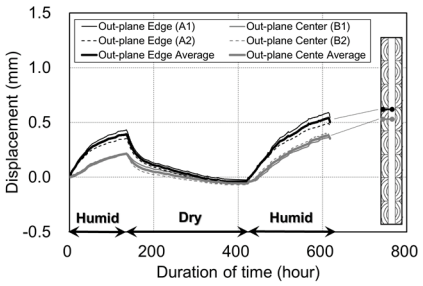

(a) Out-plane direction, Surface sap wood.

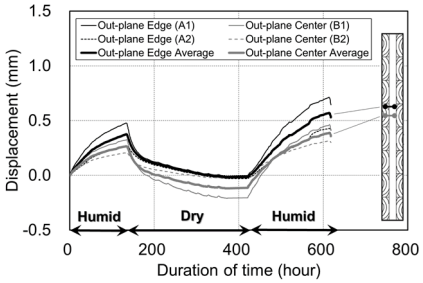

(b) Out-plane direction, Surface heart wood.

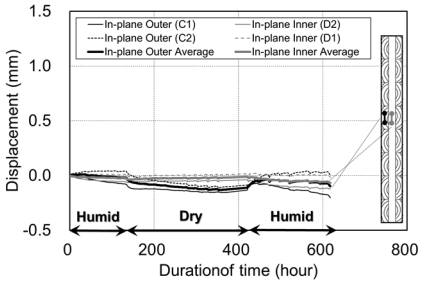

(c) In-plane direction, Surface sap wood.

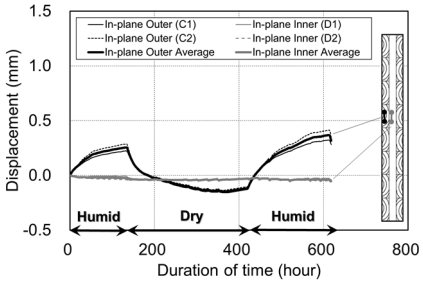

(d) In-plane direction, Surface heart wood.

Figure 11. Response of the CLT under humid and dry cyclic climate (Larch).

6 Conclusion

A series of tests were carried out to estimate the mechanism of distortion of the CLT and to evaluate the capability of surface coating or surface painting against the distortion prevention. The results are summarized as follows;

- The deformation of CLT was approximately two times larger than that of the GLT. CLT showed larger shrinkage and swelling than GLT. The arrangement of the lamination si supposed to cause this difference.
- The film forming type paint seems to work well as to reduce the deformation of CLT under humid and dry climate. And the penetrating type paint seem to not work well as for reducing the deformation of CLT.
- One solution to reduce the moisture related deformation of CLT is to arrange the out most laminations of CLT so as to cover the surface of CLT with the sap wood side of the laminations.

ORCID

Shiro Nakajima: http://orcid.org/ 0000-0002-5382-5175

Acknowledgement

This research was founded by the Taisei Foundation.

References

Oshima, A. (2017). *Survey on durability of timber buildings composed of CLT panels*, Bachelor Thesis, University of Utsunomiya, Tochigi, Japan.

Lepage, R.T.M. (2012). *Moisture Response of Wall Assemblies of Cross-Laminated Timber Construction in Cold Canadian Climates*, PhD Thesis, University of Waterloo, Ontario, Canada.

XV International Conference on Durability of Building Materials and Components
DBMC 2020, Barcelona
C. Serrat, J.R. Casas and V. Gibert (Eds)

Determination of the Deterioration Characteristics of Facade Materials: A Case Study

Nil Kokulu

Antalya Bilim University, Faculty of Fine Arts and Architecture, Çıplaklı Mh. Akdeniz Blv. Pk:07190 Döşemealtı, Antalya, nil.kokulu@antalya.edu.tr

Abstract. *Deterioration of the facade materials of a building and its importance are topics that are not getting the attention that they deserve and need. If a material can't meet its accepted performance criterion during its service life then deterioration may occur on the surface, inside, under or at the structure of the material. Environmental, construction related, and human related agents collaborate with the mechanisms and make an effect which concerns the durability. Therefore, detecting the deteriorations of the materials play an important role for the maintenance planning. This study aims to detect the agents, mechanisms and effects of the deteriorations of a case building. A systematic approach was developed by making literature review. Hostile environmental analysis and building facade inspection have been made by the visual observations on a specific day. Deteriorations occurred at granite, wood composite, aluminum, glass and ceramic materials have been discussed.*

Keywords: *Environmental Deterioration, Facade Inspection, Agents, Mechanisms, Durability.*

1 Introduction

Building components are expected to maintain their required performance levels over their service life. In order to succeed in this process, identifying the environment and the future cause of the deteriorations are a precondition. During the literature reviews, it is seen that facade materials such as granite, wood composite, aluminium, glass and ceramic are exposed to deteriorations as time progresses.

According to Grelk *et al.* (2007), bowed granite cladding is a problem caused by the temperature differences and the moisture. Also, Marie (2013), in her article, states that natural stone facades perform differently over time and the colour of the facade may change according to cracking, dirt, corrosion, carbonation and biological colonization. This change causes visual aesthetic problems and the problems may differ according to person's characteristics.

Morrel *et al.* (2010), state that as a biological agent, white rot fungi and brown rot fungi can easily deteriorate wood in wood plastic composites (WPC) and may cause loss of weight depending on the climate. The most important factor was determined as moisture for fungal decay. They also argue that WPC's bending properties change when exposed to fungi. The authors go on to say that physical agents are also important when deterioration of WPC's is the subject. Although the damage seems like it is on the surface, chemical discoloration occurs beneath the surface and it is very difficult to remove. Also, UV degradation changes the characteristics such as colour, surface composition and mechanical changes of WPC's.

According to Honfi *et al.* (2014), in their article about the glass structure failures, they described two kinds of exposures which are faults and errors. Faults are the physical reason for the failures such as excessive loading, surface damage and moisture, while errors are the logical reason of the exposures such as modelling and calculation errors, poor manufacturing and detailing errors.

Corrosion is most common in metals and observed to some extent in ceramics. Khanam *et al.* (2015), state that corrosion on aluminium has seen because of the saline environment. They state that chloride ions attack to aluminium film and made pits on the top. This causes structural failure of the material.

Besides the obvious problems of breakage, ceramics deteriorate during their service life according to temperature, external loads, vibrations and environment. They may contain soluble salts which can crystallize at or near the surface and destroy the material. Also, unstable glazes of the ceramics may cause crumbs on the surface (Museum Management Programme, 2018).

In this study, the deteriorations formed in granite, wood composite, ceramic, aluminum and glass and their causes have been explained systematically. Agents, mechanisms and effects of the deteriorations were identified. Results and expected damage are explained at the end.

2 The Case Study

2.1 Preparing the Data Analysis

In this section, specific data, information and analysis of the front facade of the building are intended to provide a proper method for conducting the deteriorations. The first part of this section provides a draft of the proposed systematic approach to study that reflects on an individual understanding and perception of the research process. The second part consists the inspections of the hostile environment and the facade of the building. For the hostile environmental analysis, site selection, building information and the climate data were studied. For the facade of the building, facade materials and their structure system were investigated.

2.2 Systematic Approach to Study

A systematic approach is an outline of the researcher for determining the steps of the case study (Figure 1).

Macro environment analysis focuses on the continental observations consisting of location, orientation of the building, surrounding buildings, traffic and pedestrian roads and vegetation at the site. Meso environment analysis consist of climate type, dominant wind direction, temperature, precipitation, air content, pollution and soluble salts which influence the building. Micro environment analysis consist of age, height, architectural form, function, facade materials, material types, their characteristics and material structure system.

Data collected after the macro, meso and micro analysis and was used as a component while making the visual observations. Visual observations consist of the sunny and rainy-day conditions of the east facade. According to this conditions, agents of the deterioration have been analyzed by taking the feedback from the literature review. According to Kuş (2018), agents in the built environment very rarely act alone but neither work together. The effect of the agent occurs when a mechanism reveals its appearance.

Performance deteriorates at a rate depending on the environment, the design of the building, building materials, maintenance and usage (Song and Lim, 2016). In this case, since the building is at a very young age, it is not possible to visually observe the deteriorations but estimate them with the help of site analysis and visual observations.

Although all the visual information and the literature review provided, it is not possible to be certain about the future deteriorations.

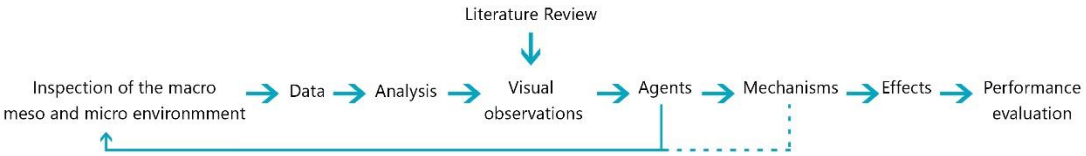

Figure 1. A systematic approach.

2.3 Macro Environment

The building is located on the intersected corner of Portakal Çiçeği street and 1460 street in Antalya, Turkey. It is a seven storey-high residential building on the right with a distance of 8.40 meters, ten storey-high residential building on the back with a distance of 14 meters and front with a distance of 40 meters and two storey-car parking on the southwest with a distance of 21.5 meters. The main entrance faces to east (Figure 2). This facade always takes the sun directly without having any shading areas. The temperature and the light play a crucial role on materials. 1460 street and Portakal Çiçeği street have intense traffic. This causes air pollution which may create deterioration. The distance from the sea is 1 km and the height of the building from the sea is 22.5 m. The pedestrian roads and the vegetation around the building can be seen in Figure 3. There is an open area in front of the main facade. There are also car parking areas on the east and the west facade.

Figure 2. East facade of the building.

2.4 Meso Environment

Antalya has a hot humid climate with rainy winters. The dominant wind direction is from northeast to southwest (Figure 3). The temperature changes 10°C to 35°C through the year. October, November and December are the months that take most of the rainfall (Holiday-weather, 2018).

The air contaminates soluble salts because of the distance within the sea. This may cause material deteriorations by collaborating with the mechanism. According to SİM Project, Sulphur dioxide and particulate matter has been diagnosed in the air (Sürekli Eğitim Merkezi, 2019). Sulfur dioxide and its acid derivations are known to cause considerable damage to materials. The east and north facade is open whereas the south and west facade are in the shade caused by surrounding buildings. There isn't so many people around the building except the Wednesdays because of the local bazaar. The building welcomes the animals.

Figure 3. The site plan, the section of the site (on the left) and dominant wind direction and the movement around the building (on the right).

2.4 Micro Environment

The six-storey office building is three years old. It has a rectangular form with the dimensions of 42.50 meters to 18.95 meters. The height of the building is 18.60 meters. The facade materials of the modern designed building are ceramic, aluminum, glass, granite and wood composite (Figure 4). The properties of the materials can be seen on Table 1.

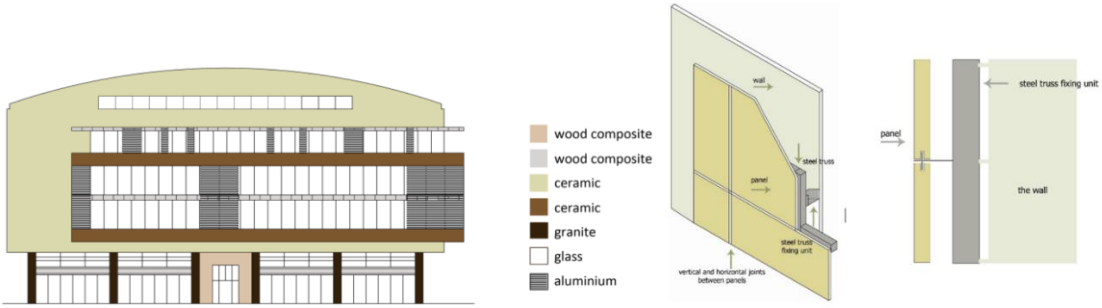

Figure 4. Facade materials of the building and the structure system of the materials.

Table 1. Properties of the facade materials.

Materials	Color	Surface finish
Ceramic	beige	unglazed
Ceramic	brown	unglazed
Granite	black	polished
Aluminium	white	polished
Wood composite	white	flat
Wood composite	light brown	flat
Glass	blue	flat

Steel truss metal panel curtain wall system has been used for the facade system. A cross or vertical steel truss is installed on the structure first. Then, a panel is fixed to the steel truss. Finally, the vertical and horizontal joints between the panels are filled with back-up materials and then finished with sealant. No anchorage system and no joints can be seen from the external (Figure 4) (Song and Lim, 2016). The corner adjoining parts of the granites are unpolished. This part may take water and air to the inside and different types of deteriorations may occur.

3 Analysis

3.1 Visual Observation Information

For the case study, visual observations are made. The observations took two hours from 12.00 to 14.00. The materials on the east facade have been examined according to their instant conditions in a sunny day and in a rainy day (Table 2). Also, future deterioration problems are discussed.

Table 2. Visual observation conditions.

	Sunny day conditions	**Rainy day conditions**
Observation day	10.11.2018	17.11.2018
Climate type	Winter	Winter
Temperature	17°C	14°C
Humidty	43%	86%
Wind direction	NE to SW	NW to SE
Wind speed	3 km/h	21 km/h
Rain ration	0%	70%

According to sunny-day and rainy-day conditions shading areas of the building have been examined. The facade of the building takes most of the sun except upper part of the facade of the ground floor in a sunny day, while it is totally in shade in a rainy day.

3.2 Agents, Mechanisms and Effects

Agents of deteriorations have been analyzed while making environmental analyses. 5 types of agents have been observed. These agents are grouped as; physical agents (temperature, moisture, light and wind), chemical agents (water, air, salts), biological agents (plants, birds, mold), design decisions, vandalism.

There exist 4 major typical mechanisms of deterioration, which lead to failure. These are grouped as; mechanisms caused by material properties, mechanisms caused by material structure properties, environmental mechanisms, construction related mechanisms.

A review of the causes of failure identified twelve of the most frequent sources of deterioration in facade materials are; dirt and dust accumulation, spalling, biological colonization, staining, corrosion, efflorescence, gypsum crust, cracks and breakage, discoloration, UV degradation, chipping, scratches. Agents, mechanisms and effects of the deterioration for each facade material can be seen in Table 3.

4 Results and Discussions

In this study, visual observations have been made to determine the future deteriorations. Since the building is only three years old, only the dirt deposition and the discoloration on the surface of the granites and discoloration on the WPC's caused by the rain have been observed. Expected deteriorations of the materials are discussed below.

Dirt and dust deposition occur on the cracks and on the surfaces of the panel with the help of the wind. High traffic areas cause great accumulation of dirt (Museum Management Program, 2018). The east facade is located on one of the most intense traffic areas. Dirt and dust deposition would be seen on the granite columns in the future. Wind can bring salts in the

air to the panel surface which can cause spalling (Museum Management Program, 2018). Spalling couldn't be seen on the front side of the columns. But it is seen on the north side of the columns. The reason is, the east side takes the sun more than the north side and can easily dry whereas the north side is always on shade. Biological agents such as bacteria, algae, fungi, and moss grow on stone surfaces and cracks with the help of humidity (Museum Management Program, 2018). The lower side of the columns can easily deteriorate because they are exposed to water more than the higher parts. Color changes on the panel surfaces may be caused by the design decisions. The sun plays an important role for this type of deterioration. This may also effect visual aesthetics (Mauko *et al.*, 2006).

Bowing and expansion due to temperature changes (Grelk *et al.*, 2007) may occur on the front side of the columns with the help of the temperature. Staining from water absorbtion or vapour condensation may occur on granite (ICOMOS, 2019). The corners of the granite are capable of water intake. Corrosion occurs when the chemical reactions happen (Shaw and Kelly, 2006). The corners of the granite have started to corrode and may cause structural problems in the future. Ceramics may contain soluble salts that can crystallize at or near the surface and destroy the panel (Museum Management Program, 2018). The adjoining parts of the ceramics are capable of salt intake. So, the efflorescence is possible.

Because of the location of the facade, air pollution may cause wet deposition where there is no rain-wash. This may cause gypsum crust (Agnes *et al.* 2012). Observations after the rain showed that, some part of the ceramics dry longer than the other parts. Condensation can lead to mold growth, noxious odors and deterioration of building finishes of the panels (Campante and Paschoal, 2002). Biological activity would be seen on the cracks of the ceramics (Agnes *et al.* 2012). Cracking occurs when thermal movement isn't provided (Goldberg, 2002).

Figure 5. Facade of the building (on the left), facade of the building in 30 years (on the right).

The panels would be affected by the temperature. It is clearly seen that no expansion joint was used, either vertical or horizontal. This may cause cracks and/or breakage even falling of the panels. Corrosion may occur on the metal structural supports and anchors of ceramic tiles (Campante and Paschoal, 2002). The panel joints may easily take water and air inside of the structure. Color changes create visually unproper aesthetic that can be seen on the ceramic tiles (Song and Lim, 2016). The reason of this can be dirt deposition which comes with the wind. Biological agents may use wood as a food source or for living with the help of water intake from the cracks or joints. This may cause weight loss of the panel (Morrell *et al.*, 2010). The WPC's on the east facade can easily take water from the rain. It is clearly seen that air pollution

came with the rain and created a color change at the surface. Because of the absorption characteristics of the WPC's moisture may cause damage of the material especially on the shading areas (Morrell *et al.*, 2010). The lower parts of the wood composite look better than the upper parts. It is probable that the upper parts would have a mechanical degredation in the future. Especially in the summer, the sun plays an important role. Wood absobs the UV lights. This causes loss of surface quality and change in the mechanical properties. UV degradation would be seen at the WPC's especially on the unshaded areas in the future.

Table 3. Agents, mechanisms and effects of the deteriorations.

GRANITE	**Agents**	**Mechanisms**	**Effects**
	Wind	Pollution caused by traffic	Dirt and dust accumulation
	Moisture + wind	Salts on the surface	Spalling
	Mositure + wind	Cracks	Biological colonization
	Design decisions	Sun	Color changes
	Temperature	No gaps between the panels	Bowing and expansion
	Moisture	Panel joints	Staining
	Air + water	Panel joints	Corrosion
CERAMIC	**Agents**	**Mechanisms**	**Effects**
	Soluble salts	Adjoining parts of the ceramic	Efflorescence
	Design decisions	Air pollution	Gypsum crust
	Moisture	Shading areas	Mold growth, Noxious odors
	Temperature	No gaps between the panels	Cracks, Breakage
	Air + water	Panel joints	Corrosion
	Wind	Air pollution	Discoloration
WOOD COMP.	**Agents**	**Mechanisms**	**Effects**
	Biological agents	Water intake from the cracks	Weight loss of the material
	Wind	Air pollution	Discoloration
	Moisture	Absorption characteristics of wood	Damage
	Light	The color of the panels	UV degradation
ALU MINI UM	**Agents**	**Mechanisms**	**Effects**
	Air + water	Profile properties	Corrosion
	Design decisions	Sun	Color changes
GLASS	**Agents**	**Mechanisms**	**Effects**
	Wind	Design decisions	Breakage
	Birds	Structural problems	Chipping
	Human related	-	Scratches
	Moisture	Application failures	Discoloration

Because of the design decisions, wind cause breakage of the glass panels which are not in a proper location of the facade (Honfi *et al.,* 2014). This may occur on the northeast side of the building because of the dominant wind direction. Birds cause chipping on the edges of the panels arised from the structural problems (Honfi *et al.,* 2014) This may occur on the upper parts of the façade. Vandalism may occur on the lower parts of the building on glass. Cleaning the panels with inappropriate materials may lead to deterioration. Moisture may ruin the mechanical and physical properties of stone and this causes discoloration. Since most of the building gets rain-washed, the glass panels can easily lose their visual aesthetics.

The method presented in this paper was developed as a tool for the prediction of the service life of building components. Deteriorations have been anaylzed by a systematic approach using environmental analysis, visual observations and literature review. It is clearly seen that, deteriorations on the facade of the building will occur in the future (Figure 5).

Acknowledgement

This research has been supported by a PhD class called Performance of Building Elements Under Environmental Effects given by Professor Doctor Hülya Kuş at İstanbul Technical University. I thank her for comments that greatly improved the study.

ORCID

Nil Kokulu: https://orcid.org/0000-0002-7057-7601

References

Agnes, B., Toth, M., Bajnoczi, B. and Szabo, C. (2012). Deterioration of Building Ceramics by Environmental Factors, A case study on Zsolnay Ceramics from the Museum of Applied Arts (Budapest), *Geosciences and Engineering*, 1(2), 7–14.

Campante, E. and Paschoal, J. (2002). Durability of Facades with Ceramic Coverings, *IX International Conference on Durability of Building Materials and Components*, Brisbane, Australia, 60, 1-10.

Goldberg, R.P. (1994). The Effects and Control of Moisture in Ceramic Tile Facades, *III World Congress on Ceramic Tile Quality*, Castellon, Spain, 231-247.

Grelk, B., Christiansen, C., Schouenborg, B., Malaga K., Hoigard, K., Scheffler, M. and Dean, S.W. (2007). Durability of Marble Cladding-A Comprehensive Literature Review, *Journal of ASTM International*, 4(4). doi: 10.1520/JAI100857

Holiday-weather (2018, December). *Antalya, Turkey: Annual Weather Averages*. https://www.holiday-weather.com/antalya/averages/

Honfi, D., Reith, A., Vigh, L.G. and Stocker, G. (2014). Why glass structures fail? - Learning from failures of glass structures, Louter, Bos, Belis & Lebet (Eds), C*hallenging Glass 4 & COST Action TU0905 Final Conference*, London, England, Taylor & Francis Group. doi: 10.1201/b16499-109.

ICOMOS (2019, January). *Illustrated Glossary on Stone Deterioration Patterns, Monuments and Sites*. https://www.icomos.org/publications/monuments_and_sites/15/pdf/Monuments_and_Sites_15_ISCS_Glossary_Stone.pdf

Khanam, Z., Singh V. and Zaidi, M.G.H. (2015). Effect of Environment on Corrosion Behaviour of Aluminium, *International Journal on Environmental Sciences,* 6(2), 281-286.

Kuş, H. (2018). *YAB 615E Performance of Building Elements under Environmental Effects: Agents, Mechanisms and Effects*, PhD class, fall lecture notes.

Marie, I. (2013). Perception Of Darkening of Stone Facades and The Need For Cleaning, *International Journal of Sustainable Built Environment*, 2(1), 65-72. doi: https://doi.org/10.1016/j.ijsbe.2013.09.001.

Mauko, A., Mırtic, B., Mladenovic, A. and Grelk, B. (2006). Deterioration of the Granodiorite Facade, *Materials and Geoenvironment*, 53(1), 23-37.

Morrell, J.J., Stark, N.M., Pendleton, D.E. and McDonald, A.G. (2010). Durability of Wood-Plastic Composites, *10th International Conference on Wood & Biofiber Plastic Composites*, 16(3), 7-10.

Museum Management Program (2018, December), *Museum Handbook Part 1, Appendix P: Curatorial Care of Ceramic, Glass, and Stone Objects*. https://www.nps.gov/museum/publications/MHI/AppendP.pdf

Shaw, B.A. and Kelly, R.G. (2006). *What is Corrosion?*, The Electrochemical Society Interface. Retrieved January 5, 2019 from https://www.electrochem.org/dl/interface/spr/spr06/spr06_p24-26.pdf

Song, S.Y. and Lim, J.H. (2016). Evaluation of Alternatives for Reducing Thermal Bridges in Metal Panel Curtain Wall Systems, *Energy and Buildings*, 127(1), 138–158. doi: https://doi.org/10.1016/j.enbuild.2016.05.078

Sürekli İzleme Merkezi (January 2019). http://www.havaizleme.gov.tr/Services/AirQuality.

XV International Conference on Durability of Building Materials and Components
DBMC 2020, Barcelona
C. Serrat, J.R. Casas and V. Gibert (Eds)

Durability Assessment of GFRP Rebars Exposed to High pH-Seawater

Alvaro Ruiz Emparanza[1], Carlos N. Morales[2], Juan Manuel Palacios[3], Francisco De Caso[4], and Antonio Nanni[5]

[1] University of Miami, College of Engineering, Dept. of Civil Architectural and Environmental Engineering, 1251 Memorial Dr, Coral Gables, FL 33146, alvaro.ruiz@miami.edu

[2] University of Miami, College of Engineering, Dept. of Civil Architectural and Environmental Engineering, 1251 Memorial Dr, Coral Gables, FL 33146, cnm32@miami.edu

[3] University of Miami, College of Engineering, Dept. of Civil Architectural and Environmental Engineering, 1251 Memorial Dr, Coral Gables, FL 33146, jxp1698@miami.edu

[4] University of Miami, College of Engineering, Dept. of Civil Architectural and Environmental Engineering, 1251 Memorial Dr, Coral Gables, FL 33146, fdecaso@miami.edu

[5] University of Miami, College of Engineering, Dept. of Civil Architectural and Environmental Engineering, 1251 Memorial Dr, Coral Gables, FL 33146, nanni@miami.edu

Abstract. *There is a continued process to implement innovative materials to enhance the sustainability and durability of the built infrastructure. Technologies developed over the last two decades have facilitated the use of glass fiber reinforced polymer (GFRP) composites as internal reinforcement bars (rebars) for concrete structures, which have proven to be an alternative to traditional steel reinforcement due to significant advantages, such as magnetic transparency and, most importantly, corrosion resistance, equating to durability and structural life extension. This study evaluates the durability of three different available and most commonly used GFRP rebar types, based on exposure to aggressive environments, such as those experienced in coastal areas. For that, the specimens were expose to high pH seawater solution (that simulates the alkalinity of the concrete exposed to seawater), at 60 ºC for different periods of time: 45, 90, and 180 days. The durability of these GFRP rebars was assessed by testing four different physio-mechanical properties, including: tensile strength, elastic modulus, and transverse and horizontal shear strength. Preliminary results show that the resilience of the GFRP rebars after being exposed to high pH seawater at high temperature, varies considerably among the three different types. The tensile strength was the most affected physio-mechanical property.*

Keywords: *Composites, Durability, GFRP Rebars, Resilience.*

1 Introduction

The use of GFRP bars (Glass Fiber Reinforced Polymer) is gaining importance as internal reinforcement for reinforced concrete (RC) structures, primarily due to the corrosion-resistant properties. One of the most important applications for this alternative reinforcement is its use in coastal RC structures where corrosion of traditional steel rebars is critical (Nolan, Rossini and Nanni, 2018) and poses significant issues for the longevity and cost of the infrastructure. This is especially important in marine environments due to: i) salt water in direct contact with concrete structures, through foundations or by air and ii) the need to increase the infrastructure's future resilience and sustainability to sustain the numerous effects related to climate change, such as the sea level rise. These critical needs may no longer be of concern with the use of

GFRP bars; which are composite reinforcing bars made of glass fibers embedded in a resin matrix and are non-corrosive. Because the driving force for such alternative reinforcement bars is the lifespan extension of RC structures, the durability of GFRP rebars must be carefully evaluated, as these aspects are fundamental for the expansion and extended application of this technology.

Concrete is considered a highly alkaline material, with typical pH values for freshly placed concrete above 12.5 to 13.9 for concrete made with high alkaline cement (Grubb, Jennifer A., *et al.,* 2007). When using steel reinforcement, the high alkalinity of the concrete provides corrosion protection to the steel by providing a passive layer of iron oxide (Fe_2O_3). Throughout the service life of the reinforced concrete structures, different phenomena such as carbonation, ingress of corrosive agents through voids and cracks, etc. lead to the breakdown of this passive layer, favouring the corrosion of steel. With GFRP rebars, however, the high alkalinity of concrete does not have a protective effect as for the steel, but it appears to affects the durability of the rebars in a negative way instead.

In the literature, different studies exist that have proven the deterioration of the tensile properties of GFRP rebars embedded in concrete or subjected to high pH solutions which simulate the alkalinity of the concrete, through accelerated aging protocols (Dejke and Tepfers, 2001; Chen, Davalos and Ray, 2006; Robert, Cousin and Benmokrane, 2009; Robert and Benmokrane, 2013; Wang, X.-L. Zhao, *et al.*, 2017). In addition, Wang *et al.* (2017) evaluated the effect of the simulated seawater and sea sand concrete on the horizontal shear properties of GFRP rebars, while Ruiz Emparanza *et al.* (2018) Yan *et al.* (2017) and Dong *et al.* (2016) assessed the resilience of bond properties of GFRP rebars embedded in concrete and exposed to seawater. Each of these studies are focused on the resilience of a single mechanical property, and to the best knowledge of the author, no research exists that integrates a combined durability assessment of different mechanical characteristics, which would help to have a better understanding of the degradation mechanism affecting GFR bars.

Therefore, this study is comprised by the evaluation of the durability of three different commercially available GFRP rebars exposed to a combination of high pH and seawater, simulating coastal reinforced concrete structures. The rebars were aged for up to 180 days at 60°C to accelerate the degradation process. High temperature is used since it is expected that the rate of reaction will double every 10°C (Pauling 1988). A temperature of 60°C was chosen based on the practices found in the literature (Dejke and Tepfers, 2001; Chen, Davalos and Ray, 2006; Robert, Cousin and Benmokrane, 2009; Robert and Benmokrane, 2013; Wang, X.-L. Zhao, *et al.*, 2017). Four different mechanical properties were tested: tensile strength, modulus of elasticity, transverse shear strength and horizontal shear strength.

2 Experimental Program

Three types of GFRP bars, denoted as A, B and C, were tested for comparison purposes due to diversity of the products in the GFRP rebar market (Ruiz Emparanza, Kampmann and De Caso Y Basalo, 2017). All tested bars in this study had a nominal diameter of 10-mm and were made of continuous EC-R glass fiber and impregnated with a vinyl ester resin. However, the manufacturing process and surface enhancements varied among them: Type-A bars were sand-coated, Type-B were helically wrapped, while Type-C were ribbed (see Figure 1).

Figure 1. GFRP rebars Type A, B and C (from left to right).

The focus of this study was to assess the mechanical performance of three GFRP bar types before and after being aged in simulated seawater concrete pore solution. Four different mechanical properties such as tensile strength, modulus of elasticity and transverse and horizontal shear strength were evaluated. For every property and exposure condition, a minimum of three specimens were tested. Table 1 summarizes the test matrix with the corresponding standardized test method used in this study.

Table 1. Test Matrix for durability assessment.

Rebar type	Temp. °C	Duration Days	Mechanical Property	Test Method
A B C	60	45 90 180	Tensile Strength Modulus of Elasticity	ASTM D7205
			Transverse Shear Strength	ASTM D7617
			Horizontal Shear Strength	ASTM D4475

In addition to the tests run on specimens that were aged at 60 °C for 45, 90 and 180 days as seen in Table 1, three repetitions per mechanical property were tested on non-exposed specimens. These results were used as benchmark to assess the resilience of the mechanical properties after the accelerated aging protocol.

2.1 Simulated Environmental Exposure Condition

The accelerated aging of the GFRP bars specimens was achieved by completely immersing the bars into a to high pH seawater solution at 60 ºC and different exposure times (45, 90 and 180 days). The seawater used was directly taken from Key Biscayne (Florida, USA). The solution was made by dissolving calcium hydroxide, sodium hydroxide and potassium hydroxide in seawater (2 g of $Ca(OH)_2$ + 2.4 g of NaOH + 19.6 g of KOH per liter of seawater). The mass concentrations of the solution were chosen according to Chen et. al 2006 (Chen, Davalos and Ray, 2006). The high alkalinity solution simulates the pore solution of normal concrete with a pH value of about 13.6.

2.3 Specimen Preparation

After each exposure condition, the GFRP rebars were extracted from the solution and prepared for testing according to the corresponding ASTM standards. The preparation of the specimens used to test the transverse shear strength consisted of cutting the rebars to 230 mm specimens while the samples for horizontal shear were cut to a length of 6 times the diameter (60 mm). The preparation of the tensile samples to assess the ultimate tensile strength and modulus of elasticity, was more extensive: after the rebars were cut to length of 1000 mm, protective anchors were installed at both ends of the samples to protect the rebar when being gripped by the loading machine. The anchorage system was accomplished by a 300 mm long steel pipe filled with expansive grout which will reduce lateral stresses during griping, since GFRP rebars are weak in the transverse direction compared to the longitudinal one.

2.3 Testing Procedure

Each of the tests were conducted in accordance with the corresponding ASTM: the test setups are shown in Figure 2.

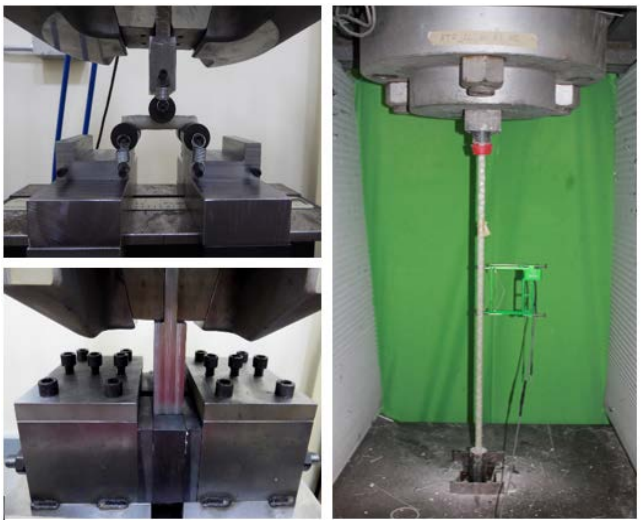

Figure 2. Test setup: horizontal shear test (top left), transverse shear test (bottom left), and tensile test (right).

In this study, all tests were performed by applying displacement-controlled loading using a Baldwin machine with a capacity of 890-kN for the tensile test, and a 133-kN Instron test frame

for transverse and horizontal shear tests. The test rate for the tensile test was 2 mm/min, while for transverse and horizontal shear test specimens were tested at a rate of 1.3 mm/min. As per the corresponding ASTMs (see Table 1), for transverse and horizontal shear tests, the crosshead displacement and the load were recorded. For the tensile tests, in addition to the load, each of the specimens were instrumented with a 100 mm long extensometer to record the strain, which was then used to determine the modulus of elasticity.

3 Results and Discussion

For the three different types of rebars within the scope of this research project, four mechanical properties of unaged and aged specimens were evaluated.

3.2 Unaged Samples

The mechanical properties for 'as-received' GFRP bars used in this study are summarized in Table 2. Mechanical characterization of pristine GFRP bars provided unconditioned values as a reference for residual strength after exposure.

Table 2. Nominal mechanical properties of 10mm diameter reference GFRP bars.

Rebar type	Tensile Strength		E-Modulus		Transverse Shear Strength		Horizontal Shear Strength	
	Avg.	CoV	Avg.	CoV	Avg.	CoV	Avg.	CoV.
	MPa	%	MPa	%	MPa	%	MPa	%
A	953.8	5.5	51570	5.1	212.4	4.8	42.9	7.7
B	834.0	5.5	55340	2.0	194.5	3.3	45.3	5.4
C	982.5	4.3	54570	6.0	211.2	2.6	50.3	5.6

3.2 Aged samples

After being exposed to high pH seawater solution for 45, 90 and 180 days, the aged samples were tested, and the results obtained for each of the four mechanical properties were compared to the benchmark values obtained from the unaged specimens, to obtain the retention over time, as shown in Figure 3 ,4 and 5.

For all the rebar types, the tensile strength was the most affected property with a reduction of up to 41% for Type-A, while the tensile capacity for Type B and C decreased 29% and 20% respectively. Compared to the literature, Chen *et al.* (2006) saw higher degradation (about 70% of degradation after 180 days) when exposing GFRP rebars to the same solution (except they used tab water instead of seawater to mixed with the same proportions of hydroxides).

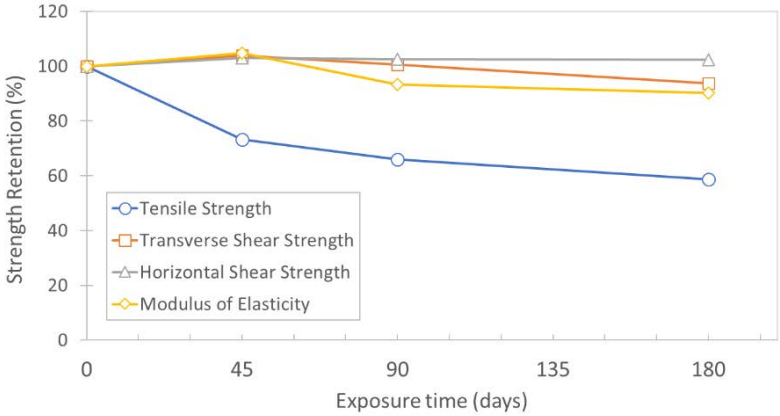

Figure 3. Retention of the tested mechanical properties for Type-A rebars.

This could be due to the lesser development of the GFRP products back in 2006. More recent research conducted by Robert *et al.* (2013) showed a lower reduction (about 10%), but the simulated seawater pore solution had a lower pH (12.15 compared to 13.5 of the current study) and the aging temperature was of 50 °C instead of 60°C.

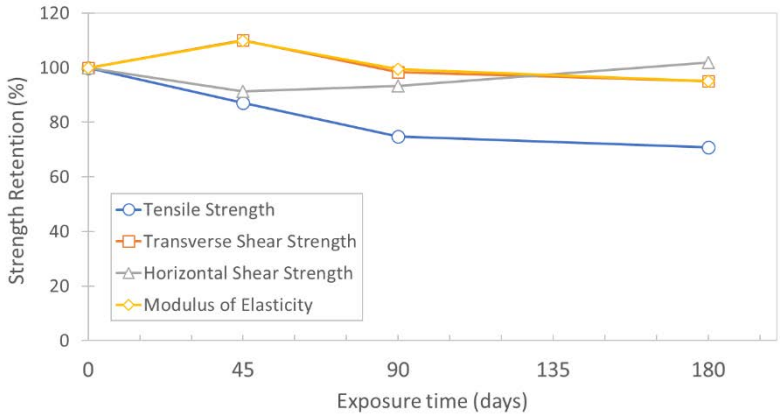

Figure 4. Retention of the tested mechanical properties for Type-B rebars.

The second most affected property was the modulus of elasticity, even if the reduction was relatively low: between 5% and 13%. These values are aligned with the data found in the literature (Robert, Cousin and Benmokrane, 2009; Robert and Benmokrane, 2013), where it was seen that that degradation of the modulus was insignificant compared to the reduction of the maximum tensile capacity. It is believed by the authors that a degradation of the fiber and resin interface takes place with the time, which affects the stress transfer between fibers. This reduction is more noticeable at a critical strain (related to the maximum tensile strength) where the decrease in the stress transfer capacity may lead to the inability to activate all the fibers of the cross section of the rebar which will result in higher strains in those fibers that are being engaged. This will then cause failure of individual fibers at an earlier stage, leading to a premature failure of the rebar. However, since the elastic modulus is not related to individual

or incremental fiber failures but rather to the sum of the elastic strain all along the coupon or rebar gage length, is not that heavily affected.

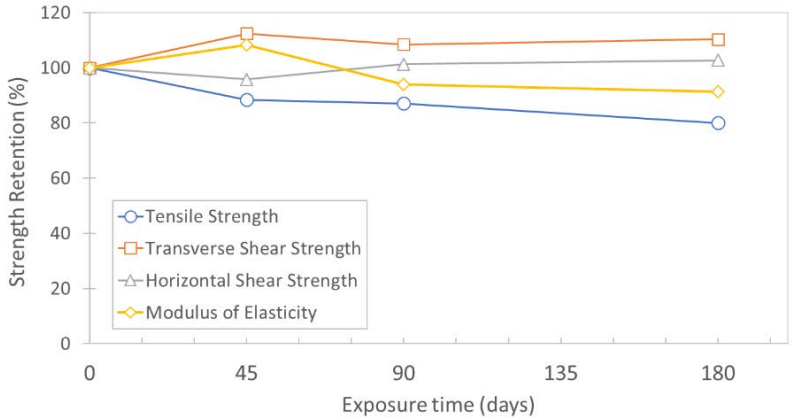

Figure 5. Retention of the tested mechanical properties for Type-C rebars.

Finally, for all the rebar types, the deterioration in terms of transverse and horizontal shear capacity was insignificant. Similar behavior has been reported by Benmokrane *et al.* (2015), in which GFRP bars (vinyl ester resin matrix with E-glass fibers) where exposed to alkaline solution (pH 12.6 – 13.0) and resulted in horizontal and transverse shear strength reduction of 5% and 10%, respectively, after 5,000 h at 60°C. This was also seen by Dejke *et al.* (2001), even though Wang *et al.* (2017) saw a decrease in the horizontal shear capacity after the rebars being aged in a high pH solution. This decrease can be related to the use of different types of rebars, specially to the type of fiber the rebars tested by Wang *et al.* (2017): E-Glass was used instead of E-CR Glass, being this last one the upgraded version of E-Glass, with corrosion resistance features.

4 Conclusions

In this study, the durability of three different GFRP rebar types was assessed after being exposed to a high pH seawater solution at 60 ºC and different exposure times (45, 90 and 180 days). Four different mechanical properties were tested: tensile strength, modulus of elasticity, transverse shear strength and horizontal shear strength. It was seen that the resilience after the accelerated exposure depended on the type of rebar. However, for all of them, the tensile strength was the most affected mechanical property, with a reduction of 20 and 41%, followed by the elastic modulus, which decreased between 5% and 13%. Finally, the horizontal and transverse shear strength capacities were almost unaltered after the aging process. These preliminary results were aligned with the findings reported by other researchers in the literature.

Regarding the significant difference in the reduction between the tensile strength compared to the modulus of elasticity, authors believe that it could be related to the degradation of the fiber and resin interface, which affects the stress transfer between fibers. This reduction is more noticeable at a critical strain (related to the maximum tensile strength) where the decrease in the stress transfer capacity may lead to the inability to activate all the fibers of the cross section of the rebar which will result in higher strains and, therefore, premature failure in those fibers

that are being engaged. But, since the elastic modulus is not related to individual or incremental fiber failures but rather to the sum of the elastic strain all along the coupon or rebar gage length, is not that heavily affected.

However, the authors of the article acknowledge that more data is needed to confirm these preliminary conclusions. Future research activities include the extension of the aging time and addition of extra exposure temperatures. This data will be then used to model the durability and predict the service life. Finally, it needs to be noted that the durability prediction values should be compared to results obtained from existing structures, to calibrate the durability model.

ORCID

Alvaro Ruiz Emparanza: https://orcid.org/0000-0001-9781-5107
Carlos N. Morales: https://orcid.org/0000-0003-4279-6839
Antonio Nanni: https://orcid.org/0000-0003-2678-9268
Francisco De Caso: https://orcid.org/0000-0001-5585-7819

References

Chen, Y., Davalos, J. F. and Ray, I. (2006). 'Durability prediction for GFRP reinforcing bars using short-term data of accelerated aging tests', *Journal of Composites for Construction*. American Society of Civil Engineers, 10(4), pp. 279–286.

Dejke, V. and Tepfers, R. (2001). 'Durability and service life prediction of GFRP for concrete reinforcement', in *Proc., 5th Int. Conf. on Fiber-Reinforced Plastics for Reinforced Concrete Structures (FRPRCS-5)*. Thomas Telford London, pp. 505–516.

Dong, Z. *et al.* (2016). 'Bond durability of BFRP bars embedded in concrete under seawater conditions and the long-term bond strength prediction', *Materials and Design*, 92, pp. 552–562. doi: 10.1016/j.matdes.2015.12.066.

Nolan, S., Rossini, M. and Nanni, A. (2018). 'Seawalls, SEACON and Sustainability in the Sunshine State', in *Transportation Research Board 97th Annual Meeting. Washington, DC.*, pp. 123–129. doi: 10.1039/b908937c.

Robert, M. and Benmokrane, B. (2013). 'Combined effects of saline solution and moist concrete on long-term durability of GFRP reinforcing bars', *Construction and Building Materials*, 38. doi: 10.1016/j.conbuildmat.2012.08.021.

Robert, M., Cousin, P. and Benmokrane, B. (2009). 'Durability of GFRP reinforcing bars embedded in moist concrete', *Journal of Composites for Construction*. American Society of Civil Engineers, 13(2), pp. 66–73.

Ruiz Emparanza, A. *et al.* (2018) 'Evaluation of the Bond-To-Concrete Properties of GFRP Rebars in Marine Environments', *Infrastructures*, 3(4), p. 44.

Ruiz Emparanza, A., Kampmann, R. and De Caso Y Basalo, F. (2017). 'State-of-the-Practice of Global Manufacturing of FRP Rebar and Specifications', in *ACI Fall Convention*. Anaheim, CA.

Wang, Z. and Zhao, X. L., *et al.* (2017). 'Durability study on interlaminar shear behaviour of basalt-, glass- and carbon-fibre reinforced polymer (B/G/CFRP) bars in seawater sea sand concrete environment', *Construction and Building Materials*, 156, pp. 985–1004. doi: 10.1016/j.conbuildmat.2017.09.045.

Pauling, L. C. (1988). General Chemistry. Dover Publications.

Wang, Z. and Zhao, X.-L., *et al.* (2017). 'Long-term durability of basalt-and glass-fibre reinforced polymer (BFRP/GFRP) bars in seawater and sea sand concrete environment', *Construction and Building Materials*. Elsevier, 139, pp. 467–489.

Yan, F. and Lin, Z. (2017). 'Bond durability assessment and long-term degradation prediction for GFRP bars to fiber-reinforced concrete under saline solutions', *Composite Structures*. Elsevier, 161, pp. 393–406.

Grubb, J. A.; Limaye, H. S.; and Kakade, A. M., "Testing pH of Concrete," *Concrete International*, V. 29, No. 4, Apr. 2007, pp. 78-83.

Benmokrane, B., Elgabbas, F., Ahmed, E. and Cousin, P. (2015). Characterization and Comparative Durability Study of Glass/Vinylester, Basalt/Vinylester, and Basalt/Epoxy FRP Bars. Journal Of Composites For Construction, 19(6), 04015008/1-04015008/12.

XV International Conference on Durability of Building Materials and Components
DBMC 2020, Barcelona
C. Serrat, J.R. Casas and V. Gibert (Eds)

Durability Assessment of Gypsum Boards with Glass Mat Reinforcement Used in Light Facade Systems

Mauricio M. Resende[1], Douglas C. Meirelles[2], Gustavo R. Boriolo[3] and Luciana A. Oliveira[4]

[1] Institute of Technological Research of State of São Paulo – IPT, Building Technological Center – CETAC, and São Judas University, mresende@ipt.br

[2] Saint-Gobain Brasil, douglas.meirelles@saint-gobain.com

[3] Saint-Gobain Research Brasil, gustavo.boriolo@saint-gobain.com

[4] Institute of Technological Research of State of São Paulo – IPT, Building Technological Center – CETAC, luciana@ipt.br

Abstract: *Gypsum boards with glass mat reinforcement are used in light weight facade systems. These boards were recently brought to the Brazilian market. Therefore, there are few studies and little practical knowledge of their performance over time, mainly concerning to durability. The gypsum boards manufacturers set that these boards always need to be coated, however they can be exposed to natural conditions during the construction site period. A study is necessary to evaluate the feasibility of using these boards in Brazil, since the exposure conditions relating to humidity, temperature and solar radiation are different from Europe and North America. The aim of this paper is to show the approach used to evaluate the durability of the gypsum board with glass mat reinforcement, and also show the test results. In order to establish the durability approach, standards were adopted, as well as the functional performance concept. In addition, the tests considered that such boards would be used on the facade and should behave similarly to other boards used in facades in Brazil, such as fiber cement boards. Thus, mechanical tests were done in steady state, saturated and after aging in cycles of immersion, drying and heating. Other evaluations were made on gypsum boards applied on exposed walls. The results showed that even the board strength decreases after the accelerated aging cycles, the final value remains in an acceptable level. In addition, boards applied on exposed walls for 12 months have been presenting a good performance; meaning no cracks neither detachments, even though the follow-up still needs to be maintained longer.*

Keywords: *Gypsum Boards with Glass Mat Reinforcement, Durability, Performance, Aging.*

1 Introduction

Gypsum boards with glass mat reinforcement[1] were recently brought to the Brazilian market and it has been used in light weight facade systems[2]. There are no Brazilian standards concerning these boards, however, there are American and also European standards (ASTM C1177, 2017 and EN 15283-1, 2009) and some publications relating to moisture resistance

[1] Gypsum boards with mat reinforcement are composed of set gypsum plaster core reinforced with inorganic fibers which are arranged in a woven or non-woven mat to form flat rectangular boards. Admixtures, fillers and fibers dispersed in the core may also be present (definition of EN 15283-1, 2009).

[2] Site of construction products in Brazil, available in<https://www.aecweb.com.br/emp/p/usg-brasil_34433_1>

(CMHC, 2007; Randall *et al*., 2016). Although, these standards and publications, there are few studies and little practical knowledge of the performance of these boards over time in Brazil, mainly concerning to durability requirements. Singh and Garg (1992) have defined the durability of glass reinforced gypsum composite by assessing its behavior in water, in natural weathering exposition and after wetting and drying aging cycles.

The use of glass mat gypsum boards in external facades is recommended only as a substrate to a coating system – whether a Direct Applied Finish System (DAFS) or an External Insulated Finish System (EIFS). Glass mat board manufacturers set that these boards cannot stay apparent, meaning no coating, during their entire service life. However, they may be exposed to natural conditions during the construction site period during one year at most.
The boards are used as a component of a facade system. Once assembled in facades, they must contribute to ensure the design life (DL) of the complete system. This is an actual discussion in Brazil, mostly because of the residential building performance standard, ABNT NBR 15.575-1 (2013), set a minimum DL of 40 years for façade systems of residential buildings.

A study is necessary to evaluate the feasibility of using these boards in Brazil, because of the design life requirement set on NBR 15575 and because of the exposure conditions relating to relative humidity, temperature and solar radiation are different among Europe, North America and Brazil. For example the average temperature in South East Brazil is around 23°C and 76% of relative humidity, with an average solar radiation of 18 MJ/(m2.dia) (Tiba, 2000, Inmet site – available in < http://www.inmet.gov.br/portal/>.

In this context, the aim of this paper is to show the approach settled to evaluate the durability of the gypsum board with glass mat reinforcement for use in facades of multi-story building in Brazil, and also show the tests results. Therefore, this study is related to the durability assessment of the glass mat product (board), does not considering the whole facade system.

2 Research Method

The durability approach settled here is according to ISO 15686-2 (2012) concepts: a) definition of user needs, material requirements and characterization; b) preparation – identifications of aging agents, mechanisms and effects, choice of performance characteristics and evaluation techniques; c) exposure and evaluation – short-term exposure (accelerated exposure) and long-term exposure (field exposure); and analyzing and interpretation. The table 1 shows the durability approach developed to this study based on the authors experience and knowledge.

Table 1. Durability approach developed to this study, based on ISO 15686-2 (2001) concepts.

Stage	Descriptions/ Definitions	Reference
Definitions		
User needs	The intention is to use this gypsum board in facades of multi-story building in Brazil façades in Brazil	Principles set to this work
Performance requirements relating to gypsum board durability	Strength reversability Moisture resistance	CMHC (2007); Randall *et al*. (2016) and Singh and Garg (1992)
Material characterization	Density, water absorption, dimensional changes due to moisture and bending strength	Characteristic from ASTM C1177 (2017), EN 15283-1(2009) and NBR 15498
Preparations		
Identification of aging agents	Water, solar radiation, hot temperature	Adapted of ISO 19208 (2016)
Mechanisms and effects	Water is the main agent of plaster degradation due to the solubility of the gypsum. By the action of wet-dry cycles of the environment, the gypsum dissolves and precipitates continuously, but the attached crystals are deposited on the surface and do not have the same imbrication of the first formation.	John, V.; Cincotto, M.A. (2017)
c) exposure and evaluation – short-term exposure (accelerated exposure) and long-term exposure (field exposure);	All characteristics were evaluated before and after stress by immersion in water associated to differents temperatures (Figure1)	Proposal of this paper. The most tests were carried out considering the NBR 15498

The tests (characteristics evaluation before and after short term exposure) were designed considering that gypsum boards with glass mat reinforcement will be used on the facade and should behave similarly to other boards applied in facades in Brazil, such as fiber cement boards, even they will be coated after at maximum one year (Figure 1)**.** Then, mechanical tests were done in steady state, saturated and after aging (cycles of immersion in water and drying), since the water is the most important aging agent for these boards (Figure 1).

In additional, a field exposure is carrying on since four gypsum boards were assembled on exposed walls it has been twelve months. These walls are in São Paulo city, West region, placed directed to North.

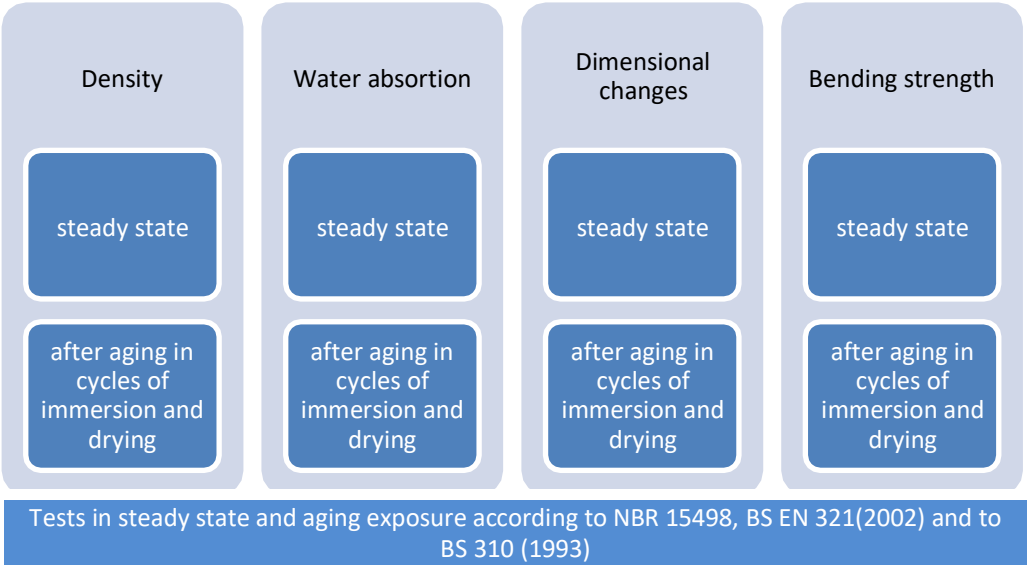

Figure 1. Tests of gypsum boards under stress condition.

The test in normal condition, steady state, means keeping the samples for three days to (20±2) º C and (50±5) % of relative humidity. Two kinds of short aging exposure were carried on: one adopting the fiber cement standard (ABNT NBR 15498, 2016) and the other adopting the OSB board standard (BS EN 321, 2001).

The aging test specified by ABNT NBR 15498 (2016) consists of subjecting the samples to 50 aging cycles. Each cycle consists of the following steps: immersion in water at 20°C for 18 hours and exposure at 60°C for 6 hours. The aging test specified by BS EN 321 (2002) consists of subjecting the samples to 3 aging cycles. Each cycle consists of the following steps: immersion in water at 20°C for 72 hours, then exposure at -12°C for 24 hours and finally exposure at 70°C for 72 hours. At the end of the aging cycles, the samples were conditioned at 20°C and 65% relative humidity until they reached constant mass (equilibrium condition). In the state condition, it determined the flexural tensile strength and the modulus of elasticity of aged and non-aged samples according to BS EN 310 (1993).

3 Results and Discussion

3.1 Density

According to NBR 15498 (2016) samples of gypsum boards were measured and weighed; the average results can be seen in Table .

Table 2. Gypsum boards with glass mat reinforcement densities.

Steady state	After aging in cycles of immersion and drying [(1)]	Difference between normal and aging conditions
798,6 ± 6,30 g	784,13 ± 19,45 g	14,47g (1,81%)
[(1)] aging exposure according to NBR 15498		

3.2 Water Absorption

Moisture content was calculated, according to NBR 15498, using 250x100 mm samples for gypsum board, which are the same sizes of the bending test samples. The results shown in Table 3 are the average of 10 samples at 21ºC and 65% RH.

Table 3. Moisture content of Gypsum boards with glass mat reinforcement (average result).

Steady state	After aging in cycles of immersion and drying (1)	Difference between normal and aging conditions
(36,6 ± 0,95) %	(55,5 ± 3,4)%	18,9%
(1) aging exposure according to NBR 15498		

In additional, the moisture content tested according to EN 15283-1 (standard for Gypsum boards with fibrous reinforcement), is around 4%, which means these boards is Type H1, with reduced water absorption rate.

3.3 Dimensional Changes

The dimensional changes relating to width and length were tested using 250x100 mm samples for gypsum board, which are the same sizes of the bending test samples. The results shown in Table are the average of 10 samples.

Table 4. Dimensional change in width and length.

	Steady state	After aging in cycles of immersion and drying (1)	Difference between steady and aging conditions
width	1,15 %	1,23%	0,08%
length	0,26%	0,18%	0,08%
(1) aging exposure according to NBR 15498			

3.4 Bending Strength after Immersion and Dry

The bending strength according to NBR 15498 (2016) was tested using 250x100 mm samples for gypsum board. The results shown in Table 5 are the average of 10 samples.

3.5 Bending Strength and Modulus after Immersion, Freezing and Heating

The bending strength and modulus of gypsum board was tested using 250mmx50 mm according to BS EN 310 (1993), in steady conditions and after short aging exposure, that was based on BS EN 321 (wood board) as showed in Table 6.

Table 5. Bending strength results before and after short term exposure.

Requirements	Steady state	Saturated condition – immersion in water for 24hours	Steady state, after aging in cycles of immersion and drying**	Satured condition, after aging in cycles of immersion and drying
Bending strength Longitudinal direction (MPa)*	7,9 ± 0,5	4,7 ± 0,4	5,9 ± 0,2	2,6 ± 0,2
Bending strength Transversal direction (MPa)*	6,0 ± 0,8	4,3± 0,5	4,5 ± 0,6	2,2 ± 0,2

* the samples were removed from the gypsum board considering longitudinal and transversal direction

** at the end of the aging cycles, the samples were conditioned at 20°C and 65% relative humidity until they reached constant mass (equilibrium condition).

Table 6. Average results obtained from the characterization of gypsum board according to BS EN 321.

Requirements*	Steady state	Steady state, after aging in cycles of immersion freezing and heating **	Variation (%)
Bending strength (MPa)	7,11 ± 1,26	6,03 ± 0,9	-18%
Modulus of elasticity (GPa)	2,65 ± 0,3	2,02 ± 0,4	-19%
* the samples were removed from the gypsum board only considering the longitudinal direction			
** at the end of the aging cycles, the samples were conditioned at 20°C and 65% relative humidity until they reached constant mass (equilibrium condition).			

The variation between the results of the physical characteristics of gypsum board mat reinforcement in steady state and after aging exposure were under 20%; density was almost zero, water absorption was around 18% and dimensional changes were around 0,08%. Relating to bending strength, the results in the saturated state were greater than 50% of the results in the steady state. The ratio of bending strength in the transversal by the longitudinal direction was greater than 70%, both in the steady and saturated state. These bending strength results meet the NBR 15498 specifications. Once considering a severe condition, the bending strength in saturated state after aging was 50% of the bending strength of the saturated boards in steady state. Relating to the exposure to wetting / freezing / heating cycles by BS EN 321, it can be seen from the analysis of Table 4 that both the bending strength and the modulus of elasticity after the aging cycles presented values above 80% of the initial values.

3.6 Long-Term Exposure (Field Exposure)

Gypsum boards mat reinforcement were installed in two walls structured by steel frame, forming a wall of 2400 mm wide x 2400 mm length. After 12 months of exposure, no significant occurrences (no cracks neither detachments or wraps) were found on the boards.

4 Conclusions

This paper shows an approach to evaluate the durability of gypsum boards mat reinforcement used in the facade, considering water as the main aging agent, since the board may have contact with rainwater and solubilize the plaster. Then, tests were made to evaluate the physical and mechanical characteristics of these boards under normal condition (steady state) and after aging, cycles of immersion in water and drying. It was assumed that glass mat gypsum boards should behave similarly to other facade sheets, such as fiber cement and wood boards. For this reason, it was adopted the aging exposure methods indicated in both standards.

Concluding, the tests results show that the difference between physical characteristics before and after aging is less than 20%. Regarding to the mechanical characteristics, the bending strength losses after aging were on average less than 50%. However, after conditioning under normal conditions there is a resistance return, the strength after aging, at steady state, is similar to the resistance in the initial saturated state (table 5). Concerning the natural exposure, the boards have been providing good results, even though the follow-up still needs to be maintained longer.

ORCID

Maurício Marques Resende: https://orcid.org/0000-0001-6496-0762 Douglas Meirelles: https://orcid.org/0000-0001-5203-0365 Gustavo Boriolo: https://orcid.org/0000-0001-5201-2191
Luciana Oliveira: http://orcid.org/0000-0001-6772-3252

References

ABNT. (2016). *NBR 15498 (Placa de fibrocimento sem amianto - Requisitos e métodos de ensaos).* Associação Brasileira de Normas Técncias, Brasil.

ABNT. (2013). *NBR 15575-1 (Edificações Haitacionais - Desempenho - Parte 1: Requisitos Gerais)*. Associação Brasileira de Normas Técncias, Brasil.

ABNT. (2013). *NBR 15575-4 (Edificações Haitacionais - Desempenho - Parte 4:Requisitos para os sistemas de vedações verticais internas e externas – SVVIE).* Associação Brasileira de Normas Técncias, Brasil.

ASTM. (2017). *ASTM C1177 (Standard Specification for Glass Mat Gypsum Substrate for Use as Sheating).* American Standard Tecnhical Materials, USA.

BSI. (1993a). *BS EN 310 (Wood-based panels - Determination of modulus of elasticity in bending and of bending strength).* British Standards Institution, UK.

BSI. (2002b). *BS EN 321 (Wood-based panels - Determination of moisture resistance under cyclic test conditions).* British Standards Institution, UK.

Canada Mortgage and Housing Corporation – CMHC (2007). Technical Series 07-100. Relationship Between Moisture Content and Mechanical Properties of Gypsum Sheathing. Montreal.

CEN. (2009). *BS EN 15283-1 (Gypsum boardas with fibrous reinforcement - Definitions, requirements and test methods - Part 1: Gypsum boards with mat reiforcement).* Comité Européen de Normalisation, UK.

ISO. (2016). *ISO 15686-2 (Buildings and constructer assets - Service life planning - Part 2: Service lefe prediction procedures). International Standard Organization.*

ISO. (2016). *ISO 19208 (Framework for specifying performance in buildings). International Standard Organization.*

John, V. and Cincotto, M.A. (2017). Gesso para construção Civil. In: Isaia, G. Materiais de Construção Civil e princípios de ciência e engenharia dos materiais. 3ª edição. São Paulo: Ibracon, Capítulo 23. ISBN: 978-85-98576-27-5.

Randall, B.G., Barber,W. and Goodman, T. (2016). *Use of Glass Mat Gypsum Sheathing as a Substrate for Exterior Insulation and Finish Systems (EIFS).* ASTM Symposium on Exterior Insulation and Finish Systems (EIFS): Performance, Progress, and Innovation. ASTM - STP 1585. Available online at www.astm.org / doi: 10.1520/STP158520140110.

Singh, M. and Garg, M. (1992). Glass fibre reinforced water-resistant gypsum-based composites. *Cement & Concrete Composites, 14*, 23-32.

Tiba, C. *et. al.* (2000). Atlas Solarimétrico do Brasil : banco de dados solarimétricos / coordenador Recife : Ed. Universitária da UFPE, 111.

XV International Conference on Durability of Building Materials and Components
DBMC 2020, Barcelona
C. Serrat, J.R. Casas and V. Gibert (Eds)

Durability of FRP Immersed in Water. Changes in Mechanical Properties

Ernest Bernat-Maso[1], Manuel J. Lis[2], Luis E. Mercedes[3] and Lluís Gil[4]

[1] Serra Húnter Fellow. Department of Strength of Materials and Engineering Structures, Universitat Politècnica de Catalunya-BarcelonaTECH, ESEIAAT, 08222-Terrassa, Spain, ernest.bernat@upc.edu

[2] Department of Chemical Engineering, Universitat Politècnica de Catalunya-BarcelonaTECH, ESEIAAT, 08222-Terrassa, Spain, manuel-jose.lis@upc.edu

[3] Department of Strength of Materials and Engineering Structures, Universitat Politècnica de Catalunya-BarcelonaTECH, ESEIAAT, 08222-Terrassa, Spain, luis.enrique.mercedes@upc.edu

[4] Department of Strength of Materials and Engineering Structures, Universitat Politècnica de Catalunya-BarcelonaTECH, ESEIAAT, 08222-Terrassa, Spain, lluis.gil@upc.edu

Abstract. *Fibre Reinforced Polymers (FRP) have been widely used to strengthened construction structural elements in the last years because of their mechanical pros. However, the durability of these materials is always controversial. In particular, the effect of long-term contact with water on the mechanical properties of FRPs is studied in this research throughout the implementation of accelerated degradation tests. Samples of Carbon FRP and Glass FRP were immersed into supply water, water with salts and surfactants and highly chlorinated water. In all cases, electrical current passing through the samples was also imposed. Tensile tests on pristine and degraded samples were carried out to determine the influence of these aggressive environments on the tensile strength and the Young's modulus of the specimens. Finally, superficial (ATR) FT-IR analyses were conducted to assess possible chemical changes in the samples surfaces. Results indicated that the chemical composition of used resins was not modified due to the water exposure. No hydrolysis process took place during testing time on the surface. However, mechanical properties were reduced, especially when samples were exposed to plain supply water, which may be related to the physical degradation caused by moisture intake by diffusion.*

Keywords: *Composites, Hydrolysis, Mechanical Properties, Accelerated Degradation, Waste Water.*

1 Introduction

Fibre Reinforced Polymers have been commonly used to strengthen existing building structures in the last years. Their significant stiffness, outstanding strength and low weight make FRP an interesting building material for retrofitting, rehabilitation or strengthening concrete or masonry structures. In addition, one of the main advantages pointed out by FRP suppliers is its corrosion resistance in wet environments, although this statement is not always proved.

In fact, FRP durability have been a controversial topic from the very beginning because of the organic nature of the matrix where fibers are embedded into. In this line, several researches may be found in the literature.

Some researchers investigated the durability of FRP components. In this line, carbon fiber has been proved to be resistant to acid and alkali environments and it can only be oxidized by strong oxidants (Zhu and Hu, 2017). In contrast, glass fiber is known to degrade in presence of water, especially in alkaline environments (Bank, Gentry, and Barkatt, 1995), where greater alkalinity is directly correlated with faster rate of glass fiber erosion. The strength of glass fiber

is permanently reduced after soaking in water because of the chemical reaction of glass fiber and water (Zhu and Hu, 2017). This fact is increased by alkalinity. Regarding corrosion, glass fiber can be affected by hydrofluoric acid but it shows a good corrosion resistance.

According to (Department of Defense USA, 2002) epoxy shows good chemical resistance but its mechanical properties are clearly reduced in the presence of moisture because it is composed by a large number of polar OH groups that facilitate attractive interaction with polar molecules like water (Panda and Mamta, 2010). Polyester durability mostly depend on their typology. Hence, orthophthalic polyester is far more affected by water presence than isophthalic polyester. According to Shaoru Zhu *et al.* (Zhu and Hu, 2017), the chemical medium can penetrate into the polymer, react with it and cause the polymer to swell. This process can produce salts, hydrolysis, saponification, sulfonation, oxidation or nitrification, which causes the breaking of the main valence bond. In general, resins have a significant cross-linking degree that brings resistance to medium corrosion. Hence, controlling curing degree is essential and it is mainly related to the hydrolytic activation energy of its hydrolyzed groups in the corresponding acid-base medium. Thus, corrosion resistance of the matrix highly depends on the curing/hardening agent.

Regarding the durability of the FRP composite material, it is stated (Cromwell, Harries, and Shahrooz, 2011; Karbhari *et al*., 2003) that hydrothermal effects are dominant. Water or moisture absorbed by the FRP matrix can result in physical changes to the matrix (including plasticization and a reduction in glass transition temperature) which result in a breakdown of the resin matrix that makes it possible further affectation of fiber and matrix-fiber interface. According with (Karbhari *et al.*, 2003), moisture diffuses into all organic polymers, leading to changes in thermophysical, mechanical, and chemical characteristics. Additionally, the primary effect of the absorption is on the resin itself through hydrolysis, plasticization, saponification, and other mechanisms, which cause both reversible and irreversible changes in the polymer structure.

Several absorption studies, like (Sun and Li, 2011) proved that the diffusive and capillary processes were the main ways composites absorb moisture. The existence of water molecules in the FRP can weak the performance of interface between the fiber and matrix. This effect can reduce the shear performance of the FRP and cause the progression of delamination between layers.

Beside moisture, chemical attack (*e.g.* acid and alkali solutions) also contributes to degradation of FRP by accelerating the hydrolysis process (Karbhari *et al.*, 2003; Liu, He, and Xiong, 2017). It is demonstrated that the tensile strength of FRP composites immersed in acid and alkali solutions decreases faster than those immersed in distilled water (Liu *et al*., 2017). Additionally, scanning electron microscope (SEM) analysis shows that immersion in alkali solution causes degradation of the fiber-matrix interface and that degradation leads to significant reduction in the tensile properties of basalt and glass FRP composites. Moreover, ingress of alkaline media into fiber can cause surface pitting, hydroxylation, hydrolysis and leaching that not only affect the integrity of fiber but also expose fiber to further degradation. This was especially observed for glass fiber composites because the reaction between glass fibers and alkali substances led to increase water uptake (Sun and Li, 2011). Similar response was observed for acidic media (Liu *et al.*, 2017). According to the wet-dry cycles test results, degradation of aramid and basalt FRP sheets in sulfate and chloride solutions were more significant than in alkali and acid solutions because sulfate and chloride solution promoted

crystallization, which accelerated the degradation. Carbon and aramid FRPs were more stable although. In contrast, glass FRPs were susceptible to moisture extracting ions from glass fiber showing lower chemical resistance.

Two processes are observed when a FRP is exposed into an aggressive media: physical adsorption of the medium caused by swelling and resulting in the destruction of the resin structure; and chemical effect on the bonds of resin molecules resulting in a performance decrease (Zhu and Hu, 2017). It is also stated that the chemical attack involves specific chemical reaction of the polymer with the fluid in the case of polyesters. In this case, the most common failure mode is the hydrolysis by water, acids and alkalis. Esters, and carbonate groups are particularly susceptible to this hydrolysis process (Bagherpour, 2012).

Hydrolysis is a reaction that involves the breaking of a bond in a molecule using water. Molecule polarity promotes moisture sensitivity. Therefore, using hardening or catalytic systems which provide a less polar molecular structure are preferred to avoid water absorption and reduce hydrolysis problems (Ellis, 1993).

Regarding the effect of saline environment, it was proved (Bank *et al.*, 1995) that the rate of strength degradation of aramid/epoxy composites in saline solution was less than that in distilled water. This behavior was justified because the presence of "massive" salt molecules slowed down the absorption rate of water, resulting in a slower rate of hydrolysis process. This fact was also proved by (d'Almeida, 1991).

Regarding the effect of chlorinated environment, it is known that chlorinated water is normally more corrosive than distilled water because of the higher conductivity and the penetrating power of the chloride ion through surface films on metals. The rate of corrosion is controlled by the chloride content, oxygen availability, and the temperature. However, the effect of the presence of chlorides is not specifically investigated for FRPs.

Regarding the effect of degradation of the mechanical properties, tensile strength of FRPs is more affected than elastic modulus because of environmental exposure, as stated by (Cromwell *et al.*, 2011).

As a conclusion of the literature review, it is stated that chemical and physical affectations are possible on FRPs exposed to aggressive media, mostly involving resin matrix. Studying the particular effects of salts and surfactants rich water and highly chlorinated water is necessary for the application of these materials on water treatment plants.

2 Materials and Methods

Two types of FRPs were produced and tested: glass fiber and polyester resin FRP (GFRP) and carbon fiber and epoxy resin FRP (CFRP). Tensile tests were performed on unaltered samples, samples immersed in supply water, samples immersed in water with salts and surfactants representing increased aggressivity of waste water and water highly chlorinated to represent a long term effect of chloride in supply water.

2.1 Materials

The used glass fiber was E-Glass Chopped Strand Mat with no orientation and a density of 225g/m^2. Filaments of the fibers were covered by silane to enhance chemical compatibility with polyester resins. The used carbon fiber was unidirectional 300g/m^2 0.165mm thickness fiber.

The polyester was an unsaturated resin of orthophthalic type and standard glycols, dissolved

in styrene (acts as hardener). The catalyst was methylethylketone peroxide. Epoxy resin was a combination of formaldehyde (polymer with 2-(chloromethyl)oxirane and phenol) and bisphenol A epichlorohydrin polymer. As hardener for the epoxy resin, a mixture of Isophoronediamine and Trimethylolpropane was used.

2.2 Sample Production

FRPs were manually laminated on a glass plate previously prepared with unmolding agents. Four layers of carbon fiber and seven layers of glass fiber were respectively used. Over each fiber layer the corresponding resin was manually applied with a brush (see Figure 1 (a)) at a ratio of 50% fiber and 50% resin. Finally, perforated release film and non-woven breather felt were placed below weight application tools to absorb excessive resin during curing process.

Resulting CFRP plate was 1mm thickness whereas GFRP plate was 4mm thickness. These plates were manually cut to the desired dimensions of 12.5mm x 200mm in the case of CFRP and 25.0mm x 200mm in the case of GFRP. Twelve specimens of each FRP type were obtained. These were divided in four groups of three samples. Each group was subjected to a different media type (unaltered specimens, supply water, waste water and chlorinated water) before tensile testing.

2.3 Degradation Method

Artificial concentrated wastewater containing 100g of urea, 50g of detergent powder (25% of sodium carbonate, 10% of sodium percarbonate, 10% of benzensulfonic acid, 3% of no ionic surfactant, 3% of silicic acid), 35g of NaCl per 1L of supply water was produced according with typical compounds found in wastewater as by (Garcia, 1985). Artificially highly chlorinated water was produced by adding 35g of NaCl per liter of supply water. Additionally, three samples of each FRP were also immersed into supply water for comparison with artificial concentrated wastewater and highly chlorinated water.

All immersed samples were subjected to an imposed electrical current according with (International Standardisation Organisation, 2017) which corresponded to 2.4mA for CFRP samples and 20mA for GFRP samples. Immersion lasted two weeks. Surface of GFRP specimens showed different coloring depending on the treatment as presented in Figure 1(b).

(a) (b)

Figure 1. (a) CFRP production and (b) GFRP specimens state before tensile tests; from left to right supply water, wastewater, chlorinated water and untreated.

2.4 Tensile Testing

Before performing tensile tests samples were prepared to avoid local stress concentration failure mode. This was achieved by covering the endings of the samples by two thin aluminum sheets bonded to both sides of the sample with epoxy resin. These sheets avoided clamp indentation on the sample during tensile test.

Tensile tests were performed with an electromechanical press at a constant displacement rate of 2mm/min, acquiring force and displacement at 50Hz until tensile failure.

2.5 ATR FTIR Testing

Samples were subjected to Fourier-transform infrared spectroscopy analysis (FTIR) after tensile test. This test was conducted to observe if there were changes of chemical bonds on the specimens after being treated by supply water, waste water or chlorinated water. Attenuated total reflection (ATR) technique was used because it is able to examine directly the sample without further preparation but obtaining only the chemical characteristics of the surface of the sample. The FTIR spectrometer used in this study was FTIR-8300.

3 Results

Quantitative results from the tensile tests and qualitative observations of the FTIR analysis are summarized in this section.

3.1 Tensile Strength

The tensile strength (f_t) of each sample was calculated assuming a uniform stress distribution on the cross section, so dividing the maximum applied force by the cross area of the specimen. All specimens broke by material tensile failure so no sliding respect clamps neither local stress effects were observed. Tensile strength results are summarized in Table 1.

Table 1. Results of the tensile tests.

	Supply water		***Wastewater***		***Chlorinated water***		***Untreated***	
	f_t (MPa)	*E (MPa)*	*f_t (MPa)*	*E (MPa)*	*f_t (MPa)*	*E (MPa)*	*f_t (MPa)*	*E (MPa)*
CFRP	1108	34364	1294	30556	1331	26912	1311	25967
	921	31561	1246	34375	1020	24359	1495	30351
	1049	28378	1413	28399	1246	27616	1033	26257
GFRP	139.3	3333	143.0	3590	150.1	4043	164.2	3613
	149.1	3784	115.7	2881	138.7	2765	159.9	3711
	157.4	3824	160.0	3243	155.8	3522	147.4	3120

3.2 Elastic Modulus

Elastic modulus (E) was calculated as the slope of the linear part of the stress-strain curve, which was set between 20MPa and 100MPa for GFRP and between 100MPa and 600MPa for CFRP. Strain was calculated as the measured axial displacement divided by the total length of the sample. Results are summarized in Table 1.

3.3 FTIR Analysis

Representative FTIR analysis results are showed Figure 2. The analyses have to be performed by qualitative comparison of the presence/absence of particular peaks in the specific ranges of the corresponding compounds. Hydroxyl groups, which are related with hydrolysis processes, are supposed to appear around 3500 cm^{1} (red line in Figure 2).

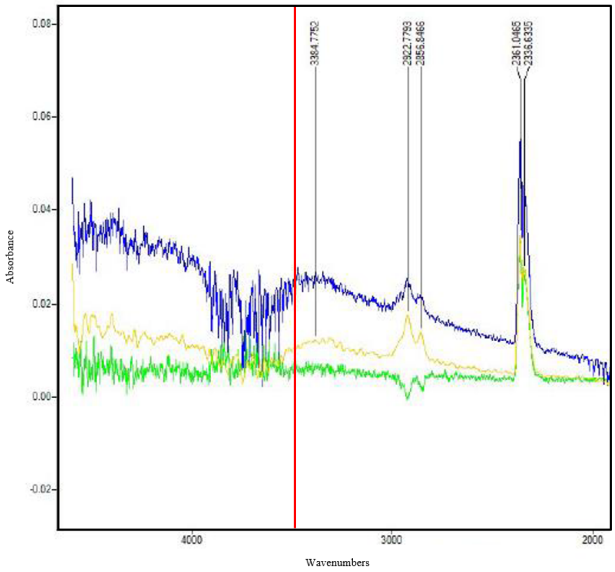

Figure 2. Effect of waste water and supply water on CFRP (left). Yellow for untreated, blue for waste water and green for supply water treated specimens.

4 Discussion

Regarding quantitative results about tensile strength and elastic modulus it is observed that immersing GFRP with an electrical current causes the decrease of the tensile strength in all cases. This strength reduction is equivalent for specimens immersed into supply water and into chlorinated water (-5.5% and -5.7% respectively), so adding NaCl makes no apparent effect on the tensile strength reduction of GFRP. Immersing GFRP in wastewater brought the higher tensile strength reduction (-11.2%). It is also associated with the most significant reduction of the elastic modulus (-7.0%) whereas immersion of GFRP in chlorinated water has no effect (-1.1%) on this parameter and immersion in supply water showed an increase (+4.8%).

In relation with CFRP specimens, the greater reduction of the tensile strength (-19.8%) is observed for specimens immersed in supply water. Treatment in chlorinated water also causes a decrease of this parameter (-6.3%) whereas immersion into wastewater showed an apparent increase (+3.0%) of the tensile strength. Elastic modulus of CFRP is increased when immersing it into supply water (+14.2%) or wastewater (+13%) with no significant difference among them. However, it is reduced when immersed in chlorinated water (-4.5%).

Looking at the results on the whole, it may be stated that chlorinated water caused the reduction of tensile strength and elastic modulus for both FRPs. Wastewater causes the reduction of mechanical properties of GFRP but increases the ones of CFRP. Finally, exposure to supply water reduces the tensile strength but increase the elastic modulus.

Incorporating the results of the ATR-FTIR analysis, it is noted that no hydrolysis happened because hypothetically resulting hydroxyl group was not detected in any case. The corresponding peak (3500cm^{-1}, red line in plot of Figure 2 as example) were not qualitatively observed in any case. Results of CFRP may indicate the physical resin adsorption of the medium, which caused the swelling of polymer, also induced by the electrical field. This adsorption is restrained by the presence of massive ions like salts and surfactants at the sample surface. In this line, surfactants are really likely to move on to the exposed sample surface. In addition, the imposed electrical current would have polarized the specimen surface, changing the properties of the solid-liquid interface and making it easier for the salt ions to adhere on to this surface. The combination of electrical polarization, so promoting ions adhesion to the surface, and superficial attachment of surfactants explained the lower water adsorption, so the lower reduction or even increase of the tensile strength for CFRP immersed in chlorinated and wastewater, respectively. The same tendency should be valid for glass fiber. In fact, surfactants were detected in resin surface of GFRP specimens. However, in the case of GFRP another process plays an important role in the opposite direction: glass fiber is sensitive to alkaline environments and higher alkalinity of wastewater may explain the greater degradation of the specimens immersed in this media because of fiber degradation. Supply water and chlorinated water showed similar tensile strength reduction because of the sensitivity of glass fiber to the moisture, which had greater effect than water adsorption restrain for chlorinated water.

Finally, inclusion of water molecules into resin structure of the matrix may explain the apparent increase of the elastic modulus, which is more evident for the cases in which water molecules adsorption was not limited, so for specimens immersed in supply water. Similar effect was observed for CFRP into wastewater but, in contrast, glass fibers really degraded in this alkaline media so a reduction of elastic modulus of GFRP was observed. Finally, variation of the elastic modulus of specimens immersed in chlorinated medium was not significant, reaching a balance between stiffening because of hypothetic adsorption of water molecules and degradation of material for both FRPs.

5 Conclusions

Combining mechanical analysis and chemical ATR FTIR analysis makes it possible to understand the underlying causes of the observed changes in the mechanical properties of FRPs immersed in aggressive water environments. The following conclusions are obtained:

- Exposure to supply water reduces the tensile strength and increases the elastic modulus of GFRP and CFRP. In contrast, exposure to chlorinated water causes the reduction of both parameters, whereas wastewater causes the reduction of mechanical properties of GFRP but increases the ones of CFRP.
- Water adsorption causes the swelling of the polymer, which is accelerated by the polarization induced by the electrical field, reducing the tensile strength.
- Media with massive ions or surfactants that tend to adhere resin surface, even more under an imposed electrical field, showed lower water adsorption by the matrix, so less degradation of the tensile strength results.
- Inclusion of water molecules into resin structure may result in a stiffer response of FRPs although further research is required to confirm this point.

As practical conclusion, plain water is showed to be the most aggressive media for the matrix

resin and a real problem to be faced for improving FRPs durability.

Acknowledgements

Authors want to acknowledge the support of AZVI S.A. company through the development of research project COMPOSITO funded by CDTI Spanish Government Agency. Authors also want to acknowledge the laboratory support of Nur Hasanah binti Mat Rais and Muhamad Arif bin Wahid. First author is a Serra-Húnter Fellow.

ORCID

Ernest Bernat-Maso: http://orcid.org/0000-0002-7080-0957
Manuel J. Lis: http://orcid.org/0000-0002-2026-085X
Luís E. Mercedes: http://orcid.org/0000-0003-2520-8599
Lluís Gil: http://orcid.org/0000-0002-2007-4846

References

Bagherpour, S. (2012). Fibre Reinforced Polyester Composites. In *Polyester*. InTech. https://doi.org/10.5772/48697

Bank, L. C., Gentry, T. R. and Barkatt, A. (1995). Accelerated Test Methods to Determine the Long-Term Behavior of FRP Composite Structures: Environmental Effects. *Journal of Reinforced Plastics and Composites*, *14*(6), 559–587. https://doi.org/10.1177/073168449501400602

Cromwell, J. R., Harries, K. A. and Shahrooz, B. M. (2011). Environmental durability of externally bonded FRP materials intended for repair of concrete structures. *Construction and Building Materials*. https://doi.org/10.1016/j.conbuildmat.2010.11.096

d'Almeida, J. R. M. (1991). Effects of distilled water and saline solution on the interlaminar shear strength of an aramid/epoxy composite. *Composites*. https://doi.org/10.1016/0010-4361(91)90203-S

Department of Defense USA. (2002). *Composite materials handbook*. (Materials Science Corporation, Ed.) (Vol. 2). Fort Washington.

Ellis, B. (Ed.). (1993). *Chemistry and Technology of Epoxy Resins*. Dordrecht: Springer Netherlands. https://doi.org/10.1007/978-94-011-2932-9

Garcia, E. (1985). Aguas Residuales: Composicion. *Aguas Residuales. Composición*, 22. Retrieved from http://cidta.usal.es/cursos/EDAR/modulos/Edar/unidades/LIBROS/logo/pdf/Aguas_Residuales_composicion.pdf

International Standardisation Organisation. (2017). ISO 11130:2017. Corrosion of metals and alloys — Alternate immersion test in salt solution. ISO.

Karbhari, V. M., Chin, J. W., Hunston, D., Benmokrane, B., Juska, T., Morgan, R., … Reynaud, D. (2003). Durability Gap Analysis for Fiber-Reinforced Polymer Composites in Civil Infrastructure. *Journal of Composites for Construction*, *7*(3), 238–247. https://doi.org/10.1061/(ASCE)1090-0268(2003)7:3(238)

Liu, F. T., He, G. H. and Xiong, J. H. (2017). Experimental study on durability of FRP sheets under wet-dry cycles in various solutions. *Procedia Engineering*, *210*, 61–70. https://doi.org/10.1016/j.proeng.2017.11.049

Panda, G. and Mamta, K. (2010). *Damage and degradation study of FRP composite*. National Institute of Technology, Rourkela.

Sun, B. and Li, Y. (2011). Effects of chemical environment on the durability performances of glass fiber/epoxy composites. *ICCM International Conferences on Composite Materials*.

Zhu, S. and Hu, F. (2017). Experimental study on durability of FRP tendon under acid - Base erosion in civil engineering. *Chemical Engineering Transactions*, *59*, 397–402. https://doi.org/10.3303/CET1759067

XV International Conference on Durability of Building Materials and Components
DBMC 2020, Barcelona
C. Serrat, J.R. Casas and V. Gibert (Eds)

Durability Studies of Polyurethane-Based Structural Adhesives Used in Engineered Wood Products in New Zealand

Catherine L. Nicholson

BRANZ Ltd, 1222 Moonshine Road, RD1, Porirua, 5381, New Zealand,
catherine.nicholson@branz.co.nz

Abstract. *The New Zealand Building Code is unique in the world in requiring evidence of a minimum durability of 50 years for all structural building elements. This prescriptive durability requirement equally applies to the adhesives used in structural applications such as engineered wood products (EWPs), including glulam, CLT and LVL. Conventional resorcinol-based structural adhesives have a long history of use in New Zealand, providing evidence of their ability to meet stringent durability requirements. Structural adhesives based on polyurethanes (PURs) are used extensively in other parts of the world and are rapidly gaining increasing interest in New Zealand due to their perceived environmental and production advantages. However, without a sufficiently long history of use, and a lack of data around their performance in the preservative treated pine EWPs typically manufactured in New Zealand, it is difficult to provide evidence of long-term durability for PURs in our domestic building industry. In this work, attenuated total reflectance Fourier transform infrared (ATR FTIR) spectroscopy in conjunction with multi-component analysis (chemometrics) was used to understand the changes that accelerated ageing cause in the chemistry of five PUR-based adhesives. The effect of hygrothermal stress was investigated through exposure of samples to accelerated ageing cycles of varying temperatures and humidities for up to 3 years' duration. Different samples were affected to different extents by each cycle. Spectroscopic data were also used to build predictive models which have the potential to be used in long-term durability assessment. Spectroscopic investigation in conjunction with mechanical testing offers the opportunity to provide a robust, fit-for-purpose test methodology for assessing the long-term durability of PUR-based structural adhesives.*

Keywords: *Adhesives, Durability, Degradation, Spectroscopy, Chemometrics.*

1 Introduction

The inclusion of a materials durability clause within New Zealand's performance-based Building Code (NZBC) is unique in the world. This clause requires all building elements to demonstrate durability for a minimum specified time (NZ Government, 2014). In the case of structural building elements, the durability requirement is 50 years.

Structural adhesives are a critical component of engineered wood products (EWPs) including glulam, laminated veneer lumber (LVL) and cross-laminated timber (CLT). EWPs manufactured in New Zealand are predominantly produced using pine (*Pinus radiata*) that has been preservative treated. Chromated copper arsenate (CCA) is widely used as a timber treatment, with micronised copper azole (MCA) being a newer alternative on the market.

Traditional formaldehyde, phenolic or resorcinol-based adhesives have a long history of use in New Zealand and are known to perform well over many decades. Polyurethane (PUR) adhesives, widely used throughout Europe and North America (Lehringer *et al.*, 2014), are attracting increasing interest from EWP manufacturers in New Zealand. However, without a

sufficiently long history of use or long-term durability data available for its performance to be evaluated in products manufactured using preservative treated pine, it is difficult to demonstrate that structural building elements containing PUR adhesives will meet the minimum 50-year durability clause. There is, therefore, a continuing need for the development of standard test methods for the service life prediction of materials for specific applications such as these (Lee *et al.*, 2008; Marston *et al*., 2011). Accelerated ageing is commonly used in these tests.

This paper describes results from a research study investigating the long-term durability of PUR-based structural adhesives. The ultimate aim of this work is to develop standard test methods which can be used for the long-term durability evaluation of products containing PUR adhesives. To achieve this, two concurrent workstreams are being undertaken. The first aims to enhance our fundamental understanding of PUR materials chemistry by subjecting adhesive films to various environmental conditions and monitoring structural changes over time. The second aims to investigate the performance of the adhesive bondline in laboratory-fabricated EWP samples through conventional mechanical testing. This dual aproach has been successfully employed by other researchers (Ren *et al*., 2013), who found that the complementary advantages of both methods enhanced an overall understanding of structure – durability relationships in polyurethane adhesives used for timber bonding.

The focus of this paper is on the work that has been carried out on the PUR adhesive films. The effects of three accelerated weathering cycles of varying temperatures and humidities for up to 3 years' duration are reported for five commercially available PUR adhesives. The results are an extension of the preliminary work carried out on the same adhesives described by Nicholson *et al*. (2017) using attenuated total reflectance Fourier transform infrared (ATR FTIR) spectroscopy and chemometrics.

FTIR spectroscopy has been widely used in the analysis of construction materials (Shaw *et al*., 2016; Pellizzi *et al*., 2014; Zhang *et al*., 2013; Mitchell *et al.*, 2013; Jelle *et al.*, 2012) and polyurethanes (Bockel *et al*., 2018; Clerc, *et al*., 2017; Ren *et al*., 2013; Sterley *et al*., 2012). It is a rapid, non-destructive analytical technique which can also be used for *in situ* testing. Chemical changes in the structure of the PUR adhesive due to ageing and accelerated weathering can be monitored to predict likely degradation mechanisms, durability characteristics and expected service life.

The accelerated ageing cycles were chosen based on the likelihood that PURs would be subjected to hygrothermal stress under in-service conditions. It is known that under conditions of elevated temperature and moisture, the constituent polyol and urethane chemical entities may be hydrolysed (Dubelley *et al.*, 2018). The susceptibility to and extent of degradation of individual PURs is highly dependant on composition. Photolysis induced by UV exposure is also an important factor to consider. Photolysis results are not presented here because the adhesive films used in this study were not formulated to withstand UV exposure and were severely degraded within only days or weeks of accelerated and outdoor ageing respectively.

In the preceeding work (Nicholson *et al*., 2017), structural changes in the adhesives exposed to accelerated ageing had been monitored over a very limited timeframe. A main conclusion was that much longer ageing times were required to build a better picture of degradation mechanisms and structural changes in order to understand the durability implications of these changes. The results reported here describe the effects of longer exposure times on the samples. The additional data now provide better insight into degradation mechanisms and have also enabled predictive models to be developed for durability evaluation.

2 Materials and Methods

2.1 PUR Adhesive Samples

Five commercially available PUR-based adhesives were selected to undergo accelerated ageing tests. Adhesives were cast onto wooden sticks and pressed flat to minimise the effect of foaming during curing. All samples were allowed to cure for at least the minimum time recommended by the manufacturer under normal laboratory conditions (approximately 22°C, 55% RH) before undergoing testing. Control samples were stored in a constant climate laboratory at 20°C and 50% RH.

2.2 ATR FTIR Spectroscopy and Chemometrics

ATR FTIR spectroscopy was performed with an Agilent Technologies 4300 instrument. Spectra were collected using MicroLab PC software and a diamond ATR sampling interface over the spectral range 650-4000 cm^{-1}. A background of 16 scans was recorded before each spectrum of 64 scans with a resolution of 4 cm^{-1} was acquired. Spectra were analysed and predictive models developed using GRAMS IQ (version 9.1) software. Table 1 shows the spectral regions of interest relevant to the PUR structure. Partial least squares calibration and cross-validation was used to assess the validity of the predictive models.

Table 1. Spectral band assignments for regions relevant to PUR structure in FTIR spectra (modified from Delpech *et al*., 2012).

Wavenumber (cm^{-1})	Band assignment	Vibrational mode
800-400	N-H	Bend
1075	C-O (urethane & ether)	Stretch
1250-1240	C-O-C (ether) N-H C-N	Assymetric stretch Bend Stretch
1374	C-H (methyl)	Symmetrical bend
1450	C-N-H (urea)	C-N stretch N-H symmetrical bend
1560-1530	C-N-H (urethane)	C-N stretch N-H symmetrical bend
1715-1630	C=O (urethane & urea)	Stretch
2250-2275	O=C=N (free isocyanate)	Stretch
2970-2850	C-H (methyl & methylene)	Stretch
3335-3320	N-H (urethane & urea)	Stretch

2.3 Exposure Cycles for Accelerated Ageing Tests

The adhesive samples were exposed to a range of temperature and humidity conditions (Table 2). A complete Cycle A was 1 day in length, a complete Cycle B was 1 week in length and Cycle C represented constant exposure to elevated temperature and humidity. Controls were sampled at the same time intervals as the exposed samples.

Table 2. Description of exposure cycle conditions for accelerated ageing tests.

Cycle A	Cycle B	Cycle C
6 hours @ 30°C, 95% RH 6 hours @ 60°C, 75% RH 6 hours @ 10°C, 50% RH 6 hours @ -10°C	5 days @ 70°C, 90% RH 1 day @ -20°C 1 day @ 80°C, < 15% RH	Constant 65°C, 100% RH

3 Results

All five adhesives had broadly similar composition as determined by ATR FTIR (Fig. 1).

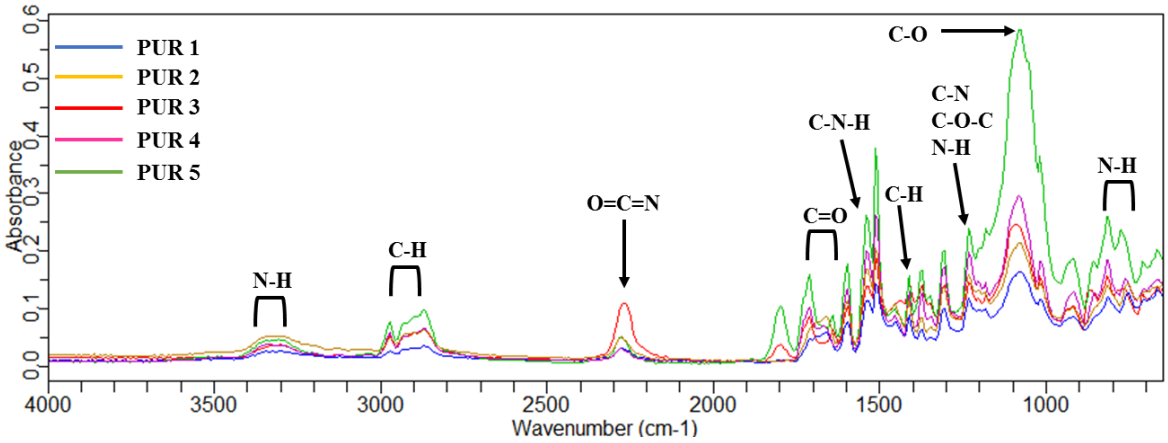

Figure 1. ATR FTIR spectra of freshly cured adhesive samples.

The adhesives were affected by the three exposure cycles in different ways. In general, PUR 1 and PUR 2 exhibited little discernible difference between the control and aged specimens. This is illustrated in Fig. 2 which shows sample PUR 1 after exposure to Cycle C for 3 years. Considerable colour changes were observed for both PUR 1 and PUR 2. Originally both cream, they turned light yellow during Cycle A, orange / brown during Cycle B and dark brown during Cycle C. Control samples did not change colour.

Structural changes were clearly evident in the FTIR spectra of PUR 3 during Cycles B and C but minimal changes were apparent during Cycle A when compared with controls. These differences were observed throughout multiple regions of interest. Fig. 3 shows sample PUR 3 after exposure to Cycle C for 3 years. Colour changes were also observed for these specimens. Originally beige, as ageing progressed they remained beige during Cycle A, turned white and powdery during Cycle B and became chocolate brown during Cycle C. Control samples did not change colour.

PUR 4 and PUR 5 behaved in a similar manner to each other. Some differences were observed in spectra when compared with the controls during all three exposure cycles. This is illustrated in Fig. 4 which shows PUR 5 after exposure to Cycle A for 18 months. Both PUR 4 and PUR 5 darkened significantly in colour during ageing in Cycles B and C but not Cycle A.

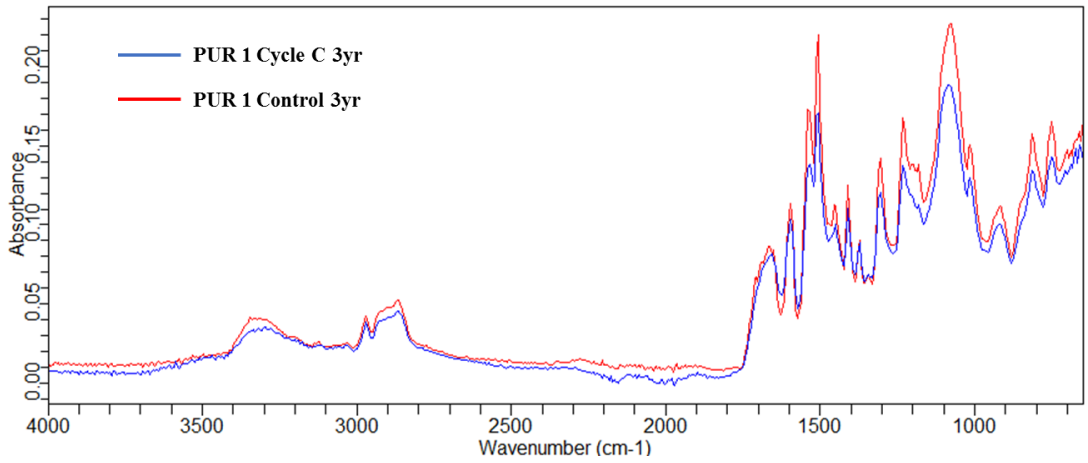

Figure 2. ATR FTIR spectra of sample PUR 1 and control after 3 years of exposure to Cycle C.

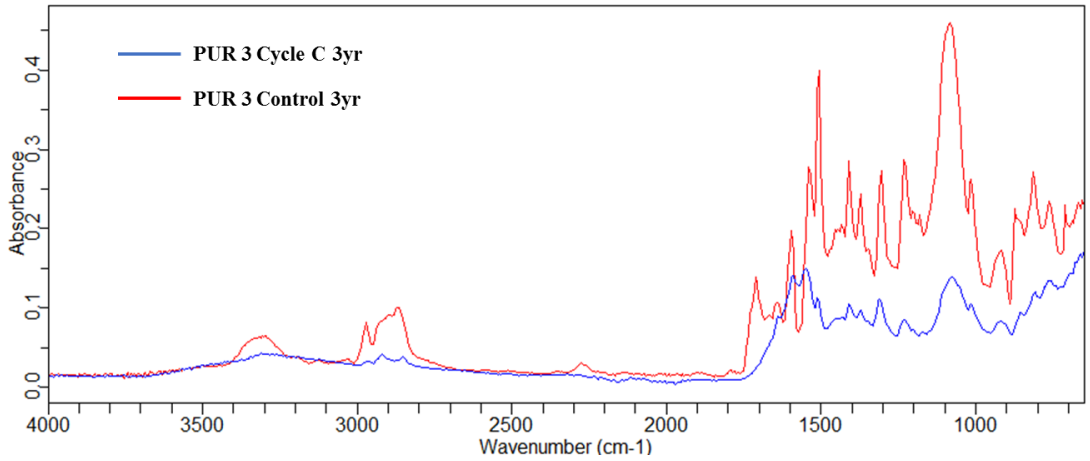

Figure 3. ATR FTIR spectra of sample PUR 3 and control after 3 years of exposure to Cycle C.

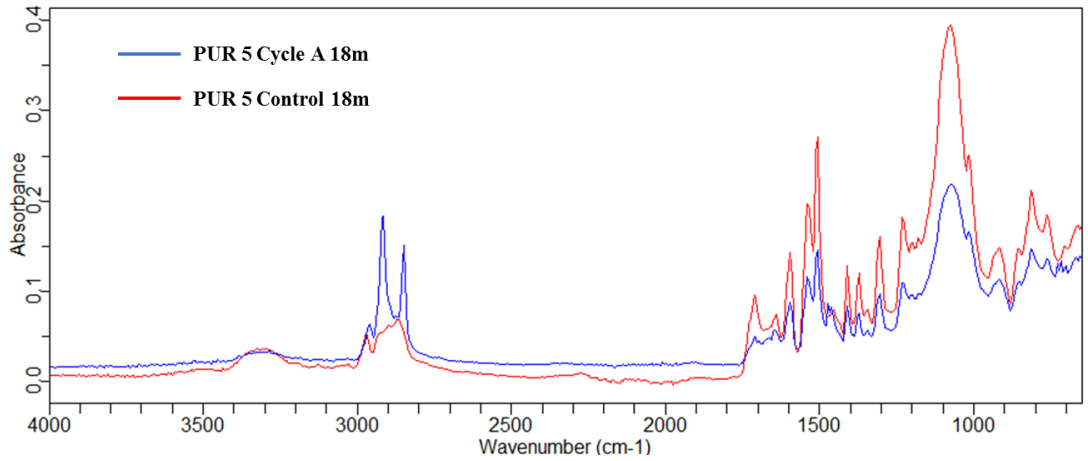

Figure 4. ATR FTIR spectra of sample PUR 5 and control after 18 months of exposure to Cycle A.

Validation results for predictive models of each adhesive sample and accelerated ageing condition were variable. Fig. 5 shows the cross-validation plot for the predictive model using PUR 1 subjected to Cycle C for up to 3 years. This had a coefficient of determination (R^2) of 0.91.

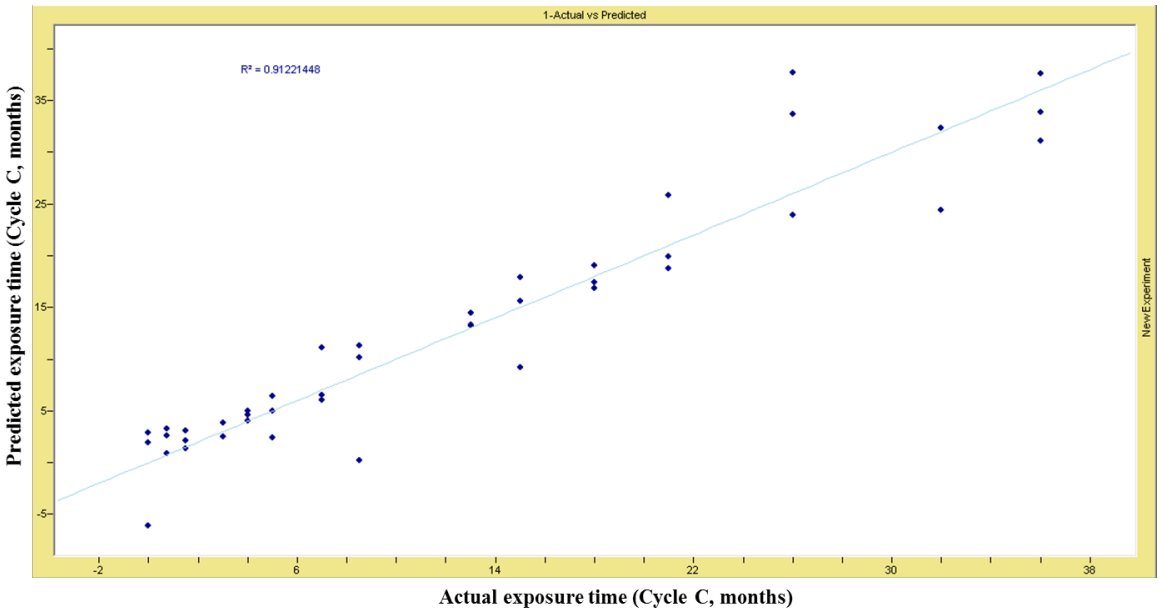

Figure 5. Cross-validation plot for the predictive model based on PUR 1 subjected to Cycle C (R^2 = 0.91).

4 Discussion

Although the five PUR adhesive samples had similar compositions, differences in spectra between control and aged samples were observed during accelerated ageing. These differences ranged from subtle to pronounced but indicate that structural changes have occurred.

PUR 1 and PUR 2 exhibited no obvious structural changes during any of the three ageing cycles (Fig. 2). The only difference noted was the reduction in intensity and eventual disappearance of the peak at around 2275 cm^{-1} (Fig. 1). This is associated with free isocyanate and its disappearance would be expected as the adhesive cured. This is confirmed by the control sample which exhibited identical behaviour. On the basis of the spectroscopy data, these samples both appear to be highly resistant to hydrolysis. However, colour changes were noted, suggesting some structural changes that were not immediately apparent by spectroscopy.

In contrast, PUR 3 showed evidence of significant hydrolytic degradation during cycles B and C (Fig. 3). There was an overall reduction in peak intensity compared with the control, and complete loss of structure in the region 1000 – 650 cm^{-1} associated with N-H bonds and over 3400 – 1800 cm^{-1}, also associated with N-H as well as C-H bonds (Table 1). Pronounced reduction in the peak at 1538 cm^{-1} asociated with C-N-H bonding is indicative of loss of the urethane structure and accounts for the observed discolouration of the samples. The disappearance of the peaks between 1750 - 1650 cm^{-1} further supports degradation of the urethane structure, being associated with the C=O bonds in urethane.

PUR 4 and PUR 5 showed evidence of some subtle structural changes around 1700 cm^{-1} associated with the C=O and C-N-H bonds in urethane and more obvious changes between 3000 – 2800 cm^{-1} associated with C-H bonding.

While the three exposure cycles were designed to be severe, they are not extreme relative to the New Zealand climate. Conditions experienced by building materials may well reach or even exceed 70ºC and 80% humidity in the north of the North Island in summer and drop to -20ºC in the south and central South Island in winter. However, it is the continuous nature of exposure under these conditions which would not be expected in-service.

It is clear that PURs cannot be treated as a generic class of adhesives that will behave identically. The wide range of PUR adhesive formulations available, and the apparent differences in resistance to hygrothermal degradation highlighted in this work, likely precludes development of a single generic test to predict the long-term durability of a given adhesive. It is more likely that new PUR adhesives will need to be tested individually to assess performance. However, the results from this work suggest that a relatively simple accelerated ageing test based on Cycle C, i.e. performed at elevated temperature and humidity over a period of several months, would give an indication of the durability of a PUR adhesive to hygrothermal stress.

The cross-validation plot for the predictive model based on PUR 1 subjected to Cycle C (Fig. 5) suggests that it may be possible to incorporate such a model into an assessment methodology for long-term adhesive durability prediction. This model will be tested using laboratory-fabricated EWP samples which are undergoing natural outdoor ageing. This will provide a measure of the reliability of the correlation that can be expected between natural weathering and accelerated ageing. Successful development of predictive models and correlation of PUR film data with mechanical testing of wood-PUR composites would assist with building a more complete picture of long-term durability.

5 Conclusions

The properties of a PUR-based adhesive, including its likely durability, are strongly related to its composition and structure. Even apparently similar PURs can exhibit pronounced differences in behaviour when subjected to hygrothermal stress. In addition, the same adhesive did not always exhibit the same structural changes when subjected to different ageing cycles. This suggests that a generic durability test for all PUR-based structural adhesives is unlikely to be feasible.

Spectral changes indicative of structural degradation had a relatively early onset within weeks or a few months of exposure to the test cycle. A simple set up consisting of sustained high temperature and humidity could be considered as a rapid screening test for new or unknown PUR adhesives.

While spectroscopy alone cannot determine long-term durability, this technique can contribute important chemical information and complement other more conventional mechanical testing methodologies. Development of predictive models may further enhance its value. A combined spectroscopic and mechanical testing approach offers the opportunity to develop a robust, fit-for-purpose test methodology for assessing the durability and expected service life of PUR-based structural adhesives used in New Zealand-manufactured EWPs.

Acknowledgements

This research is supported by the Building Research Levy.

ORCID

Catherine Nicholson: https://orcid.org/0000-0002-3541-5957

References

Bockel, S., Mayer, I., Konnerth, J., Niemz, P., Swaboda, C., Beyer, M., Harlimg, S., Weiland, G., Bieri, N. and Pichelin, F. (2018). Influence of wood extractives on two-component polyurethane adhesive for structural hardwood bonding. *The Journal of Adhesion*, *94*(10), 829-845.

Clerc, G., Brulisauer, M., Affilter, S., Volkmer, T., Pichelin, F. and Niemz, P. (2017). Characterization of the ageing process of one-component polyurethane moisture curing wood adhesive. *International Journal of Adhesion and Adhesives, 72*, 130-138.

Delpech, M.C. and Miranda, G.G. (2012). Waterborne polyurethanes: influence of chain extender in FTIR spectra profiles. *Central European Journal of Engineering, 2*(2), 231-238.

Dubelley, F., Bas, C., Planes, E., Pons, E., Yrieix, B. and Flandin, L. (2018). Durability of polymer metal multilayer: focus on the adhesive chemical degradation. *Frontiers in Chemistry, 6*, Article 459. doi: 10.3389/fchem.2018.00459.

Jelle, B.P., Nilsen, T.-N., Hovde, P.J. and Gustavsen, A. (2012). Accelerated climate ageing of building materials and their characterization by Fourier transform infrared radiation analysis, *Journal of Building Physics, 36,* 99-112.

Lehringer, C. and Gabriel, J. (2014). Review of recent research activities on one-component PUR-adhesives for engineered wood products. In: *Materials and Joints in Timber Structures*, RILEM Bookseries 9, 405-420.

Lee, N.P., Bennett, J.M., Jones, M.S., Kear, G. and Marston, N.J. (2008). A durability assessment tool for the New Zealand Building Code. In *Proceedings of the XI International Conference on Durability of Building Materials and Components,* Istanbul, Turkey.

Marston, N.J., Jones, M.S., and Vohora, S.R. A residual service life assessment tool for New Zealand. (2011). In *Proceedings of the XII International Conference on Durability of Building Materials and Components*, Oporto, Portugal.

Mitchell, G., France, F., Nordon, A., Tang, P.L. and Gibson, L.T. (2013). Assessment of historical polymers using attenuated total reflectance-Fourier transform infra-red spectroscopy with principal component analysis. *Heritage Science, 1*, 28.

Nicholson, C.L., Shaw, P. and Marston, N. (2017). Preliminary investigation of the durability of structural adhesives using FTIR spectroscopy and chemometrics. In *Proceedings of the XIV International Conference on Durability of Building Materials and Components,* Ghent, Belgium.

NZ Government, Ministry of Business, Innovation and Employment. (2014). *Acceptable solutions and verification methods for New Zealand Building Code Clause B2 Durability*. 2nd edition, amendment 8.

Pellizzi, E., Lattuati-Derieux, A., Lavedrine, B. and Cheradame, H. (2014). Degradation of polyurethane ester foam artifacts: chemical properties, mechanical properties and comparison between accelerated and natural degradation. *Polymer Degradation and Stability, 107*, 255-261.

Ren, D. and Frazier, C.E. (2013). Structure/durability relationships in polyurethane wood adhesives: neat films or wood/polyurethane composite specimens? *International Journal of Adhesion and Adhesives, 45*, 77-83.

Ren, D. and Frazier, C.E. (2013). Structure-property behavior of moisture-cure polyurethane wood adhesives: influence of hard segment content. *International Journal of Adhesion and Adhesives, 45*, 118-124.

Shaw, P. and Martson, N. Reliable durability prediction of polymeric materials. (2016). *Chemistry in New Zealand*, *80*, 137-142.

Sterley, M., Trey, S., Lundevall, A. and Olsson, S. (2012). Influence of cure conditions on the properties of a one-component moisture-cured polyurethane adhesive in the context of green gluing of wood. *Journal of Applied Polymer Science, 126,* E296-E303.

Zhang, Y., Maxted, J., Barber, A., Lowe, C. and Smith, R. (2013). The durability of clear polyurethane coil coatings studied by FTIR peak fitting. *Polymer Degradation and Stability, 98*, 527-534.

XV International Conference on Durability of Building Materials and Components
DBMC 2020, Barcelona
C. Serrat, J.R. Casas and V. Gibert (Eds)

Effect of Carbonation in Mortars with Different Types of Metakaolin and Curing Procedures

Helena Carasek, Mônica E. Jungblut, Paulo M. Passos and Oswaldo Cascudo

PPG-GECON, Universidade Federal de Goiás-UFG, Av. Universitária, nº 1488, 74605-220-Goiânia, Brazil, hcarasek@ufg.br; monicaengel.j@hotmail.com; paulompengc@gmail.com and ocascudo@ufg.br

Abstract. *This study aimed to evaluate the influence of different types of metakaolin and curing conditions on mortars depth of carbonation. To do so, prismatic mortar specimens were produced by using three different 1:2 mix proportions (binder: sand): a reference mix proportion (without mineral addition) and two mixes with partial replacement of the cement by metakaolin, in the content of 10% by mass of cement. Two types of metakaolin with different characteristics were used in order to verify their capacity of changing the mortar microstructure and the pore solution, modifying this way the carbonation behavior of these materials. Three curing conditions for the test specimens were defined: no wet curing and wet curing (by immersion in water) for 3, 9 and 28 days. After the accelerated carbonation procedure in a CO_2 chamber (in an atmosphere of 10% of CO_2), with a relative humidity of 70% and a temperature of 20°C, for a period of 7 days, the carbonation depth was measured by using pH-indicators based on phenolphthalein and thymolphthalein. The results indicated influence of the type of curing in the carbonated depth and the significant interaction between curing and the type of metakaolin. When wet curing was not performed, the carbonation was more intense in the reference mortar. The effect of curing in the mortars with metakaolin was much less significant compared to that in the reference mortar. A global discussion about carbonation behavior of metakaolin modified mortars will be performed, based on the characteristics of the metakaolins.*

Keywords: *Carbonation, Durability, Metakaolin, Curing Procedures, Mortar.*

1 Introduction

The durability of structures fits into an important context for building performance, as well as sustainability and economy.

Among the phenomena responsible for the deterioration of reinforced concrete, there is the reinforcement steel corrosion due to carbonation or chloride attack. This pathological manifestation causes the most damage due to the technical difficulty of long-term recovery and to the cost involved (Castro *et al.*, 2008). Carbonation is a natural phenomenon that occurs by the chemical reaction between carbon dioxide, presents in the atmosphere, with cement hydration products, thus reducing the concrete pH. As a result of the phenomenon, the depassivation of reinforcement steel occurs, facilitating the onset of corrosion.

In this context, mineral additions play an important role in the improvement of concrete and mortars properties, regarding mechanical resistance and durability, since its use in concrete improves the interfacial transition zone, densifies the cement paste, refining pores and reducing their interconnectivity. On the other hand, when considering carbonation, additions can lead to a negative effect, namely: a reduction in the carbonation resistance of the concrete, due to the reduction of the "alkaline reserve" of the cementitious system. This effect is influenced by the type and content of mineral addition used, as well as by the water/binder ratio and curing

conditions (Cascudo; Carasek, 2011).

Several authors have studied the effect of mineral additions on durability parameters, such as porosity, permeability, carbonation, chloride attack and others (Hossain *et al.*, 2016; Papadakis, 2000; Lim; Mondal, 2015). Some authors report that the replacement of cement by metakaolin increases the carbonation depth (Meddah *et al*., 2018; Fikhailenko *et al.*, 2018), whereas other researchers have observed smaller depths (Duan *et al.*, 2012, 2013; Rossignolo; Oliveira, 2006). So, there are still divergences in relation to the behavior of concrete or mortar modified with metakaolin, with regard to its performance against carbonation.

Thus, this work aims to analyze the influence of different metakaolins and curing conditions in the accelerated carbonation of mortars, trying to understand this behavior from the point of view of the characteristics of metakaolin. In addition, it was sought to analyze the relationship between the measurements of carbonated depth using two pH indicators: phenolphthalein and thymolphthalein based solutions.

2 Experimental

2.1 Materials

The mortars were produced with a washed riverbed quartz sand, with a fineness module of 1.65 and a maximum size of particles of 1.18 mm. The cement used was a Brazilian-type CP II F-40 portland cement, with a specific surface area of 4120 cm²/g and chemical characteristics according to Table 1. A polycarboxylic ether based superplasticizer admixture (density of 1.09 g/cm³ and solids content of 30%), water from public supply network, and two metakaolins derived from different deposits (Table 2) completed the constituent materials of the produced mortars. Brazilian-type CP II F – 40 is a portland cement similar to European CEM II/A-L 42,5 R (NF EN 197-1: 2012), being composed of 75-89% of clinker and calcium sulfate, and 11-25% in mass of limestone filler, according to the Brazilian standard NBR 16697: 2018.

Table 1. Chemical characterization of cement (C) and metakaolins (J1 and J2).

	Chemical (%)									
	Al_2O_3	SiO_2	Fe_2O_3	CaO	MgO	SO_3	Loss Ignit.	Free CaO	Insoluble Residues	Alkali Content
C	4.24	18.48	2.63	61.02	4.33	2.76	4.99	0.78	1.10	0.66
J1	37.1	52.7	2.3	0.1	1.0	---	2.7	---	---	1.5
J2	39.5	47.6	5.3	0.1	0.3	---	4.7	---	---	0.5

The two metakaolins showed different chemical compositions. J1 has higher SiO_2 content and the reddish coloration of metakaolin J2 is explained by the higher iron oxide content in this material. Regarding fineness, J2 is 30% finer than J1. Despite these differences, the two metakaolins studied showed very similar pozzolanic activity (modified Chapèlle - NF P18-513: 2012).

Table 2. Metakaolins' complementary characterization.

Metakaolin	Aspect/Colour	Specific gravity (g/cm^3)	BET Fineness (m^2/g)	Chapèlle (mg $CaOH_2$/ g)
J1		2.58	22.13	1037
J2		2.60	28.71	1075

2.2 Preparation of Specimens and Test Methods

Three different mortars were produced, one as reference and the other two with 10% replacement of cement by metakaolin J1 or J2, in mass. The mortars were produced with a 1:2 mixture (binder:sand, in mass), since this is a mix proportion commonly used in the mortar fraction of various concrete mix designs (1:2:3-binder:sand:gravel). The consistency index was maintained in 320±20 mm (according to ASTM C230: 2014). After mixing, two mortar specimens were cast, under controlled conditions, in prismatic dimensions of 40x40x160 mm (ASTM C349: 2018). The mortars' composition and identification are shown in Table 3.

Table 3. Mortars' identification and composition (kg/kg).

Identification	Cement	Metakaolin	Sand	Water/Binder	Superplasticizer Admixture
A – R	1.0	0,0	2	0.55	0
A - J1	0.9	0.1 (J1)			0.022
A - J2		0.1 (J2)			0.037

After 24 hours of molding, the specimens were demolded and subjected to four different curing conditions: no wet curing and curing by immersion in lime saturated water for 3, 9 and 28 days. For the specimens without wet curing, they were packed in PVC plastic after demolding and stored in a laboratory until the tests performing. For those specimens cured for 3 and 9 days, they were air-dried for about two hours (after the curing period) and then packed by means of PVC plastic until they reached the testing age of 28 days, in order to prevent natural carbonation.

At 28 days of age, the accelerated carbonation test (7 days) was started. Before the start of carbonation, the specimens were preconditioned with humidity (70±5%) and temperature (20±1°C) controlled (no CO_2), according to standard ISO 1920-12 (2015). It was used one CO_2 incubator, model 6034-1, Caron brand, with temperature of (20±1)°C, relative humidity of (70±5)% and CO_2 content of 10%. The carbonation depth was measured by spraying the pH indicators (thymolphthalein and phenolphthalein-based solutions) and using a digital calliper with an accuracy of 0.01 mm, as shown in Figure 1. Each specimen was sliced two times, resulting in a four-sided measurement of 40 x 40 mm, a specimen. In 2 faces the phenolphthalein was applied, and in the other two it was the thymolphthalein. On each side 4

measures were taken (in the central region on each side), which implies that the mean results of carbonation depth were obtained using 16 individual measures.

The compressive strength test (ASTM C349:2018) was performed with the mortars subjected to wet curing for 28 days.

a) 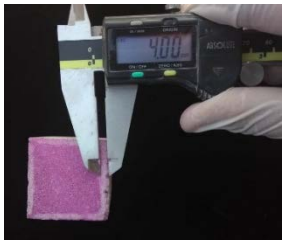 b) 

Figure 1. Measurement of carbonated depth using a) phenolphthalein and b) thymolphthalein.

For result analysis, the data was treated with Dixon statistic test (ASTM E178: 2016) in order to remove spurious values, and then analyzed using variances analysis (ANOVA) to identify the study's significant variables. In addition, multiple comparisons of means were performed by the Duncan test.

3 Results and Discussion

3.1 Compressive Strength

Table 4 presents the results of mortars' compressive strength. It can be noted that the metakaolin mortars achieved higher strengths compared to the reference mortar; in addition, there was no significant difference in strength between A-J1 and A-J2.

Table 4. Compressive Strength at 28 days of age.

Mortar	A - R	A – J1	A – J2
Compressive Strength - mean (MPa)	34	43	42
Standard Deviation (MPa)	10.4	5.0	2.7

3.2 Carbonation

The results of mortars' carbonation depth, for different curing situations, are presented in Figure 2. The carbonation depth is reduced with wet curing, showing the importance of performing curing in order to increase the durability of reinforced concrete. Comparing carbonation depths of mortars submitted to wet curing for 28 days and mortars not submitted to wet curing, it is possible to observe a reduction in carbonation up to 70% for A-R, and 45 % for A-J1 and A-J2.

The increase of wet curing time from 3 to 28 days reflected in a less pronounced depth reduction, about 50%, 25% and 30% for mortars A-R, A-J1 and A-J2, respectively. It is interesting to note that the type of curing exerts a greater influence on the reference mortar than on the metakaolin mortars (A-J1 and A-J2). It was found that concretes modified with metakaolin without the application of any curing procedure show superior carbonation resistance compared to reference concretes. From the literature, it is known that mineral additions such as blast furnace slag and fly ash require wet curing for a long time to consolidate

the pozzolanic reactions (Sulapha *et al.*, 2003), and that superpozzolans such as silica fume, nanosilica and metakaolin are generally not sensitive to wet curing (Couto *et al.*, 2003). This was verified in the present work for metakaolin and the main argument on the issue is based on the physical transformation capacity of the cement paste by the action of pozzolan, which reduces porosity and refines pores, thus increasing the volume of micropores capable of retaining water in its capillary structure (Duan *et al.*, 2013). In these cases, it can be said that self-healing occurs due to changes in the material's microstructure.

The analysis of variance - ANOVA (Table 4) confirms the statement that the type of curing exerts a strong influence on the carbonation depth, while type of mortar did not present significant effect on the results of this research.

Table 4. Carbonation depth ANOVA.

Efect	**SQ**	**GL**	**MQ**	$\mathbf{F_{calc}}$	$\mathbf{F_{tab}}$	**Result** (5% significance)
Model	652.73	11	59.34	78.5	1.8	Significant
Residual Error	278.02	368	0.76			
Total	930.75	379				
Type of curing	574.50	3	191.5	253.5	2.6	Significant
Mix design	2.80	2	1.40	1.9	3.0	Not Significant
Type of curing x Mix design	64.14	6	10.69	14.2	2.1	Significant
Residual Error	278.02	368	0.755			
Coefficient of Determination (R^2) = 0.70				**Coefficient of Correlation (R)** = 0.84		

The multiple comparison of means (Figure 2), where dashed lines indicate separation into different groups, shows that the mortars with metakaolin present a tendency to be similar regarding the carbonation for all the curing conditions. The behavior similarity of mortars A-J1 and A-J2 can be explained by the fact that the metakaolins presented similar reactivity (Chapèlle - Tab. 2), confirmed by the compressive strength results (Tab. 4), despite the chemical, coloring and fineness differences of the two pozzolans. When comparing the metakaolin mortars with the reference mortar (A-R), a distinct behavior is observed. In intermediate curing, the three mortars show same pattern from the statistical point of view.

However, when no wet curing is performed, the reference mortar presents a higher carbonation depth than the mortars with metakaolin. When wet curing is performed for 28 days, this behavior is reversed; this explains the significant interaction between Type of curing x Mix design found in ANOVA (Tab. 4). The approximately 50% increase in carbonation depth for A-J1 and A-J2 regarding A-R, in the wet curing for 28 days situation, can be explained by the hydration process and the pozzolanic reactions, in which the increased time of wet curing allowed better conditions for the hydration and pozzolanic reactions to occur, improving mortars' microstructure, but with pozzolanic reactions there is also reduction in alkaline reserve of mortars with mineral additions (Thomas; Matthews, 1992; Cascudo; Carasek, 2011). In contrast, the shorter depth for A-J1 and A-J2 without wet curing, regarding A-R, can be explained by the greater influence of curing on reference mortar, in addition to the filler and pozzolanic effects of mineral additions, which refined the mortars' porosity and microstructure (Duan *et al.*, 2013), as previously discussed.

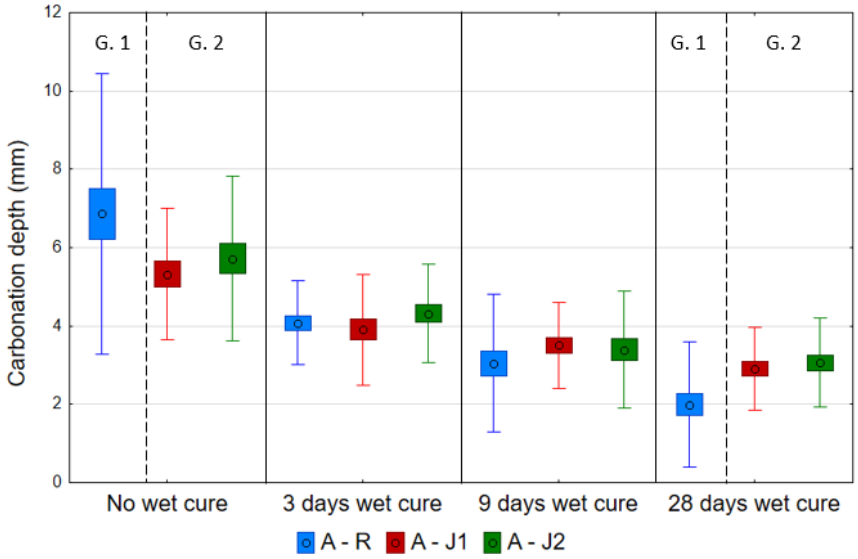

Figure 2. Carbonation depth results analyzed with multiple comparison of means.

3.3 Relationship Between pH Indicators

Figure 3 shows the relationship between the carbonated depth measurements made with thymolphthalein and phenolphthalein, and the strong correlation between these two variables ($R^2 = 0.89$). It is noted that, in general, the thymolphthalein indicated greater depths than the phenolphthalein, which can be attributed to the difference between the indicators' pH turning ranges (phenolphthalein from 8.0 to 9.8 and thymolphthalein from 9.3 to 10.5). Other authors (such as: Kazmierczak; Lindenmeyer, 1996; Yu; Lee; Chung, 2010, Reis; Camões; Ribeiro, 2016; Revert *et al*., 2016, Thiel; Gehlen, 2019) have worked with indicators and discussed the relationships between the measurements obtained.

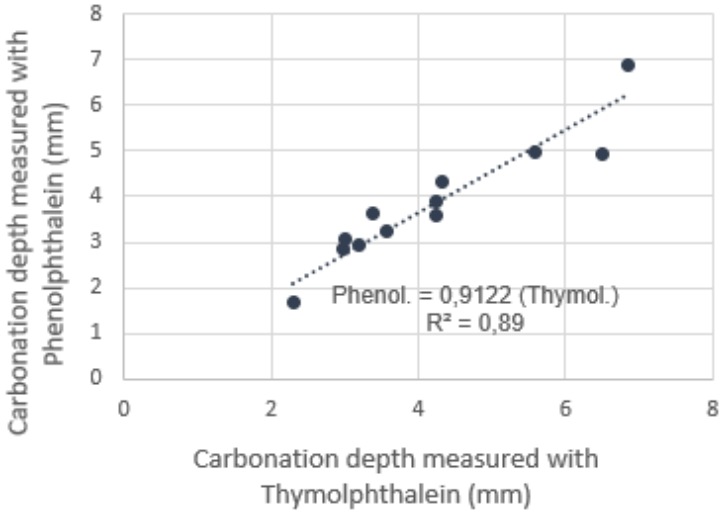

Figure 3. Relationship between carbonated depths with different pH indicators.

The equation obtained for this correlation can be highlighted; the carbonated depth readings with phenolphthalein are equivalent to 0.9 times the readings taken with thymolphthalein. An interesting aspect, and perhaps new, was noticed: this relationship between the variables matches the relationship between the two extremes of the pH ranges nominated by the different pH indicators (9.3 / 10.5 = 0.9; where 9.3 is the maximum pH indicated by phenolphthalein and 10.5 is maximum by thymolphthalein).

4 Conclusions

Based on the research presented, the following conclusions can be drawn:

Despite of the chemical, coloring and fineness differences of both metakaolins studied, there were no statistically significant differences regarding the carbonated depths of the mortars prepared with them. These metakaolins had similar pozzolanic activity (measured by the Chapèlle method), showing that this characteristic is very relevant to explain the carbonation of mortars with metakaolin.

The curing condition had a strong influence on carbonated depths of mortars. This depth is reduced with wet curing and with the increased time of immersion in water, showing the importance of wet curing for increasing the durability of reinforced concrete. However, metakaolin mortars are less affected by wet curing when compared to the non-pozzolan mortars (reference cementitious mortars). This is certainly due to a self-healing action exerted by a microstructure with refined pores, referring to systems with metakaolin, with greater water retention capacity.

As for the carbonate depth measurements performed with phenolphthalein and thymolphthalein based indicators, a strong linear correlation was observed between the two variables ($R^2 = 0.89$). The carbonated depth readings with phenolphthalein are equivalent to 0.9 times the measured readings with thymolphthalein. This relationship between the variables is exactly the relationship between the two extremes of the indicators' pH turning ranges (phenolphthalein = 9.8 and thymolphthalein = 10.5).

Acknowledgements

The authors would like to thank: Coordenação de Aperfeiçoamento de Pessoal de Nível Superior (CAPES) – Brazil, Eletrobras FURNAS and the technicians of LABITECC-UFG - Brazil.

ORCID

Helena Carasek: https://orcid.org/0000-0002-1170-0980
Mônica E. Jungblut: https://orcid.org/0000-0003-2111-0666
Paulo M. Passos: https://orcid.org/0000-0002-2934-9279
Oswaldo Cascudo: https://orcid.org/0000-0003-1879-6396

References

Cascudo, O. and Carasek, H. (2011). Ação da Carbonatação no Concreto. In G. C. ISAIA (Ed.), *Concreto: Ciênica e Tecnologia.* São Paulo, SP: IBRACON, 849-885.

Castro, A., Ferreira, R., Lopes, A., Couto, A. P., Braun, V., Carasek, H. and Cascudo, O. (2007). Influência das adições minerais na durabilidade do concreto. In *IV Congresso de Inovação Tecnológica em Energia Elétrica*. Araxá: ANEEL, 1-8.

Couto, A. B. P. ; Cascudo, O. ; Carasek, H. and Lopes, A. N. M. (2003). Influência das condições de cura na

durabilidade de diferentes concretos. In *45. Congresso Brasileiro do Concreto*, Vitória. Anais de CD-ROM. São Paulo: IBRACON, 1, 1-15.

Duan, P., Shui, Z., Chen, W. and Shen, C. (2012). Influence of metakaolin on pore structure-related properties and thermodynamic stability of hydrate phases of concrete in seawater environment *Construction and Building Materials*, 36, 947-953. doi: 10.1016/j.conbuildmat.2012.06.073

Duan, P., Shui, Z., Chen, W. and Shen, C. (2013). Enhancing microstructure and durability of concrete from ground granulated blast furnace slag and metakaolin as cement replacement materials *Journal of materials Research and Technology*, *2*(1), 52-59. doi: 10.1016/j.jmrt.2013.03.010

Hossain, M. M., Karim, M. R., Hasan, M., Hossain, M. K. and Zain, M. F. M. (2016). Durability of mortar and concrete made up of pozzolans as a partial replacement of cement: A review *Construction and Building Materials*, 116, 128-140. doi: 10.1016/j.conbuildmat.2016.04.147

Kazmierczak, C. S. and Lindenmeyer, Z. (1996). Comparação entre metodologias utilizadas para a determinação da profundidade de carbonatação em argamassas. In *Proceedings of the International Congress on High-performance and Quality of Concrete Structures*, Florianópolis, Brazil, 402-413.

Lim, S. and Mondal, P. (2015). Effects of incorporating nanosilica on carbonation of cement paste *Journal of Materials Science*, *50*(10), 3531-3540. doi: 10.1007/s10853-015-8910-7

Meddah, M. S., Ismail, M. A., El-Gamal, S. and Fitriani, H. (2018). Performances evaluation of binary concrete designed with silica fume and metakaolin *Construction and Building Materials*, 166, 400-412. doi: 10.1016/j.conbuildmat.2018.01.138

Papadakis, V. G. (2000). Effect of supplementary cementing materials on concrete resistance against carbonation and chloride ingress *Cement and concrete research*, 30, 291-299. doi: 10.1016/S0008-8846(99)00249-5

Reis, R., Camões, A. and Ribeiro, M. (2016). Using Thymolphthalein for Accelerated Carbonation Testing of High Volume Fly Ash Cementitious Blends. In *Service Life and Durability of Reinforced Concrete Structure*, Marne-la-Vallée, France, 17-30.

Revert, A., De Weerdt, K., Hornbostel, M. and Geiker, M. (2016), Carbonation Characterization of Mortar with Portland Cement and Fly Ash, Comparison of Techniques, Nordic Concrete Research, publication N. 54 1/2016, 60-76

Rossignolo, J. A. and Oliveira, I. L. (2006). Concreto leve estrutural com metacaulim *Revista Minerva: Pesquisa e Tecnologia*, *3*(2), 177-187.

Sulapha, P., Wong, S. F., Wee, T. H. and Swaddiwudhipong, S. (2003). Carbonation of Concrete Containing Mineral Admixtures *Journal of Materials in civil engineering*, 15, 134-143. doi: 10.1061/(ASCE)0899-1561(2003)15:2(134)

Thiel, C. and Gehlen, C. (2019) On the Determination of Carbonation in Cementitious Materials. In *RILEM Spring Convention and Sustainable Materials, Systems and Structures Conference*, Rovinj, Croatia, 373-380.

Thomas, M. D. A. and Matthews, J. D. (1992). Carbonation of fly ash concrete *Magazine of Concrete Research*, *44*(160), 217-228. doi: 10.1680/macr.1992.44.160.217

Yu, M., Lee, J and Chung, C. (2010), The Application of Various Indicators for the Estimation of Carbonation and pH of Cement Based Materials, Journal of Testing and Evaluation 38, no. 5: 534-540

XV International Conference on Durability of Building Materials and Components
DBMC 2020, Barcelona
C. Serrat, J.R. Casas and V. Gibert (Eds)

Effect of Cement Type and Micro-cracks on Chloride Penetration in Concrete

Nicoletta Russo[1], Matteo Gastaldi[1], Luca Schiavi[2], Alberto Strini[2], Riccardo Zanoni[2] and Federica Lollini[1]

[1] Politecnico di Milano, Department of Chemistry, Materials and Chemical Engineering "Giulio Natta", Piazza Leonardo da Vinci 32, 20133 Milano, Italy, nicoletta.russo@polimi.it matteo.gastaldi@polimi.it federica.lollini@polimi.it

[2] Consiglio Nazionale delle Ricerche, Istituto per le Tecnologie della Costruzione, Viale Lombardia 49, 20098 San Giuliano Milanese, Italy, luca.schiavi@itc.cnr.it alberto.strini@itc.cnr.it riccardo.zanoni@itc.cnr.it

Abstract. *Chloride-induced corrosion of reinforcing steel rebar is one of the major durability issues affecting reinforced concrete structures (RC). Various models have been developed to assess the durability design with regard to corrosion prevention in chloride-bearing environments, which refer mainly to uncracked concrete. Cracks, however, are frequently present in real RC structures and accelerate corrosion initiation of steel reinforcement, resulting in a shortened service life. This paper presents preliminary results concerning chloride-penetration resistance of different types of uncracked and cracked concrete, made with Ordinary Portland (OPC), Portland-Limestone (PLC) and Pozzolanic cement (PC) and a water/cement ratio of 0.45. Load-induced micro-cracks were obtained with a specifically developed technique. Cracked and uncracked concrete specimens were immersed in a sodium chloride solution for 32 and 90 days. The chloride penetration front was detected on split surfaces, perpendicular to the exposed surface, with a colorimetric technique to evaluate the combined effect of cracks and cement type on the chloride-penetration resistance of different concretes. Results showed that in uncracked conditions cement type strongly affected chloride penetration depth in concrete. A mathematical model was applied to evaluate chloride diffusion coefficient (D) from chloride penetration depth measurements and exposure time. The lowest value of D was found for PC concrete, that can be attributed to a higher pore refinement in the cement paste, five times higher for OPC and nine times higher for PLC. In cracked conditions, an additional penetration of chlorides occurred in correspondence of crack, even for micro-cracks 10-50 μm wide and 8-30 mm deep, leading to a decrease in chloride penetration resistance. The model however did not provide for an estimation of D in correspondence of the crack.*

Keywords: *Reinforced Concrete Durability, Cracked Concrete, Chloride Penetration Resistance.*

1 Introduction

Reinforced Concrete (RC) is one of the most widely used construction materials for the realization of modern structures and architectures. The considerable efforts made in the recent past to understand the degradation processes affecting RC constructions led to the development of useful tools and design models aimed at preventing corrosion of steel reinforcement rebar, which is the main cause of premature failure of RC structures (Bertolini *et al.*, 2004). These tools and models require several durability-related design parameters, among which the chloride penetration resistance of concrete is of particular relevance for the evaluation of the service life of a RC structure in chloride-contaminated environment.

Several studies have been carried out to investigate the main influencing factors of chloride penetration resistance of concrete, such as, for instance, the cement type. However, these studies - as well as current durability design models - often refer to uncracked concrete, a condition that is rarely met in real RC structures. Cracks in the concrete cover represent a privileged path for chlorides and it is therefore of fundamental importance to evaluate the effects of cracks on chloride penetration resistance of concrete (ACI 201.2R-16, 2016).

In recent years, an ever increasing number of studies has been addressed to this topic (Gu *et al.*, 2015) and, as a general result, it seems that even micro-cracks (crack opening smaller than 100 μm) can locally affect chloride penetration in concrete (Yoon and Schlangen, 2014). In some tests the chloride penetration resistance is evaluated by means the so called colorimetric method. One of the advantages in applying this method to cracked concrete is that it provides a visual detection of chloride penetration in correspondence and in the vicinity of crack. In literature, this method has often been applied to concrete specimens with wide artificial cracks (notches) subject to accelerated exposure test (Audenaert *et al.*, 2007, Marsavina *et al.*, 2009, Li *et al.*, 2016). Few studies, however, have been addressed to the application of colorimetric technique on cracked specimens subject to natural exposure conditions.

In this study, preliminary results are presented within a wider research project concerning the effects of cracks on RC durability. The chloride penetration resistance of three different types of concrete, obtained with water/cement ratio of 0.45 and different cements, was evaluated in uncracked and load-induced micro-cracked configurations. After the immersion of the concrete specimens in NaCl solution for 32 and 90 days, the chloride penetration was evaluated via colorimetric technique, and was correlated with crack geometrical parameters.

2 Experimental Procedure

2.1 Materials and Specimens

Concrete specimens were realized with three different mixes, considering three different types of cement. Details on concrete mixing proportions, and properties at fresh and hardened state are reported in Table 1.

Table 1. Concrete mixing proportions and properties.

	OPC	PLC	PC
Cement, kg/m^3	422	422	422
Water, kg/m^3	190	190	190
Aggregate, kg/m^3	1731	1731	1731
w/c	0.45	0.45	0.45
Superplasticizer, mL	15.5	10	12
Slump, mm	130	170	165
Density, kg/m^3	2496	2526	2477
$f_{c,cube,7days}$, MPa	54.0	56.9	54.6
$f_{c,cube,28days}$, MPa	76.9	60.8	67.4
$f_{c,cube,120days}$, MPa	86.9	76.8	81.4

It was considered an Ordinary Portland Cement (OPC) type CEM I 42,5R as reference, a Portland-Limestone Cement (PLC) type CEM II/A-LL 42,5R, which is one of the most widely used in Italy, and a cement with pozzolanic additions, Pozzolanic Cement (PC) type CEM IV/A(V) 42,5R-SR. The concrete mixes were obtained with 422 kg/m^3 of cement and 190 kg/m^3 of water (w/c ratio equal to 0.45), and 1731 kg/m^3 of limestone aggregates with maximum diameter of 9 mm. To improve workability at fresh state, an acrylic-based superplasticizer was added to each mix. For each concrete type, six cubic specimens 100 mm side were cast for compressive strength, which was executed after 7, 28 and 120 days of moist curing on two specimens per time. For chloride penetration resistance six prismatic specimens of dimensions 120×90×50 mm were manufactured for each concrete type. To promote the formation of the crack during the cracking procedure, four prismatic specimens were provided with a central V-shaped notch, about 5 mm deep, along the longitudinal direction on the casting surface. After casting, all concrete specimens were covered with a plastic film. The subsequent day were demoulded and placed in the curing chamber (four of them after the cracking procedure), where they were kept at 20°C and RH>90% for 28 days. Table 1 shows the average concrete properties at hardened state. An increase of compressive strength in time was observed, with compressive strengths of 77, 61 and 68 MPa reached respectively by OPC, PLC and PC concretes after 28 days of moist curing.

2.2 Cracking Procedure

A mechanical loading procedure was developed in order to induce cracks on the casting surface of specimens. A universal testing machine was used to reproduce a sort of tree-point bending test, as shown in Figure 1. The procedure was executed 24 hours after casting, on specimens presenting the longitudinal notch, for details see (Russo *et al.*, 2019). At the end of the cracking procedure the specimens were placed in the curing chamber.

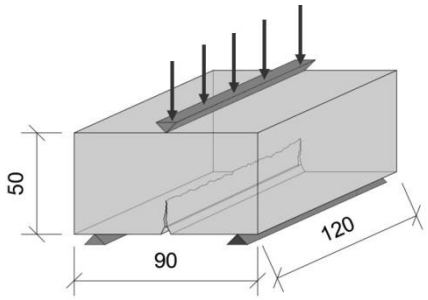

Figure 1. Specimen geometry (dimensions in mm) and cracking procedure.

2.3 Chloride Penetration Resistance

Uncracked and cracked concrete specimens were exposed to chlorides by immersion (EN 12390-11:2005). After 28 days of curing the specimens were vacuum saturated with demineralized water. At the end of the saturation procedure they were left immersed in water and within 24 hours removed from water in order to seal with epoxy resin all the surfaces, except for the casting surface. After 24 hours the specimens were immersed in a saturated solution of calcium hydroxide for 18 hours. Finally, all the specimens were immersed in a 3%

by mass sodium chloride solution, for 32 and 90 days (concrete will be henceforth identified with a code indicating the cement type and the days of exposure, *e.g.* OPC-90 for specimens obtained with Ordinary Portland Cement and exposed to chlorides for 90 days). At the end of the exposure time, the specimens were split with a hydraulic press in one point along the longitudinal direction, and therefore perpendicular to the crack plane for cracked specimens.

On the freshly split surfaces a silver nitrate solution (0.1 M) was sprayed, in order to evaluate the chloride penetration profile. The chloride penetration depth was measured in seven different positions, i.e. in the central point and at a distance of 10 mm, 20 mm and 30 mm on each side. For cracked specimens, the central measure was done starting from the tip of the notch, in order to exclude its influence on the penetration profile. A further measure was also done for cracked specimens, corresponding to the maximum penetration depth starting from the tip of the notch. For each concrete type, two cracked specimens were provided for each exposure time, while the same two uncracked specimens were used for both the exposure times. The fracture surfaces of the uncracked specimens analyzed after 32 days of exposure were sealed with epoxy resin, and the day after were exposed again to chlorides, in order to be analyzed also after 90 days of exposure. After chloride penetration measurements the split surface was impregnated with a colored superfluid two-component epoxy resin. The following day, a thin concrete slice, parallel to the split surface where chloride penetration depth was evaluated, was cut with a water cooled cutting saw. The concrete thin slice was then polished and observed at the stereoscopic microscope in order to detect the two main crack geometrical parameters, crack width and crack depth.

3 Results and Discussion

3.1 Crack Geometrical Parameters

Figure 2a reports, as an example, a wide field image of a cracked PC-90 specimen, obtained combining three different images at 6× of magnification. Wide field observation was done in order to detect the main path of the crack and to identify crack tip. The parameter crack depth was then measured with a caliper, as the distance between the notch tip and the crack tip.

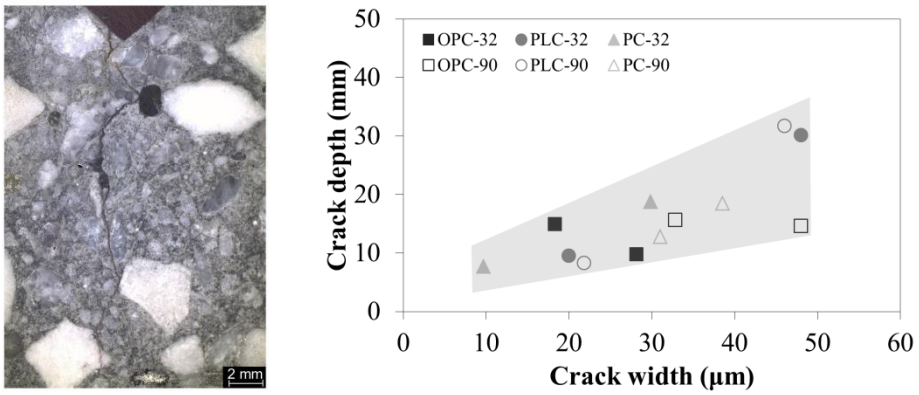

(a) (b)

Figure 2. (a) Microscopic image of cracked PC-90 specimen; (b) Crack width as a function of crack depth.

The parameter crack width is intended as the crack opening at the exposed surface, in correspondence of the tip of the notch. Five measurements were done at 50× of magnification, in a range of about one millimeter from notch tip, and then averaged. Figure 2b reports the results obtained for the two replicated samples of the three concrete types after the two exposure times. Crack widths resulted to be included in the range 10-50 μm, while crack depth included in the range 8-30 mm. Despite data were characterized by a quite high dispersion, increasing crack width an increase also in crack depth was observed, which was independent from the cement type and the exposure time.

3.2 Chloride Penetration Resistance

A colorimetric technique was used to evaluate the chloride penetration profiles on the split surfaces of different cracked and uncracked concretes. Figure 3a and 3c show, as an example, the chloride penetration profile in PLC uncracked and cracked specimens respectively, after 32 days of exposure. The penetration depths in different points after 32 days of exposure for the three cement types are reported in Figure 3b for sound and 3d for cracked configuration.

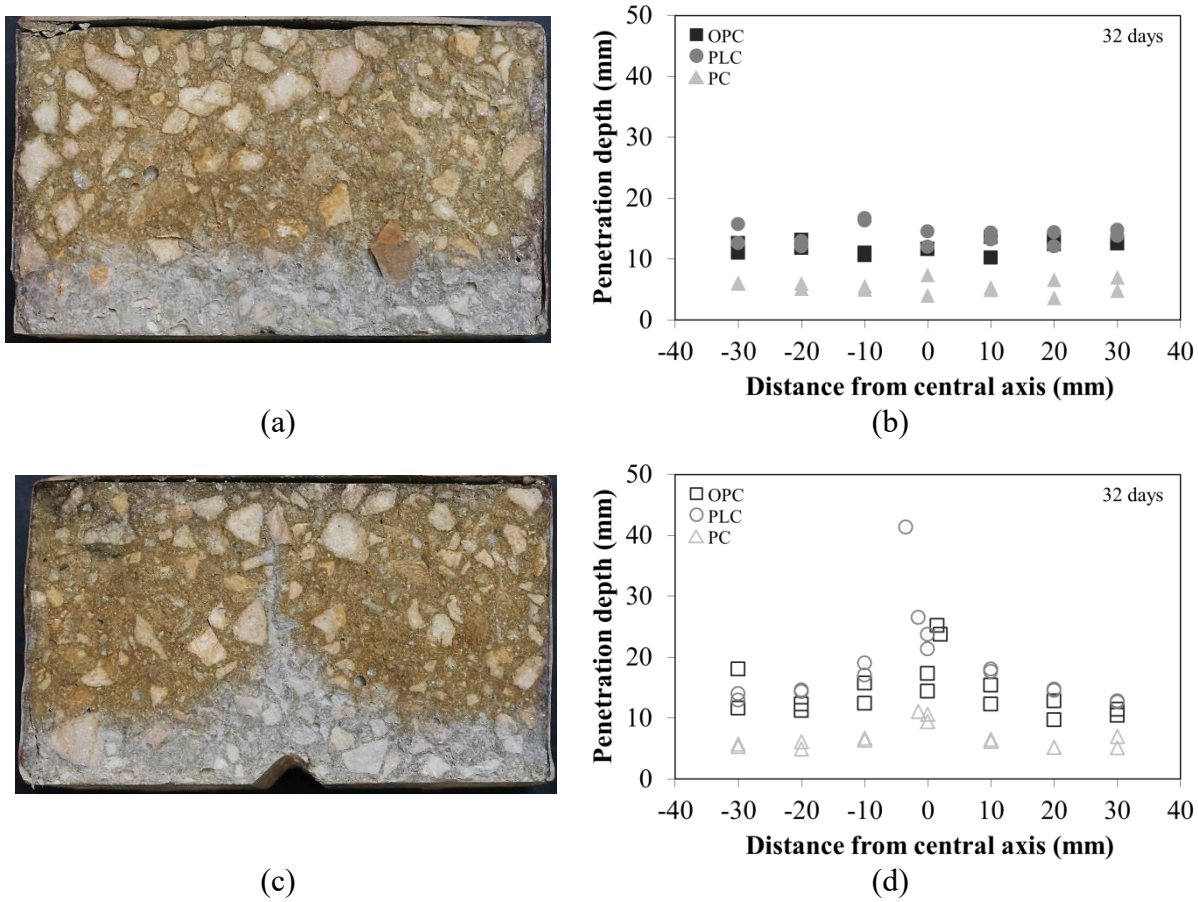

Figure 3. Chloride penetration in PLC-32 (a) uncracked and (c) cracked specimen; Chloride penetration depth measured in different points at different distances from the central axis of the specimen for different concrete types in (b) uncracked and (d) cracked specimens after 32 days of exposure.

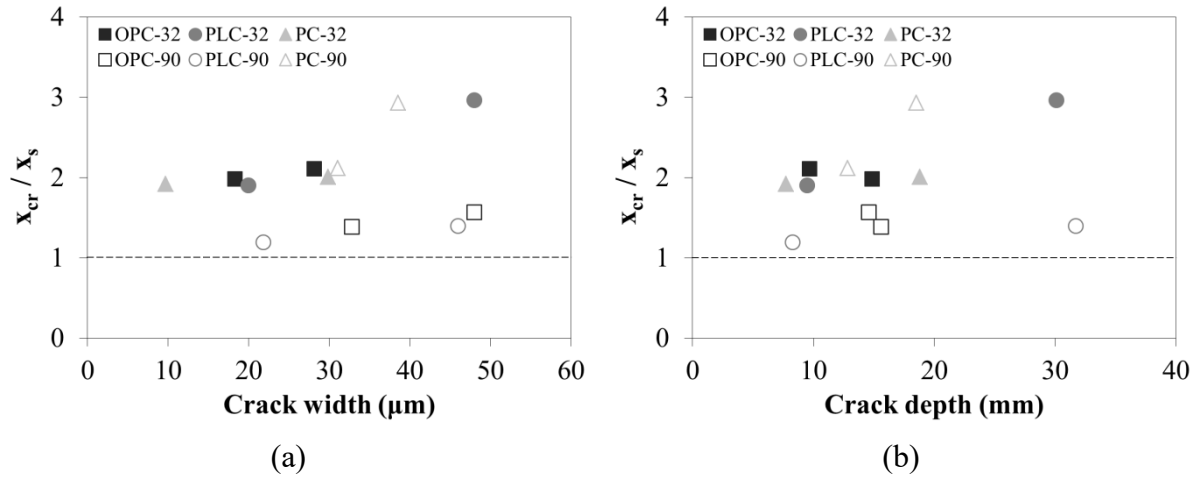

Figure 4. Local increase of chloride penetration depth in correspondence of the crack with respect to sound conditions, as a function of (a) crack width and (b) crack depth.

In Figure 3b it can be observed that, in sound conditions and for each type of concrete, the penetration depth was almost constant along the specimen and comparable between the two replicate specimens. As expected the lowest chloride penetration profiles were referred to the PC cement type, showing a chloride penetration depth of about 5 mm after 32 days of exposure. This can be attributed to a higher pore refinement in the cement paste, and therefore a higher chloride penetration resistance of this concrete type. On the other hand, despite the results of compressive strength, OPC and PLC resulted to have similar chloride penetration depths, of about 10 to 15 mm after 32 days of exposure. The same trend of penetration profile was detected on cracked specimens, except for the measurements carried out in the vicinity of the central axis, where penetration profiles were clearly altered by the presence of the crack (in this point the measurements were done starting from the tip of the notch).

In order to account for the influence of crack geometrical parameters, in Figure 4 is shown the local increase in chloride penetration depth in correspondence of the crack with respect to sound conditions (x_{cr}/x_s) as a function of crack width and crack depth for both the exposure time. x_{cr}/x_s represents the ratio between the chloride penetration depth in the crack and the average penetration depth in sound specimens. It can be observed that chloride penetration in the crack resulted always higher with respect to uncracked conditions, until a maximum of 3 times higher. The local increase of penetration depth in the crack after 32 days of exposure resulted always doubled for crack widths included in the range 10-30 μm and crack depth about 10-20 mm, independently from the concrete type, indicating that micro-cracks could lead to a significant increase of the chloride penetration. After 90 days of exposure, for PC concrete the local increment in correspondence of crack was still similar, while for OPC and PLC a lower local increment was detected, included in the range 1.2-1.5, although crack parameters were comparable to those at 32 days of exposure. This effect will be further investigated to understand if it is due to some self-healing effects, or simply to data scattering.

From the measurements of penetration depths, an attempt was made in order to evaluate chloride penetration resistance of the different concretes in terms of chloride diffusion coefficient. The diffusion coefficient was calculated considering a linear correlation between

the chloride penetration depth and the square root of time, according to the relationship proposed by Collepardi *et al.*, 1970:

$$x = 4\sqrt{Dt} \tag{1}$$

where x is the chloride penetration depth, t is time and D is the chloride diffusion coefficient of concrete.

Figure 5 shows the relationship between the chloride penetration depths for different concretes and the square root of time. It seems that for all cement types in uncracked conditions there is a general decrease in the chloride penetration rate over time (i.e. ageing effect), which has already been detected (Collepardi and Biagini, 1989), although for longer exposure times with respect to those considered in this study. Anyway, a single linear interpolation was done for each type of concrete, and the values of the diffusion coefficient are reported in the chart legend. The highest chloride penetration resistance was detected for the PC concrete, whose chloride diffusion coefficient resulted equal to 0.34×10^{-12} m^2/s, while D was more than 5 times higher for OPC concrete (1.79×10^{-12} m^2/s) and nine times higher for PLC (3.06×10^{-12} m^2/s), consistent with literature data (Collepardi and Biagini, 1989). The determination of the diffusion coefficient from the correlation (1) in the case of cracked configurations resulted to have some limitations, not only because of the ageing effect but also because of crack geometrical parameters, which were different in correspondence of different measurement surfaces. For PC the linear correlation was still able to fit results, and the value of the diffusion coefficient in the crack resulted to be equal to 1.82×10^{-12} m^2/s, more than five times higher than the value measured in uncracked conditions. Conversely, for OPC and PLC cement types, a linear correlation, in correspondence to the crack, could not be detected. This is a direct consequence of the effect previously detected, *i.e.* OPC and PLC showed lower local increase in chloride penetration depths independently from crack parameters at 90 days of exposure.

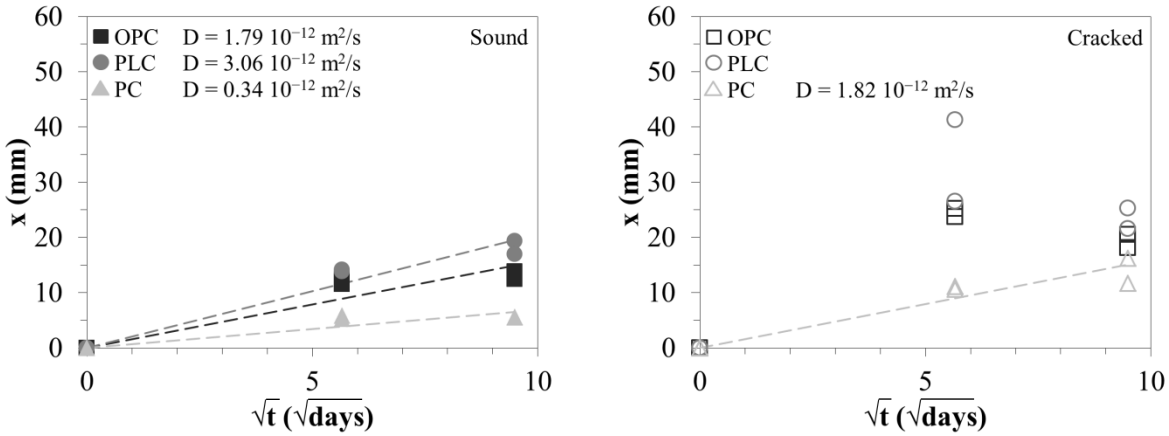

Figure 5. Chloride penetration depths as a function of the square root of time for the different concretes in (a) sound and (b) cracked conditions.

4 Conclusions

Chloride penetration in concretes made with Ordinary Portland (OPC), Portland-Limestone (PLC) and Pozzolanic (PC) cement was investigated through a colorimetric technique in uncracked and cracked configurations. Cracked specimens were obtained with a sort of three-point bending procedure able to generate V-shaped micro-cracks, with crack opening included in the range 10-50 μm and crack depth included in the range 8-30 mm. In uncracked configuration, PC was the concrete type showing lowest chloride penetration depths, due to a higher pore refinement. In cracked configuration the chloride additional penetration in the crack (x_{cr}/x_s) was evaluated as a function of two main geometrical parameters, crack width and crack depth. Independently from the concrete type, x_{cr}/x_s was always included in the range 1.2-3. Chloride penetration resistance of different uncracked and cracked concretes was investigated also in terms of chloride diffusion coefficient (D). In uncracked conditions D resulted to be equal to 1.79×10^{-12} m^2/s for OPC, 3.06×10^{-12} m^2/s for PLC and 0.34×10^{-12} m^2/s for PC concrete. The application of the same mathematical model to cracked concrete resulted limited by the fact that crack geometrical parameters were not considered.

ORCID

Nicoletta Russo: https://orcid.org/0000-0003-3919-0094
Matteo Gastaldi: https://orcid.org/0000-0002-1392-2691
Luca Schiavi: http://orcid.org/0000-0001-5574-1584
Alberto Strini: http://orcid.org/0000-0001-9585-2748
Federica Lollini: http://orcid.org/0000-0002-8706-7915

References

ACI Committee 201, (2016). *ACI 201.2R-16 Guide to Durable Concrete.* American Concrete Institute.

Audenaert, K., De Schutter, G. and Marsavina, L. (2009). Influence of cracks and crack width on penetration depth of chlorides in concrete. *European Journal of Environmental and Civil Engineering*, 13(5), 561-572. doi: 10.3166/EJECE.13. 561-572

Bertolini, L., Elsener, B., Pedeferri, P. and Polder, R. (2004). *Corrosion and protection of steel in concrete: prevention, diagnosis, repair.* Wiley.

Collepardi, M. and Biagini, S. (1989). Effect of water/cement ratio, pozzolanic addition and curing time on chloride penetration into concrete. In *Proceedings of the ERMCO '89*, Stavanger, Norway, 606-615.

Collepardi, M., Marcialis, A. and Turriziani, R. (1970). La cinetica di penetrazione degli ioni cloruro nel calcestruzzo. *Il Cemento*, 67, 157-164.

Gu, C., Ye, G. and Sun, W. (2015). A review of the chloride transport properties of cracked concrete: experiments and simulations. *Journal of Zhejiang University-SCIENCE A,* 16, 81-92. doi: 10.1631/jzus.A1400247

Li Y., Chen X., Jin L. and Zhang R. (2016). Experimental and numerical study on chloride transmission in cracked concrete. *Construction and Building Materials*, 127, 425-435. doi: 10.1016/j.conbuildmat.2016.10.044

Marsavina, L., Audenaert, K., De Schutter, G., et al., (2009). Experimental and numerical determination of the chloride penetration in cracked concrete. *Construction and Building Materials*, 23(1), 264-274. doi: 10.1016/j.conbuildmat.2007.12.015

Russo, N., Gastaldi, M., Marras, P., Schiavi, L., Strini, A. and Lollini, F. (2019). A preliminary study on the effects of cracks on chloride penetration in different concretes. In *Proceedings of the V Workshop on The New Boundaries of Structural Concrete*, Milan, Italy, 315–324.

Yoon I.S. and Schlangen E. (2014). Experimental examination on chloride penetration through micro-crack in concrete. *KSCE Journal of Civil Engineering*, 18, 188-198. doi: 10.1007/s12205-014-0196-9

XV International Conference on Durability of Building Materials and Components
DBMC 2020, Barcelona
C. Serrat, J.R. Casas and V. Gibert (Eds)

Effect of Coexisting Materials on Secondary Ettringite Formation

Kennosuke Sato[1], Tsuyoshi Saito[2] and Tatsuhiko Saeki[2]

[1] Department of Civil & Environmental Engineering, University of Yamanashi, 4-3-11, Takeda, Kofu, Yamanashi, 400-8511, Japan, satok@yamanashi.ac.jp

[2] Department of Civil Engineering, Niigata University, 8050, Ikarashi Ninocho, Nishiku, Niigata, 950-2181, Japan, tsaito@eng.niigata-u.ac.jp

Abstract. *The expansion of cement paste can occur as a result of secondary ettringite formation due to attack by sulfates. It has been proposed that this expansion is affected by coexisting hydration products such as calcium-silicate-hydrates (C-S-H), although the mechanism has not yet been clarified. The present study experimentally examined the effects of coexisting materials on secondary ettringite formation. Synthesized monosulfate and coexisting materials such as C-S-H were mixed with a sodium sulfate solution. The secondary ettringite proportion was markedly increased by the presence of C-S-H, and calcium-aluminate-silicate-hydrates (C-A-S-H) containing four-coordinate Al were formed in these samples. It is evident that ettringite is likely to form from four-coordinate Al, and that C-S-H promotes secondary ettringite formation because it transitions six-coordinate Al derived from the monosulfate to four-coordinate Al by substituting Al in the Si chains.*

Keywords: *Sulfate Attack, DEF, Secondary Ettringite Formation, Coexisting Materials, C-S-H.*

1 Introduction

Expansion due to sulfates is typically referred to as either external or internal sulfate attack, depending on the sulfate source. Internal sulfate attack after high temperature curing is also referred to as delayed ettringite formation (DEF) (Collepardi, 2003). Both external and internal sulfate attack are attributed to secondary ettringite formation in the cement paste.

Ettringite has the composition $C_6A\bar{S}_3H_{32}$ and is formed from tricalcium aluminate (C_3A) in Portland cement or from aluminum in supplementary cementitious materials during the early stages of hydration. Ettringite is subsequently converted to a monosulfate (Ms) form having the formula $C_4A\bar{S}H_{12}$ as the sulfate ion concentration in the liquid phase decreases. When sulfate ions are supplied to the hardened cement paste they react with the Ms to reform so-called secondary ettringite. However, the mechanisms which can explain all expansions due to secondary ettringite formation in a unified manner has not yet been proposed.

It has been suggested that the expansion due to secondary ettringite formation is affected by the properties of hydration products coexisting with the ettringite, such as calcium-silicate-hydrates (C-S-H). Taylor *et al.* (2001) proposed the DEF expansion mechanism in a mortar. According to this mechanism, ettringite may have a greater degree of expandability when it is formed in the outer C-S-H near the boundary between two C-S-H phases (outer C-S-H and inner C-S-H) than when it is formed in the outer C-S-H far from the boundary.

The goal of the present study was to experimentally examine the effects of coexisting materials on secondary ettringite formation. This was accomplished using a synthesized Ms sample in conjunction with coexisting materials such as C-S-H. The Ms and other materials were mixed and hydrated using a sodium sulfate solution, followed by analysis.

doi:10.23967/dbmc.2020.153

2 Methods and Materials

2.1 Preparation of Materials

The Ms was prepared from a suspension of a 1:1 molar mixture of C_3A, which was prepared by calcining of $CaCO_3$ and Al_2O_3, and $CaSO_4$ in deionized water, at a water to solid mass ratio of 10:1. The solid and aqueous phases were separated after curing at 20 °C for 14 d.

C-S-H, calcium hydroxide (CH) and hydrogarnet (HG) were used as the coexisting materials in this work. Because silica stone does not react at ambient temperature and pressure, silica stone powder (SSP) was also used for the purposes of comparison with other coexisting materials. In addition, amorphous silica (AS) and Al-substituted C-S-H (C-A-S-H) were used in verification experiments. Three C-S-H samples having different CaO to SiO_2 molar ratios (C/S ratio) (of 0.80, 1.00 and 1.50) were synthesized by reacting mixtures of CH, ethyl silicate and deionized water for 2 d at 40 °C, after which the solid and aqueous phases were separated by vacuum filtration. HG was synthesized via the reaction of C_3A with deionized water at a water to solid mass ratio of 1:1. Samples were cured for 28 d at 40 °C, after which the solid phase was separated by vacuum filtration. C-A-S-H was synthesized based on the method of Pardal *et al.* (2009). The CH, AS and SSP (purity > 96%) used in this work were all commercially-available products.

These materials were dried under 110 °C in a drying oven (defined as 0% RH), and subsequently crushed into particles smaller than 90 μm. The H_2O to SiO_2 molar ratios of C-S-H having the C/S ratios of 0.8, 1.0 and 1.5 dried at 110 °C were 0.63, 0.67, 0.82, respectively.

2.2 Mixing with a Sodium Sulfate Solution

The mixing proportions of the Ms and the coexisting materials are summarized in Table 1. Herein, the C-S-H and C-A-S-H specimens are termed CSH0.8, CSH1.0, CSH1.5, CASH0.8, CASH1.0 and CASH1.4, where the numerical portion of the name gives the C/S ratio. The effects of the chemical composition of the mixture were assessed by simultaneously

Table 1. Specimen proportions.

Sample name	Powder composition (mass%)										
	Ms	CSH 0.8	CSH 1.0	CSH 1.5	CH	HG	SSP	AS	CASH 0.8	CASH 1.0	CASH 1.4
Ms+CSH 0.8	50	50	–	–	–	–	–	–	–	–	–
Ms+CSH 1.0	50	–	50	–	–	–	–	–	–	–	–
Ms+CSH 1.5	50	–	–	50	–	–	–	–	–	–	–
Ms+CH	50	–	–	–	50	–	–	–	–	–	–
Ms+HG	50	–	–	–	–	50	–	–	–	–	–
Ms+SSP	50	–	–	–	–	–	50	–	–	–	–
Ms+AS	50	–	–	–	–	–	–	50	–	–	–
Ms+(CH+AS)1.0	50	–	–	–	27.61	–	–	22.39	–	–	–
Ms+(CH+AS)1.5	50	–	–	–	32.46	–	–	17.54	–	–	–
Ms+CASH 0.8	50	–	–	–	–	–	–	–	50	–	–
Ms+CASH 1.0	50	–	–	–	–	–	–	–	–	50	–
Ms+CASH 1.4	50	–	–	–	–	–	–	–	–	–	50

combining CH and AS with the Ms. In these trials, the CH and AS were mixed so that the C/S ratio was either 1.00 or 1.50 and the mixture was combined with the Ms at a mass ratio of 1:1.

Each mixture of the Ms and the coexisting materials were mixed with a 0.5 M sodium sulfate solution at a liquid to powder mass ratio of 2:1. They were manually mixed for 3 m and transferred into a plastic bottle and cured at 20 °C for 1 d.

After the curing, the samples were broken into small pieces and immersed in acetone for 2 d to prevent further hydration. These specimens were subsequently placed under vacuum to remove the acetone and stored in a vacuum desiccator in the presence of silica gel for 2 d. The samples were crushed into particles smaller than 90 μm and dried at 20 °C and 11% RH using a saturated LiCl solution in a vacuum desiccator until the sample mass no longer changed.

2.3 Analysis

Powder XRD was used for the identification and quantification of hydration products after mixing with the sodium sulfate solution.

For the measurement of the pH and ionic composition of the liquid phase, a Ms specimen together with coexisting materials were mixed with a 0.5 M sodium sulfate solution at a liquid to powder mass ratio of 3:1. After mixing, each sample was placed in a plastic bottle and then cured at 20 °C for 1 d, after which the solid and liquid phases were separated by centrifugation. The pH of the liquid phase was measured using a glass electrode pH meter and the concentrations of Na^+, Ca^{2+} and SO_4^{2-} ions in the liquid phase were analyzed.

Solid state ^{27}Al nuclear magnetic resonance (NMR) was employed to determine the chemical state of Al in each sample after mixing with the sodium sulfate solution. The ^{27}Al magic angle spinning (MAS) NMR experiments were performed with a ECA800 operating at 18.79 T with a 3.2 mm probe and a spinning frequency of 20 kHz. ^{27}Al spectra were recorded with a 0.6 μs pulse width and a recycle delay of 1 s between scans.

3 Results

3.1 Formation Characteristics of Secondary Ettringite

Figure 1 shows the XRD patterns of Ms samples with each coexisting material after mixing with the sodium sulfate solution. SSP does not react at ambient temperature and pressure, and so does not contribute to secondary ettringite formation. The ettringite peaks of the Ms+CH and Ms+HG were not increased in intensity as compared with Ms+SSP. Thus, when CH and HG coexist (that is, even when the Ca and Al necessary for the formation of the secondary ettringite are supplied), there was almost no secondary ettringite formation. In contrast, the diffraction peaks due to Ms almost disappeared while those resulting from ettringite increased when C-S-H was added to the Ms.

3.2 Effects of pH and Calcium Leaching

The pH values and ionic compositions of the liquid phases after mixing with the sodium sulfate solution are provided in Table 2. In all cases, the pH was in the range of 11.57 to 13.39, which is associated with the stable formation of ettringite (Stark and Wicht, 2003; Shimada et al., 2005). The Ms+CSH1.5 had the highest Ca^{2+} concentration, and the values for the Ms+CSH0.8 and Ms+CH were especially close. The pH of the Ms+CH was higher than that

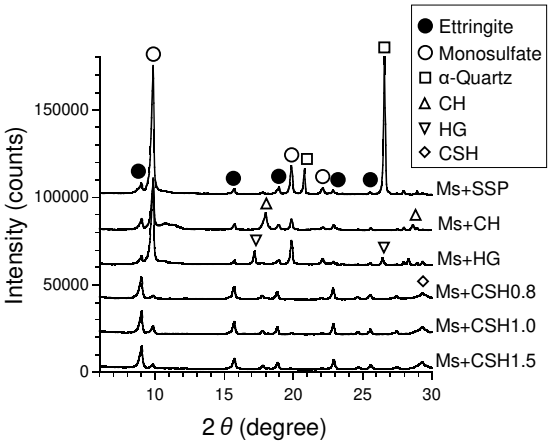

Figure 1. XRD patterns of monosulfate specimens with coexisting materials after mixing with a sodium sulfate solution.

Table 2. pH values and ionic compositions of the liquid phases.

	pH	Na^+ (mol/L)	Ca^{2+} (mol/L)	SO_4^{2-} (mol/L)
Ms	12.38	1.81	0.01	0.35
Ms+SSP	12.54	1.13	0.02	0.38
Ms+HG	12.43	1.11	-	0.34
Ms+CH	13.39	1.09	0.04	0.05
Ms+CSH0.8	11.68	0.78	0.04	0.24
Ms+CSH1.0	12.60	0.88	0.06	0.28
Ms+CSH1.5	11.57	0.86	0.12	0.13

of the Ms+CSH0.8, although the amount of secondary ettringite in the latter material was significantly greater than that in the former. Kunther *et al.* (2015) reported that of the extent of Ca^{2+} leaching decreases with decreases in the C/S ratio of the C-S-H, such that the supersaturation of ettringite in the pore solution decreases and expansion of the mortar is suppressed. This suggests that a higher Ca^{2+} concentration in the liquid phase will promote secondary ettringite formation. However, the results of this study show large differences in the extent of secondary ettringite formation, even when the Ca^{2+} concentration in the liquid phase is constant. Moreover, although the Ca^{2+} concentration of the liquid phase was slightly higher in the case of the Ms+CSH1.0 compared with the Ms+CSH0.8, and both pH values were in the range required for ettringite to be stable, the amount of secondary ettringite in the latter material was greater. Thus, the promotion of secondary ettringite formation due to the presence of C-S-H is not completely explained by conventional theories regarding the effects of the pH and Ca^{2+} concentration of the liquid phase.

3.3 Effects of Ca and Si-Based Materials

Si in the C-S-H is thought to have played an important role in secondary ettringite formation in the present work. Figure 2 shows the XRD patterns of Ms specimens with added Ca and Si-based materials after mixing with the sodium sulfate solution. For comparison, the XRD patterns generated by the Ms+SSP, Ms+CH, Ms+CSH1.0 and Ms+CSH1.5 are also provided

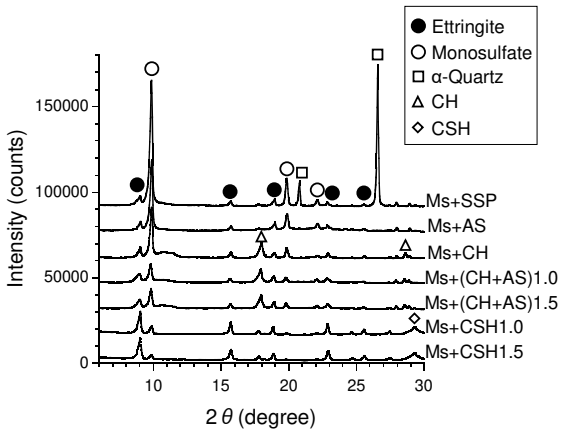

Figure 2. XRD patterns of monosulfate specimens with added Ca and Si after mixing with a sodium sulfate solution.

in the figure. These patterns demonstrate that the Ms diffraction peaks produced by the Ms+AS were slightly less intense than those in the Ms+SSP pattern. When both CH and AS were present, the Ms peaks were further decreased. Therefore, it appears that the simultaneous addition of both Ca and Si promoted the dissolution of the Ms. Conversely, the ettringite peaks did not increase significantly even when both CH and AS coexisted. Thus, even when the chemical composition in the sample is the same as that of C-S-H, the amount of secondary ettringite is greatly increased only when C-S-H is present.

3.4 Evaluation of the Chemical State of Al

The chemical state of Al, which is an important constituent element of both Ms and ettringite, was investigated using ^{27}Al NMR. Figure 3 shows the ^{27}Al NMR spectra of Ms specimens with each coexisting material after mixing with the sodium sulfate solution. For all coexisting materials, two peaks corresponding to six-coordinate Al appeared. These two peaks are attributed to Ms and ettringite (Skibsted *et al.*, 1999; Andersen *et al.*, 2004). The Ms+HG also generated a HG peak close to the ettringite peak (Cuesta *et al.*, 2017). In the case of the sample without C-S-H, a six-coordinate Al peak produced by the Ms is clearly present. In contrast, the spectra obtained from the samples with C-S-H contain a significantly reduced Ms peak along with a much more intense ettringite peak. Thus, these ^{27}Al NMR data also demonstrate that the coexistence of C-S-H promoted secondary ettringite formation.

Moreover, each of the three samples containing C-S-H generated a broad peak corresponding to four-coordinate Al. This peak is also generated by C-A-S-H, in which Al is substituted for Si in the silicate chains of C-S-H at pairing and bridging sites (Richardson, 2004). Because the bridging sites in the silicate chains are increased as the C/S ratio decreases, Al is more readily substituted for Si at these sites (Pardal *et al.*, 2012; Renaudin *et al.*, 2009). It is therefore apparent that, in samples containing C-S-H, the Si in the silicate chains were substituted with Al released by dissolution of the Ms to generate C-A-S-H.

3.5 Effect of the Presence of C-A-S-H

Figure 4 presents the XRD patterns of Ms specimens with added C-A-S-H after mixing with the sodium sulfate solution, along with the patterns of the C-S-H samples for comparison

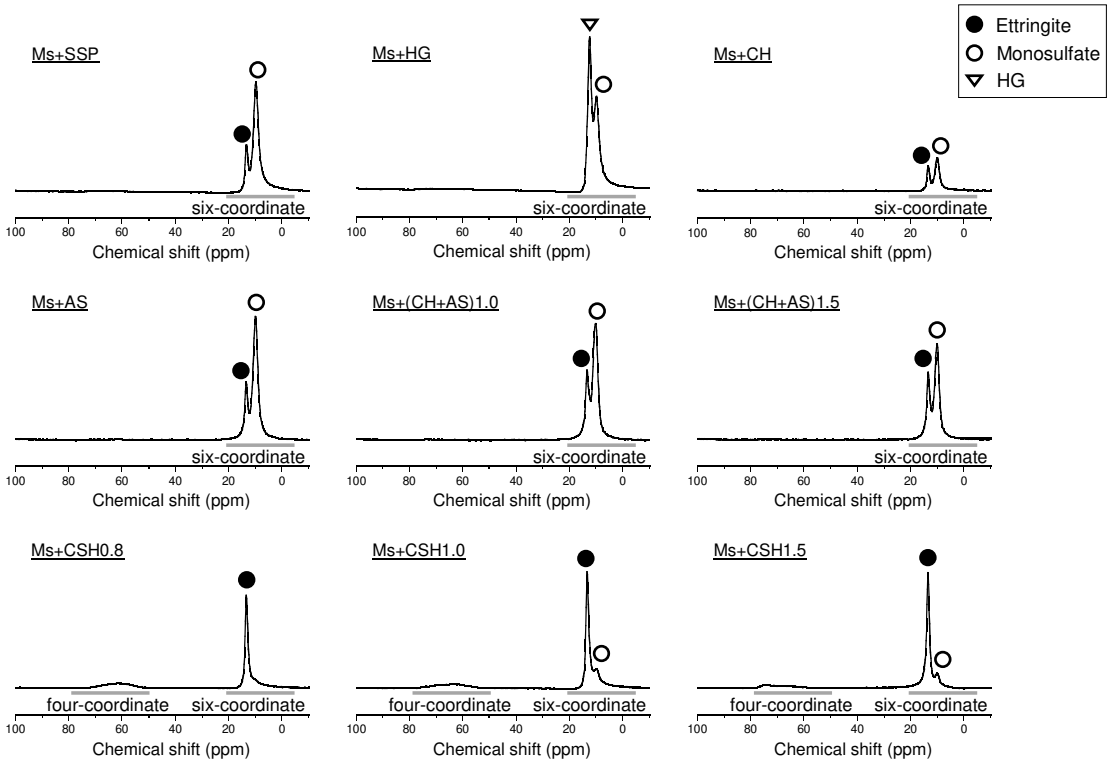

Figure 3. ^{27}Al NMR spectra of monosulfate specimens with coexisting materials after mixing with a sodium sulfate solution.

purposes. The Al/Si ratio in the C-A-S-H was 0.05. These data confirm that the Ms+CASH generated more intense Ms peaks than the Ms+CSH at equivalent C/S ratios. In addition, although the ettringite peaks were less intense than those generated by the samples containing C-S-H, these peaks were more intense compared with those generated by samples with other coexisting materials. Therefore, in the case of the Ms+CASH, the reaction of the Ms did not proceed as readily, although the ettringite peak was relatively high. These results suggest that C-A-S-H contributed to the formation of secondary ettringite by supplying Al.

Figure 5 provides the ^{27}Al NMR spectra of Ms samples with C-A-S-H after mixing with the sodium sulfate solution. These spectra confirm that the peak ascribed to six-coordinate Al in the Ms was more intense than those generated by specimens made with C-S-H. The samples with C-A-S-H as the coexisting material also produced six-coordinate Al peaks corresponding to ettringite that were comparable to those obtained from the C-S-H samples.

The combined XRD and NMR data suggest that the presence of C-A-S-H promoted secondary ettringite formation primarily by consuming four-coordinate Al in the C-A-S-H.

4 Discussion

This work demonstrates that only the presence of C-S-H markedly increased the amount of secondary ettringite in the samples. The ^{27}Al NMR spectra show that four-coordinate Al appeared only in samples in which C-S-H coexisted with the Ms, and this Al is attributed to the C-A-S-H (Richardson, 2004). Samples containing C-A-S-H were mixed with the sodium sulfate solution and examined by XRD and ^{27}Al NMR. The level of ettringite was found to be

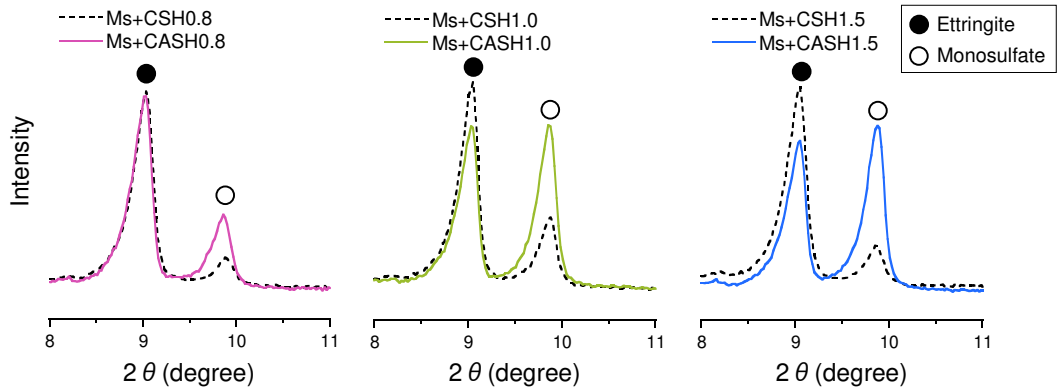

Figure 4. XRD patterns of monosulfate specimens with C-S-H or C-A-S-H after mixing with a sodium sulfate solution.

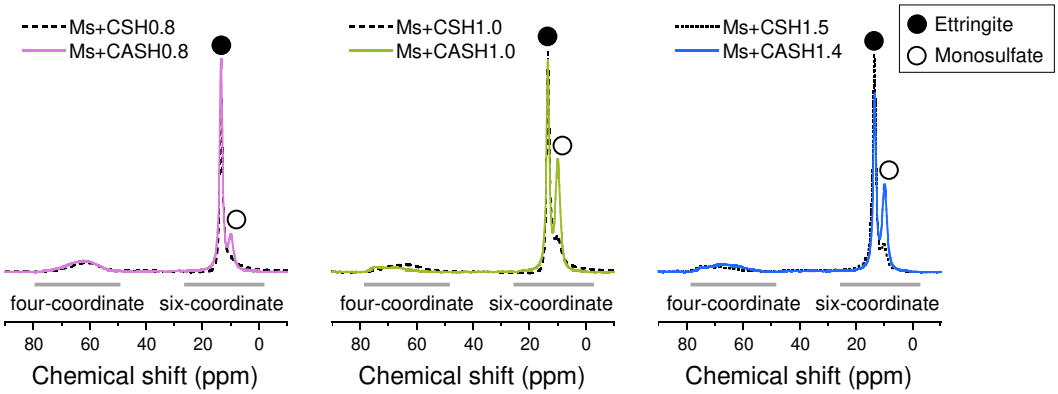

Figure 5. ^{27}Al NMR spectra of monosulfate specimens with C-S-H or C-A-S-H after mixing with a sodium sulfate solution.

equal to that in samples containing C-S-H, although the Ms peaks were not deceased.

These results suggest that the presence of four-coordinate Al is closely related to se condary ettringite formation, hence we assessed the Al coordination numbers in the samples. In the absence of coexisting materials, or when materials other than C-(A)-S-H coexist with the Ms (that is, when four-coordinate Al is not present), ettringite having six-coordinate Al is directly formed from Ms having the same six-coordinate Al. Under such conditions, the formation of secondary ettringite does not readily proceed.

In the case that C-S-H is present, Al released from the Ms is substituted into the silicate chains in the C-S-H. As a result, C-A-S-H is formed with four-coordinate Al. If a sufficient concentration of sulfate ions is available, ettringite is more likely to be formed from four-coordinate Al than from the six-coordinate Al in the Ms. That is, the presence of C-S-H promotes secondary ettringite formation by changing the Al coordination number.

As such, ettringite is likely to be formed from four-coordinate Al, and C-S-H promotes secondary ettringite formation by substituting Al into the silicate chains and converting six-coordinate Al to four-coordinate. On the other hand, using SCMs is beneficial to decrease sulfate attack, while the production of C-A-S-H is increased with the amount of added SCMs. Based on the results of the present study, ettringite is likely to be formed when SCMs are used,

however; the expansion is actually suppressed. Because of that, the expansion due to secondary ettringite formation may be related not only to the amount of ettringite but also to the location of ettringite formation.

5 Conclusions

The purpose of this study was to investigate experimentally the effects of coexisting materials on secondary ettringite formation. The conclusions can be summarized as follows.

- When monosulfate and C-S-H are mixed with a sodium sulfate solution, the amount of secondary ettringite is increased in comparison with other coexisting materials.
- The ^{27}Al NMR results confirm that C-A-S-H containing four-coordinate Al is formed in samples made with C-S-H. In addition, when C-A-S-H is added to the monosulfate, secondary ettringite is generated at a comparable level to that found in the C-S-H samples, although the monosulfate remains intact. It appears that ettringite is likely generated from four-coordinate Al, and that C-S-H promotes secondary ettringite formation as a result of transitioning six-coordinate Al to four-coordinate Al by substituting Al in the Si chains.

ORCID

Kennosuke Sato: http://orcid.org/0000-0002-3456-4037
Tsuyoshi Saito: http://orcid.org/0000-0002-2335-5790
Tatsuhiko Saeki: http://orcid.org/0000-0002-7436-5673

References

Andersen, M., D., Jakobsen, H., J. and Skibsted, J. (2004). Characterization of white Portland cement hydration and the C-S-H structure in the presence of sodium aluminate by ^{27}Al and ^{29}Si MAS NMR spectroscopy. *Cement and Concrete Research*, 34, 857-868.

Collepardi, M. (2003). A state-of-art review on delayed ettringite attack on concrete. *Cement and Concrete Composites*, 25, 401–407.

Cuesta, A., Ichikawa, R., U., Londono-Zuluaga, D., Torre, A., G., Santacruz, I., Turrillas, X. and Arenda, M., A., G. (2017). Aluminum hydroxide gel characterization within a calcium aluminate cement paste by combined Pair Distribution Function and Rietveld analysis. *Cement and Concrete Research*, 96, 1-12.

Kunther, W., Lothenbach, B. and Skibsted, J. (2015). Influence of the Ca/Si ratio of the C-S-H phase on the interaction with sulfate ions and its impact on the ettringite crystallization pressure. *Cement and Concrete Research*, 69, 37-49.

Pardal, X., Brunet, F., Charpentier, T., Pochard, I. and Nonat, A. (2012). ^{27}Al and ^{29}Si Solid-State NMR Characterization of Calcium-Aluminosilicate-Hydrate. *Inorganic Chemistry*, 51, 1827-1836.

Pardal, X., Pochard, I. and Nonat, A. (2009). Experimantal study of Si-Al substitution in calcium-silicate-hydrate (C-S-H) prepared under equilibrium conditions. *Cement and Concrete Research*, 39, 637-643.

Renaudin, G., Russias, J., Leroux, F., Cau-dit-Coumers, C. and Frizon, F. (2009). Structural characterization of C-S-H and C-A-S-H samples - Part II: Local environment investigated by spectroscopic analysis. *Journal of Solid State Chemistry*, 182, 3320-3329.

Richardson, I., G. (2004). Tobermorite/jennite- and tobermorite/calcium hydroxide-based models for the structure of C-S-H: Applicability to hardened pastes of tricalcium silicate, β-dicalcium silicate, Portland cement, and blends of Portland cement with blast-furnace slag, metakaolin, or silica fume. *Cement and Concrete Research*, 34, 1733-1777.

Skibsted, J., Henderson, E. and Jakobsen, H., J. (1993). Characterization of calcium aluminate phases in cements by aluminum-27 MAS NMR spectroscopy. *Inorganic Chemistry*, 32, 1013-1027.

Taylor, H. F. W., Famy, C. and Scrivener, K. L. (2001). Delayed ettringite formation. *Cement and Concrete Research*, 31, 683-693.

XV International Conference on Durability of Building Materials and Components
DBMC 2020, Barcelona
C. Serrat, J.R. Casas and V. Gibert (Eds)

Effect of Crack Repair by Bio-Based Materials Using Alginate and Bacillus Subtilis under Wet and Dry Environment Part-I

Keiyu Kawaai[1], Takahiro Nishida[2] and Atsushi Saito[3]

[1] Civil and Environmental Engineering, Ehime University, 3, Bunkyocho, Matsuyama, Ehime, Japan, kkawaai@cee.ehime-u.ac.jp

[2] National Research and Development Agency, National Institute of Maritime, Port and Aviation Technology, Port and Airport Research Institute, Japan, nishida-ta@p.mpat.go.jp

[3] Reseach Center, Hazama Ando Corporation, Japan, atsushi.saito@ad-hzm.co.jp

Abstract. *This study examined crack repair methods using alginate gel films (1.5 wt.%) mixed with healing agents under wet and dry actions. The healing agents consist of Bacillus subtilis (natto) as an aerobic microorganism and glucose as an organic carbon source, thereby producing insoluble calcium carbonate in the gel films in the presence of calcium ions. In this study, repaired surface in cracked mortar specimens (ϕ50×100mm) was observed by microscope. In addition, water absorption test was carried out in assessing the effectiveness of crack repair for the cases of alginate gel films with or without calcium carbonate precipitation induced by the microbial activities. Based on the observations made by microscope, precipitates in white color were clearly observed after 8 weeks on the cracked surface of specimens especially under wet conditions. In the case of the specimens with higher sealing rate of crack repair, the alginate gel films were remained intact under dry and wet actions, which is advantageous to keep moisture by swelling. Water absorption test was carried out using repaired mortar specimens with average crack size of 0.5 mm. Based on the results obtained, water absorption rate is substantially decreased in the specimens with increasing sealing rate of crack repair. The results suggest that higher crack sealing rate associated with calcium carbonate precipitation leads to higher resistance against water absorption tested in accordance with ASTM C 1585.*

Keywords: *Self-Healing, Aerobic Microorganisms, Bio-Composite, Water Absorption.*

1 Introduction

Recently, repair materials associated with microbial induced calcium carbonate precipitation (MICCP) have been intensively studied in the field of self-healing concrete *e.g.* (Jonkers *et al.*, 2010). We proposed a liquid based repair system comprising dry yeast, organic carbon sources, calcium sources mixed with Tris alkali buffering solution (Kawaai *et al.*, 2016; Putri *at el.*, 2016). The grout used for repairing cracks in concrete is supposed to seep into deeper zones in cracks, joints and gaps spatially distributed in larger areas. Then, calcium carbonate precipitation mainly contributing to the sealing effect can be formed in the cracks well before 24 hours (Kawaai *et al.*, 2016). It has been reported that the precipitation rate was largely dependent on the concentration of constituents, pH levels, and ambient environment such as temperature. The effect of temperature is significant in facilitating the precipitation process (Putri *et al.*, 2016), thus leading to a larger amount of precipitates formed compared to those tested in normal room conditions.

Apart from the grout system, the activity of Bacteria added to mixing water was observed to be limited owing to the pore solution with highly alkaline environment (Jonkers, 2011). In order

to protect them from corrosive agents and the severe environment, much research has been carried out in the development of encapsulation techniques including expanded clay particles, glass tubes, superabsorbent polymer, more recently alginate-based systems (Jonkers, 2011; Tittleboom *et al.*, 2011; Wang *et al.*, 2014; Palin *et al.*, 2016).

According to past research reported by Kawaai *et al.*, (2017), precipitation of calcium carbonate in alkaline environment has been confirmed by precipitation tests using aerobic Bacillus subtilis (natto) encapsulated in calcium alginate capsules. Sodium alginate extracted from brown seaweed could provide viscosity in aqueous solution, which varies depending on the concentrations. When sodium alginate dissolved in a liquid is used for repairing cracks in concrete, there is a strong possibility that the alginate reacts with calcium ions available on the cracked surface, thus forming a polymer comprising calcium alginate via ion-link on the cracked surface. This could result in in-situ encapsulation for the microorganism and nutrients in the cracks. Generally, there are two types of microorganisms, anaerobic and aerobic microorganisms. The former can metabolize an organic carbon sources in an oxygen-free environment. On the other hand, the latter requires oxygen for the metabolic activity. In this study, we selected Bacillus subtilis (natto) as an aerobic microorganism. The liquid-based mixture is supposed to be applied to concrete structures in tidal zones under marine environment. Dissolved oxygen is expected to be available during the wet and dry cycles. Based on the above background, this study examines the effect of crack repair using the viscosity modified mixture containing the Bacillus subtilis (natto) and nutrients via liquid-based approach under wet and dry conditions

2 Experimental Programs

2.1 Materials

First, culture solution of Bacillus subtilis (natto) containing sodium alginate is stirred using a stirrer for 30 minutes until the sodium alginate dissolves. Subsequently, Tris buffer solution or glucose is added. The concentrations of each constituent of the mixtures are shown in Table 1.

The experimental parameters include the presence (N1 mixtures) and absence (W mixture) of Bacillus subtilis (natto), the concentration of sodium alginate is specified as 1.5 wt.% for all the mixtures tested. The use of Tris buffer solution with concentrations of 0.1 mol/L is also considered as a testing parameter. In this study, three mixtures were totally prepared.

Table 1. Concentrations of each constituent of mixtures.

Mixtures		Sodium Alginate (%)	Glucose (mol/L)	Tris buffering solution (mol/L)
N1	N1-G1-T0	1.5	0.4	-
	N1-G1-T1	1.5	0.4	0.10
W	W -G0-T0	1.5	-	-

2.2 Cultivation of Bacillus Subtilis (natto)

In this study, Bacillus subtilis (natto) was cultivated using culture media mainly comprising NH_4Cl, NH_4NO_3, Na_2SO_4, $MgSO_4$, $CaCl_2$, K_2HPO_4, KH_2PO_4 in this study. The round rod shape of Bacillus subtilis (natto) forms a spore per a bacterial cell in the bacterial body. Spores are formed when it becomes an environment not suitable for growth such as oxygen, water and nutrient sources. And then, they become dormant and inactive. However, if the environment is set, the spore dormancy state ends, and germination begins. And then it becomes vegetative cell and the activity starts. Therefore, the Bacillus subtilis (natto) has higher resistance to environmental fluctuation compared to other microorganisms. In this study, the culture solution of the Bacillus subtilis (natto) after 24 hours was used as repair mixtures. Before preparing the mixtures, the dissolved oxygen concentration in the culture solution was measured to confirm the metabolic activity of Bacillus subtilis (natto) without an aeration apparatus.

2.3 Specimen Preparation and Exposure Tests

In this study, a mortar specimen with a water cement ratio of 0.5 and unit water content of 316 kg/m^3 and unit weight of crushed sand 1264 kg/m^3 was prepared using a cylindrical mold of ϕ 50×100 mm. Specimens were demolded after 24 hours and sealed curing was carried out until the age of 28 days. In order to simulate the cracks generated in the concrete member, split cracks were induced using a loading machine. The experimental set-up is similar to tensile strength test. The crack width was targeted around 0.5 mm. And then, the repair mixtures were poured into the cracks. After 1 week, exposure tests were carried out either through wet conditions (12 hours) and dry conditions (12 hours) or only wet conditions (24 hours). Wet cycles were executed using distilled water containing NaCl (3%) for both cases.

2.4 Measurement of Crack Width and Sealing Rate

The crack width and sealing rate by MICCP are measured using microscope (Dino-Lite Edge AM7915, ANMO) as shown in Figure 1. The five points highlighted in the figure are consistently measured using two specimens subjected to each exposure condition. The sealing rate is calculated based on the ratio of widths occupied with the precipitates over crack widths at each measurement point.

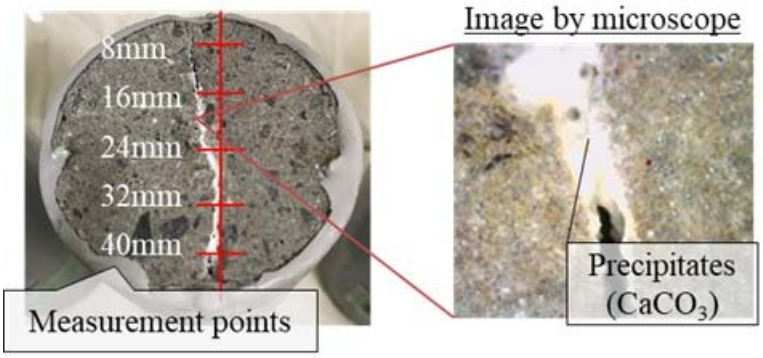

Figure 1. Measurement of crack width and sealing rate by microscope.

2.5 Measurements of Rate of Absorption of Water

The rate of absorption of water was measured in accordance with ASTM C 1585-13 using the specimens subjected to wet and dry cycles or wet condition. The test is carried out in such a way that the repaired surface was exposed to the distilled water and the water is basically absorbed through the capillary suction as shown in Figure 2. The measurements were carried out up to 7 days at predetermined intervals. Based on the changes of weight of the specimens, the rate of absorption of water is calculated using Eq. (1).

$$I = \frac{m_t}{ad} \tag{1}$$

where I: rate of absorption of water, m_t: changes of weight of the specimen, a: area of the immersed surface, d: density of water.

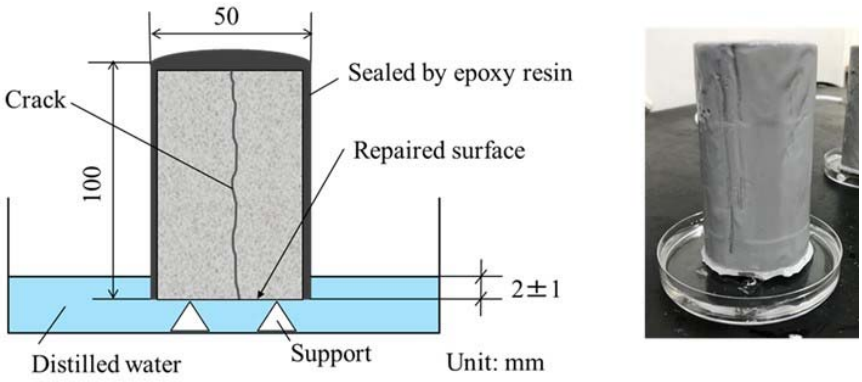

Figure 2. Testing set-up of absorption of water.

3 Experimental Results and Discussion

3.1 Exposure Tests Under Wet and Dry Cycles

For the mortar specimens repaired with each mixture, the materials formed on the cracked surface were firstly observed by microscope. The observations were made before repaired, 7 days later before the specimens were exposed to the dry and wet cycles and 56 days after the exposure. It should be noted that the average crack width was about 0.57 mm for the specimens tested. As can be seen in Figure 3, precipitates in white colour were not observed by microscope on the specimens for all the mixtures tested after the specimens were exposed to the room conditions controlled at 20°C for a week. Subsequently, precipitates were clearly observed on the specimens repaired with each mixture. However, the distribution of precipitates was largely varied, thus resulting in differences in the sealing rate. The sealing rates were 25.8% (N1-G1-T1), 40.0% (N1-G1-T0), 10.0% (W-G0-T0), and 13.8% (No repair). As observed by microscope, the sealing rate is clearly higher in the cases of specimens repaired with the N1 mixtures. It should be noted that the self-healing could naturally take place in the absence of

the microorganism owing to the unhydrated cement and carbon dioxide dissolved in the distilled water. The difference observed in the sealing rate could be also affected by the gel films formed on the cracked surface. It is partly because the moisture kept in the gel films can be released to the crack even under dry conditions in the exposure conditions. Thus, the sealing effect could be obtained even under the dry conditions in such a case. As observed on the repaired surface after the exposure tests, the higher sealing rate obtained in the case of N1-G1-T0 mixture can be explained by the fact that the gel films were present and remained intact through the dry and wet actions.

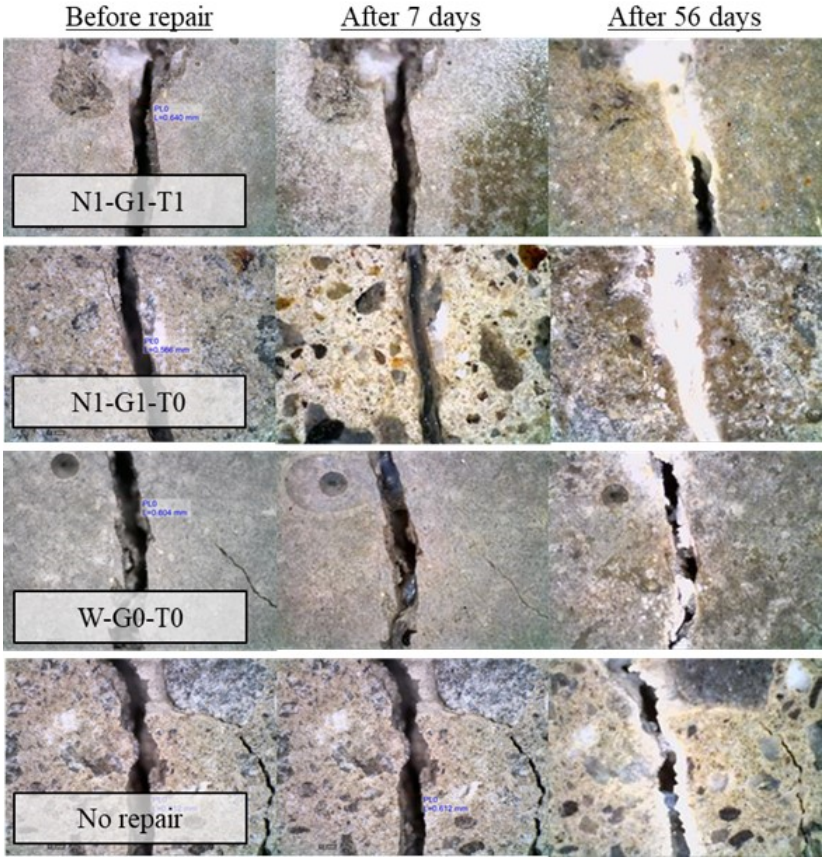

Figure 3. Observations by microscope on the repaired surface (wet and dry condition).

3.2 Exposure Tests Under Wet Condition

For the specimens exposed to the wet condition, the average crack width ranged from 0.48 to 0.51 mm. As shown in Figure 4, similar to those observed in the specimens subjected to the wet and dry conditions, precipitates in white color were clearly observed by microscope on the specimens especially repaired with the N1 mixtures after 56 days exposure. The sealing rates were 53.0% (N1-G1-T1), 74.4% (N1-G1-T0), 35.4% (W-G0-T0), and 37.9% (No repair). The effect of repair with respect to the sealing rate was found to be higher in the case of the wet conditions compared to those observed in the specimens exposed to the wet and dry environment. This could be attributed to the higher availability of moisture and dissolved oxygen for the MICCP processes in the N1 specimens. It should be noted that the gel films were

remained intact especially in those specimens. This contributed to the bio-composite formation accompanied by the calcium carbonate precipitations inside the gel films. The specimens repaired with each mixture and exposed to the exposure tests were further tested by the water absorption tests, which is discussed in Section 3.3.

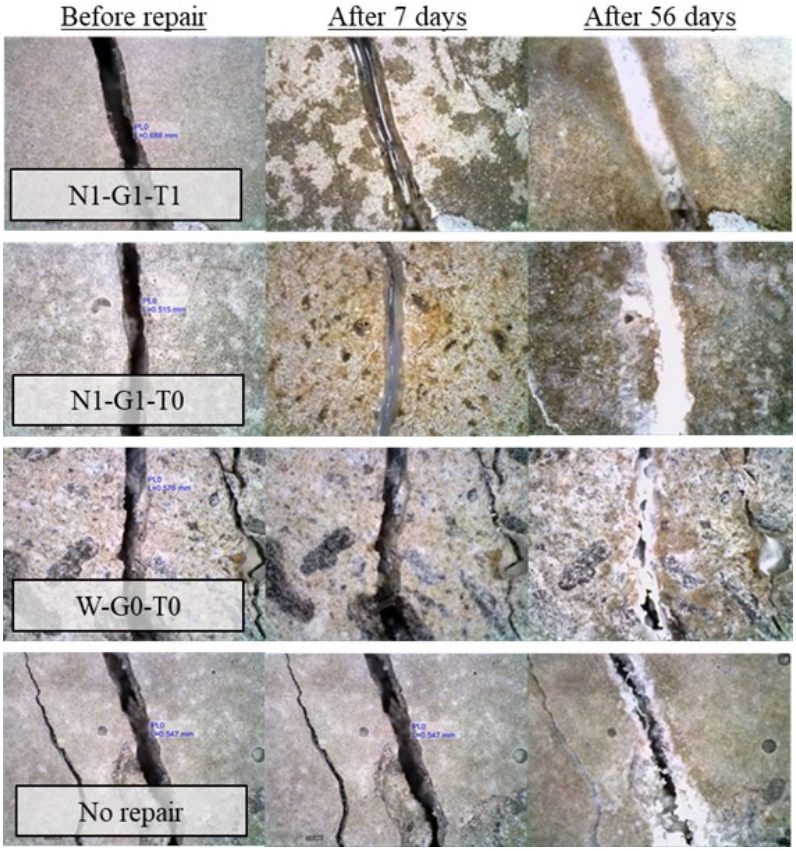

Figure 4. Observations by microscope on the repaired surface (wet condition).

3.3 Rate of Absorption of Water

Water absorption test was carried out based on modified procedure in accordance with ASTM C 1585. According to the standard, the primary gradient is obtained based on the changes of weight up to 24 hours, and the subsequent changes of weight are classified into secondary gradient. Figure 5 shows the primary gradients calculated based on the testing results for the all the mixtures including specimens without repair. As can be seen in the figure, the primary gradients are decreased with increasing rate of sealing effect of crack repair. In particular, the smallest gradient was obtained in the case of N1-G1-T0 mixture. This is consistently observed in each exposure condition, thus suggesting that the crack repair using the N1-G1-T0 mixture contributed to higher resistance against the ingress of water through the cracks. Although the sealing rate is slightly lower in the case of specimens exposed to wet and dry environment as reported in Section 3.1, the resistance against the water absorption could be enhanced using the crack repair though the MICCP. As discussed in Section 3.1 and 3.2, the presence of gel films are significant factors contributing to higher sealing effect in both exposure cases, which led to

the formation of bio-composite through the calcium carbonate precipitation. The results suggest that higher sealing rate of crack repair associated with calcium carbonate precipitation leads to higher resistance against water absorption tested in accordance with ASTM C 1585 in this study.

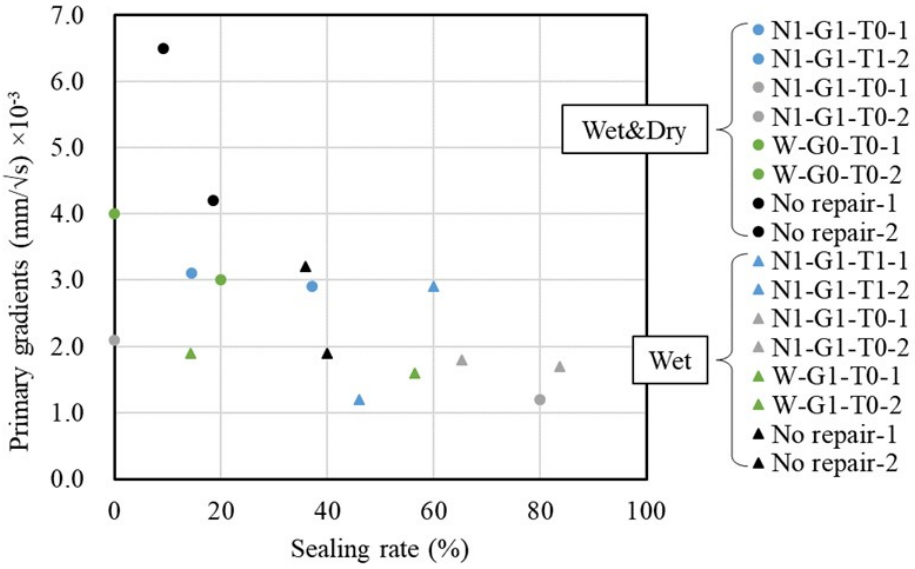

Figure 5. Primary gradient of water absorption test and sealing rate of crack repair.

4 Conclusions

- Based on the observations made on the sealing rate of crack repair, the presence of gel films remained intact on the cracked surface under exposure conditions could contribute to higher sealing effect in the cases of the N1 mixtures.
- The results suggest that higher sealing rate of crack repair associated with calcium carbonate precipitation leads to higher resistance against water absorption especially in the case of the N1-G1-T0 mixture under both exposure conditions (wet&dry and wet) tested in this study.

Acknowledgements

This study is financially supported by JSPS KAKENHI Grant-in-Aid for Scientific Research (B), Grant numbers 19H02216.

ORCID

Keiyu Kawaai: https://orcid.org/0000-0003-4767-4355
Takahiro Nishida: https://orcid.org/0000-0002-2018-6928
Atsushi Saito: https://orcid.org/0000-0001-6866-1882

References

Jonkers, H.M. (2011). Bacteria-based self-healing concrete, Heron, 56 (1/2).
Jonkers, H.M., Thijssen, A., Muyzer, G., Copuroglu, O. and Schlangen, E. (2010). Application of bacteria as self-healing agent for the development of sustainable concrete, Ecological Engineering, 36, 230-235.

Kawaai, K., Ujike, I., Yamamoto, S. and Putri, P.Y. (2016). Some considerations on precipitation rate of calcium carbonate in bio-based materials used for concrete repair, Concrete Solutions 2016, 6th International Conference on Concrete Repair, 571-578.

Kawaai, K., Nishida, T. and Saito, A. (2017). Calcite-alginate bio-composite formation in alginate gel films for self-healing concrete application, Proceedings of the 5th Seminar Workshop on the Utilization of Waste Materials in conjunction with the 2nd International Symposium on Concrete and Structure for the Next Generation, Manila Philippines, 5.

Palin, D., Wiktor, V. and Jonkers, H.M. (2016). A bacteria-based bead for possible self-healing marine concrete applications, Smart Materials and Structures, 25(8).

Putri, P.Y., Kawaai, K., Ujike, I. and Yamamoto, S. (2016). Effect of Temperature on Precipitation Rate of Calcium Carbonate Produced through Microbial Metabolic Process of Bio Materials, Civil Engineering Dimension, 18(2), 103-108.

Tittelboom, K.V., De Belie, N., Loo, D.V. and Jacobs, P. (2011). Self-healing efficiency of cementitious materials containing tubular capsules filled with healing agent, Cement and Concrete Composites, 33, 497-505, 2011.

Wang, J., Snoeck, D., Vlierberghe, S.V., Verstraete, W. and De Belie, N. (2014). Application of hydrogel encapsulated carbonate precipitating bacteria for approaching a realistic self-healing in concrete, Construction and Building Materials, 68, 110-119.

XV International Conference on Durability of Building Materials and Components
DBMC 2020, Barcelona
C. Serrat, J.R. Casas and V. Gibert (Eds)

Effect of Internal Hydrophobization on the Properties of Porous, Cementitious Materials

Kalina B. Grabowska[1] **and Marcin Koniorczyk**[2]

[1]Department of Building Physics and Building Materials, Lodz University of Technology, Al. Politechniki 6, Łódź, 90-924, Poland, kalina.grabowska@edu.p.lodz.pl

[2]Department of Building Physics and Building Materials, Lodz University of Technology, Al. Politechniki 6, Łódź, 90-924, Poland, marcin.koniorczyk@p.lodz.pl

Abstract. *Water is one of the main factors affecting the durability of porous materials and it is one of the most common causes of their degradation. Physical phenomena such as freezing or salt crystallization, as well as the development of fungi and moulds, are caused by the presence of moisture. In wet material thermal conductivity coefficient increases and the heat loss begins to rise. Hydrophobization is one of the protecting methods of porous materials against water. Two different type of water-repellent agents were used for the internal hydrophobization. The first of them is an aqueous emulsion of silane: triethoxy(octyl)silane (OTES) and the second one is also an aqueous emulsion but the matrix is poly(dimethylsiloxane) (PDMS). The paper focuses on the use of organosilicon water repellents. The main purpose of this paper is to determinate the possibility of use organosilicon agents as admixtures to internal hydrophobization. We compared results obtained for two different silicon-based admixtures. We investigated influence of both water-repellents on basic characteristics such as: absorbability, capillary water absorption and mechanical properties of cement mortar as well as heat of hydration of cement paste.*

Keywords: *Internal Hydrophobization, Cement Mortar, Silane, Siloxane.*

1 Introduction

In 2018, in Poland, cement sales amounted to 18 million tons (Polish Central Statistical Office, 2019). And it is growing every year. Cement-based building materials are one of the most commonly used one. But, as all we know, they are porous, which means that their resistance to water is insufficient. Water is one of the main factors affecting the durability of porous materials and it is one of the most common causes of their degradation. Physical phenomena such as freezing or salt crystallization, as well as the development of fungi and moulds, are caused by the presence of moisture. In wet material thermal conductivity coefficient increases and the heat loss begins to rise. Not to mention aesthetic features (*e.g.* stains) and deterioration of the microclimate. The appropriate design and composition of building material may already be a part of protection against water. The hydrophobization process might complement to these actions. Hydrophobization can be carried out in two ways from the technological point of view. The material may become hydrophobic by applying water-repellent coatings on the surface or by using suitable admixtures as one of the components. Internal hydrophobization carried out with the hydrophobic admixtures causes, contrary to surface treatment, the hydrophobization of the surface and internal surface (Barnat-Hunek, 2016).

There are very limited number of regular studies or they are insufficient in determining the effectiveness of internal hydrophobization of cement-based building materials with

organosilicon compounds. In this paper we investigate the influence of two different silicon-based admixtures on fundamental properties of cement mortar/paste. The addition of hydrophobic admixtures to the batch water was intended to create a hydrophobic material in its whole volume.

2 Hydrophobizing Agents

Considering the chemical nature of porous building materials, it can be seen, that silicon compounds (silicon dioxide, silicates, aluminosilicates etc.) are part of natural and manufactured building materials. Therefore, organosilicon compounds have found practical use in the hydrophobization of building objects. They are mainly based on and silicon-oxygen (Si-O) and silicon-carbon (Si-C) bonds. The basic structure of organosilicon compounds is a polysiloxane chain (O-Si-O-Si-O) and the type of substituents affects the diversity of spatial arrangements that can be created from the basic chains (Barnat-Hunek, 2016).

Science the 1950's silicon-based compounds have been used in industrial applications. Hydrophobic agents based on organosilicon compounds are the youngest, and the most promising, group of hydrophobic agents for internal treatment. The main groups of these compounds are alkylsilanes, arylsilanes, halosilanes, silanols, siloxanes, silylamines and silyl esters. Among all different kind of hydrophobic products developed for the building industry, silicone resins, silanes, oligomeric and polymeric siloxanes have proved to perform best in surface hydrophobization. Until recently stearates and oleates were used as waterproofing admixtures. Effective surface hydrophobization with organosilicon agents caused attempts to use them as admixtures. It turned out that organosilicon compounds used as water-repellent admixtures are the most efficient in protecting from water penetration (Barnat-Hunek, 2016; Grabowska *et al.,* 2019; Roos *et al*., 2008).

2.1 Triethoxy(octyl)silane

Silanes are monomeric molecules (have one atom of silicon) with low molecular weight of 178. They are a silicon analogue of methane. Silane derivatives of the general formula: R_nSiX_{4-n} have the most important practical significance (R can be a hydrogen atom, an alkyl or aryl group, X can be a halogen atom or an alkoxy group). Longer alkyl chain-length provides desired water resistance of the modified material and steric protection to the silicon-oxygen bond. Initially silanes undergo hydrolysis and polycondensation reactions. Subsequently they cross-link under elimination of alcohol and as a result of which polymers, with polysiloxane chain, are formed. (Ciabach, 2001; Roos *et al*., 2008). Triethoxy(octyl)silane is an alkyl alkoxy silane with three ethoxy groups and one octyl group in its structure (Fig 1).

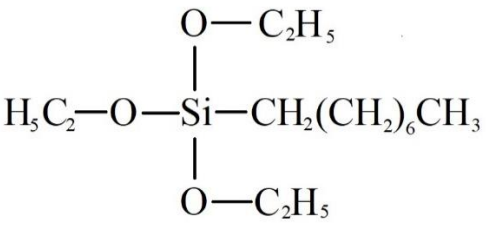

Figure 1. Structure of triethoxy(octyl)silane.

2.2 Poly(dimethylsiloxane)

Siloxanes are oligomeric molecules with a molecular weight about 400-600. The basic structure of siloxanes is a polysiloxane chain (O-Si-O-Si-O). Polysiloxanes are versatile materials. They have an excellent chemical, physical, and electrical properties. Poly(dimethylsiloxane) (PDMS) is an important example and the most common polysiloxane of this class of polymers. The chains of polysiloxanes consist alternately connected silicon and oxygen atoms. Inorganic chain and the presence of strong bonds (Si-O and Si-C) provide significant thermal and oxidative resistance as well as resistance to UV radiation of polysiloxanes. Despite of the polar character of siloxane bonds (Si-O bonds have ionic character in 50%) organosilicon compounds show similarity to paraffins in terms of low critical surface tension. Siloxanes have very low surface energy and exceptional hydrophobicity. PDMS chains are arranged in helixes and present of the methyl groups ($-CH_3$) give hydrophobic character of modified materials. Weak intermolecular interactions, characterizing PDMS, provide a significant gas diffusion coefficient. Organosilicon compounds, compared to other polymers, are characterized by very high oxygen, nitrogen and water vapor permeability (Chruściel *et al.*, 2008, Cypryk *et al.,*2007; Grabowska *et al.,* 2019;).

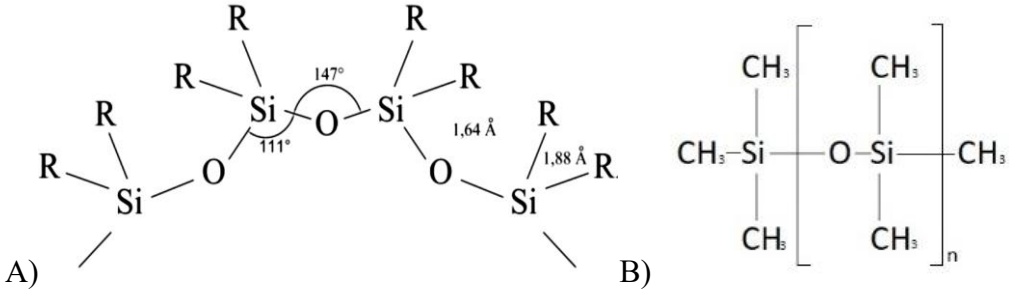

Figure 2. A) Polysiloxane chain (Cypryk *et al.,*2007), B) Structure of PDMS.

3 Materials

The Ordinary Portland Cement 42.5 R was used. Table 1 shows composition of investigated cement mortars. They were prepared according to Polish standard PN-EN 196-1 with a water-cement ratio (w/c) equal to 0.5. Prismatic samples of mortar, with dimensions160x40x40 mm, were prepared for mechanical, absorbability and capillary water absorption tests. Isothermal calorimeter was used to determine the influence of organosilicon admixtures on the heat of hydration of cement paste.

Two different type of water-repellent agents were used for the internal hydrophobization. The first of them is an aqueous emulsion of silane: triethoxy(octyl)silane (OTES). The second admixture is also an aqueous emulsion but the matrix is poly(dimethylsiloxane) (PDMS). The amount of the hydrophobic admixture in cement mortar or paste was 0%, 1%, 2% or 3% (refer to cement mass). They were added to the batched water. Both admixtures are recommended for volume hydrophobization.

Table 1. Composition of cement mortar.

	Water repellent agent		
	OTES/ PDMS		
	1%	***2%***	***3%***
W/C	0.5		
Cement [g]	450		
Sand [g]	1350		
Water [g]	225		
Admixture [g]	4.5	9.0	13.5

4 Results

4.1 Mechanical Test

Table 2 shows the results of mechanical test received after 1, 2, 7 and 28 days of curing for hydrophobized cement mortars. Results shown in Table 2 represent the average value taken over six samples. The compressive strength test was carried out on halved, prismatic samples left after flexural strength test. Results of each test of cement mortar admixed PDMS show substantial decrease in mechanical strength. After 28 days of ageing addition of poly(dimethylsiloxane) (PDMS) based admixture decreases the mechanical properties by almost a factor of two. The addition of 1% silane admixture does not decreases significantly compressive strength after 1, 2, or 7 days of curing. Noticeable loss of the strength is observed for 2% and 3% addition of silane after 1, 2, 7 and 28 days and for 1% of OTES after 28 days.

Table 2. Compressive strengths after 1, 2, 7 and 28 days of curing.

Water repellent agent	**Amount**	**Compressive strength [MPa]**			
		1 day	2 days	7 days	28 days
Reference	0%	14.40	23.04	31.16	45.25
OTES	1%	13.17	22.34	32.71	38.35
	2%	8.27	18.22	28.72	38.19
	3%	7.05	17.18	27.59	36.36
PDMS	1%	5.03	8.76	10.47	25.84
	2%	3.83	8.31	9.02	23.53
	3%	3.65	9.07	11.91	22.16

4.2 Absorbability

Absorbability of hydrophobized cement mortar is shown in Table 3. The test was carried out on three specimens for each composition. After 28 days of curing prismatic samples were dried and, after that, progressively flooded with water. Subsequently mortar samples were weighed

every 24 hours until constant weight was received. The addition of silane admixture and 2% of PDMS admixture decrease significantly absorbability. Lower values was observed for silane.

Table 3. Results of absorbabilty test of hydrophobized cement mortar.

Water repellent agent	Amount	Absorbability
Reference	0%	7.6%
OTES	1%	3.9%
	2%	2.3%
	3%	2.2%
PDMS	1%	6.3%
	2%	3.7%
	3%	6.5%

4.3 Capillary Water Absorption Test

One of the most common tests to show hydrophobic effect is capillary water absorption test. Table 4 presents the results taken over three halved, prismatic samples (six in total). Test was carried out according to PN-EN 1015-18. After 28 days of curing mortar samples were dried at 80ºC. Thereafter sealing material was applied on the side surfaces of mortar specimens (40 x 80 mm). Mortar prisms were vertically immersed in water to a depth of 1 cm and weighed after 10 min, 30 min, 60 min, 90 min, 2h, 3h, 4h and 24h. Both used admixtures decrease capillary water absorption coefficient. Lower values were observed for silane.

Table 4. Results of capillary water absorption test of hydrophobized cement mortar.

Water repellent agent	Amount	Capillary water absorption coefficient, $\frac{kg}{m^2 * min^{0,5}}$
Reference	0%	0.206
OTES	1%	0.042
	2%	0.023
	3%	0.020
PDMS	1%	0.115
	2%	0.106
	3%	0.098

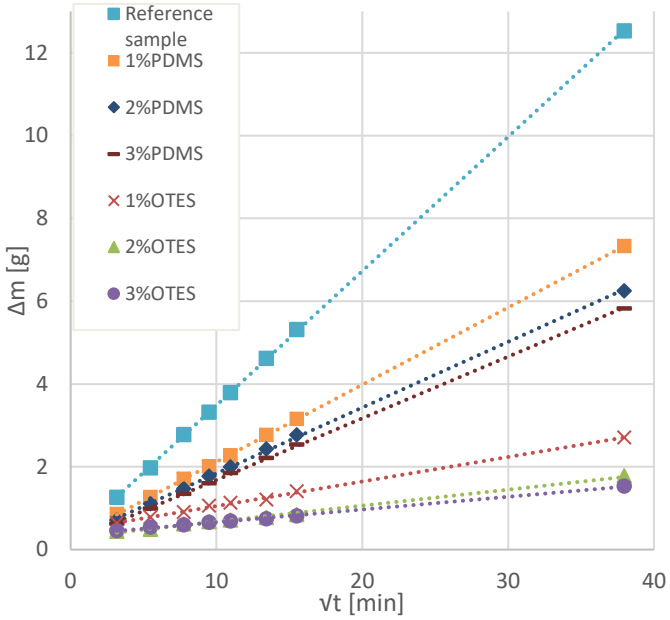

Figure 3. Mass changes of cement mortar samples during capillary water absorption test.

4.4 Heat of Hydration

The heat of hydration of cement paste with organosilicon admixtures was measured. The w/c ratio was 0.5 and the Portland Cement 42.5 R was used. Test was carried out in an isothermal calorimeter TAM Air, at temperature T=20°C. The heat was measured during 7 days for each sample. Two samples were analyzed for each composition of cement paste. 1%, 2% or 3% of organosilicon admixture was added per cement mass. The heat of hydration after 41 hours is shown in Table 5.

Table 5. Influence of organosilicon admixtures on heat of hydration.

Water repellent agent	Amount of admixture	Average hydration heat after 41 h [J/g]
Reference	0%	217.25
OTES	1%	180.00
	2%	157.78
	3%	149.12
PDMS	1%	187.10
	2%	199.70
	3%	182.05

5 Discussion

The presented test results unequivocally demonstrate the interaction between used admixtures and the cement matrix. Both admixtures gave a visible hydrophobic effect. The addition of admixture based on PDMS successfully reduces capillary water absorption. For reference sample capillary water absorption coefficient was 0.21 kg/(m^2*$min^{0.5}$) and 0.098 kg/(m^2*$min^{0.5}$) for cement mortar containing 3% of PDMS admixture. Absorbability of hydrophobized cement mortar decrease to 3.7% from 7.6%. As it was shown in Table 5 poly(dimethylsiloxane) also interacts with Portland cement. The heat of hydration of Portland cement decrease from 217,25 J/g to 182,05 J/g. Even better hydrophobic results in reducing capillary water absorption and absorbability were obtained for the second admixture based on triethoxy(octyl)silane. This water-repellent agent decreases capillary water absorption by almost 90% (from 0.21 kg/(m^2*$min^{0.5}$) to 0.02 kg/(m^2*$min^{0.5}$)) and reduce absorbability by 70% (from 7.6% to 2.2%) at the maximum amount of admixture. Also, in case of silane admixtures heat of hydration was reduced. The lowest value was obtained for 3% of OTES (149.12 J/g). Unfortunately, both admixtures decrease compressive strength of cement mortar. The largest decreases in compressive strength were observed for the content of 3% of silicon-based admixtures. PDMS admixture reduce mechanical strength of cement mortar by an average of 50% and OTES one only by 15%.

The present of non-polar such as methyl groups (-CH_3) and octyl groups (-C_8H_{17}) attached to the silicon atom provide desirable effect of internal hydrophobization of cement mortar. For the same reason the compressive strength of cement mortar might have been decreased. Changes in the heat release, during hydration process**,** indicate that the admixtures can bind to the cement phases (alite, belite or tricalcium aluminate) making water-cement reaction more difficult. This may cause incomplete hydration of the cement and thus a subsequent decrease in strength.

6 Conclusions

From the obtained results obtained the following conclusions can be drawn:

- Internal hydrophobization by using organosilicon admixtures is possible, but it has its own limitations. The hydrophobic effect depends on type of used organosilicon compound.
- Both admixtures were recommended for internal hydrophobization of cementitious materials by the producers. But treatment with triethoxy(octyl)silane gives better hydrophobic effect than poly(dimethylsiloxane) by reducing the capillary water coefficient by 90%.
- Both admixtures decrease in compressive strength, but OTES based admixture reduce it by 15% and PDMS one by up to 50%.

As a conclusion, it can be said that triethoxy(octyl)silane is an efficient water-repellent agent for cementitious materials. However, the first results are very promising, but this issue still requires more studies. Especially when it comes to mechanical properties.

ORCID

Kalina Grabowska: http://orcid.org/ 0000-0003-1232-8399
Marcin Koniorczyk: http://orcid.org/ 0000-0002-6887-4324

References

Barnat-Hunek, D. (2016). *Swobodna energia powierzchniowa jako czynnik kształtujący skuteczność hydrofobizacji w ochronie kostrukcji budowlanych* (in Polish). Wydawnictwo Politechniki Lubelskiej, Lublin, Poland.

Chruściel, J., Leśniak, E. and Fejdyś, M. (2008). *Karbofunkcyjne silany i polisiloksany. Cz. II. Otrzymywanie i zastosowania karbofunkcyjnych polisiloksanów* (in Polish). Polimery, 53 (11-12), 817-828.

Ciabach, J. (2001). *Właściwości żywic sztucznych stosowanych w konserwacji zabytków* (in Polish). Wydawnictwo Uniwersytetu Mikołaja Kopernika, Toruń, Poland.

Cypryk, M., Delczyk, B., Pospiech, P. and Strzelec, K. (2007). *Modyfikacje polimerów siloskanowych* (in Polish). Polimery, 52 (7-8), 496-502.

Grabowska, K. and Koniorczyk, M. (2019). *The effect of hydrophobic treatment by organosilicon admixtures of cement mortar.* Cement Wapno Beton, 4, 320-329.

Polish Central Statistical Office ("GUS") (2019). *Outlays and results in industry in 2018.* Statistical information.

Roos, M., König, F., Stadtmüller S. and Weyershausen B. (2008). *Evolution of Silicone Based Water Repellents for Modern Building Protection.* 5th International Conference on Water Repellent Treatment of Building Materials Hydrophobe V, Aedificatio Publishers, 3-16.

XV International Conference on Durability of Building Materials and Components
DBMC 2020, Barcelona
C. Serrat, J.R. Casas and V. Gibert (Eds)

Effect of the Type of Concrete with Mineral Additions on the Reinforcement Corrosion Induced by Chlorides - Analysis in the Same Mechanical Strength Class

Andrielli Morais de Oliveira[1], Oswaldo Cascudo[1] and Alexandre de Castro[2]

[1] GEDur - Durability Study Group, Laboratory of Technological Innovation in Civil Construction – LABITECC, PPG-GECON, Civil and Environmental Engineering School, Federal University of Goiás (Universidade Federal de Goiás - UFG), 74.605-220. Praça Universitária, Goiânia – GO, Brazil, andriellimorais@ufg.br, ocascudo@gmail.com

[2] Furnas Centrais Elétricas, Rodovia BR 153, s/n - Zona Rural, Aparecida de Goiânia - GO, 74923-650, Brazil, alexcasp@furnas.com.br

Abstract. *The environment in which the concrete structure is inserted has a great influence on its durability and its service life. Thus, the present work aims to study of the performance of 5 types of concretes of same compressive strength (35 MPa at the age of 28 days) and considers kinetic and thermodynamic aspects of the corrosion induced by chlorides. The 5 types of concretes studied were produced with the use of mineral additions in partial replacement on cement mass (10% of silica fume, 30% of fly ash and 20% of metakaolin), besides the control situation (without mineral addition). The water-to-cementitious materials ratio was different for the concretes ranging from 0.30 to 0.55. Specifically, for the concrete with fly ash, two water/binder ratios were studied (0.30 and 0.40) with the goal of verifying if there are or not significant differences on properties of corrosion with little change of water quantity in the mix. The chloride attack consisted by 308 days (44 weekly cycles) in immersion in aggressive solution rich in chlorides and subsequent drying in a laboratory environment. During this period, the corrosion potentials (E_{corr}) and corrosion rate (i_{corr}) from polarization resistance (R_p) of steel bars were monitored. As a general result, it was possible to compare the performance of concretes at the same class of compressive strength to denote which systems have the longest durability in view of attack by chloride. The results have shown that the concretes produced with mineral additions did not show steel bar corrosion, thus configuring major service life for them. Control concrete presented depassivation of reinforcing steel, E_{corr} more electronegative and higher i_{corr} over time.*

Keywords: *Concrete, Mineral Additions, Chlorides, Corrosion, Durability.*

1 Introduction

Brazilian energy matrix is composed of approximately 60.8% of hydroelectric power plants that have vulnerability in periods of drought (Gomes *et al.*, 2019). The energy policy covers tax incentives for the generation of energy from alternative sources, such as wind energy that shows its low environmental impact, low gas emissions and towers deployment.

The Brazilian northeast region was the first to house these wind farms in the country and a large number of towers are being deployed in these coastal. The wind potential of other regions of the country has been studied. In these wind farms, the base of the wind towers is made of reinforced concrete and both humidity and chloride ions may be present. This combination is extremely deleterious for concrete, since chloride ions, when in critical concentration level near the reinforcement, they can trigger the corrosion process.

For preventing corrosion at the base of wind towers, concrete of high performance can be designed. The concrete improved composition makes difficult for aggressive agents to enter from exterior to its internal structure, increasing the material's service life, safety and durability and reducing maintenance costs (Oliveira and Cascudo, 2018).

In this sense, concretes of the same strength class, with or without supplementary materials, can have different durability and service life, when exposed to harsh environments, especially containing chlorides. The use of supplementary materials, i.e. mineral additions in the composition of concretes and their benefits, has been extensively studied in recent years by literature (Ferreira, 2003; Ramezamianpour *et al*., 2012; Figueiredo *et al.*, 2014, Shi *et al.*, 2017; Rattanashotinunt *et al.*, 2018). These materials can increase concrete durability making the ingress of aggressive agents, such as chloride ions, more difficult. On the other hand, these materials can also change the pH´s pore solution, leading to a reduction of its alkalinity, which can make the steel bars in the concrete vulnerable to corrosion. However, among the mineral additions, some of them may present better performance and increase the service life of the structures, specially the so-called super pozzolans of high reactivity and fineness.

In Brazil, concretes are specified and purchased based on compressive strength, maximum water/binder ratio and environmental aggressiveness class (ABNT NBR 6118: 2014). Thus, the C35 compressive strength class is an intermediate class for most constructions and also meets the construction of wind tower concrete bases.

The aim of the present paper is to evaluate the protection ability of concretes against the steel bar corrosion. The compared concretes have the same compressive strength (C35 MPa) at the age of 28 days and the same exposure condition in harsh environment, containing chlorides. Concrete with fly ash (FA), silica fume (SF), metakaolin (Mk) and without mineral addition – Control (CR) were studied. Additionally, for the concrete with fly ash, the influence of a water/binder ratio also were measured (0.30 and 0.40). Thermodynamic (E_{corr}) and kinetic (i_{corr}) parameters of reinforcement corrosion were evaluated.

2 Experimental Program

2.1. Materials

The concrete mix proportions were based on previous studies from the durability´s study group of the Federal University of Goiás (Carasek and Cascudo, 2001; Ferreira, 2003). The composition was a combination of Portland Brazilian cement (composed by 6–10% in mass of limestone filler and by 90–94% of clinker – with a small amount of calcium sulfate), whose mechanical strength requirement is a minimum of 32 MPa of compressive strength of the age of 28 days – similar to European CEM II/A-L, mineral additions (silica fume, fly ash or metakaolin), fine sand aggregate (river sand) and coarse aggregate (stone from mica schist metamorphic rock), plasticizer, superplasticizer and tap water (potable water from the public distribution network). In the concrete mixtures, 10%, 30% and 20% of cement (by weight) were replaced by silica fume, fly ash and metakaolin, respectively. Furthermore, a control concrete (without mineral additions) was studied.

The water-to-cementitious materials ratio was different for the concretes ranging from 0.30 to 0.55. However, all concretes showed compressive strength at the age of 28 days of 35 MPa. Specifically, for the concrete with fly ash, two water/binder ratios were studied: 0.30 and 0.40.

Table 1 shows the compositions of the concretes and Table 2 shows the compressive strength of concretes at the age of 7, 28 and 91 days. The slump test was fixed in (80±10) mm. Steel bars with a nominal diameter of 10 mm (0.4 in.) were used to evaluate the corrosion.

Table 1. Composition of concretes used under this investigation.

Materials	Concretes*				
	Control	Silica Fume	Fly Ash		Metakaolin
Portland cement (kg/m^3)	552	331.2	525.0	487.5	294.4
Water/binder ratio	0.40	0.55	0.30	0.40	0.55
Mix Unit (kg) (cement: mineral addition: sand: stone)	1,0: 0.0:0.8:2.1	1.0:0.1:1.9:3.5	1:0.3:0.7:2.1	1:0.3:0.7:2.3	1:0.3:2.1:3.9
Plasticizer (%)	0.03	0.05	0.03	0.03	0.05
Superplasticizer (%)	0.00	0.15	0.08	0.01	0.00

*10%, 30% and 20% of cement (by weight) were replaced by silica fume, fly ash and metakaolin, respectively.

Table 2. Average of compressive strength of concretes studied at the ages of 7, 28 and 91 days.

Age (days)	Average compressive strength and water/binder ratio				
	Control	Silica Fume	Fly Ash		Metakaolin
	0.40	0.55	0.30	0.40	0.55
7	27 (0.8)	25 (0.4)	29 (1.0)	27 (0.1)	28 (1.3)
28	36 (1.4)	36 (0.4)	36 (1.9)	33 (1.4)	32 (1.3)
91	41 (0.3)	42 (0.6)	49 (0.9)	44 (1.8)	39 (1.7)

*Standard deviation is given in parentheses.

From Table 2, it was possible to observe that although all concretes have the same mechanical strength at 28 and 91 days (except fly ash concretes at the age of 91 days, in which their values of strength are slightly higher, in the order of 45 MPa to 50 MPa), they have different microstructure and porosity characteristics. As the water/binder ratios are different (among some of these concretes), the global porosity and the pore size distribution are, in fact, different among them. This interferes with important aspects related to durability, such as: interconnectivity and tortuosity of pores, in addition to the compactness characteristics of the paste - aggregate interfacial transition zone (Oliveira and Cascudo, 2018). Although the mechanical strengths are similar (premise of the present work), it is important to note that there are different cementitious systems being compared.

The steel bar used in the specimens was of a single type, having been used a Brazilian CA-50 carbon steel (for reinforced concrete structures). This steel meets the Brazilian standard of steel for reinforced concrete structures (ABNT NBR 7480: 2007) and it featured a yield strength higher than 500 MPa.

In order to standardize the surface conditions of the bars, they were initially chemical cleaned using a solution of (Hexamethylenetetramine) (Figure 1a). The general appearance of steel bars after chemical cleaning can be seen in Figure 1 (b). However, this procedure did not allow the complete removal of visible oxides from the bars. So, it was necessary to perform a mechanical cleaning performed with a circular brush attached to emery, as shown in Figure 1 (c). The

appearance of the bars before and after mechanical cleaning can be seen in the Figure 1 (d). Finally, the steel bars were identified (Figure 1 e). These bars had a total length of 15 cm (6 in.) and they were partially inserted into of concrete´ specimens, constituting 2.5 cm (1 in.) of cover thickness. Just a portion of steel, as showed Figure 1 (f) (5 cm = 2 in.) was exposed to corrosion induced by chloride ions (Figure 1 f). The surface area of rebar exposed to corrosion was 12.88 cm^2 (5.15 in^2) (Figure 1 g).

Cubic concrete specimens of 1500 mm side were produced and they were reinforced with four longitudinal rebars of 10 mm of nominal diameter. These test specimens were designed for the electrochemical tests, while for the electrical resistivity test, the same cubic specimens were used, but without steel bars. Oliveira and Cascudo (2018) used the same specimen shape. After manufacturing, the test specimens were under cure for 28 days in a controlled room (temperature of 22±2ºC and a minimum relative humidity of 95%). Thereafter, the specimens remained until the age of testing in the laboratory environment, which corresponded to the age greater than 91 days.

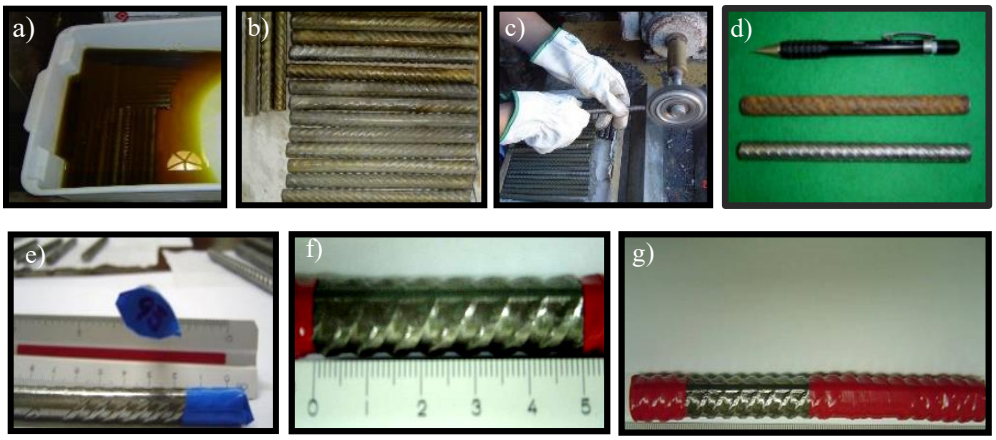

Figure 1. Preparation of steel bars: (a) chemical cleaning with (Hexamethylenetetramine), (b) final appearance of the bars after chemical cleaning, c) mechanical cleaning, (d) before and after mechanical cleaning, (e) bar identification, (f) bar ends wrapped with electrical tape and (g) bar center detail (5 cm) ready to be placed in the molds.

2.2. Methods

The corrosion was induced by wet–dry cycles in NaCl solution (NaCl diluted to 5% by mass or 0.855 M). The weekly cycles were 2 days of partial immersion of the specimen until 15 cm of its height in NaCl aggressive solution and subsequent drying during 5 days in a controlled environment (40ºC of temperature and 50 ± 5% of relative humidity).

The NaCl solution was replaced every four cycles (28 days) to facilitate aeration in a sufficient level so that the corrosion could develop. Specimens were subjected to total of 44 cycles or 308 days of attack in aggressive solution containing chlorides. The definition of the cycles was based on the studies of Cascudo (2000), considering the fact that concrete absorbs water much faster than it loses (during drying), reason why it was adopted 2 days of wetting and 5 days of drying. The importance of cycles to accelerate the phenomenon of corrosion was explained by Oliveira and Cascudo (2018).

The techniques of half-cell potential - E_{corr} (ASTM C 876: 2015) and polarization resistance (R_p) were used, the latter making it possible to estimate the instantaneous corrosion rate (i_{corr}).

These electrochemical measurements were performed by means of a three-electrode arrangement using a Voltalab 40 PGZ potentiostat, managed by Voltamaster software.

A working electrode (rebars embedded in concrete), a saturated calomel electrode – SCE (as the reference electrode) and a counter electrode of stainless steel (externally in contact with one of the faces of the concrete test specimen) were used connected to the potentiostat. In order to avoid interferences from external electric field, the measuring set up (i.e. the concrete test specimen with the 3 electrodes) were inserted inside a Faraday cage, where all the electrochemical measurements were taken. The criteria of ASTM C 876: 2015 were considered to evaluate the results of E_{corr} (mV). These criteria consider that if E_{corr} is more positive than -126 mV (SCE), the steel is passive and the probability of corrosion is smaller than 10%. Also, if E_{corr} is more negative than -276 mV (SCE), they consider that active corrosion is developing. Finally, there is a range of uncertainty with potentials between -126 mV and -276 mV (SCE).

From polarization resistance or linear polarization (R_p), it was possible to assess corrosion current density (i_{corr}). The Stern–Geary equation (Equation 1) and the proportionality factor (B Stern-Geary constant) were used.

$$i_{corr} = B/Rp \quad (1)$$

It was adopted a value of 26 mV for corroding steel and a value of 52 mV for passive steel, as established by Andrade and Alonso (2001). The criteria were adopted, which associate corrosion rates with the intensity of corrosion on corrosion levels.

3 Results and Discussion

Figure 2 (a and b) shows E_{corr} and i_{corr} against the number of cycles, respectively. The results are the average results of 4 rebars for each type of concrete. Table 3 shows the magnitude of the corrosion potentials for the studied concretes.

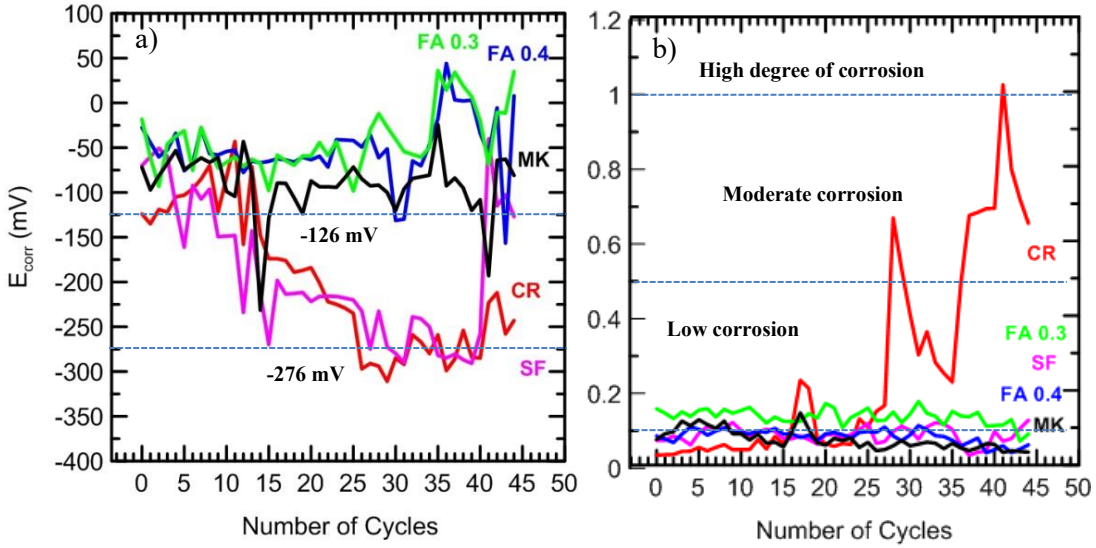

Figure 2. Influence of the type of concrete in terms of initiation and propagation of corrosion induced by chlorides on the concretes performance: representative curves of (a) E_{corr} (SCE) and (b) i_{corr} *versus* attack time by chlorides (number of wet-dry cycles in NaCl solution) according to ASTM (ASTM C 876: 2015) and Andrade

and Alonso (2001) criteria, respectively.

Table 3. Magnitude and average of E_{corr} during the 44 cycles of immersion in aggressive chloride-containing solution.

Concretes	Partial replacement of cement, by weight (%)	Water/binder ratio	E_{corr} – magnitude* (mV)	Probability of corrosion - Criteria of ASTM C 876 (ASTM, 2015)	E_{corr} - average (mV)	Time for depassivation of reinforcing steel (cycles)
CR	0	0.40	-311	> 90%	-199	28
SF	10	0.55	-291	> 90%	-192	No**
FA	30	0.30	-157	Uncertain	-51	No***
		0.40	-98	< 10%	-42	No***
MK	20	0.55	-231	Uncertain	-90	No***

* Magnitude in the table means the maximum individual value obtained. ** There were no signs of depassivation of reinforcement. *** This concrete meets the criterion adopted to define the depassivation of reinforcement and is in the uncertainty range regarding the probability of corrosion. The kinetic aspects can confirm if the reinforced is really depassivated.

From the Figure 2 and Table 3, for concretes with the same compressive strength (35 MPa), it is clear the beneficial effect that the supplementary cementitious materials – SCMs (mineral additions) provide to the concretes, regardless of the water/binder ratio, promoting significantly more electropositive corrosion potential values in relation to the reference concretes. Thus, it can be seen that the control concrete, compared to the concretes with SCMs, exhibit a greater tendency to the depassivation of reinforcement when inserted in environments containing chloride ions. Silica fume, contrary to expectations, did not achieve the best corrosion potential performance. These results are in accordance with the literature (Andrade and Buják, 2013; Jin *et al.,* 2017).

It is worth mentioning the good performance of fly ash concretes, with behaviors close to concrete with metakaolin. The silica fume concrete did not present a good performance regarding E_{corr}, and the lowest performance was presented by the control concrete. Thus, the effectiveness of SCMs in physically and chemically protecting the rebar keeping it passivated as long as possible became evident. This result is important because even though the corrosion induction method used in this work is accelerated, it reports the time until the depassivation of reinforcement, which means that, comparatively, there is a very significant response concerning the differences in performance of the various concretes analyzed (in terms of their actual expectations of durability). Only control concrete gave unequivocal evidence of reinforcement depassivation over the 44 attack cycles. With the exception of the silica fume concrete, the other concretes with mineral additions presented regions with low probability of corrosion or uncertain probability. The E_{corr} average values for metakaolin (water/binder ratio of 0.55) and fly ash (w/b = 0.3) concretes were similar. This evidences the overperformance of metakaolin as a mineral addition, since the difference in terms of w/b ratios for these two concretes is very high.

The silica fume concrete showed E_{corr} magnitude more negative and an indication of active corrosion after some few cycles. In spite of this behavior, the silica fume system did not evidence active corrosion in the period of test, based on i_{corr} results (corrosion rates obtained by

determining R_p). This can be seen in Figure 2b. This apparently different behavior for concrete with silica fume regarding the values of E_{corr} (compared to the concretes with metakaolin and fly ash) certainly reproduces some level of perturbation at the steel–concrete interface in terms of the passive layer (Oliveira and Cascudo, 2018). Probably due to local pH changes (because pore solution is different in silica fume modified systems), it is possible that thermodynamic changes occur at the interface, with changes in the state of electric charges on the electrode (reinforcement), perceived by drops in potential values (to more electronegative values).

Finally, the control concrete showed increase of values of i_{corr} (corrosion rates) in the beginning of dry-wet cycles. This denotes reduction of service life and durability. For the silica fume concrete, in terms of the corrosion rates, there was no increase in i_{corr} values over time, as well as there was no indication of depassivation of steel or significant corrosion for these concretes, within the test period. Thus, despite the negative E_{corr} values, there seems to be no depassivation and active corrosion in concrete with silica fume.

4 Conclusions

The following conclusions can be drawn from the present paper:

- More than one technique is important to diagnose the condition of the reinforcement and to assess the protection capacity of concrete.
- Control´s concrete protected less the steel bar against corrosion induced by chlorides, indicating E_{corr} more negatives and higher corrosion rates (i_{corr}).
- According to E_{corr} values, the concretes with mineral additions have showed similar performance among them (the silica fume concrete initially showed doubt, but later it was confirmed that there was no corrosion) and significantly better behaviors compared to control concrete.
- All concretes with mineral additions have not presented significant corrosion induced by chlorides for the 44 cycles (or 308 days - analyzed period).
- The influence of the small change in water/binder ratio on fly ash concretes was not significant, both for E_{corr} and i_{corr}.
- Metakaolin showed high performance as a supplementary cementitious material, even in a higher water/binder ratio.
- Among the concretes studied, those with mineral additions had higher durability and thus major service life.

Acknowledgements

The authors acknowledgement Eletrobras Furnas Company and the ANEEL – Agência Nacional de Energia Elétrica (National Electric Energy Agency - ANEEL).

ORCID

Andrielli Morais de Oliveira: https://orcid.org/0000-0001-8977-785X
Oswaldo Cascudo: https://orcid.org/0000-0003-1879-6396
Alexandre de Castro https://orcid.org/0000-0001-5089-9788

References

American Society For Testing And Materials. (2015). *ASTM C 876: Standard Test Method for Half-Cell Potentials Of Uncoated Reinforcing Steel In Concrete,* Annual Books of ASTM Standards, Philadelphia, 03 (02).

Andrade, C. and Alonso, C. (2001). On-site measurements of corrosion rate of reinforcements, *Construction and Building Materials,* 15, 141–145. https://doi.org/10.1016/S0950-0618(00)00063-5

Andrade, C. and Buják R. (2013). Effects of some mineral additions to Portland cement on reinforcement corrosion, *Cem. Concr. Res*. 53, 59–67. https://doi.org/10.1016/j.cemconres.2013.06.004

Brazilian Standard NBR 6118 (2014). *Design of concrete structures: procedure*. Associação Brasileira de Normas Técnicas (ABNT) (in portuguese).

Brazilian Standard NBR 7480 (2007). *Design of concrete structures: procedure*. Associação Brasileira de Normas Técnicas (ABNT) (in portuguese).

Carasek, H. and Cascudo, O. (2001). *Integrated design: characteristics of concrete cover and its role in the durability of reinforced concrete structures* (in portuguese). Goiânia, Brazil (research project)

Cascudo, O. (2000). *Influence of the characteristics of carbon steel intended for use as reinforcement for reinforced concrete in corrosion behavior* (in portuguese). PhD thesis – Polytechnic School, University of São Paulo, São Paulo, Brazil.

Ferreira, R.B. (2003). *Influence of mineral additions on the characteristics of cover concrete and its effect on chloride-induced reinforcement corrosion (in portuguese).* Master's Dissertation – Master's Course of the School of Civil Engineering, Federal University of Goias, Goiania, Brazil.

Figueiredo, C.P., Santos, F.B., O. Cascudo, H. Carasek, P. Cachim and A. Velosa (2014). The role of metakaolin in the protection of concrete against the deleterious action of chlorides, *Revista IBRACON de Estruturas e Materiais*, 7, 685–708. https://doi.org/10.1590/S1983-41952014000400008 (in portuguese).

Gomes, M. S.de S., Paiva, J.M.F., Moris, V.A.S. and Nunes A.O.N. (2019). Proposal of a methodology to use offshore wind energy on the southeast coast of Brazil. *Energy,* 185 (15), 327-336. doi.org/10.1016/j.energy.2019.07.057.

Jin, M., Jiang, L. and Zhu, Q. (2017). Monitoring chloride ion penetration in concrete with different mineral admixtures based on embedded chloride ion selective electrodes, *Construction and Building Materials,* 143, 1–15. doi.org/10.1016/j.conbuildmat.2017.03.131

Oliveira, A. M. and Cascudo, O. (2018). Effect of mineral additions incorporated in concrete on thermodynamic and kinetic parameters of chloride-induced reinforcement corrosion. *Construction and Building Materials*, 192, 467 – 477. doi.org/10.1016/j.conbuildmat.2018.10.100

Ramezanianpour, A.A.A. and Bahrami Jovein, H. (2012). *Influence of metakaolin as supplementary cementing material on strength and durability of concretes*, *Construction and Building Materials*, 30, 470–479. doi:10.1016/j.conbuildmat.2011.12.050.

Rattanashotinunt, C., Tangchirapat, W., Jaturapitakkul, C., Cheewaket, T. and Chindaprasirt, P. (2018). Investigation on the strength, chloride migration, and water permeability of eco-friendly concretes from industrial by-product materials, *Journal Clean Production,* 172, 1691–1698. doi:10.1016/J.JCLEPRO.2017.12.044.

Shi, Z., Geiker, M.R. ., De Weerdt, K., . Østnor, T.A, Lothenbach, B. ., Winnefeld, F. and Skibsted, J. (2017). Role of calcium on chloride binding in hydrated Portland cement–metakaolin–limestone blends, *Cement and Concrete Research*, 95, 205–216. doi.org/10.1016/j.cemconres.2017.02.003

XV International Conference on Durability of Building Materials and Components
DBMC 2020, Barcelona
C. Serrat, J.R. Casas and V. Gibert (Eds)

Evaluation of the Effects of Environmental Exposure on the Performance Decay of ETICS

Maurizio Nicolella[1], Roberto Landolfi[2] and Alessio Pino[3]

[1] University of Naples Federico II, Department of Civil, Architectural and Environmental Engineering, Piazzale Vincenzo Tecchio, 80, 80125 Naples, Italy, maurizio.nicolella@unina.it

[2] University of Naples Federico II, Department of Civil, Architectural and Environmental Engineering, Piazzale Vincenzo Tecchio, 80, 80125 Naples, Italy, roberto.landolfi@unina.it

[3] University of Naples Federico II, Department of Civil, Architectural and Environmental Engineering, Piazzale Vincenzo Tecchio, 80, 80125 Naples, Italy, alessio_pino@hotmail.it

Abstract. *The performance decay of a building component is influenced by a huge variety of parameters, interacting between them and determining different results in terms of service life and performance over time. For this reason, evaluating and modeling the performance of a component requires the comprehension of the way and the measure the single factors affect it, and turning this into an analytical model is a very complex operation. Moreover, components of existing buildings are subjected to an additional incognita: the characteristics and the durability of the materials, which is hardly a certain information, and can vary between similar buildings, affecting the accuracy of the evaluation. This study, conducted according to the guidelines of ISO 15686:7 code, investigates on a common solution for interventions on existing buildings, the ETICS, surveying their current performance degree through thermographic camera tests. The aim is to appreciate the difference in the performance decay between different façades of the same building – a homogeneity that allows to estimate this parameter alone - in order to reach an analytical expression of the variation of performance decay according to the difference in the exposure. The sample is constituted by buildings of large dimensions and well-known original projects and details of successive interventions, located in the city of Naples. The data obtained with in-field measurements were subjected to statistical analysis, to allow the quantitative determination of the impact of this parameter.*

Keywords: *Durability, ETICS, in-field Measurement.*

1 Introduction and State of the Art

In the last decades, together with the acknowledgement of the necessity to plan the maintenance of a building in advance, an increasingly higher importance has been given to the role of the comprehension of the dynamics of performance decay of building materials and components. In fact, knowing the trends and the times of performance decay is a required item, in order to predict the performance levels that will be reached through time, according to which maintenance interventions can be chosen.

Since diseconomies in terms of maintenance choices evidently lead to a waste of resources, the consequences of a scarce knowledge about the performance decay of components rapidly produce effects on the aspects of sustainability and energy consumption, which is a critical topic in the current situation of the construction industry. Despite that, accomplishing a high level of detail in the understanding of the processes that determine the performance decay of building components is definitely not an easy task. On one hand there are the intrinsic

characteristics of the materials, which can also be determined through laboratory tests which simulate the passing of time (i.e. accelerated aging tests), but on the other hand the actual in-use condition of building components has several possible variations: the micro-context, and macro-context of the building, the compatibility with other components, and many more. This evidence is also embodied in the structure of the Factor Method, which attributes a separate weight for the external and internal environment.

It seemed interesting to refer to a specific component for which the environmental impact of the maintenance activity has been emphasized (Minarovičová, 2015), that is used to produce benefits in terms of durability of the system, and improvement of thermal – so, energy – performance: the ETICS or External Thermal Insulation Composite Systems.

They consist in an insulation board bonded onto a new or existing masonry or concrete wall, and mechanically fixed with anchors. The insulation board is then protected by a base coat, usually 3-4 mm thick, made of the cement mortar with resin used as adhesive, but reinforced with a glass fibre mesh. Onto the base coat a 'key coat', or primer, is applied, and then the finishing, which is usually a thick (1.5-2 mm) top coat. This technology is very common all over Europe, thanks to its low cost and the possibility it offers to accomplish a very good improvement of the thermal properties of the building envelope.

The research investigates the variation of the trend of its performance decay according to the environmental exposure, and in particular the cardinal exposure: considering that very often it is applied on the whole surface of buildings, then the differences in the behavior of the ETICS on the single façades are an interesting item.

This kind of solution is defined in UNI/TR 11715 code, “Thermal insulation products for buildings - Design and in-situ installation of External thermal insulation composite systems with renders (ETICS)”, and its aspects related to durability have attracted a strong interest, in the field of research. The most part of the experimentations has focused on laboratory tests, making use of climatic chambers by simulating the aging process through specific cycles, among which the first attempts were performed by Daniotti and Paolini (2005), who realized qualitative comparisons between the durability of different solutions of ETICS, without developing re-scaling factors to relate it to natural time. In the same year, Bochen *et al.,* (2005) performed other climatic chamber tests, also determining the equivalence to natural aging. Years later, Griciuté *et al.,* (2013) made more experimentations involving the accelerated ageing of ETICS.

Other researchers investigated specific aspects of the durability of ETICS, among which Topcu and Merkel (2008), who focused on the moisture absorption, Künzel and Zirkelbach (2008), who studied the influence of rain water leakage on the hygrothermal performance of ETICS. There has been, in general, a much higher number of laboratory experimentations than field tests, including computational and theoretical modelling of the durability of this solution, such as the computational analysis performed by Koči *et al.,* (2012) and the multi-physics modelling by Daniotti *et al.,* (2014). On the other hand, there has been a much lower, and more recent, number of field researches on the durability of ETICS, realized by De Freitas (2016) and Kvande (2018). In these and other cases, little use of the thermographic camera has been noticed.

2 Materials and Methods

The investigated solution of ETICS has the following structure:
- skim “Klebocem”, width 0.5 cm;
- SK insulating panel “Stiferite”, width 4 cm;
- mechanical anchors in PVC, 2 per m^2;
- primer “Klebocem”;
- glass fiber mesh, width 0.3 cm;
- primer “Klebocem”;
- colored top coat “Rivaton”, width 0.2-0.3 cm.

The research has been carried out as a thermographic and photographic analysis on ten buildings in Naples, Italy – in Via Attila Sallustro - which have been built in 2012-2013. They are all buildings in reinforced concrete, consisting of seven floors and a total lateral surface, constituted by hollow bricks and ETICS, of 25000 m^2. The device used for the thermographic survey was a thermographic camera IR FLIR 250T, and the output consisted in a total of sixty thermographic pictures, taken from the ground level, which show several relative differences in the superficial temperature, highlighting phenomena of detachment which could not, in most of the cases, be noticed by simple visual inspection. The individuation of the performance level of the various parts of the building followed the procedure suggested in ISO 15686-7 code.

Also, in accordance with the recommendations from UNI EN ISO 4628-1 code, it is necessary to define performance degrees as numbers from 1 to 5, detailed in Table 1, in order to attribute quantitative scores to each of the thermographic and photographic frames, which represent the in-use condition that they display.

Table 1. Performance degrees for the in-use conditions of the ETICS.

Degree	Type of symptoms	In-use condition of the ETICS
1	No symptoms	No performance decay
2	Slight symptoms	Cracking and blistering phenomena on the surface (millimetrical size)
3	Medium symptoms	Macro-cracking and macro-blistering phenomena on the surface (centimetrical size)
4	Strong symptoms	Slight detachment of the panels
5	Totally unacceptable	Partial/total detachment of the panels

The definition of the performance degrees displays two typologies of anomalies: the “slight symptoms” and the “medium symptoms” refer to the finishing layers, which have a basically protective performance and effect on the panels, while the “strong symptoms” and the “totally unacceptable” state are related to the panels themselves, and therefore have a much stronger significance in terms of performance decay of the ETICS.

In several cases, the thermographic frames show thermal gradients – caused by detachments - also in locations where no performance decay is visible by sight and by photographic frames, nor is related to an anomaly in the superficial layers, as acknowledged through tactile contact: this means that their origin has to be linked to an anomaly in the inner layers, presumably the panels themselves.

Figure 1 shows the distribution of the optical cones of the thermographic and photographic frames, numbered from 1 to 17; for each of them, 3-5 shots have been taken.

Figure 1. Distribution of the optical cones of the thermographic and photographic frames.

The photographic survey shows that the main typology of anomalies consist in cross-shaped cracks in correspondence of some mechanical anchors, and in the form of horizontal lines, in correspondence of the contact between two adjacent panels, as shown in Figure 2.

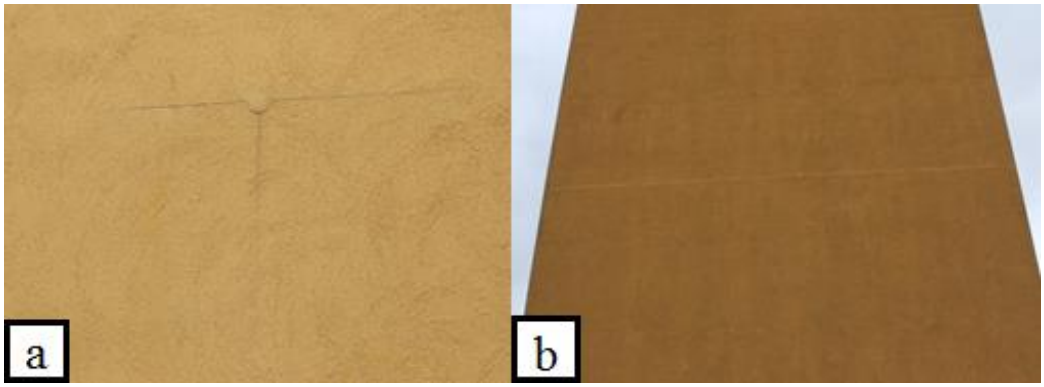

Figure 2. Photographic frames: a) cross-shaped crack in correspondence of a mechanical anchor; b) line-shaped crack in correspondence of the contact between two adjacent panels.

Thermographic frames show color – corresponding to temperature – variations both in the shape of lines, which confirm the detachment revealed by the photographic information, and in the form of diffuse areas, as in Figure 3.

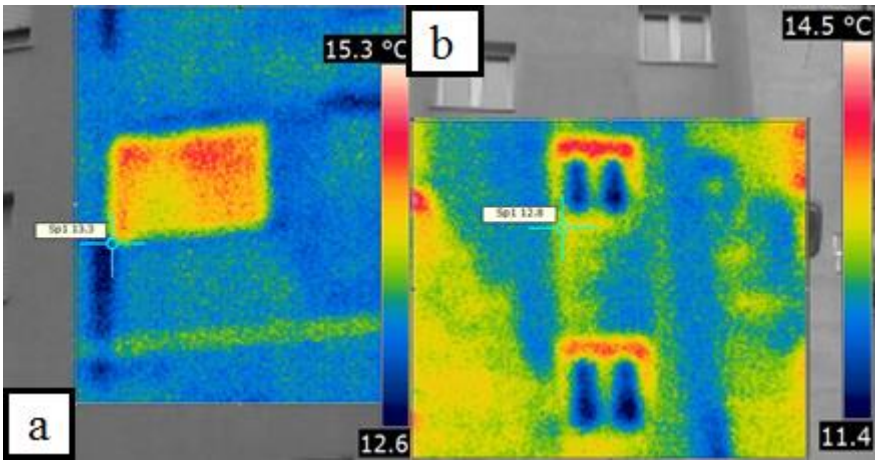

Figure 3. Thermographic frames: a) horizontal line at different temperature; b) diffuse thermal gradient on the surface.

3 Results and Discussion

A score between 1 and 5 was attributed to each of the photographic and thermographic frames, according to the typology and distribution of decay; the score of 5, corresponding to an unacceptable performance, was never attributed. Then, statistical analysis were performed on the sample, leading to the Gauss distribution shown in Figure 4.

Figure 4. Gauss distribution of the state of decay of the ETICS in the experimentation, measured in the performance degrees of Table 1.

The mean value of the performance decay is equal to 1.74, while the standard deviation is 1.28. The result seems coherent with the age of the sample buildings, and is strongly dependent on the output of the thermographic survey. In fact, as it was partially pointed out in the previous paragraphs, several areas did not present any visible – nor sensible - decay in the external layers, but the thermographic frames showed a thermal gradient, which had to be related to a detachment of the panels, signalling a more consistent state of decay.

In order to break down the obtained data, it was chosen to perform also separate analyses by dividing the output according to the cardinal direction of the façades. This led to four

different gauss distributions, respectively for the main cardinal directions of the building: E-NE, N-NW, W-SW and S-SE, reported in Figure 5.

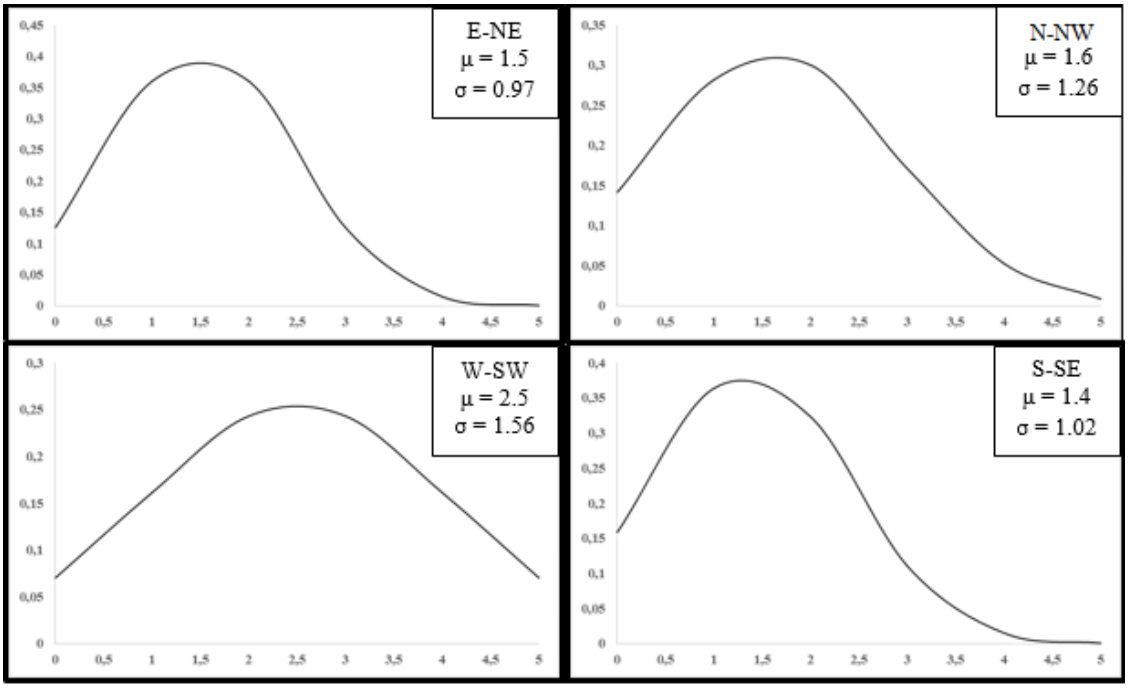

Figure 5. Gauss distribution of the state of decay of the ETICS in the experimentation for each cardinal exposure, with the detail of mean value (μ) and standard deviation (σ).

It can be noticed that, differentiating the analysis on the single façades, the results generally become more accurate: in 3 cases out of 4, the deviation is lower than in the analysis on the whole surface. Moreover, it emerges that values of higher decay correspond to the W-SW façade, while the other cardinal exposures have better performances. Since there is a higher frequency of detachment of panels, associated with higher performance degrees, this is also probably the reason behind the higher deviation.

The more negative value of performance decay in the W-SW direction seems particularly strong, reaching a ratio of 1.5-1.8 with the values in the other directions. Qualitatively, this phenomenon could be explained in relation to the less favorable conditions that insist on this façade, in particular solar exposure.

4 Conclusions

As for many materials in the sector of building constructions, the large use of ETICS in the current building industry does not find its counterpart in a sufficient quantity of field experimentations, compared to the notable number of theoretical models and laboratory tests; considering the complexity of the factors that influence this aspect in relation to the context, it is certainly necessary to encourage a more frequent use of field experimentations to enrich the database concerning the states of decay.

The aim of the experimentation carried out in this work was not to try to produce a relation

between time and decay, as the collected data only refer to a single year, then it is not realistic to hypothesize a trend on its base, but rather the focus was on two significant aspects:
- the opportunities to make use of different tools and instruments for the monitoring activity, questioning their utility and the typology and level of information that they can provide;
- the qualitative differences that may exist in the decay of the same component, as a consequence of the variation of micro-contextual aspects.

The first point clearly refers to the use of the thermographic camera, and surely this case has provided a good proof of its peculiarities: incipient detachments between the panels could be noticed only thanks to the use of this instrument, allowing a much clearer picture of the state of decay; looking forward to the availability of quantitative data about the evolution of this anomaly, this is certainly an interesting information in the field of predictive maintenance.

At the same time, it has to be noticed that thermographic surveys do not show the dimension of the detachment, but only its existence; then, it is not possible to deduce the entity of the reduction of the thermal performance that the ETICS have to provide. So, an interesting development can be individuated in the possibility to link thermographic surveys to partially destructive tests, aimed to ascertain the dimension of the detachment, associate it to the output of the thermographic survey, and quantitatively determine its influence on the thermal performance of the ETICS.

Concerning the second aspect, the strong difference between the higher performance decay observed on one of the façades (W-SW) and the one on the others (E-NE, N-NW and S-SE) is certainly an interesting result, which is probably better not to refer yet to a single parameter, as the solar exposure might be, but rather to consider as an item of future interest, in the perspective of more detailed assessments of the weight of the micro-climatic factors that influence the durability of the single components. On this side, for future experimentations, it will be interesting to gather data from thermographic surveys on similar buildings in different geographic locations, in order to evaluate the entity of the differential performance degree with other climates. In this way, more light can be shed on the mechanism of the environmental influence on the performance of ETICS, and of buildings components in general.

ORCID

Maurizio Nicolella http://orcid.org/0000-0002-7140-6759
Roberto Landolfi http://orcid.org/0000-0002-5196-880X
Alessio Pino http://orcid.org/0000-0002-5774-6378

References

Bochen J., Gil S. and Szwabowski J. (2005). *Influence of ageing process on porosity changes of the external plasters*, Cement and Concrete Composites, 27, 769–775.

Daniotti B. and Paolini R. (2005). *Durability Design of External Thermal Insulation Composite System with Rendering*, Proceedings of the X International Conference on Durability of Building Components, Lyon, France.

Daniotti B. and Paolini R. (2008). *Experimental programme to Assess ETICS cladding Durability*, Proceedings of the XI International Conference on Durability of Building Materials and Components, Istanbul, Turkey.

Daniotti B., Re Cecconi F., Paolini R., Cocchetti G., Galliano R. and Cornaggia A. (2014). *Multi-physics modelling for durability evaluation of ETICS*, Proceedings of the XIII International Conference on Durability of Building Materials and Components, Sao Paulo, Brazil.

Daniotti B., Spagnolo S. L. and Paolini R. (2008). *Climatic Data Analysis to Define Accelerated Ageing for Reference Service Life Evaluation*, Proceedings of the XI International Conference on Durability of Building Materials and Components, Istanbul, Turkey.

De Freitas S.S. and de Freitas V.P. (2016) *Cracks on ETICS along thermal insulation joints: Case study and a pathology catalogue*, Struct. Surv. 34, 57–72.

Minarovičová K. (2015). *Environmental impact of ETICS Maintenance*, Proceedings of the International Conference on Advanced Building Construction and Materials, Stražnice, Czech Republic.

Griciuté G., Bliūdžius R. and Norvaišienė R. (2013). *The Durability Test Method for External Thermal Insulation Composite System (ETICS) used in Cold and Wet Climate Countries*, Journal of Sustainable Architecture and Civil Engineering, 1, 50-56.

Koči V., Madera J. and Robert Č. R. (2012). *Exterior thermal insulation systems for AAC building envelopes: Computational analysis aimed at increasing service life*, Energy and Buildings, 47, 84–90.

Künzel H., Zirkelbach D. (2008). *Influence of rain water leakage on the hygrothermal performance of exterior insulation systems*, Proceedings of the 8th Symposium on Building Physics in the Nordic Countries, Copenhagen, Denmark.

Kvande T., Bakken N., Bergheim E. and Thue J.V. (2018). *Durability of ETICS with Rendering in Norway – Experimental and Field Investigations*, Buildings 7, 1-17

Topcu D. and Merkel H. (2008). *Durability of External Wall Insulation Systems with Extruded Polystyrene Insulation Boards*, Proceedings of the XI International Conference on Durability of Building Materials and Components, Istanbul, Turkey.

XV International Conference on Durability of Building Materials and Components
DBMC 2020, Barcelona
C. Serrat, J.R. Casas and V. Gibert (Eds)

Experimental Study on Carbonation Resistance and Water Absorbing Property of Concrete Crack with repair

Naoko Tsuchiya[1] **and Kaori Nemoto**[2]

[1] Building Department, National Institute for Land and Infrastructure Management, Tsukuba, Japan, tuchiya-n92ta@mlit.go.jp

[2] Housing Department, National Institute for Land and Infrastructure Management, Tsukuba, Japan, nemoto-k92ta@mlit.go.jp

Abstract. *Existing RC Buildings have some cracks and the repairing service might last the buildings for long life. The durability of the RC component is evaluated by several ways as like as carbonation resistance test, permeability test, water penetration test, and so on. Therefore, it need to be measured how much advantage the concrete crack with repair have for the durability. The aim of this paper is to study on advantage of repairing a crack of concrete to the carbonation resistance and the water-absorbing property by the experimental way. The specimens were prepared in the following point. The finishing (direct finishing and mortal tile finishing), crack width (0, 0.05, 0.5, and 2mm), and choice repairing or not. All concrete specimens were formed 10 x 10 x 20cm and those W/C were 0.55. Then, the specimens were tested by the accelerated carbonation. After 4, 8 and 26weeks accelerated carbonation, the carbonation depth and the carbonation shape of the concretes were measured by 1% phenolphthalein reaction. Also, the amount of absorbed water from the bottom were measured at 1, 3, 6, 24, 48, 72 and 168h. From the results, the carbonation went rapidly located in 2cm around the crack in the case of the no-repair specimens, regardless of any finishing. But in the case of the specimens repaired, it went evenly from the exposure side. And water absorbing test results show a trend that water amount of the concrete with a crack more increase than one of the no-crack concrete.*

Keywords: *Concrete, Crack with Repair, Carbonation Resistance, Water Absorption.*

1 Introduction

Existing RC buildings ordinary have some cracks. These expand air permeation and water penetration (D. Breysee *et al.*,), which cause irregular carbonation (Xiao-Hui *et al.*, 2018), and rebar corrosions rapidly.

On the other hand, cracks of the reinforced concrete components sometimes have been repaired, and that might last the buildings for long life.

And now, the durability of the reinforced concrete components is evaluated by several way as like as the carbonation resistance test, the permeability test, the water penetration test, and so on. Therefore, it need to be measured how much advantage the concrete crack with repair have for the durability. The aim of this paper is to study on advantage of repairing a crack of the concrete to the carbonation resistance and the water-absorbing property by the experimental way.

doi:10.23967/dbmc.2020.066

2 Specimens

2.1 Specimens Type

Table. 1 shows specimen type. 2piece of each type specimens were prepared. 10 x 10 x 20 cm rectangular column concretes were made. Many have a man-made crack at the center of oneself, and half of those were repaired.

Table 1. Specimen type.

No.	Finishing	crack (mm)	Repair material
1	Direct finishing	-	-
2	Direct finishing	0.5	-
3	Direct finishing	0.5	Soft epoxy resin grouting
4	Direct finishing	2	-
5	Direct finishing	2	U cut and filling with sealing agent
6	Direct finishing	0.05	-
7	Direct finishing	0.05	Coating with flexible synthetic resin emulsion
8	Mortal tile	0.5	-
9	Mortal tile	0.5	Soft epoxy resin grouting
10	Mortal tile	0.5*1	-
11	Mortal tile	2	-
12	Mortal tile	2	U cut and filling with sealing agent
13	Mortal tile	-	-

*1 Motal tile have no crack but concrete 0.5mm crack

2.2 Mix Proportion of Concrete

Table 2. shows the mix proportion of the concrete. Portland cement was used, and form off 3days after cast. Then, 20℃ RH 60 % air curing for not less than 28 days.

Table 2. Mix proportion.

SL	W/C	s/a	BVg	W	C	S	G
(mm)	(%)	(%)	(m^3/m^3)	(kg/m^3)			
18	55.0	45.8	0.59	180	327	793	961

2.3 Concrete Crack Width

The crack width of concrete were 0mm (no-crack), 0.05mm, 0.5mm, and 2mm. After air curing of the concrete, bending the concrete and put ones together carefully so as to being each crack wide. So, a man-made crack which pass through to another side was at the center of the specimens. Mortal tile also have a crack in response to each concrete crack, except No.10 in Table 1, which mortal tile have no-crack but concrete has a 0.5mm-wide-crack .

2.4 Finishing

Finishing type were direct finishing and mortal tile finishing. Making the mortal tile finishing, 2cm mortal were plastered after making concrete crack and cured for not less than 28days by oneself. Except some specimens, mortal tile finishing also have a crack. The crack of mortar bed were made by the way of putting a rubber in and remove it while mortar set. And, the tile were cut ahead and put on mortar bed adjusting a crack.

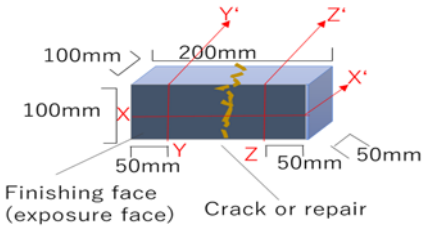

Figure 1. Cut directions after accelerated carbonation test.

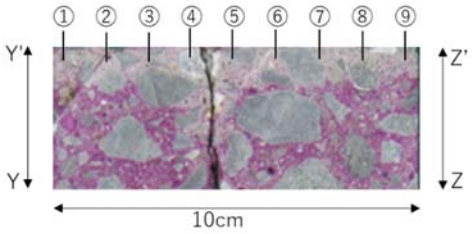

Figure 2. Measurement spots on x-x'cut side.

2.5 Repair Materials and Methods

Used repair materials and methods were shown in table 1. These repair material and method were select corresponding with the crack width. The soft epoxy resin grouting applied for 0.5mm crack, U cut and filling with the sealing agent applied for 2mm crack of either finishing. Also, coating with the flexible synthetic resin emulsion were applied for 0.05mm crack of direct finishing specimens.

3 Experiment

3.1 Accelerated Carbonation Test

The specimens were sealed with aluminium tape so that only the finishing face were exposure in 20℃, RH60%, and CO_2 5% room. And, the term of accelerated carbonation were 4, 8 and 26 weeks.

3.2 Measurement Carbonation Depth

After the accelerated carbonation, specimens were cut along x-x', y-y' and z-z' directions as Figure 1. by diamond cutter, and then solution of 1% phenolphthalein in water were sprayed. Carbonation depths were measured at 5spots on y-y' and z-z' cut side. In case of x-x' cut side, 9spots located in 10cm around the crack were measured as shown in Figure 2.

3.3 Water Absorption Test

After the curing and sealing, specimens were set on the water and measured the amount of the absorbed water at 1, 3, 6h and 1, 2, 3, 7 days. Water were absorbed from the bottom of the specimens.

4 Results and Discussion

4.1 Carbonation Depth on y-y' and z-z' Cut Side

This paragraph shows the results of the carbonation depth from exposure side on y-y' and z-z' cut side. Averaged value of y-y' and z-z' are shown.

4.1.1 The results of the no-repair case

Figure 3. shows the carbonation depth on y-y' and z-z' cut side of the no-repair case. In case

(a) Direct finishing (b) Mortal tile finishing

Figure 3. The carbonation depth on y-y' and z-z' cut side of the no-repair case.

(a) Direct finishing (b) Mortal tile finishing

Figure 4. The carbonation depth on y-y' and z-z' cut side of the repair case.

of the direct finishing, the carbonation depth at 4, 8 and 26 weeks were 7～13mm, about 12mm, and 16 ～24mm respectively. Also, it were under 3mm, 4mm and 6mm respectively in case of the mortal tile finishing.

4.1.2 The results of the repair case

Figure 4. shows the carbonation depth on y-y' and z-z' cut side of the repair case. Except No.7, the carbonation depth at 4, 8 and 26 weeks were 10～12mm, 12～14mm and 18～23mm respectively in case of the direct finishing, that was close to the results of the no-repair case. Also, it were under 2mm, 3mm and 5mm respectively in case of the mortal tile finishing, that was also close to the results of the no-repair case. Note, No.7 were coated at all face with the flexible synthetic resin emulsion, so carbonation did not go.

4.1.3 Discussion

From the results in Figure 3. and Figure 4., the carbonation depth at each term were same, regardless of repair or not. That shows the process of carbonation located on 5cm away from a crack were not relate with a crack or repair.

Add to that, the mortal tile finishing have larger resistance for carbonation than the direct finishing have, as well as the previous studies on preventive effect of finishing materials against carbonation (Kono *et al.*, 2008).

4.2 Carbonation Depth on x-x' Cut Side

This paragraph shows the results of the carbonation depth from the exposure side on x-x' cut side. In the following figures, the symbol 'Max' means the maximum value in the 9 spots results on x-x' cut side as shown in Figure 2., the symbol 'ave. of 2cm around crack' means average of the results of the spots of ④, ⑤, ⑥ in Figure 2., and the symbol 'ave. of 10cm around crack' means average of 9 spots results.

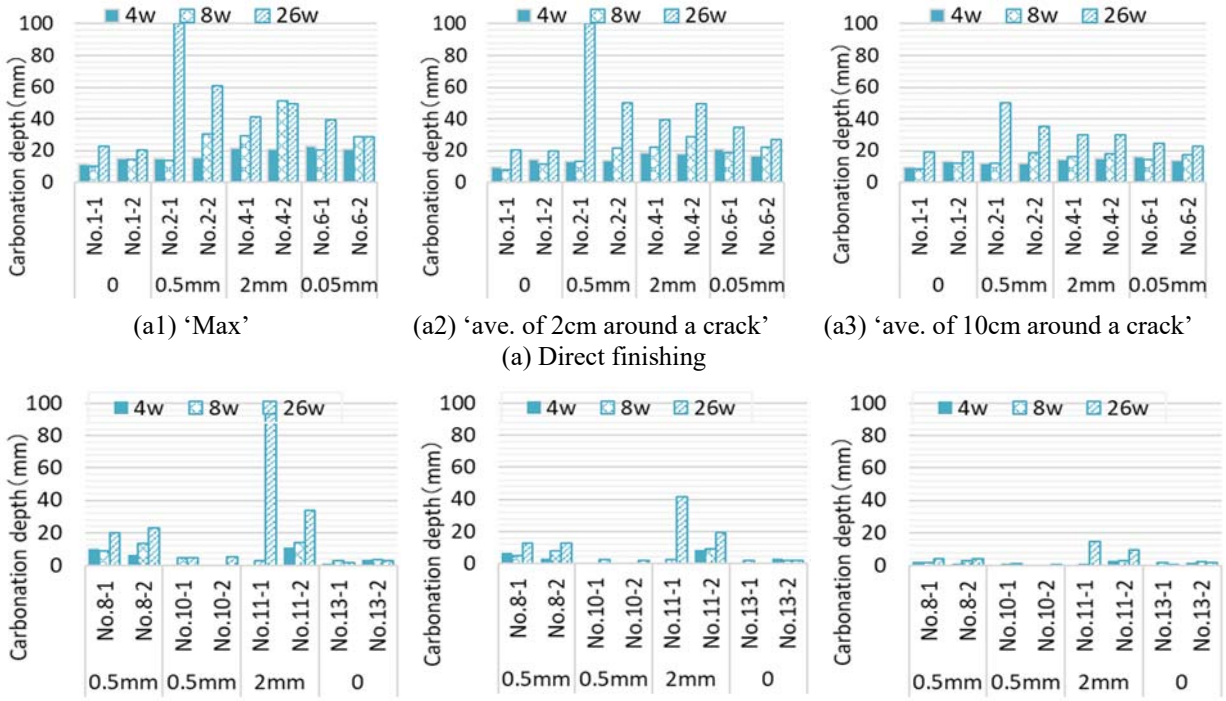

(a1) 'Max' (a2) 'ave. of 2cm around a crack' (a3) 'ave. of 10cm around a crack'

(a) Direct finishing

(b1) 'Max' (b2) 'ave. of 2cm around a crack' (b3) 'ave. of 10cm around a crack'

(b) Mortal tile finishing

Figure 5. The carbonation depth on x-x' cut side of the no-repair case.

4.2.1 The results of the no-repair case

Figure 5. shows the carbonation depth on x-x' cut side of the no-repair case. From the results of 'max' of No.4 and No.6, the carbonation depth were about 20mm at 4weeks, that was twice of the result of y-y' and z-z' cut side at Figure 3 (a). And the results at 8 and 26weeks were so large as 30mm and 50mm. Also, the results of 'ave. of 2cm around a crack' of No.2, No.4, and No.6 were about 15～20mm at 4weeks, that was about half time of the result of y-y' and z-z' cut side. And No.2 at 26weeks were 100mm. Meanwhile, the result of No.1, which don't have cracks, at 4, 8 and 26weeks were about 10mm, 10mm and 20mm each, regardless of 'Max', 'ave. of 2cm around crack', and 'ave. of 10cm around crack', that was close to the results of y-y' and z-z' cut side.

And then, focused on the mortal tile finishing specimens, the carbonation depth of No.8 'Max' at 4, 8 and 26 weeks were about 9mm, 12mm and 20mm, also that of No.8 'ave. of 2cm around a crack' were 5mm, 7mm and 13mm, and also that of No.8 'ave. of 10cm around a crack' were 3mm, 3mm and 4mm respectively. Likewise, that of No.11-2 'Max' at 4, 8 and 26 weeks were about 11mm, 14mm and 34mm, also that of No.11-2 'ave. of 2cm around a crack' were 9mm, 9mm and 20mm, and also that of No.11-2 'ave. of 10cm around a crack' were 3mm, 3mm and 10mm respectively.

Both 'Max' and 'ave. of 2cm around a crack' results were more than double for that of y-y' and z-z' cut side as showed in Figure 3. So, these 'Max' and 'ave. of 2cm around a crack' results of x-x' cut side were so larger than that of y-y' and z-z' cut side.

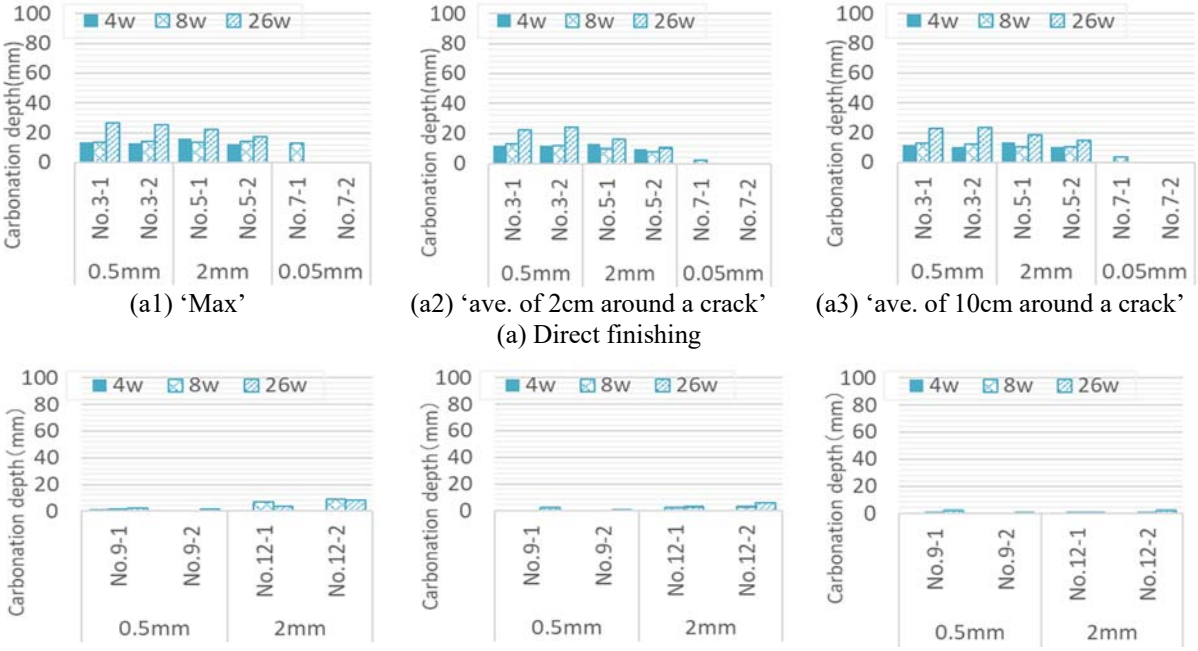

(a1) 'Max' (a2) 'ave. of 2cm around a crack' (a3) 'ave. of 10cm around a crack'

(a) Direct finishing

(b1) 'Max' (b2) 'ave. of 2cm around a crack' (b3) 'ave. of 10cm around a crack'

(b) Mortal tile finishing

Figure 6. The carbonation depth on x-x' cut side of the repair case.

And, results of 'ave. of 10cm around a crack' of x-x' cut side were not differ greatly from that of No.13 which have no crack as showed in Figure 3 (b). By the way, No.10 results show that carbonation didn't go at all as 0mm at 8weeks and 5mm at 26weeks, because this specimen have a concrete crack but no crack of tile.

4.2.2 The results of the repair case

Figure 6. shows the carbonation depth on x-x' cut side of the repair case. The 'Max' of No.3 and No.5 at 4, 8 and 26 weeks were about 13mm, 13mm and 23mm, also that of 'ave. of 2cm around a crack' were about 11mm, 11mm and 18mm, and also that of 'ave. of 10cm around a crack' were 11mm, 11mm and 20mm respectively. So, these have no difference in measurement field. Add to that, these results were close to the results of No.1 (no-crack case) as well as y-y' and z-z' cut side showed at Figure 4.

And, No.7 were coated at all face with the flexible synthetic resin emulsion, so carbonation have not gone.

As an exception case, the results of No.11 which have 2mm-wide crack shows the carbonation depth were small until 8weeks but it were large at 26weeks. Because of the repair method that block up by buried only surface layer but the filling didn't reach to deep part, the carbonation went rapid where the filling didn't reach.

And then, focused on the mortal tile finishing, the 'Max' of No.12 at 4, 8 and 26 weeks were about 0mm, 8mm and 6mm, also that of 'ave. of 2cm around a crack' were 0mm, 3mm and 4mm, and also, that of 'ave. of 10cm around a crack' were 0mm, 1mm and 2mm respectively. And the carbonation depth of No.9 at 4, 8 and 26 weeks were under 2mm regardless of the symbol. These were close to the results of the no-crack case as well as the results of y-y' and z-z' cut side.

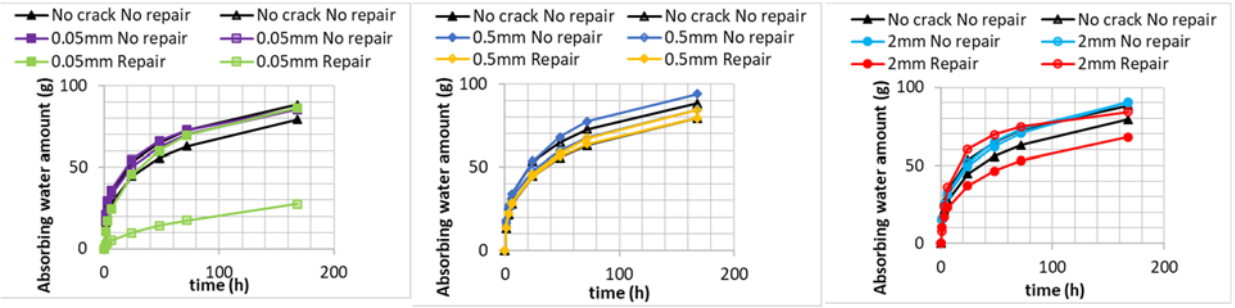

(a1) 0.05mm-crack-wide (a2) 0.5mm-crack-wide (a3) 2mm-crack-wide

(a) Direct finishing

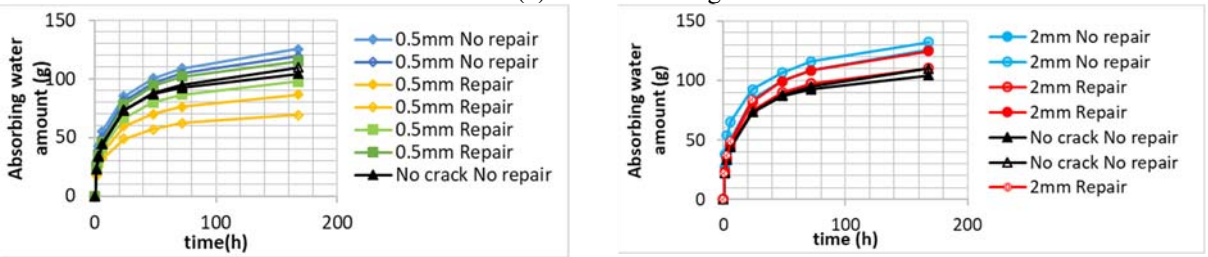

(b1) 0.5mm-crack-wide (b2) 2mm-crack-wide

(b) Mortal tile finishing

Figure 7. The amount of absorbed water

4.2.3 Discussions

In the case of the no-repair, the carbonation went rapidly located in 2cm around the crack but not rapidly at 10cm far from a crack, regardless of any finishing.

On the other side, the carbonation of the specimens repaired went evenly from the exposure side and that were similarly to the no-crack case, although there is an exception.

From these, the repairing service have advantage of the carbonation resistance compared to crack left case, though it is not confirmed durability of the repair materials in itself.

On a side note, the carbonation depth averaged located at 10cm around the crack of the no-repair specimens were close to that of the area far from a crack, and close to the no-crack case. It indicate that the influence of a crack appear little in large mass.

4.3 The Amount of Water by Absorption Test

Figure.7 shows the results of the amount of absorbed water from the bottom side. From the results, the amount of absorbed water of the specimens having a crack were bigger than the no-crack specimens. Also, those of the specimens repaired were smaller than that of the no-repair, however there were exceptions.

5 Conclusions

- The aim of this paper is to study on advantage of the repairing a crack of concrete for the carbonation resistance and water absorption resistance by the experimental way. Then, this paper shows the results of the accelerated carbonation test and water absorption test. Prepared concrete specimens were distinguished as the finishing type,

the crack width, taking repair or not, and the repair materials. The results in this study indicate as following.

- The mortal tile finishing have larger resistance to the carbonation than the direct finishing have.
- The carbonation went rapidly located in 2cm around the crack in the case of the no-repair specimens, regardless of any finishing.
- From the results of the repair case, the carbonation went evenly from the exposure side. It was the same process as the no-crack case.
- The amount of the absorbed water of the specimens having a crack were bigger than the no-crack specimens, and some specimens repaired a crack were smaller than that of the no-repair case.
- Many repairing service have advantage of the carbonation resistance as well as water absorption resistance compared to a crack left, though it is not confirmed durability of the repair materials in itself.

ORCID

Naoko Tsuchiya: http://orcid.org/0000-0002-9500-9811
Kaori Nemoto: http://orcid.org/0000-0002-1177-9959

References

D.Breysee and B.Gerard. (1997). *Transport of fluids in cracked media, penetration and permeability of concrete*, H.W.Reinhardt, ed., RILEM Report 16, Vol.164, pp. 123-153

Hosoda A., Hayashi K., Shimoda T. and Yoshida S. (2009). *Effects of microcrack of surface layer concrete on surface absorption and surface permeability* (in Japanese), Cement Science and Concrete Technology, No.63, pp. 196-203

Kono. M, Nagase K., Tsuduki M., Kanamori M., Kubota H. and Inoue K. (2008). *Evaluation of various finishing materials contributing to suppressive of concrete in structures Part9 Verification test of carbonation suppressive effects of tile* (in Japanese), Summaries of Technical Papers of Annual Meeting of Architectual Institute of Japan (Tohoku), 957-958

M. Kanematsu，I. Maruyama，T. Noguchi，H. Iikura and N. Tuchiya. (2009). *Quantification of Water Penetration into Concrete through Cracks by Neutron Radiography*, Nuclear Instruments and Methods in Physics Research Section A: Accelerators, Spectrometers, Detectors and Associated Equipment, Vol.605, Issues 1–2, 154-158

Saya M., Takahiro S., Yoshiteru O. and Ichizo K. (2008). *Experimental study in carbonation of concrete occurred flexural crack* (in Japanese), Proceedings of Annual Convension of Japan Concrete Institute, vol. 30, No.1, 657-662

Hasegawa T., Senbu O., Fukuyama T. and Inoue T. (2017). *Deterioration and preventive effects of finishing materials against carbonation and corrosion of reinforcing bars in concrete based on 20year outdoor exposure test using model building* (in Japanese), Journal of Structural and Construction Engineering, Vol.82, 733, 337-346

Ujike I., Sato R. and Nagataki S. (1996). *A study on deterioration of tightness of cover concrete due to internal cracking based on air pearmiability* (in Japanese), Proceedings of the Japan Society of Civil Engineers, No.550, V-33, pp.163-172

Xiao-Hui wang, Dimitri V. Val, Li Zheng and M. Roderick jones. (2018). *Influence of loading and cracks on carbonation of RC elementsmade of different concrete types*, Construction and Building Materials, Vol.164, 12-28

XV International Conference on Durability of Building Materials and Components
DBMC 2020, Barcelona
C. Serrat, J.R. Casas and V. Gibert(Eds)

Gold Leaf Murano Glass *Piastras*' Performance in the *Trencadís* Catalan Modernism Mosaic: Recognition of Primary Alteration Patterns

Héctor Y. Orozco Camargo[1] **and Joan Ll. Zamora i Mestre**[2]

[1]Master's Degree in Advanced Studies in Architecture-Barcelona (MBArch), Universitat Politècnica de Catalunya-BarcelonaTECH, ETSAB, Av. Diagonal, 649, 08028-Barcelona, Spain, Arq-HO@hotmail.com

[2] Laboratori d'Innovació i Tecnologia de l'Arquitectura (LiTA), Universitat Politècnica de Catalunya (UPC) - BarcelonaTECH, Pere Serra, 1-15, 08173-Sant Cugat del Vallès, Catalunya, Spain, joan.lluis.zamora@upc.edu

Abstract. *Gold leaf Murano glass is a unique product that over the centuries, especially during Byzantine period, has been used as facing forming big flat or curved mosaics that result in an architecture full of light and symbolism. This product is presented in a format of squared piastras with the same approximate dimensions that the gold leaves ones have (8x8 cm). Piastras are cut in smaller squares (1-1,5cm) in order to obtain the tiles that form mosaic's cladding. This cladding technique was incorporated during Catalan Modernism. Through this technique, beautiful pieces of tesseras of gold leaf Murano glass combined with others of opaline glass. In order to overcome the artistic challenges from this architectural movement, new mosaics were placed outdoors in order to shine by the incident sun beams and the square tiles were replaced by irregular tiles that form polygonal meshes capable of coating double curvature surfaces with great elegance. This location and prolonged exposure to the weather cause, over time, a deteriorated appearance, despite being composed of great resistant materials such as gold and glass. Studies oriented to know the phenomenology of this deterioration are being carried out and its impact on the expected durability of this coating. Being a handmade product and completely manual execution, the first studies have aimed to identify the primary anomalies that are originally generated in the different layers of this product at the time of manufacture, transport and handling. Knowing these primary anomalies must allow to prevent their occurrence and reduce their incidence in the manifestation of so-called secondary anomalies. All this in order to prolong the useful life of this appreciated architectural cladding.*

Keywords: *Brightness, Mosaic, Modernism, Trencadís, Gold leaf Murano Glass, Alteration Patterns.*

1 Introduction

Gold Leaf Murano glass consists of two external layers of different thickness and different glasses and a thin inner layer of gold leaf inserted between both. The main purpose of this product is to provide a glazed surface with the maximum brightness, colouring and texture. These features are given by the gold leaf itself. The two layers of glass provide to the gold leaf protection and transparency.

Gold is a ductile and soft material that does not corrode when it contacts with air. Gold it is not reactive not toxic. In contrast, it is an excellent reflector of infrared radiation. It is also a good heat absorber and it has a great capacity to reflect light. Within its chemical peculiarities, it should be mentioned that gold is easily lacklustre by sulphur (lost of brightness), attacked by

chlorin and for cyanide solutions in the presence of oxygen and insoluble in acids. Since gold leaves are a handmade material, occasionally, their alloys are made with other metals to reduce its cost and to obtain nuance variations in its colour appearance. Currently, there are different active gold leaf Murano glass producers. This research has been carried out on *piastras* with dimensions of 8x8cm, and with an approximate thickness of 6mm, without any treatment or alteration, as delivered by the distributor. Samples of gold leaf Murano glass consist of a first layer of transparent common glass of 6mm of thickness approximately (face A) + a gold leaf layer with a thickness of between 0,1 and 0,001µm approximately + a transparent blown glass with a thickness between 0,2mm and 0,5mm (face B), which is shown in the image 1.

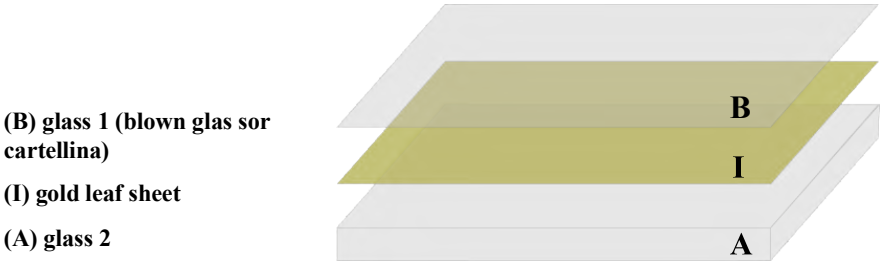

Figure 1. Composition of a gold leaf Murano Glass *piastra*.
(source: authors).

2 Interpretation of the Manufacturing Process of Gold Leaf Murano Glass

Gold leaf Murano glass is made overlapping the different layers in succession and applying final treatments to ensure the unity of the group.

2.1 Manufacturing Process of Gold Leaf Sheets

Although there are some small variations specific to each company at some point in the production process, the following basic steps are followed in order to obtain the gold leaf:

1. Heavy: gold from other remains is weighed.
2. Melting: by melting, a ingot of approximately 1cm thick is obtained.
3. Laminate I: it is the first forming that is done by inserting the ingot between two horizontal rollers. This process is done very slowly so as not to lose gold's malleability.
4. Measurement and cut: a measure is made with a compass in order to know where to cut the tapes that have already left the laminate. After this, the various plates are put together to continue with the next step.
5. Laminate II: through this second lamination by other rollers flat pieces of 4x4 cm are obtained.
6. Counterbalancing and cut: previously laminated the gold leaf sheets are counterbalanced one on the other, in the middle of it, is bent perpendicularly with a wooden dowel and cut in half. They are then counterbalanced and cut again, resulting in pieces of 2cm x 2cm.

From these pieces obtained from 2 cm x 2cm, hammering processes are applied with different levels of force to progressively reduce the thickness of the sheets.

7. Step for devastate: The first step in achieving this part of the process is to reduce as much as possible the humidity of the devastating device that will receive the gold, a process called

the "preparing". Followed by this, the gold is loaded into the devastating and then the smoothing process, which consists of constantly hitting the sheets while they are spinning. They are then cut again into 4cm x 4cm sheets.

8. Movement of the brazed: the same steps of the previous process are performed again with the aim of further reducing the thickness.

9. Movement of the mould: it is the final stage of hammering, in which it is sought that the centre of the surface of the bread and the rest perimeter have the same thickness and not present differential defects.

10. Transfer into books: it is the last step and consists of passing gold leaf sheets to white silk paper books to preserve it from humidity. The usual final measurement of the surface of the sheets is 8cm x 8cm.

During the manufacturing process of the gold leaf, the gold leaf may turn sour. This can happen repeatedly. In that case, the gold loses malleability, so it has to be cooked again and a resurrected is generated in which a greater molecular cohesion is created by which the gold increases its density.

2.2 Manufacturing Process for Murano Gold Leaf Glass

The primary anomalies can occur in any of the different processes that are carried out for the manufacture, transport and handling of the product so it is important to know the development of each of the phases.

1. The production process of Murano gold leaf glass begins with the manufacture of transparent blown glass balloons in order to obtain the minimum possible thickness, which are then cut into square segments slightly larger than those of gold leaf and left to cool.

2. The gold leaf is then manually extracted from the books and also applied manually to these glass segments.

3. The next step is the application of the thicker melting layer of transparent glass: the melted glass is poured onto the exposed face of the gold leaf and reheated to the gold leaf and the fine transparent base glass.

4. While the assembly is malleable, it is passed successively through several rollers to reduce the thickness to the desired thickness (approximately 5.95 mm) and the flat shape.

5. The *piastras* thus formed are raised with pliers and rotated to allow the best integration of the different layers.

6. Once the sheets of gold leaf are fully protected by both glasses, the whole is taken to the oven with the aim of sealing and definitively joining the different layers.

7. The parts removed from the furnace are again passed through the rollers because, having been subjected again to high temperatures, their thickness may have varied.

8. During the slow cooling, but even if the set is malleable, the pieces are cut again with the measurements of the format of the gold leaf (8cm x 8cm).

The product is stored until transport, the truck being the most common means of transport. For this purpose, the pieces are grouped and packed in honeycomb plastic film to avoid any possible external friction and are deposited inside boxes

3 Research Methodology

Since manufacturing is done by hand, this results in visually noticeable variations within the same batch of product; is why this study has been carried out using a comparative methodology of different samples in order to identify the most frequent anomalies. Similarly, this product is not covered by any regularity and its characteristics must be assessed by assimilation with other standards.

3.1 Scanning by Flat Scanner

Firstly, a cursory inspection of the parts was carried out, the parts were carefully washed and numbered. The parts have subsequently been digitized on both sides by the use of the flat scanner, obtaining digital images in .jpg. The use of the flat scanner model EPSON GT-15000 has proved to be the most efficient way of keeping a record and a detailed survey of all the pieces studied. The stored digital images have not had any kind of digital processing or subsequent manipulation.

The observation of this survey has confirmed that Murano gold leaf glass is a translucent and heterogeneous product, characterized by the light and shadow contrasts generated by the variation of the surface density between the different areas of the same sheet of gold leaf.

3.2 Visual-Instrumental Analysis Under Optical Microscope

Once those areas with unique features have been identified, these areas are inspected in greater detail using the Dino-Lite AM41115T model digital optical microscope, a portable instrument that allows in a very simple way to make a more detailed enlargement of the structure of these singularities or anomalies. A first discrimination, thanks to the focusing capacity of this device, is to identify in which of the different layers of the piece the alteration is manifested. Indirectly, the position of the anomaly may indicate when the production process occurred.

For the development of this study, three types of zoom have been carried out, depending on the face and the approach, in order to determine in which layer of the sample the anomaly is located; if they are on the inside face of the glass (a)on the sheet of gold leaf (b) or on the outer faces of protective glass (c):

- First, a 19X zoom was performed on side B (the smallest glass thickness) in order to observe the anomalies between layers.
- The same procedure is carried out on side A, but this time a 20X zoom is used as a thicker glass is being analysed and, Therefore, the focus for observing the golden material is at a greater distance from the surface.
- The last increase is made to 160X on both sides since with this increase it is interesting to analyse what is happening on the surface of the glasses.

Finally, these identified anomalies have been compiled in different groups, according to the layers in which they manifest:

- Group 1, anomalies located on the inside face of the glass (a) or on the sheet of gold leaf (b) and
- Group 2, anomalies located on the outer faces of the protective glass (c).

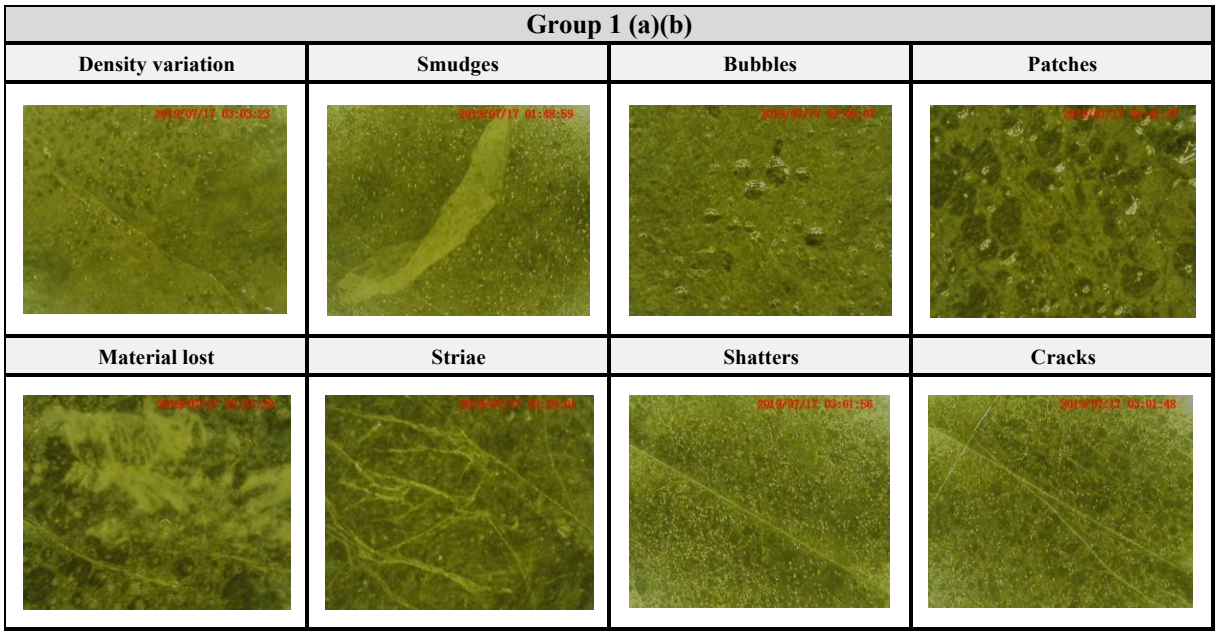

Figure 2. Alteration patterns in Group 1: On the inside face of the glass (a) or on the sheet of gold leaf (b). (source: authors).

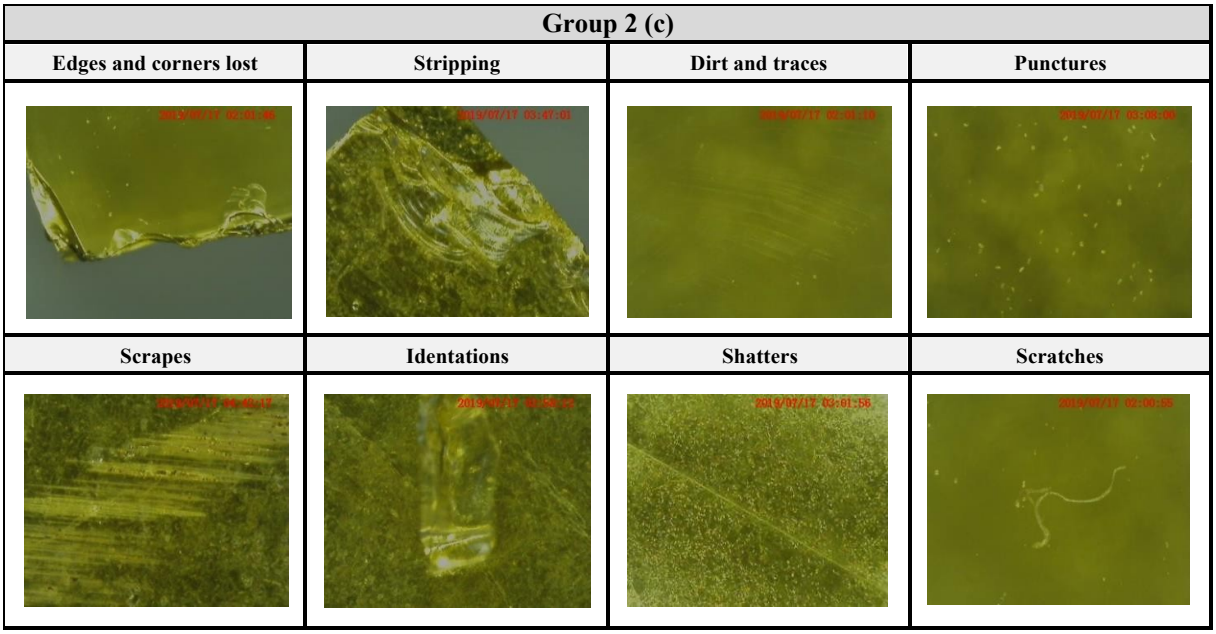

Figure 3. Alteration patterns in Group 2: On the outer faces of the protective glass (c). (source: authors).

3.3 Properties of Murano Glass Gold Leaf in Laboratory

In order to assess the durability of this product in a standardised way, a series of laboratory tests have been carried out following the UNE-EN ISO 10545 regulation for ceramic tiles; This decision was taken on the grounds that ceramic tiles are the alternative material most commonly used in the Catalan Modernism *trencadís* exterior cladding.

The tests that have been carried out are: determination of water absorption, open porosity, relative density and bulk density; determination of resistance to bending and breaking load; determination of chemical resistance; Determination of stain resistance; Determination of thermal shock resistance; Determination of surface abrasion resistance of enamelled tiles; Determination of scratch hardness; Determination of linear thermal expansion and Determination of freezing resistance. The 9 tests were carried out by a company specialising in this field.

- After the test on five *piastras* for the determination of water absorption, open porosity, relative and apparent density was obtained as a result of the mean values that the absorption of water from gold leaf Murano glass is 0.01%, the apparent porosity of 0.02% and both the relative and apparent density of 2,51 g/cm3, the common density of a glass.
- In order to determine the bending strength and the breaking load, seven samples were submitted with an average breaking strength of 2262 N, a resistance similar to that of rustic sandstone. While the maximum bending strength is 84.5 N/mm2, a value very close to the strength of a tempered glass.
- The test for chemical resistance showed that Murano gold leaf glass did not leave visible effects and therefore belongs to the first class: A, for resistance to cleaning products and pool salts. Similarly, resistance to strong and weak concentrations of acids and bases gives it the first class: HA and LA respectively.
- Three groups of 5 *piastras* have been subjected to different types of stains where it is found that the resistance of the product to stains is the maximum as they are easily removed by hot water.
- To determine the resistance to thermal coke, 5 *piastras* are subjected to 10 cycles of temperature variation between 15ºC and 145ºC by immersion. From the second cycle the product begins to crack and already in the third, pieces begin to fall off. The Murano glass of gold leaf having a metallic element between its layers, possesses a cohesion that helps to keep the whole together.
- The surface abrasion resistance test is evaluated by the PEI method (wet abrasion method) which measures the surface wear resistance of tiles and is classified in 5 degrees, where class 5 corresponds to the highest resistance. After the tests carried out on the samples, a result is given where the product corresponds to class 2 where the visible effects start to appear from 600 revolutions.

- For the determination of scratch resistance, the Mohs scale is used which, although already out of print, is not yet available for the determination of this type of test. After testing according to the Mohs scale, gold leaf Murano glass belongs to hardness 4, that is to the mineral: fluorite. A result far below the classification of glass strength.

- The results of the test to determine the resistance to linear thermal expansion, conclude with a variation of the expansion of the material with respect to the origin of 7,4x10-6/ºC in longitudinal direction and 7,6x10-6/ºC in a transverse direction, a result that is not significant.

- Finally. The test carried out to determine the resistance to frost results in 0% absorption and no defects.

4 Conclusions

- From the moment of its production, gold leaf Murano glass already presents substantial anomalies that can alter its future behaviour and durability.
- The manufacture and treatment of this product in its early stages should be more careful to reduce the risk of the occurrence of primary abnormalities which may be a risk factor for accelerating the occurrence of secondary abnormalities.
- The control of primary anomalies should not be to the detriment of the visual markings of this product.
- The first tests carried out in the laboratory indicate the appropriate quality of the glass and confirm some initial forecasts such as its weakness in the face of thermal shock or its low surface hardness.
- The durability of the product therefore falls heavily on the gold leaf itself; this stability will depend strongly on the perimeter sealing of the edges and the polluting products that can be introduced between the two glasses, during the manufacturing process (dust, gases, moisture, etc.), and on the rough surface of the gold leaf.
- There is not an adequate regulation for testing resistance to gold leaf Murano glass as the tests currently applied are governed by the characteristics of a very different product (ceramic tile) and, a more suitable element such as the case of a mirror, it lacks tests in the regulation that applies to it.

  The evaluation of the durability of this product according to the standard product of the flat glass industry, which is the mirror, has been pending for future research. The standard UNE-EN 1036 Silver-coated glass mirrors for internal use, even if it is confined to indoor situations, includes some environmental actions such as humidity and temperature in bathrooms. The conventional mirrors are flat, transparent, colourless, sodochalcium silicate glasses with parallel and polished faces, the rear face of which is covered with a sheltered silver reflecting reservoir, all this with a thickness between 2 and 10 mm allowed.
- It has been pending for future studies to evaluate the integrity of the whole when mechanical fractionation of the *piastras* is carried out by shear to obtain the irregular polygonal tesserae typical of the *trencadís*: in the case of glass of different composition and thickness, the mechanical fracture may give rise to weaknesses which leave the gold leaf unprotected from the external environment.

ORCID

Héctor Orozco: https://orcid.org/0000-0002-7436-2843
Joan Ll. Zamora: https://orcid.org/0000-0002-7705-6171

References

AENOR. (2009). Norma española. UNE-EN 1036. *Vidrio para la edificación. Espejos de vidrio recubiertos de plata para uso interno* (in Spanish). Madrid, Spain

AENOR. (2015). Norma española. UNE-EN ISO 10545. *Baldosas cerámicas* (in Spanish). Madrid, Spain

Dal Bianco, B. and Russo, U. (2012). Basilica of San Marco (Venice, Italy/Byzantine period): Nondestructive investigation on the glass Mosaic Tesserae. *Journal of Non-Crystalline solids, 358*(12–13), 1629. https://doi.org/10.1016/j.jnoncrysol.2011.10.006

De la Colina Tejeda, L. (2001). *El oro en hoja: aplicación y tratamiento sobre soportes móviles tradicionales, muro y resinas* (in Spanish). PhD Thesis, Universidad Complutense de Madrid. Spain. http://eprints.ucm.es/7082/

Neri, E., Verità, M., Biron, I. and Guerra, M.F. (2016). Glass and gold: Analyses of 4th-12th centuries Levantine mosaic tesserae. A contribution to technological and chronological knowledge. *Journal of Archaeological Science, 70,* 158-171, https://doi.org/10.1016/j.jas.2016.05.003

Römich, H. (1999). *The Conservation of Glass and Ceramics. Historical glass and its interaction with the environment*. James & James, Londres, Inglaterra, Norman H. Tennent Ed. ISBN 1-873936-18-4

Verità, M. (2006). *Tessere vitree a foglia d'oro nei mosaici di Aquilea* (in Italian). Quaderni Friulani di Archeologia XVI/2006, Murano-Venecia, Italia: Stazione Sperimentale del Vetro.

Verità, M., James, L., Freestone, I., Henderson, J., Nenna, M.D. and Shibille, N. (2009). *Glossary of Mosaic Glass Terms*. Centre for Byzantine Cultural History 2009, Brighton, Inglaterra: University of Sussex.

Whitehouse, D. (2006). *Glass. A pocket Dictionary of terms Commonly Used to Describe Glass and Glassmaking.* Nueva York, Estados Unidos: The Corning Museum of Glass.

XV International Conference on Durability of Building Materials and Components
DBMC 2020, Barcelona
C. Serrat, J.R. Casas and V. Gibert (Eds)

How to Determine when a New Building Product is Suitable – Certifications and Experience

Ernst J. de Place Hansen[1], Jørgen Nielsen[1], Eva B. Møller[2] and Ruut H. Peuhkuri[1]

[1] BUILD, Aalborg University, Campus Copenhagen, A.C. Meyers Vænge 15, 2450 Copenhagen SV, Denmark, deplace@build.aau.dk, jn1@build.aau.dk, rup@build.aau.dk

[2] Dept. of Civil Engineering, Technical University of Denmark, 2800 Kongens Lyngby, Denmark, ebmo@byg.dtu.dk

Abstract. *Previously, only solutions with long-term experience were used in the building sector and it was sufficient to describe, e.g. in the building regulations, how they should be constructed. However, the innovation rate has gradually increased, encouraged by industrialization and by building regulations becoming more functional based. As a result, the required performance is often described for the whole building or for a building component, but not at product level. Furthermore, CE marking makes it possible to market and sell a product in any country within the European Union if only one or a few properties are declared, and these may even not be the most relevant ones for a specific application in a technical solution. A CE mark is therefore neither a quality mark nor an approval of the product for a specific application, although clients and consultants often believe this is the case. It is therefore a major challenge for the building sector to determine if a new building product is suitable in a specific technical solution (wall, roof, etc.). The paper identifies a gap between performance-based requirements for a technical solution and specific requirements to properties of building products. Two cases (flat roofs with no slope, MgO-containing boards used as wind barriers) show the possible economic consequences of not closing this gap; the technical solution failed, as one of the products was not suitable for Danish weather conditions. The first case initiated the formation of the Danish Building Defects Fund in 1986, the second one from 2015 shows that the gap still exits, 30 years later. The cases show how difficult it can be even for professionals to understand different certifications, especially when a product seems to be well suited for a specific use. Based on the cases, the paper presents a systematic approach that guides users through important issues relating to requirements for a moisture-safe building envelope.*

Keywords: *CE Marking, Building Products, Performance-Based Requirements, Documentation of Properties, Decision Chart.*

1 Introduction

Previously, only solutions with long-term experience were used in the building sector and it was sufficient to describe how the solutions should be constructed; consequently the innovation rate was low. In Denmark, this was more or less the case until construction of buildings became gradually industrialized in the late 1950s and early 1960s, to accommodate the increased demand of dwellings after the Second World War. Industrialization is characterized by innovation and construction of a large number of buildings with almost the same technical solutions, reducing the construction time and/or the manpower. However, this means that a mistake can be reproduced many times before a lack of performance is discovered, and by then the economic consequences may be large. The innovation rate has gradually increased,

encouraged by building regulations becoming more functional based. As a result, technical solutions used in building projects are often only described by the required performance.

The challenge of how to handle a high innovation rate has been recognized for many years, both nationally, *e.g.* (Blach & Christensen, 1974) and internationally *e.g.* (CIB, 1982). Normally, the way to evaluate a new product is to compare it with an existing product with a known performance, although this presupposes that the properties of the existing product are relevant and sufficient. A technical solution (a wall, a roof, etc.) is normally composed by several products (bricks, insulating materials, membranes, wood panels, etc.), for which specifications may be available. The challenge is to close the gap between performance-based requirements (durability, thermal insulation, etc.) specified for a technical solution, and specific requirements to properties of products included in the solution. This is especially important when new or not fully tested products are introduced, or when well-known products are used in new combinations.

The cases presented in Section 2 illustrate how expensive it may be if the gap of documentation has not been closed. Therefore, the building sector needs guidance to evaluate if technical specifications of products lead to the fulfilment of performance-based requirements for a complete technical solution. A method for systematic review of products is described and discussed in Section 3 and 4.

2 Expensive Experiences

In several cases, new products have been used in many buildings before it was discovered that the product was unsuitable for the used purpose. Two Danish cases are described; the second showed that the problem still exists despite lessons learned from *e.g.* the first case.

2.1 Case 1: Flat Roofs

Flat roofs became popular in Denmark in the late 1950s and early 1960s. At that time the building process became more industrialized using roofing felt and building elements made of concrete, replacing labor-intensive construction work using bricklayers and brick masonry. Until 1972, the building regulations required that roofs had a slope towards drain, but in a ten-year period until 1981, when many large industrialized housing projects were constructed, there was no minimum requirement for roof slope. Unfortunately, complete flat roofs were difficult to execute with sufficient quality and the roofing materials were not durable for this solution. Therefore, many roofs leaked and resulted in expensive renovation projects and claims corresponding to 4 % of the contract sum for dwellings with flat roofs (Bunch-Nielsen, 2019).

This experience and similar cases initiated the formation in 1986 of the Danish Building Defects Fund (www.bsf.dk), a mandatory insurance-based system for social housing projects, combined with a guidance on quality assurance in construction that counts for governmental and publicly subsidized building projects (National Building Agency, 1986). This was based on the expectation that preventing damage and defects is less expensive than doing repairs, for the society as a whole as well as for the building sector. Today, claims on flat roofs are down to 0.1-0.2 % and the service life of this type of roof construction has increased from 10-15 years to 30-40 years (Bunch-Nielsen, 2019).

2.2 Case 2: Magnesium Oxide Containing Boards as Wind Barrier

Around 2007, a new type of building boards was introduced in Denmark as an alternative to traditional products used as wind barrier on the cold side of the insulation layer in a lightweight facade construction. The boards were strong, fire resistant, light, cheap and good for the working environment. The boards were quickly taken up by the market as a new, interesting product. However, in 2015 it was realized that these new boards were not at all suited as wind barrier under normal Danish weather conditions.

The boards contain MgO, which is a salt with a relatively low equilibrium moisture content, taking up moisture from the surrounding air when the relative humidity is high. Once saturated, the boards release salty liquid (Figure 1) that make screws, fittings and staples corrode and eventually initiate wood rot in surrounding wooden elements. In the longer run, the boards may disintegrate and lose their fire resisting, wind protecting and stabilizing properties. The Danish Building Defects Fund (2015a) declared promptly that they would not cover new claims related to building projects using MgO containing boards. They had by then been used in almost 20.000 social housing homes in Denmark and in an unknown number of single-family homes, private housing, schools, day care centers, hospitals, and industrial and commercial buildings. The cost of replacing boards alone in social housing dwellings has been estimated to around 1 billion DKK (Danish Building Defects Fund, 2015b).

Figure 1. Wetting of a concrete foundation revealing that salty liquid has been released from MgO boards in the above lightweight external wall. Photo: Tommy Bunch-Nielsen.

A legal sequel is on-going; In one case, the architect/consultant was judged as being responsible for not having presented clearly enough to the client, that the product was not thoroughly tested. In another case, the contractor was acquitted as he had followed recommendation from BYG-ERFA published in 2013 (BYG-ERFA, 2013) stating that MgO-containing boards were used as wind barriers, indicating that it had become a well-known product for this use. Since 2015, BYG-ERFA warns against this use of the boards (BYG-ERFA, 2015).

The binder in MgO board is formed by a chemical reaction between MgO and $MgCl_2$. Boards containing $MgSO_4$ were later introduced to the market because of the less hygroscopic behavior of $MgSO_4$ compared to $MgCl_2$ but they showed not to be a feasible alternative in Denmark and countries with a similar humid climate (Wøhler Nielsen *et al.*, 2019).

3 Systematic Review of New Products

To reduce the risk of using unsuitable products in technical solutions, decision makers need a way to review products. A method for a systematic review presented in this section is based on (Peuhkuri, Nielsen, and Møller, 2020) and (BYG-ERFA, 2017). It is a guideline to buyers of building products and other partners in a building project, who are supposed to demand documentation of relevant properties for new products or products used in a new way. Determination of requirements for products used in lightweight external walls is used as an example. The client should expect the consulting architect/engineer to:

- Identify new solutions in the building design
- Make sure that all relevant requirements for documentation of each product in each new solution is detailed and highlighted in the project documents (further detailed below)
- Ensure that suppliers' information about the product and documentation for critical parameters is present and critically evaluated.

Function of a product in a given solution. The function of a product must be identified before it is possible to identify the relevant properties. Opposed to a solid masonry wall, the functions of a lightweight exterior wall often are highly divided between products, so that one product acts as a vapor barrier, another as load bearing structure, etc. This makes it easier to develop new solutions where one product can be replaced by another disregarding all the other functions that the wall has to fulfil, provided that the products do not harm each other. In addition, there is a general requirement for durability. Further, not only the performance of the wall itself but also the joints with adjacent building elements is important.

Loads. The product may be exposed to a number of different loads in a construction. For a lightweight exterior wall, the position of the product in the wall determines the degree of the moisture load. Every load, including fire, freezing point passages, UV-exposure etc., must be quantified if relevant, including loads during the construction phase.

Relevant properties. The intended function of a specific product as part of a planned solution (*e.g.* that it contributes to the thermal insulation) and the loads it will be exposed to in the actual position in the solution, including loads during the construction phase, must be defined. This forms the basis for deciding which technical properties the product must be in possession of to function as expected in the solution.

Specification of requirements. A list of the specific requirements for a product to be used as intended in the technical solution can be based on a relevant harmonized European standard or a European Technical Assessment (ETA) in case the product is not covered by a standard. However, standards covering specific types of products, *e.g.* plasterboard or insulation, normally relate to product properties only and not to properties related to the technical solution, *e.g.* strength, fire resistance and sound insulation. In case a standard covers a technical solution, for example a lightweight wall, it usually focuses on statics and fire safety issues.

This means that where moisture loads are important, it is necessary (and legal) to supplement with requirements for moisture related properties, assuming these properties cannot be declared based on harmonized standards. This may be requirements related to moisture content at a specified relative humidity in the surrounding air, free water uptake, drying rate after water uptake, mechanical and chemical stability associated with moisture absorption, and durability in relation to moisture content. In addition, requirements for buildability must be included. In case it is decided to replace a product by another, the alternative product have to meet all the requirements, and not only one of them.

Documentation of product properties. For each of the listed requirements reference to a test standard shall be made. If a relevant harmonized European standard exists, it must be used.

4 Discussion

The cases in Section 2 illustrates, as previously stated in (de Place Hansen, 2013), that the buildings regulations' increasing use of performance-based requirements highlights the need for recommendations for levels of requirements for technical solutions and for communication about the experience with building products and solutions. Further, that building professionals should reflect more on the feasibility of a product or solution in a specific context, without having 40 years of experience from practice, as a lack of service life data not necessarily prevents new products and solutions to be promoted (de Place Hansen and Møller, 2015).

The introduction of CE marking makes it possible to market and sell a specific product in any country within the European Union (EU). However, a CE mark handled by EU, declaring specific properties of a building product, does not guarantee that the product complies with performance-based building requirements, being national based. Further, a CE mark is neither a quality mark nor an approval of the product for a specific application, although clients and consultants often believe this is the case. A product can get a CE mark simply by meeting a minimum requirement for a single property, *i.e.* CE marking does not ensure that the building product has all the relevant properties.

The producer might have had a specific use in mind, *e.g.* related to fire resistance or a specific climate, and not that it would be used in a climate where moisture related properties would be more relevant to document, but national authorities cannot force remaining properties to be declared. Further, a new product or a new use of a product is often not covered by a harmonized standard and an ETA is not necessarily issued, *i.e.* a CE mark is not required. It is therefore a major challenge for the building sector to determine if a new product is suitable in a specific technical solution, *e.g.* being able to withstand hygrothermal load during 40 years of use in a building envelope. Experience from the Danish Building Defects Fund has shown that requirements in relation to moisture are not sufficiently well formulated.

Further, by combining existing products with new products in a technical solution, it is necessary to expose how both new and existing products behave, to estimate how the combination will react, although this is not always sufficient (Ingeniøren, 2019). In general, the more products that are part of a technical solution, the harder it is to formulate product specifications for a solution adequate for a specific geographical location.

To close the gap between performance-based requirements and product specifications in an economical way, a simple, straightforward decision chart is suggested (Figure 2), combining the information presented in Section 3.

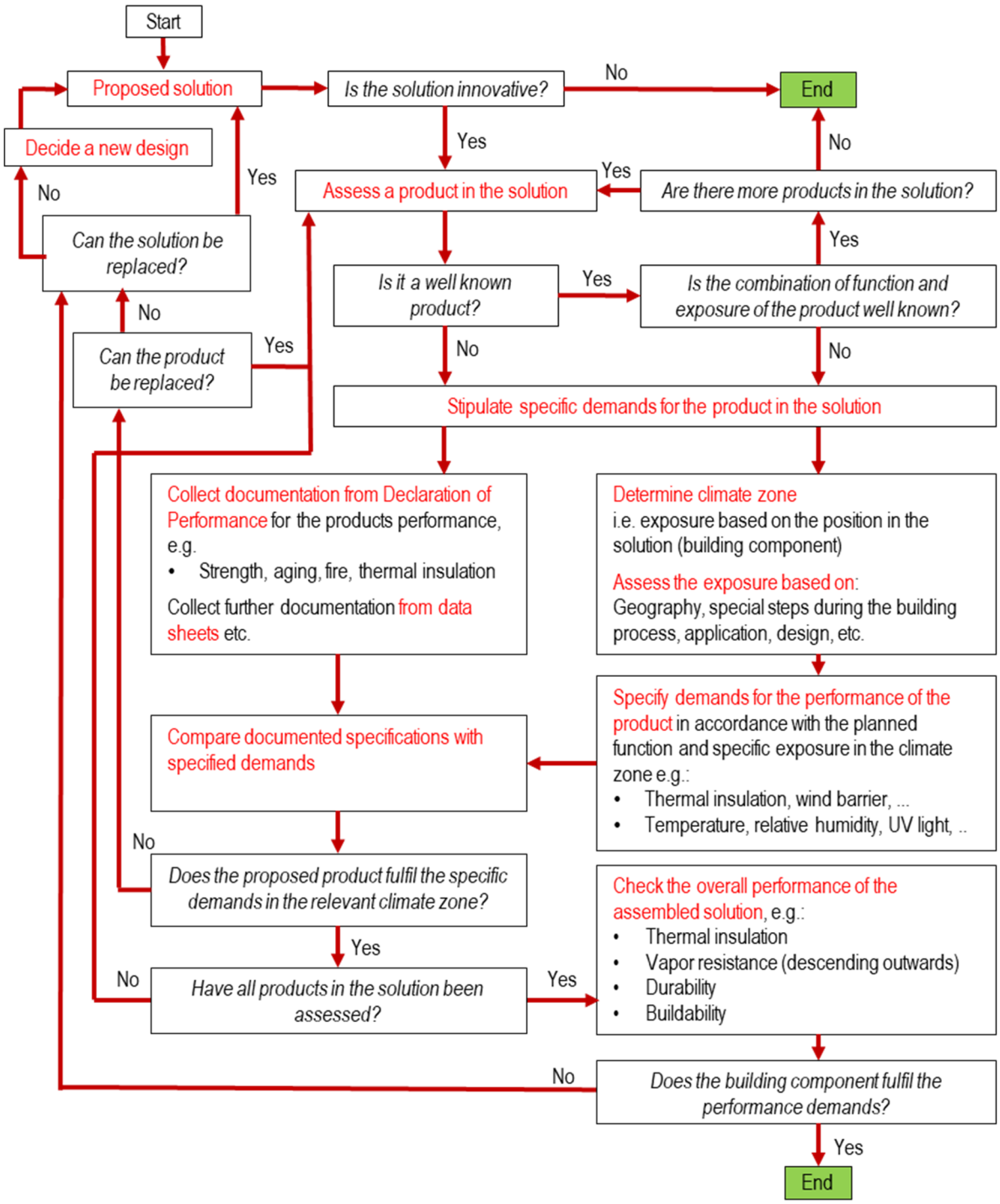

Figure 2. Decision chart guiding the user to ensure a suitable solution for an external lightweight wall, focusing on moisture related properties. Green boxes: A usable solution has been reached. Text in italic: Questions to be answered by the user. Boxes with text in red: Actions to be taken by the user. A guideline and eventually a checklist should expand each of these boxes.

The decision chart forces the user to consider different function-based requirements and guides the user through the most important issues to ensure a suitable solution for the building envelope, using a lightweight wall as an example. To use the chart for other types of external walls or other building elements, guidelines/checklists detailing the content of boxes with text in red should focus more on issues relating to statics, fire resistance, etc. The chart clarifies whether the risks the client takes are reasonable compared with the economic benefits. It can be used for both well-proven solutions with many years of good experience, as for new, innovative products or solutions. The more new products a technical solution includes, the harder the work to make it to the end of the decision chart.

The consultant must decide which requirements are needed for products used at a specific position in a specific technical solution for a building component. A documentation of this could be a part of a statement/declaration on risky conditions, including a description of how to minimize the risk. Together with an evaluation of the costs, the client has now a basis to decide whether he will accept the suggested innovative solution. For products used as roofing underlay this work has already been done in Denmark with the introduction of DUKO in 2004, an independent company that classifies roofing underlays and (since 2013) vapor barrier systems (https://duko.dk). Although this is a voluntary scheme, within a few years DUKO has increased the quality of roofs and reduced the amount of defects (Møller and Hansen, 2017).

In other wall types or in technical solutions used in other parts of the building envelope, the products involved may not have as specific functions as in lightweight walls. Nonetheless, it is still relevant to follow a systematic approach to ensure that all the relevant considerations are made when evaluating whether a suggested solution is suitable. As an example, a wall element that functions both as a load bearing structure, as thermal insulation and as a vapor barrier of course has to document all the properties relevant to comply with these functions when used at a specific geographical location.

For each new product, it can be costly to carry out tests to document whether it fulfils specific requirements, especially if the product can be used in many combinations with other products. Moreover, the producer may have a specific use in mind when putting it on the market, not considering other kinds of use. Consequently, producers may be reluctant to test for more properties than necessary for the intended use. Likewise, consultants and contractors neither have the time nor money to organize testing for more properties.

5 Conclusion

A gap between performance-based requirements specified for a technical solution and specific requirements to properties of products has been identified. Cases show that this gap still exists (second case) although problems with identification of relevant product requirements has been known for at least 30 years (first case). Further, cases show that it can be very expensive to use new products or technical solutions in a specific context if not all relevant properties are documented or if the products are not used as intended.

Closing the gap simply by asking for more documentation is not trivial as testing is expensive, and often the consultant lacks knowledge to identify what is relevant without a systematic approach. A decision chart was developed to guide the consultant into the needed systematic approach when deciding whether a specific product or solution is acceptable.

Acknowledgements

The development of the proposal for a systematic review of products and the decision chart presented in Section 3 and 4 was made possible by a grant from the Danish Building Defects Fund.

ORCID

Ernst J. de Place Hansen: https://orcid.org/0000-0002-6906-3793
Jørgen Nielsen: http://orcid.org/0000-0001-8065-4036
Eva B. Møller: http://orcid.org/0000-0001-8404-0859
Ruut H. Peuhkuri: https://orcid.org/0000-0001-7682-8515

References

Blach, K. and Christensen, C. (1974). *Ydeevne – hvorfor, hvordan?* (In Danish; author's translation: Performance – why, how?). Danish Building Research Institute, Copenhagen.

Bunch-Nielsen, T. (2019). Written communication.

BYG-ERFA (2013). *Vindspærrer i facader – materialevalg og afdækning i byggeperioden* (In Danish; author's translation: Wind barriers in facades – choice of material and covering in the building period) (BYG-ERFA Experience sheet (21) 13 12 27). Copenhagen.

BYG-ERFA (2015). *Fugtsugende vindspærreplader* (In Danish; author's translation: Moisture absorbing wind barrier boards (BYG-ERFA Experience sheet (21) 15 05 05). Copenhagen.

BYG-ERFA (2017). *Byggevarer og CE mærkning* (In Danish; author's translation: Building products and CE marking) (BYG-ERFA Experience sheet (99) 17 06 05). Copenhagen.

CIB (1982). *Working with the performance approach* (CIB Report, Publication 64). Working Commission W060, CIB, Rotterdam, The Netherlands. http://www.irbnet.de/daten/iconda/CIB_DC23969.pdf

Danish Building Defects Fund (2015a). https://www.bsf.dk/media/1542/orientering-06-03-2015.pdf

Danish Building Defects Fund (2015b). https://www.bsf.dk/media/1595/mgo-plader-omfang-omkostning.pdf

de Place Hansen, E.J. (2013). Carrot and stick – how to reduce the amount of defects in Danish construction. In *Proc. 19th CIB World Building Congress, Brisbane 2013: Construction and Society (CIB Proceedings, Vol. 2013).* (S. Kajewski, K. Manley, K. Hampson (Eds.)). Brisbane: Queensland Univ. of Technology.

de Place Hansen, E.J. and Møller, E.B. (2015). How to promote new building products and technologies without knowing their service life. In *Proc. 1st Int. Symp. on Building Pathology ISBP2015: Porto, 24 - 27 March 2015.* Peixoto de Freitas, V., de Angelis, E., Corvacho, H., Delgado, J. M. P. Q. & Guimarães, A. S. (red.). Porto: FEUP Edicões, s. 309-316

Ingeniøren (2019). *Bekymrende overraskelse: Ufarlige byggematerialer bliver til en giftig cocktail.* (In Danish; author's translation: Disturbing surprise: Harmless building materials become a toxic cocktail). Ingeniøren, 21 Oct 2019. Copenhagen. https://ing.dk

Møller, E.B. and Hansen, T. (2017). Artificial aging of air and vapour barriers. In *Proc. 14th International Conference on Durability of Building Materials and Components (XIV DBMC), 29-31 May 2017*, Ghent University, Ghent, Belgium, 285, 1-12.

National Building Agency (1986). *Vejledning om kvalitetssikring i byggeriet* (In Danish; author's translation: Guidance on quality assurance in construction) (VEJ nr. 4024 af 31/12/1986). Copenhagen

Peuhkuri, R., Nielsen, J. and Møller, E.B. (2020). *Specifikation af krav til bygningsdele i klimaskærmen* (In Danish; author's translation: Specification of requirements for solutions in the building envelope) (SBi 2020:11). Department of the Built Environment, Aalborg University, Copenhagen.

Wøhler Nielsen, S., Rode, C., Bunch-Nielsen, T., Kielsgaard Hansen, K., Kunther, W. and Grelk, B. (2019). Properties of magnesium oxide boards used as sheathing in exterior walls. 4th Central European Symposium on Building Physics (CESBP), Prague, 2-5 Sep 2019, *MATEC Web of Conferences* vol. 282, 02091. https://doi.org/10.1051/matecconf /201928202091

XV International Conference on Durability of Building Materials and Components
DBMC 2020, Barcelona
C. Serrat, J.R. Casas and V. Gibert (Eds)

Impact of Portland Cement Content on Alkali Activated Bottom Ash

Luís Tambara Júnior, Malik Cheriaf and Janaíde C. Rocha

Laboratory of Waste Valorization and Sustainable Materials (ValoRes), Department of Civil Engineering, PPGEC, Federal University of Santa Catarina (USFC), Campus Trindade, 88040-900 Florianópolis, Brazil, luistambara@gmail.com, malik.cheriaf@gmail.com, janaide.rocha@ufsc.br

Abstract. *This study explores the behavior of blended mortars of low reactive bottom ashes (BA) and ordinary Portland cement (OPC) in an alkaline solution. Mortar mixtures incorporating OPC with different replacement levels (0% to 30% mass) were studied. Isothermal conduction calorimetric analysis was studied and 28-and 60-day mechanical strength values were found. SEM images was used to identifies porosity structures at 28-day. Water absorption was also investigated. The results revealed different behaviors to low (OPC 2.5 and OPC 5) and moderated (OPC 10 and OPC 30) OPC content. Increase in percentage of Portland accelerated hydration kinetics. There is a second peak formation for moderated OPC content, associated with C-A-S-H gel formation. The partial replacement of bottom ash by OPC tend to reduce the absorption. There is a slower initial water absorption to low OPC content. This behavior is due the higher unreacted BA content, that works as a filler. Otherwise, the increase of water absorption for OPC content is due to the coexistence of Portland cement hydrates and alkali activated reactions.*

Keywords: *Blended Mortars, Alkali Activation, Porosity, Bottom Ash.*

1 Introduction

Bottom ash (BA) represents 40% of ashes from the coal-fired thermoelectric power plants (Cheriaf *et al.*, 1999), it is estimated 4.5 million tons of BA per year in Brazil (IEA, 2016). Unlike fly ash, the disposal of bottom ashes goes to settling basin. Studies have shown the use of bottom ashes as an alternative aluminosilicate source for alkali activations (Topçu *et al.*, 2014, Tambara Júnior *et al*., 2018). However, its performance is worse than fly ash. This is due the less amorphous content, higher unburned coal and low reactive SiO_2 and Al_2O_3.

An alternative to improving alkali activation BA properties is to increase surface area (through grinding) and to reduce unburnt material, through calcination (Sathonsaowaphak *et al.*, 2009). Currently in the literature hybrid or blended cements are used to obtain better responses of the material (Garcia-Lodeiro *et al.,* 2016).

Durability remains a property requiring further studies on alkali activations. A problem reported about alkali activation materials is the higher sorptivity when compared with Portland cement. Some works (Collins and Sanjayan, 2000) affirm that this is due the large proportion of fine pores which results in micro-cracks in the matrix, increasing the water capillarity. To reduce the water sorptivity it is necessary add some material that densifies the sample (Rostami and Behgarnia, 2017).

In this article was investigate the influence of ordinary Portland cement (OPC) on the mechanical strength, kinetic of water absorption and pore structure (scanning electron microscope) of blended alkali activation mortar of BA/OPC. The reaction was monitored with isothermal conduction calorimetry to evaluate the heat flow variations in the pastes in the early time of reaction. The OPC was blended from 0%, 2.5%, 5%, 10% and 30%.

doi:10.23967/dbmc.2020.180

2 Experimental Procedure

2.1 Materials Characterization

A Mastersizer 2000 laser granulometer was used to obtain particle size distribution of OPC and BA (Figure 1) and the powder was dispersed in isopropanol. It is seen that the BA used in this study contained a finer particle size than BA. Where 86% of OPC and 99.9% of BA particle size measured under 45μm, in agreement with the size particle parameter used to improve ash reactivity (Fernández-Jiménez e Palomo 2003).

The BA and OPC oxide analysis and clinker phase compositions are presented in Table 1. To the cement the phase was estimated based on Bogue calculation method. To BA was performed a Rietveld refinement method (Rietveld, 1969) using X-ray diffraction test data. To determine the amorphous and crystalline content in the BA sample, the analytical reagent corundum (Al_2O_3) was added in a total of 10% by mass as an internal standard. The OPC is a type III and the BA is classified as ash type F (low calcium content).

The sand used in the mortar mixtures was a natural fine sand. It was obtained a relative specific density of 2600 kg/m³, water absorption of 1.6%, maximum grain size of 1.2 mm and minimum grain size of 0.15mm. The sand showed a fineness modulus of 1.83.

Table 1. Chemical composition.

Oxide analysys			Phase composition results			
(%)	OPC	BA		OPC		BA
SiO_2	19.36	40.82	C3S	60.05	Quartz	7.19
CaO	63.71	1.73	C2S	10.22	Mullite	26.24
Al_2O_3	5.10	37.46	C3A	8.41	Amorphous	69.57
Fe_2O_3	3.02	5.71	C4AF	9.19		
SO_3	2.84	0.29	CS	4.83		
Others	2.17	7.32	free lime	1.25		
LOI[a]	3.80	6.67				

[a]Loss of ignation

A combination of sodium hydroxide (NaOH) pellets, water distilled and sodium silicate solution (Na_2SiO_3) was used as an alkaline activator (SiO_2 = 26.5%; Na_2O = 10.6%; H_2O = 62.9%; and density of 1.39 g/cm^3). Initially a 14M NaOH solution was prepared with distilled water, waiting up to room temperature. After that a ratio of 1:2 Na_2SiO_3 to NaOH solution were prepared. A superplasticizer additive based on polycarboxylate ether, with solids content of 0.22, was used to adjust the workability (flow value > 250 mm) required for self-leveling mortars.

To evaluate the effect of OPC content on the microstructure of blended alkali-activated mortars, it was prepared 5 mixtures. The sum of OPC and BA was considerate as binder. Hydrated mortars were prepared using the same liquid-to-binder (l/b) ratio of 0.55. The substitution in mass of BA for Portland cement was: 0% (*i.e.*, only bottom ash), 2.5%, 5%, 10% and 30%. The binder and sand ratio were kept constant from 1:2 (in mass). The molar ratios were between 2.6-3.1 to Si/Al, 0.27-0.30 to Na_2O/SiO_2 and equal to 12.3 to H_2O/Na_2O.

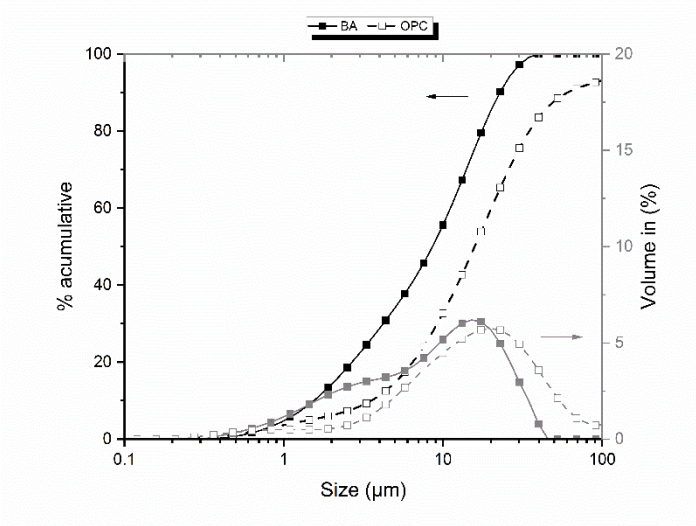

Figure 1. Particle size of OPC and BA.

2.2 Experimental Procedure

The mixing method consisted of an initial premix of the solutions (NaOH and Na_2SiO_3) until room temperature. After that, a dry mix powder of cement, bottom ash and sand of each proportion was executed. The solid/liquid mixing was performed in a planetary mixer, the first 2 minutes at 150 rpm and one last minute at 300 rpm. Then the mortars were added to the molds and cured for 24h at 80ºC.

Compressive strength was performed in cubic molds (4cm x 4cm), according to Brazilian Standard NBR 13279. To each mixture 6 samples were tested at 28 and 60 days of reaction. Calorimetric tests were performing to determine the heat evolution and the total heat through a conduction isotherm calorimeter TAM Air-Thermometric. The pastes were manually mixed for a period of 3 min with the same w/b ratio than mortars and then sealed. The samples were immediately placed in the calorimeter, under the same conditions as the mortars (80º ± 1ºC).

To stop the reaction at the test ages for microstructural analysis, the samples were kept in an oven at 40ºC until constancy of mass. Water absorption was evaluated over time for 24 hours through a method of Mariotte's bottle developed of laboratory ValoRes-UFSC. To analyze the microstructure images, the samples were carbon-coated and mounted on electron microscope slides for study under a JEOL JSM-6390SL (15.0kV) with energy-dispersive X-ray spectroscopy (EDS) performed at Central Laboratory of Electron Microscopy (LCME-UFSC).

3 Results and Discussion

3.1 Isothermal Calorimetry and Compressive Strength

The effect of OPC content on the rate of heat release and total heat release during alkali activation of the BA is shown in Figure 2. For all the samples is seen a faster reaction at 80ºC, due to this it was not possible to detect the first peak associated aluminosilicate dissolution, as observed in literature (Palomo *et al*., 1999; Garcia-Lodeiro *et al*., 2013). For the alkali

activation only with BA (OPC0) it is seen the lowest heat release and total heat. This is due its insufficient dissolution phases that start the formation of N-A-S-H gel.

Two different behaviors were observed according to the OPC content on the hybrid cements. Results are presented as low OPC content (OPC2.5 and OPC5) and moderate OPC content (OPC10 and OPC30). Even in small quantities, increasing OPC content accelerates the activation reaction. To low OPC content (Figure 2a) it is noticed the formation of a single peak in heat evolution. The increment of OPC content resulted in a higher heat release and total heat, this indicates an increase of reaction degree. OPC2.5 and OPC5 showed a total heat at 6 h of 59.79 J/g and 77.73 J/g, respectively.

Figure 2b shows heat flow curve and total heat for the alkali activation with moderate OPC content. It is observed a more intense and rapid first peak compared with low OPC content, followed by a short dormant period (occurs up to 15 minutes of activation). OPC10 and OPC30 presented a total heat at 6 h of 148.48 J/g and 126.76 J/g, respectively.

The quick first peak formation may be associated with an accelerated Si and Al dissolution and N-A-S-H formation. Also, a secondary peak starts after 15 minutes of activation. After the first gel formation the pH of pore solution decreases by which the calcium provided from OPC begins to react and form a (N,C)-A-S-H gel type (Garcia-Lodeiro *et al*., 2016).

OPC30 showed the highest total heat up to 1h of activation, however, OPC10 overcame the total heat in higher period. Martinez-Ramirez and Palomo (2001) showed that OPC hydration is retarded when alkali concentrations increases. This suggests that is greater amount of inner anhydrous cement to OPC30 than OPC10.

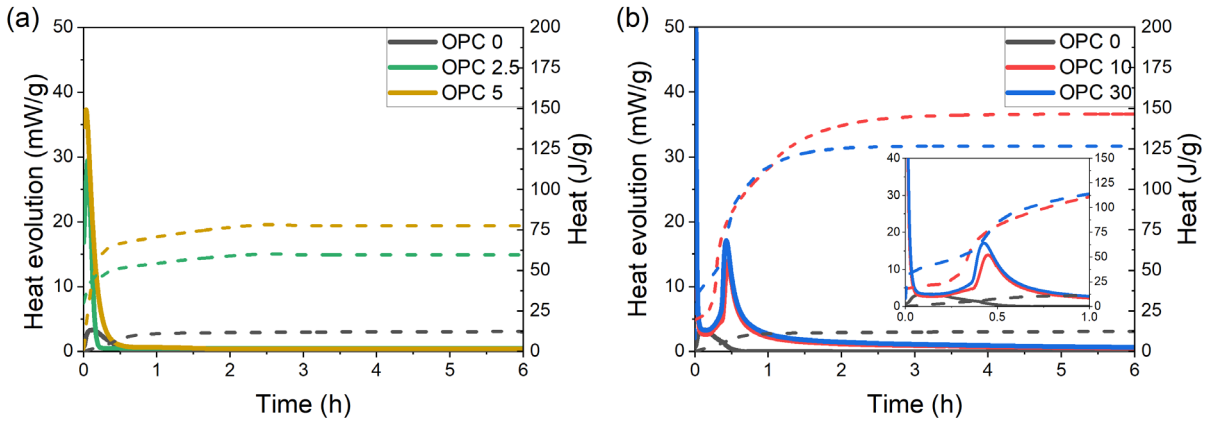

Figure 2. Heat flow and cumulative heat from the low OPC content (a) and moderate OPC content (b) alkali Activation.

Compressive strength was evaluated to later ages of 28 d and 60 days (Figure 3). OPC0 showed no strength development over the time of 60 days. This result shows that the exclusive alkali activation of BA results in a very slow evolution of reaction. The gain of compressive strength from 28 d to 60 d of OPC2.5, OPC5 correspond to 8.8%, 12.8% to low OPC content, a result in agreement with heat flow calorimetric analysis. To moderate OPC content the compressive strength for 28 d and 60 d increases 19.9% and 11.6% to OPC10 and OPC30, respectively. There is observed an optimum OPC content of 10% to blended mortar, increasing the bottom ash reaction.

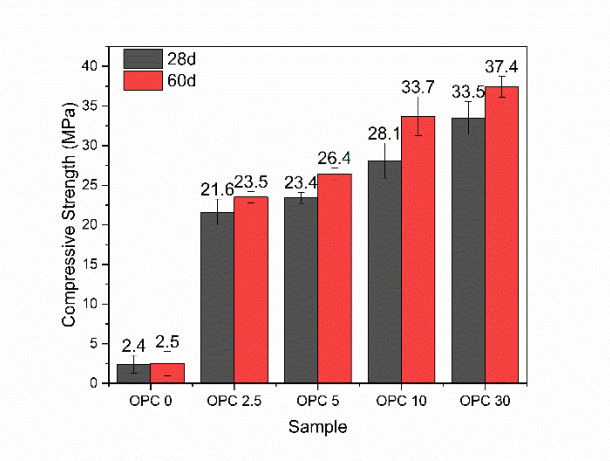

Figure 3. Compressive strength to 28 d and 60 d.

3.2 Water Absorption

Water transportation of mortars is an important property that mainly influences its durability. Figure 4 shows water absorption over a 24 h of experiment to low and moderate OPC mortars at 1 d and 28 d. The water absorption of the blended mortars reported in this work were obtained in the final rage of 2.27%-10.01% and 1.57%-4.30% for 1 d and 28 d, respectively. At 1 d of hydration, it is observed higher absorption of activation with increased OPC dosage.

At 28 d was observed to all samples a reduction of water absorption. Compared with 1d of hydration, OPC30, OPC10, OPC5 and OPC2.5 presented a water absorption reduction of 57.04%, 81.17%, 68.59% and 30.84%, respectively. Water absorption reduction is greater for moderate OPC mortars. It was observed that OPC10 showed the lowest water absorption to 28 days. The authors associate this behavior to the pore filling due best compatibility of last formation of (N,C)-A-S-H gels observed through microscopy analysis (Tambara Júnior *et al.*, 2018).

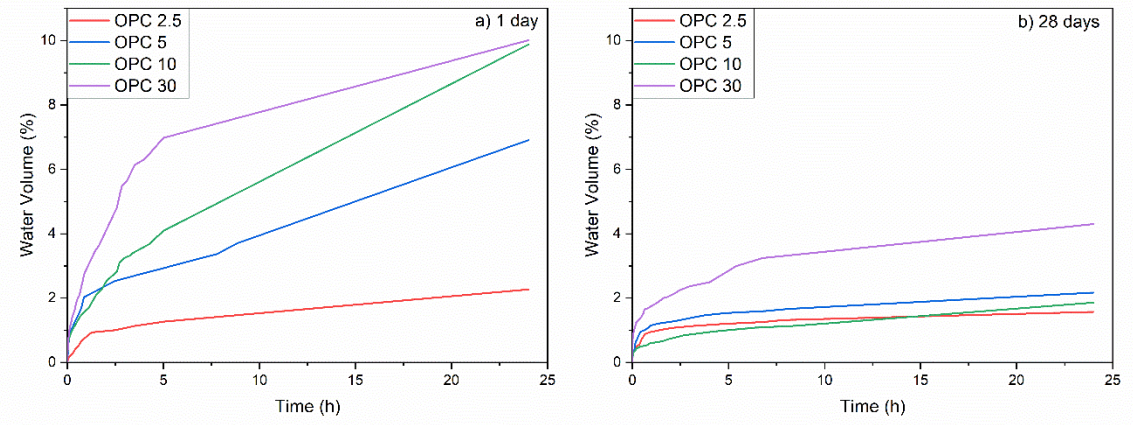

Figure 4. Water absorption of low OPC moderate OPC content at 1 day (a) and 28 days (b) of reaction.

3.3 SEM

As Figure 5a shows, the bottom ash after treatment presented predominance of irregular particles with few spherical particles, which difficult the activation. Figure 5b shows the OPC0 at 28 days of activation, where there is a larger presence of unreacted BA and insufficient gel formation, featuring in a higher porosity and low compressive strength (Figure 3).

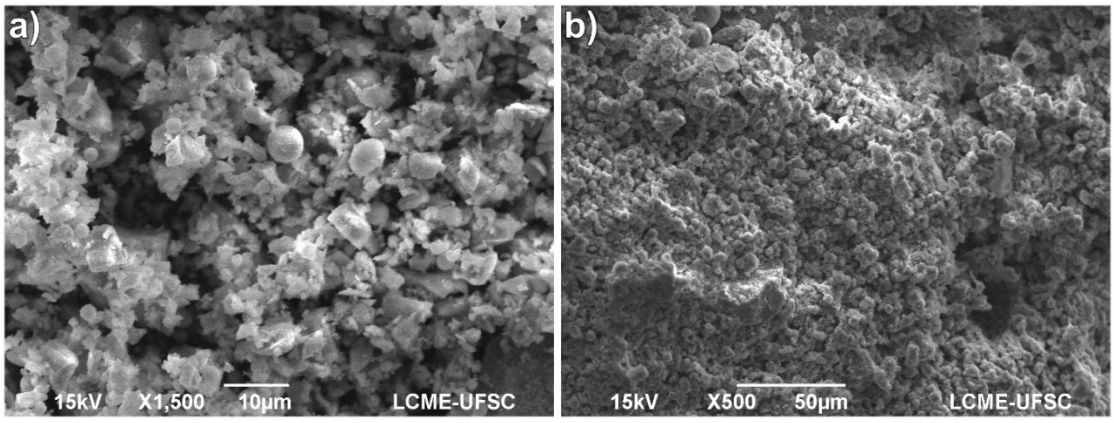

Figure 5. SEM images of a) BA and b) OPC0 hydrated at 28 days.

As visual criteria, analysis of pores size was evaluated through an image analysis software tool of SEM images. Figure 6 shows micrographs of low and moderated OPC samples at 28d. To OPC2.5 is the sample with the largest pore presence. It is observed a great presence of macropores 50 µm - 400 µm. To OPC5 was observed a reduction in the content of smaller macropores, with no significant difference to pores larger than 300 µm.

There is observed higher pore formation and unreacted bottom ash to low OPC content mortars. As calorimetry analysis shows, the improve of OPC content results in a higher energy release. This fact can be associated with the reduction of porous sizes, where this improves the silicon dissolution, resulting in a denser N-A-S-H/C-A-S-H gels.

Moderate OPC mortars resulted in a reduced presence of the larger porous size. OPC30 and OPC10 presented similar pore size range of 20 µm – 140 µm. Otherwise, it was observed the lower water absorption to the OPC10, that can be associated to a higher microporosity to OPC30 mortar.

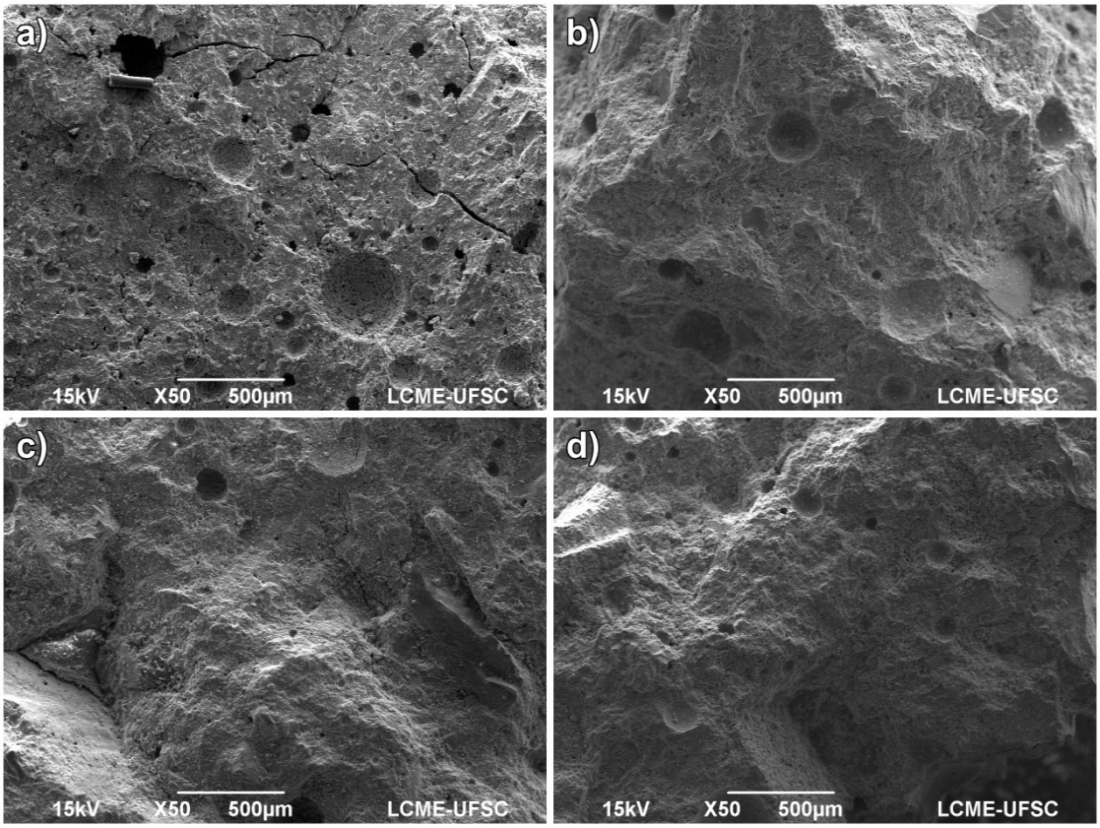

Figure 6. SEM images of 28 days a) OPC2.5, b) OPC5, c) OPC10, d) OPC30.

4 Conclusions

This study evaluated the OPC content on the blended mortars of bottom ash and Portland cement. It is concluded that there is different behavior between low to moderate OPC replacement, but even in low content (2.5% and 5%) there is a good contribution to activate bottom ashes with low reactivity.

To all the samples, as the OPC replacement increased the mechanical strength and the water absorption increases. This improved performance may be due to a denser microstructure generated to C-A-S-H gel formation observed through microstructural and calorimetry analysis that showed a secondary peak to moderate OPC content.

Furthermore, the 10% substitution of OPC significantly improved the parameters of durability, associated with the higher strength development at later ages and lower water absorption, due to its suitable Ca^{+} content provided by OPC. The increase of compressive strength and water absorption of OPC30 may be associated with a reduction of macroporosity but higher microporosity.

Acknowledgements

This study was sponsored by the Coordenação de Aperfeiçoamento de Pessoal de Nível Superior (CAPES), Conselho Nacional de Desenvolvimento Científico e Tecnológico (CNPq). We are grateful CNPq, CAPES and LCME-UFSC for assistance in scanning electron microscopy operation.

ORCID

L. Tambara Júnior: https://orcid.org/0000-0002-3269-4911
Malik Cheriaf: https://orcid.org/0000-0001-5440-2636
Janaíde C. Rocha: https://orcid.org/0000-0003-1074-3230

References

ABNT (2005). NBR 13279: Mortars applied on walls and ceilings – Determination of the flexural an the compressive strength in the hardened stage. (*In Portuguese*).

Cheriaf, M., Cavalcante Rocha, J. and Péra, J. (1999). Pozzolanic properties of pulverized coal combustion bottom ash*, Cem. Concr. Res.* 29 1387–1391. doi:0008-8846/99/$.

Collins F. and Sanjayan G.J. (2000). Effect of pore size distribution on drying shrinkage of alkali-activated slag concrete, *Cem Concr Res* 30 1401-1406.

Fernández-Jiménez and A. Palomo, A. (2003). Characterisation of fly ashes. Potential reactivity as alkaline cements. *Fuel*, 82(18), 2259-2265. doi: 10.1016/S0016-2361(03)00194-7

Garcia-Lodeiro, I. Fernandez-Jimenez and A. Palomo, A. (2013). Hydration kinetics in hybrid binders: Early reaction stages. *Cement and Concrete Composites*. 39, 82-92. doi: 10.1016/j.cemconcomp.2013.03.025

Garcia-Lodeiro, I., Donatello, S., Fernández-Jiménez, A. and Palomo, A. (2016). Hydration of hybrid alkaline cement containing a very large proportion of fly ash: A descriptive model, *Materials*. 9 doi:10.3390/MA9070605.

IEA, International Energy Agency Coal Information 2015 with 2015 data. (2016). Energy Technol. Perspect, https://www.oecd-ilibrary.org/energy/coal-information-2016_coal-2016-en, Accessed date: 14 October 2019

Martínez-Ramírez, S. and Palomo, A. (2001). OPC hydration with highly alkaline solutions. *Advances in Cement Research* 13(3) 123-129.

Palomo, A., Grutzeck, M.W. and Blanco, M.T. (1999). Alkali-activated fly ashes A cement for the future, *Cem. Concr. Res.* 29 1323–1329.

Rietveld, H. M. (1969). A profile refinement method for nuclear and magnetic structures. *Journal of Applied Crystallography*, 2(2), 65-71. doi: 10.1107/s0021889869006558

Rostami, M. and Behfarnia, K. (2017). The effect of silica fume on durability of alkali activated slag concrete. *Construction and Building Materials*. 134 262-268. doi: 10.1016/j.conbuildmat.2016.12.072

Sathonsaowaphak, A., Chindaprasirt, P. and Pimraksa, K. (2009). Workability and strength of lignite bottom ash geopolymer mortar. *Journal of Hazardous Materials* 168 (1) 44-50. doi: 10.1016/j.jhazmat.2009.01.120.

Tambara Júnior, L.U.D., Cheriaf, M. and Rocha, J.C. (2018). Development of Alkaline-Activated Self-Leveling Hybrid Mortar Ash-Based Composites. *Materials.* 11, 1829.

Topçu, I.B., Toprak, M.U. and Uygunoğlu, T. (2014). Durability and microstructure characteristics of alkali activated coal bottom ash geopolymer cement*, J. Clean. Prod*. 81 211–217. doi:10.1016/j.jclepro.2014.06.037

XV International Conference on Durability of Building Materials and Components
DBMC 2020, Barcelona
C. Serrat, J.R. Casas and V. Gibert (Eds)

Influence of Different Types of Metakaolin on Compressive Strength and Chloride Migration of Concrete

Rodrigo Teodoro[1], Helena Carasek[2] and Oswaldo Cascudo[3]

[1] Laboratory of Technological Innovation in Civil Construction (LABITECC), Federal University of Goias (UFG), Goiania, Brasil, rodrigoteodoro.eng@gmail.com

[2] Laboratory of Technological Innovation in Civil Construction (LABITECC), Federal University of Goias (UFG), Goiania, Brasil, hcarasek@ufg.br

[3] Laboratory of Technological Innovation in Civil Construction (LABITECC), Federal University of Goias (UFG), Goiania, Brasil, ocascudo@ufg.br

Abstract. *The use of mineral admixtures in concrete has grown in recent years, specially the high-performance ones, such as silica fume, nanosilica and metakaolin. Metakaolin has been extensively studied due to its high reactiveness. Thus, an experimental program was conducted to evaluate the behavior of compressive strength and non-steady state chloride migration due to differences of metakaolin characteristics. Three different metakaolins were characterized, then used in a 10% replacement ratio (of mass of cement), among two water/binder ratios (0.40 and 0.60) in concrete mixes. The results show that metakaolin increased compressive strength in every age tested. Moreover, durability properties were significantly enhanced due to the addition of metakaolin. Non-steady state chloride migration coefficient of metakaolin concretes were noticeably lower than plain concrete. In general, the addition of metakaolin in concrete caused pore refinement and reduction in total porosity, which lead to enhancements of mechanical e durability properties of concrete.*

Keywords: *Durability, Chloride Migration, Metakaolin, Compressive Strength.*

1 Introduction

Metakaolin (MK) is a relatively new supplementary cementing material (SCM), although there are studies and research in the past century, it was in the last two decades that MK was broadly studied. In Federal University of Goias (UFG), in Brazil, since 2000's several experiments were conducted with MK and other pozzolans (Cascudo, Mendes, Carasek, and Ferreira, 2014; Ferreira, Pereira, Lopes, Carasek, and Cascudo, 2004; Figueiredo *et al.*, 2014; Oliveira and Cascudo, 2018; Pereira, Lopes, Hasparyk, Carasek, and Cascudo, 2005). The results of these researches suggest that the overall good performance of highly reactivity metakaolin owes mainly to its fineness which leads to an enhancement of filler effect on concrete microstructure.

On the other hand, MK is obtained from the calcination of kaolinitic clay, mainly composed of kaolinite (hydrated aluminosilicate), which means that it's major composition is alumina (Khatib, Baalbaki, and ElKordi, 2018; Murat and Comel, 1983; Siddique and Khan, 2011). In this sense, some studies observed that MK can react with chloride ions in concrete resulting in a stable compound knows as Friedel's salt (Friedel, 1897). This means that the addition of metakaolin in concrete can improve the chloride resistance (Cascudo *et al.*, 2014; Talero, 2012), therefore improve the durability of concrete.

doi:10.23967/dbmc.2020.079

Thus, a research conducted to verify the influence of physical, chemical and mineralogical characteristics of highly reactivity metakaolins in mechanical and durability related properties of concrete. In the present paper the changes in compressive strength and chloride migration caused by MK properties were assessed.

2 Experimental Program

This paper is a part of a broader experimental program in which the influence of different types of highly reactivity metakaolins in the microstructure of concrete is evaluated.

2.1 Materials

Eight different types of concrete were mixed: with two water/binder ratios – 0,40 and 0,60 – as well as three different metakaolins – MK1, MK2 and MK3 – all from the same Brazilian manufacturer in a 10% content in substation of cement, in mass, and a plain concrete – with no MK - R. The complete composition of all eight mixes is presented in table 1.

Table 1. Compostion of concrete mixes.

Concrete mixes	Cement content (kg/m³)	Mix proportions, in mass (cement : metakaolin) : sand : crushed stone	w/b	Super-plasticizer (%)
40R	450	(1.00 : 0.00) : 1.68 : 2.37	0.40	0.36%
40MK1	405	(0.90 : 0.10) : 1.67 : 2.37	0.40	0.66%
40MK2	405	(0.90 : 0.10) : 1.67 : 2.37	0.40	0.64%
40MK3	405	(0.90 : 0.10) : 1.67 : 2.37	0.40	0.67%
60R	300	(1.00 : 0.00) : 2.98 : 3.53	0.60	0.33%
60MK1	270	(0.90 : 0.10) : 2.96 : 3.53	0.60	0.46%
60MK2	270	(0.90 : 0.10) : 2.96 : 3.53	0.60	0.38%
60MK3	270	(0.90 : 0.10) : 2.96 : 3.53	0.60	0.60%

Once the characteristics of the metakaolins are relevant to further understand the possible changes in concrete, some of their physical, chemical and mineralogical properties were analyzed: BET fineness, chemical composition by X-ray fluorescence, quantification of crystalline phases by X-ray diffractometry. Among of them, the pozzolanic index of metakaolin was measured by the Chapèlle's modified test (ABNT, 2010).

An ordinary Portland cement (OPC) (Brazilian type CP II F 40, similar to CEM II/A-L 42.5) was used in all concrete mixtures.

There were also used two different fine aggregates – both quartz sand, one with a fineness modulus of 2.09 and the other one with a MF = 3.54 – and two different coarse aggregates – both gneiss crushed stone, one with a MF equals to 5.71 and the other one with MF = 6.80. Also, a polycarboxylate-based superplasticizer was used in order to maintain the slump in a constant range, without changing the w/b ratio.

2.2 Methods

Concretes were tested in fresh state in which slump test was conducted to be kept in the range that was proposed (120 ± 20 mm). Then cylinder specimens were molded for tests in hardened state. Then they were cured immersed in water saturated of calcium hydroxide, at (23 ± 2)°C until the age of 28 days. Compressive strength tests were conducted with cylinder specimens (100 x 200 mm) of every concrete mix in four ages: 7, 28, 91 and 140 days.

The chloride resistance was measured by the Nordtest method, described in NT Build 492 (Nordtest, 1999). 100 mm × 50 mm cylindrical specimens were cut from the middle of 100 mm × 200 mm cylinders; subsequently, the apparatus, as described in the method, was assembled. This method, that was primarily proposed by Tang and Nilsson (1993), consists in forcing the chloride ions to migrate, with a direct electrical current applied in both cathodic and anodic solutions in which a specimen is immersed. This test, after some calculations based in some equations provided by the Nordtest standard, results in a coefficient of migration of chlorides in a non-steady state. This coefficient of migration is close to the coefficient of diffusion, which is the real mass transport of ions that occurs in concrete.

The results were also submitted the statiscal analysis of variance (ANOVA) and multiple mean comparison, from which some charts are presented herein.

3 Results and Discussion

Once the results of metakaolins characteristics are relevant to explain the changes in the properties of concrete, the results are presented in two section: first, the metakaolin results and then the concrete results.

3.1 Metakaolins Characterization

Although the metakaolins are produced by the same manufacturer, they are quite different, as can be seen in their chemical composition, presented in table 2.

Table 2. Chemical compostion of metakaolins.

Test Method	Content	MK1	MK2	MK3
X-ray Fluorescence Spectroscopy	SiO_2 (%)	56.46	52.58	51.43
	Al_2O_3 (%)	32.17	44.61	42.53
	Fe_2O_3 (%)	2.23	0.35	2.00
	CaO (%)	0.17	0.06	0.16
	MgO (%)	0.7	0.02	0.28
	K_2O (%)	2.16	0.09	0.95
	Na_2O (%)	0.04	0.04	0.02
	L.O.I. (%)	4.27	1.95	1.28
	Others (%)	1.65	0.11	1.14

It is known that MK1 and MK3 are obtained from the same raw material, while MK2 comes from another deposit. MK2 is white, so it is expected that it is the purest of all three, verified by chemical analysis, with around 97% of silica+alumina. The differences between MK1 and MK2 are also expressive, which may be due from the difference in the processing of raw material in the deposit (mainly a better refinement of the kaolin).

Table 3 shows other properties of metakaolins. The differences in their fineness are relevant. Although MK2 is the purest, it is the coarser metakaolin, which in theory may lead to lower reactivity. Also, it is interesting to observe the difference between the amorphous content, mainly between MK1 and MK3, which can be also explained by differences in the processing of material, especially in the calcination process.

Table 3. Physical and mineralogical properties of metakaolins.

Test Method	MK1	MK2	MK3
BET specific surface area (ASTM C 1069) (m^2/g)	19.75	8.13	30.99
XRD Quantification – Amorphous Content (%)	60.8	70.1	75.6
Chapèlle's Modified Method (ABNT NBR 15895:2010) - Pozzolanic index (mg $Ca(OH)_2/g$)	859	1027	1440

Finally, the pozzolanic index measured by the Chapèlle's modified method gives a overall understanding of the reactivity of the metakaolin, once it emulates the pozzolanic reaction (Quarcioni, Chotoli, Coelho, and Cincotto, 2015). According to this method, MK3 is the higher in reactivity, followed by MK2 and MK1.

3.2 Compressive Strength and Chloride Migration

Results of compressive strength along the age of concrete are presented in figure 1.

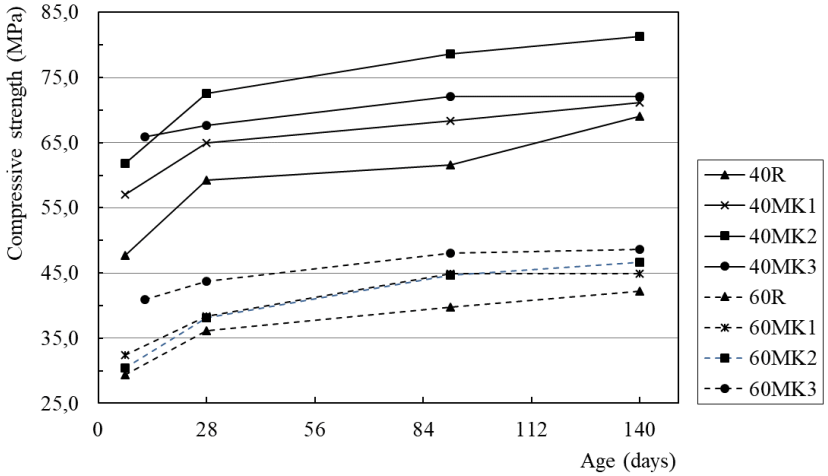

Figure 1. Results of compressive strength of concrete at ages of 7, 28, 91 and 140 days.

The difference between the w/b ratio is noticeable, as expected. It can be also seen that even in early ages MK concrete showed better results, which may be explained by the filler effect that is instantaneous. Also, at later ages MK concretes still showed better results. At 91 days a great part of the pozzolanic reactions have already occurred, it can be observed that mechanisms of action of MK in concrete changes depending on the w/b ratio. For the 0.60 concretes, MK3 presented the highest results, though for the 0.40 concretes, MK2 showed the higher value. This can be explained by the differences in the pore structure of the two groups of concrete, as the 0.40 concretes tends to be less porous, the filler effect is not that important compared to those of w/b of 0.60, so the coarser MK, although purer, showed better results, meaning that in this case the chemical reactivity took place.

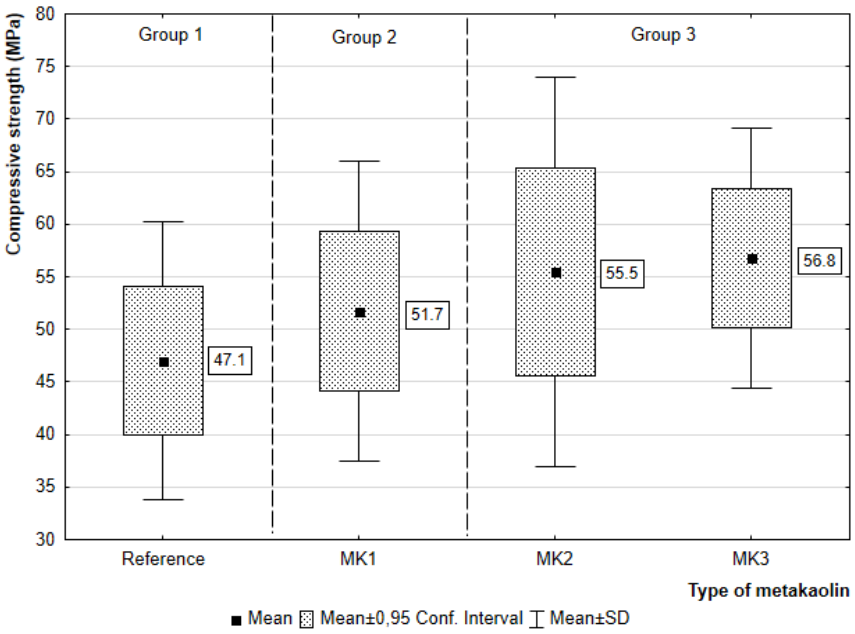

Figure 2. Multiple mean comparison of compressive strength and type of metakaolin.

Analyzing the ANOVA results, it showed that both variables (w/b and type of metakaolin) and their interaction were significant to explain the changes in compressive strength. The coefficient of determination of the model is 0.99. Figure 2 shows the multiple mean comparison segregation of the groups of statically equivalent concretes. It can be concluded that both MK2 and MK3 performed very well, in comparison to MK1 and plain concrete.

In chloride migration tests, MK concretes significantly outperformed plain concretes. Figure 3 shows the results of the non-steady state chloride migration coefficient. The w/b ratio was significant in the ANOVA model, as expected. So it was the type of metakaolin and their interaction, resulting in a R^2 equals to 0.98. Different that compressive strength, the Tukey's test from multiple mean comparison segregated the groups of statically equivalent results with some intersection. This means that it is possible to assure that the MK3 is superior than MK1 and plain concrete, but statically equivalent to MK2.

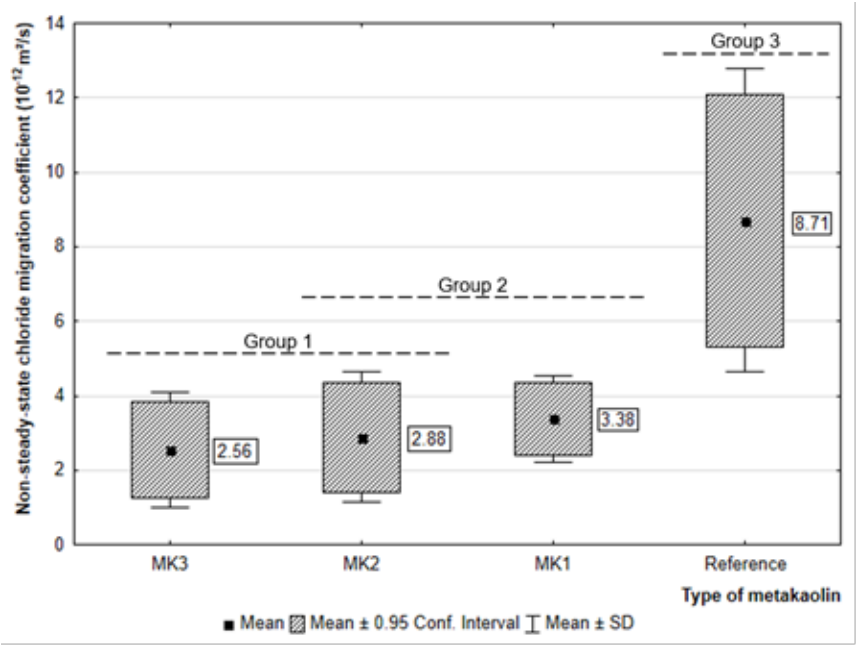

Figure 3. Multiple mean comparison of chloride migration coefficient and type of metakaolin.

It is noteworthy that even the worse result of MK concretes is way better than plain ones, as can be seen in figure 4. This means that MK can significantly improve the chloride resistance of concrete, and it is more efficient in doing it than a reduction of w/b ratio.

A possible explanation for this behavior can be due to the reaction of the chloride ions with the alumina present in metakaolins, thus forming the Friedel's salt (Talero, 2012). It can be also combined with the densification of the cement matrix that is assumed to occur with the addition of MK, once the compressive strength was also improved.

Besides that, with 0.40 w/b concretes, the differences of the three types of MK was more prominent. This may be due to the lower porosity of these concretes, and in this case, MK benefits are more evident, surpassing the effects of w/b ratio itself. Besides this, the correlation of these results and the results of Chapèlle's pozolanic index of the metakaolins are higher. This leads to the theory of chemical combination of aluminous phases with chloride ions.

Another interesting point is that every MK concrete is classified, according to Nilsson, Ngo and Gjørv (1998), as a very high or extremely high resistance to chloride attack. This means that MK concretes are significantly more durable than plain concrete. Plain concrete with w/b of 0.60, for example, is classified as a moderate chloride resistance.

It is clear that metakaolin concretes showed better results in comparison to plain concretes. The addition of MK in concrete seems to be more effective in improving the chloride resistance than the w/b ratio, evidenced by the fact that concrete with a higher w/b ratio and with the worser MK showed better results than a concrete with lower w/b ratio and without MK.

Also, for the compressive strength the enhancements caused by MK are noticeable, but in this case w/b ratio seems to be more relevant to determine.

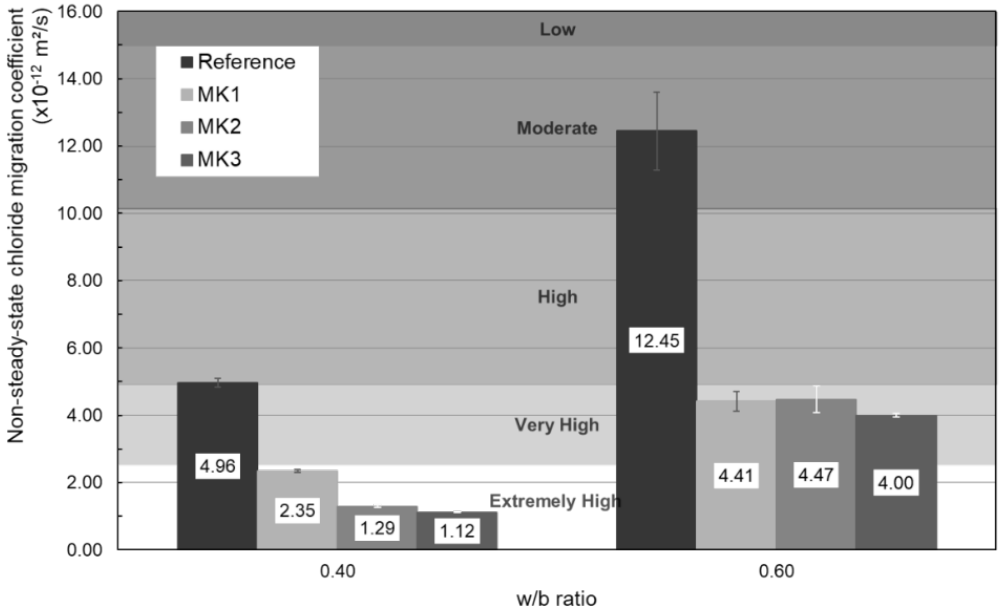

Figure 4. Mean values and standard deviation of non-steady-state chloride migration coefficient of all concrete mixtures, and the classification of chloride resistance from Nilsson, Ngo and Gjørv (1998).

5 Conclusions

- The pozzolanic activity index measured by the Chapèlle's modified method showed to be accurate to describe the overall behavior of the metakaolin, compiling the physical, chemical and mineralogical characteristics of the pozzolana in one result.
- Compressive strength was improved by the addition of metakaolin, and the interaction of the SCM was different depending on the w/b ratio.
- Metakaolin significantly enhanced the chloride attack resistance of concretes with both w/b ratio, even the worst MK with the 0.60 w/b presented better result than the 0.40 plain concrete, which demonstrate the effectiveness of MK to prevent chloride attack.

Acknowledgements

The authors acknowledge the contribution of Metacaulim do Brasil Company, which donated material, supported and financed this research. They also thank the company Eletrobras Furnas for all the support given in the experiments, as well as the following laboratories: LEDMa/UFBA for the XRD tests, LABMIC/UFG for the SEM analysis. Finally, the authors would like to thank CAPES and CNPq (Brazilian governmental institutions), which provided grants to researchers, as well as UFG and PPG-GECON.

ORCID

Rodrigo Teodoro: http://orcid.org/0000-0002-7302-456X
Helena Carasek: http://orcid.org/0000-0002-1170-0980
Oswaldo Cascudo: http://orcid.org/0000-0003-1879-6396

References

ABNT, A. B. N. T. (2010). *NBR 15895 - Materias pozolânicos - Determinação do teor de hidróxido de cálcio fixado - Método Chapelle modificado* (p. 6). p. 6. Rio de Janeiro.

Cascudo, O., Mendes, M. V. A. S., Carasek, H., and Ferreira, R. B. (2014). Eficiência dos concretos contendo adições minerais frente à ação de cloretos. *1º Encontro Luso-Brasileiro de Degradação Em Estruturas de Concreto Armado*, *1*, 1–16. Salvador: Universidade Federal da Bahia - UFBA.

Ferreira, R. B., Pereira, A. C., Lopes, A. N. M., Carasek, H., and Cascudo, O. (2004). Monitoring corrosion and determining of the gravimetric corrosion rate of concretes with high and low reactivity additions subject to chloride action. *International RILEM Conference: Use of Recycled Materials in Buildings and Structures*, Vol. 2, pp. 700–710. Barcelona.

Figueiredo, C. P., Santos, F. B., Cascudo, O., Carasek, H., Cachim, P., and Velosa, A. (2014). The role of metakaolin in the protection of concrete against the deleterious action of chlorides. *RIEM - IBRACON Structures and Materials Journal*, *7*(4), 685–708.

Friedel, G. (1897). Sur un chloro-aluminate de calcium hydraté se maclant par compression. *Bulletin de La Société Française de Minéralogie*, 122–136.

Khatib, J. M., Baalbaki, O., and ElKordi, A. A. (2018). Metakaolin. In *Waste and Supplementary Cementitious Materials in Concrete* (pp. 493–511). https://doi.org/10.1016/B978-0-08-102156-9.00015-8

Luping, T., and Nilsson, L. O. (1993). Rapid Determination of the Chloride Diffusivity in Concrete by Applying an Electric Field. *ACI Materials Journal*, *89*(1), 40–53. https://doi.org/10.14359/1244

Murat, M., and Comel, C. (1983). Hydration reaction and hardening of calcined clays and related minerals III. Influence of calcination process of kaolinite on mechanical strengths of hardened metakaolinite. *Cement and Concrete Research*, *13*(5), 631–637. https://doi.org/http://dx.doi.org/10.1016/0008-8846(83)90052-2

Nilsson, L.-O., Ngo, M. H., and Gjørv, O. E. (1998). High-performance repair materials for concrete structures in the port of Gothenburg. 2th INTERNATIONAL CONFERENCE ON CONCRETE UNDER SEVERE CONDITIONS - ENVIRONMENT and LOADING, Vol. 2, pp. 1193–1198. E and FN Spon.

Nordtest. (1999). *Concrete, mortar and cement-based repair materials: Chloride migration coefficient from non-steady-state migration experiments (NT BUILD 492)*. p. 8. Espoo.

Oliveira, A. M. de, and Cascudo, O. (2018). Effect of mineral additions incorporated in concrete on thermodynamic and kinetic parameters of chloride-induced reinforcement corrosion. *Construction and Building Materials*, *192*, 467–477. https://doi.org/10.1016/J.CONBUILDMAT.2018.10.100

Pereira, A. C., Lopes, A. N. M., Hasparyk, N. P., Carasek, H., and Cascudo, O. (2005). Microstructural analysis of carbonated concretes containing mineral admixtures. *Revista IBRACON de Materiais*, *1*(1), 15–33.

Quarcioni, V. A., Chotoli, F. F., Coelho, A. C. V, and Cincotto, M. A. (2015). Indirect and direct Chapelle's methods for the determination of lime consumption in pozzolanic materials. *Revista IBRACON de Estruturas e Materiais*, *8*(1), 1–7. https://doi.org/10.1590/s1983-41952015000100002

Siddique, R., and Khan, M. I. (2011). *Supplementary Cementing Materials* (Vol. 37). Retrieved from http://dx.doi.org/10.1007/978-3-642-17866-5_4

Talero, R. (2012). Synergic effect of Friedel's salt from pozzolan and from OPC co-precipitating in a chloride solution. *Construction and Building Materials*, *33*, 164–180. https://doi.org/http://dx.doi.org/10.1016/j.conbuildmat.2011.12.040

XV International Conference on Durability of Building Materials and Components
DBMC 2020, Barcelona
C. Serrat, J.R. Casas and V. Gibert (Eds)

Influence of Drying on Accelerated Carbonation Testing of Concrete

Jean Louis Gallias [1], Bruno Fiorio [1], Yunyun Tong [2] and Mehdi Benaissa [1]

[1] Laboratory of Materials and Mechanics of Civil Engineering (L2MGC), University of Cergy-Pontoise, 95000, Cergy-Pontoise France, jean-louis.gallias@u-cergy.fr

[2] School of Architecture and Civil Engineering, Zhejiang University of Science & Technology, 310023, Hangzhou, China, 2195838307@qq.com

Abstract. *The aim of this work is to better understand the influence of drying conditions and moisture content of concrete on the carbonation kinetics during accelerated tests. Cylindrical specimens of a typical concrete formulation for buildings were dried, after 28 days wet curing, under three different conditions: 80°C, 45°C and 20°C and 50% RH. The carbonation depth and the height of water absorption were measured during 70 days testing under 3% CO_2, 20°C and 65% RH. The results show that there is a significant difference in the drying behavior of cylindrical specimens between the lateral cast surface and their circular free surface. But, the drying cycle before accelerated carbonation tests has more influence on the carbonation rate than the type of exposed surface.*

Keywords: *Concrete, Drying, Accelerated Carbonation Test, Water Absorption.*

1 Introduction

Natural carbonation of concrete is one of the main reasons of steel reinforcement corrosion. The moisture conditions of concrete exposure have an important impact on carbonation kinetics. According to NF EN 206 (2014) standard, environments with medium relative humidity (between 50 and 70%) induce higher carbonation of concrete than drier or damper environments.

Accelerated tests are generally carried out to determine carbonation resistance of concrete and to assess the influence of various parameters of formulation, curing or ageing (Fattuhi, 1988; Alahmad *et al.*, 2009) Varying experimental conditions are used for the tests. In European level, there is not consensus for accelerated carbonation tests. For example, the Belgian standard recommends exposure of concrete specimens to 1% CO_2 while the French standard (NF XP P18-458, 2008) recommends 50% CO_2. The conditioning of specimens before CO_2 exposure varies even more strongly. For example, the European project of standard (prTS 12390-12, 2010) recommends 14 days drying in room conditions while the French standard recommends 14 days drying at 45°C. Different drying conditions before testing lead to different moisture content of concrete and consequently to varying carbonation kinetics (Parrott, .1996) (Galan, 2013).

The aim of the present work is to better understand the influence of drying conditions and moisture content of concrete on its carbonation kinetics during accelerated test.

2 Materials and Methods

A formulation of concrete with 275 kg/m^3 of CEM II/A-LL 42.5 R cement (according to EN 197.1 standard), 0.7 water-cement ratio and siliceous aggregates was used for the tests (Table

1). The compressive strength at 28 days was 26 ± 2 MPa and the density 2367 ± 10 kg/m^3. The formulation is representative of that used in France for building constructions in 50's and 60's presenting today many problems of reinforcement corrosion.

Table 1. Composition of concrete.

	kg/m^3
CEM II/A LL 42.5R	275
Sand 0/4	833
Coarse aggregate 4/16	1062
Water	193

Cylindrical Ø11x22 cm specimens were prepared and cured under water till 28 days. At 28 days, they were sawed into Ø11x7 cm specimens including the free surface of concrete of initial cylinders and into Ø11x11 cm specimens which excluded the bottom of the initial cylinders. The Ø11x7 cm specimens were covered with aluminum sheet in order to expose only the circular free surface of concrete of the initial cylinders. The Ø11x11 cm specimens were also covered with aluminum sheet in order to expose only the lateral cylindrical cast surface. With this setup, it could be expected that the free surface of specimens is representative of the free surface slabs and the cast surface of specimens is representative of cast surface of columns, beams or shells in buildings.

Both types of specimens were exposed to three different drying conditions before accelerated carbonation testing:

- 14 days at 80 ± 2°C plus 7 days at 20 ± 2°C and 65± 5% RH;
- 14 days at 45 ± 2°C plus 7 days at 20 ± 2°C and 65± 5% RH;
- 87 days at 20 ± 2°C and 50 ± 5% RH plus 7 days at 20 ± 2°C and 65 ± 5% RH.

The drying at 45°C for 14 days is recommended by the French standard NF XP P 18-458 (2008) for accelerated carbonation tests on concrete. The drying at 20°C and 50% RH for 87 days was chosen in order to reach almost the same loss of water per unit of exposed surface then that obtained in 14 days at 45°C. The drying at 80°C was applied to obtain strong and deep drying of the surface layer of concrete even if the concrete microstructure could be modified. A complementary drying for 7 days at 20°C and 65% RH was applied in all cases in order to stabilize moisture content of concrete in the same hydrothermal conditions than that used during accelerated carbonation tests. In fact, after drying, accelerated carbonation tests were carried out in 3% CO_2, 20 ± 2°C and 65 ± 5% RH for 70 days. According to Auroy et al. (2018), 3% CO2 is representative of natural carbonation. On the other hand, the hydrothermal conditions of accelerated tests are those of the French standard and close to those of the project of European standard prTS 12390-12 (2010): 20 ± 2°C and 55 ± 5% RH.

The carbonation depth was measured at 0, 28, 56 and 70 days testing by 0.2% alcoholic solution of phenolphthalein spayed to the fracture surface obtained by splitting of cylindrical specimens. In addition, on a second series of specimens exposed at the same conditions for the same periods, the height of water capillary absorption was measured after immersion in colored (by a small amount of fluorescein) water for one week. For this measure, the specimens were split and the thickness of saturated by colored water layer was determined on the fracture surface under ultraviolet light in the same way as the carbonation depth.

3 Results and Discussion

3.1 Drying

Figure 1 presents the loss of weight per unit of exposed surface of both types of cylindrical specimens during drying. The first observation is that the loss of weight, through the free (circular) surface of concrete, is between 2 and 2.5 times higher than that then that through the cast (cylindrical) surface for the different drying conditions. This happens because the surface layer of concrete has higher water content than the bulk material because of a small bleeding after casting.

The second observation is that drying at 80°C for 14 days eliminates an amount of water between 2 and 2.5 times higher than that at 45°C for 14 days or at 20°C and 50% RH for 87 days.

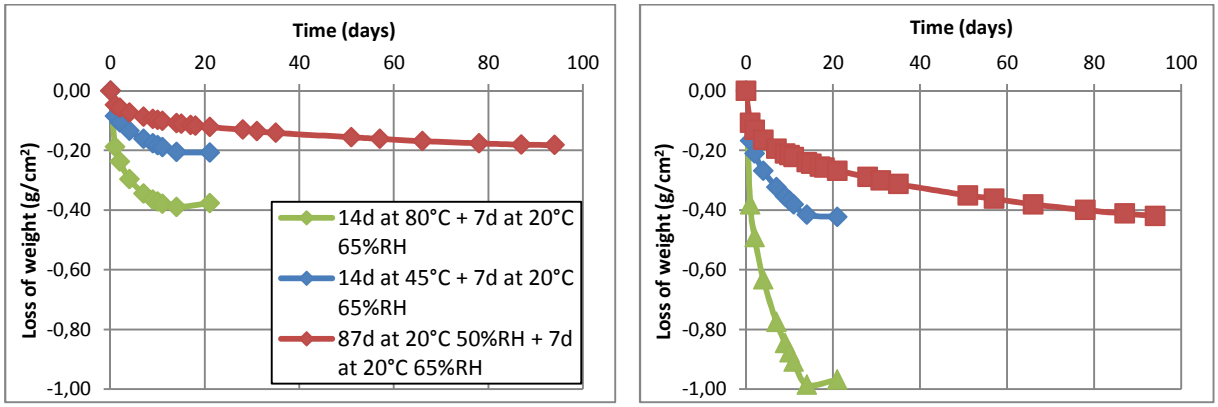

Figure 1. Loss of weight during drying. (a) Drying through the cast (cylindrical) surface of the Ø11x11 cm specimens. (b) Drying through the free (circular) surface of the Ø11x7 cm specimens.

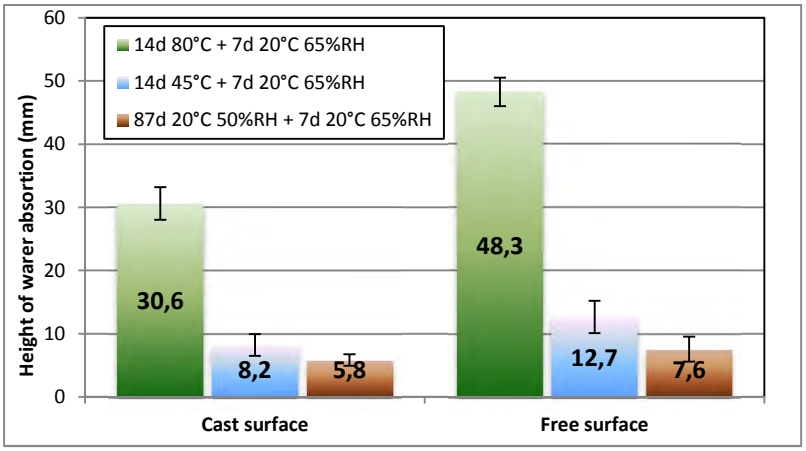

Figure 2. Height of water absorption at the end of drying.

The stronger or weaker elimination of water, according to the type of exposed surface (free or cast) and the drying condition, leads to higher or lower height of water capillary absorption

at the end of drying (Figure 2). However, the height of water absorption through the free surface is only between 1.3 and 1.5 times higher than that through the cast surface while the loss of water was between 2.0 and 2.5 times higher (Figure 1), leading to the conclusion that the surface layer of concrete presents differences in porosity and in porous size distribution comparatively to the bulk concrete. In fact, the breeding of concrete on the free surface leads to higher porosity and probably larger porous size distribution than in the bulk concrete.

The differences in porosity and in porous size distribution could be considered also to explain the significant difference of height of water absorption after 45°C drying for 14 days comparatively to that after 20°C and 50% RH drying for 87 days (Figure 2) even if in both cases the loss of weight per unit of exposed surface at the end of drying is almost the same (Figure 1). In fact, at the end of 20°C and 50% RH drying the concrete is more than 2 months older than that at the end of 45°C drying. During this time, the cement hydration progresses leading generally to lower porosity and to smaller porous size distribution.

3.2 Accelerated Carbonation

Figure 3 presents the carbonation depth during accelerated tests of both types of specimens for different drying conditions. It should be noted that the carbonation depth is negligible before carbonation test (0 mm for 80°C and 45°C drying and less than 0.5 mm for 20°C and 50% RH drying). It can be seen also that, in all cases, the carbonation depth progresses almost linearly with the square root of testing time, consequently a carbonation rate can be calculated for any case expressed in millimeter per square root of days (mm/days$^{1/2}$) presented in Figure 4.

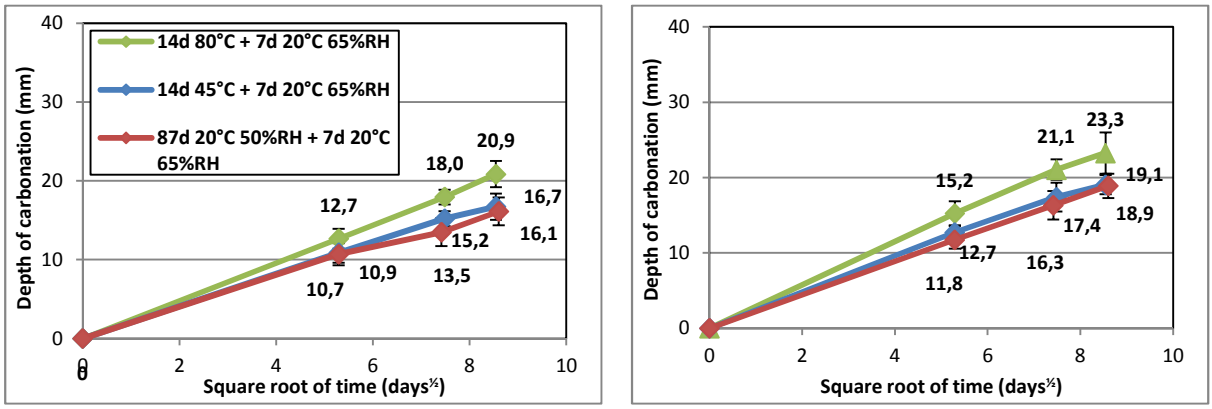

Figure 3. Carbonation depth as a function of square root of testing time (a) Carbonation through the cast (cylindrical) surface of Ø11x11 cm specimens. (b) Carbonation through the free (circular) surface of the Ø11x7 cm specimens.

The carbonation rate is higher through the free surface and after 80°C drying but is far from being proportional to the loss of water per unit of exposed surface during drying or to the height of water absorption at the end of drying. In fact, firstly the carbonation rate of specimens exposed du CO_2 through the free surface is only 13-19% higher than that through the cast surface for the different drying conditions. Secondly, the carbonation rate after 80°C

drying for 14 days is only 22-23% higher than that after 45°C drying for 14 days. Thirdly, the rate of carbonation obtained after 45°C drying is slightly higher (3 to 7%) to that obtained after 20°C and 50% RH drying for 87 days. These values allow to conclude that, firstly, a strong drying cycle (at 80°C) before accelerated carbonation tests has globally stronger influence on the carbonation rate than the type of the exposed surface (free or cast) and, secondly, the progress of hydration during the longer drying at 20°C and 50% RH does not have a very important influence on carbonation rate.

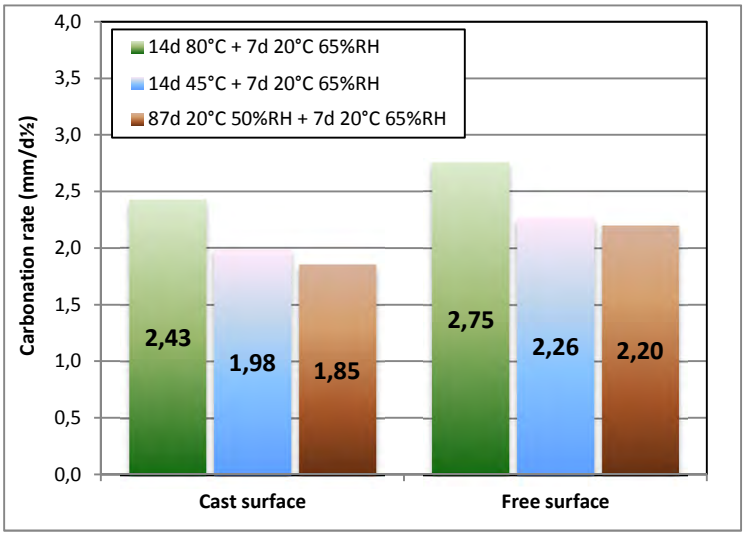

Figure 4. Carbonation rate during accelerated tests for different drying conditions and types of exposed surfaces.

3.3 Carbonation Depth and Height of Water Absorption

Figure 5 presents the comparison between the carbonation depth and the height of capillary absorption of colored water during the accelerated carbonation tests for all drying conditions and both types of specimens. It can be seen that, in all cases, the carbonation depth is systematically lower than the height of water absorption, leading to the conclusion that, for our tests, the carbonation occurs only into the unsaturated layer of concrete.

It can be seen also that the height of water absorption increases during accelerated tests. This means that the unsaturated layer of concrete becomes thicker during testing. This is particularly interesting in the light of the fact that carbonation reaction releases water (Verbeck, 1958; Parrot, 1991) and that the specimens didn't present any loss of weight during testing, rather a gain of weight. Taking into account that there is not any similar observation in literature, we can explain these results considering, firstly, the carbonation-induced changes in porosity and in porous size distribution (Galan, 2013; Auroy, 2018) leading to higher capillary absorption and, secondly, that moisture redistribution takes place in concrete during and because carbonation. In fact, Johannesson and Ulgenannt (Johannesson, 2001) based on sorption-desorption isotherms have concluded that well-carbonated cement mortar requires higher energy to absorb water molecules at its material surfaces accelerating the desorption isotherm and holding less water comparatively to noncarbonated cement mortar.

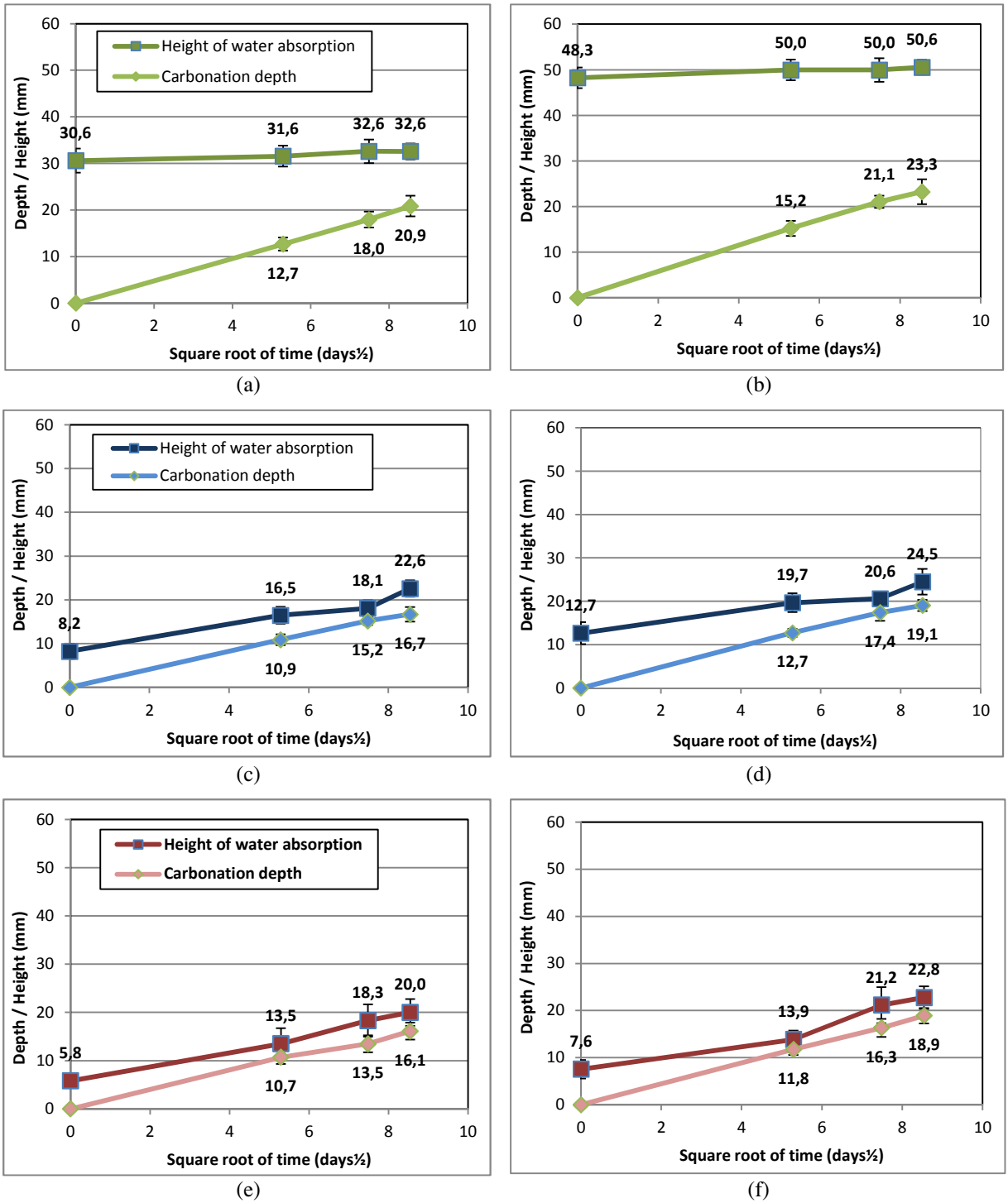

Figure 5. Carbonation depth and height of water absorption as a function of square root of testing time. (a) Through the cast surface after 80°C drying for 14 days. (b) Through the free after 80°C drying for 14 days. (c) Through the cast surface after 45°C drying for 14 days. (d) Through the free after 45°C drying for 14 days. (e) Through the cast surface after 20°C and 50% RH drying for 87 days. (f) Through the free after 20°C and 50% RH drying for 87 days.

The increasing of the height of water absorption follows mainly a proportional progression with the square root of testing time, allowing the determination of a rate of height increasing of water absorption during accelerated tests, expressed, just as the rate of carbonation depth, in millimeters per square root of days (mm/days^{½}) presented in Figure 6.

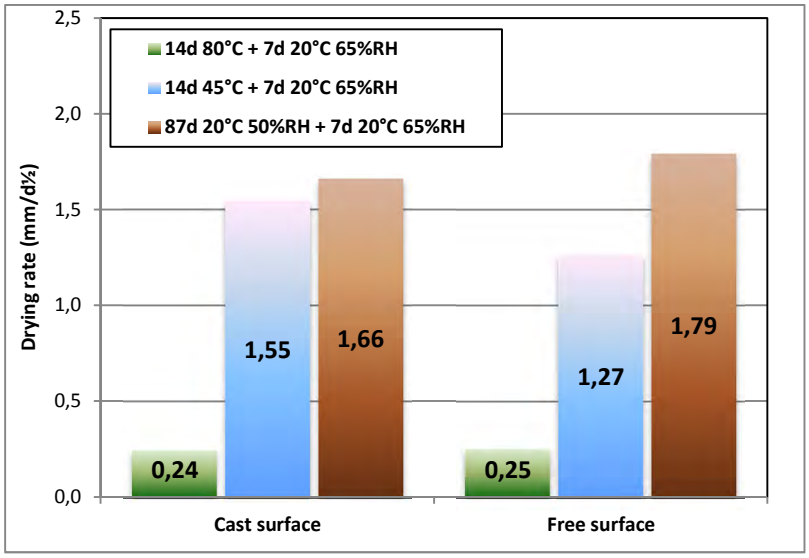

Figure 6. Rate of height increasing of water absorption during accelerated tests for different drying conditions and types of exposed surfaces.

The results of the Figures 5 and 6 show that the thickness increasing of the unsaturated concrete layer during accelerated testing is all the more important that the depth of carbonation is close. So, 20°C and 50% RH drying for 87 days leads to a relative low initial height of water absorption which progress quickly during accelerated tests with a rate close to the carbonation rate (1.66 and 1.85 mm/d^{½} respectively for exposure through the cast surface and 1.79 and 2.20 mm/d^{½} for exposure through the free surface). On the contrary, 80°C drying for 14 days leads to a relative high initial height of water absorption which progress slowly during accelerate tests staying away from the carbonated layer.

4 Conclusions

Accelerated carbonation tests were carried out after three different drying conditions through the cast and the free surface of specimens made with a typical concrete formulation for buildings construction in the 50's and the 60's. The height of water absorption was also measured at different stages of testing and compared to the carbonation depth.

The results show that there is a significant difference in the loss of weight per unit of exposed surface through the cast and the free surface of specimens. The height of water absorption through the cast and the free surface is also significantly different. But, the drying condition before accelerated carbonation tests has more influence on the carbonation rate of concrete than the type of the exposed surface. The carbonation rates through both types of surfaces and for 45°C and for 20°C and 65% RH drying are close, in accordance with literature. The carbonation rate for 80°C drying is significantly higher because of strong and

deep elimination of water modifying the concrete microstructure.

The comparison of carbonation depth and height of water absorption during accelerated tests show that the height of water absorption was systematically higher than the carbonation depth. Moreover, the height of water absorption increases during testing while the carbonation releases water and the specimens present globally a gain of weight. The hypothesis of moisture redistribution in concrete during accelerated carbonation tests was advanced to explain the increase of the unsaturated layer thickness in concrete. However, more tests are necessary to validate this hypothesis starting with the determination of the water quantity absorbed till saturation of concrete at each stage of accelerated tests in comparison with the loss of water at the end of drying. To the same end it would be also interesting to follow the carbonation rate and the height of water absorption beyond 70 days in order to identify what happens when the carbonation depth reaches the thickness of unsaturated concrete.

ORCID

Jean Louis Gallias: https://orcid.org/0000-0002-4354-9226
Bruno Fiorio: https://orcid.org/0000-0003-3039-6339
Yunyun Tong: https://orcid.org/0000-0002-1078-7017

References

NF EN 206 (2014). Béton - Spécification, performance, production et conformité.

XP P18-458 (2008). Essai pour béton durci - Essai de carbonatation accélérée - Mesure de l'épaisseur de béton carbonaté.

prTS 12390-12 (2010). Essai pour béton durci - Essai de carbonatation accélérée - Mesure de l'épaisseur de béton carbonaté.

Alahmad S., Toumi A., Verdier J. and François R. (2009). Effect of crack opening on carbon dioxyde penetration in cracked mortar samples. *Materials and Structures,* 42 (5), 559-566.

Auroy M., Poyet S., Le Bescop P., Torrenti J. M., Charpentier T., Moskura M. and Bourbon X. (2018). Comparison between natural and accelerated carbonation (3% CO_2): Impact on mineralogy, microstructure, water retention and cracking. *Cement and Concrete Research,* 109, 64-80.

Galan I., Andrade C. and Castellote M. (2013). Natural and accelerated CO2 binding kinetics in cement paste at different relative humidities. *Cement and Concrete Research,* 49, 21-28.

Fattuhi, N. I. (1988). Concrete carbonation as influenced by curing regime. *Cement and Concrete Research,* 18(3), 426-430.

Johannesson B. and Ulgenannt P. (2001). Microstructural changes caused by carbonation of cement mortar. *Cement and Concrete Research,* 31, 925-931.

Parrot L. J. (1996). Some effects of cement and curing upon carbonation and reinforcement corrosion in concrete, *Materials and Structures*, 29 (3), 164-173.

Parrot L. J. (1991). Carbonation moisture and empty pores, *Advances in Cement Research*, 4, 111-118.

Verbeck G. J. (1958). Carbonation of hydrated Portland cement, ASTM Special Technical Publication 205, 17-36.

XV International Conference on Durability of Building Materials and Components
DBMC 2020, Barcelona
C. Serrat, J.R. Casas and V. Gibert (Eds)

Influence of Fly Ash on Strength Development of Concrete and its Temperature Dependence

Hiromi Yanokura[1], Isao Kurashige[2], Naoyuki Sugihashi[1], Keiichi Takahashi[3] and Yasuhiro Kuroda[3]

[1] Shimizu Corporation, Civil Engineering Technology Division, No.16-1, Kyobashi 2-chome, Chuo-ku, Tokyo, 104-8370, Japan, h-yanokura@shimz.co.jp, n-sugihashi@shimz.co.jp

[2] Central Research Institute of Electric Power Industry, Civil Engineering Research Laboratory, 1646 Abiko, Abiko-shi, Chiba, 270-1194, Japan, kurasige@criepi.denken.or.jp

[3] Shimizu Corporation, Research Institute, No.4-17, Etchujima 3-chome, Koto-ku, Tokyo, 135-8530, Japan, keichi.takahashi@shimz.co.jp, y.kuroda@shimz.co.jp

Abstract. *Experiments on the development of compressive strength and static and dynamic Young's moduli were performed by the following mix proportions of concrete: the first uses different types of Portland cement without fly ash (FA) with a water-cement ratio of 45%, keeping at different curing temperatures; the second partially use FA in place of the cement, with the other conditions same as above; the third uses only blast furnace cement B instead of Portland cement. With these specimens, we comparatively examined in terms of temperature adjusted concrete age, how the mechanical properties change with the use of cement only, FA replacement for cement and with variation in curing temperatures. As a result, it was confirmed that the replacement of cement by fly ash enhanced the long-term mechanical properties of concrete regardless of the curing temperature applied in this experiment.*

Keywords: *Fly Ash, Curing Temperature, Compressive Strength, Static Young's Modulus, Dynamic Young's Modulus.*

1 Introduction

Recently, in Japan, fly ash (FA) has been often used as a mineral admixture of concrete from the viewpoint of effective use of industrial waste and reduction of carbon dioxide (CO_2) emissions. (Takafumi, 2014) The use of FA as an admixture in concrete is said to be effective in improving concrete performance such as increasing workability of concrete, reducing thermal cracks, development of long-term strength, and suppressing salt damage and alkali-silica reaction. For this reason, in overseas countries, in particular in Asian countries, the trend of effective utilization of FA for concrete has become active due to the increasing number of coal power plants, because FA can be obtained at low cost as industrial waste. The pozzolanic reaction peculiar to FA is activated beneficially to develop the strength of concrete as the curing temperature increases. On the contrary, when the curing temperature is low, the strength enhancement due to the pozzolanic reaction does not progress and, in some cases, the expected effect may not be obtained.

Therefore, in order to understand the temperature dependency of the mechanical properties of the concretes using FA, three kinds of Portland cements which are partially replaced with FA were comparatively studied in terms of the impact by temperature on the development of

mechanical properties of concrete. Note that we obtained basic data on the mechanical properties of cement types and curing temperatures in order to make full use of the effect of fly ash used in place of cement.

2 Experiment Plan

2.1 Outline of the Experiment

Regarding the use of cements and FA, one case is that different mix proportions for concrete are prepared at curing temperatures of 5, 10, 20, and 30°C, using only normal Portland cement (N), moderate heat Portland cement (M), or low heat Portland cement (L) respectively with no FA, and another case is that the mix proportions are prepared in the same condition as above, except 30 % of the proportion of the cement was substituted by FA. The specimens of concrete prepared were tested to obtain the strength development (for the case of N, 15% substitution of FA was also applied). For comparison, a mix proportion using blast furnace cement B instead of cement was used in the experiment.

2.2 Materials and Mix Proportions

Table 1 shows the list of materials used, Table 2 the quality of FA, and Table 3 the mix proportions (blending). The FA used is JIS A 6201 FA II class product from Noshiro Thermal Power Plant, and water to binder ratio (W/B) is set to be constant at 45%. Limestone fine powder (LP) was used to stabilize the fresh properties of mix proportions (blending) with the FA replacement ratio of 30%.

Concrete mixing was carried out in an environment of 20 ± 3 ℃ using a horizontal biaxial forced mixing mixer with a nominal capacity of 100 liters. The target slump 60 minutes after the concrete is mixed up was 18.0 ± 2.5 cm, the target air content was 5.5 ± 1.5%, and the rates of air-entraining water reducing agent (AD) and air-entraining agent (AE) were determined by test kneading.

Table 1. List of materials used.

Material	Symbol	Name and quality
Binder	N	Normal Portland cement Density 3.16 g/cm^3
	M	Moderate heat Portland cement Density 3.21 g/cm^3
	L	Low heat Portland cement Density 3.22 g/cm^3
	BB	Blast furnace cement B Density 3.04 g/cm^3
Mineral admixture	FA	Fly ash Density 2.19 g/cm^3
	LP	Limestone fine powder Density 2.70 g/cm^3
Fine aggregate	S	Limestone crushed sand Surface dry condition density 2.67 g/cm^3
Coarse aggregate	G	Limestone crushed stone Surface dry condition density 2.70 g/cm^3
Chemical admixture	AD	AE water reducing agent
	AE	AE agent (the agent for FA is used for FA concrete.)

Table 2. Quality data of FA.

Test item		Test result
Silicon dioxide (%)		66.6
Moisture (%)		0.1
Ignition loss (%)		2.0
Density (g/cm^3)		2.19
Fineness	Specific surface area by Blaine method (cm^2/g)	3,880
Flow value ratio		104
Activity index (%)	Concrete age 28 days	86
	Concrete age 91 days	100

2.3 Test Items and Methods

Test items and test methods are shown in Table 4. Specimens were taken after confirming that the slump and air content satisfied the target values at a test of fresh concrete 60 minutes after the mixing. After curing 24 hours in an initial curing room at a temperature of 20 ± 2°C with a relative humidity of 95% or more, the specimens were removed from their forms to be cured in the water at specified temperature conditions until specified ages when the specimens were subjected to various tests.

3 Test Results and Discussions

3.1 Test Results of Fresh Concrete

Table 5 shows the test results of fresh concrete. At every mix proportion, the slump and air content after 60 minutes met the targets. Remarkably, the mix proportion with 30% FA replacement, despite the high use of AE agent, recorded a more than 0.5% decrease in air content presumably due to unburned carbon of FA. In particular, the mix of LF30 had an extremely high decrease of 2.4% in air content.

Table 3. Mix proportion of concrete.

Symbol	W/B (%)	s/a (%)	Slump (cm)	Air content (%)	Unit weight (kg/m^3)								Chemical admixture (%)	
					Water W	Cement				Mineral admixture		Aggregate		
						N	M	L	BB	FA	LP	S	G	AD	AE
N	45.0	44.0	18.0	5.5	165	367	—	—	—	—		780	1004	0.90	0.003
M						—	367	—	—	—		782	1007	0.80	0.003
L						—	—	367	—	—		782	1007	0.75	0.002
BB						—	—	—	367	—		774	997	0.80	0.003
NF15					160	303	—	—	—	53		782	1004	0.93	0.007
NF30					155	241	—	—	—	103	62	757	974	1.23	0.029
MF30							241	—	—	103	62	758	976	1.30	0.026
LF30						—	—	241	—	103	62	759	976	1.10	0.023

Table 4. Test items and methods.

Test item	Test method	Description
Slump	JIS A 1101	Tested 5 minutes and 60 minutes after being mixed up
Air content	JIS A 1128	
Mass of unit volume	JIS A 1116	
Concrete temperature	JIS A 1156	
Compressive strength	JIS A 1108	Tested at the age of 7 days, 28 days, 56 days, 91 days, 182 days, 364 days
Static Young's modulus	JIS A 1149	
Dynamic Young's modulus	JIS A 1127	

Table 5. Test results of fresh concrete.

Sym-bol	Slump (cm)		Air content (%)		Mass of unit volume (kg/m^3)		Concrete temperature (°C)	
	5 min	60 min	5 min	60 min	5 min	60 min	5 min	60 min
N	20.0	19.5	6.1	5.7	2324	2319	21	21
M	18.5	20.0	6.5	6.7	2303	2296	19	19
L	21.5	20.5	6.3	6.1	2312	2309	19	19
BB	19.5	20.0	4.9	5.3	2333	2322	19	19
NF15	18.0	18.0	5.3	5.4	2325	2315	21	21
NF30	18.0	17.5	7.1	6.5	2255	2277	21	21
MF30	17.0	20.0	7.0	6.5	2263	2279	21	21
LF30	19.5	18.5	8.5	6.1	2282	2294	22	21

3.2 Relationship between Age and Compressive Strength

Figure 1 shows the relationship between age and compressive strength for each mix proportion. The strength at the age of 7 days of the mix proportions using only Portland cement without FA increased in the order of N> M> L, and the higher the curing temperature, the faster the development of strength. However, at a high curing temperature of 30°C, their increase of strength tended to slow down in an earlier stage: N peaked after age 28 days; M after 56 days; L after 91 days. On the other hand, it was observed that all the mix proportions with FA replacement for cement did not reach the peak and still continued to develop their strengths. The substitution of FA for cement demonstrates a high effect on strength increase.

The compressive strength of BB at the age of 7 days varied largely due to curing temperature, and at the temperature of 30°C, was equivalent to N, and at 5°C equivalent to M, with a large difference from the mix with Portland cement without FA. At the curing temperature of 30°C, the growth in strength of BB slowed down after 56 days of age.
On the other hand, the strength for mix proportions with FA developed in the order of NF15> NF30> MF30> LF30, and grew for a long period regardless of differences in binder type and curing temperature.

3.3 Relationship between Temperature Adjusted Concrete Age and Compressive Strength

The strength development of concrete is closely related with the maturity (time considering temperature ingredient) (Fuminori *et al.*, 1991), and this tendency is more pronounced for the case of a mix proportion using FA (pozzolan material). We studied on the relationship between temperature-adjusted concrete age （te） and compressive strength （f） (CEB, 1990) which are shown in Equation (1); maturity law.

$$t_e = \sum_{i=1}^{n} \Delta t_i \cdot \exp\left[13.65 - \frac{4000}{273 + T(\Delta t_i)}\right] \tag{1}$$

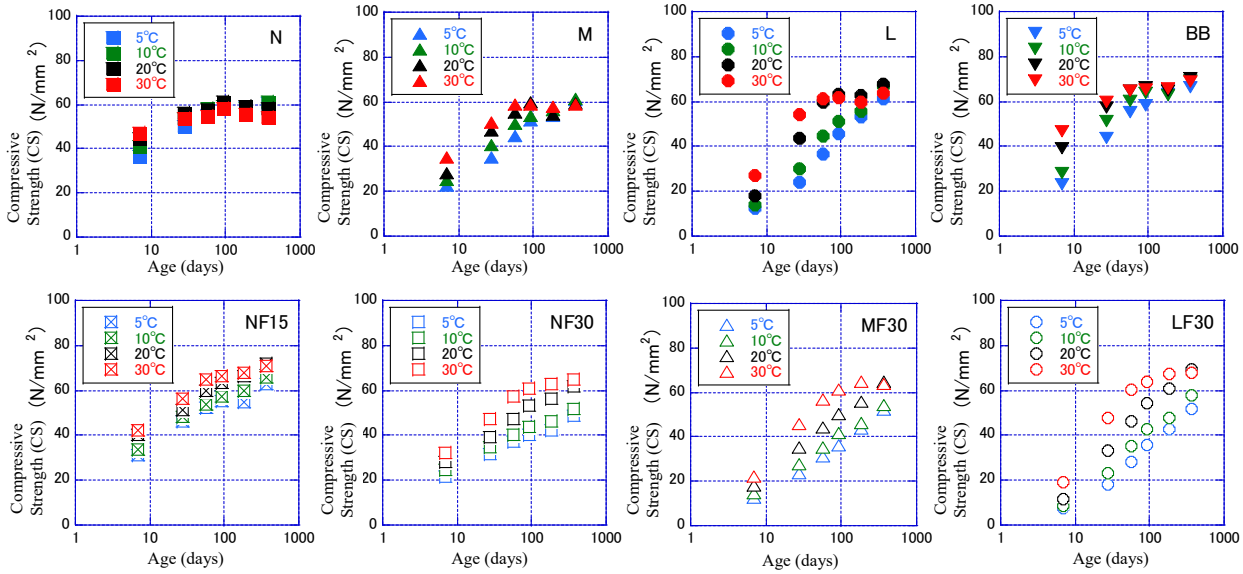

Figure 1. Relationship between concrete age and compressive strength in each mix.

Figure 2 shows the results of the relationship between temperature-adjusted concrete age and compressive strength for each mix proportion. The results of the regression analysis using Equation (2) are shown in Table 6 and Figure 2.

$$f(t_e) = a \cdot \log_{10} t_e + b \tag{2}$$

For N, M, L and BB, the data were regressed in the range with high linearity. “a” and “b” are regression coefficients obtained from experimental results.

Figure 2 indicates that the relationship between temperature adjusted concrete age and compressive strength for the mix proportions using FA keeps linearity for one year, while the relationship not using FA has limited linearity up to 91 days, from which we learn that strength development by FA continues for a long span of time. In the case of N without FA, the long term strength peaks at 60N/mm^2, while NF15 with 15% of cement replaced by FA still keeps increasing its strength even at about 80 N/mm^2, and NF15 with 30% replaced by FA does not peak even at 65N/mm^2. In the case of N, it was discovered that the effect of strength increase was greatly enhanced by about 15% replacement of cement by FA.

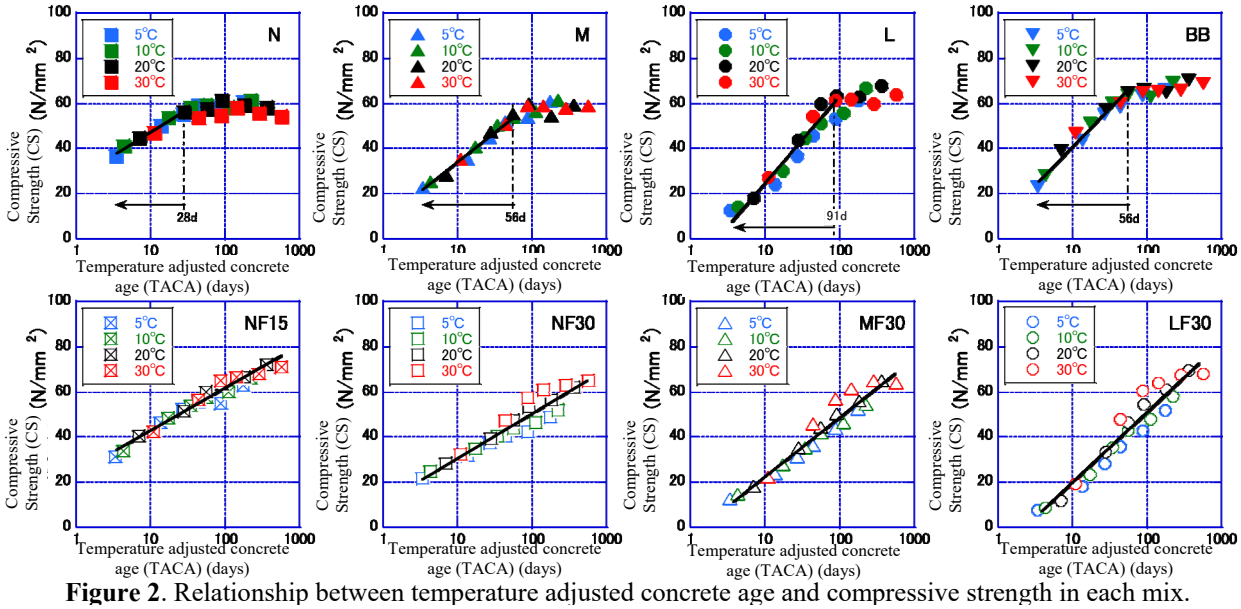

Figure 2. Relationship between temperature adjusted concrete age and compressive strength in each mix.

Table 6. Results of regression analysis for temperature adjusted concrete age and compression strength.

Symbol	Regression coefficient		Correlation coefficient	Regression interval
	a	b	R	
N	20.1	27.4	0.989	Up to Temperature Adjusted Concrete Age (TACA) 28 days
M	26.9	7.2	0.994	Up to TACA 56 days
L	36.3	-10.9	0.972	Up to TACA 91 days
BB	31.9	9.5	0.983	Up to TACA 56 days
NF15	18.1	24.8	0.976	Up to TACA 364 days
NF30	19.5	11.2	0.952	Up to TACA 364 days
MF30	26.1	-3.1	0.971	Up to TACA 364 days
LF30	31.5	-12.5	0.967	Up to TACA 364 days

Table 7. Results of regression analysis for temperature adjusted concrete age and static Young’s modulus.

Symbol	Regression coefficient		Correlation coefficient	Regression interval
	a	b	R	
N	5.61	35.1	0.964	up to Temperature Adjusted Concrete Age (TACA) 28 days
M	6.70	29.9	0.990	up to TACA 56 days
L	9.69	24.9	0.976	up to TACA 91 days
BB	7.34	32.0	0.972	up to TACA 56 days
NF15	4.02	36.0	0.964	up to TACA 364 days
NF30	4.61	31.0	0.971	up to TACA 364 days
MF30	6.60	26.4	0.974	up to TACA 364 days
LF30	8.66	22.8	0.951	up to TACA 364 days

Table-6 shows the list of calculation results of regression coefficients “a” and “b”. The larger the regression coefficient “a”, the faster the increase in long-term strength, and the regression coefficient “b” represents the initial strength. The regression coefficients “a” for the mixes using FA respectively are close to those of Portland cement as the base material (87～97% to each cement). As is the case with the ranking of “a” of base cement (L> M> N), the ranking of the mix proportions using FA was in the order of LF30> MF30> NF30> NF15, and the regression coefficient “a” for BB was between that of M and L.

On the other hand, it was found from the ranking of regression coefficients “b” that the initial strengths of mix proportions are ranked in the order of N> NF15> NF30> BB> M> MF30> L> LF30. The initial strength of the mix proportion using FA decreases as the initial strength of the base cement decreases and as the FA replacement rate increases.

3.4 Relationship Between Temperature Adjusted Concrete Age and Static Young’s Modulus

Figure 3 shows the relationship between temperature adjusted concrete age and static Young’s modulus, and Table 7 shows the results of linear regression analysis. The range of regression analysis was the same as that of the compression strength regression analysis in Section 3.3.

The static Young’s modulus tended to develop in the same manner as the compressive strength. In other words, in the concretes without FA, the regression coefficient “a” was ranked in the order of L> BB> M> N, and in the concretes using FA, in the order of LF30> MF30> NF30> NF15. However, it was smaller than the regression coefficient “a” of compressive strength, generally with a small difference resulting from the temperature adjusted concrete age. On the other hand, the regression coefficient developed in the order of N> NF15> BB> NF30> M> MF30> L> LF30, and had an almost same tendency as the compressive strength, except for the fact that BB was slightly larger than NF30.

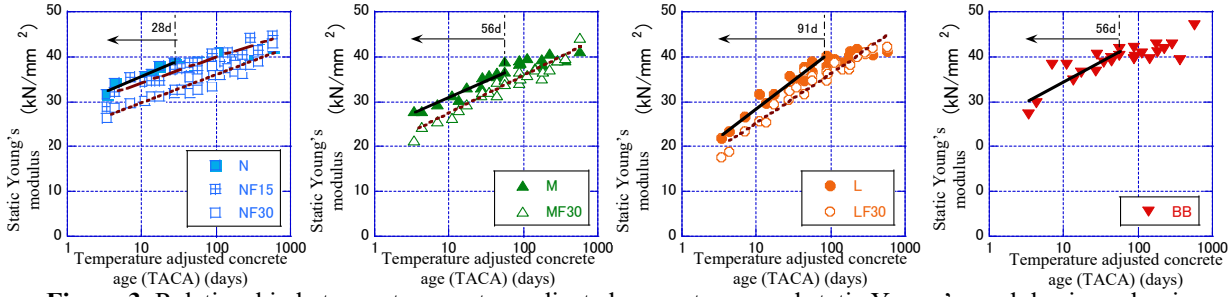

Figure 3. Relationship between temperature adjusted concrete age and static Young’s modulus in each mix

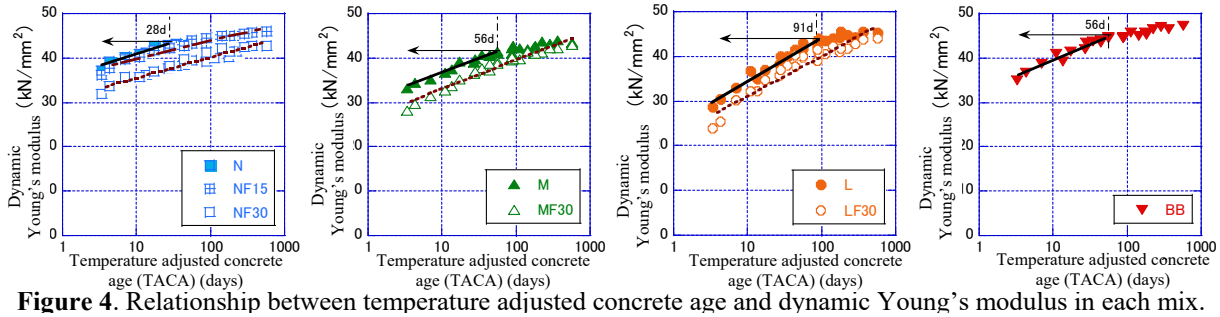

Figure 4. Relationship between temperature adjusted concrete age and dynamic Young’s modulus in each mix.

3.5 Relationship Between Temperature Adjusted Concrete Age and Dynamic Young's Modulus

Figure 4 shows the relationship between temperature adjusted concrete age and dynamic Young's modulus, and Table 8 the results of linear regression analysis. The range of regression analysis was the same as in Section 3.3.

From the difference in regression coefficient of "a", it was confirmed that the dynamic Young's modulus developed earlier than the compressive strength and static Young's modulus and tended to level off earlier with the age. The magnitude relationship of the regression coefficients "a" and "b" demonstrated the same tendency as in the static Young's modulus.

3.6 Relationship Between Compressive Strength and Young's Modulus

Figure 5 shows the relationship between compressive strength and static Young's modulus, Figure 6 shows the relationship between compressive strength and dynamic Young's modulus, and Figure 7 shows the relationship between static Young's modulus and dynamic Young's modulus.

Regardless of the types of binder or the use of FA, the relationship between compressive strength and static Young's modulus and the relationship between compressive strength and dynamic Young's modulus were constant. Moreover, the dynamic Young's modulus tended to fluctuate less than the static modulus.

The dynamic Young's modulus is generally given by the specimen's flexural vibration at which the specimen underwent resonant vibration. Since this modulus represents a status where almost no load works, it tends to grow larger than the static Young's modulus. (Ohmsha, 2004) In this experiment, as shown in Figure 7, the dynamic Young's modulus was larger than the static Young's modulus. This trend was more noticeable at young ages.

Table 8. Results of regression analysis for temperature adjusted concrete age and dynamic Young's modulus.

Symbol	Regression coefficient		Correlation coefficient R	Regression interval
	a	b		
N	5.61	35.1	0.964	up to Temperature Adjusted Concrete Age (TACA) 28 days
M	6.70	29.9	0.990	up to TACA 56 days
L	9.69	24.9	0.976	up to TACA 91 days
BB	7.34	32.0	0.972	up to TACA 56 days
NF15	4.02	36.0	0.964	up to TACA 364 days
NF30	4.61	31.0	0.971	up to TACA 364 days
MF30	6.60	26.4	0.974	up to TACA 364 days
LF30	8.66	22.8	0.951	up to TACA 364 days

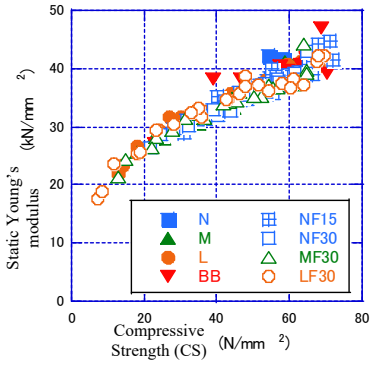

Figure 5. Relationship between compressive strength and static Young's modulus.

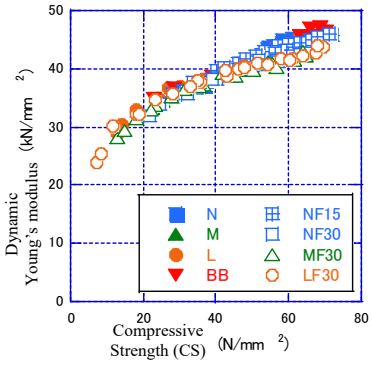

Figure 6. Relationship between compressive strength and dynamic Young's modulus.

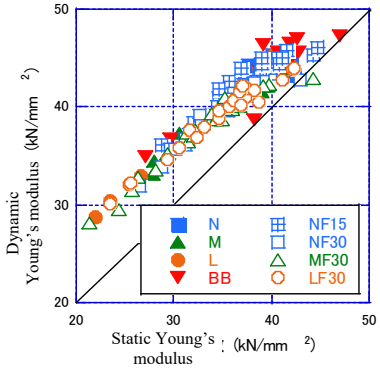

Figure 7. Relationship between static Young's modulus and dynamic Young's modulus.

4 Conclusion

The following two types of concrete, one using three Portland cements (N, M, L) with no FA and the other using the same cements but partially replaced by FA, at a water-binder ratio of 45% and cured at different curing temperatures, were comparatively studied in terms of the compressive strength up to one year of age as well as of static and dynamic Young's moduli, including an experiment using blast furnace cement B (BB). We compared the data of these specimens to determine their relationship with temperature adjusted concrete age. The obtained results obtained are as follows:

(1) The mix proportion with 30% of cement replaced by FA, despite increasing AE agent, recorded more than 0.5% decrease in air content which is presumably due to the effect of FA's unburned carbon.

(2) In the mix proportions (blending) of N, M, L and BB, the higher the temperature, the faster the strength developed. However, strength increase slowed down early and reached a peak. On the other hand, the mix proportions (blending) using FA steadily developed long-term strength regardless of the difference in binder and curing temperature, exceeding the long-term strengths of N and M. Especially N15, which is a mix proportion of N with 15% FA replacement, did not peak even at about 80 N/mm^2 of compressive strength which is 1.3 times N's peak of 60 N/mm^2, and we learned that FA substitution has a high impact on the compressive strength.

(3) In the mix proportions (blending) using N, M, L, and BB, it was shown that the strength increased highly correlated with the temperature adjusted concrete age (in logarithm) up to the moment its growth rate in strength slowed down. On the other hand, the mix proportions (blending) using FA developed the strength for a long span of time, keeping a close correlation with the temperature adjusted concrete age.

(4) It was found that for the mix proportions (blending) using FA, the lower the initial strength of the base cement or the higher the replacement rate of FA, the slower the strength development and that they demonstrate the characteristics of strength development which correspond to those of the base cement. The mix proportion (blending) using the binder with a slower initial strength development tended to result in the larger strength.

(5) Regardless of the use of FA in the mix, the relationship between compressive strength and static Young's modulus and the relationship between compressive strength and dynamic Young's modulus were constant. The dynamic Young's modulus demonstrated a larger value than the static Young's modulus, and this trend was more conspicuous at young ages.

ORCID

Takafumi Noguchi: https://orcid.org/0000-0001-6115-2292

References

CEB-FIP Model Code 1990 (1990). *Comite Euro-international du Beton*

Fuminori Tomosawa. and Sakae Ushijima (1991). *Development and application of recent cumulative temperature systems, Cement/Concrete,* No.527, pp.66-75

Ohmsha, Ltd (2004). Relationship between static Young's modulus and dynamic Young's modulus, by Kazusuke Kobayashi, supervising editor

Takafumi Noguchi (2014). *Issues and perspective on the active use of additives for architecture, Concrete Engineering*, Vol.52, No.5, pp.368-372

XV International Conference on Durability of Building Materials and Components
DBMC 2020, Barcelona
C. Serrat, J.R. Casas and V. Gibert (Eds)

Influence of Surface Treatment of Fresh Concrete on its Resistance to Drying Shrinkage

Pavel Reiterman[1] and Vendula Davidová[2]

[1] Czech Technical University in Prague, University Centre for Energy Efficient Buildings, Trinecka 1024, 273 43 Bustehrad, Czech Republic, pavel.reiterman@fsv.cvut.cz

[2] Experimental Centre, Faculty of Civil Engineering, Czech Technical University in Prague (CTU), Thákurova 7, 166 29 Prague 6, Czech Republic, vendula.davidova@fsv.cvut.cz

Abstract. *The volume changes of cement-based composites are significantly exhibited during the hardening process. Initial phases of the hardening are complemented by the expansion due to the heat evolution that is subsequently alternated by the shrinkage. Both could cause the crack initiation causing significant loss of the durability and service-life shortage. The present paper focuses on the experimental investigation of the surface treatment of fresh concrete, which is applied to prevent sudden loss of the moisture during a hardening process, especially during the concrete highway construction. The technology of concrete highway production is extremely costs demanding, but its efficiency is determined by the longer lifespan in comparison with the asphalt pavement. However, negative impacts of the drying shrinkage could significantly reduce the durability. The efficiency of used treatment was investigated in terms of restrained shrinkage tests, water adsorption and mechanical testing. In addition, there were studied two types of conventional Portland cement. Performed program confirmed great sense of the curing on the concrete durability; in addition, there was well illustrated the efficiency of the utilization of blended binder systems in the paper.*

Keywords: *Concrete Permeability, Drying Shrinkage, Surface Treatment.*

1 Introduction

The concrete is the most used material for the construction of civil infrastructure worldwide. The fundamental part of the structural concrete is Portland cement, which exhibits hydraulic properties and sufficient mechanical and also durability performance. There is a number of various types of cements, that are based on Portland clinker, however these cement types were primarily developed for the specific applications (Aitcin, 2000). For example, blended systems are preferably used for massive structures for the reduction of total hydration heat and also volume changes (Lotenbach *et al.* 2011; Vinkler and Vítek, 2019). On the other hand, due to rapidly increasing price of human work there are currently preferred technologies limiting number of craftsmen on the construction site and approaches significantly accelerating the process of construction.

These technologies often lead to the supressing of specific technological steps, such as curing. Portland cement based concrete is hydraulic material, which is sensitive for a sudden loss of moisture during hydration. Surface treatments in form of thin films are applied to prevent the drying of concrete after its casting, because hardened mass of concrete significantly reduces its diffusivity. The quality of surface layer of concrete is crucial in relation to the durability, because this thin part of structure determine final resistance to the impact of external environment. The deterioration of the concrete "skin" during hardening is the most frequent

reason of the damage during structure operation. Traditional exhibition of the problem in concrete surface layer is the presence of micro cracks or tendency to release dust particles. These failures of concrete surface subsequently lead to the increased transport of water, which significantly contributes to the gradual degradation of the structure (Reiterman *et al.,* 2019; Holcapek *et al.,* 2014). The ingress of deicers and freezing-thawing are the main mechanisms causing the degradation of concrete infrastructure (Glinicki *et al.,* 2016). The effect of frost causes propagation of cracks and their depth, and deicers, mostly on the basis of chlorides, lead to the chemical corrosion of concrete, surface scaling and corrosion of the embedded steel rebars. Hence, the permeability of concrete surface has crucial sense in relation to the lifespan of concrete structures.

2 Experimental Program

Conducted experimental program was focused on the evaluation of the quality of concrete surface layer, of which properties were modified by the application of surface treatment to prevent sudden evaporation of the moisture. This technology is used during the production of concrete pavement by the roller, and also after production of continues concrete guardrails. This effect was studied on standard cement mortars with the fraction of sand to cement 3:1, water to cement ration was set to 0.45. There were used two types of Portland clinker-based cements – CEM I 42.5 (SC) and CEM II 32.2 B-S, of which properties are introduced in Table 1.

Table 1. Properties of used cements.

Properties	CEM I 42.5 R (SC)	CEM II 32.5 B-S
CaO	63.80 %	50.51 %
SiO_2	20.60 %	27.24 %
Al_2O_3	4.80 %	7.85 %
Fe_2O_3	3.40 %	2.72 %
MgO	1.40 %	3.75 %
SO_3	3.20 %	2.85 %
K_2O	0.74 %	0.77 %
NaO	0.20 %	0.36 %
LOI	1.40 %	1.1 %
Blaine	311 m^2/kg	345 m^2/kg

CEM I 42.5 (SC) is a specific type of Portland cement, produced in Czech Republic, which is intended for the utilization during the construction of road pavement and transport structures. Its significant feature is low content of C_3A and lower value of specific surface by Blaine. CEM II 32.2 B-S performs cement with the content of blast furnace slag, which stands out from low hydration heat, low shrinkage and long-term evolution of mechanical properties.

Fresh mortars were prepared in laboratory mixer and sets of specimens were casted. Standard prismatic specimens 40×40×160 mm were used for the determination of mechanical properties in terms of EN 196-1.

Transport properties of cement mortars were studied using cylindrical specimens of height 50 mm and diameter 150 mm. A half of these samples were approximately 5 minutes after casting sprayed by surface agent to prevent evaporation. A commercial product Novapor HV,

on the basis of ethoxylated alcohol was used in the program. Recommended amount of the treatment is 200 – 250 g/m^2. A second half of samples served as a reference set. These cylindrical specimens were subsequently weighed to monitor the loss of the moisture in time. After 28 days were cylinders extracted from plastic molds, sealed on the lateral sides and they were subjected to the determination of water adsorption test to assess the surface quality. Samples were partially wetted into the water basin with downward orientation and the gradual ingress of water mass was gravimetrically determined.

The loss of the moisture has direct influence on the values of the shrinkage, respectively to drying shrinkage, because ultimate level of shrinkage is affected also by the mineralogy and properties of used cements (Davidova and Reiterman, 2020; Deboucha *et al.*, 2017; Nili and Ehsani, 2015). The dimensions of the ring are rather small, which enables quicker testing of mortar susceptibility to cracking. The method consists of casting a ring of mortar around a polished ring of steel and its following spontaneous hardening and drying under normal laboratory conditions. As the mortar attempts to contract against the restraint of steel ring, tensile stress develops in the mortar ring and it might crack. The crack initiation is usually monitored visually in selected time intervals. The mortar rings had cross-section 25 mm in radial thickness and 38 mm deep. With respect to nature of testing, fresh surface of a half of samples was treated by surface agent as well. Subsequent drying was conducted only through upper part of the ring, because the rings were kept in the mold during to test to prevent drying of the part, which cannot be treated.

3 Results and Discussion

The conducted experimental program was focused on the properties of concrete surface in terms of the restrained shrinkage and transport properties, which determine final durability of the concrete and life-span of the structure. Part of the samples was treated by surface agent, which protect fresh concrete surface from the sudden loss of the moisture. Also two types of cement with different properties and hydration kinetics were studied in the paper.

Obtained results of the loss of the moisture of all sets of samples are introduced in Figure 1. It is evident, that reference and treated samples are very sensitive for the evaporation of the water during initial hours of the hardening, where the effect of the treatment is very low. However, after the setting, when solid structure occurs, the studied process is controlled by the diffusion, what well declare obtained curves. There is evident contribution of used treatment from the long-term point of view. There is also visible difference in the efficiency for single cement types. In case of blended system was the improvement over 20 %, however in case of pure Portland cement is the improvement only just about 5 %. It is caused by the different hydration kinetics; rapid setting is more suitable.

Determination of mechanical properties confirmed expected slower development of mechanical performance in case of blended cement. Detailed values are introduced in Table 2. On the other hand, values of compressive strength after 28 days of curing are relatively high. Nevertheless, high kinetics of the setting usually lead to the cracking. Conducted tests of restrained shrinkage did not confirmed this hypothesis, what is well visible on Figure 2.

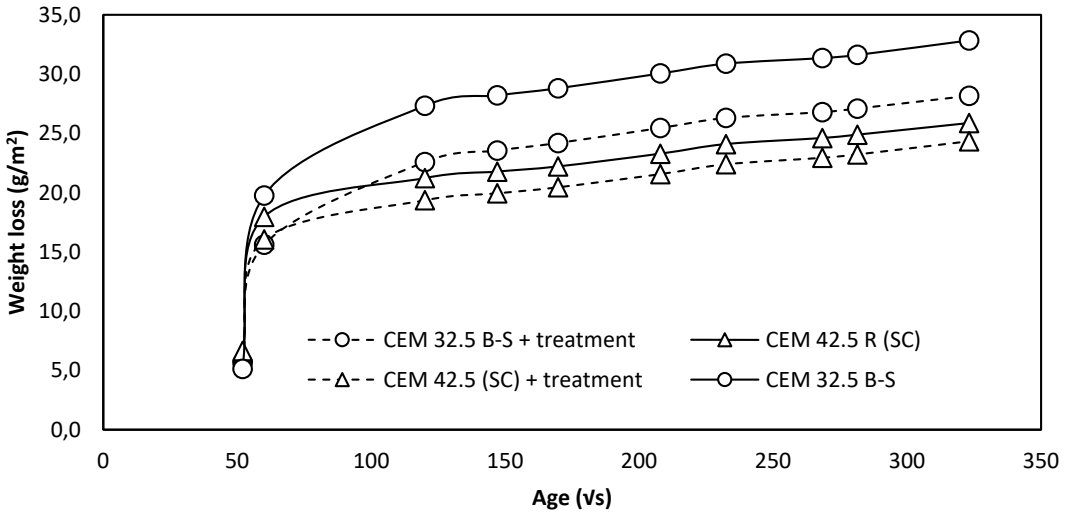

Figure 1. Monitored loss of the moisture in time.

Sudden change of the strain signalizes the moment of the rupture of mortar ring. The measurement of shrinkage declared, that mortar made of CEM I 42.5, which is specially prepared for transport structures, treated by surface agent is well resistant to the cracking. The remaining set of samples cracked approximately after 30 days of drying. However, it is necessary to note, that the time of rupture is dependent on the organization of the test. Only upper surface was exposed to the drying, what significantly extended the rupture time. Previous experiment declared, that in case of three-side drying, the rupture time could achieve a few days.

Table 2. Mechanical properties of used cement mortars.

Flexural strength [MPa]	CEM I 42.5 R (SC)	CEM II 32.5 B-S
1 day	2.9	1.8
3 days	8.1	2.7
7 days	9.7	5.7
28 days	9.8	9.5
Compressive strength [MPa]		
1 day	27.4	4.6
3 days	49.4	12.7
7 days	57.0	24.2
28 days	68.1	52.7

Results of water adsorption test are shown in Figure 3, there is well visible an improvement of the impermeability due to applied surface treatment, used type of cement respectively. On the other hand, obtained differences in non-treated samples are very low, especially up to 15 minutes. Just this short-term water adsorption has significant sense in case of the durability. For both set of samples was the achieved level of improvement about 20 %.

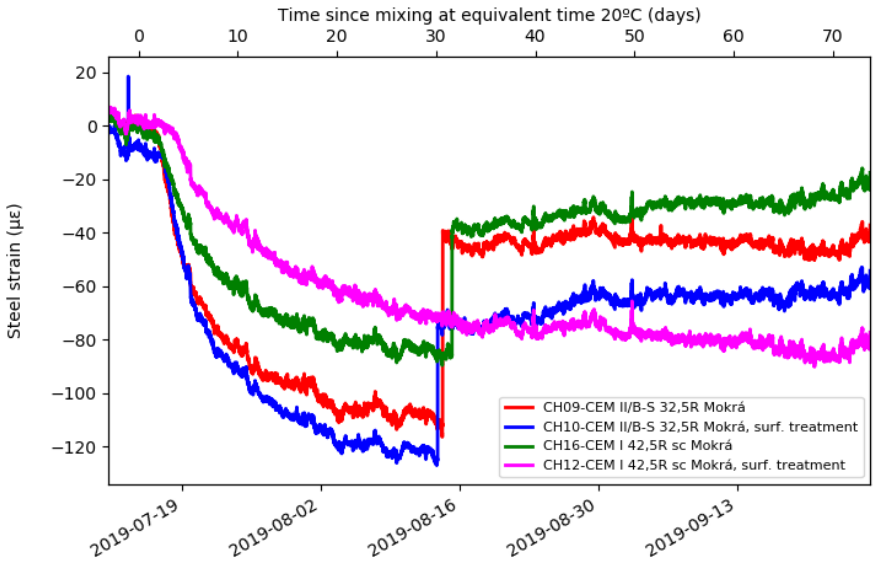

Figure 2. Results of the restrained shrinkage tests.

These results document the problem of concrete cracking during production of concrete pavement. Drying shrinkage, which is controlled by the diffusion, motivates to use binder with higher kinetics of hydration. On the other hand, higher kinetics contributes to the evolution of hydration heat and initial chemical shrinkage resulting in microcracks initiation. Generally, it is necessary to balance both preventive intervention. During past years CEM II 42.5 N/ B-S was often used during production of concrete pavement, the motivation for the selection of this type of cement was lower hydration kinetics, which positively mitigates risks of cracking. However, number of cracks has occurred shortly after the casting. It was caused by increased finesses of the cement to fulfill a required mechanical parameters, which caused higher hydration kinetics in comparison with CEM I 42.5.

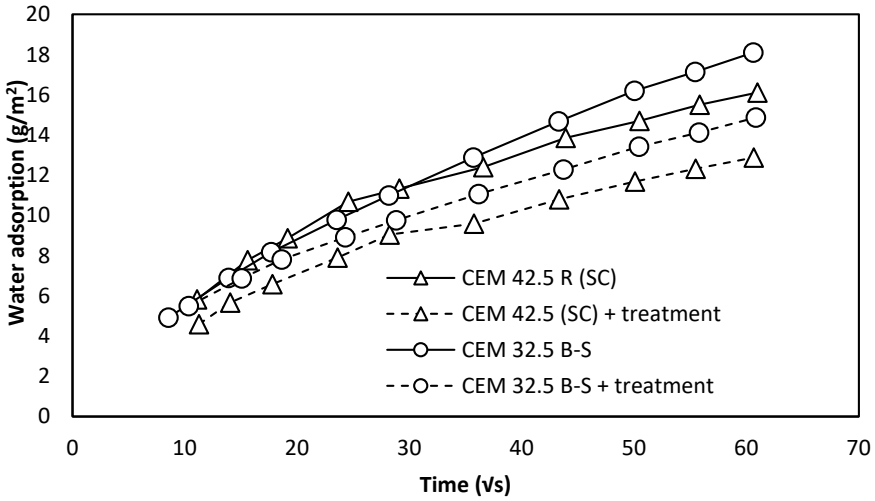

Figure 3. Results of water adsorption test.

4 Conclusions

Performed experimental program was focused on the evaluation of the efficiency of surface treatment, which is applied to prevent sudden evaporation of the water and subsequent progress of cracks due to drying shrinkage. The program conducted on standard cement mortars declared, that blended binding systems are prone to loss of the moisture. In addition, blended cement exhibited higher tendency to cracking in terms of restrained shrinkage test, the studied surface treatment did not improve this property as well. Achieved results confirmed the improvement of water impermeability, however short-term water adsorption was nearly similar for all sets of samples, except of samples made from road cement, which were treated on their surface; they exhibited slightly lower permeability of the surface layer. Obtained results indicate suitability of Portland cement, which is produced for the specific application in transport concrete structures.

Acknowledgements

This research work was financially supported by project of over project COST No. LTC18063 and FV30062.

ORCID

Pavel Reiterman: https://orcid.org/0000-0002-3918-3647
Vendula Davidová: https://orcid.org/0000-0001-9727-6860

References

Aitcin, P. (2000). Cements of yesterday and today. *Cement and concrete composites, 26,* 521-530. doi: https://doi.org/10.1016/s0008-8846(00)00365-3

Davidova, V. and Reiterman, P. (2020). Shrinkage of various types of Portland clinker-based cements with respect to their hydration degree. *Acta Polytechnica 60*(2). 88-97. doi: https://doi.org/10.14311/AP.2020.60.0088

Deboucha, W., Leklou, N., Khelidj, A. and Oudjit, M.N. (2017). Hydration development of mineral additives blended cement using thermogravimetric analysis (TGA): Methodology of calculating the degree of hydration. *Construction and Building Materials, 146,* 687-701. *d*oi: https://doi.org/10.1016/j.conbuildmat.2017.04.132

EN 196-1: *Methods of testing cement - Part 1: Determination of strength, Czech Republic* (2005).

Glinicki, M.A., Jaskulski, R. and Dabrowski, M. (2016). Design principles and testing of internal frost resistance of concrete for road structures - critical review. *Roads and Bridges - Drogi i Mosty, 15,* 21–43. doi: https://doi.org/10.7409/rabdim.016.002

Lothenbach, B., Scrivener, K. and Hooton, R.D. (2011*).* Supplementary cementitious materials. *Cement and Concrete Research, 41*. 1244–1256. doi:https://doi.org/10.1016/j.cemconres.2010.12.001

Nili, M. and Ehsani, A. (2015). Investigating the effect of the cement paste and transition zone on strength development of concrete containing nanosilica and silica fume. *Materials & Design, 75,* 174–183. Doi: https://doi.org/10.1016/j.matdes.2015.03.024

Reiterman, P., Holčapek, O., Zobal, O. and Keppert, M. (2019). Freeze-Thaw Resistance of Cement Screed with Various Supplementary Cementitious Materials. *Reviews on advanced materials science, 58,* 66–74. doi: https://doi.org/10.1515/rams-2019-0006

Vinkler, M. and Vítek, J.L. (2019). Drying and shrinkage of massive concrete wall segments—3 years experiment and analytical observations. *Materials and Structures, 52. d*oi: https://doi.org/10.1617/s11527-019-1329-x

XV International Conference on Durability of Building Materials and Components
DBMC 2020, Barcelona
C. Serrat, J.R. Casas and V. Gibert (Eds)

Influence of the Particle Size Distribution of Natural Sands in the Accelerated Alkali-Silica Expansion Test (AMBT)

Patricia E. Vila[1] **and María N. Pereyra**[2]

[1] Instituto de Estructuras y Transporte, Facultad de Ingeniería, Universidad de la República, Montevideo, Uruguay, pvila@fing.edu.uy

[2] Instituto de Estructuras y Transporte, Facultad de Ingeniería, Universidad de la República, Montevideo, Uruguay, mpereyra@fing.edu.uy

Abstract. *The accelerated mortar bar test (AMBT) is used to evaluate the potential expansion of the aggregate for the alkali-silica reaction. In this test, the aggregate should meet a certain distribution of particle size. In Uruguay it is usual that for concrete the fine aggregate is constituted by a mixture of sands, one of coarse size and another of fine size. Therefore, coarse sand must be crushed for the test and the fine sand is weighted accumulated in the smallest sieve in which there is enough material according to its particle size distribution. The aim of the work is to evaluate the influence of the particle size distribution of natural coarse sands, without crushing, in the result of the AMBT test. Mortars with different grading composition and single particle size were elaborated, and the differences obtained in the expansion, in the formation of efflorescence on the surface of the bars and in the presence of the reaction gel in the solution where the bars were immersed were analyzed. A greater expansion was observed in the samples with a continuous size distribution, compared with a single particle size. In addition, in the bars elaborated with the largest particle size, a greater amount of gel on its surface and in the solution was observed. The relevance of the work was to improve the reliability of the result in the AMBT test to evaluate the reactivity of the natural coarse sand. Natural sands of siliceous quartz-feldespathic origin were evaluated, without pessimum effect.*

Keywords: *Alkali-Silica Reaction, Accelerated Mortar Bars Test, Natural Sand, Grading Composition.*

1 Introduction

Concrete is subject to numerous pathological manifestations during its service life. The origin of these pathologies is commonly related to their constituents and their interaction with the environment. The alkali-silica reaction (ASR) is an internal reaction in concrete that occurs between certain components of aggregates considered “reactive” (opal, chalcedony, quartz, tridymite, cristobalite, chert and volcanic glass) and ions form the pore solution of concrete (hydroxyls, alkalis and calcium ions). The reaction products expand in presence of moisture, causing cracking, displacements, structural deformations, pop-outs and reduction in mechanical performances. Service life of structures may be severely affected. In addition, the reaction products can cause leaching stains on concrete surfaces (Nixon and Sims, 2016).

Great efforts have been made to develop test methods to evaluate the aggregate reactivity and the deleterious degree of the reaction. Nowadays, there are several internationally recognized standardized tests, such as the accelerated mortar bar test (ASTM, 2014; IRAM, 1997; ABNT, 2009; AENOR, 2018) the semi-accelerated concrete prism test (IRAM, 2013; Nixon and Sims, 2016) and long-term concrete prism test (with a duration of one year or more) (ASTM, 2015; IRAM, 2013; ABNT, 2009b). The criteria to define the reactivity of the

doi:10.23967/dbmc.2020.085

aggregate arises from the expansion obtained after the mortar or concrete bars have been submitted in an aggressive environment for a predetermined period of time (Nixon and Sims, 2016; IRAM, 2016; IRAM 2013; ASTM 2018; ABNT, 2009b).

In Uruguay, given the availability of natural sands, the fine fraction of the aggregate in the concrete – portion of an aggregate passing 4.75mm sieve and predominantly retained on the 0.15mm sieve - usually is obtained by two sands, one identified as "fine sand" and the other as "coarse sand". Coarse sands present large particle size generally the highest proportion in these is retained in the sieves of greater aperture (between 2.36 mm and 0.30 mm). The fine sands usually present particle size between 0.30 mm and 0.15mm. Both types of fine aggregates must be mixed to form a suitable particle size distribution to be used in concrete.

The accelerated mortar bar test AMBT test consists in evaluating the variation in length of mortar bars immersed in an aggressive solution of sodium hydroxide at (80±5) °C for a period of 14 to 28 days. This standard procedure indicates that the aggregate under evaluation shall have a specific size distribution. The material must be used in a dry condition, previously washed, with all particle passing through sieve 4.75mm and retained at sieve 0.15mm (10% retained at 2.36mm, 25% retained at 1.18mm, 0.60mm and 0.30mm and then 15% retained at 0.15mm).

In cases where it is necessary to evaluate the reactivity of a coarse sand-without the presence or with low quantity of the smallest fractions, the standard's procedure indicates that it should be crushed to obtain these fractions. However, the aggregate's textural and microstructural characteristics are altered by the crushing process, affecting its reactivity (Cosentino et al. 2011). In addition, when the process is carried out with a jaw crusher, it is difficult to reach the necessary quantities for the test in particle size smaller than 0.6mm.

The aim of the work was to analyses the influence of the particle size distribution in aggregate in the expansive behavior of the mortar in the AMBT test and to evaluate the amount of material leached to the NaOH (sodium hydroxide) solution in which the bars are immersed. The relevance of the work was to improve the reliability of the result to evaluate the reactivity of the natural coarse sand, without the need to grind the material.

2 Methodology

2.1 Materials

Two natural sands (identified AGA and AGB) of siliceous quartz-feldespathic origin were taken from the Santa Lucía river. Both sands present potentially reactive component to ASR and after being evaluated in the AMBT test have a higher expansion than the limit of 0.10% at 14 days of immersion and 0.19% at 28 days. They do not have a pessimum effect. Table 1 shows the characteristics of the sands used.

Both samples have a Fineness Modulus greater than 2.70 and contain a low quantity of particles smaller than 0.30mm (0.6% in sample AGA and 1.5% in sample AGB). At the same time, the AGA sand has only 11.9% of particles smaller than 0.60mm. For this reason, they are identified as coarse sand. In Uruguay these sands are used to produce concrete mixture combined with another fine sand.

Table 1. Characteristics of the sand used for the analysis.

Sample Id.	AGA	AGB
Origin	Paso Pache, Canelones	Aguas Corrientes, Canelones
Summary description	Natural coarse sand. Quartz-Feldespathic sand.	Natural coarse sand. Quartz-Feldespathic sand.
Potentially reactive component to ASR	5% of quartz microcrystaline (smaller size than 0.15mm)	4% of quartz microcrystaline (smaller size than 0.15mm)
Expansion in AMBT test (IRAM 1674)	0.147% (14d) – 0.236% (28d)	0.124% (14d) – 0.208% (28d)
Sieve distribution		
Retained at 4.75 mm (%)	6.0	0.2
Retained at 2.36 mm (%)	15.5	2.2
Retained at 1.18 mm (%)	31.3	16.4
Retained at 0.60 mm (%)	35.2	47.7
Retained at 0.30 mm (%)	11.3	31.9
Retained at 0.15 mm (%)	0.4	1.4
Plan	0.2	0.1
Fineness Modulus	3.69	2.86

A Normal Portland Cement - identified as CPN by the standard UNIT 20 (UNIT, 2017) - was used to produce the mortars. This cement is for general use in concrete and contains only clinker as the main component, without additions. The samples used have an equivalent alkali content (Na_2Oeq) between 1.16% to 1.29%, an average autoclave expansion of 0.11% and a specific surface (Blaine) of 330 m^2/kg.

2.2 Accelerate Mortar Bars Test (AMBT)

The accelerated mortar bars test was performed according to IRAM 1674 (IRAM, 1997) except for the particle size distribution of the aggregate which was conformed as indicated in item 2.3. Three bars were casted for each mortar. The bar sizes were in all cases 25x25x285 (mm x mm x mm) with a nominal length of 250 mm.

The initial length, the one at intermediate test times - 3, 7, 10, 14 and 21 days - and the one at the end of the immersion period were recorded for each bar during 28 days of immersion in the aggressive solution of 1N NaOH at (80±5) °C. The expansion of each bar at a certain immersion age *ti* was calculated as the difference between the length at the age *ti* and the initial length at *t0.* This was referred to the nominal length of the bar (250mm) in percentage.

The mortar expansion is calculated as the average expansion of the three bars tested. The coefficient of variation per sample was calculated to verify the accuracy of measurements of the different bars, according to the limits indicated by the ASTM C1260 (ASTM, 2014).

2.3 Particle Size Distribution in AMBT Test

Five particle size distribution were analyzed for each sand: four mixtures were fabricated with a single grading size (2.36 mm, 1.18 mm, 0.60 mm or 0.30 mm) and one mixture (identified as reference) was fabricated with different grading size composition according to the particle size distribution and considering the standard procedure but without crushing the sample (Table 2).

Table 2. Particle size distribution for mixture in AMBT test.

Sieve size		AGA sample					AGB sample				
passing (mm)	retained (mm)	AGA (reference)	236 AGA	118 AGA	600 AGA	300 AGA	AGB (reference)	236 AGB	118 AGB	600 AGB	300 AGB
4.75	2.36	10	100	-	-	-	10	100	-	-	-
2.36	1.18	25	-	100	-	-	25	-	100	-	-
1.18	0.60	65	-	-	100	-	25	-	-	100	-
0.60	0.30	-	-	-	-	100	40	-	-	-	100
0.15	pan	-	-	-	-	-	-	-	-	-	-

The AGA sample presented low quantities of particles smaller than 0.6 mm. For this reason, the reference mortar included 10% retained at 2.36 mm, 25% retained at 1.18 mm and 65% retained at 0.60 mm. In the AGB sample the reference mortar included 10% retained at 2.36 mm, 25% retained at 1.18 mm and 0.6 mm and 40% retained at 0.30 mm.

2.4 Concentration and Chemical Composition of Leachate in NaOH Solution.

The suspended solid content in the NaOH solution in which the bars were previously immersed during 28 days in AMBT test was determined. This was made by filtering a fraction of the solution on Filter Paper Grade 43 and quantifying the mass of solids retained in dry condition.

The elemental chemical composition (percentage referred to the mass of the suspended solid in dry condition) was then determined using a portal X-ray fluorescence spectrometer. The main interest of this analysis was to detect the presence of silica (Si) in the NaOH solution. This would be indicating that alkali silica reaction took place, but the gel leached into the solution, eventually without causing expansion.

The equipment used was considered adequate for this determination. However, it only quantifies elements with an atomic number greater than or equal to 12 (among the elements that cannot be detected are sodium, oxygen and calcium).

This analysis was carried out in AGA (reference), 236AGA, 600AGA and 300AGA mortars.

3 Results

3.1 Expansion and Appearance of the Bars in AMBT Test

Figure 1 shows the expansion evolution for mortar bars fabricated with AGA sand samples and Figure 2 shows the expansion evolution for mortar fabricated with AGB samples.

For AGA (reference) with particle size composition two identical mortars were fabricated (identified as AGA M1 and AGA M2). At 236AGA three identical mortars were fabricated (identified as 236AGA M1, 236AGA M2 and 236AGA M3). For 118AGA one mortar was fabricated (id. as 118AGA M1). For 600AGA two identical mortars were fabricated (id. as 600AGA M1 and 600AGA M2). For 300AGA one mortar was fabricated (id. as 300AGA M1).

For AGB (reference) with particle size composition two identical mortars were fabricated (identified as AGB M1 and AGB M2). For 236AGA three identical mortars were fabricated (identified as 236AGB M1, 236AGB M2 and 236AGB M3). For 118AGB two mortars were fabricated (id. as 118AGB M1 and 118AGB M2). For 600AGA two identical mortars were fabricated (id. as 600AGB M1 and 600AGB M2). For 300AGA two identical mortars were

fabricated (id. as 300AGB M1 and 300AGB M2).

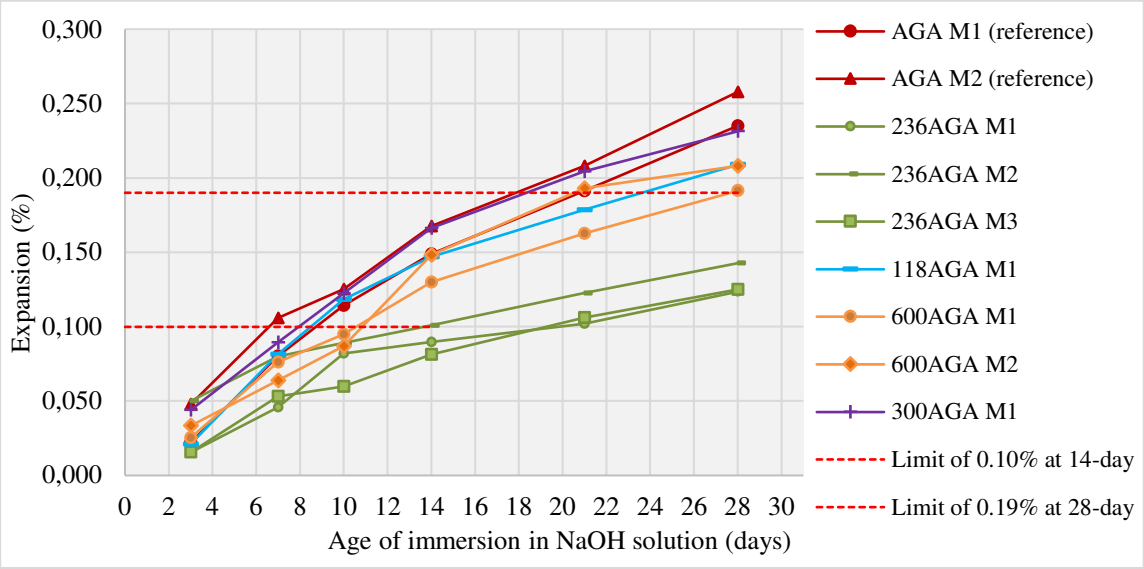

Figure 1. Expansion evolution in AMBT test. AGA sand sample.

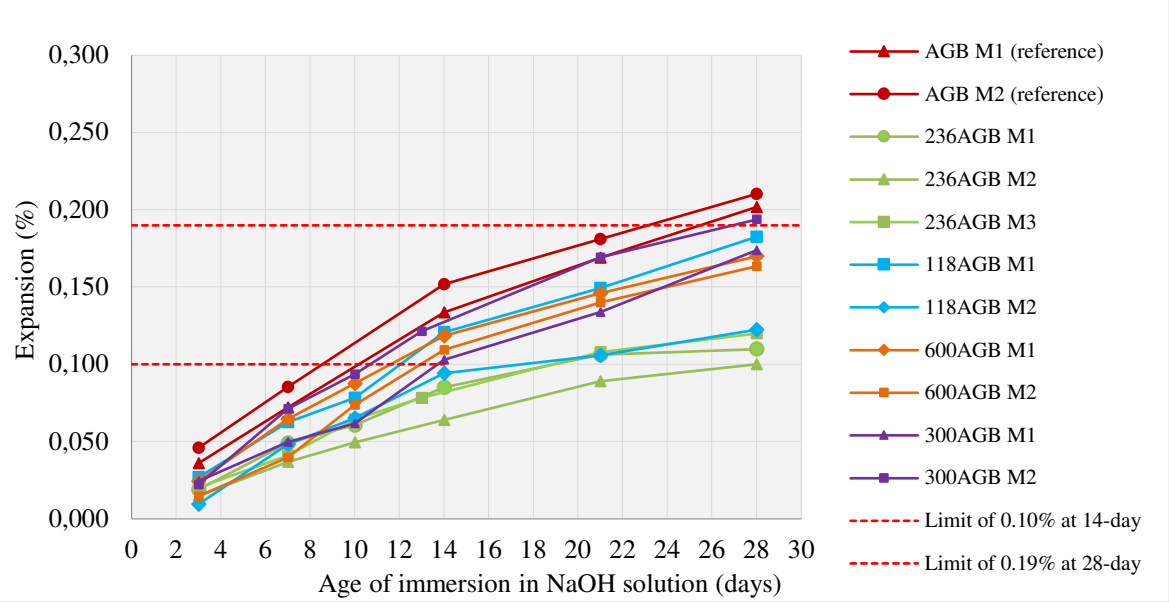

Figure 2. Expansion evolution in AMBT test. AGB sand sample.

Mortar fabricated with grading composition size (reference) according to Table 2 presented the greatest expansion in both AGA and AGB sand. In these cases, the expansion is above standard limits considered in AMBT test (0.10 % at 14 days and 0.19 % at 28 days).

Mortars fabricated with a single particle size of 2.36 mm (identification 236AGA and 236AGB) presented the slowest expansion in both sand samples. In both cases, the expansion is below the standard limits.

Mortar fabricated with a single particle size of 0.60 mm (600AGA, 600AGB) and 0.30 mm (300AGA, 300AGB) presented an intermediate expansion. In these cases, all mortars exceeded the expansion limit at 14 days; while at 28 days some samples present an expansion above and others below the limit.

In the case of the 118AGA and 118AGB mortars fabricates with a single particle size of 1.18 mm, two of them presented an intermediate expansion (118AGA M1 and 118AGB M1) and one (118AGB M2) presented a low expansion, similar to 236AGB M1.

During the test and once it was finished, the bars were visually inspected. Cracking on its surface was not observed to the naked eye but different efflorescence degrees, depending on the mortar, were observed (Figure 3). In addition, a leachate to the NaOH solution was observed in some mortars.

	AGA (ref.) (28 days)		AGB (ref.) (28 days)
	236AGA M3 (28 days)	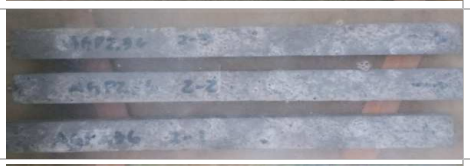	236AGB M2 (28 days)
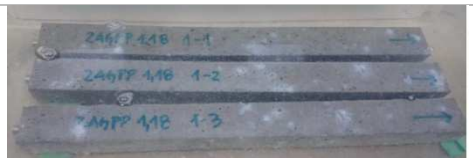	118AGA M1 (14 days)		118AGB M1 (28 days)
Without Image	-		118AGB M2 (28 days)
	600AGA M1 (28 days)		600AGB M2 (14 days)
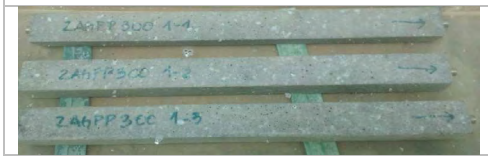	300AGA M1 (28 days)	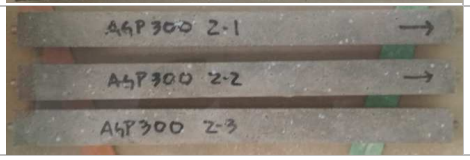	300AGB M2 (28 days)

Figure 3. Images of bars fabricated with different particle sizes at the end of the AMBT test.

Bars fabricated with a single particle size of 0.30 mm (300AGA and 300AGB) had a small amount of tiny efflorescence on their surface.

Bars fabricated with a single size of 0.60mm (600AGA, 600AGB) and 1.18mm (118AGA and 118AGB M2) had the highest amount of efflorescence. However, the surface of the 118AGB M1 mortar looked different from the 118AGB M2 mortar but it was similar to mortars

fabricated with a single particle size of 2.36mm (236AGA and 236AGB). In those cases, a discoloration of the surface and leached material in the NaOH solution were observed.

The bars fabricated with the reference mortar (AGA and AGB) presented a discoloration of the surface, similar to 236AGA and 236AGB.

3.2 Concentration and Chemical Composition of Leachate in NaOH Solution

Concentration and chemical composition of the leachate from the bars to the NaOH solution were determined. The evaluation was carried out only in mortars fabricated with AGA sand (Table 3).

Table 3. Leachate in the NaOH solution analyzed.

Id. sample	Concentration	Chemical composition of elements with an atomic number greater than or equal to 12 (% referred to the mass of the suspended solid in dry condition)					
	g/l	Si	Ca	K	S	Al	Fe
AGA (ref.) M2	0.91	22.7	55.2	2.1	1.5	4.6	0.9
236AGA M3	1.34	18.8	32.9	2.0	1.3	2.1	0.5
600AGA M2	0.81	8.1	14.1	1.2	2.4	0.4	0.3
300AGA M1	0.01	-	-	-	-	-	-

The 300AGA M1 bars did not present significant amounts of leached material to the solution (0.01 g/l).

Bars fabricated with 600AGA M2 presented leached material (0.81 g/l). The presence of Si (silica) was detected in 8.1% using the X-ray technique.

Bars fabricated with 236AGA M3 presented leached material (1.34 g/l). The presence of Si (silica) was detected in 18.8%.

Bars fabricated with AGA (reference) M2 presented leached material (0.91 g/l). The presence of Si (silica) was detected in 22.7%.

4 Conclusions

- The influence of the particle size distribution on the expansion of the mortar in AMBT test was observed. The potential reactivity of the aggregate arises from the expansion parameter. This could lead to erroneous conclusions when evaluating natural sands considering they do not present a continuous particle size distribution. For both sand samples, the greatest expansion was presented in mortars fabricated with different grading size composition (reference) and the lowest expansion was presented in mortars with a single size of 2.36mm.
- At the same sand sample, different behaviors - discoloration, efflorescence, leached material- were observed to the naked eye according to the particle size composition in both sands included in the analysis. This difference was caused by a change in the mortar microstructure. The greatest surface efflorescence was presented in mortars fabricated with a single particle size of 1.18mm and 0.60mm.
- The evaluation of the leachate concentration and its chemical composition allowed detecting the presence of the silica in the NaOH solution. Bars fabricated with the smallest size particle of 0.30mm exhibited negligible leachate. However, the bars

fabricated with the largest particle size of 2.36mm presented the largest amount of leached material. In this cases silica was detected in the NaOH solution so the alkali silica reaction took place, but the gel leached into the solution. The evaluation was performed only on a sand sample (id AGA).

Acknowledgements

Thanks to the Structures and Transport Institute (IET) of the Engineering University (UdelaR) for the equipment and laboratory necessary to carry out the test, as well as the CSIC (Science Investigation Committee - UdelaR) and Concrexur S.A. for the project financing and the private companies that provided the materials for the study.

ORCID

Patricia Vila: https://orcid.org/0000-0001-8902-5180
María Noel Pereyra: CVuyMPereyra

References

Nixon, P and Sims, I. (2016). RILEM Recommendations for the Prevention of Damage by Alkali-Aggregate Reactions in New Concrete Structures, State-of-the-Art. Report of the RILEM Technical Committee 219-ACS.

ASTM (2014). *ASTM C1260: Standard Test Method for Potential Alkali Reactivity of Aggregates (Mortar-Bar Method),* ASTM International, West Conshohocken, PA, 2014, www.astm.org.

IRAM (1997). *IRAM 1674 Agregados. Determinación de la Reactividad Alcalina Potencial Método Acelerado de la Barra de Mortero* (in Spanish), Instituto Argentino de Normalización y Certificación, Argentina.

ABNT (2009). *ABNT NBR 15577-4. Agregados. Reatividade álcali-agregado. Parte 4: Determição de expansão em barras de argamassa pelo método acelerado (In Portuguese)*. Associação Brasilera de Normas Técnicas, Brasil.

AENOR (2018). *UNE 146508 EX. Ensayos de áridos. Determinación de la reactividad potencial álcali-sílice y álcali-silicato de los áridos. Método acelerado en probetas de mortero* (in Spanish). Asociación Española de Normalización y Certificación, España.

IRAM (2013). *IRAM 1700. Agregados. Método para la determinación del cambio de largo en prismas de hormigón, debido a la reacción álcali-agregado* (in Spanish). Instituto Argentino de Normalización y Certificación, Argentina.

ASTM (2015). *ASTM C1293-08b: Standard Test Method for Determination of Length Change of Concrete Due to Alkali-Silica Reaction*, ASTM International, West Conshohocken, PA, 2015, www.astm.org.

ABNT (2009a). *ABNT NBR 15577-6. Agregados-Reatividade álcali-agregado Parte 6: Determinação da expansão em prismas de concreto (In Portuguese)*. Associação Brasilera de Normas Técnicas, Brasil.

IRAM (2016). *IRAM 1531. Agregdo gureso para hormigón de cemento. Requisitos y métodos de ensayo* (in Spanish). Instituto Argentino de Normalización y Certificación, Argentina.

IRAM (2013). *IRAM 1512. Agregdo fino para hormigón de cemento. Requisitos* (in Spanish). Instituto Argentino de Normalización y Certificación, Argentina.

ASTM (2018). *ASTM C33 C33M-18, Standard Specification for Concrete Aggregates,* ASTM International, West Conshohocken, PA, 2014, www.astm.org.

ABNT (2009b). *ABNT NBR 15577-1. Agregados-Reatividade álcali-agregado. Parte 1: Guia para avaliação da reatividade potencial e medidas preventivas para uso de agregados em concreto (In Portuguese)*. Associação Brasilera de Normas Técnicas, Brasil.

Cosentino, J. Sota, J. and Avid, F. (2011). Forma y tamaño de las partículas y su incidencia en el resultado del método de ensayo ASTM C-1260 (in Spanish). *Concreto y Cemento. Investigación y Desarrollo*. 2011, 3(1), 14-24. ISSN: 2007-3011. Available in: https://www.redalyc.org/articulo.oa?id=361233549002

UNIT (2017). *UNIT 20. Cemento pórtland para uso general. Definiciones y requisitos* (in Spanish). Instituto Uruguayo De Normas Técnicas, (Montevideo, Uruguay), p. 13.

XV International Conference on Durability of Building Materials and Components
DBMC 2020, Barcelona
C. Serrat, J.R. Casas and V. Gibert (Eds)

Innovative Approaches to Increase Service Life of Poplar Lightweight Hardwood Construction Products

Joris C.R. Van Acker, Xiuping Jiang and Jan B.B. Van den Bulcke

Ghent University (UGent), Laboratory of Wood Technology (UGent-Woodlab), Coupure links 653, 9000 Ghent, Belgium, joris.vanacker@ugent.be

Abstract. *During the second half of last century the forestry-wood chain has evolved and today ecosystem services in a sustainability framework are important. Forests are intended to provide services for the bio-economy, human health, biodiversity and climate control. An increased need for more renewable resources both for material and energy use has initiated extra interest for the potential to produce more lignocellulosic biomass, in short to increase wood production. One option is to provide in complementary production in planted forests. Both forestry and agriculture can take part in this. The cultivation of poplar hybrids in the temperate regions is a key option for the current and future bio-economy. These fast-growing trees are producing lightweight hardwood with a low natural durability, but with an important potential as construction material especially as engineered wood products. All wood protection methods are of interest to be evaluated for this wood resource, making it suitable even for high quality applications. Poplar, for many reasons, has been nominated as hardwood with the best potential to perform similarly as softwoods for applications in wood construction. Benchmarking with wood species like spruce is relevant for several engineered wood products like plywood, LVL and even CLT. Wood treatments to increase durability have evolved from traditional wood preservation towards modification techniques such as thermally modified timber. Innovative poplar based products have been assessed on their performance and are designed to fit for purpose in relation to a specific combination of use class and service life. Introducing innovative poplar based construction product for green building requires adequate testing tools. Performance based assessment should allow to integrate different protective measures. Related to moisture dynamics and the linked fungal decay risk, opportunities to extend service life are manifold. Treatment can be differentiated e.g. for cladding (building envelope) and loadbearing construction components. Simple or sophisticated modification processes can alter the equilibrium moisture content. The use of wood based panels and new engineered wood products allow for better moisture control impacting fungal decay risk, but also alter the probability of insect damage. This paper intends to present several innovative poplar based construction products and show some cases of benchmarking in relation to an integrated service life approach.*

Keywords: *Poplar, Engineered Wood Products, Wood Protection, Wood Modification.*

1 Introduction

In recent decades, the interest for building taller all-timber structures using engineered timber materials such as cross-laminated timber (CLT) has increased substantially, especially in the framework of sustainable use of resources and the positive carbon footprint of wood materials. The specific structure of CLT panels improves the dimensional stability, bending strength and other mechanical properties, thus enabling its use as load-bearing elements in various constructions. Especially in Europe, mainly spruce (*Picea abies*) is used for this purpose, while other wood species have been largely overlooked. Poplar, for example, is considered a potential species to be used in CLT as a substitute of spruce. Poplar is of interest as fast-growing tree

species providing lightweight material. It is a majorly important tree species in planted forests and agroforestry worldwide.

However, since poplar in general has a very low natural durability, we need to acquire sufficient knowledge on its behavior when incorporated in CLT. Therefore there is a need to focus on moisture dynamics (Van Acker 2017), which are in direct relation to the fungal susceptibility and thus decay resistance and service life of the product. Hence investigations should deal with moisture sorption properties (including *e.g.*, equilibrium moisture content, fiber saturation point and thermodynamic analysis) of unmodified and modified poplar products, and test the fungal susceptibility as well, aiming at incorporation in CLT products.

2 Durability Challenges for CLT (Cross Laminated Timber)

Wood, as a renewable and environmentally friendly material, has been widely exploited and used in the construction industry. However, sawn wood, timber and lumber have limited dimensions related to the tree's dimensions. This can be overcome by producing engineered wood products and especially mass timber. In recent decades, the interest for building taller all-timber structures using such EWPs has increased substantially. Engineered wood, also called composite wood, man-made wood or manufactured board, includes a range of derivative wood products which are manufactured by binding or fixing the strands, particles, fibers, or veneers or boards of wood, together with adhesives, or other methods of fixation to form composite materials. Mass timber construction uses large prefabricated engineered wood members for wall, floor and roof construction that replace steel and reinforced concrete in many building projects. These products include for example glued-laminated timber (glulam or GLT), nail laminated timber (NLT) and cross-laminated timber (CLT). While GLT is considered a 1D element (bar/trusses), CLT is mainly used as 2D element (plate/slab) as shown in Figure 1.

Figure 1. GLT ('1D' elements at the left hand side) vs CLT('2D' element at the right hand side). (Canada Wood, 2018)

GLT exists since long and more recently also CLT has become popular. The production of CLT is about 0.8 million m³ worldwide, with 90% of the CLT production in Europe. An increase of 10% on an annual basis of CLT as a building product shows potential for not only softwood species, but also hardwood species. Within the next decade, therefore, CLT could become as important as glue-laminated timber, and it is likely to extend the limits of tall wooden buildings upwards. At present, most central European producers are using spruce (*Picea abies*) as main wood species in CLT. New studies began to focus on hybrid CLT, where the hybrid build-up can be designed as a rigid composite with small error on exact analysis. The novel investigations reveal the potential to overcome low rolling shear properties in cross layers of mixed softwood-hardwood (*e.g.* beech and spruce) CLT build-ups for structural elements in

the building sector (Aicher *et al.* 2016). These approaches show potential to use also other species than spruce. New technologies such as CLT (cross laminated timber) have accelerated the construction of multi-story wooden buildings and weather protection during construction has not always been used but moisture safety remains important (Mjörnell and Olsson, 2019).

Although CLT is clearly an engineered wood products with great potential and by many considered adequate for high rise buildings in relation to mechanical and structural properties as well fire safety (Brandner *et al.* 2016, Barber 2018) the topic of sensitivity to wood rotting fungi might be underestimated. Several authors have already indicated that increased moisture in the framework of building physics, both condensation and leakage cannot be fully avoided and some preventive protection or monitoring might be required. Treatment options for mass timber products, particularly cross laminated timber (CLT) remain however to be addressed (Mankowski *et al.* 2018). Since wood species currently used to fabricate CLT are non-durable, and current design standards do not properly address incorporation of preservative treatments into these systems some experiments using a ground proximity test were proposed. Using mass timber such as CLT, but also GLT (glulam) and related engineered wood products require special attention when used in exterior applications (Morris 2015). Already some recommendations on feasible treatments of CLT have been compiled to increase awareness of decay risk and possible preventive measures (Wang *et al.* 2018). For tropical regions this could even be extra underpinned (Oliveira *et al.* 2018).

3 Assessing the Potential of Poplar

With the increasing demand of wood materials, plantations or planted forest consisting of fast-growing tree species increasingly contribute in providing a complementary wood resource and as such lower the pressure on natural forests. The cultivation of hybrid poplar is an eminent fast-growing species. As a fast-growing tree species in China (8.5 million ha) and Europe (close to 1 million ha), the major poplar hybrid plantations are now mainly focusing on plywood production. For traditional products like plywood, but also constructional timber, poplar or aspen are readily available. Aspen-OSB is an established product since decades in North-America. Specific strength and stiffness are interesting characteristics, but the ability to select quality trees with a major impact on production yield are an asset as well. Today researchers are reassessing the potential of solid timber products using poplar wood. Dimensional stability and biological durability are improved using modern wood modification methods besides traditional treatments. In this respect both glulam and CLT (cross laminated timber) show major potential eventually in combination with *e.g.* thermal modification.

In literature, it has been assessed that poplar and poplar products like plywood are considered non-durable (De Boever *et al.* 2008), thus protection can be necessary to comply with service life expectations in harsh environments (Zannutini *et al.* 2003; De Smet and Van Acker 2006; Van Acker 2008). When considering moisture dynamics some plywood products can perform quite well in outdoor conditions without ground contact (Van den Bulcke *et al.* 2011, Li *et al.* 2016). The potential of poplar is worth exploring. In some studies, poplar has been assessed as alternative for softwood to produce glulam, and combinations with other hardwoods are investigated. One study revealed that the beams composed using a specific eucalyptus clone, by its own or in combination with poplar, showed outstanding mechanical performance and the best structural efficiency. Additionally, the bonding quality, at the interface between the two

species, proved to be excellent (Castro and Paganini 2003). Clearly, poplar is a promising wood species to obtain enhanced quality in very good products based on both thermal and chemical wood modification, as well as by several other treating processes used adequately (Fraanje 1998). As such wood protection and modification can increase the potential use of poplar and poplar products considerably. Some Garnica plywood products developed recently are good examples (Sufrategui *et al.* 2016) and prove that they can be used to produce building products in a fit-for-purpose concept.

4 Innovation and Treatments to Enhance Service Life

Plywood has been the model material to investigate the impact of moisture dynamics on service life prediction. Plywood outperforms in practical circumstances what can be expected from fungal testing (Van den Bulcke *et al.* 2011, De Windt *et al.* 2018). Although in many cases low durability wood species are used and the impact on fungal growth of the glue is only temporarily, many plywood products last quite long in outdoor out of ground contact applications. The fact that such wood products under use class 3 (EN 335) circumstances can exhibit limited moisture uptake in combination with ease to dry, is not yet fully considered as an extra resistance to decay. These moisture dynamics can be assessed as time of wetness (ToW) and simulated using exterior continuous moisture measurements (CMM) as well as soaking – drying lab methods as defined in the standard CEN/TS 16818 (Van Acker *et al.* 2017b). The service life approach combining performance in relation to end use based on biocidal components, structural properties and moisture dynamics allows anyhow to provide more info than the simple material resistance only based on natural durability as in EN 350. This will provide a tool towards better integration of wood protection in the forestry wood industry chain (Van Acker 2019).

Although poplar CLT based on a range of poplar hybrid timber resources is providing important parameters for design, a second focus is to select treatments with focus on low level biocidal treatments, and on low impact thermal and chemical modification that improves moisture dynamics up to levels suitable for overall or specific conditions in a timber construction based on poplar CLT. Such treatments need to be explicitly selected based on minimal requirements and can relate to less than perfect wood protection but fit for purpose (Van Acker *et al.* 2017a). Recently Singh *et al*. (2019) showed that untreated OSB and CLT based on radiate pine were very susceptible to decay, while LVL was less susceptible. Simple boron surface treatments are suggested as potential option to lower the risk for decay. Furthermore this research indicated that moisture sorption behavior is important for experimental work especially when products treated by selected protection or modification methods. Such experiments under different experimental conditions (by changing the temperature and relative humidity) allow to provide equilibrium moisture content (EMC) modeling based on statistical analysis linked to identified significant effects from the modification. Empirical models can be compared and selected to fit the data (Jiang 2019) providing moisture sorption isotherms (MSI). Based on these data hysteresis will be analyzed and a thermodynamic analysis will be carried out.

To face the durability performance, fit for purpose and environmental challenges, the concept of introducing innovative engineered wood products is to focus on lightweight poplar, being at one hand strategically important in European forestry, while at the other hand the

technology can be transferred to other lightweight hardwoods, as well as softwoods. To achieve the performance requirements with increased cost-effectiveness, an integrated approach is applied combining wood modification (wood engineering), protection (preservation and coating) and fire resistance, the latter governing for many high-end building applications such as multi-story buildings. This leads into a specific new generation of products which are emerging: engineered and multi-level treated wood in the form of LVL, CLT, LSL and I-beam or I-joists made thereof.

Wood modification technologies like acetylation, furfurylation and different thermal modifications are intended anyhow to alter chemical and physical properties. When carried out to a sufficient level throughout the wood, these processes protect it from rot by making it "inedible" to most micro-organisms and fungi, without requiring biocides. It greatly reduces the wood's tendency to swell and shrink, making it less prone to cracking and ensuring that, when painted, it requires dramatically reduced maintenance. The innovation potential of engineered wood products from modified poplar wood is huge. TMT (thermally modified timber) poplar is already considered a SoA product. However it is always critical on lower mechanical strength, and therefore a load bearing application can be hard to achieve. Specific research on THM (thermo-hydro-mechanical) densification treatments on trembling aspen and hybrid poplar can alter some mechanical properties in a positive sense (Fang *et al.* 2019) and is considered an opportunity for future environmentally friendly wood products (Sandberg *et al.* 2013). This type of treatments are often considered of interest for low density hardwoods (Bao *et al.* 2017). Some treatments even do not focus on fungal decay resistance but are intended to improve delamination resistance (Han *et al.* 2017).

Contrary to thermal modification, chemical modification of poplar is not yet fully established. Treatability of poplar can be considered rather straightforward but still requires some technicalities due to difficult to impregnate transition zones. Chemical impregnation processes, *e.g.* with self-polymerizing and crosslinking agents can furthermore imply that the mechanical strength will be preserved (or even increased) and thus giving the innovative potential of creating renewable structural building materials from European poplar. Similarly, the use of low molecular resins can be applied on solid wood but is also valuable for *e.g*. stand based products like OSB (Wan and Kim 2004). Chemical modifications and in particular the curing step when resin treatments are applied, can lead to some embrittlement (Xie *et al.* 2013).

Building with poplar can be considered a forgotten reality that is picked up recently in an attempt to use lightweight hardwoods in construction (Kesteloot and Hudel 2016). Poplar CLT has been explored alongside GLT by several researchers (Kramer *et al.* 2014, Wang *et al.* 2014) and several companies in Europe have recently started producing this product at pilot scale. For poplar we can integrate all these trends by combining a fast growing wood resource from specific poplar cultivation, introducing this for construction and applying fit-for-purpose treatments to enhance material resistance. An example being explored in this context is poplar CLT, optionally thermally treated when decay could be a risk. Thermal treatment of poplar wood has been identified as having good potential (De Boever *et al.* 2016), being however only one of the options to increase service life under different use classes.

In Table 1 an overview is provided on how the service life of different engineered wood products could be increased. The different engineered wood products are subdivided in categories depending on the components constituting the product: strands, veneer and timber. For each category a wood based panel product as well as a beam like product is used as example.

The use of durable wood species is clearly related to the use of primarily heartwood which is often difficult to achieve in full. Vacuum pressure based wood preservation of the final product is often limited by the treatability. Glue-line additives are mainly useful when thin veneers or strands need to be protected. A third option related to wood preservation technology is spraying a diffusible component based product (*e.g.* borates) on the surface. Modification technologies might have some impact on mechanical properties and hence not fully adequate for loadbearing applications, but thermal modification for full panel products and chemical modification of strands prior to incorporation in a panel is potential technology. Finally resin treatments have similar or even better potential than glue-line additives and could also be applied as modification methods for timber based products. Applying coatings to control moisture dynamics is mainly useful for veneer and timber based products.

Table 1. Options to increase service life of Engineered Wood Products (EWP).

Component	EWP	Durable wood	Vacuum pressure[1]	Glue-line additive	Surface spray[2]	Thermal modification	Chemical modification	Resin[3]	Coatings
Strand	OSB	-	-	±	+	+	+	+	-
	LSL	-	-	±	±	-	-	+	-
Veneer	Plywood	+	+	+	+	+	±	+	+
	LVL	±	±	+	±	±	±	+	+
Timber	CLT	+	+	-	+	+	±	±	+
	GLT	+	+	-	±	±	±	±	+

Legend: +: existing option, ±: feasible option, -: less probable option

[1]: deep impregnation with biocides; [2]: surface biocide application with potential diffusion, *e.g.* borates, [3]: analogue to glue used for production or a hydrophobing agent; Abbreviations: EWP = engineered wood product; OSB = oriented strand board; LSL = laminated strand lumber; LVL = laminated veneer lumber; CLT = cross laminated timber; GLT = glue laminated timber or glulam.

5 Conclusions and Future Perspectives

The overall concept of introducing innovative engineered wood products based on fast growing plantation trees like hybrid poplars to achieve results, relate to the following objectives: (1) to link methodology (service life prediction) and product development (poplar EWP's – glulam & CLT; plywood & LVL; OSB and LSL); (2) to focus on European hardwood species; and (3) to integrate options for untreated and protected products through both biocidal and non-biocidal treatment. A holistic approach is needed to combine resistance to fungal decay, insect attack, fire, dimensional stability; in due consideration of different applications: construction (both loadbearing and not) from damp up to marine environments, interior and exterior applications (cladding, garden furniture,…), transport (caravans, containers, automotive,…) and their requirements in terms of time of wetness, aesthetics, weathering, maintenance, long-term mechanical properties (creep, mechano-sorptive behaviour, impact of treatment), as well as in terms of life cycle assessment and life cycle costing performance. All wood protection and modification methods are of interest to be evaluated for this plantation wood resource, making it suitable even for high quality applications. Poplar, for many reasons, has been nominated as

hardwood with the best potential to perform similarly as softwoods for applications in wood construction. Benchmarking with wood species like spruce is relevant for several engineered wood products like plywood, LVL and even CLT. Wood treatments to increase durability have evolved from traditional wood preservation towards modification techniques such as thermally modified timber depending on the performance required or fit-for-purpose in relation to a specific combination of use class and service life.

Acknowledgements

The authors gratefully acknowledge the support by the Flemish Research Institute for Nature and Forest (INBO) in relation to research on hybrid poplars as well as the CSC grant 201906320060 provided for Xiuping Jiang.

ORCID

Joris Van Acker: https://orcid.org/0000-0002-8961-0176
Xiuping Jiang: https://orcid.org/0000-0002-0752-2691
Jan Van den Bulcke: http://orcid.org/0000-0003-2939-5408

References

Aicher S., Hirsch M. and Christian Z. (2016). Hybrid beech and spruce cross-laminated timber. Proceedings of WCTE World conference on timber engineering, Vienna, Austria, 7p.

Bao, M., Huang, X., Jiang, M., Yu, W. and Yu, Y. (2017). Effect of thermo-hydro-mechanical densification on microstructure and properties of poplar wood (*Populus tomentosa*). J Wood Sci 63:591–605

Barber, D. (2018) Fire safety of mass timber buildings with CLT in USA. Wood and Fiber Science 50:83-95.

Brandner, R., Flatscher, G., Ringhofer, A., Schickhofer, G. and Thiel, A. (2016) Cross laminated timber (CLT): overview and development. European Journal of Wood and Wood Products 74(3):331-351.

Canada Wood (2018). Differences between the various engineered wood products. Retrieved from http://www.sohu.com/a/220390337_661558

Castro G. and Paganini F. (2003). Mixed glued laminated timber of poplar and *Eucalyptus grandis* clones. Holz als Roh- und Werkstoff 61:291-298.

De Boever, L., Van Acker, J., Vansteenkiste, D. and Stevens, M. (2008). Preservative treatment of willow wood (*Salix alba*): product retention and spatial distribution. Wood Research 53: 29–42.

De Boever L., Van den Bulcke J. and Van Acker J. (2016). Potential of thermally modified poplar wood for construction products. Proceedings of the 2nd Conference on Engineered Wood Products based on Poplar/Willow Wood, León, Spain: 107-112.

De Smet, J. and Van Acker, J. (2006). Testing methodology and CE-marking for biological performance of plywood for exterior construction purposes. Proceedings of the COST Action E44/E49 conference on Wood resources and panel properties, Valencia, Spain.

Defoirdt, N., Sen, A., Dhaene, J., De Mil, T., Pereira, H., Van Acker, J. and Van den Bulcke, J. (2017). A generic platform for hyperspectral mapping of wood. Wood science and technology, 51(4), pp.887-907.

De Windt, I., Li, W., Van den Bulcke, J. and Van Acker, J. (2018). Classification of uncoated plywood based on moisture dynamics. Construction and Building Materials.158:814-822.

Fang, C-H., Cloutier, A., Jiang, Z-H., He, J-Z. and Fei B-H. (2019). Improvement of Wood Densification Process via Enhancing Steam Diffusion, Distribution, and Evaporation. BioResources 14(2):3278-3288

Fraanje, P.J. (1998). Poplar wood for purlins; an evaluation of options and environmental aspects. Holz als Roh- und Werkstoff 56:163-169.

Han, Y., Park, Y., Chang, Y-S., Chung, H., Eom, C-D. and Yeo, H. (2017). Improvement of shear strength, wood failure percentage and wet delamination of cross-laminated timber (CLT) panels made with superheated steam treated (SHST) layers of larch wood. Holzforschung 71(11).

Jiang, X., Li H., Ramaswamy, H. S., Zhu S. and Yu Y. (2019). Moisture sorption isotherms and isosteric heats of sorption of high-pressure treated paulownia wood under different storage conditions. Transactions of the ASABE. 62(1), 105-114. DOI: 10.13031/trans.12899

Kesteloot, S. and Hudel, M. (2016). Study of the stress-grading of poplar for a structural use. Proceedings of the 2nd Conference on Engineered Wood Products based on Poplar/Willow Wood, León, Spain: 51-56.

Kramer, A., Barbosa, A., and Sinha, A. (2014). Viability of Hybrid Poplar in ANSI Approved Cross-Laminated Timber Applications. Journal of Materials in Civil Engineering, 26(7)

Li, W., Van den Bulcke, J., De Windt, I., Dhaene, J. and Van Acker, J. (2016). Moisture behavior and structural changes of plywood during outdoor exposure. European Journal of Wood and Wood Products 74(2):211-221.

Mankowski, M.E., Shelton, T.G., Kirker, G. and Morrell, J.J. (2018). Field Evaluation of Douglas-fir Cross Laminated Timber in A Ground Proximity Protected Test in Mississippi, Porceedings of the American Wood Protection Association Volume 114: 132-137.

Mjörnell, K. and Olsson, L. (2019). Moisture Safety of Wooden Buildings – Design, Construction and Operation. Journal of Sustainable Architecture and Civil Engineering. 1:29-35.

Morris, P. (2015) Optimizing the Design of Mass Timber in Exterior Applications. FP Innovations, cwc.ca. 23p.

Oliveira, G.L., de Oliveira, F.L. and Brazolin, S. (2018). Wood preservation for preventing biodeterioration of Cross Laminated Timber (CLT) panels assembled in tropical locations. Procedia Structural Integrity 11:242-249.

Sandberg, D., Haller, P. and Navi, P. (2013). Thermo-hydro and thermohydro-mechanical wood processing: An opportunity for future environmentally friendly wood products. Wood Material Science & Engineering, 8(1): 64-88.

Singh, T., Page, D. and Simpson, I. (2019). Manufactured structural timber building materials and their durability. Construction and Building Materials. 217:84-92.

Sufrategui, M.A., Albiñana, J., Alvarez, J. and Crespo, O. (2016). The Garnica brick: a structural insulated sandwich panel based on modified poplar plywood and an XPS core. In Van Acker J. (eds) Proceedings of the 2nd Conference on Engineered Wood Products based on Poplar/willow Wood. León, Spain.

Van Acker, J. (2008). Development of decay in preservative treated poplar plywood. In J. Van Acker and Y. Hua (eds) Proceedings of the Conference on Engineered Wood Products Based on Poplar/Willow Wood. Nanjing, PRChina, ISBN 9789080656574. 83-97.

Van Acker, J. (2017) Moisture dynamics defining service life performance of wood products. Pro Ligno 13(4):8-26.

Van Acker, J., De Windt, I., Defoirdt, N., Vanpachtenbeke, M. and Van den Bulcke, J. (2017a). Fit for purpose selection of wood materials. Proceedings of XIV DBMC – 14th International Conference on Durability of Building Materials and Components. p7.

Van Acker, J., Van den Bulcke, J., De Windt, I. and De Boever, L. (2017b). Continuous moisture measurements of exterior wood to simulate time of wetness. Proceedings of XIV DBMC – 14th International Conference on Durability of Building Materials and Components. p299.

Van Acker, J. (2019). Towards better integration of wood protection in the forestry wood industry chain, case study on hybrid poplar. Proceedings of the International Research Group on Wood Protection Doc. N° 19-50359, 19p.

Van den Bulcke, J., Boone, M., Van Acker, J. and Van Hoorebeke, L., (2009). Three-dimensional X-ray imaging and analysis of fungi on and in wood. Microscopy and Microanalysis, 15(5), pp.395-402.

Van den Bulcke, J., De Windt, I., Defoirdt, N., De Smet, J. and Van Acker, J. (2011). Moisture dynamics and fungal susceptibility of plywood. International Biodeterioration & Biodegradation 65(5):708-716

Wan, H. and Kim, M.G. (2006). Impregnation of southern pine wood and strands with low molecular weight phenol-formaldehyde resins for stabilization of Oriented Strandboard. Wood and Fiber Science. 38(2):314-324

Wang, J.Y., Stirling, R., Morris, O.I., Taylor, A., Lloyd, J., Kirker, G., Lebow, S., Mankowski, M.E., Barnes, H.M. and Morrell, J.J. (2018). Durability of mass timber structures: a review of the biological risks. Wood and Fiber Science, 50:110-127.

Wang, Z., Fu, H., Chui Y-H. and Gong, M. (2014). Feasibility of using poplar as cross layer to fabricate cross-laminated timber. Proceedings of the World Conference on Timber Engineering (WCTE), 5p.

Xie, Y., Fu, Q., Wang, Q., Xiao, Z. and Militz, H. (2013). Effects of chemical modification on the mechanical properties of wood. Eur. J. Wood Prod. 71:401–416

Zanuttini, R., Nicolotti, G. and Cremonini, C. (2003). Poplar plywood resistance to wood decay agents: efficacy of some protective treatments in the light of the standard ENV 12038. Annals of Forest Science 60:1-7

XV International Conference on Durability of Building Materials and Components
DBMC 2020, Barcelona
C. Serrat, J.R. Casas and V. Gibert (Eds)

Innovative Environment-Friendly Interior Finishing Technologies Resistant to Mold Growth

Piotr Czerski[1], Elżbieta Radziszewska-Zielina[2], Wojciech Ł. Grześkowiak[3], Patrycja Kwaśniewska-Sip[4] and Paweł Krzyściak[5]

[1] EXIMRENO Sp. z o.o. Makowskiego 5/5 Street, 30-322 Cracow, Poland,e-mail:biuro@eximreno.eu

[2] Faculty of Civil Engineering, Cracow University of Technology, Warszawska 24 Street, 31-155 Cracow, Poland, e-mail: eradzisz@l7.pk.edu.pl

[3] Faculty of Wood Technology, Poznan University of Life Sciences, Wojska Polskiego 38/42 Street, 60637 Poznan, Poland, e-mail: wojciech.grzeskowiak@up.poznan.pl

[4] Łukasiewicz Research Network - Wood Technology Institute, Winiarska 1 Street, 60654 Poznan, Poland, e-mail: p_kwasniewska@itd.poznan.pl>

[5] Department of Mycology, Jagiellonian University, Czysta 18 Street, PL-31-121 Cracow, Poland, e-mail: pawel.krzysciak@uj.edu.pl

Abstract. *Excessive mold development in interior spaces can be the cause of health problems in their users, as well as of a decrease in the comfort of use of internal spaces. The aim of our study was the development of a service that can ensure the long-term elimination of the cause and effects of mold in buildings by using new compositions of materials and finish application techniques. For this purpose, the most mold-resistant variants of construction material compositions and the technology of their application were selected. The study features an analysis of 18 variants of samples taken from climatic boards with various building finishes, which were tested for resistance to three species of mold: A. versicolor, Ch. globosum and P. funiculosum, under different climate and humidity combinations. The results of the study pointed to the most effective anti-mold technology. One comprehensive solution that can improve the conditions of the use of interior spaces is an external wall interior thermal insulation application system that employs silicate and lime sheets.*

Keywords: *Mold, Durability, Interior Finishing, Silicate and Lime System.*

1 Introduction

Fungi and the remediation of living quarters have been a problem that has accompanied mankind for many years. Exposure to harmful biological agents in the interior environment of living quarters has been identified by the WHO as a significant health risk. There is mounting evidence that mold growth in damp buildings is an important risk factor in the development of respiratory diseases. Air contamination by biological agents is associated with moisture and inadequate ventilation. A WHO study (2007) showed that there is a significant number of European homes that can be affected by mold and damp. Available publications indicate that in European Union Member States, the problem of mold or damp affects 10% of social housing (over 14 million cases) (Bonnefoy *et al.* 2003).

Worldwide observations indicate that in newly-built buildings, over 60% of mold problems apply to bathrooms, up to 40% to kitchens and only a few percent in other rooms. The dynamics of the indoor microclimate are related to the finishing materials and the organisms

themselves, which can in turn affect the materials. For example, porous substances can retain moisture and provide a reservoir for it, creating spaces with high humidity that are convenient for mold growth in otherwise dry indoor conditions. Molds are an extensive taxonomic group. Some of them need small amounts of organic nutrients and can grow on plasters, walls and construction materials in places with increased humidity (Fedorczak-Cisak *et al.,* 2019; Fedorczak-Cisak *et al.,* 2020; Radziszewska-Zielina and Śladowski, 2017). Molds develop actively at elevated mass humidity values, which differ between the species of mold and type of material (Gutarowska, 2010). Molds cause the biodegradation of building materials, reduce the aesthetics of the interior, destroy stored products and adversely affect the well-being and health of people and animals. They develop on surfaces, forming variegated mycelium deposits, the coloration being usually caused by numerous conidial spores (Gutarowska and Piotrowska, 2007). The second important factor affecting mold growth is the pH of a material. In particular, the alkaline nature of materials *e.g.* a high pH value of around 12-14, has been observed to show a lack of active growth of mold, which resulted from the existence of conditions unfavorable to the development of these microorganisms (Andersson et al., 1999). Excessive development of molds in utility spaces has been observed to cause health problems. The disease factor, in the form of spores, mycelium or metabolites, enters the human body by inhalation, ingestion or through the skin. The effects of these factors are not always immediate, many of them are revealed after a longer period of time (WHO 2009; Nielsen *et al.* 1999; Guo *et al.* 2004).

Control of the occurrence of molds in buildings and its reduction requires a holistic approach to the construction and occupancy process, taking into account the aspects of thermal insulation, heating, ventilation and proper finishing of materials, as well as the proper maintenance of indoor spaces (Radziszewska-Zielina *et al.* 2020). The use of comprehensive solutions consisting of the improvement of thermal and humidity conditions in an indoor space can lead to the elimination or reduction of the causes of fungal infestations. Using an internal insulation system comprised of Epatherm silicate-lime slabs is one such comprehensive solution.

2 Materials

Several dozen samples were prepared in laboratory conditions, using various finishing materials (mortars, thin coat plasters, paints (KFI, etf, acrylic (ap), latex (lp), emulsion (ep)), while the base consisted of silicate and lime sheets of varying thickness (from 15 to 100 mm). The proposed thermal insulation sheets include silicone in their composition, which gives them hydrophobic properties, making them more resistant to dampness and therefore the development of microorganisms (Hippelein and Rügamer 2004). The resistance of the analyzed sheets to the effects of molds was also a result of the existence of conditions that are unfavorable to the development of these microorganisms, particularly stemming from the alkaline character of the proposed set of materials, *e.g.* their high pH value of 12-14. In addition, based on laboratory studies, a lack of application differences was observed in the case of using these material compositions in atmospheric conditions, i.e. in temperatures ranging between 5˚C and 30˚C, with a relative air humidity of 40% to 80%. The materials used in the system are mineral products, composed of lime, quartz sand and water, which

results in a lack of toxins or other substances that are not allowed in construction.

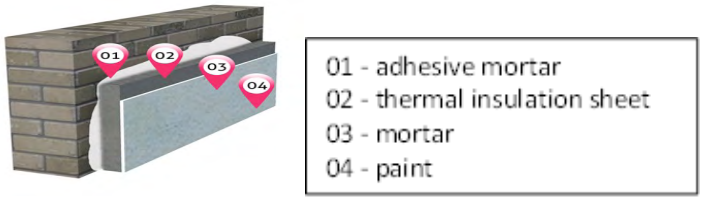

Figure 1. Layers of the proposed interior thermal insulation application system (www.eximreno.eu).

45 compositions of material and ready-made application solutions with different construction finishes (Table 1) were examined in the study:

Table 1. Material samples and technologies of their application and finishing.

No	Thickness [mm]	Finishing	No	Thickness [mm]	Finishing
1	15	factory	**24**	30	priming etg + mortar m-eti + lp
2	15	priming	**25**	30	priming etg + mortar m-eti + ap
3	15	priming, mortar m-eti	**26**	30	priming etg+thin coat plasters 5w1+ap
4	15	priming, mortar bs	**27**	30	priming etg+thin coat plasters 5w1+lp
5	15	priming, thin coat plasters ekp	**28**	30	priming etg+thin coat plasters ekp+etf
6	15	priming, mortar m-eti, KFI+priming KFV	**29**	30	priming etg + white mortar + gypsum
7	20	factory	**30**	30	Priming, mortar, lime paint KFI
8	20	priming etg	**31**	40	priming etg + mortar m-eti
9	20	priming + mortar m-eti	**32**	50	factory
10	20	priming etg, mortar m-eti, etf	**33**	50	priming etg + mortar m-eti
11	20	priming etg + mortar m-eti + ap	**34**	50	priming etg + mortar m-eti
12	25	factory	**35**	50	priming etg + mortar m-eti + etf
13	25	priming	**36**	50	priming etg + mortar m-eti + ep
14	25	priming, mortar m-eti	**37**	50	priming etg + mortar + ap
15	25	priming, mortar bs	**38**	50	priming etg + glue
16	30	factory	**39**	50	priming etg + thin coat plasters ekp
17	30	priming etg	**40**	50	priming etg+thin coat plasters 5w1+etf
18	30	priming, thin coat plasters ekp	**41**	50	priming etg+thin coat plasters 5w1+ap
19	30	priming etg + mortar m-eti	**42**	50	priming etg+thin coat plasters 5w1+lp
20	30	priming etg + mortar m-eti + etf	**43**	50	priming etg + Knauf + ap
21	30	priming etg + mortar m-eti + ep	**44**	50	priming+thin coat plasters KnaufMP75
22	30	priming etg + thin coat plasters 5w1+ etf	**45**	60	priming etg + mortar m-eti
23	30	priming etg+ thin coat plasters 5w1+ep			

3 Methods

3.1 Resistance to Molds

The study used 18 sets of 45 samples taken from climate boards with different construction finishes, which were treated with three species of mold: *Aspergillus versicolor*, *Chaetomium globosum* and *Penicillium funiculosum* in 9 climate combinations. The test was performed in compliance with American standards (ASTM C1338-08; ASTM International E104-02; ASTM International D6329-98). According to this document, stable humidity conditions are

provided by saturated solutions of selected inorganic salts, while the temperature is provided by external devices. In this study, a refrigerator chamber and an incubator were used. Radio-controlled thermohygrometers in an environmental chamber were used for the control. The conditions of the experiment and the means of ensuring them in the environmental chambers have been presented in the Table 2.

Mycological tests were carried out based on prepared spore suspensions of three selected molds with a density of 10^6/ml in two types of media (sterile distilled water and a liquid medium), which were sprayed on the test samples. The inoculated materials were placed in environmental chambers with humidity, which were then placed at three temperatures (Table 2). In total, 18 sets of 45 samples with different finishes were used in the study. A mycological evaluation of the cultures was performed after two days of incubation - 0 - determining the recovery of mold without the influence of climatic conditions. Further assessments of the size of the cultures were performed at 1 and 2 weeks of incubation. Cultures were extracted from the samples through a 1 cm^2 smear of the top layer of the sample and, after the disinfection of the surface, scraping the material from a depth of 0.5 cm on a surface of 1 cm^2. The cultures were cultivated on two media: Malt Extract LAB-AGAR™ (MEA) and Rose Bengal LAB-AGAR™ (RBA) in triplicate. When assessing the susceptibility of materials to mold, a total of over 20,000 cultures were assessed, while the total number of records in the database was about 82,000 in total, nearly 823,000 mold colonies were counted. The results were subjected to a statistical analysis.

Table 2. Conditions of the experiment.

Temperature [ºC]			Relative Humidity (%)		
Categories	**climatic conditions**	**Value**	**Categories**	**climatic conditions**	**Value**
Low	refrigerator chamber	2.6 ±1.0	Low	silicate	44.5 ± 11
Low		3.9 ± 0.6	Medium	magnesium nitrate	80 ± 1
Low		4.7 ± 1.0	High	potassium chloride	92 ± 1
Medium	room temperature	22.1 ± 1.4	Low	silicate	53 ± 1
Medium		21.8± 1.2	Medium	sodium nitrite	77 ± 1
Medium		22.6 ± 1.3	High	potassium nitrate	96 ± 1
High	laboratory incubator	36.4 ± 0.3	Low	silicate	23 ± 8
High		36.9 ± 0.2	Medium	sodium nitrite	57 ± 6
High		36.0 ± 0.3	High	potassium sulfate	86 ± 2

3.2 Statistical Analysis

The authors used one-way analysis of variance (ANOVA) to analyze the relationship between the number of mold colonies (dependent variable) and the tested variant sample "plate number" (grouping variable). The dependent variable was measured in various configurations. An ANOVA test was performed for the following configurations of experimental conditions. Afterwards, Fisher's multiple comparison tests were conducted for all identified relationships between the dependent and grouping variables, in order to detect differences between the means. A default significance level of 0.05 was adopted. The dependent variable was measured in configurations that were selected based on an analysis of the literature and the observations made during the seed test. It was found that the samples most exposed to mold fungi were those with average temperature "TEMP = SR" and high humidity "RH = WYS"

(Pasanen, 2000) conditions. The statistical analysis took into account the results after the maximum incubation time of samples from inoculation, i.e. after a period of two weeks of incubation in the above climatic conditions, "Culture = 2". A suspension in the spore medium in the MEB medium "IV = P" was selected, at which a higher number of spores was obtained relative to the spore suspension in sterile water. Spore collection from the sample surface was carried out using two methods (selected for analysis): a swab from the sample surface "V = W" and a sample groove to the depth "V = S". RBA "VI = R" medium was selected for analysis because of the low amount of impurities/infection. It has been proved that filamentous fungi depend on the presence of organic matter in the environment, they can even use house dust as a source of nutrition in conditions of high humidity (Buchmiet and Żakowska, 2009). Primary colonizers of building materials include xerophilic species that also develop in dry conditions, *e.g.* fungi of the genera *Penicillium* and *Aspergillus* (Gutarowska and Piotrowska, 2007). The dependent variable analysis was performed separately for three species of molds: "VII = A" - *A. versicolor*, "VII = P" - *P. funiculosum*, "VII = Ch" – *Ch. globosum*.

4 Results

One of the assumptions of the project was to develop a method of long-term mold removal in variously used internal spaces, one that could be introduced to the construction market. Over the course of laboratory research, material compositions with the greatest resistance to mold growth were selected and then various methods of applying them in actual construction conditions were analyzed. An analysis of the method of base surface preparation for the application of the system's sheets was performed, as well as that of their finishing depending on the type of internal space and the manner of its use. A significant relationship was found between the variable dependent number of colonies and the sample number (p value <0.05).

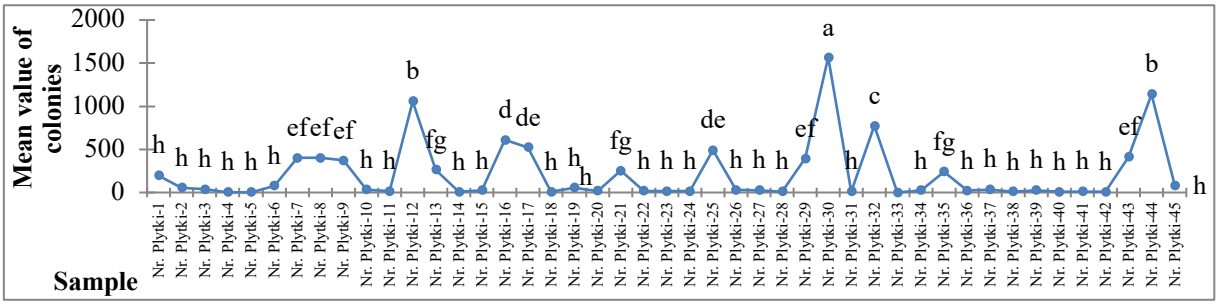

Figure 2. Experimental setup (sampling - Scraping, *A. niger*), TEMP = SR, RH = WYS, Culture = 2, IV = P, V = S, VI = R, VII = A.

For the experimental system (sampling - Scraping, *A. versicolor*), the analysis of multiple comparisons includes all samples in which the average number of colonies does not exceed 82.67 in one homogeneous class, H (this corresponds to sample 45). Samples in a homogeneous class H showed the highest resistance to *A. versicolor*. Samples 30, 44 and 12 proved to be the least resistant to *A. versicolor*, etc. (Fig. 2). Compared to variants not resistant to *A. versicolor*, samples in the G-F class also showed fungistatic activity against the

tested mold (Fig. 2). In the case of samples treated with *P. funiculosum*, variants for which the average number of colonies does not exceed 31. 33 (this limit is determined by sample No. 5) were observed to be the most resistant (Figure 3). Analysis of samples exposed to *Ch. globosum* found no significant difference between the samples (p value 0.52). Thus, all samples were observed to behave homogeneously (well) under the selected experimental setup (Fig. 4).

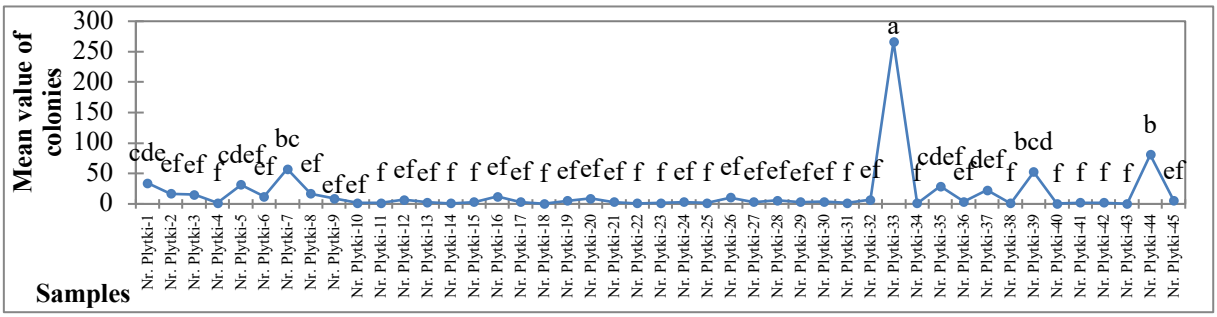

Figure 3. Experimental setup (sampling - Scraping, *P. funiculosum*), TEMP = SR, RH = WYS, Culture = 2, IV = P, V = S, VI = R, VII = P.

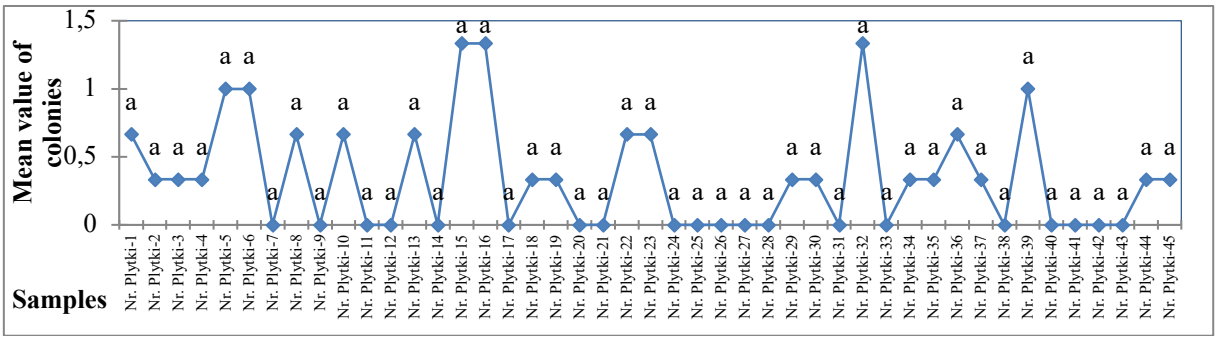

Figure 4. Experimental setup (sampling - Scraping, *Ch. globosum*)

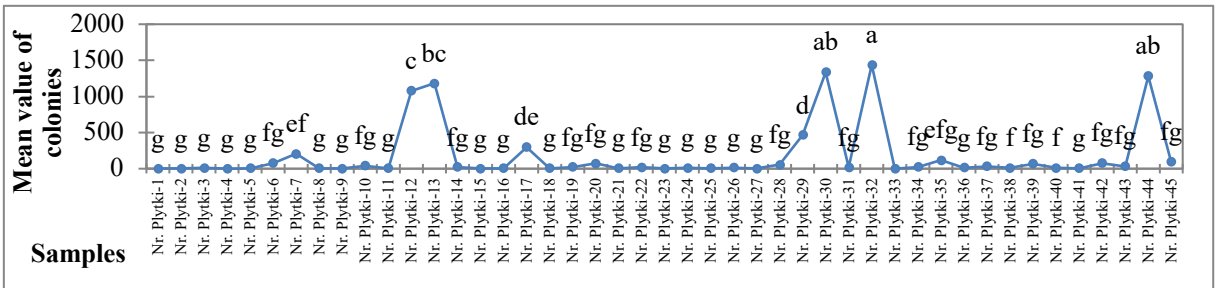

Figure 5. Experimental setup (sampling - Swab, *A. niger*), TEMP = SR, RH = WYS, Culture = 2, IV = P, V = W, VI = R, VII = A.

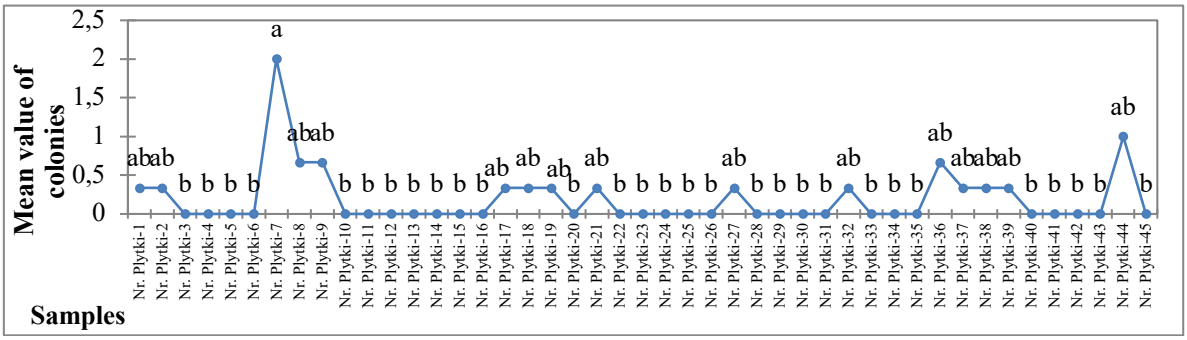

Figure 6. Experimental setup (sampling - Swab, *Ch. globosum*).

For the experimental system (sampling - Swab, *A. versicolor*), multiple comparison analysis classified all samples resistant to *A. versicolor* into one homogeneous class, G. The limit of the most resistant samples is determined by option No. 35 (Fig. 5). Additionally for the experimental system (sampling - Swab, *P. funiculosum*), multiple comparisons analysis determined the variants that were the least resistant to the action of *P. funiculosum*, which include variant No. 33. The remaining samples were within homogeneous classes B or C (not presented in figure).

Sample No. 7 was found to be the least resistant to *Ch. globosum* in this experimental setup, which is a separate class. For the remaining samples, no significant differences were observed, placing them all in the B homogenous class (Figure 6).

5 Conclusions

A review of the obtained results has shown that all building materials can be a convenient substrate for the growth of molds that contribute to their destruction. Therefore, it is necessary to know the susceptibility of currently used construction materials to colonization by these microorganisms, as well as the factors that facilitate this process.

Most often, the presence of mold was observed on samples numbered 7, 8, 9, 12, 13, 16, 17, 30, 32, 33, 44. Differences between the ability to grow mold in laboratory conditions were observed in inorganic materials (gypsum, plaster). The reason for these differences in fungal growth may have been the presence of additional sources of nutrients that stimulate said growth, e.g. in the form of dust or a microbial medium.

The results show that variants number 35 and 40, which are characterized by high vapor permeability (water vapor diffusion coefficient = 3), prevent the development of mold on their surface. Climatic boards, which have silicone in their composition, which gives them hydrophobic properties, will be more resistant to moisture, and thus to the development of microorganisms.

Acknowledgements

The project was supported as a part of the competition 3/1.1.1/2017 POIR 2014-2020 organised by National Centre for Research and Development of Poland (no. POIR.01.01.01-00-0535/17).

ORCID

Elżbieta Radziszewska-Zielina: https://orcid.org/0000-0002-3237-4360
Wojciech Ł. Grześkowiak: http://orcid.org/0000-0002-6781-8187
Patrycja Kwaśniewska-Sip: https://orcid.org/0000-0002-2084-7044
Paweł Krzyściak: https://orcid.org/0000-0002-2554-9409

References

Andersson, M.A., Nikulin, M., Koljalg, U., Andersson, M.C., Rajney, F., Rejula, K., Hintikka, E.L. and Salkinoja-Salonen, M. (1997). Bacteria, molds and toxins in water-damaged building materials. *Applied and Environmental Microbiology, 2,* 387-393.

ASTM C1338-08. *Standard Test Method for Determinining Fungal Resistance of Insulation Materials and Facing.*

ASTM International D6329-98. *Standard Guide for Developing Methodology for Evaluating the Ability of Indoor Materials to Support Microbioal Growth Using Static Environmental Chambers*, (Reapproved 2015).

ASTM International E104-02. *Standard Practice forMaintaining Consistant Relative Humidity by Means of Aquous Solutions.*

Bonnefoy, X., Braubach, M. and Krapavickaite, D. (2003). Housing conditions and self-reported health status: A study in panel block buildings in three cities of Eastern Europe. *Journal of Housing and the Built Environment, 18,* (329-352). https://doi.org/10.1023/B:JOHO.0000005757.37088.a9

Buchmiet, E. and Żakowska, Z. (2009). Toksynotwórczość pleśni na materiałach budowlanych. V Konferencja Naukowa Rozkład i korozja mikrobiologiczna materiałów technicznych, Łódź, 129.

Fedorczak-Cisak, M., Kowalska-Koczwara, A., Nering, K., Pachla, F., Radziszewska-Zielina, E., Śladowski G., Tatara, T. and Ziarko, B. (2019). Evaluation of the Criteria for Selecting Proposed Variants of Utility Functions in the Adaptation of Historic Regional Architecture*, Sustainability, 11*(4), 1094.

Fedorczak-Cisak, M., Kowalska-Koczwara, A., Pachla, F., Radziszewska-Zielina, E., Szewczyk, B., Śladowski, G. and Tatara, T. (2020). Fuzzy Model for Selecting a Form of Use Alternative for a Historic Building to be Subjected to Adaptive Reuse, *Energies, 13*(11), 2809.

Guo, H., Lee, S.C. and Chan, L.Y. (2004). Indoor air quality investigation at air-conditioned and non-air-conditioned markets in Hong Kong. *Science of The Total Environment, 323*(1–3), 87-98.

Gutarowska, B. (2010). Metabolic activity of moulds as a factor of building materials biodegradation. *Polish Journal of Microbiology, 59*(2), 119-124.

Gutarowska, B. and Piotrowska, M. (2007). Methods of mycological analysis in buildings. *Building and Environment, 42,* 1843-1850.

Hippelein, M. and Rügamer, M. (2004). Ergosterol as an indicator of mould growth on building materials. *International Journal of Hygiene and Environmental Health, 207,* 379-385.

Nielsen, K.F., Gravesen, S., Nielsen, P.A., Andersen, B., Thrane, U. and Frisvad, J.C. (1999). Production of mycotoxins on artificially and naturally infested building materials. *Mycopathologia, 145,* 43-56.

Pasanen, A.L., Kasanen, J.P., Rautiala, S., Ikaheimo, M., Kaariainen, H. and Kalliokoski, P. (2000). Fungal growth and survival in building materials under fluctuating moisture and temperature conditions. *International Biodeterioration and Biodegradation, 46,* 117-127.

Radziszewska-Zielina, E., Czerski, P., Grześkowiak, W. and Kwaśniewska-Sip, P. (2020). Comfort of Use Assessment in Buildings with Interior Wall Insulation based on Silicate and Lime System in the Context of the Elimination of Mould Growth, Archives of Civil Engineering, 2.

Radziszewska-Zielina, E. and Śladowski, G. (2017). Proposal of the Use of a Fuzzy Stochastic Network for the Preliminary Evaluation of the Feasibility of the Process of the Adaptation of a Historical Building to a Particular Form of Use, WMCAUS IOP Conf. Series: *Materials Science and Engineering, 245,* 072029.

WHO (2007). *Large analysis and review of European housing and health status (LARES)* http://www.euro.who.int/__data/assets/pdf_file/0007/107476/lares_result.pdf?ua=1

WHO (2009). *WHO guidelines for indoor air quality :dampness and mould.*

XV International Conference on Durability of Building Materials and Components
DBMC 2020, Barcelona
C. Serrat, J.R. Casas and V. Gibert (Eds)

Long-term Performance of Repairs to Reinforced Concrete Exposed to Coastal Conditions

Sachie Sato[1], Yoshihiro Masuda[2] and Masaru Kakegawa[3]

[1] Department of Architecture, Tokyo City University, 1-28-1, Tamazutsumi1-28-1, Setagaya, Tokyo,158-8557, Japan, s-sato@tcu.ac.jp

[2] Department of Architecture and Urban Design, Utsunomiya University, 7-1-2, Yoto, Utsunomiya, Tochigi,321-8585, Japan, masuday@utsunomiya-u.ac.jp

[3] Taiheiyo Materials Corporation, Tabata ASUKA Tower,6-1-1, Tabata, Kita-ku, Tokyo, 114-0014, Japan, Masaru-Kakegawa@taiheiyo-m.co.jp

Abstract. *Reinforced concrete (RC) specimens were treated using different combinations of surface coating and/or patch repair methods and materials, left in a coastal region with frost damage risk, and their properties characterized after 25 years of exposure. Specimens were prepared by chipping away concrete from one section of concrete block with embedded reinforcement bars to expose the bars, followed by patch repair and then surface coating. Four types of material were used for patch repair: cement mortar, styrene–butadiene rubber (SBR) polymer cement mortar, rust-resistant SBR polymer cement mortar, and lightweight epoxy mortar. Two types of material were used for surface coating: multi-layer textured and thin textured coating. Following exposure, cracks were visible only on the surfaces of untreated specimens, apparently due to rebar corrosion; they were absent from all specimens that had undergone surface coating and/or patch repair. In addition, the corrosion resistance of these methods and materials was investigated by measuring and comparing the surface areas of corroded rebar between three segments: the repaired part, the unrepaired part, and the boundary between them. Concrete carbonation and rebar corrosion were greatly dependent on surface coating material, with the multilayer-textured coating especially effective at blocking chloride penetration. In addition, rebar corrosion was more effectively prevented by patch repair with the SBR polymer cement mortar than with the lightweight epoxy mortar.*

Keywords: *Exposure Test, Corrosion, Cracking, Patch Repair Methods, Surface Coating.*

1 Introduction

Various recent initiatives around the world have paralleled our transition to a sustainable society. In the construction industry, efforts have focused on reviewing and optimizing the resource usage of buildings: to this end, priority has been given to improving techniques to repair, renovate, and maintain existing concrete structures to extend their lifespan and ensure their long-term integrity.

Reinforced concrete (RC) buildings are designed with high durability in mind, with purported lifetimes of over 100 years. The fact is, however, that such structures can show signs of degradation such as cracking and peeling very soon after their completion, in as little as 10–20 years. To guarantee the durability and safe usage of RC buildings in the long term, their susceptibility to different deterioration factors present in their environment should be assessed, and used to inform suitable management strategies.

The present study models an RC structure located near the coast, at risk of salt damage from

ambient chloride (Sato. K *et.al.* 2002) Specimens were initially treated using a selection of surface coating and/or patch repair methods and materials, left exposed, and then evaluated in terms of several physical characteristics to characterize the durability afforded by each combination. Exposure tests were performed in a coastal region of Hokkaido, the cold, northernmost prefecture of the long Japanese archipelago. Evaluation data from 25-year-old specimens were additionally compared with those of similar specimens exposed for 4.8 and 8 years.

2 Experimental Overview

Table 1 shows the types of materials used in the repairs. Table 2 details the content and properties of the concrete; Table 3 shows its mix composition. The concrete used had a 28-day compressive strength of 30.8 N/mm^2.Figure 1 is a structural schematic of the RC specimens. First, concrete was chipped away from a designated area of the RC slab, which had two reinforcing steel bars ("rebar") embedded in it. Next, this area was patched and its surface coated using a specific combination of materials. Concrete was removed to two different depths ("chipping depth"), defined relative to the embedded rebar: (A) chipping extended below the bar, allowing it to be completely covered with mortar, or (B) chipping reached the same depth as the rebar axis, meaning only half of it was covered with mortar. Figure 2 explains the notation of the specimen IDs in the Results section. Two-symbol IDs denote RC specimens, while three-symbol IDs denote the rebars embedded in them.

Table 1. Repair materials.

Process	Symbol	Type
Patch repair	N	None
	CM	Cement mortar
	PS	SBR* polymer cement mortar
	PI	SBR* polymer cement mortar with anti-rust additive
	LE	Lightweight epoxy mortar
Surface coating	N	None
	L	Thin textured coat
	S	Multi-layer textured coat

*SBR: styrene–butadiene rubber

Table 2. Concrete content and properties.

Materials	Properties
Cement	Ordinary Portland cement Density: 3.16 g/cm^3
Fine aggregate	River sand Density 2.62 g/cm^3, F.M.2.64
Coarse aggregate	Crushed hard sandstone Density 2.64 g/cm^3, F.M.6.71
Air entraining agent	Natural resinate
Rebar	Round steel bars with mill scale and acetone defatting: φ13 mm, SR235 (SR24) (JIS G 3112)

Table 3. Concrete mix composition.

Target slump (mm)	Target air content (%)	W/C (%)	S/a (%)	Water	Cement	Fine aggregate	Coarse aggregate	AE (*cement weight (%))
				kg/m^3				
180	4.0	65.0	48.0	185	285	862	940	0.020

These 'repaired' specimens were left at the exposure test site for predetermined lengths of time (43.025N, 140.53E, ~40 m from coastline: Figure 3). At each timepoint, several specimens were broken apart and the rebar inside removed to measure the surface area affected by corrosion ("corrosion area") and the weight lost due to corrosion ("corrosion mass loss"). Carbonation depth and chloride penetration were measured in the broken concrete in parallel. Figure 4 shows the mean monthly temperatures of the region where the specimens were left exposed.

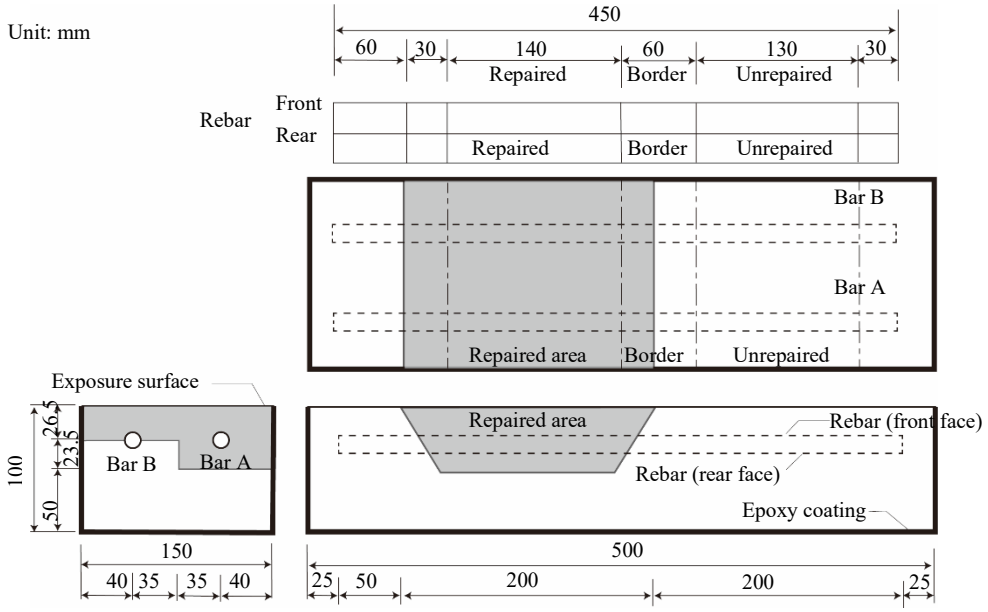

Figure 1. Schematic of RC specimen.

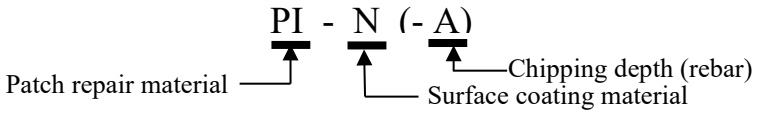

Figure 2. Specimen notation.

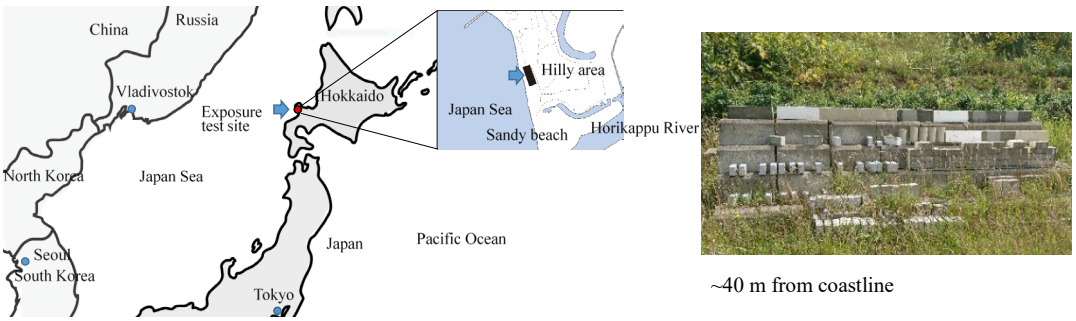

Figure 3. Exposure test site.

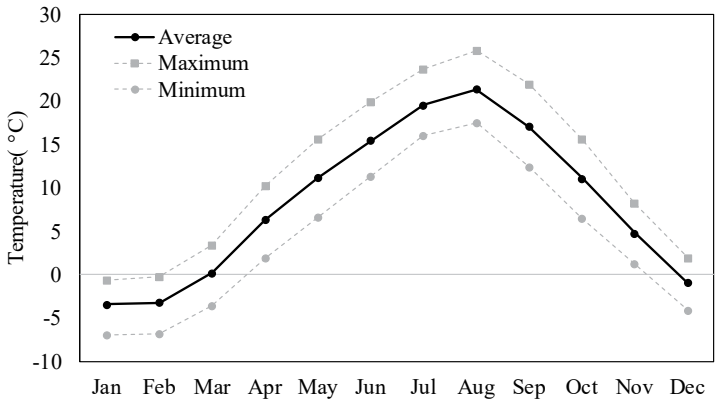

Figure 4. Mean air temperature by month at exposure test site.

3 Results and Discussion

3.1 Carbonation Depth

Figure 5 shows the measurement data for carbonation depth. Carbonation depth was most affected by the presence of surface coating itself, consistently measured deeper in specimens whose surfaces had not been coated at all (-N). When present, multilayer textured coating (-S) provided superior protection to thin textured coating (-L): specimens treated with it experienced almost no carbonation at all, irrespective of patching mortar type, evidencing its excellent resistance to carbonation.

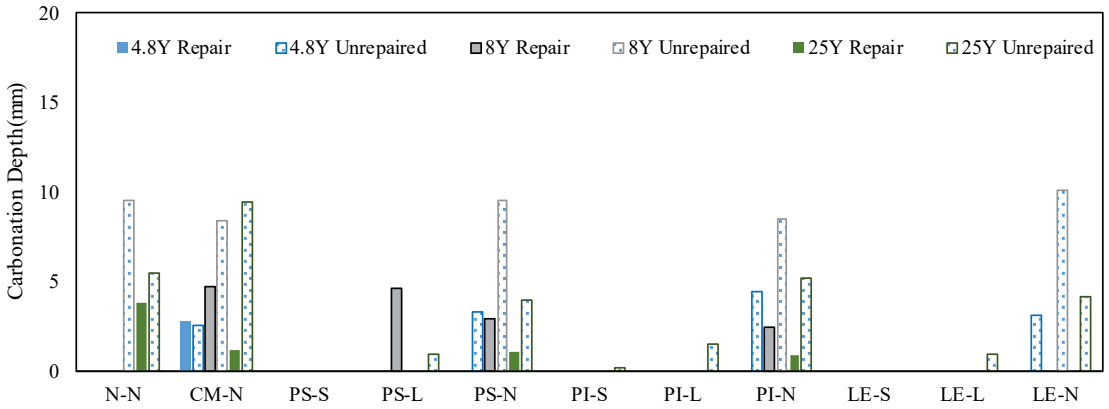

Figure 5. Carbonation depth.

3.2 Rebar Corrosion

Once removed from concrete, steel rebar was first visually graded, and then its degradation quantified by tracing and measuring the surface area of the regions affected by corrosion. Figure 6 contains photos of two bars affected by corrosion taken from a representative specimen (CM-N). Corrosion behavior clearly differs greatly between the repaired and unrepaired regions: interestingly, in the repaired part, it seems dependent on chipping depth (*i.e.* A versus B rebar).

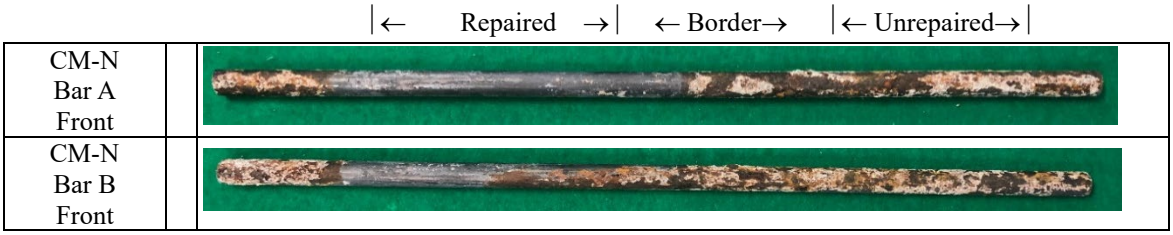

Figure 6. Rebar corrosion (CM-N, 25 years).

Next, rust was removed from the extricated bars by immersion in 10% di-ammonium citrate. Each bar was sectioned into three parts according to Figure 1 (Repaired, Border, and Unrepaired), and the corrosion mass loss calculated for each part (Nishimura N. *et al.*,2012, Kakegawa, M.*et al.*,2012). Corrosion speed was then calculated based on the mass loss using the following equation (Sato K. *et al.*,2002).

$$\Delta Ws = \frac{\Delta Wc \times W_0}{\varphi \times l \times \pi \times t} \quad (1)$$

Where ΔWs is the rebar corrosion speed (10-6g/mm^2/y), ΔWc is the mass loss due to rust (%), W_0 is the initial weight of the rebar (g), φ is its diameter (13 mm), l is its length in the part under analysis (mm), and t is the exposure length (year).

Figure 7 depicts correlations of rebar corrosion speed in the unrepaired versus border and repaired sections. Corrosion was effectively prevented by the repair techniques utilized, by and large proceeding at slower speeds in repaired than unrepaired rebar. Corrosion speed was quite high in the border region after eight years of exposure following repair with the rust-resistant SBR polymer cement (PI). This behavior could be attributable to a macrocell formed by a major differential in corrosion potential between the repaired and unrepaired parts due to the anti-rust additive in the mortar. However, the same tendency was not apparent in the 25-year-old specimens repaired using the same material, suggesting this variation likely originated in individual differences between specimens.

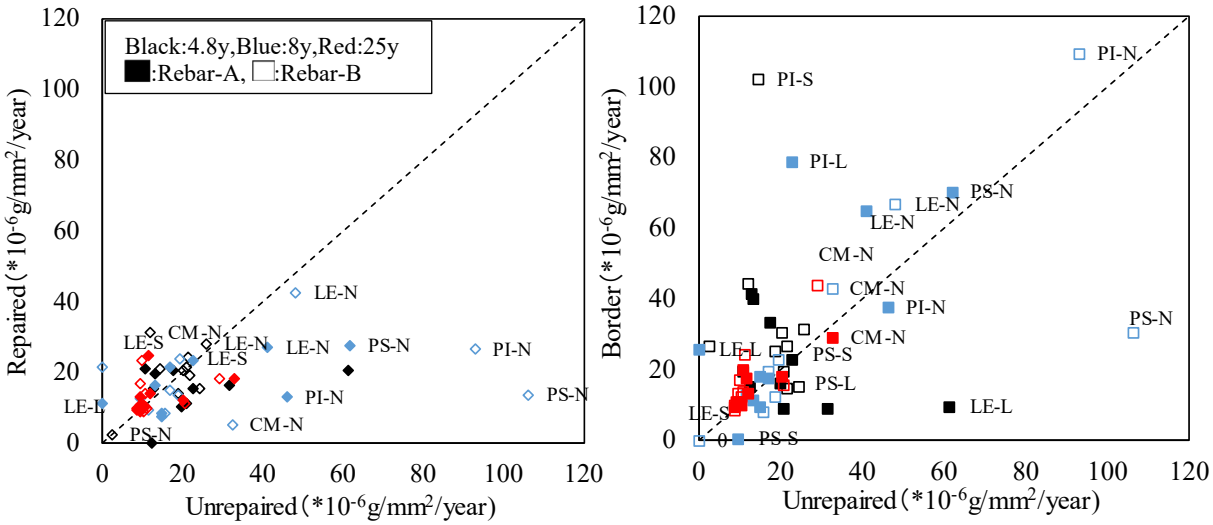

Figure 7. Rebar corrosion speed.

Figure 8 separately depicts the associations between the rebar corrosion area (itself affected by chipping depth) and corrosion mass loss by type of patching material. Specimens not treated by patch repair or surface coating (N-N-) experienced major mass loss, directly proportional to

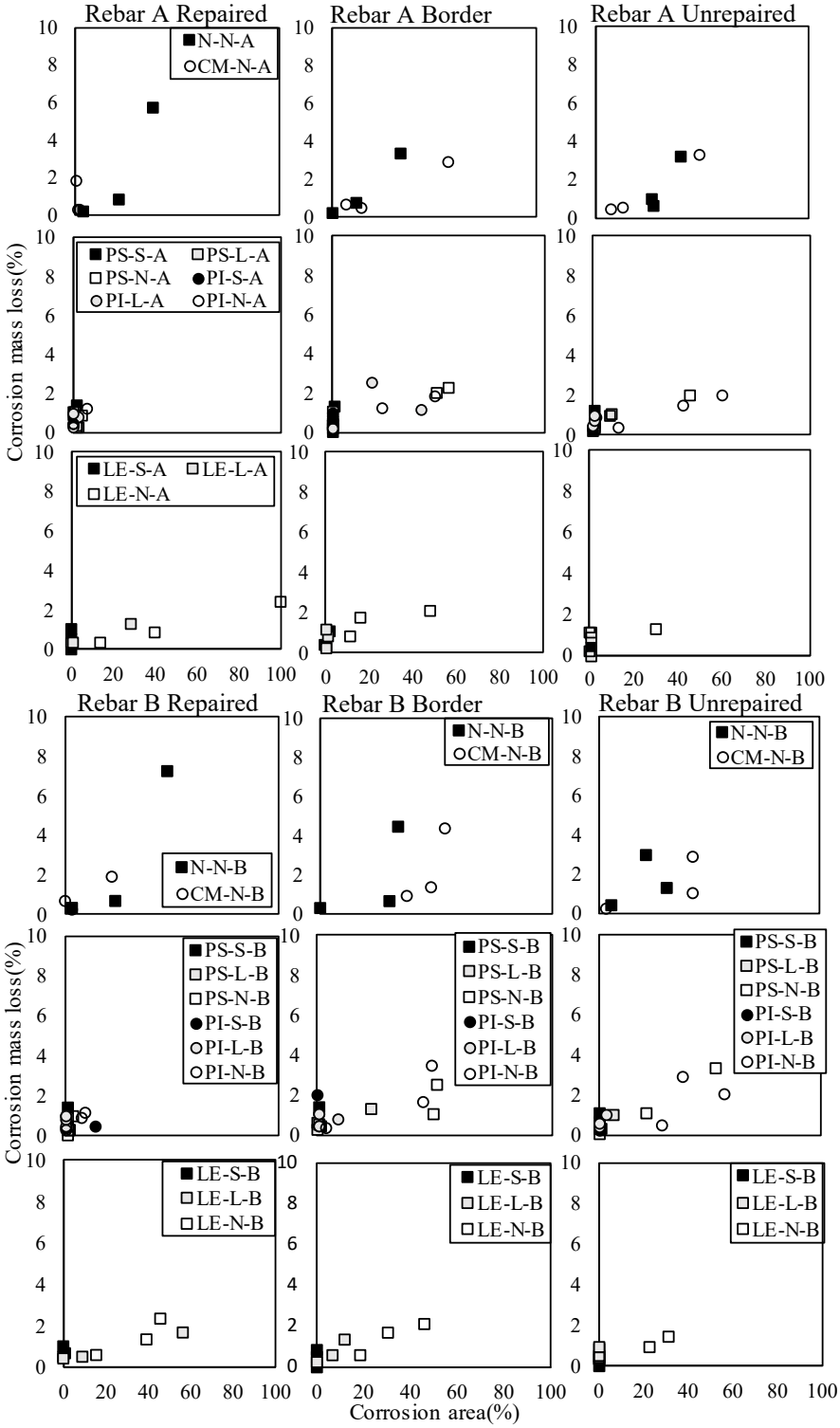

Figure 8. Rebar corrosion area versus mass loss by repair material and chipping depth.

corrosion area. In addition, corrosion progressed not only along the surface of rebar, but also towards its interior. When cement mortar was used for patch repair (CM-), the corrosion area and mass loss of the repaired region tended to be greater for B rebar than for A rebar. This suggests that chipping away enough concrete so that the entire area surrounding the rebar can be coated with patching mortar should effectively protect against corrosion. In addition, the corrosion area and mass loss of the repaired region were lower when SBR-type polymer cements (PS, PI) were used as the patching mortar than for lightweight epoxy (LE), evidencing the former materials' superior ability to protect against corrosion in patch repairs. Corrosion was prevented rather poorly by LE: when it was used, corrosion tended to spread widely across the rebar surface in the repaired region. No matter which material was used for patch repairs, the usage of multi-layer textured coating (-S-) was associated with significant drops in both corrosion area and weight loss, suggesting this material effectively resists corrosion and block the penetration of chloride ions. The only difference between PI and PS is the presence of an anti-rust additive in the former. Figure 8 shows that both materials well protect against rebar corrosion in the repaired region, with only marginal benefits afforded by the anti-rust compound.

However, specimens repaired using PI or PS tended to experience greater rebar corrosion along the border and non-repaired parts, especially in the absence of finish: this suggests the occurrence of macro-cell corrosion due to differential susceptibility to chloride penetration between the repaired and unrepaired segments. Notably, the multi-layer textured finish was the thickest of all types tested, achieving high chloride resistance and little penetration in the border and unrepaired segments on the whole. This characteristic may be why serious rebar corrosion was never really observed in the border and unrepaired parts of specimens coated with it.

4 Conclusion

This study's findings illustrate how the corrosion resistance of a repaired RC structure is affected by the materials chosen for patch repair and surface coating, as well as by chipping depth, based on experimental data from exposure tests lasting ~25 years. They can be summarized as follows:

- Carbonation was most effectively prevented by the multi-layer textured coating material.
- Corrosion protection was greater when concrete chipping extended below the rebar than merely to the same depth.
- Rebar corrosion, as with carbonation, was most effectively prevented by the multi-layer textured coating material.
- Rebar was more resistant to corrosion following patch repair with SBR polymer cements than with lightweight epoxy. However, when surface coating was not performed, macrocell corrosion may have been triggered by a high differential in chloride environment between the boundary/unrepaired and repaired regions.

Going forward, the authors plan to analyze chloride penetration depth in order to further scrutinize its relationship with rebar corrosion.

Acknowledgements

This work was supported by JSPS KAKENHI Grant Numbers JP16K06591 and JP19K04695.

ORCID
Sachie Sato: https://orcid.org/0000-0002-2299-2149
Yoshihiro Masuda: N/A
Masaru Kakegawa: N/A

References

Kakegawa.M., Masuda, Y., Matsubayashi, Y. and Kage, T.(2012). *Long-term outdoor exposure test on the rate of corrosion test of reinforcing bar in concrete containing chloride ion, Journal of Structural and Construction Engineering (Transactions of AIJ), 77(672),* 143-151, (In Japanese), doi:10.3130/aijs.77.143

Nishimura N.,Masuda, Y., Kage. T. and Matsubayashi, Y.(2010). *Evalulation of effect on repaire of section repaire method of construction based on reinforcing bars mass decrease rate of the long-term exposure test body, Journal of Structural and Construction Engineering (Transactions of AIJ). .77(655),* 1601-1608,(In Japanese) doi:10.3130/aijs.75.1601

Sato, K, Masuda, Y. *et al.,* (2002). *Outdoor exposure test on evaluation of repair reinforced concrete, Summaries of technical papers of annual meeting, Architectural Institute Japan,A-1,* 625-626(In Japanese)

XV International Conference on Durability of Building Materials and Components
DBMC 2020, Barcelona
C. Serrat, J.R. Casas and V. Gibert (Eds)

Measurement of Moisture Content and Volume Change Distribution Inside Cement Paste Specimens Using X-Ray CT Imaging

Takayuki Fumoto[1], Masaru Abuku[2] and Stephen A. Hall[3]

[1] Department of Civil and Environmental Engineering, Faculty of Science and Engineering, Kindai University, 3-4-1, Kowakae, Higashi-osaka, 577-8502, Osaka, Japan, fumoto@civileng.kindai.ac.jp
[2] Department of Architecture Faculty of Architecture, Kindai University, 3-4-1, Kowakae, Higashi-osaka, 577-8502, Higashi-osaka, Osaka, Japan, abuku@arch.kindai.ac.jp
[3] Department of Solid mechanics, Faculty of Engineering, Lund University, P.O. Box 118 SE-221 00, Lund, Sweden, Stephen.Hall@solid.lth.se

Abstract. *The purpose of this study was to clarify the internal change of concrete structures during drying. Therefore, we used X-ray CT to investigate water content and volume changes inside cement paste specimens during drying. Changes in the CT image intensities and measurements on the images indicated water content and volume changes, including local changes detected with digital volume correlation. Next steps will be to understand the link between volume changes and the local water content.*

Keywords: *Cement Past, Drying Shrinkage, Moisture Content, X-Ray CT, Digital Volume Correlation.*

1 Introduction

Concrete contains a lot of free water. When free water evaporates by drying, volume changes can occur. Such volume changes due to drying can cause cracks on the surface of concrete structures, resulting in a decreased durability of the structure.

The estimation of volume changes in concrete have usually been calculated based on the length change of a specimen (JIS A 1129-3). However, it is not only the shrinkage of cement paste that should be considered, but also shrinkage and distribution of aggregates also influence volume changes in concrete, for example Zhanga, W. *et al* (2013) and Alexander, MG. (1996). Furthermore, as moisture is transferred from the surface, the moisture content is different between the surface and the interior. For these reasons, it is difficult to estimate the complicated volume change only by the apparent externally measured size change of a specimen.

For the above reasons, we considered that a method that can measure the moisture content and volume change inside concrete in three dimensions (3D) is necessary. Previously, Sant, G. and Weiss, J. (2009). and Hong, S., *et al* (2019) used an X-ray CT apparatus to mesurement changing of water content and cracking inside the specimen. T. Fumoto also developed an X-ray CT system to estimate moisture content and composition of concrete after high temperature heating and to measure 3D volumetric strain fields in concrete under loading stress, for example Fumoto, T. and Hall, S (2019) and Fumoto, T., Mizuno, S. and Ozawa, M. (2016). Here we extend this previous work to examine the moisture content and volume change inside specimens during drying.

In this study we performed a length-change test on a cylindrical specimen of cement paste, which is a basic approach for measuring drying shrinkage, but we study the distribution of volume changes inside the sample using X ray CT and make image measurements at different

stages of the drying.

2 Experiment Methods

2.1 Specimen

To maximise the possibility of being able to make 3D measurements of the internal specimen changes during drying, a paste specimen that would give a large volume change was prepared. In addition, to study the effect of aggregates (crushed stone, in this case) on the internal deformation, paste specimens were prepared with a particle of crushed stone or crushed brick placed in the centre. Only a single particle was included to be able to visualize the effects around the aggregate without the influence of adjacent particles.

Table 1 shows the mixture proportions of the paste used in this study. In addition to ordinary Portland cement, zirconia balls with a particle size of 0.3 mm (density 6.07 g / cm^3) were mixed into the paste (the samples had 0.75% of the paste volume as zirconia balls) to provide more enhanced intensity patterns in the tomography images for improving the accuracy of the image measurements.

Table 1. Mixture proportions of paste.

W/C (%)	Unit content (kg/m^3)				
	Water	Cement	Thickener agent	Thickener agent	Zirconia ball
60	652	1088	32.6	0.326	45.4

5 L of paste was mixed in a planetary mixer, from which three specimens were made. Figure 1 shows an image of one of the specimens and the coordinate system used. The dimensions of the specimens were 75 mm in diameter and 144 mm in height. When placing the paste into the moulds, bolts with a diameter of 6 mm and a length of 35 mm were attached to the upper and lower surfaces of the specimen. For two specimen, crushed stones (surface dry density 2.63g / cm^3, water absorption 1.6%, particle size about 30mm) and crushed bricks were placed in the centre in a saturated surface‐dry condition.

The samples were demoulded the next day and, immediately after, an epoxy resin was applied to the upper and lower surfaces of the specimen so that moisture could escape only from the sides. In addition, a PVC pipe embedded with 12 ceramic balls (diameter 5 mm) was attached to each specimen to reduce mechanical errors and enabling an affine transformation to align images, following Ura, T., Fumoto, T and Takehara, K. (2016). The PVC pipe had 32 holes, with a diameter of 1 cm, arranged from the vertical-centre to the bottom to not prevent moisture dissipation. The specimens were stored in a constant temperature and humidity chamber at a 20 ± 1 ° C and a humidity of 60 ± 5%.

2.2 Measurement Method

Length change measurements and X-ray CT scans were performed after drying periods of 0, 5, 8, 13, 21, 35 and 134 days. Shrinkage strain was measured according to the measurement method of JIS A 1129-3. The X-ray CT imaging was performed using an apparatus that were shows in Fumoto, T. (2013) in detail. For each CT measurements, the center height of the specimen ± 35mm was scanned using the imaging parameters shown in Table 2 and with a

cubic image voxels with a side length of 0.123 mm. 3D deformation measurements inside the specimens were made using digital volume correlation (DVC) with the software *TomoWarp2* of Tudisco et al.(2017). For the DVC measurements, the correlation window for the correlation calculation was a cube of about 3 mm side length and the distance between correlation windows (the node spacing) was about 1.5 mm.

Table 2. X ray scan condition.

Tube voltage (kV)	Tube current (μA)	frame rate (frame/sec)	projection	Resolution (mm)	cupper plate (mm)
170	100	4	2000	0.123	3

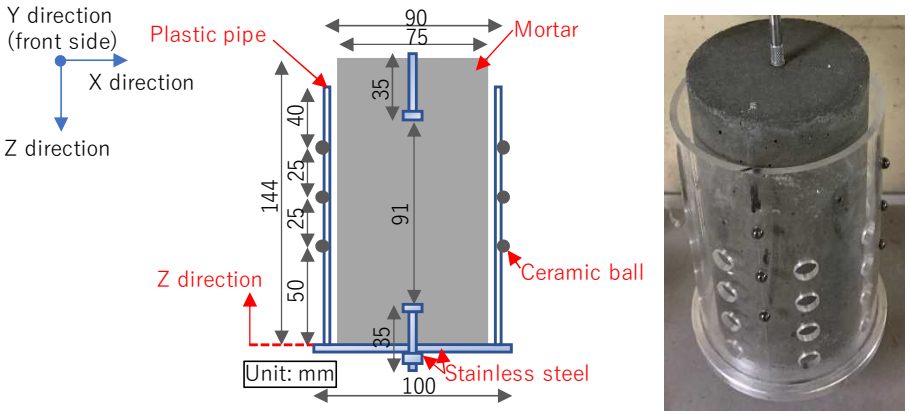

Figure 1. Design and photo of the specimen.

From the measurement results, the apparent length change of the specimen and the internal volumetric strain distribution were calculated. The apparent length change was calculated from the average value of the DVC-derived z-displacement in two cross-sections positioned at ± 20 mm from the centre in the z-direction and dividing the difference between these values by 40 mm. DVC strains were determined from the difference of displacement between adjacent subsets and the local volume strain was calculated by,

$$\varepsilon_{vol} = \varepsilon_x + \varepsilon_y + \varepsilon_z \tag{1}$$

where ε_x, ε_y and ε_z are the normal strains in each direction.

In the X-ray CT images, the intensity indicating the relative value of X-ray absorption is affected by the density and composition. Since the apparent density decreases due to drying from the side of the specimen, the apparent density reduction may be indicated as a decrease in the intensity of the X-ray CT image. Therefore, the moisture content variations were estimated using the intensity distribution in the radial direction over a series of concentric virtual cylinders, centred on the axis of the sample, of 2.5 mm thickness and spanning a height of ± 25 mm from the z-direction centre of the specimen in the X-ray CT images. The average value of the intensity distribution was calculated over each cylinder, and the transition of the average intensity from the surface to the inside of the specimen was calculated.

3 Experimental Results and Discussion

3.1 Shrinkage Strain

Figure 2 shows the shrinkage strain as a function of time obtained from the length change measurements. In the case of the paste, shrinkage strain began to increase from the start of drying and increased linearly until the drying period of 35 days, reaching about 3200 × 10^{-6}. After that, the shrinkage strain increased to about 6000 × 10^{-6} after 134 days of drying and appear to have reach a steady state. The length change for the crushed stone and crushed brick samples was smaller than that of the paste by about 500 × 10^{-6} at 35 days and about 300 × 10^{-6} at 134 days of drying. This is considered to result from the reduced paste volume due to the presence of the stone/brick particles.

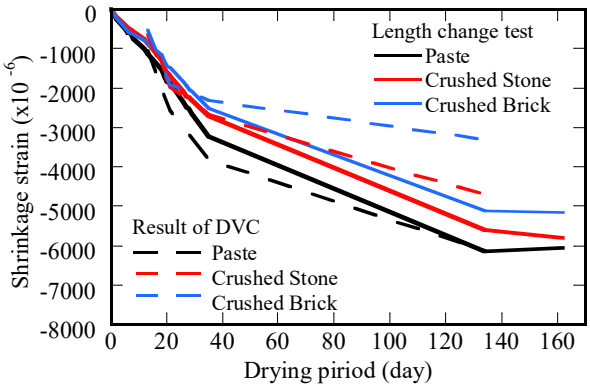

Figure 2. Drying period vs length change.

The apparent length change calculated from the DVC calculation has been included in Figure 2. For the paste, the DVC calculated value was larger than length change value until 35 days of drying period, but it converged to the the same value by the end. On the other hand, for the crushed stone, the DVC calculated length change was about 1000 × 10^{-6} smaller, and for the crushed brick it was about 1700 × 10^{-6} smaller. These tendencies are attributed to the fact that the DVC-based calculation of the length change considered the z-direction displacement over the entire cross section of the specimen and, thus, included changes in the drying condition from the surface as well as expansion due to cracks.

3.2 Observation of X-Ray CT Images

Figure 3 shows XZ cross-section images for each drying time the three samples. For the paste sample, the image intensity is seen to decreased as the drying period increases and the specimen has only a small crack after 35 days of drying. However, for the samples containing a particle, cracks can be seen at early drying stages, which became longer and wider as the drying progresses. Some of the cracks appear to have occurred at positions where there is an abrupt change in the particle surface angle. These cracks are thought to have formed due to constraints through adhesion at the particle surface.

Figure 4 shows the intensity change as a function of position from sample surface for the paste specimen. The intensity can be seen to have decreased near the surface at 5 - 8 days of drying. After about 8 days, the intensity changed significantly near the centre. After 134 days

of drying, the intensity reached almost the same value at the centre as at the surface. As shown in Figure 2, it is expected that the water movement had reached an equilibrium by this time.

Figure 5 shows the intensity rate based on intensity difference between saturation and equilibrium, which can be regarded as the rate of water reduction until reaching equilibrium under this condition. After drying for 5 days, 5 - 50% of the water up to 20 mm depth evaporated through the surface. After 13 days of drying, the water content in the first 5 mm in depth reduced very slowly. On the other hand, the water from more than 5 mm in depth moved rapidly.

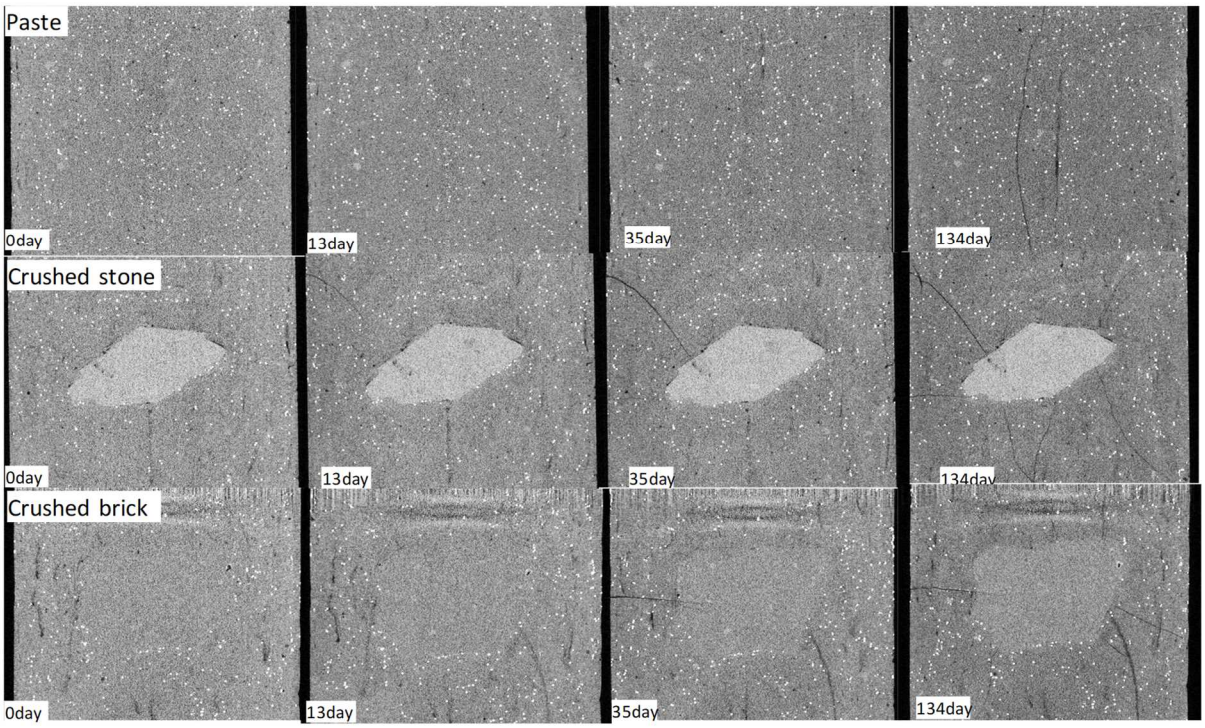

Figure 3. XZ cross-sectional images for each dry material age for paste, crushed stone, and crushed brick.

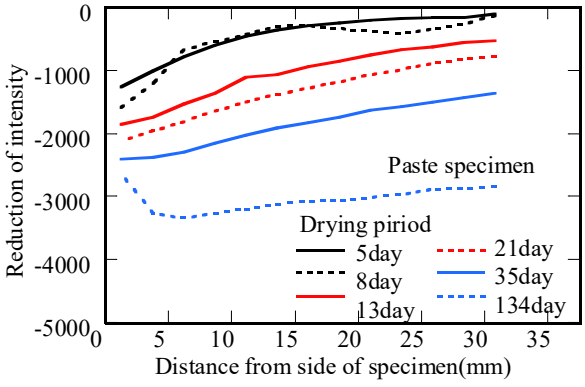

Figure 4. Intensity change from surface.

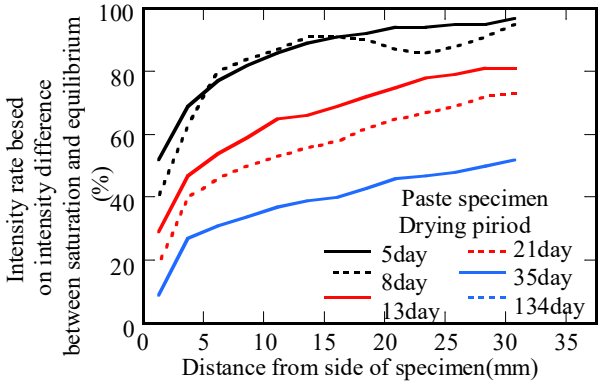

Figure 5. Intensity rate based on intensity difference between saturation and equilibrium.

3.3 Measurement Results Using DVC

Figure 6 shows the volumetric strain distribution inside the 3 specimens based on DVC measurement.

In the case of the paste specimen, there was no particular change over the first 8 days drying period. However, the shrinkage strain region can be seen to extend from the side surface after 13 days and extends to about 20 mm depth from the side at 21 days. From 35 to 134 days of drying, the shrinkage strain region widened on the whole. Localised regions of high dilation indicate the formation of cracks.

In the case of the specimens containing the particles of crushed stone and crushed brick, it can be seen that the shrinkage strain increased with drying, as in the case of paste. However, after 35 days of drying, the shrinkage strain around the particles appears to be smaller than in

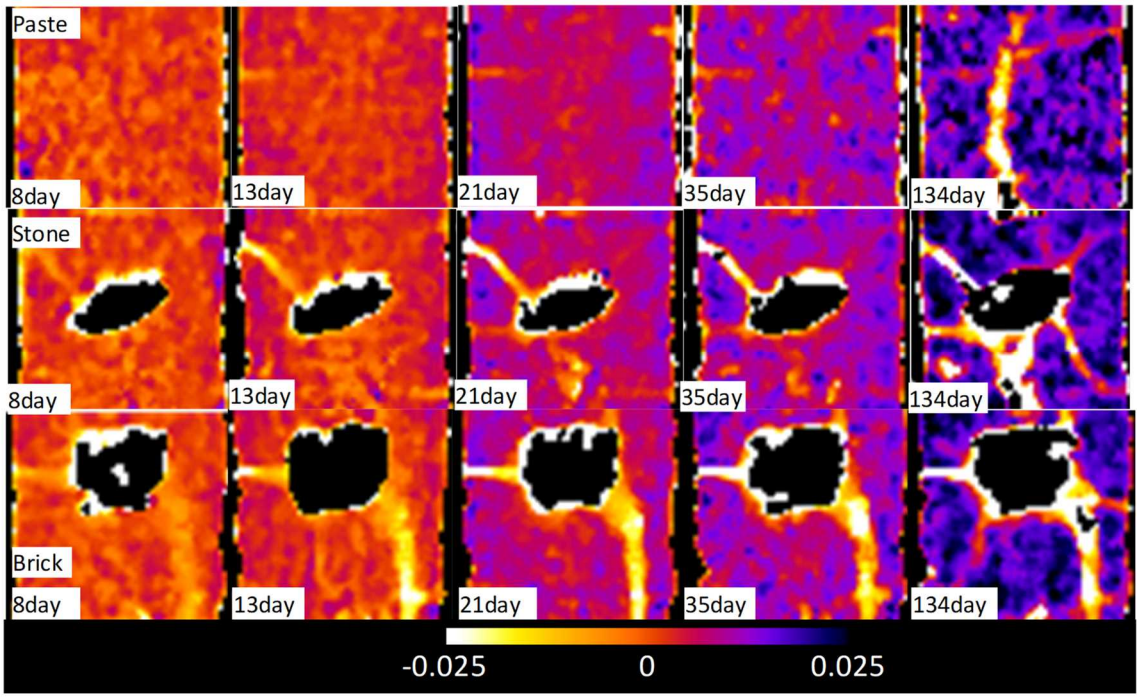

Figure 6. Volumetric strain distribution inside the specimen based on DVC measurement.

other regions. Several areas of minor dilation can be observed after 8 days of drying which evolve to cracks in the later stages, these appear to form from the particle surfaces early in the drying sequence and then their width increases with further drying. It is likely that the cracks initiated at the particle surfaces due to adhesion between the particles and the paste constraining the shrinkage process.

The results presented above show that the shrinkage strain distribution in the cement paste due to drying from the surface could be measured. In addition, the relaxation of the shrinkage strain was observed around particles, but it was obscured, in part, due to the occurrence of cracks. In future work, specimens that do not crack easily, such as mortar specimens, could avoid this issue.

In addition, the results for the paste specimen in Figures 2 and 3 show that a noticeable shrinkage strain occurred when there was over 50 % difference in the moisture content between saturation and equilibrium. This is considered to indicate that relationships between the internal moisture and volumetric strain can be investigated using X ray CT.

4 Summary

The purpose of this study was to perform length change tests on cylindrical specimens of cement paste using X ray CT as a basic study for measuring drying shrinkage distribution inside concrete and to make measurements using X-ray CT images at different stages of drying. The key conclusions from this work are:

- it was shown that the moisture content inside the paste specimen could be estimated from the intensity changes in the X-ray CT images;
- measurement by DVC analysis of the X-ray CT images showed volumetric shrinkage strain distributions inside the paste specimen and the process of cracking due to the restrictions by the aggregates;
- By integrating the results on image intensity changes and the volumetric strain, it will be possible to clarify the coupling of the local the volume change and the local water content change inside a specimen.
- In this study and the given conditions, a noticeable shrinkage strain occurred when the of the difference of moisture content between saturation and equilibrium was above 50 %.

In summary, this study has demonstrated that internal moisture movement and volume changes due to drying can be considered by image measurements on X-ray CT images, which opens the door to further investigations in the future.

Acknowledgment

This work was supported by JSPS KAKENHI Grant Number JP17K06522.

ORCID
Takayuki Fumoto: https://orcid.org/0000-0001-8478-4145
Masaru Abuku: https://orcid.org/0000-0001-7090-4732
Stephen A. Hall: https://orcid.org/0000-0002-5232-4942

Reference

Alexander, MG. (1996). Aggregates and the Deformation Properties of Concrete, ACI Materials Journal, Vol. 93, No. 6, pp. 569-577.

Fumoto, T. (2013). Development of a new Industrial X-Ray CT System and its Application to Compression Test of Polymer Concrete (in Japanese), Journal of Japan Society of Civil Engineers E2 (Materials and Concrete Structures), Vol. 69, No. 2, pp. 182-191. doi: 10.2208/jscejmcs.69.182

Fumoto, T. and Hall, S (2019). Deformation of Mortar around an Aggregate in a Trial Specimen Under Compressive Stress Using X ray CT and DVC, International Conference on Tomography of Materials & Structures.

Fumoto, T., Mizuno, S. and Ozawa, M. (2016). Evaluation of Fire Damage Distribution of Concrete by X-Ray Computed Tomography, Fourth International Conference on Sustainable Construction Materials and Technologies, http://www.claisse.info/Proceedings.htm

Hong, S., Liu, P., Zhang, J., Xing, F. and Dong, B. (2019) Visual & quantitative identification of cracking in mortar subjected to loads using X-ray computed tomography method, Cement and Concrete Composites, Vol. 100, pp. 15-24. doi: 10.1016/j.cemconcomp.2019.03.010

JIS A 1129-3 (2010). Measuring method for length change of mortar and concrete-Part 3: Dial gauge method.

Sant, G. and Weiss, J. (2009). Using X-Ray Absorption to Assess Moisture Movement in Cement-Based Materials, Journal of ASTM International, Vol. 6, No. 9, pp. 1-15, doi: 10.1520/JAI102234

Tudisco E., Andò, E., Cailletaud, R. and Hall, S. (2017). TomoWarp2: A local digital volume correlation code, SoftwareX, Vol.6, pp. 267-270, 2017

Ura, T., Fumoto, T and Takehara, K. (2016). Basic research on accuracy of internal displacement measurement using the newly developed X-ray CT system (in Japanese), Proceedings of the Japan Concrete Institute, Vol.38, No.1, pp.429-434.

Zhanga, W., Zakariaab, M. and Hama, Y (2013). Influence of aggregate materials characteristics on the drying shrinkage properties of mortar and concrete, Volume 49, pp. 500-510.

XV International Conference on Durability of Building Materials and Components
DBMC 2020, Barcelona
C. Serrat, J.R. Casas and V. Gibert (Eds)

Microstructural Evaluation of Durability of Different Cementitious Mixtures in Microbial Induced Corrosion Environments

Chunyu Qiao[1] **and David Rothstein**[2]

[1] DRP, A Twining Company, 80301-Boulder, USA, joe@drpcinc.com

[2] DRP, A Twining Company, 80301-Boulder, USA, petro@drpcinc.com

Abstract. *Sound and durable concrete mixtures are essential in environments where microbial induced corrosion (MIC) is a concern. In this study three concrete mixtures prepared with different binders (ordinary portland cement (OPC), calcium aluminate cement (CAC) and alkali-activated cement (AAC) were petrographically examined after exposure to laboratory-controlled MIC conditions. Analytical techniques included reflected light microscopy, polarized and fluorescent transmitted light microscopy (FLM) and scanning electron microscopy equipped with an energy-dispersive X-ray spectrometer (SEM/EDX). SEM/EDX analyses obtained from the same areas provided information on chemical and mineralogical alteration, while quantitative image analysis with FLM affords an opportunity to quantify the variation in capillary porosity of the paste within alteration zonation. The microscopic observations indicate that the change in normalized capillary porosity coincide broadly with different alteration zones, which are in turn dependent on the type of binder. The OPC concrete shows the greatest deterioration where the paste is largely replaced by gypsum and high capillary porosity is lined to leaching of a calcium. The formation of ettringite densifies the paste and lowers the capillary porosity inboard of the gypsum zone in the OPC concrete. The CAC and AAC mixtures show better resistance to leaching than the OPC mixture, which explains their superior resistance to MIC. These findings are consistent with independent macroscopic observations that indicate the OPC mixture deteriorated more rapidly and severely than the CAC and AAC mixtures.*

Keywords: *Microstructure, Fluorescence Microscopy, Microbial Induced Corrosion, Cementitious Materials, Image Analysis.*

1 Introduction

Microbial Induced Corrosion (MIC) is a significant concern for the condition of concrete infrastructure elements in a variety of environments (Grengg *et al.*, 2015). There is a longstanding recognition that one of the most significant of these environments include wastewater treatment plants (WWTP) and sewer lines, where biological activity from bacteria such as *Acidithiobacillus thiooxidans* lead to rapid rates of deterioration as hydrogen sulfide gas forms sulfuric acid on concrete surfaces above flow lines in sewers and in digesting basins within WWTP (Parker, 1945). In the United States, much of the concrete WWTP infrastructure was built in the 1970s and is approaching its design life of ~ 50 years. Prolonging the use of these facilities and the sustainability of the built infrastructure requires the use of sound and durable repair materials. Because these repairs are often the responsibility of local municipalities with limited financial resources, repair and remediation strategies and materials must also be economically viable.

This study assesses the resistance of three of the most commonly used and widely available (and therefore economic) materials for WWTP facilities: ordinary portland cement (OPC),

calcium aluminate cement (CAC), and alkali activated fly ash and slag (AAC). Optical and electron microscopical methods are used to characterize the response of these materials to MIC simulated in a biogenic corrosion chamber. In particular, we use fluorescence light microscopy to measure the evolution of the capillary porosity of the different binders as they undergo MIC.

2 Mixtures and Experimental Procedures

2.1 Mixtures

This study investigates three concrete mixtures made with different binders: ordinary portland cement (OPC), calcium aluminate cement (CAC), and alkali activated fly ash and slag (AAC). Table 1 summarizes the mixture proportions used to produce specimens that were cast in molds measuring 400 mm by 100 mm by 100 mm. The specimens were demolded after 24 hrs and then cured in a moist room for OPC concrete, in water for CAC concrete and in a regular room for AAC concrete. All of the specimens were cured for 28 days at 22 ± 1 °C. Coupons that measure 100 mm by 70 mm by 70 mm were cut for the biogenic acid exposure testing.

Table 1. Mixture Proprotions of three concretes (kg/m^3).

	OPC concrete	CAC concrete	AAC concrete
Binder	450	450	450
Coarse aggregate	1025	1035	1045
Fine aggregate	730	768	790
Water	160	189	195
w/b	0.36	0.42	0.43

2.2 Experimental Procedures

The exposed surface of each coupon was pre-treated to facilitate the growth of the acidophilic microorganisms prior to placement in the corrosion chamber. This involved spraying the surface with sulfuric acid (H_2SO_4) to reduce the surface pH to 2 – 4. The coupons were then partially submerged in real sewage water in an enclosed chamber at 25 °C and 100% relative humidity (RH). The exposure test lasted for 12 months. The coupons were then removed from the chamber and washed to remove loose material. Measurements of the mass of the coupons before, during and after the exposure testing indicated the most significant mass loss and deterioration on a macroscopic scale in the OPC, followed by the CAC and then the AAC.

A slab representing a cross section of each coupon was cut, lapped and polished with progressively finer diamond-embedded pads following procedures outlined in ASTM C457. The polished slabs were oven dried overnight at ~ 40°C and examined using Nikon® SMZ-25 stereomicroscope following ASTM C856.

A billet measuring 40 mm by 25 mm in area was cut from the remaining portion of each coupon. The billets were rinsed in an aqueous solution, oven dried overnight at ~ 40°C and then vacuum impregnated with an epoxy containing a fluorescent dye. Thin sections were prepared from the impregnated billets using a Pelcon® Automatic Thin Section Machine. The thin sections were examined using a Nikon® E-Pol 600 petrographic microscope. Images were obtained in fluorescence mode and image analysis software (Image J) was used to create gray-scale images and make measurements of the capillary of the paste.

Another billet impregnated with fluorescent epoxy was cut and polished for examination using a FEI™ Quanta 250 Environmental Scanning Electron Microscope (ESEM) coupled with an EDAX® Apollo X Silicon Drift energy dispersive X-ray spectrometer (EDX). The specimens were examined under low vacuum conditions (~ 70 Pa) with an accelerating voltage of 15 kV, a spot size of 5 and a working distance of ~ 10 mm.

3 Results and Discussions

3.1 OPC Concrete

Leemann *et al.* (2006) used fluorescence microscopy to investigate variations in porosity across the interfacial transition zone (ITZ) in self consolidated concrete. A similar analysis is performed in this paper to measure changes in capillary porosity across alteration zones. As a benchmark, the grey level histograms of paste (in Fig. 1a) and a void (in Fig.1b) were analyzed and statistically fitted assuming normal distributions, as shown in Fig. 1c. Since the void in Fig. 1b is filled with epoxy containing a fluorescent dye and has 100% porosity, a "normalized capillary porosity" of the paste is proposed by normalize the mean grey level of the paste to that of the air void. The standard deviation is used as the error bar, as shown in Fig. 2g.

Optical and scanning electron microscopical examination of the sample revealed several distinct mineralogical and chemical alteration zones (Fig. 2a-2e). The alteration zones are as follows, moving inward from the exposed surface: (a) coarse-grained gypsum; (b) medium-grained gypsum; (c) a transition zone with ettringite and iron oxide staining; (d) a carbonated zone; and (e) a zone of calcium leaching. Fluorescent transmitted light microscopy reveals changes in the capillary porosity of the paste in these zones (Fig. 2f-2g).

The alteration of the OPC concrete is typical of biogenic sulfuric acid attack commonly observed in OPC concretes exposed to MIC. Menéndez *et al.* (2013) described a sequence of reactions typical of these environments. The formation of gypsum ($CaSO_4 \cdot 2H_2O$) consumes calcium hydroxide ($Ca(OH)_2$) and calcium silicate hydrates (CSH) in the paste matrix. The leaching of cementitious phases and deposition of gypsum produces a higher capillary porosity in Zone (a) and Zone (b). In particular, because Zone (a) is in contact with an acidic solution, there is widespread dissolution of CSH and a dramatic increase in capillary porosity (Fig. 2g). Ettringite forms in Zone (c) because the pH sufficiently high to stabilize it this far inboard of the exposed surface. The iron staining in Zone (c) is due to the oxidization of iron-bearing accessory minerals in the aggregate that is mainly basalt and andesite. These reactions are expansive, which lowers the capillary porosity inboard of the outer alteration zones, compared to that of the intact paste (Fig. 2g). The carbonated zone, which is relatively thin, also shows decreased capillary porosity. Inboard of the carbonated zone, the leaching of Ca^{2+} in Zone (e) results in a slight increase in capillary porosity, compared to the intact paste (Fig. 2g).

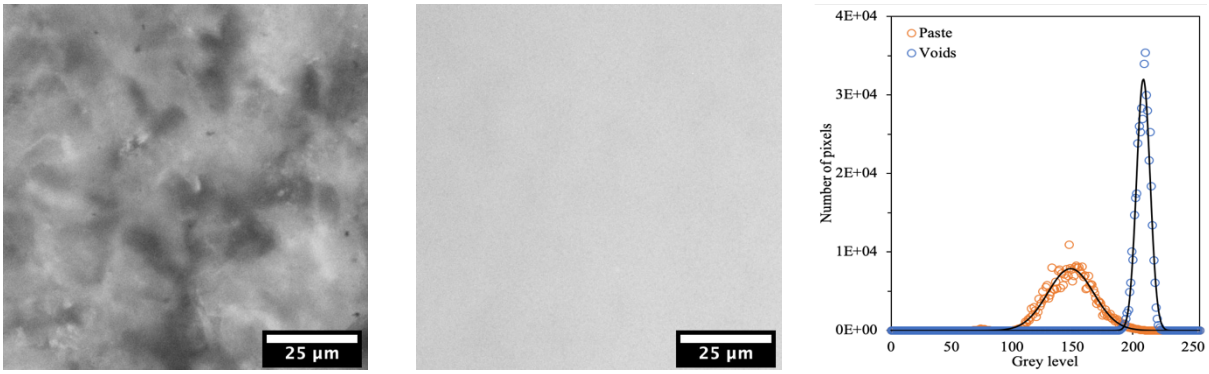

Figure 1. Determination of normalized capillary porosity in OPC: (a) paste; (b) voids; (c) grey level histograms

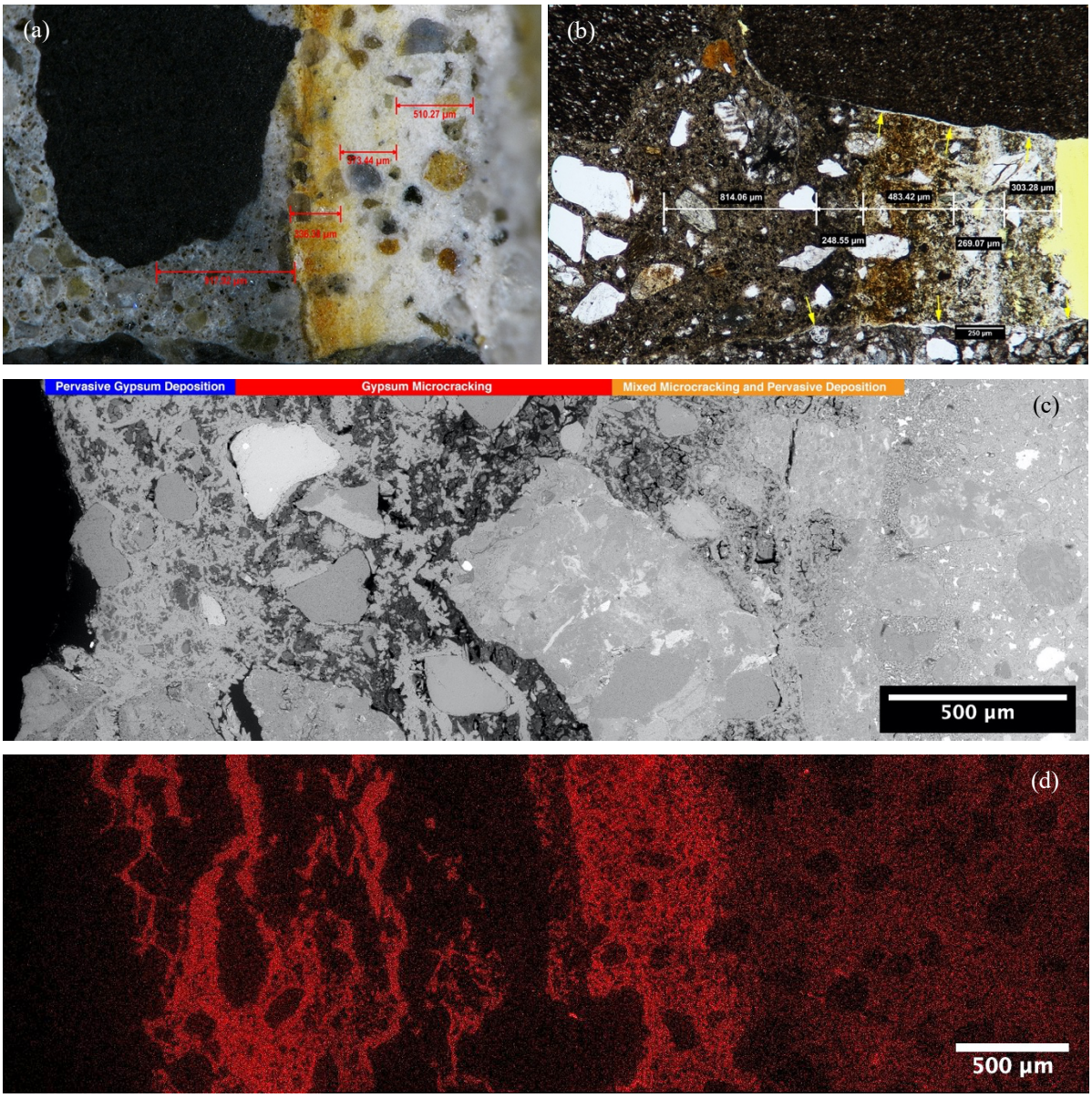

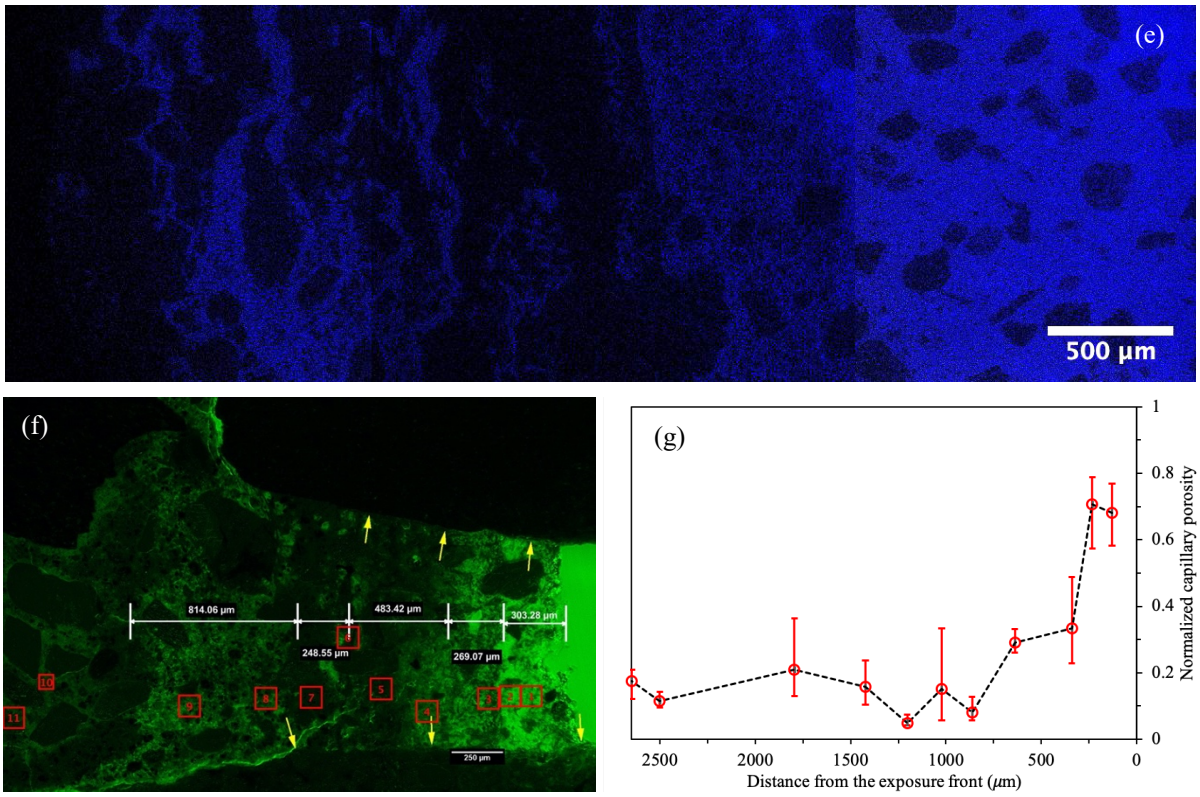

Figure 2. Alteration zones in OPC. (a) Reflected light photomicrograph of the polished surface; (b) transmitted plane-polarized light photomicrograph of the thin section; (c) backscatter electron image of alteration zones; (d)-(e) EDX elemental maps for S and Ca, respectively; (f) transmitted fluorescent light photomicrograph of the thin section; (g) Line plot showing changes in grey level and capillary porosity of the paste in the alteration zones

3.2 CAC Concrete

Fig. 3a-3d shows the alteration of the CAC concrete exposed to MIC revealed by optical and electron microscopy. The alteration zones are as follows (inwards from the exposure surface): (a) a zone of pervasive cracking with deposition of gypsum (in Fig. 3a), which was lost on the thin section during the sample preparation (in Fig.3b); (b) a transition zone that contains gypsum, ettringite and iron oxide staining; and (c) sulfate diffusion zone. As shown in Fig. 3f, the capillary porosity of the paste decreases from the intact paste to Zone (b). This indicates the sulfate attack lowers the capillary porosity to some extent before there is sufficient internal expansion to crack the concrete.

The main hydration products of the CAC concrete depend on the curing conditions (RH and T), w/b ratio and curing time (Schmitt *et al.*, 2000). The main hydration products of CAC concrete (cured in water at 22 ± 1 °C) include hydrogarnet ($3CaO{\cdot}Al_2O_3{\cdot}6H_2O$, C_3AH_6) and gibbsite ($Al(OH)_3$, AH_3). Khan *et al.* (2019) described the alteration of CAC in such environments. The most significant reactions involve the formation of gypsum and gibbsite from hydrogarnet in the presence of sulfuric acid. These reactions are expansive and lead to cracking in Zone (a). In the transition Zone (b), gypsum reacts with hydrogarnet to form ettringite (Khan *et al.*, 2019), which densifies the microstructure of the paste before the internal stress cracks the concrete. This explains the lower capillary porosity in Zone (b) and Zone (c),

compared to the intact paste (Khan *et al.*, 2019; Nishikawa *et al.*, 1992).

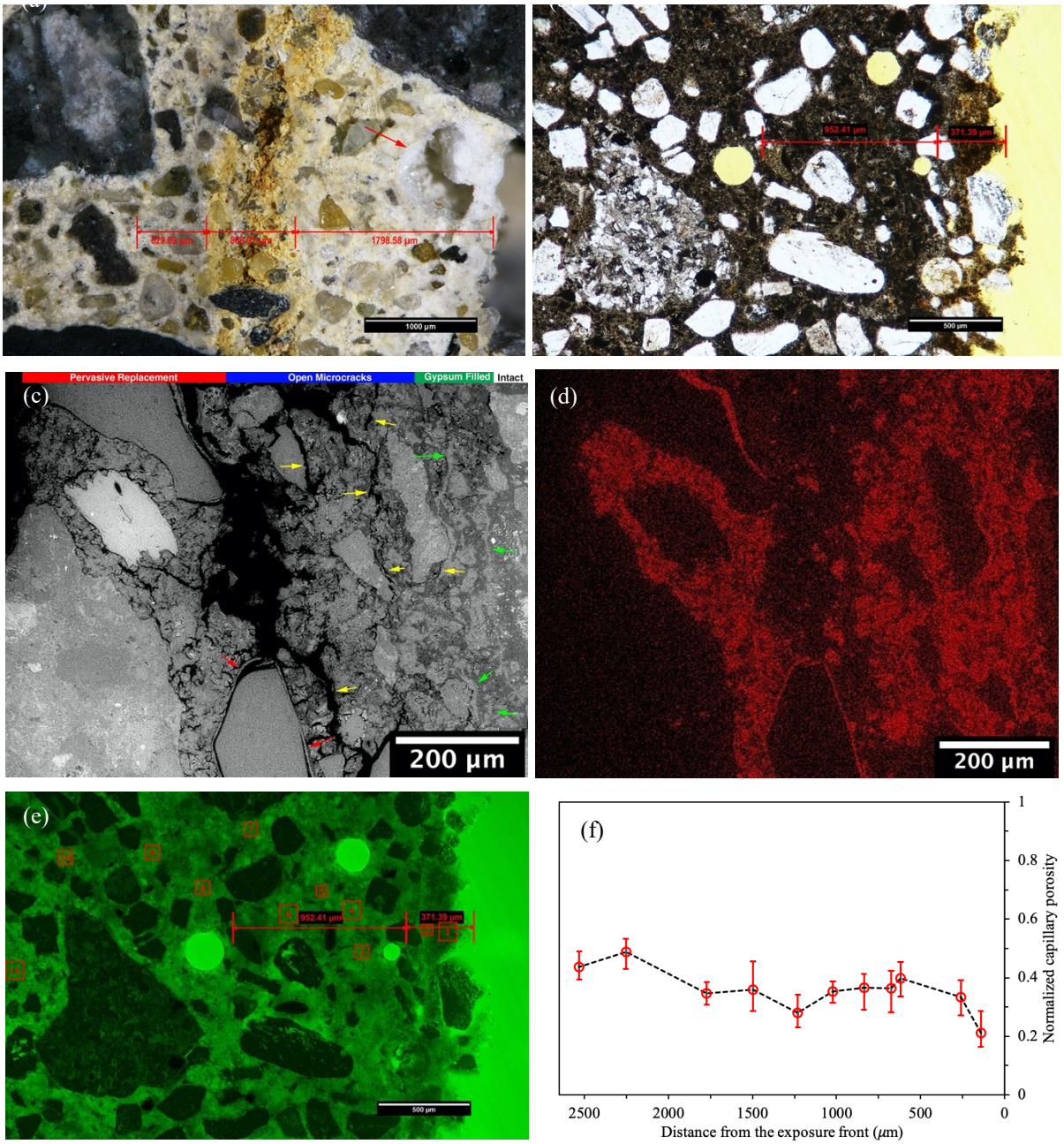

Figure 3. Alteration zones in the CAC concrete. (a) Reflected light photomicrograph of the polished surface; (b) transmitted plane-polarized light photomicrograph of the thin section; (c) backscatter electron image of alteration zones; (d) EDX elemental map for S; (e) transmitted fluorescent light photomicrograph of thin section; (f) Line plot showing changes in grey level and capillary porosity of the paste in the alteration zones.

3.3 AAC Concrete

Fig. 4a-4d shows the alteration zones observed in the AAC concrete exposed to sulfate attack. Similar to the alteration observed in CAC concrete, the alteration in AAC concrete involves the

following: (a) a zone of pervasive gypsum deposition and cracking; (b) a transition zone that contains a mixture of gypsum, ettringite and iron oxide staining; and (c) a sulfate diffusion zone. Calcium (alkali) aluminosilicate hydrate (C-(N)-A-S-H) and monosulfate (AFm) are two of the main hydration products in AAC concrete (Myers *et al.*, 2017). These react with H_2SO_4 to form gypsum, which results in pervasive gypsum deposition, leaching of the paste and cracking in Zone (a). Higher capillary porosity was observed in Zone (a) compared to that of the intact paste (Fig. 4e-4f). In the transition Zone (b) and diffusion Zone (c), the formation of ettringite from AFm densifies the microstructure and a lower capillary porosity, compared to that of the intact paste, is observed.

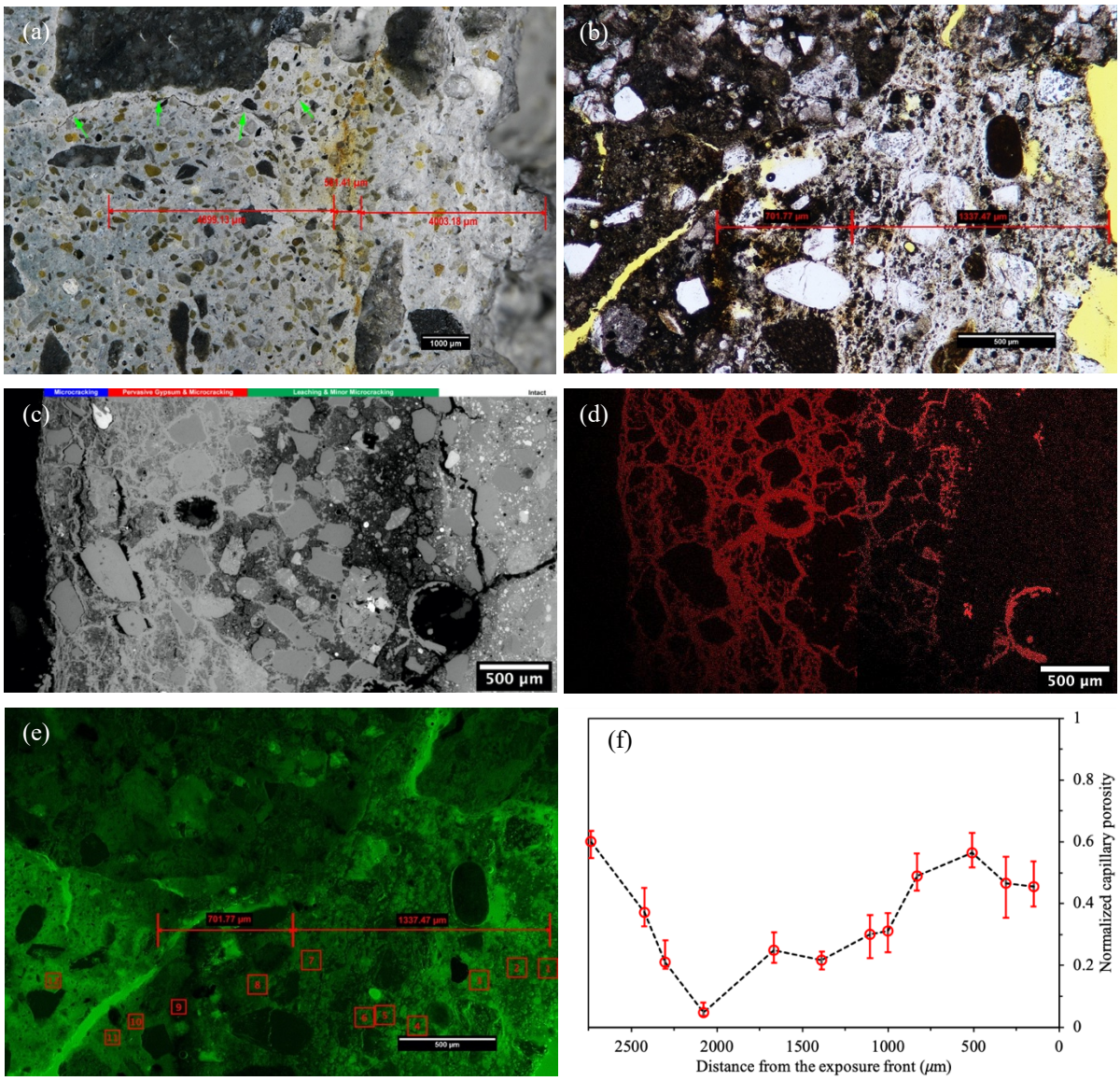

Figure 4. Observations of alteration zones in the AAC. (a) Reflected light photomicrograph of the polished surface; (b) transmitted plain-polarized light photomicrograph of the thin section; (c) Backscatter electron image of alteration zones; (d) EDX elemental map for S; (e) transmitted fluorescent light photomicrograph of the thin section; (f) Line plot showing changes in grey level and capillary porosity of the paste in the alteration zones.

4 Conclusions

Petrographic examination of three concrete mixtures prepared with different binders and subjected to MIC under controlled laboratory conditions provides insight toward the durability of these materials in WWTP environments. Observations obtained from optical and electron microscopy clearly delineate alteration zones characterized not only by distinct mineralogy, but also by distinct changes in the capillary porosity or density of the paste. The OPC mixture shows the great deterioration where the outer alteration zones show both increased capillary porosity of the paste associated with the leaching of $Ca(OH)_2$ and CSH and zones of significant cracking associated with the pervasive deposition of gypsum. Inboard of these zones the formation of ettringite actually densifies the OPC paste. The CAC and AAC mixtures show greater resistance to the sulfuric acid conditions associated with MIC than the OPC mixture. The outermost alteration zones in these mixtures have markedly lower capillary porosity than the OPC mixture. As such, the alteration zones are more cohesive and remain adhered to the intact paste, which explains why these samples show lower mass loss in macroscopic testing. The higher resistance is consistent with better resistance to leaching than the OPC mixtures, which is in turn due to the lack of $Ca(OH)_2$ and CSH in these materials.

Acknowledgements

The authors thank Mr. Gaines Green for the preparation of samples for optical and scanning electron microscopy, Mr. James Aldred for comments on a report describing some aspects of the work presented here and Mr. Stephen Grace for providing background information regarding the biogenic corrosion testing.

ORCID:

Chunyu Qiao: http://orcid.org/0000-0002-2583-5296
David Rothstein: http://orcid.org/0000-0002-5677-3139

References

Grengg, C., Mittermayr, F., Baldermann, A., Böttcher, M. E., Leis, A., Koraimann, G., Grunert, P. and Dietzel, M. (2015). Microbiologically induced concrete corrosion: A case study from a combined sewer network. *Cement and Concrete Research, 77*, 16-25. doi:10.1016/j.cemconres.2015.06.011

Khan, H. A., Castel, A., Khan, M. S. H. and Mahmood, A. H. (2019). Durability of calcium aluminate and sulphate resistant Portland cement based mortars in aggressive sewer environment and sulphuric acid. *Cement and Concrete Research, 124*, 105852. doi:10.1016/j.cemconres.2019.105852

Leemann, A., Münch, B., Gasser, P. and Holzer, L. (2006). Influence of compaction on the interfacial transition zone and the permeability of concrete. *Cement and Concrete Research, 36*(8), 1425-1433. doi:10.1016/j.cemconres.2006.02.010

Menéndez, E., Matschei, T. and Glasser, F. P. (2013). Sulfate Attack of Concrete. In M. Alexander, A. Bertron, & N. De Belie (Eds.), *Performance of Cement-Based Materials in Aggressive Aqueous Environments: State-of-the-Art Report, RILEM TC 211 - PAE* (pp. 7-74). Dordrecht: Springer Netherlands.

Myers, R. J., Bernal, S. A. and Provis, J. L. (2017). Phase diagrams for alkali-activated slag binders. *Cement and Concrete Research, 95*, 30-38. doi:10.1016/j.cemconres.2017.02.006

Nishikawa, T., Suzuki, K., Ito, S., Sato, K. and Takebe, T. (1992). Decomposition of synthesized ettringite by carbonation. *Cement and Concrete Research, 22*(1), 6-14. doi:https://doi.org/10.1016/0008-8846(92)90130-N

Parker, C. D. (1945). THE CORROSION OF CONCRETE. *Australian Journal of Experimental Biology and Medical Science, 23*(2), 81-90. doi:10.1038/icb.1945.13

Schmitt, N., Hernandez, J.-F., Lamour, V., Berthaud, Y., Meunier, P. and Poirier, J. (2000). Coupling between kinetics of dehydration, physical and mechanical behaviour for high alumina castable. *Cement and Concrete Research, 30*(10), 1597-1607. doi:10.1016/S0008-8846(00)00342-2

XV International Conference on Durability of Building Materials and Components
DBMC 2020, Barcelona
C. Serrat, J.R. Casas and V. Gibert (Eds)

Monitoring the Early-Age Shrinkage Cracking of Concrete with Superabsorbent Polymers by Means of Optical Fiber (SOFO) Sensors

José R. Tenório Filho[1,2], Didier Snoeck[1] and Nele De Belie[1]

[1] Magnel Laboratory for Concrete Research, Department of Structural Engineering, Faculty of Engineering and Architecture, Ghent University, Technologiepark Zwijnaarde 60, B-9052 Ghent, Belgium; email: roberto.tenoriofilho@ugent.be, didier.snoeck@ugent.be, nele.debelie@ugent.be

[2] SIM vzw, Technologiepark 48, Zwijnaarde B-9052 Ghent, Belgium

Abstract. *Concrete structures are subjected to shrinkage since the moment when the water makes contact with the cement. From that moment on, depending on the concrete composition and its curing conditions, chemical, autogenous and drying shrinkage might increase the risk of early-age cracking. Once a crack is formed, it may become the preferential path for the ingress of many aggressive agents inside the structure increasing the probability of damage due to corrosion, carbonation and other mechanisms. The use of superabsorbent polymers (SAPs) has been extensively studied to reduce the shrinkage cracking risk in mortar specimens by acting as internal curing agent to mitigate autogenous shrinkage. In this paper, a commercially available SAP was investigated as shrinkage reducing agent by means of internal curing in concrete specimens. The shrinkage of the concrete was monitored for 28 days with both a demountable mechanical strain gauge (DEMEC) and optical fiber sensors (SOFO). The SAP-containing concrete showed a complete mitigation of autogenous shrinkage during 28 days of measurement, for both methods. The SOFO sensors showed the occurrence of cracks after 7 days for the reference mixture, while for the SAP containing mixture, no crack was identified during the 28 days of measurements.*

Keywords: *Early-Age Cracking, Superabsorbent Polymers, Internal Curing, SOFO Sensors.*

1 Introduction

Shrinkage in concrete structures has been the focus of many studies, and lately, a lot of attention has been given to autogenous shrinkage. The autogenous shrinkage occurs in all kinds of concrete structures at different levels. In ordinary concrete structures (with water-to-cement ratio above 0.42) it is not such a prominent phenomenon but it may increase the risk of cracking, especially when supplementary cementitious materials are used (Jian *et al*., 2014; Wu *et al*., 2017). On the other hand, it may be the main cause of early-age cracking in systems with water-to-cement/binder ratio lower than 0.42 (ultra-high performance concrete, for example) (Jensen and Hansen, 2001a; Jensen and Hansen, 2001b).

Recently, a lot of research has been developed aiming to use the SAPs to reduce/mitigate shrinkage in cementitious materials, most of it at mortar or paste level (Jensen, 2008; Snoeck, 2015; Snoeck and De Belie, 2015; Snoeck *et al*., 2017; Tenório Filho *et al*., 2018; De Meyst *et al*., 2019; Snoeck *et al*., 2018; Geiker *et al*., 2004) and some in high performance concrete compositions (HPC) (Jian *et al*., 2014; Wu *et al*., 2017; Craeye *et al*. 2011; Pierard *et al*., 2006), all showing that a dosage of SAPs in the range of 0.2-0.6% with respect to the cement mass should be enough to considerably reduce or complete mitigate the deformation due to autogenous shrinkage.

Superabsorbent polymers (or hydrogels) are a natural or synthetic water-insoluble 3D network of polymeric chains cross-linked by chemical or physical bonding. They possess the ability to take up a significant amount of fluids from the environment (in amounts up to 500 times their own weight) (Mechtcherine and Reinhardt, 2012). Once in contact with the mixing water of the cementitious material, the SAPs absorb and retain a certain amount of the water (depending on their absorption capacity), later on acting as water reservoirs for the system, keeping its levels of internal relative humidity high for a considerable time frame (depending on the SAP used, even up to 28 days (Snoeck *et al*., 2017)).

Up to now, most of the studies investigating the deformation due to autogenous shrinkage of concrete have relied on test methods based on linear measurements performed with the use of length transducers placed on the top surface of prismatic specimens, with the measurements starting at different times (for example at 6 h, 9 h and 24 h) (Craeye *et al*., 2011; Pierard *et al*., 2006; Sven and Reinhardt, 2006; ASTM, 2017; Barcelo *et al*., 2005).

For the case of concrete structures, the crack formation or presence of internal voids and discontinuities might lead to different responses in different locations. For that reason, the use of long-gauge deformation sensors allows a more global and precise understanding of the material/structure under investigation.

In this paper, long-gauge deformation sensors based on low-coherence interferometry in optical fiber sensors are used to investigate the influence of superabsorbent polymers on the autogenous shrinkage of concrete mixtures. The material response due to shrinkage deformation is also evaluated by a more traditional approach, using a demountable mechanical strain gauge (DEMEC).

2 Experimental Program

2.1 Materials and Characterization of the SAP

The experimental program consisted of the shrinkage measurement of concrete specimens with and without SAPs by means of manual measurements with a demountable mechanical strain gauge (DEMEC) and automatic measurements with optical fiber sensors (SOFO).

All tests were performed on concrete mixtures produced with cement type CEM III-B 42.5N – LH/SR (CBR, Belgium); a polycarboxylate superplasticizer (Tixo, 25% conc., BASF, Belgium, at a constant dosage of 1.8 % in relation to the cement mass); sea sand 0/4 (absorption of 0.4% in mass); sea sand 0/3 (absorption of 0.3% in mass); limestone 2/20 (absorption of 0.5% in mass) and a commercial superabsorbent polymer identified as SAP1. More details about the compositions of the concrete mixtures are given in Table 1.

SAP1, made by SNF Floerger (France) is a cross-linked acrylate copolymer produced by bulk polymerization and has a mean particle size (d_{50}) of 360 μm. It has been previously studied as internal curing agent and self-sealing/healing promoter for mortar mixtures (Snoeck, 2015; Tenório Filho *et al*., 2018).

Table 1. Composition of the studied concrete mixtures, values in kg/m^3.

Mixture	Cement	Sand 0/3 - Sand 0/4	Limestone 2/20	Superplasticizer	SAP	Additional water	w/c$_{(total)}$ [-]
REF0.46	356	421 - 343	1086	6.35	0	0	0.46
REF0.57	340	406 – 331	1046	6.12	0	0	0.57
C_SAP1	340	406 – 331	1046	6.12	1.70	37.42	0.57

Dry materials were first mixed for 1 min (including SAPs, when present), then the mixing water and superplasticizer were added and mixed for an additional 2 min. When SAPs were present, the additional entrained water was added during the third minute and the mixing proceeded for an additional 2 min. The total mixing time was 3 min for the reference mixture and 5 min for the SAP-containing mixtures. Prior to the concrete mixing and testing, the superabsorbent polymers were tested to assess their absorption capacity. The filtration method was performed in compliance with Snoeck *et al*. (2018). The SAPs were tested in demineralized water and in a cement filtrate solution prepared with the same cement used to produce the concrete mixtures. The cement filtrate was produced with cement and demineralized water at a proportion of 1:5 in mass.

The absorption capacity was also studied in cement pastes and concrete mixtures by means of slump tests. The measurements were performed exactly 10 min after the first contact of the SAPs with the mixing water.

2.2 Shrinkage Measurement

For the measurements with the DEMEC, for each mixture, four prismatic specimens (100 mm x 100 mm x 400 mm) were cast and cured for 23 h in a room with controlled atmosphere of 20 ± 2 °C and RH > 95%. Right after casting, the free surface of the specimens was covered with a layer of plastic foil, attached to the mold with a thin layer of vaseline to improve the adhesion and prevent drying.

After the curing period, the demolded specimens were wrapped with aluminum tape to avoid moisture exchange with the environment, in this way, reducing the effects of drying shrinkage. Two measuring points were glued to the surfaces of the specimens (except for the troweled surface due to the fact of shape irregularities that could hinder the measurements), placed 200 mm apart on the central line of the specimens' surface. In total, each specimen had three measuring surfaces. The measurements were performed once per day for 28 days and started 24 h after the first contact of cement with the mixing water. The test was conducted in a room with a controlled atmosphere of 20 ± 2 °C and 60 ± 5% RH.

For the measurements with the SOFO sensors, given the availability and the costs, only REF0.46 and the SAP-containing mixture were tested. The sensors used were produced by SMARTEC (Switzerland). The sensors consist of an active part, that measures the deformation, and a passive part, which transmits the data to a reading unit (Figure 1). The sensors used in

this investigation had an active length of 250 mm and a passive length of 10 m.

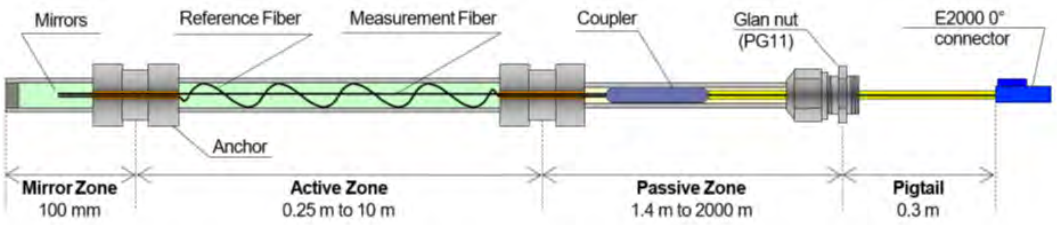

Figure 1. Illustration of the sensor. Courtesy of SMARTEC.

The specimens used for the measurements with the sensors had the same dimensions as the ones used with the DEMEC device (100 mm x 100 mm x 400 mm). The sensors were embedded in the concrete, attached to a steel rebar with a diameter of Ø 6 mm and length of 440 mm, placed at the middle height of the mold in order to ensure a correct position of the sensors. After casting and during the test, the specimens were covered with plastic foil to prevent drying. The specimens were cured for 23 h in a room with controlled atmosphere of 20 ± 2 °C and RH > 95%.

The measurements were performed automatically, every 10 min for 28 days, starting 30 min after concrete mixing. The tests were performed in a room with a controlled atmosphere of 20 ± 2 °C and 60 ± 5% RH. The values of strain were zeroed at the fluid-solid transition point. The transition point was determined considering the moment where the rate of autogenous strain became zero (Tenório Filho *et al*., 2019), corresponding to the knee point in measuring autogenous shrinkage.

3 Results and Discussion

Figure 2 shows the water uptake (g of water/g of SAP) of the SAPs in demineralized water, cement filtrate solution, and concrete.

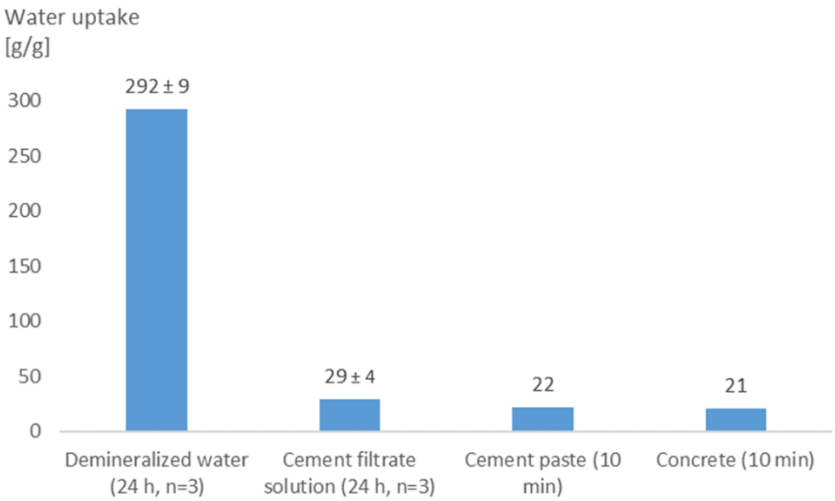

Figure 2. Water uptake [g/g SAP] of the SAP in demineralized water, cement filtrate solution, cement paste and concrete.

The absorption capacity is noticed to decrease from demineralized water to cementitious fluids, which was already expected due to presence of monovalent and divalent ions (i.e. Na^+, K^+, Ca^{2+}) in the cement filtrate, cement paste and concrete (Kang *et al*., 2017; Kang *et al*., 2018). The results with the cement paste show that such method can be used as a suitable estimation for the absorption capacity of the SAPs in concrete.

Figure 3 shows the shrinkage strain measured with the DEMEC for the mixtures REF0.46, REF0.57 and C_SAP1. The reference mixtures shows both only shrinkage during the whole time of tests and the strain values are comparable to those found in literature for concrete mixtures with similar composition and the same type of cement (Lura *et al*., 2001). On the other hand, the SAP-containing mixture show a complete mitigation of the shrinkage strain during the 28 days.

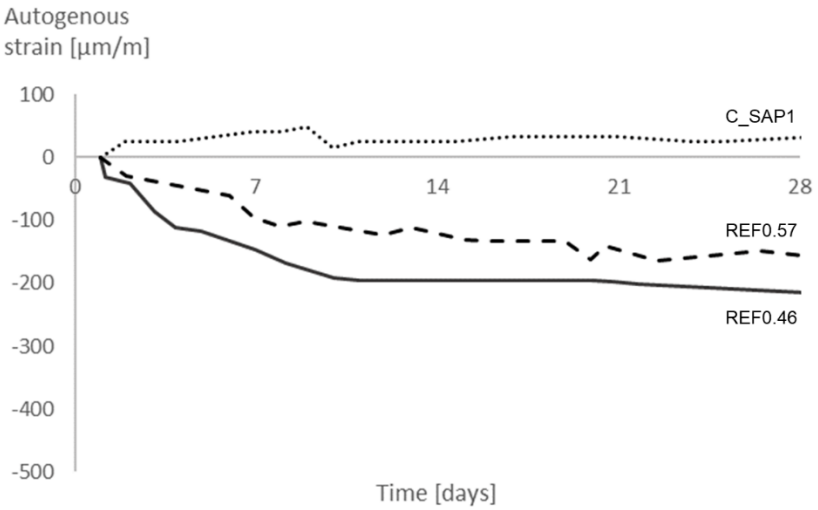

Figure 3. Autogenous strain of concrete specimens measured with DEMEC. Measurements started 24 h after mixing. The lines represent the average values for two specimens with three measurements per specimen. The maximum standard deviation found was ± 50 µm.

When comparing the mixtures REF0.57 and C_SAP1, even though they were produced with the same water-to-cement ratio (0.57), the mixture REF0.57 is not able to mitigate the shrinkage strain (but only to reduce it in comparison with the mixture REF0.46).

In such mixture, the total water content is available for being used in the hydration from the beginning, which might increase the effects of the chemical shrinkage. With the use of SAPs, part of this water is stored inside the polymer particles being released at the appropriate time to mitigate the autogenous shrinkage. In this way, the used SAPs can be considered very efficient to be used as internal curing agent, completely mitigating the autogenous shrinkage and preventing the formation of early-age cracks (which was also verified with the use of the SOFO sensors).

Figure 4 shows the autogenous strain measured with the SOFO sensors for the mixtures REF0.46 and C_SAP1. As also observed in Figure 3, the SAP-containing mixture shows a complete mitigation of shrinkage while the reference mixture (REF0.46) only shows shrinkage. Another interesting feature noticed is the existence of some “jumps” in the graph that are only

observed for the reference mixture. These "jumps" are assumed to be indications of crack-formation.

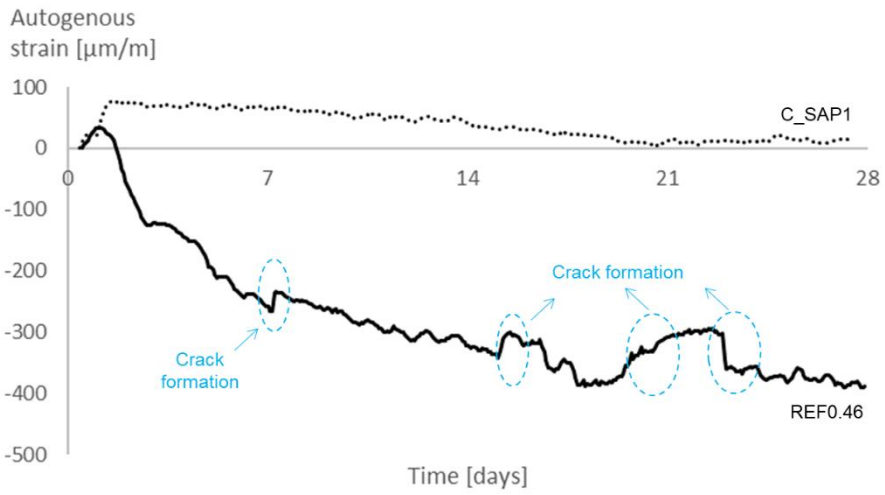

Figure 4. Autogenous strain of concrete specimens measured with SOFO sensors. Measurements zeroed at the fluid-solid transition point for each mixture. Crack formation is also indicated.

To verify whether the samples possessed internal micro-cracking, after the 28 days of measurements, the specimens were cut and investigated by means of an optical microscopy. This analysis confirmed the existence of small cracks (up to 50 µm) in the reference mixture along the length of the sensor (Figure 5). The same cracks were not observed in the mixture C_SAP1. Also, no debonding was noticed between the sensors and the cement matrix.

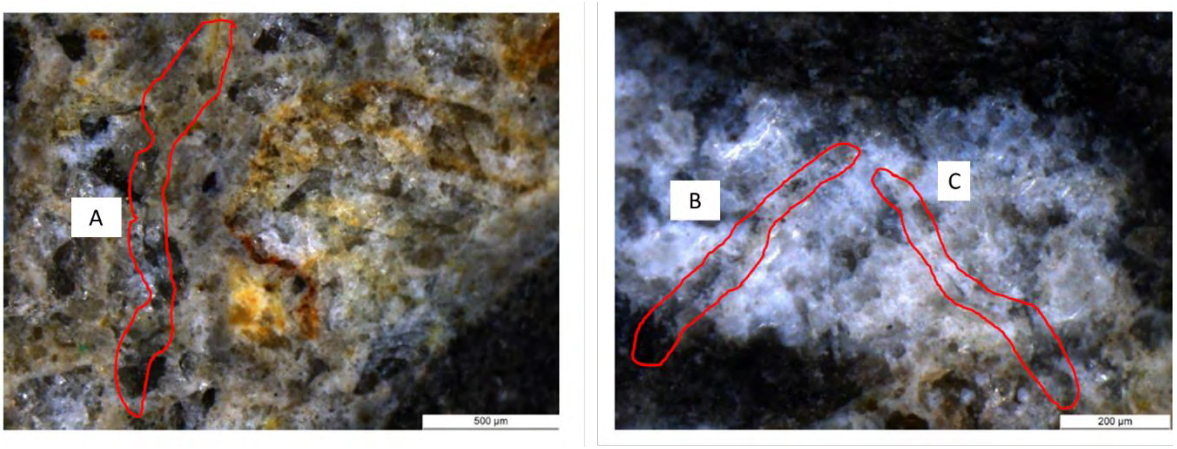

Figure 5. Micro-cracks identified in the cement matrix in the surroundings of the sensor.

4 Conclusions

- The SAP-containing mixture was able to show a significant reduction in the shrinkage strain in comparison to the reference mixtures with and without additional water, fully mitigating the autogenous shrinkage;
- Both the DEMEC and the SOFO sensors efficiently captured the effect of the SAPs in

comparison to the reference mixture, but the absolute values of strain are different. This was the case especially for the reference mixture, as a consequence of the different coverages used to avoid drying;
- The optical fiber sensors were able to provide an indication for the moment of crack formation without the need of additional tests or indirect measurements;
- While they might represent a costly investment, in comparison with other techniques, the use of the embedded sensors brings more advantages, higher level of precision and reduced person-hours in the monitoring of shrinkage deformation in the concrete, which can be even more valuable when considering the monitoring of larger scale specimens and structures.

Acknowledgements

The authors thank Tom Stulemeijer, Dieter Hillewaere and Tommy De Ghein for the help with the experimental work. As a Postdoctoral Research Fellow of the Research Foundation-Flanders (FWO-Vlaanderen), D. Snoeck would like to thank the foundation for the financial support (12J3620N).

Funding

The work has been financed by SIM program SHE (Engineered Self-Healing Materials) within the ICON project iSAP (Innovative SuperAbsorbent Polymers for crack mitigation and increased service life of concrete structures).

ORCID

José Roberto Tenório Filho: https://orcid.org/0000-0002-3135-5694
Didier Snoeck: https://orcid.org/0000-0001-9427-6312
Nele De Belie: https://orcid.org/0000-0002-0851-6242

References

Barcelo, L., M. Moranville and B. Clavaud (2005). *Autogenous shrinkage of concrete: a balance between autogenous swelling and self-desiccation*. Cement and Concrete Research, 35(1): p. 177-183.

De Meyst, L., *et al*. (2019). *Parameter Study of Superabsorbent Polymers (SAPs) for Use in Durable Concrete Structures*. Materials, 12(9).

Geiker, M.R., D.P. Bentz and O.M. Jensen (2004). *Mitigating autogenous shrinkage by internal curing*. High-Performance Structural Lightweight Concrete, 218: p. 143-154.

International, A., ASTM C157 / C157M-17 (2017). *Standard Test Method for Length Change of Hardened Hydraulic-Cement Mortar and Concrete*. West Conshohocken.

Jensen, O.M. and P.F. Hansen (2001a). *Autogenous deformation and RH-change in perspective*. Cement and Concrete Research, 31(12): p. 1859-1865.

Jensen, O.M. and P.F. Hansen (2001b). *Water-entrained cement-based materials I. Principles and theoretical background*. Cement and Concrete Research, 31(4): p. 647-654.

Jensen, O.M. (2008). *Use of Superabsorbent Polymers in Construction Materials*. Microstructure Related Durability of Cementitious Composites, Vols 1 and 2, 61: p. 757-764.

Jiang, C.H., *et al*. (2014). *Autogenous shrinkage of high performance concrete containing mineral admixtures under different curing temperatures*. Construction and Building Materials, 61: p. 260-269.

Kang, S.H., S.G. Hong and J. Moon (2017). *Absorption kinetics of superabsorbent polymers (SAP) in various cement-based solutions*. Cement and Concrete Research, 97: p. 73-83.

Kang, S.H., S.G. Hong and J. Moon (2018). *Importance of monovalent ions on water retention capacity of superabsorbent polymer in cement-based solutions.* Cement & Concrete Composites, 88: p. 64-72.

Lura, P., K. van Breugel and I. Maruyama (2001). *Effect of curing temperature and type of cement on early-age shrinkage of high-performance concrete*. Cement and Concrete Research, 31(12): p. 1867-1872.

Mechtcherine, V. and H.W. Reinhardt (2012). *Application of Super Absorbent Polymers (SAP) in Concrete Construction*, in State-of-the-Art Report Prepared by Technical Committee 225-SAP. RILEM. p. 165.

Snoeck, D. (2015). *Self-Healing and Microstructure of Cementitious Materials with Microfibres and Superabsorbent Polymers*, in Faculty of Architecture and Engineering. 2015, Ghent University: Ghent, Belgium.

Snoeck, D. and N.D. Belie (2015). *Effect of superabsorbent polymers, superplasticizer and additional water on the setting of cementitious materials*. International Journal of 3R's, 5(3): p. 721-729.

Snoeck, D., C. Schrofl and V. Mechtcherine (2018). *Recommendation of RILEM TC 260-RSC: testing sorption by superabsorbent polymers (SAP) prior to implementation in cement-based materials*. Materials and Structures, 51(5).

Snoeck, D., L. Pel and N. De Belie (2018). *Superabsorbent polymers to mitigate plastic drying shrinkage in a cement paste as studied by NMR*. Cement & Concrete Composites, 93: p. 54-62.

Snoeck, D., L. Pel and N. De Belie (2017). *The water kinetics of superabsorbent polymers during cement hydration and internal curing visualized and studied by NMR*. Scientific Reports, 7.

Snoeck, D., O.M. Jensen and N. De Belie (2015). *The influence of superabsorbent polymers on the autogenous shrinkage properties of cement pastes with supplementary cementitious materials*. Cement and Concrete Research, 74: p. 59-67.

Snoeck, D. (2015). *Self-Healing and Microstructure of Cementitious Materials with Microfibres and Superabsorbent Polymers*, in Faculty of Architecture and Engineering. 2015, Ghent University: Ghent, Belgium.

Sven Mönnig and H.-W. Reinhardt (2006). *Results of a comparative study of the shrinkage behaviour of concrete and mortar mixtures with different internal water sources*. in International RILEM Conference on Volume Changes of Hardening Concrete: Testing and Mitigation. 2006. Lyngby, Denmark: RILEM Publications SARL.

Tenório Filho, J.R., D. Snoeck and N. De Belie (2018). *The effect of superabsorbent polymers on the cracking behavior due to autogenous shrinkage of cement-based materials*. in 60th Brazilian Concrete Conference. Foz do Iguacu, Brazil: Brazilian Concrete Institute.

Tenório Filho, J.R.; Pereira Gomes de Araújo, M.A.; Snoeck, D. and De Belie, N. (2019). *Discussing Different Approaches for the Time-Zero as Start for Autogenous Shrinkage in Cement Pastes Containing Superabsorbent Polymers*. Materials, 12, 2962.

Wu, L.M., *et al*. (2017). *Autogenous shrinkage of high performance concrete: A review*. Construction and Building Materials, 149: p. 62-75.

XV International Conference on Durability of Building Materials and Components
DBMC 2020, Barcelona
C. Serrat, J.R. Casas and V. Gibert (Eds)

On the Effects of Relative Humidity and CO_2 Concentration on Carbonation of Cement Pastes

Quoc Tri Phung[1], Anna Varzina[1,2], Janez Perko[1], Diederik Jacques[1], Norbert Maes[1] and Özlem Cizer[2]

[1]Waste & Disposal, Belgian Nuclear Research Centre (SCK CEN), Boeretang 200, 2400 Mol, Belgium, {qphung, avarzina, jperko, djacques, nmaes}@sckcen.be

[2]Building Materials and Building Technology Section, KU Leuven, 3001 Leuven, Belgium, ozlem.cizer@kuleuven.be

Abstract. *Many environments to which concrete is exposed are highly aggressive due to various chemical components. In such environments, concrete is subjected to processes of chemical degradation, among which carbonation is one of the most frequently seen degradation processes. Though, the influence of saturation degree (or relative humidity - RH) of the specimen and CO_2 concentration on the carbonation of cementitious materials is still not comprehensively described with respect to carbonation rate/degree as well as alteration in microstructure and mineralogy. This work aims at thoroughly investigating how these two key parameters affect the carbonation under accelerated conditions. Furthermore, the effect of initial moisture state of the specimen on the carbonation rate is also demonstrated. For such purpose, a numerical model at continuum scale is developed to investigate the effects of RH and CO_2 concentration on the carbonation depth, phase changes in phases and porosity of hardened cement pastes due to carbonation under accelerated conditions. Verification with experimental results from accelerated carbonation tests shows a good agreement. The modelling results with supporting experimental data help to better understand the modification of material properties under different carbonation conditions and to optimize the carbonation conditions.*

Keywords: *Carbonation, CO_2 Concentration, Microstructure, Cement Paste, Relative Humidity.*

1 Introduction

The carbonation process in cement-based materials is typically considered as a deterioration phenomenon because it results in a pH decrease, which accelerates the corrosion of reinforcing bars in concrete. On the other hand, carbonation also results in beneficial effects including decreases in transport properties and refines the pore structure of cement-based materials (Phung *et al.*, 2015; Phung *et al.*, 2016b). The extent of modification in transport properties and microstructure significantly depends on carbonation conditions (*e.g.* CO_2 concentration, relative humidity) and cement types (*e.g.* OPC or blended systems). The reduction of transport properties is the result of the precipitation of carbonation products in the pore structure, which leads to a significant reduction of the total porosity (Phung, 2015).

A number of models have been proposed based on Fick's law for diffusion with an analytical relation between the carbonation depth and square root of time. Instead of giving an explicit formula to predict the carbonation depth, a large number of models have been developed in order to solve the carbonation problem numerically (Bary *et al.*, 2004; Muntean *et al.*, 2011). These approaches are based on conservation laws with a complex form to capture the most important factors (including other transport rather than diffusion and time-dependent variables, *e.g.* porosity) influencing the carbonation process. However, identification of parameters for complex models may require several experiments and is not an easy task, for example to parameterize a constitutive relation between relative humidity, porosity changes and diffusivity

of CO_2 during carbonation. In a previous study (Phung *et al.*, 2016a), the authors have successfully developed a comprehensive 1-D reactive transport model accounting for both advective and diffusive transports under an applied CO_2 pressure gradients. The model enables to predict carbonation depth and changes in permeability, diffusivity, and porosity due to carbonation. In this study, a reduced form of the previous model with only diffusive transport is used in order to investigate the key parameters (*e.g.* RH, CO_2 concentration, w/c ratios), which are applied in conventional accelerated carbonation experiments. In such a common way, the samples are put in a controlled chamber at a wide range of CO_2 concentrations (*e.g.* 0.1% to 10%) and an optimized relative humidity (50-70%) to speed up carbonation. Results from such accelerated carbonation data are scattered and sometimes contrary due to wide ranges of carbonation conditions. Moreover, the moisture content of the tested samples is not always similar or even different from the surrounding environment in accelerated carbonation chamber. This leads to a big uncertainty despite of the same carbonation conditions. The above issues are intensively discussed in this work by numerical simulation in combination with preliminary validation with experimental data.

2 Model Development

The proposed model is based on a macroscopic mass balance for CO_2 in gaseous and aqueous phases. The model only considers the carbonation of portlandite and C-S-H, which are the main hydrated phases in CEM I ordinary Portland cement (OPC) paste. Continuous hydration of the samples during carbonation is not taken into account as the experiments were conducted on 28-day-old samples and the time for carbonation was quite limited.

2.1 Mass Conservation of CO_2

2.1.1 Transport of CO_2

The total concentration of CO_2 in the porous media is the sum of the amounts of CO_2 in the gaseous and aqueous phases:

$$c = \phi(1-S)c_g + \phi S c_l \tag{1}$$

where ϕ is porosity; S is water saturation degree; c_g and c_l are the concentrations of gaseous and dissolved carbon dioxide, respectively, which can be related by using Henry law and Clapeyron equation,

$$c_g = c_l K_H / RT \tag{2}$$

where and K_H denotes the Henry constant; R is universal gas constant; T is absolute temperature. The total flux of CO_2 includes both the CO_2 fluxes in the gaseous and aqueous phase, expressed as:

$$J = D_g \frac{\partial c_g}{\partial x} + D_l \frac{\partial c_l}{\partial x} = \left(\frac{K_H}{RT} D_g + D_l \right) \frac{\partial c_l}{\partial x} \tag{3}$$

where D_g and D_l are effective diffusion coefficients of gaseous and aqueous phase, respectively. In porous media, the effective diffusion coefficient depends on the pore structure (Phung *et al.*, 2019a). For the effective diffusion coefficient D_l of dissolved CO_2, we account for the changes in porosity, tortuosity, carbonation degree ($k_{Dl}^*(\phi,\tau)$) and saturation degree ($k_{Dl}(S)$) during carbonation followed as (Phung *et al.*, 2016a):

$$D_l = D_{l0} \times k_{Dl}^*(\phi,\tau) \times k_{Dl}(S) \tag{4}$$

For CO_2 diffusion in the gaseous phase, a similar approach as in the aqueous phase is adopted. However, Knudsen diffusion is taken into account through the factor k_{Knu} because carbonation shifts the pore size distribution towards smaller pores (Phung *et al.*, 2015) which results in a smaller effective diffusivity for carbonated material.

$$D_g = D_{g0} \times k_{Dg}^{*}(\phi,\tau) \times k_{Dg}(S) \times k_{Knu} \tag{5}$$

Details of these models for the diffusivity can be found in (Phung *et al.*, 2016a).

2.1.2 Evolution of porosity during carbonation

The change in porosity is obtained from the change in solid phases by carbonation of portlandite and C-S-H.

$Ca(OH)_2 + CO_2 = CaCO_3 + H_2O$

$$\Delta\phi_{CH} = \left[\left(C_{CH0} - C_{CH}\right)/M_{CH}\right]\left(V_{CH} - V_{CC}\right) \tag{6}$$

$y_0CaO{\bullet}SiO_2{\bullet}z_0H_2O + (y_0\text{-}y)CO_2 = yCaO{\bullet}SiO_2{\bullet}zH_2O + (y_0\text{-}y)CaCO_3 + (z_0\text{-}z)H_2O$

$$\Delta\phi_{CSH} = C_{CSH0}/M_{CSH0}\left[\left(y_0 - y\right)V_{CC} - \left(V_{CSH0} - V_{CSH}\right)\right] \tag{7}$$

where $\Delta\phi_{CH}$ and $\Delta\phi_{CSH}$ are porosity changes [-] due to portlandite and C-S-H carbonation, respectively; y and z are the average Ca/Si ratio and stoichiometric ratio of H_2O in C-S-H, respectively; C_{CH} and C_{CSH} are portlandite and C-S-H contents, respectively; M_{CH} and M_{CSH0} are molar masses of portlandite and C-S-H, respectively; V_{CH}, V_{CC} and V_{CSH} are molar volumes of portlandite, calcite and C-S-H, respectively. Subscript 0 denotes the initial condition. The molar volumes of portlandite and calcite are well defined in literature. However, data for molar volume of C-S-H are scarce and it is a stoichiometry-dependent parameter. An experimental study (Morandeau *et al.*, 2014) showed that the molar volume of C-S-H is proportional to the Ca/Si ratio as:

$$V_{CSH0} - V_{CSH} = \omega\left(1 - y/y_0\right) \tag{8}$$

where $0.02 < \omega < 0.04$ [l/mol]. The total porosity of sample during carbonation is expressed as follows:

$$\phi = \phi_0 + \Delta\phi_{CH} + \Delta\phi_{CSH} \tag{9}$$

where ϕ_0 is initial total porosity. The change in capillary porosity is mainly due to the carbonation of portlandite as majority of portlandite particles are located near the capillary pores (Phung *et al.*, 2015). However, C-S-H carbonation might partially contribute to the capillary porosity change, especially under accelerated conditions. The partial contribution of C-S-H carbonation to capillary porosity is captured by a coefficient υ ($0 \le \upsilon \le 1$) as:

$$\phi_c = \phi_{c0} + \Delta\phi_{CH} + \upsilon\Delta\phi_{CSH} \tag{10}$$

where ϕ_{c0} is initial capillary porosity. The value of υ is set to be 0.5 for OPC cement paste which gives a good fit with capillary porosity change determined by MIP (Phung *et al.*, 2016a).

2.1.3 Carbonation reaction

Instead of separately modelling the carbonation reactions of CH and C-S-H, we combine both reactions as in a single reaction between Ca^{2+} (dissolved from CH and C-S-H) and CO_3^{2-} ions:

$$Ca^{2+}{}_{(total)} + CO_3^{2-} \rightarrow CaCO_3 \tag{11}$$

We consider that the reaction (11) is of the first order with respect to Ca^{2+} and CO_3^{2-} concentration. The rate of the combined carbonation reaction, r, is written as:

$$r = k_C f(S) k_r \frac{C_{Ca}}{M_{Ca}} \frac{C_{CO_3}}{M_{CO_3}} \tag{12}$$

where k_C is the temperature-dependent reaction rate coefficient, M_{Ca} and M_{CO3} are molar masses of Ca^{2+} and CO_3^{2-}, respectively. The factor *f(S)* corrects the kinetic carbonation reaction rate coefficient for the effect of water saturation degree. Following the approach of (Papadakis *et al.*, 1991),

$$f(S) = S^n \tag{13}$$

where the parameter *n* is suggested to be 3.7. The carbonation products are mainly formed around CH/C-S-H particles. Consequently, the reaction rate will reduce because Ca ion and CO_2 have to diffuse through the product layer. Therefore, a retardation factor is added into Eq. (12) as:

$$k_r = \left(C_{Ca}^s / C_{Ca0}^s \right)^{\Theta} \tag{14}$$

where C_{Ca}^s is total concentration of solid Ca except for Ca in calcium carbonate, subscript 0 denotes the initial concentration; Θ is exponential factor which is suggested to be 2 for OPC cement paste (Phung *et al.*, 2016a).

The mass balance of dissolved CO_2 is written as:

$$\frac{\partial \left(\left[\phi(1-S) \frac{K_{CO_2}^H}{RT} + \phi S \right] c_l \right)}{\partial t} - \frac{\partial \left(\left[\frac{K_{CO_2}^H}{RT} D_g + D_l \right] \frac{\partial c_l}{\partial x} \right)}{\partial x} = -f(S) \phi k_C k_r \frac{C_{Ca}}{M_{Ca}} \frac{C_{CO_3}}{M_{CO_3}} M_{CO_2} \tag{15}$$

The partial differential Eq. (15) describes the one-dimensional reaction-transport phenomenon in cement-based materials and is solved numerically using the COMSOL Multiphysics® FEM based simulation tool.

2.2 Mass Conservation of Calcium

Following the same approach for CO_2, the mass balance equation for total dissolved Ca is given as:

$$\frac{\partial \left(\phi S C_{Ca} \right)}{\partial t} - \frac{\partial \left(D_{Ca} \frac{\partial C_{Ca}}{\partial x} \right)}{\partial x} = -\phi r \frac{M_{Ca}}{M_{CO_2}} + r_d \tag{16}$$

where D_{Ca} is the effective diffusivity of calcium ion; r_d is the dissolution rate of CH and C-S-H [kg/m^3.s] which is calculated from the mass balance equation of total amount of Ca in CH and C-S-H as follows:

$$\frac{\partial C_{Ca}^s}{\partial t} M_{Ca} = -r_d \tag{17}$$

Note that in Eq. (17) the release rate of Ca due to hydration is neglected. The solid-liquid equilibrium curve of Ca based on the experimental data collected by (Berner, 1992) is used to establish a relation between the aqueous and solid calcium concentration which is expressed as an mathematical form based on a discretization of the decalcification of CH and C–S–H (Phung *et al.*, 2016a). The Ca fraction in CH and C-S-H can be estimated from the hydration of minerals (C_2S, C_3S) in cement which can be estimated by the Bouge calculation.

2.3 Mass Conservation of Moisture

2.3.1 Liquid water transport

The mass balance equation for liquid water (excluding bound water) is given as:

$$\frac{\partial(\phi S \gamma_l)}{\partial t} = -\mu_E - \mu_R \tag{18}$$

where μ_E is the vapour-liquid water exchange rate; and μ_R is the released water rate due to carbonation. The amount of water released is derived from the carbonation reactions Eqs. (6) and (7), for CH and C-S-H, respectively. For CH, there is a 1-1 relation between Ca consumption and water release. However, for C-S-H carbonation, y mol of Ca in C-S-H will release z mol H_2O. The stoichiometry values of y and z are only slightly different (Allen *et al.*, 2007). Therefore, we assume that ratio $y/z = 1$. With this assumption, it is possible to calculate the amount of released water rate based on the change of total Ca in solid phase.

$$\mu_R = \frac{\partial\left(\left(C_{Ca}^{s} - C_{Ca}^{s0}\right) M_w\right)}{\partial t} \tag{19}$$

where M_W is molar weight of water, C_{Ca}^{s0} is initial Ca content in the solid phases.

2.3.2 Vapour transport

Vapour is transported due to diffusion. The mass balance equation for vapour is given as:

$$\frac{\partial(\phi c_v (1-S))}{\partial t} + \frac{\partial\left(\phi(1-S) D_v \frac{\partial c_v}{\partial x}\right)}{\partial x} = \mu_E \tag{20}$$

where c_v is the concentration of vapour which is calculated as

$$c_v = P_v M_w / RT \tag{21}$$

where P_v is the partial pressure of vapour which is depended on relative humidity,

$$P_v = RH \times P_{vs} \tag{22}$$

where P_{vs} is the average saturation pressure of vapour; D_v is the diffusivity of vapour.

3 Description of Carbonation Experiments

Accelerated carbonation experiments were performed on cement pastes at three w/c ratios of 0.4, 0.5 and 0.6. Type I ordinary Portland cement (CEM I 52.5 N) was used. The chemical and physical properties of the cement can be found in (Phung *et al.*, 2019b). Cement pastes were cast in a cylindrical tube with an inner diameter of 98 mm and cured in sealed conditions. After 28 days of curing, the samples were cut into small disks of 25 mm thick by a diamond saw. Prior to the carbonation experiment, the samples were conditioned to different target internal relative humidity of 55%, 65% and 75% in a climate chamber. Note that sample conditioning is an essential step that would significantly affect the carbonation results as shown later in section 4.4. In our case the samples is ensure to reach the targeted RH when the mass of sample is stable. The accelerated carbonation tests were performed in 28 days at constant temperature of 20°C. Two CO_2 concentrations of 0.3% and 1% and three RH of 55%, 65% and 75% were investigated. Details of the setup and experimental procedure were described in (Varzina *et al.*, In preparation).

After carbonation, a number of post-analysis methods were used to quantitatively and qualitatively analyse the carbonated samples. The carbonated sample was sawn and sprayed by phenolphthalein solution to determine the phenolphthalein carbonation depth (Phung *et al.*, 2015). Portlandite and calcium carbonate profiles of a carbonated sample were quantified by thermo-gravimetric analysis (TGA) of the dust collected at different depths. A hole with a diameter of 10 mm was longitudinally drilled in the carbonated sample. Drilling was halted

every 3 mm to collect the dust before continuing drilling. To prevent cross contamination, the hole was carefully cleaned by compressed air before continuing drilling. TGA was performed in a NETZSCH STA 449F3 thermal analyzer. A weighed sample, usually between 30 and 40 mg was heated from room temperature to 1100°C with a heating rate of 10°C per minute under a constant nitrogen flow rate of 120 ml/min.

Mercury intrusion porosimetry (MIP) provided information on how pore structure changes during carbonation. MIP experiments were performed in a PASCAL 140/440 porosimeter in which the mercury pressure was continuously increased up to a maximum pressure of 200 MPa. The samples were taken from the reactive surface up to 3 mm in depth and referred as "carbonated samples". Furthermore, the mass of samples were followed as a function of carbonation time, which allows calculating the mass gain due to carbonation.

4 Results and Validation

4.1 Carbonation Degree

The term "carbonation depth" is typically determined by a phenolphthalein indicator. However, it is not easy to mathematically define the carbonation depth. In this study, we relate the carbonation depth to total concentration of Ca in the solid phases (C_{Ca}^{s}). In such way, carbonation depth is linked to a maximum depth at which portlandite (CH) is completely carbonated, and referred as carbonation degree of 1. The carbonation degree, d_c, is then formulated as:

$$d_c = \begin{cases} 1 & CH < 0 \\ \dfrac{C_{Ca}^{s0} - C_{Ca}^{s}}{C_{Ca}^{CH}} & CH \geq 0 \end{cases} \tag{23}$$

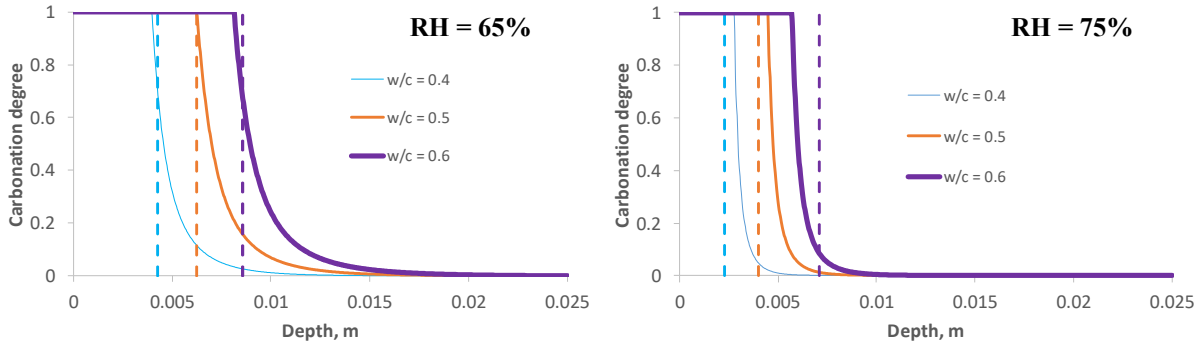

Figure 1. Carbonation degree of samples carbonated at RH of 65% and 75%, CO_2 concentration of 1% - dashed lines mark the carbonation depths determined by phenolphthalein spraying.

The carbonation degree of samples with different w/c ratios carbonated with CO_2 concentration of 1% at RH at 65% and 75% is shown in Figure 1. It is clearly seen that the higher w/c ratios, the larger carbonation degree. A higher RH results in a lower carbonation degree. Interestingly, the transition zone (*i.e.* d_c<1) is wider for carbonation at lower RH, meaning a sharp carbonation front might not be observed in this case. This is explained by a faster diffusion of CO_2 under lower RH condition. Comparing with carbonation depth determined by phenolphthalein indicator, the carbonation degree agrees very well with the phenolphthalein front (i.e. the front is corresponded to carbonation degree of 1) for 65% RH. Results at higher RH is in less agreement, especially for the sample with w/c ratio of 0.6.

4.2 Mass Gain

In this study, the sample mass gain is considered as the sum of CO_2 uptake and change in moisture content of carbonated sample. We can easily calculate the total CO_2 uptake due to the carbonation reactions of portlandite and C-S-H. Considering Eq. (11), the number of moles of solid Ca consumed equals the number of moles of CO_2 uptake. The moisture content change is related to the differences in saturation degree (mass change due to different RH is negligible). Therefore, the mass gain (normalized to initial sample mass) due to carbonation can be expressed as:

$$Mass = 100\% \int_0^L \left\{ \left[\left(C_{Ca}^{s0} - C_{Ca}^{s} \right) + \left(C_{Ca}^{0}\phi_0 - C_{Ca}\phi \right) \right] M_{CO_2} + \left(S\phi - S_0\phi_0 \right) \rho_w \right\} A / m_{sam} dx \qquad (24)$$

where A and m_{sam} are the cross section and initial mass of the sample, respectively.

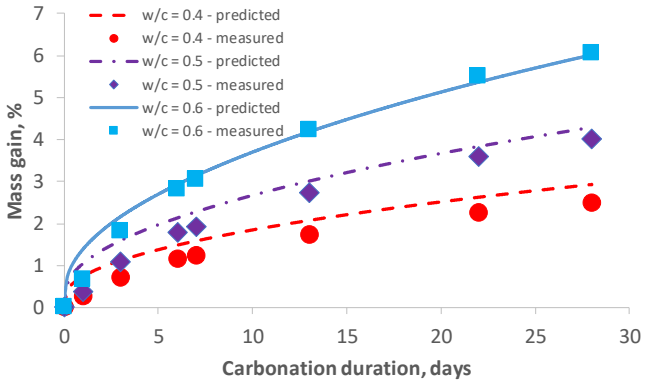

Figure 2. Mass gain of samples carbonated at RH of 65% and CO_2 concentration of 1%.

As expected, higher w/c ratio results in higher mass gain as seen in Figure 2. The predicted results agree very well with the measured data. Note that the mass gain is not equal to the CO_2 uptake because of the moisture content exchange of the samples with surrounding environment during carbonation, which is well captured in the model.

4.3 Effect of Carbonation Conditions

4.3.1 Relative humidity

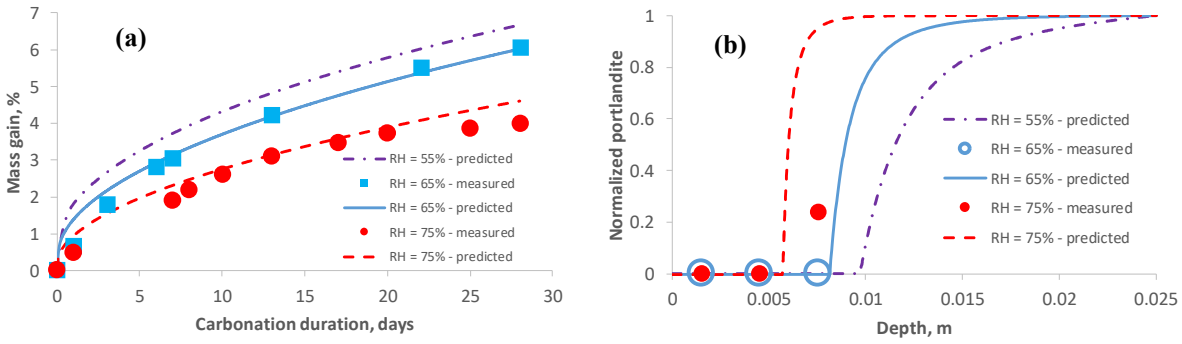

Figure 3. Effects of RH on mass gain (a) and change in portlandite content after 28 days of carbonation (b) – measured data for RH = 55% is not yet available.

Typically, a wide range of RH is used in accelerated carbonation experiments. The European standard EN 12395 even allows the tests performing with RH = 60%±10%. We therefore simulate the carbonation under various RH of 55%, 65% and 75%. Results show that the carbonation rate is significantly depended on the RH of the surrounding environment. The lower

RH, the higher mass gain and percentage of carbonated portlandite (Figure 3). The mass gain is increased 30% if RH decreases from 75% to 55%. Similarly, the depth of complete portlandite carbonation increases from 6 mm to 10 mm with a decrease of RH from 75% to 55%.

As a consequence, the drop in capillary porosity due to carbonation is more visible for lower RH as shown in Figure 4. The effects of RH is much clearer in case of higher w/c ratio.

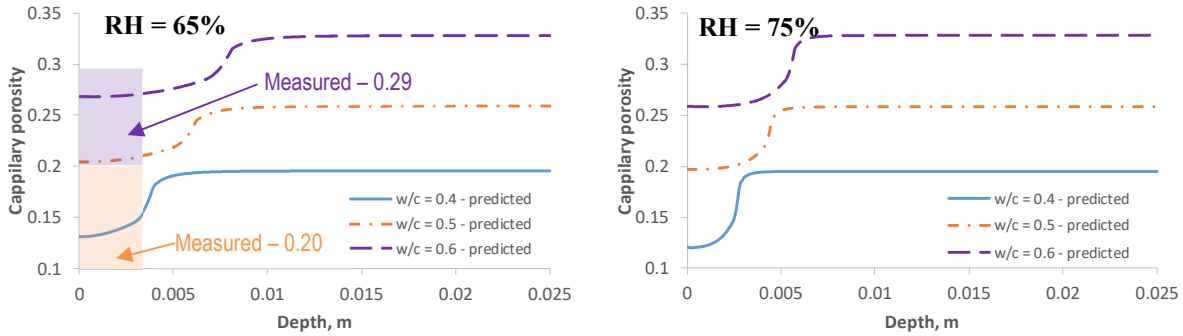

Figure 4. Effects of RH on capillary porosity decrease due to carbonation at 1% CO_2 concentration.

4.3.2 CO_2 concentration

The CO_2 concentration significantly influences the carbonation in terms of mass gain. Increasing CO_2 concentration from 0.3% to 3% triples the mass gain as seen in Figure 5a. This is a consequence of a higher amount of portlandite carbonation as shown in Figure 5b. The C/S ratio of C-S-H is also significantly reduced in the portlandite depletion zone, which is in agreement with thermodynamic modelling results showing that initially no C-S-H should decalcify. However, this sometimes does not comply with experimental findings, e.g. (Auroy *et al.*, 2018; Phung *et al.*, 2015) which showed evidences that carbonation of portlandite and other hydrated phases may occur simultaneously. In case of highest CO_2 concentration, the C/S ratio can be lower than 0.4 near the reactive surface. Interestingly, C-S-H is carbonated with the highest extent not at the reactive surface, but around 3 mm far away the reactive surface indicating that the optimal carbonation conditions (*i.e.* reaction rate, available CO_2 and Ca) occur a bit far away from the reactive surface if higher CO_2 concentration is applied.

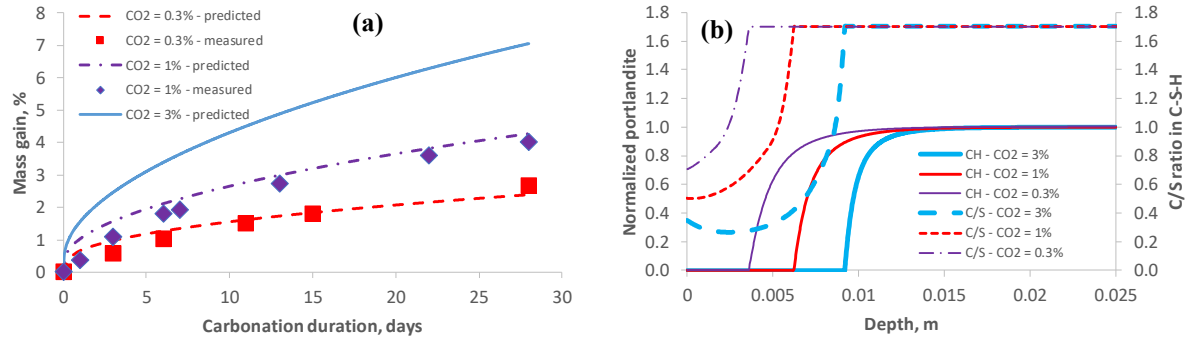

Figure 5. Effects of CO_2 concentration on mass gain (a) and changes in portlandite content and C/S ratio of C-S-H after 28 day carbonation (b) - samples with the same w/c ratio of 0.5 and carbonated under 65% RH, measured mass gain for case CO_2 = 3% is not yet available.

4.4 Effect of Sample Preparation – Initial Relative Humidity

In practice, the samples are not always well-conditioned to reach the targeted RH humidity in the carbonation chamber. The conditioning process could take few weeks to months (depended on sample size and w/c ratio) to bring the initial moisture state (RH>95%) to the optimal

carbonation RH of around 65%. If the initial RH of samples differs from the RH of carbonation chamber, the results can be significantly scattered. Figure 6 illustrates such uncertainty by investigating 3 initial RH levels of 65%, 80% and 85%. All samples with w/c ratio of 0.5 are carbonated under the same conditions with RH of 65% and CO_2 concentration of 1% at 20°C. It is clearly seen that higher initial RHs significantly reduce the carbonation degree. This is because the internal RH and saturation of these samples are much higher than the one with initial RH of 65% (Figure 6b), resulting in much slower transport of CO_2 into the samples. It is interesting to observe that a maximum RH is obtained at the depth where carbonation degree starts decreasing. This is explained by the accumulation of water released by carbonation, which does not have enough time to transport to the surrounding environment. The slower transport of CO_2 in samples with higher initial RH also induces higher C-S-H carbonation resulting in lower C/S ratio as seen in Figure 6a.

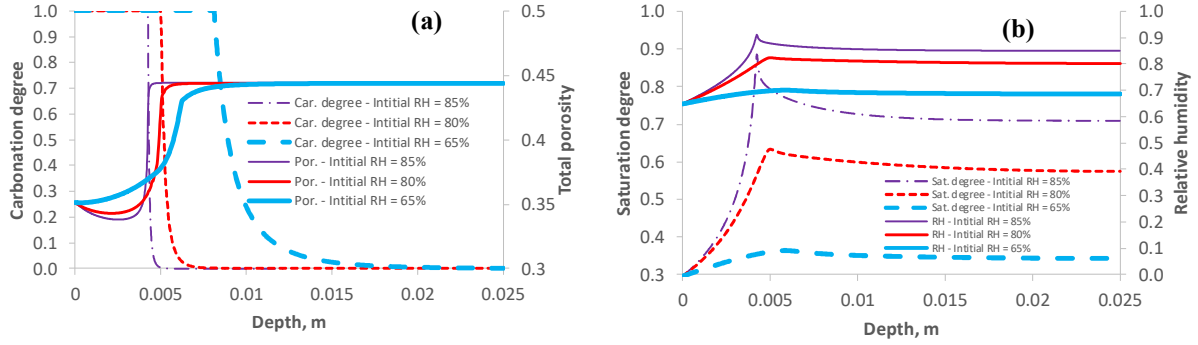

Figure 6. Effects of initial RH of samples on carbonation degree and total porosity alteration (a) and saturation degree and internal RH of carbonated samples (b).

5 Conclusions

A one-dimensional reactive transport model coupling moisture – CO_2 – Ca transport, which is adapted from a previous work (Phung *et al.*, 2016a), is implemented to investigate the effects of RH and CO_2 concentration and initial moisture state of the samples on the carbonation degree, phase changes and porosity of hardened cement pastes due to carbonation under accelerated conditions. The model enables to predict the carbonation degree, mass gain, portlandite content, C/S ratio and porosity change over time and space. A parametric study confirms that two key parameters, i.e. CO_2 concentration and RH, play an important role in accelerated carbonation of cement pastes. Variation of these parameters in a common testing range could significantly change the carbonation degree; however, their effects also depend on the microstructure of the samples which is controlled by the w/c ratios. The higher the w/c ratios, the larger the contribution of RH and CO_2 concentration. The model helps to better interpret the experimental observations and highlights underlying phenomena such as the formation of a gradual carbonation front due to carbonation of both portlandite and C-S-H or changes in moisture state along the sample depth. Furthermore, the modelling results confirm the vital contribution of initial moisture state of the samples to the carbonation process and estimated carbonation rate. Poor sample conditioning (i.e. too short time to lower the initial RH after curing to targeted testing RH) could dramatically reduce the carbonation efficiency.

Preliminary verification of the modelling results with accelerated carbonation experiment gives a good agreement even though more experimental data is still required to validate and improve the model, especially to better capture changes in transport properties due to carbonation.

Acknowledgements

This work is financially supported from ENGIE via the project 068 'CARBOCRACK'.

ORCID

Quoc Tri Phung: https://orcid.org/0000-0001-9859-860X

References

Allen, A. J., Thomas, J. J. and Jennings, H. M. (2007). Composition and density of nanoscale calcium-silicate-hydrate in cement. *Nature Materials*, *6*(4), 311-316. https://doi.org/Doi 10.1038/Nmat1871

Auroy, M., Poyet, S., Le Bescop, P., Torrenti, J.-M., Charpentier, T., Moskura, M. and Bourbon, X. (2018). Comparison between natural and accelerated carbonation (3% CO2): Impact on mineralogy, microstructure, water retention and cracking. *Cement and Concrete Research*, *109*, 64-80. https://doi.org/https://doi.org/10.1016/j.cemconres.2018.04.012

Bary, B. and Sellier, A. (2004). Coupled moisture-carbon dioxide-calcium transfer model for carbonation of concrete. *Cement and Concrete Research*, *34*(10), 1859-1872. https://doi.org/DOI 10.1016/j.cemconres.20004.01.025

Berner, U. R. (1992). Evolution of pore water chemistry during degradation of cement in a radioactive waste repository environment. *Waste Management*, *12*(2–3), 201-219. https://doi.org/10.1016/0956-053x(92)90049-o

Morandeau, A., Thiéry, M. and Dangla, P. (2014). Investigation of the carbonation mechanism of CH and C-S-H in terms of kinetics, microstructure changes and moisture properties. *Cement and Concrete Research*, *56*(0), 153-170. https://doi.org/http://dx.doi.org/10.1016/j.cemconres.2013.11.015

Muntean, A., Bohm, M. and Kropp, J. (2011). Moving carbonation fronts in concrete: A moving-sharp-interface approach. *Chemical Engineering Science*, *66*(3), 538-547. https://doi.org/DOI 10.1016/j.ces.2010.11.011

Papadakis, V. G., Vayenas, C. G. and Fardis, M. N. (1991). Experimental Investigation and Mathematical-Modeling of the Concrete Carbonation Problem. *Chemical Engineering Science*, *46*(5-6), 1333-1338.

Phung, Q. T. (2015). *Effects of Carbonation and Calcium Leaching on Microstructure and Transport Properties of Cement Pastes* [PhD thesis, Ghent University]. Belgium.

Phung, Q. T., Maes, N., Jacops, E., Jacques, D., De Schutter, G. and Ye, G. (2019a). Insights and issues on the correlation between diffusion and microstructure of saturated cement pastes. *Cement and Concrete Composites*, *96*, 106-117. https://doi.org/https://doi.org/10.1016/j.cemconcomp.2018.11.018

Phung, Q. T., Maes, N., Jacques, D., Bruneel, E., Van Driessche, I., Ye, G. and De Schutter, G. (2015). Effect of limestone fillers on microstructure and permeability due to carbonation of cement pastes under controlled CO2 pressure conditions. *Construction and Building Materials*, *82*(0), 376-390. https://doi.org/http://dx.doi.org/10.1016/j.conbuildmat.2015.02.093

Phung, Q. T., Maes, N., Jacques, D., De Schutter, G., Ye, G. and Perko, J. (2016a). Modelling the carbonation of cement pastes under a CO2 pressure gradient considering both diffusive and convective transport. *Construction and Building Materials*, *114*, 333-351. https://doi.org/http://dx.doi.org/10.1016/j.conbuildmat.2016.03.191

Phung, Q. T., Maes, N., Jacques, D., Schutter, G. d. and Ye, G. (2016b). Effect of Limestone Fillers on Ca-Leaching and Carbonation of Cement Pastes. *Key Engineering Materials*, *711*, 269-276. https://doi.org/10.4028/www.scientific.net/KEM.711.269

Phung, Q. T., Maes, N. and Seetharam, S. (2019b). Pitfalls in the use and interpretation of TGA and MIP techniques for Ca-leached cementitious materials. *Materials & Design*, *182*, 108041. https://doi.org/https://doi.org/10.1016/j.matdes.2019.108041

Varzina, A., Phung, Q. T., Perko, J., Jacques, D., Maes, N. and Cizer, Ö. (In preparation). Carbonation of fractured cement paste – synergistic effects of w/c ratio, relative humidity and CO2 concentration on microstructural and mineralogical alteration. *Cement & Concrete Composites*.

XV International Conference on Durability of Building Materials and Components
DBMC 2020, Barcelona
C. Serrat, J.R. Casas and V. Gibert (Eds)

OSB and Marine Plywood: Performance Comparison for use with Light Steel Frame Walls in Brazil

Max Junginger[1], Maurício M. Resende[2], Luciana A. Oliveira[3] and Vanderley M. John[4]

[1] Polytechnic School, University of São Paulo, São Paulo, SP, Brazil. maxjgg@gmail.com

[2] São Judas Tadeu University, São Paulo, SP, Brazil, Rua Taquari, 546, mauresende@yahoo.com

[3] Inst. de Pesq. Tecnológicas, São Paulo, SP, Brazil, Av. Prof. Almeida Prado, 532, Luciana@ipt.br

[4] Polytechnic School, University of São Paulo, São Paulo, SP, Brazil, Vanderley.John@lme.pcc.usp.br

***Abstract**: The use of light steel frame and wood frame in Brazil is still recent, hence there is little information about the durability of these technologies applied in Brazilian climate conditions. The wood-based boards are used as a part of the light steel or wood frame walls and are designed to contribute to the wall structural behavior (horizontal reinforcement and resistance to suspended loads). Once the information if such boards meet the DL (design life) set in the Brazilian code of residential building performance is still unknown, this paper analyses the technical characteristics of two wood-based boards - OSB and marine plywood - aiming to gather more information concerning durability under liquid water action. Thus, tests were carried out on samples of these two boards to evaluate their behavior against liquid water and after accelerated ageing test. In all cases, OSB showed to be more sensitive to early degradation than plywood.*

***Keywords**: OSB, Marine Plywood, Durability, Light Steel Frame.*

1 Introduction

The use of light steel frame and wood frame in Brazil is still recent. The first researches and publications were conducted in the last decade (Crasto, 2005; Milan, Novello, and Dos Reis, 2011; Oliveira and Mitidieri Filho, 2011; SiNAT, 2016), because of that there is little information about the durability of these technologies applied in Brazilian climate conditions, which can be around 23°C and 76% of relative humidity (RH) in the South East, with an monthly average solar radiation between 16 and 24 MJ/m^2.day (Tiba, 2000).

Wood-based boards are used as a part of the light steel frame or light wood frame walls. Mostly, the outer part of these external walls is formed by four layers (from exterior to interior): basecoat (mortar-based layer around 6mm thick), cementitious board, weather resistive barrier (sheathing membrane) and wood-based board (OSB or marine[1] plywood), the last one improving the wall structural behavior (Campos, 2014; Rego, 2012). The basecoat is directly

[1] In Brazil there is no standard setting the minimum requirements for plywood; however, there are two main types of plywood in the market: one used for making wood-based products, like cabinets (simply called "plywood") and another one, known as "marine plywood", used in situations where the presence of liquid water and high levels of relative humidity are rather frequent, like in boat hulls; hence the designation "marine" before the word plywood. According to APA (www.apawood.org), a product like that could receive the classification "APA marine". The boards used in this paper were supplied by a big manufacturer in Brazil.

adhered to the cementitious board, which is fastened (screws) to the OSB with the sheathing membrane in between. Also, in Brazil is quite common to have a wood-based board (usually OSB) at the inner side of the wall right behind the gypsum board as a way of improving the wall resistance to suspended loads; since shelves, frames and other loads can be fastened everywhere, whether there is a steel stud or not, a continuous layer is a need.

In terms of durability, the outer board might be directly affected by the wind-driven rain and the inner board by the high level of relative humidity (RH) inside the building. Water vapor movement is a matter of vapor pressure and it normally goes from outside to inside during the summer and from inside to outside during the winter (for cold countries). But the thing is not as "simple" as that, since there is no requirement for airtightness of light steel frame walls in Brazil: penetrations, holes and electrical fixtures are not sealed. Hence, air leakage (exfiltration) might be so high that the use of vapor barriers on the inner part of exterior walls is useless and a waste of money. To sum up with, knowing that keeping windows open is a cultural behavior in Brazil, the RH inside the house is probably close to the RH outside during warm seasons, which means that, basically speaking, RH all around the wall will be like the exterior RH. There might be some exceptions, though, mainly during the winter in southern cities, but in any case, interior air conditions are uncontrolled most of the time. A deeper discussion about this subject is out of the scope of this text, but it can be found elsewhere (Quirouette, 1985; Straube, 2002; Kumaran, 2009; Lstiburek, 2009; NRC, 2015; ABCB, 2016).

According to ABNT NBR 15575 (ABNT, 2013), Brazilian code of residential building performance, the design life (DL) of the main structural elements (steel and wood profiles) and of the other elements whose maintenance is not easy is at least 50 years. Since the wood-based layer contributes to the wall structural behavior and its maintenance is quite laborious, the design life (DL) of it should be equivalent to that of the main structural elements (steel and wood studs).

Once the information if such boards meet this DL in Brazilian climate is still unknown, this paper analyses the technical characteristics of two wood-based boards - OSB and marine plywood - in terms of bending strength, MOE - modulus of elasticity, internal bond, swelling in thickness and dimensional changes, all of them according to European Standards, aiming to get more information concerning durability of these boards when subjected to liquid water action. Thus, tests were carried out on samples of these two boards to evaluate their behavior before and after accelerated ageing tests.

2 Experimental Work

Samples of OSB (11.1 mm thick, OSB/3 (APA, 2017) and marine plywood (12 mm thick) were tested according to EN standards to gather information about density, EN 323 (CEN, 1993a); moisture content, EN 322 (CEN, 1993b); swelling in thickness, EN 317 (DIN, 1993); bending strength and modulus in bending, EN 310 (BSI, 1993a); internal bond, EN 319 (BSI, 1993b); dimensional changes, EN 318 (BSI, 2002a) and moisture resistance, EN 321 (BSI, 2002b).

EN standards were used because there is no Brazilian standard about the subject; in addition, regardless of having their own specific standards, samples of plywood were also tested according to OSB standards so that mechanical properties can be compared under the same conditions.

Such mechanical properties were measured for both axis: major strength (L = longitudinal)

and minor strength (T = transversal) using a universal testing machine (EMIC DL 10000). To determine the properties related to dimensional changes, a climatic chamber (model Thermotron 2800 programable controller) was used.

For each panel type, 10 50x50mm samples were used for internal bond and swelling in thickness; 10 50mm wide samples for bending properties and ageing and 4 (four) 50mm wide samples for dimensional changes. For the sake of simplicity, the terms mass and weight will be used interchangeably in this text.

2.1 Results and Discussion

2.1.1 Properties of the boards

After reaching constant mass at 21ºC and 65% RH, the main properties of the boards were evaluated, and the results can be seen in Table 1.

Table 1. OSB and marine plywood properties (average).

Board type	Density (kg/m^3)	Layers	MC (%)	MOE (N/mm^2)	BS (N/mm^2)
OSB	639.9 ± 24.6	Homogeneous	10.5 ± 0.3	4607 ± 649	32.7 ± 6.4
Plywood	623.9 ± 20.9	Five	10.3 ± 0.4	7039 ± 559	60.3 ± 8.6

MC - moisture content BS - bending strength MOE - modulus of elasticity

2.1.2 Swelling in thickness

The thicknesses and weights of the specimens (50x50mm) were taken seven times during the 24h bath at 20 ± 2ºC so that was possible to see the increasing rate of both (Figure 1).

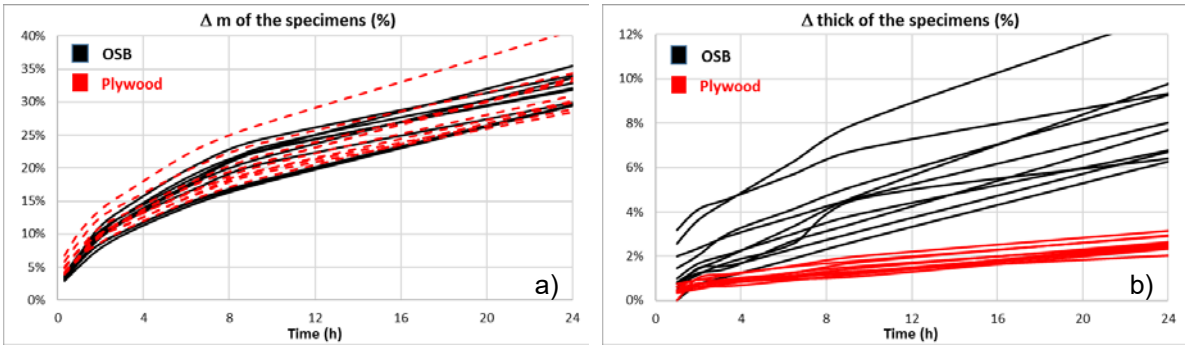

Figure 1. Changes in the a) weights and b) thicknesses of OSB and plywood for the first 24 hours.

In Figure 2 is possible to see the total thickness of all the specimens when put together side by side. It is rather evident the difference between OSB and plywood.

After the first 24h of the soak bath, all the specimens were kept under water for more 24h and, then, remained inside a room at 20 ± 2ºC and uncontrolled RH levels (around 55%) for a drying session. The results are shown in Figure 3 and here it is important to notice that the moisture content is related to the initial weight of the specimens, not to oven-dry weight. It is possible to see that both OSB and plywood show almost the same wetting and drying curves and practically the same water uptake coefficient (note that X-axis is the square root of time).

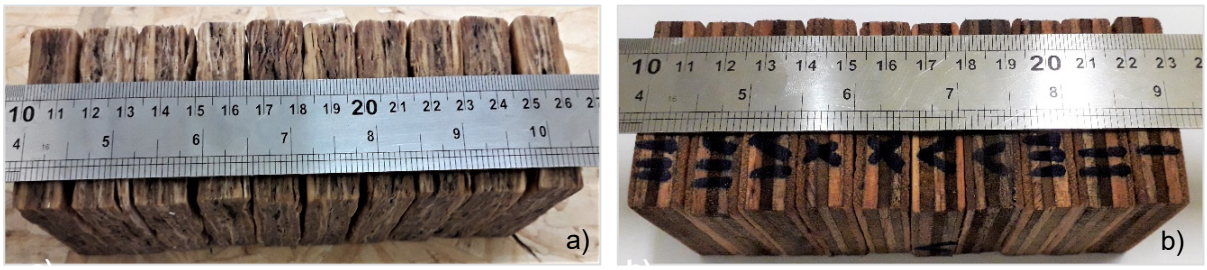

Figure 2. Appearance of a) OSB and b) Plywood after swelling.

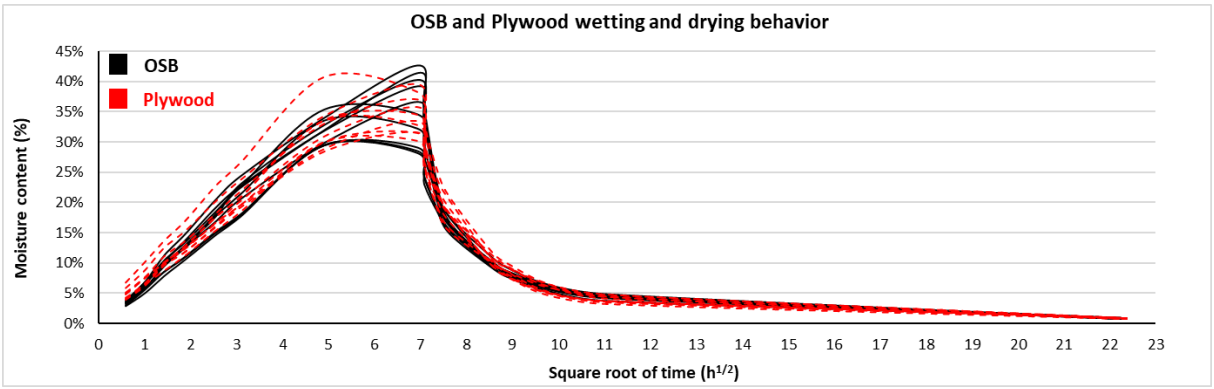

Figure 3. Wetting and drying time of OSB and plywood.

Although both OSB and plywood show quite the same water absorption and drying curves, OSB samples went through a much higher swelling after only one cycle, which can lead to problems with loose screws and nails.

2.1.3 Modulus of Elasticity (MOE) and bending strength

These tests were carried out in three conditions: with the samples acclimatized to 65% RH at 21ºC (Natural), after cyclic test (Aged) EN 321 (BSI, 2002b) and with the samples after 24h under tap water (Soak). For each set, 10 specimens were tested, which meant a total of 120 specimens (two boards, three conditions, two axis and 10 specimens each).

The distance between the supports was 20 times the thickness, i.e., 222mm for OSB and 240mm for plywood and both loading head and supports had a diameter of 20mm. Figure 4 presents the retention rate for MOE and bending strength (BS) for each set according to the axis: L stands for longitudinal and T stands for transversal (longitudinal means the axis with the highest strength).

Since the mechanical strength is deeply related to the moisture content of the specimens, the moisture contents of OSB and plywood after soak bath were determined as follows: values taken immediately after the bending test and, then, after 48h in an oven at 103ºC. So, when soaked, moisture contents (in percentage, oven-dry basis) were 36.9 ± 2.1 for OSB and 41.8 ± 4.0 for plywood.

All OSB samples presented great deterioration after soaking and cyclic test, so it was difficult to reach good accuracy and precision when measuring the thickness, which means the values presented in Figure 4 vary around ±5%. Mechanical strength loss due to water action is also described by other authors (Kojima and Suzuki, 2011; Korai, Kojima and Suzuki, 2015)

and the results in this paper are in good agreement with those ones; more similar results are also described by Okino et al (2004), when studying OSB with Brazilian wood strands.

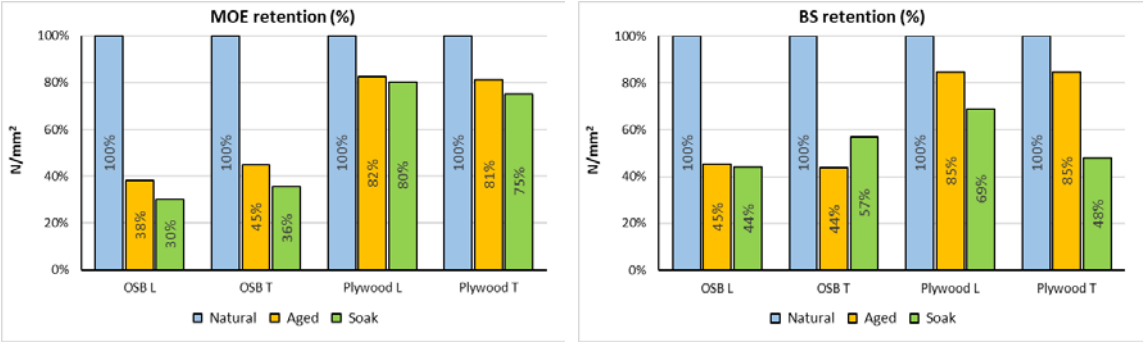

Figure 4. MOE and BS retention rates for OSB and plywood.

2.1.4 Internal bond

Internal bond tests were carried out under five circumstances: 1) original board acclimatized at 65% RH, 21ºC (Natural); 2) after swelling (soak bath); 3) after boiling; 4) oven-dry after swelling and 5) oven-dry after boiling (Figure 6). Specimens in situation 4) and 5) were oven-dried for 48h after swelling and boiling tests; then, all the samples from 2) to 5) were acclimatized at 65% RH and 21ºC before the internal bond test. Due to the mechanical damage OSB samples went through during swelling and boiling tests (see Figure 2), it was not possible to measure their internal bond.

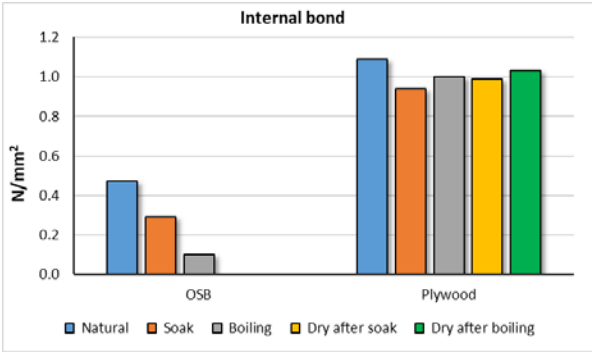

Figure 5. Internal bond of OSB and Plywood under different conditions.

2.1.5 Dimensional changes

All the samples in this test had the nominal dimensions of 300x50mm and the following charts show the mass of each specimen over time (dashed line, right vertical axis) and also the percentual variation of the mass in the last 24 hours (solid lines, left vertical axis). These last ones are important to see how long the specimens take to reach the equilibrium as required by EN 318 (BSI, 2002a): up to 0.1% in 24 hours. While Figure 6 shows the result for the cycle 30-65-85, Figure 7 shows the data for the cycle 85-65-30.

All the charts follow the same reasoning as explained here for the cycle 30-65-85: the specimens were taken from room temperature and put into the climatic chamber at 30% RH.

After the mass reaches the equilibrium, the RH level is changed to 65% and the charts show this as the first bump. Afterwards, the RH level is increased to 85% and a second bump show up; then, the specimens remain in the chamber until equilibrium.

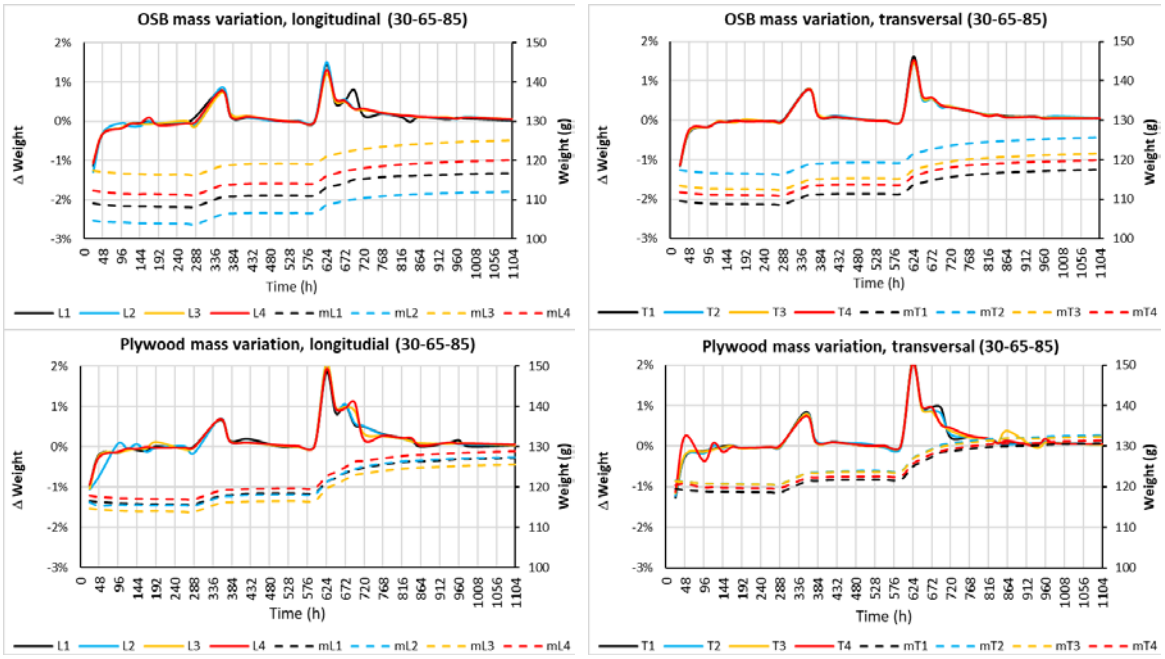

Figure 6. OSB and plywood mass variations under the cycle 30-65-85.

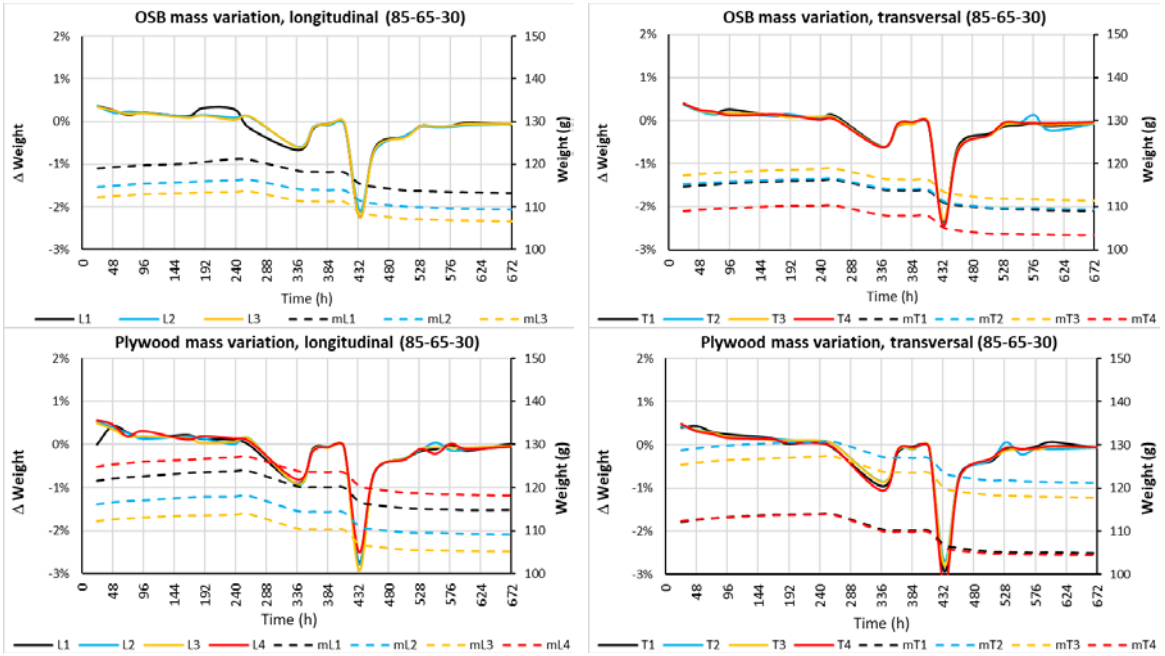

Figure 7. OSB and plywood mass variations under the cycle 85-65-30.

The two following charts, in Figure 8, show the changes of the samples length for both cycles

as well: set 1 for $L_{65,85}$ and set 2 for $L_{65,30}$.

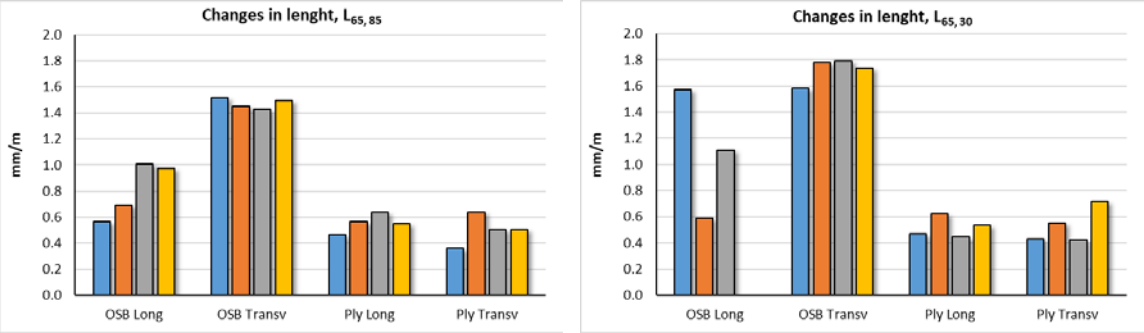

Figure 8. Changes in length of OSB and plywood: $L_{65,85}$ and $L_{65,30}$.

3 Conclusions

- Water can reach wood-based boards either due to high levels of relative humidity or because of wind-driven rain infiltration, usually taken as 1% of the rain load over the wall (ASHRAE, 2016), whether through crackings, openings, sealant failures and so on. Regarding the materials evaluated in this experiment, OSB is much more sensitive to water than plywood. Hence, its low resiliency against the most abundant degradation agent, together with the fact maintenance is not a common action in Brazil, is an alert that OSB might not the best option for a country whose climate is hotter and more humid than cold countries that already have issues with wood-based boards;
- Even with boards intended for use in humid conditions, it is important to note that "humid" means "temperature of 20°C and a relative humidity of the surrounding air only exceeding 85 % for a few weeks per year" according to EN 300 (CEN, 2006). Since in most cities of Brazil the relative humidity goes beyond this level many weeks per year, the conditions are very good to obtain high levels of mold index (ASHRAE, 2016; Ojanen et al., 2010); also, temperatures in Brazil are almost always above the minimum threshold for mold growth;
- In all tests OSB showed lower performance when compared to plywood, even where there was no direct contact with liquid water but only with different humidity levels, which means a higher stress level over time due to the greater dimensional changes.

ORCID

Max Junginger: https://orcid.org/0000-0002-7112-8584
Luciana Oliveira: https://orcid.org/0000-0001-6772-3252
Maurício Resende: https://orcid.org/0000-0001-6496-0762
Vanderley John: https://orcid.org/0000-0002-0588-8382

References

ABCB. (2016). *Condensation in Buildings Handbook* (2nd ed.). Canberra: Australian Government and States and Territories of Australia.

ABNT. (2013). *NBR 15575-1* (Edificações habitacionais - Desempenho. Parte 1: Requisitos gerais). ABNT, Rio de Janeiro.

APA. (2017). *Oriented Strand Board—Product Guide* (No. W410E; p. 12). Washington: APA HEADQ.

ASHRAE. (2016). *ASHRAE 160* (Criteria for moisture-Control Design Analysis in buildings). ASHRAE Standards Committe, Atlanta, GA.

BSI. (1993a). *BS EN 310* (Wood-based panels - Determination of modulus of elasticity in bending and of bending strength). British Standards Institution, UK.

BSI. (1993b). *BS EN 319* (Particleboards and fibreboards: determination of tensile strength perpendicular to the plane of the board). British Standards Institution, London.

BSI. (2002a). *BS EN 318* (Wood-based panels - Determination of dimensional changes associated with changes in relative humidity). British Standards Institution, UK.

BSI. (2002b). *BS EN 321* (Wood-based panels - Determination of moisture resistance under cyclic test conditions). British Standards Institution, UK.

Campos, P. F. (2014). *Light Steel Framing: Uso em construções habitacionais empregando a modelagem virtual como processo de projeto e planejamento* (Dissertação (mestrado)). University of Sao Paulo, São Paulo.

CEN. (1993a). *BS EN 323* (Wood-based panels - determination of density). Comité Européen De Normalisation, UK.

CEN. (1993b). *EN 322* (Wood-based panels - Determination of moisture content). Comité Européen De Normalisation, Brussels.

Crasto, R. (2005). *Arquitetura e Tecnologia em Sistemas construtivos Industrializados – Light Steel Framing* (Dissertação (mestrado), Universidade Federal de Ouro Preto). Retrieved from http://www.repositorio.ufop.br/handle/123456789/6246

DIN. (1993). *DIN EN 317* (Particleboards and fibreboards: determination of swelling in thickness after immersion in water). Deutsches Institut für Normung, Berlin.

Kojima, Y. and Suzuki, S. (2011). Evaluating the durability of wood-based panels using internal bond strength results from accelerated aging treatments. *Journal of Wood Science*, *57*(1), 7–13. https://doi.org/10.1007/s10086-010-1131-4

Korai, H., Kojima, Y. and Suzuki, S. (2015). Bending strength and internal bond strength of wood-based boards subjected to various exposure conditions. *Journal of Wood Science*, *61*(5), 500–509. https://doi.org/10.1007/s10086-015-1494-7

Kumaran, M. K. (2009). Fundamentals of Transport and Storage of Moisture in Building Materials and Components. In M. Bomberg and H. Trechsel (Eds.), *Moisture control in buildings: The key factor for mold prevention* (2nd ed, pp. 1–15). West Conshohocken, PA: ASTM International.

Lstiburek, J. W. (2009). *Moisture control for New Residential Buildings* (No. Building Science Digest 012). Somerville, MA: Building Science Corporation.

Milan, G. S., Novello, R. V. and Dos Reis, Z. C. (2011). The light steel frame system viability for residential buildings. *Revista Gestão Industrial*, *7*(1). https://doi.org/10.3895/S1808-04482011000100010

NRC. (2015). *National Building Code of Canada*. National Research Council.

Okino, E. Y. A., Teixeira, D. E., de Souza, M. R., Santana, M. A. E. and de Sousa, M. E. (2004). Properties of oriented strandboard made of wood species from Brazilian planted forests: Part 1: 80 mm-long strands of Pinus taeda L. *Holz Als Roh- Und Werkstoff*, *62*(3), 221–224. https://doi.org/10.1007/s00107-004-0472-3

Oliveira, L. and Mitidieri Filho, C. (2011). Sistemas construtivos tipo light steel frame para unidades habitacionais—Aspectos relativos à durabilidade.pdf. *Techne*, (176), 78–83.

Quirouette, R. L. (1985). *Building practice note n 54—The difference between a vapour barrier and an air barrier*. Ottawa: NRCC.

Rego, D. (2012). *Estruturas de Edifícios em Light Steel Framing* (Dissertação (mestrado), Universidade Técnica de Lisboa). Retrieved from https://fenix.tecnico.ulisboa.pt/downloadFile/395144743152/ MScThesis%20 Diogo%20Rego.pdf

SiNAT. (2016). *Sistemas construtivos estruturados em perfis leves de aço zincado conformados a frio, com fechamentos em chapas delgadas (Sistemas leves tipo "Light Steel Framing")* (No. Diretriz SiNAT 003, rev 2). Retrieved from Ministério do Desenvolvimento Regional website: http://pbqp-h.cidades.gov.br/projetos_sinat.php

Straube, J. F. (2002). Moisture in buildings. *ASHRAE Journal*, (January 2002), 5.

Tiba, C. (Ed.). (2000). *Atlas Solarimetrico do Brasil—Banco de dados terrestres*. Retrieved from http://www.cresesb.cepel.br/publicacoes/download/Atlas_Solarimetrico_do_Brasil_2000.pdf

XV International Conference on Durability of Building Materials and Components
DBMC 2020, Barcelona
C. Serrat, J.R. Casas and V. Gibert (Eds)

Performance of European Wood Species in Above Ground Situations After 10 Years of Weathering: Evidence of a Positive Impact of Proper Design

Magdalena Kutnik, Martine Gabillé and Mathilde Montibus

Technological Institute FCBA, Allée de Boutaut, BP 227, 33028 Bordeaux Cedex, France.
magdalena.kutnik@fcba.fr, martine.gabille@fcba.fr, mathilde.montibus@fcba.fr

Abstract. *Most of European native wood species used outdoors are expected to last less than 10 years if left untreated and exposed to severe environmental conditions such as high humidity and biological agents. However, the current classification of wood's natural durability based on EN standards does not fully reflect real end-use conditions, often underestimating wood's performance in use. In addition, the importance of design details and the role they play in enhancing service life, especially in the case of outdoor applications, is often neglected. With the aim of evaluating the positive impact of proper design on wood's service life, large-scale experimental devices, manufactured according to different designs (water draining / trapping) from six native wood species, were installed in 2009 in two French cities benefiting from different climatic conditions (oceanic / continental). The results of the evaluation carried out after 10 years of natural weathering demonstrated that (1) significant differences in the ability to withstand decay over time exist depending on the selected design details and the climatic conditions encountered in the experimental fields; (2) high variability in the resistance of non-durable spruce and poplar wood against fungal decay was noticed for each tested design, but with an unexpected high percentage of elements performing very well; (3) the moderately durable heartwood of larch, maritime pine and Douglas fir was mostly unaffected by decay even under severe conditions of exposure to rain (decking modules), suggesting these species may have greater value for outdoor applications without any preservative biocidal treatment than previously assumed.*

Keywords: *Natural Durability, Service Life, Performance, Design, Natural Weathering, Decay.*

1 Introduction

The service life of a wooden structure is the period of time after installation during which it meets the initial performance requirements, such as mechanical strength, and before replacement is needed. This depends on many factors, some being natural and beyond human control, such as wood's inherent characteristics and environmental factors (wind, rain, sun, biological decay agents), and some a result of man's actions, such as design and maintenance.

The majority of European native timber species of economic importance for the building sector are regarded as naturally moderately or poorly durable with regards to biological degradation when used for outdoor applications, such as cladding and decking. In geographical areas where biological risk is high, they are frequently expected to last less than 10 years when left untreated and exposed to severe environmental conditions such as high humidity. As a consequence, in order to ensure long-lasting products, architects tend to choose durable tropical hardwoods or native woods with enhanced durability (modified or preservative treated) rather than moderately durable European wood species whose performance over time is doubtful.

However, the importance of design details and the role they play in enhancing wood's service life, especially in the case of outdoor applications, is often neglected. Indeed, premature fungal degradation of wood is frequently the consequence of inappropriate use, poor design or mistakes made during the installation, generating water traps and thus increasing the wood's

moisture content up to a level allowing the initiation of decay.

The performance of wooden structures in terms of service-life relies both on wood's natural durability and on its exposure to weathering and biological risk. Natural durability is beyond our control, but the severity of exposure to environmental parameters can be reduced by good practices such are proper design, proper installation and proper maintenance. The objective of this study is to demonstrate that proper design of wooden structures meant for outdoor use is crucial to providing products whose service life meets the market's needs and the final users' expectations.

2 Experimental Set-up

Large experimental structures were constructed from six wood species, selected for their economic importance for the construction industry and different natural durability against fungal decay according to EN 350 (2016). They mimicked wooden constructions used outdoors above ground: cladding, decking, posts, inclined beams, assemblies, and log house outer walls (Figure 1). In order to compare their performance under different climatic conditions, the test devices were installed in 2009 in the French cities of Bordeaux and Charrey-sur-Saône (oceanic and continental climates, respectively). The full description of the experimental set up is given in Kutnik *et al.,* (2011).

2.1 Selected Timber Species

Douglas fir (*Pseudotsuga menziesii*), maritime pine (*Pinus pinaster*) and larch (*Larix decidua*) are commonly used for manufacturing outdoor structures, mainly for cladding and decking. The natural durability of their heartwood against Basidiomycete decay fungi ranges from moderately (DC 3) to poorly (DC 4) durable (EN 350, 2016), which makes them hardly suitable for use class (UC) 3.2 and UC 4 applications (EN 335, 2013) without any preventative preservative treatment, especially where long service life is expected (> 10 years).

Spruce (*Picea abies*) and poplar (*Populus sp.*) are classified as poorly (DC 4) to non-durable (DC 5) against fungal decay. In practice, they are not used untreated for UC 3.2 and UC 4 applications. In our study spruce and poplar were used as reference non-durable species, expected to decay to some extent over a period of 10 years of exposure to weathering. Different levels of decay were expected depending on the design selected for manufacturing particular experimental devices. European oak (*Quercus robur*), classified as durable (DC 1-2), was used as the reference durable wood species.

2.2 Design Details

Each type of construction comprised both water-trapping and water-draining design details. The results presented in this paper mainly concern the decking modules and the post-to-beam connections, with the design details used for manufacturing them being described in subsequent sections. Since, based on visual inspection only, the remaining construction types (log walls, posts and inclined beams) provided less interesting input, it was decided that they will be the subject of further investigation involving other tools later on.

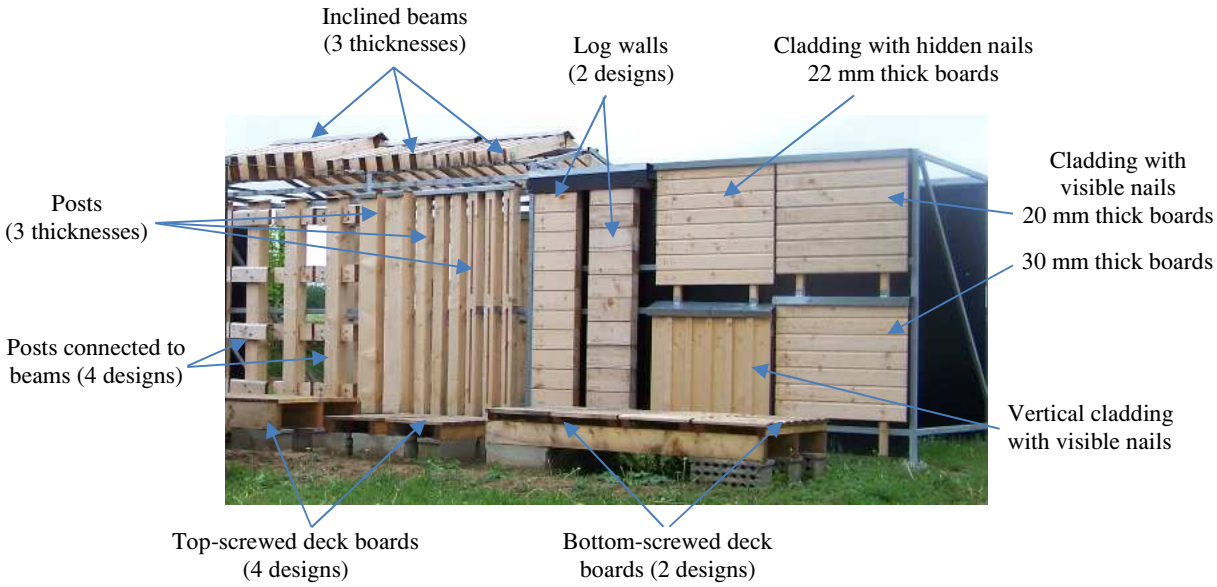

Figure 1. Experimental site in Charrey-sur-Saône, France – examples of devices made from poplar.

2.2.1 Decking Modules

The decking modules were designed to simulate exterior residential decking. They consisted of deck boards fixed on wooden joists, placed on concrete blocks to avoid direct contact with the ground. The four corners of the decking modules were also placed on concrete masonry so that their bases were at least 20 cm above ground (Figure 1). Fifty-centimeter-long boards were cut as much as possible from heartwood, pre-drilled with one or two holes near each end and mounted in two uniformly spaced rows of 5 to 16 replicates on a sub-frame (joists and/or beams) using stainless steel screws.

The modules were manufactured according to designs simulating either UC 3.2 (outdoor unprotected, without permanent water accumulation) or UC 4 (horizontal, above ground, with water accumulation over long periods of time) conditions according to the French FD P 20-651 (2011), thus representing different levels of risk with regard to the probability of fungal decay. The differences between the selected designs were the thickness, width and shape of the deck boards, the way of screwing the boards on the joists beneath (top or bottom screwing) and the typology of the wood-to-wood contact zones (water draining or water-trapping).

Design A, being the most traditional decking design, was expected to represent the worst-case scenario of exposure to water accumulation (on the wood's surface, on the screws' top, at the interface between the boards and the joists beneath). Designs B and C employed thicker boards, wider (B) or thinner (C) than design A. Designs D, E and F included different details avoiding water trapping and/or improving water drainage of the deck's surface and thus were expected to perform better than designs A, B and C.

Six decking modules were constructed from spruce and poplar (one according to each design type). Two modules were constructed from maritime pine, larch, Douglas fir and oak, according to designs A and F, expected to represent respectively the worst and the best case scenario with regard to fungal decay. The construction details are described in Kutnik and Montibus (2019).

2.2.2 Cladding Units

Cladding units of 1m x 1m were built according to four different designs, the main differences being the thickness (20 or 30 mm) of the test boards, the way of assembling and screwing them on the battens (tongue and groove boards with visible nails or lap joint boards with hidden nails) and the orientation of the wood's fibers (three horizontal and one vertical cladding) (Figure 1). Sixteen cladding units (8 spruce + 8 poplar) were installed in a setting that either allowed (4 + 4) or prevented (4 + 4) their direct exposure to wind-driven rain. The end-grain of the vertically exposed boards was protected from rainwater by stainless steel sheets.

2.2.3 Posts Connected to Beams

Posts were screwed to metallic frames, with end-grain protected from rainwater by stainless steel sheets. Beams were connected to posts using two joining types representative of traditional carpentry: the mortise-and-tenon joint and the cross lap joint. Two innovative types of joints, reducing the wood-to-wood contact zones and allowing for efficient water drainage from the two connected elements, were manufactured as well (Figure 2). All elements were connected using stainless steel fasteners. Sixteen posts (8 spruce + 8 poplar) were installed in a setting that either allowed (4 + 4) or prevented (4 + 4) their direct exposure to wind-driven rain.

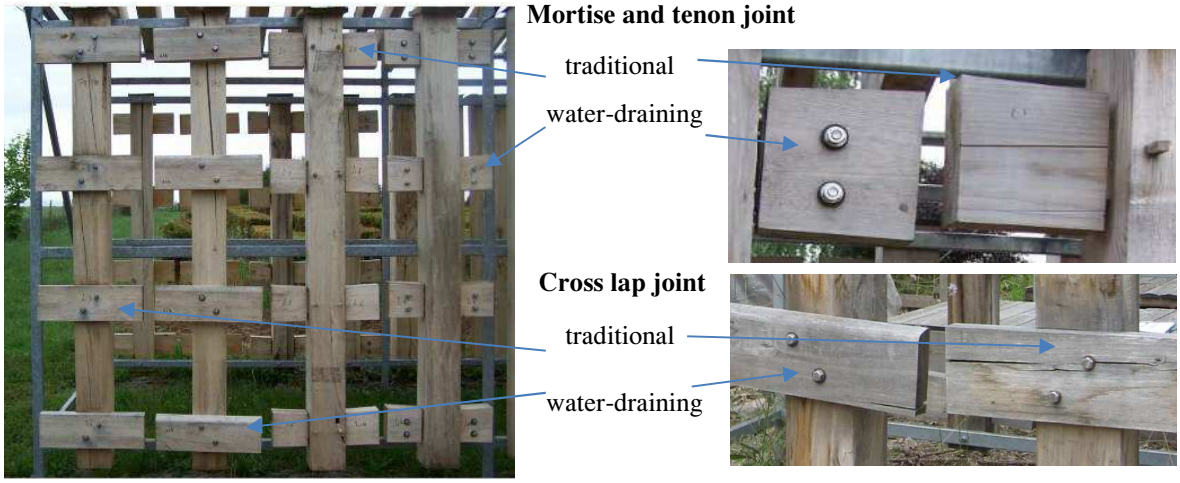

Figure 2. Poplar posts connected to beams in Charrey-sur-Saône, France.

3 Rating of the Fungal Decay

Non-destructive inspections of the deck boards were performed periodically according to a procedure similar to the one recommended in the standard AWPA E25-13 (2014). The decay inspection method consisted of gentle probing of board surfaces, checks and end-grain with a dull metal spatula for signs of softening or cavities. Special attention was paid to areas of high moisture content, discoloration or collapse that were visible on the surface and to areas sounding hollow or dull when tapped with the blunt end of the spatula.

The fungal degradation of exposed wooden elements was evaluated in 2019, after 10 years of exposure to weathering, following a rating scale ranging from “0” (sound, no evidence of fungal attack) to “4” (structural breakdown caused by decay). The rating scale used was adapted

from EN 252 (2014) and AWPA E25-13 (2014) (for more details see Kutnik and Montibus, 2019). The scale and the description of the corresponding damage are presented in Table 1.

Table 1. Description of the rating scale used for the assessment of fungal decay.

Rating level	Description of boards' degradation
0 – not degraded	• Little/surface checks • No evidence of decay, no degradation of the fixation points
1 – slight degradation/very limited extent, no immediate impact on boards' usability, no maintenance action required	• Numerous surface checks and/or few deep checks • Maximum 1 fixation point with evidence of decay • Minor softening on end-grain or on sides of checks • Decayed area <2 cm^2
2 – moderate decay, no immediate impact on boards' usability, maintenance action might be required within the next few years	• At least 2 fixation points with evidence of decay • Decayed area: max depth 2-3 mm over max 5 cm^2 OR depth of 5 mm over max 2-3 cm^2
3 – severe decay, replacement to be scheduled shortly	• All fixation points decayed OR extensive decay area > 5 cm^2 and/or > 3 cm^3 • Visible fungal activity and/or mycelium and/or fruiting body • Severe decay, likely to seriously affect the loadbearing capacity but not broken when stepped on sharply by a person of moderate weight
4 – failure, replacement needed	• Very severe decay with greater than 50% of a cross section affected • Breakage of the board or severe surface collapse • Failure when stepped on sharply by a person of moderate weight

4 Results of the Inspection Carried Out After 10 Years of Weathering

The cumulative impact of wood's natural durability, exposure conditions and effectiveness of design-based protective measures on the service life of the tested wooden constructions were quantified based on the evaluation of fungal decay. The results presented are those of the evaluation of the decks and the post-to-beams assemblies.

4.1 Assessment of the Decking Modules With Regard to Fungal Decay

The results of the evaluation are presented in Table 2 for each wood species, design type and location ("Bord" for Bordeaux and "Charr" for Charrey-sur-Saône).

The upper surface of the decks manufactured from oak, Douglas fir, larch and maritime pine (the latter in Charrey-sur-Saône only) showed either no or very little visible decay or decay limited to parts of the boards which were assumed to be residual non-durable sapwood. For this reason, the decks were left in place in order to allow future evaluation and only the top side of the boards was rated. After 10 years of weathering, the impact of the selected design details used in the decks manufactured from these four wood species was not measurable yet.

Oak (the durable reference species) resisted fungal deterioration over time, with 14 out of the 16 boards rated "0" for both design A and F in Bordeaux and all 16 in Charrey-sur-Saône rated likewise. Deck boards made from moderately to slightly durable larch and Douglas fir resisted deterioration over time on both test sites, the great majority of deck boards being rated "0" for fungal decay. A few boards reached the decay level of "2" and "3", but this degradation concerned only the residual sapwood parts. Deck boards made from maritime pine resisted degradation in Charrey-sur-Saône to the same extent as larch and Douglas fir, but high

variability was observed in Bordeaux (deck boards rated from "0" to "4"). Maritime pine boards comprised a lot of sapwood and this is certainly the main cause of their premature decay.

Table 2. Number of deck boards of each wood species and design type rated 0 to 4.

Wood species	Design type	Location	Number of boards per rating level					Number of boards
			Rating 0	Rating 1	Rating 2	Rating 3	Rating 4	
oak	A	Bord	14	1	1	0	0	16
		Charr	16	0	0	0	0	16
	F	Bord	14	2	0	0	0	16
		Charr	16	0	0	0	0	16
larch	A	Bord	13	3	0	0	0	16
		Charr	15	1	0	0	0	16
	F	Bord	13	1	2	0	0	16
		Charr	14	1	0	1	0	16
Douglas fir	A	Bord	10	2	3	1	0	16
		Charr	15	1	0	0	0	16
	F	Bord	10	1	2	3	0	16
		Charr	14	1	0	1	0	16
maritime pine	A	Bord	6	3	2	4	1	16
		Charr	13	1	0	2	0	16
	F	Bord	4	0	3	4	5	16
		Charr	15	0	0	1	0	16
spruce	A	Bord	0	2	6	6	2	16
		Charr	0	5	8	3	0	16
	B	Bord	0	1	1	8	0	10
		Charr	0	0	3	4	5	10
	C	Bord	5	18	6	5	2	36
		Charr	0	13	6	14	3	36
	D	Bord	1	5	5	1	4	16
		Charr	0	5	5	4	3	16
	E	Bord	7	4	3	1	0	16
		Charr	2	10	2	0	2	16
	F	Bord	5	5	1	1	4	16
		Charr	9	5	0	2	2	18
poplar	A	Bord	0	0	8	5	3	16
		Charr	0	12	2	1	1	16
	B	Bord	0	1	4	5	0	10
		Charr	0	10	1	1	0	10
	C	Bord	0	7	16	7	2	36
		Charr	0	16	11	9	0	36
	D	Bord	0	0	6	7	3	16
		Charr	0	10	3	3	0	16
	E	Bord	0	4	6	5	1	16
		Charr	0	11	4	0	1	16
	F	Bord	0	4	6	5	1	16
		Charr	0	6	6	2	2	16

Bordeaux/Charrey: dark orange/green colour = highest number of decks with the same rating; light orange/green colour = dispersion of ratings over the deck boards

Non-durable poplar and spruce decks were dismantled and the boards were individually rated for fungal decay. High variability was recorded in the extent of fungal degradation depending on the tested design and exposure site.

Spruce bottom-screwed deck boards (design types E and F) were significantly less decayed (high number of boards with no - rating "0" - or very little - rating "1" - decay) than top-screwed ones, except boards assembled according to design C (5 cm wide, 1 screw at each end). These boards showed high variability in their resistance to fungal decay and better overall performance than types A, B and D, especially in Bordeaux. The general trend is that decks installed in Bordeaux were slightly less decayed than in Charrey-sur-Saône.

Poplar deck boards were significantly less decayed in Charrey-sur-Saône than in Bordeaux. However, the impact of the design was less obvious than in the case of spruce. Similar performance was found for all decks irrespectively of their design in Charrey-sur-Saône and slightly better performance of bottom-screwed boards was observed in Bordeaux.

4.2 Post–to-Beams Assemblies

The assemblies evaluated on the test devices made from oak, larch, Douglas fir and maritime pine were all found sound after 10 years of exposure, irrespective of the tested design.

Spruce and poplar wood mortise-and-tenon and cross lap assemblies constructed according to water-draining designs were all sound in both test sites, irrespective of whether they were or were not directly exposed to wind-driven rain. Assemblies constructed according to water-trapping designs were decayed to different extent, depending on the wood species (spruce was less decayed than poplar) and test site (test devices installed in Charrey-sur-Saône were less decayed than those in Bordeaux). Decay fungi degraded the wood-to-wood contact zones of both elements (posts and elements connected to them) leading in many cases to the breakdown of the assembly. Figure 3 shows that mortise-and-tenon (1) and cross lap (2) assemblies were either sound, when constructed according to water-draining design (WD) or extensively decayed by fungi, when constructed according to water-trapping design (WT).

Several wooden elements connected to the posts were affected by superficial decay (larch, maritime pine, poplar and spruce), located mostly on their upper part and/or in sapwood parts.

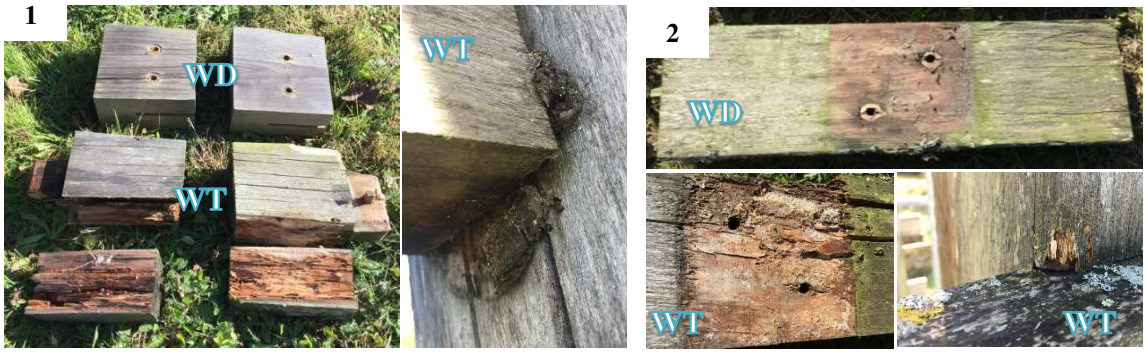

Figure 3. Poplar posts connected to beams in Charrey-sur-Saône, France.

13 Conclusions

- Significant differences in the ability of wood to withstand decay over time were observed depending on the selected design details used and the surrounding climatic conditions, especially in the case of non-durable spruce and poplar wood;
- The continental climate was less favorable to decay fungi than the oceanic one;
- A positive effect of the water draining designs was demonstrated for decks and assemblies made from non-durable spruce and poplar wood, with fewer elements being affected by fungal decay and lesser extent of decay;
- The moderately durable heartwood of larch, maritime pine and Douglas fir was unaffected by decay, even under severe conditions of exposure to rain and water accumulation (decking). This suggests that these wood species could be used without any preservative treatment, provided the sapwood has been removed, for manufacturing outdoor structures whose service life could by far exceed 10 years;
- Wooden structures made of non-durable spruce and poplar showed high variability in terms of resistance against fungal decay, but with a high percentage of elements being still sound or below their limit state of use after 10 years;
- European standards provide keys to proper selection of timber species (EN 350:2016), understanding of the biological risks associated with their use (EN 335:2013) and proper treatment where necessary (EN 599-1:2014). However, given the diversity of conditions under which wood may be in service, there is no direct, simple and reliable method to predict service life under real-use conditions based on durability classification alone. To accomplish this more reliable service life prediction tools need to be developed.

Acknowledgements

We thank “Région Bourgogne - Franche Comté” for their financial support for this study.

ORCID

Magdalena Kutnik: https://orcid.org/0000-0002-5522-5413
Martine Gabille: http://orcid.org/0000-0002-6614-5320
Mathilde Montibus: https://orcid.org/0000-0002-3033-017X

References

AWPA E25-13 (2014). Standard field test for evaluation of wood preservatives to be used above ground (UC 3B). Decking test.

EN 252 (2014). Field test method for determining the relative protective effectiveness of a wood preservative in ground contact. CEN.

EN 335 (2013). Durability of wood and wood-based products. Use classes: definitions, application to solid wood and wood-based products. CEN.

EN 350 (2016). Durability of wood and wood-based products – Testing and classification of the durability to biological agents of wood and wood-based materials. CEN.

EN 599-1+A1 (2014). Durability of wood and wood-based products - Efficacy of preventive wood preservatives as determined by biological tests - Part 1: Specification according to use class. CEN.

FD P 20-651 (2011). Durabilité des éléments et ouvrages en bois. Ed. AFNOR

Kutnik M., Jequel M. and Le Nevé S. (2011). Improving the Durability and Service Life of Wooden Components in Outdoor Applications: the French Approach. Proceedings of the 12th International conference on Durability of Building Materials and Components, 12-15 April 2011, Porto, Portugal.

Kutnik M. and Montibus M. (2019). Durability by design: a case study of the performance of wooden decks after 9.5 years of natural weathering. Proceedings of the Annual Meeting of the International Group on Wood Protection, Québec City, Québec. IRG/WP 19-20648

XV International Conference on Durability of Building Materials and Components
DBMC 2020, Barcelona
C. Serrat, J.R. Casas and V. Gibert (Eds)

Performance of Fibre-Reinforced Slag-Based Alkali Activated Mortar in Acidic Environment

Priyadharshini Perumal[1], Tirthankar Paul[2], Tero Luukkonen[1], Juha Röning[2], Paivo Kinnunen[1] and Mirja Illikainen[1]

[1] Inorganic Binders Group, Fibre and Particle Engineering Research Unit (FPERU), University of Oulu, Pentti Kaiteran katu 1, 90014 Oulu, Finland, Priyadharshini.perumal@oulu.fi

[2] Biomimetics and Intelligent System Group, Information Technology and Electrical Engineering, University of Oulu, Pentti Kaiteran katu 1, 90014 Oulu, Finland, tirthankar.paul@oulu.fi

Abstract. *The main aim of the work is to study the effect of different fibres (steel, glass and basalt) on resistance of blast furnace slag-based alkali-activated mortar in acidic environment. The alkali-activated slag mortars were exposed to 5% sulfuric and acetic acid solutions for 30 days. Mass change, compressive strength and microstructural changes were evaluated. In plain mortar, it was observed that 70% of the strength was retained in acetic acid environment whereas only 20% of residual strength remains in sulphuric acid environment. FTIR spectroscopy shows the degradation of the matrix, which implies the alkali-activated mortar was more vulnerable in sulphuric acid environment due to its aggressive nature compared to acetic acid. Decalcification and formation of calcium acetate also hinders the further progress of damage in acetic acid attack. Fibres helped in improving the performance of the mortar by holding the matrix together when the degradation occurred in acidic environment. Compared to plain mortar, incorporation of steel fibres exhibited a maximum strength retention of 19% in acetic acid and 7% in sulphuric acid, followed by glass and basalt fibres. SEM images clearly show the debonding of fibres and disintegration of matrix in acidic environment, which resulted in strength loss.*

Keywords: *Slag, Alkali Activation, Fibre-Reinforced Mortar, Acid Attack, Durability.*

1 Introduction

Interaction of cementitious materials with acidic environment is an important factor to be considered for the durability of structures exposed to harsh environment such as industrial waste water, sea water and acid rain. Alkali activated materials (AAM) are alternative cementitious system that is extensively studied in recent years (Mehta and Siddique, 2016). AAM does not involve Ordinary Portland cement (OPC) and can use 100% industrial side streams as the binding material, making them an energy efficient alternative for construction (Heath *et al*., 2014). The properties of AAM are mainly affected by the type of binder material used. AAM shows similar mechanical characteristics as that of OPC concrete, however still further studies are needed about its long-term durability performances (Provis *et al*., 2007). In specific, the chemical attack in aggressive environments like acidic, chloride, sulphate and carbonate, are to be focused.

In OPC concrete, calcium is considered to be the weakest link in the hydration product as it leaches out in acidic environment (Bernal *et al*., 2012). Though there are published studies on the low solubility and high resistance of AAM in aggressive environments (Aiken *et al*., 2018; Fernández-Jiménez and Palomo, 2009), there are also limitations in understanding their

performance in the presence of different type of fibers. In this study, an effort is made to study the effect of sulphuric (H_2SO_4) and acetic (CH_3COOH) acid on alkali activated slag (AAS) mortar with steel, glass and basalt fibers. Mainly, strength retention, microstructural changes associated with the structural damages are focused.

2 Experimental

2.1 Materials

Alkali activated slag mortar (G1) was made with ground granulated blast furnace slag (GGBFS) which was obtained from Finnsementti, Finland. Granules of anhydrous sodium metasilicate (SS, 1 mm size) with SiO_2/Na_2O ratio of 0.9 was procured from Alfa Aesar. SS was mixed with GGBFS in the ratio of 1:9 and co-grinded in a ball mill for 30 mins. Four different fibers were used in this study (Fig. 1). Table 1 lists the properties of these fibers. Fiber reinforced mortar can be identified by a nomenclature that G1S6 represents G1 mix with steel fiber of 6 mm length. Similarly, G and B were used for glass and basalt fibers, respectively. Additionally, a mix with combination of 6 mm and 12 mm steel fibers in the ratio of 1:1 (G1SM) was made. Deionized water was used for mortar production.

Figure 1. Different type of fibers.

2.2 Methods and Test Procedures

To produce mortar specimens, co-grinded slag and fine aggregate in the ratio of 1:2 was dry mixed for about a minute. Water was added to it (water-binder ratio = 0.35) and further mixed for 3 min. Fibers (1% weight of binder) were introduced to this slurry gradually while mixing was continued until a homogenous distribution was achieved. The fresh fiber-reinforced alkali-activated slag mortar was cast into cubic (50 × 50 × 50 mm^3) molds. The specimens were demoulded after 24 h and cured in 20 ˚C with 100% RH for 28 days.

Table 1. Properties of fibers.

Properties	Type of fibre			
	Steel		Glass	Basalt
Length (mm)	6	12	6	6
Density (g/cm^3)	7.88	7.85	2.68	2.67
Modulus of Elasticity (GPa)	200	200	72	85
Tensile strength (MPa)	2200	2000	1400	3500

Compressive strength before exposure (three cubic specimens) to acidic environment was determined using 3000 kN capacity with a displacement rate of 1.8 mm/min. Resistance to acid attack was studied by exposing three cubic specimens each in 5% acetic (pH 2.4) and sulphuric (pH 0.8) acids for 30 days. Later, compressive strength of the acid attacked specimens were measured. Broken pieces after testing the strength were milled to powder and used for further analysis. Deterioration mechanism of the acids in different mixes were further investigated using X-ray diffraction (XRD), Fourier transform infrared spectroscopy (FTIR) and scanning electron microscopy (SEM).

One of the cubic specimens was reserved for image analysis. Images of the cross-section of the specimen was captured as 1 cm cubes with optical microscope. Hence 25 images for each mix was analyzed and used to quantify the area of deterioration in the acid medium. In the color-based image analysis, the k-means clustering is an oft-used algorithm (Qi *et al.*, 2016). In one of each partition, the algorithm detects 'k' centroid from the 'n' number of datasets (here, pixel value), k<n. This algorithm is an iterative process which updates its centroid based on squared Euclidean distance of the data from the centroid within the cluster. Concrete is a composite with many particles of different colors and acid attacked region is not uniform in color too. However, the undisturbed core can be identified as a first step. The 'k' value has been chosen randomly and subsequently the clusters are arranged in order to minimize the intra-cluster variances and maximize the inter-cluster variances. The square error function ($\boldsymbol{E_{sq}}$) of the algorithm is given by equation (1),

$$E_{sq} = \sum_{j=1}^{k} \sum_{i=1}^{n} \left\| x_i^{(j)} - C_j \right\| \quad (1)$$

Where, C_j is the centroid,

$$C_j = \frac{1}{n_j} \sum_{i \in S_j} x_i^{(j)} \quad (2)$$

$\|-\|$ is the distance measurement (here, Euclidean distance), between centroid C_j and the data $x_i^{(j)}$ in the cluster S_j.

3 Results and Discussion

3.1 Influence of Type of Acid

Visual examination of the AAS mortar shows very small change in appearance with acetic acid environment, however there is visible disintegration of the specimen when exposed to sulphuric acid (Fig. 2). This is because acetic acid is a weak acid (only partially deprotonated), whereas sulfuric acid is a strong acid (complete deprotonation). Further exploring the chemical/ mineralogical changes on the acid exposed specimens explains that the reaction products formed by interaction of different acids plays an important role. Most important changes of acid attack would be the decalcification of the calcium silicate hydrate (C-S-H) in the hydration product. This resulted in shifts in aluminosilicate spectral bands that happens in the region 900 to 1200 cm^{-1} of FTIR curves of the acid attacked samples (Bakharev, 2005). Further, the formation of calcium acetate with acetic acid is confirmed with the presence of a C-O stretching vibrations at 1556 cm^{-1} (Fig. 3 (a)). This can also be clearly identified with XRD peaks in Figure 3 (b). The dealumination and condensation caused increase in siloxane chain length and

corresponding increase in intensity at 980 to 1100 cm^{-1}. This is not significant in sulphuric acid samples, rather shifting of peak at this region was observed. This shows that sulphuric acid resulted in delamination due to depolymerization of the AAS binders.

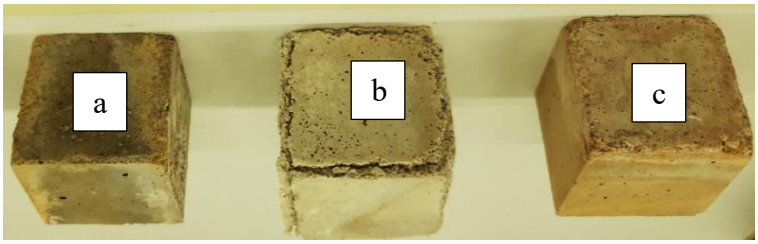

Figure 2. Cubic specimen before (a) and after 30 days exposure in sulphuric (b) and acetic (c) acid.

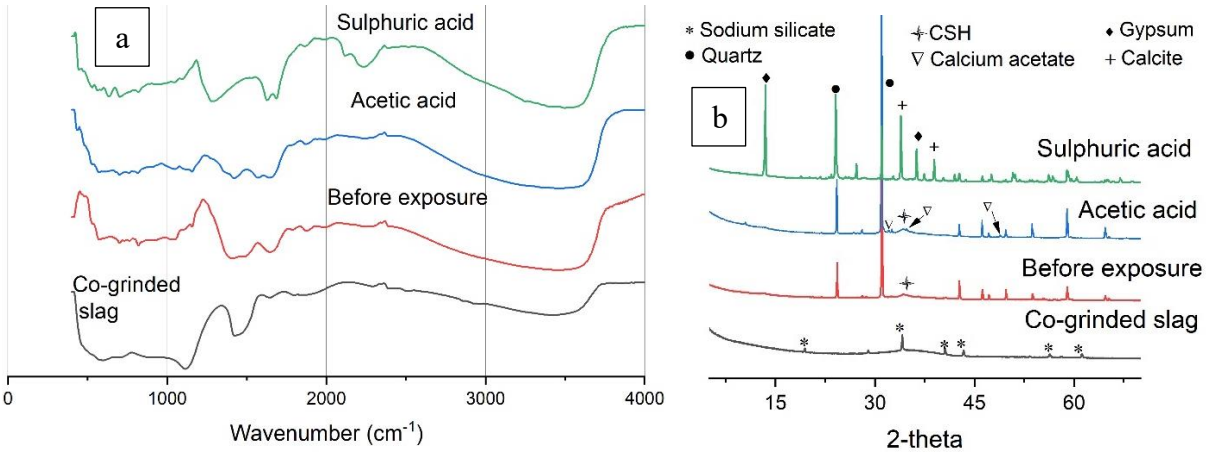

Figure 3. FTIR (a) and XRD (b) spectra of AAS mortar before and after exposure to acid.

SEM images of the acid attacked samples are shown in Figure 3. In both cases, damaged layer and the core area can be identified in the microstructure level. However, it is clearly visible that the sample is vulnerable for debonding in sulphuric acid (Fig. 4 (c)) than in acetic environment (Fig. 4 (a)). The formation of calcium acetate as an intermediate layer (Fig. 5, L2) is well observed in the optical microscopic image of acetic samples. This layer, infact acted as a protection to the core matrix from further attack (Fig. 4 (b)). Though there is also formation of similar layer with sulphuric acid, the reaction products are mainly gypsum and calcite (Fig. 3 (b) and 4 (d)) which were not stable enough to stop the progress of the sulphuric acid in to the core (Koenig and Dehn, 2016; Khan *et al*., 2018).

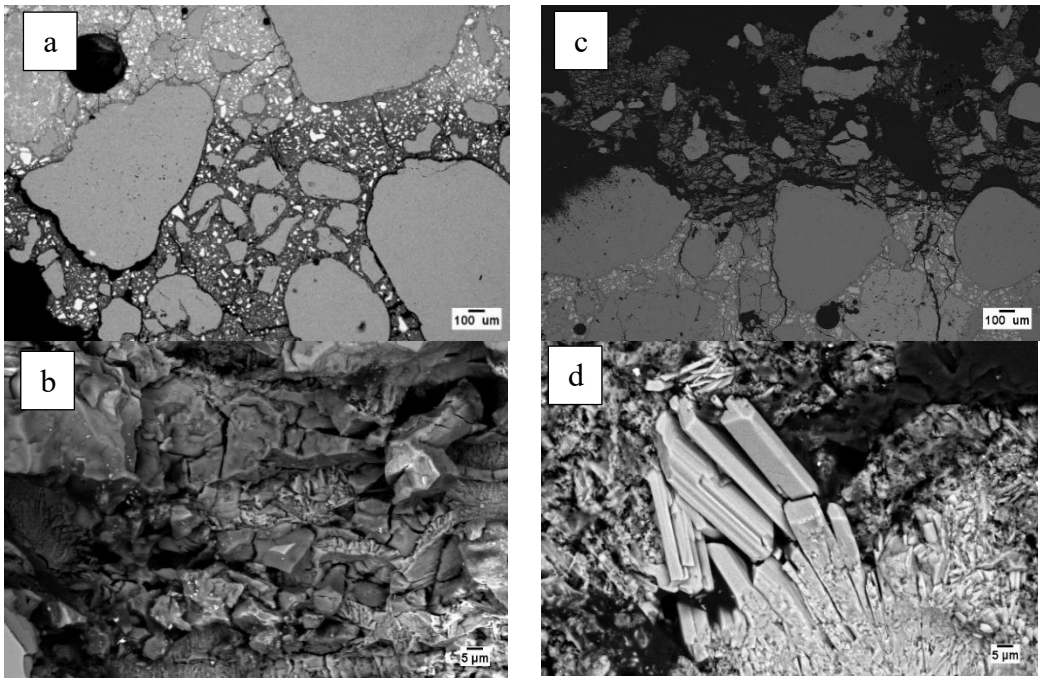

Figure 4. Representative SEM images of AAS mortar exposed in acetic (a,b) and sulphuric (c,d) acid.

An attempt was made to further quantify the different layers formed and their effect on the binder matrix in Figure 5. Based on the image analysis, core area (27%) is similar in both the acid medium. However, the damage caused by these acids looked different. Layer L2 (7%) in the acetic sample looks denser which could be due to the filling up of pores with calcium acetate. Layer L1 in both the samples looks disintegrated and deteriorated with lower binder content.

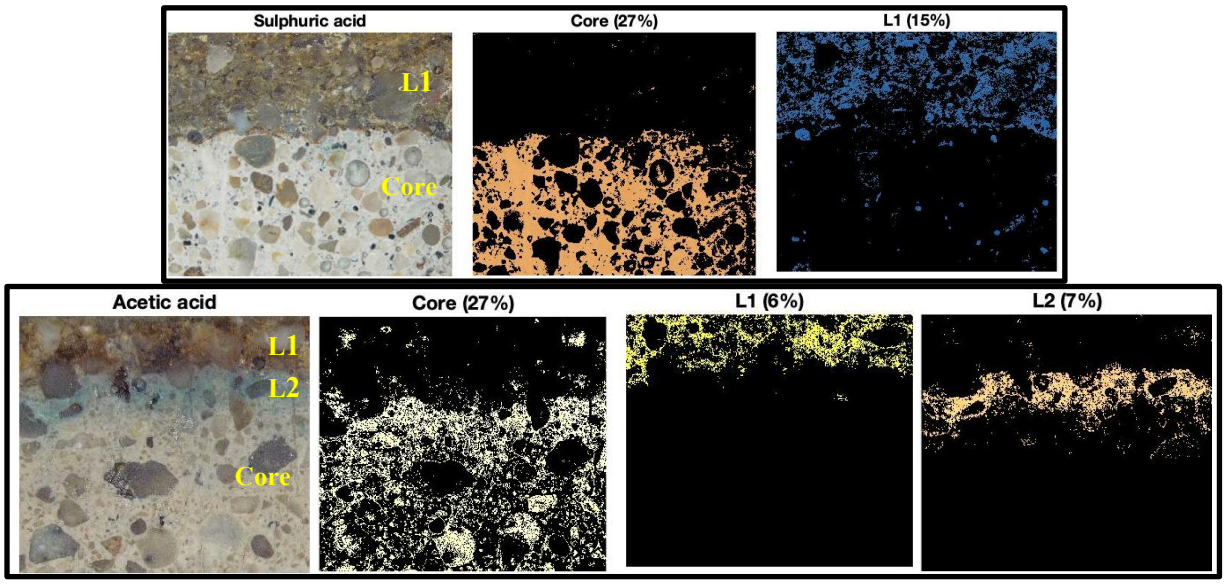

Figure 5. Representative image analysis of acid attacked AAS mortar specimens.

3.2 Role of Fiber and Their Type

Figure 6 (a) displays the effect of fibers on the compressive strength of AAS mortar before and after exposed to acetic and sulphuric acid. It also indicates the percentage reduction in strength with different mix in acidic medium. The addition of steel fibers increased the compressive strength of AAS mortar significantly whereas it was not the case with glass and basalt fibers. Strength reduction with acetic acid exposure is within 10% for the fiber reinforced AAS mortar except basalt fiber. This could be due to the use of uncoated basalt fiber which might have been damaged in the high alkaline medium (Wei *et al*., 2010). However, SEM microstructure shows the presence of basalt fibers in the matrix of the acetic attacked samples (Fig. 9 (b). Residual strength of the specimens corroded by acetic acid depends on the fiber used and it is in the order, mixed steel > 6 mm steel > 6 mm glass > 12 mm steel > 6 mm basalt. This could also be related to the unaffected area and area of the second layer (L2) which protects the core unaffected area from further corrosion (Fig. 6 (b)). SEM images of the acetic affected mixes (Fig. 9 (b), (e), (h)) shows similar structural damage as that of plain AAS mortar (Fig. 4 (a)). The improvement in residual strength of fiber reinforced AAS mortar could be due to the physical action of fibers in holding the disintegrated binder phase to some extent (Kim *et al*., 2015).

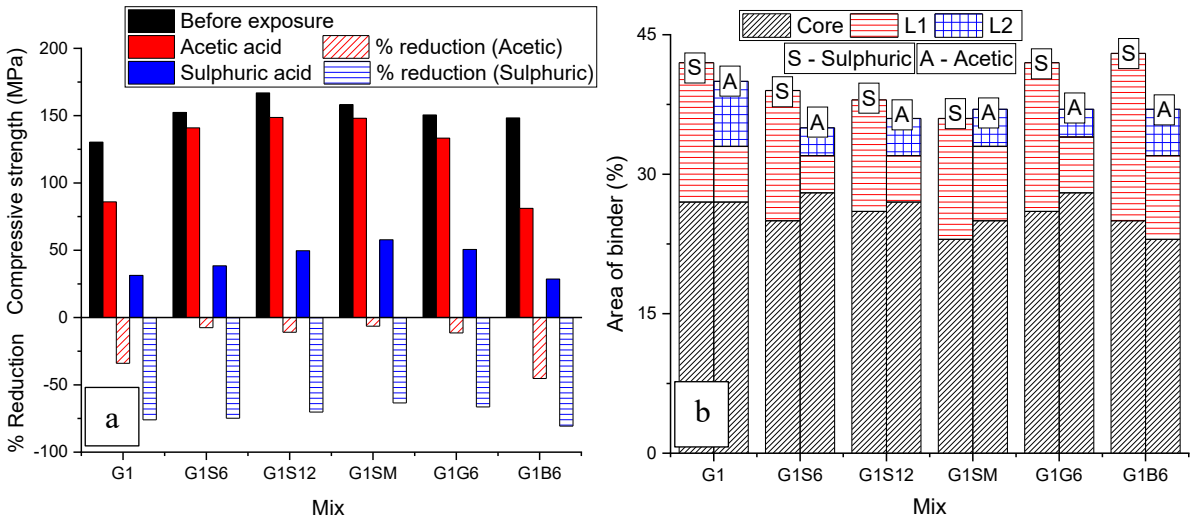

Figure 6. Compressive strength (a) and acid affected area (b) of alkali activated slag mortar.

As mentioned earlier, the effect of sulphuric acid on the AAS mortar was detrimental which is also the case with fiber reinforced AAS mortar. However, with incorporation of fibers, the residual strength improved in the corroded specimens irrespective of the type of acid. The order of resistance to sulphuric acid attack by fibers are, mixed steel steel > 6 mm glass > 12 mm steel > 6 mm steel > 6 mm basalt. This order is also maintained in the unaffected area (core) as identified in image analysis (Fig. 6 (b)). It can be seen from the SEM images that sulphuric acid corroded the sample and debonded the fibers completely (Fig. 9 (c), (f), (i)). The basalt fibers could not be even located in the corroded samples, making it clear that they need to be treated for such harsh environments (Fig. 9 (i)).

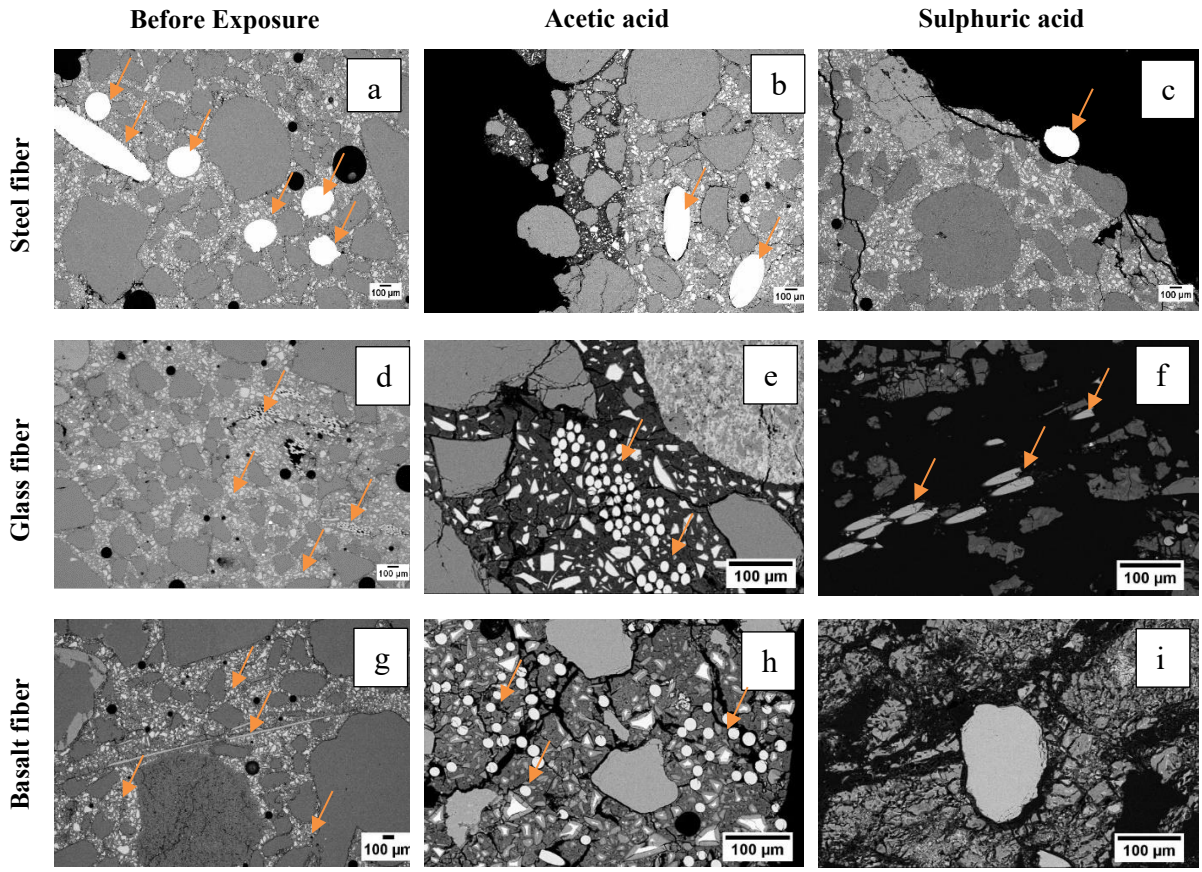

Figure 9. Representative SEM images of AAS mortar with (steel, glass, basalt) fibers before ((a), (d), (g)) and, after exposure in acetic acid ((b), (e), (h)) and sulphuric acid ((c), (f), (i)).

4 Conclusions

The influence of acetic and sulphuric acid on alkali activated slag mortar is investigated. Damage of alkali activated slag can be related to the decalcification and dealumination of the calcium silicate gels and the aluminosilicates, respectively. In acetic environment, the formation of calcium acetate acted as a barrier for further diffusion of acid protecting the unaffected core. However, sulphuric acid is corrosive and resulted in disintegration of binder matrix. Presence of fibers improved the performance of AAS mortar in corrosive environment. Residual strength of AAS mortar specimens are 19% and 7% higher with the reinforcement of mixed steel fibers (6 and 12 mm) in acetic and sulphuric acid exposure, respectively. Basalt fibers needs to be coated to use them in highly corrosive environment.

Acknowledgements

This work was supported by the Finnish Funding Agency for Technology and Innovation (Tekes) (project GEOBIZ, grant number 1105/31/2016). Authors acknowledge Business Finland (grant # 1215/31/2015) and Academy of Finland (grant #292526, #319676 and #326291) for financial support.

ORCID

Priyadharshini Perumal: http://orcid.org/0000-0002-7731-2016

Tirthankar Paul: https://orcid.org/0000-0002-1115-0843
Tero Luukkonen: https://orcid.org/0000-0002-1124-775X
Juha Röning: https://orcid.org/0000-0001-9993-8602
Paivo Kinnunen: https://orcid.org/0000-0001-8490-1890
Mirja Illikainen: https://orcid.org/0000-0001-7545-4574

References

Aiken, T. A., Kwasny, J., Sha, W. and Soutsos, M. N. (2018). Effect of slag content and activator dosage on the resistance of fly ash geopolymer binders to sulfuric acid attack. *Cement and Concrete Research*, Elsevier, 111(April), 23–40. doi: 10.1016/j.cemconres.2018.06.011

Bakharev, T. (2005). Resistance of geopolymer materials to acid attack. *Cement and Concrete Research*, 35(4), 658–670. doi: 10.1016/j.cemconres.2004.06.005

Bernal, S. A., Rodríguez, E. D., Mejía, R. and Gutiérrez, D. (2012). "Performance of alkali-activated slag mortars exposed to acids. *Journal of Sustainable Cement-Based Materials,* 1(3), 138–151. doi: 10.1080/21650373.2012.747235

Fernández-Jiménez, A. and Palomo, A. (2009). *Chemical durability of geopolymers*. *Geopolymers: Structures, Processing, Properties and Industrial Applications*, Woodhead Publishing Limited. doi: 10.1533/9781845696382.2.167

Heath, A., Paine, K. and McManus, M. (2014). Minimising the global warming potential of clay based geopolymers. *Journal of Cleaner Production*, 78, 75–83. doi: 10.1016/j.jclepro.2014.04.046

Khan, H. A., Khan, M. S. H., Castel, A. and Sunarho, J. (2018). "Deterioration of alkali-activated mortars exposed to natural aggressive sewer environment." *Construction and Building Materials*, 186, 577–597. doi: 10.1016/j.conbuildmat.2018.07.137

Kim, B., Boyd, A. J., Kim, H. S. and Lee, S. H. (2015). "Steel and synthetic types of fibre reinforced concrete exposed to chemical erosion." *Construction and Building Materials*, 93, 720–728. doi: 10.1016/j.conbuildmat.2015.06.023

Koenig, A. and Dehn, F. (2016). "Biogenic acid attack on concretes in biogas plants." *Biosystems Engineering*, 147, 226–237. doi: 10.1016/j.biosystemseng.2016.03.007

Mehta, A. and Siddique, R. (2016). An overview of geopolymers derived from industrial by-products. *Construction and Building Materials*, 127, 183–198. doi: 10.1016/j.conbuildmat.2016.09.136.

Provis, J. L., Muntingh, Y., Lloyd, R.R., Xu, H., Keyte, L.M. and Lorenzen, L., et al., (2007). *Will Geopolymers Stand the Test of Time?* Developments in Porous, Biological and Geopolymer Ceramics, John Wiley & Sons, Inc.

Qi, J., Yu, Y., Wang, L. and Liu, J. (2016). "K∗-means: An effective and efficient k-means clustering algorithm." *Proceedings - 2016 IEEE International Conferences on Big Data and Cloud Computing, BDCloud 2016, Social Computing and Networking, SocialCom 2016 and Sustainable Computing and Communications, SustainCom 2016*, IEEE, 242–249.

Wei, B., Cao, H. and Song, S. (2010). "Tensile behavior contrast of basalt and glass fibers after chemical treatment." *Materials and Design*, 31(9), 4244–4250. doi: 10.1016/j.matdes.2010.04.009

XV International Conference on Durability of Building Materials and Components
DBMC 2020, Barcelona
C. Serrat, J.R. Casas and V. Gibert (Eds)

Preconditioning of Specimens - Drying Influence on Alkali-Activated and Geopolymer Mortar

Vincent Trincal, Virginie Benavent, Hugo Lahalle, Gabriel Samson, Cédric Patapy, Yoann Jainin and Martin Cyr

Laboratoire Matériaux et Durabilité des Constructions (LMDC), Université de Toulouse, INSA/UPS Génie Civil, 135 avenue de Rangueil, 31077 Toulouse cedex 04, France
vincenttrincal@gmail.com

Abstract. *Alkali-activated materials (AAM) are now seriously considered by the cement industry as an economical alternative to Portland cement, especially for its low CO_2 footprint. However, their durability still remain to be assessed in more details. The aim of this study is to focus on the sample preconditioning conditions required for testing, especially the drying stage involved in most of the current tests. Four alkali-activated binders were studied: a geopolymer (Na-silicate activated metakaolin), a Na-carbonate activated slag (GGBS), a Na-silicate activated slag and a Na-silicate activated mixture of 50% metakaolin with 50% GGBS. After an endogenous cure of 28 days at 20°C, mortar specimens were dried at different temperatures (from 20°C to 125°C) until mass stabilization. Drying kinetics and released water contents were evaluated, as well as physical, mechanical and mineralogical analyses at the end of drying. Optimal drying temperature for each alkali-activated binder was determined by coupling mechanical strength measurements and mercury intrusion porosimetry. This study revealed that an inappropriate drying temperature could modify the porosity of some classes of AAM, and reduced the compressive strength by up to 30 to 40%. Antagonistic behaviors were observed in the four alkali-activated materials studied, therefore one should be careful about selecting preconditioning protocols for assessing the properties and the durability of these binders.*

Keywords: *Alkali-Activated Binder, Geopolymer, GGBS, Drying Conditions, Durability.*

1 Introduction

Alkali-activated binders are produced from a source of aluminosilicates (precursor) mixed with a highly alkaline solution (*e.g.* sodium (Na) or potassium (K) silicate solutions) called the activating solution (Davidovits, 1991; Provis and Van Deventer, 2009). There are two main types of alkali-activated binders, based on the calcium content of the precursors. They differ from the chemical mechanism that takes place and from the reaction products. For those rich in calcium, such as ground granulated blast-furnace slag (GGBS), chemical reactions are based on dissolution/precipitation steps. The main reaction products are C-A-S-H type phases (CaO-Al_2O_3-SiO_2-H_2O) (Pacheco-Torgal *et al.*, 2015). For precursors with low calcium content, such as metakaolins and type F fly ashes, the term geopolymer is used (Davidovits, 1991). This time, the chemical reactions consist in a dissolution/polycondensation steps, leading to a 3D-aluminosilicate network. In this network, silicon and aluminium are IV-fold coordinated and the alkali cation plays the role of a charge-balancing ion (Rowles *et al.* 2007).

An abundant literature is available regarding the alkali-activated materials (AAM) formulation, but only few studies deals with durability (Luukkonen *et al.*, 2018). Accelerated procedures for durability testing of Portland cements mixtures are often applied to AAM

without any modification, although the raw material used and physico-chemical reactions are different. These tests usually require a preconditioning of the specimens at temperatures ranging from 45°C (*e.g.* accelerated carbonation XP-P-18-458_2008), 80°C (*e.g.* permeability XP-P-18-463_2011), or even at 105°C (*e.g.* porosity NF-EN-18-459_2010). Alkali-activated binders contain gels and hydrates that can be affected and even destroyed at these temperatures (*e.g.* Zhang *et al.*, 2019). Thus, the effects of the preconditioning conditions on AAM need to be assessed, in order to avoid a deterioration of the specimens that could lead to misleading interpretations of durability tests.

2 Material and Methods

2.1 Samples Preparation

The raw materials used are Argicem metakaolin from the ARGECO Company; GGBS from ECOCEM; Betol 47T Na-silicate solution from Woellner (SiO_2/Na_2O = 1.7), Na-carbonate powder (Na_2CO_3) from Solvay, tap water from Toulouse city and standardized sand (NF EN 196-1_2016 and ISO 679_2009). Metakaolin and GGBS properties are available elsewhere in literature (*e.g.* Sabir *et al.*, 2001; Pouhet and Cyr, 2015; Pouhet and Cyr, 2016a; Samson *et al.*, 2017a).

Four alkali-activated mortars with a water/binder ratio of 0.4 were studied (see Table 1). The first formula is a metakaolin-based geopolymer developed by Pouhet *et al.* and which has been the subject of several publications (Pouhet and Cyr, 2014; 2015; 2016a; 2016b; Cyr and Pouhet, 2015a; 2015b; Pouhet *et al.*, 2019). Two formula of activated GGBS were prepared, with either a Na-Carbonate or a Na-silicate activating solution (GGBS-carbonates and GGBS-silicates). Finally, a mixture of 50% metakaolin with 50% GGBS activated by silicates is proposed in this study (Mk-GGBS-silicates) to test the coupling of the two hardening systems (based on Ca or Na). This formula has been previously tested on paste (Samson *et al.*, 2017a).

Table 1. Mix design, masses in grams.

	Metakaolin	GGBS	Na-silicate	Na-carbonate	Tap water	Sand
Geopolymer	450		354.9		46.2	1350
GGBS-silicates		450	101.3		141.8	1350
GGBS-carbonates		450		45	198	1350
Mk-GGBS-silicates	225	225	228.1		94	1350

Mortar specimens 4x4x16 cm^3 were made according to the standard protocol NF EN 196-1_2016. Most of samples were demolded 24 hours after pouring, except the GGBS-carbonates formula which was demolded at 48 hours because of its low mechanical properties at early age. The specimens were then endogenously cured (wrapped in plastic film and sealed in humidified plastic bags) for 28 days at 20°C. After this cure, some samples were kept in endogenous conditions, other were dried in different environments (20°C-95% RH, 20°C-50% RH, 20°C under vacuum, 40°C, 60°C, 80°C, 105°C and 125°C). Depending on the drying rate, the mortar specimens were analyzed at different times (the drying time varies from 12 to 49 days) and most of them at 60 days, and then compared to the mortar specimens kept in endogenous conditions for each due date. As regards the geopolymer specimens

placed in the vacuum desiccator, the pump operated only during laboratory's office hours (8 hours a day, otherwise the vacuum was maintained over the test period).

2.2 Characterizations

Several analyses were carried out in order to assess the effect of drying on the four alkali-activated materials:
- Mass monitoring was performed until mass stabilization, *i.e.* until the mass loss is less than 0.01 % between 7 consecutive days (except with 20°C-50%RH conditions which would take months to dry).
- Compressive strengths were determined using a standardized 3R press (NF EN 196-1_2016). Three measurements per mortar prism were made using a ramp of 5 kN / second. Measurements were carried out on the dry specimens as well as on control ones stored under endogenous conditions over the same period. In order to evaluate the dispersion of data, three specimens by drying condition were analyzed for each formula.
- Mercury intrusion porosimetry was performed using an AutoPore IV 9500 Porosimeter from Micromeritics according to the ISO 15901-1_2005 standard. Unlike what is recommended in the standard, samples did not undergo pretreatment for mercury intrusion analysis (*i.e.* 110°C heating in a vacuum oven at 3 Pa for 4 h). Endogenous samples containing water are therefore not dried, but dehydrated during evacuation step in the porosimeter. In order to be consistent for all samples, the test did not start until the exhaust pressure was ≤ 50 µmHg assuming complete removal of pore water.

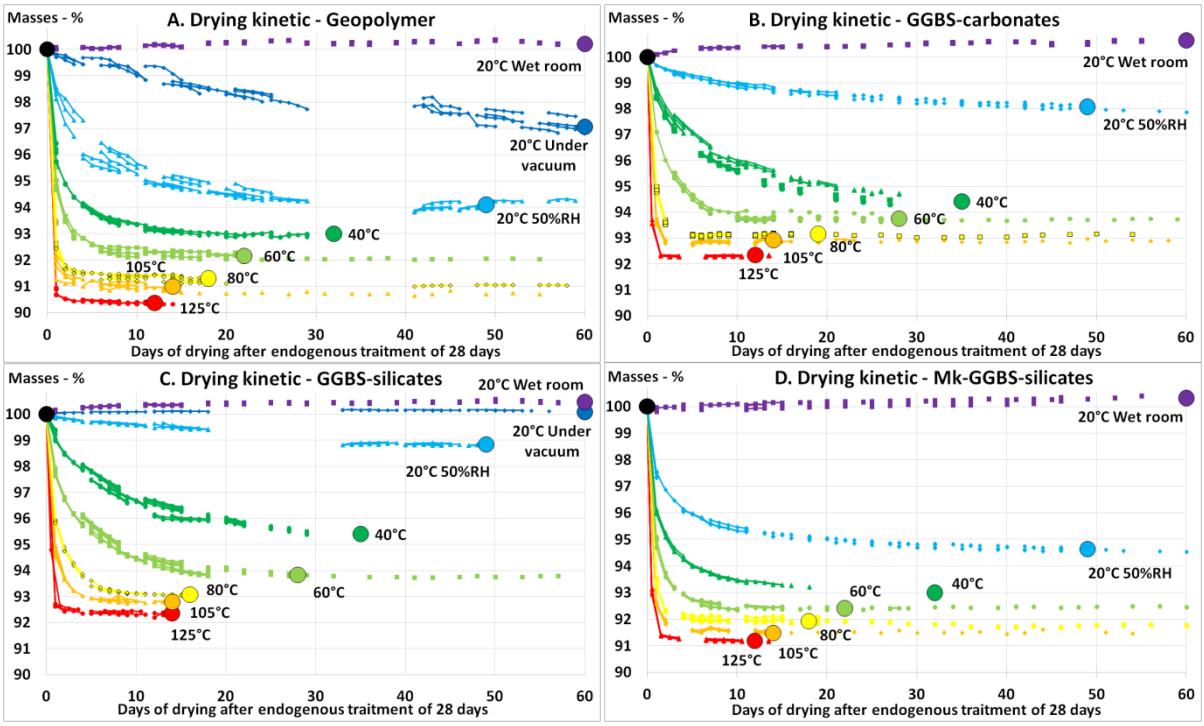

Figure 1. Mass evolution during drying at different temperatures of Geopolymer (A), GGBS-silicates (B), GGBS-carbonates (C) and Mk-GGBS-silicates (D). The circles represent the mass stabilization point.

3 Results and Discussion

3.1 Mass Monitoring

The mass variations recorded during the different drying processes show that the higher the temperature, the faster and more important the drying process (Figure 1). The comparison between the four materials shows different drying kinetics and different water content trapped in the structure of the material depending on the type of AAM. The drying rate is quicker when metakaolin is used as a precursor (Figures 1A and 1D), especially at lower temperatures, *i.e.* 20°C, 40°C and 60°C. Besides, almost all the mixing water has been evaporated in geopolymers at 105°C while almost 8% is remaining in GGBS-silicates (results not shown here). This can be explained because in geopolymers, all the water initially introduced is located in the porosity of the materials or in the alkali hydration sphere in the structural cavities of the Si-Al network (Rowles *et al.*, 2007), while in GGBS systems part of the water is bound in reaction products (C-A-S-H).

3.2 Mechanical Compressive Strengths

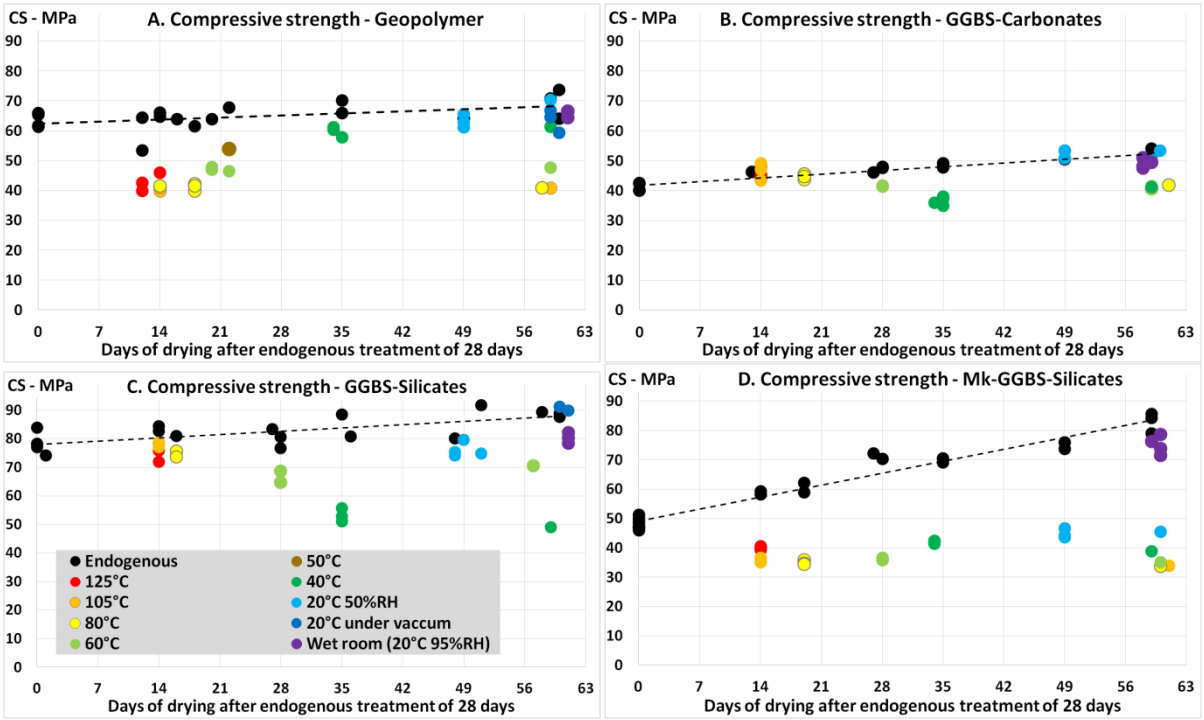

Figure 2. Compressive strengths (CS) of mortars cured in endogenous conditions (black spots) or dried at different temperatures (after endogenous treatment of 28 days). Geopolymer (A), GGBS-carbonates (B), GGBS-silicates (C) and Mk-GGBS-silicates (D). The legend inserted in C is valid for all figures.

In endogenous conditions, geopolymer samples show a slow increase of mechanical compressive strengths (CS) from 61 ± 6 MPa at 28 days to 70 ± 5 MPa at 88 days (Figure 2A). This increase seems to be stabilized after three months, as confirmed by six-months sample analyses. For GGBS-carbonates and GGBS-silicates, CS start from 41 ± 2 MPa and

77 ± 6 MPa at 28 days, respectively, then reach 54 ± 2 MPa and 89 ± 4 MPa two months later (Figure 2B-C). The CS increase is greater than for the geopolymer, and seems stabilized beyond 6 months. CS of the Mk-GGBS-silicates formulation increase from 49 ± 1 MPa at 28 days to 75 ± 4 MPa at 77 days (Figure 2D). To conclude, all four formulations show a progressive CS increase during the first months in endogenous conditions, probably linked to the pursue of chemical processes with time.

When the mortar specimens are dried (after endogenous curing for 28 days), the mechanical strength depends on both formula and drying conditions. For a drying temperature ≥ 50°C, geopolymer shows an important CS loss (up to - 36 %), even if the temperature conditions are extended for several weeks (Figure 2A). On the other hand, at drying temperature ≤ 40°C, CS were similar to endogenous ones. For GGBS-carbonates and GGBS-silicates, drying with temperature ≥ 80°C or at 20°C (with several humidities) does not decrease the CS, which are similar to those of samples stored under endogenous conditions (Figure 2B-C). However, drying at 60°C or more significantly at 40 °C decreases the CS up to -24% and -29% for GGBS-carbonates and GGBS-silicates, respectively. As for geopolymer, when the drying is maintained for a longer period than required, CS do not evolve anymore whereas in endogenous conditions the CS slightly increases, probably due to the wet storage that enable the further reaction of the materials. Finally, drying of the Mk-GGBS-silicates formulation considerably reduce CS (from - 30% to - 50%) whatever the temperature used (Figure 2D). Only samples cured in wet room (20°C 95% RH) retain similar mechanical strengths before and after curing.

3.3 Hg Porosity

In endogenous conditions, the total porosity of the four formulas does not change significantly between 28 and 88 days. Also, only the average value has been reported in Figures 3 and 4. Mean porosity is closed to 18 % for geopolymer, 15 % for GGBS-carbonates, 12.5% for GGBS-silicates and 15.5 % for Mk-GGBS-silicates. GGBS blends therefore have a lower porosity due to the formation of hydrates, when in geopolymers the water expulsed during condensations reactions is responsible for more porosity.

In drying conditions, the total porosity evolves differently for each system, as it seems to increase with the temperature level for the geopolymer (Figure 3A, 3B and 4A), to be quite stable for GGBS-carbonate (Figure 4B), having a maximum value for a drying temperature of 40°C as regards of GGBS-silicates (Figure 4D) and to be higher but stable for Mk-GGBS-silicates (Figure 4D).

Concerning the pore size distribution, geopolymer kept in endogenous conditions has half of the porosity attributed to pores < 10 nm, a quarter to 10-100 nm and the last quarter to > 100 nm (Figure 4A). However, this does not mean that half of the porosity is < 10 nm, but that the access to half of the porosity is possible by a diameter lower than 10 nm (according to inkbottle effect, *e.g.* Benavent *et al.*, 2016; Muller and Scrivener, 2017). Except desiccation under vacuum which is not an efficient drying, even a smooth drying at 20°C has the effect of replacing all the porosity < 10 nm by the category 10-100 nm. A strong drying replaces half of the 10-100 nm by the 0.1-1 µm and there is an increase of the 1-10 µm pore size. In summary, for the geopolymer, the more intense the drying, the greater the pore size (or at least the size of the necks).

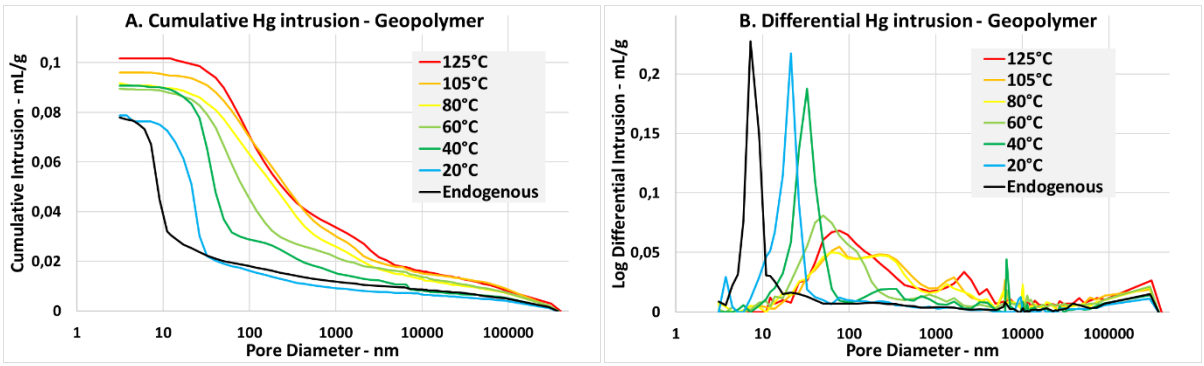

Figure 3. Geopolymer mortars mercury porosimetry as a function of drying: cumulative intrusion vs. pore diameter (A); differential intrusion vs. pore diameter (B).

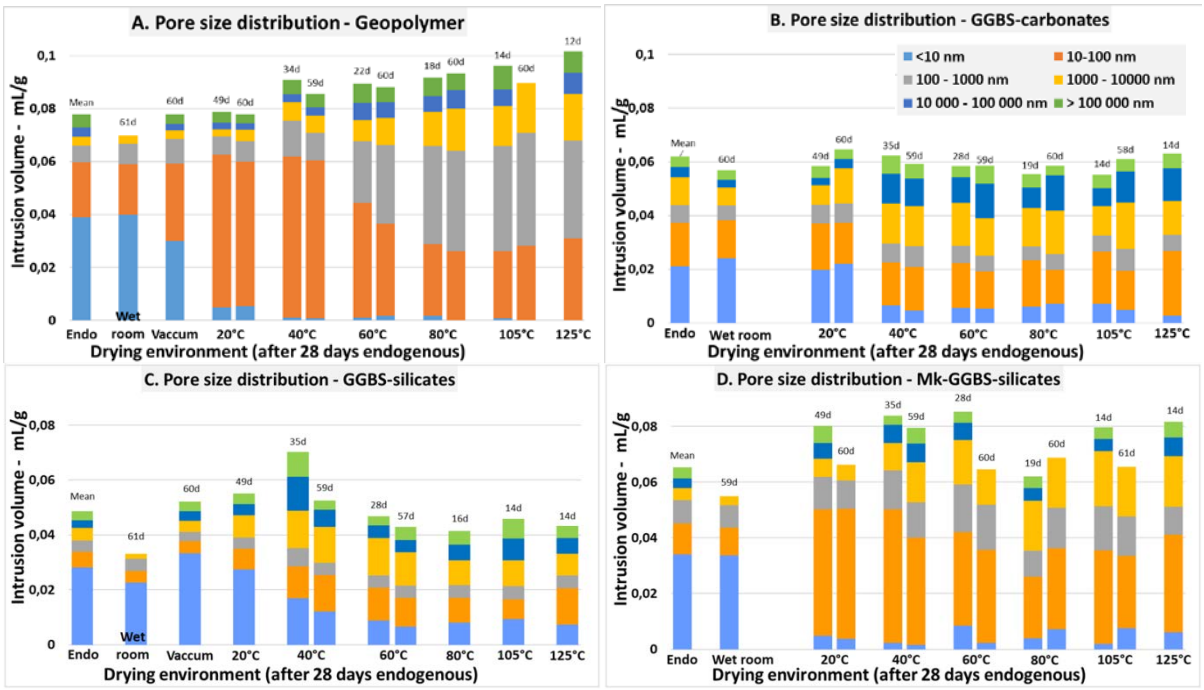

Figure 4. Pore size distribution for mortars of geopolymer (A), GGBS-carbonates (B), GGBS-silicates (C) and Mk-GGBS-silicates (D). Endo column represents the average of the samples conserved under endogenous conditions, analyzed at different ages (28 to 88 days), and showing similar properties. 50% RH for 20°C column. Up to 10 µm porosities are sometime missing due to porosimetry low vacuum problem.

Globally the same pore size distribution trend was observed for the other three formula, *i.e.* a pore size augmentation linked with drying temperature strength. However, pore size distribution modes slightly differ from one formula to another, for example with a < 10 nm pore contents varying from one third to half of the total porosity in endogenous conditions. Furthermore, the change in pore size family towards bigger sizes occurs starting from 20°C for the metakaolin materials, and from 40°C for the GGBS ones (Figure 4). Both geopolymer and Mk-GGBS-silicates show an evolution of the porosity with the increase of temperature from 20°C up to 125°C, while this evolution is limited to the range 20-60°C for GGBS materials (the pore size distribution remains constant for temperatures ranging from 60°C to

125°C). It should be noted, however, that the GGBS-silicates has a sharp increase in porosity for a drying temperature of 40°C, possibly related to micro-cracking induced by mineralogical transformations as suggested on GGBS alkali-activated concrete (Azar *et al.*, 2020).

Preconditioning recommendations must be a compromise between the drying efficiency and the impact on both the porous structure and the mechanical resistances. However, in the absence of mineralogical and microstructural data, results presented in this study should be interpreted with caution. As it has been demonstrated on Portland cements, capillary stress, the loss of physically or chemically bonded water from gels or hydrates, the potential micro-cracking as well as mineralogical changes within the material can lead to misestimating pore volumes (Gallé, 2000).

4 Conclusions on Preconditioning Drying

The effect of drying 4x4x16 cm samples at different temperatures has been assessed on four alkali-activated materials, in order to give recommendation for durability test preconditioning. The drying rate and level depend not only on the nature of the binder, in particular if chemically bonded water is present or not, but also on the porous arrangement. The results showed AAM mortars are sensitive to drying, with modifications of porosity and mechanical strengths. From mercury intrusion measurements, the pore diameter access increases starting from a drying at 20°C for the formula containing metakaolin as a precursor, and from 40°C for formula containing GGBS only.

Geopolymer drying at a temperature above 60°C is fast, but increases the measured pore size, and affects the compressive strength by 40% as a consequence. It is likely that this will affect the permeability of the material. Using a temperature below 20°C takes a lot of time, is not efficient, but does not affect the CS and the pore size. Between 20°C and 60°C there may be a drying optimum to find. A drying temperature of 40°C may be more appropriate for geopolymer, as it has less impact on the mechanical strength. Drying ramps could be tested to see if the fall of strength is due to the kinetics of drying or to the temperature itself.

As regards to GGBS-carbonates and GGBS-silicates, drying at $T \geq 80°$ C is fast, does not affect CS and slightly increases the measured pore size. In contrast, this study highlights that the material should not be dried at temperature closed to 40°C, otherwise it could lead to significant loss of mechanical strengths.

Finally, the Mk-GGBS mixture activated with silicates seems to cumulate the drawbacks of both alkali-activated systems. Whatever the temperature used, a high degree of damage to the mechanical strengths is observed, correlated with an increase of the porosity. For such mixtures, a drying by solvent exchange or by freeze-drying might be interesting, but this type of drying can only be performed on small samples.

Acknowledgements

This work is part of the L2A chair (alkali-activated binders) grouping industrial partners EDF, VINCI, ECOCEM, ARGECO, VICAT and BASF with the LMDC research laboratory.

ORCID

V. Trincal: https://orcid.org/0000-0003-4804-6617
V. Benavent: https://orcid.org/0000-0002-0263-1178
H. Lahalle: https://orcid.org/0000-0002-9201-1596

G. Samson: https://orcid.org/0000-0002-3472-8089
C. Patapy: https://orcid.org/0000-0003-3538-7893
M. Cyr: https://orcid.org/0000-0002-5012-9131

References

Azar, P., Samson, G., Deby, F., Lahalle, H., Benavent, V., Trincal, V. and Cyr, M. (2020). Comparison of the resistance against chloride-induced corrosion between ordinary and alkali activated concrete. Presented at the ACI/RILEM international conf. on cementitious materials and alternative binders for sustainable concrete.

Benavent, V., Frizon, F. and Poulesquen, A. (2016). Effect of composition and aging on the porous structure of metakaolin-based geopolymers. Journal of Applied Crystallography, 49, 2116–2128.

Cyr, M. and Pouhet, R. (2015a). Resistance to alkali-aggregate reaction (AAR) of alkali-activated cement-based binders. In Handbook of Alkali-Activated Cements, Mortars and Concretes pp. 397–422. Elsevier.

Cyr, M. and Pouhet, R. (2015b). The frost resistance of alkali-activated cement-based binders. In Handbook of Alkali-Activated Cements, Mortars and Concretes pp. 293–318. Elsevier

Davidovits, J. (1991). Geopolymers - Inorganic polymeric new materials. Journal of Thermal Analysis and Calorimetry, 37, 1633–1656.

Gallé, C. (2001). Effect of drying on cement-based materials pore structure as identified by mercury intrusion porosimetry: a comparative study between oven-, vacuum-, and freeze-drying. Cement and Concrete Research, 31, 1467–1477.

ISO 679 (2009). Cement — Test methods — Determination of strength.

ISO 15901-1 (2005). Evaluation of pore size distribution and porosimetry of solid materials by mercury porosimetry and gas adsorption.

Luukkonen, T., Abdollahnejad, Z., Yliniemi, J., Kinnunen, P. and Illikainen, M. (2018). One-part alkali-activated materials: A review. Cement and Concrete Research, 103, 21–34.

Muller, A.C.A. and Scrivener, K.L. (2017). A reassessment of mercury intrusion porosimetry by comparison with 1H NMR relaxometry. Cement and Concrete Research, 100, 350–360.

NF EN 196-1 (2016). Méthodes d'essais des ciments - Partie1 détermination des résistances.

NF P 18-458 (2008). Essai de carbonatation accélérée, mesure de l'épaisseur de béton carbonaté.

NF EN 18-459 (2010). Essai pour béton durci - Essai de porosité et de masse volumique.

Pacheco-Torgal, F., Labrincha, J.A., Leonelli, C., Palomo, A. and Chindaprasirt, P. (2015). Handbook of Alkali-Activated Cements, Mortars and Concretes. Elsevier.

Pouhet, R. and Cyr, M. (2014). Studies of Natural and Accelerated Carbonation in Metakaolin-Based Geopolymer. Advances in Science and Technology, 92, 38–43

Pouhet, R. and Cyr, M. (2015). Alkali–silica reaction in metakaolin-based geopolymer mortar. Materials and Structures, 48, 571–583.

Pouhet, R. and Cyr, M. (2016a). Carbonation in the pore solution of metakaolin-based geopolymer. Cement and Concrete Research, 88, 227–235.

Pouhet, R. and Cyr, M. (2016b). Formulation and performance of flash metakaolin geopolymer concretes. Construction and Building Materials, 120, 150–160.

Pouhet, R., Cyr, M. and Bucher, R. (2019). Influence of the initial water content in flash calcined metakaolin-based geopolymer. Construction and Building Materials, 201, 421–429.

Provis, J.L. and van Deventer, J.S.J. (2009). Geopolymers: structures, processing, properties and industrial applications. Elsevier.

Rowles, M.R., Hanna, J.V., Pike, K.J., Smith, M.E. and O'connor, B.H. (2007). 29 Si, 27 Al, 1 H and 23 Na MAS NMR study of the bonding character in aluminosilicate inorganic polymers. Applied Magnetic Resonance, 32, 663.

Sabir, B.B., Wild, S. and Bai, J. (2001). Metakaolin and calcined clays as pozzolans for concrete: a review. Cement and Concrete Composites, 23, 441–454.

Samson, G., Cyr, M. and Gao, X.X. (2017). Formulation and characterization of blended alkali-activated materials based on flash-calcined metakaolin, fly ash and GGBS. Const. and Building Materials, 144, 50–64.

XP P 18-463 (2011). Bétons - Essai de perméabilité aux gaz sur béton durci.

Zhang, Z., Zhu, Y., Zhu, H., Zhang, Y., Provis, J.L. and Wang, H. (2019). Effect of drying procedures on pore structure and phase evolution of alkali-activated cements. Cement and Concrete Composites, 96, 194–203.

XV International Conference on Durability of Building Materials and Components
DBMC 2020, Barcelona
C. Serrat, J.R. Casas and V. Gibert (Eds)

Prolonging the Durability and Conservation of Historic Materials by Microclimatic Monitoring in the Archaeological Areas

Elisabetta Rosina and Alessandra Pili

Politecnico di Milano, ABC Dept. Piazza Leonardo da Vinci 32, 20133 Milano; email elisabetta.rosina@polimi.it, alessandra.pili@polimi.it

Abstract. *Many factors have to be considered for the correct conservation of cultural heritage, in particular, the exposition of the object/site to open air, as the archaeological sites have. The risk factors can be intrinsic (durability of materials, construction and decorative techniques) and extrinsic (environmental and microclimatic conditions). The consideration of the conservation issue regarding the second has to take into account the effects the microclimatic parameters on the objects and the variation of microclimate for the use, as well as the modification due to the improvement of accessibility, safety and installations (for example plant and architecture addition/modification). In fact, the main objective of the conservation/fruition of the archaeological areas is achieving the project choices most integrated, functional and adequate to meet the needs of conservation. Monitoring and diagnostics are a necessary condition to be able to correctly define the design choices. The proposed contribution aims to specify how monitoring the microclimatic values play a fundamental role in the whole process of conservation, since the early study to the management of the site, to ensure the greater conservation and durability of the material and, ultimately, the best fruition at present and in the future.*

Keywords: *Archaeological Site, Historic Materials, Roman Tombs, Accessibility, Durability, Management Plan.*

1 Introduction

The valorization of cultural heritage, achieved together with the conservation goals, must take into account the control of the condition of use.

The valorization of the wide range of types of cultural heritage includes many different possible uses, always respectful of the compatibility with the cultural goods and sites. In all the cases, the proper management of cultural heritage includes the conscious use(Sanchez-Moral, 2005), and it is a warrant the conservation: the use is opposed to abandonment, that causes consequently to the loss of historical material, due to the natural effects of aging, waste, human activities etc.

The final goal is to achieve an integrated design that manages to coexist the architectural and plant engineering aspects with the cultural value that the site represents.
In the case of archaeological sites, it is evident that re-use is not functional as it is in historical buildings (Thompson, 2007); however, valorization activities include the correct management of the site, for achieving the conservation goals and economic sustainability.

The Conservation Plan, defined in the cultural heritage code as the tool of the conservation process, includes information related to the constant control of the asset; among these, the code lists diagnostics and instrumental monitoring.

doi:10.23967/dbmc.2020.238


Figure 1 and 2. Aerial view of the archaeological area of Tuvixeddu in Cagliari and sign of the paths and open tombs at the park entrance (credits to Intercral Ass.).

The different complexity of the archaeological sites, compared to other cultural assets, requires to articulate the design to solve the specific problems, above all the mitigation of the effects of the environment and the context (Huisman *et al.,* 2009) including also how the site is used. In fact, the estimation of risks necessarily includes the evaluation of the impact of visitor presence on microclimatic conditions and therefore on the conservation of historical materials: together with the microclimatic perturbance, the accessibility of visitors can require more modifications than in Historical buildings, especially if the archaeology site is underground or if it is a ruin. Additional fragility of open air sites consists of the continuous ageing, weathering, growth of vegetation and in isolated places random or usual passage/nesting of animals too.

Therefore, in the project of conservation and valorization, it is fundamental to recognize, know and understand these factors and the interferences they can generate. Diagnostics and monitoring are in a key position for acquiring that information, therefore they have an important role in the design and management of sites.

The biggest challenge, still ongoing, is to find an optimal threshold between conservation and valorization. The contribution presented here aims to understand the role of diagnostics and microclimatic monitoring within the cognitive process, both in the preliminary and fruition phases. The final goal is to prolong the durability of the materials, assuming that the material is the manifestation of cultural and historical value. Diagnostics and monitoring are therefore a fundamental activity for understanding and mitigating risk factors that affects the durability of goods and sites (Rosina *et al.,* 2011; Cecchini, 2012; Rosina, 2012; Camuffo *et al.,* 2015; Rosina *et al.,* 2019). In the following, the paper presents the investigation, monitoring, management of an underground Roman tomb in the Necropolis of Tuvixeddu in Cagliari (Figures 1 and 2).

The tomb is built inside a limestone bench and the internal surfaces are decorated with wall paintings and lime mortar stuccos.The assessment of the site regarded materials (surface sampling and chemical analysis for the characterization), degradation (sampling and chemical and biological investigations), archaeological (excavation and acquisition of results), environmental and microclimatic. The latter, which began in July 2017, includes continuous monitoring of microclimatic values (still in progress) and various psychrometric and

thermographic campaigns with the aim to understand the behaviour of the microclimate at static conditions, how it varies during the seasons, the effects of opening and presence of visitors inside it. Regarding this last aspect, continuous monitoring has allowed the recording and analysis of data also during the phases of archaeological excavation and restoration of the surfaces, when up to 10 people remained inside for many hours a day. The monitoring lasted during the discovery of new burial environments and the lowering of the walking surface to the original height, that changed of the air volume. The measurement made it possible to verify the trend of the microclimatic parameters as the volumetric conditions changed, as well as the variations due to the ventilation conditions and the presence of people.

The microclimatic data were cross-checked with the results of the chemical and biological analyses, that supported also the choice for design and size of the light system (type, lighting localization and time), air conditioning and control to be installed.

2 Method and Tools

Diagnostic and monitoring of the tomb case study cover a time span of 30 months. During this period several analyzes and data collection were carried out:
- Monitoring of T and RH by means of sensors
- Monitoring of T and RH by means of a psychrometer
- Thermography scanning
- Sampling and measurement of the quantity of water present on the surfaces - Sampling and quantification of the salt content
- Sampling and characterization of the biological degradation phenomena

Thermography and psychrometric measurements were performed on a seasonal basis. In particular, the thermograms recaptured wall and ceiling surfaces a to investigate any variations due to the presence of water in the limestone rock bank due to rain, natural sources and the above garden that has been regularly watered for years. The seasonal acquisition campaigns with psychrometer were carried out in double stroke, in the morning and in the afternoon, and detecting the values at two different heights (about one meter from the floor and near the ceiling). Finally, biological analyzes were performed for the characterization of some fungal formations that occurred only in certain periods and at specific external climatic conditions. All instrumental analyzes and investigations were carried out according to the regulatory standards contained in UNI 9252/88, UNI EN 16.714-1: 2016, UNI EN 13187: 2000.

3 Results

3.1 Monitoring

Prolonged monitoring over time has allowed researchers to build the so-called ”historical climate” (Camuffo *et al.,* 2015). The goal was to understand how and under which events the values of T and RH varied over time. The evaluation included the comparison with the environment data outside the tomb; a main the result was the identification of the time windows throughout the year in which the values of the microclimatic parameters were

almost similar, leading to the consideration that any opening could not cause large imbalances and therefore potential risk situations for the interior decorated surfaces.

Moreover, the data processing made it possible to observe the distribution of the T and RH values within the room and the side niches: the greatest variations resulted near the entrance. In that area, the imbalance is due to the poor insulation of the door and the presence of a closing wall made of concrete and brick blocks (that was built years ago to close the tomb after the demolition of a part of the rocky bank). The variations in the temperature parameters, evident in the thermograms, are clearly due to the different thermal transmittance of the concrete and the brick compared to the limestone. The phenomenon of the temperature increase is also favored by the orientation of the entrance front to the south-west without any screen or shadowing object, therefore it is subject to solar radiation in the hottest hours of the day.

Today the conformation of the tomb has changed compared to the situation in which the psychrometric and thermographic shot were made. New sepulchral rooms and the original level of the floor, that over time had been covered, emerged during the archaeologicalexcavation carried out before the restoration works. Furthermore, the presence of archaeologists and restorers made it necessary to open the tomb with a much higher frequency than in the previous period. After the works inside have been completed, a new campaign of measurements with the psychrometer and thermographic acquisition is planned, to compare and analyse the changes that have taken place and formulate the appropriate design choices for the use of the site.

The acquired data have shown that the distribution of temperatures is almost homogeneous throughout the whole year, with seasonal variations of around 2°C and Relative Humidity between 90% and 100%. The thermograms made it possible to highlight some thermal anomalies near the entrance wall, for the reasons described above, and in some points of the vaults of the side niches. This last phenomenon can be explained by a probable variation in the thickness of the rocky bank. In addition, the moisture could be due to the presence of a private garden above, which is regularly watered also in the periods of absence of rain. As a conclusion, it is probable that the concomitance of the presence of water in the ground practically constant and the reduced rock thickness make the infiltrations possible in some weak points.

As regards the laboratory analyzes carried out on the samples, it emerged that the quantity of water is particularly high, also confirming the humidity values detected with continuous monitoring and with the psychrometer. The analyzes however revealed a difference in the results between the samples taken near the entrance and those taken in the innermost parts. An explanation is that the ventilation conditions are different; in fact, the brick and block masonry and the uninsulated door felt higher ventilation than inside, thus favoring the surface evaporation of humidity. In natural conditions, the analysis of the internal values showed a variation of 0.5° C every ten days, approximately. After reporting the internal data compared to the external data, it emerged that the internal average values have variations that do not follow the external ones, as well as having a delay between the peaks (both maximum and minimum) of about two months compared to those detected externally. Instead, during the permanence of the archaeologists and restorers (December 2018) monitoring registered higher variations in temperature and more modest variations in humidity.

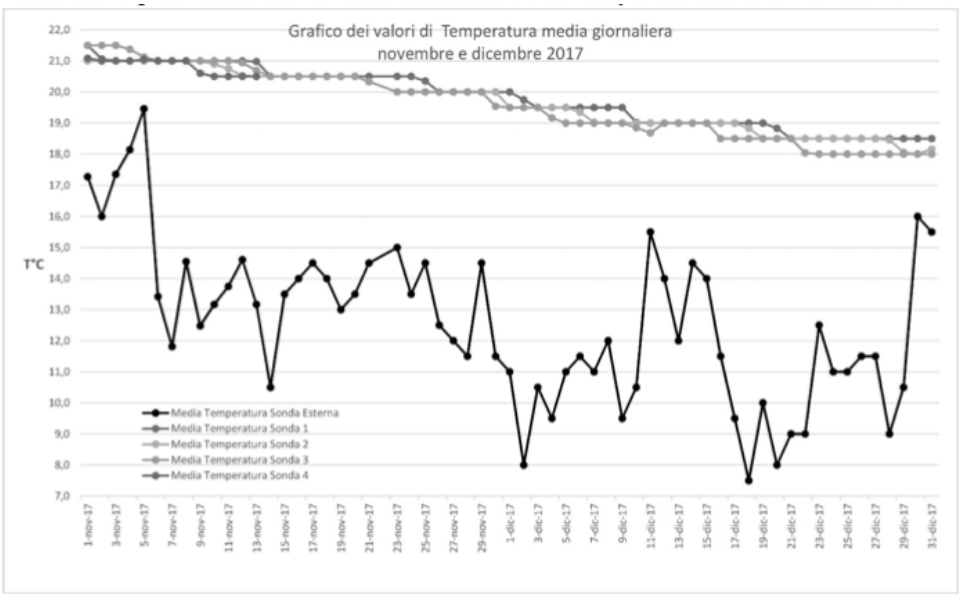

Figure 3. Graph of the daily average Temperature values recorded between November and December 2017 .

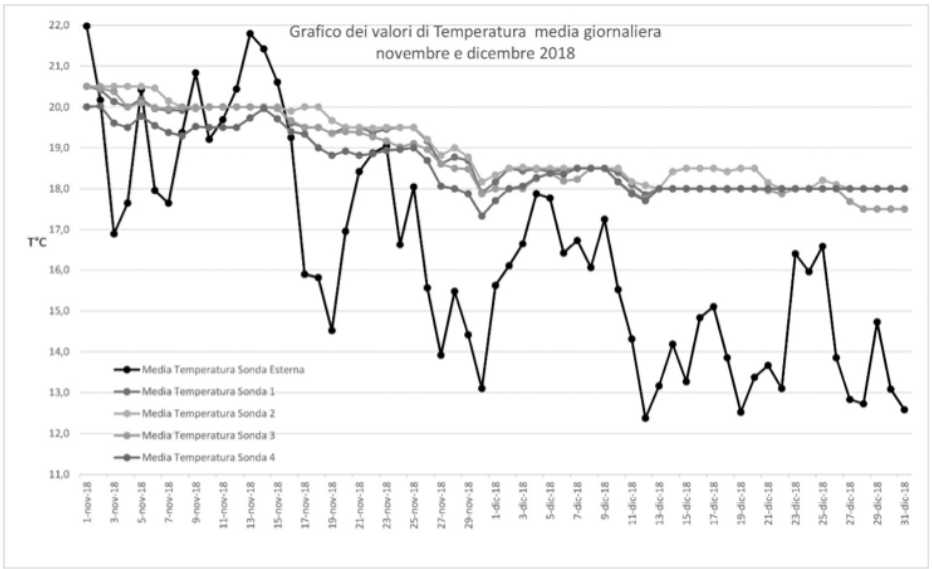

Figure 4. Graph of the daily average Temperature values recorded between November and December 2018.

3.2 Risk Factors

Concerning the above and the results obtained from the diagnostics, the following risk factors have been identified:

- Variability of microclimatic values in different conditions
- Different conditions of exposure to the presence of water in the overlying layer (heterogeneity of shapes and dimensions of the rocky bank)
- Presence of people within the site

To the first point, in addition to the implementation of an air control system, the insertion of an inlet bush that acts as an isolation environment for the passage of people could be particularly effective to avoid instantaneous and frequent imbalances in ventilation and microclimatic values. This aspect is strictly connected to the good knowledge of the optimal valuesthat must be respected for the conservation of the surfaces.

To the second point, particular attention must be paid to the critical points when designing the systems which, due to the intrinsic construction characteristics, are more exposed to infiltrations.

Last aspect, the presence of people (meaning both visitors and other subjects who can access the rooms for various reasons), in addition to an accurate programme of times, frequency and maximum number of people admitted, the systems should guarantee the possibility of adjusting the air control according to the changes to maintain the optimal conditions stably, avoiding unbalances that are harmful to the surfaces.

4 Opening Versus Conservation?

The availability of scientific literature and the present capability to conduct more appropriate restorations with the investigation of the chemical-physical properties allowed to safely open some tombs, through the study of air control and the management of the number of accesses. The environments resulted with good thermal inertia due to the thickness and the quality of the rocks. On the contrary this determines that the environments are particularly humid and, with scarce possibility to reduce the humidity. The major thermal unbalances are located near the entrances and during their opening.

Therefore, to improve the durability of historic materials in such severe ambient conditions, the scientist and competent authorities took the choice to open only the tombs with more durable materials in open air and provide a consistent plan of conservation for periodic inspection and preventive activities.

Moreover, another analysis conclusion is that only few people at time can access. The installation of a narrow suspended path above the floor has been another help to reduce the passage of many visitors at the same time. The material of the walkway will be aesthetically compatible and waterproof to stand the high humidity and do not stain with rusty the underneath structure of the tomb. Special care has been devoted, design the entrance room, with the aim to create a double space isolate the microclimate from the external variation and guarantee an intermediate space for disables Although conservation goals seem to contrast the valorization ones, that include to visit the site, the experiences conducted in the last decades showed that is possible to combine such divergent issues by keeping under control the condition and constantly updating and revising the management plan. Especially in a time

of possible variation in the climate, monitoring ambient conditions is crucial for any decision regarding the management of the fragile heritage exposed outside. The installation of visitor centers, in which it is possible to have virtual visits, watch videos, documentation and any multilevel shared knowledge, can highly decrease the pressure of real visitors. Nevertheless, opening the tombs remains a necessity that has to take into account and be possible also for technical purposes of the conservation itself. The design of the accessibility and its boundary remains one of the central focus of the conservation of archaeological sites, although sharing experiences and knowledge is far from any possible standardization of the solutions. What is possible, instead, is to share the best practices for acquiring data and monitoring in any phase of the long process of conservation, starting from the preliminary overview up to the maintenance and regular inspection after the restoration.

ORCID

Elisabetta Rosina: http://orcid.org/0000-0002-5137-1624

References

Blasco, M.F., Recuero, N., Aldas, J. and Garcia-Madariaga, J. (2018). Tourism sustainability in asrchaeological sites. *Journal of Cultural Heritage Management and Sustainable Development, 8*(3)*,* 276-292.

Camuffo, D. and Bertolin, C. (2015). New insights and meaning of "historic climate" and reburial of archaeological monuments. *International colloquium and round table in "modern methods for the protection of newly uncovered archaeological structures. Emergency conservation, protective covering, historical climate and reburial of archaeological monuments"*, Sofia and Haskovo, 10-13 Nov, 113-125.

Cecchini, A. (2012). *Le tombe dipinte di Tarquinia, vicenda conservative, restauri, tecnica di esecuzione*. Kermes quaderni, Nardini Editore.

Della Torre, S. (2003). La conservazione programmata del patrimonio storico architettonico, Milano, Guerini e Associati.

Della Torre, S. (2010). Preventiva, integrata e programmata: le logiche coevolutive della conservazione, in Pensare la prevenzione. Manufatti, Usi, Ambienti, Atti del convegno *Scienza e Beni Culturali*, Bressanone, G. Biscontin and G. Driussi (Eds.), Venezia, Arcadia ricerche, 67-76.

Guirguis M. (2017). Le necropoli e i riti funerari in: a cura di M. Guirguis. La Sardegna fenica e punica. Storia e materiali, ed Ilisso, Nuoro.

Huisman, D.J., Borenhout, M., Smit, A., Van Os, B.J.H. and Manders, M. (2009). Preservation and monitoring of archaeological sites, Ch. 11, in *Degradation of archaeological remains*, D.J. Huisman ed., publ. Sdu, 177-212.

Rosina, E. (2012). Non-destructive investigations: a case study of a convent in Lombardy (Italy), *Annales*, *2*, 9-22

Rosina, E. and Suma, M. (2019). The complexity of conservation of outfitting, historic sites and buildings under everyday uses, Convegno *Scienza e Beni Culturali*, Bressanone.

Rosina, E., Zanelli, A., Beccarelli, P., Gargano, M. and Romoli, E. (2011). New procedures and Materials for Improving Protection of Archaeological área. *Materials Evaluations, 69*(8), 979-989.

Salvi, D., Sarigu, M., Pusceddu, V. and Zamora Lopez, J.A. (2016). Sepolture tardo puniche dal lotto 7 di Tuvixeddu: due storie di bambini mai nati e alcune osservazioni epigrafiche.

Salvi, D. (2005). Cagliari, Tuvixeddu – Quartucciu, Pill'e Matta. Notizie da due necropoli puniche, A.M. Arruda (ed.). Fenicios e punicos, por terra e mar, Actas do *VI Congresso Internacional de Estudos Fenicios e Púnicos,* Lisboa, 1100-1117.

Sanchez-Moral, S., Luque, S., Cuezva, V.S., Benavente, D., Laiz, L., Gonzalez, J.M. and Saiz-Jimenez, C. (2005). Deterioration of building materials in Roman catacombs: The influence of visitors, Science of the Total Environment, *349*, 260-276.

Standard for the procedures of gravimetric test UNI 11085/03 “Beni Culturali”, Materiali lapidei naturali e artificiali. Determinazione del contenuto d'acqua: metodo ponderale.

Standard for the procedures of psicrometry and probes to monitor the microclimate UNI 10829 del 1999 Beni di interesse storico e artistico, Condizioni ambientali di conservazione, Misurazione ed analisi.

Stiglitz, A. (2014). Urbanistica di una necropoli: il caso di Tuvixeddu-Tuvumannu a Cagliari (Sardegna), *ArcheoArte. Rivista elettronica di Archeologia e Arte*, *3*, 127-146.

Thompson, J. (2007). Conservation and management challenges in a public/private partnership for a large archaeological site (Herculaneum, Italy). *Conservation and Management of Archaeological Sites, 8*, 191-204.

XV International Conference on Durability of Building Materials and Components
DBMC 2020, Barcelona
C. Serrat, J.R. Casas and V. Gibert (Eds)

Residual Strength and Durability of Glass fiber FRCM and CRM Systems Aged in Alkaline Environments

Valeria Rizzo[1], Francesco Micelli[2], Marianovella Leone[3], Antonio Bonati[4] and Maria Antonietta Aiello[5]

[1] Department of Engineering for Innovation, University of Salento, Lecce, Italy, valeria.rizzo@unisalento.it
[2] Department of Engineering for Innovation, University of Salento, Lecce, Italy, francesco.micelli@unisalento.it
[3] Department of Engineering for Innovation, University of Salento, Lecce, Italy, marianovella.leone@unisalento.it
[4] National Research Council (CNR), Institute for Construction Technologies (ITC), Viale Lombardia 49, San Giuliano Milanese, 20098, Italy, bonati@itc.cnr.it
[5] Department of Engineering for Innovation, University of Salento, Lecce, Italy, antonietta.aiello@unisalento.it

Abstract. *Fabric Reinforced Cementitious Matrix (FRCM) and Composite Reinforced Mortar (CRM) systems are used as Externally Bonded Reinforcements (EBR) in civil and historical construction. These materials are made by fibrous reinforcement, in forms of dry (FRCM) or cured (CRM) meshes embedded in a cementitious/hydraulic lime matrix. At present, this technology is considered very promising in the field of structural strengthening, retrofitting and repair existing structures. This is true especially in those cases of masonry and historical buildings, due to the specific criteria of conservation and compatibility with the substrate that need to be fulfilled. These materials, in fact, results more compatible with masonry substrate because of the inorganic matrix, instead of polymeric resin used for the well-known FRP systems (Fiber Reinforced Polymers). The recent use of these new materials in civil engineering needs appropriate and complete guidelines, that regard not only the design aspects but also the durability features. This paper presents the results of a large experimental program focused on the durability of FRCM and CRM systems and their single components, in different alkaline environments. For the whole experimental campaign, the samples have been immersed into three different alkaline solutions, for four exposure times (500, 1000, 2000 and 3000 hrs). In addition, in order to study the different accelerating effects due to temperature, three different temperatures were maintained during the ageing periods: 23°C, 40°C and 70°C. The results about the mechanical characterization of residual properties are discussed in order to highlight the influence of alkaline environments on the mechanical properties of single elements and the whole strengthening systems that were tested herein.*

Keywords: *Durability, FRCM, CRM, Alkaline Environments, Accelerated Aging.*

1 Introduction

Masonry buildings are a significant part of the architectural heritage in Europe and all over the world. A large number of these buildings, in consequence of earthquakes or other degradation processes, require repair and reinforcement because of their high seismic vulnerability and brittleness. In the last 20 years, innovative systems called EBR (Externally Bonded Reinforcement) became a common strengthening solution to replace the ordinary techniques and traditional materials in retrofitting of existing buildings. EBRs are typically composite materials, constituted by fibers of various nature (carbon, steel, basalt, glass, aramid or natural

fiber) embedded in a matrix. The most common systems are known as FRP (Fiber Reinforced Polymers), in which the matrix is constituted by a polymeric thermoset resin. During the last years, a new generation of fibrous materials was conceived and designed, by replacing the polymeric resin with inorganic matrix. These materials are called FRCM (Fabric Reinforced Cementitious Matrix) or CRM (Composite Reinforced Mortar). The difference between them is that in FRCM a soft dry net of fibers constitutes the internal reinforcement, while in CRM a rigid FRP grid is used as internal reinforcement embedded in a cementitious or lime mortar. This last technique can be considered a replacement of the traditional reinforced plaster, in which steel grid is replaced by FRP mesh. The mortar-based strengthening materials represent a valid alternative to the well-known FRP in those cases of reinforcement of existing masonry buildings. In fact, FRCMs and CRMs ensure compliance with the requirement for the conservation of architectural heritage (ICOMOS/ISCARSAH 2005). The application of FRCM and CRM provides a better compatibility with masonry substrates because of the high vapor permeability of mortar, but not only. In fact, these materials are sustainable and reversible, can be easy applied also on irregular substrates, on wet support and have better performance at elevated temperature. Due to the low costs, to the absence of galvanic corrosion (as same as traditional composites) and to the installation requirements that recall the traditional mortars, the interest of many researcher was addressed to these materials. However, many issues still require further investigation in order to guarantee the effectiveness of this technique. In fact, for both types of inorganic EBR systems, the investigation on short- and long-term behavior is essential. The durability of polymer composite materials was investigated in depth. Instead, the long-term behavior of FRCM and CRM systems represents a new research frontier, because of the lack of experimental data and poor knowledge of the possible chemical or physical degradation mechanism that may be activated in harsh environments. Only few works exist in technical literature about this important issue. Most of them are focused on Carbon (Arboleda 2014; Nobili and Signorini 2017; Donnini *et al.* 2017) and AR-Glass (Nobili 2016; Colombo et al. 2011) FRCM, in some cases following the procedures defined by Acceptance Criteria (AC434 2011), and others include the study of the durability of the constituent materials, fibers (Nobili 2016; Micelli and Aiello 2017) and mortar (Nobili 2016). In order to better understand all the possible effects due to aggressive environments in which these external reinforcement systems may work during the service lifetime, a large experimental program is presented in this paper. The research was focused on the durability of FRCM and CRM systems and their single components, namely dry glass fibers, pre-cured glass fiber grids and mortar matrix, in alkaline environments. In fact, it is important to investigate in depth, not only the behavior of the entire system, but also the effects on the chemical, physical and mechanical properties of constituents. The obtained results, in terms of residual mechanical properties and physical damages, are discussed in the paper in order to highlight the influence of alkaline environments on the mechanical properties of the tested specimens.

2 Materials and Method

The experimental program for the determination of FRCM/CRM's mechanical properties after alkaline attack consisted of two different groups. The first, called System 1 is a FRCM reinforcement while the second one, labelled System 2, is a CRM material. For both groups, not only the systems have been considered, but also their constituent elements (matrix and

reinforcement). For System 1, in fact, FRCM, dry grid of AR (alkali-resisted) glass fiber and mortar samples have been tested. The System 2 consists only of dry yarns and the corresponding pre-cured mesh of E-CR (electric grade) glass fibers reinforced polymer (GFRP), utilized to make CRM.For both groups, the alkaline treatments had been performed by immersing the samples in three different alkaline solutions, varying the chemical ions and the pH values. The first solution, called A, wanted to simulate the lime mortar matrix, with a pH equal to 12.6 (Micelli and Aiello 2017). The solution B, corresponding to Portland matrix, is a saturated solution of 0.16% $Ca(OH)_2$ + 1% Na(OH) + 1.4% K(OH) in weight, achieving a pH=12.8 (Litherland et al. 1998; Micelli and Aiello 2017). The last one, solution C, follows the standard protocol (ASTM D7705/D7705M - 12 2015), with the highest pH equivalent to 13.8. Four periods of treatment are considered, i.e. 500, 1000, 2000 and 3000 hours. In addition, with the aim to accelerate the ageing, the solutions were maintained at three incremental temperatures, 23°C, 40°C and 70°C.The samples have been labeled using the following alphanumeric code: first part means the type of specimens (for System 1 DG=Dry Grid, M=mortar, FRCM=Fabric Reinforced Cementitious Mortar; for System 2 GG=GFRP Grid, DY=Dry Yarn); second part states for treatment temperature (U=Untreated sample, 23, 40, 70°C); third letter distinguishes the alkaline environments (A=lime solution, B=Portland solution, C=standard alkaline solution); fifth part sets out the ageing time (500, 1000, 2000, 3000 hrs.). The whole experimental program consisted of 824 samples, of which: 23 untreated specimens, i.e. 5 samples for DG_U, FRCM_U, DY_U, GG_U and 3 samples for M_U); 801 aged specimens, i.e. 5 samples for each type of materials excluded mortar M (3 samples), for each alkaline environment, for each temperature and for each time. The mechanical properties of untreated samples, that constituted the reference ones, have been preliminary determined.

Single yarns of DG_U materials, i.e. the internal fibrous reinforcement of FRCM samples, have been cut from the dry grid, obtaining samples 350 mm long, and tested by performing direct tensile tests. The mechanical properties acquired are the follows: tensile strength, $\sigma_{f,DG}$, 1373 MPa (CoV=9%); maximum strain, $\varepsilon_{f,DG}$, 1.6 % (CoV=4%); elastic modulus, $E_{f,DG}$, 91 GPa (CoV=7%). The matrix of System 1 is a typical pre-mixed mortar based on lime and cement. Prismatic samples, that have the standard dimensions for three-points flexural tests, according to (CEN 1999 1999), i.e. 40x40x160 mm, have been tested for three-point bending test and the flexural strength has been determined. The compression test was carried out on the two parts of each mortar prisms derived from the flexural tests. A maximum compressive stress, $f_{c,M}$, of 20.6 MPa (CoV=7%) and a maximum flexural stress, $f_{f,M}$, of 4.0 MPa (CoV=12%) were experimentally measured for the mortar. The reinforced system was made by one sheet of DG embedded in 10 mm of mortar. Two thin layers of water-based adhesion promoter were applied before and after the introduction of the glass fabric, as recommended by the manufacturer. The dimensions of FRCM were 440x50x10 mm. They have been tested following the Italian guidelines (Consiglio Superiore dei Lavori Pubblici 2018) and the mechanical properties obtained are: ultimate stress, $\sigma_{u,FRCM}$ = 1632 MPa (CoV=16%) and corresponding maximum strain $\varepsilon_{u,FRCM}$ = 1.3 % (CoV=29%). For the second group of specimens, a pre-cured mesh of glass fibers reinforced polymer (i.e. GFRP grid) and the dry glass yarns have been tested, carrying out tensile test in both cases. The mechanical properties of GG samples result the follows: elastic modulus, $E_{f,GG}$, 48 GPa (CoV=6%); tensile strength, $\sigma_{f,GG}$, 1485 MPa (CoV=5%); the corresponding strain, $\varepsilon_{f,GG}$, is 3,0 % (CoV=8%). The dry yarns DY, that are used to manufacture the GFRP grid (GG), have been characterized, according to the Italian

technical standard. The ultimate tensile force, obtained from tensile test, was equal to 617.2 N (CoV=10%) and the elongation at break resulted 19.1 mm (CoV=19%). To immerse samples in the three different alkaline solutions, ad-hoc supports have been designed and fabricated, in order to promote a uniform distribution of the ageing solutions. All samples have been located into different stainless steel containers with transparent and plastic lid, for each alkaline solution and for each temperature.

3 Experimental Results and Discussions

After each curing period, DG, FRCM, DY and GG samples have been tested by performing direct tensile tests, while for mortar specimens (M) both three-points flexural test and compressive test have been carried out. In this way their principal mechanical properties have been determined and compared with those of control specimens. In the following section, a synthesis of the numerous outcomes has been reported.

3.1 DG Samples

The stress vs strain behavior of glass fibers yarns was pseudo-linear. At high loads, prior to failure, in some cases, sudden discontinuities were found in the curves. This was due to the progressive rupture of single filaments. In fact, the failure mode (Figure 1a) was characterized by a gradual tensile rupture of single filaments of the yarns, regardless of the alkalinity of the solution or the immersion time. With the increment of the temperature, the alkalinity of the solution C has caused the higher reduction of the mechanical properties of DG samples, while for the solution B the alkaline products have been less damaging. At the higher treatment temperature, i.e. 70°C, the tensile behavior is still linear (Figure 1b), but the influence of the different alkalinity of the three solutions, with the increase of curing time, results more evident regard to the treatments at 23°C and 40°C.

(a)

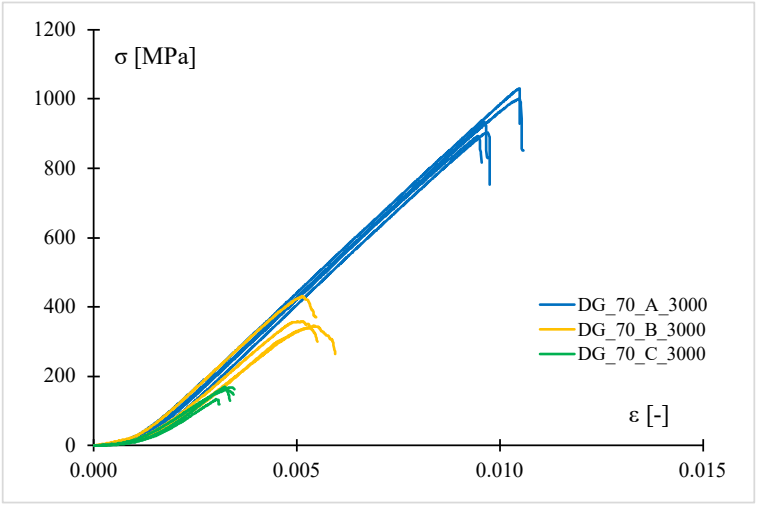

(b)

Figure 1. Typical failure mode of DG samples (a) and an example of stress-strain curves, for specimens aged at 70°C after 3000 hours (b).

3.2 M Samples

For mortar samples, the solution B turned out to be the most aggressive alkaline environment. The detrimental effects of its alkaline ions (Ca^{2+}, Na^{+} and K^{+}) are improved by the high temperature, causing the loss of compressive strength equal to 88%, after 125 days of treatments (Figure 2b). For shorter period of immersion, the reduction of the mechanical properties was obviously less (Figure 2a). In this case, after an immediate decrease of both flexural and compressive strength of mortar, no matter the alkalinity level, the immersion in aqueous solutions allows the delayed hydration of inorganic matrix and its self-healing. This results into a slight ascent of mechanical properties.

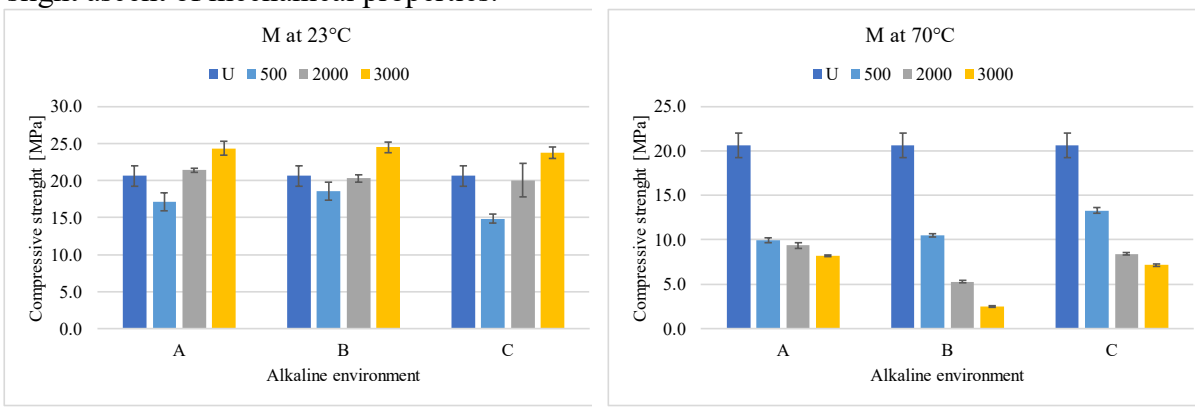

(a) (b)

Figure 2. Comparison of compressive strength of (c) M_23 and (d) M_70.

3.3 FRCM Samples

The three alkaline solutions at room temperature (23°C) seem to be not very aggressive against the tensile properties of FRCM coupons, even after 3000 hours of immersion. This is underlined by the histograms in Figure 3a, in which the values of strength of FRCM_23 samples have been plotted together with the reference one. By comparing the three solutions, the second one, that reproduces the Portland cement, has caused the greater damaging effects on the treated specimens, but, even in this case, they are very limited. The behavior of samples resulted more deformable but also more brittle. The formation of the first crack in the matrix often corresponds to the ultimate condition of samples cured for longer time. In fact, very few cracks predict the tensile failure of glass yarns.

3.4 DY Samples

The decay of mechanical features of DY specimens, contrary to what obtained from mechanical tests on dry glass fabric (DG), was activated to room temperature as early as 500 hours. This could be related to the different nature of glass fibers. Indeed, DG are constituted of alkali-resistant (AR) glass fibers, that are made by a specific formulated glass composition with addition of Zirconia (ZrO_2), and they are suitable for use in inorganic matrix. On the other hand, DY consist of the ordinary electrical grade glass fibers (E-glass). This kind of fibers are a low alkali glass, without any inclusion of Zirconia and then they are prone to chemical degradation in presence of alkaline species. The evident degradation of DY samples is due to a combination of mechanisms which may occur within the microstructure of the composite materials, i.e. an

effect of the ions $(OH)^-$, which produces corrosion of the fibers, and a second effect due to the precipitation of hydration products, which may reduce the flexibility of the fibers (Bentur 2000; Majumdar, West, and Larner 1977). All of this has been evident carrying out SEM (Scanning Electronic Microscope) analysis on damaged glass filaments. Figure 4a-b, which relate to specimens treated with CVD (Chemical Vapor Deposition) of gold particles (O'Brien 2001), show the typical morphology of the etching on the glass surface, as also seen by (Guo *et al.* 2018) in glass and basalt, and by (Aghamohammadi *et al.* 2018) in basalt fibers. In the present case, the attack appeared more extensive due to the extreme ageing conditions adopted by enhancing the temperature up to 70°C.

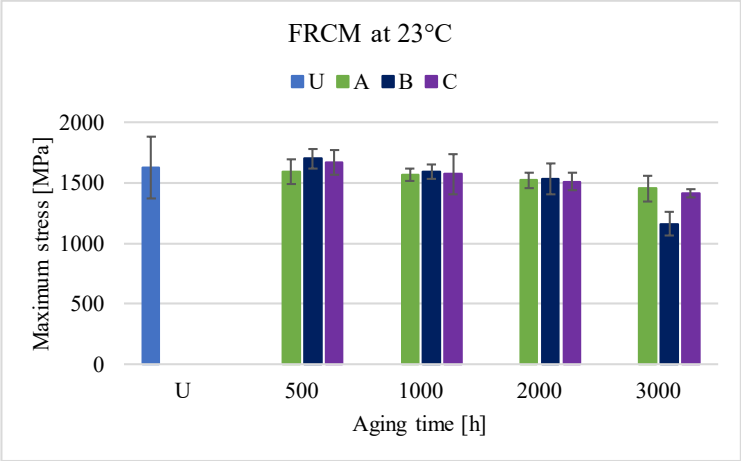

(a)

Figure 3. Tensile strength, varying the curing time of (a) FRCM_23; comparisons of stress-strain curves of FRCM at (b)40°C and (c) 70°C.

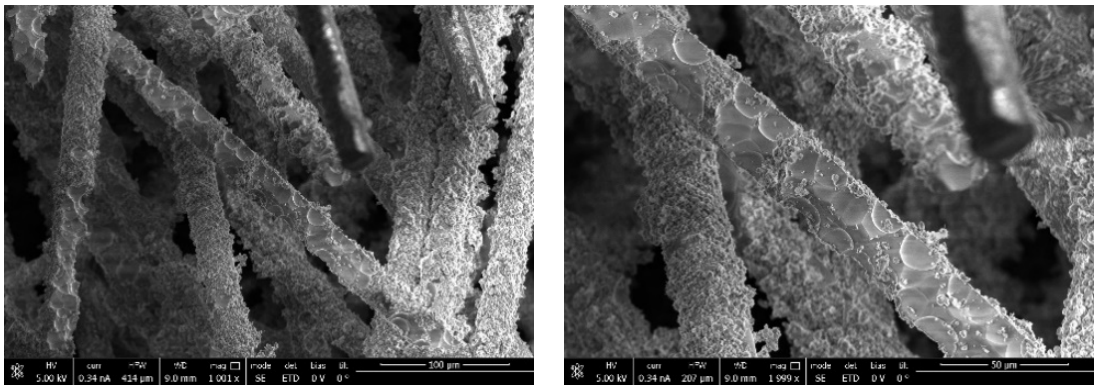

(a) (b)

Figure 4. Images of DY_70_A_3000 specimen with (e) 1001x, (f) 1999x of magnification.

3.5 GG Samples

As underlined by the histograms in Figure 5a, the most aggressive treatment is constituted by the solution B: σ decreases drastically already after 500 hours of immersion at 23°C (decline of 20%). As expected, higher temperature accelerates the detrimental effect of ions dissolved into the solution and the gap between the mechanical feature of reference samples and

GG_40_B_3000 is more that 80% (Figure 5b). The different between the maximum tensile stress of untreated samples (blue column) is more than 95% for samples treated at 70°C. For the two other solutions, A and C, the reduction does not exceed the range of variability of the standard deviation, for treatments at standard temperature, while increase at the highest temperature (-77% and -73% for the solution A and C respectively), however less than in case for solution B.

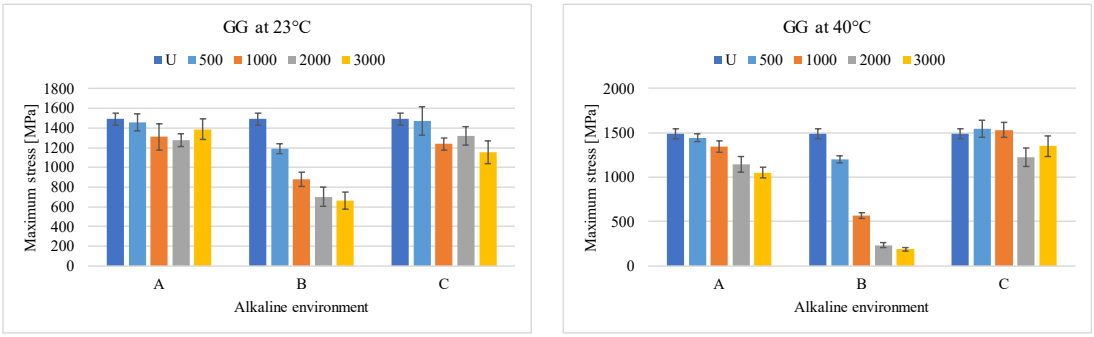

(a) (b)

Figure 5. Maximum tensile stress, varying the solutions of GG_23, GG_40

4 Conclusions

In the present paper, a large experimental program on long-term behavior of composite systems has been briefly reported. Two groups of samples, called System 1 and System 2, have been treated into three different alkaline conditions and four exposure times (500, 1000, 2000 and 3000 hrs.). The ageing was accelerated by increasing the temperature, from 23°C to 40°C and 70°C. The outcomes of the mechanical characterization of residual properties of two different systems highlighted what in the follow:

- Aging at 23°C results not very aggressive for samples of System 1, while the effects were more visible for dry yarns of E-glass fibre and the GFRP specimens (System 2)
- A particular behaviour has been observed in case of mortar samples, especially when they have been aged at 23°C. The immersion in an aqueous solution leads to self-healing process and the mechanical properties do not decrease because of the alkaline environments, but rather increase as effect of the delayed hydration of inorganic matrix.
- The treatments at 70°C, as expected, have provoked an extremely detrimental impact and until the completely break-up of the E-glass dry yarns.
- For these last samples SEM analysis has been performed, in order to detect the surface morphologies and fracture surface of E-glass corrupted filaments. In particular, in case of solution A, at 70°C and after 3000 hours of immersion, the filaments result completely covered by precipitated calcium carbonate and the massive damage that occurred have caused an evident reduction of the cross section, almost to zero in some regions. This is due to etching on the glass surface and to the extreme ageing conditions adopted by enhancing the temperature up to 70°C.

Acknowledgements

The authors would like to acknowledge the support of the staff of the Fibre Net S.p.A and of the Construction. Division of the National Research Council (CNR) for their strong support in developing the ongoing research. The support of the RELUIS Project 2019-21 is strongly appreciated too.

ORCID
Valeria Rizzo: https://orcid.org/0000-0003-1267-7484
Francesco Micelli: https://orcid.org/0000-0002-1751-7343
Marianovella Leone: https://orcid.org/0000-0001-9929-6785
Antonio Bonati: https://orcid.org/0000-0002-7221-6180
Maria Antonietta Aiello: https://orcid.org/0000-0001-6533-7008

References

AC434. 2011. "ACCEPTANCE CRITERIA FOR MASONRY AND CONCRETE STRENGTHENING USING FIBER-REINFORCED CEMENTITIOUS MATRIX (FRCM) COMPOSITE SYSTEMS."

Aghamohammadi, Hamed, S. Navid Hosseini Abbandanak, Reza Eslami-Farsani, and S. M.Hossein Siadati. 2018. "Effects of Various Aluminum Surface Treatments on the Basalt Fiber Metal Laminates Interlaminar Adhesion." *International Journal of Adhesion and Adhesives* 84 (February): 184–93. https://doi.org/10.1016/j.ijadhadh.2018.03.005.

Arboleda, D. (2014). "*Fabric Reinforced Cementitious Matrix (FRCM) Composites for Infrastructure Strengthening and Rehabilitation : Characterization Methods*" *PhD Thesis*, 1–131.

ASTM D7705/D7705M - 12. 2015. "Standard Test Method for Alkali Resistance of Fiber Reinforced Polymer (FRP) Matrix Composite Bars Used in Concrete Construction" i: 1–5. https://doi.org/10.1520/D7705.

Bentur, A. (2000). "Role of Interfaces in Controlling Durability of Fibre-Reinforced Cements." *J. Mater. Civ. Eng.* 12 (February): 2–7.

CEN (1999). 1999. "EN 1015-11: Methods of Test for Mortar for Masonry - Part 11: Determination of Flexural and Compressive Strength of Hardened Mortar." *European Committee for Standardization*, 12. http://www.docin.com/p-279781425.html.

Colombo, I., Colombo, M., Magri, A., Zani, G. and di Prisco, M. (2011). "Textile Reinforced Mortar at High Temperatures." *Applied Mechanics and Materials* 82: 202–7. https://doi.org/10.4028/www.scientific.net/AMM.82.202.

Consiglio Superiore dei Lavori Pubblici. (2018). "Linea Guida per La Identificazione, La Qualificazione Ed Il Controllo Di Accettazione Di Compositi Fibrorinforzati a Matrice Inorganica (FRCM) Da Utilizzarsi per Il Consolidamento Strutturale Di Costruzioni Esistenti," in Italian, 1–5. https://doi.org/10.1109/ChiCC.2015.7260208.

Donnini, J., De Caso, F., Corinaldesi, V., Lancioni, G., and Nanni, A. (2017). "Fabric-Reinforced Cementitious Matrix Behavior at High-Temperature: Experimental and Numerical Results." *Composites Part B* 108: 108–21. https://doi.org/10.1016/j.compositesb.2016.10.004.

Guo, F., Al-Saadi, S., Singh Raman, R. K. and Zhao, X. L. (2017). "Durability of Fiber Reinforced Polymer (FRP) in Simulated Seawater Sea Sand Concrete (SWSSC) Environment." *Corrosion Science* 141: 1–13. https://doi.org/10.1016/j.corsci.2018.06.022.

ICOMOS/ISCARSAH. (2005). "*Recommendations for the Analysis, Conservation and Structural Restoration of Architectural Heritage*" 2005. https://www.icomos.org/en.

Litherland, K.L., Oakley, D.R. and Proctor, B.A. (1981). "The use of accelerated aging procedures to predict the long term strength of GRF composites". *Cem Conc Res* 1981;11: 455-466.

Majumdar, A. J., J. M. West, and L. J. Larner. (1977). "Properties of Glass Fibres in Cement Environment." *Journal of Materials Science* 12 (5): 927–36. https://doi.org/10.1007/BF00540975.

Micelli, F., and Aiello, M.A. (2017). "Residual Tensile Strength of Dry and Impregnated Reinforcement Fibres after Exposure to Alkaline Environments." *Composites Part B: Engineering*. https://doi.org/10.1016/j.compositesb.2017.03.005.

Nobili, A. (2016). "Durability Assessment of Impregnated Glass Fabric Reinforced Cementitious Matrix (GFRCM) Composites in the Alkaline and Saline Environments." *Construction and Building Materials* 105: 465–71. https://doi.org/10.1016/j.conbuildmat.2015.12.173.

Nobili, A, and Signorini. C. (2017). "On the Effect of Curing Time and Environmental Exposure on Impregnated Carbon Fabric Reinforced Cementitious Matrix (CFRCM) Composite with Design Considerations." *Composites Part B* 112: 300–313. https://doi.org/10.1016/j.compositesb.2016.12.022.

O'Brien, P. (2001). "Chemical Vapor Deposition." In *Encyclopedia of Materials: Science and Technology*, 1173–76. Elsevier. https://doi.org/10.1016/B0-08-043152-6/00219-9.

XV International Conference on Durability of Building Materials and Components
DBMC 2020, Barcelona
C. Serrat, J.R. Casas and V. Gibert (Eds)

Resistivity Measurements to Assess the Freeze - Thaw Attack on Concrete – Lab Specimen and Real Structure

Frank Spörel

Federal Waterways Engineering and Research Institute (BAW), Kussmaulstraße 17, 76187 Karlsruhe, Germany, frank.spoerel@baw.de

Abstract. *Waterway structures like locks are exposed to a severe freeze-thaw-attack. A sufficient resistance of concrete against this exposure has to be assured. In Germany the concrete for the exposure class XF3 of federal waterway structures has to be tested in the laboratory by the CIF-Test in addition to descriptive requirements. To establish this procedure experiences on concrete mix designs which have been applied in the past were considered as well as research concerning the transferability of laboratory tests to practical experience. One important aspect was a service life study on the degree of water saturation of the concrete under practical conditions in combination with the temperature exposure. The paper presents the results of freeze-thaw tests on lab specimens and cores of concrete elements stored differently and tested at different ages. For a better understanding of the processes of the freeze-thaw attack during the freeze-thaw tests monitoring data of resistivity has been analyzed and compared to hardened concrete properties. The water absorption inside the specimen during capillary suction and the freeze-thaw-cycles could be monitored at different distances to the surface. Correlations of the water absorption to the initiation and development of internal damage were observable. A consideration of the results of the freeze-thaw tests and the resistivity measurements enables a better evaluation of long-term resistivity monitoring data of a lock. It allows for an assessment of the transferability of results of the CIF-Test to practical experience.*

Keywords: *Freeze-Thaw Attack, Resistivity, Monitoring, Concrete Core, Lab Specimen.*

1 Introduction

In Germany for hydraulic structures like locks or weirs there are special requirements concerning concrete properties. As they are massive structures a low heat of hydration of the concrete to reduce restrain is important and on the other hand a high durability for a service life of hundred years. Freeze-thaw resistance is a very important durability aspect for those structures as the high water saturation of the lock chamber walls between head and tail water results in a severe freeze-thaw attack. During the initial test of the concrete intended for parts of the structures in XF3 exposure a performance test is required for new structures under the responsibility of the Federal Ministry of Transport and Digital Infrastructure. The CIF-Test according to (BAW, 2012) has to be passed. The procedure is similar to the RILEM recomendation (Setzer *et al.*, 2004).

Before the mandatory introduction of this test questions concerning the transferability of the results of laboratory tests to practical experience were intensively discussed. To address that question the monitoring of the temperature and moisture exposure of real structures was supposed to be an adequate way to get reliable information on this question. Different structures like bridges, tunnels and locks were equipped with sensors for long term monitoring campaigns. A detailed analysis of the freeze-thaw attack on concrete structures based on monitoring data of real structures is published in (Spörel, 2013). The main

differences between XF1 and XF3 exposure have been worked out for an example of a lock. The monitoring of the lock has been continued for 16 years during the whole service life of the lock so far and can be evaluated. As the monitoring data gives an impression of the complete history of the freeze-thaw attack during the previous service life of the structure (Spörel, 2016) it can be considered in evaluating the surface scaling observed at the structure.

To support the evaluation of the long-term resistivity monitoring of the lock the paper describes resistivity monitoring results on the freeze-thaw attack during the CIF-Test on lab specimens and concrete cores which were equipped with the same sensors as the lock.

2 Principles to Monitor the Freeze-Thaw Attack on Concrete

2.1 General

Concerning freeze-thaw attack the temperature and the degree of saturation are decisive parameters. If a critical degree of saturation is reached a freeze-thaw damage can occur (Fagerlund, 1977). As a continuous direct measurement of the degree of saturation is not possible an indirect determination of the degree of saturation by means of resistivity measurements was chosen. A calibration is required to account for different influencing parameters on the resistivity (Elkey and Sellevold, 1995; Spörel, 2013).

2.2 Monitoring System

The resistivity measurement was conducted using a multiring electrode (MRE). The MRE is a sensor consisting of several rings of stainless steel, each with a thickness of 2.5 mm, with an insulating plastic ring between two steel rings. It enables AC resistance measurements of the concrete between two adjacent steel rings in eight steps at a frequency of 10.8 Hz and at a distance of 7 to 87 mm to the concrete surface (Raupach, 1992). A multitemperature probe (MTP) is installed near the MRE. The MTP is equipped with eight PT 1000 sensors to enable temperature measurements at eight different distances to the concrete surface. A typical arrangement of a measuring point is shown in Figure 1.

Figure 1. MRE and MTP (left), Sensor installation in a structure (right) (Spörel, 2019).

2.3 Focus of Data Evaluation

One aspect to evaluate the intensity of a freeze-thaw attack is the number of freeze-thaw cycles. As the freezing temperature of water in the pore structure of concrete depends on the pore size (Brun *et al.*, 1977; Setzer, 2000) a simple evaluation of temperature data might be

misleading concerning the intensity of a freeze-thaw attack. The freezing of water in the pore structure is decisive to activate the micro-ice-lens pump according to (Setzer, 2002). Resistivity measurements indicated that a minimum degree of saturation is required for the freezing of water in the pores (Spörel, 2013). In a hygroscopic saturation state only finer pores are filled with water and no freezing of water was observed at certain temperatures below 0 °C. The approach of (Brun *et al.*, 1977; Setzer, 2000) could be detected by resistivity measurements (Spörel, 2013; Spörel, 2016).

The effect of temperature on the resistivity has to be compensated to monitor concrete saturation. The investigations have shown that the Arrhenius approach (equation 1) is working well at concrete temperatures higher than 0 °C if the activation energy is determined and considered adequately (Spörel 2013, Spörel 2016). The constant b correlates to the degree of saturation of the concrete and has to be adapted at changing degrees of saturation.

$$\rho_{el} = \rho_{el,0} \cdot e^{b \cdot \left(\frac{1}{T} - \frac{1}{T_0}\right)} \quad (1)$$

ρ_{el} Resistivity at temperature T in Ωm
$\rho_{el,0}$ Resistivity at temperature T_0 in Ωm
T, T_0 Absolute temperature in K
b Constant in K

At temperatures below 0 °C the Arrhenius approach is not effective if the degree of saturation of concrete is high. There is an abrupt increase of the temperature compensated resistivity if temperature decreases below 0 °C. This takes place in a much shorter time than observed when wet concrete is drying. These observations were attributed to freezing of water in the pore structure (Spörel, 2013; Spörel, 2016) and are very helpful as it enables to monitor freeze-thaw attack in laboratory tests as well as for the data interpretation of the long-term monitoring of the lock. The potential of resistivity measurements to detect freezing of water was also observed for cement pastes (Sato and Beaudoin, 2011; Wang *et al.*, 2016).

To evaluate the intensity of a freeze-thaw attack an analysis of meteorological data is not sufficient. There are relevant differences between freeze-thaw-cycles analyzed on meteorological data and on the temperature measured in the concrete cover zone. The difference even rises if freezing effects detected by resistivity measurements in the concrete are compared to meteorological data (Spörel, 2013).

Using this approach resistivity measurements by means of MREs were used for monitoring the freeze-thaw attack in lab specimen, small concrete elements and concrete cores. This enables to evaluate the transferability of results of freeze-thaw lab test to practical application.

3 Investigation Concept

The transferability of results of freeze-thaw tests to practical experience has always been discussed concerning adequate testing ages and storage conditions of the lab specimens. The pore structure of the concrete is influenced by that and important as transport mechanisms play an important role. In (BAW, 2012) the storing conditions for the CIF- and CDF-test are described for different testing ages. As usually concrete with a slow strength development is used for hydraulic structures the standard testing age is 56 d after storage in water for 14 d.

To address this question investigations were realized on a concrete with the same composition and the same source of raw materials as used in the lock described in (Spörel, 2013; Spörel 2016). A concrete with 270 kg/m³ CEM III/A 32.5 N LH, 80 kg/m³ fly ash, a water content of 143 kg/m³ and an aggregate content of 1876 kg/m³ was investigated.

A set of five lab specimen for the CIF-Test at different ages were cast as well as two concrete elements. The concrete elements and two additional lab specimens for each test series were equipped with MREs and MTPs to monitor the resistivity during the CIF-Test and the storage of the elements under natural exposure up to a distance to the surface of 42 mm. The testing ages were set at 28 d, 56 d and 365 d for the lab specimens. At the testing age of 365 d two different storing conditions were applied (demoulding after 14 d; 351 d 20°C, 85 % rel. humidity; demoulding after 2 d, water storage at 20 °C for 321 d, 20°C/65% rel. humidity for 42 d). Additionally concrete cores were taken from the concrete element stored in the field. The cores were tested at an age of 56 d, 365 d and 6.5 a. As example results of the 6.5 years old cores are presented. The design of the element and the position of the cores and sensors are shown in Figure 2.

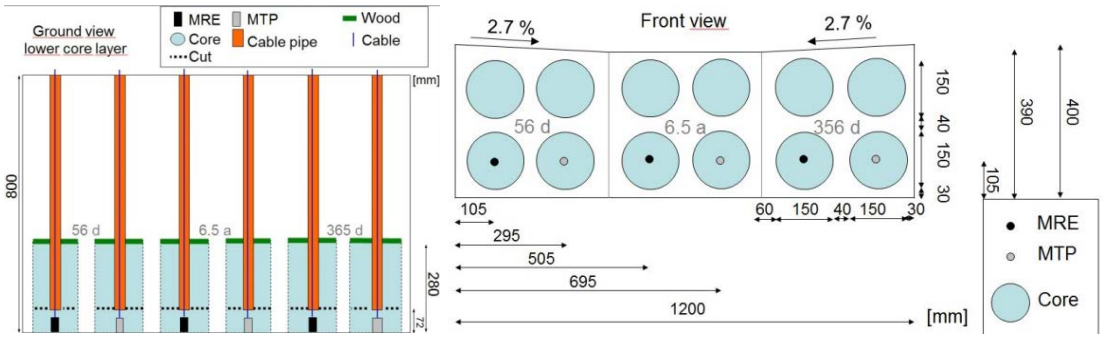

Figure 2. Dimensions of the concrete element and positions of the sensors and cores.

4 Concrete Properties

Additionally the strength development of the concrete was determined and summarized in Table 1 for cylindrical specimens with a height to diameter ratio of 2.0 for the lab and core specimens. The strength of the core specimens is lower than of the lab specimens. This confirms findings in the literature (The Concrete Society 2004; DIN EN 13791/A20 (2017).

The carbonation depth was determined on slabs 100x100x500 mm which were stored under the same conditions as the specimens for the CIF-Test and the concrete element. For slag cement concrete the carbonation depth might influence the scaling of concrete during the CIF-Test. Results are summarized in Table 1.

Table 1. Test Results for compressive strength and Carbonation.

Concrete age	f_{cm} [N/mm²]		d_c [mm]			
	Lab specimen	core	20/65	20/85	water	outdoor
56	37.3	31.8	**1.8**	1.0	0.0	2.7
365	47.4	37.2	5.4	**4.3**	**1.0**	5.1
6.5 a	-	33.3	13.0	-	8.0	**8.0**

Results of the CIF-tests for selected storage and testing age versions according to section 3

are presented in figures 3 and 4. Besides the standard testing age of 56 d two test series at an age of 365d and results of cores at a high age of 6.5 years representing a situation at a structure at a higher age are compared as examples. The test results are evaluated concerning scaling and internal damage measured by the relative dynamic Young´s modulus. The testing of cores of a structure in a freeze-thaw test includes effects of concrete casting, curing and exposure as well as influences of the coring process on the freeze-thaw resistance. This has to be kept in mind when comparing the results to those of standard lab specimens at a defined testing age and storing conditions.

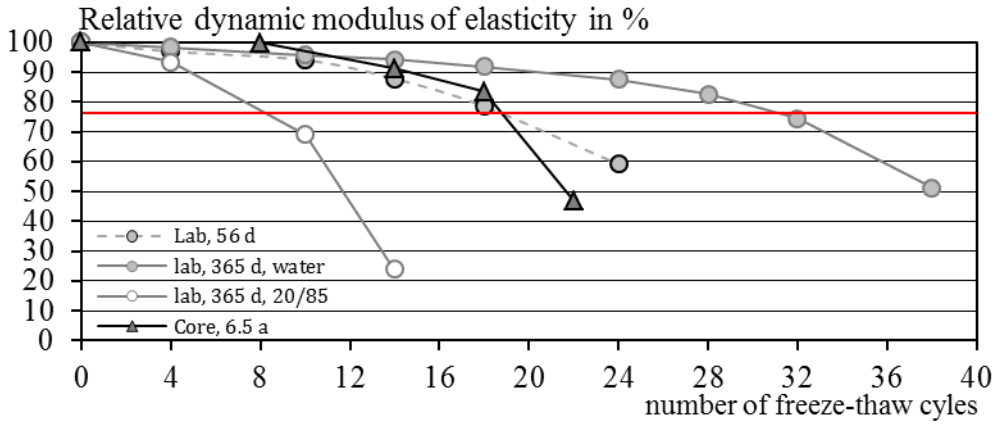

Figure 3. Relative dynamic modulus of elasticity.

Concerning internal damage the significantly lowest freeze-thaw resistance was observed for the concrete stored in climate 20/85 for one year. After 10 freeze-thaw cycles the results fall below the criteria of 75 %. The highest resistance was determined for the water stored specimens. The results of the standard conditions were congruent with the cores at high age.

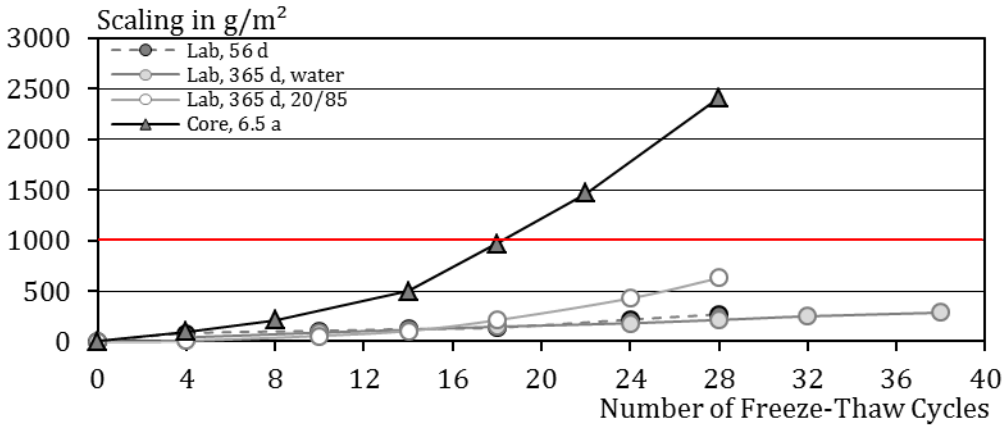

Figure 4. Scaling during the CIF-Test.

Looking at the lab specimens scaling was affected only slightly by the investigated storing conditions. The lab specimens tested at standard age and curing conditions showed

comparable results to the water stored specimens tested at an age of 365 d. The storage in climate 20°C/85% rel. humidity resulted in the highest scaling for the lab specimens but still passed the criteria of 1000 g/mm² according to (BAW 2012). Considerably higher scaling was observed for the cores tested at an age of 6.5 years correlating to the carbonation depth.

Both for the scaling and the internal damage development the testing age is not the decisive parameter concerning the freeze-thaw resistance of the concrete. The effect of the curing regime on the internal damaged was very dominant for the lab specimens. The stronger impact of the storing conditions than the testing age was observed for the scaling as well. The scaling results of the cores yet showed a strong deviation of the lab specimens. Influences of the carbonation depth at the start of the CIF-Test might have an impact on the test results. A low carbonation for the standard and water storage, and higher values for the storage at 20 °C and 85 % rel. humidity and for the cores were measured (Table 1, Bold type values).

5 Resistivity Measurements

For a better understanding of the processes during the CIF-Test the monitoring data was evaluated. An important parameter is the water absorption during the capillary suction phase and during the freeze-thaw cycles. As an example in Figure 5 results of the resistivity measurements in a distance of 32 mm to the surface and the weighing of the samples for the period of capillary suction before the start of the freeze-thaw-cycles are shown. The weighing data illustrate the great influence of the storage conditions of the specimens. By oven drying at 105 °C the degree of saturation of the differently stored specimens was determined before and after capillary suction (Table 2). The degree of saturation of the water stored specimens is already high before the capillary suction starts whereas the specimens stored for one year in climate 20° C/85% rel. humidity has a very much higher absorption potential.

Table 2. Degree of saturation at the beginning of capillary suction.

	Storing conditions			
	56 d, 20/65	365 d, 20/85	385 d, water	6.5 a, outdoor
Degree of saturation before capillary suction [%]	51	57	82	67
Degree of saturation after capillary suction [%]	63	79	90	78

The resistivity data illustrate that in a measuring depth of 32 mm from the surface only for the concrete stored for one year in climate 20 °C/85 % rel. humidity a decrease in resistivity is observed during the capillary suction period. The decrease of resistivity is caused by a rising degree of water saturation in that measuring depth of 32 mm. The resistivity of the other specimens was not affected by water absorption in that measuring depth. According to Table 2 the highest rise of the degree of saturation during the capillary suction phase was observed for the specimen stored in 20 °C/85 % rel. humidity. This indicates that it might be plausible that only this specimen showed a change in resistivity at that measuring depth. Closer to the surface also for the other specimens a decrease of resistivity was observed.

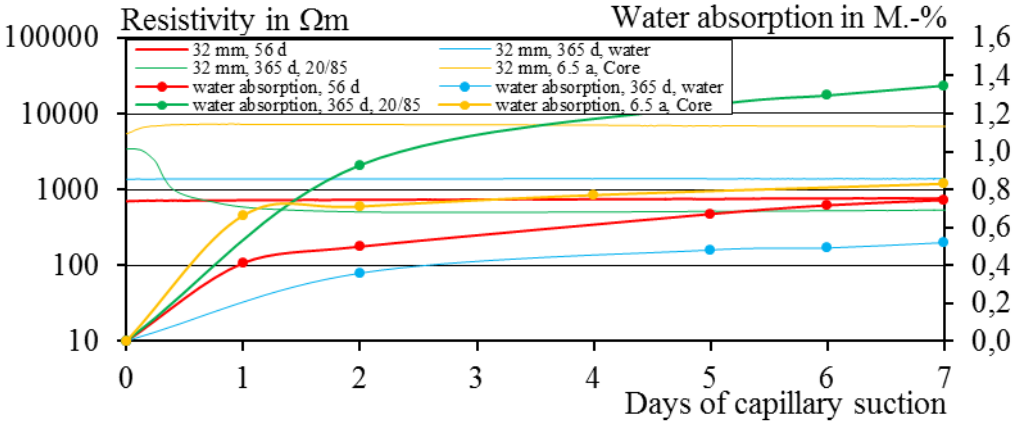

Figure 5. Water absorption during capillary suction.

Figure 6 shows the resistivity in a measuring depth of 42 mm during the freeze-thaw-cycles which was compensated for temperature effects according to equation (1) and the development of the relative dynamic modulus of elasticity. As described in (Spörel, 2013; Spörel, 2016) a typical increase and decrease of the resistivity is observed during the freeze-thaw cycles caused by freezing and melting of water in the pore structure. High resistivity is measured at concrete temperatures down to –20 °C when water in the pore structures is frozen and low values are measured at temperatures between 0 and 20 °C when the water is present in a liquid state. The Arrhenius approach is unable to compensate the effects of the freezing of water on the resistivity.

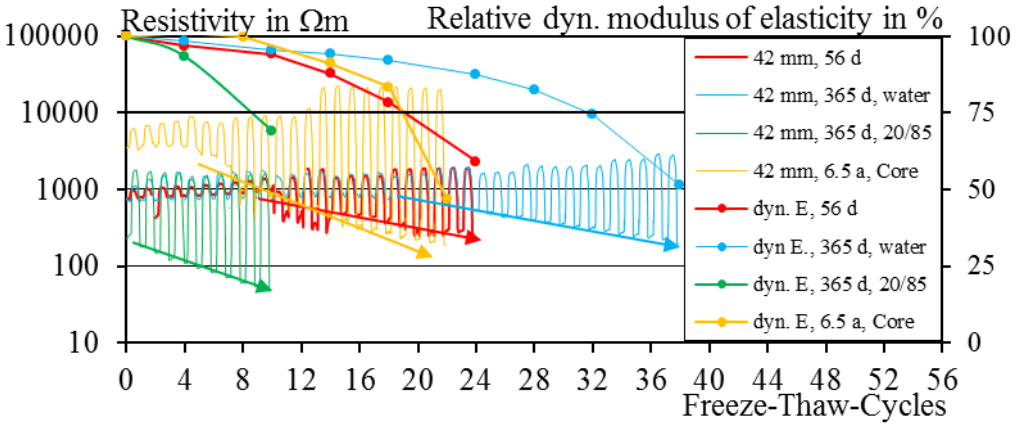

Figure 6. Temperature compensated resistivity and dynamic modulus of elasticity during the CIF-Test.

The low resistivity values decrease over time which is marked by arrows. This indicates the rise of the degree of saturation in that measuring depth. Analogue with that the dynamic modulus of elasticity starts to decrease. For the water stored concrete at an age of 365 d the decrease of resistivity starts at about 20 freeze-thaw cycles in that measuring depth. About at that time the relative modulus of elasticity also starts to decrease more rapidly as before. For the other samples similar correlations are observed. As proposed by (Fagerlund, 1977) the

results seem to confirm that after reaching a critical degree of saturation the concrete is damaged. The water absorption according to the micro-ice-lens theory (Setzer, 2002) also seems to be confirmed. At certain distances to the surface no water transport was detectable during the capillary suction whereas during the freeze-thaw cycles a water transport occurred.

6 Conclusions

By means of monitoring the resistivity of concrete at different distances to the surface the micro-ice-lens theory (Setzer, 2002) and the theory of the critical degree of saturation (Fagerlund, 1977) seem to be comprehensible. The effect resulting from the freezing of water in the pore structure of concrete on the resistivity will be a helpful tool to further analyze the monitoring data of the lock concerning the frequency of such freezing incidents under practical conditions. The results of the resistivity monitoring in lab tests and the long-term monitoring of a lock in combination with a consideration of the surface damages at the lock enable to better evaluate the transferability of results of the CIF-Test to practical conditions.

References

BAW Code of Practice (2012). *Frost Resistance Tests for Concrete.* Federal Waterways Engineering and Research institute (BAW), Karlsruhe, Germany

Brun, M., Lallemand, A., Quinson, J.-F. and Eyreaud, C. (1977). A new method for the simultaneous determination of the size and shape of pores: the thermoporometrie. *Thermochemica Acta 21 (1)*, 59-88

DIN EN 13791/A20 (2017). *Assessment of in-situ compressive strength in structures and precast concrete components; Amendment A20*, Beuth Verlag, Berlin.

Elkey, W., Sellevold, E.J. (1995). *Electrical resistivity of concrete*, Norwegian Road Research Laboratory, Publication No. 80

Fagerlund, G. (1977). The critical degree of saturation method of assessing the freeze-thaw resistance of concrete. *Materials and Structures 10*, No. 58, 217-229.

Raupach, M. (1992). *Zur chloridinduzierten Makroelementkorrosion von Stahl in Beton.* Berlin: Beuth Verlag GmbH. Schriftenreihe des DAfStb, Nr. 433 (in German), PhD thesis, RWTH Aachen University

Sato, T. and Beaudoin, J. J. (2011). Coupled AC Impedance and Thermomechanical Analysis of Freezing Phenomena in Cement Paste. *Materials and Structures 44*, 405-414

Setzer, M.J. (ed.) (2000). Micro Ice Lens Formation. *3rd Intrn. Bolomey Workshop - Pore solution in Hardened Cement Paste* Essen 1998. Aedificatio, Freiburg, 89-112

Setzer, M. J. (2002). Development of the micro-ice-lens model. *International RILEM Workshop on Frost Resistance of Concrete.* RILEM Publications SARL, 133-145

Setzer, M.J. et al. (2004). RILEM TC 176-IDC: Internal damage of concrete due to frost action. Final recommendation: Test methods of frost resistance of concrete: CIF Test: Capillary suction, internal damage and freeze-thaw test – Reference method and alternative methods A and B. *Materials and structures 37*, 743-753

Spörel, F. (2013). *Frostbeanspruchung und Feuchtehaushalt in Betonbauwerken.* Berlin, Beuth Verlag GmbH. Schriftenreihe des DAfStb, Nr. 604 (in German), PhD thesis, RWTH Aachen University

Spörel, F. (2016). Freeze-Thaw-Attack on concrete structures -laboratory tests, monitoring, practical experience. *Proceedings PRO 114 Conference on Materials, Systems and Structures in Civil Engineering - Frost Action in Concrete.* Paris / RILEM Publications S.A.R.L., 151-160

Spörel, F. (2019*).* Monitoring of the freeze-thaw attack on concrete. *The nordic concrete federation workshop proceedings No. 16 "Concrete in arctic conditions"*, 75-78

The Concrete Society (2004). *In situ concrete strength. An investigation into the relationship between core strength and standard cube strength.* Concrete Society Project Report No. 3, Camberley, UK.

Wang, Z., Wang, L., Yao, Y. (2016). Percolation in cementitious materials under freeze-thaw cycles investigated by means of electrical resistivity. *Proceedings PRO 114 Conference on Materials, Systems and Structures in Civil Engineering - Frost Action in Concrete.* Paris/RILEM Publications S.A.R.L., 201-210

XV International Conference on Durability of Building Materials and Components
DBMC 2020, Barcelona
C. Serrat, J.R. Casas and V. Gibert (Eds)

Restoration of Historic Windows: Methodology and Case Studies

Edward A. Gerns[1] **and Sarah K. Van Domelen**[2]

[1] Wiss, Janney, Elstner Associates, Inc., 10 South LaSalle, Suite 2600, Chicago, Illinois, USA, egerns@wje.com

[2] Wiss, Janney, Elstner Associates, Inc., 10 South LaSalle, Suite 2600, Chicago, Illinois, USA, svandomelen@wje.com

Abstract. *All too often, the original windows are unnecessarily removed and replaced from historic buildings. In some instances, replacement is justified due to the extent of deterioration resulting from years of deferred or inappropriate maintenance. However, often historic windows are unnecessarily replaced as a result of incorrect assumptions or misinterpretation of their condition. Alternatively, a designer may believe that a new window will perform better, require less maintenance, increase energy efficiency, or just last longer than the existing original windows. This may not be the case. This paper will address issues related to the evaluation and restoration of historic wood and metal windows. An overview of the methodology used by the authors to evaluate the condition of windows and determine repairs that are necessary to maintain structural integrity, repairs that are necessary to address air and water infiltration, and repairs relative to aesthetics and function, will be presented.*

Keywords: *Wood Windows, Steel Windows, Evaluation, Restoration.*

1 Introduction

Windows are a character defining architectural feature of almost all buildings. At a functional level, windows provide natural light and fresh air, and sometimes a means of egress, to interior spaces. Over the years, many building owners have opted to replace rather than restore original historic windows. Replacement window manufacturers tout these products as a means of providing increased thermal performance and 'no maintenance.' However, in reality, replacement windows may have unrealistic payback periods, and many new windows are actually 'not maintainable.' Alternate materials such as aluminum, and more recently vinyl and fiberglass, have been used to replace historic original windows. In many instances, when considering life cycle costs as well as maintaining historic fabric, repairing and restoring historic windows is not only environmentally and preservation sensitive, but also economical. Thermal upgrades are also possible by installing storm windows at a macro scale, or replacing or installing weather-stripping at a micro level.

2 Evaluation Methodology

Determining the general condition of any historic window is critical to developing a restoration program. The condition of windows can vary significantly based on orientation and location within the facade. Often, coatings and/or previous interventions may be misleading relative to the actual condition of the window components. Determining the extent and location of hazardous materials is also critical to accurately developing an appropriate scope of work. Based on the findings, special provisions for remediation may be required. In some instances,

hazardous materials may have been installed during original fabrication or installation and may be concealed by the various components of the windows.

The general methodology used by the authors when evaluating historic windows includes document review, comprehensive or representative close-up interior and exterior surveys, investigative openings, and partial or complete window disassembly. Based on the available funds and access, all of these tasks may not be possible or practical. Much like any aspect of building restoration, building owners should understand that gathering more information during the initial evaluation can reduce the potential for unanticipated added costs once work begins.

2.1 Document Review

When existing building drawings or specifications exist, review of these documents can provide insight into the construction of the windows, as well as the method of anchorage to surrounding construction. Particularly in the case of wood windows, the windows were often constructed onsite to accommodate variation in the as-built openings, and original drawings may be limited or nonexistent. In the case of metal windows, the original manufacturer can sometimes be determined by comparing window profiles with resources such as Sweet's Catalogue. Review of documents detailing past maintenance or repairs can also help identify existing conditions.

2.2 Visual Survey: Exterior

Close-up observation of the exterior portions of the windows is critical to determine the extent of intervention that may be required. While a comprehensive review of all windows is ideal, selected review must often suffice due to access considerations. If possible, windows from all facades and different floors should be reviewed. If there are different types of windows, a sample of each should be included. Observations should include the condition of the coatings, perimeter seals, and glazing putty and stops, but perhaps more critical is the evaluation of the substrate material. Peeling paint and missing putty can often be misleading when the substrate materials are actually in relatively good condition. Typically, the lower portions of the jambs and side rails of the sash, and the sill and bottom rail of the sash exhibit the most deterioration. Probing these areas with an awl can be an effective means to assess the condition of the substrate for both wood and metal windows. In the case of wood windows, the awl will readily penetrate rotted areas. Areas of corrosion or section loss in metal windows may be visually apparent, previously installed fillers can often be detected by tapping areas with the awl.

If the water resistance of the windows is in question, performing water testing using various techniques can provide an indication of the source(s) of the leakage. It is important to understand, however, that historic windows cannot meet standardized testing criteria for new windows, and that failure to meet current standards for water resistance is not a basis or justification, in and of itself, to replace the windows.

2.3 Visual Survey: Interior

A close-up examination from the interior is also critical to evaluate the existing window conditions. Depending on the building occupancy, it may be easier to perform a comprehensive survey from the interior, but if that is not possible, rationale similar to that described above should be applied when selecting specific locations for review.

Review of the windows from the interior can provide an indication of the water resistance of

the existing assemblies. Damage such as peeling paint, blistering plaster, and discoloration of finishes may be an indication of water infiltration. Review of the specific location of the damage can provide an indication of the source of water. While the window itself may be the source of the infiltration, other factors may be contributing including lack of flashings, failed perimeter sealant, condensation, or thermal bridging. Inventorying the existing hardware and operation of the sash should be included if the intent is to restore functionality of the windows. Often the windows have been painted or sealed closed, so evaluation of functionality can be challenging.

2.4 Investigative Openings and Disassembly

Investigative openings can be helpful in determining window anchorage details, as well as the configuration of the window-to-wall interface at the perimeter of the assembly. Concealed conditions and deterioration may also be revealed. Removing selected windows, in part or as a whole, can also provide valuable information with respect to the assembly and components. The geometry of weather-stripping and component profiles can be difficult to determine without removing operable portions and the frames.

3 Restoration Approaches

Once the investigation has been completed, gaining an understanding of the Owner's expectations is necessary to develop an appropriate restoration approach. While comprehensive restoration is ideal to achieve a consistent end result, it is often not necessary or justified. The approach will determine the maintenance cycle for the windows. Less invasive approaches will have a lower initial cost, but a shorter service life. Likewise, more invasive approaches will have higher initial costs, but a longer service life prior to required maintenance. Regardless of the approach, the cost of access and general conditions will generally be consistent. A combination of approaches could also be appropriate based on available funds, window location or exposure, or other factors. A brief description of various restoration approaches follows.

3.1 Scraping and Painting

If the substrate is generally in good condition, removing areas of loose coating, sanding, and applying a new coating system can protect the historic fabric of the windows. Replacing deteriorated glazing putty is often performed concurrently. This approach is obviously the least invasive and lowest cost when considering the entire window assembly.

3.2 Stripping and Painting

Based on the condition of the substrate material, or to determine the condition of the substrate, complete removal of the existing coating may be necessary. In the case of wood windows, paint strippers are most effective. If the existing coatings contain lead, certain strippers can both remove and capture the coatings for disposal. For steel windows, paint strippers can also be used, but abrasive blasting can frequently be more effective and economical. If performed properly, blasting can effectively remove existing coatings at inside corners and crevasses. For wood windows, hand tools are often necessary to remove remnants from these areas. It is important that all chemicals and other residue be completely removed from the surface of the window prior to performing repairs or applying a new coating system.

3.3 Localized Repairs, Dutchman Repairs, and Component Replacement

Depending on the size and extent of substrate deterioration, repairs can vary from patching of localized areas of rotted wood or corrosion, to replacement of complete members. Localized rot in wood windows and corrosion of metal windows can be removed and the area filled with a compatible repair material such as an epoxy filler. In both instances, particularly wood, it is important avoid applying the filler as a means of building up the surface of non-deteriorated areas. This can lead to accelerated deterioration of the wood, since the filler can trap moisture. This is less of an issue with metal windows, but achieving a uniform surface is not necessary unless the area has the potential to hold water (e.g. the upward facing surface of a sill).

More extensive deterioration may require replacing portions of a member (dutchman repair) or a complete member. The most common application of dutchman repairs is for the lower portions of jambs, while complete replacement is often necessary for sills. Ideally, rot resistant old growth woods such as mahogany are desirable for dutchmen in wood windows. Deteriorated portions of the members are cut away and the new piece is anchored to sound substrate. Treatment of the joint between the dutchman and the original material should be considered to limit the potential for water to reach the untreated end grain of both pieces. Fasteners can be countersunk and concealed with a wood plug.

In the case of steel dutchmen, it is likely that the original profile of the steel assembly is no longer manufactured, and the new pieces may need to be fabricated by building up smaller pieces to generally match the profile. A perfect match using this approach is typically not possible due to the differences in fabrication. Welding is typically the preferred installation approach for steel dutchmen. Testing the original steel for compatibility and determining a weld procedure should be part of the process. Once the welding is completed, the area can be ground smooth to the adjacent material and coated.

3.4 Glazing

Removing the existing glass in a window that is being restored, either temporarily or for replacement, is preferred to achieve optimal performance. By removing the glass, the glazing pocket can be prepared and coated prior to reglazing. From a preservation perspective, the glass should ideally be retained and reused. However, a relatively high rate of breakage is almost unavoidable in many instances, which can increase the appeal of comprehensive reglazing.

Often, installing replacement insulating glass units (IGUs) is considered as a thermal improvement. This approach can introduce challenges relative to the width of the glazing pocket and the weight of the sash. Conventional IGUs are typically 1 inch thick, while historic glass is typically between 1/8 inch and 1/2 inch thick, depending on the size of the opening. With thicker replacement glass, the glazing pocket must be made wider by either modifying the sash component, reducing the profile of the putty and glazing points, or modifying the glazing stops, all of which have the potential to significantly reduce the wind load resistance of the window. The frame and hardware should also be evaluated to ensure that they can support any added weight. Recently, glass manufacturers have introduced thinner IGUs that can fit into existing glazing pockets, but at a significant cost increase over reusing the existing glass or using conventional IGUs. Other replacement glazing options, such as laminated glass, can also be considered, but many of the same considerations discussed above will still apply.

3.5 Hardware

Based on the condition of the existing hardware, replacement hardware may be necessary. Matching original hardware may be possible, but is often challenging if the components are no longer manufactured. Options can include salvage sources or potentially using hardware from other windows on the building. If limited original hardware is available, sets of original hardware and replacement hardware can be grouped by window.

3.6 Weather-Stripping

Historic windows typically used metal weather-stripping at all operable interfaces. For wood windows, the geometry of the weather-stripping is somewhat forgiving, and a similar metal profile is often available that can fit the assembly. At concealed interfaces, modern weather-stripping materials such as foams and plastics may also be used. Historic weather-stripping for metal windows was typically fabricated specifically for a particular profile, and is most likely no longer available. Salvage and reuse of weather-stripping may be possible under certain circumstances, but given the tolerances of fabrication and operation, once removed, it is likely not realistic to reinstall. For this reason, weather-stripping options for metal windows generally include custom fabrication of new weather-stripping to match the original, or creative application of readily available modern components.

4 Case Study: Wood Windows

Second Presbyterian Church, located in Chicago, Illinois, is a National Historic Landmark that was constructed in 1874. Bell tower facade repairs, including masonry and window restoration, were recently performed. Because the interior of the bell tower encompasses predominantly unoccupied space, and the height of the tower makes exterior access challenging, maintenance of the existing historic windows had been infrequent over the years (Figure 1).

Figure 1. Typical window conditions before (left) and after restoration (right).

The exterior evaluation of the windows was performed from an aerial lift, which allowed access to all of the tower windows. The surfaces were probed with an awl, but no investigative openings were created. On the interior, access was limited based on the proximity of an interior stair. Conditions included wood decay at various exterior locations including sills, the base of jambs, and at decorative tracery. Several of the sash were missing, and the frames had been boarded up. Portions of the leaded art glass were broken or missing. Since the windows were likely built on site during construction, no original drawings or specifications existed.

Based on the owner's inability to ensure that resources could be dedicated to future maintenance of the windows, a comprehensive restoration approach was selected to maximize service life. Repairs included complete removal of existing coatings using a chemical stripper, replacement of deteriorated sills and tracery, dutchman repairs at the lower portions of jambs, replacement of sash, hardware, and weather-stripping, removal and restoration of the art glass, interior and exterior painting, and perimeter sealant replacement (Figure 2). The replacement sash were fabricated to match the profiles of the limited sash that remained. Although the original sash were likely glazed with leaded glass based on historic photos, the new sash were glazed with clear laminated glass due to budgetary constraints. The decision was also made to seal the perimeter of the glass with silicone sealant, rather than traditional glazing putty, to reduce the overall maintenance cycle. Based on the location of these windows, the substitution is not visually apparent. Finally, the colors of the new exterior coatings were selected based on paint analysis performed on other windows at the church and the historic photos.

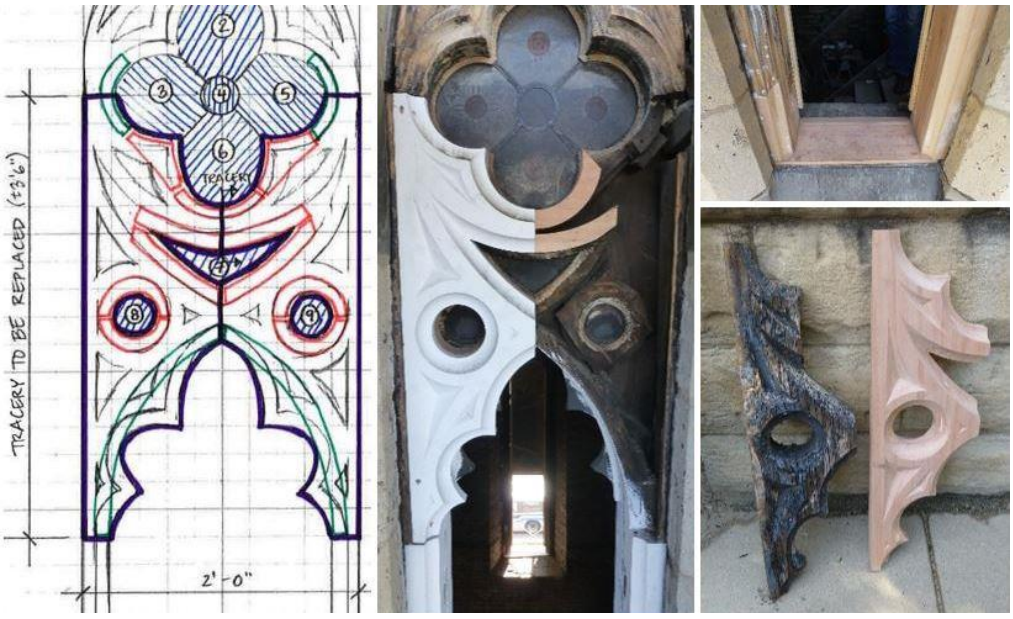

Figure 2. Sill replacement and jamb dutchmen (upper right) and tracery replacement.

Various challenges were encountered throughout the project. At the outset, it was difficult to find an experienced window restoration contractor that could perform the necessary onsite restoration of the existing frames. Once on board, the contractor encountered challenges obtaining the desired wood species for replacement elements and dutchmen. In the end, the challenges were overcome, and the end result was a successful wood window restoration.

5 Case Study: Steel Windows

30th Street Station, located in Philadelphia, Pennsylvania, is the second busiest train station in the United States. The building is iconic in the Philadelphia community and is listed on the National Register of Historic Places. Constructed in 1934, one of the defining architectural features is the fenestration system, which includes rolled steel casement windows set into cast iron curtain walls that are located between limestone clad piers (Figure 3). As part of a comprehensive facade restoration project, an evaluation of the windows was performed. Due to security and access restrictions, the evaluation was limited. The window assessment included a visual survey of select areas on the interior and exterior. In addition, one of the steel windows was removed to document the interface geometry and concealed conditions. Materials testing of the steel and cast iron, and a finish analysis to determine the original color scheme, were performed. A hazardous materials survey and testing were performed by the owner.

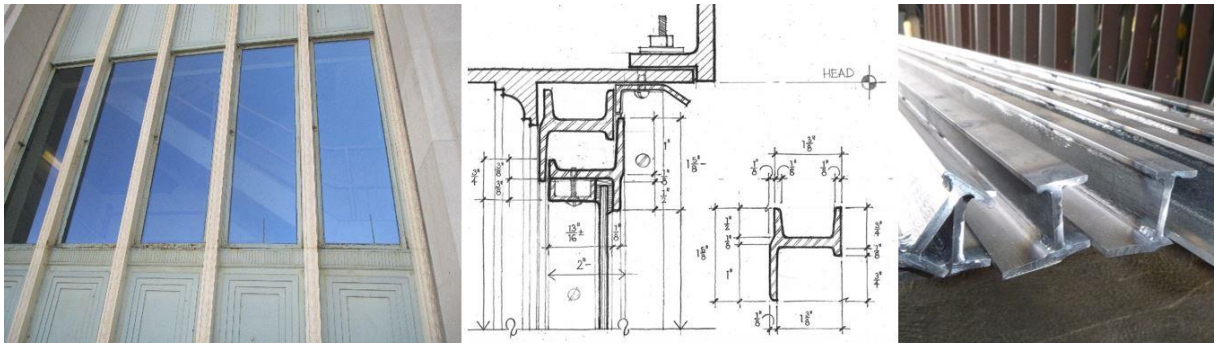

Figure 3. Cast iron curtain wall and steel casement windows (left and center); built up dutchman sections (right).

Our investigation revealed that limited repairs and intervention could extend the service life of the system, but a more comprehensive restoration could provide a significantly longer service life and limited maintenance schedule that were more in line with the owner's goals. Detailing and profiles were found to be generally consistent throughout the station, but window sizes varied. The original manufacturer of the windows was determined through archival research, and product data, including original profiles, was located in historic product literature.

A comprehensive facade restoration program, including the stone masonry facade, steel frame windows, and cast iron curtain wall, began in 2012. The restoration scope included off-site restoration of the steel sash and frames, including comprehensive glass replacement, and in-situ restoration of the cast iron curtain wall. Coating removal was accomplished by abrasive blasting with a garnet media to achieve SSPC-SP10 (near white metal blast with a surface profile between 1 and 2 mils). Where necessary, dutchmen were created by building up steel plates and stitch welding them to mimic the original profile. The original steel was tested for weldability and a weld procedure was provided. A high performance coating system was applied to the blasted surface, consisting of a zinc-rich primer, epoxy intermediate coat, and fluoropolymer top coat. Finally, a blast and solar protection film was applied to the new glass prior to being glazed into the restored sash. To improve the overall thermal performance of the building, custom fabricated aluminum storm windows were installed on the interior of the building at office locations.

Figure 4. Steel frame blasting and surface profile measurement (left and center); coating mockup (right).

Several challenges were encountered at the beginning of the project that had to be resolved. Hazardous materials were found in concealed portions of the window assembly that required remediation. In addition, the weather-stripping had to be custom fabricated, as an off-the-shelf product replicating the profile could not be located by the contractor. A comprehensive quality control and quality assurance program was also established that included inspection and surface profile measurements of the window frames following blasting, and coating thickness measurements following each layer of coating application.

6 Conclusions

A successful historic window restoration project requires a clear understanding of the existing window conditions and the owner's expectations for window maintenance and service life. When possible, a comprehensive investigation of the existing windows can more accurately customize a restoration approach that achieves the desired end result.

ORCID

Edward A. Gerns: http://orcid.org/0000-0003-3640-4114
Sarah K. Van Domelen: http://orcid.org/0000-0002-1171-7862

References

Rex, J. and Society for Protective Coatings. (2000). *Systems and Specifications, SSPC Painting Manual: Volume 2.* Pittsburgh, PA: SSPC.

Sweet's Catalogue Service, Division of F. W. Dodge Corporation (1932). *Sweet's Architectural Catalogues*. New York, NY.

XV International Conference on Durability of Building Materials and Components
DBMC 2020, Barcelona
C. Serrat, J.R. Casas and V. Gibert (Eds)

Smalti Murano Glass *Tessella's* Applied Outdoor in the *Trencadís* Catalan Modernism Mosaic: Recognition of Preliminary Alteration Patterns

Raül Serra i Fabregà[1], Joan Ll. Zamora i Mestre[2] and Paloma Arias[3]

[1] PhD in Architecture, Building and Urban Technology, Universitat Politècnica de Catalunya (UPC) - BarcelonaTECH, ETSAB, Av. Diagonal, 649, 08028-Barcelona, Spain, raul.serra@upc.edu

[2] Laboratori d'Innovació i Tecnologia de l'Arquitectura (LiTA), Universitat Politècnica de Catalunya (UPC) - BarcelonaTECH, Pere Serra, 1-15, 08173-Sant Cugat del Vallès, Spain, joan.lluis.zamora@upc.edu

[3] Programa de Doctorado Tecnología de la Arquitectura, de la Edificación y del Urbanismo Universitat Politècnica de Catalunya (UPC) – BarcelonaTECH, Av. Diagonal, 649, 08028- Barcelona, Spain, paloma.arias@upc.edu

Abstract: *This contribution presents previous results of a study carried out with the aim of achieving better results in the restoration processes by replacing the tiles of an exterior mosaic tiling of the Trencadís type of Catalan Modernism. In this case the trencadís tiles come from the cutting of pieces, called piastras, of opaque and mass-colored glass called Smalti Murano glass. These companies have extensive color catalogs that, although not exactly the same as they were a century ago, are close enough for these replacement tasks. Each color corresponds, however, to a different composition of glass and a slightly different manufacturing process. These differences favor that the differences of color always go accompanied also of differences of superficial aspect. However, not all color references currently available have the same surface quality since this product, during its manufacture, acquires primary defects typical of artisanal processes. So far the predominant criteria for the selection of the new references of piastras that must replace the product damaged by the extensive exposure to the weather as a coating are based primarily on color. However, durability requirements must also be part of the selection criteria for substitution references. The primary defects that a product already presents in its superficial quality are often indicators of either a more irregular quality or of circumstances that favor the early appearance of secondary defects throughout its useful life. The main objective of this study is to ensure, in restoration work by substitution, the selection of the best piastras from the point of view of surface quality, to apply on site the most similar tiles of tone and with greater durability. This study is part of a collaboration between the study group LiTA (Laboratori d'Innovació i Tecnologia de l'Arquitectura) (UPC) and a private non-profit organization.*

Keywords: *Colour, Murano Glass, Smalti, Trencadís, Preliminary Alteration Patterns.*

1 Introduction

Murano Smalti glass has been used for centuries as a tile in colored mosaics as a coating for interior walls. Smalti glass, by its nature is very bright, chemically stable and has a solid color mass. Given its intense mass coloration, the glass tiles were placed sideways with what they always had small dimensions (of the order of the thickness of the glass) and parallel faces.

The trencadís is a coating typical of the architecture of Catalan Modernism that is composed of small pieces of materials, irregularly cut, such as enameled ceramics or marble, arranged randomly supported by its main face (table) on a layer of mortar forming a colorful polygonal mesh that has three-dimensional architectural motifs. It thus differs from the traditional historical mosaic by the arbitrary arrangement of the carved tiles with irregular shapes, by its ability to solve the coating of three-dimensional surfaces and because it is very often in situations of full weather where it manifests itself with all its brightness and color. (Fig.1)

The uniqueness of Murano Smalti glass is due to the fact that this mass-colored opal glass is still handcrafted today using traditional techniques. The same techniques used during Catalan Modernism. The producing companies continue to supply hundreds of different colors that cover almost all shades.

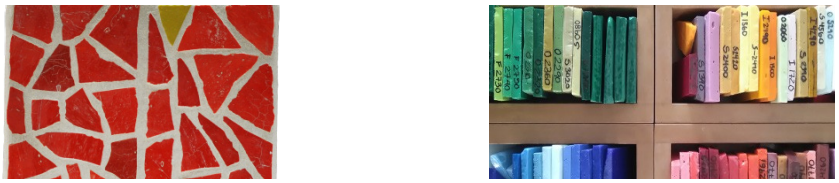

Figure 1. Left: test piece for trencadís coating tests made with smalti Murano glass tiles. Right: referenced glass samples analyzed in this study(source: authors).

2 The Material

In this study the piastras are made of opal glass, called Smalti. In the world of glass mosaics, smalti indicates a bright, opaque, mass-colored glass with high lead content, generally obtained by adding a crystalline material (*corpo*) and colored crystals (*anima*) to a molten transparent glass.

Figure 2. Left: Murano Smalti glass forming process by lamination until flat piastras are obtained. Center: glass piastras shown on Side 1. Right: manual cutting process (source: authors).

The traditional coloring agents commonly used for glass are a limited number of metal ions which, by absorbing part of the incident light, give rise to a great diversity of colorations. The apparent color of each glass depends on the nature of the ion, its oxidation state and the composition of the glass in which it melts.

Once the desired mixture is mixed in the corresponding crucible, homogenized and reached the appropriate temperature, masses of molten material are removed from the oven to form the piastras.

During the process of mixing, melting, forming and subsequent cooling of the piastras, they acquire various primary defects that alter their surface quality. These primary defects not only devalue their appearance but can also reduce their durability expectations as they are the source of new secondary anomalies that appear with the passage of time and exposure to the weather.

Due to the glass forming process, the surface quality obtained on both sides is not the same as that the face in contact with the table is kept in contact with the metal while the face in contact with the laminator is kept in contact with the atmosphere of the premises.

Since the face of the Murano glass in the trencadís lining will not be the edge but the table of the piastra, it will be necessary to select the one with the least primary defects present. This is how the face of each piastra is seen, called (A) in this study and the hidden face of each piastra, called (B) in this study.

The visual difference (brightness, color, surface homogeneity) of the faces is significant and should be taken into consideration at the time of restoration, since it can alter the assessment of the final overall quality of the trencadís lining.

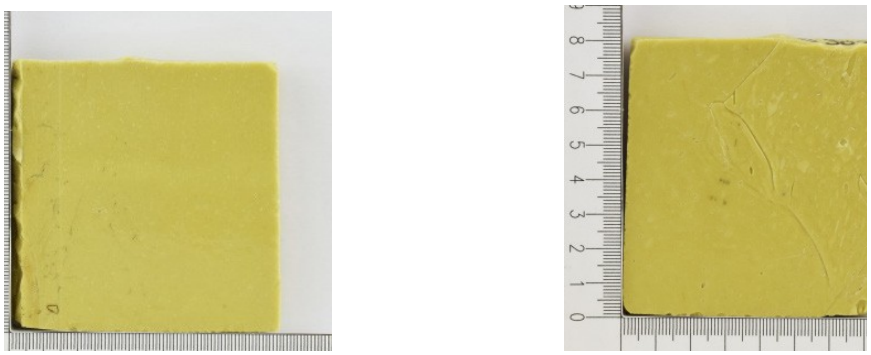

Figure 3. On the left the Face (A) of the reference glass S 3020 and on the right the Face (B) of the same glass reference where bubbles and folds often present in the hidden face of these glasses are appreciated (source: authors).

The objective of this research is to develop a procedure that allows grouping and ordering the various references available according to their apparent surface quality, so that artisans can select and use those references that, for the same color, have fewer primary defects. In order to favor this objective, the following inspection methodology, census and assessment of surface quality were proposed.

3 Methodology

With this objective a campaign was made to capture digital images on a universe of 77 references and 2 pieces for each reference, of approximate dimensions 8x8 cm, which constitute the basic sample ceded for this study by a company mainly oriented to the elaboration of this product.

Each of the 77 references has a different tonality, but these can be grouped into 11 color ranges:

Brown (17 references), violet (3 references), white (5 references), blue (11 references), green (16 references), orange (7 references), yellow (5 references), red (5 references), pink (4 references), black (2 references) and gray (2 references).

The samples are identified according to the manufacturer's catalog code. These codes are composed of an initial letter and 4 numbers, the letters refer to the type of smalti, differentiating them into: C: Skin (3 references), F: Smalti Fino (9 references), I: Imperial (25 references), OR: Ordinary Smalti (28 references), S: Special (12 references), and the numbers below identify the hue of the color.

This leads us to show that the same color range can be found in different types of smalti glass. Since the same color can be prescribed in different types of glass, it is about adopting the one that presents less primary defects and that is probably why it will age more adequately throughout its useful life, increasing its durability.

3.1 Digitization

All received parts have been digitized using a scanner corresponding to the "HP Deskjet F2200 series" model. The image has been executed following the following process:

- Cleaning the face of the piece of glass to be scanned with a fiber cloth, including the removal of the identification sticker if necessary.
- Placement of the pieces on the scanning area (each piece on both sides), forming sets of 20 pieces chosen at random, without corresponding to any sorting or classification.
- Scan of the set of parts, using the software "HP Solution Center", typical of the hardware referenced above and used for that purpose. Generating JPEG files with a horizontal and vertical resolution of 600 dpi and a variable dimension, about 10 MB.

3.2 Digital Image Editing

The JPG files corresponding to the scans of the groups of 20 glass samples and the subsequent edition of the images of the individual samples have been treated with the software "Adobe Photoshop CS6 version: 13.0.1 service pack: 1".The result of this work was the images of individual pieces, making a distinction between the two faces of each piece and calling them "sight" for the face generated by having a work view (face A), and "hidden" for the face generated to be arranged in contact with the mortar (face B). Generating jpg files of 1146 x 1146 pixels and a horizontal and vertical resolution of 600 dpi.

Figure 4. Overall images of the various image scanning processes with flatbed scanner (source: authors).

3.3 Characterization of the Identifying Color of the Samples

The characterization of the identifying color of the samples has been made from the images obtained in the previous process, and responds to the following sequence:

- superposition of 5 arbitrary markers on all images of individual samples.
- measurement of RGB color values in the center of each marker superimposed on the image of the sample piece, with the aim of parameterizing its color.
- overlay the histogram, in each of the images of individual samples.

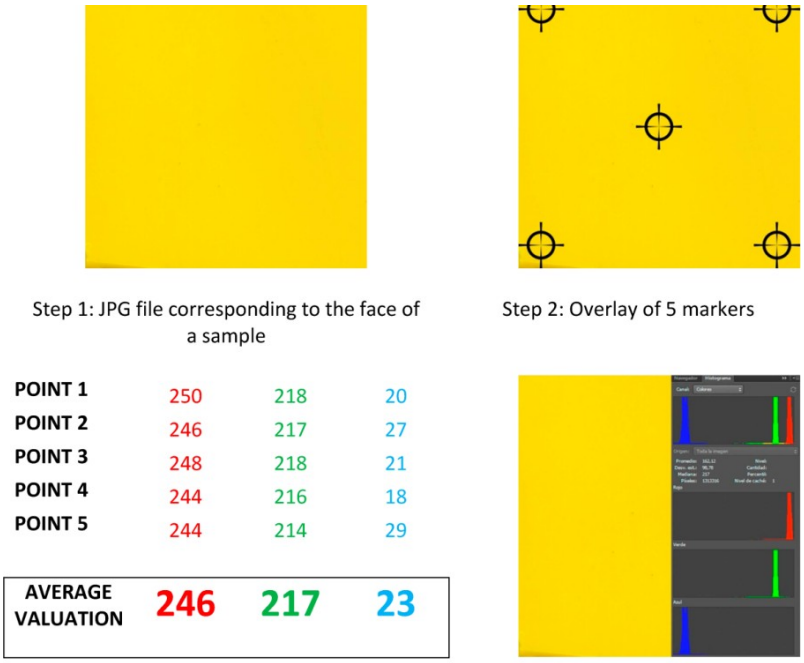

Figure 5. Model type of file for the evaluation of the color of the sample (source: authors).

3.4 Sample Defect Assessment

To assess the visible surface quality of each sample on each face:

- An initial value of 10 has been granted to each face
- For each face of each piece examined, a qualitative assessment of each defect has been made, giving a value of -1 if the said defect is generalized or 0 if it is punctual or non-existent.

3.5 Census of Surface Defects

The 10 primary defects observed on this face during the visual inspection are listed below, accompanied by their description:

- A1 Scales: Presence of half uncoiled sheets of the sample piece.
- A2 Fissures: Presence of marked fissures in the observed face of the sample.
- A3 Cracks: Presence of lesions with differently separated lips and variable depth.
- A4 Polygonal microfisuration: Presence of microcracks showing a cracking structure on the observed face.
- A5 Wound: Presence of discontinuities more or less deep and with well-defined lateral limits.
- A6 Longitudinal mark: Presence of unidirectional longitudinal marks, often accompanied by air pockets and very elongated spots.
- A7 Stain: Presence of spots of different coloration, more or less rounded.
- A8 Color: Presence of traces of colors other than the color of the piece, in the form of water or stains with a certain contour definition.
- A9 Flatness: Presence of irregularities in the plane of the analyzed face.
- A10 Bubbles: Presence of discontinuities in the material of the analyzed face, of more or less depth and with a rounded shape.

4 Evaluation and Interpretation of Results

The first interpretation of the results (Table 1) shows that there are different evaluations:

Table 1. Average concurrence of defects on both faces.

	View face (A) analysis	Hidden face (B) analysis
Concurrence of more than 5 defects	6.17%	24.69%
Concurrence of 5 defects	20.99%	22.22%
Concurrence of 4 defects	22.84%	17.90%
Concurrence of 3 defects	21.60%	24.07%
Concurrence of 2 defects	18.52%	7.41%
Presence of a single defect	7.41%	3.70%
Without any defect	2.47%	0%

About the analysis between different samples of a same reference, the average additional defects on both faces (Table 2) are the following:

Table 2. Average additional defects on both faces.

	View face (A) analysis	Hidden face (B) analysis
The same defects are found	30.86%	33.33%
There is 1 additional defect	35.80%	32.10%
There are 2 additional defects	12.35%	14.81%
There are 3 additional defects	14.81%	13.58%
There are 4 additional defects	6.17%	2.47%

Since the objective of the study was to order the different references observed according to their surface quality (primary defects), to offer information to the artisan before the task of transferring the color's design choice to the product code for the highest quality execution, has been considered a new variable that corrects the scores regarding the characterization of this material. This variable is the variability of defects observed in different samples of the same code.

Thus, understanding that a lower variability of valuations between different samples of the same code is preferable, from the point of view of the reliability of the valuation performed, and a greater variability of valuations is inconvenient due to the lower reliability of the same valuation, the criterion of correcting the results has been adopted according to the following criteria:

Table 3. Criteria of modification of the sample's score.

Criteria	Modification
If the difference in defects between the various samples is 0	+1
If the difference in defects between the various samples is 1 or 2	±0
If the difference in defects between the various samples is 3	-1
If the difference in defects between the various samples is 4 or 5	-2

5 Final Qualification of References

The absolute final qualification of the samples, for pragmatic reasons, has been reduced to a double score for each company code: a preponderant score for the face and an accessory score for the hidden face, based on a 5-star system such as maximum and 1 star minimum. To capture this fact graphically, generic files have been formulated that contain the information for each code of the company analyzed.

Finally, a relative final qualification of the samples with respect to the results of the samples belonging to codes of the same color range has been established. The objective is to help the selection of codes in the translation of the design color to the nomenclature of the execution material:

- A high quality code, that is, the best quality available (green color rating),
- A medium quality code (orange rating): its substitution is recommended with the recommended green references ordered.
- A low quality code (red rating): mandatory replacement is prescribed by the ordered orange references.

About the references of Murano glass, the results are as follows:

Table 4. Average distribution of quality by smalti types.

	C: Skin	F: Fine	I: Imperial	O: Ordinary	S: Special
High quality	0%	0%	20%	14.29%	8.33%
Medium quality	100%	88.89%	60%	53.57%	50%
Low quality	0%	11.11%	20%	32.14%	41.67%

And in terms of color spectrum:

Table 5. Average distribution of quality by colours.

Quality	Brown	Violet	White	Blue	Green	Orange	Yellow	Red	Pink	Black	Grey
High	11.76%	33.33%	40%	9.09%	0%	14.29%	60%	0%	0%	0%	0%
Medium	52.94%	66.67%	40%	54.55%	68.75%	57.14%	40%	60%	100%	100%	100%
Low	35.28%	0%	20%	36.36%	31.25%	28.57%	0%	40%	0%	0%	0%

6 Conclusions

Murano Smalti glass has been revealed as a material with a high amount of concurrent surface primary defects, defects that affect similarly to its two faces, although they predominate on its face (B). It can be concluded because most of the primary defects observed are inherent to the product as it is currently produced and few others are inherent to the face (B), which is in contact with the forming table.

The results of this preliminary study, although they illustrate quite clearly the primary defects that this material suffers, should still be considered indicative, since several limiting causes must be considered:

- these are parts from references of a single manufacturer and have been voluntarily selected by the manufacturer itself to be a sample.
- these are cut pieces of larger piastras; In the reality of the work, this intermediate format is not used, but each tile is extracted, by fractionation, from any area of the piastra.
- the number of references and colors analyzed in each range is not equivalent.

ORCID

Raül Serra Fabregà: http://orcid.org/0000-0002-5500-1858
Joan Ll. Zamora: http://orcid.org/0000-0002-7705-6171
Paloma Arias: http://orcid.org/0000-0002-8334-8269

References

Arias, P. and Zamora, J. (2018) *Evaluación de las características cromáticas del vidrio de Murano utilizado en revestimientos exteriores de trencadís.*Euro-American Congress on Construction Pathology, Rehabilitation Technology and Heritage Management,7th REHABEND Congress: Caceres (Spain), May 15th-18th. Santander (Cantàbria): Universidad de Cantabria, 2018, p. 1254-1263. http://hdl.handle.net/2117/131486

Gómez, J. (2015) *Los pináculos de la Sagrada Familia: restauración y obra nueva* (Tesis doctoral) Universitat Politècnica de Catalunya. http://hdl.handle.net/2117/95689

Verità, M., James, L., Freestone, I., Henderson, J., Nenna, M.-D. and Schibille, N. (2009), *Glossary of Mosaic Glass Terms*, edited by B. Bjornholt (Centre for Byzantine Cultural History, University of Sussex, 2009)

Verità, M. (2000) *Technology and deterioration of vitreous mosaic tesserae, Studies in Conservation*, 45: sup 3, 65-76, DOI: 10.1179/sic.2000.45.s3.007.

XV International Conference on Durability of Building Materials and Components
DBMC 2020, Barcelona
C. Serrat, J.R. Casas and V. Gibert (Eds)

Study of Autogenous Self-Healing in Different Mortar Formulations

Nohelia Gutiérrez, Laia Haurie, Antonia Navarro and Joan Ramon Rosell

Universitat Politècnica de Catalunya, Barcelona School of Building Construction, Av. Doctor Marañon 44, 08028 Barcelona, Spain, csn.gutierrez@gmail.com, laia.haurie@upc.edu, antonia.navarro@upc.edu, joan.ramon.rosell@upc.edu

Abstract. *Autogenous self-healing of cement-based materials is a topic of current interest. This research evaluates autogenous self-healing in four types of mortars based on Portland Cement, one containing CEM II and the other 3 formulated with CEM I and different additions: fly-ashes; nanosilica and hydraulic lime. The evolution of longitudinal cracks caused by a point load has been evaluated measuring the water absorption by capillarity and studying the evolution of the crack by optical microscopy. Besides the mortar composition, it has been evaluated the effect of the environmental conditions on the crack repair. The different specimens were exposed to three different environments: water immersion, curing chamber at 20 ± 2°C and 95 ± 5% of relative humidity (RH) and the laboratory at 25 ±5°C and 65% ± 5% RH. The results obtained allow us to establish that constant hydration is an essential factor for the development of self-healing mechanism. If the samples are kept in water immersion self-healing occurs no matter the additions of the mortar formulation. Size of the crack is also an important factor to allow self-healing. The product formed during self-healing to fill the crack is mainly calcium carbonate.*

Keywords: *Self-Healing, Cement, Environmental Conditions, Cracks, Water Absorption Test.*

1 Introduction

Currently, several research fields have been dedicated to studying self-healing materials; among these smart materials are cement-based materials. Cracking is inherent to the material, however, the crack width should not exceed a prescribed limit because it can affect its durability and resistance against aggressive substances (Ghosh, 2009).

This research focuses on the autogenous self-healing of the cracks of mortars based on Portland cement at early stages. Autogenous self-healing is a natural phenomenon (Joseph, 2008) and this process mainly relies on chemical, physical and mechanical interactions (Kishi, Ahn, Hosoda, Suzuki, and Takaoka, 2007).

Several authors have demonstrated that the presence of water is fundamental in order to obtain autogenous self-healing. For instance (ter Heide and Schlangen, 2007) concluded that hydration was the mechanism for crack healing that leads to the strength recovery of the prismatic specimens. Similarly (de Rooij, Schlangen, De Belie, and Van Tittelboom, 2011) indicated that one of the two chemical processes for self-healing is the continuous hydration of cement. Regarding the influence of environmental conditions, the investigation of (Argouges, 2012) showed evidence of natural self-healing in cracked specimens stored in a humid environment 23º C and 100% RH, for up to 5 months. The incorporation of cementitious materials is another factor influencing self-healing. The investigations of

(Huang, Ye, and Damidot, 2014) and (Van Tittelboom, Gruyaert, Rahier, and De Belie, 2012) studied the effect of blast furnace slag and fly-ash on self-healing of cracks in cementitious materials. Likewise, the research of (De Nardi, Cecchi, Ferrara, Benedetti, and Cristofori, 2017) showed that the presence of crystalline admixtures speeds up the sealing of the cracks and the recovery of the mechanical properties. In order to evaluate self-healing ability there are several methods, (Wang, De Belie, and Verstraete, 2012) used the capillary absorption test to show that the specimens had a low water absorption, which indicated that the precipitation inside the cracks increased the water penetration resistance of the cracked specimens. In the same way, (Qureshi, Kanellopoulos, and Al-Tabbaa, 2016) concluded the improvement in terms of capillary absorption of healed samples was significant after 28 days of healing. Microscopic methods had also been used extensively to evaluate both autogenous and autonomous self-healing. The specimens are observed before and after the healing process (Tang, Kardani, and Cui, 2015).

In this study, the effect of different environment conditions on the autogenous self-healing of different Portland mortar admixtures was evaluated by means of the capillary absorption test and by optical microscopy.

2 Experiment

2.1 Materials

In this study, there were used four mortar formulations based on Portland Cement, one containing CEM II /A-V 42,5 R and the other 3 formulated with CEM I 52,5 R and different additions: fly-ash from the Bocamina Thermoelectric Power Plant of Chile; nanosilica with a SiO_2 content of 99.998% and calcium hydroxide CL-90. The mass ratio between sand and cementitious conglomerate (s/c) was 3 and it was established a superplasticizer/cement mass ratio (sp/c) of 0.012. Table 1 presents the composition of the different mortars. The specimens were cast in large plastic molds of 100x100x500 mm^3 and were reinforced with electro-welded galvanized steel mesh (12.7 mm x 12.7 mm and Ø 0.8 mm), which was embedded at the top and the bottom of the pieces as can be seen in figure 1a. The pieces were kept 2 days in the mold and after demolding were cured 5 days in the curing chamber at 20 ± 2° C and 95 ± 5% of relative humidity (RH). The next day, the pieces were removed from the curing chamber and divided into small specimens of 100x100x40 mm^3. Mortar specimens were fabricated to evaluate cracks at very early stages; therefore, at the age of 9-d, longitudinal cracks were caused to the specimens by a point load (figure 1b). The cracking process started with a constant average loading speed and then it was decreased to 0.2 mm/s.

2.2 Environmental Exposure

The effect of the environmental conditions on self-healing of concrete has been previously reported (Suleiman and Nehdi, 2018). Therefore, cracked specimens of the four mortar formulations were exposed for 60 days to 3 different environments: water immersion at laboratory conditions, curing chamber at 20 ± 2°C and 95 ± 5% of RH and the laboratory at 25 ±5°C and 65% ± 5% RH. This last group received a weekly amount of water to simulate an environment with the presence of average humidity.

In addition, in each environmental condition, the specimens were divided into two groups: cracked and control specimens (without cracks). The comparison between both specimens reaffirmed the evolution of the longitudinal cracks.

Table 1. Mix design of the four mortar formulations.

Material (g)	Formulation M1	Formulation M2	Formulation M3	Formulation M4
CEM II/A-V 42,5 R	7000			
Natural sand	21000	21000	21000	21000
Water	3710	3850	4760	4550
Superplasticizer	84	84	84	84
CEM I 52,5 R		5950	5950	5950
Fly-ash		1050		525
Nanosilica			700	
Filler			350	
CL-90				525

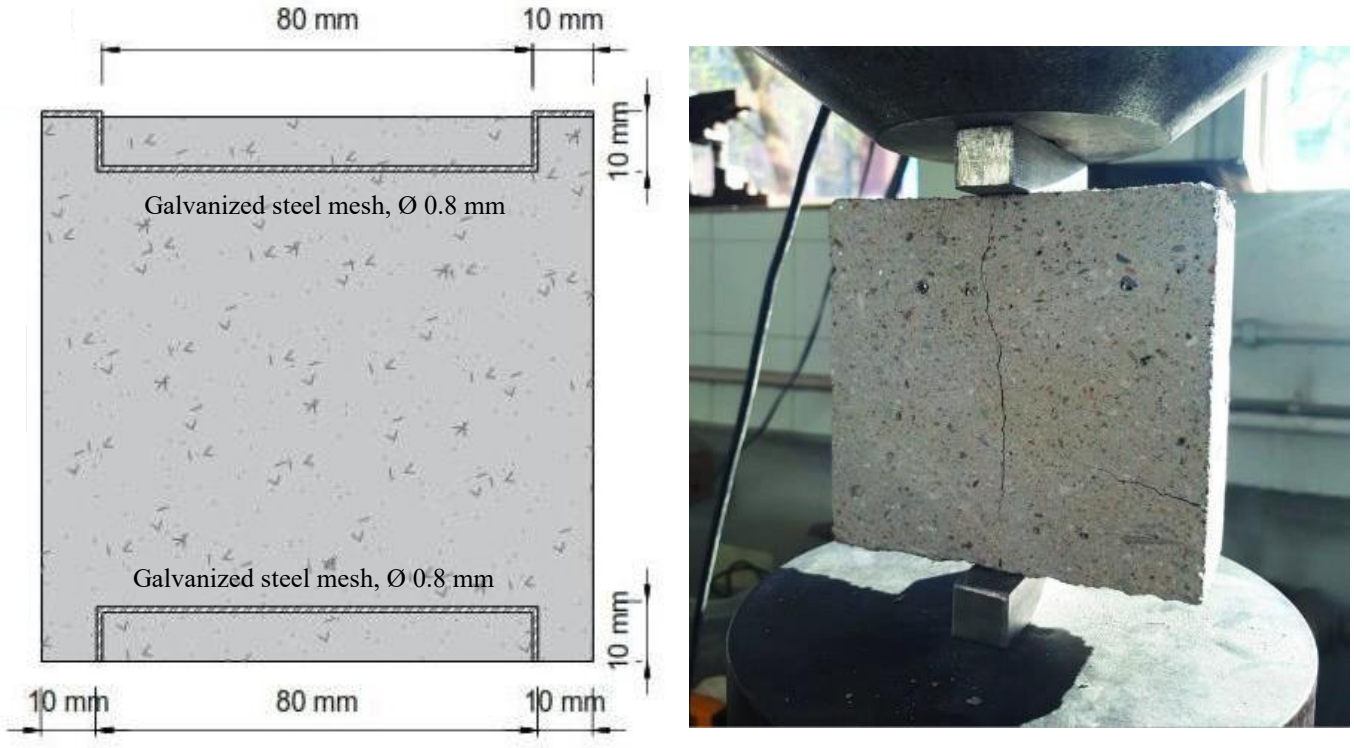

Figure 1. (a) Steel mesh scheme and (b) cracking of the specimen by a point load.

2.3 Analysis of Self-Healing Products

2.3.1 Water absorption test by capillarity

The water absorption test could effectively evaluate the self-healing performance of cement-based materials (Park and Choi, 2018). This test was performed according to UNE-EN 1925 *Natural stone test methods. Determination of water absorption coefficient by capillarity*. All 100x100x40 mm^3 specimens were oven-dried at 70 ± 5º C. The samples were weighted and the bottom surface was measured before they were immersed in water at a depth of 5 ± 1mm. The mass of water absorbed by the samples was measured at: 1, 9, 16, 36, 49, 64, 81, 121, 225 and 361 minutes. The test was carried out before cracking, upon cracking and after 7, 15, 30 and 60 days of exposure to the three different environmental conditions.

The mass of water absorbed per square meter was plotted against the square root of time and the water absorption coefficient (S) was determined using linear regressions.

2.3.2 Self-healing evaluation by optical microscopy

Optical microscopy was used to observe the cracks surface (Homma, Mihashi, and Nishiwaki, 2009). In this investigation the evolution of the longitudinal cracks surface was monitored just upon cracking, and after 7, 15, 30 and 60 of exposure to the different environments. The device used was a Motic Stereoscopic Microscope with Euromex 10 Megapixel Image Sensor. Each crack was divided into sectors to analyze the evolution of the cracks in each specimen.

3 Results and Discussion

3.1. Autogenous Crack Healing

3.1.1 Water absorption test

The results showed the relationship between the self-healing efficiency and the variation of the absorption coefficients over time (before, upon, and after cracking) of the specimens in the three different environmental conditions (immersion, humidity chamber and laboratory). With this information, for each environment and for each mortar formulation, exponential adjustments were made and the mean of the cracked and control (non-cracked) specimens was calculated, as can be seen in figure 2.

A first general observation was that all cracked specimens that were fully immersed in water showed absorption coefficients that decreased over time, this confirmed the crack healing and the formation of hydration products. In the case of cracked specimens exposed to the curing chamber, the absorption coefficients also decreased over time. However, the absorption coefficients were higher than for the immersed samples. This could be due to an incomplete crack healing of the mortars. For cracked specimens conditioned in the laboratory, their absorption coefficients remained almost similar over time and were higher than the aforementioned cases. This was attributed to the absence of crack healing in the specimens conditioned in the laboratory.

Another remarkable observation, were the differences between control and cracked

specimens. At the beginning of the test just upon cracking, the absorption coefficients of the cracked specimens were always higher than that of the control specimens. However, after 60 days, the absorption coefficients of the cracked specimens that were fully submerged in water were lower or similar than that of control specimens. This observation clearly indicates that a mechanism of self-healing had occurred, and furthermore, the cracks had a major influence on the capillary water absorption of cementitious materials (Van Belleghem, Van Tittelboom, and De Belie, 2018).

The properties of each mortar formulation were part of this investigation, one of the essential characteristics that make a significant impact on water resistance of mortar is porosity and pore structure (Gulbe, Vitina, and Setina, 2017), graphically it was observed the absorption coefficients of the M2 specimens were higher than the other mortar formulations. This fact indicated that at early ages, fly-ash increases the porosity of the mortar, however, it decreased as the age increased (Termkhajornkit, Nawa, Yamashiro, and Saito, 2009). On the other hand, the absorption coefficients of the M3 and M4 specimens were lower than the other mortar formulations. This was because nanosilica diminishes the total volume of accessible pores in cement mortars (Tobón and Kazes, 2008) and the addition of hydrated lime lowered the total porosity of fly-ash cement pastes (Barbhuiya, Gbagbo, Russell, and Basheer, 2009).

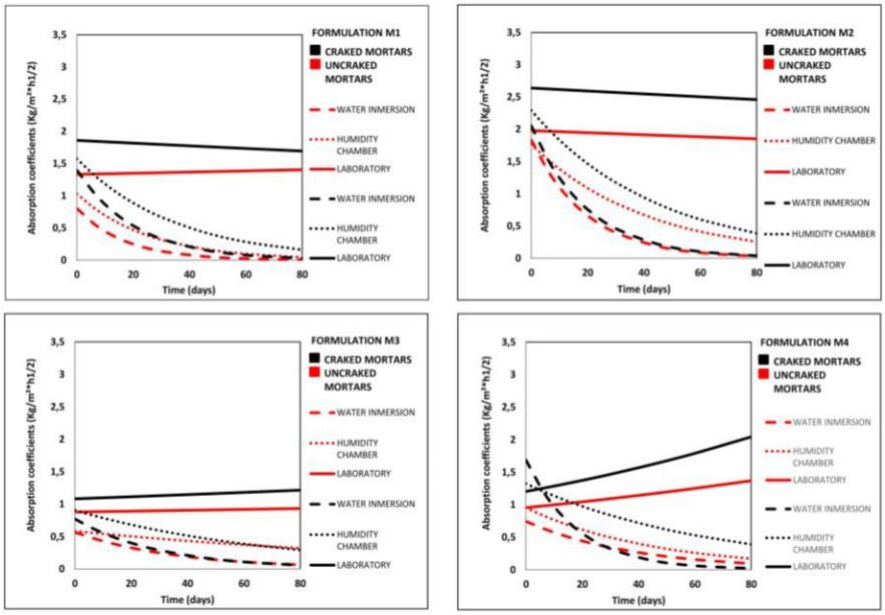

Figure 2. Exponential adjustments that show the variation of the absorption coefficient of the cracked and control specimens exposed to water immersion, humidity chamber and laboratory for a period of 60 days.

3.1.2 Optical microscopy

The evolution of the surface crack width of the specimens was measured using a microscope. Four sector images were taken along the crack, before and after the healing

process. After 60 days, cracks of the specimens immersed in water showed sealing or the formation of healing products along the surface of the crack of the specimens (inside and outside the crack). It must be highlighted that only cracks with a width smaller than 150 µm exhibited sealing. The images of the crack evolution can be observed in figure 3. In the case of the cracks of the specimens exposed to the curing chamber, only in some of the cracks occurred healing. For all the cracks of the specimens conditioned in the laboratory, no evolution or healing products were observed, due to the minimum contact they had with water. These findings were in good agreement with the results of the water absorption test by capillarity.

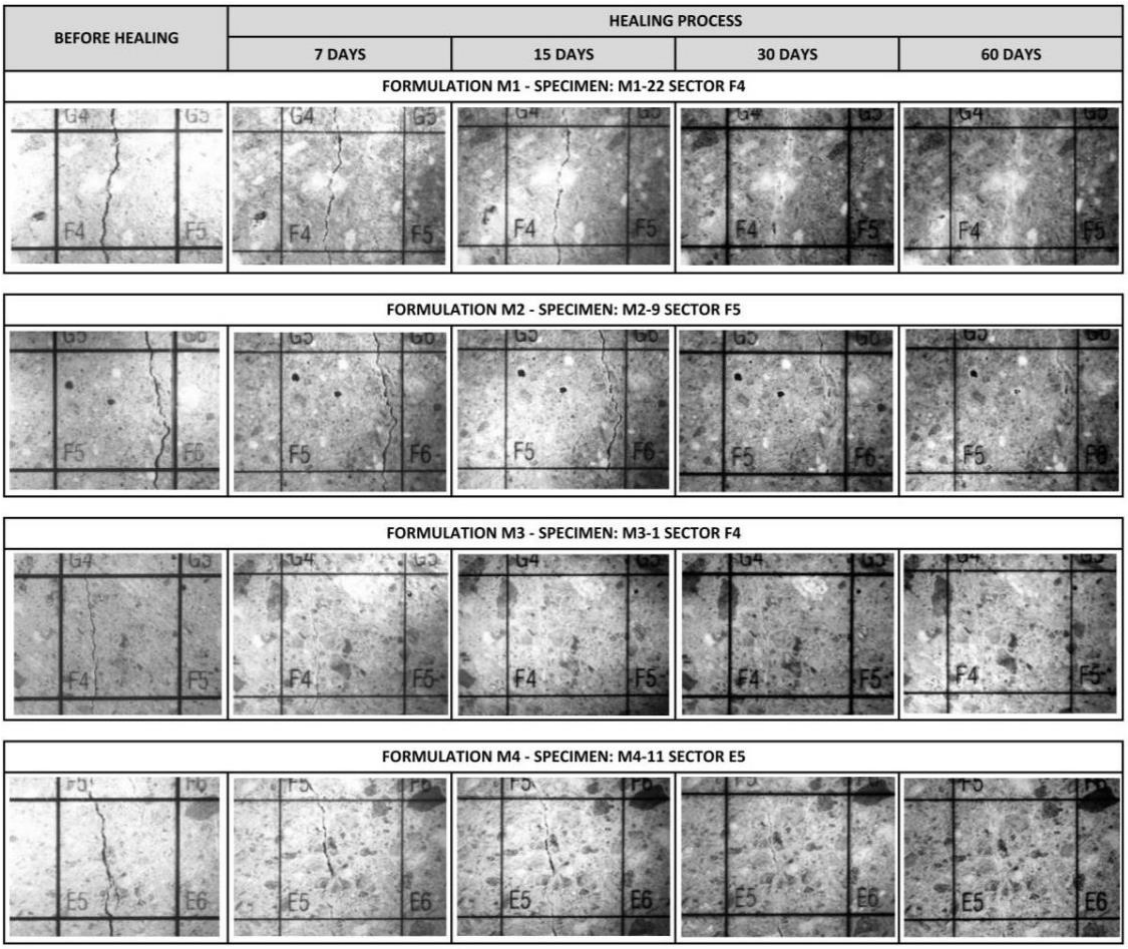

Figure 3. Evolution in the surface crack of different mortar formulations exposed to water immersion. The evolution was analyzed upon cracking and during the healing process.

4 Conclusions

This research analyzed the self-healing ability of four mortar formulations of cracked specimens exposed to different environmental conditions. Based on the experiments, the following conclusions were obtained:

- Constant hydration was an essential factor for the development of the autogenous self-healing mechanism.
- Width of the crack was an important factor to allow self-healing and from the absorption coefficients could be concluded that wider cracks exhibit higher absorption rates. Nevertheless, the form and path of the cracks were other parameters that had a big influence on self-healing.
- The product formed during self-healing to fill the crack was mainly calcium carbonate.
- The incorporation of additions to cement-based mortars did not influence self-healing of the mortars. In the cracked specimens that were kept in water immersion, self-healing occurred no matter the additions of the mortar formulation.
- High humidity environment conditions influenced only in some of the cracked specimens, probably in a longer period of exposure, the self-healing of the cracks could be carried out completely.
- Although the water absorption test by capillarity measured effectively the self-healing performance of the cracked specimens, in some cases, the evaluation by optical microscopy was more accurate to validate self-healing.

ORCID

Laia Haurie: http:// orcid.org/0000-0002-0732-8928
Antonia Navarro: http:// orcid.org/0000-0001-6212-8593
Joan Ramon Rosell: http:// orcid.org/ 0000-0001-5034-8388

References

Argouges, M. (2012). A study of the natural self-healing of mortars using air-flow measurements. *Materials and Structures*, 1625–1638. https://doi.org/10.1617/s11527-012-9861-y

Barbhuiya, S. A., Gbagbo, J. K., Russell, M. I. and Basheer, P. A. M. (2009). Properties of fly ash concrete modified with hydrated lime and silica fume. *Construction and Building Materials*, *23*(10), 3233–3239. https://doi.org/10.1016/j.conbuildmat.2009.06.001

De Nardi, C., Cecchi, A., Ferrara, L., Benedetti, A. and Cristofori, D. (2017). Effect of age and level of damage on the autogenous healing of lime mortars. *Composites Part B: Engineering*, *124*, 144–157. https://doi.org/10.1016/j.compositesb.2017.05.041

Gulbe, L., Vitina, I. and Setina, J. (2017). The Influence of Cement on Properties of Lime Mortars. *Procedia Engineering*, *172*, 325–332. https://doi.org/10.1016/j.proeng.2017.02.030

Homma, D., Mihashi, H. and Nishiwaki, T. (2009). Self-Healing Capability of Fibre Reinforced Cementitious Composites. *Journal of Advanced Concrete Technology*, *7*(2), 217–228. https://doi.org/10.3151/jact.7.217

Huang, H., Ye, G. and Damidot, D. (2014). Effect of blast furnace slag on self-healing of microcracks in cementitious materials. *Cement and Concrete Research*, *60*, 68–82. https://doi.org/10.1016/j.cemconres.2014.03.010

Joseph, C. (2008). *Experimental and numerical study of the fracture and self-healing of cementitious materials*. Cardiff University, UK.

Kishi, T., Ahn, T., Hosoda, A., Suzuki, S. and Takaoka, H. (2007). Self-Healing Behaviour By Cementitious Recrystallization of Cracked Concrete. *First International Conference on Self Healing Materials*, (April), 1–10.

Ghosh, S. K. (2009). *Self-healing Materials: Fundamentals, Design Strategies, and Applications.* Wiley-VCH Verlag GmbH and Co. KGaA.

Park, B. and Choi, Y. C. (2018). Quantitative evaluation of crack self-healing in cement-based materials by absorption test. *Construction and Building Materials*, *184*, 1–10. https://doi.org/10.1016/j.conbuildmat.2018.06.206

Qureshi, T. S., Kanellopoulos, A. and Al-Tabbaa, A. (2016). Encapsulation of expansive powder minerals within a concentric glass capsule system for self-healing concrete. *Construction and Building Materials*, *121*, 629–643. https://doi.org/10.1016/j.conbuildmat.2016.06.030

Suleiman, A. R. and Nehdi, M. L. (2018). Effect of environmental exposure on autogenous self-healing of cracked cement-based materials. *Cement and Concrete Research*, *111* (May), 197–208. https://doi.org/10.1016/j.cemconres.2018.05.009

Tang, W., Kardani, O. and Cui, H. (2015). Robust evaluation of self-healing efficiency in cementitious materials - A review. *Construction and Building Materials*, *81*, 233–247. https://doi.org/10.1016/j.conbuildmat.2015.02.054

Ter Heide, N. and Schlangen, E. (2007). Self healing of early age cracks in concrete. In *Proceedings of 1st International Conference on Self Healing Materials*, Noordwijk aan Zee, The Netherlands.

Termkhajornkit, P., Nawa, T., Yamashiro, Y. and Saito, T. (2009). Self-healing ability of fly ash-cement systems. *Cement and Concrete Composites*, *31*(3), 195–203. https://doi.org/10.1016/j.cemconcomp.2008.12.009

Tobón, J. I. and Kazes, R. (2008). Desempeño del Cemento Portland adicionado con Calizas de diferentes Grados de Pureza. *Dyna*, (156), 177–184.

Van Belleghem, B., Van Tittelboom, K. and De Belie, N. (2018). Efficiency of self-healing cementitious materials with encapsulated polyurethane to reduce water ingress through cracks. *Materiales de Construcción*, *68*(330). https://doi.org/10.3989/mc.2018.05917

Van Tittelboom, K., Gruyaert, E., Rahier, H. and De Belie, N. (2012). Influence of mix composition on the extent of autogenous crack healing by continued hydration or calcium carbonate formation. *Construction and Building Materials*, *37*, 349–359. https://doi.org/10.1016/j.conbuildmat.2012.07.026

Wang, J. Y., De Belie, N. and Verstraete, W. (2012). Diatomaceous earth as a protective vehicle for bacteria applied for self-healing concrete. *Journal of Industrial Microbiology and Biotechnology*, *39*(4), 567–577. https://doi.org/10.1007/s10295-011-1037-1

XV International Conference on Durability of Building Materials and Components
DBMC 2020, Barcelona
C. Serrat, J.R. Casas and V. Gibert (Eds)

Sulfate Resistance of Blended Cements (Limestone Illite Calcined Clay) Exposed Without Previous Curing

Agustín Rossetti[1], Tai Ikumi[2], Ignacio Segura[2] and Edgardo F. Irassar[3]

[1] Comisión de Investigaciones Científicas de la Provincia de Buenos Aires, CICPBA- LEMIT, La Plata, Argentina. email: agustin.rossetti@ing.unlp.edu.ar
[2] Department of Civil and Environmental Engineering, Universitat Politècnica de Catalunya Barcelona Tech, Jordi Girona 1-3, C1, E-08034 Barcelona, Spain.
[3] Facultad de Ingeniería, CIFICEN (UNCPBA-CICPBA-CONICET), B7400JWI Olavarria, Argentina. email: firassar@fio.unicen.edu.ar

Abstract. *Durability in aggressive environments is an important factor to extend the service life of concrete and the use ternary blended cements (limestone filler + calcined clays) can contribute to this purpose. In sulfate environments, the effects of supplementary cementing materials depend on the concentration, Portland cement and the progress of hydration reactions. Low level of limestone filler replacement influences the stabilization of AFt due to formation of monocarboaluminate, but high replacement increases the effective w/c and the capillary porosity promoting sulfate penetration. The use of active pozzolans suppresses the sulfate attack by minimizing both ettringite and gypsum formation. It is generally assumed that curing prior to sulfate exposure should be extended to allow the development of the pozzolanic reaction and subsequent reduction of portlandite content, pore size structure refinement and permeability reduction. However, in most field applications, concretes exposed to sulfate attack are cast in situ and thus, these are exposed to sulfate since early ages. This paper evaluates the sulfate resistance of an illitic-calcined clay and limestone filler when the cement is exposed immediately to aggressive environments. In this paper, the external sulfate resistance of blended cements containing 30% replacement of limestone filler and/or calcined clay (C30F, C30CC and C15F15CC) are analysed. Two different calcined clays from Buenos Aires, Argentina were selected. Mortar prisms and cement paste cubes were fabricated and exposed to a sodium sulfate solution after 2 days. Comparison of sulfate resistance was based on the expansion, mass variation, visual appearance and compressive strength . Furthermore, the evolution of microstructure of blended cements exposed to sodium sulfate solution was characterized by XRD tests on the external surface and the core of cement-blended pastes*.

Keywords: *Illite Calcined Clay, Limestone Filler, Sulfate Attack, Curing, Early Exposure.*

1 Introduction

Illite is one of the most abundant clayed minerals of the earth's crust coming from the alteration of feldspars and micas of rocks due to the weathering process. Illite clays develop pozzolanic properties when are thermally treated at 950 °C (Lemma *et al*, 2015) causing dehydroxylation and collapse of its structure to form a metastable or amorphous aluminosilicate (Ramachandran, 1995). These pozzolanic properties combined with the large availability of this mineral place illite calcined clays as a key supplementary material for the future mineral admixtures used in concrete.

Despite the promising characteristics of calcined clays described, a safe introduction of these

materials in the concrete technology requires the assessment of other aspects, such as the durability against different aggressive environments. External sulfate attack (ESA) has been recognized as a complex degradation phenomenon that may cause severe damage in cement based materials (Neville, 2004). High resistance to ESA in Na_2SO_4 solutions is normally associated with a segmented pore structure and low levels of portlandite (CH) and aluminate phases available to limit sulfate ingress and ettringite formation (Wild *et al*, 1997). Another important issue hardly ever evaluated for ESA resistance is the early sulfate exposure. In reality, the source of external sulfate ions is usually found in sulfate-rich soils and underground waters in contact with concrete. Therefore, ESA is especially significant in underground structures like foundations, tunnels or waste containers. Due to their large size, these structures are usually build in situ, hence being exposed to sulfates since casting. However, currently most studies about the ESA performed in laboratory rely on testing specimens cured several days in lime water prior to immersion in the aggressive sulfates solution (Ikumi *et al,* 2017).

The aim of this paper is to make a comparative study of the performance of blended cements with the addition of filler and two different illite calcined clays against sulfate attack without the previous curing prescribed by the standards to evaluate sulfate resistance when supplementary materials are used. Different proportions of cement, filler and calcined clay were used to make pastes and mortars to evaluate the mineralogical changes (X-Ray diffraction) and the evolution of physical and mechanical properties (mass variation, visual aspect, expansion and compressive strength) during ESA.

2 Materials and Methods

Portland cement (CEM I 52.5 R) with high C_3A-content (8.2%), limestone filler composed by high purity calcite (LF) and two different illitic calcined clays (ICC) were used. Calcined clays are identified by their colour: Red (ICCR) and Orange (ICCO). Their chemical composition determined by XRF are reported in Table 1. These two different illitic clay-stones are from quarries near to Olavarria, Buenos Aires Province (Argentine) and were calcined in oven at 950 °C and ground in laboratory ball mill until 90% of particles were less than 45 μm. Both calcined clays meet the chemical requirements for Class N pozzolan (ASTM C 618): S+A+F > 70%; SO3 < 4 % and LOI < 10%. XRD analysis reveals low intensity peaks of dehydroxilated illite in both clays and the associated minerals are quartz and hematite for ICCR and, quartz, hematite, oligoclase and spinel for ICCO. For these two ICCs, the Frattini test was positive after 14 days. Additionally, strength tests were performed and presented in another publication (Lemma *et al*, 2015).

Table 1. Chemical composition and mass loss on ignition of cement, filler and ICC, %.

Material	CaO	SiO_2	Al_2O_3	Fe_2O_3	MgO	SO_3	K_2O	Na_2O	LOI
Cement	60.92	16.58	4.21	1.80	2.16	1.77	0.67	0.28	2.05
Filler	59.53	<0.01	1.10	0.52	0.48	0.06	0.060	<0.01	39.98
ICCR	0.33	66.30	16.28	9.23	1.46	<0.01	5.60	0.08	0.58
ICCO	1.13	63.43	13.82	7.89	2.71	0.04	4.29	1.52	0.2

Physical characteristic of the materials are summarized in Table 2. Density was determined by the ASTM C 188 procedure, retained on 75 and 45 µm sieves (ASTM D 422 and C 618) and Blaine specific surface (ASTM C 204) and the particle size distribution (PSD) were determined using the laser granulometer (Malvern Mastersizer, 2000). The particle size distribution by volume of materials are shown in Figure 1.

Table 2. Physical characteristic of cement, clays and filler.

Property / Material		Cement	Filler	ICCR	ICCO
Density		3.10	2.70	2.63	2.65
Particle size distribution	Dv10, µm	1.8	1.7	1.6	1.3
	Dv50, µm	20.1	6.6	8.8	7.3
	Dv90, µm	65.1	72.2	33.7	36.9
Specific Surface Area	BET, m^2/g	1.10	3.74		
	Blaine, m^2/kg			522	724

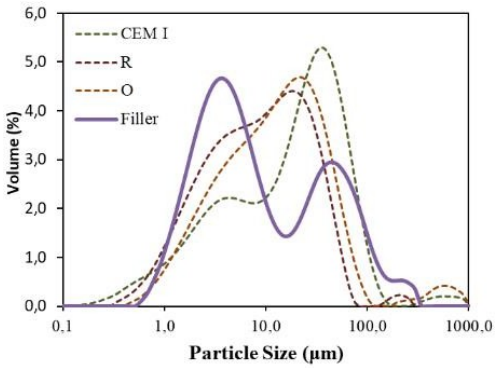

Figure 1. Particle size distribution of materials.

For this study, the SCM replacement in all binders was set to 30% by cement weight. By this way, all compositions present the same initial C_3A content and thus, the different behaviours observed can be solely attributed to the effects of the SCMs introduced. Five different blended cements were prepared: a binary filler cement (70% CEM + 30% LF), a binary illitic red calcined clay cement (70% CEM + 30% ICCR), a binary illitic orange calcined clay cement (70% CEM + 30% ICCO), a ternary red illitic blended cement (70% CEM + 15% ICCR + 15% LF) and a ternary orange blended cement (70% CEM + 15% ICCO + 15% LF). The nomenclature adopted is C30F, C30CCR, C30CCO, C15F15CCR and C15F15CCO, respectively.

Pastes were prepared using a water to binder ratio of 0.485 (as prescribed by ASTM C1012) and mixed using high speed mixer. Eighteen cubes of 20 x 20 x 20 mm were cast for each blended cement and cured in moist cabinet. After 24 hours, cubes were demolded and immersed in water for 24 hours to ensure full saturation of the samples prior to sulfate exposure. Then, twelve cubes were immersed in 50 g/l Na_2SO_4 solution and the remaining cubes in water at 20 °C. At 7, 14, 28, 56, 96 and 204 days, the change of mass and the visual appearance was evaluated. Both sulfate solution and water were replaced after each determination.

Changes in phase composition were examined using X-ray diffraction (XRD) at 28 and 204

days. Surface and core samples of the same size were cut from the paste cubes, dried by solvent exchange with acetone, crushed and the powder was pressed in cylindrical standard sample holders of 16 mm diameter and 2.5 mm height. XRD measurements were made using a PANalytical X'Pert PRO MPD Alpha Θ/2Θ.

The evaluation of expansions during sulfate exposure was based on the mortar bar expansion tests defined by the ASTM C 1012. Mortar specimens of 25 x 25 x 297 mm elaborated with w/c=0.485 and cement:graded sand = 1:2.75 were cast. Before sulfate immersion, the standard proposes a 24 h curing in molds at 38°C and further curing after demolding in lime water until the compressive strength reaches 20 MPa. For this experience, the initial curing was made in the molds during 24 hours in a moist cabinet at 20°C. After one day, the specimens were demolded and immersed in lime-water at 20°C during 24 hours. Finally, the initial length was measured and the bars were immersed in the 0.352M Na_2SO_4 solution (50 g/l) at 20°C. The expansion was determined at 7, 14, 21, 28, 56, 91, 105, 120 and 180 days and the solution was renewed after each measurement period. Reported expansions are the average of six specimens. According to ASTM C 1157, blended cement is sulfate resistant (HS) when the expansion does not exceed 0.05% at 6 months and 0.10% at 1 year.

For compressive strength, mortars bars were cast following the procedure described above and cut with diamond saw in 25 mm-cubes before immersion in the sulfate solution. Complementary, a set of 12 cubes continues curing in lime-water. These cubes allow comparing change mass and compressive strength on the specimens with the same dimension when they were exposed to sulfate solution.

3 Results and Discussion

3.1 Mass Variation of Paste

Figure 2 shows the relative mass variation rate for each blended cement immersed in sulfate solution (grey-red-orange) and in water (blue bar) during 6 months. As can be seen, all pastes presented positive relative mass variations throughout the period evaluated, which indicates increments of mass during the attack. However, this mass increment is produced at different rates depending on the binder composition. During the first 28 days, all specimens follow similar trends, with a gradual decrease on mass gain over time, regardless of the binder and the exposure condition. This behaviour is associated with the pore filling caused by normal hydration processes, relevant here as the samples were immersed only 2 days after casting.

After 28 days, the specimens submerged in non-aggressive conditions maintain similar mass variation rates until the end of the test, as the main hydration reactions occur during the first weeks. However, the samples stored in sulfate solution show an increase of mass gain from this age, which is more significant in the composition C30F, followed by the C15F15CC (more in R than O) and C30CC (again more in R than O). This mass gain observed after 28 days of aggressive curing is associated with the sulfate uptake and the progressive formation of sulfate attack compounds such as gypsum and ettringite. These results suggest that the use of calcined clay reduces the amount of sulfate ions penetrating the matrix and delays the formation of expansive phases. The higher weight gain over time in pastes with ICCR versus ICCO could be attributed to a different interaction of the red calcined clay with sulfates than the orange calcined clay, but this interaction would not be related to greater damage.

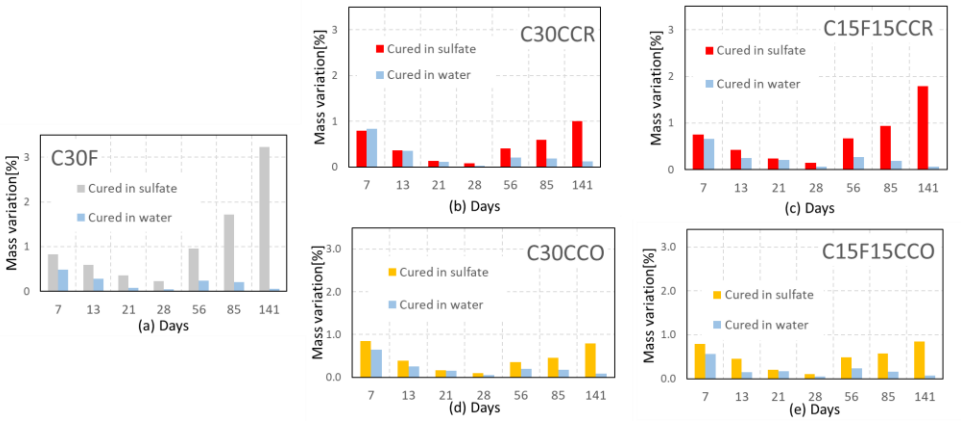

Figure 2. Relative mass variation of pastes cured in water and in sulfate solution.

3.2 Visual Appearance of paste

Figure 3 shows the evolution of visual appearance of paste cubes immersed in sulfate solution for some selected photographs at 28, 90 and 180 days. Figure 3 shows that the integrity of cubes for all blended cements is not compromised during the first 28 days of sulfate exposure. At 90 days, C30F presents a remarkable cracking along the edges, which is the typical cracking pattern associated with the ESA. At this age, pastes with ternary cements (C15F15CCO and C15F15CCR) show a slight cracking near the corners of the cubes, being its intensity considerably lower than for C30F. On the other hand, the composition with 30% ICCR presents no signs of damage after 90 days of sulfate exposure, but for the 30% of ICCO a small crack can be seen at the edge. At 180 days, C30F cubes are completely cracked as the external layers and regions close to the corners can be easily shelled by hand. The damage in the composition C15F15CCO and C15F15CCR has progressed after 180 days of exposure and the initial cracks observed at 90 days are now connected throughout the entire external edges of the cube. On the other hand, the C30CCR and C30CCO cubes only developed very slight and fine cracks along the edges, being slightly more developed in C30CCO pastes. These results suggest that the incorporation of calcined clays up to a 30 % replacement limit significantly more the amount of cracking developed during the ESA than the use of limestone filler.

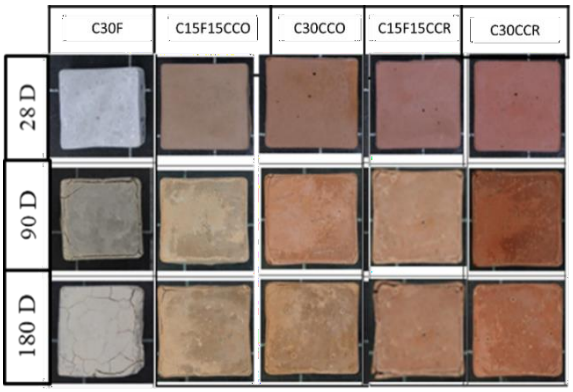

Figure 3. Visual appearance of paste: photographs of cubes at 28, 90 and 180 days.

3.3 XRD-Analysis of Pastes

Figure 4 shows the XRD patterns obtained from the surface and core samples of the paste cubes exposed to sulfate attack at 204 days. On the surface (Fig. 4a), ettringite and gypsum formation are detected in all samples. Peaks of ettringite and gypsum were more intense for C30F. In this paste, gypsum is confirmed by the presence of peak at 20.72° 2θ. For paste containing 15% of ICC, a hump before the quartz peak at 20.82° 2θ is detected; also, the high peak intensity at 31.16° and 33.36° 2θ is attributed to gypsum. For C30CCR and C30CCO pastes, the hump and secondary peak of gypsum have a weak intensity, and some doubt to assign completely the 11.63° and 23.3° 2θ peaks to gypsum arise due to a possible mismatched with the monocarboluminate. In the core of the cubes (Fig. 4b), ettringite and monocarboaluminte were assigned as the peak hump at 20.7° 2θ is absent, the peak intensity at 31.16 and 33.36° 2θ were too weak. In addition, the intensity of CH peaks were too large in the core of the specimens, indicating its consumption on the surface to from ettringite and gypsum. Some reduction of CH is attributed to the pozzolanic reaction of illite calcined clays.

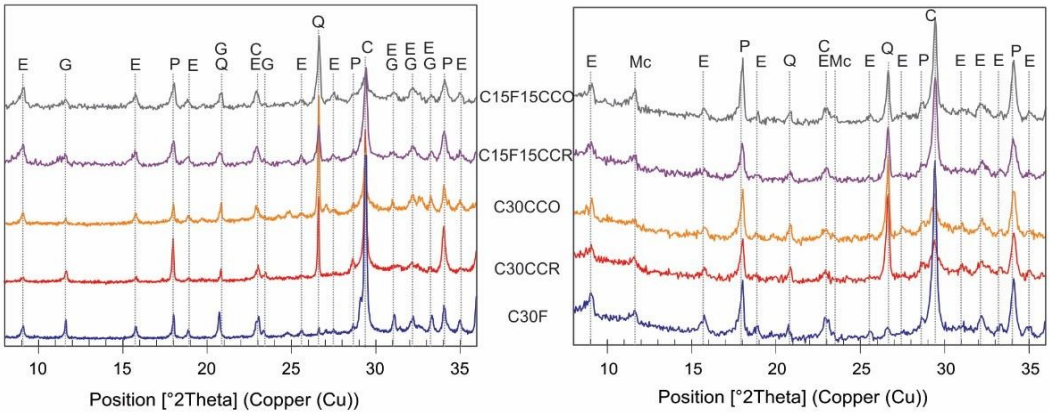

Figure 4. XRD pattern on pastes exposed to sulfate solution for 204 days. (a) Surface and (b) Core.

3.4 Expansion of Mortar

Expansions of mortar bars in sulfate solution are shown in Fig. 5. During the initial exposure up to 28 days, the expansions of the five blended cements present a similar rate, being slightly higher for C30F. After 28 days, the C30F expansion rate increases exponentially reaching the limit of 0.10% at 38 days. At 90 days, the attack on C30F has been so severe that it is no longer possible to measure the length variations since the specimens are practically disintegrated.

On the other hand, C30CCR mortars show a very slow expansion rate and the limit of 0.05% is only reached at 252 days, which is after the threshold of 6 months established by the ASTM standard to be considered as a sulfate resistant cement. For the C30CCO the expansion is also lower but the limit of 0.05% is overpassed at 3 months, so this blended cement is not sulfate resistance according to the standards. The low expansion when 30% of ICC (O and R) is mixed with the cement is attributed to the pozzolanic reaction of the calcined clays, which consumes the CH formed during hydration and reduce the availability of calcium for ettringite formation and specially blocking the pores to prevent the ingress of sulfates into the matrix. This pozzolanic reaction progresses after the immersion in the sulfate solution as occurred in non-aggressive water curing.

For C15F15CCR mortar, the expansion is similar to C30CC up to 90 days, but from this point, the slope increases and exceeds the limit of 0.10% at 161 days, qualifying this cement as not sulfate resistant. The C15F15CCO mortar, the expansion is similar to C30CC up to 56, then the expansion grows faster than the other ternary cement and the limit of 0.05% is passed at this age. Here it can be seen that the ICCR has better pozzolanic activity than the ICCO, because it produces lower expansion on sulfate for the binary and ternary cements.

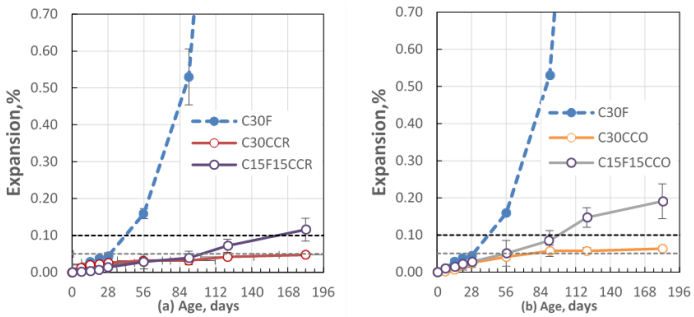

Figure 5. Expansion on sodium sulfate of mortar following ASTM 1012. (a) Blended cements with ICCR and (b) blended cements with ICCN.

3.5 Compressive Strength

Figure 6 shows the compressive strength of mortar for blended cements immersed in sulfate solution (Fig 6 a and c) and in distillate water (Fig 6 b and d). For C30CCR and C30CCO, the compressive strength of mortar cubes cured in water and those cured in sulfate increases from 28 to 90 days confirming the pozzolanic reaction. On the other hand, C30F shows a slight increase due to the dilution caused by limestone filler addition.

At 90 days, C30F cured in sulfates has practically lost its compressive strength, indicating severe degradation caused by ESA. Compositions with the 30 % ICC replacement (C30CCR and CC30CCO) present a significant increase of the compressive strength during the 28 - 90 days period in aggressive conditions. At 90 days, the strengths obtained even reach higher values than the ones obtained in non-aggressive conditions. This behaviour might be attributed to ettringite formation in quantities below the damage onset threshold, which only causes a densification of the matrix. Mixtures with 15 % ICC replacement also develop strength improvements from 28 to 90 days. However, in this case the strength gained is lower than the one observed in 30 % ICC replacement mixtures, specially in the ICCO material.

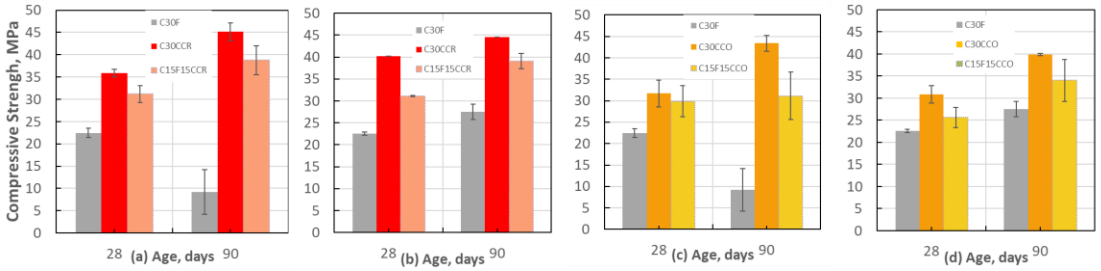

Figure 6. Compressive Strength of mortars, (a) C30CCR, C15F15CCR cured in sulfate, (b) C30CCR, C15F15CCR cured in water, (c) C30CCO, C15F15CCO cured in sulfate, (d) C30CCO, C15F15CCO cured in water.

4 Conclusions

Preliminary results of this study related to the sulfate attack with limestone filler and two different illitic calcined clay exposed immediately to the aggressive environment shows that:

- Limestone filler addition to Portland cement causes the formation of monocarboaluminate, which is unstable in sulfate environment and rapidly forms ettringite causing cracking and massive influx of sulfate ions promoting the gypsum formation, expansion and compressive strength reduction.
- The pozzolanic reaction of calcined clay in mortars is similarly developed in aggressive and non-aggressive curing conditions, consuming the CH and blocking the sulfate ingress due to pore size refinement. The AFm phases formed during hydration in water were converted to ettringite when pastes are exposed to sulfate solution, but the mortar shows no expansion and retains the compressive strength at 6 months.
- These experiences show that despite the lack of curing prior to sulfate exposure, cement with the replacement of 30% of an illitic calcined clay (in this case the ICCR better than ICCO) shows great resistance to ESA, while limestone cements presented a worse performance.

ORCID

Agustin Rossetti: https://orcid.org/0000-0002-0809-2320
Tai Ikumi: https://orcid.org/0000-0001-9547-5241
Igancio Segura: https://orcid.org/0000-0001-6519-9899
Edgardo Irassar: https://orcid.org/0000-0003-4488-0014

References

Ikumi, T., Segura, I. and Cavalado, S.H.P. (2017). Influence of early sulfate exposure on the pore network development of mortars. *Construction and Building Materials, 143*, 33-47. doi: 10.1016/j.conbuildmat.2017.03.081

Lemma, R., Irassar, E.F. and Rahhal, V. (2015). Calcined illitic clays as portland cement replacements. In K. Scrivener and A. Favier (Eds.), *Calcined Clays for Sustainable Concrete,* 269-276. doi: 10.1007/978-94-017-9939-3_33

Neville, A. (2004). The confused world of sulfate attack on concrete. *Cem. Concr. Res. 34*

Ramachandran, V.S. (1995). *Concrete Admixtures Handbook: Properties, Science and Technology*. 2nd ed, ed. V.S. Ramachandran. United States of America: Noyer Publication

Wild, S., Khatib, M. and O'Farrell, M. (1997). Sulphate resistance of mortar, containing ground brick clay calcined at different temperatures. *Cem. Concr. Res., 27,* 697-709. doi: http://dx.doi.org/10.1016/S0008-8846(97)00059-8

XV International Conference on Durability of Building Materials and Components
DBMC 2020, Barcelona
C. Serrat, J.R. Casas and V. Gibert (Eds)

Testing Joints of Air and Vapour Barriers, Do We Use Relevant Testing Methods?

Eva B. Møller[1] **and Torben V. Rasmussen**[2]

[1] Department of Civil Engineering, Technical University of Denmark, Brovej 118, 2800 Kgs. Lyngby, Denmark, ebmo@byg.dtu.dk

[2] Danish Building Research Institute, Aalborg University Copenhagen, A.C. Meyers Vænge 15, 2450 Copenhagen SV, Denmark, tvr@sbi.aau.dk

Abstract. *This article describes testing of peel and shear resistance and airtightness of joints of air and vapour barrier systems before and after artificial aging. The testing of peel and shear resistance was based on standardised methods while the test of airtightness was a method invented for this project. The results show that while peel and shear strength increased with aging, the airtightness was significantly reduced. As these two results seem to contradict each other, the methods are discussed, especially whether the standardised tests are too far from the conditions on site or joints should be tested on other materials as well. Furthermore, weaknesses in the airtightness method is also pointed out.*

Keywords: *Peel Resistance, Shear Resistance, Airtightness, Artificial Aging, Air and Vapour Barrier.*

1 Introduction

To reduce energy consumption some building regulations (*e.g.* BR18, 2017) require test of airtightness in newly erected buildings. Membranes are widely used to ensure the required airtightness but often their purpose is twofold; increased airtightness and reduced diffusion. Independently of whether a vapour barrier or an air barrier is needed, the tightness of the joints is crucial. Furthermore, the joints must stay tight throughout the service life of the membrane.

By joints are meant joints between two lengths of membrane and joints between membrane and other building parts. Tapes or adhesives can be used as sealants, most manufacturers sell membranes and sealants as systems, preferably including collars for pipes that may penetrate the membrane. This is a way to ensure that membrane and sealant are compatible. In Denmark, an independent company (DUKO) classifies vapour barrier systems and roofing underlays, the requirements for obtaining classification include tests of peel and shear resistance.

There are different standardised ways to test joints, *e.g.*:

- Peel resistance according to EN 12316-2:2013 or E DIN 4108-11:2016
- Shear resistance according to EN 12317-2:2010 or E DIN 4108-11:2016

Systems can be tested just after installation or after ageing. Although tests of airtightness are only required in new buildings, evaluation of durability requires tests of performance of aged joints. Methods for artificial aging are described by Møller and Hansen (2017), together with detailed descriptions of resistance test methods and a new way of testing airtightness.

This article describes the outcome of tests of resistance against peel and shear of nine vapour or air barrier systems before and after aging and the result of the non-standardised test of airtightness. It also discusses whether the result from standardised test methods corresponds to what can be observed on building sites and the new way of testing airtightness.

2 Method

All test methods are based on the standardised methods described in ISO or DIN standards except for the test of airtightness, which has been invented for this project. To ensure a uniform pressure when taping the joints, samples for peel or shear resistance testing were placed on a plane surface and a 50 mm wide 2 kg rubber coated roller was pulled over the joint.

2.1 Materials

Nine air or vapour systems were selected for testing, the selection was made by contacting manufacturers and suppliers of air or vapour barrier systems. It was asked whether they would be interested in having their product tested. The characterisation of the materials as given by the manufacturers is shown in Table 1. All systems used tape for joints.

Table 1. Materials used for testing with descriptions given by the manufacturers, VB and AB denotes Vapour Barrier and Air Barrier, respectively. PE = Polyethylene, PP = Polypropylene.

ID	Description	Membrane material	Thickness [mm]
A	VB	PE	0.11
B	VB	Multi-layer PE	0.20
C	VB	LDPE	0.15
D	VB	PE	0.12
E	VB	PE	0.15
F	AB	3-layer with woven reinforcement	Unknown
G	VB	3-layer: PE, PP (reinforcement and fleece)	0.20
H	VB	PP nonwoven + PP foil	Unknown
I	AB	PP fibre cloth with PP coating	0.20

2.2 Artificial Aging

All tests were performed on non-aged as well as aged samples, except peel resistance for membrane joint with membrane, which were only tested on non-aged samples. The artificial aging was performed by placing the samples for 84 days in a climate chamber at 70 °C and 90 % relative humidity followed by 84 days in a ventilated oven at 70 °C.

2.3 Peel Resistance

Peel resistance was tested on joints of two membranes and joints of membrane and aerated concrete (AAC). The tests were performed according to EN 12316-2:2013 that specifies how to test peel resistance of a joint between two pieces of a membrane. A sample was placed in a testing machine with the grips 200 mm apart. During testing the grips moved apart at a constant speed. The force used for peeling was recorded. The method was adjusted for the test with AAC because of the thickness of the AAC.

In addition, the speed of the tests was reduced from a separating speed for the grips from 100 ± 10 mm/min to 10 ± 1 mm/min. Samples used for membrane/AAC tests were approx. 14 cm wide instead of the standardised 50 mm, that were used for the membrane/membrane joints. The measured force was converted to the equivalent force for 50 mm samples. Figure 1 shows the principle of the tests as well as pictures from the testing. Five samples were tested for each material combination.

Figure 1. Test of peel resistance, sketch from the side and photo from the front. Left: Membrane taped to AAC. Right: Two pieces of membrane taped together.

2.4 Shear Resistance

Shear resistance was tested on aged and non-aged joints of membrane/membrane (see Figure 2) and according to EN 12317-2:2010. Similar to the peel test, the ends of the samples were placed in the grips of a testing machine with a constant separating speed and the shear strength was recorded. The separating speed was reduced from 100 ± 10 mm/min to 10 ± 1 mm/min.

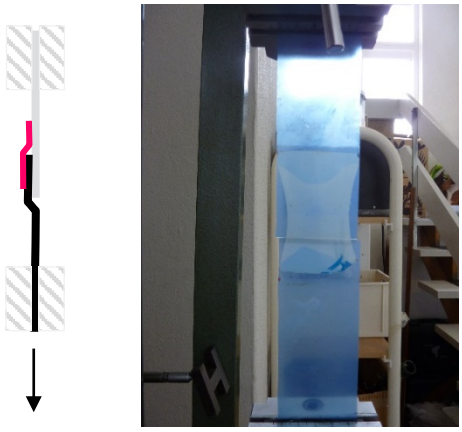

Figure 2. Test of shear resistance, sketch from the side and photo from the front.

2.5 Test of Airtightness

The test of airtightness was not a standard test but a test especially invented to simulate conditions in an older attic where it would be difficult to establish an airtight barrier. The aim was to test airtightness before and after artificial aging. The method is described in (Møller and Hansen, 2017). In short, it consisted of a wooden frame supplied with angled boards and a pipe in the middle. The inside of the frame was lined with the membrane to be tested and fixed to the frame with the system's tape. To secure airtightness around the pipe the system's collars were used and the pipe sealed. The frame was placed in a box leaving a small space between membrane and box, see Figure 3. It was ensured that the frame was airtight and so was the

connection between box and frame. Through a hole in the box a ventilator created a pressure difference between box and frame. The flow necessary to obtain pressurisation of 10, 22, 34, 46, 58, 70 and 82 Pa was recorded. The test was repeated three times and again three times with the same negative pressure differences. By linear regression, the results from the different pressure differences were combined to a single value for a pressurisation of 50 Pa. The test was inspired by the blower door test (EN/ISO 9972: 2015). After 164 days of artificial aging, the tests were repeated. One frame of each system was tested.

Figure 3. Test equipment for test of airtightness. Left: wooden frame with lining of membrane taped to the frame, pipe with collar in the middle. Right: wooden frame placed in box, a ventilator created a pressure difference between frame and box through a hole in the box (not visible on photo).

3 Results

To evaluate the tests results, these are compared to the requirements given by DUKO (2014) when manufacturers want to obtain a certification of their product. Therefore, a line, representing the requirements given by DUKO, has been added to the presentation of results.

3.1 Peel Tests

The DUKO requirements for non-aged joints of membrane/membrane and membrane/AAC is > 10N/50 mm. There are no requirements for aged joints. The results of the peel resistance tests are shown in Figure 4. All systems fulfilled the DUKO requirements. Except for system B, all membrane/ACC became stronger with aging. All non-aged membrane/membrane joints, except for system C, were more than 20 % stronger than non-aged membrane/ACC joints.

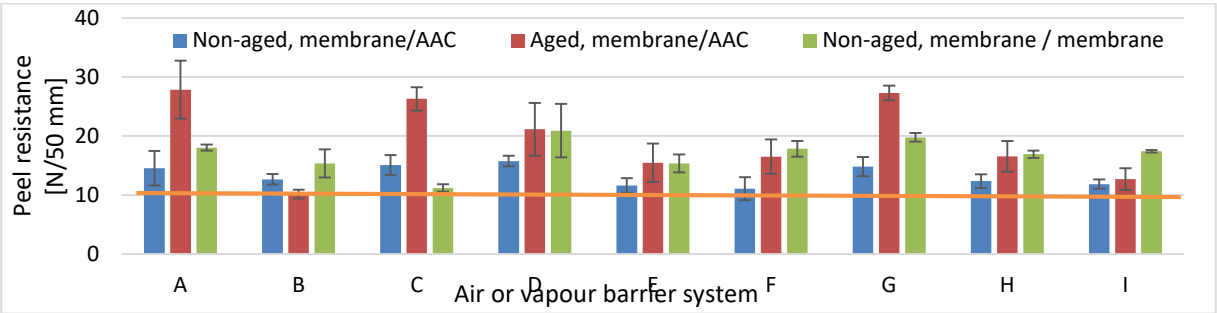

Figure 4. Result of test of peel resistance, average of five samples, with standard deviations. The orange line marks the DUKO requirements for non-aged joints, there are no requirements on aged joints.

Tapes consist of an adhesive and a carrier layer. As shown in Figure 5 there were different places where the adhesive could fail; either the bonding to AAC or to the carrier layer. Where the adhesive stayed showed where the best bonding took place.

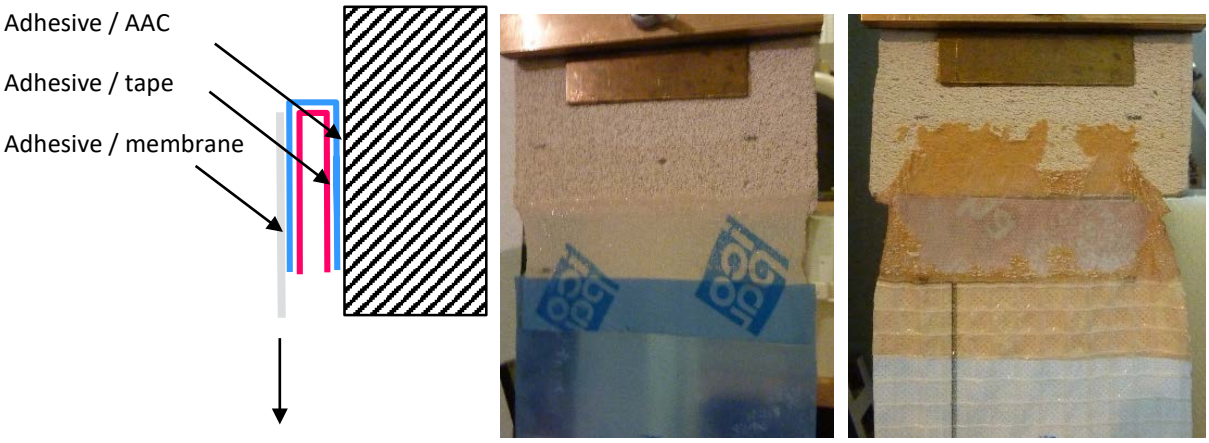

Figure 5. The failure of the adhesive could appear in different places, the sketch shows three possibilities in membrane/AAC connections. The photos show examples, Left: Failure between adhesive and AAC (very little adhesive left on AAC). Right: Failure between adhesive and tape as the adhesive left the carrier layer of the tape.

In some tests, the failure was not clearly between two layers, but parts of the adhesive would stay at the tape and other parts would be peeled of the tape or the failure layer was not the same in all tests of the same system. Consequently, some systems have two failure modes, which can be seen in Table 2, where the failure modes are presented.

Table 2.Point of failure in peel test. In no test did the membrane break.

	Point of failure	A	B	C	D	E	F	G	H	I
Non-aged, membrane/AAC	Adhesive/tape			x						
	Adhesive/AAC	x	x	x	x	x	x	x	x	x
	Adhesive/membrane									
Aged, membrane/AAC	Adhesive/tape	x	x			x	x	x	x	x
	Adhesive/AAC	x			x			x		
	Adhesive/membrane			x						
Non-aged, membrane/membrane	Adhesive/tape	x				x	x		x	x
	Adhesive/membrane	x	x	x	x			x	x	

3.2 Shear Tests

The results of the shear tests are shown in Figure 6, all systems fulfilled the DUKO requirements. The non-aged samples of system A did not come apart; the membrane, however, was stretched to more than the double of its length, without enhancing the force of the machine. In the rest of the systems, the adhesive did not stick to the tape. In the aged samples, the tape broke in system A and G, in the other systems the adhesive did not stick to the tape.

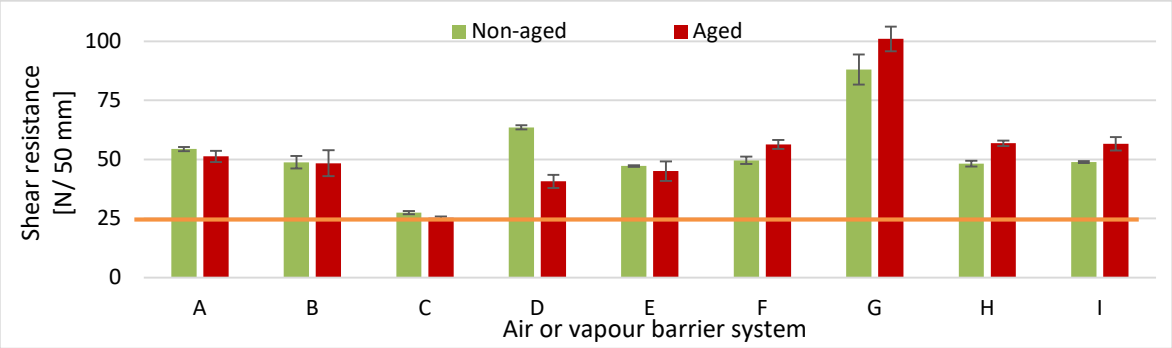

Figure 6. Shear strength, average of 5 samples with standard deviations. Orange line: DUKO requirements for non-aged and aged joints.

3.3 Airtightness

The results of the airtightness tests are shown in Figure 7. All systems needed higher air flow after aging, i.e. all systems were leakier after aging, typically 2-3 times more than before aging.

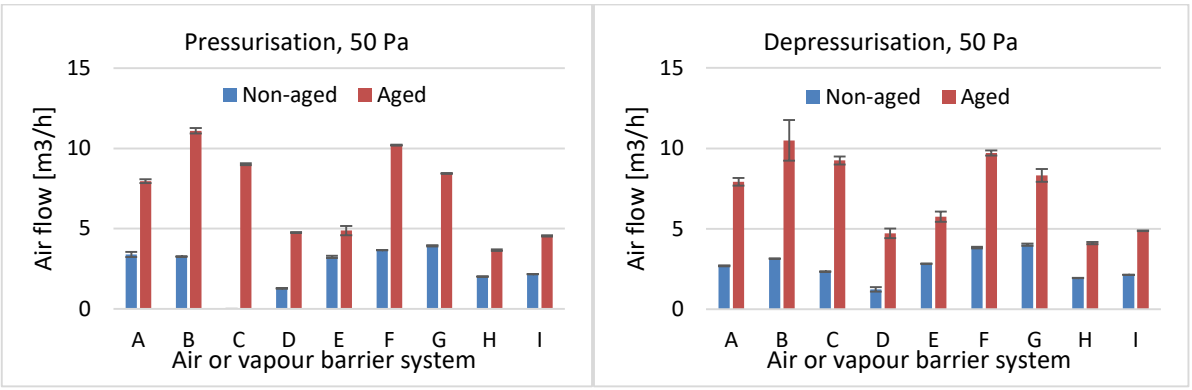

Figure 7. Test of airtightness of non-aged and aged systems, positive and negative pressure difference of 50 Pa. With standard deviations.

4 Discussion

Whether the aging method is the most relevant will not be discussed here, as this method has been discussed by Møller and Hansen (2017). Furthermore, there is no clear picture of which systems perform best, consequently, the discussion is limited to general results and the methods.

4.1 Testing of Peel and Shear Resistance

Although the testing of peel and shear resistance are two different tests, there are many similarities between the results, therefore, these are discussed collectively.

It was expected that peel and shear strength would decrease because of aging. However, the results contradict this; except for system B, peel strength on AAC was generally enhanced and shear strength on membrane/membrane was enhanced or only reduced by less than 10 % in all cases except system D where the shear strength was reduced by more than 1/3.

This is surprising, as practitioners have reported how some tapes, with time lose their ability to adhere to membranes, and from that generalised to all types of surfaces. Unfortunately, these

statements have not been verified systematically, and are only built on specific cases that experienced craftsmen have come across. Change of bonding may vary with aging and be surface/material dependent. Therefore, testing with a larger variety of surfaces seems needed.

However, it also raises the question whether the tests can predict the behaviour of the systems on site. The samples were made under ideal conditions: The joints were assembled on a plane horizontal support with a 2 kg roller under relatively clean laboratory conditions; this ensured the reproducibility of the test. Unfortunately, this may be in contradiction to conditions on site, where there should be a solid support, but the surface may not be plane and clean, the pressure used on the tape is not well defined. Hence, air leakage may not only be related to aging but to bad adhesion in the first place and consequently more sensible to aging than the tests foresee. It underlines the importance of correct workmanship, but questions the relevance of the tests.

In the peel tests of non-aged samples with AAC the adhesive was generally peeled of the AAC, while in the aged test the adhesive was more often peeled of the tape; apparently bonding to the AAC grew with aging. It is not clear why; maybe the heat decreased the viscosity of the adhesive, consequently, the adhesive could penetrate the pores of the AAC and thereby enhance the bonding. Maybe the outcome would have been differently if beech had been used instead of AAC, as prescribed in E DIN 4108-11:2016, the pores in beech are much finer than in AAC.

In the aged samples and most of the membrane/membrane joints, the failure occurred between the adhesive and the carrier layer of the tape. This means that it is not a problem to ensure bonding to membranes in shear tests or to AAC in general; the weak spot is in the tape itself, a better tape would be one where the adhesive bonds better to the carrier layer.

4.2 Testing of Airtightness

While the peel and shear tests are standardised, the test of airtightness was a new method, it is therefore relevant not only to evaluate the results but also the method itself.

The results of the airtightness tests were reproducible; each test was performed at least three times and the results were very close to each other; apparently, tests with pressure difference of up to 82 Pa did not influence the airtightness in the following test. The outcome of the test did also not depend on the operator, something that was also tested.

Contrary to the peel and shear tests, the testing of the airtightness showed a significant reduction caused by aging. Probably the uneven support made it impossible to make as perfect joints as in the standardised plane test samples; possibly tension in the joints caused leakage if these tensions opened the joints over time. The test was designed to simulate realistic conditions in a building and - contrary to the standardised peel and shear tests - the results agreed with statements from practitioners. The test might therefore be relevant. Unfortunately, the samples were not tightened to the same level of tightness level before testing, but only tightened to a level, where it was possible to obtain the needed pressure difference. In many cases additional tightening had to be done immediately before testing the non-aged samples. Consequently, the test only shows the influence of ageing of systems with a tightness above a certain level. Artificial aging seemed to be important, however, it is possible that the release of tension in the joints happened within relatively short time. The testing should probably have been performed more than 24 h after final tightening just as the peel and shear tests were. Other test methods that involve membranes, e.g. test of radon membranes, require a relaxation period of at least 40 hours after installation (Rasmussen and Cornelius, 2017).

DUKO (2014) has a method of testing airtightness that involves a mock-up of a wooden framework resembling a 12 m² wooden building. It is tested for airtightness twice with one week apart, but no artificial aging. By comparing the two tests methods, it might be possible to determine if artificial aging is important for the test.

5 Conclusion

The tested systems all fulfil the requirements for obtaining a DUKO certification on peel and shear resistance. In peel tests of aged samples on AAC and almost all shear tests, the weak layer was at the intersection between carrier layer of the tape and the adhesive, thus, improvement of the peel resistance should be an improvement of the tape itself not the bonding to AAC.

Surprisingly, the peel resistance increased with aging for taped joints to AAC, and shear resistance increased generally. Contrary to this, the test of airtightness showed significant loses in airtightness after aging performed in a wooden box. This raises the question whether the standardised tests of peel and shear resistance are performed under conditions that are too far from the conditions on site and therefore irrelevant. Additionally, it may be necessary to test on more surfaces than only membrane and ACC, *e.g.* wood.

The airtightness test was an attempt to find a different but relevant and reproductive test method. The method still needs to be improved, and compared with other test methods, but the result seemed to be reproductive and in concordance with experience from practice.

Acknowledgements

The work was carried out when both authors were employed at the Danish Building Research Institute. The authors thank The Danish Building Defects Fund (Byggeskadefonden) for financial support of this research project.

ORCID

E. B. Møller: http://orcid.org/0000-0001-8404-0859
T. V. Rasmussen: http://orcid.org/0000-0003-1779-8963

References

BR18 (2017). *Bekendtgørelse af offentliggørelse af bygningsreglement 2018* (Danish building regulations, in Danish), Trafik-, Bygge- og Boligstyrelsen, Copenhagen, Denmark.

DUKO (2014) Information on www.duko.dk: Krav til dampspærresystemer under DUKO – Dampspærre- og Undertagsklassifikationsordning (in Danish, authors translation: Requirements on vapour barrier systms under DUKO): https://duko.dk/userfiles/Klassifikationskrav_dampspaerresystemer-udgave01_20140414.pdf

E DIN 4108-11 (2016). Entwurf: *Wärmeschutz und Energie-Einsparung in Gebäuden – Teil 11: Mindestanforderungen an die Dauerhaftigkeit von Klebeverbindungen mit Klebebändern und Klebemassen zur Herstellung von luftdichten Schichten* (in German). E = Entwurf i.e. draft, not implemented yet.

EN/ISO 9972: (2015) *Thermal performance of buildings – Determination of air permeability of buildings – Fan pressurization method*

EN 12316-2: (2013) *Flexible sheets for waterproofing – Determination of peel resistance of joints – Part 2: Plastic and rubber sheets for roof waterproofing*

EN 12317-2 (2010) *Flexible sheets for waterproofing – Determination of shear resistance of joints – Part 2: Plastic and rubber sheets for roof waterproofing*

Møller, E.B. and Hansen, T. (2017). Artificial aging of air and vapour barriers. In *Proceedings of the XIV International Conference on Durability of Building Materials and Components*, Ghent, Belgium, 285, 1-12.

Rasmussen, T.V. and Cornelius, T. (2017). Radon barrier: Method of testing airtightness - 2. Edition. In *Proceedings of 11th Nordic Symposium on Building Physics, NSB2017, 11-14 June 2017, Trondheim, Norway.*

XV International Conference on Durability of Building Materials and Components
DBMC 2020, Barcelona
C. Serrat, J.R. Casas and V. Gibert (Eds)

The Efficiency of Fly Ash Concrete in the Context of the Combined Action between Chlorides and Carbonation

Raphaele Malheiro[1], Gustavo Camacho[1], Gibson Meira[2] and Aires Camões[1]

[1] Centre for Territory, Environment and Construction (CTAC), University of Minho, Campus Azurém, Guimarães, Portugal, raphamalheiro@gmail.com, gustavo92@live.com.pt, aires@civil.uminho.pt

[2] Federal Institute of Education, Science and Technology of Paraíba, R. Dep. Balduíno M. de Carvalho, 155/1104,58.036-860 João Pessoa, Paraíba, PB, Brazil, gibsonmeira@yahoo.com

Abstract. *The fly ash concrete (FAC) has often been used in chloride contaminate environments. The aluminates present in fly ash (FA) react with free chlorides binding them and reducing the amount of chlorides able to penetrate into concrete. However, $Ca(OH)_2$ present in FAC is easily consumed by pozzolanic reactions, making easier the advance of carbonation. In this context, it is important to know the FAC behaviour in environments subjected simultaneously to chlorides and carbonation. Chloride diffusion coefficient (D) increases in environments containing chlorides and CO_2 when compared to one containing only chlorides. This increase is related to the effects of carbonation on concrete. Therefore, this paper investigates the efficiency of FAC in context of the combined action of chlorides and carbonation. Two different concretes were cast, a FAC (40% FA) and a reference concrete (RC), that is a concrete with similar properties to FAC but without FA. After 90 days humid curing, half of specimens were subjected to accelerated carbonation (20ºC, 55% RH and 4% CO_2) during 1, 2 and 7 months. The other half was protected and remained in laboratory during the same period. Afterwards, non-steady-state migration tests were performed. The results show that, under the studied conditions, the efficiency of the FAC against chloride penetration is not affected when compared to the results obtained for RC. The carbonation depth in FAC is higher than in RC, but the D in FAC remain lower than in RC. This behaviour can be attributed to the higher capacity of FAC binding chlorides.*

Keywords: *Chloride, Carbonation, Fly Ash, Combined Action, Migration Test.*

1 Introduction

The building sector plays a significant role in the global energy use and carbon emissions. The concrete is one of most consumed materials in the world and the annual worldwide CO_2 emissions from cement manufacturing, main component of concrete, add up to almost 2.3 billion mt, which is nearly 7% of the global emissions from fossil fuel combustion (Mehta & Monteiro, 2014). To reduce the environmental impact of the building sector is essential to reduce the cement consumption and to guarantee the long-term durability of concrete structures.

The incorporation of fly ash (FA) in cementitious matrices has been used in two main ways. First, to reduce the cement consumption without loss of mechanical strength. Second, to increase the concrete structures durability, making its cementitious matrix more resistant to the action of chlorides. The SiO_2 present in FA reacts with $Ca(OH)_2$ resulting from cement hydration and produces C-S-H structures that strongly decrease the concrete porosity and hence reduces the transport of aggressive agents such as chloride ions. In addition, the aluminates present in FA chemically react with free chlorides binding them and reducing the amount of free chlorides able to penetrate into concrete (Alonso Alonso, Acha and Andrade, 1994).

Therefore, the FA concrete has showed a high perform in chloride presence (Cheewaket, T., Jaturapitakkul, C. and Chalee, 2010; Chindaprasirt, Rukzon and Sirivivatnanon, 2008; Varga, I., Spragg, R., Bella, C., Castro, J., 2014). However, the consumption of $Ca(OH)_2$, due to the pozzolanic reactions, decreases the alkalinity of the concrete and resulting in a more rapid carbonation when compared to a concrete made without FA (Neville, 1997). In this sense, it is necessary to investigate the efficiency of FA concrete in the context of the environment containing chlorides and carbon dioxide.

In the present work, an experimental investigation is carried out to understand the behaviour of FA concrete against the coupled effect of chloride and carbonation. The effect of carbonation on chloride diffusion coefficient is evaluated.

2 Experimental Program

2.1 Materials and Concrete Mixtures

Ordinary Portland Cement (OPC), CEM I 42.5R, and FA were used as binder materials in the concrete specimens, which chemical compositions are presented in Table 1. The chemical composition of FA was determined using x-ray fluorescence spectroscopy. In addition, Scanning Electron Microscopy was used to observe FA morphology (Figure 1), revealing that it is mainly composed by cenosphere particles (Malheiro *et al*., 2018). These FA were obtained from the burning of South African and Colombian coal in Portuguese thermoelectric power plants.

Table 1. Chemical composition of OPC and FA.

	SiO_2	Al_2O_3	Fe_2O_3	CaO	MgO	SO_3	K_2O	Na_2O	Cl^-	TiO_2	P_2O_5	LOI	IR	RE
OPC (%)	20.33	4.59	3.06	62.30	2.12	3.10	0.76	0.19	0.07	-	-	1.78	1.21	0.49
FA (%)	55.10	26.60	5.70	2.58	1.30	-	1.41	0.26	-	1.33	0.73	3.07	-	1.92

LOI – Loss on ignition IR – Insoluble residual RE – Remaining elements

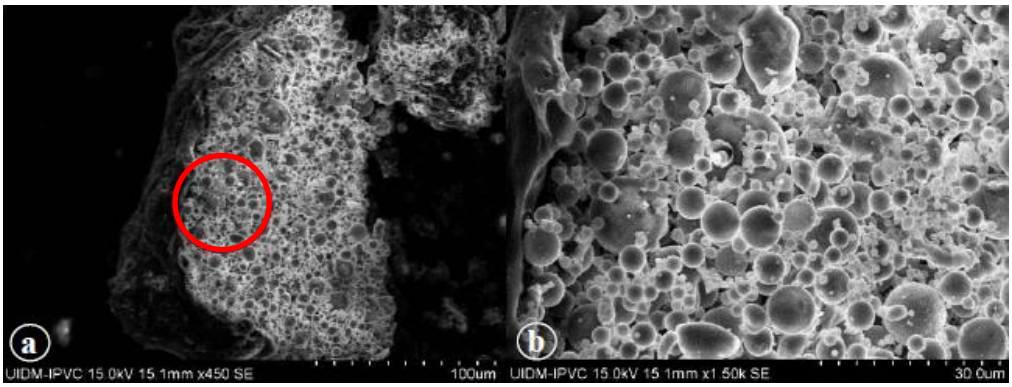

Figure 1. SEM FA images: a - 100µm (x300) and b – 30µm (x1500).

In addition to knowing the behavior of FAC under combined situation, it is also important

to compare its behavior to RC behavior, that is a concrete with similar properties to FAC but without FA, under same situation. Thus, two mixtures were adopted in this study, which are presented in Table 2. Crushed sand with a fineness modulus of 2.96 and two types of granitic crushed coarse aggregate, one with fineness modulus of 6.07 and the other with 6.94, were used. Tap water, maximum value of chlorides in the water was 10 mg/l, was used for mixtures.

Table 2. Materials and main properties of the mixtures.

Properties	FAC	RC
FA (%)	40	0
Cement (kg/m^3)	228	380
FA (kg/m^3)	152	0
Water/binder ratio	0.50	0.50
Slump (mm)	110	95
Compressive strength 365 days (MPa)	51.59	53.45
Immersion water absorption (%)	9.99	10.75
Capillary water absorption (kg/m^2/min$^{1/2}$)	0.116	0.104

Cylindrical concrete specimens with ϕ100x200 mm were casted with the mixtures presented. After casting, the specimens were covered with a plastic sheet and were stored in a humidity chamber (21 ºC and 98% RH) for one day. Then, they were removed from the moulds and were cured immersed in water for 90 days. The choice of this curing period was to give enough time for pozzolanic reactions in specimens containing FA to occur. After the curing period, all specimens were cut in three slices (ϕ100x50 mm). The top and bottom of the samples were discarded.

2.2 Accelerated Tests

The efficiency of FAC in the context of the combined action between chlorides and carbonation was studied in two ways: combined situation and reference situation. In the combined situation the specimens were subjected to carbonation test and, after, to chloride migration test. In the reference situation, the specimens were subjected only to the chloride migration test. The Figure 2 shows the test scheme.

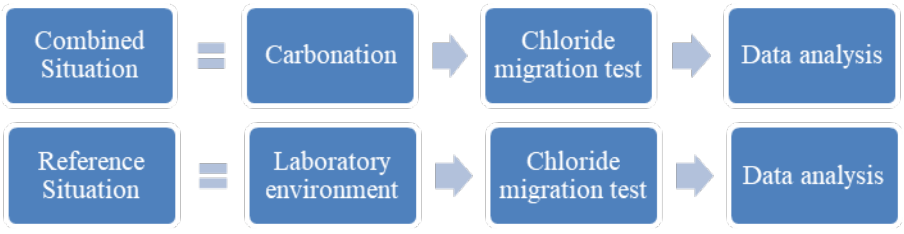

Figure 2. Laboratorial procedure scheme.

Before the tests, the specimens (FAC and RC) were subjected to preconditioning procedures

in order to achieve the equilibrium with environmental humidity near 60% and accelerate the carbonation process (in the combined situation case). This preconditioning had three stages. In the first stage, the specimens remained in a chamber with controlled temperature and humidity (20ºC and 60% RH) until reaching constant mass. Second, they had the lateral and the bottom face covered with paraffin in order to guarantee the one dimensional attack of aggressive agents through the top of the specimen. Third, in order to distribute the humidity inside the concrete specimens, they were protected with several layers of plastic film and put in a ventilated oven (40ºC), for 20 days. The specimens were weighed before and after being in oven and one has verified that the water loss was not bigger than 0.1%.

In the combined situation, after preconditioning procedures, the plastic film was removed and the specimens were subjected to accelerated carbonation in carbonation chamber (4% CO_2, 20ºC and 55% RH), following the recommendations of the European Standard (CEN/TS12390-12, 2010), during three different periods: 1, 2 and 7 months. Finished the test, the specimens were not broken and the paraffin coating was removed in order to permit the chloride migration test to be carried out. In the reference situation, the specimens remained wrapped in laboratory environment (20ºC and 60% RH) until chloride migration test time.

After, the chloride migration test was performed according the Portuguese specification (LNEC E 463, 2004). Finished the test, the specimens were broken perpendicular to the penetration direction of the aggressive agents. In the combined situation, the specimens were tested after each carbonation period studied. In this case, the halves were used in different ways: one half was sprayed with a solution of 1% phenolphthalein in 70% ethyl alcohol (RILEM TC CPC-18, 1988) in order to determine the carbonated front and the other half was sprayed with 0.1 N $AgNO_3$ to determine the chloride penetration depth. In the reference situation, the halves were used to determine the chloride penetration depth.

2.3 Capillary Water Absorption Test

The capillary water absorption test was carried out in order to study the open porosity of concrete (LNEC E 393, 1993). The test consisted in measuring the amount of absorbed water through only one face of a no saturated concrete specimen immersed in a water film of 5 ± 1 mm. The absorption of water through capillarity is the difference between concrete hardened mass, M_i (g), that had one face in contact with water during a time ti and the dry concrete mass, M_0 (g), divided by the superficial area that was in contact with water, a (mm).

3 Results and Discussion

3.1 Effect of Carbonation on the Chloride Diffusion Coefficient in Specimens with FA Incorporation

The effect of carbonation on the chloride diffusion coefficient in FAC is evaluated in Figure 3. This figure gathers the chloride diffusion coefficient values achieved for concrete subjected to the combined situation and reference situation. The values were determined for the three different carbonation test periods studied: 1, 2 and 7 months.

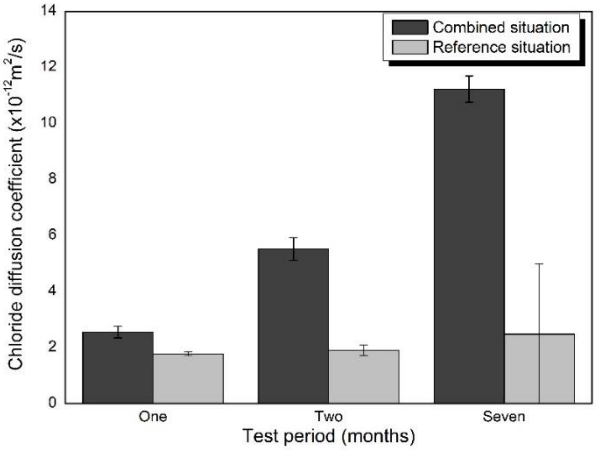

Figure 3. Chloride diffusion coefficient for FAC for the different situations: combined and reference.

According Figure 3, under conditions studied, there is a significant increase in chloride diffusion coefficient for FAC subjected to the combined situation when compared to the reference situation. This increase is quite high since the first month and gradually increases, until reaching the value of 352% in the seventh month.

The relationship between chloride diffusion coefficient and carbonation depth for FA concretes studied is showed in Figure 4. In this case, the chloride diffusion coefficient is closely related to the carbonation depth, through of an exponential equation with high coefficient of determination, $R^2 = 0.93$. In this sense, the increase in the carbonation depth leads to a significant increase in the chloride diffusion coefficient for FAC.

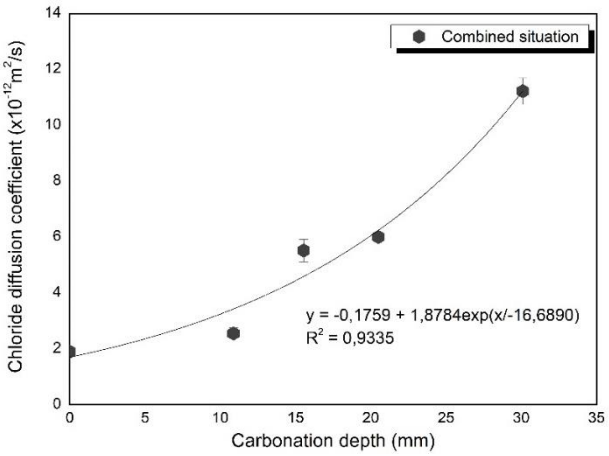

Figure 4. Relationship between chloride diffusion coefficient and carbonation depth for FAC.

The increase in the chloride diffusion coefficient can be related to: the increase in the large capillary pores, caused by carbonation (Ngala, V. and Page, 1997), which, in this case, can provides a "privileged path" for the chlorides penetration; and the chloride binding capacity reduction in carbonated concrete, consequently, there are more free chlorides available to penetrate in the cementitious matrix. The hypothesis of the increase in the large capillary pores

is investigated through the study of open porosity. The Figure 5 shows the capillary absorption results, after seven months, for FAC.

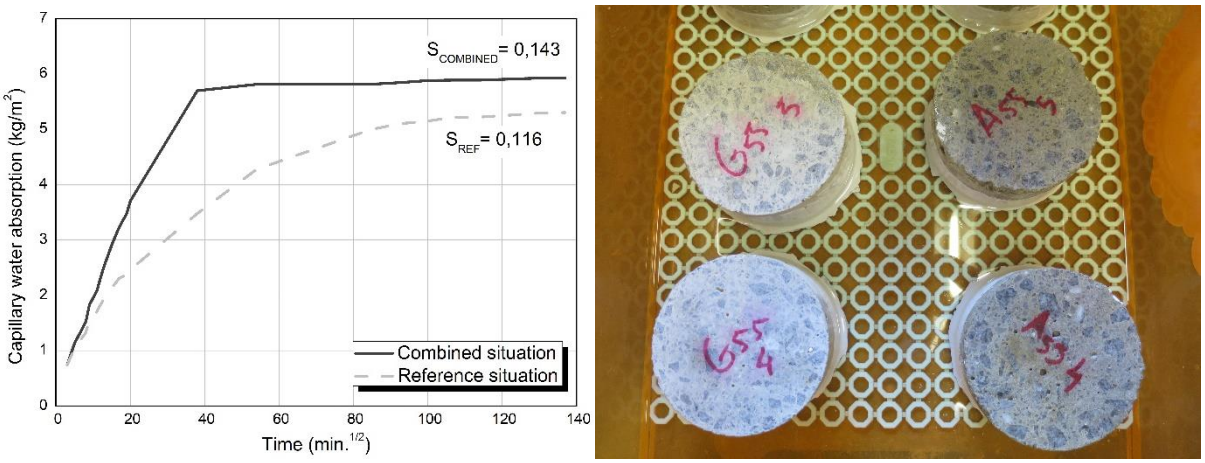

Figure 5. Capillary water absorption kinetics (left) and capillary water absorption test (right) after seven months testing.

In Figure 5 (left) is observed a higher capillary absorption coefficient for the specimens under combined situation when compared to the specimens under reference situation. It can indicate an increase in the fraction of the large capillary pores in FA concrete carbonated. Furthermore, the specimens subjected to the combined situation reached the stability (capillary pore saturation) more quickly, around 40 $min^{1/2}$, than ones under reference situation. The "superficial perspiration" verified in the specimens subjected to the combined situation (Figure 5, right) can be related to this capillary pore saturation. The results corroborate the hypothesis that the increase in the large capillary pores was one of the responsible for the increase in the chloride penetration in the carbonated FAC.

In this sense, it is possible to say that the FAC carbonated, under studied conditions, can work as a "privileged path" for the free chlorides penetration. This path can be seen in FAC specimens after combined test (Figure 6): XM1 is carbonation depth (left) and XM2 is chloride penetration depth (right). The chlorides completely cross the carbonated front, XM1, but only penetrate a few millimeters (XM2 - XM1) after this front.

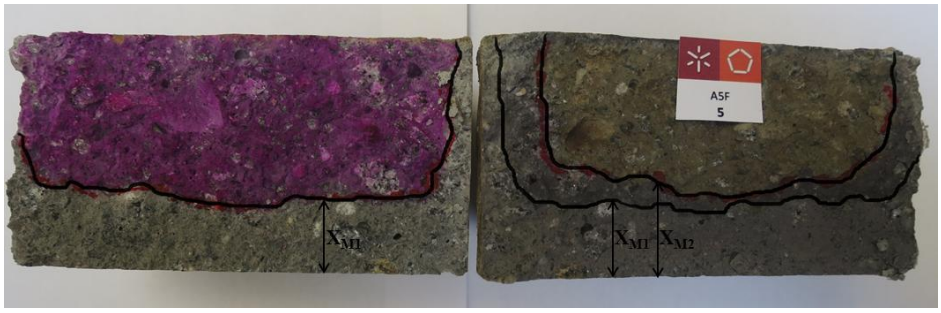

Figure 6. FAC specimens after combined situation (carbonation plus migration test).

3.2 Comparison between the Results Obtained for Specimens with FA Incorporation and Equivalent Specimens without FA

It is important to understand the FAC behavior in environments containing chloride and carbon dioxide but it also important to compare its performance to RC performance in the same environment. The Figure 7 gathering the chloride diffusion coefficients and the carbonation depths achieved for these two types of concrete in different test periods.

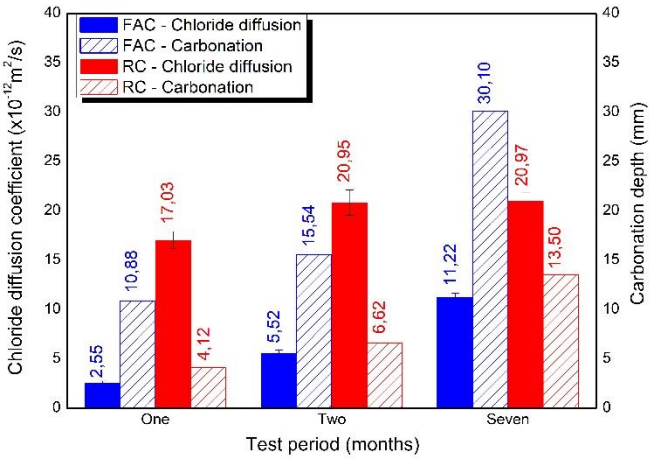

Figure 7. Chloride diffusion coefficients and carbonation depths achieved for FAC and RC under combined situation.

Regardless the test period and carbonation depth, the chloride diffusion coefficients for FAC is always less than the chloride diffusion coefficients for RC. This difference in chloride diffusion coefficients values tends to decrease over time, from 85% in the first month of testing to 53% in the seventh month (it is still a very significant difference). This result corroborates the efficiency of FAC against the chloride penetration, under conditions studied, even when the concrete structures are inserted in environments subject to chloride ions and carbon dioxide.

However, it is important to note that, regardless the test period, the carbonation depths for FAC is always higher than the carbonation depth for RC. In the seventh month, the carbonation depth for FAC is very close 30 mm. Taking into account the minimum coatings recommended by standards for carbonation environment, 25 – 40 mm (LNEC E 464, 2007), in this case, carbonation front can be close to the concrete reinforcement.

4 Conclusions

By experimental investigations on FAC subjected to chloride and carbonation environment, under conditions studied, the main conclusions can be drawn:

- There is a significant increase in chloride diffusion coefficient for FAC subjected to the combined situation when compared to the reference situation. This increase is related to the carbonation depth through an exponential relationship.
- This increase can be related to the increase in the large capillary pores, caused by carbonation, and the chloride binding capacity reduction in carbonated concrete.
- Despite the increase mentioned above, under chloride and carbon dioxide presence, the

chloride diffusion coefficient for FAC is always less than the chloride diffusion coefficient for RC. However, the carbonation depth is significant.

Acknowledgements

The authors thank the Foundation for Science and Technology (FCT) for supporting this research. The au-thors also thank the SECIL for making available cement used in this research and the CIMENTEIRA DO LOURO for providing the aggregates used.

ORCID

Raphaele Malheiro: https://orcid.org/0000-0001-6922-9813
Gibson Meira: http://orcid.org/0000-0003-4473-4308
Aires Camões: https://orcid.org/0000-0002-9677-3627

References

Alonso Alonso, M. C., Acha, M. and Andrade, P. (1994). Incidencia de la adición de cenizas volantes en la durabilidad de las estructuras de hormigón armado. *Hormigón y Acero*, *45*.

CEN/TS12390-12, E. C. for S. (2010). FprCEN / TS 12390-12 Testing hardened concrete - Part 12 : Determination of the potential carbonation resistance of concrete : Accelerated carbonation method.

Cheewaket, T., Jaturapitakkul, C. and Chalee, W. (2010). Long term performance of chloride binding capacity in fly ash concrete in a marine environment. *Construction and Building Materials*, *24*, 1352–1357.

Chindaprasirt, P., Rukzon, S. and Sirivivatnanon, V. (2008). Effect of carbon dioxide on chloride penetration and chloride ion diffusion coefficient of blended Portland cement mortar. *Construction and Building Materials*, *22*(8), 1701–1707. https://doi.org/10.1016/j.conbuildmat.2007.06.002

LNEC E 393. E 393 - Determination of the absorption of water through capillarity (1993). Lisbon, Portugal.

LNEC E 463. E 463 - Determination of diffusion coefficient of chlorides from non-steady-state migration test (2004). Lisbon: LNEC.

LNEC E 464. E 464 - Concrete - Prescritive methodology for a design working life of 50 and of 100 years under the environmental exposure (2007). Lisbon, Portugal.

Malheiro, R., Camões, A., Meira, G., Amorim, M. T., Castro-gomes, J. and Ferreira, R. M. (2018). Behaviour of cementitious matrices subjected to the combined action of chloride ions and carbonation. *Revista Materia*, *23*(3).

Mehta, P. K. and Monteiro, P. J. M. (2014). *Concrete: microstructure, properties, and materials* (4th ed.). McGraw-Hill.

Neville, A. M. (1997). *Propriedades of concrete* (2nd ed.). São Paulo: PINI.

Ngala, V. and Page, C. (1997). Effects of carbonation on pore structure and diffusional propertiesof hydrated cement pastes. *Cement and Concrete Research*, *27*, 995–1007.

RILEM TC CPC-18. (1988). RILEM RECOMMENDATION CPC-18 Measurement of hardened concrete carbonation depth. *Materials and Structures*, 453–455.

Varga, I., Spragg, R., Bella, C., Castro, J., B. D. and J. W. (2014). Fluid transport in high volume fly ash mixtures with and without internal curing. *Cement and Concrete Composites*, *45*, 102–110.

XV International Conference on Durability of Building Materials and Components
DBMC 2020, Barcelona
C. Serrat, J.R. Casas and V. Gibert (Eds)

The Palace of Westminster Courtyards Project: Sourcing Stone for Repair and Conservation

Elizabeth Anne Laycock[1], David Jefferson[2] and Steven Hetherington[1]

[1] Department of the Natural and Built Environment, Sheffield Hallam University, City Campus, Sheffield, S1 1WB UK, e.a.laycock@shu.ac.uk

[2] Jefferson Consulting Limited, The Old Armoury, Crown Business Park, Old Dalby, Melton Mowbray, Leicestershire, LE14 3NQ, UK. enquiries@jeffersonconsulting.co.uk

Abstract. *The Palace of Westminster, commonly known as the Houses of Parliament, serves as the meeting place of the House of Commons and the House of Lords and is situated on the north bank of the River Thames in London, England. The site is part of the UNESCO Westminster World Heritage Site. The building was constructed of magnesian limestone, selected following a nationwide survey of building stones carried out by a Government Select Committee. However, some of this stone began to decay soon after construction in the mid 1800s. As the majority of the stonework has survived very well the aim of the work was to source a demonstrably durable material with characteristics which align with the majority of the existing stonework. Samples were taken from the building for petrographic analysis in order to identify compatible material in quarries, either working or which could be re-opened. Durability of the magnesian limestone was assessed using both accepted tests and novel methodology. Large scale walls were constructed in the laboratory and exposed to accelerated frost weathering with realistic temperature parameters. The logistical problems with sourcing the original building material, the nature of the transport and the masons' unfamiliarity with the stone may all have played a part in undermining its durability. When magnesian limestone is properly selected and used correctly, its reputation for being of poor durability is largely unfounded. Suitable sources for replacement stone were located which provided several options for both immediate and long-term sourcing for repair and conservation.*

Keywords: *Magnesian Limestone, Durability, Restoration, Weathering, Freeze Thaw.*

1 Introduction

As with all historic buildings, natural wear and tear results in the necessity of repairing the fabric of the Palace of Westminster from time to time. Wherever possible this is undertaken with either the original stone where this is still available, or a stone which is petrographically, chemically and visually similar to the original, when the original source is unknown or has been worked out or sterilised by development. Unfortunately, over the years a number of stories regarding the unsuitability of the stone used by Barry to build the 'New' Houses of Parliament after the disastrous fire of 1834, have become to be regarded as fact (Shenton, n.d.).

2 The Historic Construction

The original stone for the Palace of Westminster selected by the Commissioners appointed by Parliament, was magnesian limestone from Bolsover Moor. The rate of extraction of acceptable stone with suitable bed heights could not be maintained and production was switched to Mansfield Woodhouse. The required bed heights again proved impossible to achieve. In 1834, only three years after the foundation stone had been laid, and with the walls of the new building about four to five metres in height, all the external stone was being supplied from the Anston

area. The Anston quarries finally fulfilled one of the main criteria for the supply of stone, being both of acceptable bed height and able to meet a supply rate which matched the planned speed of construction.

Stone was transported from the site using horse-drawn wagons to the Chesterfield canal and loaded into boats at Dog Kennel's Wharfe after storage at Kiveton Park. (Richardson, 1999). From there it was carried to West Stockwith to be transferred on to Trent sloops for the rest of the two-week journey to the Humber and then down the North Sea coast to the Thames and Westminster. Lott and Richardson (1997) highlight the 'formidable' scale of the operation as 400 imperial tons were carried by barge each month (approximately 4880 metric tons per annum). Anston Stone was used in the whole building except 'the upper part of the towers and the front towards Abingdon Street' (Elsden and Howe, 1923).

Soon after the building was completed signs of degradation started to appear on some of the stonework. These problems were almost certainly a result of the demand for large quantities of stone in relatively short time, compounded by the complexities of the formation of the of magnesian limestone (Smith, 1995). While acceptable building stone is available, in a range of bed heights, its quality can be variable and requires careful selection of appropriate material.

There were pressures to complete the building quickly and at minimum cost. Many of the masons involved in constructing the building would have been unfamiliar with magnesian limestone. A government select committee in 1861 reported that there were 17 beds in various thicknesses from 1 ft to a few inches but that both the good quality Anston and the poorer were 'worked indiscriminately' with no supervision within the quarries and as a result "*So little stone was rejected at the quarries that almost the only waste was that derived from the cutting of the blocks*" following which "*the stone was sent to London within a fortnight of quarrying, even throughout the Winter*" i.e. without seasoning to allow any weak material to fail before processing (Elsden and Howe, 1923). The stone had not been marked to show the bed orientation and thus much of the ashlars "*were sur-bedded – an example of unpardonable slackness*" (Elsden and Howe, 1923).

Despite often repeated comments that the magnesian limestone was not suitable for use in the polluted atmosphere of London, the majority of the stonework has survived extremely well. The quality of properly selected Anston stone was demonstrated by Sir Henry de la Beche, the first Director of the Geological Survey, who was involved in selecting the stone for the Palace of Westminster, when he used it for the new Museum of Practical Geology on Jermyn Street. Magnesian limestones have been used successfully in polluted atmospheres outside London; in Mansfield and Doncaster for example. Petrographic and electron microscope studies have shown that one reason for this durability may be the thin layer of crystalline gypsum which can develop on the surface of the stone, protecting it from further reaction.

3 The Original Stone

The magnesian limestones were originally formed in a shallow near-shore environment, ranging from sabkha muds to lagoonal oöidal banks, shell banks, patch reefs and detrital deposits. These strata were petrographically variable even before dolomitisation which overwrites original depositional fabrics. Thin beds of marl are not uncommon, and this clayey material is also present as very thin films within some of the limestone. In terms of petrography, chemistry and physical properties, a considerable range of stones exists as is evidenced by the colour and texture of the stones in historic buildings from Nottingham to the Tyne. The fine-grained nature of some of the stones and dolomitisation often make it impossible to identify the type and source of stone purely from a visual study of the surface alone. There are probably as many different types of magnesian limestone in the area from which the stone was sourced as there are different

types of ordinary limestone in the UK.
In order to determine the types of stone which may be required for the conservation work in the Courtyards, and elsewhere on the exterior of the Palace, it is first necessary to study and sample all the stonework within the seven courtyards, aiming to identify the existence of significant variations and, if they do exist, the number of stone types present and their distribution. Although all the fabric is relatively contemporaneous, the problems encountered with the supply of stone to the 'New' Houses of Parliament between 1839 and about 1852, and possible modifications since that time, may well have resulted in individual elevations utilising different building stones (Bolsover Moor, Mansfield Woodhouse, North Anston), and all three magnesian limestones may conceivably be present in at least some of the elevations.
Careful sampling of the fabric was therefore undertaken and 15 samples of magnesian limestone were taken from locations in the Chancellor's Court, The State Officers Court, The Peer's Court and The Star Chamber Court. A further piece of stone was provided, having become detached at some point in the past. The original context of this stone was unknown and was found to be Caen and not magnesian limestone (Yates, 2014; Palmer 2014) and is not discussed further. The lack of supervision and selection throughout the process in an attempt to finish the original work as speedily as possible and at minimum cost can be witnessed upon survey of the fabric of the building. It appears likely that the most damaged stonework involving the Anston stone is where softer material has been used for carved work, where poor stone selection has allowed flawed stone to be inserted in the building and where the stone has been incorrectly laid.
Petrographic analysis indicated that all the stones were originally detrital limestones formed in a lagoonal environment which were heavily recrystallised during the dolomitisation process. Three of the samples were relatively coarse-grained, the remainder finer grained, the typical clast size being about 140 microns. The original sediment consisted largely of spherical and sub-spherical particles, the exact nature of which cannot be determined due to the effects of the recrystallisation. However, when considered in the context of the Permian limestone elsewhere along its outcrop, these grains are most likely to be a mixture of rounded intraclasts, shell and other fossil fragments, spherical algal bodies and coated grains as well as true oöids. Some of the samples indicate that some of the shell and other fossil fragments could have been quite large. Although the finer-grained matrix is largely amorphous due to the dolomitisation, there are areas which suggest that algal mats may have been present. Overall, the assemblage suggests a typical Permian shallow water reefal and lagoonal environment, typical of the much of the Permian magnesian limestone outcrop.
There was no pattern in the use of the stone according to the study of the petrography and the fabric from which the samples were obtained. This apparent mixing of stone types within the fabric does have an advantage when conservation is undertaken. Due to the variation in the fabric there is no requirement for the exact matching of petrographies when a stone is repaired or replaced. Providing that the replacement material originated in a similar limestone facies to the original stone, and the degree and type of dolomitisation together with its physical characteristics, is similar, the most appropriate new stone for the location within the building can probably be selected.

4 Locating Replacements

Given the importance of the building, very careful consideration must be paid to the potential sources which most closely matched the fabric both visually and petrographically, and with acceptable chemical characteristics (*e.g.* the concentrations of silica, magnesium and iron),

similar porosity, permeability and compressive strengths, and of the same geological age. Sources that most closely matched these were available from quarries not operating commercially at the time of assessment. The type of dolomite fabric seen in the samples from the Courtyards, and elsewhere on the exterior of the building, is typical of that found in the area between Doncaster and Mansfield. However, the colour of the stone within this area can vary between pure white and pale brown. Obtaining a good colour and texture match restricts the search area for new stone to within about 20 kilometres of Anston.

All the magnesian limestone quarries within the target area were visited in order to determine whether or not stone with the correct texture and colour was potentially available. This included closed and mothballed quarries, as well as ones which were operating. Where it was not possible to obtain permission for access to a quarry, the visual appearance of the stone, and in particular its colour, bed height and jointing, was observed from the perimeter. Closer analysis of the stone in such cases was obtained by studying exposures outside, but close to, the quarry. Although there were a considerable number of quarries in the area in the second half of the 19th century, very few now remain. The result of the field studies indicated that Tarmac's quarry at Harrycroft was potentially a suitable source of stone for the repairs and conservation at the Palace of Westminster. Although not active at the time of the survey, reserves of stone remained in a consented area. The quarry is now fully consented and operational. The geology of the site is complex, with the rock being a mixture of patch reefs separated by bedded lagoonal deposits. Structurally the stone is also variable, being cut by faults and, more importantly, by joint features caused by differential compaction within and round the perimeter of the individual reefs. The reef limestones are not suitable for use as a building stone and any resource must therefore be extracted from the inter-reefal areas.

While the petrography of the material was consistent with that sampled from the palace, an assessment of the durability of the magnesian limestone was required and sample blocks were collected and tested by Sheffield Hallam University using an environmental chamber. At the request of the architects and following Stage 1 of the work, a second stage used stone from the commercially operating Cadeby Quarry.

5 Durability Assessment

For the first stage of work, four blocks of magnesian limestone were selected. These were chosen in order to represent the variation within the non-biohermal beds at the quarry. The bioherms, or patch reefs, have not been sampled since the stone is irregular and unbedded and contains numerous joints and cracks, probably due to the irregular compaction suffered after burial; it is not suitable for masonry use. The blocks were cut at the masonry yard at the Dean and Chapter quarry at Lincoln Cathedral. All cut blocks were 350mm length, 200mm depth and 200mm height. Block 1 was slightly variable and produced 14 blocks. Block 2 was far more uniform and yielded 8, Block 3 was found to contain a number of vent features in the stone and block 4 was very fractured and contained cavities and both were deemed unacceptable. Block 5 was from a different quarry in the Warmsworth area which was also under consideration at Phase 1 (should there be any problems with obtaining stone from Anston). From each set (1,2 and 5) a total of three blocks were selected as representative for inclusion in the first stage wall. Type-t thermocouples were embedded in one block of each stone type to allow the monitoring of response to freezing and ensure that the conditions required for damage were created, while working within realistic temperatures. A test wall was built using 1:3 St Astier NHL 3.5 and coarse graded sand which has been used in previous work and was found to be of suitable strength to prevent premature sacrificial weathering of mortar (Laycock *et al*, 2008; Laycock, 2002). Panels were isolated from the

surrounding chamber using polystyrene sheeting and were sealed to prevent water ingress from above or around the sides of the panels (Figure 1). Chamber conditions were verified by test run with the wall in situ to confirm thermal performance. Testing commenced as soon as chamber conditions were confirmed. A study of data from the Meteorological Office suggested that a moderate frost cycle should be utilised. Chamber temperatures were initially set at -4 but the frost front did not penetrate deeply enough into the stone to initiate damage (Laycock, 1997). It was therefore incrementally lowered when the panel was in situ in order to ensure that the frost front passed through the block to a depth of 30mm and released during the thaw cycle. This regime was found in previous work on the Magnesian Limestone to cause damage. This resulted in a final cycle between +8 to -10ºC, cooling and warming at 0.45ºC/min, 2 minutes of simulated rain and 10 cycles per day. The chamber was maintained at -10ºC for 14 minutes. A total of 300 freeze/thaw cycles were carried out. Phase 2 repeated this regime with 9 blocks of Cadeby stone cut to the same sizes as before.

Figure 1. Test wall installed into climate chamber for frost testing.
1a. Exterior, prior to installation. 1b. Interior, after sealing.

5.1 Salt Resistance Test

Analogous stones from the fabric of the building were tested with a variety of salt solutions identified from the literature as having significant deleterious impact. Samples are created such that the salt solution is forced to evaporate through the faces of the exposed prism, thus simulating conditions required to produce efflorescence and sub-florescence. The experimental method for salt decay by capillary rise and evaporation was used by Scherer (2004) and Lee and Kurtisb (2017). Salt concentrations were based on those used by other authors (Table 1).

Table 1. Salts selected for resistance testing

Salt	Relevance to decay	Conc.	Examples of previous work
NaCl	commonly used as a de-icing salt, may be present in older brickwork	5%	Goudie (1986) Lopez-Arce (2008) *
NaSO4	Salt used in standard testing as known to have highly deleterious effect.	14%	EN 12370 Benavente et al (2001)
MgSO4	Decay product from deterioration of dolomite	35%	Cardell et al (2008)

*used 5.3 wt.% NaCl

6 Results

Visual logging using the method reported in Laycock *et al.* (2008) of over 300 cycles of simulated weathering confirms that the performance of the Cadeby stone and types 2 and 5 were of similar and low order of deterioration both in terms of area and extent (Figure 2a) and severity of damage. Type 1 manifested significantly more severe damage, over a greater areal extent. This is in direct contrast to the performance of Type 1 in the EN 12370 sulphate crystallisation test (Figure 2b) in which types 2 and 5 demonstrated variable and poorer performance. However, when compared to other samples of magnesian limestone building stone tested in the same way indicate that all types tested in both phases of this work demonstrated excellent resistance to deterioration. The material from Cadeby was found to perform consistently well in all tests carried out.

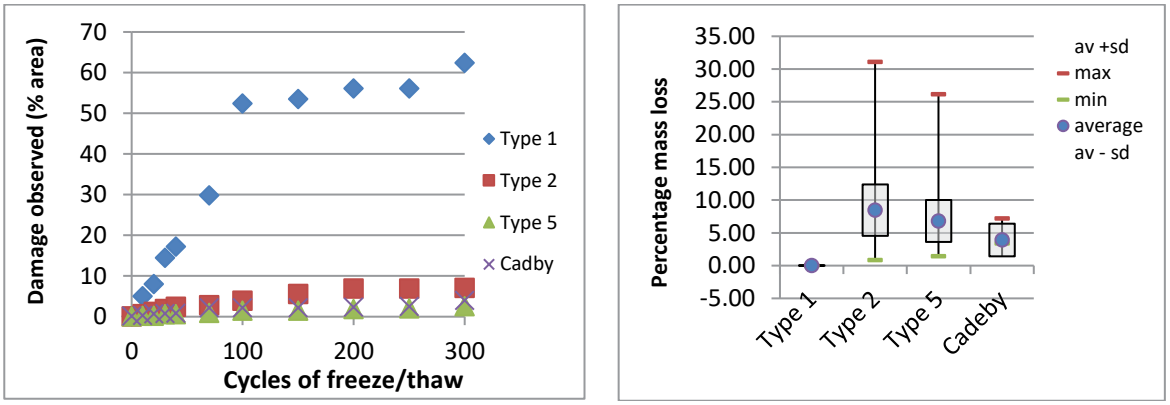

Figure 2. Comparison of the results (Phase 1 and 2). Left:2a) Freeze Thaw testing. Right: 2b) Sodium sulfate crystallisation test.

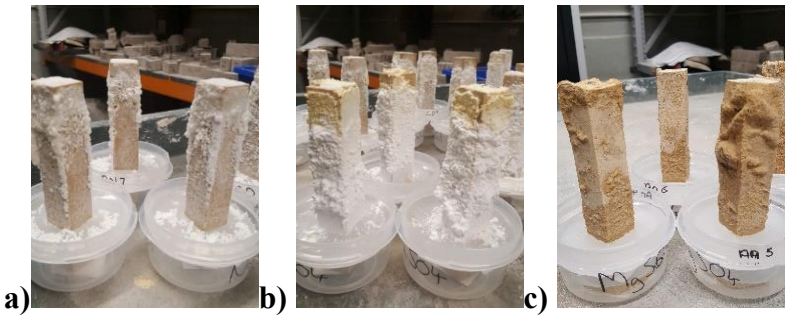

Figure 3. Salt resistance. 2a Anston (type 1) after 120 hours NaCl; 2b Anston (type 1) after 120 hours after 22 days $NaSO_4$; 2c Anston (type 1) after 30 days $MgSO_4$

Results from the capillary rise and evaporation test included prisms of Clipsham stone, a non-magnesian stone of good reputation previously used in repair interventions. In this test the Clipsham showed noticable material loss from crystallisation of magnesium sulphate after 24 hours and sodium sulphate after 48 hours. In contrast the Cadeby and Anston stones were affected to a much lower degree by these salts. All stone types tested in the 5% NaCl showed low rates of material loss despite rapid evaporation and crystals tended to form as efflorescence rather than sub-fluorescence. Magnesium sulphate solution caused no early damage to the samples, however blistering of the Cadeby was noted in one prism by 120 hours. This test confirms that the Cadeby and Anston stones provided show good resistance to decay by the development of salt crystallisation.

7 Conclusion

The bulk of the original stone for Barry's Palace of Westminster was obtained from quarries at North Anston west of Worksop. Although some of the stone reportedly failed soon after its inclusion in the building, this was almost certainly due to poor quality control during extraction and shipping as well as during construction. This could be attributed demands for a high quantity of stone required in a relatively short period and with a tight budget. This poor project management is evidenced by the mixture of stone petrographies, a result of the distance the stone had to be brought and the likelihood of mixing of stone from different extraction areas at the loading wharf on the Chesterfield canal, again when being off-loaded and re-loaded on to sea-going barges, and again when stockpiled at Westminster. This contrasts with accepted good practice to select the appropriate stone for a specific location in the fabric at the quarry. Furthermore, as stone was used and replaced with new stocks shipped in from Anston, the range of various types of petrography would also vary with time. These problems may well have contributed to the reported weathering of some of the stone soon after the building was completed, potentially unsuitable stone being used on occasion for features such as windows or copings.

Where used elsewhere, and with due diligence, magnesian limestone has had a perfectly acceptable durability. There is no reason why the fabric should not be repaired with magnesian limestone with due consideration to the factors outlined in the Technical Advice Note 2016 (Jefferson and Henry, 2016). While some authors have suggested to the contrary (Hunt, 2015), it is completely unacceptable to repair such as building in this with a pure limestone, even one of the highest quality (Jefferson, 2015). Fortunately, the use of the Clipsham stone introduced into the Palace has largely been for the construction of extensions to the building in some of the courtyards, in order to provide increased accommodation. Only a relatively small quantity of the Lincolnshire limestone has actually been used for repairs to the Anston, and other, magnesian limestones in the original fabric.

This work assessed sources of carefully selected magnesian limestone which was deemed to be compatible with the original stone from South Yorkshire. In the large-scale frost testing very little damage was observed to the stone. Where damage did occur during the frost testing this was of a cosmetic nature rather than causing severe material loss. Salt crystallisation testing also showed low levels of losses in standard and non-standard regimes. The Cadeby stone is likely to decay eventually by surface blistering due to magnesium sulphate crystallisation, but this is not anticipated for an extended interval. In conclusion both Anston (Harrycroft) and the Cadeby magnesian limestone materials tested were found to be durable. Both quarries contain variable stone, Cadeby has produced six different types of building stone. If the stone tested is representative of the materials exploited from the quarries, then an extended life span in use is suggested. The work highlights the difficulties in evaluation of likely stone performance from a single test. By using a variety of methods, the differential performance observed can be balanced. The results show that the magnesian limestone can be expected to be durable, but that the natural variability of the stone is such that considerable care must be exercised to ensure that the correct quality of stone is used. Durability is not the only consideration when selecting a stone for conservation use; petrographic, permeability, strength and colour after a period of weather are all important factors.

Acknowledgements

The authors wish to acknowledge T Brindley for construction of the wall, the input of the Harmer 2004 technical team (particularly Carl James for supporting the frost work; Callum McPherson for the sulphate testing; Steve Williams for technical team leadership). Proof reading by M Laycock and B Nightingale.

ORCID

Elizabeth A Laycock http://orcid.org/0000-0003-3758-6829
Steven Hetherington http://orcid.org/0000-0002-9851-8478

References

Benavente, D. García Del Cura, M.A. Bernabéu, A and Ordóñez, S. (2001). *Quantification of salt weathering in porous stones using an experimental continuous partial immersion method*. Engineering Geology, Vol.59(3), 313-325 DOI: 10.1016/S0013-7952(01)00020-5

Cardell C. Benavente and D.Rodríguez-Gordilloa, J. (2008*). Weathering of limestone building material by mixed sulfate solutions. Characterization of stone microstructure, reaction products and decay forms.* Materials Characterization 59 1371–1385 DOI: 10.1016/j.matchar.2007.12.003

Elsden, J. V. and Howe, J. A. (1923). *The Stones of London*., Colliery Guardian, London

EN 12370 (1999). Natural stone test methods - Determination of resistance to salt crystallization. BSI:London.

Goudie, A. S. (1986). *Laboratory simulation of 'the wick effect' in salt weathering of rock*. Earth Surface Processes and Landforms Vol 11 275-285

Hunt, B (2015). *The stone that has rescued the Houses of Parliament*. Natural Stone Specialist, May 2015

Jefferson (2015). *Letter Dr David Jefferson, Jefferson Consulting* 10 July 2015. Stone Specialist https://www.stonespecialist.com/news/letter-dr-david-jefferson-jefferson-consulting

Jefferson D. and Henry A. (2016). *Identifying and Sourcing Stone for Historic Building Repair*. Historic England Technical Advice Note. Historic England: Swindon

Laycock, EA Spence, K, Jefferson, David P, Hetherington, S, Martin, B and Woods, Christopher (2008) *Testing the durability of limestone for Cathedral façade restoration*. Environmental Geology. https://doi.org/10.1007/s00254-008-1333-x

Laycock, E.A. (2002). *Ten years of frost testing at Sheffield Hallam University*. Construction and Building Materials. Volume 16, Issue 4, June 2002, Pages 195-205 https://doi.org/10.1016/S0950-0618(02)00006-5

Laycock, E.A. (1997). *Frost degradation and weathering of the Magnesian Limestone building stone of the Yorkshire provinc0.e* PhD Thesis University of Sheffield. ASIN: B001ABK27O

Lee, B.Y. Kurtis, K.E. (2017). *Effect of pore structure on salt crystallization damage of cement-based materials: Consideration of w/b and nanoparticle use*. Cement and Concrete Research 98 61–70DOI: 10.1016/j.cemconres.2017.04.002

Lopez-Arce, P. Doehne,E. Martin, W. Pinchin, S. (2008). *Sales de sulfato magnésico y materiales de edificios históricos: simulación experimental de laminaciones en calizas mediante ciclos de humedad relativa y cristalización de sales.* Materiales de Construcción Vol. 58, 289-290 125-142 ISSN: 0465-2746

Lott, G. K. and Richardson, C. (1997). *Yorkshire stone for building the Houses of Parliament (1839-C.1852)* Proceedings to the Yorkshire Geological Society., 51 (4), 265-272.

Palmer, T (2014). *Understanding the Weathering Behaviour of Caen Stone.* Journal of Architectural Conservation. Volume 14, Issue 3. 43-54 https://doi.org/10.1080/13556207.2008.10785030

Richardson, C (1999). *History Summary of the Chesterfield Canal*. Kiveton Park and Wales History Society (http://www.kivetonwaleshistory.co.uk/heritage/chesterfield-canal/chesterfield-canal-history)

Shenton, C (n.d.). *The Fire of 1834.* The History of Parliament, British Political Social and Local History. Institute of Historical Research © Crown copyright and The History of Parliament Trust 1964-2019 https://www.historyofparliamentonline.org/periods/modern/fire-1834

Scherer, G.W.(2004). *Stress from crystallization of salt.* Cement and Concrete Research 34 1613–1624 DOI: 10.1016/j.cemconres.2003.12.034

Smith, D.B., (1995). *Marine Permian of England. Geological Conservation Review Series, No. 8,* Chapman and Hall: London, 205pp http://www.jncc.gov.uk/page-2953

Yates, T (2014). *Identifying Caen Stone for Remedial Work. An Example from Cloister Court, Palace of Westminster.* Journal of Architectural Conservation. Volume 14 Issue 3 55-58 https://doi.org/10.1080/13556207.2008.10785031

XV International Conference on Durability of Building Materials and Components
DBMC 2020, Barcelona
C. Serrat, J.R. Casas and V. Gibert (Eds)

Transport of Moisture and Chlorides into Sprayed Concrete

Diego Aponte, Marilda Barra, Susanna Valls and Lucia Fernandez

Department of Civil and Environmental Engineering (DECA), Universitat Politècnica de Catalunya-BarcelonaTECH, Campus Nord UPC, 08034-Barcelona, Spain, diego.fernando.aponte@upc.edu

Abstract. *This contribution is a study of the durability and transport properties of sprayed concrete used in an actual construction site. It considers whether concrete spraying can generate different porosities as the thickness of the sprayed layer increases. The work consisted of a study of the properties of the interior and exterior concrete layers with a particular focus on chloride penetration. A few of the methodologies and techniques used are compressive strength at 28 days, depth of penetration of water under pressure UNE EN 12390-8, boiled absorption and volume of permeable voids ASTM C642, and accelerate chloride penetration NT BUILD 443. Calculated transport property values included absorption (A) and volume of permeable voids (VPV), porosity interconnection, and chloride diffusion coefficient (De). The conclusion obtained is that there are no significant differences between the physical microstructural properties of the interior and exterior sprayed concrete layers, they present a similar porosity, and behave in the same way under a chloride attack when test tubes are completely saturated.*

Keywords: *Sprayed Concrete, Moisture Movement, Chloride Penetration, Chloride Diffusion Coefficient, and Durability.*

1 Introduction

Sprayed concrete is typically used in the construction and stabilization of tunnels, underground structures, and other construction sites where the application of traditional cast-in-place concrete is particularly challenging (Wang *et al.*, 2015). Unlike conventional concrete, sprayed concrete has a short setting time as well as high mechanical properties due to the incorporation of set accelerating additives (Austin *et al.*, 2002; Galobardes, 2013). At the same time, sprayed concrete presents more porosity than cast-in-place concrete, which can affect its durability by making it more vulnerable to damages caused by moisture, chemicals, and other external agents (Galobardes *et al.*, 2014).

This study conducted a characterization of the physical, mechanic, and durability properties of sprayed concrete with two goals in mind. The first is to determine if, when studied by layers, sprayed concrete shows different transport properties depending on its proximity or direct contact with the projected surface. The second is to study the impact of the presence of chlorides introduced by moisture via the sprayed concrete's transport mechanisms to determine potential durability issues.

2 Methodology

This study was conducted with wet-mix sprayed concrete, using a CEM I 52.5 R, water/cement ratio 0,35 and 450 kg /m^3 of cement, a superplasticizer type

MASTERCLENIUM SKY 554-BASF, and the accelerating additive MasterRoc SA 172 (which is non-alkaline and presents no alkalis or chlorides). Table 1 shows the dosage used in the shotcrete.

Table 1. Sprayed concrete dosage.

Material	Quantity (kg/m^3)	Quantity (%)
Cement	450	19.4
Water	155	6.7
Sand 1 (0/2mm)	750	32.4
Sand 2 (0/6mm)	485	20.9
Medium Ag. (4/12mm)	435	18.8
Superplasticizer	4.5	0.2
Accellerator	38.2	1.7

The wet mix concrete was sprayed on 4 mm-thick metallic test panels located at an ongoing construction site, using 7-15 m^3 air pressure per minute at a 90° angle, and maintaining a 0.5 – 1.5m distance to ensure all samples would be sprayed with similar speed, compaction, and adherence.

After the spraying, the mixes were transported to the Construction Materials Laboratory of the Universitat Politècnica de Catalunya, and they were left outdoors for 28 days to simulate the environment to which they would have been exposed at the construction site. After the initial 28 days, the next step was to extract 7.5 cm diameter cores (cylindrical specimens) from the test panels (Figure 1a) and divide each sample into two equal parts of 5 cm each, which are called parts A and R (Figure 1b).

Part A is the first layer, which under real conditions would have been in contact with the terrain. Part R is the second layer, which is adhered to the first layer and has a surface that was used to simulate exposure to open air.

Three specimens of each type of sample (part A or part B) are used for density, water penetration, suction test and compressive strength . Two specimens of each type of sample are used for chloride penetration test.

Figure 1. Extraction of sprayed concrete specimens (a) and division of samples into part A and part B.

2.1 Density, Absorption, and Porosity

These specimens did not undergo any special preparations to test for density, absorption, or porosity. The test was conducted following the standard ASTM C642.

2.2 Moisture Penetration under Pressure

Epoxy paint was used to cover the lateral parts of the specimens, leaving only the two opposite faces of the cylinder exposed to ensure that the moisture flow would be vertical and ascending without lateral losses. This test used pressurized water under the surface of the hardened sprayed concrete for 72 hours, applying a 500±50 kPa pressure, as foreseen under norm UNE-EN-12390-8.

2.3 Capillary Cuction

The epoxy paint used to avoid moisture losses described above also prepared the specimens to undergo the capillary suction tests, which were conducted under the standards of norm ASTM C1585-04.

2.4 Chloride Determination

This test was based on the NT BUIL 443 method to determine the resistance of hardened concrete to chloride penetration. The specimens used for this test also received epoxy paint treatment to ensure the moisture would only flow in the desired direction and presented no visible cavities or cracks. Each specimen was cut through the layers of A and R, to study the penetration properties of each layer separately. Each sample tested was hence 50 mm high, in pairs originated from the same original sample.

An aqueous NaCl solution was prepared with a concentration of 165 ± 1g NaCl per dm3, which means that initially, the chloride concentration was 100,09 g Cl-/l ± 0,607 g Cl-/l. The samples were afterward inserted into the NaCl solution and underwent the following steps:

- Three type-A samples and three type-R samples were extracted, originating from three different specimens at 35, 60, and 90 days.
- After extracting the samples at 35 days, we replaced the aqueous solution with a new one with identical characteristics to the one used initially.
- Each time the samples were extracted, we conducted proceedings to determine the distance of penetration of the chlorides and the concentration of chlorides at each depth.

The results from the chloride penetration tests are presented as the average of two A samples and two R samples at 35, 60, and 90 days. This test did not consider the metallic test panels from which each sample originated. However, samples A and R came from the same specimen.

2.5 Compressive Strength

The samples were cut and polished at their extremes to obtain a 2 – 1 relation on the specimens that would be used to test the compressive strength, meaning that they were twice as high as the diameter of the cylinder. The norm used for this test was UNE 83-302.

3 Results

3.1 Physical Properties

Concerning the physical properties of the samples, the test shows only slight differences between the dry density and the apparent density. The average values of samples A and R are practically the same (Figure 2).

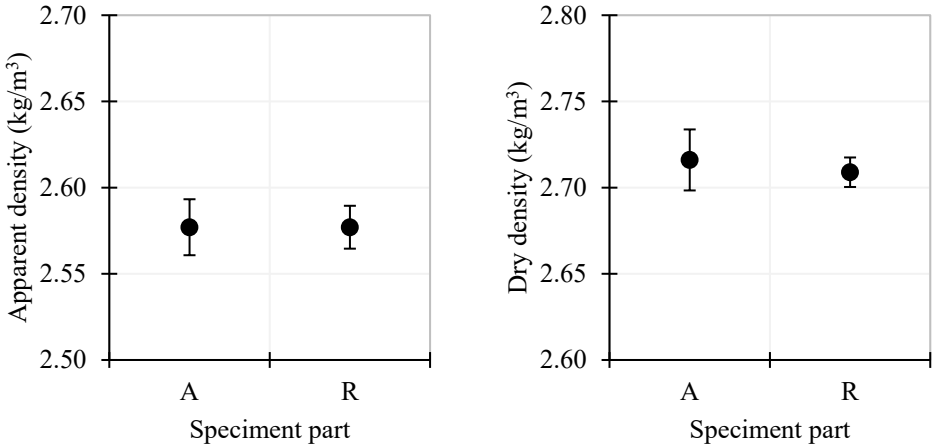

Figure 2. Apparent density and dry density of the samples.

Some differences were observed when it comes to the absorption capacity and porosity of the samples. R-type samples presented more porosity than A-type samples, and in consequence, a larger absorption capacity (Figure 3).

With regards to water penetration under pressure, we observed that there is a significant porous interconnection in both type-A and type-R samples. Throughout the 3-days test, moisture completely penetrated both samples.

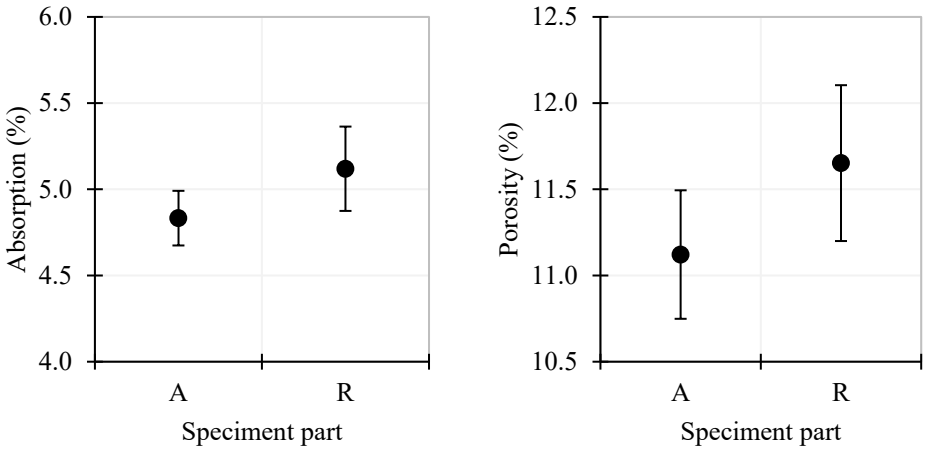

Figure 3. Absorption and porosity of the samples.

The capillary suction test confirmed the porous interconnectivity in both A and R samples, reaching almost a saturation level of 100% (Figure 4a). The only significant difference between the type-A and type-R samples performance is that during the first 6 hours of the test, the maximum free absorption was higher on type-A samples (Figure 4b). Forced absorption tests indicated that there were few isolated pores since, when dried, we observed very little water filling those pores.

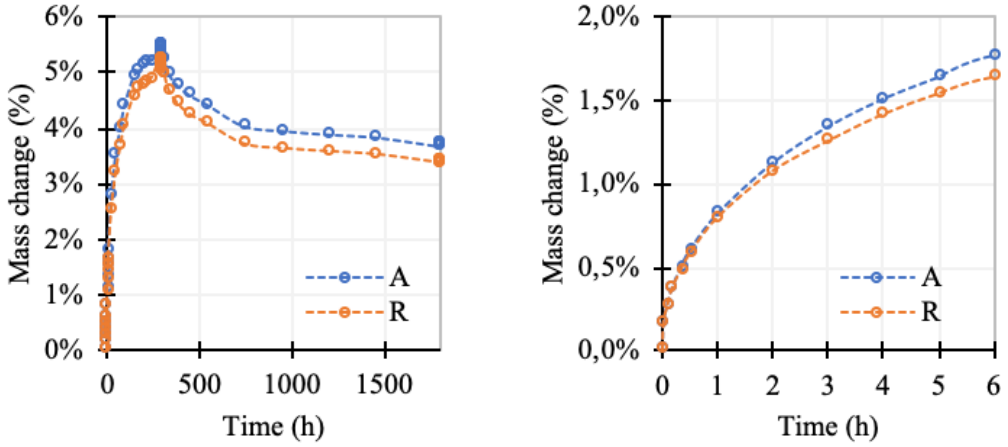

Figure 4. Capillary suction and drying of the samples (a). Capillary suction during the first 6 hours (b).

There is also no significant difference between the loss of water of samples A and R. This confirms that the porosity structure of both samples is very similar, being capable of retaining and losing the same quantity of moisture (Table 2).

Table 2. Mass of water absorbed during the free and forced absorption test.

Speciment part	Total water (g)	Free absorption (%)	Forced absorption (%)
A	29.59	5.1 (94.6%)	5.4
R	28.36	4.8 (93.0%)	5.2

3.2 Durability – Chloride Penetration

The test followed the directions of norm NT BUIL 443 to determine the chloride penetration profiles for samples type-A and type-R at immersion ages 35, 60, and 90 days. Figure 5 shows that there are no significant differences between the profiles determined on both types of samples at their different ages. The test shows that, as the exposure time increases, the concentration of chlorides on the surface increases significantly between 35 and 60 days, but from 60 to 90 days, the increase was not relevant.

It is important to notice that, according to the results of the penetration profiles, the diffusion coefficient decreases as the exposure time increases. Using the square minimums method as dictated by norm NT BUIL 443, the test determined the diffusion coefficients for all cases and showed that the differences are not relevant. (Table 3).

Table 3. Chloride coefficient of the samples at different ages ($x10^{-11}m^2/s$).

Specimen part	35 days	60 days	90 days
A	4.55	3.55	1.97
R	5.14	2.42	2.26

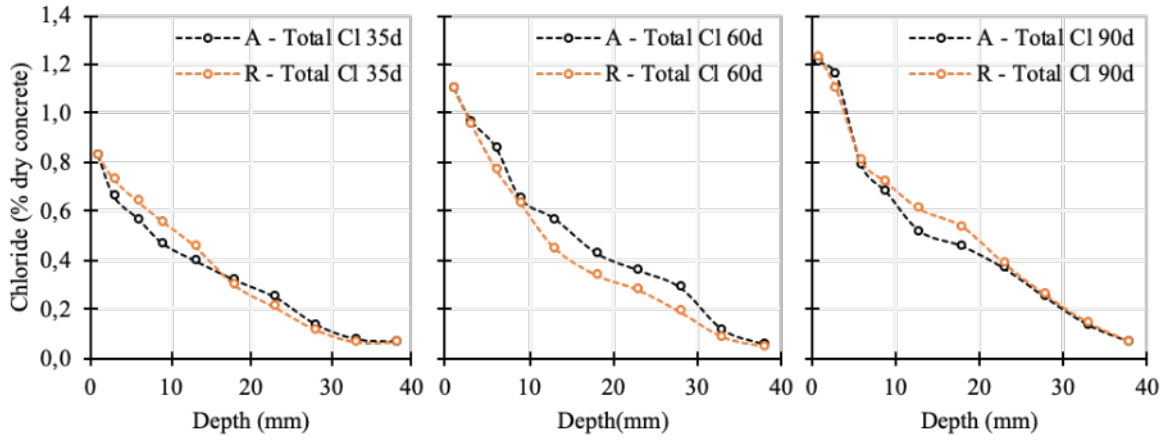

Figure 5. Chloride profiles at 35, 60, and 90 days fo the samples.

This data indicates that an increase of exposure time does not imply a higher accumulation of chlorides at the penetrated depths since, over time, the chloride ions in the solution accumulate at the walls of the sample's pores. The pores hence become progressively saturated, slowing down the aqueous solution's capacity of penetration.

3.3 Compressive Strength

For the mechanical tests, samples were obtained from three metallic test panels containing the

same type of sprayed concrete. Samples originated from the different test panels presented different results despite having used the same sprayed concrete at all of them (Table 4). This can be due to differences in the aggregate distribution during the spraying of the concrete, leading to differences in behavior. In order to verify the distribution of the aggregates in the different samples, a visual analysis was performed. Figure 6 shows that the specimens originated from test panel 2, the one where the aggregate distribution is most homogeneous, presented higher compressive strength.

Table 4. Compressive strength at 28 days of different test panels (MPa).

Sample	Test Panel 1	Test Panel 2	Test Panel 3
C. S	41.7	51.2	44.3

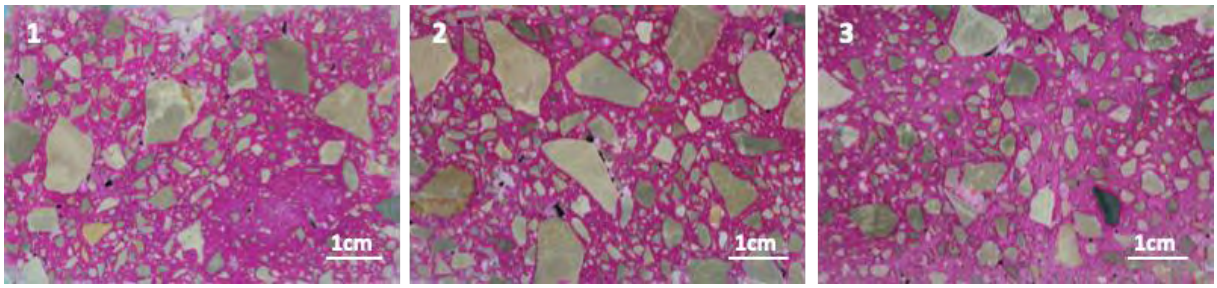

Figure 6. Visual analysis of the distribution of aggregates in the samples.

4 Conclusions

The experimental work carried out in this study presents the following conclusions:

- The samples used for the density tests show slightly different behavior compared to the ones used at the capillary suction tests. However, these differences are not relevant.
- The distribution of aggregates in concrete generates a difference in the mechanical properties of the different samples tested, but this difference does not show a significant impact on the moisture or chloride transport properties.
- On a microstructural level, there are no significant physical differences between shot concrete sample parts A and R. Both parts present a porosity network of similar characteristics.
- The samples of sprayed concrete analyzed in this study presented larger pore interconnectivity compared to regular concrete, which contributed to increase the speed of diffusion of chlorides. This indicates that sprayed concrete could be more vulnerable to chloride penetration than regular concrete.
- There are no noticeable performance differences in terms of chloride penetration between the concrete parts which were exposed to the surface, and the layers exposed to open air. Therefore, there is no proof that the chloride penetration is not homogeneous throughout all the shot concrete layers.
- The high level of concordance of the results obtained from different tests indicates that A and R behave similarly under a chloride attach when completely saturated.

Acknowledgments

The authors gratefully acknowledge to the competitive project BIA2016-78740-R: "Materiales proyectados ligeros para refuerzo y la rehabilitación del patrimonio urbano" funded by the Ministry of Economy and Competitiveness, within the 2016 Call for projects "Excelencia y Retos". General Directorate of Scientific and Technical Research. Subdirectorate General for Research Projects.

ORCID

Diego Fernando Aponte Hernández: http://orcid.org/0000-0001-5737-7819
Marilda Barra Bizinotto: http://orcid.org/0000-0002-1417-1615
Susanna Valls: http://orcid.org/0000-0001-8586-7700
Lucia Fernandez: http//orcid.org/0000-0002-2379-3782

References

Austin, S. and Goodier, C. (2002). *Construction and repair with wet-process sprayed concrete and mortar*. Shotcrete magazine, Vol 4.

Galobardes, J. (2013). *Characterization and control of wet mix sprayed concrete with accelerators*. Ph.D. Thesis, Universitat Politècnica de Catalunya-BarcelonaTECH, Barcelona, Spain.

Galobardes, J.,Cavalaro, S., Aguado, A., Garcia, T., and Rueda, A. (2014). *Correlation between the compressive strength and the modulus of elasticity of sprayed concrete.* 7th International symposium on sprayed concrete, Modern use of wet mix sprayed concrete for underground support, Norway.

Wang, J., Niu, D., and Zhang, Y(2015). *Microstructure and mechanical properties of accelerated sprayed concrete*. Materials Structures, Vol. 49, p. 1469–1484.

XV International Conference on Durability of Building Materials and Components
DBMC 2020, Barcelona
C. Serrat, J.R. Casas and V. Gibert (Eds)

Building Circular Economy: a Case Study Designed and Built Following a BIM-Based Life Cycle Assessment Approach

Mauro Manca[1], Zuzana Prochazkova[1], Umberto Berardi[2], Licinio Alfaro [3] and Felipe Pich-Aguilera[1]

[1] CEIM, Universitat Internacional de Catalunya, Carrer de la Immaculada, 22,08017 Barcelona, Spain
m.manca@picharchitects.com

[2] Ryerson University Toronto, 350 Victoria St, Toronto, ON M5B 2K3, Canada, uberardi@ryerson.ca

[3] ITEC, Carrer de Wellington, 19, 08018 Barcelona, Spain, lalfaro@itec.cat

Abstract. *The awareness of the environmental impact of buildings during their entire whole life cycle has seen a growing interest in recent years. In fact, as buildings become more energy-efficient, life cycle impacts become increasingly important. Investors in the building sector are becoming aware of the direct and indirect benefits of a design process that enables the control of the impact of the building, ensuring the higher quality, intrinsic value of materials under a circular economy point of view. The durability is, together with reusability and recyclability, one of the main characteristics of construction materials. In this framework, the purpose of this paper is to describe a BIM-based approach to life cycle assessment (LCA) from the initial stages of the design of the Socrates Building in Viladecans. For this scope, a digital model in the TCQi GMA software was created to assist in the evaluation, optimization, and comparison of different design and construction alternatives. An integrated project delivery contract was adopted. These aspects altogether showed the potential of increasing the real estate value and the profitability of the building. This paper discusses problems that emerged during the digital project management, assessing criticalities and opportunities.*

Keywords: *LCA, Circular Economy, Prefabricated Construction.*

1 Introduction

The Socrates Building is a mixed-use building that allows to explore the challenges of a new model of design and construction based on the circular economy. The building is located in Viladecans Business Park, close to Barcelona, a new business development area dedicated to emerging companies and new business models. The basis of achieving a building of circular economy was to ensure that the building could adapt to a wide range of uses that span from offices to tertiary. This goal was pursued with the following main directives: maximum spatial flexibility, structural durability, material disassembling and traceability and comfortable and healthy occupied spaces, followed an approach often only fully presented in theory (Berardi, 2015).

An industrialized and dry construction systemic approach was chosen as the best option to respond effectively to life cycle strategies and to reduce the negative impact of the operational phase and deconstruction phase. Construction materials were chosen according to their level of traceability, fostering the use of Cradle to Cradle materials, and the commitment of the contractor to select products with a material passport or Environmental Declaration of Product

(EPD). The decision-making during the design process was supported with a Life Cycle Assessment (LCA) developed with a digital BIM model and implemented with environmental impact data of the BEDEC database.

An important part of the process was dedicated to conceiving a building with an increased value during its operational phase, which is usually the highest impact in the life cycle (Asdrubali *et al.*, 2013). Therefore spaces were designed utilizing energy simulations to ensure optimal lighting and thermal comfort (Bernstein, 2011), and to give a direct benefit to energy conservation and a subsequent reduction in operating costs.

Another keystone in the design was to support direct access to nature and open spaces with vegetation, natural ventilation and direct access to daylight and views. Each floor plan possesses open space equipped with vegetation, irrigated with recovered rainwater. The LEED v.4 certification protocol was adopted to better structure all of the aspects related to sustainability, this decision was taken in accordance with an analysis of the office buildings market in Barcelona where the majority of buildings with environmental certifications have a higher real estate value and higher rental potential (Eje Prime, 2018). A final practical aspect of the design and construction phase was the implementation of an integrated delivery process (IDP) that aligned every stakeholder towards the common goal of conceiving a circular economy building.

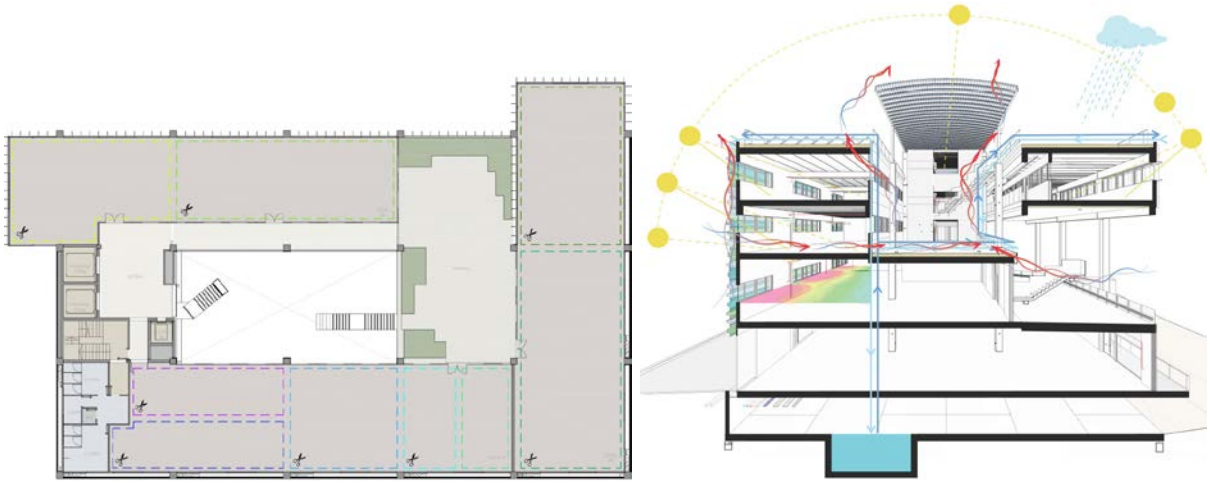

Figure 1. Type floor plan with interior subdivision schemes (left) and section (right) of the Socrates building.

2 Main Building Characteristics

The building comprises four levels: the first two stories are accessible to automated vehicles whereas the upper floors are designed according to office criteria. Open common spaces are provided on each floorplan and located to the core of the building, also serving as connection and circulation zones. The rooftop hosts a common terrace partially covered with a green substrate and an area dedicated to HVAC plant equipment and PV.

2.1 Construction Elements

Particular attention was dedicated to structural design as it is considered to be one of the most influential components of the building, remaining practically unchanged through the whole life cycle affecting its duration and the resulting building economy (Manganelli, 2014). The

building is designed to be fully industrialized and assembled onsite. This process guarantees a more effective construction process by reducing the construction time schedule, minimizing onsite waste production, facilitating the traceability of each material and its revalorization at the end of the lifecycle.

The structure is constructed from a prefabricated concrete frame composed of 0,60m x 0,80 m pillars that span the full height of the building as a single element without vertical interruption in addition to horizontal beams with a section of 60 x 80 cm that connects to the vertical structure. Pillars are distributed across a 10 x 10-meter grid, with a 100m^2 free areas that guarantee the highest spatial flexibility for any tertiary and light industrial use. Prefabricated hollow-core slabs complete the horizontal enclosure and give structural stability to the frame.

Figure 2. Prefabricated structure during the construction phase of the Socrates building.

2.2 Envelope

The façades are composed of a sandwich panel with 8 cm of mineral wool, held by a steel frame substructure and finished on the interior with plasterboard panels and an additional 4cm of insulation. The Eastern and Southern façades are covered by metallic perforated panels that leave sufficient space for natural ventilation and HVAC ducts and piping.

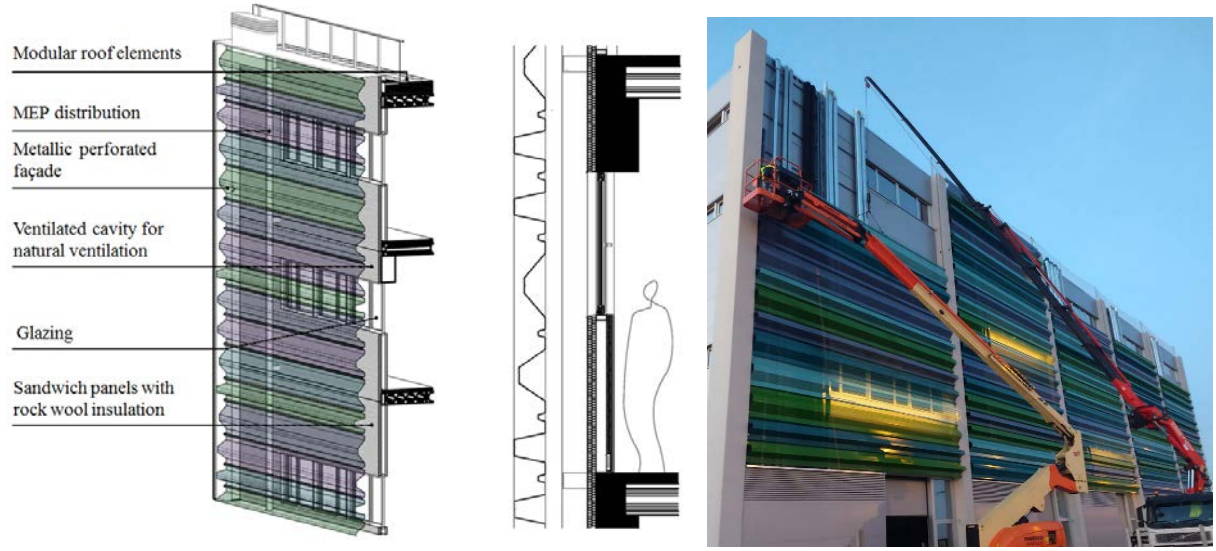

Figure 3. 3D of the façade (left), façade section (center) and construction phase (right) of the Socrates building.

All the horizontal enclosures in contact with occupied spaces present a waterproof layer covered by 10 cm of XPS thermal insulation. The roof garden consists of an industrialized green roof, modular elements that include the irrigation system. The remainder of the roof and terraces are covered with concrete floor tiles. Interior spaces are left without any additional finishing.

2.3 Mechanical, Electrical, and Plumbing

The HVAC system, linked with a geothermal heat pump of 303 kW, acts as the primary system and covers 80% of the demand for heating and cooling power. A water to air heat pump of 316kW supports the system during peak demand. The installation of 45 kWp of PV panels is estimated to produce 60.000 kWh, covering 38% of the expected energy consumption. The distribution systems run along the façade, connecting to the ventilation system of each interior space. This configuration was chosen to facilitate ease of maintenance and to improve internal spatial flexibility, offering multiple options of connection to services externally with no implication to the interior spaces.

3 Methodology

3.1 Application of an Integrated Process for the Building Life Cycle

Energy simulations with Energy plus were performed to optimize the building envelope for the thermal comfort. Daylight analysis determined the volumetric and spatial definition of the building, assisting with the interior design considerations that according to a different range of options in favor of maximum spatial flexibility. At the same time, an LCA was performed with the digital BIM model of the architectural proposal, then integrated with a personalized database of construction products, based on BEDEC (BEDEC), the Catalan online database of construction products with technical details, costs, and environmental information. The whole process took place within the TCQi-GMA software (TCQi-GMA).

3.1.1 Software TCQi-GMA, its development, and LCA

The TCQi-GMA (TCQi) is used for life cycle assessment and other applications of construction projects developed by IteC. It is based on TCQ2000 (TCQ), a software developer for the construction sector, formed by a set of applications to support the activities of the edition, contracting, planning and control of projects and construction sites. It includes indicators on time, cost, quality, security, waste generation and embodied energy. A specific methodology is used to calculate the environmental data, similar to the one used in eco-labels type III. The categorization of products and services for the construction sector, as defined by the European standard EN 15804 (EN 15804), is applied. Materials durability, joints disassemblability, and material positioning within a layer play a vital role in the process.

3.1.2 Application of the process in the Socrates building

The inputs for the LCA of the Socrates building were:

- The budget of the project in Excel, created by the construction contractor and;
- A set of 3D models converted to .IFC file format from various 3D modeling software. The 3D models provided consisted of b1) a foundations model, b2) a structural model,

created in Tecla by the provider of prefabricated structure b3) an HVAC model provided by the installation engineer, and of b4) an architectural model produced by the architects.

Eight chapters of LCA were defined for the project: demolition & groundworks, foundations, structure, building services, civil works, rainwater storage system, private urbanization, elevators, and extra modifications.

Each chapter was assigned a construction system as defined in the BEDEC database and given a specific code associated with detailed information about its construction process and the cost. During the next phase, the IFC models are associated with the TCQ2000 structure. Each of the four 3D models is integrated within the software. The different components were then manually selected and associated with the corresponding chapters of the created structure. The unit to import the BOQ is selected, and the BOQ is imported to the TCQ2000 structure. Some of the elements presented in the original budget file did not have representation in the 3D model, therefore the BOQ data comes from various sources: a) from the 3D model; b) from the Excel file, and c) calculated manually when incomplete in both inputs. Once the digital model has been defined, the LCA is performed, using the TCQi-GMA software. When uploading the structure from the TCQ2000 to TCQi, the software analyses the provided data and evaluates how complete the environmental data is, as defined by the structure.

In the Socrates Building, the information related to the waste generation is 100% complete, while the information referring to Energy and CO2 generation is missing in 9.09% (Gris and Alfaro, 2019). In order to complete the information, the incomplete chapters can be adapted, assimilated or completed manually. The last source is to integrate data coming from the material supplier, such as volume, mass, LoW (2014/955/EU) code, embodied energy and associated CO2 emission. Once all the data has been completed, the environmental impact of the construction phase is determined. Finally, the TCQi-GMA software allows the integration of data about the use phase, as well as the end-of-life phase, based on the existing database, as well as maintenance manuals, when specific information is not available.

4 Results

As a result of the implementation of energy simulation during the design process, the maximum depth of the volumes on the 2nd and 3rd floors was set to 10 meters, ensuring a 10-meter patio to the core. This strategically allowed openings towards an interior zone with better acoustic conditions. This choice guaranteed at least 2% of Daylight Factor (DF) across 75% of working areas and an efficient level of natural ventilation. The overall energy consumption of the proposal is reduced by 40% compared to the corresponding baseline model designed according to ASHRAE 90.1.

Concerning the LCA, detailed data related to the product, construction, use, and end of life phases have been studied. 8 chapters of the construction work divided into earth movement, foundations, structure, civil works, rainwater storage, private urbanization, elevators, and extra modifications. The BEDEC database was used for product and construction phases. Relationship with use and end of life future phases has been created, but not completed due to lack of information. At the current stage, the total LCA information for the foundations and structure phases has been created (Fig. 4).

The overall results considering the product and construction phase show the largest impact during the product phase (2.453.247 kg CO_2 eq). The construction phase impact is low (448.129 kg CO_2 eq). In the product phase the impact is distributed mostly between the foundations (542.000 kg CO_2 eq,), structure (846.885 kg CO_2 eq,) and civil works (883.000 kg CO_2 eq,). The civil works contain all the non-load bearing elements of the building envelope, interior partitions, and finishing. The rest of the construction categories in total count less than 181.000 kg CO_2 eq. The prefabricated concrete structure causes the largest impact during the construction phase, with 409.028 kg CO_2 eq compared to the second-largest impact by the earth moving with 25.000 kg CO_2 eq.

To achieve the total LCA, relations are being created between the different work items and the future items of works during the use phase and end of life phase. This process requires an important time dedication because each item that defines the construction work needs several works items to calculate the future impact. However, once the relationship has been created, it can be applied or adapted for future use in another project, becoming part of the company's own knowledge and future business. Unlike other LCA software that performs generic calculations in different scenarios, the methodology used in this paper identifies each material and associated construction processes, creating relationships reflecting the real construction work in detail, in order to conduct in-depth analysis, introduce the disassembly capacity or the material passport identification.

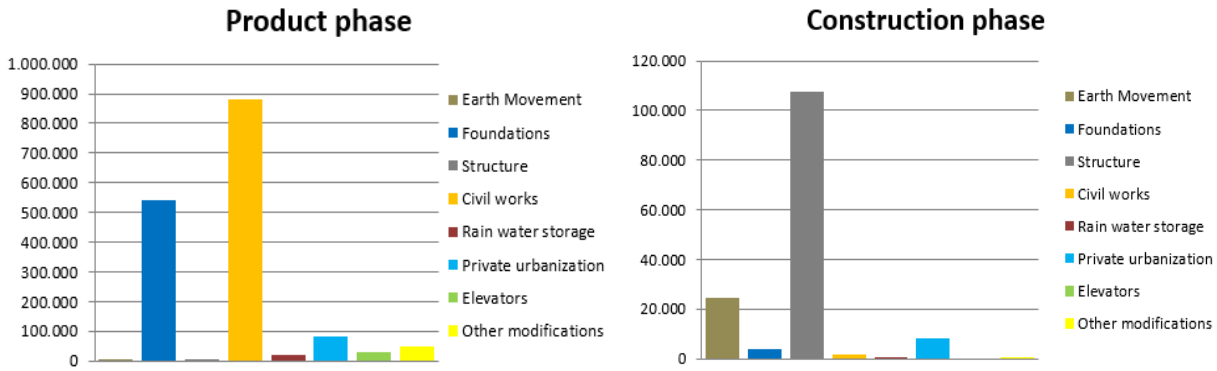

Figure 4 Global Warming potential in kg CO_2 eq: Product phase (left), and Construction phase (right).

Finally, in the Socrates Building, 88% of the construction materials have been identified and defined for its recyclability at the end of life, amounting to 7.800 tons. Moreover, 84%, accounted for its weight has a Cradle-2-Cradle certificate. The design and construction process has guaranteed a minimum waste production calculated for 25 tons of waste material, including excavation consisting of only 4 kg of waste per square meter of construction: 100% of this waste can be traced by a waste management protocol and 99,3 % is re-valorized.

5 Discussion and Conclusions

The new Socrates Building close to Barcelona was designed to be an example of the integration of circular economy in the construction sector. This experience has outlined some criticalities and opportunities, as discussed here.

As a first consideration, it is worth highlighting the importance of an integrative process during design and construction. The integration of all the stakeholders with an IDP was beneficial for technical and construction decisions, giving the opportunity to incorporate synergy to the whole value chain, allowing constant control on cost and quality. However, the IDP contract was introduced just before the construction works, causing initial maladjustment that produced an increase in technical costs. This could have been avoided by including this strategy from the start of the design phase.

As a general consideration of the circular economy, the Socrates Building is presented as a dynamic system of parts and functions attached to specific uses that can vary during its life cycle. The concept of the circular economy includes not only the life cycle of construction material but also the operational phase and the increased value derived from spatial flexibility, the health and comfort of occupants that can give greater performance, energy and economic savings during use and maintenance. This aspect is crucial for the generation of a different business model for tertiary buildings, moving the focus from only the environmental impact to include the quality of the service and the sub-sequential impact on occupant satisfaction and employee retention. In fact, employee cost is usually estimated to reach up to 90% of building cost (Attema *et al.*, 2018) and every improvement under this aspect can have much higher savings if properly quantified.

Concerning the lifecycle analysis, data availability is an important issue in the construction sector. In the Socrates project it was enhanced, as most of the products were Cradle-2-Cradle certified or had the Environmental Product Declaration (EPD). However, one of the main barriers in applying the LCA methodology in the design process is the lack of precise and consolidated data, especially considering the environmental impact of specific construction systems in the use phase. The availability of information about maintenance, repair, replacement, and refurbishment plays an important role in the development of this methodology. In order to overcome this barrier, ITeC is currently working on enabling the BEDEC users to create their own online database of construction systems, using the elements available in the existing database. The users will be able to share their database with one another and integrate them into their TCQi Software for LCA. This offers more flexibility in the exchange of information and in the acquisition of information for specifications, planning and construction tracking. Furthermore, with the increasing implementation of big data analysis and artificial intelligence, the statistical data will allow us to determine the most appropriate systems and installation methods for any geographical orientation or location, as well as being able to determine product needs or the capacity for growth based on existing resources in a specific area.

In order to consider the environmental impact of the construction beyond the system boundary, the reuse, recovery and recycling potential has to be considered in the life cycle assessment. Another issue identified in the process was the interoperability of software and the diverse needs of the LCA methodology on how to create the 3D model of the building.

Finally, the Socrates Building can be considered as one of the first real case studies for the integration of circular economy in the building sector. The next step required for a business model of the circular economy will be to consider each component of the life cycle in terms of intrinsic economic value in the real estate market so that buildings will increase its value beyond standard indicators and so enhancing the interest in sustainable buildings.

ORCID

Umberto Berardi: https://orcid.org/0000-0002-0508-6195

References

ANSI/ASHRAE/IES Standard 90.1-(2010). Energy Standard for Buildings Except Low-Rise Residential Buildings

Asdrubali F., Baldassarri C., Fthenakis V. (2013). Life cycle analysis in the construction sector: Guiding the optimization of conventional Italian buildings, Energy and Buildings 64, 73-89

Attema, J.E., Fowell, S.J., Macko, M.J. and Neilson, W.C. (2018). The Financial Case For High PerformanceBuildings. San Francisco: Stok, LLC.

BEDEC. Retrieved from https://itec.es/servicios/bedec/

Berardi U. (2015). Sustainability assessment of buildings, communities and cities, chapter in the book, Assessing and Measuring Environmental Impact and Sustainability, ed. Jiri Klemeš, Elsevier.

Berardi U. (2017). A cross country comparison of building energy consumption and their trends, Resource Conservation and Recycling, 123, 230-241.

Bernstein H. M. (2011). Outlook 2011 Executive Conference, McGraw-Hill Construction Reports 2011 EjePrimeEdiciones, SLU (2018). Retrieved from :https://www.ejeprime.com/oficinas/las-oficinas-en-busca-del-sello-el-14-de-los-edificios-de-madrid-y-barcelona-son-sostenibles.html

CEN/TC 350 Sustainability of construction works

EN 15804:2012(2014). Sustainability of construction works - Environmental product declarations - Core rules for the product category of construction products

EN 15978: (2011). Sustainability of construction works. Assessment of the environmental performance of buildings: Calculation method

Finkbeiner M., Schau E. M., Lehmann A., Traverso M., Towards life cycle sustainability assessment, Sustainability 2 (10), 3309-3322

Gris R., Alfaro L. (2019). Análisis del ciclo de vida de un edificio aplicado a un modelo digital (in Spanish), grade thesis, Universitat Politècnica de Catalunya, Barcelona, Spain.

ISO 14040: (2006). Environmental management — Life cycle assessment — Principles and framework

List of Waste. Commission Decision 2014/955/EU

Manganelli B. (2014). Economic life prediction of concrete structures. Advanced Materials Research Vols. 919-921 (2014) pp 1447-1450

Socrates Building website, Retrieved from https://www.edificio-socrates.com

TCQ/ TCQi. Retrieved from https://itec.es/programas/tcq/

TCQi-GMA. Gestión del modelo ambiental. Retrieved from https://itec.es/programas/tcqi/gestion-ambiental/

XV International Conference on Durability of Building Materials and Components
DBMC 2020, Barcelona
C. Serrat, J.R. Casas and V. Gibert (Eds)

Development of 3D Printing Technology for Geopolymers

Kinga Korniejenko, Michał Łach, Janusz Mikuła, Maria Hebdowska-Krupa, Dariusz Mierzwiński, Szymon Gądek and Marek Hebda

Institute of Materials Engineering, Faculty of Materials Engineering and Physics, Cracow University of Technology, Jana Pawła II 37, 31-864 Cracow, Poland, michal.lach@pk.edu.pl

Abstract. *The article presents the first results of the project under the title: 'Development of 3D printing technology for construction and facade prefabricated elements made of concrete composites and geopolymers', grant no. POIR.04.01.04-00-0096/18, funded by the National Centre for Research and Development in Poland, within the framework of programme: 'Smart Growth Operational Programme 2014-2020, IV Increasing the research potential, 4.1.4: 'Application projects'. The main aim of the project is design and development of the innovative large-format printer using geopolymers for 3D printing for residential houses. It allows the development of a technology for the production of a universal residential building, with a construction that is easy to transport and fast to assemble, as well as with the possibility of simple and quick expansion depending on the needs of users. The article shows the main idea of the advanced large format 3D printing for geopolymers with using an ergonomic printing method as well as materials research in modern filaments in the form of geopolymers.*

Keywords: *Geopolymer, 3D Printing, Additive Manufacturing, Large-Format 3D Printer, 3D Printing in Civil Engineering.*

1 Introduction

Additive Manufacturing is a rapidly developing industrial sector and potentially a disruptive technology. It can provide new horizons in the construction sector, especially in terms of geometrical flexibility, reduction of labour costs, improvement of efficiency and safety, construction in harsh environments, and sustainability (Nematollahi *et al.*, 2019; Labonnote *et al.*, 2016; Panda and Tan, 2019; Soltan and Li, 2018). Unfortunately, the full exploitation of 3D printing processes is currently limited due to the in-process and in-service performance of the available materials' sets, especially in application in construction industry.

Nowadays, the using geopolymers for 3D printing in the large-format printer is a great challenge. It offers a new perspectives for the construction industry, but the development of this technology is slowed down by a lot of barriers. The article shows the possibility of development the 3D printing. The main idea of development the advanced large format 3D printing for geopolymers is using an ergonomic printing method as well as materials research in modern filaments in the form of geopolymers. The article is focused on problems that appear during the first trials of development 3D printing technology.

The first research were connected with basic properties of the materials – key factors of effectiveness 3D printing process, such as: viscosity and time of bonding (Labonnote *et al.*, 2016; Rahul *et al.*, 2019). This basic properties are related with the thixotropic, and allow to understood as high yield strength and low viscosity behavior of the materials, including (Labonnote *et al.*, 2016; Panda and Tan, 2019):

- pumpability - reliability with which material is moved through the delivery system,
- extrudability - depositing material through a deposition device,

- buildability - resistance of wet material to deformation under loads,
- and open time - period during which the aforementioned properties remain consistently within acceptable tolerance.

The basic challenge in 3D printing is received the material that is sufficiently fluid and at the same time has sufficient viscosity to retain its shape after the printing process (Panda and Tan, 2019; Panda *et al.*, 2018). Moreover, not only the material properties decided about the possibilities of effective process. The other elements associated with technology are also important. All of this factors happen that there is only a limited understanding of the material requirements for 3D printing technology (Labonnote *et al.*, 2016; Rahul *et al.*, 2019).

2 Materials

The samples for small scale prototyping were prepared with metakaolin with pigment addition. The samples for large scale were prepared as geopolymer concrete, based on:

- metakaolin and sand (ratio: 1:1),
- fly ash and sand (ratio: 1:1).

Both raw material, fly ash as well as metakaolin, were thoroughly investigated as a possible raw material for the production of the geopolymers. The chemical composition was determined by X-ray fluorescence (WD-XRF). They oxide composition is shown in Table 1.

Table 1. Oxide composition of fly ash and metakaolin.

	Oxide composition (wt.%)							
	SiO_2	TiO_2	Fe_2O_3	Al_2O_3	CaO	MgO	K_2O	Na_2O
Fly ash	55,9	1,09	5,92	23,49	2,72	2,61	3,55	0,59
Metakaolin	53,01	0,74	1,34	41,54	0,27	0,38	0,71	0,82

Geopolymers were made from fly ash from the metakaolin or fly ash and sand in ratio 1:1. The fly ash was delivered from the bituminous coal power plant 'Skawina'. This power plant is located in Skawina in Lesser Poland region on the south of Poland. The fly ash is obtained as combustion by-product through the electrostatic precipitation of fine particles from the exhaust gases from coal-fired furnaces. The chemical composition of this fly ash is relevant for the geopolymerization process – it is typical for class F (Łach et al., 2016). The detailed oxide composition is presented in Table1. This raw material contains less than 5% of unburned material and less than 10% of iron compounds. Additionally it has low amount calcium compounds. The amount of the reactive silica in the material is ca. 36%. Moreover, it has physical parameters relevant to geopolymers manufacturing, especially it contains a lot of spherical particles and has good workability (Łach et al., 2018) as well as large amount of amorphous phase (Łach et al., 2016). The process of activation has been made by 10M sodium hydroxide solution combined with the sodium silicate solution (the ratio of liquid glass - 1:2.5).

3 3D Printing of Small Scale Elements

Samples were prepared using sodium promoter for activation the metakaolin with some pigment addition. The trials has been made on the laboratory 3D printer for concrete – WASP 2040 with pneumatic feeder.

The samples some multilayers plate have been prepared using 3D printing method – Figure 1. The printed samples were characterized by different quality.

Figure 1. Page layout.

The most important problem was viscosity of the material. In the first trials the material was too solid and the process was impossible to print effectively (Figure 2b), but the layers in this case were created effectively. The samples had ratio between liquid and solid parts: c/s = 0.25. Because of the lack of possibility of printing the viscosity was regulated by ethanol addition. After receiving the required viscosity the main challenge was layer stability. The samples had ratio between liquid and solid parts: c/s = 0.3. This materials were very easy to printability, but the main problems was connected with lack of proper stiffness of the layers (Figure 2a), because of that the product loss they shape.

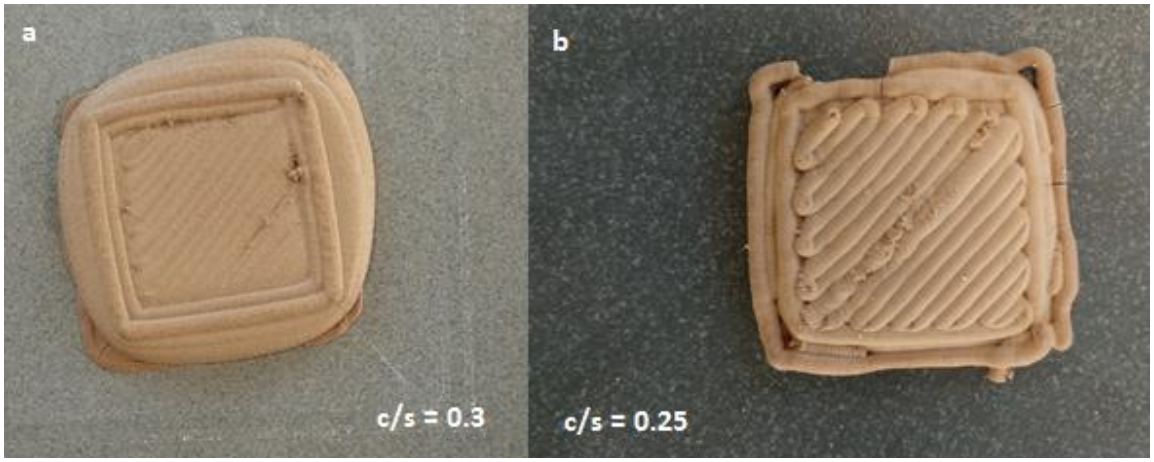

Figure 2. Samples after 3D printing with different liquid/solid ratio a) 0.3, b) 0.25.

The ratio between c/s required modification, but main problem is too long period for receiving the proper stiffness it must be analyzing once again and modify by proper addition on introducing some factors that accelerate the bonding such as additional sources of

temperature (Bong *et al.*, 2019; Nematollahi *et al.*, 2019).

The other challenge was brittle material behavior after the curing time and cracking during the drying process (Figure 3).

Figure 3. Samples after drying with visible cracks.

The problem of the cracks required introducing the additives to the geopolymer. It could be for example fibers addition that reduced the brittle material behavior (Korniejenko *et al.*, 2018; Nematollahi *et al.*, 2018; Silva *et al.*, 2020).

4 3D Printing for Large-Scale Elements – Manual Prototype for 3D Printing Process

The other trials was performed on large scale samples made on the self-produced manual 3D printing machine (Figure 4). The construction given material using a rotating screw (own design for determining the optimal consistency and speed of material reproduction).

The samples were prepared using metakaolin and fly ash mixed with sand in ratio 1:1.

Figure 4. Self- produced manual 3D printing machine.

The trials were conducted on the large form with using different ratio liquid and solid parts – Figure 5.

Figure 5. Samples after 3D printing with different liquid/solid ratio a) 0.3, b) 0.25.

The achieved results did not fulfil the requirements. The samples produced with different kind of ratio were too liquid to application for building elements. The material need further modification.

5 Conclusions

The article is focused on problems that appear during the first trials of development 3D printing technology, especially materials issues. It shows similar problems that appeared for small and large scale elements as well as for different raw materials used. The most important problem was viscosity the material. It was regulated by ratio between liquid and solid parts and additives such as ethanol. This problem was partly solved, but after receiving the required viscosity the main challenge was layer stability. There are planned further work on material stabilization.

The other challenge was brittle material behavior after the curing time and cracking during the drying process. The solving of this challenge required further works, especially connecting with design of proper curing process.

Acknowledgements

This work has been supported by Smart Growth Operational Programme 2014-2020, IV Increasing the research potential, 4.1.4: Application projects, funded by the National Centre for Research and Development in Poland, within the framework of the grant: Development of 3D printing technology for construction and facade prefabricated elements made of concrete composites and geopolymers, grant no. POIR.04.01.04-00-0096/18.

ORCID

Kinga Korniejenko: https://orcid.org/0000-0002-8265-3982
Michał Łach: https://orcid.org/0000-0001-5713-9415
Janusz Mikuła: https://orcid.org/0000-0001-9514-7870
Maria Hebdowska-Krupa: N/A
Dariusz Mierzwiński: https://orcid.org/0000-0003-2292-3546
Szymon Gądek: N/A

Marek Hebda: https://orcid.org/0000-0002-8583-9459

References

Bong, S.H., Nematollahi, B., Nazari, A., Xia, M. and Sanjayan, J. (2019) Method of Optimisation for Ambient Temperature Cured Sustainable Geopolymers for 3D Printing Construction Applications *Materials*, *12*, 902. doi: 10.3390/ma12060902

Korniejenko, K., Łach, M., Hebdowska-Krupa, M. and Mikuła J. (2018). The mechanical properties of flax and hemp fibres reinforced geopolymer composites *IOP Conference Series: Materials Science and Engineering*, *379,* 012023. doi: 10.1088/1757-899X/379/1/012023

Labonnote, N., Rønnquist, A., Manum, B. and Rüther, P. (2016). Additive construction: State-of-the-art, challenges and opportunities *Automation in Construction, 72*(3) 347–366. doi: 10.1016/j.autcon.2016.08.026

Łach, M., Korniejenko, K. and Mikuła J. (2016). Thermal insulation and thermally resistant materials made of geopolymer foams *Procedia Engineering*, *151*, 410-416. doi: 10.1016/j.proeng.2016.07.350

Łach, M., Mierzwiński, D., Korniejenko, K. and Mikuła, J. (2018). Geopolymer foam as a passive fire protection *MATEC Web of Conferences*, *247*, 00031. doi: 10.1051/matecconf/201824700031

Nematollahi, B., Vijay, P., Sanjayan , J., Nazari , A., Xia, M., Nerella, V.N. and Mechtcherine, V. (2019). Effect of Polypropylene Fibre Addition on Properties of Geopolymers Made by 3D Printing for Digital Construction *Materials, 11(12),* 2352. doi: 10.3390/ma11122352

Nematollahi, B., Xia, M. and Sanjayan J. (2019). Post-processing Methods to Improve Strength of Particle-Bed 3D Printed Geopolymer for Digital Construction Applications *Frontiers in Materials, 6*, 160. doi: 10.3389/fmats.2019.00160

Panda, B. and Tan, M.J. (2019). Rheological behavior of high volume fly ash mixtures containing micro silica for digital construction application *Materials Letters, 237*, 348–351. doi: 10.1016/j.matlet.2018.11.131

Panda, B. Unluer, C. and Tan, M.J. (2018). Investigation of the rheology and strength of geopolymer mixtures for extrusion-based 3D printing *Cement and Concrete Composites, 94*, 307–314. doi: 10.1016/j.cemconcomp.2018.10.002

Rahul, A.V., Santhanam, M., Meena, H. and Ghani, Z. (2019). 3D printable concrete: Mixture design and test methods, *Cement and Concrete Composites, 97*, 13–23. doi: 10.1016/j.cemconcomp.2018.12.014

Silva, G., Kim, S., Aguilar, R. and Nakamatsu J. (2020). Natural fibers as reinforcement additives for geopolymers – A review of potential eco-friendly applications to the construction industry *Sustainable Materials and Technologies, 23*, e00132. doi: 10.1016/j.susmat.2019.e00132

Soltan, D.G. and Li, V.C. (2018). A self-reinforced cementitious composite for building-scale 3D printing *Cement and Concrete Composites, 90,* 1-13. doi: 10.1016/j.cemconcomp.2018.03.017

XV International Conference on Durability of Building Materials and Components
DBMC 2020, Barcelona
C. Serrat, J.R. Casas and V. Gibert (Eds)

Environmental Monitoring System Based on Low-Cost Sensors

Behnam Mobaraki[1], Seyedmilad Komarizadehasl[2], Francisco J. Castilla Pascual[3] and José A. Lozano-Galant[1]

[1] Department of Civil and Building Engineering, Universidad de Castilla La Mancha.
Av. Camilo Jose Cela s/n, 13071, Ciudad Real, Spain.
behnam.mobaraki@uclm.es,Joseantonio.lozano@uclm.es

[2] Department of Civil Engineering and Environmental Engineering, Universitat Politècnica de Catalunya BarcelonaTech, C/ Jordi Girona 1-3, 08034, Barcelona, Spain
seyedmilad.komarizadehasl@upc.edu

[3] Department of Civil Engineering,Universidad de Castilla La Mancha, Cuenca, Spain
fcojavier.castilla@uclm.es

Abstract. *Temperature and humidity measurements provide useful information on multiple areas of civil engineering application such as Structural Health Monitoring (SHM), Structural System Identification (SSI) and structures rehabilitation. Majority of the existing commercial systems are so costly and also these measurement paradigms need many reference spots for a full-scale structure. The aforesaid paradigms are based on collecting data through smart devices, transferring information to each other and in the final stage processing the obtained information collaboratively through cloud computing or the others technologies. Taking into account the above information and obstacles, utilizing the Open Source Platforms (OSP) microcontrollers like Arduino as well as low cost sensors are attracting more and more attention. This paper gives a comprehensive information about the most determinant aspects of the aforementioned kits in terms of their pros and cons, installation procedure, communication protocol, number of the required connections and specific characteristics of the data acquisition system.*

Keywords: *Thermal Analysis, Low-Cost Sensors, Building Information Modeling, Open Source platforms, Structural Health Monitoring.*

1 Introduction

Climate change has drastically affected crops, wildlife and people's livelihoods. One of the main elements that can prevent this tragedy is to lessen the energy consumption since this incident could also be caused by burning of the fossil fuels for the human needs. In this way, one of the most efficient solution is to control the waste of energy in the buildings and public places. The development of economically viable Building Information Modelling (BIM) using different software and hardware has become increasingly popular in recent years. An economic Arduino-based embedded system can be defined as combination of Arduino open source platform and low-cost environmental sensors. Studies of the Arduino-based as well as

BIM-based controlling systems in different engineering fields were conducted by many scholars.

Barroca *et al.,* (2013) have designed and Arduino-based controlling system for concrete structures. They have prepared thermal and temperature sensors inside the concrete in order to measure temperature and humidity of the concrete at different levels. Different low-cost particle sensors were assessed by calibration methods adapted from the US EPA 2013 Air Sensor Workshop recommendations. The six different elements of the examinations were linearity response, precision of measurements, limit of detection, dependence on particle composition, dependence on particle size, relative humidity and temperature influences (Wang *et al.,* 2015). Bamodu *et al*., (2017) have used various types of humidity and temperature low cost sensors such as LM35 and DHT11 in order to control the indoor environment parameters of the buildings, heating, Ventilation, Air-Conditioning (HVACs).

Monitoring ventilation as well as thermal/humidity comfort level of the public places are vital issues since variation of the mentioned parameters might occur in different spaces. For instance, these variations may affect energy consumption and health of passengers in the subway. Marzouk and Abdelaty (2014) stablished Wireless Sensor Network (WSN) and BIM-based model in order to be able to monitor thermal condition in the different places of a subway. Kim *et al.* (2015) presented the development of Modelica Llibrry for BIM-based building energy simulation using an Object-Oriented Physical Modeling (OOPM) approach and Modelica, an equation-based OOPM language. Using the ModelicaBIM library they have prepared system interfaces between BIM and energy simulation, aiming to stablish semi-automatic translation from BIM to building Energy Modeling (BEM). Garcia and Kamsu-Foguem (2019) presented a new approach for automation of building construction when dealing with the energy efficiency for the purpose of predicting comfort levels elements such as heating, ventilating, air conditioning and etc. moreover they stablish BIM for thermal performance of prefabricated construction system (Mobaraki *et al.,* 2018).

As is evident from the aforementioned studies, the advantage of using the low-cost sensors for establishment of BIM in thermal performance of different structures has already proven. Along with the undertaken studies, it has to be mentioned that the accuracy of the low-cost sensors is a decisive parameter in reliability of the BIM. Therefore, in the section 2 of this article, a comprehensive information about the Arduino mechanism, types of smart connections and types of low-cost sensors will be presented. In the third section a detail explanation related to the performed experiments in terms of performance of low-cost sensors DHT22 will be explained.

2 Arduino Sensors

Arduino UNO is an open source software/hardware for making interactive electronic objects. The physical programable part is of 6.8 cm * 5.3 cm board which has 14 digital input/output pins, 6 analog inputs, 5 power pins (VIN, 5V, 3.3V and GND) with different performances, a 16 MHz crystal oscillator, a USB connection for compiling the data as well as using power supplied form the laptop/computer, a DC power jack (7 – 12V), a reset button for restarting the program/Arduino from the beginning and some small parts (Garin *et al.,* 2018). For talking to the sensors through Arduino as well as programing the board through compiling the sketches the open- source Arduino Integrated Development Environment (IDE) software has

been presented (Philips, 2019). This cross-platform application has written in Java, C and C^{++} and is compatible with all Windows, MacOS and Linux. The Arduino environment is extendable by utilizing the libraries. These libraries have written in C/ C^{++} and they increase functionality of the sketches for working with hardware as well as manipulating data. One of the main capabilities of microcontroller is to read sensors and capture the values. In other words, it can be express that sensors are sort of objects, capable of converting physical quantity (like temperature or humidity) into an electrical quantity. For measuring different parameters through Arduino various types of sensors exist. For instance, temperature, motion, humidity, vibration, displacement, pressure and etc. these measurements might be done for several purposes such as smartening systems of metering, retail, logistic, agriculture and security. For the connection of a sensor to the Arduino and observing the measured parameters, sensor's library which defines a canonical set of predefined sensors and control ability, should be used. The Arduino's sensors are categorized as digitals and analogs. Analog sensors observe the external changes such as temperature and humidity variations and yield analog voltage that represents the measured parameter. For instance, 2V might mean 23 degrees Fahrenheit. Normally this output voltage is between 0 to 5V. Analog signals might be influenced by the ambient noise which leads to produce errors in the output signals. However, the digital sensors generate discrete values like 0 and 1 which are so called digital/binary signals. They have lower range of calculation than the analog ones. Therefore, the analog sensors are more appropriate for wide range of measurements. As far as the analog outputs are liable to change rapidly and unpredictably, digital sensors are preferred over the analog ones.

3 Arduino-Based Thermal Controlling System

Temperature and humidity are one of the decisive factors measured in many projects. In order to evaluate the accuracy of the low-cost temperature sensors, it was decided to stablish an Arduino-based thermal controlling system. This system is going to measure variation of the temperature in an oven located in Universidad de Castilla-La Mancha (UCLM). The Arduino-based thermal measurement system is depicted in Fig.1.

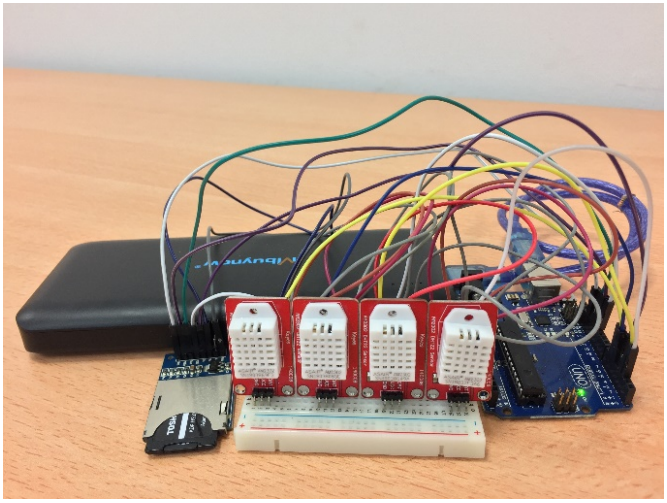

Figure 1. The Arduino-based thermal measurement system.

3.1 Hardware Description

Fig.2 shows all the used particles for establishment of this measurement system Arduino UNO, DHT22 sensor, breadboard and SD Card/Reader. The proposed system is based on the open source Arduino UNO platform and low-cost temperature/humidity sensor DHT22. The operating temperature of this sensor is between -40° C to 80° C with accuracy of 0.5° C. It is also capable of measuring humidity from 0-100% with resolution of 0.01 and accuracy of 2-5% RH. DHT22 sensor was chosen since it is one of the most employed and common low-cost humidity and temperature sensors in the engineering and environmental projects. The communication system of the sensor is a custom protocol which use a single wire/bus communication. Fig.2 illustrates the utilized oven for measuring the DHT22 accuracy (Sensor, 2019).

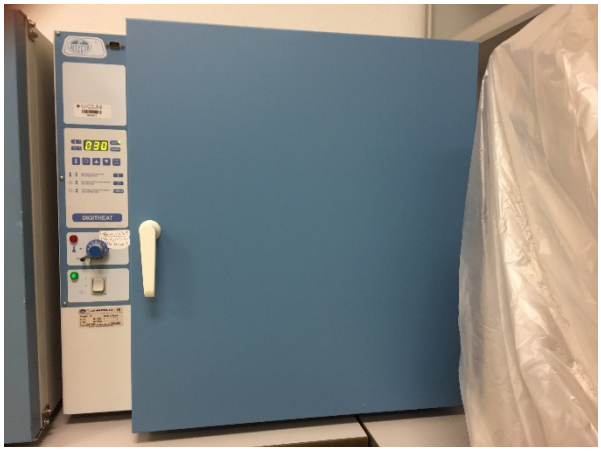

Figure 2. The utilized oven SELECTA-2001244 for the experiment.

3.2 Comparative Sensors Result

To estimate the responses of DHT22 sensor as well as their precision, variation of the temperature versus time related to the 4 sensors shown in the Fig.3. The sensors adjusted to record the temperature with frequency of 2 seconds. All of them have been registered to measure the temperature inside an oven in the laboratory of Universidad de Castilla-La Mancha (UCLM). Model of the oven is SELECTA-2001244, Capable of changing temperature from 10° C to 250° C with precision of 2% and resolution of 1° C. In order to figure out the precision of the sensors, the oven adjusted to reach to the temperature of 30° C and keep working for period of time. As shown in the Fig.3, variation of the temperature has been divided to two parts. The first part shows variation of the temperature for reaching to the adjusted temperature and the second part depicts behavior of the sensors at the fixed temperature of 30° C. In the second part the sensor number 1, number 2, number 3 and number 4 are showing constantly the temperature of 29.6° C, 29.4° C, 29.4° C and 29.6° C respectively. These observations indicate the discrepancy between the low-cost sensor DHT22 for recording the homogenous temperature in the oven. It has to be mentioned that in our measurements not only we are facing with error of the sensors, but also the oven has its own range of error, 2%, as mentioned in the above.

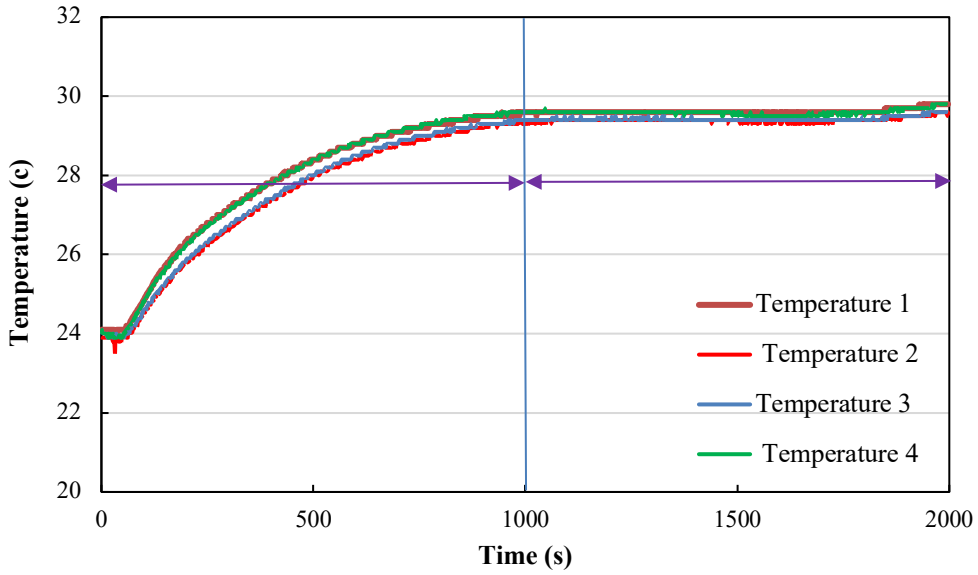

Figure. 3. Variation of the temperature related to the four DHT22 sensors.

By this graph it is clearly visible that the accuracy tolerance of the temperature sensor DHT22 is around 0.5° C. The obtained range of accuracy is almost as equal as the one indicated by the manufacturer in the DHT22 datasheet, 0.5° C (Zarnik and Papa, 2019). Low cost environmental sensors are so useful for determining the thermal parameters of buildings (Mobaraki and vaghefi, 2018). Moreover, they are applicable for determining characteristic of structures and inferring variation humidity and temperature of concrete during the construction procedure (Mobaraki *et al.,* 2020).

In order to have better recognition of the sensors' accuracy it is better to have a statistic view on the obtained results. In statistic standard deviation is defined as amount of dispersion of a data set. In this criterion, a low range of standard deviation shows that the values are tending to get close to the average/mean of the dataset however, the high range of that demonstrate that the set of data are dispersed and has a wider range. It can be seen from Fig. 4 that the derived standard deviation related to the four sensors vary from 0.04 to 0.13 which shows a good performance trend. These 1000 measured point are belong to the second part of the measurement when the homogenous temperature of 30° C starts in the oven.

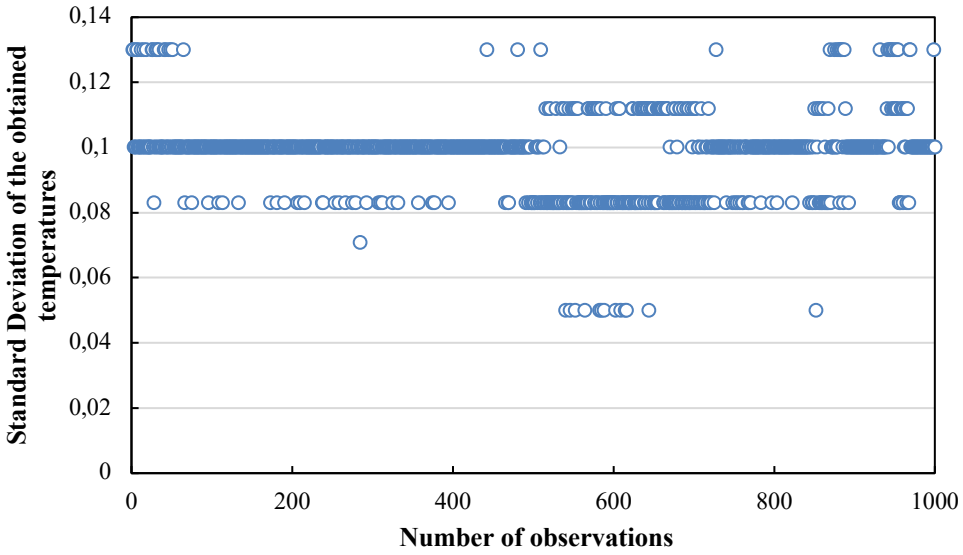

Figure 4. Variation of the standard deviation related to the 1000 measurements of temperature.

Fig.5 shows dispersion of standard deviation (in the case humidity) calculated for the four sensors by 1000 measurements at the third step of Fig. 5. Standard deviation is always positive number. Majority of the observations were extended above 1.25 close to 1.3 (1.25≤Standard deviation ≤1.3). A low range of standard deviation same as Fig.4 (related to temperature) shows that the observations tend to be close to the average temperature, however the higher one presents (Fig. 7) the wider range of observations discrepancy (Mobaraki and Vaghefi, 2016).

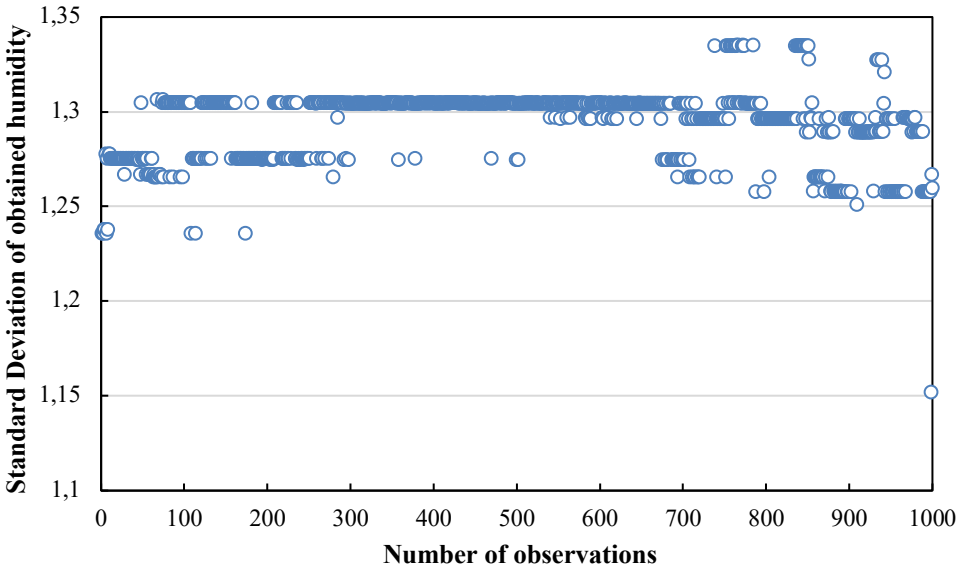

Figure 5. Variation of the standard deviation related to the 1000 measurements of humidity.

4 Conclusion

Low-cost environmental sensors are so practical in building rehabilitation projects for enhancing thermal resistance of buildings. Evaluation the accuracy of the low-cost temperature/humidity sensors through an Arduino-based system has been done for the environment sensor DHT22. Four sensors have hooked up to the digital ports 2, 3, 4 and 5 of the Arduino and variation of temperature and humidity related to the oven SELECTA were presented in this article. Lower range of standard deviation acquired for the temperature data set (0.04≤Standard deviation ≤0.13) rather than humidity (1.15≤Standard deviation ≤1.33). Which means that the sensor DHT22 is more accurate in terms of measuring temperature rather than humidity. From the obtained results it is clearly visible that the range of accuracy or in the other word the precision of the temperature sensor DHT22 is around 0.5° C which is almost equal to the one mentioned in the DHT22 datasheet, 0.5° C.

Acknowledgements

The authors are indebted to the Spanish Ministry of Economy and Competitiveness for the funding provided through the research projects BIA2013-47290-R, BIA2017-86811-C2-1-R, and BIA2017-86811-C2-2-R founded with FEDER funds It is also to be noted that funding for this research has been provided to Mr. BEHNAM MOBARAKI by the Spanish Ministry of Economy and Competitiveness through its program for his Ph.D. It is also to be noted that part of this work was done through grant number 2018-COB-9092 from Universidad de Castilla La Mancha (UCLM).

ORCID

Behnam Mobaraki: https://orcid.org/0000-0002-2924-643X
Seyedmilad Komarizadehasl: https://orcid.org/0000-0002-9010-2611
Francisco Javier Castilla Pascual: https://orcid.org/0000-0003-1961-6174
Jose Antonio Lozano-Galant: http://orcid.org/0000-0003-0741-0566

References

Bamodu, O. Xia, L. and Tang L. (2017). An indoor invironment monitoring system using low-cost sensor network. *Procedia*. 606-666.

Barroca, N. Borges, L.M., Velez, F.J., Monteiro, F., Gorski, M. and Gomez, C.J. (2013). Wireless sensor networks for temperature and humidity monitoring within concrete structures. *Construction and Building Material.* 1156-1166.

Garin, A.M. Millan-Garcia. J.A., Bariri. A., Millan-Medel J. and Lizzaraga J.M. (2018). Environmental monitoring system based on an open source platform and the internet of things for a building energy retrofit. *Automation in Construction*. 201-214.

Garcia, L.G. and Kamsu-Foguem, B. (2019). BIM-oriented data mining for termal performance of prefabricated buildings, *Ecological Informatics*. 61-72.

kim, J.B. Jeong, W. Clayton, M.J. Habrel, J.S. and Yan, W. (2015). Developing a physical BIM library for building termal energy simulation. *Automation in construction.* 16-28.

Marzouk, M. and Abdelaty, A. (2014). Monitoring termal confort in subways using building information modeling. *Energy and Buildings.* 252-257.

Mobaraki, B. Komarizadehasl S. Castilla-Pascual F.J. and Lozano-Galant, J.A. (2020). Application of low-cost sensors for accurate indoor environmental monitoring. *J. Automation in Construction*.

Mobaraki. B. and Vaghefi. M. (2018). Investigation of dynamic behavior of concrete bridge columns under surface blasting, *Sharif Journal of Civil Engineering.* 133-141.

Mobaraki. B. and Vaghefi. M. (2015). Numerical study of the Depth and cross-sectional shape of tunnel under Surface explosión, *Tunnelling and underground space technology*. 114-122.

Mobaraki. B. and Vaghefi. M. (2016). Effect of soil type on the dynamic response of a tunnel under surface detonation. *Combustion, Explosion. Shock waves*, 363-370.

Philips Semiconductors, (2019). Arduino datasheet.

The Sensor Company, (2019). SHT21 datasheet.

Wang, Y., Li, J., Jiang, H., Zhang, J., Jiang, Q. and Biswas, P. (2015). Labratory evaluation and calibration of three low-cost particle sensors for particulate matter measurements. *Aerosol science and technology.* 1063-1077.

Zarnik, M.S. and Papa, F.N.G. (2019). Thermal phenomena in LTCC sensor structures. *Sensors and Actuators A: Physical*. 198-206.

XV International Conference on Durability of Building Materials and Components
DBMC 2020, Barcelona
C. Serrat, J.R. Casas and V. Gibert (Eds)

Integration of Durability Data of Construction Elements Within a BIM-Based Environment

Leticia Ortega[1], Begoña Serrano[2], Isaac Villanova[3] and Andreea R. Ilies[4]

[1] Valencian Institute of Building (IVE), Avenida Tres Forques, 98, 46018-Valencia, Spain, lortega@five.es

[2] Valencian Institute of Building (IVE), Avenida Tres Forques, 98, 46018-Valencia, Spain, bserranol@five.es

[3] Valencian Institute of Building (IVE), Avenida Tres Forques, 98, 46018-Valencia, Spain, ivillanova@five.es

[4] Valencian Institute of Building (IVE), Avenida Tres Forques, 98, 46018-Valencia, Spain, anil1@arq.upv.es

Abstract. *In the unavoidable way to achieve more sustainable buildings, it is essential to provide the architects with data on the environmental impact and the durability of the different components of the building, and make it available in the format they are using in the design phase. In this regard, the use of the building information modelling (BIM) tools has arisen as a new trend in the construction industry to improve the sustainable assessments of buildings in the design phase. In order to improve an existing tool developed by the Valencian Institute of Building in cooperation with the Valencian Regional Government, on providing the characteristics of the most common construction elements within a BIM-based environment, a database of durability and environmental impact data of construction elements and materials has been developed for integration within the tool. The reference service lives database has been created from a multicriteria study consisting in the analysis of sixty service life data bases published in recent decades. The work developed allows the architects working in Spain to have the durability required data of the construction elements from the design phase, for the integration and information exchange within a BIM-based environment to be able to use the existing BIM-based LCA/LCC.*

Keywords: *BIM-Based Software, Durability, Life Expectancy, Cost, Maintenance.*

1 Context

As it is considered to be a basic industry, the construction sector in Spain is one of the major sources of economic growth and development. So far, the most extended strategy among the construction companies applied to improve the efficiency and become more competitive has been to decrease the buildings construction costs without taking into account the life cycle of buildings. Trying to lower the initial construction costs had a negative impact on the quality of its processes and materials.

In this context, voices are being raised in the academic field that demand a change in the production model of the construction sector proposing solutions taking into account the whole life cycle of the building and the impact it has on the environment. The economic assessment of estate projects beyond the construction phase becomes an essential tool for cost optimization,

allowing realistic comparison between different investment options (García-Erviti, Armengot-Paradinas, and Ramírez-Pacheco, 2015).

The science of life cycle cost analysis is a fundamental tool to make changes in the Spanish construction sector. That is the reason why it is necessary to provide the stakeholders of the sector with the necessary tools to modify the decisions in the design stage based on the global cost. As an agent of the construction sector, The Valencian Institute of Building seeks to help technicians to apply the life cycle cost methodologies during the design phase by providing them with tools and data.

The Valencian Institute of Building (IVE), as a public interest incorporated foundation in the construction sector subjected to private law, constituted in 1986, promoted by the Second Vice Presidency of the Valencian Government and Regional Ministry of Housing and Bioclimatic Architecture and directed by a board committee, brings together a collective of professionals involved in the building and urban process. Its main interests, among others, lie in improving the processes linked to the edification and urban space, encouraging research and enhancing life quality, sustainability, safety, accessibility and durability standards through the smart development in the built environment.

2 Objective

During the last decades there has been rising concerns about the service life in terms of stability, safe functioning and appearance of the constructions already built and the ones to be built. The problem is not only to make the buildings and products last longer, which can be advantageous from the point of view of the scarcity of resources (MIT CSHub Cambridge, s.f.), but to know the reference service life of the systems mostly used (and therefore their global cost) to take knowledge based decisions.

The final purpose of the research is not to find out how to increase the durability of the products and systems, but to compile the maximum quantity of durability data available in order to have the ability to compare different constructive solutions. For this purpose, a reference service life database has been developed, not from tests, but from an analysis of different existing worldwide databases.

The developed database is due to be included in a BIM-based computer software so that architects and construction professionals can use it to predict how much their buildings will last and how much they will have cost at the end of their service life.

3 Methodology: Multiple-Criteria Decision-Making

Obtaining reliable data regarding the durability of building materials and systems was one of the difficulties in achieving the final goal. Instead of selecting a specific database, it was decided to rely on a multiple-criteria decision analysis applied to existing databases.

Multiple-criteria decision-making (MCDM) or multiple-criteria decision analysis (MCDA) studies, as part of the operational research linked to applying advanced analytical methods to provide a wide range of problem-solving techniques through applied mathematics methods, are a scientific method of obtaining information to aid in decision making by providing a comparative judgement between complex data. It is based in relating different indicators and giving each one of them certain degree of importance. (Mardani, 2011)

Even though it's a comprehensible and rational method which helps finding solutions in complex situations, it is difficult defining the comparison criteria, researching available data and, maybe the most important of all, the time factor.

Stage 1. Scope of application

To correctly evaluate the different sources, a taxonomy of the components of the constructive elements was developed, so the comparison can be as accurate as possible when compared to other sources under the same conditions.

Stage 2. Available databases

The next step was a thorough research to locate the most majority of available databases worldwide.

There were identified sixty service life databases published in the recent decades, from Spain, Germany, Portugal, UK, US, Canada, Australia, Italy, Sweden, Switzerland and Israel.

Stage 3. Indicators

Four indicators were defined to evaluate the weight each database should have when pondering the data: data affinity, which refers to the climate zone of the country were the study was made; data obsolescence depending on the publishing year; reliability of the source, depending on the authors and investigation center where the study was made and the level of expertise of the data base related to the different constructive elements. For each indicator 2 or 3 levels were created in order to rank the databases depending on the level achieved in each indicator, as seen in the tables below.

Table 1. Data Afinity.

Climate zone (country)	Score
Mediterranean climate zone (Spain, Portugal, Italy)	3
Temperate climate zone (Germany, UK, Sweden, Switzerland)	2
Cold and sunny climate zone (UK, Canada, Australia)	1

Table 2. Data Obsolescence.

Year	Score
2012 to present	3
2000-2005	2
Before 2000 or unknown	1

Table 3. Data Reliability.

Reliability	Score
High	3
Medium	2
Low	1

Table 4. Level of expertise.

Level of expertise	Score
High	2
Low	1

Stage 4. Multiple-criteria weigh

The analyzed databases were scored for each of the indicators mentioned above. As seen in the tables above, the maximum score that could be obtained was set in 11 points. Each database was scored a total number of points after evaluating the four indicators.

Stage 5. Multiple-criteria decision-making

After scoring the databases, to obtain a service life data for each construction element, a weighted average was applied to each durability data of every constructive element obtained from the different data bases. The weighted average was based on the weigh that each database obtained. Aberrant data was not taken into account.

For instance, considering a constructive element such as a wooden beam of which 3 different durability data were gathered, a weighted average was applied having more weight in the average the data gathered from sources closer to Spain, more reliable, more specialized and more recent.

Multiple-criteria decision-making results

The reference service life of the constructive materials database was a result of the multiple-criteria decision-making.

The service life data to be used with the objective of including it into a BIM-based environment tool was the one resulted from the process explained above. However, with research purposes, the results were also organized and sorted into a table including more complex information as the minimum and maximum service life or an average service life having considered only one of the four indicators or the critical value. The Image 1 below shows the results of the analyzed and processed data of the constructive elements of a brick wall façade. The data used for the BIM-based tool was the Multiple-criteria average service life column.

Image 1. Example. Durability data results.

Construction material: TAXONOMY			Construction material	Group										
03 Facade	3.1 Wall	3.1.1 Brick: cooked clay	Fabrica ladrillo cerámico	Brick clay pieces	23	High	40	150	79	90	77			
03 Facade	3.2 Exterior cladding	3.2.3 Plastered	Cement mortar reviewed	Plastering	15	Medium	5	60	32	40	32			
03 Facade	3.5 Others	3.5.2 Thermal insulation in 2-layer	Non-hidrofilic mineral w	Thermal insulation in two-layered facade	14	Medium	25	80	46	55	46			
03 Facade	4.2 Interior cladding	4.2.2 Plastered and trimmed	Plastered plaster	Plaster	14	Medium	5	62	38	48	38			

The database created allowed the extraction of a variety of relations between the analyzed elements. The Graphic 1 below shows an example of comparison between the durability of different types of curtain wall façade depending on the indicator taken into account. The first bar refers to the multiple-criteria, that is all the indicators, and the rest of them have into account just one indicator.

Graphic 1. Curtain wall façade durability comparison results.

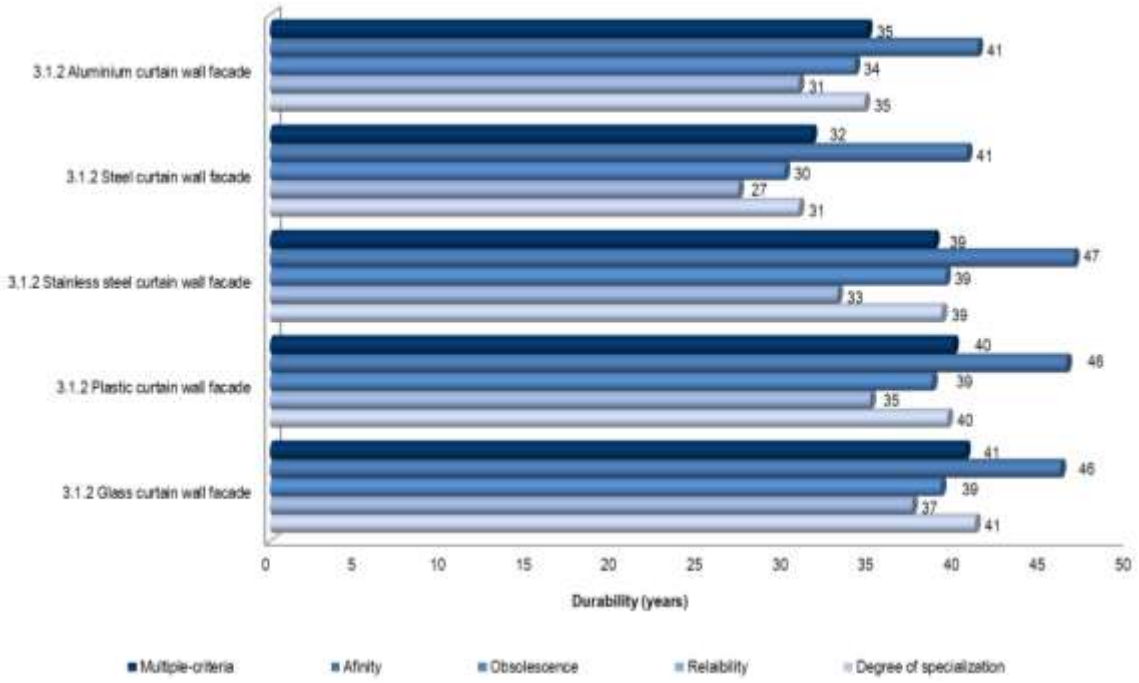

4 Durability Into BIM-Based Computer Software

The Valencian Institute of Building in cooperation with the Valencian Regional Government, has been gathering information and created a database about the most common construction materials characteristics and put it together in the Catalogue of Construction Materials.

Complementary information such as materials durability, maintenance and costs are being added to the already existing Catalogue of Construction Materials in order to improve it and update it to nowadays needs.

It is well known that Building Information Modelling (BIM) as a method of developing architecture projects is as its peak and the big majority of architects and construction professionals are already using BIM-based computer software to efficiently plan, design, construct and manage buildings and infrastructure. The construction materials' information gathered and applied when planning buildings will allow knowing the service life of buildings and its cost from the design phase.

The current catalogue was released to the public as a software program tool in 2010 and it's being updated at the moment with the purpose of turning it into a web application. The catalogue provides tools for designing custom constructive solutions, calculate their properties and check them according to the Spanish law. The image 2 below is part of the Catalogue of Construction Materials being developed and it shows different façade types and its properties.

Table 5. Example. Façade types and properties. Catalogue of Construction Materials under development.

Tipos | Subtipos | Soluciones de Catálogo

Modificar Parámetros | Ver sólo habilitadas

		Código	Sección	E (mm)	M kg/m²	Caso cámara aire	DB-SI	DB-HS		DB-HR		
							R/E/I	G.I.(h)	G.I.(nh)	R_A dBA	$R_{A,tr}$ dBA	U
✓	ⓘ	FC01a03M3205(		265	361		EI120	1	2	52	47	
✓	ⓘ	FC01a04M3205(	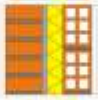	285	383		EI180	1	2	52	47	
✓	ⓘ	FC01b01M3205(		195	172		EI120	1	2	43	38	

The Valencian Institute of Building has been working on integrating construction materials data, characteristics, durability data from the latest databases and information from other IVE tools in a BIM-based environment. Therefore, users will be able to know constructive information and characteristics from the design phase.

This web application will let users define and choose a bundle of constructive solutions for their project, downloading them in IFC and RFA formats with the properties of each solution, such as durability. It is currently in development and it is not released yet to the public, although it is expected to be available by the beginning of 2020.

Assessing the building over its life cycle (planning, construction, use and demolition phase) provides an insight into the real quality of the building (Federal Ministry for the Environment,

Nature Conservation and Nuclear Safety (BMUB), 2016). The application of the durability data into BIM software will allow professionals to previously assess buildings' life cycle.

The final input lies in the integration of the present research results and information gathered from other IVE tools into BIM software in order to be applied to projects from the design phase. A web application will let users define and choose a bundle of constructive solutions for projects, download them in IFC and RFA formats with the properties of each constructive element, such as durability. It is expected to be released to the public by the beginning of 2020.

5 Conclusions

The previous and numerous worldwide studies carried out in the field of predicting the construction materials service life and the latest research here displayed allowed us to carry out data extraction, process it and apply it to our nearby environment (Spain).

In these moments in which the construction sector needs to change the model that has been applied in the last decades, the progress achieved with the present research allows to take steps in order to improving quality and sustainability, encouraging a better understanding of the construction systems we use, as well as its components and materials. We cannot improve the functioning of the construction systems if we do not know their behavior.

The present study provides with data that architects and technicians need in order to be able to consider the reference service life of the buildings from the design phase, allowing the advance in multiple aspects that result in the improvement of the construction sector efficiency, such as maintenance plans, better forecast of life cycle costs, buildings and construction systems design, information given to clients accuracy... etc.

Nevertheless, in order to successfully carry out this process, it is necessary to raise awareness in the construction sector and to be supported by public policies. The Valencian Institute of Building works in parallel in this line together with the regional government for the improvement of quality and sustainability in the construction sector with a holistic and comprehensive vision of the entire construction process.

Acknowledgements

Special thanks to the Valencian Government and Regional Ministry of Housing and Bioclimatic Architecture.

ORCID

Leticia Ortega: https://orcid.org/0000-0001-5934-4324
Begoña Serrano: https://orcid.org/0000-0002-9606-0029

References

CLF. Carbon Leadership Forum. (n.d.). Recommended guidelines for building component lifespans in the whole building life cycle assessment.

Federal Ministry for the Environment, Nature Conservation and Nuclear Safety (BMUB). (2016). Guideline for Sustainable Building. In *Guideline for Sustainable Building. Future-proof Design, Construction and Operation of Buildings* (p. 176). Berlin: Druckrei Conrad, Berlin.

García-Erviti, F., Armengot-Paradinas, J., & Ramírez-Pacheco, G. (2015). Life cycle cost analysis as an economic evaluation tool for sustainable building. State of art.

Ginebra: International Organization for Sandardization . (2010). ISO 15686 Buildings and constructed assets-Service Life Planning.

Instituto Valenciano de la Edificación. (2010). Catálogo informático de elementos constructivos.

Mardani, A. (2011). *Multiple Criteria Decision Making. From early history to the 21st century.* Singapore: World Scientific Publishing CO. Pte. Ltd.

MIT CSHub Cambridge. (n.d.). *MIT Concrete Sustainbility Hub*. Retrieved from https://cshub.mit.edu/durability

National Institute of Building Sciences. High performance building council. (n.d.). National Performance Based Design Guide.

Ortega Madrigal, L. (2012). Propuesta metodológica para estimar la vida útil de los sistemas constructivos de fachadas y cubiertas utilizados actualmente con más frecuencia en la edificación española a partir del método propuesto por la NORMA ISO-15686. *Tesis doctoral*, 265.

Perera, O. (2011). Procuring Green in the Public Sector: a checklist for getting started. *IISD International Institute for Sustainable Development*.

The British Standards Institution. (2015). In *Guide to durability of buildings and building elements, products and components* (p. 50). UK: BSI StandardS Publication.

UNEP United Nations Environment Programme. (2002). *Global Environment Outlook 3. Past, present and future perspectives.* London: Earthscan Publications Ltd.

WBDG. Whole Building Design Guide . (n.d.). Mechanical Insultation Design Guide. *National Institute of Building Sciences*.

WBDG. Whole Building Design Guide. (n.d.). Building Envelope Design Guide. *National Institute of Building Sciences* .

XV International Conference on Durability of Building Materials and Components
DBMC 2020, Barcelona
C. Serrat, J.R. Casas and V. Gibert (Eds)

Maintenance-Oriented Design in Architecture. A Decision Support System for the Evaluation of Maintenance Scenarios Through Bayesian Networks Use. A Case Study: the Headquarters of ING Groupe in Amsterdam

Michele Di Sivo[1], Daniela Ladiana[2], Federico Novi[2] and Caterina Salvatori[2]

[1] Dipartimento di Ingegneria dell'Energia, dei Sistemi, del Territorio e delle Costruzioni dell'Università di Pisa (DESTEC), Largo Lucio Lazzarino, 2, 56122 - Pisa, Italy, michele.disivo@unipi.it.

[2] Dipartimento di Architettura di Pescara, Università degli Studi "G. d'Annunzio" di Chieti e Pescara, Viale Pindaro, 42, 65127 – Pescara, Italia
d.ladiana@unich.it, fn@officinadiarchitettura.net, caterinasalvatori@libero.it

Abstract. *This study was developed at the Department of Architecture of Pescara and Department of Energy, Systems, Territory and Construction Engineering of the University of Pisa as part of an experimental thesis that led to the implementation of a Decision Support System. The objective of the work was to implement a tool capable of evaluating - in relation to the choices concerning the morphology of the building, the construction technologies, the materials and the design of the architectural elements - the levels of maintenance quality implemented in the various phases of the project, from the first phases, in which few relevant decisions are made, to the executive phase characterized by a multiplicity of choices. The aim was to construct a tool in which the reliability of the evaluations was related to the quantity and quality of the data that feeds the decision-making process, but which is also able to evaluate preliminary decisions based on the elements of choice that characterize the first phases of the project. The conceptual model has been defined through the construction and implementation of a Bayesian Network or a graphical system of probabilistic inference able to represent the set of stochastic variables and their conditional dependencies through the use of a direct acyclic graph. Through the interrogation of the network it is therefore possible to evaluate through the expression of a synthetic index, a real overall rating of the different aspects that contribute to define the maintenance quality. The use of Bayesian Networks, in the light of the analyses carried out on an experimental basis - exemplified here on the case study of ING Groupe headquarters - for the ability to control a multitude of factors linked to the durability of materials, the morphology of systems and ease of intervention, seems capable of generating useful, effective and expandable tools to support the design decision-making process.*

Keywords: *Design, Durability, Maintenability, SSD, Bayesian Networks.*

1 Introduction

The architectural design of buildings is increasingly characterized by a new morphological, functional and technological complexity that requires, from coordination to control, maintenance and management of the entire life cycle, new skills to effectively implement a process in which the act of conception and the moment of construction are continuously intertwined over time (Daniotti, 2007; Latouche, 2015; Di Sivo, 1994; Ladiana, 2009).

The use of Bayesian Networks is in this experimentation proposed for the construction of

an open model of a useful tool to manage uncertainty through the creation of conceptual maps of reality that aim to highlight the variables and links in a clear and rigorous way.

The study described in this paper has been developed at the Department of Architecture of Pescara with and the Department of Energy, Systems, Territory and Construction Engineering of the University of Pisa, starting from an experimental thesis that led to the implementation of a Decision Support System (SSD).

For the tool described, in addition to the purposes related to the operating mode and the possible implementation of databases, there is the structural purpose of being able to operate within an "open system" that can be progressively expanded, on which it would be possible, as the study and experimentation progresses, to graft new areas of evaluation, increasing its operations.

2 Research Objectives and Methodological Approach

The objective of the research developed was to implement a tool capable of evaluating - in relation to the choices concerning the morphology of the building, the construction technologies, the materials and the design of the architectural elements - the levels of maintenance quality implemented in the various phases of the project, from the first phases, in which few relevant decisions are made, to the executive phase characterized by a multiplicity of choices (Di Sivo, 1994).

It was intended to build a tool in which the reliability of the evaluations would be related to the quantity and quality of the data that feeds the decision-making process, but able to operate also in a preliminary way on the basis of the elements of choice that characterize the first phases of the project.

The fundamental aim was to achieve a design support tool capable of operating according to the logic of design optimization dictated by the criteria of maintainability consolidated in the scientific culture (D'Alessandro, 1994), while allowing, at the same time, to draw on databases, existing or gradually implementable, relating to: incompatibility of materials, forms of degradation resulting from the morphology of components and connections, size of maintenance equipment, ergonomic schemes related to maintenance operations, etc.

In order to be easy to use, the SSD was based on the evaluation and expression of maintenance quality through a rating index. From the methodological point of view, the work has been developed in the direction of the construction of a system capable of managing the large number of variables that distinguish maintenance-oriented architectural design from the initial phase.

The current reality of projects is in fact extremely complex, especially when analyzing problems related to maintainability, where the multitude of variables at stake and uncertainty factors characterize the entire life cycle of the project (Talamo, 2019). It is therefore necessary to be able to use a "interrogable" modelling tool capable of providing support for the automation of evaluation processes formalized on the basis of maintenance criteria that can be applied to the entire architectural organism or to a part of it, such as a façade system. A quantitative approach to integrate uncertainty and the multitude of variables in an objective and rigorous way into reasoning can be implemented through the use of the so-called Bayesian Networks.

The conceptual model for the decision support system has in fact been developed through

the construction and implementation of a Bayesian Network, a representation of a probabilistic inference model capable of describing the set of stochastic variables and their conditional dependencies through the use of a Direct Acyclic Graph (DAG) (Novi, 2018).

Following a "data driven" strategy, a space-time analysis tool has been developed to support decisions in order to reach a maintainability index. First of all, the knowledge network was built (directly through the Hugin Expert software) by defining a conceptual model consisting of nodes (variables) that represent the "maintainability criteria" defined, then linked together according to criteria of causal dependence (cause - effect).

In order to simplify the operational phase of compiling the values of the variables of the individual nodes - variables, a simple tabular interface has been created with the help of a spreadsheet that makes the input of data by the designer clear and simple and automates the numerical output with a compilation and update link directly to the nodes of the BN created in the Hugin Expert software.

Once the available values are propagated, the network allows to obtain through the expression of a synthetic index, a rating about the maintenance quality of the described project and to perform in real time multi-scenario simulations, diagnostic evaluations, sensitivity analysis, simply by directly modifying the values in the network or in the tabular interface. The tool thus obtained, even in the presence of partial or inhomogeneous data, allows to perform a multitude of simulations and obtain in real time functional results at the level of knowledge of the problem, guiding the designer in a conscious way in the evaluation and the necessary choices throughout the lifecycle design.

3 Implementation of the DSS on a Case Study: The Headquarters of ING Groupe

The method described has been tested through the application on case studies with different technologies and construction methods with the intent to test the flexibility and compliance of the project support tool developed to operate in cases of uncertainty and complexity.

Here is described the analysis carried out on a well-known existing building: the headquarters of ING Groupe in Amsterdam (Fig.1), built by Meyer and Van Schooten Architects (MVSA) in 2002; this building was chosen as a case study because it is characterized by a high design attention to the maintenance theme, in order to carry out the evaluation by simulating different possible scenarios related to different technical solutions as may happen in a possible design process. In the experimentation, the maintainability of the building has been tested in three areas: vertical closure - plant engineering system - upper closure but is exemplified here for exposure limits for the evaluations related to the facade.

ING Group is an example of sustainable, innovative and energy-efficient architecture.

The glass and aluminum structure of the building is raised on metal pillars whose height varies between 9 and 12m. The façade consists of two layers of glass spaced apart which contain a passage to allow both access for maintenance and natural ventilation.

The external glass is hooked through 6 fixing points that guarantee the support of the façade by means of glass elements (thickness 20mm), bound to the floor by stainless steel components. The sheets of 1800 x 3300mm size, are made of tempered or tempered - laminated glass 12 or 19mm thick.

Figure 1. Headquarters ING Group, Amsterdam. MVSA Architects.

The sheets are separated vertically by silicon joints of 12mm; horizontally by a glass opening element with a height of 410mm for the ventilation of the facade. The internal facade is made up of inward opening wooden frames 950mm wide and 2900mm high. The cleanability and periodic control of the facade cladding is also guaranteed thanks to the accessible roof on the tenth floor. A system of tracks that runs through the entire building is designed to ensure a high level of inspection and maintenance: thanks to the installation of mobile trolleys on the roof, the easy cleaning of all the windows has been ensured.

In the experimentation of the decision support system, the building was analyzed considering two possible configurations: in the first case, it was evaluated deprived of some of the solutions related to maintainability; in the second case, it was analyzed how it looks today, with the current technical characteristics related to maintainability.

The flexibility of the method, allows to perform multi-scenario analysis by intervening on probability distributions, i.e. to verify how simulations in real time, allow to take strategic decisions. Therefore, each case has been subjected to a double analysis: in the first one the method is tested as a tool for evaluating the building, while in the second one its potential as a support system for decision making has been verified.

The maintainability index of the building is obtained from the analysis of three guiding criteria:

- MATERIALS for assessing the durability not only of the intrinsic properties (quality of the component), but also in relation to the design and execution techniques and the environmental context to which it belongs (design quality - execution quality - environmental quality);

- the MORPHOLOGY OF SYSTEMS for the determination of the morphological quality through the analysis of the sub-requisites of maintainability such as: durability - not dirtiness - self-cleaning capacity - cleanability, in order to make more appropriate choices during the design phase to avoid possible pathologies;

- EASE OF INTERVENTION for the determination of accessibility and spatial ergonomics through the evaluation of the sub-requirements of maintainability such as: maintainability by the user - serviceability - serviceability - reparability - disassembly - replaceability.

3.1 Analysis of Cases and Evaluation of Alternatives

CASE 01 assumes the construction of the curtain wall using insulating glass on a single layer and without the equipment and access routes to the envelope.

Analysis 01: the first step consists in the realization of three tables on a spreadsheet (information database) in which the parameters of the sub-requirements related to the maintainability of the façade are analyzed, in order to determine the three criteria of the system (durability of the materials - morphology of the systems - ease of intervention) in relation to the materials and components used for the realization of the proposed case study.

The second step provides, in order to obtain the evaluation of the maintainability index, the use of Bayesian Networks. This consists in the realization of a second grid (Fig. 2) that allows to translate the parameters on Hugin (software for the use of Bayesian Networks).

In the third step, the saving of each parameter under examination and the subsequent export to Hugin, implements an automation process at the end of which you get a node for each parameter exported.

Figure 2. Database construction and data link.

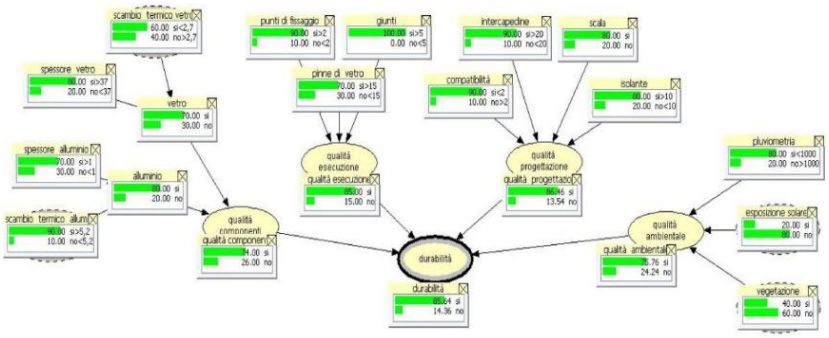

Figure 3. Each node-parameter is linked to a reference table with Boolean values.

The result is a relationship network (Fig.3) in which each node-parameter is linked to a reference table with values 1 or 0, indicating whether or not the requirement previously verified on the spreadsheet has been met. From the connection between the nodes it is possible to determine the maintainability of the facade under examination, which in this case expressed an index for maintainability of 48%.

The results obtained show that the main cause is to be attributed to the ease of intervention.

The system of vertical closures and the components integrated in it must be structured in such a way as to make their inspection easy. During the design, especially in relation to the surface conformation of the materials, dust and atmospheric pollution, it is necessary to provide easy access structures to facilitate cleaning operations.

In the *Analysis 02*, the implementation of a series of operations allows to verify the compliance of the instrument as a support to decision-making choices.

In intervention A the insertion of paths to overcome the difficulties connected to the periodic cleaning of the curtain wall was foreseen. The integration of this aspect has led to a 50% increase in inspectability, with an improvement also in terms of the cleanability of the facade.

Intervention B, consisted in the insertion of equipment (ladders - trolleys), particularly recommended for buildings with curtain walls, as they facilitate periodic cleaning and maintenance operations, avoiding the use of particularly expensive external means with consequent time savings. The integration of this aspect has led to reparability from 40 to 80%.

Finally, intervention C considered all ergonomic aspects with the aim of improving user satisfaction and the overall performance of the system. The intervention concerned the relationship between the dimensions and the geometry of the operating space, in order to take into account the body and limb positions of the operators and their movement in relation to the specific maintenance actions and the use of the required tools and utensils. The ergonomic aspect, therefore, allows to perform those periodic cleaning and maintenance operations without which the use of external means would be required.

The *Analysis 02*, through the progressive incorporation of the operations described above, has led to an increase in the sub-requisites of ease of intervention, which overall have led to an increase in terms of maintainability of 15% (from 48 to 63%).

In CASE 02, the insulating glass facade consisting of a transparent double skin was analyzed, with the presence of the inspectionable cavity, the accessible staircase and the tracks that allow the passage of the trolleys throughout the casing.

At the end of the process already described for the previous case here, the Evaluation 01 provided a rating index for maintainability of 71 %. Therefore, action was taken where the system had the lowest rating value, which in this case, among the three criteria examined, was the morphology of the systems.

During the design phase it is necessary to pay particular attention to the internal and external factors of the system in order to minimize the inconveniences due to the degradation caused by atmospheric agents on the walls. It was therefore considered, in this case, to provide a geometric configuration of the façade and a morphology of the components such as to allow a homogeneous washout of the surfaces while avoiding stagnation, accumulation, water absorption and the fixing of dust. Therefore, the 02 analysis simulated different conditions on some aspects related to the morphology of the system.

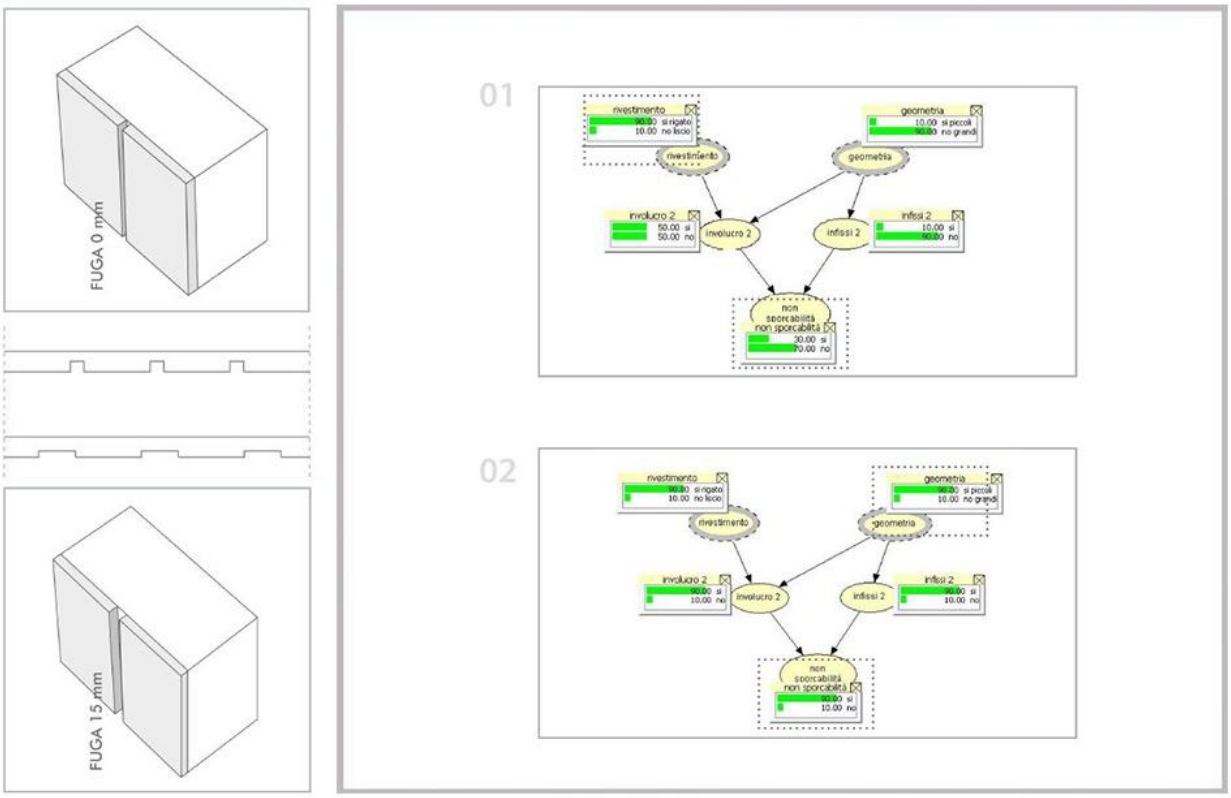

Figure 4. Evaluation of maintenance scenarios related to different forms of external panels.

Intervention D has provided for the use of smaller smooth panels in order to facilitate better washing of the facade and easier disassembly, with a 20% increase in non-dirtability.

Intervention E assumed the use of striped panels, with sufficiently wide and shallow joints to create preferential water flow paths; on the contrary, narrow and deep joints would lead to the deposit of debris and dirt with the need for specialized personnel for periodic cleaning operations. This intervention has led to 30 to 90% non-soiling.

The example described denotes how the Bayesian Networks offer the possibility to verify in real time how much each single intervention can affect, in percentage - probabilistic terms, the degree of maintainability of the project.

In the second analysis of Case 02 of ING, the progressive incorporation of the components led to an increase in the sub-requirements of the morphology of the systems, which on the whole led to an improvement in the maintainability of the system with an increase of 10% more (from 71 to 81%).

The results obtained from the proposed analyses show that certain choices, made during the design phase, can have a high impact on maintainability. Although it is a simple qualitative evaluation, the analysis highlights not only an objective comparison between the two scenarios, but also clarifies and makes explicit all the variables that significantly affect the results.

4 Conclusions

The use of Bayesian Networks, in the light of the analysis carried out on an experimental basis, for the ability to control a multitude of factors related to the durability of materials, the morphology of the systems and the ease of intervention, seems capable of generating a valuable tool not only useful as a support in decision-making ex-ante in the project phase of new construction but also ex-post for the identification of rehabilitation interventions in existing buildings. The system developed allows to determine the impact that determined variables, chosen from the point of view of maintainability, bring to the whole project allowing to establish what attention should be paid to the estimates of probability to obtain certain services of interest or at the same time what corrective actions are essential to be taken.

Future developments in the research of the SSD model are oriented in the direction of the integration of cost parameters for a more complete and effective evaluation and comparison of alternative intervention scenarios and the identification of implementable protocols for an objective comparison between contractors during the awarding of a contract.

ORCID

Michele Di Sivo: http://orcid.org/0000-0002-2140-9513
Daniela Ladiana: http: // orcid.org/0000-0001-6008-1365

References

D'Alessandro, M. Ed.(1994). *Dalla manutenzione alla manutenibilità*. Milano: Franco Angeli.

Daniotti, B. and Lupica Spagnolo, S. (2007). "Service life prediction for buildings' design to plan a sustainable building maintenance", *Conference Sustainable construction, materials and practices*, Lisbon, Portugal.

Dave, B., Koskela, L., Kiviniemi, A., Owen, R. and Tzortzopoulos, P. (2013). *Implementing Lean in construction: Lean construction and BIM*. CIRIA C725.

Di Sivo, M. (1994). *Il progetto di manutenzione*, Firenze: Alinea Editrice.

Di Sivo, M. and Ladiana, D. (2010). "Building maintenance: a technology for resource conservation", *WIT Transactions on Ecology and the Environment*, Vol 128, 2010 WIT Press, doi:10.2495/ARC100371.

Ladiana, D. (2009). "Durata e sostenibilità del ciclo di vita degli edifici. L'importanza dell'approccio maintenance-oriented." *Manutenzione Tecnica e Mangement*, anno XVI, n.3, (Marzo)

Latouche, S. (2015). *Usa e getta. Le follie dell'obsolescenza programmata* [Use ant throw. The Madness of Planned Obsolescence], Torino: Bollati Boringhieri

Novi, F. (2018). "Bayesian networks as a resilience tool for decision – making processes in uncertainty conditions", *TECHNE - Journal of Technology for Architecture and Environment*, Vol. 15, p 341-347.

Talamo, C., et al. (2019). "Incertezza epistemica, gestione dei rischi e informazione: il ruolo del progetto esecutivo". *TECHNE - Journal of Technology for Architecture & Environment*. Vol. 18, p164-173.

XV International Conference on Durability of Building Materials and Components
DBMC 2020, Barcelona
C. Serrat, J.R. Casas and V. Gibert (Eds)

Metamodel Development for Predicting Hygrothermal Performance of Wood-Frame Wall under Rain Leakage

Lin Wang[1], Hua Ge[2] and Liangzhu (Leon) Wang[3]

[1]Postdoctoral Fellow, Department of Building Civil and Environmental Engineering, Concordia University, 1455 de Maisonneuve O., Montreal, QC H3G 1M8, Canada, forestwang2013@gmail.com

[2]Associate Professor, Department of Building Civil and Environmental Engineering, Concordia University, 1455 de Maisonneuve O., Montreal, QC H3G 1M8, Canada, hua.ge@concordia.ca

[3]Associate Professor, Department of Building Civil and Environmental Engineering, Concordia University, 1455 de Maisonneuve O., Montreal, QC H3G 1M8, Canada, leon.wang@concordia.ca

Abstract. *In recent years, stochastic modeling has been increasingly applied to investigate the uncertainties of input parameters in hygrothermal simulation and the moisture damage risks of building envelopes. Generally, stochastic modeling requires hundreds or even thousands of simulations to take into account the uncertainties of input parameters, which is computationally intensive and time-consuming. This paper aims to apply polynomial and neural network metamodel as a substitute for the traditional hygrothermal model, to predict the hygrothermal performance of building envelopes. In the previous study carried out by the authors, stochastic simulations have been performed based on the traditional hygrothermal model, to investigate the hygrothermal performance of wood-frame walls under different rain leakage levels. The material properties and rain deposition factors were considered as stochastic variables, and stochastic simulations were performed under three rain leakage scenarios: 1%, 0.5% and 0.1% of wind-driven rain. In this paper, the stochastic inputs (the hygric material properties and rain deposition factor) and outputs (the maximum moisture content and mold growth index over a 5-year period of the simulation) of a conventional 2×6 wood-frame wall are used to develop the metamodels through polynomial regression and neural network methods. The metamodels are developed for each rain leakage scenario, and the stochastic data of the three rain leakage scenarios are aggregated together to train another metamodel. It is found that the metamodels generally perform well to predict the maximum moisture content and mold growth index. The metamodels for low rain leakage scenarios are better than those for high rain leakage scenarios and the neural network metamodel is more accurate than polynomial metamodel for high rain leakage scenarios, i.e. 1% of rain leakage.*

Keywords: *Neural Network Metamodel, Polynomial Metamodel, Hygrothermal Simulation, Wood-frame Wall, Rain Leakage.*

1 Introduction

In recent years, the stochastic modeling approach has been increasingly applied to investigate the uncertainties of input parameters in hygrothermal simulation and the moisture damage risks of building envelopes. Generally, stochastic modeling requires hundreds or even thousands of simulations to take into account the uncertainties of input parameters, which is computationally intensive and time-consuming. To improve computational efficiency, a statistical meta-model can be developed as a substitute for the traditional hygrothermal model, to predict the hygrothermal performance of building envelopes.

There are several comparative studies to investigate the performance of different metamodeling methods (Van Gelder *et al*., 2014; Janssen *et al*., 2015; Ostergard *et al*., 2018). And the hygrothermal performance of the building envelopes have been approximated by various metamodel methods, such as generalized additive model, polynomial regression and neural network (Zewdu Taffese and Sistonen, 2016; Zanetti Freire *et al*., 2017; Marincioni *et al*., 2018; Ostergard *et al.,* 2018; Tijskens *et al*., 2019). According to the comparison study by ANNEX 55, the best metamodeling techniques are polynomial regression (PR), multivariate adaptive regression splines (MARS), and sigmoidal transfer function neural networks, and it was suggested that the metamodel can only be used within the range of the training data values. (Janssen *et al*., 2015). On the contrary, the data set in different ranges may need different metamodels to ensure their reliability. Most of the previous studies have focused on the performance of different types of metamodels, however, there is a lack of studies investigating the reliability of the metamodels at different data ranges.

According to the stochastic analysis performed by Wang and Ge (2019), the rain leakage level significantly influences the moisture performance of building envelopes. This paper develops metamodels for predicting moisture performance of a conventional 2x6 wood-framed wall under different rain leakage scenarios. The polynomial regression and sigmoidal transfer function neural network methods are employed to develop the metamodels. Metamodels are developed for three rain leakage scenarios: 0.1%, 0.5% and 1% of wind-driven rain. Additionally, a metamodel representing all the three scenarios is developed by training the aggregated stochastic data. The performance indicators- Root Mean Square Error (RMSE) and Maximum Absolute Error (MAE) are used to evaluate the reliability of the developed metamodels.

2 Methods

2.1 Hygrothermal Model

The metamodels are developed based on a hygrothermal model of a conventional 2×6 wood-framed wall. Figure 1 shows the configuration of the investigated wall, and Table 1 shows the mean values of the material properties of each component in the wall.

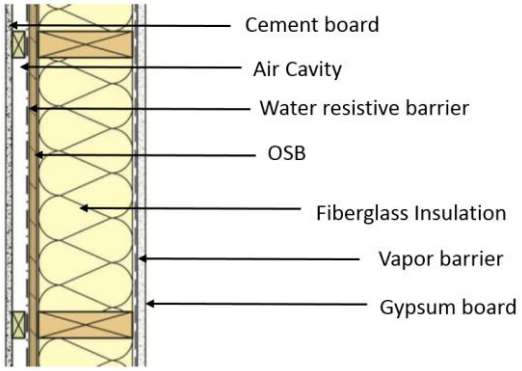

Figure 1. Configuration of 2x6 wood framed wall.

Table 1. Material properties.

	ρ (kg/m^3)	θ_{por} (m^3/m^3)	W_f (kg/m^3)	μ_{Dry} -	D_{ww} (m^2/s)	c (J/kg·K)	λ (W/m·K)
Cement Board	1130	0.479	152	905	2.16E-8	840	0.24
Air Gap	1.3	0.999	-	0.56	-	1000	0.13
Water Resistive Barrier	400	0.001	0.9	328	-	1500	2.4
OSB	650	0.9	377	994	1.29E-10	1880	0.1
Fiberglass	30	0.99	208	1.35	-	840	0.036
Vapor barrier	130	0.001	-	4E6	-	2300	2.3
Gypsum Board	625	0.706	430.625	172	3.47E-11	870	0.16

ρ- bulk density; θ_{por}- porosity; W_f – saturation water content; μ_{Dry} – vapor resistance factor at dry state; D_{ww}- moisture diffusivity at saturation wáter content; c- specific heat capacity; λ- termal conductivity

The boundary conditions are listed in Table 2. and the Canadian Weather Year for Energy Calculation (CWEC) data of Vancouver is used as weather data except for the rain data, which are extracted from the WUFI weather database. The wind-driven rain is calculated based on the semi-empirical model in ASHRAE 160 (2016). The equation of the semi-empirical model is presented as follows:

$$r_{bv} = F_E \cdot F_D \cdot F_L \cdot U \cdot \cos\theta \cdot r_h \quad (1)$$

where

F_E - rain exposure factor

F_D - rain deposition factor

F_L - empirical constant, 0.2 ($kg \cdot s/m^3 \cdot mm$)

U - hourly average wind speed at 10m (m/s)

θ - the angle between wind direction and normal to the wall

r_h - rainfall intensity, horizontal surface (mm/h)

Table 2. Boundary conditions.

α_{in} ($W/m^2 \cdot K$)	α_{ex} ($W/m^2 \cdot K$)	β_{in} (s/m)	β_{ex} (s/m)	α_s -	α_l -	F_E -	F_D -
8	17	5.6E-8	1.19E-7	0.6	0.9	1.0	0.35

To investigate the impact of rain leakage on the hygrothermal performance of the wall assembly, hygrothermal models are created for three rain leakage scenarios: 0.1%, 0.5%, and 1 % of wind-driven rain. The wall is assumed to face east orientation, which receives the highest amount of wind-driven rain. The penetrated rain wáter is assumed to be deposited on the exterior surface of OSB. The moisture content and mold growth index at the interior surface of OSB are used for performance evaluation. The details of the model setup can be found in Wang and Ge (2019).

2.2 Data Preparation

To evaluate the moisture problem and mold growth risks, stochastic simulations were performed for 5 years starting from Oct. 2012 based on DELPHIN and MATLAB (Wang and Ge, 2019). The stochastic input and output data are used for training the metamodels.

The input data includes stochastic hygric material properties of OSB and fiberglass and the rain deposition factor. The material properties are assumed to follow the normal distribution, the mean values and standard deviations are determined from literature (Kumaran *et al.*, 2003; Mukhopadhyaya *et al.*, 2007). The rain deposition factor is assumed to follow uniform distribution from 0.35 to 1.0 as prescribed in ASHRAE 160 (2016). The stochastic inputs are sampled by the Latin Hypercube Sampling technique, and the stochastic models are generated for the three rain leakage scenarios. For each scenario, 100 stochastic models are generated. In total, simulations are performed for 300 stochastic models. Table 3 shows the mean values and standard deviations of the stochastic inputs. Other parameters of the hygrothermal model are kept as deterministic values. The output data used for training the metamodel is the stochastic results of maximum moisture content and mold growth index for the 5-years' simulation.

Table 3. Stochastic inputs.

Material properties					Boundary condition
OSB			Fiberglass		Rain deposition factor
W_f	μ_{Dry}	A	W_f	μ_{Dry}	Fd
kg/m^3	-	$kg/m^2 \cdot s^{0.5}$	kg/m^3	-	
337 (54)	994 (38)	0.0022 (0.00055)	208 (14.5)	1.35 (0.034)	0.35 to 1

2.3 Metamodel Development

2.3.1 Polynomial Regression

The polynomial regression method is one of the most widely used meta-modeling methods. The metamodel is nth polynomial, which is fitted by input and output samples. The equation of the metamodel can be written as follows (Jin *et al.*, 2001):

$$\hat{y} = b_0 + \sum_{n=1}^{m}\sum_{i=1}^{p} b_{ni} x_i^n + \sum_{n=1}^{m}\sum_{k=1}^{m}\sum_{i=1}^{p}\sum_{j=1}^{p} b_{nkij} x_i^n x_j^k \quad (2)$$

where

$\hat{y}$- estimated output

x- input vectors

p- the number of inputs

m- the order of the polynomial

b- regression coefficients

In general, the regression coefficients can be determined based on the least square method. The accuracy of polynomial regression metamodel is influenced by sample size and order number. According to ANNEX 55 (Janssen *et al*., 2015), a third-order polynomial performs the best for approximating an original model with 14 parameters, while a second-order model significantly reduces the number of coefficients with only slightly worse performance than the third-order model. The Root Mean Square Error (RMSE), which measures the accuracy of the metamodel, has no significant reduction after the sample size is higher than 100. Therefore, in

this paper, the sample size is 100 for each rain leakage scenario, and the metamodel is developed based on the second-order polynomial. For the metamodel representing all the three rain leakage scenarios, there are 300 samples. The polynomial metamodels are developed using the Polyfitn toolbox in MATLAB (D'Errico, 2012).

2.3.2 Neural Network Metamodel

A neural network is composed of an input layer, an output layer, and one or more hidden layers in between. Figure 2 shows a typical architecture of the neural network. These layers are interconnected so that the information can be transferred from one layer to another through transfer function. At each hidden layer, there are several neurons that contain the transfer function. The number of neurons in the hidden layer is defined by the users and the transfer function can be radial basis function or sigmoidal transfer function. According to Van Gelder et al. (2014), the radial basis function network needs more training samples to obtain the same accuracy with a sigmoidal transfer function network. And the performance of one hidden layer neural network with 9 neurons could be better than that of two hidden layers with 17 and 19 neurons at each layer when predicting the number of hours with room temperature higher than 25 ℃ in a semi-detached dwelling model. Therefore, in this paper, the sigmoidal transfer function network is used to develop the metamodel, and there is only one hidden layer with 10 neurons. The number of neurons in the input layer and the output layer is equal to the number of input and output parameters. In this paper, there are six input parameters (the six stochastic variables shown in Table 3) and one output parameter (stochastic maximum moisture content or mold growth index). The training algorithm used in this paper is the Bayesian regularization, which shows a better performance than the Levenberg-Marquardt algorithm (Kayri, 2016). The neural network metamodels are developed using Neural Net Fitting APP in MATLAB.

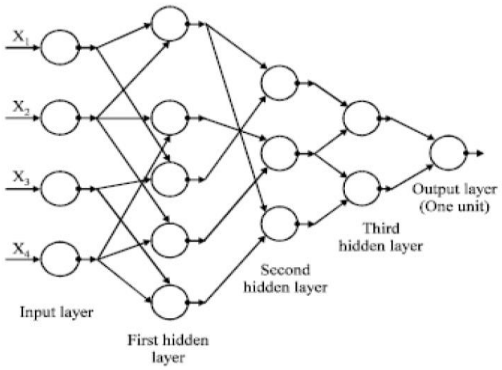

Figure 2. A typical neural network model (Galkin and Lawell, 2013).

3 Results and Discussion

3.1 Metamodels for Moisture Content

Figure 3 shows the comparison of maximum moisture content between metamodels and the originals model for the test data that are not participated in training the metamodels. In this paper, 85% of the sample data set are used for training, and 15% are used for testing. And Table 4 shows the RMSE and MAE of the two types of a metamodel for each scenario. It can be seen

from Figure 3 that the metamodels for 0.1% rain leakage scenario have the best performance.

All the metamodel outputs are almost on the 45-degree line, and the trendline of the outputs from metamodel is almost overlapping with the 45-degree line for both polynomial and neural

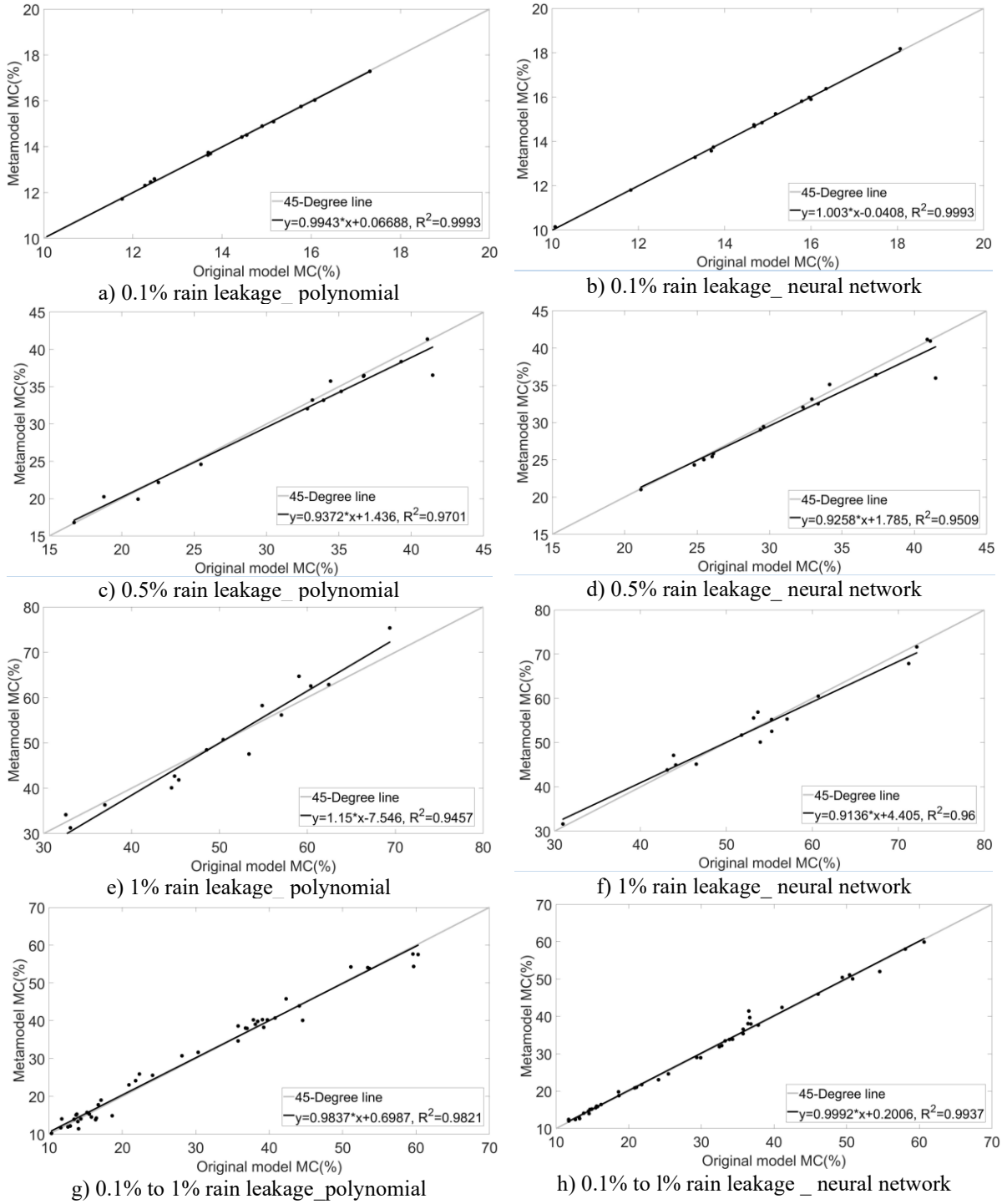

a) 0.1% rain leakage_ polynomial

b) 0.1% rain leakage_ neural network

c) 0.5% rain leakage_ polynomial

d) 0.5% rain leakage_ neural network

e) 1% rain leakage_ polynomial

f) 1% rain leakage_ neural network

g) 0.1% to 1% rain leakage_polynomial

h) 0.1% to l% rain leakage _ neural network

Figure 3. Comparison of the outputs (maximum moisture content) between original models and metamodels for different rain leakage scenarios.

Table 4. Comparison of the metamodel performance between polynomial regression and neural network methods for different rain leakage scenarios (maximum moisture content).

	Polynomial				Neural network			
	0.1%	0.5%	1%	0.1% to 1%	0.1%	0.5%	1%	0.1% to 1%
RMSE	0.05	1.49	3.29	2.05	0.06	1.50	2.11	1.12
MAE	0.11	4.93	5.99	5.31	0.12	5.49	3.80	4.91

network methods. Therefore, the predicted values from the metamodels are almost equal to those from original models and the metamodels perform very well for predicting the maximum moisture content. For the 0.5% and 1% rain leakage scenarios, the outputs from metamodels are distributed around the 45-degree lines, and the trendlines deviate from the 45-degree lines.

The outputs of 1% rain leakage scenario is more spreading than those of 0.5% rain leakage scenario, which means the accuracy of the 1% rain leakage metamodels is lower than that of 0.5% rain leakage metamodels. Figure 3 g and h show the metamodels representing the whole range of rain leakage from 0.1% to 1%. It can be observed the outputs of the neural network metamodel are closer to the 45-degree line than those of the polynomial metamodel, which means the neural network metamodel has a better performance than polynomial metamodel.

The performance of these metamodels can be verified by observing their RMSE and MAE as presented in Table 4. It can be seen that the 0.1% rain leakage scenario has the lowest RMSE and MAE, it is followed by 0.5% and 1% scenarios. The metamodels representing all the rain leakage scenarios have higher RMSE and MAE than the 0.1% and 0.5% rain leakage scenarios, but lower than the 1% scenario. For the 0.1% and 0.5% rain leakage scenarios, the RMSE and MAE of neural network metamodels are slightly higher than those of polynomial metamodels. While, for the 1% rain leakage scenario and the metamodels representing all the rain leakage scenarios, the neural network method has a lower RMSE and MAE than the polynomial regression method.

3.2 Metamodels for Mold Growth Index

Table 5. Comparison of the metamodel performance between polynomial method and neural network method for different rain leakage scenarios (maximum mold growth index).

	Polynomial				Neural network			
	0.1%	0.5%	1%	0.1% to 1%	0.1%	0.5%	1%	0.1% to 1%
RMSE	0.10	0.14	0.15	0.39	0.07	0.16	0.09	0.12
MAE	0.23	0.39	0.24	1.01	0.12	0.36	0.20	0.37

Table 5 shows the performance of the metamodels for predicting the maximum mold growth index. The conclusions that can be drawn from this table are similar to those for the maximum moisture content. The scenarios with higher rain leakage have higher RMSE and MAE, and the neural network method has lower RMSE and MAE than the polynomial method, particularly at higher rain leakage levels.

4 Conclusions

This paper developed polynomial and neural network metamodels to simulate the maximum

moisture content and mold growth index of a conventional 2x6 stud wall under different rain leakage levels. The main conclusions of this paper are: 1) In general, the developed metamodels are performing well to substitute the original hygrothermal models. 2) The metamodels for lower rain leakage levels (from 0.1% to 0.5% rain leakage) perform better than those with higher rain leakage levels (from 0.5% to 1% rain leakage). 3) Neural network metamodel performs better than polynomial metamodel, especially for the scenarios with higher rain leakage level.

OCID

Lin Wang: https://orcid.org/0000-0002-6529-1123
Hua Ge: http://orcid.org/0000-0003-1368-4301
Liangzhu (Leon) Wang: https://orcid.org/0000-0002-3656-7020

References

ASHRAE. (2016). ANSI/ASHRAE Standard 160-2016 Criteria for moisture-control design analysis in buildings. Atlanta, GA: American Society of Heating Refrigerating and Air Conditioning Engineers Inc.

D'Errico, J. (2012). Matlab function 'polyfitn', http://www.mathworks.com/matlabcentral/fileexchange/34765-polyfitn , last accessed on Oct. 20, 2019

Galkin, I. and Lowell, U.M. (2013). Polynomial neural networks. http://ulcar.uml.edu/~iag/CS/Polynomial-NN.html, last accessed on Oct. 20, 2019.

Janssen, H., Roels, S., Gelder, L. V. and Das, P. (2013). Final report of IEA Annex 55- Subtask 2: Probabilistic tools. Gothenburg, Sweden: International Energy Agency.

Jin, R., Chen, W. and Simpson, T. W. (2001). Comparative studies of metamodelling techniques under multiple modelling criteria. Structural and Multidisciplinary Optimization. 23(1), 1-13.

Kayri, M. (2016). Predictive ability of Bayesian Regularization and Levenberg-Marquardt algorithms in artificial neural networks: a comparative empirical study on social data. *Mathematicl and Computational Applications*. 21(2), 20

Kumaran, M.K., Lackey, J.C., Normandin, N., Tariku, F. and van Reenen, D. (2003). Variation in the hygrothermal properties of several wood-based building products. In Proceedings of Second International Building Physics Conference, Leuven, Belgium.

Marincioni, V., Marra, G. and Altamirano-Medina, H. (2018). Development of predictive models for the probabilistic moisture risk assessment of internal wall insulation. Building and Environment. 137, 257-267.

Mukhopadhyaya, P., Kumaran, M.K., Lackey, J.C., van Reenen, D. and Tariku, F. (2007). Hygrothermal properties of exterior claddings, sheathing boards, membranes and insulation materials for building envelope design, NRCC-50287. National Research Council of Canada, Ottawa, Canada.

Ostergard, T., Lund Jensen, R. and Enersen Maagaard, S. (2018). A comparison of six metamodeling techniques applied to building performance simulations.Applied Energy. 211, 89-103.

Tijskens, A., Roels, S. and Janssen, H. (2019). Neural networks for metamodelling the hygrothermal behaviour of building components. Building and Environment. 162, 106282.

Van Gelder, L., Das, P., Janssen, H. and Roels, S. (2014). Comparative study of metamodelling techniques in building energy simulation: guidelines for practitioners.Simulation Modelling Practice and Theory, 49, 245-257.

Wang, L. and Ge, H. (2019). Effect of rain leakage on hygrothermal performance of highly insulated wood-framed walls: a stochastic approach. Canadian Journal of Civil Engineering. Special Issue: Durability and Climate Change.

Zanetti Freire, R., dos Santos, G.H. and dos Santos Coelho, L. (2017). Hygrothermal dynamic and mould growth risk predictions for concrete tiles by using least squares support vector machines.Energies. 10(8), 1903.

Zewdu Taffese, W. and Sistonen, E. (2016). Neural network based hygrothermal prediction for deterioration risk analysis of surface-protected concrete facade element. Construction and Building Materials. 113, 34-48.

XV International Conference on Durability of Building Materials and Components
DBMC 2020, Barcelona
C. Serrat, J.R. Casas and V. Gibert (Eds)

Practical Application of Low-Cost Sensors for Static Tests

Seyedmilad Komarizadehasl[1], Behnam Mobaraki[2], Jose A. Lozano-Galant[2], and Jose Turmo[1]

[1]Department of Civil and Environment Engineering, Universitat Politècnica de Catalunya, BarcelonaTech. C/ Jordi Girona 1-3, 08034, Barcelona, Spain. Seyedmilad.komarizadehasl@upc.edu, jose.turmo@upc.edu

[2]Department of Civil Engineering, Univesidad de Castilla-La Mancha. Av. Camilo Jose Cela s/n, Ciudad Real, 13071, Spain. behnam.mobaraki@uclm.es, Joseantonio.lozano@uclm.es

Abstract. *Structural Health Monitoring (SHM) is essential to assess the accuracy of durability predictions of structures. Using low-cost sensors on structural evaluation has gained significant attention compare to high-cost sensors. Although these may not be as accurate and sensitive as the expensive electronic devices, with efficient code and right use, there is a possibility of getting useful information from them. These sensors can vary based on their functionality and the measurements they provide. For example, one is highly sensitive to the light of its environment while the other kind would give different results in different temperatures. In this paper, three different displacement measuring sensors have been studied. An ultrasonic sensor (HC-SR04) and two different types of laser sensors (VL53L0X and VL53L1X) are investigated in the paper. An Arduino Mega has captured their measured data, and a raspberry pi has made the acquisition. Not only issues regarding coding and placing of these sensors have been presented ultimately, but precise solutions for the aforementioned problems as well as an efficient way of assembling all the sensors are also presented in this paper. The data generated from these electronic devices can be used for Structural Health Monitoring applications.*

Keywords: *Low-Cost Sensors, Distance Measurement, Internet Of Things (IoT), Accuracy and Sensibility, Structural Health Monitoring.*

1 Introduction

Recently, the need for using sensors in structures for monitoring and inspection of their health state is growing. With this, the need for more economical means of doing SHM is getting very great attention. In this paper, a few models of static sensors have been presented. Moreover, the characteristics of each of them have been explained. Each type could be used in specific situations, and each one has advantages as well as disadvantages in different ambient (Komarizadehasl *et al.,* 2020a; Komarizadehasl *et al.,* 2020b). For being able to work with these sensors, first briefly, Arduino Uno (which is the central programable logic controller (PLC) in this project) would be introduced. Secondly, three different types of ranging sensors would be introduced along with their specifications. Each type of sensor may use a different way to send its data. Thirdly, different ways of communicating with this PLC will be presented. Finally, the results of these sensors against different situations, objects, and colors would be illustrated (Mobaraki *et al.,* 2020; Mobaraki and Vaghefi, 2016).

doi:10.23967/dbmc.2020.207

2 State of the Art

In this section, the sensors and a microcontroller that has been used in the project will be reviewed along with their technical descriptions.

2.1 Arduino Uno

Arduino (Figure 1) is an open-source electronics platform based on easy-to-use hardware and software. Arduino Uno is a microcontroller board based on the ATmega328P. It has 14 digital input/output pins, six analog inputs to measure and convert the voltage to a digital value. It facilitates numerous interfaces to communicate with other microcontrollers and computers such as Inter-Integrated Circuit (I2C), Serial Peripheral Interface (SPI), and Universal asynchronous receiver/transmitter (UARTA). The board can work on an external power supply via a USB port or a power jack. An integrated development environment (IDE) is available for writing, compiling, and developing the code. This IDE supports a dialect of C/C++ using specific regulation of code organizing (Pasha, 2016).

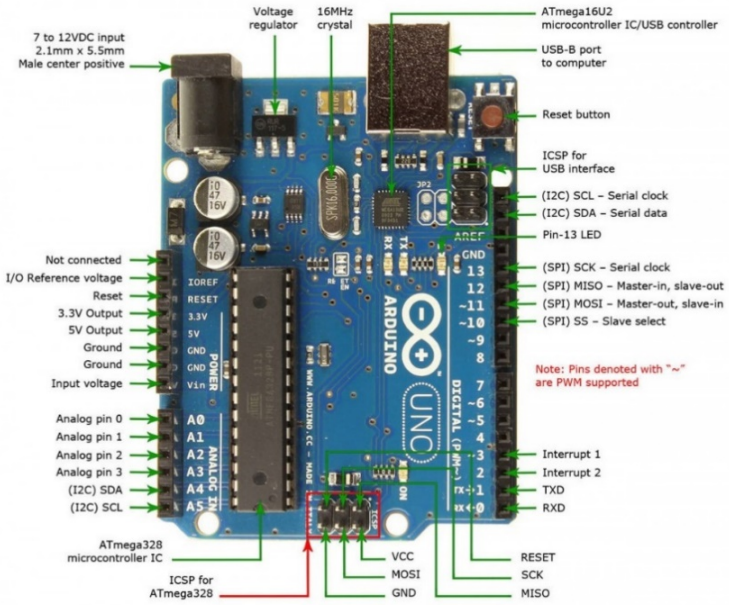

Figure 1. Schematic of the Arduino Uno.

2.2 Ultrasonic Sensors

Ultrasonic ranging module HC - SR04 (Figure 2) provides 2cm - 400cm non-contact measurement function, the ranging accuracy can reach to 3mm. The modules have transmitters, receivers, and processing circuits. The basic concept of work is: firstly, using the I\O trigger for at least 10uS (microsecond) high-level signal. Secondly, The Module automatically sends a frequency of 40 kHz and detects whether there is a pulse signal back. Finally, the range can be calculated through the time interval between sending trigger signals and receiving an echo signal. Test distance = (time × velocity of sound (340M/S)) (Kamal and Hemel, 2019). The technical specification of the use sensor is in Table 1.

Figure 2. Schematic of an Ultrasonic ranging module HC-SR04.

Table 1. Technical specification of the ultrasonic sensor.

Working Voltage	DC 5 V
Working Current	15mA
Working Frequency	20Hz
Max Range	4m
Min Range	2cm
Measuring Angle	15 degree
Trigger Input Signal	10uS TTL pulse
Echo Output Signal	Input TTL lever signal and the range in proportion
Dimension	45*20*15mm

The speed of sound can vary based on temperature and humidity. For calibrating the speed of sound, another kind of sensor had to be used.

2.2.2 Temperature and humidity sensor

As it has been written in section 2.2, for measuring the distance using that sensor, the speed of sound is needed. The sound travels at different speeds in different temperatures and humidity. DHT22 (Figure 3a) has already been calibrated during the production process and provides accurate information (Liu, 2013). The technical specification of the use sensor is in Table 2. Wire connecting illustration is as follows:

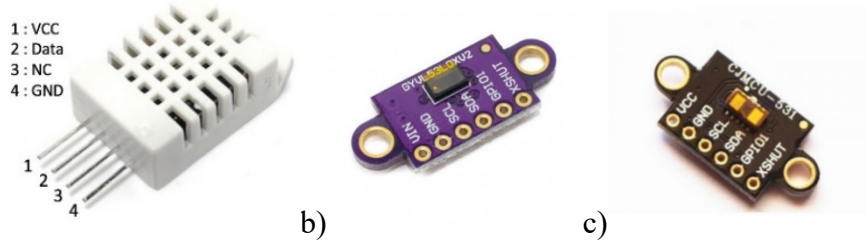

a) b) c)

Figure 3. a)Schematic of a DHT22, digital temperature, and humidity sensor, b) Schematic of a VL53L0X, c) Schematic of a VL53L1X.

Table 2. Technical specification of DHT22.

Working Voltage	3.3-6V DC
Working Current	0.3mA
Sensing element	Polymer capacitor
Operating range	Humidity: 0-100%RH Temperature: 40~80Celsius
Accuracy	Humidity: +-2%RH(Max+5%RH) Temperature: <+0.5Celsius
Resolution or sensitivity	Humidity: 0.1%RH Temperature: 0.1Celsius
Repeatability	Humidity: +-1%RH; Temperature: +-0.2Celsius
Humidity hysteresis	+-0.3%RH
Long-term Stability	+-0.5%RH/year
Sensing period	Average: 2s
Interchangeability	fully interchangeable
Dimensions	14*18*5.5mm

2.3 The VL53L0X

The VL53L0X (Figure 3b) is a new generation Time-of-Flight (ToF) laser-ranging module housed in the smallest package on the market today, providing accurate distance measurement whatever the target reflectance, unlike conventional technologies. The technical specification of the use sensor is in Table 3.

Table 3. Technical specification of VL530L0X.

Working Voltage	2.6-5.5V DC
Working Current	10mA up to 40mA
Working Frequency	50Hz
Output format (I^2C)	16-bit distance reading (in millimeters)
Distance measuring range	Up to 2m with a minimum range of 3cm
Weight without header pins	0.5 g
Dimension	13*18*2mm

It can measure absolute distances up to 2m, setting a new benchmark in ranging performance levels, opening the door to various new applications. The VL53L0X integrates a leading-edge SPAD array (Single Photon Avalanche Diodes) and embeds ST's second generation FlightSenseTM patented technology. The VL53L0X's 940 nm VCSEL emitter (Vertical-Cavity Surface-Emitting Laser), is invisible to the human eye, coupled with internal physical infrared filters, it enables longer ranging distances, higher immunity to ambient light, and better robustness to cover glass optical crosstalk (Adafruit, 2016).

2.4 The VL53L1X

The VL53L1X (Figure 3c) is a state-of-the-art, Time-of-Flight (ToF), laser-ranging sensor, enhancing the ST FlightSense™ product family. It is the fastest miniature ToF sensor on the market with accurate ranging up to 4 m and fast ranging frequency up to 50 Hz Housed in a miniature and reflowable package, it integrates a SPAD receiving array, a 940 nm invisible Class1 laser emitter, physical infrared filters, and optics to achieve the best ranging performance in various ambient lighting conditions with a range of cover window options. Unlike conventional IR sensors, the VL53L1X uses ST's latest generation ToF technology, which allows absolute distance measurement, whatever the target color and reflectance. It is also possible to program the size of the ROI on the receiving array, allowing the sensor FoV to be reduced. The technical specification of the use sensor is in Table 4.

Table 4. Technical specification of VL53L1X.

Working Voltage	2.6-5.5V DC
Working Current	10mA up to 40mA
Working Frequency 1-Short: up to ~130 cm 2-Medium: up to ~300 cm in the dark 3-Long: up to 400 cm in the dark	1-50 Hz max sampling rate (most immune to interference from ambient light) 2- 30 Hz max sampling rate 3- 30 Hz max sampling rate
Output format (I^2C)	16-bit distance reading (in millimeters)
Distance measuring range	Up to 2m with a minimum range of 4cm
Weight without header pins	0.5 g
Dimension	13*18*2mm

2.5 Price

In Table 5, information regarding prices of the introduced sensors has been given, VAT included.

Table 5. Price of used electronic gadgets.

Arduino Uno	10.99€
Ultrasonic Sensor	3.00€
VL53L0X	6.5€
VL53L1X	15.0€
DHT22	6.5€
16 GB SD card + Sd card module	5.56€+2.5€

3 Communication Ways

While many sensors use digital and analog ports for uploading the measured data to the microcontroller, some sensors use the inter-integrated circuit (I2C) protocol. This is a protocol that allows multiple "slave" digital integrated circuits (Sensors) to communicate with one or more "master" chips (Arduino). Like the Serial Peripheral Interface (SPI), which is only intended for short-distance communications within a single device. The ultrasonic sensor and DHT22 have been connected to the Arduino's digital ports. The laser ones had to be connected to I2C port (SCL, SDA) on the board. Since both of these laser sensors had the same board addresses, introducing them to the Arduino raised a problem. For solving this issue, the X shut pin of these two sensors has been used to change their circuit address. The code was written on the Arduino platform and uploaded to the board via a USB cable. For getting the main characteristics of these sensors, a few tests have been carried on. All the different types of ranging circuits have been connected and glued together like Figure 6, so data from all 3 of them would be measured almost the same and simultaneously.

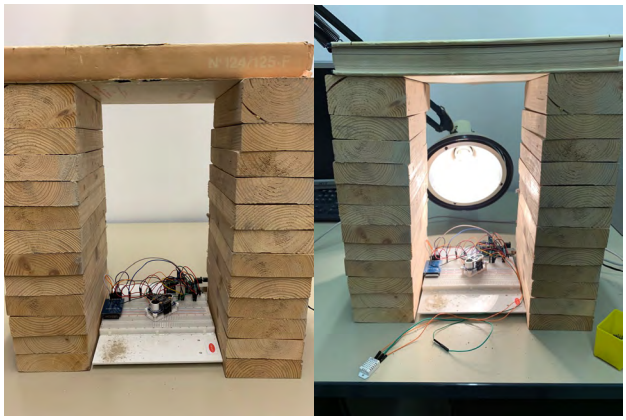

Figure 6. Experiment formation.

4 Experiments

The device was tested against the same measurement against different materials. In Figure 6, 2 tests with and without extreme ambient light have been done for getting the distance from the big book. For the one with the light bulb, the temperature sensor has been moved a bit far from the source of the light and heat. The reason was that the excruciating heat coming from the light bulb would not harm the sensor. The other tested objects were a white paper, a black paper, a clear and transparent plastic cover, and some thin tissues. In Table 6, standard deviations driven from the performed tests have been illustrated.

Table 6. Ranging results of the same experiment under different circumstances.

Tests / Sensors type	a thick book	a white paper	a black paper	a transparent plastic cover	a tissue	Extreme ambient light	Extreme ambient light*
Ultra	0.61	1.87	1	0.7	352	3.23	_
Laser1	2.5	2.67	7.18	5.46	4.66	3607	39.86
Laser2	1.5	1.48	1.87	3.12	1.62	21.94	_

On this table, the last column has been created to provide filtered data from the first laser sensor due to the extreme environmental light and heat test. The filter has deleted the ranging out-puts equal to 8190. When this sensor is not able to read, or the measurement distance is more than its capacity, it declares this number.

It should be mentioned that the ultrasonic sensor, which was the chipset sensor and the easiest one to install, had shown better performances compared to the laser ones. On the downside, this sensor needs 5v interaction digital ports and needs at least 4 volts for its full functionality. The only problem with this sensor could be its data providing speed. Although the laser has a faster rate (50Hz data production), this sensor has a frequency of only 20Hz. In other words, this sensor can provide up to 20 data each second. The biggest problem with the ultrasonic sensors would be their dependence on ambient temperature and humidity, since the speed of sound changes from an environment to another. This sensor needs an accurate speed of sound for its calculations. The proposition of this paper would be using the ultrasonic sensor with a laser sensor if there was the probability of changing temperature or of extreme ambient light. Using the first laser sensor or the second one is due to what range and circumstances the experiment may experience.

5 Conclusion

Notwithstanding that the laser sensors did not have as good results as the ultrasonic one, they can be useful as well. They are smaller, lighter, and faster than the ultrasonic sensors. Moreover, have noise-free technology (no noise can enter from the wires). Moreover, they work independently of the temperature of their testing situation. Best results will only appear if an ultrasonic sensor (attached to its temperature and humidity sensor) be used alongside a Laser sensor. They can cover the downsides of each other and provide an accurate, useful set of data. The selection of Laser type one or two depends on the circumstances of the experiment. If there is enough budget, Laser type 2 provides a way better set of data and is less sensitive to ambient light.

Acknowledgments

The authors are indebted to the Spanish Ministry of Economy and Competitiveness for the funding provided through the research project BIA2017-86811-C2-1-R directed by José Turmo and BIA2017-86811-C2-2-R, directed by Jose Antonio Lozano-Galant. All these projects are funded with FEDER funds. Authors are also indebted to the Secretaria d' Universitats i Recerca de la Generalitat de Catalunya for the funding provided through Agaur (2017 SGR 1482). It is also to be noted that funding for this research has been provided for MR. SEYEDMILAD KOMARIZADEHASL by Agencia Estatal de Investigación del Ministerio de Ciencia Innovación y Universidades grant and the Fondo Social Europeo grant (PRE2018-083238).

ORCID

Seyedmilad Komarizadehasl: https://orcid.org/0000-0002-9010-2611
Behnam Mobaraki: https://orcid.org/0000-0002-2924-643X
Jose Antonio Lozano Galant: http://orcid.org/0000-0003-0741-0566
Jose Turmo: https://orcid.org/0000-0001-5001-2438

References

Adafruit, (2016). Adafruit VL53L0X Time of Flight Micro-LIDAR Distance Sensor Breakout data-sheet.

Kamal, A. and Hemel, S. (2019). Comparison of Linear Displacement Measurements Between A Mems Accelerometer and Hc-Sr04 Low-Cost Ultrasonic Sensor. ieeexplore.ieee.org.

Komarizadehasl, S., Mobaraki, B., Lozano-Galant, J.A. and Turmo, J. (2020)a. Detailed evaluation of low-cost ranging sensors for structural health monitoring applications, in: *International Conference of Recent Trends in Geotechnical and Geo-Environmental Engineering and Education*. "RTCEE/RTGEE 2020, 8–12.

Komarizadehasl, S., Mobaraki, B., Lozano-Galant, J.A. and Turmo, J. (2020)b. Evaluation of low-cost angular measuring sensors, in: *International Conference of Recent Trends in Geotechnical and Geo-Environmental Engineering and Education.* "RTCEE/RTGEE 2020,17–21.

Liu, T. (2013). Digital-output relative humidity & temperature sensor/module DHT22 (DHT22 also named as AM2302) Capacitive-type humidity and temperature module/sensor.

Mobaraki, B., Komarizadehasl, S., Castilla-Pascual, F.J. and Lozano-Galant, J.A. (2020). Determination of Enviromental Parameters Based onArduino Based Low-Cost Sensors, in: *International Conference of Recent Trends in Geotechnical and Geo-Environmental Engineering and Education.* "RTCEE/RTGEE 2020.

Mobaraki, B. and Vaghefi, M. (2016). Effect of the Soil Type on the Dynamic Response of a Tunnel under Surface Detonation. Combust. Explos. Shock Waves 52, 119–127. https://doi.org/10.1134/S0010508216030175

Pasha, S. (2016). Thingspeak Based Sensing and Monitoring System for IoT with Matlab Analysis. Int. J. New Technol. Res. 2, 19–23. https://doi.org/ISSN : 2454-4116

XV International Conference on Durability of Building Materials and Components
DBMC 2020, Barcelona
C. Serrat, J.R. Casas and V. Gibert (Eds)

A Nonparametric Statistical Model for the Selection of Significant Variables Acting in the Deterioration of Built Façades

Carles Serrat[1], Vicenç Gibert[2], Joan R. Casas[3] and Jacek Rapinski[4]

[1] IEMAE-EPSEB, Dept. of Mathematics, Universitat Politècnica de Catalunya-BarcelonaTECH, Av. Dr. Marañón, 44-50, 08028-Barcelona, Spain, carles.serrat@upc.edu
[2] LABEDI-EPSEB, Dept. of Architectural Technology, Universitat Politècnica de Catalunya-BarcelonaTECH, Av. Dr. Marañón, 44-50, 08028-Barcelona, Spain, vicenc.gibert@upc.edu
[3] Dept. of Civil and Environmental Engineering, Universitat Politècnica de Catalunya-BarcelonaTECH, Jordi Girona, 1-3, 08034-Barcelona, Spain, joan.ramon.casas@upc.edu
[4] Institute of Geodesy, University of Warmia and Mazury, Oczapowskiego, 2, 10719-Olsztyn, Poland, jacek.rapinski@uwm.edu.pl

Abstract. *Serrat and Gibert (2011) introduced the use of survival analysis techniques for the study of time-to-failure in the facades of a building stock. Those techniques have been implemented in a predictive system that incorporates the inspection methodology together with the statistical methodology. The system proposes a network of urban laboratories for building research analysis and information with the aim of modelling the degradation time based on the information from all the cities participating in the project, from a multiscale perspective. The approach is population based, that is from the manager of the building stock point of view, in order to obtain information on the evolution of the stock across time, and to help the manager with decision making process on global maintenance strategies. However, for an efficient decision making it is crucial to determine those covariates -like materials, morphology and characteristics of the facade, orientation or environmental conditions- that play a significant role in the progression of different failures along the façade service life. The proposed platform also incorporates an open source GIS plugin that includes survival and test moduli that allow the investigator to model the time until a damage when taking into account the variables collected during the inspection process. The aim of the paper is to introduce the methodology and the modelling strategy for the deteriorating process of an urban front. The contribution will be illustrated with a case study located in the city of L'Hospitalet de Llobregat (Barcelona, Spain) in which more than 14,000 facades have been inspected and analyzed.*

Keywords: *Non-Parametric Modelling, GIS for Building Durability, Inspection Methodologies, Survival Analysis, Collaboratory.*

1 Introduction

In order to design a multiscale predictive platform for the analysis of the deterioration process of the facades in a building stock, we will focus on determining a reliable inspection method that fits to any urban laboratory. The system proposes a network of urban laboratories for building research analysis and information (BRAIN) with the aim of modeling the degradation time based on the information from all the cities participating in the project, from a multiscale perspective.

On the other hand, the methodology must study the morphology of the architectural elements and the states of the damages in the facades, from a general perspective. Basic fundamentals

and definitions on the methodological parts and preliminary works have been previously introduced by Serrat and Gibert (2011) and Gibert *et al*. (2014).

The manuscript is organized as follows. In Section 2 the main predictive and methodological issues will be presented. Section 3 will be devoted to the non-parametric estimation of the statistical model and Section 4 will fully illustrate with a case study the Geographic Information System tool as well as the results and interpretation of the significant variables acting on the deterioration of built facades. The paper ends with a summary and the main conclusions of the conducted research.

2 A Predictive System

In this section we will introduce, in a short manner, the four ingredients of the predictive system that we are proposing. That is a) the collaborative approach in order to join and analyze the information from the nodes in the network of urban labs, b) the inspection methodology to be applied to the urban lab, c) the survival analysis methodology as a statistical technique for the durability and modeling estimation and, d) the GIS platform as a tool for managing the information and the analyses. Details of these components can be found in Gibert (2016).

2.1 A Collaborative Perspective

The research focuses the prospecting campaign of the facades at a multiscale level. Indeed, it concentrates the interest within the concept of the urban laboratory that collects the envelope of the buildings and constitutes the urban front. This approach defines the urban canyon as the U-shape location where the facades are exposed and the time-to-event variables as well as the territorial and environmental covariates occur and determine the facades durability over time. Figure 1 shows the urban laboratory and the urban canyon (Gibert, 2016).

The project is a translatable study to any city in the world in a networking manner. The net has a neuronal analysis center, the Collaboratory, as a coordination unit, able to store and analyze the information from the cells in order to test for similarities and differences accros the participants (cities, *i.e.* urban labs). Right-hand part of the Figure 1 illustrates the network. The main goal is to join efforts into the predictive knowledge of the deterioration of the urban fronts and facilitate the design of common standards as well as protocols of follow-up and intervention strategy.

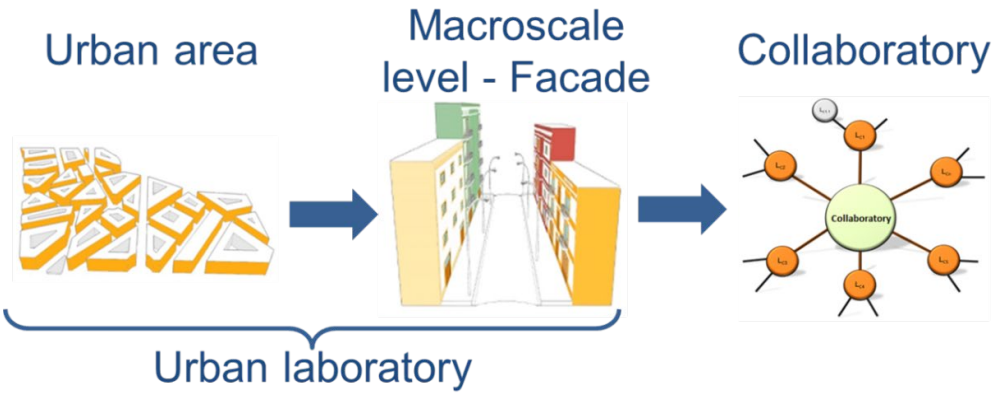

Figure 1. Urban laboratory network and Collaboratory for the BRAIN project.

2.2 Inspection Methodology

The main goal of the monitoring part is the follow-up of the facades in order to detect in which particular moment of the service life of the facade the damages occur and progress. From this perspective Gibert *et al.* (2014) designed the inspection protocol based on a list of requirements in order to apply a population approach and as a result an inspection document was derived. The document consists of two parts. Part a) allows to collect field data, cartographic data, cadastral data as well as plot/building/facade data and architectural characteristics. Part b) is made for collecting the existing elements and materials and the state of damages at the time of inspection.

2.3 Survival Analysis Methodology

Let T be the time from the beginning of the follow-up (time zero) until the failure (the event of interest) happens. T is our random variable of interest. Let $f(t)$ and $F(t)$ be the density and the cumulative distribution function of the random variable T. Based on f and F we can derive statistics of interest like, the quantiles of the distribution. This will allow us to estimate the time until a proportion of damaged buildings in the population or, in the reverse sense, the proportion of damaged buildings at certain time for a particular damage. In the service life setup, time zero will mean the date that the building is built and by failure we will understand the successive grades of gravity, or the successive grades of extent, of the damages. The survival (*i.e.* durability) function for the random variable T is the complement to one of the distribution function F, that is,

$$S(t) = 1 - F(t) = 1 - \mathrm{P}(T \leq t) = \mathrm{P}(T > t) \tag{1}$$

Our sample will be inspected at different inspection times (t_1, t_2, …) and the information on the failures times for the damages that the inspector collects will be interval censored, in the sense that the investigator only can ensure with probability one that the time to failure is in a time interval (l_i, r_i) (Serrat and Gibert, 2011).

In the context of our research on facades durability, since there are no references on the distribution functions that failure times follow, we will estimate the durability function and the hazard function in a non-parametric manner. That is, our estimates will be only based on the data and we will not suppose any hypothetical (and non-testable) distributions family for the unknown density f. We will use the Turnbull's estimator (Turnbull, 1976) based on an iterative algorithm that maximizes the non-parametric likelihood function

$$L = \prod_{i \in O} \big(F(o_i) - F(o_i^-)\big) \prod_{i \in R} \big(1 - F(r_i)\big) \prod_{i \in L} F(l_i) \prod_{i \in I} \big(F(r_i) - F(l_i)\big), \tag{2}$$

where O, R, L and I are the subsets of exact, right-censored, left-censored and interval-censored observations, respectively. From the resulting probabilities, durability and hazard functions can be derived. From the computational point of view, in order to obtain the proper estimates for the survival model, we will use the Turnbull's estimator implemented in the statistical environment R (R Core Team, 2014) in the Icens package (Gentleman and Vandal, 2016) available at Bioconductor website.

2.4 GIS Platform

In order to visualize and analyze, in a territorial and multiscale approach, the available information on the urban canyon, we have implemented a QGIS plugin for the Linux environment (QGIS Development Team, 2016). The application allows the manager the visual follow-up (*i.e.* location and characteristics at a multiscale level) of the ageing process of the urban laboratory. The language used to implement this application has been Python (van Rossum and the Python development team, 2016), open source language, object-oriented, which allows the use of other external programs, such as the case of R used for the statistical analysis. More details on the plugin and its development can be found in (Gibert, 2016).

3 A Modelling Strategy

As a first result the proposed platform allows the investigator to select a subsample of facades of interest, a particular failure in a particular element and to estimate and draw the durability functions for each level of severity and each level of extent, in a marginal way. This output allows to compute the percentiles distribution as well as the cumulative distribution function of the overall subsample. In a similar manner, the plugin offers the possibility of adding one specific covariate value (material, orientation, environmental condition…) and to derive the durability function for this specific value of that covariate. Based on these features it is possible to visually identify which variables could be significantly involved in the deterioration process.

In order to select the significant variables that take part in a non-parametric model for the deteriorating process we will use the extension of the Fleming-Harrington class of tests proposed for interval censored data by Oller and Langohr (2015). These tests allow to compare for equality of distribution functions and to check for ordered survival distributions among the categories of a covariate.

3.1 Proposed Selection Algorithm

The algorithm that we have designed to select, from a set of candidates, the sequence of covariates in the model for a given significance level, α, is:

- STEP 1: Perform an equality test for each one the covariates candidates to explain the failure of interest. Choose, if exists, the covariate that shows the minimum p-value lower than α. In case none of the candidates satisfies the constrain this would mean that none of the covariates would be significative enough to explain the deteriorating process.
- STEP 2: Branch the subsample according the selected covariate and compute the sample size of each one the categories. Explore and validate the possibility of recoding those values. In case of recodification, apply equality tests in order to ensure the significance of the just restratified covariate.
- STEP 3: Repeat steps 1 and 2 for each one of the resulting branches by considering the remaining candidate covariates, until none of them becomes significative.

Figure 2 illustrates, in a global manner, the three steps of the proposed algorithm. The final non-parametric model will identify a significantly different behavior in the aging process among the branches in the resulting classification tree.

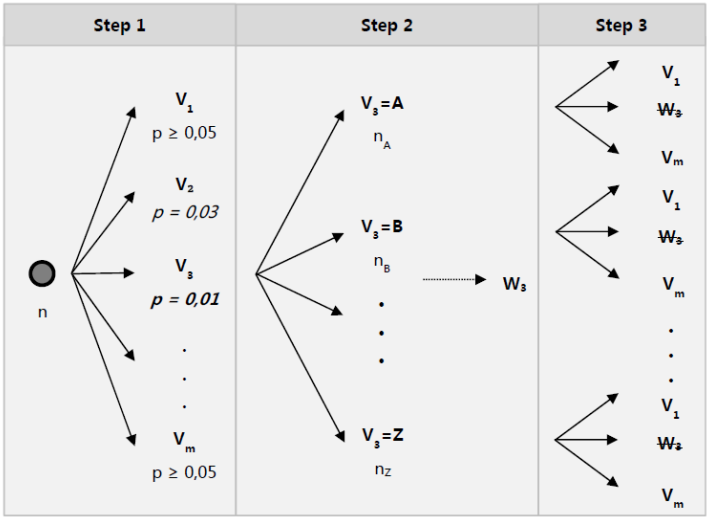

Figure 2. Algorithm for the selection of the covariates of interest from a given set V_1, V_2, … V_m of candidates (for a supposed significance level $\alpha = 0.05$, *i.e.* a 95% of confidence level).

4 A Case Study: L'Hospitalet de Llobregat

The collaborative strategy has been introduced in a variety of countries and cities, as a strategy for building stock management (Serrat and Gibert, 2011). As an illustration of the modelling strategy we will use the analysis of a particular failure in L'Hospitalet de Llobregat (hereafter L'Hospitalet) in the metropolitan area of Barcelona. L'Hospitalet is the city having the second largest population and is among the twenty most populated cities in Spain. The municipality covers an area of 12.5 square kilometers next to Barcelona, and it is divided in 12 neighborhoods.

A first group of 13,193 inspections were done by 2001 across all the city. Later on, by 2016, 1,308 facades have been reinspected. We will focus in the dwelling buildings located in the Centre, Collblanc and Santa Eulàlia neighborhoods as a statistical population of interest. The sample size is 814 and we are talking almost 150,000 square meters of exposed facades. Figure 3 shows the subsample of interest.

After computing the Weighted Severity Index (Gibert, 2016) for all the failures of interest in the selected sample we saw that the most relevant failure is the moisture in the deck railing plasters. The subsample at risk of suffering this failure is made by 512 facades. Figure 4 shows, numerically and graphically, the estimated survival functions for each one of the levels of extent (low, medium and high). We will focus now in obtaining a model non-parametric for the moisture in the deck railing plasters in a low level of extent (*i.e.* the dark green stepwise line in Figure 4).

The covariates that have been considered of interest to be in the model are: V_1: the morphology of the facade, V_2: the construction period, V_3: the material, V_4: the neighborhood and V_5: the orientation. After applying the selection algorithm described in the previous section we obtain the model

$$T \sim V_2 + W_1 + W_4 \tag{3}$$

Figure 3. QGIS map of the subsample of interest in L'Hospitalet de Llobregat (inspected facades in light blue, n = 814).

where V_2 stands for the construction period stratified in two groups (before and after 1960), W_1 describe the morphology of the facade (flat versus no flat) and W_4 indicates if the facade belongs to the Centre neighborhood. In Figure 5 we can see the characteristics of the resulting four groups, named G_1, G_2, G_3 and G_4.

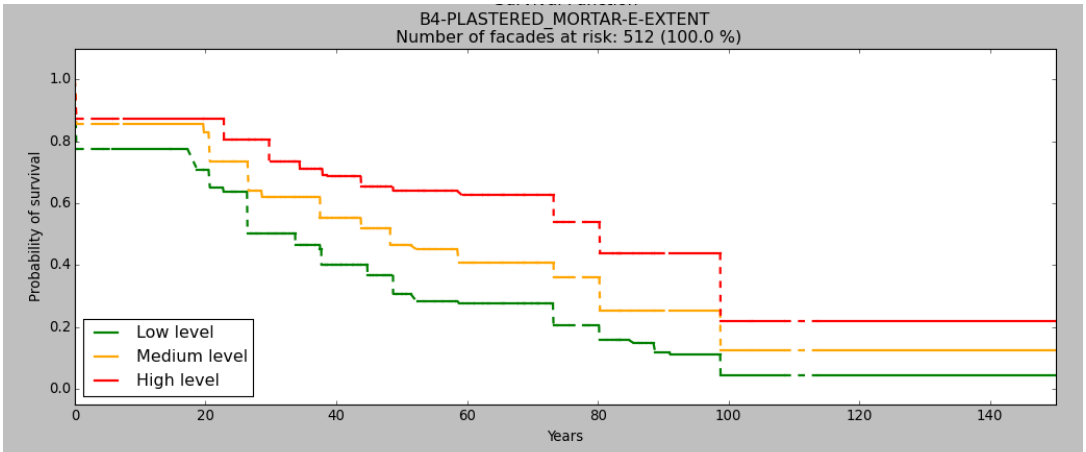

	LC %	IC %	RC %	10%	25%	50%	75%	10.0	25.0	50.0	100.0
Low	56.2	14.6	29.1	0.1	17.8	33.7	73.2	22.4	36.3	69.3	95.7
Medium	43.0	11.5	45.5	0.2	20.6	48.2	98.7	14.5	26.4	53.4	87.4
High	29.7	6.8	63.5	0.2	29.7	80.3	98.8	12.5	19.5	36.0	78.0

Figure 4. Durability functions for moisture in the deck railing plasters, in our subsample of interest in L'Hospitalet de Llobregat (% of censoring –in pink–, quantiles –in blue– and cumulative of failures across time –in green–).

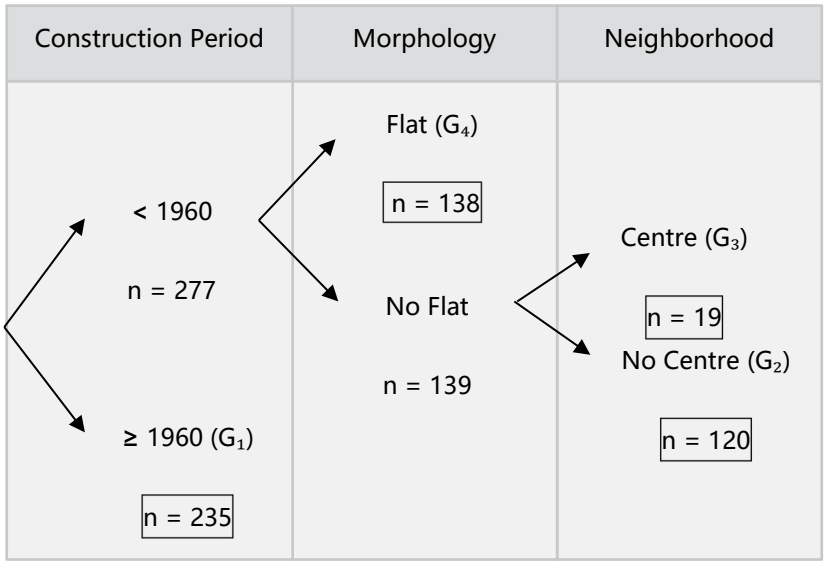

Figure 5. Classification tree for the time until the occurrence of puntual humidities in the plaster of the deck railing in the facades of residential buildings of L'Hospitalet de Llobregat.

By performing pairwise tests we can prove that the durability functions are ordered according to the groups in which the subsample has been split. In fact, the survival distributions follow the sequence

$$S_{G3} > S_{G2} > S_{G4} > S_{G1} \tag{4}$$

as it is shown in Figure 6.

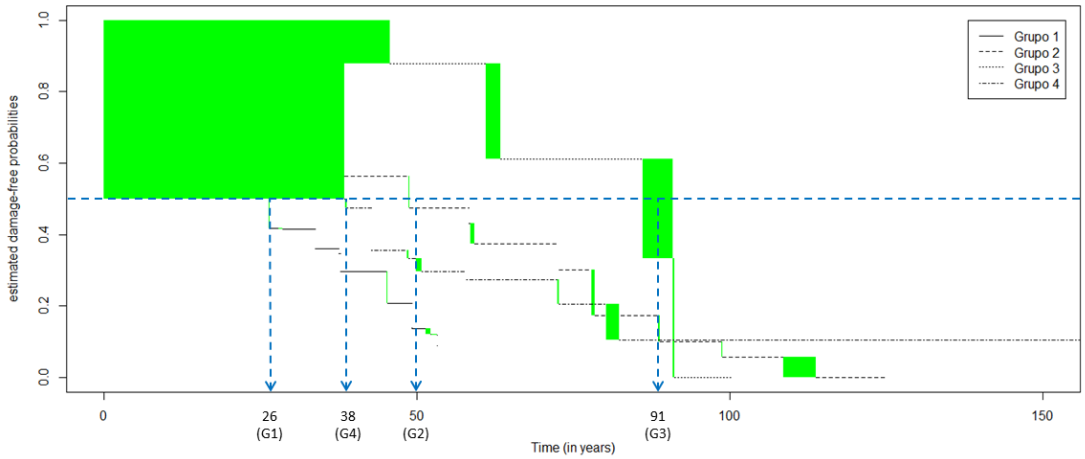

Figure 6. Stratified durability functions for puntual humidities in the plaster of the deck railing according the model defined by the construction period, the morphology and the neighborhood covariates, and estimated median time for each group.

It is interesting to highlight the improvement introduced in the predictive estimation from the proposed model with respect to the marginal estimation in Figure 4. For example, the estimation of the median time to injury is approximately 34 years in the marginal model, whereas, when the model is known, this median is estimated in about 26, 38, 50 and 91 years, for the facades of groups G_1, G_4, G_2 and G_3, respectively.

It can be observed that young facades (the ones in the group G_1) fails before than the others. In contrast, the facades with a better durability (the ones in the group G_3) are the older ones, located in the Centre neighborhood and with a no flat morphology (*i.e.* with other elements in the facade like balconies and tribunes). This fact poses a new and interesting debate on the constructive models and the associated building technology.

5 Conclusions

From a non-parametric approach it is really convenient to model how different covariates can play a significant role in the aging process of the elements of the facades. When data are interval censored this goal is actually more challenging due to the uncertainty in the data. The main benefit of the proposed algorithm is that it allows to build a model in which at every step the most significative covariate is chosen and validated, in a sequential manner. This is a powerful strategy in order to identify priorities and to guide the decision making. Through the case study it has been illustrated the advantages of the proposed modelling strategy overcoming the limitations of not being available a parametric alternative.

Acknowledgements

This research has been partially supported by grants MTM2015-64465-C2-1-R (MINECO / FEDER) from the Ministerio de Economía y Competitividad (Spain) and 2017 SGR 622 from the Departament d'Economia i Coneixement de la Generalitat de Catalunya. Authors are grateful to members of the IEMAE, LABEDI and GRASS-GRBIO groups their valuable comments and suggestions in the development of the work. Special thanks to Laura and Sandra for their implication and efficient collaboration in the project.

ORCID

Carles Serrat: http://orcid.org/0000-0002-1504-5354
Vicenç Gibert: http://orcid.org/0000-0001-6341-5762
Joan Ramon Casas: http://orcid.org/0000-0003-4473-4308
Jacek Rapinski: http://orcid.org/ 0000-0002-8954-7963

References

Gentleman, R. and Vandal, A. (2016). *Icens: NPMLE for Censored and Truncated Data*, R package version 1.44.0.

Gibert, V. (2016). *Sistema predictivo multiescala de la degradación del frente urbano edificado* (in spanish), PhD Thesis, Universitat Politècnica de Catalunya-BarcelonaTECH.

Gibert, V., Serrat, C. and Casas, J.R. (2014). Determination of criteria for the exploration and for obtaining indicators in evolutional analysis of degradation in urban facades. In *Proceeding of the 13th International Conference on Durability of Building Materials and Components*, Sao Paulo, Brasil, 656–663.

Oller, R. and Langohr, K. (2015). *FHtest: Tests for Right and Interval-Censored Survival Data Based on the Fleming-Harrington Class*, R package version 1.3.

QGIS Development Team (2016). *QGIS Geographic Information System*. Open Source Geospatial Foundation Project URL. http://www.qgis.org/

R Core Team (2014). *R: A language and environment for statistical computing*. R Foundation for Statistical Computing, Vienna, Austria, URL http://www.R-project.org/

Serrat, C. and Gibert, V. (2011). Survival analysis methodology for service live prediction and building maintenance. In *Proceeding of the 12th International Conference on Durability of Building Materials and Components*, vol. II, Porto, Portugal, 599–606.

Turnbull, B.W. (1976). The empirical distribution function with arbitrarily grouped, censored and truncated data. *Journal of the Royal Statistical Society, Series B, 38,* 290–295.

van Rossum, G. and the Python development team (2016). *The Python Language Reference*, release 2.7.12. URL: https://docs.python.org/2.7/

XV International Conference on Durability of Building Materials and Components
DBMC 2020, Barcelona
C. Serrat, J.R. Casas and V. Gibert (Eds)

Degradation of Concrete Structures from the Climate Change Perspective

Pablo Benítez[1,2], Fernanda Rodrigues[2], Sudip Talukdar[3] and Sergio Gavilán[4]

[1] *FIUNI*, Facultad de Ingeniería, Universidad Nacional de Itapúa, Encarnación, 6000, Paraguay, pablo.benitez@fiuni.edu.py

[2] *RISCO*, Department of Civil Engineering, University of Aveiro, Aveiro, 3810-193, Portugal, mfrodrigues@ua.pt

[3] Department of Civil Engineering, British Columbia Institute of Technology, Burnaby, BC 3700, Canada, stalukdar1@bcit.ca

[4] *FIUNA*, Faculty of Engineering, National University of Asuncion, San Lorenzo, 2160, Paraguay, ingsergiogavilan@gmail.com

Abstract. *The negative effects of climate change are underway despite the global efforts to mitigate them and the future scenario are unsettling. Climate change poses critical challenges to urban environments and highlights the need for research its impacts on the built environment. One of the most significant effects of climate change on reinforced concrete structures is associated with the carbonation of these structures. The increase of parameters such as temperature and carbon dioxide jeopardise the degradation of such structures by carbonation-induced corrosion. This paper presents the results of the monitoring and analysis of a set of buildings that determine carbonation as the main degradation mechanism of structures in Paraguay. Through the application of a previously developed carbonation model, the worsening of the carbonation-induced degradation has been determined after considering the climate change effects in the coming 50 years. The outcomes of the study determined that the poor quality of the structures in Paraguay cause premature degradation in them. Furthermore, considering climate change effects, it has been determined that this phenomenon could accelerate corrosion failure times in reinforced concrete structures.*

Keywords: *Carbonation, Climate Change, Real Carbonation Data, Reinforcement Corrosion.*

1 Introduction

Nowadays, ensuring that structures can withstand the environmental factors that determine their degradation has become a big challenge for engineers, who often are subject to a limited budget when are designing their projects. The study of the degradation of structures caused by environmental phenomena did not reach a significant interest until a few decades ago when climate change became tangible as a critical problem that affects the daily integrity of human beings. Furthermore, such as the buildings built in earlier times (*e.g.*, bridges, cathedrals, castles, and so on), it is now possible to classify several of the 20th-century concrete structures as modern heritage, whose maintenance has cultural and historical value for each country.

Rehabilitation, maintenance and repair of buildings play an important role in ensuring its performance in the long term, so they have a significant impact on the adaptation of buildings to climate change. Recent studies have shown widespread concern regarding the regulations in the construction industry in relation to durability, which are based on historical climate data. Therefore, a comprehensive study of the climate change impacts on the degradation of the structure is necessary (de Wilde and Coley, 2012). Perhaps one of the most meaningful

conclusions of the Intergovernmental Panel on Climate Change (IPCC) in its fifth assessment report was that the climate change effect comprises a problem that cannot be removed immediately. That is, the concentrations of greenhouse gases in the world are so high that their reduction or stabilization could not be possible for several centuries (IPCC, 2013).

Although civil engineering historically has covered its knowledge based on physical and mechanical stresses to establish the durability conditions of a structure, the effect of climate change has forced to expand knowledge in a deeper way towards the environmental and chemical stresses that influence directly on the integrity of infrastructures worldwide. Therefore, a neglected area is the impact of climate change on RC structures, where it is necessary to adapt future designs to ensure that infrastructures have adequate capacity and have sufficient durability to deal with the consequences of climate change (Talukdar, 2013).

Under this context, the degradation of reinforced concrete (RC) structures could be significant considering carbonation-induced corrosion. Carbonation is a natural phenomenon produced by the chemical reaction between cement hydroxides and the atmospheric carbon dioxide (CO_2) (Broomfield, 2007). This degradation mechanism is directly influenced by three climatic parameters that are associated to the effects of climate change: CO_2 concentration, temperature and relative humidity. Therefore, the study of the carbonation phenomenon as a degradation mechanism of concrete structures has been a spotlight of engineers since the emergence of climate change.

2 Carbonation in RC Structures

Regarding carbonation-induced degradation, the interpretation of reinforcement corrosion requires a quantitative understanding of the environment, physical deterioration process, transport mechanism through the concrete, cracking process and the corrosion phenomenon (Taffese and Sistonen, 2013). Corrosion in the reinforcement causes cracking of the surface of the structure and subsequent the spalling of the cover due to the expansion of the corroded rebar. Then, the corrosion rate directly affects the extension of the service life of the RC structures (Ahmad, 2003).

2.1 Effects of Climate Change on Concrete Degradation

Several studies agree that climate change will cause new considerations and establish new conditions for the construction industry. Due to climate change, the risks of damage induced by carbonation in concrete can increase by more than 16% by the year 2100, which means that one in six structures will suffer additional and costly corrosion damage due to this phenomenon. It has also been found that, as a consequence of climate change, the corrosion rate could increase by 15% if the temperature increases by 2 °C (Stewart *et al.,* 2011, 2012).

Research developed for concrete infrastructures in China has determined, taking into account the same climatic parameters mentioned above, that the depth of carbonation could increase by 45% in reinforced concrete structures by the year 2100 (Peng and Stewart, 2016). On the other hand, Stewart *et al*. concluded that in some regions of Australia, the risks of damage induced by carbonation can increase even by more than 400% by the year 2100 (Stewart *et al.,* 2011). Later, other studies showed that global warming could advance the time of failure by 31% or decrease the service life up to 15 years for moderate levels of aggressiveness (Bastidas-Arteaga *et al*., 2013).

The long life of the buildings is perhaps the most palpable problem since most of the buildings built now must continue in service within the next 50-100 years. However, the most efficient way for adaptation is taken the proper actions before these buildings are built, i.e. during the design stage. Therefore, it is crucial to develop policies and strategies that reduce long-term risks for new buildings, encourage early adaptation where possible to existing buildings and, at least, adopt a precautionary approach to the uncertain risks of climate change (Camilleri *et al.,* 2001).

2.2 Carbonation-Induced Degradation in Paraguay

Carbonation is one of the most frequent phenomenon that leads to degradation problems in structures located in Paraguay. The index of relative humidity and the tropical temperature makes a propitious place for the carbonation to propagate in the structures and jeopardise its durability due to the reinforcement corrosion. In this paper, a database with 327 carbonation depth measurements in different structures of Paraguay has been analyzed in order to know the real carbonation rate in RC structures. The construction industry in Paraguay has had significant growth in the last decade. However, the first infrastructures built in the country lacked adequate control, whereby currently a poor quality in buildings is evidenced that compromises its durability.

The carbonation data of the case study corresponds to buildings located in urban area. Considering that the study was conducted in existing buildings, the carbonation depth was measured by applying the phenolphthalein test. Three measurements were taken for each structural element and the average of these values was computed. The year of construction of these structures was between 1986 and 1997, although some of them were built in the current century. On the other hand, the interventions were made between 2013 and 2019. As for their constructive characteristics, these buildings are constructed with Ordinary Portland Cement. It should be noted that in several cases, the concrete structure was completely exposed. These cases correspond to unfinished buildings, a very common case in the country when construction projects do not end (usually due to budget problems) and remain exposed to weathering in some cases for more than ten years even.

Through a statistical analysis of the real carbonation data, the mean value and the standard deviation for the cover thickness and the carbonation depth are shown in Table 1. These results suggest that can be expected a carbonation depth that has almost the same thickness than the cover. This result is quite important since the probability of corrosion onset is too high considering the loss of alkalinity of concrete due to carbonation. On the other hand, the results shown in Table 1 have been classified according to the structural elements of the building. After this classification, it has been seen that the slabs were the most compromised elements from the point of view of the corrosion initiation by carbonation. This is deduced since the mean cover thickness (12.30 mm) was practically equal to the mean of the carbonation depth (12.15 mm) in the structures.

Considering the carbonation tests results, an analysis was performed in order to determine the carbonation-induced corrosion risk. It was possible to classify three conditions of degradation for the analysed structures: with corrosion risk, without corrosion risk, and the condition of imminent corrosion initiation. For this purpose, a structure without corrosion risk has been considered when the cover of the structure is not yet carbonated or, at least, the

carbonation front is not in a critical zone that may induce corrosion. This consideration is specifically referred to that an immediate carbonation-induced corrosion is not expected. However, as has been studied in the literature, corrosion could be induced by other mechanisms and this study has focused only on carbonation.

Table 1. Results for carbonation depth and concrete cover of the case study.

Variable	Main Value	Standard Deviation
Carbonation Depth (mm)	18.0	7.13
Cover Thickness (mm)	18.1	8.32

Furthermore, the condition referring to structures with corrosion risk includes those where the carbonation front had exceeded the cover thickness. This implies that the reinforcement is wholly embedded in a carbonated concrete, leaving it vulnerable to corrosion due to the suppression of the passive protection layer. The last condition referred to imminent initiation of corrosion considers what has been established in Yoon *et al*. (2007), in which the corrosion begins when the carbonation front is located at least within 5 mm of the rebar surface, being necessary an immediate intervention.

Then, this analysis has shown that almost half of the cases analysed (49.91%) present a considerable corrosion risk or imminent corrosion initiation caused by carbonation. That means the carbonated thickness in the concrete is higher than the cover thickness, and that the durability of the structure is in a critical condition. Thereby, it can be said that almost 50% of the buildings analysed in the urban area of Asunción, whose were built no more than 30 years ago, can be considered as structures at the beginning of the last stage (corrosion propagation) of its corrosion degradation. Such degradation conditions correspond to the time in which the interventions were carried out in the structures of the case study. Hence, the structures without corrosion risk could also be considered under carbonation-induced corrosion risk in the next years if appropriate maintenance actions are not performed. Over the 327 real carbonation data, the result of the analysis is depicted in Figure 1.

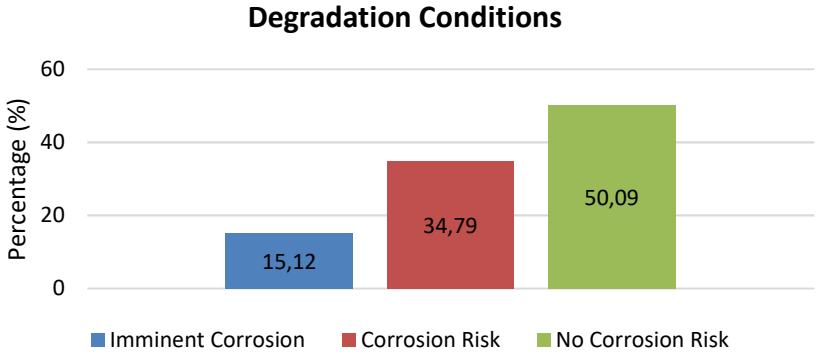

Figure 1. Degradations conditions considering inspection results.

In essence, through the case study shown in this section, it was possible to illustrate that carbonation is a common problem in the concrete structures of Paraguay. The lack of control

during the execution of the works often triggers in structures without the adequate conditions that guarantee their durability. Therefore, according to the study developed in this section, the cover thickness is referred to as the most influential parameter to reduce the time to corrosion initiation. In this way, a rigorous control is recommended during the elaboration of these structures that guarantee, not only the adequate thickness but a good cover quality through a low porosity.

3 Carbonation Modelling

Recently, many degradation models have sought to link the phenomenon of climate change and its influence on degradation parameters, which represents a significant advance. On the other hand, the estimation of the service life of structures under the influence of cracking or the system of loads to which a real structure is subjected is still insufficiently studied due to its complexity. The numerical degradation model applied in this paper to estimate the carbonation depth in structures due to the climate change effect was the model developed in (Talukdar *et al*., 2012). This model was considered suitable to represent the estimated carbonation-induced degradation over time since it is formulated as a function of a climatic scenario and concrete properties. This feature allows the model to predict the degradation of concrete structures under consideration of climate change, which is directly related to the context of this research.

The carbonation model applied in this research is a deterministic one-dimensional numerical diffusion model for a gaseous medium through a porous substrate based on Fick's Second Law. The model has been validated based on experimental results obtained in an accelerated carbonation chamber. Then, the model develops an extensive analysis of the carbonation phenomenon considering parameters such as porosity, relative humidity, temperature, diffusion and concentration of gases. Therefore, as it is considered parameters such as relative humidity, temperature and carbon dioxide concentration into the numerical model, the climate change effects can be included within the carbonation model. In this way, the model allows to determine the concentration of CO_2 and $Ca(OH)_2$ within the concrete as a function of time by applying the following equations:

$$\frac{\delta}{\delta t}\left[CO_{2(aq)}\right] = D\frac{\delta^2}{\delta x^2}\left[CO_{2(g)}\right]HRT - k\left[CO_{2(aq)}\right]\left[Ca(OH)_{2(aq)}\right] \quad (1)$$

$$\frac{\delta}{\delta t}\left[Ca(OH)_{2(aq)}\right] = D\frac{\delta^2}{\delta x^2}\left[Ca(OH)_{2(aq)}\right] - k\left[CO_{2(aq)}\right]\left[Ca(OH)_{2(aq)}\right] \quad (2)$$

Where $CO_{2(aq)}$ and $Ca(OH)_{2(aq)}$ are the aqueous concentration of CO_2 and $Ca(OH)_2$ respectively(mol/m^3), D is the effective diffusivity of the carbon dioxide into the concrete (m^2/s), *HR* is the relative humidity (%), *T* is the temperature (K), *k* is the reaction rate constant (m^3/mol/s), $CO_{2(g)}$ is the atmospheric concentration of carbon dioxide (mol/m^3). Therefore, by solving Equations (1) and (2) simultaneously, it is possible to obtain the concentrations of both solutions involved in the carbonation reaction using the "*Method of Lines*" proposed by Cutlip and Shacham (Cutlip and Shacham, 2007). Further details of the mathematical derivation of the model and the values of the parameters in both equations can be found on (Talukdar *et al*., 2012).

Equations (1) and (2) model the corrosion initiation stage. For the corrosion propagation stage, the model employs an analytical thick-walled uniform cylinder which assumes that the generation of a volume of corrosion products (rust) around the corroding steel causes an expansion in the diameter of the steel. Within the formulation of this stage of corrosion degradation, the model considers parameters such as the activation energy and the reference current flow density which are not generally taken as constants by other models. These parameters may depend on the interaction between the concrete resistivity, the saturation level and the cover thickness.

3.1 Carbonation Simulation Results

The carbonation model provides a valuable perspective on how the carbonation front advances over time through concrete structures under the influence of climate change. After running the carbonation model in MATLAB, the results are shown in Table 2 regarding the ultimate carbonation depth (UCD) for two typical RC structures of Paraguay (20 and 25 MPa) considering two different climatic scenarios of the IPCC (RCP 4.5 and RCP 8.5). The UCD represents the maximum depth reached by the carbonation front during the simulations.

Furthermore, a control scenario is considered to be able to monitor the expected increase in the carbonation depth caused by the climate change effect. This control scenario is a scenario where the relative humidity and the mean annual temperature were held to the current values for Paraguay as 75.1% and 23.7 °C, respectively. On the other hand, it is also possible to determine through the degradation model what are the times of corrosion initiation caused by carbonation, as well as the corrosion propagation time.

Table 2. Carbonation modelling - Simulation results.

Climatic Scenario	Corrosion Initiation (years)	Propagation Time (years)	Ultimate Carbonation Depth (mm)
Strength: 20 MPa – Cover thickness: 25 mm			
Control	20.15	2.32	35
RCP 4.5	19.27	2.95	35.6
RCP 8.5	18.24	2.88	40
Strength: 25 MPa – Cover thickness: 25 mm			
Control	26.65	2.66	30
RCP 4.5	23.69	2.69	30.8
RCP 8.5	22.57	2.76	35

After the application of the carbonation model, some conclusions can be drawn regarding the corrosion risk by carbonation in the concrete structures of Paraguay. Concrete structures would reach an UCD between 30 and 40 mm corresponding to a service life of 50 years, depending on the concrete quality and the climatic scenario predicted. Herein, the ultimate carbonation depth is considered as the maximum depth of carbonation front reached in the simulation and this parameter is subjected to the boundary conditions of the model. Moreover, it can be said that the RC structures in Paraguay would be under considerable corrosion risk considering the forecasting climate changes. Moreover, simulations have not shown alteration

regarding the UCD between the control scenario and the best scenario. The difference was concerning the time, where the UCD is reached in the best climate scenario between 12% and 20% earlier than in the control scenario. On the other hand, the carbonation depth could increase between 14% and 16% for the worst-case scenario.

On the other hand, it has been found that the higher the strength of the structure, the greater the carbonation resistance, which is reflected in the corrosion initiation times. The main reason for this behaviour is the porosity of the material. The concrete strength is directly related to the porosity of the material so that the diffusion of gases within the concrete is limited in the materials of greater resistance.The numerical model applied in this paper considers that before the expansive pressure of the oxide is generated, it is necessary that the porous zone of the concrete/steel interface be wholly filled with the corrosion products (rust). This porous zone has been initially considered in the numerical model with a value of 10 μm. However, many other studies consider different values for this parameter ranging from 50 μm to 100 μm (Siemes *et al*., 1985; Broomfield, 2007). If the porous zone is increased by 50%, the corrosion propagation time can be increased between 10 and 60%. Therefore, the limit pf rust generation to fill this zone is quite influential in the simulation results obtained. That is, the concrete quality will always be a critical factor regarding the durability of RC structures.

4 Conclusions

Although there are several investigations related to the corrosion of concrete reinforcements in countries such as China, the United States, Australia and European countries, at the Latin American level it was possible to confirm a lack of available research that can describe the same problems under the specific circumstances of the region. In the specific case of Paraguay, as it is a developing country, the accessibility to information and the low number of it does not allow to describe the state of degradation of the infrastructures scientifically.

It was found that quality control during the construction process is of utmost importance to ensure a minimum concrete cover, which is one of the most critical factors on the initiation of corrosion time. Furthermore, structures and infrastructures in Paraguay are not appropriately designed and executed according to the consideration of environmental effects. Regarding the degradation prediction models, one of the most significant handicaps is the difficulty in adopting the parameters in a precise and quantifiable way. It is true that these numerical models seek to describe, in an increasingly precise way, the natural behaviour of the degradation processes of structures. However, it is still necessary to carry out a lot of research in this area to achieve this objective entirely.

Concerning the carbonation model results for the structures of Paraguay, can be expected early degradation in the next years due to climate change effects. Thus, for the worst climate scenario, in the second half of this century is expected an average increase by 16 %, in the maximum carbonation depth regarding a control scenario for RC structures of 20 and 25 MPa. Meanwhile, the time to reach the same maximum carbonation depth of the control scenario can be reduced even in 8 years for the best climate scenario, depending on the quality of the concrete. After a sensitivity analysis through the carbonation model, it was found that the reduction of the concrete cover to a value of 10 mm provides a significant acceleration in the corrosion initiation time. Therefore, not only the concrete strength has to be monitored, but also the concrete cover. Perhaps one of the most concerning conclusions is given by the fact that the

carbon dioxide accumulated in the earth's atmosphere cannot be reduced to acceptable levels until within a few centuries, even considering that greenhouse gas emissions were entirely and immediately reduced. Then, this situation suggests that the best strategy to deal with this problem involves adaptation measures rather than mitigation measures. From the engineering and constructions approach, this strategy must be proposed dynamically considering the accelerated change in the expected climate according to the IPCC scenarios.

Acknowledgments: This wok was funded by Project PTDC/ECI-EST/28439/2017 - POCI-01-0145-FEDER-028439 - funded by European Regional Development Fund (ERDF) through COMPETE2020 and with financial support from FCT/MCTES through national funds (PIDDAC).

ORCID

Pablo Benítez: https://orcid.org/0000-0002-3607-0559
Fernanda Rodrigues: https://orcid.org/0000-0001-9127-7766

References

Ahmad, S. (2003). Reinforcement Corrosion in Concrete Structures , Its Monitoring and Service Life Prediction – – a Review. *Cement and Concrete Composites 25:459–71.* doi: 10.1016/S0958-9465(02)00086-0

Bastidas-Arteaga, E., F. Schoefs, M. Stewart and X. Wang. (2013). Influence of Global Warming on Durability of Corroding RC Structures: A Probabilistic Approach. *Engineering Structures 51:259–66.* doi: 10.1016/j.engstruct.2013.01.006

Broomfield, J. (2007). *Corrosion of Steel in Concrete. Understanding, Investigation and Repair* - 2nd Edition. Taylor & F. New York, USA.

Camilleri, M., R. Jaques and N. Isaacs. (2001). Impacts of Climate Change on Building Performance in New Zealand. *Building Research and Information 29(6):440–50.* doi: 10.1080/09613210110083636

Cutlip, M. and M. Shacham. (2007). *Problem Solving in Chemical and Biochemical Engineering with Polymath, Excel, and Matlab*. Second Edition. U.S.: Prentice Hall.

de Wilde, P. and Coley, D. (2012). The implications of a changing climate for buildings. *Building and Environment*, *55*, 1–7. doi: 10.1016/j.buildenv.2012.03.014

IPCC. (2013). Summary for policymakers, in: I.P.C.C. Stocker, T.F.,D. Qin, G.-K. Plattner, M. Tignor, S.K. Allen, J. Boschung, A. Nauels, Y. Xia VB (Eds.), *Climate Change 2013: the Physical Science Basis.* Contribution of Working Group I to the Fifth Assessment Report of the Intergovernmental Panel on Climate Change. [Internet], United Kingdom and New York. Available from: http://www.climatechange2013.org/

Peng, L. and M. Stewart. (2016). Climate Change and Corrosion Damage Risks for Reinforced Concrete Infrastructure in China. *Structure and Infrastructure Engineering 12(4):499–516.* doi: 10.1080/15732479.2013.858270

Siemes, A., A. Vrouwenvelder and A. van den Beukel. (1985). Durability of Buildings - A Reliability Analysis. *Heron*, *30(3):3–48.*

Stewart, M., X. Wang and M. Nguyen. (2011). Climate Change Impact and Risks of Concrete Infrastructure Deterioration. *Engineering Structures 33:1326–37.* doi: 10.1016/j.engstruct.2011.01.010

Stewart, M., X. Wang and M. Nguyen. (2012). Climate Change Adaptation for Corrosion Control of Concrete Infrastructure. *Structural Safety 35:29–39.* doi: 10.1016/j.strusafe.2011.10.002

Taffese, W. and E. Sistonen. (2013). Service Life Prediction of Repaired Structures Using Concrete Recasting Method: State-of-the-Art. *Procedia Engineering, 57:1138–44*. doi: 10.1016/j.proeng.2013.04.143

Talukdar, S. (2013). *The Effects of Global Climate Change on Carbonation Induced Corrosion of Reinforced Concrete Structures*. PhD Thesis, University of British Columbia. Vancouver, Canada.

Talukdar, S., N. Banthia and J. Grace. (2012). Carbonation in Concrete Infrastructure in the Context of Global Climate Change – Part 1 : Experimental Results and Model Development. *Cement & Concrete Composites 34:924–30.* doi: 10.1016/j.cemconcomp.2012.04.011

Yoon, I., O. Çopuroğlu and K. Park. (2007). Effect of Global Climatic Change on Carbonation Progress of Concrete. *Atmospheric Environment 41:7274–85.* doi: 10.1016/j.atmosenv.2007.05.028

XV International Conference on Durability of Building Materials and Components
DBMC 2020, Barcelona
C. Serrat, J.R. Casas and V. Gibert (Eds)

Relationships between Outside and Interior Appearance Inspection and Actual Bio-Deterioration of Structural Members in Existing Wood Houses

Takahiro Tsuchimoto[1], Satoshi Takahashi[2], Hideaki Sumikura[3] and Takafumi Nakagawa[4]

[1] Dept. of Building Materials and Components, Building Research Institute (BRI), Tachihara 1, Tsukuba, Ibaraki 305-0802, Japan, tutti@kenken.go.jp

[2] Dept. of Production Engineering, Building Research Institute (BRI), Tachihara 1, Tsukuba, Ibaraki 305-0802, Japan, s-taka@kenken.go.jp

[3] Dept. of Architecture, Hiroshima University, 1-4-1 Kagamiyama, Higashi-Hiroshima City, Hiroshima 739-8527, Japan, sumikura@hiroshima-u.ac.jp

[4] Research Institute for Sustainable Humanosphere, Kyoto University, Gokasho, Uji, Kyoto 611-0011, Japan, nakagawa@rish.kyoto-u.ac.jp

Abstract. *The inspection of the used house which is necessary to be evaluated is carried out without removal of the interior or exterior finishing materials. However, where the interior or exterior appearance was degraded, there was not always a bio-deterioration of the wooden structural member in the existing wood houses. Therefore, the interior or exterior appearance of the 103 used wood houses were inspected and the bio-deterioration of all wooden structural members were investigated after removal of the finishing materials. Then, the relationships between the appearance degradation and the actual bio-deterioration of the wooden structural members in the used wood houses were studied. The results were summarized as follows:*

1) *The bio-deterioration of the wooden structural members were found much on 1st story rather than 2nd story, in the elder building age, in case of short eaves and in case of low foundation. The issues known experience empirically were verified numerically.*
2) *The tendency of the appearance degradation occurrence were the same as the tendency of the bio-deterioration partially, but didn't match it entirely.*
3) *About 90 % of the portions whose interior or exterior appearance were degraded didn't have the bio-deterioration of the wooden structural member.*
4) *The ratio of the portion with the bio-deterioration of the wooden structural member without appearance degradation were only 1.6 %.*

Keywords: *Appearance Inspection, Degradation, Bio-Deterioration, Used Wood House.*

1 Introduction

It is not uncommon in Japan for wood houses to be scrapped after a family has finished using it and for a new house to be rebuilt for a new family. This makes the market for the used houses inactive and disturbs the growth of the sustainable society. Revitalizing the market for the used houses is one of the most important social issue in Japan (MLIT, 2015). One of the main factors disturbing the distribution of used wood houses is the difficulty in grasping whether structural components are decayed or damaged by termites (Cho *et al.*, 2013). Therefore, a visual inspection of the current state of more than 100 wooden houses was carried out, and after all the finishing materials and interior / exterior materials were removed, a biological deterioration survey of all structural members was carried out. Then, we analyzed the relationship between

appearance defects and biological deterioration of structural members.

2 Appearance Inspection and Bio-Deterioration Survey Methods

2.1 Attribution of Inspected and Surveyed Houses

Houses to be demolished for removing or renovated houses were selected (Tsuchimoto *et al.*, 2016). This was a necessary condition for exposing all structural members and surveying the state of bio-deterioration. Since the durability can be affected by the building age, the construction methods, and the site condition, we made an effort so that the attribution of the inspected and surveyed houses didn't have any bias. Most of the construction method of the inspected and surveyed houses were Japanese conventional post and beam construction. The wood frame construction and the prefabricated wood construction were only 4 and 2 houses, respectively. It was difficult to find the relatively new house for inspection and survey. The building age distribution of the inspected and surveyed houses are shown in Table 1. The minimum and maximum building ages were 14 and 63, respectively. As for the story of the houses, most were 2-story houses, excluding ten 1-story houses and a 3-story house. The distribution of the building locations of the inspected and surveyed houses are shown in Table 2. As mentioned above, though the houses needed to be chosen without bias, the houses built at the standard region were most and occupied about 73 %. Because most of the houses in Japan were built in the standard region including Tokyo and Osaka.

Table 1. Building age distribution of the inspected and surveyed houses.

Building age	20 years or less	21-30 years	31-40 years	41-50 years	51-60 years	61 years or more	Un-known	Total
Number of houses	4	26	36	25	7	1	4	103

Table 2. Building locations distribution of the inspected and surveyed houses.

Region	Cold region			Standard region		Hot and humid region		Total
Zone No.	1 & 2	3	4	5	6	7	8	
Example of place	Hokkaido	North Tohoku	South Tohoku	Cool area*	Warm area*	South Kyushu	Okinawa	
Number of houses	0	5	11	18	57	12	0	103

*: The cool area and the warm area respectively indicate the relatively cool and warm district of North Kyushu, Shikoku and the main island of Japan excluding Tohoku.

2.2 Method of Appearance Inspection

As the appearance inspection, the interior and exterior materials and the finishing material of the house, for example, shown in Photo 1(a) were observed (Photo 1(b)), and their degradation such as rain leak marks, cracks, discoloration and so on were grasped. The location and degree of these deteriorations were visually measured with reference to "Durability design and maintenance / deterioration diagnosis of wood houses" (2002) issued by the Japan Housing and

Wood Technology Center.

2.3 Method of Bio-Deterioration Survey of All Structural Members

The bio-deterioration survey were conducted to all structural members after the removal of all sheathings and finishing materials (Photo 1(c)). The visual and tactile inspection were conducted to survey all structural members for bio-deterioration. The bio-deterioration includes the decay and the termite damage. The position and degree of the deterioration were grasped and recorded with reference to the above-mentioned manual issued by HOWTEC.

Photo 1. Overview of (a) inspected house, (b) appearance inspection and (c) bio-deterioration survey.

3 Database of Inspection and Survey Results

3.1 Objective

Although there are several factors that disturb the market distribution of the used wood houses, it is not too much to say that the largest factor among them is that they include degraded parts, or that the range and the degree of deterioration are unknown. Many studies of the degradation of old wood houses have revealed whether the house contains degraded components and the tendency for degradation to exist. But even if you know these things, the buyers cannot decide whether the used wood house needs to be repaired or whether they can live as it is, if they can endure. Therefore, it is necessary to evaluate not only whether or not the degradation has occurred but also in what range and how serious the bio-deterioration is.

Then, the inspected and surveyed houses were divided into square segments of approximately 900 mm, each linked to the results of appearance inspections and to the results of bio-deterioration survey of all structural members, including the degree of decay or termite damage. Each segment is not necessarily independent, but the number of segments indicates the range of degradation. In other words, minor deterioration is one segment, but widespread degradation is two or more segments. And, the relationship between the appearance defect and the bio-deterioration of the structural member was analyzed.

3.2 Compilation Method into Database

At first, the investigated houses were divided into roofs, walls, and floors of the 1st and 2nd story, respectively. The roof segment and the 2nd floor segment include the ceiling and the 1st story's ceiling, respectively. The wall segments included the interior sheathings and the exterior finishing material. Next, as shown in Figure 1, the wall, floor and roof were divided into approximately 900 mm square segments. The wall with the opening was divided into the

hanging wall and spandrel wall segments. As a result, 103 homes were divided into approximately 65,000 segments. Each segment linked to the attribution of the investigated houses and the information of the appearance degradation and the bio-deterioration of the structural members included in it.

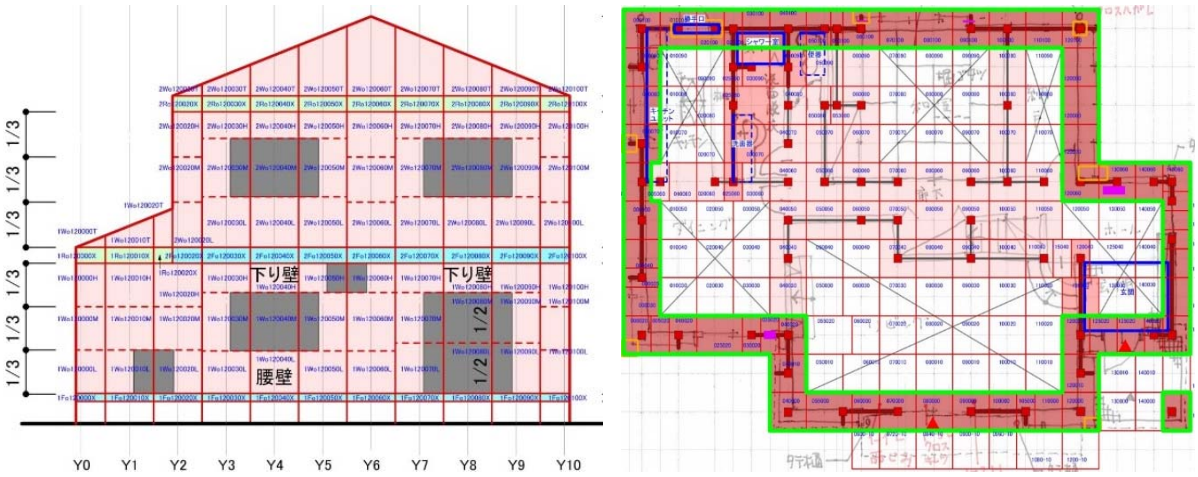

(a) Wall divided into segments. (b) Floor divided into segments.

Figure 1. Dividing method of investigated house into segments.

4 Frequency of Appearance Degradation and Bio-Deterioration

All of the 103 houses had the degradation in appearance, and 97 houses had the bio-degradation. Out of 65,000 segments, the appearance degradation was found in 5,667 segments, corresponding to 8.7 %, and the bio-deterioration of the structural members was found in 1,421 segments, corresponding to 2.2 %. In other words, most existing wood houses have the bio-deterioration of structural members, but their range is generally limited. Figure 2 and 3 shows the frequency of the appearance degradation and the bio-deterioration of the structural members for each building age and each construction area, respectively. The incidence of the appearance degradation and the bio-deterioration increased with older building age, except for over 50 years whose sample was very few. The incidence of them was lowest in zone No. 7 with high temperature and humidity. In others, the incidence increased in warmer zone, except for zone No. 3 where the sample was very small.

Figure 4 shows the incidence of them for each building part. Both of the appearance degradation and the bio-deterioration of the structural member often occurred on the 1st story and outside rather than the 2nd story and inside, respectively.

Figure 5 shows the relationships between the construction method and height of the foundation and the bio-deterioration of the structural member in the 1st story. The incidence of the bio-deterioration was lower in the order of the concrete mat foundation with footing, only the footing with the moisture barrier concrete and the one without the moisture barrier concrete. The mat foundation and the moisture barrier concrete are effective in preventing the bio-deterioration of the structural member in the 1st story. Although there were some exceptions, the incidence of the bio-deterioration almost decreased as the foundation height raised.

Figure 6 shows the effect of the segment orientation on the incidence of the appearance degradation and the bio-deterioration of the structural members. The orientation of the segments

had no obvious effect on the incidence of them.

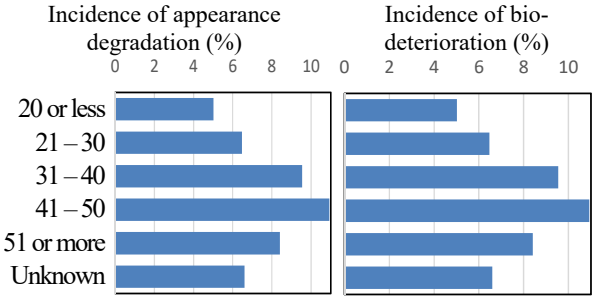

Figure 2. Incidence of the appearance degradation (left) and the bio-deterioration (right) for each building age.

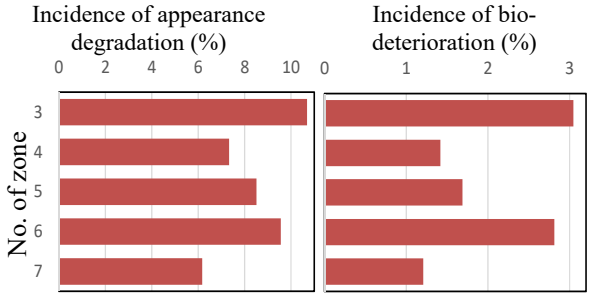

Figure 3. Incidence of the appearance degradation (left) and the bio-deterioration (right) for each building location.

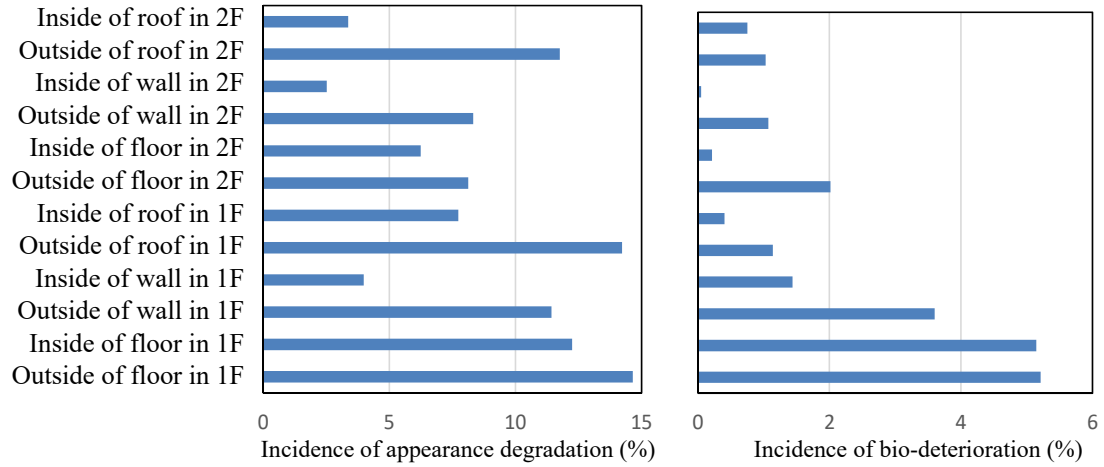

Figure 4. Incidence of the appearance degradation (left) and the bio-deterioration (right) for each building part.

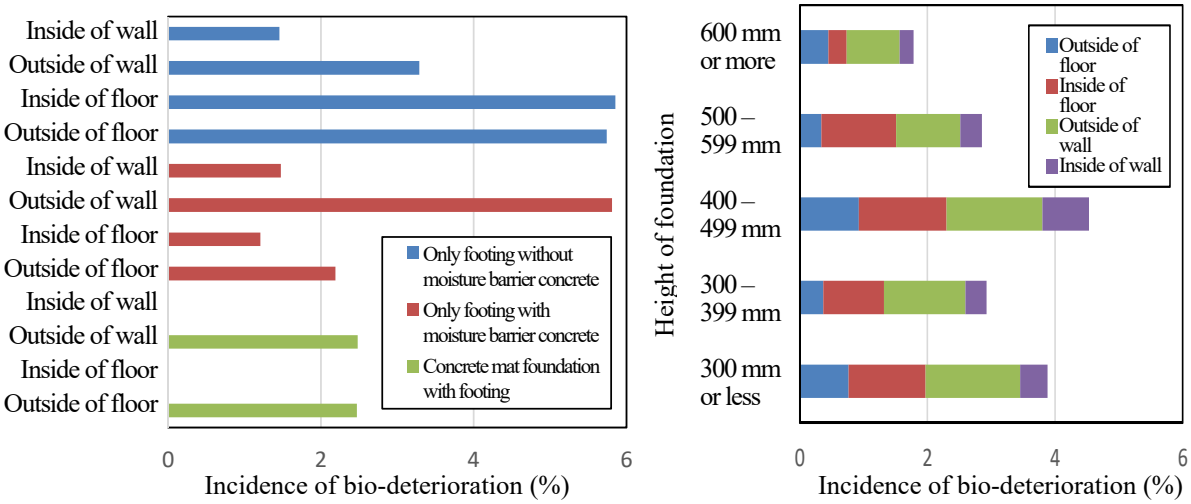

Figure 5. Relationships between the construction method (left) and height (right) of the foundation and the bio-deterioration of the structural member in the 1st story.

Figure 7 shows the effect of the eaves length on the incidence of the appearance degradation and the bio-deterioration of the structural members. The length of the eaves didn't clearly affect the incidence of the appearance degradation. However, as the length of the eaves increased, the incidence of the bio-deterioration almost decreased.

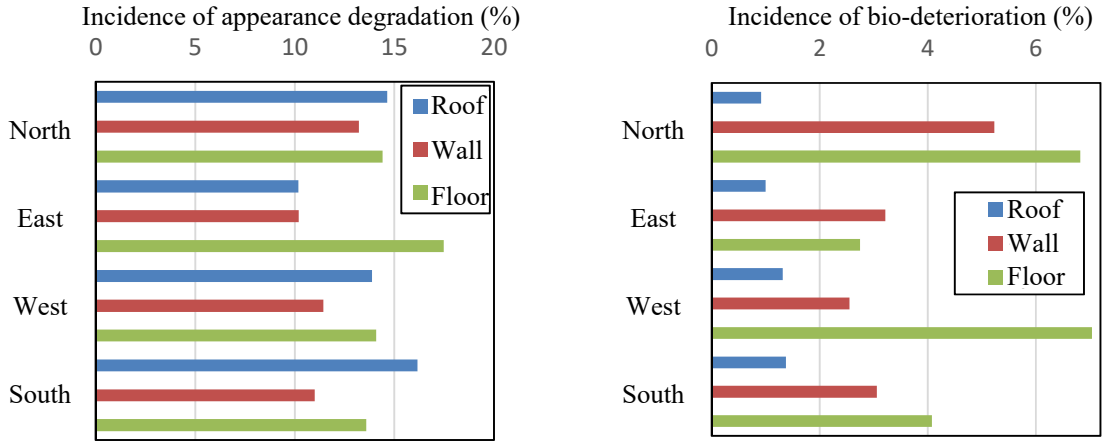

Figure 6. Relationships between the incidence of the appearance degradation (left) and the bio-deterioration (right) and the orientation of the segments.

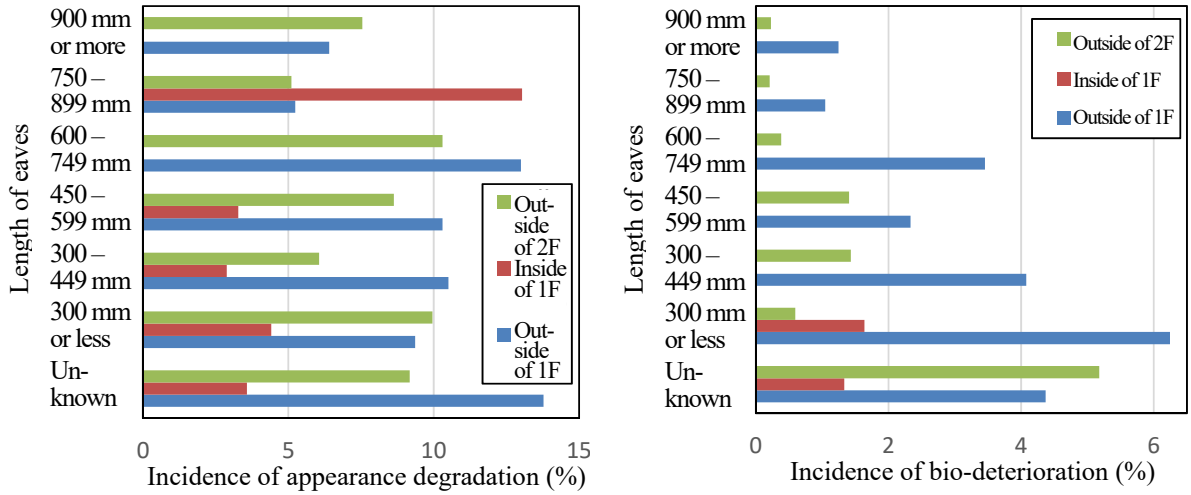

Figure 7. Relationships between the incidence of the appearance degradation (left) and the bio-deterioration (right) and the length of the eaves.

5 Difference between Appearance Degradation and Bio-Deterioration

On the most of the dealing with the used houses, only the appearance inspection is conducted. So, the result of the appearance inspection needs to match the position of the bio-deterioration. However, the occurrence of the appearance degradation and the bio-deterioration of structural members were not the same, as mentioned above. For example, there was no decayed member in the 2nd floor system near the position of the rain leak mark on the ceiling of the 1st story found by the appearance inspection, as shown in Figure 8. And, the bottom of the column decayed even though no degradation were found by the appearance inspection, as shown in Figure 9.

Figure 8. Not decayed structural member of floor system in 2F (right) in spite of the rain leak mark on the ceiling (left).

Figure 9. Decayed bottom of column (right) in spite of no degradation found by the appearance inspection.

Then, we analyzed the differences between the appearance degradation and the bio-deterioration of the structural members. The number of the segments with/without appearance degradation and those with/without the bio-deterioration of the structural member were subjected to the cross tabulation, as shown Table 3. It was clarified that there was no bio-deterioration in more than 90 % of segments out of all with the appearance degradation (*e.g.* Figure 8), and that there was the bio-deterioration in only 1.6 % of segments of all without the appearance degradation (*e.g.* Figure 9).

Table 3. Cross tabulation of the number of segments with/without the appearance degradation and those with/without the bio-deterioration of the structural members.

			Appearance degradation			
			Found		Not found	
			Number of segments	Ratio	Number of segments	Ratio
Bio-deterioration of structural member	Found	Total	484	8.5 %	**937**	**1.6 %**
		2F	88	5.1 %	**129**	**0.5 %**
		1F	396	10.0 %	**808**	**2.3 %**
	Not found	Total	**5,183**	**91.5 %**	58,416	98.4 %
		2F	**1,649**	**94.9 %**	23,698	99.5 %
		1F	**3,534**	**89.9 %**	34,718	97.7 %
Total			5,667	100 %	59,353	100 %
		2F	1,737	100 %	23,827	100 %
		1F	3,930	100 %	35,526	100 %

Next, the distribution of segments including those differences for each building part was studied, as shown in Figure 10. The incidence of the segments with the bio-deterioration in spite of the no appearance degradation in the 1st story was higher than that in the 2nd story and high in the order of the floor, the wall and the roof. From these, even if the occurrence rate of such differences depends on the incidence rate of biological deterioration, the appearance degradation, the structural members in the 1st story, especially in the floor, should be inspected or surveyed carefully, regardless of the appearance degradation. On the other hand, the distribution of the segments without the bio-deterioration in spite of the appearance degradation didn't have clear tendency for each building part and in each part the incidence was over 80%. One possible reason is that it takes time for the outside rain leak to penetrate the structural members, and the water evaporates before the water reaches the structural members.

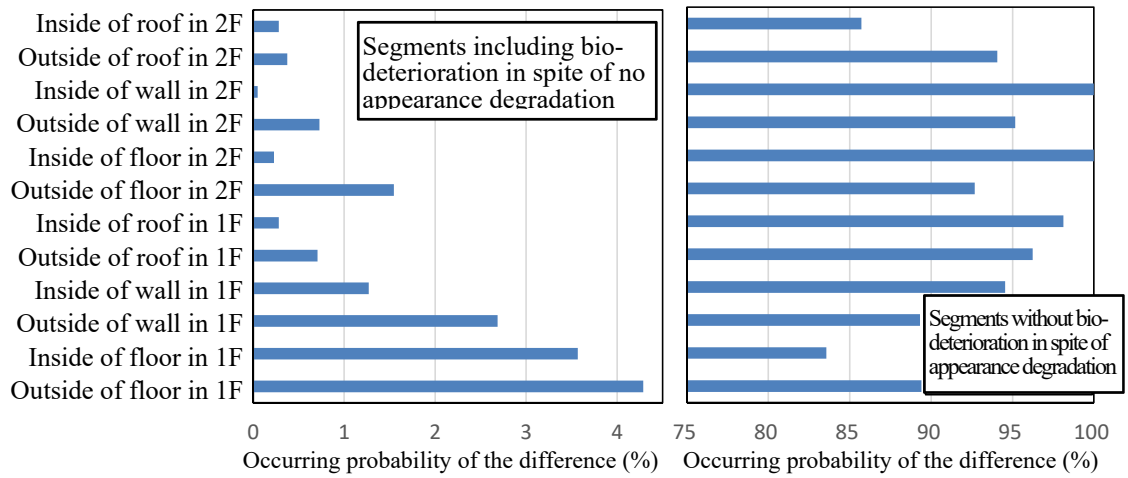

Figure 10. Distribution in each building part of the segments including the bio-deterioration in spite of no appearance degradation (left) and without the bio-deterioration in spite of appearance degradation (right).

6 Conclusions

The relationships between the appearance degradation and the actual bio-deterioration of the structural members obtained by the investigation for over 100 used wood houses were analyzed and concluded as follows:

- The bio-deterioration of the wooden structural members were found much on 1st story rather than 2nd story, in the elder building age, in case of short eaves and in case of low foundation. The issues known experience empirically were verified numerically.
- The tendency of the appearance degradation occurrence were the same as the tendency of the bio-deterioration partially, but didn't match it entirely.
- About 90 % of the portions whose interior or exterior appearance were degraded didn't have the bio-deterioration of the wooden structural member.
- The ratio of the portion with the bio-deterioration of the wooden structural member without appearance degradation were only 1.6 %.

Acknowledgements

The inspection and survey for over 100 used wood houses were conducted as a part of the R&D Project "Development on performance evaluation technologies for home inspection to reduce uncertainty of existing house" funded by The Ministry of Land, Infrastructure, Transport and Tourism (MLIT). The compilation of the inspection and survey results into the database was conducted as a part of the R&D Project of Building Research Institute "Development of durability evaluation method of buildings materials and components for strategic maintenances".

ORCID

Takahiro Tsuchimoto: https://orcid.org/0000-0003-4925-1831

References

Cho, H. and Takada, M. (2013). A study on the characteristics of home buyer's demand and the obstructive factors of existing housing circulation - Based on the survey of targetiong existing home buyers in Osaka Prefecture - (in Japanese), *J. Architecture Planning*, 78(8), 1817-1825, Architectural Institute of Japan, Tokyo Japan.

Ministry of Land, Infrastructure, Transport and Tourism in Japan (MLIT, 2015). *Preparing a market that facilitates the smooth trading of existing houses*, White Paper on Land, Infrastructure, Transport and Tourism in Japan, Chapter 5, 167-168, MLIT, Tokyo, Japan.

Tsuchimoto, T., Takahashi, S., Sumikura, H., Nakagawa, T. and Hanawa, K. (2016). Study on the differences between visual inspection and degradation diagnosis on old wood houses (in Japanese), *Summaries of Technical Papers of Annual Meeting*, C-1, 591-592, Architectural Institute of Japan, Tokyo, Japan.

XV International Conference on Durability of Building Materials and Components
DBMC 2020, Barcelona
C. Serrat, J.R. Casas and V. Gibert (Eds)

State of Maintenance in Relation to Property Regime, Tenancy and Uses of a Large Sample of Residential Buildings Located in the Most Vulnerable Areas of the City of Barcelona

Sara Vima-Grau[1], Còssima Cornadó[2] and Pilar Garcia-Almirall[3]

[1] PhD researcher and Teaching Assistant of the Department of Technology in Architecture, FPU Grant by MECD, Universitat Politècnica de Catalunya, ETSAB, Barcelona, sara.vima@upc.edu

[2] Lecturer professor Serra Húnter Fellow, PhD architect of the Department of Technology in Architecture, Universitat Politècnica de Catalunya, ETSAB, Barcelona, cossima.cornado@upc.edu

[3] Professor of the Department of Technology in Architecture, Universitat Politècnica de Catalunya-BarcelonaTECH, ETSAB, Barcelona, pilar.garcia-almirall@upc.edu

Abstract. *In a context of downturn of public investment after the financial crisis of 2007, an increase of social and economic inequality takes place in territories and cities. Socio-residential vulnerability is intensified in certain urban areas where processes of socioeconomic and socio-spatial regression are related with the resident population difficulties to access resources for the intervention and maintenance of an aging residential building stock that gradually decays. Mediterranean cities in Southern Europe and precisely the city of Barcelona face the added difficulty of counting with a residential built stock of mostly private property, accounting many situations of horizontal property in which each building is managed by a community of owners who are not necessary householders and users. The present study consists of an analysis of the relation between the state of maintenance of residential buildings and the property regime, tenancy and uses, based on the observation of common spaces and elements of a large sample of buildings located in the most vulnerable areas of the city of Barcelona. The provided results can contribute to foster improvements in future public rehabilitation programs and policies. Particularly according to local challenges to guarantee and promote durability of a mostly privately-owned residential built stock that is located in areas where socioeconomic difficulties hinder the residents' capacity to carry out rehabilitation or maintenance actions. Management of the maintenance of the residential built stock must take into account the repercussion of particularities in property regimes, tenancy and uses, especially when it refers to common spaces and elements of residential buildings.*

Keywords: *State of Maintenance, Property Regime, Form of Tenure, Building Pathology, Vulnerable Housing Stock.*

1 Introduction

In the current context of regression of public and private investment in the construction sector, the obsolescence of the existing residential building stock in areas of the city that are particularly vulnerable is a matter of high concern in the city of Barcelona (Ajuntament de Barcelona, 2016). A city where the design and provision of public policies to support maintenance and rehabilitation faces the challenge to address the predominance of a privately-owned residential building stock mostly characterized by a horizontal structure of ownership. This fact places the inhabitants, both users and owners, in a central role for the implementation of maintenance and rehabilitation actions of an aging housing stock (Cerezo, 2018).

In this context, current debates regarding the lack of maintenance and obsolescence of the existing urban fabric consider not only the decay of the built environment at different scales but also the increasing risk of social and residential exclusion affecting its inhabitants. The distinction between physical factors, related to the building stock material and technical processes, and behavioural factors, related to human actions, possibilities and struggles, is at the same time explanatory of the causes and descriptive of the effects of the progressive deprivation of the urban existing tissue. (Thomsen *et al*. 2015 and 2017).

The present paper provides a cross-analysis of quantitative and qualitative indicators of the state of maintenance of a large sample of residential buildings located in five of the most vulnerable neighbourhoods of the city of Barcelona, in relation to the property regime, tenancy and risk of residential exclusion as well as occupancy and uses within the building. This contribution can provide tools to consider the impact of this socioeconomic aspects on the issue of obsolescence and it aligns with the aim of the Council of Barcelona to foster the design of specific integral public rehabilitation programs that can support the most vulnerable tenants and householders to access maintenance and improvement actions at present and in long term. (Diari Oficial de la Generalitat, 2018).

2 Objectives

The main objectives of this research are:

- To describe the building stock in different vulnerable neighbourhoods according to the type of observed damages and the state of maintenance and conservation.
- To analyse and detect the impact of socioeconomic issues such as property regime, tenancy and risk of residential exclusion, forms of occupancy and uses in relation to the state of maintenance and conservation of the residential building stock.

3 Methodology

3.1 Sample of Study and Data Collection

The main sources for this paper are, firstly, a study on the detection of the most vulnerable areas of the city of Barcelona (Garcia-Almriall *et al*., 2017), and the following study on the prediagnosis of the state of conservation of the building stock in 16 vulnerable neighbourhoods (Cornadó *et al*., 2017).

This paper presents a cross-analysis of data of a total sample of 2434 buildings located in five of the previously studied vulnerable neighbourhoods that are selected for their very diverse characteristics. El Raval (1119/1685 analysed buildings) and La Barceloneta (737/1074 buildings) are central neighbourhoods with a historic urban tissue with mainly constructions of the XIX century. Ciutat Meridiana (54/78 buildings) and El Besòs (188/281 buildings) are peripheric neighbourhoods in the north and south of river Besòs and consist of a modern urban tissue with mainly open block and tower constructions built between 1950 and 1975. Trinitat Vella (345/592 buildings) is also a peripheric neighbourhood built in the same period, but its urban tissue consists of attached constructions between party walls conforming a closed urban block (Figure 1).

Figure 1. Different type of buildings of the five analysed neighbourhoods. From left to right: El Raval, La Barceloneta, Ciutat Meridiana, El Besòs and Trinitat Vella.

3.2 Data Analysis

3.2.1 Building pathology: type of observed damages

Firstly, this paper provides an analysis of a series of observed damages according to their relevance on the studied areas. The available data was obtained during a fieldwork campaign (Cornadó *et al*., 2017) (Figure 2). The described damages are: cracks in bearing walls, façade buckling, risk of material detachment in facades and roofs, dampness (rising damp, moisture and rainwater leaks), degraded windows and woodwork, rusty metal elements, cracks in the facing, stains and dirt.

Figure 2. Fieldwork images of observed damages.

3.2.2 State of maintenance and conservation in relation to property, tenancy and uses

Secondly, this paper presents qualitative and quantitative indicators to statistically analyse the state of maintenance and conservation of the building stock: a qualitative indicator that describes the need of rehabilitation of the building stock obtained in a campaign of fieldwork (Cornadó et al., 2017) (Figure 3), a quantitative indicator of the superposition of the previously described damages within one single building (Cornadó et al., 2017), and finally a quantitative indicator of the existence of administrative requirements and orders of conservation provided by the Council of Barcelona (Garcia-Almirall et al., 2017).

Figure 3. Fieldwork images of buildings with different results the need of rehabilitation indicator.

Results from the three indicators are classified according to four levels in relation to the state of maintenance and conservation of the building stock (Table 1), and they are further analysed according to socioeconomic variables related with property, tenancy and uses (Table 2):

Table 1. Qualitative and quantitative indicators of the state of maintenance and conservation.

Indicators	Level 1	Level 2	Level 3	Level 4
- Need of rehabilitation	High	Regular	Low	Very low
- Superposition of damages	7-9	4-6	1-3	0
- Administrative requirements	More than 2	2	1 (interior)	1 (façade)
Sate of maintenance	**Very low**	**Low**	**Regular**	**Adequate**

Table 2. Socioecnomic variables, data and sources.

Variables	Data	Source
- Property regime	· Horizontal Property · Vertical Property: legal entity or natural person	Garcia-Almirall, 2017 Statistical Database
- Risk of residential exclusion	· Application for public rental aid · Number of evictions	Garcia-Almirall, 2017 Statistical Database
- Tenancy and uses of the building	· Blocked and empty premises · Empty premises in ground floors · Private uses in ground floors · Public uses in ground floors	Cornadó *et al*., 2017 Fieldwork

4 Results

4.1 Observed Damages in Relation to the State of Maintenance of the Building Stock

The graphic in Figure 4 presents the distribution and relevance of the different observed damages in the total sample of studied buildings according to each neighbourhood:

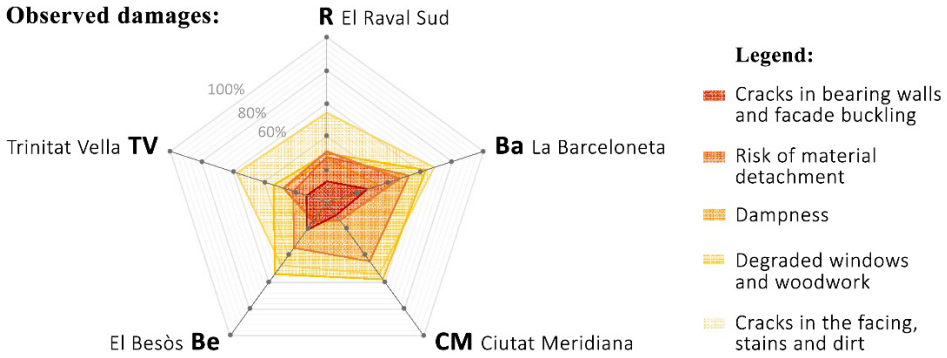

Figure 4. Proportion and distribution of observed damages.

The most abundant observed damages are those that are strictly related with a lack of ordinary and extraordinary maintenance actions: cracks in the facing, stains and dirt, as well as damages in windows and woodwork and carpentries. Their proportion according to neighbourhood varies between 55-68%. The proportion of cases with dampness is still quite relevant and a little bit more variable among neighbourhoods: between 50% in La Barceloneta

and Ciutat Meridiana, 30% in El Besòs and El Raval, and 20% in Trinitat Vella. There is a considerable number of cases with risk of material detachment, particularly in La Barceloneta (near the 50%), and still importantly in El Raval and Trinitat Vella (around the 30%), while it is very low in El Besòs and Ciutat Meridiana (15%). Finally, the proportion of cases presenting damages of mechanic structural origin such as cracks in the bearing walls is a lot lower and it presents high variability from La Barceloneta and el Besòs, the locations with a highest percentage (25%), to Ciutat Meridiana (10%). The graphic in Figure 5 presents the distribution of three groups of indicators that are classified in four levels in order to assess the state of maintenance of the whole sample:

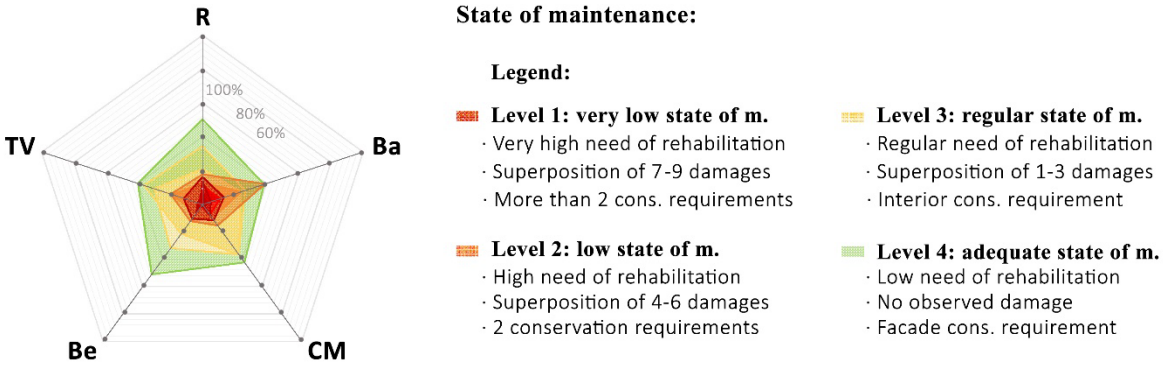

Figure 5. Proportion and distribution of four levels in relation to the state of maintenance.

The highest proportion of cases (between 40-50%) correspond to Level 4 and thus present an adequate state of maintenance and conservation, although this proportion is slightly lower in La Barceloneta, Ciutat Meridiana and Trinitat Vella. The proportion of cases included in Level 3, if we consider both the quantitative and qualitative indicators, is rather homogeneous around the 40% with slightly less cases in La Barceloneta. Instead, La Barceloneta presents a peak in the proportion of cases included in Level 2, with a 40% of cases that present a low state of maintenance according to the quantitative indicator. A proportion that is qualitatively less important but still accentuated: 25% of cases in Level 2 in La Barceloneta in comparison to a 18% in Trinitat Vella and between 7-13% in the rest of areas. Finally, the qualitative indicator provides an almost homogeneous distribution of cases included in Level 1 between 10% in El Besòs to 16% in El Raval, including cases with a very poor state of conservation. Even though the proportions of administrative requirements are very low (mostly under 10%), there is a 16% of cases with administrative requirements for interior conservation in El Raval.

4.2 Building Pathology and State of Maintenance in Relation to the Property Regimes

The cross-analysis of the distribution of damages and the indicators of the state of maintenance according to different property regimes is presented in Figure 6. The proportion of observed damages within cases of horizontal property is slightly higher if compared to the results of the full sample in Figure 4, and clearly higher if compared to the results for cases with a vertical property regime. Besides, there is a clear decrease of the proportion of cases presenting damages of mechanic structural origin as well as risk of material detachment for vertical properties. More particularly, vertical juridical properties clearly present lower percentages of all types of damages in comparison to vertical physical properties.

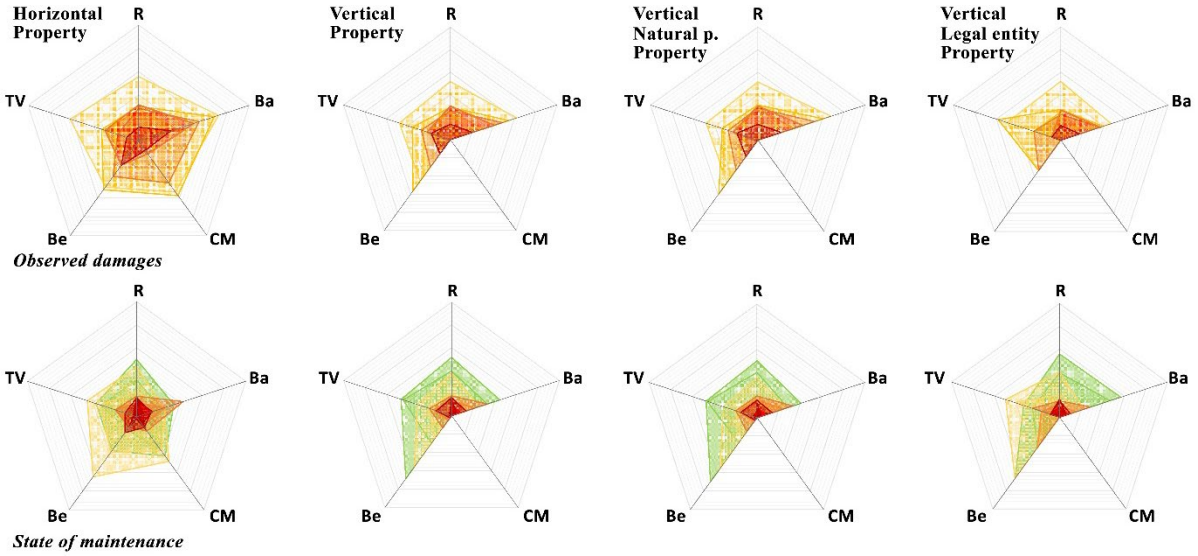

Figure 6. Proportion of observed damages and the state of maintenance in relation to property regimes.

Regarding quantitative and qualitative indicators of the state of maintenance and conservation of the building stock, similar results can be observed. The proportion of cases presenting an adequate state (Level 4) is clearly inferior for horizontal properties. Vertical properties include a much higher percentage of buildings in an adequate state, particularly in El Besòs, and most specifically in the case of vertical properties owned by of La Barceloneta. Instead, vertical properties owned by natural persons in Trinitat Vella concentrate the major number of cases with an adequate state. Regarding the poorest state of maintenance and conservation, the proportion of cases is more elevate for horizontal properties in all studied neighbourhoods and it is particularly lower in the case of vertical juridical properties in la Barceloneta and El Besòs.

4.3 Building Pathology and State of Maintenance in Relation to Tenancy and Risk of Residential Exclusion

In comparison to the results presented in Figures 4 and 5, Figure 7 clearly shows how the proportion of observed damages and the proportion of cases with a lower state of maintenance is much higher for those buildings in which the resident community has faced eviction processes in the last years. Results according to buildings in which many residents apply for rental social aid are very similar. This observation is particularly clear in La Barceloneta, El Besòs and Trinitat Vella, while it is also significant in El Raval and Ciutat Meridiana.

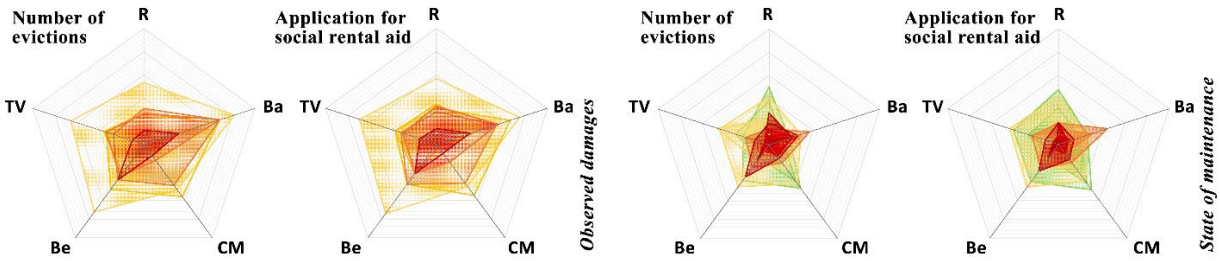

Figure 7. Proportion of observed damages and state of conservation according to risk of residential exclusion.

4.4 Building Pathology and State of Maintenance According to Occupancy and Uses of Residential and Ground Floors

The results presented in Figure 8 highlight the very high impact of the existence of blocked unused spaces both in residential and ground floors in relation to the observation of damages and the very poor state of conservation for all coincident cases. Remarkably, empty premises in ground floors present a similar correlation, particularly in Ciutat Meridiana and El Besòs.

Additionally, it is interesting to consider the impact of a different use of ground floors, be it of private access (housing, garage or storage) or of public access (commercial and services). In the case of El Raval, the percentage of cases with a very low state of maintenance is higher in buildings with housing or storage uses on the ground floor. Nevertheless, both the proportion of observed damages and of buildings with a very low state of maintenance tend to increase in buildings with commercial and services in the ground floor, with exceptions in El Besòs where the proportion of some types of damages decreases significantly while there is a higher proportion of buildings in an adequate state.

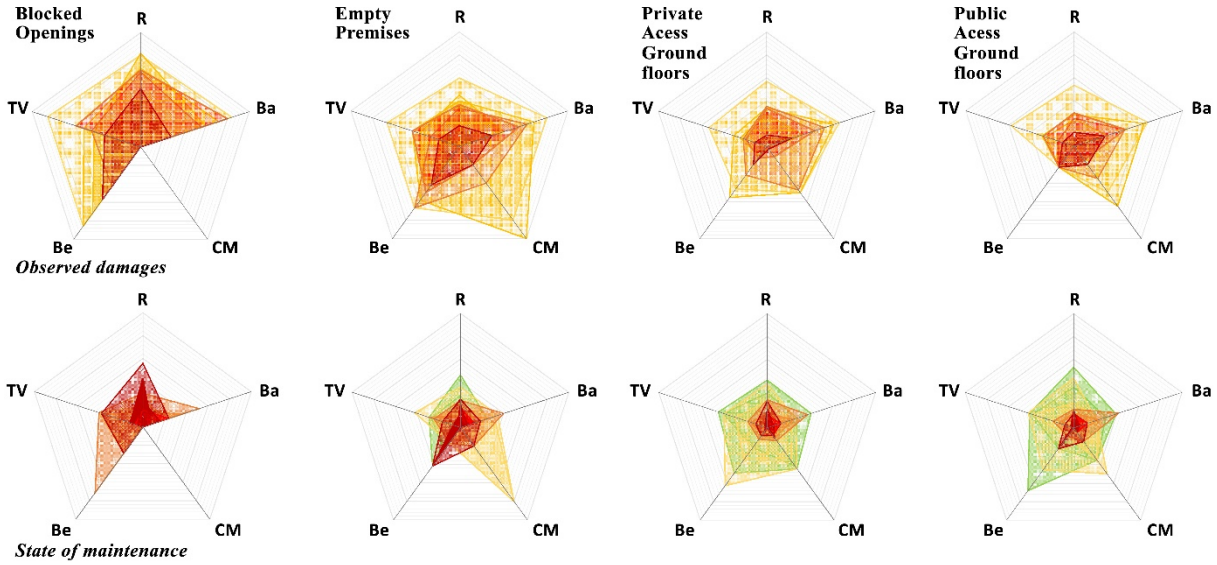

Figure 8. Proportion and distribution of observed damages and four levels of the state of conservation according to the occupancy and uses of residential and ground floors.

5 Conclusions

First of all, there is a clear relation between the abundance of most observed damages in common elements and spaces of buildings and lack of ordinary or extraordinary maintenance actions. Results regarding the qualitative indicators of the state of maintenance and conservation also confirm the existence of a low percentage of buildings that need an urgent intervention of rehabilitation, while they highlight a considerable proportion of cases in which the state of maintenance is not yet adequate.

In this context, the higher proportion of observed damages and lower state of maintenance of privately-owned buildings with a horizontal structure of property confirms the consequences of what can be pointed as an added difficulty hindering the implementation of maintenance

actions. The particularly lower proportions of damages and the increase of the adequate states of maintenance for the specific case of vertical juridical property in La Barceloneta and El Raval can be explained by the speculative pressure in the historic central areas, where the acquisition and renovation of entire buildings is frequent.

Secondly, the clear impact of socioeconomic variables that are closely related to the risk of residential exclusion in communities, confirms how socioeconomic difficulties and residential instability are also explanatory factors of the gradual decay of the residential building stock.

Finally, the high correlation between the existence of empty premises both in residential and ground floors and the accumulation of severe damages and a poor state of maintenance explains the high impact of a usually prolonged lack of activity. Besides, in most studied neighbourhoods where the common ground floor activity is housing, buildings with commercial ground floors present a lower state of maintenance. While in the case of El Raval, in which the common ground floor activity is commercial, the presence of other activities of private access such as housing, provides a sign of deprivation. The correlation between ground floor uses and state of maintenance must be interpreted according to the location and urban activities of each site.

Results from this paper confirm that the design and management of public programs aiming at improving the state of maintenance and conservation of the residential building stock must adapt and consider seriously socioeconomic aspects related with property, tenancy, occupancy and uses, particularly in contexts where the risks of socioresidential exclusion are high.

Acknowledgements

The main sources of this research have been provided or supported by the Council of Barcelona, by means of several contracts that have been crucial for the development of fieldwork and database elaboration. The present paper has been written with funding of the Ministry of Education thanks to an FPU Grant for Doctoral research. Finally, this research has been carried out in the framework of the ongoing R&D Project: Re-Inhabit. *Indicadores socio-espaciales para la mejora del stock habitacional en zonas vulnerables. Criterios de actuación en los casos de las áreas metropolitanas de Barcelona y Bilbao*. RTI 2018-101342-B-I00, supported and funded by the Ministry of Science and Innovation.

ORCID

Sara Vima Grau: http://orcid.org/0000-0002-9912-8201
Còssima Cornadó Bardón: http://orcid.org/0000-0003-0553-7176
Pilar Garcia Almirall: http://orcid.org/0000-0002-5918-118X

References

Ajuntament de Barcelona (2016). *Pla pel Dret a l'Habitatge de Barcelona 2016-2025. Resum executiu*.

Cornadó, C., Garcia-Almirall, P. and Vima, S. (2017). *Prediagnosi de l'edificació residencial en els àmbits de vulnerabilitat de la ciutat de Barcelona*. Ajuntament de Barcelona.

CVE-DOGC-A-18157071-201 (2018). *Anunci de la Convocatòria del Programa de Finques d'Alta Complexitat*. Diari Oficial de la Generalitat de Catalunya (DOGC). Núm 7642-14.6.2018.

Garcia-Almirall, P., Vila, G., Vima, S. and Uzqueda, A. (2017). *Estudi i detecció a la ciutat de Barcelona d'àmbits de vulnerabilitat residencial*. Ajuntament de Barcelona.

Cerezo, Á. (2018). Evolución del derecho de propiedad en cuanto al deber de conservación en la legislación de suelo y urbanismo desde 1956 a 2018, de la triada clásica a la actuación sobre el medio urbano. *ACE: Architecture, City and Environment = Arquitectura, Ciudad y Entorno, 13* (38): 81-100, 2018.

Thomsen, A., Van der Flier, K. and Nieboer, N. (2015). Analyising obsolescence, an elaborated model for residential buildings. Structural Survey 33, 3: 210-227.

Thomsen A., Nieboer, N. and Van der Flier, K. (2017). Obsolescence - understanding the underlying processes. ENHR 2015 Conference Lisbon.

XV International Conference on Durability of Building Materials and Components
DBMC 2020, Barcelona
C. Serrat, J.R. Casas and V. Gibert (Eds)

Statistical Analysis on Belgian Building Defects

Jasmijn De Vos, Anke Blommaert and Nathan Van Den Bossche

Ghent University, Faculty of Engineering and Architecture, Building Physics Group. Sint Pietersnieuwstraat 41 B4, 9000 Ghent, Belgium. *Nathan.vandenbossche@ugent.be

Abstract. *The lack of systematization in the collection of building defects leads to a wide range of data that is not used to its full potential. Unfortunately, this opportunity is missed since lessons could be drawn from analyzing this data by systematically mapping and investigating building defects. This paper presents the results of a statistical analysis on 27074 cases of building defects provided by a Belgian insurance company, ranging from 1991 up to 2019. This analysis focuses on the types of damage, the occurrence in relation to the construction time and the typology of the claims. Spearman correlation tests, X^2 tests, and Kruskal-Wallis tests are performed to assess the significance of correlations. Moisture problems constitute 49% of all technical defects, followed by structural issues (19%), and cracking (17%). Within the category of moisture problems, the roof is the dominant location for problems to occur, followed by basements, façades, windows, and rising damp. 50% of the judicial cases were closed after 3 years, whereas cases without lawsuit are typically settled after 1-2 years.*

Keywords: *Building Defects, Pathology, Catalogue, Statistical Analysis, Insurance Company.*

1 Introduction

Currently, an immense amount of information is available about building defects in the Belgian construction industry. Details about the causes, the damage caused by the defects, the associated repair cost, the liability, etc. can be found in reports of insurance companies, law offices and expertise bureaus, since they are appointed to deal with damage claims. However, the existing information is not fully used to prevent similar mistakes and to limit the number of damage claims in the future, since there is no harmonized data collection, no classification, no structure and no consent in processing the data.

In different countries, initiatives have been taken to create databases on building pathologies. 'Système de collecte des désordres' (France), 'Danish Building Defects Fund' (Denmark), 'Defect Action Sheet' (United Kingdom), 'Patorreb' (Portugal) and 'Learning from Mistakes' (Italy) are only a few initiatives where countries create databases on building pathologies. The CIB (International Council for Research and Innovation in Building and Construction) is a worldwide network concerned with the exchange of information to learn from past and current building pathologies. It achieves what the previously mentioned countries do at national level, on an international level.

Statistical analysis of these data may reveal unidentified patterns and provide insights on the dominant failures in terms of building component, type of damage, cause, time of occurrence, geographical location, building exposure, cost, and the like. Consequently, these insights may help in identifying aspects that need attention, additional guidelines, quality assurance protocols, or prevention, in order to reduce the failure cost in the building industry. This is of great importance since building defects often lead to discussions, and generate high costs, time

delay, reputation damage, litigations and decreased sustainability.

For property developers, architects and construction managers, the results of the analysis may provide a series of lessons on the critical aspects in order to minimize building defects. The insights derived from the analysis can be used by building professionals, leading to innovative ideas regarding materials, design concepts and construction methods. As a consequence, the quality of the buildings can be enhanced. Higher quality implies better durability, longer service life, lower life cycle cost, lower waste production, and higher sustainability.

2 Methodology

A qualitative and representative dataset is a prerequisite for statistical analysis to derive conclusions that can be extrapolated to the Belgian building industry. The analysis presented in this paper was based on the database of the largest Belgian insurance company in the building industry (containing 27 074 documented cases), representing the larger share of architects and engineering offices in that field.

Firstly, data are extracted from the insurance company's database, recoded and cleaned. The cleaning of the data is not discussed in this paper, but proved to be essential for the quality of the final dataset and analysis. Note that no statistical data-imputation for missing fields was done. A second step concerns the selection of the statistical tests and their graphical representation in the search for statistical correlations, associations and differences. Because of the size of the database (26 392 cases remaining after cleaning the database), it could be assumed that the variables are normally distributed and parametric tests can be performed (based on the Central Limit Theorem (CLT)). However, since the database contains a high number of outliers and extreme values and some combinations in the subdivisions contain a limited number of cases, the CLT cannot be applied for a more in-depth analysis. Therefore, non-parametric statistical testing is executed.

The following three tests are used: Spearman correlation, X^2 and Kruskal-Wallis. The focus is on the detection of correlations, trends and differences for the level of occurrence, cost and time. The trends and statistical differences are discussed and interpreted in chapter 4, Results. Finally, the last chapter provides some conclusions and future perspectives.

3 The Database

The database from the insurance company contains 27 074 documented cases, which have been processed and filed by either jurists or engineers between 1991 and 2019 working at the company. Since jurists are not trained in building science, there is perhaps a possibility that some damage cases are incorrectly diagnosed or documented in the database. However, for technical more complex cases a construction expert is always consulted, and given that this paper focusses mainly on the overall analysis, it is considered that this effect is negligible for the analysis presented here.

It must be considered that unconscious selection bias is present, as the insurance company mainly focuses on the insurance of the professional liability of architects and contractors. Hence, failures in which an insurance company is not involved (*e.g.* contractor makes a mistake

and repairs it) are not covered here. By consequence, the analysis does not provide insights into the complete overall fault cost or construction failures. Nonetheless, this database is a relevant sample of the real 'population' of construction failures, as it can be assumed that the more complex cases are covered, and as well the important failures in terms of associated costs.

4 Results

4.1 Damage Categories

Using descriptive statistics, the occurrence hierarchy of the nine categories of damage is shown in figure 1.

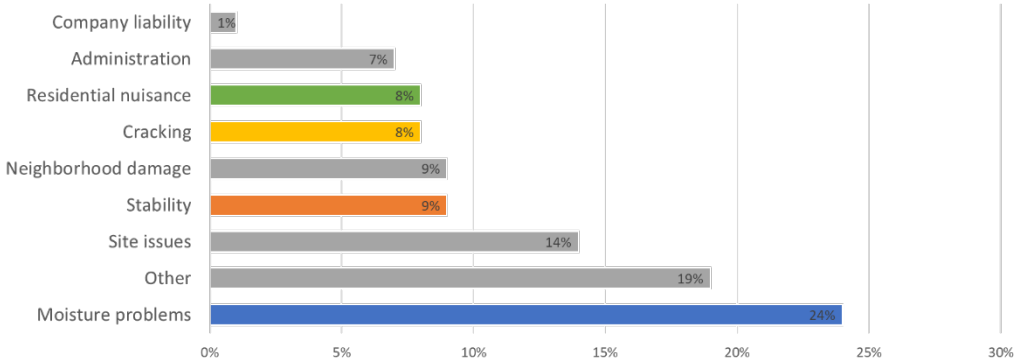

Figure 1. Distribution of the 9 categories of damage for 26 392 cases.

Five of the nine categories do not involve building defects and are therefore not further discussed. The category 'other' will not be taken into account even though this category also contains damages due to building defects. Due to the size of this category, we cannot analyze each case individually. Thus this category is eliminated to ensure homogeneity. Four categories remain: moisture problems, stability, cracking and residential nuisance (figure 2), containing 13 068 cases. Most building related damage claims are caused by moisture problems (49%). Cracking, residential nuisance and stability have a similarly smaller share of 16-19%.

The distribution of the damage types within the different categories is also shown in figure 2. For moisture problems, the two mayor problems are concerning water infiltration in the roof (24%) and the basement (21%), while all other problems only occur less than 10% of the time. It must be noted that the subcategories contain labels according to location and type. This makes it unclear how, for example, 'condensation problems in the roof' should be categorized.

For stability, the roof (27%) is the most affected apart from the 49% of cases which is categorized as "General stability problems". These general stability problems regard the general load-bearing structures like walls, beams and columns with the exclusion of the separate categories.

For cracking, the lack of a detailed categorization obstructs the opportunity for a more in-depth analysis. Cracks could have been formed due to stability or moisture problems.

For residential nuisance, the damage is the most often categorized as sewage problems (22%), defective material (12%), heating problems (11%) and finishing (11%).

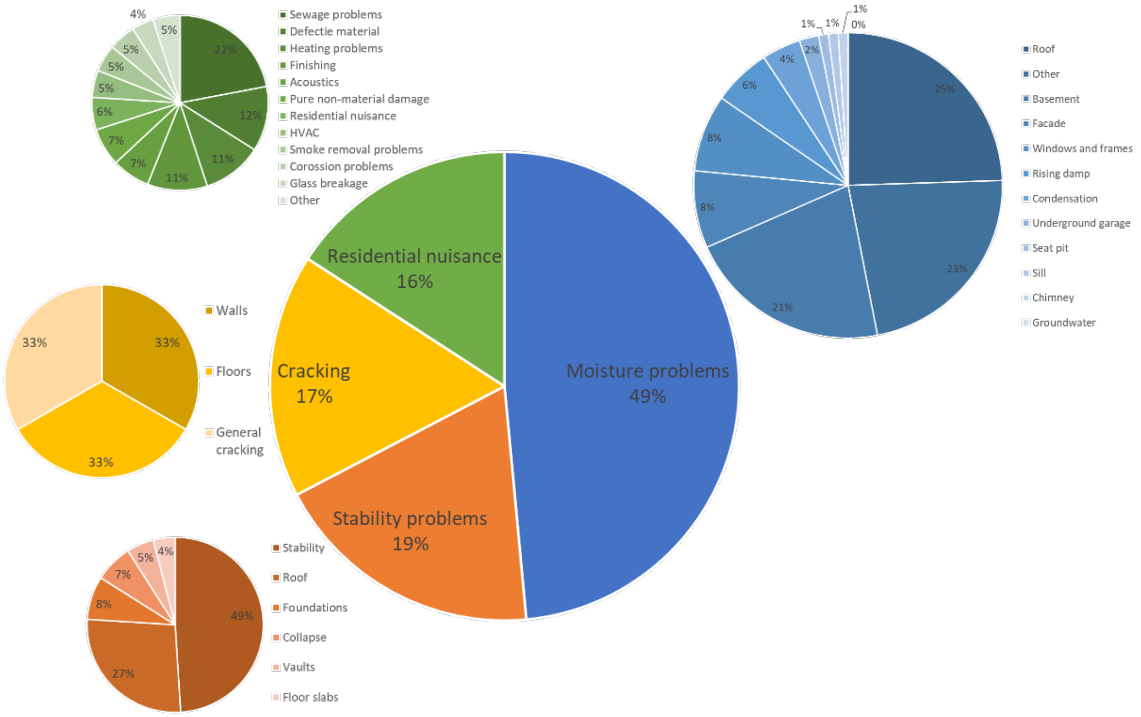

Figure 2. 4 categories of construction damage and their respective subdivisions for 13 068 cases.

4.2 Temporal Evolution of Claim Distribution

The number of claims evolves over time. Between 1991 and 2003, there is an almost constant number of claims, then the number starts to increase until 2010 when it slowly decreases again.

The reason why numbers start to increase in 2003 is that the insurance took over a competitor in that year. The decrease in claims starts a few years after the financial crisis in 2008, which of course had an impact on the construction market. In addition, in 2008, a new law was also introduced regarding the compensation of court costs: the losing party must pay the winning party a fee to compensate juridical costs. In 2010, the insurance company also decided to introduce prevention measures to cover contract initiations and contract problems and starts to provide advice and assistance to the insured professionals when a rise of the imminent defects can be noticed, which also might partially explain the decrease over the last decade. However, it can be concluded that the overall number of cases in the database is affected by the company structure, the variable market share over time, the work volume in the construction industry (business cycle), evolution of construction standards and guidelines, prevention measures, and the like. Although it is generally acknowledged that the introduction of the EPBD in 2006 has had a clear impact on the building sector and changed building component compositions drastically, it is yet unclear to what extent that change has resulted in an associated rise (learning curve for new methods) or decline (more quality control and larger buffers) in failures.

When we look at the distribution of the types of damage per year, it is observed that the percentages fluctuate over time. From 2001, an increase of ‘neighborhood damage’, is detected.

The latest ten years a small decrease in the number of 'site issues' (measurement and calculation errors, delivery problems, delays, budget exceedance,…) is noticed (figure 3).

When only the four main types of damage are considered (moisture problems, stability, cracking and residential nuisance), we see that 'moisture problems' remains the most occurring damage type.

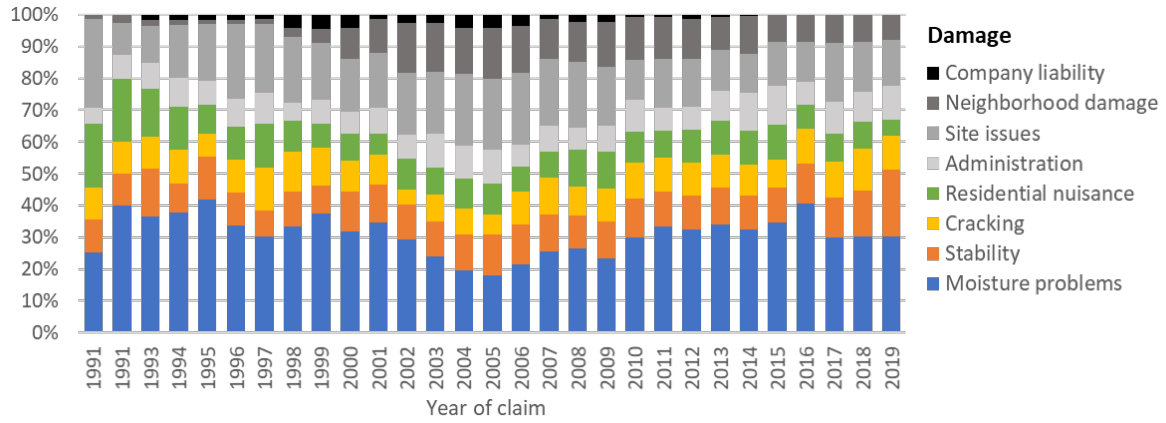

Figure 3. Evolution of the distribution of types of damage over time.

4.3 Moment of Occurrence in the Building Process

Damage claims can occur at different times. The milestones considered here are the provisional acceptance (PA), the final acceptance (FA), the fifth year after the final acceptance and the tenth year after the final acceptance (the end of the ten-year liability period).

In figure 4 it is observed that in 47% of the cases, damage occurs before the provisional acceptance and in 28% of the cases, damage occurs in the five years following the final acceptance. It makes sense that there are almost no damages found after more than 10 years. These cases are less relevant for the insurance company because there is only a 10 year liability. There is only a 1 year difference between PA and FA, explaining the lower percentage (13%) in this interval.

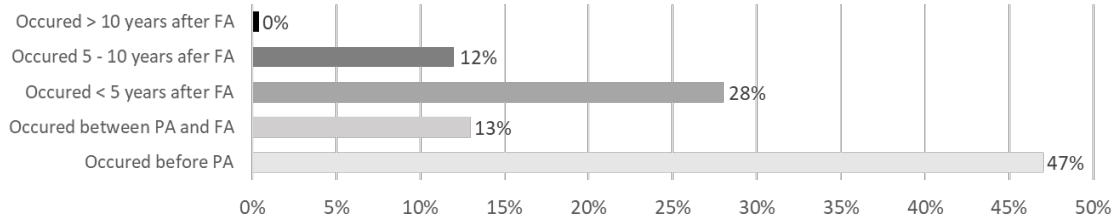

Figure 4. Bar chart: Distribution time (delivery).

The X^2 - test for 'Damage' and 'Time delivery' indicates various significances. Figure 5 shows that stability problems mainly arise even before the final acceptance has taken place and that moisture problems mainly occur within five years after the final acceptance. Only 15% - 25% of the cases are reported between five and ten years after the final acceptance. Therefore,

from these data, it can be concluded that stability problems occur early in the construction process and that cracking and moisture problems arise later.

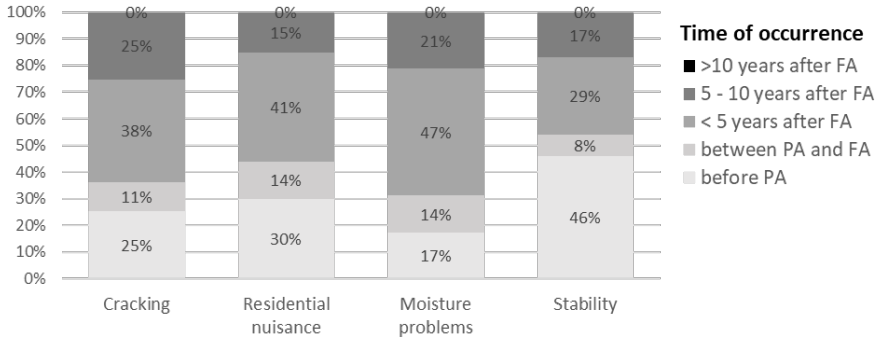

Figure 5. Analysis of time of occurrence in the building process (delivery) for the 4 main categories

Next, the four main categories are considered separately and conclusions are drawn for aspects for which relevant significances were found. No extreme exceptions are found for moisture problems. Water infiltration of roofs and basements occurs in more than 30% of the cases before the final acceptance. At first sight this appears to be in contrast to the general conclusion above on the occurrence of moisture problems. However, it should be noted that these building components typically adopt a perfect barrier watertightness concept: flat roofs and basements do not incorporate drainage or buffering systems which may result in a quick appearance of building defects. Next to that, both building components are subjected to water loads irrespective of co-occurrence of wind and rain events (resulting in wind driven rain loads on buildings). Although cathedral roofs typically include drainage systems, moisture mass buffering is not present. Rising damp occurs in 30% of the cases between five and ten years after delivery, while for the other moisture problems this is only around 20%-25%. Thus rising damp is a phenomenon that takes more time to develop, while water infiltration to roofs and basements occurs rather quickly.

For stability, it is observed that for the subcategories collapses, stability problems of foundations, and roofs, more than 50% occurs before final acceptance. On the other hand, for the stability of vaults and floor slabs this is between five and ten years after final acceptance. Collapses are probably mainly attributed to demolition and renovation works.

It seems remarkable that residential nuisance is already reported before the provisional acceptance (figure 5). However, this result can be explained by looking more in detail to the specifications of residential nuisance (figure 6). Damage related to finishing, color, aesthetics and pure non-material damage occur mainly before the provisional acceptance. These defects are detected when the material is supplied or when the construction is still in progress. As expected, corrosion and moss growth occur later in time.

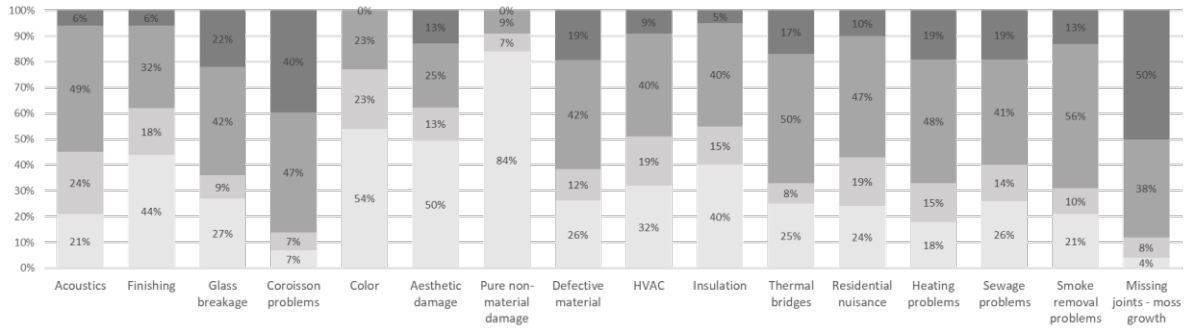

Figure 6. Specification residential nuisance versus time of occurrence (delivery)

4.4 Damage and Type of Settlement

The type of settlement reveals information on the complexity. There are three types of settlement: Amicable settlements without appointment of experts, amicable settlements with appointment of experts and juridical files with appointment of lawyers. An amicable settlement of a dispute is a settlement that satisfies both the parties. Juridical files are generally speaking more difficult. The different categories all have about the same amount of judicial files.

Therefore, the X^2 - test for 'Damage' and 'Type of settlement' indicates that specific types of damage are more complicated than others. Since stability is more complex, it is less classified as amicable settlements without the appointment of experts (only 18% of cases in this category) than residential nuisance (32%), moisture problems (27%) or cracking (23%).

4.5 Time of Occurrence and Type of Settlement

The X^2 - test between 'Time delivery' and 'Type of settlement' shows a significant difference. Damages occurring in the tenth year after the acceptance are mainly judicial files (56%) or amicable settlements without appointment of experts (38%). The type amicable settlements with appointment of experts is almost completely missing. This can be explained by the tight timeframe for lodging the complaint: the ten-year liability is coming to an end. Therefore, if necessary, it is classified as judicial, but if it can quickly be solved in an easy way, it is classified as amicable settlement without appointment of experts.

5 Conclusions

The database analyzed here comprises four main types of damage related to building defects: moisture problems, stability, cracking and residential nuisance. It was concluded that moisture problems, mainly water infiltration and rising damp, account for about half of the building defects. Even though the number of damage claims evolves over time, water infiltration remains the prominent claim. It must be noted that there are a lot of inconsistencies regarding the categorization of the cases. The subcategories, for instance, contain labels according to location and type. This makes it unclear how certain cases should be categorized.

Some types of damage are more complex than others. Stability is more complex since they are less classified as amicable settlements without the appointment of experts than residential

nuisance, moisture problems or cracking.

Most problems occur before the final acceptance. When we look at each type of damage individually, we notice that each type of damage occurs at different times. Moisture problems, cracking and residential nuisance occur later in time, compared to stability problems. Within the cases considering stability, especially collapses or damage arising at the foundations are the ones to occur before the provisional acceptance. For the cases considering moisture problems, rising damp occurs later than all other types of water damage.

For damages occurring in the tenth year after the acceptance, there are almost no amicable settlements with appointment of experts. This can be explained due to the tight timeframe for lodging the complaint, the ten-year liability is coming to an end. Therefore, if necessary, the complaint is classified as judicial, but if it can be easily solved, it is classified as amicable settlement without appointment of experts.

Acknowledgements

The authors would like to thank the insurance company for the access to the database, information and insights, and fruitful collaboration.

ORCID

Nathan Van Den Bossche: https://orcid.org/0000-0002-8738-7249
Anke Blommaert: https://orcid.org/0000-0002-8427-7300

References

Carretero-Ayuso, M.J., A. Moreno-Cansado, and J. de Brito (2017). *Failure and damage determination of building roofs*, Revista De La Construccion, 16(1): p. 13.

de Freitas, V.P. (2013). *A state-of-the-art report on building pathology*, Internation Council for Research and Innovation in Building and Construction. p. 195.

De Vos, J. (2019). *Building defects in the Belgian construction industry: trend analysis* (Unpublished master's thesis), Ghent university, Faculty of Engineering and Architecture.

Duncan, A. and L. Ward (2017). *A building pathology system in New Zealand-what is possible?*, BRANZ Study Report SR366: Judgeford,New Zealand. p. 36.

Molnárka, G.J.B. (2000). *Problems in Failure Analysis in Building Pathology*, p. 129-142.

W086, C. (1993). *Building pathology_A state-of-the-art report*, Internation Council for Research and Innovation in Building and Construction. p. 78.

Abdul-Malak, M.A.U., M.M.H. El-Saadi, and M.G. Abou-Zeid (2002). *Process model for administrating construction claims*, Journal of Management in Engineering, 18(2): p. 84-94.

Ferraz, G.T., et al. (2016). *State-of-the-Art Review of Building Inspection Systems*, Journal of Performance of Constructed Facilities, 30(5): p. 8.

Wetenschappelijk en Technisch Centrum voor het Bouwbedrijf (2014). *Contact 2014*. (in dutch)

IBM SPSS. Available from: https://www.ibm.com/analytics/spss-statistics-software.

Protect (2013). *Bulletin 56*, p. 12 (in dutch).

Protect (2002). *Tekst analyse van schadegevallen*, p. 25. (in dutch)

Notten, F. (2019). *Uit de bouwput?,Crisis en opleving in de bouwketen (2005-2015),* p. 30. (in dutch)

National Bank of Belgium Online statistics. [cited 2019 18 May]; Available from: http://stat.nbb.be/?lang=en&SubSessionId=1ad83e70-cd97-4da7-98c0-7f6b7fc6edd6#.

Van Den Bossche, T. (2016). *Cursus_Verzekeringen*, Hogeschool Gent. p. 69.

Van Daele, L. (2017). *Een catalogus van bouwgebreken-uitbreiding en analyse*, Universiteit Gent. p. 121. (in dutch)

XV International Conference on Durability of Building Materials and Components
DBMC 2020, Barcelona
C. Serrat, J.R. Casas and V. Gibert (Eds)

Strategies to Support Facility Management Resourcing Building Information Modelling

Raquel V. Matos[1], Fernanda S. Rodrigues[2], Hugo F. Rodrigues[3] and Aníbal G. Costa[4]

[1] RISCO, Civil Engineering Department, University of Aveiro, Campus Universitário de Santiago, 3810-193 Aveiro, Portugal, rvpm@ua.pt.

[2] RISCO, Civil Engineering Department, University of Aveiro, Campus Universitário de Santiago, 3810-193 Aveiro, Portugal, mfrodrigues@ua.pt.

[3] RISCO, Civil Engineering Department, University of Aveiro, Campus Universitário de Santiago, 3810-193 Aveiro, Portugal, hrodrigues@ua.pt.

[4] RISCO, Civil Engineering Department, University of Aveiro, Campus Universitário de Santiago, 3810-193 Aveiro, Portugal, agc@ua.pt.

Abstract. *The significant growth of the building stock in the 20th century allied to the low rate of building retrofitting over the last years results in the current low conservation level of the Portuguese building stock. The building natural aging, associated with the lack of planned maintenance actions and the climate changes consequences contributed to accelerating the degradation of building materials in the existing buildings, leading to a poor conservation of Portuguese public building stock. So, to extend the service life of the materials, the application of appropriate maintenance actions is imperative. This work aims to assess the building performance and to prioritize the maintenance actions employing Key Performance Indicators using Building Information Modelling (BIM) as a supporting tool for building condition assessment and maintenance management. To achieve these goals the following methodology was applied to a case study: 1)Building Information Collection; 2) Building Life Cycle Cost Estimation, and 3) Automated calculation of Building Performance Indicator supported by BIM, using Revit software and Dynamo programming. The application of this maintenance management automated strategy shows the importance of BIM in Facility Management; permits the model's permanent update of information decreasing the probability of information loss and the consequent investment in data collection, and has high potential to prioritise the building maintenance actions, extending the materials service life and building durability.*

Keywords: *Building Condition Assessment (BCA), Key Performance Indicators (KPIs), Building Service Life, Durability, Dynamo, Building Information Modelling (BIM).*

1 Introduction

To slow down the buildings` degradation processes and consequently the increase of the materials lifetime is essential to implement suitable, cost-benefit maintenance actions through cost and time effective maintenance management systems. A consistent building performance evaluation taking advantages of quantifiable tools to evaluate Building Condition Assessment (BCA) is crucial to meet an efficient and sustainable maintenance strategy in the scope of the Facility Management (FM) (Abbot *et al.,* 2007; Marmo *et al.,* 2019).Therefore, the main objective of this work is to assess the building performance by the integration of KPIs in a BIM software - the Autodesk Revit - and through this software to prioritize the maintenance actions in a practical and automated way. These KPIs were applied to the building of the Civil

Engineering Department of the University of Aveiro to support FM systems and maintenance planning. For this purpose, the research pursued a methodology with the following steps: 1) Building information collection; 2) Building Life Cycle Cost estimation; 3) Automated calculation of BPI supported by BIM, using Revit software and Dynamo programming. This study contributes to optimize the maintenance management of the Aveiro's University campus and to provide an easy instrument to prioritize maintenance, based on existing and reliable performance metrics and leveraging new technologies like BIM. In the next sections, some important concepts are approached to understand the methodology applied that is presented and validated by applying them to a case study. In the end the results are presented and discussed.

2 Conceptual Review

According to Crawford (2011) and Ngwepe *et al.* (2015) there are six building life cycle stages, consuming the last three stages, namely the construction, operation and demolition, approximately 15% of world's freshwater resources, 36% of the world's energy; and produce about 40% of the world's greenhouse gas emissions (Ngwepe, 2015; Maslesa *et al.,* 2018; IEA, 2020). As almost all the buildings have a lifespan of over 50 years the operation stage is the longest, during which the performance of buildings relies on the proper operation and maintenance (O&M) (Lai *et al.*, 2007). For this purpose, the continuous monitoring at regular intervals is needed to identify indicators that precede failures and to perform necessary maintenance work at the right time. So, the so-called predictive maintenance starts with the BCA, which can be monitored by parameters that indicate the performance level, detecting early signs of failure leading to the beginning of maintenance procedures (Selcuk, 2017; Bortolini; *et al.*, 2016).

2.1 Building Condition Assessment

Building Condition Assessment (BCA) should be the basis for management and maintenance decisions in the built environment towards sustainable construction (Abbot *et al.,* 2007). BCA techniques have been studied and should be applied to measure assets performances during their service life, to consequently maintain them most effectively (CEN/ TS 17385:2019; Dejaco *et al.,* 2017; Wahida *et al*., 2012). According to Dejaco *et al.* (2017) and Marmo *et al.* (2019) to a BCA successfully oriented, the KPIs are the best way to measure the buildings' performance allowing to have accessible and useful information about buildings and their parts.

2.2 Key Performance Indicators (KPIs)

KPIs system aims to provide a measure of current performance and a clear statement of performance targets, as well as an evaluation of performance progress (Maslesa *et al*., 2018).

Building owners claim KPIs, mainly to understand the conditions of their assets and consequently, to allocate a suitable budget for maintenance or refurbishment and support their maintenance choices. Accordingly, the importance of measuring building performance through KPIs have been emphasized (Marmo *et al.,* 2019). Nevertheless, these methodologies mostly tend to evaluate the performance of the whole building and not the single components, mainly using analyses of users' satisfaction. For this reason, a Building Performance Indicator (BPI) was chosen for this study application, since it evaluates the performance of buildings and its systems.

2.2.1 Building Performance Indicator

The Building Performance Indicator (BPI) was developed by Shohet (a) *et al.* (2003); Shohet (c) (2003) Shohet (2006). A value between 0 and 100 defines this indicator, that expresses the building's state, by the performance evaluation of its various systems (Pn). The BPI is obtained by equation 1.

$$\text{BPI} = \sum_n P_n \times W_n \quad (1)$$

Where:

BPI - Building Performance Indicator (on a scale of 0-100):

Pn – Performance level for system n (on a scale of 0 to 100) as determined by equation 2.

Wn – Weight of each building system n, as determined by Life Cycle Costs (LCC).

The BPI value indicates the performance level of the building studied, according to the followed categories: BPI>80 indicates that the use of the building, and its subsequent performance, are good or better; 70<BPI<80 indicates that the state of the building is such that some of the systems are in marginal condition; 60<BPI≤70 reflects the deterioration of the building; BPI < 60 means that the building is run-down.

Each building's system is evaluated according to three criteria: actual physical performance of the systems (Cn); frequency of failures in building systems (Fn); and actual preventive maintenance carried out on the systems (PMn) and their correspondent weights $W(C)_n$, $W(F)_n$ and $W(pm)_n$. The combination of these three elements represents the performance level of the entire system (Pn) (Equation 2). This indicator has an economic component since it depends on the LCC.

$$P_n = C_n \times W(C)_n + F_n \times W(F)_n + PM_n \times W(pm)_n \quad (2)$$

For every system n, the sum $W(C)_n + W(F)_n + W(pm)_n = 1$.

Also, P_n and its components are graded according to performance scales between 0 and 100, like BPI. The weighting of each building system (Wn) is accomplished by weighting the contributions of the system's components to the total cost erection, maintenance, and replacement. The selection of this indicator is related to its reliability, and because it was previously validated by 6 experienced facility managers in maintenance (Lavy & Shohet, 2004).

2.3 KPIs integration within Building Information Modelling

According to ISO 29481-1(2014) BIM is a shared digital representation of the physical and functional characteristics of any built object, to facilitate design, construction and operation processes to form a reliable decision basis. In FM, BIM includes unified information base, consisting in a Big Data database, providing a building owner's manual, useful support for analysis, support for emergency response, security management and scenario planning (IFMA, 2013; Rodrigues et al., 2019). Revit is a BIM software offering a multi-disciplinary and collaborative approach to the design and construction process. To add extra functionalities to import/export data parameters from Revit to Excel, Dynamo tool can be used, as an add-in for extending Revit's parametric functionality and information retrieval (Autodesk Dynamo, 2020; Sadeghi *et al.*, 2019). Aboumoemen *et al.* (2017) verified that the linkage between BIM and KPIs to measure the building performance is an untimely task. So, in the present study, the potential of the linkage between BIM and KPIs to demonstrate the agility of the FM strategy researched is explored and verified.

3 Case Study

After the theoretical approach, the automated building performance indicator calculation and its extraction were applied to the Civil Engineering Department of Aveiro's University, built in 2004/2005, located in Aveiro, mainland Portugal.The methodology applied is described in the following points.

3.1 Building Information Collection

The Civil Department of Aveiro's University aims to provide an educational environment for its students and professors. With a plan area of 1613 m2, it is a building with four floors, one below the ground floor and three above the ground level, including the ground floor. Its main facade has a northeast orientation. Figure 1 is a plan of Aveiro's University Campus of Santiago representing in yellow the case study building location. The structural foundations are in reinforced concrete piles. The major part of the structure (columns and beams) are metallic, and the slabs are in reinforced concrete. The roof structure consists of steel columns and beams and tubular sections that support the metallic tile. The rainwater drainage system is characterized by galvanized zinc gutters and the dropp tubes in PVC-U. In terms of building interior finishing, the floors are in vinyl coating in the classrooms, and in the professors' offices the floor coating is in cork mosaic. The ceilings are mainly covered with plasterboard painted and in exposed concrete. The exterior doors and windows are in metallic profiles. In Figure 2, it is possible to observe a 3D model of the civil engineering department developed in Revit by Tavares (2019).

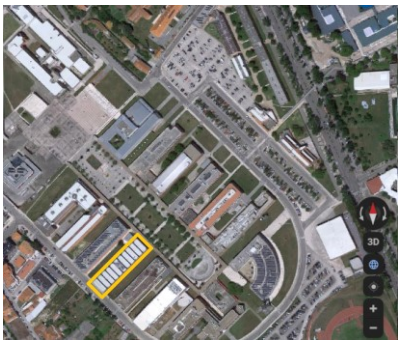

Figure 1. Building location in Aveiro's University Santiago Campus.

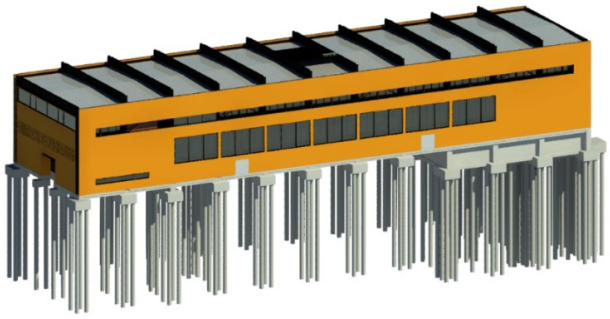

Figure 2. Revit model of the Civil Engineering Department of Aveiro's University (Tavares, 2019).

To understand the current periodicity of maintenance actions and to identify the main building anomalies, interviews with employees, lecturers and pivots in charge of management and maintenance of the building were carried out. The building plans, elevations, costs estimation and maintenance records were requested. Afterwards, a building inspection was accomplished and a report related to the assessment of buildings' deterioration state was done. Then, a set of building systems was selected to be evaluated by Pn's criteria such as windows, roofs, structural framing, structural columns, interior and exterior walls, mechanical and safety equipment, doors, drainage system, electric system, and lifts.

3.2 Building Life Cycle Cost Estimation

The economic contribution of each building system (Wn) selected to include in the BPI was

calculated by life cycle cost estimation. The contribution of each building system was given in percentage for the three alternative scales to include in BPI calculation: 1) Construction costs, 2) Maintenance Costs index, 3) Life Cycle Cost index. Despite being an essential step of this study, the results obtained in this step are not herein presented since it is out of this paper focus.

3.3 Automated Evaluation of BPI Supported by BIM

In this step, the integration of BPI into the Revit software with shared parameters and resourcing Dynamo to extract them as a final value to Microsoft Excel took place. In Revit software, the shared parameters are parameters attributed to the different object families with several types of information, which in this case allows associating the Cn, Fn, PMn, Wn(Cn), Wn(Fn) and Wn(Pmn) criteria and its contribution to each family objects. After the parameters attribution and based on the building inspection and the LCC calculated in the previous step of this methodology, it is possible to attribute to each system a quantifiable evaluation and contribution as depicted in the Revit schedule, automatically extracted, in Figure 3.

<KPI window>

A	B	C	D	E	F	G	H	I
EFM	Mark	Cn	Fn	PMn	Wn (Cn)	Wn (Fn)	Wn (PMn)	PN
Vão Envidraçado	F1	80	100	20	37.5	37.5	25	72.5
Vão Envidraçado	FX_2.1	60	80	20	37.5	37.5	25	57.5
Vão Envidraçado	FX_2.2	80	100	20	37.5	37.5	25	72.5
Vão Envidraçado	FX_2.3	60	80	20	37.5	37.5	25	57.5
Vão Envidracado	FX 2.4	60	80	20	37.5	37.5	25	57.5

Figure 3. Revit schedule with the parameters' values of the Building Performance Indicator.

The extraction of global values of each parameter for each building system to an Excel file is an essential task, after this one, to calculate the final value of the BPI. This task was accomplished through Dynamo programming tool.

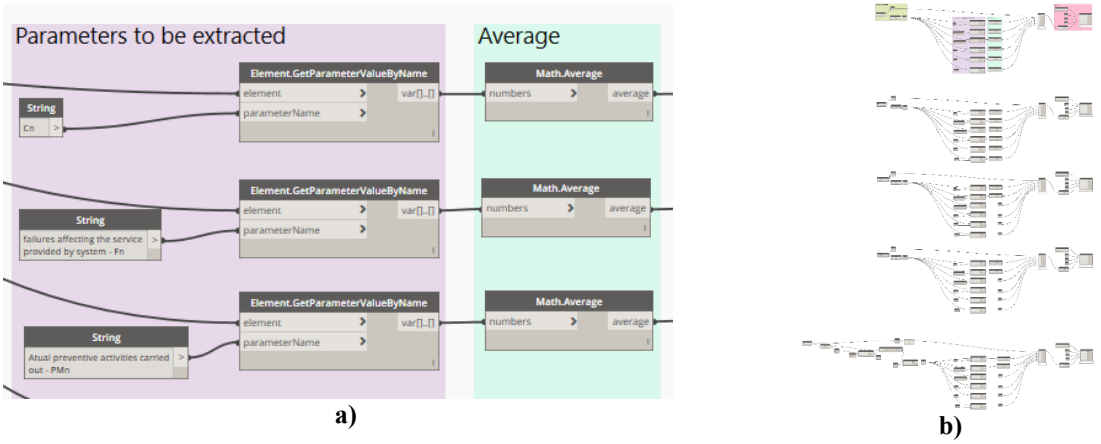

Figure 4 – **a)** Selection of parameters to be extracted and the calculation of the global value of each one. **b)** Piece of work from visual programming in Dynamo BIM to extract parameters from every category.

The interaction between the three software pretends to take advantage of its interoperability (Revit-Dynamo and Excel), to create an automated method that allows prioritizing maintenance actions. Thus, the Dynamo BIM allows selecting the category of elements and the parameters which is pretended to extract, generating the global value of each parameter correspondent to

each category of elements. Figure 4 shows part of the visual programming developed on the interface of Dynamo BIM software.

Then, the contribution of each element calculated for the total LCC in step 2 was included in the Excel sheet. After this, the BPI was calculated as presented in Figure 5.

Element	Cn	Fn	PMn	W(Cn)	W(Fn)	W(PMn)	Pn	Wn	BPI
Windows	73.78	79.49	21.54	37.50	37.50	25.00	62.86	7.86	4.94
Roofs	40.00	60.00	40.00	37.50	37.50	25.00	47.50	8.96	4.26
Structural Framing	78.39	100.00	20.00	45.00	45.00	10.00	82.28	9.85	8.10
Structural Columns	78.72	98.72	20.00	45.00	45.00	10.00	81.85	9.85	8.06
Walls Exterior	80.00	80.00	20.00	37.50	37.50	25.00	65.00	7.86	5.11
Walls Interior	80.00	80.00	20.00	35.00	35.00	30.00	62.00	17.49	10.84
Mechanical Equipment	20.00	20.00	20.00	20.00	20.00	50.00	18.00	2.45	0.44
Doors	79.62	80.00	40.19	35.00	35.00	30.00	67.92	17.49	11.88
Drainage system	80.00	80.00	50.00	37.50	37.50	25.00	72.50	3.18	2.31
Electric system	100.00	90.00	50.00	25.00	25.00	50.00	72.50	5.25	3.80
Elevators	100.00	100.00	80.00	30.00	30.00	40.00	92.00	8.28	7.62
Security (Fire, CTV)	100.00	100.00	60.00	37.50	37.50	25.00	90.00	1.49	1.34
							Total	100.0	68.70

Figure 5. Excel file with parameters and categories exported from Revit software by Dynamo software and BPI calculation.

3.4 Results Analysis

The value of the BPI obtained indicates the deterioration level of the building, meaning that preventive and break-down maintenance activities must be carried out since the value obtained is between $60<BPI\leq70$, according to the anomalies detection during the building inspection. Besides being a global performance indicator of the building, the BPI also allows defining the priorities of the maintenance actions about the building's systems. The Pn indicator should establish the intervention action priority of the systems. Through Figure 5, it is possible to observe that the HVAC system (Mechanical Equipment) has the lower Pn indicator, indicating that is the one that needs more urgent maintenance actions (preventive and corrective), followed in the second place by the roof system, and then by the windows framing, which is according to the building inspection done.

3.5 Application of "Color Splasher" to BIM Model

To simplify the maintenance management process, the values obtained in Figure 5 were categorized by colours, resourcing the color splasher BIM plug-in, which allows a quick recognition about building condition systems as it is presented in Figure 6.

The colour categorization to express the actual system's condition was done, in which red colour indicates urgency in system intervention and green colour indicates the satisfactory condition of the system.

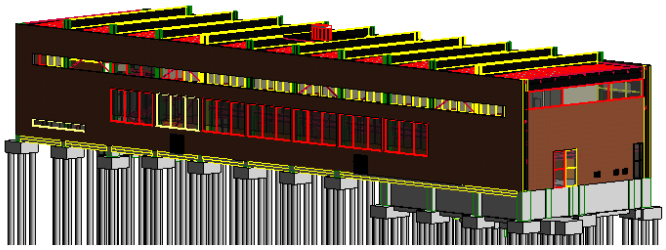

Figure 6. "Color splasher" application to 3D View of the building model.

With Figure 6, it is possible to observe easily and quickly that HVAC system, roof system, and windows framing are the ones that more urgently need maintenance actions, as mentioned above.

4 Final Conclusions

The methodology developed is innovative because it allows collecting and analyse the diversified information about building systems condition, permits calculating the systems' and the whole building`s performance in an automated way. This calculation is possible through shared parameters attributing the BPI parameters to Revit object families, and through interoperability Revit-Dynamo-Excel. Besides that, to facilitate the process of setting priorities of maintenance actions, the maintenance priorities were categorized by colours in the BIM model.

This methodology can be applied to any building typology and it is very relevant because its application allows prioritizing the maintenance actions in existing buildings, optimizes the building information sharing and facilitates building anomalies record and analysis. Moreover, its application leads to the easier building life cycle information retrieval, contributing to facility managers time and money-saving. The evaluation of systems performance leads facility managers in identifying anomalies early enough to minimize the impact of operational interruptions. So, faster maintenance processes and shorter periods of information disruption by using BIM was proved, and it motivates the FM implementation, which contributes to increasing the materials service life.

As a future study is proposed the development of an assessment approach, based on a set of KPIs, for measuring environmental building performance and green maintainability.

Acknowledgemnts

This research work was funded by the Portuguese Government through the FCT under the PhD grant SFRH/BD/147532/2019, awarded to the first author.

ORCID

Raquel V. Matos: https://orcid.org/0000-0002-0171-7842?lang=pt
Fernanda S. Rodrigues: https://orcid.org/0000-0001-9127-7766
Hugo F. Rodrigues: https://orcid.org/0000-0003-1373-4540
Aníbal G. Costa: https://orcid.org/0000-0001-8950-4843

References

Abbot, G. R. McDuling, J. J. Parsons, S. and Schoeman J.C. (2007). Building condition assessment: A

performance evaluation tool towards sustainable asset management. *CIB World Building Congress 2007. pp. 649-662: Construction for Development,* Cape Town, South Africa, 14-17 May.

Aboumoemen, A. and Underwood, J. (2017). A Bim Maturity-KPI Assessment : Literature Review. *13th International Postgraduate Conference,* September 2017, University of Salford, Salford, UK.

Autodesk Dynamo. (2020). What is Dynamo?. Available in https://primer.dynamobim.org/01_Introduction/1-2_what_is_dynamo.html

Bortolini, N. Forcada, M. and Macarulla, M. (2016). BIM for the integration of building maintenance management - a case study of a university campus. *In C. & Scherer (Ed.), eWork and eBusiness in Architecture, Engineering and Construction. Taylor & Francis Group.* ISBN 978-1-138-03280-4.

Crawford, R. (2011). *Life Cycle Assessment in the Built Environment.* In Book. In Spon Press (Ed.), Society. Taylor & Francis.

CEN / TS 17385. (2019). *CEN TS 17385: Method for Condition Assessment od Immobile Constructed Assets*. https://doi.org/ISBN:9780580519024.

Dejaco, M. C. Re Cecconi, F. and Maltese, S. (2017). Key Performance Indicators for Building Condition Assessment. *Journal of Building Engineering*, *9*, 17–28. https://doi.org/10.1016/j.jobe.2016.11.004.

IEA. (2020). International Energy Agency - Buildings - A source of enormous untapped efficiency potential. Available in https://www.iea.org/.

IFMA. (2013). *BIM for Facility Managers*. In Book. P. Teicholz (Ed.), John Wiley & Sons, Inc., Hoboken, New Jersey. ISBN: 978-1-118-38281-3.

ISO 29481-1. (2014). *International Organization for Standardization - ISO 29481-1:2014 - Building Information Models - Information delivery Manual - Part1: Methodology and format*.

Lai, J. H. K. and Yik, F. W. H. (2007). Monitoring building operation and maintenance contracts. *Facilities*, 25(5–6), 238–251. https://doi.org/10.1108/02632770710742200.

Lavy, S. and Shohet, I. M. (2004). Integrated maintenance management of hospital buildings: A case study. *Construction Management and Economics,* 22(1), pp.25–34.

Marmo, R. Nicolella, M. Polverino, F. and Tibaut, A. (2019). A Methodology for a Performance Information Model to Support Facility Management. *Sustainability*, 11(24), 7007. https://doi.org/10.3390/su11247007.

Maslesa, E. Jensen, P. A. and Birkved, M. (2018). Indicators for quantifying environmental building performance: A systematic literature review. *Journal of Building Engineering*, 19(March), pp.552–560. https://doi.org/10.1016/j.jobe.2018.06.006.

Ngwepe, L. (2015). A theoretical review of building life cycle stages and their related environmental impacts. Available at: https://core.ac.uk/download/pdf/54198925.pdf.

Rodrigues, F. Teixeira, J. Matos, R. and Rodrigues, H. (2019). Development of a web application for historical building management through BIM technology. *Advances in Civil Engineering*, 2019.

Sadeghi, M. Elliott, J. W. Porro, N. and Strong, K. (2019). Developing building information models (BIM) for building handover, operation and maintenance. *Journal of Facilities Management*, 17(3), 301–316. https://doi.org/10.1108/JFM-04-2018-0029.

Selcuk, S. (2017). Predictive maintenance, its implementation and latest trends. *Proceedings of the Institution of Mechanical Engineers, Part B: Journal of Engineering Manufacture, 231(9),* pp.1670–1679. https://doi.org/10.1177/0954405415601640.

Shohet (a), I. M. Lavy-Leibovich, S. and Bar-On, D. (2003). Integrated maintenance monitoring of hospital buildings. *Construction Management and Economics, Vol. 21(2),* pp.219–228.

Shohet (b), I. M. (2003). Key performance indicators for maintenance of health-care facilities. *Facilities, Vol.21*, pp. 5–12. https://doi.org/10.1108/02632770310460496.

Shohet (c), I. M. (2003). Building evaluation methodology for setting maintenance priorities in hospital buildings. *Construction Management and Economics, Vol.21(7),* pp.681–692. https://doi.org/10.1080/0144619032000115562.

Shohet, I. M. (2006). Key performance indicators for maintenance of healthcare facilities. *Journal of Construction Engineering and Management, Vol. 21(April),* pp.5–12.

Tavares, E. (2019). *Gestão do Património Edificado com Recurso ao BIM*, (In Portugueses), Master Thesis, Universidade de Aveiro, Aveiro, Portugal.

Wahida, R. N. Milton, G. Hamadan, N. Lah, N. M. I. B. N. and Mohammed, A. H. (2012). Building Condition Assessment Imperative and Process. *Procedia - Social and Behavioral Sciences, Vol. 65*(November 2015), pp.775–780. https://doi.org/10.1016/j.sbspro.2012.11.198.

XV International Conference on Durability of Building Materials and Components
DBMC 2020, Barcelona
C. Serrat, J.R. Casas and V. Gibert (Eds)

Assessment of Building Resistance to Accidental Actions in the Social Aspect of Sustainable Construction

Aleksandra Radziejowska[1] **and Anna Sobotka**[2]

[1] AGH University of Science and Technology in Cracow, Faculty of Mining and Geoengineering, Av. Mickiewicza 30, 30-059 Cracow, Poland, e-mail: aradziej@agh.edu.pl
[2] AGH University of Science and Technology in Cracow, Faculty of Mining and Geoengineering, Av. Mickiewicza 30, 30-059 Cracow, Poland, e-mail: sobotka@agh.edu.pl

Abstract. *In the article is considered one of the categories of social aspect of sustainable construction as specified in the standard EN 16309:2014 - namely: safety and security. The authors analyzed the component of the above-mentioned category with a subcategory called: resistance of buildings for accidental actions. The assessment criteria are: earthquake resistance, explosion resistance, fire performance and traffic impacts. A model of building's assessment of random interactions is presented, which will allow to make comparisons of the object's safety in the investigated ranges with other residential buildings, as well as with a reference building.*

Keywords: *Social Aspect, Security and Safety, Sustainable Construction, Accidental Actions.*

1 Introduction

Civil engineering is one of the main branches of the economy in which the goals of sustainable development are realized. According to (ISO 15392, 2008), three main aspects have been identified in sustainable construction: environmental, social and economic. Due to a number of studies and publications related to both the environmental and economic aspects, the authors focused on finding a model for assessing the social aspect, which is important for the user's comfort and health, especially in residential buildings (Yılmaz and Bakış, 2015).

Assessing the social aspect of a building is a difficult process. Only part of the assessed elements of the considered criteria can be quantified, compared with the parameters specified in legal acts and standards. On the other hand, such assessment allows to determine whether the object meets the examined criteria, thus allowing to obtain information about the facility's ability to meet the needs and expectations of users.

In this study, one of the subcategories of the sixth category (K_6) of social assessment regarding safety and security will be discussed and developed. Category K_6 Safety and security consists of four subcategories, which include: K_{61} *Resistance to climate change*, K_{62} *Safety and security against accidental actions*, K_{63} *Safety and security against intruders and vandalism* and K_{64} *Security against interruptions of utility supply* (EN 15643-1, 2011), (EN 15643-3, 2012). The subgroup that the authors presents concerns on K_{62} *Safety and security against accidental actions*, which consists of four criteria that will be included in the proposed assessment: K_{621} *Earthquake (rockburst mining),* K_{622} *Explosions,* K_{623} *Fire resistance* and K_{624} *Resistance to dynamic external actions* (Fig. 1). This publication is part of the work, which aims to present a comprehensive method of assessing the social aspect of sustainable construction.

2 Subcategory K_{62} Safety and Security Against Accidental Actions

The safety and security category is a measure of the building's ability to withstand current and future anticipated loads such as: rain, strong wind, snow, flood, fire, earthquake, explosion, landslide, etc., as well as protection against vandalism and crime and safety during use. It is a measure of the ability of buildings to provide safe shelter during exceptional events that may affect user safety.

In random impacts is assed building resistance (protection / forces / deformation / stability and safety) against accidental loads resulting from one-off events, e.g. earthquakes, explosions, fire and traffic, and their secondary effects (*e.g.* projectiles, toxic gases, crushed glass, etc.).

Figure 1 shows the division of the subcategory *Safety and security against accidental actions* (K_{62}), which is a component characterizing the *Safety and security* (K_6) category (EN 16309, 2014+A1). K_{62} is assessed by the criteria marked later in the article by the symbols $K_{621} \div K_{624}$. For the assessment of the criteria a discrete five-point scale was adopted, in which the most advantageous solution will assume the highest value equal to 5 (Radziejowska, 2018).

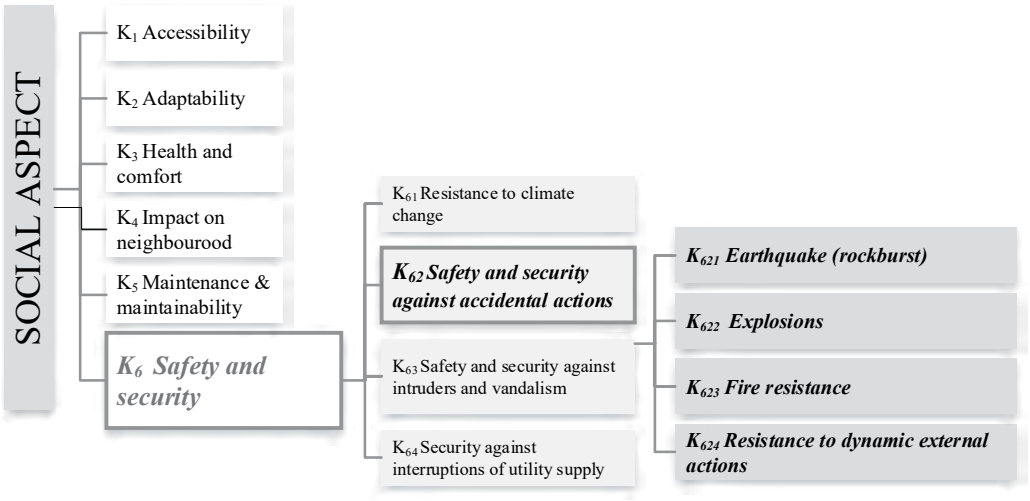

Figure 1. Fragment of the base structure of the criteria included in the proposed assessment (own elaboration).

3 Determining the Method of Evaluation of the Criteria

3.1 Determining the Scale of Parameter Values Characterizing the Criterion K_{621}

Criterion K_{621} *Earthquake resistance; rockburst mining* should be assessed through the use of protective measures in the building, which can be implemented by increasing structural stability, assembly of elements ensuring flexibility and shock resistance, resistant to breaking glass or alarm systems and gas and water shut-off valves.

Poland is located outside the areas of active tectonic plates, it is classified as aseismic zone. The specificity of our country, and more specifically the areas of mining basins, is the occurrence of paraseismic shocks, which are a consequence of underground mining operations. The phenomenon during which rapid destruction of the rock structure surrounding the excavation occurs as a result of exceeding their strength is called rockburst. The effect of such

a dynamic phenomenon in the rock mass (rapid rock relaxation) is the emission of vibrations, *i.e.* the seismic shock effect. Shock (seismic) waves propagate to the surface, which induce vibrations of buildings (Fig. 2 &3).

Figure 2. Cracks formed in a residential building in post-mining areas, around Bytom in Poland, 22/05/2011.

Figure 3. The uncontrolled dilatation of the building was created as a result of post-mining burst, around Bytom, 22/05/2011.

At the Central Mining Institute has been developed so-called Mining Scale of Intensity (Barański, 2014) for the area of the Upper Silesian Coalfield, based on the correlation of observed effects in buildings with the values of vibration parameters - so this is an empirical scale. The shock parameters necessary to assess the degree of vibration intensity on the surface for the GSIGZWKW-2012 scale are: the amplitude of the vibration speed and their duration.

Based on the existing GSIGZWKW-2012 scale, concerning the level of nuisance and related technical requirements necessary to be implemented shall be assessed the building's resistance to earthquakes (rock bursts) - criterion K_{621} - depending on the determined shocks according to a 5-point scale with levels with the following meaning: 5 - imperceptible nuisance, 4 - low nuisance, 3 - medium nuisance, 2 - high nuisance, 1 - very high nuisance (Table 1).

Table 1. Assessment of building resistance depending on the established level of nuisance and technical requirements for objects located in mining areas.

Scale of evaluation	Nuisance level					Technical requirements fulfilled
	Level 0	Level I	Level II	Level III	Level IV	
5	Fulfilled technical requirements for the considered level					
4		X				-
3			X			-
2				X		-
1					X	-

- not fulfilled technical requirements
+ technical requirements fulfilled

3.2 Determining the Scale of Parameter Values Characterizing the Criterion K_{622}

Criterion K_{622} *Explosions*, similarly to the previous one should be assessed by the applied protective measures or avoiding the use of explosive gases in buildings, installation of break-proof glass and separation of shelters inside

During the operation of residential buildings, there are two causes of disasters caused by explosions:

- gas explosion
- terrorist attack.

Construction disasters caused by an explosion are not common events, however, the consequences they carry are disproportionately high (Koccaz, Fatih Sutcu i Torunbalci, 2008).

In both causes of explosions in buildings, the method of protection should be similar and consist of the use of solutions that increase the building's resistance in this type of threat (Table 2).

Table 2. Assessment of residential buildings resistance to explosions.

Scale	Wired gas		Propane-butane gas		Gas detectors	Construction	
	with valve	without valve	with valve	without valve		resistant	no resistant
5	+				+	+	
4	+				+		+
			+		+	+	
3		+			+		
2			+				+
1				+			+

3.3 Determining the Scale of Parameter Values Characterizing the Criterion K_{623}

The next criterion for the assessed subcategory is K_{623} *Explosions*. In order to improve fire resistance, fire resistance of materials of higher classes than recommended can be used, which will improve the load-bearing capacity, integrity and / or insulation performance of building elements, improve access for fire brigades, make evacuation routes taking into account the needs of people with disabilities, install warning systems, smoke detectors, fire extinguishing systems in public areas, separate fire-cutting zones for the spread of fire, use fire-resistant products in places most exposed to fire (Fig. 4) (Phan, McAllister i Gross, 2010).

Figure 4. Fire extinguisher placed in the underground garage of a multi-family building 02/02/2016.

Figure 5. Entrance to the underground garage with a display informing about the concentration of carbon monoxide 12/06/2016.

Figure 6. Emergency exit from the underground garage in a residential building 11/10/2016.

An important element is also the users' awareness of the measures used in the event of

random events, which should be implemented by e.g. placing appropriate instructions in the common parts regarding evacuation or operating instructions for the use of fire-fighting equipment (Fig. 5&6).

For the assessment of *Fire safety* - criterion K_{623} - depending on the established safeguards, as in previous, a five-degree discrete scale was adopted, as is shown in Table 3.

Table 3. Fire safety assessment of buildings $\boldsymbol{K_{623}}$.

Scale	The degree of compliance with the requirements according to the Table 3				
	All 5 met	4 + 1 met to a limited extent	3 + 2 met to a limited extent	2 + 3 met to a limited extent	1+4 met to a limited extent
5	+				
4		+			
3			+		
2				+	
1					+

Where the requirements are:

1. *The proper load-bearing capacity of the structure in a timely manner after the fire*
2. *Limiting the spread of fire and smoke in the building*
3. *Limiting the spread of fire to neighboring buildings*
4. *The possibility of evacuating people*
5. *Ensuring the safety of rescue teams* (Infrastructure, 2002 and its subsequent amendments)

3.4 Determining the Scale of Parameter Values Characterizing the Criterion K_{624}

The last criterion in this subcategory is K_{624} *Resistance to dynamic external actions*, which can be implemented by applying measures for increased resistance to traffic influences, among which solutions such as: constructing barriers or strengthening the construction of building facilities located in areas at risk (Fig. 7&8).

Figure 7. Tram line running right next to multi-family buildings, Lisbon 31/12/2015.

Figure 8. Tram line and busy two-lane road in the Borek Fałęcki district in Krakow, 25/10/2016.

After consultation with an expert in the field of the impact of vibrations on people and buildings, it was assumed that the assessment of criterion K_{624} should be carried out separately

for both sub-criteria: *The impact of vibrations on people* (Table 4) i *Impact of vibration on buildings* (Table 5). It was determined that the final value less favorable from both grades obtained will be adopted.

Table 4. The impact of vibrations on people.

Scale	$a < a_{dop}$ *for direction x & y*	$a < a_{dop}$ *for direction z*	$a = a_{dop}$ *for direction x & y*	$a = a_{dop}$ *for direction z*	$a < a_{dop}$ *dla for direction x & y*	$a < a_{dop}$ *for direction z*
5	+	+				
4		+	+			
	+			+		
3			+	+		
2				+	+	
			+			+
1					+	+

where:
a – measured vibration acceleration
a_{dop} *- limit values for vibration acceleration*

Assessment of the impact of *vibration transmitted through the ground to buildings*, depending on the determined vibration results, a discrete five-degree scale with levels was adopted with the following meaning:
5 – imperceptible vibrations,
4 – noticeable but harmless,
3 – harmful,
2 – highly harmful (danger to the building and people's safety),
1 – causing building failure.

Table 5. Impact of vibration on buildings.

Scale	Impact of vibration on buildings				
	Zone I	Zone II	Zone III	Zone IV	Zone V
5	+				
4		+			
3			+		
2				+	
1					+

4 A Method Proposal for Assessing Building Resistance to Random Influences

The authors while developing the classes of standards in the assessed criteria for selected categories used, among others:

- national standards and regulations on technical conditions to be met by buildings and their location,
- expert research,
- direct surveys conducted among users,

– in situ research.

The proposed method assesses both quantitative and qualitative features. Qualitative features had to be processed into quantitative form by using the appropriate mathematical apparatus, e.g. fuzzy sets. Then all values were processed into non-denominated values, finally all criteria are evaluated using a discrete 5-point Likert scale, which allows comparison of features that were initially found in different physical measures. In addition, developing a method for quantifying grades required determining the weighting of the criteria. The final characteristics of the selected subcategory of the social aspect of the building is expressed in the form of a scalar function taking into account the weight of each criterion.

The vector below characterizes the subcategory (K_{62} *Safety and security against accidental actions*) of the social aspect together with the matrix of weights assigned to it.

$$O_{2j}^{6} = \left[o_{2,1}^{6} \quad o_{2,2}^{6} \quad o_{2,3}^{6} \quad o_{2,4}^{6}\right] \tag{1}$$

$$\Lambda_{2j}^{6} = \left[\lambda_{2,1}^{6} \quad \lambda_{2,2}^{6} \quad \lambda_{2,3}^{6} \quad \lambda_{2,4}^{6}\right] \tag{2}$$

where:

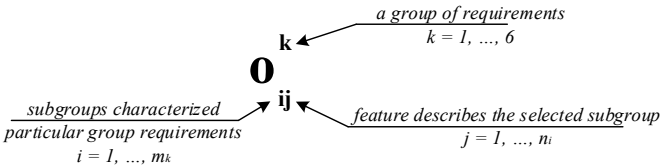

In the presented assessment it is proposed to use a corrected summation index (3), thanks to which a scalar function can be easily formulated, which allows the obtained result to be unequivocally interpreted.

$$O_i^k = \sum_{j=1}^{n_i} o_{ij}^k \ \lambda_{ij}^k = o_{i1}^k \ \lambda_{i1}^k + \cdots + o_{in_i}^k \ \lambda_{in_i}^k \tag{3}$$

where:

$o_{ij}^k = \left[o_{i1}^k, \ldots, o_{in_i}^k\right]$ – vector of the assessed features of the subgroup and,

$\lambda_{ij}^k = \left[\lambda_{i1}^k, \ldots, \lambda_{in_i}^k\right]^T$ – weight vector for features included in the assessment.

The above calculations should be made for the tested building as well as for the reference building. The reference building (reference building) will be treated as a hypothetical building designed in accordance with applicable standards and common practice and having the same technological, construction and functional parameters as the building being assessed. The reference building is to be used for carrying out comparative calculations with the analyzed object (Owczarek, 2006) .

The obtained values should be compared with the assessment obtained by the reference object, which will allow to assess how well the examined object is assessed in the scope of this subcategory. The information obtained from the calculations will indicate the weakest features that the analyzed building has, which will allow it to take appropriate action in the refurbishment policy in the future (Radziejowska, 2018).

5 Conclusions

The method of standardizing subcategory evaluations proposed in the work on the example of

K_{62} is a contribution to the unification of the assessment of social performance of sustainable construction. The established threshold values, the adopted scale of assessments for the considered criteria, as well as the weights assigned to individual criteria and subcategories are largely based on expert research.

The presented method of assessing the social aspect of sustainable construction based on the example of subcategory K_{62} allows to make a comparison regarding the building's resistance to random events between the tested building and the reference object, as well as between buildings made in different technologies. In the longer term, it will determine the scope of the planned refurbishment of the building, and may also be helpful in valuing the property.

Acknowledgements

The work was carried out as part of statutory research no. 11.11.100.197 in the Department of Geomechanics, Civil Engineering and Geotechnics of Faculty of Mining and Geoengineering, AGH University of Science and Technology in Cracow.

ORCID

Aleksandra Radziejowska: https://orcid.org/0000-0002-3190-7129
Anna Sobotka: https://orcid.org/0000-0002-4477-8821

References

Barański, A. K. (2014). Intensity scale GSIGZWKW-2012 in relation to the dynamic resistance of buildings. *Bezpieczeństwo Pracy i Ochrona Środowiska w Górnictwie*, strony 3-10.

EN 15643-1, s. (2011). Sustainability of construction works. Assessment of social performance of buildings. Calculation methodology. Standardization Committee.

EN 15643-3, s. (2012). Sustainability of construction works. Assessment of buildings. Framework for the assessment of economic performance. Standardization Committee.

EN 16309, s. (2014+A1, 12). Sustainability of construction works - Assessment of social performance of buildings - Calculation methodology. Standardization Committee.

Infrastructure, M. o. (2002 and its subsequent amendments, April 12). The Regulation on the technical conditions that should be met by buildings and their location (Dz. U. Nr 75, poz. 690 z późn. zm.).

ISO 15392, s. (2008). Sustainability in building construction -- General principle.

Koccaz, Z., Fatih Sutcu, F. and Torunbalci, N. (2008, October 12-17). Architectural and structural design for blast resistant buidlings. Beijing, China: The 14th World Conference on Earthquake Engineering.

Owczarek, S. O. (2006). Reference building - basis of estimate building condition. *Prace Naukowe Instytutu Budownictwa Politechniki Wrocławskiej. Studia i Materiały*, strony 333-339.

Phan, L., McAllister, T. and Gross, J. (2010, November). Best Practice Guidelines for Structural Fire Resistance Design of Concrete and Steel Buildings. *NIST Technical Note 1681*. National Institute of Standards and Technology, U.S. Department of Commerce.

Radziejowska, A. (2018). A method of assessing the social performance of residential buildings in the aspect of sustainable construction. *dissertation*.

Yılmaz, M. and Bakış, A. (2015, July). Sustainability in Construction Sector. *Procedia - Social and Behavioral Sciences*, strony 2253-2262.

XV International Conference on Durability of Building Materials and Components
DBMC 2020, Barcelona
C. Serrat, J.R. Casas and V. Gibert (Eds)

Behaviors of Concrete with Recycled Clay Brick as Fine Aggregate

Wencui Yang, Xiaoping Cai and Duojie Jiangjiu

School of Transportation Science and Engineering, Harbin Institute of Technology, 73 Huanghe Road, Nangang District, 150090, Harbin, China, yangwencui@hit.edu.cn, caixiaoping@hit.edu.cn

Abstract. *Massive waste materials were produced by the construction and demolition industry every year. In residential constructions, clay bricks are a dominant material and they account for a large proportion of construction and demolition waste. Using crushed bricks in cement concrete is an effective way to preserve natural aggregate and to reduce construction and demolition waste. The mechanical properties, the permeability and the carbonation resistance of concrete with recycled clay brick as fine aggregate were studied in this paper. The results showed that the compressive strength, the flexural strength and the impermeability of concrete decreased with the increasing of the replacement percent of recycled clay brick. However, the permeability of concrete with the water to cement ratio of 0.35 was still at the "Low" level when the replacement percent was less than or equal to 75%. The carbonation resistance of concrete using recycled clay bricks as fine aggregate was degraded.*

Keywords: *Construction and Demolition Waste, Fine Recycled Aggregate, Clay Brick, Durability.*

1 Introduction

Vast amounts of waste materials are produced by the construction and demolition industry every year. The volume of these materials has reached an unacceptable level from an environmental, economic and social point of view (Vieira *et al*., 2016). In residential construction, clay bricks are a dominant material, so they account for a large proportion of construction and demolition waste (Crowther, 2000; Formoso *et al*., 2002). Since concrete is the most widely used construction materials in the world, using crushed bricks in concrete is an effective way to preserve natural aggregate and to reduce construction and demolition waste.

Several studies have been conducted to investigate the potential of using clay brick as aggregates. Poon and Chan (2006) investigated the possibility of using crushed clay brick as aggregates in sub-base materials. A study by Lan Zong showed the permeability of water, air and chloride ions increased when recycled coarse aggregates were used. Additionally, the recycled concrete containing clay brick waste had increased porosity and exhibited a loose paste matrix (Zong *et al*., 2014). Schackow used a powdered（<45μm）fired clay brick clean waste to replace Portland cement, and 28 and 90 days-compressive strength, water absorption, apparent porosity, absorption by capillarity, chloride retention, carbonation depth and sulphate resistance were evaluated. According to the results, they suggested that a moderate clay brick clean waste addition (up to 10 wt.%) is desirable if a comparable workability is desired (Schackow *et al*., 2015). Adamson's research (2015) showed that the natural coarse aggregates can be replaced by crushed bricks, without significant change in the durability of concrete when the steel is not present. However, when concrete is reinforced with steel, replacing natural aggregates with crushed brick is not recommended. Bektas's study (2009)

doi:10.23967/dbmc.2020.016

indicated that as the brick replacement level increased, the mortar flow ability reduced. The 10% and 20% brick replacements had no negative effect on the mortar compressive strength and very limited effect on the mortar shrinkage.

This paper reports a study with the aim to investigate the mechanical properties and durability of concrete with recycled clay brick as fine aggregate. By conducting a sort of laboratory experiments, the compressive strength, flexural strength, permeability and carbonation resistance of concrete with recycled clay brick were studied.

2 Experimental Program

2.1 Materials

Ordinary Portland Cement (P·O 42.5) was used in accordance with China National Standard GB/175-2009, and Table 1 summarized its properties.

Table 1. Chemical and physical properties of cement.

Initial setting time (min)	Final setting time (min)	Tensile strength (MPa)		Compressive strength (MPa)	
		3d	28d	3d	28d
190	250	4.2	7.1	22.9	43.8

Natural river sand was used as fine aggregate, the fineness modulus of river sand was 2.9. Crushed limestone was used as coarse aggregate, and the grading of coarse aggregate is given in Table 2. Recycled clay bricks were broken into pieces. And the grading of recycled clay brick was controlled as the requirements of Chinese National Standard GB/T 25176-2010. Table 3 and Table 4 show the properties and the gradation of the recycled clay bricks as fine aggregate. A super plasticizer was used to adjust the workability of concrete.

Table 2. The grading of coarse aggregate.

Sieve pore size (mm)	19.0-26.5	16.0-19.0	9.5-16.0	4.75-9.5
Percentage (%)	25	25	35	15

Table 3. The properties of recycled clay brick.

Apparent density (g/cm^3)	Packing density (kg/m^3)	Close packing density (kg/m^3)
2.34	899	994

Table 4. The grading of recycled clay brick as fine aggregate.

Sieve pore size (mm)	4.75	2.35	1.18	0.6	0.3	0.15	<0.15
Percentage (%)	2	7	10	30	36	13	2

2.2 Mix Proportions and Sample Preparation

The proportions of reference concrete with the water to cement ratio of 0.35 and 0.47 are given in Table 5. The recycled clay brick was introduced as volume percentage of the

concrete fine aggregate, and four levels of replacement, 25%, 50%, 75% and 100%, were investigated.

Due to the high water absorption of recycled clay brick, it is suggested to soak the brick aggregate in water prior to adding to concrete [Khalaf, 2005; Khalaf, 2006; Cachim, 2009]. Therefore, this procedure was adopted in this work for recycled clay brick. The recycled clay brick aggregate was soaked in water for 24h and added to concrete mixture in a saturated condition.

Table 5. Mixture proportions of reference concrete (kg/m^3).

W/C	Water	Cement	Sand	Gravel	Super plasticizer
0.35	175	500	629	1106	4.5
0.47	175	372	702	1151	4.5

2.3 Methods

2.3.1 Mechanical properties

The compressive strength and flexural strength of concrete were tested at 28d age. The compressive strength specimens with the size of 100mm×100mm×100mm and the flexural strength specimens with the size of 100mm×100mm×400mm were tested in accordance with the Chinese standard GB/T 50081-2002.

2.3.2 Carbonation resistance

The concrete cubes with the size of 100mm×100mm×100mm were casted, and the samples were demoulded after 24h and cured in the standard curing condition until 28 days, then the samples were placed in a carbonation chamber with the CO_2 concentration of 20%, the temperature of 20°C and the RH of 70%. The carbonation depth was determined at the start of exposure and after 3, 7, 14 and 21 days according to Chinese standard GB/T 50082-2009.

2.3.3 Permeability

The permeability of concrete was measured at 28d age according to the Chinese standard GB/T 50082-2009, and the size of specimen was φ100mm×50mm.

3 Test Results and Discussion

3.1 Mechanical Properties

Table 6 demonstrates the compressive strength and the flexural strength obtained from the concrete samples with different replacement of recycled clay bricks. Each data represents the average of three samples. It was observed that with the increasing of recycled clay brick content, both the compressive strength and the flexural strength decreased. When the water to cement ratio was 0.35, the compressive strength loss of approximately 20% at 28 days was observed in concrete produced with 25% recycled clay brick replacement ratio. The reduction in compressive strength was observed more significantly in concrete with 75% or more replacement ratio as it decreased over 30%. The compressive strength of concerte with the

water to cement ratio of 0.47 showed the similar change, and the decrease of compressive strength was more than 30% when 25% recycled clay brick was added. It was shown the replacement of recycled clay bricks had more influence on the concrete with higher water to cement ratio.

Table 6. Mechanical properties of concrete (28d).

W/C	Replacement percentage (%)	Compressive strength (MPa)	Flexural strength (MPa)
0.35	0	51.8	6.0
	25	42.3	4.8
	50	41.5	4.1
	75	35.2	3.8
	100	32.3	3.6
0.47	0	48.3	4.5
	25	33.2	4.1
	50	31.2	3.7
	75	26.8	3.4
	100	24.3	3.1

3.2 Permeability

The electric flux method was used to evaluate the permeability of concrete to chlorides, and the results was described in Figure 1. It can be found that with the increasing of the recycled clay brick content, the impermeability decreased. According to ASTM C1202, the permeability of concrete to chlorides could be divided into 5 classes by charge passed, which is shown in Table 7. When the water to cement ratio was 0.35 and the replacement percent of recycled clay brick was less than or equal to 75%, the permeability of concrete could be evaluated as “Low”. When the water to cement ratio was 0.47 and the replacement percent of recycled clay brick was less than or equal to 25%, the permeability of concrete could be evaluated as “Low”.

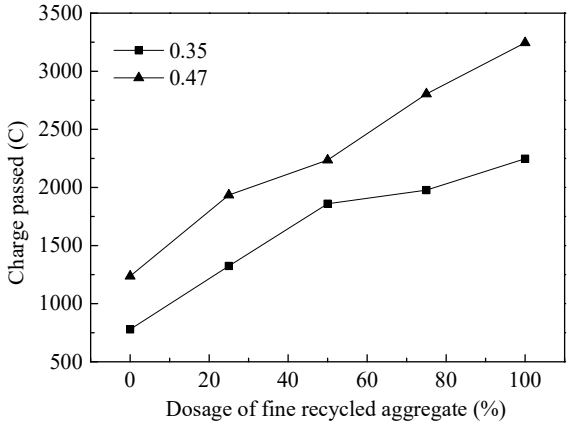

Figure 1. Effect of the dosage of fine recycled aggregate on the permeability of concrete.

Table 7. Chloride ion penetrability based on charge passed.

Electric flux（6h, C）	Permeability
＞4000	High
2000-4000	Moderate
1000-2000	Low
100-1000	Very low
＜100	Negligible

3.3 Carbonation Resistance

The effect of the dosage of fine recycled aggregate on the carbonation depth of concrete is described in Figure 2. Generally, concrete with higher water to cement ratio has more pores, and CO_2 could get into concrete much easier through these pores. Consequently, the carbonation depth increased with the increasing of water to cement ratio for all test age. The carbonation depth also increased with the increasing of the test age and the replacement level of recycled clay brick. The porous recycled clay brick may carbonate considerably faster than the concrete with natural aggregate, causing a increase of the carbonation depth which was shown in Figure 3.

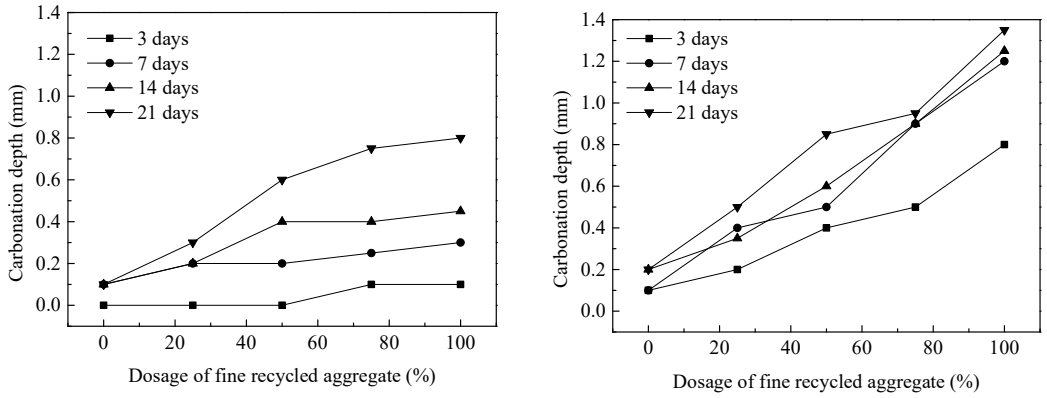

(a) *W*/*C*=0.35. (b) *W*/*C*=0.47.

Figure 2. Effect of the dosage of fine recycled aggregate on the carbonation depth of concrete.

Figure 3. Surface of split concrete cube with the replacement level of 100% used in the carbonation test after being sprayed with phenolphthalein at 21days (*W*/*C*=0.47).

4 Conclusions

Based on the above experimental results, some conclusions could be drawn below:

- Both the compressive strength and the flexural strength decreased with the increasing of the replacement percent of recycled clay brick.
- The impermeability of concrete decreased with the increasing of the replacement percent of recycled clay brick. But the permeability of concrete with the water to cement ratio of 0.35 was still kept at "Low" level when the replacement percent was less than or equal to 75%.
- The carbonation resistance of concrete using recycled clay bricks as fine aggregate was degraded.

Acknowledgment

The investigation and results reported in this paper are supported by Technology Program (Technology-2014-04-002) from Guang Dong Province Department of Transportation, Technology Program (JCYJ20150831200925298) from Science and Technology Innovation Committee of Shen Zhen, and Technology Program (JX2016CG-F014) from Housing and Construction Bureau of Shen Zhen.

ORCID

Wencui Yang: https://orcid.org/0000-0002-5006-9888

References

Adamson. M, Razmjoo. A and Poursaee. A. (2015). Durability of concrete incorporating crushed brick as coarse aggregate [J]. *Construction and Building Materials*, 94, 426-432.

Bektas. F, Wang. K and Ceylan. H. (2009). Effects of crushed clay brick aggregate on mortar durability [J]. *Construction and Building Materials*, 23, 1909-1914.

Cachim P.B. (2009). Mechanical properties of brick aggregate concrete. *Construction and Building Materials*, 23, 1292-1297.

Crowther P. (2000). Building deconstruction in Australia. Overview of Deconstruction in Selected Countries, *CIB Report*, No. 252, 28.

Formoso. C.T, Soibelman. L, Cesare. C.D and Isatto E.L. (2002). Material waste in building industry: main causes and prevention [J]. *Journal of Construction Engineering and Management*, 128, 316-325.

Khalaf. F.M. (2005). Properties of new and recycled clay brick aggregates for use in concrete [J]. *Journal of Materials in Civil Engineering*, 17, 456-464.

Khalaf F.M. (2006). Using crushed clay brick as coarse aggregate in concrete [J]. *Journal of Materials in Civil Engineering*, 18, 518-526.

Poon. C.S and Chan. D. (2006). Feasible use of recycled concrete aggregates and crushed clay brick as unbound road sub-base. *Construction and Building Materials*, 20, 578-585.

Schackow. A, Stringari. D and Senff. L. et al. (2015). Influence of fired clay brick waste additions on the durability of mortars [J]. *Cement and Concrete Composites*, 62, 82-89.

Vieira. T, Alves. A and Brito. J. de, et al. (2016). Durability-related performance of concrete containing fine recycled aggregates from crushed bricks and sanitary ware [J]. *Materials and Design*, 90, 767-776.

Zong Lan, Fei Zhengyue and Zhang Shiping. (2014). Permeability of recycled aggregate concrete containing fly ash and clay brick waste [J]. *Journal of Cleaner Production*, 70, 175-182.

XV International Conference on Durability of Building Materials and Components
DBMC 2020, Barcelona
C. Serrat, J.R. Casas and V. Gibert (Eds)

Durability of Mortars Packaged with Production Waste of Autoclaved Aerated Concrete

Maurizio Nicolella[1], Claudio Scognamillo[2] and Federica Vitale[3]

[1] Department of Civil, Architectural and Environmental Engineering (DICEA), University of Naples Federico II, 80125-Naples, Italy, maurizio.nicolella@unina.it

[2] Department of Civil, Architectural and Environmental Engineering (DICEA), University of Naples Federico II, 80125-Naples, Italy, claudio.scognamillo@unina.it

[3] Department of Civil, Architectural and Environmental Engineering (DICEA), University of Naples Federico II, 80125-Naples, Italy, federica.vitale@unina.it

Abstract. *The building sector is responsible for the introduction of about 40% of the waste in the environment (60 Mtons per year in Italy), with serious consequences for our future. Therefore, the statistics of the last few years have induced many researchers and many companies to investigate more sustainable products and technologies. Among these strategies, the re-use of waste materials has been widely encouraged. Many solutions have been proposed in the field of mortars for which the use of waste products such as ceramic materials, polystyrene, clay, concrete, has been tried out. The results have often been encouraging, especially for masonry mortars. Nevertheless, very few attempts have been made to place this type of products on the market. Moreover, the "younger" building materials such as Autoclaved Aerated Concrete have not been fully investigated in their potential use as recycled aggregates. The goal of this research was to evaluate the characteristics of mortars packaged with different percentages of production waste of Autoclaved Aerated Concrete components as aggregates, in order to assess the possible use of these conglomerates as masonry mortars or as plasters. The first campaign included tests for determining mechanical resistance, density, capillary water absorption, adherence to substrate, resistance to carbonation. The tested mortars had satisfactory mechanical characteristics and generally exhibited a good capacity to withstand the actions of atmospheric agents. Finally, the results highlighted the direct connection between Autoclaved Aerated Concrete percentage and mechanical and durability properties.*

Keywords: *Building Materials Production Waste, Carbonation, Lightweight Aggregates, Recycled Conglomerates, Sustainability.*

1 Introduction

The reuse of building waste materials in sustainable concretes or mortars has raised over the last years due to the environmental impact of building constructions. Building materials production waste is preferred rather than Construction and Demolition one due to its controlled chemical composition. The replacement of ordinary aggregates with production waste ones generally affects the mechanical performances of concretes or mortars owing to the low density of recycled aggregates (de Brito *et al.,* 2005; Ćosić *et al.*, 2015).

Nepomuceno, Isidoro and Catarino (2018) suggested a 30% threshold value of volume-replacement percentage of natural coarse aggregate with recycled ceramic in case of structural concrete. Actually, an increase of porosity and of average pore diameter is observed when the recycled aggregates are used (Anastasiou *et al.,*2018; Dang *et al.*, 2019). The accretion of

macropores and the reduction of micropores increases the resistance to external sulphate attack as a consequence of the lower capillary pores transport phenomena (Coppola *et al*., 2018). Moreover, the porosity improves the thermal insulation performances of mortars (Khan, 2002; Mendes *et al*., 2019).

Despite the raising interest on recycled lightweight aggregates, it is presently unclear whether the high porous structure of the recycled conglomerates affects their durability due to the microstructural changes induced by the aggregates. In particular, the relation between recycled mortars morphology and their carbonation resistance has not been fully investigated.

In order to analyze the effects of the use of a production waste lightweight material on the physical, the mechanical and the resistance to carbonation properties of conglomerates, five groups of mortars packaged with an increasing percentage by mass of Autoclaved Aerated Concrete (AAC) recycled aggregates were tested and compared. The changes in density, porosity, water adsorption, mechanical strengths and carbonation depths were measured.

The results of this study may be used to define the threshold of AAC aggregate percentage with the respect to the application of conglomerate as masonry mortars or as renderings and plasters.

2 Materials and Methods

2.1 Materials

The tested mortars were packaged with natural hydraulic lime (NHL 5 according to UNI EN 459-1:2010 standard) supplied by TSCcalce.

A natural siliceous sand and a recycled Autoclaved Aerated Concrete were used as aggregates. The natural sand was provided by Bacchi s.p.a and its apparent density, stated by the manufacturer, was 1460 kg/m^3. The recycled aggregate was supplied by Bacchi s.p.a, resulted from the production waste of Autoclaved Aerated Concrete (AAC) wall components. The particles size distribution of the recycled aggregate was measured through the dry sieving method according to UNI EN 933-1: 2012 and it is shown in Figure 1.

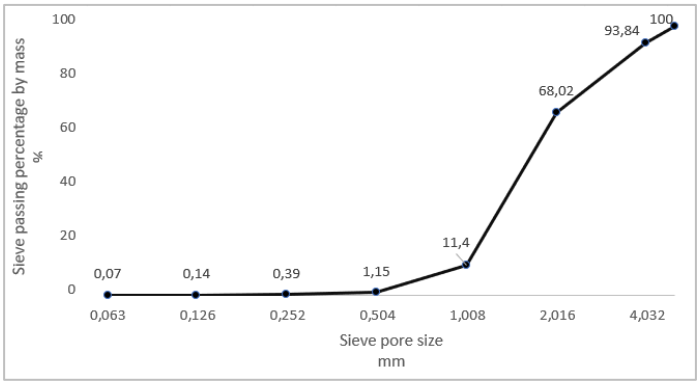

Figure 1. Particle size distribution of Autoclaved Aerated Concrete recycled aggregates according to the sieving test method.

The particle density and the water adsorption of AAC aggregates were analyzed according to UNI EN 1097-6:2013 pycnometer method for aggregate particles passing 4 mm test sieve and retained on the 0,063 mm test sieve. The outcomes are shown in Table 1.

Table 1. Particle density and water adsorption of Autoclaved Aerated Comcrete recycled aggregates.

M1 (g)	M2 (g)	M3 (g)	M4 (g)	ρ_{rd} (kg/m^3)	ρ_{ssd} (kg/m^3)	ρ_a (kg/m^3)	W (%)
77,93	477,73	452,29	45,11	860	1480	2290	72,76

M1, saturated and surface dried mass in air; M2, mass of pycnometer containing the saturated aggregate sample and the water; M3, mass of pycnometer filled with water only; ρ_{rd}, oven dried particle density; ρ_{ssd}, saturated and surface dried particle density; ρ_a, apparent particle density; W, water adsorption.

The chemical composition of the recycled aggregates was determined by a ThermoGravimetric Analysis (TGA) using a Netzsch- STA 409 PC Luxx apparatus. The mass losses of an AAC aggregate sample of 20 mg were monitored over time as the sample was heated in a controlled atmosphere. The temperature ranged from 23° to 1200° with a 10°/min heating rate. The mineralogical composition of AAC aggregates was analyzed by X-ray Diffraction (XRD) technique using a Philips X'pert PRO multipurpose powder diffractometer with X-ray wavelength of 1,54 Å. The outcomes were compared with the standard patterns of the International Centre for Diffraction Data database. The main mineralogical phases were Silicon Oxide, Calcium Carbonate, Calcium Hydroxide Hydrated Silicates and Calcium Sulfate Hydrated. A distilled water was used as kneading water.

Five groups of mortars with five specimens in each group were analyzed. All the tested specimens were packaged using the hydraulic lime and a binder-aggregate ratio of 1:3 by mass. The first group – noted 1 - was taken as reference and it was composed of mortars with 100% natural aggregate percentage. In the other four groups – noted 2,3,4,5 - the natural sand was gradually replaced with an increasing percentage by mass of recycled aggregate from 12,5% to 50%. The water – binder ratio of 2,3,4,5 was adjusted due to AAC aggregate water adsorption. Table 2 shows the compositions of the tested mortars.

Table 2. Compositions of tested mortars.

	HL (g)	SS (g)	AAC (g)	W (g)	W/B	RA (%)
1	450	1350	0	225	0,50	0
2	450	1181,25	168,75	337,5	0,75	12,5
3	450	1012,50	337,50	450	1,00	25
4	450	843,75	506,25	562,5	1,25	37,5
5	450	675	675	675	1,50	50

HL, hydraulic lime; SS, siliceous sand; AAC, Autoclaved Aerated Concrete recycled aggregates; W, kneading water; W/B, water/binder ratio; RA, AAC percentage by mass on the total aggregates.

2.2 Methods

2.2.1 Mixing procedure of mortars and testing program of physical, mechanical and resistance to carbonation properties

Physical, mechanical and resistance to carbonation tests were performed on prismatic specimens according to UNI EN 196-1:1996 specifications. The natural sand and the recycled

aggregates were dry premixed before they were blended with the hydraulic lime and the kneading water. The specimens were molded in prismatic casts (40x40x160 mm) and cured in a climatic chamber (MSL Humichamber EC 125) under controlled conditions according to UNI EN 1015-11:2007. Three specimens of each group were tested for density, porosity, water adsorption, compressive and flexural strength, two specimens of each group were tested for resistance to carbonation.

2.2.2 Apparent and bulk dry densities, open porosity and water adsorption

The tests were conducted according to UNI EN 1936:2007 specifications. The prismatic specimens were dried in an oven at 70±5° temperature until a constant mass was recorded.

As the mass was stabilized, the three specimens of each group were weighted and their dry mass M1 was recorded. Then the dry specimens were stored for 24h under vacuum in a vessel in which the pression was gradually lowered to 15±5 mmHg. After this period a volume of water was introduced in the vessel so that the specimens were immersed for at least 5 mm. The specimens were kept under vacuum and immersed in water for 24h with the same pression of 15±5 mmHg. Finally, the pression was returned to the atmospheric value and the specimens were left immersed for other 24h. After the 72h storage the immersed specimens were weighted and the M2 value was recorded. The mortars were then wiped with a cloth and the mass of the saturated specimens, noted M3, was measured.

The apparent (ρ_a) and the bulk (ρ_r) densities, the open porosity (p) and the water adsorption (W) were finally calculated using the UNI EN 1936:2007 equations.

2.3 Mechanical Properties

The compressive and the flexural resistance tests were performed according to UNI EN 1015-11:2007 procedure using the Alpha Technologies Tensometer 2020 machine. The compressive load cells were of three types: groups 3,4,5 were tested with 5kN, group 2 with 10kN and group 1 with 15kN. The flexural load cells were 5kN for groups 4,5 and 10kN for groups 1,2,3.

2.3.1 Adherence on substrates test

The adhesive strength of mortars on substrates was measured according to UNI EN 1015-12:2016 procedures. Three different substrates - brick, tuff and lapil-cement - were tested and their fracture patterns were compared.

2.3.2 Resistance to carbonation

The resistance to carbonation test and the analysis of the results were conducted according to UNI EN 13295:2005 indications. The carbonation depth was measured according to UNI EN 14630:2003 procedures. The measurement was repeated only two times - on 15th and on 30th day- because all the specimens were fully carbonated after thirty days.

3 Results

3.1 Apparent and Bulk Dry Densities, Open Porosity and Water Adsorption

The apparent and the bulk dry densities, the open porosity and the water adsorption of the tested

mortars are shown in Table 3. The mean values for the three specimens of each group are reported. The reference mortar -1- exhibited an apparent density 66% higher than the group 5.

The open porosity and the water adsorption of group 5 were respectively twice and three times as high as group 1.

Table 3. Apparent and bulk dry densities, open porosity and water adsorption. Mean values of the three specimens of each group are reported.

	ρ_a (g/cm^3)	ρ_r (g/cm^3)	*p* (%)	*W* (%)
1	1,75	2,24	22	12,58
2	1,51	2,13	29	19,35
3	1,27	1,95	35	27,12
4	1,20	1,91	37	31,07
5	1,05	1,87	44	41,53

ρ_a, apparent dry density; ρ_r, bulk dry density; p, open porosity; W, water adsorption

3.2 Mechanical Properties

The mean values of flexural and compressive strength are reported in Table 4. The flexural resistance of group 4 was tested only on two specimens due to the breakage of one sample during the curing period. The group 5 exhibited a flexural and a compressive resistance fifteen and ten times, respectively, as low as mortars of group 1.

Table 4. Flexural and compressive strength. Mean values of the three specimens of each group* are reported.

	σ_f (MPa)	σ_c (MPa)
1	2,62	6,93
2	1,54	4,53
3	0,67	1,49
4	0,13	0,90
5	0,17	0,57

* Except for flexural resistance of group 4 (mean values of two specimens); σ_f , flexural resistance; σ_c, compressive resistance.

The compressive strength values were compared to UNI EN 998-2:2016 and to UNI EN 998-1:2016 specifications with respect to the classes of masonry and rendering or plastering mortars, respectively. The classification of the tested mortars is reported in Table 5.

3.3 Adherence on Substrates Test

The adhesive strength of mortars on each of the tested substrates is shown in Table 6. Mean values of recorded resistance are reported along with UNI EN 1015-12:2016 fracture pattern classification. The A, B, C pattern types referred to an adhesion fracture at the interface between mortar and substrate, to a cohesion fracture in the mortar itself and to a cohesion fracture in the substrate material, respectively.

Table 5. Classification of the tested mortars according to UNI EN 998-1,2:2016.

	UNI EN 998-2	UNI EN 998-1	
	Table 1	Table 1	Table 2
1	M5	CS III/ IV	GP-LW-CR-OC
2	M2,5	CS II/ III	GP-LW-CR-OC-R-T
3	M1	CS I	GP-LW-CR-OC-T
4	/	CS I	GP-LW-CR-OC-T
5	/	CS I	GP-LW-CR-OC-T

/ not classified; GP general purpose; LW lightweight rendering/plastering; CR coloured rendering mortar; OC one coat rendering mortar for external use; R renovation mortar; T thermal insulation mortar

Table 6. Adhesive strength on substrates. Mean values of resistance and fracture pattern type are reported.

	Brick		Tuff		Lapil-cement	
	f_u (MPa)	FP	f_u (MPa)	FP	f_u(MPa)	FP
1	0,24	A	0,29	B/C	0,56	A
2	0,34	A	0,34	B/C	0,26	B
3	0,30	B	0,04	B/C	0,14	B
4	0,16	B	0,05	A	0,12	B
5	/	/	/	/	0,09	B

f_u, adhesive strength; FP, fracture pattern; / it was not possible to measure the strength

3.4 Resistance to Carbonation

The results of the resistance to carbonation test are shown in Figure 2. On the 15th day the group five was carbonated twice as high as the reference mortar whereas all the specimens were fully carbonated on the 30th day.

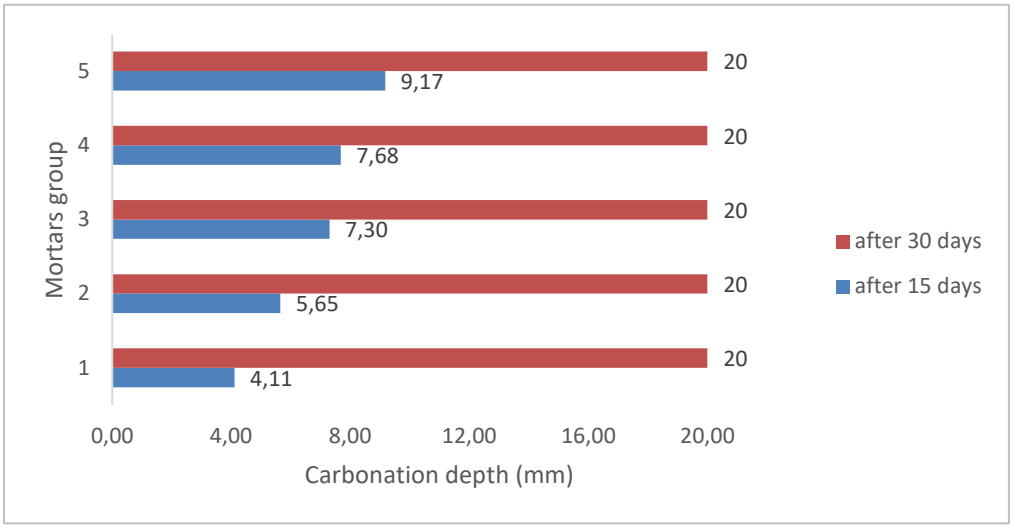

Figure 2. Resistance to carbonation test. Carbonation depth on 15th and 30th day are reported.

4 Discussions and Conclusions

The aim of the research was to investigate the influence of Autoclaved Aerated Concrete waste production aggregates on the mechanical and the durability properties of mortars, with specific respect to the resistance to carbonation. Results indicate that the replacement of the ordinary siliceous sand with AAC aggregate impacts on the hard-state properties of mortars.

The density and the mechanical properties – compressive and flexural strengths – and the adhesive strength to substrates decreased as the recycled aggregate percentage grew. Concerning the adhesive strength to substrate, the adherence to tuff rapidly lowered as the sand was replaced with AAC. Moreover, the open porosity and the water adsorption increased as AAC replaced the natural sand. Actually, the mortars with a higher percentage of AAC needed more kneading water due to the AAC adsorptive properties. Finally, the highest AAC mortar exhibited a short-term low resistance to carbonation, whereas the same value of carbonation depth was observed on 30^{th} day measurement for all the specimens.

Similar trends were reported by Blanco *et al.* (2000) who recorded a strong correlation between the use of lightweight aggregates and the physical and the mechanical properties of concretes. Moreover, the discussed results are consistent with Zhao *et al.* (2015) who measured the reduction of flexural and compressive strength of concretes due to the use of recycled aggregates. Tewar *et al.* (2017) also investigated the substitution of natural sand with AAC waste production aggregates and they reported the growing of kneading water mass and the lowering of compressive strength as AAC percentage was kept higher. Finally, the higher porosity of recycled-aggregates conglomerates was found responsible for a higher CO2 uptake, similar to Evangelista *et al.,*(2010); de Oliveira Andrade *et al.,*(2018).

However, the tested mortars were packaged with only one type of binder and one particle sizes distribution of aggregates, mainly ranged between 2 and 4 mm. Therefore, further studies are necessary to find if the type of binder and the packing of aggregates can modify the discussed results. The resistance to carbonation test needs to be repeated with a shorter time interval between the measures in order to better evaluate the evolution of the phenomenon. Finally, a mechanical test on the carbonated specimens has to be executed to investigate the effects of CO2 diffusion on the compressive and the flexural strength of the mortars.

In conclusions, the substitution of natural sand with AAC aggregates seems to be useful to package both masonry and rendering or plastering mortars. Moreover, the increased porosity and the reduced density of higher AAC percentage mortars suggest their potential thermal insulating properties. Conversely, a threshold for AAC percentage is necessary for masonry mortars packaged with hydraulic lime due to the reduction of mechanical performances and resistance to carbonation.

ORCID

Maurizio Nicolella: http://orcid.org/0000-0002-7140-6759
Claudio Scognamillo: https://orcid.org/0000-0002-0954-7323
Federica Vitale: https://orcid.org/0000-0003-4297-3372

References

Anastasiou, E., Papachristoforou, M., Anesiadis, D., Zafeiridis, K. and Tsardaka, E. C. (2018). Investigation of the use of recycled concrete aggregates originating from a single ready-mix concrete plant. *Applied Sciences (Switzerland)*, *8*(11). https://doi.org/10.3390/app8112149

Blanco, F., Garciéa, P., Mateos, P. and Ayala, J. (2000). Characteristics and properties of lightweight concrete manufactured with cenospheres. *Cement and Concrete Research*, *30*(11), 1715–1722. https://doi.org/10.1016/S0008-8846(00)00357-4

Coppola, B., Courard, L., Michel, F., Incarnato, L., Scarfato, P. and Di Maio, L. (2018). Hygro-thermal and durability properties of a lightweight mortar made with foamed plastic waste aggregates. *Construction and Building Materials*, *170*, 200–206. https://doi.org/10.1016/j.conbuildmat.2018.03.083

Ćosić, K., Korat, L., Ducman, V. and Netinger, I. (2015). Influence of aggregate type and size on properties of pervious concrete. *Construction and Building Materials*, *78*, 69–76. https://doi.org/10.1016/j.conbuildmat.2014.12.073

Dang, J. and Zhao, J. (2019). Influence of waste clay bricks as fine aggregate on the mechanical and microstructural properties of concrete. *Construction and Building Materials*, *228*, 116757. https://doi.org/10.1016/j.conbuildmat.2019.116757

de Oliveira Andrade, J. J., Possan, E., Squiavon, J. Z. and Ortolan, T. L. P. (2018). Evaluation of mechanical properties and carbonation of mortars produced with construction and demolition waste. *Construction and Building Materials*, *161*, 70–83. https://doi.org/10.1016/j.conbuildmat.2017.11.089

Evangelista, L. and de Brito, J. (2010). Durability performance of concrete made with fine recycled concrete aggregates. *Cement and Concrete Composites*, *32*(1), 9–14. https://doi.org/10.1016/j.cemconcomp.2009.09.005

M.I. Khan. (2002). Factors affecting the thermal properties of concrete and applicability of its prediction models. *Building and Environment*, *37*, 607–614.

Mendes, J. C., Barreto, R. R., de Paula, A. C. B., Elói, F. P. da F., Brigolini, G. J. and Peixoto, R. A. F. (2019). On the relationship between morphology and thermal conductivity of cement-based composites. *Cement and Concrete Composites*, *104*(October 2018), 103365. https://doi.org/10.1016/j.cemconcomp.2019.103365

Nepomuceno, M. C. S., Isidoro, R. A. S. and Catarino, J. P. G. (2018). Mechanical performance evaluation of concrete made with recycled ceramic coarse aggregates from industrial brick waste. *Construction and Building Materials*, *165*, 284–294. https://doi.org/10.1016/j.conbuildmat.2018.01.052

Tewar, B., Shah, P. M. and Patel, P. B. (2017). Effect of Partial Replacement of Sand with Wastage of Manufactured AAC Block in Concrete. *Materials Today: Proceedings*, *4*(9), 9817–9821. https://doi.org/10.1016/j.matpr.2017.06.273

Zhao, Z., Remond, S., Damidot, D. and Xu, W. (2015). Influence of fine recycled concrete aggregates on the properties of mortars. *Construction and Building Materials*, *81*, 179–186. https://doi.org/10.1016/j.conbuildmat.2015.02.037

UNI EN 13295:2005. Products and systems for the protection and repair of concrete structures. Test methods. Determination of resistance to carbonation

UNI EN 1015-11:2007. Determination of flexural and compressive strength of hardened mortars

UNI EN 1936:2007. Determination of real density and apparent density, and of total and open porosity

UNI EN 14630:2007. Products and systems for the protection and repair of concrete structures. Test methods. Determination of carbonation depth in hardened concrete by the phenolphthalein method

UNI EN 196-6:2010. Methods of testing cement − Part 6: Determination of fineness.

UNI EN 459-1:2010. Building lime - Part 1. Definitions, specifications and conformity criteria

UNI EN 933-1:2012. Tests for geometrical properties of aggregates – Part 1: Determination of particle size distribution – sieving method

UNI EN 1097-6:2013. Tests for mechanical and physical properties of aggregates − Part 6: Determination of particle density and water absorption

UNI EN 998-1:2016. Specification for mortar for masonry – Part 1: Rendering and plastering mortars

UNI EN 998-2:2016. Specification for mortar for masonry – Part 2: Masonry mortar

UNI EN 1015-12:2016. Methods of test for mortar of masonry - Part 12: Determination of adhesive strength of hardened rendering and plastering mortars on substrates.

XV International Conference on Durability of Building Materials and Components
DBMC 2020, Barcelona
C. Serrat, J.R. Casas and V. Gibert (Eds)

Effect of Supplementary Cementitious Material and Fine Recycled Aggregates on Shrinkage Properties of Self-Compacting Microconcrete

Miren Etxeberria and B.T. Purandhar Reddy

Department of Civil and Environmental Engineering (DECA), Universitat Politècnica de Catalunya-BarcelonaTECH, Campus Nord UPC, 08034-Barcelona, Spain, miren.etxeberria@upc.edu

Abstract. *An increase in the population has led to the progressive construction of infrastructures and buildings. This causes severe environmental problems, firstly high emissions of CO2 are caused in cement production; secondly, a high volume of construction and demolition waste is landfilled and thirdly, it is necessary to look for new, no natural resources for the production of construction materials. The objective of this work is to analyse the influence of fine recycled aggregates and high volumes of fly ash in the properties of high-performance self-compacting (SC) microconcrete. The experimental work presented in this paper was carried out in two phases. In phase 1, SC- microconcrete were produced with 100% of Portland cement, and natural sand was replaced by both mixed and ceramics recycled aggregates in 30% and 50%. In phase 2, SC- microconcretes were produced with the replacement of 50% of Portland cement by fly ash, and natural sand was replaced by both mixed and ceramics recycled aggregates in 30% and 50%. In each phase, the drying and autogenous shrinkage of all mortars was measured via their storage in a climate chamber after 24 hours of casting and the determining of properties during 90 days. In order to assess the influence of the shrinkage effect on the mechanical properties, the prismatic samples were also stored in a climatic chamber, and the compressive strength at several ages was determined in all of the SC mixtures. The results showed that the microconcretes produced employing mixed and ceramic fine aggregates achieved higher compressive strength and lower autogenous shrinkage. Although the C-N achieved the lowest drying shrinkage, the mixtures with 30% of CRA and MRA were found to have similar values. The employment of the CRA aggregates improved the drying shrinkage and compressive strength of the C-FA-N mixture.*

Keywords: *Self-Compacting Microconcrete, Fly Ash, Fine Recycled Aggregates, Shrinkage.*

1 Introduction

The portland cement (PC) industry is one of the major contributor to CO2 emissions. In recent years, Fly Ash (FA) has been widely used as supplementary cement material in replacement of part of PC in concrete construction. In addition, the mixtures employing FA require low water content in order to achieve good workability (Abdalhmid, Ashour, and Sheehan, 2019; Duran-Herrera, De-León-Esquivel, Bentz, and Valdez-Tamez, 2019; Kristiawan and Aditya, 2015; Matos, Foiato, and Prudêncio, 2019). Dinakar *et al.* (Dinakar, Kartik Reddy, and Sharma, 2013) described that about 30% -50% of FA content was ideal for the production of self-compacting concrete (SCC). It was determined that the replacement of 50 wt.% of PC by siliceous fly ash resulted in a low contribution to the hydration at early ages (up to 2 days of age). Between 12 h and 2 days after casting, the hydration is influenced by the so called "filler effect" of FA. Between 2 and 7 days, the fly ash reaction was detected by measuring the increase in chemical shrinkage, bound water and reduced portlandite contents (Deschner *et al.*, 2012). According to Matos *et al.* (Matos *et al.*, 2019), the compressive strength gains in SCC with FA were significant up to 180 days. According to certain researchers (Abdalhmid *et al.*, 2019; Duran-Herrera *et al.,* 2019; Kristiawan and Aditya, 2015) a higher cement replacement of FA tends to

decrease both drying and autogenous shrinkage. According to Altoubat *et al.* (Altoubat, Junaid, Leblouba, and Badran, 2017), the high strength SCC tested employing high degree of restraint (ASTMrings) showed that cement replacement of up to 35% of FA does not compromise the cracking resistance of the mix. The free shrinkage and thus the shrinkage potential of the SCC mixes decreases. It is also known that the employment of high absorption capacity recycled aggregates (RA) are able to reduce the autogenous shrinkage of high performance RA concrete (Etxeberria, Miren, Gonzalez-Corominas, 2018; Suzuki, Seddik Meddah, and Sato, 2009). The drying shrinkage of concrete increases when RA are employed. However, Behera *et al.* (Behera, Minocha, and Bhattacharyya, 2019) determined that in SCC concrete produced with fine RA and the ternary blend binder was more effective in controlling the shrinkage strain of concrete. Internal Curing can reduce autogenous shrinkage and improve concrete quality. Internal curing is necessary for designing HPC, and conventional concrete with low water–cement ratio, when RA have been employed (Al Saffar, Al Saad, and Tayeh, 2019).

In this research work the influence of the FA, supplementary cementitious material, as well as the employment of mixed and ceramic recycled aggregates (MRA and CRA, respectively) on the shrinkage and compressive strength of SC-microconcrete exposed to drying and sealing curing condition were analysed.

2 Materials

2.1 Binder

Portland cement (PC) CEM I 52.5 N-SR with a density of 3.22 kg/m^3 was employed for SC-microconcrete production. Class F Fly ash (FA) with a density of 2.21 kg/m^3 was also employed in up to 50% of replacement of cement volume.

2.2 Aggregates

Natural Silica sand (NA) with a fraction of 0/4 mm was employed for SC-microconcrete production. Its dry density and water absorption capacity at 24 hours were 2.47 kg/m^3 and 2.43%, respectively.

Fine MRA and CRA aggregates were employed in replacement of up to 50% of natural aggregates. The MRA aggregates were composed of approximately, 70% ceramic, 20% of concrete, 9.4% of raw aggregates, 0.5% of gypsum, and 0.1% of other components. The composition of the CRA aggregates was 100% ceramic material. The fraction of both RA was 0/4 mm, but their grading distribution was coarser than that of the NA aggregates, however they proved to have more particles finer than 63µm, which were 2%, 11% and 14.5% in the NA, MRA and CRA aggregates, respectively. The dry density (determined following UNE-EN 1097-6) of MRA and CRA were 1.92kg/dm^3 and 1.97kg/dm^3, respectively. The water absorption capacity of MRA and CRA was determined following UNE-EN 1097-6 specification proved to be 15.5% and 14.0%, respectively. The absorption capacity which was determined following the NY703-19 specification was 15.4% and 12.2%, respectively. Those last values were employed for concrete mixture design.

A superplasticizer based on PAE polymer technology was employed in all mixtures.

3 Mix Design and Production Process

Two series of the SC-microconcrete production were carried out, with five different mixtures produced in each of the series, see Table 1.

In Series 1 all the mixtures were produced employing 100% PC. In series 2, the same volume of binder employed in series 1 was used, but the binder was composed of 50% of PC and 50% of FA. In both series five SC-micrococrete mixtures were produced, one with 100% of natural sand and the other four mixtures employing MRA and CRA in 30% and 50%. In all mixtures the effective water-cement ratio of 0.27 was maintained. The RA was employed in saturated conditions (the value determined according to NY 703-19 standard).

A planetary mixer BE-20, in a low –medium speed was employed for SC-microconcrete production. The same production process was applied for all the SC-microconcretes. Firstly PC, FA and the 95% of effective water amount were mixed; secondly NA, the pre-saturated MRA/CRA were added to the mixer and mixing continued at a low speed. Thirdly, the chemical admixture was added together with the 5% of effective water amount. Finally, all the accumulated material was removed manually from the bottom and mixing continued for a few minutes. On finalizing the SC-microconcrete production, a slump flow test was performed according to EFNARC (Ankush, Rajeev, and Koshta, 2014; European Federation for Specialist Construction Chemicals and Concrete Systems (EFNARC), 2005). The spread diameter, D, of all the mixtures kept within the range of 250 ± 10 mm (see Table 3). The flow of the mixtures was adequate, and did not present bleeding and segregation. In series 2, the SC-microconcrete produced employing CRA needed a higher amount of admixture in order to achieve adequate fluidity. While following NY703-19 specifications which gave the CRA absorption capacity as 12.2% we believe it to be more advisable to follow UNE-EN-1097-6 which determined it to be 14%.

4 Test Procedure

All specimens were demoulded after 24 hours of casting and were exposed in a climatic chamber in drying condition (23 ±3ºC and 50%±3% of RH) and sealed condition (23 ±3ºC) in order to determine the drying and autogenous shrinkage after 24 hours of casting. The compressive strength of samples exposed to those curing condition was also determined.

4.1 Shrinkage (Autogenous-Sealed and Drying)

The shrinkage of the SC-microconcrete was determined following UNE-EN 12617-4 specifications. Six 25x25x287 mm specimens were produced for each type of SC-microconcrete. After casting, they were covered with plastic film, in order to avoid water evaporation, and place in the humidity room for 24 hours. After 24 hours of casting, all the specimens were demoulded. Half of the specimens were employed for autogenous (sealed) shrinkage determination and the other half for drying shrinkage (both shrinkage measurements were determined 24 hours after casting). A digital length comparator was employed for length measurements at different ages. According to their autogenous shrinkage values, the specimens were sealed with aluminium adhesive tape immediately after demoulding and placed in the climatic chamber at 23 ±3ºC. It was then that the first length (control length) measurement was carried out and periodically over 90 days. In order to determine the drying shrinkage value, after demoulding, the specimens were place in a climatic chamber at 23 ±3ºC and 50%±3% of

RH and the initial length was measured. The length measurements were carried out periodically for 90 days.

Table 1. Mix proportions of Series 1 and Series 2 microconcrete mixtures. The values are given of kg of component/m^3 of concrete production.

	Cement	Fly Ash	Sand	AR	total water	Super (%)*	Efect. w/c	D (mm)
	SERIES 1							
C-N	925.5	-	1111.5	0.00	268.9	0.70	0.27	250
C-MRA30	925.5	-	778.1	259.8	300.8	0.68	0.27	275
C-MRA50	925.5	-	555.8	433.0	322.1	0.68	0.27	275
C-CRA30	925.5	-	778.1	266.0	292.1	0.68	0.27	27.5
C-CRA50**	925.5	-	555.8	443.3	307.6	0.68	0.27	30
	SERIES 2							
C-FA-N	462.7	317.6	1111.5	0.00	274.9	0.65	0.32	27.7
C-FA-MRA30	462.7	317.6	778.1	259.8	306.7	0.65	0.32	28.7
C-FA-MRA50	462.7	317.6	555.8	433.0	328.0	0.65	0.32	30
C-FA-CRA30	462.7	317.6	778.1	266.0	298,1	0.68	0.32	29
C-FA-CRA50**	462.7	317.6	555.8	443.3	313.5	0.68	0.32	26.5

*Admixture is the % with respect to cement weight ** C-CRA50-ABS or C-FA-CRA50-ABS: the absorption capacity of RCA was considered of 14% determined following UNE-EN 1097-6

4.2 Compressive Strength

The compressive strength was determined following UNE-EN 12390-3 specifications (according to the dimensions and mechanical test procedure). Prismatic specimens of 40x40x160mm were produced for all mixtures. They were demoulded after 24 hours of casting and were exposed in a climatic chamber in identical conditions to those of the specimens employed for shrinkage testing. Four samples were employed for compressive strength determination.

5 Results

5.1 Autogenous (Sealed) Shrinkage and its Mechanical Properties

5.1.1 Shrinkage

The sealed- autogenous shrinkage in hardened state of each mixture produced in series 1 and series 2 are illustrated in Figure 1. According to the results of the autogenous shrinkage in S1 samples, it was clear that the C-MRA50 mixture achieved the lowest shrinkage. The 50% of MRA, which had the highest absorption capacity, was efficient reducing initial shrinkage. The C-N mixtures achieved the highest shrinkage during the first 2 days. In all probability this difference was higher during the first 24 hours after casting. In series 2, due to higher water and lower cement amount, the initial shrinkage values were lower than those in Series 1. After 28 days, the autogenous shrinkage of the C-MRA50 mixture was still found to be the lowest. However, the shrinkage caused by the hydration of the cementitious material was found to increase with time (see figure c) and d)). In all probability was due its to very high cementitious

material. The mixtures produced employing 30% of MRA and CRA, and 50% of CRA were not able to release enough water in order to reduce the shrinkage value in series 1. In series 2, the RA worked more efficiently probably due to the slightly higher water amount employed in this series and the presence of FA.

5.1.2 Compressive strength

Figure 2 illustrates the compressive strength at 2 and 28 days of the recycled aggregate microconcretes produced in series 1 and series 2 with respect to those of the conventional microconcrete. The compressive strength values of C-N and C-FA-N at 2 days (2D) and 28 days (28D) are also described in figure 3. In series 1, all the Sc-microconcretes produced with RA achieved more than 95% of the compressive strength achieved by the C-N mixture after 2 days (1 day in mould and 1 day in the chamber). At 28 days , all the RA microconcrete obtained higher strength than that of the C-N microconcrete. The C-MRA30 and C-CRA50 microconcretes achieved the highest strength. The internal curing capacity of the RA improved the compressive strength of the SC-microconcretes. However, the weak properties of the mortar present on the MRA reduced the strength of the SC-microconcrete when it was produced with 50% of MRA.

As expected the early strength value of SC-microconcretes was considerably reduced by using a high percentage of fly ash (Abdalhmid *et al.,* 2019). The samples produced in series S2 achieved 50% lower compressive strength than its corresponding sample in series S1 after 28 days. In series 2, the mixtures produced with RA achieved a lower early compressive strength than that of C-AF-N during the first 2 days. However, this increased after 28 days, and they achieved the same strength of the C-FA-N mixture.

In general, the SC-microconcrete produced employing MRA and CRA achieved a higher increase of strength from 2 to 28 days than that of C-N and C-FA-N mixtures.

5.2 Drying Shrinkage and its Compressive Strength

5.2.1 Drying shrinkage

Figure 3 a) and b) show the drying shrinkage values obtained by each mixture produced in series 1 and series 2, respectively, exposed to a climatic condition for 90days. In both series, the C-N and C-FA-N mixtures obtained the lowest drying shrinkage value. While in series 1 (100% of PC) the C-MRA50 and C-CRA50 mixtures achieved the highest shrinkage, in series 2 the SC-microconcrete produced with CRA achieved similar drying shrinkage to that of the C-FA-N mixture. The FA reduced the rate of hydration and thus the drying shrinkage of the microconcrete containing FA was considerably lower than that of the S1 mixtures (Abdalhmid *et al.*, 2019).

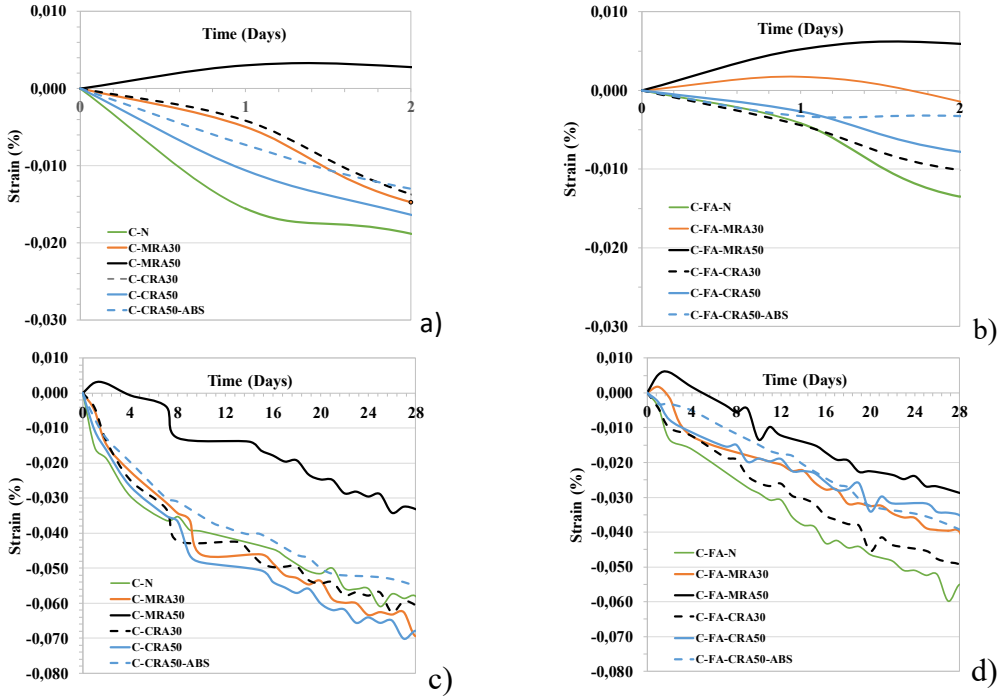

Figure 1. Autogenous (sealed) shrinkage values of Series 1 mixtures a) 2days, c) 28 days and Series 2 b) 2 days and d)28 days. (the time of 0 day is referring to 24hours after casting).

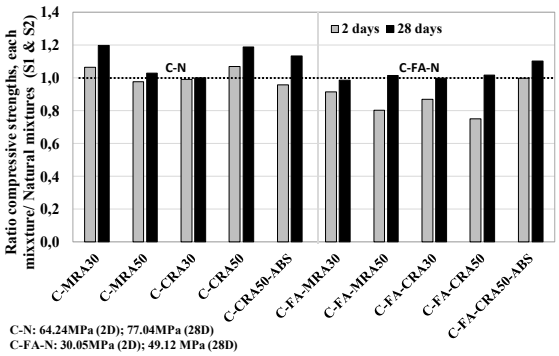

Figure 2. Ratio of compressive strength of recycled microconcretes with respect to conventional one at 2 days and 28 days after sealed condition at 23ºC.

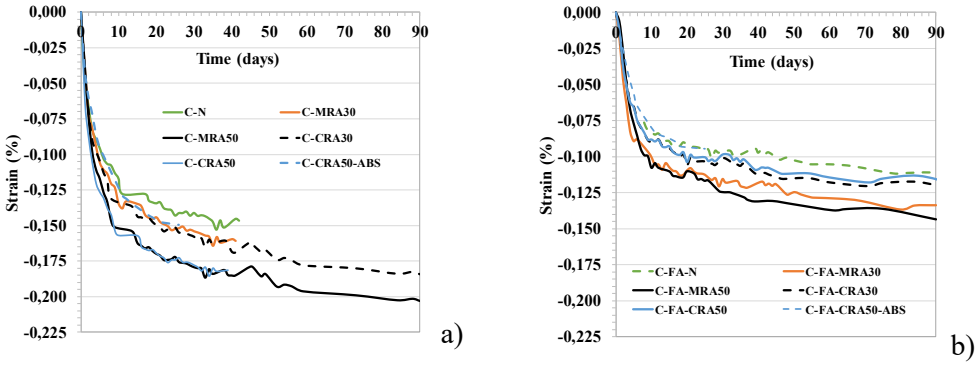

Figure 3. Drying shrinkage of the samples produced at series 1 (a) and series 2 (b).

5.2.2 Compressive strength

Figure 4 illustrates the compressive strength of SC-microconcretes produced with RA with respect to those of the conventional SC-microconcrete, series 1 and series 2, after 2 and 28 days. The compressive strength values of C-N and C-FA-N at 2 days (2D) and 28 days (28D) are also shown in figure 4. The SC-microconcretes produced in Series 1 achieved much higher strength than those produced in series 2, due to the fast drying process, in all probability the high volume of FA was not hydrated.

In series 1, the C-CRA mixtures achieved higher compressive strength than that of the C-N mixture at 2 and 28 days. However, the increase of compressive strength, from 2 to 28 days, was lower in all RA mixture than that of C-N, with the exception of the C-CRA30 mixture.

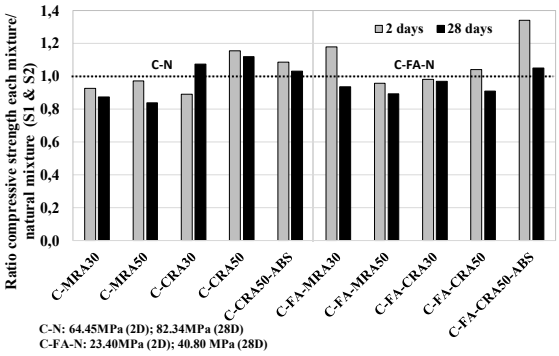

Figure 4. Ratio of compressive strength of recycled microconcretes with respect to conventional one at 2 days and 28 days (1days in mould and 27 days in drying condition).

In series 2, the mixture C-FA-CRA50-ABS achieved the highest compressive strength (the absorption capacity of 14% was the optimum). In general, the microconcrete produced with RA reached similar o higher strength values to that of C-FA-N after 2 days, all the RA microconcretes achieved lower strength values to those of the C-FA-N after 28 days.

6 Conclusions

The following conclusions can be drawn based on the results presented above:

- The autogenous shrinkage was effectively reduced by employing the MRA and CRA aggregates in SC-microconcrete mixtures made with 100% of PC, achieving also a higher compressive strength to the mixtures produced with NA. The C-MRA50 mixture achieved the lowest shrinkage value. However, due to the low mechanical properties of MRA aggregates, the C-MRA30 and C-CRA50 mixtures achieved a higher strength.
- The employment of 50% FA as a binder caused a reduction of up to 40-50% of the autogenous shrinkage value. The compressive strength was also reduced when compared to the mixtures produced with 100% of PC. The use of RA in FA mixtures also produced a favourable effect on lowering of the shrinkage value and the increasing of the strength value with respect to those SC-microconcrete produced employing NA and FA after 28 days.
- Although the C-N achieved the lowest drying shrinkage, the mixtures with 30% of CRA and MRA were found to have similar values. In addition, the mixtures made with CRA achieved the highest compressive strength when 100% of PC was employed.

- The employment of FA reduced the drying shrinkage as well as the compressive strength in up to 40-60% with respect to values obtained by mixtures produced with 100% of PC. The employment of the CRA aggregates improved the drying shrinkage and compressive strength of the C-FA-N mixture.

Acknowledgements

The authors want to thank the Ministry of Economy, Industry and Competitiveness (Ministerio de Economia, Industria y Competitividad, Spain) for the funding of the project BIA2017-85657-R (-HACCURACEM). The authors also want to thank the staff of the LATEM-UPC Laboratory for their support.

ORCID

Miren Etxeberria: https://orcid.org/0000-0003-2208-6207

References

Abdalhmid, J. M., Ashour, A. F., and Sheehan, T. (2019). Long-term drying shrinkage of self-compacting concrete: Experimental and analytical investigations. *Construction and Building Materials*, *202*, 825–837. https://doi.org/10.1016/j.conbuildmat.2018.12.152

Al Saffar, D. M., Al Saad, A. J. K., and Tayeh, B. A. (2019). Effect of internal curing on behavior of high performance concrete: An overview. *Case Studies in Construction Materials*, *10*, e00229. https://doi.org/10.1016/j.cscm.2019.e00229

Altoubat, S., Junaid, T. M., Leblouba, M., and Badran, D. (2017). Effectiveness of fly ash on the restrained shrinkage cracking resistance of self-compacting concrete. *Cement and Concrete Composites*, *79*, 9–20. https://doi.org/10.1016/j.cemconcomp.2017.01.010

Ankush, G., Rajeev, C., and Koshta, M. K. (2014). Influence of Fine Aggregate Particle Size and Fly Ash on the Workability Retention of Mortar for SCC, *3*(2), 23–28.

Behera, M., Minocha, A. K., and Bhattacharyya, S. K. (2019). Flow behavior, microstructure, strength and shrinkage properties of self-compacting concrete incorporating recycled fine aggregate. *Construction and Building Materials*, *228*, 116819. https://doi.org/10.1016/j.conbuildmat.2019.116819

Deschner, F., Winnefeld, F., Lothenbach, B., Seufert, S., Schwesig, P., Dittrich, S., Goetz-Neunhoeffer F., and Neubauer, J. (2012). Hydration of Portland cement with high replacement by siliceous fly ash. *Cement and Concrete Research*, *42*(10), 1389–1400. https://doi.org/10.1016/j.cemconres.2012.06.009

Dinakar, P., Kartik Reddy, M., and Sharma, M. (2013). Behaviour of self compacting concrete using Portland pozzolana cement with different levels of fly ash. *Materials and Design*, *46*, 609–616. https://doi.org/10.1016/j.matdes.2012.11.015

Duran-Herrera, A., De-León-Esquivel, J., Bentz, D. P., and Valdez-Tamez, P. (2019). Self-compacting concretes using fly ash and fine limestone powder: Shrinkage and surface electrical resistivity of equivalent mortars. *Construction and Building Materials*, *199*, 50–62. https://doi.org/10.1016/j.conbuildmat.2018.11.191

Etxeberria, Miren, and Gonzalez-Corominas, A. (2018). The assessment of ceramic and mixed recycled aggregates for high strength and low shrinkage concretes. *Materials and Structures*, *51*(5), 1–21. https://doi.org/10.1617/s11527-018-1244-6

European Federation for Specialist Construction Chemicals and Concrete Systems (EFNARC). (2005). *The European Guidelines for Self-Compacting Concrete Specification, Production and Use*. (E. F. for S. C. C. and C. Systems, Ed.). Norfolk, UK. Retrieved from http://www.efnarc.org/pdf/SCCGuidelinesMay2005.pdf

Kristiawan, S. A., and Aditya, M. T. M. (2015). Effect of high volume fly ash on shrinkage of self-compacting concrete. *Procedia Engineering*, *125*, 705–712. https://doi.org/10.1016/j.proeng.2015.11.110

Matos, P. R. de, Foiato, M., and Prudêncio, L. R. (2019). Ecological, fresh state and long-term mechanical properties of high-volume fly ash high-performance self-compacting concrete. *Construction and Building Materials*, *203*, 282–293. https://doi.org/10.1016/j.conbuildmat.2019.01.074

Suzuki, M., Seddik Meddah, M., and Sato, R. (2009). Use of porous ceramic waste aggregates for internal curing of high-performance concrete. *Cement and Concrete Research*, *39*(5), 373–381. https://doi.org/10.1016/j.cemconres.2009.01.007

XV International Conference on Durability of Building Materials and Components
DBMC 2020, Barcelona
C. Serrat, J.R. Casas and V. Gibert (Eds)

Identification of the Influence of Concrete Cover Thickness and Ø/ρ Parameter on Crack Spacing.

Chavin N. Naotunna, S.M Samindi M.K Samarakoon and Kjell T. Fosså

Department of Mechanical and Structural Engineering and Material science, Faculty of Science and Technology, University of Stavanger, Stavanger, Norway, chavin.guruge@uis.no

Abstract. *Cracks due to the service load in the reinforced concrete structures are controlled at the design stage, by limiting the calculated crack width. Widely used crack width calculation models (Eurocode 2 and Model code 2010), estimates the crack width by multiplying the crack spacing with the mean strain difference of concrete and reinforcement. Concrete cover thickness and the ratio of diameter to reinforcement area to effective tensile area of concrete ($Ø/\rho_{p,ef}$) are the two main crack spacing governing parameters in the aforementioned models. The existing models are mostly applicable when concrete cover thickness is within the specified limit. For example, Model Code 2010 model limits the concrete cover thickness to 75 mm. In order to identify the influence of aforementioned two governing parameters on crack spacing, the results of recent experiments have been considered. According to some recent studies, it is found that the concrete cover thickness has a significant influence and the $Ø/\rho_{p,ef}$ parameter has a negligible effect on crack spacing. To investigate the reasons why the $Ø/\rho_{p,ef}$ parameter has a negligible effect on crack spacing, the involvement of bond properties is needed to study. Some authors have specified that the large diameter bars consist of higher bond force per unit surface area than the small diameter bars, due to the high rib area. Due to this reason, the similar bond behavior could be identified, from low number of large bar diameters and high number of small diameter bars. A literature review has been carried out to study the bond behavior on specimens subjected to pure tension. With the facts and available data, it is further verified that the $Ø/\rho_{p,ef}$ parameter has a negligible influence and concrete cover thickness has a significant effect on crack spacing.*

Keywords: *Crack Spacing, Concrete Cover, Bond Stress-Slip, Axial Tension.*

1 Introduction

Cracks in the reinforced concrete (RC) structures create issues to the durability, aesthetic appearance and the liquid or gas tightness of the structure. Among the various types of cracks that can generate in a structure, the cracks due to service load is controlled at the design stage by limiting the calculated crack width. In the most widely used codes of practices (Ex. Eurocode 2, 2004; Model code 2010, 2013; etc.), the calculated crack width is governed by multiplying the crack spacing with the mean strain difference between reinforcement and concrete. Therefore, the crack spacing parameter can be identified as an important factor in crack controlling criteria. However, it has identified many limitations in the above-mentioned available crack controlling methods (Ex. limitation for the maximum value of concrete cover thickness). Further, there are many experimental evidences from previous literatures, that the experimental predictions do not match with the code prediction values.

In the aforementioned codes, the concrete cover thickness and $Ø/\rho_{p,ef}$ parameter (ratio of diameter to reinforcement area to effective tensile area of concrete) have identified as the two most governing factors of the crack spacing model. In order to improve the existing models, the authors have studied the behavior of aforementioned parameters with the help of available literatures. The crack width or crack spacing models developed in the mentioned codes are based on the axial tension experiments of an RC tie subjected to pure tension. Because a RC tie in pure tension can be represented the tensile region of a bending member with or without axial tension (Debernardi *et al.,* 2013). There are many previous experiments reported, which have

studied about the cracking behavior of RC members. Among them, it can be found various types of data to identify the crack width governing parameters. However, with the advancement of material and geometrical properties of concrete and reinforcement, the authors have selected two recent axial tensile experiments mentioned in (Tan *et al.,* 2018; Tan *et al.,*2019) and (Rimkus and Gribniak, 2017), to identify the crack spacing governing parameters. The selected experiments consist of the RC ties with multiple reinforcement bars, which are more similar to the RC members in practice.

The concrete cover parameter and $\emptyset/\rho_{p,ef}$ parameter is available in the existing crack governing models are due to the 'no-slip theory' and 'bond-slip theory' respectively (Saliger,1936; Broms, 1965). The 'no-slip theory' assumes a perfect bond between reinforcement and surrounding concrete. The 'bond-slip theory' considers that a slip occurs between the reinforcement-concrete interface. From the selected experimental data, it could identify that concrete cover thickness has a significant impact on crack spacing, and therefore to the crack width. When considering the effect of $\emptyset/\rho_{p,ef}$ parameter, it could identify that the parameter has a negligible effect on the crack spacing (Beeby, 2004; Rimkus and Gribniak, 2017). When trying to identify the reasons for this controversial conclusion, Ålander in (Beeby *et al.,* 2005) makes a statement, that when the bar diameter increases, the rib area also increases (even with similar rib pattern). This increased rib area in larger bar diameters cause to have a higher bond force per surface unit area, than the smaller bar diameters (Noghabai, 1995). This effect is not considered in the existing EC2 or MC 2010 models. The mentioned models assume the bond-stress is only a factor of tensile strength of concrete. For example, MC 2010 assumes that the mean bond stress between concrete and reinforcement is equal to 1.8 times the mean tensile strength of concrete in the stabilized cracking stage.

Balaz (1993), introduces a mathematical model to identify crack widths by using the well-known Ciampi-Eligehausen (Ciampi *et al.,* 1981; Eligehausen *et al.,* 1982) bond-slip model. Ciampi-Eligehausen, bond-slip model is based on Rilem-type pull-out test (RILEM, 1994) results. Therefore, at first this paper reviews literatures focusing on the effect of rebar size on bond properties in Rilem-type pull out tests. However, many existing literatures concluded that, bond strength and stiffness decrease with the increase of bar diameter (which is opposite to the expected results). Therefore, this paper investigates the actual bond-slip behavior of specimens subjected to 'axial tension'.

2 The Behavior of Concrete Cover and $\emptyset/\rho_{p,ef}$ Parameter on Crack Spacing from the Recent Experiments

Table 1 shows the test results of axial tensile experiments of RC ties mentioned in Tan *et al.,*(2018) and Tan *et al.,* (2019). Table 1 confirms that the increase of concrete cover, cause to increase crack spacing. When comparing the specimen 1 and 3, with the increase of concrete cover, the maximum crack spacing (Table 1) increases. Likewise, the crack spacing values and specimen 2 and 4 behaves similarly.

Table 1. Crack spacing values measured in stabilized cracking stage (Tan *et al.,* 2019).

Specimen No.	Width × height × length (m × m × m)	No. of bars	Diameter (mm)	Cover (mm)	$\emptyset/\rho_{p,ef}$	$S_{r,mean}$ (mm)	$S_{r,max}$ (mm)
1	0.4 × 0.4 × 3	8	32	40	796	178	240
2	0.4 × 0.4 × 3	8	20	40	1274	163	250
3	0.4 × 0.4 × 3	8	32	90	796	266	320
4	0.4 × 0.4 × 3	8	20	90	1274	217	290

Considering specimen 1 and 2 (likewise, 3 and 4) with the same concrete cover thickness, specimen size and material properties, the effect of $\emptyset/\rho_{p,ef}$ parameter on crack spacing cannot be compared, due to difference in steel areas (Specimen 1 and 2 have $8\times\pi\times16^2$ mm^2 and $8\times\pi\times10^2$ mm^2 steel areas respectively). The same steel area can be represented with different sizes of reinforcement. If small diameter bars are used, the circumference area of the rebar are higher than when the same steel area is replaced by large diameter bars. For example, if one 16 mm bar is replaced with four 8 mm bars (similar steel area), the circumference area is doubled [$(4\times\pi\times8) / (1\times\pi\times16) = 2$]. Therefore, the higher number of smaller diameter bars consist of higher concrete-reinforcement interface area than the few number of large diameter bars arrangement. When bond area becomes large, transfer length will be low. In theory, the RC specimens with similar cross-sectional area and similar steel area, the larger bar diameter has the higher $\emptyset/\rho_{p,ef}$ value. According to the EC2 and MC 2010 crack spacing models, this cause to predict larger crack spacing values than the specimens with smaller bar diameter.

Rimkus and Gribniak (2017) have studied the effect of $\emptyset/\rho_{p,ef}$ on crack spacing, by keeping the steel area and other previously mentioned crack spacing governing parameters constant. In the study, the different values for $\emptyset/\rho_{p,ef}$ has been obtained by changing the rebar diameters. This experiment had tested 21 number of specimens with 150 mm x 150 mm (Height x width) cross section size and 30 mm concrete cover thickness. The study have tested three different steel areas of 315 mm^2, 450 mm^2 and 607.5 mm^2 (Steel ratio ($\rho_{p,ef}$) of 1.4 %, 2.0 % and 2.7 % respectively) and used different deformed bar sizes of 5 mm, 6 mm, 8 mm, 10 mm, 12 mm and 14 mm diameters to change the $\emptyset/\rho_{p,ef}$ ratio. However, the final conclusion of the experiment is that, the crack spacing has a negligible influence from the $\emptyset/\rho_{p,ef}$ parameter.

The conclusions of the aforementioned results in Rimkus and Gribniak (2017), gives a good agreement with the statement of Beeby (2004). Moreover, Beeby (2004) compares previous experiment results of (Farra and Jaccoud, 1994; Haqqi, 1983) and concluded that the $\emptyset/\rho_{p,ef}$ parameter does not influence on crack width or crack spacing. However, when the experiments in (Farra and Jaccoud, 1994; Haqqi, 1983) have altered the $\emptyset/\rho_{p,ef}$ parameter for the comparison, the reinforcement ratios also differed unlike in the experiments of (Rimkus and Gribniak, 2017). Therefore, the statement of Beeby (2004) is further confirmed from the experimental results of (Rimkus and Gribniak, 2017).

3 The Involvement of The Bond-Properties to the Crack Spacing Models.

It is vital to investigate reasons why the previous experimental findings shows that $\emptyset/\rho_{p,ef}$ parameter, (which appears from the 'bond-slip approach') does not influence on crack spacing. Alander, who had studied the reinforcement rib geometry on crack widths in Alander (2002), have made a good explanation for this reason in the discussion paper Beeby *et al.* (2005). According to their findings, the bond per surface area of every reinforcement is not similar, due to the different rib geometry. Moreover, when the diameter of a bar increases, the bond strength increases, due to the increase in rib area and height relative to the smaller bar diameters (nominal bar diameter to rib height is generally used as 22). Therefore, the assumption made on developing the existing crack spacing models that the bond stress is similar among every bar diameter have to be reconsidered.

The rib pattern or height are considered as the governing factors of the bond-strength and bond-stiffness of a reinforcement. The ratio of the nominal bar diameter to rib height is generally used as 22 in reinforcement (Metelli and Plizzari, 2014). Bond-index parameter quantitatively represent the effect of rib-pattern and rib-height of a specific reinforcement. The

bond-index is identified as the most governing rib parameter that influences bond-strength and bond-stiffness and EC2 specifies to have a minimum bond index of 0.056 for a bar exceeding the diameter of 12 mm. To investigate the statement made by Alander in Beeby *et al.* (2005) discussion paper, a literature review has been studied on the size effect of the bars on the bond between concrete and reinforcement. The details and the conclusions of some existing literatures are listed in the Table 2.

Table 2. Summary of the previous studies on the bond behavior for size effect.

Publication	Experiment	Diameter (mm) - [Bond Index]	Results
Bažant *et al.* (1995)	Unconfined Pull-out test	3.175, 6.35, 12.7, 25.4 [smooth bars]	Size effect presents. Bond strength is low in large bars.
Noghabai (1995)	Confined (steel casing) Pull-out test.	8, 16, 32 [Deformed bars]	Bond strength increases with the diameter. The embedded length is short (2.5*diameter).
Bamonte and Gambarova (2007)	Confined (steel casing) Pull-out and push-in tests.	Machine Ribbed 5, 12, 16, 28 – [0.086]	Bond strength decreases with the increase of bar diameter
Metelli and Plizzari (2014)	Unconfined Pull-out test	Machine Ribbed 12, 16, 20 – [0.04-0.105] Commercial (hot-rolled) 12 - [0.095,0.105] 20 - [0.079, 0.089] 40 - [0.054, 0.072] 50 - [0.04, 0.063]	Bond strength increases with the increase of bond index (rib area). Bond strength and stiffness decreases with the increase of bar diameter.
Shima *et al.* (1987)	Confined Pull-out test for long embedded length (40 times diameter).	Ribbed Bars 19.1 25.4 31.8	Bar Diameter has a small effect and bond strength is proportional to 2/3 power of concrete compressive strength.
Morita (1994)	Confined (large covers (5.5*dia.)) Axial tensile test.	3, 7, 13, 19, 25, 51 [Deformed bars]	Size effect does not present in specimens subjected to axial tension with large covers.

According to the Table 2, except in Noghabai (1995), other experiments have concluded that the bond strength decreases with the increase of bar diameter. These results does not agree with the previously mentioned statement by Alander in Beeby *et al.* (2005) discussion paper. This can lead to another direction, whether the pull-out or push-in tests represents the bond-behavior of an RC tie subjected to axial tension or flexure. The authors in (Alander, 2002; Beconcini *et al.,* 2008; Mazzarolo *et al.,* 2012) explains that the traditional Rilem-type tests (RILEM, 1994) does not represent the bond condition of a member subjected to bending or axial tension. The main reasons for the discrepancy are identified as the short anchorage length (embedded length is five times the bar diameter), one-way loading method (the concrete parallel to the reinforcement is in compression), failure mode (splitting failure that occurs in unconfined tests) in the standard pull-out tests. The short embedded length is decided in the Rilem-type test is to ensure the uniform distribution of the bond stress along the bar (Mazzarolo *et al.,* 2012) and to reach the bond-failure before rebar yields (Bamonte and Gambarova, 2007; Mazzarolo *et al.,*

2012). In order to make the experimental conditions closer to the practical situation, Shima *et al.,* (1987) have used longer embedded lengths (40 times diameter) and studied the size effect on bond stress (Table 2).

It has observed that the reinforcement-concrete interface in axial tensile members does not subject to the range of slip value as observed in the Rilem-type tests. The experimental investigation of the crack widths at the level of reinforcement in (Borosnyói and Snóbli, 2010; Husain and Ferguson, 1968; Tammo and Thelandersson, 2009) have proved that the slip is in the range of hundredth of a millimeter (ex. 0.01 mm to 0.06 mm). These studies have observed the crack width propagation along the concrete cover thickness by sealing the crack, with a hardened epoxy and examining by cutting the specimen. (Borosnyói and Snóbli, 2010; Caldentey *et al.,* 2013) have explained the reason for the relatively small crack widths at the reinforcement face. They have considered that it is due to the accumulation of strains in secondary cracks, which are identified as Goto cracks in Goto (1971). These secondary cracks are developed around the primary cracks (Debernardi *et al.,* 2013; Debernardi and Taliano, 2016) and therefore the 'slip' is considered as spread at the vicinity of primary crack. However, Yannopoulos (1989) has conducted experiments to study the variation of crack widths along the concrete cover thickness. During, the experiment, the increase length of specimens was measured using gauges that were fixed at the both end-faces perpendicular to the reinforcement of the axial tensile tie. One measurement was obtained 2.2 mm away from the reinforcement and the other measurement was obtained at the edge (i.e. at a distance of concrete cover) of the specimen. The obtained average change in length were 0.06 mm and 0.13 mm respectively. The conclusion is that, even the internal cracks do exist, their accumulation does not equal with the crack widths at the concrete surface. Therefore, the internal cracks (spread around primary cracks) cannot be considered as a contributor to the slip.

The experiment mentioned in Beeby (2004), contributes to the fact that, slip does not occur between reinforcement and concrete interface in axial tensile members. A layer of grout is applied at the end faces of RC tie (faces perpendicular to reinforcement) and observed no cracks in the reinforcement-concrete interface after the tensile load is applied. Due to these facts, the slip between reinforcement and concrete can be expressed as negligible and the cracking is according to the 'no-slip theory'. However, to ensure this fact, the authors have studied through the aforementioned bond-slip experiments conducted for axial tensile experiments. The method of slip and bond-stress measurements in conducted axial tensile experiments are listed in Table 3. Except for the experiment mentioned in Doerr (1978), other listed experiments have not measured the concrete strain separately to obtain the slip. Either the researcher has neglected the concrete strain or calculated it from the force equilibrium using only the reinforcement strain. There is a possibility that these calculated concrete strain can be due to 'no-slip' conditions. The experiment mentioned in Doerr (1978), which had separately measured the 'concrete strain' with strain gauges, 16 mm away (one diameter length) from the reinforcement face. This measurement does not represent the slip at the reinforcement – concrete interface. Based on above reasons it is not clear whether the experiments given in Table 3 have measured the actual value of slip.

Table 3. Details of the axial tensile experiments focused on bond-slip.

Experiment	Details	Bond stress	Slip
Doerr (1978) Cylindrical specimen dia.= 150 mm. Length = 600 mm. Bar dia. = 16 mm Strain gauge on rebar and concrete. Spacing = 28 mm	Concrete strain gauges were placed 16 mm away from concrete, while casting. Electrical resistance wire strains were used. Specimen were sectioned to 28 mm size parts along the length.	Bond stress ($\tau_{(x)}$) along the bar $\tau(x) = -\frac{1}{\pi\varphi}.\frac{dP(x)}{dx}$ $P_{(x)}$- Force in reinforcement. Where P(x) can be identified by interpolating the steel strain at each segment.	Slip of the element 'a+1' ($s_{(a+1)}(x)$), $s_{(a+1)}(x) = \varepsilon_{s,a}.dx - \varepsilon_{c,a}.dx$ $\varepsilon_{s,a}$ – Strain in 6einforcement $\varepsilon_{c,a}$– Strain in concrete dx – spacing of strain guages
Morita (1994) Rectangle specimens Square c/s = 12*φ Length = 60*φ Strain gauge only on rebar. Spacing = 5* φ	Concrete strain is neglected when calculating the slip, assuming the domination contributor to the slip is the internal cracks.	Bond-slip model identified by (Muguruma, Morita, and Yoshida, 1967) $\frac{d^2y\ s(x)}{dx^2} = \frac{4\ (1+np)}{Es}.\tau(x)$ s(x) – Slip n – Modulus ratio p – Steel Ratio	Slip is identified from the steel strain, neglecting concrete strain. Slip of the element 'a+1', $s_{(a+1)}(x) = \varepsilon_{s,a}.dx$
Beconcini *et al.* (2008) Cylindrical specimen dia.= 132 mm. Length = 1000mm. Bar dia. = 16 mm Strain gauge only on rebar. Spacing = 25mm	Specimen were sectioned to 25 mm size parts along the length. Concrete and steel stresses and strains of each section were identified with a constitutive model based on Ramberg Osgood formation and with the force equilibrium F = Fs+ Fc.	Equilibrium of a rebar portion $d\sigma s\ .\frac{\pi\varphi^2}{4} = \pi\varphi\tau(x)$ σs – Steel stress calculated from steel strain	From the definition of slip $\frac{ds}{dx} = \varepsilon s - \varepsilon c$

When considering the bond-slip behavior of the specimens subjected to axial tension, it can be concluded that the 'bond-slip' theory can cause a negligible influence on crack spacing. Therefore the involvement of $\emptyset/\rho_{p,ef}$ parameter on crack spacing behavior have to be reconsidered. Further This description ends with agreeing the conclusion of Beeby (2004), that the $\emptyset/\rho_{p,ef}$ parameters has a negligible effect, while concrete cover thickness has a significant effect on crack spacing and therefore to the crack width.

4 Summary and Conclusions

Concrete cover thickness and $\emptyset/\rho_{p,ef}$ parameter have identified as governing parameters of crack spacing models in Eurocode 2 and Model code 2010. From the recent experimental results, it

could be identified that the concrete cover thickness has a significant effect on crack spacing. However, the $\emptyset/\rho_{p,ef}$ parameter, which present in the crack spacing model due to the 'bond-slip theory' has an negligible influence to the crack spacing. A possible reason for that can be the effect of different rib indexes of different bar sizes, which is not taken into account in the above-mentioned crack spacing models. Experimental results showed similar crack spacing values using low number of large bar diameters and high number of small bar diameters. Therefore, the bond per unit surface area have to be higher in large diameter bars than small diameter bars. A literature survey is carried out to identify the aforementioned effect and it is found that, the bond per unit surface area is getting lower with the increase of bar diameter. Moreover, it is vital to investigate the applicability of Rilem-type pull-out test results to study the bond behavior in a RC tie. The main contradiction is the, obtained slip value in axial tension is significantly smaller than Rilem-type pull-out tests. Further, there is an argument that the internal cracks contribute to the slip. However, the results of Yannopoulos (1989) have proved that the internal cracks do not have a significant contribution to the slip. Further, Beeby (2004) have experimentally proved that there is no slip occurred at the reinforcement-concrete interface of an RC tie in pure tension. Moreover, as mentioned in the available studies on bond-slip behavior subjected to axial tension, have not measured the concrete strain separately, to measure the slip value. Therefore, it can be concluded that the mentioned crack spacing models have overestimated the effect of bond-slip behavior.

ORCID

Chavin N. Naotunna: https://orcid.org/0000-0003-4994-2675
S.M Samindi M.K Samarakoon: https://orcid.org/0000-0002-6847-972X

References

Alander, C. (2002). *The effect of rib geometry on crack widths and the service life of structures.* Paper presented at the 3rd International Symposium on Bond in Concrete.

Balazs, G. L. (1993). Cracking analysis based on slip and bond stresses. *Materials Journal, 90*(4), 340-348.

Bamonte, P. and Gambarova, P. G. (2007). High-bond bars in NSC and HPC: Study on size effect and on the local bond stress-slip law. *Journal of Structural Engineering, 133*(2), 225-234.

Bažant, Z. P., Li, Z. and Thoma, M. (1995). Identification of stress-slip law for bar or fiber pullout by size effect tests. *Journal of engineering mechanics, 121*(5), 620-625.

Beconcini, M. L., Croce, P. and Formichi, P. (2008). *Influence of bond-slip on the behaviour of reinforced concrete beam to column joints.* Paper presented at the Proceedings of International fib Symposium "Taylor Made Concrete Structures: New Solutions for our Society.

Beeby, A. W. (2004). The influence of the parameter ϕ/ρ eff on crack widths. *Structural Concrete, 5*(2), 71-83.

Beeby, A.W.,C. Å., J. Cairns, R. Eligehausen, U. Mayer, S. Lettow, Daniele Ferretti, I. Iori, Pietro G. Gambarova, Patrick Bamonte, Ezio Giuriani, Giovanni A. Plizzari, Stavroula Pantazopoulou and Souzana Tastani. (2005). Discussion : The influence of the parameter φ/ρeff on crack widths. *Structural Concrete, 6(4):155-165*. doi:10.1680/stco.2005.6.4.155

Borosnyói, A. and Snóbli, I. (2010). Crack width variation within the concrete cover of reinforced concrete members. *Építõanyag, 62*(3), 70-74.

Broms, B. B. (1965). Crack width and crack spacing in reinforced concrete members. *Paper presented at the ACI Journal Proceedings.*

CEN. (2004). EN: EN 1992-1-1, Eurocode 2: Design of concrete structures - Part 1–1: General rules and rules for buildings In. Brussels: European Committee for Standardization.

Ciampi, V., Eligehausen, R., Bertero, V. V. and Popov, E. P. (1981). Analytical model for deformed bar bond under generalized excitations.

Ciampi, V., Eligehausen, R., Bertero, V. V. and Popov, E. P. (1982). *Analytical model for concrete anchorages of reinforcing bars under generalized excitations*: College of Engineering, University of California Berkeley, CA, USA.

Debernardi, P. G., Guiglia, M. and Taliano, M. (2013). Effect of secondary cracks for cracking analysis of reinforced concrete tie. *ACI Materials Journal, 110*(2), 207.

Debernardi, P. G. and Taliano, M. (2016). An improvement to Eurocode 2 and fib Model Code 2010 methods for calculating crack width in RC structures. *Structural Concrete, 17*(3), 365-376.

Doerr, K. (1978). *Bond behavior of ribbed reinforcement under transversal pressure.* Paper presented at the Nonlinear behavior of reinforced concrete structures; contributions to IASS symposium.

Farra, B. and Jaccoud, J.-P. (1994). *Influence du béton et de l'armature sur la fissuration des structures en béton: rapport des essais de tirants sous déformation imposée de courte durée*. Retrieved from

fib. (2013). fib Model Code for concrete structures 2010. In *Structural Concrete*. Berlin: Ernst and Sohn.

Goto, Y. (1971). *Cracks formed in concrete around deformed tension bars.* Paper presented at the Journal Proceedings.

Haqqi, S. (1983). *Serviceability of reinforced concrete subjected to tension.* Polytechnic of Central London,

Husain, S. I. and Ferguson, P. M. (1968). Flexural crack width at the bars in reinforced concrete beams.

Mazzarolo, E., Scotta, R., Berto, L. and Saetta, A. (2012). Long anchorage bond–slip formulation for modeling of rc elements and joints. *Engineering Structures, 34*, 330-341.

Metelli, G. and Plizzari, G. A. (2014). Influence of the relative rib area on bond behaviour. *Magazine of Concrete Research, 66*(6), 277-294.

Morita, S. (1994). Experimental study on size effect in concrete structures. *Size effect in concrete structures*, 27-46.

Muguruma, H., Morita, S. and Yoshida, H. (1967). Fundamental study on bond between steel and concrete. *Transaction of Architectural Institute of Japan, 131*, 1-6.

Noghabai, K. (1995). *Splitting of concrete in the anchoring zone of deformed bars: a fracture mechanics approach to bond.* Luleå tekniska universitet,

Pérez Caldentey, A., Corres Peiretti, H., Peset Iribarren, J. and Giraldo Soto, A. (2013). Cracking of RC members revisited: influence of cover, ϕ/ρs, ef and stirrup spacing–an experimental and theoretical study. *Structural Concrete, 14*(1), 69-78.

RILEM, T. (1994). RC 6 Bond test for reinforcement steel. 2. Pull-out test, 1983. *RILEM recommendations for the testing and use of constructions materials*, 218-220.

Rimkus, A. and Gribniak, V. (2017). Experimental investigation of cracking and deformations of concrete ties reinforced with multiple bars. *Construction and Building Materials, 148*, 49-61.

Saliger, R. (1936). High grade steel in reinforced concrete. *Paper presented at the Preliminary Publication, 2nd Congress of IABSE*. Berlin-Munich: IABSE Publications.

Shima, H., Chou, L.-L. and Okamura, H. (1987). Micro and macro models for bond in reinforced concrete. *Journal of the Faculty of Engineering, 39*(2), 133-194.

Tammo, K. and Thelandersson, S. (2009). Crack widths near reinforcement bars for beams in bending. *Structural Concrete, 10*(1), 27-34.

Tan, R., Eileraas, K., Opkvitne, O., Žirgulis, G., Hendriks, M. A., Geiker, M., Brekke, D. and Kanstad, T. (2018). Experimental and theoretical investigation of crack width calculation methods for RC ties. *Structural Concrete, 19*(5), 1436 - 1447.

Tan, R., Max, A. N., Hendriks, Mette, G. and Terje, K. (2019). Analytical calculation model for predicting the cracking behavior of reinforced concrete ties. *Structural Engineering*.

Yannopoulos, P. (1989). Variation of concrete crack widths through the concrete cover to reinforcement. *Magazine of Concrete Research, 41*(147), 63-68.

XV International Conference on Durability of Building Materials and Components
DBMC 2020, Barcelona
C. Serrat, J.R. Casas and V. Gibert (Eds)

Influence of High Volume Fly Ash and Recycled Aggregates in Chloride and Carbonation Resistance of Concrete

Miren Etxeberria and Fernando Álvarez

Departament of Civil and Environmental Engineering, Universitat Politècnica de Catalunya-BarcelonaTECH, Campus Nord UPC, 08034-Barcelona, Spain, miren.etxeberria@upc.edu

Abstract. *This paper deals with the evaluation of the influence of recycled concrete aggregate (RCA) and the employment of high volume of fly ash (FA) on the physical, mechanical and durability (chloride ion penetration and carbonation) properties of concretes. The obtained values of which, being compared to those of conventional concretes. Concrete was produced using 0%, 25% and 50% FA in replacement of Portland cement, and 0% and 50% of RCA in substitution of natural aggregates. All the concretes were produced employing an effective water-cement ratio of 0.50. The physical properties at 28 days and the compressive strength at 7, 28 and 90 days were determined in all the concretes produced as well as the assessment of durability (penetration of chlorides and depth of carbonation) on all concrete mixtures. The depth of the carbonation was determined after submitting every concrete sample to a series of accelerated tests at 20% of CO_2 concentration during 7, 14 and 28 days after the curing period in the humidity room and pre-condition in the laboratory. The chloride penetration was determined at 28 and 90 days of curing. It was concluded that the employment of 50% of un-carbonated RCA increased the early strength of concrete produced using FA, and at late ages, RCA concretes achieved similar strength when 25% of FA was employed. The concrete produced with 50% of FA achieved the highest resistance to chloride ion penetration also when RCA was employed. Although the use of FA increased the carbonation depth of the concrete samples, the employment of the un-carbonated RCA reduced that effect. The employment of RCA with CEM II or binder with 25% of FA caused the lowest carbonation depth.*

Keywords: *Fly Ash, Recycled Aggregates, Concrete, Carbonation, Chloride Resistance.*

1 Introduction

Concrete production has a high impact on our environment due to the abundant consumption of energy and a large amount of CO_2 emissions in cement production. In addition, the demolition of concrete structures causes a considerable volume of waste to end up in landfills. These problems may be reduced, achieving a green concrete, by employing fly ash (FA) as supplementary cementitious materials and recycled concrete aggregates (RCA) in replacement of cement and natural aggregates, respectively for concrete production (Marinković, Dragaš, Ignjatović, and Tošić, 2017).

It is known that the RCA is suitable for concrete production (Chen *et al.*, 2019), in addition the employment of recycled aggregate concrete (RAC) as structural material has been widely analysed and validated for many applications (Pedro, De Brito, and Evangelista, 2014). However, the durability of concrete produced with RCA is actively being studied in order to improve its qualities (Guo *et al.,* 2018). According to Guo *et al.* (Guo *et al.,* 2018) RAC has lower chloride ion diffusion resistance than conventional concretes due to the RCA's high porosity. According to the results of a carbonation resistance test, when the RAC were produced employing at least 70% of RCA, the resistance was found to be higher due to the larger amount of mortar in recycled concrete. In contrast, the results of studies by Silva *et al.* (Silva *et al.,*

2015) determined that the carbonation of concrete produced with 100% of RCA was 2.5 times higher than that produced with natural aggregates.

On the other hand, today the use of FA up to 15-20% (Chandra and Bendapudi, 2015) or up to 15-30% (Xu and Shi, 2018) in concrete production is considered usual and it has been determined that the employment of high amount of FA controlled the temperature of concrete and achieved adequate mechanical and durability properties. It is known that the concretes produced with FA have low strength at initial ages, this effect being more evident when higher percentages of FA are employed in concrete production and less evident when concrete are produced with a low water/cement ratio. However at later ages, the strength of concrete increases due to the reaction of its FA with Portlandite (Kocak and Nas, 2014; Xu and Shi, 2018). According to Lam *et al.* (L. Lam, Y.L. Wong, 1998) the chloride ion penetration resistance of concrete is higher when FA is employed. Dinakar *et al.* (Dinakar, Kartik Reddy, and Sharma, 2013) described that concretes achieve their highest strength and chloride ion resistance when up to 30% of FA is employed for concrete production. However, several other researchers (Kurda, De Brito, and Silvestre, 2019) determined that concrete produced with FA achieves lower carbonation resistance than the concrete produced employing 100% of Portland cement.

In this paper, the influence of RCA and the employment of high volumes of FA on the physical, mechanical and durability (chloride ion penetration and carbonation) properties of concretes have been evaluated, and those values were compared to those of conventional concretes. Concretes were produced using 0%, 25% and 50% FA in replacement of Portland cement, and 0% and 50% of RCA in substitution on natural aggregates

2 Materials

2.1 Binder

The cement types of CEM II A-L 42.5R (with 12% limestone, named CEMII) and CEM I 52.5R (high strength-rapid hardened, named CEMI) with the densities of 3.1 kg/dm^3 were employed. Class F fly ash (FA) with a density of 2.16 kg/dm^3 was also employed.

2.2 Aggregates

Three fractions of natural limestone aggregates were used for concrete production: fine (NS of 0/4mm,) and coarse aggregates (CA1 of 5/10mm and CA2 of 8/20 mm). The dry density of NS, CA1 and CA2 were 2.58kg/dm^3, 2.67kg/dm^3 and 2.67kg/dm^3, respectively. The absorption capacity was of 1.79%, 0.75% and 0.57%, respectively.

The recycled concrete aggregate (RCA) was produced via the crushing of a parent concrete, namely one-year-old waste, 30 MPa concrete specimens from a concrete company. The component of the parent concrete being CEM II A-L 42.5R cement and limestone aggregates. The RCA was used for concrete production immediately after the parent concrete was crushed, and the RCA aggregates were un-carbonated. The grading distribution was defined by the fraction 5/20mm. Its density was of 2.33 kg/dm^3 and an absorption capacity of 5.35%.

3 Mix Design and Production Process

Two stages of concrete productions were carried out. In stage 1, all the concretes were produced

employing 100% of natural aggregates. Four different concretes were produced in which different binders were employed. CC, 100% of CEMII; CFA25, 25% (in weight) of CEMII was replaced by FA; CFA50: 50% of CEMII was replaced by FA and CFA50.2: 50% of binder was CEMI and 50% of FA (see Table 1). In stage 2, all the mixtures were produced employing 50% of the aggregates volume defined in the CC mixtures replaced by RCA. Four different concrete mixtures were produced: CRA, 100% of CEMII; CRAFA25, 25% (in weight) of CEMII was replaced by FA; CRAFA50, 50% of CEMII was replaced by FA and CRAFA50.2, 50% of binder was CEMI and 50% of FA (see table 1).

The effective w/c ratio of 0.50 was maintained constant in all concretes. In stage 1, in order to determine the effective w/c ratio, the effective absorption capacity of 90%, 50% and 50% of the total absorption capacity of NS, CA1 and CA2, respectively were determined. In addition, in stage 2, the effective absorption capacity of RCA was determined as being 80% of its total absorption capacity. The RCA was used with high humidity, having 75-80% of water absorption capacity, and their moisture content was measured prior to their use.

The concrete specimens were produced and cured following UNE EN 12390-2:2001 regulations and were manually compacted using a steel rod. The concrete specimens were then covered with a plastic sheet and air-cured for the first 24 h. After 24 h of casting, the specimens were demoulded and then stored in a humidity room and kept at 21ªC and 95% of humidity until the test ages were reached for the physical, mechanical and chloride ion penetration test. The specimens taken from the humidity room after 28 days for carbonation resistance testing were sent to the laboratory to undergo pre-conditioning for 14 days at 400ppm, 24ºC and 55% humidity before being placed in the CO_2 chamber.

A superplasticizer based on modified polycarboxylates was employed in all mixtures. A 0.50% with respect to cement weight was needed in all the concrete mixtures in order to achieve a slump test of 17-19cm. The density at fresh state of all the concrete mixtures was also determined. Table 1 shows that the employment of FA increased the density of concrete due to its capacity to densify the cement paste, in contrast the employment of RCA decreased the density of concrete (Etxeberria *et al.*, 2007).

Table 1. Mix proportions of Stage 1 and Stage 2 concrete mixtures. The values are given of kg of component/m^3 of concrete production (W: water, Ad: admixture, Effect: Effective).

	CEM	FA	W Total	NS	CA1	CA2	RCA	Ad. (%)	Effect. w/c	Density (kg/dm^3)
STAGE 1										
CC	350		192.5	900	275.2	647	0	0.50	0.5	2.24
CFA25	262.5	87.5	192.5	867.9	275.2	647	0	0.50	0.5	2.34
CFA50	175	175	192.5	835.9	275.2	647	0	0.50	0.5	2.36
CFA50.2	175	175	192.5	835.9	275.2	647	0	0.50	0.5	2.36
STAGE 2										
CRA	350		213.4	900	137.6	323.5	400	0.50	0.5	2.31
CRAFA25	262.5	87.5	213.4	867.9	137.6	323.5	400	0.50	0.5	2.30
CRAFA50	175	175	213.5	835.9	137.6	323.5	400	0.50	0.5	2.31
CRAFA50.2	175	175	213.5	835.9	137.6	323.5	400	0.50	0.5	2.33

4 Test Procedure

4.1 Physical and Compressive Strength

Physical properties were measured according to ASTM C 642 ‘‘Standard Test Method for Density, Absorption and Voids in Hardened Concrete” at 28 days after casting. Three cubic specimens were used in this test for each concrete mixture produced.

The compressive strength of concretes at 7, 28 and 90 days were determined following UNE-EN 12390-3:2009 specifications. Three cylindrical specimens were used for each concrete mixtures.

4.2 Carbonation and Chloride Resistance

The concretes were submitted to accelerated carbonation test, following GB T50082-2009 standards, in order to assess the carbonation penetration resistance of each concrete produced employing different types of binders as well as the RCA. The concrete specimens were placed in a CO_2 chamber at 20% CO_2, 20ºC and 60% of RH for 7, 14 and 28 days after their curing process of 28 days and pre-conditioning period of 2 weeks. The concentration of the CO_2 employed was very high. It is known that the carbonation coefficient increases with an increase in carbon dioxide concentration (Shah and Bishnoi, 2018). In addition, at long test periods, the high concentrations of CO_2 cause a change of the cement paste microstructure compared to that of samples placed in natural exposure (Castellote *et al.,* 2009). However, the high concentration of CO_2 conditions, in short periods of testing, allow the concrete's resistance to carbonation to be characterized (Hyvert *et al.,* 2010). Two specimens of each concrete were employed for carbonation depth measurement. The compressive strength of each concrete was also determined.

The chloride penetrability of concrete was determined following the ASTM C1202 (1997) standard. The chloride ion penetration resistance of concrete is represented by the total charge passed in Coulombs during a test period of 6 h. In this study, the chloride ion penetrability test was carried out on the concrete specimens at the ages of 28 and 90 days and each result was the average of two measurements.

5 Results

5.1 Physical and Compressive Strength

Table 2 shows the physical properties obtained by all the concretes analysed. The employment of FA increased the density and decreased the absorption capacity of concrete due to its reaction with $Ca(OH)_2$ (Deschner *et al.,* 2012). The CFA50.2 produced with 50% of FA in substitution of CEMI achieved the lowest absorption capacity. The employment of RCA, in stage 2, decreased the density of its Stage 1 corresponding concrete. The CRA achieved 18% higher absorption capacity than that of CC concrete. Similar results were obtained by Kurda *et al.* (Kurda, de Brito, and Silvestre, 2019). The absorption capacity of recycled aggregate concrete was lower when FA was employed in its production. The CRAFA50.2, produced with CEMI, achieved the lowest absorption capacity. CRAFA50 and CRAFA50.2 achieved a higher density, lower absorption and porosity than that of the CC concrete.

Table 2 also shows the compressive strength at 7 days, 28 days and 90 days of all the

concretes produced. The CC mixture achieved the highest compressive strength at 7, 28 and 90 days. In addition, the concretes produced employing 25% of FA achieved the strength of CC concrete. Similar results were obtained by Nath and Sarker (2011) at 28 and 90 days. The concretes produced with 50% of FA achieved lower strength than the CC concrete in all the tested ages. Although the employment of CEMI improved the properties achieved by concrete produced using CEMII, the CFA50.2 proved to have 14.8% lower strength than that of CC after 90 days (see figure 1). This in all probability was due to a none reaction in some of its high volume of FA (Hemalatha and Ramaswamy, 2017; Xu and Shi, 2018). In stage 2, the concrete CRA achieved the highest strength at 7 and 28 days, and the CRAFA25 concrete after 90 days.

Table 2. Physical properties of concretes produced in Stage 1 and 2, Compressive strength of concretes at 7, 28 and 90 days.

	Physical properties			Compressive strength (MPa)		
	Absorption (%)	**Dry Density (kg/dm3)**	**Vol. of accesible porous (%)**	**7 days**	**28 days**	**90 days**
			STAGE 1			
CC	4.70	2.19	10.29	36.7	42.0	49.6
CFA25	3.98	2.28	9.09	29.0	39.3	49.4
CFA50	3.95	2.29	9.04	17.5	29.1	39.5
CFA50.2	3.70	2.32	8.38	22.1	32.7	42.2
			STAGE 2			
CRA	5.56	2.16	12.04	34.5	41.3	47.5
CRAFA25	4.52	2.24	10.11	31.5	38.7	48.1
CRAFA50	4.16	2.24	9.32	19.2	26.9	37.8
CRAFA50.2	4.06	2.23	9.06	23.7	30.5	41.8

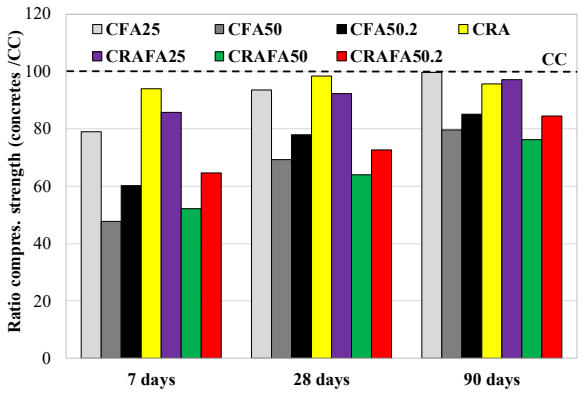

Figure 1. Ratio of the compressive strength of all the concrete with respect to that of CC concrete.

At 7 days of curing, the concretes produced employing RCA and FA achieved a higher strength than that of the concretes produced employing FA and NA (see Figure 1). The rough surface and attached un-carbonated mortar of the RCA caused adequate ITZ in CRA (Etxeberria *et al.,* 2007).

At 28 days and 90 days, the concrete produced with RCA achieved a slightly lower strength

to the concretes produced employing natural aggregates. In stage 2, the CRAFA25 achieved the highest strength at 90 days due to the pozzolanic effect of FA and its reaction with Ca(OH)2, similar behaviour was determined by Kou and Poon (2013).

In addition, the two concretes produced employing 25% of FA achieved the strength of the CC concrete. Cement type I 52.5R (CEMI) was required for concrete employing 50% of FA in order to avoid a high strength reduction at 90 days.

5.2 Carbonation and Chloride Resistance

Figure 2a shows the chloride penetration resistance of each concrete at 28 and 90 days, in accordance with the total charge passed value obtained, which are categorized as low, moderate and high corrosion risk.

At 28 days, almost all of the concretes were classified with moderate risk for corrosion, except the CC and CRA concretes, which were classified as high risk of corrosion. The employment of a higher percentage of FA reduced the corrosion risk. The concretes produced employing 50% of FA and RCA (CRAFA50 and CRAFA50.2) achieved the lowest value of the total charge passed. At 90 days, the concretes produced with 50% of FA, CFA50.2 and CRAFA50.2, achieved the lowest value. The CRA concrete was found to still have a high risk of corrosion after 90 days of curing.

In stage 1, the concretes produced with 50% FA and natural aggregates achieved the highest decrease of the total charge passed value from 28 days to 90 days. The reduction of the total charge passed of the CFA50.2, CFA50, CFA25 and CC concretes were 53%, 40%, 25% and 19% respectively. In stage 2, the reduction rate of CRAFA50.2, CRAFA50, CRAFA25 and CRA were 27%, 10%, 41% and 9%, respectively. The RCA was also found to have an influence on the chloride resistance.

The average carbonation depth of each concrete specimen after their exposure to 20% of CO_2 during 7 days, 14 days and 28 days is shown in Figure 2b. After 7 days of exposure, the concretes produced with 50% of FA and NA suffered the highest carbonation depth, the use of 50% of RCA reduced the CO_2 penetration.

It is clear that the employment of FA increased the depth of carbonation within the concrete samples. Several researchers have also determined this (Khunthongkeaw, Tangtermsirikul, and Leelawat 2006; Kurda, De Brito, *et al.,* 2019). The concretes produced with 100% of CEMII as well as employing 25% of FA achieved the highest resistance to carbonation at any time, being higher when RCA was employed for concrete production. In this research work un-carbonated RCA aggregate was employed, which was carbonated during their contact with CO_2, increasing the concretes carbonation resistance. Similar results were obtained by Thomas et al. (Thomas *et al*., 2013). Most of the research work carried out up to date define that concrete produced employing RCA achieved lower carbonation resistance due to its high porosity of RCA (Kurda, De Brito, *et al.,* 2019; Leemann and Loser 2019), however the carbonated or un-carbonated state of RCA could modify this behaviour. After 28 days of CO_2 exposure, the concretes produced with 50% of RCA and 50% of FA suffered a greater carbonation process. In all probability, the result was due to a higher presence of cement paste which became modified as a result of a high CO_2 concentration (Castellote *et al.*, 2009). However, this effect will be lower at natural exposure.

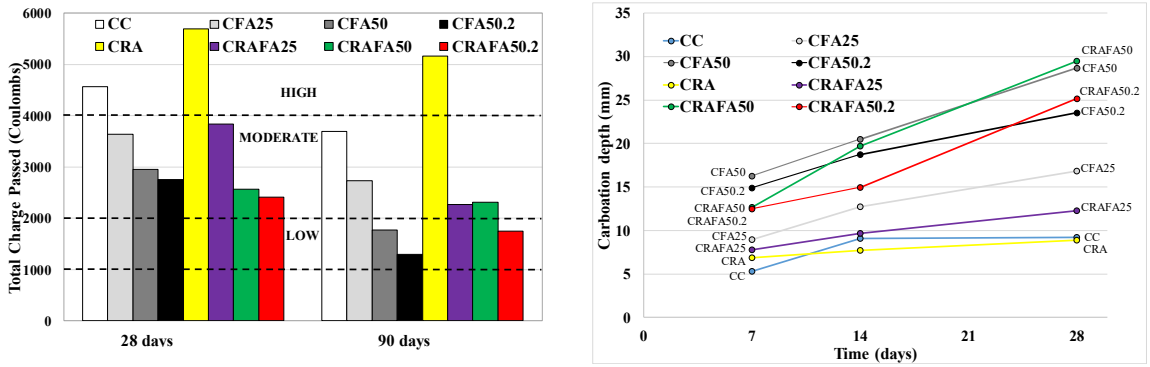

Figure 2 a) Chloride-ion penetration of concrete mixtures and ASTM corrosion ranges. b) carbonation depth of concrete mixtures.

6 Conclusions

The following conclusions can be drawn based on the results presented above:

- The effect of RCA in decreasing and increasing the density and absorption capacity, respectively, of concretes was lessened by employing FA. The CRAFA50 and CRAFA50.2 achieved a higher density, lower density and porosity than that of the CC concrete.
- The results of compressive strength test at 7 days determined that the concretes produced employing FA achieved higher strength when RCA was used than the concretes produced with NA. At 28 and 90 days. The concrete produced with 50% of RCA with or without employing 25% of FA achieved similar strength to that of the CC concrete. At 90 days, the concretes produced with CEM I and 50% FA achieved 14% lower strength than the CC concrete
- Chloride ion penetration was more influenced by the type of binder employed than the type of aggregates used. The concrete produced with 50% of FA achieved the highest resistance to chloride ion penetration. The concrete produced with 50% of RCA achieved high resistance to corrosion when 25% or 50% of FA was employed for concrete production. CRA (the concrete without FA) proved to achieve the lowest resistance to chloride ion penetration.
- The employment of FA increased the depth of the carbonation of the concrete samples. After 7 days of 20% CO_2 exposure, the use of RCA was shown to reduce the carbonation depth of the concretes produced with 50% FA and NA. The employment of RCA in concrete production with CEM II or employing 25% of FA caused the lowest carbonation depth.

ORCID

Miren Etxeberria: https://orcid.org/0000-0003-2208-6207

References

Castellote, M., Fernandez, L., Andrade, C., and Alonso, C. (2009). Chemical changes and phase analysis of OPC pastes carbonated at different CO2 concentrations. *Materials and Structures/Materiaux et Constructions*, *42*(4), 515–525. https://doi.org/10.1617/s11527-008-9399-1

Chandra, S., and Bendapudi, K. (2015). Contribution of Fly ash to the properties of Mortar and Concreteb h,u h /,.,. *International Journal of Earth Sciences and Engineering*, *04*(October 2011), 1017–1023.

Chen, W., Jin, R., Xu, Y., Wanatowski, D., Li, B., Yan, L., and Yang, Y. (2019). Adopting recycled aggregates as sustainable construction materials: A review of the scientific literature. *Construction and Building Materials*, *218*, 483–496. https://doi.org/10.1016/j.conbuildmat.2019.05.130

Deschner, F., Winnefeld, F., Lothenbach, B., Seufert, S., Schwesig, P., Dittrich, S., and Neubauer, J. (2012).

Hydration of Portland cement with high replacement by siliceous fly ash. *Cement and Concrete Research*, *42*(10), 1389–1400. https://doi.org/10.1016/j.cemconres.2012.06.009

Dinakar, P., Kartik Reddy, M., and Sharma, M. (2013). Behaviour of self compacting concrete using Portland pozzolana cement with different levels of fly ash. *Materials and Design*, *46*, 609–616. https://doi.org/10.1016/j.matdes.2012.11.015

Etxeberria, M., Vázquez, E., Marí, A., and Barra, M. (2007). Influence of amount of recycled coarse aggregates and production process on properties of recycled aggregate concrete. *Cement and Concrete Research*, *37*(5), 735–742. https://doi.org/10.1016/j.cemconres.2007.02.002

Guo, H., Shi, C., Guan, X., Zhu, J., Ding, Y., Ling, T. C., and Wang, Y. (2018). Durability of recycled aggregate concrete – A review. *Cement and Concrete Composites*, *89*, 251–259. https://doi.org/10.1016/j.cemconcomp.2018.03.008

Hemalatha, T., and Ramaswamy, A. (2017). A review on fly ash characteristics – Towards promoting high volume utilization in developing sustainable concrete. *Journal of Cleaner Production*, *147*, 546–559. https://doi.org/10.1016/j.jclepro.2017.01.114

Hyvert, N., Sellier, A., Duprat, F., Rougeau, P., and Francisco, P. (2010). Dependency of C-S-H carbonation rate on CO2 pressure to explain transition from accelerated tests to natural carbonation. *Cement and Concrete Research*, *40*(11), 1582–1589. https://doi.org/10.1016/j.cemconres.2010.06.010

Khunthongkeaw, J., Tangtermsirikul, S., and Leelawat, T. (2006). A study on carbonation depth prediction for fly ash concrete. *Construction and Building Materials*, *20*(9), 744–753. https://doi.org/10.1016/j.conbuildmat.2005.01.052

Kocak, Y., and Nas, S. (2014). The effect of using fly ash on the strength and hydration characteristics of blended cements. *Construction and Building Materials*, *73*, 25–32. https://doi.org/10.1016/j.conbuildmat.2014.09.048

Kou, S. C., and Poon, C. S. (2013). Long-term mechanical and durability properties of recycled aggregate concrete prepared with the incorporation of fly ash. *Cement and Concrete Composites*, *37*(1), 12–19. https://doi.org/10.1016/j.cemconcomp.2012.12.011

Kurda, R., de Brito, J., and Silvestre, J. D. (2019). Water absorption and electrical resistivity of concrete with recycled concrete aggregates and fly ash. *Cement and Concrete Composites*, *95*, 169–182. https://doi.org/10.1016/j.cemconcomp.2018.10.004

Kurda, R., De Brito, J., and Silvestre, J. D. (2019). Carbonation of concrete made with high amount of fly ash and recycled concrete aggregates for utilization of CO2. *Journal of CO2 Utilization*, *29*(October 2018), 12–19. https://doi.org/10.1016/j.jcou.2018.11.004

L. Lam, Y.L. Wong, and C. S. P. (1998). Effect of fly ash and silica fume on compressive andfracture behaviors of concrete. *Cement and Concrete Research*, *28*(2), 271–283.

Leemann, A., and Loser, R. (2019). Carbonation resistance of recycled aggregate concrete. *Construction and Building Materials*, *204*, 335–341. https://doi.org/10.1016/j.conbuildmat.2019.01.162

Marinković, S., Dragaš, J., Ignjatović, I., and Tošić, N. (2017). Environmental assessment of green concretes for structural use. *Journal of Cleaner Production*, *154*, 633–649. https://doi.org/10.1016/j.jclepro.2017.04.015

Nath, P., and Sarker, P. (2011). Effect of fly ash on the durability properties of high strength concrete. *Procedia Engineering*, *14*, 1149–1156. https://doi.org/10.1016/j.proeng.2011.07.144

Pedro, D., De Brito, J., and Evangelista, L. (2014). Influence of the use of recycled concrete aggregates from different sources on structural concrete. *Construction and Building Materials*, *71*, 141–151. https://doi.org/10.1016/j.conbuildmat.2014.08.030

Shah, V., and Bishnoi, S. (2018). Carbonation resistance of cements containing supplementary cementitious materials and its relation to various parameters of concrete. *Construction and Building Materials*, *178*, 219–232. https://doi.org/10.1016/j.conbuildmat.2018.05.162

Silva, R. V., Neves, R., De Brito, J., and Dhir, R. K. (2015). Carbonation behaviour of recycled aggregate concrete. *Cement and Concrete Composites*, *62*, 22–32.https://doi.org/10.1016/j.cemconcomp.2015.04.017

Thomas, C., Setién, J., Polanco, J. A., Alaejos, P., and Sánchez De Juan, M. (2013). Durability of recycled aggregate concrete. *Construction and Building Materials*, *40*, 1054–1065. https://doi.org/10.1016/j.conbuildmat.2012.11.106

Xu, G., and Shi, X. (2018). Characteristics and applications of fly ash as a sustainable construction material: A state-of-the-art review. *Resources, Conservation and Recycling*, *136*(August 2017), 95–109. https://doi.org/10.1016/j.resconrec.2018.04.010

XV International Conference on Durability of Building Materials and Components
DBMC 2020, Barcelona
C. Serrat, J.R. Casas and V. Gibert (Eds)

Modernization of Housing Estates Towards Sustainable Development: What do Housing Estate Managers Provide, What do the Users See?

Anna Ostańska

Department of Architecture and Urban Planning, Faculty of Civil Engineering and Architecture, Lublin University of Technology, Nadbystrzycka 40, 20-618 Lublin, Poland, a.ostanska@pollub.pl

Abstract. *Modernizing multi-family residential estates in operation for about 40 years is a multifaceted and complex process. In Poland, these assets cannot be considered "degraded" yet, they are not an obvious object of deep retrofit actions. The literature on the subject and the author's own research confirm that the management of Polish housing estates is carried out with the focus on current repairs and improving energy efficiency by insulating the buildings' envelopes. Poland lacks long-term programs to implement retrofitting actions based on the analysis of both social and technical needs and aimed at improving the estate's sustainability parameters. The author puts forward an original approach to the programming of sustainable housing stock retrofit based on the PEARS model (People-Environment-Actions-Resources-Sociology). The paper focuses on the social research part of the model and presents the case-based analysis – the results of the recurring survey conducted to provide input for sustainable planning of the estate improvements. The paper is a summary of over ten years of research and studies on practices of maintenance of infrastructure and buildings, changing user needs, and user opinions on the possible directions towards sustainable housing.*

Keywords: *Housing Stock, Deep Retrofit, Sustainable Housing, Recurrent Survey.*

1 Introduction

Polish housing estates with prefabricated buildings, created between nineteen-sixties and -nineties, are still considered a valuable asset (Zyga, 2014). This is due to their generally satisfactory technical condition (Nowogońska, 2017), good location and presence of local amenities, as well as the shortage of affordable housing. However, the maintenance of these assets becomes a challenge because of the scale of the problem (Ostańska, 2019) (buildings of this type and age are present in practically all towns and cities, as shown in Fig. 1), complex ownership structure (obstacle in the decision-making process (Radziszewska-Zielina, 2006)), and changing regulations (promoting individual ownership of flats (Radziszewska-Zielina and Gleń, 2013, 2014). The growing expectations towards energy efficiency, user safety, and comfort, accompanied by growing requirements of the building codes, make the "prefab blocks" becoming obsolete. Therefore, keeping the buildings fit for purpose requires (Runkiewicz *et al*., 2014) not only repairs, but also investment (Yiu and Leung, 2005; Taczanowska and Ostańska, 2012; Radziszewska-Zielina and Gleń, 2013; Komar, 2014, Wójtowicz, 2014; Stevenson and Baborska-Narozny, 2017). She wrote about the types and needs of surveys in architecture, among others, about the types and needs of surveys in architecture Niezabitowska (2014).

The residents of the housing estates have the greatest knowledge on the functional deficiencies of the flats, the buildings, and the infrastructure and amenities of the estates. As flat owners, members of the housing cooperatives, or just clients-users, they have also the power

to oppose the investment plans proposed by the estate management as well as the power to affect them. As observed in practice, the residents rarely use the opportunity of the latter, so they rarely participate in the management of the estates in an active way.

The aim of the research presented in this paper was twofold: to collect input for planning improvement measures customized for a particular estate directly from the users, and to stimulate the interest of the residents in the possibilities of influencing the managers' decisions, especially regarding the current needs and corrective or improvement actions aimed at "reviving" the estates (Ostańska, 2009, 2015).

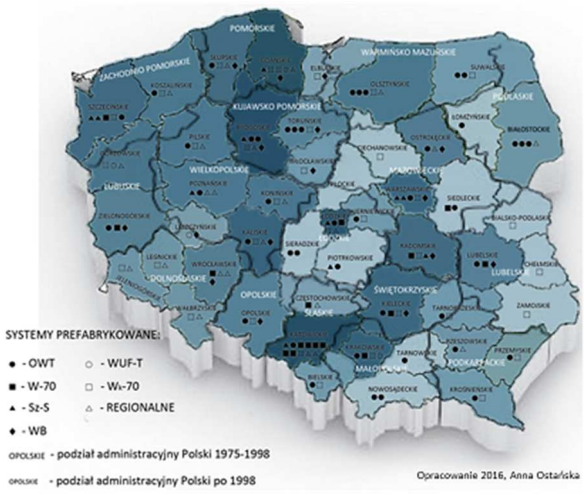

Figure 1. Distribution of prefabricated housing systems in Poland (1975-1985) according to location of prefabrication plants.

The author conducted a number of surveys in selected housing estates in three voivodships (Fig. 2). Most of them were carried out in Lubelskie Voivodship and repeated in regular intervals to juxtapose physical changes in the estate with changes of the residents' opinions on most urgent or most wanted improvements.

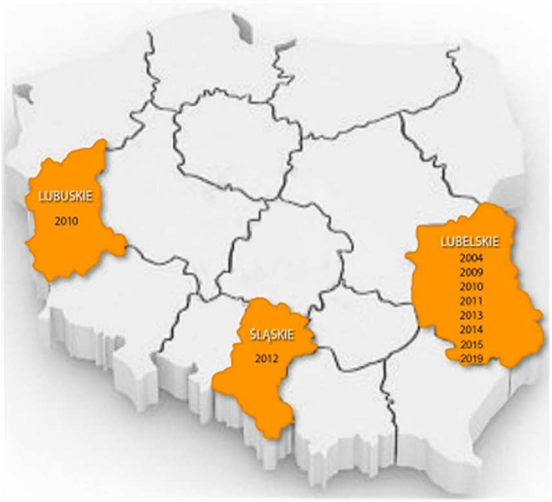

Figure 2. Location of surveys.

The paper presents the methodology behind the research and discusses results obtained in three particular housing estates in Lubartów (Ostańska, 2018). The surveys consisted in a questionnaire-based direct interview with the residents conducted first in 2010, and repeated in 2014.

2 Methods

The idea of the survey is presented in Figure 3. Its starting point was the selection of the object of research: an estate. After obtaining the estate management's consent to conduct the survey, a preliminary "in situ" assessment of the condition of the buildings and infrastructure was conducted and clusters of buildings representative for the estate were selected to serve as the sample. The residents of these buildings were then approached at home to provide answers to a set of questions on both renovation (*R*) and modernisation needs of the estate, the building and the flats. The modernisation comprises sustainability (*Me*) and functional (*Mf*) aspects.

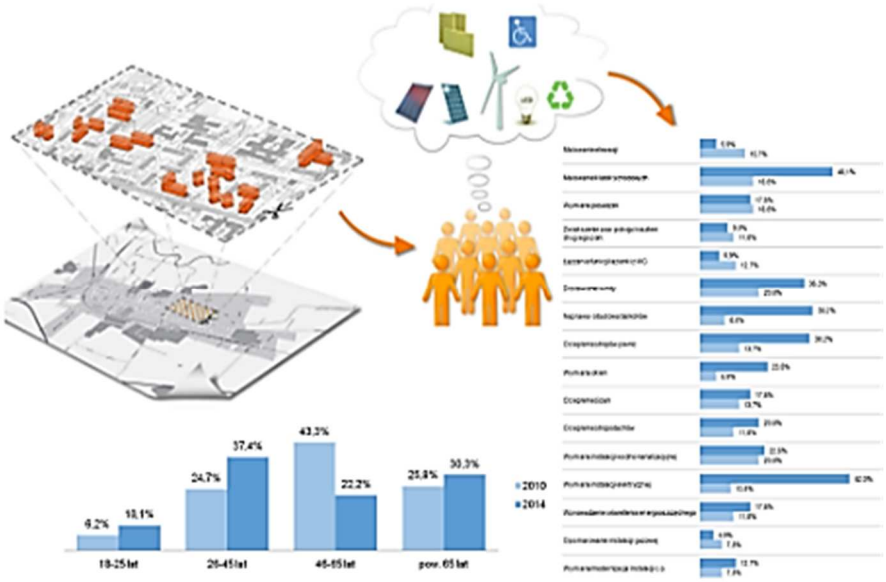

Figure 3. The idea of the survey on the opinions of the housing estate residents.

The interviews were intended to be repeated according to the same questionnaire in regular intervals. The purpose of repeating the survey was to update the insight into the modernization needs based on the opinion of the residents, and analyzing the perceived effects of the estate managers' activities.

The participants of the research were limited to adults living in the blocks of flats selected as the sample. Only one person per flat was asked to give answers.

The interviews were conducted on the basis of an original questionnaire: a standard form adjusted to the particularities of the housing estate in question. The questionnaire contained a total of 26 questions, including open-ended, closed-ended single-choice and closed-ended multiple-choice questions. Semi-open questions (logically open, technically closed) provided a list for multiple choice of feasible corrective actions, including measures for saving energy and improving functionality. Other semi-open questions concerned the list of common-use facilities

present in the estate to check if they are still in use. A single logically and technically open question concerned the works the residents conducted on their own in their flats. The classification and demographic questions concerned: age, education, migration and participation in the costs of renovation.

Thus, the full scope of the survey questions comprised:

- deficiencies in local amenities,
- condition of the estate's infrastructure,
- comfort of living (buildings and dwellings),
- opinion on the priorities for corrective actions.

The complete questionnaire form can be found in Ostańska (2018) (Appendix 3a, Questionnaire C/2010).

3 Results

In the particular case presented in this paper, the survey was conducted twice to answer the following questions:

1) Did the residents' priorities on "the most urgent needs" change over time and with the measures actually taken in the estate?
2) Did the preferences of the housing estate residents' needs change in terms of repair/renovation works (*R*), modernization measures aimed at environment protection (*Me*), and functional modernization (*Mf*)?
3) Did the housing cooperative's spending stay in proportion to the preferences of the residents?

The research conducted on three housing estates in Lubartów produced 102 filled questionnaires in 2010 and 102 questionnaires in 2014. Analysis of the results of three housing estates in Lubartów shows that the age structure of people surveyed in 2010 and 2014 is significantly different ($\chi 2[3, n = 196] = 10.46$; $p = 0.015$; $\phi = 0.231$). It should be noted that the number of people aged over 65 slightly increased (25.8% in 2010 vs. 30.3% in 2014). However, significant differences (decrease in 2014 compared to 2010) are observed in the age group 46-65. The remaining groups do not differ from each other in particular years (Figure 4).

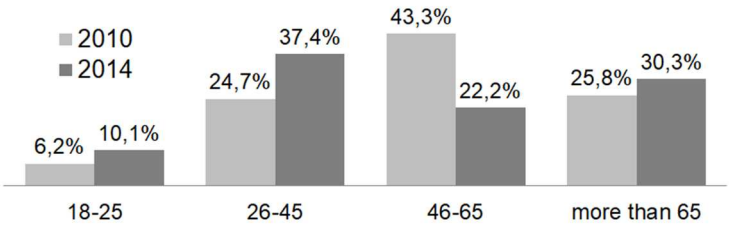

Figure 4. Age structure of the respondents: 2010 and 2014.

Considering the residents' responses to the perceived "most urgent needs" (Figure 5), it was observable that the average number of unsatisfied "most urgent needs" per respondent in 2014 (2.63) was lower than in 2010 (3.95) ($t(204) = 2.96$; $p = 0.003$). The detailed analyses confirmed differences in seven of the sixteen areas studied:

- Facade painting ($\chi 2[1, n = 204] = 5.10$; $p = 0.024$; $\phi = 0.158$) - increase from 5.9% to 15.7%,

- Painting staircases ($\chi 2[1, n = 204] = 19.02$; $p < 0.001$; $\phi = -0.305$) – a drop from 46.1% to 18.6%,
- Installing a lift ($\chi 2[1, n = 204] = 6.17$; $p = 0.013$; $\phi = -0.174$) – a drop from 36.3% to 20.6%,
- Repair or replacement of balconies ($\chi 2[1, n = 204] = 25.81$; $p < 0.001$; $\phi = -0.356$) – a drop from 39.2% to 20.6%,
- Basement ceiling insulation ($\chi 2[1, n = 204] = 15.93$; $p < 0.001$; $\phi = -0.279$) – a drop from 38.2% to 13.7%,
- Window replacement ($\chi 2[1, n = 204] = 12.66$; $p < 0.001$; $\phi = -0.249$) – a drop from 23.5% to 5.9%,
- Replacement of electrical installation ($\chi 2[1, n = 204] = 40.16$; $p < 0.001$; $\phi = -0.444$) – a drop from 52.0% to 10.8%.

No significant differences were noted in other aspects. Interestingly, only one aspect (facade painting) received a significant increase of residents' interest, almost by 10%, in relation to the results obtained in the first study.

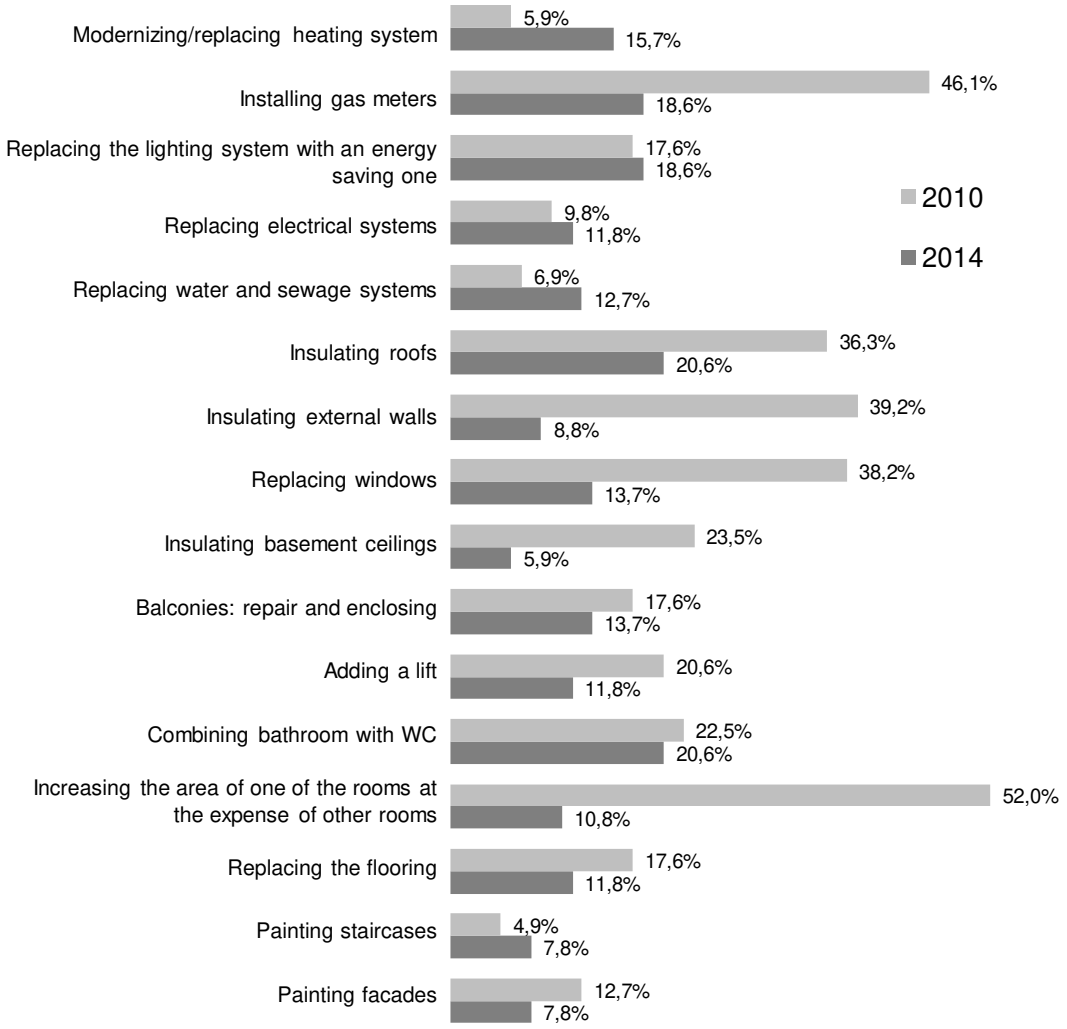

Figure 5. Priorities of improvements according to the respondents (share in the number of all indications).

Comparing the results of 2010 and 2014 (Figure 6), differences were observed in the category of "modernization measures aimed at environment protection" (*Me*) (decrease from 68.6% to 58.3%; $t(204) = 3.975$; $p < 0.001$) and functional modernization (*Mf*) (increase from 16.7% to 30.3%; $t(204) = -2.436$; $p = 0.016$).

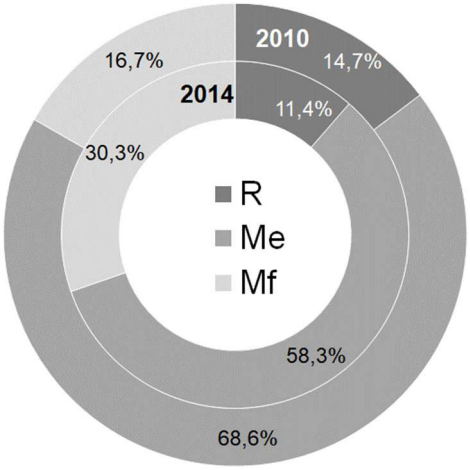

Figure 6. The residents' priorities of "most urgent" improvements according category and the year of the survey (description in the text).

The next step was to compare the priorities of the estate management with the priorities of the residents. This was done by juxtaposing the shares of actual spending on repair/renovation activities (*R*), modernization measures aimed at reducing the estate's environmental impact (*Me*), and functional modernization (*Mf*) with the proportions of the numbers of the residents' indications of the most urgent needs that belong to these categories (Figure 7). As expected, significant discrepancies were found.

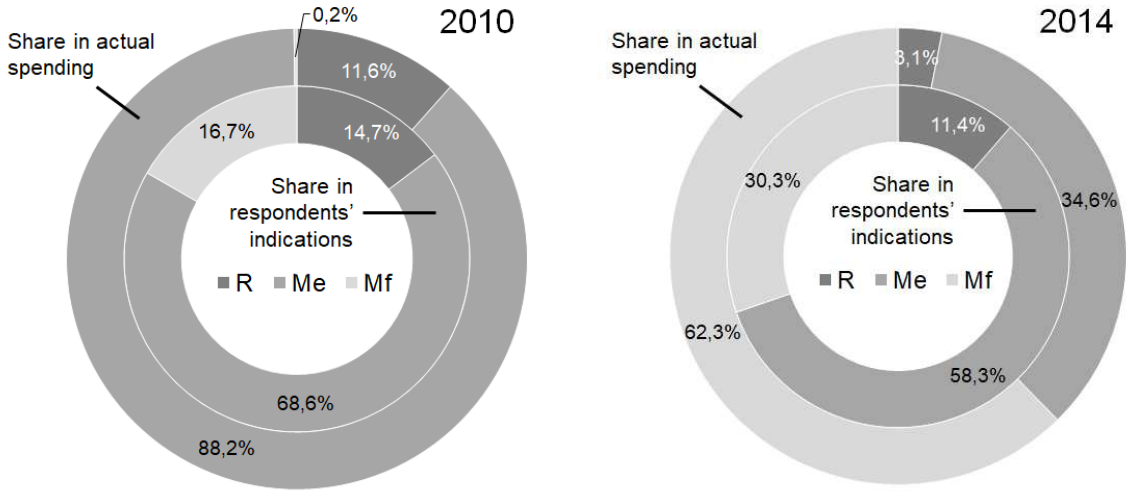

Figure 7. Users' perceived "most urgent" needs for improvements vs. actions taken by the estate managers expressed as the share in total spending (description in the text)

In 2010, 68.6% of all residents' indications on the "most urgent needs" concerned *Me*, whereas the housing cooperative spent 88.2% of its budget on actions within this category ($t(211) = -7.544$; $p < 0.001$). As for *Mf*, the cooperative spent practically nothing, while 16.7% of the inhabitants pointed to the urgency of actions from this category ($t(211) = 7.000$; $p < 0.001$).

In 2014, current repairs consumed only 3.1% of the cooperative's budget, though the residents' indications on actions from this category were 11.4% of all indications. The *Me*-related "most urgent" needs constituted 58.3% of all residents' indications, whereas the housing cooperative's spending on them constituted 34.6% of their total expenditures ($t(102) = 4.940$; $p < 0.001$). The "most urgent needs" in functional modernization had 30.3% of residents' indications, but the cooperative spent as much as 62.3% of the budget on this category ($t(102) = -6.666$; $p < 0.001$). This was possible due to extra funds from an EU-sponsored urban regeneration grant.

4 Summary and Conclusions

The residents' opinions on "urgent needs" related with maintenance and improvements to the fabric of their housing estates evolve over time (between the first survey in 2010 and the next one in 2014) and with the measures actually taken by the estate management. In particular, the repair/renovation needs seemed to be at least partly satisfied, as less people pointed to the items from this category in the second survey. A similar number of items from the list of "modernization measures aimed at environment protection" were selected as worth implementing in 2010 and in 2014. The need for "functional modernization" visibly increased, which may be related to the growing age of the residents and growing needs for comfort and accessibility.

The proportion between the housing cooperative's expenditures on maintenance and modernization measures does not correspond to the reported needs of the residents, especially in terms of functional modernization: in the case of the presented housing estate, no investment was done in functional modernization at all. Despite the passage of time, the actions taken by the estate management are not consistent with the expectations of the inhabitants.

The method of monitoring the residents' needs adopted in the presented research, so a direct interview, proved feasible. The results provide a valuable input on user expectations, and this input was successfully used in practice to define the scope of modernization projects in several housing estates in Lubartów. Keeping up to date with user needs, the housing estate managers are able to revise the action plans.

Though the face-to-face interview is a labor-intensive way of collecting input, both the cost and effort related with data collection and analysis proved acceptable. However, the surveys should be continued on a regular basis. To facilitate the dialog between the residents and the estate management and to streamline the data collection process in the future, it is advisable to construct an Internet platform. Its design is the current subject of the author's research.

ORCID

Anna Ostańska: http://orcid.org/ 0000-0002-1789-4288

References

Komar, B. (2014). *Współczesna jakość spółdzielczej przestrzeni osiedlowej w świetle zasad rozwoju zrównoważonego na wybranych przykładach* [Quality of space of the cooperative housing estates in the light of the principles of sustainable development on the basis of selected examples]. Gliwice:Wydawnictwo Politechniki Śląskiej.

Niezabitowska, E.D. (2014). *Metody i techniki badawcze w architekturze* [Research methods and techniques in architecture]. Gliwice: Wydawnictwo Politechniki Śląskiej.

Nowogońska, B. (2017). *Diagnoza w procesie starzenia budynków mieszkalnych wykonanych w technologii tradycyjnej* [Diagnosis in the process of aging of residential buildings erected using traditional methods]. Warszawa: Komitet Inżynierii Lądowej i Wodnej PAN.

Ostańska, A. (2009). *Podstawy metodologii tworzenia programów rewitalizacji dużych osiedli mieszkaniowych wzniesionych w technologii uprzemysłowionej na przykładzie osiedla im. St. Moniuszki w Lublinie* [Problems of revitalization of residential quarters of prefabricated buildings on the basis of Stanislaw Moiuszko Quarter in Lublin]. Lublin: Politechnika Lubelska.

Ostańska, A. (2015). Algorithm of revitalization programme design for housing estates, *Civil and Environmental Engineering Reports*, 18(3), 107–114.

Ostańska, A.E. (2018). *Programowanie rewitalizacji osiedli mieszkaniowych z zastosowaniem modelu PEARS* [Programming regeneration of housing estates. Application of PEARS model]. Lublin: Komitet Inżynierii Lądowej i Wodnej PAN.

Ostańska A. (2019), *Analiza wyników badań struktury zasobów mieszkaniowych w Polsce na przykładzie budynków wznoszonych w technologii prefabrykowanej* [Analysis of the results of research on the structure of housing resources in Poland on the example of buildings erected in prefabricated technology] Przegląd Budowlany, nr 5, s. 41-43.

Radziszewska-Zielina, E. (2006). *Metody badań marketingowych w budownictwie, podręcznik dla studentów wyższych szkół technicznych* [Methods of marketing research in the construction industry, a handbook]. Kraków: KNOW-HOW.

Radziszewska-Zielina, E. and Gleń, M. (2013). *Szanse i zagrożenia dla budownictwa mieszkaniowego z prefabrykatów* [Opportunities and dangers for residential construction with the use of precasts], *Inżynieria Morska i Geotechnika*, *5*, 392–396.

Radziszewska-Zielina, E. and Gleń, M. (2014). *Zrównoważone budownictwo szansą dla budownictwa mieszkaniowego z prefabrykatów* [Sustainable construction as an opportunity for prefabricated housing}. In: A. Sobocińska and M. Pisarski (Eds.), *Wybrane zagadnienia z budownictwa ogólnego* (pp. 195–210). Radom: Spatium.

Radziszewska-Zielina, E. and Gleń, M. (2013). Conducting SWOT analysis in the field of housing construction using prefabricates. *Economics and Business Management*, *11(1-2)*, 36–42.

Runkiewicz, L., Szudrowicz, B., Prejzner, H., Geryło, R., Szulc, J. and Sieczkowski, J. (2014), Diagnostyka i modernizacja budynków wielkopłytowych (cz. 1) [Diagnostics and modernization of prefabricated concrete buildings (part 1)], *Przegląd Budowlany, 7-8*, 54–60.

Stevenson, F. and Baborska-Narozny M. (2017). Housing performance evaluation: challenges for international knowledge exchange. *Building Research & Information. 46(5),* 501-512. doi: 10.1080/09613218.2017.1357095.

Taczanowska, T. and Ostańska, A. (2012). *Dokładność realizacji a potrzeba modernizacji budynków wielkopłytowych* [Assembly accuracy and the need to modernize large panel buildings], Warszawa: Medium.

Wójtowicz, M. (2014). *Wielka płyta – problem techniczny czy społeczny?* [Buildings made of large panel elements – technical or social problem?] In: A. Halicka (Ed.) *Budownictwo na obszarach zurbanizowanych: nauka, praktyka, perspektywy* (pp. 329–340). Lublin: Politechnika Lubelska.

Yiu, C.Y. and Leung A.Y.T. (2005), A cost-and-benefit evaluation of housing rehabilitation, *Structural Survey*, *23(2)*, 138–151, https://doi.org/10.1108/02630800510593701.

Zyga, J. (2014). *Ocena budownictwa wielkopłytowego przez pryzmat rynku nieruchomości* [Evaluation of prefabricated blocks of flats through the Real estate market point of view]. *Budownictwo i Architektura, 13(3)*, 57–64.

XV International Conference on Durability of Building Materials and Components
DBMC 2020, Barcelona
C. Serrat, J.R. Casas and V. Gibert (Eds)

Quality Evaluation of Granulated Blast Furnace Slag Sand Via Acid Immersion and Freeze-Thaw Tests

Takaya Kawato[1] **and Isao Kurashige**[2]

[1,2] Central Research Institute of Electric Power Industry, Civil Engineering Research Laboratory, Nuclear Fuel Cycle Backend Research Center, 1646 Abiko, Abiko-shi, Chiba, 270-1194 Japan.
[1] t-kawato@criepi.denken.or.jp [2] kurasige@criepi.denken.or.jp

Abstract. *In recent years, the use of granulated blast furnace slag (GBFS) sand as fine aggregate in concrete has been increasingly discussed from the viewpoint of environmental impact reduction and effective utilization of by-products in Japan. The various physical properties of concrete with GBFS sand, such as the compressive strength, drying shrinkage, and carbonation, were evaluated. Especially, it was demonstrated that GBFS sand can modify the hardened cement paste around it owing to the reaction of amorphous phase in the sand. Moreover, its resistance to sulfuric acid is considered to be as excellent as that of BFS powder. Therefore, in this study, we attempted to evaluate the performance of GBFS sand using a freeze-thaw (F-T) and acid immersion tests. Consequently, it was found that GBFS sand mortar had a significantly higher resistance to F-T and sulfuric acid than crushed sand mortar. In addition, it improved the resistance to freezing and thawing by prolonged curing. In our experiments, the resistance of GBFS sand mortar to sulfuric acid was measured to be approximately four times higher than that of crushed sand mortar. In contrast, in the case of nitric acid, the ratio was measured to be only two times higher. From the above results, it was concluded that the performance of GBFS sand can be easily judged by F-T and sulfuric acid immersion tests.*

Keywords: *Blast Furnace Slag, Quality Evaluation, Resistance Test, Acid, Freeze-Thaw.*

1 Introduction

From the viewpoint of environmental protection and depletion of natural resources, the use of artificial aggregates and by-products are promoted for concrete aggregate. In Japan, the JIS standard for coarse aggregate for concrete of blast furnace slag was established in 1977 and the standard for blast furnace slag fine aggregate was added in 1981 (JIS A 5011-1). However, the use of blast furnace slag as aggregate remains at approximately 0.7% of the aggregate for concrete because blast furnace slag aggregate has a poor track record and its quality is not reliable enough.

If the utilization rate of GBFS sand is improved, the environmental footprint can be reduced and a high durability concrete structure can be constructed. Therefore, the reactivity of GBFS sand is appropriately evaluated and its performance is incorporated into the concrete performance design to improve reliability. When GBFS sand is used for concrete, it is known to improve the neutralization resistance, F-T resistance, and permeability resistance to chloride ion and sulfuric acid, and reduce the drying shrinkage (*e.g.*, Ayano *et al.*, 2014; Patra *et al.*, 2018; Takahashi *et al.*, 2018). The performance of GBFS sand is determined by the reactivity depending on the composition and manufacturing method.

In this study, to establish the method for evaluating the reactivity of GBFS sand, we

doi:10.23967/dbmc.2020.116

examined the GBFS sand quality evaluation test methods and test conditions. When GBFS sand is used for concrete, the interface between the aggregate and cement paste is modified. To measure the reactivity of interface between GBFS sand and cement paste, F-T test was conducted in salt-water. In addition, acid immersion test was performed to measure the reactivity of GBFS sand with acid. Crushed sand was used for the comparison with GBFS sand.

2 Experiments

2.1 F-T Test in Salt Water Using Small Mortar Pieces

2.1.1 F-T test process

- Using a diamond cutter, from a 40 * 40 * 160 mm mortar cured under water with a temperature of 20 °C until the age of seven days, quarry test specimens that is 10 ± 2 mm cube on all sides.
- Quarried specimens were cured in water up to the planned age.
- Test solution was prepared by adding 5 mass% sodium chloride.
- Moisture was wiped from the surface of the specimens cured until the planned age, the seven pieces were formed into a set, and the total mass (m_0) was measured.
- A set of specimens and 10 ± 0.05 times the test solution was placed in a 200–300 mL test container, its lid was capped, and it was left in the F-T apparatus (Figure 1.).
- The F-T cycle consisted of a 16 h freezing step and 8 h thawing step (Figure 1.).
- At the end of 28 cycles of F-T, the surfaces of the pieces that remain on the sieve (4.75 mm) were wiped off and the mass (m_t) was measured.
- Mass residual rate (R) was evaluated using the following formula.

$$R = \frac{m_t}{m_0} \times 100 \quad (1)$$

Where,

R: Mass residual rate after t cycle (%)

m_0: Initial mass (g)

m_t: Mass after t cycle (g)

2.1.2 F-T test conditions

Table 1. shows the conditions for the F-T test. We examined the effects of the curing period and test period on the F-T evaluation test in salt-water. Furthermore, to investigate leaching during the test, it was compared with a test system using a saturated aqueous solution of calcium hydroxide (CH) as a solvent.

Table 1. Conditions for the F-T test.

Symbol	Cement	Fine aggregate	W/C	S/C	Curing	Test period	Solution
14B	OPC	BFS	0.5	2.25	14d	(7cycles) 28cycles	5% NaCl
14S		S					
14B+CH		BFS					5% NaCl +CH sat.aq.
14S+CH		S					
28B		BFS			28d		5% NaCl
28S		S					
28B+CH		BFS					5% NaCl +CH sat.aq.
28S+CH		S					

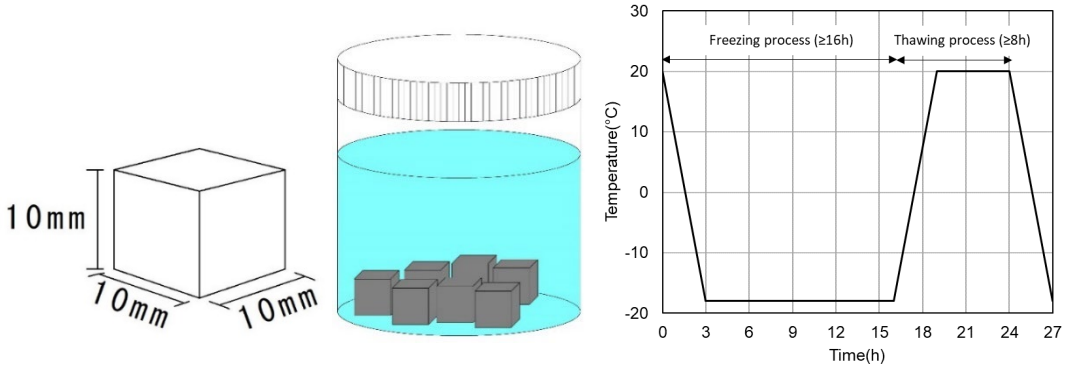

Figure 1. Conditions of F-T test.

2.2 Acid Immersion Test Using Mortar Cylinder

2.2.1 Acid immersion test process

- Cylinder specimens (diameter = 50 mm (D_0), height = 100mm) cured up to 28 days in water at 20 °C were immersed in 5 mass% acid, which is more than five times the specimen volume.
- Complete immersion of the specimen was confirmed, its container was covered, and left at 20 ± 2 °C. Figure 2. shows the conditions for the acid immersion test.
- In case of "with" exchange, all acid solutions were replaced every seven days, and the upper and lower sides of the specimen were inverted each time.
- After immersion for 56 days, a cut was made on the center of the remaining specimen height.
- Phenolphthalein solution was sprayed on the cut surface and the diameter of the colored part (D_{56}) was measured.
- Evaluation is based on the erosion depth (Ys) derived from the following equation.

$$\mathrm{Ys} = \frac{(D_0 - D_{56})}{2} \tag{2}$$

Where,

Ys: Erosion depth (mm)
D_0: Initial specimen diameter (mm)
D_{56}: Diameter of non-neutralization area after 56 days (mm)

2.2.2 Acid immersion test condition

For the acid immersion test, we investigated sulfuric acid and nitric acid. In addition, we investigated the possibility of reducing acid waste and the number of test processes by comparing the “with” and “without” test solution exchanges. Table 2. lists the conditions for the acid immersion test.

Table 2 Conditions for the acid immersion test.

Symbol	Cement	Fine aggregate	W/C	S/C	Curing	Test period	Solution	Solition exchange	Liquid-solid ratio
B-S	OPC	BFS	0.3	1.7	28d	56d	5% H_2SO_4	with	5 times or more (7.0)
S-S		S							
B-S(N/A)		BFS						without	22.5
S-S(N/A)		S							
B-N		BFS					5% HNO_3	with	5 times or more (7.0)
S-N		S							
B-N(N/A)		BFS						without	22.5
S-N(N/A)		S							

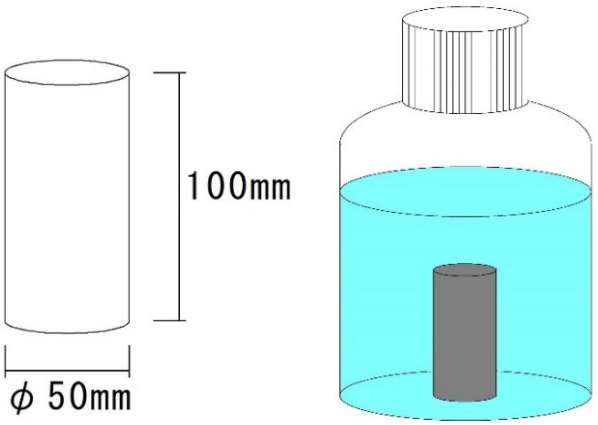

Figure 2. Conditions for the acid immersion test.

3 Results and Discussion

3.1 F-T Test Results and Discussion

Figure 3. shows the effect of curing days.
Figure 4. shows the effect of leaching.
Table 3. shows the pH of the solution after the F-T test.

3.1.1 Difference in number of curing days

Compared to crushed sand mortar, GBFS mortar clearly demonstrated the difference in mass residual rate for a curing period of 28 days. To evaluate the quality potential of GBFS, a longer curing period was considered necessary.

3.1.2 Difference in test period

GBFS with 28 days of curing could evaluate the quality even at the end of 28 cycles; however,

under other conditions, the mass residual rate was extremely low at the end of 14 cycles, making it impossible to evaluate the quality of the aggregate. When the residual mass of the mortar began to decrease, seven cycles were considered suitable for evaluation.

3.1.3 Effect of leaching

F-T using salt-water requires higher F-T resistance than when fresh water is used. Focusing on the difference in test solution during the seven cycles of 14-day curing, 5% NaCl showed a smaller value for 5% NaCl + CH sat.aq. (11% for GBFS, 13% for crushed sand). From these results, it is considered that 5% NaCl evaluates the quality of GBFS in the state of adding the influence of leaching as well as F-T. From Table 3., the initial value of 5% NaCl is pH = 7.22; however, after testing both GBFS and crushed sand, their pH exceeded a value of 12. In contrast, the initial value of 5% NaCl + CH sat.aq. was pH = 12.95 and 12 or more after the test. From the result, it was surmised that leaching is suppressed in 5% NaCl + CH sat.aq.

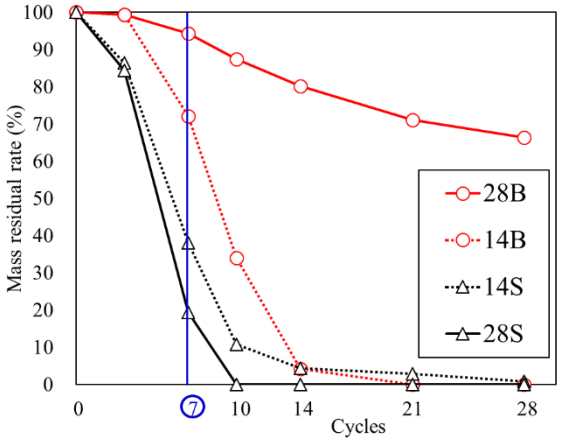

Figure 2. Effect of curing days.

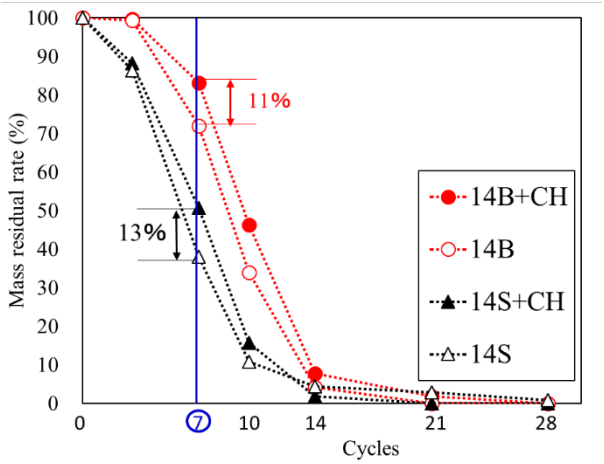

Figure 3. Effect of leaching.

Table 1. pH of the solution after the F-T test.

Symbol	5%NaCl	5%NaCl+CH sat.aq.
Initial	7.22	12.95
BFS-14	12.55	12.61
CS-14	12.45	12.54
BFS-28	12.87	12.95
CS-28	12.93	12.99

3.2 Acid Immersion Test Results and Discussion

Figure 5. shows the results of acid immersion test.
Figure 6. shows the state after the acid immersion test (no-exchange).
Figure 7. shows the shape of specimen after the acid immersion test about solution exchange.

3.2.1 Effect of liquid exchange

The depth of erosion in the sulfuric acid immersion test was reduced by 1.0 mm (28%) and

4.5 mm (34%) for GBFS and crushed sand, respectively, when the liquid was not changed because the total amount of solution in contact with the specimen during the test period was as small as 22.5 in "without replacement," as compared to 56 (7.0 times × 8 times) in "with replacement," per liquid-solid ratio. In addition, when the solution was changed, the difference in fine aggregate performance was more pronounced. The erosion depth in the nitric acid immersion test was also confirmed to decrease by 3.0 mm (48%) for GBFS and 3.2 mm (29%) for crushed sand. This is also thought to be due to the amount of solution in contact.

3.2.2 Difference between sulfuric acid and nitric acid

GBFS erosion depth in sulfuric acid immersion test decreased to 27% in comparison to crushed sand. In GBFS, calcium and magnesium were eluted by the reaction of sulfuric acid and aggregate; thus, the expansion force of the generated dihydrate gypsum was relaxed and deposited on the surface without peeling off, which is considered to suppress erosion (Jariyathitipong *et al.*, 2013). In this study as well, the suppression of peeling shown in Figure 6. was confirmed. In contrast, in the nitric acid immersion test, the erosion depth of GBFS only decreased to 58% in comparison to crushed sand. Unlike dihydrate gypsum, calcium nitrate is known to have very high solubility, which prevents the reactants from precipitating, and the calcium elution is excellent; thus, erosion proceeds (Tanaka *et al.*, 2008). This study also showed the melting of calcium and softening of the surface layer.

In nitric acid erosion, the density of the hardened body is dominant. However, in sulfuric acid, the influence of hydrate composition that affects the formation of dihydrate gypsum is also added. Therefore, it seems that the erosion depth during sulfuric acid erosion was further reduced.

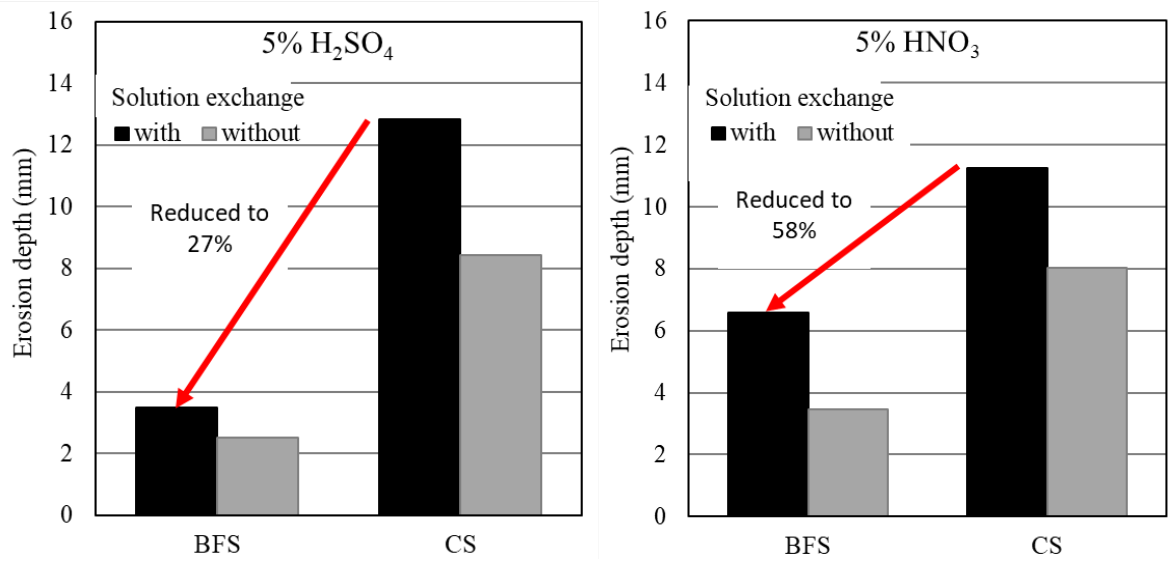

Figure 4. Results of the acid immersion test.

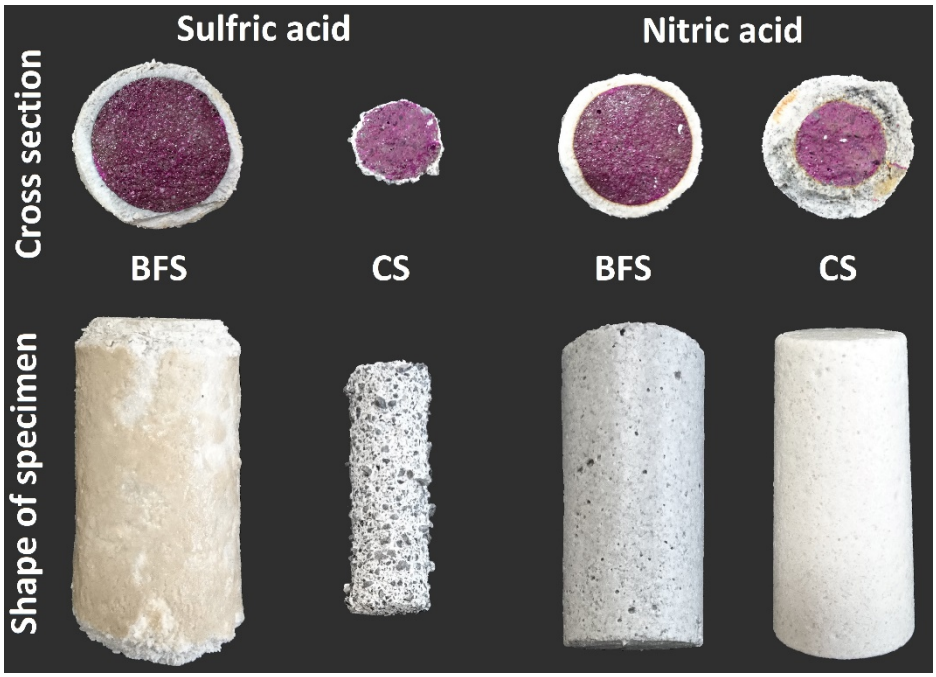

Figure 5. State after the acid immersion test (no-exchange).

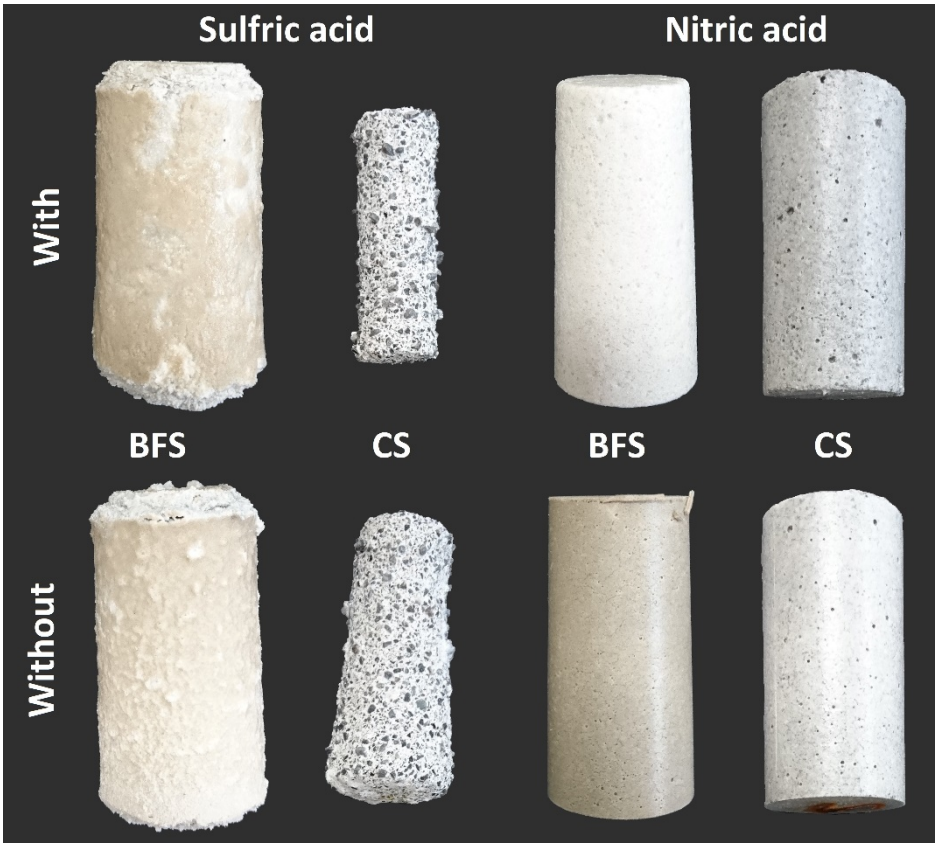

Figure 6. Shape of specimen after acid immersion test about solution exchange.

4 Conclusions

It is well known that GBFS has different performance depending on the raw iron ore and process of steel mill (Tobo *et al.*, 2015). However, few studies have evaluated the quality variation of GBFS. In this study, we examined a method that can easily determine the performance of GBFS. As a result, the following results were obtained from this study.

- The quality of GBFS sand as fine aggregate was evaluated by acid immersion test and F-T test in salt-water.
- The implementation of the F-T test evidently expressed the difference in durability depending on the reactivity of GBFS sand.
- Although leaching occurred during the F-T test by salt-water, it was found that destruction by F-T was superior to that by leaching. Or, even if leaching occurs, its effect is small when the liquid to solid ratio is 10.
- Long-cured GBFS mortar had a significantly improved resistance to F-T.
- The sulfuric acid immersion test enabled the evaluation of the resistance of GBFS sand to sulfuric acid.
- In the reaction with nitric acid, although GBFS sand mortar showed higher resistance than crushed sand mortar, it did not show special resistance like sulfuric acid immersion.

Acknowledgements

This study was conducted as part of normalization of JSCE-C 507 and JSCE-C 508. I would like to thank all the parties concerned, especially Prof. T. Ayano and Dr. T. Fuji of Okayama University.

ORCID

Takaya Kawato: http://orcid.org/0000-0003-2336-8994
Isao Kurashige: http://orcid.org/0000-0002-2773-0885

References

Hiroyuki Tobo, Keiji Watanabe, Michihiro Kuwayama, Shigeaki Goto, Hiroki Goto and Toshihiro Tanaka (2015). Effect of Water Granulation Conditions on Density and Grain Size of Granulated Blast Furnace Slag. ISIJ International, Vol. 55, No. 11, 2499–2508

Hitoshi Tanaka and Yoshihiro Masuda (2008). An experiment on progress of chemical corrosion of concrete by sulfuric acid and nitric acid. J. Struct. Const. Eng., AIJ, Vol.73 No.625, 355-361

JIS A 5011 (2013). Slag aggregate for concrete-Part 1: Blast furnace slag aggregate. Retrieved from http://kikakurui.com/a5/A5011-1-2013-01.html

Paweena Jariyathitipong, Kazuyoshi Hosotani, Takashi Fujii and Toshiki Ayano (2013). The sulfuric acid resistance of concrete with blast furnace slag. Proceeding of First International Conference on Concrete Sustainability (ICCS13),581-586

Paweena Jariyathitipong, Kazuyoshi Hosotani, Takashi Fujii and Toshiki Ayano (2013). Improvement of resistance to sulfuric acid attack of concrete by use of blast furnace slag sand. Journal of JSCE Ser. E Vol.69 No.4 337-347

Rakesh Kumar Patra and Bibhuti Bhusan Mukharjee (2018). Influence of granulated blast furnace slag as fine aggregate on properties of cement mortar. Advances in Concrete Construction, Vol. 6, No. 6, 611-629

Takahashi Katsunori, Watanabe Keiji, Niitani Kyoji, Hosotani Kazuyoshi (2018). Effect of Blast Furnace Slag Fine Aggregate for Freezing-and-Thawing Durability of Mortar and Concrete under Salt Existence Environment. JFE TECHNICAL REPORT No. 23

Toshiki Ayano and Takashi Fujii (2014). Resistance to freezing and thawing attack of concrete with blast furnace slag fine aggregate. Journal of JSCE Ser. E Vol.70, No.4, 417-427

XV International Conference on Durability of Building Materials and Components
DBMC 2020, Barcelona
C. Serrat, J.R. Casas and V. Gibert (Eds)

Risk-Based Approach for Improving Concrete Bridges' Inspection Planning

Sindre Tronsli, Samindi M.K Samarakoon and R.M Chandima Ratnayake

Department of Mechanical and Structural Engineering and Materials Science, University of Stavanger, Norway, www.uis.no

Abstract. *Visual inspection forms the basis of the inspection planning process for concrete bridges. The authority responsible for bridge inspection maintains a database to record past inspection results, in order to plan future inspections. It is a challenge to recognize and classify bridges that it is essential to inspect based on inherent requirements. This is further exacerbated by the limited budget available. This manuscript describes a methodology for classifying bridges based on risk of potential failure and distributing the annual inspection budget for carrying out inspections on bridges accordingly. The absence of such a methodology allocation of resources for bridge inspection without real need. For example, on some occasions it is not necessary to inspect certain bridges on a time basis. Hence, this study focuses on developing an inspection-planning approach based on the actual and predicted condition (i.e. based on the database of past inspection data). It enables the bridges to be classified into different categories, based on the risk of potential failures. This enables the effective distribution of annual budgets among the bridges, avoiding unnecessary inspection that incurs pointless inspection costs.*

Keywords: *Visual Inspection, Concrete Bridges, Group Technology.*

1 Introduction

Routine bridge inspections are essential for maintaining information, damage status and proper prioritization of bridge maintenance measures. In the Norwegian Public Road Administration (NPRA), bridge inspections are defined as follows: "Inspection is a visual control combined with surveying and testing of materials carried out to assess the bridges' condition and level of safety. The inspection shall reveal the need for operational measures and/or maintenance, as well as any need for reinforcement or rebuilding" (Vegdirektoratet, 2000). According to the available information on bridge maintenance and current inspection procedure at the NPRA, visual inspection has not been performed annually for over half the bridges in Norway. These are serious figures, highlighting troublesome issues with the Road Administration Inspection System. Following the disclosures, the NPRA estimated in 2017 that there is a lag in maintenance and improvements for bridges and quays, which has a cost of NOK 15 billion (Statens Vegvesen, 2017a). From 2017, the government increased funding for road and bridge maintenance in the national budget by NOK 2.9 billion, which corresponds to an increase of 7.7% (Regjeringen, 2017). But, even though the government has increased its support for bridge maintenance in recent years, it is not certain that this support will persist. The NPRA estimates that they have a huge backlog of NOK 15 billion in the maintenance of bridges and quays. At the same time, in 2013, an ambitious streamlining programme was established, which states that the NPRA must cut internal costs by 10-15% by 2023. This corresponds to cuts of around

doi:10.23967/dbmc.2020.120

NOK 1.4 billion (Statens Vegvesen, 2018). Therefore, it is vital to improve the existing inspection procedure, to optimize the available budget. This situation underlines the need for Risk Based Inspection procedures, which include optimal prioritization of inspections and the determination of optimal inspection interval. This paper proposes the use of Risk Based Inspection (RBI) for the planning of inspections, which will help to optimize and increase the efficiency of the inspection procedure carried out by the NPRA.

2 The Existing Inspection Procedure in NPRA

In the inspection programme, once a bridge needs to be inspected, visual inspection, combined with non-destructive/destructive testing, is performed to assess the condition and safety of the bridge. Then, any damage or deficiencies in the bridge's structural members (i.e. location) should be recorded in a database. Possible damage/deficiencies (i.e. corrosion, cracks, spalling, discolouring, etc.) in bridges are listed in the NPRA handbook (Vegdirektoratet, 2000) with a representing number. Moreover, the NPRA has established a bridge management system called 'Brutus' to input all the information about all bridges in Norway. Therefore, the Brutus (i.e. bridge inspection data base – BIDB) consists of the historical inspection data of the bridges. When assessing damage, it is vital to classify the type, level (use Table 1), cause and consequences of the damage to the entire bridge and/or the environment (use Tables 2 and 3). Then, to recommend the level of action required, a priority level is calculated using Equation (1). Furthermore, a higher priority level indicates a requirement for immediate action/measure (Ratnayake and Samarakoon, 2018). However, damage levels can be set based on quantitative parameters set by the NPRA, but only for cracks. Quantitative parameters for deciding the damage level for spalling/Reinforcement (RF) corrosion, leakage or other damage modes have not been set. This study will therefore develop quantitative measures to set damage levels accordingly.

According to the procedure, each bridge should initially have a General Visual Inspection (GVI) every year. Each bridge will initially have to carry out a Close Visual Inspection (CVI) every five years. A CVI is defined as a condition monitoring of the entire bridge, in order to verify that it fulfils its function, and is a more comprehensive type of inspection compared to a GVI. But the intervals of one and five years for GVI and CVI, respectively, do not always represent the optimal inspection interval. The procedure for changing the inspection interval starts with observation of serious damage during inspection, with the consequence level being set to a minimum of 3. Then, the inspection engineer evaluates the damage and the bridge as a whole, in respect of whether the inspection interval should be changed for that particular bridge. If the result of the evaluation indicates that the inspection interval should be changed, a Risk and Vulnerability Assessment (RVA) shall be carried out to determine a new inspection interval (Vegdirektoratet, 2018).

Table 1. Damage/defect level and rank. (Vegdirektoratet, 2000)

Rank	Damage/deficiency level	
1	Low (L)	
2	Medium (M)	
3	High (H)	
4	Very high (VH)	

Table 2. Consequence type and level. (Vegdirektoratet, 2000)

Consequence type	*Abb.
Damage/defect(s) threatening bearing capacity	B
Damage/defect(s) threatening road safety	RS
Damage/defect(s) that may increase maintenance costs	M/R
Damage/defect(s) that may affect the environment/ aesthetics	E/A

Consequence Level	Measures to be taken	Rank
L	No action required	1
M	Register the recommended measures in BIDB	2
H	• Register the recommended measures in BIDB, and • Inspection interval shall be recommended	3
VH	Immediate action is required	4

Abbreviation - B: Bearing capacity; RS: Road safety; M/R: Maintenance/Repair; E/A: Environment and aesthetic appearance

Table 3. Example: Damage/defect level and rank -crack width (CW). (Vegdirektoratet, 2000)

Damage level	Rank	CW in mm
Low (L)	1	CW < 0.3
Medium (M)	2	0.3 < CW < 1.0
High (H)	3	1.0 < CW <2.0
Very high (VH)	4	CW > 2.0

$$Priority\ (P) = Damage\ level \times Consequence\ of\ damage \quad (1)$$

when

$P \leq 6$: Recommended measures are normally not assessed before the next inspection

$8 \leq P \leq 12$: Recommended measures are assessed with the proposed time of execution

$P = 16$: Measures taken immediately

3 Group Technology Concept to Improve Inspection Planning

3.1 Bridge Families and Representative Bridges

In order to develop optimal inspection procedures, the concept of group technology has been used, as it has the potential to increase the efficiency of the inspection procedure (Rachman and Ratnayake, 2019). Group technology is widely used in the manufacturing industry to classify the system into subsystems and subdivide them into part families, based on design attributes and manufacturing similarities. According to the literature, the use of group technology in manufacturing processes helps to both improve the productivity and increase the efficiency of the process. However, there are limited applications of the concept in civil engineering applications. Group technology concepts are based on creating families of bridges with similar characteristics, such as building materials, degradation mechanisms and condition, and, for each bridge family, a representative bridge is designated. The representative bridge should have all the characteristics of the remaining bridges in each bridge family. The purpose of the representative bridges is that, on the basis of thorough inspections of the representative bridge, one should be able to predict future damage conditions on the remaining bridges in the bridge family. The representative bridge must undergo frequent inspections, and one should have good information about its condition. This information is used to map and predict the condition of the remaining bridges in the bridge family and should significantly reduce the number of GVIs needed.

Initially, based on building material, the bridges are grouped into primary families: reinforced concrete, pre-stressed concrete and steel. The secondary families group the bridges primarily by location and exposure. For example, they can be grouped as bridges close to the sea, inland bridges and high-risk bridges which need special attention. To classify the groups, information from the BIDB about previous inspections is used. Furthermore, a secondary family consisting of "high-risk bridges" includes bridges in poor condition and operates independently of exposure zone. The requirement for bridges in the high-risk family is a priority level > 9 on critical damage, as given in Equation (1), i.e. damage priority 12 or 16. Critical damage is damage with the highest priority level on the actual bridge. Bridges in the "High-risk" family will not have a representative bridge, because all the bridges in the bridge family are at high risk and therefore need thorough and frequent inspections on the same basis as the representative bridges. The different secondary families are as follows: bridges in coastal climates with priority level ≤ 9 on critical damage, bridges in inland climate with priority level ≤ 9 on critical damage, bridges with priority level > 9 on critical damage.

The study uses the bridges in the Rogaland, Norway, area to illustrate the method. Rogaland consists of 721 road bridges; concrete is the most typical building material, with 522 bridges. Furthermore, 133 bridges are built with pre-stressed concrete and 66 bridges with steel. Moreover, Rogaland is a region in Norway with an elongated coast, and this is evidenced by the high number of bridges located near/within the coastal area. In total, 359 of Rogaland's 720 bridges are in coastal areas, of which 48 qualify for the secondary family, "high-risk bridges". That leaves 311 bridges in the secondary family "bridges in coastal climate". Although Rogaland has an elongated coast, a large proportion of its bridges are located inland. A total of 361 bridges are located in inland areas, of which 51 are eligible for the secondary family, "high-risk bridges". That leaves 310 bridges in the secondary family, "bridges in coastal climate".

3.2 Selection of Representative Bridge

The representative bridges should have all the damage features (*i.e.* corrosion, leakage, spalling, etc.). To ensure this, the study compares the damage frequencies, as well as other characteristics like age, length and structural integrity for the individual bridges to the bridge family as a whole. This is information that is available in NPRA's database, Brutus. The study therefore involves a damage frequency analysis, and this is the decisive factor when appointing representative bridges. For this analysis, 90 bridges have been used, and the bridges are grouped. Then, damage vs frequency analysis has been carried out for each group which consists of at least 10 bridges. Figure 1 shows a Pareto chart of damage vs frequency for the reinforced concrete bridges in coastal areas, based on the registered inspections in the BIDB database until 2018. The dominant mechanisms of damage to reinforced concrete bridges in coastal areas is found to be corrosion of reinforcement and spalling (spalling/RF corrosion), leakage and cracks (80%). Based on the frequency of each type of damage, representative bridges have been assigned for each bridge group. For example, based on the damage and frequency analysis of reinforced concrete bridges in coastal areas, "Kongsbrua" has been chosen as the representative bridge for reinforced concrete bridges in coastal climate in Rogaland, Norway. It represents the remaining bridges, with an approximately equal frequency of damage to the rest of the bridging family, with damage rates of 45%, 27% and 27% for spalling/RF corrosion, leakage and cracks, respectively. An assessment of other characteristics like age, length and structural integrity also

has to be a significant factor in the process. In other words, the representative bridge should have similarities to the rest of the bridge family when it comes to damage frequencies, age, length and structural integrity.

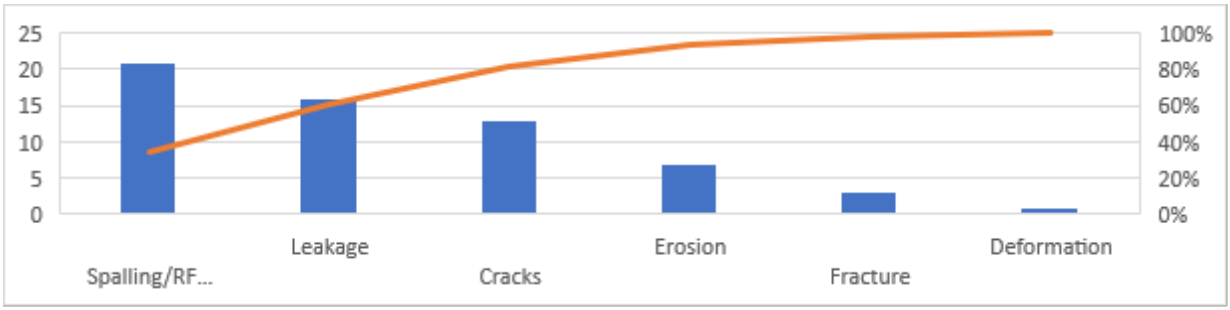

Figure 1. Different types of damage vs frequency in bridge group: reinforced concrete bridges in coastal areas.

The methodology based on the concept of group technology has great potential in inspection planning, and the use of representative bridges can significantly reduce the number of GVIs, without compromising safety. But there are several factors that determine the credibility of the method. Firstly, the bridges in the different families must be of a similar nature. This includes approximately similar damage frequencies, as well as similar characteristics like age, length and structural integrity. Secondly, the appointment of the representative bridge must be as correct as possible. In addition to having similar damage frequencies to the rest of the family, the representative bridge should both be older than and have greater damage than the majority of the bridges in the family. The process does not designate any representative bridges for the high-risk families. This is because bridges in the high-risk families are very different from each other in terms of climate, age and length. The only thing they have in common beyond common building material is one or more cases of serious damage (priority ≥ 12). It would be wrong to designate representative bridges for the high-risk families, as it is very difficult to predict future damage for serious damage whose development is already very advanced. Serious damage will often develop in an accelerating and unpredictable way, making the prediction of future condition uncertain (Vegdirektoratet, 2000). Therefore, all bridges in the high-risk families should be given priority, with frequent and thorough GVIs, on the same basis as the representative bridges. For bridges in families with a representative bridge, simple inspections can be given a lower priority, as long as inspections of the representative bridge have given satisfactory results.

3.3 Comparison of Repair Cost

In order to understand the severity of the damage in terms of repair costs, the cost of implemented measures in the most typical damage modes – crack, spalling/RF corrosion and leakage – have been studied. This was done by using the BIDB database, where both damage priority number (i.e. calculated as given in Equation (1)) and estimation of repair cost related to the damage have been recorded. The correlation between damage, damage priority number and cost of repair has been studied, to understand which damage should be prioritized in maintenance and inspection, from a cost-based perspective (Tronsli, 2019). It could be seen that spalling/RF corrosion is the most expensive to repair, followed by cracks and leakage. For

spalling/corrosion, the repair costs will, to a large extent, increase with increasing priority, compared to cracks and leakage. Therefore, from a cost-based perspective, it is beneficial to repair spalling/RF corrosion at an early phase of damage development.

3.4 Modification of the Existing Inspection Planning Process

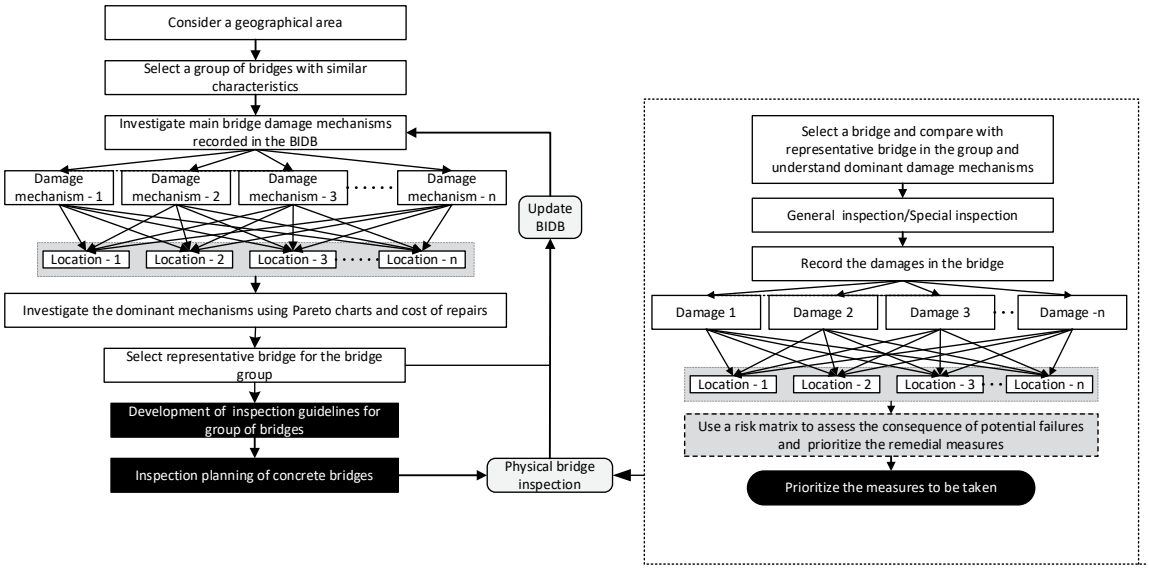

Figure 2. Modified inspection planning process.

The existing inspection procedure can be modified, as given in Figure 2, by implementing group technology and a risk-based inspection planning process. However, it is vital to develop risk matrices to assess the severity, considering consequences and repair costs. According to a repair cost comparison, the cost of repairing spalling/RF corrosion is very high. Therefore, the risk matrix has been developed to assess the severity of spalling/RF corrosion.

4 Development of Risk Matrix

To aid the inspection planning and to ensure an optimal inspection interval, the study developed risk matrices, which decide optimal interval time, based on the priority level (refer to Equation (1)) of the critical damage. The risk matrices developed are only in respect of the damage mode, spalling/RF corrosion, as the damage frequency analysis and cost analysis showed that spalling/RF corrosion are the most dominant and expensive of the damage modes. However, the method of developing risk matrices is applicable for other damage modes. Four matrices are applicable for the damage mode, spalling/RF corrosion, and they are based on the different consequence types the NPRA uses (bearing capacity, road safety, maintenance and aesthetics) when assessing damage. Table 4 shows the risk matrix developed for consequence type, “maintenance”. In order to correctly assess the level of spalling/RF corrosion damage, the study also developed a new scale, which evaluates the damage based on quantitative parameters. It assesses the damage level, based on the size of the area of damaged concrete, and is only applicable for reinforced and pre-stressed concrete bridges. The scale for consequence level is used as in the existing procedure. The exception is for the consequence type, “maintenance”,

where the consequence scale is replaced with a new scale, based on estimated cost for maintenance, worked out from the cost analysis. By adding quantitative parameters to the determination of damage and consequence levels, the accuracy of the assessment is increased, minimizing the possibility of human error or incompetence when assessing damage with consequence type, "maintenance".

Table 4. Risk matrix for assessing spalling/RF corrosion; consequence type: Maintenance.

			Consequence level for maintenance cost			
Maintenance		**Area of damaged concrete**	**1**	**2**	**3**	**4**
			<10,000 NOK	10,000-50,000 NOK	50,000-200,000 NOK	>200,000 NOK
Damage level / measure of probability of failure	**1**	Under 1m²	1	2	3	4
	2	1m²-5m²	2	4	6	8
	3	5m²-20m²	3	6	9	12
	4	Over 20m²	4	8	12	16

Priority	Risk and interval
1-2	Very low risk. Simple inspection can be abolished if the main inspection interval does not exceed 5 years.
3-4	Low risk. The range of simple inspection is 24-36 months.
5-8	Medium risk. The range of simple inspection intervals is 12-24 months.
9-12	High risk. The range of simple inspection intervals is 6-12 months.
16	Very high risk. Simple inspection should be performed as soon as possible. The maximum interval for simple inspections is 6 months.

5 Case Study: Illustrative Example

During the GVI, the bridge is checked for damage and defects according to the modified process given in Figure 2. When observing damage, damage and consequence levels shall be determined by finding the right matrix, based on the different consequence types (referring to Table 2). Then, the damage and consequence levels for the critical damage are entered into the risk matrix, and the matrix will propose a new inspection interval for future GVIs on that particular bridge. If the damage has consequence type M/R (maintenance/repair cost), a cost analysis must be performed. This is about finding the approximate cost of repairing the damage and must be done to find the consequence level, in order to find favourable inspection intervals for GVIs. Bridge 11-0307 Gyastøl, which is located in Rogaland, Norway, has been chosen. Built in 1945, it is a reinforced concrete bridge located in a coastal area. "Gyastøl" is compared with "Kongsbrua", which is the representative bridge for reinforced concrete bridges in coastal areas. Based on the representative bridge, critical damage to "Gyastøl" is spalling/RF corrosion on the bottom of the bridge slab, and the damage has been recorded with consequence level 2 and consequence type "maintenance". The damage description states that there is around 1.5m^2 of spalling, as given in Table 5, which corresponds to damage level 2. Using Table 4, a new inspection interval for future GVIs on the bridge can be estimated. The analysis shows that there is a low risk of failure, valued with priority 4 and consequence type "maintenance", and the matrix suggests a new inspection interval for upcoming GVIs of 24-36 months. Since the previous GVI on the bridge was carried out on 6.6.2018, the next GVI will be set to the period 6.6.2020-6.6.2021. The case shows that it is possible to increase the intervals of GVI using risk analysis and the risk matrix. This will ensure an optimal allocation of resources. Furthermore, this increase in efficiency will enable an increase in resources dedicated to those bridges with the greatest need for frequent inspections.

Table 5. Inspection registered in BIDB: Bridge 11-0307 Gyastøl.

Inspection								
Close visual inspection 12.09.2019 (Done)								
Damage mode				**Status**				
Spalling/RF corrosion				Open	Repaired		Expired	
Damage level				**Consequence level**				
1	2	3	4	**Bearing capacity**	1	2	3	4
Cause of damage				**Traffic safety**	1	2	3	4
Normal degradation of concrete				**Maintenance**	1	2	3	4
Damage description				**Aesthetics**	1	2	3	4
Around 1.5m^2 of spalling.								

6 Discussion and Conclusions

The existing NPRA inspection procedure shows how bridges in Norway prioritize inspections and utilize their budgets. It can be seen that the current inspection procedure does not utilize the allocated inspection budget efficiently. To improve the existing method, and to increase the efficiency of both the inspection procedure and the resource allocation in the NPRA, the concept of group technology is proposed. The proposal to group the bridges into families, according to different properties, and then to designate representative bridges for each bridge family is a new way of working that will increase both efficiency and safety. However, it must be considered that the sample size chosen in this study is small. Therefore, it is vital to carry out further work and a damage frequency analysis using a larger sample size of bridges. However, the application of the proposed improvements can contribute to a reduction in the number of simple inspections, without compromising on safety.

ORCID
S.M. Samindi M.K Samarakoon: https://orcid.org/0000-0002-6847-972X
R.M Chandima Ratnayake: https://orcid.org/0000-0003-2222-8199

References

Rachman, A.Y. and Ratnayake, R.M.C. (2019). *Corrosion loop development of oil and gas piping system based on machine learning and group technology method*, Journal of Quality in Maintenance Engineering, Accepted.

Ratnayake, R.M.C. and Samarakoon, S.M.S.M.K. (2018). *Risk based inspection planning methodology for concrete bridges*. I: Proceedings of the International Conference on Sustainable Materials, Systems and Structures (SMSS2019). Challenges in Design and Management of Structures, 20-22 March 2019 – Rovinj, Croatia. PRO 128, Vol. 4. RILEM Publications 2019 ISBN 978-2-35158-226-8, p. 184-191.

Regjeringen (2017). *Økte bevilgninger og redusert vedlikeholdsetterslep på veinettet*. Available at: https://www.regjeringen.no/no/aktuelt/okte-bevilgninger-og-redusert-vedlikeholdsetterslep-pa-veinettet/id2575305/.

Tronsli, S. (2019). *Optimization of inspection budget allocation,* Thesis, University of Stavanger, Norway.

Statens Vegvesen (2017a). *Svikt i bruforvaltningen skal rettes opp Statens vegvesen*, Available at: https://www.vegvesen.no/om+statens+vegvesen/presse/nyheter/nasjonalt/svikt-i-bruforvaltningen-skal-rettes-opp.

Statens Vegvesen (2017b). *Bedre bruvedlikehold*. https://www.vegvesen.no. Available at: https://www.vegvesen.no/fag/fokusomrader/forskning+og+utvikling/pagaende-fou-program/bedre-bruvedlikehold.

Statens Vegvesen (2018). *Årsrapport 2017*, Available at: https://www.vegvesen.no/om+statens+vegvesen/om+organisasjonen/arsrapporter/_attachment/2250466?_ts=162ddffbea0&fast_title=%C3%85rsrapport+2017.pdf.

Vegdirektoratet (2000). *Håndbok V441 Inspeksjonshåndbok for bruer*, Available at: https://www.vegvesen.no/_attachment/69833/binary/964063?fast_title=H%C3%A5ndbok+V441+Inspeksjonsh%C3%A5ndbok+for+bruer+%2836+MB%29.pdf

XV International Conference on Durability of Building Materials and Components
DBMC 2020, Barcelona
C. Serrat, J.R. Casas and V. Gibert (Eds)

Structural Reliability of Bridges Made with EAF Concretes

Mariano A. Zanini

Dept. of Civil, Environmental and Architectural Engineering, University of Padua, Via Marzolo 9, 35131 Padua, Italy, marianoangelo.zanini@dicea.unipd.it

Abstract. *The development of sustainable concretes is becoming an emerging issue in civil construction sector. The use of Electric Arc Furnace (EAF) slag aggregates in the production of concretes is one way to fulfill sustainability goals. Past research demonstrated a significant increase of mechanical properties of EAF concretes when compared with ones made with natural aggregates (NA); however, at the same time, their use implies also an increase of self-weight loads. The present contribution aims to investigate the reliability of structural systems realized with EAF concretes, with special emphasis to bridge structures. Two different bridge types, considered as case-study examples, are designed considering ordinary concrete mixes, and subsequently, a reliability analysis is run for each EAF concrete class in order to investigate the variation of structural safety margins related to the use of the sustainable EAF concretes in replacement to the ordinary NA concrete mix.*

Keywords: *EAF Slag, Reinforced Concrete, Structural Reliability, Bridges.*

1 Introduction

Among the viable solutions to improve the environmental sustainability of cement-based materials, the use of recycled materials inside concrete mixes is acknowledged to be one of the most effective. Both non-conventional binders and aggregates can be successfully used to design concrete with satisfactorily high properties, both in terms of fresh properties, mechanical strength and durability. However, less research has been devoted both in laboratory and at field-scale about other manufactured aggregate types, even if the use of some of them in concrete has shown promising results. This is the case of electric arc furnace (EAF) slag, a stony, very hard, heavy-weight crushed material, which has been successfully employed to produce concrete (Geiseler, 1996; Motz, and Geiseler, 2001; Koros, 2003). Further, many other studies (*e.g.* Papayanni and Anastasiou, 2010; Pellegrino *et al.,* 2013; Faleschini *et al.,* 2015; Santamaria *et al.,* 2017) demonstrated how concrete with enhanced properties could be designed including EAF slag as partial or full aggregate replacement, significantly reducing the environmental impacts of the mix (Faleschini *et al.,* 2014). Following the positive results achieved in small-scale specimens, some research works have been carried out to study also the structural behavior of full-scale structural elements made of reinforced concrete (RC), including EAF slag at varying replacement ratio inside the mixes (*e.g.* Pellegrino and Faleschini 2013; Faleschini *et al.,* 2017a; Faleschini *et al.,* 2017b; Faleschini *et al.,* 2017c; De Domenico *et al.,* 2018). The above literature has evidenced that EAF slag concrete can be suitably applied in gravity structures, where its heavy-weight and high strength result as positive features. However, doubts might arise about its efficacy when applied in elevation RC structures, because the enhanced mechanical strength might not sufficiently balance the increased dead loads of the RC EAF concrete elements. Accordingly, this paper aims to solve this question, analyzing three classes of EAF concrete, characterized by increasing aggregates replacement ratio, through reliability-based analyses of the capacity of RC structural elements made with EAFconcretes.

Two different bridge types, *i.e.* a single-span simply supported prestressed reinforced concrete (PRC) bridge and a two- span continuous steel/concrete composite I-girder bridge, are designed according to the 2008- Italian Building Code prescriptions and considering a classic NA concrete mix. A reliability assessment is then performed for them, investigating the impact of full replacement of NA concrete with each of the three EAF concrete classes considered (*i.e.* C1, C2, A) on structural safety, thus quantifying the variation of structural safety margins related to the use of the sustainable EAF concretes in replacement to a classic NA concrete mix.

2 Structural Reliability Index Assessment

Figure 1 shows the general structural reliability workflow herein adopted in the following analyses: the workflow briefly presents key steps followed in assessing structural reliability index β. As regards the three EAF concrete classes, Table 1 lists main properties of the selected categories. More details can be found in Zanini (2019).

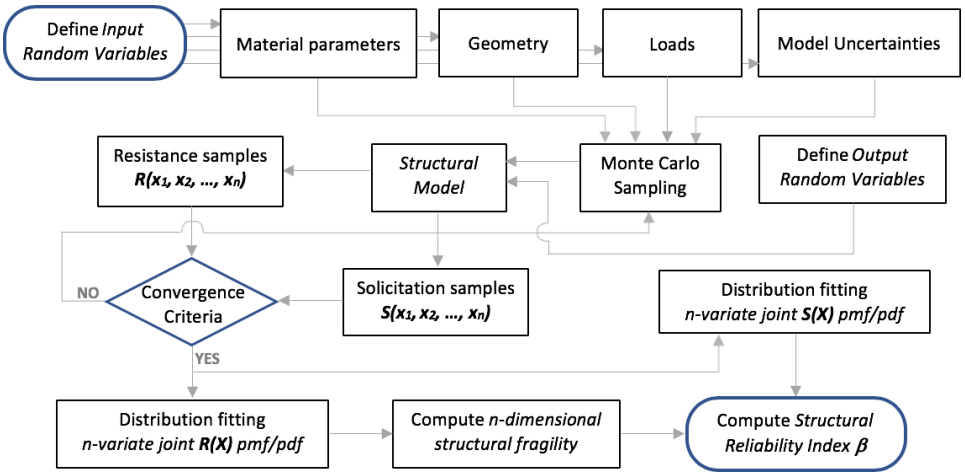

Figure 1. General structural reliability workflow.

Table 1. Properties of the selected EAF concrete categories ([a] concrete compressive strength ratio; [b] concrete specific weight ratio).

	EAF - C1	EAF - C2	EAF – A
EAF aggregates size	> 4 mm	> 4 mm	0 – 4 mm
w/c ratio	≤ 0.5	> 0.5	-
f_{c_EAF}/f_{c_NA} [a]	0.99 – 1.92	0.79 – 1.92	0.78 – 1.11
ρ_{c_EAF}/ρ_{c_NA} [b]	1.11 – 1.24	1.01 – 1.27	1.01 – 1.28

3 Application to Two Case-Study Bridges

The abovementioned structural reliability workflow was used to investigate how the use of EAF concretes can impact structural safety of two different common bridge configurations, namely a single-span simply supported PRC girder bridge (Bridge #1) and a two-span continuous steel/concrete composite I-girder bridge (Bridge #2). Both bridge types were first designed according to the 2008-Italian Building Code prescriptions (Italian Ministry for Constructions 2008), considering the use of ordinary NA concrete mixes. A reliability analysis was then carried out on the benchmark case (NA) and on the three hypothetical sustainable construction solutions (i.e. the same bridges in terms of sizing and reinforcement), realized with EAF-C1, EAF-C2 and EAF-A concrete mixes. Load analysis was conducted for both structures in accordance to Italian codes, accounting for self-weights of girders, dead loads of guard-rails and parapets, traffic loads, and in addition, taking into account wind actions and RC pier self-weight in Bridge #2.

3.1. Bridge #1: Single-Span Simply-Supported PRC Girder

The first case study is represented by a single-span simply supported PRC girder bridge. The span is 22 m-length and 13.5-m width and is composed by a RC slab of 30-cm thickness sustained by 7 PRC beams connected with transverse cast-in-situ RC beams (0.2-m x 0.9-m) located at the quarters. Each PRC beam is characterized by a double-T section of 1.3-m height h and 0.6-m width b, with wings t_f and web t_w thickness values of 0.13-m and 0.15-m, respectively. Figure 2 shows main geometrical features of Bridge #1.

For Bridge #1, the analysis was focused on the Ultimate Limit State (ULS) flexural strength of the PRC beams. PRC beams were first designed in compliance with Italian Ministry for Constructions (2008), considering a C30/37 NA concrete: acting ULS design girder bending moments were computed for self-weight of materials and load model LM1 with TS placed at mid-span, and subsequently distributed via the computation of Courbon's distribution coefficients in order to derive design acting bending moments Msd on each PRC beam. Hence, PRC beam design was performed considering a stress-block constitutive law for concrete and an elasto-perfectly plastic law for prestressing steel, assuming section wings of constant average thickness equal to 0.165 m, neglecting the contribution of ordinary steel reinforcing bars and considering a resultant prestressing cable ideally condensing all prestressing steel area Ap. Main materials parameters adopted in PRC beam design.

Once designed the most loaded PRC beam, reliability analysis was carried out in order to assess structural safety margin for the same bridge configuration realized both with NAC and the sustainable EAF concrete mixes. First, input random variables were fixed for material parameters, geometrical features, loads and model uncertainties: the type of distribution and coefficient of variation assumed for each random variable can be found in Zanini (2019). One output random variable x is here monitored, i.e. bending moment at mid-span. *MC* simulations were run sampling data from input distributions and deriving bending moment solicitation $M_S(x)$ and resistance $M_R(x)$ samples until the achievement of the convergence criterion. Hence, sampled $M_S(x)$ and $M_R(x)$ values were fitted in order to derive related pdfs parameters: Figure 3 shows bending moment M_S pdfs and M_R fragility curves for both NA and EAF concrete mixes, evidencing a lower fragility for EAF-C1 and EAF–C2 classes with respect to NA, whereas

EAF-A class shows a higher fragility, and this can be mainly attributed to the compressive strength reduction that characterizes EAF-A mix.

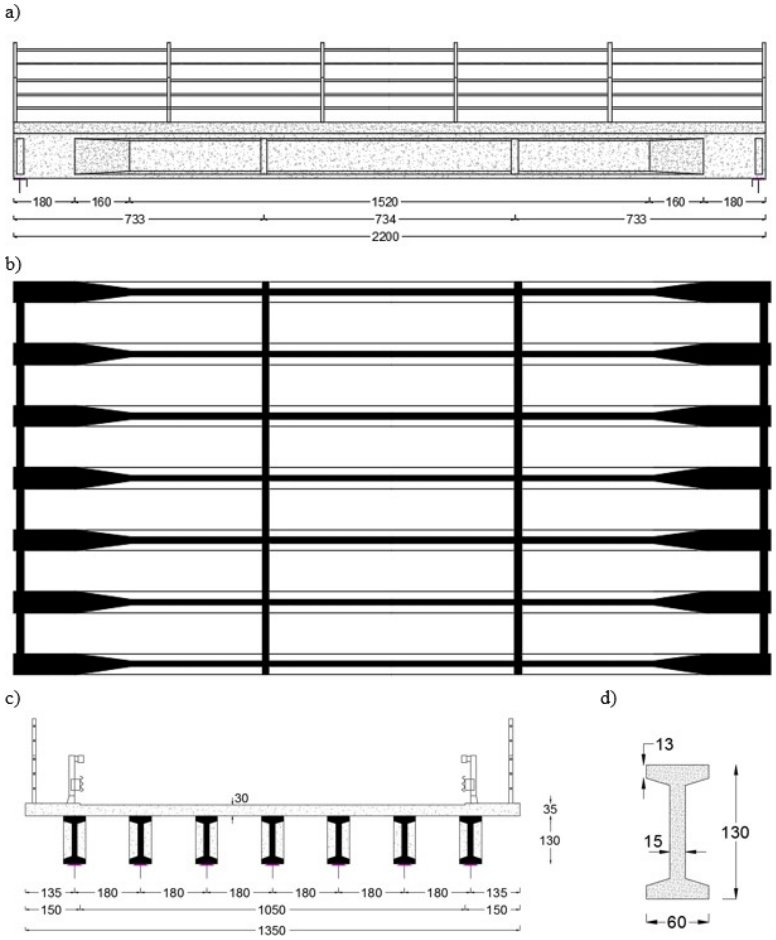

Figure 2. Bridge #1 main geometrical characteristics [in cm]: girder profile (a), girder plan (b), deck section (c) and PRC beam section (d).

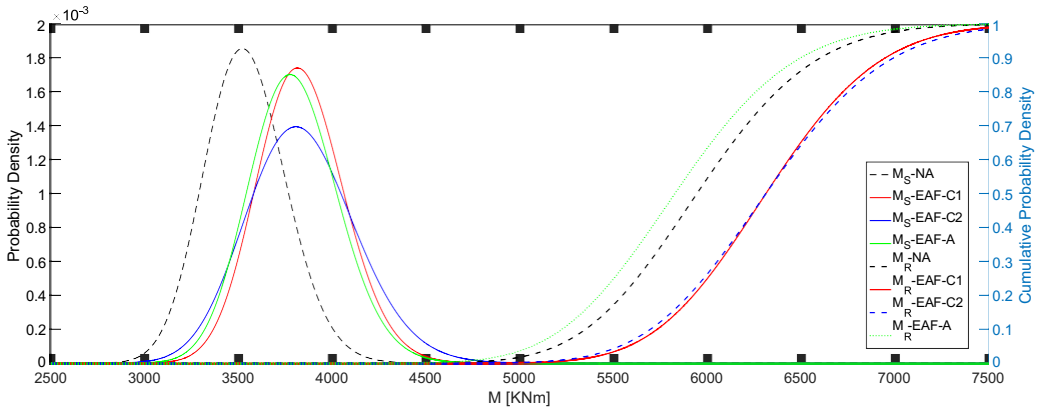

Figure 3. Bridge #1 bending moment M_S *pdf*s and M_R fragility curves for NA and EAF concretes.

In addition, slight differences can also be observed when comparing bending moment solicitations MS of the three EAF concrete classes, while their pdfs are higher with respect to the NA mix one, mainly due to their higher self-weight. Lastly, failure probabilities P_f and related Structural Reliability Index β were computed for each concrete mix, leading to P_f estimates of 1.98e-07, 7.24e-08, 3.48e-06, 2.28e-05 and β values 5.071, 5.259, 4.495, 4.077 for NA, EAF-C1, EAF-C2 and EAF-A concretes, respectively. Results highlighted how the use of EAF-C1 in this specific application leads to structural safety margins higher than NA concretes, whereas EAF-C2 and EAF-A are characterized by lower structural reliability levels.

3.2. Bridge #2: Two-Span Continuous Steel/Concrete Composite I-Girder

The second case study is represented by a two-span continuous steel/concrete composite I-girder bridge (Figure 4). Bridge #2 has two spans of 30-m length and 13.5-m width and is composed by a deck consisting in a RC slab of 30-cm thickness supported by 2 I steel profiles of variable height ranging from 1.7-m at abutments to 2.8-m at pier support, connected with open diaphragms made with coupled L steel profiles. I-steel profiles were sized according to the 2008-Italian Building Code prescriptions Italian Ministry for Constructions (2008), thus resulting in steel plates of 40-mm, 60-mm and 30-mm thickness for the upper wing, lower wing and web, with 0.9-m and 1.3-m width for upper and lower wings, respectively. The deck is supported by a 16-m height RC pier characterized by a rectangular hollow section with 2.5-m height, 1.5-m width and 30-cm thickness. In the upper part, pier has a variable section which joints with a beam cap of 1.3-height.

For Bridge #2, the analysis was focused on the Ultimate Limit State (ULS) combined axial force-bending moment of the RC rectangular hollow pier. Pier section was therefore first designed according to Italian Ministry for Constructions (2008), considering a C30/37 NA concrete and a B450C steel reinforcement. ULS design axial load-moment (P-M) solicitation points were computed considering two different load combinations (*i.e.* maximizing axial force or bending moment on pier base section) taking into account the self-weight of materials, load model LM1 with TSs placed at the most unfavorable section (*i.e.* in correspondence of pier support), and wind action computed with the following formula:

$$W = \frac{1}{2}\rho {v_b}^2 c_p c_e c_s A_{ref} \quad (1)$$

where ρ is the air mass density equal to 1.25 kg/m^3, v_b is the wind velocity measured at 10 m above the ground for open-country surface conditions, c_p, c_e and c_s stand for the pressure, exposure and shape coefficients, respectively, and A_{ref} is the surface area of the structural members impacted by wind. An equivalent rectangular $A_{ref,deck}$ area of 2.6-m height was considered for deck, also adding a 3-m height equivalent rectangular $A_{ref,traffic}$ area in order to take into account also vehicles profile, as specified in Italian Ministry for Constructions (2008). P-M solicitation points were derived for both analyzed load combinations and then reinforcing steel area was iteratively derived by computing the resistance P-M interaction diagram, adopting a stress-block constitutive law for concrete and an elasto-perfectly plastic law for reinforcing steel bars with main materials' mechanical properties listed in Zanini (2019).

Pier design process lead to identify the reinforcement solution able to equalize the worst P-M solicitation point, thus resulting in two layers of 20 mm diameter longitudinal reinforcement steel bars with 10 cm spacing (*i.e.* one inner and one outer surfaces, 28 bars in the shorter RC web and 40 bars in the longer one, see Figure 4d).

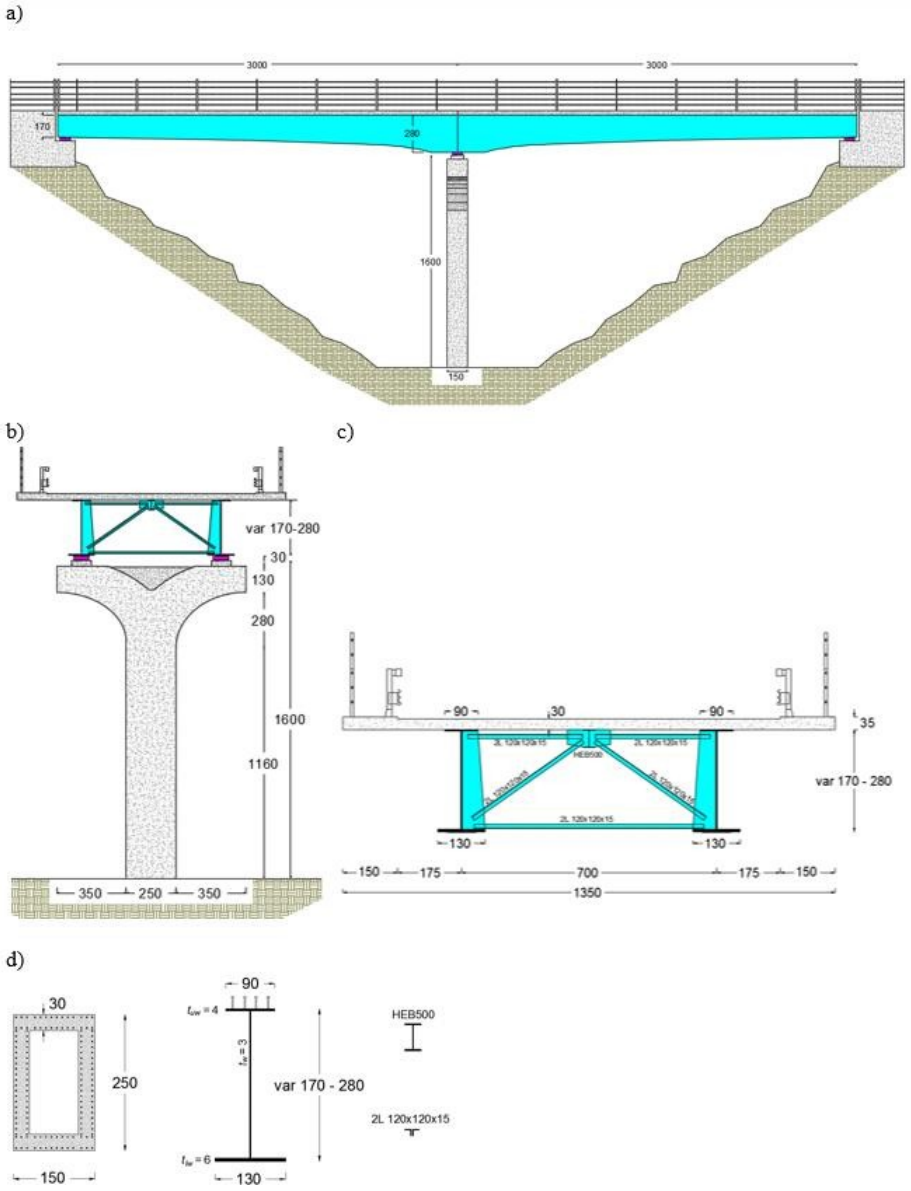

Figure 4. Bridge #2 main geometrical characteristics [in cm]: longitudinal profile (a), transversal section (b), deck section (c) and RC rectangular hollow pier and main steel profile sections (d).

Once designed the RC rectangular hollow pier, reliability analysis was carried out in order to assess structural safety margin for the same bridge configuration realized with sustainable EAF concrete mixes both in RC slab and pier elements. Input random variables were fixed, as listed

in Zanini (2019), whereas in this specific case, two output random variables x_1, x_2 were monitored, i.e. RC pier base section bending moment and axial force. MC simulations were run sampling data from input distributions, and deriving couples of bending moment-axial force solicitation $M_S(x_1)$-$N_S(x_2)$ and resistance P-M interaction diagram samples $M_R(x_1)$-$N_R(x_2)$ until the achievement of the adopted convergence criteria. Figure 5 represents fragility surfaces derived for both NA and EAF concrete mixes highlighting, as expected, a lower fragility for EAF-C1 and –C2 classes with respect to EAF-A and NA mixes.

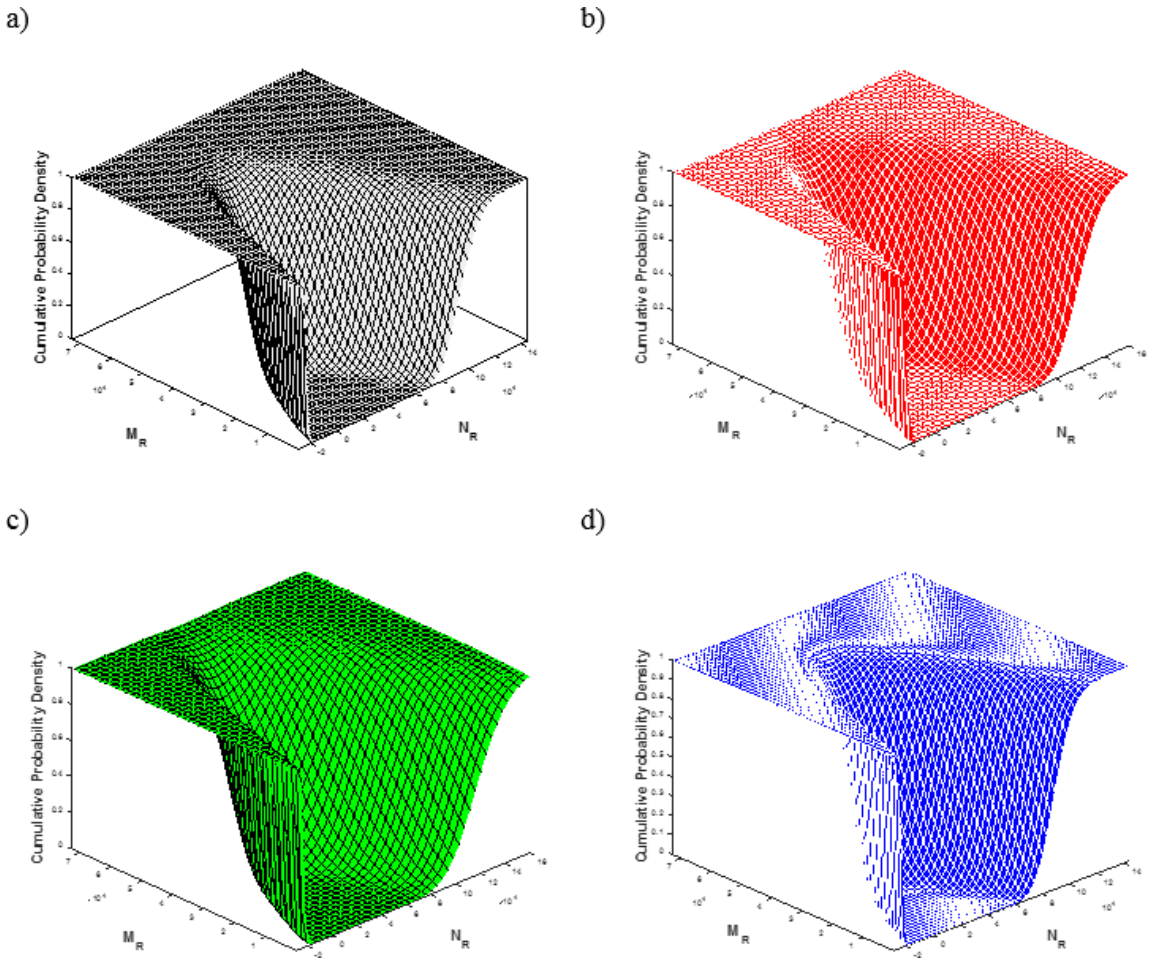

Figure 5. Bridge #2 joint bivariate fragility surfaces for NA (a), EAF-C1 (b), EAF-C2 (c) and EAF-A (d) concretes.

Failure probabilities P_f and related Structural Reliability Index β were then computed with Eqs. 1, 4 obtaining P_f estimates of 4.25e-05, 1.26e-05, 1.93e-05, 5.53e-05 and β values 3.930, 4.212, 4.116, 3.866 for NA, EAF-C1, EAF-C2 and EAF-A concretes, respectively. Results evidenced how the use of EAF-C1 and –C2 mixes in this specific application leads to structural safety margins higher than NAC, whereas EAF-A is characterized by lower structural reliability levels.

4 Conclusions

The present work investigated the influence on structural safety margins related to the replacement of common NAC mixes with EAF ones, with special emphasis to the field of the design of common bridge types. A general structural reliability workflow was proposed in order to formalize the methodology to be used in assessing the structural reliability index for a generic n-dimensional problem. Two bridge case studies were then analyzed, showing reliable outcomes when using EAF concretes for structural elements subject to compressional regimes, like bridge piers or PRC beams. Among future improvements of the present study, further efforts will also be required in order to investigate the impact of EAF concretes on seismic reliability of RC structural systems.

ORCID

Mariano Angelo Zanini: https://orcid.org/0000-0001-9326-802X

References

De Domenico, D., Faleschini, F., Pellegrino, C. and Ricciardi, G. (2018). Structural behavior of RC beams containing EAF slag as recycled aggregate: Numerical versus experimental results. *Constr Build Mater, 171,* 321-337.

Faleschini, F., Fernández-Ruíz, M.A., Zanini, M.A., Brunelli, K., Pellegrino, C. and Hernández-Montes, E. (2015). High performance concrete with electric arc furnace slag as aggregate: mechanical and durability properties. *Constr Build Mater, 101,* 113-121.

Faleschini, F., Bragolusi, P., Zanini, M.A., Zampieri, P. and Pellegrino, C. (2017a). Experimental and numerical investigation on the cyclic behavior of RC beam column joints with EAF slag concrete. *Eng Struc, 152,* 335-347.

Faleschini, F., De Marzi, P. and Pellegrino, C. (2014). Recycled concrete containing EAF slag: Environmental assessment through LCA. *Eur J Environment Civil Eng, 18*(9), 1009-1024.

Faleschini, F., Hofer, L., Zanini, M.A., Dalla Benetta, M. and Pellegrino, C. (2017b). Experimental behavior of beam- column joints made with EAF concrete under cyclic loading. *Eng Struc, 139,* 81-95.

Faleschini, F., Santamaria, A., Zanini, M.A., San José, J.T. and Pellegrino, C. (2017c). Bond between steel reinforcement bars and Electric Arc Furnace slag concrete. *Mater Struct, 50*(3), 170.

Geiseler, J. (1996). Use of steelworks slag in Europe. *Waste Manage, 16*, 59-63.

Italian Ministry for Constructions (2008). *D.M. 14/01/2008, Technical Rules for Constructions, Rome, Italy*. (in Italian).

Koros, P.J. (2003). Dusts, scale, slags, sludges... Not wastes, but sources of profits. *Metallurgical and Materials Transactions B, 34*(6), 769-779.

Motz, H., Geiseler, J. (2001). Products of steel slags an opportunity to save natural resources. *Waste Manage, 21*(3), 285-293.

Papayianni, I. and Anastasiou, E. (2010). Production of high-strength concrete using high volume of industrial by- products. *Constr Build Mater, 24*, 1412-1417.

Pellegrino, C., Cavagnis, P., Faleschini, F. and Brunelli, K. (2013). Properties of concretes with Black/Oxidizing Electric Arc Furnace slag aggregate. *Cem Concr Compos, 37,* 232-240.

Pellegrino, C. and Faleschini, F. (2013). Experimental behavior of reinforced concrete beams with electric arc furnace slag as recycled aggregate. *ACI Mater J, 110,* 197-206.

Santamaría, A., Orbe, A., Losañez, M.M., Skaf, M., Ortega-Lopez, V., González, J.J. (2017). Self-compacting concrete incorporating electric arc-furnace steelmaking slag as aggregate. *Mater Des, 115, 179-193.*

Zanini, (2019). Structural reliability of bridges realized with reinforced concretes containing electric arc furnace slag aggregates. *Eng Struc, 188,* 305-319.

XV International Conference on Durability of Building Materials and Components
DBMC 2020, Barcelona
C. Serrat, J.R. Casas and V. Gibert (Eds)

Study on Technical Standards of Reinforced Concrete Structures with Long Service Life when Using Blended Cement and Finishing Materials

Tadatsugu Kage[1], Hiroyuki Tanano[1], Naoko Tsuchiya[2] and Hiroshi Jinnai[3]

[1] Dept. of Department of Building Materials and Components, Building Research Institute, 1 Tachihara, Tsukuba-c., Ibaraki-pref., Japan, kage@kenken.go.jp

[2] Building Dept., National Institute for Land and Infrastructure Management, Ministry of Land, Infrastructure and Transport, 1 Tachihara, Tsukuba-c., Ibaraki-pref., Japan, tuchiya-n92ta@mlit.go.jp

[3] Dept. of Architecture, Faculty of Engineering, Tokyo Polytechnic University, 1583 Iiyama, Atsugi-c., Kanagawa-pref., Japan, jinnai@arch.t-kougei.ac.jp

Abstract. *It is very important to improve and secure durability of reinforced concrete (RC) building and housing, in order to extend the service life of it. In this study, these were studied experimentally that the contribution ratio of blended cement to the carbonation resistance of concrete when a part of OPC replaced to FA or BFS much more were used for concrete, and the effect of carbonation suppression required for an effective finishing materials when these were applied for concrete surface. As a result, we were able to obtain the knowledge that the contribution ratio to the carbonation resistance of concrete using blended cement with different mixture replacement ratio, and the effect of carbonation suppression required for 4 types of finishing materials and its specifications, from the viewpoint of securing durability and extending the service life of RC structures. Therefore, these were considered to be able to sufficiently contribute to the review of the evaluation method or technical standards concerning about the durability of RC structures prescribed in "Housing Quality Assurance Act" in Japan.*

Keywords: *Blended Cement, Finishing Materials, Water-Cement Ratio, Depth (thickness) of Concrete Cover, Resistance or Suppression of Carbonation.*

1 Introduction

It is very important to improve and secure durability of reinforced concrete (RC) building and housing, in order to extend the service life of it. In Japan, the technical standards concerning about the durability of RC structures and quality of concrete are prescribed in "Housing Quality Assurance Act". In the notification No.1374 shown in Table 1 related to this laws, the subjects of "phenomenon of deterioration" are the rust of rebar caused by carbonation of concrete. This table means a necessary measures have been taken to extend the period of large-scale repair work is not required up to 3 generations (generally 75-90 years) under the general conditions of environment and maintenance that are normally assumed. And, as the evaluation standards of "reduction of deterioration" for concrete, the relationship between water-cement ratio (W/C) and depth (thickness) of concrete cover is prescribed depending on the required durability (carbonation resistance) of concrete. This is because the thickness of concrete cover in the RC structures directly affects the corrosion of the rebar due to the carbonation of the cover concrete. Therefore, in order to improve the durability performance and to extend service life of RC structures, it is necessary to increase the cover thickness or reduce the W/C of concrete.

In addition, this technical standard is specified assuming concrete using ordinary portland cement (OPC), and when using fly ash (FA) or ground granulated blast-furnace slag (BFS) for concrete, the mass of cement for calculating W/C must be excluding all (100%) of FA in this certification standards. Also, the mass of cement for calculating W/C must be excluding 30% of BFS, i.e. the "contribution ratio of carbonation resistance" of FA and BFS are defined as 0 and 0.7. This concept is determined in consideration of the contribution ratio of the mixture in blended cement to the carbonation resistance of concrete. This concept is determined by the replacement ratio of FA of about 15% and BFS of about 45%, which are equivalent to "Type B" in Japanese Industrial Standards (JIS), also based on many previous research and survey such as guidelines of Architectural Institute of Japan (AIJ).

Therefore, in case of using the blended cement and using FA or BFS much more for concrete, it is necessary to reduce the W/C of concrete much more, or to use the effective finishing material for durability, for examples, tiling, mortar coating, external insulation methods, etc. Table 1 shows that an effective finishing material for durability, and W/C of 5% are equivalent to a concrete cover of 1 cm (10mm). However, tiling, mortar coating, external insulation methods, and the like are exemplified as effective finishing material for durability, but required performance is not shown.

In this study, these were studied experimentally that the contribution ratio of blended cement to the carbonation resistance of concrete when a part of OPC replaced to FA or BFS much more were used for concrete, and the effect of carbonation suppression required for an effective finishing materials when these were applied for concrete surface. This study might be so useful to get the technical data for suggesting the new certification standards and to reduce environmental load in the construction sector, and to secure durability of RC structures.

Table 1. Certification standards of RC structures with long service life in the notification No.1374 related to Housing Quality Assurance Act in Japan.

Part or members of RC structures			≦W/C50%	≦W/C55%
not contacts directly with the ground	walls except bearing walls, slab of floors	inside	2cm	3cm
		outside*	3cm	4cm
	bearing walls, columns, beams	inside	3cm	4cm
		outside*	4cm	5cm
contacts directly with the ground	walls, columns, slab of floors, beams, rising part of continuous foundation		4cm	5cm
	foundation (except the rising part of continuous foundation, and leveling concrete)		6cm	7cm

Note *: It could be reduced by 1cm (10mm) on the outside, by using an effective finishing material for durability (ex: tiling, mortar coating, external insulation methods, etc.)

2 Carbonation Resistance of Concrete Using Blended Cement

An accelerated carbonation test was performed on specimens with changed water-binder ratio (W/B), the type and replacement ratio of mixture, and the ratio of each mixture contributing to the carbonation resistance was clarified experimentally. The goal is to provide useful and technical data for durability design of RC structures using blended cement.

2.1 Outline of Experiment

Table 2 shows the experimental factors and levels and their combinations. The W/B were 30, 40, 50, 60%, and the mixture replacement ratio is selected from 2 kinds of 15 and 25% for FA and 1 to 3 kinds selected for BFS of 30, 50, and 70%. It was set as the combination. In addition, when OPC was used, specimens with W/B80% and 100% were prepared in order to confirm the compressive strength and carbonation resistance of the specimen with a small amount of cement per unit volume of concrete. In addition, in order to ascertain the carbonation resistance of specimens using commercially available portland blast-furnace slag cement (Type B), W/B50% specimens (with a replacement ratio of 40-45%) were prepared and subjected to the same tests. The accelerated carbonation test conformed to JIS A 1153 (Method of accelerated carbonation test for concrete). The pre-curing was performed under standard curing until the age of 28 days, and then in-air curing at 20°C, 60% R.H. until the age of 56 days.

Table 2. Experimental factors and levels.

Type of mixture	W/B (%)	Mixture replacement ratio (%)	Curing before carbonation test
Non (only OPC)	40,50,60,80,100	-	1) Air curing up to age of 56 days (20℃, 60% RH) after sealed curing for 5 days 2) Air curing up to age of 56 days (20℃, 60% RH) after standard curing for 28 days
ground granulated Blast-furnace slag (BFS)	30	70***	
	40,50	30*,50**,70***	
	60	30*, 50**	
Portland blast-furnace slag cement (Type B)	50	40-45**	
Fly ash (FA)	40,50,60	15**,25***	

Note *: Type A, **:Type B, ***Type C, according to the classification of blended cement by JIS

2.2 Results of Experiment and Discussion

Figure 1 shows the relationship between the compressive strength and the carbonation rate coefficient. However, the modified carbonation depth subtracts the carbonation depth immediately before the start of the test (age of 0 week). The figure shows that the standard curing 28days compressive strength and the carbonation rate coefficient have a strong correlation, and the carbonation rate coefficient tends to decrease as the standard curing 28days compressive strength increases, regardless of the type of mixture and the replacement ratio.

Figure 2 shows the relationship between W/B and the carbonation rate coefficient, in case of using BFS. There was a strong linear correlation between W/B and the carbonation rate coefficient, which was similar when FA was used. Here, the ratio that the mixture contributes to carbonation resistance as a replacement of OPC was defined as “contribution ratio of carbonation resistance (α)”. Using the contribution ratio α, the amount of binder that contributes to carbonation resistance was determined as equation (1). In this equation, the “mixture” indicates mixtures (FA or BFS).

$$\text{Amount of Binder} = \text{Amount of OPC} + \alpha \times \text{Amount of mixture} \quad (1)$$

Figure 3 shows a trial calculation of the carbonation rate coefficient when α is changed by 0.2 from 0 to 1.0, in case of BFS50%. It was assumed that the ratio of mixture that could contribute to carbonation resistance as a replacement of cement could be estimated by back-

calculating α at the intersection where the trial calculation results of each α and the line of OPC (N, in Fig) intersect. Using this estimation method, the contribution ratio (α) of the carbonation resistance according to the mixture replacement ratio of FA and BFS were calculated and shown in Table 3. For α of fly ash, FA15 was 0.07 to 0.42, FA25 was 0 to 0.17. For α of ground granulated blast-furnace slag, BFS30 was 1.04 to 1.07, BFS50 was 0.83 to 0.84, BFS70 was 0.45 to 0.69. Among the mixtures, BFS had a higher contribution ratio of the carbonation than FA, and the greater the replacement ratio of mixture, the smaller the contribution ratio.

As the results, these were obtained that the ratio excluding BFS from the mass of cement for calculating W/C may be 0% for Type A, 20% for Type B and 30% to 60% for Type C. Also, in case of FA, it may be 60% to 100% for Type B and 90% to 100% for Type C. Therefore, it was found that the current standard (Table 1) could be mitigation in some cases.

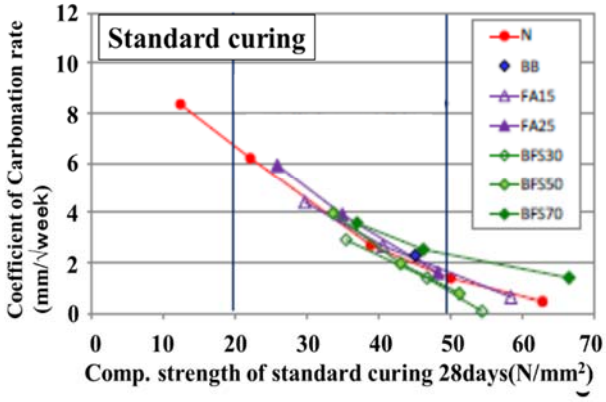

Figure 1. Relationship between compressive strength and carbonation rate coefficient (standard curing).

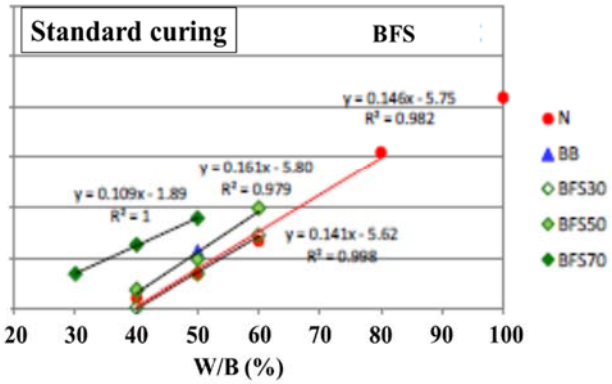

Figure 2. Relationship between water binder ratio and carbonation rate coefficient (standard curing).

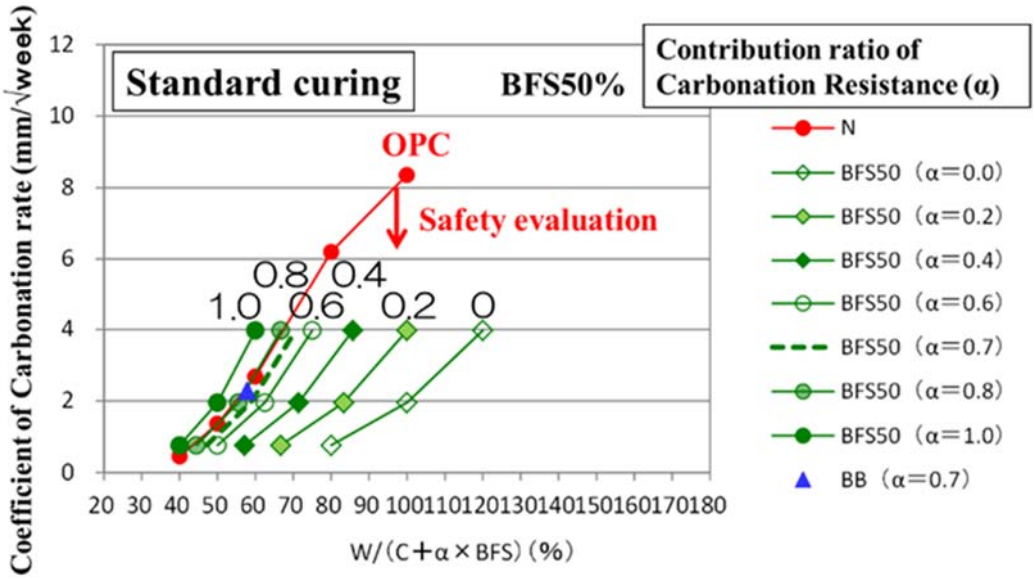

Figure 3. Calculation results of carbonation rate coefficient changing contribution ratio α.

Table 3. Calculation results of Contribution ratio for Carbonation Resistance.

Binder	Mixture replacement ratio (%)	Blended Cement (JIS)	Contribution ratio of Carbonation Resistance W/B (%)			
			30	40	50	60
OPC(N) +FA	15	Type B	-	0.42	0.21	0.07
	20	Type C	-	0.17	0.07	0.00
OPC(N) +BFS	30	Type A	-	1.04	1.06	1.07
	50	Type B	-	0.84	0.84	0.83
	70	Type C	0.45	0.59	0.69	-

3 Suppression Effect of Finishing Materials on Carbonation of Concrete

In RC structures, finishing materials that can suppress the intrusion of carbon dioxide, which causes carbonation, are often applied to the concrete surface. It is possible to use the effect of carbonation suppression of finishing materials. However, there were few experimental data that confirmed it such as tiling, mortar coating, and external insulation methods, and it was not clear how to select finishing materials that can be considered equivalent effect. Here, confirmation of the effect of suppression the carbonation of concrete of 4 types of finishing materials, which were tile, mortar, external insulation and coating materials for textured finishes, and the evaluation method of the suppression effect, were examined.

3.1 Outline of Experiment

Table 4 and Table 5 show type of finishing materials and mortar coating. Also, Figure 4 shows the experimental image. For concrete, W/C60% was used considering the upper limit of the technical standards prescribed in “Housing Quality Assurance Act”. Specimens were sealed at 20°C until the age of 4 weeks, then dried in a room with 60%R.H. and a temperature of 20°C until the age of 8 weeks, and then mortar was applied to one side of the mold surface. Thus, a specimen for the accelerated carbonation test was prepared. In each mortar, W/B was 40%, and the binder: fine aggregate = 1: 2.5 (mass ratio). The binder used for mortar was OPC, and high-early-strength portland cement (HPC), which could be expected to develop early strength, and silica fume (SF), which could be expected to be densify the concrete, 5% (mass ratio) of the binder was replaced. The type of aggregate was based on natural sand, and perlite artificial lightweight aggregate (standard weight 0.17kg/L) was also used.

The mortar coating was applied to concrete specimens, with the variable factors being the type of binder and aggregate, the amount of polymer (main component: ethylene vinyl acetate copolymer emulsion), the thickness of mortar and the curing method after mortar coating. The effect of carbonation suppression of mortar coating was confirmed.

The amount of polymer mixed in the mortar is based on B×3% as a general value in finished mortar, and B×6% with an increased amount of polymer was also examined. The thickness of mortar applied to the specimen was basically 10mm, and as shown in the Table 5, the mortar thickness was varied within the range of 5 to 30mm. The method of curing the specimens after mortar coating was based on air curing in a room at about 20°C, and examination was also made on those that were cured for 2 or 7 days after coating. The accelerated carbonation test started at concrete curing age of 12 weeks, in accordance with JIS A 1153. Also, the carbonation depth of concrete was measured at test age of 8, 13, 26 and 52 weeks.

Table 4. Type of Finishing Materials.

Type of finishing materials	Materials and symbols
Non	Concrete(C1)
Tile	Water absorption type 1(T1, T2(with M8), T3)、type 2(T4, T5(with M8))
Mortar	Primer(C-1(t=1mm(M1, M2)),C-2(t=2mm(M3, M4))), Primer(CM-1(t=10mm(M5, M6)), CM-2(t=10mm, M7, M8))) On-site mixing mortar(t=10mm,M9), (t=15mm,M10)
External insulation	Polystyrene type 4(t=30mm, IN1, IN2), Polystyrene type 3(t=30mm, IN3), Urethane foam typeA22(t=30mm, IN4)
Coating materials for textured finishes	Multi-layer coating materials for textured finishes(CM1,CM2), Coating materials for thick textured finishes(CM3,CM4), Coating materials for thin textured finishes(CM5)

Table 5. Type of Mortar Coating.

Binder (B)	Aggregate	Contents of polymer (B × wt%)	Curing after mortar coating	Thickness of mortar (mm)
-	-	-	In air without coating	0
OPC	Natural sand	3	In air after coating	5, 10, 20, 30
			2 days wet after coating, then air	10
			7 days wet after coating, then air	
		6	In air after coating	10, 30
			2 days wet after coating, then air	10
			7 days wet after coating, then air	
	Perlite ALA	3	In air after coating	10, 30
HPC	Natural sand	3	In air after coating	10, 30
			2 days wet after coating, then air	10
			7 days wet after coating, then air	
OPC+SF (95:5 wt)	Natural sand	3	In air after coating	10, 30

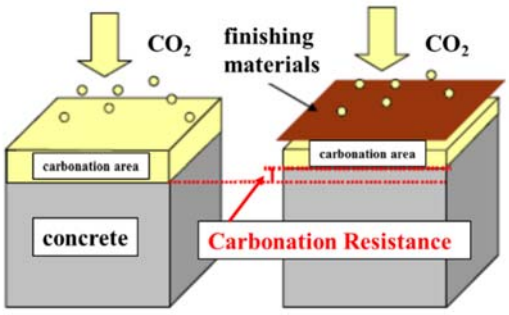

Figure 4. Outline of experiment.

3.2 Results of Experiment and Discussion

Figure 5 shows the carbonation depth of each specimen at the test age of 52 weeks. In this figure, the carbonation depth of the specimen that was not finished was also shown, and the value when the carbonation depth was 10 mm smaller than that was shown by the dotted line. As a result, it was found that the finishing material other than mortar has an effect of carbonation suppression of more than 10 mm compared to the specimen C1 (exposed concrete).

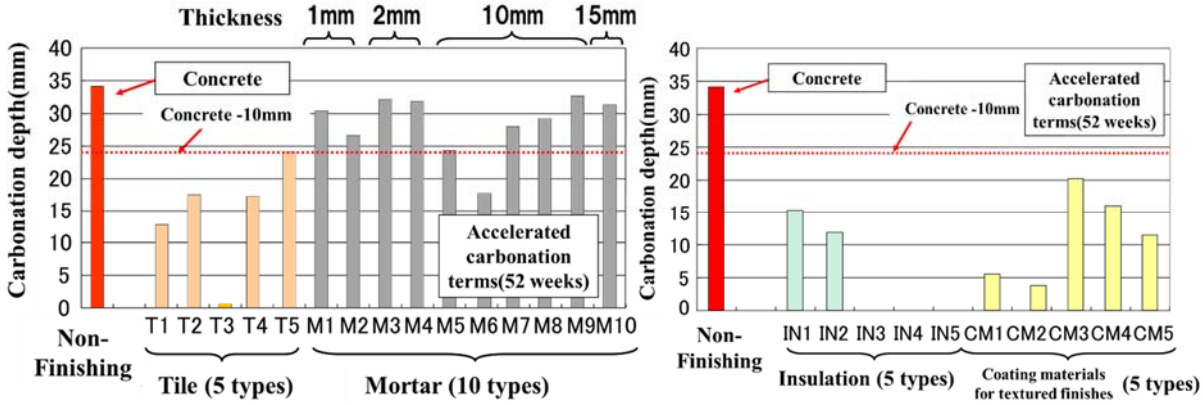

Figure 5. Carbonation depth of concrete with 4 types of finishing materials.

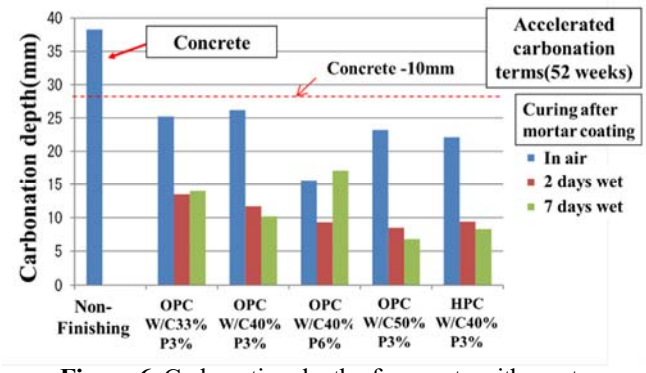

Figure 6. Carbonation depth of concrete with mortar changing curing condition.

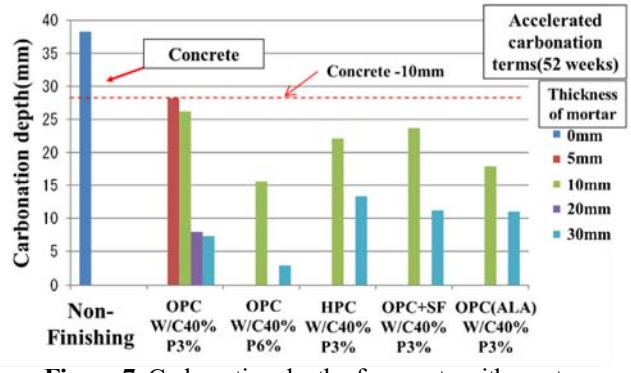

Figure 7. Carbonation depth of concrete with mortar changing thickness and materials used.

With regard to mortar coating, it was not possible to obtain a carbonation suppression effect of 10 mm or more with a primer of 1.0 to 2.0 mm, and an equivalent thickness of at least about 10 mm was required. However, not all M5 to M10 mortars with a thickness of 10 mm or more have a carbonation suppression effect.

Figure 6 shows the test results of the carbonation depth of concrete with a mortar thickness of 10 mm, at the test age of 52 weeks. The compressive strength of the mortar at the age of 28 days was greatly improved by the wet curing after mortar coating, and the carbonation suppression effect by the mortar was also greatly improved. In addition, in this experiment, it was suggested that by increasing the amount of polymer mixed in the mortar, the carbonation suppression effect equivalent to the case of wet curing can be obtained even if it was cured in the air. Figure 7 shows the test results of the carbonation depth of concrete cured in air after mortar coating at the test age of 52 weeks. As the thickness of mortar increased, the effect of suppressing carbonation increased. In this experiment, if the mortar thickness was 10 mm or more, the effect of suppressing carbonation was obtained equivalent 10 mm or more compared to the specimen C1 (exposed concrete) even if wet curing was performed. For mortar with HPC as the binder or mortar in which part of the binder was replaced with silica fume, the test results at test age of 13 weeks tended to slightly improve the carbonation suppression effect of mortar. However, the same trend was not clearly confirmed at the test age of 52 weeks. For the mortar using lightweight aggregate, the compressive strength was as low as about 40% when using natural sand, but the carbonation suppression effect was equivalent to that of mortar using

natural sand.

As the results, it was confirmed that the 4 types of finishing materials, which were tiling, mortar coating, and external insulation method and a finishing coating material, had the same carbonation suppression effect as the concrete cover thickness of 10 mm, *i.e.* W/C5%. In addition, these were obtained that the effect of carbonation suppression of mortar coating could be improved by initial curing, the amount of polymer increase and the mortar coating (thick coating) of about 30mm.

4 Conclusions

We were able to obtain the knowledge that the contribution ratio of blended cement to the carbonation resistance of concrete when a part of OPC replaced to FA or BFS much more were used for concrete, and the effect of carbonation suppression required for an effective finishing materials and its specifications when these were applied for concrete surface, from the viewpoint of securing durability of reinforced building and housing.

The results obtained were as follows:

- The ratio excluding FA from the mass of cement for calculating W/C may be 60% to 100% for Type B and 90% to 100% for Type C. Also, in case of BFS, it may be 0% for Type A, 20% for Type B and 30% to 60% for Type C.
- The 4 types of finishing materials, which were tiling, mortar coating, and external insulation method and a finishing coating material, had the same carbonation suppression effect as the concrete cover thickness of 10 mm, i.e. W/C5%.
- The effect of carbonation suppression of mortar coating could be improved by initial curing, the amount of polymer increase and the mortar coating (thick coating) of about 30mm.

As the results, these were considered to be able to sufficiently contribute to the review of the evaluation method or technical standards concerning about the durability of RC buildings and housing prescribed in “Housing Quality Assurance Act” in Japan.

Acknowledgements

We would like to thank all those who have contributed to this experimental research.

ORCID

Tadatsugu Kage: http://orcid.org/0000-0002-0767-2622
Hiroyuki Tanano: http://orcid.org/0000-0003-0165-237X
Naoko Tsuchiya: http://orcid.org/0000-0002-9500-9811
Hiroshi Jinnai: http://orcid.org/0000-0003-0810-7999

References

Architectural Institute of Japan (2007). *Recommendation for Practice of Concrete Building with Fly Ash..*

Architectural Institute of Japan (2017). *Recommendation for Design and Practice of Reinforced Concrete Building with Portland Blast-Furnace Slag Cement or Ground Granulated Blast-Furnace Slag.*

Notification No.1374, *Housing Quality Assurance Act,* JAPAN

Toshinori, O. et al. (2014-2016). Durability Performance of Blended Cement Concrete (part 1-7), *Summaries of Technical Papers of Annual Meeting,* Architectural Institute of JAPAN.

Yoshihiro,M. et al. (2011-2013). Basic Study on Carbonation Suppressive Effect of Finish Materials for Concrete (part 1-8), *Summaries of Technical Papers of Annual Meeting,* Architectural Institute of JAPAN.

XV International Conference on Durability of Building Materials and Components
DBMC 2020, Barcelona
C. Serrat, J.R. Casas and V. Gibert (Eds)

The Business Case for Re-Usable Buildings – Business Models, Systems Diagnosis and Case for Action

Kathryn P. Bourke[1] **and Katherine T. Adams**[2]

[1]Whole Life Ltd, 77 Rickmansworth Road, Watford, WD18 7JB UK,
Kathryn.bourke@wholelifeltd.co.uk

[2] Loughborough University, School of Architecture, Building & Engineering, Ashby Road, Loughborough, Leicestershire, LE1 13TU, UK, k.adams@lboro.ac.uk

Abstract. *This paper presents the results of a pathfinder project on re-usable buildings which was part funded by Climate- KIC, supported by the EIT, a body of the European Union. It places reusable buildings in the context of sustainability generally, and specifically within the general theme of circular economy transition. It includes a brief summary of the literature review undertaken, focussing on challenges and benefits to the business case for adoption of reusable buildings.*

Keywords: *Re-Usable, Sustainability, Circular Economy, Business Case, Literature Review.*

1 Introduction

This paper reports the initial results of a scoping study undertaken with partial funding from the Climate _KIC programme, which is supported by the EIT, a body of the European Union. The objective of the study was to test out the possibility of generating a critical mass of client support for re-usable buildings. Re-usable buildings for this study included those that could be adapted in use for same use or for different uses within a circular economy context. The work was undertaken by a consortium led by the London Waste and Recycling Board (LWARB), in partnership with the Sustainable Development Foundation (SDF), the Forum for the Future (FforF), the Alliance of Sustainable Building Products (ASBP) and Whole Life Ltd. (WLL).

The early part of the project involved a literature review. The later part of the project included workshops, which led to a sector routemap for the future development of the market, together with initial business models which might encourage and support the market for re-usable buildings and components. This paper is focussed on the challenges and benefits identified for the business case for re-usable buildings and components.

2 Literature Review Methodology and Scope

The literature review encompassed searches of academic papers, government and non-governmental organisation (NGO) publications and industry publications using Web of Science. A key word search was undertaken, using the term ‘reusable buildings’ in addition to sourcing works known to members of the consortium. The main aim of the literature review was to understand the outcomes of previous work in this area, and to identify the gaps with a focus on the business case.

3 Main Findings of the Literature Review

3.1 Overview

There is a perception that the application of circular economy principles to the built environment offers major opportunities, in environmental terms but also in terms of social and economic impacts. The reuse of buildings is gaining more interest; with evidence showing that conversion (from one function to another) is increasing in inner urban areas. The benefits and challenges for commercial re-usable buildings are well defined though not often quantified. There is a clear distinction in the motivations between the different development models (develop to sell, manage or occupy), with owner-occupancy driving a greater interest in adaptability. End-users preferences are for versatile and a refit-ready building that provides fewer disruptions, improved service and better quality of space.

3.2 Application of Circular Economy within the Building Sector

There are several industry studies that look at how a circular economy can be applied in the building sector, they mostly describe the different business models that could be applied, together with some of the challenges and opportunities, though they are lacking in actual costs. A few of these studies define what a circular economy in the built environment would look like and the macro-economic benefits (at a region or Country level). At the micro (business level), there is little economic information available within the literature on the financial benefits or costs for undertaking circular business models. Indeed, research by (Adams *et al.*, 2017) found that one of the largest challenges for adopting circularity in the built environment is the unclear financial case, particularly for the whole life of a product/building which ranked number one for the majority of stakeholders; having a clear business case was the most important enabler.

3.3 Re-Usable Buildings

Findings from the review of circular building case studies are limited, but some examples are shown below. They show that the client is instrumental in driving the circular building forward, along with establishing the benefits to the end user.

One of the key drivers identified within the literature is that of obsolescence which affects every building to some degree at some stage during its lifecycle (Douglas, 2006). As buildings age, the rate of decay increases and the decline in building condition escalates unless regular maintenance and upkeep is undertaken. There are 6 principal types of obsolescence; economic, functional, social, legal, physical and aesthetic (Barras and Clark, 1996). As such, when a certain level of obsolescence is reached, a building may require adaptation in some form.

Conversion (changing use or sometimes known as adaptive reuse), is a growing strategy for dealing with vacant buildings such as offices. A study in Liverpool showed that more than 60% of buildings have changed their original use during their life cycle and around 10% of them have changed their use frequently (every six years) during the last 20 years thereby signalling an increase in the rate of change (Manewa *et al*., 2016). However, the property market can be segregated and for example, office investors are not always keen on investing in the housing market. A study of 15 cases in the Netherlands displayed the following success factors: low purchase price, an adaptable floor plan, government subsidy, or clients with long- term

investment scenarios (housing associations) (Remöy and Voordt, 2014).

3.3.1 Re-use versus demolition

There is a debate of the costs of reuse verses demolition and new build, though studies tend to show that it usually lower for the former. For example, it is potentially cheaper to adapt than to demolish and rebuild, in as much as the structural components already exist and the cost of borrowing is reduced, as contract periods are typically shorter (Shipley *et al*., 2006). This is also likely to be the case if the building is designed for adaptation and re-use.

Buildings are generally demolished because they are perceived to no longer have any value (Kohler and Yang, 2007). In most cases, it is the market that sets this value, even though such an assessment may be based on incomplete information with no consideration given toward externalities. According to Ball (2002), it is generally preferable to repair a building than replace it because the value of the location and quality of a new building is not necessarily better than the old one. In contrast, O'Donnell (2004) suggests that an adapted building will not completely match a new building in terms of operational energy performance, but the shortfall should be balanced against gains in social value. Certainly, the life cycle expectancy of the materials in an older building may well fall short of those in a new building. The age of materials will also directly affect the on-going maintenance costs of an adapted building, which, as a result, may well be higher than those for a new building.

Bullen and Love, 2010 identified that there are a diverse set of issues that organisations need to consider when comparing the option to demolish or reuse a commercial building.

3.3.2 Stakeholders

In a survey of high profile UK property developers and agents, 94% saw the need for an adaptable building solution providing associated capital cost increases were minimised (Gregory, 2004). Workshops undertaken in the UK (Pinder, Schmidt and Saker, 2013) for adaptability suggested that more adaptable buildings might be suitable investment if they provide easier sales or command a price premium, but there are challenges for speculative developers (those procuring buildings to sell) as the purchaser obtains the benefits of adaptability, not the developer. Owner/occupiers may recoup the benefits through lower rates of depreciation of increased price at sale, but both funders and owners are risk-averse in respect of novel.

3.3.3 Costs of adaption of existing buildings

Cost is usually cited in the literature as the main obstacle to developing more adaptable (re-usable) buildings, with the assumption being that adaptability results in higher initial construction costs. For example, studies have shown that using solutions such as higher floor-to-ceiling heights, system walls and soundproof suspended ceilings, could increase initial construction costs by about 20–25% (Arge and Landstad, 2002). However, other adaptable design solutions, such as easily divisible building forms and floor plans, were found to be cost neutral (see Figure 2). Other studies found that on average, the design strategies employed resulted in a 1% increase in initial construction costs when compared with conventional (less adaptable) designs; one-third of the strategies resulted in longer initial construction times.

In the UK the notion that more adaptable (re-useable) buildings cost more to construct has,

to some extent, been fuelled by past attempts at 'future-proofing' buildings. Guy (1998) explains how, during the 1980s and 1990s, institutional investors' desire to reduce the risk of depreciation associated with changing occupier requirements led to the emergence of an institutional specification that involved over-specifying, among other things, floor loadings, small-power provision and comfort cooling services. Property agents insisted that all new office developments should incorporate these over-specified design features - a case of exchange value prevailing over use value.

Spending more on the initial construction costs of a building to make it more adaptable can only usually be justified if the adaptability is likely to generate some form of benefit or return on investment in the future. Slaughter (2001) estimated that all but one of the adaptable design solutions in her study would pay for themselves at the first adaptation cycle, generating, on average, a net saving equivalent to 2% of the initial construction cost. She found that three-quarters of the adaptable design strategies reduced the time required to adapt the building (thereby reducing disruption to users) and allowed for easier access when maintaining the building.

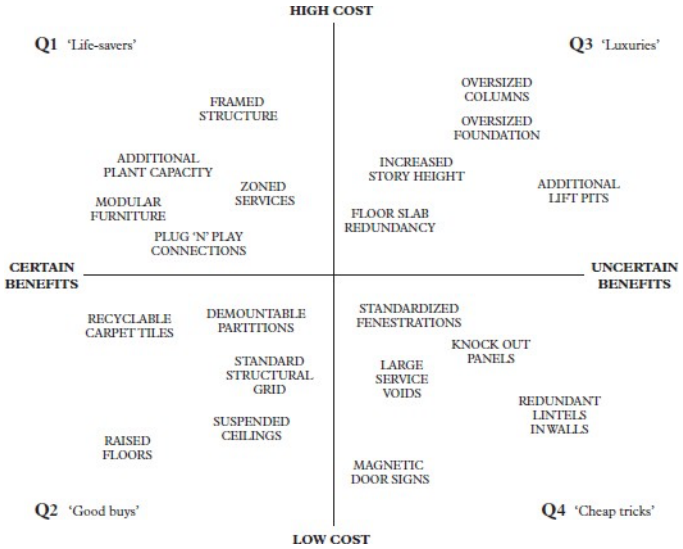

Figure 1. Cost and uncertainty in designing adaptable (re-usable) buildings (Pinder, Schmidt and Saker, 2013)

3.3.4 Whole life costs

A critical component to aid re-usable buildings is the use of whole-life costing (WLC), when all the costs and benefits (including incomes) are factored in over the projected lifecycle of the building which includes the cost of the demolished building. WLC can be used as a forecasting tool to evaluate alternative planned capital expenditures with the aim of ensuring the optimum value from capital assets considering all future costs and benefits in present day values.

An example is shown in Figure 2 of the difference in cash flow over the lifecycle of the building based on adaptable and standard design. However, the ultimate answer (for linear and circular buildings) depends on future assumptions which may involve high risk and uncertainty (which are likely to be less in the 'business as usual case' and the hidden costs/benefits associated with social and environmental issues remain untapped.

Discounting is commonly used in WLC and is based on the concept of time preference: the tendency for people to attach more value to a benefit received today than to the same benefit

received in the future. The choice of discount rate is important in the context of reuse as high discount rates give little weight to more distant entries in the cash flow and place great emphasis on the early years, thus favouring a short-term approach and the minimisation of capital investment. As such it is important to develop an economic model for circular buildings that allows the investor to benefit from day one.

BRE is also looking at how whole life cycle costing can be used within a circular building assessment methodology for the BAMB project. A number of modelling scenarios have been undertaken, and the key findings are that whilst the methodology can show benefits over one lifecycle (through adaptation), taking into account residual value within the current building is difficult, as is applying value from other building cycles. The model (similarly to life cycle assessment), is based on one building, and as such limits the opportunity to transfer value. Discounting as already recognised above, also presents issues (see Lowres and Hobbs, 2017).

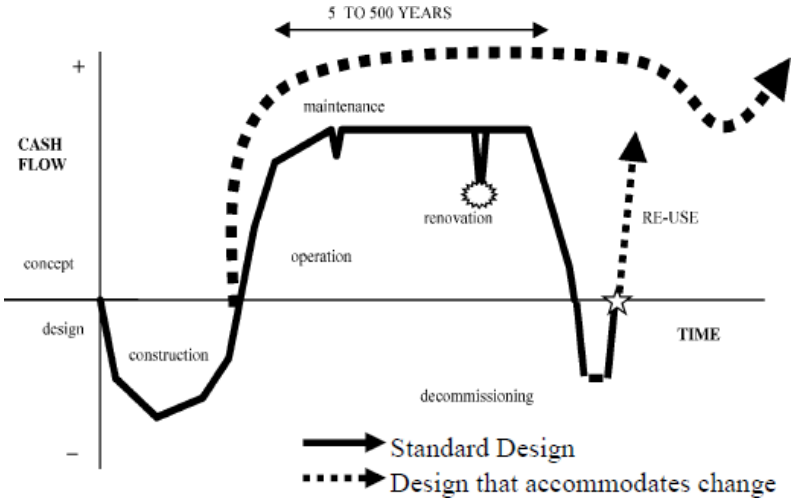

Figure 2. Illustrative whole life costs of standard design versus adaptable design (Manewa *et al.*, 2016)

3.3.5 Financing

Studies have shown that there is a fundamental shortcoming in the current financing of buildings (Circle Economy and ABN AMRO, 2017). Commonly, a bank issues a loan (mortgage) to buy a building, including the land on which it is built. However, the costs of demolition and recycling (as well as any residual value) at the end of its life are not part of the financing. The result is that it can be cheaper to leave a building vacant or not be incentivised to realise any value from the material within the building. The building and land are viewed as part of the same asset, if these were separated, financing may be easier or at least more flexible. There could be a benefit from having land that is easier to access as buildings can be dismantled quickly and reused elsewhere.

Moving towards circular buildings requires an alliance of parties that collaborate to deliver services. To do so, material reuse has to be the starting point, both during renovation (interior and exterior) and at the end of the lifecycle. This new chain is also based on an integrated

lifecycle approach to investment decisions and design. The producer or financer remains the owner of the resources and is responsible for the residual value. The residual value of materials remains on the balance sheet and can be estimated using resource model predictions.

Building in such a way that materials have a residual value instead of a negative value (disposal costs) makes investing in circular design useful. The customer pays for the performance of the building or a section of road, instead of the function. This shifts the responsibility for good maintenance and management from the customer to the owner of the materials. Investments in the adaptability of buildings generate value in the long term because the needs of (future) users are more easily met, as such there is value though utility, though there is little empirical evidence to support this within the literature.

Banks such as ABN Ambro are investigating how to allow for higher investment costs which justify lower running costs and a higher final value of the building elements. This therefore means a relatively higher loan-to-value ratio for a project, and a relatively smaller amount of equity capital relative to the loan capital. More (hybrid) financing products can further facilitate the financing. These could be equity, risk funds or other forms of financing besides bank financing. (Circle Economy and ABN AMRO, 2017)

3.3.6 Valuation

A building constructed according to a circular method has added value for investors. The value of real estate is currently linked mainly to the price of the location and the difference between rental income and operating costs. Often, the value of the raw materials in the building is of secondary importance. This view will change fundamentally in the transition from a linear to a circular economy. In addition, the purpose for which buildings are used changes with increasing regularity. A building that can be converted easily and inexpensively to another function has more potential future value than a one-purpose building. As a result, the investor knows that when the current tenant's lease is terminated, it will be relatively easy to re-let the building, possibly for a different use.

However, current investors' relatively short-term investment visions of between five and ten years and the highly limited or total absence of appreciation of this added value by surveyors often forms a barrier. Research by Ellison *et al*., (2007) suggested that only a very limited interpretation of adaptability, relating primarily to the flexibility of internal spaces, was currently factored into commercial property valuations. Consequently, valuations fail to reflect other forms of adaptability, such as the ability to accommodate changes of use.

McAllister (2009) suggests that property valuations play an important role in the property market by acting as a surrogate for prices, but he also argues that '… there is some anecdotal evidence to suggest that valuation can act as an impediment to innovation in property markets. This is because property values tend to be based on information from past transactions; in other words, if there is no evidence that a design attribute has added value to a building in the past, then valuers will not ascribe any additional value to those attributes in the present. This can result in a vicious circle, whereby developers will not include a particular design attribute in their buildings because valuers do not consider that it adds value, and valuers do not consider that it adds value because developers do not include it in their buildings.(Pinder, Schmidt and Saker, 2013).

One of the few empirical studies to (inadvertently) provide an insight into the relationship

between adaptability and rental values was undertaken by Baum (1994). Baum was interested in understanding why some buildings experience higher rates of depreciation than others, so he explored this by statistically analysing the relationship between building characteristics and rental values, using data from 125 office buildings in the City of London. He found that internal configuration (floor to ceiling height and floor layout) and internal specification (quality of finishes and services) were the most important determinants of depreciation in the sample buildings. Baum suggested that because demand for these characteristics would change over time (due to changes in working practices, fashions, etc.) property investors should look to purchase buildings that were flexible, in terms of their configuration and internal specification. He concluded that 'Flexibility reduces the risk of an irreversible and major reduction in the market value of a building'.

4 Summary of Results of the Literature Review

The reuse of buildings is gaining more interest; with evidence showing that conversion (from one function to another) is increasing in inner urban areas. The benefits and challenges for commercial Re-usable buildings are well defined though not often quantified. There is a clear distinction in the motivations between the different development models (develop to sell, manage or occupy), with owner-occupancy driving a greater interest in adaptability. The relative costs of re-use verses demolition and new build remains a matter of debate though studies tend to show that it usually lower for the former.

Where building have not been designed for reuse, then the cost of adaption of existing buildings can be greater than building them from scratch. As such building adaptation is a higher cost process, when adaptable features are not incorporated with the initial design. Cost is usually cited in the literature as the main obstacle to developing more adaptable (Re-usable) buildings, with the assumption being that adaptability results in higher initial construction costs. Though this is highly dependent on the solution adopted. Spending more on the initial construction costs of a building to make it more adaptable can only usually be justified if the adaptability is likely to generate some form of benefit or return on investment in the future.

Studies show that adaptable design solutions pay for themselves at the first adaptation cycle, generating, on average, a net saving equivalent to 2% of the initial construction cost. Investments in the adaptability of buildings generate value in the long term because the needs of (future) users are more easily met, as such there is value though utility, though there is little empirical evidence to support this within the literature.

Whole life costing is recommended to show payback, however there can be issues in its use from discounting. There is a fundamental shortcoming in the current financing of buildings with the costs of demolition and recycling (as well as any residual value) at the end of its life not factored into business case (a side effect partly of discounting but also reflecting different contractual parties at the end of life). The value of real estate is currently linked mainly to the price of the location and the difference between rental income and operating costs. Often, the value of the raw materials in the building is of secondary importance. It is unclear if property valuations consider any benefits from adaptability and 're-let ability' and how depreciation of assets is factored in.

ORCID

Kathryn Bourke:https;//orcid.org/0000-0002-5547-257X
Katherine Adams:https://orcid.org/0000-0002-7757-6396

References

Arge, K. and Landstad, K. (2002). *Generality, Flexibility and Resilience in Buildings: Principles and Properties that Provide Adaptable Office Buildings,* Project Report 336, Norwegian Building Research Institute, Oslo.

Adams, K.T. *et al.* (2017). Circular economy in construction: current awareness, challenges and enablers. *ICE Proceedings Waste And Resource Management*, 1–11.

Ball, R. (2002). Re-use potential and vacant industrial premises: revisiting the regeneration issue in Stoke-on-Trent. *Journal of Property Research, 19(2),* 93–110.

Barras, R. and Clark, P. (1996). Obsolescence and performance in the central London office market. *Journal of Property Valuation & Investment, 14*(4), 63–78.

Baum, A. (1994). Quality and property performance. *Journal of Property Valuation & Investment, 12*(1), 31–46.

Bullen, P.A. and Love, P.E.D. (2010). The rhetoric of adaptive reuse or reality of demolition: Views from the field. *Cities. Elsevier Ltd, 27*(4), 215–224.

Circle Economy and ABN AMRO (2017). A Future Proof Built Environment. Putting circular business models into practice, *Amsterdam: CircleEconomy*.

Douglas, J. (2006). *Building Adaptation*, Oxford: Butterworth Heinemann.

Ellison, L., Sayce, S. and Smith, J. (2007). Socially responsible property investment: quantifying the relationship between sustainability and investment property worth. *Journal of Property Research 24*(3), 191–219.

Gregory, J. (2004). Rehabilitation-new ways for older housing. *New South Wales Department of Housing,* Retrieved from: www/housing.nsw.gov.au/rehab.htm

Guy, S. (1998). Developing alternatives: energy, offices and the environment. *International Journal of Urban and Regional Research, 22*(2), 264–82.

Kohler, N. and Yang, W. (2007). Long-term management of building stocks. *Building Research and Information, 35*(4), 351–362.

Lowres, F. and Hobbs, G. (2017). Challenging the current approach to end of life of buildings using a life cycle assessment (LCA) approach. *International HISER Conference* 2017, Delft.

Manewa, A. *et al.* (2016). Adaptable buildings for sustainable built environment. *Built Environment Project and Asset Management, 6*(2), 139–158.

McAllister, P. (2009). Assessing the valuation implications of the eco-labelling of commercial property assets. *Journal of Retail & Leisure Property, 8*(4), 311–22.

O'Donnell, C (2004). Getting serious about green dollars. *Property Australia 18(4), 1– 2.* Retrieved from http://www.propertyoz.com.au

Pinder, J., Schmidt, R.I. and Saker, J. (2013). Stakeholder perspectives on developing more adaptable buildings. *Construction Management and Economics, 31*(5), 440–459.

Remöy, H. and Voordt, T. Van Der. (2014). Adaptive reuse of office buildings into housing : opportunities and risks. *Building Research & Information, 42*(3), 381–390.

Shipley, R., Utz, S. and Parsons, M. (2006). Does adaptive reuse pay? A study of the business of building renovation in Ontario, Canada. *International Journal of Heritage Studies, 12*(6), 505-520.

Slaughter, S. (2001). Design strategies to increase building flexibility. *Building Research & Information, 29*(3), 208–17.

XV International Conference on Durability of Building Materials and Components
DBMC 2020, Barcelona
C. Serrat, J.R. Casas and V. Gibert (Eds)

Viability of Production and Application of Concrete with Addition of Fibers of Polyethylene Terephthalate (PET) Bottles for Construction

Edson C. Rodrigues

Estácio de Sá University (UNESA), Civil Engineering Undergraduate Course, e-mail: sonia.almeida@estacio.br, web page: www.portal.estacio.br Campus: Centro IV – Praça Onze Av Presidente Vargas, 2560 – Centro – Rio de Janeiro – 20210-031 Rio de Janeiro – Brazil

Abstract: *Concrete is the main material used in the construction industry not only for the ability to produce infinite variety of shapes for precast forms and for its characteristics of high resistance to compression, but primarily for their low manufacturing cost. Nonetheless, the production by mixing cement, fine aggregate, coarse aggregate and water, using natural raw materials such as stone, sand and water, despite being plentiful, represent the consumption of millions of tons of natural resources. Thus, the continuous search for new solutions is fundamental in order to not only further lower the manufacturing costs of this essential component in construction, but also to seek alternative materials, those of origin in processes of sustainability.*

Keywords: *Recycling, Polyethylene Terephthalate, Sustainability, Construction, Materials, Concrete, Cement, Fibers, Mixing, Production, Application.*

1 Objectives

A great amount of PET bottles that were once discarded damaging the environment are gaining a new function in the construction market, and their use as fibers in concrete, an alternative that hasn't been widely studied so far, can replace the use of glass fibers, polyethylene, polypropylene and even steel. Thus, this work aims to present an analysis on the sources of the recycling of PET (Polyethylene Terephthalate) to determine the possibilities for the production and availability of PET fibers that are appropriate for the concrete mixture of Portland cement, minimizing the use of sand in the civil construction industry; to review the physical mechanical behavior of the concrete with the addition of PET bottle fibers; and verify the best application of this concrete in the construction of buildings, aiming at reducing costs and ensuring the sustainability of the sector while maintaining the necessary quality. To achieve the desired goal, initially the possibilities of production and availability of PET fibers in the Brazilian market will be determined. Following, it will reviewed the mechanical and physical behavior of concrete with the addition of PET bottle fibers, analyzing the results of workability, its axial compression strength and diametral compression tensile strength. Finally, with all the foundation generated in the previous steps, it will be analyzed the possibilities of application in civil construction.

2 Methodology

The methodology used has included laboratory tests with the molding, curing, grinding and rupture of specimens to verify the behavior of the concrete with PET fibers in relation to its

axial compression strength and diametral compression tensile strength, when compared to the fiber-free concrete.

The theoretical and conceptual basis of this work was based on the analysis of the improvement of the concrete resistance properties with the addition of fibers. The study of the bibliographic material on concretes was based, mainly, on the Brazilian standards where the step by step of the execution of the experiments carried out in this work is illustrated, contributing also to the standardization of the tests.

3 Results

3.1 PET Recycling in Brazil

The recycling of PET in Brazil is one of the most developed in the world, presenting a high productivity rate. According with the Brazilian Census of Recycling of PET, Brazil in 2006 exceeded the score of 50% recycling rate and, in 2012, 331,000 tons of PET packaging were collected. Brazil also already have more than 90% of recycling companies with more than 5 years of activity.

With the help of the advanced taken by the Brazilian national solid waste policy, there has been a growth of cooperatives decreasing the difficulty of obtaining bottles to recycle. As indicated by Business Commitment for Recycling (CEMPRE), from 2004 to 2015 the level of recovery of materials increased by 29% and the volume of packages deposited in landfill was reduced by 21.3%. In addition, in relation to cooperatives and voluntary delivery points (VDP): 802 cooperatives were supported from 2012 to 2017, 4,487 cooperatives structuring actions carried out and 364 municipalities attended in 21 states; and 2,082 PEV were installed from 2012 to 2017; 7,826 PEV structuring actions carried out and 240 municipalities attended in 24 states.

3.2 PET fibers Brazilian Production

The Brazilian industry of PET flakes has a production capacity from 2,500 kg/h to 4,500kg/h including moderns grinding lines with optical separator systems, super washing and fines screening for the production of colorless PET flake, hot-wash PET recycling system covering all the production steps including label and lid removal and separation, grinding, hot-washing and drying. Also, the Brazilian industry of PET flakes developed a national technology for PET flake super washing, providing highest level of decontamination and final quality to the PET raw material marketed. This technology could also produces PET flakes with some specials specifications: standard colors: Crystal, Blue and Green; particle size between 8.0 and 12.0 mm; PVC contamination of less than 80 ppm; contamination by olefins and non-ferrous metals of less than 100 ppm; bulk density between 350 and 500 g/L; maximum humidity of 1,0%; and absence of PET powder.

3.3 Laboratory Tests

The cement agglomerate used was the CP II E32 of the MAUÁ brand and it was weighed on a WELMY mechanical scale. The sand used in the manufacturing process of the specimens was classified as the average sand of the MARQUES BROTHERS, sifted, whose maximum allowable granulometry is 1.41 mm and weighed on a WELMY mechanical scale. For the characterization of the sand, a specific mass test was performed based on the standard NBR NM 52 – 2009 – Fine aggregates, using a Chapman Vial. The unit mass test followed the standard NBR NM 45 – 2006 – Aggregates. The test on the sand's granulometry was performed as prescribed by NBR NM 248 – 2003. The coarse aggregate used was Gravel I of the brand IRMÃOS MARQUES and the sample was weighed on a WELMY mechanical scale.

The PET fibers used in this analysis were obtained from the recycling of soda bottles that were discarded in nature, then washed and cut with the aid of a ruler, scissors and guillotine in the dimensions of 30 mm x 3 mm. The fibers were weighed on a Bel electronic scale.

For the concrete dosage characteristics, the calculations were made according to the method of the Brazilian Association of Portland Cement (ABCP) by means of a technical study (ET-67), with the title "Concrete Dosing Parameters", authored by the public engineer Penna Firme Rodrigues (revised in 1995) that presents an eminently experimental feature.

The materials measurement was made from the mortar basic trace of 1: 1.5: 1.82: 0.47 a/c (cement, sand, gravel, water, respectively). It is worth noting that the basic trace represents a proportion of each material as is usually used in the civil construction.

For compression and diametral compression tests performance, cylindrical specimens were molded with dimensions of 100x200 mm, as well as, the procedures of density and healing were performed according to ABNT NBR 5738-2015.

The consistency of the fresh concrete was determined by the slump test of a concrete cone, according to NBR NM 67: 1998.

For the axial compression test, the I-3001-C 100 Tf digital hand press produced by Contenco was used. For the evaluation of the Axial Compression Strength test, the guidelines of ABNT NBR 5739: 2007 - Concrete - Compression test of cylindrical specimens were followed.

The test of determination of tensile strength by diametral compression was performed according to ABNT NBR 7222: 2011, considering the ages of 7 and 28 days. The press used in the test was the I-3001-C 100 Tf digital hand press produced by Contenco.

The fresh concrete test has showed the slump of the concrete cone specimen come was 90 mm for concrete without the addition of PET fibers, characterizing a rich concrete, while for the trait with 2% PET fiber, the slump was 20 mm indicating a poor concrete of very low workability, as shown in Figure 1.

Figure 1. Slump test of a concrete cone.

According to Mheta and Monteiro (1994), in concrete with fibers, compressive strength is not the most important contribution of reinforcement. Figures 2 and 3 present the results of axial compressive strength according to NBR 5739 (ABNT, 2007). It can be observed that there was not much difference in the deformation presented by concrete with addition of PET fiber to concrete without fiber. Both presented type of D - conical and sheared rupture, as specified in Annex A of NBR 5739.

Figure 2. Specimen with PET fibers after cracking under axial compression.

Figure 3. Specimen with no PET fibers after cracking under axial compression.

The axial compressive strength test has demonstrated that the mixture with addition of PET fibers (2% content) showed a small reduction in axial compressive strength in relation to concrete without fiber addition at the age of 28 (3.27% reduction). In contrast to what be observed at the age of 7 days, when fiber-reinforced concrete showed higher axial compressive strength results than fiber-free concrete (an increase of 1.18%), which can be seen in the comparison with the results in Figure 4.

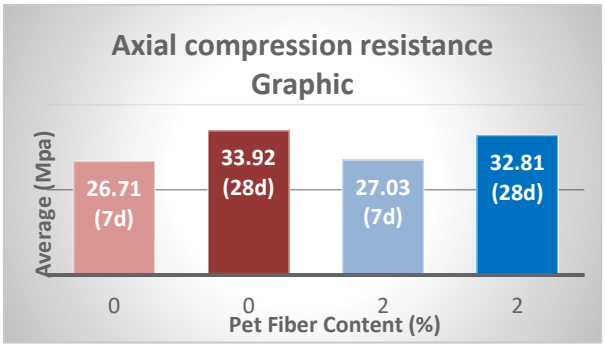

Figure 4. Comparative results of axial compression resistance tests.

The Figure 5 illustrates the specimen with PET fibers after the diametric compression test. According to NBR 7222 (ABNT, 1994), it can be observed that the crack propagated easily at the top and with some resistance at the bottom, holding the parts together. Thus, an excess load is required to break it completely. However, this is not the case with concrete without the addition of PET fiber, where the crack propagated throughout the body and abruptly breaking it, as shown in Figure 6.

Figure 5. Specimen with PET fibers after cracking under diametral compression.

Figure 6. Specimen with no PET fibers after cracking under diametral compression.

In the diametrical compression tensile strength test, we observed an increase in tensile strength by diametral compression with increasing control age (7 to 28 days), as expected. On the order hand, the results for axial compressive strength, PET fiber-reinforced concretes have presented a 18.38% increase in diametral tensile strength in relation to non-PET-reinforced concrete at both ages, which can be seen in the comparison of the results in Figure 7.

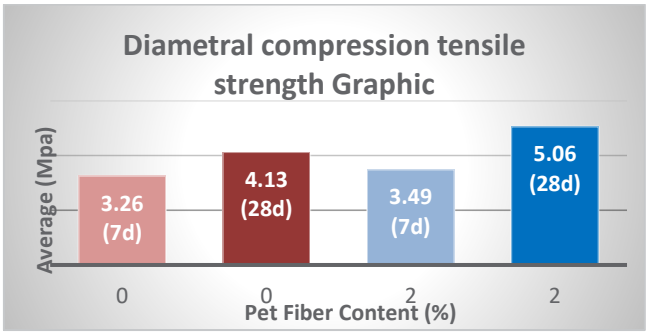

Figure 7. Comparative results of diametral compression tensile strength tests.

3.4 Application of Concrete with PET Fibers

The results have demonstrated that the greatest gains obtained with the use of fibers are associated with the increased strength of concrete to tensile stress. By adding PET fiber to concrete, it is no longer a fragile material. This is due to the increased bonding of the matrix to the concrete (transition zone), causing an increase in its mechanical characteristics, such as modulus of elasticity (Gpa), and tensile strength (MPa). Additionally, its filaments work as adhesion point of tensions between the cracks, preventing their propagation, thus making the concrete more resistant and ductile, with a post-fissure capacity.

With these results, important applications for concrete obtained from mixtures with PET fibers would be in pavement structures, hydroelectric plants, tunnel coverings, dams, slabs, which have a volumetric control of shrinkage, which would make it possible to reduce the possibilities of cracks, besides offering good protection.

In addition, there are other applications of PET fibers in construction that may be used more intensely in the future as repair materials (MRs) for degraded hydraulic surfaces, for example, to provide a satisfactory performance at lower cost compared to materials generally employed in these cases, with the advantage of an appropriate final disposal of these solid wastes.

4 Conclusions

From the analyzed aspects, the use of recycled PET fibers in concrete definitely provided considerable changes in the physical properties of the material.

- Regarding workability, the conventional concrete was workable and cohesive. It was noted a loss of rebate in the trait with 2% content of PET (20 mm slump), proving to be very consistent, a fact that, however, did not compromise the casting of the concrete;
- Regarding the axial compression strength, concrete with the addition of PET fibers at 7 days of age had a strength gain of 6.59% and a loss of 5.54% at 28 days of age. Regarding the mechanical test for axial compression at 28 days of age, there has been no significant difference for fiber-reinforced concrete compared to non-fiber concrete; and
- However, a significant increase in the results of tensile by diametral compression to 2% PET fiber concrete has been obtained with increasing control age (from 7 to 28 days), as expected. The result of increasing tensile strength was then successfully achieved. Thus, different to what has been observed in the axial strength results, the concrete with

addition of PET fiber presented a 18.38% increase in tensile strength compared to concrete with no fiber addition.

The results allow us to conclude that there is possibility of production and availability of PET fibers that are suitable for mixing in concrete, since the results of the mechanical physical behavior of the concrete were satisfactory for the performed mixing condition.

It is noteworthy that further studies are necessary to prove its applicability in structural use, aiming at a future revision of NBR 8953 (2015).

Thus, even though it has been well demonstrated academically that the tensile strength property of this technology proves superior to conventional concrete, the viability of its use at the industrial level will only occur with more government support and incentives through an infrastructure that can guarantee the stability of the production of PET fibers, establishing the necessary logistics to guarantee its offer for the civil construction, allowing construction companies to use this material for the preservation of our planet. As mentioned in the beginning of this study, the waste from PET bottles generates a major environmental problem, and any appropriate end we can find for this waste returns a great benefit to nature.

ORCID

Edson Rodrigues: https://orcid.org/0000-0002-3267-980X

References

Associação Brasileira de Normas Técnicas. (1983). NBR 7211: Agregado para concreto. Rio de Janeiro.

Associação Brasileira de Normas Técnicas. (2011). NBR 14724: Informações e documentações – Trabalhos acadêmicos - Apresentação. Rio de Janeiro.

Associação Brasileira de Normas Técnicas. (2007). NBR 11578: Cimento Portland composto – Especificação. Rio de Janeiro.

Associação Brasileira de Normas Técnicas. (2016). NBR 5738: Moldagem e cura de corpos-de-prova cilíndricos ou prismáticos de concreto. Rio de Janeiro.

Associação Brasileira de Normas Técnicas. (2007). NBR 5739: Concreto - Ensaio de compressão de corpos de prova cilíndricos. Rio de Janeiro.

Associação Brasileira de Normas Técnicas. (1997). NBR 7215: Cimento Portland – Determinação da resistência a compressão. Rio de Janeiro.

Associação Brasileira de Normas Técnicas. (1958). NBR 7222: Resistência a tração simples de argamassa e concreto por compressão diametral de corpos-de-prova cilíndricos. Rio de Janeiro.

Associação Brasileira de Normas Técnicas. (2015). NBR 7680-1: Concreto – Extração, preparo, ensaio e análise de testemunhos de estruturas de concreto partem 1: Resistência à compressão axial. Rio de Janeiro.

Associação Brasileira de Normas Técnicas. (2003). NBR NM 248: Agregados - Determinação da composição granulométrica. Rio de Janeiro.

Associação Brasileira de Normas Técnicas. (2006). NBR NM 45: Determinação da massa unitária e do volume de vazios. Rio de Janeiro.

Associação Brasileira de Normas Técnicas. (2009). NBR NM 52: Determinação da massa específica e massa aparente. Rio de Janeiro.

Associação Brasileira de Normas Técnicas. (1998). NBR NM 67:Concreto - Determinação da consistência pelo abatimento do tronco de cone. Rio de Janeiro.

Bauer, L. A. F. (2013). Materiais de Construção: Novos Materiais para Construção Civil. 1.Vol. 5. Ed, Rio de Janeiro: LTC.

Bezerra, M. N., Mancini, S. D. and Zanin, M. (1998). Reciclagem de PET Advindo de Garrafas de Refrigerante Pós-Consumo. Revista Polímeros: Ciência e Tecnologia, São Carlos, Vol. 8, n. 2, pp.68-75.

Bogio, A. and Borges, A. (1989). Dosagem de Concretos: Método do prof. Lobo Carneiro e método do ACI. Porto Alegre: UFRGS, Curso de Pós-Graduação em Engenharia Civil.

Carvalho, W. C. and Gomes, R. A. M. P. A Aplicação de Fibras de Garrafa PET como Agregado Estrutural do

Concreto. Artigo científico.
Coró, A. G. (2002). Trabalho de Conclusão de Curso. Investigação das propriedades mecânicas de concretos reforçados com fibras pet. Rio Grande do Sul.
Figueiredo, A. D. de. (2011). Concreto reforçado com fibras. 2011. 248 f. Tese (Doutorado) - Curso de Pós graduação em Engenharia Civil, Departamento de Engenharia de Construção Civil, Escola Politécnica da Universidade de São Paulo, São Paulo.
Figueiredo, A. D. (2005). Concreto com Fibras. Cap. 39. In: Isaia, G. C (Ed.). (2005). Concreto: Ensino, Pesquisa e Realizações. São Paulo, Instituto Brasileiro do Concreto IBRACON.
Gorniski, J. P., and Karzmierczac, C. S. (2007). Microestrutura dos polímeros. Cap. 12. In: Isaia, G. C (Ed.). Materiais de Construção Civil e Princípios de Ciência e Engenharia dos Materiais. São Paulo, Instituto Brasileiro do Concreto IBRACON.
John, V. M. (2000). Reciclagem de resíduos na construção civil: Contribuição à metodologia de pesquisa e desenvolvimento. 2000. 113 f. Tese (Doutorado) - Curso de Engenharia de Construção Civil, Engenharia de Construção Civil, Escola Politécnica da Universidade de São Paulo, São Paulo.
Leite, M. B. (2001). Avaliação de Propriedades Mecânicas de Concretos Produzidos Com Agregados Reciclados Com Resíduos de Construção e Demolição. 2001. 290 f. Tese (Doutorado) - Curso de Programa de Pós-graduação em Engenharia Civil, Escola de Engenharia, Universidade Federal do Rio Grande do Sul, Porto Alegre.
Marangon, E. (2004). Aspectos do comportamento e da degradação de matrizes de concreto de cimento portland reforçados com fibras provenientes da reciclagem de garrafa PET, Ijuí – RS.
Modro, N.L.R. (2008). Desenvolvimento e Caracterização de Concreto de Cimento Portland Contendo Resíduos Poliméricos de PET, Dissertação de M.Sc., UNIVILLE, Joinville, SC, Brasil.
Pelisser, F. (2002). Avaliação do Desempenho de Concreto Reforçado com Fibras de Polietileno Tereftalato (PET). 2002. 127 f. Dissertação (Mestrado) - Programa de Pós-graduação em Engenharia Civil, Universidade Federal de Santa Catarina, Florianópolis.
Salomão, R. and Pandolfelli, V. C. (2003). Concretos refratários contendo fibras poliméricas: correlação entre a permeabilidade e o comportamento de secagem, apresentado no 47° Congresso Brasileiro de Cerâmica, João Pessoa/PB. Consultado em 25/02/2018.

XV International Conference on Durability of Building Materials and Components
DBMC 2020, Barcelona
C. Serrat, J.R. Casas and V. Gibert (Eds)

A Joint Inversion Approach of Capacitive and Resistive Measurements for the Estimation of Water Saturation Profiles in Concrete Structures

Marie A. Alhajj[1], Sébastien Bourguignon[2], Sérgio Palma Lopes[3] and Géraldine Villain[1]

[1] Mast-Lames, Ifsttar, Site de Nantes, Allée des Ponts et Chaussées, CS 5004, 44344 Bouguenais Cedex France, marie-antoinette.alhajj@ifsttar.fr, geraldine.villain@ifsttar.fr

[2] Centrale Nantes, 1 rue de la Noë, 44321 Nantes Cedex 3, France, sebastien.bourguignon@ec-nantes.fr

[3] Gers-GéoEnd, Ifsttar, Site de Nantes, Allée des Ponts et Chaussées, CS 5004, 44344 Bouguenais Cedex France, sergio.lopes@ifsttar.fr

Abstract. *Concrete is a construction material that is well known for its durability. However, it is exposed to environmental attacks that lead to the penetration of aggressive agents such as water and chlorides, thus, threatening its durability and service life. Within this context and exploiting the sensitivity of the electromagnetic properties of concrete to its water content, the literature suggests determining water saturation profiles using non-destructive techniques. For instance, measuring the electrical resistivity at several points of the surface of the concrete structure can lead to an estimate of the resistivity depth profile. Then, after a calibration step, the water saturation depth profile can be obtained and the durability can be assessed. Similarly, the water depth profile can be assessed by dielectric permittivity measurements. In this paper, we propose a new inversion scheme based on the combination of both resistive and capacitive measurements: resistivity and permittivity measurements are inverted jointly to estimate the water saturation profile in concrete. Numerical experiments with simulated data show that information gathered from the two measurements enriches the inversion process, leading to the determination of more reliable water saturation profiles.*

Keywords: *Durability, Nondestructive Techniques, Capacitive and Resistive Measurements, Inversion Procedure.*

1 Introduction

Nondestructive (ND) methods are promising to assess the durability of concrete. They are non-intrusive and allow continuous structure monitoring (Balayssac, 2017). This study focuses on estimating the concrete saturation degree and handles two kinds of measurements: the DC-electrical resistivity and the dielectric permittivity. Both quantities are sensitive to the water content in concrete, and in a complementary way (Fares, 2018), and can, therefore, be used to evaluate the durability of concrete towards water ingress (Balayssac, 2017). The method consists of performing resistivity and permittivity measurements at the surface of the structure; then, an inversion procedure is required to retrieve the electromagnetic depth profiles. Finally, water saturation is obtained through calibration of the electromagnetic properties.

The inversion of measurements has been performed using either the resistivity or the permittivity data to obtain the water saturation with depth profile (Fares, 2016). However, inversion results may lack reliability, in particular, due to the small number of available data, the presence of noise in the measurements, and the lack of sensitivity of each data set to the

water saturation profile. Therefore, a possible solution to improve the inversion of ND measurements relies upon combining the two types of data, the electrical resistivity, and the dielectric permittivity, taking advantage of their complementarity (Tathed, 2018).

In Section 2, we introduce a brief description of both ND methods. Then, in Section 3, the searched saturation profile is modeled with a parametric curve, and both the forward model and the inverse problem are discussed. Our joint inversion procedure is described in Section 4. Finally, Section 5 presents numerical simulations evaluating the performance of the proposed methodology.

2 Electromagnetic Properties of Concrete

2.1 DC-Electrical Resistivity

The DC-electrical resistivity of concrete, noted ρ [Ω.m], expresses the ability of the material to oppose the flow of free electric charges when it is subjected to an electric field. In a homogeneous and isotropic material, it is expressed by the Ohm's law ratio of the measured voltage drop V [V] to the applied current intensity I [A], multiplied by a geometric factor G_r [m] :

$$\rho_a = G_r \frac{V}{I}. \tag{1}$$

The resistivity measurement principle consists of transmitting a direct current (DC) into the concrete using two electrodes and measuring the induced potential drops between one or several pairs of electrodes. Then, the 'apparent' resistivity can be calculated using Eq. (1). Since concrete is usually not a homogeneous material, the latter observable is not the 'true' resistivity of concrete but rather an integrating value over a volume depending on the electrode array configuration and size (Loke, 2004) (Presuel-Moreno, 2010) .

In this study, two electrode configurations are considered to measure apparent resistivities, the Wenner and the Schlumberger arrays (Loke, 2004). Our measuring device consists of a multi-electrode resistivity probe formed by 14-point electrodes equally spaced every 20 mm (Du Plooy, 2013). For all possible electrode combinations following the Wenner and Schlumberger configurations, a dataset consisting of about 100 apparent resistivities can be obtained.

2.2 Dielectric Permittivity

The dielectric permittivity, noted ε [F/m], is related to the phenomenon of electric polarization which results from the relative displacement of the bound charges in the material under the action of an external electric field. Due to the energy losses that accompany the polarization phenomenon, the permittivity can be expressed using a complex variable where the real part is the ability of the material to store electric energy. Consequently, the relative dielectric permittivity of concrete, ε (dimensionless), can be obtained from the system's capacitance, C [F], the vacuum permittivity, ε_0 [F/m] and the geometric factor, G_c [m]:

$$C = G_c . \varepsilon_0 . \varepsilon. \tag{2}$$

The measurement principle consists in applying an alternating current between two or more electrodes placed on the surface of the sample and measuring the resonance frequency of the

electrode-concrete system. The measuring device and consists of four different types of probes, each composed of metal plate electrodes and Plexiglas® support. The probes differ by their number of metal plates, their dimensions and the spacing between them (Fares 2016):

- electrode GE consisting of 2 plates (70xx40 mm^2) with a plate spacing of 40 mm,
- electrode ME+ consisting of 3 plates (70x15 mm^2) with a plate spacing of 15 mm,
- electrode ME consisting of 4 plates (70x10 mm^2) with a plate spacing of 10 mm,
- electrode PE consisting of 5 plates (70x5 mm^2) with a plate spacing of 5 mm.

Using this device, four apparent permittivity values can be collected for each measuring sequence, whose depth sensitivity increases with both the size and the spacing of the electrodes. Note that the measured apparent permittivity is equal to the 'true' permittivity of concrete in case of a semi-infinite homogeneous medium. Nonetheless, when the medium is of finite dimensions or is not homogeneous, the measured apparent permittivities must enter an inversion procedure to obtain the true permittivity distribution in the concrete medium.

3 Saturation Profile

In this section, a definition of the saturation degree is provided as well as the saturation profile chosen for this study. Then, the methodology for computing the forward model and solving the inverse problem for each ND electromagnetic method is briefly explained. Finally, our joint inversion approach is presented.

3.1 Definition

The saturation degree, noted S, represents the fraction occupied by water in the total pore volume. The saturation degree conditions the penetration of aggressive agents. For this, the determination of the saturation degree makes it possible to predict the degradation of concrete. Moreover, it is important to note that both resistive and capacitive properties of concrete are sensitive to saturation (Balayssac, 2017). The calibration of each of ρ and ε as functions of S is performed on the test specimen. The calibration of the electrical resistivity can be expressed by the model:

$$\rho = AS^{-B} \tag{3}$$

where A and B depend on the concrete specimen studied. Eq. (3) is consistent with Archie's empirical law (1942) proposed by geologists in the oil prospecting field for non-clayey rocks, and then for porous materials such as concrete (Fares, 2018). The calibration of the dielectric permittivity results is performed under the model (Fares, 2018):

$$\varepsilon = aS + b \tag{4}$$

where a and b depend also on the concrete specimen tested. This study aims to deal with the phenomena of drying and soaking in concrete, considered here as non-cyclic and unidirectional. As a result, the degree of saturation in concrete is assumed to evolve only in one direction, which is the depth z perpendicular to the concrete surface, and from a drier state to a wetter state or vice versa (monotonic curve). In addition to that, to better constrain the profile reconstruction, a parametric model is considered using a Weibull curve with the following expression:

$$S(z) = (\theta_1 - \theta_2)\exp(-(\frac{z}{\theta_3})^{\theta_4}) + \theta_2, \quad (5)$$

where θ_1 is the saturation ratio on the surface, θ_2 is the saturation ratio in the structure depth, θ_3 is the scale factor, and θ_4 is the shape factor. Eq. (5) provides a continuous parametric model, where the unknown saturation profile is expressed by the continuous function *S(z)* depending on the four parameters θ_i, i=1, …, 4. The inversion procedure then amounts to estimating the parameters θ_i from the apparent resistivities ρ_a or the apparent permittivities ε_a.

3.2 Forward Model

The forward model consists in the computation of the apparent observables corresponding to a given saturation profile *S(z)*. It has been implemented numerically using the commercial finite element (FE) modeling software COMSOL Multiphysics® (v.5.4). The 3D-concrete model is defined: geometry (700x900x150 mm^3 concrete block), FE mesh, electrode positions for both electrical and dielectric problems (Fig. 1). The FE mesh is finer near the electrodes with a maximum element size of 1 mm and coarser elsewhere with a maximum element size of 5 mm and consists of about 30000 elements. Then, the saturation profile is defined by the Weibull curve defined by Eq. (5). The electrode systems described in Section 2 are used for the measurement simulations.

For the DC-electric problem, 14-point electrodes (see Fig. 1a) represent the multi-electrode resistivity probe. Knowing the saturation profile in concrete depth, the imposed resistivity depth profile is obtained using Eq. (3). Then, the forward model resolution leads to the computation of the apparent resistivities using Eq. (1). For this, the module AC/DC - electric currents of COMSOL is used and positive current is injected in one electrode, negative current in another and an electric potential is simulated in the remaining electrodes. For the dielectric problem, the dielectric plates are represented by surface plates with an infinitely small thickness (Fig. 1b). Knowing the saturation depth profile in concrete, the corresponding permittivity depth profile is obtained using Eq. (4). Then, the forward model resolution leads to the computation of the apparent permittivities using Eq. (2) for each electrode set. For this, the module AC/DC - electrostatics of COMSOL is used and a potential difference is imposed on the electrode plates. For both DC-electric and dielectric models, the following conditions are considered: current conservation within the concrete block, electric insulation of the block boundaries and a null initial potential in the block.

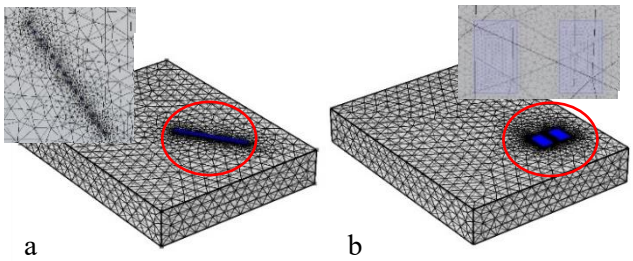

Figure 1. The meshing of the 3D model of a concrete slab (700x900x150 mm^3) with a) the resistivity probe and b) the capacitive electrodes.

3.3 Inverse Problem

The inversion procedure aims to retrieve the water saturation profile from the apparent measurements. This can be achieved by finding the parameters θ in Eq. (5) that best fit the data, by minimizing the least-squares mismatch between the measurements, say d_{mes}, and their prediction corresponding to a given saturation profile, say d_{mod}:

$$\psi = \sum_i (d_{mod_i} - d_{mes_i})^2 \tag{6}$$

In this work, we choose the Levenberg-Marquardt algorithm (Morrison, 1960), which is a standard method for non-linear least-squares optimization problems.

3.3.1 Separate inversion

In previous studies, apparent capacitive and resistive measurements were inverted separately to estimate the water profiles in concrete (Fares, 2016). A single type of measurement was considered (either the resistive or the capacitive ones) to estimate the saturation profile with depth. The method is similar for both types of measurements and is shown in Fig. 2. The goal is to minimize the cost function in Eq. (6), where:

$d_{mod} = \rho_{a_{mod}}$ and $d_{mes} = \rho_{a_{mes}}$ in the inversion of apparent resistivities,

$d_{mod} = \varepsilon_{a_{mod}}$, and $d_{mes} = \varepsilon_{a_{mes}}$ in the inversion of apparent permittivities.

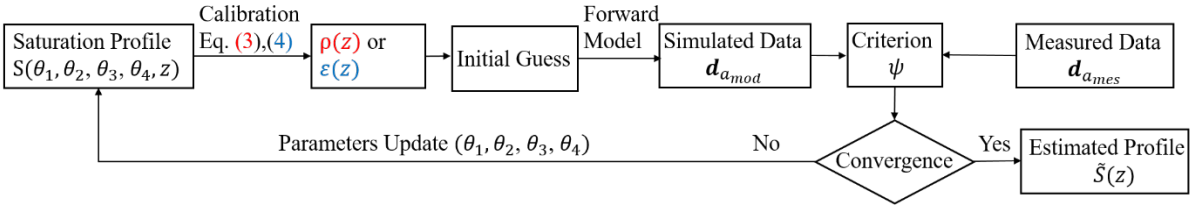

Figure 2. Scheme for the estimation of the saturation depth profile (parameters θ_i) from apparent resistivity or permittivity measurements.

3.3.2 Joint inversion

In this section, we consider a joint inversion approach. The calibration laws established by experimental studies (Eq. (3) and (4)) make it possible to connect each of the properties, electrical resistivity, and dielectric permittivity, to common property, the saturation degree. The joint inversion procedure is presented in Fig. 3. It is an iterative process, which starts with an initial saturation profile given by the initial parameters. Then the resistivity profile is obtained using Eq. (3) and the permittivity profile using Eq. (4). Afterward, the simulated data, that is, the apparent resistivities and permittivities, are computed and compared to the measured data in the joint least-squares criterion given in Eq. (7) ψ, where W_ρ and W_ε are weight parameters given to capacitive and resistive data respectively depending on the quality of these measurements.

$$\psi = W_\rho \sum_i (\rho_{a_{mod_i}} - \rho_{a_{mes_i}})^2 + W_\varepsilon \sum_j (\varepsilon_{a_{mod_j}} - \varepsilon_{a_{mes_j}})^2 \tag{7}$$

The main advantage of the joint inversion is that both measurements are sensitive to

saturation but in a complementary manner. Therefore, the information gathered may yield a better estimation of the saturation profile. Also, the joint inversion could have another advantage concerning the investigation depth of the measurements. Previous studies show that knowing the spacing between electrodes, the investigation depth of the corresponding measurements can be estimated (Loke, 2004) (Fares, 2016). The two ND methods sample differently the investigated volume concerning concrete slab thickness, therefore, combining the two methods makes it possible to better constrain the problem by information on the different regions of this volume of interest.

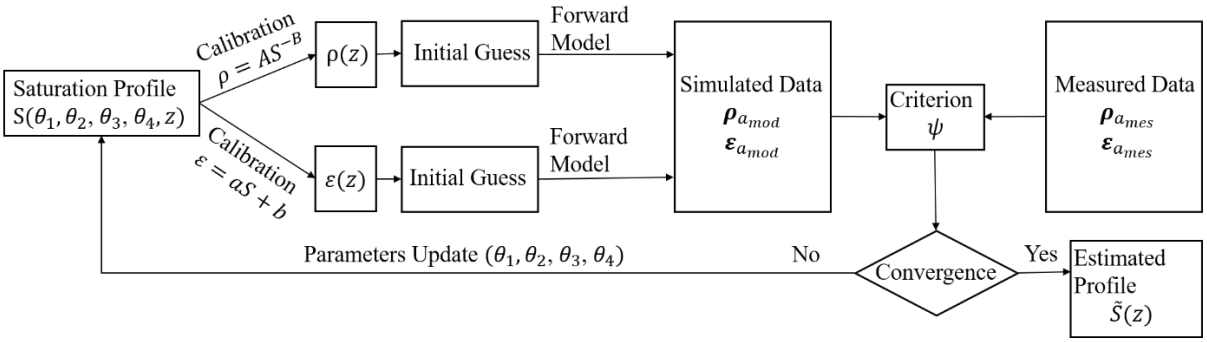

Figure 3. The joint inversion scheme to determine concrete saturation distribution in depth.

4 Numerical Experiments

In this section, numerical experiments are performed to validate the proposed joint inversion approach. Synthetic data are computed, where a saturation profile is generated according to Eq. (5) and represents the 'true' saturation profile (Table 1, column 1). The forward model is computed using the same numerical slab model and electrode simulation as presented in Section 3.2. In all simulations, the initial saturation profile in the optimization procedure is chosen such that the relative error compared to the true profile is equal to 10% (Table 1, column 2).

In the first numerical experiment, we consider noise-free data. The inversion procedure is run successively by considering only apparent resistivity data, only apparent permittivity data, and finally both data sets. The results are shown in Fig. 4. Profiles corresponding to the successive iterations of the Levenberg-Marquardt procedure are represented by the green curves. It is clear that the three inversion methods correctly converge toward the true profile. This result confirms that apparent resistivity and permittivity data, employing their corresponding calibration curves (Eq. (3) and Eq. (4)), can be jointly inverted into a unique saturation profile. In addition to that, the variability of the fitted profile between iterations is important in the inversion of apparent permittivity data (Fig. 4b); due to the smaller number of data, which is equal to the number of unknowns to be determined (the four parameters of the Weibull curve). This variability seems to disappear in the joint inversion (Fig. 4c) due to the additional number of resistivity data added to the permittivity data, which induces a faster convergence to the 'true' profile and a smaller number of iterations (15 for the joint inversion compared to 37 for the permittivity inversion alone). Note that inversion is stopped when the four following criteria are satisfied: the criterion ψ is less than 10^{-6}, the relative variation of estimated parameters between two consecutive iterations is less than 10^{-6}, the number of iterations is higher than 50 and the criterion gradient is less than 10^{-3}.

The second inversion test aims to study the influence of noise in the inversion. Referring to previous noise assessment studies done in the laboratory for capacitive and resistive data (Du Plooy, 2013), three additional sets of computations are carried out. The first one considers noisy resistivity data, such that the coefficient of variation (CV_r defined as the ratio between the standard deviation and the mean of the measurement) is 4%, and permittivity data remain noise-free. The second one considers noisy permittivity data, such that CV_p =2%, and noise-free resistivity data. Finally, the third data set considers noise on both resistivity and permittivity data (CV_r=4% and CV_p=2%, respectively). The results of this study are shown in Table 1, where the estimated profile parameters are given. For each test case, individual and joint inversions are performed. The relative error between the true profile parameters and the estimated one as well as the iteration number is given. In the first study, the two inversions have the same iteration number. However, the relative error is smaller for the joint inversion. For the second study, both the number of iterations and the relative error decrease significantly when the joint inversion is performed. Finally, in the last study, the relative error and the iteration number are the lowest for the joint inversion.

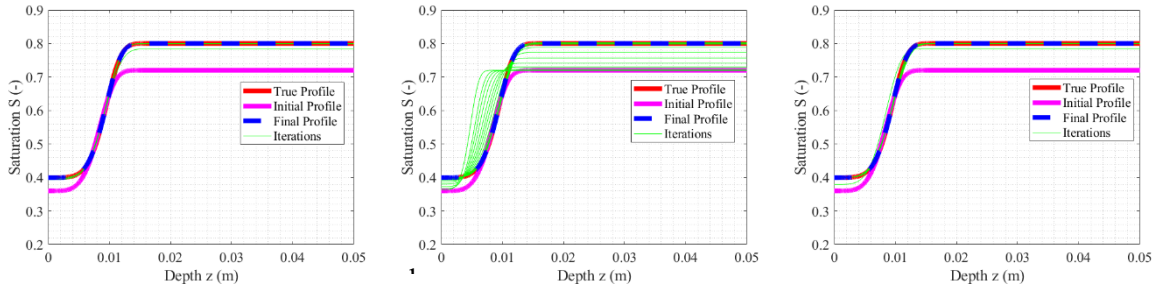

Figure 4. a) Inversion procedure using apparent resistivity data alone –b) Inversion of apparent permittivity data alone and c) Joint inversion of apparent resistivity and permittivity data.

Table 1. Separate and joint inversion results for noisy resistivity and permittivity data.

'True' Profile	Initial Profile	Noise Conditions	Resistivity	Permittivity	Joint
$\begin{bmatrix}0.4\\0.8\\0.01\\5\end{bmatrix}$	$\begin{bmatrix}0.36\\0.72\\0.009\\4.5\end{bmatrix}$	$CV_r = 4\%$ $CV_p = 0\%$	$\begin{bmatrix}0.3927\\0.8006\\0.0101\\4.4996\end{bmatrix}$		$\begin{bmatrix}0.4001\\0.8003\\0.0103\\5.1200\end{bmatrix}$
		Iteration Number	9	9	
		Relative Error	3.21 %	1.26%	
$\begin{bmatrix}0.4\\0.8\\0.01\\5\end{bmatrix}$	$\begin{bmatrix}0.36\\0.72\\0.009\\4.5\end{bmatrix}$	$CV_r = 0\%$ $CV_p = 2\%$		$\begin{bmatrix}0.4031\\0.9500\\0.0119\\10.85\end{bmatrix}$	$\begin{bmatrix}0.4030\\0.8000\\0.0100\\5.4910\end{bmatrix}$
		Iteration Number	50	9	
		Relative Error	38%	2.63%	
$\begin{bmatrix}0.4\\0.8\\0.01\\5\end{bmatrix}$	$\begin{bmatrix}0.36\\0.72\\0.009\\4.5\end{bmatrix}$	$CV_r = 4\%$ $CV_p = 2\%$	$\begin{bmatrix}0.3927\\0.8006\\0.0101\\4.4996\end{bmatrix}$	$\begin{bmatrix}0.4031\\0.9500\\0.0119\\10.85\end{bmatrix}$	$\begin{bmatrix}0.3991\\0.7967\\0.0100\\4.9811\end{bmatrix}$
		Iteration Number	9	50	6
		Relative Error	3.21%	38%	0.25%

5 Conclusion

In this study, we developed a new joint inversion approach for resistivity and permittivity data in concrete structures. Numerical experiments were carried out using synthetic data that showed that the joint inversion of DC-resistivity and dielectric permittivity data can produce a more accurate solution. Simulations using noise-free synthetic data showed good convergence to the 'true' considered saturation profile. Besides, when performing the inversion of synthetic noisy data, the profile estimation is improved by carrying out joint inversion as the relative error between the true and estimated parameters decreases as well as the iteration number compared to the separate inversions. For a complete validation of the joint inversion approach, more intensive simulation tests are required. Afterward, real lab data will be acquired to take into account furthermore the presence of noisy data and to validate the joint inversion approach.

ORCID

Marie Antoinette Alhajj: 0000-0001-7711-5103

References

Balayssac, J.-P. and Garnier, V. (2017). *Non-destructive Testing and Evaluation of Civil Engineering Structures,* Elsevier Press Ltd., London.

Du Plooy, R., Palma Lopes S. and Villain, G. et al. (2013). *Development of a multi-ring resistivity cell and multi-electrode resistivity probe for investigation of cover concrete condition.* NDT&E International.54:27-36.

Fares, M. and Fargier, Y. et al. (2016). *Determining the permittivity profile inside reinforced concrete using capacitive probes,* NDT&E Int. 79:150–161.

Fares, M. and Villain, G et al. (2018). *Determining chloride content profiles in concrete using a resistivity probe*, Cement and Concrete Composites. 94:315-326

Loke, M.H. (2004). *Tutorial: 2-D and 3-D electrical imaging surveys*.

Morrison, D. (1960). *Methods for nonlinear least-squares problems and convergence proofs*. Proceedings of the Jet Propulsion Laboratory Seminar on Tracking Programs and Orbit Determination: 1–9.

Presuel-Moreno, F. et al., (2010). *Characterization of New and Old Concrete Structures Using Surface Resistivity Measurements*, Florida, Florida Department of Transportation Research Center, p. 279.

Tathed, P. Han, Y. and Misra, S. (2018). *Hydrocarbon saturation in Bakken Petroleum System based on joint inversion of resistivity and dielectric dispersion logs,* Fuel 233 (2018) 45–55.

XV International Conference on Durability of Building Materials and Components
DBMC 2020, Barcelona
C. Serrat, J.R. Casas and V. Gibert (Eds)

A Risk-Based Approach for Quantifying Durability and Life-Expectancy of the Wall-Foundation Construction Detail in Timber Buildings

Andrea Gaspari, Ivan Giongo and Maurizio Piazza

Department of Civil, Environmental and Mechanical Engineering, University of Trento, via Mesiano, 77, 38123 Trento, Italy, andrea.gaspari.1@unitn.it, ivan.giongo@unitn.it, maurizio.piazza@unitn.it

Abstract. *Understanding and predicting the durability of timber structural components of buildings can lead to a more reliable and efficient use of this material in constructions. The work described herein presents a methodology to assess the life-expectancy of wall-foundation details in timber buildings based on the estimation of the durability of the timber structural element. Risk classes were defined starting from the inputs from the most relevant standards addressing the durability of timber available in Europe. The attribution of a risk class to the wall-foundation detail requires decision trees that consider the key aspects that affect the durability of this construction detail in the case of fungal attack. The methodology was then applied to three case studies and the results were compared to the observations from onsite inspections carried out on the decayed structural timber elements. The present work represents the first step towards the development of a tool capable of predicting the durability of timber components within the building structure. The work reported herein was carried out within the framework of the TSafe project.*

Keywords: *Timber Buildings, Wall-Foundation Detail, Durability, Risk-Based Approach, TSafe Project.*

1 Introduction

Understanding and predicting the durability of timber is of paramount importance for a more reliable, extensive and efficient use of this material in constructions. Furthermore, quantifying the durability will also allow for a more precise quantification of the carbon stocks stored into the wood products (Profft *et al.,* 2009).

Because decay caused by biotic attack is one of the most critical concerns in the long-term performance of wood, durability at the material level has been deeply investigated. In-ground and above-ground behaviour of wood has been studied through field and laboratory testing (*e.g.*: Meyer *et al.,* 2016; Meyer *et al.,* 2017). Prediction models have been also developed to predict decay caused by fungal attack or to predict mould grow (Brischke *et al.,* 2014).

The prediction of timber decay in building structural components has instead been investigated by only but a few researchers. The Australian project, reported in Leicester *et al.* (2008), is an interesting example of a comprehensive project that examines the decay of timber and the corrosion of the metal fasteners. Decay functions have been developed within the framework of the aforementioned project to predict the depth of the fungal attack on timber structural elements inside the building envelope.

The functions have been calibrated through an extensive field test campaign and on opinions of experts (Wang *et al.,* 2008c). Strong assumptions have been made by the researchers to keep these functions simple and straightforward. Moreover, a limited set of Australian structural typologies have been considered in the project.

Recently, the increasing availability of timber-based products for a diverse range of building solutions has stimulated researchers into approaching more sophisticated tools to map timber moisture distribution over time. The Heat, Air and Moisture (HAM) analysis is one of the tools adopted to predict timber moisture content with precision (*e.g.*: Carbonez *et al.*, 2015 and Chung *et al.*, 2019).

The Wall-Foundation Detail (WFD) in timber buildings can have quite different geometries, materials, wall stratigraphies and boundary conditions. The combination of these characteristics can create a very large number of possible configurations that escalates the effort of performing HAM analyses. With reference to the durability of this construction detail, finding the most critical combinations can be very important to approach this problem effectively. Another key issue to be solved when studying this detail is how to model water intrusion. Guidelines for modelling water intrusion in walls where the problem can be schematized as one-dimensional can be found in Lstiburek *et al.* (2016a-b). An equivalent of the above-mentioned guidelines for the two-dimensional problem is not available yet and because the WFD is essentially a two-dimensional problem, its study demands bigger efforts in order to run numerical analyses and perform experimental tests.

The paper presents a methodology to categorise the WFD of timber structures in relation with the durability of the timber structural element. This method permits to assign a risk class to the detail, based on decision trees that considers the most significant issues related to timber durability accounting for fungal attack. Risk classes are used both to identify the most critical configurations and to associate to them a decay estimation function that at this preliminary stage was taken from literature. Three case studies (Gaspari *et al.,* 2020) are then introduced to compare the results of this preliminary decay prediction.

The methodology proposed herein is part of the TSafe project where reliable strategies for the risk assessment of timber structures are used to create decision-making tools useful to every party involved in the construction of timber structures. The purpose of the TSafe project is to combine numerical simulations, such as HAM analyses, with artificial intelligence and machine learning algorithms to extract simple and applicable rules from complex problems solved numerically (see for example Glavind *et al.,* 2019 and Freire *et al.,* 2017).

Risk classes are defined in section 2. Then, the decision trees necessary to assign a risk class and the parameters for the quantification of the decay are presented in section 3. The results obtained are compared to three case studies in section 4. Finally, section 5 outlines the conclusions and future work.

2 Risk Classes

Risk classes were defined according to the provisions contained in the main European standards that deal with the durability of timber from the material point of view (*i.e.*: ÖNORM B 3802-1:2015, EN 335:2013 and DIN 68800-1:2019-06) and from that of a building detail (*i.e.*: ÖNORM B 2320:2017 and DIN 68800-2:2012-02). Risk classes identify a general behaviour of the construction detail in terms of protection against water intrusion, condensation, and water permanence and of timber drying performance. Moreover, the risk classes group together different building details that show similar behaviour. A definition of the risk classes for the WFD, considering the standards cited above, is reported in the following (Gaspari *et al.,* 2020).

- Risk class 1 (R1): timber is protected against outdoor weather (direct rain, bounce water,

wind-driven rain and external rain accumulation) and against rising damp. Moreover, presence of condensation is possible, but a rapid drying is ensured.

- Risk class 2 (R2): timber is protected against outdoor weather (direct rain, bounce water, wind-driven rain and external rain accumulation) and against rising damp. Presence and permanence of condensation is possible.
- Risk class 3 (R3.1 and R3.2): timber can get wet, due to outdoor weather (direct rain, bounce water, wind-driven rain and external rain accumulation) or to condensation caused by non-efficient airtightness. The class R3 is divided into the two subclasses R3.1 e R3.2 considering, respectively, the possibility of timber to dry or not.
- Risk class 4 (R4): timber can get wet due to outdoor weather (direct rain, bounce water, wind-driven rain and external rain accumulation) or to condensation. Timber is in direct contact with a porous material that can absorb water. Timber cannot dry rapidly.
- Risk class 5 (R5): timber can get wet due to outdoor weather (direct rain, bounce water, wind-driven rain and external rain accumulation) or to condensation. Timber is prevented from drying and water that comes in contact with timber cannot run out.

As a preliminary approach, a fast and straightforward evaluation of the decay is assessed through functions available in literature that estimate the depth of the fungal attack (Leicester *et al.,* 2008). According to Wang *et al.* (2008c), the decay depth d_t is evaluated through equation (1) as a function of the time *t* and the slope *r*

$$d_t = \begin{cases} 0 & , \quad t < lag \\ (t - lag)r, & t \geq lag \end{cases} \tag{1}$$

where $r = k_{wood} k_{geometry} k_{climate}$ and *lag* is a function of *r.* The parameters k_{wood} and $k_{geometry}$ are constant values that depend on the wood species, on the location of timber within the detail and on the interaction between timber and the other elements (as defined in Wang *et al.,* 2008c). The parameter $k_{climate}$ depends on the amount of water (from precipitation) penetrating the detail and on such water can dry off.

In order to consider the contribution of condensation, equation (2) is proposed, where the term $t_{wet,cond}$ is added to the equation proposed by Wang *et al.* (2008c).

$$k_{climate} = 0.03(t_{wet,rain} + t_{wet,cond})^{0.4} \tag{2}$$

$$\begin{cases} t_{wet,rain} = \sum_{i=1}^{12} (t_{rain} - t_{drying})_i \ , & (t_{rain} - t_{drying})_i \geq 0 \\ t_{wet,cond} = \sum_{i=1}^{12} (t_{cond} - t_{drying})_i \ , & (t_{cond} - t_{drying})_i \geq 0 \end{cases} \tag{3}$$

The "duration parameters" t_{cond}, t_{drying} and t_{rain} in equation (3), must be evaluated based on the assigned risk class. The relation between the risk classes and these parameters is reported in Table 1.

Table 1. Relations between the duration parameters and the risk classes.

R	$\boldsymbol{t_{rain}}$ [hour/month]	$\boldsymbol{t_{cond}}$ [hour/month]	$\boldsymbol{t_{drying}}$ [hour/month]
1	0	0	∞
2	0	To be evaluated	To be evaluated
3.1	To be evaluated	To be evaluated	To be evaluated
3.2	To be evaluated	To be evaluated	To be evaluated

4	720	To be evaluated	To be evaluated
5	720	To be evaluated	0

In the cases where t_{rain} and t_{drying} must be evaluated, suitable methods can be found in Wang *et al.* (2008c). The t_{cond} indicates the number of hours per month in which timber is wet because of condensation and it can be calculated by referring to well-established methods for the hygrothermal analysis of buildings. Leakage coming from the inside of a building was not considered in the present study for the sake of simplicity, but suitable approaches can be found in Wang *et al.* (2008c).

3 Decision Trees

The WFD in timber buildings can be classified through decision trees whose branches account for the various conditions which may occur and affect the durability of the timber structural components. For brevity, only the decision trees related to the three case studies selected to compare the results are presented.

The background material for developing the decision tree included prominent European standards in the field of durability of timber structures such as ÖNORM B 2320:2017 and DIN 68800-2:2012-02.

The most relevant parameter is the distance of the base-surface of the timber element from the ground surface. This distance *H* is positive when the position of the timber base-surface is higher than the ground surface, negative otherwise.

In the three case studies selected, *H* was always less than 10 centimetres, so two conditions were considered in the following: (a) *H* greater or equal to 0 cm, but lower than 10 cm, and (b) *H* lower than 0 cm. A decision tree was defined only for the first scenario since risk class R5 was always assigned to the second one. Figure 1 shows the two decision trees defined for the $0\ cm \leq H < 10\ cm$ (Gaspari *et al.,* 2020).

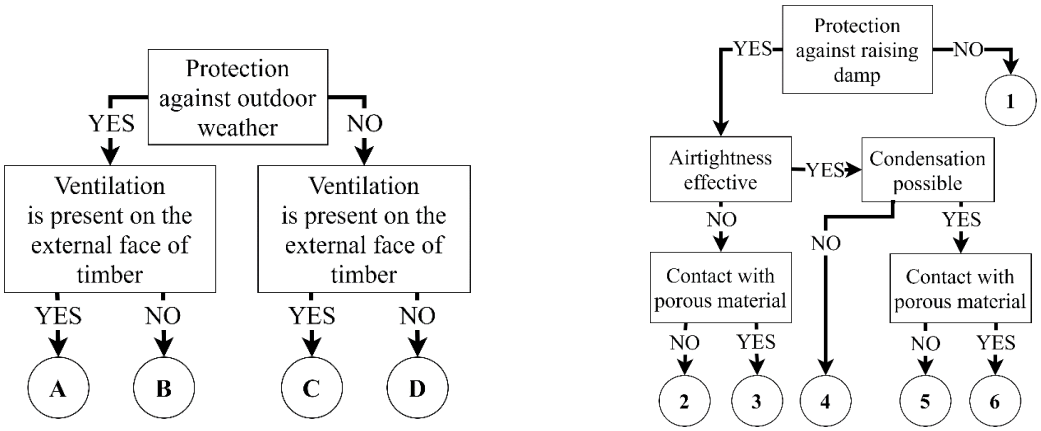

(a) (b)

Figure 1. Decision tree (a) DT1 and (b) DT2 for $\mathbf{0\ cm \leq H < 10\ cm}$.

The decision tree DT1 shown in Figure 1 (a) considers outdoor weather (direct rain, bounce water, wind-driven rain and external rain accumulation) and the possibility of timber drying off

due to ventilation. This tree results in 4 different conditions, from A to D. Decision tree DT2, reported in Figure 1 (b), takes into account the rising damp issue, the building airtightness and whether timber is in contact with porous material or not. This second tree leads to 6 conditions. These two trees are independent from one another, but both must be used for the evaluation of the detail. All combinations of the results from the two trees are shown in Table 2 (Gaspari *et al.,* 2020).

Table 2. Risk classes definition for the combination of DT1 and DT2.

	DT1			
DT2	**A**	**B**	**C**	**D**
1	4	4	4	5
2	3.1	3.2	3.1	5
3	4	4	4	5
4	1	4	3.1	5
5	2	2	3.1	5
6	4	4	4	5

In the preliminary procedure for the decay estimation, additional aspects must be specified in order to assess the decay estimation properly. In fact, decay estimation functions are typically defined for a single face of the timber element. However, depending on the geometry of the WFD and on the contact between timber and other materials, multiple faces can be affected by decay. These additional aspects are provided in Table 3.

Table 3. Additional aspects for the combination of DT1 and DT2.

	DT1			
DT2	**A**	**B**	**C**	**D**
1	A3	A4	A3	A3
2	A2	A4	A2	A3
3	A2	A4	A2	A3
4	A1	A4	A2	A3
5	A2	A4	A2	A3
6	A2	A4	A2	A3

The aspects reported in Table 3 are defined as follows, considering the internal and external faces of timber.

- A1: decay due to leakage must be evaluated solely on the internal face.
- A2: decay must be evaluated on the external face and eventually on the internal face due to leakage.
- A3: decay must be evaluated on both faces.
- A4: decay must be evaluated on the external face and eventually on the internal face due to leakage. Moreover, if the internal face of timber is in contact with a scarcely permeable material or $H_{int} < 0\ cm$, R5 risk class must be selected.

Considering a linear element (for example a post or a beam), if decay is present on both internal and external faces, the same depth of the fungal attack must be considered on the

lateral faces. The same must be done if decay is present on one face and a porous insulation is in contact with timber.

Finally, the leakage contribution must be considered only if $H_{int} \leq 5\ cm$.

4 Results

In this section the WFD of three case studies is analysed by applying the decision trees. Then, the preliminary procedure for the estimation of the decay is applied to the case studies and a final comparison is reported.

The case studies have been described in detail in Gaspari *et al.* (2020), while just a brief description is provided herein. Table 4 gives an overview on these case studies.

Table 4. Overview of the case studies.

Case study	Structural typology	Year of construction	Year of inspection	Element analysed	Dimensions [mm]	
					Thickness	Width
A	Light-frame	2007	2018	Post	140	80
B	Light-frame	2009	2018	Post	160	180
C	CLT	2015	2017	CLT	160	200

For case study C where the timber component is a CLT panel, a reference width of 200 mm corresponding to the width of a single wood-board of the CLT panel was selected.

In case study A, the distance of the base-surface of the post from the ground is set to *H = 0 cm*. In fact, in this case the base-surface of the timber element is at the same level of the ground surface. There are no waterproof membranes; protection against outdoor weather and ventilation are also absent. These conditions lead to path D in DT1 and to path 1 in DT2. The combination of paths D and 1 determines a risk class R5 with the additional condition A3. In case study A the element studied is a post and because both external and internal faces must be evaluated, then all four faces must be evaluated.

In case study C, the base of the post is set to *H = -23 cm* and consequently a risk class R5 was assigned to the detail. All faces of the post must be evaluated.

Case study C presents a CLT wall with *H = 0 cm.* The CLT wall is not properly protected against outdoor weather and ventilation is absent. Moreover, a hygro-thermal analysis verified the absence of accumulation of condensation. These conditions lead to path D in DT1 and path 4 in DT2. The combination of paths D and 1 results in assigning risk class R5 with the additional condition A3.

In order to evaluate correctly the decay of the CLT panel, the lateral faces of the board were considered. In fact, cracks and long-term effects on CLT boards usually lead to preferential paths for water to penetrate into the CLT.

Case studies A, B and C were inspected after 11, 9 and 3 years after construction, respectively. Case studies A and B showed 0 % of residual timber cross-section, where the residual cross-section is the ratio between the timber cross-section area in sound conditions at the time of the inspection and the original timber cross-section at the time of construction. Case study C showed a residual cross-section of approximately 60 %. The comparison between the outcomes of the inspections and the results of the model has been reported in Figure 2.

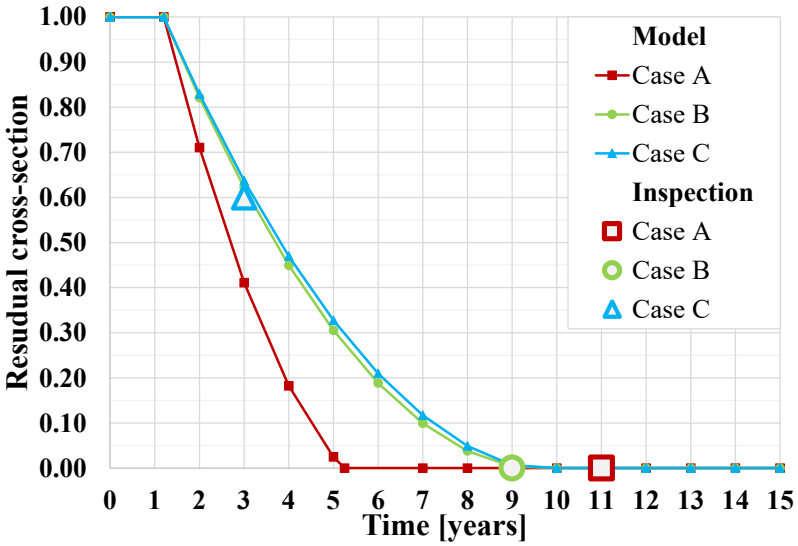

Figure 2. Comparison between the observations from the case-study inspections and the results of the analytical model.

5 Conclusions

This paper proposes a methodology to categorise the Wall-Foundation Detail (WFD) of timber structures in relation with the durability of the timber structural element. Risk classes were defined looking at the prominent standards that treat the topic of the durability of timber. The risk classes can be assigned to the WFD via decision trees designed to consider the main aspects that can affect the durability of this construction detail in relation with fungal attack. This was the first step to develop a reliable method capable of predicting the life-expectancy of timber construction details. Future research steps, as a part of the TSafe project, will involve more sophisticated tools such as Heat, Air and Moisture analysis, machine learning and a combination of both. For a preliminary validation of the overall analysis approach, three case studies were selected and studied using the methodology proposed herein. A good correspondence was observed from the comparison between the results of the proposed methodology and the onsite inspections.

Acknowledgements

The authors gratefully acknowledge FederlegnoArredo and ReLUIS Project framework 2019-2021 (funded by the Italian Emergency Management Agency, DPC) for the financial support given to the research. Ri-Legno S.r.l and ReWIS are thanked for providing the data relative to the case-studies.

ORCID

Andrea Gaspari: https://orcid.org/0000-0001-7779-6578
Ivan Giongo: https://orcid.org/0000-0002-3867-2334
Maurizio Piazza: https://orcid.org/0000-0001-6279-4860

References

ASI (2017). *ÖNORM B 3802-1:2015, Protection of timber used in buildings - Part 1: General* (in German), Austrian Standards Institute.

ASI (2017). *ÖNORM B 2320:2017, Wooden residential houses - Technical requirements* (in German), Austrian Standards Institute.

Brischke, C. and Thelandersson, S. (2014). Modelling the outdoor performance of wood products – A review on existing approaches, *Construction and Building Materials, 66*, 384-397. doi: 10.1016/j.conbuildmat.2014.05.087

Carbonez, K., Van Den Bossche, N., Ge, H. and Janssens, A. (2015). Comparison between uniform rain loads and point sources to simulate rainwater leakage with commercial HAM-models. *Proceedings of International Symposium on Building Pathology*, Porto, Portugal.

CEN (2013). *EN 335:2013, Durability of wood and wood-based products - Use classes: definitions, application to solid wood and wood-based products*, European Committee for Standardization.

Chung, D., Wen, J. and Lo, L. J. (2019). Development and verification of the open source platform, HAM-Tools, for hygrothermal performance simulation of buildings using a stochastic approach. *Building Simulation, 13,* 497-514. doi: 10.1007/s12273-019-0594-5

DIN (2019). *DIN 68800-1:2019-06, Wood preservation - Part 1: General* (in German), German Institute for Standardization.

DIN (2012). *DIN 68800-2:2012-02, Wood preservation - Part 2: Preventive constructional measures in buildings* (in German), German Institute for Standardization.

Freire, R. Z., Santos, G. H. and Coelho, L. S. (2017). Hygrothermal Dynamic and Mould Growth Risk Predictions for Concrete Tiles by Using Least Squares Support Vector Machines. *Energies, 10(8),* 1093. doi: 10.3390/en10081093

Gaspari, A., Canetti, D., Sartori, T. and Giongo, I. (2020). Analytical evaluation of the durability of timber structures - The case of the wall-foundation construction detail (in Italian), *Structural, 227*. doi: 10.12917/STRU227.05

Glavind, S. T., Sepùlveda, J. G., Qin, J. and Faber, M. H. (2019). Systems Modeling Using Big Data Analysis Techniques and Evidence. *Proceedings of the 4th International Conference on Systems Reliability and Safety (ICSRS 2019)*, Rome, Italy.

Leicester, R., Wang, C-H., Nguyen, M., Foliente, G., Cole, I. and MacKenzie, C. (2008). Engineered Durability: Completion of a 10-year Project, *Proceedings of the World Conference of Timber Engineering (WCTE2008)*, Miyazaki, Japan, Paper No. 403.

Lstiburek, J., Ueno, K. and Musunuru, S. (2016a). *Strategy Guideline: Modeling Enclosure Design in Above-Grade Walls*. Office of Scientific and Technical Information (OSTI).

Lstiburek, J., Ueno, K. and Musunuru, S. (2016b). *Modelling Enclosure Design in Above-Grade Walls*. Office of Scientific and Technical Information (OSTI).

Meyer, L., Brischke, C. and Källander, B. (2017). Testing the durability of timber above ground: Evaluation of different test methods. *European Journal of Wood and Wood Products, 75*, 291–304. doi: 10.1007/s00107-016-1137-8

Meyer, L., Brischke, C. and Preston, A. (2016). Testing the durability of timber above ground: A review on methodology. *Wood Material Science & Engineering, 11(5),* 238–304. doi: 10.1080/17480272.2014.983163

Profft, I., Mund, M., Weber, G., Weller, E. and Schulze, E. (2009). Forest management and carbon sequestration in wood products. *European Journal of Forest Research, 128*, 399–413. doi: 10.1007/s10342-009-0283-5

Wang, C. H., Leicester, R. H. and Nguyen, M. N. (2008). *Manual 3 - Decay in ground contact*, Forest & Wood Products Australia Limited.

Wang, C. H., Leicester, R. H. and Nguyen, M. N. (2008). *Manual 4 - Decay above- ground*, Forest & Wood Products Australia Limited.

Wang, C. H., Leicester, R. H. and Nguyen, M. N. (2008). *Manual 9 - Models for timber produced in building envelope*, Forest & Wood Products Australia Limited.

XV International Conference on Durability of Building Materials and Components
DBMC 2020, Barcelona
C. Serrat, J.R. Casas and V. Gibert (Eds)

A Spatially Continuous Driving Rain Map of India at 0.5°×0.5° Gridded Scale

Sneha Das[1] **and Kaustav Sarkar**[2]

[1]School of Engineering, Indian Institute of Technology Mandi, Kamand, Himachal Pradesh-175075, India, D16031@students.iitmandi.ac.in

[2]School of Engineering, Indian Institute of Technology Mandi, Kamand, Himachal Pradesh-175075, India, srkr@iitmandi.ac.in

Abstract. *Driving rain is one of the most critical sources of moisture affecting the hygrothermal and durability performance of building envelopes. The estimation of severity in terms of annual driving rain indices using annual and monthly weather data (aaDRI and maDRI respectively) aids towards contemplating potential moisture loads, and hence in the efficient design of buildings in the geographical area of interest. In this study, monthly and annual gridded datasets of wind and rainfall, pertaining to the thirty-year period of 1988-2017 have been used to design a spatially continuous driving rain map for India at 0.5°×0.5° (lat./long.) resolution. The observations reveal that the use of annually averaged data leads to underestimation of the driving rain severity thereby highlighting the inefficiency of a coarser temporal scale. A linear relationship has subsequently been developed to enable refinement of aaDRI into maDRI. The analysis of the monthly driving rain map reveals that the entire western coastal belt and a few regions in the north-eastern part of the country observe high to severe exposure conditions. Furthermore, a trend analysis of the yearly driving rain index values reveals statistically significant decreasing trends over the northern and eastern regions of the country, whereas increasing trends in the shielded regions surrounding central India is observed.*

Keywords: *Driving Rain Map, Gridded Data, Trend Analysis, India.*

1 Introduction

Durability performance of built facilities is a function of both the material characteristics and the environment to which they are exposed. The exposure conditions that primarily affect the durability include temperature and moisture conditions. The presence of moisture initiates and escalates numerous deterioration processes in building materials. Damage is often inflicted in the form of cracks and/or spalling of surface due to corrosion of reinforcement, and salt migration and crystallization (Broomfield, 2003; Charola, 2000; Neville, 1995). Prolonged dampness also leads to efflorescence and mold growth, which affects the aesthetics as well as the indoor air quality of buildings (Gaylarde *et al*., 2002; Bornehag *et al.*, 2001). Moisture accumulation in porous materials causes frost damage and a reduction in thermal insulation of the building envelope (Bhattacharjee, 2013; Jerman and Černý, 2012). The intricate and multifaceted impact of moisture on the performance of buildings invokes the need to realistically estimate the severity of moisture exposure.

Wind Driven Rain (WDR) is an important source of moisture affecting the hygrothermal performance and durability of building facades (Blocken *et al*., 2009). A significant development in the field of WDR research was associated with the field observations made

by Lacy (1965) and Hoppestad (1955), which established the proportionality of WDR intensity $\left(R_{wdr}\right)$, to horizontal rainfall $\left(R_h\right)$, and the wind speed (U). This proportionality relationship led to the development of WDR index $\left(R_h * U\right)$, and its application to map the driving rain severity in several countries (Narula *et al.*, 2017; Pérez-Bella *et al.*, 2012; Giarma, 2011; Chand and Bhargava, 2002). A schematic representation of WDR is depicted in Fig. 1.

The accuracy and reliability of such maps depend upon the spatial and temporal resolution of available meteorological data. The station records available in a country are often limited and lack temporal completeness. Gridded weather data poses a viable solution in this regard owing to their temporal and spatial consistency (Das *et al*., 2020). This study utilizes monthly average wind and rainfall gridded data to determine the *maDRI* and *aaDRI* at a spatial resolution of $0.5° \times 0.5°$ for the Indian subcontinent.

To the best of the authors' knowledge, the WDR map generated in this study offers the finest spatial resolution at which the *maDRI* and *aaDRI* have been mapped for Indian mainland. The numerical efficiency of the gridded data and the developed index is also verified by comparing the relationship between *maDRI* and *aaDRI* against previously reported studies by Chand and Bhargava (2002) and Narula *et al*. (2017). The results of this study are in close conformance with the previous studies. The study also extends to the trend analysis of driving rain index for the recent 30 years of weather records (1988-2017). Trend analysis of the WDR over India shows a receding trend of moisture loads over the country.

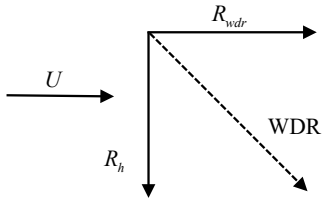

Figure 1. Components of wind-driven rain (WDR).

2 Gridded Data

Gridded datasets are interpolated products constituted using observations from sources like station observations, satellites, ships etc. and have the benefit of temporal continuity and spatial coverage. The present study uses gridded datasets of rainfall and wind for the determination of driving rain severity. The study uses thirty years of rainfall and wind data from 1988-2017.

2.1 Rainfall Data

Rainfall gridded dataset at a monthly scale has been obtained from the Climatic Research Unit (CRU) - version CRU TS v4.02. The data is based on station observations collected from reliable international agencies and covers all land masses excluding the Antarctica region at $0.5° \times 0.5°$ (lat./long.) resolution. The stations selected for the generation of data at individual grids is subjected to the criteria of minimum 75% data availability for the base period, 1961-1990 (Harris *et al.,* 2014). Out of the global dataset, rainfall data for 1179 grids pertaining to

the duration 1988-2017 have been extracted, which encompasses the geographical stretch of India lying within a rectangular region extending between 6.5°N - 37.5°N to 66.5°E - 101.5°E.

2.2 Wind Data

Monthly wind data have been obtained from the web repositories of the National Oceanic and Atmospheric Administration (NOAA). The dataset is available at a spatial resolution of $2.5° \times 2.5°$ between 90°N - 90°S and 0°E - 357.5°E (NOAA, 2019). Both horizontal and vertical components of wind records for India which comprises of 1179 grid values, have been extracted from the primary global dataset. The extracted records for the Indian region have been re-gridded to a resolution of $0.5° \times 0.5°$ for the purpose of this study using bilinear interpolation. The resultant wind vector was determined as: $\left(u^2 + v^2\right)^{0.5}$ where u and v are the horizontal and vertical wind components respectively.

3 Driving Rain Index

3.1 Calculation of *maDRI* and *aaDRI*

The procedure for determination of *maDRI* and *aaDRI* is adopted from previous studies (Chand and Bhargava, 2002; Giarma and Aravantinos, 2011). Firstly, the monthly driving rain index (*mDRI*) for each of the 12 months have been calculated using Eq. 1 and then the *maDRI* has been calculated using Eq. 2.

$$mDRI = \left(\sum_{i=1}^{N} W_{month,i} / N\right)\left(\sum_{i=1}^{N} R_{month,i} / N\right) \tag{1}$$

$$maDRI = \sum_{i=1}^{12} mDRI \tag{2}$$

where, *maDRI* is in m^2/s, W_{month} is the monthly average wind speed in *m/s*, R_{month} is the monthly total rainfall in *m*, *N* is the number of years under consideration. The estimation of *mDRI* can be carried out by including the cases for which rainfall is zero, or by excluding such instances for averaging of the rainfall. The latter approach is expected to provide a more realistic depiction. In this study, the *mDRI* values have been determined by both approaches to assess the differences in results obtained by the two approaches.

The *aaDRI* has been calculated as the product of average annual wind speed and average annual rainfall, as stated in Eq. 3.

$$aaDRI = \left(\sum_{i=1}^{N} W_{year,i} / N\right)\left(\sum_{i=1}^{N} R_{year,i} / N\right) \tag{3}$$

where *aaDRI* is in m^2/s, W_{year} is the annual average wind speed in *m/s*, R_{year} is the annual total rainfall in *m*, *N* is the number of years under consideration.

Based on the values of indices calculated using Eqs. 2 and 3, the exposure conditions have been categorized into four classes after Lacy (1977), namely, shielded, moderate, high, and severe for the ranges of [0,3), [3,7), [7,11), and [11, ∞), respectively. This classification has been subsequently used towards the development of *maDRI* and *aaDRI* maps for India.

Often meteorological data are not available at a monthly temporal scale. This study, therefore, establishes a relationship between *aaDRI* and *maDRI* to facilitate estimation of the latter from annual meteorological records which are often available.

3.2 Trend Analysis

A trend analysis of the yearly driving rain index (*yDRI*) has been carried out to ascertain the increasing or decreasing pattern of driving rain severity across the subcontinent. Mann-Kendall (MK) test is a non-parametric test commonly used to statistically assess any monotonic upward or downward trend in a time series data (Mann, 1945). The present study uses this test to identify the existence of trends in the manifestation of driving rain over the Indian mainland. In this test, the null hypothesis is that data comes from a sample of independent realizations, and hence there is no trend in the data, whereas the alternative hypothesis states that a monotonic trend exists. The MK test statistic is calculated using Eqs. 4 and 5:

$$S = \sum_{k=1}^{n-1} \sum_{j=k+1}^{n} \operatorname{sgn}\left(X_j - X_k\right) \tag{4}$$

such that,

$$\operatorname{sgn}(X_j - X_k) = \begin{cases} 1, \ if \ (X_j - X_k) > 0 \\ 0, \ if \ (X_j - X_k) = 0 \\ -1, \ if \ (X_j - X_k) < 0 \end{cases} \tag{5}$$

Here, $j \neq k$, and $j, k \leq n$, where n is the number of data points. The z-statistic is then computed as stated in Eq. 6:

$$Z_s = \begin{cases} \dfrac{S-1}{\sqrt{Var(S)}}, S > 0 \\ 0, \quad S = 0 \\ \dfrac{S+1}{\sqrt{Var(S)}}, S < 0 \end{cases} \tag{6}$$

If $|Z_s| > Z_{1-\alpha/2}$ ($Z_{1-\alpha/2}$ can be obtained from standard normal distribution level), then the null hypothesis is rejected. In the present study, the test is carried out at $\alpha = 0.05$ significance level. The trend analysis is also supported by the determination of Sen's slope. The Sens's slope (β) assists in the determination of direction of the existing trend. In the case of driving rain, the Sen's slope estimates if the driving rain severity is decreasing or increasing. This helps a designer to contemplate if a building will be exposed to a greater moisture load and thereby help towards efficient design of facade elements.

4 Results and Discussions

4.1 Driving Rain of India Based on *maDRI* and *aaDRI*

Figs. 2a and 2b represent the *maDRI* maps obtained respectively by including and excluding the cases for which rainfall is zero. It was observed that there is no significant difference between the *maDRI* maps developed using the two approaches. The plots reveal that the

shielded exposure region covers major area of northern part of the country, along with parts of central, western, and south-western India. The moderate exposure covers the entire eastern coastal belt and majority of north-eastern India, in addition to parts of western and central India. The high and severe exposure condition, is observed by the western coastal belt of India and parts of north-east. This observation is common for both the approaches adopted in the determination of *maDRI*. The percentage of land area covered by each of the exposure categories using the latter approach are 63.36%, 33.42%, 1.95%, and 1.27% respectively in increasing order of severity. This is in contrast with the observations made by Narula *et al.* (2017), in which most of the mainland of India was reported to observe moderate exposure condition. The present analysis using the most recent 30 years of data observes a shift in the severity level to the shielded conditions. This is indicative of the receding pattern of driving rain loads for the subcontinent.

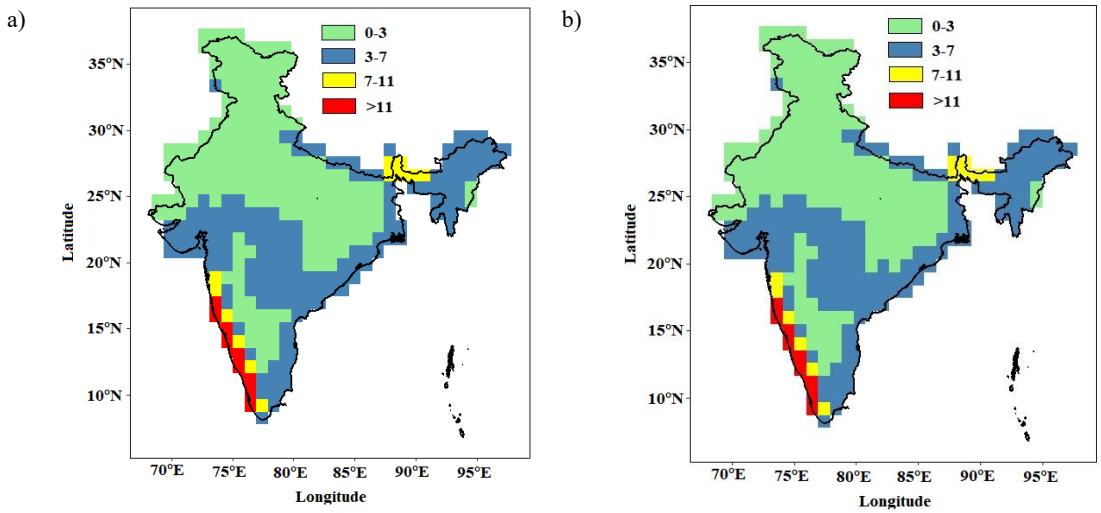

Figure 2. Driving rain map of India based on *maDRI* (a) including and (b) excluding months with no rainfall.

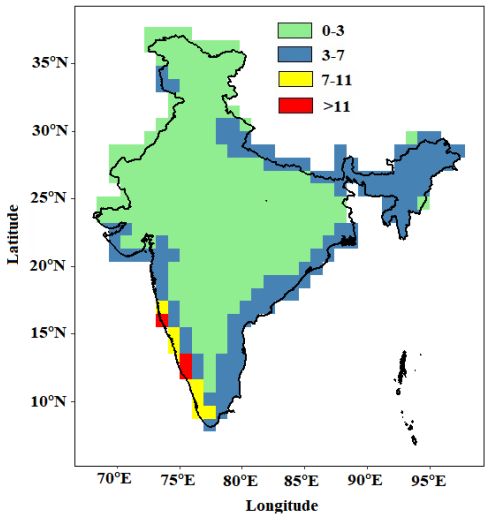

Figure 3. Driving rain map of India based on *aaDRI.*

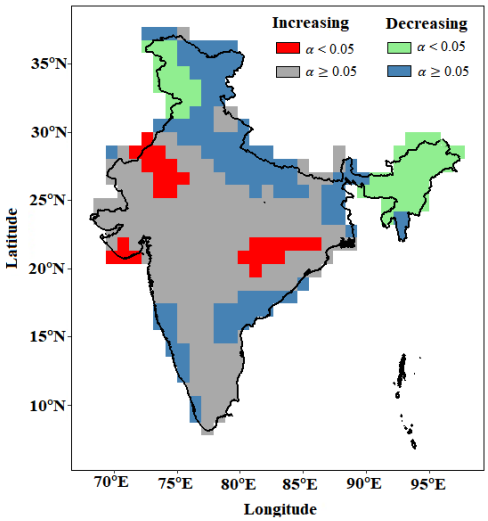

Figure 4. Trend analysis of WDR based on *yDRI.*

Fig. 3 shows the *aaDRI* map of India. Comparison of the *aaDRI* map with *maDRI* map shows a significant increase in the number of grids observing shielded exposure conditions. The percentage of area covered by each exposure category based on *aaDRI* is 77.01%, 21.37%, 1.36%, and 0.25%, respectively, in increasing order of severity. The observation suggests that implementation of *aaDRI* underestimates the driving rain severity at a given location. Therefore, *maDRI* is a more reliable choice for contemplating driving rain severity. For instances when meteorological records are not available at a finer temporal scale, the *aaDRI* can be used towards estimation of *maDRI*. In the following section, a relationship between *maDRI* and *aaDRI* has been established to facilitate the objective.

4.2 Relationship Between *maDRI* and *aaDRI*

The scatter plot between *maDRI* and *aaDRI* values presented in Fig. 5 indicates a fairly strong linear relationship between the two indices. This was also reported in previous studies for India. The relationship obtained between the two indices is given in Eq. 7 and those reported by Chand and Bhargava (2002) and Narula *et al.* (2017) are stated in Eqs. 8 and 9, respectively:

$$maDRI = 1.29 aaDRI - 0.28 \tag{7}$$

$$maDRI = 1.24 aaDRI - 0.18 \tag{8}$$

$$maDRI = 1.23 aaDRI - 0.32 \tag{9}$$

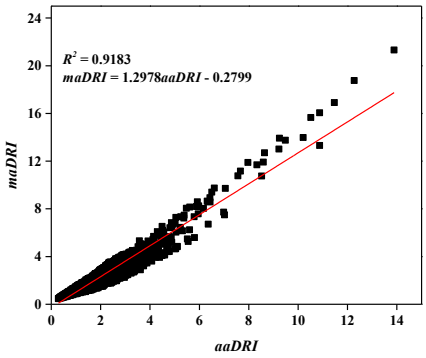

Figure 5. Relationship between *maDRI* and *aaDRI*.

A fair degree of match is observed between the expression reported in this study and those from the previous studies. This indicates the reliability of the indices determined using 0.5°×0.5° gridded data in the present study. The relationship would also aid towards the estimation of *maDRI* from *aaDRI* in instances wherein meteorological records of wind and rainfall are not available at a fine temporal resolution.

4.3 Trend Analysis Based on Yearly Driving Rain Index

This study extends to the determination of any existing trend between the driving rain index for the considered 30 years of data. This is facilitated by determination of yearly driving rain index (*yDRI)* for each year, calculated as stated in Eq. 10:

$$yDRI = (Total\ rainfall\ in\ a\ year) \times \left(Average\ rainfall\ in\ a\ year \right) \quad (10)$$

Rainfall in expressed in *m*, and the average wind speed is expressed in *m/s*. The objective is facilitated by conducting MK test and determination of Sen's slope for each of the grid as discussed in section 3.2. Fig. 4 shows the plot of trend analysis for each of the 1179 grids at 5% significance (α). It can be observed from Fig. 4 that, there exists significant negative trend in northern and north-eastern part of the country, where as significant positive trend is observed by parts of western and south-western India which observe shielded exposure condition. The value of β ranged between [-0.10, 0.04] which is fairly similar to the range of [-0.12, 0.03] as was reported by Narula *et al*. (2017). Out of the total number of grids exhibiting significant trend, 61.53% observe a negative trend in severity.

5 Summary and Conclusion

The present study assesses the severity of prevailing moisture loads on buildings in India at a spatial resolution of 0.5° × 0.5° using gridded records of wind and rainfall data. This assessment has been facilitated by the computation of *maDRI* and *aaDRI.* Trend analysis of yearly driving rain index has also been carried out at a 5% significance level to determine the temporal evolution of the relative severity of moisture loads. The major findings and contributions of this study are as follows:

- *aaDRI* and *maDRI* maps for India at 0.5°×0.5° spatial resolution have been developed.
- The *maDRI* map developed is apt for the assessment of relative severity of moisture loads for India. Zones of shielded, moderate, high, and severe exposure condition correspond to 63.36%, 33.42%, 1.95%, and 1.27% respectively of the total land area.
- There has been a decline in moisture loads manifesting on buildings. Majority of the area has been observed to be under shielded exposure condition, in comparison to a previous study wherein maximum area was reported to be under moderate exposure condition.
- *maDRI* and *aaDRI* exhibit strong linear relationship which is in compliance with previous studies, thus indicating the reliability of the equation developed (Eq. 7) for the determination of *maDRI.*
- Trend analysis of the *yDRI* values reveals statistically significant decreasing trends over the northern and eastern regions of the country whereas increasing trends in the shielded regions surrounding central India.
- The limitation of the reported results lies in the unavailability of fine resolution gridded wind data from ground observations and the lack of grid-to-point comparison of gridded datasets with respect to station data in order to assess the reliability of the gridded weather datasets.

The study can be further be extended towards the determination of daily driving rain index for the same spatial resolution subjected to the availability of data. This is expected to provide a better representation of the prevailing moisture loads on building envelopes in India.

Acknowledgements

The authors acknowledge the ECR grant (No. ECR/2016/001240) provided by SERB, DST for the project "Modelling of hydraulic diffusivity and its application in FE-simulation of moisture transport in concrete for assessing corrosion risk."

ORCID

Sneha Das: https://orcid.org/0000-0003-2262-671X
Kaustav Sarkar: https://orcid.org/0000-0002-8541-1866

References

Bhattacharjee, B. (2013). Moisture influence on the thermal properties of materials in building envelopes and sustainability in tropical climates. In *ICSDEC 2012: Developing the Frontier of Sustainable Design, Engineering, and Construction*, 765-774.

Blocken, B., Abuku, M., Roels, S. and Carmeliet, J. (2009). Wind-driven rain on building facades: some perspectives. *EACWE*, *5*, 19-23.

Bornehag, C.G., Blomquist, G., Gyntelberg, F., Järvholm, B., Malmberg, P., Nordvall L, Nielsen, A., Pershagen G. and Sundell. J. (2001). Dampness in buildings and health. review. Nordic Interdisciplinary review of the Scientific Evidence on Associations between Exposure to Dampness in Buildings and Health Effects (NOrDDAMP). *Indoor Air*, *11*, 72-86.

Broomfield, J.P. (2006). Corrosion of steel in concrete: understanding, investigation and repair. *CRC Press*.

Chand, I. and Bhargava, P.K. (2002). Estimation of driving rain index for India. *Building and Environment*, *37*(5), 549-554.

Charola, A.E. (2000). Salts in the deterioration of porous materials: an overview. *Journal of the American institute for conservation*, *39*(3), 327-343.

Das, S., Narula, P. and Sarkar, K. (2020). Design of intermittent rainfall-pattern for structures with gridded data: Validation and implementation. *Journal of Building Engineering*, *27*, 100939.

Gaylarde, C., Silva, M.R. and Warscheid, T. (2003). Microbial impact on building materials: an overview. *Materials and Structures*, *36*(5), 342-352.

Giarma, C. and Aravantinos, D. (2011). Estimation of building components' exposure to moisture in Greece based on wind, rainfall and other climatic data. *Journal of Wind Engineering and Industrial Aerodynamics*, *99*(2-3), 91-102.

Harris, I.P.D.J., Jones, P.D., Osborn, T.J. and Lister, D.H. (2014). Updated high- resolution grids of monthly climatic observations–the CRU TS3. 10 Dataset. *International journal of climatology*, *34*(3), 623-642.

Hoppestad, S. (1955). Slagregn i Norge (Driving rain in Norway). *NBI Rep*, *13*.

Jerman, M. and Černý, R. (2012). Effect of moisture content on heat and moisture transport and storage properties of thermal insulation materials. *Energy and Buildings*, *53*, 39-46.

Lacy, R.E. (1965). Driving rain maps and the onslaught of rain on buildings. In *Proc. of CIB/RILEM Symposium on Moisture Problems in Buildings, Helsinki, 1965*.

Lacy, R.E. (1977). Climate and building in Britain.

Mann, H.B. (1945). Non-parametric tests against trend. Econometria. *1945. 246*.

Narula, P., Sarkar, K. and Azad, S. (2017). Driving rain indices for India at 1°× 1° gridded scale. *Journal of Wind Engineering and Industrial Aerodynamics*, *161*, 1-8.

National Oceanic and Atmospheric Administration (NOAA), (2019). (http://www/esrl.noaa.gov/psd/data/gridded/data.ncep.reanalysis.derived.surface.html).

Neville, A. (1995). Chloride attack of reinforced concrete: an overview. *Materials and Structures*, *28(2)*, 63.

Pérez-Bella, J.M., Domínguez-Hernández, J., Rodríguez-Soria, B., del Coz-Díaz, J.J. and Cano-Suñén, E. (2012). Estimation of the exposure of buildings to driving rain in Spain from daily wind and rain data. *Building and Environment*, *57*, 259-270.

XV International Conference on Durability of Building Materials and Components
DBMC 2020, Barcelona
C. Serrat, J.R. Casas and V. Gibert (Eds)

Development of a Service Life Database of Building Elements Based on an International Data Collection

Kyriaki Goulouti, Morgane Giorgi, Didier Favre and Sébastien Lasvaux

Laboratory of Solar Energetics and Building Physics (IGT-LESBAT), HEIG-VD, University of Applied Sciences of Western Switzerland (HES-SO), Yverdon-les-Bains, Switzerland,
sebastien.lasvaux@hes-so.ch

Abstract. *This paper presents a new service life database (DUREE database) for building elements, based on international service life data. The database includes 7'000 service life data, for more than 2'000 building elements. In addition, the fitting of the data to a lognormal distribution is presented. The study contributes to the increasing demand of probabilistic building LCA and LCC and provides the possibility to define statistical distributions, with a systematic way, for a large number of building elements and different levels of details (LOD), appropriate for BIM-based assessments.*

Keywords: *Service Life, LCA, LCC, Lognormal Distribution, Probabilistic Analysis.*

1 Introduction

Reliability issues in life cycle studies, *i.e.* Life Cycle Assessment (LCA) or Life Cycle Cost (LCC) analysis have been long discussed (Björklund, 2002; Huijbregts, 1998). Different methods have been proposed to enhance the confidence in the LCA results, *i.e*. uncertainty and sensitivity analyses, as summarized in Pannier (2018) for the building sector. Reducing the variability and uncertainty of the input parameters, increase the accuracy of the LCA or LCC result. Among the different parameters that present significant uncertainty and influence the building LCA accuracy is the service life of the building elements, as it has been shown by different studies, *e.g.* (Grant and Ries, 2013). The service life mainly influences the use phase through the replacement of the building elements. For instance, in rescent LCA studies, the replacement stage can account for up to 36% of the greenhouse gas emissions (GHG) of a multifamily house (Goulouti *et al.*, 2019).

The term *'service life'* (or lifetime) can be understood and defined in various ways, depending on the scope of the final user *e.g.* building designer, owner, LCA or LCC expert (Lasvaux *et al.*, 2019). According to Thiebat (2019), the service life of a building can be classified into physical, functional or economic service life. The physical service life corresponds to the lifetime allowed by physical degradation procedures, contrary to the functional one that additionally takes into account the *'performance/requirements ratio'*, while the economic service life corresponds to the residual economic value. Furthermore, the international standard ISO 15686, (ISO 15686:2011), distinguishes among the service life, the reference service life, the estimated service life, the predicted service life and the service life during the design. In the Swiss context, the Swiss Society of Architects and Engineers (SIA) differentiates the technical service life (SIA 2047, 2015; SIA 480, 2016), from the useful life (SIA 2047, 2015; SIA 260, 2003; SIA 480, 2016) or the amortization period (SIA 2032, 2010), used for LCA calculations.

doi:10.23967/dbmc.2020.035

There are multiple studies, as summarized in Silvestre *et al.*, (2015) that discuss the ways the service life is estimated, mainly through the deterministic, the probabilistic and engineering method. However, in practice, the attribution of the building elements service life is based on standardized values, from technical standards, as for example in Switzerland, in the SIA 2032 technical book (SIA 2032, 2010). Apart from the technical parameters that affect the duration of service life, different scientific studies, as summarized in (Goulouti *et al.*, 2019; Volland *et al.*, 2019) have identified a variety of non-technical, socio-economic parameters that additionally affect the service lives of building elements.

Hence, there is a variability linked to the definition and the corresponding estimation of service life and there is no general agreement about the service life data, among the studies, as it is also stated in Dixit (2017). Furthermore, in the literature, there are different ways of decomposing buildings and attributing the service life, *i.e.* either at the functional or at the construction material level. Previous studies with service life data for specific materials have been conducted by Hoxha *et al.* (Hoxha *et al.,* 2014) and Dixit (2019), who additionally reported their variability through statistical distributions. Looking at more functional oriented databases, the Swiss eBKP-H – SN506511 (CRB, 2012) standard of construction costs provides a structured way to decompose the building into elements and sub-elements. Similar decomposition exists in Germany, too. In France, the INIES database that was developed to gather product-specific LCA studies of manufacturers (*i.e.* the "Environmental Product Declarations", EPDs), includes a hybrid building decomposition, combining both a function-oriented classification and a material orientation (*e.g.* firstly the Insulation product category, which is then decomposed into different materials like EPS, glass wool, etc.). The main limitations of the previous studies and databases are either that they are not complete, in terms of material variety (Dixit, 2019; Hoxha *et al.*, 2014) or that they report deterministic service life values and no statistical distributions can be derived (CRB, 2012; HQE, 2004).

In the context of increasing the reliability in LCA and LCC calculations, by integrating the inherent uncertainties of the different parameters, there is a necessity of providing a systematic way to take into account the service lives of building elements in LCA calculations, within a probabilistic framework. Thus, the aim of this paper is to present the development of a service life database that gathers service life data from 67 international sources. The database uses a hybrid decomposition (functional decomposition according to eBKP-H – SN506511 and material decomposition, as well) and it is thus compatible to the BIM-based LCA context, allowing calculations in different level of details (LOD), as stated in Cavalliere *et al.* (Cavalliere *et al*., 2018). Furthermore, statistical distributions are determined using the collected data, through a straightforward method.

2 Development of the DUREE Service Life Database

The literature search for service lives was conducted in English, French and German via Google, Google Scholar and Science Direct. The research of the service life data concerned data for the structural system, the technical installations, the façade elements and coatings, the roof elements, as well as for the interior layout. In total, 67 sources were identified, coming from energy standards, LCA and LCC standards, the public sector, scientific reports, private associations, banks, building management and insurance companies. Furthermore, the partners of the IEA EBC Annex 72 contributed to this research, by providing additional service life data

through a survey, conducted on national LCA methodologies, in the beginning of 2019 (Lasvaux *et al.*, 2019). Depending on the scope of the final user, the service life values were then classified in three main categories, *i.e.* LCA, LCC and Real – Estate Management. The 67 sources resulted in 95 entries and their allocation is presented in Table 1. Some documents did not only provide a single average service life but also a range of values *e.g.* min – mean – max. These values were treated as individual sources. Moreover, some service lives can be used in more than one category (*e.g.* LCA and LCC). In that case, the values were attributed to both LCA and LCC categories. This explains why the total number of sources in Table 1 is above 67. More details about the sources can be found in (Lasvaux et *al.*, 2019).

Table 1. Type and number of identified sources and service life values.

Type of sources	Total sources	Total values
LCA documentations	39	50
LCC analysis	14	23
Real – Estate Management domain	23	36

The service life data were organized in a database and formed the DUREE Database in an Excel spreadsheet, according to the eBKP-H – SN506511 that it is appropriate for different LOD calculations, in BIM-based LCA and LCC analyses. The five main groups of building elements, extracted from this functional nomenclature, include the structural work (main group C), the technical installations (main group D), the façade elements and coatings (main group E), the roof elements (main group F) and interior layout (main group G), see Figure 1. These main categories are further decomposed into two sub-categories, according to the SN 506511 nomenclature (*e.g.* the intermediate element level and the detailed element level). Five more sub-categories were added to this decomposition, in order to cover lower levels for more detailed components. Figure 1 presents an example of the database structure, for the SIA 2032 LCA perimeter. The names of the eBKP-H – SN506511 codes of the building elements are shown in Figure 2.

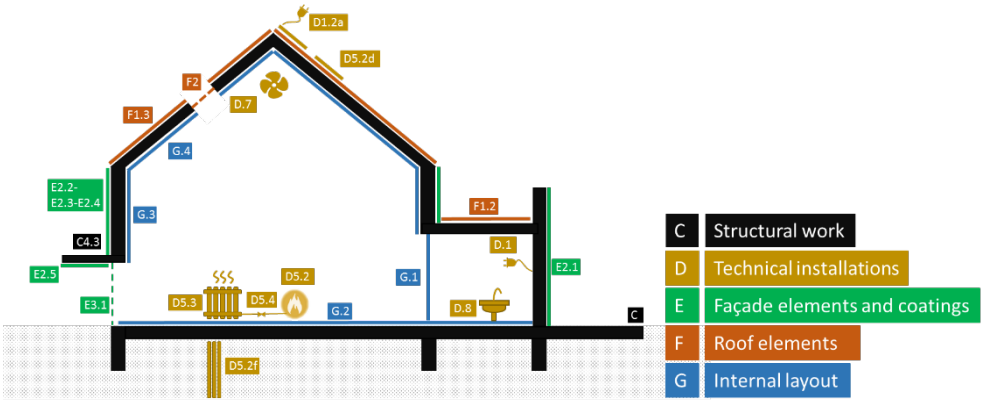

Figure 1. Main groups and intermediate element levels from the eBKP-H - SN 506511 nomenclature, for the 24 building elements, according to SIA 2032.

Each one of the 67 sources provides service life data for different components. Some sources offer data only for the main and intermediate categories, while others provide values at a lower

material level. Hence, an Excel function was created in order to calculate the statistic mean for each source for the main and intermediate categories, in case that service live data were provided at the material level. This function adds a flexibility to the database and allows calculations for the different stages of the design process, *i.e.*, for a screening analysis by taking values from the main categories (*e.g.* D Technical installations), or for a detailed analysis, by taking values from lower levels of details (*e.g*. heat producer, D5.2).

3 Descriptive Statistics

The database includes approximately 7'000 service lives data, for more than 2000 building elements. From these data, approximately 79% came from LCA and LCC sources. In addition, approximately 28% came from Switzerland and the rest were international data, mostly from European countries. The majority of Switzerland's data came from the management sector, while the majority of the international data belonged to the LCA domain.

Figure 2 presents the boxplots of the service lives for all the building elements included in the LCA perimeter of the Swiss SIA 2032 (see Figure 1). The descriptive statistics are presented for the total sample, as well as for the three sub-samples that correspond to service lives coming from LCA, LCC or Management sources. For some components such as photovoltaics, solar collectors or geothermal probes, some sub-samples (*e.g.* service life data for PVs in the LCC literature) are quite small, since there is a limited number of data found in the literature. The boxes correspond to the central 50% of the data, while the whiskers represent 80% of the data.

In general, there is a considerable variability for the most of the building elements and the different sources do not agree, as also stated in Dixit (2019). For each building element, the service life data exhibit a similar trend among the three sub-samples, regarding the variability. As far as the median values are concerned, two of the three sub-samples are relatively in accordance, but they are not systematically the same. In other words, there is no sub-sample that presents systematically lower or higher values. Hence, it is recommended to use the total sample, in order to determine a statistical distribution for the building elements' service life. Furthermore, the boxplots show that the service lives are positively or negatively skewed. The building elements exhibiting the highest variability are the technical installations (main group D), while the smallest variability is exhibited by the roof elements, (main group F). Furthermore, it should be noted that the variability of the sources diminishes, when moving towards lower levels of the database and more detailed materials, *e.g.* from D1 (electrical installations) to D1.2a (PV). The descriptive statistics for additional building elements can be found in (Goulouti *et al.*, 2019).

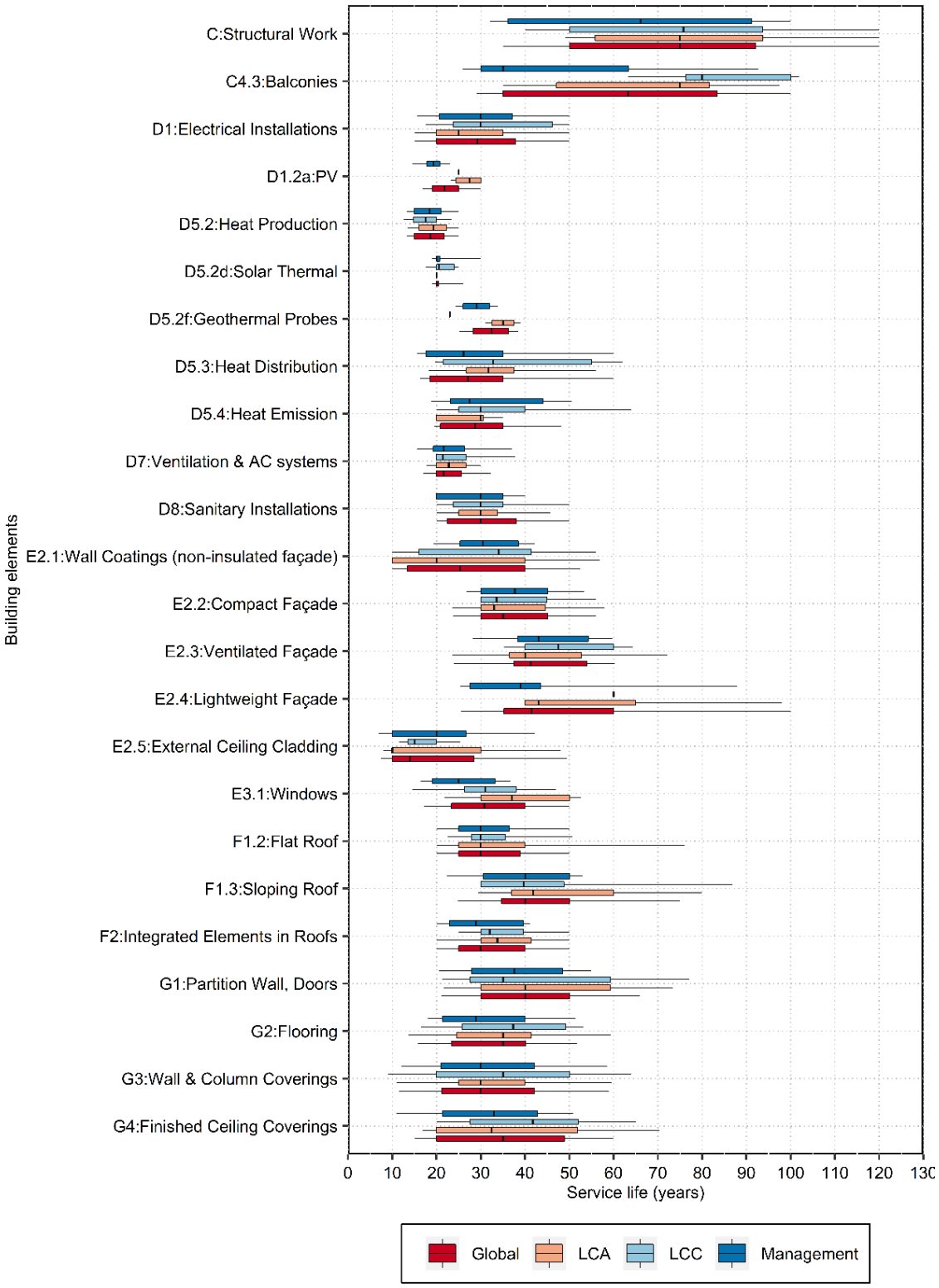

Figure 2. Boxplots for the 24 building elements, according to the SIA 2032 (see Figure 1) building LCA system boundaries.

4 Fitting to a Statistical Distribution

As stated in Dixit (2017), in order to deal with the variability of the service lives, statistical distributions can be determined, based on empirical service life data. Thus, using the DUREE database, such statistical distributions can be derived, with a systematic way for different building elements and levels of the database, *i.e.* service lives coming from the main groups or the sub-categories. Consequently, the service lives of the building elements can be taken into account, within a probabilistic framework, in further LCA and LCC calculations. In the literature, the lifetime data are often modelled using lognormal or Weibull distributions, (Aktas and Bilec, 2012; Kim and Yum, 2008). Input service life data constitute independent positive random quantities, for which the use of the lognormal process is well justified, (Voelkel, 2006), since according to the central limit theorem in the log domain, an infinite number of positive random values would approach the lognormal distribution (Limpert *et al.*, 2001). Thus, the latter can be used to model the service lives of building elements. In order to assess the goodness of fit of the lognormal distribution, two statistical methods were employed for the service lives of the building elements, using the statistical software R (R, 1997). First, the graphical method was computed, *i.e.* the Q-Q plots, which compares the theoretical and empirical distributions.

Figure 3 presents the empirical and theoretical density as well as the Q-Q plot of building element E.2 (Façade coatings above ground). The two graphs show that the two distributions are linearly related and that their points lie approximately on the line y=x. In addition, the p-value, according to the Anderson – Darling Test was calculated (R Documentation, 2002). The results confirmed the initial hypothesis of the lognormal distribution, (p-value > 0.05), (Goulouti *et al.*, 2019).

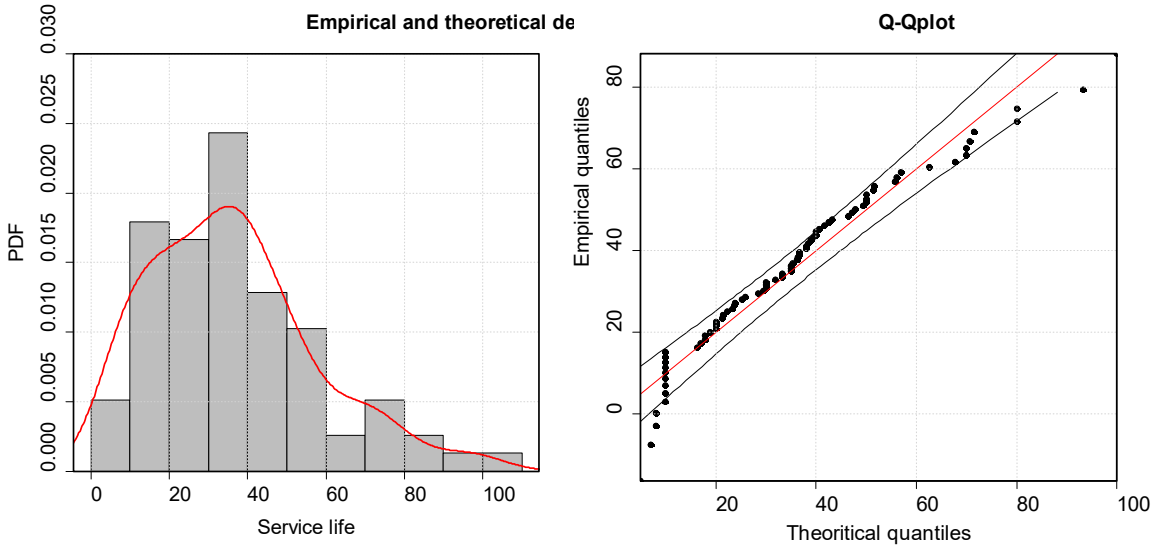

Figure 3. Example of goodness of fit (Q-Q plot) for the E.2 building element (Façade coating above ground).

5 Conclusions

This paper presents the development of a new database (DUREE database) for the service lives of building elements. International service life data were gathered and classified in three sub-samples, according to the scope of the sources application (LCA, LCC and Management sector). The main conclusions of the study are:

- The descriptive statistics show that there is a relative important variability and no general agreement, concerning the service lives of the building elements;
- There is no significant difference, among the three sub-samples, in terms of variability. As far as the median values are concerned, two of the three sub-samples present similar values, but they are not systematically the same. Thus, the total sample can be used in further LCA analysis;
- The structure of the database, *i.e.* main groups or sub-categories, offers the flexibility to the designer to attribute the service life data in different LODs, appropriate for BIM-based LCA analysis, *e.g.* screening LCA analysis (service lives from main groups), or more detailed LCA (service lives from sub-categories);
- The database offers the possibility to define statistical distributions, with a systematic way, for the service lives of the building elements. The goodness of fit for the different building elements confirmed the initial hypothesis of the lognormal distribution.

Acknowledgements

The authors wish to acknowledge the support of this work by the Swiss Federal Office for Energy (SFOE, DUREE Project No. SI/501483-01) and the Swiss National Science Foundation (SNF, Grant No. 2-77059-17). This research study has been complemented with additional service life data, provided within the framework of the IEA-EBC Annex 72, which focuses on Assessing Life Cycle Related Environmental Impacts Caused by Buildings (http://annex72.iea-ebc.org).

ORCID

Kyriaki Goulouti: https://orcid.org/0000-0002-7165-6117
Morgane Giorgi: https://orcid.org/0000-0002-1150-6811
Didier Favre: https://orcid.org/0000-0002-3351-2710
Sébastien Lasvaux: https://orcid.org/0000-0002-8723-9676

References

Aktas, C. B., and Bilec, M. M. (2012). Impact of lifetime on US residential building LCA results. *International Journal of Life Cycle Assessment*, *17*(3), 337–349. https://doi.org/10.1007/s11367-011-0363-x

Björklund, A. E. (2002). Survey of approaches to improve reliability in LCA. *International Journal of Life Cycle Assessment*, *7*(2), 64–72. https://doi.org/10.1007/BF02978849

Cavalliere, C., Habert, G.,Dell'Osso R. and Hollberg, A. (2018). Continuous BIM-based assessment of embodied environmental impacts throughout the design process. *Journal of Cleaner Production*.

CRB. *SN 506511, Code des coûts de construction Bâtiment*. , (2012).

Dixit, M. K. (2017). Life cycle embodied energy analysis of residential buildings: A review of literature to investigate embodied energy parameters. *Renewable and Sustainable Energy Reviews*, 79, 390–413. https://doi.org/10.1016/j.rser.2017.05.051

Dixit, M. K. (2019). Life cycle recurrent embodied energy calculation of buildings: A review. *Journal of Cleaner Production*, *209*, 731–754. https://doi.org/10.1016/J.JCLEPRO.2018.10.230

Goulouti, K., Padey, P., Galimshina, A., Habert, G. and Lasvaux, S. (2020). Uncertainty of building elements' service lives in LCA & LCC of buildings: What matters? *Building and Environment,*183, https://doi.org/10.1016/j.buildenv.2020.106904

Grant, A. and Ries, R. (2013). Impact of building service life models on life cycle assessment. *Building Research and Information*, *41*(2), 168–186. https://doi.org/10.1080/09613218.2012.730735

Hoxha, E., Habert, G., Chevalier, J., Bazzana, M. and Le Roy, R. (2014). Method to analyse the contribution of material's sensitivity in buildings' environmental impact. *Journal of Cleaner Production*, *66*, 54–64. https://doi.org/10.1016/j.jclepro.2013.10.056

HQE. (2004). INIES, Environmental and health reference data for building. Retrieved July 9, 2019, from https://www.inies.fr/about-the-inies-database/

Huijbregts, M. A. J. (1998). Uncertainty in LCA LCA Methodology Application of Uncertainty and Variability in LCA. *The International Journal of Life Cycle Assessment*, *3*(5), 273–280.

ISO/TC 59/SC 14. *ISO 15686-1:2011:Buildings and constructed assets - Service life planning*. , (2011).

Kim, J. S. and Yum, B. J. (2008). Selection between Weibull and lognormal distributions: A comparative simulation study. *Computational Statistics and Data Analysis*, *53*(2), 477–485. https://doi.org/10.1016/j.csda.2008.08.012

Lasvaux, S., Giorgi, M., Lesage, J., Wagner, G., Favre, D., Padey, P., … Habert, G. (2019). *DUREE Project, Analysis of lifetimes of building elements in the literature and in renovation practices and sensitivity analyses on building LCA & LCC*. Retrieved from https://www.aramis.admin.ch/Texte/?ProjectID=38626

Limpert, E., Stahel, W. A.and Abbt, M. (2001). *Log-normal Distributions*. *51*(5), 341–352. https://doi.org/10.1641/0006-3568(2001)051[0341:LNDATS]2.0.CO;2

Pannier, M. L., Schalbart, P. and Peuportier, B. (2018). Comprehensive assessment of sensitivity analysis methods for the identification of influential factors in building life cycle assessment. *Journal of Cleaner Production*, *199*, 466–480. https://doi.org/10.1016/j.jclepro.2018.07.070

R. (1997). The R Project for Statistical Computing.

R Documentation. (2002). Anderson-Darling Test For Normality. Retrieved March 31, 2019, from https://www.rdocumentation.org/packages/nortest/versions/1.0-4/topics/ad.test

SIA 2032. (2010). *SIA 2032 - L'énergie grise des bâtiments*. Zürich: Société Suisse des Ingénieurs et des Architectes (SIA).

SIA 2047. (2015). *SIA 2047 - Rénovation énergétique des bâtiments*. Zürich: Société Suisse des Ingénieurs et des Architectes (SIA).

SIA 260. (2003). *SIA 260 - Bases pour l'élaboration des projets de structures porteuses*. Société Suisse des Ingénieurs et des Architectes (SIA).

SIA 480. (2016). *SIA 480 - Calcul de rentabilité pour les investissements dans le bâtiment*. Zürich: Société Suisse des Ingénieurs et des Architectes (SIA).

Silvestre, J. D., Silva, A. and Brito, J. de. (2015). Uncertainty Modelling of Service Life and Environmental Performance To Reduce Risk in Building Design Decisions. *Journal of Civil Engineering and Management*, *21*(3), 308–322. https://doi.org/10.3846/13923730.2014.890649

Thiebat, F. (2019). *Life Cycle Design, An Experimental Tool for Designers*. Springer IInternational Publishing.

Voelkel, J. G. (2006). *Weibull vs Lognormal Data Analysis*.

Volland, B., Farsi, M., Lasvaux, S. and Padey, P. (2019). Service life of building elements: An empirical investigation. *In Progress*.

XV International Conference on Durability of Building Materials and Components
DBMC 2020, Barcelona
C. Serrat, J.R. Casas and V. Gibert (Eds)

Durability Based Service Life Estimation for Chloride Exposed Cracked and Self-Healed Concrete

Nele De Belie[1], Bjorn Van Belleghem[1], Sylvia Keßler[2], Philip Van den Heede[1] and Kim Van Tittelboom[1]

[1] Magnel-Vandepitte Laboratory for Structural Engineering and Building Materials, Ghent University, Technologiepark Zwijnaarde 60, B-9052 Ghent, Belgium, nele.debelie@ugent.be

[2] Helmut-Schmidt-University, Chair of Engineering Materials and Building Preservation, Holstenhofweg 85, Hamburg, 22043, Germany, sylvia.kessler@hsu-hh.de

Abstract. *Chloride ingress in cracked concrete leads to rapid corrosion of embedded steel reinforcement and a decrease of the expected service life. Corrosion monitoring experiments showed that a 300 µm wide crack caused initiation of corrosion of a rebar (Ø 10 mm) with a concrete cover of 26 mm within three weeks of cyclic exposure to a 33 g/l NaCl solution. After a period of unstable corrosion activity during the first 20 weeks of exposure, corrosion propagated further at a relatively high rate (0.345 to 0.718 mm³/week). Application of a theoretical pitting model revealed that a reduction of about 50% of the rebar cross-section would occur after a period of 9 to 20 years of continuous cyclic exposure to chlorides. To avoid such rapid degradation, the use of self-healing concrete can be proposed. Introduction of macro-encapsulated polyurethane into the concrete matrix, will lead to the formation of a (partial) barrier against ingress of chlorides at the moment cracks appear. Corrosion monitoring experiments showed that the autonomous crack healing could not always prevent corrosion initiation, but caused an important reduction of the corrosion rate during the 44 weeks exposure period. The mean rate of volumetric loss of steel amounted to 0.042 mm³/week, about 15 times lower than for the untreated cracked samples. The rebars also showed no or very limited signs of corrosion after visual inspection. The simplified pitting model indicated that a 50% reduction in steel cross-section would take more than 5 times longer for samples with self-healing properties versus ordinary cracked samples.*

Keywords: *Steel Corrosion, Durability, Cracking, Self-Healing Concrete, Service Life Prediction.*

1 Introduction

1.1 General Introduction

Reinforced concrete is without doubt one of the most ingenious inventions in the construction industry. By combining concrete with steel, a composite material is created which has both a high compressive and tensile strength. Numerous structures, such as buildings, bridges, tunnels and roads have been made using reinforced concrete due to its high strength and high degree of freedom in shape and design. A huge amount of steel reinforced concrete structures were built by the mid-20th century. However, these structures are now over 50 years old and several have shown major deterioration. One very common problem in reinforced concrete structures is the appearance of cracks when the concrete element is subjected to tensile stresses. These cracks form preferential pathways for chlorides or carbon dioxide to penetrate the concrete and rapidly reach the steel reinforcement. This will increase the risk for initiation and possibly further propagation of steel reinforcement corrosion. Several studies have provided proof of a

shortening of the corrosion initiation period due to the presence of cracks and chlorides (Ahmadi *et al.*, 2015; Jaffer and Hansson, 2008; B. Otieno *et al.*, 2010; Sangoju *et al.*, 2011). In some cases corrosion onset is almost instantaneous after crack appearance (Schießl & Raupach, 1997). Moreover, once corrosion has initiated, there can be an acceleration of the corrosion rate in the propagation phase as the crack provides easier supply of chlorides, moisture and oxygen to the reinforcement (Ahmadi *et al.*, 2015; Li *et al.*, 2017; Otieno *et al.*, 2010; Schießl and Raupach, 1997). Mostly, an increase in the corrosion rate was found in short term tests (< two years) while less influence of cracks on the propagation rate was found in long-term studies (Käthler *et al.*, 2017).

Thus, cracks should be repaired as soon as possible to avoid major durability issues. However, cracks in certain structures can be invisible or inaccessible, impairing repair works. Moreover, repair works have a big economic impact due to the (in)direct costs involved. Therefore, the idea of providing the concrete with the ability of restoring cracks by itself without any human interference grew during the last few decades. One promising approach to create a so-called self-healing concrete consists of the embedment of encapsulated healing agents in the concrete matrix. Brittle macro-capsules are placed in regions subjected to high tensile stresses and where cracks would cross the steel reinforcement.

In this research, autonomous crack healing through the use of encapsulated healing agents was investigated for its efficiency to reduce the ingress of chlorides into the concrete matrix and to improve the corrosion resistance of reinforced concrete.

1.2 Steel Corrosion Monitoring

Chloride ions cause breakdown of the passive layer on the steel reinforcement when present at a certain threshold concentration. As the chloride ingress in concrete is not homogenous, this leads to a very localized corrosion. Chloride induced corrosion is actually a combination of a macro-cell corrosion process (leading to a current I_{macro}) between spatially separated anodic and cathodic areas on the steel and a micro-cell corrosion process between very small anodic and cathodic parts inside the corrosion pit (leading to a current I_{micro}). The macro-cell corrosion process will usually lead to much higher corrosion rates (Schießl and Raupach, 1997). According to Ohm's law, the current which is flowing between anodic and cathodic sites on the steel surface is directly proportional to the potential difference between those areas and inversely proportional to the resistances of the system. On this basis, the macro-cell corrosion process can be represented by an equivalent electric circuit.

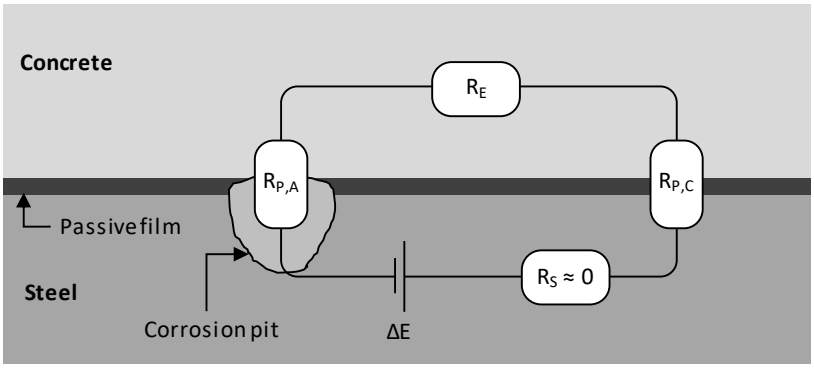

Figure 1. Equivalent circuit model for macro-cell corrosion, redrafted after Hiemer *et al.* (2015).

As can be seen from Figure 1, the equivalent circuit consists of four resistances: the resistance of the anodic partial reaction ($R_{P,A}$), the resistance of the cathodic partial reaction ($R_{P,C}$), the resistance of the concrete (R_E) and the resistance of the steel (R_S, which is assumed to be zero). The potential difference ΔE (driving potential) between the anode and the cathode can be seen as the driving force for the corrosion process. In order to estimate the rate of corrosion, the total corrosion current (I_{corr}) should be calculated, as in Equation (1).

$$I_{corr} = I_{macro} + I_{micro} = \frac{\Delta E}{R_{P,A} + R_{P,C} + R_E} + I_{micro} \quad (1)$$

2 Materials and Methods

2.1 Concrete Samples

A reference concrete as described in Van den Heede (2014) was used as a representative mixture for concrete in exposure class XS2, i.e. submerged reinforced concrete in contact with chlorides from seawater (Table 1). The mixture had a water-to-binder ratio of 0.41 and a fly ash-to-binder ratio of 15%, according to the k-value concept (NBN B15-001, 2004). The concrete had a slump class S4 and a compressive strength at 28 days of 65.2 ± 2.0 MPa.

Table 1. Mix proportions of the concrete mixture.

Sand 0/4 (kg/m³)	696
Aggregates 2/8 (kg/m³)	502
Aggregates 8/16 (kg/m³)	654
CEM I 52.5 N (kg/m³)	317.6
Fly Ash (kg/m³)	56
Water (kg/m³)	153
Superplasticizer (ml/kg binder)	3.0

Steel reinforced concrete prisms with dimensions of 120 mm x 120 mm x 500 mm were made for corrosion monitoring. The reinforcement scheme of the prisms (Figure 1), was based on Hiemer *et al.* (2015) and Keßler *et al.* (2017), and was adapted based on earlier experiments (Van Belleghem *et al.*, 2018). The steel reinforcement (BE500S) in the concrete prisms consisted of an anodic and a cathodic part which were electrically separated from each other. The anode was a central steel bar (∅ = 10 mm, L = 250 mm), partially coated with cement paste and epoxy resin to prevent crevice corrosion, with only the central 50 mm exposed. The cathode consisted of two electrically connected cages (each with four longitudinal rebars ∅ = 8 mm and five stirrups ∅ = 6 mm which were welded to each other). The anode/cathode ratio was kept small (1/58) to accurately measure the macro-cell corrosion process. Both parts were connected to the exterior by means of an insulated copper wire. In addition, two glass fiber reinforced polymer rebars (∅ = 6 mm) were placed in the compression zone. Four types of specimens were prepared (with 3 replicates): uncracked specimens (UNCR), cracked but not healed specimens (CR), and self-healing specimens containing two layers of 6 capsules filled with high (6700 mPas) or low (200 mPas) viscosity polyurethane (PU_HV_CAPS and PU_LV_CAPS). The samples contained an Ag/AgCl internal reference electrode, fixed to the coated part of the anodic rebar. After casting, the prisms were stored at 20°C and a relative humidity above 95%.

The prisms were demolded after 24 hours and stored at the same conditions until 28 days. Then, anode and cathode were connected to each other through the external copper wires.

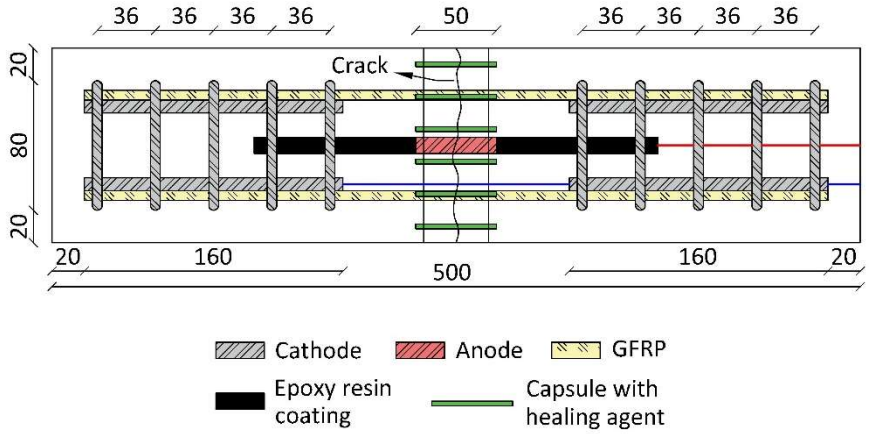

Figure 1. Reinforcement scheme and capsule positions in the concrete prisms (dimensions in mm) – top view, redrafted after Van Belleghem *et al.* (2018).

2.2 Crack Creation

At 28 days, a flexural crack with a target width of 300 µm was created in the concrete prisms by means of a three-point bending test. The concrete prisms contained a triangular notch with a height of 3.5 mm at mid-span to ensure that the cracks originated in the center of the prism and consequently crossed the anodic rebar (and the capsules). Cracks were kept open by means of a special frame (Figure 2). After crack creation, all samples were stored at 20 ± 2°C and a relative humidity of 60% for 48 hours to allow the polyurethane to cure inside the crack.

2.3 Exposure Regime

The prisms were placed with the crack facing upwards and the lateral surfaces were covered with aluminum butyl tape, extending beyond the upper surface of the samples, to create a basin with three compartments (Figure 2). The top (cracked) surface of the samples was exposed weekly to 1 d wetting and 6 d drying cycles for a total duration of 44 weeks. During the wet period, the central compartment was filled with a 33 g/l NaCl solution, while the outer compartments were filled with a 1.15 g/l $Ca(OH)_2$ solution.

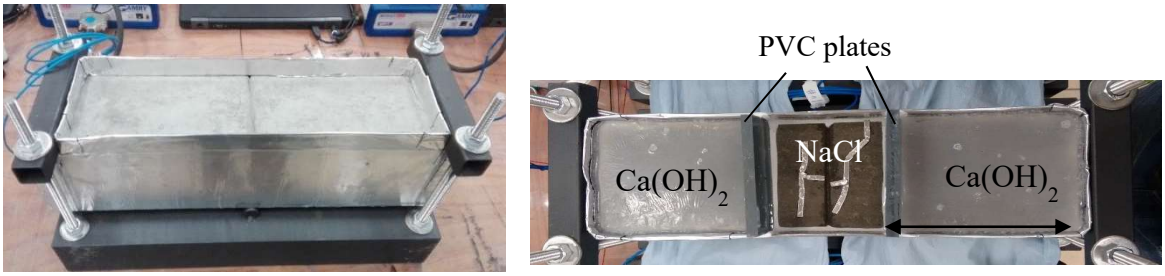

Figure 2. Concrete prism mounted in a three-point bending test frame (left); Basins on the surface (right).

2.4 Corrosion Measurements

The macro-cell corrosion current between anode and cathode (I_{macro}) was measured once every hour with a low resistance ammeter. Electrochemical measurements were performed at the end of the wet period with a potentiostat using the internal Ag/AgCl reference electrode (SAE). The corrosion potential (E_{corr}) was measured while anode and cathode were connected. Other parameters were measured as well (for results see Van Belleghem, 2018), such as open circuit potential (OCP) of anode and cathode, linear anodic and cathodic polarization resistance ($R_{P,A}$ and $R_{P,C}$), and concrete resistance (R_E). All electrochemical measurements were performed weekly during the first 12 weeks of the wet-dry cycles and thereafter every two to four weeks.

2.5 Chloride Profiling and Visual Evaluation

After the corrosion monitoring period, the chloride ingress was determined by means of chloride profile grinding (layers of 4 mm thickness) in an area of 10 mm x 30 mm around the crack next to the location of the anodic rebar. The total chloride content of each powder was determined by means of acid-soluble chloride extraction in a nitric acid solution followed by a potentiometric titration against silver nitrate. After determination of the chloride profiles, the anodic steel reinforcement bars were removed from the concrete prisms for visual inspection of the corrosion products. Next, all rebars were immersed in a chemical cleaner solution ($HCl:H_2O$ = 1:1 + 3 g/l urotropine) for 24 hours in order to remove all corrosion products and residual concrete. Afterwards, the steel rebars were visually inspected again to investigate the loss of steel due to chloride induced corrosion.

3 Results of Corrosion Experiments

3.1 Corrosion Monitoring

An overview of the measured electrochemical parameters during the 50 weeks monitoring period is given in Figure 3. The initial measurement in the uncracked state is shown as ‘week -1’, while ‘week 0’ represents the values after cracking but without exposure to a solution. From week 1 until week 44 the samples were exposed to the wet-dry cycles. The last measurement at week 50 was performed after a six week dry period.

The uncracked samples showed a non-active state of corrosion along the whole exposure period. No macro-cell corrosion current was detected and the corrosion potential was nearly constant at values of -70 to +80 mV_{SAE}. The cracked samples showed clear evidence of corrosion initiation within the first three weeks of exposure to 33 g/l NaCl solution: there is a steep rise in the macrocell corrosion current and a concurrent drop of the corrosion potential down to values between -200 and -400 mV_{SAE}. Every week a sharp increase of the macro-cell corrosion current can be seen for all the cracked samples, which corresponds to the start of each wet period. Apart from the occurrence of these peaks, the overall macro-cell corrosion current shows a decreasing trend during the first twenty weeks of exposure. It remains relatively constant in the period from 20 to 44 weeks in a range of 20 to 60 µA, which shows that the corrosion is propagating at a constant rate. The corrosion parameters measured at week 50, after a dry period of six weeks, indicate that the corrosion is propagating at a lower rate. This is logical as the continuous supply of chlorides and moisture act as catalysts for the anodic and cathodic corrosion reaction.

Generally, the corrosion behaviour of the self-healing samples with high viscosity PU (PU_HV_CAPS) was very similar to the corrosion behaviour of the cracked samples. However, the self-healing samples with low viscosity PU (PU_LV_CAPS) behaved more closely to the uncracked samples. The macro-cell corrosion current was negligible and the driving potential was comparable to the values found for the uncracked samples.

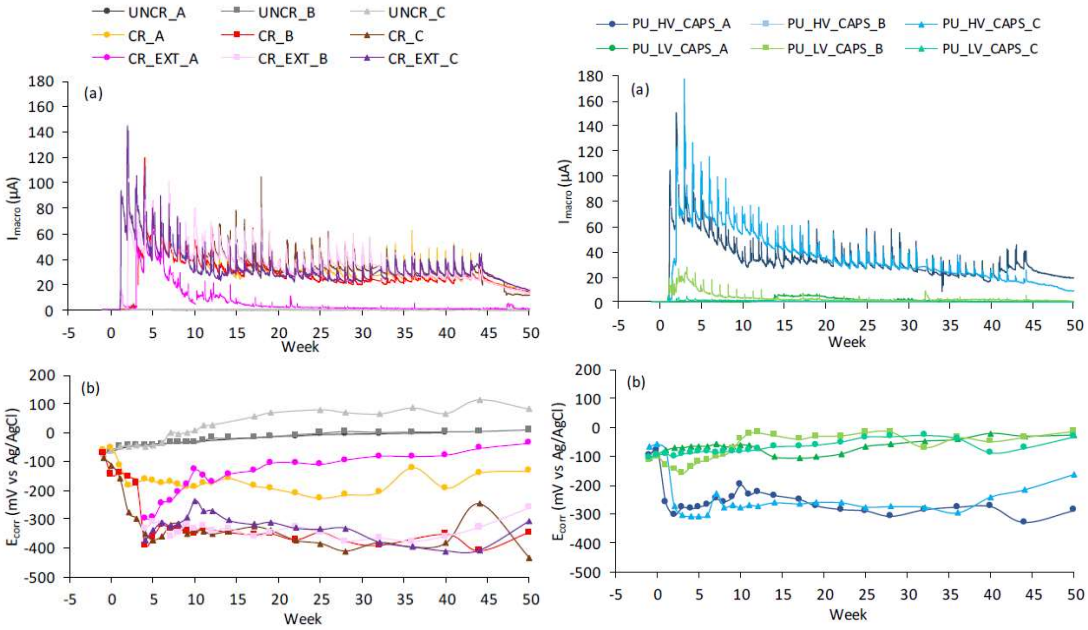

Figure 3. Macro-cell corrosion current and corrosion potential for uncracked (UNCR) and cracked (CR) samples (left) and for samples with high (HV) and low (LV) viscosity PU (right) (Van Belleghem, 2018).

3.2 Chloride Profiles and Visual Examination of the Rebars

The obtained chloride profiles are shown in Figure 4 together with the location of the rebar. For the uncracked samples the mean chloride concentration at the surface amounted to 3.43 ± 0.05 m%/binder and then dropped fast to nearly zero at a depth of 18 mm into the concrete matrix. The samples containing an untreated crack showed a very high chloride concentration close to the surface of the samples (up to 6 m%/binder). The chloride concentration drops steeply when going to the second layer (4-8 mm below the surface) and gradually decreases until a depth of 20-25 mm. At depths larger than 20 mm, the chloride concentration remained almost constant at about 1.3 to 1.5 m%/binder. Autonomous crack healing with low viscosity polyurethane (PU_LV_CAPS) led to a clear reduction of the chloride concentration compared to the cracked samples. At the level of the reinforcement the chloride concentration was about 0.26 m%/binder, which was three to seven times lower compared to the concentration found at the level of the reinforcement of the cracked samples.

Visual examination of the rebars from the uncracked samples showed no corrosion products and no visual damage to the rebars was observed after cleaning. For the cracked samples, clear formation of corrosion products on the central part of the anodic rebar was noticed. After cleaning, clear pitting corrosion was observed at the same location. The series PU_LV_CAPS showed negligible formation of corrosion products and no pitting corrosion.

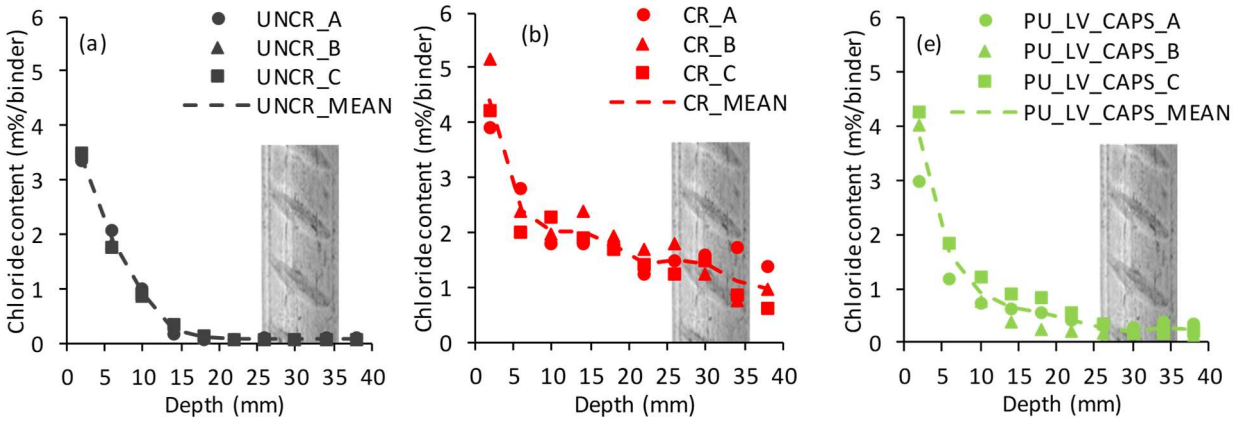

Figure 4. Chloride profiles of all sample series with indication of rebar location.

4 Prediction of Reduction of Steel Cross-Section

The mass loss of steel due to the macro-cell corrosion reaction can be determined theoretically from the measurement of the macro-cell corrosion current in time using Faraday's law according to Equation (2):

$$m = \frac{Q}{F} \cdot \frac{M}{z} \tag{2}$$

where m is the mass loss of iron (Fe) (g), Q is the total electric charge passed through the substance (C), F is the Faraday constant (= 96485 C/mol), M is the molar mass (here 55.845 g/mol) and z is the valency number (being 2 for oxidation of iron).

The total charge passed can be calculated by taking the integral of the measured current over time. The mass loss due to micro-cell corrosion is hereby not taken into account. The cracked samples showed a large mass loss ranging from 0.19 to 0.24 g at the end of the measurements. A further prediction can be made by calculating the volume loss in the initial 20 weeks of exposure (high and unstable corrosion current, leading to a volume loss of 6.36 to 15.45 mm³) and adding this to the volume loss in the secondary period, where a relatively stable macro-cell corrosion current develops (0.551 to 0.718 mm³/week). A similar calculation for the self-healing prisms with LV PU, resulted in an initial volume loss of 1.65 to 10.34 mm³ and a rate of volumetric loss of 0.042 mm³/week afterwards (14 times lower than what was found for the untreated cracked samples).

Application of a simplified pitting model proposed in Van Belleghem (2018) revealed that, for a steel bar with a diameter of 10 mm in cracked concrete, a reduction of about 50% of the cross-section would occur after a period of 9 to 20 years of continuous cyclic exposure to chlorides. However, for the self-healing concrete with LV PU, such a 50% reduction would take more than 100 years to occur.

5 Conclusions

- Cracks in concrete allow rapid penetration of chlorides and impair the durability of the structure. Within three weeks of cyclic exposure to a 33 g/l NaCl solution, the reinforcement in lab specimens with a 300 µm wide crack started to corrode. A volume loss of 6.36 to 15.45 mm³ was calculated for the initial 20 weeks of exposure, followed by a period of

relatively stable macro-cell corrosion current leading to a volume loss of 0.55 to 0.72 mm³/week. This means that 50% of the rebar cross-section (diameter 10 mm) would be lost after 9 to 20 years. Uncracked samples showed a non-active state of corrosion during the whole exposure period of 44 weeks.

- In the case of self-healing concrete with macro-encapsulated polyurethane, crack formation led to rupture of the capsules and release of healing agent in the crack. Low viscosity polyurethane induced a decrease of the corrosion rate in comparison to cracked and untreated samples. After an initial volume loss of 1.65-10.34 mm³, the mean steel loss rate amounted to 0.042 mm³/week only. At the end of the experiment the rebars showed no or very limited signs of corrosion. A 50% reduction in steel cross-section was estimated to take more than 100 years, using a simplified pitting model.

Acknowledgements

This research was performed in the framework of ISHECO (Impact of Self-Healing Engineered Materials on steel COrrosion of reinforced concrete) - program SHE (Engineered Self-Healing materials) and funded by SIM and VLAIO. Philip Van den Heede is postdoctoral fellow of Research Foundation - Flanders (FWO) (project No. 3E013917)

ORCID

Nele De Belie: http://orcid.org/0000-0002-0851-6242; Bjorn Van Belleghem: https://orcid.org/0000-0003-1294-1724; Sylvia Kessler: http://orcid.org/0000-0002-1335-1104; Philip Van den Heede: https://orcid.org/0000-0003-1307-2831; Kim Van Tittelboom: https://orcid.org/0000-0002-7718-3189

References

Ahmadi, B., Ramezanianpour, A. A. and Sobhani, J. (2015). Rebar corrosion in cracked RC prisms located in harsh marine environment. *Magazine of Concrete Research*, 66(19), 1007–1019.

Hiemer, F., Keßler, S. and Gehlen, C. (2015). Reinforcement corrosion behavior in bending cracks after short-time chloride exposure. In *Proceedings of the 4th International Conference on Concrete Repair, Rehabilitation and Retrofitting* (pp. 99–106). Leipzig, Germany.

Jaffer, S. J. and Hansson, C. M. (2008). The influence of cracks on chloride-induced corrosion of steel in ordinary Portland cement and high performance concretes subjected to different loading conditions. *Corrosion Science*, 50(12), 3343–3355.

Käthler, C. B., Angst, U., Wagner, M., Larsen, C. K. and Elsener, B. (2017). *Effect of cracks on chloride-induced corrosion of reinforcing steel in concrete – a review.* Norwegian Public Roads Administration, Report 454.

Keßler, S., Hiemer, F. and Gehlen, C. (2017). Einfluss einer Betonbeschichtung auf die Mechanismen der Bewehrungskorrosion in gerissenem Stahlbeton. *Beton- Und Stahlbetonbau*, 112(4), 198–206.

Li, W., Liu, W. and Wang, S. (2017). The effect of crack width on chloride-induced corrosion of steel in concrete. *Advances in Materials Science and Engineering*, Article ID 3968578, 11 pages.

Otieno, M.B., Alexander, M.G. and Beushausen, H. (2010). Corrosion in cracked and uncracked concrete: influence of crack width, concrete quality and crack reopening. *Magazine of Concrete Research*, 62(6), 393–404.

Sangoju, B., Gettu, R., Bharatkumar, B. H. and Neelamegam, M. (2011). Chloride-Induced Corrosion of Steel in Cracked OPC and PPC Concretes: Experimental Study. *Journal of Materials in Civil Engineering*, 23(7), 1057–1066.

Schießl, P. and Raupach, M. (1997). Laboratory studies and calculations on the influence of crack width on chloride-induced corrosion of steel in concrete. *ACI Materials Journal*, 94(1), 56–61.

Van Belleghem, B. (2018). *Effect of Capsule-Based Self-Healing on Chloride Induced Corrosion of Reinforced Concrete*. PhD thesis, Ghent university.

Van Belleghem, B., Kessler, S., Van den Heede, P., Van Tittelboom, K. and De Belie, N. (2018). Chloride induced reinforcement corrosion behavior in self-healing concrete with encapsulated polyurethane. *Cement and concrete research*, 113, 130-139.

XV International Conference on Durability of Building Materials and Components
DBMC 2020, Barcelona
C. Serrat, J.R. Casas and V. Gibert (Eds)

Environmental Deterioration Factors in Metal Claddings and GFRC Panels Implemented on Facades: An Assessment through Two Cases in Istanbul

Sahar Manafvand Ardi[1], Begum Diker[2] and Payam Kanani Bahri[3]

[1] Faculty of Architecture, Istanbul Technical University, Taskisla Campus, 34437-Istanbul, Turkey, saharmanafvand@gmail.com

[2] Faculty of Art and Design, Dept. of Architecture, Dogus University, Acibadem Campus, 34722-Istanbul, Turkey, bdiker@dogus.edu.tr

[3] Faculty of Architecture, Istanbul Technical University, Taskisla Campus, 34437-Istanbul, Turkey, payamkanani70@gmail.com

Abstract. *Decrease in performance of building facades, components, and materials before their service life is an unexpected situation. Therefore, detecting the probable causes of these anomalies plays a crucial role in maintenance planning. This study aims to determine the environmental deterioration factors which affect the performance of buildings, especially building façades, through two case buildings situated in the same university campus in Istanbul. The methodological framework of the study is based on visual observations and literature review. Through observations on a different period of time, anomalies have been detected and photographed. In the first case, it has been focused on metal claddings on building façade. In the second case, it has been focused on GFRC panels which have the majority of the North façade. Within the help of literature and observations, two cases have been compared to each other in terms of their deterioration factors and interpreted through graphs. In the first case, occurred deteriorations have been detected such as uniform dirt, corrosion, joint degradation, mechanical impacts, and delamination. in the second case, deteriorations have been observed such as biological staining, uniform dirt, moisture rising, and design failures.*

Keywords: *Environmental Deterioration Factors, Building Façade Failures, Metal Claddings, Glass Fibre Reinforced Concrete Façade.*

1 Introduction

Performance of a building deteriorates in time depending on environmental effects, usage, maintenance, detail design and type of materials which are used in building envelope. Therefore, defining the probable causes of deteriorations has high importance to propose appropriate solutions.

Environmental agents are divided into natural (wind, rain, freeze and throw, and solar radiation), and chemical and biological problems, issued by air pollution (Norvaišienė *et al*., 2003). The data reported in this paper investigates environmental agents which can affect performance of façade.

A research called "Climatic and Air Pollution Effects on Building Facades" has a deep literature review on degradation mechanisms that affect the durability of building materials (Norvaišienė *et al*., 2003). A study called "Evaluation of Damage of Building Facades in Brasilia" aims to evaluate age and climatic agents through quantitative research. Visual inspections and facade mapping were used as a method and some degradation agents such as grout and sealing failures and efflorescence are examined over the exposure to solar radiation

(Bauer *et al.,* 2014). By now, many kinds of research have been done on deterioration factors and durability of materials. Defining these factors/mechanisms correctly is essential in order to propose appropriate solutions in design, construction, and maintenance process.

2 Environmental Factors

Mechanisms are generally examined in three categories: physical, chemical, and biological (Dickinson *et al*., 1999). *Physical mechanisms* are related to the presence of water. Freezing and thawing processes with the temperature and moisture differences may cause stress and crack on the material (Norvaisiene *et al*., 2003). *Chemical mechanisms* involve some chemical compounds that can react with the building surface. Particulate matters in the air generally comprise dust, smoke and suspended particles. Dust particles being large and heavy, settle quickly and will not affect large areas. Smoke and suspended particles being smaller and lighter remain in the atmosphere for a longer time and affect larger areas (Chew *et al.,* 2003). Sulfur and nitrate have acidic concentrations, and they cause acid rain, which is a threat to human health and also building envelope (Norvaisiene *et al*., 2003). Besides, corrosion of materials can occur due to chemical interaction with the environment. If corrosion of materials does not prevent in time, it may cause even structural deteriorations.

In *biological mechanisms*, wind changing the direction of rain drops to façade and this is "one of the most important moisture sources" that effects durability of façade material. These destructive effects can be "frost damage, discoloring, biological and chemical degradations" and also structural cracking (Blocken *et al*., 2013). Also rain water is one of the reasons of stains on façade. It can wash the dirt through the façade and also is a major factor that causes biological grow on it. "Sunlight plays an important role in affecting the formation of stains on a facade. The intensity and duration of sunlight that a surface receives affect the limit of runoff flow, the type of biological stains and the pattern of staining" (Chew *et al*., 2003).

3 Case Studies

In this part, two case buildings where are located in Istanbul are selected in order to understand environmental deterioration factors. In this context, there is an approach from macro to micro scale, which begins with defining the surrounding of the buildings and continues with the building facade components.

3.1 Local Environment

Both of the case buildings are located in Maslak, where is one of the main business districts of İstanbul. The altitude is 120 meters, and distance from the sea is approximately 3 km. In the first case, the northern facade of the building is facing Buyukdere Street, which usually has heavy traffic flow. Also, there is viaduct which is passing near the case building and facing the northern facade of the first case building again. The other side of Buyukdere is a high-density urbanized area which has many commercial and residential complexes.

In the second case building, traffic direction is in North and East face. There is also a parking lot in the West side. The site plans of the case buildings are given in Figure 1:

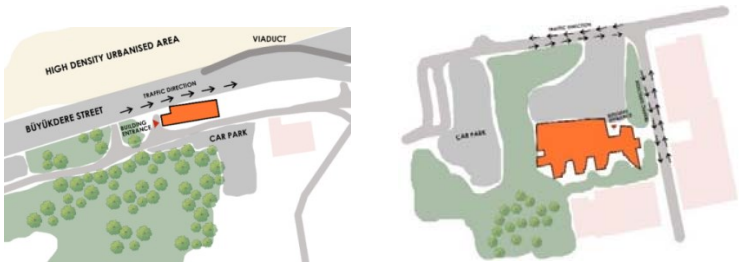

Figure 1. Site plans of the first and second case buildings.

3.2 Micro Environment

Istanbul where the case buildings are located has mild-humid climatic characteristics. According to the official statistics, the highest temperature is in July (41.5°C), and the lowest average temperature is in February (-16.1°C). The average number of rainy days is highest in January (17.3) and the lowest in July (4.3). Maximum daily precipitation is 128.9 mm (Turkish State Meteorological Service Official Web Sites, n.d.).

The dominant wind direction in the district is North – North East. Accordingly, it is assumed that the northern façade of the building is exposed to more wind and rain. Figure 2 shows the location of the case buildings in macro scale. Distance from the sea is approximately 3 km that can be an adequate distance to happen convection of salt.

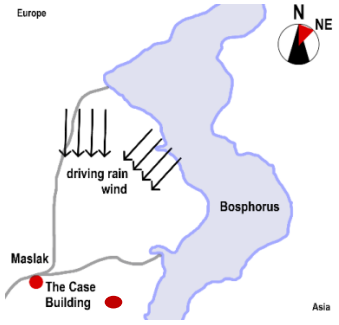

Figure 2. Location of the case buildings.

The recent measurements performed by Ministry of Environment and Urbanization show that PM10 and NO_2 values are comparatively increasing in the rush hours as a probable consequence of Buyukdere Street (SİM Project n.d.). Also, a report which has been prepared in 2018 by the Netherlands Enterprise Agency shows the existing situation within the context of air pollution in İstanbul. According to the European Directive, the number of permitted exceedances per year is 18. Figure 3 shows that NO_2 limit is exceeded more than 18 times in 6 stations in 2017 and Maslak district has the third highest exceedance level (Standards-Air Quality-Environment-European Commission, n.d.). As understood, the selected buildings are located in a highly urbanized area and air pollution in the district is quite a lot. Therefore, the selection of appropriate material for the building envelope is a critical issue.

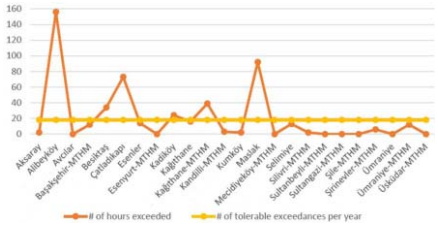

Figure 3. Frequency of hours the NO_2 limit was exceeded in 2017.

3.3 Facade Components

The first case building facade mainly has 4 mm thickness white colored *aluminum composite panel (1), siliconized glass system with an aluminum frame (2), structural steel columns (3), natural stone cladding (4),* silver-gray colored *aluminum mesh cladding (5) and white colored aluminum dynamic vertical and fixed horizontal shading elements (6)* (Figure 4).

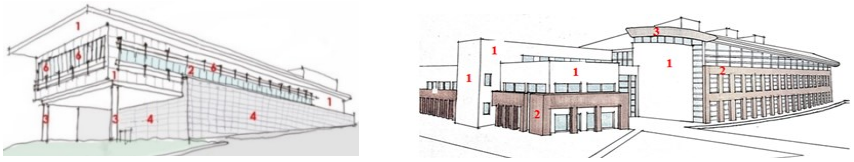

Figure 4. Façade components of the first and second case buildings.

Materials that have been used on façade for the second case building are (most to least); *glass fibre reinforced concrete (GFRC) (1), clinker based facade panels (2), aluminum (3).* It has been focused on metal claddings in the first case and GFRC panels in the second case since they have the most deterioration in comparison with other materials on the façade.

4 Preparation for Field Observation

The methodological framework of the study is based on visual observations and literature review. Firstly, façade deterioration factors have been defined in detail through literature. For the field observation, two datasheets have been prepared. The first datasheet contains the general information such as primary use of the building and construction process. The second one involves atmospheric exposures such as wind, rain, sun that affects the building façades, climate in the observation days and deterioration types. After collecting data, anomalies on building façade have been detected and shown in façade mapping (Figure 5).

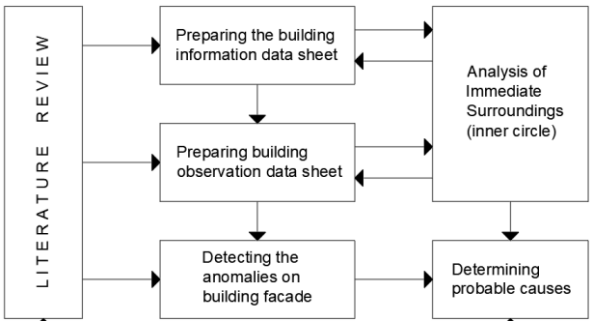

Figure 5. The methodology of the study.

5 Analysis and Discussions

For the first case building, four observations were made. The first one was made on 27th April 2015, in a cloudy day, 18°C at 09:30 am. The second one was on 25th September 2018, rainy day, 19°C. The third one was 9th October 2018, cloudy day, 16°C at 12:00 am and the fourth observation was on 4th December 2018, after rain, 10°C at 05:30 pm.

For the second case, the first observation was in 22th October 2018, 15:35 in partly cloudy weather. The second one was in 10th November 2018, 17:09 in a completely sunny weather. The last observation was made after two heavy rainy days in 19th November 2018, 14:22.

5.1 Case Study 1

According to the observations, anomalies detected on the selected building facades are examined. Deteriorations are classified into five categories. These are; uniform dirt (A), corrosion (B), joints degradation (C), mechanical impact (D), and delamination (E). The deteriorations which have been detected are shown in façade mapping (Figure 6).

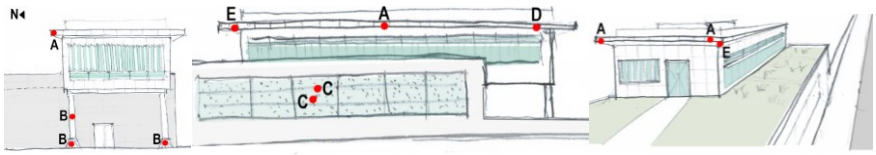

Figure 6. Deteriorations on the West, North, and East façade.

Uniform dirt has been mostly seen on the aluminum composite panels and shading elements (Figure 7). The most dirtiness has been concentrated on the overhangs that have 10-12 meter height from Buyukdere Street. Especially the North and East facade are the dirtiest facades of the building. The reason may be the viaduct which passes above the main road and brings all the pollution onto the façades within the help of dominant wind and driving rain.

Deterioration Type	**A**	**Date**	9.10.2018
		**Weather data**	Cloudy, 16°C
		Affected parts	Aluminum composite panel Overhangs and facades, shadings
		Affected facades	North, South, East, West
		Probable causes	Atmospheric pollution

Figure 7. Deterioration type A, 'uniform dirt'.

The observations which have been made in 25th September and 4th December 2018 show that two structural columns on the West façade of the building have been deteriorated by corrosion effect (Figure 8). The waterhole has been observed below the feet of the column after the rain. Accordingly, degradation on the feet is thought to be due to the wrong slope angle. Deterioration on the column head may be related with the storm water runoff.

Deterioration Type	B	Date	25.09.2018, 04.12.2018
		Weather data	Rainy, 19°C, after rain 10°C
		Affected parts	Structural steel column column head, body, and feet
		Affected facades	West
		Probable causes	Atmospheric pollution wrong slope (ground level) stormwater runoff

Figure 8. Deterioration type B, 'corrosion'.

According to the observation on 9th October 2018, joints degradations have been detected on the North façade, which has covered with aluminum mesh cladding (Figure 9). This deterioration may be the consequence of stiff breeze coming from the North and North-East direction. Also, wrong detail design may cause to happen in this situation.

Deterioration Type	C	Date	9.10.2018
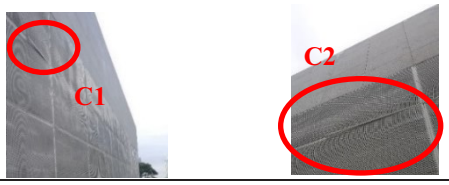		Weather data	Cloudy, 16°C
		Affected parts	Aluminum mesh cladding
		Affected facades	North
		Probable causes	Atmospheric effects (wind, rain) wrong detail design (WDD)

Figure 9. Deterioration type C, 'joints degradation'.

The observation on 9th October 2018 makes think about a mechanical impact on the North façade overhang, which is covered with aluminum composite panels (Figure 10).

Deterioration Type	D	Date	9.10.2018
		Weather data	Cloudy, 16°C
		Affected parts	Aluminum composite panels Overhang
		Affected facades	North
		Probable causes	

Figure 10. Deterioration type D, 'mechanical impact'.

According to the observation on 4th December 2018, delamination is seen on the North and East overhangs (Figure 11). Probable cause is thought to be the storm water runoff with the wind which is coming from the dominant direction. It may have penetrated from the joints and caused the delamination of layers on the composite panels.

Deterioration Type	E	Date	4.12.2018
		Weather data	After the rain, 10°C
		Affected parts	Aluminum composite panels Overhang
		Affected facades	North, East
		Probable causes	Stormwater runoff

Figure 11. Deterioration type E, 'delamination'

5.2 Case Study 2

According to the observations, anomalies detected on the selected building facades are examined. Deteriorations are classified into three categories. These are; biological staining (A), moisture rising (B), and joints degradation (C). The deteriorations which have been detected are shown in façade mapping (Figure 12).

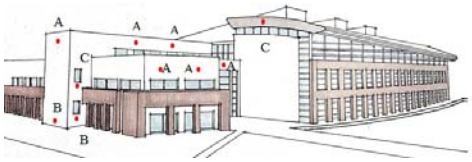

Figure 12. Façade mapping of the second case building.

According to observations, the building is exposures to the prevailing wind, which changes the direction of raindrops. As the most deteriorated part of the façade is the N/E (Figure 13), lack of sunlight slowdowns the procedure of drying after it had been wetted, and results as biological staining (due to algae, bacteria, and fungi).

Deterioration Type	**A**	**Date**	22.10.2018, 19.11.2018
		**Weather data**	Partly cloudy, Rainy
		Affected parts	GFRC panels
		Affected facades	North, East
		Probable causes	lack of sunlight after rains

Figure 13. Deterioration type A, 'biological staining'.

N/E façade is directly in contact with ground and grasses. Because of continues dampness, external wall of this part of façade is stained. As a result, mould growth appeared and there was discoloration to the wall (Figure 14).

Deterioration Type	B	**Date**	10.11.2018, 19.11.2018
		**Weather data**	Sunny, Rainy
		Affected parts	GFRC panels, Clinker panels
		Affected facades	North, East
		Probable causes	Continuous dampness, WDD

Figure 14. Deterioration type B, 'moisture rising'.

Panel joints and sealants on a façade provide for drainage of run-off on the facade. Joints affect runoff can locally rinse away deposited dirt stains at areas where a file of vertical joints is broken and where joints are slanted (Figure 15).

Deterioration Type	**C**	**Date**	10.11.2018, 19.11.2018
		**Weather data**	Sunny, Rainy
		Affected parts	GFRC panels, Aluminum
		Affected facades	North, East
		Probable causes	Atmospheric effects (wind, rain) wrong detail design

Figure 15. Deterioration type C, 'Joints degradation'.

7 Conclusion

In this study, field observation has been done for two case buildings, and probable causes on façade deteriorations have been examined with the help of literature.

The district of both cases has air pollution due to high urbanization and heavy traffic intensity. Especially in the first case, some deteriorations have been observed after only three years of usage on the North, East, and West façades which are close to the main road and the viaduct. According to the literature, aluminum composite panels should be cleaned at least once in a year. Besides, stormwater runoff should be controlled to prevent the corrosion of steel materials. To delay or prevent necessary significant renovations for the future, maintenance planning should be done and implemented periodically.

This paper helps to understand the expected behavior of GFRC panels and metal claddings for Istanbul province and similar climatic conditions. More data and laboratory analysis is required for this method to produce more reliable façade degradation mapping.

ORCID

Sahar Ardi Manafand: https://orcid.org/0000-0002-0326-017X
Begum Diker: http://orcid.org/0000-0001-9149-3880
Payam Kanani Bahri: https://orcid.org/0000-0003-1951-9534

References

Bauer, E., Kraus, E., Silva, M. N. and Zanoni, V. A. (2014). Evaluation of Damage of Building Facades in Brasilia. *XIII International Conference on Durability of Building Materials and Components* (págs. 535-542). Sao Paulo: RILEM Publications SARL.

Blocken, B., Derome, D. and Carmeliet, J. (2013). Rainwater runoff from building facades: A review, Building and Environment, Elsevier Ltd.

Chew, M. and Tan, P. (2003). Facade staining arising from design features. *Construction and Building Materials*, *17(3)*, 181–187. https://doi.org/10.1016/S0950-0618(02)00102-2

Dickinson, H. S. and C, J. J. (1999). *Effects of Air Pollution on Hİstoric Buildings and Monuments and the Scientific Basis for Conservation, Corrosion and Protection Center, University of Manchester.* Report on a Research Project Supported by Commission of the European Community.

Flores-Colen, I. and Brito, J. d. (2010). A Systematic Approach for Maintenance Budgeting of Buildings Facades Based on Predictive and Preventive Strategies. *Construction and Building Materials*(24), 1718-1729.

Galbusera, G., Brito, J. d. and Silva, A. (2014). The importance of the quality of sampling in service life prediction. *Construction and Building Materials*(66), 19-29.

Madureira, S., Flores-Colen, I., Brito, J. d. and Pereira, C. (2017). Maintenance Planning of Facades in Current Buildings. *Construction and Building Materials*(147), 790-802.

Mohaney, P. and Soni, E. G. (January 2018). Aluminium Composite Panel as a Facade Material. *International Journal of Engineering Trends and Technology (IJETT)*, 75-80.

Norvaisiene, R., Miniotaite, R. and Stankevicius, V. (2003). Climatic and Air Pollution Effects on Building Facades. *Materials Science (Medziagotyra), 9*(1), 102-105.

SIM Project. (n.d.). Retrieved September 29, 2019, from https://sim.csb.gov.tr/Services/Details?id=6b7a9840-1e13-4045-a79d-0f881c4852ad

Standards—Air Quality—Environment—European Commission. (n.d.). Retrieved September 29, 2019, from https://ec.europa.eu/environment/air/quality/standards.htm

Turkish State Meteorological Service Official Web Sites. (n.d.). Retrieved September 29, 2019, from https://mgm.gov.tr/eng/forecast-cities.aspx

XV International Conference on Durability of Building Materials and Components
DBMC 2020, Barcelona
C. Serrat, J.R. Casas and V. Gibert (Eds)

Methodology for Predicting the Service Life of Two-Ply Roofing-Felt Membrane

Erik Brandt [1] **and Martin Morelli** [2]

[1] Department of the Built Environment, Aalborg University, A.C. Meyers Vaenge 15, 2450 Copenhagen, Denmark, ebra@build.aau.dk

[2] Department of the Built Environment, Aalborg University, A.C. Meyers Vaenge 15, 2450 Copenhagen, Denmark, marmo@build.aau.dk

Abstract. *The service life of roofs depends not only on the quality of materials and components but also on several other factors such as workmanship, maintenance, design and substrate. The service life of materials is at production time estimated to a certain number of years. Later when some experience has been gained the service life can hopefully be better predicted. However, the predicted service life can always be questioned because no one knows how long the product or material will last. The durability of a two-layer roofing-felt membrane has been investigated through inspection of several 20 to 30 years old roofs that had aged naturally under in use conditions in a northern humid climate. In 50 % of the inspected roofs, samples were taken out for laboratory test. In this paper, the developed methodology to conduct a service life prediction of roofing membrane is presented. The paper includes a description of the on-site inspection; test conducted in the laboratory which was used as basis for predicting the service life of the two-layer roofing-felt membrane and how these information are extrapolated to a predicted service life. Further, it is discussed if the used methodology for prediction is generally applicable for other types of membranes.*

Keywords: *Natural Ageing, Prediction, Roofing Membrane, Building Survey.*

1 Introduction

The service life of a flat membrane roof is dependent of the material of the membrane but to a large extent also on the design of details and the workmanship. Among the factors affecting the service life are the slope, the number of details, the buildability (how easy it is to build the roof including underlay and details). However, it is a prerequisite that the membrane itself has a long service life and it is the scope of this paper to propose a way to assess the service life of the membrane material. The influence of design, workmanship and maintenance is also influencing the service life of the finished roof, however is less influencing the service life of the roofing-felt membrane as a material.

In Denmark, we use a lot of different materials for roof coverings. For flat roofs (little slope) the traditional material is (bitumen based) roofing felt, which still has the major part of this market. PVC, TPO and other plastic materials only have a small market share.

As well, the membrane materials as the underlays have undergone large changes during the years. The roofing felt was originally a cheap material with a short service life that depended on regular maintenance. Later materials with better composition and better reinforcement were developed but still the service life was very short compared to other roof coverings. One of the reasons for this was that roofs were made without slope. This meant that the membranes were exposed to water for long periods and, even worse, that they – due to the many freezing point

passages in Denmark – were exposed to forces from formation of ice. For some years, the service life for roofing felt in Denmark was only estimated to 12-15 years.

In the beginning of the 1970ies the codes were changed, so a slope of at least 1:40 were required in order to avoid standing water and problems due to ice. Since then, lots of development as regards substrates for roofing membranes and composition (including reinforcement) of roofing felt have taken place. The roofing felts used today are almost exclusively modified bitumen (SBS or APP modified) with reinforcement of polyester (sometimes supplemented with small amounts of glass fibre).

Service life of roofing materials has been a subject of many heated discussions and so far, it has in Denmark not been possible to agree on reference service lives for different roofing materials.

Some roofing materials like clay tiles and zinc have been used for a long time and their service life is relatively well known due to long times experience from practice. For membranes the composition of the materials is changing rapidly and long-term experience are consequently not available. Estimation of service life must therefore be based on other methods *e.g.* accelerated ageing or estimation of service life based on the condition of roofs in practice (which naturally means that the roofs should have a relatively long time of service under in use conditions). In the following, we set forth how estimation of reference service life for a roofing felt was performed in Denmark and give proposal to a methodology for assessing estimation of service life for roofing membranes.

2 Method

As mentioned above estimation of service life may be performed in different ways. In this small study, a combination of visual inspections and laboratory testing was used to estimate/predict the reference service life of a two-layer roofing-felt membrane.

The inspections were only related to the roofing felt itself (not to the welded joints, penetrations etc.). The roofs were located all over Denmark, and had an inclination between 1.4° and 45°. The roofing felt was laid out on an underlay of wooden boards or insulation materials. The 12 inspected roofs were chosen randomly amongst several other roofs constructed in the period 1990 to 1999, *i.e.* 20-30 years old roofing-felt membranes. Amongst the criteria for selecting, the roof was the geographical location, size and accessibility. One roof was new when the roofing felt was installed and 11 roofs were renovations. The inspected roofs had a total area of 26´639 m2. The age and history of the inspected roofs were known as they belonged to a database run by a guarantee body, and the inspected roofs were chosen from this database.

2.1 Inspections

Prior to the inspection, a systematic inspection scheme was developed to obtain a more consistent evaluation of the roofs. The evaluation of the different roof parameters, cf. Table 1, were ranked in four steps from a to d, which described the condition of the roof as

a) in good conditions,
b) with minor degradation,
c) with critical degradation,
d) in need of replacement.

The general information were determined before the inspection and validated on site; however, if a sample was not cut out it could difficult to determine the buildup of the roof and the membrane layers.

Table 1. Content of scheme used for visual inspection.

General information	Area, year of construction, type of membrane, layers, inclination, substrate, fixation
Relevant for evaluation	Overall condition, condition of slate granules, cracks in membrane, traffic areas, walkways, maintenance, biological growth, roof valley, residual service life
Other information	Quality of welded joints, depression or lump, number of details, cracks in coverings, roof light, damage at roof light, installations on roof and fastening, drainage

In connection with the inspection, samples measuring approximately 0.7 x 1.0 m were cut out of six roofs, cf. Figure 1, for later laboratory test, cf. Table 2. The sample was cut out between to welded joints thus; it was possible to repair the roof with a decent result.

a)  b) 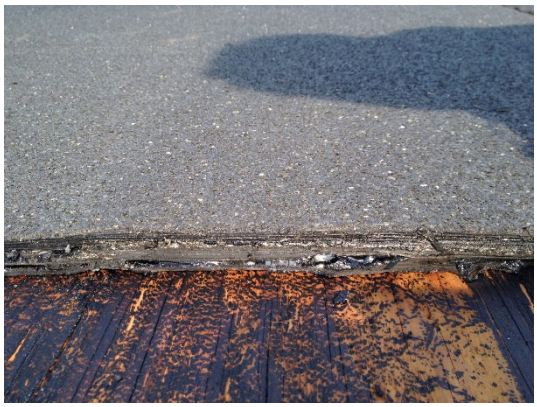

Figure 1. a) Test specimen cut out of roof with a wooden substrate and b) layers of welded roof membranes.

Table 2. The test methods used for testing of samples.

Test method	Title	Deviation
EN 13707:2013 + A2	Flexible sheets for waterproofing. Reinforced bitumen sheets for roof waterproofing. Definitions and characteristics	
FTIR-analysis	Determination of SBS content	None
EN 12311-1:1999	Flexible sheets for waterproofing - Part 1: Bitumen sheets for roof waterproofing - Determination of tensile properties	Only tested in the longitudinal direction
EN 1109:2013	Flexible sheets for waterproofing. Bitumen sheets for roof waterproofing. Determination of flexibility at low temperature	Tested on the entire system and in some cases on fewer specimens than prescribed due to lack of material
EN 12691:2006	Flexible sheets for waterproofing - Bitumen, plastic and rubber sheets for roof waterproofing - Determination of resistance to impact	Tested at -10°C on a substrate of mineral wool instead of testing at 23°C on a substrate of polystyrene or alu-board
EN 12730:2015	Flexible sheets for waterproofing. Bitumen, plastic and rubber sheets for roof waterproofing. Determination of resistance to static loading	None

2.1.1 Results of visual inspections

The results of the visual inspections are that the top membrane in all inspected roofs are assessed as being in good condition. Only minor changes compared to new membranes were visible. The protection in form of slate granules on the surface of the membrane was almost intact, and there were only minor signs of degradation even in valleys and depressions where water may gather occasionally (Figure 2a and 2b). There were in a few cases small cracks in the slate covering – known as “mud cracks” – but even here, there were no signs of degradation of the bitumen below (Figure 3a). In no cases, there were seen degradation to an extent where the reinforcement was visible. There were no signs of shrinkage of the membrane during the inspections, and there were no signs of moisture problems (neither were there reported leaks or moisture problems). On the north facing coverings biological growth was often seen (Figure 3b), which can be eliminated with a regular maintenance. Biological growth was often observed on roofs that were not maintained, however, this did not indicate any signs of degradation of the raw top-roof membrane.

a)

b)

Figure 2. Roof condition at different points. a) Condition of slate is generally good as shown, b) roof valley in equal conditions as other parts of roof membrane.

2.2 Laboratory Tests

In Denmark, we have no legal requirements to the properties of roofing materials apart from the requirement of watertightness. There are on the other hand a number of properties that are normally considered when discussing bituminous roofing membranes. These include:
tensile strength, elongation at break, flexibility under cold conditions and static and dynamic

a)

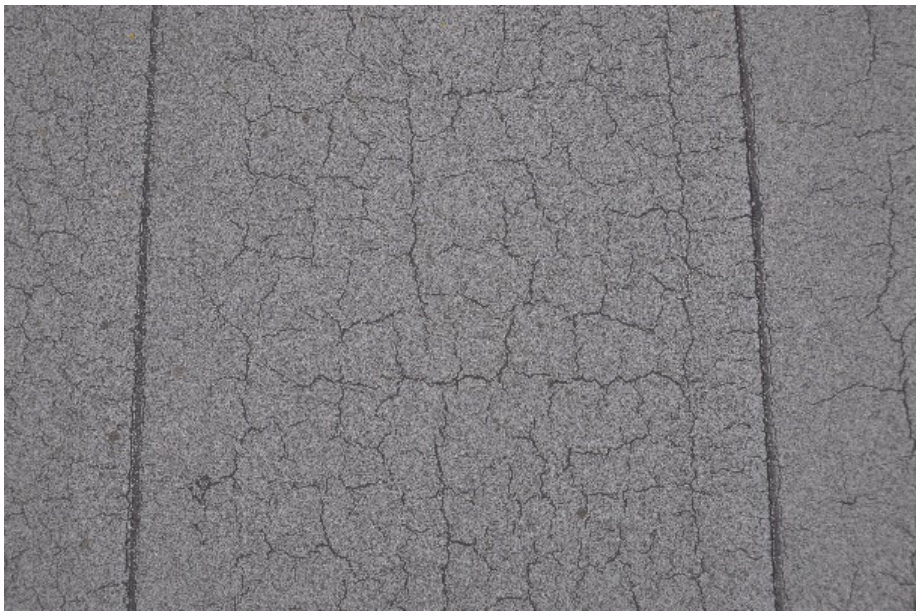

b)

Figure 3. Roof condition at different points. a) mud crack with fine amount of slate granules and b) biological growth was seen on north facing covering and surfaces, this limited biological growth is assessed not to influence the service life.

load. It seemed natural to base the study on the above mentioned properties. The testing was performed on smaller samples taken from larger samples of 0.7 x 1.0 m from the six roofs. The laboratory tests were conducted on the combined upper and lower roofing-felt membranes, because it was not possible to separate the two membranes. The results from the laboratory test were compared to a reference sample made from a virgin roofing felt (newly produced) as a combination with an upper and lower membrane welded together similar to the samples taken out from the inspected roofs.

The testing was performed at a laboratory that had all the necessary test facilities and was

approved by ETA Denmark. The test facilities was inspected and the testing was supervised by SBi (the Danish Building Research Institute /Aalborg University) and ETA Denmark A/S (that afterwards issued an ETA based on the results of the investigation).

2.2.1 Results of laboratory tests

Tensile strength is often required to be above 500 N/50 mm per sheet of bituminous roofing material and above 1000 N/50 mm for a finished solution with two layers of membrane. This requirement was fulfilled for all the tested specimens.

Elongation at break: The results achieved during testing was all above normal used requirements in many other European countries.

For *flexibility under cold conditions* results under -15 °C were achieved for membranes aged 20-30 years under in use conditions *i.e.* better than the requirements used for new membranes after accelerated heat ageing (often considered to be equivalent to 10 years of natural ageing).

Testing for *static and dynamic load* was passed by all samples with results similar to those for virgin materials.

The *SBS content* in the tested membranes lies in the same range as by production and within the deviations that may be expected by the test method.

In general, all samples that were tested performed very close to the reference samples of virgin welded material.

3 Service Life Prediction

There are no commonly accepted method to be used for prediction of service life based on tests. All predictions are consequently based on subjective judgements.

In this case the prediction of service life of the roofing membrane is based om visual inspections and tests in the laboratory. It is our opinion that both parts of the investigation are important and both should be taken into account when the service life shall be predicted. If one of the two parts gives unsatisfactory output, the service life can at best be assessed to a little longer than the actual service life of the inspected roofs. If both factors are on a good level, the service life can be assessed to be longer than the actual service life of the inspected membranes – the question is only how much longer. This depends on the actual results of both inspections and laboratory tests. Both tests should be weighted equally important and all the investigated parameters determined in the laboratory.

In this study inspections as well as laboratory tests showed very good results. Based on the results the reference service life was estimated to at least 50 years. This result is in accordance with earlier studies in Denmark performed by the Danish Roofing Advisory Board (Brandt and Bunch-Nielsen, 2008) and results from Finnish investigations (Kattoliitto, n.d.).

4 Discussion

The methodology for prediction the service life of 2-ply roofing felt was in this case chosen as explained in *3 Service life prediction* but other methodologies may be used if it appears more relevant. The laboratory test might have been complemented by other tests, cf. below, where it is explained why some test have not been part of this investigation.

Watertightness was not tested, as no leaks or moisture problems have been reported or noted

in the roofs. Further, no leaks were detected after the tests for static and dynamic load.

Strength of connections were not tested as it was impossible to separate the layers in the finished membrane (two layers welded together).

Dimensional stability was not tested as this is most important the first few years after installation (shrinkage is unwanted at installation). There were no signs of shrinkage by the inspections.

Peel and shear resistance is not relevant for 2-ply systems according to EN 13707 table A.1.

5 Conclusion

In this study we used a methodology based on a combination of visual inspections of "old" roofs in situ and test of material properties of samples taken from the inspected roofs. It is our opinion that this method is well suited for estimation of reference service life of roofing membranes. It should be noted that it is a prerequisite that the roofs to be inspected should be relatively "old" compared to the final estimated result of service life. It is also necessary to know the history of the roof membranes *i.e.* to avoid estimation of roof membranes that has been repaired or replaced roof, thus it interfere with the results. We believe that the used methodology may be used for other types of roofing membranes and maybe even more generally for estimation of service life for building materials.

When it comes to the service life of the finished roof it is necessary to take into account also the influence of design, workmanship and maintenance. In Denmark, we have for quite a long period used directions from the Danish Roofing Advisory Board as guidelines (also known as TOR and are published in Danish) for the design of bituminous membrane roofs. This has resulted in a significant decrease in the number of problems we had some 40 years ago *i.e.* good directions help to design properly and thereby reduce the number of failures.

In addition, the workmanship is important, and to ensure a good long lasting roof it is considered crucial that skilled persons are used for the job.

ORCID

Erik Brandt: https://orcid.org/0000-0003-1485-5600
Martin Morelli: https://orcid.org/0000-0002-1013-3136

References

Brandt, E. and Bunch-Nielsen, T. (2008). Service life (model) for bituminous roofing. In *Proceedings of the 11 DBMC International Conference on Durability of Building Materials and Components,* Istanbul, Turkey, T22, 1–9.

EN (1999). *EN 12311-1:1999: Flexible sheets for waterproofing - Part 1: Bitumen sheets for roof waterproofing - Determination of tensile properties.*

EN (2006). *EN 12691:2006: Flexible sheets for waterproofing - Bitumen, plastic and rubber sheets for roof waterproofing - Determination of resistance to impact.*

EN (2013a). *EN 1109:2013: Flexible sheets for waterproofing. Bitumen sheets for roof waterproofing. Determination of flexibility at low temperature.*

EN (2013b). *EN 13707:2013: Flexible sheets for waterproofing. Reinforced bitumen sheets for roof waterproofing. Definitions and characteristics.*

EN (2015). *EN 12730:2015: Flexible sheets for waterproofing. Bitumen, plastic and rubber sheets for roof waterproofing. Determination of resistance to static loading.*

Kattoliitto (n.d.). *Roof System Manual*. Kattoliitto, Finland.

XV International Conference on Durability of Building Materials and Components
DBMC 2020, Barcelona
C. Serrat, J.R. Casas and V. Gibert (Eds)

Probabilistic Approach to the Service Life Prediction of Timber Claddings

Ana Silva[1] **and Andrés José Prieto**[2]

[1] Department of Civil Engineering, Architecture and Georresources, Instituto Superior Técnico, University of Lisbon, Lisbon, Portugal, ana.ferreira.silva@tecnico.ulisboa.pt

[2] Instituto de Arquitectura y Urbanismo, Universidad Austral de Chile, Edificio Ernst Kasper (Campus Isla Teja),Valdivia, Chile, andres.prieto@uach.cl

Abstract. *The service life of buildings and components is extremely difficult to model and predict, mainly due to the uncertainty and variability associated with the degradation phenomena. These uncertainties are usually related with the intrinsic randomness of natural phenomena, such as the environmental degradation agents. In order to deal with these uncertainties, in this study, a stochastic approach is used, to model the service life of timber claddings. For this purpose, a logistic regression analysis is used to evaluate the probability of timber claddings to reach the end of their service life over time. Moreover, the impact of the environmental exposure conditions (e.g. facades orientation, distance from the ocean, exposure to damp and exposure to wind/rain action), which influence the degradation and service life of timber claddings, is also evaluated. The proposed models are applied to 150 timber claddings, located in Valdivia (South Chile), which have been analysed during an extensive fieldwork survey. The results obtained in this study aid the definition of maintenance plans, in a technically informed manner, in order to promote the conservation of these claddings, which are an important symbol of the local identity of this region, depicting a complexity of cultural values, inherited by Spanish and German colonisations.*

Keywords: *Durability, Service Life Prediction, Timber Claddings, Chile.*

1 Introduction

A rational approach to the definition of maintenance policies and strategies requires an efficient evaluation of the service life of the building or element under analysis. External claddings are one of the most vulnerable elements of a construction, since are subjected to several degradation agents and mechanisms (Silva *et al.,* 2016). The façade is considered as a building component, acting as the first durability layer, contributing to the building's performance and aesthetic appearance, functioning as the interface of the exterior and the inner environment, thus also contributing to the users' internal comfort. The deterioration rate of timber façades depends on several variables, including location, solar orientation, architectonical details, exposure level, microclimate, and intrinsic properties of materials used in construction. The use of service life prediction methodologies allows a more rational management of the maintenance of buildings and its constructed components by supporting reduced life cycle costs of built assets. This study evaluates the probability distribution of the degradation condition of timber claddings, using the evaluation of the characteristics of 150 cladding systems inspected in Valdivia, Chile. For that purpose, a logistic regression analysis is used, which allows forecasting the probability of the timber claddings to reach the end of their service life over time and according to their environmental exposure conditions. This analysis is relevant in developing countries where there are few studies related to the service life prediction of building components (façades). The scarcity of funds to maintain and preserve the built park and infrastructures needs a more rational approach to decision-making regarding the inspection, maintenance and rehabilitation.

1.1 Degradation Phenomena of Timber Claddings

In 2011, Gaspar and de Brito (2011) proposed a numerical index (severity of degradation - S_w) to express the overall degradation condition of facades claddings. The severity of degradation (S_w) index is obtained by the ratio between the weighted degraded area and the total cladding area, assuming the highest possible level of degradation (equation 1). This methodology was originally developed for rendered facades, establishing a general framework model, and was adapted to new cladding materials, as natural stone claddings, ceramic cladding systems, painted surfaces (Silva *et al.,* 2016).

$$S_w = \frac{\sum(A_n \times k_n \times k_{a,n})}{A \times \sum k_{max.}} \quad (1)$$

Where S_w represents the severity of degradation of timber claddings, expressed as a percentage, k_n is the multiplying factor of anomaly "n", as a function of their degradation level, within the range K = {0, 1, 2, 3, 4}, $k_{a,n}$ is the weighting factor corresponding to the relative weight of the anomaly detected, A_n is the area of cladding affected by an anomaly "n", in m^2, A is the facade area, in m^2, and $\sum(k_{max.})$ is the sum of the weighting factors for the highest degradation level of each anomaly type in a cladding with an area equal to A. In Table 1, the different types of anomalies detected are classified according to five degradation levels, considering the extent of the cladding affected by them. The degradation levels proposed vary between level A (very good condition) - the most favourable condition, corresponding to claddings with no visible degradation - and level E (severe degradation) - the worst possible condition, corresponding to claddings with generalised degradation.

Table 1. Degradation levels adopted for timber claddings.

Degradation level	Anomalies group	Anomalies description	$k_{a,n}$	% Area of cladding affected
Level A (Very good) $S_w \leq 1\%$	-	No visible degradation	-	-
Level B (Good condition) $1\% < S_w \leq 10\%$	Aesthetic	AA1 Staining or color change (dirty surface)	0.3	≤ 15%
		AA2 Wearing or detachment of the finishing layer	0.7	≤ 10%
	Loss of integrity	AB1 Warping, swelling or other flatness deficiencies	0.5	≤ 10%
Level C (Slight degradation) $10\% < S_w \leq 20\%$	Aesthetic	AA1 Staining or color change (dirty surface)	0.3	> 15%
		AA2 Wearing or detachment of the finishing layer	0.7	> 10% to ≤ 50%
	Loss of integrity	AB1 Warping, swelling or other flatness deficiencies	0.5	> 10% to ≤ 50%
		AB2 Cracking of elements and/or joints (possibly from substrate cracking)	0.9	≤ 20%
		AB6 Moisture (Oxyde) / Biocostra	0.5	≤ 30%
		AB8 Delamination	1.0	≤ 10%
		AB9 Crumbling	1.2	≤ 10%
Level D (Moderate degradation) $20\% < S_w \leq 40\%$	Aesthetic	AA2 Wearing or detachment of the finishing layer	0.7	> 50%
	Loss of integrity	AB1 Warping, swelling or other flatness deficiencies	0.5	> 50%
		AB2 Cracking of elements and/or joints (possibly from substrate cracking)	0.9	> 20%
		AB3 Broken or splintered elements	1.0	≤ 20%
		AB4 Detachment of elements from substrate (lack of adherence)	1.2	≤ 10%
		AB6 Moisture (Oxyde) / Biocostra	0.5	> 30%
		AB5 Rot	1.2	≤ 10%
		AB7 Xylophage attack	1.0	≤ 10%
		AB8 Delamination	1.0	> 10% to ≤ 30%
		AB9 Crumbling	1.2	> 10% to ≤ 30%
Level E (Severe degradation) $S_w > 40\%$	Loss of integrity	AB3 Broken or splintered elements	1.0	> 20%
		AB4 Detachment of elements from substrate (lack of adherence)	1.2	> 10%
		AB5 Rot	1.2	> 10%
		AB7 Xylophage attack	1.0	> 10%
		AB8 Delamination	1.0	> 30%
		AB9 Crumbling	1.2	> 30%

2 Probabilistic Analysis of Timber Claddings Reaching the End of their Service Life Over Time

A logistic regression analysis is used to model the probability of timber claddings reaching the end of their service life over time and according to their environmental exposure conditions. Logistic regression is one of the most used statistical procedures, which allows describing the relationship between a categorical dependent variable and one or more explanatory variables, in terms of the probability of a given event. In this study, the dependent variable corresponds to the question "Has the timber cladding reached the end of its service life?", and this question presents two mutually exclusive classes: "yes" and "no". For the timber claddings under analysis, it is assumed that a cladding reaches the end of its service life, when presents a set of anomalies corresponding to a severity of degradation of 20%. Figure 1 shows an illustrative example of a timber cladding in the end of its service life. The limit to establish the end of service life is conventionally defined and is related to the Chilean context, and with the users' acceptance criteria. This theoretical limit can change according to the buildings' economic and social context or even funds available for maintenance actions. The sample analysed is composed by 150 timber claddings, located in Valdivia (South Chile), and only 8% of the claddings have reached the end of their service life. In the first analysis performed, only the age of the claddings is used as explanatory variable.

Figure 1. Case study that exemplifies the end of the service life of timber claddings.

The proposed model, described by Equation (2), allows evaluating the probability of a timber cladding reach the end of its service life according to its age. The goodness-of-fit of the proposed models to the dataset under analysis is evaluated through the Chi-square test (χ^2) and the Chi-square test of Hosmer-Lemeshow (χ_{HL}^2). These tests are easy to compute and are present in the statistical software used in this study; furthermore, as mentioned in Silva et al. (2016), these tests have been widely used mainly due to the nonexistence of better approaches. For the Chi-square test (χ^2) test, a *p*-value around 1 reveals a better fit to data than a model that only has the constant; on the other hand, a *p*-value around 1 for χ_{HL}^2 test, reveals that the age of the claddings or the other independent variables included in the model, are relevant for the end of service life of timber claddings. The model summary ($\chi^2(148) = 17.826$, $p = 1.00$) and the Hosmer and Lemeshow test ($\chi_{HL}^2(8) = 0.133$, $p = 1.00$) reveal an adequate adjustment of the model to the sample under analysis. The Wald test (χ_{Wald}^2 (1) = 12.163, with $p = 0.00$) shows that the age is statistically relevant to predict the probability of timber claddings reaching the end of their service life.

$$P(Y = "End\ of\ service\ life") = 1 - \frac{1}{1+e^{-18.200+0.539Age}} \quad (2)$$

Figure 2 shows the probabilistic distribution of timber claddings reaching the end of their service life over time. As expected, the probability of timber claddings reaching the end of their service life increases with the claddings' age. After 33.8 years, a timber cladding presents a probability higher than 50% of have reached the end of its service life, after 35.8 years, this probability is higher than 75% and after 37.9 years, it is higher than 90%.

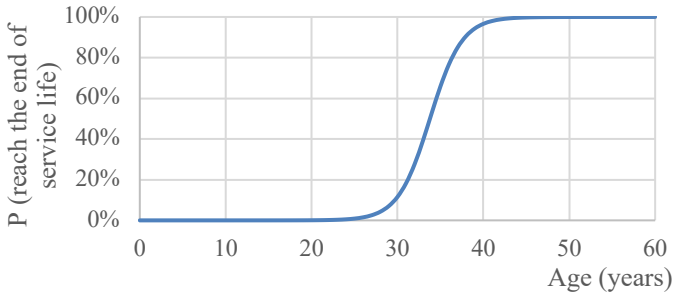

Figure 2. Distribution of probability of timber claddings reaching the end of their service life over time.

Table 2 shows the classification table of the proposed model, which allows evaluating the percentage of timber claddings correctly classified by the model, i.e. the classification table provides the accuracy of the model, evaluating the capability of the model discriminate the case studies that has reached the end of their service life from the case studies that has not reached this limit. The proposed model classifies correctly 97.3% of the timber claddings analysed, revealing that the model presents a good classification capability.

Table 2. Classification table of the proposed model.

Observed		*Predicted*		
		Has the timber cladding reached the end of its service life?		**Percentage correct**
		No	Yes	
Has the timber cladding reached the end of its service life?	No	136	2	98.6
	Yes	2	10	83.3
Overall percentage				97.3

3 Probabilistic Analysis of Timber Claddings Reaching the End of their Service Life according to the Environmental Exposure Conditions

Wood is frequently used as external cladding, mainly due to aesthetic, ecological or architectural reasons. Nevertheless, wood is extremely susceptible to various degradation agents and mechanisms (e.g. wetting, microorganisms, fungi or algae, xylophage agents), especially related with the environmental exposure conditions (Brischke *et al.,* 2017). In this sense, in this study, the influence of the environmental exposure conditions in the service life of timber claddings, located in Valdivia (Chile) is analysed. For this purpose, the influence of the exposure to damp, the façades orientation, the wind-rain action and the exposure to sea salts (distance from Pacific Ocean) is evaluated. In Figure 3, the probability of timber claddings reaching the end of their service life over time, according to their exposure to damp, is analysed. For the exposure to damp, two categories are considered (Silva *et al.,* 2016): i) high, for claddings located near to damp sources, in contact with the terrain, in areas with high relative humidity, and not protected by adjacent buildings; and ii) medium, for claddings that are not directly exposed to damp sources. Equation (3) allows estimating the probability of a timber cladding to reach the end of its service life over time and according to its exposure to damp, where the variable "Age" must be replaced by the age of the timber claddings and the variable "Damp" must be replaced by 1 if the timber cladding presents a high exposure to damp and by

0 if the cladding shows a medium exposure to damp. This model correctly classifies 97.3% of the timber claddings under analysis.

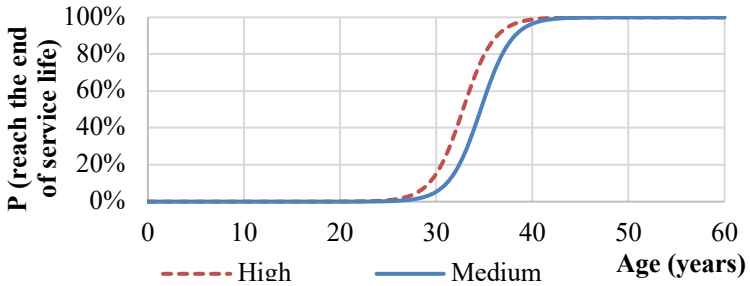

Figure 3. Distribution of the probability of timber claddings reaching the end of their service life over time, according to their exposure to damp.

$$P(Y = "End\ of\ service\ life") = 1 - \frac{1}{1+e^{-21.462+0.620Age+1.143Damp}} \quad (3)$$

Figure 4 shows the probability of timber claddings reaching the end of their service life over time, according to façades orientation. This probability can be estimated using Equation (4), where in the variable "façades orientation", the symbol of the category corresponding to the timber cladding analysed should be replaced by 1, and the remaining categories' symbols by 0. The logistic regression model obtained, adopting the variable age and façades orientation correctly classifies 98% of the sample analysed.

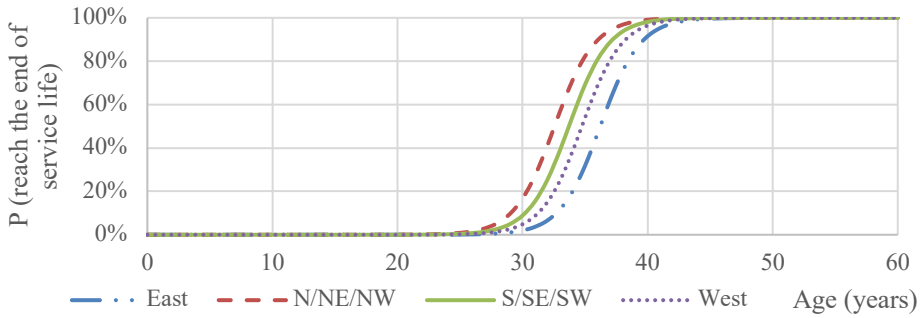

Figure 4. Distribution of the probability of timber claddings reaching the end of their service life over time, according to façades orientation.

$$P(Y = "End\ of\ service\ life") = 1 - \frac{1}{1+e^{-21.826+0.628Age-0.921E+1.375N/NE/NW+0.652S/SE/SW}} \quad (4)$$

Figure 5 presents the probability of timber claddings reaching the end of their service life over time, according to their exposure to wind-rain action. In this study, two categories are adopted to characterise the exposure conditions of timber claddings to the combined action of wind and rain: i) unfavourable, for claddings located in tall buildings, located in areas unsheltered by surrounding buildings or vegetation, thus exposed to prevailing winds; and ii) current, for claddings protected from the direct incidence of rain and prevailing winds. Equation (5) allows evaluating the probability of a timber cladding to reach the end of its service life according to its age and exposure to wind-rain action, where the variable "Wind" must be replaced by 1 if the timber cladding presents an unfavourable exposure to wind-rain action and by 0 if the cladding shows a current exposure. This model correctly classifies 97.3% of the timber claddings analysed.

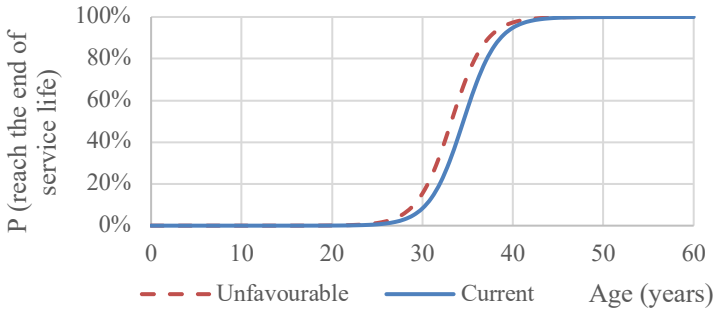

Figure 5. Distribution of the probability of timber claddings reaching the end of their service life over time, according to their exposure to wind-rain action.

$$P(Y = "End\ of\ service\ life") = 1 - \frac{1}{1+e^{-18.369+0.532Age+0.703Wind}} \quad \textbf{(5)}$$

In Figure 6, the probability of timber claddings reaching the end of their service life over time, according to their distance from the Pacific Ocean, is shown. In this analysis, two categories are considered: i) claddings located at more than 5km from the Pacific Ocean; and ii) claddings located at less than 5km from the Pacific Ocean. Equation (6) allows estimating this probability, where the variable "Ocean" must be replaced by 1 if the cladding is located at less than 5km from the Pacific Ocean and by 0 if the cladding is located at more than 5km. This model presents a classification capability of 97.3%.

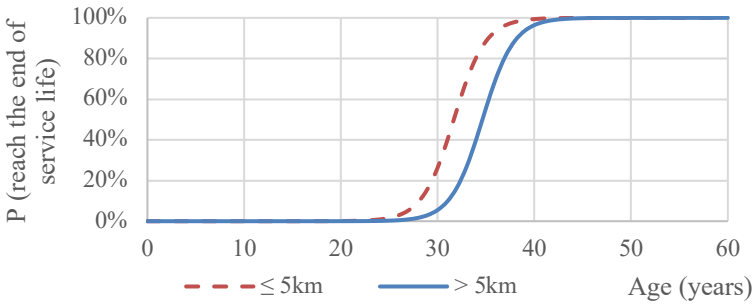

Figure 6. Distribution of the probability of timber claddings reaching the end of their service life over time, according to their distance from the Pacific Ocean.

4 Results and Discussion

Bio-materials, as timber, when applied in façade claddings, are exposed to several degradation agents, which generally are biotic agents (fungi, insects, moulds, algae) and abiotic agents (water, solar radiation, gradient of temperature, pollutants) (Sandak *et al.,* 2019). Other factors, such as the building orientation and its surrounding environment, presence of adjacent buildings, vegetation, and the proximity of water reservoirs (Silva *et al.,* 2016; Prieto and Silva, 2019), can also compromise the durability of timber claddings. Moreover, the degradation mechanisms usually occur simultaneously, affecting the degradation pattern over time and the extent damages among the different timber claddings analysed. Based on the sample analysed (150 timber claddings located in South Chile), and according to the stochastic models proposed, the following conclusions can be drawn (Table 3).

This analysis reveals that after 33.8 years, a timber cladding presents a probability higher than 50% of have reached the end of its service life and after 37.9 years, this probability is higher than 90%. These results are in accordance with the literature related with the durability of timber claddings, which suggests an estimated service life between 30 to 35 years for wood materials in outdoor exposure environments.

The weathering of timber claddings occurs mainly due to abiotic agents, which present a significant impact in the degradation process of timber claddings in South Chile due to their exposition to severe climatic conditions. In most cases, weathering leads to cracking, colour changes or alterations in the finishing layer (Sandak *et al.,* 2019).

A high exposure to damp contributes to the presence of fungi decay, insects, moulds and algae growth, among other biotic factors (Sandak *et al.,* 2019). Although the presence of mould does not affect the structural properties of wooden façades, it has a large effect on the aesthetical service life of the cladding. Mould leads to the claddings' discolouration, unpleasant odour, and health problems. This factor usually appears in environmental conditions like in Valdivia, where relative humidity (RH) is higher than 75% and the temperature ranges between 0 and 45 ºC. Algae, which promotes the colour change of timber claddings, normally occurs in contexts with RH > 95% and temperature fluctuations from 0ºC to 45ºC. Timber claddings with high exposure to damp reach the end of their service life sooner (with a probability of 95% of have reached the end of its service life after 37.5 years - Table 3), than claddings with a low exposure, which reach the end of their service life around two years later (39.4 years). In the sample analysed, timber claddings with high exposure to damp have a higher incidence of rot and xylophage attack.

Regarding the surfaces' orientation, claddings facing North are more exposed to UV radiation, suffering significant thermal gradients. On the other hand, timber claddings facing South, in Chile, are more exposed to the presence of damp. Claddings facing East and West are the most affected by wind-rain action in Valdivia. Table 3 shows that timber claddings facing North reach the end of their service life sooner (with a probability higher than 95% of reaching the end of their service life, after 37.2 years), followed by claddings facing South (38.4 years) and by the claddings facing the remaining orientations (West - 39.4 years; East - 40.9 years) (Table 3). The main anomalies detected in claddings facing North orientation were related with wearing or detachment of the finishing layer, broken or splintered elements and detachment of elements from substrate.

Table 3. Analysis of the probability of timber claddings reach the end of their service life, according to their environmental exposure conditions.

Environmental exposure conditions		Age where a timber cladding achieves a probability of 50% of have reached the end of its service life	Age where a timber cladding achieves a probability of 75% of have reached the end of its service life	Age where a timber cladding achieves a probability of 90% of have reached the end of its service life	Age where a timber cladding achieves a probability of 95% of have reached the end of its service life
Exposure to damp	High	32.8	34.6	36.4	37.5
	Medium	34.7	36.4	38.2	39.4
Facades orientation	N	32.6	34.3	36.1	37.2
	S	33.7	35.5	37.2	38.4
	W	34.4	36.5	38.3	39.4
	E	36.2	38.0	39.7	40.9
Exposure to wind and rain action	Unfavourable	33.2	35.3	37.4	38.8
	Current	34.5	36.6	38.7	40.1
Distance from the Pacific Ocean	< 5km	31.7	33.5	35.5	36.5
	> 5km	34.6	36.4	38.2	39.3

The level of exposure to the combined action of wind and rain is influenced by the façades orientation, as well as by the height of the building, the presence of adjacent buildings or even vegetation. In this study, façades with an unfavourable exposure to wind-rain action reach the end of the service life sooner (with a probability higher than 95% of reaching the end of their service life, after 38.8 years), when compared with façades with a current exposure (40.1 years).

In the sample analysed, timber claddings with a high exposure to wind and rain are more prone to present staining or colour change, cracking and presence of crumbling.

Finally, timber surfaces close to the Pacific Ocean (< 5 km) reached the end of their service life sooner (with a probability higher than 95% of reaching the end of their service life, after 36.5 years) than cases located at more than 5 km from the Ocean coastline (39.3 years) (Table 3). Timber claddings closer to the seashore show a higher incidence of anomalies such as cracking of elements and/or joints and wearing or detachment of the finishing layer.

5 Conclusions

In this study, a logistic regression analysis is used to evaluate the probability of timber claddings to reach the end of their service life over time and according to the claddings' environmental exposure conditions (*e.g.* facades orientation, distance from the ocean, exposure to damp and exposure to wind/rain action). According to the proposed model, the 150 timber claddings analysed present a probability higher than 50% of reaching the end of their service life after 34 years, which is in accordance with the literature and the empirical knowledge related with the degradation of these claddings. As expected, timber façades with unfavourable conditions (closer to the Pacific Ocean, facing North (N) and South (S) orientations and with high exposure to environmental agents, i.e. damp and wind-rain actions) are more prone to reach sooner the end of their service life. In the sample analysed, the most common anomalies detected were staining or colour change; wearing or detachment of the finishing layer; cracking of elements and/or joint; warping, swelling or other flatness deficiencies; and broken or splintered elements.

This model allows predicting the end of service life of timber claddings, i.e. the instant after which is necessary to intervene, in order to improve the claddings' condition, ensuring that the cladding is able to fulfil the users and owners' demands and expectations, in a probabilistic way. In this sense, the model allows knowing the risk associated with the service life values estimated by the model, and the risk of failure of the timber claddings over time and according to the environmental degradation agents that influence the degradation of the timber claddings under analysis. The results obtained can be useful for a further knowledge of the durability and service life of timber claddings and can be employed to aid the adoption of rational and adequate maintenance policies. In fact, the analysis of the timber claddings' degradation and service life in South Chile (Los Rios region), allows establishing new and adapted strategies and maintenance plans, to reduce the repair costs and to optimise the use of scarce resources, as well as promoting new approaches to maintain cultural identities of the southern regions of Chile, in which the wood is one of the main natural resources.

ORCID

Ana Silva: http://orcid.org/0000-0001-6715-474X
Andrés José Prieto: http://orcid.org/0000-0003-0604-0364

References

Brischke, C., Meyer-Veltrup, L. and Bornemann, T. (2017). Moisture performance and durability of wooden façades and decking during six years of outdoor exposure. Journal of Building Engineering, 13, 207-215. DOI: 10.1016/j.jobe.2017.08.004.

Gaspar, P. and de Brito, J. (2011). Limit states and service life of cement renders on façades. Journal of Materials in Civil Engineering, V. 23, Issue 10, pp. 1393-1404.

Prieto, A. J. and Silva, A. (2019). Service life prediction and environmental exposure conditions of timber claddings in South Chile. Building, Research and Information, 48(2), 191-206.

Sandak, A., Sandak, J., Brzezicki, M. and Kutnar, A. (2019). Portfolio of Bio-Based Façade Materials. In Bio-based Building Skin (pp. 155-177). Springer, Singapore.

Silva A., de Brito J. and Gaspar P.L. (2016). Methodologies for service life prediction of buildings. With a focus on façade claddings. 1st Edition, Springer International Publishing, Switzerland.

XV International Conference on Durability of Building Materials and Components
DBMC 2020, Barcelona
C. Serrat, J.R. Casas and V. Gibert (Eds)

Reliability Assessment of Pressurized Pipes with Inclined Defects

Yanlin Wang[1,a], Weigang Wang[1,b], Wei Yang[2] and Chun-Qing Li[1,c]

[1] School of Engineering, RMIT University, Melbourne, 3001, Australia, [a]s3733192@student.rmit.edu.au, [b]weigang.wang@rmit.edu.au, [c]chunqing.li@rmit.edu.au

[2] Faculty of Architecture, Design and Planning, The University of Melbourne, Melbourne, 3010, Australia, wei.yang@unimelb.edu.au

Abstract. *Inclined defects in pipelines can lead to failures in the form of mixed mode fracture. A review of the literature suggests that few studies have been carried out on reliability assessment of pipelines considering mixed mode fracture. This paper intends to present a reliability-based method for assessing fracture failures of pressurized pipes with inclined defects. Richard's criterion is employed in the development of the limit state function for reliability assessment. A Stochastic model of load effects is developed, and first passage method with a developed analytical solution is used to predict the pipe failures. A worked example is provided to illustrate the application of the proposed method. The method presented in this paper can help pipe engineers and asset managers to develop a reliability-based maintenance strategy for better management of pipelines.*

Keywords: *Pressurized Pipes, Inclined Crack, Mixed Mode Fracture, Time-Dependent Reliability, First Passage Probability.*

1 Introduction

Pipelines are widely used as one of the safest and most economical structures to transport gas or liquid (*e.g.*, water; natural gas) in industries (Keshtegar and Miri, 2014). However, most of them have been in service for a long time, and the exposure to the corrosive environment increases the likelihood of failures before the end of the intended design life (Carbal and Kimber, 1997). The consequences of pipeline failures can be economically, socially, and environmentally devastating (Mahmoodian and Li, 2017). Therefore, it is essential to fully understand the failure mechanisms of pipes and accurately predict its service life.

A literature review suggests that most of the previous researches on the pipe failure assessment mainly considered the loss of strength due to the reduction of wall thicknesses of pipes (*e.g.*, Ahammed and Melchers, 1997; Mahmoodian and Li, 2017; Liu *et al.*, 2019). Nevertheless, it has been found that pipe failures are more likely to be fracture type due to the stress concentration near the tips of crack-like defects (Li and Mahmoodian, 2013; Fu *et al.*, 2019). As the cracked structures often fail unexpectedly at the applied stress much below the material strength (Anderson, 2005), it is necessary to assess the integrity of pipeline based on fracture mechanics. Also, the defects on the pipe walls are often caused by corrosion, which can grow in any directions depending on the heterogeneity of surrounding soil properties (Wang *et al.*, 2018; Wang *et al.*, 2019). Moreover, the crack-like defects in pipes most likely grow in an inclined manner because of the complex stress state (Li *et al.*, 2016). As a result, in these pipes (*e.g.*, Figure 1), the failures can be induced by a mixed mode loading interaction. Some previous researches (*e.g.*, by Erdogan and Shih, 1968; Chang *et al.*, 2006) indicated that the single mode fracture failure criterion is seldom appropriate for assessing the integrity of structural components with inclined cracks. Thus, a method based on mixed mode fracture criteria is more appropriate to assess the fracture failures of pipes. To predict the pipe failures, time-dependent reliability methods have been successfully used since the parameters associated with pipe

failures are highly uncertain and changing with time (Fu *et al*., 2019). Although several researchers, *e.g*., Li and Mahmoodian (2013); Fu *et al*., (2019); Wang *et al*., (2019), have assessed the probability of pipe failures using time-dependent reliability methods for different defect types (*e.g*., sharp corrosion pit; elliptical corrosion pit), these works only focuses on Mode I (opening mode) fracture failure. The reliability assessment of pipelines with inclined defects considering mixed mode fracture, in comparison, is highly limited.

This paper presents a time-dependent reliability method for pressurized pipe based on first passage probability theory. The cast iron pipe with an external inclined crack-like defect is considered in this paper. A stochastic model of the stress intensity factor is developed by incorporating Richard's criterion into the limit state function. A case study is presented to illustrate the proposed method. The proposed method can be applied to the risk-based maintenance strategy for pipelines.

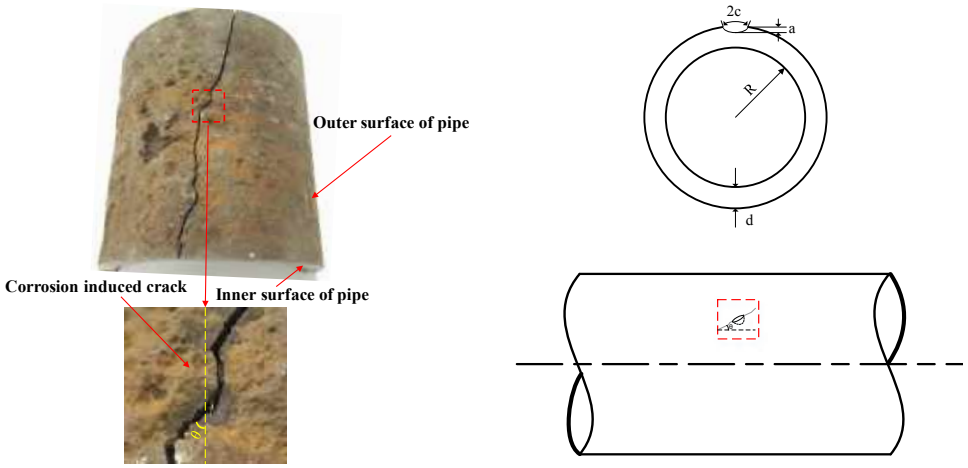

Figure 1. A pressurized pipe with inclined external surface defects.

2 Problem Formulation

To determine the probability of failure of a pipe, a failure criterion must be established. In the structural reliability theory, the criterion can be expressed in the form of a limit state function as follows (Melchers, 1999):

$$G(L,R,t) = L(t) - R(t) \tag{1}$$

where $L(t)$ is the load effect on the structures at time t; $R(t)$ is the acceptable limit (resistance) at time t. As both load effect ($L(t)$) and acceptable limit ($R(t)$) are time-dependent, all or some of the basic variables should be modelled as stochastic processes. For reliability problems involving the stochastic processes, the structural failure event is that the stochastic processes of the load action process $L(t)$ initially pass upwards an acceptable limit (threshold) $R(t)$ during the service life. With the assumption of Poisson processes, the probability of failure can be determined as follows (Melchers, 1999):

$$P_f(t) = 1 - [1 - P_f(0)]e^{-\int_0^t v\,dt} \tag{2}$$

where P indicates the probability of an event; $P_f(0)$ is the probability of failure at time $t = 0$ and v is the mean rate for the load action process $L(t)$ to cross upwards the threshold $R(t)$. The up-crossing rate v can be determined by the Rice formula (Rice, 1944)

$$v = v_R^+ = \int_{\dot{R}}^{\infty} (\dot{R} - \dot{L}) f_{L\dot{L}}(L, \dot{R})\, d\dot{L} \tag{3}$$

where v_R^+ is the up-crossing rate of the load action process $L(t)$ relative to the threshold $R(t)$; $\dot{R}$ is the slope of R with respect to time; $\dot{L}$ is the time derivative process of L; $f_{L\dot{L}}$ is the joint probability density function for L and $\dot{L}$. Li and Melchers (1993) derived an analytical solution to Equation (3) when $L(t)$ is a Gaussian process and the threshold R is deterministic. It is expressed as follows:

$$v_R^+ = \frac{\sigma_{\dot{L}|L}}{\sigma_L} \phi\left(\frac{R - \mu_L}{\sigma_L}\right) \left\{ \phi\left(\frac{\dot{R} - \mu_{\dot{L}|L}}{\sigma_{\dot{L}|L}}\right) - \frac{\dot{R} - \mu_{\dot{L}|L}}{\sigma_{\dot{L}|L}} \Phi\left(-\frac{\dot{R} - \mu_{\dot{L}|L}}{\sigma_{\dot{L}|L}}\right) \right\} \tag{4}$$

where μ and σ are the mean and standard deviation of random variables represented by subscripts L and $\dot{L}$; $'|'$ denotes the condition; ϕ and Φ indicate the standard normal density and distribution functions. For a given Gaussian stochastic process with mean function $\mu_L(t)$ and auto-covariance function $C_{LL}(t_i, t_j)$, all terms in Equation (4) can be determined as follows:

$$\mu_{\dot{L}|L} = E\left[\dot{L} \middle| L = R\right] = \mu_{\dot{L}} + \rho_L \frac{\sigma_{\dot{L}}}{\sigma_L} (R - \mu_L) \tag{5a}$$

$$\sigma_{\dot{L}|L} = [\sigma_{\dot{L}}^2 (1 - \rho_L^2)]^{1/2} \tag{5b}$$

where $\mu_{\dot{L}} = d\mu_L(t)/dt$; $\sigma_{\dot{L}} = \left[\partial^2 C_{LL}(t_i, t_j) / (\partial t_i \partial t_j)\big|_{i=j}\right]^{\frac{1}{2}}$; $\rho_L = C_{L\dot{L}}(t_i, t_j) / [C_{LL}(t_i, t_j) \cdot C_{\dot{L}\dot{L}}(t_i, t_j)]^{\frac{1}{2}}$; and $C_{L\dot{L}}(t_i, t_j) = \partial C_{LL}(t_i, t_j)/\partial t_j$.

For Equation (4) to be of practical use, the key is to establish an appropriate limit state function for the mix mode fracture failure of pipes. Richard (2001) developed a fracture criterion to simplify the prediction of crack growth under multiaxial loadings. According to Richard (2001), unstable crack growth in brittle materials would occur if the local loading condition along the crack front reaches a critical value, which described by the following expression (Richard, 2001):

$$K_v = \frac{K_I}{2} + \frac{1}{2}\sqrt{K_I^2 + 4(\alpha_1 K_{II})^2 + 4(\alpha_2 K_{III})^2} \geq K_{IC} \tag{6}$$

where K_v is an equivalent stress intensity factor; K_I, K_{II}, and K_{III} are the Mode I (opening mode), Mode II (in-plane shear mode), and Mode III (out-of-plane shear mode) stress intensity factors, respectively; K_{IC} is the Mode I fracture toughness which quantifies the material resistance to crack extension; $\alpha_1 = K_{Ic}/K_{IIc}$ and $\alpha_2 = K_{Ic}/K_{IIIc}$ with K_{IIc} as the fracture toughness for pure Mode II and K_{IIIc} as the fracture toughness for pure Mode III. With $\alpha_1 = 1.155$ and $\alpha_2 = 1.0$, Equation (6) was found having an excellent agreement with other criteria (*e.g.*, developed by Schöllmann *et al*., 2002) and the experimental data in brittle materials (Richard *et al*., 2014). Based on Richard's criterion, Equation (1) can be expressed as:

$$G(t) = \frac{K(t)_I}{2} + \frac{1}{2}\sqrt{K(t)_I^2 + 5.3361 K(t)_{II}{}^2 + 4 K_{III}{}^2} - K(t)_{IC} \tag{7}$$

The determination of stress intensity factors is presented in the next section.

3 Model of Load Effects

The stress intensity factor (K) represents the magnitude of the stress fields surrounding the tip of crack or crack-like defect. Its magnitude depends on the far-field stress level σ, the size of crack a, and the geometries of the bodies. For a pipe with an external inclined defect as shown in

Figure 1, the stress intensity factor K can be generalised as follows (Li *et al*., 2016):

$$\boldsymbol{K} = \frac{pR}{d}\sqrt{\pi\frac{a}{Q}}\boldsymbol{F}\left(\frac{a}{d},\frac{a}{c},\frac{d}{R},\xi,\theta\right) \tag{8}$$

where $\boldsymbol{K} = \{K_I, K_{II}, K_{III}\}^T$; p is the internal pressure; pR/d is the average hoop stress in pipes; ξ is used to define the position of an arbitrary point along the semi-elliptical crack; θ, c, d, and R are defined in Figure 1; Q is the shape function which can be expressed as follows (Shiratori and Miyoshi, 1986):

$$Q = 1 + 1.464\left(\frac{a}{c}\right)^{1.65}; \quad \frac{a}{c} \leq 1 \tag{9}$$

In Equation (8), $\boldsymbol{F}\left(\frac{a}{d},\frac{a}{c},\frac{d}{R},\xi,\theta\right) = \{F_I, F_{II}, F_{III}\}^T$, where F_I, F_{II}, and F_{III} are the influence coefficient functions for Mode I, II, and III, respectively. Li *et al*., (2016) have developed the influence coefficients of stress intensity factors for inclined cracks in pipes under internal pressure using three-dimensional finite element analysis. The approximations of the influence coefficients can be expressed as follows:

$$F_I = M_I N_I sin^2(h_I^{11} + h_I^{12}\theta) \tag{10a}$$

$$F_{II} = M_{II}[h^6(\xi) + h^7(\xi)^3]\, sin(h_{II}^8 + h_{II}^9\theta) \tag{10b}$$

$$F_{III} = M_{III} N_{III}\, sin(h_{III}^{11}\theta) \tag{10c}$$

where $M_i = h_i^1 + h_i^2\left(\frac{a}{d}\right) + h_i^3\left(\frac{a}{d}\right)^2 + h_i^4\left(\frac{a}{d}\right)^3 + h_i^5\left(\frac{a}{d}\right)^4$; $N_i = h_i^6 + h_i^7(\xi)^2 + h_i^8(\xi)^4 + h_i^9(\xi)^6 + h_i^{10}(\xi)^8$ with the coefficients, h_i^n $(n = 1 - 12)$ are given in Table 1.

The crack size a can be represented by the corrosion pit depth. A widely accepted model for corrosion pit depth is employed in this paper, which is expressed as follows (Kucera and Mattsson, 1987):

$$a(t) = kt^n \tag{11}$$

where k and n are empirical coefficients to be determined from field data.

Apart from the growth of corrosion pit, the operating internal pressure and pipe wall thickness also change with time. Therefore, it is justifiable to model the load effect $L(t)$ as a stochastic process. The randomness of the load effect can be taken into account by introducing a random variable, ξ_L. This variable is defined in such a way that its mean is unity, i.e., $E(\xi_L) = 1$, and its coefficient of variation, λ_L, is a constant (Mahmoodian and Li, 2017). The load effect can be expressed as follows:

$$L(t) = L_c(t) \cdot \xi_L \tag{12}$$

where $L_c(t)$ is treated as a pure time function determined by the load effect function. The mean and auto-covariance functions of $L(t)$ can be expressed as follows (Li and Melchers, 2005):

$$\mu_L(t) = E[L(t)] = L_c(t) \cdot E[\xi_L] = L_c(t) \tag{13}$$

$$C_{LL}(t_i, t_j) = \lambda_L^2 \rho_L L_c(t_i) L_c(t_j) \tag{14}$$

where ρ_L is the auto-correlation coefficient for $L(t)$ between two points in time t_i and t_j.

Table 1. Values of h in Equation (10) with $d/R = 0.1$ and $a/c = 0.4$ (Li *et al*., 2016).

Constant	i = I	i = II	i = III
h_i^1	0.957	-0.427	0.742
h_i^2	0.504	-0.123	0.076
h_i^3	0.256	0.114	-0.070
h_i^4	0.155	-0.019	0.073
h_i^5	0.088	-0.346	0.309
h_i^6	0.983	0.454	0.618
h_i^7	-0.059	0.186	-0.101
h_i^8	-0.044	3.142	-0.604
h_i^9	0.023	-2.001	1.279
h_i^{10}	-0.166		-1.016
h_i^{11}	1.589		1.997
h_i^{12}	0.994		

4 Worked Example

The proposed methodology is applied to a case study in which a cast iron pipe with inclined corrosion pits is considered. To calculate the stress intensity factors, the influence coefficient functions for Mode I, II, and III are determined by means of the constants in Table 1 and the assumption of aspect ratio $a/c = 0.4$. According to Li *et al*., (2016), for $a/c = 0.4$, the critical stress intensity factor occurs at the deepest points along the crack front. The crack front normalized coordinate ξ is assumed to be 0.1. The pipe characteristics and the geometric information of corrosion pit are summarised in Table 2.

Table 2. Values of variables for reliability analysis in the worked example.

Basic variables	Mean	C.O.V	Reference
k	2.540	0.197	Mahmoodian and Li (2016)
n	0.320	0.188	Mahmoodian and Li (2016)
R	127 mm	-	Li and Mahmoodian (2013)
d	16 mm	-	Li and Mahmoodian (2013)
P	0.45 MPa	0.27	Sadiq *et al*., (2004)
K_{Ic}	7.66 MPa/m$^{0.5}$	-	Marshall (2010)

The load effect is calculated by Equation (8), (9) and (10). The mean of function μ_L and standard deviation σ_L can be calculated as a function of time using Monte Carlo simulation together with the proposed model of pit depth. The up-crossing rate v_R^+ can be obtained from Equation (5) for a given auto-correlation coefficient, and the probability of failure can be calculated by Equation (2).

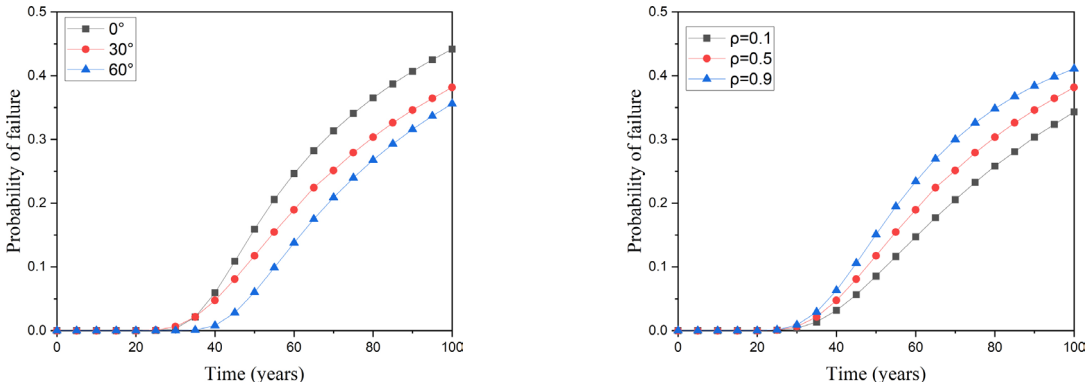

(a) (b)

Figure 2. Probability of pipe failure: (a) for different inclination angles with $\rho\rho = 0.5$; (b) for different auto-correlation coefficients with $\theta\theta = 30°$.

The calculation results of the probability of failure with different inclination angles and auto-correlation coefficients are shown in Figure 2. The probability of pipe failure increases with the exposure time due to the growth of pit depth. Also, it can be seen that the probability of failure decreases with the increase of the inclination angles since the equivalent stress intensity factor KK_{vv} in Equation (6) drops markedly with the increase of angles $\theta\theta$. Moreover, the auto-correlation coefficients affect the pipe fracture failure significantly since the fracture failure of pipes depends on many factors. These factors, such as pipe geometries, internal pressure, and corrosion pit depth, are interrelated at different time points in service life. As a result, the load effect is correlated in the time domain. The considerable difference in the probability of failure under different $\rho\rho$ justifies the necessity of using a time-dependent reliability method based on the concept of first passage probability theory.

5 Conclusion

In this study, the time-dependent failure probability of pipes with inclined crack-like defects was calculated, in which a mixed mode fracture criterion was used to establish the limit state function. First passage probability theory was employed to predict the pipe failures. A case study was provided to illustrate the proposed method. From the results of the case study, it has been found that the stress intensity factors increase rapidly with the increase of corrosion pits depth, and the probability of pipe failure increases for longer service time. Moreover, the probability of failure is highly sensitive to both the auto-correlation coefficients and inclination angles. The smaller the inclination angle is, the higher the probability of failure. As such, for engineering assessment of pipes with inclined defects, more attention should be paid to the defects with smaller inclination angles. The proposed method can be applied to the development of rehabilitation strategies for existing pipe networks.

Acknowledgements

Financial support from the Australian Research Council under DP140101547, LP150100413 and DP170102211, and National Natural Science Foundation of China with Grant No. 51820105014 is gratefully acknowledged.

ORCID

Yanlin Wang: https://orcid.org/0000-0002-4589-9975
Dr. Weigang Wang: https://orcid.org/0000-0002-5803-3572
Dr. Wei Yang: https://orcid.org/0000-0002-3673-6488

Reference

Ahammed, M. and Melchers, R.E. (1997). Probabilistic analysis of underground pipelines subject to combined stresses and corrosion. *Engineering structures*, *19*(12), 988-994.

Anderson, T.L. (2005). *Fracture mechanics: fundamentals and applications*. CRC press.

Carbal, M.A. and Kimber, M.J. (1997). Pipeline fracture experiences in Australia and North America. *Pipeline fracture experience*, 1-21.

Chang, J., Xu, J.Q. and Mutoh, Y. (2006). A general mixed-mode brittle fracture criterion for cracked materials. *Engineering Fracture Mechanics*, *73*(9), 1249-1263.

Erdogan, F. and Sih, G.C. (1963). On the crack extension in plates under plane loading and transverse shear. *Journal of basic engineering*, *85*(4), 519-525.

Fu, G., Yang, W., Deng, W., Li, C.Q. and Setunge, S. (2019). Prediction of Fracture Failure of Steel Pipes With Sharp Corrosion Pits Using Time-Dependent Reliability Method With Lognormal Process. *Journal of Pressure Vessel Technology*, *141*(3), 031401.

Keshtegar, B. and Miri, M. (2014). Reliability analysis of corroded pipes using conjugate HL–RF algorithm based on average shear stress yield criterion. *Engineering Failure Analysis*, *46*, 104-117.

Kucera, V. and Mattsson, E. (1987). Atmospheric corrosion. *Corrosion mechanisms*, *28*, 211-284.

Li, C.Q. and Mahmoodian, M. (2013). Risk based service life prediction of underground cast iron pipes subjected to corrosion. *Reliability Engineering & System Safety*, *119*, 102-108.

Li, C.Q. and Melchers, R.E. (1993). Outcrossings from convex polyhedrons for nonstationary Gaussian processes. *Journal of engineering mechanics*, *119*(11), 2354-2361.

Li, C.Q. and Melchers, R. E. (2005). Time-dependent reliability analysis of corrosion-induced concrete cracking. *ACI Structural Journal*, *102*(4), 543.

Li, C. Q., Fu, G. and Yang, W. (2016). Stress intensity factors for inclined external surface cracks in pressurised pipes. *Engineering Fracture Mechanics*, *165*, 72-86.

Liu, A., Chen, K., Huang, X., Chen, J., Zhou, J. and Xu, W. (2019). Corrosion failure probability analysis of buried gas pipelines based on subset simulation. *Journal of Loss Prevention in the Process Industries*, *57*, 25-33.

Mahmoodian, M. and Li, C.Q. (2016). Structural integrity of corrosion-affected cast iron water pipes using a reliability-based stochastic analysis method. *Structure and Infrastructure Engineering*, *12*(10), 1356-1363.

Mahmoodian, M. and Li, C.Q. (2017). Failure assessment and safe life prediction of corroded oil and gas pipelines. *Journal of Petroleum Science and Engineering*, *151*, 434-438.

Marshall, P. (2001). *The residual structural properties of cast iron pipes: structural and design criteria for linings for water mains*. UK Water Industry Research.

Melchers, R.E. (1999). *Structural reliability analysis and prediction 2nd edition.* John Wiley & Sons, Chichester.

Rice, S.O. (1944). Mathematical analysis of random noise. *Bell System Technical Journal*, *23*(3), 282-332.

Richard, H.A. (2001). Experimental and numerical simulation of mixed-mode crack growth. In *Proceedings of the Sixth International Conference on Biaxial/Multiaxial Fatigue &* Fracture, 623-630.

Richard, H.A., Schramm, B. and Schirmeisen, N.H. (2014). Cracks on mixed mode loading–theories, experiments, simulations. *International Journal of Fatigue*, *62*, 93-103.

Sadiq, R., Rajani, B. and Kleiner, Y. (2004). Probabilistic risk analysis of corrosion associated failures in cast iron water mains. *Reliability Engineering & System Safety*, *86*(1), 1-10.

Schöllmann, M., Richard, H. A., Kullmer, G. and Fulland, M. (2002). A new criterion for the prediction of crack development in multiaxially loaded structures. *International Journal of Fracture*, *117*(2), 129-141.

Shiratori, M. and Miyoshi, T. (1986). Analysis of stress intensity factors for surface cracks subjected to arbitrarily distributed stresses. In *Computational Mechanics' 86*, 1027-1032.

Wang, W., Li, C.Q. and Shi, W. (2019). Degradation of mechanical property of corroded water pipes after long service. *Urban Water Journal*. DOI: 10.1080/1573062X.2019.1687744.

Wang, W., Robert, D., Zhou, A. and Li, C. Q. (2018). Factors Affecting Corrosion of Buried Cast Iron Pipes. *Journal of Materials in Civil Engineering*, *30*(11), 04018272.

Wang, W., Shi, W. and Li, C.Q. (2019). Time dependent reliability analysis for cast iron pipes subjected to pitting corrosion. *International Journal of Pressure Vessels and Piping*, *175*, 103935.

XV International Conference on Durability of Building Materials and Components
DBMC 2020, Barcelona
C. Serrat, J.R. Casas and V. Gibert (Eds)

Seismic Performance of the Reinforced Concrete Girders Obtained from an Existing Building Constructed in 1961

Hideo Araki

Faculty of Engineering, Hiroshima Institute of Technology, Asakita-ku Miyake 2-1-1, Japan,
h.araki.k4@it-hiroshima.ac.jp

Abstract. *This study examines, through experiments, two reinforced concrete girders obtained from a residential building constructed in 1961. The average concrete strength obtained from the material tests was approximately consistent with the specified strength. Honeycombs were observed in girders; hence, one of the girders was repaired using an epoxy resin injection to investigate the effect of retrofitting. The original and retrofitted girders were subjected to reverse loadings with displacement control and had a sectional area of 250 mm × 800 mm, according to the structural draft. Both girders were designed to exhibit a common shear span length of 1,200 mm to evaluate the validity of the current equations for shear capacity in seismic evaluation, as recommended in the criteria for seismic assessment in Japan. Using these equations, the ratio of the shear strength to flexural strength of the test girders was found to be 1.67. No significant difference was observed in the crack patterns of both girders. Their maximum strength reached the calculated flexural strengths; however, the shear cracks apparently progressed with the increase in drift angle. The hysteresis loops were slip-type because of the bond slippage of the main bars. The final failure mechanism was shear failure mode. The equation for flexural strength predicted the observed value of the original girder; the maximum strength of the retrofitted girder was approximately 1.1 times that of the original. Consequently, the epoxy resin injection recovered the seismic performance of the girders in this building.*

Keywords: *Reinforced Concrete Girder, Existing Building, Seismic Performance, Shear Capacity, Retrofitting.*

1 Introduction

The seismic performance of existing buildings in Japan is typically evaluated based on their structural drawings in accordance with the standards established in the Japanese Building Disaster Prevention Association's (JBDPA) 2001 guidelines. However, the actual components of the existing buildings frequently differ from their structural drawings; this complicates the accurate evaluation of their seismic performance. The equations recommended in the seismic evaluation were empirically derived using small scaled test specimens manufactured in the laboratory. In the field of building engineering, few experimental tests have been conducted on the actual reinforced concrete (RC) members of buildings constructed decades ago; however, full-scale loading tests were conducted on existing buildings by Osawa *et al*. (1968) and Matsushima (1970). Therefore, the research by Aoyama *et al*. (1983) and Araki *et al*. (2013, 2017) on the seismic performance of RC members obtained from old buildings is extremely valuable. In this study, the mechanical properties of concrete and the seismic performance of actual RC girders were investigated through experimental evaluations.

doi:10.23967/dbmc.2020.123

(a) (b) (c)

Figure 1. Existing building (a) comprehensive view of the test building; (b) concrete core boring; (c) cutting girder with a wire saw.

2 Existing Building

The building under investigation is a five-story RC building; it was constructed in 1961 and was used for residual purposes. Fig. 1(a) shows an image of the building. Its standard plan is star shaped, which was very popular in Japan between 1956 and 1964. The design of this building was based on the old structural code established by the Architectural Institute of Japan (AIJ) in 1958; the building's poor seismic performance could be attributed to a low amount of shear reinforcement. To estimate the mechanical properties of concrete, concrete cylinders were obtained from the first, the fourth, and the fifth stories by concrete core cutter when the building was demolished in 2017 as shown in Fig. 1(b). Additionally, two girders were obtained from the roof floor without any damage using a wire saw as shown in Fig.1(c).

3 Experimental Procedure

The material tests were performed using concrete cores and steel bars and seismic tests for the girders were performed to check the validity of the present equations used in the standard.

3.1 Materials

The mechanical properties of the concrete in existing RC buildings are directly related to the seismic performance of the structures and are important for seismic evaluations. Therefore, compressive and splitting tensile tests were performed. Table 1 summarizes the mechanical properties of concrete. The average concrete strengths of the roof floor were 19.2 N/mm^2. The concrete's strength in the building was distributed over a wide range from 14.3 N/mm^2 to 28.4N/mm^2. Although the average compressive strength exceeded the specified concrete strength, the COV of the compressive strength (0.263) exceeded the applicable upper limit of 0.25 for the seismic evaluation of existing buildings, as shown in a previous study by Sezen *et al*. (2011). The tensile splitting strengths were distributed over a range: from 1.13 N/mm^2 to 2.85 N/mm^2. The average yield strength of the main bars ϕ19 and the stirrups ϕ9 obtained by the tensile tests were 325 N/mm^2 and 292 N/mm^2, respectively.

Table 1. Mechanical properties of concrete.

Floor level	Compressive strength [N/mm^2]	Modulus of elasticity [kN/mm^2]	Tensile strength [N/mm^2]
5F	19.2 (0.263)	17.9 (0.238)	1.72 (0.305)

(COV): Coefficient of variation

3.2 Test Girders

The sectional area of the girders in the structural drawing was 250 mm × 800 mm. The obtained girders were designed with shear span lengths of 1,200 mm, to investigate the validity of the shear capacity equation currently used for seismic evaluation. The original test girders were termed SG-1 and SG-2, respectively. The structural drawing indicated that the main and shear reinforcements were plain round bars (22 ϕ and 9 ϕ, respectively). Table 2 presents the details of the original test girders. Their flexural Q_{mu} and shear strengths Q_{su} were calculated using Eqs. (1) and (2), respectively, which are provided in the JDBPA standard (2001). The failure modes of the members are very important factors for the seismic performance of existing buildings; therefore, valuating the strength of the RC members is necessary.

$$M_u = 0.9at \cdot \sigma_y \cdot d$$
$$Q_{mu} = {}^{2M_u}\!/_{L} \tag{1}$$

where M_u is the yield flexural moment [N·mm], a_t is the area of main reinforcement in tension [mm^2], σ_y is the yield strength of main reinforcement [N/mm^2], d is the effective depth [mm], Q_{mu} is the strength at the flexural failure [N], and L is the length of shear span [mm].

$$Q_{su} = \left\{ \frac{0.053 p_t^{0.23} (18 + F_c)}{M/(Q \cdot d) + 0.12} + 0.85\sqrt{p_w \cdot \sigma_{wy}} + 0.1\sigma_0 \right\} b \cdot j \tag{2}$$

where Q_{su} is the strength at the shear failure [N], p_t is the tensile reinforcement ratio [%], F_c is the compressive strength of the concrete [N/mm^2], M/Qd is the shear span ratio, p_w is the shear reinforcement ratio, σ_{wy} is the yield strength of the stirrup [N/mm^2], and j is the distance between the resultant internal forces (7/8d) [mm]. Eq. (2) denotes the minimum shear strength as empirically proposed by Arakawa (1960), which is most commonly used in Japan. M/Qd = 1 was assumed in the equation following the RC standard when M/Qd was less than 1. The yield strength of reinforcements (SR24) was assumed to be 294 N/mm^2. This strength is recommended in the standard (JDBPA, 2001), because tensile tests for the reinforcing bars were not required in the seismic evaluation. The estimated concrete strength of 16.7 N/mm^2 was obtained by subtracting half the standard deviation of the concrete strength from the average value in accordance with the standard (JDBPA, 2001). Using Eqs. (1) and (2), the ratio of Q_{su} 314 kN to Q_{mu} 186 kN of the original test girder was 1.66. RC stubs were manufactured at both ends of each girder to enable fixing to the testing machine. Steel plates (t = 10) mm were welded at both ends of the main reinforcements for anchorage before casting concrete for the stubs. Shear connectors of 24-D16 were installed to the girder sides with epoxy mortar to ensure that the original girder was connected to the stub concrete. Fig. 2 presents the details of the test girder.

Table 2. Details of the test girders.

Test Girder	Concrete (N/mm^2)	Section [mm]	Shear span [mm]	Main bar [SR24]	Stirrup [SR24]
SG-1	16.67	250 × 800	1200	2-19ϕ	2-9ϕ@250
SG-2				Pg = 0.61%	Pw = 0.20%

Specified concrete strength in the structural draft Fc: 17.6 [N/mm^2] (180kg/cm^2)

3.3 Loading and Measurement of Girders

The test setup was designed to subject the test girders to shear – force reversals. The top stub was fixed to an L-shaped steel beam, while the bottom stub was fixed to the reaction floor with high-tension bolts. Shear force was applied using a horizontal jack under displacement control. One cycle was attempted per peak displacement level with drift angle R = 1/800, 1/400, 1/200, 1/133, 1/100 rad for both the girders. A pantograph system was used to ensure that the top and bottom stubs remained parallel during the reverse loadings. Fig. 3 shows the test setup. The shear displacement between the top and bottom stubs was measured using a linear viable differential transducer (LVDT). To measure the local displacements of the test girders, 17 LVDTs were mounted on one side of the test girder. Finally, the lateral load was measured using a load cell.

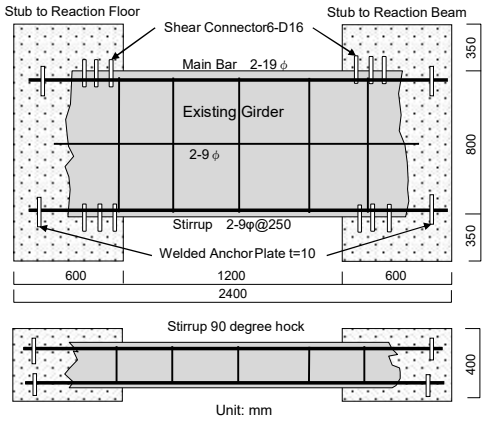

Figure 2. Dtails of the test girder.

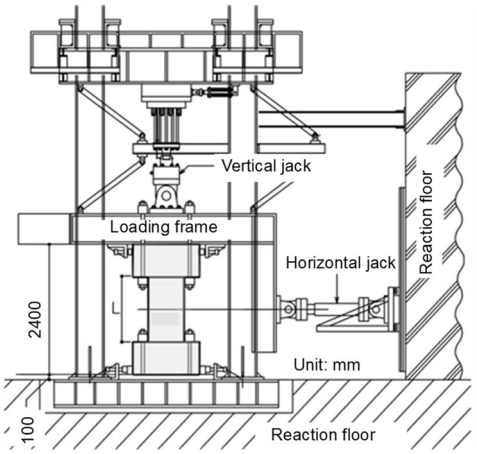

Figure 3. Test setup.

3.4 Retrofitting

Epoxy resin was injected into one of the original girders before loading to investigate the retrofitting effect. The injected epoxy resin filled the vacant space in the concrete and bonded the concrete and the reinforcing bars together. The epoxy resin injection alone may improve the seismic performance of moderately damaged buildings, although epoxy resin injection is usually associated with wrapping steel plates or CFRP sheets. In contrast to the conventional

(a) (b) (c)

Figure 4. Retrofitting process of test girder SG-2: (a) perforation; (b) sealing and attachments for capsules; (c) epoxy resin injection with capsules.

method in which epoxy resin injected at the concrete surface of the members, epoxy resin was injected with spring capsules at the position of the reinforcing bar or at the distance of 50 mm from the concrete's surface. The epoxy resin was also injected at the location of deficiencies as honeycombs. Fig. 4 presents the retrofitting process. The total amounts of epoxy resin injected into the original test girder SG-2 was 5.73 kg.

4 Experimental Results

4.1 Crack Patterns

The figures below show the location the slabs on the right side of the girders. Slight flexural cracks developed in the ends of both girders during the positive loading of the first cycle at drift angle R = 1/800 rad. The shear cracks started to occur around the small openings; then, the shear cracks appeared throughout the entire girders under increasing controlled displacement until drift angle R = 1/50 rad. The specific width of the shear cracks increased, whereas the flexural cracks did not progress. Shear cracks of 45 degrees were observed at both ends of the test girder SG-1, and diagonal shear cracks were observed in the retrofitted test girder SG-2. The final collapse mechanisms were the shear failure type. Fig. 5 (a) and (b) illustrate the crack patterns of the test girders at the final stage at drift angle R = 1/30 rad.

(a) SG-1 (b) SG-2

Figure 5. Crack patterns at final stages.

4.2 Shear Force and Drift Angle Response

Fig. 6 depicts the relationships of the shear force Q with drift angle R in both the test girders. The calculated flexural and shear strengths of the original girders were 186 kN and 314 kN, based on the standard. The stiffness degradations for both the test girders were observed at the first loading cycle. In both girders, the peaks of the shear forces were measured at drift angle R = 1/200 rad. The maximum shear forces exceeded the calculated flexural strength and did not reach the calculated shear strength. Although the shear cracks progressed, the apparent strength degradations were not observed. Therefore, the main bars were estimated to be yielding. In contract, the hysteresis loops were of a slip - type from the initial stage. The bond slippage of the main bars from the concrete may have occurred because the reinforcement was a plain round bar, and the concrete strength was low. No significant degradation of the shear force Q was observed until drift angle R = 1/50 rad. The maximum strength of the retrofitted girder (297

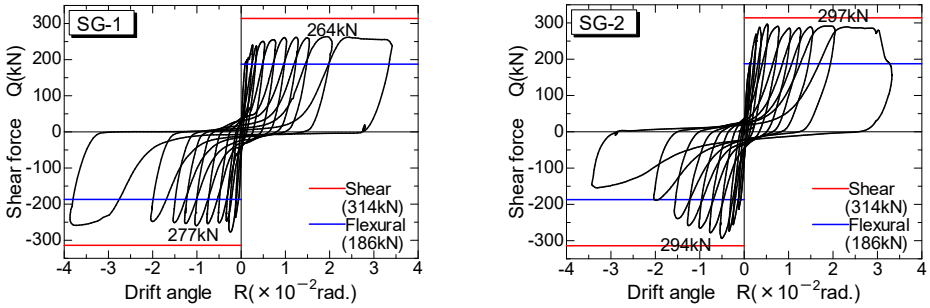

Figure 6. Shear force and drift angle response.

kN) slightly increased in comparison with those of the original test girder (277 kN). Those values were much greater than the flexural strength calculated with Eq. (1) using the recommended material strength based on the standard (JBDPA, 2001).

5 Discussions

5.1 Strength

5.1.1 Shear cracks strength

Investigating the shear crack strength is important for guaranteeing serviceability under a long-term load. The following two equations for the shear crack strength are commonly used in Japan. Eq. (5) is theoretically derived from the principal stress theory, and Arakawa (1960) empirically derived Eq. (6) from the broad experimental data on RC members. The tensile stress σ_T was recommended by Collins *et al*. (1991).

$$V_c = \sigma_T \frac{b \cdot D}{\kappa} = 0.33\sqrt{\sigma_B}\frac{b \cdot D}{\kappa} \tag{5}$$

$$Q_{sc} = \left\{ \frac{0.085 k_c \left(50 + \sigma_B\right)}{M/\left(Q \cdot d\right) + 1.7} \right\} b \cdot j \tag{6}$$

where σ_T is the tensile stress [N/mm^2], κ (= 1.5) is the shape factor of the section in Eq. (5), and k_c (= 0.72) is the scale factor in Eq. (6). For the concrete strength σ_B of the test girders, an average concrete strength of 19.2 N/mm^2 was used. The comparisons of the observed and calculated strengths of the shear cracks are shown in the first half of Table 3. The shear crack strength as calculated by Eq. (5) was underestimated, while that calculated by Eq. (6) was overestimated.

5.1.2 Maximum strength

The validity of the present equation for the shear strength was compared with that of the observed maximum strength. The flexural strength was calculated using Eq. (1). The yield strength of the reinforcement in the equation was obtained through tensile tests. The test pieces for the tensile test were taken out from the test girders after loading. Bar arrangements in the girders were inspected by removing the concrete cover after the loadings. The stirrups (9ϕ)

$$Q_{su} = \left\{ \frac{0.068 p_t^{0.23} (18 + F_c)}{M/(Q \cdot d) + 0.12} + 0.85\sqrt{p_w \cdot \sigma_{wy}} \right\} b \cdot j \tag{7}$$

were arranged with a 300 mm - 600 mm space, unlike the structural draft, and a 600 mm space was used in the calculation. The empirical equation for the shear strength was used in this study. Eq. (7) expresses the mean values of the test results taken from previous studies on RC members. This equation was also proposed by Arakawa (1960) and was used for the direct comparison of the observed maximum strength in shear failure. The observed and calculated values for maximum strength are summarized later in Table 3. The predicted maximum strengths, as calculated by Eq. (1), were consistent with the observed values of the original girders. The maximum strengths of the girders were 277 kN and 297 kN, respectively. Those maximum values were 7% and 15% greater than the flexural strengths calculated by Eq. (1). However, the researchers noted that the crack patterns of both girders through the loadings were mainly shear failure modes.

5.2 Effect of Retrofitting

The maximum strength of the retrofitted girder was 1.07 times that of the original girder, although the girders before repair contained some honeycombs. Researchers estimated that the epoxy resin injected into the honeycombs or around the main bars protected the progress of the flexural failure or the bond slippage. Fig.7 shows the comparisons between the observed envelope curves of the shear force responses and the shear strength calculated by Eqs. (1) and (7).

Table 3. Lists of strength.

Test Girder	Cracking strength [kN]			Maximum strength [kN]		
	Obs.	Eq.(5) V_c	Eq.(6) Q_{sc}	Obs.	Eq.(7) Q_{su}	Eq.(1) Q_{mu}
SG-1	198	193 (1.03)	257 (0.77)	277	360 (0.77)	259 (1.07)
SG-2	209	193 (1.08)	257 (0.81)	297	360 (0.83)	259 (1.15)

* ( ): Observed/Calculated

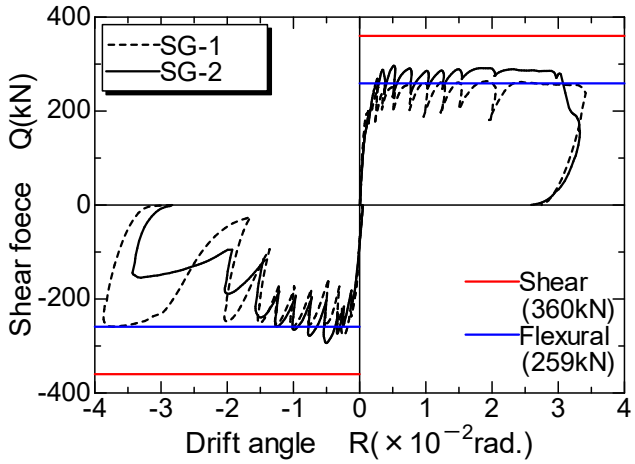

Figure 7. Envelopes of shear force and drift angle response.

6 Conclusions

The following conclusions are drawn from the results of the experimental investigation on actual RC girders obtained from an existing building constructed in 1961:

- Material tests revealed that eight concrete cylinders obtained from each floor of the building exhibited average compressive strengths of 19.2 N/mm^2 and an average tensile splitting strength of 1.72 N/mm^2.
- The failure modes of the girders could be appropriately predicted through the method recommended in the standard. However, the phase of the bond slippage was observed in the hysteresis loops because of the plain round bars.
- The predicted flexural strengths were consistent with the observed maximum values.
- Epoxy resin injection improved the seismic performance of the RC girders.
- The researchers noted that the crack patterns of both the girders through the loadings were mainly shear failure modes.

Further experimental investigation with actual RC members from the building is required to evaluate the validity of the current equations and the quantitative effect of epoxy resin.

Acknowledgements

This experimental research has been supported by the Japan Ministry of Education, Culture, Sports, Science and Technology under Grant-in-aid No.16H04458. The author would like to thank the students of the Structural Earthquake Engineering Lab. of the Hiroshima Institute of Technology and Mr. Kagawa, the president of SG Engineering, Japan.

References

Aoyama, H., Hosokawa, Y, Shiohara, H. and Katsumata, h. (1983). Study on earthquake resistance of a historic SRC building (Old AIJ Building) Part 1-3, Summaries of Technical of Annual Meeting Architectural Institute of Japan, pp.2465-2470.

Araki, H., Sauod, M., Tokugawa, T. and Kagawa, J. (2013). Seismic performance of actual RC members retrofitted with CFRP and epoxy resin, *Proceedings of APFIS2013*, Melbourne

Araki, H., and Segawa Y. (2017). Seismic Performance of Actual Members Retrofitted with Epoxy Resin Injection, *Proceeding of 16WCEE 2017*, Santiago, Chili, Paper No. 1706

Arakawa, T. (1960). Shear resistance of reinforced concrete beam, Transactions of Architectural Institute of Japan, No.66, pp.437-440.

Architectural Institute of Japan, (1991, 1971, 1962, 1958). Standard for structural calculation of reinforced concrete structures

Collins M. P. and Mitchell D. (1991). Prestressed Concrete Structures, Prentice Hall, Englewood Cliff, NJ

Japan Building Disaster Prevention Association (JBDPA), 2001, Standards of seismic evaluation of existing RC buildings Revised Edition.

Matsushima, Y. (1970). Experimental tests reported of full scale destruction of the reinforced concrete wall-type five-story apartment, *Concrete Journal*, Vol.8, No.1, pp.11-21.

Osawa, Y. Aoyama, H. and Funabashi, I. (1968). Destruction of the old building vibration and Tokyo Marine Building, Part Examination of safety against seismic force, *Concrete Journal,* Vol.6, No. 6, pp.16-26.

Sezen, H., Hookham, C., Elwood, K. J., Bartlett, N. and Moore, M. A. (2011). Core Testing Requirements for Seismic Evaluation of Existing Structures, Concrete International, pp.43-48.

Yamamoto, Y. (2005). Points at low strength concrete in seismic retrofitting for existing building (Earthquake and strengthening), *Japan association of architectural firms*, pp.77-91.

AUTHORS INDEX

XV | DBMC

15th International Conference on Durability of Building Materials and Components

50 ANYS
UNIVERSITAT POLITÈCNICA DE CATALUNYA BARCELONATECH
sense Limits

- Barcelona School of Building Construction
- Barcelona School of Civil Engineering
- Barcelona School of Architecture
- Vallès School of Architecture

CIMNE
International Center for Numerical Methods in Engineering